Geotechnique, Construction Materials & Environment

VOLUME 5(1)

Edited by

Zakaria Hossain
Akira Kobayashi
Shinya Inazumi

PROCEEDINGS OF FIFTH INTERNATIONAL CONFERENCE – GEOMATE 2015
GEOTECHNIQUE, CONSTRUCTION MATERIALS AND ENVIRONMENT OSAKA, JAPAN
16-18 NOVEMBER, 2015

Geotechnique, Construction Materials and Environment

Edited by

Zakaria Hossain
Department of Environmental Science and Technology
Graduate School of Bioresources
Mie University, Japan

Akira Kobayashi
Department of Civil, Environmental and Applied System Engineering
Faculty of Environmental and Urban Engineering
Kansai University, Japan

Shinya Inazumi
Department of Civil Engineering
National Institute of Technology
Akashi College, Japan

THE GEOMATE INTERNATIONAL SOCIETY

Published by:
The GEOMATE International Society
Tsu city, Mie, Japan
E-mail: society@geomate.org
http://www.geomate.org/

ISBN Number: 978-4-9905958-4-5 C3051

Table of Contents

Preface

On behalf of the GEOMATE 2015 Organizing Committee, we would like to welcome you in attending the International Conference on Geotechnique, Construction Materials and Environment held at the Osaka International Convention Center, Japan in conjunction with Kansai University, Japan Geotechnical Society, GEOMATE International Society, AOI-Engineering, Useful Plant Spread Society, HOJUN and Glorious International.

On Friday 11 March 2011, at 14:46 Japan Standard Time, the north east of Japan was struck and severely damaged by a series of powerful earthquakes which also caused a major tsunami. This conference was dedicated to the tragic victims of the Tohoku-Kanto earthquake and tsunami disasters. The 2015 Geomate conference covers three major themes with 17 specific themes including:

The conference covers three major themes with 17 specific themes including:

- Advances in Composite Materials
- Computational Mechanics
- Foundation and Retaining Walls
- Slope Stability
- Soil Dynamics
- Soil-Structure Interaction
- Pavement Technology
- Tunnels and Anchors
- Site Investigation and Rehabilitation
- Ecology and Land Development
- Water Resources Planning
- Environmental Management
- Public Health and Rehabilitation
- Earthquake and Tsunami Issues
- Safety and Reliability
- Geo-Hazard Mitigation
- Case History and Practical Experience

This year we have received many paper submissions from different countries all over the world, including Albania, Algeria, Australia, Bahrain, Bangladesh, Brazil, Canada, China, Colombia, Czech Republic, Egypt, France, Hong Kong, India, Indonesia, Iran, Israel, Japan, Jordan, Malaysia, Nigeria, Pakistan, Poland, Romania, Russia, Saudi Arabia, South Korea, Sudan, Taiwan, Thailand, Tunisia, United Arab Emirates, UK, USA and Vietnam. The technical papers were selected from the vast number of contributions submitted after a review of the abstracts. The final papers in the proceedings have been peer reviewed rigorously and revised as necessary by the authors. It relies on the solid cooperation of numerous people to organize a conference of this size. Hence, we appreciate everyone who support as well as participate in the joint conferences.

Last but not least, we would like to express our gratitude to all the authors, session chairs, reviewers, participants, institutions and companies for their contribution to GEOMATE 2015. We hope you enjoy the conference and find this experience inspiring and helpful in your professional field. We look forward to seeing you at our upcoming conference next year.

Best regards,

Prof. Dr. Akira Kobayashi, Conference Chairman — Akira Kobayashi

A/Prof. Dr. Shinya Inazumi, Conference Vice-Chairman — Shinya Inazumi

Prof. Dr. Md. Zakaria Hossain, Conference General Secretary

Organization

Conference Honorary Chairmen:

Emeritus Professor Dr. Sohji Inoue, Mie University, Japan
Emeritus Professor Dr. Teruo Nakai, Nagoya Institute of Technology, Japan
Emeritus Professor Dr. Fusao Oka, Kyoto University, Japan

Scientific Committees:

Conference Chairman: Professor Dr. Akira Kobayashi, Kansai University, Japan
Conference Vice Chairman: Associate Professor Dr. Shinya Inazumi, National Institute of Technology, Akashi, Japan

Conference Organizing Committee:

Professor Dr. Akira Kobayashi, Kansai University, Japan
Professor Dr. Tatsuaki Nishigata, Kansai Univ., Japan
Associate Professor Dr. Shinya Inazumi, National Institute of Technology, Akashi, Japan
Professor Dr. Akira Murakami, Kyoto University, Japan
Professor Dr. Kazuhiro Oda, Osaka University, Japan
Emeritus Professor Dr. Sohji Inoue, Mie University, Japan
Professor Dr. Toshinori Sakai, Mie University, Japan
Professor Dr. Zakaria Hossain, Mie University, Japan

National Advisory Committee:

Professor Dr. Fumio Tatsuoka, Tokyo University of Science, Japan
Professor Dr. Junichiro Takeuchi, Kyoto University, Japan
Professor Dr. Kazunori Uchida, Kobe University, Japan
Professor Dr. Kingshuk Roy, Nihon University, Japan
Associate Professor Dr. M.S. Hossain, Islamic University of Technology, Bangladesh
Associate Professor Dr. Sayuri Kimoto, Kyoto University, Japan
Associate Professor Dr. Inoue Kazuya, Kobe University, Japan
Professor Dr. Jing-Cai Jiang, University of Tokushima, Japan
Professor Dr. Noriyuki Yasufuku, Kyushu University, Japan
Professor Dr. Masuya Hiroshi, Kanazawa University, Japan
Professor Dr. Toshihiro Morii, Niigata University, Japan
Professor Dr. Nishimura Tomoyoshi, Ashikaga Institute of Technology, Japan
Professor Dr. Yoshihiro Kimura, Tohoku University, Japan
Professor Dr. Kimitoshi Hayano, Yokohama National Univ., Japan
Associate Professor Dr. Kenichiro Nakarai, Hiroshima University, Japan
Professor Dr. Hiroyuki Ii, Prof. Wakayama University, Japan

International Advisory Committee:

Professor Dr. Sai Vanapalli, University of Ottawa, Canada
Professor Dr. Musharraf Zaman, University of Oklahama, USA
Professor Dr. Rafiqul Tarefder, University of New Mexico, USA
Professor Dr. M. Bouassida, National School of Engineering of Tunis
Professor Dr. L.R. Austriaco, Angles Univ. Found., Philippines
Professor Dr. A.S.M. Abdul Awal, University Technology Malaysia
Professor Dr. M. Ibn Ibrahimy, International Islamic University, Malaysia
Professor Dr. Mohammad Shariful Islam, BUniversity of Engineering and Technology, Bangladesh

Professor Dr. Bujang B.K. Huat, University Putra Malaysia
Professor Dr. Nemy Banthia, University of British Columbia, Canada
Professor Dr. Ian Jefferson, University of Birmingham, UK
Professor Dr. John Bolander, University of California, USA
Professor Dr. Shamsul Chowdhury, Roosevelt University, USA
Professor Dr. Isabel Pinto, University of Coimbra, Portugal
Professor Dr. Mark Jaksa, University of Adelaide, Australia
Associate Professor Dr. Jim Shiau, University of Southern Queensland, Australia
Professor Dr. Hj. Ramli Bin Hj. Nazir, University Technology Malaysia
Associate Professor Dr. Raja Rizwan Hussain, King Saud University, Saudi Arabia

International Technical Program Committee:

Prof. Sai Vanapalli, University of Ottawa, Canada
Prof. Alaa Masoud, Tanta University, Egypt
Prof. Aly Ahmed, Beni-Suef University, Egypt
Prof. Aminaton Marto, Universiti Teknologi Malaysia, Malaysia
Prof. Bandari Shankar, Osmania University, India
Prof. Bashir Ahmed Mir, National Institute of Technology, India
Prof. Hamidi Abdul, Aziz, Universiti Sains Malaysia (USM), Malaysia
Prof. Hussein Elarabi, University of Khartoum, Sudan
Prof. M. Shohidullah Miah, International Univ. of Business Agriculture &Tech., Bangladesh
Prof. Michele, Casagrande, Pontifical University Catholic of Rio De Janeiro, Brazil
Prof. Radim Cajka, Technical University of Ostrava, Czech Republic
Prof. Rajaraman Jambunathan, AMET University, India
Prof. Reshma Chandran T., Global Institute of Architecture, India
Prof. Roslan Hashim, University of Malaya, Malaysia
Prof. Seyed Naser Moghaddas Tafreshi, K.N. Toosi University of Technology, Iran
Prof. Valeriy Perminov, Tomsk Polytechnic University, Russia
A/ Prof. Abdoullah Namdar, Sichuan University, China
A/ Prof. Abdul Naser Abdul Ghani, Universiti Sains Malaysia, Malaysia
A/ Prof. Alaeddinne Eljamassi, Islamic University of Gaza, Palestine
A/ Prof. Alina Paranina, Herzen State Pedagogical University of Russia, Russia
A/ Prof. Ashraf Elmoustafa, Ain Shams Univeristy, Egypt
A/ Prof. Bindu C S, Cochin University of Science& Technology, India
A/ Prof. Chee-Ming Chan, Universiti Tun Hussein Onn Malaysia, Malaysia
A/ Prof. Chidanand Naik, Anjuman Instistute of Technology and Management, India
A/ Prof. Dahlia Hafez, Cairo University, Egypt
A/ Prof. Deepa G Nair, Isfahan University of Technology, India
A/ Prof. Dolrerdee Hormdee, Khon Kaen University, Thailand
A/ Prof. Farhad Behnamfar, Isfahan University of Technology, Iran
A/ Prof. Gabriela B. Cazacu, Geotech Dobrogea, Romania
A/ Prof. Hadi Khabbaz, University of Technology, Sydney (UTS), Australia
A/ Prof. Homayoon Ganji, Herat Univercity Badghis, Afghanistan
A/ Prof. Hudson Jackson, US Coast Guard Academy, United States
A/ Prof. Inazumi Shinya, National Institute of Technology, Akashi, Japan
A/ Prof. John Smith, RMIT University, Australia
A/ Prof. Kasinathan Muthukkumaran, National Institute of Technology, India
A/ Prof. Lindrianasari Lindrianasari, Universitas Lampung, Indonesia
A/ Prof. Mahdi Karkush, Baghdad University, Iraq
A/ Prof. Mohamed Redha Menani, Batna University, Algeria
A/ Prof. Navid Khayat, Ahvaz Branch, Islamic Azad University, Iran
A/ Prof. Salam, Bash AlMaliky, AlMustansiriya University, Iraq
A/ Prof. Shailesh Kumar Jha, Indian Institute of Technology, India
Dr. Abdul Karim M. Zein, University of Khartoum, Sudan
Dr. Abdull Halim Abdul, Universiti Teknologi MARA, Malaysia
Dr. Afshin Asadi, University Putra Malaysia, Malaysia
Dr. Ahmad Safuan A Rashid, Univeristi Teknologi Malaysia, Malaysia

Conference Correspondence:

Prof. Dr. Zakaria Hossain, General Secretary,
Dept. of Env. Sci. & Tech., Mie University, Japan,
Prof. Dr. Akira Kobayashi (Chairman)
Dept. of Civil and Environmental Engineering, Kansai University, Osaka, Japan,
A/Prof. Dr. Sinya Inazumi (Vice-Chairman),
National Ins. of Tech., Akashi, Japan,
E-mail: conference@geomate.org
Tel & Fax: +81-59-231-9578

Editorial Committee and Executive Committee:

Keynote Paper

Fifth International Conference on Geotechnique, Construction Materials and Environment, Osaka, Japan, Nov. 16-18, 2015, ISBN: 978-4-9905958-4-5 C3051

BEARING CAPACITY OF AN OPEN-ENDED PILE

Yoshiaki Kikuchi [1]
[1] Professor, Department of Civil Engineering, Tokyo University of Science, Japan

ABSTRACT

In recent years, large-diameter steel pipe piles embedded deeply have come to be often used in port construction in Japan. This is greatly different from how the situation used to be. However, the procedure used to estimate the bearing capacity of a pile has hardly changed. In this paper, the bearing capacity mechanism of an open-ended pile was examined. Plugging phenomenon was studied in field loading tests, laboratory experiments both on a large and small scale. The following conclusions were presented in this report: (1) Many loading test results have shown that the plugging effect is mainly affected by pile diameter. (2) From the field pile loading test results, it was shown that a pile with secondary critical resistance, which is considered to show ultimate bearing capacity, had a very low plugging condition. (3) Inner friction that causes plugging was mostly mobilized in 2D from the pile tip.

Keywords: Open-Ended Pile, Toe Bearing Capacity, Plugging Effect, Inner Friction

INTRODUCTION

The pile foundations of port facilities in Japan have been constructed by pile driving with steel pipe piles for the past 50 years. Although pile diameters and pile lengths have changed a lot in this time, the design method has hardly changed. However, evaluating the toe bearing capacity of a pile has always been a problem. Because of the use of open-ended piles with a large diameter in recent years, there have come to be many uncertainties about the toe bearing capacity. This problem has been taken into account in the design as a plugging ratio. However, the argument made in the method of estimating a plugging ratio is not fully encompassing. Under these circumstances, this paper introduces the latest method of examining the toe bearing capacity of an open-ended pile.

PREVIOUS STUDIES

To precisely estimate the toe bearing capacity of open-ended piles, it is important to evaluate the plugging effect at their bottom end. Therefore, many studies on the mechanism of the plugging of open-ended piles have already been done both analytically and experimentally. The results of those studies have suggested several types of algorithms, and they have been adopted in several design codes in Japan, such as the Specifications for highway bridges [1] and Recommendation for the design of building foundations [2]. In the Recommendation for the design of building foundations, the toe bearing capacity of an open-ended pile is evaluated to be equal to ηR_{PC}, in which R_{PC} indicates the toe bearing capacity of a closed-ended pile, and η is a coefficient of the plugging effect. If L_B/d_I, which is the ratio of embedded depth to stiff layer (L_B) to the pile diameter (d_I), is less than 5, η equals 0.16 (L_B/d_I), and if L_B/d_I is larger than 5, then η is equal to 0.8.

Thus, it has been assumed that the condition of the plugging effect depends on the ratio of the embedded depth to the diameter of the pile. If the embedded depth is smaller than the regulation value, the toe bearing capacity of the open-ended pile is reduced at a fixed rate which bears no relation to the characteristics of the ground in the construction site. This can be one of the causes of underestimating the toe bearing capacity of open-ended piles.

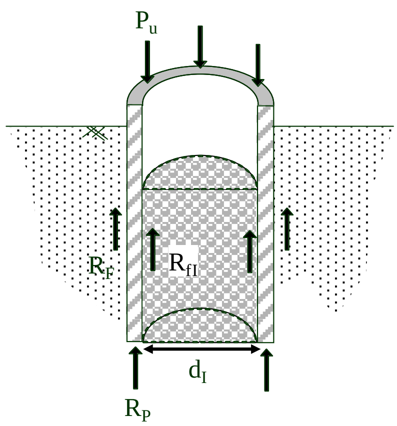

Fig. 1 Diagram of the bearing capacity of an open-ended pile.

Considering the toe bearing resistance of an open-ended pile, total resistance will be the sum of the resistance of the annular part, R_P, and inner friction between the pile and the soil, R_{fI} as shown in Fig. 1. Considering this, the theoretical plugging effect, η, will be the ratio of the sum of the toe bearing capacity of an open-ended pile and that of a closed-ended pile, R_{PC} [2].

$$\eta = \frac{R_P + R_{fl}}{R_{PC}} \quad (1)$$

In this case, estimating R_{fl} is the most important and difficult point in estimating η.

TOE BEARING CAPACITY ESTIMATION METHODS AND MEASURED TOE BEARING CAPACITY IN THE FIELD

The bearing capacity of a single pile is commonly divided into toe bearing capacity and shaft resistance force [3].

The calculation formulae for static bearing capacity of piles used in the port construction standards of Japan (JPTS), and Eurocode7 (EC7) and the standard for the U.S. Army Corps of Engineers (USCOE) as typical examples of the calculation formulae, are compared in Table 1 [4]-[6]. As shown in the table, in every standard, the bearing capacity calculation condition of a pile is divided into a sandy layer and a clayey layer. Moreover, bearing capacity is separated into shaft resistance and toe resistance.

Table 1 Comparison of static bearing capacity calculation methods in each design code

		JPTS	Eurocode 7 (EC7)	USCOE
Sandy ground	Base resistance q_p(kN/m^2)	300N	$N_q\sigma_{v0}'$	$N_q\sigma_{v0}'$
	Shaft resistance q_s(kN/m^2)	2N	$K_s\ \sigma_{v0}'\tan\delta$	$K_s\ \sigma_{v0}'\tan\delta$
Clayey ground	Base resistance q_p(kN/m^2)	6c_u	9c_u+ σ_{v0}'	9c_u
	Shaft resistance q_s(kN/m^2)	c_u	αc_u	αc_u

In JPTS, the SPT-N value is used for estimating the bearing capacity of piles in sandy ground. For piles in clayey ground, the shear strength from an unconfined compression test is used. A similar estimation method is used for the bearing capacity of piles both in EC7 and USCOE. That is, the toe bearing capacity of a pile in sandy ground is estimated by the product of the coefficient of bearing capacity and the overburden pressure. The shaft resistance in sandy ground is assumed to be proportional to the normal stress at the pile surface. The bearing capacity of the pile in clayey ground is estimated based on the undrained shear strength in each code.

This comparison shows that bearing capacity estimation for a pile in clayey ground is similar in the three codes. However, the bearing capacity estimation methods for a pile in sandy ground differ greatly. The method in JPTS is originally what Meyerhof [7] proposed from the relationship between unit toe resistance and SPT-N value (q_p = 400 N). However, the constant of the equation is modified in many instances in Japan [8] and shaft resistance is proposed based on many measurement examples [8]. Thus, the bearing capacity estimation technique in JPTS mainly relies on experiential results.

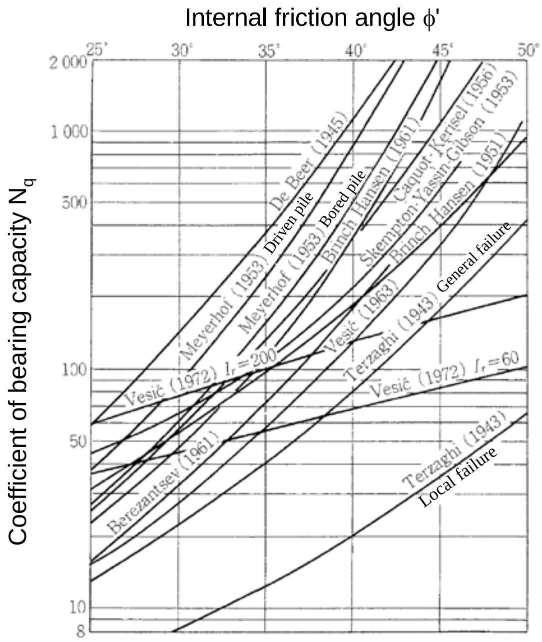

Fig. 2. Relationship between Nq and ϕ proposed by researchers.

The coefficient of bearing capacity N_q for estimating toe bearing capacity of a pile in sandy ground used in EC7 and USCOE is calculated by supposing the failure mechanism of the ground around the pile toe. The bearing capacity coefficient N_q is determined from the internal friction angle ϕ. Although this method is rational, the coefficient of bearing capacity varies with the assumption of a failure mechanism that is more than 10 times greater. For this reason, the relationship between Nq and ϕ proposed by many researchers varies greatly (Fig. 2) [9]. Moreover, there is a difference in the assumption of effective overburden pressure. In EC7, it is assumed that all overburden pressures are effective. On the other hand, in USCOE, it is proposed that the effective overburden pressure in bearing capacity calculation of a deeply embedded pile should be reduced from the total overburden pressure according to the proposal by Meyerhof [6].

Shaft resistance force is premised on the frictional resistance along a shaft, and such an assumption is rational. However, it is difficult to precisely determine the earth pressure coefficient at the pile shaft.

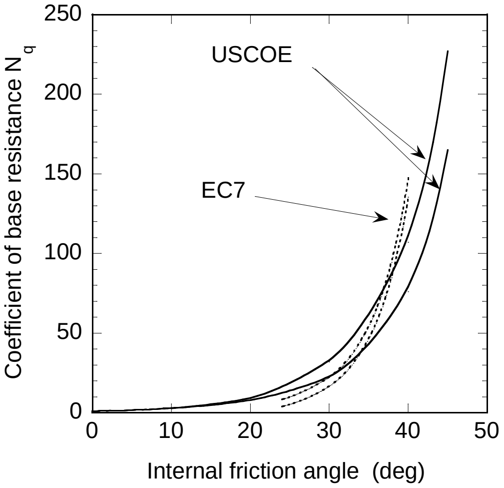

Fig. 3. N_q used in EC7 and USCOE.

Coefficients of bearing capacity N_q shown in Fig. 3 are used in EC7 and USCOE. They give moderate numbers comparing the variance of N_q shown in Fig. 2. Internal friction angle should be defined when calculating N_q. Here, the following equation is used for estimating the internal friction angle from the SPT-N value and is introduced in the present JPTS. This equation is constructed from two proposals by Meyerhof [10], [11] about the relationship between SPT-N value and relative density and between relative density and internal friction angle. If this equation is used, ϕ will become smaller if the depth increases under the condition of the SPT-N value independent from the depth.

$$\phi = 25 + 3.2\sqrt{\frac{100N}{p'_{v0} + 70}} \tag{1}$$

where N: SPT-N value and p'_{v0} : effective overburden pressure at sounding. Maximum of SPT-N should be 50.

Although the toe bearing capacity per unit area is determined by only the SPT-N value using the method in JPTS, it is determined from the SPT-N value and effective unit volume weight in EC7 and USCOE. Furthermore, in USCOE, the maximum effective overburden pressure is considered to be affected by the pile diameter and ground conditions. In equation USCOE, overburden pressure applied to calculate toe bearing capacity is constant when the penetration depth exceeds 20 times of pile diameter. This assumption is quite conservative and gives too small bearing capacity when deeply embedded piles. From this reason, I don't consider USCOE method hereafter.

Other methods for estimating the bearing capacity of piles are presented. One of them is the cavity extension theory. This theory used for estimating the bearing capacity of a pile was originally proposed by Vesic [12]. Yasufuku et al. [13] revised it as follows:

$$q_p = \frac{3(1+\sin\phi_{cv}')}{(1-\sin\phi_{cv}')(3-\sin\phi_{cv}')}[I_{rr}]^{(4\sin\phi_{cv}'/(3(1+\sin\phi_{cv}')))}\left(\frac{3-2\sin\phi_{cv}'}{3}\right)\sigma_{v0}' \tag{2}$$

$$I_{rr} = \frac{I_r}{1+I_r\Delta_{av}} \tag{3}$$

$$I_r = \frac{3G}{(3-\sin\phi'_{cv})\sigma'_{v0}\tan\phi'_{cv}} \tag{4}$$

where q_p: unit bearing capacity of pile toe (kN/m²)

I_{rr}: reduced rigidity index

I_r: rigidity index

ϕ_{cv}': critical state friction angle (degrees), which can be $\phi_{cv}' = 30 + \Delta\phi_1 + \Delta\phi_2$. Values of $\Delta\phi_1$ and $\Delta\phi_2$ can be referred from Table 2.

Δ_{av}: average volumetric strain for plastic zone around a cavity. It is a function of I_r: $\Delta_{av} = 50(I_r)^{-1.8}$.

G: shear stiffness, which can be calculated from $G = 7000\ N^{0.72}$(kN/m²). N is the SPT-N value around a pile toe.

Figure 4 shows the difference in estimated toe bearing capacity using these four methods. Here, the SPT-N value is assumed to be 50 independent of the depth. Effective unit weight of the ground is assumed to be 7 kN/m³. In this case, according to the USCOE code, if the embedded depth is at least 20 times greater than the pile diameter, the effective overburden pressure in bearing capacity estimation will become constant at 20Dγ'.

Table 2. $\Delta\phi_1$ and $\Delta\phi_2$ for sandy soil and gravel

(a) $\Delta\phi_1$

Angularity	$\Delta\phi_1$(°)
Round	0
Sub- angular	2
Angular	4

(b) $\Delta\phi_2$

Grading of soil	Δϕ2(°)
Uniform (Uc < 2)	0
Moderate grading(2 < Uc < 6)	2
Well graded (6 < Uc)	4

The estimated toe bearing capacity using JPTS is independent of the embedded depth, as shown in Fig. 4. This has an odd effect in that the bearing capacity does not change in the depth direction. EC7 shows the highest bearing capacity at almost all depths.

However, estimated bearing capacities by the three methods become almost the same when the embedded depth of the piles is 15–40 m and they show a big difference when the embedded depth is deeper.

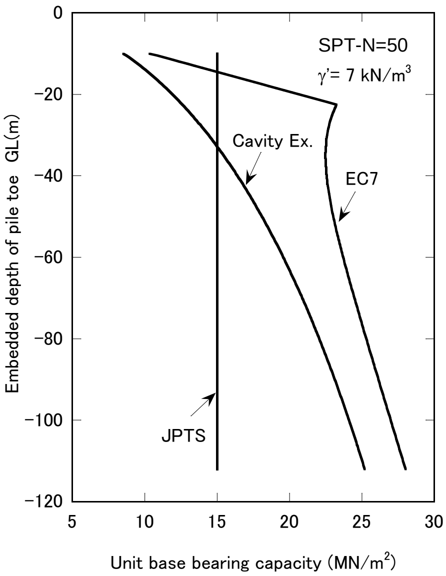

Fig. 4. Comparison of toe bearing capacity in JPTS, EC7, and Cavity Expantion.

The estimated values should be compared with measured values to discuss the validity of the methods. Figure 5 a) shows a comparison between the measured toe bearing capacity per unit area and the estimated value in the case of a pile diameter of 1000 mm or less. The measured data used for this comparison were from the Japanese Association for Steel Pipe Piles [14] and the latest data. This result shows that the measured values are smaller than the estimated values. The estimated values by JPTS and the cavity expansion method become closer to the measured values compared to those by EC7. However, when the embedded depth of the pile becomes deep, the values using JPTS were underestimated compared to the measured values.

Figure 5 b) shows the same type of comparison for the case of a pile diameter of 1000 mm or more. It turns out that the measured values are considerably smaller than the estimated values on the whole. This is because forming of the plug of a pile toe portion becomes inadequate and the bearing capacity is smaller than the calculated bearing capacity based on a closed-end pile, when the pile diameter becomes large.

Since the toe resistance at the plug portion of an open-ended pile may decrease if the pile diameter is increased, it is possible that the resistance at the real portion of the pile will differ from that of the plug portion even if the pile diameter is 1000 mm or less. When considered in this way, there is no reason to believe that even the EC7 results are overestimated or that the JPTS results are preferable for estimating measured data.

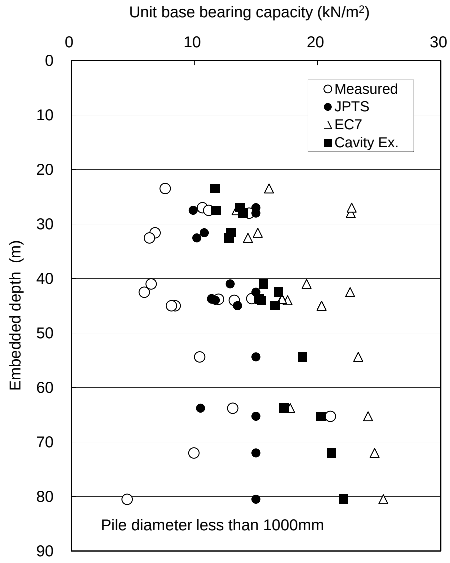

a) Pile diameter 1000 mm or less

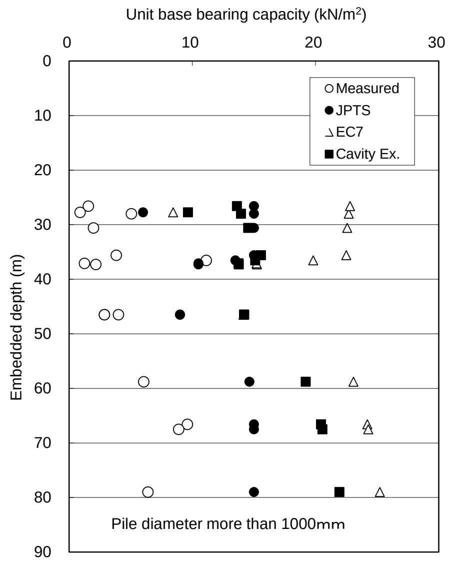

b) Pile diameter 1000 mm or more

Fig. 5. Comparison between measured and estimated bearing capacity.

Most piles presently used in port facilities are deeply embedded large-diameter steel pipe piles. Popular pile diameters are around from 1400mm to 1600mm. Embedded length of piles are up to 90m. When estimating the bearing capacity of these types of piles, the toe bearing capacity poses a big problem, referred to as the problem of plugging ratio.

Figure 6 provides a reference for considering the plugging of a large-diameter steel pipe pile. The figure shows the relationship between the pile diameter and the ratio of measured toe resistance and the estimation results of JPTS. Since the embedded depth is not considered in the figure, the data shows some variation, but it is clear that there is a tendency for the toe bearing capacity of the pile per unit area to be small when the pile diameter is large. This means that the resistance per unit area of the portion of a plug becomes small when the pile diameter becomes large.

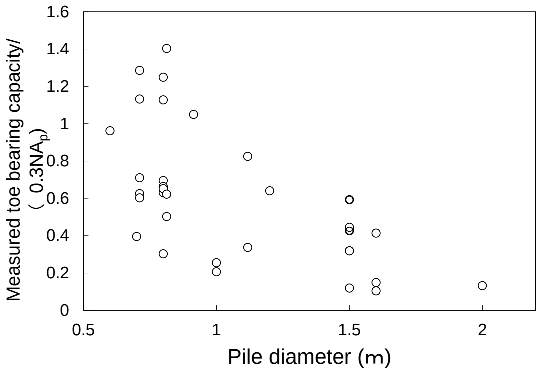

Fig. 6. Relationship between pile diameter and the ratio of measured and estimated bearing capacity.

EXAMINATION OF BEARING CAPACITY MECHANISM OF OPEN-ENDED PILES

The Tokyo Port Seaside Road was designed so that the Tokyo Gate Bridge would cross over Channel No. 3 of the port. The subject of this study is a steel-pipe-sheet pile foundation that features large-diameter steel pipe piles serving as the pier foundation between the principal meridians of the Tokyo Gate Bridge. As its bearing capacity has not been fully proved, load tests (including a static axial compressive load test, rapid load test, and dynamic load test) were conducted, as shown in Fig. 7, to obtain information about the bearing mechanism of the foundation piles at the site of the planned bridge construction, and the test results were used for designing the bridge. The characteristics of vertical bearing capacity obtained from in-situ tests on actual size large-diameter open-ended steel pipe piles are discussed.

Overview of Static Axial Compressive Load Test

Figure 8 shows the ground conditions where the tests were conducted and the embedded depth of test piles. It can be seen from the figure that the water depth at this site is AP-7 m. A soft, cohesive alluvium layer continues down to AP-40 m, followed by laminated ground (alternating sandy and cohesive layers) down to AP-65 m, and then a diluvial sandy gravel layer (Tokyo gravel layer) appears around AP-69 m. Following a few weak layers in the sandy gravel layer around AP-80 m, a solid sandy layer appears around AP-82 m.

Fig. 7. View of static axial compressive load test.

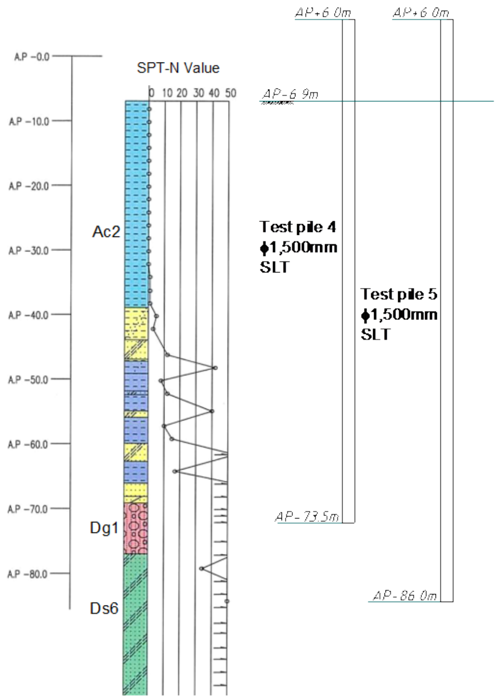

Fig. 8 Overview of soil boring log and embedment of test piles.

The results of static axial compressive load tests are presented here. In the tests, steel pipe piles 1,500 mm in diameter were hammer-driven into a sandy gravel layer and a sandy layer, in order to obtain the characteristics of bearing capacity under two conditions (in sandy gravel layer and sandy layer).

In these load tests, the axial force acting on a pile was measured by attaching strain gauges to the pile; at the same time, the settlement of the pile (both at the toe and the head) was measured using settlement gauges. Multi-stage repeated loading was conducted in accordance with the static axial compressive load test method proposed by the Japanese Geotechnical Society [15]. Particular care was taken when a virgin load was applied; that is, the load was maintained for 30 min or longer to wait for settlement of the pile, before moving to the next loading stage.

Vertical Bearing Capacity

Figure 9 shows the axial force distribution when a virgin load was applied to Pile No. 4. What should be noted here is the axial force distribution around the lower end of the test pile. As the lower end was being embedded into the sandy gravel layer, the subgrade resistance increased, with a large change in the axial force in the depth direction. At the point where the pile head load exceeded 22,000 kN, the axial force distribution showed a large bend around the pile toe. This suggests that transferred axial pile force rapidly decreased toward the pile toe.

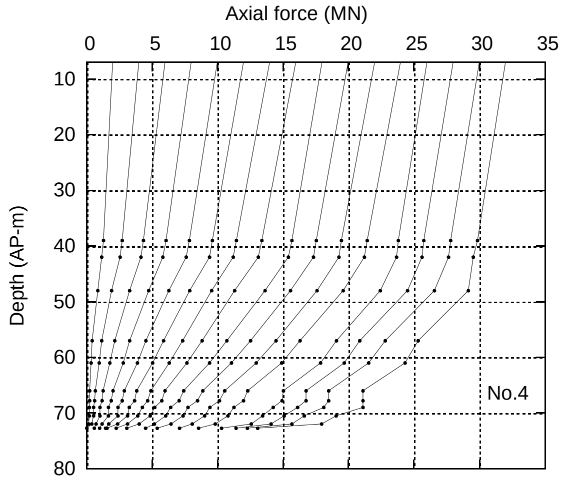

Fig. 9. Axial force distribution in Pile No. 4 load test.

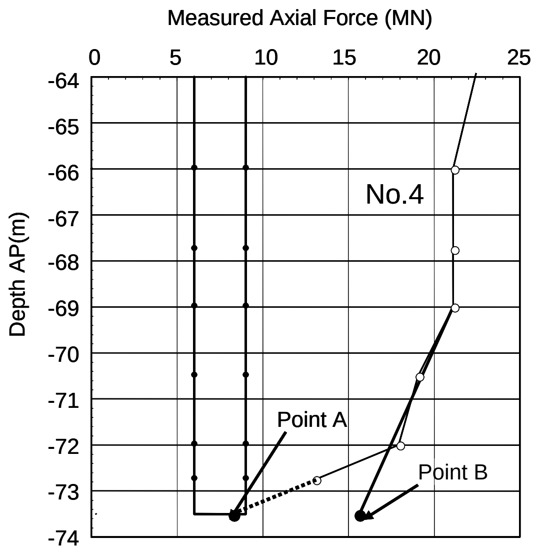

Fig. 10. Axial force distribution at the base of Pile No. 4.

Figure 10 shows an enlarged view of the situation around the pile toe. Here, assuming the load at Point B in Fig. 10 to be the toe resistance, load settlement curves for both the head and lower end of the pile can be obtained as shown in Fig. 11.

The loading test results for Pile No. 5 are shown in Figs. 12 to 14. Although the embedded length differed from Pile No. 4, the pile was inserted into a stiff sandy layer. The features of the axial force distribution were similar to the results of the load test on Pile No. 4, such that the transferred axial pile force rapidly decreased toward the pile toe when the load applied to the pile head was close to the bearing capacity.

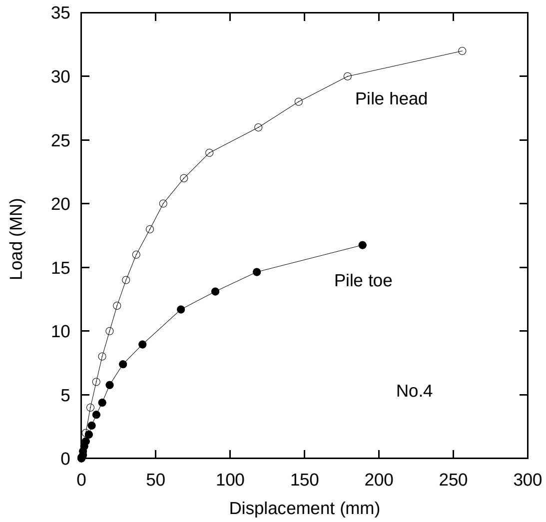

Fig. 11 Relationship between load and displacement on Pile No. 4.

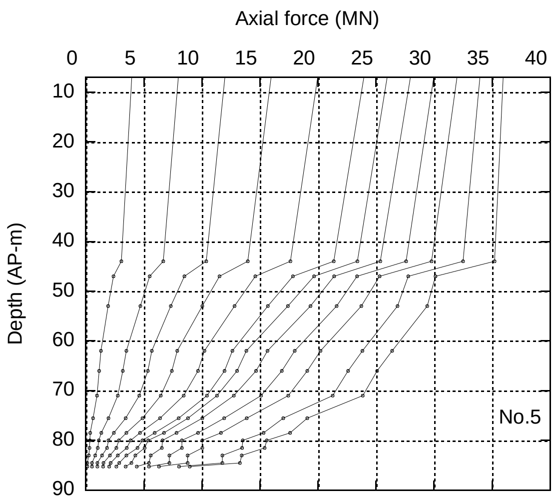

Fig. 12. Axial force distribution in Pile No. 5 load test.

End Bearing Capacity of Pile

The axial force distribution around a pile end under the secondary critical resistance is shown in Figs. 10 and 13. Axial force suddenly became smaller than at the upper part at the point where the strain gauge was set near the lower pile end. The point showing a sharp change in axial force was 1D (D: pile diameter) above the lower pile end.

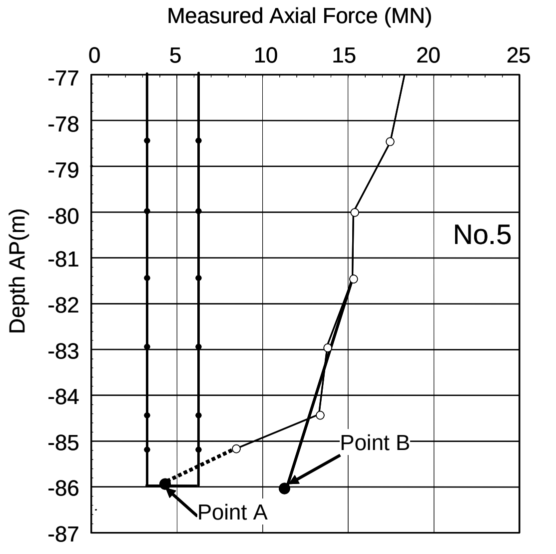

Fig. 13. Axial force distribution at the base of Pile No. 5.

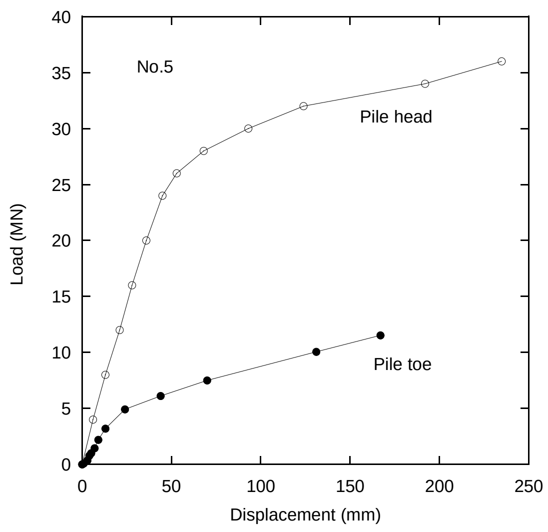

Fig. 14. Relationship between load and displacement on Pile No. 5.

Based on the relationship between vertical axial compressive load and pile displacement shown in Figs. 11 and 14, the primary and secondary critical resistance (when the toe displacement is 10% of the pile diameter) were obtained as shown in Table 3.

Focusing on the phenomena at the pile toe of No.4 pile, ground solidity did not change around the lower pile end, Judging from the test results for Pile No. 5 that was more deeply embedded, it was unlikely that peripheral friction became large only at this point (see Fig. 15). Moreover, the results of a cone penetration test (CPT) showed that the penetration resistance of the inner soil at the pile base clearly became larger than the outer ground after the loading test. Thus, it can be concluded that a sharp change in axial force might have been caused by skin friction at the inner side of the pile. As shown in Fig. 15, the total bearing capacity at the pile toe could be obtained by extrapolating the measured values of axial force within the assumed bearing layer to the level of the lower pile end (Point B).

Table 3. Critical resistance (MN).

	Pile No. 4	Pile No. 5
Primary critical resistance	20	26
Secondary critical resistance	32	36

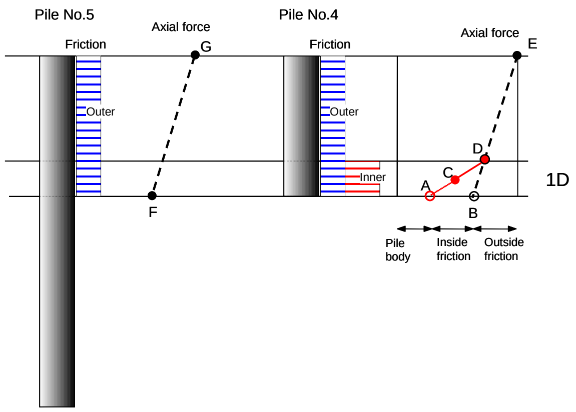

Fig. 15. Relationship between axial force distribution and friction.

Assuming that the axial force at Point A obtained by extrapolating the measured value that curved at the pile end should be the resistance of the pile body, the difference between the axial force at Point B and the axial force at Point A could be regarded as the plug resistance due to inner friction. Figures 16 and 17 show the relationship between total base resistance, inner friction resistance, and resistance of the pile body. In both figures, at the secondary critical resistance, the total base resistance shows an increase. The resistance of the pile body reached nearly the maximum level when the settlement of the pile end was about 50 mm, about 3% of diameter, while inner friction resistance was still increasing.

Yamagata and Nagai [16] and Nicola and Randolph [17] proposed an equation to obtain the ultimate resistance of a unit sectional area, based on their assumption that the base resistance of the open-ended pile can be expressed as the sum of resistance at the sectional area of the lower end of a pile, At, and inner friction.

Yamagata and Nagai [16] proposed the following equation to estimate this resistance from the SPT-N value: $q_t = 0.4NA_t$ (MN/m^2).

Nicola and Randolph [17] proposed a correlation between the resistance of the real portion of an open-ended pile, q_t, and CPT resistance, q_c:

$$q_t = \left(\frac{\lambda m(w_t / D)}{(w_t / D) + c}\right) q_c A_t \quad (6)$$

where m = 0.7, c = 0.015, w_t/D: normalized settlement of the pile toe.

$\lambda := 1.75 - (\sigma'_v/200)$ ($\sigma'_v \leq 200$ kPa)

$= 0.75$ ($\sigma'_v \geq 200$ kPa)

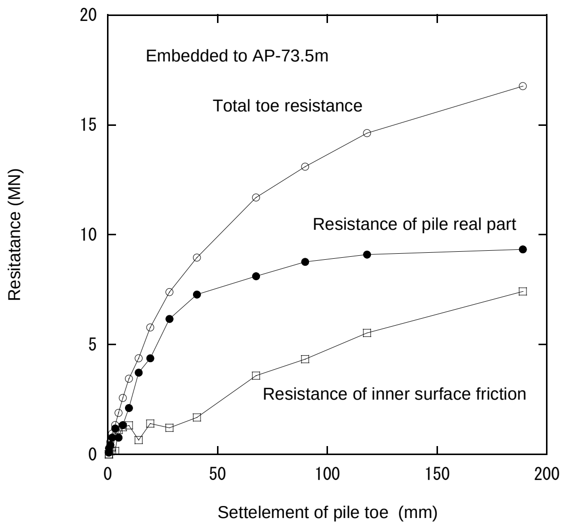

Fig. 16. Resistance at base of Pile No. 4.

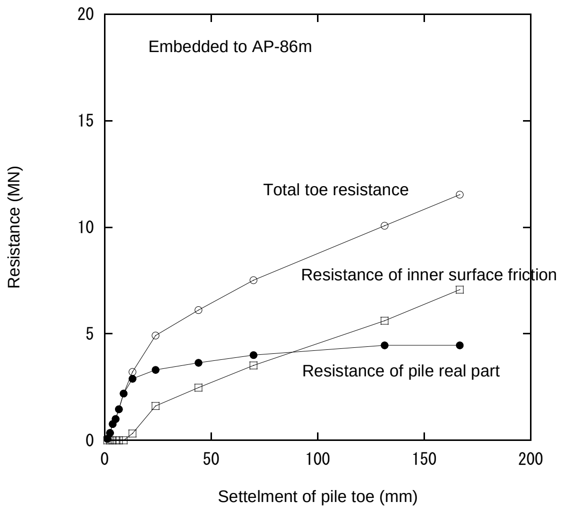

Fig. 17. Resistance at base of Pile No. 5.

When converting the equation proposed by Nicola and Randolph under the test pile embedment condition and the secondary critical load condition, the resistance of the unit sectional area q_b can be obtained from the cone penetration resistance q_c as follows: $q_b = 0.46q_c$ (kN/m^2). Thus, the ultimate resistance R_t of the sectional area of a pile can be obtained using the proposed equations, based on the SPT-N value measured at the pile base and the CPT results, as shown in Table 4.

The axial forces at Point A on Pile No. 4 and No. 5 in Figs 10 and 13 under the secondary critical load condition were 8.2 and 4.6 MN, respectively, as shown in Figs. 16 and 17. Both loads were close to the R_t values shown in Table 4.

It might appear less accurate to assume that the end bearing capacity of a pile at Point C, where was the nearest axial force measuring point from the pile toe, is the sum of the resistance of the sectional area of the pile end and the inner friction, and that the load at Point B is the resistance of the sectional area of the pile toe, as shown in Fig. 15. However, the results coincide relatively well with the existing proposals, so the above assumption can be considered to be fairly correct. Table 5 shows the results obtained from load tests. Inner friction resistance was estimated to be 7.5 MN on Pile No. 4 (accounting for 48% of the end bearing capacity of the pile) and 6.7 MN on Pile No. 5 (accounting for 59% of its bearing capacity). Inner friction resistance showed similar values whether the bearing layer was the sandy gravel layer or the sandy layer. Thus, it can be said that the difference in pile base resistance under the secondary critical load in a sandy gravel layer and a sandy layer largely depends on the difference in pile body resistance.

As shown in Table 4, the pile body resistance depends on the penetration resistance (CPTq_c value or converted SPT-N value) of a relatively limited area around the pile base. However, the inner friction in a sandy gravel layer and a sandy layer can apparently be determined independently regardless of the penetration resistance.

Table 4. Resistance at sectional area of pile end R_t (MN)

Proposed by	Yamagata and Nagai (1973)		Nicola and Randolph (1997)	
R_t proposed equation	$0.4NA_t$		$0.46q_cA_t$	
Pile No.	4	5	4	5
Converted SPT-N value	125	68	-	-
CPT: q_c value (MPa)	-	-	97	50
Resistance R_t	8.6	4.7	7.7	4.0
Load at Point B	8.2	4.6	8.2	4.6

Table 5. Bearing capacity at pile toe based on results of static axial compression load test (MN)

Pile No.	4	5
Bearing capacity at pile toe	15.7	11.3

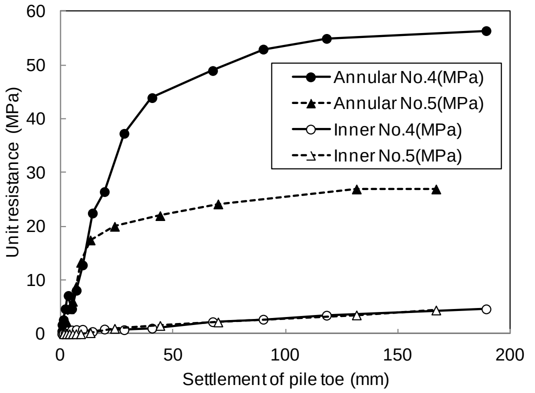

Fig. 18. Unit resistances of the annular and inner parts of a pile. Each unit resistance is the resistance divided by the cross-sectional area.

The loading test results show that the toe resistance could be divided into inner friction and resistance of the pile body. It is also shown that the maximum resistance of the pile body can be reached with a relatively small settlement, whereas a large settlement is required for exhibiting inner resistance.

Figure 18 shows unit resistances for the annular part and inner friction. The unit toe resistance of the annular part is R_t/A_t, where A_t is the cross-sectional area of the steel. The unit toe resistance due to inner friction was $R_{fI}/(A_p\text{-}A_t)$. A_p was the total cross-sectional area and $A_p\text{-}A_t$ is the inner cross-sectional area of the pile. The intensities of the unit frictional resistance for both piles were almost the same, although the unit annular resistances were different.

EXPERIMENT FOR MEASURING INNER FRICTION OF MODEL OPEN-ENDED PILE

Material and Experimental Procedure

The model ground was made of Souma sand #4. Dried Souma sand was pluviated into a container, which was 2 m in length, 2 m in width and 1.5 m in depth, through a pipe with a diameter of 3 cm. The height of the sand fall was kept at 30 cm while the sample was being prepared. The relative density of the model ground was about 40%.

After the ground preparation was completed, model piles were driven into the ground. The model pile, which was a triple-tube pile with a length of 1656 mm with the inner plate, was made of steel as shown in Fig. 19. The outer pile diameter was 24.6 cm and the inner pile diameter, D, was 20 cm. The cross-sectional area ratio of the inner pile and annular part was 0.66:0.34. The position of the inner plate could be changed from the bottom of the model pile to 40 cm above the pile end and also the inner plate could be removed. The distance between the pile end and inner plate, d_{TP}, was a parameter of this study.

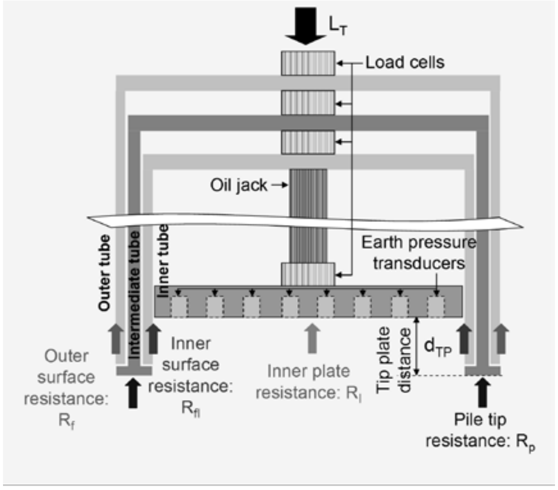

Fig. 19. Diagram of the pile used in this study.

Fig. 20. Set-up of the penetration experiment with large-diameter pile.

The model piles were penetrated into the model ground statically at a speed of 10 mm a minute. Four load cells were used to measure the penetration resistances of various components such as outer surface resistance, annular part resistance, inner surface resistance, and inner plate resistance. Eight earth pressure transducers were attached to the inner plate to measure the earth pressure acting on the plate. The penetration depth of the pile was measured with a retractable displacement meter.

Figure 20 shows the set-up of the experiment.

Results

Figure 21 shows the relationship between penetration resistance and penetration depth. Figure 21 (a) shows the results obtained with a closed-ended pile; on the other hand Fig. 21 (c) shows those obtained for an open-ended pile. Figure 21 (b) shows those obtained for d_{TP} = 20 cm. In each figure, L_T represents the total resistance, R_f the outer friction resistance, R_p the annular part resistance, R_I the inner plate resistance, and R_{fI} the inner friction resistance.

Figure 21 (b) shows how R_I increased after 210 mm of penetration and R_I, R_{fI} rapidly increased and R_p decreased after about 10 mm of the following penetration. These results mean the inner plate came into contact with the soil at penetration of around 210 mm and the pile was fully plugged at penetration of around 220 mm.

In Fig. 21 (c), clear plugging was not observed but a small vibration of the penetration resistance was observed after a penetration of about 730 mm and it shows the generation of plugging.

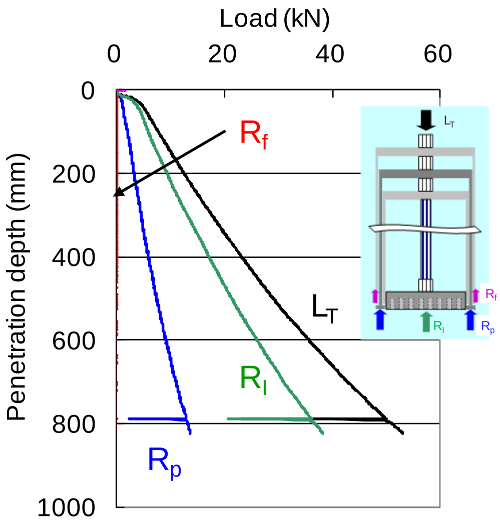

(a) d_{TP}= 0 cm

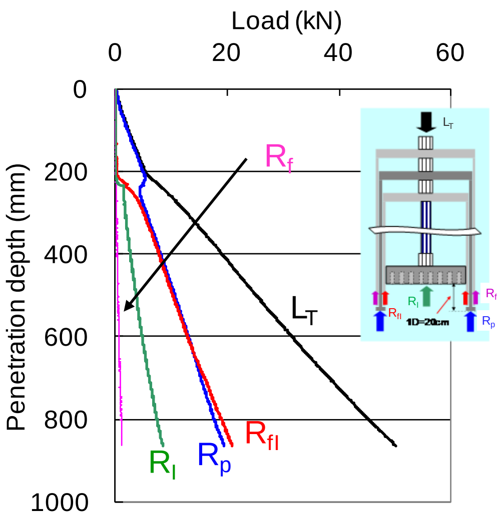

(b) d_{TP}= 20 cm

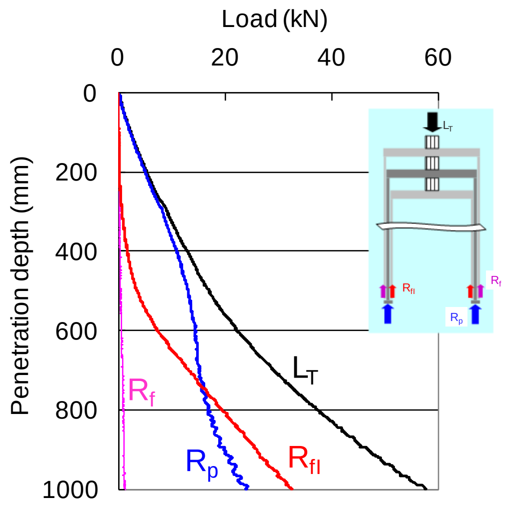

(c) No inner plate.

Fig. 21. Penetration resistance change with depth.

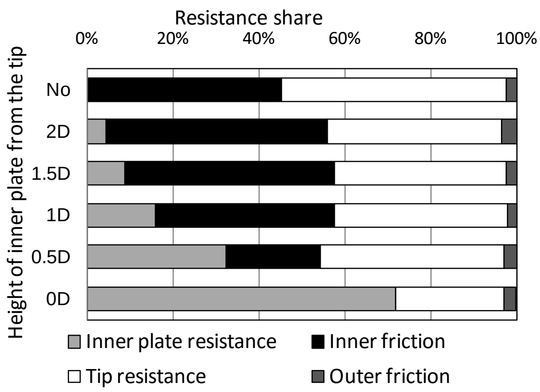

Fig. 22. Resistance share of each inner plate condition at a penetration depth of 700 mm. At around this penetration depth, almost full plugging was observed in the open-ended condition.

Figure 22 shows the sharing of each resistance component at a penetration depth of 700 mm in each inner plate condition. In these experimental conditions, the outer friction was negligible. The share of annular part resistance was about 40% in each experimental condition except no inner plate condition and 0D of d_{TP} condition. These results mean that the reaction of the ground on the pile toe was almost uniform, as the cross-sectional area ratio of the inner pile and annular part was 0.66:0.34. The share of inner friction increased as d_{TP} increased. When d_{TP} was 2.0D, the share of inner plate resistance was less than 5% and the share of inner friction was about 54%. In this experiment condition, if an inner plate exists, the inner friction observed can represent the inner friction with sufficient plugging. Inner friction required to cause plugging was mostly mobilized in 2D from the pile toe.

Vertical stress acting on the horizontal plane of inside of the pile in each height can be assumed to be uniform in a very simple way of consideration. This way is consideration is the same as Yamahara's [18], [19]. The force balance of the thin soil disc with *dx* thickness inside the pile will be drawn as shown in equation (6)

$$\Delta\sigma = \gamma_t \left(1 + \frac{\mu K_h \sigma_1 D\pi}{A_s}\right) \cdot dx \qquad (6)$$
$$A_s = D^2\pi/4$$

Where σ_1 is the vertical stress acting on the lower surface of the soil, $\Delta\sigma$ is the vertical stress difference acting on the lower and the upper surface of the soil in *dx*, μ is the friction coefficient between the pile and soil, K_h is the horizontal earth pressure coefficient on the pile surface, D is the inner pile diameter, *dx* is the thickness of the soil considering, and A_s is the horizontal cross-sectional area inside the pile.

From equation (6), equation (7) can be drawn when x axis is vertical axis, x=0 is at the pile toe, and x is positive in the pile.

$$\sigma = \left(\sigma_0 + \frac{\gamma_t D}{4\mu K_h}\right)\exp\left(\frac{4\mu K_h}{D}(-x)\right) - \frac{\gamma_t D}{4\mu K_h} \qquad (7)$$

Where σ_0 is the vertical stress acting on the horizontal plane of the pile toe, σ is the vertical stress acting on the horizontal plane at x upper than the pile toe.

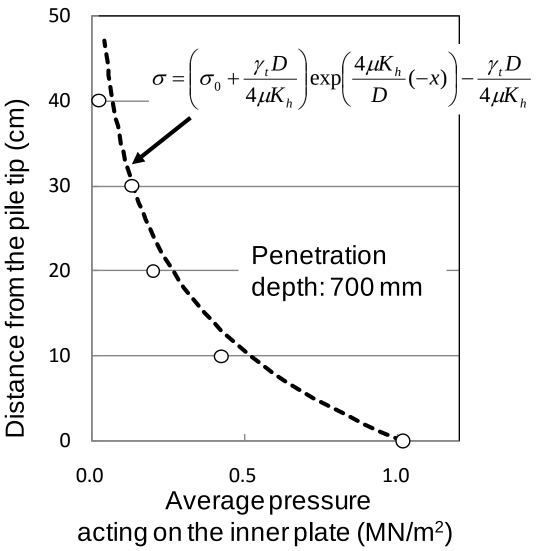

Fig.23. Average vertical stress acting on the inner plate.

Figure 23 shows a comparison between the experimental results and equation (7). In this figure, the data used were those measured at a penetration depth of 700 mm. At this penetration depth, the total resistance of the pile in each case was almost the same. The dotted line shows the calculation results from equation (7). In this case μK_h was 0.34 for fitting the experimental data. Friction angle between the pile wall and the sand, δ will be $(2/3)\phi$ - ϕ. As ϕ is about 38 degree, δ will be 26 – 38 degree, then μ is considered to be between 0.49 and 0.78. As a result, K_h will be between 0.44 and 0.69.

The equation can simulate the tendency of the stress acting on the inner plate to be reduced.

The difference in inner friction between different tip plate distances may present the inner friction of that area in the condition of full plugging.

CONCLUSIONS

This paper introduced the problem of the estimation of open-ended large diameter piles. Also presented was an international comparison of methods for evaluating bearing capacity used in design, which is particularly important for open-ended piles. Then this paper introduced a series of field loading test results which was conducted for large diameter long embedded open-ended piles. The results gave us strong impression for the importance of researching inner friction of open-ended piles. From this reason, this paper finally introduced a series of laboratory model experiment for estimating inner friction of fully plugged piles.

Following are the conclusions reached in this study:

(1) Comparison between measured toe bearing capacities of open-ended piles and three major methods for evaluating the toe bearing capacity shows difficulties of estimation of large diameter deep embedded open-ended piles. Difficulty consists from two part; one is difficulty of evaluation of toe bearing capacity of deep embedded closed-ended piles and the other is evaluation of plugging ratio of large diameter open-ended piles.

(2) From the field loading test, it was concluded that a sharp change in the axial force might have been caused by skin friction of the inner side of the pile only one or two times the length of the pile diameter from the pile toe.

(3) From the field pile loading tests results, a very low level of plugging was performed at secondary critical resistance, which is considered to show ultimate toe bearing capacity.

(4) Inner friction for plugging was mostly mobilized in 2D from the pile toe when the pile with an outer diameter of 24.6 cm and inner diameter of 20 cm, penetrated from the surface to a depth of about 3.5 times the pile diameter.

This paper consists of some previously presented contents. I reconstructed this paper for this presentation.

ACKNOWLEDGEMENTS

The research work presented in this keynote papers was conducted a lot of colleagues. I will not show all the name of my colleagues, but I sincerely thank to all the colleagues involved in this research.

REFERENCES

[1] Japan Road Association, "Specifications and Comments for Highway Bridges", Vol. IV Substructures. (in Japanese), 2002.

[2] Architectural Institute of Japan, "Recommendations for design of building Foundations", 2001, p. 207. (in Japanese)

[3] Fleming, W.G.K., A.J. Weltman, M.F. Randolph and W.K. Elson, "Piling Engineering 2nd edition", Blackie, Glasgow, 1992.

[4] Overseas Coastal Area Development Institute of Japan, "Technical standards and commentaries for port and harbour facilities in Japan", Daikokusha, 2002, pp. 286-287.

[5] Orr, T.L.L, E.R. Farrell, "Geotechnical Design to Eurocode 7", Springer, 1999, pp. 106-113.

[6] ASCE, "Design of Pile Foundations. Technical Engineering and Design Guides as adapted from the US Army Corps of Engineers". No. 1, ASCE, 1993, pp. 17-22.

[7] Meyerhof, G.G., "Penetration tests and bearing capacity of cohesionless soils". Journal of SMFE, Vol. 82, No. SM1, ASCE, 1956, pp. 1-10.

[8] Yamagata, K., "Allowable bearing capacities of a pile constructed in various installation methods", Tsuchi to Kiso, Vol. 23, No. 7, Japanese Geotechnical Society , 1975, pp. 13-20. (in Japanese).

[9] Japanese Geotechnical Society, "3.4 Pile foundations", Hand book for Geotechnical Engineering, Japanese Geotechnical Society, 1999, pp. 783-872. (in Japanese).

[10] Meyerhof, G.G., "Discussion on soil properties and their measurement", Discussion 2. Proc. of the IV International Conference on SMFE, Vol. III, ASCE, 1957, p. 110.

[11] Meyerhof, G.G., "Compaction of sands and bearing capacity of piles". Journal of SMFE, Vol. 85, No. SM6, ASCE, 1959, pp. 1-29.

[12] Vesic, A.S., "Expansion of Cavities in Infinite Soil Mass". Journal of SMFE, Vol. 98, No. SM3, ASCE, 1972, pp. 265-290.

[13] Yasufuku, N., H. Ochiai and S. Ohno, "Pile End-bearing Capacity of Sand Related to Soil Compressibility". Soils and Foundations, Vol. 41, No. 4, Japanese Geotechnical Society, 2001, pp. 59-71.

[14] Japanese Association for Steel Pipe Piles, "Steel pipe pile – its design and construction", 2000, p. 130 (in Japanese).

[15] Japanese Geotechnical Society, "Standard for Method for Static Axial Compressive Load Test of Single Piles", JGS1811-2002, 2002.

[16] Yamagata, K. and K. Nagai, "Consideration of an open ended steel pipe pile (No. 2)", Journal of Architecture and Building Engineering. No. 213, 1973. (in Japanese).

[17] Nicola, A. and Randolph, M.F., "Plugging behaviour of driven and jacked piles in sand", Geotechnique Vol. 47, No. 4, 1997, pp. 841-856.

[18] Yamahara, H., "Plugging effects and bearing mechanism of steel pipe piles", Trans. of the Architectural Inst. of Japan, 96, 1964, pp. 28-35 (in Japanese).

[19] Yamahara, H., "Plugging effects and bearing mechanism of steel pipe piles (Part 2)", Trans. of the Architectural Inst. of Japan, 97, 1964, pp. 34-41. (in Japanese).

INTRODUCING ADVANCED TOPICS IN GEOTECHNICAL ENGINEERING TEACHING

Jim Shiau, PhD (Newcastle)
School of Civil Engineering and Surveying, University of Southern Queensland, Australia

ABSTRACT

This paper demonstrates a strategy to integrate research into geotechnical engineering teaching at advanced postgraduate level. It involves the use of simple small-scale physical models, the introduction of particle image velocimetry (*PIV*), and a numerical model of a tunnel heading. The effectiveness of using a project-based learning (*PBL*) assignment is also presented. Based on staff experience and student feedback, it is concluded that this is an effective and satisfying way to engage students with the subject matter. It is hoped that discussing and displaying some of these advanced topics will encourage further student interest in geotechnical engineering research.

Keywords: Tunnel, Heading, Modelling, PIV, Education

INTRODUCTION

The current methods of engineering education are under significant pressure to reform. Increasing complaints from industry regarding graduates being inadequately prepared, high failure rates among most engineering programs, and results from a number of engineering education research studies showing problems with traditional teaching methods; this is forcing a push towards different approaches.

The complex nature of geotechnical engineering in general leads to a heavy reliance on computer modelling both in research and development as well as in practice, and this makes it difficult to teach using conventional 'chalk, book and talk' methods that have been found lacking by [1] who stated that it is too inflexible, and the amount of students that were responding poorly was increasing as more people were going to university. This is consistent with [2] who state that student centric methods, where the teacher responds to students, were shown to be more effective as opposed to teacher centric methods where students respond to the teacher.

Changing technology, increasing reliance on computers and software, and expectations of students and industry are different [3]. Where students used to use textbooks and libraries, they now use the internet. Everyone expects to be able to use a computer, or even a smartphone, and results are expected over a much shorter period. With the limited time allocated to geotechnical engineering by some universities, finding efficient ways of teaching is critical [4]. The benefits of hands-on teaching and using laboratory work have been widely published. Both teaching staff and students can benefit from such an approach [5], as it is more enjoyable for the staff and more engaging for the student.

Physical modelling has long been used by geotechnical engineering researchers with success for a number of years. It is an effective way of simplifying and visualizing a particular problem [6] and will likely always be necessary at some level to validate increasingly popular numerical modelling. It is particularly useful in assisting the transition from basic soil mechanics into the analysis and design of geotechnical structures [7-9] who successfully demonstrated a number of flow net problems and concluded that such inexpensive development can be used efficiently to complement the theoretical approach and serve to visualise phenomena of geo-structural failures in two-dimensional space.

The concept of Project Based Learning (*PBL*) is not new, but rarely can be found in geotechnical engineering teaching. *PBL* is referred to as an integrated approach to teaching, in which students learn the required material in the course of a realistic problem. This is opposed to the traditional deductive method, where students are taught fundamentals and analytical approaches, and then move onto applying them to textbook problems. The critical difference between the two is the motivation and enthusiasm that the student feels towards the content. In the integrated approach, the theory and background is brought in as needed for the problem, and thus the student is able to connect to the material better [1-2]

When *PBL* is combined with modern technology it may appear a very interesting and unique approach to teaching. However, the concept that people learn best through active engagement is not new, and is often credited to philosophers Socrates and Aristotle. Its relevance to modern universities is often credited to [10], who recommended more interactive approaches to engineering teaching. While praise of

PBL is fairly widespread, unsuccessful implementation can lead to very high student disapproval if the problem is inappropriate, and/or the required theory and background information isn't easier enough to access. The difficulty of creating a suitable assignment dissuades many staff, particularly in the engineering area where the potential gains are actually very high.

There is demand for alternative assessment of geotechnical engineering due to its complexity, and the need to be realistic and relevant for its industry. It is the objective of this paper to demonstrate the successful development of a tunnel heading model and a *PBL* assignment based on the 2009 Shanghai building collapse; both of which are ready to be adopted in any advanced geotechnical engineering course.

EXAMPLE 1: TUNNEL HEADING MODEL

Background

Physical modelling of tunnels is generally split based on whether it has been done in a centrifuge (*n*g) or under normal conditions (1g). The former can more accurately model realistically larger structures; the model can be scaled up by a factor of *n*. It is, however, expensive and time-consuming. The latter are easy to develop and cost-effective, more suited for qualitative and educational purposes. These simple models can give valuable insight into the stability and settlement problems.

The aim of this example is to demonstrate a way in which physical modelling can be used to enrich a technical course. It is believed that showing some aspects of an advanced topic such as tunnelling and *PIV* may help to reinforce earlier learnings such as the concept of a soil model, and show the possibilities and breadth of the geotechnical area.

Problem statement and the physical model

Tunnelling has undergone significant research using physical modelling; a comprehensive review can be found in [11]. The critical geotechnical aspects for tunnel design as discussed by [12]-[14] are: stability during construction, ground movements, and the determination of structural forces for the lining design.

Fig. 1 shows the problem definition: C is the overburden height, D is the tunnel diameter, σ_s is the surface surcharge, σ_t is the tunnel support pressure, γ the unit weight and φ is the angle of internal friction. The purpose of this model is to investigate tunnel heading stability and soil movement upon collapse in cohesionless soil over a range of cover to diameter ratios (*C/D*).

To do this, the following methods will be used: physical modelling using scale models with a transparent face, and *PIV* to demonstrate the movement of the soil in these models. The sand used will be kept constant and the properties of this sand will then be used in future numerical modelling using *FLAC*.

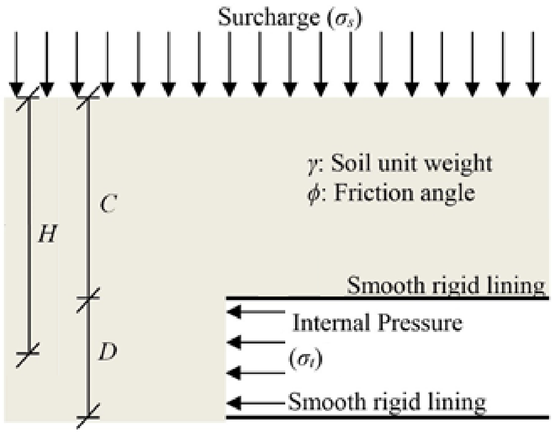

Fig. 1 Schematic Diagram of tunnel heading during construction

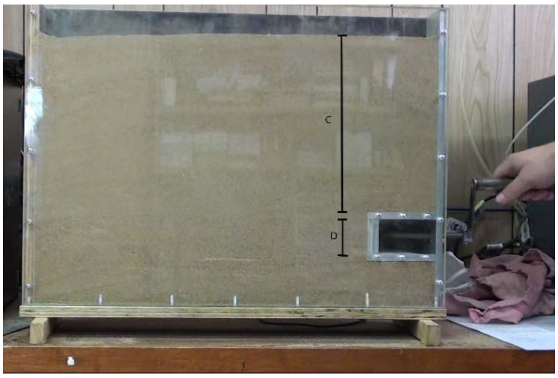

Fig. 2 Photograph of the tunnel heading model

Physical models are used themselves to study the behaviour of soil and its impacts, but quite commonly also to verify numerical models. If the soil of interest is sand, using 1g scale models is particularly attractive, as there is no need for a centrifuge as the soil fails under its own self weight. The models can be relatively simple to construct and operate, whilst still yielding good results. Therefore for this exercise, 1g scale models have been used to conduct the physical modelling.

The aim of the experimental tests was to gain an understanding of the failure mechanisms in front of the tunnel face, and to examine the settlement characteristics of the soil with varying overburden (*C/D* ratios). To do this, the modelling tanks needed to be designed and constructed and the properties of the sand in question needed to be identified. The design of the models draws inspiration from other r external research projects, namely from [15]-[17]. A picture of the models used is shown in Fig. 2.

A total of five boxes were constructed to cater for the six *C/D* cases that were to be examined. They are

50 cm long and 5cm in breadth, with a totally transparent Perspex front panel. The crank handle rotates the screw which slowly withdraws the heading. The tunnel has been approximated to a rectangle to simplify construction. The sand was blended with coloured sand (for the *PIV*), and was constant for all experiments. The density was determined to be 1800 kg/m^3, and the friction angle to be 35 degrees.

The procedure for the physical modelling was kept as similar as possible through the six cases. The heading is slowly withdrawn using the crank handle. The screw that has been used is calibrated for 1mm/revolution. Thus, the handle was rotated at approximately 1 revolution every two seconds, which therefore leads to the heading being retracted at 0.5mm/sec. This is stopped when the sand is no longer touching the heading, and this was considered as the total failure of the tunnel heading. After this, measurements were taken of settlement parameters: S_{max}, *L*, and *B* as shown in fig. 3.

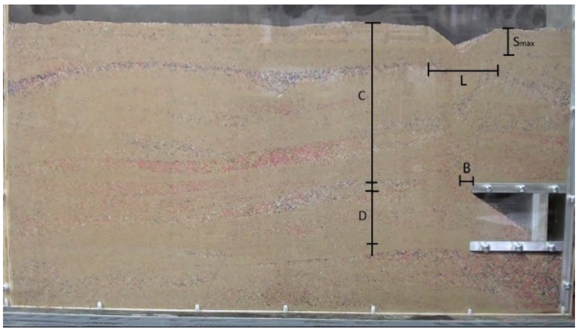

Fig. 3 Definition of Settlement Parameters

While the heading is being retracted, a full HD camera is recording the soil movement from beginning to end. This footage is then used for the particle image velocimetry.

Particle Image Velocimetry (*PIV*)

PIV is a technique that allows investigation of plane displacement patterns [14]. It was first used in fluid dynamics to demonstrate flow fields, but it has since become widely used in various fields, from aerospace, thermodynamics, and also geotechnical research. It is non-invasive, requires relatively minimal setup, and can analyse a soil sample on a grain-scale level [14]. This combined with rapid technological advances in computing during the last few decades, has meant that *PIV* has become very widely used in the geotechnical area.

In this research project, a qualitative investigation using *PIV* of the tunnel face collapse is used to identify displacement patterns and demonstrate failure behaviour. Layers of coloured sand were used in the physical modelling to better allow *PIV* to track the soil particles. There are many possible software alternatives that can do *PIV* analysis, but the program that was selected was Geo*PIV*, created by [17].

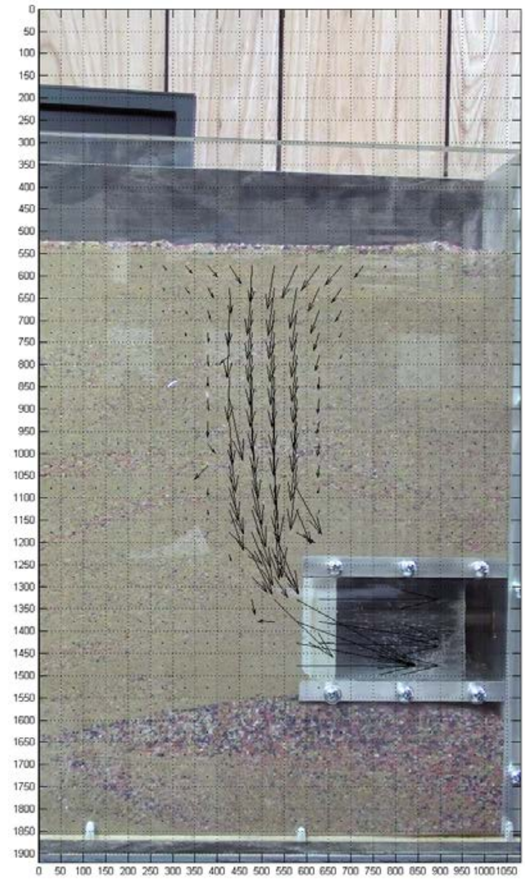

Fig. 4 A *PIV* analysis of the *C/D*=3 case

As the analysis software requires images rather than a video file, the first step once the testing is completed is to export images out of the video. A freeware program named "VirtualDub" has been used for this purpose. As the raw footage has been recorded at 50 frames per second (fps), only every 100th frame is exported, this corresponds to one image every two seconds. More frames may increase accuracy but there will be diminishing returns the more frames that are included, and this will also dramatically increase the computing time. Then *Adobe Photoshop* was used for a slight adjustment to the levels to increase spatial variation in brightness and contrast across the image.

From the physical modelling results, the relationship among maximum settlement (S_{max}), *C/D*, and the position (*B*) of this maximum settlement can then be studied. Figs. 6 and 7 show the *PIV* analyses of cases with *C/D* = 3 and 7 respectively. These *PIV* plots of the physical modelling appear to somewhat confirm these observations.

Using the *PIV* analyses in such a qualitative manner means other observations can be made regarding the failure behaviour. For instance, the failure mechanism observed using an animation of all the frames analysed using *PIV* is consistent with what is described in [10], of a staged failure.

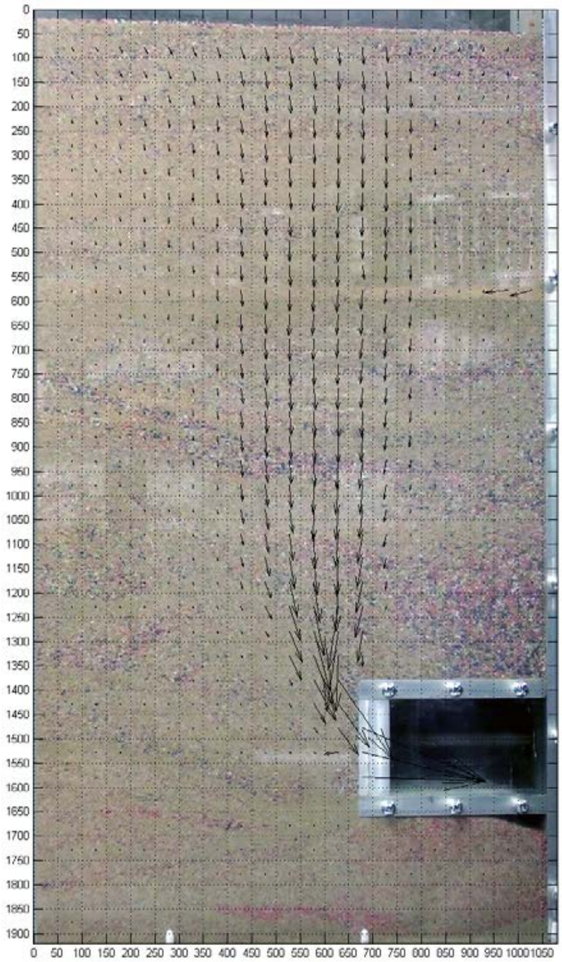

Fig. 5 A *PIV* analysis of the *C/D*=7 case

The numerical model

Geotechnical problems in reality are very difficult to model with 100% accuracy because of the number of variables involved. Although numerical modelling has significantly improved in quality and quantity over the past few decades, it is still somewhat bound by these restrictions. This combined with the need for numerical modelling to be verified means that physical modelling is still a large part of geotechnical research.

A numerical model has been developed for simulating a tunnel heading [9]. The developed *FLAC* model uses the built-in *FISH* language that automatically generates grid dimensions, solution commands and outputs relevant plots for prescribed condition. The developed model is user friendly with only limited soil parameters and dimension inputs required by the designer to achieve relatively accurate and meaningful results for preliminary design and construction purposes. A typical mesh generated by *FLAC* using the developed script is shown in fig. 6.

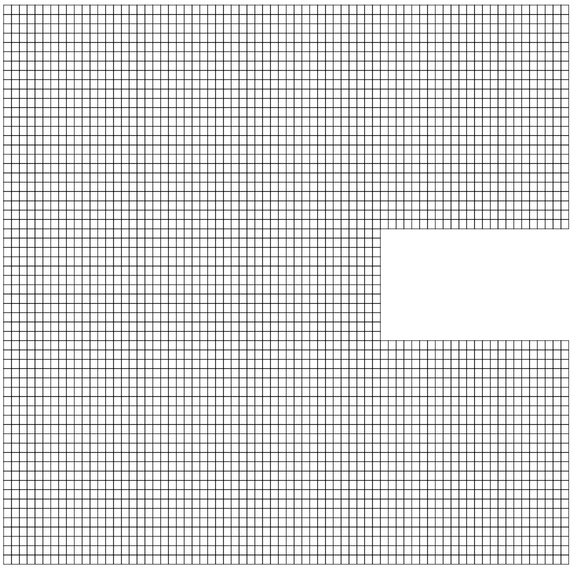

Fig. 6 A typical mesh of a tunnel heading (*C/D*=2)

The model assumes a Mohr-Coulomb material, and *2D* plane strain conditions. While the real soil conditions and tunnel/soil interactions are three-dimensional, the model uses these assumptions for simplicity, such that the tool could be used in the preliminary stages. The tunnel lining is assumed to be rigid and soil conditions homogenous having uniform properties with increasing depth. The problem is similarly defined using fig. 1.

The tunnel heading problem can be approached by making use of a pressure relaxation technique whereby the internal pressure (σ_t) is gradually reduced until a point of failure is detected. During the operation of a tunnelling machine, it is the slurry or earth pressures at the tunnel heading that is controlled. Therefore, the use of a pressure relaxation technique would provide a more realistic result when compared to other methods such as the displacement method, as the relaxation method better reflects the conditions at the cutter head.

When the heading pressure is relaxed, the heading stability decreases until yielding occurs at the point of instability. This point is also where a sudden change in tunnel face movement takes place. While reaching this point of collapse would be avoided in practice, it does provide a meaningful bound to designers in understanding the sensitivity of the soils response to changes in face pressures during construction.

The overall heading stability is commonly presented using the dimensionless quantities $\gamma D/S_u$ and $(\sigma_s - \sigma_t)/S_u$ and in conjunction with the geometry ratio *C/D*. These dimensionless quantities would help to define the point of instability, providing designers and TBM operators with minimum heading pressures to prevent collapse and to estimate the sensitivity of the soil response to the tunnel boring and changes to face pressures.

The aforementioned point of collapse is identified by examining the force history plot, which describes how convergent the solution is, in that particular stage. A convergent solution indicates that the retaining soil forces (shear strength and internal pressure) have reached equilibrium with the destabilising forces (weight). As this numerical method gradually reduces the internal pressure, there is eventually a stage where it is reduced enough for an equilibrium to be unattainable. A typical history plot is shown in fig. 7. After approximately 80,000 steps, an equilibrium can't be found, this is identified as the collapse stage.

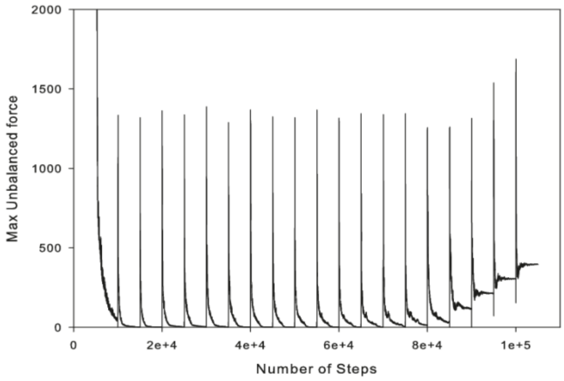

Fig. 7 Typical unbalanced force history plot

Figs 8-12 present typical plots of velocity vector, plasticity indicator, shear strain rate (SSR), vertical displacement contour, and principal stress tensor. These plots are useful for student learning in observing and comparing model responses. They also provide an increased understanding for soil behaviour and the failure mechanisms of a tunnel heading collapse

Classroom integration

The above developments were implemented into an advanced geotechnical engineering course over a four week period, where each week constitutes a three hour session. The contents of these four weeks are given below. Week 1 is an introductory lecture covering some of the required material; basics of tunnelling and a discussion about physical modelling in geotechnical engineering. In week 2, the physical models are actually used by the students, and a brief demonstration of the *PIV* analysis as well as the computer modelling is conducted. Week 3 is for the *PIV* analysis and the computer simulations, while week 4 involves an activity to complete a group report which is due two weeks after.

Week 1: There is a short lecture including:

- Introduction to tunnelling: history, methods of construction, discussion of design criteria (stability, settlement, lining forces), and define the problems that engineers face.
- Discuss stability and settlement – how these are measured, and how are they managed in tunnel boring machines (TBM's)
- Brief explanation of the 1g model in the laboratory, *PIV* analysis and numerical modelling techniques using *FLAC*. Show what to expect in the following weeks.
- A number of journal and conference papers are given to students for reading activity at home.

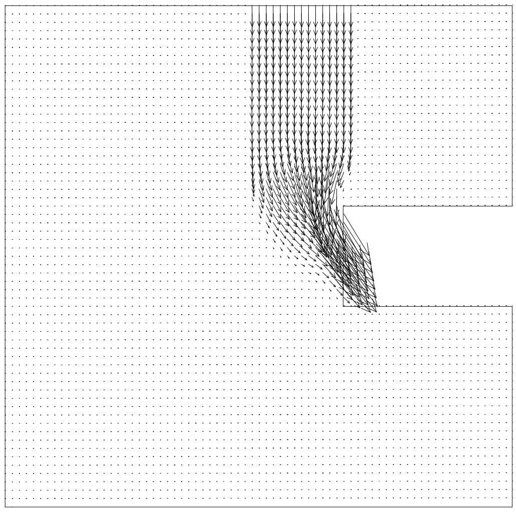

Fig. 8 Velocity vector plot at collapse for C/D=2, φ=40°

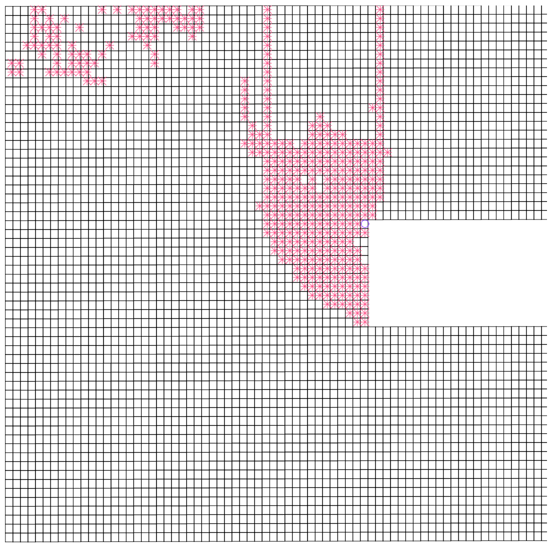

Fig. 9 Plasticity indicator plot at collapse for C/D=2, φ=40°

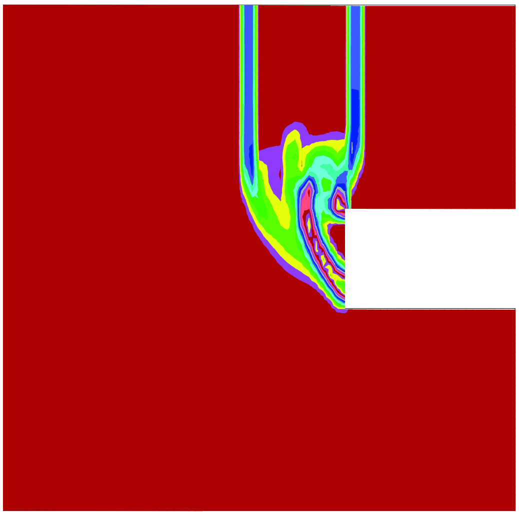

Fig. 10 Shear strain rate (SSR) plot at collapse for C/D=2, φ=40°

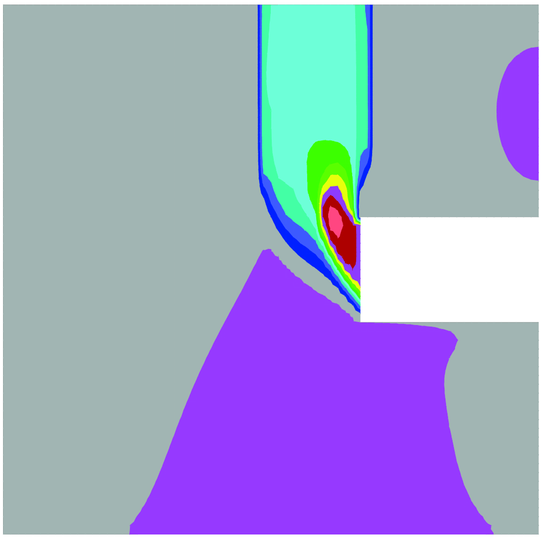

Fig. 11 Vertical displacement contour plot at collapse for C/D=2, φ=40°

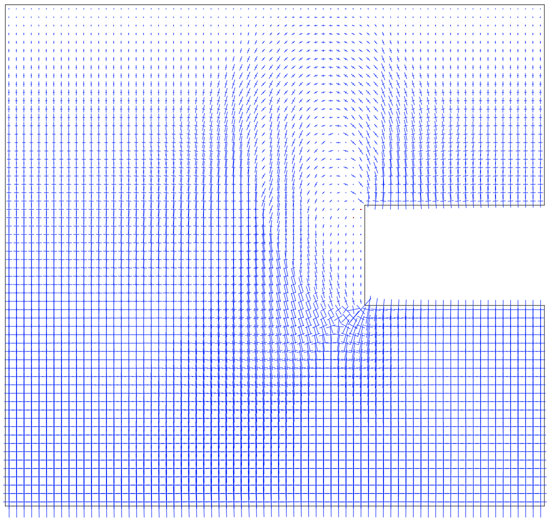

Fig. 12 Principal stress tensor plot at collapse for C/D=2, φ=40°

Week 2: Class meets in the soil laboratory:

- Five groups are formed (one for each box), and they are each set the task of investigating a different *C/D* (between 1 and 7)
- Students are asked to draw diagrams showing deformed shapes and failure planes, and participate in a discussion with questions such as: what is the effect of *C/D?* What effect would the strength of sand have? What are the assumptions involved?
- A demonstration of the *PIV* process – series of images extracted from video, mesh generation, processing, and post-processing (vector animation, final picture)
- A demonstration of the numerical model using *FLAC*. Show input of parameters, explain operation, analysis of outputs – identify the collapse stage.
- Both *PIV* and *FLAC* script are given to students for preparing Week 3 activities.

Week 3: Class meets in the computer laboratory:

- Complete *PIV* analysis using the images captured in Week 2. Does the *PIV* match with observations?
- Perform stability and settlement analysis using *FLAC* and the developed script provided by the lecturer. Complete parametric studies on the effects of depth ratio *C/D* and the frictional angle of sand φ.

Week 4: Class meets in the tutorial room:

- Students begin a group technical report of approximately 15 pages summarising all their findings.
- There is no fixed structure of this report, it needs to demonstrate that they have learnt and understood from this subject matter.

Summary

A four week teaching activity was developed to facilitate student learning in tunnel analysis and design. This activity involves physical modelling in geotechnical engineering, using advanced computing techniques (*PIV*), and employing a numerical model (*FLAC*). This development would suit a part of a postgraduate course; it could also suit a short tunnel engineering course for practising engineers. It can also be tailored to fit an advanced undergraduate course.

According to some student feedback and general observation of the activity as it is in progress, outcomes from this activity seem to be quite positive. Using a more interactive class style such as this leads to better student engagement than a traditional classroom method. These extra activities also introduce students to tunnelling and some of the methods of geotechnical research. It is hoped that this helps increase awareness and interest in the field of geotechnical engineering.

EXAMPLE 2: PROJECT BASED LEARNING

Background

In a traditional assignment, students may be given a very basic 'textbook' version of a problem that normally requires the employment of a procedure and formulae taught in class, by hand or by the use of a standard spreadsheet, or possibly very basic usage of software to solve.

One of the problems here is that geotechnical engineering deals with a high level of uncertainty, where judgment and simplifications frequently need to be made in order to be able to produce a solution. These problems also have no context, and so students can be left wondering what the linkage is to real design and construction. Students can only see the "trees", but not the forest. Besides, students are not able to experience that important part of technical writing experience.

A novel *PBL* assignment was developed with the concept behind the development and the required process as follows:

- Pick a problem which is relevant to the content and difficulty of the course.
- It must have enough information for students to research.
- The software must be available and easy enough to learn to do the problem before the due date.
- There must be enough 'room' in the problem for HD students to achieve better than A students.

The *PBL* assignment

The developed one-page assignment given to students is shown below.

At around 5:30am on June 27 2009, an unoccupied 13-storey building in the Minhang district of Shanghai city toppled over killing one worker.

It was reported in the Wall Street Journal that: "According to the Shanghai Daily, initial investigations attributed the accident to the excavations for the construction of a garage under the collapsed building. Large quantities of earth were removed and dumped in a landfill next to a nearby creek; the weight of the earth caused the river bank to collapse, which, in turn, allowed water to seep into the ground, creating a muddy foundation for the building that toppled."

Fig. 13 Shanghai building collapse (Source: <http://www.wsj-asia.com>

A team of experts and government officials examined the cause of collapse and prepared a report that was made available from CIV3403 Study Desk. It was noted that a theoretical analysis was not included in the report.

The assigned task was to conduct slope stability analyses using computer software Slope/W or/and FLAC/Slope and prepare a technical report to support the final outcome of investigation.

The rubric

Students were provided with a comprehensive rubric which was to be used to mark the assignments. This matrix identified the main headings, such as presentation, research and theory, and assignment requirements, and set out under 15 subheadings, the levels of return which would justify a grade of HD, A, B, C or F. This clearly told the students the levels of effort staff were expecting. A complete marking rubric can be found in the appendix of this paper. As demonstrated in the marking rubric in the Appendix, marks were awarded for:

- the quality of the problem definition and its justification;
- the approach with which they were trying to solve the problem;
- the quality of the computer modelling; and
- the quality and organization of the technical report.

Other than this very little information about the problem was given, and thus the first step was for the students to redefine the problem in terms which made it solvable within the limitations of their knowledge and the available software. This required a substantial amount of research on the geometry and properties of the building site, soil properties, and groundwater conditions. Many aspects of these required assumptions and simplifications to be made, and thus there was no absolute correct answer.

Reflection

As might be expected, a wide range of quality of assignments was submitted, with more than 150 scripts in each of three years. As well as the report from the Shanghai Daily, a number of other newspaper reports are available on the internet, and a common thread among many was sensational reporting for maximum news benefit, with a frequent lack of technical justification. It was necessary for the students to be able to sift through these, and extract the useful factual data without being biased by the unsupported conclusions.

Since first setting the assignment, some authoritative technical publications have appeared on the same subject, so it was also necessary for students to assimilate these, but not to plagiarize the results and conclusions, often from more advanced software than they had available.

Responses ranged from about 12 to over 100 pages, with one or two each year failing to submit a reasonable effort, but the vast majority having a fair go.

The *PBL* approach also highlighted some fundamental misunderstandings amongst the students, and one of the most common arose from the confusion surrounding undrained shear strength, "undrained cohesion", and apparent cohesion. Loose terminology and use of symbols in published papers was a major contributor, which would not affect those well versed in geotechnical engineering, but is a trap which easily ensnares those still engaged in the learning process.

Another similar problem frequently arose because of the special use which we, as geotechnical engineers, have given to words which occur in everyday use. This is particularly true of drained behavior, and saturated soils. Students may not actually read all the text book material assigned to them, find it hard to understand how a soil can be simultaneously saturated and drained. Aspects such as this made marking quite difficult, because it is so fundamental to the subsequent analysis that failure to grasp these concepts makes most of any subsequent analysis meaningless.

Since there are no "exact answers", it is necessary for markers to read every script, which takes considerable time and effort. With over 150 assignments to mark in a short period, it has also been essential to share the workload. Means need to be found to ensure that a consistent scheme is being applied.

Student responses

The university has a feedback procedure whereby students are able to provide feedback online. Questions that are asked include commenting on effective and ineffective aspects of the course, as well as general suggestions for the course.

<u>Positive responses</u>

I am working in a very active geotechnical environment, and the comments are very positive from my professional geotechnical colleague: seniors, juniors and a PhD.

The assignment was great, which helped me with understanding the course material better, and problems were realistic. It's great experience to make the connection between theories and the real life scenario, which gave me a taste of my future career.

For a subject that I thought I would just 'do' and try and pass to get it out of the way, I ended up really enjoying this subject. And I have also found myself wanting to understand these areas more and wanting to investigate the areas in my own time. I now have an interest in it!

Over all I think this course was fantastic. I actually remember the contents of the assignments and I actually understood them! I think back to so many other courses and I don't remember hardly anything to do with the assignments!

<u>Negative responses</u>

Trying to learn the geotechnical packages was a little hard, need a session dedicated to introducing the software.

Assignment 2 needs a bit more direction. It had good intentions, and while I know it was meant to test student's ability for analysis and problem solving, I was always a little confused.

Summary

A *PBL* assignment has been developed for an undergraduate geotechnical engineering course. This assignment follows an integrated approach where students are given a realistic problem and learn the geotechnical and other aspects in the process of solving it. Students learn geotechnical fundamentals and concepts, the process of problem definition, technical writing, and are introduced to the commercially used software packages.

The challenges in setting up this type of assignment are considerable: finding a suitable problem that fulfils the required conditions is not an easy task, initial student disapproval can be dissuading, and marking can be more time-consuming. Despite this, it is recommended for geotechnical teaching as it is more suitable and relevant than traditional classroom teaching. Student feedback and response from the course has been very positive. It is more engaging for the student, and more satisfying for the staff.

ACKNOWLEDGEMENT

The author would like to thank his project students for their direct and indirect efforts in the past 12 years at University of Southern Queensland. Special thanks are given to his recent students Mathew Sams, Michael Hobson, Brian Lamb and Ryan Kemp, as well as his colleague Dr. Stephen Buttling.

REFERENCES

[1] Felder, R. M., and Silverman, L. K. (1988). Learning and teaching styles in engineering education. *Engineering education*, *78*(7), 674-681.

[2] Prince, M., & Felder, R. (2007). The many faces of inductive teaching and learning. *Journal of College Science Teaching*, *36*(5), 14.

[3] Quintela, A., & Santana, T. (2007). *Teaching geotechnical works using professional practice.* Paper presented at the Proceedings, International Conference on Engineering Education (ICEE), Coimbra, Portugal.

[4] Haury, D. and Rillero, P. (1995). North Central Regional Educational Laboratory. *Perspectives of Hands-On Science Teaching. Viewed 05/02.* <http://www.ncrel.org/sdrs/areas/issues/content/cntareas/science/eric/eric-2.htm>

[5] Wartman, J. (2006). Geotechnical physical modeling for education: Learning theory approach. *Journal of Professional Issues in Engineering Education and Practice*, *132*(4), 288-296.

[6] Meguid, M. A., Saada, O., Nunes, M. A., & Mattar, J. (2008). Physical modeling of tunnels in soft ground: a review. *Tunnelling and Underground Space Technology*, *23*(2), 185-198.

[7] Shiau, J. S., Selvan, P. and Ayers, R. (2006). *Developing physical models for geotechnical teaching and research*. International Conference on Physical Modelling in Geotechnics, Hong Kong.

[8] Shiau, J. S., and Hobson, M. (2011). *Teaching Earth pressure theory using physical models: an example in civil engineering*. International Engineering and Technology Education Conference. Kuala Lumpur, Malaysia.

[9] Shiau, J. S., Sams, M. S., & Kemp, R. J. (2014). *Physical modelling and PIV analyses of an underground tunnel heading*. In Geotechnical Aspects of Underground Construction in Soft Ground, Seoul, 61-66.

[10] Dewey, J. (2007). *Experience and Education*. Simon and Schuster.

[11] Peck, R. B. (1969). Deep excavations and tunnelling in soft ground. In *Proc. 7th int. conf. on SMFE* (pp. 225-290).

[12] Ward, W. H., & Pender, M. J. (1981). Tunnelling in soft ground: general report. In *Proceedings of the 10th International Conference on Soil Mechanics and Foundation Engineering, Stockholm* (Vol. 4, pp. 261-275).

[13] Mair, R. J., & Taylor, R. N. (1997). Theme lecture: *Bored tunneling in the urban environment*. *of XIV ICSMFE [131]*, 2353-2385.

[14] Kirsch, A. (2010). Experimental investigation of the face stability of shallow tunnels in sand. *Acta Geotechnica*, *5*(1), 43-62.

[15] Chen, R. P., Tang, L. J., Ling, D. S., & Chen, Y. M. (2011). Face stability analysis of shallow shield tunnels in dry sandy ground using the discrete element method. *Computers and Geotechnics*, *38*(2), 187-195.

[16] Chen, R. P., Li, J., Kong, L. G., & Tang, L. J. (2013). Experimental study on face instability of shield tunnel in sand. *Tunnelling and Underground Space Technology*, *33*, 12-21.

[17] White, D. J., Take, W. A., & Bolton, M. D. (2003). Soil deformation measurement using particle image velocimetry (*PIV*) and photogrammetry. *Geotechnique*, *53*(7), 619-631.

[18] Itasca Consulting Group Inc (2003). "*FLAC* User's Manual". Minneapolis, USA.

APPENDIX: MARKING RUBRIC GIVEN TO STUDENTS

	Component (% of marks allocated)	F 0-49%	C 50-64%	B 65-74%	A 75-84%	HD 85-100%
Presentation (10%)	*Marking requisites*	No				Yes
	Overall presentation	No effort	Poor	Adequate	Good	Excellent
	Language skills	Unacceptable	Basic – many mistakes	Adequate – some mistakes	Good – few mistakes	High level – very few mistakes
Research (10%)	*Evidence of research*	None	Some – not beyond the set text	Adequate – attempt has been made	Good – decent research	Excellent – extensive research
	Quality of resources	None or unacceptable	Basic	Adequate	Good	High level
	Knowledge of study materials	None	Limited	Adequate	Considerable	Excellent
	Reference list	None or unacceptable	Basic	Adequate	Good – a range of sources	Excellent – authoritative sources
Technical Matter (80%)	*Executive Summary*	None or unacceptable	Basic – not clear	Adequate – provides enough info.	Good	Excellent – clear, concise, with required info
	Table of Contents	None	Basic		Comprehensive	
	Introduction and background	None or unacceptable	Basic	Adequate information	Good	Excellent – provides all required information
	Problem Definition (discussion, justification, etc.)*	Inadequate - little to no discussion	Basic level of discussion	Adequate – many aspects are covered	Good – most aspects are discussed	Excellent – all required aspects defined and justified
	Discussion of methods (FLAC/slope and Slope/w)	Little or no discussion on topic	Basic discussion on topic	Adequate discussion on topic	Good discussion on topic	High level – extensive research is evident

*Numerical Analysis of the problem**	None, unacceptable, many aspects incorrect	Basic analysis, simplistic approach	Adequate analysis, inconclusive approach	Good analysis, a good approach	Excellent, approach is comprehensive
Supplied computer files	No				Yes
Conclusions and recommendations	None	Basic	Adequate	Good – has made many conclusions	Excellent – problem has been solved, recommendations given

*High weighting given to these sections

FRP STRENGTHENED REINFORCED CONCRETE PILES UNDER STATIC LATERAL LOADS – A FIELD STUDY

Dr. K. Muthukkumaran
Associate Professor, Department of Civil Engineering, National Institute of Technology, Trichy, India
Dr. M. Murugan
Former Ph.D. Scholar, Department of Civil Engineering, National Institute of Technology, Trichy, India
Dr. C. Natarajan
Professor, Department of Civil Engineering, National Institute of Technology, Trichy, India

ABSTRACT

Piles could be damaged under major lateral loading environment for a long period. The sources of lateral loads are lateral earth pressure, wind loads, seismic loads, impact loads from ships (berthing and mooring) eccentric loads on columns, river current and mud movement loads in alluvial settings (foundations subject to scour), ocean wave forces, slope movements, and cable forces on transmission towers. Hence it is important to improve the lateral load capacity of pile foundation. In recent years, Fiber Reinforced Polymer (FRP) jacketing has become popular to retrofit existing deficient piles. The lightweight, high strength and corrosion resistance of FRPs made them particularly suitable for repair. This paper presents the experimental study on Glass Fibre Reinforced Polymer (GFRP) strengthened Reinforced Concrete (RC) piles subjected to lateral loads. The effects of GFRP strengthening on RC piles were studied.

Keywords: Strengthening, RC piles, GFRP, Lateral Loads

INTRODUCTION

Foundation of any structure plays an important role in safety and satisfactory performance of the structure as it transmits the loads from structure to earth. Piles are structural elements in a foundation which have the function of transferring load from the superstructure through weak compressible strata or through water, onto stiffer or more compact and less compressible soils or onto rock. Pile foundations are often necessary to support large structures when the surface soil conditions are not strong enough to support the structure with shallow foundations. Piles are also subjected to significant amounts of lateral loads and overturning moments besides axial loads when used under tall chimneys, high-rise structures, and coastal and offshore structures. Piles are also designed for lateral loads, when they are required to restrain forces causing sliding or overturning of structures. Lateral loads are in the order of 10-15% of the vertical loads in the case of onshore structures, whereas coastal and offshore structures these lateral loads can exceed 30% of the vertical loads. Therefore, proper attention has to be given in designing such pile structures under lateral loads. In recent years, many investigations have addressed the externally bonded GFRP composites for strengthening and retrofitting the piles subjected to heavy lateral loads. Alkhrdaji and Nanni (2000) studied the flexural strengthening of bridge piers using FRP composites. Test results indicate that FRP strengthening technique is effective in increasing the flexural capacity of the piers. Test results also indicate that the capacity and failure modes of the bridge piers are closely related to the superstructure/substructure interaction and the pier boundary conditions. Chaallal and Shahawy (2000) studied the performance of fiber-reinforced polymer-wrapped reinforced concrete column under combined axial-flexural loading. Results indicate that the strength capacity of beam-columns improved significantly as a result of the combined action of the longitudinal and the transverse weaves of the bidirectional composite fabric. Richard et al. (2003) investigated the retrofit of square concrete columns with carbon fiber reinforced polymer for seismic resistance. Results indicate that added confinement with CFRP at critical locations enhanced ductility, energy dissipation capacity and strength of all substandard members. Bousias et al. (2004) studied the effectiveness of fibre reinforced polymers in retrofitting of rectangular reinforced concrete columns. Wrapping with FRP is found to greatly improve seismic performance of columns that suffer from both lack of seismic detailing and reinforcement corrosion. Sen and Mullins (2007) studied the application of FRP composites for underwater piles repair. They suggested that the bidirectional material should be preferred over uni-directional material and carbon fibre over glass fibre. Ilki et al. (2008) studied the axial behavior of RC columns retrofitted with FRP composites. The study concluded that the external confinement of columns with CFRP sheets resulted in an increase in the strength and ductility. Bournas and Triantafillou (2009) studied the flexural strengthening of reinforced concrete columns with near-surface-mounted (NSM) FRP and stainless steel. The results demonstrate that NSM FRP and stainless steel reinforcement is a viable solution towards enhancing the flexural resistance of RC columns subjected to seismic loads. Ilki et al. (2009) investigated the seismic performance of reinforced concrete columns constructed with low quality of concrete and insufficient transverse reinforcement before and after retrofitting. The test results showed that all reference specimens, which were not retrofitted, failed with a premature loss of performance either due to buckling of longitudinal reinforcement or loss of bond, while retrofitted ones exhibited a significantly superior performance, particularly in terms of ductility. Purushotham Reddy et al. (2009) studied the retrofitting of RC Piles using GFRP Composites. The authors concluded that the axial and lateral load carrying capacity of the GFRP retrofitted pile increases with the conventional pile. Sangeetha and Sumathi (2010) investigated the behavior of Glass fibre wrapped concrete columns under uniaxial compression. The study concluded that confinement increased the strength of the concrete columns loaded axially.

Goksu et al. (2012) investigated the possibility of using CFRP reinforcement for the flexural retrofit of low-strength reinforced members under reversed cyclic loading conditions. The longitudinal CFRP reinforcement effectively contributes to the reversed cyclic flexural capacity of the existing low-strength member. The laterally load pile behaviour under different conditions were studied by Muthukkumaran et al. (2008), Almas Begum & Muthukkumaran (2009) and Muthukkumaran (2015).

FAILURE MECHANISMS

Collapse of a laterally loaded pile foundation occurs when a failure mechanism forms in each pile within a pile group. The pile behavior is dependent on the characteristic length of the pile. When the length of the pile exceeds 4T, the pile is considered as long pile and when the pile length is ≤ 2T, the pile is considered as short rigid pile (IS 2911). Where, T is the relative stiffness factor

$$T = \left[\frac{EI}{k_1}\right]^{\frac{1}{5}} \tag{1}$$

in which, EI is the flexural rigidity of pile and k_1 is the co-efficient of subgrade reaction of soil.

Failure of a short rigid pile occurs when the lateral resistance of the soil this been exceeded. The failure mechanisms of short rigid pile for free headed and fixed head condition are shown in Figs. 1a and 1b respectively. In case of long flexible pile, the failure is associated when the moment at one or more points exceeds the moment of resistance and the failure takes place by formation of one or two plastic hinges along the pile length. The failure modes of long flexible pile for free headed and fixed head condition are shown in Figs. 1c and 1d respectively.

In case of long flexible-free headed pile, the failure takes place by formation of one plastic hinge along the pile length. This distance from ground level is termed as depth of fixity. Generally the lateral strength of piles can be improved by increasing the stiffness of the soil around the pile by compaction (or special grouting) or by increasing the pile stiffness for the portion above depth of fixity. In this paper, the performance of long flexible-free headed piles subjected to lateral loads was studied by increasing the pile stiffness by GFRP confinement.

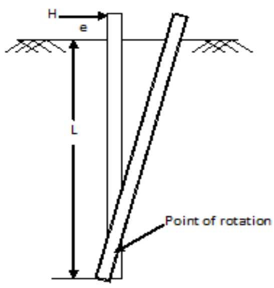

1a. Free headed pile-Short rigid pile

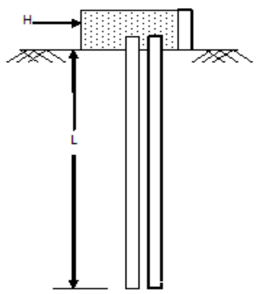

1b. Fixed head pile-Short rigid pile

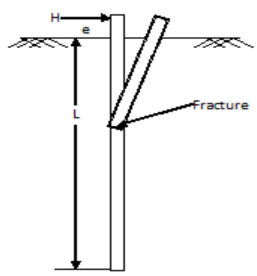

1c.Free headed pile-long flexible pile

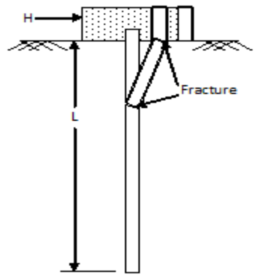

1d. Fixed head pile-long flexible pile

Fig. 1. Typical failure modes in short rigid piles and long flexible piles

MATERIAL PROPERTIES

Concrete

The characteristic compressive strength of concrete used for the study was 30 MPa. The mix ratio adopted for casting the specimens was 1: 1.204: 2.755 (Cement: Fine aggregate: Coarse Aggregate) with water-cement ratio of 0.385. The compressive strength of cubes after 28 days water curing was 41.44 MPa.

Reinforcement

The yield strength of steel used for the study was 415 MPa. Six numbers of 8 mm bars were used as longitudinal reinforcement with a cover thickness of 40 mm. Bars of 6 mm dia. at 175 mm spacing were used as lateral reinforcement (ties).

Properties of Glass Fibre Reinforced Polymers

Glass fibre reinforced polymers were used in the study. Properties of GFRP materials are given in the Table 1.

Table 1 Properties of GFRP materials

Properties	GFRP	
	Unidirectional	Bidirectional
Weight of fibre, g/m2	920	750
Fibre thickness, mm	0.90	0.6
Nominal thickness per layer, mm	1.5	1
Fibre tensile strength, N/mm2	3400	3400
Tensile modulus, N/mm2	73000	73000

Soil Characteristics

Disturbed and undisturbed soil samples were collected from the field to study the engineering properties of soil. Engineering properties of the soil are listed in Table 2. The soil was classified as clayey sand (SC) according to IS 1498 – 1970.

Table 2. Engineering properties of the soil

Depth (m)		1	2	3
% Passing	4.75 mm	99	97	94
	425 µ	64	64	62
	75 µ	49	44	41
Atterberg Limits	LL (%)	47	46	39
	PL (%)	26	26	23
	Ip (%)	21	20	16
UCC	(kN/m^2)	894.67	1028.09	1126.19
SPT value	(N)	26	28	31
Type of soil	(IS 1498)	SC	SC	SC

CASTING OF RC PILES

A pile of 230 mm dia. and 4 m length (3 m below and 1 m above the ground level (GL)) of bored-and-cast-in-situ (reinforced concrete piles) were cast in the field already surveyed. The center to center spacing between the piles are 1.18 m and all the test piles were located at a distance of 1.5 m from the reaction pile which is located at the center as shown in Fig. 2. Theoretical lateral strength of 230 mm dia. pile is 25 kN. The following steps were followed to cast the piles in the field.

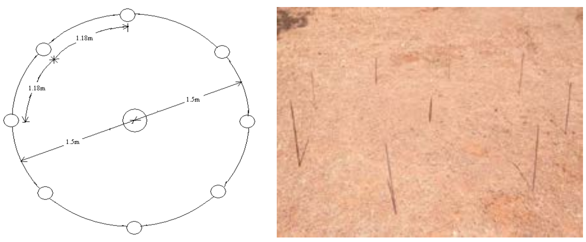

Fig. 2. Pile layout

Boring

Power auger equipment was used for the drilling work in bored-and-cast-in-situ piles. Boring was carried out up to the depth of 3 m from ground level. Fig. 3 shows the power auger boring at the field.

Concreting

Pre-fabricated reinforcements were inserted in the boreholes and concreting was done. Fig. 4 shows the concreting of RC piles in the field.

Curing

Piles were covered with gunny bags for water curing immediately after demoulding since gunny bags can hold water for long time. Fig. 5 shows the water curing of concrete piles.


Fig. 3. Power auger boring


Fig. 4. Concreting


Fig. 5. Curing of RC piles

GLASS FIBRE REINFORCED POLYMER WRAPPING

After sufficient water curing for 28 days, the RC piles were prepared for GFRP wrapping. The following steps were followed for FRP wrapping

Soil Excavation

Soil around the pile was excavated for FRP wrapping. For laterally loaded piles, the depth of fixity is important for the designer since the maximum bending moment will be at depth of fixity. The pile is mainly designed for maximum bending moment. In the present study, the depth of fixity was estimated as 1.23 m below ground level based on the soil properties. The depth of excavation (1.5 m) made was slightly higher than the depth of fixity

Chiselling

Chiselling was carried out to make the uneven concrete surface as even surface using chisel and hammer.

Plastering

Cement mortar was applied over the uneven concrete surface to make even for GFRP wrapping.

Rubbing

The surfaces of the RC piles were rubbed with sand paper to remove loose and deleterious material from the surface with a silicon carbide water-proof paper sheet.

Primer Coating

The mixed material of Nitowrap 30 epoxy primer was applied over the prepared and cleaned surface.

Saturant Coating

The saturant system used in this work was made of two parts, namely, resin and hardener. The components were thoroughly hand mixed for 3 minutes before application.

GFRP wrapping

The first coat of saturant was applied over the primer coat and GFRP sheet was then wrapped directly on the surface. GFRP layer was wrapped around the pile with an overlap of ¼ of the perimeter to avoid sliding or debonding of fibres during tests and to ensure the development of full strength. Fig. 6 shows the wrapping process done on piles.

Earth Filling

Excavated soil was filled in layer by layer. Sufficient compaction was done for each layer to achieve the same density as obtained during excavation. Fig. 7 shows the filling of excavated soil.


Fig. 6. GFRP wrapping


Fig. 7. Filling of excavated soil

EXPERIMENTAL SET UP AND PROCEDURE

Lateral Load Application

The lateral load test was performed in accordance with IS : 2911(Part 4) - 1985. The pile was loaded horizontally at a distance of 0.85 m above ground level. The lateral load to the pile was applied through a hydraulic jack, which was placed between the supporting and testing piles. The reaction was obtained from the central supporting pile. The capacity of the jack is 200 kN and ram diameter is 75 mm with 150 mm ram travel. The jack is connected to a hydraulic pump. The load applied is displayed on pressure gauge and also measured through proving ring.

Installation of Dial Gauges

Three dial gauges were installed to measure the lateral displacement of pile. Dial gauges used for these tests were accurate to 0.01 mm. Dial gauges were clamped on specially fabricated steel frame with 30 cm apart from one another. The steel frame was fixed in the ground in such a way that there was no deflection in the steel frame. One dial gauge was placed behind the loading point.

Loading Procedure / Loading Sequence

The loading sequence adopted in the test is in accordance with IS : 2911(Part 4) - 1985 section 6.2. Maintained Load Method was adopted in the test. In this method application of increment of test load and taking of measurement or displacement in each stage of loading was maintained till rate of displacement of the pile either 0.1 mm in first 30 minutes or 0.2 mm in first one hour or till 2 hour whichever occur first. In the static lateral load test, the load was applied in increment of 20% of the working load until it reaches ultimate lateral load. After this stage, the load was released and then brought to "no load" condition. Each load step was maintained as mentioned above. The pile lateral movement readings were taken at 0, 15 and 30 minutes after each load step. In the cyclic lateral load test, each load was applied in increment of 20% of the working load until it reaches ultimate lateral load. After each load step, the load was released and then brought to "no load" condition then the next increment load was applied. Each load step was maintained as mentioned above. Test set up is shown in Fig. 8

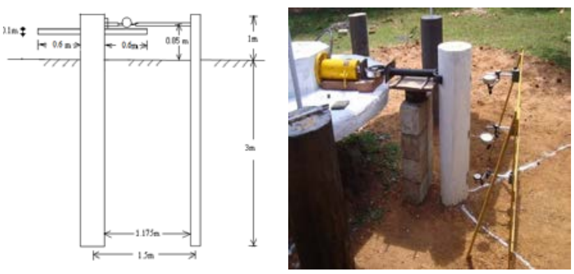

Fig. 8. Test setup

RESULTS AND DISCUSSIONS

GFRP Strengthened RC Piles Subjected to Static Lateral Loads

Experimental investigations have been conducted on 4 RC piles. Out of the 4 piles, one reference pile was tested without any wrapping and the remaining 3 piles were wrapped with GFRP composites of varying configurations. The static lateral load test was performed in accordance with IS : 2911 (Part 4) - 1985. At each stage of loading, lateral displacement of piles were measured. Displacement at ground level was interpolated from the three dial readings since the three dial gauge readings were linearly varied. Lateral load versus ground level displacement of piles is shown in Fig. 9. Lateral load corresponds to 5 mm and 12 mm displacements at ground level were calculated from the Fig. 9 and it is tabulated in Table 3. As per IS : 2911(Part 4) - 1985, safe load of the pile was taken as 50% of final load at which the total displacement increases to 12 mm or final load at which the total displacement corresponds to 5 mm at ground level. However, the safe load of the pile is taken as the minimum of the above two. In all the cases it was observed that the first condition is the minimum

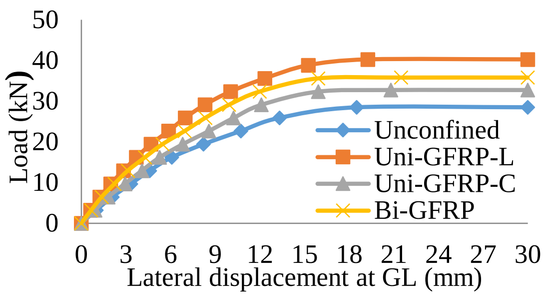

Fig. 9. Lateral displacement of piles at ground level

Soil Behavior around the Pile

In the analysis of soil-pile interaction under lateral load, the behavior of soil around a pile is an important parameter which has a great influence on the results. Most of the research about piles under lateral loads has to date been performed to investigate the load-bearing capacity of the piles, pile deflection, pile rotation and internal forces created in the pile. Only a few physical models have been created to investigate the behavior of the soil around the pile and its deformation pattern. Therefore it is necessary to investigate the soil deformation pattern around laterally loaded piles and pile-soil interaction in order to improve the level of knowledge on this subject. It can be observed that there is a cap between pile and soil surface in the loading side of the ground. This cap is extended to some depth below ground level depends on the type of FRP wrapping. It was also noticed that the top surface of the ground around the pile opposite to loading slightly heaved. Considering Fig. 10 the maximum horizontal displacement occurs in the ground level and decreases gradually with depth. At greater depths (depths about 2 to 3D, where D is the diameter of pile) the displacements of soil around the pile are negligible which was confirmed by visual observation as well as measurement by thin rod.

Table 3. Lateral load carrying capacities of tested piles

Type	Ultimate Load, P_u (kN)	Load corresponding to 12 mm displacement at GL (kN)	50 % of Load corresponding to 12 mm displacement at GL (kN)	Load corresponding to 5 mm displacement at GL (kN)	Safe load (kN)
Unconfined pile	28.5	24.26	12.13	13.81	12.13
Uni-GFRP-L	40.27	35.12	17.56	20.29	17.56
Uni-GFRP-C	32.77	28.96	14.48	15.45	14.48
Bi-GFRP	35.81	32.37	16.18	18.16	16.18

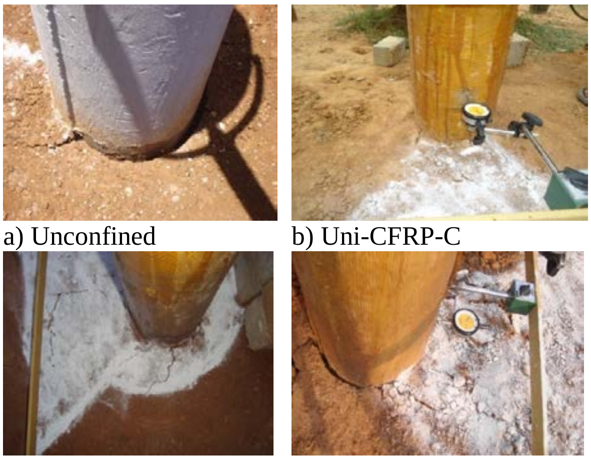

a) Unconfined b) Uni-CFRP-C

c) Bi-GFRP d) Uni-CFRP-L

Fig. 10. Soil behavior around the pile

Shear Strains around a Laterally Loaded Pile

It can be observed that the maximum shear strain occurred in pile-adjacent soils near the surface. A triangular strain wedge to the side of the displaced pile is created. Fig. 10 shows that in front of a laterally loaded pile a passive zone is established and the propagation of this zone is purely depend on the imposed displacement, since the soil condition is identical for all pile locations.

Effects of Pile Stiffness on Soil Deformation Patterns around a Pile

In flexible piles, the pile stiffness is an effective parameter in lateral load capacity. This parameter significantly influences the deformation of the surrounding soil. From the observation it can be seen that the mobilized depth of the strain wedge was increased and the mobilized angle was decreased with increasing pile stiffness.

Failure Mode of Piles

The failure of all piles occurred below the ground level, at a distance of about 1.4 to 2.4 times the diameter of the pile. The failure modes of all the piles were long pile failures that occurred by bending moments, as shown in Fig. 11

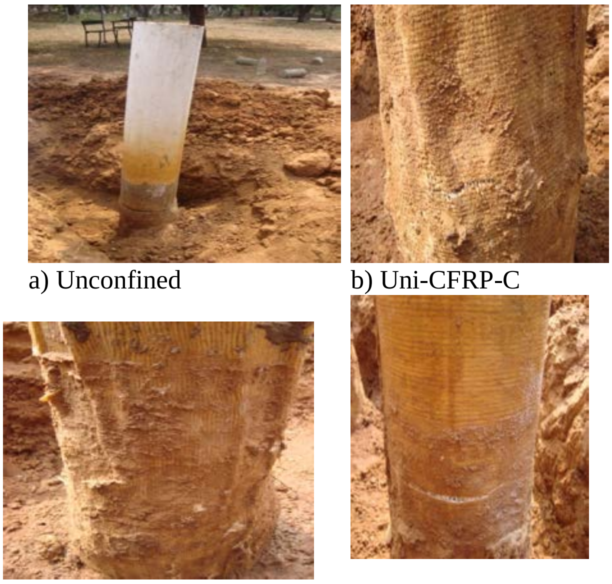

a) Unconfined b) Uni-CFRP-C

c) Bi-GFRP d) Uni-CFRP-L

Fig. 11. Failure mode of piles

Under lateral loading, the unconfined pile failed at 0.32 m from the ground level which is about 1.4 times its diameter. Whereas, unidirectional GFRP confined piles with fibres along the length and circumference of piles failed at 0.54 m and 0.51 m (about 2.3 to 2.4 times diameter) respectively. The displacement of soil around the pile (width and depth of gap) was measured by visual observation as well as measurement by thin rod. The width and depth of gap depends on soil type and loading condition. This experimental study was conducted on C - φ soil. Table 4 presents the gap width & depth and the depth of pile failure from ground level. It shows very clearly that the GFRP confined piles are taken much more lateral load than unconfined piles. It is also noticed that the GFRP confined piles depth of fixity is about 1.6 to 1.8 times more than unconfined piles which means that the GFRP confined piles moment carrying capacity is almost more than 1.5 times than unconfined piles.

Table 4. Gap formation and pile failure

Type of piles	Unconfined pile	Unidirectional GFRP-L	Unidirectional GFRP-C	Bidirectional GFRP
Maximum width of gap at GL (cm)	1.8	2	1.9	1.8
Maximum depth of gap from GL (cm)	42	67	58	71
Pile failure (depth from GL in cm)	32 (1.39D)	54 (2.32D)	51 (2.19D)	56 (2.41 D)

CONCLUSIONS

Based on the experimental results, the following conclusions are made.

1. The GFRP wrapped piles lateral capacity is significantly higher than the conventional pile of the same depth and diameter. The GFRP wrapped piles depth of fixity is about 60 to 70% higher than conventional concrete piles. It shows that the moment carrying capacity of GFRP wrapped piles are much more than the conventional concrete piles.
2. GFRP piles with fibre orientation along the length of the pile indicated about 41% more lateral strength than unconfined pile. However, the increment in the lateral load carrying capacity was only about 15% for fibres oriented in circumferential direction. The percentage increase in lateral strength of pile strengthened with bidirectional GFRP mat was 26% than unconfined pile. This clearly indicates that the GFRP strengthening is an effective method for strengthening of existing piles.

REFERENCES

[1] Almas Begum, N. & Muthukkumaran, K. (2009). Experimental investigation on single model pile in sloping ground under lateral load. International Journal of Geotechnical Engineering 3, No.1, 133-146.

[2] Alkhrdaji, T., and Nanni, A. (2000). “Flexural strengthening of bridge piers using FRP composites.” ASCE structures congress 2000, M. Elgaaly, ed., Philadelphia.

[3] Bournas, D. A., and Triantafillou, T. C. (2009). “Flexural strengthening of reinforced concrete columns with near surface mounted FRP or stainless steel.” ACI Struct. J., Vol. 106, No. 4, pp.495–505.

[4] Bousias, S.N., Triantafillou, T.C., Fardis, M.N., Spathis, L. and O’Regan, B.A. (2004). “Fiber-reinforced polymer retrofitting of rectangular reinforced concrete columns with or without corrosion”, ACI Structural Journal, Vol. 101, No. 4, pp. 512–520

[5] Chaallal, O. and Shahawy, M. (2000). “Performance of fiber-reinforced polymer-wrapped reinforced concrete column under combined axial-flexural loading”, ACI Structural Journal, Vol. 97, No. 4, pp. 659–668.

[6] Goksu, C., Polat, A. and Ilki, A. (2012). “Attempt for seismic retrofit of existing substandard RC members under reversed cyclic flexural effects”, Vol. 16, No. 3, pp. 286-299.

[7] Iacobucci, R.D., Sheikh, S.A. and Bayrak, O. (2003). “Retrofit of square concrete columns with carbon fiber-reinforced polymer for seismic resistance”, ACI Structural Journal, Vol. 100, No. 6, pp. 785–794.

[8] Ilki, A., Peker, O., Karamuk, E., Demir, C., and Kumbasar, N. (2008). “FRP retrofit of low and medium strength circular and rectangular reinforced concrete columns.” Journal of Materials in Civil Engineering, Vol. 20, No. 2 , pp.169-188.

[9] Ilki, A., Demir, C., Bedirhanoglu, I. and Kumbasar, N. (2009). “Seismic retrofit of brittle and low strength RC columns using fiber reinforced polymer and cementitious composites”, Advances in Structural Engineering, Vol. 12, No. 3, pp. 325-347

[10] IS : 2911 (Part 1/Sec 2) - 1979 Code of practice for design and construction of pile foundations. Bureau of Indian standards.

[11] IS : 2911 (Part 4) - 1985 Code of practice for design and construction of pile foundations. Bureau of Indian standards.

[12] IS : 1498 - 1970 Classification and identification of soils for general engineering purposes. Bureau of Indian standards.

[13] Muthukkumaran, K., Sundaravadivelu, R. & Gandhi, S.R. (2008). Effect of slope on P-Y curves due to surcharge load. Soils and Foundations 48, No.3, 361-365.

[14] Muthukkumaran, K. (2014). Effect of slope and loading direction on laterally loaded piles in cohesionless soil. International Journal of Geomechanics, ASCE, 14(1): 1-7.

[15] Purushotham Reddy, B., Alagusundaramoorthy, P., and Sundaravadivelu, R. (2009). “Retrofitting of RC Piles using GFRP Composites.” KSCE Journal of Civil Engineering, 2009, Vol. 13, No.1, pp. 39-47.

[16] Sangeetha, P., and Sumathi, R. (2010). “Behaviour of glass fibre wrapped concrete columns under uniaxial compression.” International Journal of Advanced Engineering Technology, Vol. 1, No. 1, pp.74-83.

[17] Sen, R., and Mullins, G. (2007). “Application of FRP composites for underwater piles repair.” Journal of Composites: Part B 38 (2007) pp.751–758.

Technical Paper

Geotechnique Paper

Fifth International Conference on Geotechnique, Construction Materials and Environment, Osaka, Japan, Nov. 16-18, 2015, ISBN: 978-4-9905958-4-5 C3051

A NEW LOOK AT PAVEMENT MANAGEMENT

John Yeaman, Stuart Yeaman[2] and John W Yeaman[3]
[1]Queensland Pavement Centre, University of The Sunshine Coast, Australia [2] Jacobs Engineering,, Australia,
[3]Pavement Management Services, Australia

ABSTRACT

Pavement Management embraces the full range of engineering activities (Design, Construction, Operation, Maintenance and Renewal), throughout the life cycle. Over the past 4 years, The Queensland Pavement Centre at the University of the Sunshine Coast, Australia, has been studying the various parameters that influence pavement behaviour and those parameters that impact the whole of life of a road pavement under real operational conditions. By 2015 five sites have been installed in operational pavements, designed to monitor the performance of critical parameters as a function of material properties, climatic changes and the complete spectrum of traffic usage. One site (Sippy Downs Drive – East) has been operational for over 1000 days. This paper is based on the findings from that study. The paper will address a design aspect of Pavement Management, in particular the critical strains as measured in the subject pavement every minute of every day for the past two years and demonstrate how the performance parameters can be utilised in a simulation method to predict whole of life performance based on operational data, obtained from real life, rather than assumed parameters.
The configuration of other sites and a test suite for installation and analysis are recommended.

Keywords: Transfer Function, Layer Temperature, Design, Simulation, Field Sampling

INTRODUCTION

The Engineering Science of Pavement Management has stagnated for the past 20 years, with practioners reducing the Science to becoming an inventory of the stock of road assets and a means of justifying decisions that are often based on very little knowledge of the performance of the asset under an extensive range of conditions and manufacturing methods.

Pavement Management, as many people understand it, does not involve the fundamental requirements of a triple bottom line in engineering, engineering, economics and sustainability, embracing the principles of risk management.

Pavement Management must consider the component paradigms:

- Design
- Construction
- Operation
- Maintenance
- Renewal

Whilst all of these aspects are necessary for the effective management of pavements throughout the life cycle, the design of a pavement to meet the conditions of its use must be paramount, since if the design is unsuitable or simply incorrect then the remainder of the management process is useless Mathematics and computing power mean that we no longer have the need to design pavement for one season (The Mean Monthly Average Pavement Temperature), One Load (An equivalent Standard Axle) and one material (defined by Stiffness at one temperature and one time of loading).

This paper will examine will examine the use mathematical simulation process , using statistical data from data collected from operational pavements and materials to determine the probability of a pavement meeting its whole of life expectancy, for the conditions pertinent to its use**..**

THE FUNDAMENTAL ISSUES OF PAVEMENT MANAGEMENT

Construction

The pavement constructor can make or break the design, particularly when it comes to preparation of the subgrade and compaction of the structural layers. Many industry associations go to great lengths to train construction operators in the correct use of equipment, but if the material supplied is a little segregated, cold , or containing " off -spec" materials the resultant variability in the as built quality can easily make the finished product less than that assumed for the design.

Structure

We assume one structure for the design, but natural materials have a latent coefficient of variability in the order of thirty percent for almost all of their properties. Manufactured materials such as quarried and crushed products, Hot Mix Asphalt (HMA) and Concrete have much lower coefficients of variation and can be laid with great accuracy. Layer thicknesses and compaction can be assumed with a lot more certainty but what about the subgrade stiffness? We use a modulus (stiffness) mostly calculated from a Californian Bearing Ratio (CBR) test. If we are fortunate to have determined the Resilient Modulus of the Subgrade material, what is its variability across the project?

Environment

Solar Radiation is a critical parameter impacting on the pavement's environment. The quantum of solar radiation drives the pavement surface temperature, oxidation and polymerisation of the bitumen binders in HMA mixtures and surface treatments. The predominate pavements adopted in Queensland. Fortunately Solar Radiation is an unique commodity in that it can be calculated for any point on the earth's surface for any time of the day and day of the year, for example at the Sippy Downs Campus – Latitude 26° 43'23"South ; Longitude 153° 04'02"East ,Solar Radiation is at its peak at 12:03 pm every day. Moisture content also has a serious impact on pavement performance. In Queensland we are not subjected to Freeze Thaw cycles but the State is subject to "drought and flooding rains". Pavements can be dried by the environment to well under optimum and can be totally inundated for weeks on end.

Traffic

Over the past few years we have become more aware of the impact of heavy trucks and vehicle speed on the performance of pavements. It will be shown that often Four Wheel Drives, Armoured Cars ,innocent looking Coffee Carts and mobile food vans are exerting stresses onto a pavement as much as a Bus or Truck.

Maintenance

The timing, treatment, quality and methods will have a significant impact on the performance of a pavement throughout its life. Serviceability (water proofing, riding quality) Safety (skid resistance, potholes, rutting) and Structural Capacity (ability to carry changing loads, fatigue cracking and permanent deformation) all can be modified by maintenance, provided that the cause not the effect of the problem is rectified

THE RELATIONSHIP BETWEEN CRITICAL STRAINS AND FATIGUE CRACKING

For the purposes of this paper we will adopt the transfer function adopted throughout Australia Reference[1]

$$Nf=\left[\frac{6918(0.856Vb+1.08)}{S\,Mix^{0.36}\mu\varepsilon}\right]^{5} \quad \text{Equation 1}$$

Where

Nf = the number of cycles to fatigue failure

Vb is the Voids filled by bitumen in the target HMA

Smix (|E*| the Stiffness of the HMA obtained from the Mixture Master Curve

με is the horizontal tensile strain at the base of the HMA layer

Other transfer functions such as those developed in reference [2] are equally suitable for the local conditions

$$\boldsymbol{Nf = 18.4\,(18.4(0.00432\mu\varepsilon^{-3.291})E^{-0.654}}$$

Equation 2

Where symbols are as defined above

For this study we will only discuss the influence of the Critical horizontal strain με.

DESCRIPTION OF SIPPY DOWNS PAVEMENT MONITORING SITE

During the latter part of 2012, Sunshine Coast Council (SCC), undertook a upgrade of a major arterial road, adjacent to the University Campus. It was suggested by SCC officers that this would provide an opportunity to instrument the road and determine some of the critical parameters under operational conditions. The description and equipment at the site is described in Reference [3] a paper prepared following an extreme weather event shortly after the road as opened to traffic.

Following this event, Pavement Management Services (PMS) added to the equipment at the site to enhance further study and analysis capability

Weather Station	**Air temperature**	**In Pavement**	**Horizontal Strain Gauge @ 75mm**
	Relative Humidity		**Vertical Strain Gauge @ 650mm**
	Atmospheric Pressure		**Thermocouple on Surface**
	Rainfall		**Thermocouple @ 75mm**
	Wind Speed		**Moisture Gauge @**
	Wind Direction		**Moisture Gauge @**
	Solar Radiation		**Camera**
Solar panels provide electrical energy			
Data are collected every minute 24/7 and transferred dally at 6:am to the researcher's computer			
The camera records a photograph of the road surface every day at 10:00 am and a photograph of any vehicle that exceeds a nominated strain level			

Table 1 Elements of Pavement Monitoring Site at Sippy Downs Drive

RELATIONSHIP BETWEEN LAYER TEMPERATURE AND HORIZONTAL TENSILE STRAIN

The surface layer temperature has a major influence on the strains obtained under operational conditions, even diurnally. In general, surface layer temperature rises to a maximum around 3:30 pm on a summers day, this is around 3 hours after peak solar radiation (figure 4) to be noted here that in general the Strains as measured in the pavement are general positive in format which indicates that the surface layer is in compression and there is unlikely to be development of fatigue failure during this period.

On the other hand, during a winter cycle (19 June 2014) it can be seen that again peak strain occurs about 3:30pm about 3 hours after peak solar radiation (figure 3), but here the Strain lies in the negative zone of the chart, signifying that the pavement is likely to be developing fatigue strain.)

Figure 1 Relationship between Strain 1 and Surface Layer Temperature for 20 December 2014

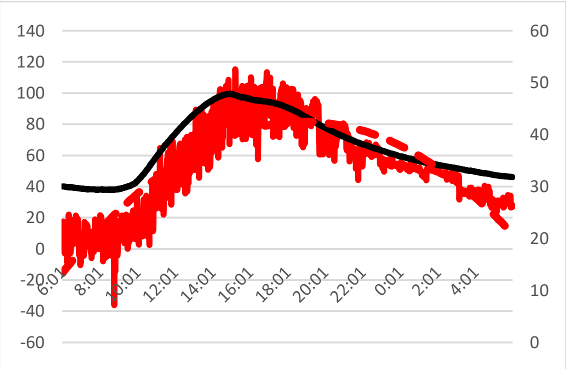

Area under Curve	MEAN STRAIN	Mean Temperature
76,355	53	37.7

Figure 2 Relationship between Strain 1 and Surface Layer temperature for 19th June 2014

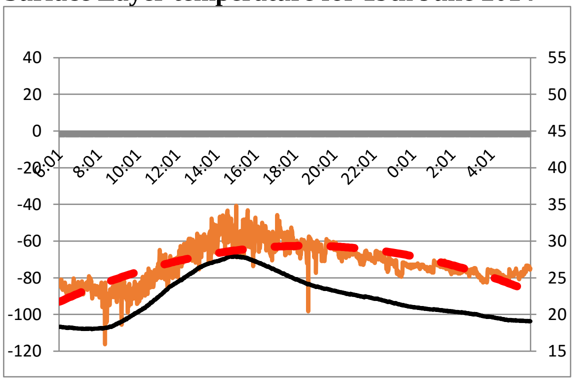

Area under Curve	MEAN STRAIN	Mean Temperature
-103,480	-72	22.3°C

These results can be compared in table 2, where it can be observed the major differences between parameters as a function of season.

One must therefore query the efficacy of using one strain in the transfer function (Equation 3 or Equation 4) to calculate the Cycles to failure

Table 2 Seasonal Comparison between Strain 1 and surface layer Temperature

	Summer		Winter	
	STRAIN	Temperature	STRAIN	Temp.
Area Under Curve	76,355	54,357	-109,408	30,771
Mean	53	37.7°C	-76	21.3°C
Standard Deviation	29.5	6.05	11.53	3.54 °C

Annual Drift

A comparison of daily results for the same date 1 year apart fails to yield a significant trend at this time (750 days) (table 3). What we can see here is the variability in surface layer temperature, which may explain some of the differences

Table 3 Strain and temperature parameters 1 year apart

	Area under Curve	MEAN	Standard Deviation	Mean Pavement Temperature
Dec 12	9,511	6.6	15.1	34.3°C
Dec 13	-7827	-5.4	29.7	40.9°C
Dec 14	76,355	53	29.5	37.7°C

It was therefore decided to examine the strain distribution month by month. Figure 3 provides this information

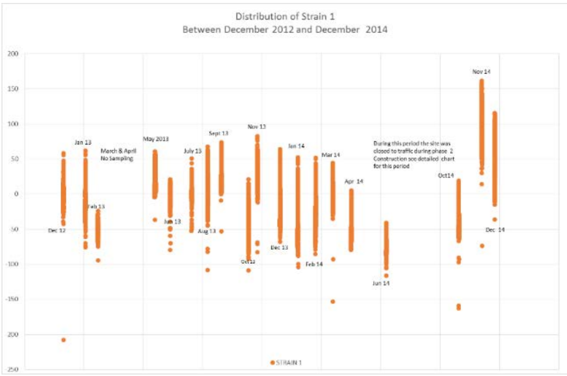

Figure 3 Distribution of Strain Data over 750 days

From Figure 3 , it can be seen that range in strain values, in fact, varies month by month. With strain values at a minimum (largest negativity) in June of each year to date. It is interesting to note the slight increase in strain range (greater positivity) in December of each year. Is this the permanent set of Hooke's Law?

STRAIN DISTRIBUTION WITH SEASON

A statistical analysis (Histogram and Cumulative Distribution function) of all results between 20th December 2012 (the first day opened to traffic) and 20th December 2014 are given in Figure 7

Analysis of this data provides the following statistics:

MEAN = -1.4 με

Standard Deviation = 42.37 με

Number of samples = 30,240

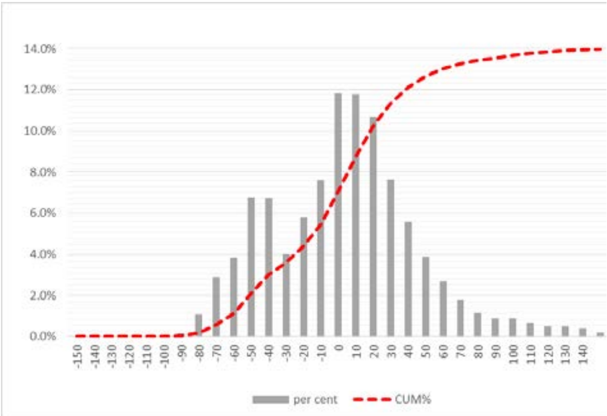

Figure 4 Distribution of Horizontal strain data over 750 days

ABERRATIONS TO STRAIN TEMPERATURE RELATIONSHIP

In the period July to October 2014 that section of road containing the monitoring station was closed due to new construction being undertaken to the west of the monitoring site. This provided a unique opportunity to observe the strain behaviour without traffic and only influenced by pavement temperature. The relationship between Strain and temperature in this period is shown in Figure 10

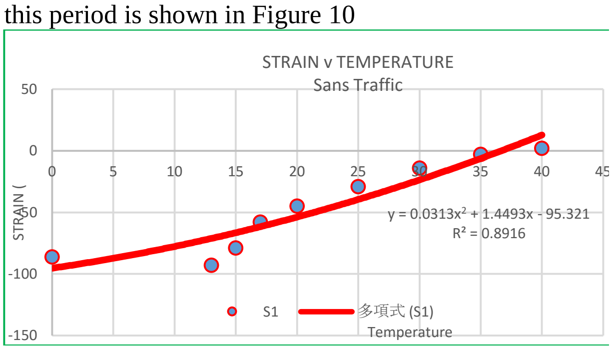

Figure 5 Relationship between Strain 1 and Temperature (without traffic) July to October 2014

The range for the strain during this period is best illustrated by a Histogram and a Cumulative Distribution function (Figure 10) from which it can be observed that the 90th percentile of strain 1 results fall within the range -70 to +10 Micro strain

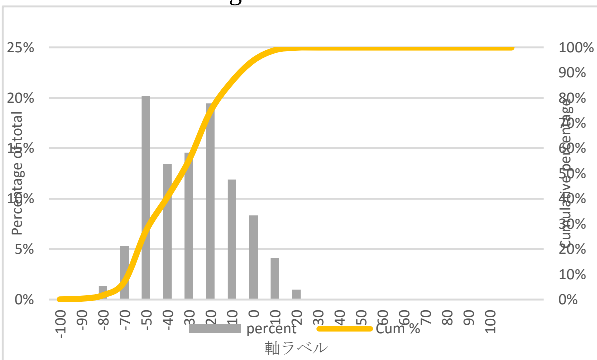

Figure 6 Distribution of Strain 1 without Traffic July to October 2014

Further extension of this data without traffic (between 11 July and 3 October 2014) can be illustrated in the following Figure 5

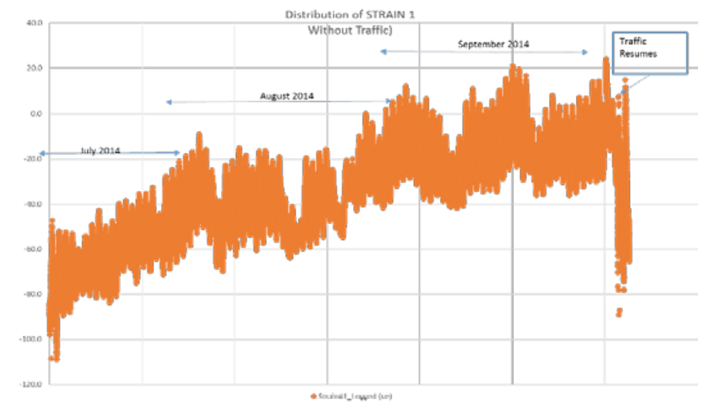

Figure 7 Daily Range of Strain (without traffic)

Superimposing the Temperature profile for the same period demonstrates the impact of temperature on the pavement as a function of Surface layer temperature

These figures illustrate, not only, the narrow band of strains occurring in a pavement, (0 to -70 με at the 90th percentile range but also the fact that there is some strain developed in a pavement by thermal changes only

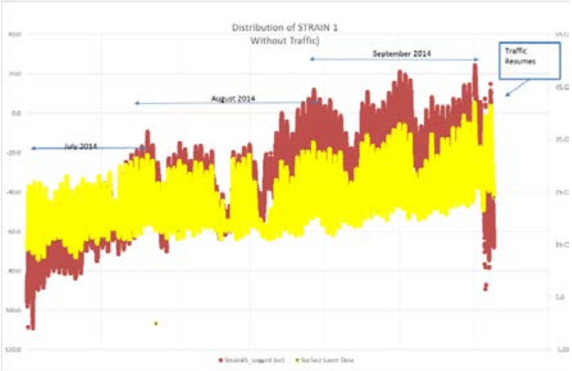

Figure 8 Daily Range of strain (without Traffic) with daily range of temperature superimposed

DISTRIBUTION OF SURFACE LAYER TEMPERATURE

Clearly there is a very strong relationship between horizontal strain and temperature with a much greater effect that many of us realise; of significance is the maximum value for surface layer. Surface layer temperature over two full years of study has indicated that the surface layer temperature at this site exceeds 50°C less than 2% of the time. Figure 8 following illustrates the distribution of Surface Layer (top 75mm) over 750 days

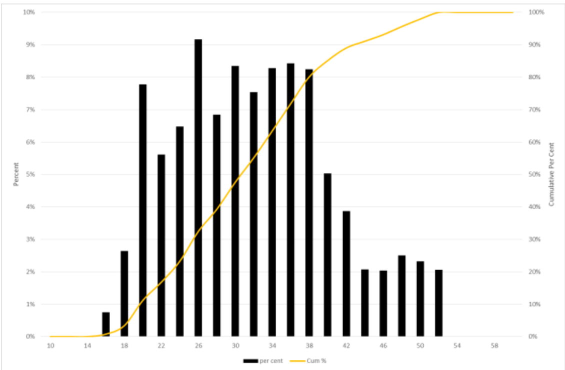

Figure 9 Distribution of Surface Layer Temperature for Latitude 26° 43'23"S; Longitude 153° 04'02"E
From Dec 2012 to Dec 2014

THE EFFECT OF TRAFFIC

The camera at the monitoring site is configured to take a photograph of the pavement surface at 10:00 am daily. These photographs are scanned visually to assess any visible deterioration in the pavement. To date there has only been one issue with cracking,, which on investigation was found to be a blocked sub soil drain. A significant outcome for the efficacy of the technology

The camera is also configured to take a photograph of the same area should the measured strain exceed 160 με at either gauge.

In figure 10 we can see that a similar vehicle, bus, makes a different impact on the pavement at a different time of the day. In the first photo, when the pavement is relatively cool (8:00 am and 27°C) the bus triggers a reaction in the Strain 1 gauge (the upper one) of around 200 με, but around 3:00 pm when the temperature is at its maximum (around 45 °C) and the pavement is considerably less stiff, a similar bus triggers a reaction in Strain Gauge 2 (the lower one) of around -60 με. The stiffnesses from the Master Curve Catalogue for this subject HMA are

Speed = 45kph, Temperature = 25°C Dynamic Modulus = 11,400 MPa

Speed = 45kph, Temperature = 45°C the Dynamic Modulus =4,350 MPa

This further highlights the risk associated with continuing to use one, only, strain in the transfer equation – Equation 3

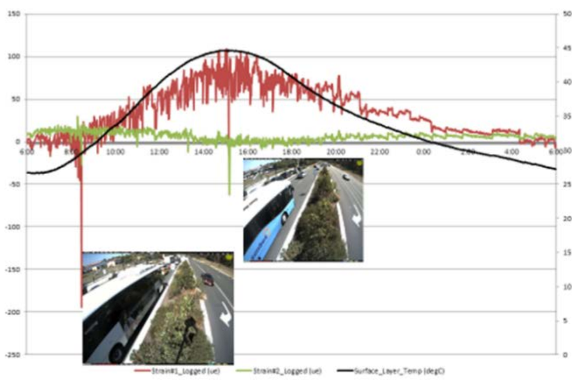

Figure 10 Comparison of field measured Strains for Similar Vehicles at different temperature conditions

D is the fraction of life consumed by cycles at the different strain levels. In general if the damage fraction reaches 1 failure occurs.

This linear summation of cycle ratios is fundamental to pavement analysis

PAVEMENT ANALYSIS BY SIMULATION

Monte Carlo Simulation is a computation method that is based on taking random readings from a physical law or mathematical model numerous times in order to obtain a numerical integration, an optimum value or a probability distribution.

In this application by Jopson Reference [4], Monte Carlo Simulations were used to determine the values for Nf using the statistical data for εt (Figure 7) above. The HMA Master Curves were determined by analysis of the HMA taken from the failed section of the road and compacted in the Shear Box compactor and the real life data obtained from the Pavement Monitoring Site.

These values together with volumetric properties of the HMA (obtained from the HMA testing such as Voids filled by Bitumen (Vb) were used within the Transfer function (Equation 3) to determine the number of cycles to failure (nf). The damage factor (Nf calculated by this method divided but the design life).

The probability density function was determined to determine the probability of failure within the design life.

This analysis provided a predictive time to failure under actual traffic of 6 years compared with an actual result of 7 years

INPUTS FOR SIMULATION ANALYSIS

The following inputs were required to start the system

Analysis Period

The analysis period is the "whole of life" desired "for the pavement. This will determine the number of iterations in the simulation. For Example if the desired life is 20 years the process will be iterated 10 Million times (20 years X 365.25 days per year x 1440 minutes per day).

Pavement Thickness

A value chosen by the designer, through experience, as to the approximate thickness required by the site conditions and the traffic spectrum. This will be tested by simulation and increased or decreased in the analysis until the desired thickness for the conditions is met.

PERFORMANCE PARAMETERS

Traffic Spectrum

The traffic data from the proposed site together with typical strains obtained for the spectrum of vehicles provides statistics as to the strains to be exerted on the pavement, (vide Figure 7).

Asphalt Master Curve

A suitable mixture provided by the supplier is nominated and the Master Curve obtained for that mixture. This data is used to populate Equation 3 and determine the stiffness of the mix at any temperature and time of loading.

Solar Radiation and Surface Temperature

The solar radiation for the proposed site can be calculated for any minute of any day for the analysis period, from this the surface temperature (taking into account, Albedo, Emissivity and Conductivity for the nominated HMA can be provided

ANALYSIS

The Damage factor for each iteration is determined by simulation via the input data and the transfer function

The Design thickness

The design thickness is that one that is obtained at D= 1 (*vide* Equation 7) from the application of Miners Hypothesis

CONCLUSION

The use of Field data from a permanent pavement monitoring site, together with laboratory CHARACTERIZATION of materials can be adopted to provide a fully mechanistic approach to pavement analysis and design

REFERENCES

[1] Austroads "Guide to Pavement Technology-Part2 : Pavement Structural Design , 2008 pp 76

[2] Tanquist, BA August 1, 2001, "Development of a Quick Reliability Method for Mechanistic-Empirical Asphalt Pavement. , Minnesota Department of Transportation

[3] Fairweather H and Yeaman J 2014 "A study of the Parameters Affecting the Performance of Roads Under an Extreme Rainfall Event" Int. J of GEOMATE , Sept, 2014 Vol. 7, No. 1 (SI No.13) pp 99 -960.

[4] Jopson K "A forensic analysis of premature pavement failure of a road pavement using Asphalt Master Curves and Computer simulation-"Final Year Thesis , University of the Sunshine Coast, Australia

.

Fifth International Conference on Geotechnique, Construction Materials and Environment, Osaka, Japan, Nov. 16-18, 2015, ISBN: 978-4-9905958-4-5 C3051

SPATIAL ANALYSIS OF COLLAPSE-RELATED SOIL PARAMETERS

M. Mohammad Ali

California Public Utilities Commission. 180 Promenade Circle #115, Sacramento, CA 95834, USA.

ABSTRACT

Application of various techniques for spatial analysis to the field of civil engineering is well documented. In this paper a case study is presented, where kriging is applied for estimating collapsing soil parameters, which exceeds a critical threshold value for high, medium and low collapse susceptibility, with the estimation variance, at certain depth of Tucson, Arizona area. The estimate is based on existing criteria with spatial analysis used to build up model variograms and utilizing its parameter in the linear interpolation technique of simple kriging.

.

Keywords: Collapsing soil, geostatistics, variogram, krigging,

INTRODUCTION

Analyzing and providing an appropriate interpretation of data obtained from the phenomenon whose distribution is spatial in nature are challenging tasks. Due to availability of fast computing system such studies are becoming common in the fields of health, environment, geology, engineering, and many others. Besides visual perception of the spatial distribution of the phenomenon, the analysis is useful to translate the existing patterns in to objective and measureable quantities by estimating parameters at an unknown location. Since the emphasis of spatial analysis is to measure properties and relationship, taking in to account the spatial localization of the phenomenon under study, such analysis is being applied in geotechnical field [7], and significant amount of works have been published in the literature [6] [3] [4] . Geostatistical technique of simple kriging can be used with the geostatistical model to develop the contour of estimated parameters with the contour of estimation variance for parameters of a soil deposit having vertical as well as horizontal anisotropy.

In general, parameters of a soil deposit vary due to the inherent properties from its formation in the geological process. A soil deposit in a region may be either residual or transported. Also a transported soil may be either *alluvial* (stream borne) or a*eolian* (wind borne) or *colluvial* (gravity transported). When alluvial soils are deposited in an arid or a semi-arid environment, they develop larger voids and undergo a large decrease in bulk volume upon saturation or load application and are known as collapsing soils. However, it is difficult to identify collapse susceptible soils with this definition due to the existence of many different types of clay minerals and many other factors that contribute to the collapse phenomenon. Therefore, geostatistical methods in analyzing collapsing soil parameter would provide an optimum solution.

In this study geostatistical techniques of simple kriging were applied to selected collapsing soil parameters for soil in Tucson, Arizona. Previous works on this topic was limited only to studies involving either specific areas or specific soil parameters. The purpose of this study was to gather as much information as possible from reliable sources and to use this data with geostatistical technique to estimate parameters at un-sampled locations with the determination of estimation variance.

MATHEMATICAL DETAILS:

Kriging is a geostatistical technique to interpolate the value $Z(x_0)$ of a random field $Z(x)$ at an unobserved location x_0 from observations $z_i=Z(x_i)$, $i= 1,\ldots,n$ of the random field at nearby locations $x_1,\ldots,x_n$. Kriging computes the best linear un biased estimator $\hat{Z}(x_0)$ of $Z(x_0)$ based on a stochastic model of the spatial dependence quantified either by the variogram $\gamma(x,y)$ or by the expectation $\mu(x)=E[Z(x)]$ and the covariance function $c(x,y)$ of the random field.

The kriging estimator is given by a linear combination $\hat{Z}(x_0) = \sum_{i=1}^{n} w_i x_0 Z(x_i)$ of the observed value $z_i = Z(x_i)$ with weights $w_i(x_0)$, $i=1,\ldots,n$ chosen such that the variance, known as kriging variance or kriging error is as given by Eqn.(1) is minimized subject to the unbiasedness condition given in Eqn (2):

$$
\begin{aligned}
&\sigma_k^2(x_0) : \\
&= Var\left(\hat{Z}(x_0 - Z(x_0)\right) \\
&= \sum_{i=1}^{n}\sum_{i=1}^{n} \sum_{j=1}^{n} w_i(x_0) w_j(x_0) + Var(Z(x_0)) \\
&- 2\sum_{i=1}^{n} w_i(x_0) c(x_i, x_0) \ldots\ldots\ldots\ldots\ldots\ldots\ldots(1)
\end{aligned}
$$

$$
E[\hat{Z}(x) - Z(x) = \sum_{i=1}^{n} w_i(x_0)\mu(x_i) - \mu(x_0) = 0 \ldots\ldots\ldots(2)
$$

The kriging variance must not be confused with the variance as given by Eqn. (3) f the kriging predictor $\hat{Z}(x_0)$ itself.

$$
\begin{aligned}
&Var\left(\hat{Z}(x0)\right) \\
&= Var\left(\sum_{i=1}^{n} w_i Z(x_i)\right) = \sum_{i=1}^{n}\sum_{j=1}^{n} w_i w_j c(x_i, x_j) \ldots(3)
\end{aligned}
$$

Types of kriging

Depending on the schochastic properties of the random field different types of kriging apply. The type of kriging determines the linear constraint on the weights wi implied by the unbiasedness condition. Therefore, the method of calculating weights depend upon the type of kriging.Common types of kring are: simple kriging, ordinary kriging, universal kriging,indicator kriging, Multiple-indicator kriging,disjunctive kriging, andLognormal kriging.

Simple kriging interpolation:

The interpolation by simple kriging is given by

$$
\begin{aligned}
&\hat{Z}(x_0) = \\
&\begin{pmatrix} z_1 \\ \vdots \\ z_n \end{pmatrix}' \begin{pmatrix} c(x_1, x_1) & \cdots & c(x_1, x_n \\ \vdots & \ddots & \vdots \\ c(x_n, x_1) & \cdots & c(x_n, x_n) \end{pmatrix}^{-1} \begin{pmatrix} c(x_1, x_0 \\ \vdots` \\ c(x_n, x_n) \end{pmatrix} \ldots\ldots(5)
\end{aligned}
$$

The kriging error is given by:

Simple kriging

Simple kriging is mathematically the simplest, but the least general. It assumes the expectation of the random field to be known, and relies on a covariance function. However in most applications neither the expectation nor the covariance is known beforehand.

Assumption

The practical assumptions for the application of simple kriging are i) wide sense stationary of the field, ii) The expectation is zero everywhere: μ(x)=0, iii) Known covariance function c(x,y)=Cov[Z(x),Z(y)].

Simple kriging equation

The kriging weights of simple kriging have no unbiasedness condition and are given by simple kriging equation system:

$$
\begin{pmatrix} w_1 \\ \vdots \\ w_n \end{pmatrix} = \begin{pmatrix} c(x_1, x_1) & \cdots & c(x_1, x_0) \\ \vdots & \ddots & \vdots \\ c(x_n, x_1) & \cdots & c(x_n, x_n \end{pmatrix}^{-1} \begin{pmatrix} c(x_1, x_0) \\ \vdots \\ c(x_n, x_0) \end{pmatrix} \ldots\ldots(4)
$$

$$
\begin{aligned}
&Var\left(\hat{Z}(x_0) - Z(x_0)\right) \\
&= \underbrace{c(x_0, x_0)}_{Var(\hat{Z}(x_0))} - \underbrace{\begin{pmatrix} c(x_1, x_0) \\ \vdots \\ c(x_n, x_1) \end{pmatrix}' \begin{pmatrix} c(x_1, x_1) & \cdots & c(x_1, x_n) \\ \vdots & \ddots & \vdots \\ c(x_n, x_1) & \cdots & c(x_n, x_n) \end{pmatrix}^{-1} \begin{pmatrix} c(x_1, x_0) \\ \vdots \\ c(x_n, x_0) \end{pmatrix}}_{\mathrm{var}(\hat{Z}'(x))} \ldots\ldots(6)
\end{aligned}
$$

Which leads to the generalized least squares version of the Gauss- Marcov theorem [4]:

$$
\begin{aligned}
&Var\left(Z(x_0)\right) = \\
&Var\left(\hat{Z}(x_0)\right) + Var\left(\hat{Z}(x_0) - Z(x_0)\right) \ldots\ldots\ldots(7)
\end{aligned}
$$

Ordinary kriging equation

The kriging weights of ordinary kriging fulfill the unbiasedness condition

$$\sum_{i=1}^{n} \lambda_i = 1 \text{.................................(8)}$$

and are given by the ordinary kriging equation system:

$$\begin{pmatrix} \lambda_1 \\ \vdots \\ \lambda_n \\ \mu \end{pmatrix} = \begin{pmatrix} \gamma(x_1, x_1) & \cdots & \lambda(x_1, x_n) & 1 \\ \vdots & \ddots & \vdots & \vdots \\ \lambda(x_n, x_1) & \cdots & \lambda(x_n, x_n) & 1 \\ 1 & \cdots & 1 & 0 \end{pmatrix}^{-1} \begin{pmatrix} \lambda(x_1, x* \\ \vdots \\ \lambda(x_n, x*) \\ 1 \end{pmatrix} \text{.....(9)}$$

The additional parameter μ is a Lagrange multiplier used in the minimization of the kriging error $\sigma^2{}_k(x)$ to honor the unbiasedness condition.

The interpolation by ordinary kriging is given by

$$\hat{Z}(x*) = \begin{pmatrix} \lambda_1 \\ \vdots \\ \lambda_n \end{pmatrix}' \begin{pmatrix} Z(x_1) \\ \vdots \\ Z(x_n) \end{pmatrix} \text{.........................(10)}$$

The kriging error is given by

$$\operatorname{var}\left(\hat{Z}(x*) - Z(x*)\right) = \begin{pmatrix} \lambda_1 \\ \vdots \\ \lambda_n \\ \mu \end{pmatrix}' \begin{pmatrix} \lambda(x_1, x*) \\ \vdots \\ \lambda(x_n, x*) \\ 1 \end{pmatrix} \text{.......(11)}$$

Collapse Criteria and Related Parameters:

In arid regions soil deposits become partially saturated with large voids due to high evaporation rate. Application of loads on such soils causes small deformation at low degree of saturation. However as soon as the soil becomes saturated, large deformations take place due to the collapse of the intergranular structure and the phenomenon is referred to as collapse. In general, if the dry density of the soil is sufficiently low to give a void space larger than that required to hold the liquid limit water content, then collapse upon saturation is likely. Otherwise collapse generally occurs only when the soil is loaded.

Collapsing soils has been recognized in Africa, part of Asia, Europe as well as in the United States. In the United States the severity of the problem has been observed in the Midwestern and Western United States, where soil deposits are generally either *aeolian* or *alluvial.*

Many criteria for predicting the collapsing potential of a soil are available in the literature (Ref from ASCE). Some of the criteria are derived theoretically from consolidation test results and some are empirical. The methods for evaluating collapse susceptibility vary from simple to very complex. Considerable effort has been given to establish criteria for predicting the collapse potential and the critical values for severity of a soil. Some of the more commonly used criteria are described below.

The parameter C_p is known as collapse parameter and is obtained from consolidation test as shown in Fig1. [9]

$$C_p(\%) = \frac{e_1 - e_2}{1 + e_0} \times 100 = \frac{\Delta e}{1 + e_0} \times 100 = \frac{\Delta H}{H_0} \times 100 \text{....(12)}$$

Where e_1, e_2 are initial and final void ratio upon wetting, Δe and ΔH are changes in void ratio and sample height after saturation under a pressure of 200 kPa, and H_0 is the initial height of sample.

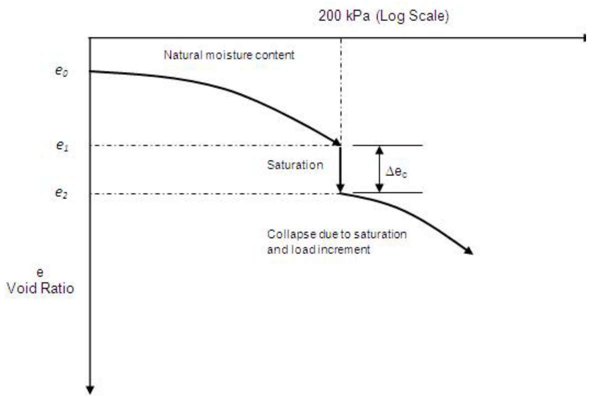

Fig. 1. Typical collapse potential in one dimensional consolidation test

[3].

R, known as Gibb's parameter is obtained from the following relation:

Table 1.Critical Values for and High Collapse (HC) Medium Collapse (MC) and Non-Collapsing(NC), Soil Parameters.

Parameters	High Collapsing (HC)	Medium Collapsing (MC)	Non-Collapsing(NC)
C_p (%)	> 5	$2 < C_p \leq 5$	≤ 2
R	≥ 1.4	$1.0 \leq R$ <1.4	< 1.0
e_0	≥ 0.82	$0.67 \leq e_0$ <0.82	< 0.67
γ_d, *pcf* (kN/m^3)	≤ 90(14.3)	90(14.3) $< \gamma_d$ ≤99(15.6)	>99(15.6)

$$R = \frac{\frac{\gamma_w}{\gamma_d} - \frac{1}{G_s}}{w_l} \qquad (13)$$

Where γ_d is the dry unit weight, w_l is the liquid limit moisture content, γ_w is the unit weight of water, and G_s is the specific gravity of soil solids.

Denisov (1964) criteria of collapse susceptibility is expressed as the ratio e/e_{LL}.If the ratio is greater than 1 then the soil is collapse susceptible.

Where e_{LL} is the void ratio at liquid limit and e is the void ratio at natural moisture content.

Beside the established criteria for soil collapse, there are other parameters that contribute to collapse phenomenon. These related parameters are : initial dry unit weight (γ_d), initial moisture content (w_0), initial void ratio (e_0), initial porosity (n_0), initial degree of saturation (s_0) and plastic limit (*PL*). Specific cut-off values for selected parameters are given below in Table 1

For this study field and laboratory test data were collected from local consulting engineers' offices and from the reports of previous researchers[3]. The raw data were reduced to obtain parameters in two categories: established criteria, such *as* C_p , *R*, and collapse-related soil parameters, such as, γ_d,w_0,e_0,n_0,s_0 and *PL*.. Analysis on selected parameters are presented in this paper.

Modelling of variogram:

Modelling of variogram is the first and most important step in applying the technique of kriging ,which is the method used here for obtaining unbiased estimate of parameters in un sampled location. A considerable amount of computation is necessary to obtain an adequate estimate of the variogram because of the empirical and subjective nature of the estimation process [2]. Parameters of interest with critical values are listed in Table 1. The various data sets containing number of data points of the parameters are listed in Table 2.

Table 2. Data sets used in the Analysis

Data set Number	Range of depth, m	Number of Data
1	0.0-0.3	125
2	0.3-0.6	286
3	0.6-0.9	254
4	0.9-1.2	100
5	1.2-1.8	104
6	1.8-12.2	123
7	0.0-12.2	219

Representative variograms were obtained for each of the parameters in each of the seven data sets, but only few are presented here. Since modeling of a variogram is, in part, an art requiring some subjective judgment, multiple trials are usually necessary in order to obtain a satisfactory variogram. The important parameters for a variograms are the range of influence, a, and the sill C, .

Nested Model:

$$\boldsymbol{\gamma(h) = C\left[\frac{3h}{2a} - \frac{1h^3}{2a^3}\right] + C_0 \quad for\ h < a} \qquad (\mathbf{14})$$

$$= C + C_0 \qquad \text{for } h \geq a$$

and

$$\gamma(0) = C_0 \qquad \text{for } h = 0$$

In geostatistical modeling, the most commonly used model is the nested models as shown in Figure 2. This model bears the same significance as the Normal distribution bears to statistics.

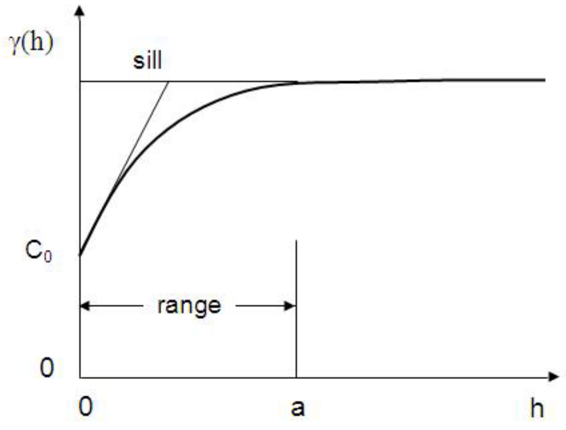

Fig.3. The Nested Model (Spherical with Nugget)

Variograms were obtained for the analysis for all the parameters , however few of them are presented here. Figures 3 and 4 show the variograms for Cp and γ_d of data set 5, respectively. In several cases a pure "nugget effect" model was obtained, indicating a complete lack of geological structure, Figure 5, shows such a model for the parameter e_0 of data set 6.

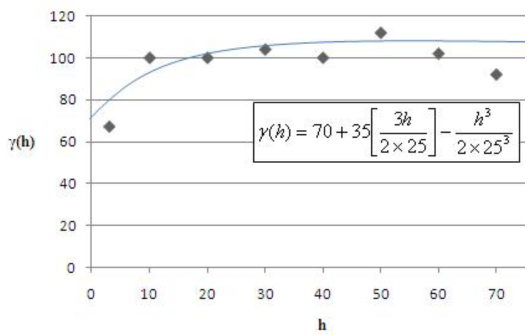

Fig.3. Semi-variogram and fitted equation for C_p of Data Set 5

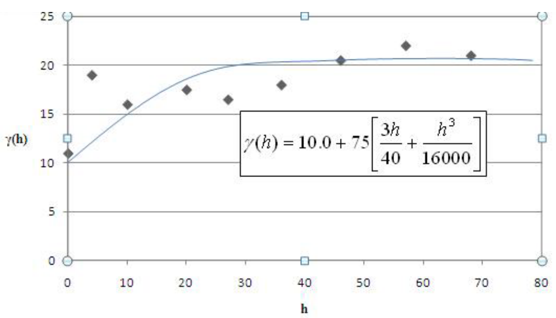

Fig.4. Semi-variogram and fitted equation for γ_d of Data Set 5

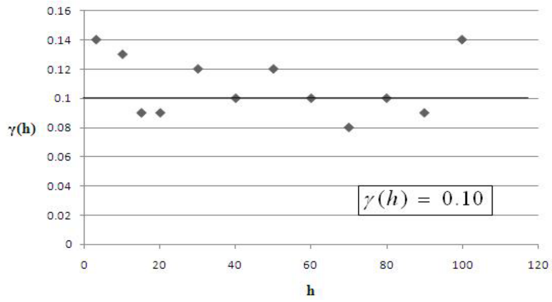

Fig.5. Semi-variogram and fitted pure nugget model for e_0 of Data Set 5

Fitting a Model

Constructing a variogram is to find theoretical model that best fits the experimental variogram. The choice is often limited to linear or spherical models, with a spherical model being the most common as the parameters are estimated subjectively. However, it is important that the chosen theoretical model y(h) fits well to the experimental semi-variogram within the model's limits of reliability [10] The choice of a theoretical model is generally made by examining the experimental variogram and taking in to account the fact that variograms are subject to significant fluctuations at large distances. Since most of the experimental variograms could be approximated by a spherical model, such a model was fitted to all the computed variograms in this study.

The key parameters of the selected spherical model, after cross-validation with different trial models for Data set 1 is presented in Table 3. The nugget value C_0 which is the estimate of y at h=0, provide an indication of short distance variation. The greater the value of C_0, the greater is the variance of the data set. Some of the model, e_0, for example shows a "pure nugget" effect indicating lack of spatial correlation.

Table 3. Parameters of Spherical Models fitted to Data Set 2

Data Set	Parameter	Nugget C_0	Range, a	Sill C
2	C_p	18.5	-	-
	γ_d	12.5	35.0	100.0
	n_0	32.4	35.0	45.0
	s_0	102.0	30.0	148.0
	w_0	0.002	25.0	0.0025
	e_0	0.042	30	0.053

The range , a, of the variogram can be interpreted as the diameter of the zone of influence which represents the average maximum distance over which a soil property is spatially related. In our study this distance was found to be 5.5 to 8 miles which is large relative to the distance over which soils are usually sampled for laboratory tests for a particular project, This suggest that , geostatistical concept can be applied successfully to the study of geotechnical problems.

There are three methods of krigging: punctual, block, and universal. Puntual kriging, which provides estimates for values of a random variable at points where there is no drift, has two forms: simple kriging if the mean value of the variable is known, and ordinary kriging, if the mean value is not known. Drift is defined as a non-stationary expectation of a random function. Block kriging is used when an estimation of the spatial average is required over a volume or an area. Universal kriging is an optimal method of interpolation that applies in all cases where drift must be taken in to account because of lack of data to make stationary or quasi-stationary estimates.`

In this study, variograms were estimated for each collapse criterion and collapse related soil parameters (Table 1) using a discrete number of values obtained from test data at incremental distances corresponding to sampling locations throughout the area. These variograms (Table 3) are then used in conjunction with ordinary kriging to estimate values of the parameters at un-sampled locations. Simple kriging [10] was then utilized to produce contour plots of estimated probability and associated kriging variance for each parameter in each data set.

Results and discussion

Results of kriging analyses showing contour of estimated valur of soils parameter γ_d (pcf) within 5 ft. (0.30 m) of surface having high collapse susceptibility based on collapse criteria with estimation variance are shown are in Fig 6 (a) and 6(b). If the critical values for any specific areas are known, areas containing high. Medium or low collapse susceptible soils can be obtained from these contour plots with known confidence. Areas where no data points are available are easily detected by discontinuities in the contour lines. Similar plots were developed for all of the other collapse criteria and collapse-related soil parameters for each of the seven data sets, however, they are not presented here due to space limitations.

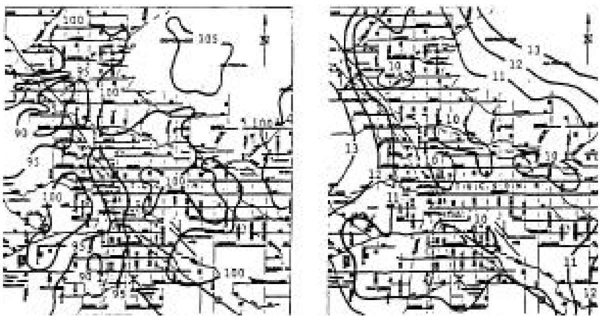

(a) **(b)**

Fig.6. Contour plots of a) Estimated value of γ_d in pcf, and b) Estimation variance

CONCLUSION

1. Collapsing soil parameters can be considered as regionalized variable and the concept of geostatistics may be applicable where a large amount of data are available from reliable sources.
2. Linear estimation method of kiriging was found to be a valuable tool for characterizing and modeling the spatial variability of geotechnical parameters.
3. The parameters under investigation can be best be fitted by a spherical model variogram
4. Simple Kriging method provides a means for estimating soil parameters at an un-sampled location with known variance of estimation. Therefore, the method can be applied to estimate any collapsing soil parameter in an area with a known degree of confidence. This information is extremely valuable to planners and Government officials.

REFERENCES

[1] Ali, M.M., E.A. Nowatzki, D.E. Myers, (1989), "Geostatistical Techniques to Estimate Collapse-related Soil Parameters", *Proc. 25th symposium on Engineering Geology and Geotechnical Engineering*, Reno, Nevada, March, pp. 289-296.

[2] Ali, M.M., E.A. Nowatzki, D.E. Myers, (1989), "Geostatistical Methods to Predict Collapsing Soil", *Proc. XII ICSMFE, Rio de Janeiro, Brazil,* Vol. VII, No.2, August, pp. 567-570.

[3] Andrew Richmond (2003) Financially Efficient Ore Selection Incorporating Grade Uncertainty, Mathematical Geology, Vol 35, N.2p 195-215,

[4] Chiles JP, P Delfiner (1999) Geostatistics,Modeling Spatial Uncertainty, Willey Seriesin Probability And Statistics.
[5] Clark I, (1979) Practical geostatistics, Applied Science Publishing, Ltd, Essex, London.
[6] David JC, (2002) Statistical and Data analysis in Gelogy, 3rd Ed, New Rork, John Wiley & Sons.
[7] Hammah, RE, and Curran, JH (2006) Geostatistics in Geotechnical Engineering: Fad or Empowering, GeoCongress, Geotechnical Engineering in the Information Technology Age, Proceedings, Atlanta, USA.
[8] Harman, H.H (1969) Modern Factor Analysis, 2nd Edition, Univ. of Chicago press. Chicago, Illinois.
[9] Jennings, JE and Knight K. (1957) The additional Settlement of foundations due to collapse of sandy subsoils on wetting. Proceedings,4th ICSMF.
[10] Journel, AJ and Huijbregts, C,J. (1978). Mining Geostatistics, Academic Press, New York,
Matheron, G.(1963) Principles of Geostatistics. Econ. Geology, 58, 1246-1266.

Fifth International Conference on Geotechnique, Construction Materials and Environment, Osaka, Japan, Nov. 16-18, 2015, ISBN: 978-4-9905958-4-5 C3051

A 3D INVESTIGATION INTO UNDRAINED CLAY SINKHOLE FORMATION

Brian Lamb[1] and Jim Shiau[1]
[1]School of Civil Engineering and Surveying, University of Southern Queensland, Australia

ABSTRACT

The main focus of this paper is to use 3D analysis to investigate sinkhole formation behavior. This is completed by analysing different square sinkhole cavity opening sizes and overburden properties with trapdoor analysis. The research is conducted by closely examining sinkhole structures through finite difference software FLAC 3D. Once the cavity trapdoor roof is released, the effect of the trapdoor on the overbuden of the sinkhole can be analysed. The sinkholes models are computed via the strength reduction method, which can produce the factor of safety of the formation along with the final overburden displacements and sinkhole shape. The completion of 3D numerical models allows for numerous sinkhole simulations, with varying material properties and different overburden depth to cavity width ratios. It is expected that this research would increase the understanding of the phenomena of sinkholes by making use of three dimensional numerical simulations.

Keywords: 3D Investigation, Sinkhole, Geotechnical, Trapdoor, FLAC

INTRODUCTION

Sinkholes are a global phenomenon which can have devastating consequences. A sinkhole is a hole or depression viewable on the ground surface. Sinkholes often make headlines for causing structural damage, damage to property or simply because of their size and their immediate unpredictable impact. Current well known sinkhole cases include the three examples which formed in Siberia, being up to 80m wide and 70m deep. Locations such as Florida are known for their likeliness of spontaneous sinkhole collapse due to the limestone geology present [1]. The nature of how sinkholes occur spontaneously makes them of constant public interest.

They have many different causes but all are based on the overburden soil pressures increasing to a breaking point, were then the overburden material collapse. The material above an underground cavity is known as the overburden. This collapse into the underground cavity leaves, in many cases, a conical shape and circular ground opening. The shape of the extent of the sinkhole appears to be influenced mainly by the cavity roofs aspect ratio. If the overall width and length of the cavity roof has an aspect ratio of around 1:1, it is hypothesised no matter the actual shape of the cavity roof then the surface extent of the sinkhole will be principally circular.

Causes of sinkhole failure include those produced from manmade activities such as collapse of underground mines, tunnels and pipelines as well as manmade ground disturbances such as drilling and compaction. Natural causes of sinkholes include the suffusion of carbonate rocks, most commonly limestone [2]. Other soil materials that lead to suffusion are chalk, gypsum and basalt. Suffusion is the process of non-cohesive soil material falling into underground cracks or soil material being washed into cracks. These cracks are caused by weathering of the underground rock.

3D FLAC MODEL

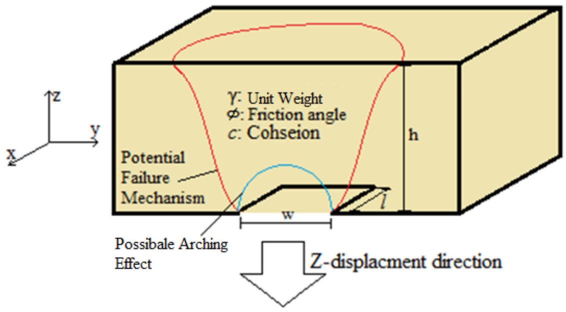

Fig. 1 Idealised trapdoor cavity sinkhole in 3D space

While physical soil conditions and overburden to trapdoor cavity interactions have high complexity, the model uses simplification and assumptions to aid with predicting theoretical soil responses within the trapdoor cavity opening and overburden soil. Figure 1 shows the idealised trapdoor cavity in 3D space. The height (h) representing the height of the overburden material above the cavity and width (w) representing the length or diameter of the cavity roof. (l) represents the length or depth of the trapdoor cavity in the x-direction as shown in Figure 1. The sinkhole model assumes the use of Mohr-Coulomb failure criteria with set soil characteristics of mass-density, elastic modulus, Poisson's ratio, cohesion and friction angle. The overburden soil properties are assumed to be homogenous throughout the height of the overburden. Artificial boundary conditions are required to allow for the explicit finite difference to function. This goes against the endless continuum of soil strata in which sinkholes form in real life. Artificial boundaries are necessary to set the quantity of overburden to be tested, which has a large control on computation time. However these boundaries can be set to minimise their effect on the final results. Undrained clay was analysed. The major characteristic of the undrained clay was the non-zero cohesion and zero friction angle.

Plotted were the maximum shear strain rate plots, displacement and velocity contour plots, maximum unbalanced force ratio history and z-displacement history. Each material has six different cases, ranging from shallow to deep each case had its own height to width ratio. The trapdoor width to length ratio is *2w:1L* for each case. Therefore the results present half symmetry of a square trapdoor. The results are presented in a dimensionless ratio, $FoS = f(h/w, c_u/\gamma h)$

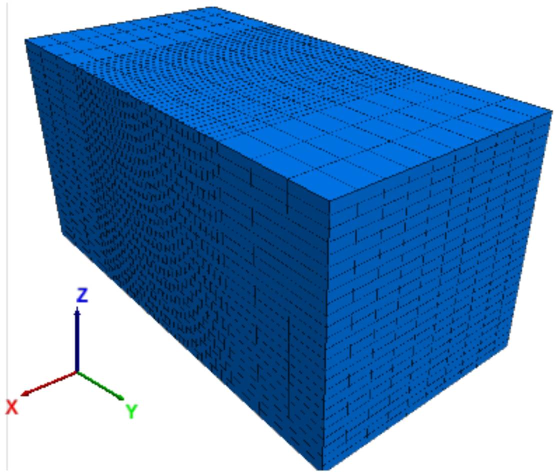

Fig. 2 Generated 3D mesh

RESULTS AND DISCUSSION

The trapdoor cavity opening can cause structural failure and the soil body will reach a new deformed equilibrium state. The change in location of a particle from its original location is the shear strain. Shear strain rate is an indication of the rate of deformation and thus is also a representation of the slip failure plane of sinkholes.

The displacement contours plots indicate areas of similar displacements. The displacement for each case is at its maximum at the geometrical center. Figure 3 shows example plots.

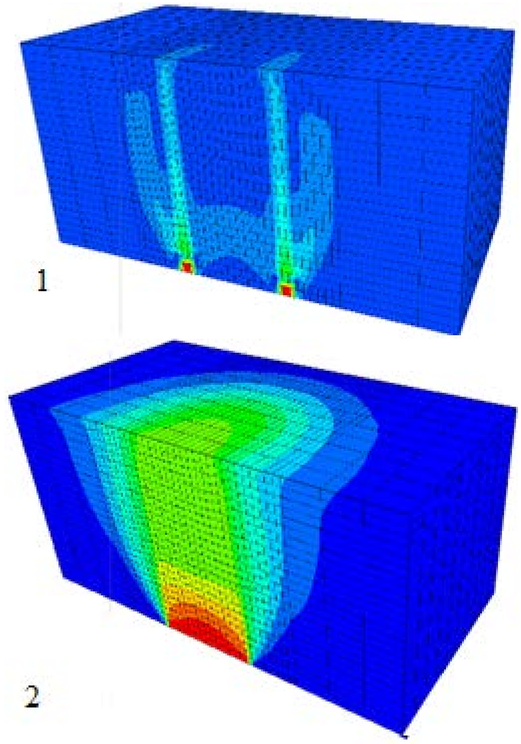

Fig. 3 3D Undrained clay case 2 (*h/w=10*), Picture 1 Max Shear Strain Rate, Picture 2 Displacement Contours.

Figure 3 shows the 3D plots for shear strain rate, and displacement contours for undrained clay case 2. The shear strain rate plot indicates a curved failure plain, with a major amount of the shear strain occur at the cavity extents.

The maximum displacement in the displacement plot occurs over the cavity opening. Minimum displacement occurs again on the sides of the funnel shape where the displacement becomes zero. The funnel shape created in 3D matches sinkholes which form in reality. The 3D model left a circular extent on the surface despite the cavity roof representing a square. As discussed it is thought that the main contributing factor to the shape of the surface extent is the aspect ratio. Neglecting the form of the shape, if the cavity shape falls into an aspect ratio of around *1:1*, then the surface deformation extent should be circular. The aspect ratio can be defined as width (w) x length (l) of a square surrounding the extents of the cavity roof. The aspect ratio of the cavities here are *1:1* (w:l) with the cross-section taken representing a whole sinkhole. The maximum displacement appears to form a dome shape above the cavity opening. The displacement contours then open up to create the funnel shape. The contours have a smaller magnitude than case 1, due to the smaller cavity size here.

Effect of Depth Ratio *h/w*

As expected smaller the h/w ratio larger the displacement contours extent and value. The displacement contours acted very similarly to those calculated in 2D. This circular extend of the displacement contours also matches that of two physical model tests [3], [4]. As displacement contours represent areas of similar displacement, they also can represent the possible locations of slip planes.

For case 2 of the undrained clay six deformation factors (DF) plots were generated to illustrate the behaviour of the collapse of this modelled sinkhole. The deformation factor is a built in changeable attribute of a plot which allows the user to see how the soil body will deform and has the ability to exaggerate the deformation as shown in the supplied plots to see how the soil body behaves.

Table 1 Factor of Safety for Undrained Clay (h = 10, w/l = 2, square) Strength Ratio $c_u/\gamma h$ = 1.58

case	*h/w*	*FOS (3D)*	*FOS (2D)*
1	1.667	0.82	0.51
2	2	1	0.592
3	2.5	1.06	0.682
4	3.333	1.32	0.795
5	5	1.41	0.947
6	10	1.86	1.189

Table 1 shows the undrained clay factor of safety results for both the 2D and 3D calculations. Both the factor of safety for 2D and 3D analysis follows a very similar trend as expected, this is also shown in Figure 4.

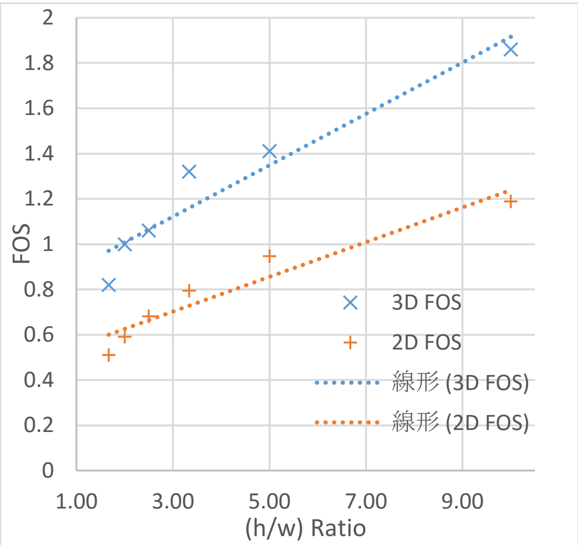

Fig. 4 FOS 3D & 2D plot w/l = 2, $c_u/\gamma h$ = 1.58

Figure 4 is a plot of the undrained clay factor of safety for both 3D and 2D for comparison. Both 2D and 3D have near linear trends. With increasing (*h/w*) ratio the factor of safety increased. Also note that the same points for both 2D and 3D results fall on the same side of the trend line. 2D underestimates the factor of safety by roughly 30% when compared to the 3D results. This is because 2D cross-sections have no constraint in length (*l*) going into the model. On the other hand 3D models have their model dimension fully specified.

As the width decreases the factor of safety increases. 3D analysis appears to have a more realistic factor of safety calculated than the 2D analysis. 2D analysis underestimates the factor of safety, this is due to the fact with 2D analysis the cross section taken has no given depth or length (l) into the page. With 3D analysis the cavity opening has given dimension (*wl*) and thus the 3D model is more constrained, which produces a higher factor of safety. The factor of safety for 3D analysis is roughly 30% greater than the 2D results, these matches previous 2D to 3D analysis results.

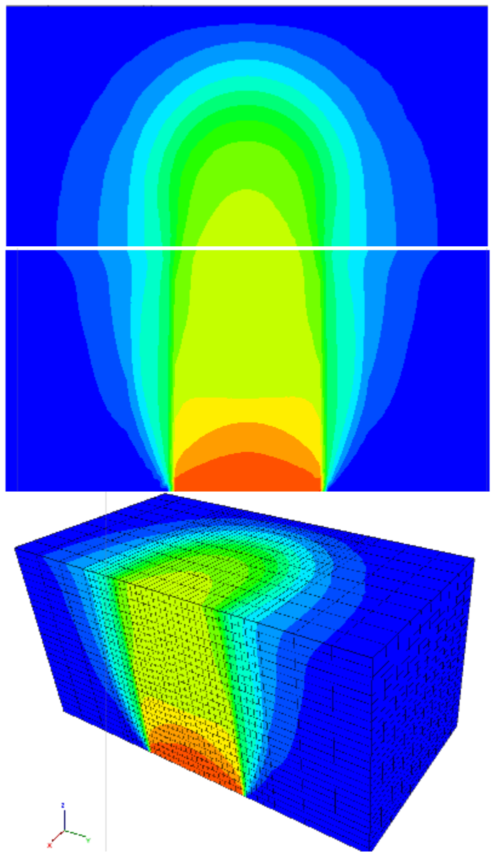

Fig. 5 Case 1 (*h/w*) = 1.667, displacement contours of top, front and 3D view

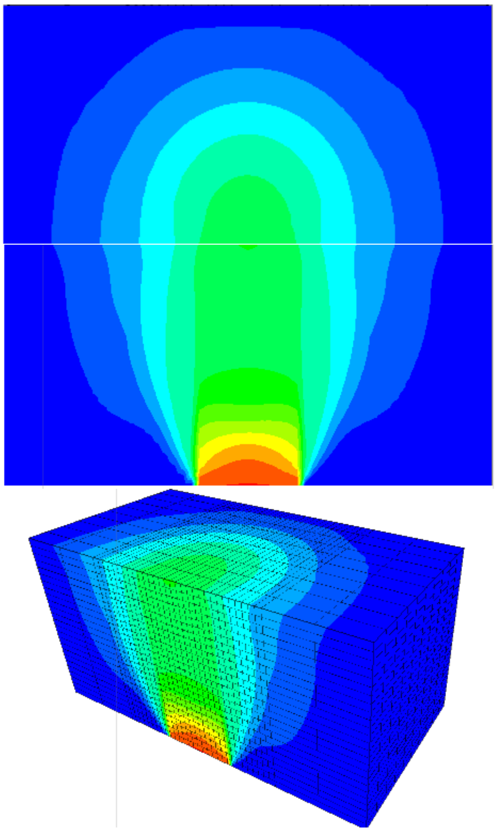

Fig. 6 Case 3 (h/w) = 2.5, displacement contours of top, front and 3D view

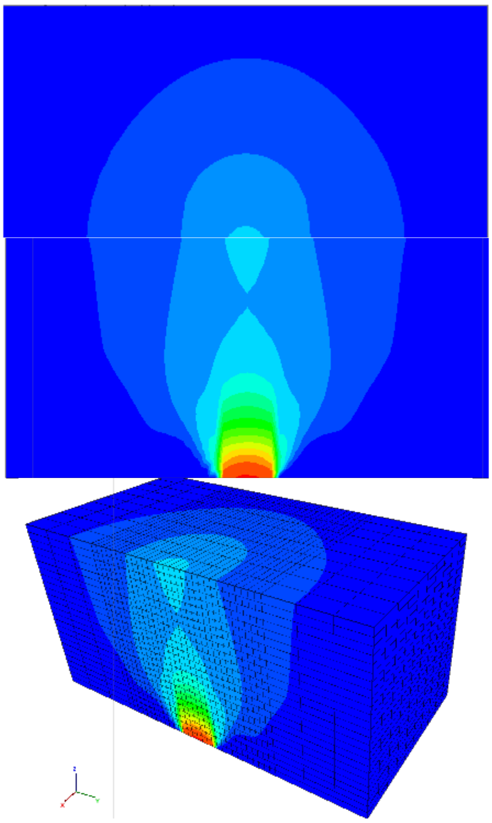

Fig. 7 Case 5 (h/w) = 5, displacement contours of top, front and 3D view

Figure 5, 6 and 7 show the displacement contours for cases 1, 3 and 5 resectively. As this h/w ratio increases the magnitude and extent of the displacement contours become smaller. This is as expected as smaller cavity roof should produce smalleer displacment magnitudes. It is evident from the top view of the displacement contours that the magnitude of the contours increased with the increasing cavity opening area.

Investigation of Effect of Shear Strength Ratio

As an additional study, four cases were examined. All parameters for the undrained clay were kept constant apart for the cohesion. Case 1 has cohesion of 10kPa, case 2 c_u = 20kPa, case 3 c_u = 30kPa and case 4 c_u = 40kPa. Effectively here is a study of the undrained strength ratio. The undrained strength ratio is defined as $\gamma D/c_u$, a dimensional less ratio where γ represents the self-weight of the soil, D represents the cavity opening w and c_u represents the uniform undrained shear strength. As the strength ratio is dimensionless, it can be redefined as $c_u/\gamma D$, this way when conducting this parametric study and increase the cohesion of the soil from 10 to 40, the ratio will increase with the factor of safety. However if the ratio was left as defined as $\gamma D/c_u$ then the strength ratio would decrease as the cohesion is increased. Undrained strength ratio = $\gamma D/c_u$ redefined as = $c_u/\gamma D$

Table 2 FOS results Effect of Shear Strength Ratio, *h/wl = 10/(5x2.5)*

case	*Strength ratio* ($c_u/\gamma D$)	*3D FOS*
1	1.05	0.33
2	2.11	0.66
3	3.16	1.00
4	4.21	1.33

Table 2 shows the factor of safety results for this investigation. Note again the trapdoor width to length ratio is always $w=2l$. As expected the factor of safety increases linearly as the cohesion is increased. This is due to the increased undrained shear strength increases the stability of the overburden. Therefore increase of factor of safety should generate displacement contours with lesser and lesser displacement magnitude.

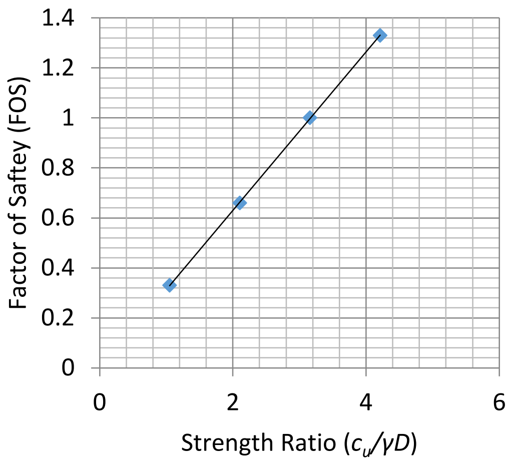

Figure 8 Effect of cohesion on the FOS of the undrained clay plot

Figure 8 depicts the factor of safety plot vs the undrained strength ratio in terms of $c_u/\gamma D$. By linear interpolation, Figure 8 should give the factor of safety for any sinkhole by this analysis with a cavity ratio of w/l = 2 with an undrained strength ratio defined as $c_u/\gamma D$.

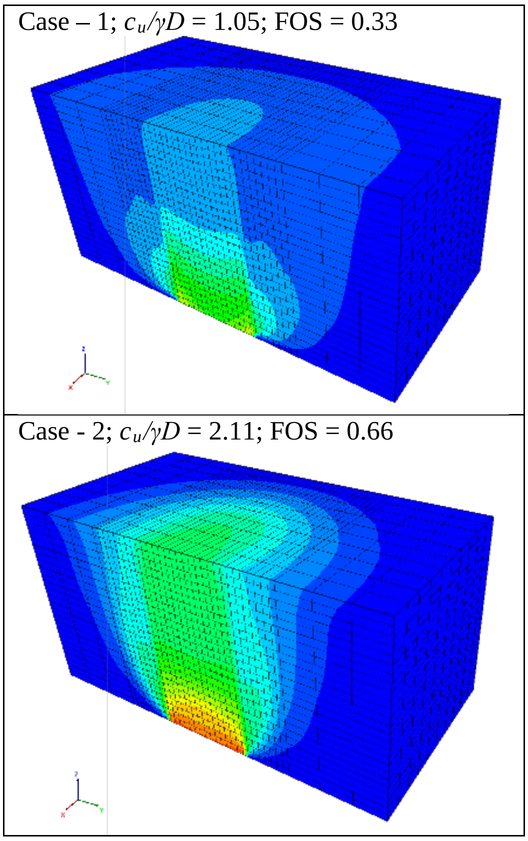

Figure 9 Effect of Shear Strength Ratio, displacement contour plots *h/w*=2, *w/l*=2

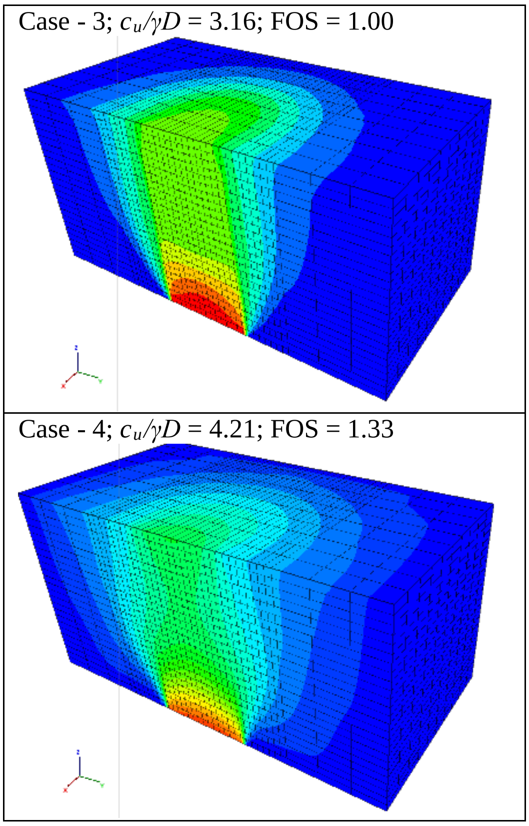

Figure 10 Effect of Shear Strength Ratio, displacement contour plots *h/w*=2, *w/l*=2

Figure 9 & 10 shows the displacement contours for the four cases studied in this section. As stated all cases have the same cavity opening, instead this study is for the effect of the cohesion. This also can be taken as the effect of changing the undrained strength ratio. All the displacement contour plots exhibit funnel shape contours. The maximum displacement is occurring over the cavity opening. For the weakest case, case 1 with a factor of safety of 0.33 the displacement contours shows a unique formation. The contours show a localised caving around the cavity opening. They also show a chimney type failure with the same displacement magnitude as the localised caving in around the cavity opening. The overall displacement contour extent of case 1 is very wide.

Every case has a circular surface extent. This shows that the undrained strength ratio does not affect the shape of the surface extent of the sinkhole in a homogenous soil body.

CONCLUSION

Trapdoor openings can cause structural failure, causing the soil body to reach a new deformed equilibrium state. This was successfully shown with the shear strain rates plots, measuring deformation.

As expected, smaller the *h/w* ratio, larger the displacement contours extent and value. The displacement contours acted very similarly to those calculated in 2D. These results can be found in [3], [4]. Displacement contours have circular extents, which match existing sinkholes. Future work is required to determine if the circular surface displacement extents is irrespective of the cavity trapdoor opening.

As the trapdoor cavity width decreases the factor of safety increases. 3D analysis appears to have a more realistic factor of safety calculated than the 2D analysis. 2D analysis underestimates the factor of safety, this is due to the fact 2D analysis neglects depth or length of a 3D problem. The 3D models constrained by all three dimensions, producing a higher factor of safety. The factor of safety for 3D analysis is roughly 30% greater than the 2D results, these matches previous 2D to 3D analysis results.

REFERENCES

[1] Zisman, ED 2005, 'Sinkhole Case Studies-Is it or Isn't it a Sinkhole?', Sinkholes and the Engineering and Environmental Impacts of Karst.

[2] Augarde, CE Lyamin, AV Sloan, SW 2003, 'Prediction of Undrained Sinkhole Collapse', Journal of Geotechnical and Geoenvironmental Engineering, pp. p.197-205, viewed 20 November 2013.

[3] Lamb, B 2014, 'Physical and Numerical Investigation into Sinkhole Collapse', BENG (honours) Thesis, University of Southern Queensland.

[4] Lamb, B and Shiau, J 2014, 'Physical and Numerical Investigation into Sinkhole Collapse', Fourth International Conference on Geotechnique, Construction Materials and Environment, Brisbane, Australia.

EFFECT OF LIQUID ALKALINE ACTIVATOR CONTENT ON UNIT WEIGHT AND STRENGTH OF A WATER TREATMENT SLUDGE–FLY ASH LIGHTWEIGHT CELLULAR GEOPOLYMER

Cherdsak Suksiripattanapong[1], Suksun Horpibulsuk[2] and Arul Arulrajah[3]
[1]School of Civil Engineering, Faculty of Engineering and Architecture, Rajamangala University of Technology Suvarnabhumi Suphan Buri Cumpus, Thailand
[2]School of Civil Engineering, Institute of Engineering, Suranaree University of Technology, Thailand
[3]Faculty of Science, Engineering and Technology, Swinburne University of Technology, Australia

ABSTRACT

A lightweight water treatment sludge-fly ash geopolymer is investigated in this research with the intention to develop an alternative green construction and building materials, without the usage of Portland cement as a cementing agent. Two waste by-products namely water treatment sludge from the Bang Khen water treatment plants of the Metropolitan Water Work Authority of Thailand (MWA) and Fly Ash (FA) from the Mae Moh power plants of the Electricity Generating Authority of Thailand (EGAT) were used in this research. The liquid alkaline activator, L used was a mixture of sodium silicate solution (Na_2SiO_3) and sodium hydroxide solution (NaOH). This article investigates the effect of liquid alkaline activator on unit weight and strength of lightweight water treatment sludge-fly ash geopolymer. The various influential factors studied are mixing ingredient (air content and Na_2SiO_3/NaOH) and heat condition. Test results show that the influence of liquid alkaline activator on unit weight is classified into two zone: (zone 1 is the amount of L less than 1.0LL and zone 2 is the amount of L greater than 1.0LL). For zone 1, the unit weight of lightweight water treatment sludge-FA geopolymer is constant although the amount of L increases. For zone 2, the unit weight of lightweight water treatment sludge-FA geopolymer decreases significantly as amount of L increases. The maximum compressive strengths of lightweight sludge-FA geopolymers are at L of 1.0LL for all the Na_2SiO_3/NaOH ratios, heat duration and air content.

Keywords: Lightweight, Geopolymer, Sludge, Fly Ash

INTRODUCTION

Water production requires the extraction of water from natural sources. The water treatment process results in a muddy sludge by-product. The clarifier system employed in water treatment plants results in the sludge flocculating and falling in the bottom of the treatment tank. <u>This method is similar to that used by other water treatment plants worldwide</u> The liquid sludge is subsequently drained to sludge lagoons for disposal. The increasing demand of treated water produced by the Metropolitan Waterworks Authority of Thailand (MWA) has resulted in increasing quantities of sludge by-products generated annually. For MWA, the water treatment sludge is generated with the maximum capacity of 300 tons per day in the dry season and about 700 tons per day in the wet season. With the continuous increase in water demand due to growing population in many developed and developing countries including Thailand, the quantity of water treatment sludge is subsequently increasing at ever increasing rate and hence the urgent need to find a sustainable reuse option for the growing stockpiles of sludge, which in the past have been disposed to landfills.

Alkali-activated alumino-silicate cement, known as 'geopolymers' has become increasingly popular in recent years as an environmental friendly alternative to ordinary Portland cement [1]. Geopolymers are furthermore touted for their high performance (high strength and durability), low CO_2 emission and low energy consumption. Silica rich materials such as clay or kaolin [2], fly ash, and bottom ash [3] can be used as a precursor to react with the liquid alkaline activator.

Fly Ash (FA) derived from coal-fired electricity generation provides the greatest opportunity for commercial utilization of this technology due to the plentiful worldwide raw material supply [4,5]. Palomo et al [6] found that the different FA activated with 8-12 M NaOH cured at 85^{o}C for 24 hours produced a material with compressive strength of 35-40 MPa and about 90 MPa if sodium silicate (Na_2SiO_3) is added to the NaOH solution. Xie & Yunping [7] reported that the hardening process of FA activated with Na_2SiO_3 is mainly attributed to the gel-like reaction products that bind FA particles together. FA is extensively used as a precursor for geopolymers in Thailand [8, 9]

Sukmak et al. [10, 11] previously investigated the possibility of using FA as a raw material and silty clay as aggregates to develop the clay-FA geopolymer brick. The liquid alkaline activator (L) was a mixture of Na_2SiO_3 and NaOH. The suitable ingredient for the clay-FA geopolymer is Na_2SiO_3/NaOH ratio of 0.7 and L/FA ratio of 0.6, which are lower than those of FA geopolymer. The 7-day strength of the clay-FA geopolymer is greater than 10 MPa, suitable as bearing masonry unit according to the Thailand Industrial Standard. The strength requirement is 2.5 MPa for non-bearing and 7.0 MPa bearing masonry units. It has been illustrated that the durability against sulfate attack of clay-FA geoplymer is better than that of clay-cement; i.e., there is no major change in the microstructure and pH of clay-FA geopolymer when exposed to sulfate solutions [12].

Recently, Suksiripattanapong et al. [13] investigated strength development in water treatment sludge-FA geopolymer. The optimum ingredient providing maximum unit weight and strength is NaOH/Na_2SiO_3 ratio of 80:20 and L/FA ratio of 1.3, irrespective of heat condition and curing time. The optimum heat temperature and duration for the optimum ingredient are 75°C and 72 hours, respectively. The durability against wet-dry of sludge-FA geoplymer is better than that of clay-cement [14]. The research develops a new lightweight Cellular (LC) FA-sludge geopolymer as a sustainable lightweight masonry unit. The air foam is used to make this LC FA-sludge geoplymer.

This research investigates the effect of liquid alkaline activator, L on unit weight and strength of lightweight cellular sludge-FA geopolymer. The scanning electron microscopy (SEM) analysis is undertaken to analyze the role of L on unit weight and strength. This research will enable WTS traditionally destined for landfill to be used as an aggregate in the lightweight geopolymer masonry product, which is significant from engineering, economical and environmental perspectives.

MATERIALS AND METHODS

Materials

The sludge was collected from the Bang Khen water treatment plant of the Metropolitan Waterworks Authority of Thailand. The sludge consists of 0.15% sand, 99.65% silt and only 0.20% clay. The grain size distribution, mineral and chemical compositions of the sludge were obtained from laser particle size analysis and X-ray Fluorescence (XRF) analysis as shown in Figure 1 and Table 1, respectively. The specific gravity is 2.60. The liquid limit is 64% and is classified as a non-plastic material.

FA was obtained from the Mae Moh power plant of the Electricity Generating Authority of Thailand (EGAT) in the northern region of Thailand. Table 1 summarizes the chemical composition of FA using X-ray fluorescence (XRF). Total amount of the major components (SiO_2, Al_2O_3 and Fe_2O_3) are 67.31% while the CaO content is 30.24%; therefore, it is classified as Class C. Figures 1 shows the grain size distribution curve of FA, which was tested by laser particle size analysis. It is shown that the sludge particles are larger than the FA ones. The average grain size of FA is 13.25 micron. The specific gravity of FA is 2.35. The morphology of the sludge and the FA is shown in Figure 2. The FA particles are fine and spherical whereas the sludge particles are irregular in shape. The liquid alkaline activator (L) is a mixture of Na_2SiO_3, which consists of 9% Na_2O and 30% SiO_2 by weight, and NaOH with a concentration of 10 molars.

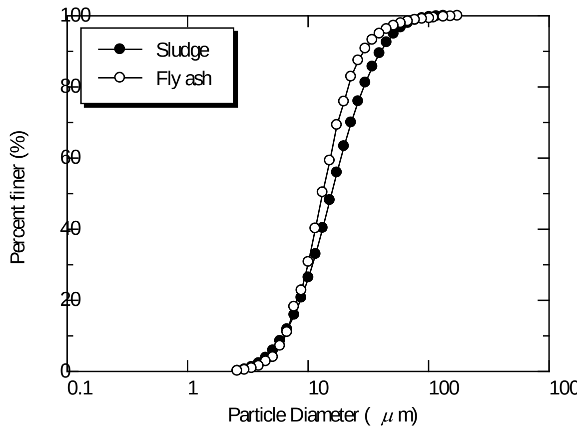

Fig. 1 Grain size distribution of Sludge and FA.

Table 1 Chemical composition of sludge and fly ash.

Chemical composition (%)	Sludge	Fly ash
SiO_2	61.84	47.51
Al_2O_3	24.80	13.14
Fe_2O_3	9.52	6.66
CaO	0.60	30.24
MgO	N.D.	N.D.
SO_3	0.59	N.D.
Na_2O	N.D.	0.41
K_2O	1.90	1.63
LOI	0.75	0.42

Air foam agent, Sika Poro 40 from Sika (Thailand) Company limited, were used in this study.

Sika Poro 40 is a blend of anionic surfactants and foam stabilizers. It is a liquid air entraining agent used in various types of mortar, concrete and cementitious material. The air foam was prepared by mixing the foaming agent with water at a ratio of 1:50 by weight.

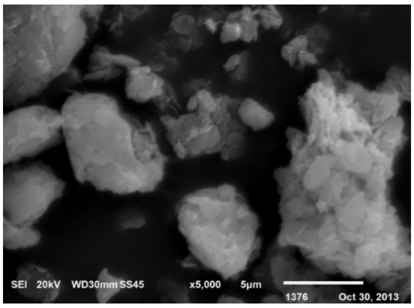

Sludge

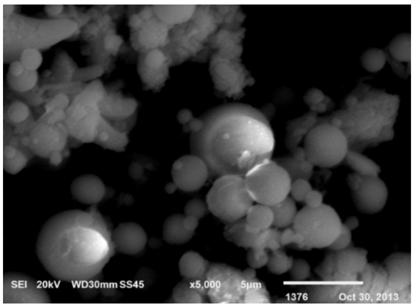

FA

Fig. 2 Scanning electron microscopy (SEM) images of sludge and FA.

Sample Preparation

The LC sludge-FA geopolymer sample is a combination of sludge, FA, liquid alkaline activator (Na_2SiO_3 and NaOH) and air content (A_c). The sludge/FA ratio was fixed at 70:30. The Na_2SiO_3/NaOH ratios were 90:10, 80:20 an d 70:30. The air-dried sludge and FA were mixed for 5 minutes in a mixer to ensure homogeneity of the mixture. The mixer was stopped and the mixture was activated by the liquid alkaline activator and mixed for additional 5 minutes. The mixture with various Na_2SiO_3/NaOH ratios was taken to determine L content at liquid limit state (LL). LL was determined using Casagrande's method, which is the same for determination of liquid limit of soil and used as a reference for mixing lightweight sludge-FA at various Na2SiO3/NaOH ratios to ensure that the sludge-FA-L mixture before mixing with air foam had similar flowability [15]. Figure 3 shows the relationship between L/FA ratio at liquid limit state and Na_2SiO_3/NaOH ratios. The test result shows that L/FA ratio at liquid limit state varies with Na_2SiO_3/NaOH ratio which is between 1.92 and 2.04 by fly ash content. The L/FA ratio at liquid limit state decreases with decreasing Na_2SiO_3/NaOH ratio (increase of NaOH) until the minimum L/FA ratio is 1.92 at Na_2SiO_3/NaOH ratio of 80:20. Beyond this minimum, L/FA ratio at liquid limit state increases with decreasing Na2SiO3/NaOH ratio.

To prepare lightweight sludge-FA, the input L contents in the lightweight sludge-FA vary from 0.8 to 1.5 times LL, in which LL for each Na_2SiO_3/NaOH ratio can be determined from Figure 3. The air form was added into the sludge-FA-L mixture and mixed for 5 minutes. The air content (Ac) values were 100, 300 and 500% by total volume of dry soil (V_s). The V_s value was determined from the dry weight of sludge and FA (W_s) and specific gravity values of sludge and FA. The air form was then added into this sludge-FA geopolymer mixture and mixed for additional 5 minutes. The uniform lightweight sludge-FA geopolymer was transferred to containers of 50x50x50 mm. The samples were dismantled, wrapped within vinyl sheet and then heated at 65ºC for heat durations of 24, 72 and 120 hours. After heating, the samples were subsequently cured at room temperature (27-30ºC). Unit weight and strengths of lightweight sludge-FA geopolymer samples were measured after 7 days of curing in accordance with ASTM C138 and ASTM C69-09, respectively.

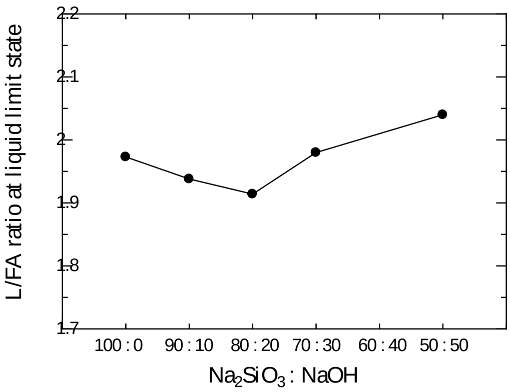

Fig. 3 Relationship between L/FA and Na_2SiO_3/NaOH

UNIT WEIGHT AND STRENGTH OF LIGHTWEIGHT WATER TREATMENT SLUDGE-FA GEOPOLYMER

Figure 4 shows the relationships between 7-day unit weight versus liquid alkaline activator of LC sludge-FA geopolymer for Na_2SiO_3/NaOH ratios of 90:10, 80:20 and 70:30. The samples were heated at 65ºC for 24, 72 and 120 hours. The amount of liquid alkaline activator is 0.8LL, 0.9LL, 1.0LL, 1.1LL, 1.3LL and 1.5LL where LL is liquid alkaline activator at liquid limit. The air content (*Ac*) values varied between 100 and 500% by volume of dry soil (*Vs*). The test result shows that the unit weight of LC sludge-FA geopolymers decreases as air content and L increases. The L on unit weight is classified into two zones: (zone 1 is L less than 1.0LL and zone 2 is L greater than 1.0LL). For zone 1, the unit weight of LC sludge-FA geopolymer is constant although the L content increases. For zone 2, the unit weight of lightweight water treatment sludge-FA geopolymer decreases significantly as the L content increases. The L content at liquid limit is designated as transitional liquid alkaline activator.

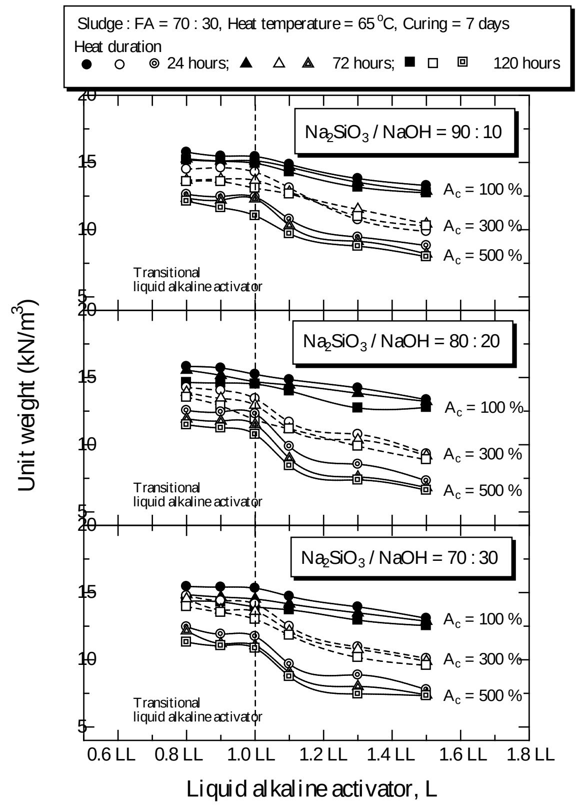

Fig. 4 Relationship between unit weight and Liquid alkaline activator of lightweight sludge-FA geopolymer at different air content and Na_2SiO_3/NaOH.

Effect of L on 7-day strength of LC sludge-FA geopolymer is shown in Figure 5. The amount of L was 0.8LL, 0.9LL, 1.0LL, 1.1LL, 1.3LL and 1.5LL at Na_2SiO_3/NaOH ratio of 90:10 80:20 and 70:30 and air content of 100, 300 and 500%. The samples were heated at 65ºC for 24, 72 and 120 hours, respectively. The test result shows that the 7-day strength of LC sludge-FA geopolymer depends on the L content for all Na_2SiO_3/NaOH ratios, heat duration and air content. The 7-day strength of LC sludge-FA geopolymer increases with increasing L until the maximum strength is attained at a transitional L value. Beyond this transitional L value, the compressive strength decreases as the amount of L increases. It is because the excessive liquid alkaline activator resulting in the bleeding in sample [16]. The maximum compressive strengths of LC sludge-FA geopolymers are at L of 1.0LL for all the Na_2SiO_3/NaOH ratios, heat duration and air content. Compressive strengths on wet side (1.1LL, 1.3LL and 1.5LL) and dry side (0.8LL and 0.9LL) of transitional L are similar. Even through the increase of L greater than transitional L results in the decreases in unit weight of LC sludge-FA geopolymer, the compressive strength of this sample decreases. In order to reduce cost (reduction of L), the increase of air content is the most appropriate to reduce unit weight and provides the high compressive strength. For example, at the same Na_2SiO_3/NaOH ratio of 90:10 and unit weight (13.53 kN/m^3), the sample with L = 1.0LL and A_c = 300% has 10.33 MPa strength while the sample with L = 1.5LL and A_c = 100% has 3.84 MPa strength.

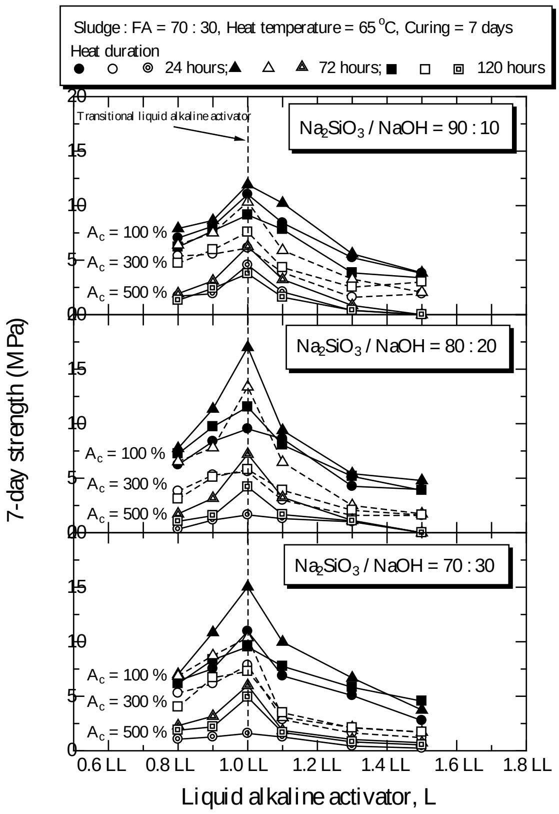

Fig. 5 Relationship between compressive strength and Liquid alkaline activator of lightweight sludge-FA geopolymer at different air content and Na2SiO3/NaOH.

Figure 6 shows the scanning electron microscopy (SEM) images of 7-day cured geopolymer samples with Na_2SiO_3/NaOH ratio of 80:20 and air content of 300% for different L (0.8LL to 1.5LL). The samples were heated at 65ºC for 72 hours. The SEM images show that the low L content (0.8LL and 0.9LL) was not enough to manufacture homogenous sample though air content is greater than 300%. In addition, the low L content is not sufficient to dissolve silica and alumina oxide from FA for producing geopolymerization products. On the other hand (L content greater than transitional L), the FA particles are etched obviously (reaction alkali dissolution). Furthermore, it is found that the holes in FA particles are filled with smaller FA particles and welded by the geopolymerization products (Sodium aluminosilicate hydrate, N-A-S-H), which is typical of geopolymerization reaction [3]. The SEM images (L = 1.1LL, 1.3LL and 1.5LL) show that the L content is enough to react with FA. Even through the amount of geopolymerization products increases as the L content increases, the compressive strength of lightweight sludge-FA geopolymer decreases as amount of L increases (Figure. 5). The decrease of this strength is due to the loss of the pore fluid between structure of sludge and FA particle while the samples were heated. The excessive amount of L causes shrinkage resulting in the micro-cracks (Figure. 6) (L=1.1LL, 1.3LL and 1.5LL) this report is in agreement with Sukmak et al. [10,11]. When compared SEM images of sample at L of 1.0LL and SEM images of samples at L of 0.8LL and 0.90LL, the geopolymerization products are clearly observed on FA particle for L of 1.0LL. This result is agreement with the compressive strength of lightweight sludge-FA geopolymer (Figure. 5) which gives maximum compressive strength.

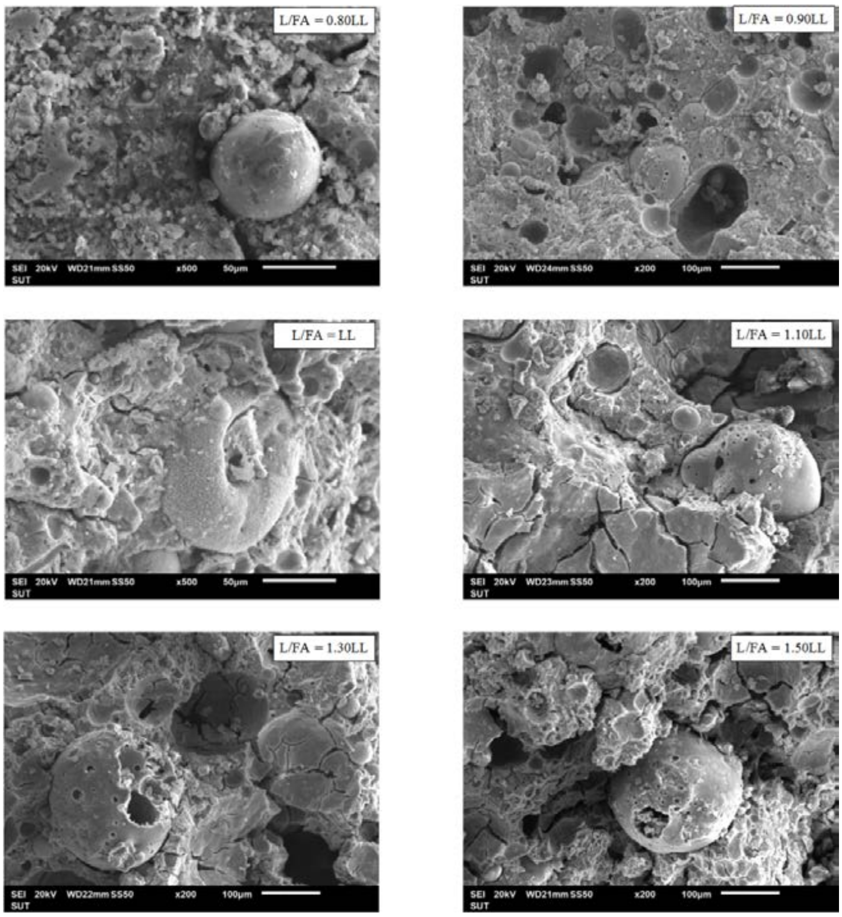

Fig. 6 SEM images of the lightweight sludge-FA geopolymer at curing time of 7 days at Na_2SiO_3/NaOH ratio of 80/20 and heat temperature of 65 ^oC for 72 hours air content of 300% for different L.

CONCLUSIONS

The effect of liquid alkaline activator on unit weight and strength of lightweight sludge-FA geopolymer is researched in this study. The conclusions can be drawn as follows.

1. The influence of liquid alkaline activator on unit weight is classified into two zone: (zone 1 is L less than 1.0LL and zone 2 is L greater than 1.0LL). For zone 1, the unit weight of LC sludge-FA geopolymer is essentially constant although the L increases. The L at liquid limit is designated as transitional liquid alkaline activator. For zone 2, the unit weight of LC sludge-FA geopolymer decreases as amount of L increases clearly.

2. The 7-day strength of LC sludge-FA

geopolymer increases with the increase in L and gives maximum compressive strength when L ratio is 1.0LL which is Transitional L. Beyond this maximum value, compressive strength of LC sludge-FA geopolymer decreases as the L increases. It is because the excess liquid alkaline activator results in the bleeding in sample. The maximum compressive strengths of lightweight sludge-FA geopolymers are at L of 1.0LL for all the Na_2SiO_3/NaOH ratios, heat duration and air content.

3. The low L content is insufficient to dissolve silica and alumina oxide from FA for producing geopolymerization products. On the other hand (amount of L greater than transitional L), the FA particles are etched obviously (reaction alkali dissolution). In addition, it is found that the holes in FA particles are filled with smaller FA particles and welded by the geopolymerization products (Sodium aluminosilicate hydrate, N-A-S-H) which is typical of geopolymerization reaction.

ACKNOWLEDGEMENTS

This work was financially supported by Metropolitan Waterworks Authority of Thailand in the fiscal year 2013, the Thailand Research Fund under the TRF Senior Research Scholar program Grant No. RTA5680002. The financial support from the Office of Higher Education Commission under NRU project of Thailand, as well as Suranaree University of Technology are also very much appreciated. The first author also acknowledges the financial support from the Rajamangala University of Technology Suvarnabhumi.

REFERENCES

[1] Davidovits J., “Geopolymers”, Journal of Thermal Analysis and Calorimetry Vol. 37, 1991, pp. 1633-1656.
[2] Buchwald A. & Kaps Ch., “Property controlling influences on the generation of geopolymeric binders based on clay”, Geopolymer (Melbournd Australia), 2002.
[3] Davidovits J., Buzzi L., Rocher R., Gimeno D., Marini C.. & Tocco S., “Geopolymeric cenment based on low cost geologic material”, results from the European Researh project GEOCIS-TEM. In: Davidovits et al., editors., Proceedings of the second international conference gropolymere Vol. 99, 1999, pp.83-96.
[4] Mohapatra R. & Rao J.R., “Some aspects of characterisation, utilisation and environmental effects of fly ash”, Journal of Chemical Technology and Biotechnology Vol.76, 2001, pp.9-26.
[5] Van Jaarsveld J., Van Deventer J. & Lorenzen L., “Factors affecting the immobilization of metals in geopolymerized fly ash”, Metall Mater Trans B Vol.29, 1998, pp.283-91.
[6] Palomo A., Grutzek M.W. & Blanco M.T., “Alkali-activated fly ashes. A cement for the future”, Cement and Concrete Research Vol.29, 1999, pp.1323-1329.
[7] Xie Z. & Yunping X., “Hardening mechanisms of an alkaline-activated class F fly ash”, Cement and Concrete Research Vol.31, 2001, pp.1245-1249.
[8] Chindaprasirt C., Chareerat T. & Sirivivatnanon V., “Workability and strength of coarse high calcium fly ash geopolymer” Cement and Concrete Composites, Vol.29, 2007, pp.224-229.
[9] Sata V., Sathonsaowaphak A. & Chindaprasirt P., “Resistance of lignite bottom ash geopolymer mortar to sulfate and sulfuric acid attack” Cement and Concrete Composites Vol.34, 2012, pp.700-708
[10] Sukmak P., Horppibulsuk S. & Shen S.L. “Strength development in clay-fly ash geopolymer”, Construction and building Materials Vol.40, 2013, pp.566-574.
[11] Sukmak P., Horppibulsuk S., Shen S.L., Chindaprasirt P. & Suksiripattqanapong C. “Factors influencing strength development in clay-fly ash geopolymer”, Construction and Building Materials Volo.40, 2013, pp.1125-1136.
[12] Sukmak P., Silva P-D., Horpibulsuk S. & Chindaprasirt P., “Sulphate resistance of clay-Portland cement and clay-high calcium fly ash geopolymer”, Journal of Materials in Civil Engineeing, 2014, pp.04014158(1-11).
[13] Suksiripattanapong C., Horpibulsuk S., Chanprasert P., Sukmak P. & Arulrajah A., “Compressive strength development in fly ash geopolymer masonsy units manufactured from water treatment sludge”, Construction and Building Materials, 2015, Vol.82, pp.20-30.
[14] Horpibulsuk S., Suksiripattanapong C., Samingthong W., Rachan R. & Arulrajah A., “Durability against wet-dry cycles of water treatment sludge-fly ash geopolymer”, Journal of Materials in Civil Engineeing (Accepted for publication)
[15] Neramitkornburi A, Horpibulsuk S, Shen SL, Arulrajah A and Disfani MM, Engineering properties of lightweight cellular cemented clay-fly ash material. Soils and Foundations 2014; 55: doi: 10.1016/j.sandf.2015.02.020.
[16] Posi, P., Teerachanwit, C., Tanutong, C., Limkamoltip, S., Lertnimoolchai, S., Sata, V., Chindaprasirt, P. “Lightweight geopolymer concrete containing aggregate from recycle lightweight block.” Materials and Design Vol.52, 2013, pp.580–586.

PREDICTING THE STRESS-STRAIN BEHAVIOR OF MINE TAILINGS USING MODIFIED HYPERBOLIC MODEL

Mary Ann Q. Adajar[1] and Mark Albert H. Zarco[2]
[1]Associate Professor, De La Salle University, Manila, Philippines
[2]Professor, University of the Philippines, Quezon City, Philippines

ABSTRACT

The shear strength behavior of mine tailings was investigated through direct shear test to determine its applicability as embankment material. Tailings in dry condition manifested a strong particle interlock as indicated by high critical state friction angle ranging from 36.6º to 38.4º. Friction angles at failure of saturated tailings were lower at an average of 4º as compared to those obtained in dry condition. Modified hyperbolic model was formulated to predict the shear stress against shear strain and volumetric strain against shear strain responses of tailings to different stresses. The modified hyperbolic model provides a good approximation to the stress-strain and volumetric strain-shear strain responses measured during the tests of tailings that exhibited a ductile failure and compressive volumetric strain. However, the model does not give a good prediction of stress-strain response for specimens that exhibited brittle failure with dilative volumetric strain. The model cannot capture the strain softening phenomena, but it can be used to model the behavior leading to the strain softening as well as during the ductile stage.

Keywords: Mine Tailings, Shear Strength, Friction Angle, Stress-strain Behavior, Modified Hyperbolic Model

INTRODUCTION

The abundance of solid wastes in the environment can pose risk to the health of the exposed population and damage to the environment. One way to respond to this environmental issue is to find useful application for these wastes materials. Numerous studies have been undertaken to determine the applicability of solid wastes as an alternative construction material. Ceramic waste and quarry dust aggregates were used as a possible replacement for conventional crushed stone coarse and fine aggregates [1]. Ashes from a wastewater treatment facility that incinerates its treatment sludge were evaluated for possible use as partial clay substitute for brick manufacture and as a soft soil stabilizing admixture [2].

In the Philippines, one of the most abundant solid wastes found in the environment are wastes from mining operations called mine tailings. The most common environmental issue associated with mining activities is the disposal of the enormous amounts of tailings regularly produced from mining operations. The use of mine tailings as embankment materials is one possible option that alleviate disposal problem and reduce the negative environmental effects. To evaluate the applicability mine tailings as embankment materials, thorough study of its geotechnical characteristics is needed. Geotechnical characterization includes the determination of its physical properties and hydraulic conductivity characteristics [3]. A study of its compaction behavior, compressibility and hydrocompression settlement describes its consolidation behavior [4]. This research study investigates the shear strength behavior of mine tailings through direct shear test. The determination of the shear strength parameters and understanding of the stress-strain response to different stresses are essential steps to completely evaluate the suitability of mine tailings for geotechnical application.

Different methods have been developed to model the stress-strain behavior of soils prior to failure. The catastrophic failure of Merriesspruit gold tailings dam in South Africa led to the study of Fourie, AB, et.al. on the stress-strain behavior of Merriesspruit tailings under undrained loading to establish the steady state line using critical state soil mechanics [5]. Onur, M. et.al. determined the shear strength parameters of saturated clayey soils under unconsolidated undrained condition using the Mohr-Coulomb model with the aid of PLAXIS software program [6]. Hyperbolic stress-strain equations were developed by Duncan and Chang as a means for modeling the isotropic nonlinear elastic stress-strain behavior of soils prior to failure [7]. In this study, the critical state model and a modified version of the Duncan and Chang hyperbolic model were used to describe the stress-strain and volume change behavior of tailings. The shear strength behavior of tailings must be established because this is a determining factor for the stability of earth structures built using this waste material.

EXPERIMENTAL PROGRAM

Mine tailing samples came from three (3) mining sites in the Philippines namely: wastes from concrete aggregate quarry in Cavite and designated as TS#1, gold mine tailings from gold processing plant in Davao del Norte and designated as TS#2, and gold mine tailings from mining site in Aroroy, Masbate and designated as TS#3. These tailings are non-plastic, considered as fine-grained consisting of fine sands and silts. The physical properties, hydraulic conductivity, and consolidation behavior of the tailing samples are discussed in Adajar and Zarco (2013, 2014) [3][4]. In this study, direct shear test was carried out with samples in dry and saturated conditions following the procedures described in ASTM D3080. Samples are prepared at initial relative densities of 60% (medium dense), 80% (dense) and 90% (very dense) both in dry and fully saturated conditions.

For dry condition, test runs for each tailing samples used five (5) different vertical stresses of 13.63 KPa, 20.44 KPa, 27.25 KPa, 54.50 KPa and 87.50 KPa. The first two vertical stresses (13.63 KPa and 20.44 KPa) represent the low-stress conditions. The other three (3) vertical stresses of 27.25 KPa, 54.50 KPa and 87.50 KPa correspond to the overburden pressure in the field at the depth of 1.5m, 3.0m and 4.5m, respectively. The horizontal stress was applied at a fast rate of 1.25mm/min.

For the saturated condition, four (4) vertical stresses (13.63 kPa, 20.44 kPa, 27.25 kPa and 54.50 kPa) were used. The sample was allowed to come into drained equilibrium under the application of these vertical stresses before subjecting to horizontal load. A very slow strain rate of 0.12mm/min was used to simulate the drained condition.

.

SHEAR STRENGTH PROPERTIES

Stress-strain and Volume Change Behavior of Tailings in Dry Condition

The typical stress-strain and volume change relationship of dry tailing samples is presented in Figs. 1. The stress-strain plot shows the typical response of soil to shearing forces at monotonic loading. The shear stress at failure is greater for specimens subjected to greater normal effective stress (σ') as compared to specimens with lower normal effective stress. The shear stress at failure, termed as the critical state shear stress is described as the shear strength at which continued shearing occurs without change in shear stress and volume for a given normal effective stress. The three (3) tailing samples exhibited similar stress-strain behavior. It can be noted that at very dense condition (Dr = 90%) and lower normal effective stresses (σ' ≤ 27.25 KPa), the specimen showed a rapid increase in shear stress reaching a peak value at low shear strains and then decreases with increasing shear strains indicating strain softening until the critical shear stress is attained. This indicates that specimen failed in brittle manner, typical for dense sands and over-consolidated clays. The determination of brittle failure is potentially important when dealing with embankment and slopes as this leads to progressive failure which may be sudden and catastrophic. At higher normal effective stresses and relative density of 90%, all the tailing samples behaved like loose sands or normally consolidated clays. There is a gradual increase in shear stresses as the shear strain increases until an approximately constant shear stress is attained. The stress-strain behavior suggests that tailings failed in ductile manner. For test specimen with relative densities of 60% and 80%, the peak shear stress was not observed even at lower stresses for all the tailing samples. The samples behaved like a ductile material at every normal effective stress.

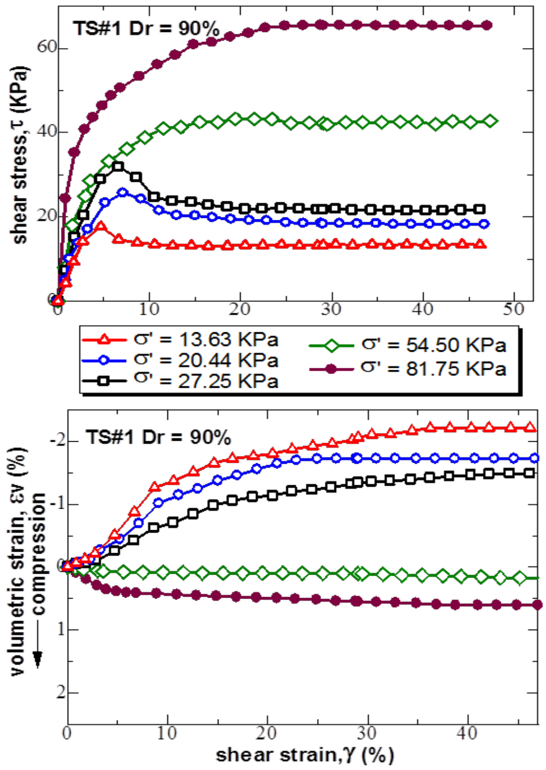

Fig. 1 Typical stress-strain and volumetric strain-shear strain plots of dry tailing

The volumetric strain plot shows that tailings followed a well-established behavior trends for granular materials. As the normal effective stress was increased, the tendency for the specimen to dilate was decreased. Specimens achieved greater compressive volume change as the normal effective stress is increased. Samples that exhibited peak shear stress showed an initial compressive behavior and then continued to increase in volume with shear strain manifesting a dilative behavior. This behavior arises because tailing, like soil, is essentially a particulate material. The particles must take up a suitable arrangement of packing before continued shearing can take place. If the particles are initially more densely packed, some loosening which corresponds to an increase in volume change, that is dilation, will have to occur before the critical shear can takes place.

Stress-strain and Volume Change Behavior of Saturated Tailings

The typical stress-strain and volume change behavior of saturated tailings are shown in Fig. 2. All specimens exhibited the same trend in stress-strain behavior. Peak shear stress was not observed even at very dense condition and low normal stresses. The samples behaved like loose sands and normally consolidated clays where strain hardening was observed indicating a ductile failure. The increase in shear strength was coupled with decreased in volume. This compressive behavior increased as the normal effective stress is also increased. The rearrangement of soil particles into a denser configuration was easily facilitated because of the presence of moisture, thus resulted to ductile and compressive behavior of the saturated tailings.

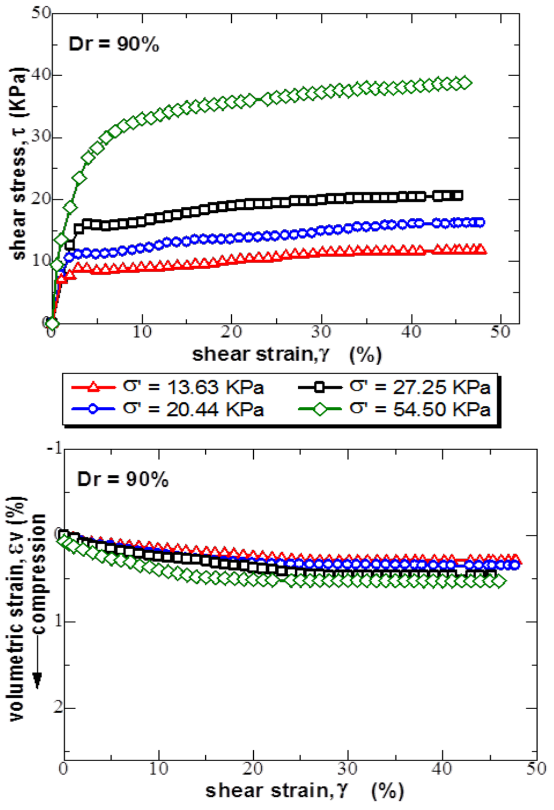

Fig. 2 Typical stress-strain and volumetric strain-shear strain plots of saturated tailings

It is expected that all soils reach an approximately constant shear stress irrespective of their initial state. In the case of saturated tailings in this study, the samples continued to gain strength until the end of the test. The ductile behavior manifested by tailings is preferable as this will not lead to progressive collapse. Many of the design procedure in geotechnical engineering assume that the soil can be relied on to behave in a ductile manner, where it will undergo continued deformation at constant load. This is in contrast to a brittle material, which at failure breaks and loses it load carrying capacity entirely.

Friction Angles

Tailings in dry condition reached a critical state in which unlimited shear strain could be applied without further changes in volume, normal effective stress or shear stress. Test results revealed that the critical state reached by the specimen depends on the normal effective stress at which it is sheared. The initial void ratio, as expressed by relative densities, has no significant effect on the critical shear strength. The critical state shear stress when plotted on a graph of τ against σ' lies in a straight line with slope tan (ϕ_{cs}) and can be described by equation $\tau = \sigma' \tan\phi_{cs}$. This line represents the failure line or termed as critical state line (CSL) and ϕ_{cs} is called the critical state friction angle. Soil states below the CSL will cause the soil to behave in a ductile manner and is desirable in engineering design. Soil states above the CSL and bounded by the peak shear strength envelope will cause the soil to behave in brittle manner which can cause sudden failure or collapse. Although high shear strengths (peak) are observed in this region, there is no guarantee that the high shear strengths will be uniformly mobilized at `the same time and this will present high safety risk which should be avoided. High values of friction angles are obtained from the tests indicating that dry tailings have strong particle interlock resulting to high shear strength.

For tailings in saturated condition, the shear stress corresponding to 15% horizontal displacement or approximately equal to 29% horizontal strain was considered as the shear stress at failure and friction angle obtained using this shear strength is referred to as friction angle at failure (ϕ_f). Similar to the test results in dry condition, the values of shear strength at failure of each tailings is unaffected by its initial void ratio. The friction angles at failure for saturated tailings were lower at an average of 4^o as compared to those obtained in dry condition. The moisture serves as lubricant that reduces frictional resistance between particles, therefore, it resulted to lower values of friction angles. Cohesion values are almost zero. The saturated tailings did not exhibit cohesive behavior since samples are classified as non-plastic. The friction angles in both dry and saturated condition are summarized in Table 2 together with some values of friction angles from literature. The values of friction angles derived from this study are within the range of values obtained from studies of other researchers.

Table 2 Friction angle at failure of tailings

Type of Tailings	Friction angle at failure		Source
	Dry condition ϕ_{cs} (deg.)	Saturated condition ϕ_f (deg.)	
TS#1	38.4	34.4	This study
TS#2	36.8	32.5	This study
TS#3	36.6	33.3	This study
Gold Slimes	20 – 40.5		Vick [8]
Fine Coal Refuse	22 – 39		Vick [8]
Copper Slimes	24 – 37		Shamsai [9]

The Modified Hyperbolic Model

Strain hardening manifested in all test runs of saturated tailings. The stress-strain curves reflect an asymptotic behavior, as such, hyperbolic fitting techniques were applied to characterize the stress-strain and volume-change behavior of tailings in saturated condition determined from direct shear tests. The hyperbolic model is one of the most frequently used models for predicting the behavior of soils especially if one wishes to apply the finite element method to describe the non-linear movement within soil masses. The Duncan and Chang [7] hyperbolic model was developed based on data obtained from the triaxial tests. In this study, the stress-strain data are obtained from direct shear test; hence, there is a need to modify the method in the hyperbolic model to obtain the hyperbolic parameters from the direct shear test.

The modified model approximates the stress-strain behavior from direct shear tests by the following hyperbolic relation:

$$\tau = \frac{\gamma}{a + b\gamma} \tag{1}$$

where τ is the shear stress, γ is the shear strain, a and b are parameters evaluated from the tests data.

The stress-strain data is represented in a transformed plot where the value of shear strain, γ measured during the test is divided by the corresponding value of shear stress, τ and plotted against the shear strain (γ/τ vs. γ). If the stress-strain relationship measured during the test is hyperbolic, the transformed diagram is a straight line. The hyperbolic parameters a and b of Eq. (1) is the intercept and slope of this straight line, respectively. The intercept a of this straight line on the γ/τ axis is the reciprocal of initial shear modulus, G_i of the tailing sample while the slope of the line, b is the reciprocal of the asymptotic shear stress, τ_{ult}.

The variation of the initial shear modulus, G_i in response to change in normal effective pressure can be represented using the power law approach as suggested by Janbu:

$$G_i = K \cdot P_a \left(\frac{\sigma'}{P_a} \right)^n \tag{2}$$

The parameters K (shear modulus number) and n (shear modulus exponent) describing initial shear modulus (G_i) are obtained from a best-fit straight line drawn through data points of the logarithmic diagram showing the values of normalized shear modulus (G_i/P_a) against the values of normalized normal effective stress (σ'/P_a), where the normalizing parameter P_a is the atmospheric pressure equal to 101.325 KPa.

The failure ratio R_f that relates the asymptotic shear stress with shear stress at failure is defined as the ratio of the shear stress at failure, τ_f to the asymptotic shear stress, τ_{ult}. Since the stress-strain plot exhibited an asymptotic behavior, the value of shear stress at failure, τ_f from stress-strain plot of the test is taken as the shear stress at 15% horizontal displacement.

The variation of angle of internal friction ϕ' with respect to normal stress, σ' is described in terms of hyperbolic parameters ϕ_o and $\Delta\phi$. The angle of internal friction, ϕ' is given by the expression,

$$\phi' = \phi_o - \Delta\phi \log\left(\frac{\sigma'}{P_a} \right) \tag{3}$$

The parameter ϕ_o is the value of angle of internal friction, ϕ' at σ' equal to P_a and $\Delta\phi$ is the reduction in ϕ' for a ten-fold increase in σ' which are obtained from best-fit line through data points on the plot of ϕ' vs. logarithm of normalized σ'/P_a.

The volumetric strain vs. shear strain behavior can also be approximated by hyperbolic equation of the form,

$$\varepsilon_v = \frac{\gamma}{\alpha + \beta\gamma} \tag{4}$$

where ε_v is the volumetric strain, α and β are volumetric strain parameters that can be determined from test data presented in transformed plot of γ/ε_v vs. γ. The value of α is the intercept of the best fit line of the data points while the value of β is the slope of the plot and represents the asymptotic value of ε_v. The parameters α and β vary with normal effective stress and can be represented by the following expressions:

$$\alpha = K_a P_a \left(\frac{\sigma'}{P_a} \right)^m \quad (5)$$

$$\beta = K_b P_a \left(\frac{\sigma'}{P_a} \right)^r \quad (6)$$

The values of K_a and m are determined in a logarithmic diagram of normalized α/Pa versus normalized σ'/Pa while the values of K_b and r are determined in a logarithmic diagram of normalized β/Pa versus normalized σ'/Pa. The parameters K_a and K_b (volumetric strain numbers) are the values of normalized α and β, respectively, for a confining stress of 1 atm. The slope of the best fit line is the value of parameters m and r (volumetric strain exponents).

After the hyperbolic parameter values are determined, the stress-strain and volumetric strain-shear strain responses of tailings as a function of normal effective stress, σ' can be predicted using the following expressions:

The shear stress is given by equation,

$$\tau = \frac{\gamma}{\dfrac{1}{K \cdot P_a \left(\dfrac{\sigma'}{P_a} \right)^n} + R_f \left(\dfrac{\gamma}{\tau_f} \right)} \quad (7)$$

The volumetric strain is calculated using the equation,

$$\varepsilon_v = \frac{\gamma}{K_a P_a \left(\dfrac{\sigma'}{P_a} \right)^m + \gamma K_b P_a \left(\dfrac{\sigma'}{P_a} \right)^r} \quad (8)$$

The hyperbolic parameters to describe the shear modulus (*Gi*) and volumetric strain parameters (α and β) of tailings in saturated condition are presented in Table 3 and Table 4, respectively.

The modified hyperbolic model was also applied to tailings in dry condition. This is to verify if the proposed model is applicable to samples with stress-strain and volumetric strain- shear strain curves that do not exhibit an asymptotic trend. It can be noted that it was not possible to obtain the hyperbolic parameters (*Ka, m, Kb, r*) to describe the volumetric strain parameters α and β for specimens that exhibited dilation. The volumetric strain against shear strain curve of dilatant samples is not hyperbolic and the transformed plot produced negative values of α and β, thus, the determination of *Ka, m, Kb* and *r* using the normalized α and β in logarithmic diagram was not possible. It was observed that the modified hyperbolic model does not give a good prediction of the stress-strain response for dry tailings. This is because the stress-strain curves do not exhibit an asymptotic trend.

Table 3 Hyperbolic parameters describing stress-strain response from test data of tailings in saturated condition

Type of tailing	Dr (%)	Shear modulus hyperbolic parameters				
		K	*n*	Øo (deg.)	ΔØ (deg.)	R_f
TS#1	90	36.11	1.20	31.61	8.09	0.897
	80	28.39	1.04	31.75	5.85	0.888
	60	23.84	1.02	32.13	4.70	0.902
TS#2	90	17.84	0.894	30.89	4.42	0.882
	80	15.95	0.842	31.22	3.29	0.868
	60	13.91	0.831	30.55	4.18	0.856
TS#3	90	34.69	1.115	30.97	6.85	0.899
	80	18.11	0.917	31.81	2.86	0.892
	60	15.39	0.604	31.68	2.67	0.907

Table 4 Hyperbolic parameters describing change in volumetric strain of tailings in saturated condition

Type of Tailing	Dr (%)	Volumetric strain parameter, α		Volumetric strain parameter, β	
		K_a	*m*	K_b	*r*
TS#1	90	0.0357	-1.130	1.369	-0.307
	80	0.0212	-0.911	0.822	-0.350
	60	0.0220	-0.997	0.625	-0.342
TS#2	90	0.0094	-1.080	0.281	-0.188
	80	0.0149	-0.759	0.247	-0.280
	60	0.0120	-0.639	0.223	-0.280
TS#3	90	0.0139	-1.024	0.342	-0.191
	80	0.0107	-1.013	0.221	-0.357
	60	0.0071	-0.868	0.220	-0.372

Using the determined hyperbolic parameters, the model's response to the test data was compared with experimental data using Eqs. (7) and (8). The comparison of the test data and the calculated hyperbolic response is shown in Fig 3.

The comparison showed that the modified hyperbolic model provides a good approximation to the stress-strain response measured during the tests for tailings with ductile behavior since the stress-strain curve shows a hyperbolic trend. However, the model does not give a good prediction of stress-strain response for specimens that exhibited brittle failure. The model cannot capture the strain softening phenomena, but it can be used to model the behavior leading to the strain softening as well as during the ductile stage. The volumetric strain-shear strain response using the modified hyperbolic model also compares fairly well with the test data for specimens with compressive volumetric strain. However, the model does not apply to dilatant samples because the present model cannot account for the change in sign of the volumetric strain.

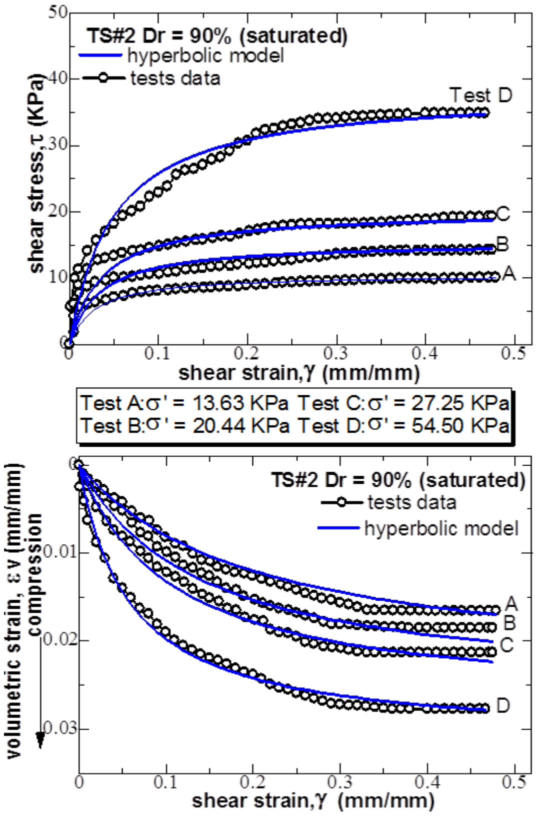

Fig. 3 Comparison of hyperbolic model and test data for saturated tailing.

CONCLUSION

The shear strength behavior of tailings from aggregate quarry and gold mining sites in the Philippines were investigated through direct shear tests. Experimental results showed that:

Dry tailings at very dense initial state and lower normal stresses exhibited peak shear strength and strain softening with dilative behavior, indicating that tailing samples failed in brittle manner. At relative densities lower than 90%, samples reached the critical state even at lower normal stresses indicating that tailings have ductile and contractive behavior.

Saturated tailings exhibited strain hardening indicating a ductile failure with contractive volumetric strain. Friction angles at failure were lower at an average of 4^o as compared to those obtained in dry condition.

The modified hyperbolic model provides a good approximation to the stress-strain response measured during the tests of tailings that exhibited a ductile failure. However, the model cannot capture the strain softening phenomena, but it can be used to model the behavior leading to the strain softening as well as during the ductile stage.

The volumetric strain-shear strain response using the modified hyperbolic model also compares fairly well with the test data specifically for specimens which have compressive volumetric strain. However, the model does not apply to dilatant samples.

REFERENCES

[1] Abdullah, M, et.al., “Concrete with ceramic wastes and quarry dust aggregates”, 5th Annual Conf. Management in Construction Researchers Asso., Malaysia, 2006, pp.383 – 388.

[2] Tempest, BQ and Pando, MA, “Characterization and demonstration of reuse applications of sewage sludge ash”, Int. J. of GEOMATE, Vol. 4, No. 2 (Sl. No. 8), June 2013, pp. 552-559.

[3] Adajar, MQ and Zarco, MH, “An empirical model for predicting hydraulic conductivity of mine tailings”, Int. J. of GEOMATE, Vol. 7, No. 2 (Sl. No. 14), Dec., 2014, pp. 1054-1061.

[4] Adajar, MQ and Zarco, MH “Estimating hydrocompression settlement of mine tailings” Philippine Engineering J., Vol. 34, No.1, June 2013, pp. 11 – 30.

[5] Fourie, AB and Papageorgiou, G, “Defining an appropriate steady state line for Merriespruit gold tailings”, Canadian Geotechnical J., Vol. 38, 2001, pp. 695-706.

[6] Onur, MI, et.al., “Modelling of shear strength parameters of saturated clayey soils”, Int. J. of GEOMATE, Vol. 7, No. 2 (Sl. No. 14), Dec. 2014, pp. 1107-1110.

[7] Duncan, J and Chang, C, “Nonlinear analysis of stress and strain in soils”, Proc. of the American Society of Civil Engineers, Vol. 96, 1970, pp. 1629 – 1653.

[8] Vick, SG, Planning, design, and analysis of tailings dams, John Wiley & Sons, New York, 1990.

[9] Shamsai, A, et.al., “Geotechnical characteristics of copper mine tailings: a case study”, Geotechnical Geological Engineering J., Vol. 25, 2007, pp. 591-602.

Fifth International Conference on Geotechnique, Construction Materials and Environment, Osaka, Japan, Nov. 16-18, 2015, ISBN: 978-4-9905958-4-5 C3051

STABILITY OF UNDRAINED TWIN CIRCULAR TUNNELS

Jay Lobwein[1], Mathew Sams[1] and Jim Shiau[1]
[1]Faculty of Engineering and Surveying, University of Southern Queensland, Australia

ABSTRACT

This paper investigates the stability of horizontally aligned 2D twin circular tunnels in tresca material under plane strain conditions. Finite element limit analysis based on classical plasticity theory is used to determine rigorous upper and lower bounds from *Optum G2*. The upper and lower Factor of Safety (FoS) bounds are defined in terms of gravitational accelerations in an unsupported greenfield problem. A new unit factor of safety design stability chart is developed as a function of dimensionless parameters, including the depth ratio, strength ratio and spacing ratio. Amplified factor of safety design stability charts are illustrated and compared for shallow, medium and deep twin tunnels. It was found the greater the depth, the lesser the FoS. Additionally, increased depth ratios, presents tunnel stability interaction, reducing the spacing ratio impact on the failure. These charts can be used in the preliminary stages of design for practicing engineers.

Keywords: Circular Tunnel, Twin Tunnels, Undrained Clay, FOS, Design Chart

INTRODUCTION

Subsurface infrastructures are becoming more important with the growing demand of transportation systems in major cities around the world. Tunnel construction is a key focus in the advancement of underground construction. There are number of different tunnel designs evolving based on construction techniques, soil settlement and tunnel stability.

Many research studies have been conducted in the field of tunnel stability for different types of soils and geometries. Early studies by Broms and Bennermark [1] introduced a stability number as shown below in Eq. (1).

$$N = \frac{\sigma_s - \sigma_t + \gamma(C + \frac{D}{2})}{S_u} \qquad (1)$$

Where σ_s is the uniform surcharge pressure on the surface and σ_t is the internal normal tunnel pressure, C is the cover depth above the tunnel roof, D is the tunnel diameter, γ corresponds to the unit weight, and S_u is the undrained shear strength of the soil. Commonly, from early stages the stability number was formulated by increasing the surcharge pressure whilst setting the tunnel pressure to zero in an active collapse mechanism.

An active tunnel collapse mechanism is triggered by the surface pressure and self-weight of the soil, whilst the internal tunnel pressure is the resistance against tunnel failure. For a passive tunnel collapse, the tunnel pressure is increased in a ‘blow out’ situation, whilst the self-weight and surface pressure are the resistance against failure [2].

The work by Broms and Bennermark [1] extended across numerous experimental and theoretical studies for tunnel stability, predominantly modelling circular headings. The experimental studies were conducted using a centrifuge which enhanced the gravity until tunnel collapse [3]–[5]. The definition of the stability number was extended using a number of dimensionless parameters [5].

Basing the stability number on dimensionless parameters, stability charts are produced. These stability design charts are based on a unit factor of safety for all cases. This study will determine factor of safety values to produce new stability charts for twin circular tunnels. Upper and lower bound solutions were produced using limit analysis for the stability number shown below in Eq. (2). The stability number was regarded as a function of the depth ratio and strength ratio for a homogenous soil.

$$N = \frac{\sigma_s - \sigma_t}{S_u} = f(\frac{C}{D}, \frac{\gamma D}{S_u}) \qquad (2)$$

Upper and lower bounds on the stability parameter were extensively described by Lyamin and Sloan [6], [7]. These numerical techniques modelled arbitrary geometries, varying soil layers, and complex loading conditions. However, most importantly the continual refinement of the limit analysis using upper and lower bounds increased the accuracy of the collapse loads, and hence the accuracy of the design stability charts for tunnels.

With further refinement of the finite element limit analysis (FELA) techniques, numerous geotechnical engineering problems have been solved rigorously through upper and lower bounds [8]. This development has led to a number of studies in the field of tunnel stability for circular, square and heading tunnel profiles [9]–[12].

Studies by Wilson et al. [9], [10] investigated the stability of circular and square tunnel headings, respectively. The shear strength was assumed to increase linearly with depth. In this instance, the stability problem is defined with an extra dimensionless variable, as shown in Eq. (3).

$$N = \frac{\sigma_s - \sigma_t}{s_u} = f(\frac{C}{D}, \frac{\gamma D}{s_u}, \frac{\rho D}{S_u}) \tag{3}$$

Where ρ is the strength factor which determines the rate of strength increase with depth. Both studies modelled ρ incrementally, from zero (homogeneous case) to one. For square tunnels, D refers to the side length instead of the diameter.

Semi-analytical rigid block mechanisms were used as a comparison to the numerical formulation of the upper and lower bound theorems. Both upper and lower bounds were bracketed to a true collapse load to within 5% for all cases considered.

A similar approach was opted for wide rectangular tunnels, with an additional dimensionless parameter, B/D, representing the aspect ratio of the tunnel, where B is the width and D is the depth [11].

Furthermore, an infinitely long flat wall was modelled by Augarde et al. [12], where only the face of the heading was free to move and subject to a uniform surface pressure (σ_s). This model can also be assumed to be the longitudinal section of a tunnel. The tunnel floor and roof were assumed to be fixed in a rigid lining situation. This plain strain heading problem presented a number of stability design charts similar to studies completed by Wilson et al. [9], [10].

In relation to twin tunneling stability analysis, only a limited amount of study has been completed. Reference [13] investigated the finite element optimization of the tunnel positioning in three different configurations; aligned horizontally, vertically and inclined. It concludes that the best design in soft soil is the horizontal side-by-side configuration, based on lining forces and settlement. Therefore, this paper will only investigate the horizontal alignment.

By defining the problem with two tunnels, another variable is introduced, that being the tunnel spacing. This spacing distance is given by S and is normalized with respect to the tunnel diameter D, which together establish the dimensionless spacing ratio parameter defined as S/D.

In-line with the studies completed on various tunnel profiles, Wilson et al. [14], [15] extended the theory into square and circular tunnels respectively. Both studies presented 2D horizontally aligned dual tunnels for undrained homogenous soil. Shown below in Eq. (4) is the stability number for the dual circular tunnels, with the problem now also being dependent on tunnel spacing.

$$N = \frac{\sigma_s - \sigma_t}{s_u} = f(\frac{C}{D}, \frac{\gamma D}{C_u}, \frac{S}{D}) \tag{4}$$

The dual tunnels were investigated using FELA and compared with rigid block analysis under plane-strain conditions with uniform tresca material. The true collapse loads, were found to differ by at most 5% and presented in stability design charts. Similar to the work completed by [9]–[12], the failure of the structure was induced by uniform surface surcharge for upper and lower bounds.

The ultimate purpose of this paper is to study the parameters of the unsupported-greenfield twin tunnel problem. A factor of safety approach is used, and a practical range of dimensionless parameters has been selected.

PROBLEM DEFINITION

This paper investigates only the homogeneous case for varying twin circular tunnels. Tresca material is used for all models of analysis, where the angle of friction (φ) is zero. Fig. 1 shows the problem in this study. The soil properties include the unit weight γ, and undrained shear strength S_u. The geometry of the system is described by the cover depth C, the tunnel diameters D, and the tunnel spacing S.

The surcharge surface pressure σ_s and internal tunnel pressure σ_t are both ignored. With this unsupported greenfield condition, the stability of the system would then simplify considerably, as expressed in [15], but would need to be defined using a factor of safety approach, as described in Eq. (5). The developed FoS is a function of the depth ratio C/D, strength ratio $S_u/\gamma D$ and the spacing ratio S/D.

$$FoS = (\frac{C}{D}, \frac{S_u}{\gamma D}, \frac{S}{D}) \tag{5}$$

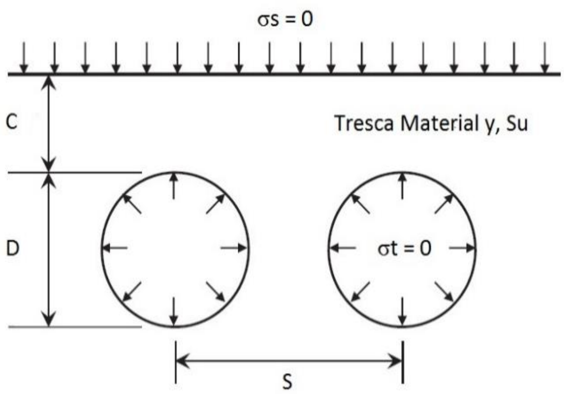

Fig. 1 Problem Definition

The system is described using dimensionless ratios as described in Eq. (5). A range has been selected based on its practicality; this study will calculate a factor of safety for: C/D = 1–6, $S_u/\gamma D$ = 0.05–2, and S/D = 1–14. Other Tresca material properties that had minimal effect on the factor of safety outcome included: Poisson's ratio ν = 0.49 and Young's Modulus E = 30MPa.

FELA MODELLING

Optum G2 is a finite element software used for strength and deformation analysis of geotechnical boundary value problems. The program differs by commuting rigorous upper and lower bounds to an exact limit load or strength reduction factor.

Each 2D model was restrained in the base and sides in both the x and y dimensions. There was allowance of enough model space between each tunnel, base and sides. This ensured the assumption of an infinitely wide and constant soil medium; however this might not be the case in reality. Shown in Fig. 2 identifies the model space and boundary restraints for a twin tunnel profile of depth ratio C/D = 1 and spacing ratio S/D = 3. Over allowance of the model would deteriorate the accuracy of the finite element limit analysis, as more elements would need to cover the entire soil area.

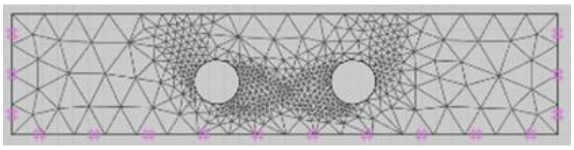

Fig. 2 Typical twin tunnel mesh (C/D = 1, S/D = 3)

The number of finite elements used was 1000 for each model for all cases. Mesh adaptivity was enabled with three iterations starting at 1000 elements. Fig. 2 shows 10,000 mesh elements with mesh adaptivity of three iterations starting at 1000 elements to illustrate the failure mechanism for twin circular tunnels.

The FoS value was developed by prompting the gravity multiplier. The gravity multiplier is iterated in the software code until a state of collapse is reached, whilst all other properties are constant. The upper and lower bound gravity multiplier values are essentially the factor of safety values. For example, if a lower bound gravity multiplier is 1.5, then the gravity on the model would have to be amplified by 1.5 times the gravity ($9.81 m/s^2$) to produce a tunnel collapse. Therefore, the initial unit weight of the soil has increased also by 1.5.

The strength ratio was developed with respect to the diameter. The undrained soil shear strength was ranged from 2.7kPa–108kPa for the ranging strength ratios. The range of strength ratios are used to verify the factor of safety values.

Subsequently, each strength ratio value is divided by the calculated factor of safety value to produce a new stability number. The stability number is averaged out across the range of strength ratios for constant depth and spacing ratios. It is important to note that the stability number calculated is for a unit factor of safety.

Table 1 illustrates the procedure for an upper and lower bound twin circular tunnel with a depth ratio C/D = 1 and spacing ratio S/D = 3 for strength ratios 0.05, 0.5, 1.0, 1.5 and 2.0. The constant values are the diameter D = 3m and unit weight of the soil γ = $18 kN/m^3$ used throughout all calculations. The averaged stability numbers calculated are 0.630 for the lower bound and 0.579 for the upper bound.

Table 1 Average stability number calculations

SR	FoS(LB)	FoS(UB)	N(LB)	N(UB)
0.05	0.079	0.086	0.633	0.581
0.5	0.794	0.864	0.630	0.579
1.0	1.589	1.728	0.629	0.579
1.5	2.383	2.592	0.629	0.579
2.0	3.177	3.455	0.630	0.579

RESULTS AND DISCUSSION

Collating all the averaged stability numbers across a range of depth and spacing values, a new design stability chart is shown in Fig. 3. This chart is based on an exact bound unit factor of safety with a percent difference equal to 11.7 percent. The exact bound is found by averaging the upper and lower bounds to calculate a true collapse FoS. Averaging the stability number across a range of strength ratios, simplifies the unit factor of safety chart as a function of the depth ratio, strength ratio and spacing ratio.

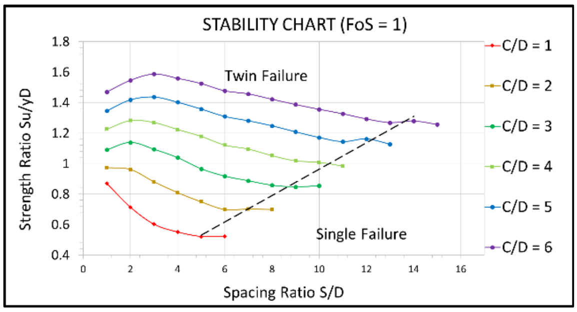

Fig. 3 Conditions at collapse state.

By inspection, the spacing ratio was increased until a singular tunnel failure occurred for the respective depth ratio. The failure was governed either by an upper or lower bound failure, with an additional space ratio calculated to confirm and extend the singular failure. A linear line of best fit was elected to dissect the two failure zones.

This chart can be used to determine whether a particular twin tunnel profile will fail or not. This is based on required information based on the depth, spacing, diameter and soil properties of the dual tunnels. Due to the fact soil can behave in an uncertain and complex matter, it would be rare for an engineer to base dual tunnels on a FoS = 1.

Consequently, an extension of the design stability chart is completed.

Table 2 identifies the lower bound factor of safety values for varying strength and spacing ratios, at a constant depth ratio = 3. By inspection a unit factor of safety value is achieved when the strength ratio approximately equaled to 1.1 and the spacing ratio = 5 at a constant depth ratio = 3. This figure can also be identified by inspection on the design stability chart presented in Fig. 3.

Table 2 Lower Bound FoS values (C/D=3)

SR	S/D=1	S/D=3	S/D=5	S/D=7
0.05	0.045	0.044	0.049	0.053
0.3	0.267	0.262	0.296	0.32
0.7	0.624	0.612	0.692	0.747
1.1	0.980	0.961	1.087	1.174
1.5	1.336	1.311	1.482	1.600
2.0	1.782	1.748	1.976	2.134

Design Stability Charts

Three design stability charts were constructed for depth ratios 1, 3 and 6 to identify the comparisons between shallow, medium and deep twin tunnel stability behavior. Both upper and lower bound FoS values are determined for each chart until singular failure is induced. Furthermore, each design stability chart illustrates the failure boundary between twin and singular tunnel failure.

It can be noticed for all charts that the spacing between the tunnels and the strength of the soil has a significant effect on the factor of safety values.

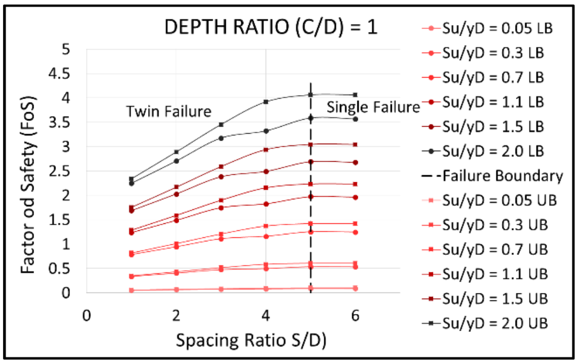

Fig. 4 Design stability chart (C/D = 1)

Shown in Fig. 4 is the shallow stability chart with a twin tunnel depth ratio C/D = 1, for varying spacing and strength ratios. The limiting spacing ratio for dual stability is S/D = 5 for both upper and lower bounds.

The shallow design stability chart shows the largest extent of factor of safety values, maximizing at a FoS = 4, when the strength ratio $S_u/\gamma D$ = 2 and the spacing ratio S/D = 5. This concludes that for shallow tunnels the strength ratio has much greater effect on the tunnel stability. For the shallow tunnels, a steep linear gradient is projected up until singular failure is induced, where all the strength ratios sharply plateau over the failure boundary when S/D = 5. There is no initial tunnel stability interaction between the tunnels at close spacing ratios.

Fig. 5 presents the design stability chart for a twin circular tunnel depth ratio C/D = 3, for varying spacing and strength ratios with increasing upper and lower bound strength ratios. The limiting spacing ratio for dual stability is S/D = 9 triggered by both upper and lower bounds. This chart is presented as a medium depth dual tunnel profile.

Comparably, the extent of the factor of safety values is less with FoS maximizing at 2.5, when the strength ratio $S_u/\gamma D$ = 2 and the spacing ratio S/D = 9. There is a rising curved plateau over the failure boundary line when S/D = 9 for all strength ratios. Furthermore, there is minor tunnel stability interaction when the spacing ratio is less than 2, where the tunnels interact with each other under reducing conditions.

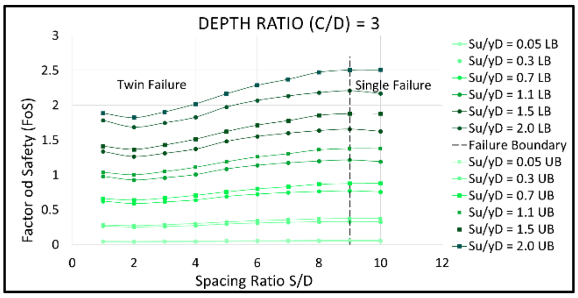

Fig. 5 Design stability chart (C/D = 3)

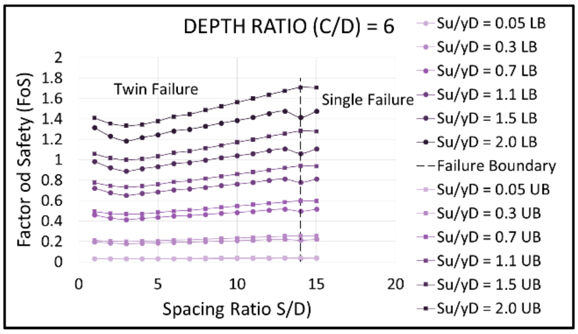

Fig. 6 Design stability chart (C/D = 6)

The deep design stability chart for a twin circular tunnel with a depth ratio C/D = 6, for varying spacing and strength ratios is illustrated in Fig. 6. The limiting spacing ratio for dual stability is S/D = 14 triggered only by the lower bound.

The FoS values have the lowest extent of tunnels maximizing at 1.7, for a strength ratio $S_u/\gamma D$ = 2.0 and spacing ratio S/D = 14. The stability tunnel interaction is more prominent for spacing ratios less than 3. The rising FoS plateau is further reduced until the failure boundary when the spacing ratio S/D = 14. At this point for all strength ratios, only a singular lower bound failure is induced which can be identified as a drop in the FoS results along the failure boundary line. This indicates a slight tunnel stability interaction just prior to singular collapse

Referring to all the design charts, the greater the depth and/or strength ratios, the less the FoS. Furthermore, the greater the depth and/or strength ratios the less the spacing ratio impacts the failure and the more tunnel stability.

Plasticity and Shear Strain Rate

The plastic multiplier is a direct measure of the plastic strain increment. The contour plots shown in (Figs. 7 to 9) indicate the failure mechanism for each tunnel configuration, with a spacing ratio just prior to singular collapse. Each tunnel depth illustrates a symmetrical elliptic failure contour that branches from the inner aspect of the walls to a center point. As the tunnel depth increases, the ecliptic failure contour engulfs the tunnel roof and base entirely. The shallow tunnel failure mechanism is positioned in the pillar and extending from both sides shown in Fig. 7. The pillar is positioned at a distance equal to the diameter. As the tunnel is increased with depth the pillar width is extended to a distance six times the diameter from the external walls for a deep tunnel shown in Fig. 9. Lastly, the tunnel depth increases, the complexity is enlarged by floor heave.

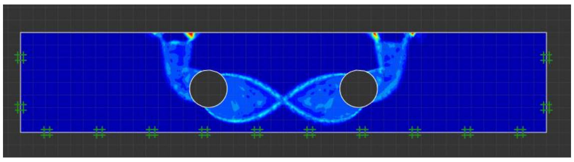

Fig. 7 Plastic multiplier plot (C/D = 1, S/D = 4)

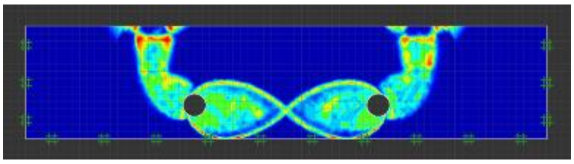

Fig. 8 Plastic dissipation (C/D = 3, S/D = 8)

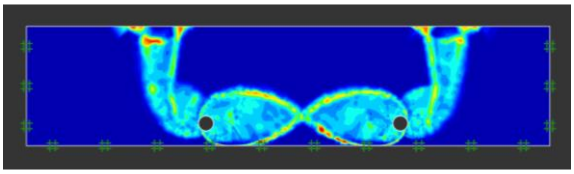

Fig. 9 Plastic dissipation (C/D = 6, S/D = 13).

Principle Elemental Stresses

The principle stresses were plotted for shallow, medium and deep tunneling (Figs. 10 to 12). The blue vectors indicate the major principle stresses, whilst the red vectors indicate the minor principle stresses. For all cases, the vector fields are similar. The major principle vectors are actively shown in the symmetric ecliptic contour area, whilst the minor principle vectors are predominantly shown in the pillar areas closer to the surface. With greater depth the stress complexities are increased around the tunnel voids.

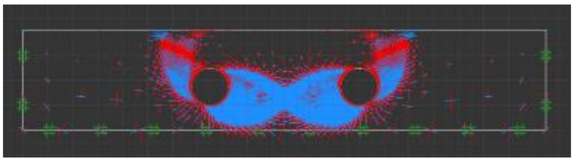

Fig. 10 Principle stress vectors (C/D = 1, S/D = 4).

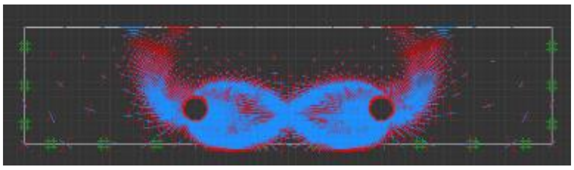

Fig. 11 Principle stress vectors (C/D = 3, S/D = 8).

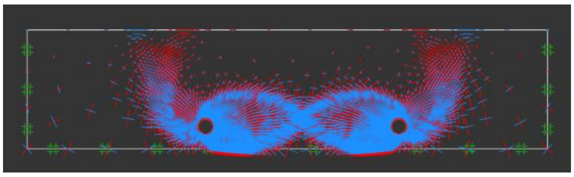

Fig. 12 Principle stress vectors (C/D = 6, S/D = 13).

Displacement Vectors

The displacement vectors represent the deformation in the x and y direction for each tunnel void. Deformations for shallow, medium and deep tunnels are shown in (Figs 13 to 15). For a shallow configuration, the major displacements are projected on the inner wall and invert of the void towards the center of the tunnel. There is no displacement on the crown and the external invert of the tunnel. As the depth increases, the vector field surrounding the tunnel void becomes greater.

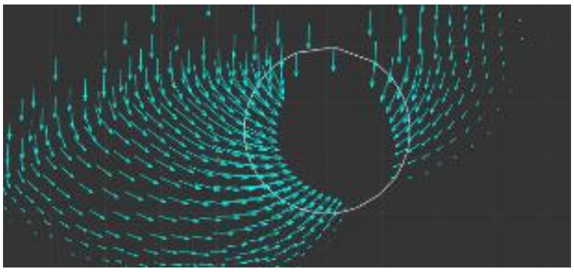

Fig. 13 Displacement vectors (C/D = 1, S/D = 4)

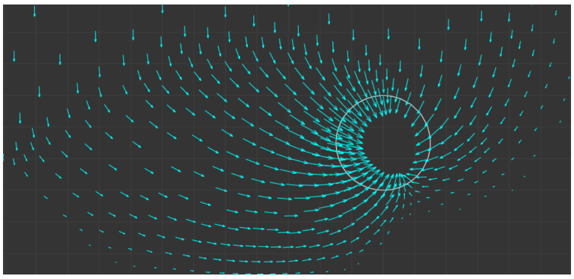

Fig. 14 Displacement vectors (C/D = 3, S/D = 8)

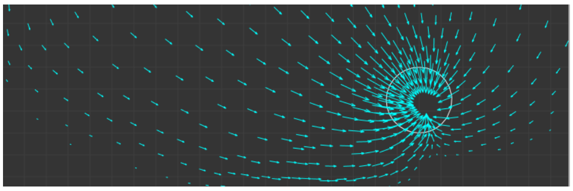

Fig. 15 Displacement vectors (C/D = 6, S/D = 13).

CONCLUSION

The stability of twin circular heading tunnels horizontally aligned in tresca material under plane strain conditions were investigated using FELA. The upper and lower FoS bounds were defined in terms of gravitational accelerations in an unsupported greenfield analysis using the software *Optum G2*.

The factor of safety results are a function of three dimensional properties; depth ratio C/D, strength ratio $S_u/\gamma D$ and spacing ratio S/D. A new unit factor of safety stability chart was created to determine the failure. Design stability charts were developed for depth ratios 1, 3 and 6 to compare the failure behavior of the different tunnel depths.

It was concluded the greater the depth, the less the FoS. Additionally, the greater the depth the less the spacing ratio impacts the failure and the more tunnel stability interaction. Further work includes to model square twin tunnel stability and to further investigate the stability tunnel interaction for undrained clay.

REFERENCES

[1] Broms BB & Bennermark H, “Stability of clay at vertical openings”, Journal of the Soil Mechanic and Foundations Division, Proceedings of the American Society of Civil Engineers, 1967, vol. 93, pp. 71–93.

[2] Assadi A & Sloan S, “Undrained Stability of Shallow Square Tunnel”, Journal of Geotechnical Engineering, 1991, vol. 117, pp. 1152–1173.

[3] Atkinson JH & Cairncross AM, “Collapse of a shallow tunnel in a Mohr-Coulomb material”, Cambridge, pp. 202–06.

[4] Peck RB, “Deep excavations and tunneling in soft ground”, Proceedings of 7th International Conference on Soil Mechanics and Fundamentals Engineering, Mexico, 1969, vol. 3, pp. 225–290.

[5] Davis EH Gunn MJ Mair RJ & Seneviratne HN, “The stability of shallow tunnels and underground openings in cohesive material”, Geotechnique, 1980, vol. 30, no. 4, pp. 397–416.

[6] Lyamin AV & Sloan SW, “Lower bound limit analysis using non-linear programming”, International Journal for Numerical Methods in Engineering, 2002a, vol. 55, no. 5, pp. 573–611.

[7] Lyamin AV & Sloan SW, “Upper bound limit analysis using linear finite elements and non‐linear programming”, International Journal for Numerical and Analytical Methods in Geomechanics, 2002b, vol. 26, no. 2, pp. 181–216.

[8] Sloan SW, “Geotechnical stability analysis”, Geotechnique, 2013, vol. 63, pp. 531–572.

[9] Wilson DW Abbo AJ Sloan SW Lyamin AV, “Undrained stability of a square tunnel where the shear strength increases linearly with depth”, Computers and Geotechnics, 2013, vol. 49, pp. 314–325.

[10] Wilson DW Abbo AJ Sloan SW Lyamin AV, “Undrained stability of a circular tunnel where the shear strength increases linearly with depth”, Canadian Geotechnical Journal, 2011, vol. 48, pp. 1328–1342.

[11] Abbo AJ Wilson DW Sloan SW Lyamin AV, “Undrained stability of wide rectangular tunnels”, Computers and Geotechnics, 2013, vol. 53, pp. 46–59.

[12] Augarde CE Lyamin AV Sloan SW, “Stability of an undrained plane strain heading revised”, Computers and Geotechnics, 2003, vol. 30, pp. 419–430.

[13] Chehade F Shahrour I, “Numerical analysis of the interaction between twin-tunnels: Influence of the relative position and construction procedure”, Tunneling and Underground Space Technology, 2008, vol. 23, pp. 210–214.

[14] Wilson DW Abbo AJ Sloan SW Lyamin AV, “Undrained Stability of Dual Circular Tunnels”, International Journal of Geomechanics, 2014, vol. 14, pp. 69-77.

[15] Wilson DW Abbo AJ Sloan SW Lyamin AV, “Undrained Stability of Dual Square Tunnels”, 12th International Association for Computer Methods and Advances in Geomechanics Conference, 2008, Goa, India, pp. 4284–429.

Fifth International Conference on Geotechnique, Construction Materials and Environment, Osaka, Japan, Nov. 16-18, 2015, ISBN: 978-4-9905958-4-5 C3051

RELATING THE TUNNEL SETTLEMENT PARAMETER WITH VOLUME LOSS

Mathew Sams and Jim Shiau
School of Civil Engineering and Surveying, University of Southern Queensland, Australia

ABSTRACT

This paper describes the development, verification and use of a numerical model for investigating settlement induced by circular tunnels in cohesive soils. The model aims to simulate the movement and relaxation of the soil around the shield and lining annulus that occurs due to the overcutting and grouting of the tunnel void by a tunnel boring machine. To achieve this, the model uses a pressure relaxation technique that progressively reduces the tunnel support pressure from a specific amount until a point of failure is detected. For three separate stages before this point of failure, the surface settlement data is exported for analysis. Using a regression of the commonly used Gaussian equation on the settlement data, i_x values can be determined for each case. This is done for a number of geometry and soil ratios which will cover the most practical range for soft cohesive soils. The results of this study are quite positive, settlement results compare well with previous experimental and observational results. Design charts using dimensionless ratios have therefore been presented.

Keywords: Tunnel, Settlement, Undrained, Cohesive, Volume loss

INTRODUCTION

Population increases, increased urbanisation, and the rapid development of emerging countries have driven research into the better management of transport services and infrastructure. Tunnels have increasingly become a common solution; with limited scope for changes above ground, better use of the underground space is an effective solution. With the development of tunnel boring machines (TBM's) over the past few decades tunnels can now be produced increasingly difficult ground conditions, such as very soft ground. In such conditions where the soil mechanics are more critical, responsibility increasingly falls to the geotechnical engineer.

These problems arise in modern tunnel boring machines (TBM's) because of the small amount of overcutting, resulting in the inevitable delay between when the tunnel is bored and when the lining and the grout is installed. During this period, there is always a degree of soil movement.

The three primary design criteria of underground tunnels from a geotechnical perspective are: stability during construction, long and short term settlement, and determination of lining structural loading as discussed by [1], [2], [3], and [4]. This paper considers the settlement problem.

SETTLEMENT ANALYSIS OF TUNNELS

Surface settlement induced by tunnelling is a complex phenomenon that is dependent on many factors such as soil and groundwater conditions, tunnelling dimensions and construction techniques. Therefore, much modern tunnelling research has been given to better predict the soils response to changes in stress resulting from tunnel construction by determining analytical solutions for these problems. ([5], [6], [7], and [8])

However, with the rapid development of computer technology, numerical modelling using finite element or finite difference methods has become the preferred method for geotechnical design and analysis. These models are generally compared to field observations and experimental results for validation. In some cases however, empirical and semi-empirical methods are still applicable, and indeed quite capable. For tunnel settlement in particular, the empirical method is still widely used, due to its suitability and ease of use. ([9] and [10])

This empirical method for estimating surface settlements generally follows a Gaussian distribution curve, as in Eq. (1). This approach was first suggested by [11], who observed that it matched settlement patterns of deep excavations remarkably well. For the particular application to tunnels, research by [1] indicated a close fit with experimental and observational results. This method requires the input of a trough parameter (i_x) which influences the physical width of the profile, and also relates the volume loss and the maximum settlement, as shown in Eq. (2).

In practice, a target volume loss (V_s) will likely be known (based on experience or client specified); this and the estimated i_x can be used to predict a S_{max}, which can then be used in Eq. (1).

$$S_x = S_{max} e^{-\frac{x^2}{2{i_x}^2}} \quad (1)$$

$$V_s = \sqrt{2\pi}\, i_x S_{max} \quad (2)$$

Figure 1 shows the nature of this equation. D is the diameter of the tunnel, H is the to-axis tunnel depth, C is the overburden, S_x is the settlement profile at the surface, S_{max} is the maximum vertical settlement, and i_x is the trough width parameter which, physically, is the distance from the tunnel axis to the point of inflection of the curve.

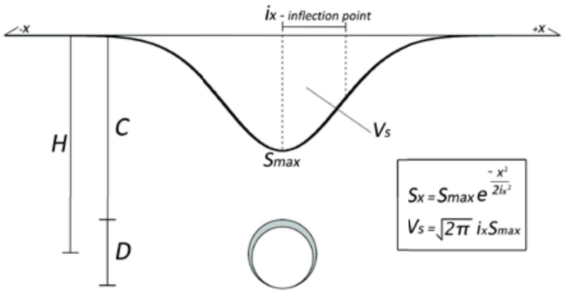

Fig. 1 Typical settlement profile of a tunnel

Further examination of this method has been extensive. Centrifuge modelling has been one of the methods used to test its adequacy, with results from [12], [13], [3], [10], and [14]. It has also been extensively compared with measurements from constructed tunnels in [15], [16], [17], and [18], reporting settlement profiles of the shape suggested by a Gaussian equation.

Estimations of the inflection point parameter, i_x have been attempted, the most notably by [19], [3], [20] in Eq.'s (3), (4), and (5) respectively. However, these only take into account the geometry of the system, volume loss and soil strength aren't definable parameters. The most widely used method is the one suggested by [17], which through analysing data collected from tunnels in London suggested that i_x is linearly proportional to the to-axis tunnel depth, H, as in Eq. (6).

$$i_x = 0.5D^{0.2}H^{0.8} \tag{3}$$

$$i_x = 0.75D\left(\frac{C}{D}\right)^{0.8} \tag{4}$$

$$i_x = 0.29\left(\frac{H}{D}\right) + 0.5 \tag{5}$$

$$i_x = kH \tag{6}$$

This equation wouldn't be suitable for very shallow cases (C/D < 1), as the diameter would become a more dominant parameter. However, this equation allows the coefficient of proportionality (k) to vary with other parameters such as volume loss and soil type. Commonly assumed values of k range from 0.4 for stiff clays to approximately 0.7 for soft clays [21]. However, these haven't been thoroughly defined using dimensionless parameters.

PROBLEM DEFINITION

The circular tunnel problem is shown in Fig. 2. In this study, only greenfield settlement has been analyzed. Thus, the surcharge load (σ_s) is set to 0 kPa. The soil is considered as homogenous undrained clay following the Mohr-Coulomb model. The system will be described in terms of dimensionless ratios: C/D, $\gamma D/s_u$, and E/s_u.

This paper will study the following parametric range: C/D = 1 - 5, $\gamma D/S_u$ = 1.5 - 6, and E/s_u = 100 - 800. Using this approach, the results can be studied methodically, and practical design charts employing these ratios can be produced that should cover a practical range.

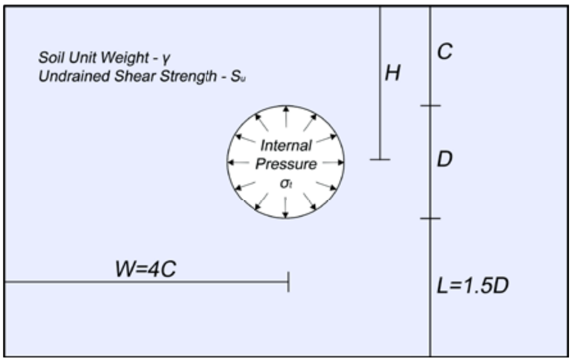

Fig. 2 Problem Definition

The problem is modelled using 2D plane strain conditions in *FLAC* [22]. Despite the fact that tunneling is a three-dimensional activity, transverse settlement under greenfield conditions can be modelled quite accurately with this simplification [23].

3D numerical programing is much more complex requiring more parameters which sometimes can be difficult to determine in practice. Three-dimensional analysis is also much more time consuming and computationally demanding. For simplicity, the tunnel can be reasonably considered to be very long and at a consistent depth. It is the focus of this paper to study 2D transverse surface settlement.

PRESSURE RELAXATION TECHNIQUE

With the development of powerful computers over the last two decades, numerical modelling has proceeded to become a dominant technique for problem resolution. The finite difference method is one such technique that has been successfully used in the past for modelling tunnels using shear strength reduction method [24], and it has again been used in this study. Using *FLAC*, the problem is solved by a pressure relaxation method [25], developed in this paper using the built-in program language *FISH*.

After defining boundary conditions, soil properties and tunnel geometry, the developed model slowly reduces the internal supporting pressure from a set amount, at each relaxation step. In this study, the model was set to fully relax from the starting amount in 1% increments. At each of these relaxation steps, the surface settlement data is recorded.

A typical finite difference mesh of the problem in this study is shown in Fig. 3. The boundary conditions shown in the figure are important as they ensure that the entire soil mass is modelled accurately despite using a finite mesh. It should be noted that the soil domain size for each of the cases was chosen so that the failure zone of the soil body is placed well within the domain. Using Fig. 2, *L = 1.5D* and *W = 4C* are adopted in all analyses of the paper.

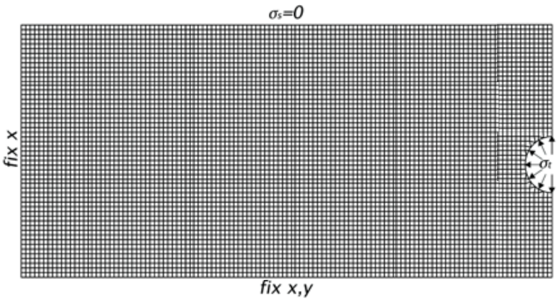

Fig. 3 Typical mesh of the problem (*C/D*=2)

The internal pressure σ_t, is reduced by multiplying the at-rest pressure, where no movement occurs, by a reduction factor which is based on the number and range of relaxation steps. At each subsequent relaxation step, the internal pressure is less than the at-rest pressure, and consequently the soil moves into the tunnel void until the internal forces in the soil reach equilibrium, balanced or otherwise.

In the elastic state, internal forces have reached a balanced state (nodal unbalanced force approaches zero), no more movement takes place and the circular tunnel is considered to be stable. Once the internal pressure is reduced to the extent where the internal forces are no longer sufficient to retain the earth pressures, nodal forces become unbalanced and the tunnel is considered to be unstable.

The failure point occurs when the unbalanced forces fail to reach zero equilibrium during a particular relaxation stage. This point of instability is quite abrupt and can be identified relatively easily by observing the unbalanced force history (Fig. 4). It can also be clearly observed using plasticity indicator and velocity plots (Fig. 5).

The surface settlement data is recorded for every relaxation step. Thus, settlement analysis can be done for any arbitrary step. In this study, the analysis has been based on the relaxation steps of 10%, 25%, and 50% of the collapse stage (i.e. if the collapse stage was 52% relaxation; the stages being analyzed are: 5%, 13%, and 26%).

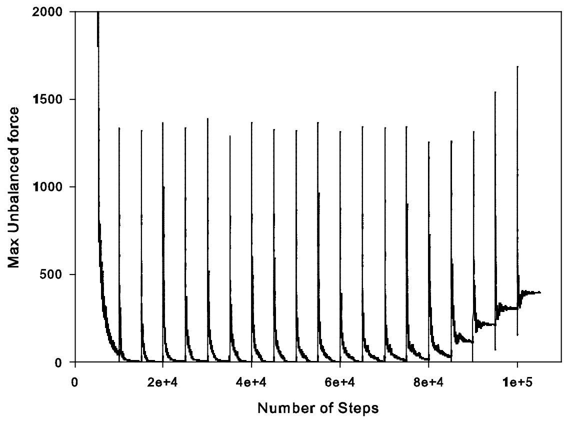

Fig. 4 Unbalanced force history plot (*C/D*=3, $\gamma D/S_u$ =4, E/s_u =200)

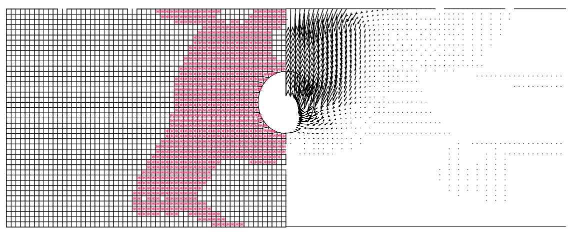

Fig. 5 Plasticity (left) and velocity (right) plots at the stage of collapse (*C/D* =1, $\gamma D/S_u$ =3)

The volume loss can then be back-calculated by integrating the surface settlement data. It should be noted that this numerical model controls the internal tunnel pressure; the volume loss isn't a controlled parameter.

RESULTS AND DISCUSSION

As previously discussed, these settlement profiles are commonly represented by the Gaussian equation, as in Eq. (1). In this study, this equation has been used for a regression with the data collected at the collapse stage of each of the cases. This has been done using *MATLAB*, and the curve fitting toolbox. A typical example of this is shown in Fig. 6. It was found that using this equation to model settlement can be considered accurate, with r^2 values of greater than 0.97 achieved for all cases, where an r^2 of one would indicate a perfect fit. The example shown in Fig. 6 is for *C/D* = 4, $\gamma D/S_u$ = 3, and this particular example has r^2 = 0.987.

In Fig. 7, the depth ratio *(C/D)* is varied and the strength ratio $(\gamma D/S_u)$ and Young's modulus *(E)* are kept constant. The profiles are as expected, with the shallow case producing a narrow but deep trough, that become shallower and wider as *C/D* increases. In Fig. 8, *C/D* and *E* are kept constant, and $\gamma D/S_u$ is varied. Once again, the trend is as expected, when the strength ratio is increased (i.e. soils become weaker), the settlement at the point of collapse is greater. Fig. 9 similarly shows the impact of Young's modulus, with the stiffer soils (higher *E*) having proportionately lower settlement.

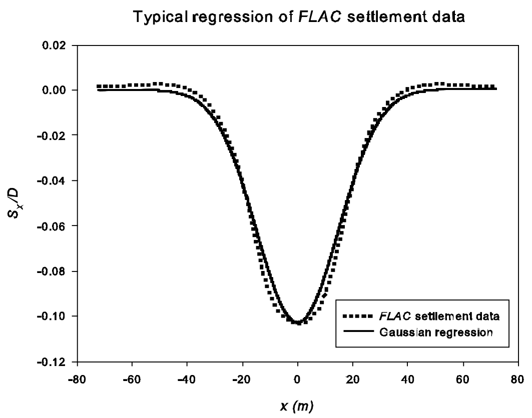

Fig. 6 Typical regression analysis (*C/D* =4, *γD/S*$_u$ = 3)

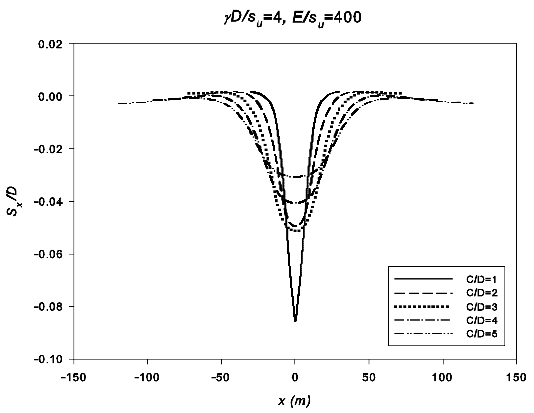

Fig. 7 Settlement profiles with varying *C/D*

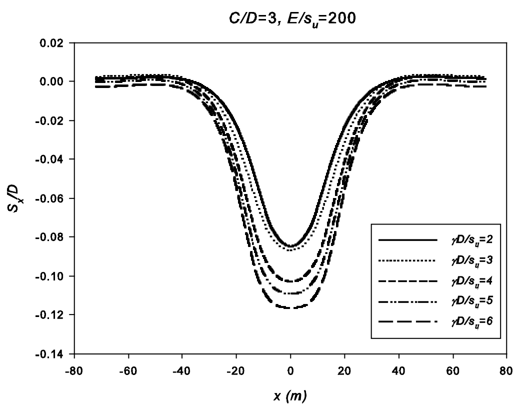

Fig. 8 Settlement profiles with varying *γD/S*$_u$

Figures 10-12 show displacement vectors and y-displacement contours of a particular case (*C/D*=1, *γD/S*$_u$=3, *E/S*$_u$=200) during 10%, 25%, and 50% of the collapse relaxation, as previously discussed. In Fig. 10, there is too much internal pressure being applied, resulting in some local blowout; as relaxation continues, the displacement pattern becomes more as expected. The y-displacement contours show similar behavior.

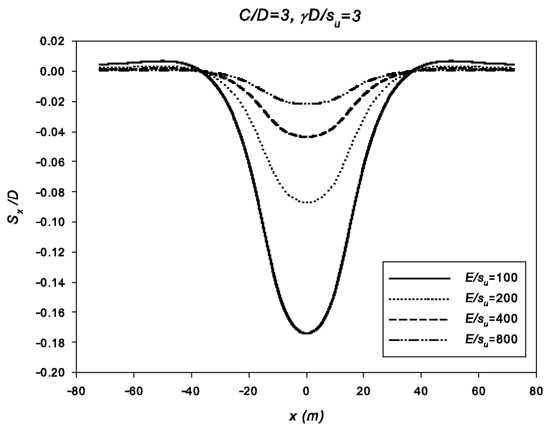

Fig. 9 Settlement profiles with varying *E/ S*$_u$

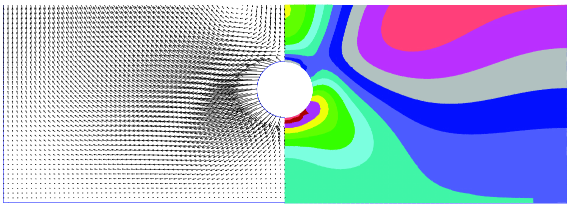

Fig. 10 Displacement vector and y-displacement contour of 10% of collapse (*C/D*=1, *γD/S*$_u$=3, *E/S*$_u$=200)

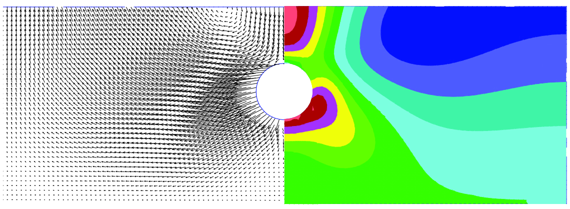

Fig. 11 Displacement vector and y-displacement contour of 25% of collapse (*C/D*=1, *γD/S*$_u$=3, *E/S*$_u$=200)

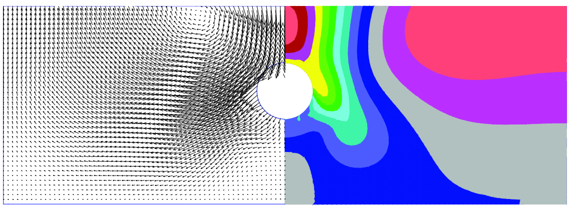

Fig. 12 Displacement vector and y-displacement contour of 50% of collapse (*C/D*=1, *γD/S*$_u$=3, *E/S*$_u$=200)

Fig. 13 contains a comparison with experimental results by [1], and suggested equations by [19], [3], and [20]. These equations are given in Eq.'s (3), (4), and (5). It should be noted that these equations are based on *γD/S*$_u$≈*1*.8, γD/S$_u$=2.6, and *γD/S*$_u$≈*3* respectively.

These equations appear to match quite well with the results of this study, appearing in approximately in the expected positions according to the strength ratio ($\gamma D/S_u$) with which they were obtained.

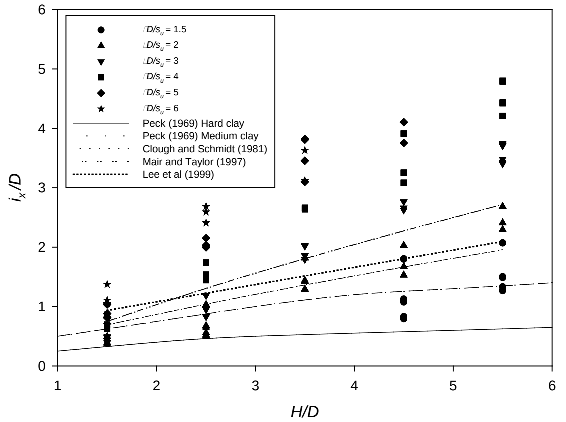

Fig. 13 Comparison with previous results

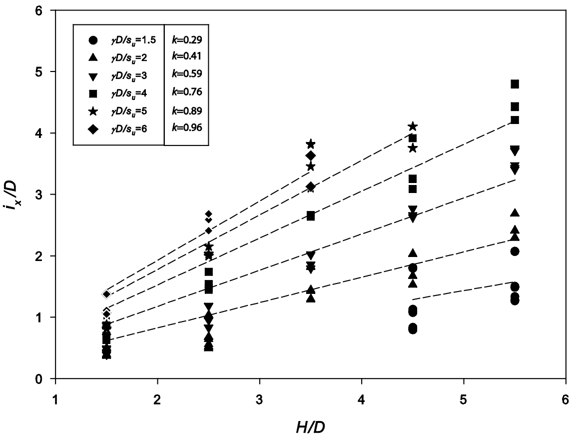

Fig. 14 Comparison with O'Reilly's and New equation (eq. 6)

Using the widely known equation from [17], the results can be compared, as in Fig. 14. These results concur strongly with this equation, with the stronger soils achieving the lowest k (0.29 for $\gamma D/S_u$=1.5), and the weaker soils achieving the highest k (0.96 for $\gamma D/S_u$=6). Therefore, the general use of k = 0.5 for clay may not be a good approach; will be very conservative for strong soils and very un-conservative for weak clay.

From Fig. 14, it also becomes clear that a k value could be reasonably selected based solely on the strength ratio. For each $\gamma D/S_u$, there is some variation being caused by differing levels of volume loss, but its impact is relatively small. The overall values of k for each $\gamma D/S_u$ are taken from Fig. 14, and graphed against $\gamma D/S_u$, as shown in Fig. 15. An equation describing the relationship between k and $\gamma D/S_u$ can then be acquired, as shown in Eq. (7).

Reference [3] supported a recommendation that k =0.5 could be used for clay. That study used clay with $\gamma D/S_u$=2.6. If this strength ratio is used in Eq. (7), a result of k =0.55 is obtained. Therefore, it can be said that the results of this study and this proposed equation correlate quite well with [3]. It should be noted however, that this equation is for soft clay, using for harder clay ($\gamma D/S_u$ < 1) will result in unrealistically low settlement trough parameters (k).

$$\frac{i_x}{H} = k = 0.5 ln\left(\frac{\gamma D}{s_u}\right) + 0.07 \qquad (7)$$

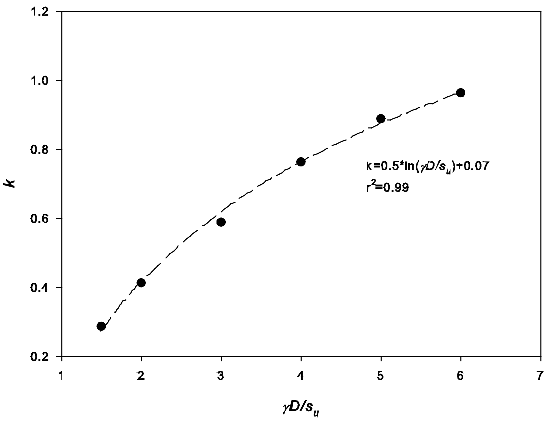

Fig. 15 Equation for practical estimation of *k*

CONCLUSION

A pressure relaxation approach has been developed to simulate a circular tunnel and the relaxation of the soil that occurs during construction. The stage of relaxation that induces collapse can be determined using outputs from the *FISH* script that automatically generates the mesh and outputs surface settlement data for each relaxation step. Using this, the settlement data at three previous 'pre-collapse' stages are exported to *MATLAB* where a Gaussian curve is fitted. This allows reliable estimation of i_x for all cases.

This study compares favorably with previous published results, and it is concluded that volume loss makes only a small difference to the resulting trough parameter. By using the O'Reilly and New relationship, a k value can be selected based purely on the soil strength ratio, $\gamma D/S_u$.

REFERENCES

[1] Peck, R.B., (1969). "Deep Excavations and Tunneling in Soft Ground". In: Proceedings of the 7th International Conference on Soil Mechanics and Foundation Engineering, Mexico City, State-of-the-art Volume, pp. 225-290.

[2] Ward, W., & Pender, M. (1981). "Tunnelling in soft ground: general report". Paper presented at the Proceedings of the 10th International Conference on

Soil Mechanics and Foundation Engineering, Stockholm.
[3] Mair, R. J., and Taylor, R. N. (1997). “Theme lecture: Bored tunnelling in the urban environment”. In Proc., 14th Int. Conf. on Soil Mechanics and Foundation Engineering, Hamburg, Balkema, Rotterdam, Netherlands, 2353–2385.
[4] Mair, R. (2008). “Tunnelling and geotechnics: new horizons”. Geotechnique, 58(9), 695-736.
[5] Rowe, R. K., Lo, K. Y., & Kack, G. J. (1983). “A method of estimating surface settlement above tunnels constructed in soft ground”. Canadian geotechnical journal, 20(1), 11-22.
[6] Sagaseta, C. (1987). “Analysis of undraind soil deformation due to ground loss”. Geotechnique, 37(3), 301-320.
[7] Loganathan, N., & Poulos, H. G. (1998). “Analytical prediction for tunneling-induced ground movements in clays”. Journal of Geotechnical & Geoenvironmental Engineering, 124(9), 846.
[8] Pinto, F., & Whittle, A. J. (2013). “Ground movements due to shallow tunnels in soft ground. I: Analytical solutions”. Journal of Geotechnical and Geoenvironmental Engineering, 140(4), 04013040.
[9] Gunn, M. J. (1993). “The prediction of surface settlement profiles due to tunneling”. In Predictive Soil Mechanics. Proceedings of the Wroth Memorial Symposium, 27-29 July, St Catherines College, Oxford.
[10] Taylor, R. (1998). “Modelling of Tunnel Behaviour”. Proceedings of the ICE-Geotechnical Engineering, 131(3), 127-132.
[11] Martos, F. (1958). “Concerning an approximate equation of the subsidence trough and its time factors”. In International strata control congress, Leipzig, 191-205.
[12] Atkinson, J. H., & Potts, D. M. (1977). “Subsidence above shallow tunnels in soft ground”. Journal of the geotechnical engineering division, 103(4), 307-325.
[13] Mair, R. J. (1979). “Centrifugal modelling of tunnel construction in soft clay”. PhD Thesis.
[14] Osman, A. S., Mair, R. J., & Bolton, M. D. (2006). “On the kinematics of 2D tunnel collapse in undrained clay”. Géotechnique, 56(9), 585-595.
[15] Attewell, P., & Farmer, I. (1974). “Ground deformations resulting from shield tunnelling in London Clay”. Canadian Geotechnical Journal, 11(3), 380-395.
[16] Cording, E. J., and Hansmire, W. H. (1975). “Displacement around soft ground tunnels”. General Report: Session IV, Tunnels in soil. In Proc., 5th Panamerican Congr. on Soil Mech. and Found. Engrg.
[17] O'reilly, M. P., & New, B. M. (1982). “Settlements above tunnels in the United Kingdom-their magnitude and prediction”. In Tunneling ’82. 173-181.
[18] Rankin, W. (1988). “Ground movements resulting from urban tunnelling: predictions and effects”. Geological Society, London, Engineering Geology Special Publications, 5(1), 79-92.
[19] Clough, G. W., & Schmidt, B. (1977). “Design and performance of excavations and tunnels in soft clay”. Dept. of Civil Engineering, Stanford University.
[20] Lee, C.J., Wu, B.R., Chiou, S.Y., (1999). “Soil movements around a tunnel in soft soils”. Proceedings of the National Science Council, Part A: Physical Science and Engineering 23 (2), 235–247.
[21] Guglielmetti, V., Grasso, P., Mahtab, A., & Xu, S. (Eds.). (2008). “Mechanized tunnelling in urban areas: design methodology and construction control”. CRC Press.
[22] Itasca Consulting Group Inc (2003). “FLAC User’s Manual”. Minneapolis, USA.
[23] Ghaboussi, J., Ranken, R. E., & Karshenas, M. (1978). “Analysis of subsidence over soft-ground tunnels”. Paper presented at the Evaluation and Prediction of Subsidence.
[24] Shiau, J.S., Lamb, B. R., and Sams, M.S. (2015). “Stability Charts for Unsupported Circular Tunnels in Cohesive Soils”. Submitted for consideration.
[25] Panet, M., & Guenot, A. (1983). “Analysis of convergence behind the face of a tunnel”. Tunnelling 82, proceedings of the 3rd international symposium, Brighton, 7–11 June 1982, P197–204. Publ London: IMM, 1982. Paper presented at the International Journal of Rock Mechanics and Mining Sciences & Geomechanics Abstracts.

EFFICIENCY OF SAND-NATURAL EXPANSIVE CLAY MIXTURE AS A HYDRAULIC BARRIER

Abdullah A. Shaker[1] and Tamer Y. Elkady [1 2]
[1] Eng. AbdullahBugshan Research Chair in Expansive Soils Civil Engineering Department, College of Engineering, King Saud University, Riyadh, Saudi Arabia

[2] Soil Mechanics and Foundation Research Laboratory, Faculty of Engineering, Cairo University, Giza, Egypt

ABSTRACT

The aim of this study is to evaluate the hydraulic performance of a sand-natural expansive clay mixture in comparison with sand-bentonite mixture. Natural expansive clay used in this study was obtained from Al-Qatif region, Saudi Arabia. The saturated hydraulic conductivity was evaluated for different mixtures of sand-Al Qatif clay with clay contents ranging from 10% to 60% clay. Similarly, the saturated hydraulic conductivity of sand-bentonite mixtures with different bentonite contents (0%, 5%, 10% and 20%) was also evaluated. All hydraulic conductivity tests were performed under different confining pressures. Test results revealed that sand-Al-Qatif clay mixtures can perform adequately as a hydraulic barrier; however, with Al-Qatif clay contents greater than that used for sand-bentonite mixtures. This is attributed to difference between clay mineralogy between Al-Qatif clay and bentonite. In addition a quantitative approach is proposed to assess the hydraulic conductivity of sand-Al-Qatif clay mixtures in comparison to that for sand-bentonite mixtures. Finally,soil fabric of mixtures was examined using scanning electron microscope (SEM) technique to observe differences in fabric between sand-Al-Qatif clay and sand-bentonite mixtures.

Keywords: Expansive clay, Hydraulic conductivity, Sand, Mixture, Barrier

INTRODUCTION

The rapid growth of oil industry in the eastern region of Saudi Arabia generates enormous quantities of hazardous wastes. In order to avoid the ground water contamination with these hazardous wastes provision of proper hydraulic barriers is of utmost importance. These barriers are usually constructed using sand-clay mixtures.Current practices employ construction of hydraulic barriers using mixture of high plastic expansive clay with sand. Bentonite is commonly used in these mixtures because of its high swelling potential that provide better sealing characteristics with small clay content (Chapuis. 1990).

The call for utilizing local resources is always well received as it provides an alternative to costly imported foreign materials.Several researchers investigated the use of natural clays as a hydraulic barrier. Rawas et al (2006) investigated the use of Oman shale in liners. Obrike et al (2009) investigated the use of some type of shale in waste disposal landfills in Nigeria. Langdon et al (1996) studied the permeability of clay liners of some geological formations and different depositional basins in Turkey.

General specifications of hydraulic barriers can vary from one project to another. Some tolerance on the amount of water to be allowed to pass can be considered. Daniel (1993) and Rowe et al (1995) suggested specifications for liner material in which the coefficient of hydraulic conductivity (cm/s) was put as ($10^{-6}< k <10^{-8}$).

The aim of this paper is to investigate the efficiency of a mixture of sand-Al Qatif (natural) expansive clay as a hydraulic barrier.The main efficiency criteria considered in this study is hydraulic conductivity. Test parameters considered in this study included clay content (10%, 20%, 30%, 40% and 60% by dry weight of sand and confining pressure (50, 100, 200 and 400 kPa). The relative performance of the proposed sand-Al-Qatif clay mixture with respect to sand bentonite mixtures with bentonite contents ranging from 5% to 20% by dry weight of sand was evaluated. In addition, SEM technique was used to examine the different fabrics emerged for sand-Al-Qatif clay and sand-bentonite mixtures at different clay contents.

MATERIALS

The sand used in this study was locallyprocessed sand which is typically used in concrete construction in Saudi Arabia. The grain size distribution of sand is presented in Fig. 1 and its specific gravity is 2.66.Values corresponding to coefficients of uniformity and curvature are C_u = 1.737 and C_c=1.078;respectively.

The naturalexpansive clay used in this study was sampledfrom the town of Al-Qatif. Al-Qatif, which is a historic, coastal oasis region located on the western shoreline of the Arabian Gulf in the Eastern Province of Saudi Arabia.Geotechnicaland mineralogical characterization of this expansive clay was documented by Dhowian et al. (1985), Abduljawad (1992) and Al-Shamrani et al. (2010). This expansive clay is considered highly expansive in nature due to the presence of high smectite mineral content (Azam, 2003). Soil samples were obtained from a test pit excavated to a depth of about three meters. Samples were transferred to laboratory for complete geotechnical, chemicaland mineralogical characterization. Tables 1 and 2 summarize the Geotechnical and chemical properties of Al-Qatif clay, respectively. Figure 2 shows the X-Ray diffraction X-Ray diffraction (XRD) intensity diagram. From this figure (Fig. 2), it is apparent that the main swelling clay minerals are montmorillonite and attapulgite (palygorskite).

The bentonite used in this study was sodium type obtained by a local supplier. Bentonite is commercially used as drilling mud for boring activities in Saudi Arabia. Tables 1 and 2 summarize the geotechnicaland chemical characteristics of bentonite, respectively. The mineralogical analysis of bentonite using XRD technique indicated that the main clay mineral is montmorillonite minerals along withquartz, feldspar and hematite minerals as shown in Fig. 3.

Table 1 Geotechnical characteristics of Al-Qatif clayand bentonite

Property	Al-Qatif Clay	Bentonite
	Index parameters	
Specific gravity, G_s	2.75	2.70
Liquid limit, LL (%)	140	480
Plastic limit, PL (%)	45	50
Plasticity index, PI (%)	95	430
USCS	CH[1]	--
	Swelling Characteristics	
Swelling pressure(kN/m^2)	550-600	--
Swelling potential(%)	16-18	--

[(1)]CH refers to clay with high plasticity

Table 2 Chemical composition of Al-Qatif clayand bentonite

Chemical Compound	Al-Qatif Clay	Bentonite
Na_2O	0.5	0.83
MgO	4.92	3.07
Al_2O_3	15.82	14.38
SiO_2	55.86	47.25
K_2O	5.22	0.57
CaO	1.74	3.87
FeO	9.39	21.36
ZnO	---	0.92

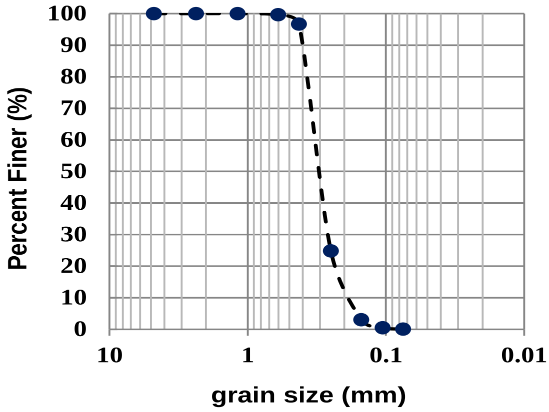

Figure 1: Grain size distribution of sand

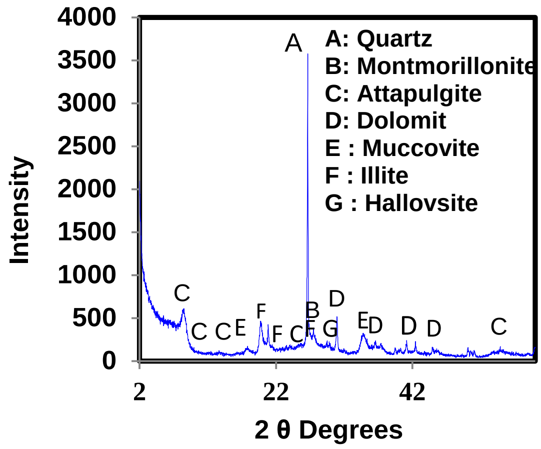

Figure 2: X-Ray diffraction of Al-Qatif clay

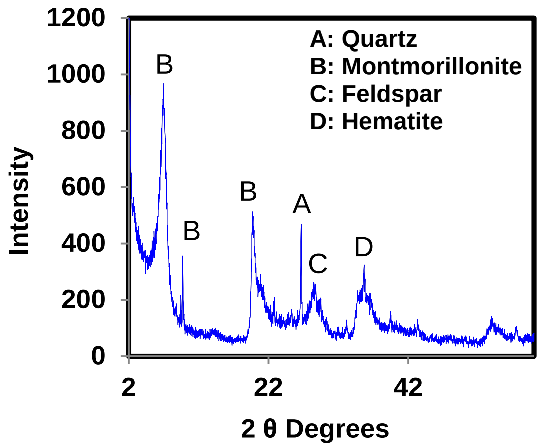

Figure 3: X-Ray diffraction of bentonite

TESTING METHODS

Sample Preparation of Mixtures

In this study, two types of mixtures were fabricated for the laboratory testing program. The first was sand-Al-Qatif expansive clay mixtures with clay contents of 0%, 10%, 20%, 30%, 40% and 60% by dry weight of sand. The second mixtures were sand-bentonite with bentonite contents of 0%, 5%, 10% and 20% by dry weight of sand. The sand-bentonite mixture was used to provide basis of comparison for the sand-Al-Qatif clay mixtures.

The natural expansive clay (Al-Qatif) obtained from the field was air-dried, pulverized and sieved using sieve No. 40 to form clay powder. Desired proportions of oven-dried sand and powder clay (whether Al-Qatif or bentonite) were hand mixed under dry conditions to obtain a homogenous blend. Desired water content was then added and mixed thoroughly and stored in plastic bags overnight in humid environment to allow time for the soil particles to hydrate as recommended by ASTM D 698 (2000) Test samples were statically compacted to initial molding conditions corresponding to maximum dry unit weight and optimum moisture content for each sand-clay mixture. Final dimensions of samples were 70 mm in diameter and 34 mm high for hydraulic conductivity tests.

Index Properties of Mixtures

The basic index properties of sand-Al-Qatif clayand sand-bentonitemixtures were evaluated for different clay contents. Tests performed included specific gravity tests (ASTM D854-02) and Atterberg limits (ASTM D 4318-00). Specific gravity values are summarized in Table 3.As shown in Table 3, a notable increase in specific gravity with increase in clay content. The liquid limit, plastic limit and plasticity index values for sand-Al-Qatif clay and sand-bentonite mixtures at different clay contents, are presented in Tables 4and 5; respectively.

Table 3 Specific gravity values for different sand-Al-Qatif clay and sand-bentonite mixtures

Clay Content (%)	Specific Gravity	Bentonite Content (%)	Specific Gravity
0	2.66	0	2.66
10	2.67	5	2.67
20	2.67	10	2.68
30	2.68	20	2.7
40	2.68		
60	2.69		

Table 4 Atterberg limits of sand-Al-Qatif clay mixtures

Clay content (%)	LL (%)	PL (%)	PI (%)
0	NA	NA	NA
10	NA	NA	NA
20	29	17.6	11.4
30	36	18.5	17.5
40	43	19.9	23.1
60	60	22.2	37.8

Table 5Atterberg limits of sand-bentonite mixtures

Bentonite content (%)	LL (%)	PL (%)	PI (%)
0	NA	NA	NA
5	NA	NA	NA
10	36	23.6	12.4
20	62	27	35

Compaction Curves for Mixtures

The compaction curves for all sand-Al-Qatif mixtures and sand-bentonite mixtureswere carried out in accordance with standard proctor compaction method (ASTM D698 - 00). Figures 4 and 5 show the variation of compaction curves as a function of clay content for sand-Al-Qatif clay and sand-bentonite mixtures; respectively.For sand-Al-Qatif clay mixtures (Fig. 4), it is apparent that as, the clay content increases,the maximum dry unit weight increasesreaching a peak value between 20% and 30% clay content. However, as the clay content increased beyond this value (i.e., 25%), the maximum dry unit weight decreases with increase in clay content. Similar trend was observed for sand bentonite mixtures (Figure 5) with the peak value of maximum dry unit weight observed at 10% bentonite content. These compaction curves will be used to determine the initial molding conditions considered in this study.

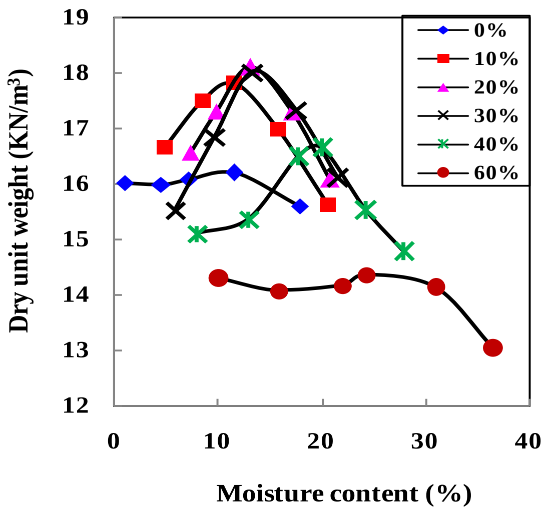

Figure 4: Compaction curves of sand-Al-Qatif claymixtures with different clay contents

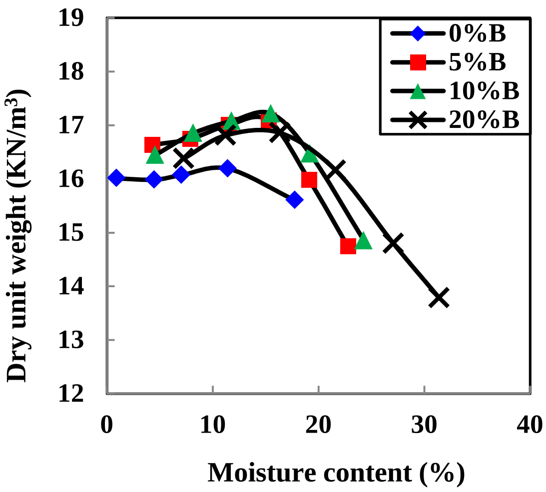

Figure 5: Compaction curves ofsand-bentonitemixtures with different bentonite contents

Hydraulic Conductivity Test

Thesaturated hydraulic conductivities of sand-Al-Qatif clayand sand-bentonitemixtures were evaluated using flexible wall constant head permeameter. Confining pressures considered in this test series rangedfrom 50 to 400 kPa.Tests were performed under constant tin accordance with ASTM D5084 (2003). This procedure includes four test stages: specimens soaking, backpressure saturation, consolidation and permeation. Permeation through the test samples was conducted under a constant hydraulic gradient (i)of 30.

DISCUSSION AND TEST RESULTS

A comparison of hydraulic conductivities of evaluated for sand-Al-Qatif clayand sand-bentonite mixtures are presented in Fig.6. From this figure, it is observed that the hydraulic conductivity of sand-bentonite mixtures is much lower than that for sand-Al-Qatif claymixtures. This is attributed to differences in clay mineralogy between Al-Qatif and bentonite clay. In other words, bentonite has a high swelling ability due to the presence of high percentage of montmorillonite mineral as compared to Al-Qatif clay.This swelling ability promote the the better sealing of sand voids even under low clay content.

Furthermore, it is noted that sand-bentonite mixtures with 5% bentonite content can produce a hydraulic conductivity equivalent to that of 30% Al-Qatif clay content, also the 10%, 20% bentonite content can produce a hydraulic conductivity equivalent to that of 40%, 60% Al Qatif clay content; respectively. Sand-Al-Qatif clay mixtures with clay contents greater than 40% can match the hydraulic conductivity requirementsof hydraulic barrier ($K=10^{-7}$ cm/s) as shown in Fig. 6.

To quantitatively assess the hydraulic conductivity of sand-Al-Qatif clay mixtures in comparison to that for sand-bentonite mixtures, a simple index termed hydraulic conductivity performance ratio (HCPR) was proposed and is defined as follow:

$$(\text{HCPR}) = \frac{Log(K\ of\ _{\text{sand-Al\_Qatif clay}})}{Log(K\ of\ _{\text{sand-bentonite}})} \quad (1)$$

The HCPR of sand-Al-Qatif clay mixtures are summarized in Table 6 for samples at 10% and 20% clay content. From this table, it is noted that the hydraulic conductivity performance ratio depends on confining pressure and ranges between 0.48 and 0.59.

Table 6 Hydraulic conductivity performance ratio of sand-Al-Qatif claymixture at 10% and 20% clay content

Confining Pressure (kPa)	Performance ratio (HCPR) of mixture	
	10%	20%
50	0.57	0.48
100	0.57	0.48
200	0.56	0.5
400	0.59	0.5

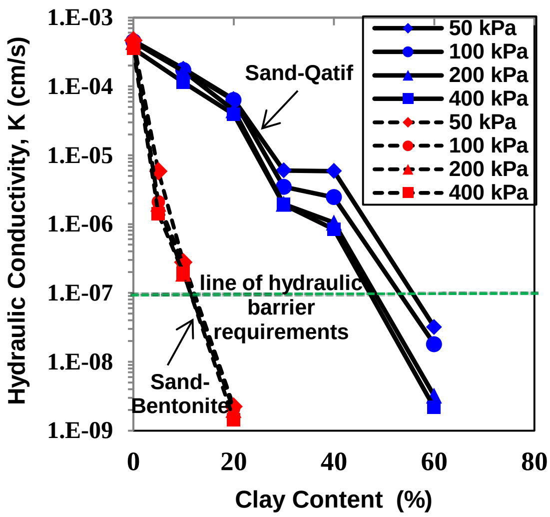

Figure 6: Variation of hydraulic conductivity of sand-Al-Qatif clay mixtures and sand-bentonitemixtures with clay content

SEM Investigation

The fabric of sand-Al-Qatif clayand sand-bentonite mixtures was observed using scanning electron microscope (SEM) technique. SEM was performed using Joel apparatus (Model JSM-6380 LA). Micrographs of SEM investigations for both mixtures at 20% clay content are shown in Figs 7 and 8 for sand-Al-Qatif clayand sand-bentonite mixtures; respectively. From these micrographs, it was observed that, for sand-Al-Qatif claymixtures clay partially filled the void and coated the sand grains while grain-to-grain contacts are maintained which, in turn, control the behavior of the mixture. Micrographs for sand-bentonite mixture with same clay content (i.e., 20%) showed that the clay particle assemblages were observed to occupy the voids between sand grains and develop connectors between sand grains. This leads to a significant reduction in hydraulic conductivity of sand-bentonite mixtures Compared to the hydraulic conductivity of sand-Al-Qatif claymixture at same clay content.

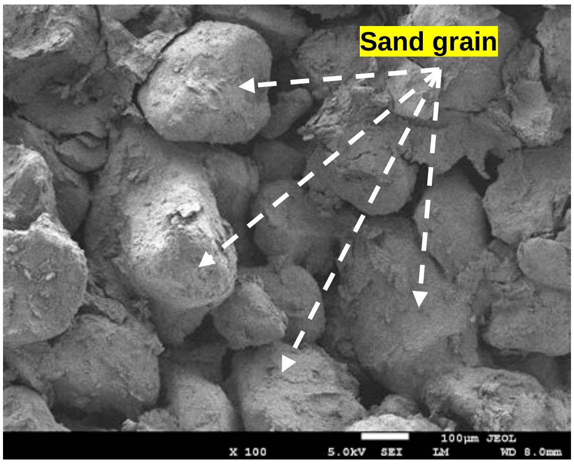

Figure 7: SEM of sand-Al-Qatif claymixtures mixture with 20% clay content

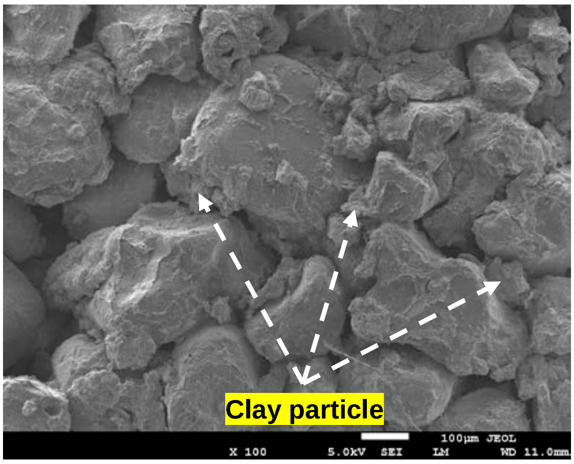

Figure 8: SEM of sand-bentonite mixtures mixture with 20% clay content

CONCLUSIONS

Based on this investigation, the following conclusions can be derived:

1- The clay content had a significant impact on the hydraulic conductivity of sand-Al-Qatif clay mixtures; whereas, confining pressure was observed to have a pronounced effect on K at clay contents greater than 30%.

2- The hydraulic conductivity of sand-bentonite mixtures was to be much lower than that for sand-Al-Qatif clay mixtures. This difference is attributed to the difference in clay mineralogy of Al-Qatif and bentonite clay.

3- The HCPR proposed in this study can be used as a quantitative approach to evaluate the hydraulic conductivity of sand-natural clay mixtures with respect to that of sand-bentonite mixtures. The HCPRfor sand-Al-Qatif clay ranged between 0.48 and 0.59.

4- The SEM investigation for sand-Al-Qatif clay mixtures showed thatthe part of the clay particles reside in the voids between the sand grains at clay contents 20%. As for sand-bentonite mixtures at the same clay content observed, the gaps between sand grains are hardly visible and filled with clay causing a significant decrease in hydraulic conductivity.

5- Al-Qatif clay was found to satisfy the hydraulic conductivity requirements for liners when 40 % clay or more is used.

ACKNOWLEDGEMENTS

This paper was financially supported by King Saud University, Vice Deanship of Scientific Research Chairs.

REFERENCES

[1] Abduljauwad, S N, "Characterization and chemical treatment of Expansive clay in AlQatif.", International Journal of Rock Mechanics and Mining Sciences &Geomechanics Abstracts, Volume 29, Issue 4, July 1992, Page 226.

[2] Al-Shamrani, M.A., Mutaz,E., Puppala, A.J., and Dafalla, M.A. "Characterization of Problematic Expansive Soils from Mineralogical and Swell Characterization Studies.".American Society of Civil Engineers,Geoflorida, Florida, 2010, No.199, pp. 793-802.

[3] ASTM D854-02. “Standard test methods for specific gravity of soils.” Annual book of

ASTM standards, section 4, vol. 04.08, Soil and rock; Building stones, ASTM, PA

[4] ASTM D 698-00. “Standard Test Methods for Laboratory Compaction Characteristics of Soil Using Standard Effort.” Annual Book of ASTM Standards, Section 4, vol. 04.08, Soil and Rock; Building Stones, ASTM, PA.

[5] ASTM D4318-00. “Standard Test Methods for Liquid Limit, Plastic Limit, and Plasticity Index of Soils.” Annual Book of ASTM Standards, Section 4, vol. 04.08, Soil and Rock; Building Stones, ASTM, PA.

[6] ASTM D5084-03. “Standard Test Methods for Measurement of HydraulicConductivity of Saturated Porous Materials Using a Flexible Wall Permeameter.”American Society for Testing and Materials, West Conshocken, PA.

[7] Azam. S, Influence of mineralogy on swelling and consolidation of soils in eastern Saudi Arabia. Can Geotech J, 2003, 40(5):964–975.

[8] Chapuis, R.R. “Sand-bentonite liners; Predicting permeability from laboratory tests.” Canadian Geotechnical Journal, 1990, 27, 47–57.

[9] Daniel, D.E, "Geotechnical practice for waste disposal."Chapman and Hall, London, 1993.

[10] Dhowian, A.W., Ruwiah, I., AndErol, A."The Distribution and Evaluation of the Expansive Soils in Saudi Arabia."2nd Saudi Engineering Conference, KFUPM, Dhahran, Vol.4, 1985.

[11] Langdon, N.J., Al Hussaini, M.J.,Walden,P.J., and Sangha, C.M, “An assessment of permeability of clay liners: two case histories”. Geological society,London, Engineering Geology Special publications, 1996.

[12] Obrike, S.E., Osadebe, C.C., and Omoniyi, S.S, "Geotechnical analysis of two Nigerian soils for use as clay liners."Bulletin of Engineering Geology and the Environment, 2009, Volume 68, issue 3, p. 417 – 419.

[13] Rawas,A.A.,Yahiae, A.M., Abdulaziz, S.A., and Salem, A. "sand–attapulgite clay mixtures as a landfill liner."Geotechnical and Geological Engineering, 2006, 24: 1365–1383.

[14] Rowe RK, Quigley RM, Booker JR,"Clayey barrier systems for waste disposal facilities". E and FN Spon, 1995.

MECHANICAL PROPERTY OF SAND CEMENTED WITH CALCIUM PHOSPHATE COMPOUNDS USING PLANT–DERIVED UREASE

R.A.N. Dilrukshi[1], Jun Watanabe[1] and Satoru Kawasaki[2]
[1]Graduate School of Engineering, Hokkaido University, Sapporo 060-8628, Japan
[2]Faculty of Engineering, Hokkaido University, Sapporo 060-8628, Japan

ABSTRACT

The effect of plant-derived urease enzyme to induce the precipitation of calcium phosphate compounds (CPCs) and hence to improve the unconfined compressive strength (UCS) of sand was examined as a novel, eco-friendly ground improvement method. Initially, Toyoura sand test pieces were cemented only from CPC solution. Furthermore, another sand test pieces were cemented by different concentrations of urea, concentration fixed plant seed extract (Watermelon) to obtain optimal cementation and different concentrations of CPC solutions made from calcium and phosphate stock solutions. All test pieces were cured up to 28 days in an airtight container at high humidity at 25ºC. The UCS tests and scanning electron microscope (SEM) observations of sand test pieces were carried out. The UCS of test pieces cemented with CPC and plant extract were significantly higher than that of test pieces cemented without plant extract and increases with time. The best ratio of Ca: P in CPC solution was 0.75 M: 1.5 M, reaching a maximum UCS of 125.6 kPa after 28 days of curing. In addition, pH concentration was measured after UCS test and it has increased with time. Results indicate that the best pH for optimal cementation is 8.0. A specific crystal structure could not be identified from SEM observations in the segments of the test pieces cemented with CPC in all cases in this study. These results suggest that the addition of plant extract to CPC significantly enhances the mechanical properties of sand.

Keywords: Plant-based Urease, Calcium Phosphate Compound, Unconfined Compressive Strength, Ground Improvement

INTRODUCTION

In recent years, development of infrastructures with scarcity of useful land has become a major issue and the engineers are compelled to resolve the problem. Possible alternative solutions may be one of among as avoid the particular land, removal/ replace unsuitable soils, designing the planned structures (flexible/ rigid), and modifying existing ground using ground improvement techniques. However, currently, the engineers are focusing on modifying existing ground using ground improvement techniques by ensuring sustainability in land use. Ground improvement refers to a technique that improves the engineering properties of the soil mass treated and hence to enhance bearing capacity of soil for successful foundation design and use as a countermeasure against natural disasters, including ground liquefaction of saturated sand.

Currently, ground improvement techniques such as grouting via cement, chemical, compaction, fracture and jet, micro piles, jacked piers, driven piers, ground anchors, shoring, soil nailing, vibro compaction, concrete columns, piers, etc. are practicing widely [1]. However, these techniques are related with major environmental issues such as large CO_2 emissions during cement production, and high energy cost for cement production and re-excavation of cement improved ground. Therefore, in recent years, biogrout- based ground improvement practices have been introduced.

The process of using biological means to obtain ground improvement is known as biogrouting [2]. Different mineral formation mechanisms are involved in the formation of biogrouts. Carbonate precipitation using urea and ureolytic bacteria [3] or urea and purified/crude extracts of plant species having urease activity [4]-[6] or using glucose and yeast [7], iron/manganese compound precipitation though iron-oxidizing bacteria [8], siloxane bond formation using glucose and yeast [9], calcium phosphate compound (CPC) based chemical grouts (CPC-Chem) formation by its self-setting mechanism [10], CPC biogrout (CPC-Bio) formation in relation to the addition of ureolytic microorganisms and an ammonia source to CPC-Chem [11]. The solubility of CPC-Bio which is generated as a result of the biological action is dependent on its pH (Fig.1 and Table 1) [12]. CPC-Chem is easy to obtain, safe to handle, non-toxic, and can be recycled in the form of a fertilizer. These advantages make it suitable for geotechnical applications [10]. When CPC-Chem was converted to CPC-Bio by the addition of urease producing microorganisms and an ammonia source, the unconfined compressive strength (UCS) increased from 42.9 kPa to 57.6 kPa [11].

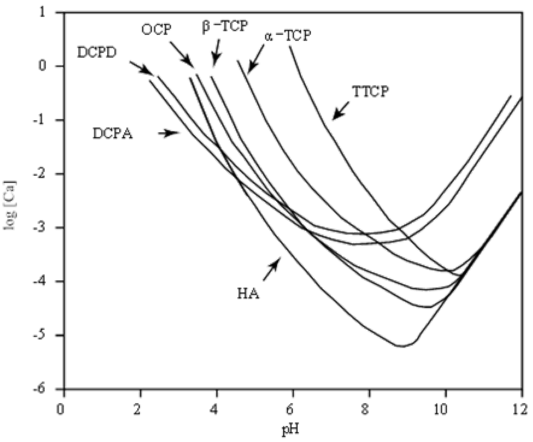

Fig. 1 Solubility phase diagrams for the ternary system, $Ca(OH)_2$-H_3PO_4-H_2O, at 25^0C, showing the solubility isotherms of $CaHPO_4$ (DCPA), $CaHPO_4.2H_2O$ (DCPD), $Ca_8H_2(PO_4)_6$. $5H_2O$ (OCP), α-$Ca_3(PO_4)_2$ (α-TCP),β-$Ca_3(PO_4)_2$ (β-TCP), $Ca_4(PO_4)_2O$ (TTCP), and $Ca_{10}(PO_4)_6.(OH)_2$ (HA) [12].

Table 1 Biologically relevant calcium orthophosphates [13]

Ca/P ratio	Compound	Abbreviation
0.5	Monocalcium phosphate monohydrate ($Ca(H_2PO_4)_2.H_2O$)	MCPM
0.5	Monocalcium phosphate anhydrate ($Ca(H_2PO_4)_2$)	MCPA
1	Dicalcium phosphate dihydrate ($CaHPO_4.2H_2O$)	DCPD
1	Dicalcium phosphate anhydrate ($CaHPO_4$)	DCPA
1.33	Octacalcium phosphate ($Ca_8(HPO_4)_2(PO_4)_4.5H_2O$)	OCP
1.5	A-tricalcium phosphate (α- $Ca_3(PO_4)_2$)	α-TCP
1.5	B-tricalcium phosphate β- $Ca_3(PO_4)_2$	β-TCP
1.2-2.2	Amorphous calcium phosphate ($Ca_x(PO_4)_y.nH_2O$)	ACP
1.5-1.67	Calcium-deficient hydroxyapatite ($Ca_{10-x}(HPO_4)x(PO_4)_{6-x}(OH)_{2-x}$) ($0<x<1$)	CDHA
1.67	Hydroxyapatite ($Ca_{10}(PO_4)_6(OH)_2$)	HA
2	Tetracalcium phosphate ($Ca_4(PO_4)_2O$)	TTCP

The purpose of this study was to discover a plant species that contains urease activity unrelated to ureolytic microorganisms. This activity can then be used to increase the pH that is favorable for CPC precipitation by catalyzing the hydrolysis of urea, which can then use to precipitate CPC and increase the UCS of small scale, cylindrical Toyoura sand test pieces more than 100 kPa, which is the required strength for mitigating ground liquefaction [14].

SELECTION OF A PLANT-DERIVED UREASE SOURCE FOR CPC PRECIPITATION

The importance of urease enzyme is to catalyze the reaction of urea hydrolysis to form ammonium ion (NH_4^+) and carbonate ion (CO_3^{2-}) (Eq. (1)). The NH_4^+ and CO_3^{2-} produced from this reaction represent the final products of the reaction. However NH_4^+ ions actually start out as NH_3. When NH_3 reacts with water, it creates OH^- ions, which raise the pH of the system. A number of common plant families are very rich in urease; for example, melons and squash, the pine family, bean varities [15] such as Jack beans (*Canavalia ensiformis*), soybean (*Glycine max*) leaf and seed, pigweed (*Chenopodium album*) and mulberry leaf (*Morus alba*) [16].

$$CO(NH_2)_2 + 2H_2O \rightarrow 2NH_4^+ + CO_3^{2-} \quad (1)$$

In this study, we investigated urease active plant species to increase the pH that is favorable for CPC precipitation. Hence, initially, we studied three types of plant seeds in cucurbit family such as watermelon, melon and pumpkin. Out of them, a solution made by dissolving 0.08 g of urea in 3.44 mL of watermelon seed extract (prepared by soaking 1g of crushed seeds about 30 min. in 10 mL of distilled water) showed pH value ranging from 8.5 to a constant value of 9.5 within 1 hour. This range of pH is favorable for CPC precipitation (See Fig. 1), and therefore, watermelon seeds were selected for further investigations of this study.

MATERIALS AND METHODS

Chemical reagents such as calcium acetate-$Ca(CH_3COO)_2$ (CA), and dipotassium phosphate-K_2HPO_4 (DPP) was used as CPC chemicals. Urea was selected as the ammonia source and watermelon seeds (*Citrullus vulgaris*) that leftover as food waste were used for catalyzing the hydrolysis of urea. Seed extract was prepared by soaking crushed seeds in water or another liquid as required, about 30 min. and collecting the filtrate. Toyoura sand with particle density ρ_s = 2.64 g/cm^3, minimum density ρ_{min} = 1.335 g/cm^3, maximum density ρ_{max} = 1.645 g/cm^3, mean diameter D_{50} = 170 μm was used for UCS test specimen preparation. The final concentrations of CA: DPP = 0.75 M: 1.5 M and CA: DPP = 0.75 M: 0.75 M, which have yielded largest UCS at the initial investigation were used for further investigations of this study.

Initially, the pH variability in relation to different concentrations of plant seed extract (different solid-liquid ratios) and urea was investigated to ascertain optimal concentrations for maximum CPC precipitation. Solid-liquid ratio (dry weight of crushed seeds, (g) /volume of liquid, (mL)) ranging from 0.0005 to 0.005 were selected and prepared in a CA solution with 0.75 M. Amount of urea ranging from 0.08 g to 0.8 g was selected and dissolved in a DPP solution (0.75 M and 1.5 M). Small scale sample mixtures consisting of 15 g of Toyoura sand, 1.72 mL of plant seed extract prepared using CA solution and 1.72 mL urea solution made by dissolving urea in 1.72 mL DPP solution were used for the pH determination. Hence, the final volume of the solution was 3.44 mL.

Ca^{2+} ion concentration in a CPC solution gives an indication about CPC precipitation. A low Ca^{2+} ion concentration in the solution indicates high CPC precipitation rather than high Ca^{2+} ion concentration. Therefore, Ca^{2+} ion concentration in a mixture consisted with CPC- Chem, seed extract and urea was measured with time using a Ca^{2+} ion meter to get an indication about CPC precipitation with time. Best solution mixture that gives favorable pH from first investigation explained in above paragraph was considered for assessing Ca^{2+} ions. According to that, 5 mL of plant seed extract having best solid-liquid ratio, was prepared using CA solution with 0.75 M and 5 mL urea solution was made by dissolving urea in 5 mL of DPP solution (0.75 M and 1.5 M). Hence, the volume of the final solution was 10 mL. Ca^{2+} ion concentration of prepared solution was measured just after mixing, after 1 day, 3 days, 7 days, 14 days, and 28 days. Controls were prepared using only CPC solution for the comparison purpose and measured Ca^{2+} ion concentration with time.

Urease activity test was conducted according to a method based on conductivity [17]. Conductivity was measured using a conductivity meter to investigate the change in urease activity using different solid-liquid ratios of seed extract and urea. Urea dissolved in 10 mL of distilled water was mixed with 10 mL of seed extract and the final mixture with the volume of 20 mL was used for measuring conductivity and hence to calculate urease activity of watermelon seed extract contacted with urea.

After completing basic investigations, such as pH variability test, Ca^{2+} ion measurement and urease activity test, best solid-liquid ratio and amount of urea were selected to prepare of test specimens for UCS test. As mentioned above, CA with 0.75 M and DPP with 0.75 M and 1.5 M concentrations were selected to prepare of test specimens for UCS test. Crushed seeds were soaked in the concentration known CA solution by maintaining required solid-liquid ratio. The required weight of urea, which had been weighted in advance, was then dissolved in the concentration known DPP solution. A volume of 36.65 mL from both the seed extract in the CA solution and the urea in the DPP solution were added to 320.09 g of Toyoura sand. The mixture was uniformly mixed in a stainless steel ball for 2 min and then divided into quarters. Each quarter was then placed in to a plastic mold (inner diameter φ = 5 cm, height h = 10 cm). The inner wall of each mold was covered with an overhead projector sheet (0.1 mm thick) to avoid any disturbance of the test pieces during their removal from the mold. The mixture was tamped down 30 times by a hand rammer when each quarter was filled into the mold. Finally, the upper edges of the test pieces were slightly trimmed so that they were flat, and covered with Parafilm M (Structure Probe, Inc., West Chester, PA) to avoid desiccation. The molded test pieces were subsequently cured in an airtight container at high humidity. After curing, test pieces were removed carefully from the mold, and the UCS of the test pieces was measured with a UCS apparatus T266-31100 (Seiken-sha Co. Ltd., Japan) at an axial strain rate of 1% /min. All test pieces were prepared, cured and tested at 25 ºC. Two test pieces were made for each test case under same condition, in order to investigate the repeatability of measurements of UCS test. The pH of the test pieces was calculated as an average of three measurements (at the top, bottom, and middle of each test piece) using a pH Spear (Eutech Instruments Pte., Ltd., Singapore).

RESULTS AND DISCUSSION

According to the results of pH variability with different amount of urea and solid-liquid ratio, pH was increased and became constant with time and it has shown favorable pH for CPC precipitation, in the mixture of 0.08 g of urea and 0.005 of solid-liquid ratio.

Ca^{2+} ion concentration of the mixture of CPC solution consisted with 0.233 g urea (0.08 g*5 mL/1.72 mL) instead of 0.08 g of urea used in pH variability test, and 0.005 of solid-liquid ratio was decreased gradually with the time and that indicated the increment of the precipitation of CPC with time. The behavior of control solutions were similar and decrement rate with the time was low compared with the solution consisted with urea and seed extract. Furthermore, this investigation showed that CPC precipitation was closely related with pH. As an example, Ca^{2+} ion concentration with time in the test case only with CPC (CA = DPP = 0.75 M) and the test case with CPC (CA = DPP = 0.75 M), urea and seed extract are shown in Fig. 2. According to the Fig. 2, low Ca^{2+} ion concentration (high CPC precipitation) could be expected with urea and seed extract rather than using CPC only. The reason to get high precipitation is the availability of favorable pH for CPC precipitation. (See Fig. 1). Moreover, the precipitation of CPC could be observed in the solution only with CPC. However the amount and the rate of precipitation were low compared with CPC having urea and seed extract due to low pH (pH around 6). There is a tendency to solubilize CPC at pH around 6 rather than the pH in the range of 8-9 (See Fig.1).

Urease activity values of the mixture of watermelon seed extract and urea are presented in Table 2.

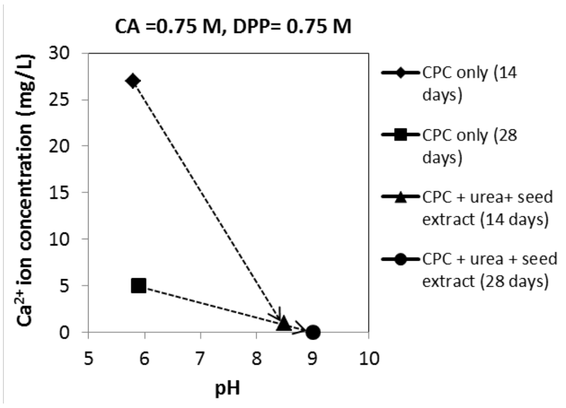

Fig.2 Temporal variation of Ca^{2+} ion concentration

Table 2 Quantitative values of urease activity

Case No.	Weight of urea (g)	Solid/liquid ratio	Conductivity (mS/cm)	Urease activity (u/L)
1	4.65	0.005	0.0438	520.54
2	2.33	0.005	0.0617	733.28
3	0.93	0.005	0.0608	722.58
4	0.465	0.005	0.0722	858.06
5	0.0465	0.005	0.0798	948.39
6	4.65	0.0025	0.0149	177.08
7	4.65	0.0005	0.0013	15.45

As shown in Table 2, when the urea content increased then the urease activity decreased and when the solid-liquid ratio of the seed extract was increased, the urease activity increased. Furthermore, best combination of urea and seed extract (0.08 g of urea/1.72 mL and 0.005 of solid/liquid ratio) selected from pH variability test showed a high urease activity from urease activity test (Case No. 4 in Table 2).In Case No. 4, weight of urea was 0.465 g instead of 0.08 g to match the concentration of urea (0.08 g*10 mL/1.72 mL). It is clear that the property of urease activity supported to increase the pH by catalyzing urea in to NH_4^+ and CO_3^{2-}.

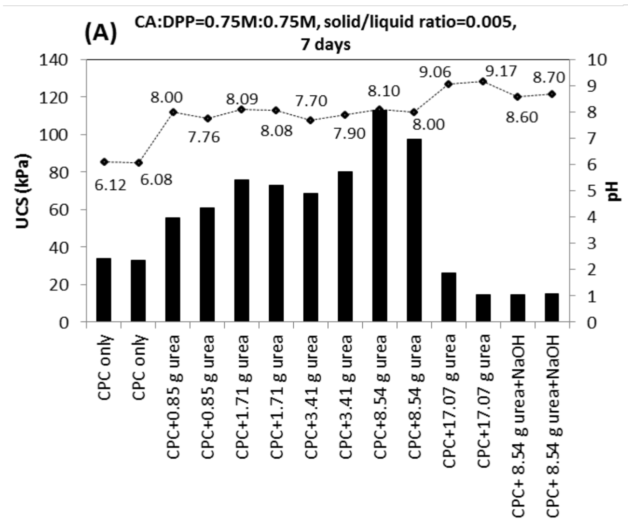

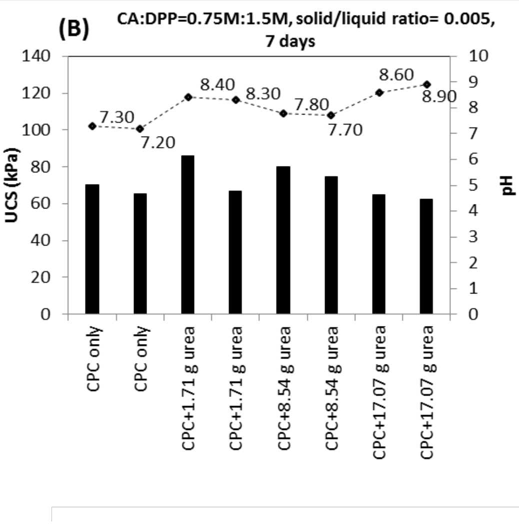

Fig.3 Effect of pH on UCS

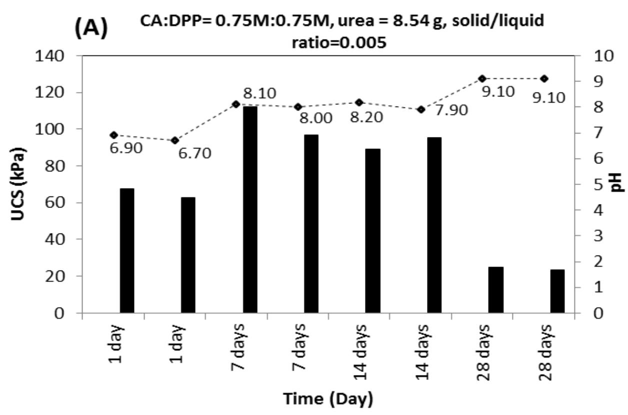

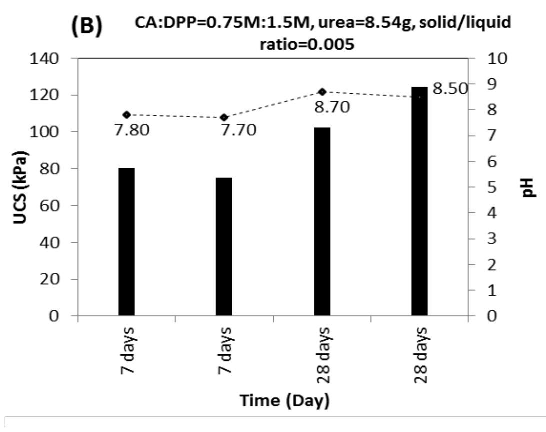

Fig.4 Temporal variation of UCS

Finally, the UCS test was conducted for the test specimens made using best combination of urea and seed extract. According to that, 1.71 g (0.08g * 36.65 mL /1.72 mL) was used to prepare the first UCS test pieces and later, more test pieces were made by changing urea in the range of 1.71 g-17.07 g to observe the behavior of UCS. As shown in Fig.3 (A), while using CA = DPP = 0.75 M, the increment of urea caused to increase the UCS up to certain level and afterward increment of urea caused to decrease the UCS. When the maximum UCS achieved was decreased by adding more urea, the pH of the sample has changed from around 8 to more than 9. It was clear that an increase of urea caused the release of greater number of NH_4^+ ions in relation to urea hydrolysis, and that caused an increase in the pH of the specimen that was unfavorable for CPC precipitation. It was thus ascertained that the UCS value has been decreased after a certain level of urea was used. The maximum value of UCS was obtained after 7 days with 8.54 g of urea. At the same way, while using CA: DPP = 0.75 M: 1.5 M, the behavior of UCS was observed by changing the amount of urea. The maximum average value of UCS was obtained after 7 days with 8.54 g of urea (Fig.3 (B)) as in the case with CA = DPP = 0.75 M. We therefore further considered temporal variations in values of the UCS using 8.54g of urea for both cases (CA = DPP = 0.75 M and CA = 0.75 M, DPP = 1.5 M) (Figs. 4 (A) and 4 (B)). In the case of CA = DPP = 0.75 M, the UCS began to gradually decreased after 14 days and dramatically decreased after 28 days. The pH of the test pieces after 28 days was more than 9. That was unfavorable for precipitating CPC relevant to CA = DPP = 0.75 M that means Ca/P = 1. The possible precipitates are DCPA and/or DCPD (See Table 1). Unfavorable pH caused to decrease the UCS value dramatically after 28 days. Furthermore, the decrease of the UCS after 14 days was not related to the value of pH. As we mentioned earlier, it is possible to precipitate two CPCs in the case of Ca/P ratio of 1. The solubility of DCPD is higher than that of DCPA for the same value of pH and this could thus cause a decrease in UCS after 14 days rather than 7 days, even if both cases indicated nearly the same pH values (See Fig. 4 (A)). In case of CA = 0.75 M and DPP = 1.5 M, the pH value of the test pieces increased and pH of around 8 was observed after 28 days. This favorable pH caused to precipitate maximum CPC. In this respect, the UCS value increased with time and had a value of more than 100 kPa after 28 days by achieving our goal.

According to the compressive stress (σ) – strain (ε) curves for the test pieces made using 8.54 g of urea, (Fig. 5) to study the temporal variations of the UCS, the two stress- strain curves obtained for two identical test pieces made at each test case showed almost the same behavior in terms of shape. Furthermore, the compressive strain (ε) was decreased and moved leftward, and Young's modulus increased with the increments of UCS. A comparison of all the stress (σ) - strain (ε) curves in relation to the maximum UCS values, shows a distinctive peak at approximately 2% of the failure strain. The above discussion confirms that the aim of this study was achieved after 28 day curing period with CA: DPP = 0.75 M: 1.5 M in relation to the use of seed extract at solid-liquid ratio of 0.005 and 8.54 g of urea for 320.09 g of Toyoura sand.

CONCLUSION

The efficacy of plant-derived urease enzyme (watermelon seed extract) to induce the precipitation of CPC-Bio and hence to improve the UCS of sand was examined in small scale, cylindrical, laboratory samples. The results show that,

- the UCS of more than 100 kPa was achieved after 28 days, due to generated CPC-Bio with the help of CA: DPP = 0.75 M: 1.5 M in relation to the use of watermelon seed extract at a solid-liquid ratio of 0.005 and 8.54 g of urea for 320.09g of Toyoura sand.

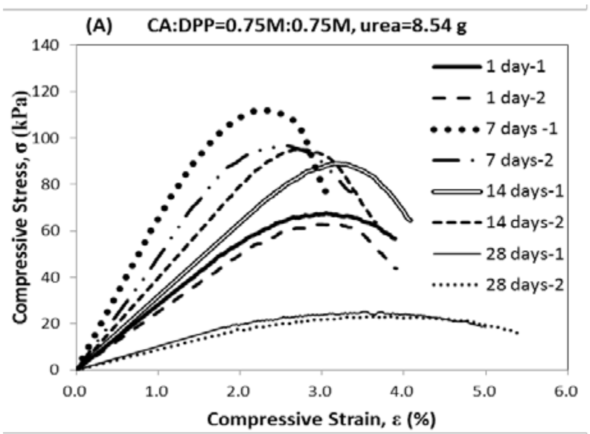

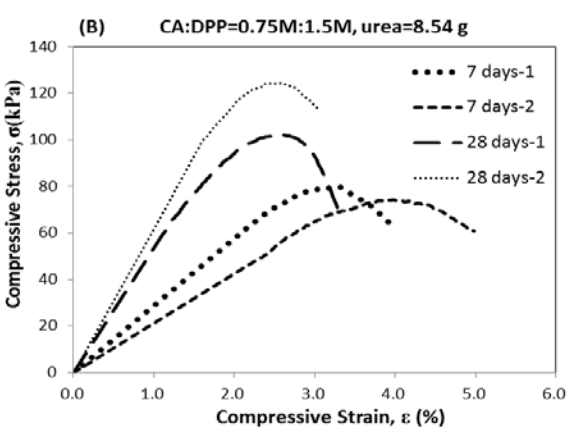

Fig.5 Compressive stress (σ) - compressive strain (ε) curves of test pieces with different curing time (Day) – (Solid/liquid ratio =0.005)

- the pH was the governing factor to precipitate CPC as CPC-Bio and watermelon seed extract having urease activity helps to increase the pH by catalyzing the process of urea hydrolysis and best pH observed for optimal cementation was around 8.0.

According to the results of this study, plant urease- induced CPC precipitation technique has the potential to be utilized as an environmental friendly grouting material to respond to soil liquefaction by improving the ground. In addition to the geotechnical engineering issues, knowledge gathered from this technique may also provide satisfactory solutions for solving problems in the fields of geoenvironmental and rock engineering. However, the relationship between the strength and the various CPC precipitation parameters such as concentration and pH of reaction mixture, and long term curing time should be examined and understood more clearly in further to facilitate practical applications.

ACKNOWLEDGEMENTS

The work was partly supported by a Grant-in-Aid for Scientific Research (No. 24300299) from the Japanese Ministry of Education, Sports, Science, and Technology; this support is gratefully acknowledged.

REFERENCES

[1] Karol RH, “Chemical grouting and soil stabilization”, 3rd ed., CRC Press, Boca Raton, FL, 2003.

[2] Van Paassen LA, Harkes MP, Van Zwieten GA, Van der Zon WH, Van der Star WRL and Van Loosdrecht MCM, in Proc. 17th Int. Conf. on Soil Mechanics and Geotechnical Engineering, 2009, pp. 2328-2333.

[3] Harkes MP, Van Paassen LA, Booster JL, Whiffin VS and Van Loosdrecht MCM, “Ecological Engineering”, Vol. 36, 2010, pp. 112-117.

[4] Park SS, Choi SG and Nam IH, “Effect of Plant-Induced Calcite Precipitation on the Strength of Sand”, J. of Materials in Civil Engineering, 2014, pp 1-5 (06014017).

[5] Neupane D, Yasuhara H, Kinoshita N and Unno T, “Applicability of Enzymatic Calcium Carbonate Precipitation as a Soil-Strengthening Technique”, J. of Geotechnical and Geoenvironmental Engineering, Vol. 139 No. 12, Dec. 2013, pp. 2201-2211.

[6] Nam IH, Chon CM, Jung KY, Choi SG, Choi H and Park SS, “Calcite Precipitation by Ureolytic Plant *(Canavalia ensiformis)* Extracts as Effective Biomaterials”, KSCE J. of Civil Engineering, (0000) 00(0), 2014, pp 1-6.

[7] Kawasaki S, Murao A, Hiroyoshi N, Tsunekawa M and Kaneko K, “ Fundamental study on novel grout cementing due to microbial metabolism”, J. of the Japan Society of Engineering Geology, Vol. 47, 2006, pp. 2–12 (in Japanese with English abstract).

[8] Weaver TJ, Burbank M, Lewis A, Crawford R and Williams B, “Bio- induced calcite, iron and manganese precipitation for geotechnical engineering applications” in Proc. Geo-Frontiers, 2011, pp. 3975–3983.

[9] Terajima R, Shimada S, Oyama T and Kawasaki S, “Fundamental study of siliceous biogrout for eco-friendly soil improvement”, J. of of the Japan Society of Civil Engineers, Ser.C (Geosphere Engineering), Vol. 65, 2009, pp.120–130 (in Japanese with English abstract).

[10] Akiyama M and Kawasaki S, “Novel grout material using calcium phosphate compounds: in vitro evaluation of crystal precipitation and strength reinforcement”, J. of the Japan Society of Engineering Geology, Vol. 125, 2012a, pp. 119–128.

[11] Akiyama M and Kawasaki S, “Microbially mediated sand solidification using calcium phosphate compounds”, J. of the Japan Society of Engineering Geology, Vol. 137-138, 2012b, pp. 29-39.

[12] Tung MS, “Calcium phosphates: structure, composition, solubility, and stability, in: A. Zahid (Ed.), Calcium phosphates in biological and industrial systems”, Kluwer Academic Publishers, Norwell, 1998, pp. 1-19.

[13] Dorozhkin SV and Epple M, “Biological and medical significance of calcium phosphates”, Angewandte Chemie International Edition, Vol. 41, 2002, pp.3130–3146.

[14] Yamazaki H, Maeda K, Takahashi K, Zen K and Hayashi K, “Technical Note of Port and Harbour Research Institute”, Vol. 905, 1998, pp. 1-29 (in Japanese).

[15] Das N, Kayastha AM and Srivastava PK, “Purification and characterization of urease from dehusked pigeonpea (Cajanus cajan L.) seeds”, J. of Phytochemistry, Vol.61, Issue.5, Nov. 2002, pp.513-521.

[16] Sirko A and Brodzik R, “Plant ureases: Roles and regulation - Review”, J. of Acta Biochimica Polonica, Vol. 47 (4), 2000, pp.1189-1195.

[17] Whiffin VS, “Microbial $CaCO_3$ precipitation for the production of biocement”, PhD. dissertation, School of Biological Science & Biotechnology, Murdoch University, Perth, Australia, 2004, 154 pp.

Fifth International Conference on Geotechnique, Construction Materials and Environment, Osaka, Japan, Nov. 16-18, 2015, ISBN: 978-4-9905958-4-5 C3051

EFFECTS OF BAGASSE ASH AND HYDRATED LIME ADDITION ON ENGINEERING PROPERTIES OF EXPANSIVE SOIL

Liet Chi Dang[1], Hayder Hasan[2], Behzad Fatahi[3], Robert Jones[4] and Hadi Khabbaz[5]

[1,2] PhD Candidate, School of Civil and Environmental Engineering, University of Technology Sydney (UTS), Sydney, Australia

[3] Senior Lecturer in Geotechnical Engineering, School of Civil and Environmental Engineering, University of Technology Sydney (UTS), Sydney, Australia

[4] Senior Infrastructure Engineer, Arup, Brisbane, QLD 4001, Australia

[5] Associate Professor of Geotechnical Engineering, School of Civil and Environmental Engineering, University of Technology Sydney (UTS), Sydney, Australia

ABSTRACT

The main objective of this research is to investigate the influence of hydrated lime and bagasse ash on engineering properties of expansive soil obtained from an array of laboratory tests. Bagasse ash is a readily available waste by-product of the sugar-cane refining industry causing the adverse impacts on environment. Bagasse ash is considered in this investigation in order to evaluate the potential benefits of its pozzolanic material for stabilisation of expansive soil. The preparation of stabilised soil specimens was conducted by changing the bagasse ash contents from 0 to 25% by dry weight of expansive soil along with hydrated lime dosage was increased. The bearing capacity and shrinkage properties of stabilised expansive soil were examined through a series of experimental tests including linear shrinkage and California bearing ratio (CBR) after various curing periods of 3, 7 and 28 days. The results reveal that the additions of hydrated lime and bagasse ash improved the strength and bearing capacity of stabilised expansive soil remarkably, and meanwhile significantly reduced the linear shrinkage of treated expansive soil. Hence, the application of hydrated lime and bagasse ash as reinforcing material can not only enhance the engineering properties of expansive soil, but also facilitate to cope with environmental issues and provide trivial cost construction materials for sustainable development.

Keywords: Expansive Soil, Hydrated Lime, Bagasse Ash, Linear Shrinkage, Strength and CBR

INTRODUCTION

Expansive soils are fine grained soil or decomposed rocks that show huge volume change when exposed to the fluctuations of moisture content. Swelling-shrinkage behaviour is likely to take place near ground surface where it is directly subjected to seasonal and environmental ups and downs. The expansive soils are most likely to be unsaturated and have montmorillonite clay minerals. Most of severe damage in relation to expansive soils is depended on the amount of monovalent cations absorbed to the clay minerals.

Construction of residential buildings and other civil engineering structures such as highways, bridges, airports, seaports on expansive soil is highly risky in that such soil is susceptible to cycles of drying and wetting, inducing shrinkage and swelling behaviour under building foundations, which results in cracking to structural and none structural elements of those structures. The average annual cost of damage to structures due to shrinkage and swelling is estimated about £400 million in the UK, $15 billion in the USA, and many billions of dollars worldwide [1].

An increasing number of ground improvement techniques have been suggested for dealing problematic soil such as the application of sand cushion technique, belled piers and granular pile-anchors. In addition, chemical stabilisation is the most popular method utilized to enhance the physical and mechanical properties of problematic soils consisting of soft soil and expansive soil. The chemical ground improvement approach is a proven technique in improving engineering properties of problematic soils and is highly applicable for lightly loaded structures such as road pavement and low-rise residential buildings [2].

In recent years, a growing quantity of laboratory and field experiments have been carried out and extensive studies have been conducted on problematic soil using various additives such as cement [3], [4], and lime [5]. Several by-products including fly ash [6], rice husk ash, bagasse ash [7], just to name a few have been investigated by using each alone or in combination with other additives. Hence, the potential for using by-products as chemical treatment of soft soil and expansive soil is the most promising. Although a growing number of investigations have been undertaken so as to reinforce problematic soil using waste by-products to diminish the effects of the swelling-shrinkage characteristics and enhance the mechanical properties, there are still not adequate studies on the influence of waste by-products, particularly in bagasse ash stabilised expansive soil.

Bagasse ash is an abundant fibrous waste product derived from sugar-refining industry and readily available for use without costs. This material is increasingly warned to pose problem to the environment that requires public attention and researchers on its safe disposal and searching for chances to use as recycled material as well. However, bagasse ash is considered as pozzolanic stuff rich in amorphous silica, which is effectively employed together with hydrated lime in improving the engineering properties of expansive soil. Therefore, it has become a focus of interest in recent years. Manikandan and Moganraj [8] have performed several studies on bagasse ash in searching of beneficial approaches to stabilise expansive soil. Based on the test results, they indicated that bagasse ash inclusion caused significant modification and improvement in the engineering properties of expansive soil.

Nevertheless, more investigations are essential in order to provide a comprehensive understanding of the engineering properties of black soil improved by combination of hydrated lime and bagasse ash in ground improvement. Expectantly, a couple of chief objectives associated with adopting industrial waste byproducts in line with diminishing hydrated lime dosage are likely to be acquired concurrently if the use of hydrated lime-bagasse ash inclusions treated expansive soil can give rise to the appreciable improvement of shrink-swell behavior and mechanical properties.

In this paper, an array of laboratory experiments including linear shrinkage, compaction, and CBR tests have been performed on untreated and treated expansive soil samples with different hydrate lime and bagasse ash contents after different curing time of 3, 7 and 28 days. Outcomes of this experimental investigation were analysed to obtain a better understanding of the effects of hydrated lime-bagasse ash additions on the shrinkage potential and engineering behavior of expansive soil.

MATERIALS AND EXPERIMENTAL PROGRAM

Materials

Soil

The soil samples used in this study for current experimental tests were collected from the specific area of Queensland, Australia. The soil was air-dried and broken into pieces in the laboratory. Table 1 shows the physical properties of the soil used in this investigation. In term of sizes of particles, the soil was classified as clay of high compressibility (CH) according to the Unified Soil Classification System. The specific gravity of solids (Gs) was 2.62-2.65. The grain size distribution showed that 0.1% of particles were in the range of gravel, 18.3% in the range of sand and 81.6% were fine-grained material (silt/clay). Atterberg limits of the fine portion of material were about 86% liquid limit (LL) and 37% plastic limit (PL), which yielded to a plasticity index (PI) of 49%. The average linear shrinkage and natural moisture content of the samples was 21.7% and 30.8%, respectively. Based on the high linear shrinkage and plasticity index, the soil can be classified as highly expansive soil.

Table 1 Characteristics of natural soil

Characteristics	Value
Gravel (%)	0.1
Sand (%)	18.3
Silt/Clay (%)	81.6
Natural water content (%)	30.8
Liquid limit (%)	86
Plastic limit (%)	37
Plasticity index (%)	49
Linear shrinkage (%)	21.7
Specific gravity	2.62-2.65
USCS classification of the soil	CH

Lime

Hydrated lime has 75–80% of calcium hydroxide and 7% silica that was used in this investigation. The Hydrated lime is locally purchased from Cement Australia supplier, one of the most widely used construction materials in Australia.

Bagasse Ash

Bagasse ash was collected during cleaning operation of boiler from ISIS Central Sugar Mill Company Limited, Queensland, Australia. The bagasse ash was taken from this company at a boiling temperature of 700-800°C. Table 2 provides the similarly physical and chemical properties of bagasse ash employed in this study, which are similar to the bagasse ash utilized in the previous research performed by Anumpam et al. [9]. The bagasse ash used for this research was carefully sieved and passed through 0.425mm aperture sieve to eliminate undesirable materials.

Mixing of Materials

Soil samples with particles size smaller than 2.36 mm were prepared by mixing bagasse ash or hydrated lime combined with bagasse ash at a ratio of 1:3 in the ranges shown in Table 3. Following this preparation, the specimens were mixed thoroughly. A mechanical mixer was used for the mixing of the expansive soil with hydrated lime and bagasse ash. After mixing of the material, the specimens were prepared for the conventional geotechnical experiments, including compaction and California bearing ratio tests in order to determine the optimum moisture contents, the maximum dry densities of selected admixtures and observe the stress‑strain behaviour of treated and untreated expansive soil samples.

Table 2 Characteristics of bagasse ash after Anumpam et al. [9]

Physical properties		Chemical properties	
Property	Value	Components	% by weight
Specific gravity	2.38	Ignition loss	2.11
Liquid limit (%)	41	SiO_2	65.27
Plastic limit (%)	None	Al_2O_3	3.11
Optimum moisture content (%)	48	Fe_2O_3	2.10
Maximum dry density (g/cm^3)	1.27	CaO	11.16
Lime Reactivity (kg/cm^2)	32	MgO	1.27

Table 3 Summary of mixes used in this study

Mix No.	Bagasse Ash (%)	Hydrated Lime (%)
1	0	0
2	6	0
3	10	0
4	18	0
5	25	0
6	4.5	1.5
7	7.5	2.5
8	13.5	4.5
9	18.25	6.25

Experimental Procedure

Linear Shrinkage

In this investigation, portion of a soil sample of at least 250g from the material passing the 425 μm sieve by drying method was air dried until it was dried enough to permit crumbling of the soil aggregation, which has been prepared in according with the procedure prescribed in AS 1289 [10] for the preparation of disturbed soil samples for Atterberg limits and linear shrinkage. Then, the linear shrinkage values of untreated and treated expansive soil specimens were determined as specified in accordance with in AS 1289 [10].

California Bearing Ratio Test

Unsoaked CBR tests were conducted on untreated and treated expansive soil in according with the method specified in AS 1289 [10] in order to examine the strength and bearing capacity of expansive soil as the subgrade materials in support of road and highway systems. Soaked CBR is not reported in this paper. Right after conducting the mixture process of expansive soil mixed with bagasse ash and hydrated lime, untreated and treated samples were shaped in a cylindrical metal mould of known volume, with 152 mm in internal diameter and 178 mm in height, at the maximum dry density (MDD) and optimum moisture content (OMC). In order to ensure uniform compaction, the samples were compacted in five equal layers by pressing the spacer disk of 61 mm in thickness with help of testing machine in order to obtain the targeted dry density. Then, the prepared samples were sealed by using plastic wrap to prevent moisture change, and afterward curing for various periods of 7 and 28 days at a controlled room environment of 25^{0}C temperature and relatively 80% humidity. After sample preparation and curing for different periods of 7 and 28 days, the samples were subjected to an annular surcharge of 4.5 kg put on the top and immediately set up in the conventional unconfined compression apparatus without soaking. The machine was set at a load rate of 1 mm/min, and this was kept consistent for all samples tested. An S-type load cell was used as a transducer to converting the force into an electrical signal, readable on the load cells display. A data logger was used to transfer the data to a readable output. An LVDT displacement transducer was set up against the bearing block of the machine to measure the vertical displacement of the samples under the applied load. The LVDT reading was used to plot the load-penetration curve that was commonly used to calculate the CBR values. The CBR values of untreated and treated expansive soil specimens were computed based on 2.5 mm penetration instead of 5.0 mm penetration, as penetration of 2.5 mm always gave rise to higher CBR values than that of 5.0 mm penetration. For each type of mixtures, the CBR value was obtained as the average of three CBR tests.

RESULTS AND DISCUSSIONS

Effects on Linear Shrinkage

Fig. 1 provides a comparison of linear shrinkage improvement of hydrated lime and bagasse ash additives stabilised expansive soil after curing period of 7 days. As can be seen in Fig. 1, the growing amount of hydrated lime and bagasse ash inclusions from 0 up to 25% at a given curing period was found to decrease the linear shrinkage remarkably. Particularly, when bagasse ash contents was increased from 0 up to 25%, the liner shrinkage of bagasse ash mixed with expansive soil drastically plunged by a substantial amount of 46% after only curing for 7 days in comparison with that of virgin soil specimen. The effects of hydrated lime-bagasse ash on linear shrinkage of treated expansive soil, moreover, was more pronounced than that of bagasse ash mixed with expansive soil. For example, when the 25% hydrated lime-bagasse ash addition at a ratio of 1:3 was ultilised to stabilise expansive soil, there was a remarkable reduction of linear shrinkage of approximately 80% compared to that of original expansive soil specimen. Hence, it is noteworthy to state that the additions of bagasse ash and hydrated lime-bagasse ash admixtures yielded the strongly positive effects of reducing linear shrinkage of expansive soil even with the application of bagasse ash stabilisation of expansive soil adopted only.

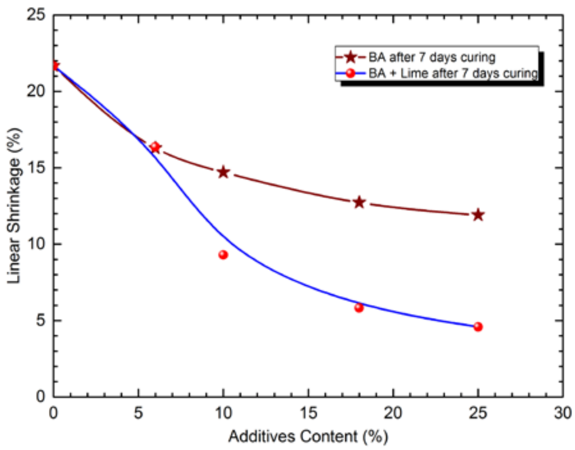

Fig.1 Influence of different bagasse ash and hydrated lime-bagasse ash combination on linear shrinkage of expansive soil after 7 days curing

In addition, Fig. 2 and Fig. 3 depict the effects of bagasse ash and hydrated lime-bagasse ash admixtures on linear shrinkage of stabilised expansive soil in line with curing time prolonged. Overall, the increase in bagasse ash and hydrated lime-bagasse ash inclusions up to 25% led to the decrease in linear shrinkage of expansive soil enormously with increasing curing periods of 3, 7, 28 days. It is obviously observed that the decrease in linear shrinkage was significant, speedy during the first 7-day curing period for both bagasse ash and hydrated lime-bagasse ash treated expansive soil specimens for most of particular additive contents. And then there was a marginally reduction of linear shrinkage of stabilised expansive soil when the curing time was further sustained up to 28 days. To be more specific, as plotted in Fig. 2 and Fig. 3, the addition of 6% bagasse ash caused lower decrease in linear shrinkage of stabilised expansive soil after curing time prolonged than that of 6 % hydrated lime-bagasse ash combination. However, the decrease in linear shrinkage of hydrated lime-bagasse ash combinations treated expansive soil in line with increasing curing time was so much lower and more pronounced than their bagasse ash-stabilised counterparts with further increasing stabilisers contents up to 25%. Subsequently, the 28 days final linear shrinkage of treated expansive soil shown in Fig. 3 fell down dramatically by almost 84% compared to that of original expansive soil when hydrated lime-bagasse ash combination contents were increased from 0 to 25%, whereas the drop of linear shrinkage of bagasse ash stabilised expansive soil as illustrated in Fig. 2 was roughly half in comparison with that of untreated soil specimen when bagasse ash inclusions were forced to rise up to 25%. It can be noted that the increasing curing time together with increasing additive contents obviously caused the substantial influence on linear shrinkage of bagasse ash and hydrated lime-bagasse ash admixtures treated expansive soil. Consequently, the use of the growing amount of either bagasse ash stabilisation or hydrated lime-bagasse ash treatment could be likely beneficial since these stabilisers could provide considerably positive effects of coping with expansive soil in terms of reducing linear shrinkage and cracking, which cause the most damage for superstructures and roads built directly on it.

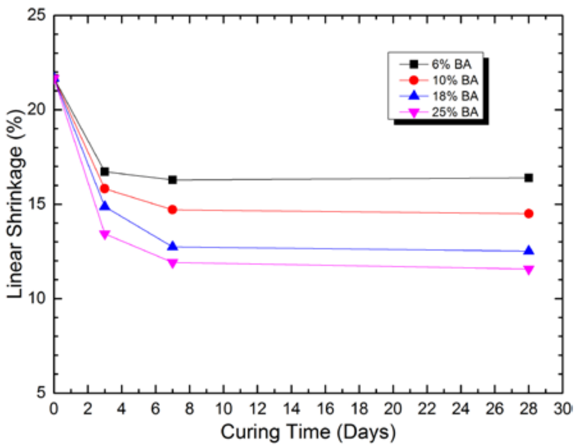

Fig. 2 Linear shrinkage of expansive soil mixed with various bagasse ash contents for different curing time

The significant improvement in linear shrinkage could be attributed to the flocculation and aggregation phenomena of clay particles induced by the presence of free lime in bagasse ash that caused a decrease in surface of clay particles, then formed the clay particles coarser, and eventually enhanced the friction and strength of treated expansive soil. As a result, the finer clay particles were replaced by relative coarser particles that could be one of the key factors resulting in the considerable decrease in linear shrinkage with increasing the additives contents and age.

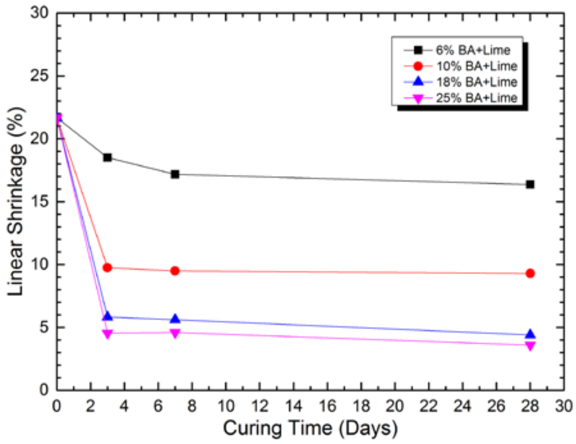

Fig. 3 Linear shrinkage of hydrated lime-bagasse ash treated expansive soil with different additives contents and curing time

Effects on the California Bearing Ratio (CBR)

The strength and bearing capacity of subgrade materials are essential factors in pavement engineering. In order to evaluate the strength of pavement resisting repetitive point loads by traffic vehicles, the CBR test is one of the most common tests used to assess the quality of base and subgrade materials for highway and road construction and design purposes. Fig. 4 and Fig. 5 represent the variation of CBR values of expansive soil specimens stabilised with different bagasse ash contents and hydrated lime-bagasse ash combinations from 0 up to 25% along with various curing periods of 7 and 28 days.

In general, the figures depict the appreciable improvement in CBR values with increase in bagasse ash and hydrated lime-bagasse ash combinations together with the increase of age. To be more specific, the CBR values of bagasse ash treated expansive soil plotted in Fig. 4 increased substantially with the additive amount increased and curing time prolonged. For instance, in comparison with the CBR value of parent soil specimen, the CBR values of bagasse ash stabilised expansive soil increased from 7.1% up to 11.5% with increasing bagasse ash additions from 0 to 25% after curing for 7 days. The amount of CBR increase was almost 62% compared with the CBR of parent soil specimen. In addition, with the curing time increased from 7 days up to 28 days, the CBR value of bagasse ash treated expansive soil at a content of 25% increased significantly by approximately 83%, 15% compared with that of untreated expansive soil and same bagasse as content treated expansive soil after 7-day curing, respectively. This obviously demonstrates that the surge of CBR values was not only with increasing bagasse as additions but also curing time prolonged. The increase in CBR values may be due to cementation and pozzolanic reactions in form of frictional resistance contributed from bagasse ash. This agreed well with the early reports presented by researchers [7], [9].

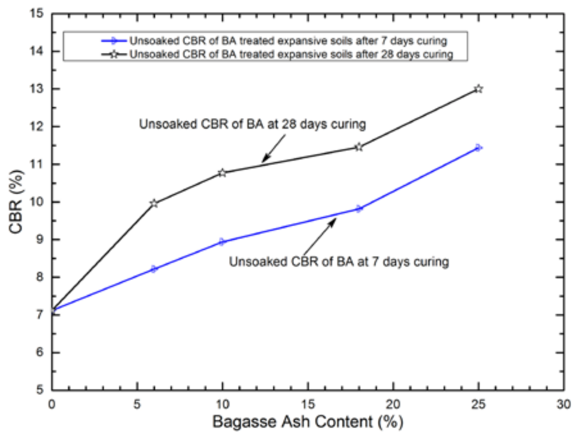

Fig. 4 Influence of bagasse ash admixtures on average unsoaked CBR of treated expansive soil with various curing time

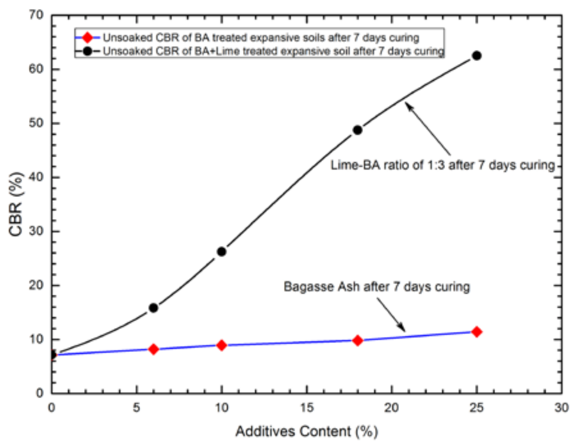

Fig. 5 Influence of hydrated lime and bagasse ash admixtures on average unsoaked CBR of treated expansive soil after curing period of 7 days

Figure 5 indicates the general effects of bagasse ash and hydrated lime-bagasse ash combinations on the CBR gain of treated expansive soil for varying hydrated lime-bagasse ash contents after curing for 7 days. As illustrated in Fig. 5, the CBR of treated expansive soil specimens rose drastically with an increasing amount of stabilisers up to 25% adopted in order to treat expansive soil for a given curing period. To illustrate this, the addition of 10% percentage of hydrated lime-bagasse ash generated the 7-day curing CBR increased by a factor of 3.7 in average, whereas with 25% content of the hydrated lime-bagasse ash addition at a ratio of 1:3 after curing for 7 days, the average CBR was significantly increased by a factor of 8.8 in comparison with that of original soil specimen, respectively. Additionally, in order to compare with the same content and curing time of bagasse ash stabilised expansive soil specimens, the 25% combination of hydrated lime-bagasse treatment of expansive soil after curing period of 7 days gave rise to the average CBR surged up by a great factor of 5.5. Hence, it is important to note that the combinations of hydrated lime-bagasse ash treated expansive soil incontrovertibly yielded higher CBR values than bagasse ash alone. This was in conformity with the previous investigations carried out by Osinubi [7].

CONCLUSIONS

The following conclusions can be drawn based on the experimental results

The increasing amount of bagasse ash and hydrated lime-bagasse ash inclusions from 0 up to 25% gave rise to the significant decrease in linear shrinkage when curing time was increased. The effects of hydrated lime-bagasse ash combinations on linear shrinkage of treated expansive soil was more pronounced than that of bagasse ash mixed with expansive soil. As a result, the application of hydrated lime-bagasse ash treatment could be likely the most promising approach in terms of construction materials being adopted in ground improvement.

There was the enormous improvement in CBR values with increase in bagasse ash and hydrated lime-bagasse ash combinations from 0 up to 25% in line with curing time prolonged. Overall, the hydrated lime-bagasse ash inclusion stabilised expansive soil could be satisfied the requirements by most of specifications for either subgrade or even subbase course materials for road and highway construction purposes on the basis of CBR.

This investigation based on experimental tests exhibits the additions of bagasse ash and hydrated lime-bagasse ash stabilised expansive soil enhance engineering properties and remarkably diminish linear shrinkage of treated soil samples. Hence, the hydrated lime-bagasse ash combination should be widely utilised in expansive soil treatment that undeniably helps not only impede the influence of waste by-product bagasse ash on the environmental issues but also provide novel construction materials for sustainable development together with a tremendous amount construction cost saving on the basis of decrease in dosages of conventional stabilisers comprising of lime, cement.

ACKNOWLEDGEMENTS

The results presented in this paper are part of an ongoing research at University of Technology Sydney (UTS) supported by Arup Pty Ltd, Queensland Department of Transport and Main Roads (TMR), ARRB Group Ltd and Australian Sugar Milling Council (ASMC). The authors gratefully acknowledge their supports.

REFERENCES

[1] Jones, L.D. & Jefferson, I., 'Expansive soils', *ICE manual of geotechnical engineering*, ICE Publishing, London, 2012, pp. 413-41.

[2] Khabbaz, H. & Fatahi, B., 'Stabilisation of Closed Landfill Sites by Fly Ash Using Deep Mixing Method', *Grouting and Deep Mixing 2012*, eds Johnsen, L.F., Bruce, D.A. & Byle, M.J., ASCE, USA, 2012, pp. 417-26.

[3] Fatahi, B., Engelbert, D., Mujic, S. & Khabbaz, H. 2012, 'Assessment of Surcharging on Strength and Stiffness of Cement Treated Clays', *Grouting and Deep Mixing 2012*, eds Johnsen, L.F., Bruce, D.A. & Byle, M.J., ASCE, USA, 2012, pp. 272-80.

[4] Fatahi, B., Khabbaz, H. & Fatahi, B., 'Mechanical characteristics of soft clay treated with fibre and cement', *Geosynthetics International*, 2012, vol. 19, pp. 252-62.

[5] Bell, F.G., 'Lime stabilization of clay minerals and soils', *Engineering Geology*, 1996, vol. 42, no. 4, pp. 223-37.

[6] Fatahi, B. & Khabbaz, H., 'Influence of fly ash and quicklime addition on behaviour of municipal solid wastes', *Journal of Soils and Sediments*, 2013, vol. 13, no. 7, pp. 1201-12.

[7] Osinubi, K.J., Bafyau, V. & Eberemu, A.O., 'Bagasse Ash Stabilization of Lateritic Soil', in E. Yanful (ed.), *Appropriate Technologies for Environmental Protection in the Developing World*, Springer Netherlands, 2009, pp. 271-80.

[8] Manikandan, A. & Moganraj, M., 'Consolidation and Rebound Characteristics of Expansive Soil by Using Lime and Bagasse Ash', *International Journal of Research in Engineering and Technology*, 2014, vol. 03, no. 04, pp. 403-11.

[9] Anupam, A.K., Kumar, P. & Ransinchung, G.D., 'Use of Various Agricultural and Industrial Waste Materials in Road Construction', *Procedia - Social and Behavioral Sciences*, 2013, vol. 104, pp. 264-73.

[10] AS 1289, *Methods of testing soils for engineering purposes*, Standards Australia, Sydney, Australia, 2001.

CLAY-SHALE MATERIALS AS LOW-COST LANDFILL LINERS: AN INTEGRATED GEOCHEMICAL AND GEOTECHNICAL ASSESSMENTS

Moshood N.TIJANI[1], Jean-Frank WAGNER[2] and Matthew E. NTON[1]
[1]Department of Geology, University of Ibadan, 20005 Ibadan - Nigeria
[2] Fachbereich Geographie/Geowissenschaften (FB VI), Universität Trier, D-54286 Trier - Germany

ABSTRACT

Increasing rate of wastes generation due to urbanization and industrialization, as well as the need for proper waste disposal management has been the concerns of many low income countries like Nigeria. Hence, this study assessed the geotechnical and chemical characteristics in respect of suitability of selected clay-shale deposits in Nigeria as low cost landfill liners for waste disposal. Twenty four (24) clay-shale samples were subjected to engineering tests, mineralogical XRD and geochemical analyses. Apart from normal kaolinitic clay, the XRD analyses revealed smectitic and mixed layer clays with Liquid Limit (LL) of 58.3 – 116.5 (av. 75.4) and 170.4 – 173.2 (av. 171.8) respectively while the Plasticity Index (PI) ranged from 20.3 – 51.6 (av. 31.8) and 80.9 – 93.3 (av. 87.1) respectively. Methylene blue adsorption index (MBI) ranges from ≈10 to 18.6 meq/100g for both smectictic and mixed layer clay-shales with corresponding surface area of 0.8−1.5m^2/g, suggesting the dominance of active clay minerals. In addition, the geochemical analyses show that the clay-shale materials contain significant amount of Al_2O_3 with average value of 17.0 and 15.9% respectively while Fe_2O_3 has average value of 8.2 and 6.5% respectively, suggesting Fe-rich smectitic clays. The overall evaluation revealed that the clay-shale materials are chemically and geotechnically suitable for application as landfill liners subject to appropriate beneficiation /amendment such as mixing with cement and other binding materials.

KEYWORDS: Geochemical, Geotechnical Assessment, Landfill, Clay-Shale, Liner Materials

INTRODUCTION

Increasing urbanization and industrialization have led to an increase in the flow of goods and services in many low income developing nations, resulting to increase in the volume and varieties of generated wastes. Thus, the environmental implications of the increasing rate of solid waste production and the need for proper waste disposal management has been the concerns of many low income countries like Nigeria. In addition, safe containment of wastes and control of leachate from landfill or waste-dump sites are paramount in the mitigation of groundwater pollution. Hence, proper design and careful selection of lining materials are vital parts of engineered waste disposal system [1].

For economical reasons, natural clays and clay-shales available within a reasonable hauling distance, can be used as landfill liners while compacted natural clays are also widely used as landfill liners due to their low hydraulic conductivity and high contaminant attenuation [2], [3]. In other words, compacted clay liner (CCL) must have a low hydraulic conductivity to control leachates from the wastes and must have sufficient shear strength to accommodate possible settlement [2], [4]. Therefore, strict specifications are usually imposed on the selection of a liner material, design and construction of the compacted clay liners in order to satisfy the above requirements [1], [2], [5].

Another major constraint to the development of properly engineered landfills is the high cost of imported synthetic liners in local markets of developing countries like Nigeria, which therefore calls for alternative local sources of materials for landfill liner. Consequently, crushed shale / clay-shale deposits appear to be inexpensive alternative that can be utilized to contain leachate in landfill and protect the underlying groundwater resources. This study, therefore, assesses the geotechnical and geochemical characteristics of shale (clay-shale) units from southern part of Nigeria, for suitability as low cost compacted clay liner (CCL) and as components of landfill barrier system in waste disposal systems.

GEOLOGICAL SETTING OF STUDY AREA

The three major rock types - igneous, metamorphic and sedimentary - abound in Nigeria. Igneous and metamorphic rocks constitute the Precambrian crystalline Basement Complex units and underlie the physical foundation of the country, while the Cretaceous-Tertiary sedimentary units, which lie unconformably on the Basement Complex constitute the sedimentary basins as depressions between basement landmass in the south, northeast and northwest [6], [7]. The Basement Complex and the sedimentary basins are equally dispersed in Nigeria with the basement rocks most extensive in northern-central, south-western parts and along the eastern margin of Nigeria (Fig.1).

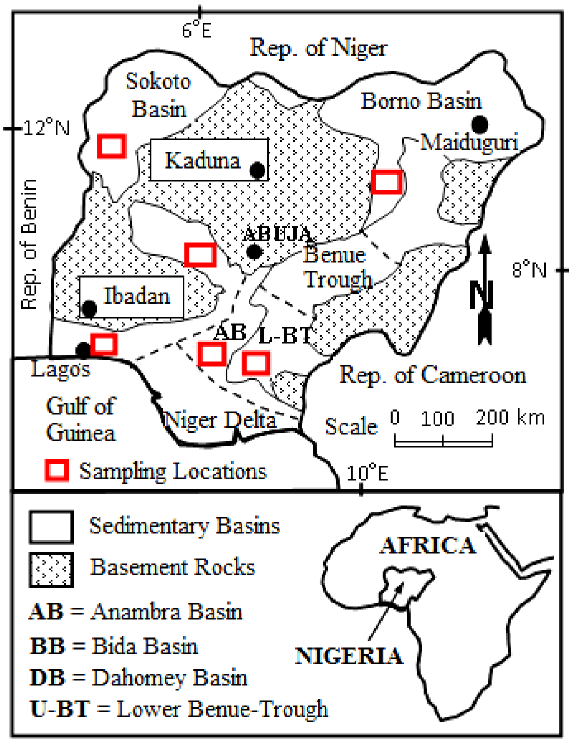

Fig. 1: Geology of Nigeria indicating Sampling Locations (Inset: Map of Africa)

The sedimentary basins occupy the central X-shaped area of the country and underlie the southern part as well as northwestern (Sokoto Basin) and north-eastern areas (Bornu Basin). The Precambrian Basement units consist of gneisses, granites, migmatitic and granitic gneisses, quartzites, slightly migmatised to unmigmatised meta-sedimentary schists and dioritic rocks [6]. The Cretaceous and Tertiary sedimentary units consist of alternating sequence of rock units ranging from shales, limestones, mudstone / siltstone intercalated with sandy units in places. The occurrences of extensive clay-shale and mudstones in many of the sedimentary basins (Fig. 1) offer an opportunity of local sourcing of materials for this study.

MATERIALS AND METHODS

For the purpose of this study, selected shale / clay-shale samples were collected from different lithologic units within the sedimentary basins in Nigeria (Fig. 1). The samples were obtained from road cut sections and in excavation pits of sand/laterite quarry sites. Efforts were made to collect fresh un-weathered samples for the laboratory tests. Most of the samples were either in forms of soft rock when wet or in blocky compact and laminated form. Physical appearance indicates that the colour of the sampled clay-shale varied from light grey, to whitish and light brown as well as light reddish when iron-stained. After drying in the laboratory, the samples were disaggregated and sieved to obtain fine-grained materials with a maximum size of about 4.75 mm (sieve number 4).

In this preliminary study, representative samples of the selected clay/shale units were subjected to tests such as Atterberg consistency limits (liquid limit, plastic limit, shrinkage) and hydrometer tests while methylene blue adsorption index (MBI) was estimated following standard method [8]. For the chemical studies, oxides of major elements (SiO_2, Al_2O_3, Fe_2O_3, CaO, MgO, K_2O, Na_2O and TiO_2) were analysed using a Philips PYE UNICAM SP9 atomic absorption spectrophotometer (AAS) and determination of the loss on ignition (LOI) using Heraus muffle furnace with sequential heating up to 1,050°C.

The mineralogical analyses for the identification of clay minerals via X-ray diffraction were carried out using a Siemens D500 Diffractometer with Cu-K_{alpha} radiation. Powdered as well as textural preparations of samples were measured in three forms; untreated, treated with ethylene glycol and heated to 550°C. The resulting diffractogram charts were analysed using the DIFFRAC-plus Evaluation programme (EVA), version 6.0 rev. 0. The criteria for the mineral identification as in [9] and [10] are presented in Table 1.

Table 1: Criteria for Identification of Major Clay Minerals

Minerals Basal d-spacing, Å (Untreated)	Glycolation Effect	Heating Effect
Kaolinite (d_1 = 7.1, d_2=3.5, d_3 = 10.4	No change / reaction	Degraded@ 550° C
Illite (d_1 = 10.0, d_2 = 5.0)	No change	No reaction
Palygor. (d_1=10.5, d_2 = 4.5, d_3 = 3.2)	No change	Degraded @ 600° C
Smectite ($d \approx 11.9-15.3$)	Peak change $d \approx 16.6-17.2$	Change to $d \approx 9.5-10.0$
Vermiculite ($d \approx 13.9 - 14.3$)	No change	Change to $d \approx 9.8-10.0$
Chlorite (d_1 =14.3, d_2 = 7.1)	No change	Change to $d \approx 13.8$

Palygor = Palygorskite

All the geotechnical, chemical and mineralogical tests, following standard laboratory procedures, as well as follow-up data evaluation and interpretations were carried out at the Department of Geology, University of Trier, Germany.

RESULTS AND DISCUSSIONS

Grain-size Distribution and Index Properties

The grain-size distribution curves for the representative samples of the clay-shales used in this study are presented in Fig. 2. The curves revealed that the crushed clay-shales are generally clayey with percentage fines (silt and clay) ranges from 90−98% for most of the samples. However, the proportion of clay fractions (<0.002mm) are in the range of 60−75% for the more plastic (smectitic) samples, 50−55% for mixed layer clay-shale materials and 15−30% for silty (kaolinitic) samples. The values are more than minimum of 20% recommended for liner materials, especially for the smectitic and mixed layer clay-shale materials [11].

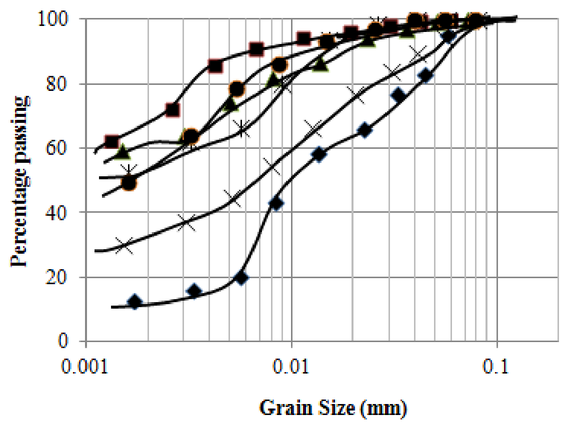

Fig. 2: Representative Grain size Distribution Curves for the clay-Shale Samples.

The NRA (1992) define suitable materials as those clays with a liquid of 30>(LL)<90% and plasticity index of 20>(PI)<65%. For this study, the results of the Atterberge limits as presented in Table 2 revealed Liquid Limit (LL) of 58.3 – 116.5 (av. 76.2) and 170.4 – 173.2 (av. 171.8 0) for smectitic and mixed layer clay materials respectively, while the Plasticity Index (PI) ranged from 20.3 – 51.6 (av. 31.8) and 80.9 – 93.3 (av. 87.1) respectively. However, the kaolinitic clay materials revealed LL of 38.8 – 75 (av. 54.6) and PI of 10.5 – 29.6 (av. 20.7), suggesting little expansive properties desirable of landfill liner materials. The implication is that the relatively low plasticity index for the kaolinitic clay will enhanced leachate attack from the landfill as a result of its potential high permeability.

As shown in the Casagrande Plasticity Chart (Fig. 3), nearly all the clay-shale samples plot below the "A" line. In other words, the clay-shale materials can be classified as inorganic silts of medium plasticity and intermediate compressibility (ML) for the kaolinitic clay-shales while the smectitic and mixed layer clay-shale materials exhibited high plasticity as inorganic clays (CL-OH) of higher compressibility.

Table 2: Geotechnical characteristics of the clay-shale materials (in %)

Para-meters	Min.	Max.	Mean	Std. Dev.
Smectitic Clays (N=10)				
LL	58.3	116.5	75.4	19.9
PL	32.2	64.9	43.4	10.4
PI	20.3	51.6	32.0	10.4
SL	25.6	52.0	35.4	8.4
Mixed layer Clays (N=4)				
LL	170.4	173.2	171.8	2.0
PL	79.9	89.6	84.7	6.8
PI	80.9	93.3	87.1	8.8
SL	56.6	69.3	63.0	9.0
Kaolinitic Clays (N=10)				
LL	38.8	75.0	52.3	10.9
PL	21.9	48.6	32.2	8.0
PI	10.5	29.6	20.2	6.1
SL	16.3	42.1	27.2	7.8

Therefore, with possible minimal beneficiation, these characteristics will be suitable for capping and bottom liner materials or as components of such, in landfill system.

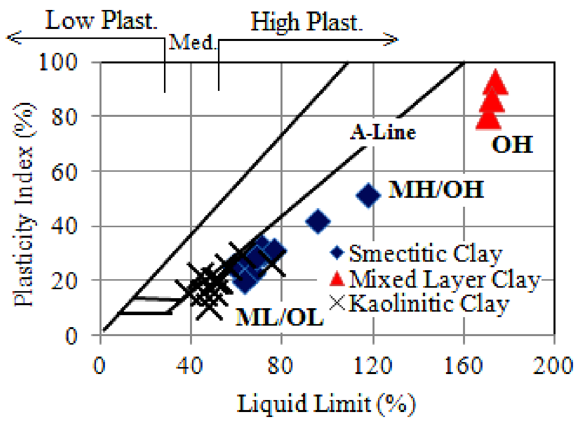

Fig. 3: Casagrande chart classification of the clay-shales

Although a moderately high plasticity index is considered important in the selection of a suitable liner material. However, under extremely high plasticity (PI>65%) the liner material becomes sticky and difficult to work with when wet and forms hard lumps when dry and at the same time more susceptible to desiccation [1], [3], [5]. In this study, the PI values of 10-30% for kaolinitic clay-shales and 20-52% for smectitic clay-shales are within the recommended range of 20-65% for most of the samples, especially for smectitic clay-shale materials. However, the values of 80-93% for the mixed-layer clay-shales are extreme enough as to warrant beneficiation with other materials, before application as liner materials.

Chemical Characterization

The summary of the results of geochemical analyses are presented in Table 3a-c. The results revealed that the smectitic clay-shales have relatively lower SiO_2 of 38.2 – 63.1wt.% (±8.4%) compared to values of 47.8 – 68.1 wt.% for the mixed layer and kaolinitic clay materials.

Table 3a: Geochemical Characteristics of the smectitic Clays (N=10)

Parameters (%)	Min	Max.	Mean	Std. Dev.
SiO_2	38.2	63.1	53.1	8.44
TiO_2	0.87	1.52	1.16	0.21
Al_2O_3	11.5	23.2	17.0	4.31
Fe_2O_3	6.37	10.9	8.19	1.40
MnO	0.02	0.17	0.08	0.05
CaO	0.01	17.2	4.50	6.04
MgO	0.81	2.82	1.52	0.58
Na_2O	0.04	0.32	0.12	0.10
K_2O	0.21	1.90	0.80	0.58
LOI	10.1	21.5	13.4	4.11

Table 3b: Geochemical Characteristics of the mixed layer Clays (N=4)

Parameters (%)	Min	Max.	Mean	Std. Dev.
SiO_2	48.84	68.0	59.6	9.09
TiO_2	1.00	1.26	1.11	0.11
Al_2O_3	12.5	18.4	15.91	2.78
Fe_2O_3	5.07	8.21	6.54	1.39
MnO	0.04	0.08	0.06	0.02
CaO	0.57	3.61	1.48	1.43
MgO	0.62	4.25	2.37	1.93
Na_2O	0.04	0.44	0.16	0.19
K_2O	0.17	2.07	1.05	0.78
LOI	7.78	15.5	12.1	3.92

The loss on ignition (LOI) values range between 10.1 and 21.5 wt.% (av. 13.4%) for smectitic clay while the mixed layer and kaolinitic clays exhibited values of 7.8 – 15.5wt.% (av. 12.0%). Furthermore, the analyzed clay-shales contain significant amount of Al_2O_3, with respective average values of 17.0% 15.9% and 24.5% for smectitic, mixed layer and kaolinitic clay materials.

Table 3c: Geochemical Characteristics of the kaolinitic Clays (N=10)

Parameters (%)	Min	Max.	Mean	Std. Dev.
SiO_2	47.8	62.8	56.7	4.52
TiO_2	1.01	3.17	1.89	0.64
Al_2O_3	17.0	30.9	24.5	5.04
Fe_2O_3	1.62	7.79	3.56	2.03
MnO	0.01	0.04	0.02	0.01
CaO	0.01	0.36	0.09	0.12
MgO	0.07	2.08	0.51	0.63
Na_2O	0.02	1.02	0.22	0.32
K_2O	0.15	2.16	0.91	0.64
LOI	8.18	15.5	12.0	2.72

LOI=Loss on Ignition

However, Fe_2O_3 have average value of 8.2%, 6.5%, and 3.6% respectively, suggesting Fe-rich assemblages for smectitic, mixed layer and kaolinitic clay-shale materials. Also average values of 4.5% and 1.5% CaO for smectitic and mixed layer clays respectively compared to 0.1% CaO for kaolinitic clay-shales suggest the dominance of Ca-montmorillonite as also supported by the XRD results.

Mineralogical Characterization

The X-ray diffraction (XRD) analyses of the clay-shale samples revealed the general presence of quartz (usually at d = 3.34A°) as the principal non-clay mineral in all the analyzed samples while calcite ($CaCO_3$) also occur in a couple of the samples. The representative X-ray patterns presented in Fig. 4 revealed the presence of kaolinite in all samples by its basal spacings at 7.1 and 3.5A°. In addition, the oriented mounts of the samples confirm the presence of divalent-cation saturated smectite (Fig. 4b and c) for the mixed-layer and smectitic clay-shale materials. The basal spacing, d_{001} of the smectite mineral ranges from 14.45–15.31A°, suggesting the dominance of Ca-montmorillonite.

In both cases, such basal spacing (d_{001}) are expanded to about 17.0 A° under glycolation (Fig. 4b and c), and clearly distinguished the observed Ca-montmorillonite from chlorite and vermiculite groups. The X-ray pattern for the smectitic clay-shale materials also exhibit two weak bands at d = 10.5 and 4.5A° (Fig. 4b), indicating the presence of palygorskite while a weak peak at d = ≈5.0A° (Fig.

4c) also suggest the presence of illite in the mixed layer clay-shale materials. Moreover, these results correlated well with the estimated activities of the clay-shales and are also clearly consistent with the results of XRD analyses presented earlier.

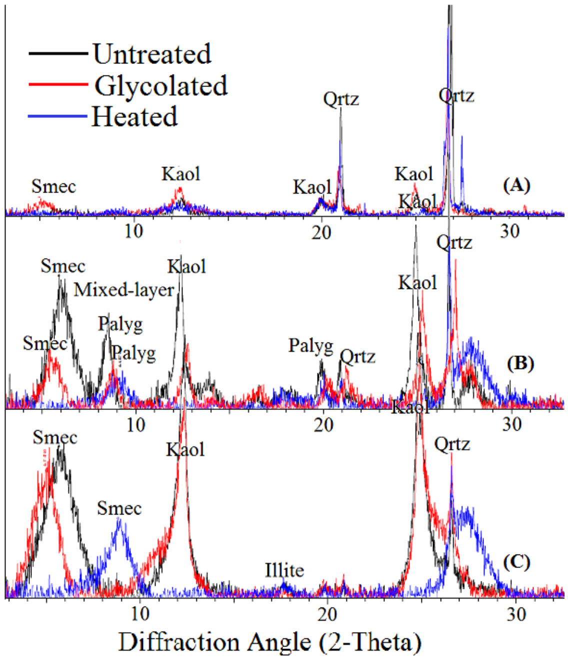

Fig. 4: Representative XRD patterns of the clay-shale samples under different treatments (A= Kaolinitic; B= Mixed layer; C= Smectitic)

Methylene Blue Index and Activity

In the field of clay chemistry, the adsorption of methylene blue to the edges, external surfaces, and accessible inter-layer regions of clay minerals dispersed in an aqueous solution is often used to measure CEC and specific surface area of clay minerals [12], [13]. In this study, the results of Methylene blue adsorption index, MBI (an estimate of CEC) and surface area of the clay-shale materials are presented in Table 4 alongside the activity.

As shown in Table 4, MBI (an estimate of CEC) range from ≈10 to 18.6 meq/100g for both smectictic and mixed layer clay-shales with corresponding surface area of 0.8−1.5m^2/g suggesting the dominance of swelling clay minerals as also revealed by the estimated montmorillonite content of 31.5 to 60.1%. However, the MBI value of 1.8−5.8 meq/100g and surface area of 0.14−0.45m^2/g for kaolinitic clay-shale materials is a confirmation of the dominance of inactive clay minerals as reflected by the low values (15.1 - 18.1%) of estimated montmorillonite content.

Clay minerals with high plasticity also generally have higher activity and corresponding high CEC [14]. These tend to plot in the upper right hand region of an expanded plasticity chart (high liquid limit and high PI) as shown earlier in Fig. 3.

Table 4: Geochemical Characteristics of the kaolinitic Clays (N=10)

Para-meter	Acti-vity	MBI (meq/100g)	SA (m^2/g)	% Mont.
Smectitic Clay (N=10)				
Min.	1.32	10.0	0.78	32.3
Max.	1.92	18.6	1.46	60.1
Mean	1.71	14.7	1.15	47.5
Std. Dev.	0.23	2.63	0.21	8.48
Mixed layer Clay (N=4)				
Min.	0.96	9.75	0.76	31.50
Max.	1.81	17.4	1.36	56.05
Mean	1.49	13.5	1.05	43.45
Std. Dev.	0.38	3.19	0.25	10.31
Kaolinitic Clay (N=10)				
Min.	0.51	1.77	0.14	5.71
Max.	0.72	5.80	0.45	18.7
Mean	0.60	3.59	0.28	11.6
Std. Dev.	0.10	1.92	0.15	6.19

MBI = Methylene blue adsorption index
Mont. = % Montmorillonite
SA= Surface Area; %

Activity provides an indirect indication of the type of clay minerals present, e.g. Allophones, Illite, Kaolinite, and Halloysite, do exhibit an activity of 0.5, while Illites and Smectites are characterized by an activity of 1 [15]. In this study, based on the grain size distribution and Atterberg limits, the estimated activity as presented in Table 4 range from 0.51−0.72 for the kaolinitic clays; suggesting the dominance of inactive clays with low CEC and little or no swelling potential. However, values of 0.96−1.92 for smectitic and mixed layer clay-shales indicate normal to predominantly active clay materials with relatively higher swell susceptibility and higher CEC. These results correlated well with the estimated activities of the clay-shales and are also clearly consistent with the results of XRD analyses, index properties and Atterberg limits (LL, PL and PI) presented earlier; thus it can be inferred that the study clay-shales are suitable as liner materials.

SUMMARY AND CONCLUSIONS

The results of the geotechnical tests conducted on the clay-shale samples revealed that smectitic and mixed layer clays have Liquid Limit (LL) of 58.3 – 116.5 (av. 75.4) and 170.4 – 173.2 (av. 171.8) respectively while the plasticity index (PI) ranged from 20.3 – 51.6 (av. 31.8) and 80.9 – 93.3 (av. 87.1) respectively. With percentage fines of more than 85%, percentage clay fraction of 60−75% (smectitic) and 50−55% (mixed-layer), most of the samples satisfy the basic requirements of clay liners according to the standard specifications (Daniel, 1993). The mineralogical analyses revealed the presence of kaolinite in all samples by its basal spacings at 7.1 and 3.5A°, however, the oriented mounts of the samples confirm the presence of divalent-cation saturated smectite for the mixed-layer and smectitic clay-shale materials. These are consistent with the geochemical data with SiO_2 of 38.2 – 63.1wt.% (±8.4%) and average Al_2O_3 of 17.0% for smectitic clay-shales and SiO_2 of 47.8 – 68.1 wt.% and Al_2O_3 of 5.9% and 24.5% respectively for mixed layer and kaolinitic clay materials. Nonetheless, average value of 8.2%, 6.5%, and 3.6% respectively, suggests Fe-rich assemblages.

In summary, based on the results of the geotechnical, mineralogical and chemical properties of the study clay-shales were generally within the range suitable for use as liners or component materials. However, higher plasticity index of 80-93% for the mixed-layer clay-shales are extreme enough as to warrant amendment or blending with other materials in order to obtain suitable plasticity property and shrinkage susceptibility, before application as liner materials. Further studies in respect of permeability, compaction behaviour and sorption characteristics of the clay-shales are recommended.

ACKNOWLEDGMENTS

The first author acknowledged, with many thanks, the assistance and supports of Dr. Oscar Baeza-Urrea and Mrs. Jutta Moschansky-Koster of the Fachbereich Geographie/Geowissenschaften (FB-VI), Universität Trier, Germany, during the laboratory phase of this study.

REFERENCES

[1] Daniel, D.E. "Landfill and impoundments". In: Daniel DE (ed) *Geotechnical practice for waste disposal.* Chapman & Hall, London, 1993. pp 97–112.

[2] Mohamedzein A; Yahia E., Amer A. A., Mohammed Y. A., Ahmed Q., Abdul-Hamid A. Assessment of crushed shales for use as compacted landfill liners. Engineering Geology 80; 2005; pp. 271–281.

[3] Nayak, S., Sunil, B.M., and Allamaprabhu, K. Assessment of Blended Lithomargic Clay as Landfill Liner Material. Current Advances in Civil Engineering (CACE); Vol. 2(40); 2014. pp. 102-117.

[4] Mitchell, J.K., Bray, J.D., Mitchell, R.A. Material interactions in solid waste landfills. Proceedings of a Specialty Geoenvironment 2000 Conference. ASCE, New Orleans, LA, USA, 1995; pp. 568– 590.

[5] Rowe, R.K., Quigley, R.M. and Booker, J.R. “Clayey barrier systems for waste disposal facilities”. E & FN Spon Lond, 1995; 390 pp.

[6] Kogbe, C.A. The Cretaceous and Paleocene sediments of southern Nigeria.In. CA. Kogbe. (Ed). 2nd ed. Lagos: Elizabeth Publishers, 1989; 273-286.

[7] Obaje N. G. Geology and Mineral Resources of Nigeria, Lecture Notes in Earth Sciences 120, DOI 10.1007/978-3-540-92685-6 1, Springer-Verlag Berlin-Heidelberg, 2009.

[8] Hang, P. and Brindley, G.. Methylene blue adsorption by clay minerals. Determination of surface areas and cation exchange capacities. *Clay and Clay Minerals*. 18: 1970; pp.203-212.

[9] Brindley, G.W., and Brown, G. (Eds.). Crystal Structures of Clay Minerals and Their X-ray Identification. Mineralogical Society, London. 1980.

[10] Moore, D.M., Reynolds Jr., R.C.,. X-ray Diffraction and the Identification and Analysis of Clay Minerals. Oxford University Press, Oxford; 1997.

[11] National River Authority North West Region, *Earthworks to landfill sites,* 1989.

[12] Omotoso, D. “Clay Characterization in the Oil Sand Industry.” 2nd CONRAD Clay Workshop Presentation, Edmonton, March, 2011.

[13] Bergaya, F., Theng, B., and Lagaly, G. (Eds). Handbook of Clay Science. 1. Elseviers. 2006; 1223p.

[14] Boxill, L. Potential for Use of Methylene Blue Index testing to Enhance Geotechnical Characterization of Oil Sands Ores and Tailings. *Proceedings Tailings and Mine Waste; Vancouver, BC, November 6 to 9, 2011.*

[15] Sobkowicz, J. and Boswell, J. “Influence of Clay Mineralogy on the Geotechnical Stability of Tailings Deposits." 2nd CONRAD Clay Workshop Presentation, Edmonton, March, 2011.

Fifth International Conference on Geotechnique, Construction Materials and Environment, Osaka, Japan, Nov. 16-18, 2015, ISBN: 978-4-9905958-4-5 C3051

LABORATORY-SCALE MACRODISPERSION IN HETEROGENEOUS POROUS FORMATION AND ITS QUANTIFICATION USING SPATIAL AND TEMPORAL MOMENT APPROACHES

Kazuya INOUE[1], Tomoki KURASAWA[1] and Tsutomu TANAKA[1]
[1] Graduate School of Agricultural Science, Kobe University, Japan;

ABSTRACT

Solute transport in groundwater is significantly influenced by the heterogeneity associated with spatial distribution of the hydraulic conductivity. Understanding solute transport behavior in heterogeneous flow fields is fundamental to develop appropriate models in aquifer management. In this study, laboratory two-dimensional tracer experiments were carried out in a 1 m length, 1 m height and 0.03 m thickness sandbox to identify macrodispersion in heterogeneous porous formation. Dye tracer of Brilliant Blue FCF mixed with NaCl was applied as a pulse type source and subsequent transport behavior of dye was recorded with digital camera. In addition to the spatial moment approach, temporal moment approach was also applied to estimate the longitudinal macrodispersivity by means of NaCl concentrations at an observation point in the flow field. The experimental results indicated that longitudinal and transverse macrodispersivity were larger than those in homogeneous formation. Moreover, it was revealed that both macrodispersivities in longitudinal and lateral directions have a non-dependency of the regional flow rates.

Keywords: Macrodispersion, Spatial moment, Temporal moment, Dye tracer experiment, Heterogeneity

INTRODUCTION

The phenomenon of dispersive mixing of solute in aquifers has been the subject of considerable research interest during the past few decades due to concerns on public health. In homogeneous porous media under laboratory conditions, the classical theory describing this spreading or dispersion of solute, based on Fickian process and flow, combines mass conservation and the time rate of change for the flux of a contaminant moving through a porous medium. On the other hand, geological media often possess very complex spatial patterns of hydraulic conductivity, leading to extremely complex solute transport behavior. That is, the Fick's law assumptions are no longer valid and the classical theory does not predict the amount of mixing. This phenomenon referred to as macrodispersion [1].

Understanding the characteristic behind such transport pathways related to macrodispersion is a crucial step to ensuring the reliable prediction of a contaminant behavior in a laboratory or a field. Field and laboratory scale experimental studies have been extensively conducted to examine macrodispersion in heterogeneous porous media. Several field experiments have also provided considerable insight into the transport process as affected by both small- and large-scale variations in the hydraulic properties [2]. The problem of field study is, however, that discrete point sampling provides only limited sampling spatially, and time required to collect samples limits sampling temporally. Such a difficulty to obtain detailed and comprehensive data sets directly in the field has led to the development of well-controlled laboratory experiments as useful tool to investigate macrodispersion process. In addition, image analysis techniques have become an attractive tool for a detailed monitoring of laboratory experiments at very high spatial and temporal resolution [3].

Macrodispersivities are often identified in the field by monitoring breakthrough curves at a limited number of observation wells [4]. However, field tracer test, in general, based on breakthrough curves cannot infer the transverse dispersivity. Contrary to the temporal moments, a snapshot of a cloud of solute particles in time expresses the dispersive variation in the aquifers, providing the estimates of spatial moments corresponding to the heterogeneity of concern [5].

The objectives of this study are to identify the laboratory-scale longitudinal and transverse macrodispersivities using a non-invasive technique in conjunction with a dye tracer and to elucidate the solute transport behavior in two-dimensional heterogeneous porous formations under saturated conditions. Spatial and temporal moment approaches linked with image data of dye tracer behavior and variations of NaCl concentration are utilized to rely on the difference between the two approaches.

EXPERIMENTAL METHODS

Materials and Experimental Apparatus

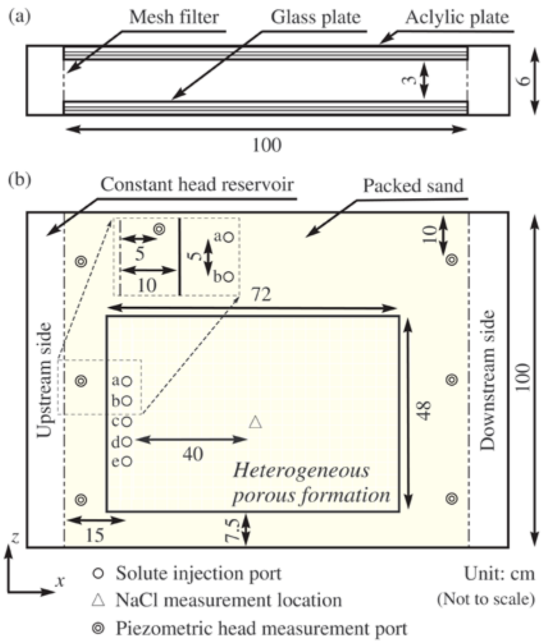

Fig. 1 Schematic diagram of experimental apparatus: (a) Plane view and (b) vertical view.

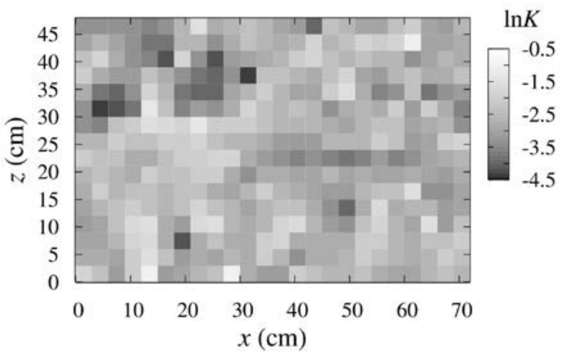

Fig. 2 The generated heterogeneous formation.

Flow and transport observations are routinely made using dye tracers that allow visual qualitative, and in some cases quantitative, evaluations of plume evolution. For the purpose of visualization of solute transport phenomena, in this study, Brilliant Blue FCF, which is a synthetic color having the nature of readily visible in soils, moderate mobile, and low toxicity [6], was used as a dye tracer. In particular, the advantage of Brilliant Blue FCF is its good visibility and against the color of the soil's background and its low toxicity [6]. NaCl was also mixed with dye tracer solution of Brilliant Blue FCF in order to observe the solute concentration of NaCl in a flow field. The initial concentrations of Brilliant Blue FCF and NaCl were adjusted to 0.40 mg/cm^3 and 5.0 mg/cm^3, respectively. The initial concentration of dye tracer was determined to be low enough to avoid density-induced flow effects.

The intermediate-scale experiments were carried

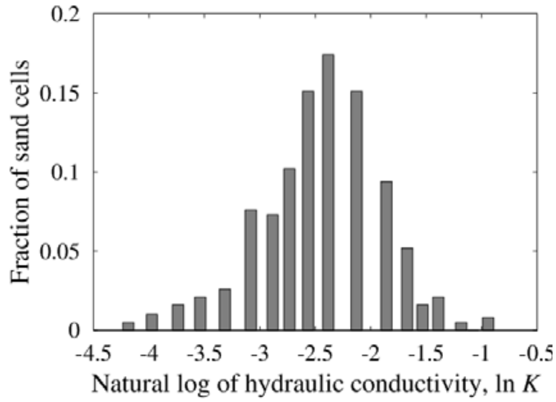

Fig. 3 The fraction distribution of the seventeen different materials.

out in a two-dimensional horizontal laboratory tank (100 cm × 100 cm × 3 cm) packed with silica sand to create a heterogeneous medium with well-defined statistical properties. The flow tank was constructed from 1.5 cm acrylic and glass plates for the front and back respectively and stainless steel for the both sides and bottom. At the front side, the glass plate provides the opportunity of visual observation of migrating dye tracer, while 6 manometers established at the perforated acrylic plate were placed in the flow tank to determine piezometric heads. Constant head water reservoirs connected to the upstream and downstream ends of the tank were used to control the water flow. Schematic diagram of experimental apparatus is shown in Fig. 1.

The area referred to as the heterogeneous formation shown in Fig. 1 was the primal area to create heterogeneous porous formation using seventeen different sands reflecting heterogeneous field sites. Hydraulic conductivity of each material was individually measured with a constant head column test. The hydraulic conductivity distribution assumed to follow a log-normal probability density function and was characterized by the geometric mean value of 0.0859 cm/s and the geometric variance of 0.3074 cm^2/s^2. The hydraulic conductivity distribution exhibits spatially-correlated structure defined by an exponential covariance function with correlation scale of 6 cm. The generated heterogeneous formation generated from block kriging and the fraction distribution of the seventeen different materials are shown on Fig. 2 and Fig. 3, respectively. Addition to the heterogeneous formation, as the base case of solute transport in homogeneous porous media, soil material ($\ln K = -2.13$) comprised a homogeneous porous formation.

Experimental procedure

Packing of the materials with 24 and 16 cells in

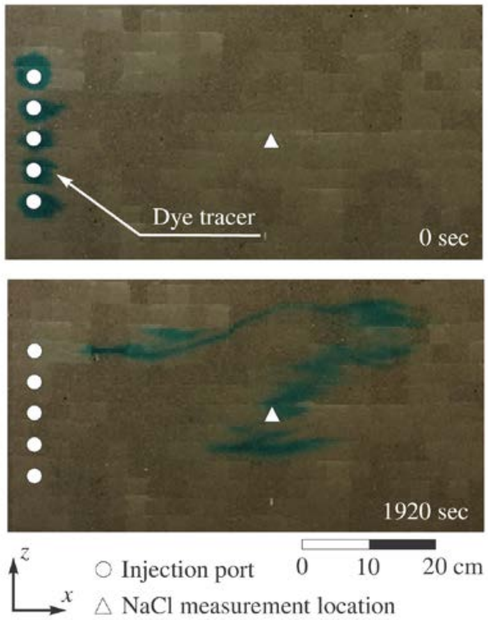

Fig. 4 Representative images of dye tracer transport in heterogeneous formation.

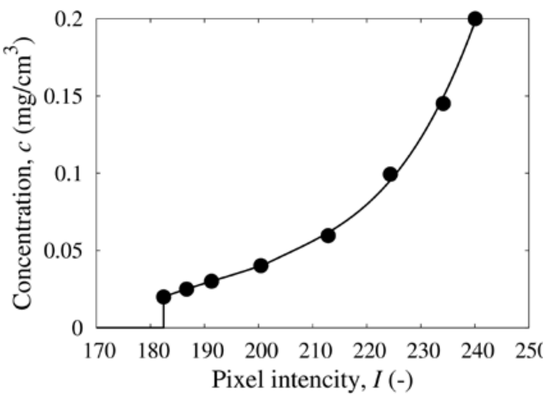

Fig. 5 Example of relation between the pixel intensity and the dye tracer concentration.

the *x* and *z* directions, respectively, was carried out under saturated conditions in order to avoid air entrapment. Each sand cell had 3 cm and 3 cm in both directions. The prescribed packing structures were established to transparent sheets described all sand cell locations and attached to the glass plate of flow tank. As the first step before creating heterogeneous porous packing, as shown in Fig. 1, the soil material with -1.18 of the geometric mean of the hydraulic conductivity was filled in 7.5 cm layer at the bottom of the tank through the process of compaction. In heterogeneous packing, the materials comprising each cell were packed in 3 cm layers using narrow dividers with the thickness of 1 cm to establish sharp connectivity between cells. The dividers were removed as packing progressed. The rest of upper area was filled by the same soil

Table 1 Experimental cases.

Case	Injection port	Flow rate (cm^3/min)
Homogeneous	1 point (c)	297
	3 points (b,c,d)	297
	5 points (a,b,c,d,e)	297
Heterogeneous	1 point (c)	297
	3 points (b,c,d)	297
	5 points (a,b,c,d,e)	101
	5 points (a,b,c,d,e)	184
	5 points (a,b,c,d,e)	297

material ($\ln K = -1.18$) in the same manner in 6 cm layers.

After packing, water was applied to the flow tank under a specific hydraulic gradient controlled by constant head water reservoirs at the upstream and downstream sides, while maintaining saturated condition of porous media. A steady saturated flow field was established in the flow tank when fluctuations in the observed drainage rate, which was effluent from the constant head water reservoir at the downstream side, and piezometer reading at water pressure measurement points could become negligible. In tracer experiments, to examine the effect of variation of flow rate on macrodispersion phenomena, the experiments were carried out for flow rates of 101, 184 and 297 cm^3/min.

After steady flow field was established, dye tracer of Brilliant Blue FCF mixed with NaCl was released from one injection port of c, three injection ports of b, c and d or five injection ports from a to e whose locations are depicted in Fig. 1. Experimental cases are listed in Table 1. The solution with 25 cm^3 in each injection port was injected for 30 seconds. During the experiment, the profiles of solute migration were recorded using a digital camera approximately 100 cm located away from the water flow tank.

Transport process and image calibration

Fig. 4 shows the typical image obtained during the tracer experiments. Each of the pixels representing an image has a pixel intensity which describes how bright that pixel is. Data recorded by the digital camera successfully indicated different pixel intensities in dye tracer distributions, suggesting different concentrations of the dye tracer. In order to establish a relationship between the color intensity and concentration, calibrations were performed and analyzed with solutes of known concentrations of dye. Example of regression curve is shown in Fig. 5.

Spatial Moment Approach

Spatial moments of aqueous concentrations distributed in space are calculated based on the spatial moment approach [7]. Spatial moments are calculated from digital image at given times as follows:

$$M_{ij}(t) = \int_{-\infty}^{\infty}\int_{-\infty}^{\infty} c(x,z,t)x^i z^j dxdz \tag{1}$$

where x and z are the Cartesian coordinates, c is the solute concentration, t is the time, M_{ij} is the spatial moments associated with the distribution of tracer plume at a certain time, and i and j are the spatial order in the x and z coordinates, respectively. Based on the regression curves relevant to the dye concentration and pixel intensity, the pixel intensity distribution can be converted to a concentration distribution by the calibration, providing an analogy between Eq.(1) and Eq.(2) [8]

$$M_{ij}(t) = \int_{-\infty}^{\infty}\int_{-\infty}^{\infty} H(x,z)I(x,z,t)x^i z^j dxdz \tag{2}$$

where $H(x,z)$ is the area per unit pixel and $I(x,z,t)$ is the intensity at a corresponding pixel. The centroid of concentration distribution is calculated as the normalized first-order spatial moment.

$$x_c = \frac{M_{10}}{M_{00}}, \quad z_c = \frac{M_{01}}{M_{00}} \tag{3}$$

where x_c and z_c are the centroid locations of plume concentration distribution in the x and z coordinates, respectively. The second order spatial moments are also computed as follows.

$$\sigma_{ij} = \begin{pmatrix} \dfrac{M_{20}}{M_{00}} - x_c^2 & \dfrac{M_{11}}{M_{00}} - x_c z_c \\ \dfrac{M_{11}}{M_{00}} - z_c x_c & \dfrac{M_{02}}{M_{00}} - z_c^2 \end{pmatrix} \tag{4}$$

where σ_{ij} is the second order spatial moments. Longitudinal and transverse macrodispersivities from spatial moments of the distributed tracer plume are calculated as [8]

$$A_L = \frac{1}{2}\frac{\sigma_{xx}}{\xi_c}, \quad A_T = \frac{1}{2}\frac{\sigma_{zz}}{\xi_c} \tag{5}$$

where A_L is the longitudinal macrodispersivity, A_T is the transverse macrodispersivity and ξ_c is the travel distance of the center of tracer plume in the mean flow direction at a given time t.

Temporal Moment Approach

The temporal moment approach was used to characterize the breakthrough data at NaCl measurement location. The jth normalized absolute temporal moments, $\mu_j(x)$, and the jth central temporal moments around the mean, $\mu'_j(x)$, are very useful descriptors of breakthrough curves (BTCs). The first-order temporal moment corresponds to the mean arrival time of solute, while the second-order temporal moment is an analogy with the statistical dispersion [9]

$$\mu_j(x,z) = \frac{\int_0^{\infty} t^j c_m(x,z,t)dt}{\int_0^{\infty} c_m(x,z,t)dt} \tag{6}$$

$$\mu'_j(x,z) = \frac{\int_0^{\infty} (t-\mu_1)^j c_m(x,z,t)dt}{\int_0^{\infty} c_m(x,z,t)dt} \tag{7}$$

where $\boldsymbol{c_m}$(x,z,t) represents the time variation of the NaCl concentrations at the monitoring locations, and j is the nonnegative integer corresponding to the order of concern. Longitudinal macrodispersivities using temporal moments are calculated as

$$A_L(\zeta_p) = \frac{\zeta_p}{2}\frac{\mu'_2(\zeta_p)}{(\mu_1(\zeta_p))^2} \tag{8}$$

where ζ_p is the distance from the source of solute injection, $\mu_1(x)$ is the first normalized absolute temporal moments and $\boldsymbol{\mu'_2}(x)$ is the second central temporal moments around the mean.

RESULTS AND DISCUSSION

Longitudinal Macrodispersivity

Longitudinal macrodispersivity values obtained from spatial and temporal moments in heterogeneous and homogeneous formations are shown in Fig. 6 as a function of the mean displacement distance of dye tracer distribution. Longitudinal macrodispersivity estimates in homogeneous formation remain constant during the course of solute transport, whereas longitudinal macrodispersivity estimates in heterogeneous formation exhibit the increase tendency with the increase of displacement distance. This is attributed

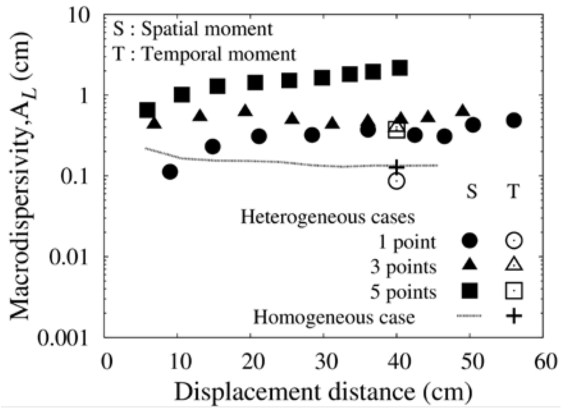

Fig. 6 Longitudinal macrodispersivity variation identified with spatial and temporal moments in heterogeneous and homogeneous formation.

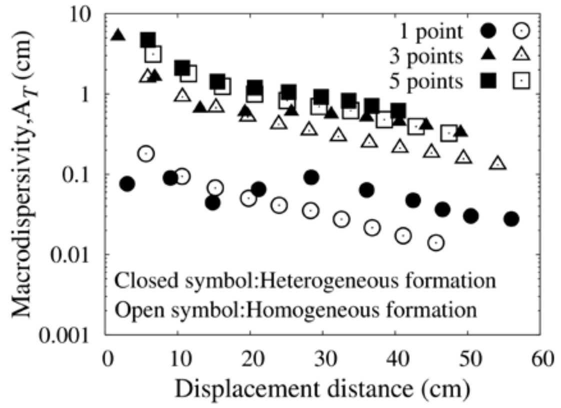

Fig. 7 Transverse macrodispersivity variation identified with spatial moments in heterogeneous and homogeneous formation.

to the distribution of hydraulic conductivity comprising flow fields and exhibits the evidence occurring macrodispersion phenomena in heterogeneous porous formation. Hence, these results demonstrate that the scale effect of macrodispersion can be observed under controlled laboratory conditions. In heterogeneous formation, longitudinal macrodispersivity values obtained from spatial moments show a dependency on the number of injection ports, or on the initial plume length in the *z* direction. This is due to the difference of the inherent heterogeneity associated with the solute transport pathway.

In homogeneous formation, longitudinal macrodispersivity estimates using temporal moments are almost identical to the macrodispersivity estimates obtained from spatial moments. This may suggest that single monitoring point leads to a plausible result in homogeneous porous formations if a direction from a solute injection port to a monitoring point is parallel to the

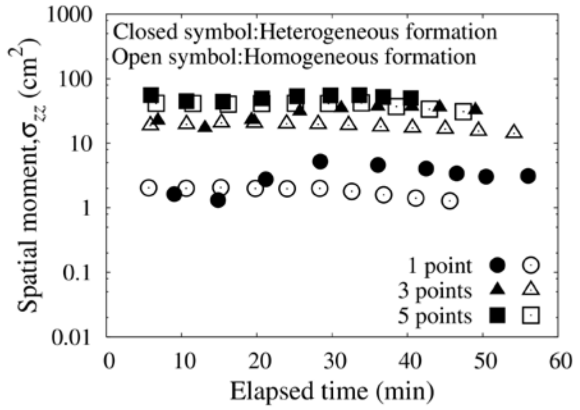

Fig. 8 Variation of spatial moment of σ_{zz} in each formation

regional flow direction. Contrary to this, in heterogeneous formation except for the case with 3 injection points, a marked difference between longitudinal macrodispersivity estimates from spatial and temporal moments appears. This indicates that single monitoring location is insufficient to capture the primal characteristics of solute transport as breakthrough curves and to identify a reliable estimate.

Transverse Macrodispersivity

The results of transverse macrodispersivity estimates obtained from spatial moments are shown in Fig. 7 as a function of the displacement distance of solute. The values of the transverse macrodispersivity indicate a dependency on the number of injection ports in the *z* direction and show the decrease tendency. To clarify this variation, the results of the second spatial moments in the *z* direction σ_{zz} as a function of elapsed time are shown in Fig. 8. The results of σ_{zz} exhibit a dependency on the plume-scale in the *z* direction. The geometrical elongation of the initial tracer distribution in the *z* direction provides a higher value of σ_{zz}. In addition, the velocity component in the *z* direction is relatively small to that in the *x* direction. Therefore, as shown in Fig. 8, the results of σ_{zz} remain constant during the solute transport, resulting in larger values of the transverse dispersivity associated with the source length in the *z* direction and a decrease tendency of the transverse macrodispersivity.

The difference of estimates between homogeneous and heterogeneous porous formations appears in transverse macrodispersivity variation shown in Fig. 7, especially in larger displacement distance. This is because the shapes of tracer plumes become complex and irregular according to the preferential pathlines of solute in heterogeneous formation, leading to the transverse

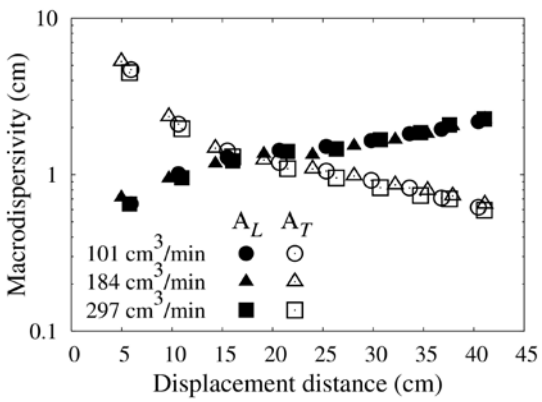

Fig. 9 Macrodispersivity estimates obtained from spatial moments at various flow rates.

macrodispersivity estimates in heterogeneous formation relative to those in homogeneous formation.

Effect of Flow Rate

In order to examine the effect of variation of flow rate on macrodispersion phenomena, three experimental cases with the initial dye release from five injection ports were performed at various flow rates of 101, 184 and 297 cm^3/min. Fig. 9 shows macrodispersivity estimates obtained from spatial moments at three flow rates. Longitudinal and transverse macrodispersivities have a non-dependency of flow rate. This agrees with earlier work [10], suggesting the reliability of estimates.

CONCLUSIONS

In this study, the behavior of macrodispersion in heterogeneous and homogeneous formations was assessed through intermediate-scale solute transport experiments. Longitudinal and transverse macrodispersivities were identified using spatial and temporal moment approaches using the dye tracer distribution and NaCl concentration, respectively. The following findings have been clarified.

1. Longitudinal and transverse macrodispersivity estimates obtained from spatial moments of the distributed dye tracer plume in heterogeneous formation were larger than those in homogeneous formation.
2. Longitudinal and transverse macrodispersivity values obtained from spatial moments in heterogeneous formation show a dependency on the plume-scale in the *z* direction.
3. In homogeneous formation, longitudinal macrodispersivity estimates using temporal moments are almost identical to the macrodispersivity estimates obtained from spatial moments. On the other hand, in heterogeneous formation, a marked difference between longitudinal macrodispersivity estimates from spatial and temporal moments appeared.
4. Longitudinal and transverse macrodispersivities have a non-dependency of the regional flow rates.

REFERENCES

[1] Gelhar LW, Welty C, Rehfeldt KW, "A critical review of data on field-scale dispersion in aquifers", Water Resour. Res., 28(7), 1992, pp.1955-74.

[2] Sudicky EA, "A natural gradient experiment on solute transport in a sand aquifer: Spatial variability of hydraulic conductivity and its role in the dispersion process", Water Resour. Res., 22(13), 1986, pp.2069-82.

[3] McNeil JD, Oldenborger GA, Schincariol RA, "Quantitative imaging of contaminant distributions in heterogeneous porous media laboratory experiments", J. Contam. Hydrol., 84, 2006, pp36-54.

[4] Adams EE, Gelhar LW, "Field study of dispersion in a heterogeneous aquifer 2. Spatial moments analysis", Water Resour. Res. 28(12), 1992, pp.3293-307.

[5] Fadili A, Ababou R, Lenormand R, "Dispersive particle transport: identification of macroscale behavior in heterogeneous stratified subsurface flows", Math. Geol., 31(7), 1999, pp.793-840.

[6] Flury M and Flühler H, "Tracer characteristics of brilliant blue FCF", Soil Sci. Soc. Am. J., 59, 1995, pp.22-27.

[7] Tompson AFB, Gelhar LW, "Numerical simulation of solute transport in three-dimensional, randomly, heterogeneous porous media", Water Resour. Res., 26(10), 1990, pp.2541-62.

[8] Inoue K, Kobayashi A, Suzuki K, Takenouti R, Tanaka T, "A new approach for estimating macrodispersivity using dye tracer and spatial moment analysis", Annual J. Hydraulic Eng., JSCE, 55, 2011, pp.613-618 (in Japanese).

[9] Fernàndez-Garcia D, Illangasekare TH, Rajaram H, "Difference in the scale-dependence of dispersivity estimated from temporal and spatial moments in chemically and physically heterogeneous porous media", Water Resour. Res., 28, 2005, pp.745-59.

[10] Zinn B, Meigs LC, Harvey CF, Haggerty R, Peplinski WJ, Von Schwerin CF, "Experimental visualization of solute transport and mass transfer process in two-dimensional conductivity fields with connected region of high conductivity", Environ. Sci. Technol, 38, 2004, pp.3916-3926.

Fifth International Conference on Geotechnique, Construction Materials and Environment, Osaka, Japan, Nov. 16-18, 2015, ISBN: 978-4-9905958-4-5 C3051

STRESS-STRAIN BEHAVIOR OF GEOSYNTHETIC REINFORCED SOIL USING A MODIFIED CBR TEST

Danny Useche Infante[1,2], Gonzalo Aiassa Martinez [1], Pedro Arrúa [1] and Marcelo Eberhardt[1]
[1] Facultad Regional Córdoba, Universidad Tecnológica Nacional, Argentina; [2] Doctoral Fellow CONICET, Argentina

ABSTRACT

In previous works several experimental investigations aimed at establishing the behavior of granular soils reinforced with geosynthetics have been conducted. It has been found that the capacity of the soil improves due to a tensile force given by the geosynthetic that thus provides a soil reinforcement function and therefore allows a better distribution of pressure in the soil. Many of these studies report the use of CBR tests to characterize the behavior of reinforced soil. The CBR test measures the vertical deformation with application of vertical loads, by which it is possible to characterize the stress-strain behavior of the material. In this paper, modified CBR tests are performed on samples of granular soils reinforced with geogrids in order to establish the behavior of reinforced soil at the load application surface from foundations; in this case the displacements are restricted in the cylinder edges of CBR test. The results are compared with those obtained by CBR testing performed without restricting displacements at the edges and without including any type of reinforcement, which were documented in previous work of the authors.

Keywords: Shallow Foundations, Geosynthetics, Reinforced Soil, CBR

INTRODUCTION

A considerable amount of literature has been published on improvements achieved by including geosynthetics in the soil mass with shallow foundations: [1]-[3]. Stress-strain behavior of geogrids reinforced soil, with use of the CBR test, has been studied in [4]. In research presented at [5], the authors conducted an investigation with a modified CBR device to characterize the behavior of soil-geotextile system and the mechanism of reinforced.

In this paper, an experimental study using the CBR test is performed to determine the stress-strain behavior of sand with the inclusion of geosynthetics. In particular the case is studied where the geosynthetic is anchored to the CBR mold, in order to reproduce the condition in which the geosynthetic is pressed by compacted ground and a tension force occurs when the geosynthetic deforms by the application of loads.

Subsequently, the results are compared with samples without anchoring of the geosynthetic to the mold. Therefore, it is possible to establish the improvement achieved in the soil mass by including geosynthetics anchored and unanchored to the mold. Some results for specimens without geosynthetic and geosynthetic layers not anchored to the mold were reported in [6], and are considered in this work to determine the effect of fixing the geosynthetic to the mold in stress-strain behavior of a soil-geosynthetic system.

MATERIALS

Sand

In tests, natural sand of Córdoba Argentina is used. This soil is commonly utilized in shallow foundations of structures and embankments bases. The Granulometric distribution of the sand is presented in Fig. 1, the sand is classified by the USCS system as SW (Well graded sand) with uniformity coefficient C_u=8.9 and curvature coefficient C_c=1.7.

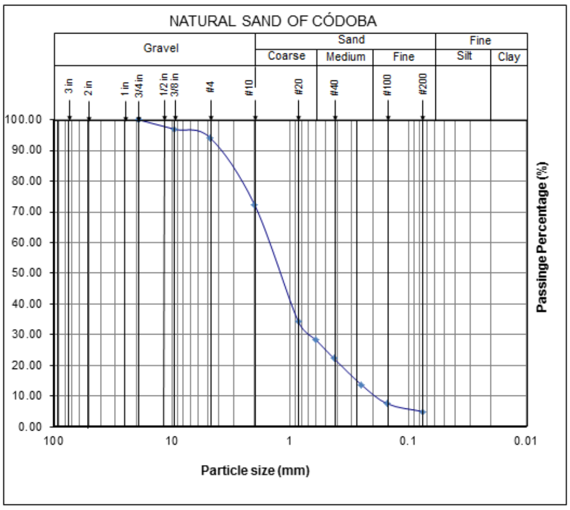

Fig. 1 Granulometric distribution of the sand.

Geosynthetic

In the soil mass uniaxial geogrids are used, commercialized by CORIPA S.A, a local company. Table 1 shows the physical and mechanical properties of the geogrid used. These geogrids are flexible mesh with shaped orthogonal grid made up of woven filaments of polyvinyl alcohol (PVA) covered with a polymeric coating, with high tensile strength, a high stiffness modulus and low susceptibility to yield.

Table 1 Mechanical properties of geogrids [7].

Property	Unit	Value
Tensile strength (to def. 5%)	kN/m	35
Functional modulus (def. 5%)	kN/m	700
Strain to break	%	5
Tensile strength (to break)	kN/m	35
Tensile strength to yield for 120 years ≤ 30ºC	kN/m	23
Mesh opening	mmXmm	20X30

LOAD TEST

A modified CBR type tests were conducted on compacted sand samples. The compacted specimens were reinforced and unreinforced by geosynthetic. Some samples were also prepared with geosynthetic anchored to the edge of the mold (Table 2).

Table 2 Tests conducted.

No. Specimen	Description of the test	Compaction of the sample
1	Without geosynthetics	Three layers, 55 blows each
2	A geosynthetic layer on the upper third part of the sample	Three layers, 55 blows each
3	A geosynthetic layer halfway the sample	Three layers, 55 blows each
4	Two layers of geosynthetics on the upper third part of the sample	Three layers, 55 blows each
5	A geosynthetic layer halfway the sample anchored in the edge of the mold	Two layers 83 blows each
6	A geosynthetic layer on the upper third part of the sample anchored in the edge of the mold	Three layers, 42 blows each

The first 4 samples were prepared in the mold used to standard proctor compaction test, preparing samples with 152.4 mm of diameter and 110 mm of height (see [6]). The geogrid was cut into the circular bore size of the mold and introduced into the soil mass as the geometry shown in Figs. 2b, 2c and 2d. For specimens 5 and 6, two rings with 152.4 mm of diameter and 53 mm of height were used in order to press the geosynthetic and thus restrict movement of the geosynthetic on the edge of the mold; for a geosynthetic layer halfway the sample, the height of the specimen after compaction was 106 mm (see Fig. 2e) and for the sample with a geosynthetic layer on the upper third part the height of the specimen after compaction was 82 mm (see Fig. 2f). Compaction of the material was using a 5.5 lb hammer (2.5 kg) with different layers according to the sample volume or the purpose of conserving constant compaction energy as can be seen in Table 2. Load readings of every 0.2 mm piston settlement up to a depth of 20 mm were taken. This was followed by readings every 1 mm until completing a depth of 25 mm, where the trial ends. The piston used to transfer the load to the soil mass had a diameter of 50.8 mm. The dry density of samples γ_d were 19 kN/m^3 with a variation of ± 1.0 kN/m^3 while the moisture content was 4% with a variation of ± 1%.

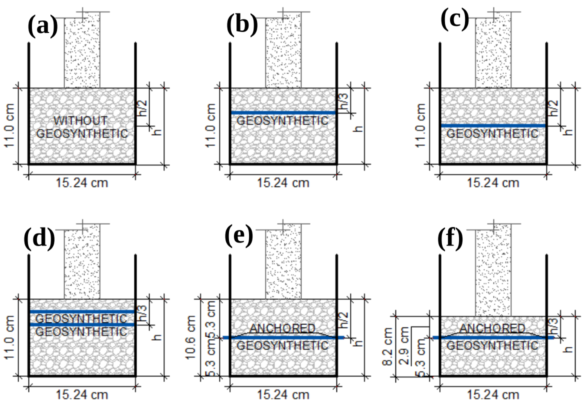

Fig. 2 Scheme of the tests described in Table 2, (a) Specimen No. 1, (b) Specimen No. 2, (c) Specimen No. 3, (d) Specimen No. 4, (e) Specimen No. 5, (f) Specimen No. 6.

EXPERIMENT RESULTS

Stress vs. Settlement graphics are performed for each specimen by obtaining values shown in Fig. 3. In these curves different behaviors for small and large deformations were observed. Growth in the slope of the curve is presented from 2.5 mm settlement typical behavior of sands in CBR type tests. From Fig. 4 to Fig. 7 stress-strain behavior for small, medium and high deformations is shown. Subsequently, vertical displacements produced in the geosynthetic for each of the reinforced soil specimens are presented.

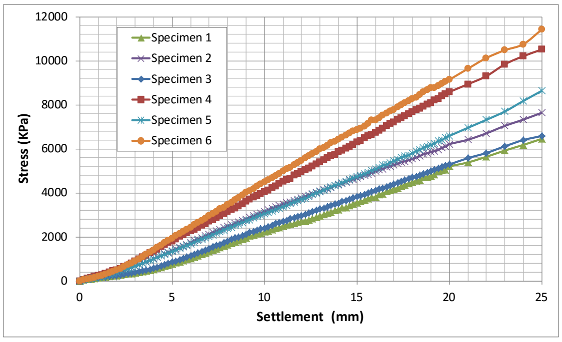

Fig. 3 Stress vs. Settlement for the specimens tested.

The values obtained for deformations below 1 mm are shown in Fig. 4. There can be seen some erratic data and in some specimens improvement is achieved. It is also shown no significant improvement for specimen 3 corresponding to the geosynthetic layer halfway. In Fig. 5, deformation behavior between 1 mm and 5 mm is presented. The data trend is shown and the improvement is seen with the inclusion of geosynthetics, except when a layer of geosynthetic is used halfway the sample (Specimen No. 3). From 2.5 mm settlement an accelerated growth curve is shown, marking stiffening.

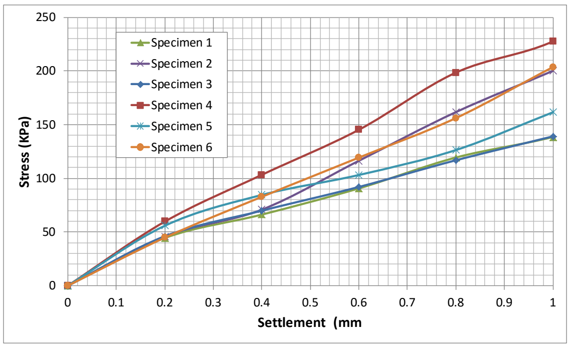

Fig. 4 Stress vs. Settlement for the specimens tested to lower strains than 1 mm.

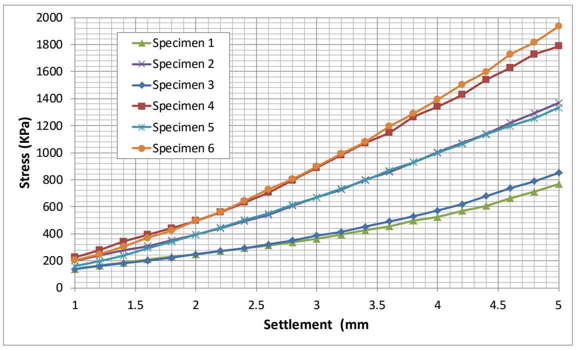

Fig. 5 Stress vs. Settlement for the specimens tested to strains between 1 mm and 5 mm.

In Fig. 6, the curves for deformation between 5 mm and 15 mm can be seen, the growth shown from 2.5 mm settlement remains. A small improvement is shown for specimen 3 (geosynthetic used halfway the sample unanchored to the mold), which had shown no increase with small deformations. Fig. 7 shows the results for high strains, namely strains from 15 mm to 25 mm; in this case the linear trend of the data is maintained.

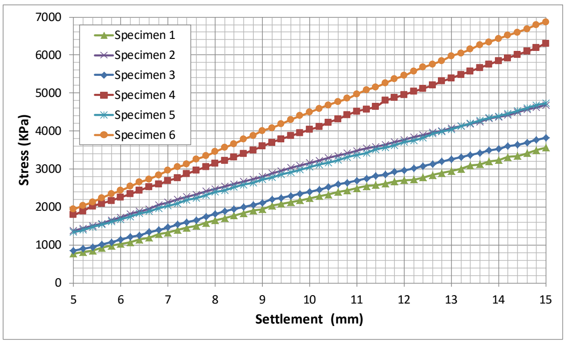

Fig. 6 Stress vs. Settlement for the specimens tested to strains between 5 mm and 15 mm.

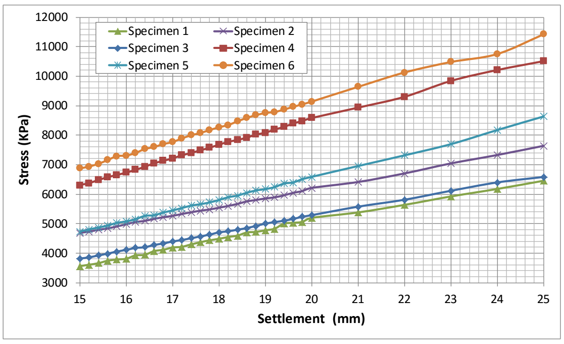

Fig. 7 Stress vs. Settlement for the specimens tested to strains between 15 mm and 25 mm.

Furthermore, vertical relative deformations in the geosynthetic were measured. These measurements were made from the upper horizontal plane of the specimen, every 2 cm from the central axis considering the directions shown in Fig 8. Before measuring, the soil above the layer of geosynthetic in the specimen was removed. Vertical profiles were performed along the coordinate axes for each layer of geosynthetic, obtaining the resulting deformation in the geogrid at the end of the test. The results of these measurements show some small initial deformations caused by soil compaction, these are located at different points of geogrid and are most evident in the samples in which the geosynthetic is not anchored to the mold. The vertical profiles for the different layers of geosynthetic according to the different geometric configurations (see Fig. 2 and Table 2) can be seen in Fig. 9 and Fig. 10.

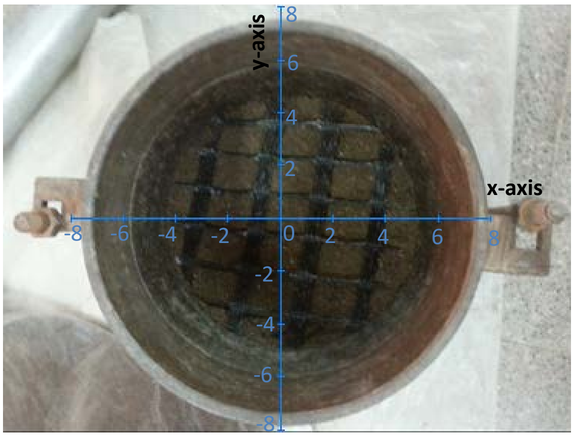

Fig. 8 Axes (Unit: cm) used to measure the vertical displacements in the geosynthetic.

The vertical displacements along the x-axis for the specimens with geosynthetics can be seen in Fig. 9 and the displacements along the y-axis are shown in Fig. 10. In these curves, greater deformation can be observed in specimen 6, in which the displacements of geosynthetic are restricted in the edges, where the geogrid layer presses the mold. The top layer of the specimen 4 (where two layers of geosynthetic are used in the upper third part of the sample) also shows greater deformations than 1.5 cm, proving that a tensile force occurs in the geosynthetic that results in an improvement in soil behavior.

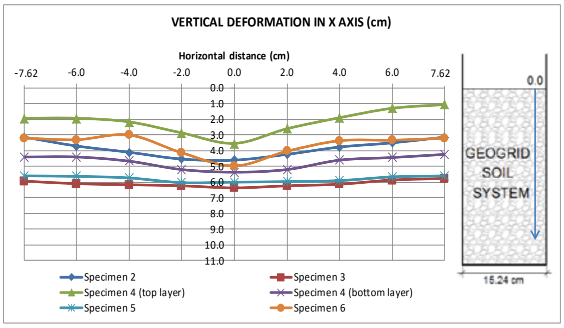

Fig. 9 Geosynthetic vertical displacement (x-axis).

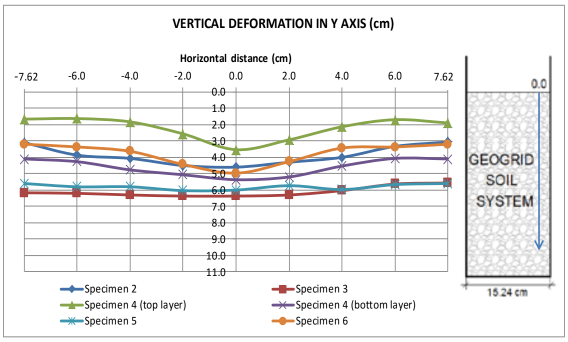

Fig. 10 Geosynthetic vertical displacement (y-axis).

ANALYSES AND DISCUSSION

In order to estimate the improvement of the soil produced by the inclusion of geogrids, a modified BCR (Bearing Capacity Ratio) as well as the index SR (Stress Ratio) are calculated for each of the samples tested.

BCR (modified Bearing Capacity Ratio)

With the results of the experiment the BCR (modified Bearing Capacity Ratio) was calculated and the data obtained from the samples anchored and unanchored to the mold were compared. As can be seen when the geosynthetic is pressed by the mold, a tension force occurs in the geosynthetic achieving a much greater improvement in the soil. The BCR was defined in [8] as the ratio of the ultimate bearing capacity of reinforced soil and ultimate bearing capacity of unreinforced soil. In the present study, the ratio is performed for vertical load between reinforced and unreinforced samples at the same settlement. So, we defined it as modified BCR as follows:

$$BCR = \frac{q_{(R)}}{q_{(U)}} \qquad (1)$$

where $q_{(R)}$ and $q_{(U)}$ are the values of the applied load during the test for reinforced and unreinforced soil respectively for the same settlement value.

The modified BCR is plotted against the ratio of settlement (s) and the width of the foundation (B) for the purpose determining the improvement in soil produced for different values of (s/B).

Fig. 11 provides the BCR versus the relation (s/B) for specimens 2 and 6 with a geosynthetic layer included in the upper third part of the sample unanchored (2) and anchored (6) to the mold (see Table 2). Evidently, a further increase in the BCR occurs when the geosynthetic is pressed by the mold (Specimen 6). A peak value can also be seen for BCR when the ratio (s/B) is closer to 0.08, namely when Settlement reaches piston 4 mm.

The results, for the specimens with a geosynthetic layer halfway the sample, are presented in Fig. 12. In this case can be seen that when the geogrid is included in the soil without being anchored to the mold edges, no significant increase occurs in the BCR, however when the geosynthetic is anchored to the mold, this value increases reaching a maximum value when the ratio (s/B) is near to 0.08 as occurs in the samples with a geosynthetic layer in the upper third part.

Fig. 13 shows the curve for specimen 4 in which two layers of geosynthetic in the upper third part of the sample are included without any anchor. It shows similar behavior to the other specimens tested with a peak in the value of the BCR when the value of the ratio (s/B) is close to 0.08. The sample in which a larger value of BCR is reached corresponds to specimen 6, with a geosynthetic layer on the upper third part of the sample anchored to the mold (see Fig. 2 and Fig. 11).

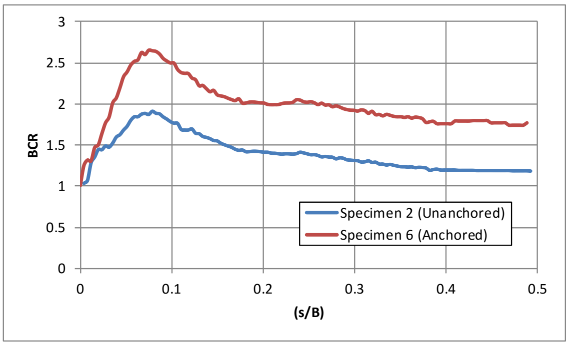

Fig. 11 BCR vs. (s/B) for a geosynthetic layer included in the upper third part of the sample; with geogrid unanchored (Specimen 2) and with geogrid anchored (Specimen 6).

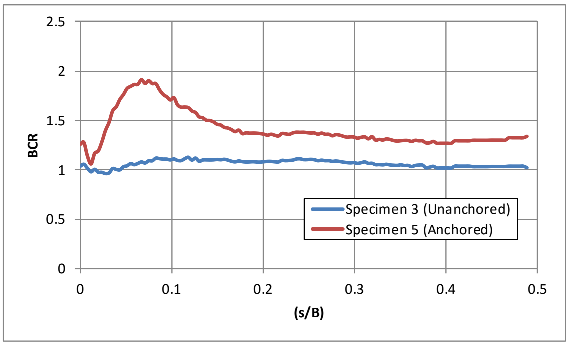

Fig. 12 BCR vs. (s/B) for samples with a layer of geosynthetic in halfway; with geogrid un anchored (Specimen 3) and with geogrid anchored (Specimen 5).

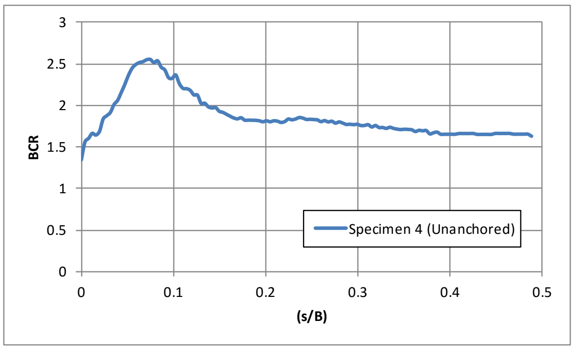

Fig. 13 BCR vs. (s/B) for the specimen 4, with two layers of geosynthetic in the upper third part of the sample unanchored to the mold.

Index calculation SR (Stress Ratio)

The SR (Stress Ratio) index relates the stress values obtained in load tests with standard values to the same deformation. It was calculated for each specimen as follows:

$$\boldsymbol{SR} = \frac{\boldsymbol{Stress\ (kPa)}}{\boldsymbol{Standard\ Stress\ (kPa)}} * \mathbf{100} \qquad (2)$$

This index is calculated for stress values corresponding to 2.5 mm and 5.0 mm of settlement obtained from stress-settlement curves, which are divided between CBR test standard stress of 1000 Psi (6900 kPa) and 1500 psi (10300 kPa) respectively. In other words, with this analysis small deformations are measured.

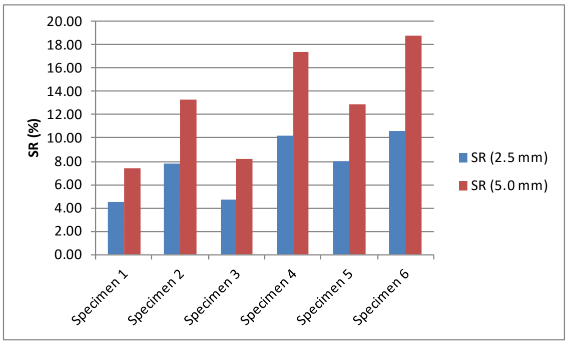

Fig. 14 SR for the specimens tested.

In Fig. 14, SR results are shown for each of the samples tested. It can be seen that no appreciable increase occurs in the SR rate for specimen 3. This means that including a geogrid layer halfway the sample produced no improvement in the soil, although when the geogrid layer is pressed by the mold (the displacements are restricted in the edge of the mold) a considerable increase occurs in the SR as is shown in the values obtained for specimen 5.

The results for the other samples show a significant increase in the SR using geogrid, especially when they are anchored to the edge of the mold. These results are similar to those achieved calculating the modified BCR.

CONCLUSIONS

In this paper, modified CBR test was performed on compacted sand samples in order to determine the effect of the geosynthetic inclusion on the behavior of soil-geosynthetic systems. From the experimental results, the following can be concluded:

For settlements, s/B, around 8%, results show a significant increase when geosynthetics are included in the soil mass. The calculated values of modified BCR show that for deformations near to 4 mm a peak value occurs in the BCR, which results in an appreciable improvement in soil behavior.

The values of SR (Stress Ratio) show a significant increase particularly when the geosynthetic is anchored to the mold edges.

The improvement obtained when the geosynthetic layer is boundary anchored by the mold, is better than when it is left unanchored. The tension force developed by the geogrid when it is anchored to the mold can clearly be seen, therefore it is important to establish a sufficient anchorage length in geosynthetic, enough to ensure that this force occurs. In the present tests, a size of geogrid three times the width of the foundation (3B) was used.

For large settlements (s/B > 10%), the results showed that although the improvement that occurs is below the peak, an asymptotic behavior occurs in the BCR, which is >1 (see Figs. 11, 12 and 13). The behavior of modified BCR vs. s/B presents a curve with two differentiated zones denominated as pre-peak and post-peak. It is estimated that this can be provisionally explained as follows: (1) First, the development of tension in the geosynthetic, and friction interaction sand-geogrid, during the first settlements produces an increased in modified BCR reaching a maximum at optimum combination between compacted soil and geosynthetic effect, (2) then the curve drops to stabilize at a given value of BCR, higher than one (asymptote) where, possibly, have been reaching a residual friction interaction sand-geogrid. However, it will be necessary to increase the experimental study and numerical analysis of the behavior, in order to confirm this explanation. For this, direct shear tests are planning, where sand-geogrid interaction can be studied.

In addition, larger scale tests are planned in order to validate the present results and establish the optimum value of the anchorage length as well as the overlapping layers.

Furthermore, other variables such as soil moisture, shape and size of the foundation should be considered. Also experiments with biaxial geogrids should be considered, as well as different forms of geometric configuration of the soil-geosynthetic system.

ACKNOWLEDGEMENTS

The authors would like to thank the NationalScientific and Technical Research Council (CONICET), the National Technological University (UTN), the Regional Faculty of Córdoba (Argentina) and CORIPA S.A. for the geogrid samples provided.

REFERENCES

[1] Chen, X.; Zhang, J. y Li, Z. “Shear behaviour of a geogrid-reinforced coarse-grained soil based on large-scale triaxial tests”. Geotextiles and Geomembranes, 42, 4, 2014, pp. 312-328.

[2] Kumar, S.; Solanki, C.H. and Pandey, B.K. “Behaviour of prestressed geotextile-reinforced fine sand bed supporting an embedded square footing” Int. J. of GEOMATE. Vol. 8, No. 2, 2015, pp. 1257-1262.

[3] Marto, A.; Oghabi, M. and Eisazadeh, A. “The effect of geogrid reinforcement on bearing capacity properties of soil under static load; a review”. Electronic Journal of Geotechnical Engineering, 18, 2013, pp. 1881-1898.

[4] Duncan-Williams, E. and Attoh-Okine, N. O. “Effect of geogrid in granular base strength - An experimental investigation”. Construction and Building Materials, 22, 2008, pp. 2180-2184.

[5] Bergado, D.T.; Youwai, S.; Hai C.N. and Voottipruex, P. “Interaction of nonwoven needle-punched geotextiles under axisymmetric loading conditions”. Geotextiles and Geomembranes, 19, 5, 2001, pp. 299-328.

[6] Aiassa, G.M.; Useche, D.J.; Arrua, P. and Eberhardt, M. “Investigación experimental del comportamiento de cimentaciones superficiales sobre arenas reforzadas con geosintéticos”. XV Congreso Panamericano de Mecánica de Suelos e Ingeniería Geotécnica. (accepted 2015).

[7] CORIPA: www.coripa.com.ar/productos/4-geogrillas.

[8] Das, B.M. Shallow Foundations: Bearing Capacity and Settlement. CRC Press, 1999.

FifthInternational Conference on Geotechnique, Construction Materials and Environment, Osaka, Japan,Nov. 16-18, 2015, ISBN: 978-4-9905958-4-5 C3051

INFLUENCE OF DIFFERENT INITIAL DENSITIES IN THE HIDROMECHANICAL BEHAVIOR OF STABILIZED LOESSIC SOILS

Alercia Biga Carolina[1], Arrúa Pedro[2], Eberhardt Marcelo[3], Aiassa Martinez Gonzalo[4]
[1,2,3,4] Grupo de Investigación y transferencia en Geotecnia, Estructuras y Fundaciones (GIGEF), Departamento de Ingeniería Civil, Facultad Regional Córdoba, Universidad Tecnológica Nacional, Argentina

ABSTRACT

Loessic soil is widely recognized for its metastable structure which, in a randomica way, presents soil particles linked together by soluble salts bridges , forming an open mineral skeleton, which therefore, in presence of cycles wetting, cause a dissolving of these links causing an internal slippage and thereby resulting a new macroscopic structural reorganization. The arrangement of the porous medium and its porosity, characterize the soil hydromechanical response. Thus, the geotechnical properties are significantly modified by using different compaction methods and the addition of natural agents as sodium motmorillonite.

This paper presents a series of tests using remoulded samples, based on the influence of different initial compaction densities and different percentages of bentonite, in the hydraulic and mechanical behavior. Infiltration assays were performed with the falling head technique, by using a flexible wall permeameter. Also, a universal compression machine was used to execute unconfined compressive tests.

The experimental results are compared to those obtained in natural soil samples remoulded at different densities. The comparatives show that, increasing the packing density in conjunction with the addition of bentonite, achieve greatly improve the hydraulic and mechanical properties of loessic soils, getting geotechnical structures more resistants and less permeable hydraulically.

Keywords: Permeability coefficient, Bentonite, Axial stress, Flexible wall permeameter, Loessic soil.

INTRODUCTION

Loess is aeolian sediment and is one of the most extensive surficial deposits on the surface of the Earth. Loess has come to be regarded as one of the most important archives of long-term dust deposition and Quaternary climate change. [1]

Loess soils are usually found in arid or semiarid climates and their physical and chemical characteristics mainly depends on their geological origin.

South American loess presents a broad geographic distribution extending across the Chaco–Pampean Plain of Argentina and neighboring areas of Uruguay, southern Brazil (Rio Grande do Sul), Paraguay, and the eastern Bolivia lowlands [2]

The largest area of loess soils is concentrated in central Argentina.

The accumulation of loess has been explained through a combined mechanism of fluvial and aeolian transport from the Andes to the eastern lowlands. [2]

It is estimated a volume of 34000-45000 cubic kilometers for the Argentine Pampas loess, estimating an average thickness of 30-40 meters and a deposition period of 2.5 million years.[3]

The mineralogical structure is composed by volcanic origin materials and is alkaline in nature. Grain-size distribution includes fine sand (1%-10%), silt (50%-80%) and clay (2%-15%) that have been deposited by wind action in areas of low energy [4][5]. In nature the loess has an open structure [6], low unit weight, and it is highly dependent on external conditions. Loessic soils are characterized by volumetric instability due to wetting and stress state changes. [7] The purpose of the addition of bentonite is to stabilize the silty loess due to low technical qualities for application in construction works. [8][9]

This paper presents an experimental study characterizing the mechanical and hydraulic loess response improved with bentonite. The variables affecting the samples manufacturing were the influence of bentonite content, water content, and dry unit weight. They were analyzed to the optimization of infiltration and compression tests.

Argentinean loessic soils Performance

Due to its random structure and its low unit weight, the stability and strength of the soil mass is highly dependent on the strength of the bonds and contacts between particles. Wetting and dissolution of salts that make contact bridges altering the behaviour of the soil mass.

Hydraulic conductivity is affected by this phenomenon. There are numerous factors that control this conductivity like porosity, degree of saturation, particle size, structure, and properties of the permeant fluid [10].

That is why it is important to know, how these factors affect the soil behaviour, to understand the geotechnical soils response against different environmental conditions.

It has been analyzed the behaviour of Cordoba loessic soil by adding materials such as bentonite. It has been reported changes in values of mechanical and hydraulic response obtained experimentally in Cordoba loess soils. [11][12].

MATERIALS

Loessic soil

The soil used was obtained from boreholes at 1m depth, in Ciudad Universitaria, Córdoba. Table 1 presents the principals geotechnical properties of the soil used in this work.

Bentonite

Sodium bentonite was used. It comes from deposits from Pellegrini Lake, Black River, located at north of Patagonia. Composed of 92% of motmorillonite, and lower percentages of quartz, gibbsite, feldspar, calcite and zeolites. It has a high sodium content product as a result of presence of soluble salts and cations retained in the thickness of the diffuse double layer. The magnesium comes from octahedral positions of the clay structure, from soluble salts and exchangeable cations. Generally show high proportions of iron between 4% and 6%. It has a high cation exchange capacity, which varies between 76 and 97 meq/100g. The exchangeable ions are Na+, Ca++, Mg++ and K+, with a predominance of sodium cations, hence its classification [13]. It has high plasticity and high swelling capacity. Table 1 presents the principals geotechnical properties of the soils used in this work.

METHODS

The materials were collected on trays at 20ºC during 24 hs. Soil passing sieve 100 was used. Soil has been drying at 105 ºC during 24 hs. The loessic soil comparison specimen was four different dry units weight, $\gamma_{d\,1}$ (kN/m^3) = 1.4, $\gamma_{d\,2}$ (kN/m^3) = 1.5, $\gamma_{d\,3}$ (kN/m^3) = 1.6 and $\gamma_{d\,4}$ (kN/m^3) = 1.7, and the compaction water content was ω_{ini} (%) = 20. Three groups of soil were selected, (a) specimens with different dry unit weight with a 3% content of bentonite respect to the dry unit weight of soil. They called SB1-1, SB1-2, SB1-3 and SB1-4. (b) Specimens with different dry unit weight with a 6% content of bentonite respect to the dry unit weight of soil. They called SB2-1, SB2-2, SB2-3 and SB 2-4. (c)) specimens with different dry unit weight with a 9% content of bentonite respect to the dry unit weight of soil. They called SB3-1, SB3-2, SB3-3 and SB 3-4 and the last group was only made of loessic soil. They called S1, S2, S3 and S4. Specimens were 0.07 m in diameter and 0.14m in high. Static compaction method was used to prepare samples, in cylindrical metallic molds. The specimen test was built and compacted in three layers of equal thickness. Extraction of samples was performed using a hydraulic jack. In order to conserve water content, plastic bags were used.

Table 1. Materials properties

Properties	Loess	Bentonite
γ_d (kN/m^3)	***12.2-14.5***	**--**
γ (kN/ m^3)	***14.9-16.8***	**---**
LL (%)	***20.8-32.2***	***301***
IP (%)	***0-8***	***231***
Gs	***2.68***	***2.71***
***Ps* 200 (%)**	***96***	***100***
Clay content< 0,002 mm	***4***	***85***
SUCS	***CL-ML***	***CH***
***Ss* (m^2 /g)**	***1***	***731(*)***
Ph	***> 8***	***7-7.5***
***Sc* (%)**	***0.38***	***< 0.1***

Note: γ = natural unit weight, LL = Liquid limit, IP = Plasticity index, Gs = Specific gravity, Ps = passing sieve, Ss = Specific surface, Sc = salt content. (*) [14]

INFILTRATION TEST

A flexible wall permeameter was used to evaluate hydraulic properties of samples. Falling head permeability test was conducted [15]. Fig.1

Loess-bentonite samples were infiltrated in unsaturated and saturated condition. At the ends of each sample, filter paper and porous stones were used. Porous stones were saturated during 24 hours. During infiltration tests, the gradient was 10 [15]. Pressures for the camera, upper and lower head were taken as 117 kPa, 114 kPa and 100 kPa respectively. Deaerated water was used as permeant fluid.

In unsatured condition, the infiltration rate (I_r) is adopted (Eq. (1)).

$$I_r = \frac{\Delta V(t)}{\Delta t \; A} \tag{1}$$

Where ΔV: volume infiltrate during time Δt, A: cross section specimen area. Under saturated condition the permeability parameter k is obtained with Eq. (2).

$$k = \frac{a\,L}{A\,\Delta t} Ln \left(\frac{PB_1 + \frac{V_{u(t_1)} - V_{l(t_1)}}{a}}{PB_2 + \frac{V_{u(t_2)} - V_{l(t_2)}}{a}} \right) \tag{2}$$

Where a: area of burette, L: length of sample, A: area of sample, Δt: lapsed time, PBi: bias pressure, V_u $(t$i): volume reading of upper burette at time i, $V_l(ti)$: volume reading of lower burette at time i. The saturation level was calculated as $B = [(u_2 - u_1)/(\sigma_2 - \sigma_1)]$. Where u_2 - u_1: increase in pore pressure, σ_2 - σ_1: increase in cell pressure. We consider that, B at 98% is saturation condition [16]. At the end of experiment, the water content was established in each sample.

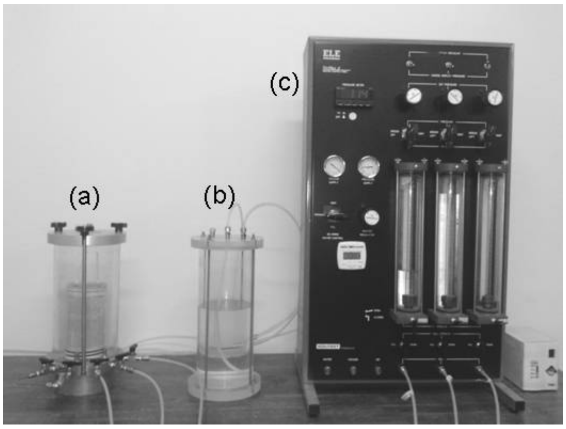

Fig.1 Flexible Wall Permeameter. (a) Infiltration cell. (b) Transfer tank. (c) pressure-volume panel

UNCONFINED COMPRESSION (UC)

For UC test a mechanical press was used instrumented with a load cell with a capacity of 50kN and a digital comparator for recording displacements with a precision of 0.001 mm, to a constant deformation rate of 2.4 mm/min. UC tests was used to evaluate the stress–strain characteristics and the stiffness properties of the Soil-Additive-Mixture. Fig. 2
Unconfined compression strengths were determinate on loess- bentonite samples and loess samples.

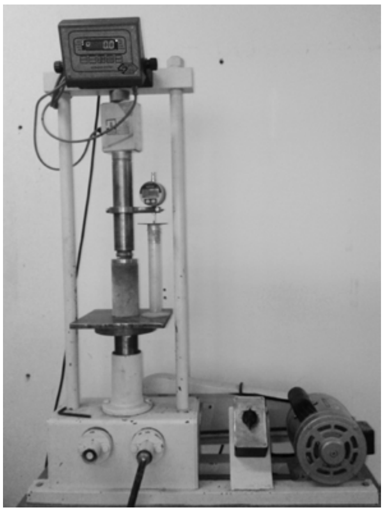

Fig.2 Mechanical Press for unconfined compression tests

Axial strain was determinate by using Eq. (3):

$$\varepsilon = \frac{\Delta l}{l_0} \tag{3}$$

Where: Δl: length change of specimen as read from deformation indicator, mm, and $L_{0:}$ initial length of the specimen, mm.

The compressive strength $s_{c,}$ for a given applied load was calculated by Eq. (4):

$$\sigma_c = \frac{P}{A} \tag{4}$$

Where P: given applied load, kpa, and A: corresponding cross sectional area mm^2.

At the end of each test, it proceeded to take moisture from each sample.

RESULTS DISCUSSION

Infiltration test

The incorporation of fine material produced a decreased on infiltration and on permeability coefficient too, on soil bentonite samples. [17] [18] [19]. Figure 3 and Fig. 4 show the experimental results obtained for each soil bentonite mixture remolded at different dry unit weight.

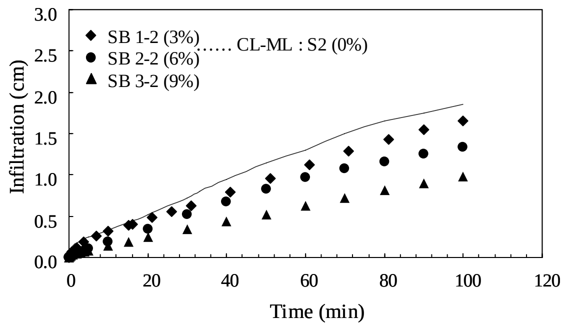

Fig. 3 Infiltration test on soil /bentonite samples with 1.5 kN/m^3 dry unit weight.

Figure 5, Fig. 6 and Fig. 7 shown how influence a particular dry unit weight to infiltration rate.

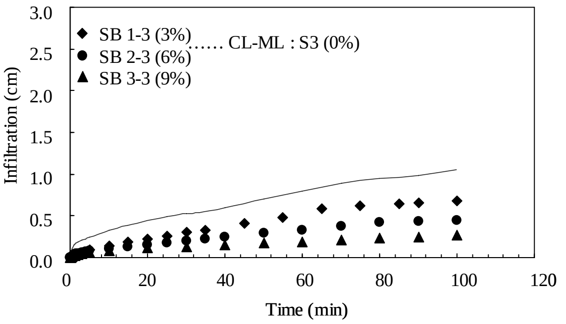

Fig.4 Infiltration test on soil /bentonite samples with 1.6 kN/m^3 dry unit weight.

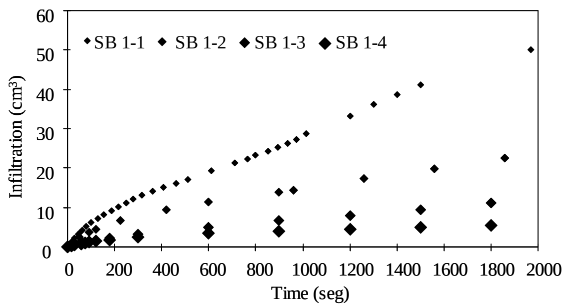

Fig.5 Infiltration test on soil /bentonite samples with different dry unit weight and 3% of bentonite content.

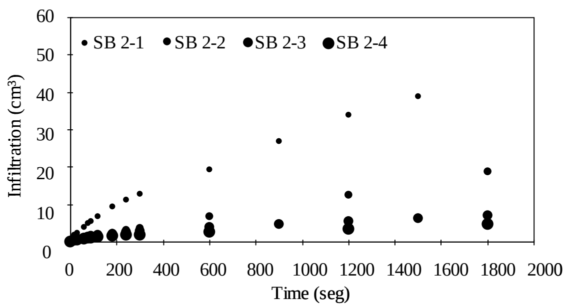

Fig.6 Infiltration test on soil /bentonite samples with different dry unit weight and 6% of bentonite content.

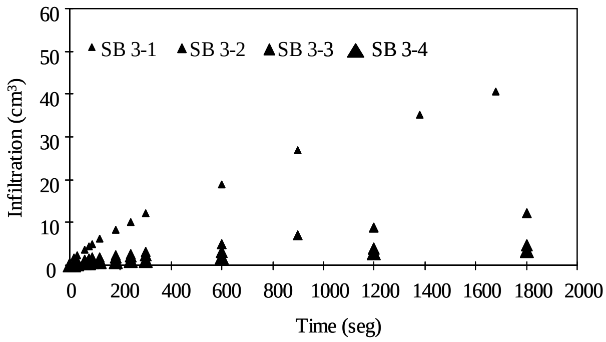

Fig.7 Infiltration test on soil /bentonite samples with different dry unit weight and 9% of bentonite content.

In saturated condition, an increase of bentonite on soil mixtures produced a decrece on infiltration volume. Similar behaviour was observed, in terms of increase in the dry unit weight.

The results were: for γ_{d1} = 1,4 kN/m^3 , k $_{SB1}$ = 9,4 x 10 $^{-9}$ m/s, k $_{SB2}$ = 6,64 x 10 $^{-9}$ m/s, k $_{SB3}$ = 1,48 x 10 $^{-8}$ m/s and k $_S$ = 4,15 x 10 $^{-8}$ m/s, for γ_{d2} = 1,5 kN/m^3 , k $_{SB1}$ = 7,10 x 10 $^{-9}$ m/s, k $_{SB2}$ = 6,65 x 10 $^{-9}$ m/s, k $_{SB3}$ = 3,11 x 10 $^{-9}$ m/s and k $_S$ = 9,91 x 10 $^{-9}$ m/s. For γ_{d3} = 1,6 kN/m^3 , k $_{SB1}$ = 4,21 x 10 $^{-9}$ m/s, k $_{SB2}$ = 1,59 x 10 $^{-9}$ m/s, k $_{SB3}$ = 1,56 x 10 $^{-9}$ m/s and k $_S$ = 4,88 x 10 $^{-10}$ m/s. For γ_{d4} = 1,7 kN/m^3 ,k $_{SB1}$ = 1,28 x 10 $^{-9}$ m/s, k $_{SB2}$ = 1,79 x 10 $^{-9}$ m/s, k $_{SB3}$ = 3,14 x 10 $^{-10}$ m/s and k $_S$ = 3,36 x 10 $^{-10}$ m/s.

A possible explanation for this behaviour is due to high cation exchange capacity sodium bentonite which has, comes from the presence of Na + ions, which become attractive to water molecules. The swelling process of these ions modifies the consistency of the mixture and changing its texture, affecting the hydraulic conductivity. This behaviour is accentuated by increasing the percentage of bentonite on soil -bentonite mixtures. [15]

Unconfined Compression (UC)

The results of unconfined compression are shown on Fig.8. The graphic shows that mechanical behavior has a better performance in relation with the increase of bentonite content.

Higher compression resistance is achieved in samples with 9% of bentonite than samples without bentonite. The compressive strength increased by 25% in samples with addition of bentonite with respect to samples without addition, for maximum experimental dry unit weight near 1.7 kN / m^3.

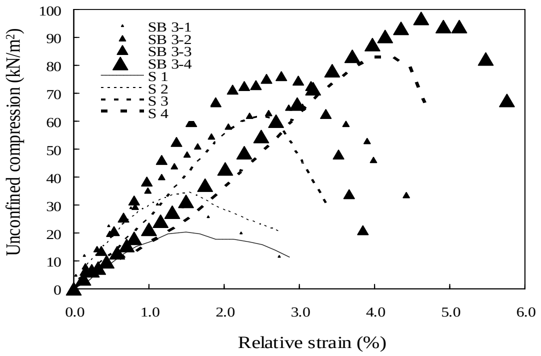

Fig.8 Unconfined compression tests on samples with 9% bentonite

Densities close to 1.7 g / cm3, and bentonite contributions greater than 3%, produced changes in the stiffness of the specimen. It was observed a ductile behaviour with relative deformations greater than 5% was observed.

The maximum unconfined compression strength registered was in samples with dry densities greater than 1.65 kN / m^3, with values close to 100 kN / m^2, and contributions from 9% bentonite.

This represented an increase of 5.3 times the compressive strength obtained for soil samples without addition of bentonite and moulded with a dry density of 1.4 kN / m3.

CONCLUSION

This paper has presented a study loess soil - bentonite mixtures and has revised the importance of bentonite content and its influence on the mechanical and hydraulically performance of additive mixtures. Water content, dry unit weight, and bentonite percentages have been studied. It has been identified the main results as follows:

Hydraulic properties: a) Increased design dry density from 1.4 kN / m3 to 1.7 kN / m3, on samples with the same bentonite percentage, it caused a decrease on the infiltration volume about 90%. The lowest rate infiltration was recorded on samples with a dry unit weight about 1.65 kN / m^3 and with 9% bentonite addition, registered a decreced of 75% in comparison with soil without bentonite. b) The use of compaction techniques to enhance natural dry density of silty loessic- soils without addition of bentonite, and designing samples with dry densities near 1.7 kN / m3, generate a decreced on permeability coefficient about two orders of magnitude, reaching values in the order of 3.14×10^{-10} m/s. This behavior also visualized on samples with 9% of bentonite and higher density about 1.6 kN / m^3.

Unconfined compression: a) The compressive strength increased by 25% in samples with addition of 9% of bentonite with respect to samples without addition, for maximum experimental dry density of about 1.7 kN / m^3.b) The maximum unconfined compression strength registered was in samples with dry densities greater than 1.65 kN / m3, with values close to 100 kN / m2, and contributions from 9% bentonite.

This represented an increase of 5.3 times the compressive strength obtained for soil samples without addition of bentonite and molded with a dry density of 1.4 kN / m3.

ACKNOWLEDGEMENTS

The authors thanks the support of Universidad Tecnológica Nacional Facultad Regional Córdoba, Ministerio de Ciencia y Tecnología, Gobierno de la Provincia de Córdoba (PID-GRF), and FONCyT Agencia Nacional de Promoción Científica y Tecnológica (PICT).

REFERENCES

[1] Muhs R. Daniel, Stephen R. Casttle, Onn Crouvi, Denis-Didier Rousseau, Jimin Sun, and Marcelo A. Zárate, Loess Records, Ed Springer Sciencie, USA, 2014, ch 16.

[2] Marcelo A. Zarate, Loess of southern South America, Quaternary Science. Vol. 22. 2003 pp.1987–2006.

[3] Bloom, A.,“Some Questions about the Pampean Loess”.Paper for the Department of Geography. University of Leicester Nº 23, 1992. pp 17-18.

[4] Teruggi, M.E. “The Nature and Origin of Argentinean Loess”. Journal of Sedimentology and Petrology, 27(3), 1957.pp 323-332.

[5] Moll, L.L. y Rocca, R.J. “Properties of loess in the center of Argentina”. Memoria. XI Pan American Conference on Soil Mechanics and Foundation Engineering. Viña del Mar, Chile. Vol. I.1991. pp. 1-14.

[6] Aiassa G, Zeballos M, Arrúa P and Terzariol R, “Infiltración en suelos limosos compactados”, XIX Congreso Argentino de Mecánica de Suelos e Ingeniería Geotécnica, Octubre 2008, La Plata, Argentina

[7] Arrúa P, Aiassa G., and Eberhardt M. “Behavior of collapsible loessic soil after interparticle cementation”, International J. of GEOMATE, Vol. 1, November-December 2011, pp. 130–135

[8] Arrúa, P.; Aiassa, G. and Eberhardt, M. Loess soil stabilized with cement for civil engineering applications. International Journal of Earth Sciences and Engineering. ISSN: 0974-5904. Vol. 5, No 1, 2012.pp.10-18

[9] Aiassa G. and Arrúa P, “Desempeño de barreras sanitarias simples de suelo loessico compactado”, Revista Tecnología y Ciencia, Año 8, Noviembre 2009, pp. 26–40.

[10] Mitchell K. James. Fundamentals of Soils Behavior. Editorial John Wiley and Sons. Inc. 1993.

[11] Alercia Biga, I. C ; Arrúa P., Eberhardt M.G; Aiassa Martinez G.A.; “Hydraulic Conductivity in Loessic Stabilized Soil”, “Fourth International Conference on Geotechnique, Construction Materials and Environment, Brisbane”, Australia (2014), ISBN 978-4-9905958-3-8 C3051.

[12] Nieva, P.M. y Francisca, F.M. “Conductividad hidráulica de mezclas de limo-bentonita compactadas”. En: Francisca, F. (ed.), Desafíos y avances de la geotecnia joven en Sudamérica, Vol. 1, 2009, pp. 193-196.

[13] Santamarina J., Klein K, Wang Y., and Prencke E. Specific surface: determination and relevance. 2002 Published on the NRC Research Press Web site at http://cgj.nrc.ca

[14] Hyang-Sig Ahn, Ho Young Jo, “Influence of exchangeable cations on hydraulic conductivity of compacted bentonite.” Journal of Applied Clay Science, Vol 44, 2009. pp.144-150.

[15] ASTM. D 5084. Standard Test Methods for Measurement of Hydraulic Conductivity of Satured porous Materials using a Flexible Wall Permeameter.

[16] Fredlund, D,G; Rahardjo, H; Soils Mechanics for unsatured soils. John wiley and Sons.. NY. USA. 1993

[17] Cuisinier,O; Auriol, J.Cl;Le Borgne, T; Deneele, D; “ Microestructure and hidraulic conductivity of a compacted lime-treated soil”, Journal of Engineering Geology. Vol. 123, (2011).187-193.

[18] Qiong Wang ,Yu-Jun Cui, Anh Minh Tang, Jean-Dominique Barnichon, Simona Saba, Wei-Min Ye “Hydraulic conductivity and microstructure changes of compacted bentonite/sand mixture during hydration”. Journal of Engineering Geology. Vol 164, (2013) ,67-76.

[19] India Sudhakar M. Rao, Ravi K., “Hydro-mechanical characterization of Barmer 1 bentonite from Rajasthan, India”. Journal of Nuclear Engineering and Design. Vol 265. (2013). 330-340.

Fifth International Conference on Geotechnique, Construction Materials and Environment, Osaka, Japan, Nov. 16-18, 2015, ISBN: 978-4-9905958-4-5 C3051

CASE STUDY ON DEFORMATION ANALYSIS DURING EARTHQUAKE OF IRRIGATION POND EMBANKMENT

Minoru Yamanaka[1], Takuya Sanei[2], Katsuhiko Koizumi[2] and Shuichi Hasegawa[1]
[1]Facultyof Engineering, Kagawa University, Japan
[2] Graduate School of Engineering, Kagawa University, Japan

ABSTRACT

A failure damage of irrigation pond embankment by earthquake was worried seriously after the 2011 off the pacific Coast of Tohoku Earthquake, Japan. It is very important to confirm a safety against sliding failure of irrigation pond embankment which is made from soil material. In order to clear a deformation of irrigation pond embankment during an earthquake, an influence of earthquake acceleration and ground water table inside the pond embankment by the geotechnical software ALID was discussed mainly in this paper. As a result, it could be clear that deformation of embankment model becomes larger as well as value of acceleration and height of ground water table. And more it turned out of influence of the location of the sandy layer with a possibility of liquefaction.

Keywords: Soil Structure, Earthquake, Deformation, Numerical Analysis

INTRODUCTION

Some irrigation pond embankments were serious damaged by washout or large subsidence during the 2011 off the pacific Coast of Tohoku Earthquake, Japan[1),2)]. About 210,000 ponds are distributed in Japan. Pond embankment, which is earth structure, causes slip failure by seismic ground motion, or it may occur a large settlement and deformation by a liquefaction of foundation ground during an earthquake. Serious damage occurrence to a pond embankment by the big earthquake in the near future is worried, therefore it is necessary to evaluate an earthquake-resistant of pond embankment by numerical deformation analysis which is considerable an influence of seismic ground motion.

The deformation amount can't be estimated by circler slip stable analysis which is generally used. Newmark method[3),4)] is very useful as an estimation method of deformation amount. But the Newmark method just analyzes the slipping length of circular surface which indicates the smallest safety factor, and can't indicate deformation shape in detail for the whole embankment.

The authors were discussed using by the analysis for liquefaction induced deformation program ALID on deformation during earthquake of pond embankment[5)]. In this paper, deformation properties for the pond embankment was discussed in detail by changing liquefaction layer, earthquake acceleration and ground water level using the ALID.

ANALYSIS MODEL AND CONDITION

Figure 1 shows the analysis model of irrigation pond embankment, and the model sets a low permeability soil ② at front zone of embankment. Each size of model used a standard length for constructing a new irrigation embankment.

Seismic accelerations of 5 steps, which ranges from 150 to 600 gal, loads on the upper surface of layer ④ and ⑤. To evaluate influence to deformation amount by the difference in the locations of the liquefaction layer distributed under the embankment,

Table 1 Input data used in the analysis

Soil Layer		Deformation Condition	$\bar{N}$	c' (kN/m^2)	ϕ' (°)	γ_t (kN/m^3)	G (kN/m^2)
①	Compacted Sandy Soil-A	Decrease of G, Liquefaction	14.5	33.6	28.2	20.6	18,000
②	Compacted Sandy Soil-B	Decrease of G, Liquefaction	16.7	16.7	29.8	20.9	18,000
③	Cohesive Soil (Old Fill)	Decrease of G, Undrained	6.0	26.9	25.5	20.3	6,316
④	Alluvial Clayey Soil	Decrease of G, Undrained	10.0	19.0	26.8	16.8	10,526
⑤	Alluvial Sandy Soil	Decrease of G, Liquefaction	4.0	13.0	28.1	18.9	4,210
⑥	Diluvia Gravel Soil	Coupled Element	50.0	38.8	41.0	19.2	52632

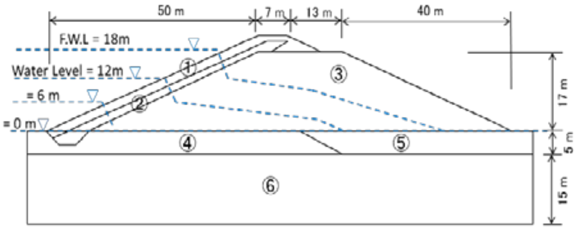

Fig.1 Analysis model

Case-1 is set the alluvial sandy soil layer ⑤ with a possibility of the liquefaction at the right side under the embankment model, and Case-2 is set the alluvial sandy soil layer ⑤ at the left side.

Table 1 shows the condition for deformation and the input data for each layer of the model. For the deformation condition under each ground water table inside the embankment model, the sandy layer was defined as the liquefaction element, and the clayey layer was defined as undrained element. On the other hand, for the deformation condition upper each ground water table, both of the sandy layer and the clayey layer were defined as the decreasing element of stiffness *G*. the *G* depends on the liquefaction resistance ratio F_L. and the F_L changes on the fine content *Fc* [6]. This analysis used ALID; the Analysis for Liquefaction Induced Deformation program.

The input data was decided by using some soil laboratory tests and geotechnical survey results. The strength parameter c' and φ' was decided from the consolidated undrained shear test; CU-bar test, and the *G* was translated by from the *N*-value by standard penetration test.

ANALYSIS RESULTS

Deformation of embankment for Case-1

Figure 2 shows the maximum shear strain counter for each height of water level and seismic acceleration *a*=300 gal for Case-1; the sandy layer ⑤ with a possibility of the liquefaction at the right side under the embankment model. For the water level = 18 m, which equivalent to the full water level F.W.L, in Fig.2(a), the shape showing the maximum

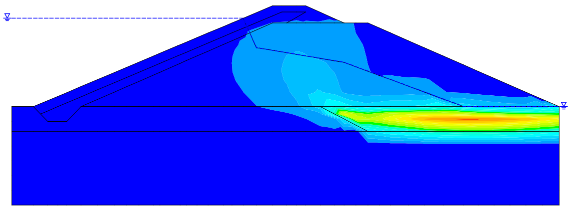

(a) Full water level F.W.L; 18 m

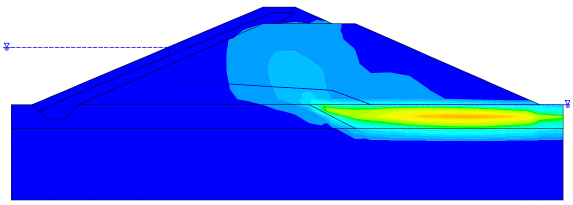

(b) Water level; 12 m

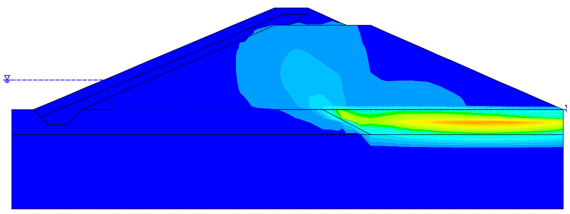

(c) Water level; 6 m

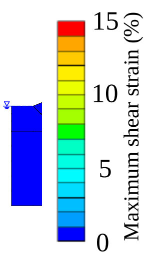

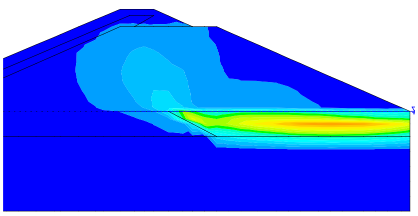

(d) Water level; 0 m

Fig.2 Maximum shear strain contour
(Case-1, *a* = 300 gal)

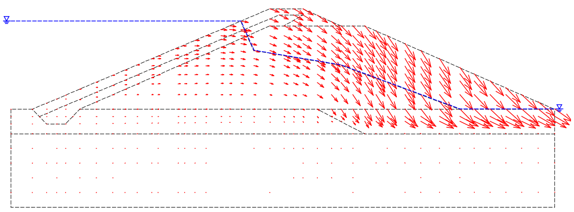

(a) Full water level F.W.L; 18 m

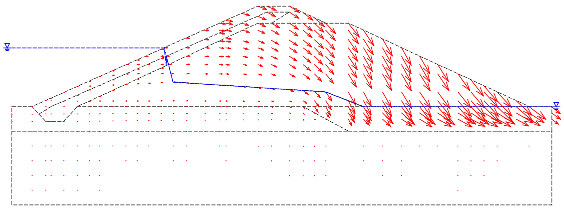

(b) Water level; 12 m

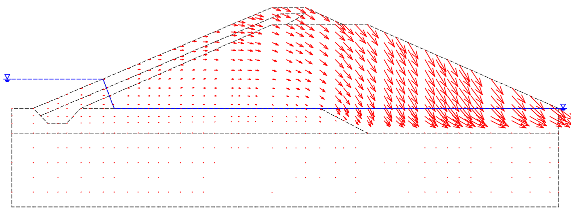

(c) Water level; 6 m

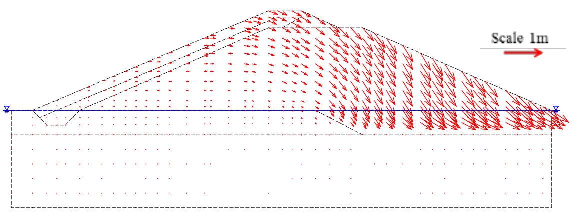

(d) Water level; 0 m

Fig.3 Deformation vector
(Case-1, *a* = 300 gal)

shear strain is distributed from the top of embankment to the sand layer ⑤ such as a circle slip surface. In particular the maximum shear strain of the sand layer ⑤ is over 10 %, it seems that the embankment slips largely such a circular shape because the sand layer occurs large-decreasing of G by liquefaction of the layer ⑤. In the other hand, for in Fig.2 (b), (c), (d) the shape of maximum shear strain and its amount is almost same as Fig.1 (a) although the water level falls.

Figure 3 shows the deformation vector for each water level and seismic acceleration *a*=300 gal for Case-1. For the water level = 18 m in Fig.3(a), the deformation vector directs toward to the downstream side of embankment, and the length of vector at the sandy layer ⑤ is larger. The maximum length of deformation vector is about 0.5 m at the toe of embankment slope. Amount and direction of deformation vector for condition with other water table in Fig. 3 (b),(c),(d) seems to almost same, therefore the deformation of embankment is not different by the height of water lever for a=300 gal.

Deformation of embankment for Case-2

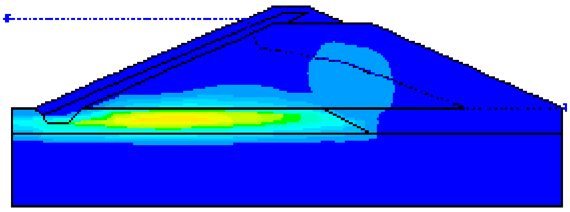

(a) Full water level F.W.L; 18 m

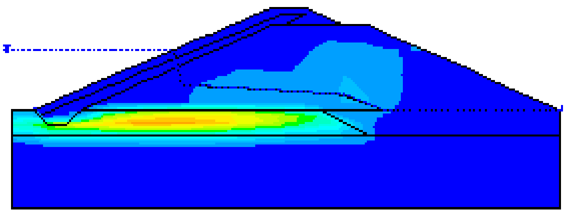

(b) Water level; 12

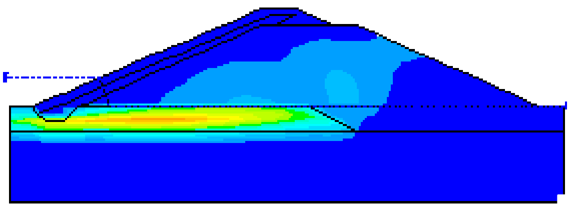

(c) Water level; 6 m

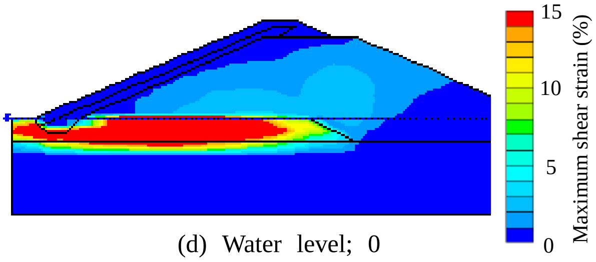

(d) Water level; 0

Fig.4 Maximum Shear strain contour
(Case-2, *a* = 300 gal)

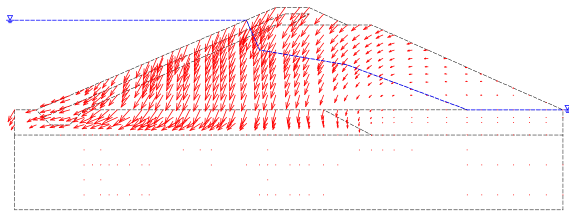

(a) Full water level F.W.L; 18

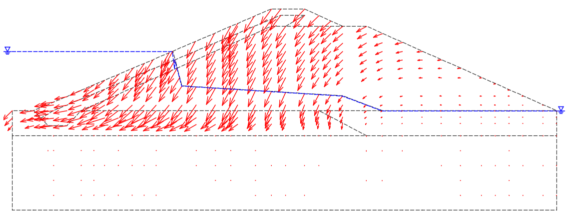

(b) Water level; 12

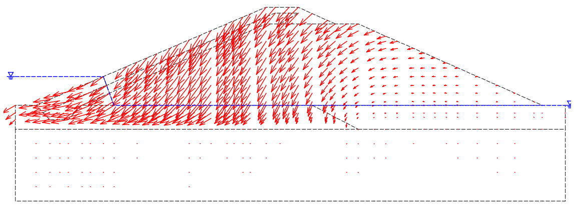

(c) Water level; 6 m

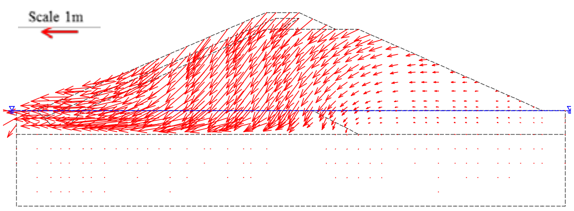

(d) Water level; 0 m

Fig.5 Deformation vector
(Case-2, *a* = 300 gal)

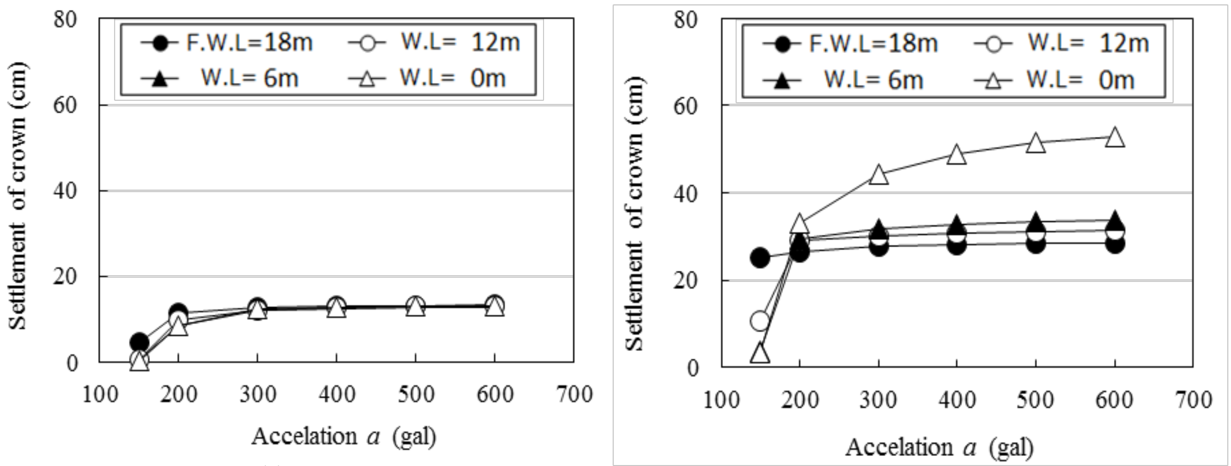

(a) Case-

(b) Case-

Fig.6 Relationship between acceleration and settlement of crown

Figure 4 shows the maximum shear strain counter for Case-2; the sandy sol layer ⑤ with a possibility of the liquefaction at the left side. For the water level = 18 m in Fig.4 (a), the range of the maximum shear strain is concentrating to the sandy layer ⑤, and the range is not reaching to the upper part of embankment. For in Fig.4 (b), (c), d) the amount of maximum shear strain at the sandy layer ⑤ is increasing as well as a decline of the water level, and the range is expanding to the upper part of embankment. The range looks like a circular slip surface.

Figure 5 shows the deformation vector for each water level for Case-2. The vector directs toward the lower left side, the length of vector is increasing toward the same side. The length of vector indicates maximum at the sandy layer ⑤ for the water level = 0 m in Fig.5 (d), the deformation of the toe of embankment slope is very large by 0.45 m

Figure 6 shows the relationship between acceleration a and settlement of embankment crown. For Case-1 in Fig.6 (a), the amount of settlement is increasing slightly from a=150gal to 200 gal, but the amount of settlement is almost constant at 13 cm over a=200 gal. For Case-2 in Fig.6 (b), the settlement is 25 cm already at a=150 gal for the water level =18 m, and is constant almost from a=150 gal to 600 gal. Therefore it is obvious that the liquefaction occurs to the sandy layer ⑤ for a=150 and it occurs at the condition of all acceleration for the water level 18m. And more the settlement of crown is increasing as well as a decline of the water level for Case-2.

CONCLUSION

The following results can be obtained in this study.

1) For Case-1 which is set the alluvial sandy soil layer with a possibility of the liquefaction at the right side under the embankment, the deformation vector directs toward to the downstream side of embankment, and the length of the vector the deformation of embankment is not different by the height of water lever for a=300 gal.

2) For Case-2 which is set the alluvial sandy soil layer at the left side, the amount of maximum shear strain at the sandy soil layer is increasing as well as a decline of the water level, and the range is expanding to the upper part of embankment. The range looks like a circular slip surface.

3) The amount of settlement at embankment crown is different from the height of water level, and the amount of Case-2 is bigger than one of Case-1.

REFERENCES

[1] Suzuki H, "Study on damage factors to earth dams for irrigation due to earthquake motions -In the Case of the 2011 offshore Pacific Coast Tohoku Earthquake-", Bulletin of the National Institute for Rural Engineering, No.54, 2015, pp.73-137 (in Japanese with English abstract)

[2] Abbas M, Takada S and Sepand S, "Fujinuma dam performance during 2011 Tohoku Earthquake, Japan and Failure mechanism by FEM", Proc. of the 15th World Conf. on Earthquake Engineering, 2012, CD-ROM, 8p.

[3] Newmark N.M, "Effects of Earthquakes on Dams and Embankments", Geotechnique, Vol.15, No.2, 1965, pp.139-159.

[4] Yasuda S. and Adachi K "Estimation of Sliding Displacement of Embankments during Earthquakes by Newmark's Method", Geotechnical Engineering Magazine, JGS, 2010, pp.52-53 (in Japanese)

[5] Sanei T, Yamanaka M, Hasegawa S and Koizumi K, "Analysis Case Study on Dynamic Deformation of Pond Embankment by using ALID", Proc. of the 49th Japan National Conf.

on Geotechnical Engineering, 2014, pp.1393-1394 (in Japanese)
[6] Yasuda S, Yoshida N, Adachi K, Kiku H, Gose S and Masuda T, “A simplified practical method for evaluating liquefaction-induced flow”, Journal of Geotechnical Engineering, JSCE,No.638/ Ⅲ -49,1999, pp.71-89 (in Japanese with English Abstract).

Fifth International Conference on Geotechnique, Construction Materials and Environment, Osaka, Japan, Nov. 16-18, 2015, ISBN: 978-4-9905958-4-5 C3051

IMAGE PROCESSING FOR GEOTECHNICAL LABORATORY MEASUREMENTS

Erica Elice Saloma Uy[1] and Tirawat Boonyatee[2]
[1]Civil Engineering, De La Salle University, Philippines; [2] Chulalongkorn University, Thailand

ABSTRACT

This research is an effort to apply image processing techniques for non-contact determination of 2D and 3D displacements of specimens in a triaxial apparatus. For the 2D measurement, a calibration procedure is applied to correct image distortions before the positions of interested points are tracked by the pyramidal optical flow algorithm (Lucas and Kanade, 1981). By considering the change of position, the displacement of an interested point can be determined. The results are compared with the measurements obtained from LVDTs and are well agreed. For 3D measurement, calibration, rectification, correspondence and 3D re-projection are performed. It is verified by an isotropic compression test of a cylindrical sponge in a triaxial apparatus. The estimated displacement and discharge of water are compared with the measured ones and are well agreed. The repeatability and resolution of the developed system are found to be in the order of 0.006 cm and 0.004 cm, respectively.

Keywords: Image Processing, Non-Contact Measurement, Optical Flow, Stereo Vision System

INTRODUCTION

Geotechnical measurements have provided the life and blood for advances in modern geotechnical engineering [1]. Since the development of soil mechanics in 1930s, innovations have been made to achieve more precise, accurate and reliable measurements. Over the years, several techniques in measuring the displacement of soil are developed. Techniques such as full-field measurements, which can also be referred to as a non-contact measurement, began to flourish by providing better understanding compared to point-wise measurements. In contrast to conventional sensors such as linear variable differential transducers (LVDTs), deformation can be determined without any direct contact with the target of measurement [2]. Image processing is becoming a trend especially in the field of Geotechnical Engineering in determining measurements. The advent of digital image processing resulted in powerful measuring techniques such as Digital photogrammetry, particle image velocimetry (PIV) and digital image correlation (DIC) [3],[4].

This study is an effort to develop a system that incorporates non-contact measurement through image processing. The system aims to determine the displacement and volume change of soil specimens in a triaxial apparatus. Lucas and Kanade pyramidal optical flow algorithm is applied to track the movement of the soil [5], [6]. Non-contact measurements are made with respect to 2D and 3D axes. Triaxial tests are performed to validate the displacements and volume change the system measured. The advantage of this technique is that on-line and off-line measurement can be done through the pictures taken. Furthermore, monitoring of the progression of failure zones within the sample as it is being tested is possible. In order to integrate this system, Labview is used as the software to develop programs that can implement image processing, optical flow and monitoring.

OPTICAL FLOW ALGORITHM

Optical flow can be defined as the changes in gray values that occur within the image plane through successive images [5]. It has the dimensions of velocity were it can be denoted as $\vec{v} = (u, v)$ where u and v are the x and y components of the optical flow vector at a point. When the optical flow is obtained from two successive images, the optical flow vector will appear as a displacement vector $\vec{d} = (d_x, d_y)$ where d_x and d_y are the x and y components of the displacement vector at a point.

An optical flow algorithm has the capability in estimating the changes in motion of a certain point within the image under the assumption that brightness is constant among the subsequent images [7]. Lucas and Kanade pyramidal optical flow algorithm is a type of feature based approach. The method establishes correspondence of feature points between the varying images at a certain time interval. Furthermore, it analyzes two grayscale images, I and J, having $\vec{x} = (x, y)$ as the pixel location within the image plane. Thus, $I(\vec{x}) = I(x, y)$ and $J(\vec{x}) = J(x, y)$. Let image $I(\vec{x})$ be the first image while image $J(\vec{x})$ the second image. When a point of concern, $\vec{s} = (s_x, s_y)$, is established in the first image the algorithm will track its location $\vec{t} = \vec{s} + \vec{d}$ in the second image. $I(\vec{s})$ and $J(\vec{t})$ must be almost equal and have a similar brightness in the two dimensional neighborhood. Equation (1) defines the expression used to track the points and determine the image displacement $\vec{d}$ where it is the vector that minimizes the residual function $\varepsilon(\vec{d})$ [5].

$$\varepsilon(\vec{d}) = \varepsilon(d_x, d_y) = \sum_{x=u_x-\omega_x}^{u_x+\omega_x} \sum_{y=u_y-\omega_y}^{u_y+\omega_y} [I(x,y) - J(x+d_x, y+d_y)]^2 \quad (1)$$

where

ω_x, ω_y = arbitrary numbers that ranges from 1, 2, 3 or more pixels

CALIBRATION

Stage 1: 2D Camera Calibration

Prior to the calibration for the stereo vision system, 2D camera calibration is performed to eliminate the distortion. Two Canon 650D cameras with 18-55 mm f/3.5-5.6 IS II Kit Lens are used and pointed parallel towards the triaxial apparatus. This stage involves the determination of the internal and external parameters of cameras. The focal length, optical center and distortion coefficients are known as the internal parameters. Tangential and radial distortion coefficients are the most common types encountered in calibrating a camera. On the other hand for the external parameters, it is composed of a rotation matrix and translation vector. Presented in this section are procedures for calibrating a single camera which were implemented in Labview.

1.) A panel of dotted grid having a spacing of 2 cm center to center is placed in front of the object of concern. The camera must capture different orientations of the panel in a range of + 20 degrees. Caution must be made to ensure that the first image is in the field of view of the camera so that the dots can be visibly seen.

2.) Threshold is performed to extract the grid feature of the calibration panel from pictures taken from the previous step.

3.) The calibration axis is established at the upper left corner of the grid.

4.) The internal, distortion and external parameters are estimated.

Stage 2: Calibration for 3D Measurement

In this stage a cube is placed inside the triaxial cell together with water to determine the appropriate focal length, baseline or separation between the two cameras and image resolution. The cube is used since its straight edges can be easily detected by image processing routines. The cube is 9.9x7.5x6 cm. The parameters were varied until they provide a good coverage area of the object of concern. From this test, the cameras must be placed at the back of the apparatus at 113 cm. Cameras are mounted on the wall so that it can have stable support. A focal length of 55 mm and base line of 20 cm is used to have a better view of the object as it is being tested. An image resolution of 1920x1280 pixels is implemented since it can capture the whole object with less distortion.

2D IMAGE PROCESSING

Accuracy Check

A rubber cylinder with a height of 12.7 cm and a diameter of 5.8 cm is used to check the accuracy of the system. An angle bar is attached on the perimeters of the specimen to serve as the support for the LVDT. Three strain gauges are also attached at the top, middle and bottom part of the specimen. Lucas and Kanade pyramidal optical flow algorithm is used to track the movements of marked points. 10 sets of readings up to a displacement of 1.27 cm are performed in steps of 0.5 mm and 1 mm. From the test, a resolution of 0.2 mm is obtained. Strains are derived from displacements obtained from image processing and compared to the readings from a strain gage. Unfortunately, there is a large discrepancy because of the difference in the size of gage length used. The strain gage measures at a single point over a gage length of 6 mm while the strain is computed over a wider distance.

Triaxial Test

Two Bangkok soft clay samples taken from depths of 6 to 7 m (BH1) and 9 to 10 m (BH2) were tested. A grid of dots is drawn on the membrane to serve as targets. A ruler is placed inside the triaxial cell to serve as a reference during the test. Consolidated drained compression unloading triaxial test is performed having a cell pressure of 50 kPa for BH1 and 100 kPa for BH2. For the compression unloading part of the test, it is done by increasing the deviator stress while reducing the cell pressure so that the mean effective stress decreased. Pictures are taken every hour with the use of timer remote controls.

The displacements, external and internal, is obtained through image processing and compared to the reading from a LVDT. The external measurement is made by selecting a region of interest at the top most part of the triaxial cell. It can be observed from Fig. 1 and 2 that the results of both measurement techniques are well agreed. For the internal measurement, the whole region within the coverage of the cameras is tracked. Among the entire region tracked, the area close to the pedestal has the best fit as seen in Fig. 3 and 4. From the test, failures occurred at the mid-section. For the region near the top cap, a small movement was observed. These observations can be clearly seen in Fig. 5 and 6.

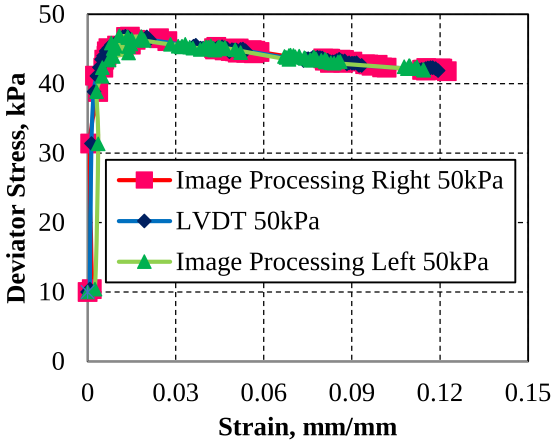

Fig. 1 Stress strain curve for BH1

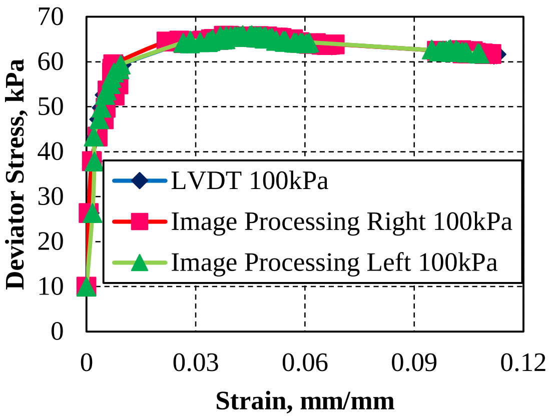

Fig. 2 Stress strain curve for BH2

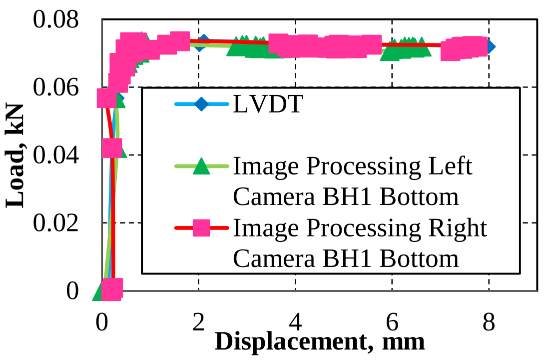

Fig. 3 Load vs displacement curve for BH1

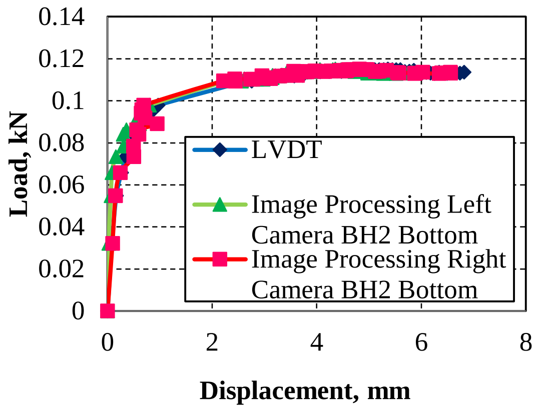

Fig. 4 Load vs displacement curve for BH2

Color Mapping

To further monitor the behavior of the soil the displacement and strain field were calculated. A color magnification mapping technique is applied to determine the areas where large deformations occur. This technique is inspired from the research done at Massachusetts Institute of Technology. The pixel values are amplified to reveal hidden information within the image [8]. Their technique can be referred to as Eulerian video magnification. From this, a program is developed in Labview where a color map containing amplified values is plotted and overlaid to the image. This served as an early detection of critical zone of the soil as seen in Fig. 5 and 6. Three base colors in the program are red, green and blue. Red represents a large displacement while blue is for a small displacement. The program developed has a capability of showing only large displacements and strains by making small values transparent. The strain is computed from the change in displacement between two points dividing by the length between them. The grid size used for this computation is 1x1 pixel or 0.26x0.26 mm.

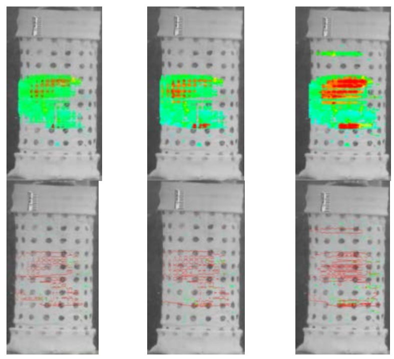

Fig. 5 Color mapping, displacement field (above) and strian field (below), for BH1 from the left camera at day 1, 2 and end of the test.

In Fig. 6, it shows that the sample BH2 tends to have a large movement at the middle in the first few days of the test. This would mean that the soil is undergoing a bulging failure. During the shearing stage, the triaxial cell is being pushed from the bottom. Therefore large displacements can also be expected near the base. Large strain localizations are visible where large displacements occurred. From the color map, non-homogeneous movement is seen as the soil experiences failure.

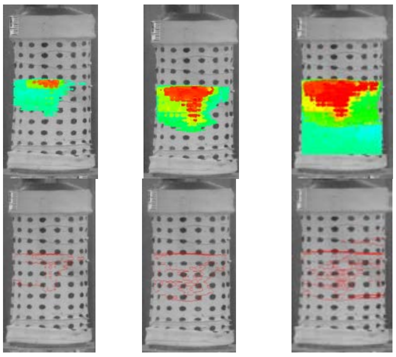

Fig. 6 Color mapping, displacement field (above) and strian field (below), for BH2 from the left camera at day 1, 2 and end of the test.

STEREO VISION SYSTEM

Stereo vision system utilizes two cameras to determine the 3D position of a desired point.

Calibration

For the stereo vision calibration there are two phases. First, the cameras are calibrated independently. The process is similar for calibrating a camera that measures 2D deformation. Second, stereo calibration is performed. This process is defined as the computation of the geometrical relationship between the two cameras [9]. Error statistics, as shown in Table 1, are also obtained to check if the calibration data is valid. The calibration quality and the rectification should be within the range of 0.7 to 1.0. Having a calibration quality of 1.0 would mean that the system is perfectly calibrated. On the other hand the maximum rectification error should not exceed 1.5.

Rectification

Stereo image rectification is a process when the image planes produced by the left and right camera are being aligned [9]. This process comes right after the stereo calibration since distortion should first be corrected. It helps simplify the stereo correspondence computation. From the error statistics obtained from the stereo calibration, the rectification error should always be satisfied. This maintains the accuracy of the system to perform mapping.

Table 1 Error statistics of stereo calibration

Error Statistics	Result
Max Projection Error	1.99
Calibration Quality	0.83
Max Rectification Error	1.45
Rectification Quality	0.9

Stereo Correspondence

Stereo correspondence is the stage when the match between the field of view of the left and right image is mapped [10]. A disparity map is obtained during this step. The overlapping view of the two cameras produces an almost equal disparity value thus the disparity image would highlight the objects within that region. To achieve this, the object of concern must be the dominant one in the scene. Furthermore, a uniform light condition is essential to avoid errors such as shadows form other objects in the scene.

Stereo correspondence is performed along the overlapping view through sum of absolute differences (SAD) window. The SAD algorithm is an area-based correspondence algorithm. It computes the intensity differences for each center pixel (i,j) in a window v_x by v_y [11]. To have a better correspondence, a bigger window size is advisable.

Depth Mapping

The depth map can be obtained through the process called reprojection. It is performed at a particular reference rectified image. For the program's case the left rectified image served as the reference. The reprojection matrix (Q), Eq. (3), is used to reproject the 2D coordinates at the rectified image together with the corresponding disparity value into its 3D position [9].

$$\begin{bmatrix} X \\ Y \\ Z \\ W \end{bmatrix} = Q \cdot \begin{bmatrix} x \\ y \\ d \\ 1 \end{bmatrix} \tag{2}$$

$$Q = \begin{bmatrix} 1 & 0 & 0 & -c_x \\ 0 & 1 & 0 & -c_y \\ 0 & 0 & 0 & f \\ 0 & 0 & -1/T_x & (c_x - c'_x)/T_x \end{bmatrix} \tag{3}$$

where
c_x = horizontal distance from the principal point to the optical center on the image plane of the left image
c_y = vertical distance from the principal point to the optical center on the image plane of the left image
f = focal length
T_x = baseline
c'_x = horizontal distance from the principal point to the optical center on the image plane of the right image
W = weight

Accuracy Check

Validation for depth reading

To thoroughly check the accuracy of the system, a small card board was attached on a micrometer. It is placed on the triaxial base at a distance of 105 cm from the cameras. Ten readings are made when the cardboard was moved in steps of 0.05, 0.1, 0.2, 0.4, 0.6, and 0.8 cm along the micrometer axis. The standard deviation from both increments are computed and used to express the repeatability of the system. The coefficient of variation of the system is found to be around 0.006381 to 0.078066. The repeatability and accuracy of the system is determined from the standard deviation and it is found to be 0.006 cm and 0.004 cm, respectively.

Validation for depth reading under tilting planes

In order to determine the capacity of the system to read depth changes under tilting planes, a laser transducer was used to get the profile of a deformed sample and it is compared to the result of the system. Oil clay is used as a sample since it is easy to manipulate. Readings are made at the center, 40º from the center and boundary of the sample. The profile is read for 10 times at the center and 40º from the center of the sample. For the profile at the boundary of the sample, only 3 readings are made. The measurements from the stereo vision system and the laser transducer are compared. From the test, errors at the center has a range of 0.39 to 0.90 mm, errors at 40º from the center has a range of 0.64 to 4.62 mm, and errors at the boundary has a range of 0.79 to 1.87 mm. Large errors are observed from the readings at 40º from the center. Stereo correspondence search is difficult to perform at this area since it is at the maximum camera coverage.

Triaxial Test

Initially tests are planned to be done on Bangkok Clay samples but a sponge is used instead to avoid non-homogeneous mode of deformation. The use of sponge provided a better control on the flow of water. Six trials are made in determining the capacity of the system. The amount of water flowing in and out of the sponge is calculated by three different techniques.

For the first technique, the reference image is taken before the beginning of test. In this manner the cumulative volume of water can be measured. This method only worked for a certain amount of time because it became difficult to estimate movements from significantly different image pair. For the second technique, the reference image is taken right after the cell pressure and back pressure has been applied. The volume obtained from this technique is also a cumulative one. Similarly the algorithm worked over a limited period. In the third technique, the change in volume between successive images is determined. For all methods**,** percentage errors in a range of 1.16 to 8.86% are observed. When the size of patch is varied to examine its influence on the calculated result, no distinct trend was observed. A large amount of water is introduced to the sponge to determine its limitation. Using the second method, the volume of inflow calculated is 43.16 cc while the measured volume is 45.88 cc and error of 6.1% is observed.

The capacity of the system to measure at displacements is also determined. 3 Unconsolidated undrained tests are performed using Bangkok clay. Unfortunately, only 1 trial can be analyzed because the images of the other trials are not in good condition. An error of 1.77 to 10.14% is observed from the measured external displacements. The internal displacements on the other hand are measured at the midsection of the soil sample since it is the critical area. Fluctuations are encountered when the displacements and strains are computed. To further investigate on this, displacements at the pedestal, 1/3 from the base and 2/3 from the base was obtained and compared with the result from the LVDT. From Fig. 7, it can be seen that fluctuations started at a deviator stress greater than 15 kPa at 2/3 from the base. To have a better understanding on what occurred during the test full-field monitoring was performed. Displacement fields are shown in Fig. 7 and it can be seen that there are localizations at the area 2/3 from the base. Due to this, it is impossible to measure the internal displacements for this data.

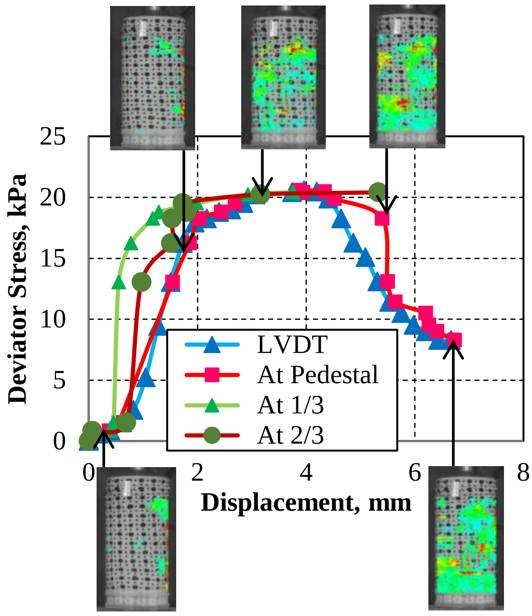

Fig. 7 Stress-displacement plot for Bangkok Clay

CONCLUSION

A non-contact measurement system was developed and it had the capacities to perform 2D and 3D measurements through image processing. Lukas and Kanade pyramidal optical flow algorithm is applied in both measurements to track the movement of interested points.

The 2D measuring system's resolution is found to be 0.2 mm. When the readings from the system are compared to those from LVDT, for a consolidated drained unloading test errors ranging from 5 to 10% are observed. For the 3D measuring system, when an unconsolidated undrained test is performed errors ranging from 1.77 to 10.14% are observed. When measuring out of plane movements, the repeatability and resolution is found to be 0.006 cm and 0.004 cm, respectively. For the readings of depth at titling planes the profile from the system is compared with a laser transducer. Large differences can be observed at 40º from the center at a range of 0.64 to 4.62 mm. Errors ranging from 1.16 to 8.86% are obtained when computed volumes are compared with measured values. The system provides an option to compute the volume of flow between any image pair. From these, it can be concluded that the system has a good capability in obtaining 2D and 3D measurements. It can be applied in monitoring the behavior of the soil during the test such as to monitor the development of localization failures in soil. However, it is only limited to the area viewable by the cameras.

REFERENCES

[1] Marr WA, "Advances and Retreats in Geotechnical Measurements", Judgment and Innovation: The Heritage and Future of the Geotechnical Engineering Profession, 2000, pp. 42-60.

[2] Viggiani, G. amd Hall, SA, "Full-field Measurements, A New Tool for Laboratory Experimental Geomechanics", Paper presented at the Proceedings of the 4th International Symposium on Deformation Characteristics of Geomaterials (Burns SE, Mayne PW and Santamarina JC (Eds.)), 2008, pp.3-26.

[3] Xing, ZX, Wells, LG, Yaping, J and Shearer, SA, "Using Image Analysis to Measure Two-Dimensional Soil Deformation", Journal of Terramechanics, Vol 34, 1997, pp. 73-82.

[4] Khosravi, M, Tang, L, Pipatpongsa, T, Takemura, J, and Doncommul, P, "Performance of Counterweight Balance in Stability of Undercut Slope Evaluated by Physical Modeling", International Journal of Geotechnical Engineering, Vol 6, 2012, pp. 193-20.

[5] Fernando, WSP, Udawatta, L, and Pathirana, P, "Identification of Moving Obstacles with Pyramidal Lucas and Kanade Optical Flow and K Means Clustering", Proceedings on the 2007 Third International Conference on Information and Automation for Sustainability, 2007, pp. 111-117.

[6] Lucas, BD and Kanade, T, "An Iterative Image Registration Technique with an Application to Stereo Vision", Proceedings of Imaging Understanding Workshop, 1981, pp. 121-130.

[7] Mahalingam, V, Bhattacharya, K, Ranganathan, N, Chakravarthula, H, Murphy, RR and Pratt, KS "A VLSI Architecture and Algorithm for Lucas-Kanade Based Optical Flow Computation", IEEE Transaction on Very Large Scale Integration (VLSI) Systems, 2010, pp. 29-38.

[8] Wu, HY, Rubinstein, M, Shih, E, Guttag, J, Durand, F, and Freeman, WT, "Eulerian Video Magnification for Revealing Subtle Changes in the World", ACM Transactions on Graphics, Volume 31, 2012.

[9] Bradski, G and Kaehler, A, "Projection and 3D Vision", Learning OpenCV Computer Vision with the OpenCV Library, O'Reilly, 2008, pp.405-458.

[10] Saidon, MS, Desa, H, Murugesa, P and Rosbi, MSM "Developing Stereo Vision System for Object Recognition and Positioning of AMAD-R Mobile Robot", Proceedings of the International Conference on Man-Machine Systems, 2009, pp. 3B8-1-5.

[11] Kuhl, K. "Comparison of Stereo Matching Algorithms for Mobile Robots", The University of Western Australia, Australia, 2005

Fifth International Conference on Geotechnique, Construction Materials and Environment, Osaka, Japan, Nov. 16-18, 2015, ISBN: 978-4-9905958-4-5 C3051

CORAL SAND SOLIDIFICATION TEST THROUGH MICROBIAL CARBONATE PRECIPITATION USING *PARARHODOBACTER* SP.

Md. Nakibul Hasan Khan[1], Suguru Shimazaki[1] and Satoru Kawasaki[2]
[1]Graduate School of Engineering, Hokkaido University, Japan
[2]Faculty of Engineering, Hokkaido University, Japan

ABSTRACT

The coastal erosion has been a problem in associate with manmade construction. The maintenance and management is expensive for repair and rebuild the coast. Compared to the concrete structure coral sand solidification would considered to minimize cost. The present experimental study was conducted to coral sand solidification through microbial carbonate precipitation (MCP) using *Pararhodobacter* sp. Ureolytic bacteria; *Pararhodobacter* sp. was isolated from the beachrock in Nago, Okinawa, Japan. ZoBell2216E as a medium for marine bacteria was used for the culture of the bacteria. Suitability for the use in MCP syringe test, growth properties of the bacteria were observed in various cultural conditions. MCP sand solidification test was carried in 30mL Terumo syringe injected bacterial culture fluid. Strength of the specimen was measured by needle penetration test. The maximum value of the absorbance at bacterial growth curve was constant if the added amount of the medium is 100mL. The correlation coefficient of determination for absorbance measurements and viable cell count measurements was obtained 0.5478. In MCP syringe test, pH of the specimen was decreased and Ca^{2+} concentration was increase with time. The estimated value of unconfined comprehensive strength (UCS) also increased with time. The maximum value of UCS of the specimen was 12MPa. The estimated UCS values of the specimen produced by sand solidification test for 14 days curing time have been achieved.

Keywords: Sand Solidification, Unconfined Compressive Strength, Microbial Carbonate Precipitation, Pararhodobacter sp

INTRODUCTION

Erosion of the sandy shore is often used to refer to changes in the coastline due to the collapse of the sediment balance. Coastal erosion has been a significant problem globally due to anthropogenic changes along the coastline. In order to prevent, or at least minimize damage from erosion, a combination of various structures and processes has been traditionally used, including embankments, revetments, jetties, artificial reefs, offshore breakwaters, and sand bypassing [1].

The use of inexpensive alternative materials should be considered, to cope with the increase in costs related to the maintenance and management of concrete structures. In this regards, we focused on alternative materials to replace beachrock to reduce lifecycle costs associated with the currently employed methods. Beachrock forms much more quickly than other sedimentary rocks within the intertidal zone and is composed of coastal sediments that have been cemented together mainly by $CaCO_3$ [2]. By using the processes that solidify beach sand, we hypothesized that could create a highly durable artificial beachrock that would be comparable in efficacy to the existing concrete structures.

For the formation of beachrock various factors have been considered. Among them, Danjo and Kawasaki (2014) [3], focused on the possibility of promoting solidification by microbial processes, specifically urea decomposition by microorganisms. In this study, the microbial induced calcium carbonate precipitation (MICP) method was utilized, which relies on the microbial metabolism of urea that generates carbon dioxide and precipitates $CaCO_3$ [4]. This low environmental impact method was assessed to determine its efficiency as an alternative means to alleviate coastal erosion. In order to create an artificial rock, the present study was conducted with the following two purposes:

(a) To solidify coral sand with an unconfined compressive strength (UCS) of 10 MPa or more, through the MICP method using ureolytic bacteria, *Pararhodobacter* sp..
(b) To examine the growth features of the *Pararhodobacter* sp. which used in the experiment.

MATERIALS AND METHODS

Absorbance Measuring Test

Materials

The test bacterium was *Pararhodobacter* sp., an ureolytic bacterium isolated from the soil near beachrock in Sumuide, Nago, Okinawa, Japan. This strain was isolated from soil samples using artificial seawater (Akuamarine, Yashima Drug Company, Osaka, Japan) (Table 1). The strain was cultured on ZoBell2216E medium (polypeptone 5.0 g/L, yeast extract 1.0 g/L and $FePO_4$ 0.1 g/L, in artificial seawater, pH 7.6~7.8), which is often used for growth of marine bacteria.

Table 1 Composition of artificial seawater

Reagent	g/20L
$MgCl_2 \cdot 6H_2O$	222.23
$CaCl_2 \cdot 2H_2O$	30.7
$SrCl_2 \cdot 6H_2O$	0.85
KCl	13.89
$NaHCO_3$	4.02
KBr	2.01
H_3BO_3	0.54
NaF	0.06
NaCl	490.68
Na_2SO_4	81.88

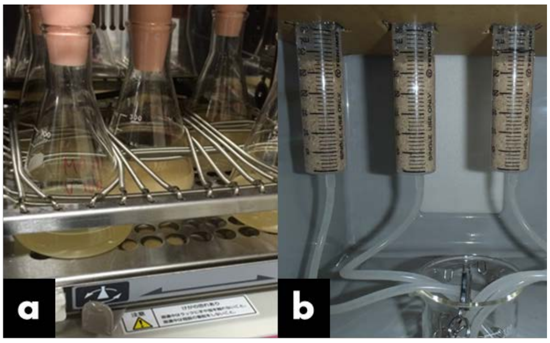

Fig. 1 State of (a) liquid culture and (b) sand solidification tests in the syringe.

Methods

The bacterial strain was cultured in liquid medium under various conditions. The change in cell density over time for each culture condition was quantified by measuring the absorbance (optical density) of the suspension using a spectrophotometer at 600-nm wavelength (OD_{600}) [5], [6]. For each culture condition, the absorbance was read and the viable cell count was determined using the plate dilution method simultaneously. Finally, the growth curve of the strain in each culture condition was obtained to investigate the effects of various conditions on bacterial growth.

Experimental condition

In order to shorten the total time for culturing the bacterial strain used in the experiment, the following three conditions were set up and analyzed, with respect to previous study [1].

(a) The initial mass of the microbe when added to the liquid culture medium was varied: 0.01 g, 0.1 g, or 1.0 g (the previously used mass was 0.1 g).
(b) The volume of liquid culture media was varied: 100 mL, 150 mL, or 200 mL (as opposed to the previously used volume of 100 mL).
(c) The shaking speed at the time of culture was varied: 80 rpm and 160 rpm (the previously used speed was 80 rpm).

MCP Test in Syringe

Materials

Pararhodobacter sp. and coral sand (the grain size distribution of the coral sand is 0.07 ~ 4.0 mm) from Okinawa, Japan, were used for the syringe solidification test. In addition, artificial seawater (Table 1) was used to recreate similar conditions to those in which the original beachrock was formed.

Methods

First, the bacterium was grown up under various experimental conditions listed above. These cultures, ZoBell2216E culture solution, were shaken for 2 days at 30°C. Then, 40 g of coral sand, dried at 110°C for at least 2 days, was placed in a 35mL syringe (diameter 2.5cm × height 7cm). Subsequently, 16mL of the culture medium (ZoBEll2216E) and 20mL of the solution for consolidation (this was the composition, mainly urea and $CaCl_2$, used for all of the various test conditions) was sequentially injected into the syringe. The solution for consolidation was then injected and drained once a day. The pH values and Ca^{2+} ion concentrations were measured every 3 days. The state of the syringe solidification test is shown in Fig. 1b. After 14 days of curing, the UCS of the specimen was estimated using a needle penetration device (SH-70, Maruto Testing Machine Company, Tokyo, Japan).

Experimental conditions

Considering the effect of conditions on the UCS of specimen, two test conditions were utilized: one with regular and other without regular, the re-injection of the culture solution. For regular test condition, the mass of the bacterial culture used was 0.01 g, 0.1 g, or 1.0 g; the concentrations of urea and $CaCl_2$ (solution for consolidation) used were 0.3 M, or 0.5 M. The standard conditions (0.1 g/0.3 M) were the same as those used by Inagaki *et al.* (2011) [7]. The test period was 14 days. In the experiment where the culture solution was re-injected, the mass of the bacteria (culture solution) was 1.0 g and urea and $CaCl_2$ (solution for consolidation) concentrations were 0.5 M each. The test period was also 14 days, where the culture solution repeatedly injected at 7th day. Both the pH and Ca^{2+} ion concentrations were measured daily.

RESULTS AND DISCUSSION

Absorbance Measuring Test

The absorbance values, which indicate the growth rate of the bacterium, under various culture conditions are described below.

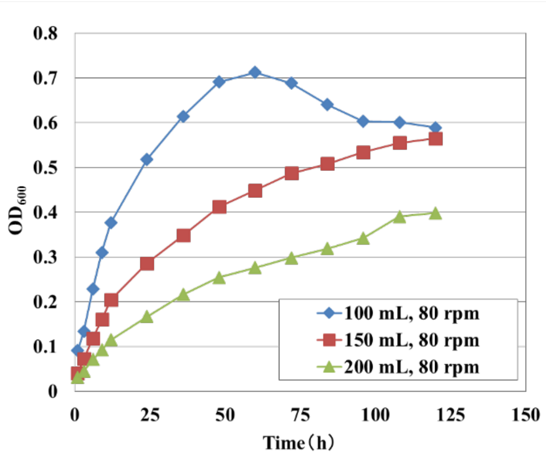

Fig. 2 The absorbance measurement results focused on the amount of liquid medium.

Importance of the volume of the culture solution

The results obtained using various volumes of culture media (100 mL, 150 mL, and 200 mL) and shaking speeds (80 rpm) are shown in Fig. 2 where microbial strain was 0.1g. With regard to shaking at 80 rpm, the absorption values for all three experiments increased with a decrease in the volume of culture medium. However, the absorbance values measured in 150mL and 200mL volumes at 80 rpm experiments were drastically different. In addition, the time required to reach the maximum absorbance was between 48 and 60 h in 100mL. In this case, it appears that the nutrient source (oxygen) was rapidly and homogeneously dispersed in the culture. If homogenization of nutrients and increased supply of oxygen in the culture fluid is assumed important, it is also explains why a decrease in absorbance is observed when the volume of the culture media is increased.

Effects of the amount of strain added and shaking speed

When more bacterial culture was added at the beginning of the experiment, the maximum value of the absorbance was obtained (Fig. 3), where culture solution was used 100mL. Since the absorbance measurement was based on the turbidity of the culture solution, this result is expected. However, as the same concentration of nutrients is available in the media, we predicted that the difference in cell densities would reach a peak regardless of the amount of cells initially added. Unlike the expected test result, regardless of the amount of strain added, the absorbance was nearly constant at approximately 80–100h (Fig. 3). It is difficult to explain the actual cause of the above result; the possible reasons could lie in the nutrients, source of dissolved oxygen and medium, but these factors were not examined. However, when the medium composition was the same, the absorbance read at the various time points were comparable regardless added amount of strain. This result is considered advantageous as it allows for the artificial control of the cell density in the medium used. The absorbance increased with a faster shaking speed, the maximum value of the absorbance was obtained when shaken at 160 rpm in comparison to 80 rpm (Fig. 3). The increase in shaking speed was considered to be effective in shortening overall time needed for the experiment to take place. When shaken at 160 rpm, the absorbance peaked approximately 24h after the start of the culture, indicating that the three-day growth is not necessary in the future.

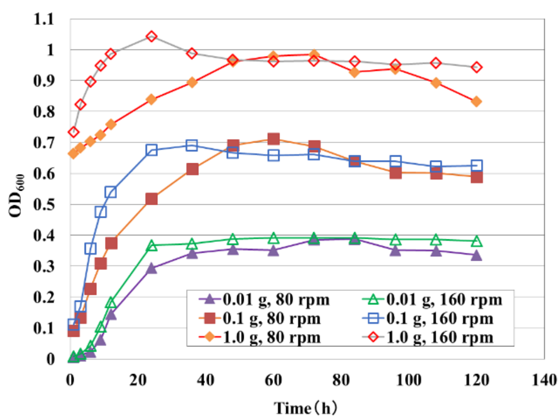

Fig. 3 The absorbance measurement results focused on the amount of strain added and shaking speed.

MCP Test in Syringe

The liquid culture medium of 100 mL and shake the culture at 160 rpm, which would provide ideal absorbance readings as well as result in optimum bacterial growth was used for syringe test. The pH and temperature for the optimal growth of the bacteria was 7.0–8.5 and 30–40°C, respectively. The above conditions were implemented for all aspects during the solidification test.

Role of pH and Ca^{2+} concentrations

The pH of all specimens during the test period tended to be lower than the pH at the beginning of the experiment (Fig. 4). However, when 1.0 g of the culture was added, regardless of the amount of urea and $CaCl_2$ added, the pH increased from days 3 through 6. The Ca^{2+} concentration was at 2.0 g/L or less in all cases when measured after 3 days (Fig. 5). After the 6th day, the Ca^{2+} concentration tended to increase markedly when the urea and $CaCl_2$ solution added was at 0.3 M and 0.5 M. The concentration of Ca^{2+}, when the 0.3 M urea and $CaCl_2$ solution were used, did not change over time and continued to be consumed until the Ca^{2+} was present in concentrations above 10.0 g/L. On the other hand, the most dramatic increase in Ca^{2+}concentration when using 0.5 M (0.01 g/0.5 M), during which the consumption of Ca^{2+} at the 12-day time point was reduced to 7.0 g/L. As can be gathered from Fig. 4 and Fig. 5, the Ca^{2+} concentration increases when the pH lowers. The diminution of urea hydrolysis with decreasing cell density is a potential cause of pH reduction. Therefore, in the specimen, if there are high concentrations of urea or $CaCl_2$ at the beginning, the amount of carbon dioxide produced by urea decomposition does not reduce Ca^{2+} consumption, in fact, eventually Ca^{2+} concentration could have increased. Alternatively, the precipitation of $CaCO_3$ for MICP begins at the cell surface of bacteria [8], [9], strains induce precipitation of $CaCO_3$ at a crystal nucleus.

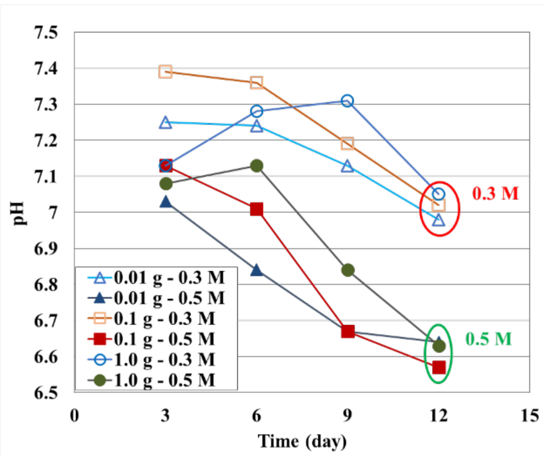

Fig. 4 The pH of the effluent over time course of different test cases in the syringe.

Estimated UCS value

The summarized results of the needle penetration test for each case are shown in Fig. 6. The estimated UCS value of the 0.3 M urea and $CaCl_2$ experiments was approximately 2 MPa, regardless of the added amount of culture added. In the cases of 0.5 M, the estimated UCS value tended to be higher than the case of 0.3 M. When the amount of bacterial strain added was 0.01 g and 0.1 g for 0.5 M urea and $CaCl_2$ solutions, the UCS showed 3~4 MPa. The specimens were significantly solidified in all experiments using 0.5 M, where the estimated UCS at some points exceeded 7 MPa. The estimated UCS tended to decreases from the top to the bottom of the specimen.

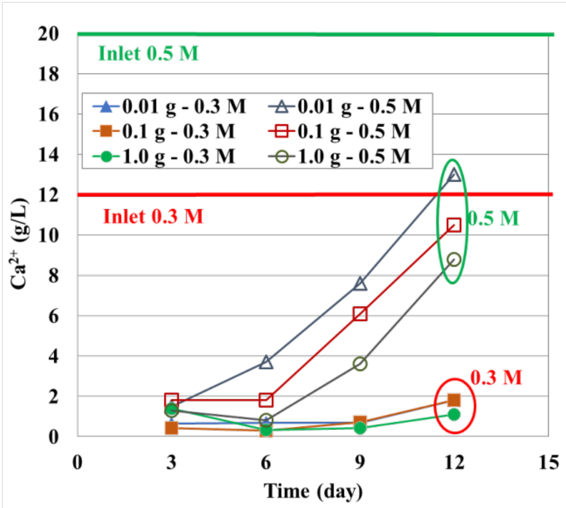

Fig. 5 Ca^{2+} concentration of effluent over time of different test cases in the syringe.

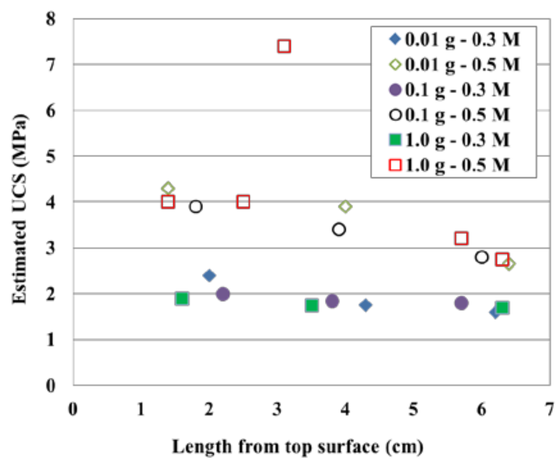

Fig. 6 Needle penetration test results of specimen in syringe in various test conditions.

Relationship between Ca^{2+} concentration and the estimated UCS in the specimen

From Fig. 6, in the case of 0.5 M solutions of urea and $CaCl_2$, the estimated UCS value of the specimen ranged from 3 to 4 MPa; the intensity distribution tended to decrease from the top to the bottom of the specimen. In this case, the Ca^{2+} concentration in the effluent demonstrated a tendency to increase in the latter half of the study period (Fig. 5). The collected effluent was estimated to have a pH and Ca^{2+} concentration of the lower part of the specimen. Furthermore, since this strain was cultured in aerobic conditions, it is possible that oxygen concentration played a role in strain activity. Since it can be considered that the bottom of the specimen approaches anaerobic conditions, the lower portion of the specimen may demonstrate reduced strain activity when compared to the top of the specimen. Therefore, the estimated UCS value of the specimen was expected to decrease from the top to bottom. On the other hand, from Fig. 6, in the case of 0.3 M urea/$CaCl_2$, the estimated UCS of the specimen were approximately 2 MPa. In addition to the concentration of the urea and $CaCl_2$, the amount of Ca^{2+} in the effluent was generally constant throughout the test period (Fig. 5). The concentration of Ca^{2+} in the original solidification promoting solution was consumed nearly 90% by the precipitate as $CaCO_3$. Therefore, it was expected that the estimated UCS values of the specimen should also remain constant, which is consistent with the results obtained above.

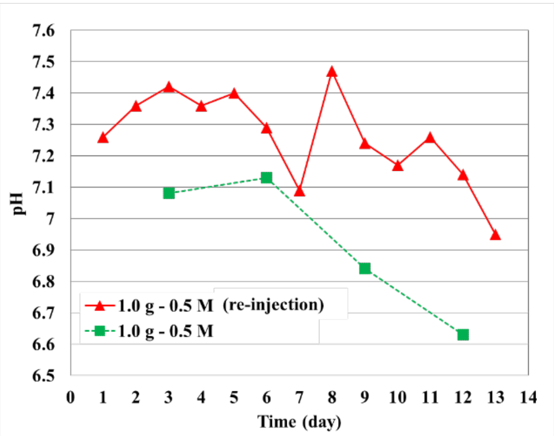

Fig. 7 Changes of pH in the effluent over time in the re-injection test in the syringe.

pH and Ca^{2+} concentration of effluent in the re-injection test

The pH of effluent in the re-injection test (1.0 g of bacterial culture was also re-injected on 7th day) is shown in Fig. 7. In the re-injection test, the pH was maintained higher as compared to the previous test, without re-injection. The pH begins to decrease after 5th day, and at 7th days it was reduced to a value close to the previous test. However, when carrying out the re-injection of the culture on day 7, pH was the maximum value during the study after 8 days thereafter decreased. However, the pH in the re-injected test remained between approximately 6.9~7.5, and did not continue to decrease (Fig. 7). The concentration of the Ca^{2+}on effluent in the re-injection test is shown in Fig. 8. The Ca^{2+} concentration in the re-injection test was approximately constant during the entire test period (Fig. 8). Overall, in the standard tests (without re-injection) the Ca^{2+} concentration increased from the beginning to the end of the experiment, which was not seen when cultures were re-injected.

The results demonstrated in Fig. 7 and Fig. 8, indicate that if the re-injection of the culture was not performed during the study in the syringe solidification test, both the pH and Ca^{2+} concentrations in the effluent decreased and increased, respectively. This trend was observed regardless of the cell density of the liquid culture injected. However, if the re-injection of the culture is completed during the study, the pH was approximately 7.0~7.3, and the Ca^{2+} concentration was constant at approximately 1.0 g/L throughout the course of the experiment (Fig. 7 and Fig. 8). The pH rise of in the effluent due to urease activity of strain increased during re-injection of the culture liquid. At the same time, the Ca^{2+} concentration decreases also to be considered due to the increase in cell concentration. After subsequent re-injection test that had remained high cell concentration in the specimen as compared to the previous test, even longer observed increase and maintenance of pH by urease activity. The precipitation of $CaCO_3$ was increased and persisted, Ca^{2+} concentration remain constant.

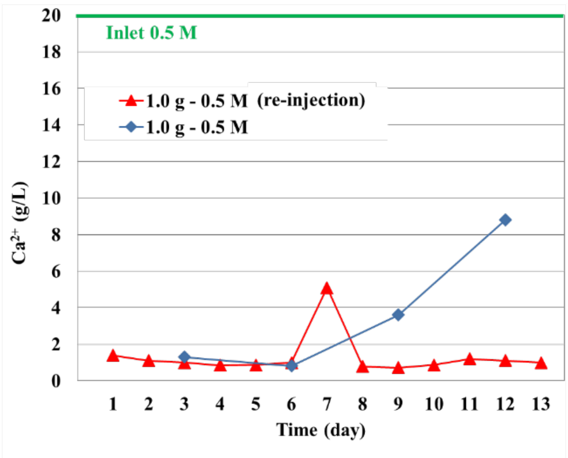

Fig. 8 Ca^{2+} concentration of effluent over time in the re-injection test in syringe.

Estimated UCS value in the re-injection test

In the re-injected 14 days test period, the UCS was approximately 8.0~13.0 MPa (Fig. 9), this value is greater than the maximum value at the time of the previous test. The UCS demonstrated a minor decreasing tendency from the upper half to the lower half of the specimen (Fig. 9). Specimens of immediately after removal of the syringe test and the re-injection syringe test is shown in Fig. 10. In the re-injection test results of the syringe shows the estimated UCS value was double that recorded using the without re-injection test. In addition, we also observed variation in solidification, which had increased the UCS value regardless of the position of the specimen, indicating that the specimen was heterogeneous and lacked problems in solidification. For this reason, there was a possibility that cell density in the specimen was not constant. From Fig. 9, the estimated UCS value in re-injection test was shown by about 2 times the needle penetration test as compared to the without reinjection. By increasing the cell concentration at 7th day, for the amount of precipitation of $CaCO_3$ and trends of Ca^{2+} concentration was kept constant, it is considered that the estimated UCS value increases. Therefore, although the estimated UCS value of the specimen was expected to be constant from the top to the bottom, variations were observed in the results.

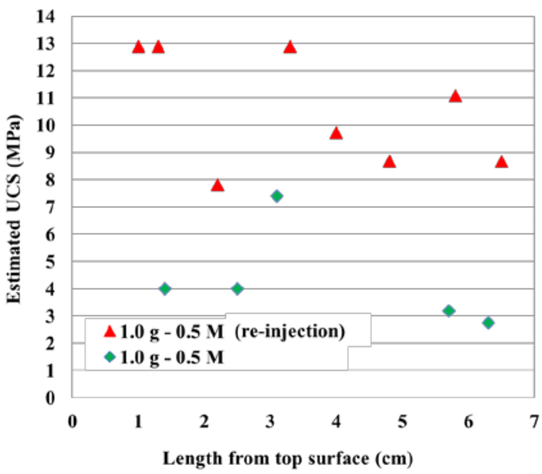

Fig. 9 Needle penetration test results of the re-injection test case in syringe.

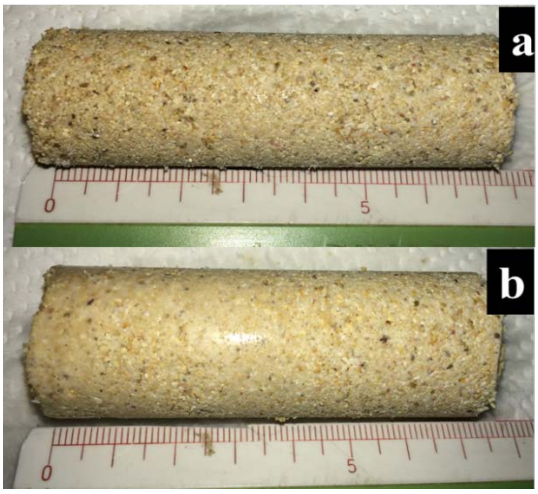

Fig. 10 appearance of specimens immediately after removal of (a) the syringe test and (b) the re-injection syringe test (photo left specimen top).

CONCLUSION

In this study, results demonstrated that the specimen solidified up to 13 MPa UCS after 14 days of curing using a microbial strain of *Pararhodobacter* sp.. Based on the findings from this study, for future attempts of the MICP method using this strain to obtain the ideal conditions for solidification in the future, four suggestions are outlined below:

(1) To facilitate solidification in a short period, the urea and $CaCl_2$ concentration should preferably be 0.5 M.
(2) For the well progress of solidification of the specimen, the pH in the specimen should be 7.0 or higher, and the Ca^{2+} concentration should be maintained at1.0 g/L.
(3) When the pH and Ca^{2+} concentrations in the specimen are out of the above range, the process can be improved by injecting more of the culture again.

REFERENCES

[1]. T. Danjo, S. Kawasaki, S. Shimazaki and K. Koizuka: Coral sand solidification test using ureolytic bacteria. Geomechanics from Micro to Macro (2013) 1521-1526.
[2]. T. Danjo and S. Kawasaki: A Study of the Formation Mechanism of Beachrock in Okinawa, Japan: Toward Making Artificial Rock. International Journal of Geomate 5(1) (2013) 633–638.
[3]. T. Danjo and S. Kawasaki: Formation Mechanisms of Beachrocks in Okinawa and Ishikawa, Japan, with a Focus on Cements. Materials Transactions 55(3) (2014) 493-500.
[4]. V. S. Whiffin, L. A. Van Paassen and M. P. Harkes: Microbial Carbonate Precipitation as a Soil Improvement Technique. Geomicrobiology Journal 24 (2007) 417-423.
[5]. H. L. Ehrlich: Geomicrobiology. Marcel Dekker, New York (2002).
[6]. J. K. Fredrickson and M. Fletcher: Subsurface microbiology and biogeochemistry. Wiley-Liss, Hoboken, NJ (2001).
[7]. Y. Inagaki, M. Tsukamoto, H. Mori, S. Nakajima, T. Sasaki and S. Kawasaki: A centrifugal model test of microbial carbonate precipitation as liquefaction countermeasure. Japan Geotechnical Journal 6 (2011) 157–167 (in Japanese with English abstract).
[8]. J. T. De Jong, B. M. Mortensen, B. C. Martinez and D. C. Nelson: Bio-mediated soil

improvement. Ecological Engineering 36 (2010) 197-210.

[9]. W. De Muynck, N. De Belie and W. Verstraete: Microbial carbonate precipitation in construction materials: A review. Ecological Engineering 36 (2010) 118-136.

Fifth International Conference on Geotechnique, Construction Materials and Environment, Osaka, Japan, Nov. 16-18, 2015, ISBN: 978-4-9905958-4-5 C3051

NUMERICAL MODELING OF ROCKING OF SHALLOW FOUNDATIONS SUBJECTED TO SLOW CYCLIC LOADING WITH CONSIDERATION OF SOIL-STRUCTURE INTERACTION

S. Mohsen Haeri* and Aria Fathi
Civil Engineering Department, Sharif University of Technology, Tehran, Iran.
*Corresponding author, smhaeri@sharif.edu

ABSTRACT

Strong Vibration of buildings during seismic or wind loading may result in an uplift or partial separation of the foundation from the underneath soil. To date, various researches have indicated that Soil-Structure Interaction (SSI) has many favorable features including a decrease in shear base demand in structures and a probable increase in natural period of soil-structure system. Furthermore, Rocking is one of the most important factors in describing the rotational behavior of structures built on shallow foundations especially on soft soils which can affect the dynamic behavior of the structures noticeably. To study the effects of rocking of shallow foundations subjected to slow cyclic loading with consideration of soil-structure interaction, a Finite Element Method (FEM) using ABAQUS software has been deployed to simulate the rocking motion of shallow foundations. For a more efficient simulation of the soil, both linear and non-linear elastic-perfect plastic behavior of the soil have been taken into account in the analysis using the sub-routine coded in FORTRAN. The results notably show that allowing the foundation to rock, may result in stiffness degradation of the soil-structure system and increase in energy dissipation of soil-structure, especially in high rise structures. Additionally, results describe that deploying the linear elastic-perfect plastic approach may result in higher uplift of the foundation in comparison to that using a non-linear elastic-perfect plastic approach, particularly in structures with lower heights.

Keywords: Soil-Structure Interaction, Rocking Behavior, Uplift, Energy Dissipation, Linear Analysis, Non-Linear Analysis, Elastic-Perfect Plastic Approaches.

INTRODUCTION

In recent years, many attempts have been carried out to predict the behavior of soil during dynamic loading such as earthquake. These predictions generally have led to safer and more efficient design of structures especially those which located on soils. One of the most important aspects of seismic design which attracts attentions among structural and geotechnical engineers is the recognition of Soil-Structure Interaction (SSI) in their design, and the significant effects of these two systems on each other under dynamic loadings. The rocking mode can be considered as one of the most important aspects of dynamic SSI to scrutinize the dynamic behavior of structures with shallow foundations located on flexible soils. Therefore, several researches have taken this aspect of the analysis into account. Primary researches on rocking have started from early 1960s when Housner [1] -with considering his observations over severe earthquakes- investigated on rigid blocks subjected to horizontal loading so as to study their separation from the underneath surface. The results of his study showed that structures which were able to rock had been less damaged in comparison to apparently more stable and state-of-the-art ones [1].

Conventional engineering design methods emphasize on preventing uplift of the foundation for preventing the overturning of the structures during strong earthquakes, however, recent studies indicate that allowing the structures to a controlled rocking may result in energy dissipation by the soil-structure system allowing some amount of uplift without jeopardizing the structure to overturn [2], [3].
In general, the non-linear behavior of the soil has many beneficial effects during seismic loading such as a probable increase in natural period of the soil-structure system and a decrease in shear base demand in structures. Furthermore it can also play a key role in energy dissipation during strong vibrations. However, permanent displacements of foundations are the most noticeable disadvantage of nonlinearity which may lead to inevitable damages [2], [3]. Importance of the rocking mode and nonlinearity of the soil encourages researchers to apply these characteristics into engineering design. Hence, geotechnical design codes are being shifted from the classical-limit analysis to the performance-based design approach. A recent study shows that, allowing foundation to yield, instead of the superstructure, can improve the overall integrity of the structure during earthquake [4]. Similarly, another study has shown that the input energy to the soil-structure system could be dissipated between superstructure and foundation by a controlled rocking [5].

In this paper, rotational behavior of 10, 20 and 30 story structures subjected to slow lateral cyclic loading, deploying SSI, have been taken into consideration. To study the rocking effects of shallow foundations on these structures, Finite Element Method (FEM) has been used. In this respect, two linear and non-linear elastic-perfect plastic soil behaviors have been taken into account for a more efficient simulation of SSI by adding two sub-routines coded in FORTRAN to the main code. Two series of analyses including six numerical models have been carried out using ABAQUS program. The purpose of these analyses is to assess energy dissipation of the soil-structure system the critical contact area, the amount of uplift and also the permanent settlement of the shallow foundations of the studied structures. The results are studied and presented in the following sections.

MODEL CHARACTERISTICS AND PARAMETERS

To study the rocking behavior of shallow foundations, six numerical models including soil, structure and foundation systems were simulated. Three different heights for the structure representing 10, 20 and 30 story buildings are considered for the analysis. Two types of behaviors, namely linear and nonlinear elastic-perfect plastic, are assumed for the soil underneath the structure. The aim of this study is to study the effect of soil nonlinearity and plasticity on the rocking behavior of these soil-structure systems under cyclic loadings. Also to study the effect of height of the structure underlain by linear or nonlinear elasto plastic soils subjected to cyclic loadings with consideration of SSI is another aim of this research.

Therefore, three structures with different heights of 30m, 60m and 90m representing respectively 10, 20 and 30 story buildings are considered for the analysis. The analyzed structures have some characteristics in common, such as length and width, elements type, and material properties; yet, their heights are different. The model of the building as an integrated rigid system consists of a foundation and the structure. The mass of the structures in conjunction with their foundations were estimated based on the mass of conventional buildings. The parameters associated with the analyzed structures are given in Table 1.

Table 1 Structure parameters

Structural Properties	10 Story	20 Story	30 Story
Height (m)	30	60	90
Weight (KN)	16620	39240	58860
No. of Elements	6850	11800	13800
E (GPa)	25	25	25
Poison Ratio	0.35	0.35	0.35

Mohr-Coulomb model has been employed in all elasto plastic cases for the soil underneath of the structural foundation. Although, there is a general consensus among researchers that shear modulus of the soils, particularly the granular soils, vary with both shear strain levels and confining pressure [6], however, in majority of numerical dynamic SSI analyses, this intrinsic feature of the soil is ignored and is considered only at static shear strain levels. Therefore, for a more realistic result, the nonlinearity, inhomogeneity and plasticity of the soil have been taken into consideration in this work by using a sub-routine coded in FORTRAN. Maximum shear modulus of the soil ($G_{\max}$), is obtained from Eq. (1) [7].

$$G_{\max(KN/m^2)} = 218.82K_{2(\max)} + (\sigma^{'})^{0.5} \quad (1)$$

$$\sigma^{'} = \frac{\sigma^{'}_1 + \sigma^{'}_2 + \sigma^{'}_3}{3} \quad (2)$$

where $\sigma^{'}$ is the mean effective confining stress, obtained from Eq. (2); $\sigma_1^{'}, \sigma_2^{'}$ and $\sigma_3^{'}$ are the maximum, intermediate and minimum effective principal stresses, respectively; and the magnitudes of $K_{2(\max)}$ vary from 35 to 70 for sandy soils (taken to be 52 for all cases which refers to fine granular soils with medium relative density).

The model proposed by Reference [8] for variation of shear modulus with shear strain was implemented, considering the variation of maximum shear modulus with confining pressure. Taking into account above points, in the first series of the analyzed cases the nonlinear elastic-perfect plastic behavior is considered for the soil.In the second series of analyses, the soil behavior is assumed to be elasto-plastic in a way that the soil behaves linear-elastic before the Mohr-Coulomb Failure Envelope, and behaves perfectly plastic when the soil yields by reaching to the shear strength or Mohr-Coulomb Failure criteria.

In dynamic analysis, damping plays a key role in the response of the structure to the motion by dissipating a part of elastic energy. In this study, the formulation proposed by Reference [9] has been used.

$$C = \alpha[M] + \beta[K] \quad (3)$$

In above relationship, [C] is the damping matrix of physical system; [M] is the mass matrix of physical system; [K] is the stiffness matrix of the system, and α and β are Rayleigh damping coefficients which can be computed by two significant natural modes by implementing Eq. (4).

$$2\xi_i\omega_i = \alpha + \beta\omega_i^2 \quad (4)$$

where ξ is damping ratio (taken to be 8% for all the soil systems and 5% for the structure systems).

One of the most delicate measure for obtaining Rayleigh damping coefficient, is the selection of the most efficient natural frequency modes to be implemented in formulations. Park and Hashash [10] suggested to use the first mode as well as the first odd mode which its frequency is higher than the loading frequency for solving the Eq. (4)

Lateral Cyclic Displacements on Structures

Figure 1 shows a schematic view of soil-structure system in conjunction with the external loads applied to the structure and the forces which are translated to the base center point of the soil-structure interface.

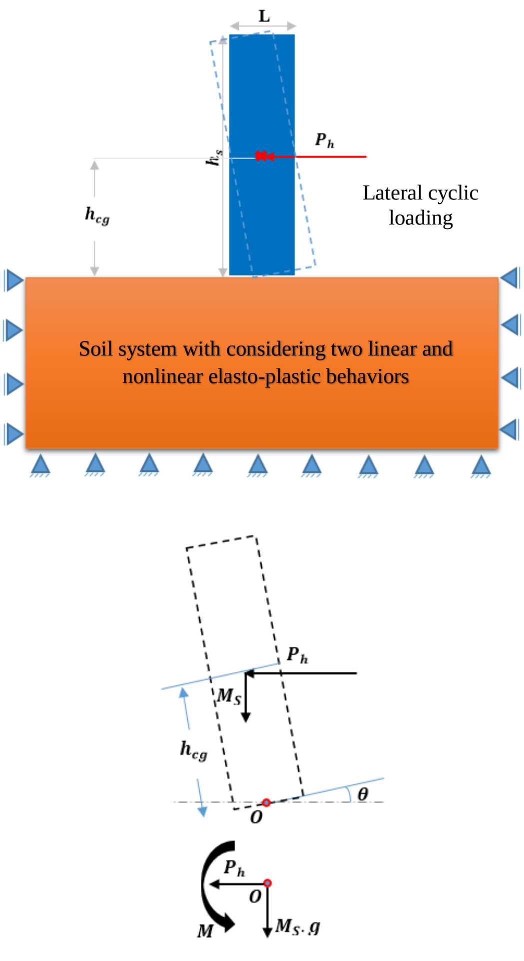

Fig. 1 Schematic model of soil-structure system as well as the external loads applied on the structure.

Based upon the Fig.1, the external loads are obtained by:

$$P_h = P_{act} \tag{5a}$$

$$M = P_h.P_{cg} + M_s.g.h_{cg.\sin(\theta)} \tag{5b}$$

where P_{act} is reaction force which is obtained during the applied lateral cyclic displacement; M_s is mass of the structure; M is moment acts at the base center point; h_s is monolithic height of structure and foundation; h_{cg} is center of gravity height of the structure-foundation system; g is gravitational acceleration; and θ is rotation of the structure.

Figure 2 shows the sinusoidal slow lateral cyclic displacements were taken into consideration in analyzed structures. To assess the stiffness variation of the soil-structure systems at their interface, all the time history-displacements apply constant rotation to each of the structures during loading. The slow cyclic time history-displacements include three clusters with different amplitudes, that each of the clusters have three cycles as shown in Fig. 2.

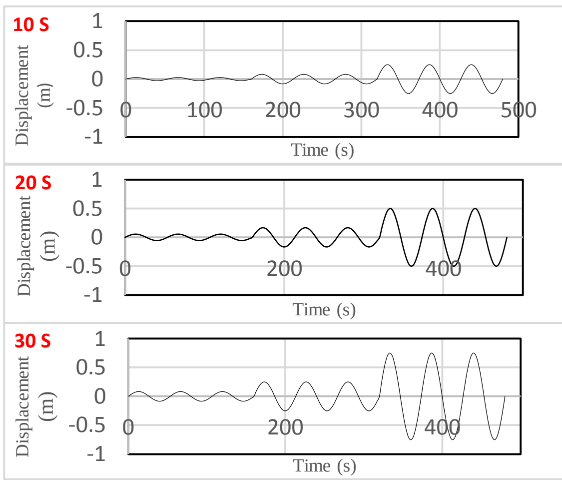

Fig.2 Slow lateral time history-displacements for 10, 20, and 30 story analyzed structures.
**Notice: S stands for story

Verification

The finite element model of rocking behavior of shallow foundations, deploying SSI effects has been verified using S21 test result which is related to second series of centrifuge tests (Krr02), provided by K. R. Rosebrook & B. L. Kutter [11]. In S21 test, a double-wall structure configuration which includes two Aluminum shear walls with parallel aluminum strip footings, has been seated on Nevada sand with a relative density of 60 percent located in a container of 20 centimeter height. The soil characteristics as well as mechanical properties of the shear walled structure are described in Rosebrook and Kutter [11]. The centrifuge was spinning with an acceleration of 20 g, to convert model data to the prototype scale. The soil-structure system in prototype scale for the S21 test is shown in Fig. 3. For verification of the numerical modeling in this study, the soil behavior is considered to be nonlinear elastic-perfect plastic.

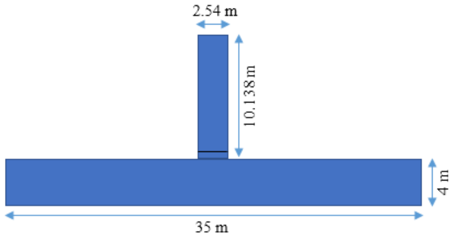

Fig. 3 The prototype scale of the soil-structure system for the S21 test.

The applied sinusoidal slow cyclic time history-displacement for the centrifuge test consisted of three cycles as shown in Fig. 4.

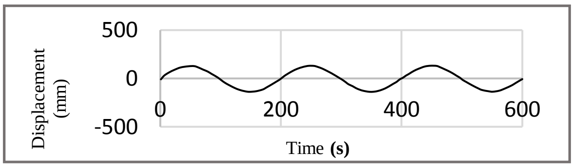

Fig. 4 Applied time history-displacement for the S21 centrifuge test [11].

Comparison of numerical model and centrifuge test

Figure 5 shows the rotation-moment relationship of soil-structure system at the center point of the base of the footing computed by proposed numerical modeling, and is that for the centrifuge test results reported by K. R. Rosebrook & B. L. Kutter [11]. The agreement between result of the numerical and experimental models is very promising, as could be seen from Fig. 5.

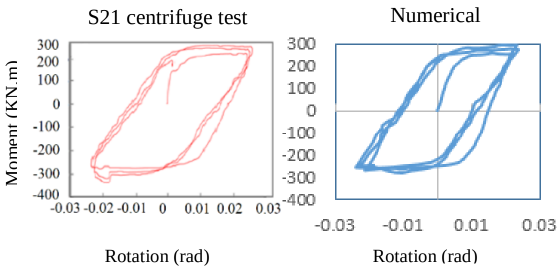

Fig. 5 Comparison of rotation-moment relationship of the proposed numerical modeling, and that for the centrifuge test results reported by K. R. Rosebrook & B. L. Kutter [11] for the aluminum shear walled structure on dense sand.

RESULTS OF THE ANALYSIS

Static Analysis Results

Immediate static settlements of the soil underneath the base centeral points of the foundations of 10, 20, and 30 story structures are computed, considering both linear and nonlinear elasto-perfect plastic behaviors for the granular soil; and are compared with the approximate initial settlement method proposed by Mayne and Poulos (1999) [12] as shown in Table 2. The results show that the immediate static settlement in linear elasto-plastic approach is closer to that resulted from approximate method. The reason is that the approximate approach is based on linear elasticity behavior of the soil. However, the values of immediate static settlement using nonlinear elasto-plastic approach are much higher due to yielding of the soil when shear modulus decrease at corresponding high shear strain levels.

Table 2 Immediate static settlements of the foundation computed by three different approaches.

Structure Properties	10 Story	20 Story	30 Story
Approximate method (mm)	9.2	18.4	27.6
Linear elasto plastic soil (mm)	7.8	15.0	23.4
Nonlinear elasto plastic soil (mm)	57.5	72.0	82.0

Dynamic Analysis Results and Rocking Behavior

Energy dissipation and rotational stiffness degradation

It is clear that a part of the input energy is dissipated by the rocking motion of the structures with shallow foundations subjected to dynamic loading, in the real world and in all kinds of analysis, and is observed in rotation-moment diagrams as shown in Fig. 6. In this regard, the hysteresis loops are wider with a larger area of dissipated energy when the nonlinear elasto-plastic behavior is considered for the soil beneath the foundation. Indeed, yielding of the soil at sides of the foundation during the rocking mode owing to increasing the shear stress and decreasing the shear modulus in these areas, eventuate in more energy dissipation through the nonlinear approach. The rotational stiffness degradation in nonlinear approach is slightly more, compared to that for the linear one, showing that the stiffness degradation as well as softening of the soil system are associated with increasing of the rotational amplitudes (Fig. 6).

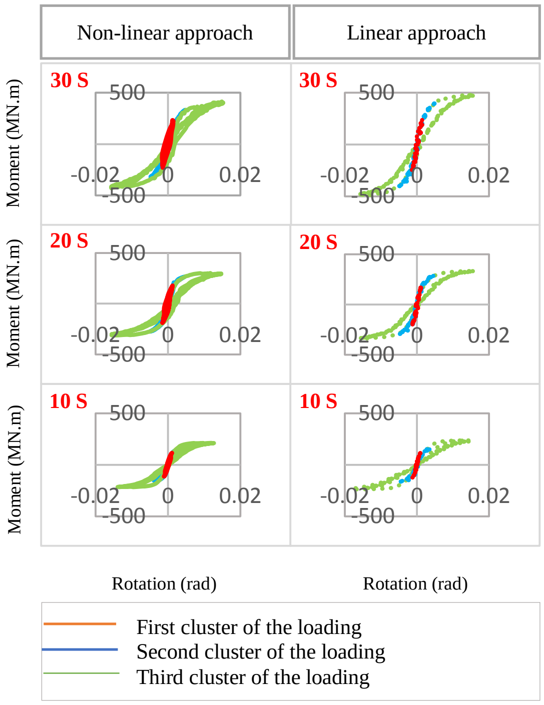

Fig. 6 Rotation-moment diagrams for the 10, 20, and 30 story structures with consideration of two linear and non-linear elasto-plastic approaches for the soil underneath the foundation.

Additionally, Fig. 6 shows that energy dissipation of soil-structure system during rocking could be enhanced not only by increasing the rotational amplitudes but also by increasing the height of the structures.

The soil settlement-time history for the center point of the soil-foundation interface has been plotted over the displacement time history of the similar point on the base of the foundation, and is shown in Fig. 7. It is evident from these two plots that a great amount of input energy is dissipated through the nonlinear elaso-plastic behavior for the soil especially in the tall, slender structure (30 story structure). In fact, the compatibility of the soil settlement and the foundation displacement plots show that the input energy can be dissipated by yielding of the soil, which result in more permanent settlement and lower reflection of foundation in nonlinear soil. The linear behavior of the soil results in much higher separation of the foundation of structure from the underneath soil showing less compatibility between the soil and the structure and more foundation separation and uplift during rocking. Moreover, during the first two clusters of the loading, in both cases the movements of soil and foundation are more compatible showing little uplift. However, in the third cluster of loading with higher load amplitude, the amplitudes of soil-foundation separation and foundation uplift is greater especially for the linear behavior of the underneath soil.

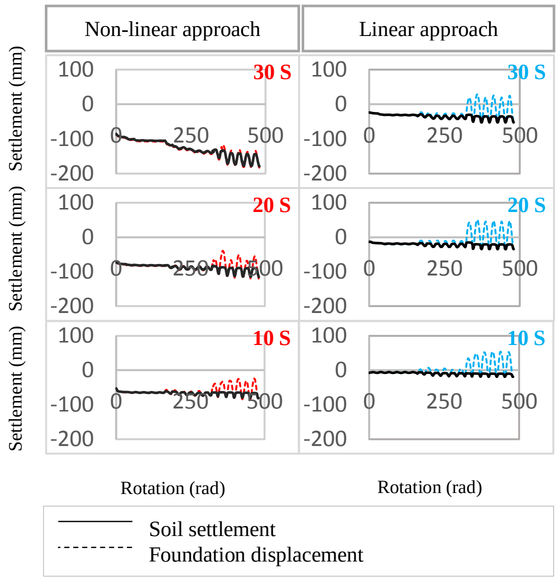

Fig. 7 Comparison of settlement and displacement-time history plots for the center point of soil-foundation interface through the nonlinear and linear approaches.

Mobilized Moment and effective contact area of the foundation

In each cycle of loading, the foundation contact area is varied by the applied rotation, therefore, mobilized moment, energy dissipation, and uplift of foundation during rocking could have a close relation with ratio of foundation contact area to foundation area which is defined by following equation.

$$\zeta = \frac{A_C}{A} = \frac{\text{Foundation Contact Area during Rocking}}{\text{Actual Foundation Area}} \tag{6}$$

Critical amount of ζ as well as its corresponding mobilized moment of soil-structure system are computed at maximum rotational amplitudes of each cluster of loading and are shown in Table 3. In this regard, maximum mobilized moment in each cluster of loading is obtained, where the foundation has the least contact area with the underneath soil at a short period of time. Based on obtained results shown in Table 3, the nonlinearity of the soil decreases the maximum mobilized moment in the structure due to cyclic loading and increases the effective contact area of the foundation during rocking which both enhances the safety of the structure against overturning and reduces the internal loads and decreases the associated material consumption when the results are compared with those of linear soil behavior.

Table 3 The ratio of foundation contact area during rocking to actual foundation area as well as the maximum mobilized moment.

			$\zeta = \frac{A_C}{A}$			Maximum Mobilized Moment (MN.m)		
			10 S	**20 S**	**30 S**	**10 S**	**20 S**	**30 S**
Nonlinear elasto plastic soil	**Rotation (rad)**	0.0015	0.83	0.87	0.96	115.76	178.08	229.09
		0.005	0.45	0.48	0.66	152.12	265.64	331.80
		0.015	0.33	0.42	0.45	212.00	301.17	411.41
		End of Loading	0.63	0.87	0.92	0	0	0
Linear elasto plastic soil	**Rotation (rad)**	0.0015	0.71	0.80	0.84	123.78	188.24	240.88
		0.005	0.37	0.39	0.47	160.11	289.39	396.65
		0.015	0.22	0.23	0.26	236.06	336.07	483.11
		End of Loading	0.47	0.53	0.58	0	0	0

CONCLUSION

The obtained results from the slender, high rise structures, which are allowed to rock show that the stiffness degradation of the soil-structure system decreases as well as increasing the energy dissipation. Although, the nonlinear elastic-perfect plastic approach result in dissipating the major amount of the input energy in comparison to the linear elastic-perfect plastic behavior considered for the soil, yet, it causes the noticeable permanent settlement which might have destructive effects on the structures.

Additionally, deploying the linear approach through the analysis eventuate in the less contact area during rocking, and it can make structures less stable against overturning. To sum up, with all this taken into account, rocking and nonlinearity of the soil have many beneficial effects for the soil-structure system during strong vibrations that should be more noticed in future engineered designs.

REFERENCES

[1] Housner GW, "The Behavior of Inverted Pendulum Structures During Earthquakes", Bulletin of the Seismological Society of America, Vol. 53, 1963, No. 2, pp. 403-417.

[2] Gajan S, Kutter BL, Phalen JD, Hutchinson TC and Martin GR, "Centrifuge modeling of load-deformation behavior of rocking shallow foundations", Soil Dynamics and Earthquake Engineering, Vol. 25, 2005, 773-783.

[3] Deng L and Kutter BL, "Characterization of Rocking Shallow Foundations Using Centrifuge Model Tests", Earthquake Engineering and Structural Dynamics, 2011, DOI: 10.1002/eqe.1181.

[4] Anastasopoulos I, Gazetas G, Loli M, Apostolou M and Gerolymos N, "Soil Failure Can be used for Seismic Protection of Structures", Bulletin of Earthquake Engineering, Vol. 8, 2009, 309-326.

[5] Weian L, Hutchinson TC, Kutter BL, Hakhamaneshi M and Gavras AG, "Balancing the Beneficial Contributions of Foundation Rocking and Structural Yielding to Improve Structural Seismic Resilience", 4th ECCOMAS Thematic Conference on Computational Methods in Structural Dynamics and Earthquake Engineering, 2013.

[6] Kramer SL, "Geotechnical Earthquake Engineering", Prentice Hall, 1996.

[7] Seed HB and Idriss IM, "Soil Moduli and damping factors for dynamic response analysis", 1970, Report No. EERC 70-10, University of California,,Berkeley.

[8] Seed HB, Wong RT, Idriss M and Tokimatsu K, "Moduli and Damping Factor for Dynamic Analysis of Cohesionless Soil", Journal of Geotechnical Engineering Division, ASCE, Vol. 112, 1986, No.11.

[9] Rayleigh JWS & Lindsay RB, "The Theory of Sound" Dover Publications, New York, 1945.

[10] Park D and Hashash YMA, "Soil Damping Formulation in Nonlinear Time Domain site Response Analysis", Journal of Earthquake Engineering, Vol. 8, 2004, No. 2, 249-274.

[11] Rosebrook KR. and Kutter BL, "Soil-Foundation-Structure Interaction: Shallow Foundations Centrifuge Data Report For KRR02", Earthquake Engineering Research Center, University of California, Davis, 2001, EEC-971568, Peer 2061999 & 2142000.

[12] Mayne PW and Poulos HG, "Approximate Displacement Influence Factors for Elastic Shallow Foundations" Journal of Geotechnical and Geoenvironmental Engineering, Vol. 125, 1999, No. 6.

FUZZY LOGIC APPLICATION TO COAXIAL AND NON-COAXIAL COMPONENTS OF SHEAR STRENGTH AND CONSOLIDATION OF SOILS

J.Rajaraman [1] K.Thiruvenkatasamy [2] and S.Narasimha Rao [3]

1, 2 Professor, Department of Harbour and Ocean Engineering,
AMET University, 135 East Coast road, Kanathur -603 112
Chennai, India
3, Director,Dredging Corporation of India (Govt. of India)

ABSTRACT

Fuzziness is explored as an alternative to randomness for describing uncertainty. The new sets –as – points geometric view of fuzzy sets is developed. This view identifies a fuzzy set with a point in a unit hyper cube and a non-fuzzy set with a vertex of the cube. In Fuzzy logic a crisp set is a set in which all members match the class concept, and the class boundaries are sharp. The degree to which an individual observation z is a member of the set is expressed by the membership function F, which can take the value of 0 or 1for Boolean sets. In fuzzy logic the membership function is a number in the range of 0.1 with 0 representing non-membership of the set and 1 representing full membership of the set. "Kosko cube" is the Starting point. A two dimensional version of Kosko cube is considered. The sediments usually consist of clay and sand. If p is percentage of clay, then (1-p) is % of sand. Clay properties relate to pure shear. Similarly the sand % represents simple shear. Fuzzy logic suits this problem when % are expressed in the range 0, 0.1, 0.2 etc. up to 1.0. The membership functions in the combination of coaxial and non-coaxial shear component (pure and simple shear) is represented in Kosko cube. Taking Skempton's experimental data (clay + Sand) points distributed in quadrants I, II, III, IV inside the cube as points are interpreted through simple Geological processes. Fuzzy logic also suits soil consolidation.

Keywords: Fuzzy Logic, Coaxial and Non-coaxial Shear, Kosko Cube, Membership function.

INTRODUCTION

Zadeh (1965) writes, " The notion of a fuzzy set provides a convenient point of departure for the construction of a conceptual framework which parallels in many a respects the framework used in the case of ordinary sets, but it is more general than the latter and, potentially, may prove to have a much wider scope of applicability, particularly in the fields of pattern classification and information processing. Essentially, such a framework provides a natural way of dealing with problems in which the source of imprecision is the absence of sharply defined criteria of class membership rather than the presence of random variables."

I. THE GEOMETRY OF FUZZY SETS: SETS- AS- POINTS (Kosko Cube) [1].

In Figure 1 consider the set of two elements X= $\{x_1 x_2\}$. The non- fuzzy power set 2^X contains four sets :
$2^X = \{\ \emptyset, X, \{x_1\},\ \{x_2\}\}$.These four sets correspond respectively to four bit vectors (0 0),(1 1), (1 0), and (0 1). This 1s and 0s indicate the presence or absence of the ith element x_i in the sub-set. More abstractly, each sub-set A is uniquely defined by one of the two – valued membership functions m_A: $X \rightarrow \{0, 1\}$.
Now consider the fuzzy sub- sets of X. The fuzzy sub-set A= $\left(\frac{1}{3}\ \frac{3}{4}\right)$ can be viewed as one of the continuum – many continuous – valued membership functions m_A: $X \rightarrow \{0, 1\}$. Indeed this is the classical Zadeh sets – as - functions definition of fuzzy sets. In this example element x_1 belongs to , or fits in, sub-set A a little bit- to degree $\frac{1}{3}$. Element x_2 has more membership than not at $\frac{3}{4}$. Analogous to the bit vector representation of finite (countable) sets , we say that A is represented by the fit vector $\left(\frac{1}{3}\ \frac{3}{4}\right)$. The element $m_A(x_i)$ is the ith fit or fuzzy unit value. The set -as –points view then geometrically represents the fuzzy sub-set A as a point in 1^2, the unit square as in figure1.The mid-point of 1^n maximally fuzzy. All its membership values are $\frac{1}{2}$. The mid point is unique in two respects.

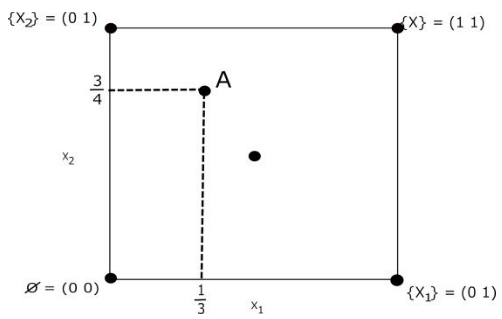

Fig. 1 Kosko cube

II. A CONCEPTUAL MODEL OF DISSOLUTION OF THE SKELETON GRAINS

Here dissolution is the ensemble of phenomenon that chemically attack the particles of various sizes, whether through solubilization or by hydrolysis. In this model the particles are sorted by size in a table. The particles of diameter $200\mu m$ will be in box no. 200. Since dissolution being gradual, it consists of translocating the particles from box to box without ever skipping a box. This process comes to a halt when the thickness taken off is dl. The following figure 2 explains such a model.

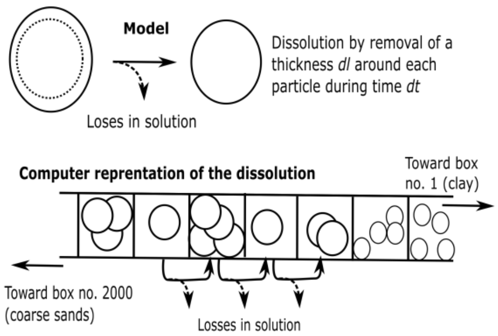

Fig.. 2 Model of Dissolution of the skeleton grains [2].

In this a collection of particles containing sands, silts and clays at the same time, the point representing which is located at the centre of the textural triangle as shown in the figure as point X. In reality, the smallest particles have a greater surface area/ mass ratio. They are therefore more susceptible to dissolution and disappear in greater proportion by weight. The result is a trajectory towards the sand corner, at the cost of a very pronounced loss in total mass as shown in the figure 3.

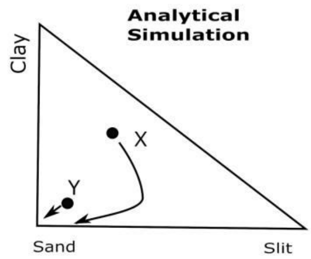

Fig. .3 Result of a simulated Dissolution in a textural triangle [2].

Dissolution at first affects mainly the particles of clay size, especially the fine clays, leading to an evolution towards the base of the triangle. Then the silts are attacked in their turn, whereby an inflexion is seen in the trajectory towards the sand corner.

If we start from a collection of already sandy particles (point y), there is no trajectory observable by simulation. The point representing the collection remains almost in place in the triangle. In other words, it is impossible to create a clayey or even silty material starting from a sand composed of particles of size $2000\boldsymbol{\mu m}$. When the diameter will be reduced to $1000\boldsymbol{\mu m}$, this sand will continue to be counted in the coarse sands (particle size class 2000 $\boldsymbol{\mu m}$ - 200 $\boldsymbol{\mu m}$). The size class will not change in the system of measurement. However it would have lost 87.5% of its mass. The chemical reduction of sands does not change the particle size class.

III. ISOTROPIC STRESS AND DEVIATORIC STRESS

The amount of water existing in the soil mass will significantly influence the engineering behavior of soil. Karl Terzaghi has said in effect, that there would be no need for soil mechanics if not for water. This is because the presence of water affects the state of stress within a soil mass. The water content also has bearing on potential volume change, progressive failure, densification, shear strength, and settlement. The mechanism of soil –water interaction is complex and its behavior is not only dependent on soil types, but is also related to the current and past environmental conditions and stress histories, Isotropic stress and deviatoric stress

Isotropic stress acts equally in all directions, it results in a *volume change* of the body. Deviatoric stress, on the other hand, changes the *shape* of a body as shown in figure 4. [3].

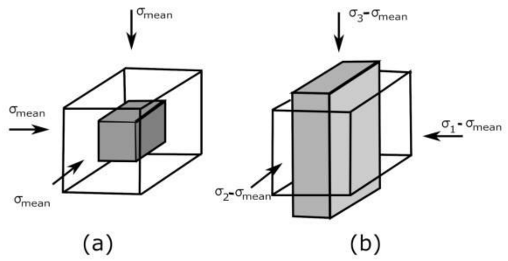

Fig.4 The mean (hydrostatic) and deviatoric components of the stress. (a) mean stress causes volume change and (b) Deviatoric stress causes shape change.

IV. THE CONCEPT OF COAXIAL AND NON- COAXIAL COMPONENTS OF SHEAR STRENGTH

In a homogeneously strained, two-dimensional body there will be at least two material lines that do not rotate relative to each other, meaning that their angle remains the same before and after strain. A material line connects features , such as an array of grains, that are recognizable throughout a body's strain history. The circle deforms and changes into an ellipse. In homogeneous strain, two orientations of material lines remain perpendicular before and after strain. These two material lines form the axes of an ellipse that is called strain ellipse. The principal incremental strain axes rotate to the finite strain axes, a scenario that is called non- coaxial strain accumulation. The case in which the same material lines remain the principal strain axes at each increment is called coaxial strain accumulation. The coaxial component of shear strength is called pure shear and the non-coaxial component of shear strength is called simple shear. The combination of simple shear (a special case of non-coaxial strain) and pure shear (coaxial strain) is called general shear or general non-coaxial strain. Two types of general shear are possible. It is explained in figure 6.

The following figure 5 explains simple shear and pure shear [3].

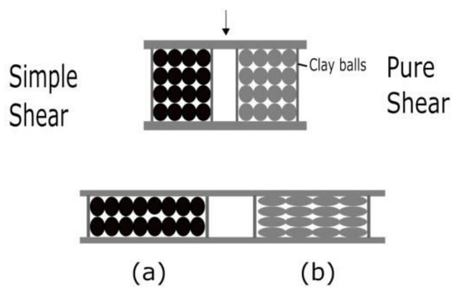

Fig. 5 Simple Shear and Pure Shear Explained

In Figure 5 The rigid spheres slide past one another to accommodate the shape change without distortion of the individual marbles . In figure 5b the shape change is achieved by changes in the shape of individual clay balls to ellipsoids, are quite different.

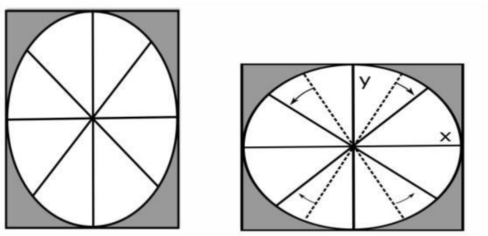

Fig.6 Homogeneous Strain

In Figure 6 Homogeneous strain describes the transformation of a square to a rectangle or a circle to an ellipse. Two material lines that remain perpendicular before and after strain are the principal axes of the strain ellipse [solid lines]. The dashed lines are material lines that do not remain perpendicular after strain; they rotate toward the long axis of the strain ellipse.

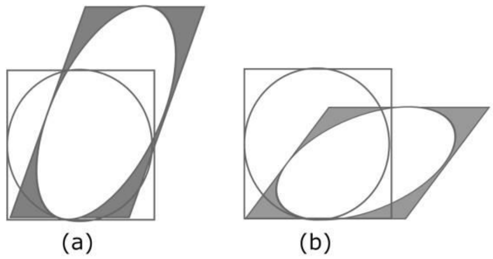

Fig.7 A combination of Simple shear and Pure shear.

In figure 7 a combination of simple shear [a special case of non-coaxial strain] and pure shear [coaxial strain]is called general shear or general non-coaxial strain. Two types of general shear are transtension [a] and transpression[b], reflecting extension and shortening components.

V. THE PROPERTIES OF SEDIMENTS DERIVED FROM SECONDARY ROCKS AND MANIFESTATION OF COAXIAL AND NON-COAXIAL COMPONENTS OF SHEAR STRENGTH

The properties of sediments derived from secondary rocks are worth mentioning in this context:

(1) Rock is aggregate of minerals. Chemical composition is a direct function of mineralogy, and mineral composition varies with grain size. The major- element chemical composition of

shales and mudstones is related also to grain size.

(2) Grain size and shape, control coaxial and non-coaxial strains of the sediments. Angular grains increase the angle of internal -friction of the soil.

(3) Because the chemical composition of siliciclastic sedimentary rocks is closely related to the mineral composition of these rocks, the chemical composition varies as a function of grain size along with variations in mineralogy. For example that SiO_2 abundance decreases progressively from fine sands to fine clays, whereas the Al_2O_3 content systematically increases.

(4) Quartz arenites composed of 90 to 95% siliceous grains quartz, chert, quartzose rock fragments).

(5) Fine grained siliciclastic sedimentary rocks, composed mainly of particles smaller than approximately 62 microns, make up approximately 50% of all sedimentary rocks in stratigraphic record.

(6) Quartz tends to be more abundant in coarse grained mudstones and shales, whereas clay minerals are more abundant in fine grain mudstones and shales.

(7) Quartz arenites are more poorly sorted and may contain high percentages of sub-angular to angular grains. Some quartz arenites exhibit textural inversions such as a combination of poor sorting and high rounding, a lack of correlation between roundness and size, such as small round grains and larger angular grains, or mixtures of rounded and angular grains within the same size fraction. These textural inversions probably result from mixing of grains from different sources, erosion of older sandstones, or environmental variables such as wind transport of rounded grains into a quiet- water environment.

(8) Angular grains may result also from development of secondary overgrowths.

(9) Now the problem has to do with the inherent relationship of parent rock grain size and size of rock fragments. Only fine size parent rocks yield substantial quantities of rock fragments of sand size. Therefore, coarse grained parent rocks are poorly represented by rock fragments in sandstones.

(10) Collectively, the changes brought about in the composition of sediment by weathering and erosion, transport, reworking at the depositional site can be significant. Provenance analysis requires that we cannot use the absence of particular constituents as a guide to provenance interpretation; we can use only the presence. The fact that feldspars and heavy minerals may be absent or scarce in sandstone, for example, does not mean that they were necessarily absent or scarce in the source rocks. Feldspars would have been converted chemically to clays.

The ultimate products of weathering following the above properties of sediments ends up in sand and clay. The coaxial and non-coaxial components of shear strength are the hidden signature to sediments in the presence of water.

VI. THE COMPLEX FUNCTION – PERMEABILITY [4].

Permeability is a complex function of particle size, sorting, shape, packing ,and orientation of sediments. These variable factors can be expressed in terms of heterogeneity factor. For a formation with a mixture of clay and sand the following equations with this heterogeneity factors C_{V_1} and c_{v_2} This variable factor C_V is believed to decrease with decreasing particle size and decreasing sorting .This factor C_V is affected by particle orientation. It is also affected by the orientation parallel to bedding plane or perpendicular to the orientation. To make it a simple factors for the purpose of calculation the heterogeneity of clay is taken as C_{V_1} and for sand as c_{v_2}.

The general eqn for C_V total is (C_V = Coefficient of variation or Heterogeneity)

$$c_{v_{total}} = \sqrt{pc_{v1}^2 + (1-p)pc_{v2}^2}$$

P = 1 (Taking element No: 1 as clay)

Element 2 sand (1 - p) = o

$$c_{v_{total}} = \sqrt{1c_{v1}^2 + (1-1)c_{v2}^2}$$

$$c_{v_{total}} = \sqrt{c_{v1}^2} = c_{v_2} \text{ (for clay)}$$

Similarly for p = 0 for clay

$$c_{v_{total}} = \sqrt{0c_{v1}^2} = (1-0)c_{v_2}^2$$

$$c_{v_{total}} = \sqrt{c_{v2}^2} = c_{v_2} \text{ (for sand)}$$

The common shear strength eqn is τ = [C + σ tan ϕ] where τ is shear strength, C is cohesion and σ is normal stress and φis the angle of internal friction of the soil.

τ = [C + σ tan ϕ] cos α, and

$$\cos\alpha = \sqrt{pc_{v_1}^2 + (1-p)c_{v_2}^2}$$

$$\tau = (c + \sigma\tan\phi)\sqrt{pc_{v_1}^2 + (1-p)c_{v_2}^2}$$

When α = 90^0, cos α = 0 for pure clay p = 1, Sand (1 - p) = 0, φ = 0.

$$\tau = (c + \sigma\tan\phi)\sqrt{c_{v_1}^2 + 0c_{v_2}^2} \text{ , for cos(90°)=0}$$

$\tau = c(c_{v_1})$ for pure clay. $c_{v_1}, \tau = c$

For pure sand p = 1. τ = (C + σ tan ϕ)

$\tau = (c + \sigma \tan\phi)\sqrt{pC_{v_1}^2 + (1-p)C_{v_2}^2}$ for cos 0=1

For pure sand p = 0.

$$\tau = (c + \sigma \tan\phi)\sqrt{0C_{v_1}^2 + (1-0)C_{v_2}^2}$$

$$\tau = (c + \sigma \tan\phi)(\sqrt{0 + C_{v_2}^2})$$

$$\tau = (c + \sigma \tan\phi)C_{v_2}$$

For clay C = 0,

$\tau = (C_{v_2})\sigma \tan\phi$, and $C_{v_2} = 1$

Heterogeneity

C_{v_1} or $C_{v_2} = 1$

τ = σ tan ϕ.

VII. THE RELATION BETWEEN COAXIAL AND NON-COAXIAL STRAIN AND SKEMPTON POINTS

This figure.8, shows the sharing of coaxial and non-coaxial strain or strength by different soil samples. No point lies in quadrant IV which is high cohesion and high friction zone but in nature high cohesion and high friction cannot exist together in a soil sediment system, when sharing the same volume or space between clay and sand (0.0,1.0 or 1.0,0.0).

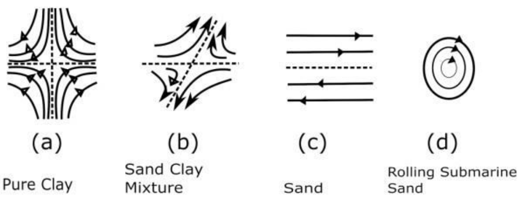

Fig.8 Particle paths or flow lines during progressive strain accumulation. [5].

These flow lines represent pure shear [a], general shear [b], simple shear [c], and rigid –body rotation [d]. The cosine of the angle α is the kinematic vorticity number,W_k for these strain histories; W_k =0,0 < W_k <1, W_k=1, and W_k = ∞ respectively. Avoiding the math, a convenient graphical way to understand this parameter is shown in fig.8 When tracking the movement of individual points within a deforming body relative to a reference line, we obtain a displacement field (or flow lines) that enables us to quantify the internal vorticity. The angular relationship between the asymptotes and the reference line defines W_k. W_k =cos α.

For pure shear W_k= 0 fig. 8a, for general shear 0< W_k <1 fig. 8b and for simple shear W_k = 1 fig 8c . Rigid- body rotation or spin can also be described by the kinematic vorticity number (in this case, W_k = ∞ fig. 8d).When α = 0^0, Cos α= 1, represents simple shear. When α = 90^0, Cos α = 0, represents pure shear. [5].

The component describing the rotation of the material lines with respect to the principal strain axis is called the internal vorticity, which is a measure of the degree of non-coaxiality.

If there is zero internal vorticity, the strain history is coaxial, which is sometimes called pure shear. The non-coaxial strain history describes the case in which the distance perpendicular to the shear plane remains constant; this is also known as simple shear.

For interpretation the data (after Skempton,1964) indicating the variations of angle of internal friction (φ) with percentage of clay content is shown in a family of nine points, distributed over the first three quadrants as shown in fig.9

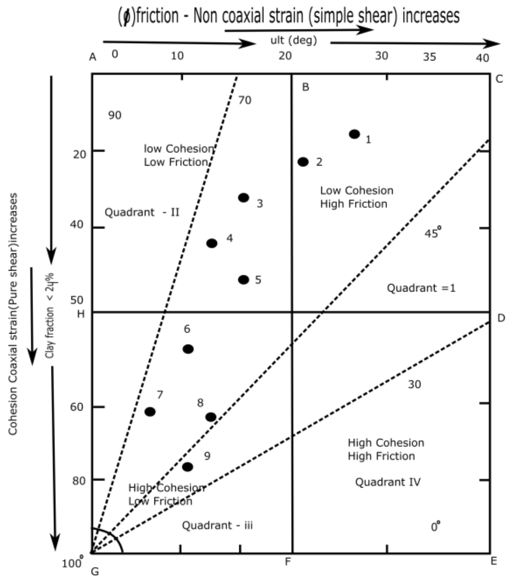

Fig..9 variation of φ_{ult} with percentage of clay content. (After Skempton 1964) All Skempton points lie in quadrants I, II,III. [6].

In the above fig.9.,if ∝ = 0, the slope line coincides with x axis , GFE, cos ∝= cos0 = 1.0. If ∝ = 90^0, the slope line becomes vertical and coincides with y axis, GHA, cos∝ = cos 90^0 = 0.0.

In Table I the activity increase from quartz to clay minerals or from frictional soil to cohesive soil or simple shear to pure shear combinations as Skempton Points is shown.

TABLE I ACTIVITY NUMBER, CLAYS AND SKEMPTON POINTS [6].

Quadrant	No. of Skempton points	Type of Quadrant
I	02	Low cohesion, High friction
II	03	Low cohesion, Low friction
III	04	High cohesion, Low friction
IV	Nil	High cohesion, High friction

VIII. FUZZY LOGIC (MEMBERSHIP FUNCTIONS) APPLICATION TO COAXIAL AND NON-COAXIAL COMPONENTS OF SHEAR STRENGTH OF SOILS

In marine environment the sea beats the waves on the sandy shores whose particles are subjected to intense dissolution, which does not, however, prevent them from remaining sandy. Now transferring the triangle in correct orientation, and ignoring gravity, to each of the quadrants (I II III IV) into the Kosco's cube the following integrated figure is obtained.

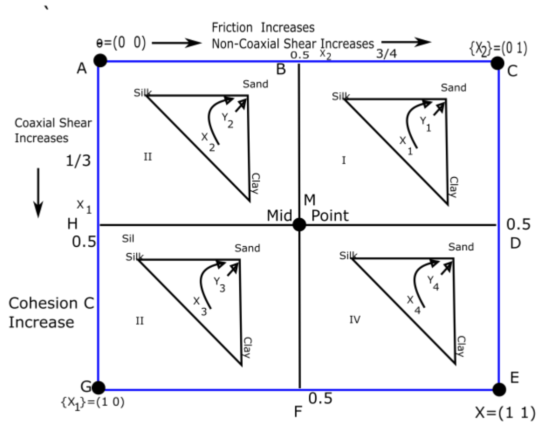

Fig.10 Fuzzy logic (Membership Functions) and Shear Strength of soils

In above integrated figure 10 the Boolean corner crisp points and the fuzzy paths and the mid –Point M with maximum fuzzy are shown. Since marine conditions are considered only dissolution is considered for the fuzzy logic. The movement from X_1 in the direction of the arrow indicates the movement of clay. It is applicable to X_2 , X_3 and X_4. The small movements of sand are indicated from Y_1, Y_2, Y_3 and Y_4. In this figure 10 the importance is given to the maximum fuzzy point M and all other Boolean crisp corner points of the cube. The sedimentation processes sometime undergo the following processes : a) sand deposit gaining clay particles in the voids b) already existing sandy clay deposits may undergo loss of clay particles c) clay deposits may gain sand in the voids d) in some cases clayey sand may undergo loss of sand. In all these cases the membership function related to Geological process will be different. For clarity only dissolution is discussed.

Table II Connecting Fuzzy logic, Fuzzy Paths, Cohesion and Frictional Components of Shear Strength of Soils

Quadrant	Fuzzy Area	Fuzzy path Away from	Fuzzy path towards destination	Geo-Tech Classification
I	BCDM	Mid point Max.Fuzzy	Cohesion (0.0) Friction (1.0) Crisp point	Low Cohesion High Friction
II	ABMH	Mid-point Max.Fuzzy	Cohesion (0.0) Friction (0.5)	Low Cohesion Low Friction
III	HMFG	Crisp corner Cohesion (1.0)	Mid point Cohesion(0.5) Friction (0.5)	High cohesion Low Friction
IV	MDEF	Friction (0.0) Cohesion (1.0) Friction (1.0)	Cohesion (0.5) Friction (0.5)	High Cohesion High Friction Cannot exist in Natural soils

IX. THE SUITABILITY OF FUZZY LOGIC (MEMBERSHIP FUCTIONS) AND INTERPRETATION OF GEO-TECHNICAL PARAMETERS

The Maximum Fuzzy, Mid-Point M:

The mid-point represents maximum fuzzy with (membership function 0.5, 0.5) and also the percentage of clay 50% and sand 50% intrinsically related to coaxial shear (pure shear) of clay and non-coaxial shear (simple shear) in a unique logic. This mid-point is a reality in fuzzy logic.

But this mid-point is forbidden to classical logic (Boolean logic) and set theory. The arbitrary insistence on bivalence or sharp crisp sets is the main reason for the restriction. At the middle point of the cube the classical theory breaks down completely because both sand and clay exist in reality with membership functions (0.5, 0.5).

Hence conclusion number 1. is, if laws of mathematics applied to reality they are not certain. This is the reason for avoiding mid-point. Fuzzy logic is for reality (in this case Geology) and therefore it admits mid-point under all conditions. In other words, when crisp sets in the four corners of the cube contracts to a mid-point, the classical (Boolean Logic fails).

The Minimum Fuzzy or Boolean or Crisp Sets:

When the mid-point expands and propagates to include all the four corners of crisp sets, then also the classical logic fails. For classical logic at the mid-point nothing is distinguishable. At the vertices everything is distinguishable. At the corners of the cube (vertices) point E representing high friction and high cohesion (1.0, 1.0) cannot exist simultaneously in nature in soils in a given sample.

There is residual friction even for very pure clay. Similarly a feeble cohesion for fine sands. The corner points (0.0) (0,1), (1,0) can exist in soil processes and samples in ideal cases. But the corner point (1, 1) can not exist in any conditions.Therefore conclusion number 2 is, if the laws of mathematics are certain (sharp or crisp sets), they do not refer to reality.

X. FUZZY LOGIC AND CONSOLIDATION [7].

Figures 11 and 12 presents an excellent pictorial idea of the process of the consolidation in an especially instructive manner. At the start of the process t = 0 and T = 0, U_Z=0 for all depths. In this process three dimensionless parameters are introduced for convenience in presenting the results in a form usable in practice. The first is Z/H, relating to the location of the point at which consolidation is considered, H being the maximum length of the drainage path. The second is the consolidation ratio, U_z defined to indicate the extent of dissipation of the hydrostatic excess pressure in relation to the initial value $U_z = (u_i - u) / u_i = [1-u/u_i]$. The subscript z is significant, since the extent of dissipation of excess pore water pressure is different for different locations except at the beginning and the end of consolidation process. The third dimensionless parameter, relating to time, and called "Time factor", T is defined as follows: $T = C_v\ t/H^2$ where C_v is the coefficient of consolidation, H is the length drainage path, and t is the elapsed timed from the start of the consolidation process. The figures 11 1nd 12 are valid for double drainage conditions.

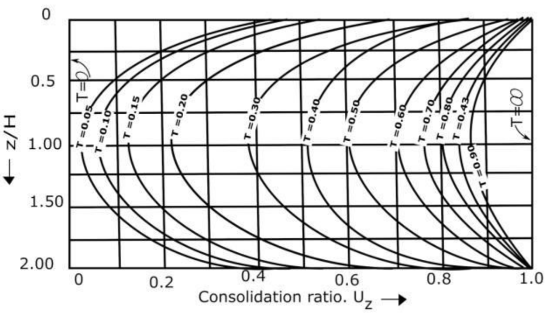

Fig.11. Graphical Solution for consolidation equation [8].

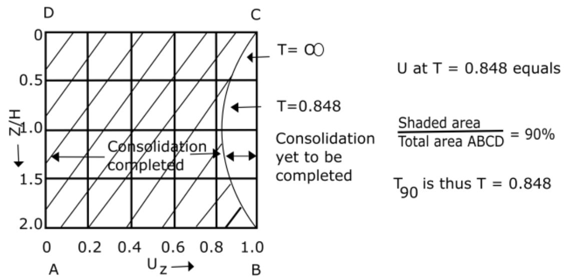

Fig. 12 Average consolidation at time factor 0.848 [8].

Fuzzy logic and membership function

In fuzzy logic two distinct rotations are most commonly employed in the literature to denote membership functions. In one of them the membership function of a fuzzy set A is denoted by $\mu_A : X \rightarrow [0,1]$ where X denotes the universal set under consideration and A is a label of the fuzzy set defined by this function. The universal set is always assumed to be a crisp set . For each x ϵ X, the value $\mu_A(x)$ expresses the degree (or grade) of membership of element x of X in fuzzy set A. Some examples of membership functions are included inside the consolidation figure 13 (the combination of consolidation and membership functions).

Separating the time factor T = 0.20 the corresponding membership function meets the time factor curve at the point P. This point p is common for time factor T = 0.2 and the membership function. Similarly different membership functions A,B,C,D,E and F meet the time factor curve at P the common point for all. This is because of the fact that Terzaghi assumed soil to be a homogeneous and isotropic medium in which consolidation process takes place. Each membership function deviates from Terzaghi's curve which the author calls as Terzaghi shift. But when the membership function assumes the shape as shown in figure F inside figure 13 almost the two curves (Terzaghi's curve and membership function curve) almost merge and become one curve only. So fuzzy logic is indirectly captures the anisotropic characteristics of the soil. So the figure F represents Terzaghi's assumptions in tune with membership functions. But the figure A to E in figure 13 represents anisotropic behavior of soil with different mineral mixture as parent material. In these isotropic conditions in figure 13 A to E, the coefficient of consolidation, permeability, coefficient of volume compressibility are different because basically the soil is heterogeneous in nature.

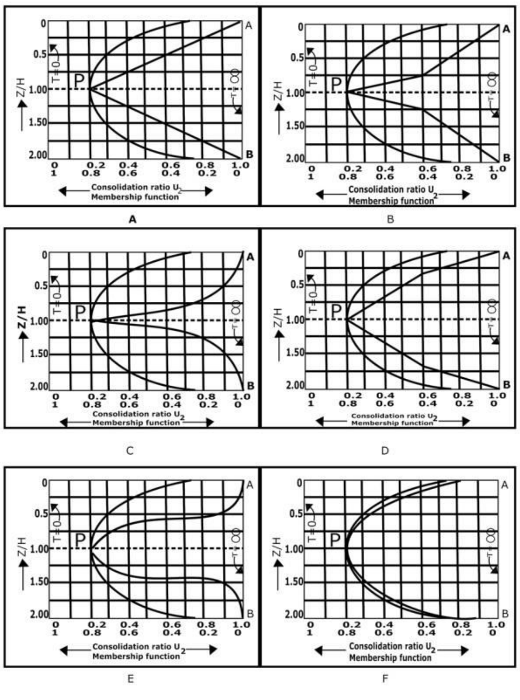

Fig. 13 A to F Consolidation of Soil and Membership Function

XI. CONCLUSIONS

(for Shear Strength of soils and fuzzy logic)

1. If the laws of mathematics applied to reality they are not certain. This is the reason for avoiding mid-point. Fuzzy logic is for reality (in this case Geology) and therefore it admits mid-point under all conditions. In other words, when crisp sets in the four corners of the cube contracts to a mid-point, the classical Boolean logic fails.

2.If the laws of mathematics are certain (sharp or crisp sets). They do not refer to reality.

3.The Boolean logic says that the shape of the Earth is a perfect sphere but as the reality demands, Geologist admit the reality and say that the the shape of the Earth is a spheroid which is ellipsoid of revolution. Seeing is always believing.

(for Consolidation of soil and fuzzy logic)

4.If we consider membership functions the fuzzy logic suits even anisotropic soils.

5.Out of six membership functions the membership functions in figure 13 F alone suits Terzaghi's assumptions for consolidation Theory.

6. The membership functions in figure 13 A to E presents anisotropic soils from different origins though they share a common point P .

REFERENCES

[1] Bart Kosko, "Fuzziness versus Probability", International Journal General Systems, vol.17, 1990,pp. 211-240

[2] Jean – Paul Legros, V.A.K. Sarma, Major soil groups of the World, CRC Press Taylor and Francis group, Chap 3, 2013,pp.100-105

[3] Van der pluijm,ben a, Earth Structure- W.W.Norton & Company inc, New York, 10110, 2003,pp.65-68

[4] Jensen Jerry, Statistics for Petroleum Engineers and Geoscientists, Prentice Hall, Cuevas,pp.32-36,chapter 6, 1993,pp. 143-150

[5] Van der pluijm,ben a, Earth Structure- W.W.Norton & Company inc, New York, 10110, 2003,pp. 68

[6] Skempton,a.w, long term stability of clay slopes, Geotechnique, vol.14, 1964,pp.77

[7] Demicco Robert V, Klir George J, Fuzzy logic in Geology, Elsevier Academic Press, 2004, pp 12 – 15.

[8] Venkatramaiah C, Geo-Technical Engineering, Wiley Eastern Ltd.1993, pp268-273

DEVELOPMENT OF A PROBABILISTIC LIQUEFACTION POTENTIAL MAP FOR METRO MANILA

Chua, Renz Anderson D.[1] and Dungca, Jonathan R.[2]
[1]Civil Engineering Department, De La Salle University Manila, Philippines;

ABSTRACT

The study aimed to create a probabilistic liquefaction potential map for Metro Manila. A liquefaction opportunity map was produced by computing the probability of an earthquake with a moment magnitude of at least 5.2 from occurring. Historical data were gathered from 7 surrounding active faults within a 150 km radius of Metro Manila to determine their recurrence. A liquefaction susceptibility map was also developed by taking into consideration the conditions of the soil. Approximately 1000+ borehole logs scattered across Metro Manila was used in developing this map. These two maps were then combined to create the probabilistic liquefaction potential map. The results show that there is only a 2% chance of an earthquake capable of triggering a liquefaction occurring in a given year but in 50 years, there is a 10% chance of exceedance coming from an earthquake with an acceleration of 0.7g. The earthquake is most likely to come from the Valley Fault System which runs straight through Metro Manila.

Keywords: PSHA, Liquefaction Potential, Liquefaction Opportunity, Liquefaction Susceptibility

INTRODUCTION

Geotechnical hazards by definition are events that are directly caused by the action of the ground that would cause adverse effects on humanity. This includes but is not limited to earthquakes, liquefaction, soil settlement, soil heaving, collapse, land-slide and scouring [1]. Among these, earthquakes and its corresponding after effects are what cause not only the loss of millions of lives but also the halt of economic growth.

The two geotechnical hazards, earthquake and liquefaction must continuously be looked out for. Since Manila is the capital of the Philippines, its vulnerability is that much greater than any other location in the country. This is why a study on the different geotechnical hazards must be done to prepare not just the professionals for their design but also for the normal individuals to protect their lives.

METHODOLOGY

Data Gathering

Determination of Source – In order to determine the active faults situated around the area of interest, the researcher first consulted the National Structural Code of the Philippines (NSCP) to see which among the known faults are within the 150km radius of NCR. This 150km radius is in accordance to [2].

Earthquake Records – Records of earthquakes from the faults determined above having values not less than 5.2 in magnitude in the Richter's scale were gathered as can be seen in Fig. 1.

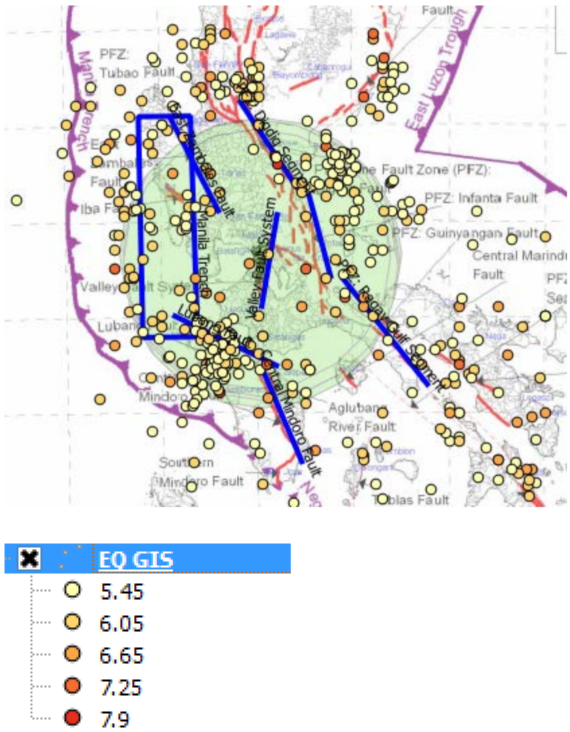

Fig. 1 Spread of EQ events in the area of study

Source Characteristics – This included its geometry, source type, and direction of movement that can affect the modelling of each earthquake generator.

Borehole Logs – These contain vital soil information that show the susceptibility of the soil at hand.

Data Analysis

Magnitude Limits – Magnitude 5.2 served as the lower limit in this study because according to [3] this surface magnitude was the smallest earthquake that was able to trigger liquefaction. This happened in Laoag city in the Northern parts of Luzon. The upper limit used was a magnitude of 8.2 since it is the largest earthquake ever recorded in the country [4]. It should be noted that both these limits are in terms of surface magnitude, the most common type of magnitude recorded in the country. It is to be expected that the data will not have a significant spread throughout all the magnitude between the said ranges above so to cover this problem, an interval of 0.6 magnitudes will be used as a range to ensure that each group will have enough data within it. This interval range was adopted from the work of [5] where he had found out that this range is the most effective way of distributing the data points without hindering the study's results.

Modelling of the Earthquake Events –First assumption is that surface magnitudes below or equal to 5.7 were considered to come from a point source since the magnitude is relatively small in comparison [6]. On the other hand, those that exceed this value were considered as either a linear fault rupture or an area rupture depending on the generator's geometry and source type. The second assumption was that both linear fault and area fault ruptures will follow the finite fault rupture model by [7] which states that the earthquake generated at the focus will propagate and felt equally along the rupture length or area. The relationship between length and the moment magnitude of a strike slip fault is expressed by Eq. (1) [8].

$$\log L = 0.74M_w - 3.55 \quad \sigma_{\log L} = 0.23 \tag{1}$$

Despite having the equation in terms of moment magnitude, the models Eq. (2) and Eq. (3) developed by [9] successfully converted the surface and body wave magnitude available in the country into moment magnitude so that it can be used in this equation.

$$M_w = e^{-0.222+0.233M_s} + 2.863 \tag{2}$$

$$M_w = e^{-4.664+0.859M_b} + 4.555 \tag{3}$$

Equation (4) on the other hand uses a model that was derived from a database containing earthquakes from subduction zones. This equation was then used to determine the area fault rupture of the event by applying the determined length value in the aspect ratio prepared by [10].

$$M = 4.532 + 0.887 \log L \qquad \sigma_M = 0.344 \tag{4}$$

where:
$L = 2W$

Probability Distribution of distance R – To determine P(R), the assumption made was that the radius used in solving for the probability is the nearest distance between the point of interest and a splice or part of the rupture area or length. This was made in accordance to the finite fault rupture model by [7] where it states that an earthquake has an equal probability of occurrence in the whole length or area of the fault rupture area or length. For an area source type, the region of permissible foci needs to be determined first. This region was then divided into 1 square kilometer, placing the focus on the center of each grid. This origin was then extended in accordance to the aspect ratio of the magnitude interval used. The shortest distance from that area to the site will be taken as R. To compute for the probability distribution of R, the number of ruptures that falls on each 10 km distance interval must be normalized by the total number of ruptures possible for the source zone. The same concept was used for linear source types except that instead of dividing into 1 square km intervals, the length of rupture was divided into 1km interval. The length was then extended from the origin of each interval. This will give the value R. The computation for P(R) was the same as above [6].

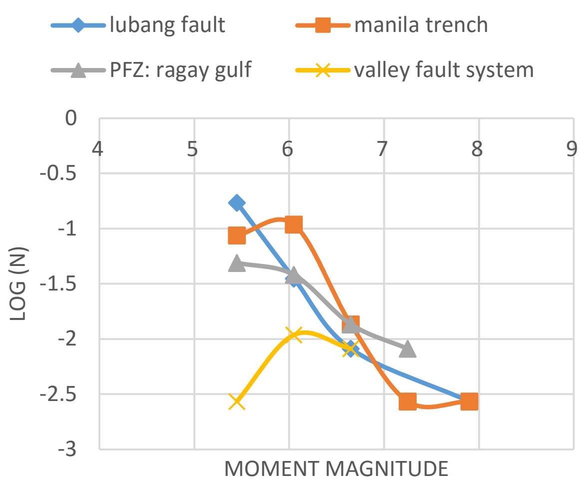

Fig. 2 Annual rate of occurrence

Annual Rates of Earthquake Activity – The annual rate of activity in Fig. 2 for each seismic generator was made by distributing each recorded earthquake event to the source nearest to its epicenter. The number of events per magnitude range per generator divided by the total number of years that has available record resulted to the annual rates of earthquake activity. This was repeated every magnitude range to every available faults. A Semi-logarithmic regression was also made from the values determined and was used for determining the next variable needed.

Probability Distribution of Earthquake Magnitude M – This can be done by using Eq. (6) by [11]. The $\boldsymbol{\beta}$ used in the equation was the absolute value of the slope determined from the regression mentioned above. Multiplying the results to the probability values of R for each interval for each source and then combining all of them will result to the probability of occurrence of earthquakes that can cause liquefaction to occur at a specific location.

$$\boldsymbol{f_M(m) = \frac{\beta \exp[-\beta(m-m_l)]}{1-\exp[-\beta(m_u-m_l)]}} \tag{5}$$

$$\boldsymbol{P[m_l \leq m \leq m_u] = \int_{m_l}^{m_u} f_M(m) \approx f_M\left(m_l + \frac{m_u}{2}\right)(m_u - m_l)} \tag{6}$$

Ground Motion Intensity – Because of the lack of strong ground motion data in the country, the attenuation relationship, Eq. 7, developed by [12] with a similar tectonic setting was used instead.

$$\boldsymbol{\log A = 0.41M - \log(R + 0.032 \times 10^{0.41M}) - 0.0034R + 130}$$

$$\boldsymbol{\sigma_{\log A} = 0.21} \tag{7}$$

Given the value of A, the probability that a target PHA (a*) was then exceeded should an earthquake of the given magnitude interval occur at the given distance range, P(A), can be estimated by computing the standard normal deviation z Eq. (8) and then obtaining the cumulative distribution function (CDF) value [6].

$$\boldsymbol{z* = \frac{\log a* - \log A}{\sigma_{\log A}}} \tag{8}$$

Correction Factors on N value – The N value shown in the borehole logs cannot be used directly in the succeeding equations needed in determining the liquefaction susceptibility. The N value needed to be adjusted first by several correction factors before it can be used. This was done by using Eq. (9) and Eq. (10) by [13]. The summary of the results can be seen in Fig. 3.

$$\boldsymbol{N_{60} = NC_N C_E C_B C_R C_S} \tag{9}$$

where:

$\boldsymbol{N_{60}}$ - corrected N value;
N - standard N value;
$\boldsymbol{C_N}$ - factor to normalize N to a common reference effective over burden stress;
$\boldsymbol{C_E}$ - correction for hammer energy ratio;
$\boldsymbol{C_B}$ - correction for borehole diameter;
$\boldsymbol{C_R}$ - correction for rod length;
$\boldsymbol{C_S}$ - correction for samplers;

$$\boldsymbol{N_{60cs} = \alpha + \beta N_{60}} \tag{10}$$

where:

$\boldsymbol{\alpha = 0 \; for \; FC \leq 5\%}$
$\boldsymbol{\alpha = e^{1.76-\left(\frac{190}{FC^2}\right)} \; for \; 5\% < FC < 35\%}$
$\boldsymbol{\alpha = 5 \; for \; FC \geq 35\%}$
$\boldsymbol{\beta = 1 \; for \; FC \leq 5\%}$
$\boldsymbol{\beta = 0.99 + \frac{FC^{1.5}}{1000} \; for \; 5\% < FC < 35\%}$
$\boldsymbol{\beta = 1.2 \; for \; FC \geq 35\%}$

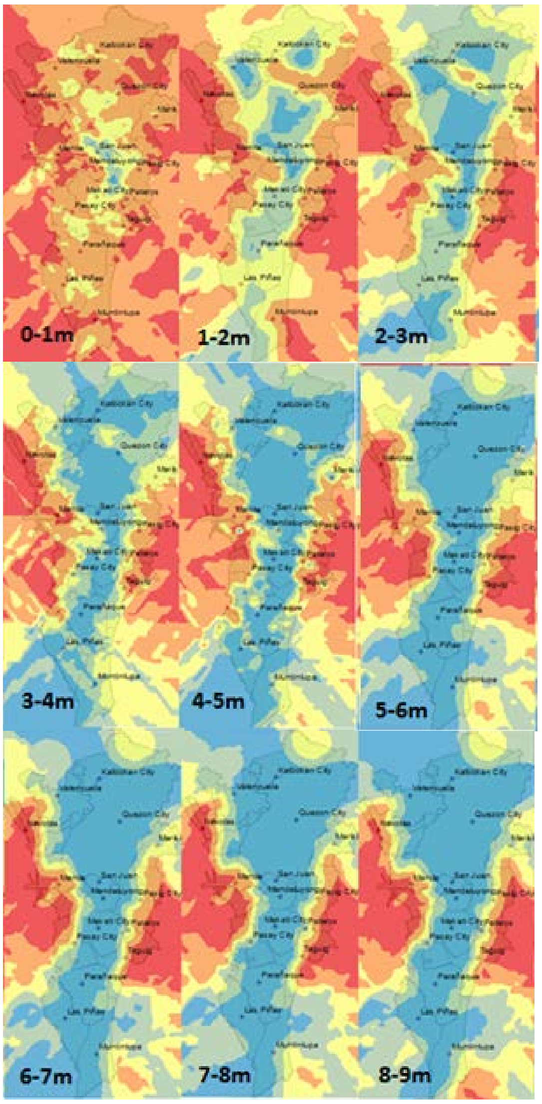

Fig. 3 SPT value per meter depth

$\boldsymbol{CRR_{7.5}}$ – With the corrected value of $\boldsymbol{N_{60cs}}$, $\boldsymbol{CRR_{7.5}}$ was then determined by Eq. (11) developed by [13]. Equation (12) and Eq. (13) were then used to adjust this value to the right magnitude and overburden pressure.

$$\boldsymbol{CRR_{7.5} = \frac{1}{34-N_{60}} + \frac{N_{60}}{135} + \frac{50}{(10N_{60}+45)^2} - \frac{1}{200}} \tag{11}$$

$$K_M = \frac{10^{2.24}}{M_w^{2.56}} \tag{12}$$

$$K_\sigma = \left(\frac{\sigma'_v}{P_a}\right)^{f-1} \tag{13}$$

CSR and the 'a' to trigger – From the value determined above, given a factor of safety of 1.3, the value for CSR was determined. This value was then equated to Eq. (14) developed by [14] to determine the acceleration needed to possibly trigger a liquefaction. This acceleration can then be used to determine the susceptibility of the area and subsequently its liquefaction potential also.

$$CSR = \frac{0.65 a_{max} \sigma_{vo} r_d}{g \sigma'_{vo}} \tag{14}$$

where:

a_{max} - peak horizontal acceleration

$$r_d = 1 - 0.00765z \; for \; z \leq 9.15m$$

$$r_d = 1.174 - 0.0267z \; for \; 9.15m < z \leq 23m$$

Results

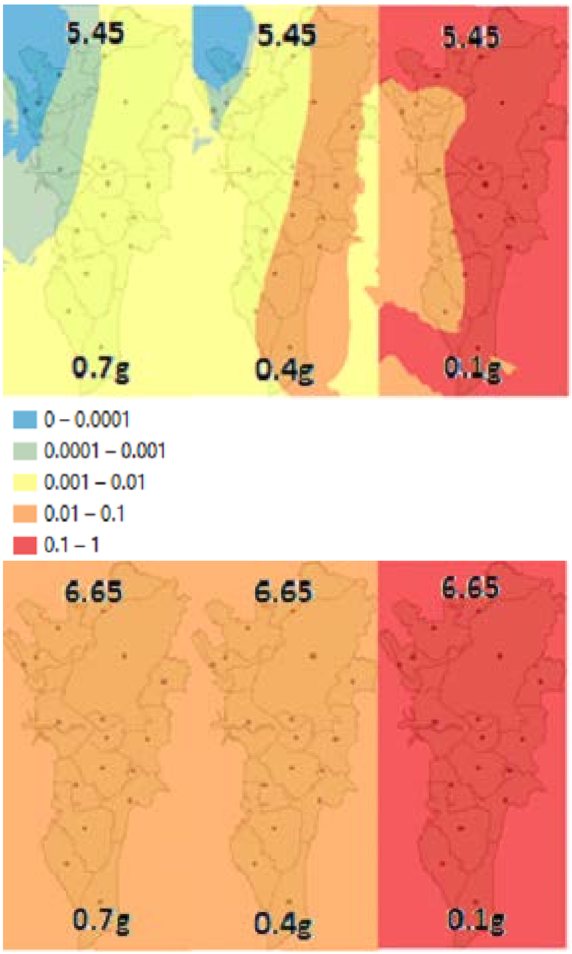

Fig. 4 Liquefaction Opportunity

Liquefaction Opportunity – Now that the values of P(R), P(A), P(M) and v_i are known for each magnitude interval. Substituting all these values into
Eq. (15) resulted to the annual exceedance rate for various target PHAs in each source.

$$\lambda[X \geq x] \approx \sum_{sources\, i} v_i \int_{Mo}^{Mmax} \int_{R|M} P[X \geq x|M,R] f_m(m) f_{R|M}(r|m) drdm \tag{15}$$

Combining them together will produce the annual rate of exceeding a target PHA when an earthquake capable of triggering liquefaction occurred at any of the sources nearby as can be seen in Fig. 4.

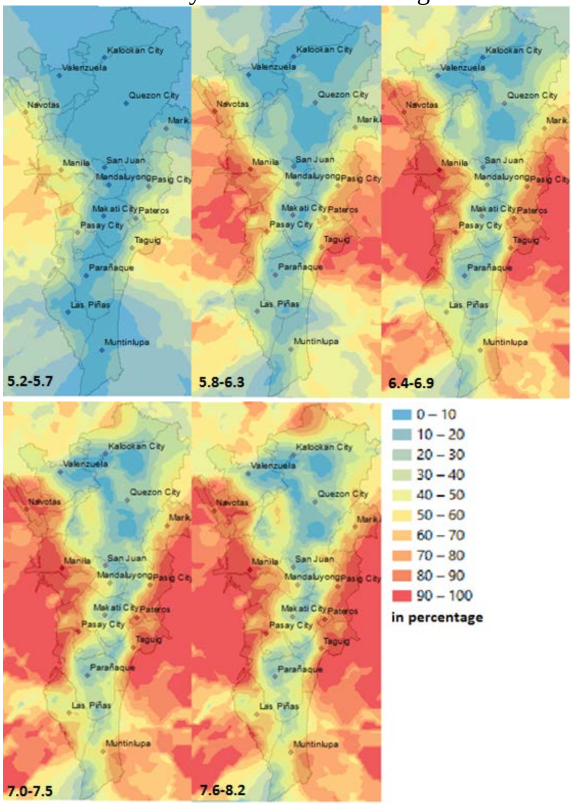

Fig. 5 Liquefaction Susceptibility

Liquefaction Susceptibility – Given that an earthquake with a specific magnitude range from a fixed distance of 15km to the target site, the probability of exceeding the target acceleration that is needed to trigger the event by the acceleration by the given magnitude range and fixed distance was then computed. Example of results can be seen in Fig. 5.
Liquefaction Potential – Assimilating both the liquefaction opportunity and susceptibility produced a liquefaction potential map for the site. Figure 7

showed the probability of exceeding the acceleration needed to trigger a liquefaction by combining every combination of magnitude and distance for every seismic generator around the area.

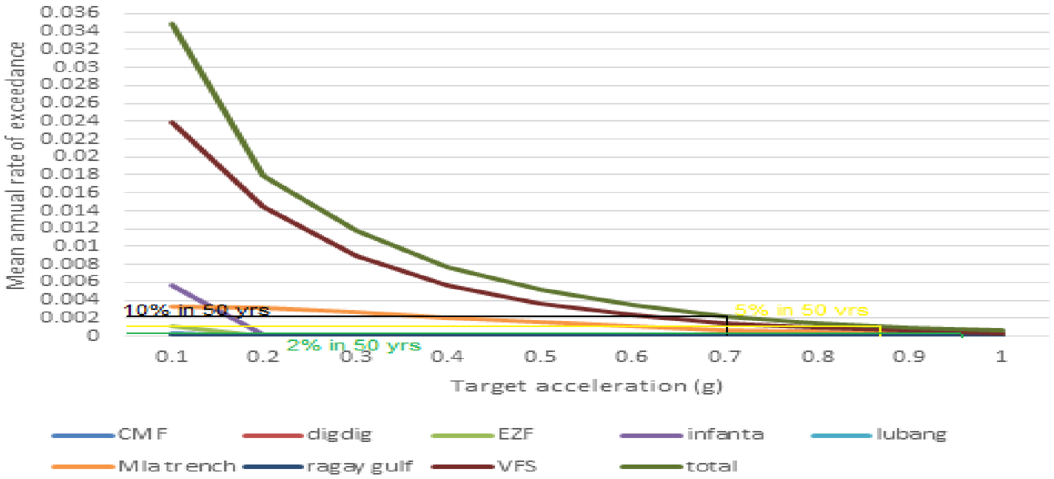

Fig. 6 Hazard Curve for all seismic generators

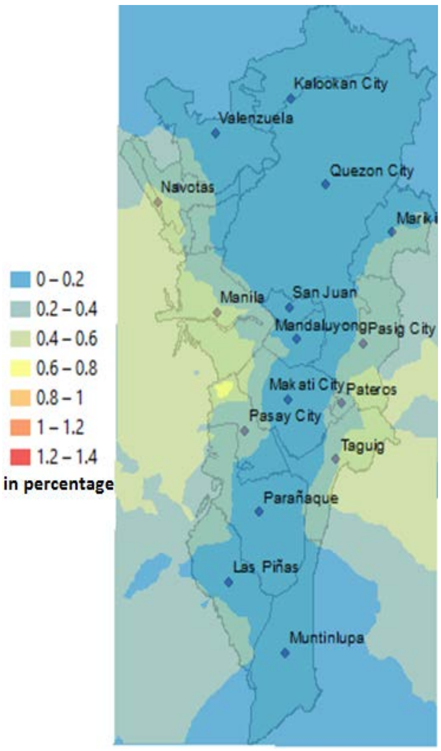

Fig. 7 Liquefaction Potential for Metro Manila

Design Ground Motion – Aside from the annual probability that the target acceleration (a*) will be exceeded should an earthquake capable of triggering liquefaction occurred in any of the source zones, $\boldsymbol{\lambda[X \geq x]}$, it is also necessary to compute the PHA corresponding to a given probability of exceedance in a given time frame. The design ground motion used in this study was a 10% probability of exceedance in a 50 year time frame Eq. (16) [6].

$$\lambda_{y*} = \frac{\ln(1-P[Y_T>y*])}{T} = \frac{\ln(1-0.1)}{50} = 0.00211 \tag{16}$$

Hazard Curve – The resulting values was then used to generate hazard curves for the liquefaction opportunity as can be seen in Fig. 6.

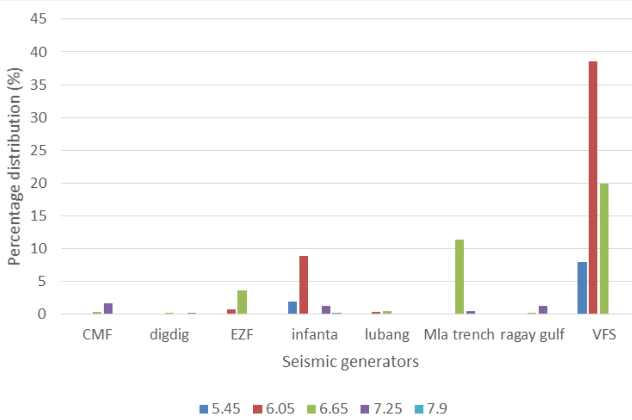

Fig. 8 Deaggregation of results

Deaggregation – The results was then be deaggregated, as shown in Fig. 8, to show which among the magnitude intervals will be responsible in the occurrence of the most probable earthquake that will cause liquefaction in the area of interest. It also showed which among the seismic generators contribute the most to the probabilities. This knowledge can then be used to make to prepare for the worst and properly mitigate and lessen the damages that will be incurred by the phenomenon.

CONCLUSION

It can be seen that there are 8 active faults surrounding Metro Manila that are capable of triggering a liquefaction in the said target area namely: Central Mindoro Fault, Manila Trench, Valley Fault System, Lubang Fault, PFZ: Digdig Segment, PFZ: Ragay Gulf Segment, PFZ Infanta Segment, and East Zambales Fault. Among the eight seismic generators, only one is an area fault rupture which is the Manila trench. Valley fault system on the other hand is the closest among them and yet the only one that has a few recorded movements in the past 368 years [15]. This gives us the idea that it could possibly move anytime now. Since it runs straight through the region, having it move would surely cause a massive damage to the city proper's.

From the earthquake opportunity analysis, the greatest probability of an earthquake with a magnitude of at least 5.2 has only 1% chance of occurring within a given year but if we look at the seismic hazard map, one could see that in the next 50 years, there is a 10% chance of having an earthquake generate an acceleration of 0.7g in the area which is a bit higher to the 0.6g value determined by [5]. The increase in value could be attributed to the increase in data within 20 years. This value, according to the deaggregation, would likely come from the valley fault system with a magnitude range of 5.8 – 6.3 from a distance range of 0 – 10km away from the site.

The vertical mid-section of the Metro Manila has rocky or very hard soil in it though they start showing at around 3m deep. Both the western and eastern part of the region has sandy top soil for the first 6 meters, beyond that it is mostly clays and silts. On the other hand, SPT values show a much more constant range of values throughout the entire 20m depth. Seeing that the top soil for all seem to be red and yellow in color even for the vertical mid-section of the region. This is because this layer of soil have not been consolidated yet. After that the red and yellow section continue to cluster in the same area where the sandy soils are found, both in the western and eastern part of the region. Since the liquefaction susceptibility of the area is largely influenced by the soil type map and SPT map, it was no surprise that the patterns shown in the susceptibility maps are pretty much the same in nature.

Finally, the liquefaction potential developed from this study shows the same pattern as that of the susceptibility except the values are very much lower, the greatest probability only having a 2% chance of exceedance in a given year. But just like with the earthquake opportunity map, this should not be underestimated since this value increases as time passes by.

REFERENCES

[1] Orense R P, Geotechnical Hazard: Nature, Assessment and Mitigation, Quezon City: The University of the Philippines Press, 2003.

[2] Yould T, Perkins D, "Mapping liquefaction induces ground failure potential" Journal of the Geotechnical Engineering Division, ASCE 104 (4), 1978, pp. 443-446.

[3] SEASEE (Southeast Asia Association of Seismology and Earthquake Engineering), Series on Seismology vol IV, 1985.

[4] Phivolcs (Philippines Institute of Volcanology and Seismology), Catalogue of Mentro Manila Earthquakes, magnitude 5.2 and above (1907 – 2013), 2014.

[5] Thenhaus P, Hanson S, Algermissen S, Bautista B, Bautista M B J P, et al., "Estimates of the regional ground motion hazard in the Philipiines. National Disaster Mitigation in the Philipines." DOST-PHIVOLCS, 1994, pp. 45-60.

[6] Beroya M & Aydin A, "Seismic hazard analysis of Laoag City, Northern Philippines for liquefaction potential assessment", Engineering Geology 96, 2008, pp. 28-42.

[7] Kiureghian D & Ang A, "A fault rupture model for seismic risk analysis", Bulletin of the Seismological Society of America 67, 1977, pp. 1173-1194.

[8] Wells D, Coppersmith K, "New empirical relationships among magnitude, rupture length, rupture width, rupture area and surface displacement" Bulletin of the Seismological Society of America 84 (4), 1994, pp. 974-1002.

[9] Giacomo D, Bondar I, Storchak D A, Engdhal E R, Bormann P, Harris J, "ISC-BEM: Global Instrumental Earthquake Catalogue (1900-2009), III. Re-computed Ms and mb, proxy Mw, final magnitude composition an completeness assessment", Physics of the Earth and Planetary Interiors, 2014.

[10] Geller R, "Scaling relations for earthquake source parameters and magnitudes", Bulletin of the Seismological Society of America 80 (5), 1976, pp. 757-776.

[11] Kramer S, Geotechnical Earthquake Engineering, New Jersey: Prentice Hall, 1996.

[12] Fukushima Y & Tanaka T, "A new attenuation relationship for peak horizontal acceleration of strong earthquake ground motion in Japan", Bulletin of the Seismological Society of America 80, 1990, pp. 1501-1523.

[13] Youd T, Idriss I, Andrus R, Seed, "Liquefaction resistance of soils summary report from 1996 NCEER and 1998 NCEER/NSF workshops on Evaluation of Liquefaction Resistance of Soil" Journal of Geotechnical and Geoenvironmental Engineering, ASCE 127. 2001, pp. 817-833.

[14] Seed H B, Idriss I M, "Simplified procedure for evaluating soil liquefaction potential", J. Geotech Engrg. Div., 1971, pp. 1249-1273.

[15] Bautista M L P & Oike K, "Estimation of the magnitudes and epicenters of Philippine historical earthquakes", Techtonophysics 317, 2000, pp. 137-169.

Fifth International Conference on Geotechnique, Construction Materials and Environment, Osaka, Japan, Nov. 16-18, 2015, ISBN: 978-4-990.3958-4-5 C3051

EFFECT OF RICE STRAW LENGTH ON MECHANICAL PROPERTIES OF QUICK LIME AND RICE HUSK ASH STABILIZED SOIL

Ayaka Oya[1], Satoru Iida [1], Masamitsu Fujimoto[2], Ryoichi Fukagawa[2]and Der-Her Lee [3]
[1]Graduate School of Science and Engineering, Ritsumeikan University, Japan, [2]Department of Civil Engineering, Ritsumeikan University, Japan, [3]Department of Civil Engineering, National Cheng Kung University, Taiwan

ABSTRACT

Riverbank collapse often occurs along the Saigon River which flows through Ho Chi Minh City (HCMC). One of the influencing factors is the soft ground which is the riverbank composed of. Our research about the ground improvement method using quicklime, rice husks ash so far. Rice straw is newly added to the improved soil in this paper. The Rice straw is expected to improve the failure strain property, that is to restrain brittle failure. These mixing materials can be obtained easily and cheaply in Vietnam. A series of unconfined compression tests are carried out to improve the mechanical properties of improved soil. Moreover pH tests are conducted to validate the chemical action of the improved soil and evaluate the effect of improved soil on surrounding environment.

Keywords: Ground improvement,

INTRODUCTION

Major cities in South East Asia have been developed on river plain. Its soft ground often causes problems such as settlement. Particularly, Riverbank failure occurs along Saigon River, which flows in the center of Ho Chi Minh City. Fig.1 shows the riverbank failure along Saigon River. Saigon River is main water resource of HCMC, and has Saigon Port, which plays an important role of trading. One of the main factors of riverbank failure is assumed to be soft ground composing riverbank [1]. It causes serious damage to buildings and agricultural land in HCMC. Fig.2 shows that the building is leaned by the riverbank failure. Such damages can be seen on many points on Saigon riverbank. However, enough countermeasures to deal with the riverbank destruction have not been fully employed because of the restraint of budget and enormous length of target riverbank. Therefore it is necessary to propose effective and economical countermeasure for reinforcing riverbank in order to contribute further development of HCMC.

To solve this problem, our research group pays attention to improved soil with quicklime and rice husks ash to stabilize the Saingon Riverbank. These materials can be obtained easily and cheaply in Vietnam. The improved soil with quicklime and rice hulk ash has been proposed and its shear strength and durability to erosion by rainfall are estimated [2], but the relationships between material mix proportion and strength properties etc. are not fully investigated. Then, we have been investigated the mechanical properties of improved soil based on a series of unconfined compression tests [3]. As the results of this study, we could experimentally make clear that appropriate quantities of quick lime and rice hulk ash improve unconfined compression strength of the soft clay soil. However, some problems remains, that is, the failure strain of the improved soil is decreased as the curing days increase, and the brittle fracture occurs in some cases.

In this paper, to overcome the problem above, rice straw is more applied to improved soil in addition to quicklime and rice hulk ash. The rice straw is assumed that it improves failure strain and restrains the occurrence of brittle failure. A series of unconfined compression tests are carried out in order to investigate the strength characteristics of the improved soil. Moreover pH tests are performed for validation of the chemical action of the improved soil and considering the effect on surrounding environment.

Fig. 1. The riverbank failure along Saigon River

Fig. 2. The Building affected by riverbank failure

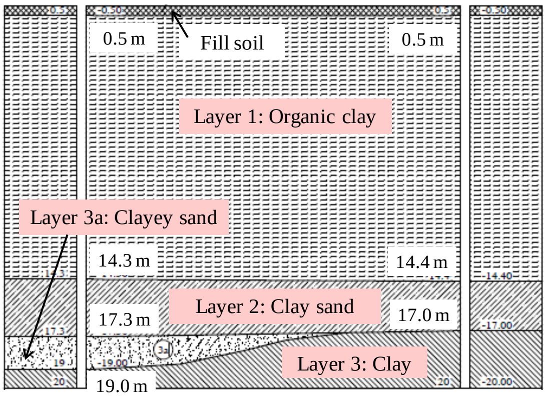

Fig. 3. The cross sectional profile of the riverbank

Fig. 4. Quicklime

Fig. 5. Rice hulk ash

Fig. 6. Rice straw

GEOTECHNICAL CHARACITERISTICS OF SAIGON RIVERBANK

Fig.3 show the cross sectional profile of the Saigon riverbank. SPT (Standard Penetration Test) s were carried out at two points at this observation site and record fill soil above either three or four compositionally distinct layers [1]. The surface of the ground is covered with a 0.5 m thickness of fill soil, which is carried from outside of the sample site. Layer 1 is organic clay with a SPT-N value of 1–2 and a thickness of 13.8–13.9 m. Layer 2 is clay sand with a SPT-N value of 12–13 and a thickness of2.6–3.0 m. Layer 3 is clay and has a SPT-N value of 7–11. Layer 3a, as shown in Fig.4, is clayey sand and has a SPT-N value of 8 and a maximum thickness of 2.7 m. In the presence, and considerable thickness of this very soft soil, is of particular importance for slope stability assessment of the Saigon riverbank. This research focuses on the soft clay soil on layer 1.

INPROVED SOIL USING THE QUICKLIME, RICE HUSKS ASH AND RICE STRAW

Quicklime, rice husks ash and rice straws are applied to stabilize the soft clay soil. The characteristics of the materials and hardening mechanism are explained in this chapter.

Characteristic of the materials

Quicklime (Fig.4) is used for soil stabilization in practical work for long time, and shows dehydration action and pozzolanic reaction. Rice hulk ash (Fig.5) includes silicon dioxide about 90 present of its weight, and this value is higher than that of fly ash, which used as pozzolanic material. Rice straw is dry stem of gramineous plant. The rice straw (Fig.6) is expected to increase the failure strain and to prevent the brittle fracture of improved material.

Hardening mechanism of the improved soil

The improved soil is hardened by dehydration action of quicklime, which is short term reaction, and pozzolanic reaction of silica, which is long term reaction.

Firstly, water in the soil vaporized by calcium oxide (CaO) which is the main component of quick lime. Then, the water content of the soil approaches optimum water content and compaction strength increases. In this process, water (H_2O) reacts with CaO and hydrated lime ($Ca(OH)_2$) is produced (Formula (1)) .

$$H_2O + CaO \rightarrow Ca(OH)_2 \quad (1)$$

Next, $Ca(OH)_2$ gently reacts with silicon dioxide

(SiO_2) which is included in both rice hulk ash and soil and calcium silicate hydrate (nCaO・SiO_2・$m$$H_2O$) is produced (Formula (2)).

$$Ca(OH)_2 + [SiO_2] \rightarrow nCaO \cdot SiO_2 \cdot mH_2O \quad (2)$$

where n and m are integer. Improved soil is hardened in this stage. This reaction is called "pozzolanic reaction". Silicate hydrate (nCaO・SiO_2・$m$$H_2O$) is similar to cement and enhances durability and water-tightness and strength of the soil increases.

In addition, it is assumed that rice straws mixed into improved soil increase the failure strain of the material because tensile force and superficial cohesion of the soil are increased by fibers of the rice straw.

UNCONFINED COMPRESSION TEST OF IMPROVED SOIL

In order to validate the effect of the length of rice straws and understand mechanical properties of the improved soil, unconfined compression is carried out. In this study, unconfined compression strength, failure strain and modulus of deformation are estimated from the unconfined compression test to evaluate the mechanical properties. In this research, the target values of unconfined compression test are unconfined compression strength: 200 kN/m^2 and failure strain: 5 % [4][5].

Test method

First of all, specimens for the test are prepared. Fujinomori clay which is similar to soft ground material of the field is applied to the tests. Fujinomori clay and water are mixed and then the quicklime, rice husks ash and rice straw is mixed with soil in the mixer sufficiently. After that, improved soil is packed in a mold, which is 10 centimeter in height and 5 centimeter in diameter. Improved soil is packed dividing into 3 parts. The weight of packed soil in the mold is 300 g in each mold. Mix proportion of the materials for specimens is indicated in Table 1. 3 testing specimens are prepared for each testing condition.

Then, the specimens are cured. The specimens are cured in the air until 3 day, after that under the water, because when improved soil is practically used in the fields, most of them are assumed to be put under the water.

After curing, unconfined compression test is conducted. Test method in this study is based on the standard of The Japanese Geotechnical Society [JGS 0511 Method for unconfined compression test of soils]. During a test, the test specimen is compressed in a standard compression rate that a compression strain produces of 1% per a minute continually.

Table 1. Mix proportion of the materials
(The weight ratio to the weight of Fujinomori clay)

Fuzinomori clay	100 %
Water	About 50 %
Quicklime	5 %
Rice husks ash	10 %

Test condition

We used 3 types of wet rice straw to validate the effect of its length, that is, the length of the rice straw for the tests are 0.3-1.0 cm, 1.0-3.0 cm and 3.0-7.0 cm respectively. The curing periods of test specimens are 1, 3, 7, 14, 28 and 56 days. The specimens are cured in the air until 3 day, after that they are put under the water, because when improved soil is practically used in the fields, most of them are assumed to be put under the water.

Test results and discussion

The stress-strain curves of the improved soil, using 0.3-1.0 cm of wet rice straw are shown in Fig. 7. Unconfined compression strength increases as the curing days. The stress-strain relationships are strongly influenced by the curing period. After curing period of 14 days, the value of failure strain is decreased. The Compression stress is dropped rapidly after yield. And, although the materials are mixed sufficiently, testing results vary more widely as the curing days. This is because the testing results highly depend on chemical reaction of the materials used in the improved soil. Validation of the strength of the improved soil should be estimated to expect deterioration of strength, which should be left for future works.

The stress-strain curves of the improved soil, using 3.0-7.0 cm of wet rice straw are shown in Fig. 8. Unconfined compression strength increases as the curing days as well as 0.3-1.0 cm rice straw specimens. The unconfined strength increases more early than that of 0.3-1.0 cm rice straw improved soil. The unconfined strength is dropped at the curing period 56 days. It is assumed that rice straws disturb the specimen, because the length of rice straws is large toward the size of specimen (5.0 cm $\times$10.0 cm). The tests with other size of specimens should be done to consider the effect of the length of rice straws.

The relationships between unconfined compression strength and curing period is shown in Fig. 9. The results of the improved soil with no rice straw [3] is shown in the graph for the comparison. The unconfined strength exceeds the target value (200

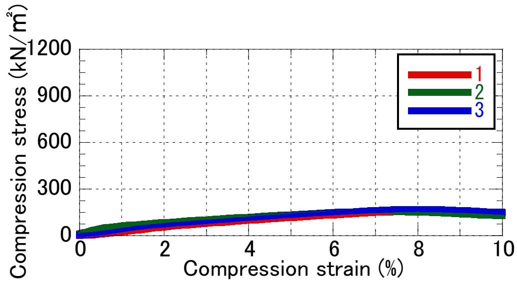

(a) Curing period 1 day

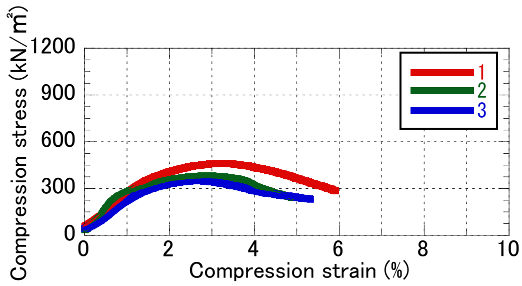

(b) Curing period 7 days

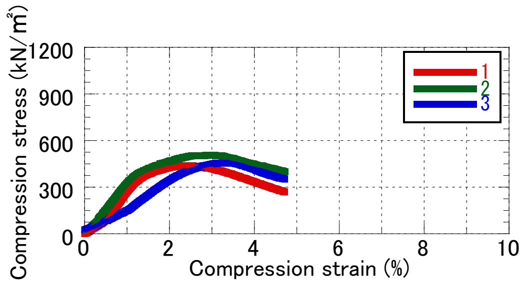

(c) Curing period 14day

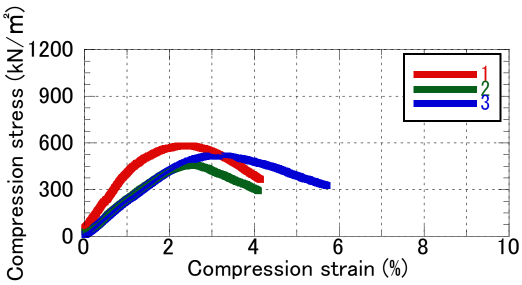

(d) Curing period 56day

Fig. 7. The stress-strain curves of the improved soil with 0.3-1.0 cm of wet rice straw

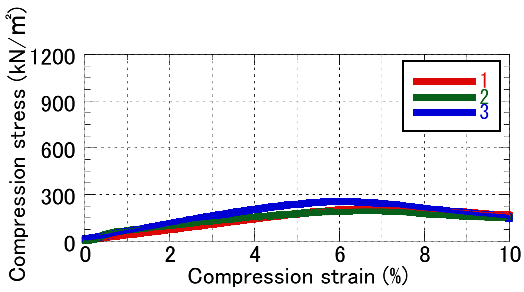

(a) Curing period 1 day

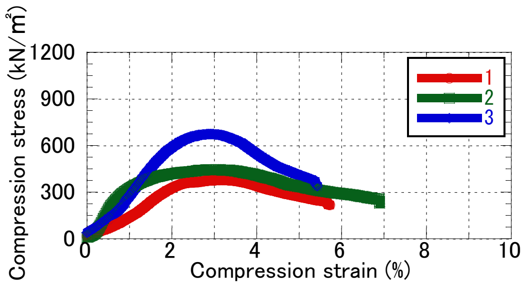

(b) Curing period 7 days

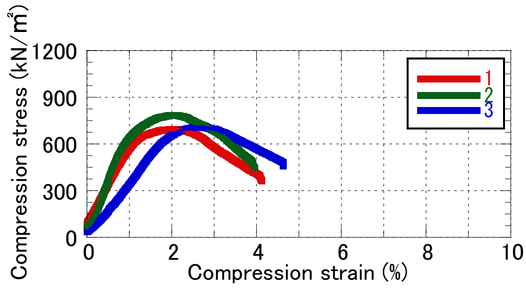

(c) Curing period 14day

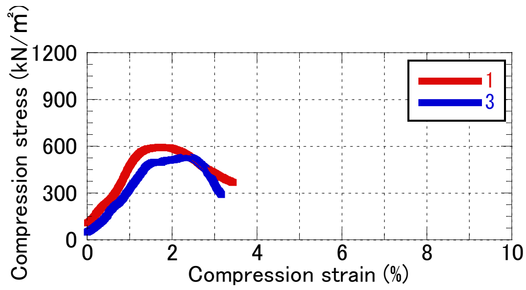

(d) Curing period 56day

Fig. 8. The stress-strain curves of the improved soil with 3.0-7.0 cm of wet rice straw

kN/m^2) in all case. In terms of the strength at curing period 56 days, 0.3 cm-1.0 cm rice straw is most suitable among the condition in this paper.

Fig.9 shows that the failure strains of the specimens mixing rice straw are higher than specimens without rice straw, so that we suppose that improved soil added rice straw can improve the failure strain property to some extent. Moreover among low failure strain, specimens corresponding to 0.3-1.0 cm rice straw are the most high failure strain comparing with other specimens although the failure strain does not reach the target value (5 %). This reason is assumed that rice straw is not long, but is much number because rice straws are broken up into small pieces, and they are mixed in entire soil. The improved soil with 0.3-1.0 cm rice straw is the best suited in the conditions which are validated in this time in terms of both the strength and the failure strain.

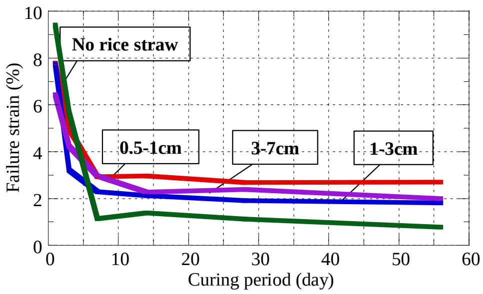

Fig. 9. The relationships between unconfined compression strength and curing period

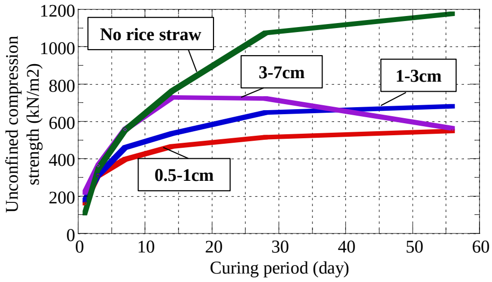

Fig. 10. The relationships between failure strain and curing period

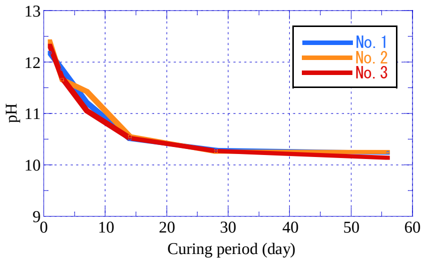

(a) Rice straw 0.3 cm-1.0 cm

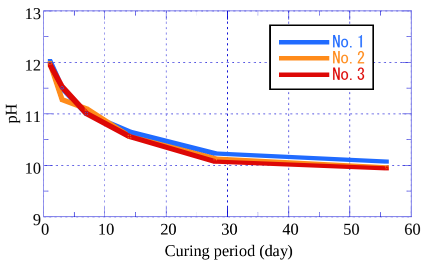

(b) Rice straw 1.0-3.0 cm

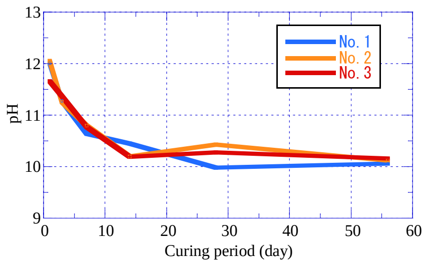

(c) Rice straw 3.0-7.0 cm

Fig. 11 The relationships between pH and curing period (Rice straw 0.3-1.0 cm)

UNCONFINED COMPRESSION TEST OF IMPROVED SOIL

pH tests are performed for validation of the soil and considering the effect on surrounding environment.

Test method

The method for PH test is based on the standard of the Japanese Geotechnical Society [JGS 211 Test method for pH of suspended soils]. A pH meter was calibrated at first by Neutral phosphate, Phthalate and Borate standard solution. Then, soil sample used for unconfined compression tests is mixed with water, and the suspension for the test is prepared. After the suspension is left for 30 minutes at least, pH is measured by pH meter (HORIBA D-51).

Test condition

The difference of test conditions is the same as the cases of unconfined compression tests. A specimen was used for unconfined compression test at first, and then the specimen was broken by hammer and next used for pH test as testing samples.

Test results and discussion

The results of pH tests corresponding to every curing period are shown in Fig. 11. The pH values distribute from about 12 to about 10 during 56 curing period at all condition. These shows that improved soil is changing reaction of alkali from neutrality. Moreover, the pH is decreasing largely not later than 7 days of curing period. It is due to dehydration action which is short term reaction. The amount of strong alkali which is in CaO reacts with water (H_2O), and weak alkali ($Ca(OH)_2$) is produced. As a result of this reaction, the pH is rapidly decreased until the period of 7 days. From the results of the pH tests, it is assumed that the dehydration action end by 7 days, and Pozzolanic reaction occurs after curing period of 7 days. Since there is not big difference between the testing conditions of rice straw length, the difference of rice straw length does not much effect on overall tendency.

CONCLUSION

This paper presented research results on the hardening mechanism of improved soil using materials of quicklime, rice husks ash and rice straw. The research was carried out based on the unconfined compression tests and the pH tests. In this paper, the improved soil with rice straw can improve failure strain property, but the failure strains are less than the target value. Among low failure strain, specimen with 0.3-1.0 cm rice straw is the most high failure strain of other specimen. This reason is assumed that rice straw is not long, but is much number and is mixed in entire soil. Unconfined compression strength is higher than the target value. pH value of the soil are 12 at curing period 1 day and about 10 at curing period 56 day. pH test can make sure reaction of alkali from neutrality.

For future works, improved soil with larger amount of straw should be tested, because there is a possibility that failure strain by increasing the compound ratios of rice straw. The tests with other mix proportions should be conducted to clarify the suitable mix proportions. In addition, it is important to keep highly alkali to maintain the strength of the improved soil [], so we should investigate validation of pH values of the improved soil.

REFERENCES

[1] Oya et al., "Seepage flow-stability analysis of the riverbank of saigon river due to river water level fluctuation", Int. J. of GEOMATE, March., 2014, Vol. 8, No. 1 (Sl. No. 15), pp.1212-121

[2] Der Her Lee, "Strength and erosion property of the stability soils", Institute for National Cheng Kung University engineering works process master's thesis, April 1976.

[3] Oya et al., "Study on mechanical characteristics of improved soil using quick lime and rice hulk ash for riverbank erosion around cultural heritage", , Journal of Disaster Mitigation for Historical Cities, Vol. 8（2014, July）pp.139-144.

[4] Anh et al., "Study on Strength and Durability of Fiber-Cement-Stabilized Soils by using Rice Straw", Proc. of the 1st Vietnam/Japan Joint Symposium on Saigon River Bank Erosion, pp.100-110.

[5] Mori et al,. "An experimental study on strength of fiber-cement-stabilized mud by use of paper sludge and durability for drying and wetting tests", Shigen-to-sozai, Vlo. 122, pp. 353-361, 2006.

Fifth International Conference on Geotechnique, Construction Materials and Environment, Osaka, Japan, Nov. 16-18, 2015, ISBN: 978-4-9905958-4-5 C3051

GIS BASED PROBABILISTIC HAZARD RISK ASSESSMENT OF ROAD ACCIDENTS

Dr. Ather Ashraf[1] and Hania Arif[2]
[1]Punjab University, Pakistan; [2] Punjab University, Pakistan

ABSTRACT

Accident is any unintentional and unplanned event happed due to lack of intention. Road Accidents are one of most common type of accidents which usually happen due to crashing of automobiles. Road traffic injury has become a serious ill health globally, inflicting over one-million deaths annually. Ninety percent of those deaths occur in the third world countries wherever they're the second leading reason behind death in older, kids and adults. Road traffic injuries square measure coupled to the atmosphere factors like road style, density of population around it and handiness of alternatives for pedestrians and two wheelers. It is very important to find the root cause analysis of road accident to avoid them in future. But before finding root cause analysis, it is required to identify most vulnerable road based on risk assessment and to explore sensitivity of results about road uncertainty. The aim of the study is to analyze and discuss possible reasons of road accidents and its impacts. The main goal was to identify vulnerable roads, risk assessment and to explore sensitivity of results about road uncertainty. We applied our study in Lahore, a major city of Pakistan. Pakistan is a developing country. Roads are not managed as they could be managed. Some roads are more vulnerable where accidents occur daily, particularly in Lahore, this ratio is very high. Identifying such vulnerable road is very important. For this we applied a GIS, geographic data systems, enabled risk assessment of road in our study. The study started with the spatial data compilation from the primary and secondary sources. The accident data is analyzed and tabulated for probability calculation which used in the development of hazard layer. The element at risk is identified based on hazard map. Their cooping capacity and with stand capacity are measured and used in the development of vulnerability and exposure map. Finally risk map is developed by overlaying hazard map, vulnerability map, exposure map and capacity map through weighted overlay technique.

Keywords: GIS, Analytic Hierarchy Process (AHP), Hazards, Vulnerability

INTRODUCTION

In big cities the road accidents are very common and a big issue. A large number of people injured and died every year. Science and technology in the modern world, devised many ways to avoid the accidents. But the fact is that number of accidents has been increased with the rapid increase in population. According to world statistics, low and middle income countries are expecting that their road accidents ratio will be increased about 80% in next 15 years. These countries have no plan to avoid/reduce this ratio. Traffic accidents are included among the top 10 causes of deaths and disabilities in the South-East Asian Region. It is also estimated that by the end of year 2020, death and injuries are mostly caused by traffic accidents in the world [7]. Road accidents have also a great negative impact on economy. Mostly male population is died and injured during accidents as compared to female population. About 70 percent of the population age group is 15-44 years that is active and take part in the development of country [25].The death or disability due to such accidents affects the education and living conditions of children, culminating further into poverty and deprivation as their savings and income can be spent on treatment. Traffic injuries and traffic accidents increased in spite of the growing burden of road traffic safety. Reasons may vary in each region, but general awareness and general health scale and serious effect of traffic accidents on the issue of the lack of specific information, including social and economic costs of falls, and interventions or measures are road traffic accidents that can prevent or reduce the damage.

In developing countries including Pakistan, there is no attention to reduce traffic accidents by the higher authorities. Traffic accidents in Lahore increased tremendously over the years. Therefore it is necessary to overcome road accidents to save the lives of the people. This study will be helpful to identify the root causes of accidents and also significant for the reduction of accidents ratio. It will also be helpful for making the transport system more efficient.

Transportation is the backbone for the development of a country. But due to extensive flow of traffic, accidents occur. In case of Pakistan, traffic accidents management is neglected. Some factors like road geometry, icebergs and surface of roads, unskilled drivers, carelessness and lack of knowledge regarding traffic rules are contributed in road accidents. These factors can be minimized and traffic can be managed which may prevent thousands of causalities and economic losses.

Mustafa Karasahin & Serdal Terzi tried to identify the sections of road highways as hazardous locations. GIS is used for the analysis of locations that were hazardous. Different layers were established and after this combined all layers. SQL (Structured Query Language) were applied to acquire the results by using GIS. Hazardous locations were marked if more accidents occurred on that place. For this purpose GPS was used to get reference points [15]. This study was conducted in Delaware. They had developed GIS based traffic accident information. Occurrence of accidents, number of accidents, accident sites and such sort of other information were recorded. These points were analyzed using GIS for the management and reduction of traffic accidents [10].

Ravin Hasseea had studied traffic accidents by using GIS for processing and analysis. For data storing, processing, displaying and querying GIS was used. Spatial analysis, proximity analysis, network analysis etc. were effective in traffic accidents management**.** GIS provided facility for spatial query and displaying results in the form of maps like chloropleth maps, thematic maps, dot maps etc. to display different results of accidents [13].

Department of Civil Engineering in University of Putra Malaysia (UPM) developed a system using GIS applications. Their observation concluded that thousands of people and vehicle were the victim of dangerous accidents each day. They developed a prototype Geographic Information System and Road Accident View System (GIS-RAVS) for the reduction of traffic accidents. According to researchers this system is very effective to identify the accident location, ranking of accidents, store and retrieve accidents database, show the roads where most of the accidents occurred and different statistical analysis were performed in a short time. Different queries were also applied on the above data for analysis [19].

Driving is essential part of daily life for almost all people. Many people driving on the road do not have same physical & psychological sense and driving any vehicle is a risky activity. US police generated a report on road accidents, 6.4 million accidents happened in US. To reduce traffic accidents, efficient traffic accident handling is very necessary for reducing impact of traffic accidents & to save millions of lives. GIS is used to store, edits, display and analyze location information. GIS have been used for many years for research, transportation and management purposes because it has powerful tools for visualization and to manage data (features) into databases. Visualization can greatly facilitate the analysis of traffic accidents.

This research conducted to make use of a analytical hierarchal process (AHP) method for analyzing accidents. This method made it possible to utilize all relevant information on traffic accidents including accurate location for earlier response, route numbers, route name, mile post, accurate event locations. These indicators help in better analyzing traffic accidents and visualization hot spot of incidents. The proposed method able to generate new datasets for accidents and it displays the accidents on the top of all existing road networks. Finally a risk map is developed based on hazard, vulnerability and capacity calculated using AHP and spatial techniques.

METHODOLOGY AND ANALYSIS

Accident data and ancillary data was acquired and was maintained appropriately in the tabular form. This data was collected for studying and identifying the accidental locations and their pattern in the Lahore district. This data was processed to frame in spatial form. Topological error were removed and thematic maps were formed. Figure 1 is showing the bar graph generated from this dataset at different landmarks.

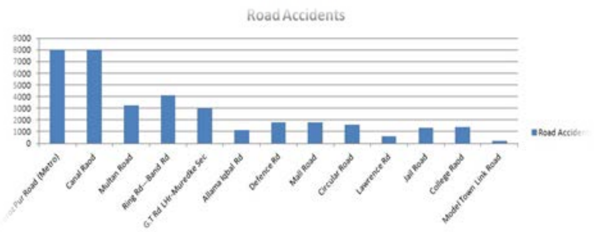

Figure 1: Road Accidents Bar Graph

Vulnerability Assessment:

In Lahore, the recorded causes of accident are mostly Carelessness (speed, Don't Obeying Law, Unskilled Drivers), Awareness (Awareness, Uneducated Drivers, and Lack of Information) and Fitness (Vehicle Fitness and Drivers Conditions). These causes are taken as vulnerability criteria in case of road accidents. This research uses AHP results to identify vulnerable roads and crossings. A risk map was developed with the help of Hazard, Capacity and Vulnerability value. A spatial risk surface was developed using IDW analysis and define safety measure on this.

In Pakistan, most of the people are hit due to carelessness. Carelessness is the fault of people. Violation of traffic rules, driving without traffic license, driving during or after drinking or having drugs, driving while using mobile phone, continuous changing of traffic lanes, over speed driving and other violation is a usual trend that is being observed on the daily basis. Most of the accidents occurred by people whose ages have less than 18. Second most important cause is awareness. In Pakistan, most people are illiterate and they have no sense to understand the signs of traffic symbols. Most of the drivers are uneducated. One of the most basic reasons of road accident is that they have no sufficient information about traffic lane and its distribution. Fitness is the last but not the least criteria of road accidents. In the whole world, after 10 years vehicles are expired and there are not allowed to run on main roads specially. Most of the vehicles are expired in Pakistan. But they are still running on roads without any check and balance. Vehicles fitness is one of the most important criteria for a safe journey. Beside the vehicle fitness, driver condition is also important. Some of accidents occurred due to the drivers who take drugs. And they drive vehicle in such condition which cause serious accidents. These accidents are in small numbers but they caused serious damage because of driving on main road.

These criteria are used in AHP for assigning weight to different situations. The processed data is used to develop a vulnerability map showing in figure 2 below.

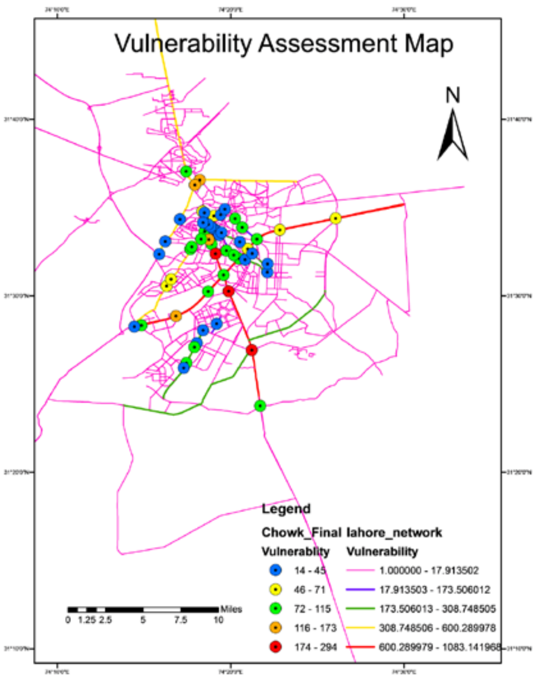

Figure 2: Vulnerability Assessment Map

Capacity of Road

In case of road, Capacity is basically used to reduce the vulnerability and road accidents. Capacity of road is the maximum potential of traffic on it. It is defined as traffic count per hour or per day. Every country has its own standards to fix the value of capacity, usually depends upon road width. Rural areas have low capacity of roads as compared to urban areas. In road accidents scenario, traffic wardens and signals are also used as capacity to reduce accident ratio.

We collected all the information related to road capacity and assign it to each crossing and roads as attribute data.

Risk Assessment

Risk assessment is done to examine the causes of accidents. The risk is calculated by following formula:

$$R = \frac{H*V*T}{C} \text{ --------------- (eq: 1)}$$

Where,

R = Risk,
H = Hazard
V = Vulnerability
T = Time and
C = Capacity

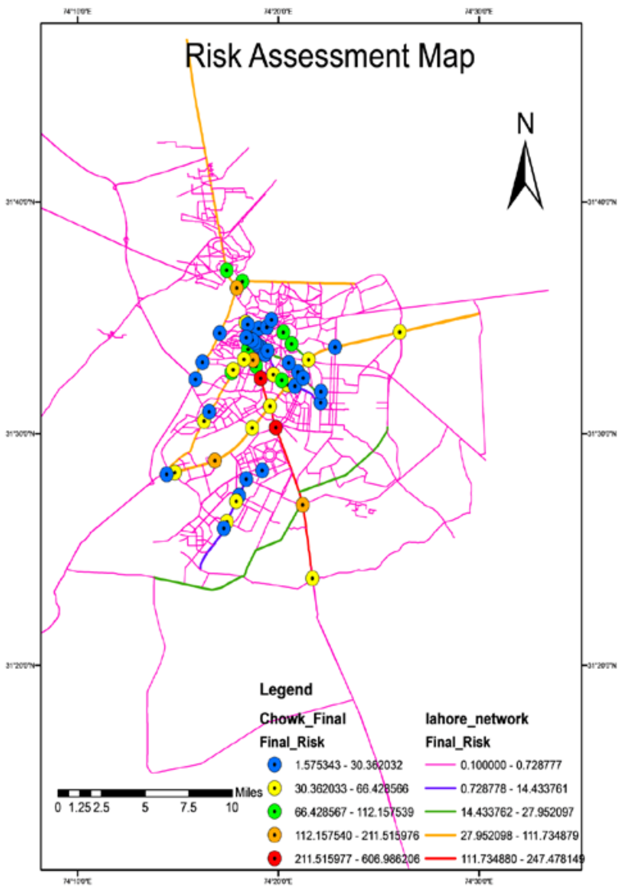

Figure 3: Risk Assessment

Figure 3 is showing the risk assessment mapping using equation 1. This map is helpful in identifying the risk pattern and can help finding solution and taking necessary precautions to prevent or lower these risks.

CROSSING ACCIDENTS

There are three types of crossing e.g. junction, cross intersection and round crossing. Junction is a place where three roads cross each other. Cross section is a place where four roads cross each other and round crossing is a place where five roads cross each other. Most of the accidents occurred on crossing. Signals are erected on crossings but some of them are not functional partially or completely and also most of people do not follow the signals that are even functional. That's why constables / wardens perform their duties on crossing to reduce the accident's ratio. But unfortunately accident's ratio is not reduced significantly yet. Figure 4 below is showing the bar graph of accident at different crossings. Most of the Road Accidents occurred on Ferozpur road and Canal road as the graph is representing it. Most of road accidents occurred on Kalma chowk (Ferozpur Road), Ichra chowk (Ferozpur Road) and Johar Town chowk (Canal Road) as shown in Figure 4.

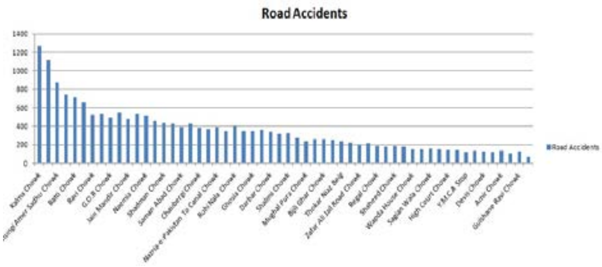

Figure 4: Road Accidents for Crossings

Vulnerability Assessment

The vulnerability criteria for crossing are same as of road, i.e., Carelessness (speed, Don't Obeying Law, Unskilled Drivers), Awareness (Awareness, Uneducated Drivers, and Lack of Information) and Fitness (Vehicle Fitness and Drivers Conditions). These criteria are used in AHP for analyzing vulnerable crossing. The AHP quantifies these crossing and a surface is developed using IDW to identify vulnerable areas and crossing. Figure 5 is showing the result of IDW with vulnerable crossings.

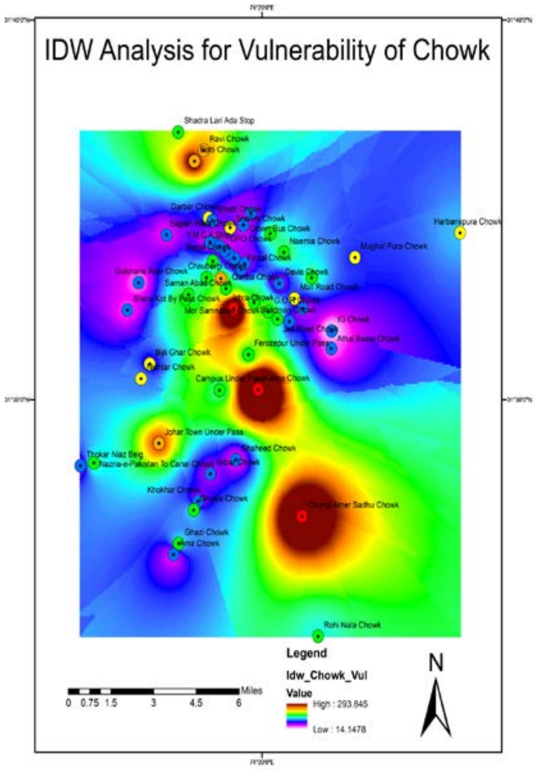

Figure 5: IDW analysis with vulnerable crossings

Capacity of Crossing

Crossing capacity is defined as traffic count per hour or per day. Every country has its own standards to fix the value of capacity. It is usually depends upon road arms. During peak hours, a crossing bears the maximum potential of traffic. Crossing capacity also included signals and constables. Accidents ratio reduced by using functional signals and constables.

Risk Assessment for Crossings

Risk at crossings is also calculated using equation 1. The hazard, vulnerability and capacity are measured as mentioned above. The result of risk assessment is shown in figure 6 below.

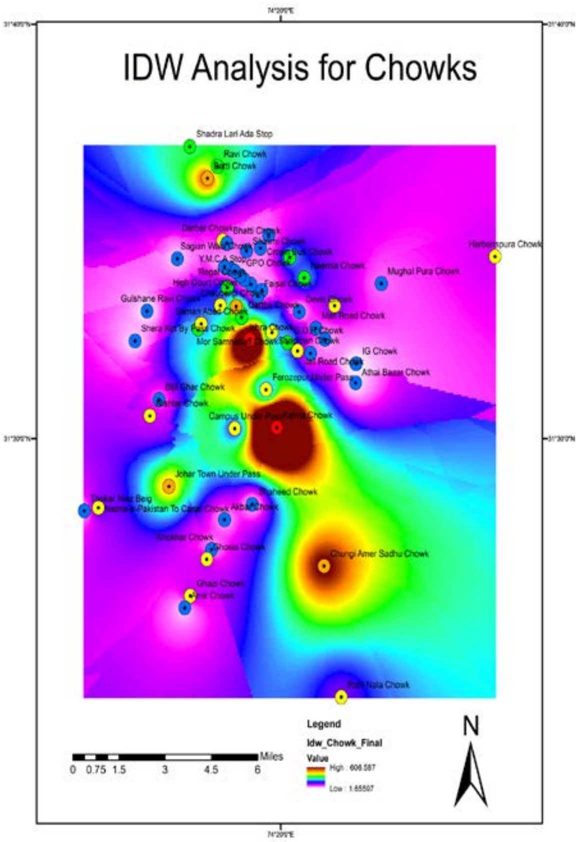

Figure 6: IDW analysis with chowks

CONCLUSION

From the analysis performed, the results shows that road accident is one of the important and serious issues which must be dealt effectively and efficiently. This research study proposed measures for the reduction of road accidents using GIS based analysis. It identifies vulnerable roads and chowks to calculate the risk and on the basis of analysis and define safety measure. According to result of road analysis, Ferozpur Road and Canal Road are most risky roads of Lahore on the basis of vulnerability and road accidents. Their road accidents value is above 8000 per year. This road accidents value is very high because this value is based on only those accidents that are rescued by Rescue 1122. Ring road, Grand Trunk Road and Multan Road have road accidents are above 4000 per year. These roads are less risky than above roads (shown in Figure 3).

.

But in case of chowks, Kalma chowk (Ferozpur Road) and Ichra chowk (Ferozpur Road) have most risk because Road Accidents value is above one thousand in one year. Johar Town Chowk (Canal Road), Batti Chowk (Grand Trunk Road) and Chungi Amer Shudu Chowk (Ferozpur road) are also very dangerous but less risky than Kalma chowk and Ichra chowk (shown in Figure 6).

Traffic Engineering & Transport Planning Agency (TEPA) is one of the major stakeholders which can play a better role in this regard. Therefore, the agency must give attention towards higher accident rates and take preventive measures to save lives of thousands of people.

The strategy generates a brand new form for managing traffic accident and shows the minimum and maximum value of risk of road network in spatial form. If this search is effectively applied then it may be very helpful to reduce road accidents. This research identifies pattern and scenario applied to reduce accidents and other traffic management matters. Some strategies must be applied to design Road geometry, to fix traffic speeds on roads, manage traffic flow and density, define lanes for different vehicles and control speed variation of vehicles.

REFERENCES

[1] (2004, September 15). Retrieved june 2011, from Pakistan Times: http://pakistantimes.net/2004/09/15/national1

[2] Agarwal, C. G. (2002). A Review and Assessment of Land-use Change Models: Dynamics of Space, Time, and Human Choice. US Dept. of Agriculture, Forest Service, Northeastern Research Station.

[3] Ahmad, A. (2007). Road safety in Pakistan. National Road Safety Secretariat, Islamabad, Islamabad.

[4] Bajwa, I.-u., Ahmad, I., & Khan, Z. (2007). URBAN HOUSING DEVELOPMENT IN PAKISTAN; A CASE STUDY OF LAHORE METROPOLITAN AREA. Lahore.

[5] Bharrat Parshad Bhatt, K. D. (2013). Using Geographic Information System and Analytical Hierarchy Process in Landslide Hazard Zonation.

[6] BLUMENTH, M. (1966, Jun.). Traffic Accident Prevention Research as a System Component. Public Health Reports (1896-1970), Vol. 81(6), pp: 569-572.

[7] C J L, M., & Lopez, A. (1996). The Global Burden of Dissease;A Comlprehensive assessment of Mortality and disability from disseases, injuries and risk factors in1990 and projected to 2020. Boston: Harvard University Press.

[8] D Thiromalaivasan, D. M. (2001). : Aquifer Vulnerability Assessment Using Analytic Hierarchy Process and GIS for upper Palar Watershed. Remote Sensing Anna University of Chennai, India.

[9] Delfino, G., Rindone, C., Russo, F., & Vitetta, A. (2005). RISK ANALYSIS IN ROAD SAFETY: A MODEL AND AN EXPERIMENTAL APPLICATION FOR PEDESTRIANS. Association for European Transport and contributors, Italy.
[10] Faghri, & Raman. (1995). GIS-based traffic accident information system for Kent County, Delaware. GIS-based traffic accident information system for Kent County, Delaware. Kent county, DEaware.
[11] FHWA. (2002). GIS based Crash Refrencing and Analysis System.
[12] Google Earth. (n.d.).
[13] Hasseea , R. (2003). A GIS based Accident System for reducing Road Accidents. Association for European Transport, UK.
[14] Iqbal, M. (2011, March 4). Lahore Urban Transport Master Plan Study: A Government of Punjab Project. Lahore, Punjab, Pakistan.
[15] Karasahin, M., & Terzi, S. (2002). Determination of Hazardous locations on Highways through GIS: A case study-Rural Road of Isparta-Antalia. International Symposium on GIS. Istanbul-Turkey.
[16] Khan, M. A., Al Kathairi, A. S., & Garib, A. M. (2004). A GIS based traffic accident data collection, referencing and analysis framework for Abu Dhabi. Abu Dhabi, United Arab Emirates.
[17] Larsen, M. A. (2010). Philadelphia Traffic Accident Cluster Analysis using GIS and SANET. In Master of Urban Spatial Analystics Capstone Project.
[18] Lawrence, R. M., David, D., & Joseph, J. H. (1986). Accident Reduction through Stress Management. Journal of Business and Psychology, Vol. 1(1), pp: 5-18.
[19] LIANG, L. Y., HUA, L. T., & MA'SOEM, D. M. (2005). TRAFFIC ACCIDENT APPLICATION USING GEOGRAPHIC INFORMATION SYSTEM. Journal of the Eastern Asia Society for Transportation Studies, pp. 3574 - 3589.
[20] Mahmud, A. R., & Zarrinbashar, E. (2009). Intelligent GIS-Based Road Accident Analysis and Real-Time. International Journal of Engineering, Vol. 2(1).
[21] Mazhar, F., & Jamal, T. (2009, June 1). Temporal Population Growth of Lahore. Journal of Scientific Research, Vol. XXXIX(1).
[22] Murray, C., & Lopez , A. (1994). Global comparative assessments in health sector: disease burden expenditures and intervention packages. (W. H. Organization, Compiler) Geneva, Switzerland.
[23] Punjab Portal. (2012). Retrieved July 6, 2012, from http://www.punjab.gov.pk/index.php?q=punjab_quick_stats: http://www.punjab.gov.pk/index.php?q=punjab_quick_stats
[24] Rescue 1122. (2012). Retrieved July 5, 2012, from http://www.rescue.gov.pk/default.aspx: http://www.rescue.gov.pk/default.aspx
[25] Shami, S. (2005, Apri 16-22). Road Traffic Safty: Cost of Government Neglect. Economic and Political Weekly, Vol. 40(16), pp. pp:1598-1602.
[26] Spring, G., & Hummer, j. (1995). Identification of Hazardous Highway Locations using Knowledge-based GIS: A case study.
[27] Tahir, N., Naseer, R., Macassa, G., Durrani, M., & Khan, M. S. (2011). Road Traffic Accidents managed by Rescue 1122: a case study from Pakistan. Lahore.
[28] Thomas J. McDonald, R. B. (2010). Saftey Analysis of low volume Rural Road in Lowa. Transportation, Lowa State University.
[29] Unknown. (2004). World Health Organization. Geneva.
[30] Unknown. (2008). Urban Road Traffic Safety GIS System.
[31] Urbanpk. (2012). Retrieved from Urbanpk: http://www.urbanpk.com/pages/content/metro/lahore
[32] Vidhya Kumaresan, V. V. (2009). Development of Gis Based Traffic Analsis System. San Diego, California.
[33] Wang, J., Shen, Y., & Khattak, A. (2010). Visualization of Traffic Accident. Virginia Modelling, Analysis and Simulation Center, Old Dominion University.
[34] Whitelegg, J. (1986). A Geography of Road Traffic Accidents. Transactions of the Institute of British Geographers, New Series,, Vol. 12(2), pp: 161-176.
[35] WHO. (2003). Retrieved from World Health Organization: http://www.who.int/vilence_injury_prevention/unintentional_injuries/road_traffic/rtip1/en.
[36] Wikipedia. (2013). Retrieved from Wikipedia: http://en.wikipedia.org/wiki/Lahore
[37] (2004). World Report on Road Traffic Injury Prevention. World Health Organisation. Geneva: World Health Organisation.

Fifth International Conference on Geotechnique, Construction Materials and Environment, Osaka, Japan, Nov. 16-18, 2015, ISBN: 978-4-9905958-4-5 C3051

PREDICTIONS FROM STANDARD PENETRATING TEST USING ARTIFICIAL NEURAL NETWORK

A.G.Mahgoub[1], Dahlia H. Hafez[2] and Mostafa A. Abu Kiefa[3]
[1]DAR AL-Handasah, Egypt; [2,3]Faculty of engineering, Cairo University, Egypt

ABSTRACT

The Standard Penetrating Test (SPT) can be considered as one of the most common in-situ popular and economic tests for subsurface investigation. Therefore, many empirical correlations have been developed between the SPT N-value, and other properties of soils. The principle objective of the current study is to demonstrate the feasibility and efficiency of using artificial neural networks (ANNs) to predict the soil angle of internal friction (Φ), the soil modulus of elasticity (E) and tip resistance (q_c) of cone penetration test (CPT) results from SPT results considering the uncertainties and non-linearities of the soil. In addition, ANNs are used to study the influence of different input parameters that can be used to improve the prediction. A large amount of field and experimental data including SPT/CPT results, plate load tests, direct shear box, grain size distribution was obtained from a project in the United Arab Emirates to be used in the training and the validation of the ANNs. The ANN results are compared with some common traditional correlations. The results show that the developed ANNs can efficiently predict the aimed parameters from the SPT results. The predicted parameters from ANN were in very good agreement with measured results compared to the predicted values from available traditional correlations.

Keywords: Angle of Internal Friction; Cone Penetrating Test; General Regression Neural Network; Soil Modulus of Elasticity, Standard Penetrating Test.

INTRODUCTION

The Standard Penetration Test (SPT) is one of the most commonly used in-situ tests for site investigation and foundation design. Many empirical correlations have been developed between the SPT N-value, and other engineering properties of soils. Despite the fact that this test has disadvantages such as discrete strength measurement and dependence on operator and apparatus, it is still the most popular and economic mean for subsurface investigation.

The current paper studies the feasibility and efficiency of using artificial neural networks (ANNs) to estimate the soil properties Φ, E and CPT results (q_c) [1]-[5] from SPT result and to investigate which parameters should be included in the soil property estimation to improve the prediction models.

Artificial neural networks have been intensively studied and applied to many geotechnical engineering problems [6], [7]. It has been applied to estimate many soil and material properties [8], [9] and it proved to be a powerful tool that can have superiority over other correlation techniques. The idea of neural network technology is similar to the brain's own problem-solving process. An ANN is composed of a large number of connected neurons which act like simple processors. Generally, when a large volume of data is available for training, ANNs offer viable solutions. It has been shown that ANNs are capable of mapping nonlinear and complex relationships in nature and are very beneficial when a problem is difficult to formulate analytically.

To train and test a neural network a large amount of data is needed. In the current study, field and experimental data including SPT/ CPT results, plate load tests, direct shear box, grain size distribution were obtained then filtered and processed from a large-scale project that covers the United Arab Emirates (UAE). The soil in UAE is mostly cohessionless soil. UAE is witnessing a lot of development and many construction projects. It is believed that using data from such active areas in construction for prediction of soil properties would be of benefit to engineers in this area specifically and to geotechnical engineers in general.

The available data used for estimating Φ (Direct shear box), E (plate loading test) and q_c (CPT results) from N (SPT results), is first presented. The different ANN models are then developed. Different input parameters were considered to study the influence of the input parameters on the ANN models. The predictions from ANN are compared to predictions from other correlations available in the literature. Conclusions highlighting the efficiency of the ANNs are finally presented.

AVAILABLE DATA

The data for this study was collected from the results of geotechnical investigation work that has been done for a large-scale project. The project extends all over United Arab Emirates UAE where the soil is mainly cohessionless soil.

The project has about 820 boreholes with variable depths and with SPT for each borehole along the project alignment. About 400 CPT were executed beside the boreholes. Moreover, there are about 630 test pits with maximum depth 3.0m along the project alignment with 260 plate loading test to determine the modulus of soil elasticity and 606 CBR tests. In addition, lab tests were performed on the soil sample for classifications such as, Grain size distribution tests (Sieve analysis and Hydrometer), and lab tests for determining the shear strength parameters such as direct shear box.

NEURAL NETWORK MODELING

The current study uses a supervised ANN. In a supervised network, a large number of correct predictions are given to the model from which it can learn. Examples of supervised networks are back propagation networks (BPN), general regression networks (GRNN) and probabilistic neural networks (PNN).

The architecture of a supervised ANN, generally, consists of an input layer, an output layer and one or more hidden layers. The input layer contains the input variables. The output layer contains the target output vector. At least one hidden layer that contains the artificial neurons (processing units) is used between the input and output to assist in the learning process. The neurons in the different layers are interconnected. Each connection has a 'weight' associated with it. Input values in the first layer are weighted and passed on to the hidden layer. Neurons in the hidden layer produce outputs by applying an activation function to the sum of the weighted input values [10], [11]. These outputs are then weighted by the connections between the hidden and output layer. The output layer produces the desired results.

Two main phases are included in neural network operation. The first is the training phase and the second is the testing phase. In the first phase the data is repeatedly presented to the network while the weights of the data are updated to obtain the desired output. In the second phase the trained network with the frozen weights is applied to data it has never seen. A properly trained network can model the unknown function that relates the input variables to the output variables. It can then be used to make predictions for a given set of previously unseen input patterns where the output values are unknown.

The neural networks used in the current study were developed using the neural network program Neuroshell 2. This program implements several different neural network algorithms. The general regression neural network (GRNN) is used in the current study. GRNNs are known for their ability to train quickly on sparse data sets [10].

The GRNN models developed were three-layer networks (input layer, output layer and one hidden layer). The number of neurons in the input layer is equal to the number of inputs and the number of neurons in the output layer is equal to the number of outputs, while the number of neurons in the hidden layer is usually equal to the number of correct patterns given to the model to learn from.

The inputs were scaled using a linear scale function [0,1]. The GRNN used was genetic adaptive; i.e. it uses a genetic algorithm to find an input smoothing factor adjustment. The genetic breeding pool size of 100 was used in the developed GRNN. An initial smoothing factor was taken as 0.3. The smoothing factor is an important parameter in the GRNN which determines how tightly the network matches its predictions to the data in the training patterns.

For each of the data sets prepared to estimate Φ, E and q_c from N, 20% of the data was randomly extracted. This 20% was used as a testing set while the rest of the data was used as a training set**.**

ESTIMATING Φ FROM SPT RESULTS

Output/Input Variables of ANN Analysis

For estimating Φ from SPT results, the SPT results (N values), direct shear test and grain size analysis were used from the available date. The readings of the SPT test were filtered to be at the same elevation of the lab tests. A total of 84 data points were prepared. The parameters that were investigated as input parameters to be included in the GRNN models developed were N (obtained from SPT results), Fc (fines content) and D_{50} (defined as grain diameter corresponding to 50% of the material being smaller) obtained from grain size analysis and δ_{eff} (the effective overburden pressure) calculated at the same level of the SPT test. The calculation of effective overburden pressure was based on a unit weight of soil of 18 KN/m^3 and the unit weight of water of 10 KN/m^3 taking into consideration the effect of ground water level.

The output of the GRNN models considered is tan Φ which was both measured (obtained from direct shear box) and estimated by the GRNN models developed. Five different GRNN models were developed with different input parameters to study the influence of the input parameters on the obtained tan Φ. To evaluate the efficiency of the GRNN models developed, the coefficient of correlation (r^2) was used. r^2 is a statistical measure of the strength of the relationship between the actual versus predicted outputs. r^2 value of 1 indicates a perfect fit, while that of 0 indicates no relationship.

Results of Neural Networks

Figure 1 shows 5 different GRNN models developed (GRNN1 to GRNN5) with 5 different input combinations and the corresponding r^2 (for all data points) obtained for each Network. GRNN2 with inputs (N, δ_{eff}) is the best model to represent the correlation predicting (tanΦ) from SPT results and effective overburden with high value of r^2 of 97.55%.

Table 1 presents the data used in GRNN2 as input and the measured tan Φ. The comparison between the predicted tan Φ from GRNN and the actual measured values is presented in Fig. 2.

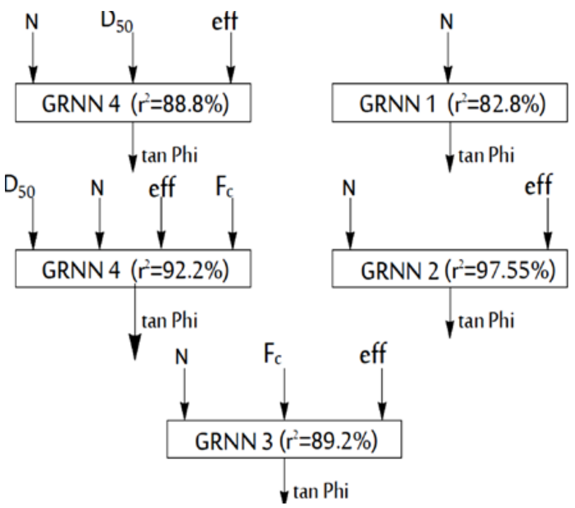

Fig. 1 Trials used to predict tan (Φ) from SPT results considering different input parameters with r2 coefficient (%)

Table 1 The used data for estimation of φ (GRNN2)

Index	Effective stress(Kpa)	N	TAN (Φ)
Min	14.85	1	0.46604
Max	89	68	0.86865
Mean	43.21941	12.667	0.60258

For GRNN2, the weight (influence) of each input parameter on the relation is reflected by the individual smoothing factor of each input parameter. The individual smoothing factors for each input are shown in Fig. 3. It is concluded from Fig. 3 that (δ_{eff}) is the Second input variable that influences the network and N- value (SPT result) is the last one.

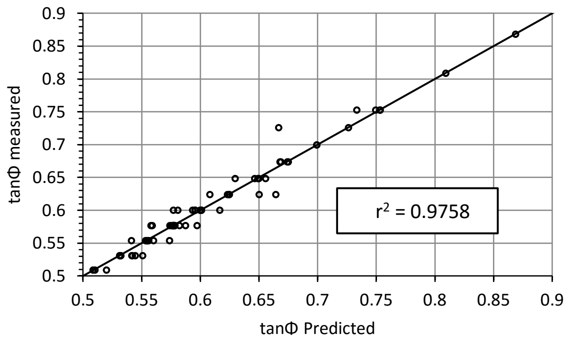

Fig. 2 Comparison between predicted and measured tan (Φ) from SPT results with r^2% coefficient

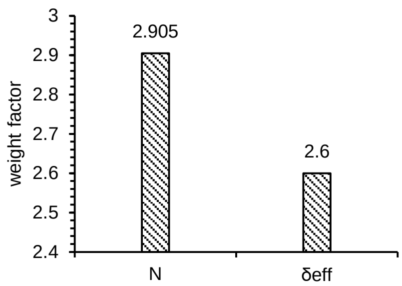

Fig. 3 The weight factors for the correlation between angle of internal friction and SPT results (GRNN2)

Comparison between Neural Networks and a Set of Traditional Methods

Table 2 shows some of the correlations used for the estimation of Φ from SPT results available in the literature. The available data is applied to the available correlations in the literature and are plotted in Fig. 4 along with the results from the ANN model developed.

From Fig. 4, it is clear that the ANN model predicted values of angle of internal friction that are very close to the measured values compared to the other available correlations. Therefore it is a good indication for the applicability of using this model in comparison with other correlations

Table 2 Different correlations for predicting (tanφ) from SPT results

Researcher	Correlation
Kulhawy and Mayne, (1990)	$\phi = tan^{-1}(N/(12.25 + 20.35\delta_{vo}/pa)^{0.34}$
Wolff, (1989).	$\phi = 27.1 + 0.30N - .00054N^2$
Shioi and Fukui (1982)	$\phi = 4.5\,N + 20$
Hatanaka and Uchida, (1996)	$\phi = \sqrt{18\,N_1} + 20$
	Where, $N_1 = \sqrt{\frac{98}{\delta_{vo}}}\,N$ & δ_{vo} in KN/m^2

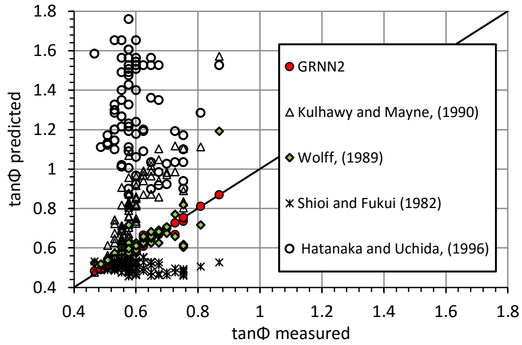

Fig. 4 Comparison between actual (measured) and predicting (tanΦ) from SPT.

ESTIMATING E FROM SPT RESULTS

Output/Input Variables of ANN Analysis

For estimating E from SPT results, the SPT-(N values) results, plate loading test and grain size analysis were used from the available date. The readings of the SPT test were filtered to be at the same elevation of the lab tests and at the zone of 120 cm below Plate loading test (influence zone while the plate width is 60cm). A total of 34 data points were prepared. The parameters that were investigated as input parameters to be included in the GRNN models developed were N (obtained from SPT results), Fc (fines content), D_{50} and depth of water below the plate loading test.

Results of Neural Networks

Figure 5 shows 7 different GRNN models developed (GRNN1 to GRNN7) with 7 different input combinations and the corresponding r^2 (for all data points) obtained for each Network. GRNN2 with inputs (N, D_{50}) is the best model to represent the correlation predicting (E) from SPT results and effective overburden with high value of r^2 of 95.46%. Fig 6 shows the influence factors for every input.

Table 3 presents the data used in GRNN2 as input and the measured E. Fig 7 shows the comparison between the predicted E from GRNN2 and the actual measured values.

Table 3 The used data for estimation of E (GRNN2)

Index	D50	N	E (Mpa)
Min	0.121	2	9.9
Max	0.2159	53	73.05
Mean	0.1557235	12.41177	29.75
St. Deviation	2.58E-02	11.80169	14.73538

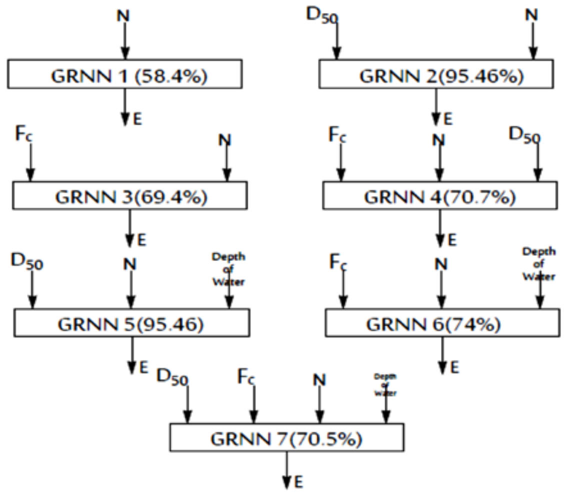

Fig. 5 Trials used to predict E from SPT results considering different input parameters with r2 coefficient (%).

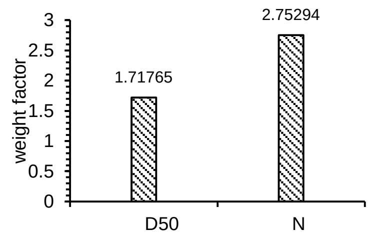

Fig. 6 The weight factors for the correlation between angle of internal friction and SPT results (GRNN2)

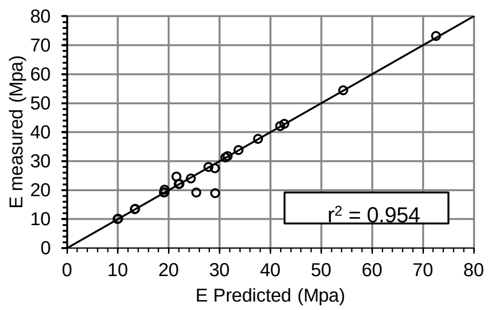

Fig. 7 Comparison between predicted and measured E

Comparison between Neural Networks and a Set of Traditional Methods

Table 4 and Fig. 8 show some of the correlations used for estimation of E from SPT results available in the literature. From Fig. 8 it is shown that the ANN model (GRNN2) was in very good agreement with measured values of E compared to the other available correlations in the literature.

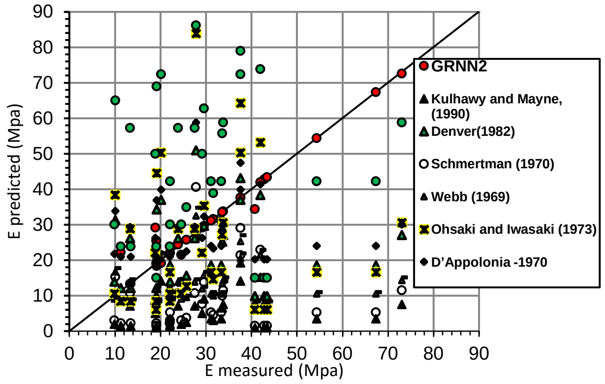

Fig. 8 Comparison between actual (measured) and predicting (E) from SPT.

Table 4 Different correlations for predicting (E) from SPT results

Researcher	Correlation
Kulhawy and Mayne, (1990)	$5N = E/P_a$
Schmertman(1970)	$E(KPa) = 766N$
Denver(1982)	$E(Mpa) = 7\sqrt{N}$
Webb (1969)	$E = 7.17 + 0.478N \quad E = kg/cm2$
Ohsaki and Iwasaki (1973)	$E = 3.5 * N\,0.8$
D'Appolonia (1970)	$E = 18.75 + 0.756N$
Schultze & Menzenbach (1960)	E= 7.46+0.517N
Trofimenkov (1974)	E= 500 log10(N)

ESTIMATING q_c FROM SPT RESULTS

Output/Input Variables of ANN Analysis

For estimating q_c from SPT results, the SPT-(N values), results of grain size analysis (Fc, D_{50}, D_{30}, D_{10}) and effective overburden pressure (δ_{eff}) were used from the available date. The readings of the CPT test were filtered to be at the same elevation of the lab tests and N-value of SPT. A total of 94 data points were prepared.

Results of Neural Networks

Figure 9 shows 10 different GRNN models developed (GRNN1 to GRNN10) with 10 different input combinations and the corresponding r^2 (for all data points) obtained for each Network. GRNN7 with inputs (N, Fc, D_{50}, D_{30}, D_{10}, δ_{eff}) is the best model to represent the correlation predicting (q_c) from SPT results and effective overburden with high value of r^2 of 90%.

Fig 10 shows the influence factors for every input for GRNN3, GRNN4, GRNN7, GRNN8 that have r^2 >90%, however, GRNN7 is considered the strong correlation between qc (CPT result) and N-value of SPT result because N value has a high influence factor of 2.77 and is considered the last factor in the other correlations (GRNN3, GRNN4, GRNN8). In addition, D50 is the last factor that has no effect on output results for GRNN7.

Table 5 presents the data used in GRNN7 as input and the measured q_c. Fig 11 shows the comparison between the predicted q_c from GRNN7 and the actual measured values.

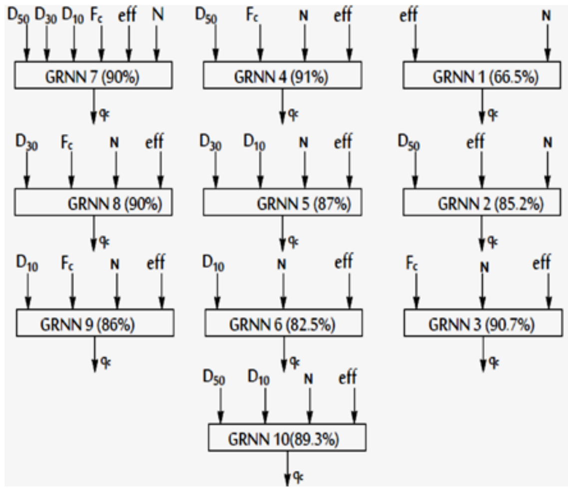

Fig. 9 Trials used to predict q_c from SPT results with r^2 coefficient (%).

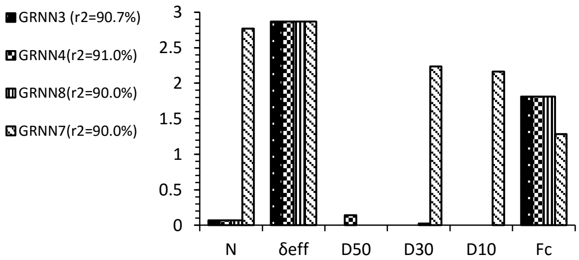

Fig. 10 The weight factors for the correlation between q_c (CPT result) and N (SPT result).

Table 5 The used data for estimation of q_c (GRNN7)

Index	D50	D30	D10	Fc %	N	EFFECTIVE PRESSURE (KN/m2)	qC (Mpa)
MIN. Value	0.03	0.013	0.0015	7.1	1	21	3.8
MAX. Value	0.3	0.1408	0.0707	65.1	47	87	53
Mean	0.15	0.10	0.06	11.83	12.42	42.58	18.53
Std. Deviation	0.03	0.02	0.01	9.85	8.48	18.25	12.04

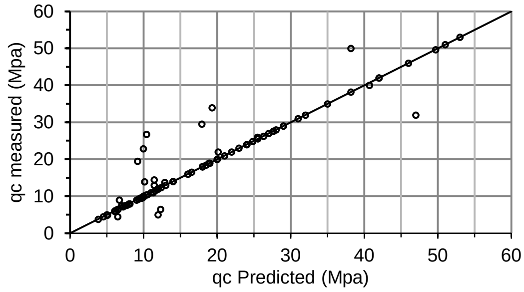

Fig. 11 Comparison between predicted and measured q_c for GRNN7.

Comparison between Neural Networks and a Set of Traditional Methods

Table 6 and Fig. 12 show some of the correlations used for estimation of q_c from SPT results available in the literature. It is clear from the figure that the ANN model yields better prediction of qc.

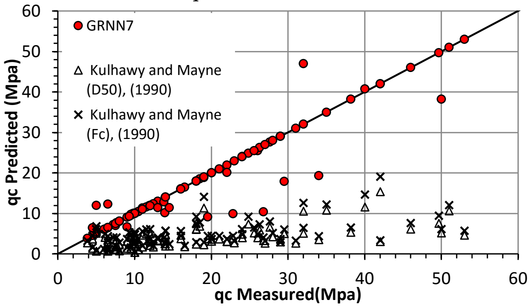

Fig. 12 Comparison between actual (measured) and predicting (q_c) from SPT.

Table 6 The variables correlations for predicting (q_c) from SPT results

Researcher	Correlation
Kulhawy and Mayne, (1990)	$({}^{qc}/_{pa})/N = 4.25 - \frac{F_c}{41.3}$ ${}^{qc}/_{pa})/N = 5.44\, D_{50}^{0.26}$

CONCLUSION

The paper studied the feasibility and efficiency of applying artificial neural networks (ANN) to predict φ (angle of internal friction), E (modulus of elasticity) and qc (CPT result) from SPT results (N values) which is one of the most commonly used in-situ tests. A large amount of data for cohesionless soil was used that was collected from a project covering most of UAE. The effect of different input parameters was investigated and ANN results were compared with other available correlations. The following can be concluded:

- The results of the ANN models developed for predicting φ, E and qc from N gave a very good agreement with actual results compared to some of the traditional methods available in the literature.
- ANN model (GRNN2) with coefficient of correlation (r^2= 97.6%) and inputs (N, δeff) was the best model to represent the correlation predicting (tanΦ) from SPT results (N) and effective overburden stresses (δeff).
- ANN model (GRNN2) with r^2= 95.6% and inputs (N, D50) was the best model to represent the correlation of predicting (E) from SPT results and mean grain size distribution.
- ANN model (GRNN7) with coefficient of correlation (r^2= 90%) and inputs (D10, N, δeff, D30, FC and D50) was the best model to represent the correlation for predicting (qc) from SPT results and results of grain size distribution tests.

REFERENCES

[1] Robertson, P.K., Guide to Cone Penetration Testing. Signal Hill: Gregg Drilling & Testing, 2010.

[2] Zervogiannis, C.S. and Kalteziotis, N.A. (1988), “Experience and Relationships from Penetration Testing in Greece”, International Symposium on Penetration Testing, ISOPT-1, Orlando, 2, 1063-71, Balkema Pub., Rotterdam.

[3] Burt Look, "Handbook of Geotechnical Investigation and Design Tables." (2007)

[4] Cem Ozan July 2003, "Estimation of Grain Characteristics of Soils by Using Cone Penetration Test (Cpt) Data." MSc. Thesis, The Graduate School of Natural and Applied Sciences of The Middle East Technical University, Turkey.

[5] Salehzadeh H., Hozouri A., Golestani A.R., "Correlation between Cone and Standard Penetration tests." 5th SASTech 2011, Khavaran Higher-education Institute, Mashhad, Iran. May 12-14.

[6] Abu Kiefa M.A (1997), “Prediciting The Driven Pile Capacity on Cohessionless Soil by Neural Networks. Pro. Of 3rd Int. Geotechnical Eng. Cof., Cairo University, 5-8 January, Cairo Egypt, pp.227-240.

[7] Abu Kiefa M.A (1998a), “General Regression Neural Networks for Driven Piles in Cohessionless Soil.” Journal of Geotechnical and Geoenvironmental Engineering, ASCE, Vol. 124, No. 12, Dec., pp. 1177-1185.

[8] D. Singh, M.Zaman and s. Commuri, "Artificial Neural Network Modeling for Dynamic Modulus of Hot Mix Asphalt Using Aggregate Shape Properties", Journal of Geotechnical and Geoenvironmental Engineering, ASCE, Civ. Eng. 2013.25, Jan. 2013, pp 54-62.

[9] Hasanadehshooiili, H. Lakirouhani, A. and Medzvieckas, J. (2012) "Superiority of Artificial Neural Networks over Statistical methods in prediction of the optimal length of Rock Bolts", V18(5):655-661.

[10] Ceryan, N, Okkan, U, and Kesimal, A. (2012) "Application of Generalized Regression Neural Networks in Predicting the Unconfined Compressive Strength of Carbonate Rocks" Rock Mech Rock Eng, V45: 1055-1072.

[11] Specht, D.F. 1991. "A general regression neural network." IEEE Trans. Neural Networks, 2(6), 568-576.

[12] Goh, A.T.C. (1995a), “Back propagation Neural Networks for Modeling Complex System,” Artificial Intelligence in Engineering, Vol.9, no.3, PP.143-151.

Fifth International Conference on Geotechnique, Construction Materials and Environment, Osaka, Japan, Nov. 16-18, 2015, ISBN: 978-4-9905958-4-5 C3051

COMPRESSIBILITY BEHAVIOR OF SIDOARJO MUD VOLCANO (LUSI)

Luky Handoko[1], Noriyuki Yasufuku[2], Ryohei Ishikura[3] and Ahmad Rifa'i[4]
[1]Department of Civil Engineering, Universitas Atma Jaya Yogyakarta, Indonesia; [2&3]Department of Civil Engineering, Kyushu University, Japan; [4]Department of Civil and Environmental Engineering, Universitas Gadjah Mada, Indonesia

ABSTRACT

Sidoarjo mud volcano (Lusi) is one of the most challenging problems regarding to the compressibility of fine grained soils in Indonesia. Understanding about compressibility behavior is essential to construct appropriate remediation program for this problems. Consolidation test has been conducted to investigate the compressibility behavior of Lusi mud volcano. In this study, the laboratory test result is compared with estimated value derived from some empirical equations. A simple equation can be used to predict e-log σ' curve very well by using the correlation between initial void ratio (e_0) and void ratio corresponding to unit pressure (e_1); and correlation between compression index (C_c) and physical properties of soils, such as liquid limit (w_L) or natural water content (w_n). This equation predict better than other available equations in literature when compared with laboratory test of Lusi mud volcano.

Keywords: High Water Content Material, Consolidation, Compression Index, Hydraulic Conductivity

INTRODUCTION

One of the most challenging problems regarding to the compressibility of fine grained soils in Indonesia is the eruption of mud volcano in Sidoarjo district, East of Java. This mud is known as Lusi. It has been erupted since May 2006 and still continues. The fresh erupted material is considered as high water content material which collected inside of 12 meters dike. Subsequently, this materials undergo sedimentation process and self-consolidation process and settled in about 640 ha area. Large amount of mud was produced and it becomes serious environmental issue in the future if not used appropriately. Appropriate remediation program need to be constructed to solve this problems and mostly required the knowledge of the compressibility behavior of this materials.

Compressibility behavior requires appropriate consideration when dealing with fine grained soils. Compression index (C_c) is one of the most important parameters that used to describe compressibility of fine grained soils. Compression index can be derived from two different ways: direct measurement by conducting laboratory test and calculation from available empirical equations. Oedometer and Rowe cell are two famous apparatuses generally used to determine compression index in laboratory. Since laboratory test requires undisturbed samples, the accuracy of this method relies on the quality of the specimens. Good quality of undisturbed specimens are difficult to be obtained. Sampling process, transportation process, and adjustment process in the apparatus may increase the disturbance degree of soil sample. Accuracy of laboratory equipment also plays important role in order to obtain reliable results. On the other hand, recently many equations are available in literature to calculate compression index based on physical properties. Physical properties of soils can be determined directly from laboratory test easily and require only disturbed samples. This method is considered to be easier to use compare with the direct measurement method. Furthermore, this method requires less cost and time compare with the other one.

This paper discuses compressibility behavior of Lusi mud volcano. One-dimensional consolidation test using Oedometer apparatus was conducted in laboratory. The results of the test were plotted in void ratio (e) and vertical effective stress (σ') (in log scale). Estimation methods from available empirical equations were conducted as well and the results were plotted together with the experimental results. Performance of some empirical equations are discussed.

AVAILABLE COMPRESSIBILITY EQUATIONS IN LITERATURE

Numerous empirical equations to estimate C_c has been proposed. The compression index of soils has been tried to be correlated with single variable of liquid limit (w_L) [1,2,3,4,5,6,7,8], plasticity index (I_P) [7,9,10,11], shrinkage index (I_S) [11], natural water content (w_n) [5,7,8,12,13,14,15], initial void ratio (e_0) [2,7,14,15,16,17,18], initial porosity (n_0) [19], dry density (γ_d) [15] and multivariable equations

Table 1 Selected empirical equations to determine compression index (C_c)

Empirical equations	Applicability	References
Intrinsic variables (liquid limit (w_L))		
$0.007(w_L-10)$	Remolded clays	Skempton [1]
$0.0046(w_L-9)$	Brazilian clays	Cozzolino [2]
$0.017(w_L-20)$	All clays	Shouka [3]
$0.009(w_L-10)$	Normally consolidated clays	Terzaghi and Peck [4]
$0.006(w_L-9)$	All clays with wL < 100%	Azzouz et al. [5]
$(w_L-13)/109$	All clays	Mayne [6]
$0.011(w_L-6.36)$	Busan clays, Korea	Yoon et al. [7]
$0.0118(w_L-20.7)$	Silts and clays, Ireland	McCabe et al. [8]
State variables (natural water content (w_n))		
$0.01(w_n-5)$	All clays	Azzouz et al. [5]
$0.01\ w_n$	All clays	Koppula [12]
$0.01(w_n-7.549)$	All clays	Herrero [13]
$0.0115w_n$	Organic silts and clays	Bowles [14]
$0.01(w_n+2.83)$	Busan clay, Korea	Yoon et al. [7]
$0.008w_n-0.044$	Remolded Iranian soils	Abbasi et al. [15]
$0.014(w_n-22.7)$	Silts and clays, Ireland	McCabe et al. [8]

combining those previously mentioned indices with other physical properties such as specific gravity (G_s)[5,7,12,15]. Physical properties of soils are classified into two groups, namely intrinsic properties and structural properties [15]. The intrinsic properties are then referred as intrinsic variables and the structural properties are the state variables [20]. The intrinsic variables consist of consistency limit (w_L, I_P and I_S). Those variables are influenced by mineralogy of soil particle and are independent from disturbance of specimen[15,20]. The state variables consist of w_n, e_0, n_0 and γ_d. Those variables are sensitive to specimen environment disturbance[15,20]. Liquid limit-based and natural water content-based empirical equation are reported to give better results compared than other indices. Table 1 presents some selected empirical equations to determine C_c available in literature.

Previously mentioned literature that propose estimation of C_c do not predict the void ratio-effective stress relationship (e-log σ'). They only predict the slope of the e-log σ' curve. The e-log σ' curve generally can be written linearly as in Eq. (1) where e_1 is the void ratio corresponding to effective vertical stress at unit pressure (e when σ'=1 kPa) and C_c is the slope of the curve. Once the e_1 can be determined, many different e-log σ' equations can be derived from different C_c equations.

$$e = e_1 - C_c \log \sigma' \quad (1)$$

Abbasi et al. [15] conducted test on 26 different Iranian remolded soils. Each specimen was prepared in three different density and subjected to one-dimensional consolidation test to obtain C_c. Based on the results, relationship between e_0 and e_1 can be obtained. Fig. 1 shows the plotted data of e_0 and e_1. The correlation between e_0 and e_1 is presented in Eq. (2) and it shows good correlation between e_0 and e_1, indicated from high coefficient of determination (r^2=0.922). Eq. (2) and one of the equation presented in Table 1 can be used to draw e-log σ' based on Eq. (1).

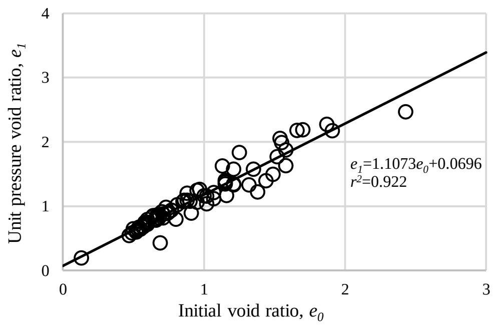

Fig. 1 Relationship between initial void ratio (e_0) and unit pressure void ratio (e_1) (data from Reference [15])

$$e_1 = 1.1073 e_0 + 0.0696 \quad (2)$$

Abbasi et al. [15] proposed Eq. (3) and (4) based on experimental results to obtain e-log σ' equation in Eq. (5).

$$C_c = -0.461\gamma_d + 0.883 \quad (3)$$

$$e_1 = -1.78\gamma_d + 3.70 \quad (4)$$

$$e = (-1.78\gamma_d + 3.7) - (-0.461\gamma_d + 0.883)\log \sigma' . \quad (5)$$

Berilgen et al. [21] proposed an empirical equation to satisfy the *A*, *Z* and *B* constants for *e*-log *σ'* equation proposed by Liu and Znidarcic [22] that presented in Eq. (6). *A*, *Z* and *B* are constants that depended on e_0, I_P and I_S. The equations to determine those constants are presented in Eq. (7),(8) and (9).

$$e = A(\sigma' + Z)^B \quad (6)$$

$$A = 2.69[\exp(0.008(I_P))] \quad (7)$$

$$B = (1 + e_0)[0.008\ln(I_P) - 0.054] \quad (8)$$

$$Z = (1 + e_0)\exp[1.97 - 3.9\ln(I_L)] \quad (9)$$

Tripathy and Mishra [23] proposed an *e*-log *σ'* equation based on Skempton's compression index equation as shown in Eq. (10); where I_v is intrinsic void index, C_c^* is intrinsic compression index and e_{100}^* is the void ratio corresponding to a vertical effective stress of 100 kPa. The equation to calculate C_c^* and e_{100}^* are presented in Eq. (10) and (11). Both constants are depended on void ratio at liquid limit (e_L). The I_v is depended on vertical effective stress (*σ'*) as presented on Eq. (13).

$$e = I_v C_c^* + e_{100}^* \quad (10)$$

$$C_c^* = 0.256 e_L - 0.04 \quad (11)$$

$$e_{100}^* = 0.016 e_L^3 - 0.089 e_L^2 + 0.679 e_L + 0.109 \quad (12)$$

$$I_v = 2.45 - 1.25\log\sigma' + 0.015(\log\sigma')^3 \quad (13)$$

METHODS

Lusi mud volcano was selected to assess the compressibility equations. Physical properties of Lusi mud volcano has been published [24]. Lusi mud volcano contains mostly of fine grained soils (84.47%) and classified as high plasticity silt (MH). It has G_s = 2.71, w_L =58.44%, w_P = 30.77%, w_S=22.27% and I_P 27.66%. One-dimensional consolidation test using oedometer apparatus was conducted to obtain compressibility behavior of lusi mud volcano. The initial water content is about 82% and corresponding to initial void ratio 2.22. The *e*-log *σ'* curve obtained from laboratory test is compared with estimated curve from several approaches.

RESULTS AND DISCUSSIONS

Eq. (1) is used as basis equation to derive estimated *e*-log *σ'* curves. The e_1 can be obtained from Eq. (2) and C_c is estimated from w_L and w_n. These two indices have been selected to represent intrinsic variables group and state variables group. Both indices has been reported to have high correlation with C_c compare to other indices within their group [8,15,20]. Fig. 2 shows the estimated *e*-log *σ'* curves in which C_c is derived from liquid limit and Fig. 3 shows the similar thing but C_c is derived from natural water content. Based on Eq. (2), unit pressure void ratio, e_1, for Lusi mud volcano is estimated to be 2.53. Both Fig. 2 and Fig. 3 indicate that most of the estimated *e*-log *σ'* curves might have similar tangent value but some of them quite far from laboratory test results plotted data. It is also indicated that *e*-log *σ'* curve from Yoon et al. [7] (Reffered as Eq. (1)-[7]) gives best prediction among group based on w_L to predict C_c and Abbasi et al. [15] (Reffered as Eq. (1)-[15]) gives best prediction among group based on w_n to predict C_c.

Performance of Eq. (1)-[7] and Eq. (1)-[15] equations are then compared with other method to generate *e*-log *σ'* curves from Abbasi approach (Eq. (5)), Berilgen approach (Eq. (6)), and

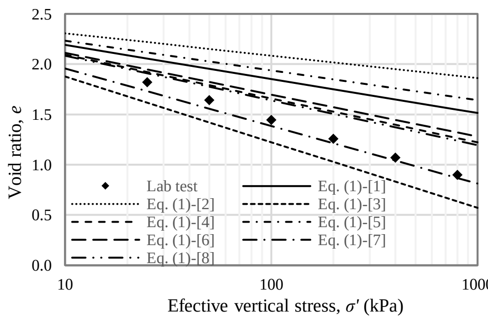

Fig. 2 Comparison of estimated *e*-log *σ'* curve based on Eq. (1) (e_1 from Eq. (2) and C_c from liquid limit-based equation) and oedometer test results

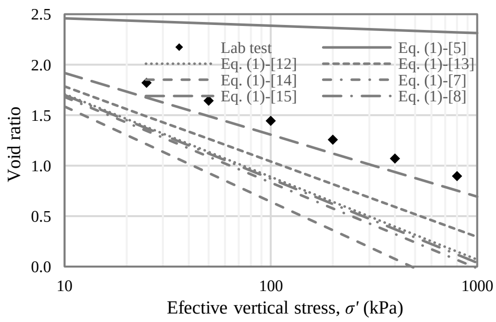

Fig. 3 Comparison of estimated *e*-log *σ'* curve based on Eq. (1) (e_1 from Eq. (2) and C_c from natural water content-based equation) and oedometer test results

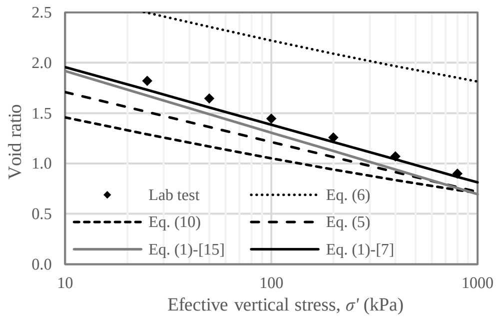

Fig. 4 Comparison of oedometer test results and estimated *e*-log *σ'* curve from different methods

Tripathy&Mesra approach (Eq. (10)). The comparison results are shown in Fig. 4. This figure indicates that *e*-log *σ'* curves derived from Eq. (1) shows the best prediction.

CONCLUSIONS

Compressibility behavior of Lusi mud volcano has been investigated from two different methods. Direct measurement from laboratory test using oedometer apparatus has been conducted. The result of test was compared with estimated *e*-log *σ'* curves. A simple equation (Eq. (1)) can predict e-log σ' very well by using the correlation between initial void ratio (e_0) and void ratio corresponding to unit pressure (σ'=1 kPa) (e_1) as presented in Eq. (2); and correlation between compression index (C_c) and physical properties of soils, such as liquid limit (w_L) or natural water content (w_n). This equation predict better than other available equations in literature when compared with laboratory test of Lusi mud volcano.

ACKNOWLEDGEMENTS

The first author would like to express his gratitude to Department of Civil Engineering of Universitas Atma Jaya Yogyakarta for funding support of this paper. The authors also gratefully for the supports from colleagues and students to conduct laboratory tests and fruitful discussions.

REFERENCES

[1] A.W. Skempton, "Notes on compressibility of clays", Quarterly Journal of the Geological Society, 100 (1944) 119-135.
[2] V.M. Cozzolino, Statistical forecasting of compression index, The 5th International Conference on Soil Mechanics and Foundation Engineering, Paris, 1961.
[3] H. Shouka, Relationship of compression index and liquid limit of alluvial clay, 19th Japan Civil Engineering Conference, Tohoku, 1964, pp. 40.41-40.42.
[4] K. Terzaghi, R.B. Peck, Soil mechanics in engineering practice, 2 ed., John Wiley and Sons, Inc., New York, 1967.
[5] A.S. Azzouz, R.J. Krizek, R.B. Corotis, "Regression analysis of soil compressibility", Soils and Foundations, 16 (1976) 19-29.
[6] P.W. Mayne, "Cam-clay prediction of undrained strength", Journal of Geotechnical Engineering, 106 (1980) 1219-1242.
[7] G.L. Yoon, B.T. Kim, S.S. Jeon, "Empirical correlations of compression index for marine clay from regression analysis", Canadian Geotechnical Journal, 41 (2004) 1213-1221.
[8] B.A. McCabe, B.B. Sheil, M.M. Long, F.J. Buggy, E.R. Farrell, "Empirical correlations for the compression index of irish soft soils", Proceedings of the Institution of Civil Engineers, 167 (2014) 510-517.
[9] V.A. Nacci, M.C. Wang, K.R. Demars, Engineering behavior of calcareous soils, Civil Engineering in the Oceans III, ASCE, Newark, 1975.
[10] A. Nakase, T. Kamei, O. Kusakabe, "Constitute parameters estimated by plasticity index", Journal of Geotechnical Engineering, 114 (1988) 844-858.
[11] A. Sridharan, H.B. Ngaraj, "Compressibility behaviour of remoulded, fine-grained soils and correlation with index properties", Canandian Geotechnical Journal, 37 (2000) 712-722.
[12] S.D. Koppula, "Statistical estimation of compression index", Geotechnical Testing Journal, 4 (1981) 68-73.
[13] O.R. Herrero, "Closure of universal compression index equation", Journal of Geotechnical Engineering Division, 109 (1983) 755-761.
[14] J.E. Bowles, Physical and geotechnical properties of soils, McGraw-Hill Book Company Inc., New York, 1989.
[15] N. Abbasi, A.A. Javadi, R. Bahramloo, "Prediction of compression behaviour of normally consolidated fine-grained soils", World Applied Sciences Journal, 18 (2012) 6-14.
[16] Y. Nishida, "A brief note on compression index of soil", Journal of Soil Mechanics and Foundation Engineering, 82 (1956) 1-14.
[17] B.K. Hough, Basic soils engineering, 1 ed., The Ronald Press Company, New York, 1957.
[18] G.B. Sowers, Introductory soil mechanics and foundation, 3 ed., The Macmillan Company, London, 1970.
[19] J.H. Park, T. Koumoto, "New compression index equation", Journal of geotechnical and Geoenvironmental Engineering, 130 (2004) 223-226.
[20] C. Lee, S.-J. Hong, D. Kim, W. Lee, "Assessment of compression index of busan and incheon clays with sedimentation state", Marine

Georesources and Geotechnology, 33 (2012) 23-32.

[21] S.A. Berilgen, M.M. Berilgen, I.K. Ozaydin, "Compression and permeability relationships in high water content clays", Applied Clay Science, 31 (2006) 249-261.

[22] J.C. Liu, D. Znidarcic, "Modeling one-dimensional compression characteristics of soils", Journal of Geotechnical Engineering, 117 (1991) 162-169.

[23] S. Tripathy, A.K. Mishra, "On the use of skempton's compression index equation", Geotechnical and Geological Engineering, 29 (2011) 129-135.

[24] L. Handoko, A. Rifa'i, N. Yasufuku, R. Ishikura, Physical properties and mineral content of sidoarjo mud volcano, The 5th International Conference of Euro Asia Civil Engineering Forum (EACEF-5), Surabaya, 2015.

AN EXACT FINITE ELEMENT MODEL FOR AXIALLY LOADED PILE IN ELASTO-PLASTIC SOIL

C. Buachart[1], C. Hansapinyo[2], J. Tanun[3], N. Tanakhum[4], and W. Sommanawat[5]
[1,2,3,4] Faculty of Engineering, Chiang-Mai University, Thailand,
[5]Ubon Ratchathani Rajabhat University, Thailand

ABSTRACT

A displacement based finite element method for analyzing axially loaded pile embedded in finite depth of elasto-plastic soil is presented. The investigation herein is conducted on the condition of shape function by which exact value may be reproduced at the nodal point regarding to a few number of element. The examined shape functions which satisfy the homogeneous governing equations in elastic and plastic soil are introduced to obtain the so-celled exact element stiffness matrix via total potential energy principle. Numerical examples of elasto-static pile embedded in elasto-plastic Winkler foundation illustrates the accuracy of proposed element compare with conventional finite element shape functions. Axial force and displacement solutions show very good agreement with data from the available literature. Then the proposed shape functions are also used to conduct free vibration analysis of axially loaded pile embedded in elastic soil. The results from finite element modal analysis show fairly accurate compare with analytical solutions.

Keywords: Axially loaded pile, Displacement method, Finite element, Shape function, Soil-pile interaction

INTRODUCTION

Accuracy of a finite element solution depends significantly on the extent to which the assumed displacement pattern is able to reproduce the actual deformation of the structure. For a one-dimensional problem with single variable, Tong [1] proved that the finite element nodal solution can be obtained exactly if the assumed shape functions satisfy the homogeneous differential equation of the problem. Kanok-Nukulchai *et al.* [2] extended Tong's concept to one-dimensional problem with several dependent variables, i.e., authors developed an exact two-node deep beam element. Ma [3] also applied concept of nodal exact shape function to solved axial vibration problems of elastic bars, exact solution was obtained for undamped harmonic response analysis. Force-based formulation of pile-embedded in elastic soil was proposed in Reference [4] and obtained the exact solution for problem taken from Li *et al.* [5]. The displacement-based formulation was also proposed in Reference [6], the exact nodal-displacements and forces was obtained for elastic soil.

In this study, the nodal exact shape function concept suggested by Tong [1] and Buchart [6] is employed to solve the elastic bar embedded in elasto-plastic soil problem. Two sets of shape functions which satisfies the homogeneous differential equation will be derived for developing a present bar element. The stiffness matrix and nodal force vector are expressed based on total potential energy
principle. Example of elasto-static pile embedded in elasto-plastic soil is solved to verify the accuracy and efficiency of proposed bar element. Free vibration of a pile embedded in elastic soil foundation using the consistent mass matrix for this pile element is also investigated.

MATHEMATICAL FORMULATION

Problem Definition

The analysis considers a single circular pile, with diameter d (cross section $A = 0.25\pi d^2$ and perimeter $U = \pi d$), embedded into soil deposit (Fig. 1). The pile has a total length L and is subjected to an axial force P_0 at the pile head which is flush with the ground surface. The soil medium is assumed to be elastio-plastic, isotropic and homogeneous, with elastic properties described by equivalent spring coefficient k_s. Once the soil displacement go beyond the yielding displacement w_*, the shear resistance will keeps constant as long as the displacement increases. The soil bearing capacity at pile's end is presented by coefficient k_b. The pile is assumed to behave as an elastic column with Young's modulus E. The Poisson's ratio of the pile material is neglected. Figure 1(a) shows the elastic and plastic zone occurred in soil due to the axial displacement w_0 at top pile head is greater than yielding displacement w_* occurred at depth z_0 from pile head.

Hence, the length of an elastic portion in Fig. 1 is denoted by ℓ, the magnitude of axial displacement in elastic portion is less than or equal to yielding displacement.

Governing Differential Equations

Consider one-dimensional element in Fig. 2, the total potential energy of this soil-pile element subjected to the axial forces P_1 and P_2 is defined as

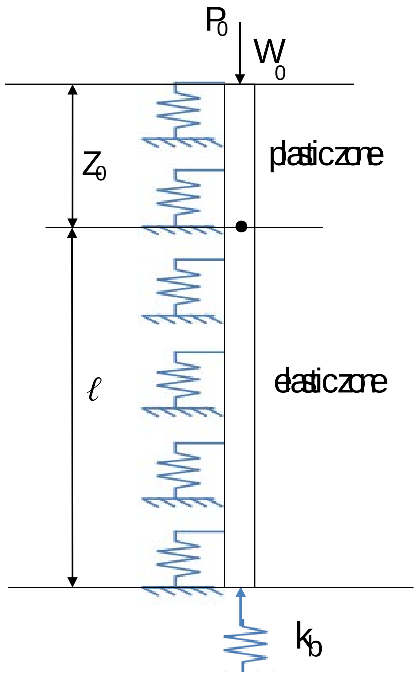

(a)

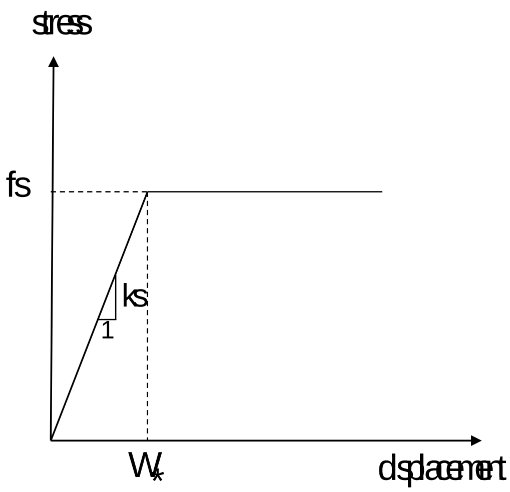

(b)

Fig. 1 Axially loaded pile and soil model

the sum of internal potential energy (strain energy) and the external potential energy due to external load as follow:

$$\Pi = \frac{1}{2}\left[EA\int_0^L \left(\frac{dw}{dz}\right)^2 dz + k_s U \int_0^L w^2 dz \right] - P_1 w_1 - P_2 w_2 \tag{1}$$

where $w(z)$ is the vertical pile displacement at depth z. The first and second terms in Eq. (1) represent the strain energy in pile and surrounding soil, respectively.

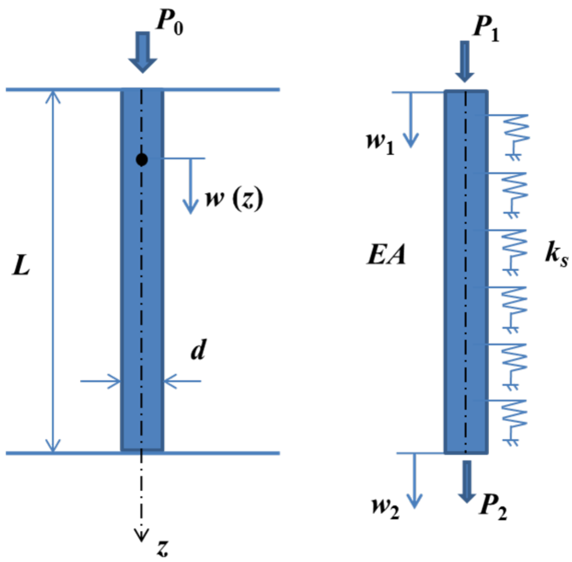

Fig. 2 Axially loaded pile embedded in soil and corresponded two-node finite element model.

The first variation of Eq. (1) leads to

$$\delta\Pi = EA\int_0^L \left(\frac{d\delta w}{dz}\right)\left(\frac{dw}{dz}\right) dz + k_s U \int_0^L (\delta w) w dz - P_1 \delta w_1 - P_2 \delta w_2 \tag{2}$$

Applying the appropriate Gauss-Green theorem to Eq. (2) and setting $\delta\Pi = 0$, gives the differential equation for equilibrium

$$-EA\frac{d^2 w}{dz^2} + k_s U w = 0 \quad \text{for} \quad 0 < z < L \tag{3}$$

and a set of natural boundary conditions as follows

$$P_1 = -EA\left.\frac{dw}{dz}\right|_{z=0} \text{ and } P_2 = EA\left.\frac{dw}{dz}\right|_{z=L}$$
(4)

Shape Functions for An Exact Pile Element

Following the concept presented by [1] and [2], a pile element is developed with the shape functions that satisfy the homogeneous differential equation, Eq. (3). Two groups of shape functions are derived following elastic and plastic soil conditions.

Elastic soil conditions

The field variable *w*, which satisfy Eq. (3), can be represented by the following hyperbolic function

$$w(z) = c_1 \cosh(\alpha z) + c_2 \sinh(\alpha z) \quad (5)$$

where $\alpha^2 = k_s U/EA$ is the characteristic parameter of pile. By applying the nodal displacement boundary conditions to elastic soil portion (Fig. 1), Eq. (5) can now be expressed in terms of nodal variables, w_1 and w_2, as follows

$$w(z) = w_1 N_1(z) + w_2 N_2(z) \quad (6)$$

where the shape functions can be expressed as

$$N_1(z) = \frac{\sinh[\alpha(\ell - z)]}{\sinh\beta} \quad (7)$$

$$N_2(z) = \frac{\sinh(\alpha z)}{\sinh\beta} \quad (8)$$

with the non-dimensional parameter $\beta = \alpha\,\ell$.

Plastic soil conditions

Consider the plastic soil portion, upper portion in Fig. 1, displacement *w* in second term of equilibrium equation (3) have to be replaced by yielding displacement w_* as follow

$$-EA\frac{d^2w}{dz^2} + k_s U w_* = 0 \text{ for } 0 < z < z_0$$
(9)

The field variable *w*, which satisfy homogeneous differential equation part of Eq. (9), can be represented by linear function of soil depth. Hence, displacement shape function of plastic portion can be expressed as a ramp function used in typical linear FEM, *i.e.*

$$N_1(z) = \frac{(z_0 - z)}{z_0} \quad (10)$$

$$N_2(z) = \frac{z}{z_0} \quad (11)$$

Derivation of Element Stiffness Matrices

Refer to first variation of strain energy terms in Eq. (2), due to the arbitrariness of δw (see also [7]), the element stiffness matrix for pile and soil can be expressed as follows:

$$K_{ij}^{pile} = EA\int_0^L \left(\frac{dN_i}{dz}\right)\left(\frac{dN_j}{dz}\right)dz \quad (12)$$

$$K_{ij}^{soil} = k_s U\int_0^L N_i N_j dz \quad (13)$$

where the indices *i* and *j* are ranged from 1 to 2.

Element stiffness for an elastic soil portion

Substituting shape functions from Eq. (7) and (8) into element stiffness formulation in Eq. (12) and (13), the component of element stiffness matrices for elastic soil portion can be explicitly expressed as

$$\begin{aligned} K_{11}^{pile} = K_{22}^{pile} &= \frac{\alpha EA}{2}\left(\beta \operatorname{csch}^2\beta + \coth\beta\right) \\ K_{12}^{pile} = K_{21}^{pile} &= -\frac{\alpha EA}{2}\operatorname{csch}\beta\left(1 + \beta\coth\beta\right) \end{aligned} \quad (14)$$

and

$$\begin{aligned} K_{11}^{soil} = K_{22}^{soil} &= \frac{k_s U}{2\alpha}\left(\coth\beta - \beta\operatorname{csch}^2\beta\right) \\ K_{12}^{soil} = K_{21}^{soil} &= -\frac{k_s U}{2\alpha}\operatorname{csch}\beta\left(1 - \beta\coth\beta\right) \end{aligned} \quad (15)$$

Element stiffness for plastic soil portion

Substituting shape functions from Eq. (10) and (11) into element stiffness formulation in Eq. (12) and (13), the component of element stiffness matrices for plastic soil portion can be explicitly expressed as

$$K_{11}^{pile} = K_{22}^{pile} = -K_{12}^{pile} = -K_{21}^{pile} = \frac{EA}{z_0}$$
(16)

and

$$K_{11}^{soil} = K_{22}^{soil} = 2K_{12}^{soil} = 2K_{21}^{soil} = \frac{k_s U z_0}{3} \qquad (17)$$

Consistent Mass Matrix

In free vibration analysis, the consistent mass matrix has to be constructed. Formula of consistent mass matrix is similar with soil stiffness matrix in Eq. (15) or (17), except the factor $k_s U$ replaced by ρA, *i.e.*

$$M_{ij} = \rho A \int_0^L N_i N_j dz \qquad (18)$$

where ρ = mass density of pile material. An explicit expression of this consistent mass matrix will be omitted for the sake of simplicity and clarity of the presentation.

NUMERICAL EXAMPLES

In this section, two numerical examples are presented to illustrate the effectiveness of the finite element proposed in the previous section. Application of this pile element to the free vibration analysis is also demonstrated by the second example. Analytical solutions of all problem tests are available in the literatures [6, 8, 9, and 10].

Static Analysis

A bored pile was installed in the medium silt clay and the end bearing layer is sandstone. The pile length is 45 m, and the diameter d = 1 m. The elastic modulus of pile shaft $E = 2.2 \times 10^7$ kPa. From soil tests, the values of equivalent soil elastic coefficient k_s = 12000 kPa/m, the yielding displacement of soil w_* = 2.6 mm, and end bearing stiffness k_b = 684000 kPa/m [8]. The value $k_b A$ is added into the last diagonal member of stiffness matrix.

The numerical test was performed using two element assembly to construct three algebraic equations. Assuming the value of plastic depth z_0, the displacement at bottom end was solved from third row of algebraic equation. Then, the displacement at pile head w_0 was obtained from second row of algebraic equation, and the value of load P_0 at pile head was computed. Two cases were run to compare the results: (i) proposed stiffness, Eqs. (14) and (15) were used to constructed element stiffness of bottom part, and Eqs. (16) and (17) for upper part, and (ii) two conventional linear elements [7] were used to constructed the global stiffness matrix.

The results from two cases are shown in Table 1. As expect, the present pile element model prove to be flawless: finite element solutions of proposed element are identical to the exact analytical solutions in reference [8]. The conventional linear element behaves stiffer than proposed element and exact solutions, greater pile head load is required to obtain yield displacement at pile head.

Table 1 Calculated loads and settlement of the pile at any values of plastic depth.

z_0 (m)	Present (Exact) P_0 (kN)	Present (Exact) w_0 (mm)	Linear FEM P_0 (kN)	Linear FEM w_0 (mm)
0	2086	2.60	2451	2.60
9	2951	3.91	3192	4.03
18	3796	5.64	3931	5.78
27	4593	7.71	4648	7.80
36	5291	9.95	5302	9.97
45	5807	11.98	5807	11.98

Free Vibration Analysis

Natural frequencies and mode shapes of a fixed-ended pile is computed with ten pile elements. A bored pile was installed in the medium clay of length 50 m and diameter d = 1 m. Equivalent soil elastic coefficient k_s = 34200 kPa/m. The end bearing stiffness is very large (fixed at the bottom). The unit mass is of pile shaft is taken as ρ = 2400 kg/m^3. To perform modal analysis, element stiffness and consistent mass matrices of proposed element and linear conventional element are constructed with assumed elastic soil condition. Result of the natural frequencies, compared with the exact theory [10] is shown in Table 2. Percent error of natural frequencies, which are obtained from conventional linear element are slightly better than present element. The first three mode shapes of proposed element are also plotted in Fig. 3 and appear to be almost indifferent from the exact ones.

Table 2 Circular frequency of fixed-ended pile

Mode	Circular Frequency (rad/sec) Ten piles (Present)	Ten piles (Linear)	Exact Theory
1	153	153	153
2	313	312	309
3	504	502	490
4	712	710	676
5	938	935	864
6	1184	1181	1053
7	1446	1443	1242
8	1711	1708	1432

9	1943	1940	1621
10	2084	2082	1811

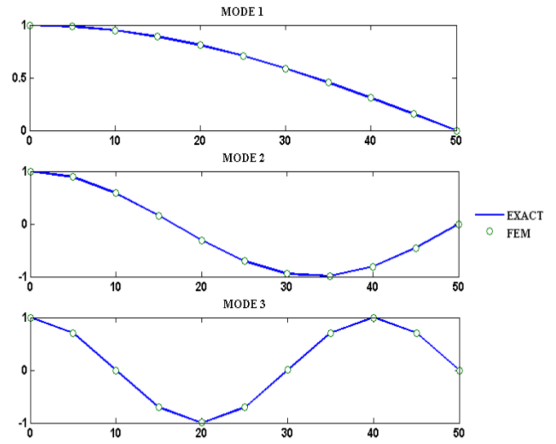

Fig. 3 Fixed tip pile problem: the first three mode shapes from the free vibration analysis of a ten-element model.

CONCLUSIONS

The new finite element model for pile subjected to axial load is proposed. A necessary condition for the present finite element model to reproduce the exact values at the nodal points is that it has to satisfy the homogeneous differential equation of the problem. Numerical example for static load pile embedded in elasto-plastic soil indicates that an exact finite element solution can be obtained even with minimum number of element used. In addition, the same shape functions can produce fairy satisfactory results in free vibration problem on three fundamental modes.

REFERENCES

[1] Tong P, "Exact solutions of certain problems by finite element method", AIAA J., Vol. 7, 1969, pp. 178-180.
[2] Kanok-Nukulchai W, Dayawansa PH, and Karasudhi P, "An exact finite element model for deep beams", Int. J. of Struc, Vol. 1, Jan. 1981, pp. 1-7.
[3] Ma H, "Exact solutions of axial vibration problems of elastic bars", Int. J. Numer. Meth. Eng., Vol. 75, 2008, pp. 241-252.
[4] Sae-Long W, Limkatanyu S, Prechasaree W, Damrongwiriyanupap N, and Kuntiyawichai K, "Natural stiffness matrix for bar with lateral interfaces: exact force-based derivation", in Proc. 18th Conf. on NCCE, 2013, pp. 110-116.
[5] Li JP, Tan YW and Liang FY, "A modified analysis method for the nonlinear load transfer behavior of axially loaded piles", KSCE J. Civ. Eng., Vol. 16(3), 2012, pp. 325-333.
[6] Buachart C, Hansapinyo C, and Sommanawat W, "An exact finite element model for axially loaded pile", in Proc. 1st Int. Conf. on ACESD, 2014, pp. 483-486.
[7] Zienkiewicz OC and Taylor RL, The Finite Element Method. Vol. I. Oxford: Butterworth-Heinemann, 2000.
[8] Chou YC and Hsiung YM, "A normalized equation of axially loaded piles in elasto-plastic soil", J. Geo Eng., Vol. 4(1), 2009, pp. 1-7.
[9] Timoshenko SP, Young Zina D H, and Weaver WL, Vibration Problems in Engineering, USA: John Wiley & Sons, 1974.
[10] Wu WB, Wang KH, Ma SJ, and Chin JL, "Longitudinal dynamic response of pile in layered soil based on virtual soil pile model", J. Cent. South Univ. T., Vol. 19, 2012. pp. 1999-2007.

APPENDIX

Exact Solution of Pile Static Load Test

Prescribe the boundary conditions (4) into the solution of governing equations (3) and (9). The load applied to the pile top could be expressed as

$$P_0 = w_* \left[\alpha EA \tanh\left(\alpha \ell + \gamma\right) + z_0 k_s U \right] \tag{19}$$

and the displacement at the pile top is therefore

$$\begin{aligned} w_0 = w_* + \frac{1}{2} w_* \left[\tanh\left(\alpha\ell + \gamma\right) + \frac{z_0 k_s U}{\alpha EA} \right]^2 \\ - \frac{1}{2} w_* \tanh^2\left(\alpha\ell + \gamma\right) \end{aligned} \tag{20}$$

The variable γ is the characteristic value of the end bearing capacity of soil at pile tip.

$$\tanh\left(\gamma\right) = \frac{k_b}{\alpha E} \tag{21}$$

In derivation of Eqs. (19) and (20), the soil of end bearing capacity is assumed in the elastic condition. Detail derivation of Eqs. (19)–(21) are described in reference [8].

Free Vibration of Fixed-Ended Pile

The governing equation for free vibration of pile is expressed as

$$-EA\frac{\partial^2 w}{\partial z^2}+k_s U w=\rho A\frac{\partial^2 w}{\partial t^2},\ 0<z<L \tag{22}$$

Assume that pile subjected to fixed boundary condition at the pile tip w = 0 at z = L. Natural circular frequency ω and mode shape ψ of pile embedded in soil can be expressed as

$$\psi_n=\cos\left(\lambda_n z\right);\ n=1,2,3,... \tag{23}$$

and

$$\omega_n=\sqrt{\frac{\left(\lambda_n^2+\alpha^2\right)E}{\rho}};\ n=1,2,3,... \tag{24}$$

where the wave number parameters λ_n are defined as

$$\lambda_n=\left(n-\frac{1}{2}\right)\frac{\pi}{L};\ n=1,2,3,... \tag{25}$$

Note that Eq. (23) always satisfies boundary condition at pile tip, *i.e.* ψ_n (L) always equal to zero.

Fifth International Conference on Geotechnique, Construction Materials and Environment, Osaka, Japan, Nov. 16-18, 2015, ISBN: 978-4-9905958-4-5 C3051

LIQUEFACTION ASSESSMENT BY MICROTREMOR MEASUREMENTS IN BABOL CITY

Asskar Janalizadeh Choobbasti[1], Sadegh Rezaei[2] and Mehran Naghizadeh[3]
[1,2] Civil Engineering, Babol university of technology, Iran; [3] Civil Engineering, IAU Zanjan branch, Iran

ABSTRACT

The recent researchers have discovered microtremor applications for evaluation of the liquefaction potential. Microtremor measurement is a fast, applicable and cost-effective method with extensive applications. In the present research the liquefaction potential has been reviewed by utilization of microtremor measurement results in Babol city. By using the fundamental frequency and amplification factor, the value of vulnerability index (K_g) was calculated and the liquefaction potential has been evaluated. For controlling the accuracy of this method, its output has compared with the results of Seed and Idriss method in 30 excavated boreholes within the study area. These two methods show an acceptable conformity with each other. Also, the artificial neural network (ANN) with different inputs was trained. Regarding the results of the three methods, we can conclude the threshold value of liquefaction potential is K_g=5. By reviewing and comparing these three methods, it will be observed that microtremors have the capability of assessing the liquefaction potential with desirable accuracy.

Keywords: Liquefaction, Microtremor, Vulnerability index, Artificial neural networks, Microzonation

INTRODUCTION

Earthquake is one of the most devastating natural disasters which has always threatens human lives and properties. The most important effects caused by an earthquake are the liquefaction phenomena. Investigations of failures of soil masses are subjects touching both geology and engineering.

On the basis of both the field and the laboratory types of observations of soil behavior attempts were made to propose methods to evaluate the liquefaction potential of a particular soil. In the literature, several simplified methods can be found to assess nonlinear liquefaction potential of soil. Derived from several field and laboratory tests, various procedures, also named as conventional methods, have been developed by utilizing case studies and undisturbed soil samples [1].

Recently, the H/V technique [2] is becoming more popular with its data collection facilities and application allowance in all areas. By employing the H/V ratio, we were able to determine the predominant frequency (F_p) and the amplification factor (A_p) of the site. Nakamura [3] also proposed the vulnerability index “K_g value” as a means to determine the extent of liquefaction. The present study mainly aims to show how the microtremor measurements can play a significant role in a liquefaction assessment [4].

Microtremor measurement was undertaken at 60 stations in the Babol, north of Iran, during 2011 and 2012. The study was conducted in Babol city for one important reason: the city is densely populated with critical buildings and infrastructures and it is built upon the recent, loose, and therefore, generally liquefaction-prone sediments of the Babolrood River. With rwgards Nakamura’s method, H/V spectral ratios, fundamental frequency and amplification factor and finally vulnerability index (K_g) were calculated for all microtremor stations.

There are geotechnical boreholes near 30 microtremor recording stations with suitable data. The Seed and Idriss method is used to assess the liquefaction potential [5].

The goal of the aim activities includes the assessment of liquefaction by a new, fast and applicable method in other stations and preparation of Babol city’s liquefaction map.

METHODOLGY

Ambient seismic noise or microtremors are feeble ground motions with displacement amplitudes of about 0.1–1 μm and that can be detected by seismograph with high magnification [6]. Recently, to assess potential hazards associated with ground failure or liquefaction, the vulnerability index (or K_g value) that is derived from microtremor data may be evaluated. Among the various approaches to microtremor study, the H/V spectral ratio technique introduced by Nakamura (1989) was chosen for this investigation due to ease of application. This technique has been described in a number of papers.

By employing the H/V ratio, we were able to determine the predominant frequency (F_p) and the amplification factor (A_p) of the site. Nakamura also proposed the vulnerability index "K_g value" as a means to determine the extent of liquefaction [3]. For this purpose, he compared the results of vulnerability index and the damage points in the Kobe earthquake and concluded that K_g is a suitable index for determining the site vulnerable points, such that each point with higher K_g value is more damage potential. The K_g value is simply derived from strain of ground structures. It can be defined as:

$$K_g = \frac{A_p^2}{F_p} \tag{1}$$

After Nakamura some scientist have used microtremor to liquefaction evaluation [7]-[9].

DATA COLLECTION AND RESULTS

Microtemor measurements were carried out at 60 stations in Babol during the period 2011 and 2012.

Fig. 1 shows the H/V spectral ratio for some stations. According to the analysis, the fundamental frequency (F_p) varies from 0.69 to 12.60 Hz within the study area. Also, the amplification factor (A_p) varies from 1.45 to 4 within the study area. Fig. 2 and fig. 3 show the fundamental frequency and amplification factor in the study area, respectively. As it can be observed in the fig. 2 and fig. 3 for ten recording stations, fundamental frequency and amplification factor have not presented. Since these stations have been surrounded by the factories and highways in the city, accurate microtremor recording was impossible all day long [10], [11].

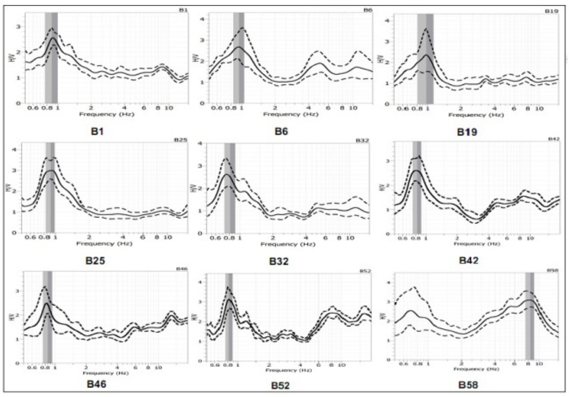

Fig. 1 H/V spectral ratio

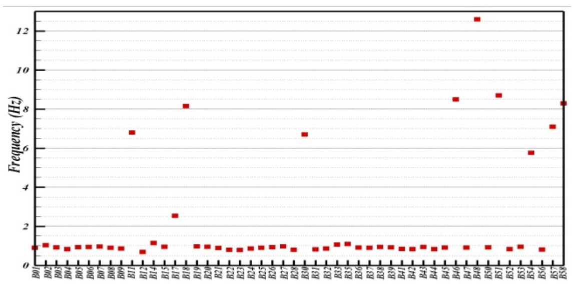

Fig. 2 Fundamental frequency

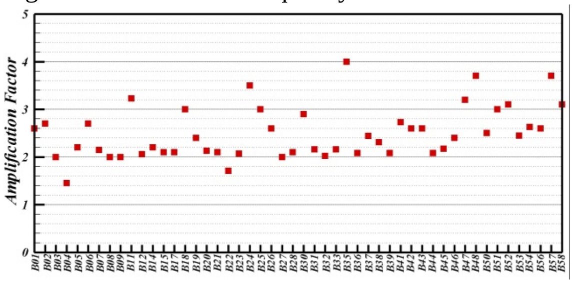

Fig. 3 Amplification factor

By using the results of figures 2 and 3, the K_g values are calculated for different stations. These results are indicated in fig. 4. By reviewing the scientific literature, it has been concluded that the higher K_g value, the more liquefaction potential will be. In fact K_g value has a qualitative meaning, for instance the possibility of liquefaction occurrence is more in recording station 35 than recording station 25.

In the next sections, firstly, the possibility of liquefaction occurrence will be evaluated by using the data of 30 geotechnical boreholes and the Seed and Idriss (1985) method. Secondly, the ANN with different inputs including type of soil, total stress, effective stress and corrected SPT blow count was trained. Subsequently, by comparing the stations in which liquefaction has occurred (using Seed and Idriss (1985) and ANN) and the values obtained from microtermor measurement, it was possible to obtain a precise value for K_g which is the threshold value for liquefaction occurrence.

ASSESSMENT AND COMPARISON OF LIQUEFACTION POTENTIAL BY USING CONVENTIONAL METHOD

Simplified procedures, originally proposed by Seed and Idriss [5], using the standard penetration test (SPT), are frequently used to evaluate the liquefaction potential of soils. This procedure has been revised and updated since its original development [12]. The method was developed from field liquefaction performance cases at sites that had been characterized with in situ standard penetration tests. Using a deterministic method, liquefaction of soil is predicted to occur if the factor of safety (FS) which is the ratio of the cyclic resistance ratio (CRR) over cyclic stress ratio (CSR), is less than or equal to one. No soil liquefaction is predicted if FS > 1 [12].

By using the 30 geotechnical boreholes in the region, we can assess the liquefaction potential in Babol city. The results of this assessment in 4 boreholes have been shown in fig. 5. In these 30 boreholes we compare the two methods of conventional and microtremor and by analyzing the results it is possible to obtain a precise value for K_g which is the threshold value for liquefaction occurrence. Table 1 shows the depths of evaluated liquefaction using conventional method against the K_g value. By reviewing table 1, it is observed that in all the stations with K_g values higher than 5, liquefaction phenomena occurred. Consequently the value of K_g=5 can be considered as a threshold value for these 30 stations, in that for all the stations of this region with K_g value higher than 5, the occurrence of liquefaction phenomena is possible and for stations with lesser values, this possibility does not exist.

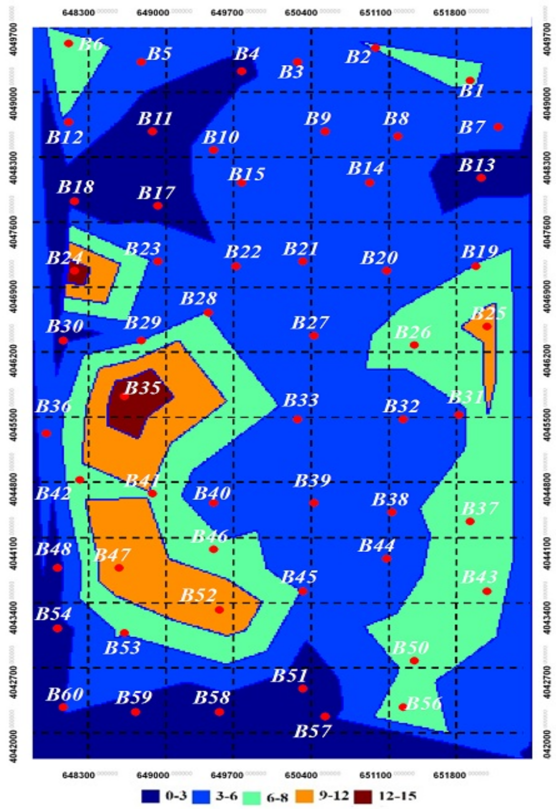

Fig. 4 map of K_g distribution in Babol city

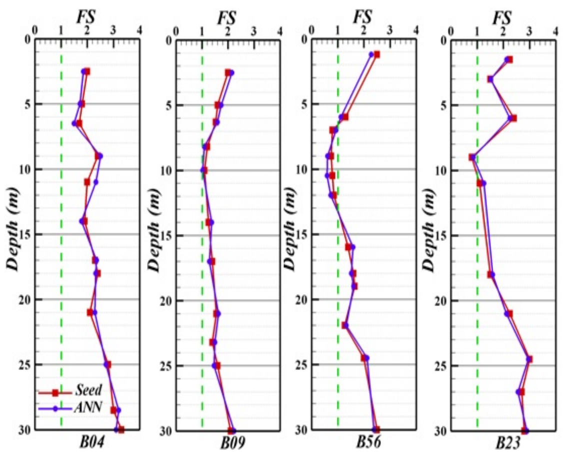

Fig. 5 Evaluation of factor of safety using conventional and ANN method

In the next section, we assess the potential of liquefaction using ANN method and the results will be compared with the results of microtremor measurement to be able to prepare the liquefaction microzonation map of Babol city.

Table 1 The liquefaction depths versus K_g value

Station	Liquefaction depths by using Seed & Idriss method (m)	K_g Value
B01	2-4.5 & 5.5-8 & 8.5-10.5	7.51
B02	5-10	7.01
B04	-	2.53
B05	5.5-7	5.21
B07	-	4.80
B09	-	4.63
B11	-	1.53
B12	5-6.5 & 8-9.5	6.15
B15	-	4.63
B18	-	1.10
B19	6-7 & 9-10	5.93
B22	-	3.65
B23	8.5-10.5	5.42
B25	3-5 & 5.5-8 & 8.5-10.5	10
B27	-	4.12
B28	5.5-8	5.51
B30	-	1.25
B32	-	4.74
B35	3-6 & 6.5-10.5	14.6
B37	6.5-9.5	6.61
B39	-	4.7
B42	5-12	8.14
B43	4.5-7 & 8-10	7.19
B44	7-8	5.2
B45	4-6.5	5.17
B50	4-6 & 7-8 & 8.5-9.5	6.79
B52	3.5-5 & 6.5-10.5	11.57
B56	6.5-11	8.34
B57	-	1.92
B58	-	1.16

ASSESSMENT AND COMPARISON OF LIQUEFACTION POTENTIAL BY USING ANN

Today, the application of artificial neural networks in the engineering world is well known to engineering sciences [13]. Considering that ANN can assess liquefaction potential in this precise manner, we will assess the liquefaction phenomena by this method in the 20 remaining stations and the results will be compared with the microtremor measurement result.

The input–output data pairs used in the present work consist of four input variables, including soil type, total stress, effective stress, corrected SPT blow count and one output factor of safety. Before using the training procedure the data were normalized to their mean value and standard deviation 1. A training set of 23 out of 30 input–output data pairs is used to train the MLP-type neural network with only one hidden layer based on BP algorithm. At the end of the training process, it is necessary to evaluate the capability of ANN model in prediction of liquefaction potential. The remaining 7 data pairs are used to test the network performance. Since there are four input variables the network has four neurons in the input layer and one neuron in the output layer. Hence there is no specific method to determine the number of neurons in the hidden layer, Trial and error was used. Fig. 6 depicts the effect of different neural network architecture (different number of neurons in the hidden layer) on the RMS error of the network obtained from the normalized data. As can be seen a network with 15 neurons in the hidden layer has an acceptable performance.

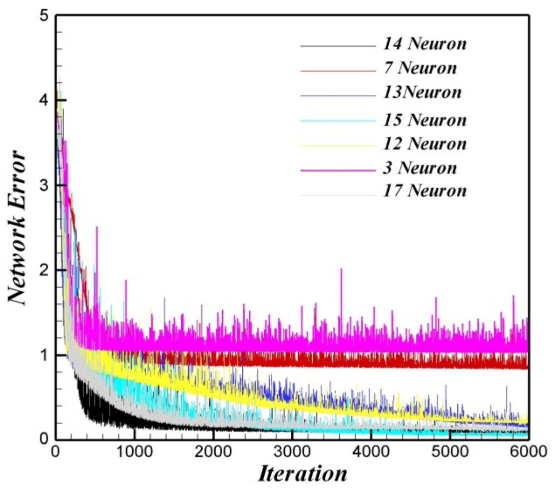

Fig. 6 Effects of the number of hidden neurons on the network performance

The excellent behavior of the MLP-type neural network is also shown in Fig. 5. The figure reveals that the trained network is able to model and predict the outputs successfully. It is evident from test data sets that the experimental ANN can be applied successfully to predict liquefaction potential.

Fig.7 shows the liquefaction microzonation by using microtremor measurements and fig.8 indicates the liquefaction microzonation by the ANN. In these two figures, the areas shown in red include the zones with liquefaction potential. By comparing the two methods, it is concluded that they have very good conformity with each other. Only in 4 stations of B32, B36, B44 and B45, the results are different. The K_g value in these stations is close to 5 which is considered the threshold value for liquefaction phenomena. The value of K_g at these stations changes with a minor change in the fundamental frequency and amplification factor. Also, we used the ANN for comparing the two methods which have a small error in prediction. For this reason, the mentioned minor difference is not taken into consideration and the value of K_g=5 is introduced as a threshold value, such that soils with higher K_g values will have liquefaction potential.

From these results, it is reasonable to conclude that K_g is clearly a value which corresponds to the site and can be considered as vulnerability index of that site, an indicator which might be useful in selecting weak points of ground especially in liquefied areas.

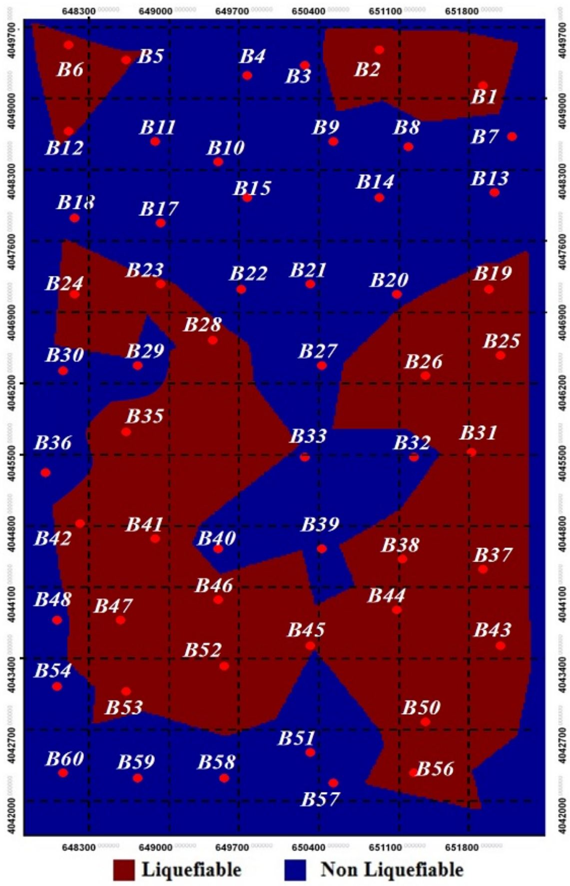

Fig. 7 Liquefaction microzonation of Babol by microtremor measurement

CONCLUSION

In the present research, the microtremor measurements were used in 60 stations in order to evaluate the liquefaction potential.

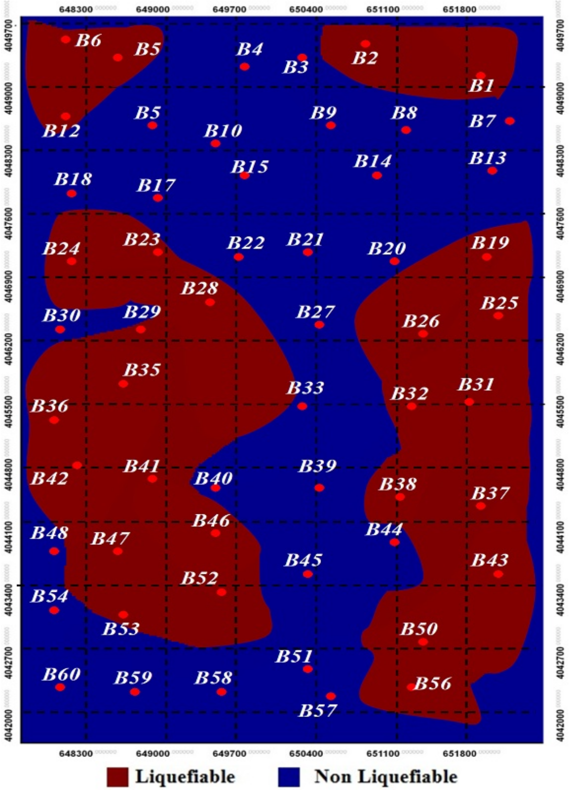

Fig. 8 Liquefaction microzonation of Babol by ANN

By using the fundamental frequency and amplification factor, the value of vulnerability index (K_g) was calculated. To obtain a precise value for K_g which is the threshold value such that at higher values, the liquefaction potential exists, the microtremor results have been compared with the conventional method results. By comparing these results, it is concluded that in Babol city, the stations with K_g values higher than 5, have the liquefaction potential. Subsequently, in order to assess the liquefaction potential, the ANN was utilized in the remaining stations. By comparing the ANN and microtremor results, it was observed that the results are in good conformity with each other and except for 4 stations, the liquefaction phenomena has occurred in all those other stations where their K_g values were higher than 5. With regards the results of the three methods, we can conclude the threshold value of liquefaction potential is K_g=5. Furtheremore, we prepared two maps for liquefaction microzonation by using the microtremor and ANN results. Finally, it can be stated that microtremor measurements are considered suitable and complementary method among conventional methods for reviewing the liquefaction potential which is fast, applicable and cost-effective.

REFERENCES

[1] Saygili G, "Liquefaction potential assessment in soil deposits using artificial neural network", M.Sc. Thesis, Concordia University, 2005.

[2] Nakamura Y, "A method for dynamic characteristics estimation of subsurface using microtremor on the ground surface". Quarterly Report of RTRI, Vol. 30, 1989, pp. 25–33.

[3] Nakamura Y, "Real-time information systems for hazard mitigation", 10th World Conference in Earthquake Engineering, Spain, Madrid, 1996.

[4] Huang HC, Tseng YS, "Characteristics of soil liquefaction using H/V of microtremors in Yuan-Lin area, Taiwan", TAO, Vol. 13(3), 2002, pp. 325–338.

[5] Seed HB, Idriss IM, "Simplified procedure for evaluating soil liquefaction potential", J Soil Mech Found Div SM, Vol. 9, 1971, pp.1249–1273.

[6] Dikmen U, Mizaoglu M, "The sesimic microzonation map of Yenisehir-Bursa, NW of Turket by means of ambient noise measurements", J Balkan Geoph Soc, Vol. 8, 2005, pp.53–62.

[7] Rezaei S, Choobbasti AJ, "Liquefaction assessment using microtremor measurement, conventional method and artificial neural network (Case study: Babol, Iran)", Frontiers of structural and civil engineering, 2014, DOI 10.1007/s11709-014-0256-8

[8] Uehan F, Nakamura Y, "Ground motion characteristics around Kobe City detected by microtremor measurement",11th World Conference on Earthquake Engineering, Acapulco, Mexico,1996.

[9] Saita J, Nakamura Y, Sato T, "Liquefaction caused by the 2011 off the Pacific coast of Tohoku earthquake and the result of the prior microtremor measurement", 9th International Conference on urban earthquake engineering, Tokyo, Japan, 2012.

[10] Choobbasti AJ, Rezaei S, Farrokhzad F, "Evaluation of site response characteristics using microtremors", Gradevinar, 65, 2013, pp.731-741.

[11] Choobbasti AJ, Rezaei S, Farrokhzad F, Heidarzadeh Azar P, "Evaluation of site response characteristics using nonlinear method (Case study: Babol, Iran)", Frontiers of structural and civil engineering, 2014, DOI 10.1007/s11709-014-0231-4

[12] Seed HB, Tokimatsu K, Harder LF, Chung RM, "Influence of SPT procedures in soil liquefaction resistance evaluations", J Geotech Eng ,Vol. (12), 1985, 1425–1445.

[13] Rezaei S, Choobbasti AJ, Soleimani Kutanaei S, "Site effect assessment using microtremor measurement, equivalent linear method and artificial neural network (Case study: Babol, Iran)", Arabian Journal of Geosciences, 2013, DOI: 10.1007/s12517-013-1201-1

Fifth International Conference on Geotechnique, Construction Materials and Environment, Osaka, Japan, Nov. 16-18, 2015, ISBN: 978-4-9905958-4-5 C3051

STUDIES ON CYCLIC LOADING OF RECYCLED CONCRETE AGGREGATE WITH ADDITION OF RUBBER CHIPS

Wojciech Sas, Andrzej Głuchowski Alojzy Szymański
[1]Facultyof Civil and Environmental Engineering, Warsaw University of Life Sciences, Poland

ABSTRACT

In this paper, tests on the reclaimed waste, Recycled Concrete Aggregate (RCA) was presented. Reclaimed concrete is still a problem which were solved usually by storing concrete debris on landfills. One of ideas to solve this issue in another manner was the introduction of recycled materials to pavement engineering. Geotechnical study was undertaken to obtain physical and mechanical properties of RCA improved with rubber grains. Such mix, could behave more elastic strain development during load cycles, typical for traffic.

For better understanding of its exceptional behavior under repeated loading, cyclic CBR test was conducted in various stages of loading. For the purpose of bearing capacity analysis, uniaxial test was also conducted. While the cyclic loading and a mechanical stabilization are a cause of aggregates crushing, created another particle size distribution, could not fulfill quality requirements. Determination of resilient modulus M_r from repeated loading test and development of strains during the tests was also presented. The paper also includes an proposition of possible guideline of RCA mix as a material in pavement subbase construction.

Keywords: Cyclic loading, cCBR, rubber chips, recycled concrete aggregate

INTRODUCTION

Developing of car industry results in increase of cars. One of wastes which are produced by the time of car exploitation and after vehicle utilization is rubber tires. Among many geo-engineering methods of recycling including rubber retaining walls, so-called rubber chips and tire shreds are one of possible ways of renew this source [1]. Intensive studies to find possible application when rubber chips (RC) is mixed with natural aggregates has been conducted lately. Takano et al. [1] tested shear behavior of RC and silica sand mix using micro focus X-ray CT scanner. Results of this tests was that under direct shear, mix of sand and RC, shear stress rises monotonically and no peak stress is observed. Also dilatancy effect was smaller when comparing to pure sand. Interesting is fact that RC additions can decrease shear strain propagation. This fact is important for road engineering where shear stress is cause of many construction damages. Also mix of gravel, fly ash and waste fibers was studied by [2]. Series of CBR tests and direct shear tests have shown increase of CBR characteristics, optimal addition of waste tyre rubber is equal from 0.2 to 2.0% of dry unit weight of soil. [3], used shredded rubber from waste to reinforcement and cement as a binding medium to soft clay with different percentages of rubber content. Series of CBR and unconfined compressive strength tests have shown improve of bearing capacity, strength and high compressibility of the material.

Recycled Concrete Aggregate (RCA) is an anthropogenic material which is a product from demolition of exploited constructions. Conducted researches on RCA recycling has lead to form many possible ways of application in bound and unbound form. Important fact is that for sustainable development of resources, non-renewable resources as sand, gravel etc. should be replaced by renewable resources as RCA [4]. Application of renewable materials can reduced green-house gas emission simply by avoiding of mining process [5].

Cyclic loading is phenomena which can be observed in many constructions. Characterization of the material subjected to repeated loading is desired mostly by road engineers and foundation engineers when industrial settlement is constructed. New area of utilization of this problem is wind plants foundation engineering where wind caused movement of the center of gravity and creates cyclically changed stresses over subgrade soils [6]

On order to understand cyclic loading phenomena for each material proper tests must be conducted. Most common method to obtain such data is to perform cyclic triaxial tests. this tests unfortunately are expensive and not widespread especially in road laboratories.

In previous article [7] authors presents a new method of dealing with cyclic loading phenomena. The cCBR method was presented as a equivalent of standard cyclic triaxial tests. The cCBR method have many advantages, it is low cost due to common standard of CBR tests, no new equipment is needed. Procedure of the cCBR test is based on the CBR method. Experienced laboratory crew can easily perform this tests.

The purpose of performing cCBR test is to find key factor which characterizes cyclic loading - resilient modulus M_r.

Resilient modulus is characteristic value of cyclic loading where resilient strain is taken to consideration as design factor. The M_r value is calculated as follows:

$$\boldsymbol{M_r} = \frac{\Delta\sigma_d}{\Delta\varepsilon_r} \quad (1)$$

where, $\boldsymbol{\Delta\sigma_d}$ is deviator stress pulse $\Delta\boldsymbol{\sigma_d} = \Delta\boldsymbol{\sigma_1} - \Delta\boldsymbol{\sigma_3}$, $\boldsymbol{\sigma_1}$ is major principal stress, $\boldsymbol{\sigma_3} = \boldsymbol{\sigma_2}$ is minor principal stress, and $\boldsymbol{\Delta\varepsilon_r}$ is resilient strain over deviator pulse $\boldsymbol{\Delta\sigma_d}$ [8].

2. MATERIAL AND METHODS

2.1 Material

Material for tests was obtained from demolished concrete from building demolition site. Concrete aggregates were an element of construction, whose strength class was estimated from C16/20 to C30/35. Aggregates were in 100% composed from broken cement concrete. Grain gradation curve was adopted according to EN ISO 14688: 2a [9] and placed between upper and lower grain gradation limits.

For estimation of physical properties, a series of tests was conducted. The sieve analysis led to classifying this material as sandy gravel (saGr), in reference to [9, 10]. Test results are shown in Figure 1. This distribution of particles from 12.0mm to 0.063mm is typical for soils used for sub-base and support another structures.

The Proctor test results are presented in Figure 2. The test procedure involved compaction in the Proctor mold, whose volume equaled 2.2dm^3, by using standard energy of compaction, equal 0.59J/cm^3. Optimum moisture content for sandy gravel was m_{opt} = 9.54% and maximum dry density of optimum moisture content was 1.97g/cm^3. For RCA with 0.5% RC addition, m_{opt} = 8.47% and ρ_{max}= 1.94 g/cm^3. for RCA with 1% RC addition, m_{opt} = 8.02% and ρ_{max}= 1.91 g/cm^3. Addition of RC caused decrease of ρ_{max} and corresponded m_{opt}. This phenomena is caused, by smaller than RCA, RC density. Decease of the moisture content seems to prove that much of water fill inner pores due to grater capillary forces than in open pores [11].

2.2 Methods

After the optimum moisture content has been estimated, the cCBR tests on samples with 0, 0.5 and 1% RC content were performed.

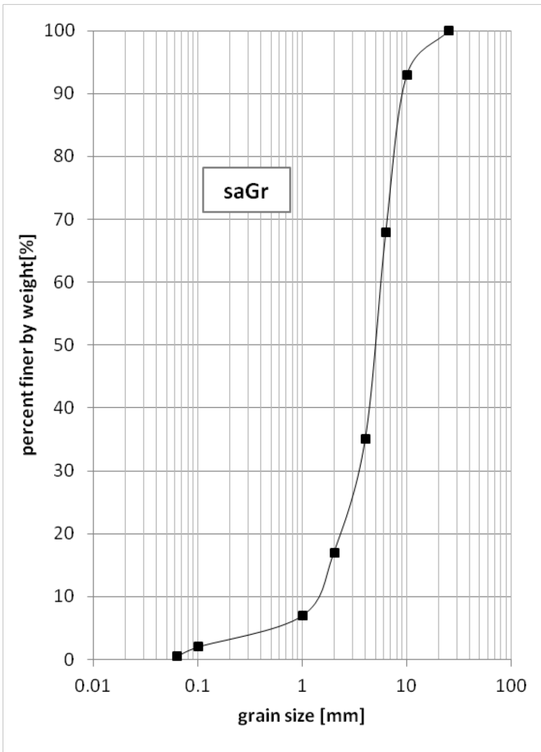

Fig. 1 Particle size distribution of tested soil.

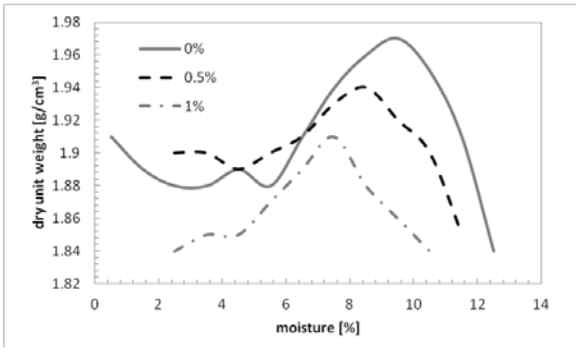

Fig. 2 The Proctor test results for sandy gravel.

The Proctor tests observations concerning the high water absorption of the RCA results in proper sample curing before compaction. RCA was compacted after leaving moisture material in hermetic box for 24h to prevent moisture loss. Material conditioned in such way give more reasonable data concerning physical properties repetition.

When curing of material and compaction in CBR mold in respect to Proctor's energy of compaction were done, cCBR tests were performed. The cCBR method was based on standard CBR test. The cCBR test bases on CBR method. Procedure of performing the cCBR test is simple and bases on standard CBR test procedure. Previous studies on cyclic loading performed on porous material was conducted by performing cyclic triaxial apparatus.

In recent years mechanistic-empirical pavement design has become more popular and traditional empirical methods of design are replaced. CBR value method of design the road construction was replaced by mechanistic approach where resilient modulus and Poisson ratio is employed for calculations of layer thickness. cCBR method is a way to compromise reliable CBR equipment with new standards of designing.

The cCBR test method bases on two parts of testing. First one is standard CBR test where loading is conducted to 2.54mm plunger penetration with velocity equal 1.27mm/min. Next step is beginning of second phase. After loading maximal stress at 2.54mm is noted. Unloading is conducted to 10% of maximal stress, called minimal stress. Loading and unloading constitutes first cycle of cCBR test. Next step is repetition of loading to maximal and unloading to minimal stress. cCBR test is terminated when plastic strains which occurs in one cycle are less than 1% of total strain in one cycle. Commonly the number of repetitions for un-cohesive soils is around to 50 cycles. The number of the cycles to obtain this condition usually oscillates around 50 [12, 13].

After cCBR test, last hysteresis loop is taken to calculations of resilient modulus M_r. To calculate M_r value. Resilient strain $\Delta\varepsilon_r$ is amount of strain during unloading where elastic response to decreasing stress is observed. Deviator stress is difference between maximal stress where elastic strains occurs and minimal stress.

Because of CBR test standards, not all area of specimen top is loaded. Therefore correct strain cannot be measured. For calculate the M_r value another equation was proposed [8] (2):

$$M_r = \frac{1.513(1-\nu^{1.104})\Delta\sigma_p \cdot r}{\Delta u^{1.012}} \tag{2}$$

where: ν –Poisson's ratio [-] (in this study 0.35 for granular materials), $\Delta\sigma_p$ – change between maximum and minimum axial stress in one cycle [MPa], r – radius of plunger [mm], Δu – recoverable displacement in one cycle.

3. RESULTS

Tests conducted on RCA have shown good performance of this material. cCBR test results for RCA with 0% RC in details is presented in figures 3, 4 and 5, Plots present results of cCBR test in function of axial stress and displacement on fig. 3. Figures 4 and 5 present the changing in time of displacement and axial stress respectively. RCA in this test presents resilient response. After 50 repetitions resilient modulus value was M_r= 495.6MPa. Elastic (resilient) displacement was 0.275mm which is 99.5% of total displacement in cycle. In terms of shakedown concept [14], material have reach steady point called plastic shakedown where plastic displacements occur but constitutes small amount of total displacements.

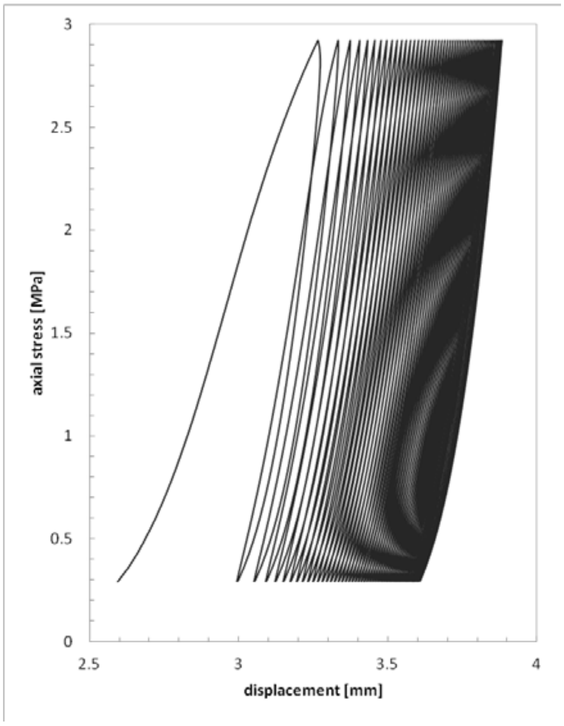

Fig. 3 Stress – displacement curve from cCBR test for RCA with 0% RC.

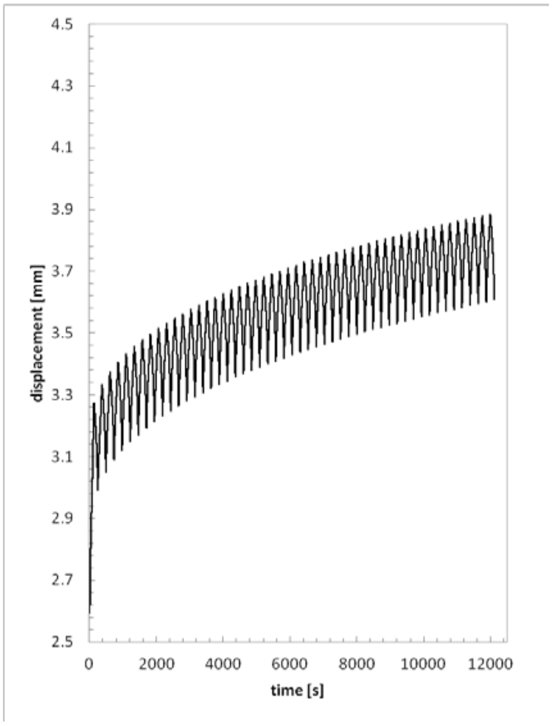

Fig. 4 Displacement – time curve from cCBR test for RCA with 0% RC.

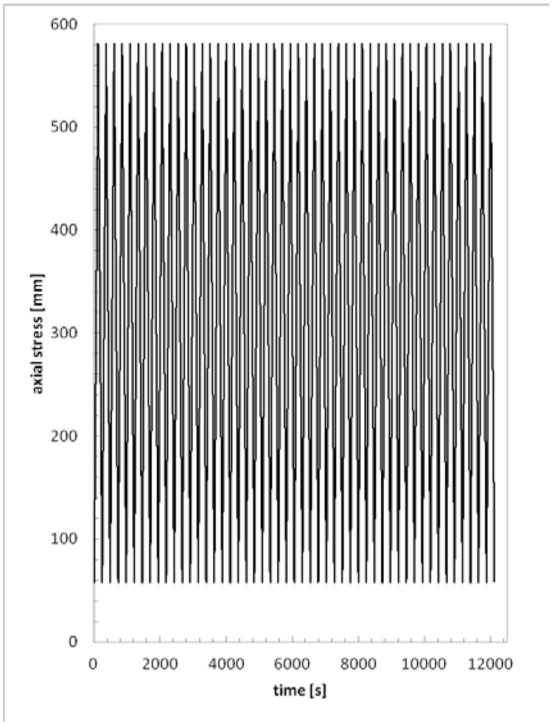

Fig. 5 Axial stress – time curve from cCBR test for RCA with 0% RC.

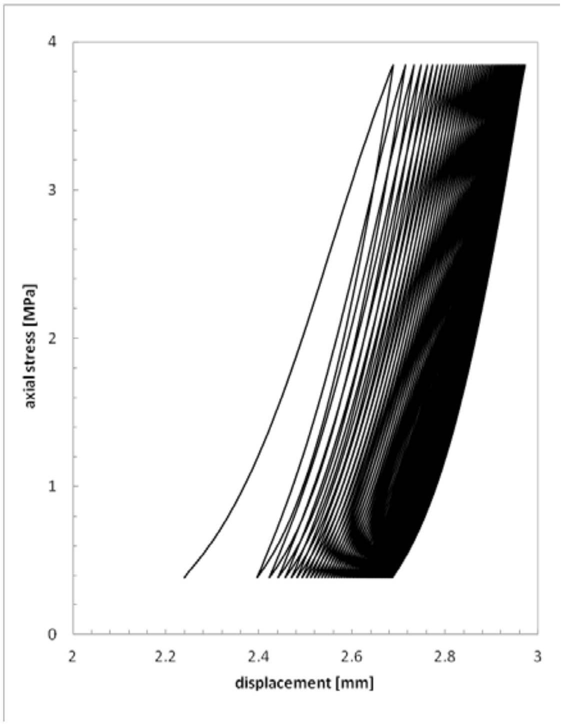

Fig. 6 Stress – displacement curve from cCBR test for RCA with 0.5% RC.

cCBR test results for RCA with 0.5 and 1% of RC content is presented in figures 6, 7, 8 and 9, Plots present results of cCBR test in function of axial stress and displacement on fig. 6 and 8. Figures 7 and 9 present the changing in time of displacement for 0.5 and 1% of RC content respectively.

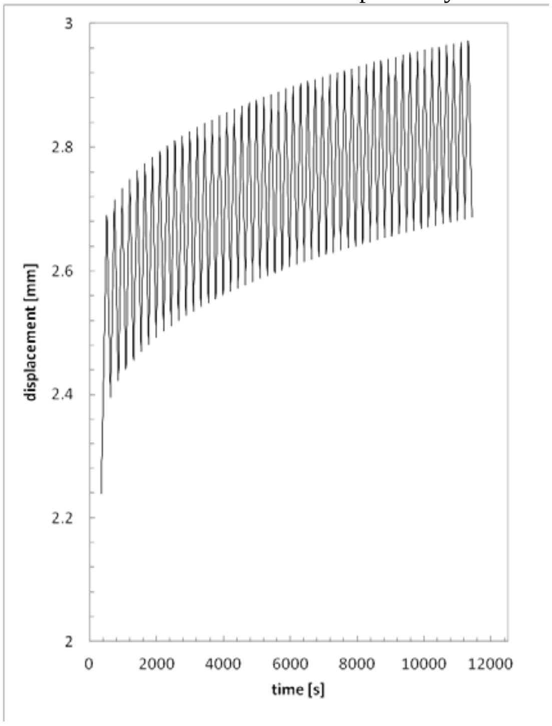

Fig. 7 Displacement – time curve from cCBR test for RCA with 0.5% RC.

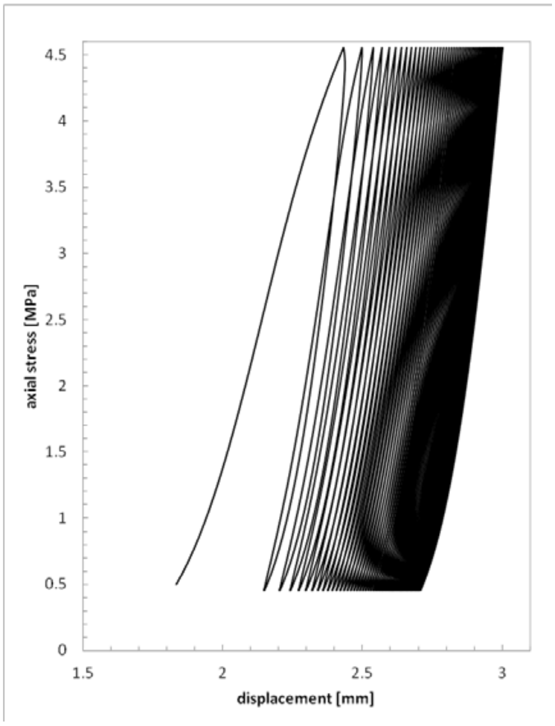

Fig. 8 Stress – displacement curve from cCBR test for RCA with 1% RC.

Addition of 0.5% RC increased CBR bearing capacity from 47% (RCA with 0% RC) to 56%.

Calculations of resilient modulus have shown increase of M_r. For 0.5%RC content RCA M_r value was M_r= 632.4MPa and was 137MPa greater than for RCA without RC addition.

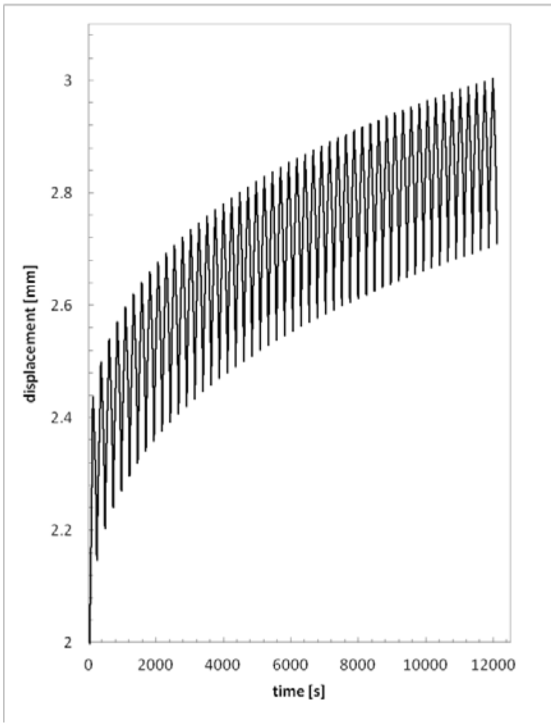

Fig. 9 Displacement – time curve from cCBR test for RCA with 1% RC.

Resilient modulus describes not only bearing capacity therefore rise in CBR value was equal 19% but rise in M_r value was 27%. This mean that grater improvement of plastic strain dissipation was observed.

For sample with addition of 1% RC CBR bearing capacity was 66% and rise to 19% in compare to 0% RC. The resilient modulus have shown increase of M_r. For 1% RC content RCA was M_r= 698.0MPa and was 202MPa greater than for RCA without RC addition. On figure 10 detailed view of results was presented. Resilient modulus value rises more when compared to CBR value. This phenomena is bounded with plastic strain increase. No RC addition, results in grater plastic strains and in one cycle amount of plastic strain is grater for 0% RC.

Addition of RC seem to improve resilient properties of material. RCA with RC addition can faster dissipate plastic strains. This may be caused by elastic properties of rubber. Stress between grain contacts may be better arranged by rubber chips. Abovementioned statement presents in details figure 11.

Properties of RCA as a anthropogenic soil material need further studies to understood mechanical properties but overall mechanical characterization proved that this material is appropriate for construction of the unbound sub-bases. Eurocode 7 EN 13286-7:2004 [15] classifies RCA by mechanical performance parameter M_r and this material reached the highest C1 class.

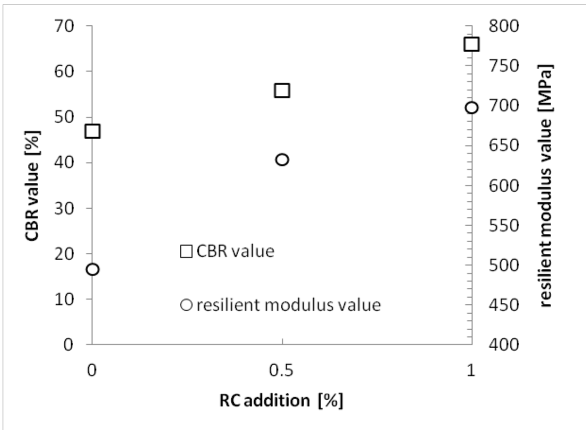

Fig. 10 CBR value and M_r value for different addition of RC from cCBR test.

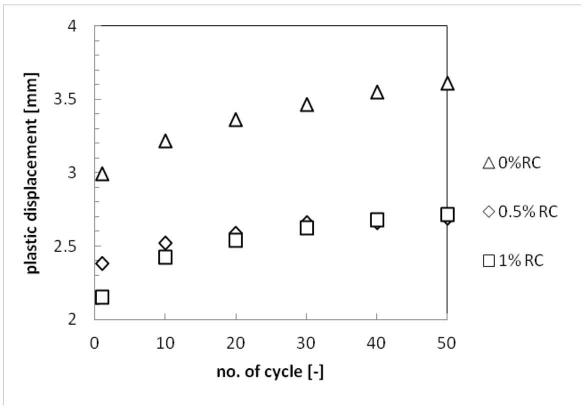

Fig. 11 **P**lastic displacement change during cCBR test for RCA with various RC content.

4. CONCLUSION

Results of cCBR test on stabilized and non-stabilized RCA presented in this paper are as follows:

1. Optimal moisture content for RCA with RC addition is lower. Also maximal dry density decrease with increasing of RC addition.
2. The CBR value for tested samples rises with increase of RC addition. For pure RCA CBR value was equal 47% for 0.5% and 1% RC content CBR value was 56% and 66% respectively.
3. The resilient modulus M_r values growth was observed with increase of RC content. For pure RCA the M_r value was 495.6MPa for for 0.5% and 1% RC content the M_r value was equal 632.4 and 698.0MPa.
4. Plastic displacements are decreasing when RC was added. For 0.5 and 1% RC content plastic displacements are smaller but between this contents, differences are not so great.

5. Resilient modulus values in compare to European standards classified this material to highest class C! and RCA with RC addition can be part of road construction as sub-base.

REFERENCES

[1] Takano D, Chevalier BJ, Otani J, "Experimental and numerical simulation of shear behavior on sand and tire chips" in Proc. 10th International Conference on Computer Methods and Recent Advances in Geomechanics, 2015, pp. 1545-1550.

[2] Srinivas A, Prasad DSV, AnjanKumar M, Prasada Raju GVR, "Utilisation of waste materials in the construction of roads", International Journal of Engineering Research and Development, Vol. 11(1) Jan. 2015, pp. 55-62.

[3] Ghatge SH, Rakaraddi PG, "Soil stabilization using waste shredded rubber tire chips", Journal of Mechanical and Civil Engineering (JMCE), Vol. 11, 2014, pp. 20-27.

[4] Tosic N, Marinkovic S, Dasic T, Stanic M, "Multicriteria optimization of natural and recycled aggregate concrete for structural use", Journal of Cleaner Production Vol.87, 2015, pp. 766-776.

[5] Soleimanbeigi A, Edil T, Benson C, "Engineering Properties of Recycled Materials for Use as Embankment Fill", In Proc. Geo-Congress, 2014, pp. 3645-3657.

[6] Randolph M, Gouvernec S, "Soil response" Offshore Geotechnical Enigineering, Spon Press, 1st ed., 2011. pp. 113-144

[7] Sas W, Głuchowski A, Szymański A, "Cyclic behavior of recycled concrete aggregate imptoved with lime addition" In Proc. 4th International Conference on GEOMATE, 2014, pp. 196-201.

[8] Araya A.A., "Characterization of Unbound Granular Materials for Pavements" PhD Delft, 2011.

[9] EN 1997-2:2007 Geotechnical design – Part 2: Ground investigation and testing.

[10] WT – 4: Mieszanki niezwiązane do dróg krajowych. GDDKiA (Unbound mix for national pavements).

[11] Deshpande YS, Hiller JE, "Pore characterization of manufactured aggregates: recycled concrete aggregates and lightweight aggregates", Materials and Structures Vol. 45(1), 2011, pp.67-79

[12] Sas W, Głuchowski A, Szymański A, "Determination of the resilient modulus M_R for lime stabilized Clay obtained from repeated loading CBR tests", Annals of Warsaw University of Life Sciences-Land Reclamation, Vol. 44, 2012, pp. 143-153.

[13] Sas W, Głuchowski A, „Metodyka wyznaczania modułów sprężystości (*E* i *Mr*) na podstawie badania CBR pod obciążeniem cyklicznym", Scientific Review – Engineering and Environmental Sciences, Vol. 57, 2012, pp. 171- 181.

[14] Werkmeister S, Dawson AR, Wellner F, "Permanent deformation behaviour of granular materials and the shakedown theory", Journal of Transportation Research Board, 2001, Vol.1757, 2001, pp. 75-81.

[15] BS EN 13286-7:2004, Unbound and hydraulically bound mixtures. Cyclic load triaxial test for unbound mixtures.

ULTIMATE BEARING CAPACITY OF FOOTING ON SANDY SOIL AGAINST COMBINED LOAD OF VERTICAL, HORIZONTAL AND MOMENT LOADS

Du L. Nguyen[1], S. Ohtsuka[2], and K. Kaneda[3]
[1]Department of Energy and Environment Engineering, Nagaoka University of Technology, Japan
[2]Department of Civil and Environmental Engineering, Nagaoka University of Technology, Japan
[3]Takenaka corporation, Japan

ABSTRACT

Rigid plastic finite element method employing the rigid plastic constitutive equation, which considers non-linear shear strength properties against confining pressure, is used for the assessment of ultimate bearing capacity of footing on sandy soils against the combined load of vertical, horizontal and moment loads. The numerical results were compared with the results predicted by semi-empirical bearing capacity formulate of Architectural Institute of Japan and others. The comparison is conducted in terms of vertical and horizontal loads plane and vertical and moment loads plane. The limit load is expressed in normalization form by the limit vertical load, Vo. Results show that the normalized vertical load decreases with the increase in the normalized horizontal load and/or moment load. Effect of non-linear shear strength on the normalized limit load space in vertical, horizontal and moment loads is clearly indicated. The normalized horizontal load is obtained greater than that of linear shear strength property.

Keywords: Ultimate Bearing capacity, Size effect, Finite element method, Inclined load

INTRODUCTION

The ultimate bearing capacity of footing related to inclined loads is an important aspect in geotechnical engineering. Because the number of superstructure buildings has increased and great earthquakes occur regularly, estimating the ultimate bearing capacity of footing with considering the effect of footing width is necessary. The strip footings are often subjected to the inclined loads and the combined loads. The ultimate bearing capacity for combined vertical and horizontal loads (with no moments) is resolved by Green (1954). The general case of vertical, horizontal and moment loads has received less attention. Several authors (notably Meyerhof (1953), Hansen (1970) and Vesic (1975)) provide procedures for a general case; however they only conduct empirical generalizations of the simpler cases without examining in detail.

In previous geotechnical research, the combined vertical and horizontal load is referred as the inclined loads. Their results showed that the vertical bearing capacity significantly decreased when the inclined angle θ = atan(H/V) increased.

By using the ultimate bearing capacity factors N_c, N_q (Prandtl), and N_γ (Meyerhof), the Architectural Institute of Japan (AIJ, 1988, 2001) developed an ultimate bearing capacity formula which considers the size effect factor and now is widely used in Japan. It was developed by semi-experiments. The ultimate bearing capacity formula is expressed as follows:

$$\mathbf{q_u} = i_c \alpha c \mathbf{N_c} + \mathbf{i_\gamma} \gamma \beta \mathbf{B} \eta \mathbf{N_\gamma} + \mathbf{i_q} \gamma \mathbf{D_f} \mathbf{N_q} \qquad (1)$$

where c: cohesion, γ: unit weight of soil, D_f: depth of embedment, B: footing width; N_c, N_q, N_γ: bearing capacity factors; i_c, i_q, i_γ: inclination factors, α and β express the shape coefficient and α = 1 and β = 0.5 are recommended by De Beer (1970), respectively; q_u is ultimate vertical bearing capacity per unit area of footing (kN/m^2). η: the size effect factor is defined as:

$$\eta = \left(\frac{B}{B_o}\right)^m \qquad (2)$$

where, B_0: reference value in footing width

m: coefficient determined from the experiment (m = -1/3 is recommended in practice).

Meyerhof (1956) introduced 'inclination factor i_γ' that is defined as follows:

$$i_\gamma = \frac{V}{V_0} = \left(1 - \frac{\operatorname{atan}(H/V)}{\phi}\right)^2 \qquad (3)$$

where ϕ: internal friction angle, H and V: horizontal and vertical of the load applied on the footing, V_o: vertical ultimate load.

Inclination factor has been estimated by FE analysis. But, there are few analyses for sandy soils except Loukidis et al. (2008). However, the effect of footing width on ultimate bearing capacity is not considered directly. As shown in Eqs. (1) and (2), the size effect of footing is large in case of sandy soil. It can be seen in the combined load space of vertical, horizontal and moment loads. This is a major topic of this study.

Recently, the numerical methods are efficient techniques for solving problems related to geotechnical engineering. The rigid-plastic finite element method (RPFEM) was applied in geotechnical engineering by Tamura (1991). In this process, the limit load is calculated without the assumption about the potential failure mode. The method is effective in calculating the ultimate bearing capacity of footing against the three-dimensional boundary value problems. Although RPFEM was originally developed based on the upper bound theorem in plasticity, Tamura proved that it could be derived directly by using the rigid plastic constitutive equation.

This paper investigated the ultimate bearing capacity of footing on sandy soils against the combined load of vertical, horizontal and moment loads. This research applied rigid plastic finite element method which employs the rigid plastic constitutive equation in which non-linear shear strength properties against confining pressure is inlcuded. The vertical load *V*, horizontal load *H* and moment *M*, which were applied at the center of the footing, were subjects in this study. The analytical method provides the reliable computational results. The relation in normalization form of H/V_0 vs V/V_0 and V/V_0 vs M/BV_0 were acquired and then were compared with the relationship by Meyerhof (1956), Architectural Institute of Japan (1988, 2001) and Loukidis et al. (2008).

RIGID PLASTIC FINITE ELEMENT METHOD

Stress – Strain rate relationship

Tamura (1987, 1991) developed the rigid plastic constitutive equation for the frictional material whose strength sastifies the Drucker-Prager yield criterion:

$$\mathrm{f}(\sigma) = aI_1 + \sqrt{J_2} - b = 0 \tag{4}$$

where I_1: first stress invariant

J_2: second invariant of deviator stress s_{ij}

The coefficients *a* and *b* express the soil constants corresponding to the internal friction angle and cohesion, respectively.

The volumetric strain rate is expressed as follows:

$$\begin{aligned}\dot{\varepsilon}_v &= \mathrm{tr}(\dot{\boldsymbol{\varepsilon}}) = \mathrm{tr}\left(\lambda \frac{\partial \mathrm{f}(\boldsymbol{\sigma})}{\partial \boldsymbol{\sigma}}\right) \\ &= \mathrm{tr}\left(\lambda\left(\alpha \mathbf{I} + \frac{\mathbf{s}}{2\sqrt{\mathrm{J}_2}}\right)\right) = \frac{3a}{\sqrt{3a^2 + 1/2}}\dot{e}\end{aligned} \tag{5}$$

where λ: the plastic multiplier, and $\dot{e}$: the norm of strain rate. **I** and **s** express the unit and the deviatoric stress tensors. The strain rate $\dot{\boldsymbol{\varepsilon}}$, which is purely plastic component, should satisfy the volumetric constraint condition which is derived by Eq. (5) as follows:

$$\mathrm{h}(\dot{\boldsymbol{\varepsilon}}) = \dot{\varepsilon}_v - \frac{3a}{\sqrt{3a^2 + 1/2}}\dot{e} = \dot{\varepsilon}_v - \hat{\eta}\dot{e} = 0 \tag{6}$$

Each strain rate, which is compatible with Drucker-Prager's yield criterion, must satisfy the kinematical constraint conditions of Eq. (6). $\hat{\eta}$ is a coefficient determined by Eq. (6) which is on the dilation characteristics. The rigid plastic constitutive equation is expressed by Lagragian method after Tamura (1991) as follows:

$$\boldsymbol{\sigma} = \frac{b}{\sqrt{3a^2 + \frac{1}{2}}}\frac{\dot{\boldsymbol{\varepsilon}}}{\dot{e}} + \hat{\beta}\left(\mathbf{I} - \frac{3a}{\sqrt{3a^2 + \frac{1}{2}}}\frac{\dot{\boldsymbol{\varepsilon}}}{\dot{e}}\right) \tag{7}$$

The first term expresses the stress component uniquely determined for the yield function, and the second term expresses the indeterminate stress component, defined to be parallel to one of the generators of the cylindrical cone of the yield surface. The indeterminate stress parameter $\hat{\beta}$ still remains unknown until the boundary value problem with Eq. (6) is solved.

In this study, the constrain condition on strain rate is introduced into the constitutive equation directly with the use of penalty method:

$$\boldsymbol{\sigma} = \frac{b}{\sqrt{3a^2 + \frac{1}{2}}}\frac{\dot{\boldsymbol{\varepsilon}}}{\dot{e}} + \kappa(\dot{\varepsilon}_v - \hat{\eta}\dot{e})\left(\mathbf{I} - \frac{3a}{\sqrt{3a^2 + \frac{1}{2}}}\frac{\dot{\boldsymbol{\varepsilon}}}{\dot{e}}\right) \tag{8}$$

where, κ is a penalty constant. This technique makes the computation more stable and faster. In rigid plastic finite element method (RPFEM), the occurrence of zero energy modes has been pointed out and some numerical techniques to avoid it have been introduced into FEM. However, zero energy modes have not been observed in computation with the rigid plastic constitutive equation using the Penalty method.

Rigid plastic constitutive equation for non-linear shear strength property

Tatsuoka (1986), and other researchers (Hettler, A. and Gudehus, G. (1988)) reported the effects of confining pressure on the internal friction angle for sandy soils by experiments. The property of the normalization between internal friction angle and first stress invariant always holds irrespective of the reference value of the confining pressure in the standardization of internal friction angle (Du N. L. et al. (2013)). From Fig. 1, the obtained results from experiment on Toyoura sand, Degebo sand, Eastern

Scheldt sand, and Darmstadt sand indicated that although internal friction angles are different between soils, the normalized internal friction angle shows the same trend for all case studies although any reference values of ϕ_0 and I_{10} are employed in normalization form. Thus, non-linear shear strength property against confining pressure is included in RPFEM in order to assess the ultimate bearing capacity of footing on sandy soils by taking account of the size effect of footing. The internal friction angle ϕ = 30^0 at I_1 as 150 kPa is employed as references through the following case studies.

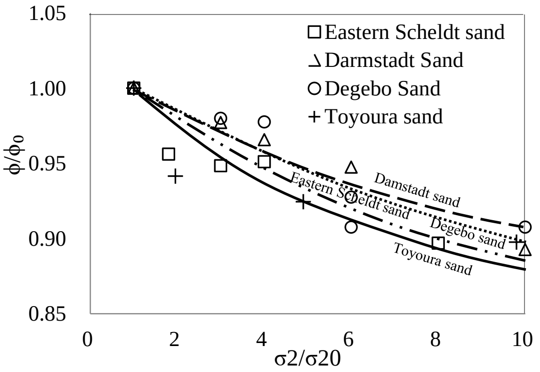

Fig. 1 Relationship between internal friction angle and first stress invariant for various kinds of sands

The high order hyperbolic function is introduced to the yield function of sandy soils as follows:

$$\mathrm{f}(\boldsymbol{\sigma}) = aI_1 + (J_2)^n - b = 0 \tag{9}$$

where a and b are the soil constants. The index n expresses the degree in non-linearity in shear strength against the first stress invariant. Eq. (9) is identical with Drucker-Prager yield function in case of n=1/2. The non-linear parameters a, b and n are identified by the testing data. In this case studies, a = 0.24, b = 2.4 kPa and n = 0.56 was set based on the experiment data from Fig. 1.

The non-linear rigid plastic constitutive equation for confining pressure is obtained as follows:

$$\boldsymbol{\sigma} = \frac{3a}{n}\left\{\frac{1}{2n^2}\left[\left(3a\frac{\dot{\mathrm{e}}}{\dot{\varepsilon}_v}\right)^2 - 3a^2\right]\right\}^{\frac{1-n}{2n-1}}\frac{\dot{\boldsymbol{\varepsilon}}}{\dot{\varepsilon}_v} + \\ + \left(\begin{array}{l} \dfrac{b}{3a} - \dfrac{1}{3a}\left[\dfrac{1}{2n^2}\left(3a\dfrac{\dot{\mathrm{e}}}{\dot{\varepsilon}_v}\right)^2 - 3a^2\right]^{\frac{n}{2n-1}} \\ -\dfrac{a}{n}\left[\dfrac{1}{2n^2}\left(3a\dfrac{\dot{\mathrm{e}}}{\dot{\varepsilon}_v}\right)^2 - 3a^2\right]^{\frac{1-n}{2n-1}} \end{array}\right)\mathbf{I} \tag{10}$$

Stress is uniquely determined for plastic strain rate and it is different from Eq. (8) for Drucker-Prager yield function in this equation.

The authors successfully proposed a rigid plastic equation using non-linear shear strength property against confining stress to RPFEM to assess the ultimate bearing capacity for the vertical load cases of rigid flat footing (Du N. L. et al. (2013)). The results of RPFEM were obtained similarly to the ultimate bearing capacity formula by Architectural Institute of Japan (AIJ, 1988, 2001), which take into account the size effect of footing.

ULTIMATE BEARING CAPACITY OF FOOTING UNDER COMBINED LOADS

Ultimate bearing capacity for combined vertical and horizontal loads

The rigid plastic finite element method was used to assess the ultimate bearing capacity of strip footings of which the width varied from 1m to 100m, subjected to the inclined load at an inclination angle θ with respect to the vertical. The boundary conditions and typical mesh for analysis are shown in Fig. 2.

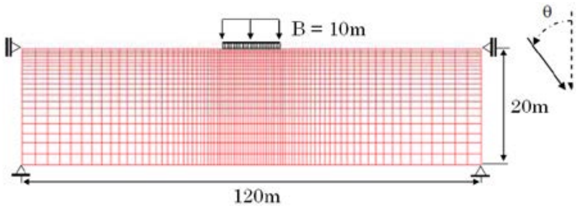

Fig. 2 Typical finite element mesh and boundary conditions

Because of the absence of loads symmetry, the entire soil domain of dimensions will be considered. The numerical simulation procedure was used for the computation of the (H, V) failure envelope (where H and V are the horizontal and vertical ultimate footing loads, respectively).

For inclined load, the application of RPFEM is limited to the case where the contact pressure between footing and ground is positive. In other words, the ratio H/V is set comparatively in small range. Further detailed discussion will not conducted in this study.

Fig. 3 provides the RPFEM result on the relationship between normalized horizontal and vertical loads on H-V space. Two cases considered include (i) linear shear strength property and (ii) non-linear shear strength property. The results by AIJ and Meyerhof formulae are also shown. Since AIJ formula employs the same coefficient with Meyerhof method, the results in normalization form from AIJ and Meyerhof show unique and coincident line. The inclination coefficient proposed by Loukidis et al. (2008) is also shown in this figure. They proposed the inclination factor i_γ based on the FE analysis for B=10m as follows:

$$i_\gamma = \frac{V}{V_0} = \left(1 - \frac{(H/V)}{\tan\phi}\right)^{(1.5\tan\phi + 0.4)^2} \qquad (11)$$

This coefficient is developed for linear shear strength, but it differs from the lines of Meyerhof and AIJ as shown in Fig. 3a. In the figure, the normalized horizontal load is indicated greater than those of Meyerhof and AIJ. The obtained results by RPFEM are plotted for various footing widths. It is apparent that the results match with the model of Eq. (11) by Loukidis et al. though they are varied for footing width.

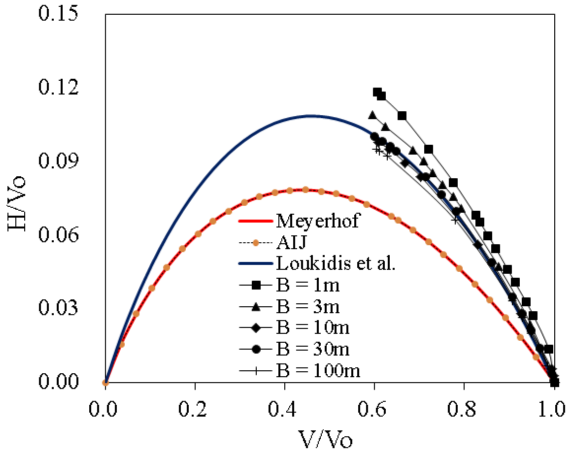

a) RPFEM with linear shear strength property

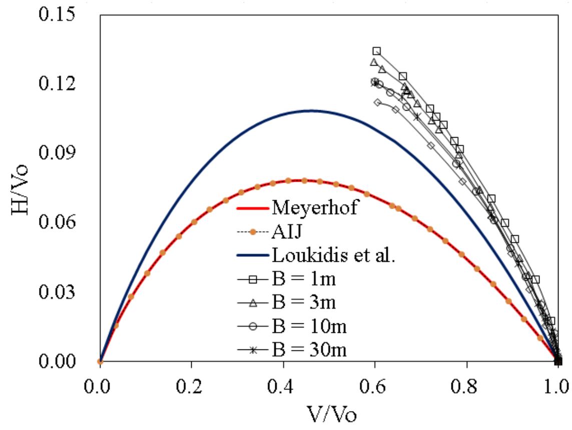

b) RPFEM with non-linear shear strength property

Fig.3 The relation between normalized horizontal and vertical loads

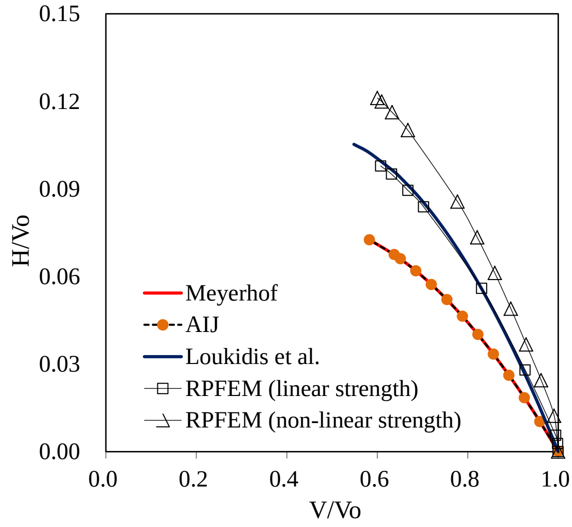

Fig. 4 Comparison inclination coefficients among the various methods at footing width B = 10m

Fig. 3b indicates the inclination coefficient in case of non-linear shear strength. AIJ formula is developed by taking account of the size effect of footing. However, since the inclination coefficient of Meyerhof is introduced into the formula, the applicability of AIJ formula for inclined load has not been examined. The results by RPFEM taking account of non-linear shear strength are plotted in the figure. Fig.4 indicates the ultimate load in H/V_0 and V/V_0 space to compare the inclination coefficient among the various methods at B=10m. It is readily seen that RPFEM affords the identical results by Loukidis et al. in case of linear shear strength, but the greater results than that by Loukidis et al. in case of non-linear shear strength. Although ϕ is constant in case of linear shear strength, ϕ decreases by confining pressure in case of non-linear shear strength. Since the decrease in ϕ mostly depends on the magnitude of vertical load, the decrease in ultimate bearing capacity is largest for vertical loading. For the inclined load, the decrease in ϕ becomes moderate with the increase in inclination angle of inclined load. It derives the normalized horizontal load in case of non-linear shear strength greater than that of linear shear strength.

Fig. 5 showed the failure modes of ground for non-linear and linear shear strength. They are similar, but the deformation area in the case of linear shear strength is larger than that in case of the non-linear shear strength. The mechanism is found composed of three different zones and similar to the mechanism assumed by Meyerhof and Hansen.

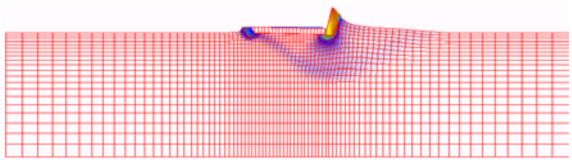

a) RPFEM with linear shear strength property

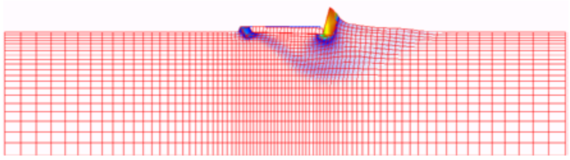

b) RPFEM with non-linear shear strength property

Fig. 5 Deformation mechanism analysis at footing width B = 10m

Ultimate bearing capacity for vertical, horizontal and moment loads

The type of loads, which is often known as combined loads, is important to the stability of superstructure where footings are subjected to vertical, horizontal and moment loads combination. Typically, the vertical force is stemmed from the weight (W) of superstructure, while the horizontal load comes from the seismic coefficient H/V, and the overturning moment load is caused by the horizontal load. In case study, vertical loads range from about 150 kN to 300 kN and the overturning moment varies from 200 kN.m to 500 kN.m. A series of finite element analysis were conducted for sandy soil with unit weight γ = 18 kN/m^3, cohesion c = 5 kN/m^2, internal friction angle $\phi = 30^0$, the height of superstructure h (10-20m), and at the footing width B = 3m. The moment load is given to the footing by the external force where the summations in vertical and horizontal loads are zero and the resultant moment at the center of footing is same with the prescribed moment load. The results demonstrated the interaction between the vertical, horizontal and moment loads. Fig. 6 shows the representative finite element meshes of analysis.

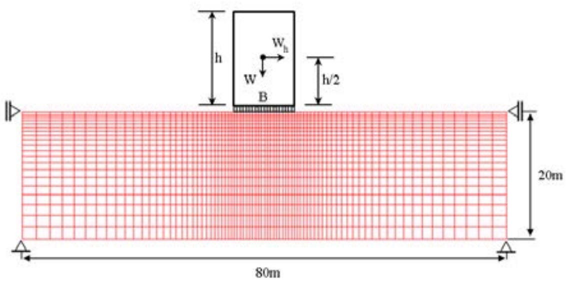

Fig. 6 Representative finite element meshes under superstructure on the strip footings condition at 3m of footing width

At each height of superstructure value, the ultimate bearing capacity of footings subjected to combined loading was computed under the condition of seismic load applied to superstructure. By changing superstructure height and the seismic coefficient H/V, the forces H, and V the moment load was computed.

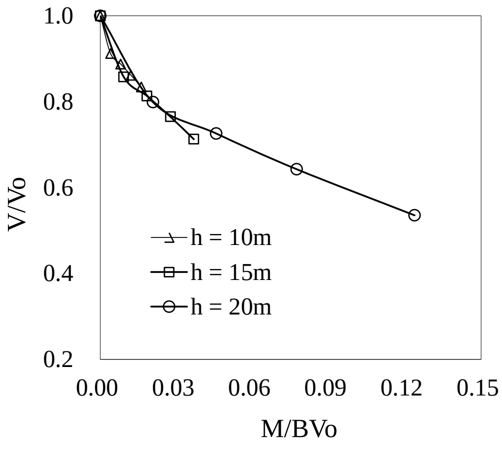

a) Linear shear strength property

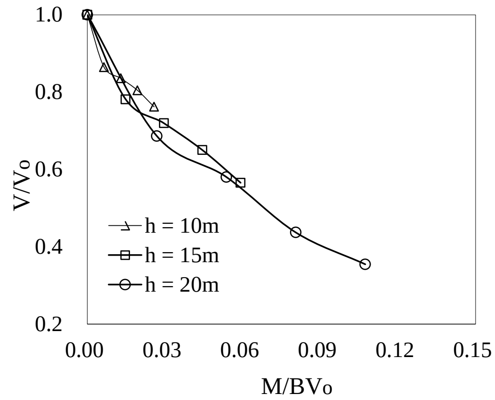

b) Non-linear shear strength property

Fig. 7 The relation between normalized vertical and moment loads

Fig. 7 shows ultimate bearing capacity of footing failure in the normalized V-M form by changing superstructure height (10m, 15m and 20m). The results showed that the normalized load V/V_0 decreases with an increase in M/BV_0. In the case of linear strength, the values that represent the relationship between the normalized V/V_0 and M/BV_0 are similar. It is not affected by height of superstructure; while in case of non-linear strength those values are discrepancy. It is explained that this case influences the internal friction angle responding to the confining stress. It means that the effect of moment load in non-linear case is clearer than that in linear shear strength property.

Fig. 8 shows examples of the deformation mechanism from evaluates at the collapse. The larger the combination loads, the smaller the limit load. The results from analysis computation also show that the failure mechanism is asymmetrical and confined to one side of the footing.

H/V = 0.1

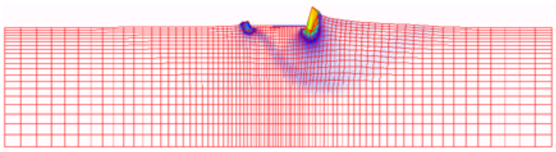

H/V = 0.4

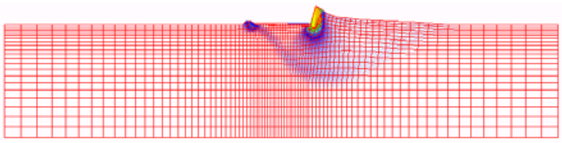

a) Linear shear strength property

H/V = 0.1

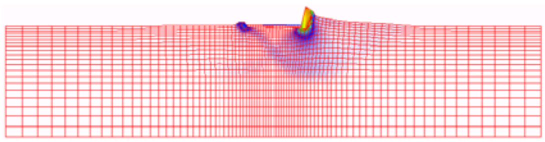

H/V = 0.4

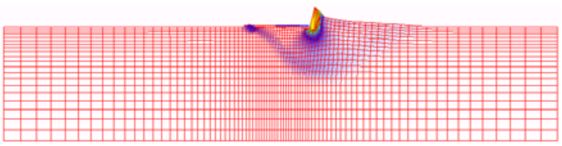

b) Non-linear shear strength property

Fig. 8 Deformation mechanism analysis subjected to combined loads

CONCLUSION

In this study, the limit load in ultimate bearing capacity is expressed in normalization form. The ultimate bearing capacity of footing that is subjected to the inclined loads and the combined loads of strip footing has been investigated in this study. The obtained conclusions can be summarized as follows:
(1) The non-linear shear strength model for sandy soil is employed in RPFEM to evaluate the size effect of footing on ultimate bearing capacity. Through the case studies the applicability of the method was clearly exhibited.
(2) Ultimate load space in normalized vertical and horizontal loads was shown to match with that by Loukidis et al. (2008) and be greater than those by Meyerhof (1956) and AIJ (1988, 2001) in case of linear shear strength. On the contrary, it is obtained greater than that by Loukidis et al. in case of non-linear shear strength. It is understood by the following reasons:
(i) The internal friction angle decreases by confining pressure and the decrease is the most for the case of vertical loading.
(ii) In inclined loading, the decrease in internal friction angle becomes smaller since the ultimate vertical load decreases with the increase in inclination angle. Thus, the computed results can be obtained.
(3) The combination of vertical, horizontal and moment loads is considered to evaluate the stability of buildings during earthquake. The effect of moment load on ultimate bearing capacity is investigated through case studies.

References

[1] Architectural Institute of Japan, AIJ (1988, 2001), “Recommendations for design of building foundations”, 430p.
[2] Du, N. L., Ohtsuka, S., Hoshina, T., Isobe, K. and Kaneda, K. (2013) “Ultimate bearing capacity analysis of ground against inclined load by taking account of non-linear properties of shear strength”, Int. Journal of GEOMATE, Vol. 5, No. 2, pp. 678–684.
[3] De Beer, E. E. (1970), “Experimental determination of the shape factors and the ultimate bearing capacity factors of sand”, Geotechnique, Vol. 20, No. 4, pp. 387 – 411.
[4] Hettler, A. and Gudehus, G. (1988), “Influence of the foundation width on the ultimate bearing capacity factor”, Soils and Foundations, Vol. 28, No. 4, pp. 81-92.
[5] Loukidis, D., Chakraborty T., and Salgado R., (2008), “Bearing capacity of strip footings on purely frictional soil under eccentric and inclined loads”. Can. Geotech. J., Vol. 45, pp. 768-787.
[6] Meyerhof, G. G. (1956), “Rupture surfaces in sand under oblique loads (discussion)”, Journal of soil mechanics and foundations division, ASCE, Vol. 82, No. SM3.
[7] Tamura, T., Kobayashi, S. and Sumi, T. (1987), “Rigid Plastic finite element method for frictional materials”, Soils and Foundations, Vol. 27, No. 3, pp. 1-12.
[8] Tamura, T. (1991), “Rigid plastic finite element method in Geotechnical engineering”, Current Japanese Materials Research, Vol. 7, Elsevier Applied Science, London, pp. 135-164
[9] Tatsuoka, F., Sakamoto, M., Kawamura, T. and Fukushima, S. (1986), “Strength and deformation characteristics of sand in plane strain compression at extremely low pressures”, Soils and Foundations, Vol. 26, No. 1, pp. 65–84.

THE PROPAGATION BEHAVIOR OF PILE-DRIVING-INDUCED VIBRATION DONE ON SOIL AT VARYING DISTANCES AND ITS EFFECTS ON EXISTING STRUCTURES

D.Y. Acosta, M.B. Juego, H.M. Sanchez and I.S. Sanchez
College of Engineering, De La Salle University Manila, Philippines

ABSTRACT

Pile driving operations are becoming a prevalent practice in Metro Manila due to the presence of soft soil conditions. However, ground vibrations are induced in the process, which could cause possible structural damages to the nearby existing structures. Ground vibration measurements were recorded at three designated sites at 3, 15, and 30 meters away from the pile-driving source through the use of three of Guralp's accelerometers. A defined attenuation behavior of the emitted vibrations was observed when the pile was in contact with the predominantly sand and silt layers, vibration prediction models for sand and silt layers were formulated and then validated with the measurements obtained at the other two sites, predicted results were correlated to existing vibration limits, a zone of influence was then generated and is capable of identifying the types of structures that are susceptible to structural damage within a radius of the source of pile driving.

Keywords: Attenuation Behavior, Zone Of Influence, Vibration Prediction Model, Vibration Limits, Structural Damage

INTRODUCTION

Pile driving operations are becoming a prevalent practice in Metro Manila due to the presence of soft soil conditions. However, ground vibrations are induced in the process, which could then cause possible structural damages to the nearby existing structures. Several vibration limits are set forth by international codes to minimize the negative effect, however, there is still a lack of proper translation of these limits for comprehensive on-site usage. Since modern construction work is usually done in urban areas, it is essential to establish vibration limits upon consideration of the structures that are vulnerable to structural damage within a certain radius of the source of pile driving.

BACKGROUND

The transmission of energy from the hammer down to the pile and then to the surrounding soil governs the entire vibration transmission process and forms a crucial part in analyzing the behavior of ground vibrations. A simple concept of the energy transmission is then presented.

When the hammer hits the pile head, energy is being transferred down to the body of the pile in the form of a compressional body wave [1]. S-waves are generated in the Pile shaft and propagate conically from the pile. Compressional (P) – waves and Shear (S) -waves are also generated in the pile toe and they propagate in spherical waveforms in all directions. As these S and P – waves reach the ground surface, a part of the waves are being converted into Rayleigh (R) –waves, as seen in Fig. 1, which attenuate in amplitude in proportion to the square root of distance [2],[3].

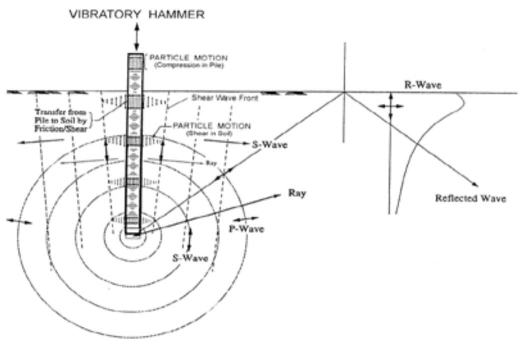

Fig. 1 Waves generated from pile driving operations [5]

Vibration Attenuation and Frequency

Ground vibrations, depending on its type and source of emission, attenuate due to geometric damping. Its attenuation is also influenced by material damping, arising due to the presence of different ground properties [5].

The Bornitz Equation considers the combined effect of both material and geometric damping, allowing the characterization of the propagation of ground vibrations as it moves away from the vibration source, it is then expressed in Eq. (1):

$$A_2 = A_1 \left(\frac{r_1}{r_2}\right)^n e^{-\alpha(r_2 - r_1)} \tag{1}$$

A_1 and A_2 are vibration amplitudes at distances r_1 and r_2, n is the geometric damping coefficient = 1 (surface waves), and α is the material damping coefficient. According to [1] and [2], the material damping coefficient (α) can be estimated as a function of vibration frequency (f), and is expressed in Eq. (2):

$$\alpha = \frac{2\pi D f}{c} \tag{2}$$

Where, c is the propagation velocity of R-waves and D is the damping ratio.

The dominant frequency of vibration can then be approximated by knowing the pile and hammer properties, specifications utilized in the pile driving operation as suggested by [11], and is given in Eq. (3):

$$f_w = k\,\left(\frac{(c)\varepsilon}{2\pi L}\right) \tag{3}$$

Where, ε is the adjustment factor which is dependent on the pile to ram weight ratio denoted by η, L is the pile length in meters, and k = 0.5 (Concrete Piles at restrike).

Table I Adjustment factors (ε) [11]

η	0.01	0.10	0.30	0.50	0.70	0.90	1.00	1.50
ξ	0.10	0.32	0.52	0.65	0.75	0.85	0.86	0.98
η	2.00	3.00	4.00	5.00	10.0	20.0	100	∞
ξ	1.08	1.20	1.27	1.32	1.42	1.52	1.57	π

Empirical Prediction Models

Two empirical vibration prediction models were utilized in the study as a basis for validation against the actual vibration measurements obtained on site. These were the empirical models presented by [6] and [7] respectively.

The model suggested by [6] only takes into account the hammer energy (W_o) and the distance away from the vibration source (r), where no consideration is made on the geological conditions of the site; it is then presented in Eq. (4):

$$v = k\left(\frac{W_o}{r}\right)^x \tag{4}$$

Values of k = 1.5 and x = 1 were adopted for conservative measurements of vibrations [4].

The said model was then utilized in contrast to a more sophisticated vibration prediction model presented by [7], wherein imperative aspects of energy transfer at the hammer – pile and pile-soil interface, and the influence of the soil properties on the vibration magnitude are considered. The model is then expressed in Eq. (5):

$$\boldsymbol{v_{sv} = k_s F_v E_T \frac{(F^H W_0)^{0.5}}{r_r} cos\theta} \tag{5}$$

Where, v_{sv} is the vertical PPV measurement in mm/s, k_s, F_v and F^H are the vibration, amplification and efficiency factors associated with the model. E_T is the toe vibration efficacy, θ is the angle of incidence of P-waves and r_r is the radial distance from the pile toe to a point on the ground surface.

Vibration Limits

Several limits were set forth by various government agencies to complement the empirical prediction models to aid in mitigating the negative effects of vibrations, specifically by providing threshold values for structural damage in relation to the magnitude of the peak particle velocity and the frequency of the vibration.

There are 4 frequently used standards on vibration limits and they were incorporated into a single graph, refer to Fig. 2, as presented by [5]. The graph served as the basis for vibration assessment in the study.

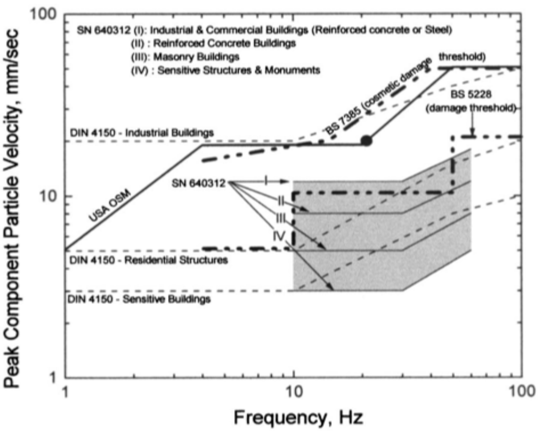

Fig. 2 Vibration Limits suggested by [1]

METHODOLOGY

Data Acquisition

Vibration measurements in terms of vertical peak particle velocity units were taken in AMAIA Steps Pasig condominium in Eusebio, Pasig City (Site A); Three E-com Center in Bayshore Avenue, Pasay City (Site B); and Meridian Park along Diosdado Macapagal Avenue, Pasay City (Site C) through the use of three of Guralp's Digital Tri-axial Accelerometers positioned at distances 3, 15 and 30 meters away from the vibration source, as seen in Fig 3.

Vibration measurements were then recorded throughout the entire duration of the pile-driving operation, they were digitally logged in a computer and were extracted through the use of the SCREAM Software, as provided by Guralp Systems.

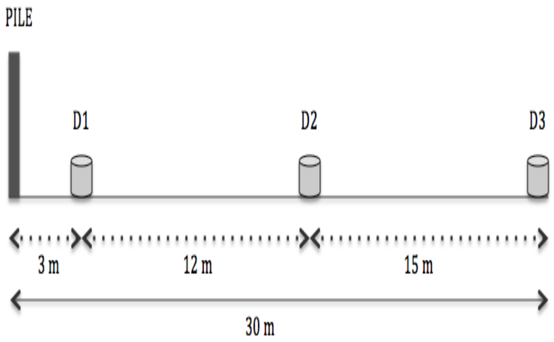

Fig. 3 Placement of accelerometers

The raw data obtained on the three sites were then exported through a Strong motion Analysis Tool, named ART, in which the vibration measurements were analyzed and documented in corresponding measurements of peak particle acceleration, velocity and displacement taken in the North, East and Vertical directions.

Site Information

Geotechnical conditions, determined through the acquisition of the borehole data, revealed that Site A was underlain with predominantly sand and silt deposits having varying soil densities across several layers. Site B was underlain with a top sand layer followed by multiple predominantly silt layers and a sandstone layer at the bottom most soil profile. While, Site C was underlain with a combination of sand, clay and silt layers, weathered rock layers were then located at the bottom most layer of the soil profile.

The number of blows needed to drive the piles down to a certain depth below the ground surface was also properly documented together with the corresponding hammer and pile specifications utilized on the three sites, refer to Table II, to aid in the analysis of the ground vibration measurements.

Table II Hammer and Pile Specifications

	Hammer		Pile	
Site	Type	Weight	Square	Length
A	Bruce	7100	450	23
B , C	NH70	7000	450	21

ANALYSIS AND RESULTS

Ground Vibrations Measurements

The retrieval of the time histories of the vibration measurements recorded at the ground surface led to the acquisition of vertical peak particle velocities (PPV) at each soil type transition at three distances away from the vibration source, they were then plotted against the pile penetration depth as shown in Fig. 4.

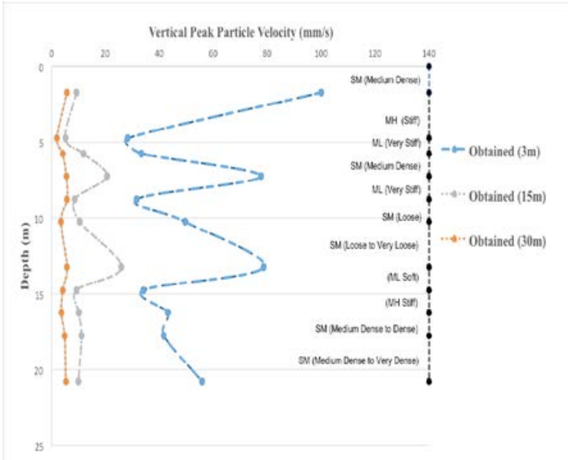

Fig. 4 Vertical PPV readings of the 3rd pile in Site A

During the entire driving process, the highest vertical PPV measurement was obtained upon driving into the medium dense silty sand layer, situated at 0 - 1.75 m below the ground surface.

It is known that in the case of pile driving in sand deposits, the surrounding soil is being compacted through static pressure [8]. The acquisition of the highest vibration magnitude can be attributed to the compaction of the surrounding soil during pile penetration and as well as the increasing shaft-soil contact area, leading to an increase in the shaft friction of the pile [9].

A sharp decline of the vertical PPV measurement followed upon the transition of the driving from the predominantly sand layer to the stiff clayey silt layer at a depth of 1.75 - 4.75 m below the ground surface. Pile driving in Clayey Silt soil layers remoulds the surrounding soil and excess pore water pressure ss are generated, which could have resulted to the decrease in the shear resistance of the surrounding soil [3],[10], thereby leading to the acquisition of a smaller magnitude of vertical PPV measurement.

The influence of the dynamic soil properties on the vibration magnitude can be evidently seen at a distance near the vibration source, but at a farther distance, it becomes more difficult to determine the influence as the vibration magnitudes cluster at a closer range and become quite similar. On the other hand, it is then crucial to analyze the attenuation behavior of the vibrations emitted on different types of soils possessing different dynamic properties at distances farther away from the vibration source.

Frequency Content

The corresponding frequency content of the vibration measurements were then obtained through the Fourier Transform of the time histories and were analyzed in the Fourier Spectra (Frequency Domain).

In Site A, the frequencies of the vertical PPV measurements ranged from 6 to 15Hz, having an average frequency of 9.33Hz, see Table III. The dominant frequency of the propagating waves due to impact sources has a span of values within 3 to 60 Hz [11] and the acquired values were found to fall within the said range.

Table III Vertical Vibration Frequency in Site A

VERTICAL FREQUENCY FOR SITE A (Hz)										
Depth (m)		1st Pile			2nd Pile			3rd Pile		
Starting Point	End Point	3m	15m	30m	3m	15m	30m	3m	15m	30m
0	0.75	11.33	10.94	8.984	10.94	14.06	10.16	9.375	14.06	9.375
0.75	1.75									
1.75	2.75	8.203	11.33	10.84	9.766	7.422	9.766	7.031	5.859	7.422
2.75	3.75									
3.75	4.75									
4.75	5.75	7.813	7.813	7.422	9.766	8.008	9.375	8.594	12.89	8.984
5.75	7.25	10.55	12.89	7.031	9.766	8.203	7.031	7.813	13.48	11.33
7.25	8.75	8.203	10.16	7.031	7.422	7.813	8.984	9.766	7.813	10.94
8.75	10.25	10.16	13.67	7.031	9.766	8.594	8.594	8.984	12.89	8.984
10.25	11.75	7.031	9.766	7.031	8.594	8.594	7.031	7.422	7.813	7.031
11.75	13.25									
13.25	14.75	10.16	9.766	8.984	8.594	8.594	7.031	8.594	7.617	8.984
14.75	16.25	10.16	9.766	8.789	8.984	8.594	7.031	8.594	8.594	8.984
16.25	17.75	10.16	9.961	8.984	7.813	8.594	10.94	8.984	12.89	10.94
17.75	19.25									
19.25	20.75	8.984	10.16	13.28	8.594	8.594	15.23	8.984	8.984	10.94
Average (Hz)		9.53			9.04			9.42		
Frequency using Svinkin's Model (Hz)		9.78			9.78			9.78		
Percentage Error		2.62			8.19			3.82		

It was interesting to see that the calculated dominant frequency of vibration in Site A upon using the model suggested by [11], having a value of 9.778Hz, yielded percentage errors ranging from 2 to 8% when compared to the measured average frequency of the vertical component of vibrations obtained on the three driven piles.

This would entail to the rationale that dominant frequencies of ground vibrations can be estimated with considerable accuracy prior to pile driving if pile-hammer properties and specifications are known. Leading the parameter to serve as reliable reference in the study of the behavior of the propagation and attenuation of ground vibrations during the pre-driving phase.

Predicted and Actual Vibration Measurements

The vertical PPV measurements obtained at the three distances were plotted against the calculated values obtained through the empirical models suggested by [6] and [7] as shown in Fig. 5 and 6 respectively.

Conservative measurements of vibration magnitudes were obtained upon using the model suggested by [6], however no consideration was made on the influence of the different soil properties on the vibration readings. On the other hand, vibration measurements obtained through the use of the model suggested by [7] have shown to satisfactorily depict the influence of the soil properties on the vibration magnitude.

However, it can be seen in Fig. 2, that overestimation of the vertical PPV measurements are made on the upper layers while there is an underestimation on the lower layers correspondingly, the overestimation of the measurements on the upper layers can be attributed to the low associated P-wave velocity in calculating the vibration magnitude, while the underestimation can be attributed to the use of the radial distance in determining the vertical PPV measurement at the lower layers.

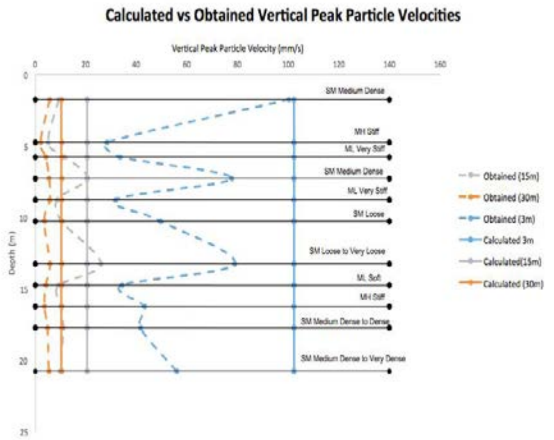

Fig. 5 Actual and Calculated Vertical PPV readings from the model suggested by [6]

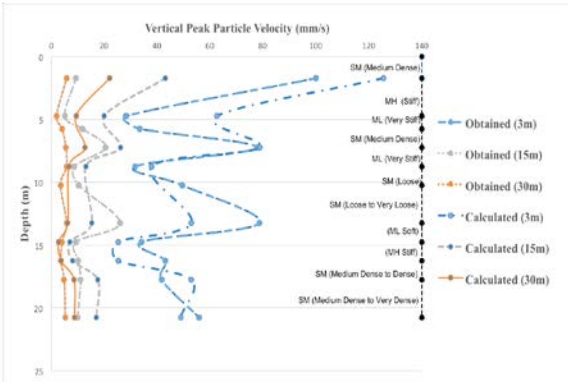

Fig. 6 Actual and Calculated Vertical PPV readings from the model suggested by [7]

Upon comparing the predicted and actual values of the vertical PPV readings, it was observed that it is still difficult to predict vibration measurements with high accuracy, as many factors such as the soil, hammer, and pile properties, and events of wave interference can greatly contribute to the change in the vibration magnitude. Despite the complex nature of predicting ground vibrations, the attenuation behavior was found to hold substantial information on the extent to which the ground vibrations would be of significance in the study.

Attenuation of Ground Vibrations

The attenuation behavior of the vertical PPV measurements in Site A were generated and analyzed by plotting the vibration readings at three different distances away from the vibration source. They were subdivided into two main groups, vibration readings emitted on the predominantly sand and predominantly silt layers respectively, this was made in order to analyze the difference between the attenuation behavior of the two different types of soils, as seen in Fig. 7 and 8.

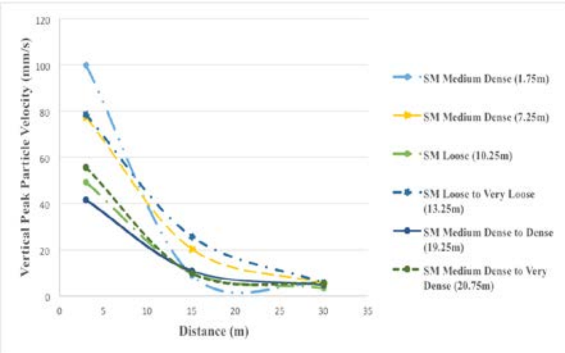

Fig. 7 Attenuation of vertical PPV in Sand Layers at Site A (3rd Pile)

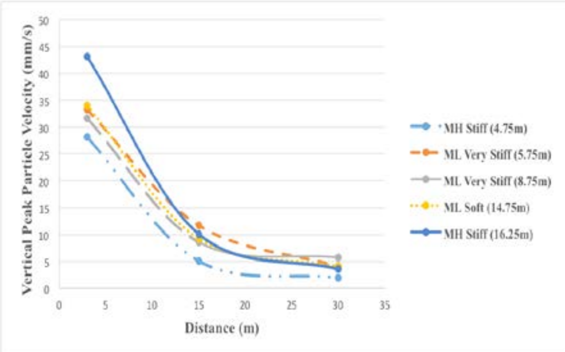

Fig. 8 Attenuation of vertical PPV in Silt Layers at Site A (3rd Pile)

The vertical PPV measurements at a distance of three meters away from the vibration source were found to be quite dispersive; this was seen on both the attenuation graphs of the predominantly sand and silt layers. The said behavior can be attributed to the influence of the dynamic soil properties on the vibration magnitude, thereby explaining the acquisition of a dispersive set of readings.

However, the measurements obtained on the predominantly sand layers damped considerably to a narrow range at a distance of 15 and 30 meters away from the vibration source. While measurements obtained on the predominantly silt layers did not come to a closer range up until a distance of 30 meters away from the vibration source.

Having observed a defined attenuation behavior on both the predominantly sand and silt layers, a best fit line was then developed through regression analysis of the field data, involving two main parameters, the dominant frequency content of the vibrations and the distance from the vibration source. Vibration prediction models for sand and silts were then generated and are expressed in Eq. (6) and (7):

$$y = e^{0.3649\ln(x_1)-1.1780\ln(x_2)+4.8072} \tag{6}$$

$$y = e^{-1.144\ln(x_1)-0.0902\ln(x_2)+5.0949} \tag{7}$$

Where, y is the vertical PPV in mm/s at a distance x_2 from the vibration source having a dominant frequency of x_1.

The vibration velocities obtained through the use of Eq. (6) and (7) showed to have correlated well with the actual vibration measurements of Site A, yielding an R square value of 0.94 and 0.86. The predicted values were then validated with the measurements of Sites B and C and good agreement was found between the predicted values and the actual vibration measurements obtained in the other two sites.

The predicted measurements obtained through the use of Eq. (6) and (7) can then be correlated with the vibration limits, referred to in Fig. 2 as suggested by [5], and a corresponding zone of influence can then be generated, refer to Fig. 10, to identify the nearby existing structures that are vulnerable to structural damage mainly due to pile-driving induced ground vibrations.

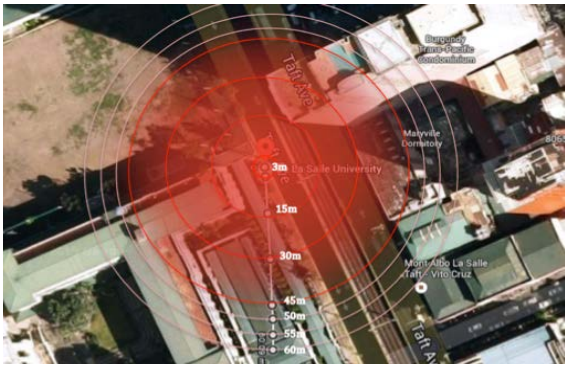

Fig. 10 Zone of Influence

Several limitations bind the use of the proposed prediction models and they are stated as follows, only vibration measurements generated through impact pile-driving operations obtained at the ground surface, at a distance of at least 15 meters away from the pile-driving source can be predicted with higher accuracy, as measurements near the vibration source were found to be dispersive. The energy imparted by the hammer unto the pile should be within the range of 41,000 – 41,130 Joules and that there should be a minimum individual layer thickness of 0.75 meters as indicated in the site borehole data for both sand and silt layers.

CONCLUSION

There has long been a concern for the damages that impact pile driving may bring to nearby existing structures. Therefore, it is necessary to establish reliable references to ensure the safety of the structures within a certain radius from the source of pile driving.

Based on the findings of the study, different types of soils, possessing varying dynamic properties, greatly influence the vibration magnitude, which makes the geological conditions of the site a highly important consideration in analyzing ground vibrations, however, the influence of the soil dynamic properties can only be evidently seen at a distance near the vibration source, in this particular case at a distance of three meters where dispersive sets of readings are obtained.

At farther distances, vibration measurements are more suited to be analyzed based on their attenuation behavior. Measurements obtained on the predominantly sand and silt layers on Site A damped considerably and clustered at a closer range at a distance of 15 and 30 meters away from the vibration source regardless of the type of soil layers the vibrations were emitted from.

Upon having observed a defined attenuation behavior, two vibration prediction models were developed through regression analysis and are capable of predicting vibration magnitudes at any distance away from the vibration source having a certain dominant frequency. The prediction models were validated on Sites B and C and good correlation was found to exist between the obtained measurements.

The prediction models can be then be correlated with the vibration limits presented in the study to map a zone of influence, where structures that are vulnerable to structural damage within a radius or source of pile driving can be identified.

ACKNOWLEDGEMENTS

The support of GEOMATE is gratefully acknowledged. The authors would also like to express their gratitude to the thesis adviser, Dr. Jonathan Rivera Dungca for his constructive comments and thorough review on this paper. Much thanks is also given to the pile driving company for granting permission to use the sites, and to Condoza Software Solutions for providing the accelerometers, which made the acquisition of data possible for this research.

REFERENCES

[1] Woods, R.D. (1997). Dynamic Effects of Pile Installations on Adjacent Structures. NCHRP Synthesis 253, National Cooperative Highway Research Program, Transportation Research Board, National Academy Press, Washington D.C., USA.

[2] Selby, A. (1991). Ground Vibrations Caused by Pile Installation. *Proceedings Of The 4Th International Conference On Piling And Deep Foundations*.

[3] Deckner, F. (2013). *Ground vibrations due to pile and sheet pile driving - influencing factors, predictions and measurements* (Ph.D). Royal Institute of Technology.

[4] Deckner, F., Viking, K., & Hintze, S. (2012). Ground vibrations due to pile and sheet pile driving – prediction models of today. *Proceedings Of The 22Nd European Young Geotechnical Engineers Conference*. *ECGD 4122-Foundation Engineering*. (2008).

[5] Athanasopoulos, G., & Pelekis, P. (2000). Ground vibrations from sheetpile driving in urban environment: measurements, analysis and effects on buildings and occupants. *Soil Dynamics And Earthquake Engineering*, *19*(5), 371-387. doi:10.1016/s0267-7261(00)00008-7

[6] Attewell, P.B. & Farmer, I.W. (1973). Attenuation of ground vibrations from pile driving. *Ground Engineering*, Vol. 3, No. 7, pp. 26-29.

[7] Massarsch, K.R., Fellenius, B.H. (2008). Ground Vibrations Induced By Impact Pile Driving. The 6th International Conference on Case Histories in Geotechnical Engineering. Arlington, Virginia.

[8] Terzaghi, K. (1996). Soil Mechanics In Engineering Practice (3rd ed., pp. 322 - 323).

[9] Hope, V.S. & Hiller, D.M. (2000). The prediction of groundborne vibration from percussive piling. *Canadian Geotechnical Journal*, Vol. 37, No 3, pp. 700-711.

[10] Rajapakse, R. (2008). Pile design and construction rules of thumb. Burlington, MA: Elsevier/Butterworth-Heinemann.

[11] Svinkin, M. R. (1992). "Pile driving induced vibrations as a source of industrial seismology." *Proc., 4th Int. Conf. on the Application of Stress-Wave Theory to Piles*, The Hague, the Netherlands, F. B. J.

[12] Dowding, C.H. (1996). Construction Vibrations. Prentice Hall, Upper Saddle River, USA.

[13] Woods, R.D.(1997).Dynamic Effects of Pile Installations on Adjacent Structures. NCHRP Synthesis 253, National Cooperative Highway Research Program, Transportation Research Board, National Academy Press, Washington D.C., USA.

[14] Svinkin, M. (2004). Minimizing construction vibration effects. Practice Periodical On Structural Design And Construction, 9(2), 108—115.

Fifth International Conference on Geotechnique, Construction Materials and Environment, Osaka, Japan, Nov. 16-18, 2015, ISBN: 978-4-9905958-4-5 C3051

SOCIAL MEDIA GIS TO SUPPORT THE UTILIZATION OF DISASTER INFORMATION

Kayoko Yamamoto and Shun Fujita
Graduate School of Information Systems, University of Electro-Communications, Japan

ABSTRACT

This study aims to design, develop, operate and evaluate a social media GIS (Geographical Information Systems) specially tailored to mash-up the information that local residents and governments provide to support information utilization from normal times to disaster outbreak times in order to promote disaster reduction. Social media GIS, an information system which integrates Web-GIS and SNS in addition to an information classification function into a single system, was operated in Mitaka City, Tokyo. The social media GIS used a design which showed information as semitransparent circles depending on its present location data and contents. This made it propose an information utilization system based on the assumption of disaster outbreak times when information overload happens as well as normal times.

Keywords: Social Media GIS, Disaster Information, Disaster Reduction, Regional Knowledge, Support for Information Utilization

1. INTRODUCTION

According to the White Paper on Disaster Management (2012) [1], measures for disaster prevention and reduction of the effects of natural disasters in Japan include “self-help”, “mutual help (cooperation)”, and “public help (rescue and assistance by public bodies)”.“Self-help” refers to local residents, businesses, and other entities protecting themselves from disaster; “mutual help (cooperation)” refers to local communities helping each other; and “public help” refers to measures by government bodies such as national and local governments. Further, the most fundamental form of help was said to be self-help, which involves measures taken by individuals. Nowadays, anybody, anywhere, anytime can use an information system to easily send, receive, and share information, and through the effective use of information systems, disaster information possessed by local residents can be accumulated and shared.

Additionally, the Science Council of Japan (2008) [2] divided “local knowledge” into “expert knowledge” based on scientific knowledge, and “experience-based knowledge” produced by the experiences of local residents, and indicated its importance. Concerning “local knowledge” that is the “experience-based knowledge” of local residents, and exists as “tacit knowledge” that is not visualized if it is not communicated to others, as a measure for disaster prevention and reduction, it is essential for the “experience-based knowledge” to be transformed into “explicit knowledge” which is of a form that can be accumulated, organized, utilized, and made publicly available through the use of information systems, and to have local related entities accumulate the knowledge together. Moreover, Committee for Policy Planning on Disaster Management – Final Report by the Central Disaster Management Council (2012) [3] particularly specified the importance of the roles of GIS (Geographic Information Systems) and social media in the collection and transmission of disaster information.

In Japan, as a disaster countermeasure, local governments provide information to local residents in the form of disaster prevention maps and hazard maps which show local hazardous places, evacuation sites and so on. However, this information is mainly published as maps that are in paper form or in PDF format on the website. Therefore, it is difficult to update the information on disaster prevention maps and hazard maps in real time, and these forms of information are not very suited to being shared during a disaster outbreak. Further, so that information can be efficiently accumulated and shared during a disaster outbreak, it is desirable that information systems which people are accustomed to using in normal times can be used as is during disasters. However, when a disaster occurs, a situation where the amount of contributed information increases, and there is an excessive amount of information can be expected; therefore, it is necessary for systems to automatically classify contributed information.

Against the above-mentioned background, the present study aims to design and develop a social media GIS for reducing the effects of natural disasters in normal times through to disaster outbreak times. This is achieved by designing and developing a social media GIS that integrates a Web-GIS with an SNS and includes a function for classifying contributed information. The social media GIS enables disaster information provided by local residents and governments to be mashed up on a GIS base map, and for the information to be classified and provided to support the utilization of the information by local residents. Further, the present study also aims to operate the social media GIS and evaluate the operation. During normal times when there is no disaster, disaster information is collected via the SNS, and local disaster information is accumulated. Through this, the system aims to improve the disaster prevention awareness of local residents. Further, during disaster outbreaks when there is an excess of information, if a communications environment (electricity, internet, information terminals, etc.) can be secured, the system aims to support evacuation activities by automatically classifying disaster information, promptly displaying it on the digital map of the Web-GIS, and ensuring its noticeability. Through having people use the system routinely and get used to it in normal times in this manner, the possibility that the system can be effectively used with no problem as a means for reducing the effects of natural disasters even in tense situations during disaster outbreaks can be anticipated.

2. RELATED WORK

The aim of the present study is to develop a social media GIS that supports the utilization of disaster information and acts as a measure for reducing the effects of natural disasters from normal times through to disaster outbreak times. Therefore, prior research in fields related to the present study [4]-[21] can be classified into the following three areas: (1) Research relating to system development which utilizes GIS; (2) Research relating to the development of social media GIS; and (3) Research relating to proposals for systems that classify contributed information.

As representative examples of research in recent years, in the research area of (1), as a measure to reduce the effects of natural disasters during normal times, Murakami et al. (2009) [4] developed a system that supports disaster prevention workshops by using a GIS. In the research area of (2), Okuma et al. (2013) [5] developed a social media GIS that integrated a Web-GIS, an SNS, and Twitter, and demonstrated improvement of local residents' disaster prevention awareness through the accumulation of disaster information, as a measure for reducing the effects of natural disasters during normal times. Further, Murakoshi et al. (2014) [6] integrated a function for classifying contributed information into the social media GIS of Okuma et al. (2013) [5], and developed a system effective as a measure for reducing the effects of natural disasters from normal times through to disaster outbreak times. Yamanaka et al. (2010) [7] proposed a support system for situation assessment which utilized text data with spatio-temporal information and was designed for use by managers of facilities. They conducted an experiment in a large-scale park which involved a hypothetical disaster outbreak, summarized contributed text data information, and displayed the congested local situation on a Web map using icons as messages. Further, Moriya et al. (2009) [8] proposed a system in which text data relating to local information in blogs was used to display the local situation (such as image, impression, and atmosphere of a place) on a Web map by using circular depictions.

In the above-mentioned prior research in fields related to the present study, measures for reducing the effects of natural disasters during normal times include development of a system which uses GIS to support disaster prevention workshops, and development of a social media GIS which accumulates disaster information. Government measures include the Japanese Ministry of Land, Infrastructure, Transport and Tourism's Hazard Map Portal Site[1)], and disaster prevention maps and hazard maps provided by local governments. Further, there is research which proposed a system which utilizes text data to display the local situation on a Web map using icons and circles which was demonstrated as being useful. However, except for in research by Murakoshi et al. (2014) [6], up to now, there has not been development of a system designed for use from normal times through to disaster outbreak times which, in order to reduce the effects of natural disasters on a sustained and continuous basis throughout such periods, supports utilization of disaster information possessed by local residents by automatically classifying disaster information provided by local residents and promptly displaying it, and providing it on a GIS base map together with disaster information provided by governments with which it is mashed up. Therefore, the present study is based on the research results of Murakoshi et al. (2014) [6] in particular, and is unique in that it uniquely designs and develops a social media GIS aimed at realizing the features outlined above. Further, the present study is unique in that it operates the social media GIS and carries out an evaluation of the operation.

3. SYSTEM DESIGN

3.1. System Features

In the present study, a social media GIS effective in supporting the utilization of disaster information has a design in which a function capable of classifying and displaying contributed information according to location information and content is included in a system which combines two web applications – an SNS and a Web-GIS, as shown in Fig. 1. The system has a structure in which the Web-GIS and the contributed information classification function are installed in the SNS. Use of the SNS enables provision of information from local residents, and enables local information concerning disasters possessed by local residents as tacit knowledge to be converted to explicit knowledge and accumulated and shared among users. During normal times, through the SNS, local residents who are the users of the social media GIS will contribute information such as information concerning dangerous and safe places in disaster outbreak times which is not noted in detail on disaster prevention maps or hazard maps produced by the government. In disaster outbreak times, through the SNS, the local residents will contribute similar information, after ensuring their own safety. Further, disaster information provided by the government in normal times, such as that concerning overall degree of danger and facilities that provide support in disaster outbreak times, will be accumulated in advance, and disaster information provided by the government during disasters will also be collected and accumulated.

The above-mentioned disaster information contributed by local residents and disaster information provided by the government will be saved in a database, and the former information will be classified according to location information and content. Together with the disaster information from the government, the classified information will be integrated into the Web-GIS, mashed up on a digital map, and visualized. Therefore, on the Web-GIS digital map, even in situations where a disaster has occurred and there is an excess of information, high noticeability of all contributed information can be maintained, and on the digital map, users can efficiently accumulate and share disaster information which includes location information among themselves.

Based on the above, the usefulness of the present system lies in the fact that it can ease the restrictions mentioned in the following three points:

1) Bidirectionality of information transmission: In this system, information contribution and viewing functions are installed in the SNS. This allows all users to contribute and view information anytime from anywhere regardless of whether it is during normal times or disaster outbreak times.

2) Mitigation of burden of obtaining information: In this system, the system automatically classifies contributed information and displays it on the digital map of the Web-GIS. Therefore information can be processed in real time and users can easily determine the riskiness and safety of places that is conveyed by the information. Further, the situation where a user does not know their own present location outside has been anticipated, and the system obtains location information and displays facilities that provide support during disasters in the neighborhood where the user is located, and also displays information contributed concerning the neighborhood where the user is located. Therefore the system can reduce the burden experienced when obtaining disaster information.

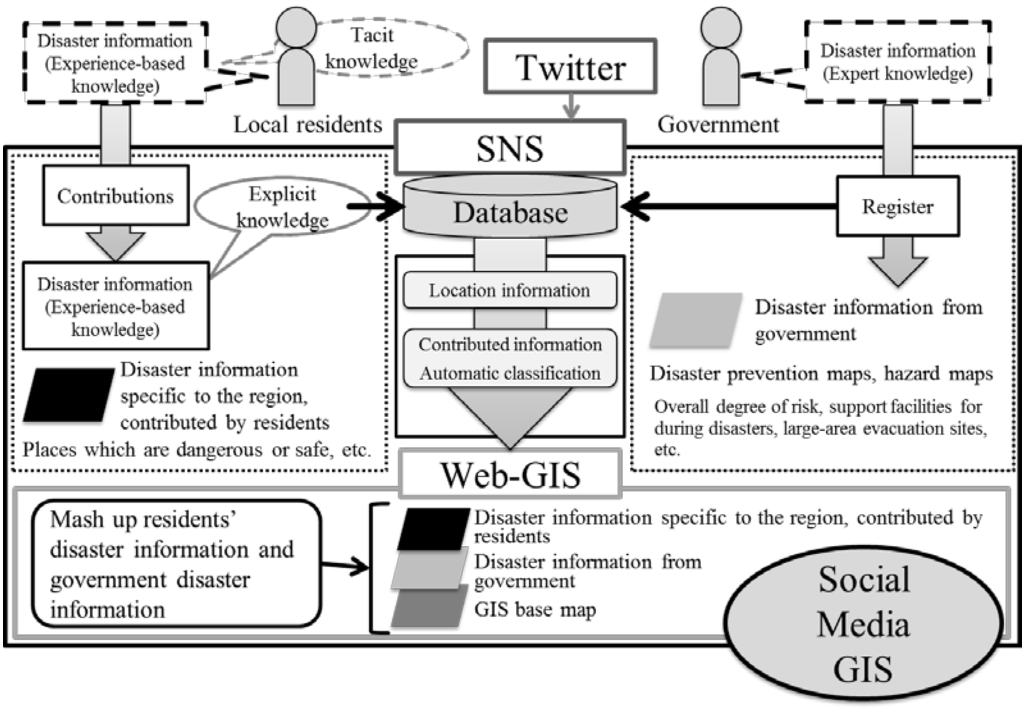

Fig. 1 Design of Social Media GIS

3) Mitigation of spatial and temporal restrictions: The information terminals that this system is designed for use with are PCs and portable information terminals. Concerning the latter, the system is designed for use with smartphones and tablet terminals, whose use has rapidly spread in recent years. Both these types of portable information terminals have touch panels with large screens, making them easy to use when dealing with digital maps, and both types allow connection to the internet from anywhere via cellular phone data communication networks. Anticipating the situation of users using the system outdoors as well during both normal times and disaster outbreak times, a system compatible with both PCs and portable information terminals has been designed and developed. Thanks to this, the system can be used anytime, regardless of whether the user is indoors or outdoors.

3.2. System Design

3.2.1. System configuration

The social media GIS of the present study is formed using three servers - a web server, a database server, and a GIS server. The web server mainly performs processing related to the SNS, and accesses the GIS server and the database server to integrate each of the functions. The SNS is operated using JavaScript and PHP, and the database server is managed using MySQL, and stores disaster information contributed by local residents which is collected through the SNS and disaster information from the government. For the web server and the database server, the rental server of the information infrastructure center of the organization to which the author of the present study belongs was used. For the GIS server, as the OS, Microsoft Corporation's Windows Server 2008 was used, and as the GIS server software, Esri's ArcGIS Server 10.0 was used.

3.2.2. Web-GIS

In the present study, for the Web-GIS, Esri's ArcGIS Server 10.0 was used, and for the GIS base map of the Web-GIS, the SHAPE version (Rel.8) of Shobunsha Publications, Inc.'s MAPPLE10000, which is part of their MAPPLE digital map data and includes detailed road system data, was used. As the map that was superimposed with this digital map data, the user interface of Google Maps was used. Among the options provided by Esri that are ArcGIS Server 10.0 API targets, the Google Maps user interface is the one that has been used the most in earlier studies in fields related to the present study. Concerning the superimposition of MAPPLE10000 (SHAPE version) and Google Maps, Google Maps employs the new geodetic system coordinates, while MAPPLE10000 conforms to the former geodetic system coordinates; therefore, ArcTky2Jgd, which is provided by Esri as product support, was used to convert the MAPPLE10000 geodetic system coordinates to the new coordinates. Furthermore, editing was performed using ArcMap 10.0 such that disaster information provided by Mitaka City and the Metropolis of Tokyo, the regions for operation, and information peculiar to each place could be input. Since the object of the present study is disaster information, users can use the Web-GIS to refer to a detailed road system that includes small streets that is output from MAPPLE10000, and by doing so they can accurately check locations related to contributed information, and in particular, precisely display disaster information related to the risk and safety of evacuation routes in disaster outbreak times. Further, the system has been set such that when the PC interface for users is used, the digital map can be viewed using full screen display. Thanks to this, users can get a general view of contributed information over a wide range, and enlarge the digital map to check information in detail.

3.2.3. SNS

In the present study, an SNS was selected as the social media for integration with the Web-GIS. The SNS was uniquely designed and developed to suit the objectives of the present study. An SNS was chosen because if an SNS is used, the system can be uniquely designed and developed to suit the objectives of use, and detailed system configuration can be performed to suit regional characteristics of the regions in which the system is to be operated. In this system, community functions limiting topics and users were not included, and functions related to user personal data registration and profile publication, information and image contribution and viewing, and commenting were uniquely designed to suit to the objectives of the present study. Since the object of this system is disaster information, for which reliability is regarded as important, the system has been designed such that it requires users to register, and each individual user can be identified by either their real name or an assumed user name. Therefore, the system is designed such that an environment in which it is difficult to make inappropriate statements or behave inappropriately has been prepared in advance, and the reliability of contributed information and comments can be improved.

Further, a button function and ranking function have been included in the SNS. Concerning the button function, it is used when users view disaster information which has already been contributed, and allows users to easily express that they have the same information. Further, a ranking function was added to the button function, and on the disaster information ranking page of the user screen, the ten information items for which the most amount of users have the same information are displayed in descending order.

3.2.4. Twitter

The present study employs a system design which allows realization of long-term operation by preventing reduction in the number of active users and allows users to contribute information anytime using portable information terminals regardless of whether they are indoors or outdoors. Therefore, Twitter was selected from among the various forms of social media, and was mashed up with the SNS which was uniquely developed, as mentioned in the previous section. Of the various forms of social media, Twitter has the easiest information contribution method, and many tweets per day can be expected, so it is essential for realizing long-term operation of the system. The system is designed such that when users contribute information from Twitter, they tag the information with the hashtag #mtkgis and with location information which employs a GPS.

3.2.5. Function for classifying contributed information

Anticipating situations where a lot of information is contributed when a disaster has occurred and there is an excess of information, a function which automatically classifies and organizes contributed information was set up and installed in the SNS. Similarly to what is described in Moriya et al. (2009) [8] in Section 2, a method in which words related to local information are obtained from contributed information, and the local situation and that location are displayed on the digital map via a circular illustration is employed. In this study, contributed information is classified into two categories according to whether it relates to either danger or safety. The system automatically classifies contributed information by searching contributed content using multiple character string searches which employ regular expressions. Specifically, when the words “danger” or “dangerous” are included in contributed information it is classified as information relating to danger, and when the word “safe” is included in contributed information it is classified as information relating to safety. Contributed information is classified right after being contributed and can be displayed on the Web-GIS digital map immediately.

Concerning this point, so that the system can accurately automatically classify and display contributed information as information related to either danger or safety, rules for making contributions which include specific illustrative examples are presented in advance on the initial page of the system and in the instructions for use of the system which are distributed to all users, so that users do not use vague expressions. Through this, due to having the users contribute information according to the above-mentioned rules during normal times, even in disaster outbreak times it can be anticipated that users will continue to contribute information in a similar manner; therefore, the probability that the system can appropriately classify contributed information can be increased.

As outlined above, when contributed information that has been classified is registered in the database, flags are added to it; therefore, the system is designed such that fields are created in advance in the database and flags can be stored in the database. When illustration is made using the Web-GIS, illustration is made using semitransparent circles that are color-coded based on the flags (red for danger, green for safety). Thanks to this, even in cases where many pieces of information are concentrated in certain areas, different types of contributed information can easily be distinguished. Further, taking into account the accuracy of acquisition of GPS location information of portable information terminals, the radius of the circles was set at 50 m.

3.2.6. Function for checking facilities that provide support during disasters

In this study, seven types of facilities included in the Tokyo Metropolitan disaster prevention maps[2)] are designated as facilities that provide support during disasters. They are temporary stay facilities, shelters, evacuation areas, water supply points, medical institutions, stations for aiding return to home (shops, etc. that provide support when people for whom it is difficult to return home are returning home on foot), and gas stands. Further, a system has been designed which enables users to check facilities that provide support during disasters in an optional range based on present location or any location, and based on any facility category. The facility names, categories, and addresses of the facilities that provide support during disasters are published, but the distance between two points cannot be calculated based on addresses. Therefore geocoding is conducted, addresses are converted to latitude/longitude, and then that data is stored in the database in advance.

Therefore, the system has a design which allows the search range to be selected from the range of 50 to 500 m, and facility categories to be selected from the seven categories mentioned above. When a request for a check of facilities that provide support during disasters is sent from an information terminal, in order to measure the distance between the designated point and disaster support facilities in the area of that point, the difference between the latitude/longitude that is sent from the information terminal and the latitude/longitude of each disaster support facility is used to calculate the distance between the designated point and each disaster support facility. Thus, facilities that are within a range designated by the user are confirmed, and further, facilities in a designated category are displayed on the digital map of the Web-GIS.

4. SYSTEM DEVELOPMENT

4.1. System Front End

In the present study, as is described in detail below, unique functions for users are operated, and support for utilization of disaster information is conducted.

4.1.1. Disaster information contribution and viewing functions

When a user contributes disaster information, they go to the contribution page using “Post disaster information”. On the contribution page, they input “Title”, “Image”, “Main Text”, “Location”, and contribute their information. Concerning input of location, when the PC interface is used, the user clicks the location on the map and location information is added; however, when the interface for portable information terminals is used, it is possible to add location information using a GPS. Concerning display of the time, as described in detail in Section 4.2.2, for this system, the development of an operation system run by multiple administrators that is operated starting from normal times of no disaster is anticipated. If users move from a dangerous place to a safe one and then contribute information, concerning contributed information that describes circumstances at a time in the past, administrators change the time display to match that time. Further, as described in Section 3.1, in both normal times and disaster outbreak times, users can contribute information about dangerous or safe places and so on, communicate by commenting about information contributed by other users, and update contributed information in real time by adding to or amending the contents of all contributed information using comments.

When users log into the system, they can check the latest ten items of contributed information on the initial page, and check contributed content and images on the disaster information list page. Further, as outlined in Section 3.2.2, users can view all contributed information on the digital map of the Web-GIS, and when using the PC interface for users, users can also view contributed information in detail using full-screen display. Further, as described in Section 3.2.5, all contributed information is automatically classified by the system and illustrated on the digital map in semitransparent circles divided into red for danger and green for safety, so users can easily distinguish between different types of information.

4.1.2. Function for viewing disaster information provided by governments

The overall degrees of danger (the degrees of danger calculated by combining the risk of building collapse and the risk of fire) published on the disaster prevention maps provided by Mitaka City and the Metropolis of Tokyo (the regions for operation of the system), and the seven types of disaster support facility described in Section 3.2.6 were input into the GIS base map using Esri’s ArcMap, and a disaster prevention map unique to the system of the present study was created. Through this, disaster information contributed by users who are local residents and disaster information provided by governments is all mashed up on the GIS base map, and users can check all this information on the one screen using the Web-GIS.

4.1.3. Function for checking facilities which provide support in disaster outbreak times

Users can search for seven types of disaster support facility by setting their choice of range and facility category. Concerning search range, a radius of 50 to 500 m from a designated point can be selected from a pull-down menu. Facility category can be selected from among seven types, and disaster support facilities in the area of a present location or a location of the user’s choice can be checked.

4.1.4. Disaster information ranking function

By viewing disaster information that has already been contributed and using the button function, users can easily indicate that they have the same information if that is the case. In addition, a ranking function has been added to the button function, so disaster information items for which the most amount of users have the same information are displayed in descending order on the disaster information ranking page of the user screen.

4.2. System Back End

4.2.1. System for classifying contributed information

When users contribute disaster information, the system classifies the contributed information. Before contributed information is stored in the database, matching using regular expressions with respect to character strings stored in PHP variables is performed. In the case when a character string which is a matching target matches when a preg_match function is used, a value returned by the function is obtained. In this case, 1 or 2 is assigned to the variable for a flag, and is stored in the database together with the contributed content. The character strings which are targets of matching are the words “danger” and “dangerous” for information relating to danger, and the word “safe” for information relating to safety. Concerning this point, misclassification due to fluctuation in expression is prevented by displaying contribution examples on the initial page of the system in advance. Information classified as outlined above is updated when the web page is loaded, and is depicted on the digital map of the Web-GIS using color-coded semitransparent circles.

4.2.2 System for management of contributed information by administrators

Every user’s contributions of information and image files are all stored as data in the database of the system. Administrators manage users and check contributed information using a list screen designed especially for the purpose. Administrators can take the measure of suspending accounts of users who have made inappropriate transmissions or behaved inappropriately, and if by any chance an inappropriate contribution is made, administrators can delete the contribution with just one click. Thanks to these features, there is no need for administrators to search to see whether or not inappropriate contributions of information have been made within the system; therefore, their burden can be lessened.

Further, for this system, it is desirable to develop a system of operation in which starting from normal times of no disaster, there are multiple administrators, consisting of government employees, people in firefighting and police organizations, and local residents. In addition, it is desirable that in the system of operation, information contributed by local residents is routinely checked on a high-frequency basis, and the reliability and consistency of information can always be guaranteed by taking the measure of deleting inappropriate contributions of information should any be discovered, and checking that contributed information is being appropriately classified by the system for classifying contributed information mentioned in the previous section. When a disaster has broken out, it is necessary to take not only the measures outlined above, but also to update published contributed information in real time and always guarantee the reliability and consistency of the information by taking the following measures. When multiple pieces of contributed information contradict each other, it is necessary to check the information by referring to information provided by other media and information systems, and then delete inappropriate information. Further, it is necessary to delete and amend information provided by local residents and governments in the case that it has become inappropriate in the circumstances of the disaster, which change by the minute.

4.3. System Interfaces

The system has three kinds of interface – a PC screen for users (Fig. 2), a portable information terminal screen especially optimized for smartphones and tablet terminals, and a PC screen for administrators.

5. TEST OPERATION AND OPERATION IN THE REGIONAL COMMUNITY

In accordance with the operation process in Table 1, test operation of the social media GIS designed and developed in the present study and evaluation of the test operation were conducted, and then full-scale operation was conducted.

5.1. Comparison with Existing Services in Region for Operation of System

In Mitaka City, the region for operation of the system, a plan for supporting the evacuation of people requiring special help during disasters was formulated in 2011, and a disaster prevention map[3)] has also been created and provided. Table 2 compares disaster prevention maps relating to Mitaka City with the features of the system of the present study. The Mitaka City disaster prevention map can be used to check locations of large-area evacuation sites designated by the city and the overall degree of danger of locations within the city (the degree of danger in Mitaka City is ranked using three levels only – 1 to 3). However, since it is published in PDF format, information cannot be viewed all at once. The Tokyo Metropolitan disaster prevention maps are published as digital maps, so it is easy for users to view information they need, and the maps include the facilities that provide support during disasters that were mentioned in Section 3.2.6 and other information. However, the maps do not have detailed disaster information concerning each region. Further, these government disaster prevention maps do not include any disaster information that is experience-based information possessed by local residents at all.

No.	Description
1	User profile publication
2	The ten most recent items of contributed information
3	The ten most important items of contributed information
4	The number of users
5	Go to my page
6	Go to the page where information can be contributed from computers
7	List of contributed information
8	Go to the page where support facilities in times of disaster can be checked
9	Go to the page where change and registration of personal data can be made
10	Logout
11	Explanation to use this system
12	Disaster information is displayed on Web-GIS digital map in the region of operation (Mitaka City)
13	General degree of risk
14	Explanation of disaster information contributed by users

Fig.2 PC screen for users

Table 1 Operation process of the system

Process	Aim	Period	Specific details
1. Survey of present conditions	To understand efforts related to tourism in the region for operation (Yokohama City)	July 2014	- Survey of government measures and internet services - Interviews with government departments responsible, tourist associations, etc.
2. System configuration	Configure the system in detail to suit the region for operation	August 2014	- Define system requirements - System configuration - Create operation system
3. Operation test	Conduct the system operation test	September 2014	- Create and distribute pamphlets and operating instructions - System operation test
4. Evaluation of operation test	Reconfigure the system based on results of interviews with operation test participants	October 2014	- Evaluation using interviews - System reconfiguration - Amendment of pamphlets and operating instructions
5. Operation	Carry out actual operation of the system	October-December 2014	- Appeal for use of the system - Distribution of pamphlets and operating instructions - System operation management
6. Evaluation	Evaluate the system based on the results of questionnaires, the results of access analysis which used log data during the period of actual operation, and the results of analysis of contributed information	January 2015	- Evaluation using web questionnaires , access analysis which used log data, and analysis of contributed information - Identification of measures for using the system even more effectively

Table 2 Comparison of features with disaster prevention map related to region for operation

	Use of digital map	Viewing means	Contributed information from local residents	Automatic classification of contributed information
Tokyo Metropolitan disaster prevention maps	Yes	Digital map	No	No
Mitaka disaster prevention maps	No	PDF	No	No
The system of the present study	Yes	Digital map	Yes	Yes

Therefore, the system of the present study is useful in that it can effectively provide detailed disaster information specific to the region where it is operated, by gathering and accumulating disaster information contributed using an SNS by users who are local residents and displaying the disaster information on the digital map of a Web-GIS. Further, it is useful in that disaster information provided by users who are local residents and by governments can all be checked visually on the digital map, useful in that the system automatically classifies contributed information and immediately displays it on the digital map, and can also handle situations during disasters when there is an information glut, and useful in that users can use the system to check facilities that provide support during disasters. Even in disaster outbreak times, if an environment in which communication can be conducted can be secured, disaster information can be gathered, accumulated, and provided by the system, in the same way it is during normal times. Therefore, the system can also supplement efforts made by governments concerning disasters.

5.2. Operation Test and Evaluation of Operation Test

Before full-scale operation was conducted, three students in their twenties who were residing or attending school in Mitaka City were selected and a one-week operation test was conducted. After the operation test, the students who participated in the operation test were interviewed. In the interviews, the students expressed the opinion that a large-sized map was desirable when viewing disaster information on the digital map. Therefore, the system was redeveloped concerning this point only – the full-screen display for the PC interface for users, mentioned in Section 3.2.2.

Table 3 Outline of users and respondents to the questionnaire

	Aged 10 to 19	Twenties	Thirties	Forties	Fifties	Sixties	Seventies	Total
Number of users (people)	1	7	6	16	15	3	2	50
Number of questionnaire respondents (people)	1	7	6	14	11	3	2	44
Valid response rate (%)	100.0	100.0	100.0	87.5	73.3	100.0	100.0	88.0

5.3. Operation

When full-scale operation was conducted, local residents aged eighteen years or over residing in, commuting to, or attending school in Mitaka City were targeted as users. Pamphlets and operating instructions were placed in the city hall and bases of citizen activities in order to appeal for use of the system. When first using the system, users registered the personal information items of “User name”, “Password”, “Age group”, “Gender”, “Region”, and “Email address”. Concerning “Age group”, “Gender”, and “Region”, which were displayed on the screen, users could set whether or not to make these items public at their discretion. After registering, users could use the system when they logged in, and after logging in, users could reset the above-mentioned items of personal information that they had registered.

Table 3 shows details of the users during the two-month period of operation. There were 50 users in total, with 28 being male and 22 being female. Users in their forties and fifties made up the greatest proportion of users, at 32% and 30%, respectively, while the proportion of users in their twenties, thirties, and sixties and over was 14%, 12%, and 10%, respectively, so it can be said that the system was used by a wide range of age groups. After having each user use the system for about one month, web questionnaires were given to users, and use of the system was evaluated. The number of valid respondents to the questionnaire was 44 (a valid response rate of 88%), with 26 valid respondents being male and 18 being female.

6. EVALUATION

In this section, according to the operation process shown in Table 1, firstly, based on results of the questionnaire, an evaluation of operation concerning use of the system is conducted. Next, based on results of access analysis utilizing log data and analysis of contributed information from during full-scale operation, an evaluation of operation concerning the aim of the system – that is, the aim of supporting utilization of disaster information in order to reduce the effects of natural disasters from normal times through to disaster outbreak times – was conducted. Further, based on the results of these evaluations, measures of using the system even more effectively were identified.

6.1. Evaluation Concerning Use of the System

6.1.1. Evaluation of usability of system

As shown in Fig. 3, an evaluation of the usability of the system was conducted focusing on the system’s unique functions. Concerning distinguishing between different types of information through the function for classifying contributed information, 89% of responses were “Easy” or “Fairly easy”, so it can be said that the system, automatically classifying contributed information and displaying the information on the digital map of the Web-GIS after color-coding it was useful. Concerning checking information using the function for checking facilities that provide support during disasters, 91% of responses were “Easy” or “Fairly easy”. It is considered that improving the method of displaying present location and facilities that provide support during disasters on the digital map led to this high rating. Concerning use of the interface for portable information terminals, 77% of responses were “Easy” or “Fairly easy”, so it can be said that developing a user interface optimized for portable information terminals was effective.

6.1.2 Evaluation concerning noticeability of contributed information

As shown in Fig. 4, an evaluation concerning the noticeability of contributed information was conducted. The evaluation asked users two questions – that is, whether it was easy to identify each piece of contributed information on the digital map of the Web-GIS even in places where contributed information was concentrated in certain parts of the map, and whether it was easy to check information in the vicinity of the user’s present location when viewing the digital map using the screen for portable information terminals. The former question relates to the ease of identifying each piece of contributed information during disaster outbreaks in situations where there is a glut of information, and 86% of responses were “Easy” or “Fairly easy”. Therefore, it can be said that displaying contributed information on the digital map in semitransparent circles colored red or green according to the content of the information was useful. Further, the latter question relates to the ease of checking information (information contributed by local residents, information relating to facilities which provide support during disasters, etc.) using portable information terminals during disaster outbreak times when users are mainly outside, and 84% of responses to this question were “Easy” or “Fairly easy”. Therefore, it can be said that along with the user interface optimized for portable information terminals, the above-mentioned color-coded display of contributed information on the digital map and the display of facilities that provide support during disasters using different icons for each category of facility (which was an improvement made to the system) were effective. Consequently, based on the above evaluation results, it is possible that the system can be used as a means for reducing the effects of natural disasters in disaster outbreak times as well if a communications environment can be secured, by using a digital map to provide disaster information for portable information terminals of users who are mainly outside, and supporting evacuation activities.

6.1.3. Evaluation concerning effects of use of the system

As shown in Fig. 5, an evaluation of the effects of using the system was conducted. The evaluation asked users two questions – that is, whether they had become interested in danger and safety in the region through using the system, and whether they wanted to use the system in the future as well. 91% of responses to the former question were “Became interested” or “Became a little interested”, so it can be said that the disaster prevention awareness (which leads to reduction of the effects of natural disasters) of more than half the users improved. Further, in response to the latter question, 94% of responses were “Want to use it” or “Lean toward wanting to use it”. Therefore, it can be anticipated that the system will continue to be used in line with its objective of supporting the utilization of disaster information in order to reduce the effects of natural disasters.

6.2. Evaluation Concerning Support of Utilization of Disaster Information

6.2.1. Access count and means of access

(1) Outline of access analysis

In order to analyze user trends, analysis was performed using access logs collected during the period of operation. In the present study, Google Analytics was used for collecting log data. Google Analytics is an access analysis service provided free of charge by Google, and is widely used. It can be used by setting up a tracking code in the source of a web page.

(2) Results of access analysis

The total access count for the period of operation was 2,537. Although there were differences in the access counts for each week, the average weekly access count was approximately 24, and it can be said that users used the system on a continual basis. Concerning the access counts for each page, the access count for the contribution page was the highest, being 34% of the total. Next was the access count for the page for checking facilities which provide support during disasters (10%), followed by the access count for the viewing page (9%). It can be seen that even if users did not contribute information, many users checked disaster support facilities and viewed disaster information. Concerning means of accessing the pages, 95% of access was from PCs and 5% was from portable information terminals; therefore, it can be presumed that use was mainly from PCs, and portable information terminals were used as a supplementary means of access. However, the fact that portable information terminals were also used shows that it is possible that the system can mitigate spatial and temporal restrictions during both normal times and disaster outbreak times.

6.2.2. Features of contributed information

Fig. 6 shows changes in the total number of users and the total number of contributions of information from week to week during the period of operation. Both the number of users and the number of contributions of information gradually increased, although there are differences in the rate of increase from week to week. The total number of contributions of information was 260 (the weekly average is approximately 26). Contributions from Twitter were all made using portable information terminals, but there were only six contributions from Twitter. Of the total number of contributions, 81% included images, and 4% of contributions were commented on. The fact that the comment function was also used and users were able to communicate with each other indicates that it can be anticipated that this function will be used not only in normal times but also in disaster outbreak times.

Information concerning danger made up 20% of the total, information concerning safety made up 68%, and other types of information made up 12%, and concerned disaster prevention storehouses, water supply points, and water wells for earthquake disasters.

Further, as shown by Fig. 7, contributions of information are dispersed over the whole area of Mitaka City, so it can be assumed that the locations of users' places of residence, commutation destinations, and schools were not concentrated in limited areas. However, there are regions where the amount of contributions of information is somewhat concentrated. In particular, there were many contributions of information concerning the area of the train station. This is considered to be due to the fact that many people come and go through this kind of area daily, and there are many places where narrow streets become even narrower due to bicycles, luggage, and the like.

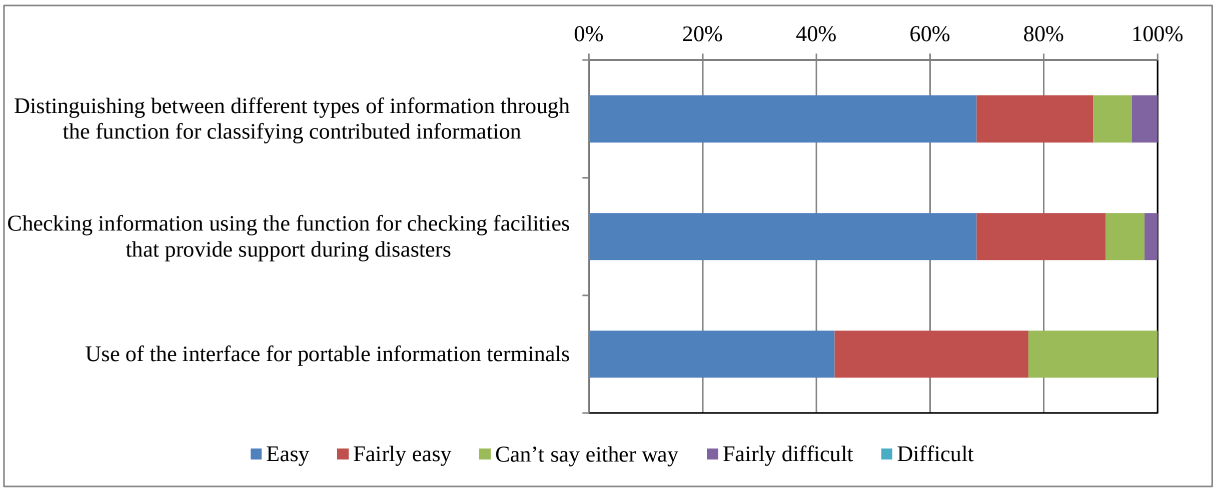

Fig. 3 Evaluation of usability of system

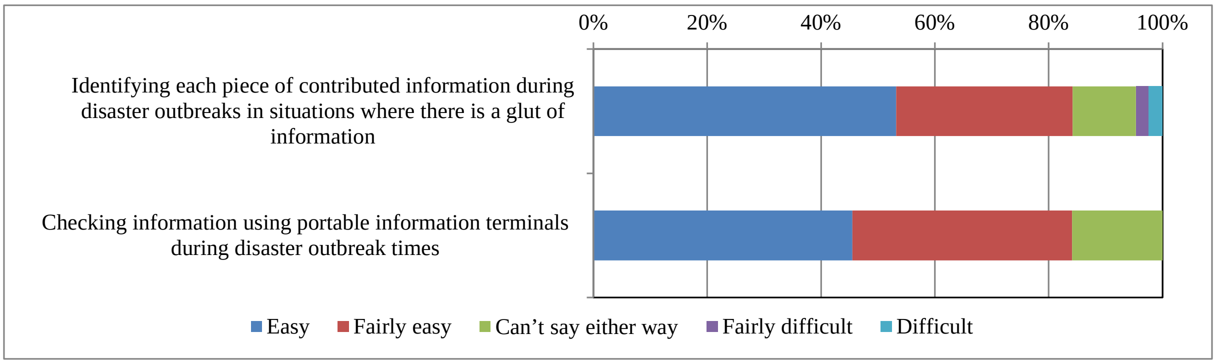

Fig. 4 Evaluation concerning noticeability of contributed information

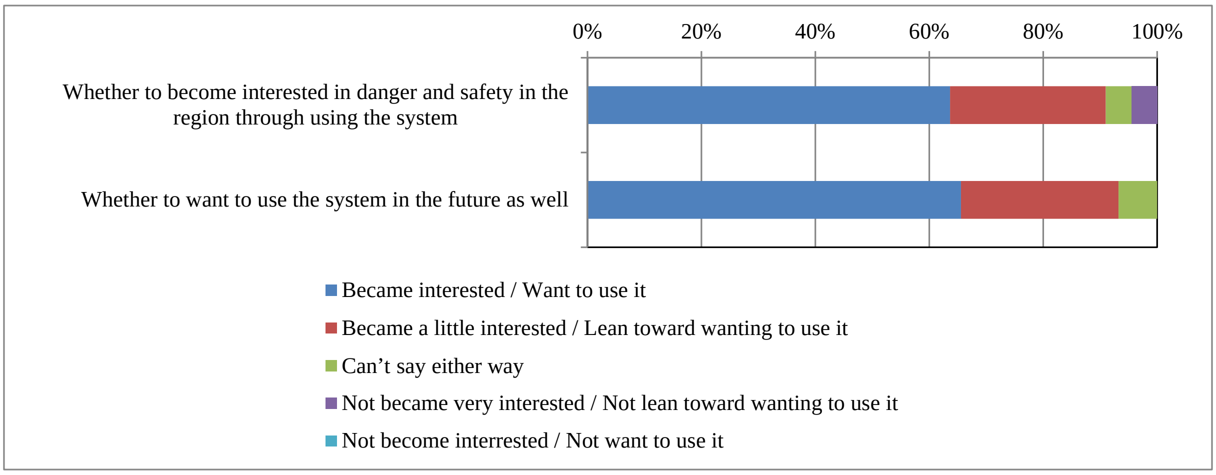

Fig. 5 Evaluation concerning effects of use of the system

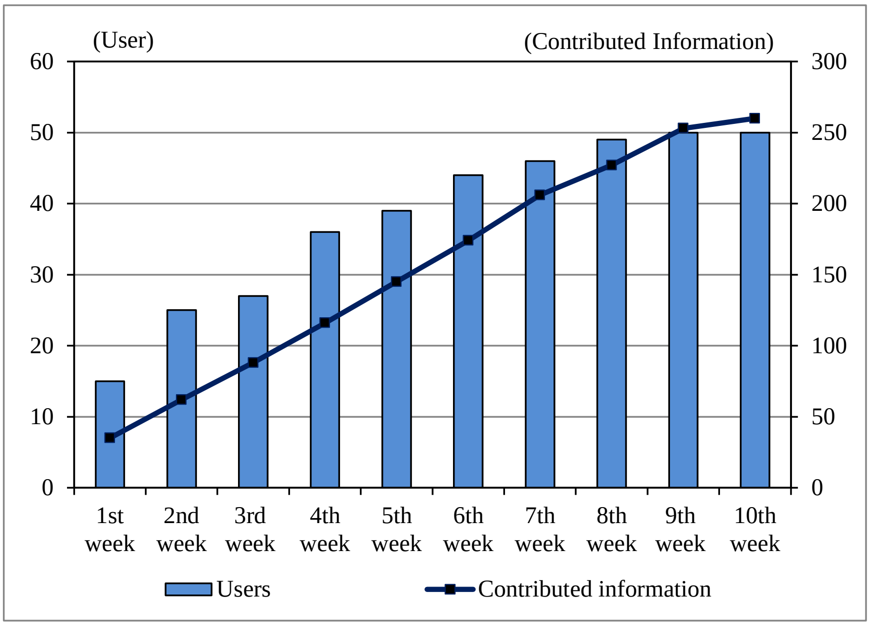

Fig. 6 Changes in the total number of users and the total number of contributions of information during the operation period

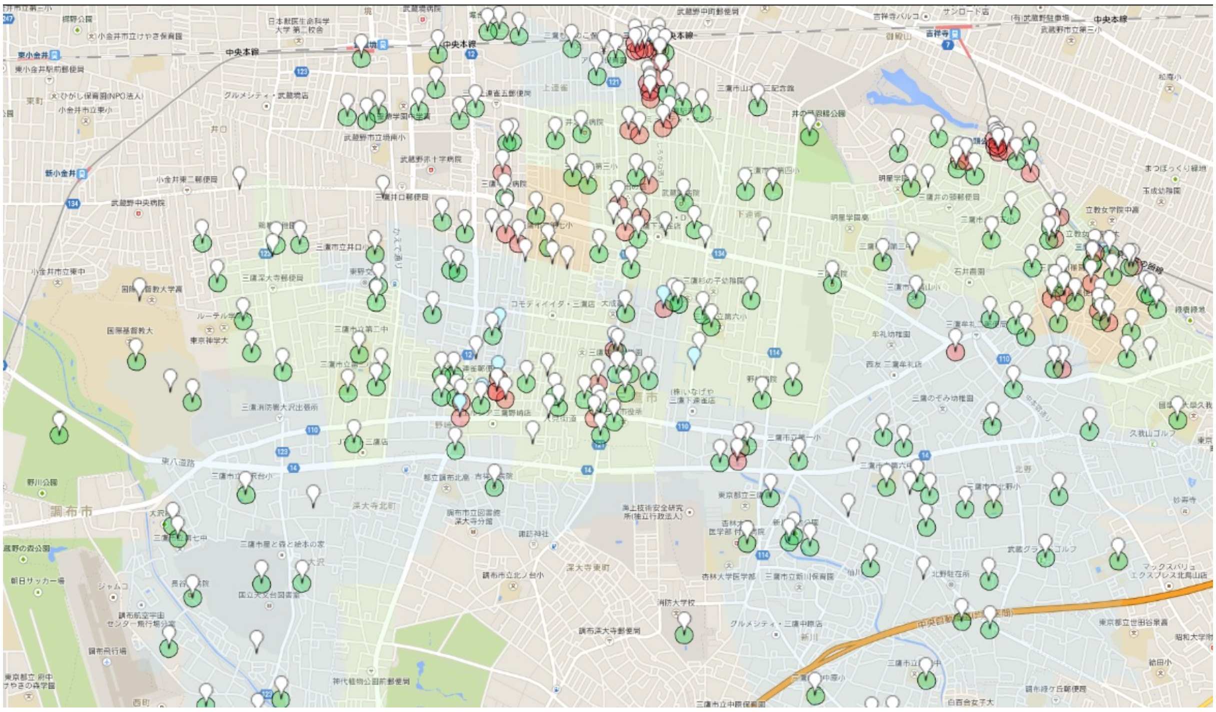

Fig. 7 Distribution of contributed information in the region for operation of the system (Mitaka City)

6.3. Identification of Measures for Using the System

Based on the results of the evaluation of the operation in this section, measures for using the system even more effectively were summarized into the two points below.

(1) Notification of information to passive users

GPS information of users' information terminals is continually obtained at a set interval, and the system searches for disaster information in the vicinity of the user and push-notifies the user of information within a set range in the vicinity of the user. Through this, passive users are notified of information.

(2) Operation of the system using cloud computing

In order to be sure the system operates even during disaster outbreaks, the system is distributed in earthquake-proof data centers. Doing this allows more reliable operation of the system than server operation by individuals. Further, combining ArcGIS Online (which is provided by Esri, Inc.)

with the system when it is used allows all servers to be operated using cloud computing.

7. CONCLUSION AND FUTURE RESEARCH TOPICS

The conclusion of the present study can be summarized into the following three points:

(1) A social media GIS which integrated a Web-GIS, an SNS, and Twitter and which included a function for classifying contributed information was designed and developed. A system which supports utilization of information in order to reduce the effects of natural disasters which anticipates use not only in normal times but also use during disasters when there is an information glut was proposed. The system supports utilization of information by depicting contributed information based on location information and content using color-coded semitransparent circles, and by displaying information based on information about present location. Mitaka City in the Metropolis of Tokyo was selected as the region for operation of the system. After a survey of existing conditions was conducted, the system was developed in detail.

(2) Since full-scale operation was to be conducted for ten weeks, a one-week operation test was conducted in advance and an area for improvement of the system was identified. After that, the system was reconfigured. People targeted as users of the system were those residing in, commuting to, or attending school in Mitaka City aged eighteen years of age or over. The number of users was fifty in total. Users in their forties and fifties made up the greatest proportion of users, at 32% and 30%, respectively, while the proportion of users in their twenties, thirties, and sixties and above was 14%, 12%, and 10%, respectively, so the system was used by a wide range of age groups. During the period of operation, users accessed the system from PCs and portable information terminals, and contributed and viewed information.

(3) An evaluation of the operation was conducted based on questionnaires to users and access log analysis. Results from the questionnaires showed that due to the function for classifying contributed information and the function for checking facilities that provide support during disasters, it was easy for users to distinguish between different types of information and check information. Further, it is possible that the system can provide disaster information to portable information terminals of users who are mainly outside during disaster outbreak times as well, and can be used as means for reducing the effects of natural disasters. In addition, an improvement in disaster prevention awareness (which leads to reduction of the effects of natural disasters) was observed as a result of use of the system, and many users responded that they would like to use the system again in the future. Therefore, it can be anticipated that the system will continue to be used in the future in accordance with its objectives. Access log analysis showed that the system was continually accessed throughout the period of operation and that 260 pieces of disaster information were contributed, dispersed throughout Mitaka City.

Future topics for research include expanding the stages of use of the system to times of post-disaster restoration and redevelopment, cooperating with firefighters, police, and so on and operating the system with the participation of a wider user base, and increasing the track record of use of the system by operating it in other regions as well, and further increasing the significance of using the social media GIS developed in the present study.

ACKNOWLEDGEMENTS

In the operation of the social media GIS and the web questionnaire of the present study, enormous cooperation was received from those in Mitaka City of Tokyo metropolis and the neighboring area in Japan. We would like to take this opportunity to gratefully acknowledge them.

NOTES

1) Japanese Ministry of Land, Infrastructure, Transport and Tourism’s Hazard Map Portal Site http://disapotal.gsi.go.jp/, Accessed 2014, August 20.
2) Tokyo Metropolitan disaster prevention maps http://map.bousai.metro.tokyo.jp/, Accessed 2014, August 20.
3) Mitaka City disaster prevention map http://www.city.mitaka.tokyo.jp/c_service/003/003310.html, Accessed 2014, August 20.

REFERENCES

[1] Cabinet Office, Government of Japan, White paper on disaster management 2012. Tokyo, 2012.
[2] Regional Research Committee, Science Council of Japan, Recommendations: towards the accumulation and utilization of “Regional Knowledge”. Tokyo, 2008.
[3] Central Disaster Management Council, Committee for policy planning on disaster management – Final report: Toward reconstruction for a Japan that is unshakable. Tokyo, 2012.
[4] Murakami M, Shibayama A, Hisada Y, Ichii T, Zama S, Endo M, “Development of an information gathering and sharing system that supports disaster prevention activities carried

out by local residents and local governments", Journal of Japan Association for Earth Engineering, Vol.9, No.2, 2009, pp.200-220.

[5] Okuma T, Yamamoto K, "Study on Social Media GIS for accumulating urban disaster information: Accumulation of disaster information during normal times for purposes of disaster reduction measures", Socio-Informatics, Vol.2, No.2, 2013, pp.49-65.

[6] Murakoshi T, Yamamoto K, "Study on Social Media GIS for supporting utilization of disaster information: For disaster reduction measures in normal times through to times of disaster outbreak", Socio-Informatics, Vol.3, No.2, 2014, pp.17-31.

[7] Yamanaka T, Tanaka Y, Hijikata Y, Nishida S, "A supporting system for situation assessment using text data with spatio-temporal information", Japan Society for Fuzzy Theory and Intelligent Informatics, Vol.22, No.6, 2010, pp.691-706.

[8] Moriya K, Sasaki S, Kiyoki Y,"A dynamic creation method of environmental situation maps using text data information", DEIM Forum 2009, 2009, pp.B1-6.

[9] Honjo S, Yuhashi H, Information society for disaster reduction –Great East Earthquake and mobile communication-. Tokyo: NTT Publishing Co., Ltd., 2013.

[10] Ikemi H, Esaki T, Mitani Y, "Sustainable data-sharing for disasters based on the Wiki and GIS technologies", Theory and Application of GIS, Vol.17, No.1, 2009, pp.93-99.

[11] Okano S, Yasui S, Okazawa K, Ebara H, Okada H, "Hybrid disaster information distribution method for community networks", IEICE Technical Report, IN, Information Network, Vol.108(458), 2009, pp.499-504.

[12] Kato T, Kobayashi M, Sato N, Yotsuyanagi T, "Towards implementing a disaster management information mashup Ssystem in the community", Monthly Journal of the Institute of Industrial Science, University of Tokyo, Vol.62, No.4, 2010, pp.377-380.

[13] Takatani T, Iwaki T, Kato Y, "Creation of a regional disaster prevention support system aimed at planning urban areas that are resistant to natural disasters", Bulletin of Mizuru National College of Technology, No.43, 2008, pp.34-50.

[14] Inoguchi M, Tamura K, Takashi Furuya T, Kimura R, Hayashi H, "Proposal aimed at realization ofeffective on-site spatial information mashup for emergency map creation teams: A case study of the 2011 Great East Japan Earthquake", Journal of Social Safety Science, No.15, 2011, pp.219-229.

[15] Kawasaki A, Meguro K, "New trends in disaster response support using web mapping, observed in the 2010 Haiti Earthquake", Monthly Journal of the Institute of Industrial Science, University of Tokyo, Vol.62, No.4, 2010, pp.409-416.

[16] Yamamori K, "Establishment of a bulletin board for times of disaster", Bulletin of Faculty of Education Mie University, No.61, 2010, pp.13-19.

[17] Korida K, Kikuchi T, Yoshiyama N, Shibata Y, Takahashi M, Takenaka M, Aoki E, "Development of community disaster prevention SNS based on the trust and relationships between local inhabitant", The Special Interest Group Technical Reports of Information Processing Society of Japan, CSEC, "Computer Security", 2011-CSEC-52(16), 2011, pp.1-6.

[18] Wasaki H, "Disaster and regional SNS: The connection effect for rescue/recovery that came to light through the Sayou Town Torrential Rain Disaster", Bulletin of the National Museum of Ethnology, No.106, 2012, pp.127-146.

[19] Yamamoto M, Ogasawara H, Suzuki I, Furukawa M, "Information dissemination network on Twitter during the Great East Japan Earthquake", Information Processing Society of Japan Magazine, Vol.53, No.11, 2012, pp.1184-1191.

[20] Yoshimura N, Inoue T, "Analysis of use of public institution accounts in the microblog service Twitter before, during, and after the Great East Japan Earthquake", The Special Interest Group Technical Reports of Information Processing Society of Japan, GN, "Groupware and Network Service", 2012-GN-83(5), 2012, pp.1-8.

[21] Yanagisawa T, Yamamoto K, "Study on information-sharing GIS for accumulating local knowledge in local communities", Theory and Applications of GIS, Vol.20, No.1, 2012, pp.61-70.

Fifth International Conference on Geotechnique, Construction Materials and Environment, Osaka, Japan, Nov. 16-18, 2015, ISBN: 978-4-9905958-4-5 C3051

CLAY-CEMENT STABILIZED CRUSHED ROCK BASE FOR WESTERN AUSTRALIAN ROADS: STRENGTH PROPERTY INVESTIGATION

Peerapong Jitsangiam [1], and Matthew Merrin [2]
[1,2] Dept of Civil Engineering, Curtin University, Australia

ABSTRACT

With the current base course material in Western Australia, namely hydrated cement treated crushed rock (HCTCRB) base, roads using HCTCRB require excessive maintenance causing from its uncertainties. This study aims to determine specific strength properties of a potential replacement material of a clay-cement stabilized crushed rock. The findings showed that a crushed rock material with a newly developed 3% clay-cement binder, possessed unconfined compressive strengths and resilient moduli significantly greater than that of HCTCRB. The developed stress dependent equation also purports that this material admixture is still exhibiting unbound performance characteristics. A material's ability to acquire the accompanying strength advantages of a 3% clay-cement binder, whilst still potentially resisting common failure methods such as shrinkage cracking, suggests that based on its potential performance as a base course layer in a pavement structure, clay-cement stabilized crushed rock base is considerable to be a viable base course material for Western Australia.

Keywords: Base course materials, Clay-cement stabilization, Crushed rock base, Pavements, Base course layers

INTRODUCTION

Flexible highway pavements in Western Australia are constructed in a layered idealistic design, with the pavement layers preferably constructed with locally sourced materials due to the associated economic benefits. When local materials do not possess sufficient strength for this purpose however, an alternative solution is to implement artificial (e.g., cement and lime) stabilization practices, providing a solution that is more economically viable, and one which allows the engineering properties of the material to be controlled [1]. Whilst this is a common practice adopted globally in pavement engineering practices, Main Roads Western Australia have been fundamentally unsuccessful when trying to implement this procedure for Western Australian pavements. The most recent artificially stabilized base course material implemented, hydrated cement treated crushed rock base (HCTCRB), has some uncertainties (i.e., drying shrinkage cracking, proper curing process and manufacturing issues), leading to roads using HCTCRB required excessive maintenance and rehabilitation. This has required a larger amount of capital expenditure than that expected. Therefore the investigation into a better base course material for Western Australian pavement structures is required. This paper therefore presents specific strength parameters developed in the laboratory investigation of a crushed rock base material stabilized with a newly developed clay-cement binder.

HISTORY OF BASECOURSE STABILISATION IN WESTERN AUSTRALIA

From the first attempted stabilization of Western Australian base course's in the 1970's, ambiguities in the resulting pavement performances have led to Main Roads Western Australia essentially prohibiting the use of stabilized pavements, and placing a number of limitations on the use of modified pavements [2].

In 1975, extensive research was commissioned into the development of a new cement binder to replace the inefficient bitumen stabilization practices that were being implemented. Initial laboratory investigations produced promising results, with limestone stabilized with 2% cement possessing strength greater than that of limestone stabilized with 3% bitumen. When sections of Leach Highway were utilized as trial pavements however, it was established that fatigue cracking was a major issue for the material due to the stiffness of the cement [3].

As a result, Main Roads Western Australia reverted back to using local materials in their virgin state, predominantly crushed rock base. After the failure of segments of the Kwinana Freeway in 1992 however, attributed to the moisture sensitivity of the crushed rock base, Main Roads once again commissioned extensive research into the development of a new base course material. After detailed laboratory testing, HCTCRB was developed, and introduced in a trial section of Reid Highway in 1997. In 2003, field testing carried out indicated that the material exhibited strong pavement performance characteristics. In 2009 however, similar testing showed that the material was exhibiting characteristics of an unbound material, due to a retardation of the cement content over time [4]. This not only reduced the strength, but also meant the crushed rock base course was far more permeable and susceptible to moisture ingress, which was the original problem faced in 1992.

Whilst periodic changes have since been made to the material specification of HCTCRB, it is speculated that the material itself may be erratic with regard to fundamental elements such as quality control, and material uniformity [5]. With no solution developed to mitigate the sporadic performance of Western Australian pavements, the investigation into a new material was carried out, with the laboratory testing regime presented in the subsequent section.

LABORATORY TESTING METHODOLOGY

With the fundamental parameter of a base course being strength [6], an investigation into specific strength properties of a clay-cement stabilized crushed rock base has been undertaken. Whilst the major faults with HCTCRB were stabilizer permanency and the subsequent moisture susceptibility, if the clay-cement stabilized crushed rock did not possess sufficient strength, then an improvement in these faults would be an insignificant development. Therefore, the unconfined compressive strength and resilient modulus of the material were determined, with these two parameters principle factors in determining the strength and performance of a cement treated pavement material [7]. To determine these material properties, two standardized tests were undertaken, namely an unconfined compressive strength test in accordance with [8], and a repeated load triaxial test in accordance with [9].

These tests were carried out on specimens of a naturally occurring crushed rock material, stabilized with a composite artificial binder. This consisted of a synthetic kaolin clay, and general purpose cement, ranging in contents of 1%, 2%, and 3% by dry mass respectively.

EXPERIMENTAL RESULTS & ANALYSIS

The initial stages of testing developed the optimal binder ratio of clay to cement required for the desired performance as a base course material. Subsequent testing was then carried out to obtain the data previously detailed in the laboratory regime, namely the unconfined compressive strength, compressive modulus, resilient modulus, and the stress dependent parameters of the clay-cement stabilized crushed rock base.

Selection of Optimal Binder Ratio

A clay-cement stabilized crushed rock base material has never been previously developed, so the ratio of clay to cement that will optimize the performance of the crushed rock base was initially determined. This involved compaction testing and unconfined compressive strength testing on the fines of a crushed rock base material, stabilized with 2% kaolin clay, 1% kaolin clay and 1% cement, and 2% cement respectively. The fines of the crushed rock base material were utilized due to soil-cement matrices developing easier around smaller sized particles [10], therefore the effect that each binder would have would be magnified.

The unconfined compressive strength of each material admixture is presented in Fig.1. As this figure details, there is a direct increase in the strength of the material with an increase in cement content. Whilst the 2% cement specimens exhibited additional strength, the 1% clay – 1% cement samples still possessed a strength greater than that of HCTCRB at the same age, of approximately 0.75 MPa. This was also sufficient for the material to be classed as a modified pavement material.

Compaction testing also detailed that the 1% clay – 1% cement samples possessed a larger maximum dry density than the 2% cement samples, with past research detailing that soil materials with a larger dry density will have an increase in strength occurring over a longer period of time [11]. With past field investigations by Main Roads also concluding that 2% cement samples are subject to fatigue failures [3], it was established that a binder of one part kaolin clay to one part cement was optimal. Therefore, for the next stage of testing, all specimens were prepared with a clay-cement binder at a 1:1 ratio.

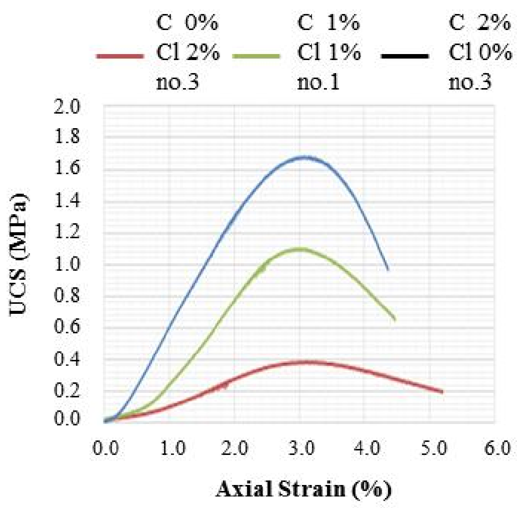

Fig. 1 Unconfined Compressive Strength of Varying Artificial Binders.

Unconfined Compressive Strength of Clay-Cement Stabilized Crushed Rock Base

The unconfined compressive strengths for crushed rock base specimens stabilized with 1%, 2%, and 3% clay-cement binder contents, at 7 and 28 days respectively, is presented in Fig.2. As this figure details, there is a strong linear correlation between an increase in binder content and an increase in the material's unconfined compressive strength for both curing time durations. There is also a distinct increase in strength over time, with the 2% and 3% specimens tested at 28 days significantly stronger than those tested at 7 days.

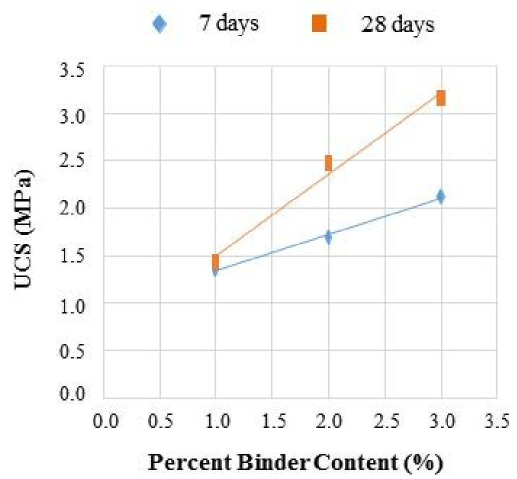

Fig. 2 Unconfined Compressive Strength with Respect to Varying Curing Time and Percent Binder Content.

All samples tested, even those stabilized with as little as 1% of a clay-cement binder, possessed unconfined compressive strengths greater than 1 MPa. Clause 1.1.12 in Main Roads Engineering Road Note 9 however, specifies that pavements must not incorporate modified granular materials with a 7 day unconfined compressive strength exceeding 1 MPa [2]. This alone would immediately suggest that that this material would not be a viable option to be utilized in pavement structures in Western Australia. With this material having never been previously developed or tested, and with Main Roads specifications primarily developed off empirical methods, it is near impossible to categorize its overall performance off of this alone however.

The 28 day unconfined compressive strength results presented in Fig.2, also enables the classification of the material based off of Austroads' established criteria. This method suggests that samples with 1% binder are modified, samples with 2% binder are lightly bound, and that samples with 3% binder are a heavily bound pavement material [12]. This criteria proposes that the 2% and 3% material admixtures exhibiting bound properties, will be susceptible to unfavorable failure modes such as transverse dry shrinkage cracking. Once again however, with Austroads' classification criteria also based off an empirical approach, it is arduous to classify a material solely based off of its 28 day unconfined compressive strength.

In comparison to the base course material presently adopted in Western Australian pavements, HCTCRB, all clay-cement stabilized crushed rock base specimens tested exhibited larger unconfined compressive strengths. With HCTCRB possessing a 28 day unconfined compressive strength of approximately 0.93 MPa, even specimens with as little as 1% clay-cement binder produced a higher compressive strength.

The unconfined compressive strength was not the only performance parameter obtained from these results, with the compressive modulus of the material also determined. Determined as the gradient of the linear sections of the stress-strain curve, the compressive modulus of crushed rock base specimens with varying percent clay-cement binder contents is presented in Fig.3. As this figure displays, there is a linear relationship between the compressive modulus and percent binder additive for clay-cement stabilized crushed rock base, for the binder contents tested in this thesis. That is, for every percent increase in clay-cement binder content, there is also a direct increase in the compressive modulus of the material of approximately 63 MPa. This suggests that whilst additional binder content is increasing the ultimate strength of the material, it is also increasing its ability to undergo smaller deformation rates when compressed, as well as its ability to resist failure phenomena such as shrinkage cracking. This is very beneficial, especially for a pavement base course material.

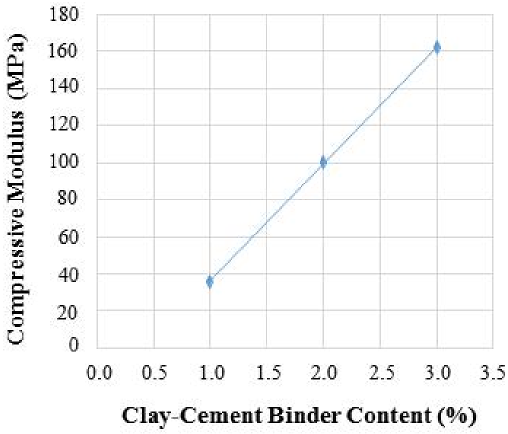

Fig. 3 Compressive Modulus with Varying Percent Binder Content.

Figure 3 also displays how specimens modified with a 1% clay-cement binder, possess a very low compressive modulus. This advocates that this material mixture is susceptible to excessive deformation under loading, which can lead to the premature failure of not only the base course layer, but the entire pavement structure. This suggests that whilst the 1% binder content samples developed sufficient unconfined compressive strength, the material mixture would not be a feasible base course material to be utilized in pavement engineering practices due to unfavorable serviceable characteristics.

Resilient Modulus of Clay-Cement Stabilized Crushed Rock Base.

The resilient moduli for crushed rock base specimens at 28 days, stabilized with 1%, 2%, and 3% clay-cement binder contents respectively, is presented in Fig.4. As this figure details, for every increase in percent binder content tested in this thesis, there is a corresponding increase in the resilient modulus of the material. That is, the materials elastic response, or ability to withstand excessive deflections under repeated traffic loading, directly increases with an increase in binder content. This reinforces the information obtained from the unconfined compressive strength and compressive modulus data. Unlike these two previous sets of data however, the relationship between the resilient modulus and the percent binder content of the material is not linear in nature.

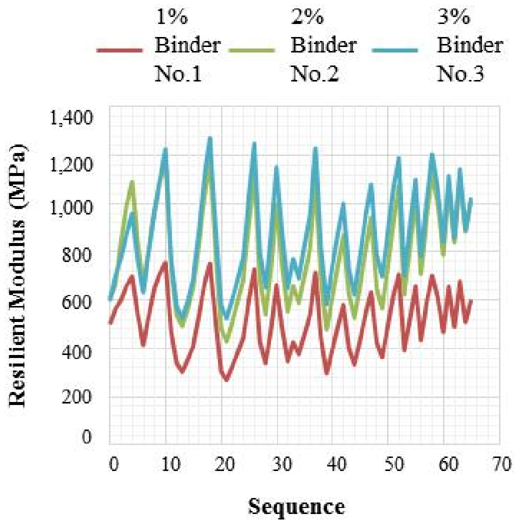

Fig. 4 Resilient Modulus of Varying Percent Binder Content.

In comparison to the peak resilient modulus of HCTCRB of approximately 1130 MPa, the 1% clay-cement binder samples exhibited a significantly lower resilient modulus of only 757 MPa, suggesting that it will be susceptible to greater deflections under the same loading. This reinforces the compressive modulus data obtained for the 1% binder samples, further reiterating that the serviceable characteristics of the material are not sufficient. This further advocates that the performance of a material cannot be characterized off of its unconfined compressive strength alone. This is supported with HCTCRB possessing a smaller unconfined compressive strength than the 1% clay- cement binder specimens, however providing a better elastic response to traffic loading.

The 2% and 3% clay-cement binder samples however exhibited larger peak resilient moduli than the HCTCRB, of approximately 1189 MPa and 1277 MPa respectively, purporting that the elastic response of these material admixtures under the same repeated loading is greater. With the 3% clay-cement binder specimens possessing the largest resilient modulus, previous testing data is reinforced, suggesting that this material admixture will exhibit the strongest performance characteristics as a pavement base course layer.

The resilient modulus data also enabled the development of the stress dependent equation of the material, with this parameter further aiding in the identification of a material's performance, denoting whether or not a material will potentially exhibit bound or unbound characteristics. Increasing the applied bulk stress increases the hardening or stiffness of materials, which results in a higher resilient modulus. It is established that bound materials that already exhibit high stiffness', present erratic resilient moduli responses with increased bulk stresses. Therefore with the bulk stresses applied to the specimen plotted against the corresponding resilient modulus, it is established that materials displaying uniform resilient moduli responses with the applied bulk stress state, are potentially exhibiting unbound characteristics [13].

The stress dependent equation for crushed rock base specimens at 28 days, stabilized with 1%, 2%, and 3% clay-cement binder contents respectively, is presented in Fig.5. With uniform resilient moduli data with applied bulk stresses enabling a strong trend line to be developed for all material admixtures, it is suggested that specimens stabilized with 1%, 2% and 3% clay-cement binder contents respectively, are potentially exhibiting unbound characteristics.

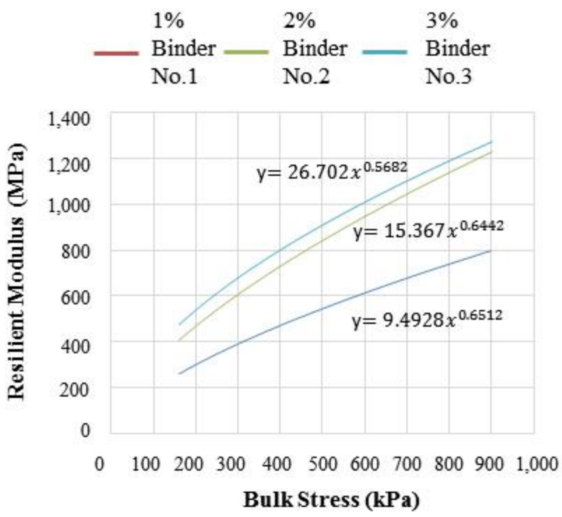

Fig. 5 Stress Dependent Equation of Varying Percent Binder Content.

Whilst, in comparison to HCTCRB, the increase in resilient modulus for the 2% and 3% clay-cement binder specimens is not substantial, the most important observation is that both admixtures are potentially exhibiting unbound properties. Whilst HCTCRB also exhibits these properties, an additional hydration phase was required for this, leading to differential performance results due to arduous material mixing and construction procedures.

The most auspicious realization from this research is the fact that the 3% clay-cement binder samples are exhibiting strength characteristics significantly better than HCTCRB, whilst still potentially displaying unbound characteristics. A material's ability to acquire the accompanying strength advantages of a 3% artificial binder, whilst still potentially resisting common failure methods such as shrinkage cracking, suggests that its performance as a base course layer in a pavement structure is very promising.

CONCLUSIONS AND RECOMMENDATIONS

With the current base course material in Western Australian pavement structures requiring excessive capital expenditure due to premature pavement failure phenomenon, this paper aimed to present the strength properties of a potential replacement material. A naturally occurring crushed rock base material, stabilized with 3% by dry mass of a clay-cement composite binder, exhibited unconfined compressive strength and resilient modulus characteristics significantly greater than that of HCTCRB. The material also potentially exhibits unbound characteristics, suggesting common pavement failure phenomena such as shrinkage cracking will be mitigated.

However, empirical evidence from Main Roads Western Australia, as well as Austroads, will suggest that this material will be subjected to unfavorable pavement failure mechanisms such as tensile fatigue cracking. Main Roads Western Australia also specify that this material cannot be incorporated into any pavement structural systems due to these reasons.

Whilst specific strength parameters are sufficient, it is arduous to classify the feasibility of the implementation of a material as a base course layer off of this alone. Evidence of this fact is presented with the performance of HCTCRB. Whilst the material possessed adequate strength, it failed due to other mechanisms of stabilizer permanency and moisture susceptibility. Therefore further investigation is required, to determine other key base course performance parameters, to establish the viability of a clay-cement stabilized crushed rock material as a base course layer in Western Australian pavements.

REFERENCES

[1] Horpibulsuk S, Chinkulkijniwat A, Suddeepong A, Neramitkornburee A and Suksiripattanapong C, “Cement Stabilization for Pavement Material in Thailand”, Geotechnical Engineering Journal, Vol.45, No.1, 2014, pp.95-102.
[2] MAIN ROADS Western Australia, Engineering Road Note 9. Perth: MAIN ROADS Western Australia, 2012.
[3] Nikraz H, and Yeo Y S, "Cement Stabilisation of Road Base Course: A Chronological Development in Western Australia.", Australian Geomechanics, Vol.44, No.3, 2009, pp.63-72.
[4] Harris D, and Lockwood N, Reid Highway Basecourse Test Sections Performance to December 2008: Revision of Report 2004/17m. WA: Main Roads Western Australia, 2009.
[5] Jitsangiam P, Chummuneerat S, Phenrat T, and Nikraz H, "Characteristics and

Performance of Cement Modified-Base Course Material in Western Australia.", Journal of Materials in Civil Engineering, Vol.26, No.9, 2013.

[6] MAIN ROADS Western Australia, A Guide to the Selection of Naturally Occurring Materials as Base and Subbase in Roads in Western Australia. Perth: MAIN ROADS Western Australia, 2003.

[7] Jiang Y J, and Fan L F, "An Investigation of Mechanical Behavior of Cement-Stabilized Crushed Rock Material Using Different Compaction Methods.", Construction and Building Materials, Vol.48, No.0, 2013, pp.508-515.

[8] Standards Australia, Methods for Preparation and Testing of Stabilized Materials - Unconfined Compressive Strength of Compacted Materials, 2008.

[9] Austroads, Determination of Permanent Deformation and Resilient Modulus Characteristics of Unbound Granular Materials under Drained Conditions. Sydney: Austroads Inc., 2007.

[10] Pakbaz M S, and Alipour R, 2012. "Influence of Cement Addition on the Geotechnical Properties of an Iranian Clay." Applied Clay Science, Vol.67–68, No.0, 2012, pp.1-4.

[11] Li H, Zhu Y, Zhang J, and Lin C, "Effects of Temperature, Strain Rate and Dry Density on Compressive Strength of Saturated Frozen Clay." Cold Regions Science and Technology, Vol.39, No.1, 2004, pp.39-45.

[12] Austroads, Guide to Pavement Technology Part 4d: Stabilised Materials. Sydney: Austroads Inc., 2006.

[13] Buchanan S, Resilient Modulus: What, Why, and How?, 2007.

Fifth International Conference on Geotechnique, Construction Materials and Environment, Osaka, Japan, Nov. 16-18, 2015, ISBN: 978-4-9905958-4-5 C3051

APPLICATION OF FUZZY SET THEORY TO SEISMIC VULNERABILITY ASSESSMENT

Kshama S. Roy[1], Md. Jakiul Hassan[2], Kamrul Islam[3], Naveel Islam[4]
[1, 4] Faculty of Engineering and Applied Science, Memorial University of Newfoundland, Canada
[2]Mechanical Engineer, Lower Churchill Project, Nalcor Energy, Newfoundland and Labrador, Canada
[3] Department of Civil Engineering, Military Institute of Science and Technology (MIST), Bangladesh

ABSTRACT

Seismic vulnerability assessment of the existing buildings has become a prime concern now-a-days due to the major threats that have been imposed by the several earthquakes all over the world. Recent studies showed that the Turkish Method may be applicable for the vulnerability assessment of the existing buildings in the developing countries. This article addresses the investigation of the significant factors that influence the performance score of the Turkish Method with particular attention to the application of the Fuzzy set theory. The results of the detailed survey that was done in the old town of the Dhaka city are extensively used for the application of the Fuzzy set theory. A comparative analysis is done with the results of a statistical analysis based on Design of Experiment (DOE) methodology. Finally the comparative evaluation shows that pounding effect, topographic effect, plan irregularity, area of the ground floor and the number of frames in the X and Y directions are the most significant factors that influence the performance score of the Turkish Method.

Keywords: Seismic Vulnerability, Turkish Method, Fuzzy Set Theory, DOE, Performance Score

INTRODUCTION

Natural disaster like earthquake causes damage to civil engineering structures resulting in deaths, economic loses, and damage of infrastructures. Most recent earthquakes in Nepal (2015), Japan (2011), New Zealand (2010 and 2011), Mexico (2011), Indonesia (2010 and 2011), China (2010) and Haiti (2010) have brought attention to researchers to predict the severity of damage of infrastructures. Many cities of the developing countries of the world contain a significant number of vulnerable buildings under considerable seismic risk. Seismic vulnerability assessments of these buildings are gaining more attention to assess correctly the degree of risk to which such critical structures may be subjected to in the event of an earthquake. Vulnerability assessment procedures found in the literature [1]-[3] are mainly based on building plan, foundation, structural system, structural and non-structural components, and structural performance. Such vulnerability assessment procedures show accurate and realistic performance of a building only if the building was built according to proper building design code and architectural features. Recent years, Bangladesh has seen the construction boom of multi-storied (mainly 6 stories and above) reinforced concrete frame (RCF) buildings in the capital city of Dhaka where standard building codes are not followed properly. Most of these buildings have open parking space in the ground floors resulting in soft story construction while some of them have structural irregularities. Moderate to severe earthquake can cause unbearable devastation and pose risk to lives of people and their assets as well as the basic infrastructure of the country. Seismic vulnerability assessment of existing buildings of Dhaka city, therefore, has gained a significant attention to the researchers and engineers. According to the opinion of a German earthquake expert [4] from the University of Kassel, Germany, Turkish method of seismic risk assessment may be applicable for a developing country like Bangladesh. In this method, the discriminant scores obtained from several discriminant functions are combined in an optimal way to classify existing buildings as “safe”, “unsafe” and “requires detailed evaluation” [1].

The Turkish method, based on the statistical analysis of observed earthquake damages of RCF buildings in Turkey, and related building attributes is expected to provide reasonable results for assessment of buildings in Bangladesh according to [5]-[6]. Several researchers in the past have used this methodology for vulnerability assessment of different cities of Bangladesh [7]-[13]. Turkish method is a two level seismic risk assessment procedure considering a number of factors described by Ozcebe et al. [5]. Considering the factors it gives a performance score for each building being assessed. But as the method uses a number of empirical equations and tables for determining the score, it is difficult to find the most significant factors that affect the performance score. The present study focuses on developing a fuzzy based technique to qualify and quantify the significant factors of Turkish method described by

Ozcebe et al. [5] and also on comparing the fuzzy set theory with Design of Experiment (DOE) methodology for seismic vulnerability assessment of RCF buildings in Dhaka city. Details of the DOE methodology can be found in authors' previous works [14] and is not repeated here.

TURKISH METHOD

The Turkish seismic vulnerability assessment method for buildings consists of two-level evaluation: (i) level one - walk down evaluation and (ii) level two - measurements at ground level and basement [5]-[6]. The walk down evaluation procedure mainly consists of taking notes of different external features of the building. Buildings are then described as belonging to high risk, moderate risk or low risk. After level 1 survey, buildings falling into the moderate and high risk levels can be subjected to more detailed level 2 surveys to determine their performance scores. Details of Level 1 and Level 2 Survey procedures can be found in Ahmed et al. [15] and Roy et al. [16] and is not repeated here. Once the vulnerability parameters of a building are obtained from two-level surveys and its location is determined, the seismic performance scores for survey levels 1 and 2 are calculated according to several empirical equations and tables [17]. A general equation (Eq.1) for calculating the seismic performance score (PS) can be formulated as follows,

$$PS = (\text{Initial Score}) - \Sigma\, (\text{Vulnerability parameter}) \times (\text{Vulnerability Score}) \quad (1)$$

The detailed procedures for vulnerability scoring can be found in Sucuoglu and Yazgan [17].

DOE METHODOLOGY

DOE Methodology involves the study of any given system by a set of independent variables (factors) over a specific region of interest (levels) and provides a straightforward technique with linear graphs to determine the relationship (interactions) between the considered factors, which can be used for practical experimentation [18]. By using DOE, it is possible to investigate the experimental process, to screen the important variables (or factors), to build a mathematical model with prediction, and even to optimize the responses where necessary. Among the different techniques in DOE method, Fractional factorial design is one of the common techniques for experimentation which is used in this study. The detailed procedures for DOE methodology applied in this study can be found in Roy et al. [14].

Strategy of Experimentation by DOE

The levels for the factors of the analysis are chosen on the basis of the survey that was done in the ward 75, 76 and 77 of the old town of Dhaka city. The details of the survey results can be found in Ahmed et al. [15]. A Microsoft Excel software program is developed for the analysis of the Turkish Method [16], and the data are analyzed by the non-commercial software, Design Expert 7.1.3. Detailed descriptions of DOE methodology can be found in Roy et al. [14]. Ten (10) parameters of the Level 2 survey of Turkish method are used as factors for the DOE analysis. The factors considered are: A) Pounding effect, B) Topographic effect, C) Plan irregularity, D) Area of the ground floor, E) Area of the above floor, F) No of frames in X direction, G) No of frames in Y direction, H) Column dimension - x, I) Column dimension -y and J) No of columns. Performance score is used as response in the DOE analysis. Among the ten factors A) Pounding effect, B) Topographic effect and C) Plan irregularity are considered as categorical factors and others are considered as numeric factors. For the categorical factors, the high and low levels are "yes" and "no" respectively. The levels of other numeric factor are given in Table 1. As ten (10) factors and two (2) levels are considered, 2^{10} = 1024 runs were required if full factorial design was used. So to minimize the runs, fractional factorial design is used which reduces the required runs from 1024 to 128.

Results from DOE Analysis

The results show that pounding effect, topographic effect, plan irregularity, area of the ground floor, number of frames in X and Y direction and the interaction between the number of frames in X and Y direction are the most significant factors. A linear regression model is developed from the DOE analysis for computing the performance score to compare with the results obtained from the Turkish Method. Regression Equation for Performance Score in terms of coded factors is shown in Eq. 2.

$$\ln(PS) = +4.12 - 0.026*A - 0.042*C - 0.038*D + 0.084*F + 0.084*G - 0.045*F*G \quad (2)$$

Details of the DOE analysis can be found in authors' previous studies [14].

FUZZY SET THEORY

A major contribution of fuzzy set theory is its capability of representing vague data. A fuzzy set is a class of objects with a membership function ranging between zero and one [19]. Fuzzy set theory resembles human reasoning in its use of approximate information and uncertainty to generate decisions. It was specifically designed to mathematically represent uncertainty and vagueness. Fuzzy set theory implements groupings of data with boundaries that are not sharply defined (i.e. fuzzy) [20].

A triangular fuzzy number (TFN) is the special class of fuzzy number whose membership is defined by three real numbers, expressed as (l, m, u) [21]. Fig. 1 depicts the structure of a Triangular Fuzzy Number (TFN). According to Tae-heon Moon the triangular fuzzy numbers is represented as follows where μ_A is triangular membership functions.

The membership function μ_A of triangular fuzzy number on $R = (-\infty, +\infty)$ is μ_A: $R \rightarrow [0, 1]$. The triangular membership function, μ_A is defined as,

$$\mu_A = \begin{Bmatrix} \frac{x-l}{m-l}, l \leq x \leq m \\ \frac{u-x}{u-m}, m \leq x \leq u \\ 0, otherwise \end{Bmatrix} \tag{3}$$

Where, $l \leq m \leq u$, and l and u stand for the lower and upper values of the support of the fuzzy number respectively, and m for the modal value [21].

Table 1 Levels for Numeric Factors, [14]

Factor	Name	Low Actual	High Actual	Low Coded	High Coded
D	Area of the ground floor	46.45 m^2	278.71 m^2	-1.0	+1.0
E	Area of the above floor	37.16 m^2	464.52 m^2	-1.0	+1.0
F	No of frames in X direction	2	20	-1.0	+1.0
G	No of frames in Y direction	2	20	-1.0	+1.0
H	Column dimension in X direction	0.076m	1.016m	-1.0	+1.0
I	Column dimension in Y direction	0.076m	1.016m	-1.0	+1.0
J	No of columns	4	50	-1.0	+1.0

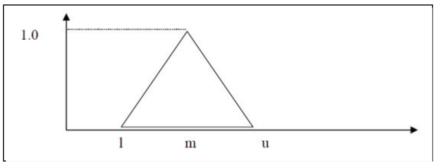

Fig. 1 Triangular membership Function

The operational laws between two triangular fuzzy numbers M_1 and M_2 are as follows in Eq. (4) and (5) [21],

$$M_1+M_2 = l_1+l_2, m_1+m_2, u_1+u_2 \tag{4}$$

$$M_1*M_2 = l_1l_2, m_1m_2, u_1u_2 \tag{5}$$

Analytical Hierarchy Process (AHP)

AHP is a method for ranking decision alternatives and selecting the best one when the decision maker has multiple criteria. With AHP, the decision maker selects the alternative that best meets his or her decision criteria developing a numerical score to rank each decision alternative [21]. An analytical way to reach the best decision is more preferable in many platforms. When variables are quantitative and number of criteria is not high, then one can use several analysis tools (for example: Multi factor evaluation process) and make his/her decision and solve the problem. However, many times beside the measurable variables, there exist qualitative variables, or peoples are supposed to prefer the best among the many choices, thus, an analytical way to make a successful decision is needed. Decision makers might have difficulties in accurately determining the various factor weights and evaluations in certain situations. In such cases, the AHP can be used. In AHP the decision maker starts by laying out the overall hierarchy of the decision. This hierarchy reveals the factors to be considered as well as the various alternatives in the decision. Here, both qualitative and quantitative criteria can be compared using a number of pair wise comparisons, which result in the determination of factor weights and factor evaluations. Finally, the alternative with the highest total weighted score is selected as the best alternative [21].

Fuzzy- Analytic Hierarchy Process (Fuzzy AHP)

The conventional AHP method is incapable of handling the uncertainty and vagueness involved in the mapping of one's preference to an exact number or ratio .The major difficulty with conventional AHP is its consistency. It is due to the transitivity property involved in the pair wise comparisons [21]. In Fuzzy-AHP, pair wise comparisons are done using fuzzy linguistic scale ranging from 0 to 10. Table 2 displays the fuzzy linguistic scale within 0 to 1. For consistency, the reciprocal fuzzy numbers are removed from the pair wise comparison matrix by using TFN corresponding to each linguistic variables used in the scale. The triangular fuzzy numbers corresponding to different verbal judgment is demonstrated using Table 2 [21].

Table 2 Linguistic levels and preference scale

Linguistic Representation	Explanation of the linguistic values	Triangular Fuzzy number(TFN)
Extremely low (EL)	Response is extremely unimportant	(0, 0, 1/6)
Very low (VL)	Response is quite unimportance	(0, 1/6, 1/3)
Slightly low (SL)	Response is slightly unimportant	(1/6, 1/3, 1/2)
Medium (M)	Response is neutral	(1/3, 1/2, 2/3)
Slightly high (SH)	Response is mildly important	(1/2, 2/3, 5/6)
Very high (VH)	Response is quite important	(2/3, 5/6, 1)
Extremely high (EH)	Response is extremely important	(5/6, 1, 1)

Fuzzy Set model for Turkish method

The membership function and triangular fuzzy function are determined by the following Eq. 6, shown by Hipeng Li [22].

$$\mu(x) = \begin{Bmatrix} 1-6x, 0 \le x \le \frac{1}{6} \\ 0, \frac{1}{6} \le x \le 1 \end{Bmatrix}$$
$$\mu(x) = \begin{Bmatrix} 0,\ 0 \le x \le \frac{k-2}{6} \\ 6x-(k-2), \frac{k-2}{6} \le x \le \frac{k-1}{6}\ (k=2,3,4,5,6) \\ 0,\ \frac{k-1}{6} \le x \le 1 \end{Bmatrix} \quad (6)$$
$$\mu(x) = \begin{Bmatrix} 0, 0 \le x \le \frac{5}{6} \\ 6x-5, \frac{5}{6} \le x \le 1 \end{Bmatrix}$$

Where, $\mu(x)$ denotes the membership function and x denotes normalized values.

ANALYSIS FOR THE FUZZY SET MODEL

Expert's judgments

For the analysis by Fuzzy Set Model, the ten factors that were used in the DOE Methodology [14] has been listed as eight factors as column dimension in X and Y direction and no of frames in X and Y direction do not need to be separated for X and Y direction due to the reason that the expert cannot distinguish the difference between the two directions. The new factors that have been selected for the analysis are given in Table 3.

Table 3 Factors for Fuzzy Analysis

Factor	Name
A	Pounding effect
B	Topographic effect
C	Plan Irregularity
D	Area of the ground floor
E	Area of the above floor
F	No of frames in the X and Y direction
G	Column dimension
H	No of columns

Table 2 and Table 3 have been sent to ten different experts of seismic vulnerability assessment to rank each of the factors of Table 3 according to Table 2 that has been made on the basis of Eq. 6.

Aggregation of Expert's Judgment

According to Lin and Wang [23], aggregation of expert's judgment should be performed to avoid conflict among expert's judgment. An operator has to be used to convert several experts' judgment fuzzy sets into a single fuzzy number. Average mean method is most common and for aggregating n experts' judgment in triangular fuzzy number $\boldsymbol{EJ_n} = (\boldsymbol{l_n}, \boldsymbol{m_n}, \boldsymbol{u_n})$ can be defined as

$$\widetilde{\boldsymbol{EJ}} = \left(\frac{1}{n}\sum_{i=1}^{n} \boldsymbol{l_i}, \frac{1}{n}\sum_{i=1}^{n} \boldsymbol{m_i}, \frac{1}{n}\sum_{i=1}^{n} \boldsymbol{u_i}\right) \quad (7)$$

Where $\widetilde{\boldsymbol{EJ}}$ is the average linguistic judgment of n expert and l, m, u are the lower, intermediate and upper values for the triangular fuzzy number.

Defuzzification

Defuzzification is a method that converts the fuzzy numbers into a crisp value [20]. The crisp value will be triggered into the Fig. 2 to calculate the importance level of the each parameter. Several techniques are available and in this paper the centroid method [24] is used for defuzzification of experts' judgment.

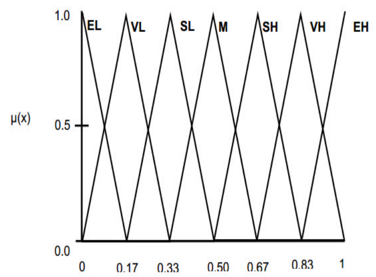

Fig. 2 Mapping linguistic importance levels values

Table 4 Aggregation of Experts' judgment and defuzzified values

Factor	Name	Aggregated value of the Experts' judgment	Defuzzified value
A	Pounding effect	0.6, 0.77, 0.93	0.7748
B	Topographic effect	0.73, 0.9, 0.98	0.8815
C	Plan Irregularity	0.47, 0.62, 0.8	0.6379
D	Area of the ground floor	0.58, 0.77, 0.95	0.7726
E	Area of the above floor	0.05, 0.22, 0.4	0.2317
F	No of frames in the X and Y direction	0.82, 0.98, 0.25	0.92
G	Column dimension	0.23, 0.4, 0.57	0.4086
H	No of columns	0.1, 0.27, 0.43	0.2748

Table 5 Comparison between results from Fuzzy Set Theory and DOE Methodology

Factor	Ranking value from Fuzzy Set theory	Coded Regression Co-efficient from the DOE methodology
Pounding effect	0.8235	-0.026
Topographic effect	0.898	-0.022
Plan Irregularity	0.636	-0.042
Area of the ground floor	0.766	-0.038
Area of the above floor	0.234	
No of frames in the X and Y direction	0.915	+0.084
Column dimension	0.415	N/A
No of columns	0.25	N/A

Defuzzified expert's judgment,

$$\widetilde{EJ}' = \frac{\int_l^u x.\mu(x)dx}{\int_l^u \mu(x)dx} \tag{8}$$

The defuzzified values have been calculated by using MATLAB 7.8.0. The results of the aggregation of the experts' judgment and the defuzzified values are given in the Table 4.

Ranking

The defuzzified values have been plotted to Fig. 2 and then the ranking for each of the factor has been calculated. The ranking shows that the pounding effect, topographic effect, plan irregularity, area of the ground floor and the number of frames in X and Y direction are the most significant factors for the performance Score in Turkish Method. The calculated ranking values are shown in Table 5.

COMPARISON BETWEEN FUZZY SET THEORY AND DOE METHODOLOGY

The most significant factors that have been found by the Fuzzy Set Theory exactly match with the results obtained from DOE methodology. For the ANOVA analysis in the DOE methodology, ten factors were taken in the model and the pounding effect, topographic effect, plan irregularity, area of the ground floor and the number of frames in X and Y direction were found as the most important factors for Turkish Method. The same ranking has been found from the Fuzzy Set Theory except the ranking values which are not same as the regression co-efficient from the DOE methodology. This is because the Fuzzy set theory is dependent on the experts' judgment which is not numerically accurate. The numerical values are not same from both of the analysis. However, the ranking from both analyses is comparable which indicates that the pounding effect, topographic effect, plan irregularity, area of the ground floor and the number of frames in X and Y direction are the most significant factors for the performance score of the Turkish Method.

CONCLUSION

This paper presents a new approach to validate the applicability of Turkish method for seismic vulnerability assessment of existing RCF buildings in developing countries like Bangladesh. Fuzzy Set Theory is a well-known approach for ranking in the AHP. This research proves the applicability of DOE methodology in the Turkish Method. The results represent that the pounding effect, topographic effect, plan irregularity, area of the ground floor and the number of frames in X and Y direction are the most significant factors for the seismic vulnerability assessment by Turkish Method which exactly matches with the results obtained from the DOE methodology. Therefore, this study primarily focused on the use of qualitative judgments as well as quantitative parameters of the various factors of Turkish method in order to rank the factors according to their significance.

REFERENCES

[1] Hassan, A.F. and Sozen, M.A. 1997. Seismic vulnerability assessment of low-rise buildings

in region of infrequent earthquake. *ACI Structural Journal*, 94(1): 31 -39
[2] Gulkan, P.and Sozen, M.A. 1997. Procedure for determining seismic vulnerability of building structures. *ACI Structural Journal*, 96(3): 336-342
[3] Kircher, C. Reitherman, R.K., Whitman, R.V., and Arnold, C. 1997. Estimation of Earthquake losses to buildings. *Earthquake Spectra, EERI*, 13(4): 703-720
[4] Dorka, U. 2005. Personal Communication.
[5] Ozcebe, G., Yucemen, M. S., Aydogan, V., and Yakut, A. 2003. Preliminary Seismic Vulnerability Assessment of Existing Reinforced Concrete Buildings in Turkey- Part I: Statistical Model Based on Structural Characteristics, Seismic Assessment and Rehabilitation of Existing Buildings, *NATO Science Series IV/29*: 29-42.
[6] Ahmed, M. Z., Islam, M. K., Ahsan, R. and Ozcebe, G. 2007. Seismic Vulnerability Assessment Methods: A Possible Application to Bangladesh, *First Bangladesh Regional Science Association (BRSA) Conference*, Dhaka.
[7] Ahmed, M. M., Jahan I., Alam M. J. 2014. Earthquake Vulnerability Assessment of Existing Buildings in Cox's -Bazar using Field Survey & GIS. *International Journal of Engineering Research & Technology (IJERT)* ,Vol. 3 Issue 8
[8] Sarraz, A., Ali, M. K.and Das, D. C. 2015. Seismic Vulnerability Assessment of Existing Building Stocks at Chandgaon in Chittagong city, Bangladesh. *American Journal of Civil Engineering*, 3(1): 1-8
[9] Sadat, M. R., Huq, M. S., Ansary, M. A. 2010 Seismic vulnerability assessment of buildings of Dhaka city. *Journal of Civil Engineering, Inst. of Engineers, Bangladesh*. 38 (2) 159-172
[10] Ishita, R. P. and Khandaker, S. 2010. Application of Analytical Hierarchical Process and GIS in Earthquake Vulnerability Assessment: Case Study of Ward 37 and 69 in Dhaka City. *Journal of Bangladesh Institute of Planners* , 3:103-112
[11] Rahman, M. A., Ullah M. S., 2013. Seismic Vulnerability Assessment of RC Structures: A Review. *Asian Transactions on Eng.*, 02(06)
[12] Ahmed, M., Khaleduzzaman, K. M., Siddique N. A. and Islam S., 2012. Earthquake Vulnerability Assessment of Schools and Colleges of Sylhet, a North-eastern City of Bangladesh. *SUST Journal of Science and Tech.*, 19(5): 27-34.
[13] Alam, M. J., Khan, M. A. R., and Paul, A. 2009. "Seismic Vulnerability Assessment of Existing RC Buildings in GIS Environment", Earthquake Engineering Research Center (EERC), Dept. of Civil Engineering, Chittagong University of Engineering & Technology (CUET), Bangladesh.
[14] Roy, K. S., Islam, K. and Arafat, M. Shams. 2011. A Novel Statistical Approach for Investigating the Significant Factors that Influence the Performan*ce Score of the Turkish Method, Proceedings of International Conference on Geotechnique, Construction Materials and Environment (GEOMAT-2011),* Tsu City, Mie, Japan.
[15] Ahmed, M.Z., Islam, K., Roy, K. S., Arafat, M. S. and Al-Hussaini, T.M. 2010. Seismic Vulnerability Assessment of RCF Buildings in Dhaka City, *Proceedings of the 3rd International Earthquake Symposium (IESB-3)*, Dhaka, Bangladesh.
[16] Roy, K. S., Islam, K. and Arafat, M. S. 2010. Seismic Risk Assessment of Existing Low-rise Buildings in Unplanned Urban Regions of Dhaka City, *Proceedings of the 2nd International Conference on Construction in Developing Countries (ICCIDC-2)*, Cairo, Egypt.
[17] Sucuoglu, H. and Yazgan, U. 2003. Simple Survey Procedures for Seismic Risk Assessment In Urban Building Stocks, Seismic Assessment and Rehabilitation of Existing Buildings, 97-118,NATO Science Series, IV/29, Editors: S.T. Wasti and G. Ozcebe, Kluwer.
[18] Lye, L. M., 2003. Some Applications of Statistical Design of Experiment Methodology in Civil Engineering. *Annual Conference of the Canadian Society for Civil Engineering, Moncton, Nouveau-Brunswick, Canada*
[19] Zadeh, L. A. 1965. Fuzzy Sets. Information and Control 8, 338-353.
[20] Klir, J.G. and Yuan, B. 2001. Fuzzy Sets and Fuzzy logic Theory and Application. Prentice, Hall of India Private Ltd.
[21] Chatterjee, D., Chowdhury, S. and Mukherjee, B. 2010. A Study of the Application of Fuzzy Analytical Hierarchical Process (FAHP) In the Ranking of Indian Banks. *International Journal of Engineering Science and Technology*: 2(7), 2511-2520
[22] Li, H. 2007. Hierarchical Risk Assessment of Water Supply Systems. *Doctor of Philosophy Thesis*. Department of Civil and Building Engineering Loughborough University, Leicestershire, UK
[23] Lin, C. and Wang, M. J. 1997. Hybrid fault tree analysis using fuzzy sets. *Reliability Engineering and System Safety*, 58: 205-213.
[24] Yager, R. R. 1980. A general class of Fuzzy connectives. *Fuzzy Sets and Systems*, 4: 235-242.

GNOMON AS SOURCE OF INFORMATION ON PLANET RHYTHMS

Alina Paranina[1], Roman Paranin[2]
[1, 2] Faculty of geography, Herzen State Pedagogical University, Russia

ABSTRACT

For millennia, humans have been using the gnomon whose shadow passes the trajectory of the light source (sun or moon) as a measurement tool. With the gnomon authors prove that the ancient stone labyrinths in Northern Europe are solar calendars, sundials and compasses. Studies of cultural heritage around the world show that the majority of them might serve as orientation in space-time. According to the authors, the collection of ancient navigational facilities can be considered as ancient astronomical and geodetic network and as a record of astronomical history of the planet. For systemic analysis of this information it is necessary to create a base of paleo-astronomical data. The acquired information may be useful for studies of the history of the Earth and the history of science: the dynamics of changes of inclination of the Earth's axis, offset of the polar circles and the tropics, the characteristics of long-period rhythms of the planet, the evolution of climatic environments and the development of navigation technologies of the past. In addition, the creation of a network of solar observatories, with the technique of automatic registration shadow or a ray of light, will provide objective information on the solar-terrestrial relations and rhythms of nature

Keywords: Gnomon, a Stone Labyrinth, Paleoastronomical research, Navigation, Rhythmic of natural processes

INTRODUCTION

Northern labyrinths can be found in England, Iceland, Norway, Denmark, Sweden, Finland, Estonia and Russia. They are located on isles, peninsulas, near harbors and in river mouths. Their picture is complicated but organized. In terms of structure, there are unispiral, bispiral, concentric and radial types. In terms of outer shape: circles, ovals, rarely squares [1].

Hypotheses about the designation of stone labyrinths can be divided into two groups: calendar and non-calendar. It should be noted that despite all the diversity of facts of non-calendar use, most part of them is often associated with time and stage of life.

Hypothesis of calendar designation of labyrinths are mainly based on the assumption of a direct projection of the trajectory of space objects on the Earth's surface (Herman Wirth, Daniel Svyatskiy, Sergei Yershov) or consider pattern of labyrinth as a record of the results of direct sight of the annual variation of the Sun (Yuri Chekmenev). However, direct sight cannot explain the technology for using the labyrinth: 1) it is impossible to explain the quantitative ratios of the trajectory of a celestial object and its reflection in the stone pattern; 2) it is even more difficult to imagine the use of the pattern - with a diameter of 20-30 meters, it is impossible "to read" from the human height; 3) the problem of monitoring the trajectory of the sun is that bright light dazzles eyes, just after sunrise its movement takes off from landmarks.

The proposed concept of the labyrinth-gnomon – a tool of back sight of the sun – from the shadow set in the center of the object, opens the possibility of its use as a sundial compass and calendar [4] - [7]. The shadow of the object is easy to observe, record, measure, and its movement reflects and a form - encodes all the movements of the sun and is consistent with the position of the elements of the structure of the labyrinth; landscape orientation on the horizon (mountains, valleys) are not necessary, on the contrary, water environment is the optimal without creating distortions of azimuths of sunrise/sunset (their normal location is on the island or cape).

Author's concept of a labyrinth-gnomon technology solves the problem of the calendar use, and is consistent with all elements of a wide range of symbolic interpretation of the signs of the labyrinth and Labrys.

Paleo-astronomical studies of natural and cultural heritage indicate the possibility of their use for orientation in space-time. The ubiquity of ancient astronomical instruments deserve systematic study to clarify the concepts of modern science and the history of rhythmic changes in the nature of the Earth.

LABYRINTH-GNOMON IN ANCIENT NAVIGATION NETWORK

The objects of study were the monuments of ancient material culture of European Russia (siedis, menhirs, stone labyrinths). From 2009 to 2013 the objects located on coast of the White Sea are investigated: in the archipelago of Kuzova, in the archipelago Solovki, in the gulf Kandalaksha, in the mouth of the river Vyg (Fig. 1).

Fig. 1 Labyrinth with a stele in the archipelago of Kuzova.

Fig. 2 Labyrinth No. 1 Big Zayatsky Island of Solovetsky archipelago.

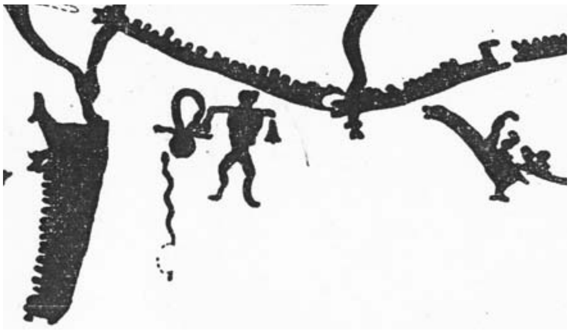

Fig. 3 White Sea petroglyphs (6000 y.o).

The applied field research methods (survey, description, observation, work with maps) and Earth remote sensing, as well as methods of mathematical, conceptual modeling and mapping. Theoretical analysis is based on the theory of reflection and systemic and chorological approach, methodological statements of historical geography by V.I. Paranin [2], [3].

Labyrinths of Big Zayatsky Island of Solovetsky archipelago as the astronomical instruments

For interpretation of a northern labyrinth the gnomon – the elementary astronomical tool was used. The shadow of a gnomon codes a trajectory of movement of the Sun on a firmament. In 2009 the authors proved that drawing of a labyrinth fixes astronomically significant points: 1) the provision of a midday shadow in days of winter and summer solstice corresponds to extreme arches of spirals, 2) the ends of spirals correspond to azimuths of risings/calling, 3) the entrance to a labyrinth notes the beginning of an annual cycle (in an equinox or a solstice) [4].

The sketch of a shadow of a gnomon in days gives the schedule similar to a pitchfork, horns, wings, a fish tail. The shadow schedule in a year fills the space whose shape form represents labris - a bilateral two-horned axe of god of light [5] - [7].

A

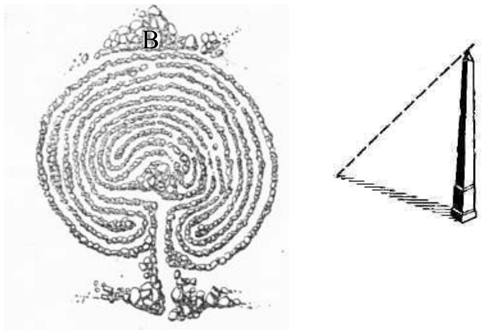

C

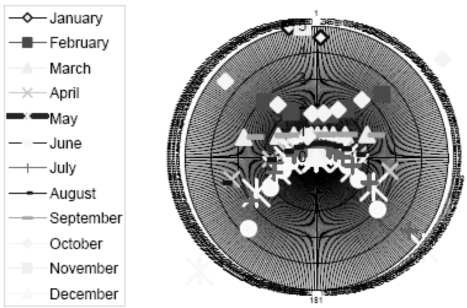

Fig. 4 Labyrinth No. 1: topographical plan (A); gnomon (B) and geometry of its shadows per year (C).

Labyrinths of Nordic countries as elements of local and regional astronomical and geodetic networks

Stone labyrinths are located, as a rule, on a plot of sea coast estuaries (at the source of fresh water) - it's convenient for rest and orientation, waiting for the desired date of astronomical calendar, in which marks of important phenological events of the area (cycles of fishing animals, climate and hydrological mode, lighting) can be made [5] - [7].

Key elements of the picture calendar are diameters of arcs and azimuths of entrance and end spirals - reflect the effect of two factors: the latitude and discrepancies of physical horizon (surface relief) with the astronomical horizon.

Polar regions differ from moderate latitudes in terms of azimuths of sunrise/sunset in the solstice that vary considerably in adjacent parallel (Table 1). If latitudes 40 - 50º rise at the summer solstice and shift by only 6.92º, and at latitudes of 50-60º only twice – 13.42º, then advancing further at only 5º (60 - 65º) to the north – rise shifts at 17.37º, and latitudinal range of 1.5º (65 - 66.5º, i.e. B. Zayatsky Island to the Arctic Circle) – to 20.03º. It is obvious that planetary space conditions of astronomical observations in the polar latitudes become the main reason for specific features of drawings.

The distorting influence of the physical horizon line on measurement of astronomical azimuths can be levelled by locating the instrument on the beach, whose calm surface coincides with the astronomical horizon, this explains the location of the labyrinth near water. This fact partly explains the abundance of labyrinths in a small area of the Big Zayatsky Island (more than 30 items on 1.25 km²): firstly, the labyrinths are located on parts of the shore, open to different sectors of the horizon, which provides accurate measurements for different astronomical dates and various astronomical objects (objects in the light of the moon cast a shadow as well); secondly, the construction of new labyrinths is associated with the retreat of the shoreline; thirdly, arranged compactly enough, they form a local network.

An equally important reason for the construction of new labyrinths is variability of subpolar latitudes of astronomical targets not only in space but also in time - here the change in slope of the Earth's axis is most visible; being observed according to displacement of the position of the Arctic Circle at other latitudes, these changes are not as dramatic (Table 1).

Table 1 Dynamics of astronomically significant directions in space and time

.

N (º)	2010 WS* 22.12	2010 SS**22.06	3000 BC WS 07.01	3000 BC SS 02.08
65	160.00	20.03	165.31	15.46
60	142.86	37.40	144.82	35.48
50	128.41	51.82	129.55	50.71
40	121.29	58.74	122.25	57.81
30	117.39	62.74	118.20	61.97
20	115.05	64.97	115.83	64.29
10	113.85	66.19	114.50	65.56
0	113.44	66.56	114.09	65.91

*WS - winter solstice;

**SS - summer solstice.

The table shows that 5,000 years ago, the azimuth of the summer solstice (SS) was significantly less than modern, therefore, the line of the Arctic Circle was located closer.

Most labyrinths are located in the most dynamic area approximately from latitude 57° to 66.5°, which primarily determines the differences in their pattern.

At the latitude of the Arctic Circle azimuths of solstices coincide with the meridian, and the boundaries of the astronomical seasons are in the shape of direct cross. In some cases the center corresponding to the polar day, is marked by a closed circle or spiral, as in a labyrinth in Iceland.

North of the Arctic Circle, only equinoxes can be reliably determined by azimuth of sunrise/sunset. To divide the year into periods between the polar night and polar day, you can use the azimuths of sunrise/sunset, which, depending on latitude, more or less rapidly move in the range of 0° +/- 180°. When the sun does not set over the horizon, length of midday shade – diameters of arcs – become the only way to divide time into days.

Labyrinths in global navigation system

Stone labyrinths and their images are known on every continent except Antarctica. In Russia, a high concentration of images is noticed in the North Caucasus (Dagestan). Single units of stone labyrinths are marked by archaeologists on the Russian plain, for example during excavations in Mostishchensky labyrinth 1 – Bronze Age settlement at the Cape of high original bank of the Don River. Mostishchensky labyrinth is located at latitude of famous astronomical observatories like Stonehenge and Archaim. On the same latitude 51-52° – one of the borders of the seven ancient climates there are a number of major European cities and sacred centers of Asia: Big Salbyksky mound in Khakassia, large burial Argens - in Tuva. Kereksur can be considered as analogue of labyrinths - concentric structures in Asia oriented to the horizon. At the same time, in the tropics there are almost no such structures.

REGIONAL FEATURES OF ANNUAL DYNAMICS OF SHADOWS

According to the terms of lighting since Aristotle five zones have been identified: tropical – hot, two moderate and two Polar – cold. They are limited by the tropics and the polar circles and different standing height of the midday sun above the horizon, the duration of the day and thermal conditions. The observation conditions of shadows in them differ substantially.

About 40% of the Earth's surface is in the hot area lying between the tropics. Day and night are slightly different in duration, and the sun is at its zenith is twice a year. 52% of the Earth falls on located between the tropics and the temperate zones of the Arctic Circle, where the sun is never at its zenith, the duration of day and night depending on latitude and time of year. Near the Arctic Circle (60° to 66.5°) for a short time in the summer sun and shallow out to the horizon, evening and morning dawns merge, and there are so-called white nights. The cold (polar) zone occupies only 8% of the earth's surface from the poles to the Arctic Circle. In winter there are polar nights and summer – polar days, which last a day or more.

Latitudinal differences in the dynamics of the shadows

Reflection of the lighting conditions in the annual dynamics of different regions of the shadows have been studied by means of building and comparison of graphs (Fig. 5) and charts of the annual dynamics of midday shade critical latitudes of the northern hemisphere parallels and all other at intervals of 10º. Models concentric labyrinths for different latitudes are shown in Figs. 6-7.

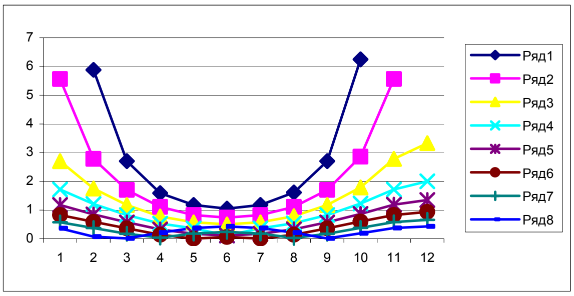

Fig. 5 Modern annual dynamics of length of midday shadow at different latitudes:
Horizontal - months of the year from January (1); vertical - length of shadow (7 m).

Fig. 5 rows 1-8 – shadows at latitudes from the equator to 70º N at intervals of 10º. In the shadow of the polar latitudes shadows of months 1, 11 and 12 are not indicated for the enlargement zoom, on 50º N the length of the shadows in December is decreased for the same purpose. The graph shows a decrease in the length of the shadow when moving to the equator, the greatest latitudinal differences for the winter, the change in the shortest shadow of the year (6) of a value equal to the height of the gnomon at 70º N (Row 1), up to half of 50º N (Row 3), and close to zero 30º N. No shade is observed on one of the tropics in the solstice at the equator – In the days of the equinoxes, at other times at different latitudes between the tropics. Coding latitude diameter of the inner circle using a standard-sized portable line or anthropometric equivalent (foot length) could be the basis of the latitudinal orientation.

Modeling of concentric labyrinth (Figs. 6, 7) was carried out for the "standard" gnomon height of 1 m, which provided an opportunity to compare them. According to the ratio of the gnomon height to the diameter of the site for monitoring annual dynamics of the shadows, the following three basic types of solar observatories can be found: "labyrinth", "staff" and "rod".

A

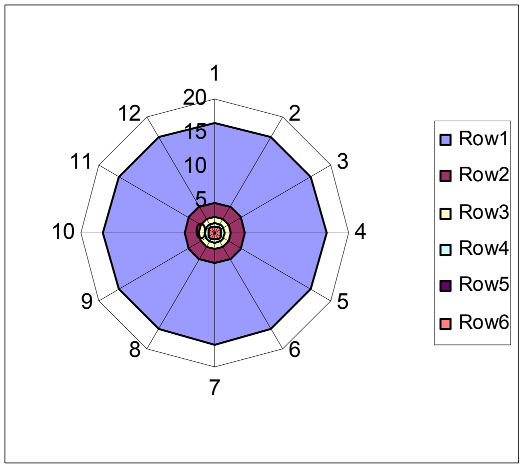

B

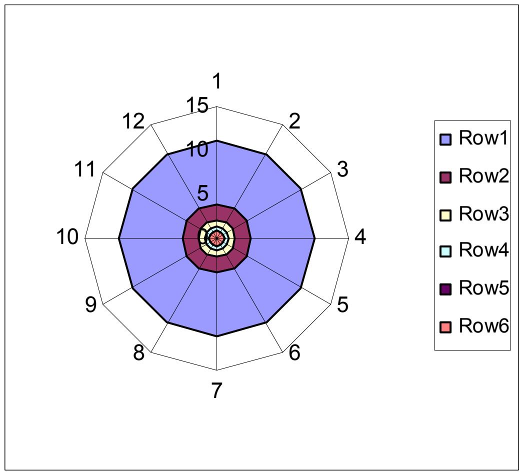

Fig. 6 Models concentric labyrinths:
A - for the Arctic Circle 66.5º N;
B - for Zayatsky island 65º N;
Row 1 - 1 and 11 months; Row 2 - 2 and 10;
Row 3 - 3 and 9; Row 4 - 4 and 8; Row 5 - 5 and 7, number 6 - June.
Winter - Rows 1 and 2; Equinox - Rows 3;
Summer - Rows 4-6.

In the subpolar regions of > 60° radius of the model exceeds the height of the gnomon many times, forcing to abandon the arc of large diameter, and summer shadows are grouped in the center – type "labyrinth 11".

At the latitude of 50 - 60° shadows of all months of the year are placed in a circle of relatively small diameter, it is convenient to use 7-arc "classic" labyrinth.

A

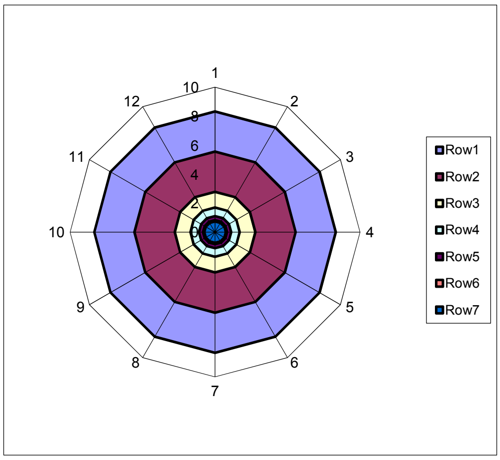

B

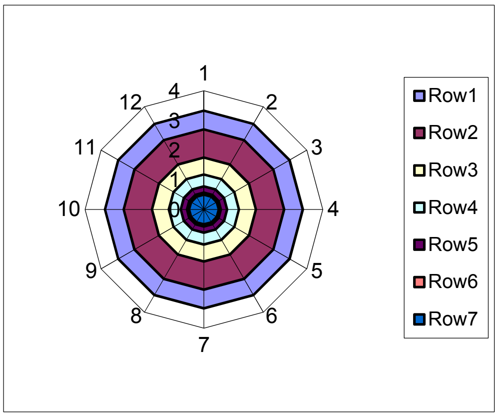

C

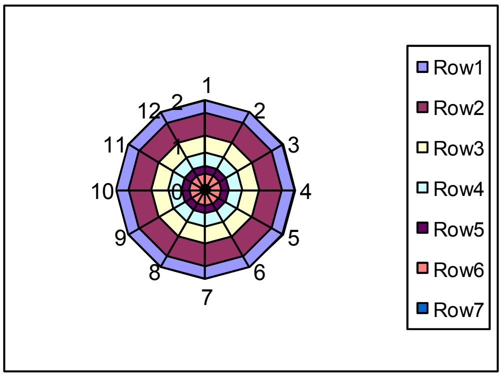

D

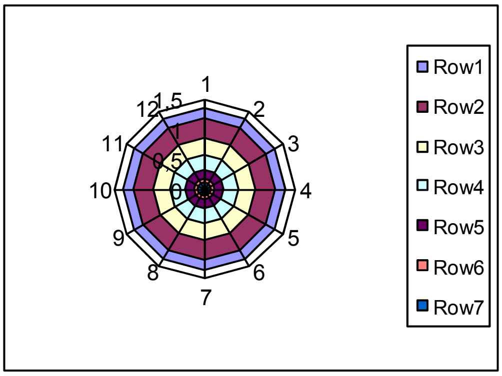

E

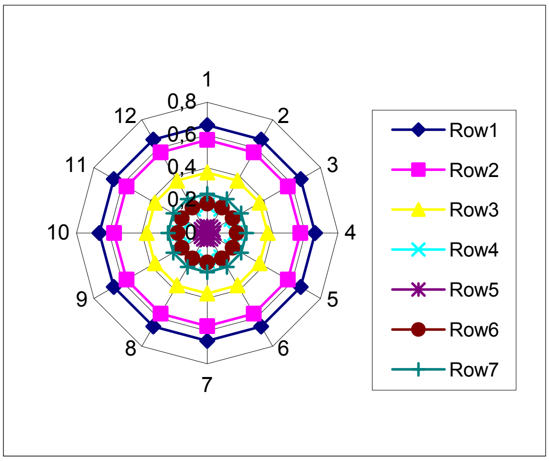

F

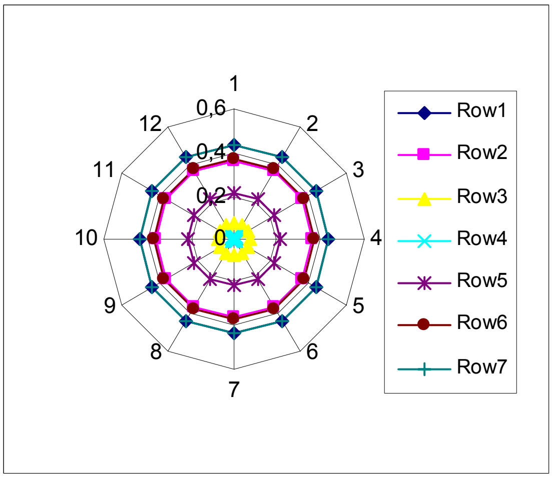

Fig. 7 Models of concentric calendars for different latitudes:
Row 1 - December;
Row 2 - January and November;
Row 3 - February and October;
Row 4 - March and September;
Row 5 - April and August;
Row 6 - May and July;
Row 7 - June;
A - 60º N; B - 50º N; C - 40º N; D - 30º N; E - 10ºN; F - 0º.

In temperate and subtropical latitudes of 40-30° radius of the outer circle of the gnomon 2-fold – a type of "staff", resorting to associations with high enough staffs Zeus, Egyptian or Babylonian rulers or deities (staves which can be of up to 5 - 7 feet) .

In the tropics, the calendar size of the shadow is placed on the gnomon – type "rod." The position of the sun at its zenith twice a year between the Tropic and the Equator makes it necessary for the formation of gnomon faces to ensure a consistent record of the provisions of the shadows without imposing seasonal sites for which it passes several times.

Thus, analysis of the graphs reveals latitude where the record of calendar positions of the shadow can be in the form of an ornament on the gnomon, or on the floor and walls of the church, in all cases, the gnomon can serve as a ruler. Marking may also include an indication of the height of the gnomon, which correspond to the length of the marked shadows (especially for staff). The calendar can be ornamental figurative sign, reproducing the stages of the year economic cycle or more abstract forms of specific forms of geometry of shadows; encoding of calendar months is possible in the animal style, which corresponds to the sequence of the zodiac animals. Calendar hexagonal rods in India and cult objects in Ancient Egypt are noteworthy as well.

Areas of space indication

Obviously, the greatest possibilities of rhythmic changes in the definition of the position of the sun belong to polar circles and the tropics. It is known that changes in the tilt of Earth's axis about 21.9º to 24.3º (according to some sources up 25.3º) causes displacement of the polar circles and the tropics for about 41,000 years. The result is a periodic expansion of the area of the temperate zone and the reduction of the polar and tropical regions.

Nutation of the Earth's axis shifts the line of the Arctic Circle to 3 meters per day and 100 per year. For example, until 2015 the Arctic Circle will move to the north, and then for 9 years, move up to 400 meters south.

The northern regions of the Earth provide other unique features of space observation targets: annual passage of sunrise / sunset 360º circle at the latitude of the Arctic Circle, the full daily observations of the zodiacal circle in 18 hours sidereal time and the position of the North Star. It is no accident ancient science allocated zone of the Arctic at a latitude of about 55° N.

It is worth mentioning that at noticeable annual dynamics of the Sun, in the North simple facilities are accurate, sensitive, accessible to a wide range of observers. In southern latitudes, the increasing the accuracy of the gnomon increase in summer is achieved by increase of its height, and in winter - the erection of screening surfaces, such projects require a significant effort (the legend of the Tower of Babel).

With regard to the influx of solar radiation of low latitudes are more stable, which is proved, in particular, by saturation of endemic and relict forms of life. At high latitudes, the smallest global climate change lead to a fundamental restructuring of the landscape and natural disasters.

Thus, a regional analysis of information resources geographic space shows that the polar regions of the planet are the most dynamic and dependent on solar energy and information. On the one hand, it creates a complexity of development, on the other it explains the appeal of the Arctic region for researchers in the past – rich material is left by ancient authors, there are numerous megalithic sites of navigation, and today – only here you can get accurate information about the current status of the planet and trends development of the global environment.

CONCLUSION

Our studies have shown that the gnomon – the simplest astronomical instrument – opens the possibility of using the primary stone labyrinths as solar calendars. The ubiquity of ancient astronomical instruments can be regarded as a source of information to clarify changes (rhythm, dynamics and evolution) of planetary parameters in the past.

The modeling of gnomon shadow during a year, presented in the article, shows the sensitivity of the structure of the labyrinth to the characteristics of lighting modes at different latitudes. It follows that for the purposes of long-term forecast rhythms of the planet it is advisable to create a network of solar observatories.

REFERENCES

[1] Kern G, Through the Labyrinth. Munich-London-New York: Prestel Verlag, 2000.
[2] Paranin VI, Historical Geography of the Chronicle of Russia. Petrozavodsk: Karelia, 1990.
[3] Paranin VI, The history of the barbarians. Ed..St. Petersburg: RGO, 1998.
[4] Paranin RV, Paranina GN, "The Labyrinth: orientation in geographic space and the evolution of the mark". in Proc. 2nd Int. Conf. Space geocultural European North: the genesis, structure and semantics. Arkhangelsk: State Pomor University of Russia. 2009. pp. 516-518.
[5] Paranina AN, "Northern Labyrinth ‑ A Key to Time, Space, Information". Scientific Research Publishing (Eastern Connecticut State Univ., USA) Natural Resources (NR). Vol. 4. Aug. 2013. pp. 349-356.
[6] Paranina AN, "Navigation in Space-Time as the Basis for Information Modeling". Scientific Research Publishing (Eastern Connecticut State Univ., USA), Archaeological Discovery (AD), Vol. 2, N3, July 2014. pp. 83-89.
[7] Paranina AN, Paranin RV, "Interaction of the nature and ancient persons on the coast of the White Sea". J. Wetlands Biodiversity (JWB). Vol. 4. Dec. 2014. pp. 131-140.

LONG TERM PERFORMANCE PREDICTION OF ROAD EMBANKMENT ON ESTUARINE DEPOSITS: A CASE STUDY IN SOUTHEAST QUEENSLAND

Jia Xie[1], Barry Wai-Choo Kok[2]
[1]Geotechnical Engineer, [2]Principal Geotechnical Engineer, Geoinventions Consulting Services, Australia

ABSTRACT

The estuarine deposits in the coastal areas of Southeast Queensland, Australia impose great challenge in assessing long term performance of highway and motorway embankments. A major transportation project was completed in Brisbane, Southeast Queensland in 2010 with a great part of road embankments constructed over soft Holocene Clay. Areas within the motorway embankments have been experiencing large after-construction settlements. A case study was carried out to back-analyze the long term settlement of the road embankment based on the most updated field monitoring data. Following the back-calculation of the key consolidation parameters by curve fitting method, the Post Construction Settlements were re-assessed by numerical analysis. This paper describes the methodology adopted to back-analyze the long term performance of road embankment. The results of the analytical and numerical analysis are presented and discussed.

Keywords: Road Embankment, Soft Holocene Clay, Post Construction Settlements, Back-Analysis, Curve Fitting

INTRODUCTION

Significant depth of soft estuarine clays with substantially varying thickness and very low strength were found along the alignments of highways and motorways in Southeast Queensland [1]. Under this circumstances, to achieve tight long term performance criteria in terms of Post Construction Settlements (PCS) is a great challenge for engineers. Areas within a major motorway project in Brisbane have been experiencing excessive PCS since construction completion in 2010. A case study was carried out to back-analyze the long term settlement of the critical embankment section with higher level of accuracy, and in turn to investigate the possible causes of under-estimation of PCS during design and construction.

This paper presents the analytical methodology and results of the long term settlement back-analysis. The establishment of sub-soil profiles is described with respect to the regional geotechnical condition. Key consolidation parameters of soft clays are back-calculated by curve fitting method. The PCS till the end of the 10-year Defect Liability Period and the end of the 40-year pavement design life are then re-assessed by using commercial software Settle3D. The back-analyzed PCS are compared to the original prediction made during construction. Possible mitigation solutions and lessons learned are discussed along with the analysis results.

REGIONAL AND LOCAL GEOLOGY

The estuarine deposits exist in Southeast Queensland are classified as originating from Holocene to Pleistocene age [2]. They are compressible clays of high plasticity and low strength. Soft clays with Holocene deposits being the primary source are commonly found in the coastal areas of Southeast Queensland with depth up to 30m [3]. Figure 1 shows the distribution of Holocene deposits in Brisbane [4].

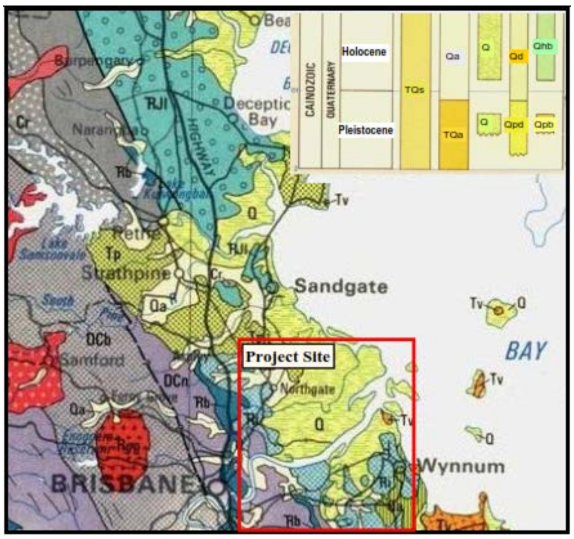

Fig. 1 Distribution of Holocene Deposits in Brisbane.

As illustrated in Figure 1, the project site is generally part of a deltaic plain formed by the Brisbane River. Embankments are situated on Holocene Clays ranging from 5m to 23m which have been sub-divided into two distinct layers: Upper and Lower Holocene Clays. The Upper Holocene Clay is very soft to soft with numerous sand lenses, while the Lower Holocene Clay is soft to firm.

METHODOLOGY

Critical Section Review

Settlement profile and criteria

An extensive field monitoring program has been implemented and settlement data have been collected periodically. Based on detailed review on the settlement profiles summarized from the monitoring data, the embankment section presented in Figure 2 was identified as the most critical with measured PCS up to 282mm till 2015 which is more than 4 times of the original prediction made during design and construction stage.

To limit the post-construction settlement and minimize the loss of serviceability the road, strict settlement criteria have been imposed on many major highway and motorway projects in Australia [1]. The project of the Authors' study was required to achieve a maximum PCS of 200mm till 2020 - the end of the 10-year Defect Liability Period. The measured settlement of the critical embankment selected has well exceeded the PCS criteria, and therefore, was adopted for long term settlement back-analysis.

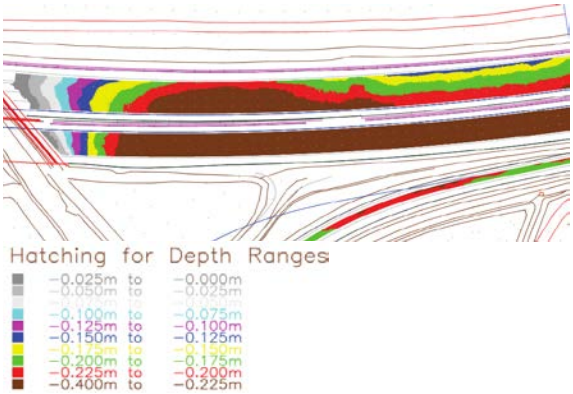

Fig. 2 Settlement profile of critical embankment section.

Sub-surface profile

The subsurface profile was anticipated based on in-depth study of the geotechnical investigation information of the project. Due to the variable ground condition encountered and different ground improvement scheme adopted, the critical section was sub-divided into two zones namely Zone 1 and Zone 2. Depends on the Holocene Clay thickness and embankment height, worst case embankment cross-sections were identified to represent each sub-zone, and site specific soil models were established accordingly. Figure 3 shows the geology long section of Zone 1 and Zone 2.

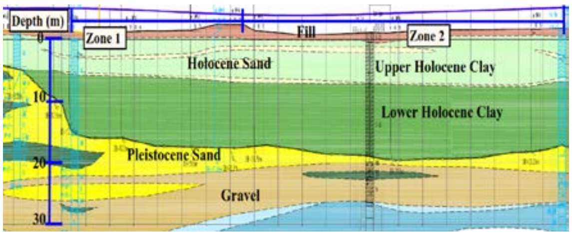

Fig. 3 Geology long section under the critical embankment section.

Ground improvement scheme

Excessive settlement caused by soft clays leads to the need of ground improvement [3]. Preloading with vertical drains is one of the most economical ground improvement methods and was adopted for the critical embankment section. Preloading on its own can decrease the total settlement facilitating the choice of foundation. The settlement process can be accelerated significantly when vertical drains are used with preloading [5]. Table 1 outlines the embankment geometry and ground improvement scheme adopted.

Table 1 Embankment geometry and ground improvement scheme

	Zone 1	Zone 2
Embankment Height (m)	4.1	3.7
Preload Surcharge Height (m)	4.5	2.3
Preload Duration (months)	4.9	9.4
Wick Drain Length (m)	20	23
Wick Drain Pattern	Triangular	Triangular
Wick Drain Spacing (m)	1.4 c/c	1.4 c/c

Embankment loading

Embankment loading is never a single-step load. The actual magnitude and rate of settlement is likely to differ significantly from the estimation due to inaccurate approximation of embankment loading [6]. Analyses in this study were based on the as-built embankment construction sequences of Zone 1 and Zone 2 recorded in the Preload Removal Documents issued during construction.

Modelling and Analysis

Curve fitting technique is commonly adopted in the industry to provide PCS prediction with higher degree of accuracy by comparing and matching the numerically computed time settlement curve to the actual time settlement curve plotted from instrumentation readings. The key element of this technique is to carefully review the settlement model and back-calculate the key consolidation parameters.

Numerical modelling

Commercial software Settle3D was employed to assess the settlement of the critical embankment section numerically. Settle3D is a 3-dimensional program for the analysis of vertical consolidation and settlement [7]. In this study, numerical models were established for the representative embankment cross-sections of Zone 1 and Zone 2. As shown in Figure 4, staged construction process were modelled according to the actual construction sequences, and time-dependent consolidation analyses were performed including primary and secondary consolidation. The baseline time settlement curves were computed by inputting the original soil parameters which were adopted during the design and construction stage by the principal designer of the project.

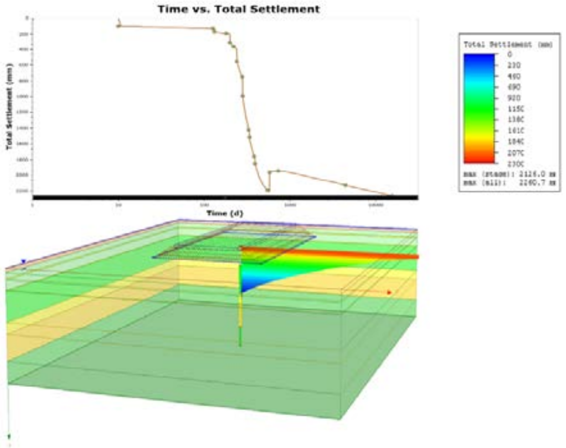

Fig. 4 Settle3D model for Zone 1 with original soil parameters.

Curve fitting and parameter back-calculation

It is important to monitor the performance of an embankment supported by soft ground during and after construction [8]. Periodic field surveys were carried out during and after the construction completion. Annual monitoring data from settlement plates till 2015 were collected. The measured settlements were adopted to plot the actual time settlement curve. The baseline time settlement curve computed by adopting original consolidation parameters were compared to the actual settlement time curve as demonstrated in Figure 5.

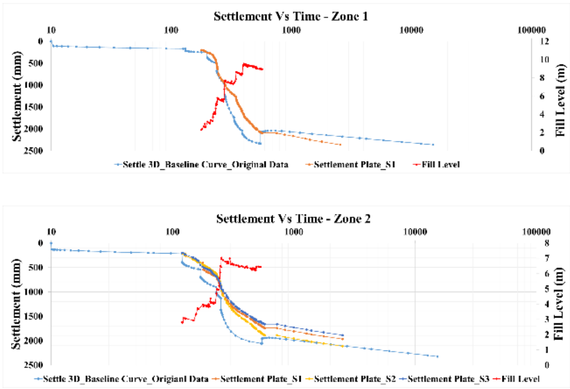

Fig. 5 Settlement time curves: baseline versus actual

The Settle3D computed curve was then adjusted in order to match the actual time settlement curve. As the focus of this study was the long term performance of the embankment, the target section of the curve fitting practice was the secondary settlement section of the curve. The new set of parameters resulted in the best fitted curves are the back-calculated parameters.

The primary consolidation parameters that were back-calculated during the curving fitting procedure are the secondary compression index ($C\alpha\varepsilon$) and over consolidation ratio (OCR) of the Holocene Clay. $C\alpha\varepsilon$ and OCR are the key parameters that could impact significantly on the long term post-construction performance of road embankments.

The original design parameters were derived from conventional laboratory oedometer tests. In this study, values of $C\alpha\varepsilon$ and OCR were back-calculated for Zone 1 and Zone 2 through curve fitting. The calculation results were calibrated by referring to laboratory test outcomes of the project and published data of local experience in Queensland.

Long term PCS prediction

The consolidation parameters back-calculated by curve fitting were input into the Settle3D models to predict the PCS from 2015 to the end of 10-year Defect Liability Period (2020) and end of pavement design life (2050). The back-analyzed PCS were compared to the original prediction assessed during construction in order to identify the difference between the original and the current assessments, and in turn to explore potential mitigation approaches.

RESULTS AND DISCUSSION

Parameter Back-Calculation Results

During the back-calculation process, particular emphasis was on the consolidation parameters of the soft Holocene Clay. Based on the results summarized in Table 2 and Table 3, the Cαε values of the Upper and Lower Holocene Clay layers under the critical embankment section generally increased from 1.0% – 1.8% to 2.0% – 3.0%. The OCR values decreased from 2.0 – 2.5 to 1.5 – 2.0 for Zone 1 while they almost remained unchanged for Zone 2.

Table 2 Consolidation parameters of Zone 1: back-calculated versus original

		Back-calculation	Original
Cαε (%)	Upper Holocene	2.5	1.0
	Lower Holocene	3.0	1.8
OCR	Upper Holocene	2.0	2.5
	Lower Holocene	1.5	2.0

Table 3 Consolidation parameters of Zone 2: back-calculated versus original

		Back-calculation	Original
Cαε (%)	Upper Holocene	2.0	1.0
	Lower Holocene	2.5	1.8
OCR	Upper Holocene	2.5	2.5
	Lower Holocene	1.6	1.5

Secondary compression is the compression that fine grained soils experience following the dissipation of excess pore pressure resulting from loading [9]. In general, the coefficient of secondary compression Cα remains constant, decreases, or increases with time [10]. In this study, the secondary compression was assessed as ratio of Cα to the compression ratio (Cc) and denoted as secondary compression index Cαε. The Cα/Cc concept was developed by Mesri and Godlewski [10] and has been recommended as a practical tool for evaluating the secondary settlement in field situations [11].

The Cαε is approximately constant [9] and Mesri and Godlewski [10] gave values ranging from 2.5% to 8.5%. Peter and David [12] examined the geotechnical compressibility of a wide variety of Queensland sediments in 2002 and found Cαε values range between 1.7% and 5.0%. Study conducted by Rankine [9] in 2007 suggested that Cαε values vary between 0.7% and 3.8% for Brisbane clays and between 0.5% and 8.1% for Sunshine Coast clays. The laboratory test results of the project of authors' study indicated Cαε values range from approximately 0.7% to 3.7% which compare well with the data from the literature.

The originally adopted Cαε values for Holocene Clays were around the lower bound of the historical data and likely to have under-estimated the secondary compressibility of the soft clays under the embankment. Although the parameter back-calculation was essentially based on the statistical analysis by curve fitting, the back-calculated Cαε values between 2.0% and 3.0% was well within the range indicated by literature and hence were adopted for PCS back-analysis.

OCR is another key consolidation parameter which is defined as the ratio of pre-consolidation pressure to the current effective overburden pressure. It is stress history dependent and not an intrinsic property of a soil. The magnitude of secondary compression in a given time was found to be generally greater in less over-consolidated clays [13]. As revealed by Figure 5, by comparing to the measured settlement plate readings, the baseline settlement time curve of Zone 1 considerably under-estimated the PCS, and hence justified the decrease on OCR values. On the other hand, the baseline settlement time curve of Zone 2 only under-estimated the PCS slightly. Therefore, a reasonably fitted curve could be achieved by moderately increasing the Cαε value without major modification on the OCR values. Empirical relations are relied on for the determination of OCR values when there are doubts on the sampling and testing quality [1]. Thus, a realistic estimation of OCR value is always difficult and literature of local experience are few.

PCS Back-Analysis Results

Long term PCS of the critical embankment section was re-assessed by adopting the back-calculated consolidation parameters in the Settle3D models of Zone 1 and Zone 2. The analysis results are listed in Table 4 and Table 5, together with the measured settlements and original predictions made during construction for comparison purposes.

Table 4 Summary of PCS back-analysis of Zone 1

	Settlement since project completion (mm)		
	Settlement Plates	Back-analysis	Original Prediction
2010		Baseline	
2012	195	183	88
2014	265	223	120

2015	282	260	130
2020	N/A	328	179
2050	N/A	594	314

Table 5 Summary of PCS back-analysis of Zone 2

	Settlement since project completion (mm)		
	Settlement Plates	Back-analysis	Original Prediction
2010		Baseline	
2012	168	168	122
2014	225	239	152
2015	245	257	170
2020	N/A	346	222
2050	N/A	586	377

Based on the above results, the original assessment under-predicted the PCS of Zone 1 by around 55% and PCS of Zone 2 by around 30%. The back-analyzed PCS from project completion in 2010 till 2015 fit well with the field measurement as presented in Figure 6. Therefore, the expected settlements from 2015 to the end of the 10-year Defect Liability Period (2020) and the end of pavement design life (2050) were predicted accordingly as summarized in Table 6.

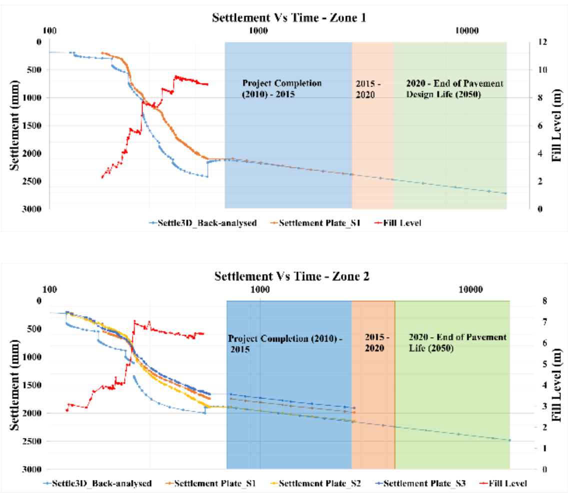

Fig. 6 Settlement time curves: back-calculation versus actual

Table 6 Expected settlements from 2015 to 2020 and 2050

	Expected Settlement (mm)	
	Zone 1	Zone 2
2015 - 2020	68	89
2020 - 2050	266	240

The predicted settlement between 2015 and 2020 indicates the severity of excess PCS and the difficulty on controlling the long term performance in accordance with the tight PCS criteria. The predicted settlement between 2020 and 2050 suggests the performance of the motorway embankments over a longer period of time till the end of the pavement design life.

Lessons Learned

Elements affecting the accuracy of long term performance prediction for road embankments constructed over soft soils are always complex. In this case study, the subsoil condition were reviewed based on information of geotechnical investigation and as-built wick drain installation. The original design process and soft soil parameter adoption were investigated based on back-calculation and in-depth literature study. Under-estimation of PCS was possibly caused by the following factors:

- Under-estimation of the secondary consolidation parameters due to the lack of understanding of the soft soil characteristics.
- Adoption of identical consolidation parameters across a large zone over deep multi-layer soft clays due to lack of awareness of possible long term problems.

CONCLUSION

This paper has focused on the long term performance back-analysis of the critical section of a major motorway project.– The numerical analysis based on consolidation parameters back-calculated through curve-fitting method indicates that the PSC was under-estimated by at least 30% in the original design. Regular asphalt rehabilitation is required to mitigate the excess long term settlement in order to conform to the project PCS criteria.

Some simple guidance notes are summarized from this study in order to predict the long term performance of road embankments on soft estuarine deposits in Southeast Queensland with a higher degree of accuracy:

- To acquire sufficient knowledge of the in-situ subsurface condition through geotechnical investigations and comprehensive review on literatures based on local experiences.
- To prevent the ignorance of localized weak zones or paleo-channels where greater long term settlements will be developed.
- To adopt a systematic review process conducted by experienced soft soil engineers during and after construction with the assistance of instrumentation monitoring.

ACKNOWLEDGEMENTS

The authors of this paper would like to express appreciation to construction consortium and the infrastructure owner for their support in providing the necessary project information for the preparation of this paper.

REFERENCES

[1] Balasubramaniam AS, Cai H, Zhu D, Surarak C and Oh EYH, "Settlements of embankment in soft soils", J. of SEAGS & AGSSEA, Vol. 41, Jun. 2010, pp. 1-19.

[2] Transport Technology, "Geotechnical Investigation: Brisbane Port Road – Stage 2 Investigation", Brisbane: Queensland Department of Main Roads, 2000.

[3] Oh EYN, "Geotechnical and Ground Improvement Aspects of Motorway Embankments in Soft Clay, Southeast Queensland", Gold Coast: Griffith School of Engineering, Griffith University, 2006, ch. 2.

[4] Whitaker WG and Green PM, "Moreton geology" [Online], Queensland: Department of Mines, 1980, Available: http//www.ga.gov.au/map/ [16 June 2015].

[5] Indraratna B, Sathananthan I, Bamunawita C and Balasubramaniam AS, "Chapter 2: Theoretical and numerical perspectives and field observations for the design and performance evaluation of embankments constructed on soft marine clay", Ground Improvement – Case Histories, 1st ed. Elsevier, 2005, pp. 199-230.

[6] Olson RE, "Settlement of embankments on soft clays", J. of Geotechnical and Geoenvironmental Engineering, Vol. 124, Aug. 1998, pp. 659-669.

[7] Rocscience Inc., "Settle3D – Settlement and Consolidation Analysis Theory Manual", Toronto: Rocscience Inc., 2009.

[8] Tan YC and Gue SS, "Embankment Over Soft Clay – Design and Construction Control", Penang: Seminar on Geotechnical Engineering, Sep. 2000.

[9] Rankine BR, "Assessment and Analysis of Queensland Clay Behavior", Brisbane: School of Engineering, James Cook University, 2007, ch 4.

[10] Mesri G and Godlewski PM, "Time and stress compressibility inter-relationship", J. of Geotechnical Engineering Division, ASCE, Vol. 103, No. 5, May. 1977, pp. 417-430.

[11] Mesri G and Choi YK, "Settlement analysis of embankments on soft clays", J. of Geotechnical Engineering Division, ASCE, Vol. 111, No. 4, Apr. 1985, pp. 441-464.

[12] Peter M and David L, "Geotechnical Compressibility and Consolidation Parameters and Correlations for Remoulded Fine-grained Marine and River Sediments", Brisbane: Sustainable Tourism, 2002, ch. 4.

[13] Craig RF, "Consolidation theory", Craig's Soil Mechanics, 7th ed. London: Taylor & Francis Group, 2004, pp. 257-258.

Fifth International Conference on Geotechnique, Construction Materials and Environment, Osaka, Japan, Nov. 16-18, 2015, ISBN: 978-4-9905958-4-5 C3051

EVALUATION OF INFILTRATION BEHAVIORS USING ADVECTIVE DIFFUSION ANALYSIS ON RADIOACTIVE SUBSTANCES IN SOILS

Yoji Ueyama[1] and Shinya Inazumi[2]

[1]Student, Advanced Course of Architecture and Civil Engineering, Akashi College, National Institute of Technology, Japan; [2]Associate Professor, Department of Civil Engineering, Akashi College, National Institute of Technology, Japan

ABSTRACT

Fukushima Daiichi nuclear disaster occurred by Great East Japan Earthquake in 2011. As a result, a lot of radioactive substances was discharged to atmosphere and deposited in surface of ground by rain. In damaged area, decontamination has been conducting. Usually decontamination for the ground is digging out for 5 cm from the surface of the ground, but its safety and validity is apprehended. In this study, per-meation behavior analysis of radioactive substance in the ground was carried out in order to prepare new decontaminations. Specifically, behavior and advection-dispersion analysis was conducted by advection-dispersion equation was embedded a term that considered half-life. As a result, we gained validity for this analysis method by comparing analysis result with result on the spot. Furthermore analytic evaluation for the current decontamination is performed.

Keywords: Radioactive substances, Osmosis, Advection-Diffusion analysis, Radioactive half-life

INTRODUCTION

Tokyo An electric power Daiichi Fukushima nuclear power plant accident has happened by the eastern Japan great earthquake in 2011. Therefore the radioactive substances released were carried by wind and fallen to the surface of the ground or the sea. Iodine-131, cesium-134 and cesium-137 have been detecting in the widespread land area such as the farmland and the ground of city area in Tohoku and Kanto [1].

Geo-Environmental pollution range by this accident was so huge that decontamination is continued now. Generally decontamination for the ground is digging and removing the ground layer about 5cm, like Fig. 1 [2]. However analysis for behavior of radioactive substances has been ever examined. So the safety and validity for it is apprehended. And the construction site of the radioactive material storage container becomes a problem. It is necessary to comprehend behavior of radioactive substances in soils in order to prepare new decontamination for the ground.

In experimental investigation handling radioactive substances is danger in experimental investigation. Therefore in this study, we embedded a term that considered radioactive half-life to advection-dispersion equation in the order to evaluate osmosis behaviors of radioactive substances in the soils. The aim of this study is confirming validity for this analysis method by comparing analysis result with result on the spot. Furthermore examining various the soils have effects on osmosis behavior in the soils.

BEHAVIORS OF RADIOACTIVE SUBSTANCES IN THE SOILS

Radioactive substances fallen to the surface of the ground have four actions. They are concentration decrement with radioactive decay, moving in the soils, scattering and flowing out by weather and absorption by the plants. However scattering and flowing out by weather and absorption by the plants are extremely small values and in order to evaluate osmosis behavior in the soils, in this study, density decrement with radioactive decay and moving in the

Fig. 1 The decontamination for the ground

soils are focused on.

Concentration decrement with radioactive decay depends on radioactive half-life. Radioactive half-life of Iodine-131 is about 8 days, its survival rate becomes 0% instantly. But radioactive half-life of cesium-137 is about 30 years so that long-term examination for it is necessary.

The existence form of radioactive cesium and soil property and importance point moving in the soils. Radioactive cesium in the soils exists as monovalent cation, Cs^+. There are clay minerals and organic matter which have a lot of negative electric charge on their surface. As with other heavy metals and positive ion, radioactive cesium adsorbs them.

THE OSMOSIS AND ADVECTION-DISPERSION ANALYSIS FOR RADIOACTIVE SUBSTANCES

Generally, substances moving in the soils analysis is modeled by the advection-dispersion equation. By this equation is added a term which considered radioactive half-life, it is applicable to moving analysis for radioactive substances.

The general differential equation for two-dimensional osmosis can be expressed as

$$\frac{\partial}{\partial x_i}\left(k\frac{\partial H}{\partial x_i}\right)+Q=\frac{\partial \theta}{\partial t} \tag{1}$$

Where: H = the total head, k = the hydraulic conductivity, Q = the applied boundary flux, θ = the volumetric water content, and t = time.

The advection-dispersion equation which including radioactive half-life can be written as

$$\theta\frac{\partial C}{\partial t}+\rho_d\frac{\partial S}{\partial C}\frac{\partial C}{\partial t}=\frac{\partial C}{\partial x_i}\left(\theta D_{ij}\frac{\partial C}{\partial x_j}\right) -U_i\frac{\partial C}{\partial x_i}-\lambda(\theta C-S\rho_d) \tag{2}$$

Where: C = the concentration of radioactive substance, ρ_d = the dry mass density of the soils, D_{ij} = the dispersion tensor, U_i = the D'arcian velocity, λ = the decay coefficient and S = the adsorption.

The advection-dispersion equation is added a term with the decay coefficient λ that expresses the concentration decrement by radioactive half-life. It is leads to

$$\lambda=\frac{\ln(2.0)}{T_{1/2}} \tag{3}$$

Where: $T_{1/2}$= the radioactive half-life.

INSPECTION OF THE VALIDITY FOR THE OSMOSIS AND ADVECTION-DISPERSION ANALYSIS

We compare the analysis result with concentration distribution measurement results of Cs-137 in the area struck by Tokyo An electric power Daiichi Fukushima nuclear power plant accident in order to validate appropriateness of this analysis method. The measurement results was measured by Pref. Saito in the spot approximately 70km away from the Daiichi Fukushima nuclear power plant three times, 9 months progress, 18 months progress and 20 months progress [3]. According to the result, as depth becomes big, concentration becomes the tendency to be small exponentially. Besides Cs-137 had stayed by about 5 cm a long period of time. And by soils size measurement at the same time, the soils of the spot was proved to be the silt layer.

Then the analysis soils is set to the silt layer. The representative figures of each parameter of the silt is shown to Table 1 [4], [5]. On the other hand, about the radioactive substances, the coefficient of molecular diffusion and the initial concentration of Cs-137 in this point was reported in the other report are used, as shown to Table 2 [6]. The analysis is entered these values and carried out.

Figure 2 shows the measurement result and analysis result of Cs-137 concentration in the depth direction. According to it, their values are very

Table 1 Parameters of silt

the hydraulic conductivity k(m/sec)	1.0×10^{-6}
the volumetric water content θ	0.4
the dry mass density of the soils ρ_d(g/m^3)	1.2×10^{6}
the distribution coefficient K_d(g/m^3)	8.0×10^{-3}

Table 2 Parameters of Cs-137

the radioactive half-life $T_{1/2}$(years)	30.2
the coefficient of molecular diffusion D^*(m^2/day)	7.2×10^{-6}
the initial concentration C_0(Bq/m^2)	3.0×10^{8}
the dispersivity of porous medium α(m)	0.01

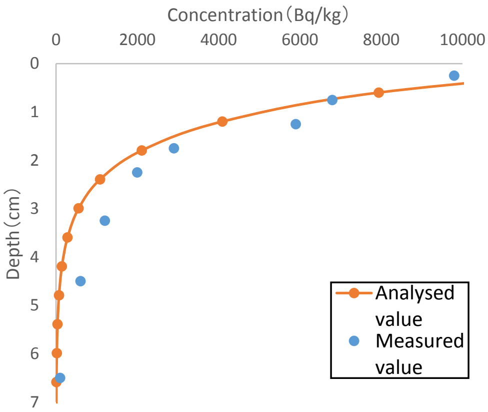

(a) 9 months progress

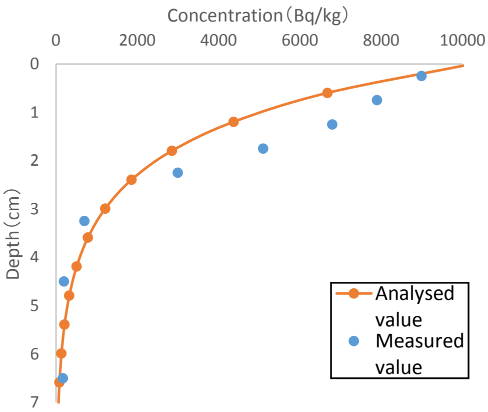

(b) 18 months progress

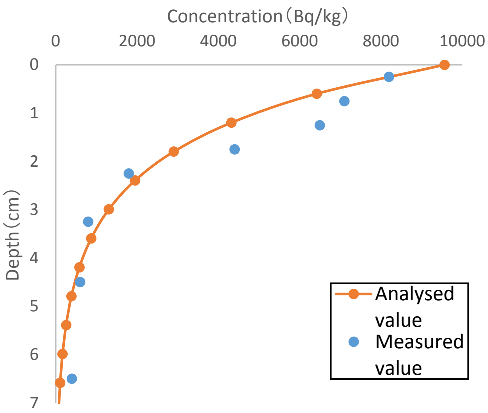

(c) 20 months progress

Fig. 2 The measurement result and analysis result of Cs-137 concentration in the depth direction

closely in every depth and the tendency to decrease of analysis result is exponentially, like measurement result. Furthermore they are the same even if time passes. Thereby the osmosis and advection-dispersion analysis including radioactive half-life has comfortable validity for the evaluation of osmosis behavior of radioactive substances in the soils.

THE ANALYTIC EVALUATION OF THE CURRENT DECONTAMINATION

The osmosis and advection-dispersion analysis including radioactive half-life is carried out in two cases, sand layer and clay layer, on the analysis section with water head difference which is descended Cs-137 which is necessary for long-term examination, like Fig. 3. Analysis section is set to the saturation state. And the boundary colored blue shows the drainage condition. The parameters of sand and clay which necessary for the analysis are used their central values showed Table 3 [4], [5]. About parameters of Cs-137, they are entered the same as the above.

Figure 4 and 5 show the transition of Cs-137 concentration in the sand and clay layers. In the sand layer, there is a large osmosis around the top of slope so that Cs-137 reaches by the foot of slope, placed depth 20cm, at five years progress. Consequently the current decontamination, digging and removing the ground layer about 5cm, has no effective in this case at five years progress. On the

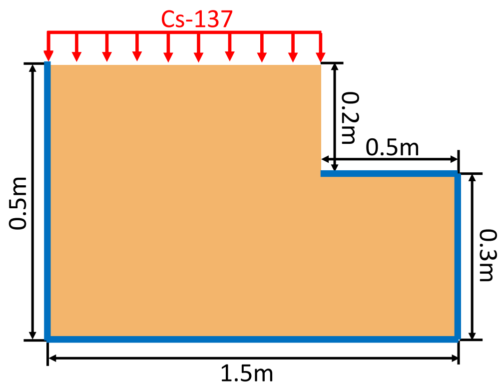

Fig. 3 The analysis section

Table 3 Parameters of sand and clay

parameter	sand	clay
the hydraulic conductivity k(m/sec)	1.0×10^{-5}	1.0×10^{-7}
the volumetric water content θ	0.4	0.4
the dry mass density of the soils ρ_d(g/m^3)	1.5×10^{6}	9.5×10^{5}
the distribution coefficient K_d(g/m^3)	4.0×10^{-3}	1.0×10^{-2}

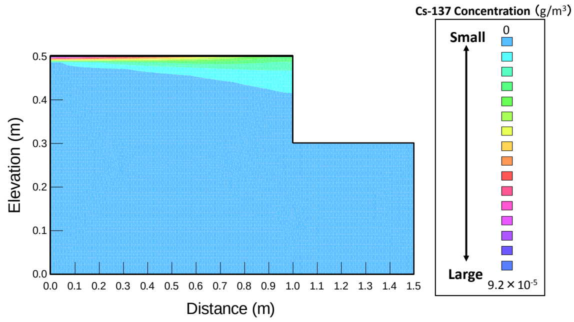

(a) 1 year progress

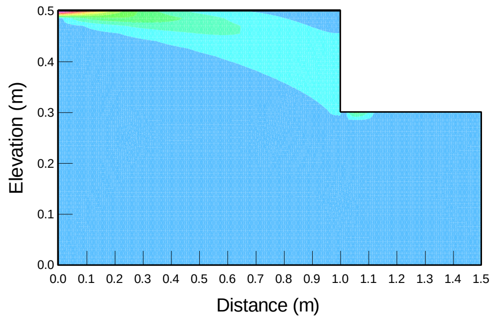

(b) 5 years progress

Fig. 4 The transition of Cs-137 in the sand layer

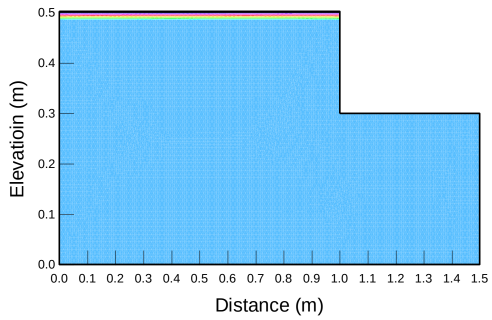

(a) 1 year progress

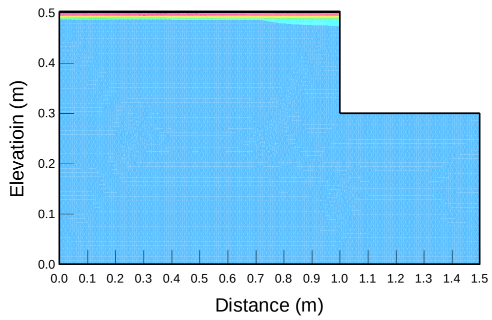

(b) 5 years progress

Fig.5 The transition of Cs-137 in the clay layer

other hand, there is, on the whole, little osmosis in the clay layer, Cs-137 stays by outer layer 5cm. Therefore the current decontamination has effective in clay layer.

From the results, the differences of the osmosis behavior of radioactive substances occurs by the soils property. For that reason, we have to select the decontamination by soils.

CONCLUSION

In this study, we embedded a term that considered radioactive half-life to advection-dispersion equation in the order to evaluate osmosis behaviors of radioactive substances in the soils. This method was confirmed the validity for it by compering measured results. Furthermore, Osmosis and advection-dispersion analysis was carried out in two cases, sand layer and clay layer. We can evaluate analytical for the current decontamination with osmosis and advection-dispersion analysis considered radioactive half-life. As a result, the decontamination should be selected by soils. Henceforth, it is necessary to evaluate the current decontamination from the analysis results that is almost the true condition, for example, implementing the osmosis and advection-dispersion analysis considered uncertainties and setting the analysis section modeled the real topography.

REFERENCES

[1] Ministry of Education, Culture, Sports, Science, and Technology “About making on a distribution map of radioactivity level by Ministry of Education, Culture, Sports, Science, and Technology”, Ministry of Education, Culture, Sports, Science, and Technology, 2015

[2] Ministry of the Environment “Decontamination guidelines revised edition”, Ministry of the Environment, 2015

[3] Saito K, Aoki K, Tanihata I “Confirming depth distribution of radioactive substances in the soils”, Japan Atomic Energy Agency, 2015

[4] Japanese Geotechnical Society “Soil tests, bases and guidance”, Japanese Geotechnical Society, 2010, p. 91

[5] Inoue Y, Morisawa S ” The distribution coefficient of radioactive substances between soil and water”, Journal of Nuclear Science and Technology, Vol. 18, 1976, pp. 524-534

[6] Suzuki K, Komiya Y, Minami, H, Mizuta M “Analysis for depth distribution of radioactive cesium in soils”, Journal of Japanese Association for Digital Humanities, Vol. 27, 2013, pp. 11-14

FLOWABILITY EVALUATION OF FLUIDIZED TREATING SOILS BASED ON MOVING PARTICLE SIMULATION

Masaki Kaneko[1], Shinya Inazumi[1], Yuji Shigematsu[2] and Hiroshi Kawamura[3]

[1]Student, Advanced Course of Architecture and Civil Engineering, Akashi College, National Institute of Technology, Japan; [2]Associate Professor, Department of Civil Engineering, Akashi College, National Institute of Technology, Japan; [3]Sanwa Co. Ltd., Japan; [4]Sumitomo Densetsu Co. Ltd., Japan

ABSTRACT

Recently, fluidized soils have come to be used as landfill material or filler in such landfill of underground space in Japan. However, the design and construction of the fluidized soil at present is based only on the rule of thumb. Therefore, taking into account the findings based on the theory is useful. This study has focused on moving particle simulation. Good results have been obtained in the numerical flow analysis by using the Bingham model to moving particle simulation. In addition, the author has developed fluidized soil with increased fluidity (super-fluidized soil). It has evaluated from two aspects of mechanical properties and flow properties of the high flow of treated soil. In the mechanical properties has showed that it meets the quality that is required for super-fluidized soils. In flow properties has showed that it has a high fluidity than the fluidized soil.

Keywords: Fluidized soil, MPS method, Bi-viscosity model, Flow simulation

INTRODUCTION

Fluidized soil is the wet stabilization soil which in principle be composed of muddy soil, the material contains the fine fraction of clay and silt enough, and solidification material to stabilize the mechanical characteristic. This fluidized soil tends to be used many as filler in a sewage pipe or the backfill of the underground (Figs. 1 and 2). However, the design and the construction are based on the heuristics of the past in the field at present. Therefore, the following points can be realized by taking into account the theoretical knowledge in addition to heuristics of the past.

(1) The most suitable combination design of the fluidized soil will enabled.
(2) It is possible to quantitatively grasp about the pumping distance and the filling distance in the field.
(3) Proper selection of equipment (apparatus) can be performed.

From these, it may be said that it is useful to take theoretical knowledge into account.

For knowledge-based theory, particle method as a method of dealing with large deformation in recent years is attracting attention. Particle method is using the particles as a method of discretization of continuum unlike the grid method. So there is no need to perform the production of the lattice requiring complicated working time. The particle method is a Lagrangian description. Therefore there is no need to calculate the convection section is required in Euler description (Table 1). The large deformation of the free boundary surface can be easily expressed. Flow analysis by the MPS method in the fresh concrete and high fluidity of concrete on the basis of the merit of particle method has been tried. Therefore, it is considered that it is possible to carry out the same way flow analysis also in the fluidized soil cement is used as the solidifying material. In this study, author focused on the MPS method. It is a kind of particle method as a

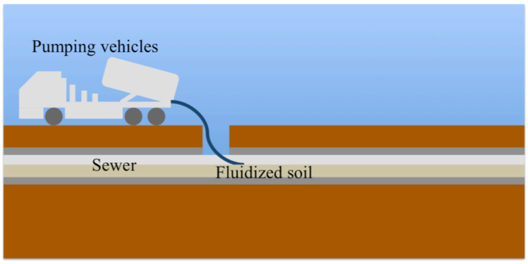

Fig. 1 Pumping of underground space

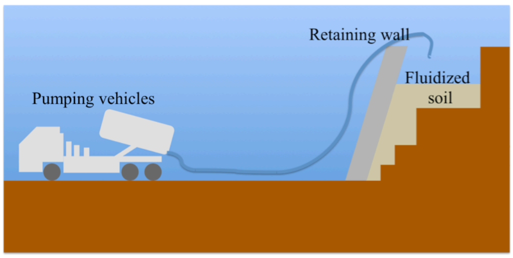

Fig. 2 The backfilling of the retaining wall

theoretical knowledge. In addition, it is conducted flow simulation of fluidized soil using the MPS method.

OVERVIEW OF THE FLUIDIZED PROCESSING SOIL

Fluidized soil is a material used at the time of backfilling and backfilling underground structure of various structures thing. In addition, it is a material that has been developed in order to make effective use of the construction waste soil. The basic concept is to expect a hardening effect by mixing a solidifying material in an appropriate amount to the muddy soil (It has a compaction unnecessary and appropriate flowability). In recent years, socially recycling has become important. Therefore the fluidized soil is widely used in urban areas [1]. In other words, to understand in relation to the characteristics of the fluidized soil also can be said that also lead to the promotion of reuse of construction waste soil.

Anamnestic research of the fluidized soil, are being carried out experimental study regarding the mechanical properties and flowability. Mechanical properties and flowability have also been studied when mixed with the fibers or changing the type of the muddy soil. However, analytical understanding with respect to the fluidity of the fluidized treated soil is not performed.

In this study, author conducted an experiment and analysis by using two fluidized Soil. As the difference between the two types of fluidized soil, the difference the stock solution (muddy soil). Namely include the difference between the maximum particle sizes. Undiluted solution of the material that is to B in this study is the particle size is composed of 74μm or less. Undiluted solution of materials that are treated as A has allowed the mixing of particle size 74μm or more fine sand.

THE PARTICLE METHOD

The particle method is a method of analyzing the motion of the continuum as the motion of a finite number of particles. It has not used mesh. Particle method is also easy to apply to three-dimensional. In recent years it has attracted attention as an analysis method for three-dimensional continuum.

Particle method is a relatively new technique. The first particle method is PAF (Particle-and-Force) method it has been proposed in 1965 in the United States Rosuaromosu National Laboratory. Then, MAC (Marker-and- Cell) method has been proposed. But the particles in this method are used as a tracer of the liquid surface. Furthermore PCI (Particle-in-Cell) method has also been proposed.

Table 1 Grid method and Particle method

	Grid method	Particle method
Discretization	Use Grid 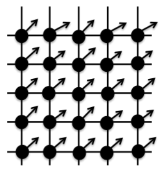	Not use Particle 

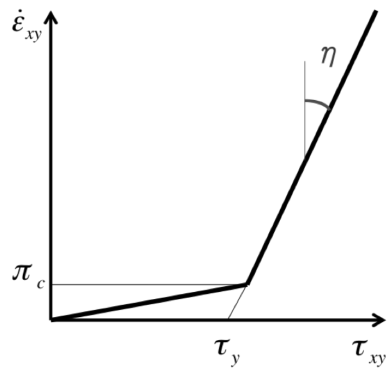

Fig. 3 Bi-viscosity model

This method uses a particle in the advection terms. The other terms it is a method of calculating a grid. Therefore, a large numerical diffusion occurs.

In the sense of using the particle only, pure particle method is SPH method has been proposed in 1977. SPH method is a method of calculating the compressible flow. So far it has been mainly handled in the area of astrophysics. In recent years, it has spread also be applied to the free liquid surface flow and solid mechanics.

Whereas SPH method was proposed as a method of calculating the compression flow, MPS method has been proposed in 1995 as a method for calculating the non-compressible flow. MPS method is calculated the incompressibility condition as a particle number density constant. This method has introduced a pressure Poisson equation. Free surface is determined by a decrease in particle number density. Therefore there is no need to draw the liquid surface shape [2][3][4].

MPS METHOD APPLYING THE BI-VISCOSITY MODEL

In this study, we have used the fluidization treated soil as the analysis material. This material can be regarded as a Bingham fluid. Therefore, it is necessary to apply the MPS method to Bingham model. However, it is very difficult to handle the Bingham model in numerical analysis. This is because the stress becomes unstable in the following yield value. Therefore, the authors are using the bi-viscosity model as an approximation model (Fig. 3). The constitutive equations employed in this model are expressed in Eqs. (1) And (2).

$$\tau_{ij} = -P\delta_{ij} + 2\left(\eta + \frac{\tau_y}{\sqrt{\Pi}}\right)\dot{\varepsilon}_{ij} \qquad \Pi \geq \Pi_c \quad (1)$$

$$\tau_{ij} = -P\delta_{ij} + 2\left(\eta + \frac{\tau_y}{\sqrt{\Pi}}\right)\dot{\varepsilon}_{ij} \qquad \Pi \geq \Pi_c \quad (2)$$

τ_{ij} $\dot{\varepsilon}_{ij}$ represent stress components and strain rate component of the viscous fluid. P represents pressure. η represent plastic viscosity. τ_y represent yield value. $\Pi = \dot{\varepsilon}_{ij}\dot{\varepsilon}_{ij}$. The governing equation obtained from these constitutive equations is expressed by Eq. (3) and Eq. (4).

$$\frac{\partial \dot{u}}{\partial t} = \frac{1}{\rho}\left(-\nabla P + \left(\eta + \frac{\tau_y}{\Pi}\right)\nabla^2 \dot{u} + 2\dot{\varepsilon}_{ij}\frac{\partial}{\partial x_j}\left(\frac{\tau_y}{\Pi}\right)\right) + \dot{F} \quad (3)$$

$$\frac{\partial \dot{u}}{\partial t} = \frac{1}{\rho}\left(-\nabla P + \left(\eta + \frac{\tau_y}{\Pi_c}\right)\nabla^2 \dot{u} + 2\dot{\varepsilon}_{ij}\frac{\partial}{\partial x_j}\left(\frac{\tau_y}{\Pi_c}\right)\right) + \dot{F} \quad (4)$$

Eq. (3) is an expression of the state in which the flowing. Eq. (4) is an expression of the state in which the immobile. $\dot{u}$ represent flow velocity vector. t represent time. ρ represent density. $\dot{F}$ represent external force vector. Π_c is using the fluidized limit strain rate(π_c) $\Pi_c = (2\pi_c)^2$.

In the MPS method, continuous body puts as particles of finite number. Particle interaction model utilizes the weighting function w represented by the Eq. (4). This force acting on arbitrary particle assumed to interact with the particles present from the particles within a certain range. In this analysis it is used a logarithmic weighting to improve accuracy than the standard weighting function [5]. It shows the weighting function in Eq. (5)

$$w(r) = \begin{cases} log\left(\frac{r_e}{r}\right) & r \leq r_e \\ 0 & r_e > r \end{cases} \quad (5)$$

Where r is the distance between particles, r_e is the radius of influence ranging interaction between the particles. Also, evaluate the density of the fluid using the particle number density. Calculation of particle number density has used the weighting function. Particle number density is determined from Eq. (6).

$$\langle n \rangle_i = \sum_{j\neq i} w\left(|\dot{r_j} - \dot{r_i}|\right) \quad (6)$$

n_i represents the particle i-th particle number density. $\dot{r_i}$ is the i-th particle position vector, $\dot{r_j}$ is the particle j-th position vector. Incompressible fluid is the density and particle number density is constant. Therefore, it is represented by n^0 the particle number density in the initial placement of the particle as a reference value of the particle number density.

The MPS method discretization is performed in first and second terms of the right-hand side of Eq. (7).

$$\frac{\partial \dot{u}}{\partial t} = -\frac{1}{\rho}\nabla P + \nu\nabla^2 \dot{u} + \dot{F} \quad (7)$$

In MPS method Gradient model and Laplacian model, as these discretization, are represented by Eq. (8) and Eq. (9).

$$\langle \nabla\phi \rangle_i = \frac{d}{n^0}\sum_{j\neq i}\frac{\phi_j - \phi_i}{|\dot{r_j} - \dot{r_i}|^2}\left(\dot{r_j} - \dot{r_i}\right) w\left(|\dot{r_j} - \dot{r_i}|\right) \quad (8)$$

$$\langle \nabla^2\phi \rangle_i = \frac{2d}{\lambda n^0}\sum_{j\neq i}(\phi_j - \phi_i)\, w\left(|\dot{r_j} - \dot{r_i}|\right) \quad (9)$$

Where $\langle\ \rangle_i$ represents that it has the approximated using a particle model in the i-th particle. d is represents the number of dimensions. λ is a coefficient for matching the analytical solution and distributed in the variable distribution. This is represented by Eq. (10).

$$\lambda = \frac{\sum_{j\neq i}\left[w\left(|\dot{r_j} - \dot{r_i}|\right)|\dot{r_j} - \dot{r_i}|^2\right]}{\sum_{j\neq i}\left[w(\dot{r_j} - \dot{r_i})\right]} \quad (10)$$

The discretization of differential operators that gradient model Laplacian model represented is a feature of the MPS method.

UNDERSTANDING AND EVALUATION OF LIQUIDITY BY THE FLOW TEST

The flow test based on "Test Method for Air mortar and air milk" (JIS A 313-1992, using an air cylinder of φ 80mm h 80mm) in order to understand the flow of the fluidized soil were performed [6]. Furthermore, author went shooting a movie at the same time. In this experiment is using a flow ability different fluidized soil in order to evaluate the flow

Table 2 The recipe of fluidized soil and Parameters of analysis

	A	B
Specific gravity	1.302	1.224
Plastic viscosity (Pa・s)	2.349	1.209
Yield value (Pa)	2	3
Distance between particles of first (m)	0.0002	
π_c	0.5	

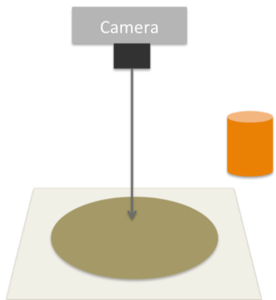

Fig. 4 Overview of image analysis

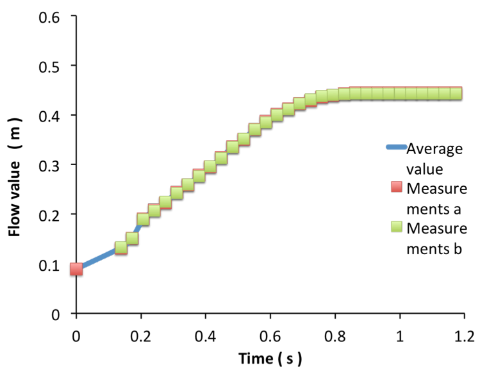

Fig. 5 Fluid behavior of A by image analysis result

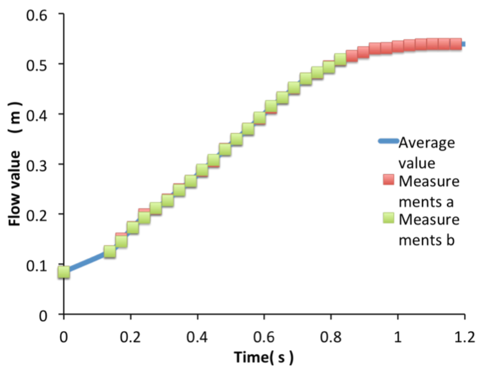

Fig. 6 Fluid behavior of B by image analysis result

ability. Formulation of the fluidized soil that was used in the experiment is shown in Table 2.

In this study has conducted an image analysis to make a comparison with the analysis. The image analysis is intended to perform grasp flow behavior. It is based on flow test video (Fig. 4). Measurement of the flow value is measured in the x and y (measured value a, measured value b) direction orthogonal. The image analysis results of the fluidized soil are shown in Figs. 5 and 6.

Looking at Figs. 5 and 6, it can be seen that A has a short flow stop time compared to B. Furthermore, A can be read that has a high fluidity. The liquidity of the difference is thought to be due to differences in particle size. In addition each fluidized soil from these figures is read that spread evenly, because the measured value 'a' and measured value 'b' are almost identical.

UNDERSTANDING AND EVALUATION OF LIQUIDITY BY PARTICLE METHOD

To understand the flow of the fluidized soil from a theoretical point of view, author has conducted flow analysis by particle method using bi-viscosity model as a response to Bingham fluid [7]. Analysis is being carried out in two-dimensional, because the flow of the fluidized soil has been carried out uniformly. Parameters of analysis used are shown in Table 2. The analysis cross section are using a flow test cross-section (Fig.7). In addition, Fig.8 and Fig.9 show the visualization of the analysis results.

It shows a diagram of a combination of 'flow behavior by analysis based on the particle method' and 'flow behavior by flow test' in each fluidized Soil. (A is shown in Fig. 10. B is shown in Fig. 11). From Figs. 10 and 11, it can be read that the flow behavior of each fluidized soil is well suited. At first glance, these figures do not seem to match. However, the range has become very small compared to the scale of the construction. Therefore, it has become a comparison at the micro range. Thus it can be said that there is validity.

Then evaluate the fluidity. From Figs. 10 and 11,

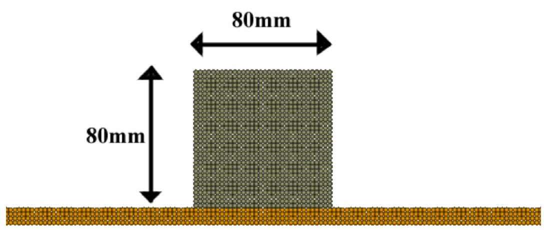

Fig. 7 Flow test cross-section

Fig. 8 The results of visualization of A

Fig. 9 The results of visualization of B

it is read that the A from the results of analysis by particle method have a high flowability. Therefore, it is expected to high filling properties and workability in B. Finally, the difference in the fluidity from the result of analysis based on the particle method it was revealed that the plastic viscosity and the specific gravity is affecting.

CONCLUSION

In this study, it has evaluated the flowability of the fluidized soil based on the experimental evaluation and particle method on the liquidity of the fluidized soil. The results and findings of this study are shown below.

(1) With regard to liquidity, high-flow fluidized soil (B) higher than the flow of treated soil (A). Comparison of the flowability of the fluidized soil with a maximum particle size of different undiluted solution, the particle size distribution of the undiluted solution showed that influence the flowability.
(2) Bi-viscosity model was apzplied particles method (MPS method) the results of flow analysis of fluidized soil is consistent with the real problem, validity has been confirmed.
(3) High-flow fluidized soil (B) from the results of flow analysis using a particle method to correspond to the bingham model was confirmed to have a high fluidity.
(4) The main factors that affect the flowability of fluidized processing soil showed that it is the specific gravity and plastic viscosity from flow analysis and test results.

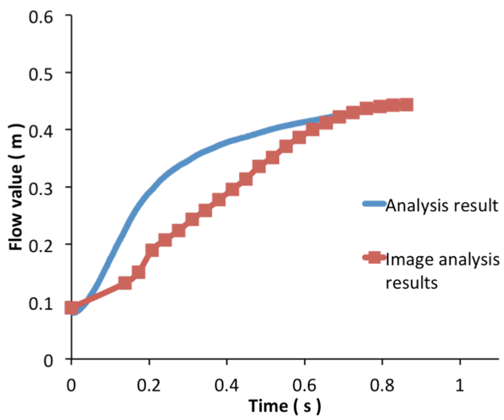

Fig. 10 Fluid behavior of A

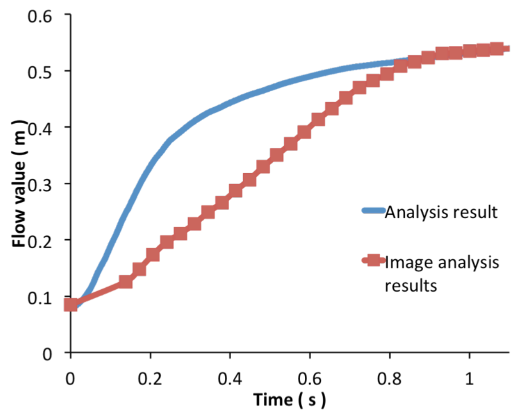

Fig. 11 Fluid behavior of B

REFERENCES

[1] Yukihiro K, “Future challenges and mechanical properties of the fluidized soil”, Japan Society of Civil Engineers Papers F, vol.62, No.4, pp.618-627, 2006.
[2] Seiichi K, “Numerical analysis of the flow by the particle method”, Nagare 21, pp.230-239, 2002.
[3] Seiichi K, Kazuya S, Kouhei M, “Particle method Introduction (From the basics of fluid simulation to parallel computation and visualization)”, Maruzen Publishing Co., Ltd., 2014.
[4] Seiichi K, “Particle method Computational Mechanics Lecture Series 5”, Maruzen Publishing Co., Ltd., 2006.
[5] Hayashi Y, Toyotani Z, Sumida K, “The water column collapse simulation by pressure stabilization particle method”, Nippondaigaku Seisankougakubu 46th Academic lecture, pp.307-308, 2013.
[6] Dokuritugyouseihouzin Dobokuzimusyo, “Fluidized soil use Technical Manual (Second edition)”, Dokuritugyouseihouzin Dobokuzimusyo, 2007.
[7] Urano S, Nemoto K, “A study on the workability of fresh concrete using flow simulation method”, Simizukensetu Kenkyuhoukokusyo, No.90, 2013.

Fifth International Conference on Geotechnique, Construction Materials and Environment, Osaka, Japan, Nov. 16-18, 2015, ISBN: 978-4-9905958-4-5 C3051

PREDICTION OF SPACE DISTRIBUTION FOR SOIL SURVEY VALUES BASED ON GEOSTASTICS

Kohei Urakami[1], Shinya Inazumi[2], Kozo Okita[3] and Tsuyoshi Okita[3]
[1]Student, Advanced Course of Architecture and Civil Engineering, Akashi College, National Institute of Technology, Japan; [2]Associate Professor, Department of Civil Engineering, Akashi College, National Institute of Technology, Japan; [3]Okita-Ko Co. Ltd , Japan

ABSTRACT

Recently, land subsidence and liquefaction are becoming evident. But neither the countermeasure nor research technique have not been established. In order to determine the cause, more detailed comprehension of soil properties is essential; therefore, in this research Improved Swedish Sounding Testing machine, or NSWS *1, capable of measuring more detailed physical properties of in-ground was utilized and conducted a subsurface investigation at a narrow detailed house at which land subsurface have occurred. Based on the result of the investigation presented physical properties of the in-ground in the plane manner using Kriging, one of geostatistics methods. Also, the comparison of converted N-value measured by the NSWS and converted N-value estimated by Kriging is presented to examine the composite capability and benefit of Kriging and NSWS for simplified on-site verification and re-measurement for reaffirmation (diagonal measurement) in the confined detached house ground.

Keywords: Geostatistics, Kriging for Swedish weight sounding test, disaster prevention

INTRODUCTION

The vast area of Urayasu city, Chiba prefecture was liquefied when 2011 Tohoku earthquake struck and followed by the permanent displacement causing heavy damage to the buildings. Although JIS standard for a research method or countermeasure construction method for liquefaction have been around for long time, they are still being developed. A technology that correspond to fast-paced changes in the natural disaster has not been established. Especially, the detached house grounds are having difficulties because they are private properties and very small in Japan. Also, due to the reasons of time, finance, vibration, a mechanical reason for installation area, and the conventional JIS method enable a limited number of data collection when conducting in-situ soil analysis. For that, in general an estimation is carried out using some methods based on a limited number of soil analysis for un-investigated area.

In this research, the NSWS was utilized at an embankment of a sunk detached house measuring converted N-value in details at each survey point. Furthermore, based on depth distribution of measured converted N-value, Kriging is used to predict space distribution of the unknown domain with unclear N-values within the survey ground. Also, the comparison of converted N-value measured by the NSWS and converted N-value estimated by Kriging is presented to examine the composite capability and benefit of Kriging and NSWS for simplified on-site verification and re-measurement for reaffirmation (diagonal measurement) in the confined detached house ground.

INVESTIGATION TESTING EQUIPMENT AND ON-SITE SUMMARY

The research conducted a ground survey at land subsidence occurred site. On this survey, the NSWS, was utilized as the survey testing machine. The machine has refined the conventional Swedish Sounding Testing machine; it evaluates soil strength by loading weight on a penetrating rod and collecting data by rotation.
The followings are the characteristics of the NSWS:

1. Maximum loading amount is 2500N possessing high penetration capability
2. It can penetrate soil layers with gravels mixed, and soft rock layers.
3. A measurement resolution is 10.8mm, very fine, enabling to collect detailed data.
4. Not only a vertical measurement but diagonal measurement are possible enabling to collect many data at the confined research area.

The next is about the venue. The venue is a detached house embankment in Nishinomiya city, Hyogo prefecture. It is a slope area with a stair-casing residential area; two two-story general detached houses are line up on the site. A part of the site caused land subsidence causing distortion on the

Fig 1. NSWS

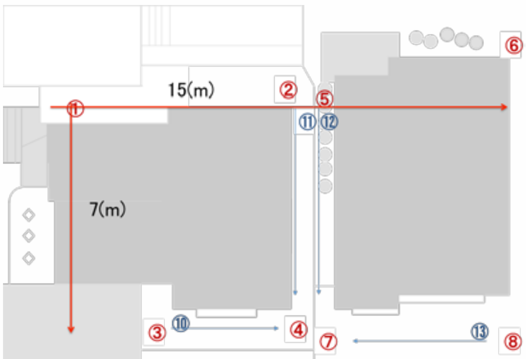

Fig 2. One-site summary

part of the building and concrete-block wall that surround the house. These phenomenon mainly happened at the South part of the site. As depicted in Fig.2 survey locations are the vertical measurement points at the North of the site (1, 2, 5, and 6) and the vertical measurement points at the South of the site (3, 4, 7, and 8), the side of the retaining wall. Also, diagonal measurement of survey locations (10, 11, 12, and 13) are meant to comprehend the bounds of weak area and insufficiency of compaction in the vicinity of the retaining wall.

.

SPATIAL DISTRIBUTION PREDICTION BY ORDINARY KRIGING

In this study interpolated a cross section among survey locations using Ordinary Kriging and estimated the distribution of converted N-value along the cross section. Ordinary Kriging is one of Krigings under the assumption of fulfillment of stationary in random variables and calculates weighted mean value of the variables. In this study, random variables are converted N-values. Also, stationary means that expected values of random variables are fixed throughout the whole targeted area, and a covariance depends solely on distance among data and is independent of the locations of data.

A general formula of Ordinary Kriging is as follows (1):

$$\hat{w}(x) = \sum_{i=1}^{n} b_i\, w(x_i) \tag{1}$$

W(x): Estimated value, W(x): Measured value, b1: Weight at each survey location

Also, formula (2) is necessary to fulfill the aforementioned stationary requirement:

$$\sum_{i=1}^{n} b_i = 1 \tag{2}$$

The formula requires the sum of weights to be equal to one; under this condition, Kriging can be applied.

In this study, Ordinary Kriging was carried out based on converted N-value measured by the NSWS. The NSWS can collect data with 1.0cm pitch. So, with this measurement resolution, or by changing the number of data analyze the change of results of interpolation and also analyze the accuracy of the estimations by changing the number of data assuming the measured values as true values. Kriging was carried out with 1.0cm pitch and 25cm pitch. And, besides comparing these two, the applicability of Kriging to the detached house grounds was examined as well.

Also, in order to make estimations on different cross sections, Kriging was utilized likewise at survey locations 3 and 7 with 1.0cm pitch. This is to judge the applicability of Kriging at different cross sections. On the cross sections created between survey locations 3 and 7 exist survey location 4 that was measured vertically, and survey location 10 that was diagonally measured from survey point 3. Therefore, by estimating this cross section and comparing with vertically and diagonally measured data, the applicability of Kriging can be judged as well as judging whether it is possible for Kriging to interpolate point data in a plane manner.

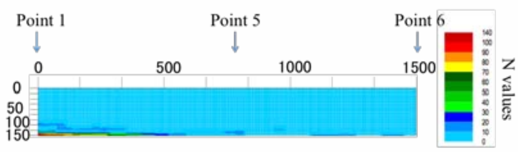

Fig 3. Result of Kriging on 1.0cm pitch

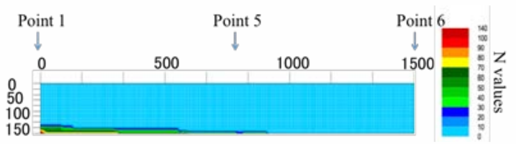

Fig 4. Result of Kriging on 25.0cm pitch

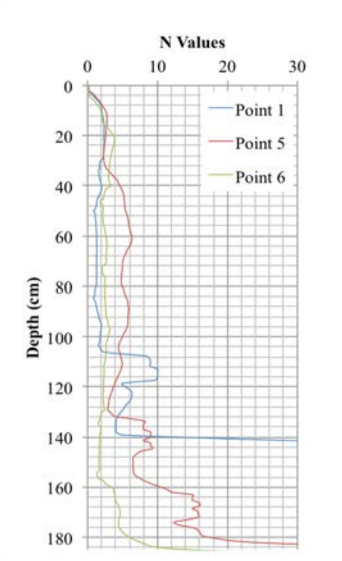

Fig 5. Actual values on Point1,5 and 6

Fig 6.

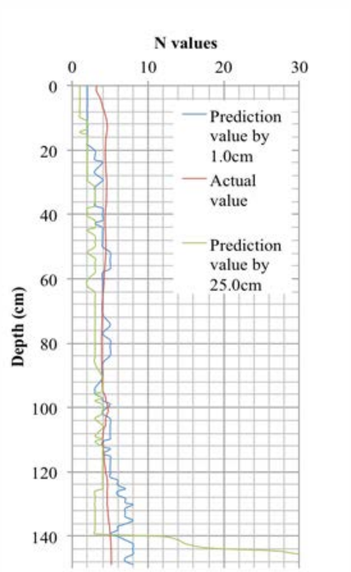

Fig 7. Compare to actual and prediction on point 2

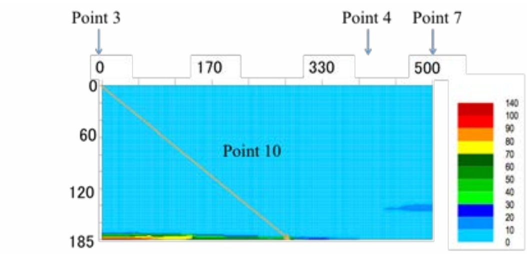

Fig 7. The result of Kriging on other cross section

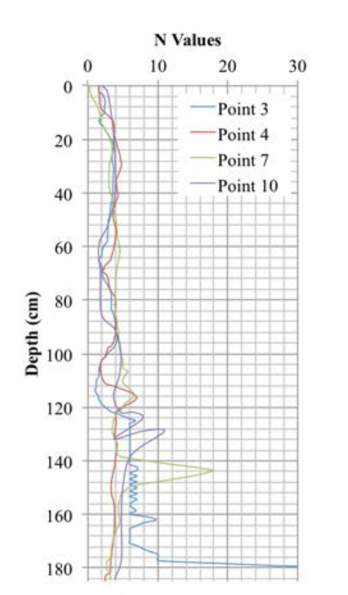

Fig 8. Actual value on Point 3, 4, 7, 10

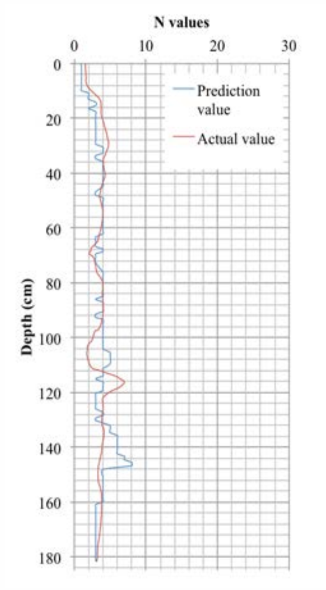

Fig 9. Compare to actual and prediction on Point4

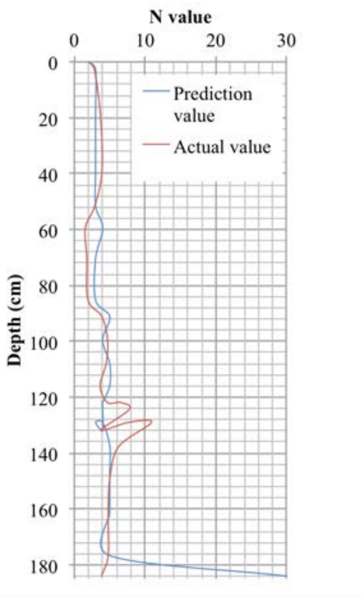

Fig 10. Compare to actual and prediction on Point10

Table 1. Relative error with the real value

Items	Relative error
Point 4	0.284210892
Point 10	0.595928736

APPLICABLE EXAMINATION BY ORDINARY KRIGING

Fig. 3 shows the results of Kriging with 1.0cm pitch at survey points 1, 5, and 6. Fig. 4 is the results of Kriging with 25cm pitch at survey points 1, 5, and 6. By comparing these two one can confirm that from about depth 130 cm to 150 cm Fig. 3 has a finer and more various distribution. Therefore, finer measurement resolution enables more detailed estimations. Fig.3 and Fig4 show the soft ground on depth 100cm. Therefore, it sees very likely to be the soft ground to depth 100cm by Kriging. Fig. 6 is a comparison of two estimations with measured converted N-value at survey point 2. One can tell that at the deep ground the estimated value with 1.0cm pitch deviates less from the measured value. From this confirmation, one can see the need to collect many data by measuring with narrow interval. Also, since both estimations have small deviations up till 140cm depth, it is safe to say the estimations have high-precision when treating measured values as true values and it thinks Kriging has applicability on vertical.

Fig. 7 shows the result of Kriging from survey point 3 to 7 with 1.0cm pitch. With Fig. 7 one can confirm the existence of soft grounds down until 120 cm deep. From there, at the vicinity of survey point 7 hard grounds appear at the vicinity of 120 cm depth, and at the vicinity of 180 cm depth a wide-ranged hard grounds appear. Fig.9 is the comparison of the measured value to estimated value at survey point 4, and Fig.10 is the comparison of the comparison of the measured value to estimated value at survey point 10. Fig.9 has overall small deviations. Next, one can confirm that down until 180 cm depth Fig.10 has small deviations. But the deviation become bigger from there. Table 1 shows relative errors of at both survey points. According to Table 1 both points have the relative errors less than one. This means both have relatively small errors. Because of these results, it is fair to say that the estimations for vertical and diagonal measurements are highly precise. Therefore, Kriging is capable of interpolating in a plane.

CONCLUSION

In this study, the followings were examined:

1. Applicability of Kriging to the detached house grounds with a small area.
2. It is possible for Kriging to interpolate point data in a plane.
3. The change in the estimation accuracy by changing the number of data.

Kriging was carried out by changing measurement data pitch. One could confirm that the increase in number of data leads to higher accuracy. Also, Kriging was applied at two cross sections, and relative errors with estimated values were small; one could support the applicability of Kriging to the vertical measurement. Lastly, the applicability of Kriging was tested against the diagonal measurement; Kriging was applied at the cross section of survey point 3 and 7. The result supports Kriging for the diagonal measurement. Therefore, it is fair to say Kriging is capable of interpolating in a plane. Therefore, it sees Kriging has applicability on detached house ground with a small area. Also each section have soft grounds to depth 100cm, it sees very likely to be the soft ground to depth 100cm on this detached house grounds by Kriging.

Kriging is used on interpolation in grounds with a small area. Thereby, on this study it thinks interpolation in grounds with a small area become precision.

This means if estimated value by Kriging has small deviation to measured value of additional search for verification, the soil survey can be finished; this helps financially as well, but if the deviation was big, additional survey needs to be conducted to find the cause.

REFERENCES

[1] Goushi N, Shinya I, Kozo O, Takumi K: Suggestion of ground investigation example and a reinforcing structure, the reinforcement method of construction for the residential land

laying earth on the ground on the slant bedrock, Ground improvement symposium memoirs Vol 11, The society of Materials Science, Japan., pp.431-438, 2014
[2] Tetsuya S, Katsuaki K: Interpolation of the space value in consideration of an error, Geothermal research society of Japan No.4, pp.183-194, 2007
[3] Yuzo O, Makoto T, Hideaki O: Basic study on estimation of physical parameters in heterogeneous ground, Journal of JSCE, No.457, Vol.21, pp.51-58, 1992
[4] Makoto H, Makoto S, Minoru U: Optimality criteria for borehole location design in the estimation of pile tip levels, Journal of JSCE, No.610, Vol.45, pp.43-45, 1998
[5] Yusuke H, Yu O, Hideaki K: A simplified scheme to evaluate spatial variability and statistical estimation error of local average of geotechnical parameters in reliability analysis, Journal of JSCE C, No.1, Vol.68, pp.41-55, 2012
[6] Kenji M, Yoshito M, Kiyoshi I, Makoto S: Probabilistic estimation of spatially distributed N-Values and its application to pile design, Journal of JSCE, No.436, Vol.16, pp.57-64, 1991
[7] Takatoshi N, Masanori T, Yoichi W, Saiichi S, Tomofumi S: Verification of 3-D visualization of ground at Tokyo International Airport, Japanese Geotechnical Journal, No.1, Vol.6, pp.69-79, 2010

Fifth International Conference on Geotechnique, Construction Materials and Environment, Osaka, Japan, Nov. 16-18, 2015, ISBN: 978-4-9905958-4-5 C3051

ALTERNATIVE MATERIALS OF SUB BASE (RESERVOIR BASE) FOR POROUS PAVEMENT

Yulvi Zaika[1] and Ludfi Djakfar[2]
[1,2]Engineering Faculty, Brawijaya University, Indonesia

ABSTRACT

This study assessed characteristic and gradation some types of stone materials as stone crush, limestone and steel slag for porous pavement and evaluate this performance based on California Bearing Ratio (CBR) and porosity. Naturally these characteristics are contrary, in which for high porosity materials will have low bearing capacity. As many as 7 gradations in 3 types soil material were prepared to test to obtain bearing capacity and porosity of material. The result showed that CBR of stone crush is high in uniform course material gradation but limestone and steel slag are in well graded material. In the term of porosity, the result completely the same for all materials in which the uniform gradation give the high porosity. It makes sign the influence of hardness and gradation of material will give contribution for bearing capacity and only gradation influence to porosity. The material are suitable for reservoir layer of porous pavement for light traffic load.

Keyword: Porous, Pavement, Reservoir, Traffic, Stone

INTRODUCTION

Climate change in various parts of the world such as rainfall is high enough to give direct effect to the pavement structure. In the beginning, road drainage system able to drain runoff to the sewer, but the increased rainfall causing puddles on the road surface. The surface flow becomes greater than the infiltration which is causes a negative effect on the structure, especially the structure of the pavement. This condition also occurred in Indonesia, where high rainfall became one of the causes of damage to the pavement structure.

One of the solutions offered in the pavement technology is the use of porous pavement that anticipate puddles of water on the road surface, in addition to increasing soil water infiltration. The pavement layer consists of base and surface layer that is able to flow the rainfall. For this purposes, material of the porous pavement must have two important properties which are able to support the weight of the vehicle and also porous. To find these characteristics in the material, CBR (California Bearing Ratio) test will conducted to determine resistance to load and porosity test to determine its ability to drain water.

California Bearing Ratio is the characteristic soil usually used as load capacity for highway construction. CBR is determined based on the rock type and gradation. There are several types of soil that has a high CBR due to rock hardness origin, but it must be supported with proper gradation such as stone crush, limestone.

In general, the use of crushed stone pavement on the foundation layer because it has a large bearing capacity. In this study used two other rock types are limestone and steel slag. The objective of study to determine the effect of soil type and soil distribution to porosity and CBR. At the end it can defined gradation band of every type of soil will provide maximum porosity at allowable CBR for porous pavement.

THE STRUCTURE OF POROUS PAVEMENT

Porous pavement is a pavement that is constructed or created using materials that allow the flow of water infiltration into the subsoil. Mechanism the porous pavement can be shown in Fig. 1. Structure of porous pavement has to resist the vehicle as live load. The characteristic layer of pavement usually represent in CBR.

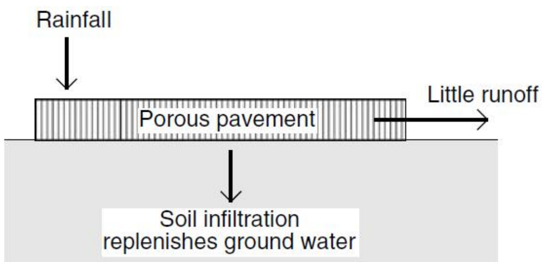

Fig. 1 Mechanism flow of rainfall in porous pavement

The Components of porous pavement has few as well as the flexible pavements consisting of a surface layer, the base layer and subgrade. Material and gradation should choos e according to the vehicle load. The material used on porous pavement are similar to water-resistant pavement material. It is just that the material has been designed or specially engineered so that it has the ability to absorb water.

Porous pavement layer components are:

(1) The surface course such as asphalt porous, porous concrete, soil filled plastics and open cell concrete block.

(2) Sub base/ reservoir course
In the structure of porous pavement, sub-base can also be called reservoir. So called because it primary function other than to resist the load, but also used for the flow of surface water over the road to drainage channel. In general, hydrological and structural function of pave ment materials are combined into a layer called the base reservoir.

In addition, the reservoir also serves to retain water before it flows into the ground or into a drainage pipe. Water storage volume is the same with the volume of void between the particles aggregate. The greater the volume of air voids, the greater the volume of water that can be accommodated

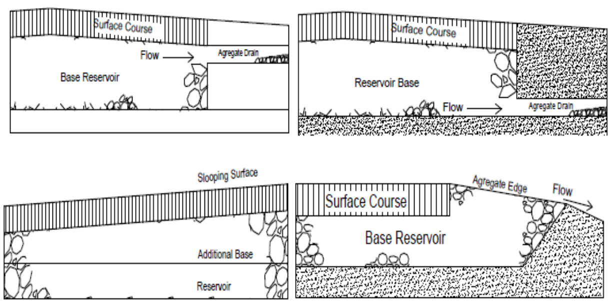

Fig. 2 Various forms of pavement base reservoir

MATERIALS

The material used as the porous pavement must the following criteria:

1. The material must have appropriate water storage capacity and is able to flow the water in a certain period without erosion.
2 The material must have sufficient rigidity to support traffic loading.
3.Materials should be able to get passed the impurities pavement.
4.Materials must be able to filtering and prevent shearing between the base, sub base and the subgrade.

Crushed stone or angular rock is, typically produced by mining a suitable rock deposit and breaking the removed rock down to the desired size using crushers. It is distinct from gravel which is produced by natural processes of weathering. Crushed stone is a rock that has been frequently used as a pavement because of the angle that produces high friction (interlocking), the large carrying capacity (CBR) of more than 80%, frost resistance and high bulk density .Because of crushed stone provided by nature so availability is limited so it is necessary to find alternative materials as a substitute.

The limestone is a sedimentary rock composed of the mineral calcite and aragonite are also used as building materials and pavement. It has high CBR is around 80% but the mineral calcite in limestone dissolves easily in water depends on the temperature and acidity (pH).

Limestone reserves is very large and almost spread across the region in Indonesia. East Java is one of the major producer of limestone. The Los Angeles Abrasion of limestone is 26.6 %.

In nature, iron, copper, steel, nickel and other metals are found in impure states called ores, often oxidized and mixed in with silicates of other metals. During smelting, when the ore is exposed to high temperatures, these impurities are separated from the molten metal and can be removed. Slag is the collection of compounds that are removed. In many smelting processes, oxides are introduced to control the slag chemistry, assisting in the removal of impurities and protecting the furnace refractory lining from excessive wear. Steel slag, a by-product of steel making, is produced during the separation of the molten steel from impurities in steel-making furnaces. The slag occurs as a molten liquid melt and is a complex solution of silicates and oxides that solidifies upon cooling.

The use of steel slag as an aggregate is considered a standard practice in many jurisdictions, with applications that include its use in granular base, embankments, engineered fill and hot mix asphalt pavement. Prior to its use as a construction aggregate material, steel slag must be crushed and screened to meet the specified gradation for the particular application. Stone dust from crushed stone are used as filler in this study. Some advantages of using slag are highly angular in shape and have rough surface texture. Typical physical and mechanical properties of steel slag are shown in Table 1 and 2.

Table 1 The Physical Properties of Steel Slag

Physical properties	Value
Specific gravity	3.2 – 3.6
Unit Weight kg/m3	1600 - 1920
Absorption	< 3%

Table 2 The Mechanical Properties of Steel Slag

Mechanical properties	Value
Los Angeles Abrasion (ASTM C131), %	20-25
Angle of Internal Friction	40-50
Hardness (measured by Mohr's scale of mineral hardness)	6 – 7
California Bearing Ratio (CBR), % top size 19 mm (3/4 inch)	>300%

In this study steel slag has 24.3 % Los Angeles Abrasion and impact is 9.49%.

Due to their high heat capacity, steel slag aggregates have been observed to retain heat considerably longer than conventional natural aggregates. The heat retention characteristics of steel slag aggregates can be advantageous in hot mix asphalt repair work in cold weather.

METHODOLOGY

California Bearing Ratio (CBR)

California Baring Ration is comparison between stress of soil and California Stress Standard that can be wrote as Eq.(1).

$$CBR = \frac{p}{ps} \tag{1}$$

Where:
P : stress of soil
Ps : California Stress Standard

Value of CBR represent quality of soil compare to stress of standard in stone crush who's CBR 100%. Standard procedure for CBR test conduct to ASTM D-1883-73 and AASHTO T-193-81. The harder material will reflect the high CBR. CBR for some type of soil material can be shown in Table 3 and for layer pavement are shown in Table 4.

Table 3 Value of CBR for Some Types of Soil Material

Material	Value of CBR (%)
Stone crush, subgrade layer	100
Natural soil aggregate as subgrade	80
Limestone	80

Table 4 Relative CBR

	CBR in Base Course	CBR in Sub Base Course
Excellent	100	50
Good	80	40
Fair		30
Poor	50	

Porosity of Soil

Soil aggregate is consist of soil particle and void between particles where water and air take place. Ratio between volume of void and total volume is called porosity as shown in Eq. (2). The porosity is usually express as a percentage and influence of density of soil, higher porosity is lower density. It means easier for water to flow in soil aggregate.

The concept of porosity testing to determine the percentage of the volume of empty space with the overall volume of the mold. To find the volume of empty space filled with air can be done by filling out a certain amount of water, the amount of water taken into the void is equal to the volume of empty space filled with air cavities.

$$n = \frac{Vv}{V} \tag{2}$$

Where:
V_v : volume of void
V_t : total volume

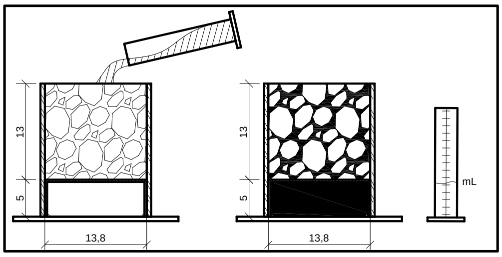

Fig. 3 Porosity Test

Some conditions will influence porosity as follows:

1. Distribution soil particle, uniformly graded soil has high porosity because volume of void bigger compare if the well graded soil.
2. Cementation of soil grand, if the soil particles have high degree cementation, the void become small and porosity is law.
3. Compaction increase the strength, lower compressibility and reduce permeability of soil by rearrange soil particle.
4. Degree of angularity, the shape individual particle is important as grain size distribution in affecting engineering response. The rounded particles have high porosity than angular.

Types and distribution soil particles

There are 4 types (stone crush, limestone, steel slag) of soil and 6 gradation variation were prepare in this study as shown in Fig. 4.

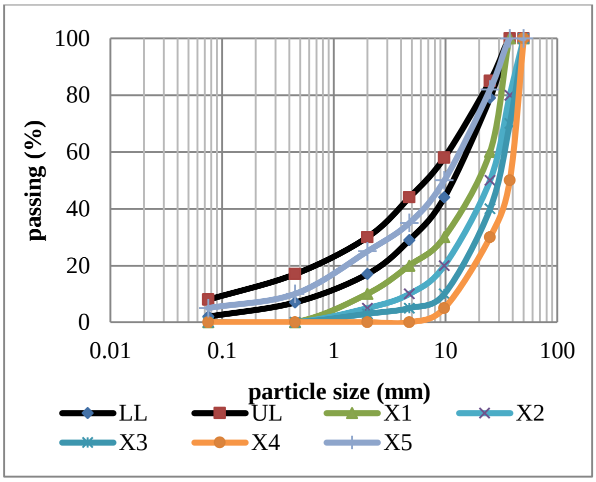

Fig. 4 Design Gradation Variation in Experiment

From that figure, X5 is control gradation because it was designed inside the gradation band as specified by Indonesia Highway Specification (Binamarga), which was represented by UL (Upper Limit) and LL (Lower Limit).

RESULT AND DISCUSTION

Several tests conducted to determine the characteristics of all the soil types with variations of gradation.

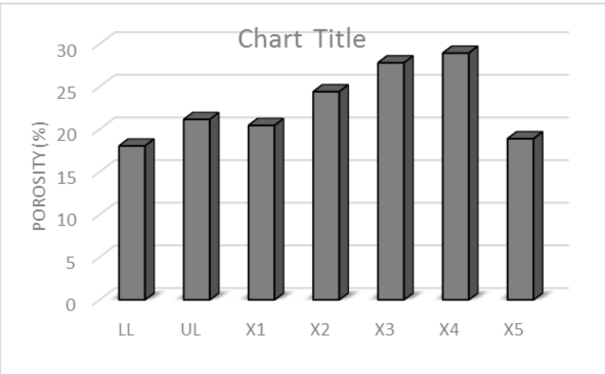

Fig. 5. Porosity of Gradation Variation of Stone Crush

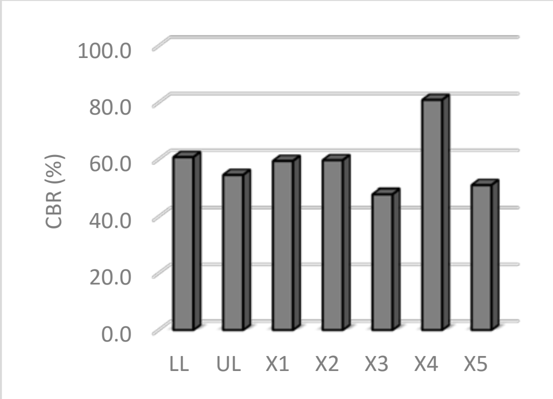

Fig. 6 California Bearing Ratio of Stone Crush

The results are porosity test and California Bearing Ratio test shown in Fig.5 and 6, where the biggest results of the two experiments were obtained from the same graded X4.

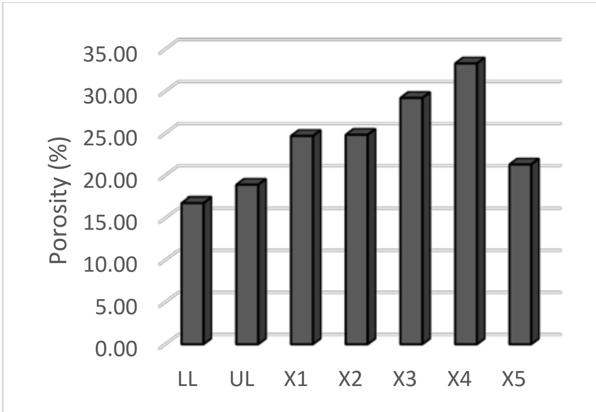

Fig. 7 Porosity of Limestone

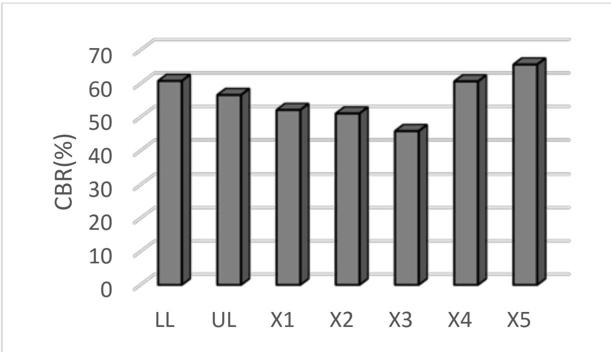

Fig. 8 California Bearing Ratio of Limestone

The limestone have different characteristic, which is the highest porosity value is derived from X4 gradation as shown in Fig. 7, but the highest CBR on gradation X5 (Fig.8). The gradation of X5 is gradation in specification of Binamarga (Indonesian Highway Specification). Due to limestone is easily soluble in water especially with high acidity, so in this study conducted CBR test in soaked conditions. The soaked CBR is lower value compare un-soaked as shown in Figure 9.

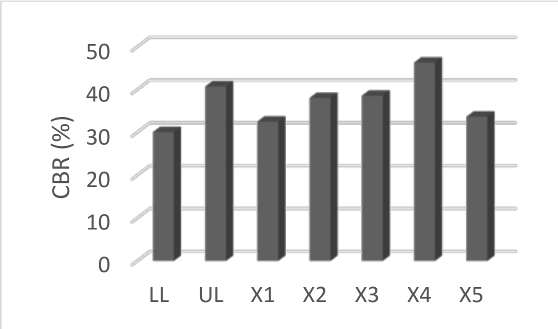

Fig. 9 Soaked California Bearing Ration of Limestone

Based on result of stone crush and limestone, 3 variation gradations steel slag were taken to analyses as that is X2, X4 and X5. The porosity and CBR of steel slag can be seen in Fig.10 and 11. Based on the figures are seen that highest porosity is in X4 and highest CBR is X5.

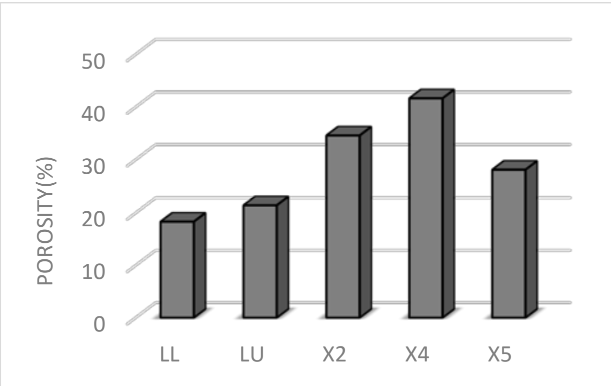

Fig.10 Porosity of Gradation Variation of Steel Slag

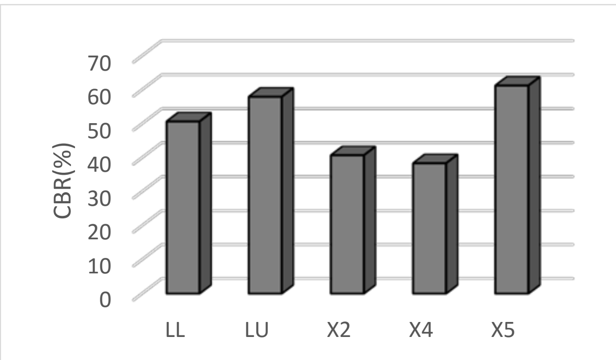

Fig.11 California Bearing Ratio of Steel Slag

From three types of soil are obtained that gradation X4 delivers maximum porosity. The number size gradation has shown that nearly uniform grain size. Based on CBR test for each trial gradation variation are obtained different results where the largest CBR value for crushed stone gradation is X4 but the limestone and steel slag is gradation X5 showed the more dominant of the gradation. It is a bit different with crushed stone, which changes the gradation eliminated even small will influence CBR value. This indicates that the strength of the rock is more dominant in bearing capacity.

CONCLUTION

1. Compared with limestone and steel slag, crushed stone has a greater bearing capacity.
2. The more uniform gradation with a larger size will give high porosity. In which porosity only determined by the gradation of the mixture.
3. California Bearing Ratio of the soil depends on the hardness of the soil and gradation.
4. Despite the porous nature of the mixture as desired but the carrying capacity is only suitable for light traffic loads that require further study of material.

REFERENCES

[1] ASTM INTERNATIONAL, “Standard Test Method for California Bearing Ratio of Laboratory Compacted Soils “,2007 (D1883-07E2).

[2] ASTM INTERNATIONAL,” Standard Test Method for Permeability of Granular Soil Constant Head “,2007,(D1883-07E2)

[3] Asphalt Institute,”Soils Manuals”, Maryland. Asphalt Institute. 1978.

[4] Binamarga,”General Specification for Aggregate Type Base Course”, (Indonesian).

[5] Chopra.M, Wanielista.M.” Performance Assessments of Portland Cement Pervious Pavement, Compressive Strength of Pervious Concrete Pavement”, Strom Water Management Academy University Florida, Central Florida, Orlando, 2007.

[6] Djakfar.L, Zaika.Y and Bowoputro.H,” Effect of More Uniform Gradation on Permeability and Strength of Base Course for Porous Pavement”, Proceedings of the Eastern Asia Society for Transportation Studies, Vol.9, 2013.

[7] Yusof .N.I.M at al, ” Utilization of Steel Slag as Aggregate Replacement in Porous Asphalt Mixtures”, Journal Teknology UTM, Vol. 69, 2014,No.1 ,67-73, eISSN 2180-3722.

[8] Kuosa.H, Niemeläinen.E, Loimula.K, “Pervious Pavement System and Material”, Research Report VVT- R- 08222- 13,2013, Finland,

[9] Roseen.R.M. Ballestero.TP, Houle.J.J ,Briggs. J,S and Houle.K.M," Water quality and Hydrologic Performance of Porous Asphalt Pavement as a Strorm-Water Treatment Strategy in a Cold Climate", Journal Environmental Engineering, Vol. 138, No.1, 2013, IO.10.1061/(ASCE)EE.1943-7870.0000459.
[10] State New Jersey Department of Environmental Protection," New Jersey Strom water Best Management Practices Manual", 2009, New Jersey.
[11] PA Department of Environmental Protection (PADEP) (2005)," *Pennsylvania Storm water Best Management Practices Manual*, Pennsylvania Storm Water Management Manual,
[12] Richardson, D.," Drain Ability Characteristics of Granular Pavement Base Material", Journal of Transportation Engineering, Vol.123, 1997, Issue 5, 385-302. DIO.10.1061/(ASCE)0733-947X.
[13] University New Hampshire Storm Water Center, "Design Specifications for Porous Asphalt Pavement and Infiltration",2009, Beds, Durham.
[14] Wang.Y and Wang.G ," Improvement of Porous Pavement" , 2011,US Green Building Councils.
[15] Zhang, L., Ong, G.P., Fwa, T.F. " A Review On The Use Of Porous Pavements To Reduce Tire-Pavement Noise", Proceedings. APTE VII, 2012, Songkhla, Thailand.

Fifth International Conference on Geotechnique, Construction Materials and Environment, Osaka, Japan, Nov. 16-18, 2015, ISBN: 978-4-9905958-4-5 C3051

CONSOLIDATION ANALYSIS OF VIETNAM SOFT MARINE CLAY BY FINITE DIFFERENCE METHOD WITH APPLICATION OF CONSTANT RATE OF STRAIN CONSOLIDATION TEST

Cong-Oanh Nguyen[1], and Thanh Thi Tran[2]

[1] Division of Soil Mechanics and Foundation Engineering, Southern Institute of Water Resource Research, and Posco Engineering Co. Ltd, Viet Nam; [2] Southern Institute of Water Resource Research, Viet Nam

ABSTRACT

There have been many reclamation projects built on the soft ground in recent years in Vietnam especially in the Southern region. Geotechnical engineers always face challenges in dealing with soft ground treatment methods. As such, ground improvement technique using preloading in combination with prefabricated vertical drains (PVD) is regularly employed to accelerate the consolidation of the thick soft clay deposits and to ensure satisfactory post-construction settlement specification. This paper presents the results from a series of numerical back-analyses using Finite Difference Method which are conducted for a case study from a typical ground improvement project in Southern Vietnam. In this study, the input consolidation parameters are established from constant rate of strain (CRS) consolidation tests on high quality soil samples obtained by hydraulic piston sampler. The approach aims at numerical solution of multi-subsoil layer model with the use of an FDM procedure coded by the authors. In comparison with field monitoring data, the back-analyses show good correlations to both magnitudes and changes with time on ground settlement, the dissipation of excess pore water pressures and interpreted gain of un-drained shear strength.

Keywords: Consolidation, CRS test, FDM, PVD, Settlement, Un-drained shear strength

INTRODUCTION

In recent years, construction on soft soil has been widely carried out over the Southern part of Vietnam. Mostly, the soft soils found in these construction projects have been improved by vertical drains and surcharge preloading method. Therefore, it is still a challenge for geotechnical engineers to estimate the correct settlement of the soft clays under surcharge load. This paper examines the results of a series of consolidation analyses using a Finite Difference Method procedure coded by the authors. The subsoil is divided into sub-layers to incorporate the change in compressibility and consolidation characteristics over the clay thickness. Input parameters of the soft Holocene soil deposit which is in Mekong Delta are determined with application of CRS test on undisturbed samples collected by piston sampler technique.

The chosen case study is Saigon Premier Container Terminal project, which is around 25 km from South West of Ho Chi Minh City, Vietnam. In general, for the container yard area the requirement is under a design net operating load of 40 kPa, the target end of construction (residual) settlement of less than 5% of estimated total settlement. Due to the presence of thick and highly compressible soft marine clay deposit at the site (between 30 and 35 meters in thickness), the widely popular construction technique using preloading method in combination with prefabricated vertical drain was employed for ground improvement. Because the area is close to the shore line of Soai Rap River estuary, surcharge sand is filled by both hydraulic method and dump trucks.

Fig. 1 shows the location map, layout plan of the whole site and arrangement of monitoring instruments including 2 settlement plates, 1 extensometer lot, 1 piezometer lot, 3 CPTU test points in tender stage, and 1 group of CPTU and FVT before surcharge removal for the investigated area, Phase II (2-2).

UNDISTURBED SAMPLING AND TESTING

Reliability of consolidation yield stress σ'_y, compression indices C_{c1}, C_{c2}, C_r and coefficient of consolidation c_v, c_h values is dependent on the quality of undisturbed samples. Some authors [4], [3] investigated the quality of soil samples retrieved by various types of samplers and concluded that stationary piston sampler provide the good quality for samples.

It was revealed that in the Mekong delta region, soft clay samples retrieved by Shelby thin wall tube shows un-acceptable quality for determine consolidation characteristics. On the review of more than thirty soil investigation reports for Mekong delta region, Bui, T. M. found that the yield stress (or pre-consolidation pressure) is smaller than over burdened pressure and is not increasing with depth, thus OCRs were less than unity [1]. From the change of void ratio by recompression to in-situ over-burdened stress, he attributed the above phenomenon to sample disturbance. The disturbance might by caused by sampling technique and other processes.

A comparison of samples taken by both piston sampler and Shelby sampler, and a comprehensive study on the soil characteristics of soft clay in Mekong Delta has been previously conducted [2]. That study reported that mechanical properties of Mekong Delta clay has not been well studied due to sample disturbance.

In this study, all the samples were collected by hydraulic piston sampler to unsure the quality of samples for laboratory tests. For the determination of consolidation characteristics of the soft soil, CRS tests are employed. This is because CRS tests can shorten the testing time and testing data are of continuous strain-time relation. Therefore, it is easier to determine required consolidation parameters for soft clays.

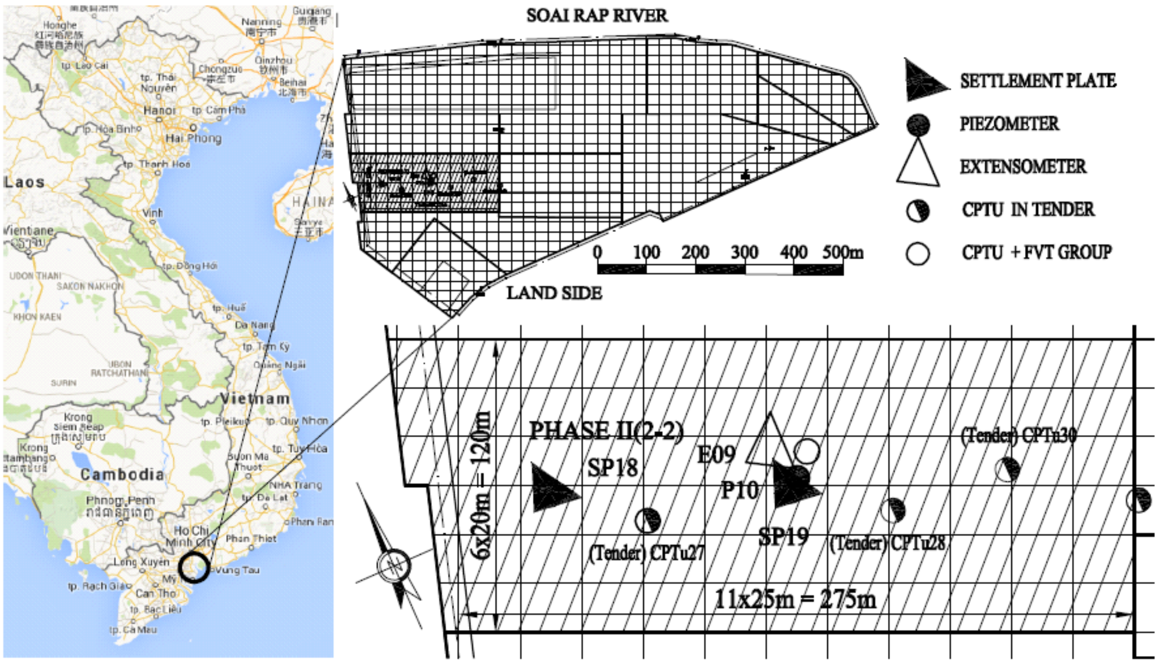

Fig. 1 Location map, layout plant and investigated zone phase II (2-2)

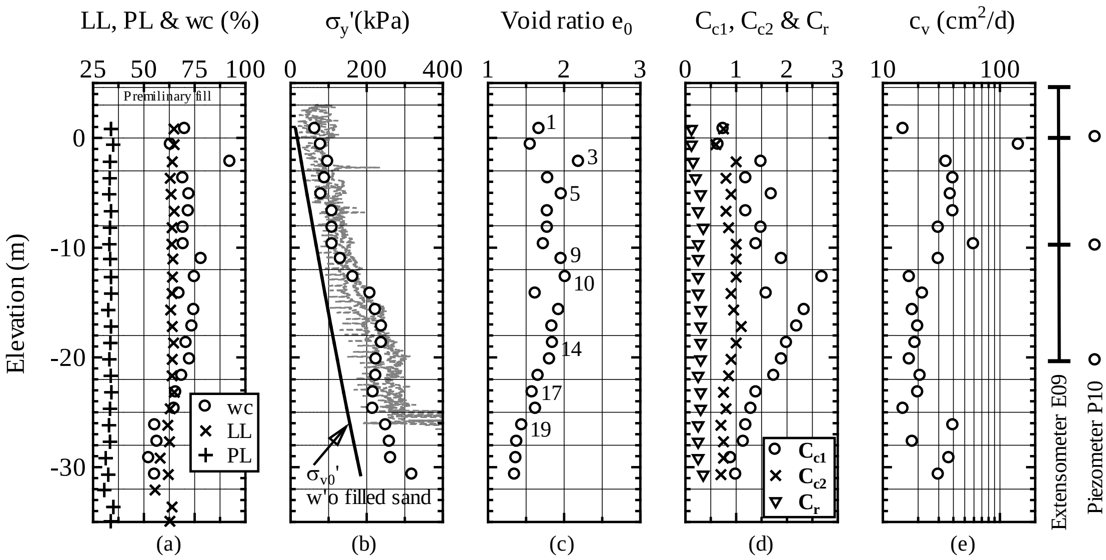

Fig. 2 Profile of soft clay properties at various depth

Table 1 Compressibility and consolidation properties of sub-layers

Sample (depth)	Ho (cm)	σ'_{v0} (kPa)	e_0	σ'_y (kPa)	σ'_b (kPa)	C_r	C_{c1}	C_{c2}	$c_{v(NC)}$ (cm^2/d)	$C_{v(OC)}$ (cm^2/d)
1(3.95)	300	13.22	1.676	65 (50)	400	0.12	0.75 (1.40)	0.75	15	150
3(6.95)	300	28.28	2.195	99 (70)	250	0.15	1.50	1.00	35	350
5(9.90)	500	43.18	1.968	81	140	0.30	1.70	0.90	38	380
9(15.8)	400	73.78	1.966	132	230	0.25	1.90	1.00	30	300
10(17.45)	600	82.36	2.020	165	320	0.25	2.70	1.00	17	170
14(23.45)	400	114.36	1.854	226	370	0.30	1.90	0.90	19	190
17(27.95)	300	139.16	1.585	218	450	0.30	1.40	0.75	20	200
19(30.95)	200	156.52	1.449	251	500	0.25	1.20	0.70	40	400

Note: Numbers in brackets are used for Model-2 in consolidation analysis at settlement plate SP18

GROUND PROFILE AND DESIGN SOIL PARAMETERS

Fig. 2(a) shows natural water content w_c, liquid limit LL and plastic limit PL for the site. It is obviously that the clay is very soft with natural water content is almost close or larger than liquid limit. Furthermore, the void ratio ranges from 1 to 2 for the first 7 sub-layers and close to 1 for the last 2 sub-layers from the top of soft marine clay as presented in Fig. 2(c). Unloading-reloading index Cr ranges from 0.10 to 0.30, Cc1 from 0.50 to 1.00 and Cc2 larger than 1.00. The figure also shows such soil parameters determined from CRS test results as the consolidation yield stress, the vertical coefficients of consolidation of sub-layers of the soft soil.

The effective over-burdened stress of intact soil is estimated without considering the load of reclaimed fill because this layer of had not consolidated the clay deposit thoroughly. The Holocene clay is still in lightly over-consolidated state with OCR ranging from 1.50 to 4.90. This proves that the undisturbed samples are in good quality enough for the engineering purposes.

Consolidation yield stresses determined by both CRS and CPTU in form of eq. 1 as indicated in Fig. 2(b) are found to be consistent to one another.

$$\sigma'_y = \frac{1}{3}(q_T - \sigma_{v0}) \qquad (1)$$

The CRS test results on 22 samples at various depths for the soft Holocene clay are showed in Fig. 4 and Fig. 5. It is clear that the soil compressibility varies with stress level with the S-shape of e-logσ'_v curves, so it can be an error for the consolidation analysis if a constant compressibility index is used. Therefore, the authors will apply three compressibility values at three different stages of loading. The first value C_r is used for unloading and reloading or over consolidated stage; the second C_{c1} is used for normally consolidated between σ'_y to σ'_p where there is a reduction in compressibility; the third C_{c2} is used for normally consolidated stage with stress level larger than σ'_p as found in Fig. 5.

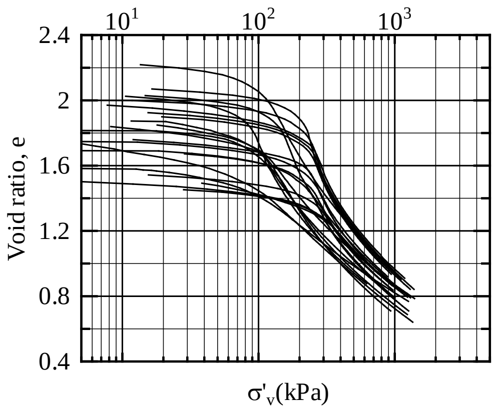

Fig. 3 e-logσ'_v by CRS tests on 22 samples at various depths of the soft clay deposit

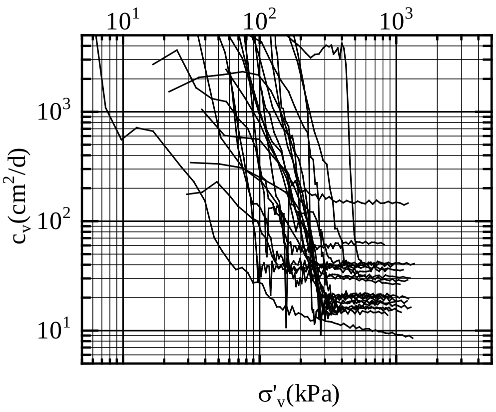

Fig. 4 c_v-logσ'_v by CRS tests on 22 samples at various depths of the soft clay deposit

As indicated in Fig. 5 for a typical CRS result, the vertical coefficient of consolidation in normally consolidated state is fluctuated around a constant value which is defined as $c_{v(NC)}$. Furthermore, the vertical coefficient of consolidation in over-consolidated stage is almost 10 times as much as that in normally consolidated stage. So, $c_{v(OC)}=10c_{v(NC)}$. The horizontal coefficient of consolidation for this soft marine clay is chosen to be as much as 3-5 times of the vertical coefficient of consolidation which is determined by CRS test results. Detailed FDM analyses are performed in the next part of this paper.

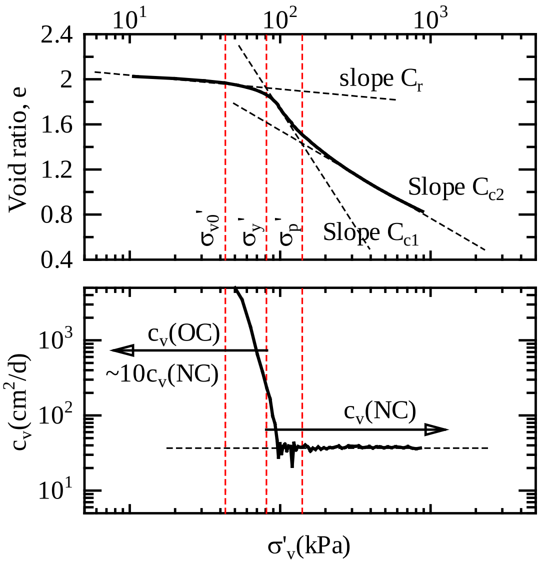

Fig. 5 Conceptual determinations of parameters

With the variation of soft soil properties over depth, average values of those parameters should not be used for the whole deposit. In order to consider the changes in over-burdened stresses, yield stresses and other consolidation characteristics as well as nonlinearity, the soft clay stratum is divided into 8 sub-layers as indicated in Fig. 2. Representative values of compressibility and consolidation parameters for consolidation analyses are chosen and tabulated in Table 1. The total thickness of soft clay in this area is ranging from 29 to 35 meters underplayed by sandy soil which works as bottom drainage boundary for prefabricated vertical drain.

MONITORING INSTRUMENTS

The monitoring instrumentation consists of 4 observation wells (Ob.01 to Ob.04) used for measuring ground steady state ground water level, 40 surface settlement plates, 19 monitoring groups with one pore water pressure transducer (piezometer) lot and one magnetic multi-level settlement lot (extensometer) for each group. They were used for the assessment of behavior of soft marine clay under preload fill for the whole project.

In this study, only one zone called phase II (2-2) is considered for the consolidation analysis by a finite difference code developed by the authors. The investigated zone of reclamation and ground improvement has one water observation well, two surface settlement plates SP18, SP19, one extensometer lot E09, and one piezometer lot P10 as indicated in the figure to evaluate the consolidation of soft ground. SP18 and SP19 were installed at the elevation of +4.650m Chart Datum Level (mCD), E09 includes one magnetic plate at +5.347m; three magnetic spiders at 0.057m, -9.872m and -19.887m; three pore water pressure transducers at +0.000m, -10.000m and -20.000m. Layout of settlement plates, piezometers and extensometers for phase II (2-2) is presented in Fig. 1, elevation arrangement of 3 pore water pressure transducers and 3 magnetic spiders as well as a magnetic plate can be found in Fig. 4.

Observation well Ob.04 was installed out of the surcharge area so it was not affected by the surcharge stress increase; then water level resulted in it is used to evaluate the dissipation of excess pore water pressure.

CONSOLIDATION ANALYSIS

Calculation method and software

This method is used for reclamation area where the loading is uniformly loaded in a wide spread zone. A unit cell around a vertical drain is considered as a drainage boundary in the coupled consolidation calculation as soon as it is installed in the ground.

Finite Difference procedure called CALPRO is developed and coded by the authors based on the general consolidation equation, dealing with the axi-symmetric meshing. The procedure allows up to 20 subsoil layers and 50 loading stages in the calculation.

The results include settlement for subsoil layers, effective stresses for each layer as well as vertical strain for each layer over each time step.

Settlement Behavior

Original ground elevation is at +3.00m (mCD). A reclamation fill of 1.6m was carried out during the first land preparation. PVDs were installed hydraulically with 150cm pitch down to the bottom of soft marine clay layer at time of 221 days and 261 days for SP18 and SP19 respectively. Drainage layer of 50cm by coarse sand was filled after the reclamation work was done; then twelve layers of 50cm of surcharge sand were filled accordingly. Besides that, PVC perforated pipe wrapped around by geo-textile fabric and water collection wells were installed to assist the water squeezing process during surcharge preloading.

As indicated in Fig. 6 the settlement at plate SP19 and E09 is almost the same in margin as long as E09 data are shifted by 45cm as correction. This is because E09 is close to, but installed 245 days after SP19.

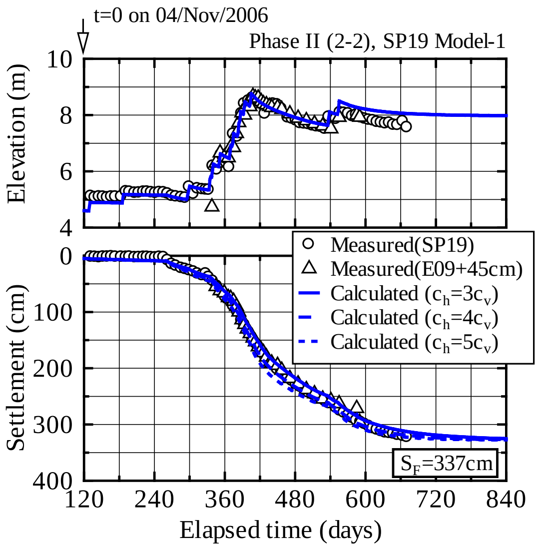

Fig. 6 Settlement by FDM calculation at SP19

A series of FDM analyses are performed with the determined parameters and various values of c_h. The calculation results show that the case with c_h=3c_v gives best fit result compared to the monitored data. Therefore, soil parameters for these two instruments are the same. The soil model for SP19 and E09 is named as Model-1. The FDM analysis result shows good agreement between measured and calculated settlement vs. time for the two above mentioned instruments. The final settlement under surcharge load for this case is 337cm.

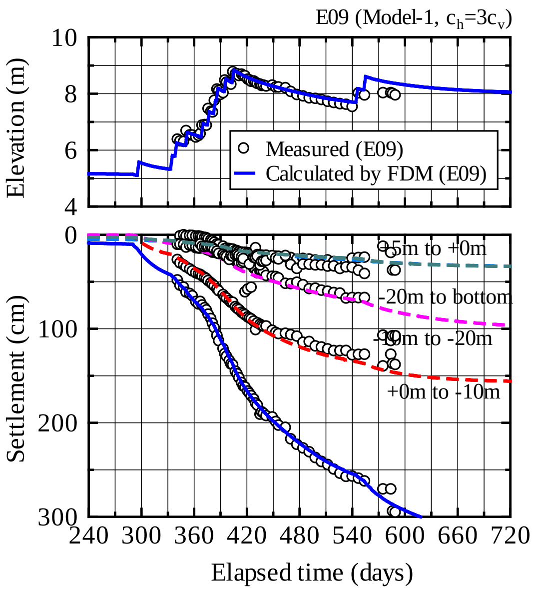

Fig. 7 Measured and calculated data at E09

Fig. 8 plots detailed calculated results by FDM at E09 for sub-layers. The settlement from +5m to +0m; +0m to -10m; -10m to -20m; and -20m to the bottom of soft marine clay are presented in the figure as dotted lines. The total settlement at the magnetic plate is the continuous line. The calculated and measured data are well consistent and plotted in the same graphs.

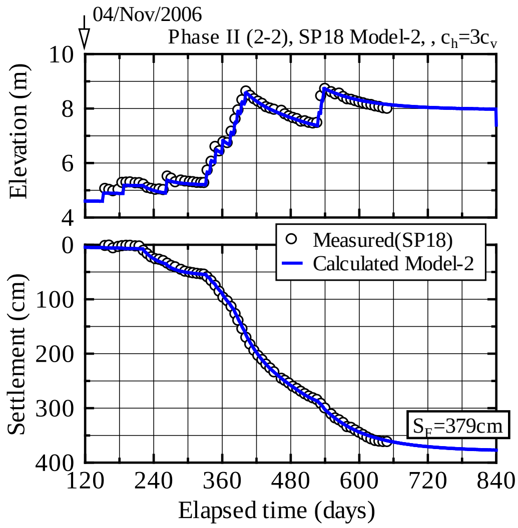

Fig. 8 Settlement by FDM calculation at SP18

Fig. 6 and Fig. 10 show the monitored data of plate SP18 is larger than those at SP19 and E09. At t=600d, the settlement at SP18 is 350cm while it is around 300cm at SP19 and E09. Based comparison of CPTu-27 at SP18 and CPTu-28 at SP19 and E09 in Fig. 9, it can be concluded that the top two sub-layers at SP18 are softer than those at SP19 and E09. Therefore, modification of yield stress for the two sub-layers is done accordingly for SP18. The new soil model for SP18 is Model-2 with a reduction in yield stress by 15kPa for the first sub-layer and 29kPa for the second sub-layer. With the new parameters as indicated in bracket in Table 1, FDM analysis shows well consistent results with the measured data. The final settlement for SP18 is 379cm.

Dissipation of Excess Pore Water Pressure

Piezometer P10 is installed close to E09 and SP19, so Model-1 is used in the FDM analysis of pore water pressure dissipation at P10. Fig. 9 shows good agreement between measured and calculated excess pore water pressure dissipated vs. time.

Dissipation rate of excess pore water pressure is well consistent to one another for both measured and calculated data at P10. Measured data from time of 570 days are a bit smaller than calculated values due to recent reduction in water level; therefore it causes the decrease in excess pore water pressure.

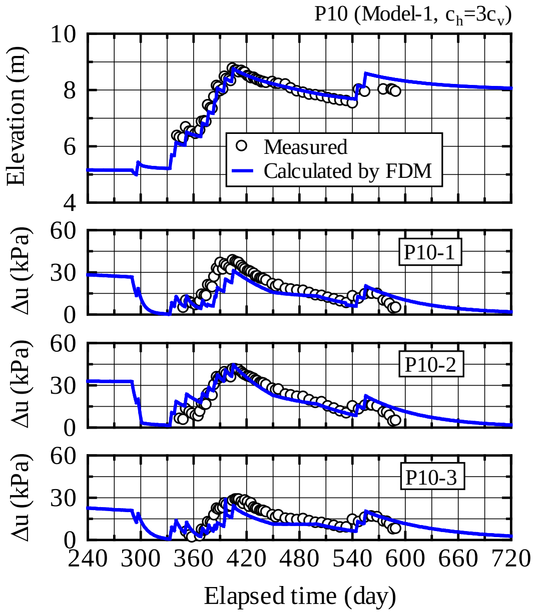

Fig. 9 Measured and calculated data at P10

Strength Gain

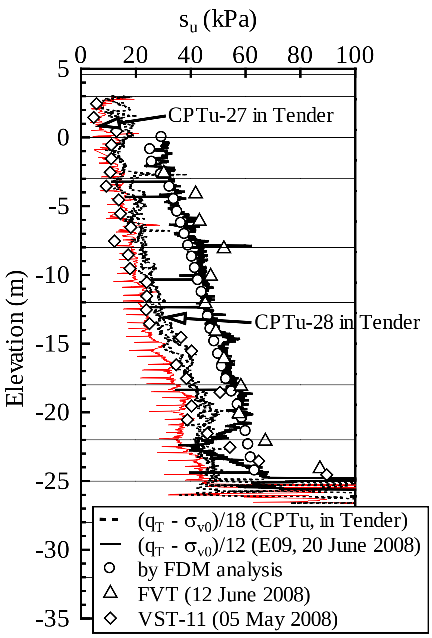

Fig. 10 un-drained strength gain by field tests and calculated by FDM

Fig. 9 presents the un-drained shear strength gain measured by field tests and calculated by FDM. Cone factors N_{kt} are 18 and 12 respectively for for CPTu done in Tender stage and before surcharge removal. These N_{kt} are determined based on un-drained shear strength tested by FVT. The difference in cone factors is due to the different cone types and manufacturers. As indicated in the figure, the strength gain is 19kPa as average value for the entire Holocene clay deposit. Furthermore, the plot also shows the consistency between measured and calculated un-drained strength gain.

CONCLUSION

Soil parameters determined from CRS test results give good consistency for the settlement analysis in both settlement and pore water pressure dissipation. Direct application of CRS test results into the consolidation analysis of Holocene soft clay gives well agreement resulted between measured and calculated data for surface settlement plates, extensometer, piezometer as well as un-drained strength gain.

For this Holocene deposit, horizontal coefficient of consolidation is as much as three times of vertical value determined by CRS test results $c_h=3c_v$. The vertical coefficient of consolidation in over-consolidated stage is almost 10 times as much as that in normally consolidated stage $c_{v(OC)}=10c_{v(NC)}$.

Consolidation analyses by FDM with consideration of multi-subsoil layers to incorporate the changes in soil parameters in the soft clay stratum can give good results in comparison between calculated and field monitored data.

REFERENCE

[1]. Bui, T. M. (2003). Initial Evaluation of Consolidation Characteristics of Mekong Soft Clay and Their Use in Engineering Practice. Hanoi Engineering Geology Workshop. Ha Noi**:** 1-13.

[2]. Takemura, J., Y. Watabe, Tanaka, M. (2007). Characterization of alluvial deposits in Mekong Delta. Characterisation and Engineering Properties of Natural Soils, Taylor & Francis Group, London. **1:** 1805-1829.

[3]. Tanaka, H. (2000). "Sample quality of cohesive soils: Lessons from three sites, Ariake, Bothkennar and Drammen." Soils and Foundations **40**(4): 57-74.

[4]. Tanaka, H., P. Sharma, et al. (1996). "Comparative study on sample quality using several types of samplers." Soils and Foundations **35**(2): 57-68.

SIMULATION OF DAMPING RATIO AND ELASTIC MODULUS CHANGES DURING THE EARTHQUAKE OCCURRENCE IN A SANDY SLOPE BY NUMERICAL MODELING

Fardin Jafarzadeh[1], Sina Heidari[2] and Hadi Farahi Jahromi [3]

[1]Sharif University of Technology, Tehran, Iran;
[2] Geotechnical Engineering, Sharif University of Technology, Tehran, Iran;
[3]Geotechnical Engineering, Sharif University of Technology, Tehran, Iran

ABSTRACT

Earthquake induced landslides endanger many structures and human life every year. Thus, many researchers and scientists have performed numerous physical and numerical modeling with various aspects of the phenomenon. This paper as a part of a thorough research project, defined and supported by Tehran Gas Company numerically evaluated a sandy slope dynamic responses under a 7.5-8.5 earthquake. The ABAQUS F.E. program was used for numerical modeling and the results were verified with the laboratory records and observations. The paper focuses on soil damping and elastic modulus changes during earthquake occurrence. Although, numerical simulations can model the soil behavior non-linearity, the varying nature of damping and modulus of elasticity during dynamic excitation as a cause of densification, cannot easily be modeled. As a compensation, the slope section was divided to three parts with different ζ and E. Finally 3 numerical analysis were performed and the best model were selected. The numerical outcomes were confirmed by comparing the displacements and acceleration responses of slope toe and crest. The process through which the models was improved showed that, "if the geotechnical parameters of materials were correctly selected and some modifications were done", the numerical calculation would be validated and could lead acceptable results. The comparisons show the effectiveness of the modifications which was verified by 1g shaking table test results.

Keywords: Land Slide, Numerical Modeling, Damping Ratio, elastic modulus, shaking table test.

INTRODUCTION

Destructive effect of dynamic slope instability endangers human life and engineering facilities worldwide. So, any method, predicting permanent ground deformations (PGD) almost accurate and acceptable, is undoubtedly applicable for both university researchers and engineering office practitioners to design any retrofitting scenario.

There are three attitudes for slope deformations prediction. The first method is laboratory testing. This method not only is an expensive one, but also need many preparations and arrangements. Beside these, preparing the test materials and dynamic testing are time consuming activities. As an alternative, anyone can use empirical formulas for slope deformation calculations. Although, this method have been improved in the last decade and many modifications have been introduced for gaining an accurate assessment, it is not a sufficient scheme which can be relied on in engineering projects. Thus, this requirement, has led the researches to examine other approaches. Through many methods, stress-deformation approaches are widely used in university theses and has been experienced many advances recent years.

But the problem is that, finite element analysis has many limitations in predicting seismically induced soil deformations as it cannot model the mesh separations through a dynamic loading. Besides that, numerical instability and other difficulties, has made the FEM results almost unreliable. To compensate the fact, a practitioner should use engineering experience and judgment to interpret FEM results.

Consequently, different approaches have been developed to investigate the stability of slopes under seismic loading conditions, including: limit equilibrium (LE) techniques, analytical sliding block techniques, and numerical modeling procedures (such as finite element (FE) or finite difference (FD) techniques) [1].

However, the first two approaches often neglect important elements such as the three-dimensional scale and the stress-strain relationship of soil, the soil deformability and nonlinear soil behavior.

As an illustration, Nian et al. (2011) used the strength reduction elasto-plastic FE method and mainly focused on the slope stability under inclined seismic loading using pseudo-static approach for three dimensional slopes [2].

It is important to understand the conditions of slopes after slope failure. Abe et al. (2013) carried out a series of shaking table tests with large-scale slope models. The models consist of a slope with weak layer which has high response acceleration at top of the slope. Results from the tests indicated that it is important to consider large deformation along slip lines in the weak layer and amplification and phase lag of response acceleration at the top. The one layered slope model was analyzed by FEM with a nonlinear model focusing on the amplification and phase lag of response acceleration at top of model [3].

Non-linear dynamic effective stress analysis is an essential tool in seismic design in geotechnical earthquake engineering. But requires analytical skills and a very thorough knowledge of soil behavior. The selection of an appropriate constitutive model for the job at hand requires knowledge of the past history of the model. The calibration of the model for the job at hand needs to be conducted on tests specimens that are representative of field conditions.

The designer needs to be aware of what the main factors controlling the results of the analysis are and make judgments as to whether any of them [4].

This paper attempts to calibrate a FEM numerical modeling with a laboratory shaking table test results, which models a dynamic slope instability in Tehran, Iran's capital. Through this approaches, a basic numerical model will be introduced and validated by a laboratory testing records.

MODEL TEST CHARACTERISTICS

The artificial slope, scaled to 1/10 of a prototype one, [5], simulates a typical slope in Tehran. The research group designed a series of dynamic sinusoidal excitations [6]. Tehran cemented soil was modeled by Babolsar coastal sand having no cohesive ingredients.

The soil rigid box frame composed from steel profiles and plates. Also, a Plexiglas plate in one side enabled the engineers to monitor slope deformations during excitations. In addition to visual observations, many accelerometers and LVDTs recorded model's dynamic responses. Figure 1 illustrates the model and sensors configuration in the rigid box (dimensions are in mm).

Using the method suggested by Prof. Seed [1], a harmonic sinusoidal record having 0.33 g amplitude, 5 HZ frequency and 25 cycles (Figure 2) was selected to model a 7.5-8.5 magnitude earthquake. Figure 3 and 4 show pre and after test situations. In order to monitor the slope displacement during the tests, 3 cm plaster strips were poured adjacent to the Plexiglas plate in each 10 cm soil layer. Through defining and analyzing the induced displacement by measuring strips horizontal movement, comparisons made between the pre and posttest slope conditions [6].

Dynamic slope responses were recorded by accelerometers and LVDTs installed in the slope. The maximum horizontal displacement of the sliding mass, vertical displacement of slope crest and acceleration time histories of slope’s toe (ACC4) and crest (ACC9) were used for numerical model verification.

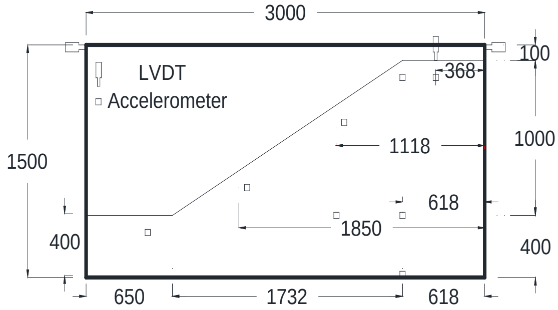

Figure 1. Soil box and sensors arrangements

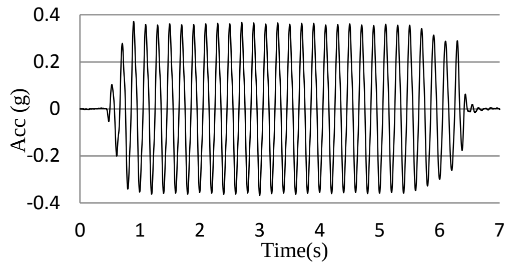

Figure 2.Induced acceleration time history


Figure 3. Constructed slope with plaster strips before test


Figure 4. Plaster strips showing deformed slope

NUMERICAL MODEL SPECIFICATIONS

The numerical model was simulated and analyzed by the FE based ABAQUS program. The slope material properties were selected as those assumed for the target slope (Table 1). In order to numerically have similar conditions to prototype situation, a discrete rigid box has been simulated. Soil-box interaction was modeled by assuming hard contact and frictional behavior in normal and tangential directions respectively. The frictional coefficient between soil-steel plates and soil-Plexiglas were 0.5 and 0.3 respectively.

Modulus reduction curves were used to define the nonlinear behavior of the soil. EPRI guidelines [7] for sandy soils were used to determine the cyclic shear strain dependency of elastic moduli at various depths.

The calculated displacements in horizontal and vertical directions are depicted in figures 5 and 6. The observed maximum horizontal displacement in laboratory scale slope (U1) were 33-35 cm at mid slope section. Also, the mid-crest settlement (U2) was 3.5 cm. Besides these two basic factors, the recorded mid crest acceleration (ACC9) was also used for numerical model verification. Regarding to figures 5 and 6, the U1 and U2 parameters were 60.6 and 17.4 cm. Figure 7 compares the recoded and calculated ACC9 parameters for these two models.

Concerning the deviations between the numerically analyzed and actual laboratory results, some modifications are required. In order to compensate these shortcomings, two basic changes in key parameters (elastic moduli and damping ratio) were introduced to the models and their effects were investigated.

Table 1 Model 1 characteristics and results

Model Name	E (Mpa)	Damping Ratio (%)	U1 (cm)	U2 crest (cm)	Acc max (g)
1	10	5%	60.6	17.4	0.5

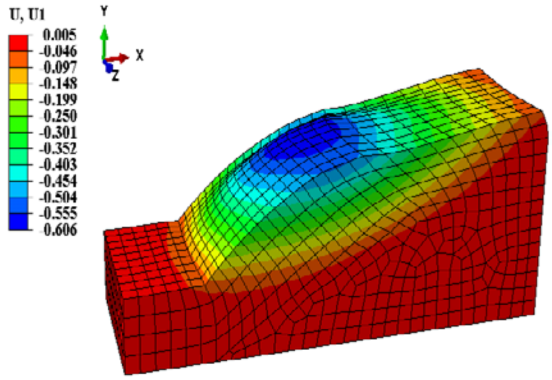

Figure 5. Horizontal displacement of model 1

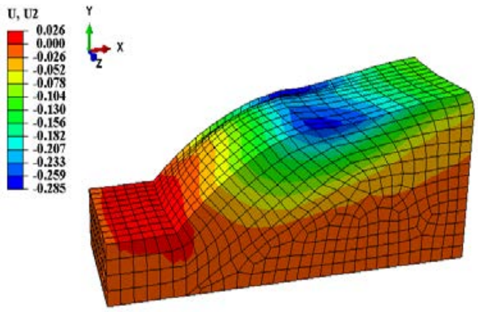

Figure 6. Vertical displacement of model 1

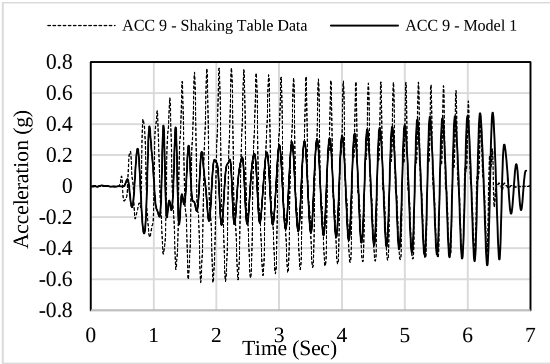

Figure 7- Crest acceleration comparison for model 1 and laboratory results

INTRODUCING ADVANCED NUMERICAL MODELS AND DISCUSSIONS

Regarding to previous discussions, although model 1 attempted to simulate a 1.3 height sandy layer, but the calculated responses were not acceptable. So a series of 3 models which gradually improved the situations are introduced hereafter. The basic concept of newly developed models is to divide the soil to a few layers having different modules of elasticity and damping ratios. Based on figure 4, 3 basic layers were recognized. The top layer, in which the first slip surface was formed, was affected in the first stage of dynamic loading (10 cycle) and had almost 20 cm depth. However, the second and the third sliding surfaces were formed in the last part of dynamic loading and occurred in the mid layer sands. Similar to the top layer, the second layers had 20 cm depth letting bottom layer (86 cm height) be almost unchanged. These almost separate layers had dissimilar geotechnical behaviors. As, the soil pouring height during model construction, was arranged to be 70, cm, it has relative density of 45-55%. However, the relative density is a vertical stress dependent parameter which can change the elasticity of layers from their initial values. Obviously low-strain stiffness (E_0) in non-cohesive soils is known to be directly proportional to the vertical effective stress by the following equation [8].

$$\frac{E_2}{E_1} = \sqrt{\frac{\sigma_2}{\sigma_1}} \qquad (1)$$

Where E1 and E2 are the stiffness moduli at two different points with vertical stresses of σ_1 and σ_2, respectively. As a result, the low-strain elasticity modulus increases with depth. Regarding to this effect, the elastic modulus of the layers at mid height were considered to be 10, 14 and 20 MPa.

Ishibashi and Zhang (1993) proved the cyclic shear strain-dependency of material damping. Figures 8 and 9 summarize various graphs of this behavior [9]. However, the ABAQUS program cannot modify the material damping values due to shear strain changes during excitations. Clearly, the three layers experienced different horizontal displacements causing the soil to have different shear strains (figure 4). As compensation, the overall damping ratios of these layers were considered 5, 10 and 10 %. It is expected that “a reasonably selected overall damping ratio could model the energy dissipation during dynamic loading”.

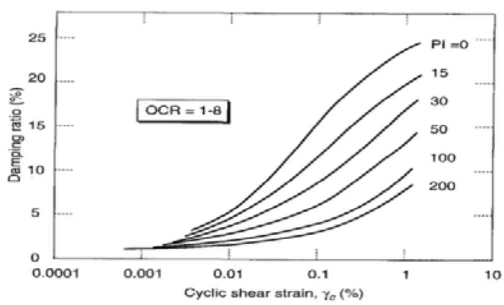

Figure 8. Damping ratio of different soil versus t cyclic shear strain [10]

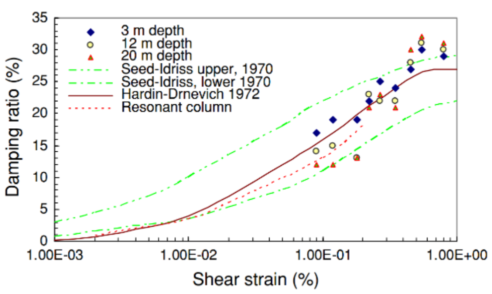

Figure 9. Damping ratio of dry sandy soil versus shear strain [11]

Figures 10, 11, 12 and table 2 summarize the numerical calculation results for the second stage simulations (model 2). The outcome were more acceptable than model 1. It is interpreted that the soil layering technique even for a laboratory scale slope, can improve the numerical result simulations. However there were some deviations between the calculated and observed records. So, the damping ratios of second and third layers were separated in the second stage of modifications. Regarding to visual observations and video films, captured during dynamic tests, different values of shear strains in the first and second layers were recognized. The third layer had no more than 1% shear strain. However the first and the second layers had γ>10% and 10%>γ>1% respectively. So, the damping of top layer was increased to 15 %. Although this division is considered helpful, but it increased the difficulty of model analysis and needed more time.

Figures 13, 14 and 15, illustrate the numerical results of model 3. The slope horizontal movement which is a key factor for model verification, was 35 cm. However, the mid-crest settlement were extremely higher than actual records (9.4 cm). Figure 15 compares the recorded and calculated slope crest acceleration. Although it experienced a clear advancement comparing to model 1 and 2, it needs more modifications. So it is decided to change the position of maximum elastic modulus assignments. In the 2nd and 3rd model, the E_0 were assigned to layers mid height. But in the 4th model, it is assigned to each layer's bottom.

Figures 16, 17 and 18 represent the horizontal and vertical displacements and response acceleration of model 4. Although the soil displacements had not changed (comparing to model 3), the acceleration response of slope crest is acceptably improved. Besides the crest acceleration, figure 19 compares the recorded and calculated toe accelerations. Although the crest settlement deviated from actual value, these comparisons confirm the validity of numerical modeling.

Table 2 Model 2, 3 & 4 characteristics and results

Model Name	Yong Modulus (Mpa)	Damping Ratio (%)	U1 (cm)	U2-crest (cm)
2		5,10,10	40.6	10.4
3	10-14-20	5,10,15	35.0	9.4
4		5,10,15	34.0	8.8

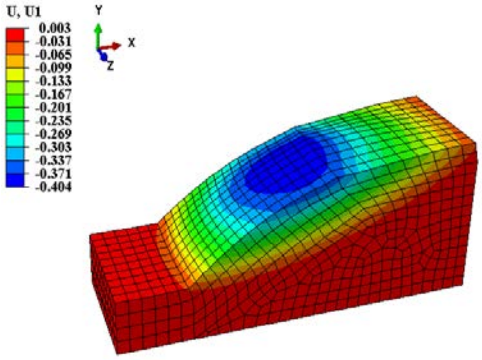

Figure 10. Horizontal displacement of model 2

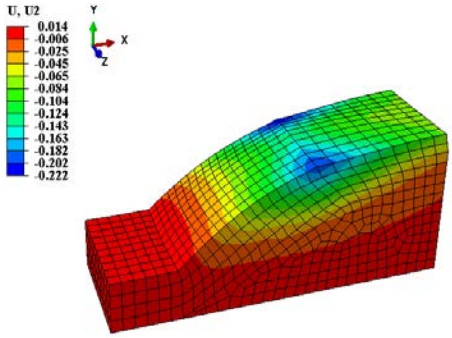

Figure 11. Vertical displacement of model 2

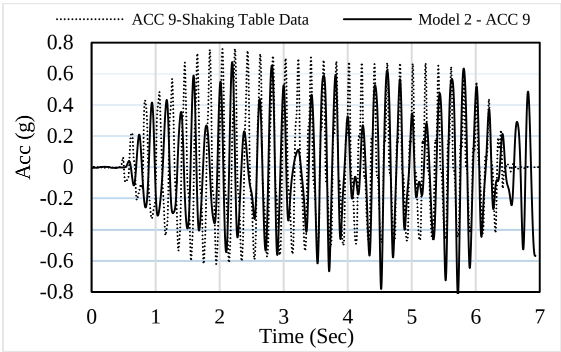

Figure 12. Crest acceleration comparison for model 2 and laboratory results

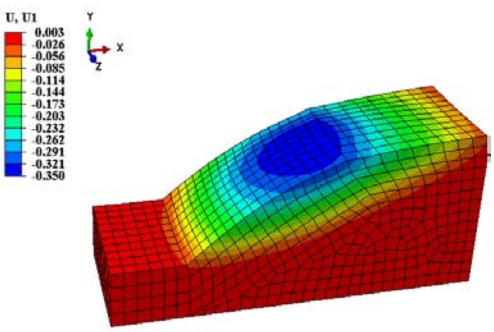

Figure 13. Horizontal displacement of model 3

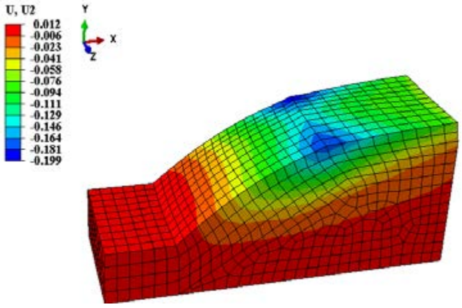

Figure 14. Vertical displacement of model 3

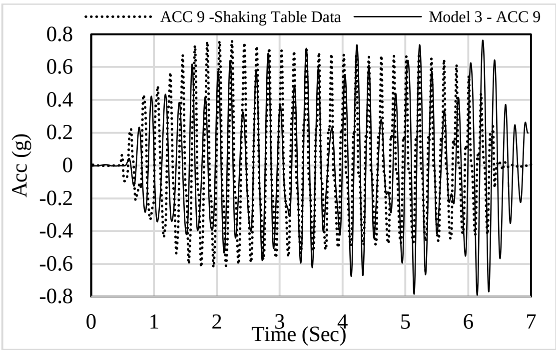

Figure 15. Crest acceleration comparison for model 3 and laboratory results

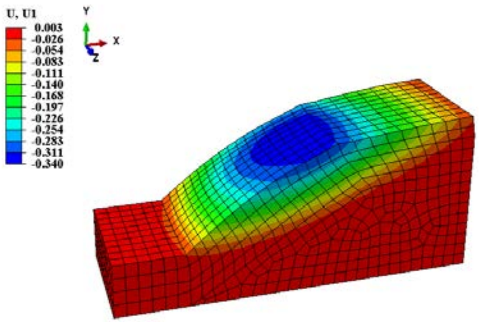

Figure 16. Horizontal displacement of model 4

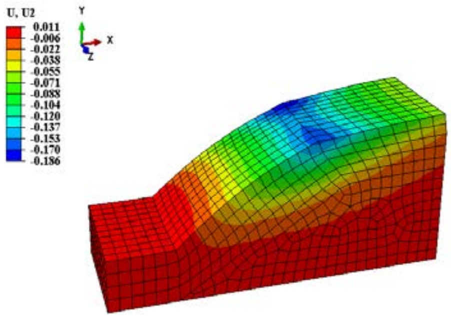

Figure 17. Vertical displacement of model 4

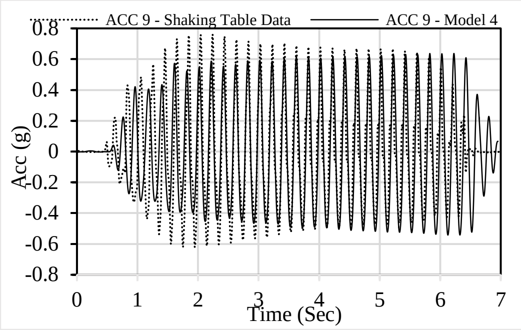

Figure 18. Crest acceleration comparison for model 4 and laboratory results

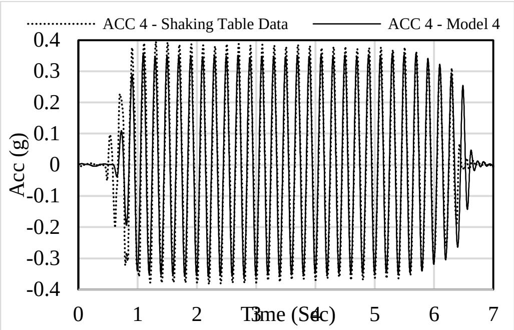

Figure 19. Toe acceleration comparison for model 4 and laboratory results

CONCLUSION

A laboratory scale sandy slope was harmonically excited to model a 7.5-8.5 magnitude by shaking table device in Sharif University of technology. Although the dynamic test, was a part of thorough research investigations, but the various numerical analysis with different aspects, were designed to compensate the shortcomings of laboratory testing. But the numerical models, need verification, and this stage was performed by comparing the recorded and calculated results. ABAQUS finite element program were selected and many models were constructed.

This paper summarizes a numerical model calibration of one dynamic test. The geometry of model and prototype was similar and model parameters were reasonably selected. Then, the first stage results were compared and some deviations were recognized.

In order to improve the numerical results, a three phase modification was performed on numerical models. The model slope was divided to three separate layers based on displacement observations. Each layer have different elastic modulus and damping ratios. The forth model which passed the verification process, had 10, 14 and 20 MPa elasticity which is assigned to each layer bottom. The damping ratios of these layers were chosen regarding to proposed graphs in the literature and shear strain observations. The three layers have 5, 10 and 15% overall material damping.

The calculated results for acceleration response which is a key factor in revealing the wave propagation algorithm verified the modelling correctness. In addition, the Horizontal displacement of 4th model coincided the laboratory observed one. However, the crest settlement was higher than actual records and need modification.

So, it is concluded that the modifications (layering) proved to be helpful and the final model is verified. Also, the authors consider the change of dilation angle in future numerical modeling to adjust the settlements.

ACKNOWLEDGEMENTS

The authors greatly acknowledge the Tehran Gas Company, which defined and financially supported the research project. The project which consists of two laboratory (shaking table testing) and numerical modeling (ABAQUS program) aspects, is really enriched by helpful scientific suggestions of IIEES (international institute of earthquake engineering and seismology) as a supervisors of the research project

REFERENCES

[1] Steven L. Kramer, "Geotechnical Erathquake Engineering", University of Washington, (1996).

[2] Nian T.K, Huang R.Q, Zhang K.L, Chen G.Q, “ Seismic stability analysis of three-dimensional slopes using elasto-plastic FE method” International Journal of Advancements in Computing Technology Volume3, Number9, 367-376. 2011

[3] Abe K., Izawa J, Nakamura H, Kawai T, Nakamura S, “Analytical study of seismic slope behavior in a large-scale shaking table model test using FEM and MPM”, Proceedings of the 18th International Conference on Soil Mechanics and Geotechnical Engineering, Paris, 1407-1410. 2013

[4] Liam Finn W.D, “Seismic Slope Stability”, Geo-Congress, 2269-2295. 2013

[5] Iai S., (1989). Similitude for shaking table tests on soil-structure-field model in 1g gravitational field. Soils and Foundations 29, 105-118

[6] H. Farahi Jahromi, M. Joshaghani, M. Sehi zadeh & S. Yousefi," comparison of dynamically induced experimental slope deformations with newmark sliding block theory“,Fifth International Young Geotechnical Engineering Conference 5iYGEC’13”,paris, France.

[7] Electric Power Research Institute (EPRI), 1996. Guidelines for determining design basis ground motions, Final Rep. No. TR-102293, Palo Alto, California.

[8] Das B.M. 1985. Advanced Soil Mechanics, McGraw-Hill
[9] Ishibashi I., Zhang X., 1993. Unified dynamic shear moduli and damping ratios of sand and clay. Soils and Foundations 33, 182-191
[10] Vucetic, m. and dobry, r, "Effect of soil plasticity on cyclic response', Journal of Geotechnical Engineering, ASCE, vol. 117, 89-107. 1991.
[11] M. H.T, Rayhani and M.H. El Naggar", Seismic response of sands in centrifuge tests, Canadian Geotechnical gournal, 45: 470-483 (2008).

Fifth International Conference on Geotechnique, Construction Materials and Environment, Osaka, Japan, Nov. 16-18, 2015, ISBN: 978-4-9905958-4-5 C3051

FURTHER DEVELOPMENTS IN THE AASHTOLIV EQUATIONS TO FORWARD-CALCULATE SUBGRADE AND PAVEMENT MODULI

Moshe Livneh[1]

[1] Civil and Environmental Engineering Faculty, Technion-Israel Institute of Technology, Haifa, Israel

ABSTRACT

Various studies have demonstrated the usefulness of the forward-calculation technique as a relevant approach to determine layered elastic moduli from in-situ load-deflection data. Recently, the well-known forward-calculation method from the 1993 AASHTO design guide was modified by this author previously to take into account the influence of (a) errors induced in the original forward-calculations as a result of correlative equations developed for the two-layer model, and (b) depth to bedrock measured from the subgrade surface. The present paper develops modifying equations that take into account the influence of a three-layer model, as opposed to the aforementioned two-layer model, on the forward-calculated subgrade and pavement moduli. Using a 3-layer model with the existing equations yields an increase in the subgrade modulus outputs by a multiplier value ranging from 1.0 to over 1.5; however, for the majority of flexible pavements with small to moderate total thicknesses, the aforementioned multiplier value is equal or very close to 1.0. In addition, using a 3-layer model with the existing equations yields an increase in the outputs of the ratio of pavement modulus to subgrade modulus, raised to the power of 1/3, by a multiplier value ranging from 1.15 down to under 0.85. Finally, practical examples of in-situ FWD measurements conducted on four flexible pavements generally support the two conclusions above, where the multiplier value for (a) the subgrade modulus values ranged from 1.0 to 1.07, and (b) the pavement modulus values ranged from 0.65 to 1.45.

Keywords: Deflection, Forward-calculation, Modulus, Subgrade, Pavement.

INTRODUCTION

Non-destructive testing (NDT) on pavements is having a significant impact on the design and evaluation of pavement systems. To determine the layer moduli of a pavement system, deflection measurements from NDT are taken. Commonly, these measurements utilize the Falling Weight Deflectometer (FWD) device, which applies an impact load to the surface of the pavement. Sensors at the load location and at fixed radii from the load center measure surface deflections. The resulting set of deflections is known as the deflection bowl or basin. Considerable background information about this method is provided in several existing studies, such as [1].

Special computer programs are available to back-calculate a modulus profile for the pavement system from the peak values of the measured input FWD force and the resulting deflection basin. These programs include (a) iterative elastic-layer back-calculation algorithms and (b) closed-form back-calculation algorithms, which are also known as direct-calculation or forward-calculation algorithms.

The closed-form back-calculation process differs from iterative back-calculation in that moduli estimates from the former are calculated directly from the load and the deflection data by means of closed-form equations, rather than iterative ones. No seed-layer moduli or other stiffness properties are needed for this closed-form method. In addition, several programs exist for this forward-calculation procedure, such as the Wiseman-Greenstein program [2], ROADHOG [3], DEFOD [4], the old 1993 AASHTO design guide equations [5, 6], ROHDE [7], MDOT [8], Romanoschi-Metcalf [9], FDOT [10], YONAPAVE [11], FHWA [12], and the new EVALIV program [13]. All these programs offer quick direct-calculation procedures that utilize a two-layer model for any given pavement structure.

Among the aforementioned forward-calculation techniques, the technique from the old 1993 AASHTO design guide is still used by several agencies around the world, including the American FHWA (Federal Highway Administration) and the Israeli National Roads Company (formerly PWD). For this matter, also see the comparison studies of the 1993 AASHTO design guide’s original equations, given in [14, 15]. As these original equations do not calculate the subgrade and pavement resilient moduli in a fully direct manner, it became necessary to replace the existing forward-calculating equations with modified ones, termed AASHTOLIV equations. The development of these equations is shown by this author in two previous papers [16, 17]. These modified equations, however, are based on the deflection characteristic of a 2-layer model; therefore, further modifications are needed to include the deflection characteristics of a 3-layer model.

Given this background, the objectives of the present paper were formulated as follows:

- to present the existing modified AASHTOLIV AASHTO equations for forward-calculating the pavement and subgrade resilient moduli;
- to develop new corrective-factor equations that take into account the deflection characteristics of a 3-layer model;
- to elaborate on the existing corrective-factor equations that take into account any given depth to bedrock measured from the pavement-subgrade interface;
- to demonstrate the use of the current developed AASHTOLIV equations by presenting four forward-calculation examples.

Finally, the following sections will detail the process of accomplishing this paper's four objectives and the consequent conclusions.

EXISTING AASHTOLIV EQUATIONS

Following the findings of [16], the suggested modified Es_{uc} equation of AASHTOLIV is given by the following expression, where Es_{uc} denotes the forwardcalculated AASHTOLIV subgrade modulus; i.e. the basic uncorrected equation:

$$Es_{uc}=\min[0.24\times P/(d_r\times r)] \quad (1)$$

where r is equal to either 900, 1,200, 1,500, or 1,800 mm, and d_r is the recorded deflections for each lateral distance, r. Note that the associated corrective expression for Eq. 1 is developed in the next section.

As for the Ep_{uc} values (i.e., the AASHTOLIV pavement modulus), numerical calculations from the AASHTO original expression lead to the following relationships to calculate these values from the calculated Es_{uc} values (i.e. those calculated from Eq. 1), the given Hp (pavement thickness), a (radius of loading plate), and d_0 (central deflection) data.

$$(Ep/Es)_{uc}=A\times[(Es\times d_0)/(1.5\times p\times a)]^{-B} \quad (2)$$

$$A=-0.3447\times[\log(Hp/a)]^3+0.8528\times[\log(Hp/a)]^2- \\ -0.5174\times\log(Hp/a)+0.8766 \quad (3)$$

$$B=-0.8883\times[\log(Hp/a)]^3+2.8376\times[\log(Hp/a)]^2- \\ -3.6121\times\log(Hp/a)+2.9094 \quad (4)$$

where A and B denote curve-fitting coefficients for calculating Ep/Es values.

Finally, it should be pointed out that all of the four equations above relate to the case of (a) deflection characteristics of a 2-layer model, and (b) infinity depth to bedrock (i.e., $D/a=\infty$).

3-LAYER CORRECTIVE EQUATIONS

In order to check the accuracy of the modified equations given in the previous section, simulated data for a surface deflection-basin was generated for various given data from a 3-layer model with infinite depth to bedrock. Surface deflection-basins can be calculated theoretically with the aid of either the Burmister equations or the Odemark-Ullidtz equations as formulated by Wiseman & Greenstein in [1]. Such theoretical calculations were performed with the latter equations for the following given data: (a) subgrade and pavement Poisson ratios of 0.5, (b) subgrade modulus of 50 MPa, (c) asphaltic modulus of either 2,500, 5,000 or 10,000 MPa, (d) granular layer modulus of 200 and 400 MPa, leading to ratio of pavement modulus to subgrade modulus that ranged from 6.2 to 25.2, (e) pavement thickness from 350 to 1,750 mm, (f) thickness of asphaltic layer of 150 mm, (g) radius of loading plate of 150 mm, and (h) reference load of 9.5889 kN (i.e. reference pressure of 135.7 kPa). The outputs of these calculations were then used to calculate, for the pavement structures characterized by the data mentioned above, the ratio of the true subgrade resilient modulus to that forward-calculated by Eq. 1 (which, along with Fig. 1, the present paper terms the AASHTOLIV subgrade modulus).

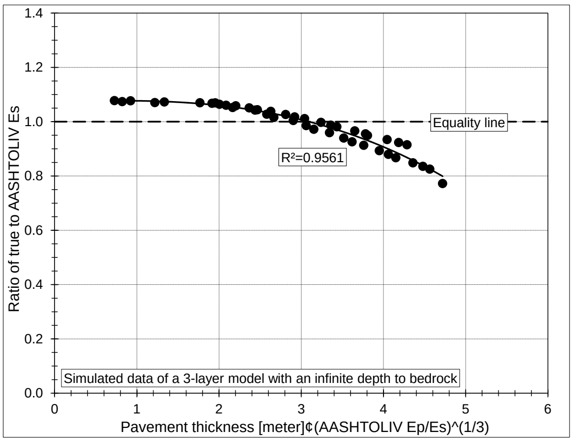

Fig. 1 Ratio of true to AASHTOLIV subgrade modulus versus apparent AASHTOLIV structural numbers for all simulated three-layer structures with infinite depth to bedrock when a=150 mm.

For the current case (i.e., the case of $D/a=\infty$ where D is the depth to bedrock from pavement and subgrade interface, and a is the radius of the loading plate), Fig. 1 shows the variation of the subgrade modulus ratio over the range of values of $Hp\times(\text{AASHTOLIV } Ep/Es)^{1/3}$, as calculated by Eqs. 2, 3 and 4, and referred to as "the apparent AASHTOLIV structural number" within the present paper. This variation possesses a high R^2 value as well as ratio values higher than 1.0 (maximum 1.08) for apparent structural numbers lower than 3.10.

The variation of the true apparent structural number in Fig. 1 clearly demonstrates the approximate nature of Eq. 1. Thus, this equation needs to be multiplied by a correction factor (Fs) equal to the variation of the ratio of true-to-AASHTOLIV subgrade modulus with apparent

AASHTOLIV structural number, as given in Fig. 1 for the D/a=∞ case. Note again that the apparent AASHTOLIV structural number was obtained from the AASHTOLIV forward-calculation equations (i.e., Eqs. 2, 3 and 4). According to Fig. 1, the formulation of Fs is as follows:

$$Fs=-0.0020\times[Hp\times(Ep/Es)_{uc}{}^{1/3}]^3- -0.0056\times[Hp\times(Ep/Es)_{uc}{}^{1/3}]^2+ +0.0138\times[Hp\times(Ep/Es)_{uc}{}^{1/3}]+1.0707 \quad (5)$$

where Fs denotes the multiplier factor for Eq. 1 to obtain corrected (true) Es values for the case of a 3-layer model with an infinite depth to bedrock (i.e., Es_m); Hp denotes the total pavement thickness in meters; and $(Ep/Es)_{uc}$ denotes the forward-calculated Ep to Es ratio by Eqs. 2, 3 and 4 (i.e. the AASHTOLIV Ep/Es).

As for the Ep values, Fig. 2 depicts the variation of the corrected (true) apparent structural numbers over the range of AASHTOLIV (uncorrected) apparent structural numbers for the same simulated 3-layer model structures that possess an infinite depth to bedrock when a=150, (i.e., again, for the D/a=∞ case, where D is the depth to bedrock and a is the radius of the loading plate). Similar to Fig. 1, Fig. 2 indicates that the R^2 value for this variation is also very high. To sum up, the formulation of this variation is as follows:

$$Hp\times(Ep/Es)_m{}^{1/3}=0.0426\times[Hp\times(Ep/Es)_{uc}{}^{1/3}]^3- -0.2929\times[Hp\times(Ep/Es)_{uc}{}^{1/3}]^2+ +1.3965\times[Hp\times(Ep/Es)_{uc}{}^{1/3}]-0.0308 \quad (6)$$

where Hp denotes the total pavement thickness, in meters; $(Ep/Es)_m$ denotes the corrected (true) Ep to Es ratio; and $(Ep/Es)_{uc}$ denotes the forward-calculated Ep to Es ratio by Eqs. 2, 3 and 4 (i.e. the AASHTOLIV Ep/Es value).

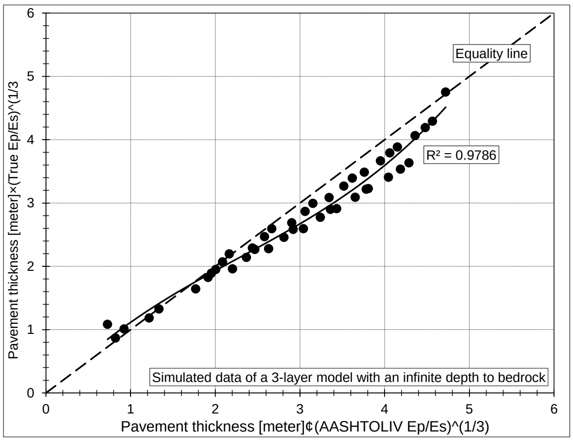

Fig. 2 True to apparent AASHTOLIV structural number versus apparent AASHTOLIV structural numbers for all simulated 3-layer structures with infinite depth to bedrock when a=150 mm.

To sum up, the corrected (true) Es and the corrected (true) Ep (termed Es_m and Ep_m, respectively) are as follows:

$$Es_m=Fs\times Es_{uc} \quad (7)$$

$$Ep_m=(Ep/Es)_m\times Es_m \quad (8)$$

where Es_{uc} is calculated according to Eq. 1, Fs is calculated according to Eq. 5, and $(Ep/Es)_c$ is calculated according to Eq. 6.

3-LAYER VERSUS 2-LAYER MODEL

As mentioned, the previous Es_m equations refer to the case of a 3-layer model structure with infinite depth to bedrock. The outputs of these equations differ from those given in [16] by the following Fs_m ratio. To recall, the equations given in [16] refer to the case of a 2-layer model with an infinite depth to bedrock (also see Fig. 3):

$$Es_m=Fs_m\times Es_c \quad (9)$$

$$Fs_m=0.0130\times[Hp\times(Ep/Es)_{uc}{}^{1/3}]^3- -0.0497\times[Hp\times(Ep/Es)_{uc}{}^{1/3}]^2+ +0.0750\times[Hp\times(Ep/Es)_{uc}{}^{1/3}]+0.9666 \quad (10)$$

where Fs_m denotes the multiplier factor of Es_c i.e. the corrected Es (subgrade modulus) for cases of a 2-layer model with an infinite depth to bedrock, as calculated by Eq. 10 given in [16] values) to obtain corrected (true) Es values for the case of a 3-layer model with an infinite depth to bedrock (i.e., Es_m); Hp denotes the total pavement thickness in meters; and $(Ep/Es)_{uc}$ denotes the forward-calculated Ep to Es ratio by Eqs. 2, 3 and 4 (i.e., the AASHTOLIV Ep/Es).

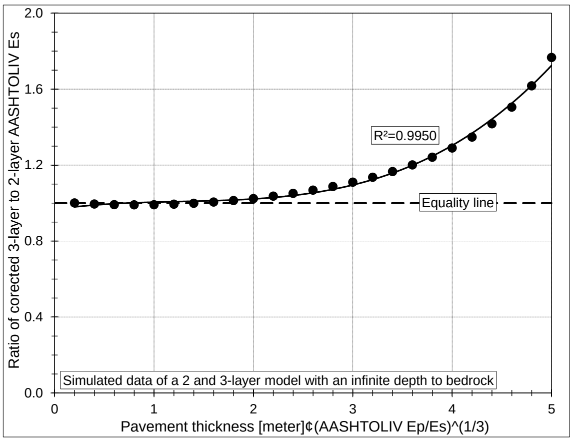

Fig. 3 Ratio of corrected 3-layer to 2-layer AASHTOLIV subgrade modulus versus apparent AASHTOLIV structural numbers for all simulated structures with infinite depth to bedrock when a=150 mm.

Fig. 3 indicates that the Fs_m values, derived from Eq. 10, vary from 1.0 to over 1.5. In addition, for the majority of conventional apparent AASHTOLIV structural numbers (i.e., up to 2.0 meters for flexible pavement with small to moderate total pavement thickness; see Fig. 4), Fs_m is equal to 1.0. At this juncture it is worthwhile noting that Fig. 4 depicts the cumulative distribution of the apparent

AASHTOLIV structural numbers forward-calculated for four given structures which are described in the following section of the present paper.

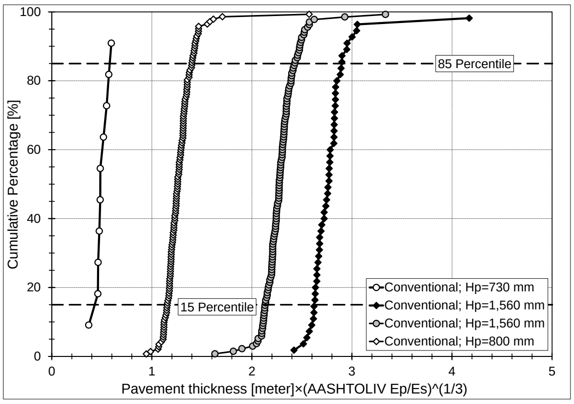

Fig. 4 Cumulative distribution of AASHTOLIV apparent structural numbers for four given flexible-pavement structures with infinite depth to bedrock.

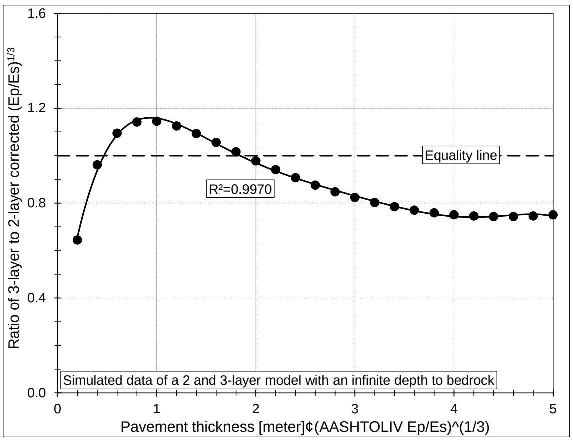

Fig. 5 Ratio of corrected 3-layer to 2-layer AASHTOLIV Ep/Es values versus apparent AASHTOLIV structural numbers for all simulated structures with infinite depth to bedrock when a=150 mm.

Similarly to Es_m, the previous $(Ep/Es)_m$ equations relate to the case of a 3-layer model structure with infinite depth to bedrock. The outputs of these equations differ from those given in [16] by the following Fp_m ratio. To recall again, the equations given in [16] refer to the case of a 2-layer model with an infinite depth to bedrock (see also Fig. 5):

$$(Ep/Es)_m^{1/3}=Fp_m\times(Ep/Es)_c^{1/3} \tag{11}$$

$$\begin{aligned}Fp_m=&-0.0034\times[Hp\times(Ep/Es)_{uc}^{1/3}]^6+\\&+0.0615\times[Hp\times(Ep/Es)_{uc}^{1/3}]^5+\\&-0.4429\times[Hp\times(Ep/Es)_{uc}^{1/3}]^4\\&+1.6273\times[Hp\times(Ep/Es)_{uc}^{1/3}]^3-\\&-3.1745\times[Hp\times(Ep/Es)_{uc}^{1/3}]^2+\\&+2.8956\times[Hp\times(Ep/Es)_{uc}^{1/3}]+0.1940\end{aligned} \tag{12}$$

where Fp_m denotes the multiplier factor of $(Ep/Es)_c$, the corrected Ep/Es values for the case of a 2-layer model with an infinite depth to bedrock as calculated by Eq. 9, given in [16] to obtain corrected (true) Ep/Es values for the case of a 3-layer model with an infinite depth to bedrock (i.e., $(Ep/Es)_m$ in order to calculate Ep_m using Eq. 8); Hp denotes the total pavement thickness in meters; $(Ep/Es)_{uc}$ denotes the forward-calculated Ep to Es ratio according to Eqs. 2, 3 and 4 (i.e., the AASHTOLIV Ep/Es).

Fig. 5 indicates that the Fp_m values of Eq. 11 vary above and below 1.0. In addition, for the majority of conventional apparent AASHTOLIV structural numbers (again, up to 2.0 meters for flexible pavement with small to moderate total pavement thickness; see Fig. 4) Fp_m varies between 0.85 and 1.15.

FINAL CALCULATING EQUATIONS

In order to forward-calculate the subgrade and pavement moduli for cases where the depth to bedrock is not infinite, it is suggested to apply the depth to bedrock effect corrective equations from the existing 2-layer model AASHTOLIV equations given in [16]. This suggestion is based on the postulation that the aforementioned corrective equations also apply to the present 3-layer model AASHTOLIV equations developed in the previous section. Thus, the final forward-calculation equations for the subgrade and pavement moduli are:

$$Es_{md}=Fs_m\times Es_d \tag{13}$$

$$Ep_{md}=Fp_m^3\times(Ep/Es)_d\times Es_{md} \tag{14}$$

where Es_{md} is the final forward-calculated subgrade modulus for the case of a 3-layer model and a given depth to bedrock; Es_d is the calculated subgrade modulus according to Eqs. 12, 13, 14, 15 and 16, given in [15] for the case of a 2-layer model with a given depth to bedrock; Fs_m denotes a multiplier factor as defined by Eq. 10 in the previous section; Ep_{md} is the final forward-calculated pavement modulus for the case of a 3-layer model with a given depth to bedrock; Ep_d is the pavement modulus calculated according to Eqs. 17, 18, 19, 20 and 21, given in [16] for the case of a 2-layer model with a given depth to bedrock; Fp_m is the multiplier factor as defined by Eq. 12 in the previous section.

FORWARD-CALCULATED EXAMPLES

In order to demonstrate the use of the new AASHTOLIV equations developed in the present paper, forward-calculations were performed on deflection bowls measured at four given flexible-pavement structures. Three of these structures (i.e. excluding the conventional structure which had a total thickness of 800 mm) were constructed at the same site, Ben Gurion International Airport, Israel, and possessed a heavy clay subgrade. The remaining structure, which was constructed at a different site (Ovda Airport, Israel), possessed a hard silty subgrade. Here it is worthy to note that all four aforementioned structures served as the -forward-calculation examples given in [16].

These forward-calculations include finding the subgrade and pavement resilient moduli for the two following cases: (a) when the depth to bedrock from the subgrade surface is infinite, and (b) when the depth to bedrock from the subgrade surface has a fixed value of 40×a=6.0 meters, where a=0.150 meters, representing the radius of the loading plate. This fixed depth was chosen according to the recommendations outlined in [18]. Figs. 6 and 7 depict the AASHTOLIV subgrade resilient moduli outputs from the 3-layer model compared to outputs from the 2-layer model for the four aforementioned structures. Fig. 6 presents the case of infinite depth to bedrock while Fig. 7 presents the case of 6.0 meters to bedrock, measured from the subgrade surface.

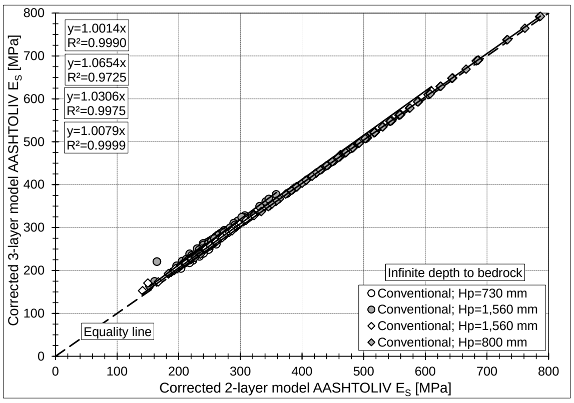

Fig. 6 Corrected 3-layer model AASHTOLIV Es versus corrected 2-layer model AASHTOLIV Es for (a) infinite depth to bedrock, and (b) the four given flexible structures.

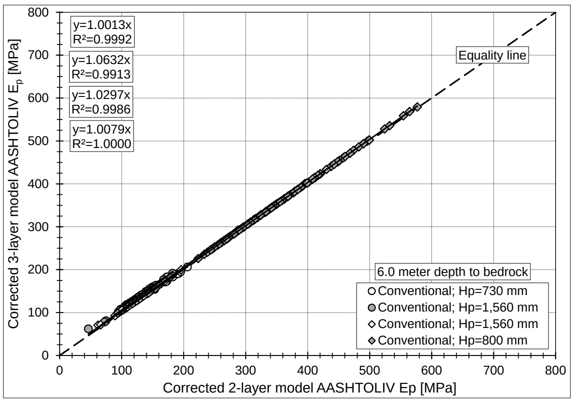

Fig. 7 Corrected 3-layer model AASHTOLIV Es versus corrected 2-layer model AASHTOLIV Es for (a) a 6.0 meter depth to bedrock, and (b) the four given flexible structures.

Figs. 6 and 7 indicate that the characterizing ratio of the corrected 3-layer model AASHTOLIV Es value versus that of the corrected 2-layer model (i.e., the slope of the linear equation obtained from the zero intercept regression) vary for the four given flexible structures from 1.00 to 1.07, where the higher average ratio value relates to the higher total pavement thickness value. This finding is consistent with that from Fig. 4 in the previous section.

In the same manner, Figs. 8 and 9 depict the AASHTOLIV pavement resilient moduli outputs from the 3-layer model compared to the 2-layer model for the four aforementioned structures. Again, Fig. 8 presents the case of infinite depth to bedrock while Fig. 9 presents the case of 6.0 meters to bedrock, measured from the subgrade surface.

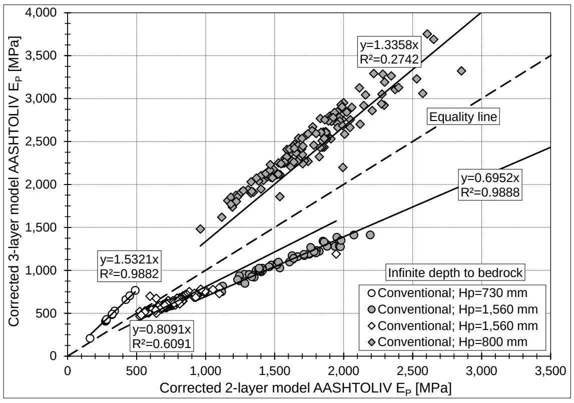

Fig. 8 Corrected 3-layer model AASHTOLIV Ep versus corrected 2-layer model AASHTOLIV Ep for (a) infinite depth to bedrock, and (b) the four given flexible structures.

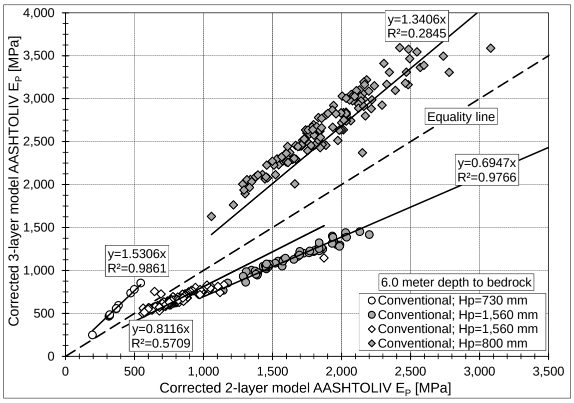

Fig. 9 Corrected 3-layer model AASHTOLIV Ep versus corrected 2-layer model AASHTOLIV Ep for (a) a 6.0 meter depth to bedrock, and (b) the four given flexible structures.

Figs. 8 and 9 indicate that the characterizing ratio (as previously defined) of the corrected 3-layer model AASHTOLIV Ep value to the corrected 2-layer model varies for the four given flexible structures from 0.70 to 1.55, where the lower average ratio value relates to the higher total pavements thickness value. This finding is consistent with that from Fig. 5 in the previous section, where its y-axis values were raised to the power of 3.

CONCLUSIONS

Findings from the current study on forward-calculation of FWD deflection-basin measurements serve as an important means to upgrade the existing AASHTOLIV equations given in [15] and [16]. The results yield the following conclusions:

- The current AASHTLOLIV equations, based on the 2-layer model for any given depth to bedrock from [15] and [16], require correction factors in order to take into account the 3-layer model effect.
- Using a 3-layer model with the existing equations yields an increase in the subgrade modulus outputs by a multiplier value ranging from 1.0 to over 1.5; however, for the majority of flexible pavements with small to moderate total thicknesses, the aforementioned multiplier value is equal or very close to 1.0
- In addition, using a 3-layer model with the existing equations yields an increase in the outputs of the ratio of pavement modulus to subgrade modulus, raised to the power of 1/3, by a multiplier value ranging from 1.15 down to under 0.85.
- The four given foreword-calculation examples generally support the two conclusions above, where the multiplier value for (a) the subgrade modulus values ranged from 1.0 to 1.07, and (b) the pavement modulus values ranged from 0.65 to 1.45.

Finally, it is important to add that despite the advantages of utilizing the current modified AASHTOLIV equations, a general statement should be made: possible results from other in-situ deflection bowl measurements may not necessarily mean that forward-calculation is always superior to back-calculation.

ACKNOWLEDGEMENTS

The data of the measured values presented in this paper were obtained in the course of engineering studies performed by the author for the Israeli Airport Authority. Thanks are therefore due to this authority.

REFERENCES

[1] Alavi, S., Lecates, J.F., Tavares M.P. & Sierra Transportation Engineers, Inc., “Falling weight deflectometer usage”, NCHRP Synthesis 381, National Cooperative Highway Research Program, Synthesis of Highway Practice, Transportation Research Board, Washington, DC, 2008.

[2] Wiseman, G., Uzan, J., Hoffman, M.S., Ishai, I. & Livneh, M., “Simple elastic models for pavement evaluation using measured deflection bowls”. In Proc. 4th Int. Conf. on Structural Design of Asphalt Pavements, Vol. II, Ann Arbor, Michigan, 1997, pp 416-426.

[3] Hall, K. D. & Elliot R. P., 1992. “ROADHOG-a flexible pavement overlay design procedure”, Transportation Research Record 1374, 1992, pp. 9-15.

[4] Sidess, A., Bonjack, H. & Zoltan, G., “Overlay design procedure for pavement maintenance management systems”, Transportation Research Record 1374, 1992, pp. 63-70.

[5] AASHTO, “AASHTO Guide for design of pavement structures 1993”, Washington, DC: American Association of State Highway and Transportation Officials, 1993.

[6] Baus, R. L. & Jonson, A.M. 1992. “AASHTO direct structural capacity method error analysis”, Journal of Transportation Engineering 118 (1), 1992, pp. 20-32.

[7] Rohde, G. T., “Determining pavement structural number from FWD testing”, Transportation Research Record 1448, 1994, pp. 61-68.

[8] Rada, G.R., Shepher, K.L., Zeigler, T.D. & Smith, T.E., “Montana's automated deflection analysis procedure”, Transportation Research Record 1570, 1997, pp. 151-162.

[9] Romanoschi, S. & Metcalf, J. B., “Simple approach to estimation of pavement structural capacity”. Transportation Research Record 1652, 1999, pp. 198-205.

[10] Badu-Tweneboah, K., Ruth, B.E. & Miley, W.G.. “Dynaflect Evaluation of layer moduli in Florida's flexible pavement systems”, Transportation Research Record 1196, 2003, pp. 96-107.

[11] Hoffman, M.S., “Direct method for evaluating structural needs of flexible pavements with Falling-Weight Deflectometer deflections”, Transportation Research Record 1860, 2003. pp. 41–47.

[12] Stubstad, R.N., Jiang, Y.J. & Lukanen, E.O., “Forwardcalculation of pavement moduli with load-deflection data”, Transportation Research Record 2005, 2007, pp. 104–110.

[13] Livneh, M., “On the reliability of excluding thickness in forward-calculating pavement parameters”, Road Materials and Pavements Design 11, 2010, pp. 171-195.

[14] Hassam, H.F., Mousa, R.M., & Gadallah, A.A., "Comparative analysis of using AASHTO and WESDEF approaches in back-Calculation of pavement layer moduli", Journal of Transportation Engineering, Vol. 129, 2003, pp. 322-329.

[15] Lee, Y.-H., Ker, H.-W., Lin, C.-J., & Wu, P.-H., "Study of backcalculated pavement layer moduli from the LTPP database", Tamkang Journal of Science and Engineering, Vol. 13, No. 2, 2010, pp. 145-156.

[16] Livneh, M., "Recent modifications to the 1993 AASHTO equations for forward-calculating subgrade and pavement moduli", in Proc. 6th Int. Conf. on Bituminous Mixtures and Pavements, Thessaloniki, Greece, 10-12 June 2015.

[17] Livneh, M., "Additional issues concerning recent modified 1993 AASHTO equations (AASHTOLIV) for analyzing measured deflection bowls", in Proc. 6th Int. Conf. on

Bituminous Mixtures and Pavements, Thessaloniki, Greece, 10-12 June 2015.

[18] Rohde, G.T. & Scullion, T., “MODULUS 4.0: expansion and validation of the modulus back-calculation system”, Report No. FHWA/TX-91/1123-3, Texas Department of Transportation, Austin, TX, 1990.

LIQUEFACTION POTENTIAL ASSESSMENT BASED ON LABORATORY TEST

Abdul Hakam[1], Febrin Anas Ismail[1] and Fauzan[3]
[1]Civil Dept. of Engineering Faculty, Andalas University, Indonesia

ABSTRACT

The physical properties of sand soil which give effect to the resistance of liquefaction include grain size and density. Those physical properties of sand soil associated to liquefaction resistance have been studied in laboratory. Based on that study, the method to assess the liquefaction potential then is proposed. In laboratory tests, the vibration source is given by using the shaking table. During the tests, the acceleration and settlement are recorded. It then concluded that there is a relationship between density and gain size particles associated with liquefaction resistance for certain acceleration of vibration. The cone penetration and relative density relationship has been developed based on experiments in laboratory. Based on the results of those laboratory tests, the liquefaction potential of a certain site then assessed. It is found that the relative density and mean gain size relationship can be used to assess liquefaction potential in sand deposits.

Keywords: Liquefaction, Earthquake, Soil particle size, Relative density, Laboratory test

INTRODUCTION

The liquefaction potential assessment in a soil deposit is an important aspect of geotechnical earthquake engineering practice since Niigata earthquake in 1964. Based on the occurrence of liquefaction and field test data a method named "simplified method" was proposed [1]. The liquefaction potential assessment at the coast of Padang using 'simplified method' has been presented [2]. The application of this method actually is not as simple as its name. It involves many factors that rarely used in civil engineering such as earthquake magnitude and depth factor. This procedure has been continuously improved based on a number of liquefaction histories around the world [3]. Based on these methods, further Shibata and Teparaksa [4] developed a method for evaluating the liquefaction potential based Cone Penetration Test results.

Based on the Cone Penetration method, the analysis of liquefaction susceptible at several locations in the city of Padang due to the 2009 earthquake has been presented [5]. Although these penetration-based methods (SPT and CPT) and cyclic stress ratio are well developed, but in the use still require advanced knowledge in choosing the parameters. The guidance for using penetration-based methods has been discussed [6].

In the past it has been summarized that the newly deposited loose sands under the shallow ground water are susceptible to liquefaction [7]. Kramer in 1996 [8] has summarized a number of methods to evaluate the liquefaction potential of a soil deposit. Those are the liquefaction history, the geological process, the soil type and fine size particles, soil density and effective stress at the time it is subjected to shaking. It has been summarized number of factors that affect soil liquefaction resistance in [9], that are:

- Relative density, D_r
- Initial stress of the soil, σ_i
- Mean grain size of the soil, D_{50}
- Applied peak acceleration, a_{max}
- Duration of the motion, t
- Over consolidation ratio, OCR
- Initial pore pressure, u_i

Even though historically, sands were considered to be the only type of soil susceptible to liquefaction, but observation showed that fine-grained soil also been suffered from liquefaction. The fine-grained soils may have a tendency to liquefy under a vibration load if they satisfy the Chinese criteria [10] that are:

- Fraction finer than 0.005 mm less than 15%
- Liquid Limit, LL less than 35%
- Natural water content more than 0.9 LL
- Liquidity Index less than 0.75

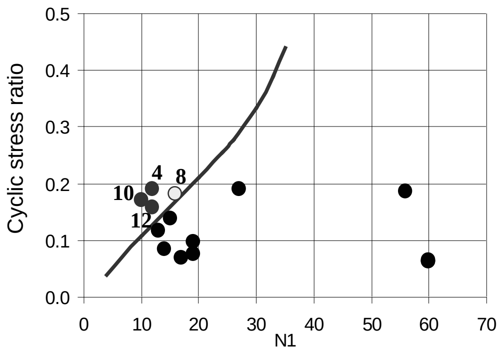

Fig. 1 Liquefaction using ‘simplified method’ [2].

Based on the grain size analysis test from several location due to Kocaeli earthquake in Turkey in 1999 [11] and due to Padang earthquake 2009, it have been reported the results of sieve analysis tests of liquefied soil samples as shown in Figure 2 (shadowed). The soil gradation of Padang is just in the middle of liquefaction boundaries from Aydan. The distribution of liquefied soil particle in Padang generally composed fine sand more than 60%. The fine content of liquefies soil of Padang is less than 20%. The mean grain size D_{50} is about 0.15mm to 0.35mm.

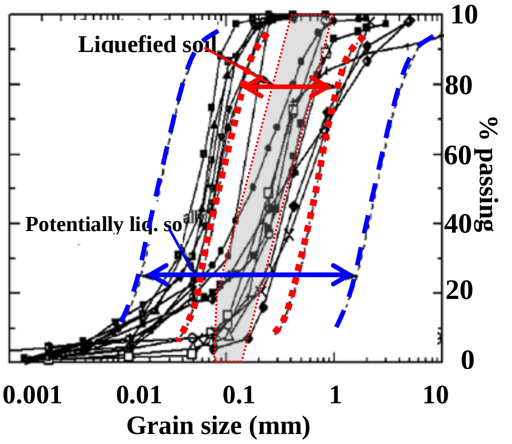

Fig. 2 Grain size limit for liquefaction [10].

Based on the field case histories on evaluation of liquefaction potential for 50-year around the world [12], mean grain size of liquefied soils are presented in Figure 3. It can be seen that from those 155 occurrences of liquefaction, 78% of liquefaction happened on the soil with mean grain size between 0.113 to 0.338 mm.

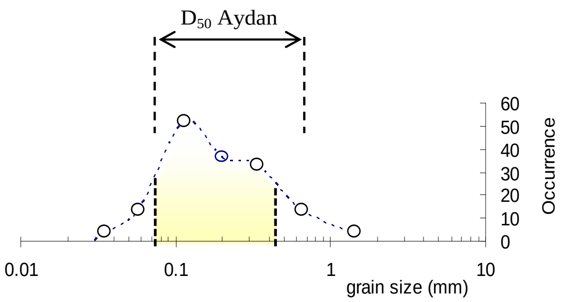

Fig. 3 D_{50} for liquefied soils, based on [12].

Therefore, this study is conducted to find out a relationship between density and gain size particles associated with liquefaction resistance for certain acceleration of vibration which is simply can be used to assess liquefaction potential of soil deposits.

The simple liquefaction potential assessment is important to have good estimation of the liquefaction problem. In this paper, the application of liquefaction potential assessment based on laboratory experiments is presented. The factors have been considered in the laboratory experiments are:

- Relative density, D_r
- Cone resistance of the soil, q_c
- Mean grain size of the soil, D_{50}
- Applied peak acceleration, a_{max}
- Duration of the motion, t

LABORATORY TEST RESULTS

A series of laboratory testing has been done by placing indicator bar on soil samples in the round container. In these tests the relative density D_r and the mean grain size D_{50} are varied. The samples are placed on the shaking table and then vibrated for 0.3g and 0.6g accelerations. During the testing the acceleration and the settlement of the indicator bar are recorded.

In field liquefaction, a seismic shaking can cause sand deposit to loose its contract and increase the water pore pressure. It happens because the seismic shaking occurs relatively fast and the soil performs an undrained loading. If soil has reached liquefaction condition then the effective stress in soil mass is decreased hence its shear strength can drop. In the liquefaction the individual soil particles are released from any confinement [13]. The same phenomenon in these experiments when liquefaction occurs in the sample, the shear strength of the soil dropped thus the indicator bar will settle down during the shaking.

The rate of settlement during shaking is approximately 0.1 cm/sec is taken as the separation criterion of settlement rate values. The rate settlement more than 0.1 cm/sec indicated that liquefaction has happened in this saturated soil samples. The general results of the tests are shown in Figure 4. The linear boundary line is made up for each acceleration 0.3g and 0.6g.

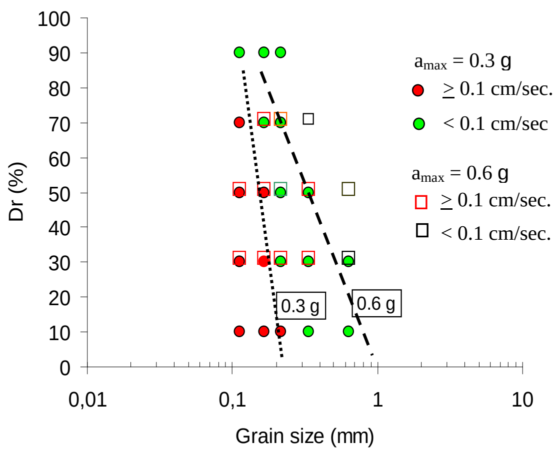

Fig. 4 $D_r – D_{50}$ for liquefaction test.

Since Cone Penetration Test is very famous in practice, the q_c – D_r relationship become essential for liquefaction potential analysis based on Cone Penetration Test (CPT). The calibration studies of the q_c is effected by sand density, in-situ effective stress and sand compressibility. Sand compressibility is controlled by grain characteristics, such as grain size, shape and mineralogy. The q_c – D_r relationships for sand then is written as follows [14]:

$$Dr = C_2^{(-1)} \ln Q/C_0 \qquad (1)$$

Where C_0=15.7, C_2=2.41 and $Q=(q_c/p_a)/(\sigma'/p_a)^{-0.5}$. Here p_a is reference pressure taken as 100kPa, in the same unit as q_c and σ'.

LIQUEFACTION ASSESSMENT

During Padang earthquake 2009, there are many locations along the shore suffered from liquefaction. One of those location is Pasir Jambak district where has sand deposit and very shallow water table. The field soil testing has been conducted to investigate soil distribution and cone resistance as presented in Figures 6 and 7.

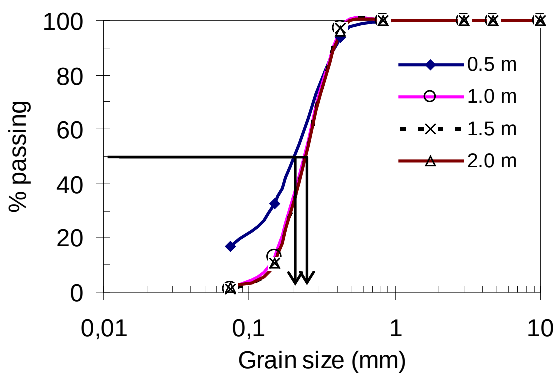

Fig. 6 Particle distribution of Pasir Jambak sand.

Table 1 shows the mean grain size of sand which is determined from the grain distribution chart and relative density is calculated using equation (1) with the unit volume of 12 kN/m^3.

Table 1 Parameter for liquefaction assessment

Name	Dept (m)	D_{50} (mm)	q_c (kg/cm^2)	D_r (%)
$D_{0.5}$	0.5	0.2	17	3
$D_{1.0}$	1.0	0.25	25	5
$D_{1.5}$	1.5	0.25	50	25
$D_{2.0}$	2.0	0.25	65	30

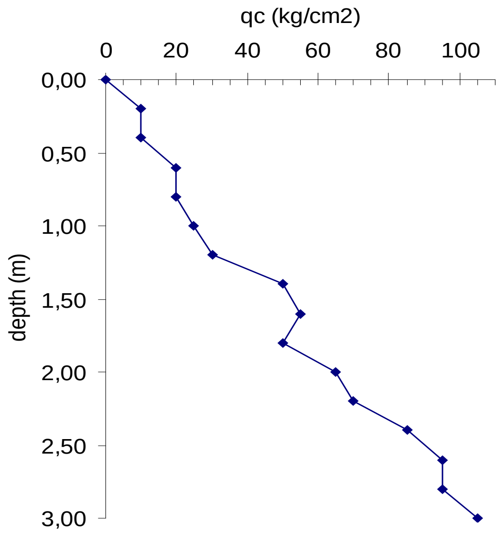

Fig. 7 CPT of Pasir Jambak.

Based on those parameters the point each depth is plotted in the Figure 8. The same value for maximum acceleration of Padang earthquake is about 0.3g. It shows that point $D_{0.5}$ just in line 0.3g which indicated that the liquefaction happed during the earthquake.

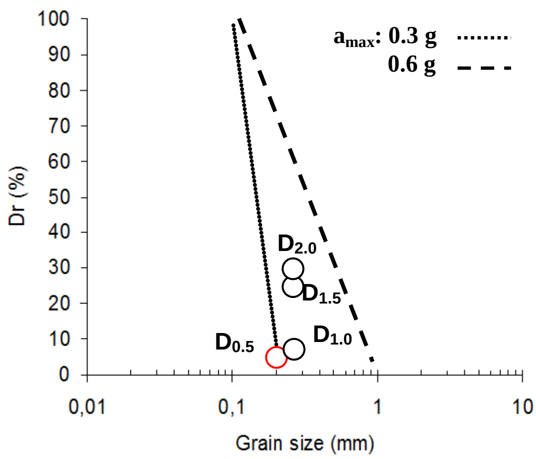

Fig. 8 D_r – D_{50} for Pasir Jambak assessment.

CONCLUSION

This paper presented that relative density and mean particle size can be associated with the liquefaction susceptibility of soil deposits. Liquefaction resistance of the sands increases with the relative density and mean particle size. Both relative density and mean particle size give unique relationship for resistance of sand soil against shaking.

Here, the liquefaction assessment of Pasir Jambak sand deposit due to Padang earthquake 2009 is presented. This analysis is practically simple to estimate the liquefaction potential. Thus, the relationship further can be used to assess liquefaction potential in certain sand deposits.

REFERENCES

[1] Seed, H. B., and Idriss, I. M., ‘‘Simplified procedure for evaluating soil liquefaction potential.’’ J. Geotech. Engg. Div. , ASCE, 97(9) , 1971, pp 1249–1273

[2] Hakam, A. and Darjanto, “Liquefaction potential assessment of Padang Beach Based on grain size and standard penetration resistance” (in Indonesia: Penelusuran Potensi Likuifaksi Pantai Padang Berdasarkan Gradasi Butiran dan Tahanan Penetrasi Standar), Jurnal Teknik Sipil – ITB, Vol. 20 No. 1, April 2013, pp. 33-38

[3] Seed, H. Bolton dan Idriss I.M., Ground Motion and Soil Liquefaction During Earthquake, Earthquake Engineering Research Institute, Berkeley, 1982

[4] Shibata, T. and Teparaksa, W., “Evaluation of liquefaction potential of soils using cone penetration tests”, J. Soils and Foundations, Vol. 28., N0. 2, 1998, pp. 49-60

[5] Hakam, A., “Soil Liquefaction of Padang due to Padang Earthquake 30s’09”, The Journal of Civil Engineering Dimension, Volume 14, no 2, 2012, pp. 64-68

[6] Youd, T. L. and Idriss, I. M. (2001). “Liquefaction resistance of soils: Summary report from the 1996 NCEER and 1998 NCEER/NSF workshop on evaluation of liquefaction resistance of soils”, J. Geotechnical and Geoenvironmental Engg., ASCE, April 2001, pp. 297-313

[7] Day R. W., , Geotechnical Earthquake Engineering Handbook, The McGraw-Hill Comp., 2002

[8] Kramer,S.L., Geotechnical Earthquake Engineering. Prentice Hall, Englewood Cliffs, N.J., 1996

[9] Das, BM., , Fundamental of Soil Dynamics, Elsevier Pub., New York, 1983

[10] Wang, W. S., “Some Findings in Soil Liquefaction”, Report Water Conservancy and Hydroelectric Power Scientific Research Institute, Beijing, China, August 1979, pp. 1-17

[11] Aydan, O., Ulusay, R. and Atak, VO., “Evaluation of ground deformations induced by the 1999 Kocaeli earthquake (Turkey) at selected sites on shorelines”, Environ Geol (2008) 54. , 2008, pp. 165–182

[12] Cetin K. O., Seed R. B., Moss R. E. S., Der Kiureghian A., Tokimatsu K., Harder, Jr. L. F., and Kayen R. E., , Field Case Histories for SPT-Based In Situ Liquefaction Potential Evaluation, Geotechnical Engineering Research Report No. UCB/GT-2000109, Department of Civil and Environmental Engineering, California University, Berkeley., 2000

[13] Ishihara. K., ”Stability of Natural Deposits during Earthquakes”, Proc. The 11th International Conf. on Soil Mechanics and Foundation Engineering, San Francisco, 1985, Vol. 1. pp. 321-376

[14] Robertson P. K. and Cabal K.L., Guide to Cone Penetration Testing, GREGG inc., 2010, pp. 42

Fifth International Conference on Geotechnique, Construction Materials and Environment, Osaka, Japan, Nov. 16-18, 2015, ISBN: 978-4-9905958-4-5 C3051

STRENGTH PROPERTIES OF ROAD BASE MATERIALS BLENDED WITH WASTE LIMESTONES

Jonathan R. Dungca[1] and Lydia Francisca T. Dychangco[2]
Gokongwei College of Engineering, De La Salle University, Philippines[1, 2]

ABSTRACT

Most areas in the Philippines experience high road construction cost due to the limited supply of suitable materials for road embankment within economic haul distances. Considering that the country is currently having extensive infrastructure development, potential use of naturally-occuring materials such as limestones was tested resulting not only as an economic alternative to the conventional materials, but leading to an improved strength of roads. Geotechnical and morphological properties of pure and blended materials were determined characterizing the behavior of the strength of the materials as limestone blend varies. A 50% blend of limestone to conventional road base materials provided optimum strength increasing the values up to 30%, 100% and 40% for unsoaked CBR, soaked CBR and UCS, respectively.

Keywords: Limestone, Road Embankment, CBR, Road Base Material

INTRODUCTION

In the Philippines, road construction is one of the prevailing infrastructure developments by the government because of the many inland transport systems used to deliver goods in different regions of the country. High haulage cost due to inflation is one of the constraints in the availability of providing high quality underlying soil layers in most areas of the country. These underlying soil layers known as subgrade, subbase and base act as the foundation of the pavement and its performance is strongly influenced by its stability, bearing strength, consolidation over time and moisture susceptibility. Hence, taking into account the materials and strength requirements of these layers are important in achieving the expected performance of the roads. The possibility of using naturally-occuring materials for road embankments was given emphasis in this study to provide economic solution to this problem.

An abundant resource recognized in this study is limestone. Limestone is a calcium carbonate type of rock that is widely available all over the world, as it constitutes more than 4% of the Earth’s crust. In the Philippines, the Mines and Geosciences Bureau (MGB) projected an estimate of 4 billion metric tons of limestone deposit in 1992. Limestones are potentially known to exhibit characteristics needed for road embankments.

The objective of the study is to determine the suitability of blending waste limestones to conventional materials as a road embankment material and to establish strength properties of different limestone blends. Strength properties considered are the California bearing ratio (CBR), unconfined compressive strength (UCS) and undrained shear strength. Regression analysis was also performed correlating the values of different strength tests with different blend proportions of limestone.

Other than geotechnical properties, physical properties were also considered since the strength is found to be greatly influenced by its mineralogical composition. The mineralogy of the materials was defined through analyzing the mineral peaks from the X-ray Diffraction (XRD) graphs. Furthermore, Scanning Electron Microscope (SEM) was also conducted to determine some of the morphological characteristics of the materials.

MATERIAL SOURCES

Limestone

Limestones coming from Guimaras Island are accredited by the Department of Public Works and Highways (DPWH) of the Philippines for use as material for road construction. Specifically, limestones tested were from Sta. Fe Lime Enterprises, located in Buenavista, Guimaras Island, Philippines. The quarry covers a total area of 350m^2 with an annual extraction rate of 70,000 mertric tons of limestone. Currently, Sta Fe. Limestone quarry have already extracted more than 60% of the area. The company is planning to expand, having an additional four (4) hectares of land to be extracted. The company is in partnership with Dorilag Cement Corp. where they supply lime as the main ingredient for cement.

Conventional Materials

In characterizing the commonly used aggregates in the Philippines, conventional materials for road bases from Batong Angono Aggregates Corporation (BAAC) were examined. Aggregates from BAAC were good representatives of the aggregates in the Philippines considering that BAAC supplied most of the DPWH road projects.

METHODOLOGY

Soil Specimen Preparation

The materials used in the study were oven dried to make sure that materials acquire 0% water content as required for testing. In addition, sieving was done for both conventional materials and limestones to meet the grading requirements provided in the study.

Index Properties

The index properties (i.e. specific gravity, Atterberg limits, particle size distribution and relative density) of both the control mix and limestone-blended conventional road base materials were identified following the ASTM procedures [1]. Index properties defined the material’s basic properties providing basis for further strength behavior analyses.

Blending of Materials

The blending of materials was arithmetically computed following a specific gradation. Specific weights of materials for each range of size were identified and measured satisfying the material requirements for subgrade, subbase and base courses as stipulated in the DPWH standards and specifications for Highways, Bridges and Airports [2]. The study required blending of limestone having different gradation to suitable aggregates to come up with a blend that will meet the gradation specifications. The materials passing No. 4 sieve (4.75mm opening) were mixed at blend proportions of 0, 20, 40, 60, 80 and 100% of limestone by weight, equivalent to 0, 7, 14, 21, 28 and 35% of limestone by total weight, respectively.

Compaction Characteristics

Following the ASTM procedure for Moisture-Density Relationship, compaction characteristics of the materials were determined. Standard Proctor Tests were obtained for each blend wherein nine (9) points were identified in order to acquire precise values of maximum dry densities and optimum moisture contents. Such property enabled the determination of the water content at which the compaction is best.

Strength Tests

CBR strength test (ASTM D1883) was performed under soaked and unsoaked conditions. Under each result, corrections were made due to surface irregularities, depicted by a concave upward behavior at the start of the Stress vs Penetration curve. The strength property is the basis for determination of the materials applicability as road embankment.

The ASTM D2166 was referenced for procedure for the determination of the unconfined compressive strength, a height-to-diameter ratio of 1.65 was considered and was remoulded following the required specimen conditions. The test was also able to estimate the undrained shear strength of the specimens in the wet state.

TEST RESULTS

Geotechnical Properties of Conventional Materials Blended with Different Percentages of Limestone

Specific Gravity

The control and blended specimens showed a decreasing trend of specific gravity as the percentage blend of limestone is increased due to the difference of the weights of minerals in material and the presence of depressed structure within particle surfaces. The behavior of values resulted to an empirical formula showed in Eq. (1).

$$Gs = 2.7775\exp^{0.0009L} \qquad (1)$$

Where:
Gs = specific gravity;
L = limestone content in percent.

Atterberg Limits - Liquid Limit

The results of soil-limestone mixture at different percentages are shown in Fig. 1. Plotting the values provided an empirical formula shown in Eq. (2).

$$LL = 15.33\exp^{0.0031L} \qquad (2)$$

Where:
LL = Liquid Limit.

Evidently, increasing limestone content increases the liquid limit of the blend since limestones have greater tendency to attract water to its particle surfaces. Changes in engineering properties of the aggregates blended with limestone may be due to the cationic exchange, flocculation of the clay, agglomeration and pozzolanic reactions as explained by Thompson [3] and Bell [4].

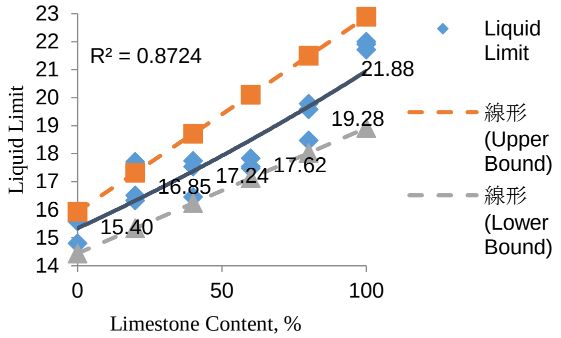

Fig. 1. Liquid Limit vs Limestone Content

Atterberg Limits -Plastic Limit

Soil-limestone mixture makes variations of plastic limit at different percentages as shown in Fig. 2. Similar to the liquid limit, changes in the engineering properties may be due to the reactions mentioned as limestone is blended to crushed aggregates. In addition, the values of plastic limit followed similar behavior as the liquid limit wherein values behaved exponentially generating a correlation shown in Eq. (3).

$$PL = 12.876\exp^{0.0025L} \quad (3)$$

Where :
PL = Plastic Limit.

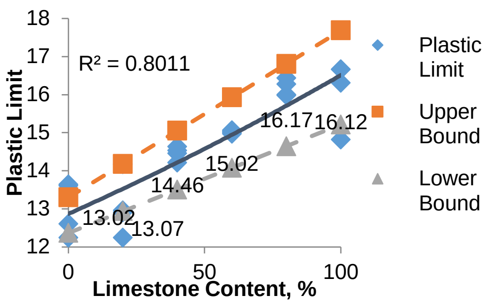

Fig. 2. Plastic Limit vs Limestone Content

Atterberg Limits –Plasticity Index

At different percentages of limestone, deviation in values of plasticity indices is measured as shown in Fig. 3. Similarly, values also formed a correlation wherein values of plasticity indices can be estimated at any limestone content as shown in Eq. (4).

$$PI = 1.8771\exp^{0.0088L} \quad (4)$$

Where:
PI = Plasticity Index.

The results confirmed that the plasticity index increases with increasing limestone content at all percentages. Because both materials exhibit low plasticity characteristics, the combination of the two materials still satisfies the general specification for road embankment which requires that plasticity index not to exceed a value of six (6).

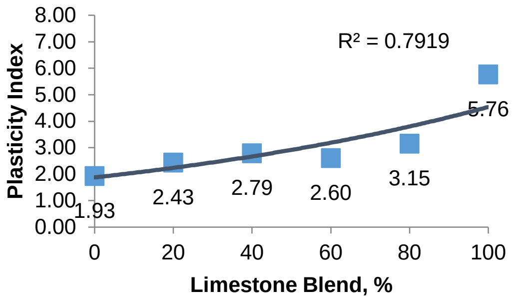

Fig. 3. Plasticity Index vs Limestone Content

Maximum and Minimum Index Densities

In performing tests for identification of maximum and minimum index densities, it was found that in both loosest and densest condition of the materials, values of index densities are decreasing as limestone content is increased. Even though the range of particle size is standardized for this test, it can still vary by volume considering that limestone is larger in volume due to its light weight. As limestone content is increased, more conventional materials are substituted by lighter particle providing drop in unit weight of the limestone- blended materials. Empirical relationships developed are as follows:

$$\text{Max. Index Density} = 22.562\exp^{0.002L} \quad (5)$$
$$\text{Min. Index Density} = 18.101\exp^{0.002L} \quad (6)$$

The exponential behavior of the data provided correlation of values wherein index densities can be obtained at any given limestone blend.

Compaction Characteristics

The Standard Proctor Test was performed following the ASTM D698 procedures in order to obtain the exact amount of moisture needed in sample preparation for strength tests. The results in the determination of optimum moisture content (OMC) and maximum dry density (MDD) are summarized in Table 1:

Table 1 Summary of OMC and MDD Values for Each Blend

Limestone Content, %	OMC, %	MDD, kN/m^3
0	5.00	24.23
20	5.56	23.05
40	5.98	22.18
60	6.63	22.09
80	7.98	21.68
100	9.54	21.08

As shown in Table 1, the MDD decreases while the OMC increases with increasing percentage of limestone. Considerable agglomerations of smaller particles of limestone occur resulted to larger ones, which prohibit the specimens to be properly compacted. This happens when there is cationic exchange wherein higher valence cations replace those with lower valence and larger cations replace those that are smaller having same valence. With the voids not filled up as much, the MDD then decreases. It can easily be seen that the limestone has lighter weight as compared to the conventional materials because of its mineralogical composition. On the other hand, the OMC increases mainly due to the additional water held within the flocculated soil structure. The increase in fines content as well as the high affinity of limestone to water caused the increase in OMC as percentage blend of it is increased. According to Akoto and Singh [5], increase in water is needed for providing more Ca^{2+} ions for the cation exchange reaction. As observed, large drop of MDD is experienced with increasing limestone content up to 40%. Okagbue and Yakubu [6] explained that the initial drop is due to the flocculation and agglomeration of the clay particles due to the cation exchange reaction. Smaller decrease in MDD as more limestone is added is due to the replacement of particles of limestone, which have comparatively low specific gravity with that of the conventional road base materials.

Plotting the behavior of MDD and OMC at different limestone content gave an empirical formulas shown in Eq. (7) and (8), respectively.

$$\text{MDD,kN/m}^3 = 23.881\exp^{0.001L} \quad (7)$$

$$\text{OMC,\%} = 4.9213\exp^{0.0061L} \quad (8)$$

Where:
MDD = maximum dry density;
OMC =optimum moisture content.

The empirical formulas obtained provided exponential behavior for both property in which values of MDD and OMC can be determined at any limestone blend.

Strength Characteristics of Conventional Materials Blended with Different Percentages of Limestone

California Bearing Ratio- Unsoaked condition

Remarkable values of CBR under unsoaked condition were obtained providing good performance for road subgrade, sub-base and base. On the average, different CBR values were obtained for each blend providing an empirical relationship shown in Eq. (9).

$$\boldsymbol{CBR_{Unsoaked}}, \% = \mathbf{-0.0107}\boldsymbol{L^2} + \mathbf{0.9194}\boldsymbol{L} + \mathbf{50.351} \quad (9)$$

Where:
$CBR_{unsoaked}$ = unsoaked CBR of the specimen.

Given this model that will produce the maximum CBR value, it can be computed that the blend accounts to blend L42.96-C57.04. This is likely to give an approximate CBR value of 70%. Comparing the unsoaked CBR strength value of 53.75% provided by the controlled specimens to the optimum blend with unsoaked CBR value of 70%, it can be concluded that optimum blend can increase the strength by 30%. The behavior of the CBR value is increasing until it reached the 42.96% blend of limestone and eventually decreases as it approaches 100%. The increase of strength of the blended materials with increasing limestone content is mainly due to the considerable plasticity of limestone. This provides binding property among particles that allows the material to gain strength. The cohesive strength limestone provided increased the over-all strength of the specimen. Other authors working on the soil-limestone mixture noted similar behavior. Newbauer and Thompson [7] explained that the increase in strength may be due to the immediate reaction endowed by the cation exchange and the flocculation and agglomeration reactions, while Van Ganse [8] postulated that this is due to the formation of crumbs of soils maintaining their individuality when the mixture is compacted.

On the other hand, increasing the limestone blend to more than 42.96% decreased the over-all strength of the specimen. Although the cohesive strength of the blend increases, there is a point in which the frictional strength is affected by the reduction of conventional materials due to the increase in volume of the limestone. Frictional strength is contributed by large particles and high cohesive strength would mean lesser contact of larger particles with each other thus, a drop of frictional strength.

California Bearing Ratio- Soaked condition

To test the strength of the limestone-blended materials at its worst condition, CBR values for soaked condition were also identified. The values demonstrated good performance resulting to CBR values greater than 20. The blend that is anticipated to attain the peak strength is L50-C50, which will give a CBR value of 60% based on the empirical relationship as shown in Eq. (10).

$$\boldsymbol{CBR_{Soaked}}, \% = -\mathbf{0.0102}\boldsymbol{L}^{2} + \mathbf{0.9976}\,\boldsymbol{L} + \mathbf{50.35} \quad (10)$$

Where:
CBR_{soaked} = the soaked CBR of the specimen.

Being able to determine the optimum strength enabled the estimation of percentage increase in strength of the optimum blend with respect to the controlled specimen. With a soaked CBR value of 30% and 60% for controlled and optimum blend respectively, a 100% increase in strength is realized.

It can be observed that CBR values from soaked condition is lesser compared to that of the CBR values under unsoaked condition. This is due to the permeation of water in soaked condition decreasing its strength. The behavior of CBR values under soaked condition is similar to that of the unsoaked condition. Reporting the swell of the materials after four (4) days of soaking period, it was observed that on the average, swell of materials on all blends have no significant value accumulating less than 1% swell.

Unconfined Compressive Strength

To further verify the results provided by CBR tests, the Unconfined Compressive Strength (UCS) test was conducted. This quickly estimates the undrained shear strength of the material. The empirical relationship was determined to describe the strength behavior as limestone content varies forming an empirical formula shown in Eq. (11).

$$\boldsymbol{UCS}, \boldsymbol{kPa} = -\mathbf{0.0087}\boldsymbol{L}^{2} + \mathbf{0.8254}\boldsymbol{L} + \mathbf{47.301} \quad (11)$$

Where:
UCS = unconfined compressive strength

With this equation, L50-C50 is found to generate the optimum strength value of 70kPa. Comparing the UCS of controlled specimen to that of the optimum blend, an increase of 40% in strength is observed. The behavior of the results followed a parabolic curve concaving downward which entails that a 50% limestone substitution to the fine aggregates would produce maximum strength of the specimen since it adds cohesion to the strength of material owing to its binding characteristics. Since undrained shear strength can be estimated with results obtained in the UCS, it can be concluded that this property exhibited similar behavior with that of the UCS. According to Lees et al. [9] and Bell [10], the increase in strength may be due to the formation of larger particles, making it behave as coarse-grained, strongly bonded, particulate material. Nonetheless, further increase of limestone would tend to decrease its over-all strength due to the drop of frictional strength as an effect of the domination of fine particles in volume. This permits less contact of coarse particles with one another leading to loss of friction.

CONCLUSION

Having analyzed the different properties and strength characteristics of road base materials blended with limestones at different percentages, the following conclusions were made:

Waste limestones from Guimaras Island, Philippines can be utilized in road construction considering that replacing 100% of the fine aggregates with limestone yielded to acceptable values of CBR for both soaked and unsoaked conditions;

From the empirical relationships given by the strength parameters considered, it can be concluded that a range of 40% to 50% blend of limestone would optimally give the most favorable strength for both unsoaked and soaked CBR and UCS. Comparing the strength values of optimum blend to purely conventional materials, a remarkable increase of up to 30% for unsoaked CBR, up to 100% for soaked CBR and upto 40% to unconfined compressive strength values were realized;

ACKNOWLEDGEMENTS

We would like to extend our deepest gratitude to DOST-ERDT for providing financial assistance for this research. We also thank LaFarge for their samples of road base materials. Also, the study would not be possible without the help of the DLSU Civil Engineering Faculty.

REFERENCES

[1] American Society for Testing and Materials (2004). “ASTM Standards on Transportation Applications”.
[2] Department of Public Works and Highways (2004) “Standard specification for Highways, Bridges and Airports”.
[3] Thompson M.R. (1965), “Influence of Soil Properties on Lime-Soil Reactions”, Public Works 96: 120-123.
[4] Bell F.G. (1993), “Engineering treatment of Soils”, Chapman and Hall, London.
[5] Akoto B.K.A. and Singh G. (1981), “Some geotechnical properties of Lime-Stabilized laterite containing a high proportion of aluminum Oxide”, Eng Geol: 85-100
[6] Okagbue, C.O. and Yakubu J.A. (2000), “Limestone Ash waste as a Substitute for Lime in Soil Improvement for Engineering construction”, Bulletin of engineering Geology and the Environment. Vol 5 No. 2, pp 107-133.
[7] Newbauer H. and Thompson M.R. (1972), “Stability Properties of Uncured Lime-Treated Fine-Grained Soils”, Highw Res Rec 381: 20-26.
[8] Van Ganse R. F. (1974), “Immediate Amelioration of Wet Cohesive soils by quick Lime”, Transp Res Rec 501: 42-53.
[9] Lees G., Abdelkader M.O., Hamdani S.K. (1982) “Effect of Clay Friction on Some Mechanical Properties of Lime-Soil Miztures”, J. Inst Highw Wng 29: 209-220.
[10] Bell F. G. (1989) “Lime Stabilization of clay Soils”, Bull IAEG 39:67-74.

Fifth International Conference on Geotechnique, Construction Materials and Environment, Osaka, Japan, Nov. 16-18, 2015, ISBN: 978-4-9905958-4-5 C3051

BEARING CAPACITY OF STRIP FOOTINGS ON CLAYS WITH INCREASING SHEAR STRENGTH

Seyednima Salimi Eshkevari[1], Andrew J. Abbo[2]
[1, 2] Australian Research Council Centre for Geotechnical Science and Engineering, School of Engineering, University of Newcastle, Australia

ABSTRACT

This paper considers the bearing capacity of surface strip footings sitting on a deep layer of clay soil with shear strength profile that increases linearly with depth. While an exact solution for the bearing capacity has previously been obtained using the method of characteristics, it is not in a form that is convenient for accurate evaluation. Significant research has been done previously in this area. In those works however, the focus has been on the techniques rather than practical application and the results are either presented for limited cases or summarised in graphs that are not easy to interpret in same range of parameters. In the present study, Finite Element Limit Analysis (FELA) is used to compute rigorous upper and lower limits on the ultimate bearing capacity of strip footings resting on the non-homogeneous clay layer. The results of the numerical limit analysis, which bracket the true bearing capacity within a range of typically less than 2%, compare well with the exact solutions available in the literature. New expressions are provided for the bearing capacity in which the bearing capacity factor is expressed as a simple function of the dimensionless rate of increase of soil strength.

Keywords: Bearing capacity, Non-homogenous clay, Increasing shear strength

INTRODUCTION

A nonhomogeneous shear strength profile is a common situation encountered in geotechnical engineering when considering normally consolidated or lightly over-consolidated clays. In such soils the undrained shear strength (c_u) tends to increase almost linearly with depth. As show in Fig. 1, the shear strength profile of such soils is usually described in terms of the rate of increase in shear strength with depth (*ρ)*. The rate of increase may be expressed as dimensionless quantity $\rho B/c_0$ where B is the footing width and c_0 is the undrained shear strength of clay at the foundation level [1]. The rate of increase in shear strength (*ρ)* is known to be an inherent soil property, varying in the range of (0.6~3.0 kPa/m) which may be estimated as a product of soil effective unit weight (γ') and $\Delta c_u/\Delta\sigma'_v$ that is the rate of increase in c_u due to the increase in the soil effective vertical consolidation stress [2]. The soil effective unit weight and $\Delta c_u/\Delta\sigma'_v$ vary in the range of (4~10 kN/m^3) and (0.15~0.3) respectively [2]. The influence of clay non-homogeneity on the bearing capacity of footings is particularly significant in the offshore engineering, where large diameter shallow foundations are installed over normally consolidated sea bed producing very high degrees of non-homogeneity; However the benefits of considering increasing shear strength profile of soil is not limited to offshore practice.

Many researchers have previously considered the influence of soil increasing shear strength on the bearing capacity of footings. The earliest recommendations on the bearing capacity of the footings over non-homogeneous clays (q_u) are given by Terzaghi [3] and Skempton [4] who suggested an average bearing capacity factor to be calculated over a shallow depth underneath the footing. Limit Equilibrium was utilised by Nakase [5], using a circular slip surface. This method was later repeated by Raymond [6] that in general, overestimates the true ultimate bearing capacity of the footing. Limit analysis techniques have been a popular approach amongst the researchers with many upper bound estimates of bearing capacity [7]-[14].

One of the best approaches to calculate the bearing capacity of footings over non-homogeneous soils is provided by Davis and Booker [1] who employed the method of characteristics to obtain the bearing capacity of both smooth and rough footings resting on clay of increasing shear strength with depth. They derived an exact expression for the bearing capacity of the form

$$q_u = F[(2+\pi) + \rho B/4] \tag{1}$$

where the factor F is a function of $\rho B/c_0$. No analytic expression was provided for F with values provided in a simple graph for $\rho B/c_0$ ranging from zero to 30. Values of F are not easy to read accurately from the graph, particularly in the lower range of $\rho B/c_0$. This method was later used by Houlsby and Wroth [15] who used the same techniques to obtain solutions for circular footings. The bearing capacity software of Martin [16] which

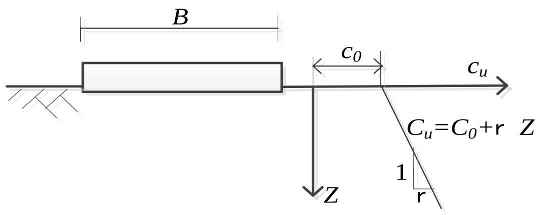

Fig. 1 The shear strength profile of the soil.

is based on the method of characteristics can also be used to find the upper and lower bounds of q_u for footings on non-homogenous clay. Tani and Craig [2] used this method to solve the problem of skirted foundations over non-homogenous clay for both plane strain and axisymmetric conditions. Other numerical methods such as finite elements and finite difference have also been utilised to investigate bearing capacity of these soils; for example Yun and Bransby [11] and others [17]-[21].

In comparison to the number of theoretical studies, there are only a few experimental results reported in the literature due to difficulties regarding the scale rule for physical modelling [2]. The centrifuge tests performed on surface strip footings by Nakase [22] and Kimura and Takemura [23] are examples of experimental studies undertaken on footings over non-homogeneous clay. In addition, some centrifuge tests performed on skirted foundations are reported by Tani and Craig [2], Prevost *et al.* [24] and more recently by Gourvenec and O'loughlin [25].

Modified bearing capacity factor defined as ($N_c=\frac{q_u}{c_0}$) is used by most researchers to present the results of the analysis which is only a function of $\rho B/c_0$. The variation of N_c is either plotted versus $\rho B/c_0$ in a graph or is given in a table for limited values of $\rho B/c_0$. It is difficult to accurately interpret N_c from these graphs, especially in the lower range of $\rho B/c_0$ and the values given in the tables are for limited number of $\rho B/c_0$. Presenting expressions that can well approximate N_c can be helpful for engineers. Bransby [26] proposed the following expression for rough strip footings using the results of Davis and Booker [1], Tani and Craig [2] and Houlsby and Wroth [15].

$$N_c = (2+\pi)+1.646\left(\frac{\rho B}{c_0}\right)^{0.662} \quad \textbf{(2)}$$

However this expression is not a safe estimate of bearing capacity as it over-estimates the results presented by abovementioned researchers [11] .

Finite Element limit Analysis (FELA) is used in the present study to investigate the bearing capacity of a rough strip footing sitting on the surface of a clay soil with increasing undrained shear strength profile. The results of the analysis provided very tight upper and lower bounds of the exact solutions for $\rho B/c_0$ ranging from zero to 30. This is done to derive accurate expressions to predict modified bearing capacity factor for a practical range of $\rho B/c_0$. Although the exact solution of Davis and Booker [1] is already available, it is not easy to accurately obtain equivalent modified bearing capacity factor from their presented graph of F. The average of limit loads were used to calculate N_c and two expressions were found using curve fitting technique to calculate N_c very accurately for rough strip footings over the whole practical range of $\rho B/c_0$.

METHODOLOGY

A parametric study was performed over a range of material properties and footing widths that are typically encountered in the design of strip footings. The study considers values of ρ between 0.1 to 3.0 kPa/m and B and c_0 varied between 1.0 to 150 m and 10 to 60 kPa respectively. FELA is a finite element method formulated from the limit theorems of plasticity. The FELA formulation used in this research is based on the method originally developed by Sloan [27] and [28] using linear programing methods. The formulations have been further developed later, applying non-linear programing as was described by Lyamin *et al.* [29] and [30]. The current formulation also benefits from adaptive re-meshing technique of Lyamin *et al.* [31] and [32].

Soil was modelled as an associated Mohr-Coulomb material. A gradient and a reference point in the geometry was introduced to the software in addition to the absolute value of the undrained shear strength of the clay to model the increasing shear strength of the clay with depth. Adaptive re-meshing technique allowed tighter upper and lower bounds of the true solutions. The target solution accuracy, number of adaptive re-meshing and the starting number of elements were set so to obtain bounds around 1% of the exact solution by Davis and booker [1]. The results of maximum power dissipation and direction of velocity vectors were used to capture the failure mechanism of the problem. The average of upper and lower limit loads was used to calculate the ultimate bearing capacity of the footing following Salgado *et al.* [33] and the bearing capacity factor N_c was calculated using the average q_u. Finally expressions were found for N_c as a function of $\rho B/c_0$ using curve fitting, which well presents the results of the analysis for all practical values of $\rho B/c_0$.

RESULTS AND DISCUSSIONS

The results of this study are presented in terms of the bearing capacity factor N_c that can be used

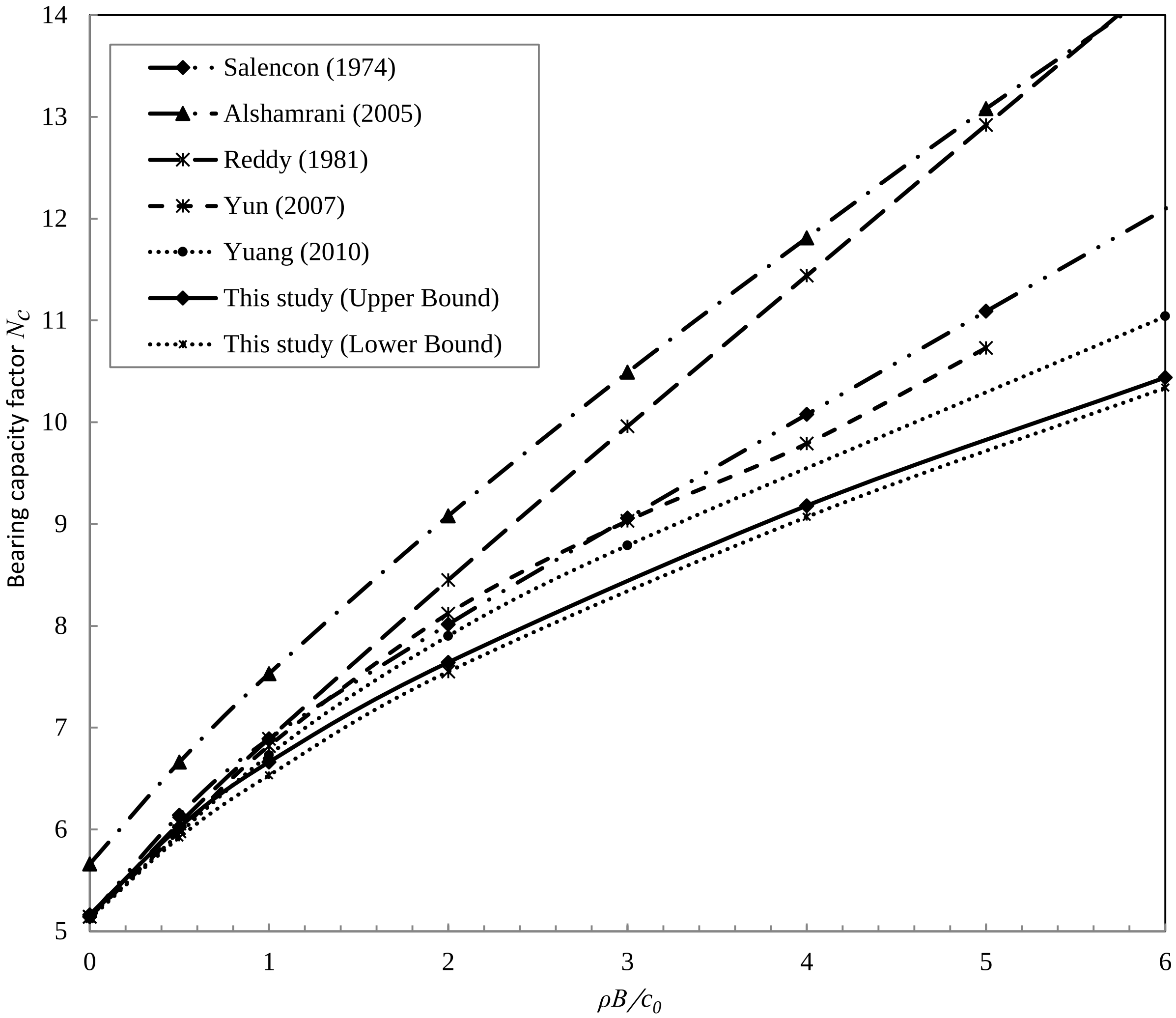

Fig. 2 Comparison of FELA results to upper bounds of others.

together with conventional bearing capacity theory. N_c is presented as a function of $\rho B/c_0$ in the graphs of Fig. 3 and Fig. 4. The range of $\rho B/c_0$ less than 2 presented in Fig. 3 is more appropriate for strip footings while the range of $\rho B/c_0$ between 2 and 30 shown in Fig. 4 may be used for large rectangular footings in offshore practice. Figure 2 indicates the upper and lower bounds of N_c obtained in this study together with the upper bound solutions of [7], [8], [10], [11] and [14]. The range of $\rho B/c_0$ shown in Fig. 2 is based on available data in the literature.

It can be seen that the upper bound of N_c is the lowest of all other available upper bound solutions in the literature and are close to those obtained from method of characteristics provided by [1], [2], [15] and [16] that are presented in Table 1. The bearing capacity factors calculated by Reddy [8] and Alshamrani [10] are over predicted significantly as ($\rho B/c_0$) increases. The accuracy of the upper bound solutions depends on the assumed failure mechanism which will be discussed later. The lower bound calculations provide very close results to these upper bounds (maximum 2% apart).

The average of the computed upper and lower bounds of N_c are plotted in Fig.3 and Fig. 4 together with the best fits for each case. The following expressions shown by Eq. (2) and Eq. (3) were obtained using curve fitting technique which is very accurate and simple to be used in design.

$$N_c = -4.29\ e^{(-0.41\rho B/c_0)} + 9.46 \qquad \rho B/c_0 < 2 \qquad (3)$$

$$N_c = 1.36(\rho B/c_0)^{0.73} + 5.37 \qquad \rho B/c_0 \geq 2 \qquad (4)$$

These expressions provide the almost exact value of the modified bearing capacity factors with excellent accuracy that can conveniently be used by engineers. Using separate expressions of N_c for cases with $\rho B/c_0$ greater than and less than two increased the accuracy of curve fitting. More over for widths of strip footings more usually encountered in engineering practice, $\rho B/c_0$ will be typically less than two. In the graphs of Fig. 3 and Fig. 4 the

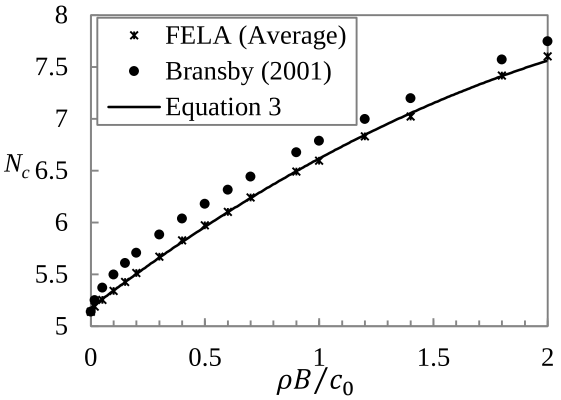

Fig. 3 Bearing Capacity Factor (N_c) for $\rho B/c_0$ <2.

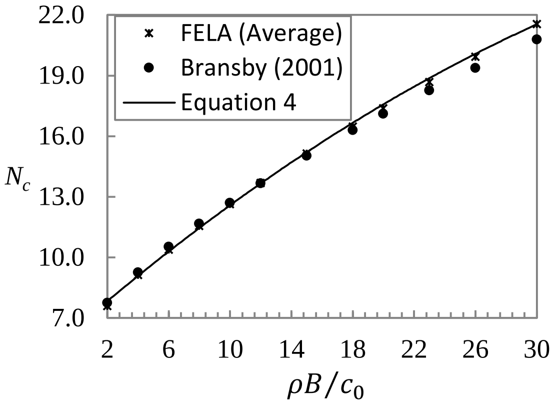

Fig. 4 Bearing capacity factor (N_c) for $\rho B/c_0$ ≥2.

Table 1 Bearing capacity factors (N_c).

Nc	FELA Lower bound	FELA Upper bound	FELA Average	Houlsby and Wroth (1984)	Tani *et.al.* (1995)	ABC Software Martin (2003)	Gourvenec and Randolph (2003)	Gourvenec *et.al* (2011)
0	5.12	5.16	5.14	5.14	5.14	5.14	5.20	5.16
0.5	5.92	6.02	5.97	-	-	5.97	-	-
1.0	6.53	6.66	6.60	-	6.84	6.61	6.70	-
2.0	7.55	7.64	7.60	7.57	7.75	7.60	7.71	-
3.0	-	-	-	-	-	8.41	8.55	-
4.0	9.07	9.18	9.13	9.08	9.23	9.13	-	-
5.0	-	-	-	-	-	9.79	-	9.82
6.0	10.34	10.44	10.39	10.37	10.49	10.42	10.62	-
7.0	-	-	-	-	-	11.01	-	-
8.0	11.51	11.61	11.56	11.52	-	11.58	-	-
10.0	12.59	12.69	12.64	12.67	12.73	12.67	12.95	-
15.0	15.05	15.21	15.13	-	-	15.14	-	-
20.0	17.31	17.44	17.38	-	-	17.40	-	17.46
30.0	21.46	21.63	21.55	-	21.69	21.58	-	-

bearing capacity factor calculated from Eq. (1) by Bransby [26] is also plotted for comparison. It is clear that Eq. (1) overestimates *Nc* in the range of $\rho B/c_0$ less than 2 and underestimates N_c for $\rho B/c_0$ greater than 20.

The best solutions for bearing capacity of strip footings over non-homogenous clays have been obtained using method of characteristic and recently by some finite element models. Some of the most accurate results published so far are presented in Table 1, together with lower bound, upper bound and the average values of *Nc* calculate in this study. The average values compare very well with the exact solution provided by Davis and Booker [1] and are in excellent agreement with the results presented by Houlsby and Wroth [15] and those obtained using the bearing capacity software written by Martin [16]. The limited cases presented by Gourvenec et.al [21] are very close to the average of FELA and the results by the above mentioned researchers, while calculated *Nc* by Tani et al. [2] and Gourvenec et.al 18] slightly over estimates the true bearing capacity factors.

Failure mechanism

The results of maximum power dissipation from the upper bound analysis indicate the failure mechanism of the footing, providing the lowest upper bound to the ultimate load on the footing. The influence of the degree of non-homogeneity on the mode of failure has been studied here and a comparison is made between the obtained failure mechanisms from this study and the ones proposed by Yun *et.al.* [11]. Figure 5a indicates the failure mechanism for $\rho B/c_0 = 2$. It can be seen that the failure mechanism is limited to much shallower depth compared to Prandtl failure mechanism [34].

The optimum failure mechanism presented by Yun *et al.* [11] is also plotted in this figure and these are representative of the collapse mechanisms that can be interpreted from the bands of high power dissipation intensity. Figure 5b shows observed failure mechanism for a higher degree of non-homogeneity. It can be seen from both the results of Yun *et al.* [11] and from the FELA analysis that as $\rho B/c_0$, increases the failure mechanism becomes shallower to the regions of the soil profile where the soil is weaker. However, the proposed failure mechanism by Yun *et al.* [11] does not quite capture the failure mechanism for the case of $\rho B/c_0$ equal to 5 in the area directly beneath the footing as it omits the wedge directly beneath the footing. The results of upper bound analysis indicated that the failure mechanism for very high degrees of non-homogeneity ($\rho B/c_0$ of 20) follows the same pattern as shown in Fig. 5b, however the triangular rigid block under the footing becomes much smaller.

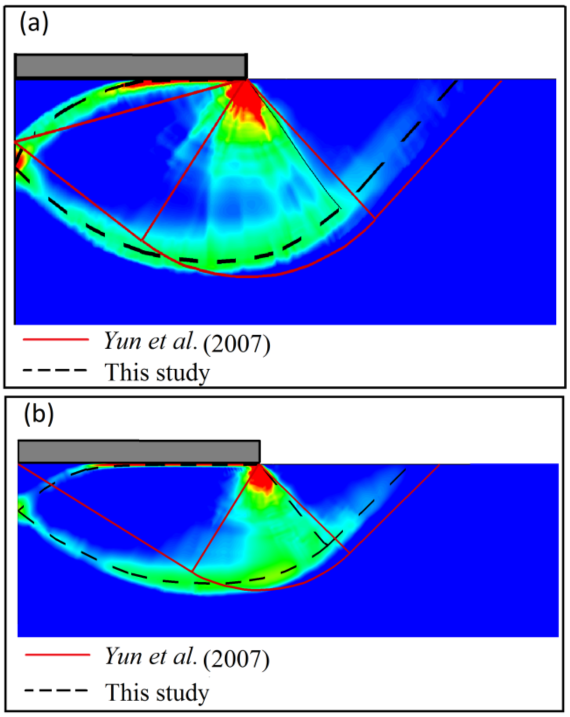

Fig. 4 Power dissipation intensity from upper bound analysis showing failure mechanism of Yun *et al.* [11] for (a) $\rho B/c_0$=2 (b) $\rho B/c_0$=5.

CONCLUSION

Rigorous upper and lower bounds on the ultimate bearing capacity of strip footing over non-homogenous clays were calculated using FELA technique. The average of the limit loads were in very close agreement with the exact solutions of Davis and Booker [1] and were used to derive expression for the modified bearing capacity factor (N_c). These expressions can conveniently be used to estimate with high accuracy the ultimate bearing capacity of strip footings over clays with increasing shear strength in depth. A comparison between the failure mechanisms observed in this study with the assumed failure mechanisms by Yun *et al.* [11] indicated that better agreement exists for lower degrees of non-homogeneity ($\rho B/c_0$=2) and the general shape of the failure mode remains the same as $\rho B/c_0$ increases but smaller rigid block is seen for higher values of $\rho B/c_0$.

ACKNOWLEDGMENT

The authors wish to express their gratitude to Professor Andrei Lyamin for providing and maintaining the Finite Element Limit Analysis software and his guidance and support in its use.

REFERENCES

[1] Davis, E. H. & Booker, J. R. The effect of increasing strength with depth on the bearing capacity of clays, Géotechnique, 23, 1973, pp. 551-563.
[2] Tani, K. & Craig, W. H. Bearing capacity of circular foundations on soft clay of strength increasing with depth, Soils and Foundations, 35, 1995, pp. 21-35.
[3] Terzaghi, K. & Peck, R. B. Soil mechanics in engineering practice, New York, John Wiley and Sons, 1948.
[4] Skempton, A. W. The Bearing Capacity of Clays, Building Research Congress, 1951, pp. 180-189.
[5] Nakase, A. Bearing Capacity of Cohesive Soil Stratum, port and Harbor Research, 1966.
[6] Raymond, G. P. The Bearing Capacity of large footings and Embankments on clays, Géotechnique, 17, 1967, pp. 1-10.
[7] Salençon, J. Discussion: The effect of increasing strength with depth on the bearing capacity of clays, Géotechnique, 24, 1974, pp. 449-451.
[8] Reddy, A. S. & Rao, K. N. V. Bearing capacity of strip footing on anisotropic and nonhomogeneous clays, Soils and Foundations, 21, 1981, pp. 1-6.
[9] Kusakabe, O., Suzuki, H. & Nakase, A. An upper bound calculation on bearing capacity of a circular footing on a non-homogeneous clay, Soils and foundations, 26, 1986, pp.143-148.
[10] Al-shamrani, M. A. Upper-bound solutions for bearing capacity of strip footings over anisotropic nonhomogeneous clays, Soils and Foundations, 45, 2005, pp. 109-124.
[11] Yun, G. & Bransby, M. F. The undrained vertical bearing capacity of skirted foundations, Soils and Foundations, 47, 2007, pp. 493-505.
[12] Huang, M., Qin, H. & Guo, Y. Upper bound solution for bearing capacity of nonhomogeneous and anisotropic clay

foundation, Yanshilixue Yu Gongcheng Xuebao/Chinese J. of Rock Mechanics and Engineering, 27, 2008, pp. 511-518.
[13] Qin, H. L., Huang, M. S., Wang, Y. J. & MA, S. K. Calculations of Nc for anisotropic and nonhomogeneous soils, Yantu Gongcheng Xuebao/Chinese J. of Geotechnical Engineering, 32, 2010, pp. 1194-1199.
[14] Yang, F., Zhao, L. H. & Yang, J. S. Upper bound ultimate bearing capacity of rough footings on anisotropic and nonhomogeneous clays, Yantu Lixue/Rock and Soil Mechanics, 31, 2010, pp. 2958-2966.
[15] Houlsby, G. T. & Wroth, C. P. Calculation of Stresses on Shallow Penetrometers and Footings, Seabed Mechanics, Denness, B. ED. Springer Netherlands, 1984, pp. 107-112.
[16] Martin, C. M. New software for rigorous bearing capacity calculations, BGA Int. Conf. on Foundations, Innovations, Observations, Design and Practice, 2003, pp. 581-592.
[17] Griffiths, D. V. Computation of bearing capacity on layered soils, Numerical methods in geomechanics, Proc. 4th Int. conference, Edmonton, Volume 1, 1982, pp. 163-170.
[18] Gourvenec, S. & Randolph, M. Effect of strength non-homogeneity on the shape of failure envelopes for combined loading of strip and circular foundations on clay, Geotechnique, 53, 2003, pp. 575-586.
[19] Zhao, S. F., Luan, M. T., Fan, Q. L., LU, A. Z. & Yuan, F. F. FLAC-based numerical analyses of bearing capacity and failure mechanism of strip and circular footings on nonhomogeneous foundations, Yantu Lixue/Rock and Soil Mechanics, 27, 2006, pp. 1909-1914+1921.
[20] Bransby, M. F. & Yun, G. J. The undrained capacity of skirted strip foundations under combined loading, Geotechnique, 59, 2009, pp.115-125.
[21] Gourvenec, S. M. & Mana, D. S. K. Undrained vertical bearing capacity factors for shallow foundations, Geotechnique Letters, 1, 2011, pp.101-108.
[22] Nakase, A., Kusakabe, O. & Wong, S.-F. Centrifuge model tests on bearing capacity of clay, J. of Geotechnical Engineering, 110, 1984, pp. 1749-1765.
[23] Kimura, T. & Takemura, J. A study on the deformations and bearing capacities of normally consolidated clay layers under strip loading, Doboku Gakkai Ronbunshu, 1987, pp. 157-166.
[24] Prevost, J. H., Cuny, B. & Scott, R. F. Offshore gravity structures: centrifugal modelling, J. of the geotechnical engineering division, 107, 1981, pp. 125-141.
[25] Gourvenec, S. & O'loughlin, C. D. Drum centrifuge tests of shallow skirted foundations on soft clay, Proc. of the 6th Int. Conf. on Physical Modelling in Geotechnics, 2006, pp. 645-650.
[26] Fraser Bransby, M. Failure envelopes and plastic potentials for eccentrically loaded surface footings on undrained soil, Int. J. for Numerical and Analytical Methods in Geomechanics, 25, 2001, pp. 329-346.
[27] Sloan, S. W. Lower bound limit analysis using finite elements and linear programming, Int. J. for Numerical and Analytical Methods in Geomechanics, 12, 1988, pp. 61-77.
[28] Sloan, S. W. Upper bound limit analysis using finite elements and linear programming, Int. J. for Numerical & Analytical Methods in Geomechanics, 13, 1989, pp. 263-282.
[29] Lyamin, A. V. & Sloan, S. W. Lower bound limit analysis using non-linear programming, Int. J. for Numerical Methods in Engineering, 55, 2002, pp. 573-611.
[30] Lyamin, A. V. & Sloan, S. W. Upper bound limit analysis using linear finite elements and non-linear programming, Int. J. for Numerical and Analytical Methods in Geomechanics, 26, 2002, pp. 181-216.
[31] Lyamin, A. V., Krabbenhøft, K., Sloan, S. W. & HJIAJ, M. An adaptive algorithm for upper bound limit analysis using discontinuous velocity fields, ECCOMAS 2004 - European Congress on Computational Methods in Applied Sciences and Engineering, 2004.
[32] Lyamin, A. V., Krabbenhoft, K. & Sloan, S. W. Adaptive limit analysis using deviatoric fields, Proc. of the 6th Int. Conf. on Adaptive Modeling and Simulation, ADMOS 2013, pp. 448-455. 2013.
[33] Salgado, R., Lyamin, A. V., Sloan, S. W. & Yu, H. S. Two- and three-dimensional bearing capacity of foundations in clay, Geotechnique, 54, 2004, pp. 297-306.
[34] Prandtl, L. Uber die Harte plasticher KBrper, Nachrichten von der KBniglichen Gesellschaft der Wissenschaften, GBttingen, 1920.

DRAINAGE SYSTEM OF PRAMBANAN TEMPLE YARD USING NO-FINE CONCRETE OF VOLCANIC ASH AND BANTAK MERAPI

Ahmad Rifa'i[1], Nor Puji Lestari[2] and Noriyuki Yasufuku[3]
[1,2]Dept of Civil and Environmental Engineering, Faculty of Engineering, Universitas Gadjah Mada, Indonesia; [3]Dept of Civil and Structural Engineering, Kyushu University, Japan

ABSTRACT

This paper focuses on the potential utilization of volcanic ash and coarse volcanic slag for no-fine concrete for drainage structure of Prambanan temple yard. This material produced from volcanic eruption also becomes environmental important issues as waste material if it is not effectively reduced or reused. Coarse volcanic slag is commonly known by local people as *Bantak.* The experimental study was conducted to determine engineering properties of no-fines concrete materials and discharge capacity of drainage system was calculated to identify the optimal dimensions of the drainage channel. In addition, a numerical analysis was carried out using SAP2000 and Plaxis to control structure stability. Based on numerical and experimental study, the utilization of no-fine concrete from volcanic ash and *bantak* by using certain mix design can be used as a porous drainage structure. By utilizing the eco-friendly material as structural material, the originality of the building will not be disturbed.

Keywords: Volcanic Ash, Coarse Volcanic Slag, No-Fines Concrete, Drainage System, Prambanan Temple Yard

INTRODUCTION

As one of UNESCO World Heritage, Prambanan Temple is the largest Hindu temple in Indonesia that needs to be preserved, maintained, and conserved. Due to heavy equipment activities during renovation period after Yogyakarta earthquake in May 2006, soil in the temple yard has become dense, and ponding often occurred during rainfall as ilustrated in Figure 1. This condition shows that existing drainage system is not sufficient and needs more effort to organize and improve the drainage systems in the First Yard of Prambanan Temple.

Fig. 1 Ponding area in Prambanan Temple Yard

The water flow in the soils has a significant influence in any civil engineering project, especially related to drainage system. Reference [1] shows the pore space in the soils or rock is a very influential factor in hydrogeological problems, because the water or its movement occured in the pore space. Water flow appearing in the soil is normally occured because of the interconnection of pore spaces or cracks and this is the potential ability of soils/ rock to drain water.

Seepage control on geotechnical structures is needed to lower the ground water level base surface that is aimed to be protected or strengthened regarding to prevent ponding water on the ground surface. Ditch or channel is an effort to collect and control water run off in the saturated soils condition. The functions of porous media are both as a drainage medium and a filter to separate suspension particles from water, so the particles won't be carried away with the water flow.

Refrence [2] shows that the use of clay and concrete as impermeable media is a misconception because the water still flows through the exposed surface of the material, but the water does not seep significantly due to the low permeability of materials. No-fine concrete is one of concrete type that use a little or even zero fine aggregate material, so it has more pores than normal concrete. No-fine concrete aggregate increase permeability and reduce the proportion of cement, but the compressive strength value obtained is lower than normal concrete.

One of the alternatives to reduce post rain-puddle in Prambanan temple yard is by application of no-fine concrete as drainage structure regarding to the ability to drain of water, so the application of the concrete will not lead reduction of the soil shear strength due to long time inundation of land surface. The aggregate developed in this study was the Merapi eruption material. Merapi eruption material is used because of the easiness to find these materials in large quantities along the river and the ineffectiveness of utilization of this material. This material is low quality of porous gravel (*bantak*) and volcanic ash.

Coarse volcanic slag is commonly known by the local people around Merapi volcano, Yogyakarta, Indonesia as *bantak*. *Bantak* are the materials product from the eruption of a volcano together with sand, which represent lightweight gravel. *Bantak* is a gravel sized as a waste material of sand mining. Based on the research conducted at the Department of Civil and Environmental Engineering UGM, structurally, *bantak* has low structural strength, so it is not too familiar for building materials.

Indonesia is one of the most countries that has a number of active volcanoes. Eruption often occurs with high intensity. Spilled lava and volcanic material out from core of the earth makes the area around the volcano has a thick layer of volcanic ash. A lot of volcanic material will become important environmental issues as a waste if it is not effectively reduced or reused. Literatures related with characterization and utilization of volcanic ash and coarse volcanic slag in geotechnical field are limited. It becomes a new approach in a view of environmental aspect.

This study focuses on replacement of cement and coarse aggregate with volcanic ash and *bantak* to produce more economical and eco-friendly concrete product. The results of this research are expected to be able to contribute on engineering practice as well as give advantages in geo-environment view. Study and analysis on no-fines concrete as a drainage structure are described and discussed.

MATERIAL AND RESEARCH METHOD

This research is located in the first yard of Prambanan Temple, which is the highest point of the series of Prambanan Temple Yard as shown in Figure 2. The land area is about 110 meters by 110 meters and a spacious courtyard of the temple of 3747 m^2. According to [3]. the stratification of the soil in Prambanan temple yard is silty sand. Some improvements have conducted in the first yard by addition of a puddle layer on top of the original soils and drainage system improvements. The drainage system applied in the temple courtyard was horizontal and vertical recharge.

Research materials were disposed volcanic ash and bantak from Mount Merapi. Volcanic ash resulted from Merapi eruption in 2010, was taken from Cangkringan, Yogyakarta, Indonesia as shown in Figure 3. The used material size of volcanic ash is the material which passed by sieve number 270. Volcanic ash is a natural pozzolan which is required in chemical reaction in concrete mixture. The mineral compositions of volcanic ash that used in this research are given in Table 1. Volcanic ash from Merapi has dissolved heavy metal content below the threshold by KEP 02/MENKLH/I/1988 for a list of criteria for water quality class D (safe water for agricultural purposes and can be used for urban businesses, industry and hydropower). Therefore, the volcanic ash was safely applied .

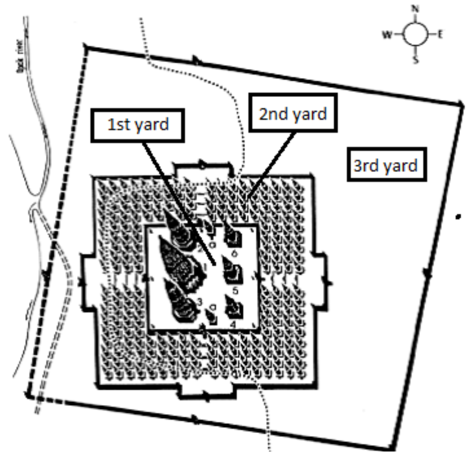

Fig. 2 Site plan of Prambanan Temple Yard (1st, 2nd, and 3rd yard)

Table 1 Physical properties of volcanic ash

Mineral composition	Value (%)
Silica (SiO_2)	57.59
Alumina (Al_2O_3)	21.36
Calcium Oxide (CaO)	4.24
Magnesium Oxide (MgO)	2.26
Iron Oxide (Fe_2O_3)	5.89
Potash (K_2O)	3.32
Natrium Oxide (Na_2O)	4.10
LOI (Loss of Ignition)	0.96

Fig. 3 Volcanic ash material

Fig. 4 Coarse volcanic slag (*bantak*)

Table 2 Physical properties of coarse volcanic slag (*bantak*)

Parameters	Value	Unit
Loose unit weight	1360.22	kg/m^3
Compacted Unit weight	1507.61	kg/m^3
Specific gravity	2.49	-
Specific gravity in SSD	2.56	-
Water absorption	4.61	%
Water content	4.40	%
Abrasion	54.75	%

Coarse volcanic slag is used as an aggregate in this experimental research. Figure 4 shows the coarse volcanic slag that was supplied from the quarry in Boyong River, Yogyakarta, Indonesia. The aggregates obtained from the quarry were screened into 10-20 mm size fractions. Table 2 shows the physical properties of coarse volcanic slag. In this study percentages of volcanic ash which added into the concrete mix design were 0% and 30%. Concrete parameters would be used as a reference standard for concrete such as unit weight, porosity, permeability coefficient of no-fines concrete, and the uniaxial compressive strength.

Rainfall analysis data was determined by using HAVARA program. The analysis obtained the characteristics of rainfall that occurs at the location including the duration and the intensity of rainfall for a certain period. The hourly rainfall data from four rain gauges around the study area for a time period from 1998 to 2012 were used. The peak discharge of rainfall calculated by using Eq. (1).

$$Q_{peak} = 0{,}278CIA \tag{1}$$

Where Q is peak rainfall discharge, C is rational method coefficient, I is rainfall intensity and A is drainage area. Meanwhile the natural infiltration capacity calculated using Eq. (2) and Eq. (3).

$$Q_i = fA \tag{2}$$

$$f_i(t) = k\left(\frac{\psi\Delta\theta}{F_i(t)} + 1\right) \tag{3}$$

Where Q_i is infiltration capacity, f is infiltration velocity, A is area, k is hydraulic conductivity, F_i is cumulative amount of infiltrated water, ψ is suction, and θD is difference between porosity with initial soil moisture.

Then, the result of rainfall analysis is used as input to calculate the drainage capacity. At this stage the analysis of the suitability of the rain discharge (Q_l) and discharge channel (Q_f) was done. If obtained $Q_l \geq Q_f$, then the redesign of trench or channel should be done. However, if $Q_l \leq Q_f$, it only needs to take some improvement, one of the improvement methods with proposed drainage channel from *bantak* and volcanic ash. Reference [4] Dimension of the channel was determined by trial and error using Eq. (4).

$$B' = \frac{-fkT}{nb\left\{ln\left(1 - \frac{fkH}{Q}\right)\right\}} \tag{4}$$

f is geometric factor which calculated by Eq. (5).

$$f = \frac{4H + 4\sqrt{bB}ln2}{ln\left\{\frac{H + 4\sqrt{bB}}{6\sqrt{bB}} + \sqrt{\left(\frac{H}{6\sqrt{bB}}\right)^2 + 1}\right\}} \tag{5}$$

Where B is length of the channel, k is permeability coefficient, T is rainfall duration time, n is porosity of material, b is channel width, H is depth of the channel, and Q is discharge capacity. According to [5] the seep discharge into the channel (Q_f) calculated by using Eq. (6).

$$Q_f = A.V_x \tag{6}$$

If the concrete channel wall were added by no-fine concrete, with $Q_1 = Q_f$, can be obtained by the minimum hydraulic conductivity value of no-fine concrete material that must be provided to the walls of the channel can be calculated using Eq. (7).

$$k_f = \frac{Q_f}{\sin\alpha\,.\,t_f} \tag{7}$$

Analysis result obtained the optimum distance between adjacent channels, water discharge that was able to enter into the channel and the minimum thickness of the channel. Based on [5] the optimum distance between two channels calculated by using Eq. (8). The representation of the subsurface flow can be seen in Figure 5.

$$S = \left[\frac{4kh_{max}}{i}\left({h_{max}}^2 - {h_w}^2 + 2dh_{max} - 2dh_w\right)\right]^{\frac{1}{2}} \quad (8)$$

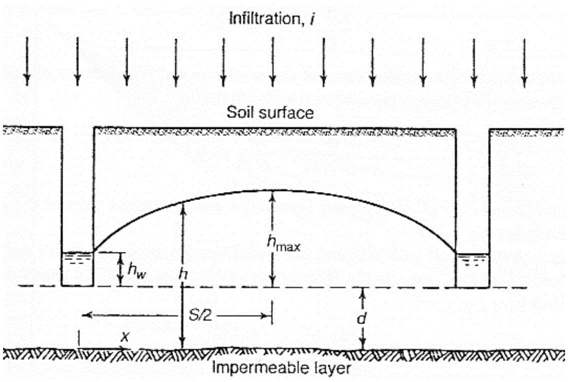

Fig. 5 The representation of the subsurface flow into the channel

The numerical analysis were carried out using SAP2000 and Plaxis assuming the drainage structure as a *plain strain model* in Plaxis and *frame model* in SAP2000. Calculation analysis about the strength of the structure channel is based on the result of the simulation using Plaxis and SAP2000 programs.

RESULT AND DISCUSSION

Table 3 shows the drainage system applied to the first yard of Prambanan temple has not been effective enough to accommodate the flood discharge that occurs on this area. There is residual discharge resulted the ponding area in Prambanan Temple yard. Therefore an improvement of drainage system, either in the form of new canals or drainage management arrangement on the drainage system, is needed to solve this problem. Based on field observations, horizontal recharges system is not functioning properly. The number of puddle distribution locations above the horizontal recharges system indicates this. The total amount of discharge (Q) used in a cross-sectional dimension of planning control in the channel is $4.63{\times}10^{-3}$ m^3/sec. This value represents the difference discharge of rain that fell in the area of the temple courtyard to natural infiltration capacity land and total discharge vertical infiltration.

The value of total run off represents the difference between the natural discharge of rain that fell in the temple courtyard and the total discharge of vertical recharge. Based on these considerations, the length of channel is determined to be planned in accordance to the existing total length of recharge channels. By trial and error using Eq. (4), the acquired new channel dimension is 0.40 meters by 0.40 meters.

Table 3 Recapitulation of drainage capacity analysis

Parameter	Value	Unit
Vertical infiltration	$7.67{\times}10^{-4}$	m^3/s
Horizontal infiltration	$2.70{\times}10^{-3}$	m^3/s
Total runoff	$3.47{\times}10^{-3}$	m^3/s
Peak rainfall discharge	$4.70{\times}10^{-2}$	m^3/s
Natural infiltration capacity	$4.16{\times}10^{-2}$	m^3/s
Residual discharge	$1.93{\times}10^{-3}$	m^3/s
Total amount of discharge	$4.63{\times}10^{-3}$	m^3/s

Effect of Merapi eruption material to concrete parameters such as porosity, compressive strength, and modulus of elasticity of no-fine concrete can be seen in Table 4. Based on laboratory tests, the unit weight of no-fine concrete (*Bj*) obtained at 2065 kg/m^3, or in other words, no-fines concrete has successfully produced according to SNI 03-2847-2002, the obtained value from the test can be categorized as lightweight concrete, because of the value of Bj < 2200 kg/m^3.

The relationship of concrete curing period for concrete compressive strength is shown in Figure 6. It shows that with the same mixture, the trend of increasing no-fine concrete strength will continue to increase with increasing curing time, as well as to the relationship of no-fine concrete strength against compaction energy applied. Based on Figure 7, the compaction energy derived from the comminution process greatly affects the strength of the concrete. However with longer curing time, no-fine concrete strength is relatively the same. The permeability coefficient of no-fine concrete generated in this study amounted to $1.33{\times}10^{-3}$ m/sec.

From the Eq. (6), the seep discharge into the channel is $Q_f = 1.49{\times}10^{-5}$ m^3/sec. If the channel wall of concrete walls were added with no-fine concrete, the analogy, with $Q_1 = Q_f$, can be obtained by the minimum hydraulic conductivity value of no-fine concrete material that must be provided to the walls of the channel at $1.49{\times}10^{-4}$ m/s. The permeability coefficient value of no-fines concrete applied to channel wall is $1.33{\times}10^{-3}$ m/s then the media will fulfill the qualification as a drainage layer. However, this condition does not make this qualified as a filtration function, so it is still necessary to carried soil particles into the channel.

Table 4 Engineering properties test result of no-fine concrete

Parameter	Value	Unit
Volcanic ash percentage	30	%
Porosity	10.03	%
Compressive strength (28 days)	9.61	MPa
Elastic modulus	2480	MPa
Density	2065	kg/m^3
Permeability	$1.33{\times}10^{-3}$	m/s

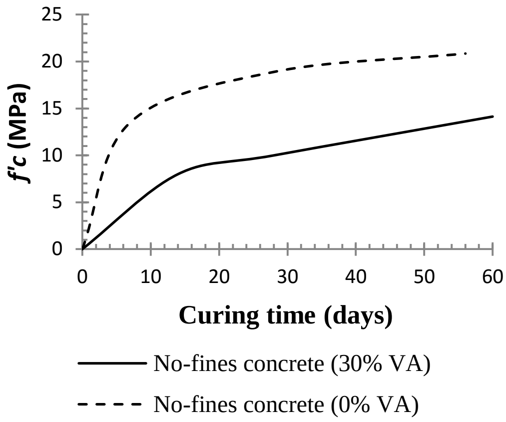

Fig. 6 Correlation of curing time with compressive strength

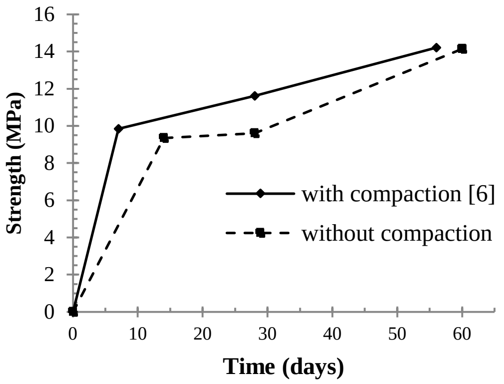

Fig. 7 Influence of the concrete compaction to increased strength

Further evaluation of reviews, these calculations were added to determine the channel spacing of subsurface drain. The optimum distance between adjacent channels is 7.50 m. To anticipate the drainage system damage due to structural failure, it would require some evaluation of loading models. Numerical analysis were performed to determine the effectiveness of Merapi eruption material for drainage channel. The proposed typical channel model proposed can be seen in Figure 8. Representation of working load location on the ground surface illustrated in Figure 9. In this analysis, simulations were assumed on the location of the ground level water table (the most critical condition).

Figure 10 shows a comparison of the bending moments value occured in the channel structure due to the influence of forklift movement and groundwater pressure from SAP2000 and Plaxis simulation. The calculation results for the thickness of channel structure are shown in Table 5. It presents that the maximum channel structure moments when loading of Condition 2 was applied (see Figure 9), then it was used as a parameter value to determine the minimum thickness of channel structure. The minimum thickness required of the channel is 0.05 m. Results of numerical analysis can be seen in Table 5.

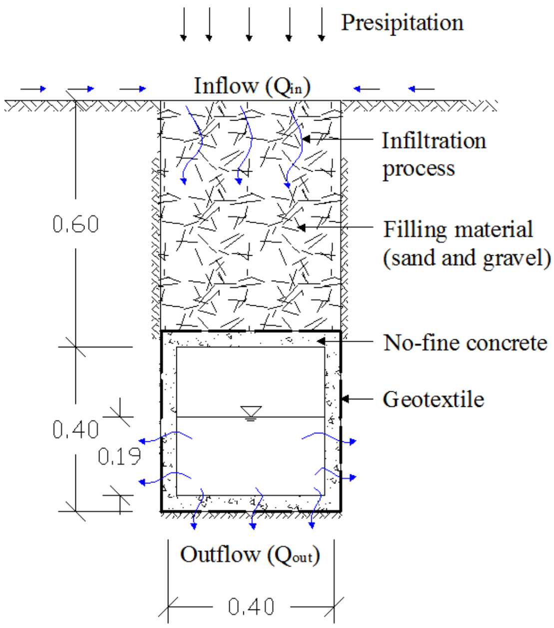

Fig. 8 The proposed drainage system

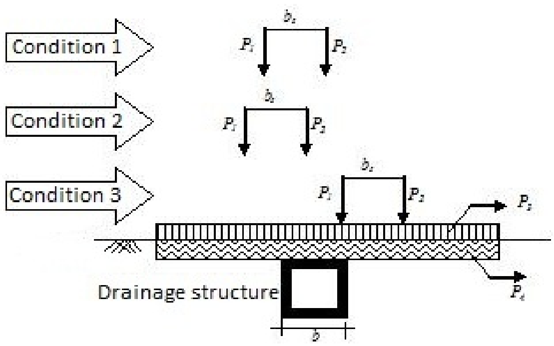

Fig. 9 Scheme of loading models on the ground surface

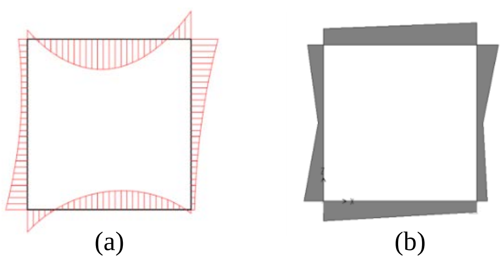

Fig. 10 Moment of channel structure simulate in (a) Plaxis and (b) SAP2000

Table 5 Results of numerical analysis

Load	Displacement (m)	M_{max} (kN.m)		Min. thickness (m)
		SAP2000	Plaxis	
1	1.63×10^{-3}	0.28	0.30	0.03
2	6.79×10^{-4}	0.56	0.56	0.05
3	6.63×10^{-3}	0.54	0.44	0.04

From the hydrological analysis and evaluation of the channel structure calculations, the typical channel model that can be applied to the first yard of Prambanan Temple is subsurface channels with the addition of filter media in the form of non-woven geotextile to avoid clogging by fine soil particles. Theoritically, the silty sand soil in Prambanan Temple yard has a low-capability of draining water (small permeability value). To avoid the impairment of soil hydraulic conductivity (k) caused by the visitor activities and the heavy equipment movements, layers formed of gravel and sand should be added on the top of slab channel to make the water completely seep into the channel.

CONCLUSION

Drainage system of Prambanan Temple yard using no-fine concrete as a porus media with volcanic ash and coarse volcanic slag are presented. The utilization of volcanic material is purposed to reduce cement need on drainage construction, which leads to global environmental problem. The experimental study was conducted to determine the optimum mix design and the engineering properties of the material. The discharge capacity of drainage system also was calculated to identify the optimal distance of two ditches. In addition, numerical analysis were carried out using SAP2000 and Plaxis to control structure stability.

The value of natural soil infiltration capacity at first yard of Prambanan Temple is of 4.16×10^{-2} m^3/sec, whereas maximum rainfalls discharge of 4.7×10^{-2} m^3/sec. This condition shows that existing drainage system was not sufficient and still need improvement using porous media of no-fines concrete. The optimum distance between adjacent channels is 7.50 m with channel dimensions of 0.4 m by 0.4 m at depth of 1.00 m as typical proposed channel model. The value of permeability of no-fine concrete using volcanic ash and *bantak* is 1.33×10^{-3} cm/sec. Meanwhile, the seep discharge into the channel has smaller value than permeability of concrete that is 1.49×10^{-4} cm/sec. According to this statement, the proposed drainage system of volcanic ash and *bantak* shows that no-fines concrete material has fulfilled the qualification as a material for drainage layer.

Based on numerical analysis and experimental study, the utilization of no-fine concrete from volcanic ash and *bantak* by using certain mix design can be used as a porous drainage structure. This can be seen from the strength of no-fine concrete based on numerical modelling and the ability to drain the water. The proposed drainage structure is very eco-friendly because the use of waste material is surely compatible to be used as structural improvement for historical site such as Prambanan Temple. By utilizing the eco-friendly material as structural material, the originality of the building will not be disturbed.

ACKNOWLEDGEMENTS

The authors express their gratitude to Directorate General Higher Education (DGHE) Ministry of Education and Culture, Indonesia and Universitas Gadjah Mada for financial supporting by Competitive Grant of International Collaboration Research and Publication with contract no. LPPM-UGM: 304/LPPM/2015, dated March 2, 2015. The authors also would like to thanks to colleagues of Department of Civil and Environmental Engineering, UGM and Preservation Center of Cultural Heritage, Prambanan Unit for their helpful and fruitful discussion and spirit in conducting field and laboratory tests.

REFFERENCES

[1] Bawono, Y.Y., “Analisis dua dimensi rembesan air pada penggalian terowongan dengan menggunakan metode elemen hingga”, Tesis, Yogyakarta: Program Pascasarjana Fakultas Teknik Universitas Gadjah Mada, 2007.

[2] Terzaghi, K. & Peck, R.B., Soil Mechanics in Engineering Practice. 3rd ed, New York, John Wiley & Sons, 1996.

[3] Rifa'i, A., “Sifat Teknis Tanah dan Struktur Fondasi Candi Wisnu Dalam Tinjauan Geoteknik”, PIT-XIII HATTI Developement of Geotechnical Engineering in Civil Construction 2009.

[4] Sunjoto, S., “The Recharge Trench as A Sustainable”, Journal of Environmental Hydrology, The Electronic Journal of the International Association for Environmental Hydrology On the World Wide Web at http://www.hydroweb.com, Vol. 16, 2008, pp.1-11.

[5] Reddi, L.N., “Seepage in soil: principles and applications”, John Wiley & Sons, 2003.

[6] Abbas, I., “Pemanfaatan abu vulkanik sebagai bahan geostruktur pada perlindungan tebing”, Tesis, Yogyakarta: Program Pascasarjana Fakultas Teknik Universitas Gadjah Mada, 2014.

MODELING OF EVAPORATION PROCESSES UNDER THE GROUND

B. Liu[1], A. Kobayashi[1], Y. Tsukada and M. Chijimatsu[2]
[1]Department of Civil and Environmental Engineering, Kasai University, Japan; [2]Hazama Ando corp., Japan

ABSTRACT

The vaporization process is modeled by incorporating the relation between pressure and enthalpy into the numerical simulation code for the coupled thermal, hydraulic and mechanical phenomena under the ground. The boundary between superheated steam and two-phase of steam and water was modeled by the previous study. On the other hand, the boundary between compressed water and two-phase of steam and liquid is modeled by the deduced equation with pressure and enthalpy in this study. Temperature is selected to be the unknown variable in the model. The enthalpy is estimated from the pressure and temperature, and then the situation of phase is examined. As an example, the situation about the disposal of the waste generating heat to 300°C is simulated by the simple 2-D and detail 1-D models.

Keywords: Groundwater, Evaporation, Coupled analysis, Nuclear Waste Disposal

INTRODUCTION

In Japanese nuclear energy policy, the high level radioactive waste from the nuclear fuel cycle is planned to be disposed in deep geology. The vitrified waste is stored for fifty years for cooling and then those are stored in overpack and disposed. This is because the stable and safe disposal is necessary. The plan, therefore, needs long time for disposal. However, since the accident at the nuclear plant Fukusima Daiichi, the disposal of nuclear waste requires urgent attention. If the nuclear fuel rod is directly disposed in the deep geology, the volume of waste may become very large and the heat generation from the waste is also very high. In this case, the effect of the high heat generation from the waste has to be examined and then repository has to be designed as most safe and stable as possible.

In this study, the vaporization process is modeled by incorporating the relation between pressure and enthalpy into the numerical simulation code for the coupled thermal, hydraulic and mechanical phenomena under the ground. The boundary between superheated steam and two-phase of steam and liquid was modeled by the previous study. On the other hand, the boundary between compressed water and two-phase of steam and water is modeled by the deduced equation with pressure and enthalpy in this study. In general, temperature is the unknown variable for the coupled problem and the boundary condition is given by temperature. Therefore, temperature is selected to be the unknown variable in the model. The enthalpy is estimated from the pressure and temperature, and then the situation of phase is examined. As an example, the situation about the disposal of the waste generating heat to 300°C is simulated by the simple 2-D and detail 1-D model.

MODEL OF PHASE CHANGE

Pressure-enthalpy Diagram

Mercer and Faust [1] and White at al. [2] gave the diagram of phase change presented by pressure and enthalpy as shown in Fig.1. By using this diagram, the phase of fluid can be recognized. The bold covex line in the graph indicates the boundary of phases, in which the boundary between area ① and ② is the phase change between liquid and steam-liquid two phase, and that between ② and ③ is the one between steam-liquid two phase and superheated steam.

Although the diagram is the plane coordinate with the vertical axis of pressure and horizontal one of enthalpy, the isothermal line can be seen in the diagram. The phase change is originally explained by three dimensional diagram adding temperature as shown in Fig.2.

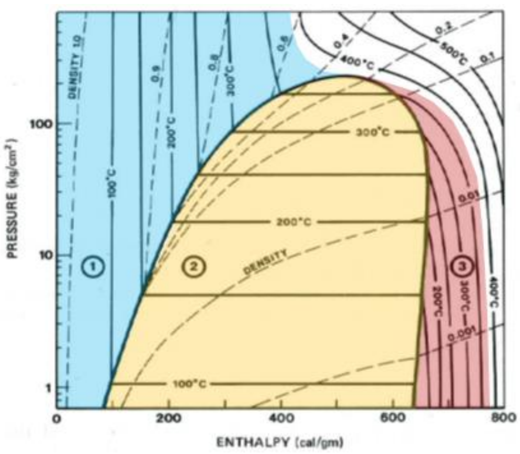

Fig.1 Pressure-enthalpy diagram for water and steam with thermodynamic regions [1], [2]

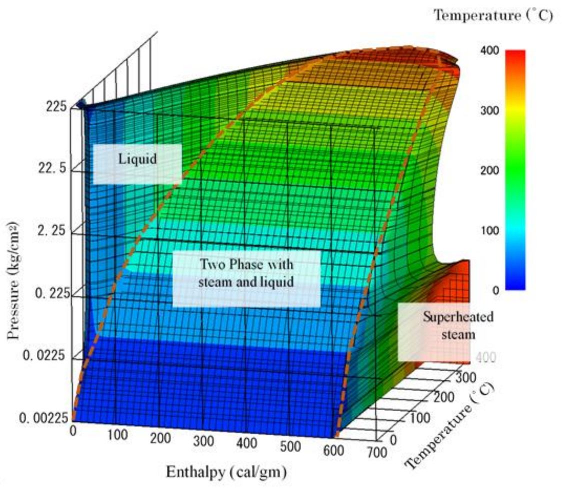

Fig.2 Pressure-enthalpy-temperature diagram for water and steam phases

Equation of Boundaries

The equation of boundary between ② and ③ in Fig.1 is given by Huyakorn and Pinder [3] as

$$h_*^g = 2822.82 - 39.952/p + 2.5434/p^2 - 0.93888p^2 \quad (1)$$

where $h^g{}_*$ is the enthalpy (kJ/kg) at the boundary between two phase region and superheated steam, and p is the pressure (dyne/cm^2). Temperature in the region ① at which enthalpy h is smaller than the enthalpy at the boundary between water and two phase region $h^l{}_*$ is given by

$$T = \psi_1(p,h) + [\psi_0(p) - \psi_1(p,h_*^l)] \quad (2)$$

where

$$\psi_0(p) = 4667.075/(12.599 - \ln(10p)) - 273.15 \quad (3)$$

$$\boldsymbol{\psi_1(p,h) = -28.152 - 0.13746p + 0.30112h + \frac{3536.4}{h} - 4.3192 \times 10^{-5}h^2} \quad (4)$$

Temperature in the region ② where enthalpy h is between $h^l{}_*$ and $h^g{}_*$ is given as

$$\boldsymbol{T = \psi_0(p)} \quad (5)$$

Temperature in the region ③ where enthalpy h is larger than $h^g{}_*$ is obtained as

$$\boldsymbol{T = \psi_2(p,h) + [\psi_0(p) - \psi_2(p,h_*^g)]} \quad (6)$$

in which

$$\boldsymbol{\psi_2(p,h) = -374.67 + 47.992p - 0.63361p^2 + 7.3939 \times 10^{-5}h^2 - \frac{3.3372 \times 10^6}{p^2h^2}h^2 + \frac{0.035715}{p^3} - 1.1725 \times 10^{-9}h^3p - \frac{2.2686 \times 10^{15}}{h^4}} \quad (7)$$

As the boundary between liquid and two phase region was not given by Huyakorn and Pinder, the following equation is reduced in this study;

$$\boldsymbol{p^l = -5 \times 10^{-11}h_*^{l\,5} + 4 \times 10^{-8}h_*^{l\,4} - 5 \times 10^{-6}h_*^{l\,3} + 0.0003h_*^{l\,2} + 0.0028h_*^l - 0.1422} \quad (8)$$

Fig. 3 shows the fitting of Eqs. (1) and (8) to the steam diagram, from which it is understood that Eqs. (1) and (7) give the relatively good approximation.

In this study, the phase of fluid is examined by using the above relations.

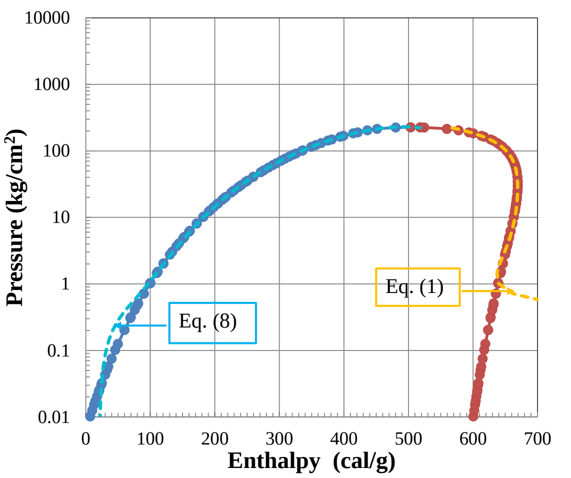

Fig. 3 Approximation relations and those fitting result

GOVERNING EQUATIONS

Mass Conservation Law

The governing equation of seepage is given as

$$-\rho_w \frac{\partial \theta}{\partial \psi}\frac{\partial P}{\partial t} - \left[\rho_w k_{ij} P_{,j}\right]_{,j} = 0 \quad (9)$$

where θ is the volumetric moisture content, ψ is the matric potential, P is the total head, ρ_w is the density of water, k_{ij} is the hydraulic conductivity, and t is time.

The density of water ρ (gm/cm^3) is given as a function of pressure p and enthalpy h by Marcer and Faust,

$$\rho^l = \begin{cases} 0.98988 + 4.0089\times10^{-4}p - 4.0049\times10^{-5}h + \\ \quad 2.6661/h + 5.4628\times10^{-7}ph - 1.2996\times10^{-7}h^2 \\ \qquad\qquad\qquad\qquad for\ h > 200 \\ 1 \qquad\qquad\qquad\qquad for\ h \le 200 \end{cases} \tag{10}$$

The density of superheated steam ρ^g is given as

$$\rho^g = -2.2616\times10^{-5} + 0.043844\ p - 1.7909\times10^{-5}ph + 3.6928\times10^{-8}p^4 + 5.1764\times10^{-13}ph^3 \tag{11}$$

The saturation degree of water S^l can be obtained by

$$S^l = \begin{cases} 1 & for\ \ h \le h^l_* \\ 0 & for\ h \ge h^g_* \\ \dfrac{\rho^g\left(h^g_* - h\right)}{h\left(\rho^l - \rho^g\right) - \left(h^l_*\rho^l - h^g_*\rho^g\right)} & for\ h^l_* < h < h^g_* \end{cases} \tag{12}$$

The saturation degree of steam S^g is given by

$$S^g = 1 - S^l \tag{13}$$

The density of water ρ_w at the two phase of liquid and steam is given by

$$\rho_w = \rho^g S^g + \rho^l S^l = \rho^g\left(1 - S^l\right) + \rho^l S^l \tag{14}$$

On the other hand, the viscosity of water μ^l and that of steam μ^g are obtained as a function of temperature T by

$$\mu^l = 10^{-6}\times239.4\times10^{[24837/(T+113)]}$$
$$\mu^g = (0.407T + 80.4)\times10^{-6} \tag{15}$$

in which the unit of the viscosity is g/(cm· s).

The relative permeability of water k^l_r and that of steam k^g_r are given as a function of saturation degree of water and steam as followings;

$$k^l_r = \left(S^l\right)^2$$
$$k^g_r = \left(S^g\right)^2 = \left(1 - S^l\right)^2 \tag{16}$$

By using above parameters, the hydraulic conductivity tensor of water k^l_{ij} and that of steam k^g_{ij} is obtained by

$$k^l_{ij} = \frac{k^l_r\rho^l gK_{ij}}{\mu^l}$$
$$k^g_{ij} = \frac{k^g_r\rho^g gK_{ij}}{\mu^g} \tag{17}$$

The hydraulic conductivity in Eq. (9) is given by

$$k_{ij} = k^l_{ij} + k^g_{ij} = \left(\frac{k^l_r\rho^l}{\mu^l} + \frac{k^g_r\rho^g}{\mu^g}\right)gK_{ij} \tag{18}$$

where K_{ij} is the intrinsic permeability of the material. By applying the van Genuchten relation to the moisture capacity of the relation between θ and ψ, Eq. (9) can be solved by considering the situation of phase change of fluid.

Energy Conservation Law

The equation describing energy transport is written as

$$(\rho C)_m\frac{\partial T}{\partial t} + \left\{S_r\rho_w c_w v_i T - (\lambda_m)_{ij}T_{,j}\right\}_{,i} + \left\{L\rho_w dS^g\right\}_{,i} + Q^h = 0 \tag{19}$$

where

$$(\rho C)_m = n\left(S^l\rho^l C^l + S^g\rho^g C^g\right) + (1-n)\rho^s C^s \tag{20}$$
$$\lambda_m = n\left(S^l\lambda^l_m + S^g\lambda^g_m\right) + (1-n)\lambda^s_m$$

in which C^l is the specific heat of water and C^g is that of steam. λ^l_m is the thermal conductivity of water and λ^g_m is that of steam. Those are the function of temperature as shown in Fig. 4. Moreover, λ^s_m is the thermal conductivity of solid and n is the porosity.

L is the latent heat and dS^g is the change in saturation degree of steam. By solving Eq. (9) and (19), total head P and temperature T are obtained. Then, the enthalpy is calculated by

$$h = E + p/\rho_w \tag{21}$$

E is the energy of the element and the second term is the pressure per unit weight (J/g or kJ/kg). The enthalpy and pressure is used to judge the phase situation.

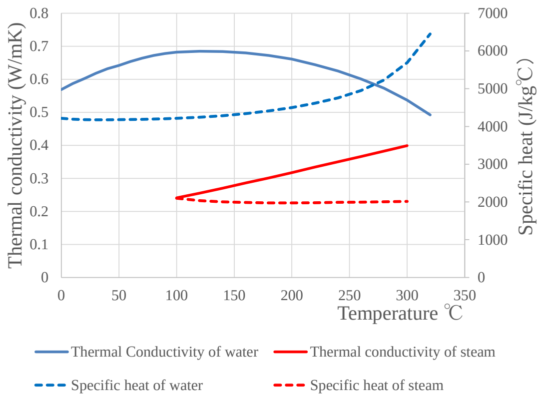

Fig.4 Nonlinear relation of thermal conductivity and specific heat to temperature

SIMULATION EXAMPLES

2-D Model

Model explanation

Fig. 5 shows the 2-D model of the situation around the waste in a repository. The horizontal length of the region is 36 m, the height is 29 m, waste is 1x1 m, tunnel with buffer material is 5x5 m and the distance between wastes is 14 m.

The thermal initial condition is 15˚C and hydraulic one is 300 m for all region. As a boundary condition, normal deformation is fixed, total head is 300 m and temperature is 15˚C for all boundaries.

Fig. 6 shows the heat generation history at the waste. Temperature increases until 300˚C by 1˚C / 10days. Table 1 shows the parameters used in the analysis.

Analysis results

Fig.7 shows the temperature distribution when temperature at waste becomes 300˚C. The rock

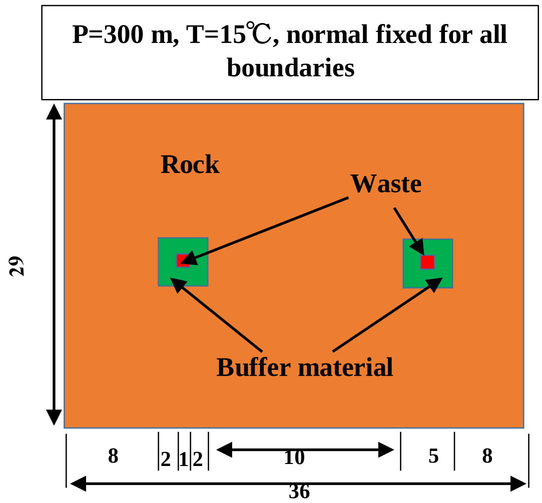

Fig. 5 Schematic view of 2-D model (unit: m)

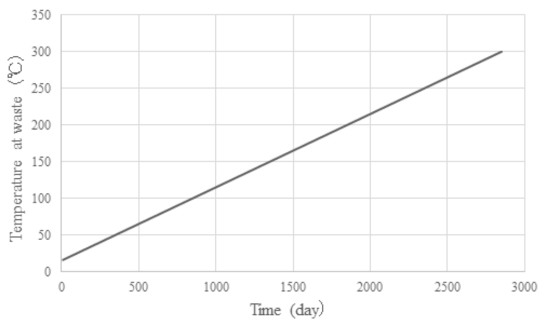

Fig.6 History of heat generation at the waste

between tunnels has temperature of over 120˚C. Fig. 8 shows the situation in the buffer material neighboring waste and rock and that in the rock neighboring buffer material when temperature at the waste reached 300˚C. The enthalpy in the buffer material neighboring waste is a little smaller than h^l_* and still evaporation does not occur. It is found that the enthalpy becomes small with the distance from the waste. Fig. 9 shows the temporal change of relation between pressure and enthalpy in the buffer material neighboring waste. It is found that the pressure and enthalpy becomes gradually large and particularly the pressure raises to about 100 kg/cm^2 by the thermal expansion of water. As the pressure becomes high, evaporation does not occur even if temperature is about 300˚C. It is, however, difficult to estimate the situation in the buffer material because the coarse mesh as shown in Fig. 7. Thus, the 1-D model is considered to estimate the detail situation in the buffer material in the following section.

Table 1 Parameters used in simulation

Parameter		Waste	Buffer	Rock
E (MPa)		2.00×10^5	3.44×10^1	1.82×10^3
v		0.30	0.30	0.21
K (m)		1.0x10^{-30}	4.0x10^{-20}	1.3x10^{-15}
VG	θ_s	0.0001	0.403	0.311
	θ_r	0.0	0.0	0.0
	α	8.0x10^{-3}	8.0x10^{-3}	3.7x10^{-1}
	n	1.60	1.60	1.13
λ_f(J/(kg˚C))			0.60	
λ_s(J/(kg˚C))		53.00	1.95	0.60
C_f(W/(m˚C))			4180	
C_s(W/(m˚C))		460	341	108
e		0.0001	0.675	0.451

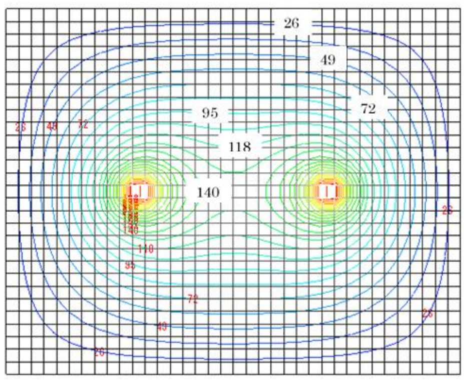

Fig. 7 Temperature distribution in the rock when temperature at waste becomes 300˚C.

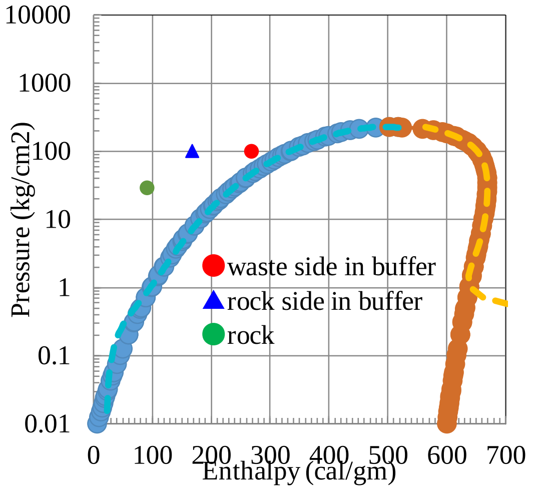

Fig. 8 Situation of phase at the different locations when temperature at waste becomes 300˚C

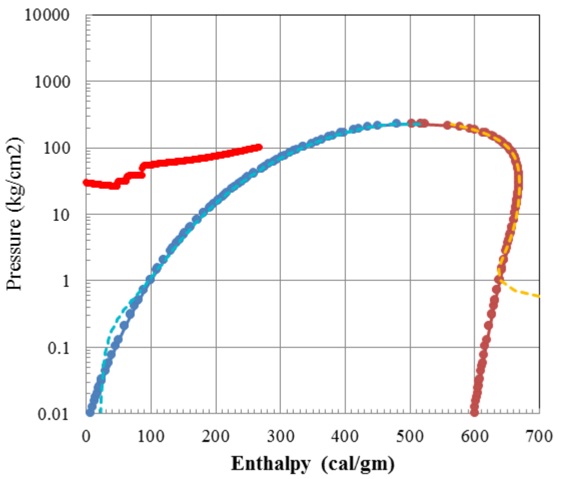

Fig.9 History of relation between pressure and enthalpy at the buffer material neighboring waste

1-D Detail Model

Model description

As mentioned above, the buffer material was made with two elements from waste side to rock mass side in 2-D model, the detail behavior in the buffer material is difficult to discuss. Fig. 10 shows the schematic view of the 1-D model, which considers the previous concept of disposal with canister containing the waste package. The analysis region extends from the center of waste to the rock mass with the constant section of 1 m^2 and length of 25 m. The buffer material of which length is 0.72 m consists of 36 elements. The boundary conditions at the edge face of waste are the prescribed temperature as same as Fig. 6, no deformation for mechanical condition and no flow for hydraulic one. Temperature at the nodes in the waste region raises as shown in Fig. 6. The boundary conditions at the edge face of rock mass are

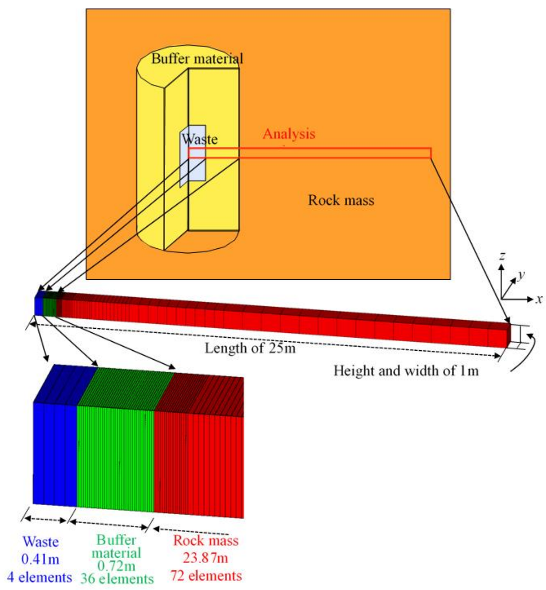

Fig. 10 Schematic view of the detail 1-D model

The prescribed temperature of 15˚C, no deformation for mechanical condition and prescribed total head of 300 m. The other boundaries have no flow for thermal and hydraulic conditions and normal deformation fixed condition.

Analysis results

Figs. 11-13 shows the histories of relation between pressure and enthalpy at the element neighboring the waste in the buffer material, the one at the center of the buffer material and the one neighboring rock in the buffer material. It is found that the buffer material neighboring the waste and rock enter into the two phase region as shown in Figs. 11 and 13. On the other hand, the part at the center of the buffer material is not at two phase region as shown in Fig. 12. This means that evaporation occurs at the both outer sides in the buffer material and evaporation does not occur at the inner parts in the buffer material.

Fig. 14 shows the distribution of pressure in the buffer material. It is found that the pressure has the largest value at the inner parts of the buffer material. The reason why evaporation does not occur at the inner parts is because the pressure of fluid at the inner parts becomes higher than that at the outer parts. Since temperature distributes mostly homogeneously in the buffer material, the high pressure may be caused from the result of fluid movement in the buffer material. This may be temporal situation and the situation of phase may change with time by depending on the boundary conditions and material properties. The verification of temporal situation change and validation of model are the remained tasks.

Moreover, the pressure becomes high at the boundary of liquid and two phase situation as shown

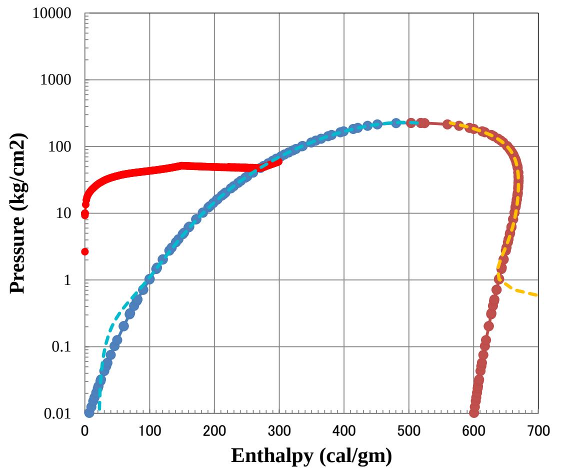

Fig. 11 History of relation between pressure and enthalpy at the element neighboring the waste in the buffer material

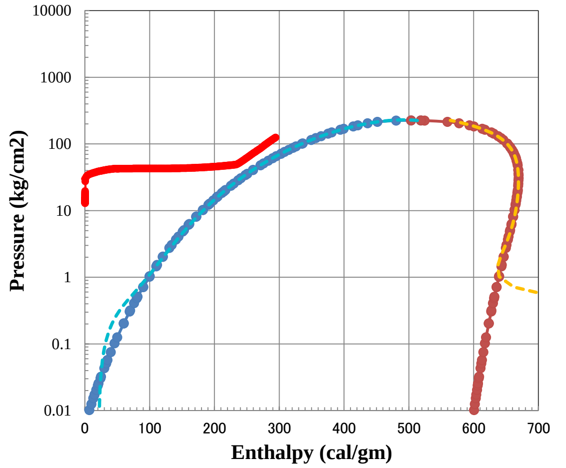

Fig. 12 History of relation between pressure and enthalpy at the element existing at the center of the buffer material

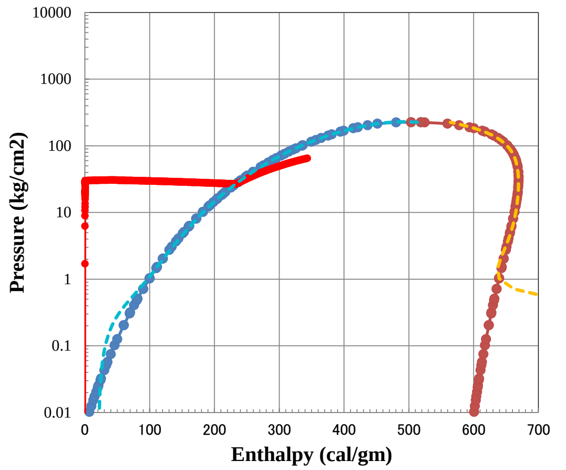

Fig. 13 History of relation between pressure and enthalpy at the element neighboring rock in the buffer material

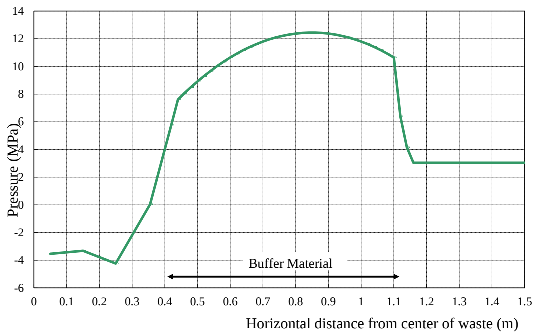

Fig. 14 Pressure distribution in the buffer material when temperature of the waste is 300 °C

in Figs. 12 and 13. The isothermal lines exit vertically at liquid region and become horizontally in two phase region as shown in Fig. 2. Therefore, the increase in temperature causes the increase in pressure close to the boundary between liquid and two phase region.

CONCLUSIONS

The disposal project of high level radioactive waste is very important for the countries having the nuclear plants. If the waste generates high heat, the effect of evaporation in the ground has to be considered for safe and stable disposal. The model to assess the effect of the evaporation of groundwater is developed in this study. The obtained conclusions are followings:

1) Evaporation process is dependent on temperature and pressure of fluid. It is found that the developed model has an ability to predict the complicated change in phase in the buffer material around the waste.

2) When temperature becomes high and the hydraulic conductivity is low, the fluid pressure may become very higher because of the thermal expansion of fluid and difficulty of movement. Such a situation may prevent evaporation according to the circumstances.

3) While the results obtained in this study is very important, the verification of the phenomena and validation of the model are the remained subject.

REFERENCES

[1] Mercer, J. M. and Faust, C. R. : "Simulation of water- and vapour-dominated hypothermal reservoirs", Paper SPE 5520, presented at the 50th Annual Fall Meeting of the Soc. Pet. Eng. AIME, Dallas, Texas, 1975.

[2] White, D. E., Muffler, L. J. P., and Trusdell, A. H. : "Vapor-dominated hydrothermal systems compared with hot-water systems", ECON. Geol. 66, 1971, pp.75-97.

[3] Huyakorn, P. S. and Pinder, G. F.: “Computational method in subsurface flow”, ACADEMIC PRESS, 1983.

A COMPARISON OF THE BASE RESISTANCE OF OPEN-ENDED PILES EVALUATED BY DIFFERENT DESIGN METHODS

Janaka J. Kumara, Yoshiaki Kikuchi and Takashi Kurashina
Department of Civil Engineering, Tokyo University of Science, Japan

ABSTRACT

Bearing capacity of an open-ended pile depends largely on the accuracy of the design method. Although the knowledge of shaft resistance is understood well, the base resistance has not yet fully understood due to the effects of soil plugging. This paper compares the base resistance of two open-ended field piles constructed in the Tokyo Bay project evaluated by CPT- and SPT-based design methods. The CPT-based design methods, which are not popular in Japan were also included to evaluate their effectiveness. The CPT-design methods discussed on this paper classify open-ended piles into plugged or unplugged modes. The results reveal that the Fugro (i.e., CPT-based) and API design methods overestimate the base resistance. On contrast, the ICP (i.e., CPT-based) and PARI (i.e., SPT-based) design methods underestimate the base resistance. On a rational approach, we recommend the UWA design method (i.e., CPT-based) as it produces the nearest results to the actual base resistance.

Keywords: Base Resistance, Cone Penetration Test, Design Methods, Open-Ended Piles, Soil Plugging

INTRODUCTION

The baring capacity of an open-ended pile consists of three parts as given in Eq. 1 (see Fig. 1 too). The base resistance is produced by the combination of plug resistance and annulus resistance (see Eq. 2). The plug resistance is the minimum of inner frictional resistance, Q_{in} or soil base resistance, $Q_{\mathrm{b,soil}}$ (see Fig. 1).

$$Q_{\mathrm{u}} = Q_{\mathrm{an}} + Q_{\mathrm{out}} + Q_{\mathrm{plug}} \quad (1)$$

Where Q_{u} is bearing capacity, Q_{an} is annulus resistance, Q_{out} is outer frictional resistance and Q_{plug} is plug resistance.

$$Q_{\mathrm{b}} = Q_{\mathrm{an}} + Q_{\mathrm{plug}} \quad (2)$$

Where Q_{b} is base resistance, Q_{an} is annulus resistance and Q_{plug} is plug resistance.

The evaluation of the base resistance is not straightforward compared to shaft resistance, due to the effects of soil plugging. In this paper, we discussed evaluation methods of the base resistance by several design methods. Nowadays, CPT-based design methods are quite popular in many parts of the world although Japanese companies still do not encourage CPT-based design methods. Three CPT-based design methods (i.e., ICP-05, UWA-05 and Fugro-05) and two non-CPT-based methods (i.e., PARI and API) were included in this study.

Data base of the field piles with both CPT q_{c} and SPT-N profiles are hard to be found, particularly in Japan. Two field piles constructed in the Tokyo Bay construction project provide both SPT-N and CPT q_{c} profiles (Kikuchi et al., 2005; Saimura et al., 2005). The base resistance of the two field piles was evaluated using the design methods. Each of the design methods has their own definitions for many parameters as explained in the following sections.

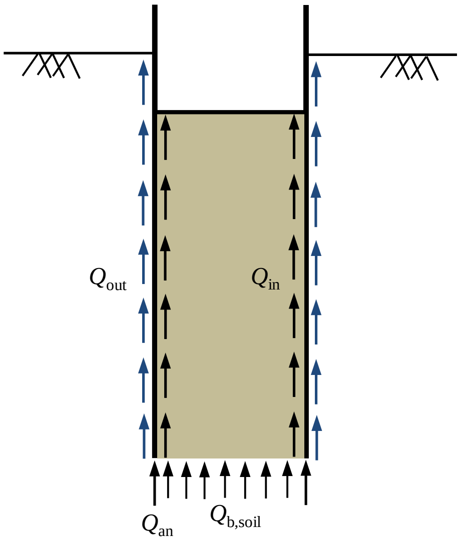

Fig. 1 The bearing capacity of an open-ended pile

ICP-05 Method

ICP-05 design method is based on the cone penetration test (CPT) results (Jardine et al., 2005). The discussion here is limited to the base resistance. The ICP-05 design methods produce design formulae for both sandy and clayey grounds. Inner frictional resistance is not evaluated separately. The base resistance of an unplugged open-ended pile driven in sandy soil is given in Eq. 3. The $q_{c,avg}$ is determined taking the average of CPT q_c within ± 1.5*D* (*D* is pile outer diameter) from the pile tip as suggested by Bustamante and Gianeselli (1982) (also known as the Dutch method).

$$q_b = A_r q_{c,avg} \tag{3}$$

Where q_b is base resistance, A_r is area ratio (see Eq. 4) and $q_{c,avg}$ is average CPT resistance.

$$A_r = 1 - \left(\frac{d}{D}\right)^2 \tag{4}$$

Where A_r is area ratio, *d* and *D* are inner and outer pile diameter respectively.

An open-ended pile is considered plugged if the following conditions are satisfied. Otherwise it is considered an unplugged pile.

$$d < 0.02(D_r - 30) \text{ and } \frac{d}{D_{CPT}} < 0.083\frac{q_c}{p_a}$$

Where *d* is inner pile diameter (in meters), D_r is relative density (in percentage), D_{CPT} is diameter of CPT probe (in meters), q_c is CPT resistance and p_a is reference pressure (i.e., 100 kPa).

The base resistance of a plugged open-ended pile is evaluated using Eq. 5. Equations 3 and 5 simply imply that a plugged open-ended pile produces a larger base resistance than a similar unplugged open-ended pile. In Eq. 5, there are two lower limits provided for a fully-plugged open-ended pile (i.e., the capacity of the unplugged pile by $A_r q_{c,avg}$ and the capacity predicted for the piles of D > 0.9 m by $0.15q_{c,avg}$ (Jardine et al., 2005).

$$q_b = q_{c,avg}\text{Max}\left(0.5 - 0.25\log\left(D/D_{CPT}\right), 0.15, A_r\right) \tag{5}$$

Where q_b is base resistance, $q_{c,avg}$ is average CPT resistance, *D* is outer pile diameter, D_{CPT} is diameter of CPT probe and A_r is area ratio (see Eq. 4).

UWA-05 Method

UWA-05 design method was developed largely from the ICP method by incorporating several modifications (Lehane et al., 2005). Hence, it considered a larger data base than the ICP and Fugro methods. This method, unlike other CPT-based design methods, introduces an effective area ratio, which combines the incremental filling ratio and annular area ratio of the pile (Gavin and Lehane, 2003; White et al., 2005). This method proposes a single equation for both closed- and open-ended piles as given in Eq. 6. The effective area ratio (see Eq. 6) becomes unity for closed-ended piles (i.e., A_{ef} = 1).

$$q_b = q_{c,avg}\left(0.15 + 0.45A_{ef}\right) \tag{6}$$

Where q_b is base resistance, $q_{c,avg}$ is average CPT resistance and A_{ef} is effective area ratio (see Eq. 7).

$$A_{ef} = 1 - FFR\left(\frac{d}{D}\right)^2 \tag{7}$$

Where A_{ef} is effective area ratio, *FFR* is final filling ratio (see Eq. 8), *d* and *D* are inner and outer pile diameter respectively.

$$FFR = \text{Min}\left[1, \left(\frac{d}{1.5}\right)^{0.2}\right] \tag{8}$$

Where *FFR* is final filling ratio and *d* is inner pile diameter (in meters).

The FFR is the incremental filling ratio (IFR) defined for the final 20 diameters of penetration. When the information of IFR is not available, Eq. 8 is used to determine the FFR. The $q_b/q_{c,avg}$ ratio in Eq. 6 depends on the annular area and the degree of soil plugging over the final stages of pile driving. This ratio varies from 0.15 for a thin-walled open-ended pile (i.e., 1 of *FFR*) to 0.60 for a fully-plugged pile (i.e., 0 of *FFR*) similar to a closed-ended pile.

The $q_{c,avg}$ is determined according to the Dutch method as simplified in Eq. 9 (Schmertmann, 1978). The CPT resistance in the zone A, $q_{c,A}$ (see Eq. 9 and Fig. 2) is the average of the envelope of minimum cone resistance recorded above the pile tip over 8*D* (*D* is pile outer diameter) distance. The CPT resistance in the zone B, $q_{c,B}$ is evaluated using Eq. 10.

$$q_{c,avg} = 0.5\left(q_{c,A} + q_{c,B}\right) \tag{9}$$

Where $q_{c,avg}$ is average CPT resistance, $q_{c,A}$ and $q_{c,B}$ are CPT resistance of zone A and B respectively.

$$q_{c,B} = 0.5\left(q_{c,avg,B} + q_{c,min,B}\right) \tag{10}$$

Where $q_{c,B}$ is CPT resistance of zone B, $q_{c,avg,B}$ is the average cone resistance recorded below the pile tip over 0.7 – 4*D* distance and $q_{c,min,B}$ is the minimum cone resistance recorded below the pile tip over the same distance of 0.7 – 4*D*.

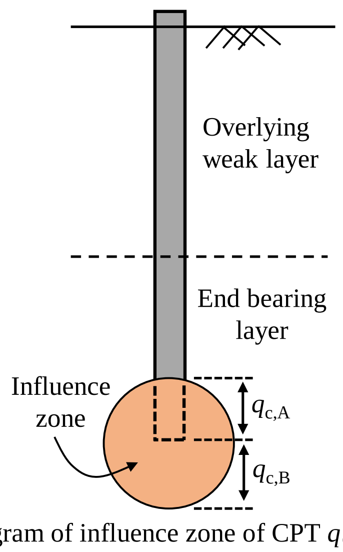

Fig.2 Schematic diagram of influence zone of CPT q_c resistance

However, in the UWA-05 design method, the pile diameter, D is used only for the closed-ended piles. It is replaced by the effective pile diameter given in Eq. 11 for open-ended piles.

$$D_{\mathrm{ef}} = D A_{\mathrm{ef}}^{0.5} \tag{11}$$

Where D_{ef} is effective pile diameter, D is pile diameter and A_{ef} is effective area ratio (see Eq. 7).

Fugro-05 Method

The Fugro design method also proposes a single equation for both closed- and open-ended piles as given in Eq. 12 (Kolk et al., 2005). The area ratio (in Eq. 12) becomes unity for closed-ended piles (i.e., $A_{\mathrm{r}} = 1$).

$$\boldsymbol{q_{\mathrm{b}} = 8.5 q_{\mathrm{c,avg}} \left(\frac{p_{\mathrm{a}}}{q_{\mathrm{c,avg}}}\right)^{0.5} A_{\mathrm{r}}^{0.25}} \tag{12}$$

Where q_{b} is base resistance, $q_{\mathrm{c,avg}}$ is average CPT resistance, p_{a} is reference pressure (i.e., 100 kPa) and A_{r} is area ratio (see Eq. 4).

The $q_{\mathrm{c,avg}}$ is determined taking the average of CPT q_{c} within ± 1.5D (D is pile outer diameter) from the pile tip same as in the ICP method.

API Method

The base resistance is evaluated using Eq. 13 (API, 2005). The dimensionless bearing capacity factor (see Eq. 13) depends on the soil type and soil density. The value of N_{q} can be read from a table given in API (2005). The table also gives the limiting base resistances for particular ground conditions (see Table 1).

$$q_{\mathrm{b}} = \sigma_{\mathrm{v}}' N_{\mathrm{q}} \tag{13}$$

Where q_{b} is base resistance, σ_{v}' is effective overburden pressure at the pile tip and N_{q} is dimensionless bearing capacity factor (see Table 1).

PARI Method

PARI design method is based on the SPT-N value (PARI, 2009). Since Japanese companies do not encourage CPT-based design methods, this is quite popular in offshore foundation designs in Japan. The base resistance is evaluated using Eq. 14. The degree of soil plugging is incorporated into the base resistance by a non-dimensional parameter, α.

$$q_{\mathrm{b}} = 300 \alpha N^* \tag{14}$$

Where q_{b} is base resistance, α is a dimensionless parameter and N^* is evaluated as given in Eq. 15.

$$N^* = 0.5(N_1 + N_2) \tag{15}$$

Where N^* is the design SPT-N value, N_1 is SPT-N value at the pile tip (≤ 50) and N_2 is the average SPT-N value recorded above the pile tip over 4D (D is pile outer diameter) distance.

Table 1 Design parameters for cohesionless siliceous soil (modified from API, 2005)

Density	Soil description	Soil-pile friction angle (degree)	N_{q}	Limiting unit end bearing resistance (MPa)
Very Loose	Sand	15	8	1.9
Loose	Sand-Silt			
Medium	Silt			
Loose	Sand	20	12	2.9
Medium	Sand-Silt			
Dense	Silt			
Medium	Sand	25	20	4.8
Dense	Sand-Silt			
Dense	Sand	30	40	9.6
Very Dense	Sand-Silt			
Dense	Gravel	35	50	12.0
Very Dense	Sand			

Unlike the CPT-based design methods, the PARI method does not take account the ground condition below the pile tip when evaluating the design SPT-N value. Table 2 briefly summaries the influence zones applied for CPT- and SPT-based design methods. It clearly indicates that the influence zone defined in each design method is different to each other except between the ICP and Fugro methods, which used the same method.

Table 2 The influence zone for the average CPT-q_{c} or SPT-N values

Design method	Above pile tip	Below pile tip
ICP	1.5D	1.5D
UWA	8D	0.7-4D
Fugro	1.5D	1.5D
PARI	4D	-

Note: D is pile outer diameter

RESULTS AND DISCUSSIONS

The details of the two field piles can be found in Kikuchi et al. (2005). Fig. 3 shows the ground profile at the T4 and T5 piles. T4 and T5 piles are embedded into sandy gravel and solid sand layers respectively. The dry density, ρ_{t} of clayey and sandy soils were taken as 1400 – 1550 and 1700 -1750 kg/m^3 respectively. The ρ_{t} of sandy gravel and solid sand were taken as 2208 and 1850 kg/m^3 respectively (Kikuchi et al., 2005). The water level is at 7 m from the pile head. The base resistance of the two piles were evaluated at 73.5 and 86 m depths for T4 and T5 piles respectively. CPT q_c and SPT-N profiles at the site is shown in Figs. 4a and 4b respectively.

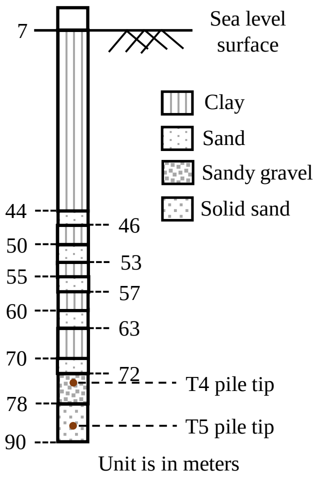

Fig. 3 The ground profile at the site (modified from Kikuchi et al., 2005)

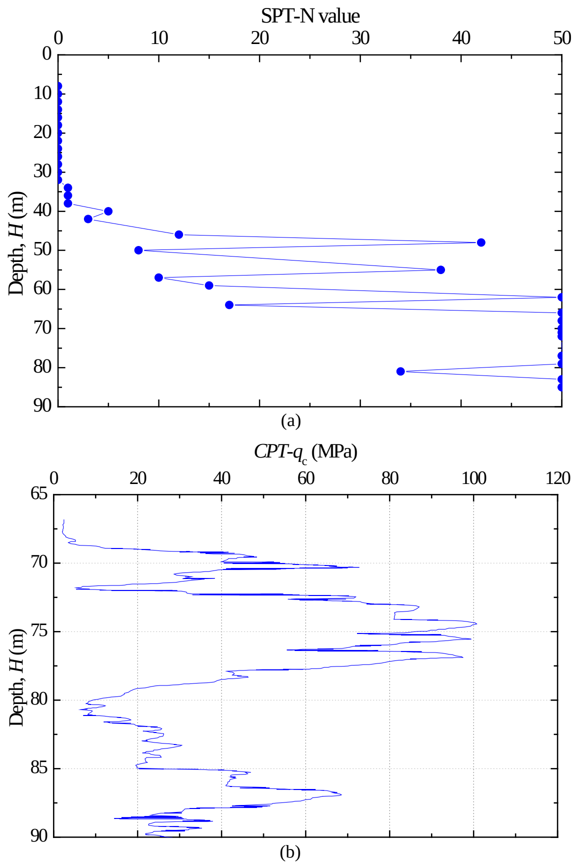

Fig. 4 (a) SPT-N profile (modified from Kikuchi, 2008) and (b) an enlarged CPT q_c profile at the pile tip (modified from Yu and Yang, 2012)

CPT resistance in the zone A and B, $q_{c,A}$ and $q_{c,B}$ respectively (see Fig. 2) for ICP-05 and Fugro-05 methods are 50.14 and 89.57 MPa respectively for T4 pile. The design CPT q_c value (i.e., $q_{c,avg}$) for ICP-05 and Fugro-05 design methods then becomes 69.86 MPa for T4 pile. $q_{c,A}$ and $q_{c,B}$ for UWA-05 method are 27.66 and 80.42 MPa respectively for T4 pile. The design $q_{c,avg}$ then becomes 54.04 MPa. Therefore, we can see that the design CPT q_c value is different among the design methods (except between the ICP and Fugro methods). The $q_{c,avg}$ for T5 pile is summarised in Table 3 along with T4 pile. $q_{c,B}$ for UWA-05 (see Eq. 10) was evaluated for 4D (D is pile outer diameter) distance below the pile tip as the variation of CPT q_c was non-uniform.

Table 3 The results of $q_{c,avg}$ for the CPT-based design methods

Design method	$q_{c,A}$ (MPa)		$q_{c,B}$ (MPa)		$q_{c,avg}$ (MPa)	
	T4 pile	T5 pile	T4 pile	T5 pile	T4 pile	T5 pile
ICP	50.14	31.16	89.57	50.75	69.86	40.95
UWA	27.66	20.90	80.42	34.78	54.04	27.84
Fugro	50.14	31.16	89.57	50.75	69.86	40.95

The value of α (see Eq. 14) was taken as 0.302 using a non-linear relationship proposed for the data available in PARI (2009) as shown in Fig. 5. Fig. 5 also indicates that a linear relationship would produce a larger value of α (i.e., 0.396) which then will produce a larger base resistance (see Eq. 14). N_1 and N_2 were found to be 50 and 45 respectively (see Eq. 15). Therefore, the design SPT-N value (i.e., N*) for the PARI method becomes 47.

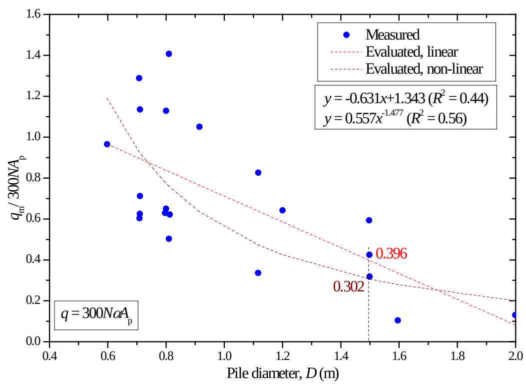

Fig. 5 The results of α parameter (modified from PARI, 2009)

Figures 6a and 6b show the base resistance of T4 and T5 piles respectively. The results clearly suggest that API and Fugro methods overestimates the base resistance in both piles. In fact, the API method gives 12.84 and 14.97 MPa for the base resistance of T4 and T5 piles respectively by Eq. 13, which are much higher than the corresponding measured values (i.e., 8.88 and 6.37 MPa respectively). However, since the API method assigns a limiting value (see Table 1), the limiting values were used in

Figs. 5a and 5b. In both T4 and T5 piles, N_q was assumed to be 40. However, given the soil condition, the use of even 50 of N_q is possible, which then would have overestimated the measured values by even a larger margin. This design method is quite tricky compared to the other methods since it does not take variations within a soil type. All other design methods discussed on this paper incorporate average behaviour of the ground at the pile tip, either as an average CPT q_c or SPT-*N* value.

On contrast, ICP and PARI methods underestimate the base resistance in both piles (see Figs. 6a and 6b). Therefore, based on a conservative approach, we can recommend the ICP and PARI methods for the evaluation of base resistance of unplugged open-ended piles. However, they underestimate the base resistance by a big margin. The PARI method considers the SPT-*N* values less than 50 (see Eq. 15). Therefore, it is worthwhile to study how a corrected *N* value might be influenced the base resistance. Also, it was understood that the PARI method does not incorporate the ground conditions below the pile tip like all the CPT-based methods do. Given the ground conditions below the pile tip is stiffer than the above it (in both piles, see Fig. 4b), a design formula incorporating it will produce a higher base resistance, which then would reduce the gap between the measured and designed values.

Among the design methods discussed here, the UWA method produces the nearest values to the measured base resistance although it overestimates the base resistance for one pile by a small margin (see Fig. 6a). Therefore, based on a rational approach, we can recommend the UWA design method. Only the UWA method incorporates the incremental filling ratio (as a function of final filling ratio) to the design base resistance. The degree of soil plugging is described by the incremental filling ratio to a greater degree. Therefore, the UWA method incorporates the degree of soil plugging in the base resistance.

As aforementioned, both the ICP and Fugro methods assign the same criterial for the design CPT q_c value (see Table 2). However, they underestimate and overestimate the base resistance respectively in both piles. Therefore, we can understand that not only the evaluation method of the design CPT q_c but also the other parameters contribute to the difference among the design methods.

The results on this paper were produced only from two field piles. Therefore, we recommend that the modifications to the existing design methods should be proposed after a number of field piles are studied. Given the field piles with both SPT-*N* and CPT q_c profiles cannot be found in Japan, the overseas projects with both SPT-*N* and CPT q_c can be studied. This study though provides the basic of a comparison of the SPT- and CPT-based design methods. We plan to extend this study further by increasing the number of field piles analysed in near future. Then, we will propose modifications to the existing design methods.

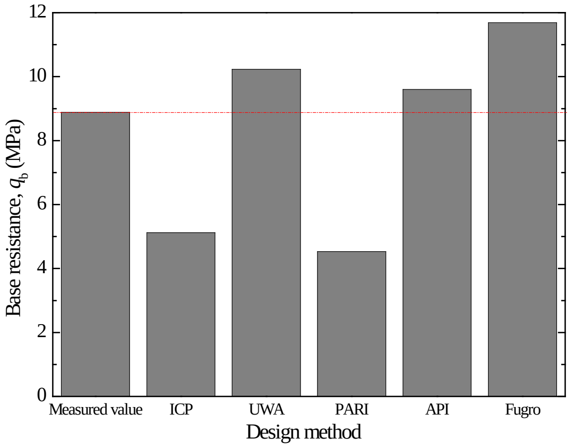

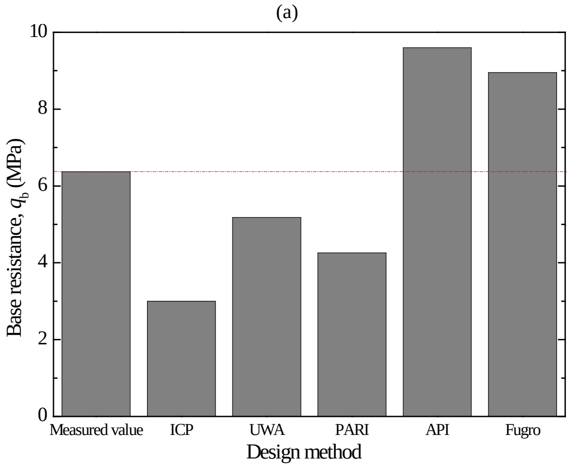

Fig. 6 Base resistance of (a) T4 and (b) T5 pile respectively

CONCLUSSIONS

The base resistance of two field piles constructed in Tokyo bay project was determined by five different design methods. The study includes both CPT- and SPT-based design methods. The following conclusions are drawn from the study.

The closest results to the measured base resistance was achieved by the UWA design method, which is the only method incorporates the incremental filling ratio (or degree of soil plugging) explicitly.

The ICP and PARI (a method practiced popularly in Japan) underestimate the base resistance, approximately by similar margins. A use of the corrected SPT-*N* value in the PARI method would have reduced the gap between the designed and measured values. Also, incorporating the ground conditions below the pile tip like in the CPT-based design methods may reduce the variation. Therefore, further study on the PARI method is recommended.

API design method overestimates the base resistance. The dimensionless parameter (i.e., N_q) suggested for the soil type and density needs a further study as it could result a base resistance deviated much from the actual value.

Fugro method gives the least matched results to the measured base resistance. Given other CPT-based design methods give better results, we do not encourage the use of Fugro method for open-ended piles.

ACKNOWLEDGEMENTS

The financial assistance to the first author through a President Postdoctoral Fellowship by Tokyo University of Science, Japan is highly appreciated. The financial supports for the research works provided by the Japan Iron and Steel Federation (JISF) and International Press-in Association (IPA) are also acknowledged.

REFERENCES

[1] Kikuchi, Y., Kusakabe, O., Fukui, J., Sasaki, H., Geshi, H., Saimura, Y., Nishimura, N. and Sakai, K. (2005), Proc. of 40th JGS Annual Conference, Hakodate, Japan, pp. 1671–1672 (in Japanese).

[2] Saimura, Y., Kusakabe, O., Kikuchi, Y., Fukui, J., Sasaki, H. and Geshi, H. (2005), Vertical bearing capacity of large diameter steel pipe piles in Tokyo port seaside road project, Proc. of 40th JGS Annual Conference, Hakodate, Japan, pp. 1673–1674 (in Japanese).

[3] Jardine, R.J., Chow, F.C., Overy, R.F. and Standing, J.R. (2005), ICP design methods for driven piles in sands and clays, Telford, London.

[4] Bustamante, M. and Gianeselli, L. (1982), Pile bearing capacity prediction by means of static penetrometer CPT, Proc. of 2nd European Symposium in Penetration and Testing, Amsterdam, 493-500.

[5] Lehane, B.M., Schneider, J.A. and Xu, X. (2005), The UWA-05 method for prediction of axial capacity of driven piles in sand, Proc. of International Symposium on Frontiers in offshore Geomechanics, Taylor and Francis, London, 683-689.

[6] Gavin, K.G. and Lehane, B.M. (2003), The shaft capacity of pipe piles in sand, Canadian Geotechnical Journal, 40(1), 36-45.

[7] White, D.J., Schneider, J.A. and Lehane, B.M. (2005), The influence of effective area ratio on shaft friction of displacement piles in sand, Proc. of International Symposium on Frontier in Offshore Geotechnics, Perth, Australia.

[8] Schmertmann, J.H. (1978), Guidelines for cone test, Performance and Design (No. FHWATS-78209), US Federal Highway Administration, Washington, D.C.

[9] Kolk, H.J., Baaijens, A.E. and Senders, M. (2005), Design criteria for pipe piles in silica sands, Proc. of International Symposium on Frontiers in offshore Geomechanics, Taylor and Francis, London, 711-716.

[10] API (2005), Recommended Practice for Planning, Designing and Constructing Fixed Offshore Platforms - Working Stress Design, American Petroleum Institute (API), Washington, USA.

[11] PARI (2009), Technical Standards and Commentaries for Port and Harbour Facilities in Japan, The Overseas Costal Area Development of Institute of Japan, Port and Airport Research Institute (PARI), Yokohama, Japan.

[12] Kikuchi, Y. (2008), bearing capacity evaluation of long, large-diameter, open-ended piles, In Proc. of 6th International Conference on Case Histories in Geotechnical Engineering, Arlinton, USA, 11-16 Aug, pp. 1-21.

Fifth International Conference on Geotechnique, Construction Materials and Environment, Osaka, Japan, Nov. 16-18, 2015, ISBN: 978-4-9905958-4-5 C3051

MEASUREMENT OF ARITHMETICAL MEAN ROUGHNESS OF CONCRETE SURFACE BY TRANSCEIVER TYPE AERIAL ULTRASONIC SENSOR

NAGAOKA Seiya*, OKAJIMA Kenji*, ISHIGURO Satoru*, ITO Ryouei*, WATANABE Ken** and ITO Tesu***

*Graduate school of Bioresources, Mie University, 1577 Machiyacho, Kurima, Tsu, Mie 514-8507, JAPAN
**Maruei concrete industry Co., Ltd., 1518 Majima, Fukujyu-machi, Gifu 501-6293, JAPAN
***X-ability Co., Ltd., 4-15 Hongo, Bunkyo-ku, Tokyo 113-0033, JAPAN

ABSTRACT

In the hydraulic performance malfunction of the concrete agriculture irrigation canal the roughness coefficient is assumed one of the evaluation criteria. The arithmetical mean roughness of the concrete surface is applied to the estimate of the roughness coefficient. In this study, we suggested the measurement method of the roughness of the concrete surface using the aerial ultrasonic wave of the transceiver type. We examined the influence of the dispersion of measured values, relations between the arithmetical mean roughness and the peak to peak value of the reflection wave, influence of wet and dry of concrete surfaces and the verification about the measurement rang. As a result, following became clear. The peak to peak value of reflection wave could estimate arithmetical mean roughness well. In addition, the arithmetic average of 15 times measurement values was sufficient accuracy. The peak to peak value of the reflection wave was little affected under wet condition. The aerial ultrasonic wave measured the diameter in the approximately range 600(mm) from distance of 1000(mm). The aerial ultrasonic wave measured the diameter in the approximately range 300(mm) from distance of 550(mm). The results of this study reveal that measurement of the arithmetical mean roughness of the concrete surface can using the aerial ultrasonic sensor of transceiver type.

Keywords: aerial ultrasonic, peak to peak value, Arithmetical mean roughness, Hydraulic performance, Functional diagnostic

1. INTRODUCTION

Japan has possessed main concrete agriculture irrigation canals that have total length of 49,239km. These were constructed since 1954-1973 of the high economy growth. When canals became too old for work, they were necessary to be repaired. Especially, the hydraulic performance malfunction is used it as the repair factor. However, visual inspection is often used in the general maintenance of the roughness of the canal. Some canals managers want to assess quantitative of the roughness of the concrete surface of the canal quantitative. Since main concrete agriculture irrigation canals have enormous length, the method is required of quantitative assessment that is simple, short time and economical.

Flow velocity decreasing and water level raising are caused by the roughness of the concreate surface. These hydraulic performance malfunction of the concrete agriculture irrigation canal the roughness coefficient is assumed one of the evaluation criteria. The arithmetical mean roughness of the concrete surface is applied to the estimate of the roughness coefficient. However, the simple, short time and economical measurement of the arithmetical mean roughness is difficult. Over the years, considerable attention has been paid to the study of measurement of the arithmetical mean roughness. The first attempt to assess the roughness of the concrete surface of the canals was made by reference [7]. Reference [7] suggested using the moulage gauge in the measurement of the arithmetical mean roughness. This method is the simple measurement, since managers only pushes the moulage gauge to the concrete surface. However, managers need complication analysis that read displacement from one by one the moulage gauge. Reference [5] suggested using the laser displacement sensor in the measurement of the arithmetical mean roughness. Measurement range of this method is line information of the concrete surface. Reference [4] suggested using the three dimensional image processing in the measurement of the arithmetical mean roughness. Measurement range of this method is line information without three dimensional image of the concrete surface. However, these method is not used in the general maintenance of the roughness of the canal. Since the agriculture irrigation canals is long total extension distance, managers request measurement of wide range.

In this study, we attempted using the aerial ultrasonic wave of the transceiver type in the measurement of the arithmetical mean roughness. The wave of the aerial ultrasonic wave has characteristic of spreading wide. Experiment date was acquired by the oscilloscope. In addition, measurement interval is 25 times per second. This method can have potential of the simple, short time and economical quantitative assessment.

In this study, first, we examined of the dispersion of the measurement value. Next, we examined relation between the peak to peak value and the arithmetic mean roughness. Next, we examined the influence of wet and dry of concrete surfaces. Last, we verified the measurement range.

2. THE MEASUREMENT EQUIPMENT

We used LZ-EZ1 (MaxBotic, Inc) as the aerial ultrasonic sensor of transceiver type. The sensor used designed for the ultrasonic measuring sensor. We selected a frequency from relationship of attenuation in the air. Since ultrasonic waves higher 80kHz in frequency attenuates from distance of 2000(mm) and ultrasonic wave of the lower 20kHz in frequency may become the audible range, we selected about the 40kHz. The ultrasonic wave of 40kHz can measure from distance of 500~2000(mm) without attenuation. Next, we compared the open type (the sensitivity: min. -80.5dB) and the waterproof type (the sensitivity: min. -58.2dB) in sensitivity. The open type has 13 times higher sensitivity than the waterproof type at each output voltage. So, we selected the open type. But measurement of the aerial ultrasonic wave must limit not to get wet. Other specification shows table.1. Experiment date of the peak to peak value was acquired by the digital oscilloscope TBS1152 (Tektronix, Inc).

Table 1 Specification the aerial ultrasonic transducer of transceiver type

frequency		42	KHz
dimension	A	16.4	mm
	B	15.5	
	C	19.9	
	D	22.1	
weight		4.3	grams

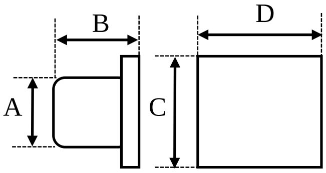

3. THE MEASUREMENT PRINCIPLE

Figure1 shows the measurement principle of measurement of the arithmetic mean roughness of the concrete surface by the aerial ultrasonic wave of transceiver type. The wave of the aerial ultrasonic wave is reflected by the concrete surface. The reflection wave was diffusely reflected by the roughness of the concrete surface. We evaluated amount of the reflection wave with the peak to peak value. The peak to peak value is difference between the maximum value and the minimum value of the reflection wave value.

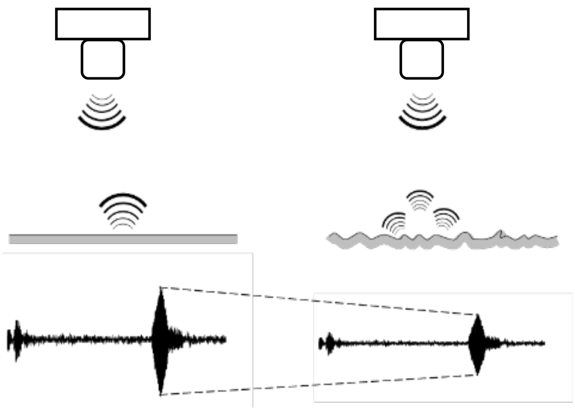

Figure 1 The measurement principle of the ultrasonic sensor

4. ARITHMETIC MEAN ROUGHNESS

4.1 The Moulage Gauge and Determination

In this study the arithmetic mean roughness was measured by the moulage gauge. The length of the moulage gauge is 147(mm). The number of steel sticks is 183. Measurement interval is 0.8(mm). Figure2 shows the measurement surface of the arithmetic mean roughness 0.30(mm).

Figure3 shows the image of the arithmetic mean roughness. The formula $\boldsymbol{f}_{(\boldsymbol{x})}$ is the roughness curve of the concrete surface. The formula $\boldsymbol{Y}_{(\boldsymbol{x})}$ is liner approximation that is calculated from the roughness curve.

R_a is calculated by ration between the integral value of $|f_{(x)} - Y_{(x)}|$ and the length of the moulage gauge.

$$R_a = \frac{1}{l}\int_0^l |f_{(x)} - Y_{(x)}|\, d_{(x)} \qquad (1)$$

R_a: The arithmetic mean roughness
$f_{(x)}$: The roughness curve
$Y_{(x)}$: The Formula of liner approximation
l: The length of the moulage gauge

Figure 2 The measurement surface of the arithmetic mean roughness in 0.30(mm)

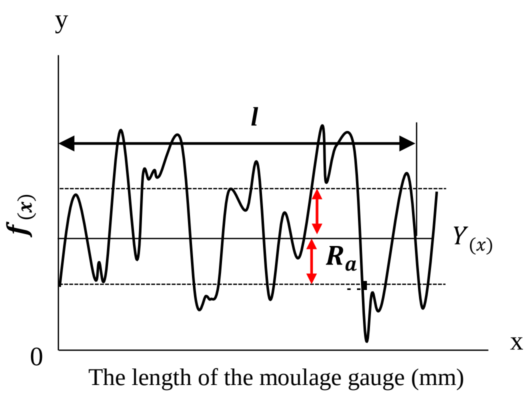

Figure 3 The image of the arithmetic mean roughness

4.2 Selected Measurement Surface

Reference [7] indicated the relationship between the arithmetical mean roughness and the number of years of the agriculture irrigation canals. The agriculture irrigation canal used 40 years, the arithmetical mean roughness becomes approximately 0.7(mm). We were selected in consideration of soundness of the canal.Table2 shows examination items and the arithmetical mean roughness.

Table 2 examination items and the arithmetical mean roughness

Ra (mm)	Dispersion	Application	Wet
0.00		○	
0.30	○	○	○
0.37		○	
0.45	○	○	○
0.67		○	

5. EXAMINATION ITEM

5.1 The Dispersion of The Measurement Value

Measurement of the aerial ultrasonic wave has the dispersion of the measurement value. Therefore, the dispersion of the measurement value needs to be decreased by the average of times. This experiment of purpose that decides the average of times of the measurement value.

We measured the peak to peak value. We measured 119 times. We got 100 sample of the moving average of 1~20 times. We evaluated ration between the standard deviation and the mean value of the moving average. The aerial ultrasonic measured from distance of 1000(mm) and 550(mm).

Figure4 indicated that the dispersion of the measurement value decreased so that the arithmetic average increased. The dispersion of the measurement value in 550(mm) tended to be larger than in 1000(mm). However, the arithmetic average of 15 times restrained the dispersion of the measurement value in 550(mm) and 1000(mm). The 15 times of average of measurement value is sufficient accuracy. In this study measurement value defines it as the average of 15 times.

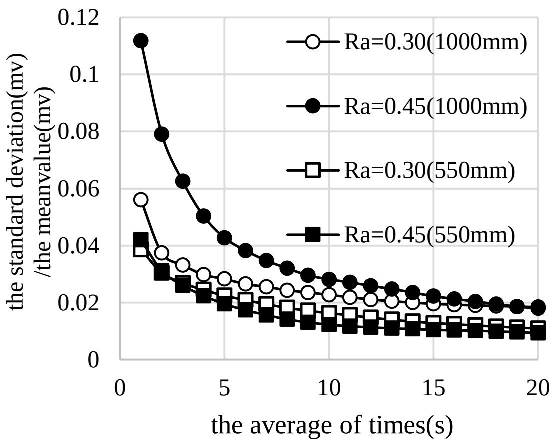

Figure 4 The dispersion of the measurement value

5.2 The Application of Measurement of The Arithmetical Mean Roughness

We measured the peak to peak value. The aerial ultrasonic measured from distance of 1000(mm). We measured five concrete surfaces that is 0.00~0.67 (mm) in the arithmetical mean roughness.

It is clear from figure5 that the peak to peak value was decreased with increasing the arithmetical mean roughness. In addition the formula of liner approximation had high correlational relationship. The formula of liner approximation is used to estimate the arithmetic mean roughness from the peak to peak. Measurement of the transceiver type aerial ultrasonic wave can estimate the arithmetical mean roughness well.

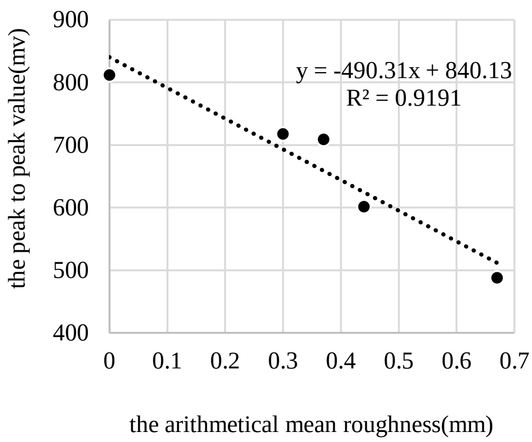

Figure 5 The relationship between the peak to peak value and the arithmetical mean roughness

5.3 Influence of Wet and Dry of Concrete Surfaces

When managers measure agriculture irrigation canals, the canals don't have the water level during non-irrigation period. But, it may rain on the measurement day before. We expected that many canals can be wet condition of the concrete surface. We evaluated the effect of the measurement value by the concrete surface condition. We compared and examined the measurement value of wet and dry of concrete surfaces.

When we reproduced wet condition of the concrete surface, we noted to be water pocket in the roughness depression. The aerial ultrasonic measured from distance of 1000(mm).

Table3 shows the measurement value of wet and dry of concrete surfaces. The measurement value of wet was a little larger than dry. We were able to guess that water filled the roughness depression of the concrete surface. Therefore, the arithmetic mean roughness was decreased. However, figure3 indicates that the standard deviation of the arithmetic average of 15 times from distance 1000(mm) was ±15.7(mv). Since the difference of the measurement value was within the range of the standard deviation, we concluded that whether wet or dry of concrete surfaces do not have influence the measurement value. Fig6 shows reflected waveforms from wet and dry of concrete surfaces. Waveforms were not different from wet and dry. Here those can be seen that the peak to peak value of the reflection wave was little affected under wet condition.

Table 3 The Measurement value of wet and dry

	wet (mv)	dry
Ra=0.30 (mm)	717.6	704.4
Ra=0.45	601.5	590.1

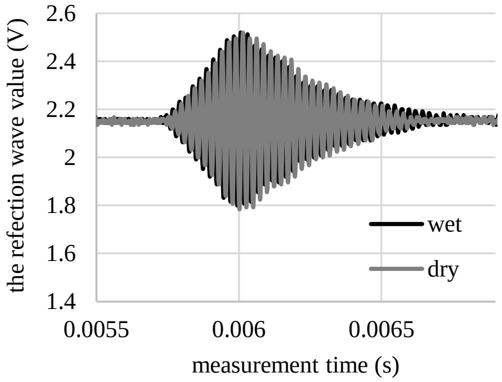

Figure 6 Reflected waveforms from wet and dry of concrete surfaces in Ra=0.30(mm)

5.4 The Verification of The Measurement Range

Measurement of the aerial ultrasonic can measure the wide range. However, the measurement range that has inference on the measurement value is uncertain. To calculate the correct measurement range is almost impossible. The purpose is to clarify the measurement range that has inference on the measurement value.

Figure7 shows the experiment principle. We examined measurement range by widening diameter of the grave on the flat board. The flat board is 0.00(mm) in the arithmetic mean roughness. The grave of particle size is 2mm. Figure8 shows the used grave. The aerial ultrasonic measured from distance of 1000(mm) and 550(mm).

Figre9 and 10 indicate that the peak to peak value was decreased with widening diameter of the grave.

Fig9 shows the relationship between peak to peak value and diameter of grave from distance of 1000(mm). When the grave diameter is 200(mm), the peak to peak was largely decreased. When the grave diameter is 200~400(mm), the peak to peak was few decreased. After 600(mm) in diameter of the grave, the peak to peak was not changed. Since 600(mm) in diameter of the grave presumably exceed measurement range, the upper limit of the measurement range is approximately 600(mm) in diameter.

Figure10 The relationship between peak to peak value and diameter of grave from distance of 550(mm). When the grave diameter is 200(mm), the peak to peak was largely decreased. When the grave diameter is 200~300(mm), the peak to peak was few decreased. After 300(mm) in diameter of the grave, the peak to peak was not changed. Since 300(mm) in diameter of the grave presumably exceed measurement range, the upper limit of the measurement range is approximately 300(mm) in diameter.

The dominant range of measurement is approximately 200(m) in diameter from distance of 550~1000(mm). The measurement range was large in proportion to the measurement range and in proportion to square of the measurement distance

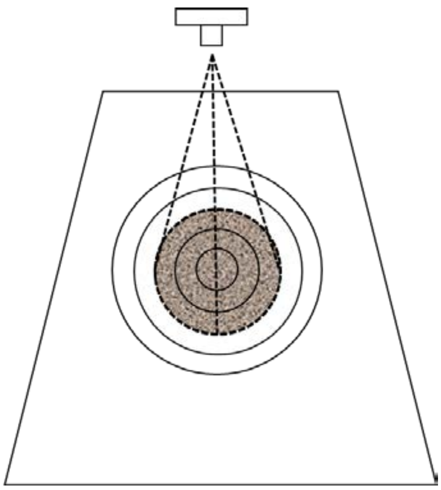

Figure 7 The diagram of experiments for searching the measuring range

Figure 8 The used grave

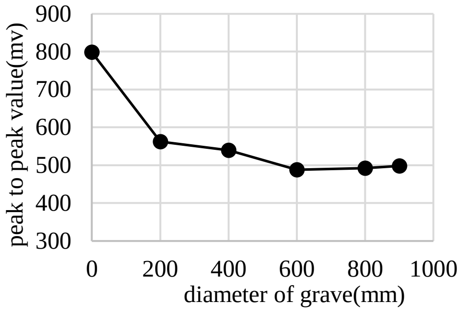

Figure 9 The relationship between peak to peak value and diameter of grave from distance of 1000(mm)

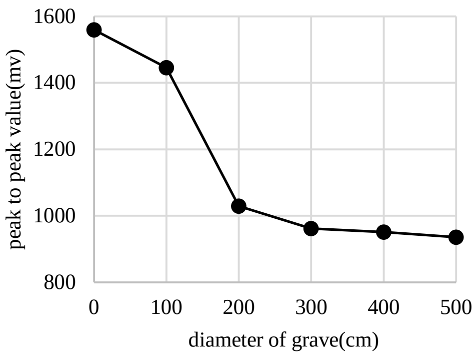

Figure 10 The relationship between peak to peak value and diameter of grave from distance of 550(mm)

6 CONCLUSION

We examined influence of the dispersion of the measurement values, relation between the arithmetical mean roughness and the peak to peak value of the reflection wave, influence of wet and dry concrete surfaces and the verification of the measurement rang. As a result, following became clear. The peak to peak value of the reflection wave could estimate the arithmetical mean roughness well. The average of 15 times of measurement values were sufficient accuracy. The peak to peak value of the reflection wave was little affected under dry condition. The aerial ultrasonic wave measured the diameter in the approximately range 600(mm) from distance of 1000(mm). The aerial ultrasonic wave measured the diameter in the approximately range 300(mm) from distance of 550(mm). The dominant range of measurement was 200(m) in diameter from distance of 550~1000(mm). Measurement range was large in proportion to measurement range and in proportion to square of the measurement distance.

When manager estimate the arithmetical mean roughness, only evaluate the peak to peak of the reflection wave. Manager can measure wet condition of the concreate surface. We think of measurement range is wide. The results of this study reveal that measurement of the arithmetical mean roughness of the concrete surface can using the aerial ultrasonic sensor of transceiver type.

It remains a challenge for future research to verification of the measurement in various weather such as temperature and wind velocity, and measurement of the canal on field.

ACKNOWLEDGEMENTS

This study is funded by the Ministry of Agriculture, Forestry and Fisheries.

REFERENCES

[1] Horiguchi K, “ Wear of concrete-The state of the Art-“, Concrete Journal, Vol. 31, No.10, pp. 17~22, Oct. 1993.

[2] Kitamura K, Honma S and Kato T, “Quantitative Evaluation for Forecast of Irrigation Canal Abrasion”, J of Water, Land and Environmental Engineering , Vol 76, No. 9, pp. 823~828, Sep. 2008

[3] Uchida K, Ishida M and Ogawa S, “Estimation of the Coefficient of Roughness for Irrigation Canals by Transcription Method for Concrete Surface”, presented at JSIDRE, pp. 432~433, 2008.

[4] Otagaki K, Hasegawa Y, Suzuki T, Matsumoto S and Sato S, “Study on Measurement Method of Surface Roughness of Concrete Canal by Three Dimensional Image Processing “, J of JSIDRE, NO. 280, pp. 7~13, Aug 2013.

[5] Nakaya T, Tokashiki M, Mori M and Mori T, “Estimation of the Coefficient of Roughness from Surface Characteristics og Abraded Concrete Channel”, Trance of JSIDRE, No. 258, pp. 23~28, Dec 2008.

[6] Tokashiki M, “ Studies on Erosion Mechanism and Accelerated Erosion Test of Concrete Irrigation Canal” Bull. Natl. Inst. Rural Eng. Japan, Vol. 52, pp. 1~57, 2013.

[7] Kato T, Honma S, Kitamura K and Imaizumi M, “Deterioration of Irrigation Canals and Change in Roughness Coefficient”, Tech. Rep. Natl. List. Rural Eng. Japan, Vol. 207, pp. 183~193. 2008.

[8] Nagaoka S, Tago Y, Okajima, K, Ishiguro S, “Measurement of roughness of concrete surface using airborne ultrasound”, presented at JSIDRE, pp 7~13, 2014.

Fifth International Conference on Geotechnique, Construction Materials and Environment, Osaka, Japan, Nov. 16-18, 2015, ISBN: 978-4-9905958-4-5 C3051

OVERTURNING AND SLIDING STABILITY OF THE GEOTEXTILE REINFORCED TIDE WALL FOR OVERFLOW

Naoki OYAMA[1], Yutaka HASHIZUME[2] and Kenji KANEKO[3]
[1,2,3]Civil Engineering, Hachinohe Institute of Techology, Japan

ABSTRACT

The authors aiming at development of new tide wall reinforced by geotextile technology. We examined the most suitable tide wall shape for tsunami energy reduction. As the results, we understood that the steep slope was more effective than the traditional tide wall for the tsunami energy reduction. In this study, we examined mechanical stability of the steep slope tide wall reinforced by geotextiles for overflow tsunami. At first, we installed pressure gauges in the rigid model and measured horizontal tsunami pressures. We considered the measured forces to the external forces and designed the tide walls which changed some parameters.

We carried out tsunami model experiments to examine for overturning and sliding stability. As the results, it were found of the following things. Tide wall were not destroyed by the first wave impulsively, it were destroyed lately by the water buoyancy after the overflow Tsunami. When we designing an advanced toughness tide wall for overflow tsunami, It must substitute the submerged unit weight instead for wet unit weight in the equation of stability calculations.

Keywords: Geotextile Reingorced Tide Wall, Overflow, Tsunami Force, Stability

INTRODUCTION

Tide wall is most important structure in the tsunami disaster prevention. it is built to defend from the tsunami a living space and life behind slightly land side from the coastline as the main purpose. In response to the 2011 earthquake, tsunami measures in soft surfaces, such as those related to refuge are bathed in the leg light, and earn the time of refuge, in order to reduce the damage of the hinterland to reduce the energy of tsunami as much as possible the embankment is still important. However, since it is a structure that functions only once tsunami decades or hundreds of years has not been performed so many studies. In 2011 the generated tsunami by Tohoku region Pacific Ocean earthquake, many seawalls have been destroyed. Therefore, Enormous human and material damage has occurred in the hinterland. From the 2011 off the Pacific coast of Tohoku Earthquake, study on the tide wall have been promoted. Many of study are attention to the erosion of scouring and tide wall of toe of slope ground by overflow tsunami [1]–[3].

Many of the civil engineering structures, its own strength and stability are primarily studied. Tide wall reducing the damage behind the main purpose is different from the general civil engineering structures. The authors, first, by tsunami Hydraulics test by rigid-body model that changing the shape of the tide wall, was examined gradient optimal seawall in reduction in the tsunami energy. As a result, compared to the gradient used in the conventional tide wall, the sea side and land side slope both in the case of a steep tide wall is greatly reduced tsunami energy [4]. As a technique for building a steep slope tide wall, it is also conceivable to use concrete. However, because it is exposed to the combined degradation environment of the freeze-thaw and salt damage, the durability becomes a problem especially in cold climates. So, for the tide wall by reinforced embankment by geotextile, to consider the stability against tsunami, stable results were obtained. However, the width of the tide wall in these experiments is set very large. In this study, we examined mechanical stability of the steep slope tide wall reinforced by geotextile for overflow tsunami.

At first, we installed pressure gauges in the rigid model and measured horizontal tsunami pressures. We considered the measured forces to the external forces and designed the tide walls which changed some parameters. We carried out tsunami model experiments to examine the stability of designed tide wall model. As the experimental results, we got the some important knowledge to design a tenacious tide wall.

MEASUREMENT OF THE TSUNAMI WAVE FORCE BY THE RIGID BODY MODEL

At first, in order to measure the wave force for overflow tsunami, an experiment was conducted by using a rigid model and open channel equipment. In this study, we measured tsunami external force for design external force. For the tide wall design,

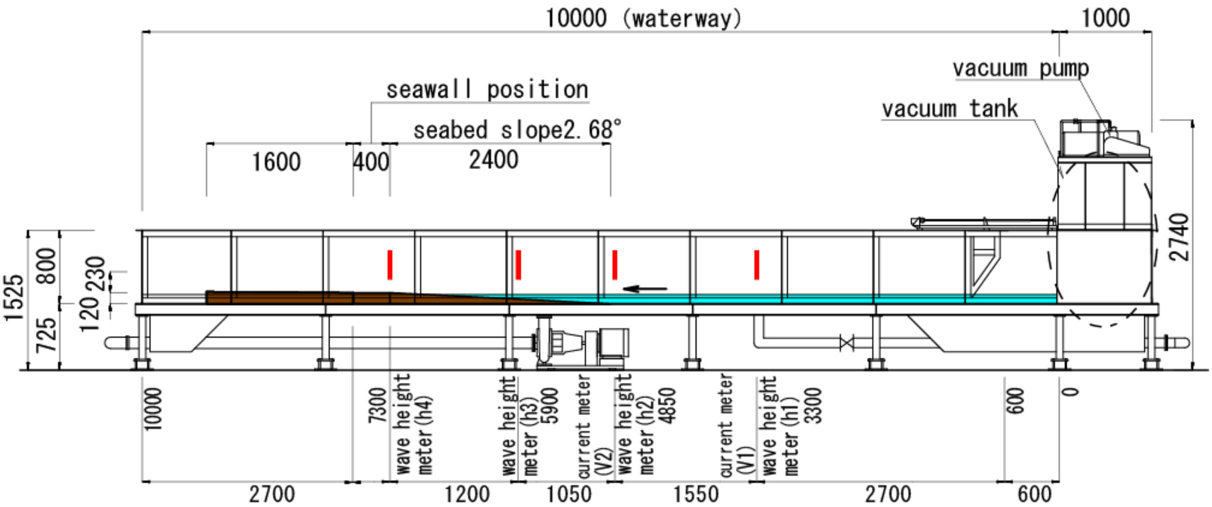

Fig.1 Open channel equipment

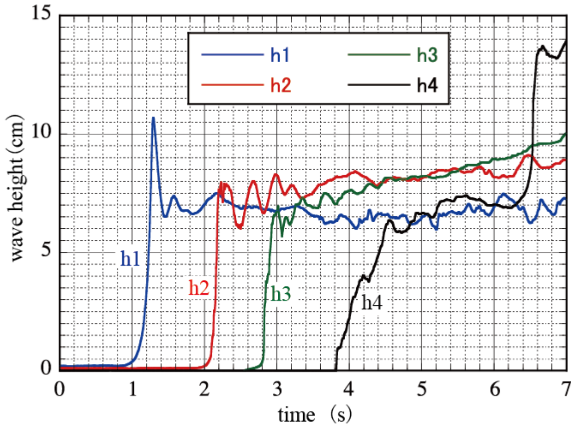

Fig.2 Results of wave height meter

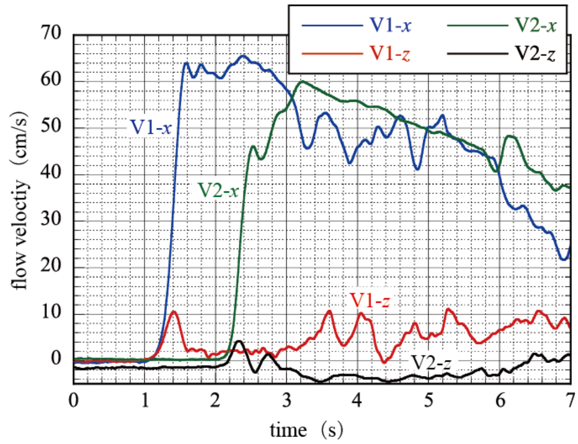

Fig.3 Results of water velocity meter

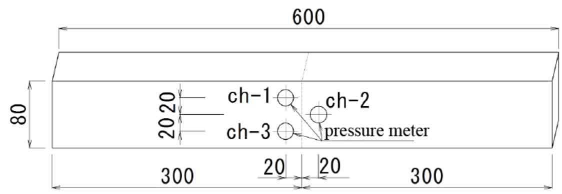

Fig.4 Installation position of the rigid model dimensions and wave pressure gauge

knowledge about the wave force to act on a tide wall by a tsunami is important. There is intended to discuss it and erforms the experiment here to set external as existing intellect.

Experiment Outline

It is shown in Fig.1 experiment device of the mimetic diagram. The experiment, fixed a rigid model after having created rigid basic ground model made by stainless steel in these open channel equipment. Rigid-body model is modeled to scale 1/100 assuming a seawall height 8.0m, it was reproduced in 80mm height of the tide wall model.

In this study, is adopt the bore wave which is the form that is the nearest to a real tsunami as an action wave in all experiment cases. The result of the wave height is shown in Fig.2 and the flow velocity is shown in Fig.3. Installation position of the wave height meter or the flow velocity meter is as shown in Fig.1. Horizontal direction of the flow rate of just before the seabed gradient maximum is about 60cm/s, the flow rate of the vertical direction is small. From the results, wave velocity is about 1.6 m/s. it will become 50 km/h if it calculation by the Froude similarity rule. Speed of tsunami observed in the vicinity of land at the time of the Tohoku-Pacific Ocean earthquake in 2011 is several hundred km/h or several decades km/h, it can be said that a reasonable flow velocity. From the figure, the reproducibility of the wave action is very good.

In order to measure the horizontal Tsunami pressure acting on the seawall, a wave pressure

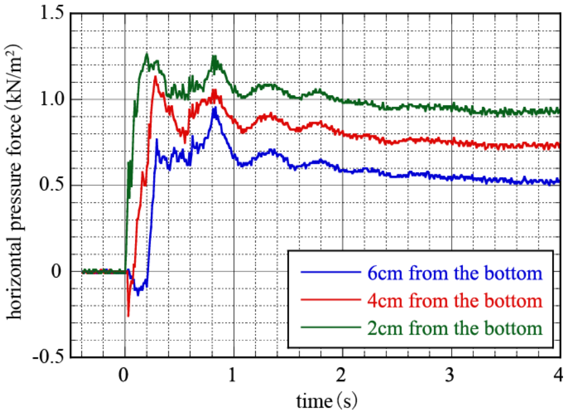

Fig.5 Measurement results of the horizontal pressure

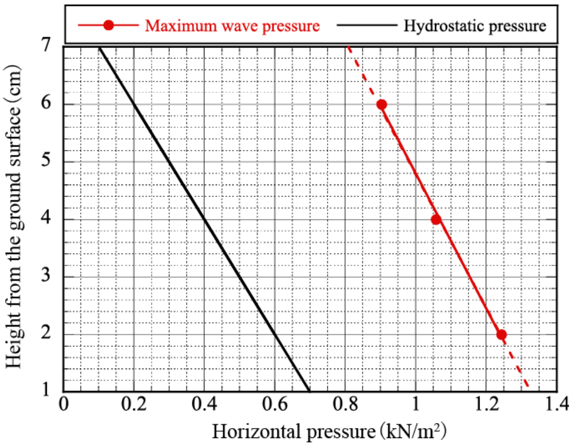

Fig.6 Vertical distribution of horizontal pressure

gauge was placed in different sea side three-point height on the rigid body model shown in Fig.4. We assume it ch-1, ch-2, ch-3 from the vertical direction top. The wave pressure meter examines it in resting hydraulic pressure and confirms that I show accurate numerical value. In addition, I decided to perform three times of experiments. In addition, as a result of having confirmed it about the horizontal distribution of the tsunami wave force preliminarily, we understand that hardly change.

Experimental Result

It is shown in Fig.5 measured change of horizontal pressure of the three waves pressure meter. From the Fig.5, The distributed over the depth direction and near to the foundation ground, it understood that the effect is greater pressure. If bore waves of such long period as a tsunami, it is considered that constant pressure is exerted over a little more time. In this study, we decided to carry out the design of tide walls based on maximum shock load. We decide to use a similar tsunami in the following experiment.

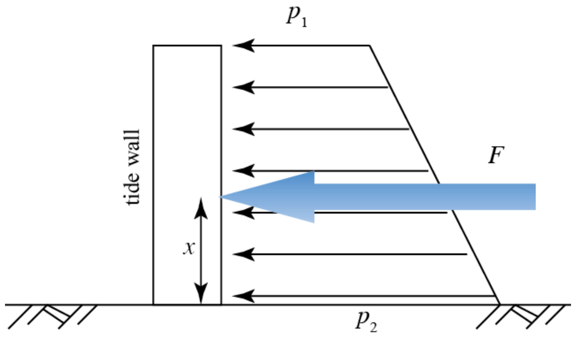

Fig.7 The horizontal external force by the assumed tsunami

Table.1 Position of the resultant force and the action point

	P_1(kN/m²)	P_2(kN/m²)	F(kN/m²)	x(m)
	124.32	90.36	854.6	3.58
Design value	—	—	860	3.6

In Fig.6, maximum shock pressure generated in shock, it shows the relationship between the height from the horizontal pressure. Here, the horizontal pressure acting on the upper part of the tide wall, as shown in Fig.7 p1, the horizontal pressure acting on the lower p2, was calculated by using these approximate straight line. Furthermore, we assumed trapezoid distribution and demanded horizontal resultant force F and action height x. I show these calculation results in table.1. In addition, in the table, similarity law in consideration of a 1/100, and is expressed in full-scale units. Three times experiment result average is 854.6 kN/m. In addition, the action height becomes 3.58m. We decided to use horizontal load 860kN/m, action height 3.6m in as design external force to perform in a following chapter.

DESIGN OF THE GEOTEXTILE REINFORCED TIDE WALL

Examination of the stability for the tsunami is a main purpose in this study. It was with the design external force the tsunami wave force (Horizontal action force) shown in the previous chapter. It examined the external stability for the tsunami of the tide wall mainly. For review of these overall stability, since even scouring measures such as the peripheral ground must be examined and taking into account, this is not performed. In addition, of the external stability, it is thought that there is not much influence by the tsunami either about the support power. From that, it was considered not covered in this study.

Table.2 Fundamental soil propetys

soil material	silica sand No.5	ferro-nickel slag
ρ_s(g/cm^3)	2.603	3.232
U_c	2.29	28.89
U_c'	1.21	0.75
w_{opt}(%)	15.492	8.282
ρ_{dmax}(g/cm^3)	1.662	2.246
Φ_d(°)	31	40

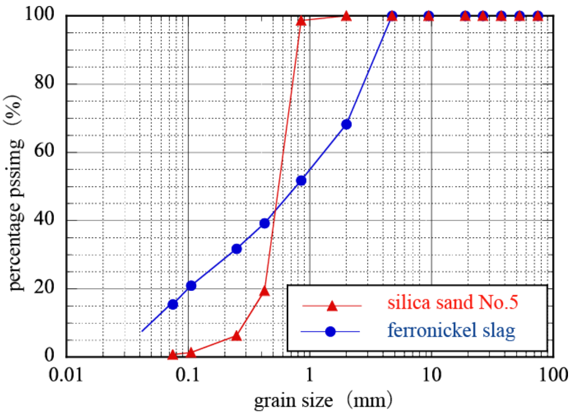

Fig.8 Grain size distrubution

Table.3 The result of the design

cese No.	embankment material	Width (cm)	F_s	M_R/M_0	$e(L/6)$
cese 1	silica sand No.5 (degree of compaction 90%)	7.5	1.010	1.823	2.057
cese 2		8.5	1.112	2.274	1.869
cese 3		10.0	1.265	3.044	1.643
cese 4	ferro-nickel slag (degree of compaction 95%)	3.0	0.902	0.498	3.010
cese 5		5.0	1.253	1.154	2.167
cese 6		6.5	1.516	1.815	1.791

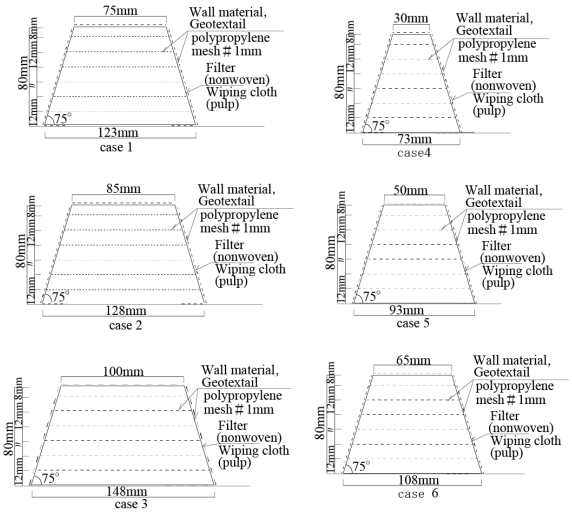

Fig.9 Figure of summary of the tide wall model

Design Condition

Tide wall height (8m), material (silica sand No. 5, ferro-nickel slag), geotextile material species and, position and spacing of the height direction was Table.2 Fundamental soil propetys unified. Fig.8 shows the grain size distribution curve of silica sand No.5 and ferro-nickel slag. Table.3 shows the basic nature. The geotextiles materials assumed standard SR-80.

Internal Stability

In this study, slope gradient of tide wall is 1:0.3. It is classified in reinforced soil wall. Here, we examine the external stability by the tsunami. In this internal stability, tide wall examined whether it could stand in the steep slope. In addition, we made a model on a scale of 1/100. The laying distance assumed it 1.2m. (The model is 1.2cm)

External Stability

The examination of the sliding stability is resistance divided by sliding-energy and it compare with the safety factor. It is shown in following equation.

$$F_s = \frac{cL + \mu \Sigma V}{\Sigma H} \geq 1.5 \qquad (1)$$

Where ΣV is vertical load in the embankment bottom (kN/m). ΣH is horizontal load in the embankment bottom (kN/m). L is the embankment bottom width. μ is the coefficient of frictionor. c is cohesion. In this case, the calculation of the vertical load by the embankment deadweight is determined by multiplying the embankment sectional area in the unit volume weight (Volume per unit length). In this study, tide wall is assumed tsunami on overflow, it becomes a situation where embankment is immersed in water. From these, wet unit weight and submerged unit weight design it with both cases, we decided to weigh it.

Consideration of overturning is all overturning moment around the embankment toe and where e is action point eccentric distance of the resultant force of resistance moment. To judge stability whether not become the middle third of the bottom width. It make a decision that we are safe if satisfied without tensile stress occurring on all parts of the bottom. As indicated by the following equation. In addition, unit volume weight is included the resistance moment calculation formula, we designed it using two kinds of unit volumes weight like a sliding calculation.

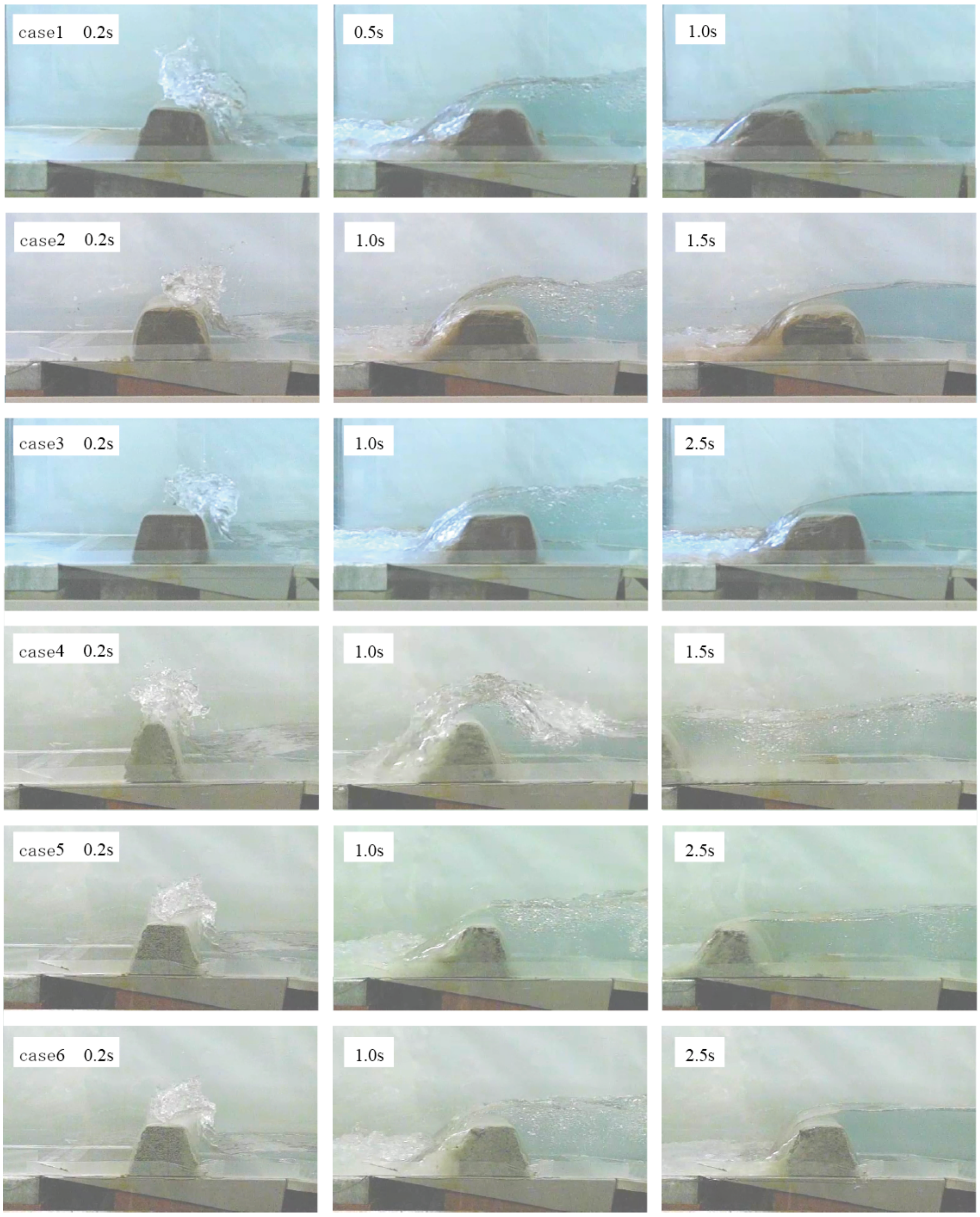

Fig.10 State of overflow of the geotextiles seawall

$$d = \frac{\Sigma M_R - \Sigma M_0}{\Sigma V} \quad (2)$$

$$e = \frac{L}{2} - d \leq \frac{L}{6} \quad (3)$$

Where $\boldsymbol{d}$ is distance from the embankment toe to the action point of the resultant force $\boldsymbol{R}$. $\Sigma \boldsymbol{M_R}$ is resistance moment around the toe. $\Sigma\ \boldsymbol{M_0}$ is overturning moment around the toe. $\boldsymbol{e}$ is resultant force. $\boldsymbol{R}$ is deviation from the embankment bottom center of the action point. The result of the design, the tide wall embankment of 6 cases in the above manner is shown in table.3. In the next chapter, we made a model of 1/100.

It produced the tsunami like two chapters. It is considerd the stability. We examine the design condition. It is shown in Fig.9.

TSUNAMI HYDRAULIC EXPERIMENT OF GEOTEXTILES REINFORCEMENT TIDE WALL

In this chapter, it was modeled on the basis of the geotextile reinforced soil tide wall of design in the previous section. We examined the experimental study of the sliding and the overturning in the external stability. Also, because the foundation ground was made of stainless, in order to ensure the boundary friction between the model and foundation, the same sand was sandwiched between them.

Outline of The Experiment

The embankment material is at same size and using readily available silica sand No.5. And, it uses a large slow cooling ferro-nickel slag of density than silica sand. That adjusted it to optimum moisture content and made soil compaction reinforcement soil model to become degree of compaction, 90% and 95%. The first layer from on the wall height and 8cm is 0.8cm, from the second layer to the sixth layer created the tide wall embankment is divided into seven layers of each 1.2cm. Geotextile reinforcement material and wall material was using polypropylene (mesh 1mm × 1.03mm). As a model of retaining sheet, used a wiping cloth made of pulp. In addition, cover the whole laying embankment in wall material to prevent the scour caused by the tsunami. Fine consistency of real thing and a model by the similarity law cry caught, also has not been carried out measurement of strain such as reinforced material.

Tsunami action waves used in the experiment is the same as Section 2. (Fig.2, 3) The tide wall model assumed it case 1-6 shown in the foregoing chapter. We photographed the state of the tsunami which did overflow by video camera, and it is observing the fracture morphology.

Experimental Result

Show a state of overflow of the tide wall model in Fig.11. In any case, integral structure of the reinforced soil wall is not lost even if can be overflow, shape by geotextile reinforcement is maintained. In Case 1, 2, 5, it is withstand the maximum pressure wave, but sliding occurred after overflow.

From a photograph, the timing to sliding by the size of the model are different but it is seen how the model is moving horizontally. In addision, in case 4, it has begun to slide in a state receiving the shock wave force after 0.5s from tsunami arrival. Even if not destroyed it by the impact load during the shock, buoyancy occurs, it is thought that vertical load becomes small very much. Case 3 and 6, it is the most top wide case in each of the embankment material. Stability was high, and the destruction such as slide, and the overturning was not seen in after overflow.

From the above, it can be that reduce the whole embankment by using large on the embankment material of the density as ferronickel slag. In addision, it is thought that it is effective to reduce costs while ensuring stability.

CONCLUSION

In this study, to examine the stability against overturning, sliding of geotextile reinforced tide wall, first, to measure the horizontal pressure of the tsunami in rigid model and determine the horizontal load using these. We designed of geotextile reinforced tide wall using the horizontal load and action point position as external force. The model examined performs the tsunami hydraulic experiment. As a result, we understood the following things,

- If it assume the horizontal external force caused by the tsunami and design it using submerged unit weight, the way of thinking of the stable calculation of basic overturning and slide is proper.
- Geotextile reinforced tide wall is possible to ensure stability by appropriate. Tsunami energy reduction effect is also large.
- From the above, it can be that reduce the whole embankment by using large on the embankment material of the density as ferronickel slag.

For the development of tenacious using the geotextile reinforced tide wall, it includes the future issues of the following,

- Examination of scouring performance of the tide wall for long time overflow.
- Detailed examination of the internal stability and whole stability.
- Examination in consideration of buoyancy is necessary.

REFERENCES

[1] Yanagisawa M, “A New Type Tsunami Barrier Seawall of Sand Dune using Reinfoecing Technology”, Journal of Japan Society of Civil Engineers, Ser. B2 (Coastal Engineering), Vol. 68, No.2, 2012, I_886-I_890.

[2] Kawabe S, “Model Test on GRS-Integral Bridge Affected by TSUNAMI”, Geosynthetics Engineering Journal, Vol. 28, 2013, pp. 245-250.

[3] Tokita K, “Hardware Measures to Advance Toughness ofEarth Bank Against TSUNAMI Flood”, Geosynthetics Engineering Journal, Vol. 28, 2013, pp. 259-264.

[4] Hashizume Y, “Fundamental Hydraulics Model Tests of Tide Embankment Reinforced by Geotextiles For TSUNAMI”, Geosynthetics Engineering Journal, Vol. 28, 2013, pp. 237-244.

Fifth International Conference on Geotechnique, Construction Materials and Environment, Osaka, Japan, Nov. 16-18, 2015, ISBN: 978-4-9905958-4-5 C3051

DEVELOPMENT OF GEOCELL REINFORCEMENT METHOT TO PREVENT THE SCOURING OF THE FOUNDATION OF TIDE WALL

Yuataka HASHIZUME [1], Naoki OYAMA [2] and Kenji KANEKO [3]
[1,2,3]Civil Engineering, Hachinohe Institute of Techology, Japan

ABSTRACT

The tsunami caused by the 2011 earthquake off the Pacific coast of Tohoku inflicted a huge damage on the tide wall of the coastal areas of Tohoku region, due to the large scale scouring of the bottom side of the landside slope. Than those reasons we need know some valid knowledge about constructing the tide wall embankment. But unfortunately we only have few research papers about the tide wall embankment against big Tsunami. In order to prevent the damage of the tide wall by tsunami, it is necessary to protect its foundation by preventing the scouring of the foundation of the landside slope. We conduct several types of comparative experiment changing number and type of reinforcement by geocell (geocell is the one of the geosynthetics material). In an attempt to examine the preventive effect of the geocell reinforcement against the scouring of the foundation of the landside slope of tide wall, in this research, we conducted an experiment using an open channel recirculating water tank and a model ground. As a result, it was found out that it is possible to prevent the scouring and the collapse of the tide wall by combining the geocell and the geogrid reinforcement without using the solidification structure like a concrete structure.

Keywords: Scouring, Tsunami, Geocell

INTRODUCTION

In 2011 the generated tsunami by Tohoku region Pacific Ocean earthquake, many tide walls have been destroyed. As one of the fracture morphology of tide wall, include the scouring of the foundation of the landside slope of tide wall. Tide wall is most important structure in the tsunami disaster, it is built to defend from the tsunami a living space and life behind slightly land-side from the coastline as the main purpose. However, I did not attract attention before the earthquake disaster other than tsunami outbreak because it was unnecessary. In addition, foundation ground scouring has not been performed many studies, because it was assumed not doing overflow. In this study, geosynthetics material examine the preventive effect of the geocell reinforcement against the scouring of the foundation of the landside slope of tide wall, we conducted hydraulic experiment.

EXPERIMENTAL OUTLINE

It is shown in Fig.1 test device of the outline figure. The size of the open channel is channel length L=10m, channel width W=0.6m, channel depth H=0.8m. It is possible to long time maintain a steady overflow for the tide wall model by circulating water using a pump. We made the tide wall model of rectangular thickness 30mm, height 350mm, and width 600mm. It was fixed by foot protection 250mm to the position of 4m from sea

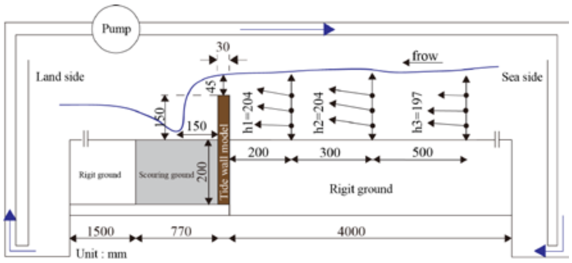

Fig.1 Open channel device

side. Therefore, the height of the tide wall is a 150mm [1]. The foundation ground assumed a rigid ground. We set up the scouring ground between 800mm of tide wall behind. In Fig.1, the part of the scouring ground carried out a preliminary experiment as a rigid ground. It shows the flow of steady overflow state in outline. Tide wall of the sea side is about depth 200mm. Water velocity is about 10cm/s. It was 45mm, and Overflow water depth of the tide wall top was around 30% of the tide wall height. In addition, after the overflow of the tide wall is the distance from the tide wall of the water flow hits the foundation ground was about 150mm.

Test case that was carried out in this study is shown in Fig.2. Test case 0 is the case of unreinforced case, and only scouring ground. Test case 1 is laying a panel made by thickness 2mm, 50mm square aluminum from a tide wall to 300mm as a concrete block model. Test case 2 is laying one layer of geocell from a tide wall to 300mm.

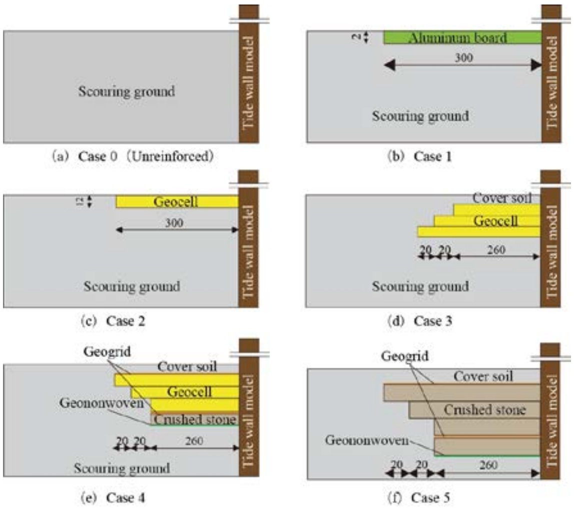

Fig.2 Test case

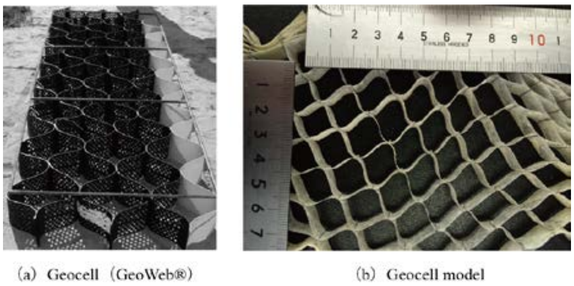

Fig.3 Geocell and geocell model

Test case 3 is pile up a geocell to three layer with cover soil of 1cm and sets it up. Test Test case 4 is laying a geogrid between cover soil and geocell and binds a geocell and a geo-grid in unity wire. Geocell is a three layers, it laying the only crushed stone in the bottom. In addition, we laid a geogrid between the geocell and crushed stone of the bedrock and laying a nonwoven between a scouring ground and the crushed stone layer. Test case 5 is laying only crushed stone to a geocell reinforcement part of Test case 4.

Geocell was created using the polypropylene OHP sheet. we assumed a geocell of 300mm in height to be 1/25 scale model and made a geocell of 12mm in height（Fig.3）. We paste silica sand No.8 of particle size 0.05-0.15mm to reproduce the material of geocell. We assumed broken stone of around 100~250mm for fill material in a geocell and used the crushed stone of 4.75mm~9.5mm. We filled crushed stone in geocell before soil compaction. The silica sand No. 8 in the void of crushed stone was filled with water compaction. In addition, I made the model of the geo-grid with the net of a screen door made by PP. And, we used wiping cloth as nonwoven. Table.1 shows the fundamental soil propatys of the nature sand used in scouring ground. Fig.4 shows the grain size distribution curve. Fig.4 shows the grain size distribution curve.

Table.1 Fundamental soil propetys

soil material	Nature sand
ρ_s(g/cm³)	2.758
U_c	20.00
U_c'	0.49
w_{opt}(%)	17.119
ρ_{dmax}(g/cm³)	1.716
D_{50}	0.70

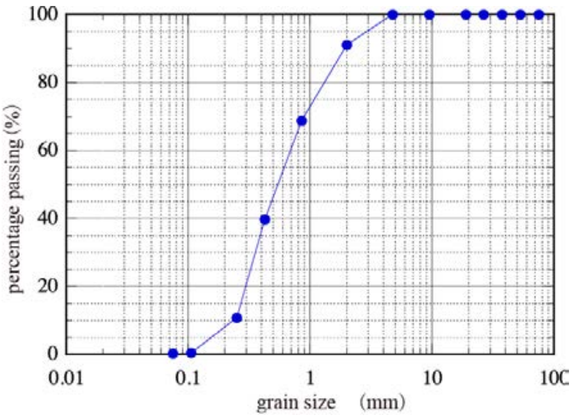

Fig.4 Grain size distrubution

The scouring ground was prepared by compaction divided into 10cm by two layer to be a degree of compaction 90%[2].

EXPERIMENTAL RESULT

It is shown in Fig.5 photos of the experiment. And shown in Fig.6 a the ground surface from the captured image. Scouring begins immediately after the overflow Looking at the case 0 is subjected to the measures, after 180s (Fig.5 (a)) scour has reached the basic bottom panel on the back of expansion Tsutsumi. Tide walls because it is rigidly connected to Shi put roots seawall to the bottom panel in this experiment are self-supporting. However, it is consider that the scouring lacks tide walls stability progressed to support ground of tide walls in the real structure. Test Case 1 is a case that was constructed aluminum panel on the surface of the scouring ground. Immediately after the overflow started (Fig.5 (b)) to begin the panel flows out scouring, the panel that has been involved in water flow faster scouring than the case 0 is observed phenomenon that scrape the sand ground was progress. Case 2 is a case constructed one layer which is reinforced soil by geocell. Immediately

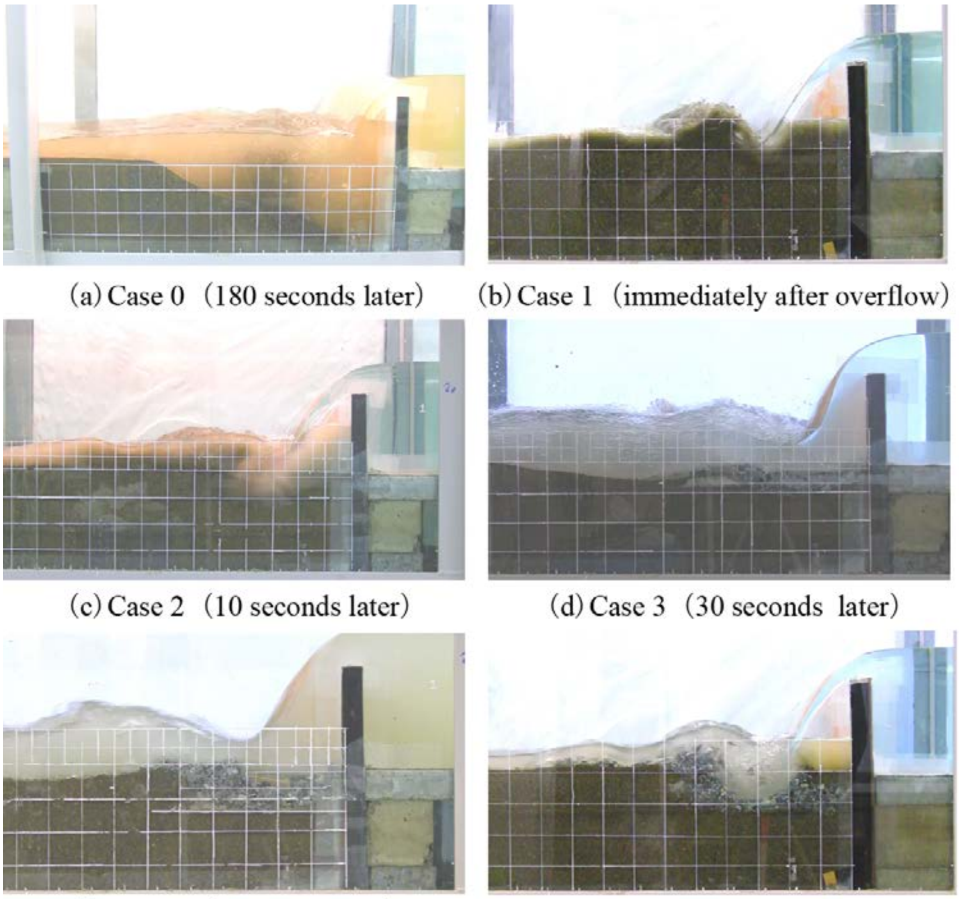

(a) Case 0 (180 seconds later) (b) Case 1 (immediately after overflow)
(c) Case 2 (10 seconds later) (d) Case 3 (30 seconds later)
(e) Case 4 (8 minutes later) (f) Case 5 (5 seconds later)

Fig.5 The conditions of scouring experiment

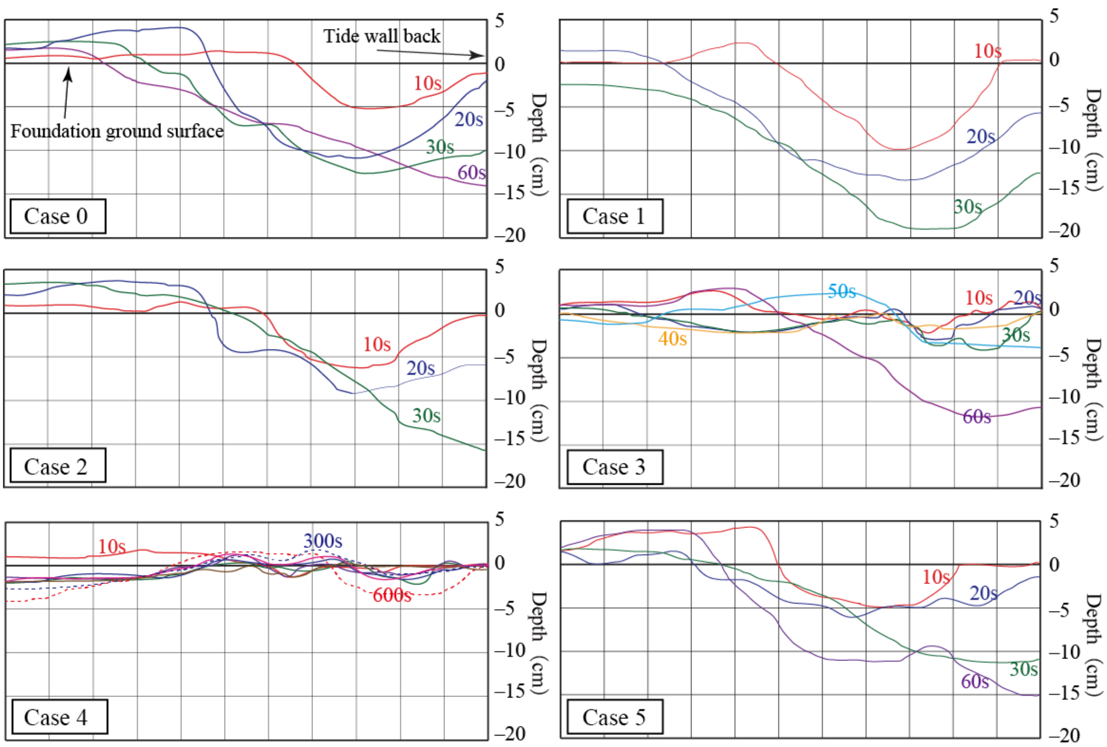

Fig.6 The changes due to scouring of the foundation ground surface

after the overflow stated, the stuffing materials had been flow out. And the geocell its self was also flow out. After the geocell layer has been shed, the scouring is progress in the same manner as the test 0, reinforcing effect of geocell cannot be confirmation almost. Test Case 3 is a case of enforcement three layers of geocell reinforcement. That case was were able to a delay ground scouring beginning over several tens of seconds compared to the three cases described above. But it is not possible to completely reduce the energy of the fluid even in the a three-layers of geocell reinforcement soil part collapse by the stuffing material was leaked in the top and that the sand beneath the geocell layer is flowing out gradually It was leaked. After the reinforcements outflow, scouring has been progress in a short period as well as the experimental cases. Case 4 is the following experiment cases.two sheets of geogrid were laid to The upper and lower surfaces of the three layers of reinforced soil by geocell so as to sandwich, further provided a gravel layer and the nonwoven fabric to the base layer. Tide walls has not occurred even eight minutes after the overflow start is scouring of enough to become unstable. Stuffed material in the top of the geocell the slightly flow out, but reinforced portion is the not collapse. It can be said that some geocell prevent flow out of stuffing materials and it can be reduce the fluid energy that reaches sandy ground. Because of the hardness of reinforced soil, the hydraulic jump has occurred. Shown by Fig.5 (e). If scour does not occur, it can be considered that the overflow tsunami energy may be reduce. For the porpoise of considering effect of scour measures by geocell, we were prepared experimental case 5 that has gravel compaction layers instead of geocell reinforced layers. Based on the result of test case 4. In the case of test 5, because of not using geocell, it cur not expected the confining effect by geocell.

CONCLUSION

In this study, we examined scouring prevention of the tide wall behind using geocell. As a result, I found out that it is possible to prevent the scouring and the collapse of the tide wall, by combining the geocell and the geogrid reinforcement.

As the future issues, the reinforcement pattern of the ground of the tide wall behind is thought about elsewhere. We want to examine rational scouring prevention method by increasing experiment case.

REFERENCES

[1] Minemura R, “A Study on Scouring by Overflow from Seawall and Applcation of an Artificial Trench”, Journal of Japan Society of Civil Engineers, Ser. B2 (Coastal Engineering), Vol. 69, No.2, 2013, I_791-I_795.

[2] Kazama M, “Experiment of The Countermeasure Using Reinforced Soil Method Sgainst to The Scouring at Back Toe of Tide Embankment”, Annual Report of Society for The Promotion of Construction Engineering, No.48, 2013, pp. 11-14.

[3] Hatogai S, “Hydraulic Model Experiments on Scour Landward of The Coastal Dike Induced by Tsunami Overflow”, Journal of Japan Society of Civil Engineers, Ser. B2 (Coastal Engineering), Vol. 68, No.2, 2012, I_406-I_410.

Fifth International Conference on Geotechnique, Construction Materials and Environment, Osaka, Japan, Nov. 16-18, 2015, ISBN: 978-4-9905958-4-5 C3051

EFFECT OF SOIL LIQUEFACTION ON THE NATURAL FREQUENCY AND DAMPING OF PILE-SUPPORTED STRUCTURES

Domenico Lombardi[1] and Subhamoy Bhattacharya[2]
[1] School of Mechanical, Aerospace and Civil Engineering, The University of Manchester, UK; [2]Department of Civil and Environmental Engineering, University of Surrey, UK

ABSTRACT

The effect induced by soil liquefaction on the natural frequency damping ratio of pile supported structures is investigated experimentally by means of a series of tests carried in a shaking table at normal gravity. The supported structures (two single piles and two pile groups) with and without superstructure mass were tested. The experimental investigation aimed to monitor the variation in natural frequency and damping of the four physical models at different degrees of excess pore water pressure generation and in full-liquefaction condition.

The experimental results showed that the natural frequency of pile-supported structures may decrease considerably owing to the loss of lateral support offered by the soil to the pile. On the other hand, the damping ratio of structure may increase to values in excess of 20%. These findings have important design consequences. In fact for low-period structures, substantial reduction of spectral acceleration is expected as a consequence of soil liquefaction.

Keywords: Liquefaction, Piles, Frequency, Damping, Seismic Demand

INTRODUCTION

The seismic design of piles in liquefiable soils is often carried out by considering simplified pseudo-static analyses. Consideration of the dynamic characteristics of the structure is employed only for the assessment of the seismic demand. This is normally determined from acceleration response spectra. In fact, according to conventional seismic methods [1], the seismic demand imposed by an earthquake on a structure can be computed from natural frequency and equivalent viscous damping ratio of the structure. In the routine practice, these are often computed neglecting soil-structure interaction effects and potential effects induced by soil liquefaction phenomena.

This paper presents an experimental investigation on the effect induced by soil liquefaction on the natural frequency damping ratio of pile supported structures. Specifically, a series of tests are carried in a shaking table at normal gravity on four structures comprising of two single piles and two pile groups. The main aim of the tests is to monitor both variation in natural frequency and damping of the four structures at different degrees of excess pore water pressure generation and in full-liquefaction condition.

SHAKING TABLE TESTS

The experimental investigation presented in this paper was performed on the shaking table facility of the Bristol Laboratory for Advanced Dynamics Engineering (BLADE) at the University of Bristol (UK). The soil container, shown in Fig. 1, consisted of a rigid box with external dimensions of 2.4 m length, 2.4 m height and 1.2 m width. The soil container was secured to the shaking table by bolting the bottom plate of the container to the aluminum platform by using a set of steel wedges. The main limitations of using rigid containers were represented by the generation and reflection of P-waves from the end walls. In a typical soil layer, which may be idealized as semi-infinite extended deposit, the energy associated with the wave propagation diminishes gradually with distance. This dissipation may be related to the combined presence of hysteretic and radiation damping as well as the fact that energy is spreading to a larger volume of soil, the so-called geometric attenuation [2]. To minimize the reflection of P waves from the end-walls as well as to aid the dissipation of energy, sheets of absorbing materials were placed on both end-walls of the container [3].

The four structures consisted of two single piles and two pile groups (see Fig. 2). Model “Single Pile – 1” and “Single Pile – 2” corresponded to the single pile models with outer diameter of 25.4 mm and 41.27 mm respectively. Model “Pile Group – 1” and “Pile Group – 2”corresponded to the pile groups, which were composed of four piles having outer diameter of 25.4 mm and 41.27 mm respectively. Aluminium alloy (type L114-T4 6082-T4) was chosen as the material for all piles. The dimensions and mechanical properties of the models are listed in Table 1.

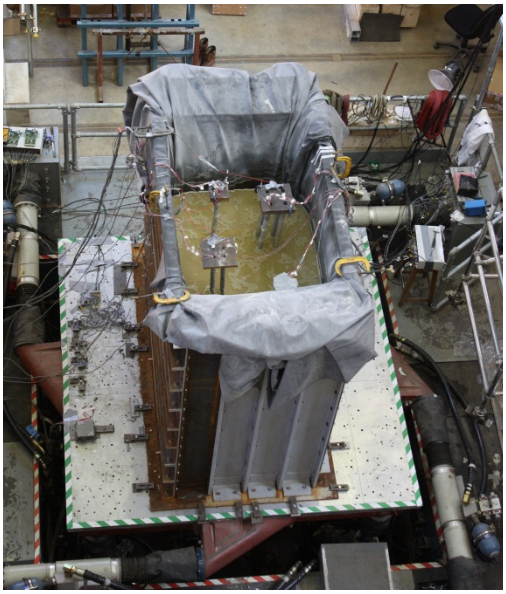

Fig. 1 Experimental rig mounted on the shaking table .

Table 1 Dimensions and mechanical properties of the physical models

Model ID	Outer diameter [mm]	EI [Nm^2]	Pile-cap weight [kg]
Single pile 1	25.4	294	1.9
Single pile 2	41.275	1305	8.44
Group pile 1	25.4	294	13.08
Group pile 2	41.275	1305	22.72

Figure 2 shows a schematic of the instrumentation layout. To estimate the modal parameters of the four structures, namely frequency and damping, each pile-cap was instrumented with an accelerometer. The input motion applied through the shaking table was also recorded by an accelerometer located on the table. Finally the ground response was measured by means accelerometers embedded in the soil deposit as illustrated in Fig. 3. Excess pore water pressure were monitored by means of pore water pressure transducers (PPTs), which were placed at four depths as shown in Fig. 3

The soil container was subjected to broadband random white noise with 0-100Hz bandwidth frequency. This was applied by the shaking table for a total duration of 300s. Specifically, three different acceleration amplitudes, i.e.: 0.02g, 0.04g and 0.15g were applied without stopping the shaking, for a total duration of 100s each. This allowed to monitor the four structures in three different conditions, namely: (i) before liquefaction; (ii) during the transition to liquefaction; (iii) at full liquefaction.

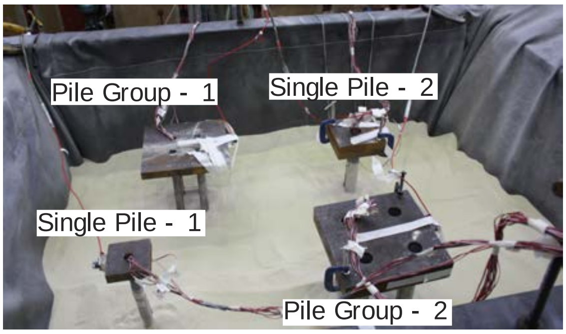

Fig. 2 Experimental rig mounted on the shaking table.

The assessment of frequencies and damping ratios were performed dividing each phase into 15 “blocks” having a duration of 20s each. Considering that the longer the record the higher the frequency resolution is, the length of each block was so determined to obtain an acceptable frequency resolution of the FRF and to ensure that all the frequencies of interest were sufficiently excited. These two considerations may be achieved by choosing a length of the block much larger than the period of the lowest mode of interest. On the other hand, the length of the block cannot be very long, due to the fact that the system under investigation is highly non-linear and therefore its modal parameters are changing with time. In particular, the effect of having blocks of longer duration may cause widening of the spectrum, which may lead to an overestimation of the damping and erroneous assessment of the natural frequency. Subsequently the FRF was evaluated for each block considering the acceleration response recorded by the accelerometer mounted on the shaking table as input, and the response measured by the accelerometer placed on the pile cap as output. To estimate the reliability of all measurements, the associated coherence function was estimated for each FRF. More details about the techniques used for the assessment of the modal parameters can be found in [4], [5].

The damping ratio of the four models was estimated from the width of the resonant peak in the FRF using the “Half-Power Bandwidth Method”. However, in order to achieve accuracy before the assessment of damping, the measured FRF was matched with a theoretical FRF of a single degree of freedom system using a curve fitting technique. The matching was carried out in the vicinity of the resonance peak by minimizing the squared error between the real response and the fitting function. The value of damping was estimated using the Half-Power Bandwidth Method, which was applied on the fitted FRF. Figure 4 shows a flow chart summarizing the different modal analysis procedures employed for the assessment of natural frequencies and damping ratios of the four physical models

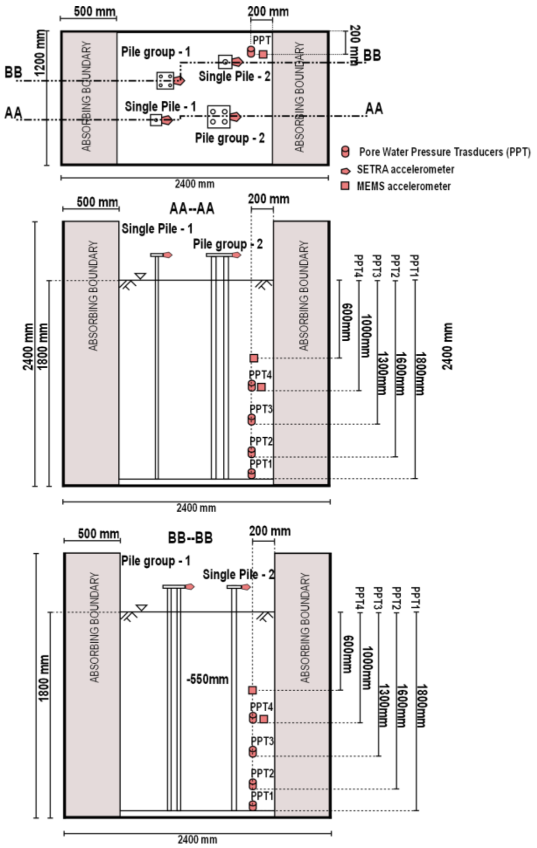

Fig. 3 Schematic of instrumentation layout

EXPERIMENTAL RESULTS (1): VARIATION IN NATURAL FREQUENCY AND DAMPING DURING SOIL LIQUEFACTION

Figure 5 plots the variation of natural frequencies and damping ratios of the structures computed from the acceleration response histories at different degrees of liquefaction. The latter is commonly expressed in terms of excess pore water ratio r_u defined as the ratio between the excess pore water pressure Δu to effective overburden stress σ'_{v0}. The change in frequency is depicted in Fig. 5 in terms of ratio f/f_{inital}, where f is the average value of natural frequency estimated considering a block of 20s, and f_{inital} is the frequency of the system measured in the first 20s of the input. The latter was assumed as the value of frequency in the initial condition.

From Fig. 5 it may be observed that, in the first phase (i.e. 0-100s), the natural frequencies of the models slightly increased with the shaking, and no significant pore water pressure built up in the soil (r_u<0.1). The small increase in frequency was caused by the densification of the soil due to the small amplitude shaking (i.e. acceleration level ~0.02g). In the second phase (i.e. 0-200s), as r_u increased (a maximum of r_u =0.35 was measured at a depth of 1m), the natural frequencies reduced by 20%-25% for models Single Pile – 2 and Pile Groups – 1 and 2 (i.e. f/f_{inital} ~0.80-0.75), although for the Single Pile – 1 this change was considerably lower, probably due to the fact this model tilted slightly during the saturation of the soil.

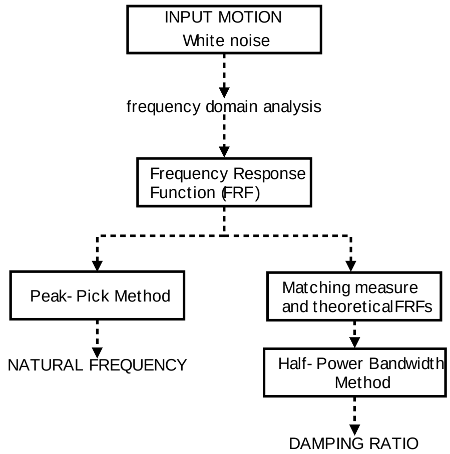

Fig. 4 Modal analysis procedures used for the assessment of the modal parameters.

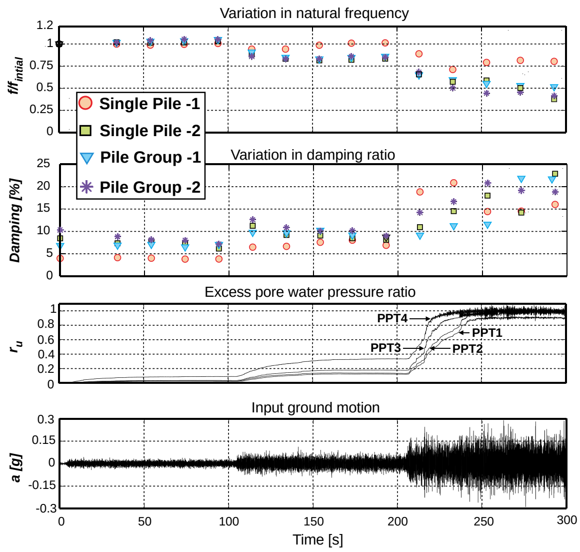

Fig. 5 Variation of natural frequency and damping ratios of the four physical models

During the last phase (200-300s), the amplitude of the input motion was incremented to 0.15g, and the soil started to liquefy from top to bottom, this can be observed from excess pore water pressure ratios plotted in Fig. 5. Full liquefaction was reached at about 250s up to a maximum depth of 1.6m. When this length was compared with the pile's length (2m), a ratio 1.6/2.0 = 0.8 was obtained (i.e. 80% of the pile was fully unsupported). At this stage, the frequency reduced to 20% for Single Pile – 1 (i.e. f/f_{inital} ~0.80), 50% for Pile Group – 1 (i.e. f/f_{inital} ~0.50) and 60% for Single Pile – 2 and Pile Group – 2 (i.e. f/f_{inital} ~0.40).

The variation of the damping ratios of the four physical models is plotted in Fig. 5. It can be recognized that the initial damping ratios of the systems were different, specifically, 5% for Single Pile – 1, around 8% for Single Pile – 1 and Pile Group – 1 and just above 10% for Pile Group – 2. In the first phase of loading (0-100 s), the damping ratios remained approximately constant for all models. In Phase 2 (100-200s), as the acceleration amplitude increased, the damping slightly increased and reached a value of about 10%. At full liquefaction (i.e. after 250s), the models experienced a significant increase in damping ratio up to values above 20%.

EXPERIMENTAL RESULTS (2): EFFECT OF SOIL LIQUEFACTION ON ACCELERATIO RESPONSE SPECTRA

The response spectrum of an earthquake represents a practical tool for determining the seismic input to be considered for designing structures in earthquake-prone areas. However in this research, response spectra are computed in order to better understand the influence of soil-structure interaction on the seismic response of the models prior to and after soil liquefaction. This was achieved by evaluating the response spectra from the time histories recorded in the soil which can be considered representative of the free-field response. Furthermore, to better identify the effects induced by the soil softening, the response spectra from data recorded on the table have been also computed and compared with the spectra associated with the free-field. The structural damping ratio used in the calculation was calculated from the damping ratios of the structures estimated during the free vibration tests before the pluviation of the soil [4], [5]. Therefore, it is important to highlight that this damping reflected only the response of the structure and neglected the additional damping introduced by the flexibility of the foundation and SSI effects. Based on this consideration a damping ratio of 3% was employed in all analyses. Figure 6 shows the computed acceleration response spectra estimated from the accelerometer at 1m depth. The spectra determined from the acceleration time histories recorded on the table have also been plotted in dotted lines for comparison.

It should be noted that the spectral values plotted in Fig. 6 are not pseudo quantities, however, these can be obtained by multiplying the spectral acceleration and velocity by the angular frequency and square angular frequency respectively.

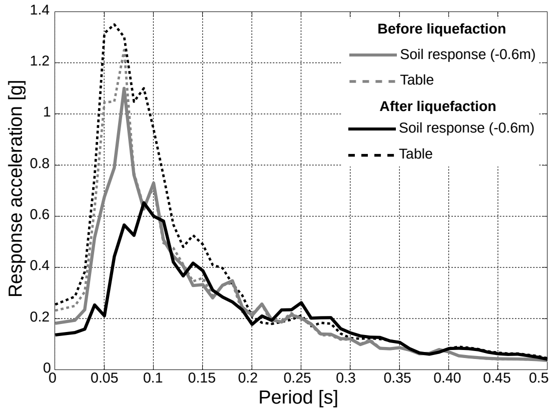

Fig. 6 Computed acceleration response spectra estimated before and at full liquefaction obtained considering an average damping ratio of the models of 3%

The results showed that before liquefaction the highest spectral peak determined from the accelerometer located at 1 m depth, i.e. 1.34g, occurred at 0.07s. It can also be observed that the response spectra of the free-field was very similar in magnitude and shapes with the one obtained from the shaking table, which considered the response at the bedrock. After soil liquefaction, the free-field response spectra exhibited a significant attenuation of the spectral acceleration in the 0.1s to 0.9s period ranges. The de-amplification factor calculated with respect to the response spectra computed on the table after liquefaction (depicted in black dotted line) was by a factor of 1.4. Finally, it can be observed that the response spectra shifted towards long periods, which in turn slightly amplified spectral acceleration beyond 0.9s.

To confirm the de-amplification of the spectral accelerations, the acceleration time histories measured by the accelerometers located on the pile heads of the four structures are plotted in Fig. 7. The measurements clearly demonstrated that with the onset of liquefaction the acceleration response of the models was considerably reduced

CONCLUSIONS

The results presented in this paper focused on the change in natural frequency and damping ratios of four structures due to generation of excess pore water pressure. It is important to note that the full liquefaction condition (i.e. r_u=1.0) was reached at a maximum depth of 1.6m, thus, the results must be interpreted bearing in mind that the ratio between the total depth of liquefaction (1.6m) and the length of the pile (2m) was 0.8.

The experimental results show that the natural frequency of four structures decreases considerably owing to the loss of lateral support offered by the soil to the pile whilst the damping ratio increases to values in excess of 20%.

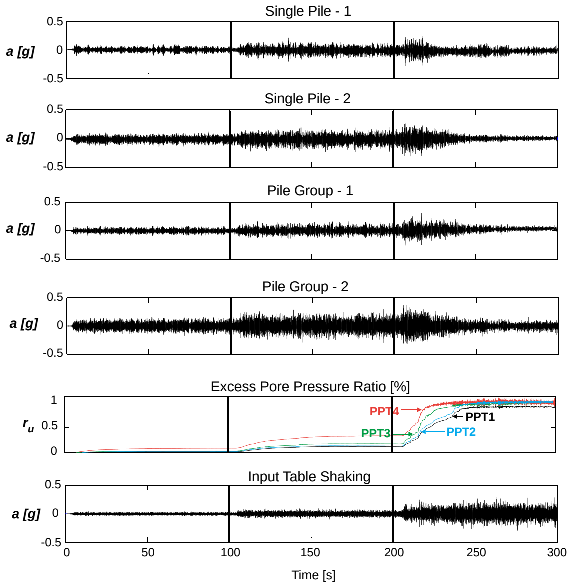

Fig. 7 Acceleration time histories recorded on the pile caps of the four models

These findings have important design consequences (a) for low-period structures, substantial reduction of spectral acceleration is expected; (b) during and after liquefaction, the response of the system may be dictated by the interactions of multiple loadings, that is, horizontal, axial and overturning moment, which were negligible prior to liquefaction; and (c) with the onset of liquefaction due to increased flexibility of pile-supported structure, larger spectral displacement may be expected, which in turn may enhance P-delta effects and consequently amplification of overturning moment.

ACKNOWLEDGEMENTS

The authors would like to acknowledge the financial support from EPSRC/H015345/1 for carrying out the test.

REFERENCES

[1] EN 1998-1:2004 Eurocode 8: Design of structures for earthquake resistance — Part 1: General rules, seismic actions and rules for buildings. European Committe de Normalisation, 2004.

[2] Bhattacharya S, Lombardi D, Dihoru L, Dietz M, Crewe AJ, Taylor CA. “Model container design for soil-structure interaction studies”, Role of seismic testing facilities in performance-based earthquake engineering. Spring Series- Geotechnical, Geological and Earthquake Engineering ISBN, 2011.

[3] Lombardi, D., Bhattacharya, S., Scarpa, F., & Bianchi, M. “Dynamic response of a geotechnical rigid model container with absorbing boundaries”. Soil Dynamics and Earthquake Engineering, 69, 2015, pp. 46-56.

[4] Lombardi D, “Dynamics of pile-supported structures in seismically liquefiable soils”. PhD Thesis, University of Bristol, Bristol, UK, 2013

[5] Lombardi D and Bhattacharya S. “Modal analysis of pile-supported structures during seismic liquefaction”, Earthquake Engineering and Structural Dynamics, 43(1), 2014, pp. 119-138.

ESTIMATION OF DISTRIBUTION OF CONE PENETRATION RESISTANCE INSIDE EARTH-FILLS WITH USE OF GEOSTATISTICAL METHOD

Kazunari Imaide, Shin-ichi Nishimura and Takayuki Shuku
Graduate School of Environmental and Life Science, Okayama University, Japan

ABSTRACT

The purpose of this study is to estimate the distribution of cone penetration resistance inside earth-fills using a geostatistical method. The spatial distribution of the strength is identified by sounding tests. In this research, the cone penetration test (CPT) is employed, and the spatial variability of the tip resistance (Q_t) is obtained. Firstly, statistical models for Q_t are determined from the CPT results. For this task, the minimization of Akaike's information criterion (MAIC) method is done to evaluate the statistical model of an embankment, which involves the mean function and the covariance function. Secondly, the Q_t distribution derived from the CPT results is spatially interpolated with the sequential Gaussian simulation method (SGSIM), which is one of the geostatistical methods. Finally, the spatial distribution of the probability that Q_t is lower than the threshold value is calculated with a sequential Gaussian simulation. In conclusion, it is found that the spatial variability of the strength inside earth-fills can be visualized in detail by applying the SGSIM to CPT results.

Keywords: Earth-fill, Static cone penetration test, Spatial variability, Geostatistical method, AIC

INTRODUCTION

There are many earth-fill dams in Japan. Some of them are getting old and decrepit, and therefore, have weakened. Making a diagnosis of the dams is an important step to stopping them from collapsing and to increasing their lifetime. An investigation of the strength inside the dam embankments is required for this task.

In the present research, the spatial distribution of the strength of earth-fills is discussed, and an identification method for this distribution is proposed. Although the strength of earth-fills is generally predicted from standard penetration test (SPT) *N*-values, the electric cone penetration test (CPT) is employed in this research to obtain the spatial distribution of the tip resistance, Q_t. The CPT is advantageous in that it is easier to make short interval exams with this test than with the SPT, and the CPT can measure the strength with high accuracy even in soft grounds, for which the *N*-values are almost equal to zero.

In general, the identification of the spatial correlation of soil parameters is difficult, since the usual sampling intervals are greater than the spatial correlation. Therefore, sounding tests are convenient for determining the correlation lengths. Tang [1] determined the spatial correlation of a ground by cone penetration tests (CPTs). Cafaro and Cherubini [2] also evaluated the spatial correlation with CPT results. Uzielli, Vannucchi and Phoon [3] considered several types of correlation functions for the CPT results. Nishimura and Shimizu [4] determined the correlation parameters of the *N*-value at a coastal dyke with the maximum likelihood method.

Although point information values are obtained from sounding tests, the information between the measuring points should be interpolated. Therefore, the sequential Gaussian simulation method (SGSIM) [5], one of the geostatistical methods, is employed here. Sounding test results are interpolated spatially with the SGSIM. Furthermore, the spatially interpolated values comply with the statistical model for embankment strength.

Firstly, statistical models for tip resistance Q_t are determined from the CPT results. For this task, the minimization of Akaike's information criterion [6] (MAIC) method is done to evaluate the statistical model of an embankment, which involves the mean function and the covariance function. Variograms [7] are also estimated to verify the statistical model determined by the MAIC. Secondly, the Q_t derived from the CPT results is spatially interpolated with the SGSIM. Finally, the spatial distribution of the strength inside an earth-fill is visualized in detail, and then the weak areas inside the embankment are identified.

SPT-*N* Compared with CPT-Q_t

In this research, an embankment at Site A is analyzed, for which CPT tests were conducted at ten points at 5-m intervals along the embankment axis, as shown in Fig. 1. The soil profile for the

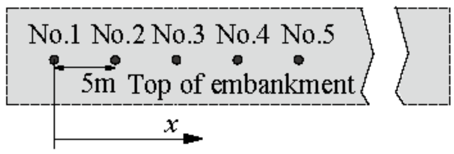

Fig. 1 Plan view of embankment and testing interval.

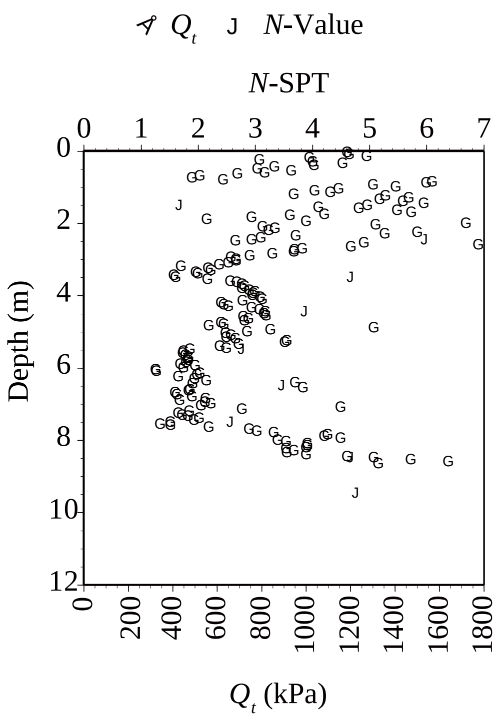

Fig. 2 Comparison between SPT *N*-Value and CPT Q_t.

embankment is categorized as intermediate soil; it consists of a sandy material with a fine content.

Standard penetration tests were conducted at the nearby location of No. 6, and the SPT *N*-value and tip resistance Q_t of the CPT are compared at the points in Fig. 2. In this figure, Q_t and the *N*-value show a similar tendency in the vertical direction, if correspondence between N=2 and Q_t= 500 kPa is assumed. Kasamatsu and Suzuki [8] derived different relationships between the *N*-value and Q_t, so that N=2 corresponds to Q_t=1200 kPa. The reason for this difference in the two studies is that Kasamatsu and Suzuki derived the relationship between the *N*-value and Q_t from a wide range of *N*-values, namely, values up to 40, and the accuracy within this range of *N*-values is not high. In this study, however, the relationship is discussed for a low range of *N*-values, namely, *N*-values smaller than 10.

STATISTICAL MODEL OF SOIL STRENGTH

Modeling Method

A representative variable for the soil properties, s, is defined by Eq. (1) as a function of location $\mathbf{X}$=(x, y, z). Variable s is assumed to be expressed as the sum of mean value m and random variable U, which is a normal random variable in this study.

$$s(\mathbf{X}) = m(\mathbf{X}) + U(\mathbf{X}) \tag{1}$$

The random variable function, $s(\mathbf{X})$, is discretized spatially into a random vector $\mathbf{s}^t$= (s_1,s_2,...,s_M), in which s_k is a point estimation value at location $\mathbf{X}$=(x_k, y_k, z_k). Symbol M signifies the number of test points. The soil parameters, which are obtained from the tests, namely, Q_t in the case of this study, are defined here as $\mathbf{S}^t$= (S_1,S_2,..., S_M). Vector $\mathbf{S}^t$ is considered as a realization of the random vector $\mathbf{s}^t$= (s_1,s_2,...,s_M). If the variables s_1, s_2,...,s_M constitute the M - variate normal distribution, the probability density function of s can then be given by the following equation:

$$f_s(\mathbf{s}) = (2\pi)^{-M/2}\left|\mathbf{C}\right|^{-1/2} \times \exp\left\{-\frac{1}{2}(\mathbf{s}-\mathbf{m})^t\mathbf{C}^{-1}(\mathbf{s}-\mathbf{m})\right\} \tag{2}$$

in which $\mathbf{m}^t$=(m_1,m_2,...,m_M) is the mean vector of random function $\mathbf{s}^t$=(s_1,s_2,...,s_M); it is assumed to be the following regression function. In this research, a 2-D statistical model is introduced; it consists of horizontal coordinate x, which is parallel to the embankment axis, and vertical coordinate z. The other horizontal coordinate, y, which is perpendicular to the embankment axis, is disregarded.

$$m_k = a_0 + a_1 x_k + a_2 z_k + a_3 x_k^2 + a_4 z_k^2 + a_5 x_k z_k \tag{3}$$

in which (x_k, z_k) means the coordinate corresponding to the position of parameter s_k, and a_0, a_1, a_2, a_3, a_4, and a_5 are the regression coefficients.

$\mathbf{C}$ is the M×M covariance matrix, which is selected from the following five types in this study:

$$\mathbf{C} = \left[C_{ij}\right] = \begin{cases} \sigma^2 \exp\left(-\left|x_i - x_j\right|/l_x - \left|z_i - z_j\right|/l_z\right) & \text{(a)} \\ \sigma^2 \exp\left\{-\left(x_i - x_j\right)^2/l_x^2 - \left(z_i - z_j\right)^2/l_z^2\right\} & \text{(b)} \\ \sigma^2 \exp\left\{-\sqrt{\left(x_i - x_j\right)^2/l_x^2 - \left(z_i - z_j\right)^2/l_z^2}\right\} & \text{(c)} \\ N_e\sigma^2 \exp\left(-\left|x_i - x_j\right|/l_x - \left|z_i - z_j\right|/l_z\right) & \text{(d)} \\ N_e\sigma^2 \exp\left\{-\sqrt{\left(x_i - x_j\right)^2/l_x^2 - \left(z_i - z_j\right)^2/l_z^2}\right\} & \text{(e)} \end{cases} \tag{4}$$

$$i, j = 1,2,\cdots,M$$

$$\begin{cases} N_e = 1 \ (i = j) \\ N_e \neq 1 \ (i \neq j) \end{cases}$$

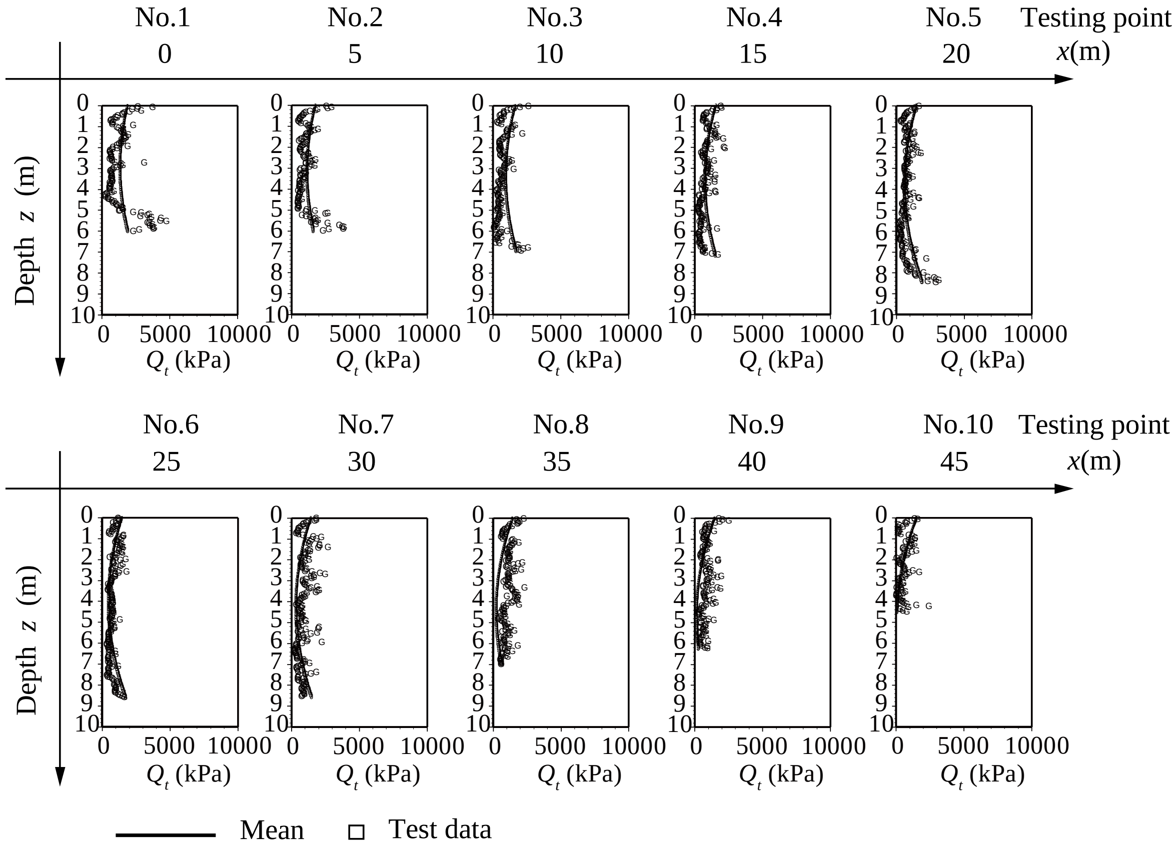

Fig. 3 Testing data, mean (trend) of Q_t in each bore hole.

in which the symbol $[C_{ij}]$ signifies an *i-j* component of the covariance matrix, σ is the standard deviation, and l_x and l_z are the correlation lengths for the *x* and *z* directions, respectively. Parameter N_e is related to the nugget effect. Akaike's Information Criterion, AIC, is defined by Eq. (5) considering the logarithmic likelihood.

$$\begin{aligned} \mathrm{AIC} &= -2 \cdot \max\{\ln f_s(\mathbf{S})\} + 2L \\ &= M \ln 2\pi + \min\{\ln|\mathbf{C}| + (\mathbf{S}-\mathbf{m})^t \mathbf{C}^{-1} (\mathbf{S}-\mathbf{m})\} + 2L \end{aligned} \tag{5}$$

in which L is the number of unknown parameters included in Eq. (2). By minimizing AIC (MAIC), the regression coefficients of the mean function, the number of regression coefficients, the standard deviation, σ, a type of the covariance function, the nugget effect parameter, N_e, and the correlation lengths, l_x and l_z, are determined.

As the correlation lengths of soil parameters are often short compared to the sampling or the testing intervals, sometimes the correlation lengths cannot be determined using the aforementioned method. For such cases, variograms are employed to identify the spatial correlation structure.

In this research, the statistical model determined from the MAIC was verified by comparing the statistical model for the variograms. The following two-step approach is proposed as a strategy for calculating the variograms. Firstly, the mean (trend) function and the standard deviation are determined by the MAIC. Subsequently, the variograms are evaluated in the horizontal and vertical directions as individual functions of the sampling intervals.

$$\begin{aligned} \gamma_x(q \cdot \Delta x) &= \frac{\sum_{j=1}^{N_z} \sum_{i=1}^{N_{x-q}} \{U(x_i, z_j) - U(x_i + q \cdot \Delta x, z_j)\}^2}{2N_z(N_x - q)} \\ \gamma_z(q \cdot \Delta z) &= \frac{\sum_{j=1}^{N_x} \sum_{i=1}^{N_{z-q}} \{U(x_j, z_i) - U(x_j, z_i + q \cdot \Delta z)\}^2}{2N_x(N_z - q)} \\ q &= 1, 2, \cdots \end{aligned} \tag{6}$$

where γ_x and γ_z are the variograms for the *x* and *z* axes, respectively, $U(x,z)$ is a measured parameter at point (x,z) from which the mean value is removed, namely, the value of $(s(x,z)-m(x,z))/\sigma$, Δx and Δz are sampling intervals, and N_x and N_z are the number of sampling points for the *x* and *z* axes, respectively.

Next, the calculated variograms are approximated by the following theoretical variogram functions, and the correlation lengths are identified. An exponential type of function, Eq. (4d), is employed here.

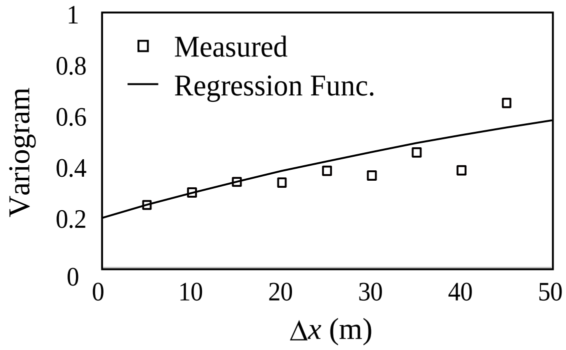

(a) Horizontal direction

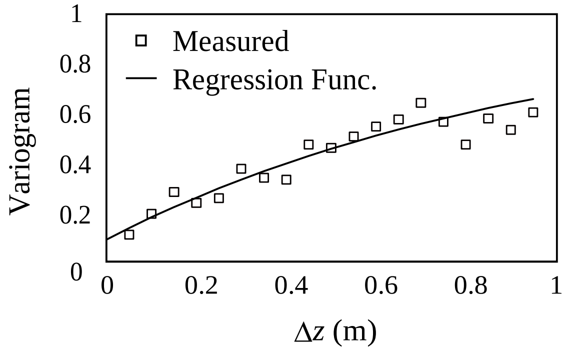

(b) Vertical direction

Fig. 4 Variograms and regression functions.

$$\begin{aligned}&\gamma_x\left(\left|x_i-x_j\right|\right)=C_{0x}+C_{1x}\left\{1-\exp\left(-\left|x_i-x_j\right|/l_x\right)\right\} \quad i\neq j\\&\gamma_z\left(\left|z_i-z_j\right|\right)=C_{0z}+C_{1z}\left\{1-\exp\left(-\left|z_i-z_j\right|/l_z\right)\right\} \quad i\neq j\\&\gamma_x(0)=\gamma_z(0)=0\end{aligned} \tag{7}$$

In Eq. (7), C_{0x} and C_{0z} are the parameters used for the nugget effect in the x and z directions, respectively, while C_{1x} and C_{1z} are the parameters used to express the shape of the variogram functions.

Statistical Model of Embankments

Figure 3 shows the distribution of Q_t and the average functions at Site A. The average functions are determined by the MAIC as nonlinear functions of the embankment axis and the vertical direction, respectively.

Figure 4 shows the variograms for the horizontal and vertical directions at Site A. In these variograms, Q_t is standardized as $(Q_t\ -m)/\sigma$ to remove the trend in which m is the mean value and σ is the standard deviation; they are obtained by the MAIC. In this figure, the regression curves given by Eq. (7) approximately correspond to the observed values. These regression curves are obtained by the least squares method, and finally, parameters C_{0x}, C_{1x}, C_{0z}, C_{1z}, l_x, and l_z are determined. Variogram values of less than 15 m in the horizontal direction and less than 0.5 m in the vertical direction are employed to identify the approximate functions of Eq. (7) for the horizontal and vertical directions, respectively, since the accuracy of the variogram values is high within the range of the small values for Δx and Δz.

Table 1 Two-dimensional spatial distribution of Q_t from CPT.

(a) Results of MAIC

Mean function			
μ=1945.26-28.87x-359.92z+0.46x^2+60.89z^2-5.14xz			
S.D.	Type	N_e	C.L.(m)
722.56	4e	0.98	l_x=10.00,l_z=0.51

μ:Mean function.
x:Horizontal coordination(m). z:Vertical coordination(m).
S.D.:Standard deviation. Type:Type of covariance matrix.
N_e:Nugget effect parameter. C.L.:Correlation length≧0.

(b) Results of variograms

C_0	C_1	C.L.(m)
C_{0x}=0.20,C_{0z}=0.09	C_{1x}=0.80,C_{1z}=0.91	l_x=77.52,l_z=0.97

Table 1 shows the statistical models determined by the MAIC and the variograms. Table (1a) corresponds to the MAIC results, while Table (1b) corresponds to the variogram results. The covariance functions are selected by the MAIC, as seen in Eq. (4e).

The lateral correlation length obtained by the MAIC is 20 times that of the vertical one. This relationship agrees with the published values [9]. However, the lateral correlation length obtained by the variograms is 50~80 times that of the vertical value. Comparing the results of the MAIC and the variograms, the lateral correlation length of the variograms is identified as being almost 5~8 times that of the MAIC. And the vertical correlation length of the variograms is identified as being almost 2 times that of the MAIC. There is a general tendency for variograms to exhibit relatively longer correlation distances in comparison to the MAIC, since the correlation length is identified along the single coordinate in the case of the variograms.

APPLICATION OF GEOSTATISTICAL METHOD

Sequential Gaussian Simulation Method

To spatially interpolate the soil parameters obtained as point information, kriging is often employed. Kriging is one of the geostatistical methods. A 2-D statistical model is also introduced in this method with horizontal coordinate x and vertical coordinate z. The other horizontal coordinate, y, is disregarded. Estimated parameter ξ^* is defined at any location as Eq. (8) in kriging.

$$\xi^*=\sum_{\alpha=1}^{n}\lambda_\alpha\xi_\alpha \tag{8}$$

in which λ_α is an interpolation coefficient, which is a function of the coordinates, x and z at the point α, and ξ_α is a sample value of a parameter at the point α. Symbol n signifies the number of sample points that are used for an interpolation. The kriging method is characterized by parameter λ_α determined from the spatial correlation of parameter values. In order to use Eq. (8), it is necessary to determine an appropriate λ_α. The way to do this is indicated simply as seen below.

Although the expansion of the middle of the formula is omitted here [7], the expected value for the square residual of a true random process $\xi(x,z)$ and the interpolated value $\xi^*(x,z)$ are given in the following equation.

The squared residual $\sigma_K^2(x,z)$ between the true parameter value ξ and estimated value ξ^* is defined as:

$$\begin{aligned}\sigma_K^2(x,z) &= \mathrm{E}\left\{\left|\xi(x,z)-\xi^*(x,z)\right|^2\right\}\\ &= \sigma_\xi^2 - 2\sum_{\alpha=1}^{n}\lambda_\alpha C_\xi(x,z;x_\alpha,z_\alpha)\\ &+\sum_{\alpha=1}^{n}\sum_{\beta=1}^{n}\lambda_\alpha\lambda_\beta C_\xi(x_\alpha,z_\alpha;x_\beta,z_\beta)\end{aligned} \tag{9}$$

Variable λ_α, is determined by minimizing $\sigma_K^2(x,z)$ in a restrained condition under which $\sum_{\alpha=1}^{n}\lambda_\alpha = 1$. The parameter, σ_ξ^2 means the variance of the covariance functions defined in Eq. (4e).

$$\frac{\partial}{\partial\lambda_\alpha}\left\{E\left[\left|\xi(x,z)-\xi^*(x,z)\right|^2\right]-2\kappa\left(\sum_{\beta=1}^{n}\lambda_\beta-1\right)\right\}=0 \tag{10}$$

From Eq. (10), the following simultaneous linear equations are given, and coefficient λ_α is obtained by solving Eq. (11).

$$\begin{aligned}&\sum_{\beta=1}^{n}\lambda_\beta C_\xi(x_\alpha,z_\alpha;x_\beta,z_\beta)-\kappa\\ &=C_\xi(x_\alpha,z_\alpha;x,z)\\ &\forall\alpha=1,2,\cdots,n\\ &\sum_{\beta=1}^{n}\lambda_\beta=1\end{aligned} \tag{11}$$

in which, κ is a Lagrange multiplier. The coefficient λ_α is determined as a function of the spatial coordinate (x,z).

Although the average value is estimated by Eq. (8) in kriging, the variance is not zero, except at the sampling point α, and then the interpolated value for the parameter has variability. Therefore, to consider the variability, many realizations are required and the simulation is repeated many times. In the present study, the sequential Gaussian simulation method is conducted; the analysis code SGSIM [5] is employed for the task. Realization $\xi_c^{(l)}$, by SGSIM, is given by Eq. (12); it is conditioned at the sample points so that the realized values coincide with the sample values.

$$\xi_c^{(l)}(x,z)=\xi^*(x,z)+\xi^{(l)}(x,z)-\xi^{*(l)}(x,z) \tag{12}$$

in which $\xi_c^{(l)}(x,z)$ means the l th realization, $\xi^*(x,z)$ is an estimated value by kriging, and $\xi^{(l)}(x,z)$ is the l th realization without conditioning. $\xi^{*(l)}(x,z)$ is the kriged estimation using the values of $\xi^{(l)}(x,z)$ at the sampling points. On the right side of Eq. (12), the first item is an estimated value of kriging as an average. The remainder of the second and third items shows an estimation error of kriging. Realization $\xi_c^{(l)}(x,z)$ is used as a Q_t value in the following chapter.

Applying SGSIM to CPT Results

The results of CPT are actual penetration resistance values; and thus, the accuracy of the measured values at the measuring points is good. However, the CPT results are point estimation values, and the interpolation of the values is needed to visualize the spatial distribution. In this research, the values for Q_t are spatially interpolated using the SGSIM. Furthermore, a Monte Carlo simulation is repeated 900 times to evaluate the probabilistic distribution of Q_t.

Figure 5 presents the analysis results at Site A. Figures (5a) and (5b) correspond to the mean and the probability that the Q_t values are smaller than 500 kPa, respectively. Due to the comparison of SPT-N and CPT-Q_t in Fig. 2, the threshold value is determined to be Q_t=500 kPa.

According to Fig. (5a), around depth z=4-8 m and x=10-30 m, the lowest value is detected. Corresponding to Fig. (5a), the highest value for the probability is obtained at the same location in Fig. (5b).

According to Figs. (5a) and (5b), the spatial distribution of Q_t and the weak areas are identified in detail; and thus, this study is effective for making a diagnosis of deteriorated earth-fill dams.

CONCLUSION

(1) Comparing the test results of the SPT-N and the CPT-Q_t values near the test points at Site A, the correspondence of N=2 and Q_t=500 kPa has been found. The relationship is available within the range of N-values smaller than 10.
(2) The correlation lengths are determined by the MAIC and the variograms. When comparing the correlation lengths obtained by the MAIC and the

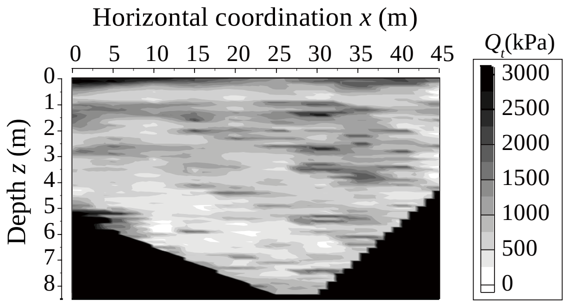

(a) Mean (Q_t)

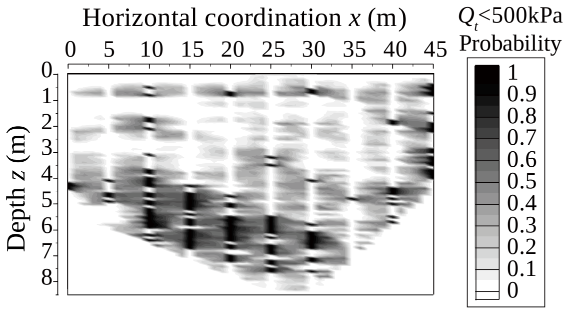

(b) Probability (Q_t<500kPa)

Fig. 5 Statistical values of Q_t by SGSIM at Site A.

variograms, the latter are longer than the former. The cause of this difference seems to be the difference in the statistic models for each method.

(3) The probability of the interpolated spatial distribution of Q_t, which is smaller than 500 kPa, is obtained by applying the sequential Gaussian simulation method to the CPT results; the vulnerable areas inside the earth-fill have been identified.

(4) Since the CPT is more sensitive to sounding tests than the SPT, and short interval tests can be conducted with it, the distribution of Q_t from the CPT is found to be more accurate for presenting the spatial distribution of the strength inside embankments than the *N*-values.

Consequently, the CPT can contribute to the appropriate maintenance of deteriorated earth-fill dams.

ACKNOWLEDGEMENTS

This research was partly supported by JSPS KAKENHI Grant Number 25292143.

REFERENCES

[1] Tang WH, “Probabilistic evaluation of geotechnical property variability”, Journal of Geotechnical Engineering, ASCE, 105(GT10), 1979, pp. 1173–1191.

[2] Cafaro F and Cherubini C, “Large sample spacing in evaluation of vertical strength variability of clayey soil”, Journal of Geotechnical and Geoenvironmental Engineering, 128(7), 2002, pp. 558-568.

[3] Uzielli M, Vannucchi G and Phoon KK, “Random field characterization of stress-normalized cone penetration testing parameters”, Geotechnique, 55(1), 2005, pp. 3-20.

[4] Nishimura S and Shimizu H, “Reliability-based design of ground improvement for liquefaction mitigation, Structural Safety, 30, 2010, pp. 200-216.

[5] Deutsch CV and Journel AG, Geostatistical Software Library and User’s Guide: Oxford University Press, 1992, ch. 5.

[6] Akaike H, “A new look at the statistical model identification”, IEEE Trans. on Automatic Control, AC-19(6), 1974, pp. 716-723.

[7] Jourel AG and Huijbregts ChJ, Mining geostatistics: Academic Press, 1978, ch. 1 and 7.

[8] Suzuki Y and Tokimatsu K, “Correlations between CPT data and soil characteristics obtained from CPT”, J. Struct. Constr. Eng., AIJ, No. 566, 2003, pp. 73-80.

[9] Nishimura S, “The investigation of the establishment method of soil parameters”, Symposium of performance design and deformation prediction of geotechnical structure during earthquake in proceedings: The Japanese Geotechnical Society, 2007, pp.121-126.

BEARING CAPACITY OF STRIP FOOTINGS ON DESICCATED CLAY CRUSTS

Qiang Xie[1], Andrew J. Abbo[2], Daniel W. Wilson[2] and Andrei V. Lyamin[2]
[1]School of Civil, Environmental and Mining Engineering, University of Western Australia, Australia
[2]Australian Research Council Centre of Excellence for Geotechnical Science and Engineering, University of Newcastle, Australia

ABSTRACT

Numerical limit analysis was used to investigate the ultimate bearing capacity of a rigid strip footing sitting on a soft clay with a stiff nonhomogeneous desiccated crust. Rigorous bounds on the ultimate bearing capacity are obtained using Finite Element Limit Analysis (FELA) in which the upper and lower bound limit theorems of classical plasticity are used as the basis of the finite element formulations. Both upper and lower bound FELA methods assume a perfectly plastic soil model, require the solutions of a large optimization problem, and produce a rigorous bound which combine to accurately bracket the true collapse load. A parametric analysis was conducted that considered varying shear strength distributions in the crust, for a range of crust thicknesses and footing widths. Results from the limit theorems accurately bracketed the true collapse load to within approximately 6%. Results show that the modelling of even a relatively thin crust can provide a significantly increase in bearing capacity over that of the underlying soft clay.

Keywords: Bearing capacity, Desiccated, Layered, Nonhomogeneous, Finite Element Limit Analysis

INTRODUCTION

The bearing capacity of shallow foundations on single-layered [1]-[3] and multi-layered [4]-[7] clay soils has attracted the interest of researchers for many decades. Most published research consider clay soils where the shear strength is constant within a soil layer. This is despite the fact that there are many situations in which soil the shear strength of clays may vary with the depth.

An undrained shear strength profile that increases linearly with depth is encountered in normally consolidated clays [8]. Despite the publication by Davis and Booker [9] of an analytical solution for bearing capacity of a strip footings on clay soils with a shear strength that increase linearly with depth, researchers have continued to consider the bearing capacity of these soils [10]-[14].

The change in shear strength with depth is also encountered in under-consolidated soils in which a surface crust may develop through the action of weathering desiccation or/ and chemical processes [15]. Such crusts are typically much stiffer than the underlying clays and exhibit a shear strength profile that decreases with depth. The underlying clay exhibits relatively constant shear strength [16] [17] or one that gradually increases with the depth [18]. These conditions are frequently encountered in newly reclaimed clay or slurry tailings [19], which makes it important to reasonably estimate the bearing capacity in such cases because of the potential failure of the stiff crust due to construction equipment's traffic load.

Park *et al*. [19] described two approaches for estimating the bearing capacity of a layered clay soils with a stiff crust. The first approached is to evaluate the bearing capacity of the footing by considering the nonhomogeneous shear strength profile directly. The alternative method determines a representative shear strength of the stiff crust and then evaluates the bearing capacity using existing solutions for two-layered clays with uniform shear strengths. Park *et al*. [19] investigated the bearing capacity of surface footings on the clay underlying stiff crust of decreasing shear strength with depth by finite element analysis and provided an insight into the failure mechanisms and design charts for some typical ratios of crust thickness to the footing width.

In this research Finite Element Limit Analysis is used to investigate the bearing capacity of strip footings sitting on a desiccated clay crust with a shear strength that decreases linearly with depth. For this study, the desiccated crust sit atop a very soft layer of clay with an undrained shear strength of 10 kPa. A parametric study was conducted for typical ranges of shear strengths and the footing geometries encountered in the design temporary working platforms. The collapse mechanisms associated with the ultimate bearing capacity of the strip footing are illustrated using plots of upper bound velocities and power dissipation intensity.

METHODOLOGY

The upper and lower bound theorems of plasticity are powerful tools when applied to geotechnical stability problems. The solution to the lower bound optimization problem defines a statically admissible stress field and provides a rigorous lower bound on the ultimate bearing capacity. A statically admissible stress field is one that satisfies equilibrium, the yield criterion and the stress boundary conditions. The upper bound optimization problem considers a kinematically admissible field and gives a rigorous upper bound on the ultimate bearing capacity. A kinematically admissible field satisfies compatibility, the flow rule and the velocity boundary conditions.

In this study Finite Element Limit Analysis methods are applied to bracket the true collapse load by computing both upper and lower bounds on the bearing capacity of a footing resting on the two-layered clays. The finite element formulations used in this study are based upon the methods originally developed by Sloan [20] and Sloan & Kleeman [21] that used finite elements with linear programming. The current FELA implementation includes the major improvements described by Lyamin and Sloan [22] [23] and Krabbenhoft *et al.* [24] [25] and importantly, the adaptive re-meshing techniques of Sloan [26]. Important features of these methods include linear elements to model the stress/velocity fields and collapsed elements to simulate the discontinuities. In addition, the global optimisation problem is solved using a bespoke conic programming scheme.

ANALYSIS AND RESULTS

Problem Definition

The footing geometry and soil profile are shown in Figure 1. The size of the soil domain is 25*B* wide by 15*B* deep, which has been checked of large enough to minimize the boundary effects to the solution. As shown in Fig. 1, the crust is modelled with a linear variation of shear strength across its depth (*H*), with the undrained shear strength decreasing from the strength at the soil surface (S_t) to that of the underlying layer (S_b).

The parametric study considered undrained shear strengths at the surface of the crust (S_t) between 10 kPa and 100 kPa. In this study, the undrained shear strength the bottom layer was limited to an extreme case of a very soft clay with S_b=10 kPa. The undrained shear strengths S_t was varied in increments of 10 kPa. The parametric study also considered a range of geometries; footing width (*B*) of 1.0m was modelled while the crust depth (*H*) was varied to obtain dimensionless crust depths (*H/B)* of 0.25, 0.33, 0.5, 0.667, 1.0, 1.667, 2.0, 2.5, 3.0, 4.0 and 5.0. The ratios of 0.25, 0.5, 1.0 and 2.0 were selected to allow accurate comparison with previous studies [7] [19].

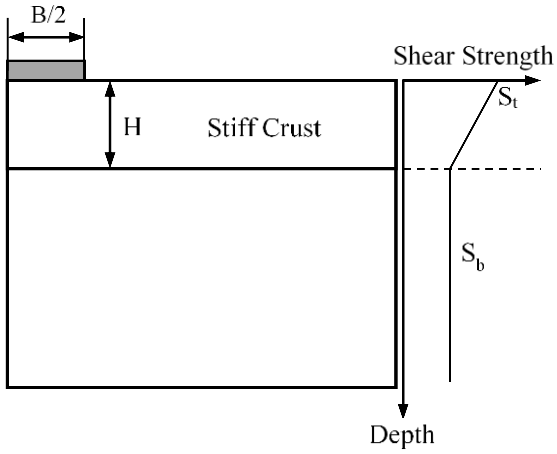

Fig.1 Footing model and shear strength profile.

Verification of the Model

The adequacy of the finite element limit analysis model was verified by comparing with the FE analysis results from Park *et al.* [19]. Figure 2 shows the bearing capacities for cases with S_t=100 kPa, S_b=10 kPa and varying *H/B* from both finite element limit analysis and FE analysis. The upper and lower solutions from finite element limit analysis closely bracket the FE analysis solutions. It can be inferred that the finite element limit analysis model used in this project is reasonable for the estimation of bearing capacity for aforementioned condition.

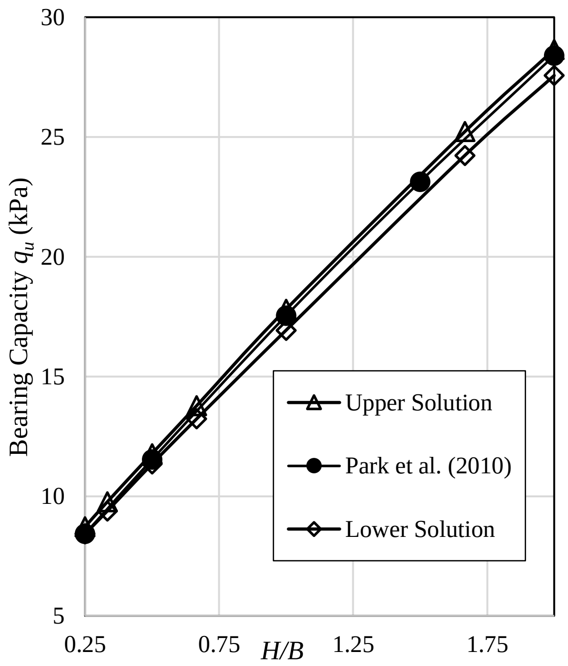

Fig. 2 Model verification with S_t=100 kPa and S_b=10 kPa

Results and Discussion

Upper and lower bound results from the Finite Element Limit Analysis accurately bracketed the bearing capacity to within 6% of the true collapse loads.

Plots of power dissipation intensity and velocities for selected cases within the parametric study are shown in Figures 3 to 7. Note that the velocity plots are not generated using results from the analyses to accurately compute the ultimate bearing capacity. The very fine meshes require for accurately have a very high density of nodes in part of the mesh and velocity vectors obscure one another. Instead, velocity plots are generate from an upper bound analyses performed with a coarse mesh of approximately 1000 elements. Figures 3, 4 and 5 illustrate the failure mechanisms for the case of a unit parametric thickness (*H/B*=1) with the shears strength of the crust ranging from stiff (S_t=100 kPa) to very soft (S_t=20 kPa). For the case of a stiff crust (Figure 3), the failure mechanism extends very wide and is characterized by plastic hinges forming in the upper layer located approximately 1.5*B* and 5*B* from the footing centerline. Unlike the usual failure mechanism associated with the bearing capacity failure, the velocity of the ground surface to the side of the footing is moving downwards with the rigid footing. These are similar to the mechanisms reported by Merifield *et al.* [7] for layered soil profiles in which a strong clay overlays a relatively weak clay. For a softer crust with S_t=50 kPa, Figure 4 shows that the failure mechanism contracts as the strength of the crust is reduced, with the plastic hinges becoming less prominent. As the shear strength of the crust approaches that of the underlying clay, Figure 5 shows that the failure mechanism reflects the general shear failure associated with a footing resting on an isotropic clay soil.

The influence of the crust depth on the collapse mechanism is shown Figures 4, 6 and 7 for cases in which S_t=50 kPa and S_b=10 kPa. For *H/B*=1, Figure 4 shows that the mechanism penetrates deep into the underlying clay layer and extends widely due to the stiff upper layer. For *H/B*=2 (Figure 6), a similar mechanism can still be observed and it extends quite deeply as well. For a very thick crust (*H/B*=5), Figure 7 shows the failure mechanism contracts to the top of the crust only reflecting a general shear failure of a footing.

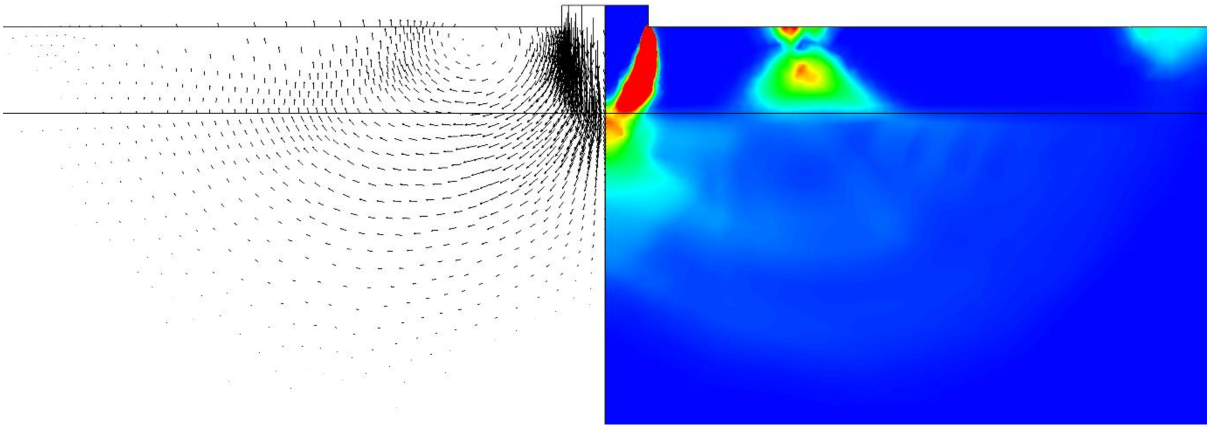

Fig.3. Velocity and power dissipation plot for case with S_t=100 kPa, S_b=10 kPa, *H*=1 m and *B*=1 m.

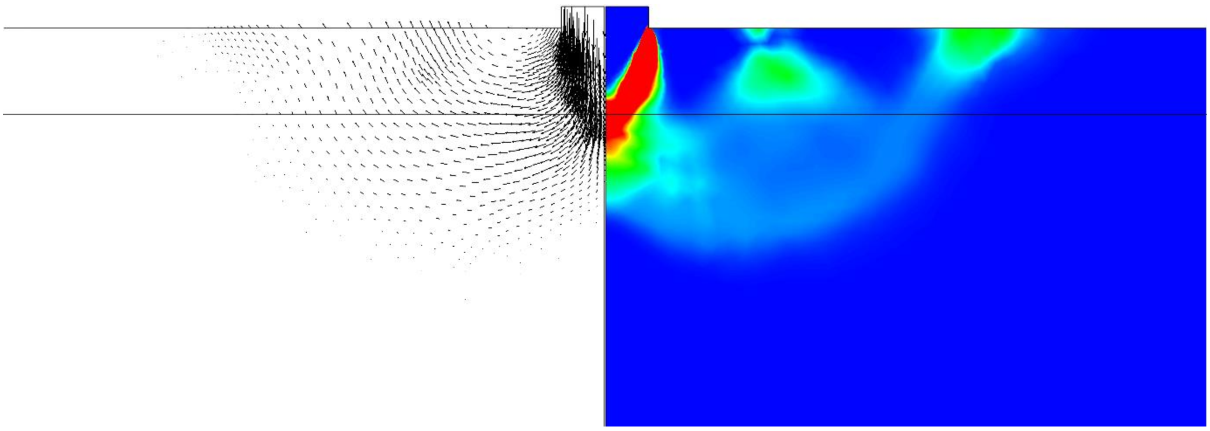

Fig.4. Velocity and power dissipation lot for case of S_t=50 kPa, S_b=10 kPa, *H*=1 m and *B*=1 m.

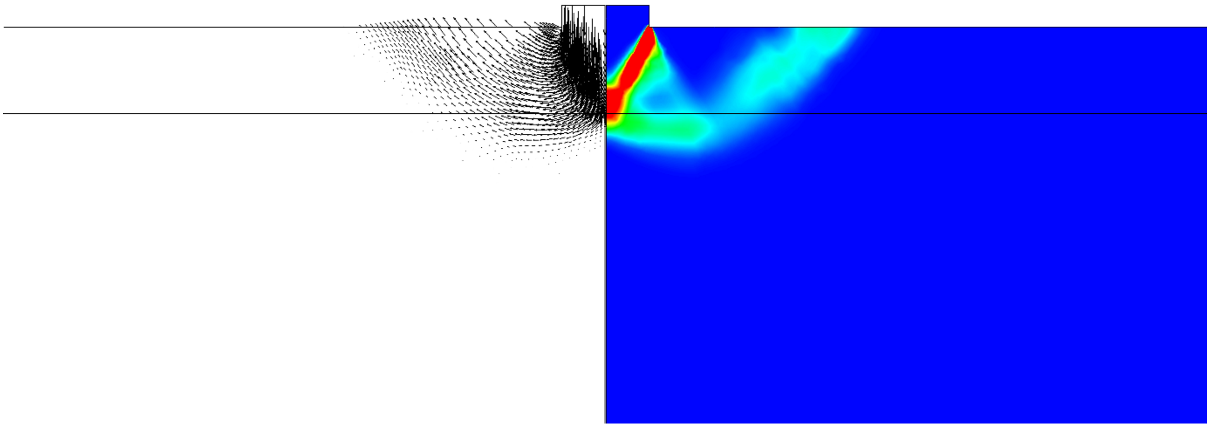

Fig.5. Velocity and power dissipation plot for case with S_t=20 kPa, S_b=10 kPa, H=1 m and B=1 m.

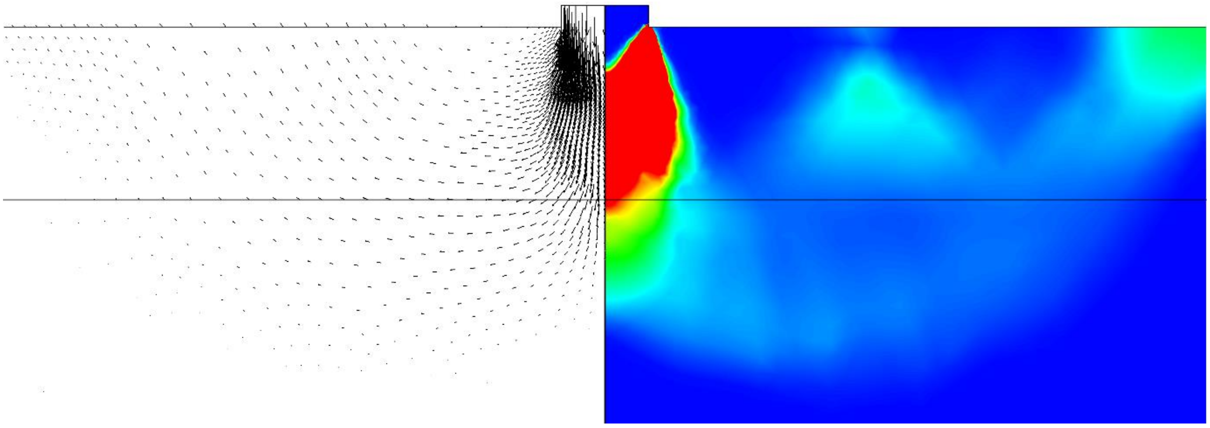

Fig.6. Velocity and power dissipation plot for case with H=2 m, B=1 m, S_t=50 kPa and S_b=10 kPa.

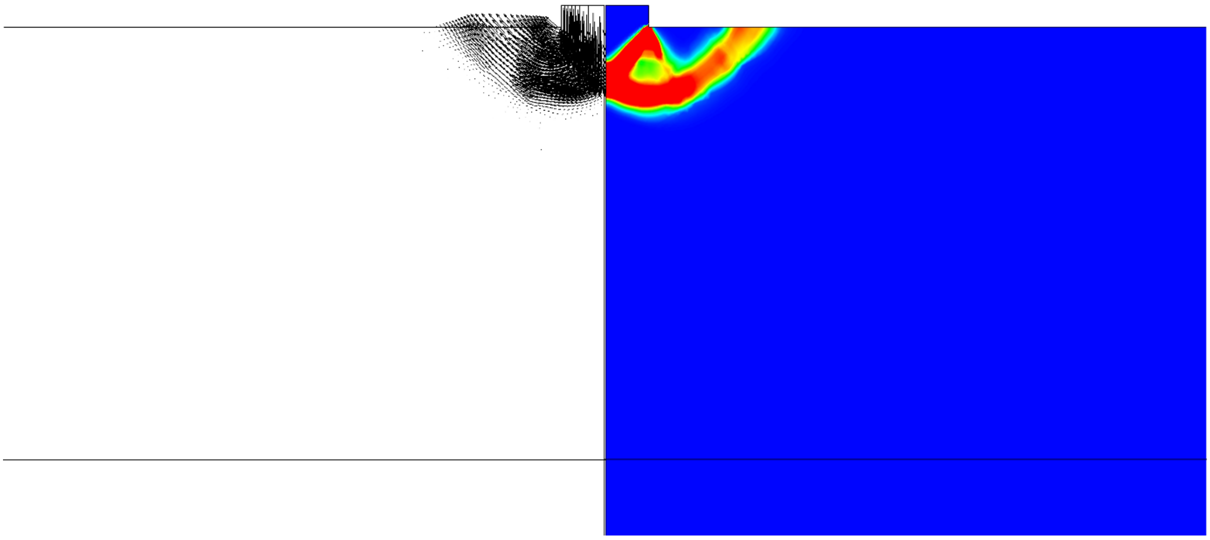

Fig.7. Velocity and power dissipation plot for case with H=5 m, B=1 m, S_t=50 kPa and S_b=10 kPa.

Results of the entire parametric study are presented in Figure 8 which plots the ultimate bearing capacity, calculated as the average of the upper and lower values computed by FELA, verse the dimensionless crust thickness. The figure shows that for a very thin dimensionless crust thickness, with a very stiff upper layer (S_t=100kPa), that the bearing capacity is approximately 40% greater than of the underlying clay. A crust thickness of H/B=1.5 is representative of the design of tracked plant working above a 1m thick desiccated crust. In this case the crust provides an increase in bearing capacity of up to over four times greater than the underlying soft clay for the range of parameters considered in this study. For the thickest of crusts considered (*H/B*=5), the failure mechanism is contained with the upper portions of the crust and the bearing capacity is greater than 90% of a strip footing on an isotropic soil with an undrained shear strength of S_t.

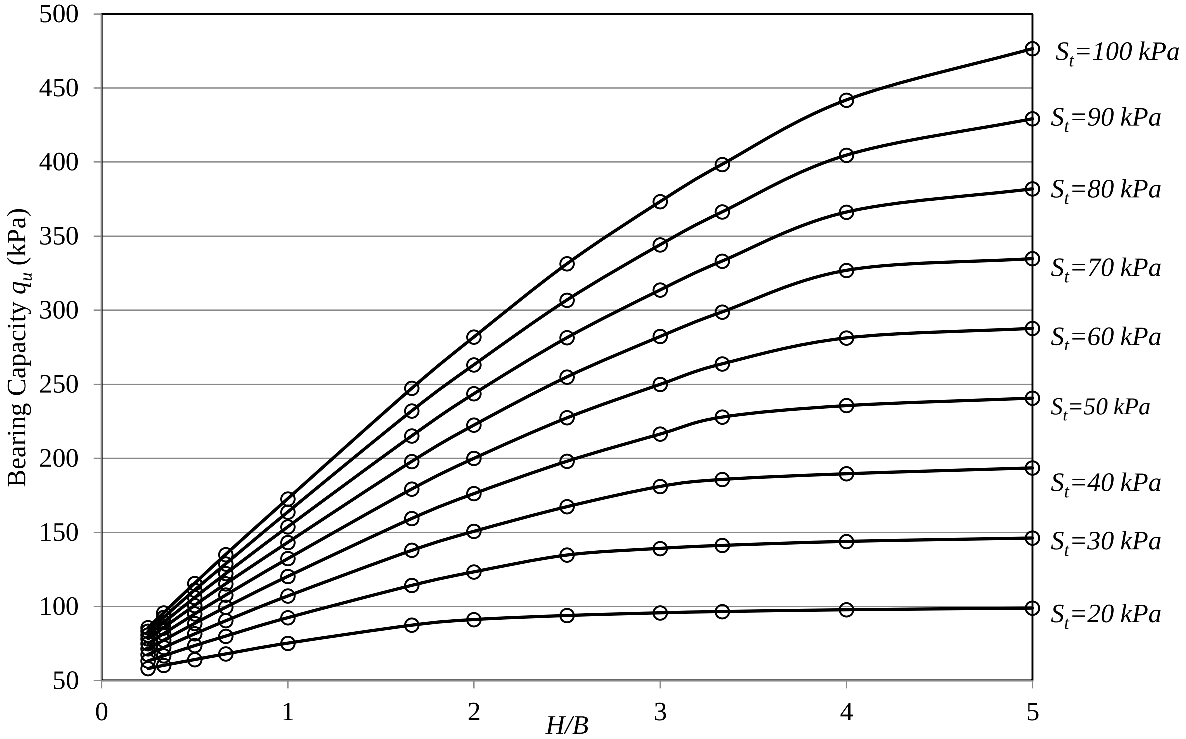

Fig.8 Ultimate bearing capacity of strip footing.

CONCLUSION

Finite Element Limit Analysis was used to investigate the bearing capacity of footing sitting on desiccated soil profile. The modelling was performed using a layered soil model that consisted of a stiff clay crust, with an undrained shear strength that decreases with depth, overlaying a very soft clay soil.

The results of the parametric study showed that a very thin crust (*H/B*=0.25) with a peak shear strength of 100kPa increased the ultimate bearing capacity by approximately 75% over and above that of the underlying very soft clay. For a thick crust (*H/B*), a very stiff crust increased the bearing capacity by nearly an entire order of magnitude.

The failure mechanisms governing the ultimate bearing capacity were also investigated. For crusts with large relative thicknesses or when the crust has a similar strength to the underlying soft clay, the failure of the footing was a general shear failure which the classical mechanism associated with the undrained bearing capacity of footings on clay. For a thin crust and/or a strong crust the mechanism extended much wider and deeper, with the crust acting as a stiff beam and developing plastic hinges. These mechanisms are consistent with those described by Merifield *et al*. [7] for the bearing capacity of layered clay soils with isotropic strengths.

KNOWLEDGEMENTS

This research was supported by the Australian Research Council Centre of Excellence for Geotechnical Science and Engineering in Newcastle University via an undergraduate vacation scholarship to support collaborative research between the University of Newcastle and the University of Western Australia.

REFERENCES

[1] Meyerhof. GG, “Some Recent Research on Bearing Capacity of Foundations”, Canada Geotech J., Vol. 1, 1964, pp 16-26.

[2] Terzaghi K, “Theoretical Soil Mechanics, New York: Wiley, 1943.

[3] Vesic AS, “Analysis of Ultimate Loads of Shallow Foundations”, J. of Soil Mechanics and Foundations Division, Vol. 99, 1973, pp 45-73.

[4] Brown JD, and Meyerhof GG, "Experimental Study of Bearing Capacity in Layered Clays", in 7th ICSFME, 1969, pp 45-51.
[5] Button, SJ, "The Bearing Capacity of Footings on Two-Layer Cohesive Subsoil", in 3rd ICSMFE, 1953, pp 332-335.
[6] Chen WF, "Limit Analysis and Soil Plasticity", Elsevier, 2013.
[7] Merifield RS, Sloan SW, and Yu HS, "Rigorous Plasticity Solutions for the Bearing Capacity of Two-Layered Clays", Géotechnique J., Vol. 49, No. 4, 1999, pp 471-490.
[8] Atkinson, J. (ed.) 2007. The Mechanics of Soils and Foundations, New York: Taylor & Francis.
[9] Davis EH, and Booker JR, "The Effect of Increasing Strength with Depth on the Bearing Capacity of Clays", Géotechnique J., Vol. 23, No. 4, 1973, pp 551-563.
[10] Tani K and Craig W, "Bearing Capacity of Circular Foundations on Soft Clay of Strength Increasing with Depth", Soils and Found, Vol. 35, No.4, 1995, pp 21-35.
[11] Lutenegger AJ, "Geotechnical Behavior of Overconsolidated Surficial Clay Crusts", Transportation Res Record, No. 1479, 1995, pp 61-74.
[12] Konrad JM and Ayad R, "Desiccation of a Sensitive Clay: Field Experimental Observation", Canada Geotech J., Vol. 34, 1997, pp 929-942.
[13] Lee SR, Byeon WY, Park HG, and Jee SH, "Trafficability Evaluation of PTM Treated Dredged Soil Deposit", in 4th ICSSE, 2006, pp 657-666.
[14] Lefebvre G, Lefebvre LM, and Rosenberg P, "Behavior of a Cemented Plastic Clay as an Embankment Foundation", Canada Geotech J., Vol. 11, 1974, pp 46-58.
[15] Raymond GP, "The Bearing Capacity of large footings and Embankments on clays", Géotechnique, Vol. 17, 1967, pp. 1-10.
[16] Salençon J, Discussion: "The effect of increasing strength with depth on the bearing capacity of clays", Géotechnique, Vol. 24, 1974, pp. 449-451.
[17] Reddy AS, & Rao KNV, "Bearing capacity of strip footing on anisotropic and nonhomogeneous clays", Soils and Foundations, Vol. 21, 1981, pp. 1-6.
[18] Kusakabe O, Suzuki H and Nakase A, "An upper bound calculation on bearing capacity of a circular footing on a non-homogeneous clay", Soils and foundations, Vol. 26, 1986, pp.143-148.
[19] Park H, Lee SR and Jee SH, "Bearing Capacity of Surface Footing on Soft Clay Underlying Stiff Nonhomogeneous Desiccated Crust", Int. J. of Offshore and Polar Engineering, Vol. 20, No. 3, Sep. 2010, pp 224-232.
[20] Sloan SW, "Lower Bound Limit Analysis using Finite Element and Linear Programing", Int. J. of Numerical Analysis Methods Geomech., Vol. 12, 1988, pp 61-67.
[21] Sloan SW and Kleeman PW, "Upper Bound Limit Analysis using Discontinuous Velocity Fields", Computer Methods in Applied Mechanics and Engineering, Vol. 127, 1995, pp 293-314.
[22] Lyamin AV, Sloan SW, "Lower bound limit analysis using nonlinear programming", Int. J. for Num. Meth. in Eng., Vol 55, 2002, pp. 573-611.
[23] Lyamin AV, Sloan SW, "Upper bound limit analysis using linear finite elements and nonlinear programming", Int. J. for Num. Meth. in Geo., Vol 26(2), 2002, pp. 181-216.
[24] Krabbenhoft K, Lyamin AV, Hjiaj M, Sloan SW, "A new discontinuous upper bound limit analysis formulation", Int. J. for Num. Meth. in Eng., Vol. 63, 2005, pp. 1069-1088.
[25] Krabbenhoft K, Lyamin AV, Sloan SW, "Formulation and solution of some plasticity problems as conic programs", Int. J. of Solids and Structures, Vol. 44, 2007, pp. 1533-1549.
[26] Sloan SW, "Geotechnical stability analysis", Géotechnique, Vol. 63(7), 2013, pp. 531–572. 51st Rankine Lecture.

Fifth International Conference on Geotechnique, Construction Materials and Environment, Osaka, Japan, Nov. 16-18, 2015, ISBN: 978-4-9905958-4-5 C3051

NUMERICAL EXPERIMENT FOR VIRTUAL PLASTER MODEL TESTS SIMULATING BLOCK SHEAR TESTS

Tatsuro Nishiyama[1] and Takashi Hasegawa[2]
[1]Faculty of Agriculture, Ehime University, Japan; [2]Professor Emeritus, Kyoto University, Japan

ABSTRACT

The strength of in-situ rock masses has been estimated by in-situ rock shear tests for a long time. However, the mechanisms for the appearance of strength in such tests have not been clarified sufficiently. This paper presents the results of a numerical analysis of virtual plaster model tests used to simulate block shear tests, which are of a kind of in-situ test. In the authors' former study, results were obtained for rock shear tests, another kind of in-situ test, along with real plaster model tests and finite element analyses. In the present study, some cases simulating block shear tests were analyzed. The appearance and propagation of cracks in the testing process were simulated with enhanced elements, which represented the displacement discontinuity in each element, as in the former analysis. The results were compared with the former results to investigate the differences between the two conditions. The shear strength in the two sets of results was found to be generally similar; however, there were some small differences. The patterns for the appearance and propagation of cracks differed from each other, while some common features also appeared. The concentration of stress in the two testing processes occurred in different parts of the materials under the two conditions, and this led to differences in both the failure mechanism and the shear strength.

Keywords: Block Shear Test, Rock Mass, Shear Strength, Crack, Finite Element Analysis

INTRODUCTION

The strength of in-situ rock masses, such as the rock foundations of large dams, has been estimated by in-situ rock shear tests for a long time. The method for such tests is constructed as a direct shear test, and the results have been treated as the shear strength with Coulomb's criteria in many practical applications. However, the mechanisms for the appearance of strength in such tests have not been clarified sufficiently.

Two kinds of methods for such tests have recently been prescribed by, for example, the Japanese Geotechnical Society [1]. One is the rock shear test, where the rock to be tested is shaped in a block form and loads are applied to the rock block. The other is the block shear test, where a concrete block is set on the rock to be tested and loads are applied to the concrete block.

The authors [2]-[3] have investigated some basic features of the rock shear test with some plaster model tests and a numerical analysis. Although the shear strength and the displacement obtained from the numerical analysis were lower than those obtained from the real plaster model tests, the mechanical features, including the failure mechanisms, generally resembled those of the real plaster model tests.

The block shear test, which is another kind of in-situ test, is different from the rock shear test in terms of the stiffness of the block to be loaded. This paper presents the results of a numerical analysis of virtual plaster model tests used to simulate the block shear test. Virtual plaster model tests were adopted because it would be tough to conduct real plaster model tests which resemble the authors' former ones for simulating block shear tests due to the difficulty in the bonding between the other materials. The results were compared with the former results to investigate the differences between the two kinds of in-situ tests.

METHODS

Object of Analysis

The loading methods used in the in-situ tests are schematically shown in Fig. 1. In this figure, (a) and (b) represent the sections of the blocks to be loaded. In each testing process, firstly, the normal force, F_{N}, is given and kept constant, and secondly, the inclined force, F_{I}, is increasingly applied. Such loading causes direct shear on the anticipated shear plane.

Figure 2(a) shows the shape of the plaster models which were used in the authors' former study. The conditions were set to be similar to those in the rock shear test, except that both surfaces were confined with clear plates to create the plane strain condition. Figure 2(b) presents the virtual model for simulating the block shear test, resembling the plaster model in Fig. 2(a), except that the block part is almost rigid.

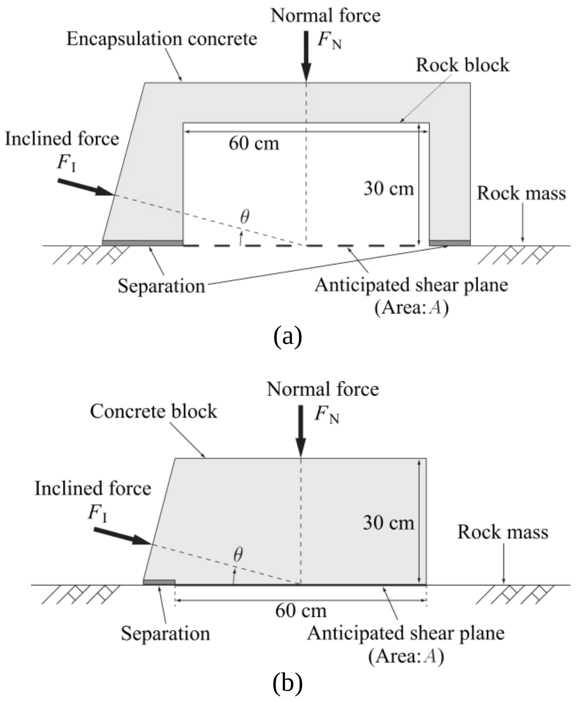

In both tests, normal stress σ and shear stress τ are given as
$\sigma = (F_N + F_I \sin\theta) / A, \ \tau = F_I \cos\theta / A$
on the anticipated shear plane. The maximum value for τ and the corresponding value for σ are used to determine the strength. Initial normal stress σ_n is given as
$\sigma_n = F_N / A$.

Fig. 1 Two types of in-situ rock shear tests: (a) Rock shear test, (b) Block shear test.

In order to compare only the rigidity of the blocks, the steel cap was kept separated from the block part even in the block shear test type (Fig. 2(b)), as was done in the rock shear test type (Fig. 2(a)).

The former plaster model tests were conducted for dozens of cases under different values for the initial normal stress, σ_n , on both intact and layered models, and all the cases were numerically analyzed (Nishiyama & Hasegawa [3]). In the new analysis, shown in this paper, tests were conducted on the intact model considering 7 different levels of initial stress, namely, σ_n = 0.375, 0.625, 1.25, 2.5, 3.75, 5, 7.5 (MPa).

Given Conditions and Procedure

The numerical model for the virtual model in Fig. 2(b) was composed of finite elements, as shown in Fig. 3. All the elements were simple constant strain triangles. The material parameters are given in Table 1; they are the same as those in the authors' former analysis.

At the boundary between the cap and the block,

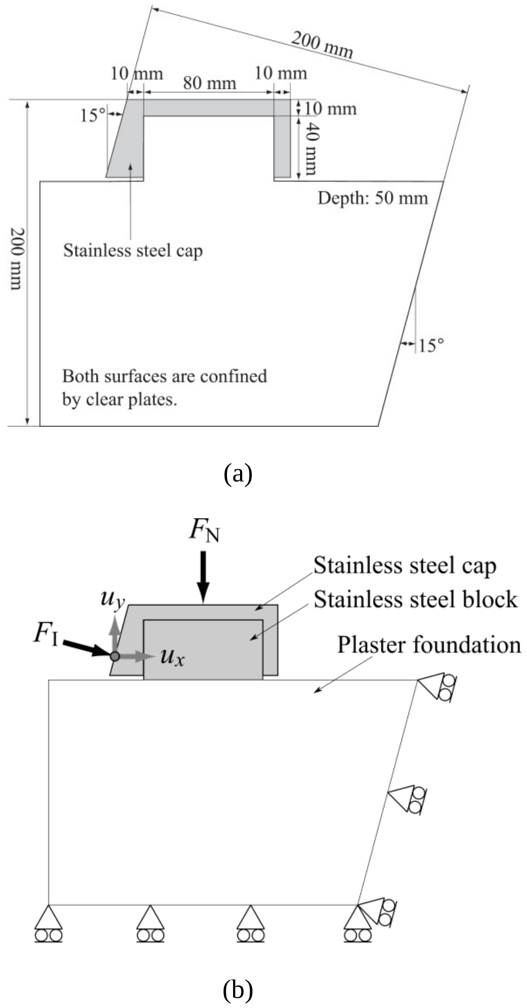

Fig. 2 Plaster models: (a) Model for simulating rock shear tests (Nishiyama & Hasegawa [2]), (b) Virtual model for simulating block shear tests.

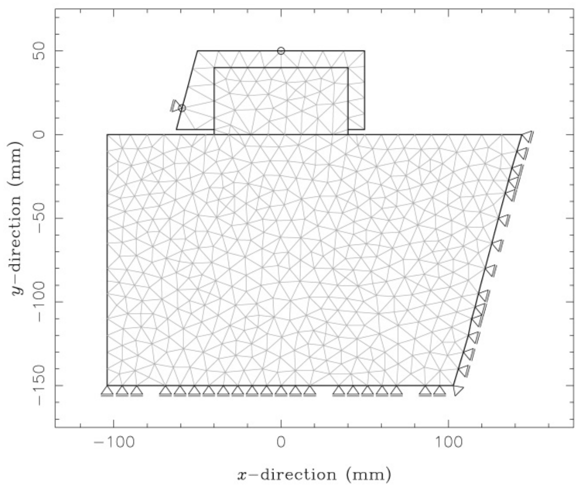

Fig. 3 Numerical model for simulating the virtual plaster model for simulating block shear tests, which are shown in Fig. 2(b).

Table 1 Material properties.

Material	Item	Value
Plaster	Density (kg/m^3) *	1,121
	Elastic modulus (MPa)	3,697
	Poisson's ratio	0.35
	Uniaxial compressive strength, σ_{ci} (MPa)	16.56
	Uniaxial tensile strength (MPa)	−2.844
	Hoek-Brown's constant, *m*	5.65
	Hoek-Brown's constant, *s*	1
Steel	Elastic modulus (GPa)	200
	Poisson's ratio	0.3

* Density was ignored in the analysis.

The strength of the plaster material was described as Hoek-Brown's failure criteria (Hoek [4]), namely,

$$\sigma_1 = \sigma_3 + \sqrt{m\sigma_{ci}\sigma_3 + s\sigma_{ci}^{\ 2}}$$

where σ_1 and σ_3 are the major and the minor principal stress values, respectively.

double nodes were adopted for the contact analysis. A simple contact analysis was also conducted on the outer boundary; however, the boundary between the block and the foundation was treated as an ordinary element boundary with single nodes because the block and the foundation should be bonded through the loading process.

An incremental analysis was conducted in the same way as in the former analysis, as follows. In every case, the boundary condition corresponding to the normal load, F_N, was given as the nodal force in the first step. Then, from the second step, the boundary condition corresponding to the inclined load, F_I, was given incrementally as the nodal displacement.

To simulate crack propagation, the CST elements whose stress had reached the material strength were replaced at every step with enhanced elements, each of which included an interface within itself (Bolzon [5]).

When the stress of the enhanced elements reached the material strength, the elastic modulus of the concerned elements was reduced to 10% of the original value to express the crushed material.

Failure was basically not considered for the steel elements. However, only the steel elements which were adjacent to the plaster elements where failure occurred were replaced with enhanced elements on account of the activation on the interface nodes of the enhanced plaster elements.

RESULTS

Figure 4 shows the macroscopic shear strength values which were obtained from the analysis. In

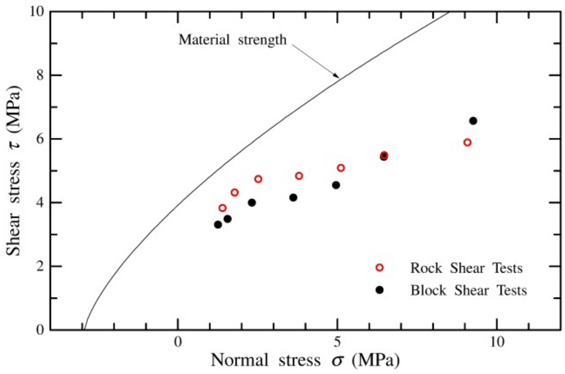

Fig. 4 Comparison of shear resistance values between the two types of tests.

this figure, the values for each type differ from one another. The shear strength for the block shear test type is smaller than that for the rock shear test type in the lower normal stress range, and such a tendency seems to make the row of data points become straighter. In the higher normal stress range, the results of the two types of tests are not the same; however, they commonly appear to be lower than the material strength.

Figure 6 shows the cracking sequence in one of the cases of the block shear test type. Referring to Fig. 5, the first small failure which localized on the side opposite to the loading side of the inclined force corresponds to the peak shear stress. Then, in Fig. 5, block heaving has already appeared. After that, small failures occurred gradually along the base of the block, and finally, the block was completely separated from the foundation. Referring to the former results for the rock shear test type, shown in Fig. 7, the width of the broken zone is narrower in the block shear test type.

The difference in the features of the cracking sequences, according to the initial normal stress, is much less noticeable than the difference in the rock shear test type. The curved propagation of a tensile crack just under the loading side happened only in the cases of the lower normal stress with the rock shear test type, whereas it occurred only in the cases of the higher normal stress with the block shear test type. Figure 8 shows the crack distribution at the residual state in one of the cases under higher normal stress.

DISCUSSION

The block is stiffer than the foundation to be broken in the block shear test type, while the stiffness is the same in the rock shear test type. Therefore, the stress distribution in the foundation under the block would need to be made to be nearly uniform in the block shear test type. On the other hand, the non-uniform stress distribution seemed to cause a reduction in strength in the model

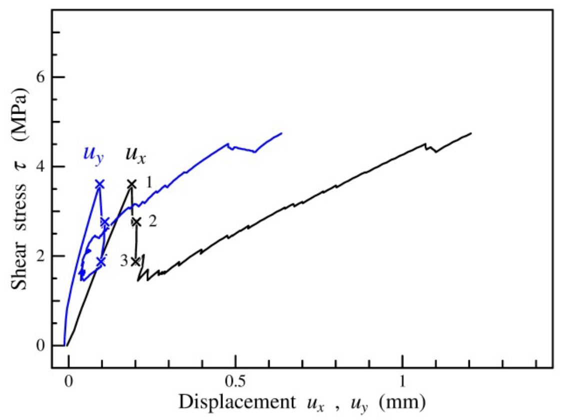

Fig. 5 Relation between the displacement and the shear stress in the case of σ_n = 0.625 MPa. The numbers correspond to those in Fig. 6.

tests of the rock shear test type because the peak shear stress appeared with a small fatal failure in every case. Before the analysis, therefore, the strength in the block shear test type was expected to be higher than that in the rock shear test type.

In the analysis of the block shear test type, uniform stress distributions certainly appeared, as shown in Fig. 9(b). However, the stress concentration caused on the side opposite to the loading side was remarkable. The reason is that it is easier to transmit the compressional stress to the opposite side with a stiffer block. Such a stress concentration caused a decrease in strength in the analysis. This reduction in strength corresponds to the knowledge reported by the Japanese Geotechnical Society [6].

In the rock shear test type, the regularity of the row of data points for the shear strength varied through the normal stress ranges according to the variation in failure mechanisms. The variation in failure mechanisms, according to the normal stress, was very little in the block shear test type; however, the obvious propagation of a tensile crack under the loading side appeared only in each case under the higher normal stress. Once again, referring to the details in Fig. 4, the row of data points appears to be divided into two straight rows which consist of three points each, and the data point in the center seems to represent the transitional state. Such a variation in failure mechanisms, including the variation in the directions of the cracks, should also be related to that in the rock shear test type.

CONCLUSION

A finite element analysis was carried out for virtual plaster model tests to investigate the basic mechanisms of block shear tests. From the analysis, some differences between block shear tests and rock shear tests were found.

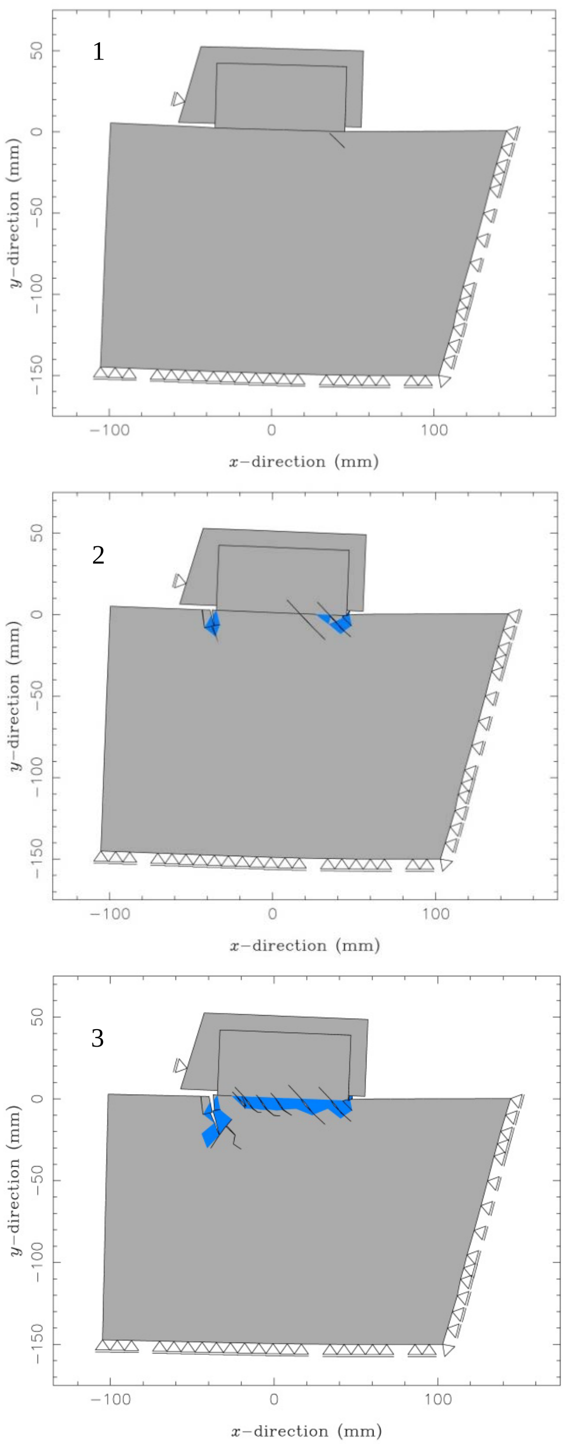

Fig. 6 Cracking sequence in the case of lower normal stress level, σ_n = 0.625 MPa, of the block shear test type. Displacement is emphasized as 30 times. The blue areas represent the regions where the elastic modulus has been reduced. The numbers correspond to those in Fig. 5.

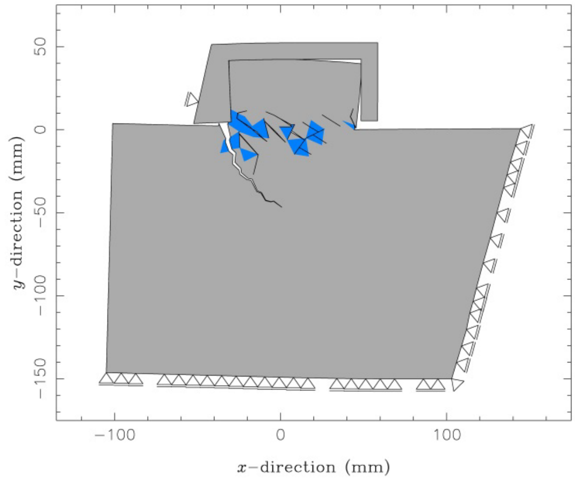

Fig. 7 Crack distribution at the residual state in the case of σ_n = 0.625 MPa of the rock shear test type (Nishiyama & Hasegawa [3]).

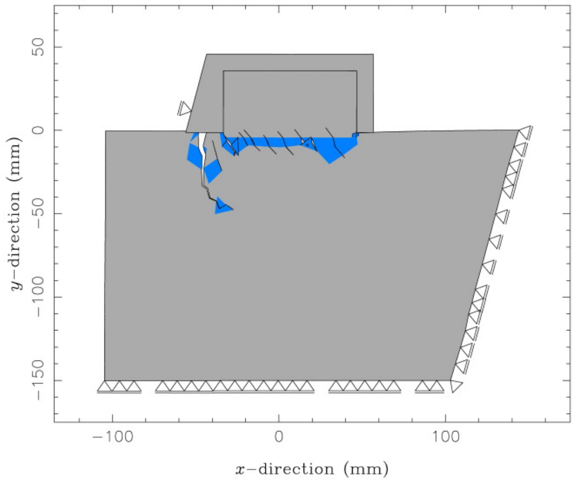

Fig. 8 Crack distribution at the residual state in the case of higher normal stress level, σ_n = 3.75 MPa, of the block shear test type.

The difference between block shear tests and rock shear tests is the degree of stiffness of the blocks. This in turn causes a difference in the distribution of stress in the rock to be broken and brings about changes in the failure mechanisms. Such a difference also leads to a difference in the macroscopic shear strength.

The macroscopic shear strength is lower in the block shear tests than in the rock shear tests under lower normal stress. Such a tendency makes the row of data points become straighter.

The above conclusions are of course only certain for the conditions given in limited cases. Further investigations in the future, for example, a detailed stress analysis or additional analyses for many different cases, are required to obtain more general conclusions.

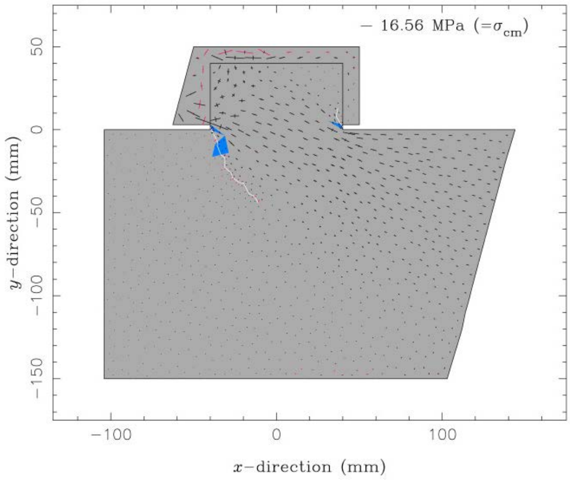

(a)

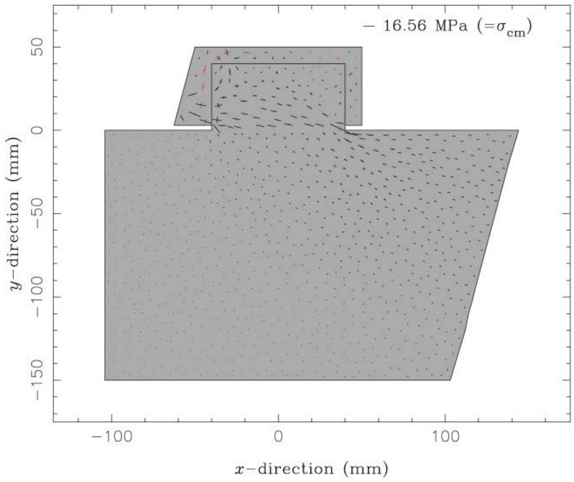

(b)

Fig. 9 Comparison of the stress distributions at the peaks of the shear stress in the cases of σ_n = 0.625 MPa: (a) Rock shear test type, (b) Block shear test type. The segments represent the principal stress axes, shown in black for compression and in magenta for tension, and $\sigma_{cm}=\sqrt{s\sigma_{ci}^2}$ represents the compressional strength of mass of the material. In the foundation part, just under each block, the compressional stress is distributed widely in (a), while there is little load in (b).

REFERENCES

[1] The Japanese Geotechnical Society, “Method for In-situ Direct Shear Test on Rocks”, JGS 3511-2004, 2004.

[2] Nishiyama T & Hasegawa T, “A fundamental study on the strength measured by in-situ rock shear tests”, in Proc. 3rd Int. Symp. on Deformation Characteristics of Geomaterials, 2003, pp. 97-104.
[3] Nishiyama T & Hasegawa T, “A practical use of the finite element with an embedded interface for simulating the direct shear on brittle materials”, in Proc. 14th IACMAG, 2014, pp. 323-327.
[4] Hoek E, “Strength of Jointed Rock Masses”, Géotechnique, Vol. 3, 1983, pp. 185-223.
[5] Bolzon G, “Formulation of a triangular finite element with an embedded interface via isoparametric mapping”, Computational Mechanics, Vol. 27, 2001, pp. 463-473.
[6] The Japanese Geotechnical Society, Methods of Determination of Geotechnical Constants for Design –Rock Mass Edition-. Tokyo: The Japanese Geotechnical Society, 2007, p. 12 (in Japanese).

CREEP AND RELAXATION BEHAVIOR OF HIGHLY ORGANIC SOIL

Shoji KAMAO[1]
[1]Nihon University, Japan

ABSTRACT

Because of the limited land area in Japan, many structures are built on peat and/or highly organic soft ground. . These soils are well known for exhibiting large settlement and secondary compression during and after construction. Preloading is suitable for ground improvement of peat and highly organic soil, as well as clay.

The author performed a series of laboratory loading/unloading creep tests to simulate the preloading method for peat and silty clay which samples collected in Japan. Previously, the author reported that the characteristics of long-term creep settlement after unloading are affected by the overconsolidation ratio, preloading time and plasticity index. In this paper, the experimental data from creep and stress relaxation tests are used to further explore the behavior of highly organic soil.

Keywords: Peat, Highly organic soil, Preloading method, Creep, Relaxation

INTRODUCTION

Recently, urban development has been brisk around large cities in Japan. Because of the limited land area, many structures are built on peat and/or highly organic soft ground, which used to be a marsh. Highly organic soil is known for its large compressibility during and after construction.

In addition, many areas along Pacific Ocean were damaged by tsunami at the time of the Great East Japan Earthquake in 2011. Therefore, developments of new revival residential land have been constructed inland and at higher places from the coastal line to prevent damage caused by tsunami. Many developments have been made inland and on higher ground that was formerly used for rice paddies or marsh. Due to the construction on highly organic soil, a geotechnical problem of large long-term settlement often occurs after construction. This paper focuses on improving the long-term settlement of soft soil by using the conventional preloading method. The effect of preloading was considered on the basis of the results of two types of experiments, i.e. the creep test with loading and unloading and the stress relaxation test that tolerates no settlement during loading. The two tests are used to clarify the reduction of long–term settlement generated after unloading the preload.

The determination of OCR (overconsolidation ratio) is often a difficult problem in the design of the preloading method, because there are only a few studies related to design and construction preloading that consider large long-term settlement for highly organic soils (e.g. Kamao et al. 1995, and Fukazawa et al. 1998).

USED SOIL

Table 1 shows the typical properties of the soil used in this study. The M soil is highly organic soil sampled in Chiba Prefecture near Tokyo. The S soil is silty clay sampled in Tokyo Bay area. The K soil is organic clay that is mixture of the M and S soils.

All specimens were used in remolded condition under reconsolidation pressure of 20 kPa. They were prepared as follows: the water content of the disturbed sample was adjusted to be twice the liquid limit (LL) and then consolidated under the reconsolidation pressure of 20 kPa for approximately two weeks.

Table 1 Soil properties

soil	Specific Gravity Gs	Water Content* w %	Liquid Limit LL %	Plasticity Index PI	Ignition Loss Lig %
M	1.83	431	349	147	35.2
K	2.38	148	155	67	14.5
S	2.60	52	50	18	5.2

* after reconsolidation

TEST PROGRAM

This study considers the long-term settlement of the soft ground as a one-dimensional consolidation phenomena like embankment of a widely spread area without lateral movement. Creep and relaxation tests were conducted in the laboratory using a conventional consolidation apparatus (Φ=60mm, h=20mm, JIS A 1217).

The Creep Test

Fig. 1 and Table 2 show the loading scheme and test conditions for the creep test.

In the first step, reconsolidation pressure (p_0) of the remolded soil specimen was loaded for 24 h. In the second step, the preload (p_P) was loaded for preloading time t_P . In the last step, Δp load was removed.

The laboratory experiments correspond to the preloading method in the field, OCR, the rate of secondary compression (ε_α) and the rebound ratio (ε_R) were chosen as parameters for evaluating preloading effects defined in Equations (1), (2) and (3). Other details are shown in Kamao et al. 1995.

$$OCR = (p_0 + p_P) / (p_P - \Delta p) = (p_0 + p_P) / p_f \quad (1)$$

$$\varepsilon_\alpha = \Delta\varepsilon / \Delta\log t \times 100 \ (\%) \quad (2)$$

$$\varepsilon_R = S_R / S \times 100 \ (\%) \quad (3)$$

where
p_0: preconsolidation pressure (kPa)
p_P: preloading pressure (kPa)
Δp: unloading pressure (kPa)
$\Delta\varepsilon$: strain during long-term settlement
S: settlement before unloading (mm)
S_R: rebound due to unloading (mm)
t: elapsed time (min)

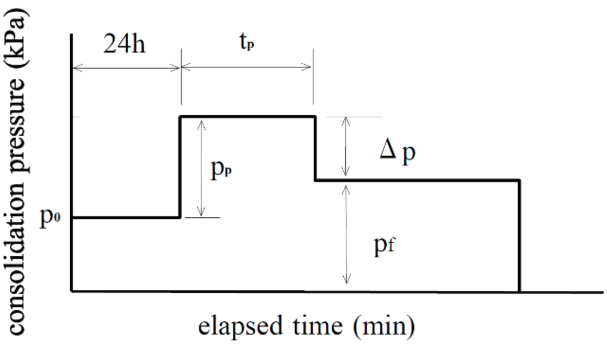

Fig. 1 Loading scheme of the creep test

Table 2 Test conditions for the creep test

p_0 kPa	p_P kPa	t_P min	Δp kPa	OCR -
20	60	60	0	1
			20	1.3
			30	1.6
			40	2
			50	2.7
			75	16

The Relaxation Test

The relaxation test was performed by reducing a load such that settlement generated in a specimen was eliminated completely when the load was reduced after loading the specimen with a preload of p_p for t_P. The relaxation tests were conducted as shown in Fig. 2 and Table 3. Each case had two relaxation phases (relaxation1 of t_1 and relaxation2 of t_2) at consolidation pressures of p_{P1} (80 kPa) and p_{P2} (160 kPa), respectively. In some cases, residual consolidation pressure was retained for a few weeks after the relaxation period (t_2) to measure the long-term resettlement.

By comparing the creep test and the relaxation test results, the author implemented to make basic data for preloading method considering the long-term settlement of highly organic soil.

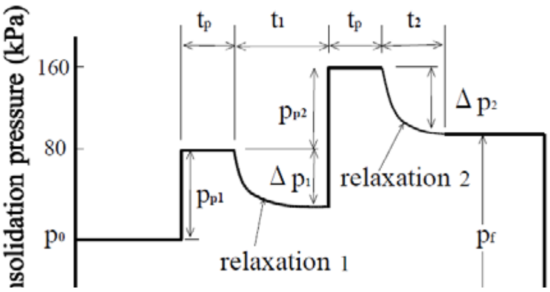

Fig. 2 Loading scheme of the relaxation test

Table 3 Test conditions for the relaxation test

cases	p_0 kPa	p_{p1} kPa	p_{p2} kPa	t_p min	t_1 min	t_2 min
1	20	60	80	120	1440	1440
2					120	720
3					360	360
4					720	120

EXPERIMENTAL RESULTS

Results of the Creep Test

Fig. 3 shows typical experimental results (S – log t curves) of the creep test. With removal of the preload at time t_P, rebound due to swelling occurred immediately for all OCRs except OCR of 1.0. Then, resettlement was observed after the rebound phase for all OCRs except the OCR of 16.0.

Relationships between the rebound ratio (ε_R) and OCR are shown in Figs. 4 and 5. Fig. 5 shows the details of Fig. 4.

From these figures, linear relationships between rebound ratio (ε_R) and OCR are obtained for each soil. The amount of rebound for soil M is 5 to 6 times larger than that for soil S and 1.6 to 1.8 times larger than that for soil K. The value of ε_R depends on the plasticity index (PI) of the soil.

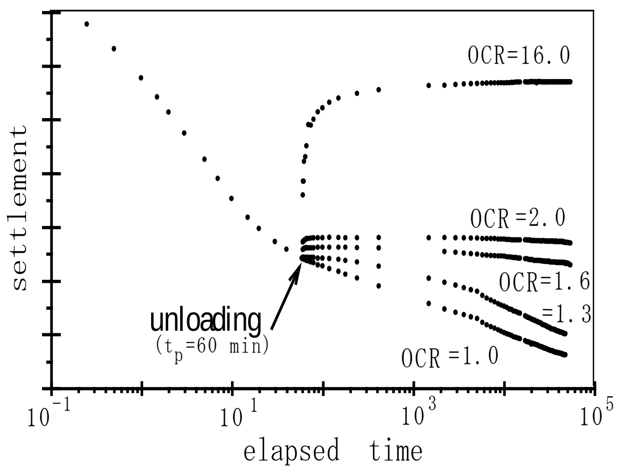

Fig. 3 Experimental results of the creep test

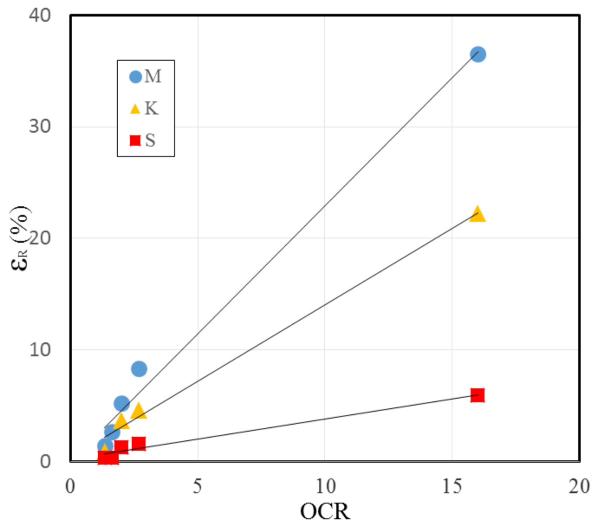

Fig. 4 Relationship between ε_R and OCR (1<OCR<16)

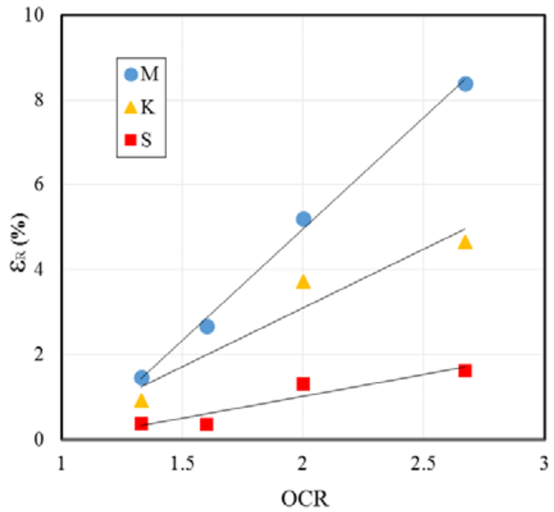

Fig. 5 Relationship between ε_R and OCR (1<OCR<3)

The rate of secondary compression (ε_α) is defined by Equation (2). Fig. 6 shows the relationship between ε_α and OCR. The rate of secondary compression (ε_α) decreases with increase of OCR. The reduction ratio (R) of the rate of secondary compression, which is seen in Fig. 6, is defined as the ratio of ε_α and $\varepsilon_{\alpha, OCR=1.0}$, as indicated by Equation (4). This value can help evaluate the preloading effect.

The relationship between R and OCR is shown in Fig. 7. The optimum OCR (i.e., which minimizes resettlement) was approximately 2.0 to 2.5 for all types of soil. Fukazawa et-al. (1984) reported the optimum OCR as approximately 1.3 to 1.5 in field measurement data. Laboratory data from the present study tended to a larger OCR number than the field data of Fukazawa et al.. The reason for this difference is considered to be the difference in the condition of the specimen. The disturbed specimen for this study has weaker soil structure than undisturbed field deposits (e. g., see Kamao, 1995).

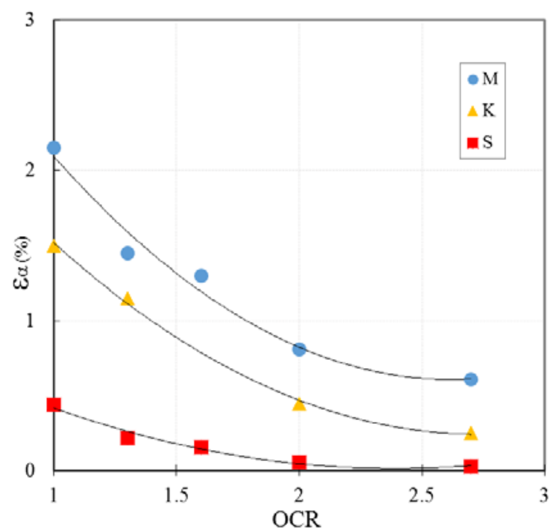

Fig. 6 Relationship between ε_α and OCR

$$R = \{1 - (\varepsilon_\alpha / \varepsilon_{\alpha, OCR = 1.0})\} \times 100\ (\%) \quad (4)$$

where

ε_α : rate of secondary compression

$\varepsilon_{\alpha,OCR = 1.0}$: rate of secondary compression at OCR = 1.0

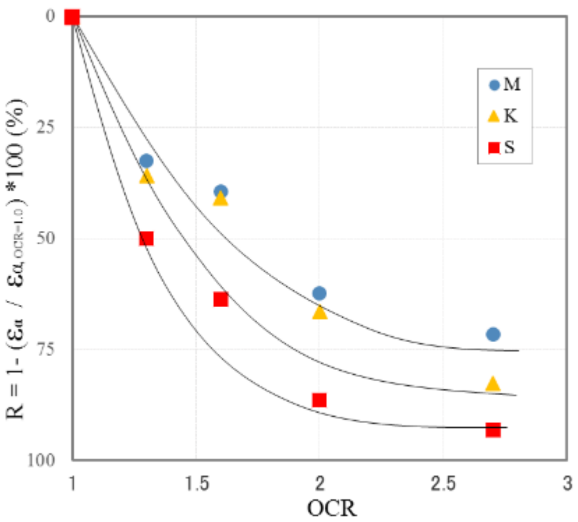

Fig. 7 Relationship between reduction ratio (R) and OCR

Results of the Relaxation Test

Figs. 8, and 9 show typical experimental results of the relaxation test. Fig. 8 shows the relationship between settlement and elapsed time before and after the relaxation phase (relaxation time is 120 min). Fig. 9 shows the relationship between consolidation pressure and relaxation time. From these figures, it can be seen that no settlement occurs after the start of relaxation time (Fig. 8), and significant reduction of the consolidation pressure was observed for all three types of soil, immediately after shifting to the relaxation phase. Then consolidation pressure gradually decreased with relaxation time to keep settlement zero (Fig. 9). Reductions were achieved by stemming rapid settlement just before shifting to the relaxation phase, proving preferable and controlling operation.

It is difficult to estimate the final decreased consolidation pressure from Fig. 9, because the consolidation pressure decreases gradually with relaxation time. The relationship between consolidation pressure p and the logarithm of the relaxation time t_1 is linear at the latter part of the test, as shown in Fig. 10. The slopes of the latter p-log t_1 curves (p/t) in Fig.10 are similar to the secondary compression settlement in Fig. 3. The magnitude of the linear slope, seems to be proportional to the amount of secondary consolidation settlement. Fig. 11 shows the linear relationship between p/t and the PI of the soil. The decreased consolidation pressure Δp_1 (Δp_2) in Fig.2, which was defined as the consolidation pressure at t=10^4 min by extending the straight line of the latter part of the test, is shown in Table 4. Consolidation theory indicates that t=10^4 min is enough consolidation time for thin specimens to undergo the laboratory oedometer test, and to undergo comparison with the creep test. The final decreased consolidation pressure is similar to the unloading of the creep test shown in Fig. 1. Using residual consolidation pressure p_f (= $p_0 + p_{p1} - \Delta p_1$), the "absolute OCR" (i.e., which has no long-term settlement ($\varepsilon_\alpha = 0$) during the relaxation phase) was calculated for each soil using Equation (1). The calculated absolute OCRs are shown in Table 4. The relationships between absolute OCR and PI for different soils are shown in Fig. 12. Regardless of the consolidation pressure p_p, OCR is well correlated with PI of soil.

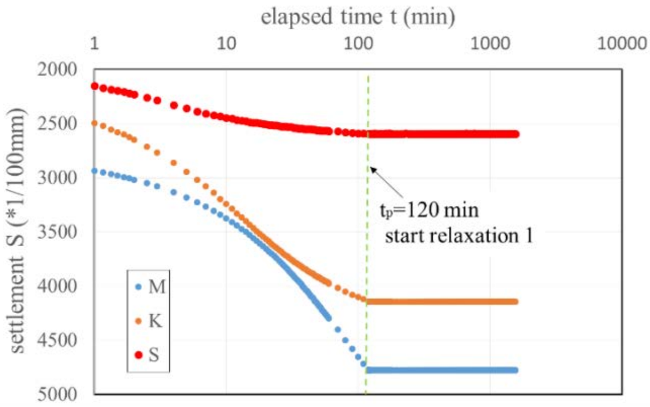

Fig. 8 Experimental result of the relaxation test (s – log t curves)

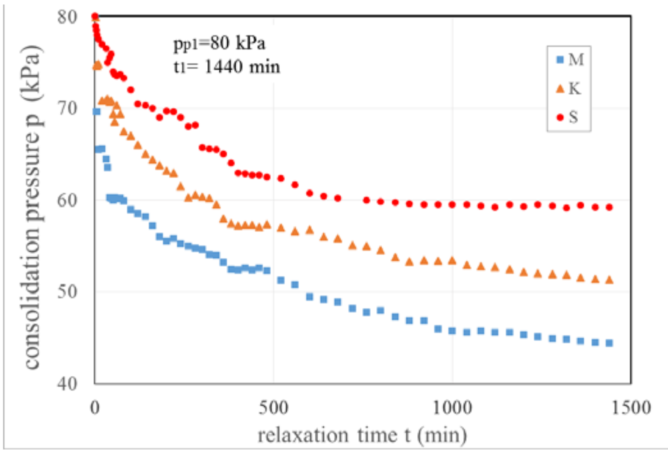

Fig. 9 Experimental result of the relaxation test (p - t curves)

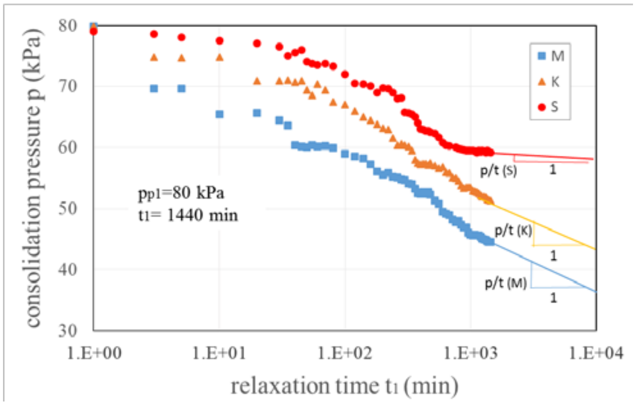

Fig. 10 Experimental result of the relaxation test (p – log t curves)

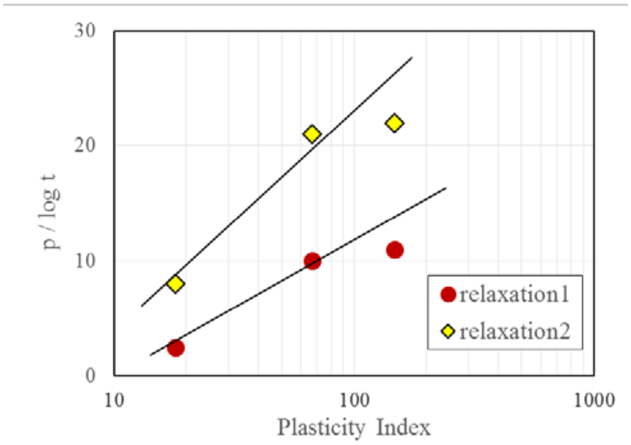

Fig. 11 Relationship between p/t and PI from the relaxation test

Table 4 Estimated residual consolidation pressure and calculated absolute OCR at the relaxation time of 10^4 min

pp1, pp2	Types of soil		
	M	K	S
80	36 (2.20)	44 (1.82)	58 (1.38)
160	77 (2.08)	88 (1.80)	122 (1.31)

unit: kPa, ( ):OCR

DISCUSSION

The OCR of the preloading method is discussed by comparing the creep test with relaxation test. The absolute OCR (which has no long-term settlement (ε_α=0)) is 2.1 to 2.2 for highly organic soil (M). For silty clay (S) and organic clay (K), absolute OCRs are 11.3 to 1.4 and 1.8, respectively.

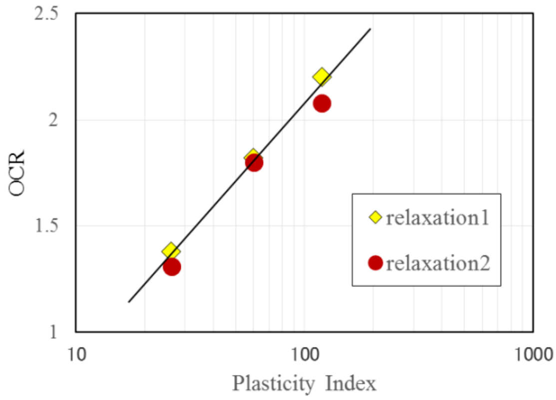

Fig. 12 Relationship between calculated absolute OCR and PI from relaxation test

These absolute OCRs were plotted on the creep test result (Fig. 7), as shown in Fig. 13. For ε_α=0 (absolute OCR), the reduction ratio (R) become 100(%) from Equation (4). Green stars on the figure indicate the absolute OCR from the relaxation test. The green lines are tendency lines.

Fig. 13 shows the tendency lines of the relaxation test are steeper than the creep test data. The differences between the relaxation test and the creep test are caused by the speed of unloading (rapid or slow unloading) and duration of loading. The estimation method for the final reduced pressure (Δp1) also seems to introduce differences. Rapid unloading (as in the creep test) allowed the specimen to swell and rebound; however, slow unloading (like relaxation test) did not allow either. Slow unloading took considerable time.

With rapid unloading, the soil structure was disturbed and changed due to the disruption of bonds between particles and aggregates (e. g., Den Haan et al., 2003). Therefore rapid unloading made the reduction ratio (R) smaller than slow unloading.

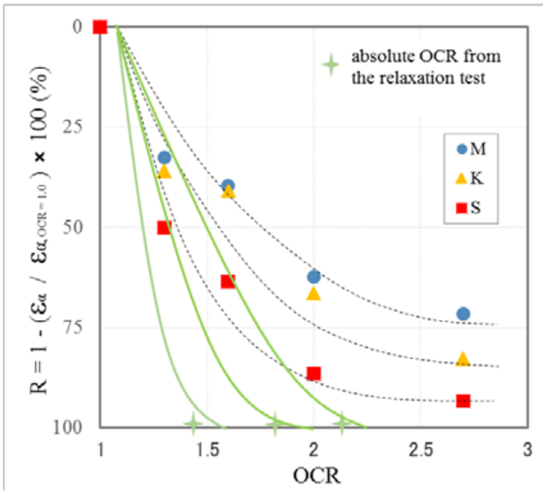

Fig. 13 Relationship between the reduction ratio (R) and OCR

CONCLUSION

Two series of laboratory model loading/unloading tests were performed. The following conclusions were reached:

(1) The creep test showed that the rebound ratio ε_R increases in accordance with increased OCR and the rate of secondary compression ε_α decreases in accordance with increased OCR.
(2) The optimum OCR (i.e., that which minimize long-term settlement) is approximately 2.0 to 2.5 for all soils.
(3) The relaxation test showed that reduction of consolidation pressure was well controlled, without settlement and rebound.
(4) The absolute OCR was obtained using estimated residual consolidation pressure.
(5) The absolute OCR was approximately 2.1 to 2.2 for highly organic soil (M). The tendency line is steeper than the creep test data for this soil.

ACKNOWLEDGEMENTS

All laboratory experiments were performed by student members of Environmental geotechnics laboratory of Nihon University.

REFERENCES

Kamao, S., Yamada, K., Sato, F. and Aita, K. (1995) Characteristics of long-term resettlement of soft ground after removal of the preload. International Symposium on Compression and Consolidation of Clayey Soils. (I.S. Hiroshima): 75-78

Fukazawa, E. and Monoi, Y. (1998) Measurement of long-term settlement of highly organic soil improved by preloading. International Symposium on Problematic Soils. (I. S. Tohoku): 75-78

Fukazawa, E., Yamada, K. and Kurihara, H. (1994) Predicting long term settlement of highly organic soil ground improved by preloading. Journal of Japanese society civil engineering, No.493, III-27, pp59-68 (in Japanese)

E. J. den Haan, Kamao S. (2003) Obtaining Isotache parameters from a C. R. S. K_0-oedometer. Soils and foundations, vol. 43, No. 4, pp203- 214

Fifth International Conference on Geotechnique, Construction Materials and Environment, Osaka, Japan, Nov. 16-18, 2015, ISBN: 978-4-9905958-4-5 C3051

INVESTIGATION OF SEISMIC BEHAVIOR OF EARTH DAM EMBANKMENTS BY USING FEM AND CENTRIFUGAL LOADING TESTS

Shohei Tsurui [1], Takahiro Sugano[1], Akira Kobayashi [3] and Akira Murakami [1]
[1] Graduate School of Agriculture, Kyoto University, Japan
[3] Faculty of Environmental and Urban Engineering, Kansai University, Japan

ABSTRACT

There are many earth dams in Japan. In particular, the number of irrigation tanks is estimated to be over 210,000. Many irrigation tanks in Japan were constructed on the basis of experience gained over one hundred years ago. Many of these tanks have suffered earthquake damage over the years. The types of damage reported include cracks at the crest in the dam-axis direction. In order to clarify this mechanism, model experiments using a small shaking table in a 1-G gravity field, which can visualize the behavior of the cross-sections, are conducted. It is found that vertical tension and compression zones appear alternatively, and that tensile stress is observed at the crest of the model from the volumetric strain distributions. Cracks at the crest are estimated to be caused by tensile stress, which is not considered in the design process. In this research, a finite element analysis and centrifugal loading tests in a 50-G gravity field are applied to examine the mechanism. As a result, it is found that the distribution where the vertical tension and compression zones exist alternatively is attributed to the heterogeneity of the dam body.

Keywords: Seismic Behavior, Earth Dam, Centrifugal Loading Test

INTRODUCTION

In Japan, there are approximately 210,000 small earth dams, which have been very important sources of water supply for irrigation. The height of the dams is shorter than 15 m, and such dams are called irrigation tanks in Japan. Many irrigation tanks were constructed on the basis of experience gained over 100 years ago. It is reported that about 20,000 irrigation tanks suffered earthquake damage in the past and are in need of repair.

As for the damage to many irrigation tanks, including those which are not considered to have an earthquake-resistant design, it is reported that cracks at the crest in the direction of the dam axis were induced by earthquakes. That mechanism is considered to be different from slide failure, which is taken into consideration in the design manual. It is difficult to repair irrigation tanks effectively because the mechanism of such cracks on the crest has not been clarified.

The most important factor in the seismic stability of irrigation tanks is the earthquake response. The material properties, including the water content of the soils and the shape of the irrigation tanks, influence the aseismic behaviour. Investigations of the seismic behavior of irrigation tanks have been conducted based on numerical analyses and model experiments.

Two types of dynamic tests have been used for the dynamic model tests, namely, dynamic centrifuge tests and 1-G shaking table tests. Dynamic centrifuge tests utilize the gravity force to simulate the behaviour of a full-scale prototype. On the other hand, 1-G shaking table tests are carried out to examine the quantitative aseismic behavior. In order to clarify the mechanism, the model experiments were conducted using a 1-G small shaking table, which could visualize the detailed behavior of the cross-section (Miyanaga et al., 2013). Figures 1 and 2 show the results of the model experiments. In the shear strain distributions, the shear strain becomes large at the foot of the slope when the specimen passes the shaking center. In the volumetric strain distributions, the tension and compression zones exist vertically and alternatively, and tension stress is observed at the top of the model. It is inferred that the seismic crack at the crest of the dam is caused by tensile stress.

In this study, the tensile stress at the crest, observed in the 1-G shaking tests, is confirmed by centrifugal loading tests with a gravity field of 50 G. Moreover, the mechanism of the tensile stress at the dam crest is examined by a numerical analysis.

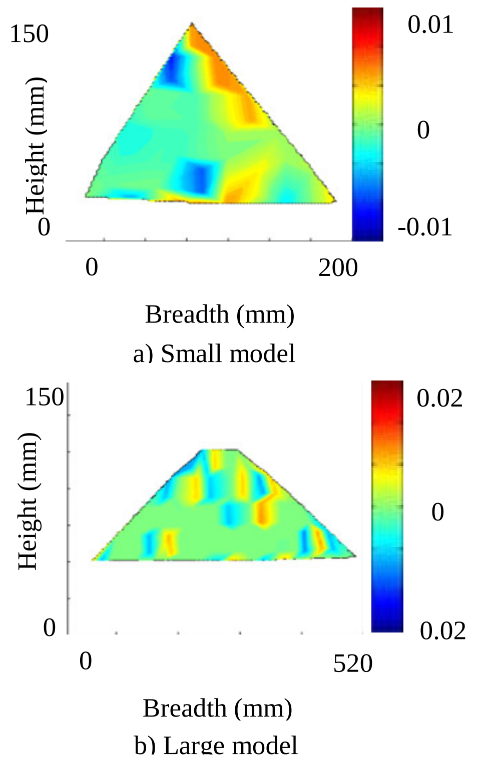

Fig. 1 Shear strain distributions of model experiments

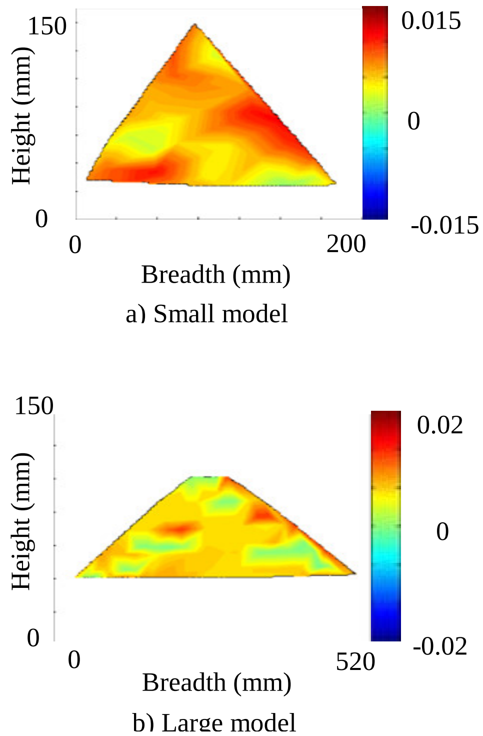

Fig. 2 Volumetric strain distributions of model

CENTRIFUGAL LOADING TESTS

Test conditions

The centrifugal loading tests were conducted under 50-G with a 1/50 scaled model. In this experiment, the model had a height of 100 mm and upstream and downstream gradients of 1:1. The model was made from No. 7 silica sand and kaolin clay with a mixture ratio of 8:2 by dry weight. The water content of the mixture was 13%. In order to evaluate the seismic behavior of the model, the gauge points were placed on the surface. Accelerometers were installed at the top of the model, the bottom of the model, and on the soil chamber. Figure 3 presents an experimental view of the model.

The model was shaken with a horizontal sine wave of 50 Hz whose amplitude was 1 mm. The input seismic wave is shown in Figure 4. The input seismic wave corresponds to the earthquake ground motion with a peak acceleration of about 300 gal.

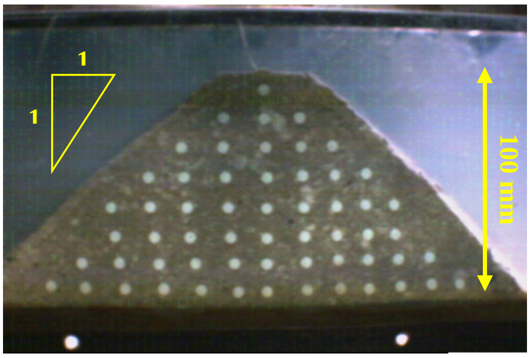

Fig. 3 Experimental view of the model

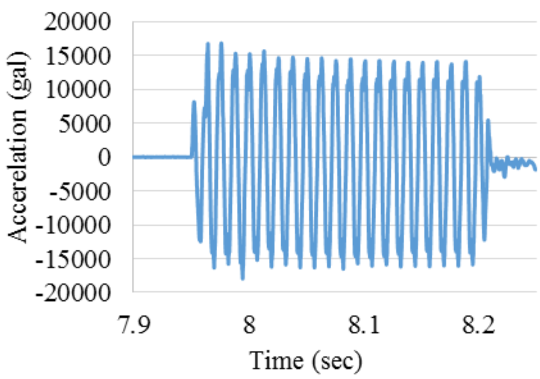

Fig. 4 Input seismic wave

Digital image analysis

In order to evaluate the displacement of the gauge points, the digital image analysis method, used in the 1-G gravity field (Miyanaga et al., 2013), is applied.

Firstly, a static image is taken before the model is shaken. While the model is shaken, continuous images are taken. The images are transformed into black and white binary images in order to make the image process quick and easy, as shown in Figure 5. Then, the coordinates of the gauge points are measured in the unit of pixels by calculating the center position of each white element representing the gauge point. Finally, the distance between two reference points on the surface of the soil chamber, which was exactly 150 mm, is measured in the unit of pixels. The scale calibration is performed using the distance of the reference points, and the coordinate of the gauge points is estimated as the relative location of the reference point in the unit of mm. By repeating this procedure for all the dynamic images, the displacement variation for each gauge point can be obtained.

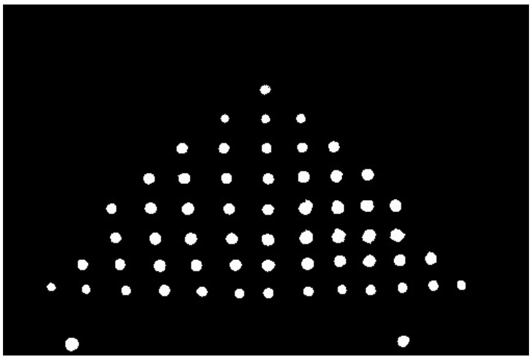

Fig. 5 Black and white binary image of model Two points at the bottom of figure are the reference points

Experimental results

Aseismic behavior

The shear strain distributions are shown in Figure 6. The shear strains become large at the top of the model. The left parts of the models have negative values, while the right parts have positive values. Figure 7 shows the displacement between two gauge points at the center of the model, which is shown by red lines in Figure 8. It is found that the displacement at the top becomes large with time. However, no change is seen for the displacements in the middle or at the bottom. Therefore, it is found that the upper part of the model expands in a horizontal direction.

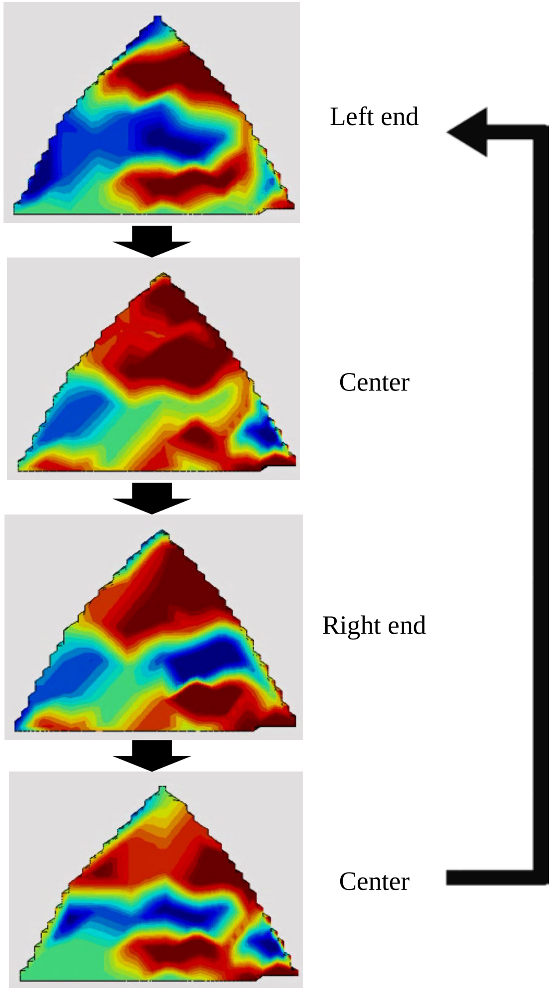

Fig. 6 Shear strain distributions of centrifugal loading tests

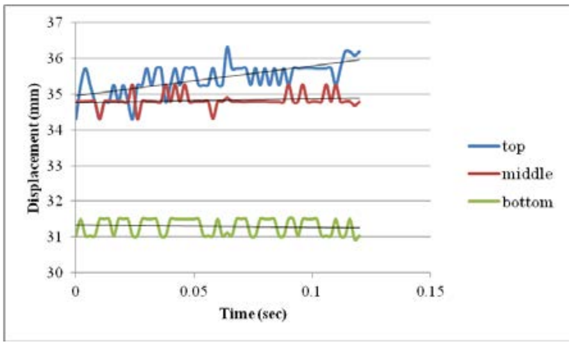

Fig. 7 Displacement between two gauge points during shaking

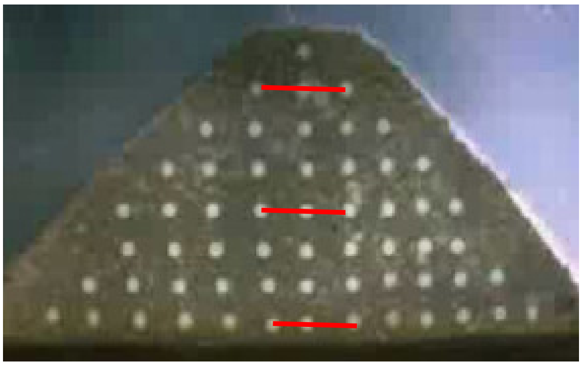

Fig. 8 Positions at which the displacement is measured

Figure 9 shows the volumetric strain distributions of the centrifugal loading tests. The volumetric strain is large at the top of the model during shaking. Moreover, the compression zones are small and are seen only in the right part at the bottom. The extension zones are observed along the slope. It is inferred that the tensile stress in the upper part causes the cracks at the crest.

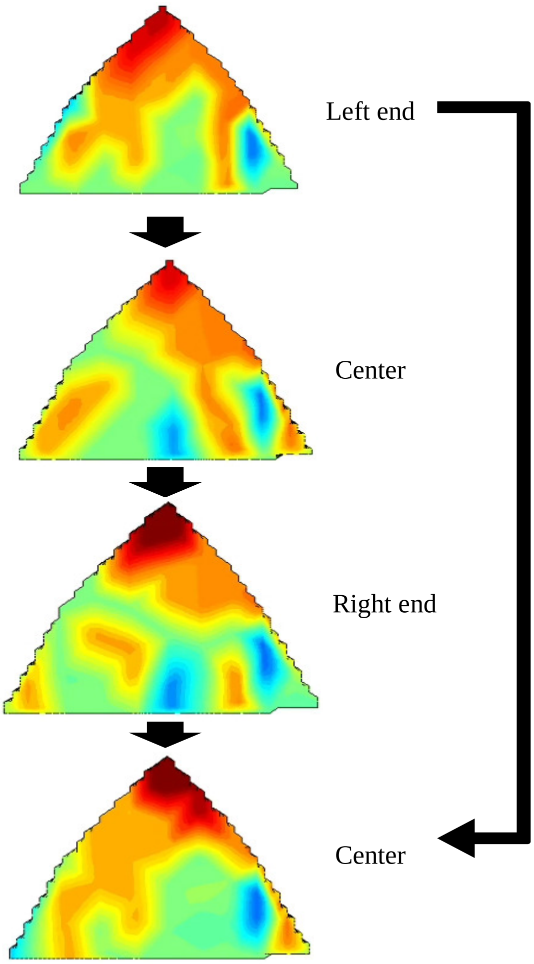

Fig. 9 Volumetric strain distributions of centrifugal loading tests

Figure 10 shows the cracks at the crest of the specimen. The cracks developed gradually and finally the depth became 5 mm. The settlement was observed at 5 mm.

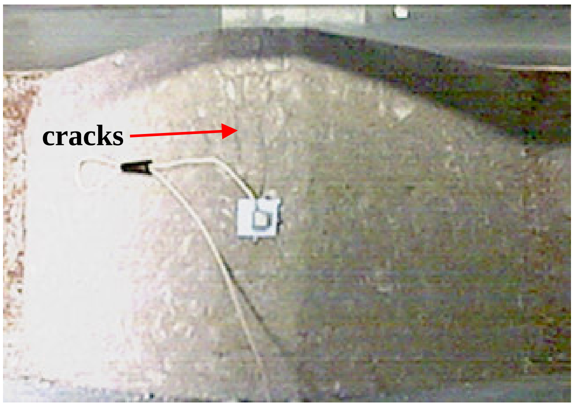

Fig. 10 Cracks observed in centrifugal loading tests

SIMULATION ANALYSIS

Model Shapes

In this study, two types of dam models with different cross-sections, examined in 1-G tests, are simulated. The first type, with a height of 150 mm and upstream and downstream gradients of 1:0.545, is called the small model. The second type, with the same height and gradients of 1:1.5, is called the large model. These model shapes are the same as those in the experiments shown in Figures 11 and 12.

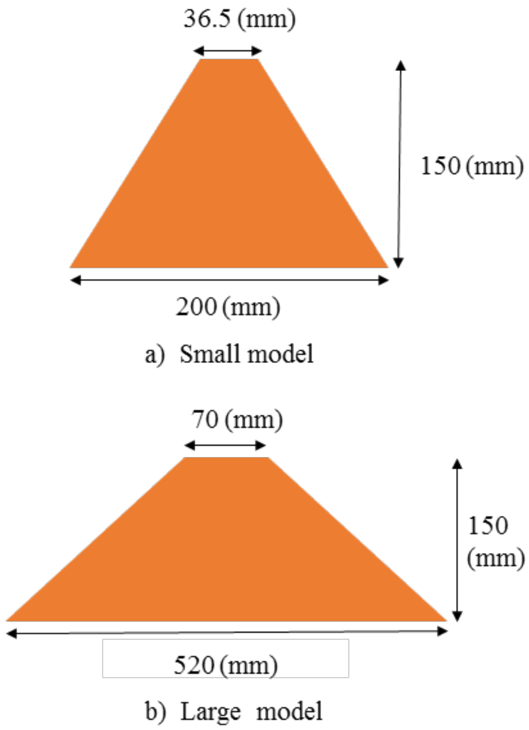

Fig. 11 Model types of numerical analyses

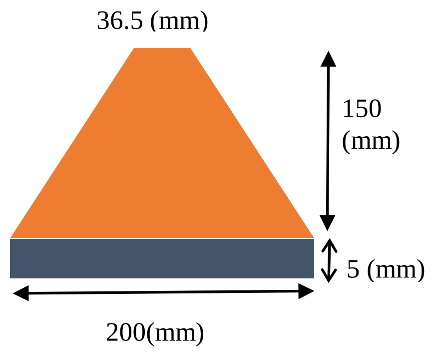

Fig. 12 Small model with base (Case 2)

Methods

To examine the strain distributions, the elasto-plastic FEM, using Mohr-Coulomb's criteria as the yield function, is applied in this study. The bottoms of the models are subjected to 2.4 Hz of horizontal sine wave. The amplitude is 280 gal. The wave is the same as that applied in the 1-G tests.

Analytical Conditions

The shear strain distributions and the volumetric distributions are examined for the following three cases;

Case 1 The basic case, with no hydrodynamic pressure

Case 2 The small model has a base whose thickness is 5 mm. Homogeneous accelerations are not input into the bottom of the dam body.

Case 3 Hydrodynamic pressure is exerted on the upstream slope of the large model.

The model and the base in Case 2 are set as shown in Figure 12. Case 2 is the case for which the input wave is not homogeneous. When the bottom of the base is subjected to a given wave, the fluctuation of the bottom of the dam body becomes a little inhomogeneous, while the amplitude is not so different.

The analytical parameters are set by reference to the measured parameters of the 1-G tests, as shown in Table 1.

Hydrodynamic Pressure

Figure 13 shows the measured hydrodynamic pressure when the model is located at the center of the shaking. The hydrodynamic pressure becomes large when the model shakes from upstream to downstream. The hydrodynamic pressure becomes small when the model shakes from downstream to upstream.

Results of Analyses

Case 1

Figure 14 shows the shear strain distributions of the small and large models when the model shakes from downstream to upstream and passes the center of shaking. It is found that the maximum shear strain is given at both ends of the bottom for the small model. On the other hand, the maximum shear strain is obtained at the central part of the bottom for the large model.

Figure 15 shows the volumetric strain distributions of the small and large models at the same time as in Figures 14 and 15. The maximum volumetric strain is shown at the top and at both ends of the bottom for the small model. On the other hand, the maximum volumetric strain is shown at the slopes for the large model. The volumetric strain observed in the small model is larger than that in the large model. The volumetric strain for both cases is distributed in a vertically striped pattern.

Table 1 Material parameters

Parameters	Dam Body	Base (Case2)
Cohesion (kPa)	15	15
Unit weight (kN/m^3)	18	18
Elastic modulus (kPa)	3,000	2,850
Internal friction angle (°)	35	35
Poisson's ratio	0.3	0.3

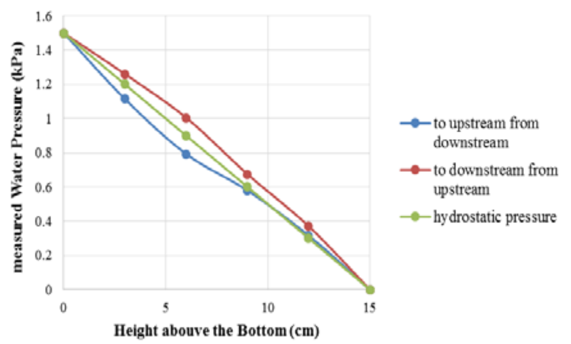

Fig. 13 Hydrodynamic pressure when the model is located at center of shaking table

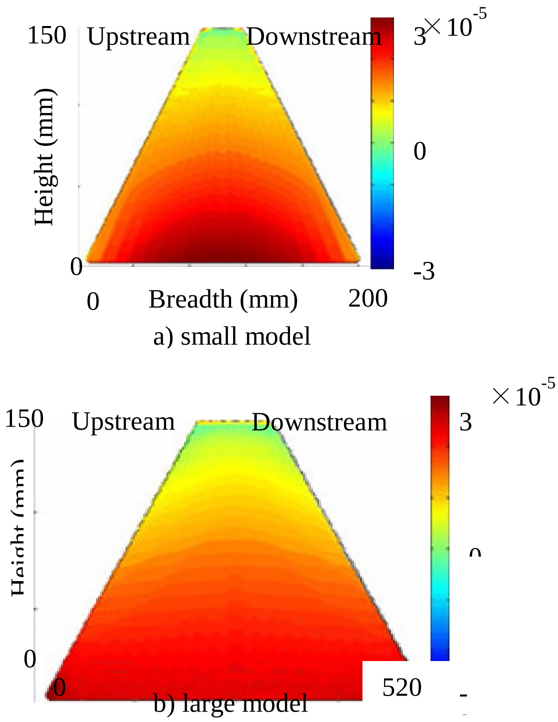

Fig. 14 Shear strain distributions of Case 1

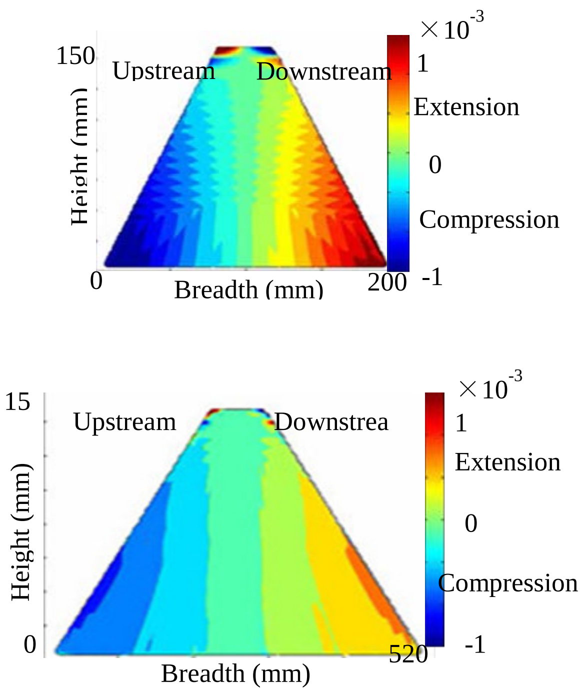

Fig. 15 Volumetric strain distributions of Case 1

Case 2

Figures 16 show the shear strain distribution of Case 2 when the models are at the center of shaking from downstream to upstream. By setting the bases, the homogeneous accelerations would not be input into the bottom of the model. The shear strain at the top is very small. As for the volumetric strain, the extension and compression zones appear alternatively at the lower part of the model.

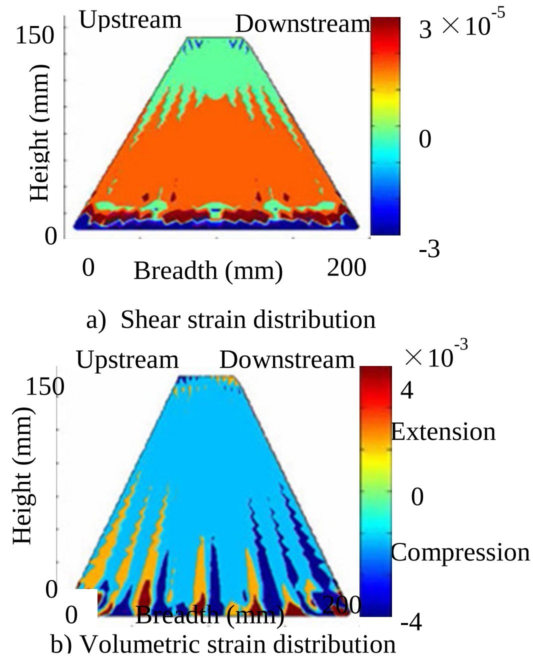

Fig.16 Strain distributions of Case 2

Case 3

In order to examine the effects of hydrodynamic pressure on embankments, the hydrodynamic pressure is applied to the upstream slope of the large model. The results are shown in Figures 20 and 21. The figures show the strain distributions when they shake from downstream to upstream and pass the center of shaking. The shear strain becomes large at the central part of the model. The parts at the slope have small strain in comparison to that shown in Figure 17. This is probably because the body is constrained by the hydrodynamic pressure. As for the volumetric strain distributions, the extension strain develops along the upstream slope and the compression strain extends to the downstream parts. The distributions are in contrast to the results without hydraulic pressure, shown in Figure 17.

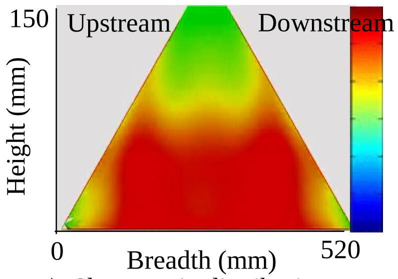

a) Shear strain distribution

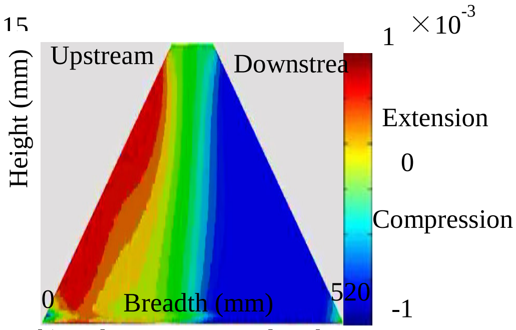

b) Volumetric strain distribution

Fig. 17 Strain distribution of Case 3

Summary of Analyses

The analysis results are different from the experimental results. In particular, large extensional volumetric strain cannot be realized at the upper part by the analyses. The distributions of shear strain are also quite different from the observed ones. As a present conclusion, the ordinary elasto-plastic model is found to unsuitable for the dynamic analysis of earth dams.

CONCLUSION

Many earth dams developed cracks in the direction of the dam axis at the crest when a large earthquake occurred. Up to now, however, design guides have not mentioned extension failure; only shear failure has been considered.

In this study, to examine the mechanism of cracks along the dam axis, 1-G shaking tests and centrifugal loading tests have been conducted. Moreover, numerical analyses have been used to examine the mechanism theoretically. The obtained results are as follows:

1) Large extension strain was observed in the upper parts of the dam in the results of both 1-G and centrifugal loading tests. In the centrifugal loading tests, a crack was observed similarly to the actual damage. Therefore, it can be concluded that the crack at the crest was caused by extension stress.

2) An ordinary elasto-plastic analysis was not able to realize the large extensional strain in the upper part. The shear strain distributions were also quite different from the results observed in the experiments. As a present conclusion, it can be said that an ordinary elasto-plastic model is not suitable for analyzing the dynamic behavior of earth dams.

3) The alternative distributions of extensional and compressional volumetric strain were realized by the inhomogeneous input of waves. However, large extensional strain was not realized by the simulation. As a result, not only the selection of the numerical model, but also the heterogeneous distribution of properties has to be examined for the theoretical consideration of cracks at the crest.

REFERENCES

[1] Miyanaga, Y., Kobayashi, A. and Murakami, A. (2013) : 1-G model test with digital image analysis for seismic behavior of earth dam, Geotechnical Engineering Journal of the SEAGS & AGSSEA, Vol. 44, No. 2, pp. 26-34.

[2] Uwabe, T., Kudo, K. and Osada, M. (1989) : Experimental Study on Hydrodynamic Pressure to Act on Composite Breakwater, Technical Note of the Port and Harbour Research Institute Ministry of Transport, JAPAN, No. 641, pp. 3-28..

[3] Suzuki, H., Nakahashi, S. and Kishino, T. (2001) : An Introduction of the Dynamic Centrifugal Loading Experimented Facility and the Shaking Experiment for Investigation of Model Embankment, Nippon Koei Technical Forum 2001 No. 9, pp. 125-137.

[4] Masukawa, S., Yasunaka, M. and Hatashida, Y. (2008): Shaking table tests by silicone rubber dam model with different ratio of crest length to dam height, Geotechnical Engineering Magazine, JGS, Vol. 56, No. 10, pp. 16-19 (in Japanese).

Fifth International Conference on Geotechnique, Construction Materials and Environment, Osaka, Japan, Nov. 16-18, 2015, ISBN: 978-4-9905958-4-5 C3051

A CYCLIC ELASTOPLASTICITY MODEL OF UNSATURATED SOILS

Tomotaka SATO, Hirotaka SAITO and Yuji KOHGO
United Graduate School of Agricultural Science, Tokyo University of Agriculture and Technology, Japan

ABSTRACT

We have been proposing a cyclic elastoplastic model for unsaturated soils. In order to obtain real cyclic stress-strain relationships, we introduced the subloading concept with a hardening rule named *jumped kinematic hardening rule*. In the elastoplastic model, two suction effects are also taken into account in order to express unsaturated soil properties. Some simulations of experimental tests for an unsaturated silt were conducted to verify the elastoplastic model. They were isotropic consolidation and triaxial compression tests with cyclic loadings. Finite element method was used for these simulations. It was found from the simulations that the model could well simulate hysteresis of loading and unloading, and different stress-strain curves with different suction values. However it was hard to estimate exactly volume changes due to cyclic shear stresses, especially, the volume reductions due to unloadings.

Keywords: Cyclic loads, Elastoplastic model, Unsaturated soils, Suction

INTRODUCTION

It is important to consider the cyclic external loads of level 2 earthquakes for embankment dams and foundations and to estimate permanent deformations simultaneously generated in order to assess long-term stabilities of the dams. The idea of level 2 earthquake, which is a motion with a large magnitude but a low frequency to occur in service, should be incorporated in the performance-based design. Those soil structures are generally constructed by compacting geo-materials. The compacted geo-materials usually exist under unsaturated conditions. Then the elastoplastic model used in the design should be capable to predict unsaturated soil behaviors. Kohgo et al. [1, 2] and Kohgo [3] have proposed elastoplastic models based on the cyclic plasticity concept in which the original or extended subloading surface models (Hashiguchi, [4]) are simplified. In the model proposed by Kohgo [3], a hardening concept named jumped kinematic hardening rule is adopted. The concept is incorporated into the generalized elastoplastic model for unsaturated soils proposed by Kohgo et al. [5]. In this paper, the model was verified by simulating isotropic consolidation tests and triaxial compression tests for an unsaturated silt (DL clay).

SUBLOADING SURFACE MODEL WITH JUMPED KINEMATIC HARDENING RULE

In the following formulation, compression stresses are assumed to be negative. In the subloading surface model, loading surfaces named subloading surface are introduced within yield surfaces (normal yield surfaces) defined in classic plasticity theory. Then smooth transition from elasticity to plasticity can be established. The subloading surfaces are defined to be similar to the normal yield surfaces. The center of similarity is fixed at the origin of stress spaces in original subloading surface model, while it can move within the yield surfaces in the extended subloading surface model. In this model, a hardening rule for the center of similarity is introduced. We will name the hardening rule *jumped kinematic hardening rule*. In the rule, the following assumptions are used: 1) the centers of similarity can move whenever reverses of loadings occur, and 2) the moved points are consistent with the stress points at which reverses of loadings occur. Other assumptions: 3) the current stress point is always on the current subloading surfaces, and 4) the subloading surfaces keep the similar shape to the normal yield surfaces, are the same as those of the original extended subloading surface model.

Figure 1 shows the schematic explanation of this concept. For simplicity, subloading and normal yield surfaces are assumed to be elliptical. It is also postulated to ignore the hardening and softening of the normal yield surface with loadings. The vertical and horizontal axes in Fig. 1 are the square root of the second stress invariant of deviator stresses (J_2) and the first stress invariant (I_1), respectively.

Supposing that the loading starts from the origin ($\alpha_{ij}{}^0$: coordinate of origin) that is also the center of similarity. The initial subloading surface (SL(0)) may expand with the loading. Here the tensor $\alpha_{ij}{}^0$ is the coordinate of the center of similarity and the superscript of the tensor denotes number of reverses of loadings. If the loading reversed at the point with the effective stress tensor $\sigma'_{ij}{}^1$, the new center of similarity should be consistent with the stress tensor: $\alpha_{ij}{}^1 \equiv \sigma'_{ij}{}^1$ (see Fig. 1(a)). This operation may be

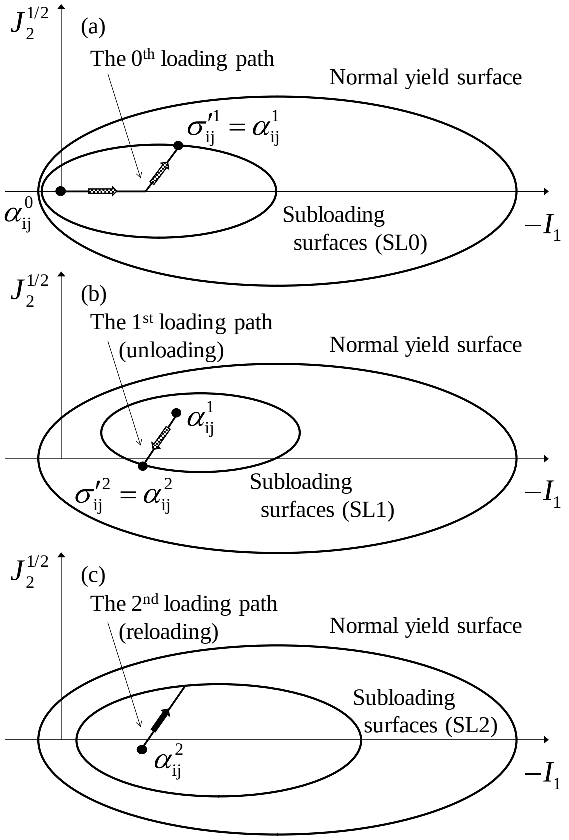

Fig. 1 Explanation of jumped kinematic hardening subloading surface model. (a) along the 0th loading path, (b) along the 1st loading path, and (c) along the 2nd loading path.

continuously done whenever the reverses of loadings occur. This operation means that once a reverse of loading occurs, the existing subloading surface disappears at the reverse point and the new subloading surface (SL(1) or SL(2) shown in Figs. 1(b) and (c)) may expand from the reverse point with the reversed direction loading. When the stress point encounters the normal yield surface, the calculation of plastic stresses will be conducted under the manner of the classic plasticity theory. The generalized return mapping algorithm (Ortiz and Simo, [6]) is used in the calculation process.

The similarity ratio $(\bar{R})^{m}_{n}$ ($0 \le (\bar{R})^{m}_{n} \le 1$) is defined geometrically as (see Fig. 2)

$$(\bar{R})^{m}_{n} = \frac{\left|(\sigma'_{ij})^{m}_{n} - (\alpha_{ij})^{m}_{n}\right|}{\left|(\hat{\sigma}_{ij})^{m}_{n} - (\alpha_{ij})^{m}_{n}\right|} = \frac{\left|(\alpha_{ij})^{m}_{n} - (\beta_{ij})^{m}_{n}\right|}{\left|(\alpha_{ij})^{m}_{n}\right|}, \tag{1}$$

where tensor $(\beta_{ij})^{m}_{n}$ = coordinate tensor of the origin of local coordinate system for subloading surface (back stress), and superscript m and subscript n express number of reverses of loading and number of load increments, respectively. The judgement whether the reverse of loading occurred is conducted by the increment of similarity ratio. If the increment

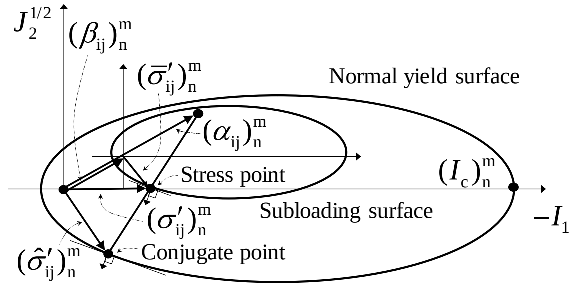

Fig. 2 Back stresses and conjugate stresses.

is negative, the reverse of loading will occur. Then,

$$d(\bar{R})^{m}_{n} < 0 \qquad \text{Reverse of loading,} \tag{2}$$

$$d(\bar{R})^{m}_{n} = (\bar{R})^{m}_{n} - (\bar{R})^{m}_{n-1}, \tag{3}$$

where $d(\bar{R})^{m}_{n}$ = increment of similarity ratio.

As the center of similarity should be always present within the normal yield surface, it may be adjusted using the following equation:

$$(\alpha_{ij})^{m}_{n+1} = \frac{(I_c)^{m}_{n+1}}{(I_c)^{m}_{n}}(\alpha_{ij})^{m}_{n}, \tag{4}$$

where I_c = yield stress (see Figs. 2).

The relationship between the conjugate point and the back stress is given by the following equations (see Fig. 2):

$$(\hat{\sigma}'_{ij})^{m}_{n} = \frac{(\bar{\sigma}'_{ij})^{m}_{n}}{(\bar{R})^{m}_{n}}, \tag{5}$$

$$(\bar{\sigma}'_{ij})^{m}_{n} = (\sigma'_{ij})^{m}_{n} - (\beta_{ij})^{m}_{n}, \tag{6}$$

where $\hat{\sigma}'_{ij}$ = conjugate effective stress; $(\sigma'_{ij})^{m}_{n}$ = current effective stress tensor; and $(\bar{\sigma}'_{ij})^{m}_{n}$ = current effective stress tensor with respect to the local coordinate system.

The hardening modulus H under isotropic hardening is assumed to be:

$$H = \hat{H} - \alpha_h \ln(\bar{R})^{m}_{n}, \tag{7}$$

where $\hat{H}$ = hardening modulus at the conjugate point, which lies on the normal yield surfaces and has the same outward normal as the current stress point does, shown in Fig. 2; and α_h = material parameter. The value of $\hat{H}$ is given by

$$\hat{H} = -\frac{\partial f}{\partial \varepsilon^{p}_{ij}} \frac{\partial \psi}{\partial \hat{\sigma}'_{ij}}, \tag{8}$$

where ε^{p}_{ij} = plastic strain tensor; f = normal yield function; and ψ = plastic potential function.

The elastoplastic stress can be calculated on the basis of the generalized plastic theory (Dafalias and Hermann, [7]) using the stress gradients at conjugate stress point. The process is as follows:

$$d\sigma'_{\mathrm{ij}} = D^{\mathrm{e}}_{\mathrm{ijkl}}\left[d\varepsilon_{\mathrm{kl}} - d\varepsilon^{\mathrm{p}}_{\mathrm{kl}}\right], \tag{9}$$

$$d\varepsilon^{\mathrm{p}}_{\mathrm{ij}} = d\lambda \cdot \hat{n}^{\mathrm{p}}_{\mathrm{ij}}, \tag{10}$$

$$d\lambda = \frac{\hat{n}^{\mathrm{f}}_{\mathrm{kl}} D^{\mathrm{e}}_{\mathrm{klqr}} d\varepsilon_{\mathrm{qr}}}{H + D^{\mathrm{e}}_{\mathrm{abcd}}\hat{n}^{\mathrm{f}}_{\mathrm{ab}}\hat{n}^{\mathrm{p}}_{\mathrm{cd}}}, \tag{11}$$

$$\hat{n}^{\mathrm{f}}_{\mathrm{ij}} = \frac{\dfrac{\partial f}{\partial \hat{\sigma}'_{\mathrm{ij}}}}{\left[\left(\dfrac{\partial f}{\partial \hat{\sigma}'_{\mathrm{kl}}}\right)\left(\dfrac{\partial f}{\partial \hat{\sigma}'_{\mathrm{kl}}}\right)\right]^{1/2}}, \tag{12}$$

$$\hat{n}^{\mathrm{p}}_{\mathrm{ij}} = \frac{\dfrac{\partial \psi}{\partial \hat{\sigma}'_{\mathrm{ij}}}}{\left[\left(\dfrac{\partial \psi}{\partial \hat{\sigma}'_{\mathrm{kl}}}\right)\left(\dfrac{\partial \psi}{\partial \hat{\sigma}'_{\mathrm{kl}}}\right)\right]^{1/2}}, \tag{13}$$

where $d\sigma'_{\mathrm{ij}}$ = increment of effective stress tensor; $D^{\mathrm{e}}_{\mathrm{ijkl}}$ = elastic modulus tensor; $d\varepsilon_{\mathrm{ij}}$ = increment of strain tensor; $d\varepsilon^{\mathrm{p}}_{\mathrm{ij}}$ = increment of plastic strain tensor; $\hat{n}^{\mathrm{f}}_{\mathrm{ij}}$ and $\hat{n}^{\mathrm{p}}_{\mathrm{ij}}$ = unit normal vector to yield function and plastic potential function at conjugate point.

MODELING OF SUCTION EFFECTS

The mechanical properties of unsaturated geo-materials may be formulated by considering two suction effects: (1) an increase in suction increases effective stresses, and (2) an increase in suction enhances yield stresses and affects the resistance to inter-particle slides (plastic deformations). The first suction effect controls changes of the shear strength for lightly overconsolidated or normally consolidated samples due to suction, volume reductions due to an increase in suction and swellings due to a decrease in suction. The second suction effect controls both changes of the shear strength for heavily overconsolidated samples due to suction and volume reductions due to a decrease in suction, namely saturation collapse (Kohgo et al., [2, 8]).

The first suction effect postulates to be estimated by the following effective stress equations.

$$\sigma'_{\mathrm{ij}} = \sigma_{\mathrm{ij}} - \delta_{\mathrm{ij}} u_{\mathrm{eq}}, \tag{14}$$

$$u_{\mathrm{eq}} = u_{\mathrm{a}} - s \qquad \left(s \le s_{\mathrm{e}}\right), \tag{15}$$

$$u_{\mathrm{eq}} = u_{\mathrm{a}} - \left(s_{\mathrm{e}} + \frac{a_{\mathrm{e}} s^*}{s^* + a_{\mathrm{e}}}\right) \qquad \left(s > s_{\mathrm{e}}\right), \tag{16}$$

$$s = u_{\mathrm{a}} - u_{\mathrm{w}}, \tag{17}$$

$$s^* = \left\langle s - s_{\mathrm{e}} \right\rangle, \tag{18}$$

where σ'_{ij} = effective stress tensor; σ_{ij} = total stress tensor; δ_{ij} = Kronecker delta; u_{eq} = equivalent pore pressure; u_{a} = pore air pressure; u_{w} = pore water pressure; s = suction; s^* = effective suction; s_{e} = air entry suction; a_{e} = material parameter; and brackets < > denote the operation $\langle z \rangle = 0$ at $z<0$ and $\langle z \rangle = z$ at $z \ge 0$.

The second suction effect can be evaluated by formulating the state surface that expresses elastoplastic volume change behavior (Kohgo et al., [8]). Here the following equations are used to estimate the state surfaces (Kohgo et al., [2]).

$$e = -\lambda^* \log\left(-p'\right) + \Gamma^*, \tag{19}$$

$$\lambda^* = \lambda + \frac{\lambda^*_{\mathrm{f1}} s^*}{s^* + a^*_1}, \tag{20}$$

$$\Gamma^* = e^0_{01} + \frac{\left(\Gamma - e^0_{01}\right)\lambda^*}{\lambda}, \tag{21}$$

where λ^* = slope of e-log $(-p')$ curves; Γ^* = void ratio of e-log $(-p')$ curves at p' = unity; e = void ratio; p' = mean effective stress; λ and Γ are values of λ^* and Γ^* at saturation, respectively; e^0_{01}, λ^*_{f1}, and a^*_1 = material parameters.

GENERALIZED ELASTOPLASTIC MODEL FOR UNSATURATED SOILS

The model described here is modified based on Kohgo's model (Kohgo et al., [2]).

At first we have to define normal yield and loading surfaces. This model has two normal yield surfaces as shown in Fig. 3 (a). One is the Mohr-Coulomb type failure surface (f_1) and the other is the elliptical cap model with corners (f_2). Both are connected on the critical state line (f). They are:

$$f = \alpha^*_{\mathrm{cs}} I_1 + \frac{\sqrt{J_2}}{g(\theta)} = 0, \tag{22}$$

$$f_1 = \alpha^* I_1 + \frac{\sqrt{J_2}}{g(\theta)} - K^* = 0, \tag{23}$$

$$f_2 = b^2\left(I_1 - I_0\right)^2 + a^2 \frac{J_2}{g(\theta)^2} - a^2 b^2 = 0, \tag{24}$$

$$g(\theta) = \frac{3 - \sin\phi'}{2\left(\sqrt{3}\cos\theta - \sin\theta\sin\phi'\right)}, \tag{25}$$

where θ = Lode angle; ϕ' = internal friction angle at failure with respect to effective stress; and I_0, a, b, K^*, P_2, α^* and α^*_{cs} are defined in Fig. 3 (a). The values of I_0, a, b, K^*, P_2 are function of I_{c}. They are given by,

$$I_0 = I_{\mathrm{c}} / (1 + R), \tag{26}$$

$$a = I_0 - I_c = -RI_0 , \tag{27}$$

$$b = -\alpha^*_{cs} I_0 , \tag{28}$$

$$K^* = -\left(\alpha^*_{cs} - \alpha^*\right) I_0 , \tag{29}$$

$$P_2 = -\frac{\left(\alpha^*_{cs} - \alpha^*\right) I_0}{\alpha^*} , \tag{30}$$

$$\alpha^*_{cs} = \frac{2\sin\phi'_{cs}}{\sqrt{3}(3-\sin\phi'_{cs})} , \tag{31}$$

$$\alpha^* = \frac{2\sin\phi'}{\sqrt{3}(3-\sin\phi')} , \tag{32}$$

where R = material parameter and ϕ'_{cs} = internal friction angle at critical state with respect to effective stress. Kohgo et al. [1] presented the details.

The following two elliptical plastic potential functions are adopted as shown in Fig. 3 (b). They are connected on the phase transformation line.

$$\psi_1 = b^{*2}\left(I_1 - P_1\right)^2 + a_1^2 J_2 - a_1^2 b^{*2} = 0 , \tag{33}$$

$$\psi_2 = b^{*2}\left(I_1 - P_1\right)^2 + a_2^2 J_2 - a_2^2 b^{*2} = 0 , \tag{34}$$

where a_1, a_2, b^* and P_1 are defined in Fig. 4(b). They are

$$P_1 = I_c/(1+R_1) , \tag{35}$$

$$a_1 = P_2 - P_1 , \tag{36}$$

$$a_2 = P_1 - I_c , \tag{37}$$

$$b^* = -\alpha_{pt} P_1 , \tag{38}$$

$$\alpha_{pt} = \frac{2\sin\phi'_{pt}}{\sqrt{3}(3-\sin\phi'_{pt})} \quad \text{at } \left(\sigma_1 = \sigma_2 > \sigma_3\right) , \tag{39}$$

$$\alpha_{pt} = \frac{2\sin\phi'_{pt}}{\sqrt{3}(3+\sin\phi'_{pt})} \quad \text{at } \left(\sigma_1 > \sigma_2 = \sigma_3\right) , \tag{40}$$

$$\alpha_{pt} = \frac{\tan\phi'_{pt}}{\sqrt{9+12\tan^2\phi'_{pt}}} \text{ at plane strain condition}, \tag{41}$$

where ϕ'_{pt} = phase transformation angle; and R_1 = material parameter.

Supposing this is an isotropic hardening model with plastic volumetric strain ε_v^p as a hardening parameter, the yield stress I_c may be evaluated by means of the state surface concept (Kohgo et al., [8]). Obtaining the value of I_c, we can easily calculate I_0, a, b, K^*, a_1, a_2, P_1, P_2 and b^* by using the relationships shown in Fig. 3.

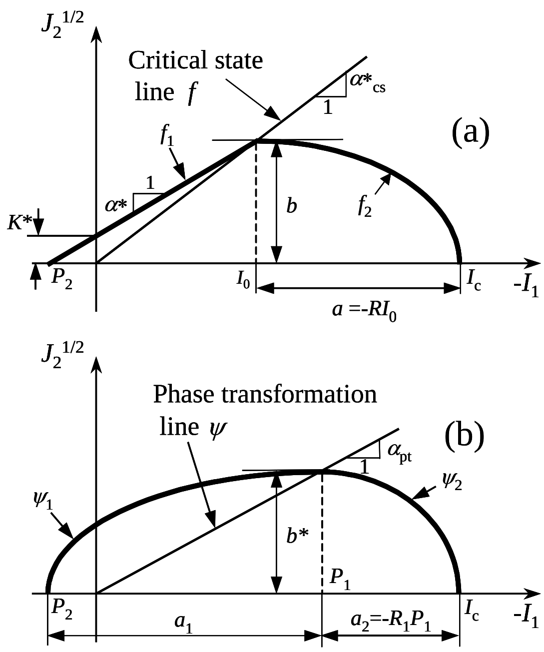

Fig. 3 Generalized elastoplastic model. (a) Normal yield functions, (b) and plastic potential functions.

SIMULATION OF LABORATORY TESTS

Some laboratory tests are simulated using the elastoplastic model described above. Finite element saturated unsaturated consolidation analysis method was used for the simulations. Tangential model (Kohgo, [9]) was used to model the soil water retention curve (SWRC). Here elastic properties are postulated to be evaluated as follows:

$$K = \frac{-2.3\left(1+e_0\right)}{\kappa} + K_i , \tag{42}$$

$$G = G_i + \gamma_j \sqrt{J_2} - \gamma_p p' , \tag{43}$$

where K = bulk modulus; G = shear modulus; κ = slope of e-log $(-p')$ curves at unloading; e_0 = initial void ratio; and K_i, G_i , γ_j and γ_p = material parameters.

The identified material parameters are shown in Table 1. The parameters concerned with unsaturated properties can be directly obtained from the triaxial compression tests and isotropic consolidation tests.

Table 1 Material parameters used for DL clay

	Elasticity				Effective stress	
κ	K_i (kPa)	G_i (kPa)	γ_p	γ_j	a_e (kPa)	s_e (kPa)
0.02	0.1	0.1	70.0	-97.0	33.3	10.0
Subloading	Plasticity			Initial Condition		
α_h	φ'	$\varphi'_{cs}=\varphi'_{pt}$	$R=R_1$	e_0	S_{r0}	s_0 (kPa)
1×10^6	26.2	30.0	0.7	1.04	0.44	20.0
State Surface						
λ	Γ	e^0_{01}	a_1^*	λ^*_{f1}		
0.152	1.306	0.508	17.4	0.044		

Simulation results of isotropic consolidation tests for an unsaturated silt are presented in Fig. 4. The test results for three specimens with different constant suction values (s = 0, 50 and 80 kPa) were simulated. In these figures, symbols with broken lines and thick solid lines denote experimental and simulation results, respectively. The each simulation result well expressed the whole void ratio- confining effective stress relationship of experimental one. The predicted lines draw the hysteresis of unloading and reloading as well as, a smooth transient stress-strain relationship from elasticity to plasticity.

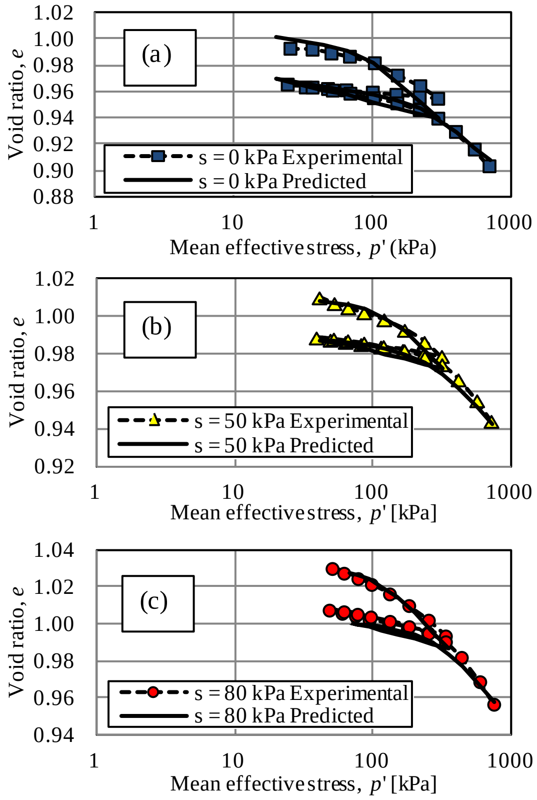

Fig. 4 Simulation results of isotropic consolidation tests for DL clay.

Figures 5-8 show the simulation results of drained triaxial compression tests of specimens with s = 0, 25, 50, 100 kPa. The specimens had the same confining pressures σ_3 = 100 kPa. These figures show the deviatoric stress q vs. axial strain ε_a and volumetric strain ε_v vs. ε_a relationships, respectively.

Figure 5 shows the simulation result in saturated case. The stress-strain relationship without cyclic loading was expressed well, and the volumetric strain – axial strain relationship was also simulated well but for the cyclic process the properties were different. Especially the compression behavior due to unloading could not be expressed well.

The simulation results for unsaturated specimens are shown in Fig. 6 – 8. Both the experimental and predicted results show 1) increasing of peak strength

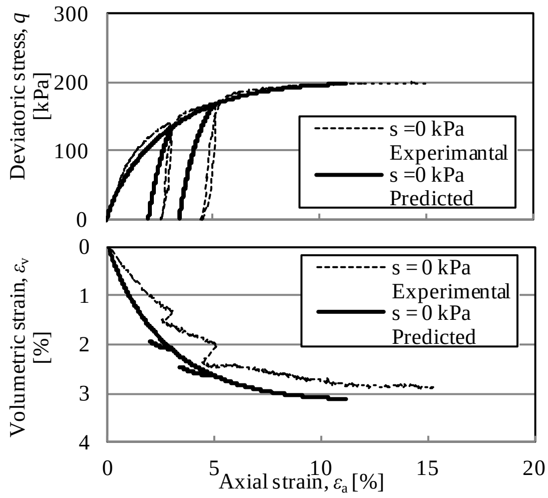

Fig. 5 Simulation results of triaxial compression tests for DL clay (s = 0 kPa).

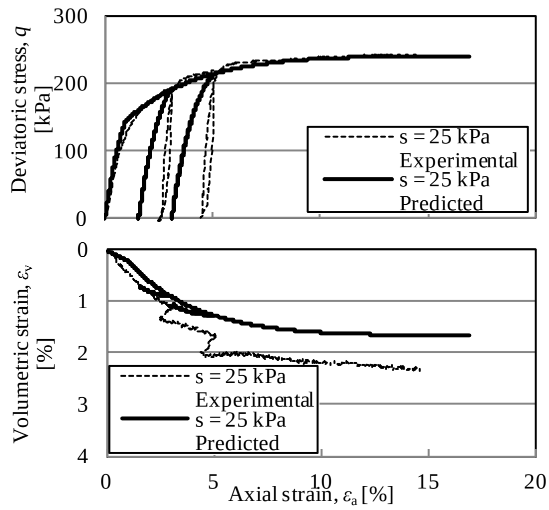

Fig. 6 Simulation results of triaxial compression tests for DL clay (s = 25 kPa).

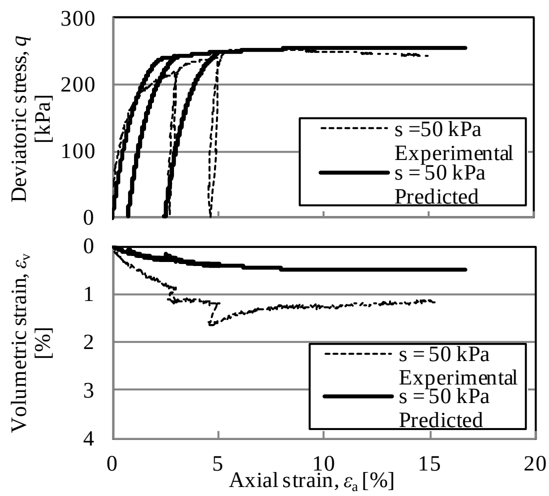

Fig. 7 Simulation results of triaxial compression tests for DL clay (s = 50 kPa).

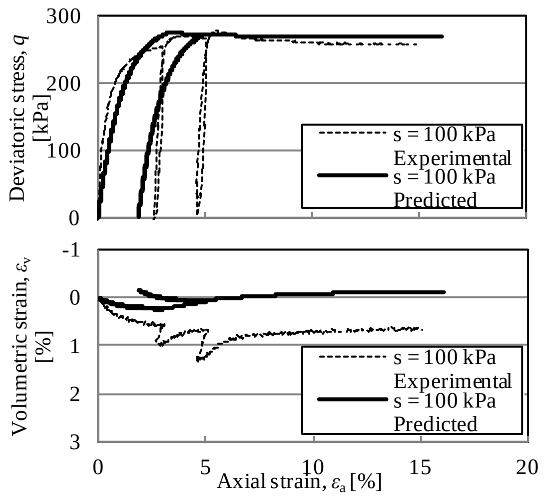

Fig. 8 Simulation results of triaxial compression tests for DL clay (s = 100 kPa).

and 2) smaller volumetric strain reduction as suction increases, and 3) strain softening behavior. As we mentioned above for saturated case, the stress – strain curves of the experimental tests were almost consistent with those of the simulation. Meanwhile in the ε_v - ε_a relationships, simulated amounts of volume change were less than those of the experimental tests. The reason was that predicted curves cannot express the compression due to unloadings. This point should be more investigated.

CONCLUSION

An elastoplastic model, which can express unsaturated soil behavior during cyclic loadings, was described in detail. In the model, we adopted a hardening concept named jumped kinematic hardening rule. The rule was incorporated into a generalized elastoplastic model with subloading surface proposed by the authors. In the concept, centers of similarity of subloading surfaces to the normal yield surfaces may jump to the reversed stress points whenever reverses of loadings occur. So the model has a potential to express anisotropic behavior due to cyclic loadings. The cyclic properties can be modeled by only one parameter α_h that was adopted in the previous model (Kohgo et al. [1, 2]). Simulations of isotropic consolidation and triaxial compression tests for an unsaturated silt named DL clay were conducted to verify the model. The simulation results in isotropic consolidation tests could successfully express cyclic properties. However in the triaxial compression test, some more investigations concerned with plastic potential functions and hardening procedures will be necessary. The verifications were only restricted for a few laboratory tests. We will try to apply the model to other cyclic laboratory tests.

ACKNOWLEDGEMENT

The research herein was supported by the Japan Society for the Promotion of Science (JSPS) (the grant No. was 26292125).

REFERENCES

[1] Kohgo, Y., Nakano, M. and Miyazaki, T. 1993b. Verification of the generalized elastoplastic model for unsaturated soils, *Soils and Foundations* 33(4), 64-73.

[2] Kohgo, Y., Asano, I. and Hayashida, Y. 2007a. An elastoplastic model for unsaturated rockfills and its simulations of laboratory tests, *Soils and Foundations* 47(5), 919-929.

[3] Kohgo, Y. 2010. An introduction of Jumped Kinematic Hardening Rule to Elastoplastic Model for Unsaturated Geo-materials, *Proc. of the 5th Int. Conf. on Unsaturated Soils*, Vol.2, 857-862.

[4] Hashiguchi, K. 1989. Subloading surface model in unconventional plasticity, *Int. J. Solids Struct.* 25, 917-945.

[5] Kohgo, Y., Hayashida, Y. and Asano, I. 2007b. A cyclic plasticity model for unsaturated soils, *Proc. of the 3rd Asian Conf. on Unsaturated Soils, UNSAT-ASIA* 2007, Nanjing China, Science Press, 365-370.

[6] Ortiz, M. and Simo, J. C. 1986. An analysis of a new class of integration algorithms for elastoplastic constitutive relations, *Int. J. Numer. Meth. Eng.* 23, 353-366.

[7] DafaliasY. F. and Herrmann, L. R. 1982. Bounding surface formulation of soil plasticity, *Chapter 10 in Soil Mechanics – Transient and Cyclic Loads*, edited by Pande, G. N. and Zienkiewicz, O. C., John Wiley & Sons.

[8] Kohgo, Y., Nakano, M. and Miyazaki, T. 1993a. Theoretical aspects of constitutive modeling for unsaturated soils, *Soils and Foundations* 33(4), 49-63.

[9] Kohgo, Y. 2008. A hysteresis model of soil water retention curves based on bounding surface concept, *Soils and Foundations* 48(5), 633-640.

Fifth International Conference on Geotechnique, Construction Materials and Environment, Osaka, Japan, Nov. 16-18, 2015, ISBN: 978-4-9905958-4-5 C3051

GEOTECHNICAL HAZARD ANALYSIS OF RIVER EMBANKMENT OF BANGLADESH AND ITS PROTECTABILITY

Md. Wasif Zaman[1], Md. Yousuf Rumi[1], Md Salequzzaman[2] and H. M. Shahin[1]
[1]Dept. of Civil and Environmental Engineering, Islamic University of Technology, Gazipur, Bangladesh
[2]Environmental Science Discipline, Khulna University, Khulna, Bangladesh

ABSTRACT

Bangladesh has a long artificial river embankment, developed mainly for the protection of its inhabitants and resources from disastrous flash floods, tidal water, cyclone surges, river currents and others. This process increases erosion of embankments and water turbidity which bring the concerned sediments from alluvial land to the inland sides and river bed that further increase vertical soil accommodation and decrease the water depth. In this research geotechnical hazard analysis has been conducted based on the statistical riverine data and flood occurrence information, obtained from various recognized institutions and secondary literatures and scientific investigation of soil structural failures from field survey. The soil characteristics and existing conditions of the embankments of the three big rivers of Bangladesh - the Ganges, the Meghna, and the Brahmaputra-Jamuna, have been investigated. The research also includes the reasons behind the failure of different embankments that were happened in last decades. A design methodology has been proposed to make these embankments more durable and to improve the strength using a pre-designed methodological case study.

Keywords: Embankment, Soil detachment, River discharge, Vetiver, Reinforcing material

INTRODUCTION

Despite being a small country, Bangladesh faces the highest number of natural calamities due to its unique geological feature which presents the country has its largest delta in the world, formed by the Ganges, the Brahmaputra and the Meghna (GBM) river system. The Bengal delta is characterized by flat terrain interlaced with an intricate network of about 700 rivers, canals and streams with a total length of approximately 22,115 km which create estuaries, tidal inlets and tidal creeks [13]. The combined catchment basin of the GBM river system measures to 1,758,000 square km, which is more than 12 times the size of Bangladesh. The amount of sediment carried annually by the rivers of the Bengal delta is about 2 billion tons. Over 92 percent of the annual runoff generated in the GBM area which flows through Bangladesh, which is only about 7 percent of the total catchment area [13]. During the rainy seasons (June to September), more than 85% rainfall occurs that brings huge amount of silts from the origin of rivers that started from the slope of Himalaya. Therefore, within a period of 4 months, nearly a trillion cubic meter of water carrying about two billion tons of silt passes through the Bengal delta. Riverine floods occur when the amount of runoff originating in a watershed exceeds the carrying capacity of natural and constructed drainage system. A total of 5695 km of embankments including 3433 km in coastal areas, 1695 flood control/regulating structures and 4310 km of drainage canals have been constructed by BWDB. Bangladesh has steady economic growth and is self-sufficient in food. So, protection is needed against the recurring flooding to make this growth sustainable.

Due to the socio-economic condition of Bangladesh most of the embankments are simply constructed with earthen materials. These earthen embankments are vulnerable to rain splash and the flow of flood water; hence they cannot solve the flood problem effectively and permanently [2]. Recent studies and news outlets has pointed out many instances of embankment failures and breaches in the past several decades. These earthen embankments are prone to breach due to their faulty design and wrong construction. For the repair and reconstruction of these existing embankments, the government has been spending a lot of money annually. So, embankments along the sea, estuaries and rivers and their associated drainage channels and systems need to be upgraded to offer greater protection from tidal activity, storm surges and water level rise. In this study the embankment failure and riverbank erosion have been investigated with respect to rainfall and flood occurrence and soil properties. Thus the study is mainly aimed to: (i) to investigate the present condition of embankments of the major rivers of Bangladesh by field observation and discussion with local community, (ii) to determine the effect of flood and rainfall on embankment and their subsequent structural collapse (iii) to provide suggestions for designing sustainable embankment (i.e. slope, factor of safety, alternate construction materials justified by present socio-economy) using pre-designed methodological case study.

STUDY AREA

For the Ganges basin we have selected Lohajang Upazila (23.46670N to 90.34170E, with an area of 130.12 km^2) of Munshiganj district, for the Brahmaputra-Jamuna basin the selection was Kazipur Upazila (24.64170N to 89.65000E, with an area of 368.63 km2) of Sirajganj district respectively. For Lohajang Upazilla, the average annual rainfall is 2102 mm, and for Kazipur Upazila, the average annual rainfall is 1649 mm [12]. In this study, a comparison of physical and geotechnical properties is carried out by field observation with the help of available previous research paper, data from government institutions, and national newspapers.

Table 1 Embankment soil characteristics at study location [12], [13].

Location		Lohajang, Munshiganj	Kazipur, Sirajganj
Soil sample		Ganges sandy soil	Brahmaputra's alluvial soil
Soil characters	Texture	Sandy loam	Loam
	OM (%)	1.37	0.8
	Type	Non-calcareous grey	Non-calcareous alluvium
	Sand (%)	0	27
	Alluvium (%)	17	72
	Clay (%)	83	1
	Percolation rate	Poor	Medium

PRESENT SCENARIOS OF EROSION AND EMBANKMENTS IN BANGLADESH

An average 256.1 ha and 622.2 ha of total land area of Gaibandha and Sirajganj respectively were eroded including embankments per year during the period of 1973-2009 [4]. During this period, the study areas i.e. Lohajang and Kazipur observed 3.82 ha and 6.89 ha erosion per year respectively [6]. Throughout June 2015, major bank erosions were estimated to take place at 48 places along a 210 km stretch of the Brahmaputra-Jamuna, Ganges and Meghna riverbank [6]. The government has built 1,209 km of embankments and has repaired 15,358 km of embankments in the 2014-15 fiscal year (April to March). Recent breaching of embankments at different location with their subsequent damages and date of breaching are shown in table 2.

CAUSES OF EMBANKMENT FAILURE

Since most of the embankments of Bangladesh are made of earth only without any surface protection, so the top soil easily washed away with the rain splash and current or flow of water. Also scouring at the toe of embankments decreases the length of slope and subsequently weakens the slope [1].

Natural Forces

1) Wave action (daily/periodic and created by constant wind):

- The impact of tidal waves are much greater on the embankments located at the vicinity of the sea.
- Cyclonic storms in the coastal zone (occurring repeatedly) act upon the water surface, which in turn moves it towards the shore with enormous hydraulic loads.

Table 2 Recent embankments breach in Bangladesh

Region/District	River	Name of embankments	Date of breach	Damages
Faridpur	Padma	Faridpur city protection embankment	May 18, 2015	20 meter bolder collapsed
Bogra, Dhonut	Jamuna	Dhonut embankment	May 05, 2015	35 meter embankment damaged
Sirajganj, Dhekuria	Jamuna	Dhekuria embankment	March 29, 2015	10 houses destroyed
Bogra; Jamalpur; Sirajganj;	Jamuna	Flood protection embankments	August 30, 2014	150 villages flooded in Bogura; 20 villages flooded in jamalpur; 600 families shelter less in sirajganj
Rajshahi	Padma	Rajshahi city protection	August 07, 2014	Soil moved and damaged
Feni, Fulgaji	Muhuri	Muhuri river embankment	June 22, 2014	30 villages flooded
Pabna, Sathiya	Ichamoti	Ichamoti river	May 20, 2014	Crops and fisheries worth 2 crore

embankment	damaged

2) Rainfall impact (from both the regular monsoon rains and torrential rains): The heaviest rainfall occurs in July and ranges from 350 mm to over 875 mm accordingly (Bangladesh Meteorological Department, 2015). The main features of rainfall impact are:

- Surface runoff caused by rainfall results in sheet erosion.
- Flooding (monsoon/periodic floods and those created by storms/cyclones).
- Monsoon rainfall causes flooding which gives rise to serious washing of embankment top soil.

3) Turbulent water currents (mainly in rivers and at coastlines):

- The high flow rate of water makes the water current turbulent which is accompanied by vortex motion in rivers and estuaries often cause erosion of the banks.
- At the originating point of a branch river or canal, especially in the surroundings of hydraulic structures, the turbulent water current erodes the banks and subsequently the embankments.

4) Wind action: The slow and steady action of wind in the relatively sparse fields and coastlines blows away the topsoil of the embankments where it is sandy or a mixture of silt and sand.

Human Interference

1) Homestead and agricultural practices: Embankments often become the privileged sites for the construction of villages and isolated homesteads. Also agricultural practices on embankments are encouraged by a high demographic pressure on the available land and accordingly a shortage of land for the rural population.
2) Cattle pasture: Cattle, mainly belonging to people living on the embankment, cause erosion by uncontrolled pasture. When the embankment is over pastured, plant species and the vegetative cover, especially the grasses, exhibits reduced growth, weaken and cannot provide adequate protection of the embankment.
3) Public cuts: Public cuts and tubes linking a river or seaside with the country side of its embankment are seen at most establishments. These have a negative effect on the strength of embankments, which makes them vulnerable to slow but continual erosive forces. During flood or cyclonic surges, collapse or major erosion occurs at those locations.
4) Unplanned afforestation of embankment slope: Afforestation without appropriate planning and management techniques destroys the undergrowth grass cover and becomes ineffective for erosion protection.
5) Improper design and construction technique: In many cases the embankments are designed with insufficient setback, resulting in increased exposure to waves and current action. This may be due to the high costs involved in land acquisition.
6) Deforestation in upstream region: Deforestation of steep slopes is assumed to lead to accelerated soil erosion and landslides during monsoon rainfall, which contributes to floods of biblical proportion in the downstream regions like that of Bangladesh.
7) Other natural and man-made reasons behind embankments collapse are- soil erosion, seepage and sliding, insufficient supervision during construction, insufficient or no clod breaking, inadequate compaction and or no insufficient laying of topsoil layers, use of inferior materials, inadequate , river migration maintenance etc.

TYPES OF EXISTING EMBANKMENTS IN BANGLADESH

Earthen Embankments

Most of the embankments are constructed by fill embankments or earthen embankments due to it are relatively cheaper and have a low initial cost.

Concrete Embankments

A very few embankments are constructed using concrete or reinforced earth methods. They have a comparatively higher cost of construction. The DND embankment which protect Dhaka, Narayanganj, and Demra from the adjoining Buriganga and Shitalkhya rivers, Brahmaputra right hand embankment which protect from Brahmaputra-Jamuna river channel are some of the examples [2].

City Protection Embankments

Almost all of the cities of Bangladesh are situated on the banks of either one or more rivers. To protect the cities from flooding, city protection embankments are constructed. The slope of the city protection embankments are often covered with concrete blocks (sometimes sand bags are also used). The Meghna-Dhonagoda embankment and others that have been constructed to protect cities and towns like Rajshahi, Shirajganj, Chandpur, Khulna and Barisal are belonging to this category [2]. These embankments let the river water remain confined only to their channels and pass directly to the sea.

DESIGN APPROACH OF EMBANKMENT

Design Methodology Followed By BWDB

According to design manual, return period is to be taken 20 years for full flood control embankment where agricultural damage is predominant. The

Embankment failed	Jamuna		Padma	
Type of analyses	Effective stress analysis		Effective stress analysis	
Water storage condition	With-out water storage	With water storage	With-out water storage	With water storage
Soil type	Saturation gradient line slope (V:H)			
Factor of	1.4			
Clay safety	1.45	1.27	1.55	1.35
Clayey	1.6			
Deviation loam(%)	1:8	14.17	14.8	
Recommeded	1:15			
F.S.(without EQ)	1.5	1.5	1.5	1.5

material to be used for the construction of embankment is classified as sandy-clay type soil. The country side slope (c/s) of embankment was determined on the basis of the saturation gradient line slope which is based on the type of soil.

Table 3 Saturation gradient line slope for different soils (standard design manual, BWDB, vol.1).

Slope Stability Analysis

Stability of the Jamuna and Padma river embankment was checked in terms of Factor of Safety (FS) values.

Table 4 Slope stability analyses for the failed sections of Jamuna and Padma flood control embankment [2].

The results show that the factor of safety is over estimated about 14-15% in case without water storage. Moreover, without water storage condition does not satisfy the recommended factor of safety. Hence, seepage analysis is necessary to solve the seepage problem as well as to get the reliable factor of safety value and safe design of embankment.

Parameters That Need To Be Considered In Design of Embankment

In Bangladesh, a very few things are considered while designing embankments i.e. slope stability of soil, type of soil, water level, cost etc. But considering parameters like river current, rain splash and effect of wind could give the embankments more resistivity against breaching so frequently.

Relationship between soil detachment rates and flow discharges

In the design of embankments, Bangladesh Water Development Board (BWDB) usually doesn't consider river inflow or peak discharge. But it is an important parameter that is responsible for embankment breaching. So, taking peak discharge for a fixed return period could give maximum soil detachment rate (i.e. soil erosion). Considering this data in design of embankments would make the structure more durable and strong. Multi–variable, non–linear regression analyses between average detachment rates, average flow discharges, and slope gradient produced the relationship is as follows [7].

$$D_c = 5.43 \times 10^6 q^{2.04} S^{1.27} R^2 \quad (1)$$

where,

D_c = soil detachment rate (kg $s^{-1}m^{-2}$),

q = flow discharge (m^3s^{-1})

Table 5 Monthly average discharge (BWDB, 2015) and predicted soil detachment rate (using eq.1) at major rivers in 2014.

Month	Slope of bed (%)	Brahmaputra		Ganges		Meghna	
		0.008		0.003		0.003	
	Stations taken for Brahmaputra, Ganges and Meghna are Bahadurabad, Hardinge bridge, Meghna-Padma confluence resp.	Flow rate (m^3/s)	Predicted detachment rate (10^{13} kg s^{-1} m^{-2})	Flow rate (m^3/s)	Predicted detachment rate (10^{13} kg s^{-1} m^{-2})	Flow rate (m^3/s)	Predicted detachment rate (10^{13} kg s^{-1} m^{-2})
April		11323	0.213	1102	0.00053	-	-
May		17772	0.535	1479	0.00096	-	-
June		36835	2.36	2605	0.00306	44170	0.99
July		79533	11.4	26583	0.35	82445	3.52
August		40819	2.92	32725	0.53	71805	2.66
September		36250	2.29	25304	0.316	60720	1.89
October		33995	2	18606	0.169	43949	0.975
November		13606	0.31	6040	0.017	-	-
December		8242	0.111	3126	0.0044	-	-
January		7181	0.0842	1629	0.00117	-	-
February		7019	0.08	1316	0.00076	-	-
March		8820	0.128	947	0.00039	-	-

S = slope gradient (%),
R = Correlation factor
The effect of slope on detachment rate increases as slope gradient becomes greater [7]. R^2 was taken as 0.97 for different soil characters of major rivers of Bangladesh [7].

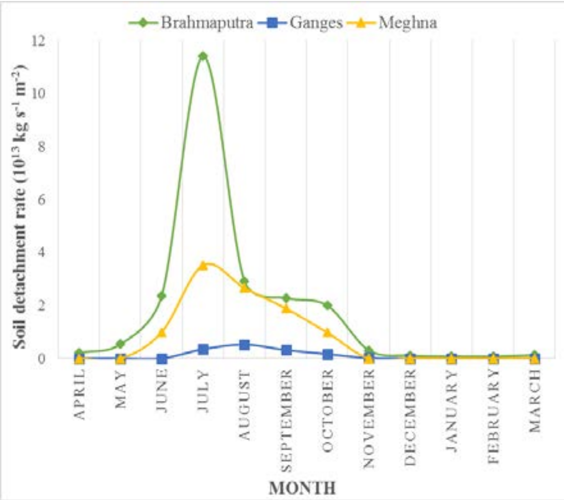

Figure 1 Predicted soil detachment rate in 2014.

Brahmaputra-Jamuna is the most erosion prone river basin in Bangladesh. Soil erosion rate is higher in Brahmaputra river basin than in Ganges and Meghna basin (Fig. 1). Greater incoming wave energy causes toe scouring, which tends to weaken the embankment and fastens the structural collapse in sloping dikes (fig.2). So, embankments in Brahmaputra basin need to be stronger than the other two as there severity of detachment of soil is larger. Naturally the steeper the slope of a field, the greater the amount of soil loss from erosion by water.

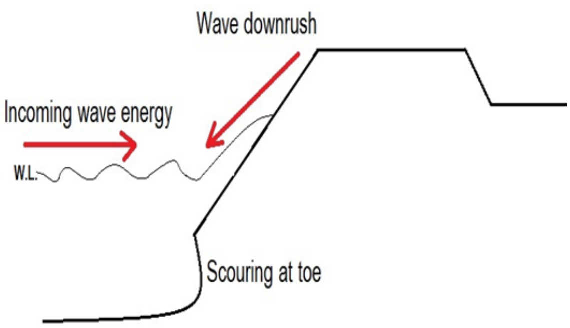

Figure 2. Cross section of an embankment showing toe scouring.

Change of river course

The major rivers of Bangladesh such as the Ganges, the Brahmaputra-Jamuna and the Meghna have a tendency to change their courses over alluvial plain. While they're en route to course change, hydraulic structures are merely adequate to restrict the rivers. There is a strong geologic possibility based on historic river course changes like that of Brahmaputra from its old Brahmaputra to present Jamuna or that of old Ganges from Bhagirathi to present Padma [8]. Although such epochal shifts are very rare instances of occurring. But, they can't be ignored also. River experts consider the Brahmaputra as one of the earth's most turbulent and dynamic rivers. They fear that the position of Brahmaputra on a fan of its own silt on the northern part of Bangladesh is tell of another possible natural shift of river change. So, it is prudent to construct and design the embankment by geographically modeling the river first based on its possibility of course change, shifting and alignment with nearby river channels.

ALTERNATIVE EMBANKMENT REINFORCING MATERIALS

Based on the socio-economic conditions of Bangladesh, a very cheaper yet effective method to protect the surface of existing earthen embankments would be the plantation of Vetiver (Chrysopogon zizanioides) grass along with the application of Jute Geo Textiles (JGT) [3]. Vetiver not only serves the purpose of slope protection but also adds environment reducing pollution. The in-situ shear test reveals that, the shear strength and effective soil cohesion of vetiver rooted soil matrix are respectively 2.0 times and 2.1 times higher than that

of bared soil [5].

Figure 3(a) Just after planting the vetiver grass along with Jute Geo-Textile (JGT);

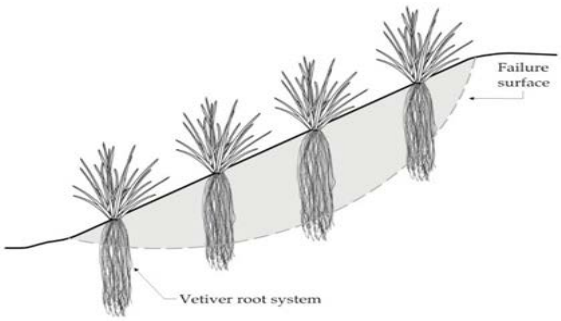

Figure 3(b) Cross section of vetiver grass on embankment showing large root depth.

During the time of vetiver root growth, the soil protection can be attained by using geo-jute. While the geo-jute degrades with time, simultaneously vetiver roots grow and take over to support the soil instead of the geo-jutes. Also to increase the solidarity of the embankment, other steps can be taken such as use of additives or reinforcing materials like soil-cement, natural or geo-synthetic fibers, geo-tubes, pressure berms etc. Pressure berms have been found quite effective in stabilizing earth retaining structures. A research project lead by the Norwegian Public Road Administration (NPRA) is presently investigating the possible use of Granulated Foamed Glass (cellular glass) as a lightweight material for road construction applications [9]. Granulated foamed glass (cellular glass) is produced by recirculating waste glass. In Bangladesh, every year huge quantity of wastes is generated which contains a significant amount of waste glass. They can be put to a good use by recycling them into granulated foamed glass.

CONCLUSIONS

The following points can be concluded from this research.

1. The soil of Ganges tidal floodplain (Lohajang, Munshiganj) has poor percolation rate indicating less water intrusion in pore spaces of soil which substantiates with lesser occurrences of soil erosion and embankment breach in the subsequent area. The soil of active Brahmaputra-Jamuna floodplain (Kazipur, Sirajganj) has medium percolation rate indicating moderate water intrusion on pore spaces of soil which substantiates with higher occurrences of soil erosion and embankment breach in the subsequent area.
2. The failure of soil mostly depends on the factor of safety. The more the safety factor the more would be the assurance of soil strength along with the less chance of failure possibility. From table 4, we can recommend Factor of Safety of 1.5.
3. While searching for alternative material to increase the solidarity of embankment, it is found that planting of Vetiver grass along with the application of Jute Geo-Textile (JGT) in the slopes of embankments as the most suitable practice in light of Bangladesh's present socio-economic aspects. Also adding pressure berms in the design, the durability of embankment can be improved.
4. Designing of embankments, effect of river water discharge is very much required to obtain more reliability in designing stable embankment.

REFERENCES

[1] Hossain M.B, Sakai T, and Hossain M.Z, (2011) River embankment and bank failure: A study on geotechnical characteristics and stability analysis, *American. J. of Environ. Sci.* Vol.7, No.2, 2011, pp. 102-107.

[2] Hossain M.Z. and Sakai T, (2008) Severity of flood embankments in Bangladesh and its remedial approach, *Agricultural Engineering International: the CIGR E-journal*, Manuscript LW 08 004, Vol.10, 2008.

[3] Islam M.S, Shahriar B.A.M. and Shahin H. M. (2013) Study on grow of vetiver grass in tropical region for slope protection, *Int. J. of GEOMATE*, Vol.5, No. 2, 2013, pp. 729-734.

[4] Rahman M.R. (2010) Impact of riverbank erosion hazard in the Jamuna floodplain areas in Bangladesh, *J. Sci. Foundation*, Vol.8 (1 &2), 2010, pp. 55-65.

[5] Islam M.S., Nasrin S., Islam M.S. and Moury F.R. (2013) Use of vegetation and geo-jute in erosion control of slopes in a sub-tropical climate. *World Academy of Science, Engineering and Technology*, Vol. 73, 2013, pp. 1162-1170.

[6] CEGIS (2005) Monitoring and Prediction of Bank Erosion along the Right Bank of the Jamuna River, Dkaka, 2005.

[7] Zhang G.H, Liu B.Y, Nearing M.A, Huang C.H. and Zhang K.L. (2002) Soil detachment by shallow flow, *American Society of Agricultural Engineers*. Vol. 45(1), 2002, pp. 1-7.

[8] Hoque M.M, Siddique M.A. (1995) Flood control projects in Bangladesh: Reasons for failure and recommendations for improvement. *Disasters*, Vol.19, No.3, 1995, pp. 260-263.

[9] Erik F.T. and Roald A. (2002) Use of waste materials for lightweight fills. *Int. Workshop on Lightweight Geo-materials*, Tokyo Japan, Mar. 2002.

[10] Cernica, J.N. (1994) Geotechnical Engineering: Soil Mechanics, New York, John Wiley and Sons Inc. 1st Edition, P.453.

[11] Anisuzzaman M, Arifuzzaman and Ridha (2013) Sub-soil characteristics of selected coastal regions of Banglades. *Int. J. of Chemical, Environmental & Biological Sciences*, Vol. 1, Issue 5, 2013, pp. 710-714.

[12] SRDI (Soil Resources Development Institute) (2000) Land and soil resource user guide, Dhaka, May 2000, June 1998.

[13] BBS (Bangladesh Bureau of Statistics (2009) Compendium of Environment Statistics of Bangladesh, Dhaka, 2009.

Fifth International Conference on Geotechnique, Construction Materials and Environment, Osaka, Japan, Nov. 16-18, 2015, ISBN: 978-4-9905958-4-5 C3051

AXIAL RESISTANCES OF OPEN-ENDED PILES DRIVEN INTO GRAVEL LAYERS: DYNAMIC LOADING TESTS OF PILES AT ROAD BRIDGE CONSTRUCTION SITE IN MIZUSHIMA PORT

Takaaki Mizutani
Head of Foundations Group, Port and Airport Research Institute, Japan

ABSTRACT

The axial resistance of a pile, in many cases, is determined using an appropriate estimating equation depending on the type of its bearing layer. However, the existing equations are not applicable to piles driven into gravel layers. A series of dynamic load tests of steel-pipe piles driven into gravel layers was conducted at a road bridge construction site in the Mizushima port for obtaining a basis for the estimation of their axial resistances. The test results indicated that both the base and shaft resistances of the piles were relatively smaller although the piles were open-ended. This paper provides the test results in detail and suggests estimating equations for determining the base and shaft resistances of piles driven into gravel layers. The safety factor necessary for utilizing the test results in the design of structures is also discussed.

Keywords: Pile, Axial Resistance, Gravel Layer, Dynamic Load Test

INTRODUCTION

The axial resistance of a pile is determined using an estimating equation selected based on the site condition. Most of these estimating equations are based on field test data whereas some of them have theoretical backgrounds. Each estimating equation has its range of applicability in terms of the configuration of piles, type of soil, etc. In the absence of an equation appropriate for the site condition, it is necessary to conduct pile loading tests at the site for designing pile foundations.

Researchers and design codes have suggested and described a large number of estimating equations for determining the axial resistance of a pile [1]-[3]. However, those for piles driven into gravel layers have not yet been established in Japan.

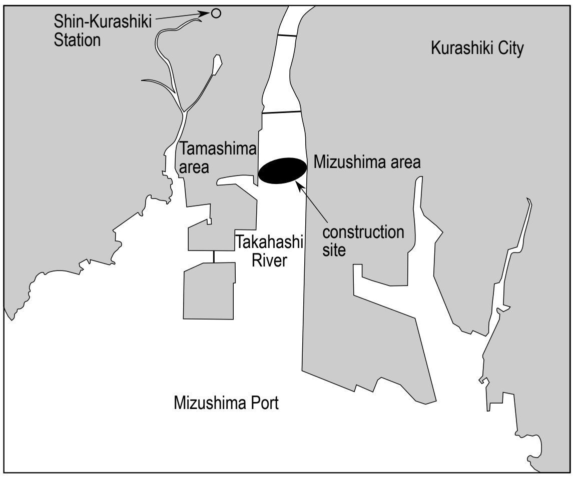

Fig. 1 Location of construction site

In the Mizushima port, the steel-pipe sheet pile structure has been employed for foundations of a road bridge with gravel layers as the bearing layer. A series of dynamic load tests of steel-pipe piles driven into gravel layers was conducted to obtain a basis for estimating their axial resistances at the construction site. This paper will provide the test results in detail and suggest a method for estimating the axial capacity of piles driven into gravel layers.

OUTLINE OF DYNAMIC LOADING TEST

Site Condition

The construction site is near the mouth of Takahashi River in Kurashiki City, in the western part of Japan. Figure 1 shows the location of the site. The width of the river is approximately 1400 m. Nineteen foundations, designated as P1–P19, are proposed to be constructed at the site at regular intervals.

Figure 2 displays the soil profile at the construction site. The profile is almost flat, with a condition similar to those at the locations of the foundations. Ag and Dg2 constitute the gravel layers, and Dg2 was selected as the bearing layer of the foundations. The issues faced during this study were the pile's base resistance in the Dg2 and shaft resistance in the Ag and Dg2 layers.

Boring surveys were conducted at the location of each foundation. The Ag layer was a medium-to-dense gravel layer comprising subrounded and subangular particles of 2–30 mm diameter. The Dg2 layer was a dense-to-very-dense gravel layer, the particles of which ranged from subrounded to

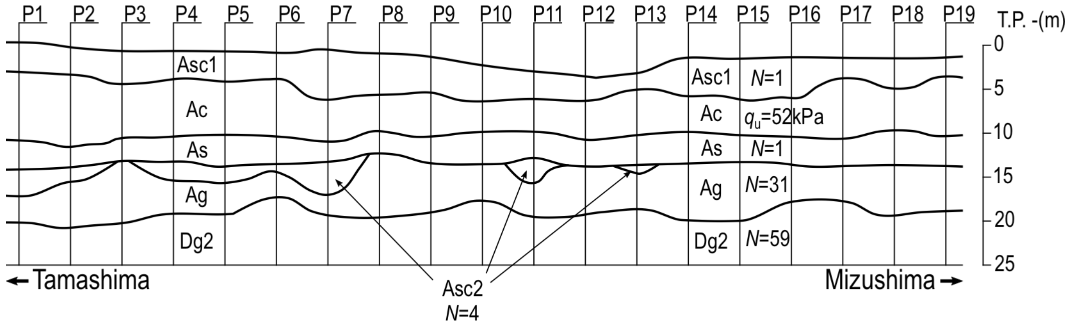

Fig. 2 Soil profile at construction site

subangular, of diameters 2–40 mm. Gravels larger than 50 mm in diameter were occasionally observed in the Dg2 layer.

Figures 3 and 4 show the depth distribution of the SPT-N values in the Ag and Dg2 layers, respectively. The values varied widely in both layers and no clear tendency was found in the obtained depth distributions. Therefore, it was decided to treat their simple mean values as the representing values of each layer: $N = 31$ for the Ag layer and $N = 59$ for the Dg2 layer, as indicated in Fig. 5, where N is the simple mean value of the SPT-N values.

Test Method

Dynamic load tests of piles were conducted according to the Japanese standard for dynamic load test of single piles [4] at the location of each foundation. The Pile Driving Analyzer (Pile Dynamics Inc.) and CAPWAP (Case Pile Wave Analysis Program) tools were used for obtaining the static axial resistances of the test piles.

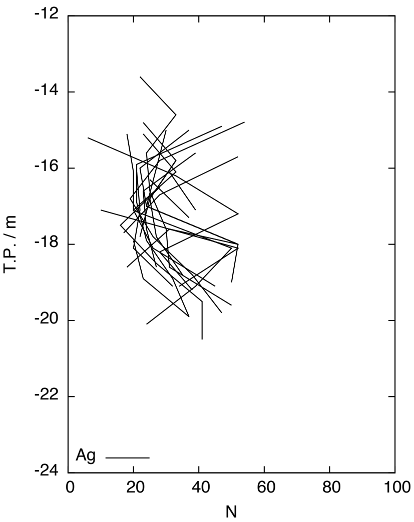

Fig. 3 Depth distribution of SPT-N values in Ag layer

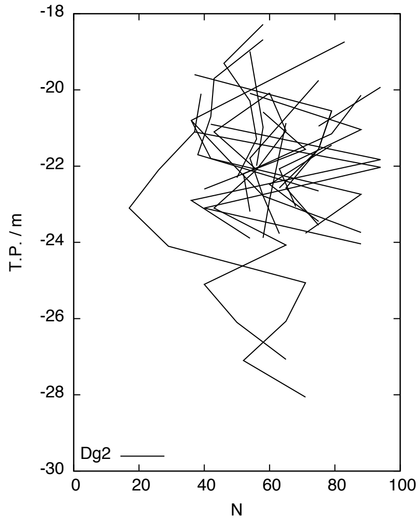

Fig. 4 Depth distribution of SPT-N values in Dg2 layer

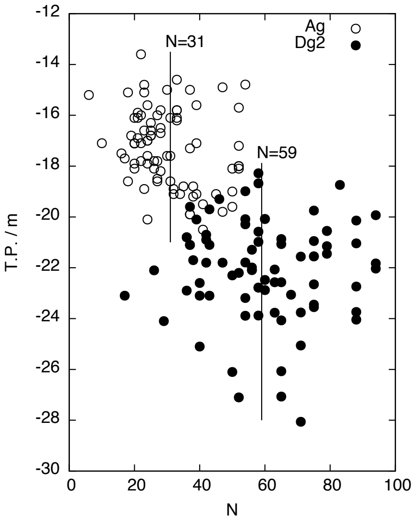

Fig. 5 N values for each layer

The test conditions are listed in Table 1. Four types of piles were tested. The label "Cross" in Table 1 denotes a pile with a rib plate at its tip. The rib plate was 2 m long from the tip and cross-shaped in sectional view. The label "Cross (3 m)" is a pile with a rib plate of 3 m length. The label "Arch" indicates a pile with three arched rib plates, each of 2 m length [5]. The plan was to collect data using a commonly-used data collection technique for dynamic load tests in Japan. The test method, in itself, was not the issue of the present study.

BASE RESISTANCE

Figure 6 shows the base resistance (R_p) obtained from the tests conducted along the bridge axis. R_p appears to depend on the geometry of the test pile.

Table. 1 Test conditions

pier	pile	pile type	curing period (days)
P1	6	Cross	9
P2	test	open-ended	7
	4	Cross	6
P3	1	open-ended	1, 9
	2	Arch	1, 9
	3	Cross	1, 9
	4	Cross (3 m)	1, 9
P4	test	open-ended	7
	test	Cross	6
P5	test	open-ended	7
	1	Cross	6
P6	test	open-ended	7
	test1 – test4	Cross	6
P7	test	open-ended	7
	1 – 4	Cross	6
P8	test	open-ended	7
	2	Cross	5
P9	test	open-ended	12
	test	Cross	7
P10	test	open-ended	11
	2	Cross	6
P11	K-1 – K-4	open-ended	0, 6
	6, 9	Cross	0
P12	test	open-ended	9
	test	Cross	7
P13	1	open-ended	13
	2 – 4	open-ended	14
P14	1 – 4	open-ended	7
P15	test	open-ended	10
	test	Cross	6
P16	1 – 4	open-ended	14
P17	1 – 3	open-ended	6
	4	open-ended	6, 28
P18	test	open-ended	7
	20	Cross	7
P19	29	Cross	7

At P3, four test piles with different tip geometries were tested after one day and nine days since the piles were driven. The test results are shown in Fig. 7. It can be seen that the R_p of the open-ended pile is smaller than that of the others. The R_p values of the non-open-ended piles were not very different. The value of R_p was observed to increase very slightly with progress in the curing period (i.e., setup capacity was observed).

The test result statistics are listed in Table 2. These statistics were calculated for open-ended and Cross piles separately. The Cross (3 m) and Arch piles were omitted because of the limited number of tests. The test results for the piles whose curing period did not exceed one day were eliminated to avoid the effect of setup, albeit it being very small.

The mean value of the test results for open-ended piles was roughly in accordance with that from a previous study, which described the results of several static load tests at a nearby area [5]. The average R_p of Cross piles was only 1.08 times larger than that of open-ended piles. It could be concluded that the rib plates at the tip of the piles had very small effect at this site. The coefficient of variation (CV) for both open-ended and Cross piles was approximately 20%.

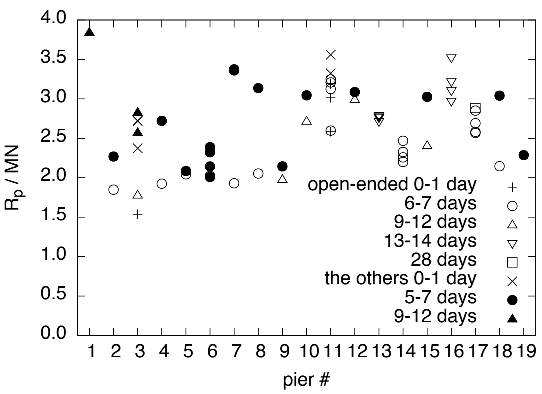

Fig. 6 R_p obtained from tests

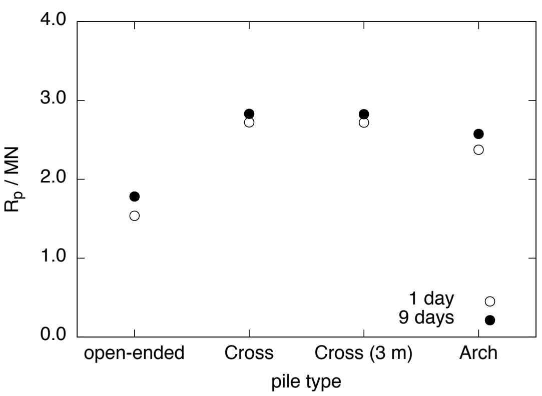

Fig. 7 R_p of different types of piles at P3

Table. 2 R_p statistics

pile type	sample size	mean (kN)	CV (%)	standard error
open-ended	33	2570	18.4	82.2
Cross	20	2790	19.6	122

The R_p of a pile driven by a hammer is most often related to its cross-sectional area and the SPT-N value of the bearing layer. The cross-sectional area (A_p) of the test pile and N of the Dg2 bearing layer were $\pi/4$ m^2 and 59, respectively. From a design reliability perspective, it is important to consider the accuracy of the test results and the characteristic value of R_p (R_{pk}) must be determined carefully. The lower limit of the one-sided, 95% confidence interval is frequently used as R_{pk}. It was easy to derive the confidence interval for R_p using the standard error values listed in Table 2. Consequently, R_{pk} was determined as 2430 kN for open-ended piles, yielding Eq. (1), as follows:

$$R_{pk} = 52NA_p \tag{1}$$

Because the piles were open-ended, Eq. (1) is likely to include the effect of plugging. Hence, the coefficient in Eq. (1) is likely to change upon altering the pile diameter, thus limiting the applicability of the equation to the site of this study.

SHAFT RESISTANCE

Strength of Shaft Resistance per Unit Area in Ag Layer

Figure 8 shows the depth distribution of the strength of the shaft resistance per unit area of the pile surface (r_f) in the Ag layer, obtained from all the tests. The data displayed a wide variety but a clear increasing trend in terms of depth. The r_f values of piles with curing period less than two days were relatively smaller. The effect of the type of pile on the r_f was not observed.

Because of the wide variety in the r_f values, it was natural to use their simple mean value as the characteristic value of the full thickness of the Ag layer. In contrast, obtaining a regression line from the data could be regarded to be better as the r_f has a tendency to increase with depth. Both results are shown in Fig. 9. Lines A and B represent the mean value and regression line, respectively whereas lines A' and B' indicate the lower limits of their one-sided, 95% confidence intervals, respectively. Here, the Cross (3 m) and Arch piles are omitted and the test results of piles whose curing period did not exceed one day are eliminated as they are the same as the statistic calculation for R_p. The regression line was obtained using the least-square method.

As shown in Fig. 9, lines A and B intersect at the centroid of the data. Consequently, both the lines conduce to the same value of total shaft friction (R_f) in the Ag layer. Therefore, even if r_f has an increasing tendency with depth, there is no need consider it for calculating the overall shaft resistance of the pile. However, it must be considered for the limit state design. The increasing tendency of r_f was neglected and the lower limit of the 95% confidence interval of the mean value (line A') was employed as the characteristic value of r_f (r_{fk}) of the Ag layer, in this study.

The mean value of r_f was 31 kN/m^2 and the lower limit of its one-sided, 95% confidence interval was 28.6 kN/m^2. This value was approximately

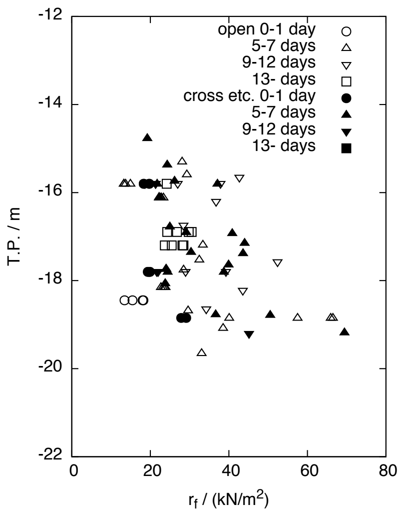

Fig. 8 Depth distribution of r_f in Ag layer

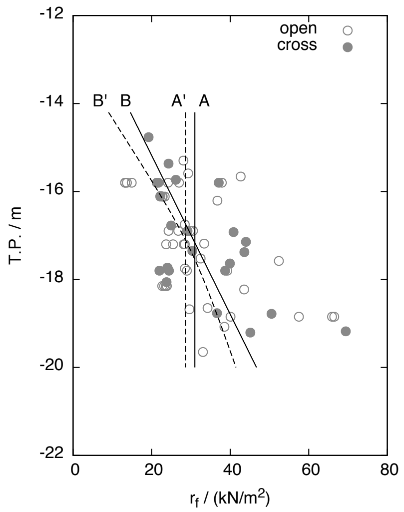

Fig. 9 Mean value (line A) and regression line (line B) of r_f in Ag layer; and lower limits of their one-sided, 95% confidence intervals (lines A' and B', respectively)

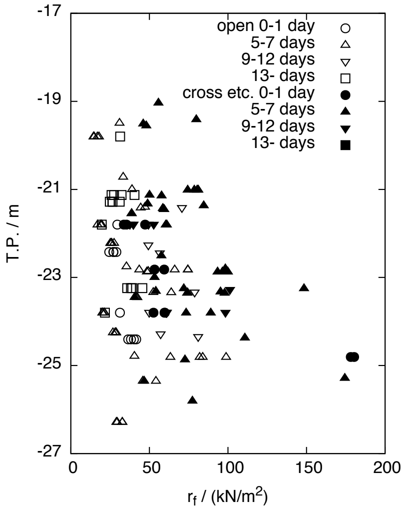

Fig. 10 Depth distribution of r_f in Dg2 layer

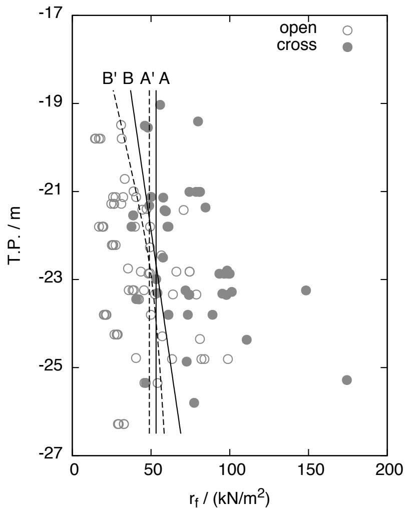

Fig. 11 Mean value (line A) and regression line (line B) of r_f in Dg2 layer; and lower limits of their one-sided, 95% confidence intervals (lines A' and B', respectively)

$0.92N$. Thus, the following equation can be derived:

$$r_{fk} = 0.92N \tag{2}$$

The CV of r_f was approximately 39%. It was observed that the r_{fk} derived from the tests had somewhat poor accuracy.

Strength of r_f in Dg2 Layer

The data processing was similar to that performed for the Ag layer. Figure 10 shows the depth distribution of the strength of r_f in the Dg2 layer and Fig. 11 shows its mean value and regression line.

The mean value of r_f in the Dg2 layer was 53 kN/m^2 and the lower limit of its one-sided, 95% confidence interval was 49 kN/m^2, which corresponds to $0.83N$. The simplest idea of the estimation equation for r_{fk} in the Dg2 layer is as follows:

$$r_{fk} = 0.83N \tag{3}$$

The CV of r_f was 53%, worse than that for the Ag layer.

CONSIDERATION FOR SAFETY FACTOR

A discussion of the safety factor is necessary for utilizing the estimating equations obtained from the above-mentioned analyses. In the Japanese specifications for highway bridges [1], the safety factor for the overall axial resistance (R_t), obtained by adding R_p and R_f, is 3.0 for end-bearing piles, and can be reduced to 2.5 if pile loading tests are appropriately conducted at the site.

Safety factors depend on the variability of the estimation equations outlined in the specifications. A past study presumed the CV of the estimation equations to be approximately 30% [6]. In this study, however, a large amount of loading test data was available, owing to which the CV of R_p and R_f could be estimated. Therefore, the safety factor could be determined more clearly.

The distribution of the characteristic value of R_t (R_{tk}) was assumed to be a normal distribution, and the load acting on the piles could be fixed without stochastic variation. As a result, the safety factor for obtaining the predefined fracture probability could be calculated easily. For example, consider the case in which the fracture probability required is <0.001.

The value of the 0.001 fractile of the standard normal distribution is approximately −3.1. The design value of R_t (R_{td}) for achieving a fracture probability of 0.001 can be calculated using the following equation:

$$R_{td} = R_{tk} - 3.1\sigma_t \tag{4}$$

Here, σ_t is the standard deviation of R_{tk}. The safety factor, which equals R_{tk} / R_{td}, is obtained as follows:

$$R_{tk} / R_{td} = 1 / (1 - 3.1\sigma_t / R_{tk}) \tag{5}$$

According to Eq. (5), the safety factor can be calculated if the value of σ_t / R_{tk}, which is the CV of R_{tk}, is known.

Because R_{tk} is the sum of R_{pk} and R_{fk}, the variance of R_{tk}, which is σ_t^2, can be obtained using Eq. (6).

$$\sigma_t^2 = \sigma_p^2 + \sigma_f^2 \tag{6}$$

Here σ_p^2 and σ_f^2 are the variances of R_{pk} and R_{fk}, respectively. The unknown parameters for calculating the CV of R_{tk} are R_{pk}, R_{fk}, and their CVs. As the values of R_{pk} and its CV are already known, it is necessary to obtain R_{fk} and its CV.

R_{fk} is the sum of the shaft resistances in each layer. Once the values of r_{fk} in each layer are known, R_{fk} can be obtained automatically. The values of r_{fk} in each layer are listed in Table 3. The values for Asc1, Ac, As, and Asc2 were derived from the test result using a method similar to that used for the Ag and Dg2 layers. Comparing the values of R_{fk} and R_f, which is the total shaft resistance of each pile obtained from the test results, the CV of R_{fk} could be estimated. Table 4 lists the statistics of R_f / R_{fk}. The CV of R_f / R_{fk} obtained was 33.6%. Therefore, the CV of R_{fk} was assumed to be approximately 35% for the study.

Based on these values and Eqs. (5)–(6), the CV of R_{tk} could be calculated. As this value depends on the pile length in each layer, the CV of R_{tk} at the location of each foundation must be calculated. The result of the calculation indicated that the CV of R_{tk} was less than 20% at any foundation. As a result, the safety factor was approximately 2.63. Owing to space constraints, detailed calculations are not shown in this paper. In this case, the calculated safety factor was comparable with that outlined in the Japanese specifications for road bridges for the case with appropriate in-situ load testing.

CONCLUSION

A series of dynamic load tests of open-ended piles driven into gravel layers was conducted at a road bridge construction site in the Mizushima port for obtaining a basis for the estimation of their axial resistances. The test results indicated that both the R_p and r_f of the piles were relatively smaller although the piles were open-ended. The average strength of the R_p per unit area of the pile tip was $52N$ kN/m^2. The r_f in the gravel layer is given by 0.8–0.9N kN/m^2.

The safety factor for utilizing the test results in the foundation design was also discussed. The derived safety factor was approximately 2.63 for a fracture probability of <0.001. This value was comparable with that outlined in the Japanese specifications for road bridges for the case with appropriate in-situ load testing. With the target fracture probability being controvertible, this procedure for determining the value of R_{tk} and the safety factor for design is regarded to be applicable extensively.

Table. 3 Values of r_{fk} in each layer

	r_{fk} (kN/m^2)
Asc1	4.8
Ac	10
As	22
Asc2	33
Ag	29
Dg2	49

Table. 4 R_f / R_{fk} statistics

pile type	sample size	mean	CV (%)	standard error
open-ended and Cross	53	1.09	33.6	0.0503

ACKNOWLEDGEMENTS

The test data discussed in this paper was provided by the Chugoku Regional Development Bureau, Ministry of Land, Infrastructure, Transport and Tourism of Japan. A part of this work was supported by a research grant from the Japan Iron and Steel Federation. We deeply appreciate the significant assistance provided.

REFERENCES

[1] Japan Road Association, Specifications for road bridges. Maruzen Co. Ltd., 2012, Part IV, ch. 12 (In Japanese).

[2] Ports and Harbours Bureau, Ministry of Land, Infrastructure, Transport and Tourism; National Institute for Land and Infrastructure Management; and Port and Airport Research Institute, Technical standards and commentaries for port and harbour facilities in Japan. Overseas Coastal Area Development Institute of Japan, 2009, Part III, ch. 2.

[3] Jardine, R., Chow, F., Overy, R. and Standing, J., ICP design methods for driven piles in sands and clays. Thomas Telford, 2005.

[4] Japanese Geotechnical Society, Method for dynamic load test of single piles. JGS 1816-2002, 2002.

[5] Tominaga, M., Nei, M., Echigo, Y., Kenmochi, S., Kage, S. and Hashimoto, S., "Kawasaki Steel Corporation", in "Foundation work of large-scale seaside plant" (feature article), Foundation Engineering & Equipment, Vol. 4, No. 5, 1976, pp. 55-90. (In Japanese)

[6] Matsui, K. and Ochiai, H., "Bearing capacity of friction piles with consideration of uncertainty of soil properties", Journal of JSCE, No. 445 / III-18, 1992, pp. 83-92.

Fifth International Conference on Geotechnique, Construction Materials and Environment, Osaka, Japan, Nov. 16-18, 2015, ISBN: 978-4-9905958-4-5 C3051

LABORATORY INVESTIGATION ON THE EFFECTS OF OVERBURDEN PRESSURE, WATER, AND TIME ON SLAKING INDUCED MATERIAL PROPERTY DEGRADATION OF COAL MINE SPOIL

Chaminda Gallage[1], Golam Mostofa[2], David Vosolo[3] and Jayasiri Rajapakse[4]
[1,2,3,4]Science and Engineering Faculty, Queensland University of Technology (QUT), Australia

ABSTRACT

In open-cut strip mining, waste material is placed in-pit to minimise operational mine costs. Slope failures in these spoil piles pose a significant safety risk to personnel, along with a financial risk from loss of equipment and scheduling delays. It has been observed that most spoil pile failures occur when the pit has been previously filled with water and then subsequently dewatered. The failures are often initiated at the base of spoil piles where the material can undergo significant slaking (disintegration) over time due to overburden pressure and water saturation. It is important to understand how the mechanical properties of base spoil material are affected by slaking when designing safe spoil pile slope angles, heights, and dewatering rates. In this study, fresh spoil material collected from a coal mine in Brown Basin Coalfield of Queensland, Australia was subjected to high overburden pressure (0 – 900 kPa) under saturated condition and maintained over a period of time (0 – 6 months) allowing the material to slake. To create the above conditions, laboratory designed pressure chambers were used. Once a spoil sample was slaked under certain overburden pressure over a period of time, it was tested for classification, permeability, and strength properties. Results of this testing program suggested that the slaking of saturated coal mine spoil increase with overburden pressure and the time duration over which the overburden pressure was maintained. Further, it was observed that shear strength and permeability of spoil decreased with increase in spoil slaking.

Keywords: Coal Mine Spoil, Slaking, Overburden Pressure, Shear Strength, Permeability

INTRODUCTION

Coal mine spoil is waste materials removed to expose coal seams during the mining process. This material is placed in spoil piles behind the active strip, creating what is commonly referred to as a low-wall. It is also called boney pile, gob pile, or pit heap. The spoil materials are typically composed of blasted fragments of mudstone, siltstone and sandstone [1]. The mean particle size of spoil is highly, ranging from fines to particles of size 0.5 m to 1.0 m depending on in-situ properties of overburden, blasting technique and equipment used. Within the coal mine industry, spoil materials are categorised into four groups; Category 1 (Cat -1), Category 2 (Cat – 2), Category 3 (Cat-3),and Category 4 (Cat -4) [2].

In open-cut strip mining, waste materials are placed in-pit to minimise mine operational costs. It is common to observe blasted rock (Cat-3 or Cat -4) being placed by draglines to form the base for spoil piles and the weaker spoil materials such as soil (Cat-1) and highly weathered rocks (Cat-2) are placed by dump trucks on the top of base material to form the final spoil profile. To accommodate increasingly high volumes of spoil within a mine pit, spoil pile heights and slope angles are increased. In the Brown Basin Coalfield of Queensland in Australian, the typical height of spoil pile is ranging from 30 m – 70 m and the slope of the spoil pile varies between 26^0 to 40^0 [3]. As spoil pile heights are increased, the foundation material is subjected to a higher stress regime that may increase the rate of disintegration (slaking) of base spoil material due mechanical breakdown. The slaking of the base material is further increased with time when this high stress is maintained in saturated conditions. In open cut mining, it is common to observe a 10 – 15 m height of water in the pit when mining and pumping is stopped temporarily. Therefore, it is assumed that the base spoil material is saturated.

Slaking has been found to transform fresh or slightly weathered Permian (Cat -4 or Cat -3) at the base of spoil pile to weaker or/and weathered Permian [2]. This mechanical breakdown leads to a decrease in particle sizes, consequently reducing the shear strength and permeability of slake affected materials. This reduction in material properties of spoil base materials have been a root cause for the failures in spoil piles during dumping, and flooding/dewatering events. The failures of spoil piles can cause human casualties, damage to equipment, delay in miming, and an increase in mine operational costs.

In order to determine safe height and slope angles for spoil piles and their appropriate dewatering rates, it is important to understand how the shear strength and permeability of saturated spoil foundation materials decrease with overburden pressure and time. Research has been conducted [4] to determine the shear strength and other properties of relatively fresh coal mine spoil under high overburden stress. However, no research has been conducted to investigate the degradation of properties of saturated spoil material due to slaking under overburden pressure and time. This paper presents the results of laboratory testing carried out to investigate the effects of slaking on classification, strength, and permeability properties of coal mine spoil (Category -3).

TEST MATERIAL AND APPRATUS

This section describes the basic properties of spoil material and testing apparatus used in this experimental program

Test Material

Fresh coal mine spoil (Category -3) was collected from an open-cut mine in Brown basin coalfield in Queensland, Australia. The particle size distribution of the collected spoil material is shown in Figure 1. According to Australian standard AS 1289.3.9, Liquid Limit, Plastic Limit, and Linear Shrinkage were determined as 34.1%, 22.0% and 4.9%, respectively. Further, the material was analysed for its mineral composition using X- ray diffraction with the results are shown in Table 1.

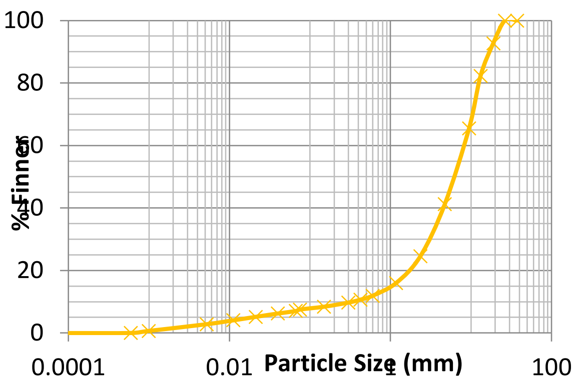

Fig. 1 Particle size distribution of test material

Table 1: Mineral composition of test material

Minerals	Amount (%)
Quartz	34.00
Albite	28.80
Kaolin	2.30
Mixed layer illite	9.20
Mica, 2M1	16.40
Anatase	8.90

Slaking Chamber

The saturated spoil material was subjected to slaking under different overburden pressures, which represent the height of the spoil pile, and time over which the overburden pressured were maintained. The pressures were achieved in the laboratory using specially designed pressure chambers. Figure 2 shows a schematic diagram and a photo of a pressure chambers used. Four such chambers were employed in this experimental program.

The chamber consists of an acrylic cylinder with internal diameter and height of 360 mm and 400 mm, respectively, and a wall thickness of 20 mm. The top and the bottom stainless steel plates are fastened by eight bolts to seal the chamber. The chamber can accommodate approximately 60 kg of spoil (assume initial unit weight of 18 kN/m3) allowing space for the piston plate. This mass is expected to be sufficient to yield results for different tests such as classification, shear strength, and permeability of slaked spoil materials. Simulated overburden pressure is achieved by means of applying air pressure to compartment above the piston which then compresses the spoil in the lower compartment with the applied pressure. A rubber seal is attached to the piston to prevent air leak through the space between the piston and the inner wall of the acrylic cylinder. A pressure of 20 kPa is needed to overcome the friction between the piston and the inner wall of the cylinder.

Two porous stones (Bronze) are embedded in the base plate and in the piston where the material is in contact. The sample can be saturated by sending water from the bottom and allowing water to freely flow through the sample and to exit from the top. Water pressure in the sample is maintained at atmospheric conditions. It is important to make sure that the water in the chamber is under atmospheric conditions so that the applied pressure on the spoil from the piston is equal to the effective stress. The consolidation of the spoil over the period of time under the applied constant overburden pressure can be measured directly from the linear variable differential transformer (LVDT) attached to the piston shaft.

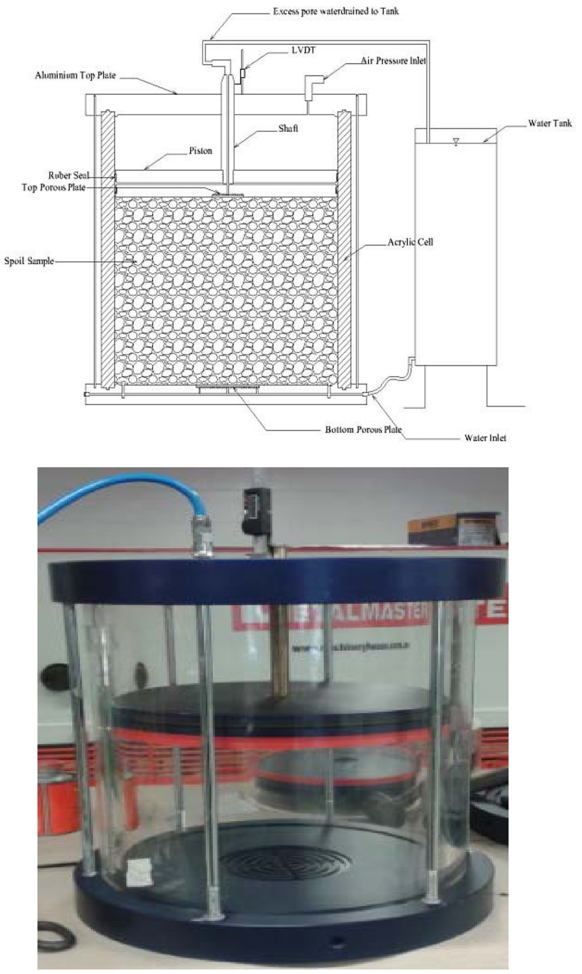

Figure 2. (a) Schematic diagram, (b) Photo of a pressure chamber used in the experimental program

TESTING PROGRAM AND METHODOLOGY

To achieve the objectives of this research, classification, shear strength, and permeability properties of spoil that would be subjected to slaking under the conditions given in Table 2 will be measured in the laboratory using standard laboratory test methods. Sample 1 is the reference material which is fresh spoil and not subjected to overburden pressure in the chamber**.**

Table 2: Slaking condition of spoil samples

Duration of slaking	Overburden pressure (kPa)		
	300	600	900
Zero (2 days)	Sample 2	Sample 3	Sample 4
3 Months	Sample 5	Sample 6	Sample 7
6 Months	Sample 8	Sample 9	Sample 10

To obtain each spoil sample given in Table 2, the following methodology was followed:

- 320 mm height of the pressure chamber was divided into 10 equal layers as shown in Figure 3a
- The water content of the spoil was measured. Bulk mass of spoil required for each layer to achieve dry unit weight of 18 kN/m^3 was calculated. Dry unit weight of 18 kN/m^3 was chosen as it was the average unit weight of spoil pile measured in the field.
- Bulk mass of spoil required for each layer to achieve the dry unit weight of 18 kN/m^3 was poured into the chamber and tamped using the weight shown in Figure 3a until the required height was achieved. This procedure was repeated for all 10 layers to achieve the spoil height of 320 mm.
- The piston and the top plate were mounted and LVDT was set to measure the vertical displacement of the piston. The vacuum was connected to the top port coming through the piston and air in the compacted spoil was sucked for about 2 hours.
- As shown in Figure 3b, the water tank was then connected to the bottom of the chamber and the system was left for 1 day (24 hours) for saturation.
- After saturation, air pressure equivalent to overburden pressure of (e.g: 300, 600,800(900) kPa) was applied in to the upper chamber and maintained for a period of 2 days, 3 months, 6 months, and 12 months.

Figure 3. (a) Compacting spoil into the pressure chamber, (b) Saturation of spoil compacted into the pressure chamber

- After the saturated spoil has been subjected to slaking over a predetermined period of time under a certain overburden pressure, the spoil was taken out from the chamber after releasing pressure and removing the top plate and the piston.
- Each sample slaked under different pressures over different time periods was tested for

particle size distribution following Australian standards

- To obtain particle size distribution down to 75 microns, wet sieving was conducted. Particle size distribution for particles smaller than 75 microns was obtained using a Malvern particle size analyser.
- To measure the permeability, the spoil was compacted into the mould measuring 150 mm diameter (see Figure 4) to achieve the dry unit weight of 18 kN/m^3 and the constant head permeability was performed.
- To measure the shear strength parameters, the specimen with 100 mm diameter and 200 mm in height compacted to achieve the dry unit weight of 18 kN/m^3 was tested in triaxial apparatus under undrained consolidation test conditions (with pore-water pressure measurement) following multi-stage test procedures. Figure 5 depicts the triaxial system used for this experimental program.

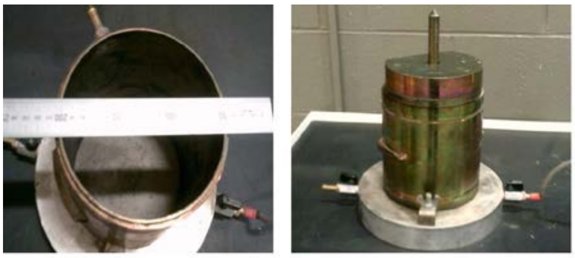

Figure 4. Permeability cell used for measuring permeability using constant head method

Figure 5. Triaxial system used for measuring shear strength properties of spoil

RESULTS AND DISCUSSION

Results of soil classification tests (particle size distribution), permeability, and shear strength tests of sample 2 - 10 are compared with those of Sample 1. Sample 1 is considered as the reference material as it is unslaked (fresh) spoil which was directly collected from an open-cut coal mine in Brown basin coalfield in Queensland, Australia. These results can be used to discuss overburden pressure and time effects on spoil slaking.

Grain Size Distribution

The effect of slaking on particles size distribution of spoil samples was determined from combined results of wet sieve analysis and laser diffraction analysis (Malvern apparatus). The Figure 6 represents particles size distribution of nine slaked and one fresh spoil sample.

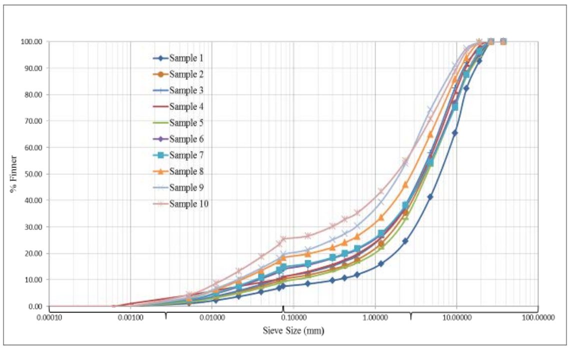

Figure 6. Particle size distribution of slaked spoil samples

As seen in Figure 6, the amount of fine particles increased with the increment of slaking time and overburden pressure. For spoil Sample 1, the amount of material finer than 75μm was approximately 8% which grew with increasing time and pressure to about 25% for spoil Sample 10 after 180 days under 900kPa overburden pressure. However, there was no significant increment of clay particles (particle size less than 0.002mm) due to slaking but had a significant increment of silt particles. The increase in the amount of fine particles in spoil samples with saturation time and pressure is an indication of more material disintegration or slaking

Hydraulic Conductivity

The influence of slaking on hydraulic conductivity was determined by the constant head permeability test. Figure 7 portrays the influence of overburden pressure and slaking time on permeability. It can be seen that the permeability decreases with an increase in overburden pressure as well as an increase in slaking time. Overburden pressure has a significant impact on permeability when it is slaked over a longer duration (e.g. 180 days). When the spoil is subjected to slaking over a long period for example, after 180 days of slaking, the permeability decreased from 0.884×10^{-06} m/sec to 0.017×10^{-06} m/sec (about 1/44), when the overburden pressure was increased from 300 to 900 kPa. For shorter slaking periods (e.g. two days), the permeability decreases from 2.1 x 10^{-06} m/sec to 0.96 x 10^{-06} m/sec (about ½) when the overburden pressure increases from 300kPa to 900kPa.

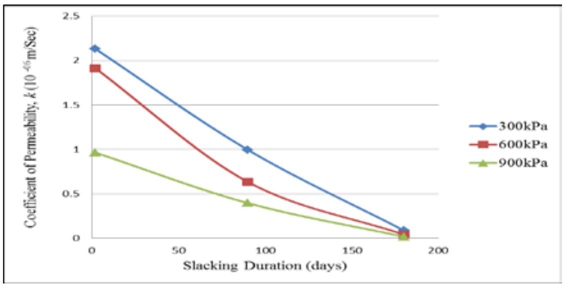

Figure 7. Effect of slaking time and overburden pressure on hydraulic conductivity

When the overburden pressure is increased, particles are crushed and compacted to decrease the volume of voids. The overburden pressure was maintained over a period of time. Spoil particles are further degraded and broken down in smaller fragments. As a result of the degradation of particle size the porosity decreased and the unit weight increased with time and overburden pressure. Permeability or flow through any sample is a function of unit weight, porosity and effective particle size and shape. Therefore, permeability decreases with increasing overburden pressure and slaking time. In brief, due to slaking over 180 days under different overburden pressures, spoil materials become low permeable gravel type materials from medium permeable.

Shear Strength

The multistage consolidated undrained triaxial tests were performed on cylindrical spoil samples. Each test specimen of 100mm diameter and 200mm height was prepared to achieve a dry density of 18kN/m^3 by wet compaction with initial moisture content of 10%. Once a specimen was enclosed in a 0.8 mm thick latex membrane, it was saturated to achieve B-value of above 0.95. Multistage triaxial tests were conducted in three stages with three different cell confining pressures of 500kPa, 600kPa and 700kPa and at the beginning of each stage back pressure was maintained at 300kPa. The effective confining pressures at the beginning of each stage were 200, 300 and 400kPa.

After consolidating the specimen for about two hours under drained conditions and stage one stress conditions (cell pressure 500kPa and backpressure 300kPa), it was sheared by applying monotonic vertical stress with a vertical strain rate of 0.05% per minute. The failure for each stage was assumed when maximum deviator stress (σ_d) was reached peak or 2% vertical strain (from the beginning of each loading stage) was achieved. Once the failure was reached for stage one, the applied vertical stress (deviator stress) was released and stage two stress conditions were applied (cell pressure, $\sigma3$ = 700 kPa and backpressure = 300 kPa). The specimen was then consolidated under drained conditions for about two hours before shearing it under undrained conditions until above mentioned failure criteria was achieved. Then, following the same steps, stage three of the test was completed. Figure 8 illustrates the observed axial strain (ε_a) versus deviator stress behavior of a multi-stage triaxial testing of the spoil specimen prepared using Sample 9. Using these values and confining pressures for each stage, total and effective major principal stresses (σ_1 and σ_1') and total and effective minor principal stresses (σ_3 and σ_3') were computed. Using effective major (σ_1') and minor (σ_3') principal stresses at failures the Mohr-Coulomb failures envelop was then drawn to obtain effective shear strength parameters: effective cohesion (c') and effective friction angle (ϕ'). Table 3 summarizes the shear strength properties of spoil samples obtained from multi-stage triaxial testing.

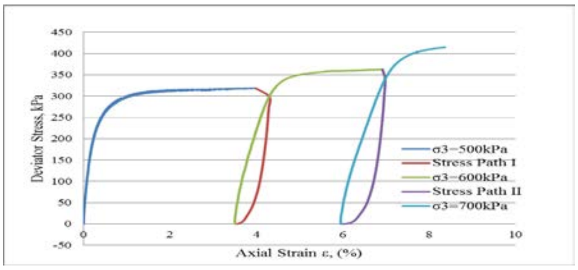

Figure 8. Deviator stress vs axial strain obtained from multi-stage triaxial test on Sample 9

The effective shear strength parameters cohesion and friction, varied from 1kPa to 40kPa and 38.62° to 33.22° due to slaking under different conditions (Table 2.4). As can be seen from Table 3, effective friction angle of spoil materials dropped due to slaking approximately 5.4° from the initial fresh condition. Furthermore, effective cohesions were exhibited by gradual increment up to 90 days and after 180 days; it dramatically increased to 40kPa. For reduction of friction angle, both slaking time and overburden pressure played similar roles whereas for effective cohesion the increment slaking time played a dominate role. The undrained friction angle and cohesion presented in table 3 indicated a similar conclusion. Due to slaking, the undrained friction angle for sample 2 was dropped to 18.47° from 26.98° (Sample 1). The friction angle gradually decreased with minor exemptions, with slaking time and overburden pressure which finally reached to 15.78° for spoil Sample 10. The undrained cohesion gradually increased from 10kPa, Sample 1 to 30kPa for Sample 7. Then, it increased dramatically to 190kPa. In fact, undrained cohesion was influenced dominantly by slaking duration

Table 3: Shear strength properties of spoil samples

Samples	Effective Cohesion, C' (kPa)	Effective friction angel, φ' (°)	Total Cohesion, C (kPa)	Total friction angel, φ (°)
Sample 1	1.00	38.62	12.00	26.98
Sample 2	2.00	34.75	12.00	18.47
Sample 3	2.00	33.29	10.00	15.83
Sample 4	2.00	34.59	15.00	18.75
Sample 5	2.00	34.74	20.00	17.05
Sample 6	3.20	33.30	19.00	16.30
Sample 7	4.00	33.83	30.00	16.90
Sample 8	10.00	33.75	40.00	17.37
Sample 9	20.00	33.52	50.00	15.68
Sample 10	40.00	33.22	190.00	15.78

CONCLUSION

The grain size distributions of spoil samples (slaked samples) suggest that this category 3 soil material is not a highly slakable material. The amount of fines (particle smaller than 0.075 mm) in the fresh soil sample (Sample 1) was about 8%. It increased to the maximum of 25% in sample 10 which was slaked over 180 days under 900 kPa overburden pressure. No significant increase in clay particles (particles smaller than 0.002 mm) were observed in sample 10 compared to sample 1 (fresh spoil).

The shear strength properties of spoil samples were obtained from consolidated undrained triaxial tests with pore-water pressure measurement. The undrained shear strength parameters from triaxial tests revealed that the material strength of spoil materials, category type 3 was medium to low with small cohesion. Triaxial tests on fresh spoil gave effective friction angle of 38.6^0, undrained friction angle of 27^0, effective cohesion of 1 kPa, and undrained cohesion of 12 kPa. Due to slaking of spoil material over six months under 900 kPa overburden pressure, the effective friction and undrained friction angles decreased by 5.4° and 11.2°, respectively. The effective and total cohesion increased by 40 kPa and 170 kPa, respectively.

The constant head permeability test results indicated a reduction in hydraulic conductivity due to slaking. The permeability property for fresh spoil was 6.99 x 10^{-6} m/sec and dropped rapidly for short termed slaked spoil samples with pressure. After six months of slaking, the effect of overburden pressure became insignificant and the permeability coefficient dropped to approximately 1.70 x 10^{-8} m/sec

ACKNOWLEDGEMENTS

The authors gratefully acknowledge the management of a coal mine in Brown Basin in Queensland, Australia who provides financial and in-kind support for this research project. Further, authors wish to express their gratitude to Mr. Glen Barnes, Senior technician at QUT for his continuous support when conducting laboratory experiments.

REFERENCES

[1] Kalinski ME, Karem WA and Little LM, “Estimating hydrocompression potential of mine spoils from a site in eastern Kentucky using dry unit weight and moisture content”, International Journal of Mining, Reclamation and Environment, Vol.24(4), 2010, pp. 350–362.

[2] Simmons J, and McManus D, (2004). “Shear strength framework for design of dumped spoil slopes for open pit coal mines”, Proceedings of Advances in Geotechnical Engineering, Vol.2, 2004, pp. 981-991.

[3] Williams DJ, Zou JS and Graham J, “Reliability index versus safety factor for coal mine slope pipe stability”, Proc. of the International Conference on Slope Stability, Isle of Wight, England, 1991, pp. 71-77,

[4] Hendrychova M, Salek M, Tajovsky K and Rechor M, “Soil Properties and Species Richness of Invertebratesons on Afforested Sites after Brown Coal Mining”, Restoration Ecology, Vol. 20(5), 2012, pp. 561–567.

Fifth International Conference on Geotechnique, Construction Materials and Environment, Osaka, Japan, Nov. 16-18, 2015, ISBN: 978-4-9905958-4-5 C3051

LIQUEFACTION ANALYSIS OF RECLAIMED GROUND IN URAYASU CITY CONSIDERING MAIN SHOCK AND AFTERSHOCK OF THE 2011 OFF THE COAST OF TOHOKU EARTHQUAKE

Sayuri Kimoto[1], Hiroshi Matsuoka[1], Hirokazu Yui[1], Fusao Oka[2]
[1]Kyoto University, Japan; [2]Professor Emeritus, Kyoto University

ABSTRACT

A wide area of the reclaimed ground in Urayasu city liquefied due to the 2011 off the Pacific Coast of Tohoku Earthquake. One of the characteristics of the earthquake is a long duration of the ground motion, which is considered to increase the damage by liquefaction. In the present study, numerical analyses have been performed for the ground in Urayasu city with an earthquake record of the 2011 off the Pacific Coast of Tohoku Earthquake including aftershock by using a liquefaction analysis program, ‘‘LIQCA2D14’’(LIQCA Research and Development Group) [1]. In the analyses, the soil is modeled as an elasto-plastic material for sandy layers including reclaimed ground layer, and an elasto-viscoplastic material for clay layers. In order to quantify the degree of liquefaction, we defined an index named LRI (Liquefaction Risk Index), which is given by the weighted integration of the effective stress decreasing ratio with respect to the depth. Moreover, the consolidation process after the earthquake motion has been analyzed in order to obtain the ground settlement with the dissipation of the pore water pressure. The simulation results of the degree of liquefaction and the settlement, are compared with the measured value.

Keywords: Liquefaction, FEM, Numerical analysis, Risk index

INTRODUCTION

Due to the 2011 off the Pacific Coast of Tohoku Earthquake, liquefaction occurred over a wide area from the Tohoku district to the Kanto district in Japan. In particular, a wide area of the reclaimed ground in Urayasu city liquefied. One of the characteristics of the earthquake is a long duration of the ground motion, which is considered to increase the damage by liquefaction. In practice, a simplified evaluation method, such as, the liquefaction potential index, P_L, is widely used in Japan to evaluate the possibility of liquefaction. There are, however, difficulties to evaluate the duration of the ground motion as well as the amplitude history which are known to affect the cyclic behavior of soil.

In order to quantify the degree of liquefaction, we introduce an index named LRI (Liquefaction Risk Index), which is calculated from the results of numerical analysis and defined as the weighted integration of the effective stress decreasing ratio with respect to the depth. Numerical analyses have been performed for the ground in Urayasu city with an earthquake record of the 2011 off the Pacific Coast of Tohoku Earthquake including aftershock, and the value of LRI is validated by comparing with the liquefaction damage in Urayasu city. Moreover, settlement during the consolidation process following the earthquake motion will be discussed.

NUMERICAL METHOD

We have numerically analyzed the deformation of a horizontally layered ground during an earthquake using a soil-water coupled method. In the numerical simulation of the dynamic behavior of the ground, we used a liquefaction analysis program, “LIQCA2D014” (LIQCA Research and Development Group, 2014) [1]. The method is a two or three-dimensional water-soil fully coupled analysis methods based on the two-phase porous theory which adopts a u-p formulation in the infinitesimal strain field [2], [3]. The equation of motion is discretized by FEM and the continuity equation is discretized by FDM. As for the time discretization in the time domain, Newmark’s beta method is used. In addition, Rayleigh’s damping is employed in the analysis, which is proportional to the initial stiffness matrix and the mass matrix.

For the constitutive model for soils, we applied a cyclic elasto-plastic model considering both the kinematical hardening rule [4] and the strain-induced degradation for sandy soils [5], and an elasto-viscoplastic model for clayey soils [6].

The model used in the present analysis is a model within a framework of continuum mechanics. Hence, the model represents the liquefaction state by the very soft continuous material with small mean effective stress. The model can describe the degradation of the material with the shrinking the overconsolidation boundary surface and the volumetric softening which is a feature of liquefaction.

SIMULATION MODEL AND BOUNDARY CONDITIONS

Fig.1 shows a map of Urayasu city. A wide area of the reclaimed ground which covers three fourths of the city liquefied due to the 2011 off the Pacific Coast of Tohoku Earthquake. We have chosen two sites of the reclaimed ground for the analyses, that is, Point Y and Point Z as indicated in Fig. 1. Point Y is located in Shinmachi area in which the reclamation began in 1972, while Point Z is located in Nakamachi area in which the reclamation began in 1965. Thus, the reclamation period is different among each site. The ground profile for the two sites are shown in Fig. 2. The thickness of the reclaimed soil layer is around 9 m and 5 m at Point Y and Point Z, respectively.

Material parameters for the elasto-plastic constitutive model are determined based on the cyclic strength curve obtained from cyclic undrained shear tests of samples taken at each site [7][8]. The parameters of the reclaimed sandy layer for each point are shown in Table 1. The cyclic shear strength curves obtained from experiments and model simulations are shown in Fig. 3.

The time discretization is based on Newmark's beta method, with β and γ set at 0.3025 and 0.6, respectively. The time increment in the calculation was set to be 0.001 s which is small enough to guarantee the accuracy of the results.

Fig.4 shows the input earthquake motions which is the recorded earthquake obtained during the 2011 off the Pacific Coast of Tohoku Earthquake at a depth of 36 m at Shinagawa seismological observatory [9]. The maximum acceleration is around 65.9 gal and the duration of the ground motion is greater than 400 sec. for the main shock. In the earthquake record, aftershock occurred after 29 minutes of the main shock. In the present analysis, however, the duration between main shock and aftershock is disregarded for saving time since we confirmed that the pore pressure dissipation occurred mainly after 29 minutes, hence it did not strongly affect the calculations. Calculations are conducted until 800000 sec. (i.e. 9.3 days) in order to investigate the dissipation process.

Fig. 1 Map of Urayasu city.

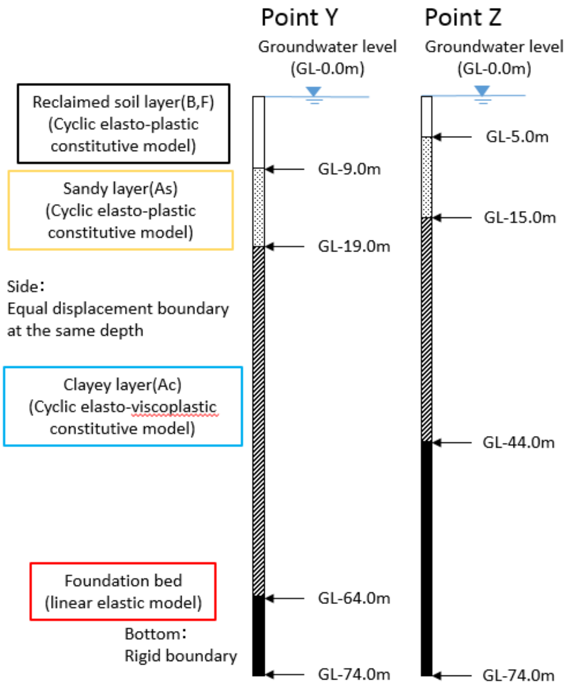

Fig. 2 Ground profile.

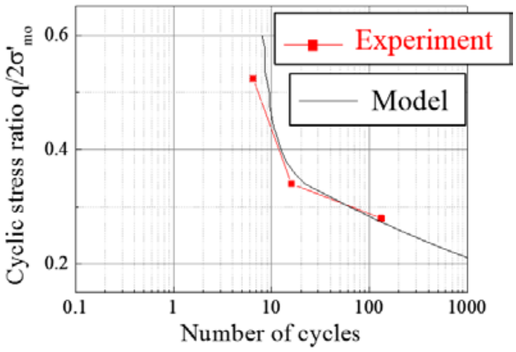

(a) Point Y, reclaimed soil layer (B, F)

(b)

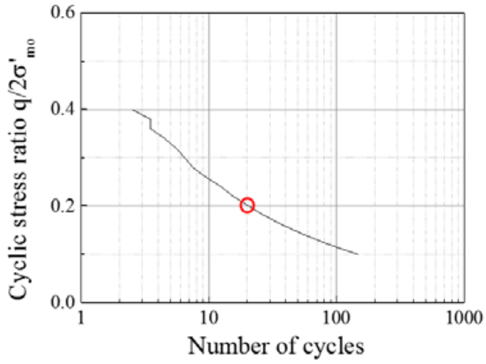

(b) Point Z, reclaimed soil layer (B, F)

Fig. 3 Cyclic strength curve of the reclaimed soil.

Table 1 Material parameters

Parameter	Point Y (B, F)	Point Z (B, F)	Sandy layer (As)
Density ρ (t/m^3)	1.68	1.68	1.93
Coefficient of permeability k (m/s)	1.0×10^{-4}	1.0×10^{-4}	1.0×10^{-3}
Shear modulus G_0/σ'_{m0}	1254	2257	527 (Y) 706 (Z)
Initial void ratio e_0	1.46	1.46	0.93
Compression index λ	0.013	0.013	0.0875
Swelling index κ	0.008	0.008	0.0142
Stress ratio at Maximum Compression M^*_m	0.8417	0.8417	1.083
Stress ratio at failure M^*_f	1.083	1.083	1.319
Quasi-OCR* $(=\sigma'_{mai}/\sigma'_{m0})$	1.0	1.0	1.25
Hardening parameter B^*_0,B^*_1,C_f	6000,80, 10	1500,15, 10	6000,150 ,15
Fading memory C_d	2000	2000	2000
Parameter of dilatancy D^*_0, n	0.9,6.0	1.0,1.0	3.75,10
Reference of plastic strain γ_r^{P*}	0.005	0.004	0.0015
Reference of elastic strain γ_r^{E*}	0.1	0.08	0.05

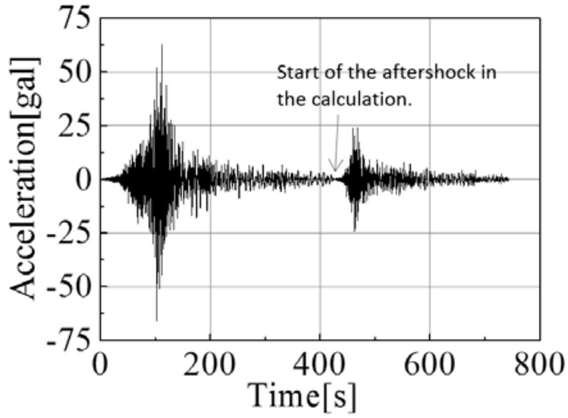

Fig. 4 Input seismic motion (Shinagawa, at a depth of 36 m).

SIMULATION RESULTS

Acceleration-time profiles of the ground surface are shown in Fig. 5. The maximum acceleration of the ground surface is 148 gal at Point Y, and 103 gal at Point Z. The input motion is amplified at both sites, and the amplification is greater at Point Y.

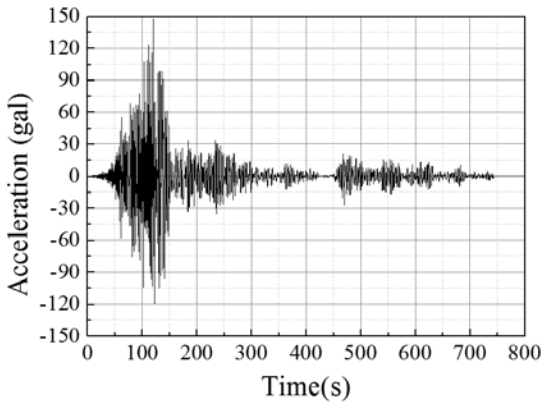

(a) Point Y

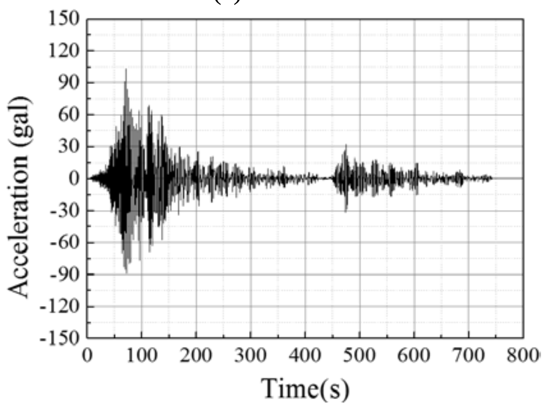

(b) Point Z

Fig. 5 Acceleration-time profile of the ground surface.

We estimate the liquefaction degree at each depth by the effective stress decreasing ratio, ESDR, as:

$$\mathrm{ESDR} = 1 - \sigma'_m / \sigma'_{m0} \quad (1)$$

in which σ'_{m0} is the initial mean effective stress and σ'_m is the current mean effective stress. When the ground liquefies completely, the mean effective stress reaches 0 and ESDR reaches 1.0. In order to quantify the degree of overall liquefaction at the point, we defined a liquefaction risk index [10], LRI, as:

$$\mathrm{LRI} = \int_0^D \mathrm{ESDR} \cdot W(z, D) dz \quad (2)$$

where z is the depth from the ground surface and $W(z, D)$ is the weighting function of z . LRI is obtained by the weighted integration of the ESDR with respect to the depth from the ground surface to a depth of D m. We adopt D=20 m in the present study and obtained LRI as:

$$\mathrm{LRI} = \int_0^{20} \mathrm{ESDR} \cdot (1 - 0.05z) dz \quad (3)$$

Distributions of ESDR obtained from the analyses are shown in Fig. 6. The values of ESDR reaches 1.0 in the reclaimed layer both at Point Y and Z after the main shock, i.e., 420 sec. Time profiles of LRI calculated using Eq. (3) for Point Y and Z are shown in Fig. 7. LRI increases during input motion in both cases and the increasing rate during the main shock is larger in the case of Point Z. This is because the cyclic shear strength of reclaimed soil layer is smaller in the case of Point Z than that of Point Y as shown in Fig. 3. Whereas the maximum value of LRI is 7.38 in Point Y and 6.35 in Point Z. It is probably because the thickness of reclaimed soil layer is larger in Point Y. In the previous research [10], we have evaluated the LRI values by data from the 1995 Hyogoken-Nanbu Earthquake. It was found that the obtained LRI values were greater than 6.0 for the points where heavy liquefaction damage had occurred. The value obtained in this research is greater than 6.0 in both sites, which is acceptable considering the heavy damage in Urayasu city. The maximum acceleration, the settlement and LRI for two cases are summarized in Table 2.

Vertical displacement-time profiles are shown in Fig. 8. The final settlement after consolidation is 0.533 m in Point Y and 0.581 m in Point Z. From a survey report, observed settlement differs among the area and the maximum settlement in the reclaimed land was around 0.4 – 0.5 m [11]. The calculated settlement after consolidation slightly overestimates the measured value.

Effective stress paths of the top element of the reclaimed layer (B, F) and the sandy layer (As) during earthquake are shown in Fig. 9 and Fig. 10, respectively. The mean effective stress of the top element approaches to zero in both two cases as shown in Fig. 9, while it decrease but does not reach zero in sandy layer as shown in Fig. 10. Effective stress paths of the top element of clay layer (Ac) are shown in Fig. 11. The mean effective stress decreases even in clay layer, and the ESDR in clay layer reaches around 0.23 in both sites.

Table 2 Maximum acceleration, settlement and LRI

	Max. acc. (gal)	Settlement after consolidation (m)	LRI (Max.)
Point Y	148	0.533	7.38 (781s)
Point Z	103	0.581	6.35 (712s)

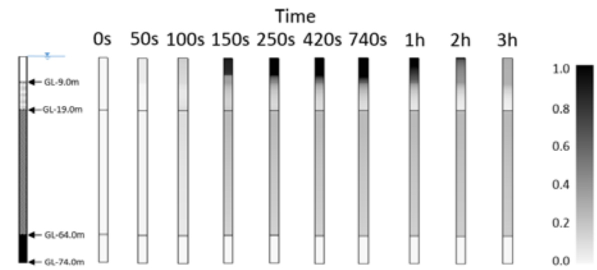

(a) Point Y

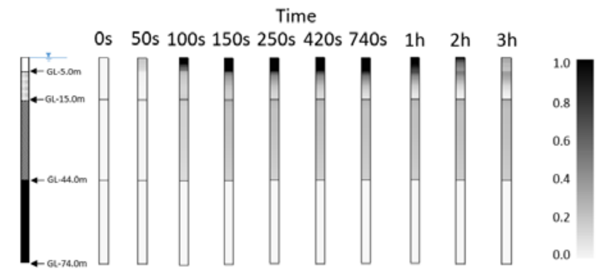

(b) Point Z

Fig. 6 Distributions of the effective stress decreasing ratio, ESDR.

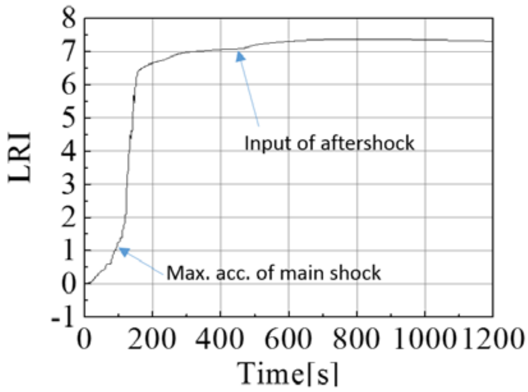

(a) Point Y

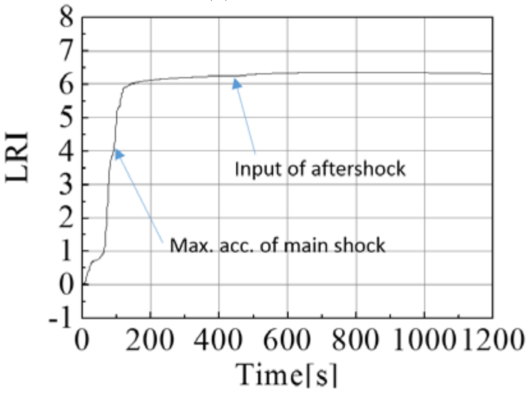

(b) Point Z

Fig. 7 Time profiles of Liquefaction Risk Index, LRI.

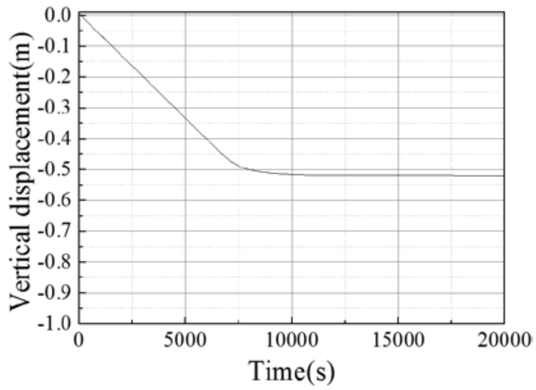

(a) Point Y

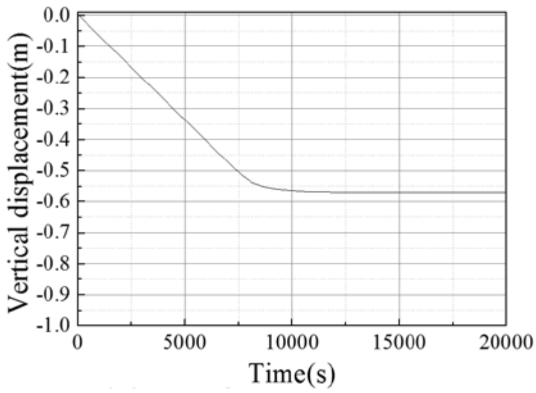

(b) Point Z

Fig. 8 Vertical displacement-time profile.

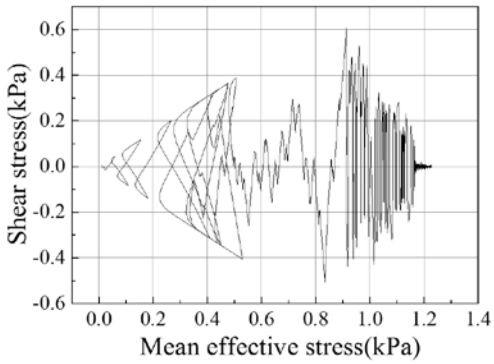

(a) Point Y

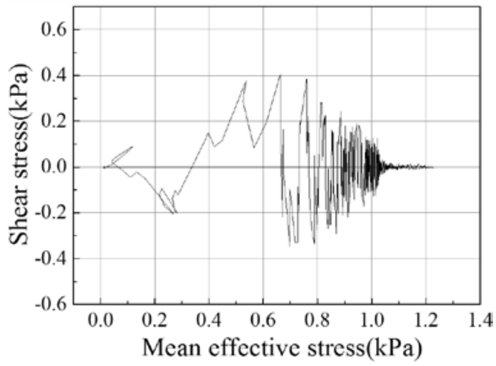

(b) Point Z

Fig. 9 Effective stress paths of the top element of reclaimed layer.

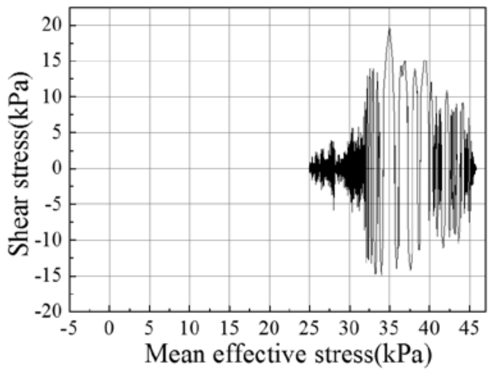

(a) Point Y

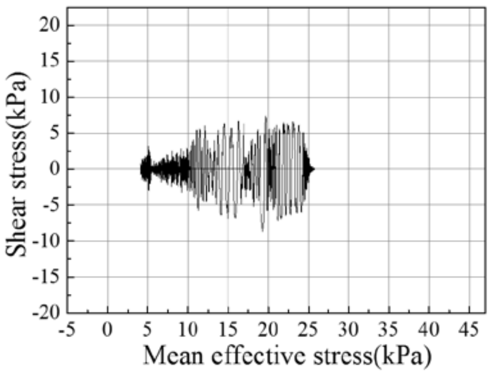

(b) Point Z

Fig. 10 Effective stress paths of the top element of sandy layer.

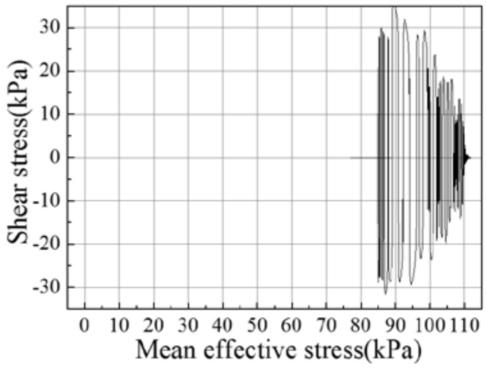

(a) Point Y

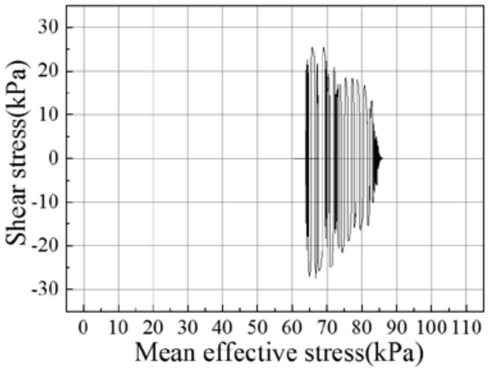

(b) Point Z

Fig. 11 Effective stress paths of the top element of clay layer.

CONCLUSIONS

In the present study, liquefaction analyses were performed for two sites in Urayasu city with an earthquake record of the 2011 off the Pacific Coast of Tohoku Earthquake including aftershock by using a liquefaction analysis program LIQCA. In order to quantify the degree of liquefaction, we introduced an index named LRI (Liquefaction Risk Index), which is given by the weighted integration of the effective stress decreasing ratio with respect to the depth. The obtained LRI values are 6.35 are 7.38 for each site, and those seem to be acceptable compared to the previous research [10]. In order to evaluate the index, we need to obtain more data indicating relationships between the liquefaction damage and the value of the index. In addition, settlement due to dissipation of excess pore pressure is evaluated. The calculated total settlement after consolidation slightly overestimates the measured settlement.

REFERENCES

[1] LIQCA Research and Development Group (Representative: F. Oka), “Materials for LIQCA2D14・LIQCA3D14 (2014 released print)”, 2014.
[2] Zienkiewicz OC, Chan AHC, Pastor M, Schrefler BA and Shiomi T “Computational Geomechanics with Special Reference to Earthquake Engineering”, John Wiley & Sons, 1999.
[3] Oka F, Yashima A, Shibata T, Kato M and Uzuoka R, “FEM-FDM coupled liquefaction analysis of a porous soil using an elasto-plastic model”, Applied Scientific Research, Vol. 52, 1994, pp. 209-245.
[4] Armstrong PJ and Frederick CO, “A mathematical representation of the multiaxial Bauschinger effect”, Report RD/B/N 731, 1966.
[5] Oka F, Yashima A, Tateishi A, Taguchi Y and Yamashita S, “A cyclic elasto-plastic constitutive model for sand considering a plastic-strain dependence of the shear modulus”, Geotechnique, Vol. 49 (5), 1999, pp. 661-680.
[6] Kimoto S, Shahbodagh Khan B, Mirjalili M and Oka F, ”A cyclic elasto-viscoplastic Constitutive model for clay considering the nonlinear kinematic hardening rules and the structural degradation”, 2013, doi:10.1061/(ASCE)GM. 1943-5622.0000327.
[7] Japanese Geotechnical Society, Workshop on constitutive model for soil, May 27-28, Tokyo, 2013 (in Japanese).
[8] Ishikawa K, Yasuda S, Aoyagi T, “Studies on the reasonable liquefaction-prediction method”, Japanese Geotechnical Journal, Vol. 9, No. 2, 2014, pp. 169-183 (in Japanese).
[9] Bureau of Port and Harbor, Tokyo Metropolitan Government, http://www.kouwan.metro.tokyo.jp/business/keiyaku/kisojoho/jishindou.html.
[10] Oka F, Yui H, Kimoto S, Kinugawa T, “New evaluation method for liquefaction of ground using dynamic liquefaction analysis method and its application”, Int. J. Geomechanics, 2015, to appear.
[11] Fukutake K, Mano H, Hotta H, Taji Y, Ishikawa A, Sakamoto T, “Studies on soil liquefaction and settlement in the urayasu district using effective stress analyses for the 2011 East Japan Great Earthquake”, Research paper, Institute of Technology, Shimizu Corporation, Vol. 89, 2012, pp.39-50 (in Japanese).

THE PERFORMANCES OF THREE SOIL RETAINING STRUCTURES: GABION, MODULAR BLOCK AND GEOCELL

STATHAS Dionysios[1], WANG Jui Pin[1]
[1]Civil & Environmental Engineering, HKUST, Hong Kong (SAR)

ABSTRACT

One of the major tasks of a geotechnical engineer is the design of earth retaining walls. Apart from the rigid reinforced concrete wall, several types of alternative facings, such as Gabion, Geocell and Modular Block, with or without soil reinforcement, are used to offer a more environmental friendly and low cost solution at the earth-retaining problem. Although several studies have been conducted investigating the performance of each of the three structures, there is no clear comparison between the mentioned earth retaining walls. We have conducted small-scale tests (1:10 scale) comparing the three types of structures in terms of load capacity, deformation behavior and failure mode. The results of this study are shown in this paper. With a total of six tests conducted, the structures were loaded until failure with and without soil reinforcement. Gabion and Modular Block miniatures were made with a 3D printer providing a more precise configuration as real ones. The Geocell is proved to perform better in terms of absolute load capacity. However, the interlock of the modular blocks provides a significant resistance parameter increasing the efficiency of the particular facing type.

Keywords: Retaining structures, Reinforced soil, Modular Block, Gabion, Geocell

INTRODUCTION

Earth retaining structures are one of the most common and important civil engineering tasks. Geotechnical engineers need to find the most suitable solution for soil retaining problems and satisfy safety, environmental and economic criteria. During the years, various types of earth retaining walls have been developed and proposed. Apart from the typical rigid reinforced concrete cantilever or gravity wall, alternative types of earth retaining walls such as gabion, modular block or geocell can also provide a reliable solution.

Gabion and Geocell are two types of elements, which can build whether a gravity wall or they can just be used as the facing of a reinforced soil structure. On the other hand, modular block is mainly used as the facing of reinforced soil systems. In the past years various studies have been conducted in order to investigate the performance of these structures. The importance of facing stiffness to the performance (Load Capacity, wall deformation, reinforcement tensile force) of reinforced soil retaining structures has been an important research topic during the last decades [1], [10].

The deformational behavior of geosynthetic reinforced soil walls with continuous facing panel has been also a discussion topic in the past [9]. Also more recently researchers proposed recommendations concerning the maximum wall displacement of segmental geosynthetic reinforced soil walls through the study of a wall data base [2].

Various studies investigating separately the performance of Gabion, Modular Block or Geocell have also been conducted recently. Geocell was proved to perform quite well under seismic loading [5], [8]. Chen and Chiu (2007) carried out small scale physical models to describe the influence of various parameters such as position of reinforcement, wall batter and load position, on the wall performance and make some design suggestions [3]. Laboratory tests to describe the behavior of Gabion wall facing under cyclic loading have also been conducted in the past years [6].

Numerical implementations are another common effort to understand and describe the performance of segmental geosynthetic reinforced walls. Most of the time numerical results are validated with laboratory tests. The numerical studies included static surcharge loading [4] as well as earthquake loading [7].

A lot of effort is being carried out to understand a structure which has many parameters influencing its behavior. This study is adding some supplementary data to the existing ones. Moreover new trends in technology are implemented to assist the physical modeling of small scale models. Finally, three common realistic structures are chosen and compared under totally same conditions, providing assistance to practical engineers in order to gain a better knowledge concerning the behavior of these structures and make decisions.

TEST SETUP

The foundation was chosen deep enough to reduce any boundary effects. The wall height was chosen 200mm and the backfill length 300mm. The model width was 210mm. Figure 1 shows the test setup. The block offset is 2mm for every modular block and geocell layer. For gabion the block offset was 6mm. The wall batter was 6º for all types of facing. Following table is summarizing the basic geometrical characteristics of every facing type. The sides of the box were covered with low friction plastic sheets to reduce side resistance.

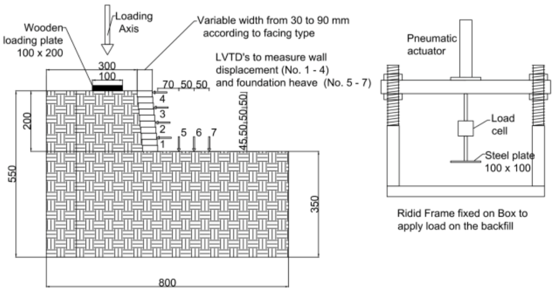

Fig. 1 Experimental setup.

Table 1 Facing geometrical characteristics

Facing	No. of Layers	Width (mm)	Offset (mm)
Gabion	4	50	6
Mod. Block	10	30	2
Geocell	10	60 - 90	2

Soil Properties

Backfill

The sandy soil used in the model tests is China Standard ISO sand. The specific gravity of this soil is 2.65g/cm^3, with the maximum and minimum dry density equal to 1.91g/cm^3 and 1.62g/cm^3, respectively. The angle of internal friction is around 38° at a relative density of 70%. This sand can be classified as poor graded sand (SP) according to the Unified Classification system (Uniformity coefficient C_u = 6.0 and coefficient of gradation C_k = 0.41).

The wetted sand used in tests had 3% water content and it was compacted to a dry density of 1.79g/cm^3, which equals 98% compaction degree. Figures 2 and 3 show the compaction test according to BS and sieve analysis results.

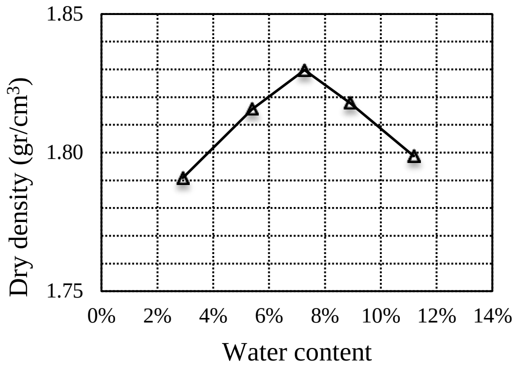

Fig. 2 Compaction curve of China Standard ISO sand.

Infill Material

The infill soil, which was used for Geocell and Modular Block was the same with the wall backfill. The Gabion baskets were filled with gravel having a grain size larger than 10mm. The specific gravity of the gravel is 2.6g/cm^3 and the porosity of the gabion baskets 50%, which resulted in an average density of 1.30g/cm^3.

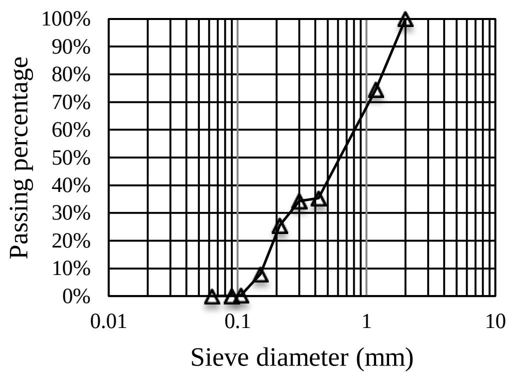

Fig. 3 Grain size distribution of China Standard ISO sand.

Miniatures

The geometrical characteristics of the miniatures were chosen according to products used in praxis. Furthermore, their dimensions, apart from being realistic, were chosen in such a way to make the three facings comparable with each other from a geometric point of view.

Gabion

Gabion sides were manufactured with a 3D printer. The material used is acrylonitrile butadiene styrene (ABS). The gabion sides were made quadratic with 50mm width and 1mm thickness. The mesh has regular hexagonal with 10mm diameter. The sides were bound together with plastic ties to form the gabion box. The average weight of each gabion box is 162g.

Modular Block

The modular blocks were also manufactured using a 3D printer with the same material as gabion sides. The size of each block is 48x30x20mm. Each block weights 34g and 7.2g, with and without sand infill respectively.

Geocell

The Geocell was made with transparent printing paper and the seams were made with staples. The height of the Geocell is 20mm and the size of an open cell is 32 x 30mm. The seams were positioned every 450mm. The total Geocell length layer is 210mm and the average width is 75mm. Each layer infilled with soil had a weight of 576g.

Reinforcement

For the soil reinforcement was used nylon sheets. The reinforcement length was chosen 30% of the wall height, which is equal to 60mm.

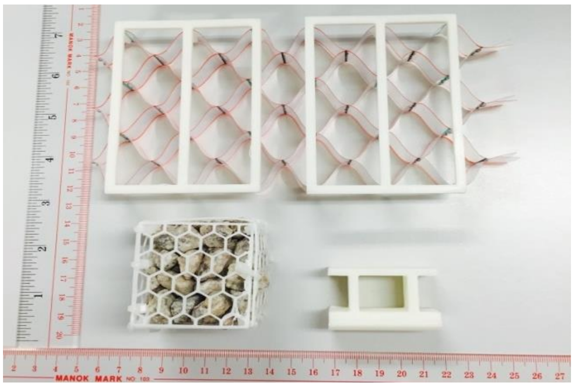

Fig. 4 Miniatures.

Testing procedure

In total there were conducted 6 tests. The first three tests were carried out without soil reinforcement. The second test set included the three types of facing with reinforcement.

The loading was applied uniformly 20mm from the back of the facing. A rigid wooden plate 100 x 200mm was used in order to distribute the load uniformly on the backfill.

A pneumatic actuator was used to generate the load, which was increased manually at steps of 2.5kPa every minute. All structures were brought to failure.

TEST RESULTS

Test without reinforcement

Gabion and Geocell failed due to sliding, whereas for Modular block the governing failure mechanism observed, was overturning. The rotation point was at 4.5cm from the foundation level (0.25H). The slip surface on the back of the wall for Gabion and Geocell has been a plane surface according to Rankine theory (Fig. 5 and 7). In case of Modular block, on the other hand, a curved surface was formed similar to a log-spiral slipping surface (Fig. 6).

Gabion and Modular block showed slight difference in terms of load capacity, 29.0kPa and 26.0kPa respectively. The Geocell, proved to have almost twice larger load capacity (48.0kPa) compared to the other two facings.

The magnitude of maximum wall deformation has been quite similar for Gabion and Modular block. On the contrary, the deformed shape observed, was quite different. The maximum deformation for the modular block occurred at the top layer, whereas for Geocell and Gabion at the height of 0.75H (Fig. 7). In case of the gabion facing type, it is necessary to mention, that LVTD 2 at 9.5cm penetrated into the gabion basket and this particular measurement should not be taken into account.

Figure 8 shows the maximum wall displacement in relation to surcharge loading on the wall backfill for each wall facing.

Table 2 Summary of test result WITHOUT reinforcement

Facing	Load Capacity (kPa)	MAX Displacement (mm)	Failure mode
Gabion	29.0	2.2 at 0.75H	Sliding
Mod. Block	26.0	1.9 at H	Overturning at 0.25H
Geocell	48.0	0.6 at 0.75H	Sliding

Note: H is 200mm the wall height

The three types of structures can be designed like a gravity wall. The weight of the structure is the main parameter, which determines their load capacity. The structure weights are 2600g, 1360g, and 5760g for Gabion, Modular Block and Geocell respectively. Gabion and modular block behaved similarly in terms of load capacity and load deformation behaviour, although modular block is a much lighter structure. This fact can be justified from the high axial rigidity of the modular block facing [10]. As reported from Tatsuoka in his Keynote lecture [10], Roles of facing rigidity in soil reinforcing, facings with a high axial rigidity can transfer through friction on the back face, part of the backfill weight effectively. Consequently, the vertical force acting as resisting force for gravity structures will be increased.

Finally, it is worth mentioning that Geocell showed no deformation until the surcharge reached the value of 44kPa. The increased load capacity can be justified from the larger weight of the structure towards the other types of facings.

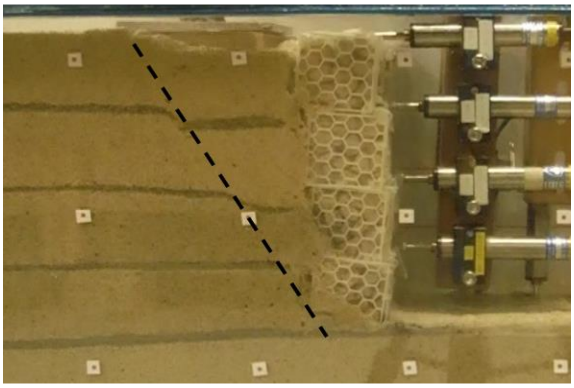

Fig. 5 Gabion without reinforcement: slipping surface

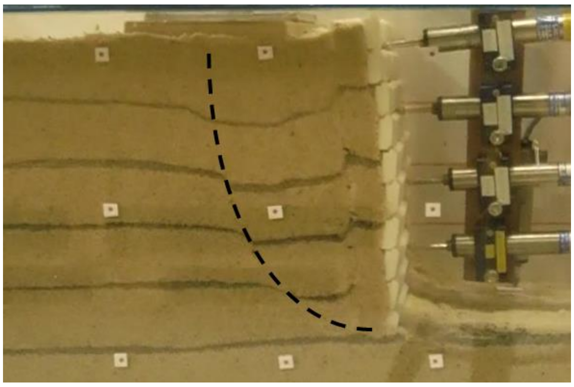

Fig. 6 Modular block without reinforcement: slipping surface

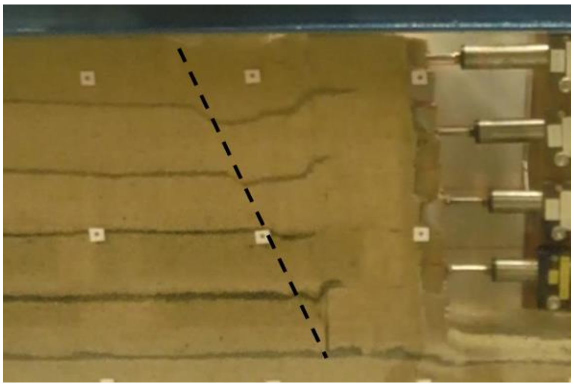

Fig. 7 Geocell without reinforcement: slipping surface

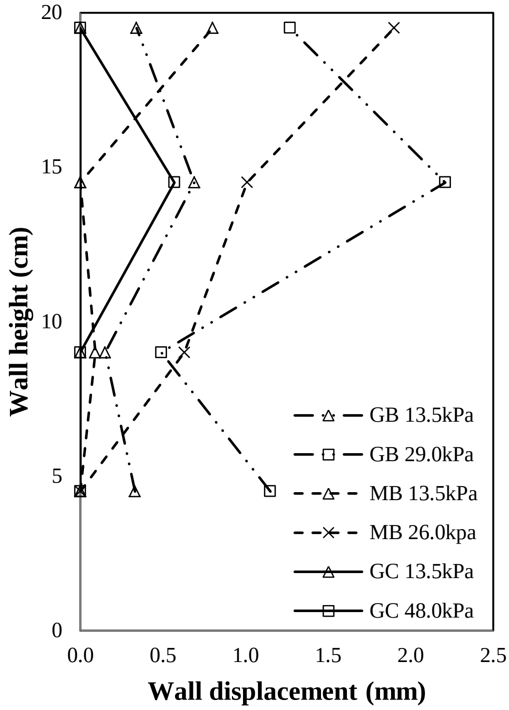

Fig. 7 Wall deformation of retaining structures without soil reinforcement

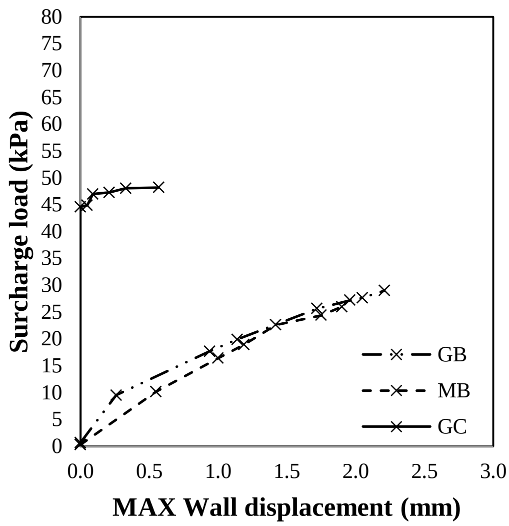

Fig. 8 Load – max displacement relation of retaining structures without soil reinforcement

Test with reinforcement

The soil reinforcement increased significantly the load capacity of the facings as expected. The failure observed for Gabion and Geocell was internal sliding. The sliding surface was at a height of approximately 0.25H from foundation level for both structures. The reinforced soil structure with a modular block facing failed due to sliding at the foundation level. The slip surface on the back of the wall formed a two wedge shape (Fig. 9 – 11).

The load capacity was quite similar for Gabion and modular block (Table 3). Geocell was proved to have the best load capacity (Table 3) from the three types of structures as well as the slightest deformation (Fig. 12) in comparison with the other two facing types.

Soil reinforcement had an influence on the wall deformed shape in case of Geocell, compared to the unreinforced case. The maximum deformation was recorded on the top of the structure (Fig. 12). For the other two cases, the position of the maximum deformation was similar to the unreinforced tests. Finally, note that the soil reinforcement reduced significantly the deformation of the wall apart from reducing increasing the load capacity.

Table 3 Summary of test result WITH reinforcement

Facing	Load Capacity (kPa)	MAX Displacement (mm)	Failure mode
Gabion	67.5	1.5 at 0.75H	Internal Sliding
Mod. Block	69.5	1.8 at H	Sliding
Geocell	79.0	1.3 at H	Internal Sliding

Note: H is 200mm the wall height

Sliding, whether internal or not, was the governing failure mechanism for all three types of structures. The Geocell had the best performance in terms of load capacity and maximum deformation. However, modular block although is the lightest structure seems to perform quite satisfactory. The interlock of the modular block provides a significant advantage to this type of structure since a sliding between facing layers is impossible.

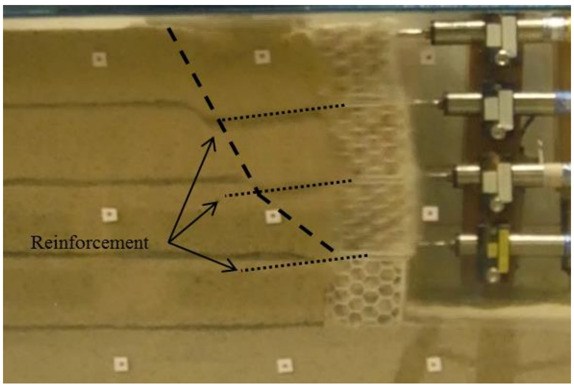

Fig. 9 Gabion with soil reinforcement: slipping surface

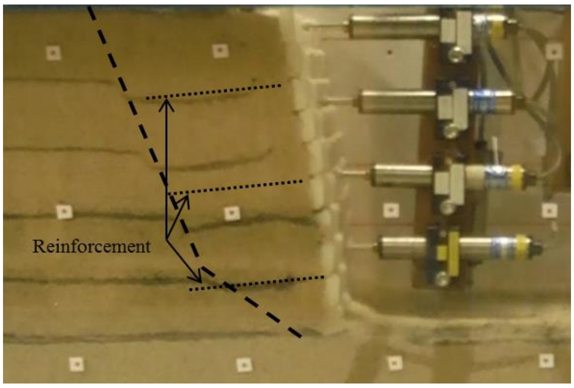

Fig. 10 Modular block with soil reinforcement: slipping surface

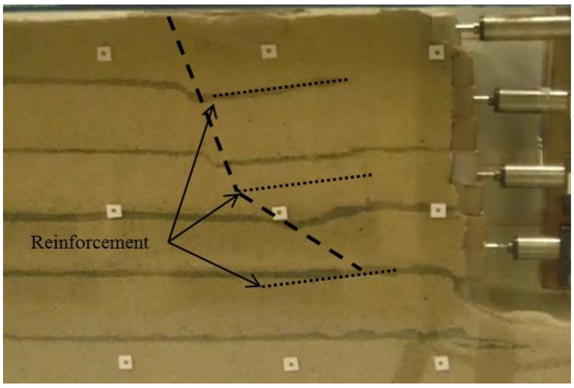

Fig. 11 Geocell with soil reinforcement: slipping surface

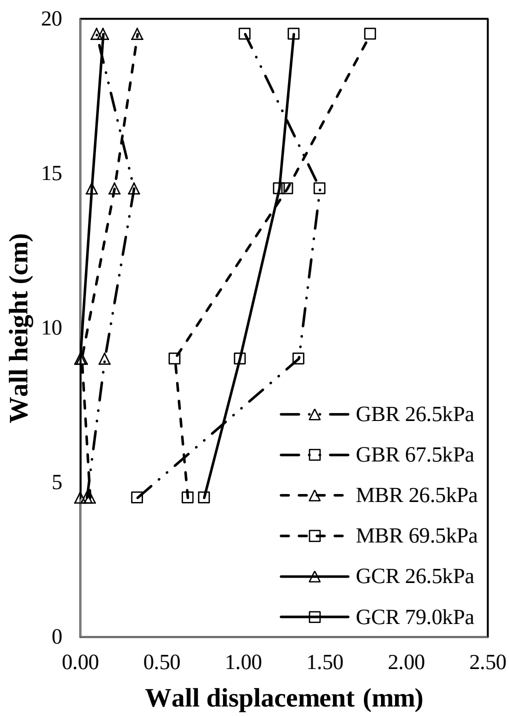

Fig. 12 Wall deformation of retaining structures with soil reinforcement

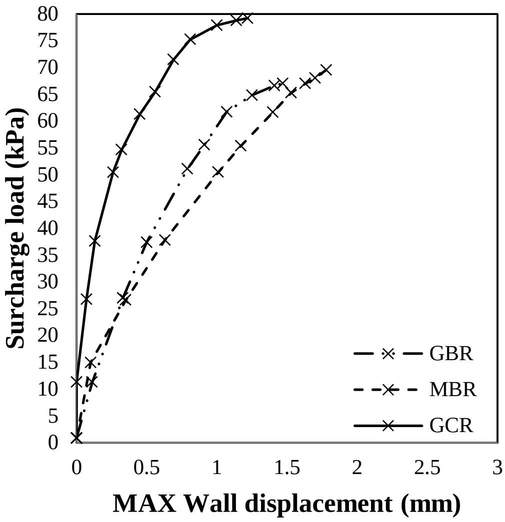

Fig. 13 Load – max displacement relation of retaining structures with soil reinforcement

CONCLUSIONS

All three types of structures are easy and quick to construct. In engineering problems, where a fast and low cost construction method is required, these types of structures can be a reliable and environmental friendly solution.

Geocell due to its larger weight was proved to have the highest load capacity. Moreover, its deformational behaviour was much better than the other two types of facing. However, in terms of relative to the structure's weight performance, modular block because of its high axial and shear rigidity can be suggested as an efficient solution especially in problems of limited space.

However, the aesthetic effect of the facing, the material availability on site and the erosion resistance of the facing should also be taken into account in the decision making process.

Finally, more and more advanced measuring and instrumentation techniques are being implemented in physical modelling in geotechnics. The use of 3D printing, which is becoming more popular day by day, can be a valuable additional tool to assist small scale physical modelling, for manufacturing complex miniatures with higher precision.

REFERENCES

[1] Bathurst, R.J., Vlachopoulos, N., Walters, D.L., Burgess, P.G., Allen, T.M., "The influence of facing stiffness on the performance of two geosynthetic reinforced soil retaining walls.", Canadian Geotechnical J. 43, 2006, pp. 1225-1237.

[2] Bathurst R.J., Miyata Y, Allen T.M., 2010, "Facing Displacements in Geosynthetic Reinforced Soil Walls", Keynote paper, Earth Retention Conference 3(ER2010), ASCE Geo-Institute, Bellevue, Washington 1-4 August, 18 p., pp. 442- 459

[3] Chen, R.H., and Chiu, Y.M., "Model tests of geocell retaining structures", Geotextiles and Geomembranes, 26,2008, 56-70

[4] Hatami, K., and Bathurst, R.J., "A numerical model for reinforced soil segmental walls under surcharge loading", J.Geotech. Geoen. Eng., ASCE, 132(6), 2006, 673–684.

[5] Leshchinsky, D., Ling, H.I., Wang, J.P., Rosen, A., and Mohri, Y., "Equivalent seismic coefficient on geocell retention systems", Geotextiles and Geomembranes, 27, 2009, pp. 9-18.

[6] Lin, Y. L., Yang, G. L., Zhao, L. H., "Engineering behaviors of reinforced gabion retaining wall based on laboratory test", Journal of Central South University of Technology, 17(6), 2010, 1351-1356.

[7] Ling, H. I., Yang, S., Leshchinsky, D., Liu, H., and Burke, C., "Finite-element simulations of full-scale modular-block reinforced soil retaining walls under earthquake loading", J. Eng. Mech. ASCE, 136(5), 2010, 653-661.

[8] Ling, H.I., Leshchinsky, D., and Wang, J.P., "Seismic response of geocell retaining walls: Experimental studies", J. Geotech. Geoenviron. Eng. ASCE, 135(4), 2009, pp. 515-524.

[9] Rowe R.K., Ho S.K., "Horizontal deformation in reinforced soil walls.", Canadian Geotechnical Journal 35, 1998, pp.312 – 327

[10] Tatsuoka, F., "Roles of facing rigidity in soil reinforcing." , Keynote Lecture. In Proceedings of the International Symposium on Earth Reinforcement Practice, IS Kyushu 1993. Fukuoka, Japan, 14 November 1993. Edited by H. Ochiai, S. Hayashi, and J. Otani. A.A. Balkema, Rotterdam, The Netherlands, vol. 2, pp. 831 - 870.

[11] Wang, J.P. ,"Full-scale shaking table test on reinforced soil structures with geocell facing", Ph.D thesis, Columbia University,2007.

Fifth International Conference on Geotechnique, Construction Materials and Environment, Osaka, Japan, Nov. 16-18, 2015, ISBN: 978-4-9905958-4-5 C3051

DEVELOPMENT OF CAPACITANCE DISPLACEMENT MONITORING SYSTEM AND ITS PERFORMANCE TESTS

LIN Wenli[1,2], Katsutoshi UENO [1], SHEN Mingrong[2], Ryosuke UZUOKA[1], Hisashi SUZUKI[1]
[1] The University of Tokushima, Japan;
[2] School of Civil Engineering, Tongji University, Shanghai 200092, China

ABSTRACT

Geological disasters caused by slope instability frequently result in great loss to human life and property, and real-time and on-line slope monitoring is a most effective method for mastering the deformation dynamics and early warning of landslide disasters. Considering the numerous landslides and high cost of slope monitoring system, three types of capacitance displacement transducer based on the principle of electrostatic capacitance were designed. Basic performance and long-term stability performance of these capacitors were examined, and the impact of temperature behavior on the capacitance measurement circuit was evaluated. The results showed that, comparing with conventional displacement transducers used for slope monitoring, capacitance type transducers can provide sufficient precision, resolution and measurement range and applying them in slope monitoring could bring obvious advantages, for their remarkable economic benefit and effectiveness.

Keywords: Linear Capacitance Displacement Transducer, Landslide, Slope Monitoring, Performance

INTRODUCTION

Landslide is a serious geological disaster and widely distributed in the global scope, which frequently causes great loss to human life and property. It is difficult to invest immense economic and technology to manage all the potential landslides. Real-time and on-line monitoring of slope is therefore, a most effective method for mastering the deformation dynamics and early warning of landslide in time [1]. However, current monitoring technology has the defects of time-consumption, costly and highly skilled, which result in their poor universal applicability in landslide monitoring. In view of this, it is of great significance to develop a simple, low-cost and easily embedded displacement monitoring instrument.

Starting with this premise, the development of low-cost slope monitoring system for consumers was presented in this paper. Based on the principle of electrostatic capacitances, three types of capacitance displacement transducers, Area-alterable Differential Type Parallel-plate Capacitor (ATPC), Area-alterable Type Cylinder Capacitor (ATCC) and Permittivity-alterable Type Cylinder Capacitor (PTCC), were designed, and performance of these transducers was examined.

1. PRINCIPLE OF THE CAPACITANCE DISPLACEMENT TRANSDUCER

Capacitance displacement transducer is used for converting a displacement caused by a change of a physical variable into an electrical signal using electrostatic capacitances [2], [3]. Ignoring edge effects, the capacitance between a pair of parallel plates is given by Eq. (1).

$$C = \frac{\varepsilon_0 \varepsilon_r S}{d} \tag{1}$$

Where ε_0 is the permittivity of free space; ε_r is the relative permittivity of the dielectric material, in the air, $\varepsilon_r = 1$; S is the overlap area of the plates (m^2); d is the distance between two plates (m).

As can be seen from Eq. (1), there are three variables, ε_r, S, d, and it is advisable to maintain any two of them as constant and adjust the other variable by changing the displacement of a movable part of the capacitance transducer, thereby establishing a linear relationship between the capacitance and the adjustable variable. A measure of the capacitance is therefore, a measure of the displacement of the movable part of the capacitance transducer, and the change in capacitance can be converted into digital signal indicating the linear displacement of the transducer by a matching measuring circuit.

1.1 Area-alterable Type Parallel-Plate Capacitor (ATPC)

The ATPC capacitor is formed by having the first and second parallel electrodes fastened on a stationary assembly to constitute the measured capacitance C_m, and the third parallel electrode 3 fastened on a movable assembly constitutes the electrostatic capacitances C_{13} and C_{32} respectively with the first and second electrodes. The electrode 3, moving with the measured object, is provided as a shield and connected to GND. The structure of ATPC capacitor is shown in Fig.1.

In this case, electrode 1 and 2 are composed of polypropylene material, the lower surface of electrode 1 and the upper surface of electrode 2 are covered with a piece of conductive paper (aluminizing paper) and electrode 3 is composed of conductive paper. The thickness of these three electrodes are 1 mm, lengths are 330 mm, which means that the measurement range of this transducer is 330 mm. Since this transducer used relatively simple material, therefore, it could be manufactured at significantly reduced cost.

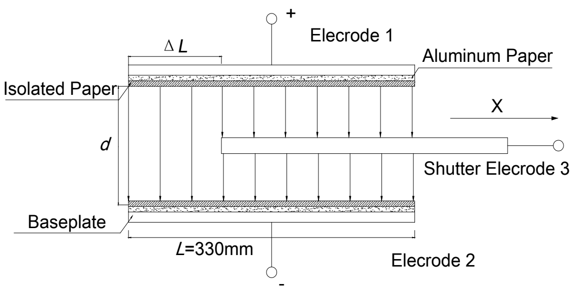

Fig.1 The structure of ATPC capacitor

We are setting permittivity ε_r and distance d remains constant and adjust the overlap area S by the movable electrode 3 of the transducer, the initial overlap area is $S_0 = a \times L$, here a is the width and L is the length of the parallel electrodes, so the initial capacitance is given by Eq.(2)

$$C_0 = \frac{\varepsilon_0 \varepsilon_r S}{d} = \frac{\varepsilon_0 \varepsilon_r a L}{d} \tag{2}$$

The change in the overlap area of the relatively fixed electrodes 1 and 2 caused by the linear displacement ΔL of electrode 3 relates to its capacitance directly, and the changed capacitance is given by Eq.(3)

$$C_m = \frac{\varepsilon_0 \varepsilon_r a (L - \Delta L)}{d} = C_0 - \frac{\varepsilon_0 \varepsilon_r a}{d} \Delta L \tag{3}$$

1.2 Area-alterable Type Cylinder Capacitor (ATCC)

This ATCC capacitor is formed by having one hollow cylindrical electrode 1 fastened on a stationary assembly and another solid cylindrical electrode 2 fastened to a moveable assembly. The inner cylinder slides within the outer cylinder so that, as the movable electrode is displaced, the overlap area of the measured capacitance changes as a function of linear displacement. Its structure is shown in Fig.2.

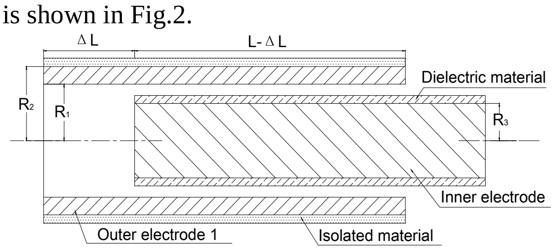

Fig.2 The structure of ATCC capacitor

In this case, both cylinders are composed of metal material. The solid inner cylinder 2 has a dielectric material affixed to its surface. Surrounding the inner cylinder 2 is the hollow cylinder 1 which has an isolated material affixed to its outer surface. The total measurement range of this capacitor is 900 mm.

Capacitance variation formula of ATCC transducer is similar to the ATPC displacement transducer and given by Eq. (4).

$$C = \frac{2\pi \varepsilon_0 \varepsilon_r a (L - \Delta L)}{\ln(R_1 / R_3)} = C_0 - \frac{2\pi \varepsilon_0 \varepsilon_r}{\ln(R_1 / R_3)} \Delta L \tag{4}$$

Where, R_1 is the inner radius of cylinder 1, R_3 is the inner radius of cylinder 2, L is the measurement length and ΔL is the displacement of movable cylinder.

1.3 Permittivity-alterable Type Cylinder Capacitor (PTCC)

The structure of PTCC capacitor is shown in Fig.3. The two relatively fixed inner and outer capacitor cylinders 1 and 2 are spaced from the inner and outer surfaces of the middle insulating cylinder 3 by a dielectric air gap. The isolating cylinder 3 is fastened to a movable assembly and slidably engaged within the inner and outer cylinders so that, as the insulating cylinder 3 is displaced, the permittivity between the two relatively fixed inner and outer cylinders changes.

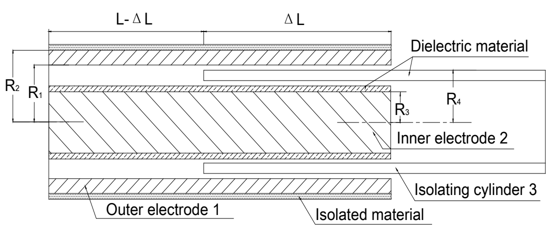

Fig. 3 The structure of PTCC capacitor

In this case, both cylinders 1 and 2 are composed of metal material. The solid inner cylinder 2 has a dielectric material affixed to its surface. Surrounding the inner cylinder 2 is the hollow insulating cylinder 3 which is composed of polyethylene material. The outer cylinder 1 has an isolated material affixed to its outer surface. In addition, the total measured range of this capacitor is 900 mm.

Here, the overlap area S_0 and distance d remains constant and the permittivity between cylinder 1 and 2 is adjusted by the displacement of the movable isolating cylinder 3, the initial capacitance is given by Eq.(5).

$$C_0 = \frac{2\pi\varepsilon_0\varepsilon_r L}{\ln(R_1/R_3)} \tag{5}$$

If the isolating cylinder 3 moves through the fixed inner and outer cylinders 1 and 2, a capacitance C_m will be formed by two sections. The first contribution on the total capacitance C_m will be the capacitance between the inner and outer cylinder for the area in which both cylinders are not overlapped by the movable isolating cylinder 3. The length corresponding to this area is designated as ΔL. The second contribution to the total capacitance C_m will be the capacitance between the inner and outer cylinders for the area in which both cylinders are overlapped by the movable isolating cylinder 3 and the length corresponding to this area is designated as $L-\Delta L$. The total capacitance C_m is given by Eq. (6).

$$C_m = C_0 - \frac{2\pi\varepsilon_0(\varepsilon_r - 1)}{\ln(R_1/R_3)}\Delta L$$

(6)

We can see from the above equation that as the movable isolating cylinder is displaced, the measured capacitance changes as a linear function of the displacement ΔL.

2. MEASUREMENT CIRCUIT OF THE CAPACITANCE DISPLACEMENT MONITORING SYSTEM

Figure 4 showed the measurement system. The variation of capacitance is induced by the displacement of the measured object. Measurement unit composed of embedded microcomputer and sensing amplifier [4]-[6] is utilized to realize real-time data transmission, processing and conversion, and finally display the result to PC to accomplish real-time monitoring the displacement of measured object.

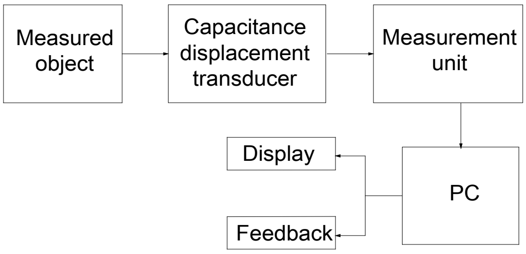

Fig.4 Measurement system of the capacitance displacement monitoring system

3. BASIC PERFORMANECE TEST AND ITS EVALUATION

The basic performance, including linearity, resolution, measurement range and the relative error of slope of transducers, were examined. The change of capacitance caused by the displacement of movable part was directly measured by the measurement circuit and recorded in value of count. Here 1 count is roughly equivalent to 3 fF capacitance. The relationship between displacement and count was drawn (see Fig.6~8) and the results were showed in Table 1.

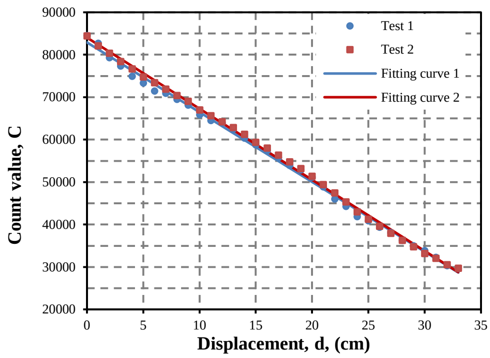

Fig.6 Basic performance test results of ATPC

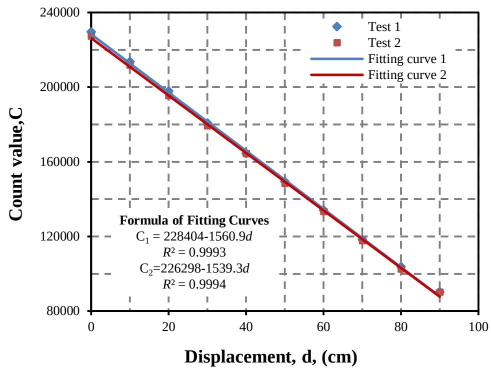

Fig.7 Basic performance test results of ATCC

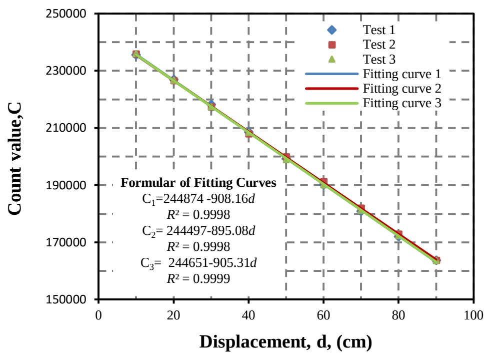

Fig.8 Basic performance test results of PTCC

Table 1 Basic performance test results of three types of capacitance transducers

Evaluation Item	ATPC	ATCC	PTCC
Type	Parallel-plate	cylindrical	cylindrical
Test Times	2	2	3
Measurement Range（mm）	330	900	900
R	0.9989	0.9997	0.9999
Sensitivity	166	153	80
Resolution（mm）	0.0060	0.0064	0.0125
Relative errors of the slope	0.899%	0.697%	0.620%
Structure	Simple manufacture	Complex wiring	Simple wiring

From Figure 6~8 & Table 1, we can see that the correlation coefficient (*R*) are all higher than 0.99. The measurement ranges of cylindrical capacitors (ATCC& PTCC) are 900mm, which is larger than parallel-plate capacitor (ATPC). The resolution of ATPC and ATCC are better than PTCC. The structure of ATPC and PTCC are simpler than ATCC. The results show that capacitance type transducers can provide sufficient precision, resolution and measurement range, comparing with conventional displace transducers used for slope monitoring. Therefore, it is feasible to develop a monitoring system based on the principle of capacitance.

4. STABILITY PERFORMANECE TEST AND ITS EVALUATION

4.1 Stable Performance of Capacitance Transducers

The long-term stability of acquisition is needed in slope monitoring. Count value of parallel-plate type and coaxial type capacitors were recorded under indoor environment for 15 hours. According to Eq. (7), the variation rate of count value can be calculated, and the relationship between variation rate of count value and time was drawn in Fig.9.

$$C_{ROC} = \frac{C_t - C_0}{C_0} \tag{7}$$

Where, C_0 is the initial capacitance; C_t is the capacitance measured in different time.

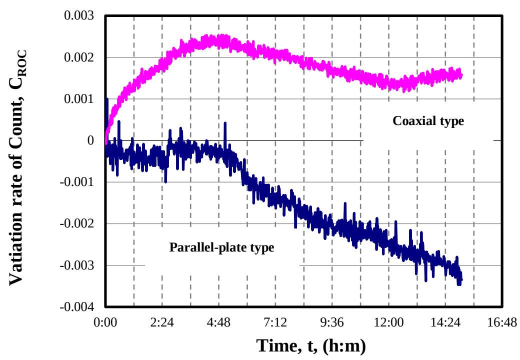

Fig.9 Long-term stability performance of parallel-plate type and coaxial type transducers

Figure 9 shows that, in the first 5 hours, the count variation rate of the parallel-plate type is basically stable, and gradually decreases with time. Its variation rate is -3.03×10^{-03}~1.00×10^{-03} within 15 hours, which is equivalent to about 0.33mm displacement. In contrast, in the first 5 hours, the count variation rate of coaxial type capacitor is increased with time, and then gradually turns to be stable. Its variation rate is 10^{-3}, which is equivalent to about 0.2 mm displacement and the error is smaller.

Based on the test result, we can see that the stability performance of the cylindrical type capacitor is more satisfied than the parallel-plate type one, while a minor change to the electrode structure of this type of displacement transducer is still necessary. Furthermore, there still remains to improve the shielding system for both types of capacitors since we did not take it into account in the tests.

4.2 Stable Performance of Measurement Circuit

It is also necessary to evaluate the stability of the measurement system under the condition of long time at different temperatures. Measurement circuit of this capacitance displacement monitoring system is composed of sensing amplifier, microcomputer and coaxial cables.

4.2.1 Temperature characteristic test of the sensing amplifier

The sensing amplifier selected in this paper is used for amplifying the measured signals obtained from the capacitor. 5 types of sensing amplifier were selected for temperature characteristic test, their difference depends on their constituent elements including IC model, silicon diodes, supply voltage and resistance (see Table 2).

Table 2 List of constituent elements of the sensing amplifier

Type	IC Model	Supply Voltage	Silicon Diodes	Resistance (Ω)
N2	74HC4538	5V	Have	1M
N4	MC14538	3.3V	Have	1M
N5	MC14538	3.3V	None	1M
N6	MC14538	5V	None	1M
N15	MC14538	3.3V	None	100k

1) Impact of silicon diodes and different IC models

Three types of sensing amplifier, N2, N4, N5, were selected for conducting the temperature characteristic test to evaluate the impact of silicon diodes and different IC models. The relationship between their variation rate of count value and temperature were drawn in Fig.10.

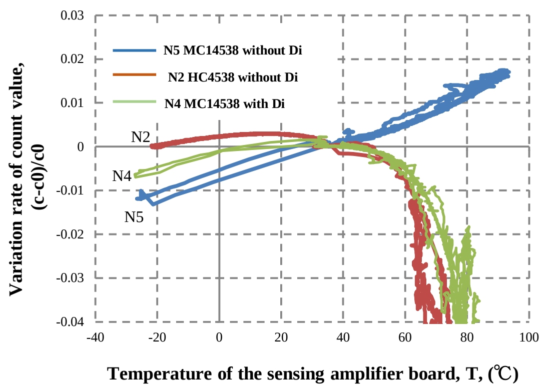

Fig.10 Temperature characteristics test result of different IC models

Figure 10 shows that:

(1) The count variation rate of N5 shows a linear growth with temperature. As the temperature increases from -30 ℃ to 90 ℃, its variation rate of count value C_{ROC} increases by 0.032 from -0.014 to 0.018. Its calculated temperature coefficient is about 2×10^{-4} /℃, which is small and can be neglected if the requirement of measurement accuracy is not high.

(2) The variation law of N2 and N4 sensing amplifiers are very similar. With the increase of temperature, both of their variation rates of count value are changed slightly when the temperature is below 50 ℃, while they all fell sharply with temperature when the temperature is higher than 60℃.

(3) Both of the N2 and N4 sensing amplifier are installed with a silicon diode. Although silicon diodes have good stability at elevated temperatures, a phenomenon of reverse leakage current which increased with temperature, still exist. When the temperature is higher than 50℃ or 60℃, reverse current will increase multiply for every 10℃increase, and decreasing its capacitance accordingly. This is why the measured count value of N2 and N4 sensing amplifiers drop dramatically as the temperature rises up to 50 ℃.

(4) In reality, when the sensing amplifier is embedded in the slope, the environment temperature would not be higher than 50 ℃. As the temperature ranges from 0℃ to 40℃, the variation rates of count value of N2 and N4 sensing amplifiers are quite smaller. When the sensing amplifier is embedded in a measurement box placed on the ground, its environment temperature would be higher in summer, and N5 sensing amplifier is more satisfactory. However, proper amount of temperature compensation is necessary for improving the measurement accuracy.

2) Impact of different resistances of RC integrating circuit

Two types of sensing amplifiers with different resistance, N5 (1MΩ) and N15 (100kΩ), were selected to evaluate the impact of different resistances. The relationship between the count variation rate and temperature was drawn in Figure.11.

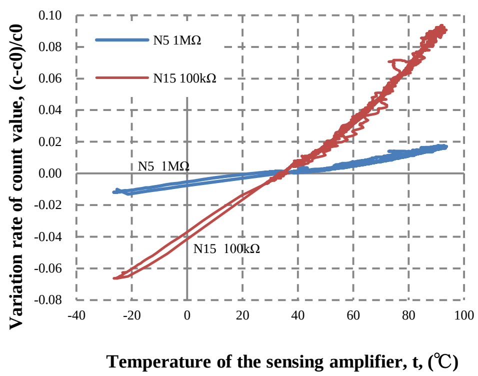

Fig.11 Test results of different resistances R

As can be seen in Figure11, the variation rates of N5 and N15 both linear increase with the increase of temperature, and the variation rate of N15 is nearly five times larger than N5. Their calculated temperature coefficients are 14×10^{-4}/ ℃ and 2×10^{-4}/℃ respectively. We can see that sensing amplifiers with a 1MΩ resistance would be more suitable for improving the measurement accuracy.

The reason is that: In the RC integrating circuit, the charging time of a capacitor is proportional to its resistance. The smaller the resistance is, the smaller the output pulse amplitude of the sensing amplifier will be. During the IC operation process, a certain time for rising and falling the pulse signal of the sensing amplifier is needed and it depends on the IC speed correlated with temperature significantly. That is, the pulse rise and fall time will be affected by the temperature. As for smaller resistance, when temperature rises up, the output pulse signal of the sensing amplifier will be smaller correspondingly, resulting in the increase of rise and fall time of pulse signal, thereby increasing the variation rate of count value.

3) Impact of different supply voltage

Two types of sensing amplifiers with different supply voltages, N5 (3.3V) and N6 (5V), were selected to evaluate the impact of different supply voltages. The relationship between the count variation rate and temperature was drawn in Fig.12.

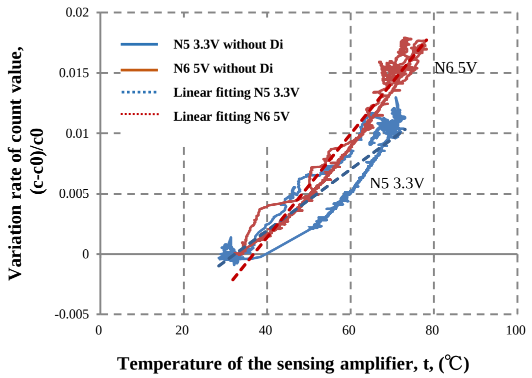

Fig.12 Temperature characteristics test results of different supply voltage

Seen from Figure12, the variation rate of count value of N5 increases from 0 to 1.3×10^{-2} as the temperature increases from 30 ℃ to 80 ℃, and its calculated temperature coefficient is 2.5×10^{-4} /℃; the variation rate of N6 increases from 0 to 1.8×10^{-2}, and its calculated temperature coefficient is 4.3×10^{-4} / ℃, which is larger than N6. Both of their variation rates are quite small, which means that temperature has very litter impact on different supply voltages.

Based on the comprehensive consideration of energy consumption, noise interference, and temperature characteristic, the sensing amplifier with 3.3V supply voltage can meet the requirements of this measuring system.

4.2.2 Temperature characteristic test of the microcomputer

Microcomputer is utilized for transforming the measured capacitance from the sensing amplifier into count value by the on-chip clock pulse generator which is composed of an external crystal oscillator and a built-in PLL loop. Since the change of temperature on the crystal oscillator and the PLL loop will change the frequency of the clock pulse generator, the measurement accuracy will also be influenced as well. Therefore, it is necessary to evaluate the temperature characteristic of the microcomputer.

Sensing amplifier has three output channels recorded, ch1, ch2 and ch4, measured data from these three channels were transformed to the microcomputer. Keeping the microprocessor in the dryer and adjusting the temperature from 30 ℃ to 100 ℃ and measuring the count value from these three channels meanwhile. The relationship between the temperature and variation rate of count value can be drawn (see Figure 13).

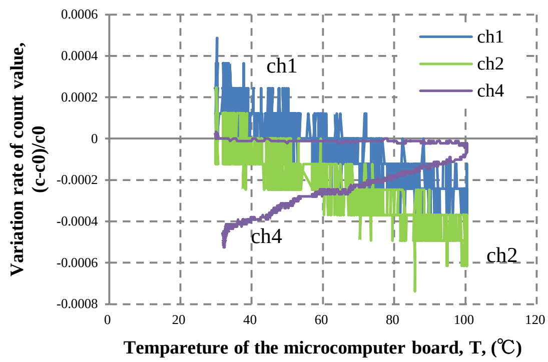

Fig.13 Temperature characteristic test results of the microcomputer

From Figure 13, we can see that the variation amount of count value is about 1×10^{-4} and its calculated temperature coefficient is about 1×10^{-6}/℃ with the temperature increasing from 30 ℃ to 100 ℃, which is very small. We can draw the conclusion that temperature has very little impact on the measurement accuracy of the microcomputer and can be neglected.

4.2.3 Stable performance test of coaxial cable

In order to be better close to the realistic situation, the temperature characteristics test of the 5D-2V coaxial cable, which is an important component for data transmission to sensing amplifier, was conducted at indoor temperature for 24 hours. Temperature was measured by the built-in temperature sensor both in sensing amplifier and microcomputer, and capacitance was measured and recorded by Teraterm software. Test results were organized in Fig.15. Curve 1 and curve 2 are the measured temperatures of sensing amplifier and microcomputer respectively, curve 3 is the variation amount of count value of coaxial cable whose initial value is 33,992.

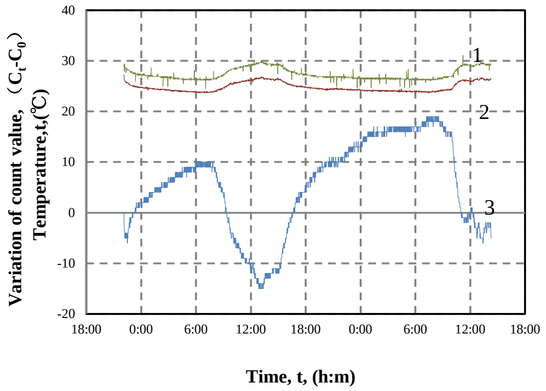

Fig.14 Temperature characteristics test result of 5D-2V coaxial cable

It can be seen from Figure14, at the beginning (from 22:30 to 6:00), as the temperature drops by 3.14℃, the variation of count value shows a trend of increase and increases by 15. Then as the temperature rise up, the count value appeares a decreasing phenomenon. It can be seen that the variation of count value is small and appears a negative increase with temperature. In order to further understand the relationship between variation rate of count value and temperature, the test data was further processed and the test curve was shown in Fig.15.

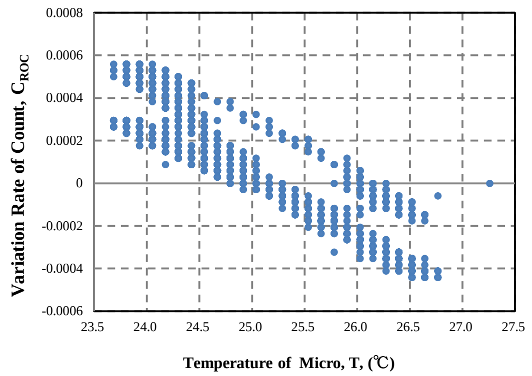

Fig.15 Temperature characteristic of coaxial cable

Figure 15 shows the variation rate of count value at different environmental temperatures. As a whole, the variation rate of count value presents a linear negative relationship with the temperature. Its calculated temperature coefficient is about 0.1deg/℃/m=2.8×10^{-4}/℃/m per electrical length, its order of magnitude is reasonable. Therefore, conclusions can be drawn that temperature has little impact on the measurement accuracy of coaxial cables, a proper amount of temperature compensation is necessary for improving the measurement accuracy though.

CONCLUSION

(1) Based on the principle of capacitance, three types of capacitance displacement transducers were designed, they are Area-alterable Type Parallel-plate Capacitor (ATPC), Area-alterable Type Cylinder Capacitor (ATCC) and Permittivity-alterable Type Cylinder Capacitor (PTCC).

(2) Basic performance of these three transducers was examined. The result shows that capacitance type transducers can provide sufficient precision, resolution, measurement range and stable performance, comparing with conventional displace transducers used for slope monitoring.

(3) Stability test of capacitance displacement transducers was conducted. The result shows that the stability performance of the cylindrical type capacitor is more satisfied than the parallel-plate type one, while a minor change to the electrode structure of this type of displacement transducer is still necessary.

(4) Temperature characteristics of capacitance measurement circuit were investigated, and results show that:

a) As for the sensing amplifier, it tends to be significantly different depending on its internal constitute elements, thus the measurement accuracy can be increased by choosing suitable internal elements of the sensing amplifier;

b) As for the microcomputer, temperature has little impact on it and the error can be basically ignored;

c) As for the coaxial cables used to connect transducers to sensing amplifiers, the count variation rate shows a linear negative relationship with temperature. Therefore, a proper amount of temperature compensation is necessary for improving the measurement accuracy.

REFERENCES

[1] Josep A Gili, Jordi Corominas, Joan Rius. Using Global Positioning System Techniques In

Landslide Monitoring [J]. Engineering Geology, 2000, 55(3):167-192.

[2] Lu Yunfeng, Zhao Jianting, He Qing, Zhong Qing. Research on Non-magnetic Displacement Measurement System Based on Capacitive Sensor [J].Chinese Journal of Scientific Instrument, 2011, 32(6):213-217, in Chinese.

[3] Joseph Habib, Jackson Mich, et al. Linear Capacitance Displacement Transducer: United States, 4961055[P].Oct.2,1990.

[4] Katsutoshi Ueno, Toshiyaki Takahara. Application of precise capacitance meter for geotechnical monitoring [J]. Proc, 45th JGS annual meeting, 2010:137-138, in Japanese.

[5] Toshiyaki. Takahara, Katsutoshi Ueno and Toshihide Sugimoto. In Situ Measurements using Developed High Resolution Capacitance Type Sensor and Its Performance Evaluation, Proc. of the Int. Workshop on ICT in Geo-Engineering, pp. 69-75, 2012, Research publishing.

[6] Katsutoshi Ueno. Capacitance type Moisture Meter and Water Gage. Patente Gazette, JP,5688731,B, 2015, in Japanese.

FifthInternational Conference on Geotechnique, Construction Materials and Environment, Osaka, Japan,Nov. 16-18, 2015, ISBN: 978-4-9905958-4-5 C3051

THE CHARACTERISTIC OF SAND-KAOLIN CLAY MIXTURE AS ARTIFICIAL MATERIAL FOR LABORATORY SOIL TESTING

Purwana Y.M.,[1], Nikraz H[2]
[1]Civil Engineering Dept., Sebelas Maret University, Indonesia;[2,]Curtin University, Australia

ABSTRACT

Laboratory soil testing is a routine activity in geotechnical engineering. For the tests, either the characteristic, behaviour of soil or the performance of the laboratory apparatus is studied. One of the most important requirements for laboratory study is that the material should have repeatability property. However, due to the heterogeneity many soil samples do not comply with this requirement. To overcome this situation, articial material might be able to be utilised. The series of laboratory tests using a new material of sand-kaolin clay mixture have been conducted. The low cohesion, no plasticity, and high internal friction possessed by sand mixed with the high cohesion, high plasticity, and low internal friction possessed by kaolin clay produce a new material. The desired new properties are obtained by changing the proportion of sand-kaolin clay mixture. The index properties, compaction characteristic, shear strength properties, and CBR results are presented. It can be concluded that sand-kaolin clay mixture is suitable material for geotechnical laboratory test.

Keywords: Artificial Material, Laboratory Testing, Repeatability Property, Sand-kaolin Clay Mixture

INTRODUCTION

Laboratory soil testing is a routine activity in geotechnical engineering. For the tests, either the characteristic or behaviour of soil or the performance of the laboratory apparatus is studied. However, due to the heterogeneity many soil samples do not comply with this requirement. To overcome this situation, articial material might be able to be utilised. Artificial material is made to resemble the characteristic and the property of original material. One of the geotechnical materials that can be used for producing artificial material is kaolin clay.

Kaolin clay is a versatile material that has a wide range of uses. It has been utilesed in wide range various industries such as : ceramic, cement, fiberglass, paint, paper filling/coating, rubber, plastic, pharmacy, textiles, detergent, and even cosmetics [1]. In geotechnical engineering, kaolin clay has been used for slope stabilization and erosion protection [2] and as a barrier for waste disposal facility. The extensive use of kaolin clay is due to its unique properties.

This paper presents the use of artificial material for laboratory soil testing made from sand-kaolin clay mixture in different proportion. The characteristic of the material is presented in term of physical and engineering properties of the material resulted from the test. A brief of each material characteristic; sand and kaolin clay is firstly described, followed by the description of new artificial material of sand-kaolin clay mixture.

THE PROPERTY OF SAND AND KAOLIN CLAY

The Properties of Sand

The most important physical characteristic of sand is particle size distribution and particle shape. The distribution alse affects the engineering properties. Other influencing factors are density, particle arrangement and isotrophy [3]. Poorly graded sand tends to have a narrower range of density compared to well-graded sand. Particle size distribution can also affect the properties of sand. The increase in the range of particle size (increase in the coefficient of uniformity,*Cu*) causes a decrease in void ratio.

In terms of strength and compressibilty, sand has relatively beneficial engineering properties compared to clay. It has high internal friction, low compressibility, non-plasticity, low swell-shrinkage potential, and in general, the behaviour of sand is rarely affected by water content. A small amount of cohesion may be generated through the capillary tension among the particles, due to the presence of water. The increase in moisture content, to some extent, can cause this increase in cohesion. With the increment of moisture, cohesion also increases significantly. However, when the moisture content reaches a certain value, cohesion will decrease and even disappear when a saturated condition is reached [4].

The shape of the particles also strongly influence the engineering properties of sand. The shape can be angular, sub angular, rounded or semi-rounded. The compaction result of sand containing angular particles tends to be less dense when compared to sand with rounded particles. For ideal uniform-size spherical particles, five different possible packing arrangements are proposed; (a) simple cubic, (b) cubic tetrahedral, (c) tetragonal sphenoidal, (d) pyramidal, and (e) tetrahedral. Simple cubic packing has the loosest stability and highest void ratio of 0.91, whereas tetrahedral packing has the densest arrangement and the lowest void ratio of 0.34.

The Properties of Kaolin Clay

The shape of kaolin clay particle is platy crystal with the length of particle being 0.2 μm to 2 μm with a thickness of 0.05 μm to 0.2 μm. Amongst other clay minerals, kaolin is a mineral with the largest particle size. Kaolin clay is categorized as a silicate mineral. Kaolin clay is one of the minerals in the kaolin group including haloysite, dickite, and nacrite. Theoretically, the main components of kaolin are alumina (Al_2O_3), silica (SiO_2), and water. Kaolin clay consists of alternating layers of one silica tetrahedral sheet and one alumina octahedral (or gibbsite) sheet tied with oxygens and hydroxyls. The common molecule formula for kaolin is $Al_2Si_2O_5(OH_4)$. Table 1 shows the typical results from chemical analyses of different sources of kaolin clay from Georgia, England, and with from Unimin Pty Ltd, Australia.

Table 1 Typical chemical analysis of kaolin clay [1] and [5]

Component (%)	Georgia	England	Unimin Australia
SiO_2	45.3	46.77	49.2
Al_2O_3	38.38	37.79	39.4
Fe_2O_3	0.3	0.56	1.01
TiO_2	1.44	0.02	0.935
MgO	0.25	0.24	0.358
CaO	0.05	0.13	0.51
Na_2O	0.27	0.05	< DL
K_2O	0.04	1.49	0.18

Compared to other clay (montmorillonite and attapulgite), kaolin clay has relatively better properties. It has lowest liquid limit, plastic limit, and activity. Active clay has a high water holding capacity, high compaction under load, high cation exchange capacity, low permeability, and low shear resistance. Therefore, very active soils can be problematic for engineers [6]. The presence of certain types of clay mineral in the soil affects its engineering properties. Soil with a high activity has high swelling when wetted and high shrinkage when dried. Activity can also be used for predicting the amount of clay fraction in the soil and is a very useful indicator for predicting the swelling/shrinkage potential of soil. Conversely, inactive soils may not cause problems for engineers, as it has little cohesion. The strength of inactive soil is mainly caused by internal friction.

PREVIOUS STUDIES ON SAND-KAOLIN CLAY MIXTURE

The effects of kaolin clay content of sand-kaolin clay mixture plus water on the void ratio with the different proportion of the mixtures has been studied [7]. The mixtures were also compacted using a static load. The results indicated that for narrowly graded fine sand, the increase in kaolin clay content led to the decreased in void ratio. However, for coarsed-finesand, the increase in kaolin clay to some extent led to a decrease in void ratio.

In addition to the study, the investigatios has also been conducted to understan the effect of kaolin clay content with different water content on the unconfined compression strength. The results indicated that with a certain water content, the increase in kaolin clay content led to an increase in strength. The results also showed that an increase in water content in the mixture caused a decrease in strength [8].

Sand-kaolin clay mixtures have also been studied by other researchers [9]. They used three different compacted sand-kaolin clay mixtures of 0%, 5%, 10% and 30% to investigate the effects of kaolin clay content on the hydraulic conductivity of the mixtures. They conculed that the increase in kaolin clay content causes the increase in hydraulic conductivity.

Some other studies concerning the engineering properties of sand-kaolin clay mixture have been conducted by several investigators [10]-[15]. However, the information about this mixture is still relatively rare and more studies are required.

TESTING PROGRAM

This study was emphasized on laboratory test for obtaining the physical and engineering properties of sand-kaolin clay mixture in different proportions, starting from index properties (gradation, atterberg limits, classification), continued by compaction characteristic, shear strength, and California Bearing Ration (CBR). To understand the effect of unsaturated condition on the mixture, the measurement of suction was also studied. Note that chemical properties test was not conducted in this study.

RESULTS

The Effect of Kaolin Clay on Index Properties

The mixture of two or more materials with different index properties may produce a material with new properties. The index property analysis on the new material was required to determine its properties. Fig 1 shows the gradation curve of sand, kaolin clay, and sand-kaolin cay mixtures.

Atterberg limits tests were also performed. The results indicated that the increase in kaolin content caused a decrease in the liquid limit and plasticity index respectively. The classification system was the performed on the new materials according to ASTM D 2487. Due to the addition of a proportion of kaolin clay to the sand, the group of specimens altered from poorly-graded sand (SP) for sand and 95:5, poorly graded sand with clay (SC-SM) for 90:10, clayey sand (SC) for 80:20 and 60:40 mixtures, and High plasticity clay (CH) for kaolin clay. Based on plasticity, the sand and 95:5 mixtures were categorized as non-plastic specimens, whereas the rest were low-plastic specimens. The summary of index properties of the mixtures is presented in Table 1.

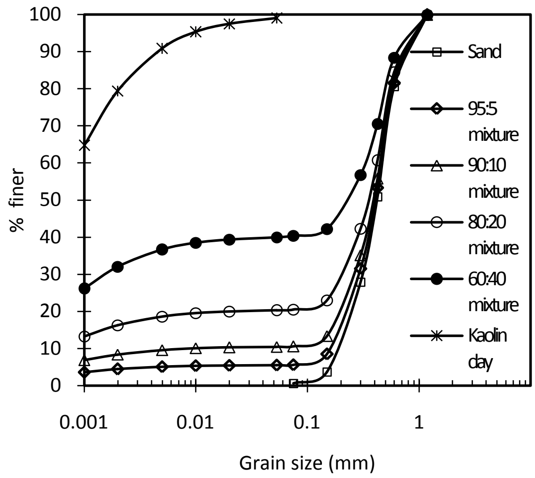

Fig. 1 Gradation curves of different mixtures

Table 2 Index properties of mixtures

Specimen	Gs	LL	PL	PI	Class.
Sand	2.63	N.A	N.A	N.P	SP
95:5 mix	2.63	N.A	N.A	N.P	SP
90:10 mix	2.63	21.3	15.4	5.9	SC-SM
80:20 mix	2.62	26.6	16.7	11.3	SC
60:40 mix	2.60	33	20	13	SC
Kaolin	2.58	58	31	27	CH

Effect of Kaolin Clay on Compaction Result

Standard Proctor test has been conducted on the aforementioned specimens. The result was presented as shown in Fig 2. For the poorly graded sand, the density due to compaction was mainly caused by rearrangement of the particles. During compaction, the particles of sand move to find the best position. The voids become narrower and the specimen becomes denser and more compact. However, due to the lack of smaller particles, the pore spaces in poorly graded sand remain relatively unfilled. Assuming that the particles of poorly graded sand are uniform and round, the packing arrangement of the specimens may be close to one of packing arrangements proposed in [3].

It can be assumed that to some extent (up to 20%), the increase in kaolin clay content would cause the increase in dry density and the decrease in void ratio. However, the void ratio starts to increase when the kaolin clay content of the mixture was > 20 %. This result is in accordance with the results in [7]. It can be concluded that the addition of kaolin clay to sand to some extent could produce a new material with better properties.

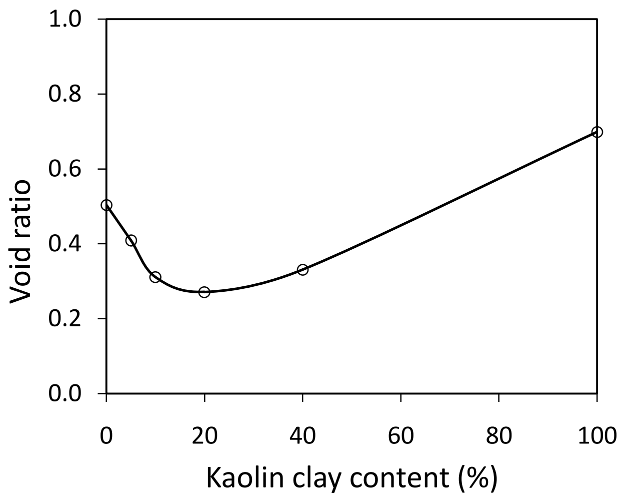

Fig. 2 Curve showing the effect of kaolin clay on void ratio

Effect of Kaolin Clay on Shear Strength

A series of direct shear test on saturated specimens was performed to obtain the effective shear strength parameters (c' and ϕ') for all mixtures. Three different normal forces of 4 kg, 14 kg, and 24 kg were given to each mixture to impose an initial normal stress of 11.2 kPa, 39.2 kPa, and 67.1 kPa. During shear, this normal stress changes due to the change in the shearing area of the sample.

The effect of kaolin clay on shear strength of saturated direct shear test of compacted samples of sand and sand-kaolin clay mixture is shown in Fig 3. A brief description on this figure has been published by authors in [15]. It can be observed that the presence of kaolin clay in the mixture contributes to the increase of cohesion. Note that the test on 60:40 mixture and kaolin clay specimens was not conducted due to the specimen condition. The higher content of kaolin clay would cause to the consistence of the mixture to be softer.

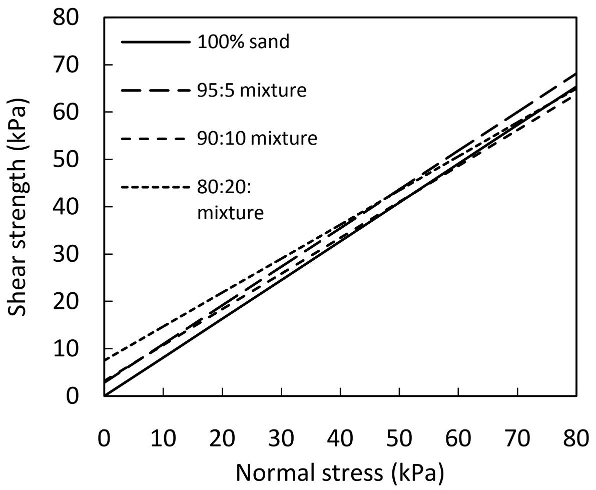

Fig 3 Failure envelopes of sand-kaolin clay mixtures as previously presented by authors in [15]

During direct shear test, sand exhibits hardening behaviour until peak value, followed by softening. The behaviour of cohesionless soil under direct shear testing is dependent on the compactness of the soil. For dense and medium sand, the shear stress increases with shear displacement to a peak value, and then decreases to an approximate constant value. For loose sand, shear stress increases with shear displacement and then remains relatively constant up until ultimate value is reached.

For 95:5 mixture, the strain hardening behaviour was taking place, starting from zero displacement to displacement at peak stress, followed by strain softening behaviour until a residual value was reached. The lowest dilation was experienced by the specimen when the normal stress of 67.1 kPa was applied, whereas the highest was when the normal stress of 11.2 was imposed. In general, the higher the normal stress, the lower the dilation. The similar (strain hardening and dilation) behaviour was also taking place in 90:10 and 80:20 mixture.

The behaviour of the specimen during the test determines the shear strength parameters. Due to limited space in this paper, the stress and strain behaviour during direct shear test is not presented. The parameters resulted from the test are presented in Table 3.

Table 3 Cohesion and internal friction angle of mixtures

Specimen	c' (kPa)	ϕ' (^{o})	Note
Sand	0	39.3	Saturated
95:5 mix	2.86	39.2	Saturated
90:10 mix	3.21	37.1	Saturated
80:20 mix	7.54	35.7	Saturated
60:40 mix	-	-	Not conducted
Kaolin	-	-	Not conducted

The Effect of Kaolin Clay on the CBR

A series of CBR tests were performed on the sand-kaolin mixture with the same proportions as the specimens in the direct shear test. The tests were carried out on soaked and unsoaked specimens. The procedure for test was conducted in reference to the ASTM D 1883-07. According to this standard, the CBR test can be performed on the specimen either in soaked or unsoaked conditions. The result of CBR test is presented in Table 4.

Table 4 Soaked and unsoaed CBR value of mixtures

Specimen	CBR		Note
	Soaked	Unsoaked	
Sand	13	13	
95:5 mix	11	12	
90:10 mix	19	25	
80:20 mix	20	40	
60:40 mix	-	-	Not conducted
Kaolin	-	-	Not conducted

It can be observed that the values of CBR are typically similar to that the result of compaction. The increase in kaolin clay to some extent (up to 20 % kaolin clay content) contributes to the increase in soaked and unsoaked CBR. Note that due to the same reason as direct shear test, the CBR test for 60:40 mixtures and kaolin clay was not conducted. However it can be easily predicted that their value might **be** relatively low.

CONCLUSION

The use of sand-kaolin clay mixture as artificial material for laboratory soil testing has been described. The behaviour of material was determined by their proportion. The low cohesion, no plasticity, and high internal friction possessed by sand mixed with the high cohesion, high plasticity, and low internal friction possessed by kaolin clay produce a new material. The desired new properties are obtained by changing the proportion of sand-kaolin clay mixture. The index properties, compaction characteristic, shear strength properties, and CBR results were presented. It can be concluded that sand-kaolin clay mixture is suitable material for geotechnical laboratory test.

ACKNOWLEDGEMENTS

The writers gratefully acknowledge the Indonesian Ministry of Education for providing funds through the DIKTI Scholarship Project.

REFERENCES

[1] Murray HH, "Overview-clay mineral application", Applied Clay Science, 5, 1991, pp. 379-395.

[2] Jotisankasa A, Sawangsurriya A, Booncharoenpanich P and Soralump S, "Influence of kaolin mixture on unsaturated shear strength of decomposed granitic silty sand", Unsaturated Soils: Research and Applications. Springer, 2012, pp. 385-390.

[3] Mitchell JK and Soga K, "Fundamentals of Soil Behavior", New Jersey, John Wiley and Sons, 2005.

[4] Wu A and Sun Y, "Granular Dynamic Theory and Its Applications", Beijing, Metallurgycal Industry Press, 2008.

[5] Shankar P, Teo J, Leong YK, Fourie A. and Fahey, M, 2010. "Adsorbed phosphate additives for interrogating the nature of interparticles forces in kaolin clay slurries via rheological yield stress", Advanced Powder Technology, 21(4), 2010, pp. 380-385.

[6] Grim RE, "Applied Clay Mineralogy", New York, Mc Graw-Hill Company Inc., 1962.

[7] Mullins CE and Panayiotopoulos KP, "Compaction and shrinkage of sands and sand-kaolin mixtures", Soil & Tillage Research, 4, 1984, pp. 191-198.

[8] Mullins CE, and Panayiotopoulos KP, "The strength of unsaturated mixtures of sand and kaolin and concept of effective stress", Journal of Soil Science, 35, 1984, pp. 459-468.

[9] Chiu TF and Shackelford CD, "Unsaturated hydraulic conductivity of compacted sand-kaolin mixtures", Journal of Geotechnical and Geoenvironmental Engineering, 124(2), 1998, pp.160-170.

[10] Frenkel H and Levy GJ, "Clay dispersion on hydraulic conductivity of clay-sand mixtures as affected by addition of various anions", Clay and Clay Minerals, 40(5), 1992, pp. 515-521.

[11] Boutin C, Kacprzak G and Thiep D, "Compressibility and permeability of sand-kaolin mixtures. Experiments versus non-linear homogenization schemes", International Journal for Numeric and Analytical Methods in Geomechanics, 2011, pp. 35: 21-52.

[12] Jigheh HS and Zare C, "Mechanical behaviour of over consolidated clay-sand mixtures", Journal of Civil Engineering and Urbanism, 2(1), 2012, pp. 40-44.

[13] Purwana YM, Nikraz H, "Experimental Study of Suction-Monitored CBR test on Sand-kaolin Clay Mixture", Int'l Journal of Geomate Vol 3 No.2, 2012, pp. 419-422.

[14] Purwana YM, Nikraz H, "The Correlation between the CBR and Shear Strength in Unsaturated Soil Conditions", Int'l Journal of Transportation Engineering, 2013, p 211-222.

[15] Purwana YM, Chegenizadeh A, Nikraz H, "Suction-monitored direct shear apparatus: a simple device for unsaturated soil testing", Australian Geomechanics 48 (3), 2013, pp. 129-139

Fifth International Conference on Geotechnique, Construction Materials and Environment, Osaka, Japan, Nov. 16-18, 2015, ISBN: 978-4-9905958-4-5 C3051

ESTIMATING UREASE ACTIVITY IN MICROORGANISM OF PEAT BASED ON ELECTRIC CONDUCTIVITY

Atsuko Sato[1], Satoru Kawasaki[2], Toshiro Hata[3] and Takahiro Yamanashi[1]
[1] Civil Engineering Research Institute for Cold Region, Japan; [2] Hokkaido University, Japan;
[3] Toyama Prefectural University, Japan

ABSTRACT

Peaty soil is widely distributed in Hokkaido. Untreated soil is too soft for use as a civil engineering material. Soil solidification improvement technologies that harness the metabolism of microbes in soil has recently been gaining attention. Such R&D has proceeded within and beyond Japan. Focus was put on a technology to achieve peat solidification by capitalizing on the ability of microbes that inhabit soil at construction sites to precipitate calcium carbonate, and consideration was given to solidifying peaty soil by harnessing the ability of those microbes. The peaty soil in Hokkaido investigated so far was confirmed to be inhabited by microbes that have urease activity. The degree of that activity, however, was unknown. Therefore, the degree of urease activity was determined based on electric conductivity. The results showed that the degree of urease activity varies depending on the kind of peat and that it is possible to solidify peaty soil without any additional treatment.

Keywords: Urease activity, Peat, Electric Conductivity, Microorganism

INTRODUCTION

Peaty soil, which is widely distributed in Hokkaido, is a highly organic and soft soil that cannot be used as an embankment material without improvement[1) 2)]. Toward developing methods for utilizing peaty soil as a material for civil engineering works, the authors have been studying a soil foundation solidification technology that relies on the urease activity of microorganisms. The authors were able to give extremely soft peaty soil unconfined compressive strength sufficient for easy transport by enhancing its urease activity[3)]. The authors thought it might be possible to predict the solidification potential of peaty soil by measuring the degree of urease activity of such soil. We conducted an experiment that addressed the electrical conductivity of peaty soil. This paper summarizes the results.

SOLIDIFICATION USING THE METABOLISM OF MICROORGANISMS

There are two common methods of soft soil solidification using the metabolism of microorganisms. One utilizes calcium carbonate[4) 5)]; the other utilizes silica[6) 7)]. The calcium carbonate method utilizes the calcium carbonate that precipitates in voids in the soil from the action of microorganisms with urease activity. The soil foundation is solidified by the action of precipitated calcium carbonate, which causes soil particles to adhere to each other. The greater is the urease activity of the microorganisms, the greater is the precipitation of calcium carbonate. The authors decided to estimate the degree of urease activity of microorganisms in the target soil samples, in order to understand the degree of solidification reaction of the soil.

METHOD

The authors focused attention on a method for evaluating the rate of urea hydrolysis[8)] as a technique to estimate the degree of urease activity of the subject peaty soil. In this method, the urease activity is estimated by measuring the electrical conductivity of the peaty soil. The microorganisms were liquid cultured on Christensen citrate agar, and urea solution was mixed in the medium. The rate of urea hydrolysis by the microorganisms was estimated by measuring the electrical conductivity of the solution. However, isolating the microorganisms that enhance solidification of peaty soil requires special knowledge and techniques that have not been considered practical for improving civil engineering materials. Therefore, the authors decided not to isolate the microorganisms but to do experiments for solidifying the peaty soil by using the microorganisms naturally living in the peaty soil. Hata et al.[8)] used a mixture of 10ml of microbe culture solution and 40ml of urea solution to measure electrical conductivity. The authors used a suspension of 10g of peaty soil in 40ml of urea solution for measuring the electrical conductivity of the soil, because the water content of peaty soil is very high. Fig. 1 shows the procedure for measuring the increase in electrical conductivity of the solution.

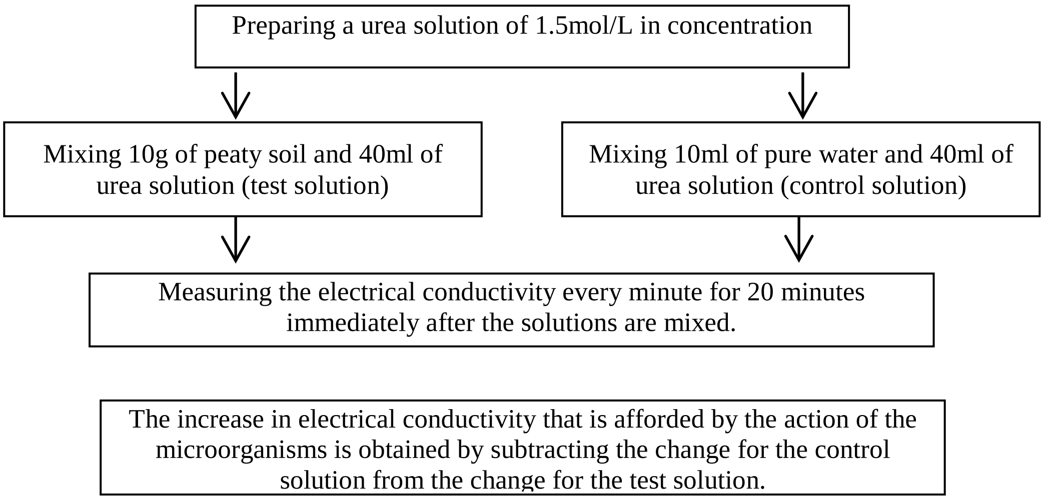

Fig. 1 Procedure for measuring the rate of urea hydrolysis
The figure in Reference #2 was partly modified and simplified.

The peaty soil samples used in the experiment were collected from the Shiribeshi, Ishikari, and Hidaka areas from among the numerous areas in Hokkaido where peaty soil is widely distributed[9]. Table 1 shows the basic properties of the peaty soil samples. Compared with common soil[10], the peaty soil samples are very high in natural water content and ignition loss, and have very small soil particle density. Peaty soil is characterized by low pH. The presence of microorganisms that have urease activity was determined by using Christensen citrate agar[11]. As shown in Fig. 2, all three media turned red. The culture results showed that microorganisms with urease activity live in the tested peaty soil.

Table 1 Basic physical properties of the peaty soil samples

Sample (sampled area)	Iwanai	Ebetsubuto	Tomikawa
Area for sample collection	Shiribeshi	Ishikari	Hidaka
Water content wn (%)	1028.64	545.92	119.55
Soil particle density ρ_s(g/cm^3)	1.557	1.895	2.206
Volatile solids L_i(%)	93.813	56.653	39.007
pH	4.5	4.1	2.5

Fig. 2 Test for urease activity

RESULTS

Conditions of the solutions

A suspension was produced as shown in Fig. 3 when the peaty soil and urea solution were mixed. All the samples from Iwanai, Ebetsubuto, and Tomikawa have a similar appearance. It was found to be possible to measure the electrical conductivity of the samples in this suspension condition.

Estimating urease activity based on electrical conductivity

Fig. 4 shows the relationship between the time after the soil and urea solution were mixed and the increase in electrical conductivity. The large increase in electrical conductivity with the passage of time indicates high urease activity. The increase in electrical conductivity with time is small in the Iwanai and Ebetsubuto samples, which means that the urease activity of these two samples is low. The increase in electrical conductivity with time is great in the Tomikawa sample, which means that the urease activity of this sample is high. The urease activity of the samples varied.

Fig. 4 also shows the data for increase in the electrical conductivity of the samples with *Bacillus pasteurii* and *Sporosarcina aquaimarina*[2]. *Bacillus pasteurii* is a land bacterium, and its effectiveness in ground solidification has been clarified and is used widely in Japan and abroad. *Sporosarcina aquaimarina* is a seawater bacterium with urease activity, whose use in soil solidification has been anticipated. The rate of increase in the electrical conductivity of the soil from Tomikawa was about one-tenth (1/10) that of *Bacillus pasteurii* and about one-fourth (1/4) that of *Sporosarcina aquaimarina*. The microorganisms in the peaty soil of Hokkaido have lower urea activity than that of the above two types of bacteria; however, the soil from Tomikawa has comparatively high urease activity. It is thought that solidification of peaty soil using the metabolism of the indigenous microorganisms is possible.

The Iwanai and Ebetsubuto samples showed relatively small increases in electrical conductivity in a short test. Therefore, their electrical conductivity was measured at 1 hour and 3 days after mixing, which were longer periods after mixing than that of the experiment by Hata et al. The measurement results are shown in Table 2. A slight increase in electrical conductivity was observed in the Ebetsubuto sample. In the Iwanai sample, the electrical conductivity increased by 340μs/cm in

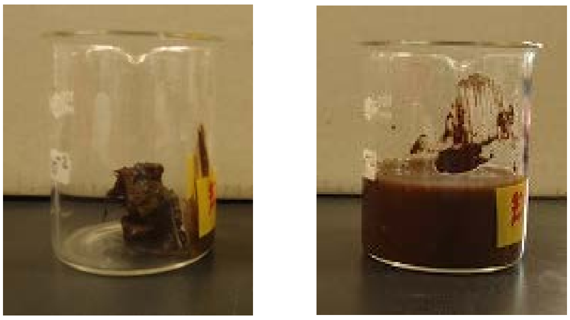

a. Peaty soil
b. Peaty soil after mixing with urea solution

Fig. 3 The appearances of the samples

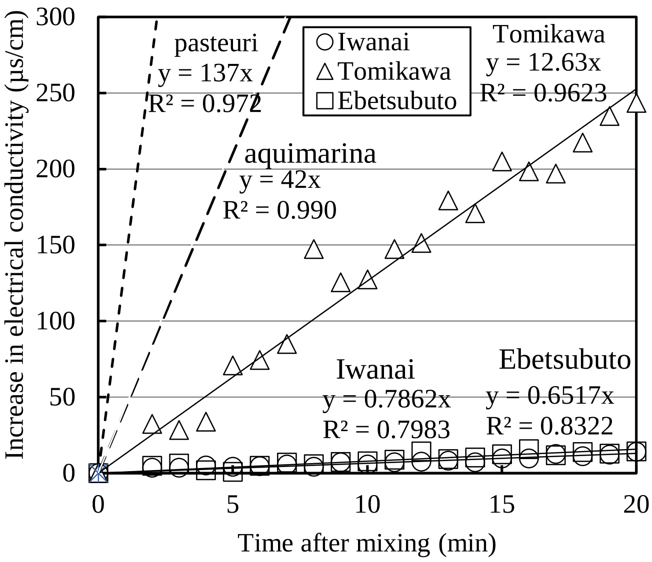

Fig. 4 Time after mixing, and the increase in electrical conductivity

three days. It was thought that by setting a longer time, the solidification of peaty soil by using the metabolism of microorganisms is possible.

CONCLUSION

The following were found as a result of the measurements.
(1) It is possible to measure the electrical conductivity of a sample in suspension without isolating the microorganisms.
(2) Microorganisms with different urease activity live in different types of peaty soil. The urease activity in the peat of Hokkaido was about one-tenth (1/10) that of *Bacillus pasteurii* and about one-fourth (1/4) that of *Sporosarcina aquaimarina*.
(3) There are some peaty soils whose urease activity is low but will increase over a longer period.

REFERENCES

[1] Public Works Research Institute, “The technical manual for recycling construction generated soil (4 th Edition)”, Dec. 2013.
[2] Ministry of the Environment , “Waste Management and Public Cleansing Act”, 1970.
[3] Atsuko Sato, Satoru Kawasaki, Toshiro Hata, and Takahiro Yamanashi, “Experiment for Solidifying Peat using Microorganisms”, Proceedings of the 69th Annual Conference of the Japan Society of Civil Engineers, Jul. 2014.
[4] Toshiro Hata, Reiko Kuwano, Hirofumi Abe, “Fundamental study of in-situ permeability control technique using microbial function”, Journal of Japan Society of Civil Engineers, Ser. G, Vol.64, No.1, pp.168-176, 2008.
[5] Yukiko Inagaki, Masayoshi Tsukamoto, Hirotoshi Mori, Susumu Nakajima, Tetsuya Sasaki, Satoru Kawasaki, “A centrifugal model test of microbial carbonate precipitation as liquefaction countermeasure”, Geotechnical Engineering Journal, Vol.6, No.2, pp.157-167, 2011.
[6] Satoru Kawasaki, Akira Murao, Masami Tsunekawa, Katsuhiko Kaneko, ”Fundamental study on novel grout cementing due to microbial metabolism”, Journal Japan Society of Engineering Geology, Vol.47, No.1, pp.2-12, 2006.
[7] Rei Terajima, Shunsuke Shimada, Tadao Oyama, Satoru Kawasaki,”Fundamental study of siliceous biogrout for eco-friendly soil improvement”, Journal of Japan Society of Civil Engineers, Ser. C, Vol.65, No.1, pp.120-130, 2009.
[8] Toshiro Hata, Tamami Yokoyama, Hiroshi Abe, “Investigation of a soil improvement technique for coastal regions on the basis of calcium carbonate precipitation by using the urea hydrolysis rate”, Japanese Geotechnical Journal, Vol. 8, No. 4, Aug. 2013, pp. 505–515.
[9] Civil Engineering Research Institute for Cold Region, “Manual for Construction on Soft Peaty Ground”, Mar. 2011, pp. 4.
[10] The Japanese Geotechnical Society, “Ground Material Testing Methods”, Nov. 2009.
[11] Toshikazu Sakazaki, Etsuro Yoshizaki, and Kanji Miki, ”In Bacterial Culture Media”, Book I, Kindai Shuppan, 1978.

STUDY OF SPH SIMULATION ON FACE COLLAPSE BEHAVIOUR AND EFFECT OF STABILIZATION METHOD AROUND TUNNEL PORTAL ZONE

T.Matsuo[1], K.Mori[2], N.Hiraoka[2], M.Sun[2], Ha H.Bui[3] and R.Fukagawa[2]

[1] Department of Technical Division, KFC, Ltd., Japan
[2] Department of Civil Engineering, Ritsumeikan University, Japan
[3] Department of Civil Engineering, Monash University, Australia

ABSTRACT

Maintenance measures for tunnel portal zones have attracted increasing interest owing to the increased collapse risk of slopes by severe torrential rain and inland earthquakes in Japan in recent years. However, these large-scale collapse behaviours cannot be simulated by finite difference method (FDM) analysis. In this study, we applied the smoothed particle hydrodynamics (SPH) method to analyse the collapse behaviour of the tunnel face under construction and the effect of the stabilization method. First, we simulated the collapse behaviour at the tunnel portal zone by two-dimensional SPH simulation and compared it with an aluminium-bar experiment, and we showed that the SPH method is effective to model the overall tendency of the large deformation and the collapse behaviour in the experiments. Second, we simulated the collapse behaviour using the SPH method in the real tunnel portal zone collapse and provided a restraint result for collapse using facebolts. Therefore, we demonstrated that the SPH method is an effective technique to evaluate reinforcement measures.

Keywords: SPH, Aluminium-bar experiment, Collapse behaviour, Tunnel face, Tunnel portal zone

INTRODUCTION

Owing to the increased risk of disasters such as torrential rains or inland earthquakes, measures to ensure long-term stability during a tunnel's service life have assumed increasing importance in recent years. However, simulations of large-scale deformation of tunnel portals using the finite element method (FEM) and finite difference method (FDM) have yielded divergent results. Furthermore, an analytical technique to treat deformation from a small to a large scale to evaluate the effect of reinforcement measures remains lacking.

This study clarified the efficiency of the smoothed particle hydrodynamics (SPH) method in modelling the large-scale deformation and collapse behaviour of the tunnel portal zone.

First, we analysed the behaviour of collapse phenomena at the tunnel face using a two-dimensional SPH simulation and compared these results with those of an aluminium bar experiment. These efforts clarified that the SPH method is effective to simulate deformation from a small to a large scale to as well as the collapse behaviour of the tunnel face.

Second, we simulated the collapse behaviour using the SPH method in an example of real portal zone collapse. Furthermore, we proposed a method for analysing the effect of reinforcement measures and verified its effectiveness.

SPH OUTLINE AND SPH APPROXIMATIONS [1-3]

The SPH method is a Lagrangian meshfree method in which particles carry field variables such as mass, density, and stress tensor and move with the material velocity. By using the SPH method, the partial differential equations for the continuum are converted into the equations of motion of these particles. Other grid-based numerical methods such as FEM and FDM suffer from mesh distortion owing to large deformations. In contrast, SPH can handle large deformations, post-failure, and complex geometries very well, and it can model complex free surfaces without any special treatments.

The SPH method has recently been applied to solving large deformations and post-failure behaviour of geomaterials [4-7]. However, it has yet to be applied to the tunnel face collapse behaviour or evaluation of effectiveness of reinforcement measures on face stability.

In the SPH method, the computational domain is modelled using a set of discrete particles. The particles have a kernel function to define their interaction range, which is called the influence domain. The field variables are calculated using an interpolation process over its neighbouring particles located within the influence domain. The interpolation process is based on the integral representation of a field function $f(x)$ as follows:

$$\langle f(x)\rangle = \int_{\Omega} f(x')W(x-x',h)dx' \qquad (1)$$

where x represents the particle location; Ω, the influence domain of the integral; W, the basis function of the approximation, which is called the kernel function; and h, the smoothing length, which defines the influence domain of W. The approximation $\langle\ \rangle$ is called a kernel approximation.

The kernel function W must be chosen to satisfy the following three conditions:

The first one is called the normalization condition:

$$\int_{\Omega} f(x')W(x-x',h)dx' = 1 \qquad (2)$$

The second condition is called the delta function property; it should be satisfied when the smoothing length approaches zero:

$$\lim_{h\to 0} W(x-x',h) = \delta(x-x') \qquad (3)$$

where $\delta(x-x')$ is a delta function

The third condition is called the compact support condition:

$$W(x-x',h) = 0 \quad when\ |x-x'| > kh \qquad (4)$$

where k is a constant which specifies the nonzero region of the kernel function for an interpolation point.

The choice of the kernel function in SPH directly affects the accuracy, efficiency, and stability of the numerical algorithm. Many kernel functions have been proposed for SPH thus far. In this study, we apply the most popular cubic spline function proposed by Monaghan and Lattanzio [8], which has the following form:

$$W_{ij} = \alpha_d \times \begin{cases} 2/3 - R^2 + R^3/2, & 0 \le R < 1 \\ (2-R)^3/6, & 1 \le R < 2 \\ 0, & R \ge 2 \end{cases} \qquad (5)$$

where α_d is the normalization factor, which is $15/(7\pi h^2)$ in two-dimensional space, and R is the normalized distance between particles i and j defined as $R = r/h$. The continuous integral representation (1) can now be discretized as a summation over the particles in the influence domain as follows:

$$\langle f(x)\rangle = \sum_{j=1}^{N} \frac{m_j}{\rho_j} f(x_j)W(x-x_j,h) \qquad (6)$$

where j = 1, 2, …, N indicate particles within the influence domain of the particle at x, the so-called neighbour; m_j and ρ_j are respectively the mass and density of particle j.

Figure 1 shows an approximation of this equation.

The approximation for the spatial derivative $\nabla f(x)$ can be obtained simply by substituting $f(x)$ with $\nabla f(x)$ in equation (1). Integrating by parts and using the divergence theorem gives

$$\langle \nabla f(x)\rangle = \sum_{j=1}^{N} \frac{m_j}{\rho_j} f(x_j)\nabla W(x-x_j,h) \qquad (7)$$

where $\nabla W(x-x_j,h)$ is a spatial derivative of $W(x-x_j,h)$.

Further details of the SPH integration scheme can be found in [3] and [5].

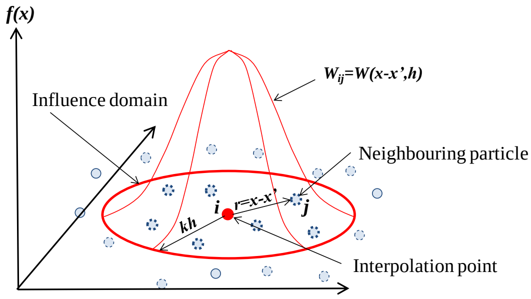

Fig. 1 Image of the SPH interpolation

SPH SIMULATION

Model of aluminium bar-experiment

We tested the behaviour at the time of the collapse of the tunnel face by the two-dimensional model experiment using an aluminium bar and compared it with simulation by SPH analysis. Table 1 shows the experimental conditions.

The tunnel height (D) is 8 cm with aluminium bars of two diameters, 1.6 mm and 3.0 mm, and 50-mm length, and four patterns of overburden, H/D = 1.0, and 2.0, are used.

Figure 2 shows the initial condition of the aluminium bar experiment.

Table 1 Specifications of aluminium bar-experiment

Items	Variable	Values
Total length	L	42 cm
Tunnel length	$L1$	12 cm
Tunnel height	D	8 cm
Overburden	H	8, 16 cm
(Ratio of H/D	H/D)	(1.0), (2.0)

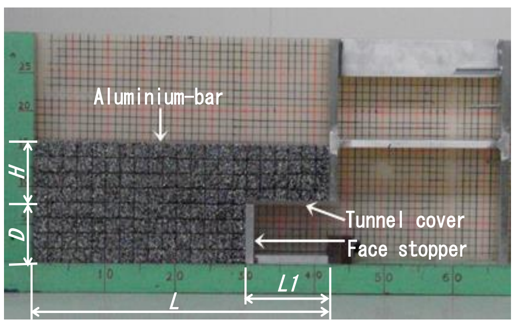

Fig. 2 Initial condition of aluminium bar-experiment (H/D=1.0)

Analysis condition

We used the two-dimensional SPH method with the elastoplastic Drucker-Prager constitutive model and the nonassociated plastic flow rule to reproduce an aluminium bar-experiment. Table 2 shows the specifications of the simulation. The soil parameters, except for the unit weight, were similar to those measured by Umezaki et al. [9]. The unit weight of the soil model is $\gamma = 21.7$ kN/m^3. Figure 3 shows the simulation model.

2280 SPH particles were used to create the model with H/D = 1.0 shown in Fig.3, with an initial smoothing length of 6 mm. Table 2 shows the total number of particles in other cases. Free-roller boundary conditions with ghost particles [10] are used at the left and right ends, and full-fixity using virtual particles [5] are used at the base and tunnel top. The initial stress condition is obtained by applying gravity loading to soil particles [5].

Then, the simulations are started by removing the face wall (A) in the side restriction shown in Fig.3.

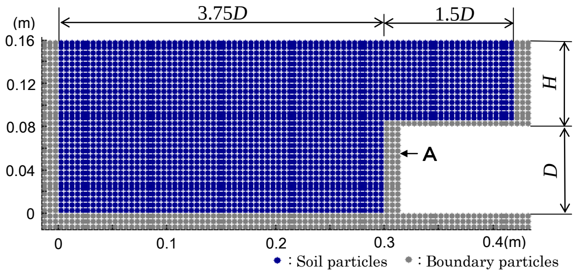

Fig. 3 SPH simulation model (H/D = 1.0)

Table 2 Specifications of SPH simulation

Items	Values
Unit weight	$\gamma = 21.7$ kN/m^3
Young's modulus	E = 5.84 MN/m^2
Poisson's ratio	$\nu = 0.3$
Cohesion	c = 0 kN/m^2
Internal friction angle	$\phi = 21.9°$

Note: Number of SPH particles is 2280 (H/D = 1.0), and 3624 (H/D = 2.0)

Comparison between experiment and SPH simulation

Figure 4 shows a comparison of the final configuration after collapse between the aluminium bar-experiment and simulation for H/D = 1.0 and 2.0. The surface configurations in both the experiment and the SPH simulation shown in Fig.4 are straight for H/D = 1.0 and H/D = 2.0.

The white dotted lines in Fig.4 indicate the boundary between the region of moved soils and nonmoved soils. These lines are equivalent to failure lines. The lines in the experiment and the simulation are similar to a straight line for two H/D values. The failure lines in the experiment are nearly straight for H/D = 1.0 and curved for H/D = 2.0.

These results clearly show that SPH analysis is effective to simulate the collapse of the tunnel face in the aluminium bar-experiment.

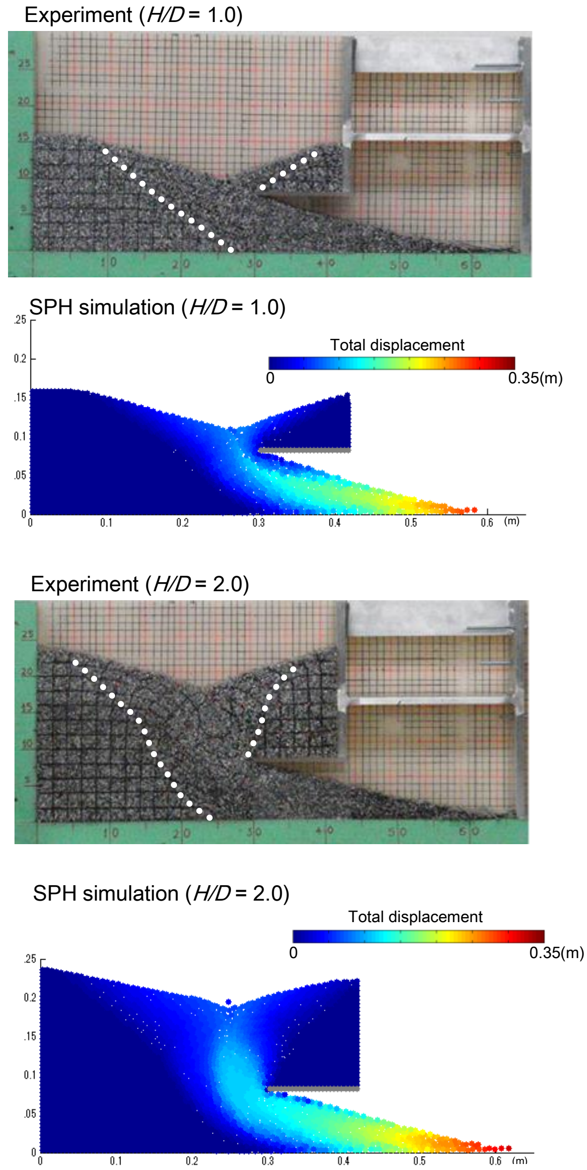

Fig.4 Comparison between SPH simulation and experiment for post-failure behavior

STUDY ON TUNNEL COLLAPSE BY SPH

Collapse process of tunnel

We tried to simulate a tunnel collapse, as shown in Photo 1 for a case of construction during torrential rains in Japan in 1995 [11], and provided a method for examining the efficacy of reinforcement by SPH. In this case, the tunnel and tunnel portal zone slope have collapsed. The geology consists of layers of sandstone, tuff, and mudstone from the Neogene period. The water seeping into the ground owing to heavy rainfall caused the collapse of the tunnel face and the entire portal zone.

Figure 5 shows the collapse mechanism. The collapse process was as follows.

Pl ıel portal zone [11]

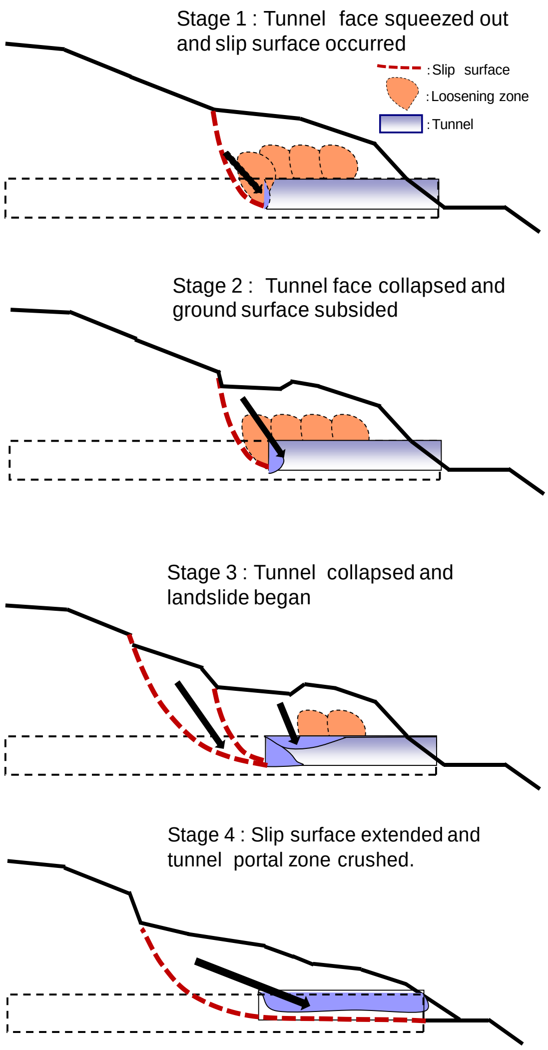

Fig.5 Process of tunnel collapse

Stage 1: The tunnel face squeezed out first and then, cracks were formed. A slip surface occurred at the ground.
Stage 2: Flaking and falling off from the tunnel face and the crown of the tunnel occurred, and large deformation or beginning of failure occurred at the tunnel face. Concurrently, the ground surface subsided vertically.
Stage 3: The tunnel collapsed, and landslide began at the ground surface.
Stage 4: The slip surface extended and the tunnel portal zone was crushed.

SPH Simulation

Figure 6 shows the analytical model and conditions of the SPH simulation. Figure 6 shows the size of the model and the soil parameters. The soil parameters are decided as follows: E, γ, ν, and ϕ values were set as those of soft rock that is common to Japan in reference to the parameters for numerical analysis [12]. Cohesion is decided based on the occurrence of failure through a parametric study by SPH, and this value is equivalent to the case of 10-m thickness of the landslide block [13]. A total of 7477 SPH particles were used to create the model with an initial smoothing length of 0.6 m.

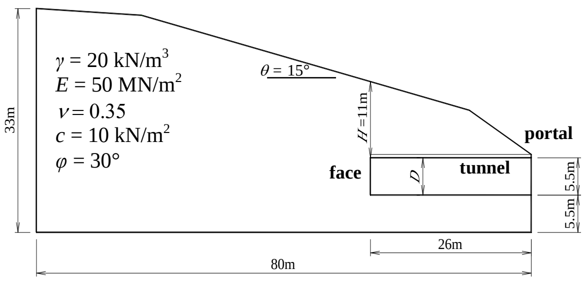

Fig.6 SPH model

Figure 7 shows a contour plot of the accumulated strain at 0.4 s and 0.8 s, which is the time just after the face collapse has started in the SPH simulation. Figure 7 shows that the slip surface extends forward and upward from the bottom of the tunnel face, and the shear band extends from the top of the tunnel at the face to the ground surface vertically.

Figure 8 shows the post-collapse configuration by SPH simulation. Figure 8 shows that the maximum displacement is 6.8 m. It is also obvious that the slip surface extending upward from the top of the tunnel reaches the ground surface, and subsidence occurs. Therefore, a second stage is simulated in the SPH, as shown in Fig.5.

In actual collapse, a landslide is caused by the crushing of the tunnel. In this simulation, the cave-in of the crown is not considered. If we incorporate the conditions under which the cave-in of the crown occurs, it should be possible to simulate the actual phenomena absolutely. However, it suffices to examine the efficacy of a reinforcement for verifying the reproducibility of early collapse behaviour by SPH.

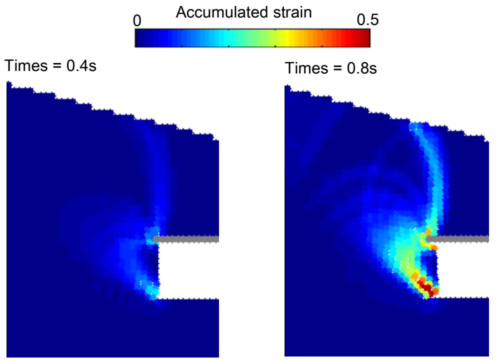

Fig.7 Contour plot of accumulated strain just after the face collapse has started

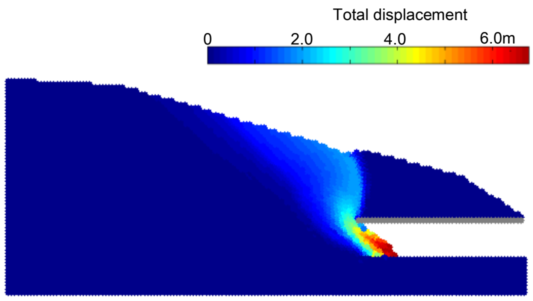

Fig.8 Final configuration after collapse

Analysis of face reinforcement

We modelled the face reinforcement using facebolts of 5-m length from the face.

In this study, we describe the reinforcing works as the equivalent of Young's modulus and the shear strength with the cross-sectional performance of the material and ground. Figure 9 shows a facebolt model and the procedure to evaluate the properties of facebolts as parameters for analysis for the improved ground.

The cross-sectional area A_1 is assumed to be equal to A_0 of 0.5 m^2, which is multiplied by the SPH particle diameter d of 0.5 m and unit width of 1.0 m. E_0 and c_0 are shown in Fig.6. We applied steel pipes with an outer/inner diameter of 76 mm/68 mm, as shown in Fig.9, for facebolts, and their properties are as follows: cross-sectional area A_s is 95 mm^2,Young's modulus E_s is 210 GN/m^2, and shear strength τ_s = 135 MN/m^2. In addition, the distance between the bolts in the width direction a is set to 1.5 m.

According to the equations shown in Fig.9, the equivalent value E_1 is 320 MN/m^2 and c_1 is 180 kN/m^2 for the improved region.

Table 3 shows the analysis case.

Figure 10 shows a contour plot of the relative strain as determined by SPH. Here, the relative strain is one divided by the maximum value of each case. The black particles denote those of the improved particles.

For one bolt, the displacement and strain are large and the tunnel face collapses. On the other hand, the displacements for two and three bolts are comparatively smaller. The time until the deformation converges is relatively short, being less than 1 s, and we could confirm that the face is stable.

However, particles attempt to inflow from the upper part of the tunnel face area, as indicated by a circle, in the case of two bolts. Therefore, three bolts are effective as a reinforcement.

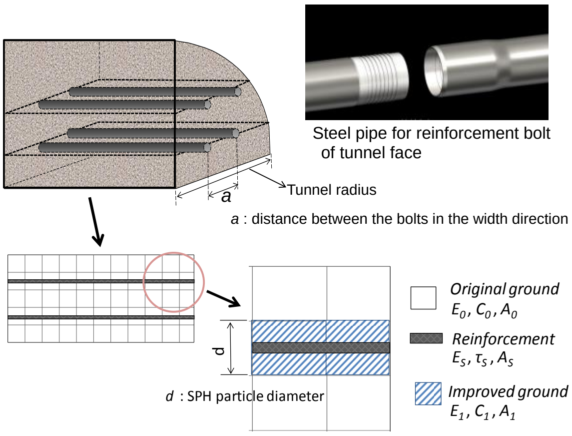

$$E_1 = \Sigma E \cdot A / A_1 = (E_s \cdot A_s / a + E_0 \cdot A_0) / A_1$$
$$c_1 = \Sigma c \cdot d / d = (\tau_s \cdot A_s / a + c_0 \cdot d) / d$$

Fig.9 Model of facebolts

Table 3 Locations of facebolts

Number of bolts	Height from bottom (m)
1	3.8
2	2.3, 4.3
3	1.8, 3.3, 4.8

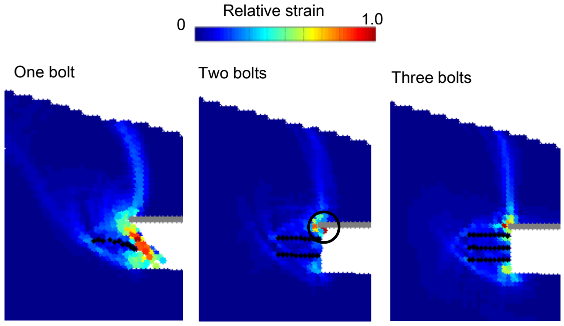

Fig.10 SPH results with facebolts

CONCLUSION

In this study, we applied the SPH method to examine tunnel collapse behaviour.

The results of our study are presented below.

・As an outline of the SPH method, we presented the basic formula of the SPH method and listed some details when this method is applied for simulating the ground deformation.

・Through a model experiment conducted using an aluminium bar and SPH analysis, we simulated the collapse behaviour of the tunnel face and confirmed that the SPH simulation results are consistent with the experimental results. These results clearly demonstrate that SPH can be used to model the two-dimensional tunnel face collapse behaviour.

・We analysed an actual case of collapse in a tunnel portal zone using the SPH method. We clearly demonstrated that the SPH method can sufficiently explain the actual collapse phenomena.

・We modelled a case in which reinforcement works are installed in the tunnel face, and we confirmed the positive effect of this model for improving the stability of the face.

The SPH method used in this study can model large-scale deformations and separation behaviour that are difficult to handle using FEM or FDM and other grid-based continuum models. In addition, this method is easier to apply compared with discrete element model (DEM) and other discontinuum models.

As a future research agenda, we plan to advance further studies on the formulation of three-dimensional models for the detailed assessment and setting of external-force conditions when caused by earthquakes, rainfall, etc..

REFERENCES

[1] Lucy L, "A numerical approach to testing the fission hypothesis", Astonom. J. 82, 1977, pp.1031-1024.

[2] Gingold RA and Monaghan JJ, "Smoothed particle hydro-dynamics theory and application to non spherical stars", Monthly Notices R.-Astronom. Soc.181, 1977, pp.375-389.

[3] Bui HH, Fukagawa R, Sako K and Ohno S, " Lagrangian meshfree particles method (SPH) for large deformation and failure flows of geomaterial using elastic-plastic soil constitutive model" , International Journal for Numerical and Analytical Methods in Geomechanics, 32, 2008, pp.1537-1570.

[4] Maeda K, Sakai H and Sakai M, "Development of seepage failure analysis method of ground with Smoothed Particle Hydrodynamics", Journal of Structual and Earthquake Engineering, JSCE, Division A, Vol.23, No.2, 2006, pp.307-319.

[5] Bui HH, "Lagrangian mesh-free particle method (SPH) for large deformation and post-failure of geomaterials using elasto-plastic soil constitutive models", Ph.D. Dissertation , Ritsumeikan University, Japan, 2007.

[6] Nonoyama H, Sawada K, Moriguchi S, Yashima A and Itoh K, "A 2D SPH simulation for real-scale slope excavation experiment", Journal of JGS, Vol.7No.4,2012, pp.543-555(in Japanese).

[7] Bui HH, Fukagawa R, Sako K, Okamura Y, "Earthquake induced slope failure simulation by SPH", Fifth Intrenational Conference on Recent Advances in Geotechnical Earthquake Engineering and Soil Dynamics, 2010.

[8] Monaghan JJ and Lattanzio JC,""A refined particle method for astrophysical problems", Astronomic and Astrophysics, 149, 1985, p.135.

[9] Umezaki T, Kawamura T and Ochiai H, "Increment of confining pressure due to pullout of reinforcement and modelling of reinforcing mechanics",Geosynthetics Engineering Journal, Vol.120,2005,pp.241-248(in Japanese).

[10] Liversky LD, Petschek AG, Carney TC,Hipp JR and Allahdadi FA, "High strain Lagrangian hydrodynamics: a three dimensional SPH code for dynamic material response" , Journal of Computational Physics, 109, 1993, pp.67-75.

[11] Japan Tunneling Association: "Physiognomy guide for tunneling engineers No.6", Tunnels and undergrounds, Vol.43, No.10, 2012, p.50 (in Japanese).

[12] Japan Railway Construction, Transport, and Technology Agency, "Standard design and construction of mountain tunnel", 2008, p.310 (in Japanese).

[13] Japan Road Association, "Earth works on Road: Guiding principle on slope works and slope stability works", 2013, p.349 (in Japanese).

Fifth International Conference on Geotechnique, Construction Materials and Environment, Osaka, Japan, Nov. 16-18, 2015, ISBN: 978-4-9905958-4-5 C3051

3D PRINTING OF GRANULAR MATERIAL AND ITS APPLICATION IN SOIL MECHANICS

Satoshi Matsumura[1], Takaaki Kobayashi[1] and Takaaki Mizutani[1]
[1]Port and Airport Research Institute, Japan

ABSTRACT

The objective of this study was to quantify the effect of particle arrangement on the macroscopic response of granular materials prepared using 3D printing. We first conducted X-ray computed tomography scanning on a specimen of packed natural gravel. Using these data as a blueprint, replicas of the gravel were created using a 3D printer and a resin-based material. Although the mechanical properties of the printing material differed from those of the natural gravel, the particle arrangement was strictly reproduced. Tri-axial compression tests were performed on both the gravel and its replicas to compare their mechanical responses. In this paper, we first describe the experimental procedures and geometrical reproducibility of 3D printing for granular materials. Then, based on the tri-axial test results, the stress–strain behaviors of the natural gravel and its replicas are compared. Finally, as a challenging application, the effect of the particle arrangement on the macroscopic response is evaluated.

Keywords: 3D printing, X-ray CT, Granular material, Particle arrangement

INTRODUCTION

Soil is composed of granular aggregation, in which the individual particles vary widely in terms of their size, shape, and physical properties. Furthermore, the structural effect of the arrangement of the particles largely affects the macroscopic response of the soil. Thus, any conventional soil tests naturally exhibit scatter because of the variation in the particle arrangement. In this context, soil “element” tests do not exist.

The objective of this study was to quantify the effect of the particle arrangement on the macroscopic response of granular materials prepared using 3D printing. Some prior works have treated the above issue of particle arrangement [1] and applied the 3D printing technique to reproduce individual particles for mechanical tests [2]. In this study, we challenged reconstructing the packing arrangement with individual particles. We first conducted X-ray computed tomography (CT) scanning on a specimen of packed natural gravel. Using these data as a blueprint, replicas of the gravel were created by a 3D printer using a resin-based material. Although the mechanical properties of the printing material differed from those of the natural gravel, the particle arrangement was strictly reproduced. Tri-axial compression tests were performed on both the natural gravel and its replicas to compare their mechanical responses. In this paper, we first describe the experimental procedures and geometrical reproducibility of the 3D printing for granular materials. Then, based on the tri-axial test results, the stress–strain behaviors of the natural gravel and its replicas are compared. Finally, as a challenging application, the effect of the particle arrangement on the macroscopic response is evaluated. The results indicate that not only the packing void ratio but also the particle arrangement significantly affects the macroscopic response of the granular material.

TESTING MATERIALS AND PROCEDURE

Figure 1 presents a flow chart of the experimental procedures used in this study. The main testing processes included X-ray CT scanning and tri-axial compression testing of the original specimen, image processing of the 3D printed tri-axial specimen, and tri-axial compression tests of the 3D printed specimen. The following sections describe each procedure in detail.

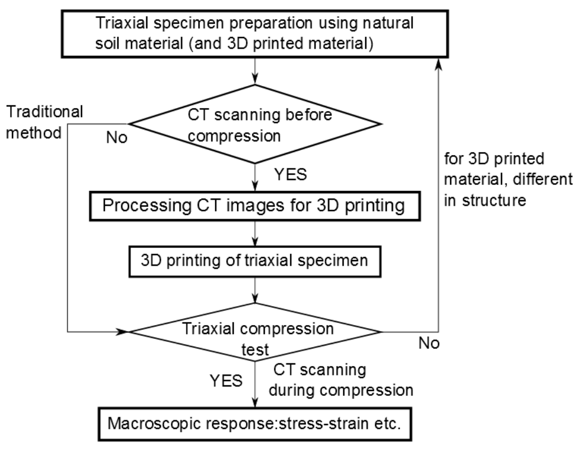

Fig. 1 General scheme of experimental procedure.

a **b**

Fig. 2 Materials used: **a**. gravel and **b**. 3D printed material.

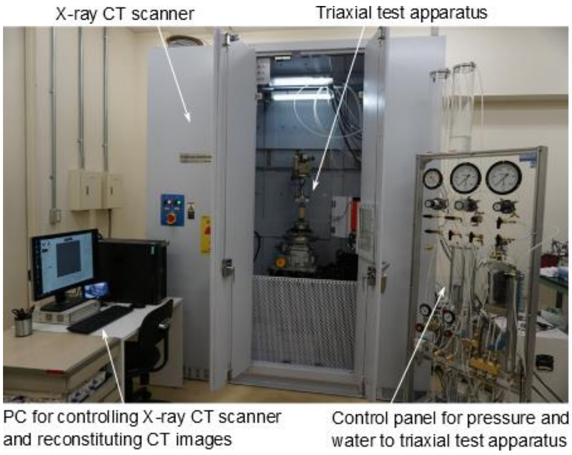

Fig. 3 Overview of X-ray CT scanner with tri-axial test apparatus.

Materials

We used natural gravel with particle sizes ranging from 4.76 mm to 9.5 mm for the prototype specimen of the tri-axial compression tests (50 mm × 100 mm). An image of the gravel is presented in Figure 2a. This relatively large particle size is due to the limitation of the resolution of the X-ray CT and the 3D printer.

Figure 2b also shows the 3D printed material created based on the X-ray CT scanning of the prototype specimen. Note that the printed gravel shown in Figure 2b was loosened after the tri-axial compression tests. The solid densities were 2765 kg/m^3 for the natural gravel and 1105 kg/m^3 for the 3D printed material at 20 °C.

X-ray CT Scanning and Tri-axial Compression Test

Figure 3 presents an overview of the X-ray CT scanner at the Port and Airport Research Institute. The voltage and current of the X-ray tube primarily ranged up to 225 kV and 600 μA. The flat panel for detecting the transmitted X-ray had dimensions of 418 mm × 418 mm, which produces X-ray CT images of 3008 × 3008 pixels at a maximum. Accordingly, the highest spatial resolution is approximately 10 μm. In the figure, the tri-axial test apparatus used is placed on a table. The round table under the apparatus rotates 360°; thus, 3D images can be produced using multiple X-ray scans from different angles.

The pressure and water in the tri-axial test can be controlled outside the X-ray scanner using the control panel, which enables the entire tri-axial compression testing with scanning to be conducted after set-up. Note that processes such as loading must be interrupted during scanning. In this study, we used the tri-axial test apparatus modified for usage in the X-ray scanner. Accordingly, by not equipping the metallic columns, only the acrylic cell bears the reaction to compression. In addition, because the compressive force range was less than approximately 2 kN, we regarded the compressive behavior of the cell as being negligible compared with the compression of the specimen.

The tri-axial compression test using the gravel was conducted as follows. The cylindrical specimen of 50 mm in diameter and 100 mm in height was reconstituted with the oven-dried gravel in the tri-axial mold by tapping. Afterwards, the specimen was consolidated under a total confining pressure of 50 kPa (with no back pressure). Moving the tri-axial apparatus into the X-ray CT scanner, as shown in Fig. 3, the specimen preparation was successfully performed before the X-ray CT scanning and compression.

To obtain the X-ray image of the gravel from which the 3D-printed specimen originated, the specimen was scanned once before loading. In the test, the spatial resolution was approximately 83.8 μm per voxel. After scanning the initial state, the specimen was compressed at a loading rate of 0.1%/min, and the exhausting condition until the axial strain reached approximately 15%.

Image Processing and 3D Printing

The newly installed Agilista-3100 developed by Keyence Corp. at the Port and Airport Research Institute was used as the high-resolution 3D printer in this study. The 3D printer uses UV-cured printing, the principle of which is demonstrated in Figure 4. The 3D printed material is formed by alternating between spraying a UV-curable resin and applying UV radiation. On the outward path from the initial position, the UV-curable resin is sprayed on the stage using the exhaust nozzles from the inkjet head with roller flattening. On the return path, UV radiation is used to harden the material. Using this instrument, the maximum printing area is 297 mm in the x-direction, 210 mm in the y-direction, and 200 mm in the z-direction. The spatial resolutions in the x- and y-directions are 600 and 400 dpi, respectively. Furthermore, in the z-direction, the model material layer can be accumulated at 15 μm per layer at a minimum.

To duplicate the inherent particle arrangement of the soil specimen, the most important feature required of the 3D printer is that the support forming the pore part in the 3D printed specimen can be removed without any external action, e.g., heating or water flow. For the 3D printer, the model and pore parts can be simultaneously and individually reconstructed using two types of resins, i.e., the model material and water-soluble support described as the white and the black areas in the figure, respectively. The water-soluble support can thus melt in the water (specifically, the water in which the same resin as the support material melts to a certain degree) simply by submerging the printed object, as schematically illustrated in Figure 5. In this study, to simplify the post-processing of the 3D printed specimen, we prepared a specimen for which the neighboring particles mutually bond slightly. Thus, the 3D printed specimen can stand alone after the water-soluble support is removed (*see* Figs. 5 and 8b).

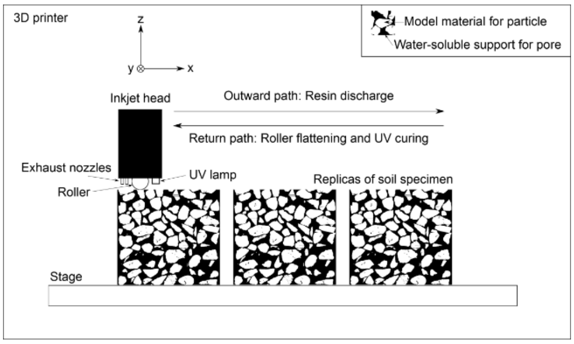

Fig. 4 UV-cured 3D printing using Agilista-3100.

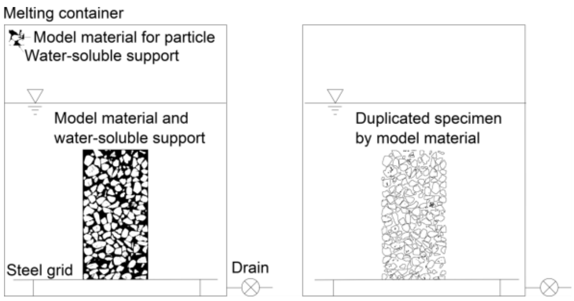

Fig. 5 Post-processing of 3D printed material. (Left) With the water-soluble support shortly after submerging the 3D printed specimen. (Right) The 3D printed specimens without the support after remaining in water for almost five days.

Figure 6 shows the image processing scheme used to make the 3D printing input file. We used "ImageJ" [3] as the image-processing tool. As shown in Fig. 6a, the X-ray scanned and reconstituted image was obtained in grayscale (of 16 bit). To distinguish the particles in the image, first, "threshold" processing was performed (*see* Fig. 6b). Using this process, the solid and pore parts were separated. In this situation, however, the neighboring particles could still bond strongly. Therefore, we employed "watershed" processing to segment the individual particles. This method enabled separation of each particle with different appearance by adding some spatial blanks between particles (*see* Fig. 6c). This figure demonstrates that the particles obviously failed to be segmented; i.e., the particle indicated by the arrow in Fig. 6c was separated into two particles. This error tends to occur for particles that are narrow in the middle. We did not address this error in this study. Finally, Fig. 6d presents an image processed by "erode" after "watershed" processing to shrink the object in the image. The above series of image processing is the result of trial and error between processing the image and actual 3D printing. Because the objective of this study was to duplicate the soil structure, we selected the X-ray CT image processing method that resulted in a 3D printed specimen that was as geometrically and mechanically close to the original gravel specimen as possible.

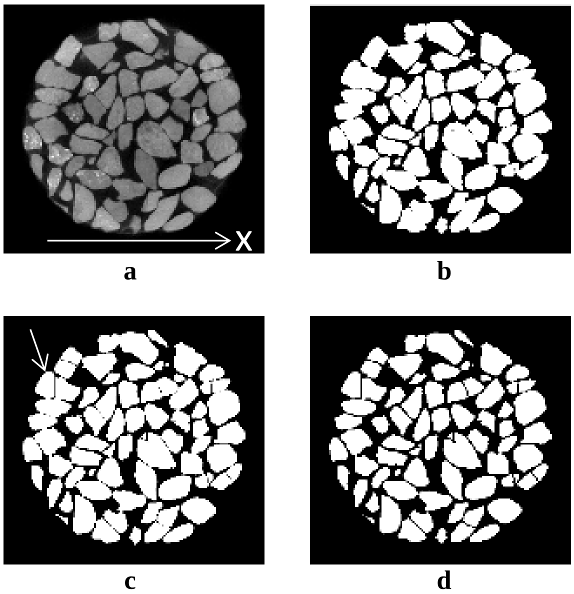

Fig. 6 Image processing for 3D printing: **a**. original image of gravel specimen, **b**. threshold, **c**. watershed, and **d**. erode.

Table 1 Specimen conditions

	Gravel	3D printed material
Soil particle density, kg/m^3	2765	1105
Dry density, kg/m^3	1640	553
Void ratio	0.686	1.008

Note: the soil particle densities were investigated at 20 °C.

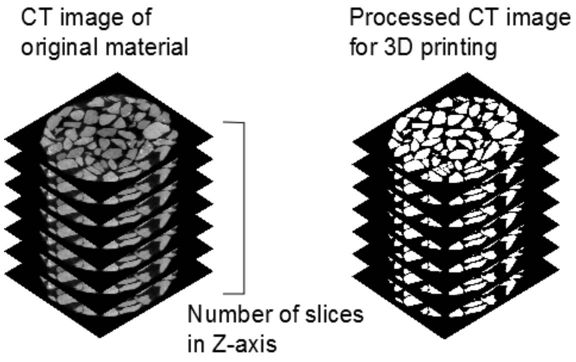

Fig. 7 3D image prepared by accumulating processed 2D images.

a b

Fig. 8 **a**. 3D printing input file and **b**. 3D printed specimen. The sample size is 50 mm in diameter and 100 mm in height, the same as the dimensions of the original gravel specimen.

Table 2 Testing condition of tri-axial specimens. The G-specimens comprised the natural gravel soil. The D-specimens were printed with the soil structure. The DR-specimens were reconstituted by the 3D printed material.

Specimen name, No.	Material used	X-ray CT scanning
G-specimen, No.1	Gravel	Yes
G-specimen, No.2		No
G-specimen, No.3		No
D-specimen, No.1	3D printed material w/ structure	Yes
D-specimen, No.2		Yes
D-specimen, No.3		Yes
DR-specimen, No.1	3D printed material w/o structure	No
DR-specimen, No.2		No
DR-specimen, No.3		No
DR-specimen, No.4		No

In this study, we generated the 3D image for printing by accumulating 2D images processed using the aforementioned method, as illustrated in Figure 7. Figure 8 shows the 3D surface image for printing and the actual 3D printed specimen. Table 1 lists the specimen conditions using the gravel and 3D printed material. The void ratio of the 3D printed specimen was 1.008, which is larger than that of the original gravel specimen. This discrepancy results from the image processing for printing explained above.

Subsequently, we performed tri-axial compression tests using the 3D printed specimen. Unlike the gravel specimen, the 3D printed specimen was set up without tapping in the tri-axial apparatus. The confining pressure and loading rate testing conditions were precisely the same as those used for the gravel specimen. The 3D printed specimen is called “D-specimen,” and the gravel specimen is called “G-specimen”.

Furthermore, to evaluate the effect of the soil structure, i.e., particle arrangement, on the mechanical response, we prepared an additional specimen reconstituted by filling the discrete 3D printed material by tapping. The material was prepared by deforming the D-specimen to make each particle discrete. Then, the void ratio of the specimen, called the “DR-specimen,” was controlled in the same manner as the D-specimen. The tri-axial compression test was conducted in the same manner as for the G- and D-specimens.

RESULTS

We now discuss the geometrical and mechanical properties of the 3D printed specimen based on the X-ray CT scanning and tri-axial test results. Table 2 lists the testing conditions.

Geometrical Property of 3D Printed Specimens

To demonstrate how accurately the soil structure can be reconstructed by 3D printing, Figure 9 presents a comparison of the particle arrangements of G-specimen No. 1 and D-specimens No. 1 to 3 (*see* Table 2). Here, we calculated the angular distribution every 20° in the longitudinal direction of each particle from the x-axis, as shown in Fig. 6a. For the calculation, we selected certain horizontal cross-sections at similar locations, i.e., 2D images, of the above four specimens. The overall tendency of the three D-specimens agrees well with that of the G-specimen. A subtle difference, however, can also be observed, which results from the insufficient accuracy of the image processing explained above rather than that of the 3D printing.

Figure 10 reveals that the content rate of the particles is smaller than the individual particle area, which is plotted along the x-axis. Although the particle areas of the duplicated specimens are consistent with one another, overall, they tend to be smaller than that of the original specimen. This result occurs because the erode processing for the 3D printing shrunk the particles. Thus, from the above simple particle analysis, it can be roughly concluded that 3D printing can duplicate granular material such as gravel.

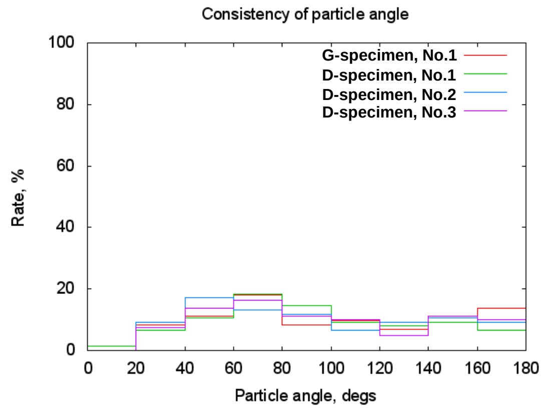

Fig. 9 Particle arrangement distribution. The particle angle was calculated based on the angle of the longitudinal direction from the x-axis shown in Fig. 6a.

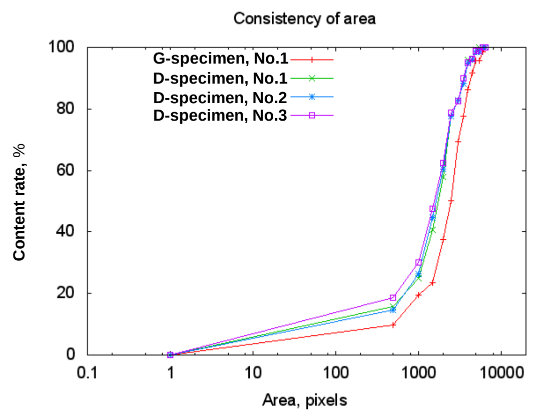

Fig. 10 Particle area distribution. The content rate of the particles is smaller than the individual particle area, which is plotted along the x-axis.

Tri-axial Compression Test Results

Figure 11 presents axial stress–strain curves of the G-, D-, and DR-specimens. The axial stress is calculated as the axial load divided by the initial cross-section area of the specimen because the volume change of the specimen during loading was not measured. Therefore, note that the stress value could contain more variation resulting from the dilatancy behavior at larger strain levels. The figures indicate that the strength and stiffness at lower strain levels of the G-specimens were both slightly higher than those of the D- and DR-specimens. In addition, the axial stress begins to fluctuate with the evolution of the axial stress. These results imply that the difference in the material—particularly, the microscopic surface friction—can be significant in exerting shear resistance even though the particle size and arrangement are duplicated similarly by the 3D printing.

In addition, the effect of the particle arrangement on the stress–strain curves is apparent. Compared with the D-specimens, for which the soil structure was duplicated for three tests, the results of the DR-specimens vary more widely. This tendency is likely to be more conspicuous for the behavior at lower strain, less than approximately 4%. In terms of these two types of specimens, because the difference is supposed to indicate only whether the duplicated structure was maintained before the axial compression, the results varying widely can be attributed to the effect of the particle arrangement.

To quantify the variation of the stress–strain curves, Figure 12 shows the relation between the resulting axial stress and the mean values of three (or four) specimens for every 0.1% of axial strain. In the figure, dashed lines representing 0.8–1.2 times the mean value are also included. From the figures, the axial stress of the G- and DR-specimens, which were reconstituted in the same manner for each uniform void ratio but with different particle arrangements, widely change from 10%–20% versus the mean value. Furthermore, this trend appears to be significant at lower stress–strain levels. In addition, little variation of the D-specimens was observed. Thus, although only three (or four) specimens were tested, the D-specimens repeated the particle arrangement result in almost the same macroscopic response against the compression. This result implies that the 3D printing technique accompanied by X-ray CT scanning enables the net effect of the soil structure on the mechanical properties of the soil to be quantified.

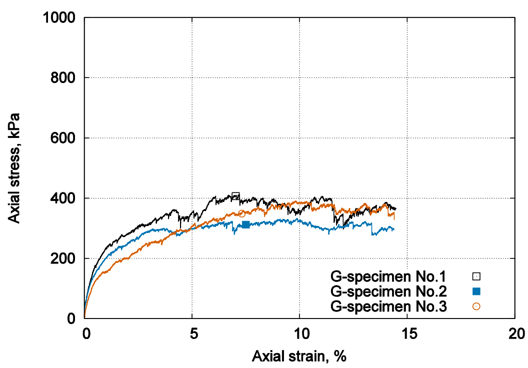

a

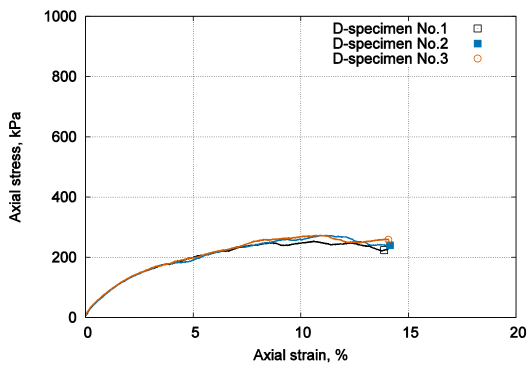

b

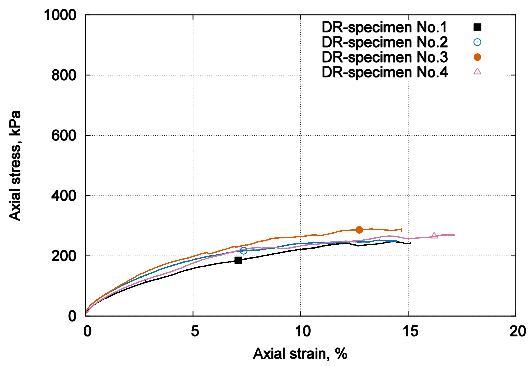

c

Fig. 11 Axial stress–strain curves: **a**. G-specimens, **b**. D-specimens, and **c**. DR-specimens.

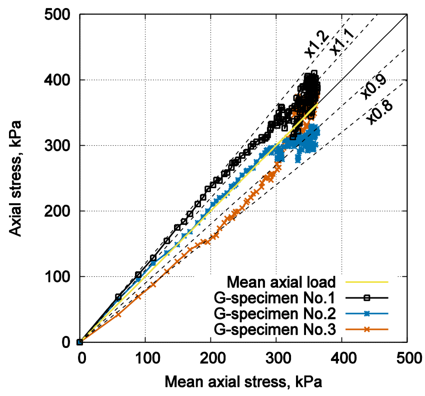

a

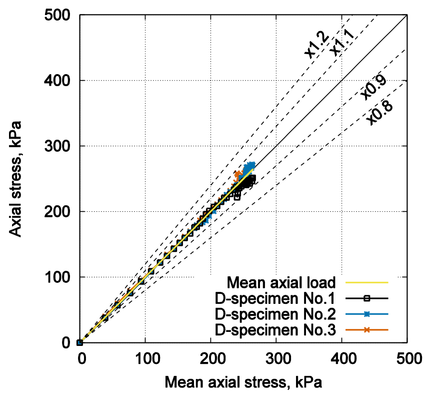

b

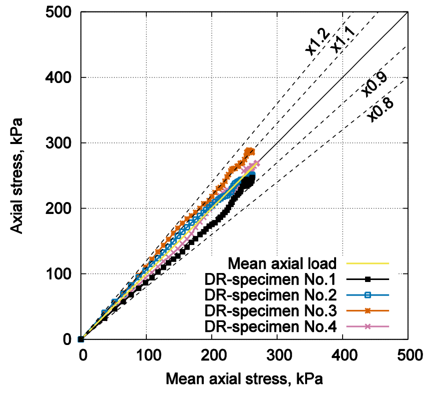

c

Fig. 12 Variation of stress due to soil structure: **a**. G-specimens, **b**. D-specimens, and **c** DR-specimens.

CONCLUSION

To quantify the effect of the soil structure, i.e., the particle arrangement, on the macroscopic response of the soil, we attempted to produce replicas of the granular material using X-ray CT scanning and 3D printing followed by tri-axial compression tests. Based on the image analysis and resulting stress–strain relations, we conclude that this approach can duplicate the granular material as a cylindrical mass with the same soil structure as that of the original. Furthermore, we emphasize that even though the granular specimen can be reconstituted at the same packing void ratio in the same manner that is usually been performed, the difference in particle arrangement causes the mechanical response to vary more widely.

ACKNOWLEDGEMENTS

This work was supported by JSPS KAKENHI Grant Number 15K14034.

REFERENCES

[1] Oda, M.: Initial fabrics and their relations to mechanical properties of granular material, *Soils and Foundations*, Vol.12, No.1, pp.17-36, 1972.

[2] Marc Z. Miskin and Heinrich M. Jaeger: Adapting granular materials through artificial evolution, *NATURE MATERIALS*, Vol. 12, pp.326-331, 2013.

[3] Rasband, W.S.: ImageJ, U. S. National Institutes of Health, Bethesda, Maryland, USA, http://imagej.nih.gov/ij/, 1997-2015.

Fifth International Conference on Geotechnique, Construction Materials and Environment, Osaka, Japan, Nov. 16-18, 2015, ISBN: 978-4-9905958-4-5 C3051

EFFECT OF SOIL MOISTURE CONDITIONS ON SEISMIC STABILITY OF EMBANKMENT SLOPE

Koichi Sumi[1], Nobutaka Hiraoka[2], Masamitsu Fujimoto[3] and Ryoichi Fukagawa[3]
[1] Graduate School of Science and Engineering, Ritsumeikan University, Japan
[2] Research Organization of Science and Technology, Ritsumeikan University, Japan
[3] College of Science and Engineering, Ritsumeikan University, Japan

ABSTRACT

Recent studies on sediment disasters have pointed out that slope failure due to earthquakes was affected by antecedent precipitation before the earthquake. Here, we focus on the variation in soil moisture conditions due to antecedent rainfall for slope failure due to earthquake. To clarify the relationship between the difference in volumetric water content of soil conditions due to elapsed time after rainfall and the scale of slope failure, we conducted a series of vibration loading experiments under different soil moisture conditions. In the experiments, 'rainfall' was applied to the model slope using an artificial rain simulator, and the model slope was subjected to seismic wave loading using a shaking table. Soil moisture sensors and laser displacement sensors were used to measure the volumetric water content of soil and displacement of the slope, respectively. The results indicated that the top of slope collapsed and, eventually, sliding failure occurred when the volumetric water content of soil was low. The crest of the model slope settled down considerably without eroding the sliding surface when the volumetric water content of soil was high. Our study indicated that the soil moisture distribution has a significant influence on the scale of slope failure.

Keywords: Slope Failure, Antecedent Rainfall, Vibration Loading Experiments, Sliding Failure

INTRODUCTION

Many slope failures happen in Japan every year and inflict enormous damage. Rainfall and seismic movements are major factors in slope failures. Previous studies examined the topographic effects on landslides triggered by earthquakes [1]-[3] and proposed a prediction method for risk assessment of seismic slope failure in mountainous area based on local topographical and mechanical conditions [4]. Although these studies pointed out the potential effects of topography and geology on seismic slope failure, they did not focus on the influences of soil moisture on seismic responses and the damage to embankment slopes due to the earthquake. The Niigata Chuetsu earthquake in 2004 was an example where soil moisture and groundwater conditions affected the slope failure. Reference [5] reported that the soil moisture and groundwater conditions were significant factors in controlling the strength of the slope in seismic slope failures and the movement of colluvial soils after the collapse. However, few studies have investigated the effects of soil moisture (groundwater) conditions on seismicity by *in situ* measurements [6] or laboratory experiments [7], [8].

In this study, we focused on variation in soil moisture conditions due to antecedent rainfall. We also conducted a series of loading experiments under different soil moisture conditions to clarify the relationship between the variation in volumetric water content of soil conditions and seismic slope failures.

EXPERIMENTS

Experimental Methods

We focused on the relationship between soil moisture conditions and the displacement of a model slope. Experiments were conducted using an artificial rain simulator (Daiki Rika Kogyo Co., Ltd., DIK-6000S) and a shaking table (Shinken Co., Ltd., G-9210). We made a model slope with granite soil (Masa soil) in a tank. Table 1 shows the properties of the soil. We provided vibration loading to the slope model via the shaking table after artificial rainfall and examined the failure configuration. In order to clarify the collapse processes, we took videos during the vibration loading experiments. A stainless steel tank, 100 cm long, 60 cm wide, and 70 cm high, was mounted on top of the shaking table. Figure 1 shows an image of the model slope and measurement points of soil moisture and displacement. The size of model slope was 65.6cm long, 60cm wide, and 40cm high. Ten soil moisture sensors (Decagon Devices, S-SMx-M005) were used to measure the variation in volumetric water content of soil and six laser displacement sensors (Micro Epsilon, ILD1300-200) were used to measure the displacement of a model slope. The vertical and horizontal displacements were measured by the laser displacement sensors of SV1-3 and SH1-3, respectively.

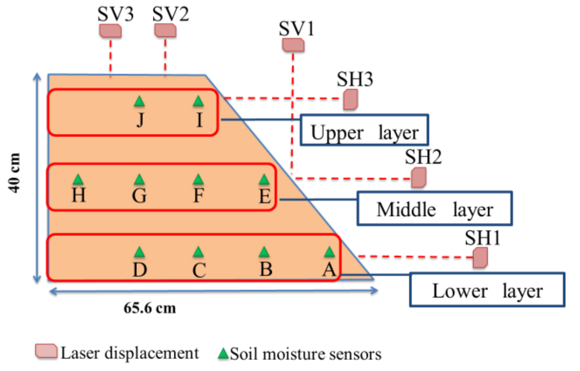

Fig. 1 Schematic figure of the embankment and the measurement points

Table 1 Properties of the Masa soil

Relative density, D_r	78%
Initial moisture content, w	10%
Dry density, ρ_d	1.60g/cm^3
Wet density, ρ_t	1.76g/cm^3
Coefficient of permeability, k	2.09×10^{-5}m/s
Void ratio, e	0.631
Porosity, n	38.7%

Experimental Conditions

In this study, six case experiments were conducted. Table 2 shows the rainfall conditions. We set a different elapsed time from the end of the artificial rainfall to provide the loading for creating differences in the volumetric water content of soil. In all experiments, the rainfall intensity was maintained at 30 mm/h. For the rainfall duration, it was 1 h in Cases 1-3 and 3 h in Cases 4-6. The bottom, rear, and the sides of the tank were undrained and the slope angle was set at 50°. Figure 2 shows waveform of acceleration. Maximum acceleration was set for about 600 gal and the frequency was set at 5 Hz.

Table 2 Experimental conditions

	Amount of rainfall per hour	Rainfall duration	Elapsed time after rainfall
Case1	30mm/h	1hour	no time
Case2			1hour
Case3			1day
Case4		3hour	no time
Case5			1hour
Case6			1day

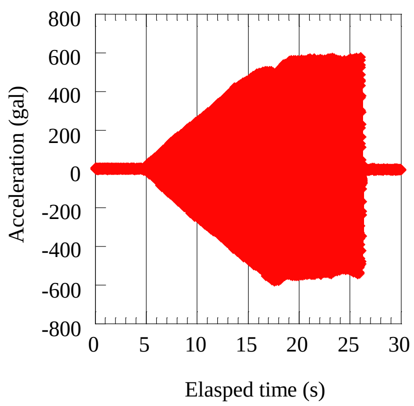

Fig. 2 Waveform of acceleration

RESULTS AND DISCUSSION

A Small Rainfall before the Loading

Figure 3 shows final longitudinal profile of slope failure and Fig. 4 shows photograph of final slope shape in Case 1. During rainfall, the increase in volumetric water content of soil from the initial value was about 8% in the lower layer and about 4% in other layers. After the rainfall ended, the decreases in volumetric water content of soil in the upper and middle layers were larger than those in the lower layer. At point D in the lower layer, the decrease in soil moisture showed little change after the rainfall ended. This result was caused by less infiltration of water from the lower layer to deeper area of slope due to the undrained condition of bottom of slope (Fig. 5). The amounts of displacement in Case 1 were larger than those in Cases 2 and 3 (Fig. 6). The time until collapse after loading in Case 3 was longer than the other cases. Although a collapse with a sliding surface in the model slope was confirmed in Cases 2 and 3, it was not in Case 1. Following settlement of the crest after providing the loading in Cases 2 and 3, collapse of the top of the slope occurred, forming the sliding surface. In Case 1, not only the surface but also the back of the model slope collapsed.

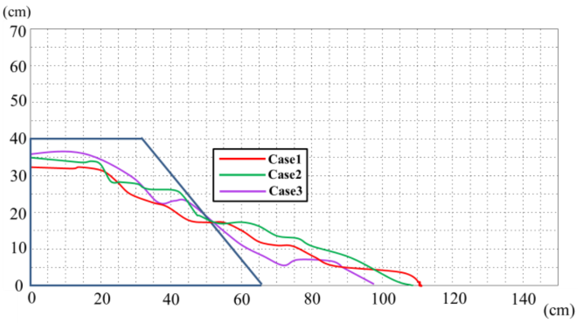

Fig. 3 The longitudinal profile of the slope failure (Cases 1-3)

Fig. 4 A photograph of the slope failure from (a) side and (b) front view (Case 1)

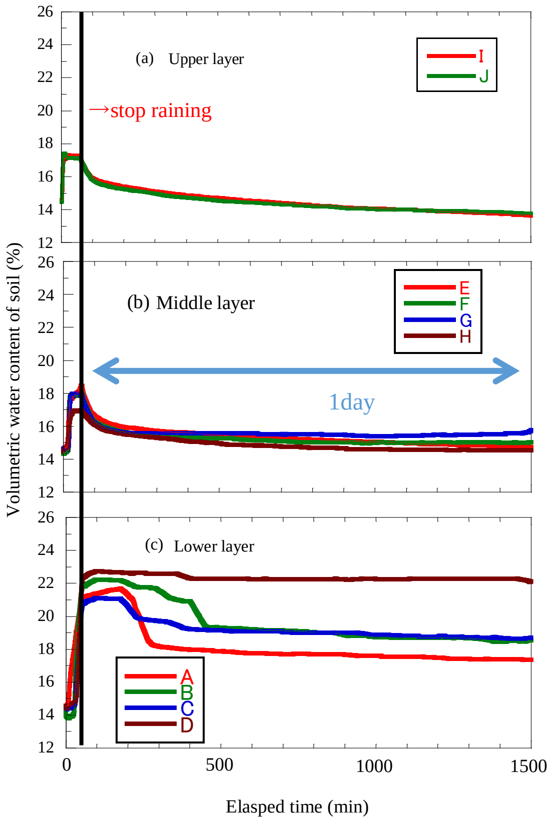

Fig. 5 The volumetric water content of soil in the (a) upper, (b) middle and (c) lower layer (Case 3)

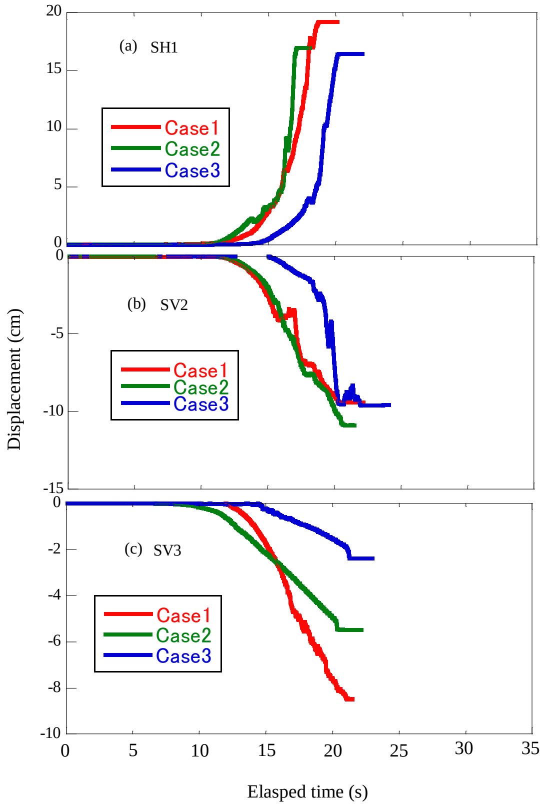

Fig. 6 Displacement after the loading at (a) SH1, (b) SV2 and (c) SV3 (Cases 1-3)

A Large Rainfall before the Loading

Figure 7 shows final longitudinal profile of slope failure and Fig. 8 shows photograph of final slope shape in Case 4. In the lower layer, the decrease in the value of soil moisture (C and D points) showed little change (Fig. 9). The decreases in volumetric water content of soil in the lower layer were similar to Cases 1-3. Although the volumetric water content of soil decreased approximately equally for both points A and B, the time to reach the minimum value was different. In Cases 4-6, settlement of the crest and collapse of the top of the slope with a sliding surface occurred, as in Cases 2 and 3. The amount of displacement in Cases 4-6 showed a large difference (Fig. 10). The time to collapse in Case 6 was longer than in Cases 4 and 5.

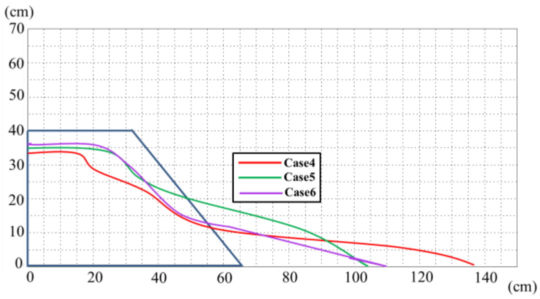

Fig. 7 The longitudinal profile of the slope failure (Cases 4-6)

Fig. 8 A photograph of the slope failure from (a) side and (b) front view (Case 4)

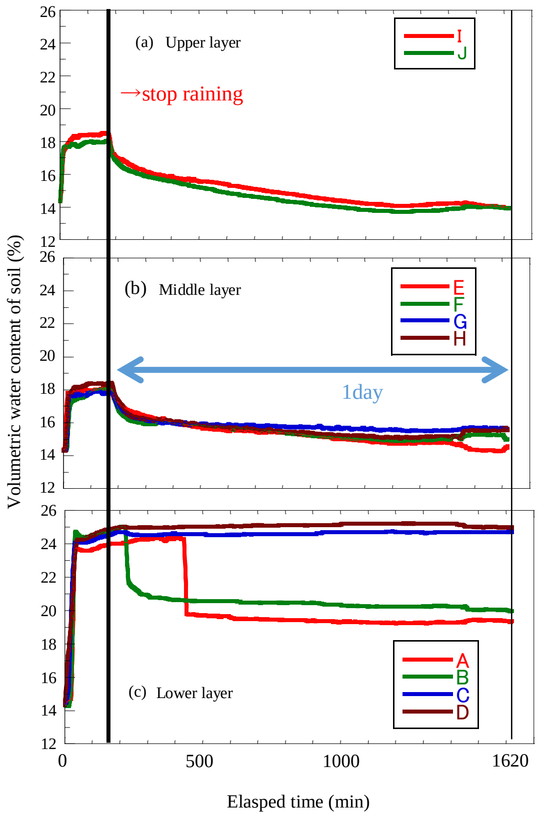

Fig. 9 The volumetric water content of soil in the (a) upper, (b) middle and (c) lower layer (Case 6)

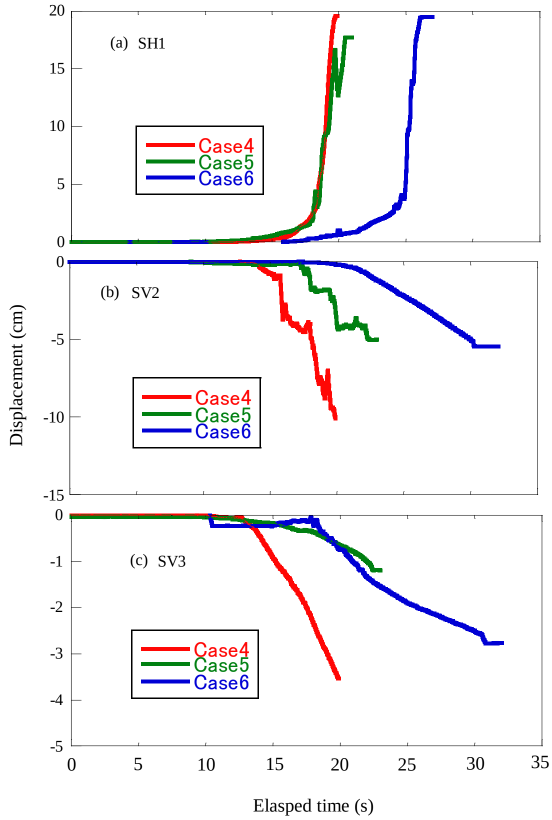

Fig. 10 Displacement after the loading at (a) SH1, (b) SV2, and (c) SV3 (Cases 4-6)

Effect of The Soil Moisture Conditions on Seismic Slope Failure

Figure 11 shows the position of the sliding surface and Fig. 12 shows a spatial distribution chart of the volumetric water content of soil before loading. Table 3 and Table 4 show time required for collapse and scale. We categorized the collapse into three stages based on visual observation: the settlement of crest, deformation of top of slope, and the formation of sliding surface during collapse. We measured the time required for the formation of three stages. The position of sliding surface became deep when the volumetric water content of soil was low. The differences in the spatial distribution of the soil moisture affected the depth of the sliding surface. Full-scale collapse occurred with a uniform soil moisture distribution and partial collapse occurred with a non-uniform soil moisture distribution. Although the volumetric water content of soil at near the top of slope was high in Case 1 and Case 4, the volumetric water content of soil in Case 1 was higher than that in Case 4 (Fig. 12). The distance of sediment movement in Case 4 was about 25cm larger than that in Case 1. The large collapse at top of slope in Case 1 with a uniform soil moisture distribution made the longer distance of sediment movement relative to Case 4. Thus, the soil moisture distribution had an effect on the failure configuration. As a result, the amount of displacement and distance of sediment movement increased, causing collapse in a shorter time after the loading when the volumetric water content of soil was high.

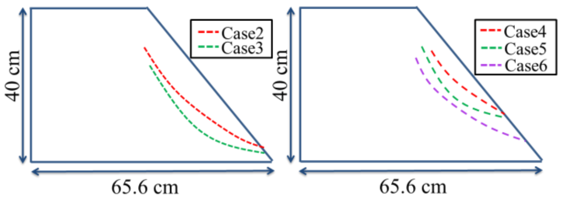

Fig. 11 Shape of sliding surface

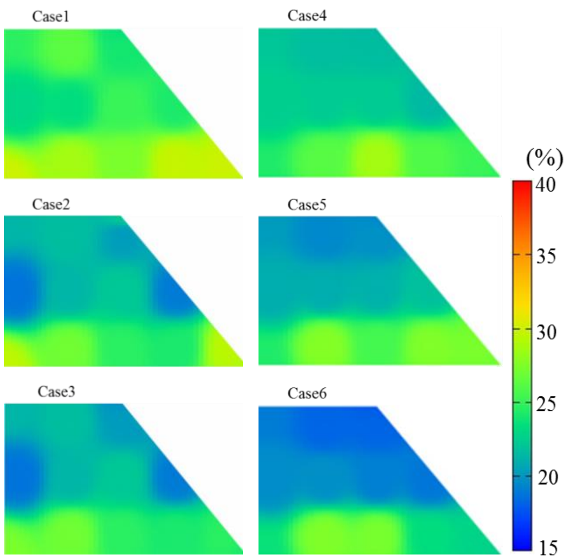

Fig. 12 Spatial distribution of volumetric water content of soil before the loading

Table 3 Time required for collapse and scale for cases of small rainfall amounts

	Case1	Case2	Case3
Rainfall amounts	30mm (30mm/hr×1hr)		
Elapsed time after rainfall	no time	1hour	1day
Time required for settlement of crest	10s	13s	14s
Time required for collapse of top of slope	12s	15s	16s
Time required for sliding failure	no sliding failure	17s	18s
Distance of sediment movement	46.9cm	42.4cm	32.8cm

Table 4 Time required for collapse and scale for cases of large rainfall amounts

	Case4	Case5	Case6
Rainfall amounts	30mm (30mm/hr×3hr)		
Elapsed time after rainfall	no time	1hour	1day
Time required for settlement of crest	10s	12s	16s
Time required for collapse of top of slope	14s	14s	12s
Time required for sliding failure	16s	19s	23s
Distance of sediment movement	71.4cm	37.4cm	43.4cm

CONCLUSION

We conducted a series of vibration loading experiments under different soil moisture conditions to examine the relationship between differences in volumetric water content of soil with seismic stability. We confirmed that seismic stability was impaired with increased volumetric water content of soil from results of the amount of displacement and the distance of sediment movement. This study demonstrated that the difference of soil moisture distribution affected the scale of slope failure. We found the soil moisture distribution is significant factor of prediction of slope failure. However, it is important to consider drainage conditions, rainfall conditions, and earthquake scales to predict the occurrence of slope failure. A problem is to reproduce the collapse mechanism accurately through analysis. We must compare the result of analysis with failure configurations on a model slope and the amount of displacement to the examine reproducibility of any analytical model.

REFERENCES

[1] Nishida K, Kobashi S and Mizuyama T, “DTM-based topographical analysis of landslides caused by an earthquake”, Journal of the Japan Society of Erosion Control Engineering, Vol. 49, No. 6, 1997, pp. 9-16 (in Japanease).

[2] Asano S, Ochiai H, Kurohara U and Okada Y, “Topographic effects on earthquake motion that trigger landslides”, Journal of the Japan Landslide Society, Vol.42, No.6, 2006, pp. 457-466 (in Japanease).

[3] Torii N and Okimura T, “Effect of torographic conditions and depth of surface soil layer on seismic response characteristics on mountain slope”, Journal of the Japan Society of Civil Engineers, Vol.64, No.2, 2008, pp. 369-382 (in

Japanease).

[4] Wakai A, Tanaka N, Abe S, Yoshimatsu H, Yamabe K and Watanabe T., “Large–area damage prediction system based on finite element method for risk assessment of seismic slope failure in mountains area”, Journal of the Japan Landslide Society, Vol.45, No.3, 2008, pp. 207-218 (in Japanease).

[5] Chigira M, “Geological and geomorphological characteristics of landslides generated by the mid niigata prefecture earthquake in 2004”, Journal of the Japan Society of Engineering Geology, Vol.46, No.3, 2005, pp. 115-124 (in Japanease).

[6] Mori T, Chiba T, Uzuoka R and Kazama M, “The relationship between change of soil moisture resulted from rainfall sand seismic response characteristics in the valley fill ground”, Journal of the Japan Association for Earthquake Engineering, Vol.10, No.4, 2010, pp. 1-13 (in Japanease).

[7] Matsumura K and Yokota Y, “Experimental study on seismic reactions of gentle slope with ground water”, Journal of the Japan Society of Erosion Control Engineering, Vol.66, No.2, 2013, pp. 48-56 (in Japanease).

[8] Tanabe T, Hiraoka N, Sumi K, Fujimoto M and Fukagawa R, “Experimental study on dynamic stability of slope failure due to earthquake after antecedent rainfall”, Journal of the Kansai Geo-Symposium 2014, pp. 223-226 (in Japanease).

Fifth International Conference on Geotechnique, Construction Materials and Environment, Osaka, Japan, Nov. 16-18, 2015, ISBN: 978-4-9905958-4-5 C3051

A METHOD FOR JUDGING THE RISK OF SLOPE FAILURE BASED ON PRECIPITATION AND SOIL MOISTURE CHARACTERISTICS

Tetsuya Iida[1], Masamitsu Fujimoto[2], Nobuyuki Kumakura[3], Daisuke Takasaki[3], Nobutaka Hiraoka[4] and Ryoichi Fukagawa[2]

[1]Graduate School of Science and Engineering, Ritsumeikan University, Japan,
[2]College of Science and Engineering, Ritsumeikan University, Japan
[3]Community Solutions Division, Toshiba, Japan
[4]Research Organization of Science and Technology, Ritsumeikan University, Japan

ABSTRACT

Slope failures often occur in Japan, and they frequently result from an increase in the moisture content of the soil. Thus, it is important to consider soil water content. In this study, we carried out a series of laboratory experiments to evaluate changes in soil moisture during rainfall. In the experiments, we constructed a model slope in which we installed 10 soil moisture sensors. The results indicated that the volumetric water content in the slope increased with rainfall, and the increments in volumetric water content were affected by the intensity of the rainfall. Then, using the experimental results, we developed a technique for judging slope failure risk based on absolute values of volumetric water content and rainfall characteristics. Our proposed method will be useful in judging the risk of slope failure because the criteria for the method are based not only on the precipitation but also on the soil moisture in-situ.

Keywords: Slope Failures, Laboratory Experiments, Soil Moisture Sensors, Volume Water Contents, Rainfall

INTRODUCTION

In Japan, many slope failures have occurred with heavy rainfall. Several models for predicting slope failure in forested areas have been proposed since the 1980s. Most studies used an approach that combined a physical model to simulate rainfall infiltration processes with slope stability analysis [1]-[9]. With regard to the physical model, one of main factors in slope failure is an increase in the moisture content of the soil. Most of these studies analyzed slope failure based on pore water pressures in the soil. The soil water content may be a good indicator to gain predictive information regarding slope failure because the soil water content responds to rainfall events as well as to pore water pressure. Although measurements of soil water content have been conducted in situ [10], [11], the role of soil water content in slope failure processes is still not well understood.

Generally, soil water conditions are measured by a tensiometer for pore water pressure and soil moisture sensors for soil moisture. A measurement system using a tensiometer and soil moisture sensors normally receives electricity by cables, leading to high costs for installing a measuring system. Thus, there is a need to develop a wireless measurement system for determining the water content in soil. Although tensiometers require regular maintenance, with degassed water in the equipment, soil moisture sensors have no such requirement. Considering the operating costs of measurements on a hazardous slope, a measurement system for soil water content would have a good return as a warning system for impending slope failure. In this study, we evaluated changes in soil moisture during rainfall using laboratory experiments, and developed a technique for judging the risk of slope failure based on the experimental results.

METHODS

We carried out two laboratory experiments to assess changes in soil water content during rainfall. We conducted one using an artificial rain simulator (Daiki Rika Co., DIK-6000S) at Ritsumeikan University. Granite soil (Masa soil) was used to make a model slope. Measurement devices for pore water pressure and soil moisture content were a tensiometer (with hydraulic gauge; Nidec Copal Electronics Corp., PA-850-102V-NGF) and soil moisture sensors (Decagon Devices, S-SMx-M005), respectively.

We performed two experiments for different purposes. The experiment in Case 1 was designed to evaluate the relationship between pore water pressure and soil moisture content and the responses in slope failure. Case 2 was conducted to determine changes in soil moisture from the start of rainfall to after the rainfall ended.

In Case 1, slope failure did not occur due to the development of gully erosion related to rainfall intensity (Photo 1). Based on these results, we do not discuss the dynamics of soil water contents for slope failure processes directly. Details of the model slope and experimental conditions for Case 1 are shown in Table 1 and Fig. 1. Details of the model slope and experimental conditions for Case 2 are shown in Table 2 and Fig. 2. We provided artificial rainfall to the model slope in the experiments to recreate natural conditions of soil moisture. The amount of rainfall per hour was changed twice in Case 1 in an attempt to provoke slope failure. The drainage condition was changed in Case 1 to raise the groundwater level in the model slope.

Photo 1 Model slope after experiment (Case 1)

Table 1 Experimental conditions (Case 1)

Moisture content	10%
Dry density	1.85 g/cm^3 (basement layer) 1.60 g/cm^3 (soil layer)
Wet density	2.035 g/cm^3 (basement layer) 1.760 g/cm^3 (soil layer)
Drainage condition	discharged water (10 hrs)
	not discharged water (11 hrs)
Preliminary rainfall condition	25 mm/hr (2 hrs)
Rainfall condition	25 mm/hr (4.5 hrs)
	50 mm/hr (15.5 hrs)
	120 mm/hr (1 hr)
Measuring interval	1 min

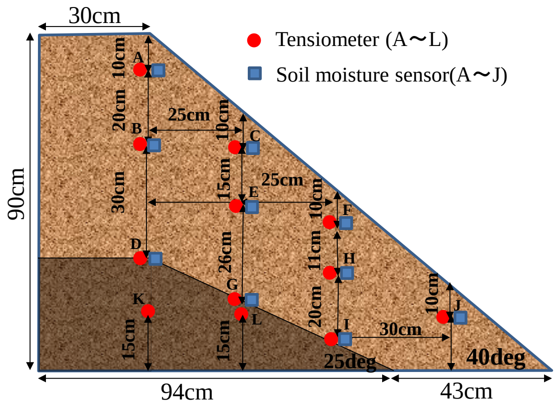

Fig. 1 Details of model slope (Case 1)

Table 2 Experimental conditions (Case 2)

Moisture content	10%
Dry density	1.60 g/cm^3
Wet density	1.76 g/cm^3
Preliminary rainfall condition	25 mm/hr (2 hrs)
Rainfall condition	15 mm/hr (14 hrs)
Measuring interval	10 mins

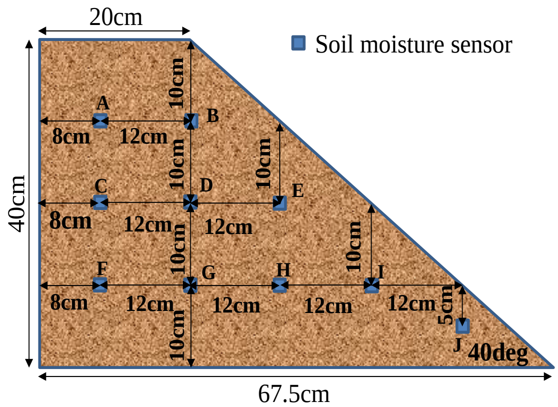

Fig. 2 Details of model slope (Case 2)

RESULTS AND DISCUSSION

Relationships between Pore Water Pressures and Volumetric Water Contents in Soil

The results of the Case 1 experiment are shown in Fig. 3, which indicates the variation in accumulated rainfall, amount of rainfall per hour, pore water pressure, and volumetric water content. The result of the Case 2 experiment are shown in Fig. 4, which indicates the time series variation in accumulated rainfall, amount of rainfall per hour, and volumetric water content.

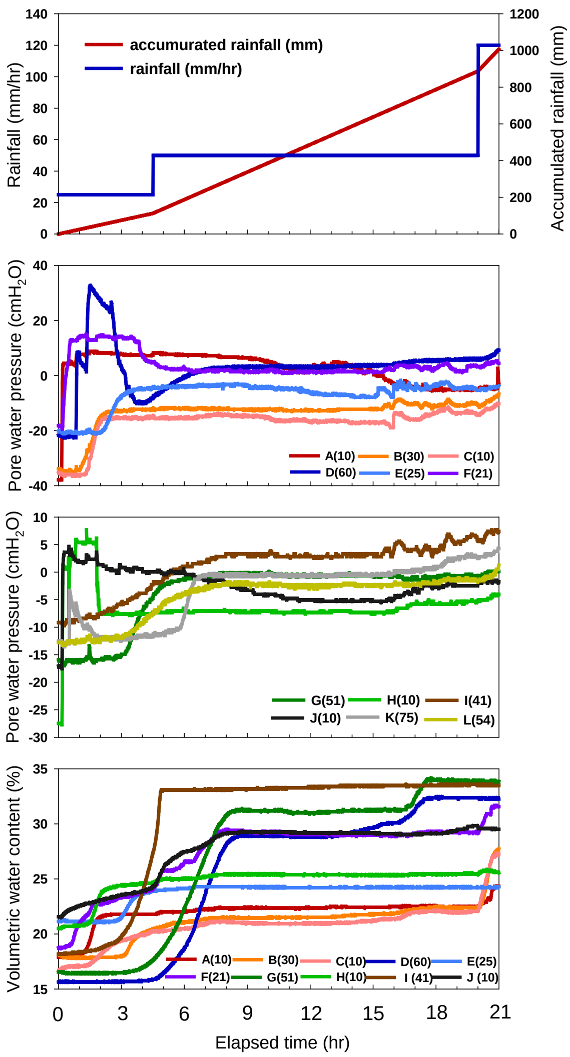

Fig. 3 Time series variation in pore water pressure and volumetric water content

In Case 1, slope failure did not occur despite changes in rainfall intensity (Photo 1), as the surface soil of the model slope in Case 1 was eroded. Most of the pore water pressure measurements in the slope increased with the rainfall. Increased pore water pressure occurred at a shallow measurement depth. Following the initial increase in pore water pressure, the values of pore water pressure became constant. Moreover, the pore water pressure of points at greater depths (D, G, and I) exceeded 0, indicating that saturation occurred at the bottom of the soil layer. The soil moisture in the slope increased due to the rainfall. Additionally, the soil water contents became constant after the increase during the rainfall, as did the pore water pressure. Moreover, the volumetric water content rose again before the end of the rainfall. The second increase in the volumetric water content may have been caused by rainfall directly on the soil moisture sensor because of the denudation of the model slope.

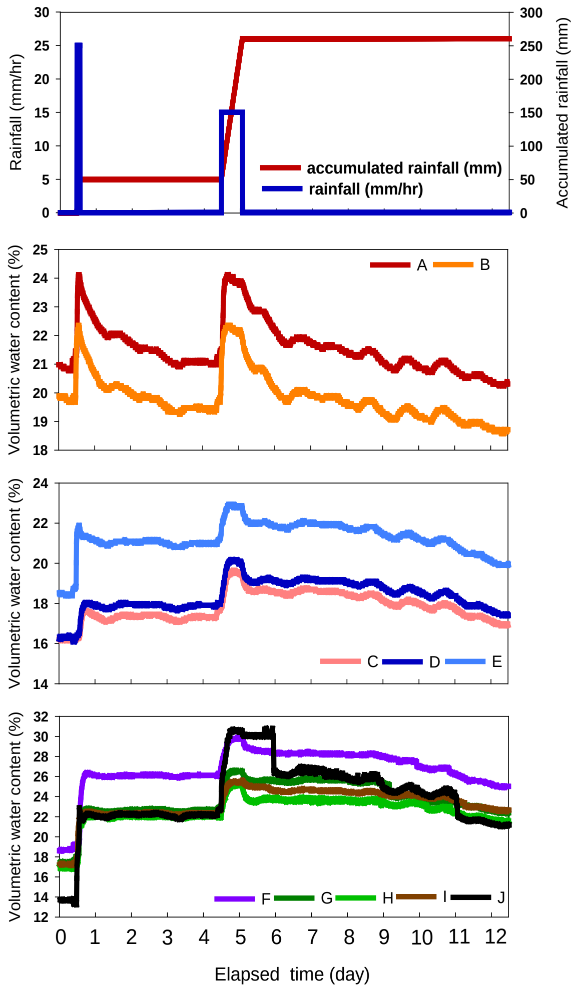

Fig. 4 Time series variation in volumetric water content

The relationship between pore water pressure and volumetric water content at D, G, and I is shown in Fig 5. When the pore water pressure exceeded 0, the value of volumetric water content had a large range, especially at point D. The increase in the volumetric water content after saturation was due to a decrease in pore air in the soil under saturated conditions. This result also indicated that soil saturation cannot be detected by a specific value of the volumetric water content of the soil. Thus, the risk of slope failure with saturation should be judged using the range of the volumetric water content.

Responses of the Volumetric Water Content at Different Measurement Depths

In Case 2, the volumetric water content in the slope rose with the initial rainfall, after which, the volumetric water content at shallow depth points (A, B) decreased due to 4 dry days between the preliminary rainfall and the subsequent rainfall. The volumetric water content of other points did not decrease, largely because of drainage conditions of the model slope. The volumetric water content measurements, which declined after the preliminary rainfall ended, then rose again with further rainfall. The range of increase in the volumetric water content differed between the preliminary and subsequent rainfall. One cause of these differences was the differing rainfall intensity between the preliminary and subsequent rainfall.

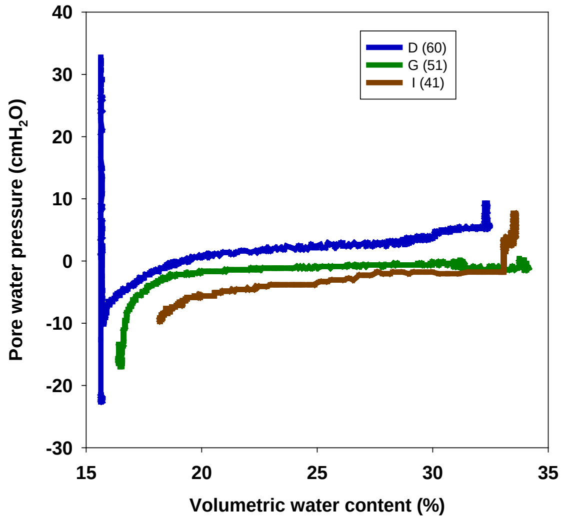

Fig. 5 Relationship between pore water pressure and volumetric water content

Method for Judging the Risk of Slope Failure

We developed a technique for judging the risk of slope failure based on the experimental results. In this study, we judged the risk for the whole slope after judging the risk based on individual soil moisture sensors. First, the risk based on individual soil moisture sensors was judged, and we then judged the risk for the whole slope using a summary of the risk values of individual soil moisture sensors.

We first tried to judge the risk of slope failure at each measurement point using an absolute value of volumetric water content. A reference value needed to be determined for an absolute value of volumetric water content. The judgment values of volumetric water contents were calculated using Eqs. (1) and (2):

$$w = \left(\frac{\rho_w}{\rho_d} - \frac{\rho_w}{\rho_s}\right) S_r \qquad (1)$$

$$\theta = w\rho_d \qquad (2)$$

where w is the moisture content (%), ρ_w is the water density (g/cm^3), ρ_d is the dry density (g/cm^3), ρ_s is the soil particle density (g/cm^3), S_r is the degree of saturation (%), and θ is the volumetric water content (%).

The dry density of the soil and the soil particle density were measured in laboratory experiments using in-situ soil samples. From the results, we determined the boundary values of volumetric water content with different degrees of saturation. Two proposed values of S_s and S_a of the degree of saturation were used in our judgment method. The volumetric water contents corresponding to the saturation degree were calculated using the equations above. The meanings of S_s and S_a are as follows: When the degree of saturation was under S_s percent (%), we assumed that the soil moisture sensor at the measurement point was in a safe state. We assumed that soil moisture was in alert status when the measured value of the degree of saturation was $>S_s$ (%). When the value of the degree of saturation is $>S_a$ (%), we assumed that the soil moisture condition was in evacuation status.

To judge the risk over whole of slope, we scored individual soil moisture sensors. We gave 1 point where the soil moisture sensor was in a safe state; 2 points if the soil moisture sensor was in alert status; and 3 points if the soil moisture sensor was in evacuation status. We judged the state (safe, alert, or evacuation) based on thresholds for the summed totals of the individual measurement points.

Application of the Method for Judging the Risk of Slope Failure

Here, we show examples of the judgment method. We determined that the values of S_s and S_a for the degree of saturation were 50% and 70%, respectively. The volumetric water content corresponding to those saturation degrees was 19.2% and 26.9%, respectively. We judged a safe state when the sum of the 10 soil moisture sensor scores was less than 15 points, alert status was 16-20 points, and evacuation status was considered to be a total score of 21 or more points. The judgment results for Cases 1 and 2 are shown in Figs. 6 and 7, respectively. In this study, we judged the potential for slope failure based on two indices of soil moisture and the characteristics of the precipitation, which were used as an index of the effective rainfall. Effective rainfall is an indicator to evaluate the residual effect of previous precipitation on soil moisture in the ground. We calculated the effective rainfall using Eqs. (3) and (4):

$$R_G = R_0 + a^1 R_1 + a^2 R_2 + \cdot\cdot\cdot\cdot\cdot a^n R_n \qquad (3)$$

$$a = (0.5)^{1/T} \qquad (4)$$

where R_G is the effective rainfall (mm), R_n is the rainfall before n minutes (mm/10min), a is a reduction factor ($0 < a < 1$), and T is the half-period. The x-axes of Figs. 6 and 7 are the effective rainfall that had a half-period of 72 h, and the y-axes are the effective rainfall where the half-period was 1.5 h.

In Case 1, the slope was judged as safe before the preliminary rainfall, and that judgment remained after the preliminary rainfall began. At 1 h and 10 min after the beginning of the preliminary rainfall, the judgment changed to alert status, which continued after the end of the preliminary rainfall. Then, at 12 h after the end of the preliminary rainfall, the judgment returned to a safe state. With regard to the later rainfall, after the preliminary rainfall, at 2 h and 50 min from the beginning of rainfall, the judgment changed to alert. Due to the continuing heavy rainfall, at 5 h and 30 min from the beginning of the rainfall, the judgment was shifted to evacuation status.

In Case 2, the judgment before the preliminary rainfall was that the slope was safe, as in Case 1, and this judgment of risk was maintained after the preliminary rainfall began. However, at 1 h and 30 min from the beginning of the preliminary rainfall, the judgment shifted to alert status. Due to the increased total amount of rainfall, at 2 h from the start of the second rainfall, the judgment entered evacuation status. At 3 h and 30 min from the end of the rainfall, the judgment of risk returned to alert status.

Although we judged the risk of slope failure, our method did not consider the measurement depth. However, it is vital to consider depth to accurately judge the risk of slope failure. When the measurement point at a deep depth was judged to be in evacuation status, the risk of slope failure was supposed to be very high. Thus, we weighted the score for evacuation status according to measurement depth. When the measuring point in the middle layer entered evacuation status, we gave it 4.5 points, and when the measurement point in the deep layer went to evacuation status, we gave it 6 points. Based on these changes in the scores of individual soil moisture sensors, we also revised the scores for the whole slope. We judged a safe state when the sum of the 10 soil moisture sensors was less than 15 points. Alert status was 16-24 points, and evacuation status was a score of 25 or more points. The results of judgments for Cases 1 and 2 are shown in Figs. 8 and 9.

In Case 1, the times in safe and alert states were the same as with no weighting, but the time of evacuation status was delayed by 40 min. Also, in Case 2, the times in safe and alert states were the same, but the time of evacuation status was delayed by 1 h and 30 min. Moreover, the time when the status reverted from evacuation to alert moved 2 h and 20 min earlier.

CONCLUSION

In this study, we carried out laboratory experiments to evaluate the relationship between pore water pressures and soil moisture conditions and assessed changes in soil moisture during and after simulated rainfall. The volumetric water content increased with the rainfall and showed a

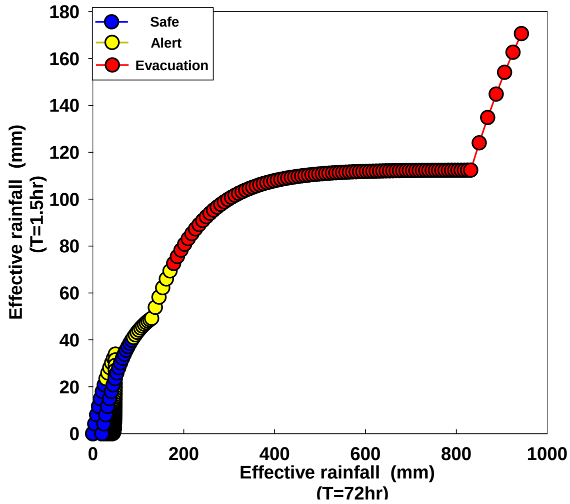

Fig. 6 Result of judgment (Case 1)

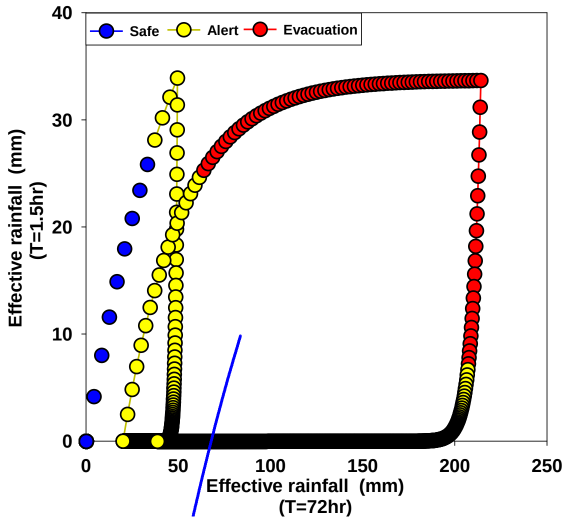

Fig. 7 Result of judgment (Case 2)

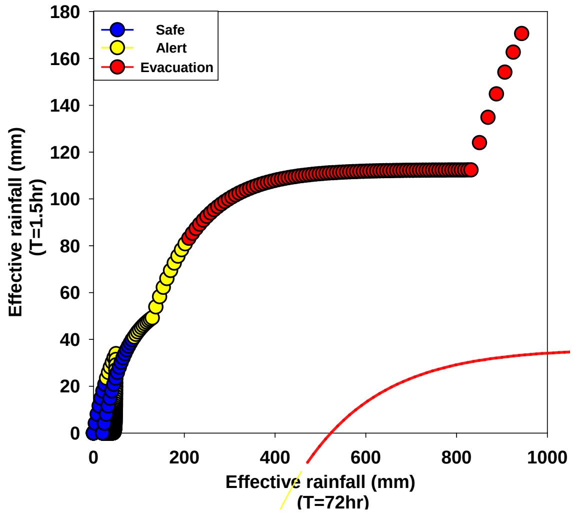

Fig. 8 Result of weighted judgment (Case 1)

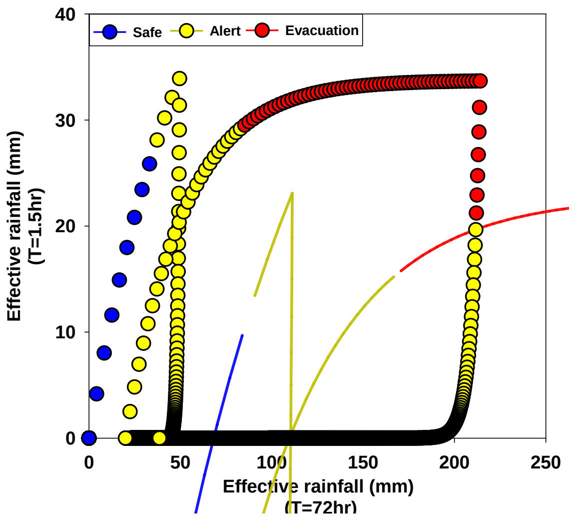

Fig. 9 Result of weighted judgment (Case 2)

large range of values after reaching saturated conditions. Then, we developed a judgment method for slope failure risk based on absolute values of volumetric water content. Soil moisture and characteristics of the precipitation were used to judge the risk of slope failure. Although the result of the judgment differed with consideration of depth, our proposed method can judge the risk of slope failure in a comprehensive manner. We must examine its applicability to an actual slope in future studies.

REFERENCES

[1] Okimura T, Ichikawa R, "A prediction method for surface failures by movements of infiltrated water in surface soil layer", Natural Disaster Science, Vol. 7, 1985, pp. 41-51.

[2] Hiramatsu S, Mizuyama T, Ishikawa M, "Study of a method for predicting hillside landslides by analysis of transient flow of water in saturated and unsaturated soils", Journal of the Japan Society of Erosion Control Engineering , Vol. 43, 1990, pp. 5-15. (in Japanese with English abstract)

[3] Montgomery DR, Dietrich WE, "A physically based model for the topographic control on shallow landsliding", Water Resources Research, Vol. 30, 1994, pp. 1153-1171.

[4] Wu W, Sidle RC, "A distributed slope stability model for steep forested basins", Water Resources Research, Vol. 31, 1995, pp. 2097-2110.

[5] Pack RT, Tarboton DG, Goodwin CN, "The SINMAP approach to terrain stability mapping", Proceeding of International Congress of the International Association for Engineering Geology and the Environment, 8, 1998, pp. 1157-1165.

[6] Khazai B, Sitar N, "Assessment of seismic slope stability using GIS modeling", Geographic Information Sciences, Vol. 6, 2000, pp.121-128.

[7] Kosugi K, Mizuyama T, Fujita M, "Accuracy of a shallow-landslide prediction model to estimate groundwater table", Journal of the Japan Society of Erosion Control Engineering, Vol. 55, 2002, pp. 21-32. (in Japanese with English abstract)

[8] Uchida T, Mori N, Tamura K, Terada H, Takiguchi S, Kamee K, "The role of data preparation on shallow landslide prediction", Journal of the Japan Society of Erosion Control Engineering, Vol. 62, 2009, pp. 23-31. (in Japanese with English abstract)

[9] Fujimoto M, Kosugi K, Hayashi Y, Tani M, Mizuyama T, "The effect of resolution of elevation model data on shallow landslide analysis", Journal of the Japan Society of Erosion Control Engineering", Vol. 64, 2011, pp. 3-10. (in Japanese with English abstract)

[10] Kubota J, Fukusima Y, Suzuki M, "Observation and modeling of the runoff process on a hillslope", Journal of Japanese Forest Society, Vol. 69, 1987, pp. 258-269. (in Japanese with English abstract)

[11] Kubota J, Fukushima Y, Suzuki M, "Observation and modeling of the runoff process on a hillslope (II)- Water budget and location of the groundwater table and its rising", Journal of Japanese Forest Society, Vol. 70, 1988, pp. 381-389. (in Japanese with English abstract)

EFFECT OF ANALYSIS FOR THE INCLINATION ANGLE OF THE BACK SUPPORT OF INCLINED EARTH RETAINING STRUCTURE

Minsu Seo[1], Jongchul Im[2], Changyoung Kim[3], Wooje Lee[4] and Jaewon Yoo[5]

[1]Graduate Research Assistant, Department of Civil Engineering, Pusan National University, South Korea,
[2]Ph.D., Professor, Department of Civil Engineering, Pusan National University, South Korea*,
[3,4,5]Pusan National University, South Korea
* Address correspondence to Jongchul Im, Professor, Department of Civil Engineering, Pusan National University, 2 Busandaehak-ro 63beon-gil (40 Jangjeon-dong), Geumjeong-gu, Busan, South Korea.

ABSTRACT

An inclined earth retaining structure (briefly called 'IER') is a structure using the earth retaining pile (front support) and a stabilizing pile (back support). The back supports are fixed to front supports in order to reduce the earth pressure acting on the front wall. In this study, in order to the effects of the installation angle of the back support, model tests were performed. As a result, excavation depth increased largely by the reduction effect of earth pressure acting on the front support by the back support. Especially, excavation depth at failure increased about 2.7 to 3.1 times by the back support.
Keywords: IER method, Inclined earth retaining structure, Front support, Back support, Installation angle

INTRODUCTION

The modern buildings have been Manhattanized by industrialization and urbanization in metropolitan cities, hence auxiliary techniques of underground excavation have been developed and used in order to increase the excavation depth and guarantee the stability during the excavation. This auxiliary method of ground anchors and soil nailing method, can cause problems interfere with the adjacent ground and the structure. And in the case of other auxiliary method of bracing method, an earth-retaining wall using struts needs a number of struts that are costly and the numerous struts that cross a construction site make excavating ground difficult.

That can be self-supporting to secure these problems Inclined Earth Retaining Structure Method (hereafter denoted as "IER method") has been developed. An IER method is a method to incline an earth retaining pile (front support) and a stabilizing pile (back support). The back supports connected to front supports reduce the earth pressure acting on the front wall and front supports by distributing it to back supports in order to increase the structural stability.

In this study, it is intended to analyze the effect according to the inclination of the front support. So, using earth pressure theory and model tests, the effect of inclination angle are analyzed. And also, the installation effect of back support was estimated by the laboratory model tests.

IER METHOD

In the IER method, inclined two piles are used and fixed each other tightly. Figure 1 shows an IER model

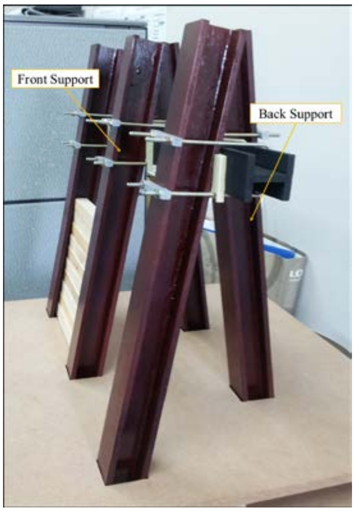

Fig. 1 IER model

Characteristics of IER method

The earth retaining wall using back support has five characteristics to increase the stability of the temporary structure as shown in Figure 2.

Firstly, the earth pressure acting on the front wall decreases by eliminating the weight of soil above the inclined front support (See 'A'). Secondly, the heads of both front support and back support are fixed with a beam connecting them in order to make the structure an integrated system transferring the force acting on the front support to back support (See ‘D’). Thirdly, the frictional resistance between the back support and soil causes the effect of ground anchor (See ‘E’). Fourthly, the back support plays a role as a stabilizing pile by resisting the activity of sliding mass (See ‘C’). Lastly, if required, an anchor can be attached to the batter pile (See ‘F’)

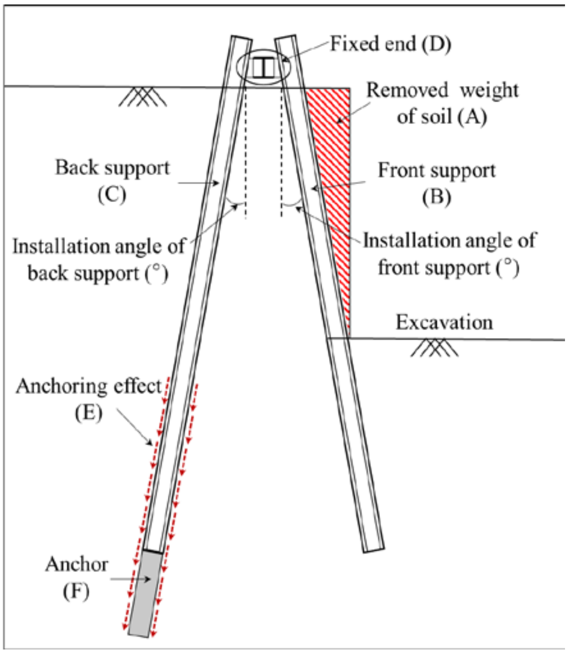

Fig. 2 Basic structure of IER Method

Field Application

Figure 3 shows the IER method applied in the field. It is located in the soft clayey ground. The front support is made by SCW (Soil Cement Wall), and installation angle of the back support was applied by 10°.

Fig. 3 Field example applied to soft clay

ANALYSIS USING EARTH PRESSURE THEORY

Theory

Coulomb’s theory [1] of the active earth pressure is expressed by Eq. (1).

$$P_{aiR} = \frac{1}{2}\gamma H^2 \frac{\cos(\theta-\beta)\cos(\theta-\alpha)\sin(\beta-\phi)}{\cos^2\theta\sin(\beta-\alpha)\sin(90^\circ+\delta+\theta-\beta+\phi)}$$
(1)

Where, P_{aiR} (=P_{ai}): active earth pressure, γ: unit weight of soil (kN/m^3), H: height, θ: Inclination angle of front support (°), case of inclined earth retaining wall : -(negative) value, ϕ: internal friction angle of soil (°), δ: wall friction angle (°), α: slope angle of back of front support (°), β: failure angle of slope (°)

The slope of front support was analyzed by increasing the slope from 0° to 20° by increments of 1°. As changing β on the slope of front support of each, maximum value of the calculated earth pressure was determined by the earth pressure of slope, and β on the value was determined by failure angle(In this case, β is increasing from 0.5° to 90° by increments of 0.5°. Table 1 presents analysis conditions.

Table 1 Analysis conditions

	Initial value (°)	Increm- -ent (°)	Maximum value (°)
Inclination angle of front support (θ)	0	1	20
Failure angle of slope(β)	0.5	0.1	90

Soil conditions

Condition of analysis ground was conducted as single layer by conditions of Coulomb earth pressure theory, was applied soil properties of general sand ground. Table 2 shows the properties of model ground (sand soil), and wall friction angle was set to 20° by applying 2/3 ϕ. Analysis height (H) is set to 6m.

Table 2 Soil Properties

Parameter	γ_t (kN/m^3)	ϕ (°)	c (kN/m^2)
Fill material	18	30	0

Results of calculations

Figure 4 shows the relationship between the inclination angle of front support and the earth pressure acting on front support. As the inclination angle is increasing, it can be seen that the earth pressure and failure angle is reduced. Figure 5 shows earth pressure ratio ($\frac{P_\theta}{P_{\theta=0}}$) on the slope of front support (θ). As a result, earth pressure at θ=10° is smaller as a 77.93%.

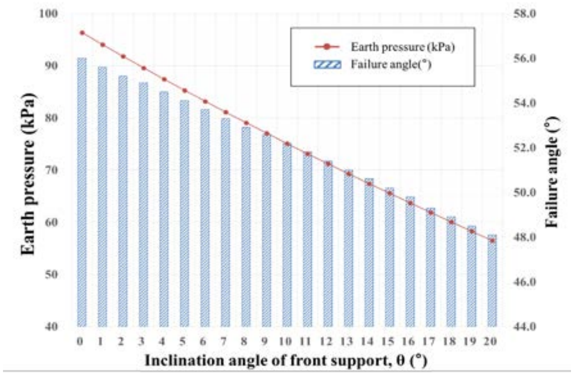

Fig. 4 Relationship between the inclination angle of front support and the earth pressure.

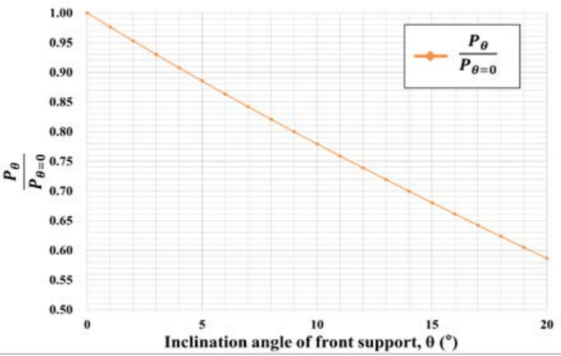

Fig. 5 Earth pressure ratio ($\frac{P_\theta}{P_{\theta=0}}$) on the inclination angle of front support (θ)

ANALYSIS OF MODEL TEST

Test equipment and soil materials

Figure 6 shows a plane strain model soil-tank applied in this study. Dimension of soil-tank is length 1,700mm, Height 760mm, and width 410mm, soil was used Jumunjin sand. Table 3 and Table 4 presents physical and mechanical properties of Jumunjin sand. Because soil change mechanical properties according to the density, soil must construct by keeping the density constant. Figure 6 shows a change of dry density according to drop height of Jumunjin sand. Figure 7 presents that density tended to converge near 1.625g/cm^3 from drop height of 0.9m. In this study, density was constructed uniformly to construct ground by soil rainer method [2] on the drop height of 1.2m considering soil-tank and height of sand rainer. The dry density at this time is 1.632g/cm^3, and the relative density is 93.8%.

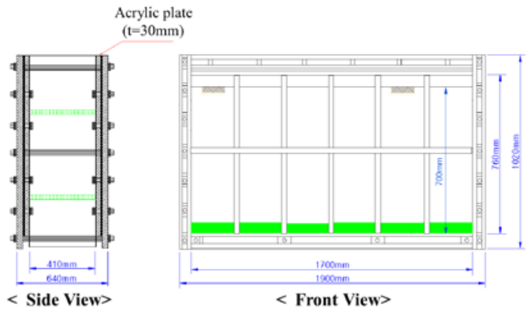

Fig. 6 Plane strain model soil-tank

Table 3 Properties of Jumunjin standard sand

Description	Index	Property
Max. void ratio	e_{max}	0.923
Min. void ratio	e_{min}	0.604
Max. dry density	γ_{dmax} (g/cm^3)	1.652
Min. dry density	γ_{dmin} (g/cm^3)	1.378
Specific gravity	G_s	2.65
Water content	w (%)	0.30
Average particle size	D50 (mm)	0.595
Effective particle size	D10 (mm)	0.443
Uniformity coefficient	Cu	1.402
Coefficient of curvature	Cg	0.912

Table 4 Variation of ϕ_{DS} with relative density for Jumunjin standard sand

Test No.	1	2	3	4
γ_d (g/cm^3)	1.378	1.468	1.522	1.561
Dr (%)	0	36.9	57.0	70.7
ϕ_{DS} (°)	31.2	33.0	35.0	37.7
Test No.	5	6	7	8
γ_d (g/cm^3)	1.572	1.602	1.632	1.646
Dr (%)	74.4	84.3	93.8	98.2
ϕ_{DS} (°)	38.0	39.2	41.1	42.0

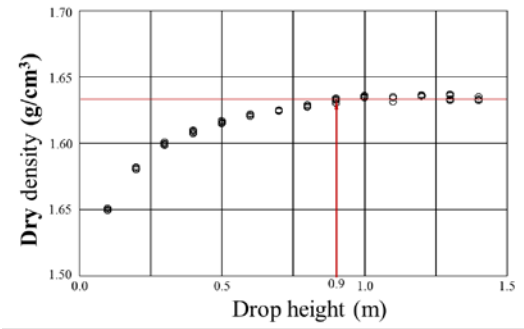

Fig. 7 Variation of Density with the Drop height

Conditions of model tests

Front and back support of IER method made to use plywood as shown in figure 8. The front retaining wall usually consists of front supports and boards at a construction site. However the front supports and boards of the model were instrumented as a unified wall since this study. The front and back support of the model had the same vertical length as the height of the model ground which was 70 cm. As shown in the Table 5, tests were conducted three kinds angles of front support inclination.

Fig. 8 Experimental model

Table 5 The types and conditions of model tests

No.		S00	S05	S10	D00	D05	D10
Form of support		Single support			Double support		
Front support	Angle (°)	0	5	10	0	5	10
	Thickness (mm)	15					
Back support	Angle (°)	-	-	-	10		
	Thickness (mm)	-	-	-	15		
	Interval (mm)	-	-	-	102		

Methods of model tests

After the model structure was installed in the plane strain soil tank, sand sprinkled the earth pressure difference don't occur between the front and back walls. And measuring a Lateral displacement of the wall was used a dial gauge capable of measuring a 1/100mm from the top of the front wall. The lateral displacements measured on the upper left- and right-side of the wall were averaged at each excavation stage. The each excavation consisted of intervals of 5 cm, the lateral displacement was measured by recording the time to convergence after the excavation.

Results of model tests

Lateral displacement of the top of the front wall by excavation depth according to the types of tests as shown in figure 9. The excavation depths at failure were estimated by using the failure criteria suggested by [3], which is the rotational displacement of retaining wall according to soil types at failure as shown in Table 6. The value of 0.00075 was used for the analysis of test results because the value is suggested in the table for range from 0.0005 to 0.001 of the dense sandy soil which was filled in the soil tank. A method of determining the rotational displacement from Eq. (2). And the excavation depths corresponding to the failure criteria of 0.00075 are tabulated in Table 7.

$$\text{Rotational displacements} = \frac{\text{Lateral wall displacement}}{\text{Wall height}} \quad (2)$$

Table 6 Rotational displacements of retaining wall at failure [3]

Soil Type	Wall rotation (Lateral wall displacement /Wall height)	
Soil Type	Active state	Passive state
Loose sandy soil	0.001-0.002	0.01
Dense sandy soil	0.0005-0.001	0.005
Soft clay soil	0.02	0.04
Stiff clay soil	0.01	0.02

Table 7 Excavation depth and Excavation depth at failure by case

No.	Excavation depth (cm)	Excavation depth at failure (cm)
S00	45	12.8
S05	45	15.5
S10	45	17.8
D00	50	40.2
D05	70	42.1
D10	70	50.1

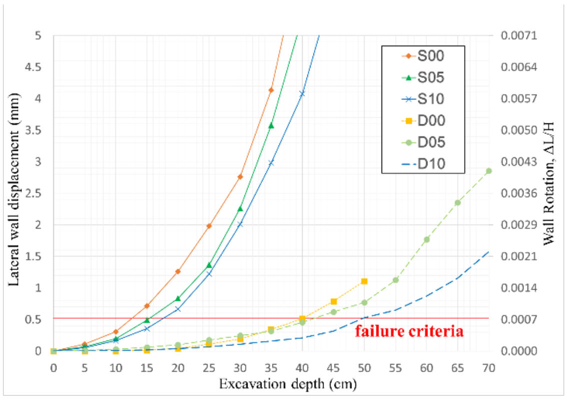

Fig. 9 Variation of tip lateral displacement with excavation depth according to the case of experiments

Analysis of model test results

Effect of the inclination of the front support

In the case of single support, the lateral displacements of S05 and S10 using the inclined front support occurred by about 54% and 45 % respectively of S00 at the 10cm of excavation depth.

And in the case of a double support, D05 and D10 compared with D00 occurred 88% and 40% respectively at the 40cm of excavation depth.

Effect of back support

Lateral displacement before failure decreased up to 88%~98% compared with single support system, regardless of inclination angle of the front support.

Excavation depth at failure increased to 3.1 times in the case that the installation angle of front support is 0° by back support. And 2.8 times in the case of 10°.

CONCLUSIONS

The results of model tests are concluded as follows.

1) Earth pressure reduces according to the inclination angle of front support by Coulomb's earth pressure theory.

2) The back support has two roles. One is to reduce the earth pressure acting on the front support, the other is to increase the stability and reduce the lateral displacement of front support wall.

REFERRENCE

[1] Coulomb, C.A. (1776). “Essai sur une Application des Règles de Maximis et Minimis àquelques Problèmes de Statique, relatifs a l’Architecture,”Mem. Roy. des Sciences, Paris, Vol.3,38.

[2] Park, L. K. (2003), “A Study on the Characteristic of Ground Behaviour and Settlement Restraining effect of Micropile during Shallow Tunnel Construction in Soft Ground”, Unpublished doctoral dissertation, Pusan National University, pp.134~145.

[3] Rankine, W.M.J. (1857). “On Stability on Loose Earth,”Philosophic Transactions of Royal Society, London, Part I, 9-27.

Fifth International Conference on Geotechnique, Construction Materials and Environment, Osaka, Japan, Nov. 16-18, 2015, ISBN: 978-4-9905958-4-5 C3051

CHARACTERISTICS OF SUBSURFACE WATER MOVEMENTS IN SOIL LAYERS ON THE HILLSLOPE BEHIND KIYOMIZU TEMPLE

Yuuki Arimitsu[1], Masamitsu Fujimoto[2], Nobutaka Hiraoka[3],Toru Danjo[4], Yuko Ishida[5] and Ryoichi Fukagawa[2]

[1]Graduate School of Science and Engineering, Ritsumeikan University, Japan,

[2] College of Science and Engineering, Ritsumeikan University, Japan,

[3] Research Organization of Science and Technology, Ritsumeikan University, Japan,

[4] Department of Storm Flood and landslide Research, National Research Institute for Earth Science and Disaster Prevention, Japan,

[5]Institute of Disaster Mitigation for Urban Cultural Heritage, Ritsumeikan University, Japan

ABSTRACT

Recently, slope failures have occurred due an increase of heavy rainfall and typhoon events. As typical examples, sediment disasters have occurred frequently at Kiyomizu-dera Temple, including debris flows in 1972 and shallow slope failures in 1999 and 2013. Kiyomizu-dera temple is a UNESCO World Heritage Site, and one of the Historic Monuments of Ancient Kyoto, Japan. An increase in shear stress and decrease in shear strength due to infiltration of rainwater led to slope failures. In this study, subsurface water movements were investigated by measuring pore water pressure changes and hydraulic gradients during rainfall events to prevent damage to important cultural assets by natural disasters. Saturation was found to occur after very small rainfall events, regardless of soil moisture conditions. Although subsurface water normally flows from upper to lower areas of the slope, water movements from the bedrock to the soil layer were observed during rainfall events, suggesting the existence of potentially hazardous slope failure conditions.

Keywords: Slope Failure, Pore Water Pressure, Hydraulic Gradient, Infiltration of Rain Water

INTRODUCTION

Recently, slope failures have occurred due to an increase in heavy rainfall and typhoon events in Japan, which cause significant damage. Kiyomizu-dera Temple is located on the slope of a mountain in Higashiyama, Kyoto Prefecture, Japan and was designated a cultural asset of national importance in 1994. Five million tourists from all over the world visit Kiyomizu-dera Temple each year [1]. Sediment disasters have occurred on a number of occasions at Kiyomizu-dera Temple, including a debris-flow event in 1972 and shallow slope failures in 1999 and 2013 [1]. Figure 1 shows a slope failure at Kiyomizu-dera Temple in 2013. It is necessary to forecast landslide and debris flow hazards, to prevent and alleviate damage to an important cultural asset and protect human life.

Previous research has noted that slope failure due to rainfall is triggered by two main factors following rainwater infiltration into the soil. Firstly, an increase in shear stress occurs due to an increase in soil weight. Secondly, a decrease in shear strength occurs due to decreasing soil cohesion. It is therefore necessary to evaluate soil moisture content, soil water movement and groundwater in the soil layer during rainfall events. In-situ measurements of pore water pressures were conducted in a catchment with granitic geology [2], [3] and sedimentary rock geology [4]. These studies showed that subsurface water movements are more complex in sedimentary rock compared to granitic sites, due to the heterogeneity of the soil structure. The complex responses of pore water pressures in soil on a slope based on sedimentary rock in Kiyomizu-dera Temple have been studied [5]–[7]. However, the subsurface water movements in the soil layer are not fully understood.

Fig. 1 Slope failure that occurred in 2013.

In this study, subsurface water movements are evaluated by investigating pore water pressure changes and hydraulic gradients during rainfall events.

METHOD

The study area is located on the hillslope behind Kiyomizu-dera Temple (Fig. 2). The soil-bedrock and measured were composed of sandstone, shale and chert. Surface layer composed of the colluvial deposit ranges 0.9 from to 4.0 m thick. A network system with data loggers was installed (Campbell, CR-1000) to record pore water pressures in real-time. Pore water pressures and rainfall were measured at 10-min intervals, using a tensiometer and tipping-bucket rain gage, respectively. Tensiometers were installed at 14 locations (Fig. 2).

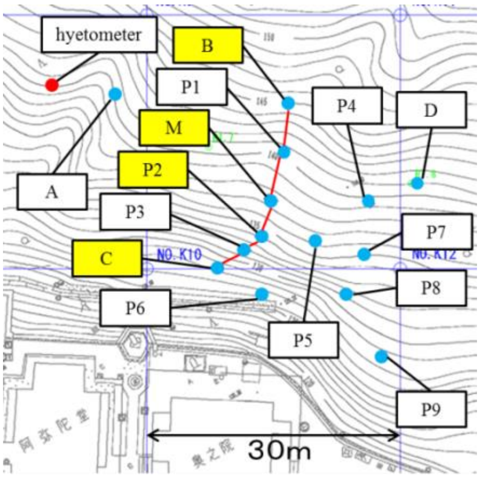

Fig. 2 Locations of observation points.

Table 1 Observation depths of tensiometers

Points	Observation depths (cm)
A	40, 80, 100
B	40, 80, 100, 200, 260
C	40, 80, 100, 230
D	40, 80, 100
M	20, 40, 60, 80, 100, 190
P1	30, 65
P2	30, 60, 100, 200
P3	30, 80
P4	30, 60, 100
P5	30, 60, 100, 200
P6	30, 60, 100, 200, 280
P7	30, 60, 100
P8	30, 60, 100, 200
P9	30, 60, 110

Table 1 shows the observation depths of the tensiometers.Tensiometer depths were decided based on the results of portable dynamic cone penetration tests. The observation period was from 13 August 2014 to 1 January 2015.

RESURTS AND DISCUSSION

Characteristic of Pore Water Pressures

Pore water pressures at points B, M, P2 and C (yellow points on Fig. 1) were evaluated to investigate subsurface water movements along the longitudinal direction of the slope. Figure 3 shows the variation of pore water pressure during the observation period (13 August 2014 to 1 January 2015). The cumulative rainfall during the period was 634 mm, with a peak rainfall of 38 mm/h at 13:00 on 16 August 2014. Pore water pressures reached positive values at each observation depth, indicating saturation at these depths. Decreases in pore water pressures after rainfall at deep observation depths (B-200 cm, B-260 cm M-190 cm and C-230) were smaller than those at shallow observation depths, indicating that deep soils retained wet conditions over a long period of time. However, at pore water

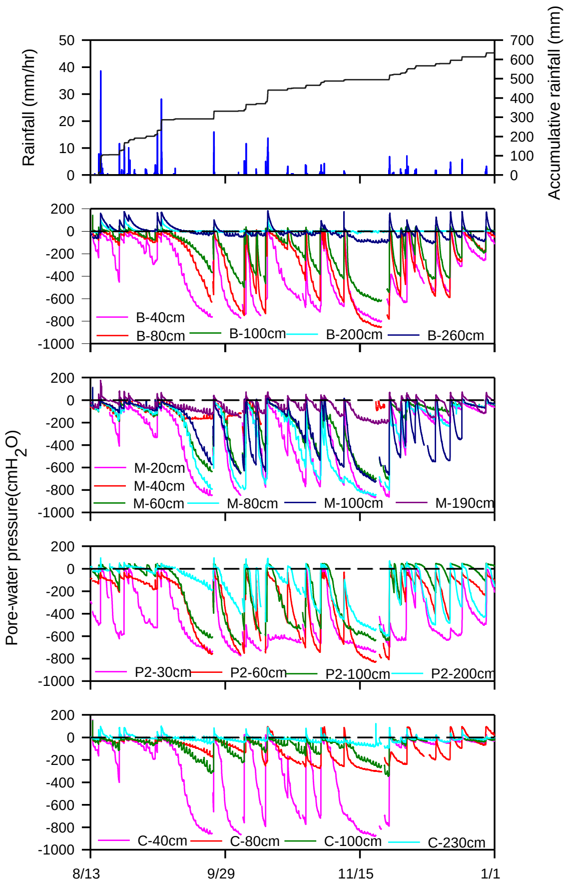

Fig. 3 Variation in the pore water pressure during rainfall events

pressures varied widely compared to other points at the soil-bedrock interface (B-260 cm, M-190 cm and C-230 cm). These results indicate that changes in pore water pressure showed different trends according to observation point and depth.

Direction of Subsurface Flow

The hydraulic gradient across the study area was investigated to evaluate groundwater flow in the soil layer. Figure 4 shows (a) hyetograph and hydraulic gradient between (b) B-40 cm and B-80 cm, (c) B-80 cm and B-100 cm, (d) B-100 cm and B-200 cm, (e) B-200 cm and B-260 cm. The hydraulic gradient was calculated from the hydraulic head and the distance between two observation depths. Hydraulic gradients with positive values indicate downward vertical flow between two observation depths at the same measurement point, while hydraulic gradients with negative values indicate upward vertical flow between two observation depths at the same point. The hydraulic gradients had negative values before the start of a rainfall event, and reached positive

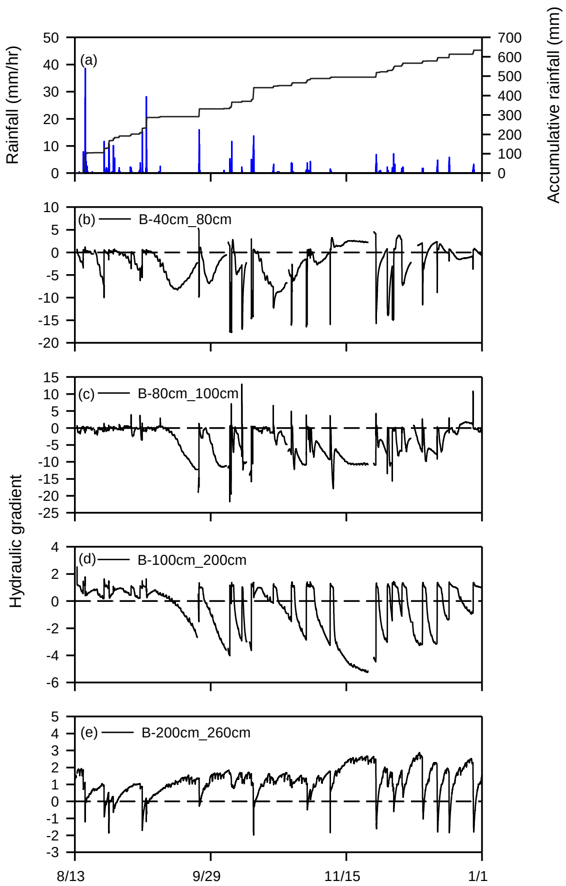

Fig. 4 (a) Hyetograph and hydraulic gradient between (b) B-40 cm and B-80 cm, (c) B-80 cm and B-100 cm, (d) B-100 cm and B-200 cm, and (e) B-200 cm and B-260 cm.

values during rainfall events (Fig. 4 b, c and d). This result indicates that the direction of soil water movement during dry conditions was from deep to shallow soil layers by evapotranspration and that infiltration occurred after rainfall events. The hydraulic gradients were positive before the start of rainfall and attained negative values during rainfall (Fig.4e). The result at point B indicated water movement from deep to shallow layers during rainfall events. This suggests that exfiltration from the bedrock layer to the soil layer occurred at this point, leading to a high probability of slope failure. Figure 5 shows (a) hyetograph and hydraulic gradient between (b) B-100 cm and M-100 cm, (c) M-100 cm and P2-100 cm, (d) P2-100 cm and C-100 cm (between each depth of 100 cm). Hydraulic gradients showed positive values during the observation period, indicating that subsurface water flows from the upper to lower levels of the slope at all times (Fig. 5b and d). Figure 5 c indicates that the hydraulic gradient reached negative values during the period 26 November 2014 to 1 January 2015. In addition, hydraulic gradients at deep observation points were positive during the entire observation period, indicating that subsurface water flows from the upper to lower areas of the slope (Fig. 6).

Effect of Soil Moisture Conditions on Subsurface Flow

To evaluate the relationships between the antecedent rainfall and the pore water pressure response, the effective rainfall was calculated using the method proposed by Suzuki and Kobashi [8].

$$M = (\ln 0.5)/\alpha \tag{1}$$

$$D_M(T) = D_M(T-1)e^{\alpha} + R(T)^{\alpha/2} \tag{2}$$

where M is the half-life, α is a reduction factor, D_M is the effective rainfall (mm), T is time (hour) and $R(T)$ is the rainfall (mm/h).

Values of effective rainfall for six half-life cases (2 h, 12 h, 24 h, 48 h, and 72 h) were calculated (Fig. 7). In the calculation, we considered the rainfall until 13 August 2014. The peaks of effective rainfall with half-lives of 2 h, 12 h, 24 h, 48 h and 72 h were 49 mm, 69 mm, 81 mm, 110 mm and 142 mm, respectively (Fig. 7). Figures 8 and 9 show the relationship between the pore water pressures at sampling points M-100 cm and M-190 cm, respectively, and the effective rainfall. The negative values of pore water pressures at 100 cm were larger than those at the soil-bedrock interface. At points M-100 cm and M-190 cm, the positive values of pore water pressure were constant throughout the

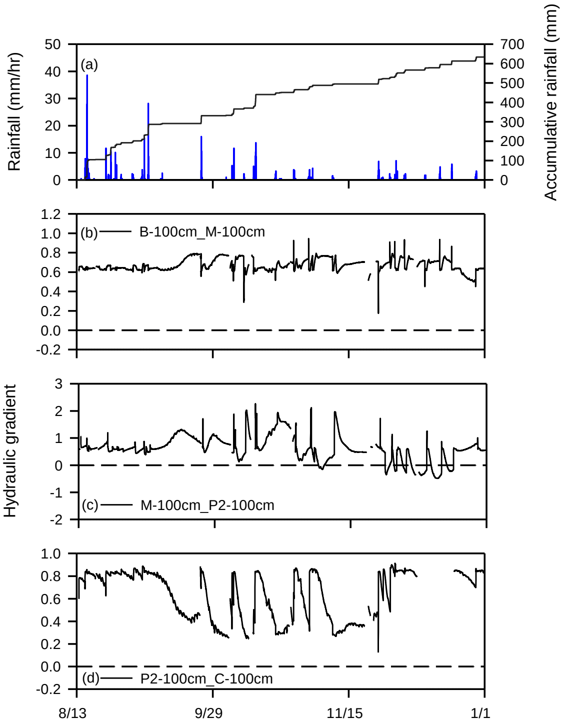

Fig. 5 (a) Hyetograph and hydraulic gradient between (b) B-100 cm and M-100 cm, (c) M-100 cm and P2-100 cm, and (d) P2-100 cm and C-100 cm (between each depth of 100 cm).

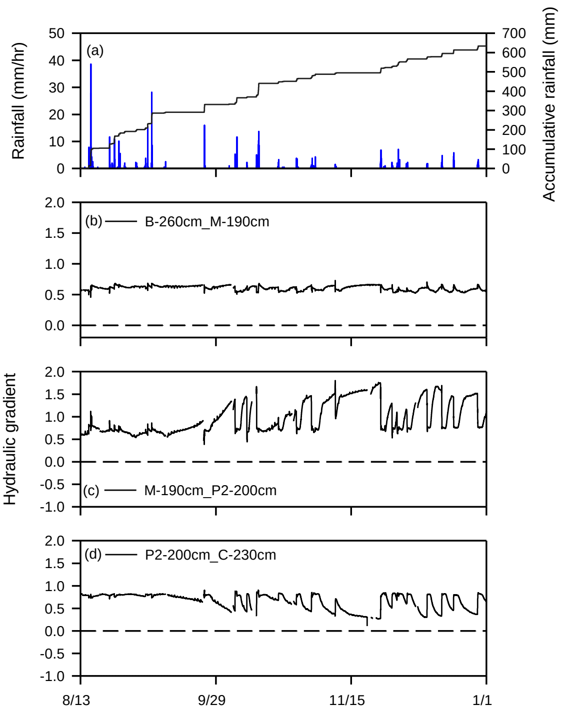

Fig. 6 (a) Hyetograph and hydraulic gradient between (b) B-260 cm and M-190 cm, (c) M-190 cm and P2-200 cm, and (d) P2-200 cm and C-230 cm.

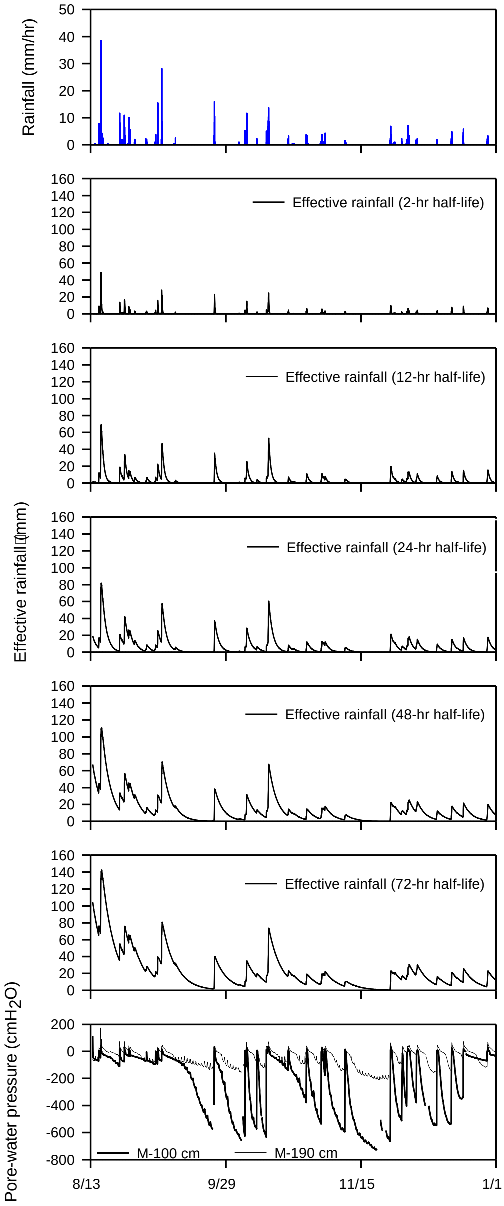

Fig. 7 Hyetograph, effective rainfall, and pore water pressure at M-100 cm and M-190 cm during the observation period.

observation period regardless of the difference in effective rainfall. In addition, the results indicate that saturation occurred at small values of effective rainfall. For dry periods, although values of pore water pressure were strongly influenced by the antecedent rainfall (i.e., long half-life), the effects were limited to a short time period after rainfall events.

CONCLUSION

In this study, subsurface water movements were evaluated by investigating pore water pressure

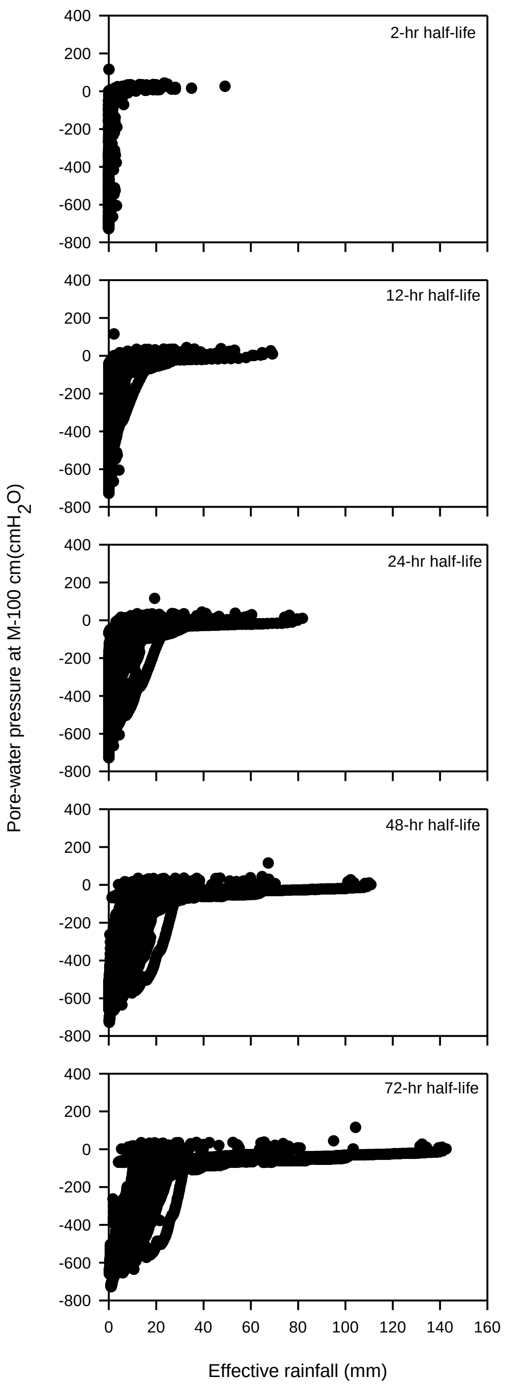

Fig. 8 Relationship between the pore water pressure at the M-100-cm point and the effective rainfall.

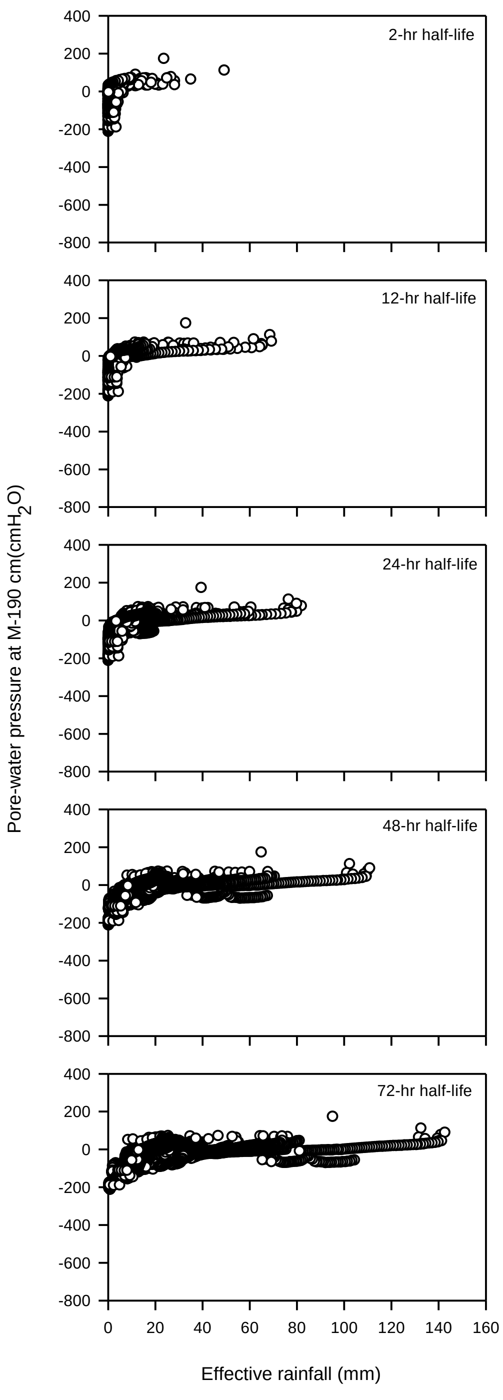

Fig. 9 Relationship between the pore water pressure at the M-190-cm point and the effective rainfall.

changes and hydraulic gradients during rainfall events. Decreases in pore water pressures after rainfall at deep observation depths were smaller than those at shallow depths, indicating that deep soil layers retained wet conditions over a long time period. The hydraulic gradient at point B indicated different trends between shallow layers and the soil-bedrock interface. Hydraulic gradients between 100-cm depth and the soil-bedrock interface were positive during the observation period, indicating that subsurface water flowed from the upper area to the lower end of the slope at all times. These results indicate that the saturation occurred after very small amounts of rainfall, regardless of soil moisture conditions.

ACKNOWLEDGEMENTS

This study was supported by grants from the Japan Society of the Promotion for Science (23221009 and 15K18714).

REFERENCES

[1] Ishida Y, Fujimoto M, Hiraoka N, Oya A, Sako K and Fukagawa R, “Study on criteria for slope failure based on rainfall intensity at Kiyomizu-dera”, Journal of Disaster Mitigation for Historical Cities, Vol.8, 2014, pp. 151-158 (in Japanese with English abstract).

[2] Uchida T, Asano Y, Mizuyama T and McDonnell J, “Role of upslope soil pore pressure on lateral subsurface storm flow dynamics”, Water Resources Research, Vol.40, 2004, W12401.

[3] Fujimoto M, Ohte N and Tani M, “Effects of hillslope topography on hydrological responses in a weathered granite mountain, Japan: comparison of the runoff response between the valley-head and the side slope”, Hydrological Processes, Vol.22, 2008, pp. 2581-2594.

[4] Onodera S, “Subsurface water flow in the Multi-Layered hillslope”, Journal of Geographical Review of Japan, Vol.64A-8, 1991, pp. 549-568 (in Japanese with English abstract).

[5] Sako K, Fukagawa R and Satomi T, “Slope monitoring system at a slope behind an important cultural asset”, Journal of Disaster Research, Vol.6, No.1, 2011, pp.70-79.

[6] Fujimoto M, Danjo T, Tsuchiyama T, Kimura T and Fukagawa R, “Detection of ground water movement using measuring method of sound of groundwater flow on the hillslope behind Kiyomizu Temple”, Journal of Disaster Mitigation for Historical Cities, Vol.8, 2014, pp.145-150 (in Japanese with English abstract).

[7] Danjo T, Fujimoto M, Kimura T, Hiraoka N and Fukagawa R, “Adamage of the slope around the Kiyomizu temple by the heavy rain from the Typhoon in 2013, and a study of the changing moisture in the ground of the slope behind an important cultural asset”, Journal of Disaster Mitigation for Historical Cities, Vol.8, 2014, pp. 115-122 (in Japanese with English abstract).

[8] Suzuki M and Kobashi S, “The critical rainfall for the disasters caused by slope failures”, Journal of Erosion Control Engineering, Vol.34, 1981, pp.16-26 (in Japanese with English abstract).

Fifth International Conference on Geotechnique, Construction Materials and Environment, Osaka, Japan, Nov. 16-18, 2015, ISBN: 978-4-9905958-4-5 C3051

SEDIMENT DISASTER RISK EVALUATION WITH THE USE OF SLOPE STABILITY ANALYSIS AT YOKOGAKI-TOGE PASS

Tsuyoshi Kibayashi[1], Yuko Ishida[2] Tatsuo Konegawa[3], Masamitsu Fujimoto[4], and Ryoichi Fukagawa[5]
[1] Graduate school of Science and Engineering, Ritsumeikan University, Shiga, Japan
[2] Research Organization of Science and Engineering, Ritsumeikan University, Shiga, Japan
[3] Mie Prefecture Mihama Town Office, Mie, Japan
[4, 5] Department of Science and Engineering, Ritsumeikan University, Shiga, Japan

ABSTRACT

The ancient road of the Kumano Pilgrimage route is one of the few world heritage sites registered by UNESCO. Yokogaki-toge, which is part of the Kumano Pilgrimage route, is located in the south of Mie Prefecture, near the center of Japan. In Yokogaki-toge, one landslide occurred in the rainy season in 2007, and three slope failures occurred due to typhoon Talas in 2011. It is important both to conserve the precious cultural heritage and to protect domestic and international visitors. Recognizing dangerous or safe sites will facilitate disaster mitigation related to slope disaster in the future. In this paper, slope failure at Yokogaki-toge was reproduced theoretically by a slope stability analysis using 2D FEM. Then, some slopes that were considered dangerous were analyzed using slope models developed in the same way, reproducing the analysis in Yokogaki-toge. Results of the analysis showed that the relative safety of these slopes could be estimated based on the slope angle. In conclusion, the correlation between safety factor and average slope angle of each slopes in Yokogaki-toge was calculated and the possibility of sediment disaster risk evaluation by only the correlation was shown.

Keywords: Kumano Pilgrimage route, groundwater level, slope stability analysis, slope risk assessment

1. INTRODUCTION

The Kumano Pilgrimage route, which runs through the Kii peninsula, was registered as a UNESCO World Heritage site in 2004. The Kumano Pilgrimage route has been familiar to many people through the ages as a sacred route to the Kii mountains. In 2011, typhoon Talas hit the Kii peninsula and inflicted much damage on the Kumano Pilgrimage route.

On the route, Yokogaki-toge is located on Nishinomine mountain, in the south of Mie Prefecture, as shown in Fig. 1. The Kounogi Rhyolite, a Kumano acidic igneous rock, is found at the crest, and a weathered mudstone of the Kumano Group is found in the lower half of Nishinomine mountain. In Yokogaki-toge, heavy rain in the rainy season of 2007 caused a landslide, and typhoon Talas in 2011 caused three slope failures, as shown in Fig. 2 [1]. It is important to identify dangerous places to ensure the safety of both this precious cultural heritage and sightseers from around the world.

2. METHOD

We tried to evaluate the risk of slope failure using numerical analysis. The evaluation model was made by reproduction analysis of slope failure at Yokogaki-toge in 2011. Understanding the groundwater level conditions at the time of slope failure is essential for reproduction analysis. In this study, we firstly focused on the relationship between rainfall and groundwater fluctuation. The groundwater fluctuation caused by the two kinds of geological conditions was considered, and groundwater levels at the time of slope failure were estimated using 4 month observational data on groundwater level and rainfall at the No. 2 landslide at Yokogaki-toge. However, the result obtained was wrong. Therefore, another groundwater level was estimated by sensitivity analysis of groundwater levels. Then, the slope failure at Yokogaki-toge was reproduced theoretically by a slope stability analysis. Finally, some dangerous slopes that had not collapsed were analyzed using the model developed for Yokogaki-toge, and a slope failure risk assessment for Yokogaki-toge was conducted. It is considered that the surface geometry and the angle of the slope have major impacts on the safety factor. We studied how the safety factor could be estimated based on the surface geometry and the slope angle.

3. RELATIONSHIP BETWEEN RAINFALL AND GROUNDWATER FLUCTUATION

The relationship between rainfall and groundwater fluctuation was considered using rainfall and groundwater level observational data from boreholes at the site of the No. 2 landslide. The soil water index was used for considering antecedent rainfall. Figure 3 shows the site of the borehole survey at the landslide location. To understand the variability of the groundwater levels caused by differences in geological conditions, spots B3 and B7 were chosen as representative points of Kounogi Rhyolite, and spot B4 was chosen as a representative point of weathered mudstone from the boring log. Figure 4 shows the relationship between the soil water index and the groundwater fluctuation. The characteristics of the groundwater fluctuation differ depending on the geological conditions. The groundwater level response at B4 (weathered mudstone) due to rainfall is sharper than that at B3 and B7 (Kounogi Rhyolite). The geological structures at B3 and B7 are the same, namely Kounogi Rhyolite on top of shale, and the behavior of the groundwater fluctuation is similar, although the altitude differed. There is a correlation between the soil water index and the groundwater level. Furthermore, the section with a high soil water index shows a strong correlation with the groundwater level. The typical peak point of the soil water index is indicated by a red sphere in Fig. 4, and the correlation coefficients between groundwater level (B3, B4) of the E survey line and the soil water index were determined, as shown in Fig. 5. The correlation coefficient for B3 is 0.328, and that for B4 is 0.754. The correlation coefficient at B4 is high.

4. ESTIMATED GROUNDWATER LEVEL AT THE TIME OF SLOPE FAILURE OCCURRENCE

The groundwater levels of the slope failure occurrence in 2011 were estimated based on the relationship between the soil water index and the groundwater fluctuation. The three slope failures were caused by typhoon Talas from September 3 to 4, 2011. The graph of Fig. 6 illustrates the presumed groundwater level based on the soil water index from July 1 to September 30, 2011, at B3 (Kounogi Rhyolite) and B4 (weathered mudstone) in the landslide area. Over 20 mm/h rainfall continued more than 10 hours, and the maximum recorded rainfall was 66 mm/h during September 3–4. This rainfall was considered to have caused the slope failure. The soil water index increased to a maximum of 376. It is physically impossible because the presumed groundwater level at B4 in this period is over ground level.

Therefore, the result suggested that estimation of groundwater level at the time of slope failure occurrence using this correlation equation is impossible. The possible cause of this wrong correlation equation is shortage of heavy rainfall data. The maximum soil water index in observed 4 months was 143. There is room for reconsidering this estimate method if more heavy rainfall data obtain.

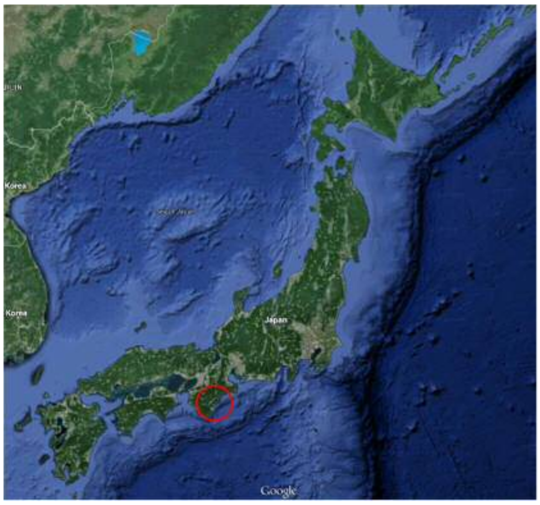

Fig. 1 Study area (add Google Maps)

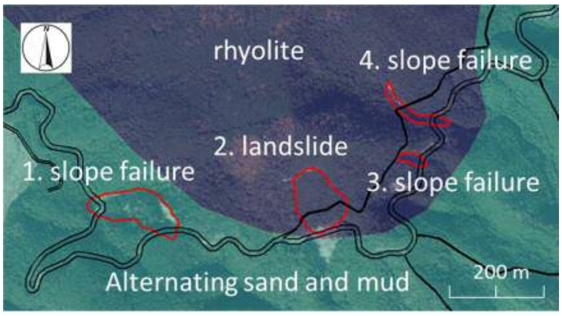

Fig. 2 Collapses and geological condition

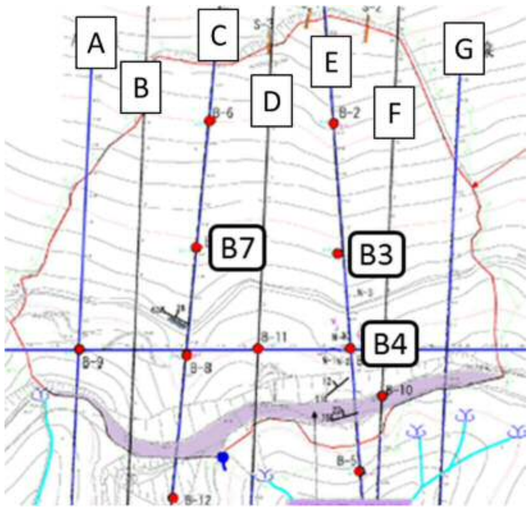

Fig. 3 Implementation site of borehole survey

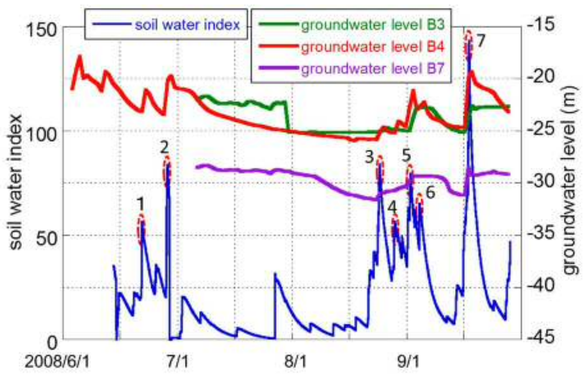

Fig. 4 Soil water index and groundwater level

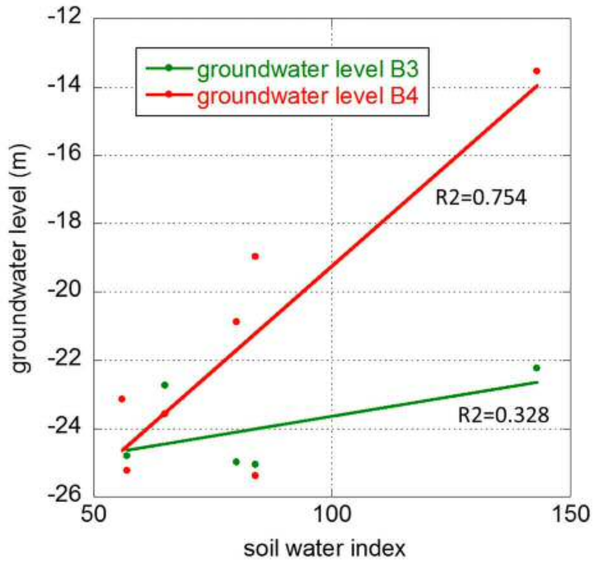

Fig. 5 Correlation between soil water index and groundwater level

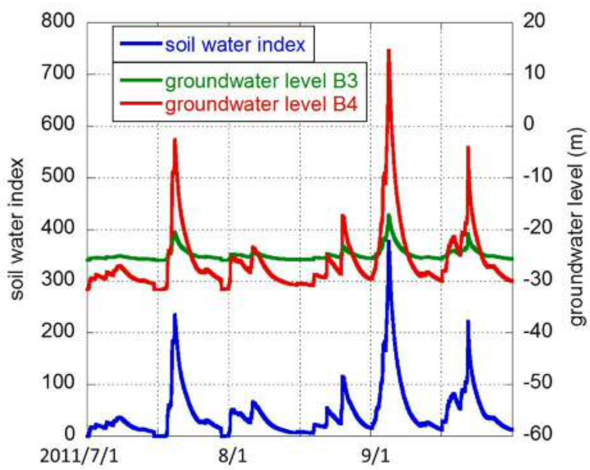

Fig. 6 Estimated groundwater level

5. DEVELOPMENT OF THE STANDARD SLOPE STABILITY ANALYSIS METHOD AT YOKOGAKI-TOGE

The standard analysis method is developed in order to evaluate slope stability of various slopes at Yokogaki-toge. Sensitivity analysis was conducted to estimate the groundwater level at the time of the No. 3 slope failure. Finite element method (FEM) analysis was performed using the commercially available PLAXIS 2D software. A constitutive model of a geological situation is an elastic–perfectly plastic model. The yield criterion in this analysis uses the Mohr–Coulomb model. A shear strength reduction method is used in slope stability analysis. The conditions for making the model slope were as follows:

- Surface geometry: 1/500 ground plan.
- Surface thickness: handy dynamic cone penetration test
- Geological boundary: the research report of landslide 2007.
- Groundwater level: changes in parallel with the geological boundary of the substratum layer and the weathered layer.

The analysis parameters were based mainly on a site investigation. Figure 7 and Table 1 show the model slope analysis and analysis parameters. The safety factor of the slope was calculated based on increases in groundwater level, calculated in 1-m increments. The relationship between groundwater depth and safety factor is shown in Table 2. The rise in groundwater level led to a commensurate decrease in the safety factor. The results of the analysis suggest that the groundwater level at the time of slope failure occurrence had increased to -8.0 m. Figure 8 shows the total displacement of pattern 4. The dotted line represents the current state line at the time of slope failure occurrence. The displacement analysis largely matched the displacement of the actual slope failure.

6. RELATIVE RISK ASSESSMENT IN "YOKOGAKI-TOGE

The 6 sites such as deep valleys and steep areas having slope failure risk at Yokogaki-toge were chosen. The analysis of these slopes was performed using the standard method developed in Chapter 4. The 6 lines in Fig. 9 shows the transversal lines of hazardous slopes from No.1 to No.6. Slope models of these sites were prepared, and slope stability analyses were conducted. The conditions for the model slope are as follows:

- Surface geometry: 1/500 ground plan.

- Slope model range: from the forest road to 15 m above the pilgrimage route.
- Surface thickness: 2.9 m (average of handy dynamic cone penetration test).
- Geological boundary: site reconnaissance results.
- Groundwater level: -9.0 m below geological boundary.

From No.1 to No.6 slope models and total displacement are shown in Fig. 10 and 11. From a result, the correlation between the model slope and the safety factor was confirmed. First, the correlation between the surface geometry and the analysis result was investigated. The displacement of each slope focused on areas with steep slopes and boundaries between gentle and steep slopes. The displacement of flat surface, such as the No. 2 slope case, covered the whole of the slope. The direct connection between surface geometry and the safety factor was not confirmed, although there is an incline in the displacement. Second, the correlation between the average slope angle and the analysis result was studied. Table 3 shows the safety factor and the average slope angle for each analysis. The safety factors of steep slopes, such as the No. 1 slope case, indicated low values compared with the others. Figure 12 shows the relationship between the average slope angle and the safety factor. The correlation coefficient for the relationship between the average slope angle and the safety factor had a high value, with increases in the average slope angle associated with decreases in the safety factor. The relationship between average slope angle and safety factor has merit as a simple evaluation method for slope stability in Yokogaki-toge.

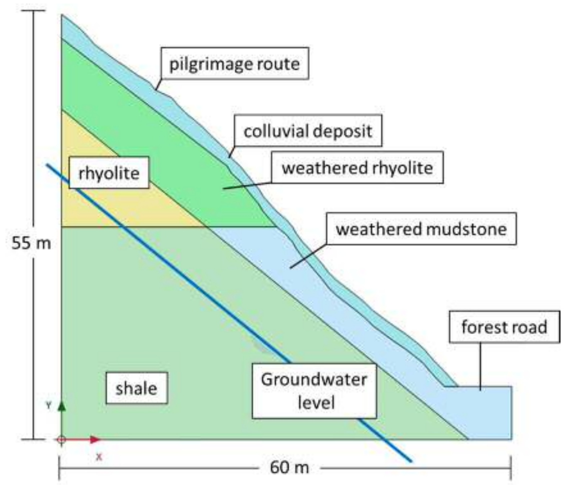

Fig. 7 Model slope

Table 1 Parameters of analysis

	colluvial deposit	weathered mudstone	weathered rhyolite	rhyolite	shale
γ_{unsat} (kN/m^3)	16.5	21.0	22.0	25.0	25.0
γ_{sat} (kN/m^3)	18.5	22.0	24.0	25.5	25.5
E (kN/m^2)	50000	55000	100000	500000	600000
ν	0.35	0.35	0.35	0.30	0.30
c (kN/m^2)	2.37	9.5	41.1	500	600
ϕ (deg)	33.2	27.8	36.0	40.0	40.0
Ψ (deg)	0	0	0	0	0
k (m/s)	1.36×10^{-3}	5.90×10^{-4}	1.00×10^{-3}	5.00×10^{-5}	1.00×10^{-5}

Table 2 Relationship between groundwater depth from the geological boundary and safety factor

pattern	groundwater depth from geological boundary (m)	safety factor
1	-12	1.110
2	-11	1.097
3	-10	1.087
4	-9	1.076
5	-8	×

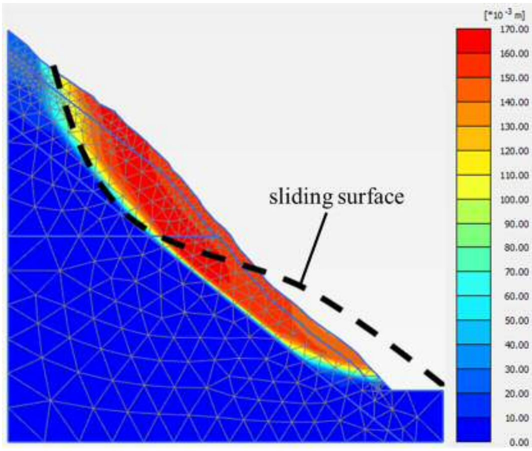

Fig. 8 Pattern 4: total displacement and sliding surface

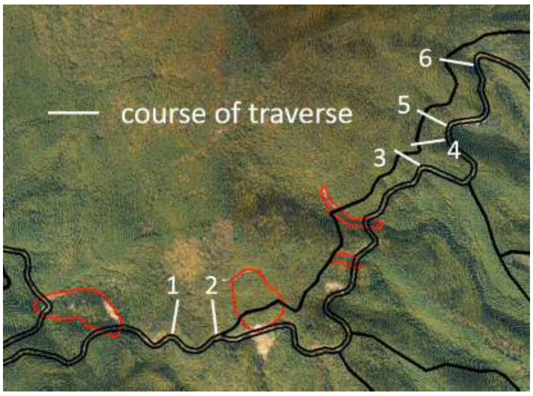

Fig. 9 Inquest cross- section surface

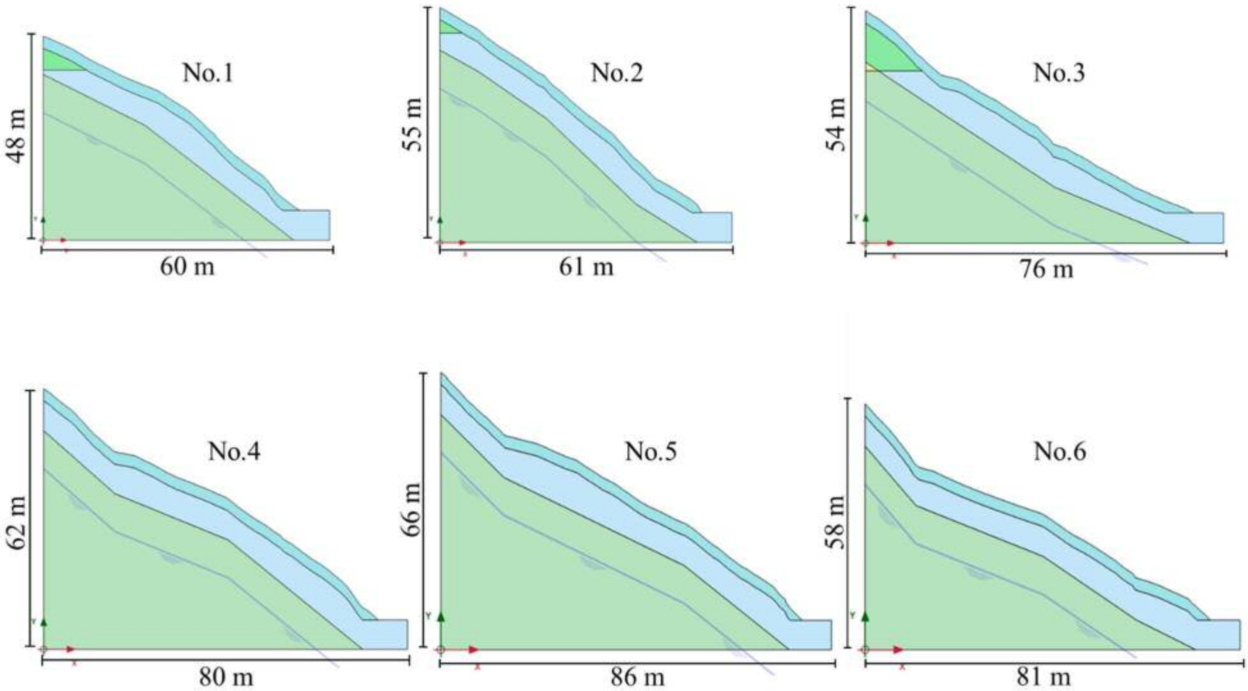

Fig. 10 Slope models

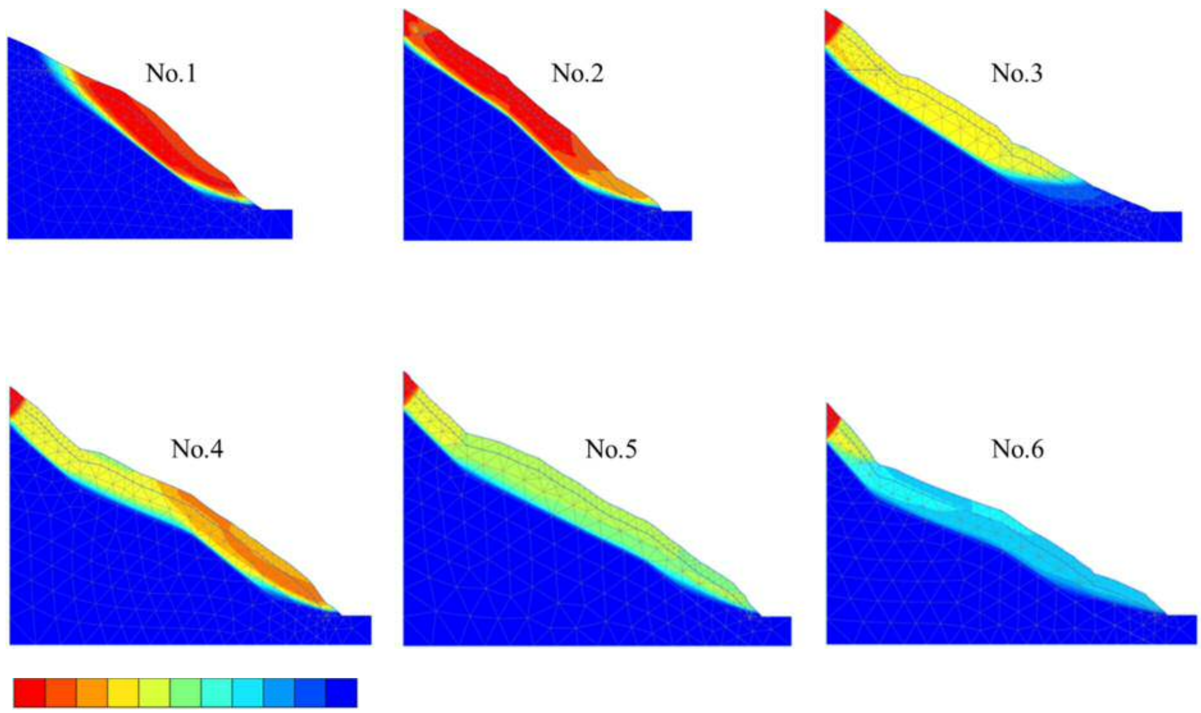

Fig. 11 Total displacement

Table 3 Safety factor and average slope angle

slope No.	safety factor	average slope angle (deg)
1	1.105	34.15
2	1.042	37.99
3	1.321	31.62
4	1.152	34.62
5	1.144	34.44
6	1.325	32.07

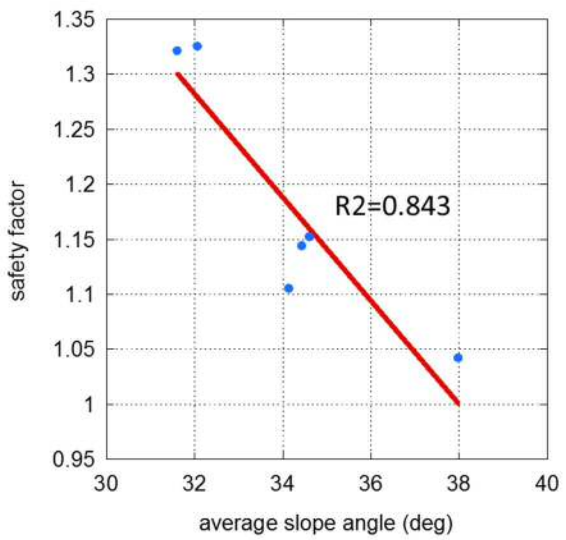

Fig. 12 Relationship between average slope angle and safety factor

7. CONCLUSION

In this study, we firstly tried to estimate the groundwater level at the time of slope failure occurrence based on the relationship between groundwater fluctuation and soil water index.

The variable characteristics of groundwater levels caused by differences in geological conditions were examined. However, we could not estimate the groundwater level at the time of slope failure occurrence, because there is no heavy rainfall data that might have caused a slope failure in the observation data. Second, a relative risk assessment using the groundwater level developed in the sensitivity analysis and standard method developed in the same way of reproduce analysis was conducted at the 6 slopes that were assumed to be potentially hazardous. The risks of each slopes were evaluated based on the safety factor. We confirmed that the average slope angle greatly affected the safety factor. The results suggested the possibility of estimating the safety factor simply based on the average slope angle.

ACKNOWLEDGEMENTS

This work was supported by Grants-in-Aid for Scientific Research (C) No. 26350380 (2014-2016) from the Japan Society for the Promotion of Science. In addition, we would like to sincerely thank Kumano agriculture and forestry office for providing groundwater level observation data.

REFERENCES

[1] Geological Survey of Japan, AIST (ed.). 2014. Seamless digital geological map of Japan 1: 200,000. Jan 14, 2014 version. Geological Survey of Japan, National Institute of Advanced Industrial Science and Technology.

DYNAMIC RESPONSE OF SINGLE PILE LOCATED IN SOFT CLAY UNDERLAY BY SAND

Deendayal Rathod[1], K. Muthukkumaran[2] and T.G. Sitharam [3]
[1]Assistant Professor, Department of Civil Engineering, NIT, Tiruchirappalli, India.
[2]Associate Professor, Department of Civil Engineering, NIT, Tiruchirappalli, India.
[3]T.G. Sitharam, Professor, Department of Civil Engineering, IISc Bangalore, India.

ABSTRACT

Piles have been extensively used for supporting axial loads and lateral loads for variety of structures including high rise buildings, transmission towers, power stations, offshore structures and highway and railway structures. Pile foundations are subjected to lateral loading due to wind action, wave action, earthquake and impact of ships in dock and harbour structures. In such cases, studying the behavior of pile foundation due dynamic loading is essential. Compare to field tests, the numerical modeling is an economical way to analyze the response of piles. This paper presents the dynamic response of a single concrete pile of 0.4m diameter, 11.5m length located in soft clay underlay by sand subjected to static vertical load as well as ground acceleration simultaneously. Finite element software PLAXIS 2D is used to analyze the pile. From the analysis, the deformation and acceleration behavior of pile with respect to time has been studied.

Keywords: Single pile, Dynamic response, Plaxis 2D, Deformation, Acceleration

INTRODUCTION

Piles are columnar elements in a foundation which have the function of transferring load from the superstructure through weak compressible strata or less compressible soils onto rock. Piles used in marine structures are subjected to lateral loads from the impact of berthing ships and from waves. Piles used to support retaining walls, bridge piers and abutments, and machinery foundations carries combinations of vertical and horizontal loads. It is found that at various sites in the coastal region, the top layer soil is soft clay with varying thickness of 5.0 to 25m and most of the structures which are constructed on soft clay. Matlock and Reese [9] gave a generalized solution in non-dimensional form for the laterally loaded pile for both elastic and rigid behavior assuming soil modulus variation linearly with depth. Broms [2] developed solutions for the ultimate lateral resistance of a pile assuming the distribution of lateral soil pressure and considering static of the problem. Singh and Verma [16] conducted large-scale model tests in sand under controlled density. Lateral load tests were conducted on single pile and pile groups. The load deflection curves were found to be non-linear and were flatter at higher load levels showing loss of soil resistance. Poulos and Davis [12] gave comprehensive collections of solutions for the design of pile foundations to resist static lateral load. Ernestn aesgaard [5] carried out full-scale field tests to assess the ability of the piles to withstand large lateral deformations that may be caused by earthquake-induced soil liquefaction. Rao et al. [13] carried out tests on model groups of piles to support dolphin-type structures. Static load tests have been conducted on instrumented model pile groups embedded in a marine clayey bed. The spacing between piles, number of piles in a group, and arrangement of pile group with respect to the direction of lateral loading have been varied. The results indicated that the capacity of pile group not only depends on the spacing between the piles, but also on the arrangement of piles in the group. Mezazigh and Levacher [11] conducted the centrifuge test on model single aluminum pile placed on horizontal ground and sloping ground surface in cohesionless soil by varying the distance from the crest of slope. The effect of distance to the slope, slope angle and soil properties were studied. The load versus deflection curves; bending-moment and p-y curves were derived for piles close to slopes and compared to the horizontal ground response. Rao et al. [14] conducted experiments on pile groups and studied the influence of parameters like flexural rigidity of pile material, embedment length of pile and arrangement of piles on the behavior of laterally loaded pile groups. The results indicated that the lateral load capacity of the pile group depends mainly on the rigidity of pile soil system for different arrangements of piles within a group. Rollins et al. [15] performed static lateral load test on a full-scale pile group to determine the resulting soil-pile interaction effects. A 3 × 3 pile group at three-diameter spacing was driven into a soil profile consisting of soft to medium-stiff clays and silts underlain by sand. It is observed that the pile group deflected over two times more than the single pile under the same average load and trailing rows carried lesser load than that of leading row, and middle row piles carried the lowest loads. Ilyas et al. [7] conducted a series of centrifuge model tests to examine the behavior of laterally loaded pile groups of 2, 2×2, 2×3, 3×3, and 4×4 piles with a center-to-center spacing of three or five times the pile width in normally consolidated and over consolidated kaolin clay. It is established that the pile group efficiency reduces significantly with increasing number of piles in a group due shadowing effect. And also, it is found that the front piles experience larger load and bending moment than that of the trailing piles. Boominathan and Ayothiraman [3] carried out the static and dynamic lateral load tests on model aluminium single piles embedded in soft clay to study their bending behavior. The results indicated that the maximum dynamic bending moment of pile in soft clay is about 1.5 times higher than the maximum static bending moment. Cubrinovski et al. [4] studied the pile response to lateral spreading by 3-D soil–water coupled dynamic analysis by shaking in the direction of ground flow. Liyanapathirana and Poulos [8] studied the analysis of pile behavior in liquefying sloping ground. Hasan Ghasemzadeh and Mehrnaz Alibeikloo [6] carried out the pile–soil–pile interaction in pile groups with batter piles under dynamic loads. Amin rahmani and Ali pak [1] studied dynamic behavior of pile foundations under cyclic loading in liquefiable soils. Therefore, the literature on the behavior of piles under static load is abundant. Very few researchers studied the fundamental characteristics of pile in soft clay under dynamic conditions. This paper aims to fill this gap through a comprehensive numerical analysis using PLAXIS 2D carried out on single piles embedded in soft clay underlay by sand subjected to static vertical load as well as ground acceleration simultaneously.

MATERIAL PROPERTIES

Single concrete pile with 0.4m diameter and 11.5m length is located in soft clay underlay by sand subjected to static vertical load as well as ground acceleration simultaneously.The pile parameters are taken as Young's modulus of concrete (E) = $3x10^7$ kN/m^2, Poisson's ratios of concrete (μ) = 0.1, Unit weight of concrete (γ_c) = 25 kN/m^3 for dynamic analysis. The properties of soft clay are taken as γ_{unsat}=16kN/m^3, γ_{sat}=18kN/m^3, E_{ref} =15000kN/m^2, R_{inter}=0.5, C=2kN/m^2, ϕ=24°, μ=0.3 and the properties of sand were taken as γ_{unsat}=17kN/m^3, γ_{sat}=20kN/m^3, E_{ref} =50000kN/m^2, E_{oed}=50000kN/m^2 E_{ur}=150000kN/m^2, P_{ref}=100kN/m^2, R_{inter} =0.67, C=1kN/m^2, ϕ=31°, μ=0.2.

FINITE ELEMENT MODEL

For dynamic analysis, the 1990 earthquake data of California having local magnitude (ML) 5.40 on Richter scale with peak horizontal acceleration -239.90cm/sec^2 is used. Fig.1 shows real accelerogram ground acceleration versus time graph used for analysis. It contained in standard SMC format (Strong motion CD-ROM) which can be read and interpreted by PLAXIS**.** The earth quake is modeled by imposing a prescribed displacement at the bottom boundary. PLAXIS has convenient default setting to generate standard boundary conditions for earth quake loading using SMC files.

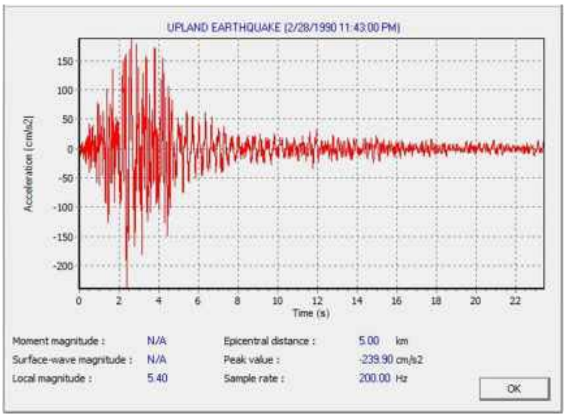

Fig.1 Ground acceleration vs. Time

The geometry is simulated by means of axisymmetric model in which the pile is positioned along the axis of symmetry. Both pile and soil are modeled with 15-noded elements. Interface elements are placed around the pile to model the interaction between pile and soil. The boundaries of model are taken sufficiently far away to avoid the influence of boundary conditions. Standard absorbent boundaries are used to avoid the spurious reflections. The presence of ground water table is neglected. Fig.2 shows the geometry model of pile. The pile is considered to be linear elastic.

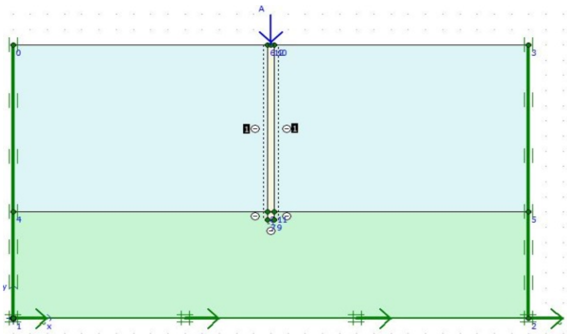

Fig.2 Geometry model of pile

The top layer of soil (clay) is modeled with simple Mohr-Coulomb model with undrain condition and the bottom layer of soil (sand) is modeled by means of hardened soil model in order to model the nonlinear deformations below the tip of pile. The pile is subjected to vertical load of 700 kN and earthquake ground excitation simultaneously. Fig.3 shows the finite element mesh generated. The mesh near the pile is observed with high concentration of stresses.

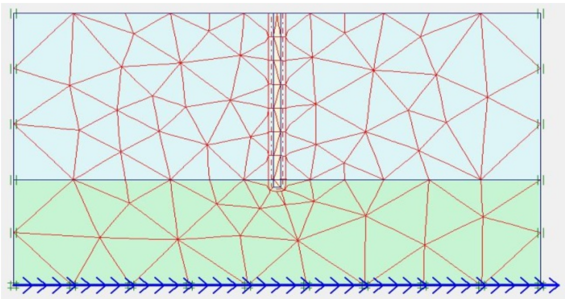

Fig.3 Finite element mesh

RESULTS AND DISCUSSION

The fig.4 shows the deformation versus time plot at top of pile surface and fig.5 shows the deformation versus time at bottom of pile surface when it is subjected to vertical load of 700 kN and earthquake ground excitation (both static and dynamic loading simultaneously).The maximum displacement of pile at top and bottom observed to be $10x10^{-7}$m at t=0.2 Seconds and $18.6X10^{-7}$ m at t=1 Seconds.

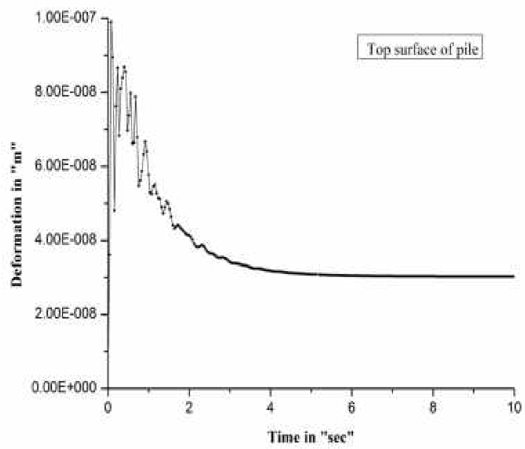

Fig.4 Deformation Vs Time at top of the pile

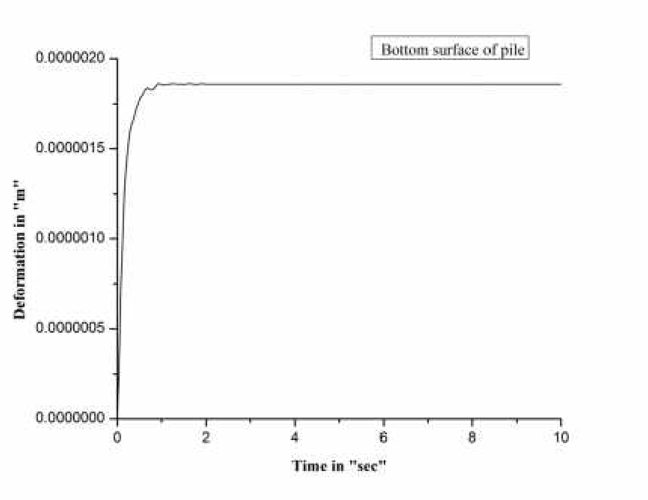

Fig.5 Deformation Vs Time at bottom surface of pile

Figs.6 and 7 shows the acceleration versus time plots at top and bottom surface of pile when it is subjected to both static and dynamic loading. The acceleration of $1.34X10^{-4}$ m/sec^2 is observed at t=0.3 sec. at top surface of pile and the acceleration of $7.7X10^{-4}$ m/sec2 observed at t=0.5sec at the bottom surface of pile.

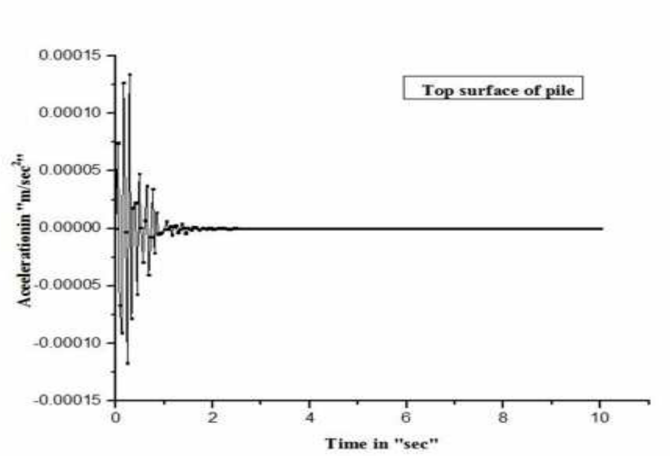

Fig.6 Acceleration Vs Time at top surface of pile

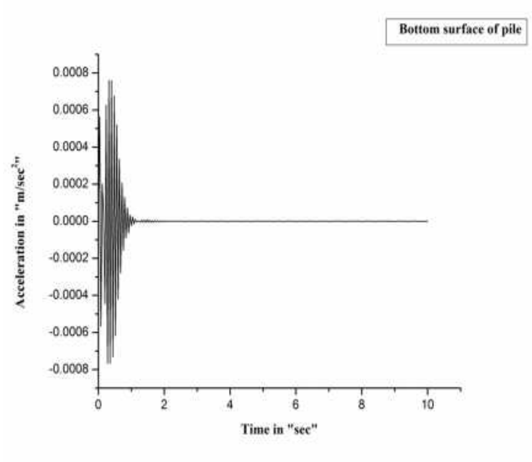

Fig.7 Acceleration Vs Time at bottom surface of pile

CONCLUSIONS

Finite element software PLAXIS 2D is used to analyze the pile. The dynamic response of a single concrete pile located in soft clay underlay by sand subjected to static vertical load as well as ground acceleration simultaneously were analysed. From the analysis, the deformation and acceleration behavior of pile with respect to time has been studied.The maximum displacement of pile at top and bottom is $10x10^{-7}$m at t=0.2 Seconds and $18.6X10^{-7}$ m at t=1 Seconds respectively. The acceleration of $1.34X10^{-4}$ m/sec^2 is observed at t=0.3 sec. at top surface of pile with less number of cycles and the acceleration of $7.7X10^{-4}$ m/sec2 observed at t=0.5sec at the bottom surface of pile with more number of cycles. The top tip of the pile is more susceptible for damage compare to bottom of pile.

REFERENCES

[1] Amin Rahmaniand Ali Pak(2012) "Dynamic behavior of pile foundations under cyclic loading in liquefiable soils" *Computers and Geotechnics 40 (2012) 114–126.*

[2] Broms, B. B. (1964)."Lateral resistance of piles in cohesive soils."*J. Soils Mech. and Found. Div., ASCE, 90(2), 27-63.*

[3] Boominathan A. and Ayothiraman R. (2007). "An experimental study on static and dynamic bendingbehavior of piles in soft clay". *Geotech.Geologic. Eng., 25, 177–189.*

[4] Cubrinovski M, R. Uzuoka, H. Sugita, K. Tokimatsu, M. Sato, K. Ishihara,Y. Tsukamoto, T. Kamata(2008) "Prediction of pile response to lateral spreading by 3-D soil–watercoupled dynamic analysis: Shaking in the direction of ground flow. *Soil Dynamics and Earthquake Engineering 28 (2008) 421–435*

[5] Ernestnaesgaard(1991) " Lateral load tests to examine large-strain (seismic) behavior of piles" Can. Geotech. J. 29, 245-252 .

[6] HasanGhasemzadeh, MehrnazAlibeikloo(2011) "Pile–soil–pile interaction in pile groups with batter piles under dynamic loads".*Soil Dynamics and Earthquake Engineering 31 (2011) 1159–1170.*

[7] Ilyas T., C. F. Leung, Y. K. Chow and S. S. Budi (2004). "Centrifuge Model Study of Laterally Loaded Pile Groups in Clay".*Journal of Geotechnical and Geo-environmental Engineering*,Vol. 130, No. 3, March 1, 2004.

[8] Liyanapathirana D.S. and H.G. Poulos(2010) "Analysis of pile behavior in liquefying sloping ground". *Computers and Geotechnics 37 (2010) 115–124.*

[9] Matlock,H.,and Reese,L.C. (1960)."Generalized solutions for laterally loaded piles". *J. of Soil Mechanics and Foundation Div., ASCE,* 86(5), 63-91.

[10] Muthukkumaran, K., R. Sundaravadivelu and S.R. Gandhi (2008) "Effect of slope on P-Y curves due to surcharge load", *Soils and Foundations* 48(3), 353 -361.

[11] Mezazigh, S. and Levacher, D(1998)" Laterally loaded piles in sand: slope effect on p-y reaction curves", *Can. Geotech. J.,* 35, (3), 433–441.

[12] Poulos, H. G. and Davis, E. H. (1980) Pile foundation analysis and design, *Wiley, New York.*

[13] NarasimhaRao, S., Ramakrishna, V. G. S. T., and Raju, G. B. (1996) "Behavior of pile-supported dolphins in marine clay under lateral loading." *J. Geotech. Geoenviron. Eng.*, 122(8), 607–612.

[14] NarasimhaRao, S., Ramakrishna, V. G. S. T., and Rao, M. B. (1998) "Influence of rigidity on laterally loaded pile groups in marine clay." *J. Geotech. Geoenviron. Eng.*, 124(6), 542–549.

[15] Rollins, K. M., Peterson, K. T. and Weaver, T. J. (1998) "Lateral load behavior of full-scale pile group in clay", *J. Geotech. Geoenviron. Eng.*, 124, (6), 468–478.

[16] Singh, A. and R.K.Verma(1973) "Lateral resistance of a field model of pile group in sand and its comparison with laboratory model". *Indian Geotech. Journal,* 3, 113-117.

Fifth International Conference on Geotechnique, Construction Materials and Environment, Osaka, Japan, Nov. 16-18, 2015, ISBN: 978-4-9905958-4-5 C3051

INFLUENCE OF MEASURED AND ANALYSIS RAINFALLS ON SEEPAGE: NUMERICAL SIMULATION ON SLOPE AT THE YOKOGAKI-TOGE PASS

Yuko Ishida[1], Tsuyoshi Kibayashi[2] , Tatsuo Konegawa[3], Masamitsu Fujimoto[2] and Ryoichi Fukagawa[2]
[1]Institute of Disaster Mitigation for Urban Cultural Heritage, Ritsumeikan University, JAPAN,
[2]Department of Science and Engineering, Ritsumeikan University, JAPAN; [3] Mihama Town, JAPAN

ABSTRACT

Many world cultural heritages are consisted of buildings, including shrines, temples, and ruins; only two such heritages are include pilgrimage routes have a figuration as roads. One of these is the Kumano Pilgrimage Route, which is a 307.6 km route in the Kii Peninsula in central Japan, on which there is a risk of sediment disasters. In 2011, Typhoon Talas caused a slope failure at Yokogaki-toge, which is part of the Kumano pilgrimage route. Risk assessment is needed to protect cultural heritage sites from sediment disasters. Seepage and slope stability analysis using a two-dimensional finite element method can be applied to slopes for risk evaluation. We have observed rainfall at multiple locations within Yokogaki-Toge, with regional variations in amount of rainfall also noted. We conducted a saturated-unsaturated seepage flow analysis of the collapsed slope using two types of rainfall, and also considered suitability of these rainfalls for risk assessment in this paper.

Keywords: Slope failure, Seepage flow analysis, Slope stability, Disaster Mitigation of Cultural heritage site.

1. INTRODUCTION

“Yokogaki-toge” is part of the world heritage site “Sacred Sites and Pilgrimage Routes in the Kii Mountain Range”. Since ancient times, the Kii Mountain Range has been considered a special place where gods dwell in Japanese mythology. This world heritage site, which is located on the Kii Peninsula in central Japan, consists of three sacred sites and pilgrimage routes that are inseparable from the nature of the Kii Mountain Range. The roads that comprise this world heritage site are approximately 307.6 km long; Yokogaki-toge is approximately 1.8 km long. Many people experience a feeling of spirituality, known as “Wabi-Sabi”, when travelling this beautiful route as shown in Fig.1, which is approximately 1,200 years old.

The majority of the pilgrimage route is vulnerable geologically and slope failures often occur along its course. In Yokogaki-toge, a landslide occurred in the rainy season in 2007, and a deep-seated landslide, slope failure, and debris flow occurred in 2011 during Typhoon Talas, as shown in Figs. 2 and 3.

To protect this precious ancient route against sediment disasters, we need to evaluate the vulnerability of the slopes. Mass movements such as landslides, slope failures, surface failures, and debris flows result from a combination of influencing factors. This study considered the occurrence of various mass movements at Yokogaki-toge, focusing on rainfall as a trigger for slope failures. Rainfall has been measured at nine points at Yokogaki-toge since August, 2014 (Fig.3) to determine the rainfall characteristics of this mountainous area.

Fig. 1 The “Yokogaki-toge” Pilgrimage Route

Fig. 2 The deep-seated landslide at Yokogaki-toge

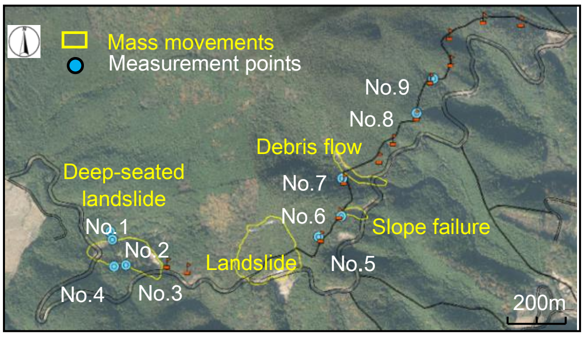

Fig. 3 Mass movements and measurement spots [1]

2. ANALYSIS OF FACTORS CAUSING MASS MOVEMENTS

To predict collapse, it is important to identify the causes of the different types of mass movement that occurred at Yokogaki-toge during the rainfall event of Typhoon Talas in 2011. Using a geographic information system and field and document surveys, we evaluated geological factors such as slope angle, aspect, and curvature, the mechanism of collapse, and rainfall. Geological structure was identified as the main cause of the collapse.

Generally, large, deep landslides result from a big total rainfall event with or without high-intensity rainfall that occurs at the end of an event, while surface failure results from high-intensity rainfall following a medium rainfall event. Since the characteristics of a rainfall event might predict the characteristics and scale of slope failures, we focused on rainfall to answer the following questions:

1. Is the rainfall at a collapse site greater than the rainfall at a non-collapsed site?
2. Would a north-facing slope collapse because the amount of rainfall on it is greater compared to a south-facing slope?

Nine rain gauges were set up on Yokogaki-toge, as shown in Fig. 3: Nos. 1 and 2 were on the south-facing slope; Nos. 3 and 4 were on the north-facing slope; and the north and south slope are approximately 100 m apart. Nos. 5–9 were placed 100–300 meters apart on the east- or southeast-facing slopes. Nos. 1–4 were on the deep-seated landslide site; No. 6 was on the slope failure site; No.7 was on the debris flow site; and Nos. 5, 8, and 9 were on non-collapse slopes. Ideally, rain gauges should be set in unobstructed open space; however, there are few such places in Yokogaki-toge because of its forest. Consequently, gauge No. 1, and Nos. 4–9, were affected by shielding from trees. Nos. 2 and 3 were set in the open space caused by the collapse.

3. CHARACTERISTICS OF MEASURED RAINFALL

During the 4-month measurement period, rain gauge No.1 had a loose connection. Therefore, the results were analyzed without including the data from this gauge.

Figure 4 compares the rainfall data for the collapsed and non-collapsed sites. The data farthest to the left (green), called Mihama, were obtained by the Japan Meteorological Agency, and used as the standard rainfall. The three right-most bars (blue) are for the non-collapsed site, and the other data (red) are the rainfall at the collapsed site. The upper figure compares the total amount of rainfall; the middle figure compares the maximum hourly rainfall; and the lower figure compares the maximum 10-minute rainfall.

The shielding effect of trees is seen in the total amount of rainfall and maximum hourly rainfall. Excluding sites Nos.2 and 3, which were not shielded by trees, the total and maximum hourly rainfall at the collapsed site did not differ markedly from that at the non-collapsed sites. However the amount of rainfall at the collapsed site was slightly greater than that at the non-collapsed site. The maximum 10-minute rainfall differed by location irrespective of collapse or non-collapse.

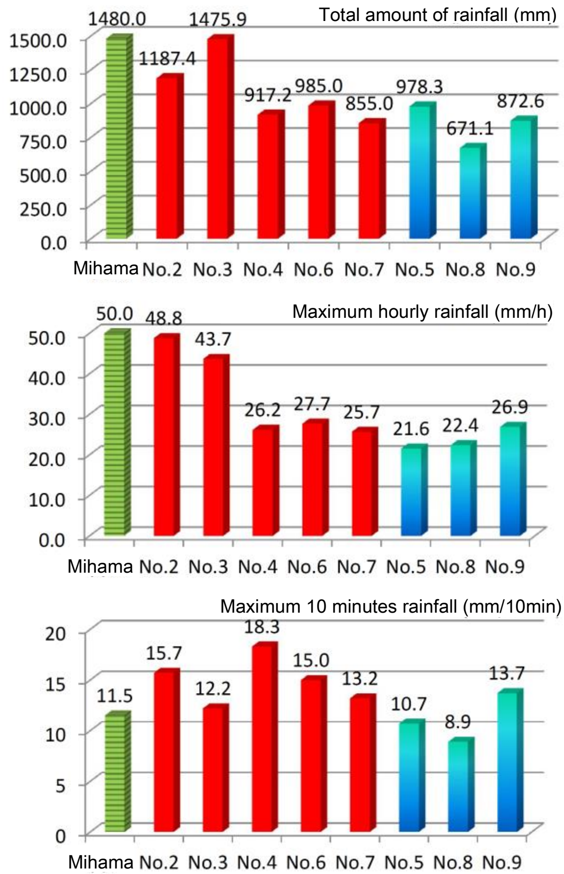

Fig. 4 Rainfall data for each rain gauge

Figure 5 shows the directions of the slopes around Yokogaki-toge. The deep-seated landslide started from the tops of the north- and west-facing slopes. Thirty rainfall events during the observation period were extracted using the following procedure: if the rain stopped for > 24 hours, a rainfall event was counted as a string of data. Rainfall events involving < 20 mm of cumulative rainfall were excluded. To investigate the influence of rainfall on collapse, the data for No. 3 (north-facing slope) and No. 2 (south-facing slope) were compared, as shown in Fig 6. The red bars in Fig 6 indicate the difference in cumulative rainfall, calculated by subtracting the data for the south-facing slope from that of the north-facing slope. The blue points in Fig 6 show cumulative rainfall of each rainfall event.

Generally, the cumulative rainfall for each event was greater on the north-facing slope than the south-facing slope. At first glance, this suggests that the collapsed slope and the slope receiving a large amount of rainfall are the same, and that there is a correlation between the cumulative rainfall during each event and the difference in rainfall between the north- and south-facing slopes. However, the trend differed for heavy rainfall events, which might trigger a collapse, as seen for events #13 and #15. The case of over 100mm cumulative rainfall as #13 and #15, their difference are very few or more rainfall is on south-facing slope than north-facing slope. Therefore, it is possible that the influence rate of rainfall for collapse is lower than that of other factors, such as geological structure. The total amount of rainfall on the north-facing slope was greater than on the south-facing slope,it means promoting weathering as an indirectly work.

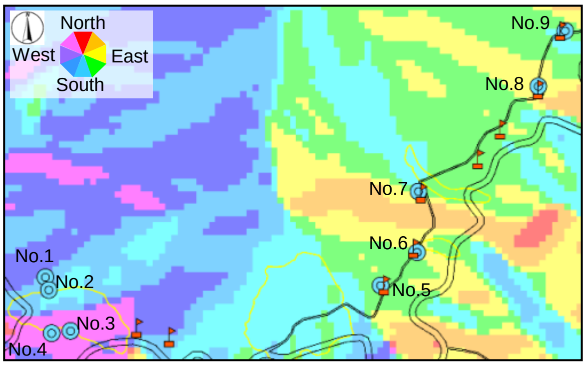

Fig. 5 Directions of the slopes at Yokogaki-toge [2]

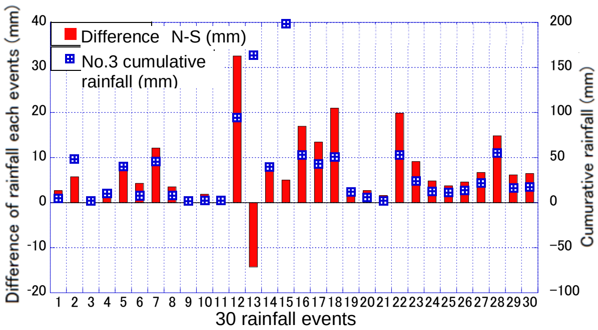

Fig. 6 Differences in rainfall
(subtracting south- facing from north-facing)

In summary:

1. Rainfall at the collapsed and non-collapsed sites did not differ so much.
2. The difference in the amount of high-intensity rainfall during a short time at each site was larger than the differences in the total and maximum hourly rainfall.
3. Rainfall has less influence on the occurrence of deep-seated landslides than other factors.
4. The greater total rainfall on the north-facing slope might promote weathering compared with the south-facing slope.

4. SATURATED-UNSATURATED SEEPAGE FLOW ANALYSIS OF THE COLLAPSED SLOPE

To evaluate slope stability, it is important to measure the rainfall at the site correctly. However, the rainfall measurement at Yokogaki-toge indicated that the observed values lacked precision due to the shielding effect of trees. Therefore, we used two types of rainfall data to evaluate slope stability: rainfall measured directly in the field, called automated meteorological data-acquisition system “AMeDAS”, and analysis rainfall obtained from rader observation. The nearest AMeDAS point is approximately 3.5 km from Yokogaki-toge, and analysis rainfall on each 1km mesh is offered.

Figure 7 shows the two types of rainfall data during the slope failure of 2011. Cases 1 to 12 in Fig. 7 indicate the time of evaluation. The difference in the two types of rainfall data is considered based on saturated-unsaturated seepage flow analysis performed using PLAXIS 2D PlaxFlow (Plaxis; Delft, The Netherlands), which is a finite element software package intended for the analysis of seepage flow. This software calculates seepage flow using Darcy’s equation. The slope model shown in Fig. 8 was determined based on a field survey and standard penetration test conducted in the landslide area. The parameters were determined based on experiments of sampling soil and values taken from the literature. Table 1 shows the hydraulic conductivity of each soil.

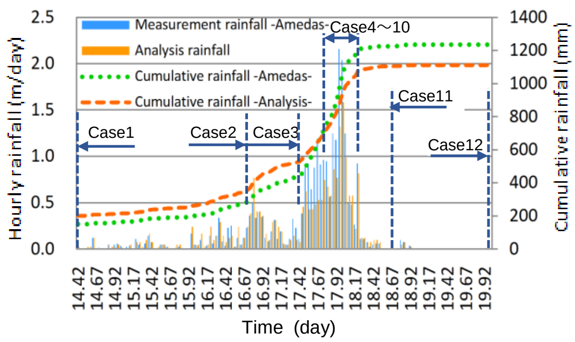

Fig. 7 Two kinds of rainfall data for the period from 17 August to 4 September, 2011

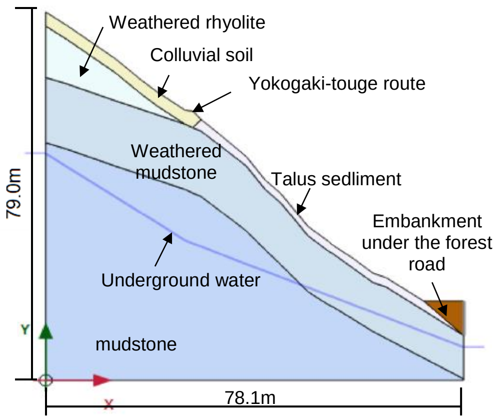

Fig. 8 Slope model

Table.1 Hydraulic conductivity of each soil

	K: hydraulic conductivity (m/day)
① colluvial soil	23.501
② weathered rhyolite	13.046
③ talus sediment	39.571
④ weathered mudstone	39.571
⑤ mudstone	8.64E+03
⑥ embankment	0.432

5. RESULTS AND DISCUSSION

The analysis was started on 17th August 2011, 2 weeks before the rainfall event that caused the collapse. The collapse was estimated to have occurred on either September 3rd or 4th. Although hourly rainfall differed, as shown in Fig. 7, the times at which the rain started and stopped were very similar. The flow velocity conditions were evaluated for the following 12 cases:

Case 1: at the end of the antecedent precipitation
Case 2: at the end of a small rainfall event
Case 3: at the beginning of the large rainfall event
Cases 4–10: near the peak rainfall, including the peak
Case 11: 17 hours after the peak
Case 12: 24 hours after the peak

Table 2 summarizes the time of analysis and cumulative rainfall in each case. The flow velocity vector diagrams for each case are shown in Fig. 9. The diagram on the left is based on the measured "AMeDAS" rainfall, and that on the right side uses the analysis rainfall.

Table.2 Cumulative time and rainfall in each case

Case	Time (day)	Cumulateve rainfall		Case	Time (day)	Cumulateve rainfall	
		Amedas (mm)	Analysis rainfall (mm)			Amedas (mm)	Analysis rainfall (mm)
1	14.42	201	151	7	18.04	985	1115
2	16.71	355	284	8	18.08	1009	1136
3	17.42	527	444	9	18.13	1033	1156
4	17.83	755	787	10	18.17	1042	1167
5	17.96	878	978	11	18.71	1105	1226
6	18.00	944	1063	12	20.00	1111	1235

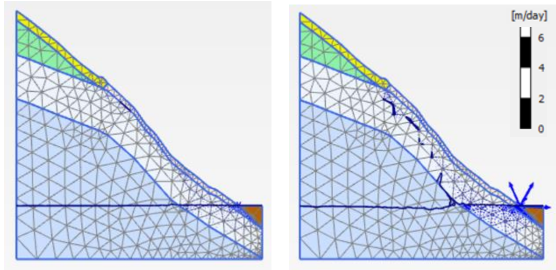

Case 1: At the end of the antecedent precipitation

- Flow velocity vectors are seen at the toe of the slope. The analysis rainfall caused a large amount of seepage.
- Phreatic lines developed in the weathered mudstone layer in the right figure (analysis rainfall).

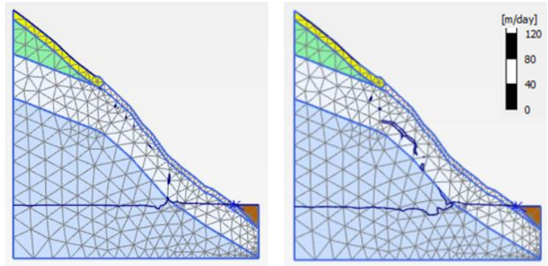

Case 2: At the end of the small rainfall

- Flow velocity vectors are seen at the toes of both slopes.
- Some phreatic lines developed in the weathered mudstone layer in the left figure (AMeDAS).

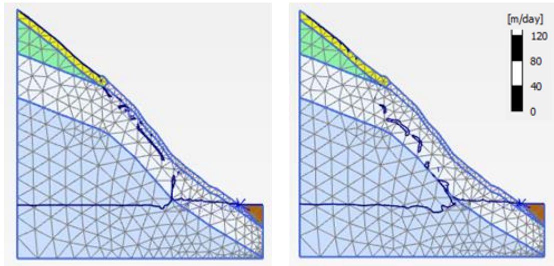

Case 3: At the beginning of the large rainfall

- Flow velocity vectors are seen at the toes of both slopes.
- Phreatic lines developed on the upper side of the weathered mudstone layer toward the geological boundary in the left figure (AMeDAS).
- Phreatic lines developed on the lower side of the weathered mudstone layer in the right figure (analysis rainfall).

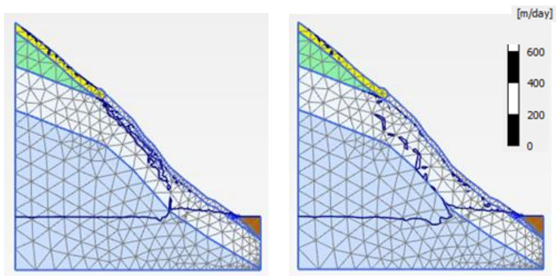

Case 4: Near the peak rainfall

- Very slight flow velocity vectors are seen at the toes of both slopes.
- Phreatic lines grew increasingly toward the geology boundary through the upper side of the weathered mudstone layer in the left figure (AMeDAS).
- Phreatic lines developed into not only the lower side, but also the upper side of the weathered mudstone layer in the right figure (analysis rainfall).
- A phreatic line arose in the surface layer of colluvial soil near the tops of both slopes.

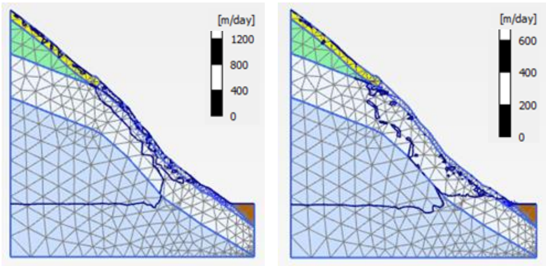

Case 5: Peak 1 (AMeDAS 2.16 m, analysis 1.32 m /3h)

- Many slight flow velocity vectors arose in the surface layer of talus sediment from the toe of the slope to the geological boundary in the left figure (AMeDAS).
- Very slight flow velocity vectors are found at the toe of the slope only in the right figure (analysis rainfall).
- The phreatic line in the mudstone layer is connected with the phreatic lines that developed on the upper side of the weathered mudstone layer toward the geological boundary in the left figure (AMeDAS).
- Marked phreatic lines developed at the toe of the slope and geological boundary in the weathered mudstone layer in the right figure (analysis rainfall).
- Phreatic lines arose at the surface layer of colluvial soil on both slopes.

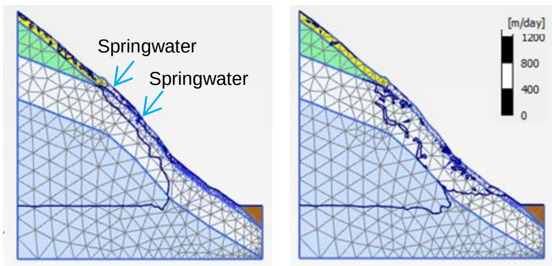

Case 6: Peak 2 (AMeDAS 2.04 m, analysis 1.58 m /3h)

- Many slight flow velocity vectors are found in the surface layer of the talus sediment near the lower slope, and some flow velocity vectors surround the springwater caused piping after the slope failure in the left figure (AMeDAS).
- Some velocity vectors are found at the boundary of the talus sediment layer and weathered mudstone layer at the middle of the slope in the right figure (analysis rainfall).
- Connected phreatic lines extend to the surface layer and weathered mudstone layer under the geological boundary in the left figure (AMeDAS).
- The bottom phreatic line moved upwards slightly, near the toe of the slope in the right figure (analysis rainfall).

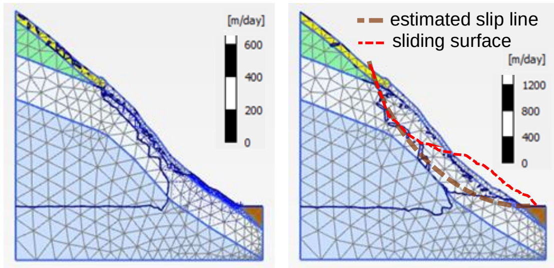

Case 7: 1 hour after the peak

- Flow velocity vectors are concentrated in the toe of the slope in the left figure (AMeDAS).
- Phreatic lines are found along the estimated slip line in the right figure (analysis rainfall).

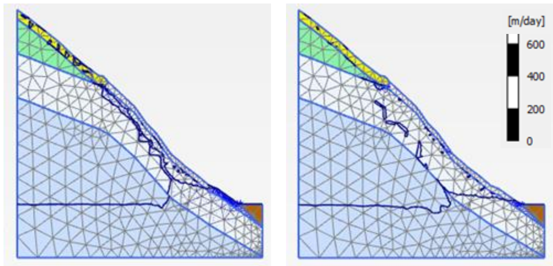

Case 8: 2 hours after the peak

- Flow velocity vectors decreased on both slopes (AMeDAS and analysis rainfall).
- Phreatic lines weakened on both slopes.

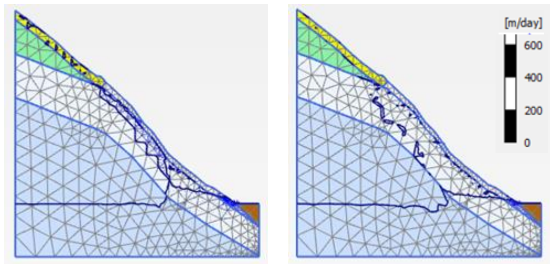

Case 9: 3 hours after the peak

- Flow velocity vectors decreased on both slopes.
- Phreatic lines weakened on both slopes.

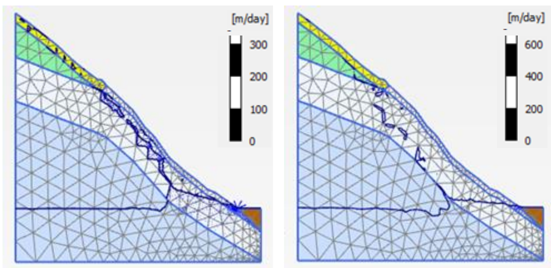

Case 10: 4 hours after the peak

- Slight flow velocity vectors are found at the toe of the slope in the left figure (AMeDAS).
- Phreatic lines weakened on both slopes.

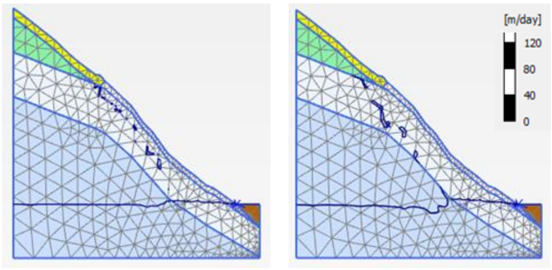

Case 11: 17 hours after the peak

- Very slight flow velocity vectors are found on both slopes.
- Phreatic lines decreased on both slopes.

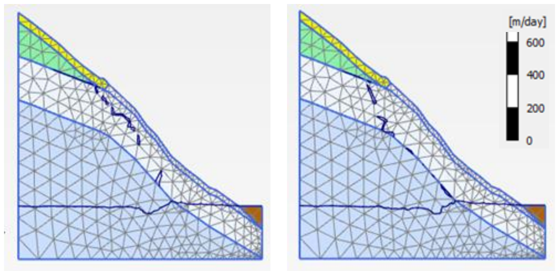

Case 12: 24 hours after the peak

- Flow velocity vectors are not found on either slope.
- The bottoms of the phreatic lines fall to a low level, and many phreatic lines that arose in the weathered mudstone layer disappeared for both slopes.

Fig.9 Flow velocity vector and phreatic lines

Flow velocity vectors based on both AMeDAS and analysis rainfall first appeared at the toe of the slope and developed toward the geological boundary on the upper side. The time lag of the maximum flow velocity based on both kinds of rainfall was 1 hour, as shown in Fig. 10. According to this result, the evaluations using either type of rainfall were similar in terms of the flow velocity arising in the slopes.

The phreatic lines based on AMeDAS rainfall were concentrated in the surface layer at the early stage, and progressed into the lower weathered mudstone layer in the middle stage. The bottom phreatic line, and many other small phreatic lines within the layers, were connected during the maximum rainfall.

The phreatic lines based on the analysis rainfall appeared at deeper positions than those based on the AMeDAS in the early stage, and appeared gradually around the toe of the slope and geological boundary of the surface. In addition, the bottom line and short lines did not connect in the weathered mudstone layer. During the most advanced stage, there were many phreatic lines around the estimated slip line.

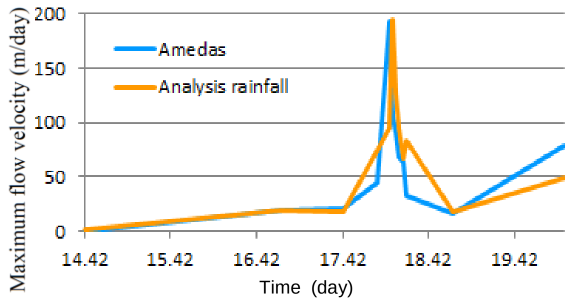

Fig.10 Transition of the maximum flow velocity

6. CONCLUSION

This study discussed the results of multi-point rainfall measurements. The amount of rainfall at each point differed slightly, while the rainfall intensity over a short period of time varied markedly. North-facing slopes catch more rainfall than south-facing slopes, which might promote the weathering of these north-facing slopes.

Saturated-unsaturated seepage flow analysis was carried out based on two types of rainfall using the before-collapse slope model. The seepage processes based on the two types of rainfall were similar, although the positions of the phreatic lines differed. With AMeDAS rainfall, seepage occurred over a broad area, while analysis rainfall resulted in phreatic lines around the estimated slip line. It might be considered that closer rainfall to actual phenomenon at Yokogaki-toge is AMeDAS by the reasons as followings:

1. More Seepage flows arise in the weathered mudstone layer over a broad area.
2. Seepage flows arise surround the springwater position at the peak.

It should verify this assumption by a coupled analysis, saturated-unsaturated seepage flow analysis as an issue in the future.

ACKNOWLEDGEMENTS

This work was supported by a Grant-in-Aid for Scientific Research (C) No. 26350380 (2014–2016) from the Japan Society for the Promotion of Science. We would also like to thank Kumano Agriculture and Forestry Office for providing the geological investigation data.

REFERENCES

[1] Mie Prefecture: aerial photo data of south part of Mie prefecture, 2012.
[2] Geospecial Information Authority of Japan: Basement map information, http://fgd.gsi.go.jp/download/, (2012.2.12 access).

EXPERIMETAL MEASUREMENT OF SOIL-PRESTRESSED FOUNDATION INTERACTION

Radim Cajka[1], Petr Mynarcik[2] and Jana Labudkova[3]
Department of Structures, faculty of Civil Engineering, VSB-Technical University Ostrava, Ludvika Podeste 1875/17, 708 33, Ostrava – Poruba, Czech Republic

ABSTRACT

Several experimental measurements of reinforced concrete slab – subsoil interaction are compared with numerical analysis of shallow foundation by means of FEM. At the Faculty of Civil Engineering VSB – Technical University of Ostrava testing device was constructed so that the phenomena of soil – foundation interaction could be experimentally investigated and compared with numerical models. The experimental model was designed as a cutout of prestressed foundation slab-on-ground and the static load test was conceived as a simulation of local loading of a square shape column. During the static load test, measurements focused on observation of horizontal deformations, tension inside the slab and on the contact surface between foundation structure and subsoil. The described static load test was part of a series of experiments realized at the Faculty of Civil Engineering, VŠB –Technical university of Ostrava.

Keywords: Foundation structure, experimental measurement, soil – structure interaction, interaction models, contact stress, FEM calculation.

INTRODUCTION

This article presents experimental static load test of post-tensioned concrete foundation model. This test was part of a series of experiments focused on problematic of interaction between concrete structures and subsoil and was realized at the Faculty of Civil Engineering, VSB – Technical university of Ostrava.

Subsoil-structure interaction problematic is international research theme and many research teams around the world produce research activity on this scope [1]-[6]. Interaction between concrete structure and subsoil is one of the main research directions at the Faculty of Civil Engineering, VSB – Technical university of Ostrava [7]-[12].

Actually, research is focused on post-tensioned concrete foundation slabs and industrial floors. For experimental static load test was concreted model of post-tensioned foundation slab and static load test was conceived as a simulation of loading by square shape column. The experiment served to a better understanding and possible improvement of these technologies from the perspective of subsoil interaction.

DESCRIPTION OF THE PRESTRESSED CONCRETE FOOR MODEL

The experimental model was designed as a cutout of prestressed concrete foundation slab. Schematic plan of experimental model is displayed on Fig. 1.

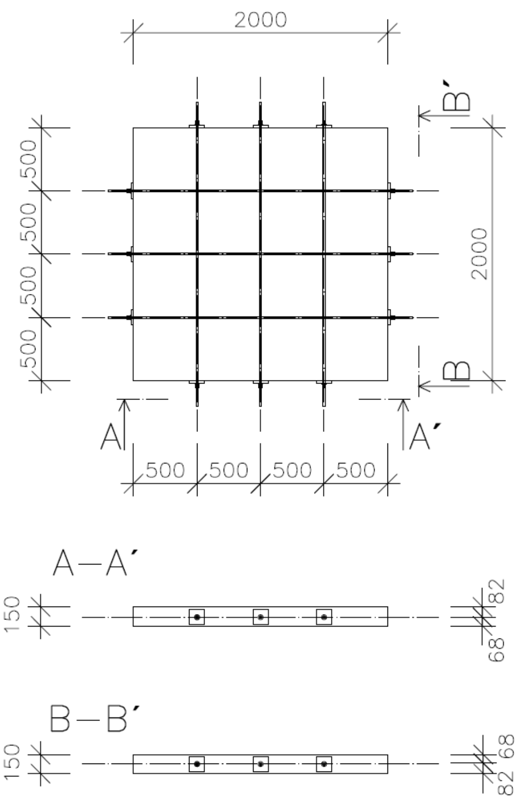

Fig. 1 The schematic plan of experimental model dimensions and prestressing threadbars positions

The basic dimensions of experimental model were 2000 x 2000 x 150 mm. The concrete type C35/45 XF1 was used for concreting. The experimental model was post tensioned by six fully threaded prestressing threadbars – displayed on Fig. 2. The materials of threadbars were from low relaxation steel with designation Y 1050 and diameters of these threadbars were 18 mm. The prestress force for each threadbar was 100 kN. The presstresing system with hollow hydraulic cylinder is displayed on Fig. 3.

Fig. 2 The steel formwork with ducts for prestressing bars

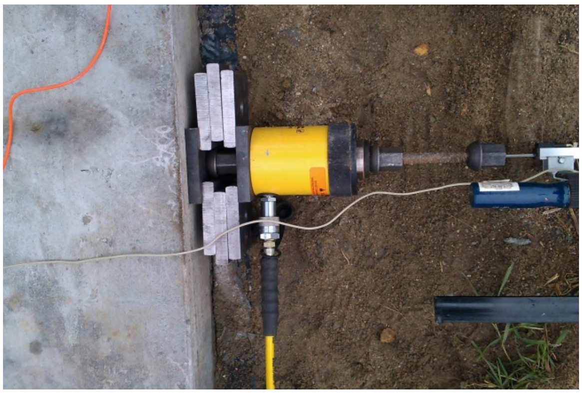

Fig. 3 The presstresing system with hollow hydraulic cylinder

Fig. 4 The complete assembly for static load test

Thredbars were anchored by domed nuts and recessed anchor plates. Positions of threadbars were designed and realized as a centric post-tensioning system. The model was laid on homogenous clay subsoil with gravel bed layer. The sliding joint was placed between contact surface of concrete foundation slab model and gravel bed layer. For this experiment was used developed sliding joint construction from parallel research direction at the Faculty of Civil Engineering, VSB – Technical university of Ostrava [13],[14].

DESCRIPTION OF SUBSOIL ATRIBUTES

The experimental model was implemented on compacted gravel bed. Gravel bed layer thickness was 300 mm and was compacted on prime clay subsoil without greensward [15],[16]. The subsoil characteristics were determined by standard geotechnical measurements. The sliding joint was made from combination of PVC foil and geotextile. The experimental model was situated in the testing device for experimental measurements of foundation slabs on the subsoil “STAND” [17].

Subsoil attributes:

- Subsoil consists of loess loam – soil classification F6 (according CSN 73 1001).
- Thickness of subsoil layer is about 5 meters.
- Volumetric weight of soil γ = 18,5 kN.m^{-3}.
- Poisson coefficient ν = 0,35.
- Static Young’s modulus EDEF = 33,86 MPa.
- Oedometric modulus of elasticity EOED= 4,27 MPa.

DESCRIPTION OF TESTING DEVICES AND MEASUREMENTS

The outdoor testing device for experimental measurements of foundation slabs on the subsoil “STAND” consists of two frames. Crossbeams enable variability of the press machine location. The frames are anchored with screws into the steel grate based in the reinforced concrete strip foundations. The construction is anchored with 4 m long micropiles. The highest possible vertical load is 1 MN [17]. The experimental static loading test on a prestressed concrete foundation slab model was the assembly of a set of measurements. Measurement gauges completed the experimental measurement line [7], [8]. Described experiment was short-term static load test without influence of concrete and subsoil creep [18], [19]. Measured data will serve for comparison with results obtained by numerical FEM modeling of soil – prestressed foundation slab interaction by [20]-[23]. The complete assembly for static load test is displayed on Fig. 4.

The experimental measurement line:

- 3 geotechnical pressure cells for measurement of the stress on the interface of the slab and subsoil. Displayed on Fig. 5.
- Built-in pressure sensor for measurement of the vertical load.
- 4 strain gauges for measurement on the surface of the slab – tension of concrete.
- 4 strain gauges for measurement inside the experimental slab – tension of concrete. Displayed on Fig. 6.
- 14 potentiometric position sensors for measurement of vertical deformations (subsidence). Displayed on Fig. 7.
- 8 temperature sensors for measurement of temperature inside and on the surface.
- Recording station for potentiometric sensors
- Recording station for geotechnical pressure cells
- Leveling device for stiffness control of outdoor testing device "STAND".

Fig. 5 Installation of geotechnical pressure cells for measurement of the stress on the interface of the slab and subsoil.

Fig. 6 Strain measurement gauges inside the experimental slab

Fig. 7 Potentiometric position sensors for measurement of vertical deformations and built-in pressure sensor for measurement of the vertical load

DESCRIPTION OF EXPERIMENTAL MEASUREMENT PROCESS

The vertical load was caused by the high tonnage hydraulic cylinder. The loaded equipment was placed between the experimental model and the steel extension fixed on the testing device for experimental measurements of foundation slabs on the subsoil "STAND" The hydraulic system was equipped with the pressure sensor. Potentiometric position sensors were installed on the surface of concrete foundation model. These gauges were connected to the same sensor station with automatic scanning and recording. Shape and size of load area simulated square shape column. Dimensions of load area were 200 x 200 mm. Fixed interval of loading process - 75kN / 30 min was chosen for this experimental testing. After each loading process a 30 minutes long relaxation step continue. Loading process and relaxation step make together one loading step.

MEASUREMENT OF VERTICAL DEFORMATION – SUBSIDENCE

Vertical deformations were measured by the set of 16 potentiometers. Potentiometers were connected to the recording sensor station. The station was programmed to automatic scanning and recording measured values. Time interval for record of deformation measurement was 10 seconds. Schematic plan of sensors is displayed on Fig. 8. Subsidence results of potentiometric position sensors – deformations at particular points are displayed on Fig.9 and subsidence of experimental post-tensioned foundation model in line 1-1´ is displayed on Fig.10.

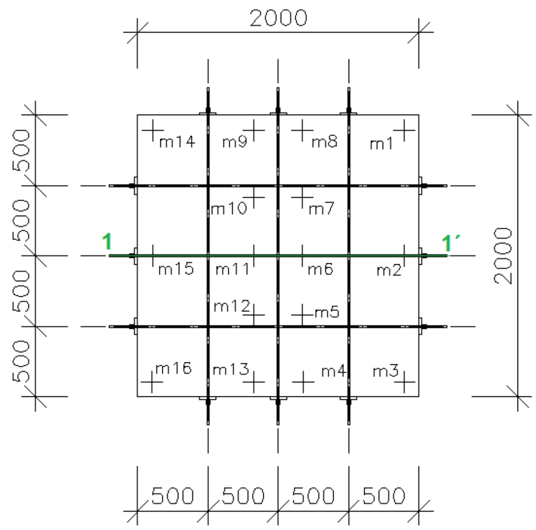

Fig.8 Schematic plan of potentiometric position sensors

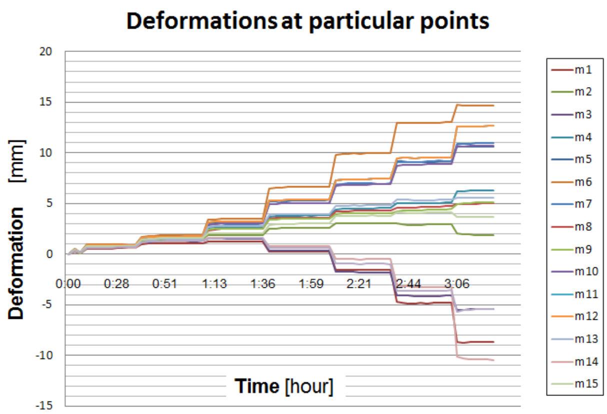

Fig. 9 Results of potentiometric position sensors – deformations at particular points

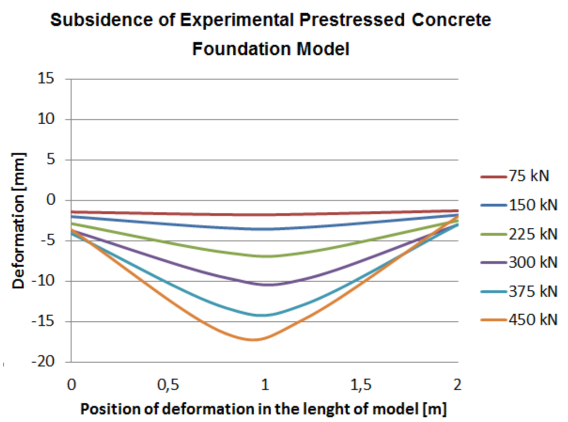

Fig. 10 Subsidence of experimental prestressed concrete foundation model (line 1-1´ on Fig.8)

STAND EXPERIMENTAL DEVICE – STIFFNESS CONTROL

During the course of the experiment, it was necessary to check the experimental device stiffness. The test stand was equipped with a leveling target and, the leveling device was targeted at this mark during the test. Thanks to this measure, the beam deflection, to which was connected a hydraulic press, could be continuously controlled.

COMPRESSIVE STRENGTH CHARACTERISTICS OF TESTED CONCRETE

Compressive strength characteristics of the tested concrete were verified in according European Standard EN 206:2013. Three pieces of test cubes were taken during the concreting. These cubes, with dimensions 150 x 150 x 150 mm, were allowed to the mature for 28 days. Cube samples were used for the strength characteristic verification in Compressive strength characteristics of the tested concrete were verified in according CSN EN 12390 - 3. Tested concrete was classified as C35/45. Tests of compressive strength characteristics were realized in the laboratory of Faculty of Civil Engineering in Ostrava.

EXPERIMENTAL EVALUATION OF THE POST-TENSIONED CONCRETE SLAB CONTACT SURFACE

The location of the test pattern inside the testing device for experimental device “STAND” and the use of available handling techniques enabled to lift the test slab. Threadbars were used for anchorage for stretching hanging straps. A pair of chain hoists was hung on the “STAND” beams. The experimental pattern was lifted and allowed the course of cracks evaluation right on concrete slab surface that was in contact with the subsoil. The crack cross is highlighted with red color on Fig.11. Punching shear damage are displayed on Fig. 12 and Fig. 13. Next cracks were localized near anchors of middle prestressing threadbars – displayed on Fig.14.

Fig. 11 The course of cracks on the contact surface of experimental post-tensioned slab

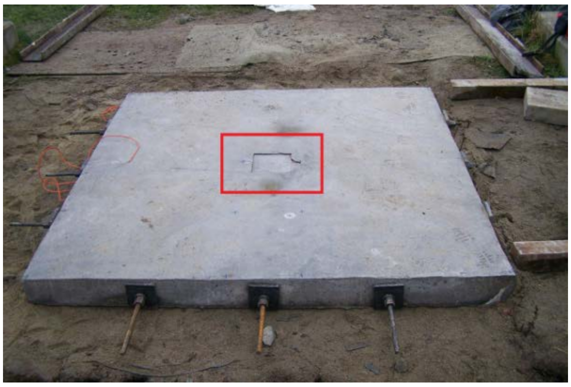

Fig. 12 Punching shear damage on the upper surface of experimental post-tensioned slab

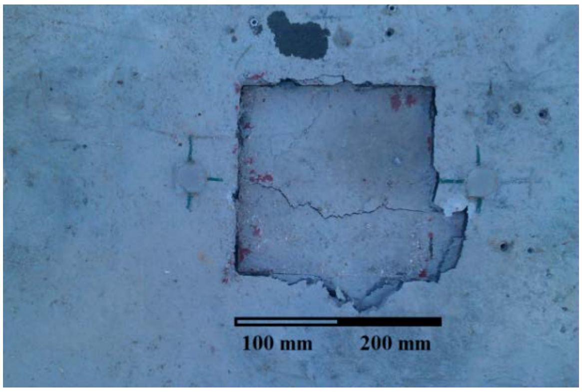

Fig. 13 Detail of punching shear damage

Fig. 14 Cracks near anchors of middle prestressing threadbar

CONCLUSION

Experimental prestressed concrete foundation slab model resist the loads exerted after seven load cycles and induced maximal load level 525 kN. First significant cracks were detected after fourth loading step Cracks were located near anchors of middle threadbars. After sixth loading step were detected first signs of punching shear. Experiment was ended in moment, when the model was strongly damaged by punching shear. Experiment bring many information about influence of prestressing to punching shear resistance. Measured data will serve for comparison with results obtained by numerical FEM modeling of soil – prestressed foundation slab interaction.

ACKNOWLEDGEMENTS

The works were supported from sources for the conceptual development of research, development and innovations for 2015 at the VSB-Technical University of Ostrava, which were granted by the Ministry of Education, Youths and Sports of the Czech Republic.

REFERENCES

[1] R. Halvonik, J., Fillo, “The Maximum Punching Shear Resistance of Flat Slabs, Procedia Engineering”, vol.: 65, 2013, pp 376-381, ISSN 1877 - 7058, doi. 10.1016/j.proeng.2013.09.058.

[2] M. Aboutalebi, A. Alani, J. Rizzuto, D. Beckett, “Structural behaviour and deformation patterns in loaded plain concrete ground-supported slabs”. Structural Concrete. 2014, vol. 15, issue. 1, pp. 81-93. ISSN 1464-4177, DOI 10.1002/suco.201300043.

[3] T. Clément, A.P. Ramos, M.F. Ruiz, A. Muttoni, “Influence of prestressing on the punching strength of post-tensioned slabs”, Engineering Structure, vol. 72, pp. 56-69 (14 p), ISSN: 0141-0296, 2014

[4] L. Nguyen-Minh, M. Rovnak, T. Tran-Ngoc, T. Le-Phuoc, “Punching shear resistence of post-tensioned steel fiber reinforced concrete flat plates”, Engineering Structure, vol. 45, pp. 324-337 (14 p), ISSN: 0141-0296, 2012

[5] J. ØVERLI, Experimental and numerical investigation of slabs on ground subjected to concentrated loads, Open Engineering, vol. 4(3), DOI: 10.2478/s13531-013-0159-9. ISSN 23915439. 2014.

[6] A. Meda, G.A. Plizzari, New design approach for steel fiber-reinforced concrete slabs-on-ground based on fracture mechanics, ACI Structural Journal, vol. 101 (3), pp. 298-303, 2004.

[7] P. Mynarcik, “The Subsidence Analysis of Experimental Post-tensioned Concrete Slab Model in the Course of the Static Load Test”, Applied Mechanics and Materials, vol. 744 – 746, pp. 1556-1559 (4 p), Trans Tech Publications, Switzerland, doi:10.4028/www.scientific.net/AMM.744–746.1556, 2015.

[8] P. Mynarcik, ”Measurement processes and destructive testing of fibre concrete foundation slab pattern”, Advanced Material Research, vol. 1020, pp. 221-226 (6 p), Trans Tech Publications, Switzerland, ISSN (Online) 1662-8985, ISSN (Print) 1022-6680, DOI: 10.4028/www.scientific.net/AMR.1020.221, 2014.

[9] R. Cajka, R. Fojtik, “Development of Temperature and Stress during Foundation Slab Concreting of National Supercomputer Centre IT4”, Procedia Engineering, vol. 65, pp. 230-235 (6 p), ISSN 1877-7058, doi: 10.1016/j.proeng.2013.09.035, 2013.

[10] R. Cajka, K. Burkovic, V. Buchta, “Foundation Slab in Interaction with Subsoil”, Advanced Materials Research, Volumes 838-841, pp. 375-380 (6 p), Trans Tech Publications, Switzerland, doi:10.4028/www.scientific.net/AMR.838-841.375, 2014.

[11] R. Cajka, P. Manasek, “Building Structures in Danger of Flooding”. IABSE Conference New Delhi, India 2005: Role of Structural Engineers towards Reduction of Poverty. New Delhi, India, pp. 551-558 ISBN 978-3-85748-111-6, WOS: 000245746100072, 2005.

[12] R. Cajka, P. Mateckova, ”Comparison of calculating methods and consequent carrying capacities of pre-stressed precast concrete roof purlin”, in proceedings of First International Workshop “Design of Concrete Structures using EN 1992-1-1, Prague, 15 March 2010, ISBN 978-80-01-04581-7, WOS: 000324078100017, 2010

[13] M. Janulikova, R. Cajka, P. Mateckova, V. Buchta, “Laboratory Testing of Asphalt Belts Rheological Properties Exposed to Shear Loads”, Transactions of the VŠB - Technical University of Ostrava, Civil Engineering Series, vol. XII, iss. 2, pp. 59–66 (8 p), ISSN (Online) 1804-4824, ISSN (Print) 1213-1962, doi: 10.2478/v10160-012-0018-2, 2013.

[14] M. Janulikova, M. Stara, “Multi-layer Rheological Sliding Joint in the Foundation Structures”, Transactions of the VŠB – Technical University of Ostrava, Civil Engineering Series, vol. XIII, iss. 2, pp. 41–46 (6 p), ISSN (Online) 1804-4824, ISSN (Print) 1213-1962, doi: 10.2478/tvsb-2013-0008, 2013.

[15] M. Janulikova, P. Mynarcik, “Modern Sliding Joints in Foundations of Concrete and Masonry Structures”, International Journal of Mechanics, vol.8, iss.1, United States: North Atlantic University Union, pp. 184 -189 (6 p), ISSN 1998-4448, 2014.

[16] M. Janulikova, M. Stara, P. Mynarcik, “Sliding Joint from Traditional Asphalt Belts”, Advanced Material Research, vol. 1020, pp. 335-340 (6 p), Trans Tech Publications, Switzerland, ISSN (Online) 1662-8985, ISSN (Print) 1022-6680, doi: 10.4028/www.scientific.net/AMR.1020.335, 2014.

[17] R. Cajka, V. Krivy, D. Sekanina, “Design and Development of a Testing Device for Experimental Measurements of Foundation Slabs on the Subsoil”, Transactions of the VŠB – Technical University of Ostrava, Civil Engineering Series, vol. XI, iss. 1, pp. 1-6 (6 p), ISSN (Online)1804-4824, ISBN 978-80-248-2332-4, doi: 10.2478/v10160-011-0002-2, 2011.

[18] J. Navratil, “Structural analysis of bridges, legitimate conservatism and obsolete theories”, Concrete Engineering International, vol.:8 (1), pp. 17-19, ISSN 14605856, 2004.

[19] J. Navratil, M. Zich, “Long-term deflections of cantilever segmental bridges”, Baltic Journal of Road and Bridge Engineering, vol.: 8, issue 3, pp 190-195. ISSN: 1822427X, DOI: 10.3846/bjrbe.2013.24, 2013.

[20] R. Cajka, “Analytical derivation of friction parameters for FEM calculation of the state of stress in foundation structures on undermined territories”, Acta Montanistica Slovaca, vol. 18, iss. 4, pp. 254-261 (8 p), ISSN: 13351788, 2013.

[21] M. Janulikova, M. Stara, “Reducing the Shear Stress in the Footing Bottom of Concrete and Masonry Structures”, Procedia Engineering, vol. 65, pp. 284 – 289 (4 p), ISSN 1877-7058, DOI:10.1016/j.proeng.2013.09.044, 2013.

[22] J. Labudkova, R. Cajka, “Comparsion of Measured Displacement of the Plate in Interaction with the Subsoil and the Results of 3D Numerical Model”, Advanced Material Research, vol. 1020, pp. 204-209 (6 p), Trans Tech Publications, Switzerland, ISSN (Online) 1662-8985, ISSN (Print) 1022-6680, DOI: 10.4028/www.scientific.net/AMR.1020.204, 2014.

[23] Cajka, K. Burkovic, V. Buchta, R. Fojtik, “Experimental soil - Concrete plate interaction test and numerical models”, Key Engineering Materials, vol. 577-578, pp. 33-36 (4 p), Trans Tech Publications, Switzerland, doi:10.4028/www.scientific.net/KEM.577-578.33, 2014.

Fifth International Conference on Geotechnique, Construction Materials and Environment, Osaka, Japan, Nov. 16-18, 2015, ISBN: 978-4-9905958-4-5 C3051

A NEW RHEOMETRICAL EQUIPEMENT FOR THE CHARACTERIZATION OF LARGE GRANULAR MATERIALS INVOLVED IN FAST LANDSLIDES

Anna Maria Pellegrino[1], Anna Scotto di Santolo[2], Aldo Evangelista[3] and Leonardo Schippa[1]
[1]Department of Engineering, University of Ferrara, Italy; [2]Pegaso University, Italy; [3]University of Napoli Federico II, Italy.

ABSTRACT

The present study focused on novel rheometrical tool for the determination of the rheological behaviour of large particle mixtures with particular interest in the application to granular materials involving in fast landslides as mud and debris flows. The main goal is the development of the Sphere Drag Rheometer (SDR), a home-made large-scale rheometer that allow to estimate the rheological properties of these mixtures considering the whole grain size distribution. The SDR is composed of a sphere rigidly joined to a support that moves at constant velocity into the mixture. Compared to standard rheometer, the SDR uses much higher volume of mixtures of wider grain size distribution next to that in situ. Several pyroclastic soils collected from the source area of debris flows occurred in Campania region (Southern Italy) were analyzed. The paper reports the experimental results on fine particles mixtures, large particle mixtures, and their comparison.

Keywords: Four or Five Keywords (First Characters of Each Word are in Capital/Uppercase Letters), Italic

INTRODUCTION

The paper focuses on an innovative rheometrical system for the determination of the rheological properties of fluids containing large particles, i.e. maximum grain size larger than 1 mm. The knowledge about the rheological properties of large particle fluids is of great and increasing importance because of their relevance in several fields like natural hazards, building materials, gas and oil, and food industry [1]. In the present study fast landslides as debris flows and the application of rheometry for debris flows are of primary interest. Debris flows put in danger people and animals, and cause damage in hilly and mountainous areas. More than 55000 people died in the last hundred years worldwide due to debris flows or combined debris flow and flood events. In Italy more than 4000 people die from 1963 to 2012 due to debris flows and flooding phenomena. In order to protect people, animals and infrastructures from damage, hazard zone mapping and warning systems as well as structural protective measures must be considered depending on the specific situation. During the definition process of such protective measures, the debris flow modeling is a fundamental task [2]-[3]. Numerical and physical modeling help in the hazard zones delineating and in the structural design and testing [4]. In order to understand and simulate the flow and the deposition process, an appropriate rheological model is a very useful physical concept for mud, debris and hyper-concentrated flows [5]. The simplest method is to assimilate the flowing mass to a continuous viscous fluid and refers to rheological models derived from the resistance formula of Newtonian and Non-Newtonian fluids [6]. When a rheological model is considered, only the material flow curve, e.g. expressing the shear rate-shear stress relation, is required. Nowadays, efficient rheometrical apparatuses for the determination of the rheological parameters of mixtures and fluids containing fine particles exist and the experimental methods related to them are widely consolidated [5]-[7]-[8]-[9]-[10]. For mixtures and fluid containing large particle, the study of the influence of the grain size is more complicated. Experimental devises equipped with a large geometrical configurations are required and such apparatuses are few and not commercially developed [11]-[12]-[13]-[14]-[15]. The debris flow materials hereby considered presents a wide grain size distribution and a small content of fine particles. Therefore, in order to estimate the rheological properties of these mixtures (i.e., considering the whole grain size distribution), a home-made experimental large-scale rheometer was design and built, the Sphere Drag Rheometer (SDR). The system could be an efficient rheometrical tool for the investigation of fluids containing particles up to 10 mm grain size.

THE SHERE DRAG RHEOMETER SDR

Characteristics and procedures

Referring to the works of [14]-[16], we developed an innovative system for measuring the motion's resistance for large particle mixtures called

SDR. The SDR is composed of a sphere, with variable diameters D, rigidly joined to a support that moves at constant velocity into the mixture. The sphere is connect to a load cell that measures the drag force necessary to move the ball through the fluid at the imposed speed. The system, illustrated in Fig. 1, is composed by a cylindrical container (i.e. having radius d_c equal to 130 mm, height h_c equal to 60 mm and sample volume equal to 0.5 l) in which the material sample are located and of an eccentric sphere (i.e. with a variable eccentricity r, relative to the motor, varying from 20 to 46 mm) fixed to a thin vertical shaft. Differently from conventional apparatus, the SDR rheometer allows to consider larger sample volume (0.5 l in SDR versus 30 ml in standard rheometers) and larger grain size distribution (up to 10 mm grain size in SDR versus 0.5 mm grain size in standard rheometer). The device can be equipped with different spheres having diameters ranging from 8 to 18 mm. The main components of the SDR apparatus are (see Fig. 1): a base station with two motors (i.e., a "slow motor" goes from 0.4 to 9.5 rpm and a "fast motor" goes to 10 to 260 rpm); a telemeter as broadcasting system; load cells having different full scale FS (i.e., one equal to 250 g and the other equal to 1000 g); a box for the electronica controlling; a reed (i.e. a magnetic position sensor); a software called SMV_V1 developed ad hoc for the SDR rheometer control.

The experiment consists in measuring the drag force F_D at a specified rotational speed Ω, while the sphere makes one full rotation within the material sample.

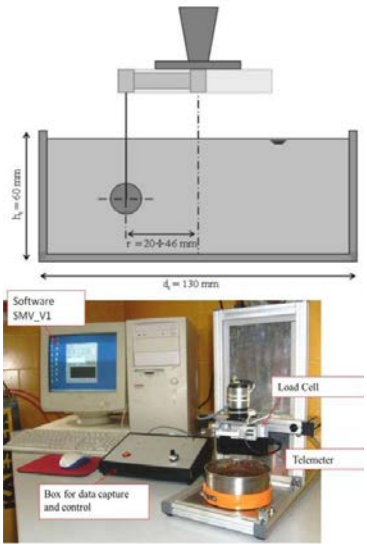

Fig. 1 Upside: geometrical scheme of the SDR rheometer. Downside: complete configuration of the SDR rheometer.

In Fig. 2a the measured points, obtained during one full rotation of the sphere, for different values of Ω, are showed. For each imposed velocity the value of the required drag force F_D (value at which the sphere starts moving through the material sample) is evaluated as the average between the measured points in a full rotation, of the sphere, as illustrated in Fig. 2b. The apparent flow curve was obtained by applying an increasing and decreasing rotational speed ramp. In order to ensure the stability of the measurements, each value of velocity was imposed for 30 seconds. This time was in agreement with the experimental results carried out with conventional rheometer on the same pyroclastic debris flow materials as described in [5].

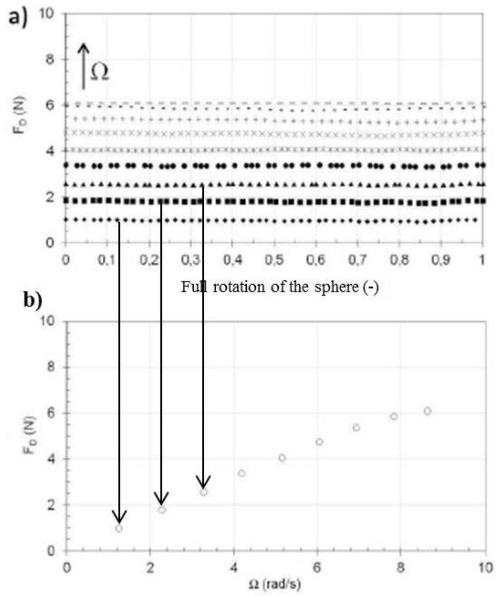

Fig. 2 Silicon oil with viscosity equal to 60 Pa·s. a) Measurements of FD during a full rotation of the sphere (D = 18 mm) at different values of the imposed rotational speed Ω (diamonds 1.24 rad/s, squares 2.27 rad/s, triangles 3.28 rad/s, circles 4.19 rad/s, stars 5.15 rad/s, crosses 6.93 rad/s, little dashes 7.83 rad/s, big dashes 8.63 rad/s); b) Resulting flow curve F_D-Ω.

Calibration of the SDR rheometer

The SDR rheometer was calibrated using several reference materials for which the rheological behaviour was already analyzed and well-known. Tests were performed on different Newtonian viscous materials (i.e. glycerin and silicone oils at different peculiar viscosity) and on Non-Newtonian viscous materials with yield stress (i.e. hair gel and tomato sauce). After, the calibration was carried out using a representative soil-water mixture, composed by water and kaolin, in order to approach the feasibility of the experimental apparatus with particles-fluid suspensions close to debris flow material mixtures tested in traditional rheometer before [5]. The kaolin-water mixture was reconstituted according to the total solid volumetric concentration Φ_T, defined as the ratio of the volume of solids to the total volume (water plus solids), as follow:

$$\Phi_T = \frac{V_S}{V_{TOT}} = \frac{V_S}{V_S + V_W} = \Phi_f + \Phi_g \tag{1}$$

where V_{TOT}, V_W, V_S are, respectively, the total volume, the volume of water and the volume of solid in the sample, and Φ_f, Φ_g are, respectively the solid volumetric concentration of fine particle and the solid volumetric concentration of coarse particle of the mixture. The complete description of the calibration is reported in [17].

Conversion of measured data into rheological parameters

Unlike traditional rheometers, the measuring system adopted for the SDR is not based on the classic shear flow between two parallel surfaces but on the flow regime around the object, a sphere that moving as in Fig. 3. For this reason it was defined an appropriate theory of conversion that allow to relate the two schemes of flow.

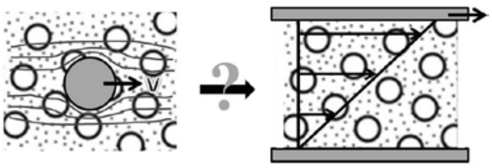

Fig. 3 Schematic principal task for the sphere drag measuring system on the left. Scheme of the classic shear flow on the right.

The analytical solution of the free motion of an object into a Newtonian fluid goes back to the work of [18]-[19] reported in [20]. The problem of the motion of an object of spherical shape through a Yield Stress Fluid is more complex than the case of Newtonian Fluid and requires a different treatment. No simple solutions were found yet and various analytical expressions were also been proposed [21]-[22]-[23]. All the theoretical works, which assume a simple yielding behavior, predict a particle velocity progressively decreasing to zero as the applied force tends to the critical value for incipient motion. The experimental results presented in the literature are in agreement with this basic expectation, namely, that the object can move through the fluid only when the force applied to it becomes greater than a critical one. In the case of Yield Stress Fluid we assume that the fluid remains perfectly rigid in its solid regime and follows a constitutive equation such as Herschel & Bulkley in its liquid regime as:

$$\tau = \tau_c + k \cdot \dot{\gamma}^n \Rightarrow \tau > \tau_c \tag{2}$$

In equation (2), τ is the shear stress (Pa), τ_c is the yield stress (Pa), $\dot{\gamma}$ is the shear rate (s^{-1}), k is the consistent coefficient ($Pa \cdot s^n$) and n is the dimensionless pseudo-plasticity index. The considered conversion theory is applicable only in the treatment of Yield Stress Fluid. As observed in [5] the soil-mixtures considered in the present study are Yield stress Fluid and their behaviour is well described using the Herschel & Bulkley model (equation (2)). In this condition the drag force F_D can be computed as following:

$$\frac{F_D}{F_C} = 1 + \frac{k}{\tau_c} \cdot \dot{\gamma}_{app}^n \tag{3}$$

Where k is an increasing, positive, dimensionless function of the surface of the object and decrease towards a critical, minimum value k_c and F_C is the critical drag force FC equal to:

$$F_C = 4\pi \cdot R \cdot \tau_c \cdot k_c \tag{4}$$

Where R is the sphere radius. Considering the numerical work of [23], the relationship between the measured sphere velocity and the apparent shear rate is the following:

$$\dot{\gamma}_{app} = \frac{v}{l} \tag{5}$$

Where v is the linear velocity of the sphere (m/s) and l is equal to 1.35 multiplied the radius of the sphere R. The complete description of the applied conversion theory is reported in [17].

MATERIALS AND METHODS

The SDR experimental results reported are related to pyroclastic soils which are representative of real pyroclastic debris flows occurred in Southern Italy. The soil mixture analyzed with SDR were before tested with standard rheometer as reported in [5]. The soil A and B derives from the most recent deposits produced by the volcanic activity of mount Somma/Vesuvius and they are sandy silt with a small clay fraction. The geotechnical and mechanical properties of such materials are well documented in literature [24]. All the experiments involved mixtures of dry soils with different amounts of water. The materials were mixed with appropriate amount of distilled water in order to obtained mixtures having different solid volumetric concentrations Φ according to equation (1). The range of solid concentration here considered was defined according to natural porosity of the soils and taking into consideration the previous study of [5]. A total amount of about 500 ml of mixture (distilled water and soils) was pre-pared and each sample was continuously mixed for the time needed to obtain a fairly homogeneous mixture. The whole sample was used performing SDR test. The entire experimental program was carried out at constant temperature equal to 23°. Fine-grained mixtures (i.e., mixtures composed by soil fraction with a particle diameter less than 0.5 mm) were tested in order to compare the data to those obtained using standard rheometer [5]. Also coarse-grained mixtures (i.e., mixtures composed by soil fraction with a particle diameter up to 0.5 mm) were tested. The complete experimental program is illustrated in table 1. A total amount of about 500 ml of mixture (distilled water and soils) was pre-pared and each sample was continuously mixed for the time needed to obtain a fairly homogeneous mixture. The whole sample was used performing SDR test. The entire experimental program was carried out at constant temperature equal to 23°.

Table 1 Experimental program.

Test (#)	Soil (-)	Φ_T (%)	Φ_f (%)	Φ_g (%)	d_{MAX} (mm)
1	A	35	35	-	0.5
2	A	38	38	-	0.5
3	A	40	40	-	0.5
4	A	42	42	-	0.5
5	A	35	28	7	5.0
6	A	38	31	7	5.0
7	A	40	32	8	5.0
8	A	35	21	14	10.0
9	A	38	24	16	10.0
10	B	32	32	-	0.5
11	B	35	35	-	0.5
12	B	38	38	-	0.5
13	B	30	21	9	5.0
14	B	32	22	10	5.0
15	B	35	25	10	5.0
16	B	38	29	9	5.0

RESULTS AND DISCUSSION

The fine-grained water-soil A and B mixtures were tested with SDR rheometer according to experimental program described in Table 1. The experimental data obtained are reported in Figures 4 and 5 for soil A and soil B, respectively, at different solid volumetric concentrations Φ. The graphs report the evolution of the drag force F_D as a function of the apparent shear rate. For each mixtures considered, the apparent shear rate was derived from the value of the imposed rotational speed Ω according to equation (5). In this way we defined the experimental flow curve in which the measured drag force F_D is related to the calculated apparent shear rate. Then the experimental flow curves (e.g., symbols in Figures 4 and 5) were compared with the theoretical curve (e.g., lines in Figures 4 and 5) obtained starting to the conversion theory and using the equations (3) and (4). First, we note that there is a good match between the measured data and those obtained through the application of the conversion theory. The water-soil mixtures behave like Non-Newtonian fluid and flow resistance increases with the increasing of shear rate regardless the value of solid concentration. The solid fraction clearly influences the rheological behavior of the materials. Although it is not possible to precisely identify the value of the critical drag force F_D associated to each mixtures, especially for more dilute mixtures (e.g., because of the lack of measurement points at very low rotational speed), even though the data show a trend equal to that obtained with tests in standard rheometer [5]. The resistance force is strictly influences by the solid volumetric concentration. The intrinsic strength of the mixtures increases as the particle fraction increases and there is a critical value of drag force below which the flow is possible. The coarse-grained water-soil A and B mixtures were tested with SDR rheometer according to experimental program described in Table 1. The experimental data obtained are reported in Figures 6 and 7 for soil A and soil B, respectively, at different solid volumetric concentrations Φ and different grain size distribution. The graphs report the evolution of the drag force F_D as a function of the apparent shear rate. For each mixtures considered, the apparent shear rate was derived from the value of the imposed rotational speed Ω according to equation (5). In this way we defined the experimental flow curve in which the measured drag force F_D is related to the calculated apparent shear rate. Also in this case, the coarse-grained water-soil mixtures behave like Non-Newtonian fluid and the flow resistance increases with imposed shear rate regardless the value of solid concentration.

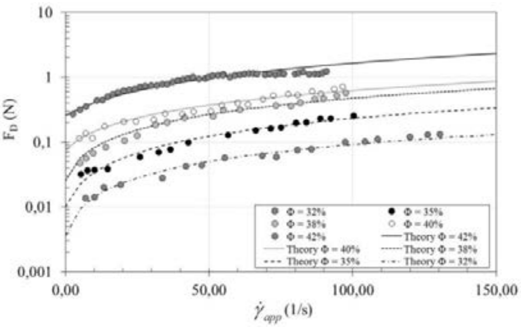

Fig. 4 Fine-grained water-soil A mixtures at several values solid volumetric concentration Φ: comparison between SDR measured data (symbols) and theoretical curve (lines).

The solid fraction also influences the rheological behavior of the materials. The data show a trend equal to that obtained with tests on fine-grained mixtures.

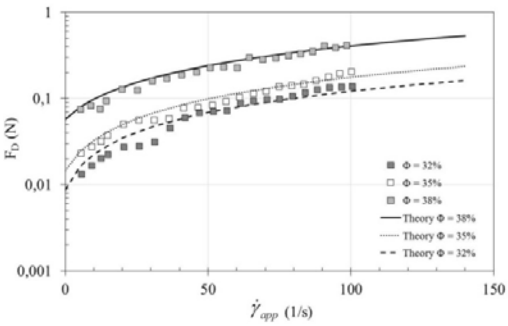

Fig. 5 Fine-grained water-soil A mixtures at several values solid volumetric concentration Φ: comparison between SDR measured data (symbols) and theoretical curve (lines).

We note that the resistance force is strictly influences by the grain size distribution and increases as the size particles increases (Fig. 6) according to [12] and [13]. The experimental results obtained on coarse-grained water-soil A and B mixtures were compared with those obtained on fine-grained water-soil A and B mixtures according to experimental program described in Table 1. The comparisons obtained are reported in Figures 8 and 9 for soil A and soil B, respectively, at different solid volumetric concentrations Φ and different grain size distribution. We observe that, at equal total solid volumetric concentration, the adding of the solid fraction with a diameter less than 5 mm brings to a reduction of the characteristic resistance of the mixture regardless the material tested. Moreover, when you consider that the addition of the fraction of particles with a diameter less than 5 mm corresponds to a solid volumetric concentration of coarse particles Φ_g of about 8-10% of the entire total solid concentration, this result becomes consistent with several previous experimental observations ([12]-[13]) and with the experimental results obtained through tests on the same coarse-grained mixtures with conventional measurement systems reported in [15]. Several studies have already demonstrated that the addition of coarse particles brings to an increase of the rheological characteristics of the mixture but, for relatively low solid volumetric concentration, a minimum depletion in fine particles fraction within the mixture does not seem to be sufficient to induce a increase of rheological parameters ([12]-[13]-[14]- [15]). Different considerations can be done when the solid fraction with a diameter less than 10 mm is added. We observe that, at equal total solid volumetric concentration, there is an increase of the characteristic resistance of the mixture. Indeed, it is noted that the addition of the fraction of particles with a diameter less than 10 mm corresponds to a solid volumetric concentration of coarse particles Φ_g of about 14-16% of the entire total solid concentration.

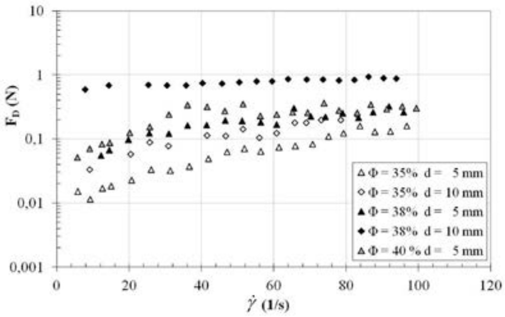

Fig. 6 Coarse-grained water-soil A mixtures at several solid volumetric concentration and grain size distribution according to Tab. 1.

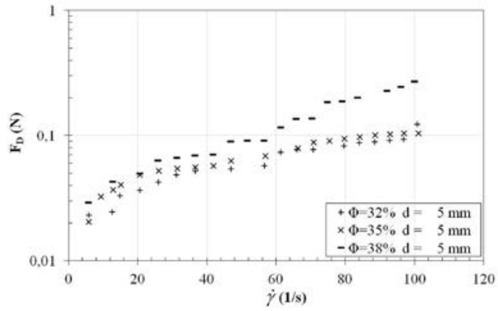

Fig. 7 Coarse-grained water-soil B mixtures at several values solid volumetric concentration Φ and grain size distribution according to Tab. 1.

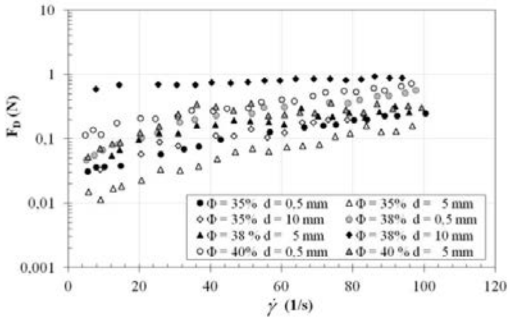

Fig. 8 Water-soil A mixtures: comparison between fine-grained and coarse-grained mixtures according to Tab. 1.

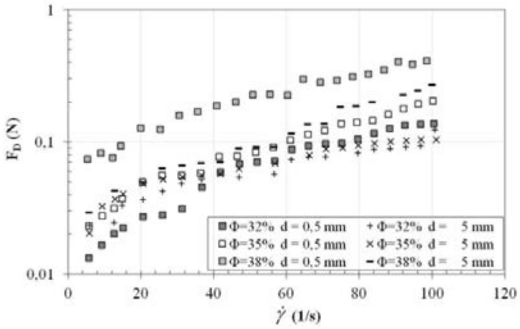

Fig. 9 Water-soil B mixtures: comparison between fine-grained and coarse-grained mixtures according to Tab. 1.

CONCLUSIONS

The obtained experimental results, conveniently converted into rheological parameters, show that the SDR rheometer is able to analyze flowing materials similar to those involved into pyroclastic debris flow.

REFERENCES

[1] Forterre Y & Evangelista A, Some observations on the prediction Pouliquen O, Flows of dense granular media, An. Rev. of Fluid Mech., 40, 2008, 1-24.

[2] Scotto di Santolo A & Evangelista A, Some observations on the prediction of the dynamic parameters of debris flows in deposits in the Campania region of Italy, International Journal of Natural Hazards, 50, 2009, 605–622.

[3] Pudasaini SP, A General Two-Phase Debris Flow Model, Journal of Geophysical Research, 117, 2012, F0310.

[4] Pellegrino AM, Scotto di Santolo A & Schippa L, Numerical modeling of a debris flow event occurred in Campania region, southern Italy: consideration on the rheological model parameters on the run-out, in Proc. Latest Trends in Engineering Mechanics, Structures, Engineering Geology, 2014.

[5] Scotto di Santolo A, Pellegrino AM, Evangelista A, Coussot P, Rheological behaviour of reconstituted pyroclastic debris flow, Geotechnique Journal, 62 (1), 2012, 19-27.

[6] Coussot P, Mudflow Rheology and Dynamics, IAHR Monograph series, Balkema.

[7] O'Brien JS & Julien PY, Laboratory analysis of mud-flow properties, Journal of Hydraulic Engineering 114, 1988, 877-887.

[8] Kaitna R, Rickenmann D & Schatzmann M, Experimental study on the rheologic behaviour of debris flow material, Acta Geotechnica 2, 2007, 71-85.

[9] Bisantino T, Fischer P & Gentile F, Rheological characteristics of debris-flow material in South-Gargano watersheds, Nat. Hazards Earth Syst. Sci. 54, 2010, 209-223.

[10] Jeong SW, The viscosity of fine-grained sediments: A comparison of low-to medium-activity and high-activity clays, Eng. Geol. 154, 2013, 1-5.

[11] Bagnold RA, Experiments on gravity-free dispersion of large solid spheres in a Newtonian fluid under shear, Royal Society A 225, 1954, 49-63.

[12] Coussot P & Piau JM, A large-scaled field concentric cylinder rheometer for the study of the rheology of natural coarse suspensions, Journal of Rheology 39, 1995, 105-124.

[13] Ancey C & Jorrot H, Yield stress for particle suspension within a clay dispersion. Journal of Rheology 45, 2001, 297-319.

[14] Schatzmann M, Bezzola GR & Minor HE, Rheological Behaviour of Fine and Large Particle Suspensions, Journal of Hydraulic Engineering 129, 2009, 796-803.

[15] Scotto di Santolo A, Pellegrino AM & Evangelista A, 2010. Experimental study on the rheologic behaviour of pyroclastic debris flow, Journal of Natural Hazards and Earth Systems Science 10, 2010, 1-8.

[16] Müller, M., Tyrach, J. & Brunn, P.O. 1999. Rheological char-acterization of machine applied plasters. ZKG International 52: 252-258.

[17] Pellegrino AM, Scotto di Santolo A & Evangelista A, A new rheometer for mud and debris flow, Accepted in Workshop on Volcanic Rocks & Soil, 2015.

[18] STOKES GG, On the effect of the internal friction of fluids on the motion of pendulums. Trans. Camb. Phil. SOC. 9 (11), 1851, 8-106.

[19] Einstein A, Investigation of the Brownian Movement, Ann. Physik 19, 1906, 289-306.

[20] Lapple CE & Shepherd CB, Calculation of particles trajectories, Industrial and Engineering Chemistry 32, 1940, 605.

[21] Ansley RW & Smith TN, Motion of spherical particles in a Bingham plastic, AIChE Journal, 13, 1967, 1193-1196.

[22] Beris AN, Tsamopoulos JA, Armstrong RC & Brown RA, Creeping motion of a sphere through a Bingham plastic, Journal of Fluid Mechanics 158, 1985, 219-244.

[23] Beaulne M & Mitsoulis E, Creeping motion of a sphere in tubes filled with Herschel-Bulkley fluids, Journal of Non-Newtonian Fluid Mechanics 72, 1997, 55-71.

[24] Picarelli L, Evangelista A, Rolandi G, Paone A Nicotera MV, Olivares L, Scotto di Santolo A, Lampitiello S, Rolandi M, Mechanical properties of pyroclastic soils in Campania Region. In Proc. of 2nd Int. Workshop on Characterisation and Engineering Properties of Natural Soils, 2007.

UNDRAINED BEHAVIOUR OF JOHOR SAND IN CYCLIC TRIAXIAL TEST

Aminaton Marto, Choy Soon Tan, Ahmad Mahir Makhtar and Siti Norafida Jusoh
Faculty of Civil Engineering, Universiti Teknologi Malaysia, 81310 UTM Johor Bahru, Johor, Malaysia

ABSTRACT

As liquefaction due to earthquake hazards may occur on both clean sand and soil comprising of sand with fines, the current research trend is more focusing on determining the boundary limits of liquefaction susceptibility of sand matrix soils. Series of laboratory testing had been carried out by researchers around the world but many of the results are contradictory. Thus, it is important to first determine the condition in which the clean sand is most susceptible to liquefaction, then only the liquefaction susceptibility of sand matrix soils could be compared and discussed under this specific condition. This paper presents the undrained behaviour of Johor sand obtained from cyclic triaxial tests. Stress controlled triaxial test apparatus was used to shear the isotropically consolidated sand samples under undrained two-way cyclic loading until the initiation of liquefaction. The liquefaction was defined based on: (i) excess pore pressure was equal to effective confining pressure or (ii) double amplitude strain of 5 % was reached, whichever was achieved first. The results of two-way cyclic triaxial tests on clean sand showed that besides the cyclic stress ratio, the liquefaction resistance of the sand under undrained loading was proportional to effective consolidation pressure and density index. The Johor sand was more liquefiable at its loose state and under low effective consolidation pressure, when subjected to earthquake loading.

Keywords: Liquefaction, density index, consolidation pressure, excess pore pressure.

INTRODUCTION

Soil liquefaction, the secondary effect of an earthquake; is a transformation of granular material from a solid state into a liquefied state with a significant increase of pore water pressure until the effective stress reaches zero [1]. For many years, research on liquefaction has been a mandatory focus on uniform clean sands, containing little or no fines; with a common assumption that the cyclic behaviour of clean sand is remarkably representing all types of in-situ sand deposits. Unfortunately, empirical evidences including the 2010 Canterbury Earthquake [2], the 2011 Christchurch Earthquake [3] and the 2011 Tohoku Earthquake [4] have shown that the sand matrix soils (sand dominant soil with limiting percentage of fine particles existed within) does actually liquefy.

Lots of the laboratory testing had been carried out by researcher worldwide [5, 6] using the cyclic triaxial testing system. Nonetheless, the research breakthroughs are somewhat conflicting. There is not enough evidence at this point to obtain a global agreement in describing how the fines particles influence the soil liquefaction resistance under dynamic loading.

Head [7] stressed that sand is largely influenced by its composition characteristics such as soil grains, packing density and void ratio. Research by Choobbasti *et al*. [5] found that when density index is fixed the finer the sand, the lower the resistance towards liquefaction. Thus, it is important to first compare at which testing environment that the clean sand is potentially liquefiable, and then only the liquefaction susceptibility of sand matrix soils could be compared under these specific conditions. This paper presents the undrained behaviour of Johor sand obtained from cyclic triaxial tests. It compares various important factors in the triaxial testing environment and determines the most susceptible environment of the Johor clean sand towards liquefaction hazards.

LABORATORY TESTING

The two-way cyclic triaxial test, in accordance to the ASTM D5311-13M Load Controlled Cyclic Triaxial Strength of Soil [8] was carried out to simulate the cyclic loading on cylindrical size reconstituted clean sand soil specimen of approximately 76 mm height and 38 mm diameter.

Material

The clean sand used in this study was the natural sand obtained from a river in Johor, Malaysia. The 'Johor' sand has a sub-angular shape with light brown colour. Based on the particle size distribution curve shown in Figure 1, the sand was poorly graded (SP) containing no fines with medium fine particle size in a narrow range. As pointed out by Choobbasti *et al*. [5], poorly graded sand is very susceptible to liquefaction than well graded sand. Hence, this soil is a suitable type for studying the role of fines in liquefaction susceptibility of sand matrix soils. The minimum and maximum densities of the sand were 1.37 Mg/m^3 and 1.59 Mg/m^3, respectively. Based on these values, the density of sand for the required density index (I_D) was calculated and prepared for the cycling loading tests.

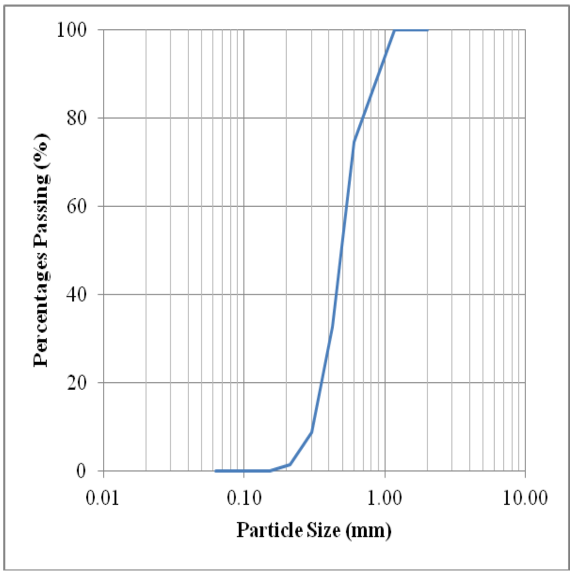

Fig. 1 Particle size distribution of Johor sand

Cyclic Triaxial Test

Prior to the saturation process, carbon dioxide gases and de-aired water was flushed through the specimens from the bottom drainage line to the top until an amount equal to the specimen's void volume was collected. Saturation process was carried out with a linear increase of cell and back pressure, keeping a constant difference of 10 kPa effective stress. This process was continued until the minimum B-value of 0.96 was achieved. Then isotropic consolidation was performed and completed in a very short period. Upon the completion of isotropic consolidation, the stress-controlled undrained cyclic triaxial tests were carried on the specimen using the back pressure of 200 kPa. In order to apply the two-way loading, the top cap was locked to the loading ram to enable the application of extension forces using an extension top cap and vylastic sleeve. The cyclic loading in terms of cyclic stress ratio (CSR) was applied to the specimen accordingly to simulate different loading amplitude. The CSR was calculated as the ratio of the applied shearing stress (one-half of the applied deviator stress amplitude) to the initial effective consolidation stress.

The sand specimens were loaded cyclically under various testing conditions; (i) effective consolidation pressure (100 and 200 kPa); (ii) density index of 20% to represent the loose state and 60% to represent the dense state and (iii) cyclic amplitude in terms of CSR at 0.1, 0.2, 0.3, 0.4 and 0.5. The nature of cyclic loading applied to the soil deposit is highly dependent on the loading source, which could be relatively uniform with single frequency or randomly with a range of frequencies. Although various researchers carried out the test with varying frequency ranging from 0.1 Hz [9] to 2 Hz [6], the testing standard of ASTM D5311-M13 [8] states that the frequency of 1 Hz is more preferable. Since the simulation of earthquake loading in a triaxial testing system is always represented by 1 Hz [10], all sand matrix soils in this study were tested with 1 Hz cyclic frequency.

The cyclic loading process was terminated either when the soil reached 10 % of axial strain or when 100 cycles of cyclic loading had been subjected to the soil specimen, whichever encountered first. In this study, the initiation of liquefaction (failure) was defined as either when excess pore pressure is equal to effective consolidation pressure [11] resulting in a temporary condition of zero effective stress in the specimen ($r_{u=1}$) or when the double amplitude strain of 5 % (ε_{DA}=5%) was reached [12, 13]. Marto [14] pointed out that the two-way cyclic loading typically generates two components of the pore pressure responses, which are known as the resilient response and the permanent response. The pore pressure for the resilient response were observed at the peak of the compression and extension zones, and known as the $u_{peak(c)}$ and $u_{peak(e)}$, respectively. In this study, the pore pressure for the permanent response ($u_{permanent}$) was used to characterise the pore pressure response due to cyclic loading.

RESULTS AND DISCUSSION

Cyclic triaxial test under undrained condition was conducted on 12 clean sand specimens subjected to different testing condition, at varying density index, effective confining pressure and cyclic stress ratio. Table 1 shows the number of cycles at the initiation of liquefaction for clean sand obtained from two-way cyclic triaxial tests. The respective testing condition and failure criteria for each test were also shown. It is found that loose specimen exhibited large strain on compression side (positive value of deviator stress) whereas dense specimen exhibited dominant deformation on extension side (negative value of deviator stress). This result was also observed by Lombardi *et al* [9].

Figure 2(a) shows the critical state line obtained from monotonic triaxial tests [15] together with the effective stress paths (ESP) of the loose sand specimen subjected to cyclic loading. It could be seen from the plot that the ESP moved to the left during the cyclic loading. This is because as the volume change of soil was not allowed in undrained test, the positive pore pressure was developed and reduced the stresses accumulated in the soil due to shearing. For the loose sand specimen, it approached the critical state line in a sudden manner when the initiation of liquefaction occurred. Figure 2(b) shows the ESP of the dense sand specimen subjected to cyclic loading. It could be seen from the plot that the ESP also moved to the left during the cyclic loading. However, the dense sand generated the characteristic of butterfly shape ESP before failure. Both the results are comparable to the stress paths of Red Hill sand subjected to cyclic loading, modelled by Lombardi *et al* [9]. The stress path was seen to have moved to the left in a sudden manner, which was caused by large deformation as a result of liquefaction. The dense sand specimen on the other hand, developed a progressive decrement in the shear stress with the addition of the number of cycle. Thus, the stress path was observed in a butterfly shape loop when the condition of zero effective stress was ascertained.

Table 1 Results of cyclic triaxial test on Johor sand

Specimen	Effective confining pressure (kPa)	Density index (%)	CSR	Failure Criteria	N_c
SAND1	100	20	0.1	ε_{DA}=5%	40
SAND2	100	20	0.2	ε_{DA}=5%	27
SAND3	100	20	0.3	ε_{DA}=5%	19
SAND4	100	20	0.4	$r_{u=1}$	14
SAND5	100	20	0.5	$r_{u=1}$	10
SAND6	100	60	0.1	ε_{DA}=5%	75
SAND7	100	60	0.3	ε_{DA}=5%	54
SAND8	100	60	0.5	$r_{u=1}$	36
SAND9	200	20	0.1	ε_{DA}=5%	67
SAND10	200	20	0.2	ε_{DA}=5%	52
SAND11	200	20	0.4	ε_{DA}=5%	34
SAND12	200	20	0.5	$r_{u=1}$	26

Note: ε_{DA}=5% : 5 % axial strain at double amplitude
$r_{u=1}$: ratio of excess pore pressure to consolidation pressure = 1
N_c : number of cycle
CSR : cyclic stress ratio

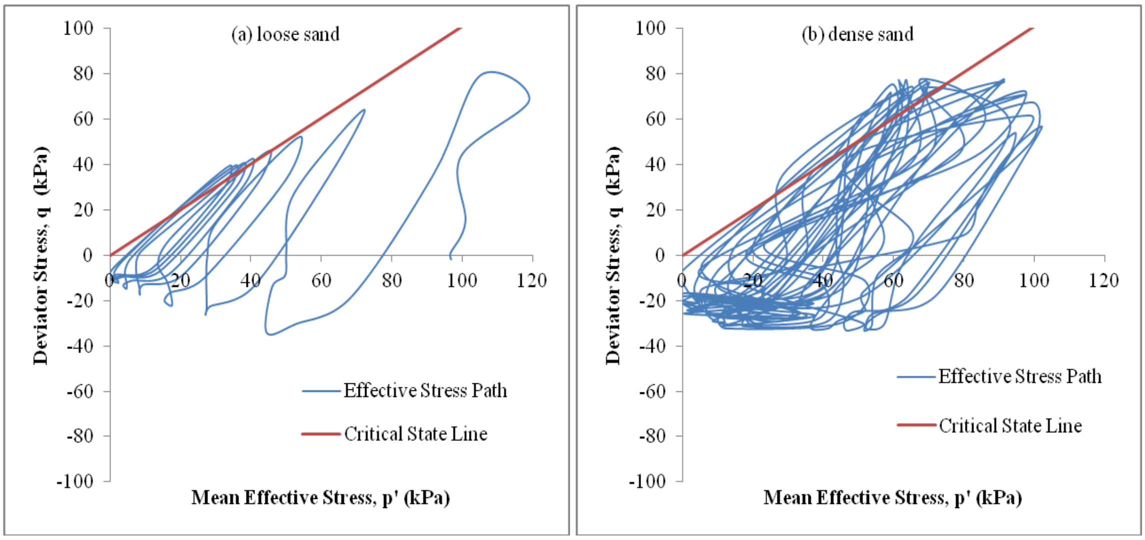

Fig. 2 Effective stress paths of Johor clean sand subjected to two-way cyclic loading

Effect of Confining Pressure

The effect of confining pressure was investigated by performing the two-way cyclic triaxial tests with initial effective confining pressure (σ'_{3C}) of 100 and 200 kPa, respectively. Figure 3 shows the effect of initial effective confining pressure towards liquefaction susceptibility of Johor clean sand under triaxial testing system. The results show that additional number of cycles (N_c) was required to initiate the liquefaction at a high initial effective confining pressure with the same CSR. The liquefaction curve shifted to the right when the initial effective confining pressure was increased from 100 to 200 kPa. For an example, it can be seen from the figure that for a constant CSR value of 0.2, the N_c for σ'_{3C} of 100 kPa was 27 while it was 52 for σ'_{3C} of 200 kPa. The findings of Della *et al* [16] and Krim *et al* [17] also showed that liquefaction resistance of sand is proportional to the effective confining pressure. The liquefaction could occur at low confining pressure but as the confining pressure increased to a higher value, the sand becomes denser thus having better resistance towards liquefaction. In addition, the results also agreed on the common ground with the general concept of liquefaction susceptibility of sand. Generally, the liquefaction only occurred to the soil at shallow depths. Youd *et al* [18] indicated in the summary of NCEER workshop that loosely deposited sand with depth of less than 15 m is susceptible to liquefaction. At shallow depths, the effective confining pressure is low.

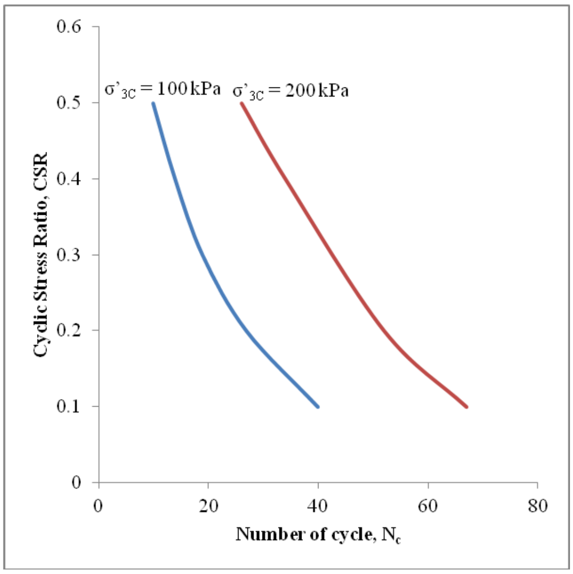

Fig. 3 Effect of confining pressure on cyclic behaviour of Johor clean sand at initial density index of 20 % and subjected to 1Hz cyclic frequency

Effect of Density Index

The effect of density index (I_D) was investigated by performing the two-way cyclic triaxial tests with initial density index of 20 and 60 %. Figure 4 shows the effect of density index towards liquefaction susceptibility of Johor clean sand under two-way cyclic triaxial tests. From the figure, for CSR of 0.3, the N_c at I_D of 20 % was 19 while the N_c at I_D of 60 % was 54. The results showed that additional number of cycles was required to initiate the liquefaction at high I_D with the same CSR. The liquefaction curve shifted to the right when the I_D was increased from 20 to 60 %. The findings of Krim *et al* [17] and Lombardi *et al* [9] also showed similar findings. From their research, they concluded that the liquefaction resistance of sand is directly proportional to the density index. Head [7] indicated that the sand is considered loose for 20 % I_D and dense for 60 % I_D. Thus, the results obtained in this study are similar to other types of sand [9, 17] in which the loose state of Johor sand is also more susceptible to liquefaction than the dense state.

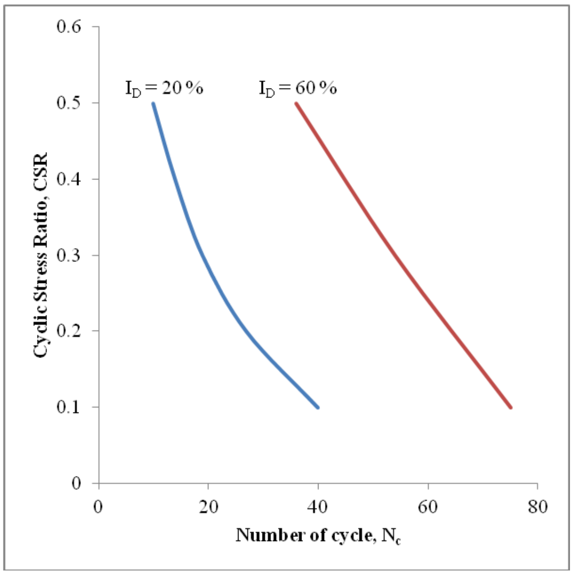

Fig. 4 Effect of density index on cyclic behaviour of Johor clean sand at 100 kPa initial effective confining pressure and subjected to 1 Hz cyclic frequency

In general, the results obtained in this study are in agreement with the concept of liquefaction susceptibility of sand as stated by Kramer [19] whereby the liquefaction is more prone to occur in loose sand. When there is an external loading exerted on saturated sand under the undrained condition, the response of cyclic softening on sand differs in accordance to density state. For loose sand of low density and with contractive tendency, the loading was too quick for the pore water to escape. In response to the compressibility of soil, the pore pressure would build up to counter the external load. At a point where the pore pressure is exceeding the contact stresses between sand grains, the soil was observed to flow like a liquid form. On the other hand, liquefaction hardly occurs to the sand in a high density state. Dense sand is not susceptible to flow liquefaction because its strength is greater in undrained condition than in drained condition [20]. Besides that, due to its dilative behaviour in nature;

the pore pressure would easily escape from the matrix of dense sand grain during cyclic loading. Hence, dense sand has more resistance to liquefaction as compared to loose sand.

Liquefaction Susceptibility

Laboratory test results showed that besides CSR, the liquefaction resistance of the sand under undrained cyclic loading was also proportional to the initial effective confining pressure and the density index. In this study, the cyclic resistance of soils had been expressed in terms of the N_c required for the liquefaction to occur. It has been found that the higher the CSR, the lower the N_c required for the liquefaction to initiate. For the effect of initial effective confining pressure, the N_c obtained was lower for 100 kPa than for 200 kPa at the same value of CSR. In term of the effect of initial density index, the N_c was lower for 20 % I_D than for 60 % I_D at the same value of CSR. Thus, from this study the most liquefiable condition for Johor clean sand under 1Hz cyclic frequency of two-way triaxial tests was being at its loose state condition (I_D = 20 %) and confined with low effective confining pressure (100 kPa).

Figure 5 shows the liquefaction susceptibility curve of sand obtained from this study under the testing condition of I_D = 20 % and confined with initial effective confining pressure of 100 kPa. The liquefaction susceptibility curve is the plot of CSR versus N_c which divided the sand into two zones; liquefaction and non-liquefaction. The shape of the curve was in general agreement with the curve obtained by previous researchers [10, 11 and 13]. However, due to different testing conditions, the curves obtained in previous studies showed different magnitude and location compared to the results obtained in this study.

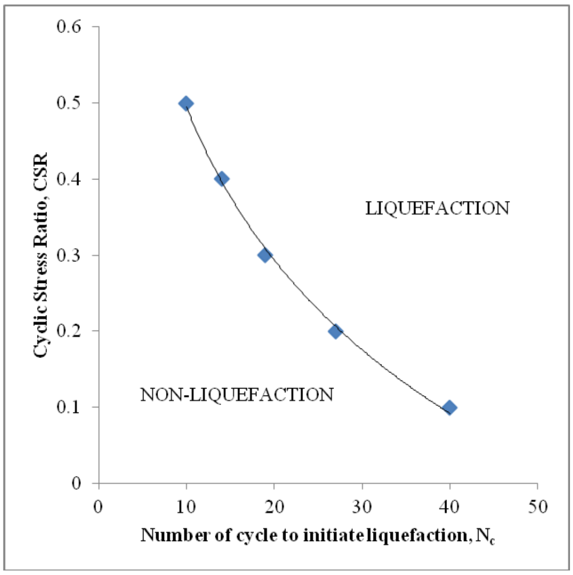

Fig. 5 Liquefaction susceptibility curve of Johor clean sand at initial density index of 20 %, initial effective confining pressure of 100 kPa and cyclic frequency of 1Hz

Through the regression analysis, the CSR was correlated with the N_c to form the liquefaction susceptibility curve in natural logarithmic relation. The coefficient of determination (R^2) of 0.99 indicated that it is a very good relation [21]. Statistically it means that 99% of the total variation of N_c, as a dependent variable, is explained by the regression line using the $\log_e$ CSR, as the independent variable. Hence, the liquefaction susceptibility curve obtained could be used to divide the liquefaction and non-liquefaction zones with great accuracy. The equation of the liquefaction susceptibility curve is as follows:

$$N_c = -18.71 \ln (CSR) - 3.17 \quad (1)$$

In which, N_c = number of cycle
CSR = cyclic stress ratio

CONCLUSION

The undrained behaviour of Johor clean sand under the two-way cyclic triaxial tests had been determined successfully and the following conclusion had been drawn:

1. The response of cyclic softening on Johor clean sand differs in accordance to density state; liquefaction was more prone to be occurred in loose sand. The loose sand approached the critical state line in a sudden manner when the initiation of liquefaction occurred while the dense sand generated the characteristic of butterfly shape effective stress path and took a longer period before eventually failed.
2. The higher the cyclic amplitude or cyclic stress ratio during cyclic loading, the smaller the number of cycles required for the initiation of liquefaction.
3. The higher the initial confining pressure, the denser the sand thus the better resistance towards liquefaction.
4. The Johor sand was more liquefiable at loose state (I_D = 20 %) and under low effective consolidation pressure (100 kPa), when subjected to earthquake loading. At this specific condition the liquefaction susceptibility curve, used as a boundary for liquefaction and non-liquefaction, had been established and could be used as a guideline for engineers in preliminary design.

ACKNOWLEDGEMENTS

The authors gratefully acknowledged the financial supports by the Ministry of Higher Education (MOHE) Malaysia, under the Fundamental Research Grant Scheme (UTM vot No.: 4F316) and also the Universiti Teknologi Malaysia (UTM) through the Zamalah program, in undertaking the research for the publication of this paper.

REFERENCES

[1] Day R, Geotechnical Earthquake Engineering. New York: McGraw Hill Professional, 2012.

[2] Wotherspoon L, Pender M and Orense RP, “Relationship between observed liquefaction at Kaiapoi following the 2010 Darfield earthquake and former channels of the Waimakariri River”, Engineering Geology, Vol. 125, 2012, pp. 45-55.

[3] Orense RP, Kiyota T, Yamada S, Cubrinovski M, Hosono Y, Okamura M and Yasuda S, “Comparison of liquefaction features observed during the 2010 and 2011 Canterbury earthquakes”, Seismological Research Letters, Vol. 82(6), 2011, pp. 905-918.

[4] Kokusho T, Nagao Y, Ito F, and Fukuyama T, “Aging effect on sand liquefaction observed during the 2011 earthquake and basic laboratory studies”, in International Symposium on Engineering Lessons Learned from the 2011 Great East Japan Earthquake, 2012, pp. 759-770.

[5] Choobbasti AJ, Ghalandarzadeh A and Esmaeili M, “Experimental study of the grading characteristic effect on the liquefaction resistance of various graded sands and gravelly sands”, Arabian Journal of Geosciences, Vol. 7(7), 2013, pp. 2739-2748.

[6] Taylor ML, Cubrinovski M, Bradley BA and Horikoshi K, “The undrained cyclic strength of undisturbed and reconstituted Christchurch sands” in NZGS Geotechnical Symposium, 2013.

[7] Head KH Manual of soil laboratory testing. Florida: CRC Press, 2006.

[8] American Society for Testing and Materials 2013 D5311M − 13: Standard Test Method for Load Controlled Cyclic Triaxial Strength of Soil

[9] Lombardi D, Bhattacharya S, Hyodo M and Kaneko T, “Undrained behaviour of two silica sands and practical implications for modelling SSI in liquefiable soils”, Soil Dynamics and Earthquake Engineering, Vol. 66, 2014, pp. 293-304.

[10] Ishihara K, Soil Behaviour in Earthquake Geotechnics. Oxford: Clarendon Press, 1996.

[11] Geremew AM and Yanful EK, “Laboratory investigation of the resistance of tailings and natural sediments to cyclic loading”, Geotechnical and Geological Engineering, Vol. 30(2), 2012, pp. 431- 447.

[12] Salem M, Elmamlouk H and Agaiby S, “Static and cyclic behavior of North Coast calcareous sand in Egypt”, Soil Dynamics and Earthquake Engineering, Vol. 55, 2013, pp. 83-91.

[13] Benghalia Y, Bouafia A, Canou J and Dupla JC, “Liquefaction susceptibility study of sandy soils effect of low plastic fines”, Arabian Journal of Geosciences, Vol. 8(2), 2015, pp. 605-618.

[14] Marto A, “Pore pressure response of undrained two-way cyclic loading of silt”, Malaysian Journal of Civil Engineering, Vol. 11(1), 1998, pp. 35-62.

[15] Marto A, Tan CS, Makhtar AM and Tiong KL, “Critical state of sand matrix soils”, The Scientific World Journal, Vol. 2014, 2014, pp. 1-8.

[16] Della N, Arab A and Belkhatir M, “A laboratory study of the initial structure and the overconsolidation effects on the undrained monotonic behavior of sandy soil from Chlef region in northern Algeria”, Arabian Journal of Geosciences, Vol. 4(5), 2011, pp. 983-991.

[17] Krim A, el Abidine Zitouni Z, Arab A and Mostéfa B, “Identification of the behavior of sandy soil to static liquefaction and microtomography”, Arabian Journal of Geosciences, Vol. 6(7), 2013, pp. 2211-2224.

[18] Youd TL, Idriss IM and Andrus RD, “Liquefaction resistance of soils: summary report from the 1996 NCEER and 1998 NCEER/NSF workshops on evaluation of liquefaction resistance of soils”, Journal of Geotechnical and Geoenvironmental Engineering, Vol. 127(10), 2001, pp.-833 817.

[19] Kramer SL, Geotechnical Earthquake Engineering. New Jersey: Prentice Hall, 1996.

[20] Das B, Advanced Soil Mechanics. Florida: CRC Press, 2013.

[21] Marto A, Volumetric compression of silt under periodic loading. University of Bradford, 1996.

INVESTIGATING THE EFFECT OF CHANGING GEOMETRIC AND RESISTANCE PROPERTIES OF MULTI-TIERED REINFORCED SOIL WALL, ON IT'S BEHAVIOR

Mohammad Reza Atrchian [1] , Ahmad Armani [2]
[1] Faculty of Engineering, Islamic Azad University, Zanjan Branch, Iran
[2] Faculty of Engineering, Islamic Azad University, Central Tehran Branch, Iran

ABSTRACT

In reinforced soil walls, whenever it is about constructing a wall with a high height, because of its increasing cost, it is necessary to consider constructing multi-tiered wall so that the cost of materials can be reduced to a large extent. In this research, performance of multi-tiered geogrid reinforced soil walls has been considered and analyzed under static loads. The research was conducted numerically and by using Plaxis software. The obtained results indicate that: By increase of the length of reinforcement and width of the step, the maximum horizontal and vertical displacement decreases. The value of horizontal and vertical displacement of wall in clay soil is more than that of sand soil. By increase of the width of the step and length of the reinforcement, the maximum deformations are transferred towards toe of the wall and the mode of deformation changes from bulging mode into slide mode in the toe of the wall. The value of safety factor in sand soils is higher than that of clay soils, and also by increase of the length of the reinforcement, the safety factor increases intensely. By increase of the length of the reinforcement and width of the wall step, the maximum effective stress decreases. The value of effective and total stress of wall in clay soils is more than that in the sand soils. Finally, it can be concluded that increasing the length of the reinforcement, width of the wall step, and using sand soil, improve the soil behavior.

Keywords: Reinforced soil, step width, multi-tiered wall, geogrid

INTRODUCTION

Geosynthetics have been used for three decades to reinforce soil masses and now their application is well accepted in soil constructions. Geosynthetics have been used in soil structures including retaining walls, slopes, embankments on soft soils, vertical embankment, and soil foundations [1]. Application of reinforcements increase resistance in soil mass through providing tensile force, decreases lateral displacements, and consequently increases general stability of soil structures [1]. The reinforced soil system has been established as a new method to improve performance of soil structures in various points and has caused advances of this method in construction projects [1]. Stepped wall, compared to simple wall with the same width, reduces the costs [2].

Multistep walls transfer a portion of their weight on the slope and naturally the volume of excavation from the natural land of the region and also the volume of backfill would be decreased [2]. Behavior of reinforced soils is subject to various factors. Particle size, soil type, reinforcement method, and structure height are considered as effective factors in soil behavior. Investigating the effect of each of these factors by using empirical or analytic methods is very difficult and costly [3]. However, using numerical methods in this field can be considered as a strong tool [3]. Therefore, the main objectives of this research is to investigate the effect of length of reinforcements, width of wall step, and changing soil properties on behavior of stepped-reinforced soil wall using numerical method.

REINFORCED SOIL SYSTEM

Generally, reinforced embankment systems have three main components [4]:

- The reinforcement
- Embankment
- Facade components

As reinforcement, both metal and non-metal materials have been used [4]. In order to meet requirements such as drainage, necessary durability, and transmitting friction stress from the reinforcement to the soil, generally, granular materials are selected for embankment. Façade components are used for maintaining embankment materials along with the wall, preventing from corrosion of reinforcement, and also providing beauty for the constructed wall (figure 1) [4]. Façade components are only designed for small horizontal pressures and they are generally made of prefabricated concrete panels, prefabricated metal sheets, wire meshes, polymer networks, and a variety of other materials [4].

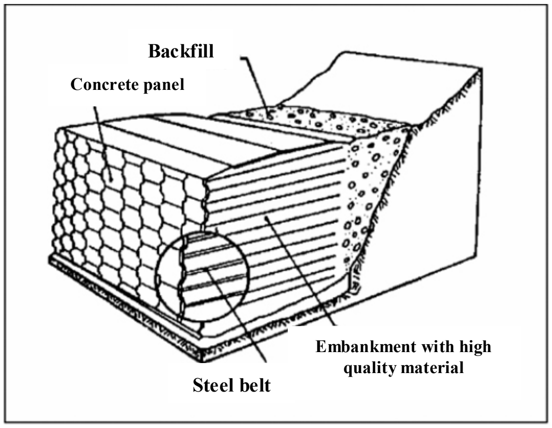

Fig.1 Components of reinforced soil wall [4]

CONSTANT AND VARIABLE PARAMETERS IN MODELING

In this research, to study the effect of properties and geometry of the wall, 50 numerical models were made so that their geometric properties and constant and variable parameters are as follows:

Reinforcement Strength

Axial elastic normal strength (EA) which is also known as stiffness range, is determined by the manufacturer. Stiffness range of geosynthetic reinforcements usually vary from 500 ($\frac{kN}{m}$) to 10000 ($\frac{kN}{m}$) [5]. The type of geogrid used in this research is the single-axis 80/20 R6. The value of its tensile stiffness in 2% strain is equal to 28 $\frac{kN}{m}$, and by considering the strain and stiffness of interest, the value of its axial elastic normal strength is obtained as 1400 $\frac{kN}{m}$.

Distance between Reinforcement Layers

In this research, face of wall is reinforced by wrapping geogrid, for this reason, there is no need for observing the vertical distance according to prefabricated concrete face. In this research, the vertical distance between reinforcing layers in all height of the wall is considered as constant and equal to 50 cm.

Wall Face

Of various types of faces used in reinforced soil walls, we can mention regular block faces of MBW, wrap-around face, prefabricated panels, integrated concrete panels, wooden façade, gabion, etc [3].

The face used in this research is of the type of wrap-around face, so that it is constructed based on each reinforcing layer and its nature is in accordance with reinforcement and geogrid with stiffness of 1400 kN/m.

Loading

To study the effect of overburden on deformation of the retaining wall, static loading was selected. The value of the static overburden considered is equal to 6 kN/m with distance of 2m from the facade of the last wall step.

Foundation Soil

The model used in this analysis is Mohr-Coulomb or the elasto-plastic model. The Mohr-Coulomb model includes 5 input parameters: Elasticity modulus (E), Poisson ratio (υ), internal friction angle (φ), cohesion (C), and dilation angle (ψ) [6].
Parameters related to soil foundation which are considered as constant are as the following table**:**

Table 1 Parameters of soils used in the foundation

Parameter	γ (KN/m^3)	γ_{sat} (KN/m^3)	E (KN/m^2)	ν
Foundation soil (GC)	21	22	60000	0.25

Parameter	Φ	C (KN/m^2)	ψ	n
Foundation soil (GC)	37	10	0	10%

Variable Parameters in Analysis

Variable parameters in the analysis are as follows:

- Widths of wall steps which are: 1m, 1.5m, 2m, 2.5m, 3m.
- Length of the reinforcements which are considered in this research based on total height of the wall
which is 15m, as follows:

L=0.5 H=7.5 m
L=0.6 H=9 m
L=0.7 H=10.5 m
L=0.8 H=12 m
L=0.9 H=13.5 m

The soils used in the body of the wall are the two types of clay and sand soils as follows:

Table 2 Parameters of soils used in the body of the wall

Parameter	γ (KN/m^3)	γ_{sat} (KN/m^3)	E (KN/m^2)	ν
Clay (CL)	19.5	22.2	10000	0.35
Sand (SC)	19	22	20000	0.3

Parameter	φ	C (KN/m^2)	ψ	n
Clay (CL)	15	30	0	27%
Sand (SC)	30	15	0	30%

OUTPUTS AND ANALYSES OF RESULTS

In this paper, according to advantages and capabilities of Plaxis software, numerical modeling was conducted by using this software. The models (50 model) were created according to various geometric models or different resistance properties explained. In the created models, the effect of changing three parameters of horizontal distance, geogrid length, and changes of soil type on behavior of reinforced soil walls, have been studied.

In order to study the effect of these three parameters, maximum stresses, maximum deformations, and safety factors have been used.

In the following figure (Fig.2), geometric properties of the reinforced soil wall related to this research are indicated schematically:

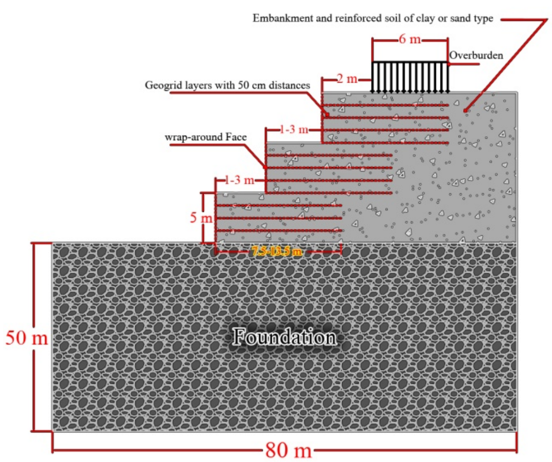

Fig. 2 Geometric properties of models

Effect of Geogrid Length, Step width, and Soil Type, on Horizontal Displacement

As it can be observed in figure 3 and 4, by increase of step width, the value of maximum horizontal displacement decreases. This issue is due to this fact that the more step width increases, the volume of soil existing in the face in which the most horizontal displacement occurs decreases, and decrease of soil volume causes decrease of pressure on face part of the wall and horizontal displacement decreases as a result. If we want to define a mathematical relation between horizontal displacement changes and step width, we can have:

W+0.5= 0.9 ~ 0.95 ΔH

Where,

W= Width of wall step

ΔH= Horizontal displacement

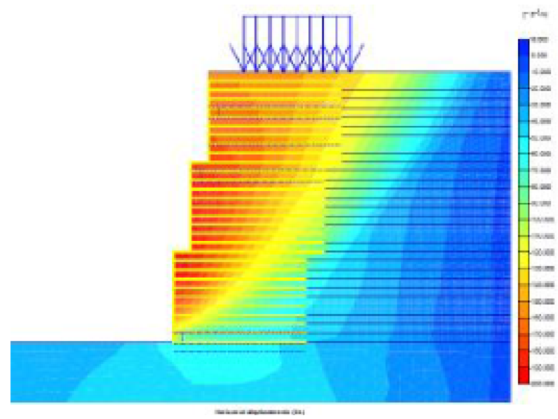

Fig.3 Output of horizontal displacement in the reinforced soil wall (Reinforcement Length 0.5H=7.5m, step width=1m, and sand soil type)

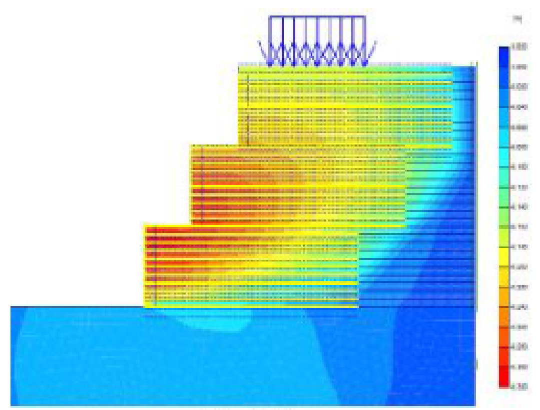

Fig.4 Output of horizontal displacement in the reinforced soil wall (Reinforcement Length 0.9H=13.5m, step width=3m, and clay soil type)

As it can be observed in figure 5 and 6, by increase of the length of the reinforcements, horizontal displacement decreases, and by increase of the length of geogrids, the surface between the soil and the reinforcement increases, and this way, increase of interaction surface causes more stabilization of the wall and decrease of extent of horizontal displacement. It should be noted that increase of step width compared to increase of geogrid length, has a higher effect on decreasing horizontal displacement. The mathematical relation which exists between changes of horizontal displacement and length of the reinforcement is as follows:

L+0.1h= 0.95 ~ 0.99 ΔH

Where,

W= Width of wall step

ΔH= Horizontal displacement

h= Total height of wall

Also the other important point which can be observed in the diagrams is that the extent of horizontal displacement of wall in sand soils is more than that of clay soils. The reason is that sand soils have a higher internal friction angle and also have more sharp corners, so such properties of soil particles and meshed shape of geogrid layers, cause a better interlock between geogrid layers and soil particles, and to the extent this interaction increases, the displacements decrease.

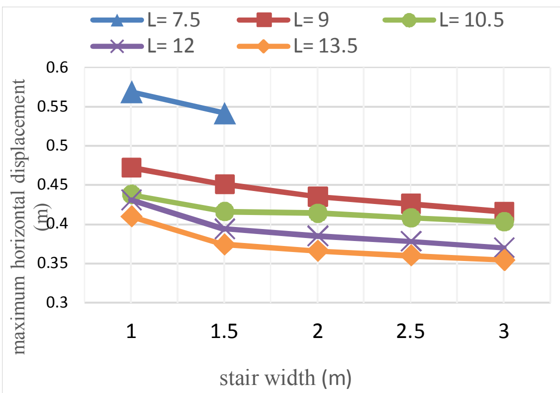

Fig.5 Maximum horizontal displacement against step width in clay soil for different lengths of geogrid

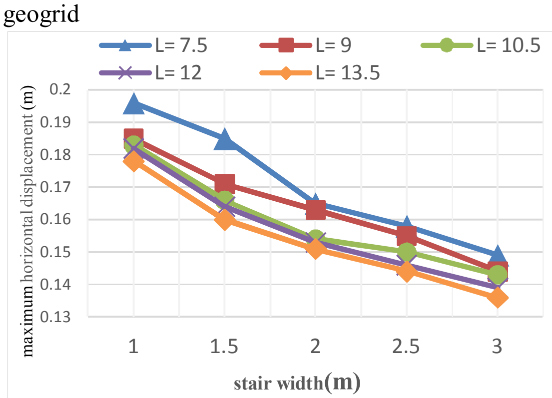

Fig.6 Maximum horizontal displacement against step width in sand soil for different lengths of geogrid

By increase of step width, the situation of the maximum horizontal displacement moves farther from the middle of wall height and moves to near the bottom of the wall. The reason of this fact is that by increase of width of wall step, volume of soil decreases and as a result of that the pressure in upper parts of the wall decreases and is transmitted to the lower layers and result in more deformations in lower parts of the wall.

Besides increase of step width, increase of the length of the reinforcement is also effective in shift of the situation of maximum horizontal displacement to lower parts of the wall face. The reason of this fact is that by increase of the length of the reinforcement and establishment of more interaction between the soil and geogrid, and also since less force is exerted to the upper layers, maximum deformations are created in lower layers of the wall.

In other words, by increase of step width and length of the reinforcement, deformation mode changes from bulging mode to sliding mode. Meaning that if horizontal displacement occurs in the highest point of the wall (peak), deformation mode changes to overturning mode, if it occurs in central parts of the façade, the deformation mode changes to bulging mode, and if it occurs in lower parts of the wall, the deformation mode changes to sliding failure [7].

Effect of Geogrid Length, Step Width, and Soil Type on Vertical Displacement

According to figure 7 and 8, by increase of step width, the extent of maximum vertical displacement decreases. In order to define a mathematical relation between step width and maximum vertical displacement we have:

W+0.5= 0.87 ~ 0.97 Δ V

Where,

W= Wall step width

Δ V= Vertical displacement

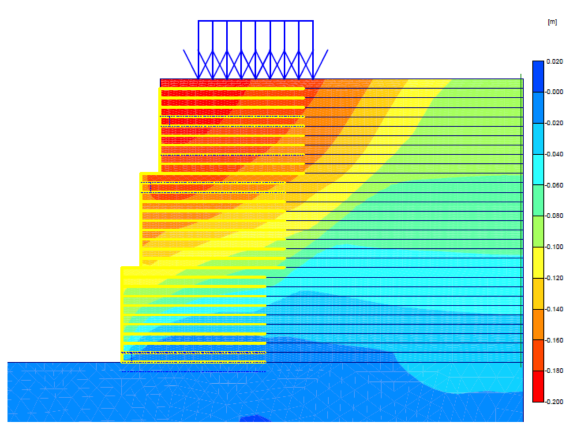

Fig.7 Output of vertical displacement in reinforced soil wall (Reinforcement Length 0.5H=7.5m, step width=1m, and sand soil type)

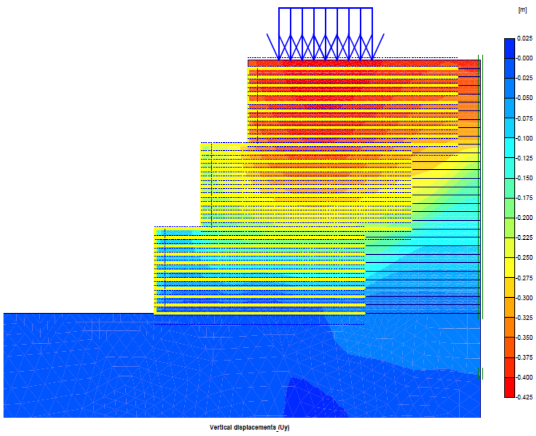

Fig.8 Output of vertical displacement in reinforced soil wall (Reinforcement Length 0.9H=13.5m, step width=3m, and clay soil type)

According to figure 9 and 10, it can be observed that by increase of length of reinforcements, the extent of vertical displacement also decreases like horizontal displacement. The reason of this fact can be

attributed to increase of interaction surface between the soil and the reinforcement. The mathematical relation between changes of vertical displacement and length of reinforcement is as follows:

L+0.1h= 0.92 ~ 0.99 ΔV

W= Wall step width

ΔV= Vertical displacement

h= Total wall height

Also the other important point which can be observed is that the extent of vertical displacement of the wall in clay soils is more than that of sand soils.

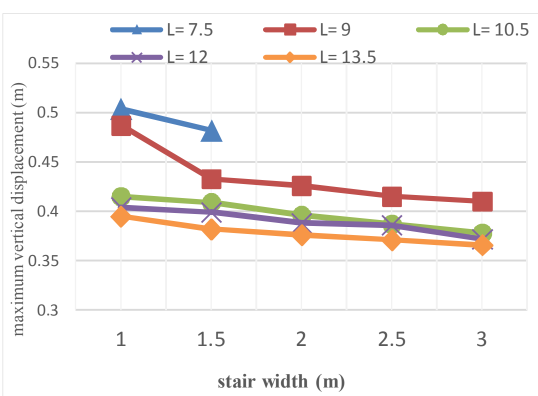

Fig.9 Maximum vertical displacement against step width in clay soil for different lengths of geogrid

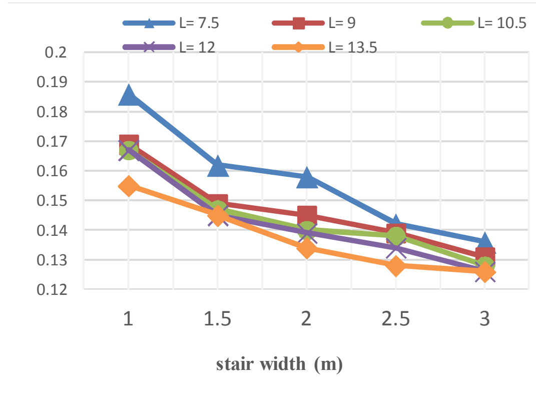

Fig.10 Maximum vertical displacement against step width in sand soil for different lengths of geogrid

By increase of wall step width and length of the reinforcement, the situation of X which is the maximum vertical displacement, moves farther from the wall face and moves towards internal part of the wall. The issue which is completely clear in the outputs is that the maximum vertical displacement occurs under the overburden and its situation in terms of its coordinate (X) is in the middle part of the overburden. The reason of this fact is that the overburden is the main factor of creating vertical displacement.

The maximum vertical displacement occurs on the last wall or under the overburden. In fact, coordinate of the height of the point of maximum vertical displacement is not subject to length of the reinforcement, step width, and soil type, and the reason is that the more we take distance from the place overburden applies, less pressure applies to the soil mass and the highest pressures occur under the overburden [8].

Effect of Geogrid Length, Step Width, and Soil Type on Effective Stress

As it can be observed in figure 11 and 12, by changing the step width, some changes would occur in extent of effective stress and by its increase, the extent of the maximum effective stress decreases. Since the effective stress is the stress between solid particles of the soil, by increase of the width of the step, volume of the solid particles decreases, and because of that the extent of maximum effective stress decreases [8].

Also by increase of the length of geogrids, because of increase of capacity of reinforcements and transmission of more force to reinforcements, the extent of effective stresses decreases [8]. In addition to step width and length of reinforcements, soil is also effective in extent of maximum effective stress. In clay soils, because the soil is fine-grained, the sum of supporting surface of grains is higher, so the effective stress in this soil type is also higher. Maximum effective stresses occur in clay soils in lower layers of the wall or on the foundation, and in sand soils, because of high friction between the georgrid and the soil, it occurs at the end of reinforcement of the first step.

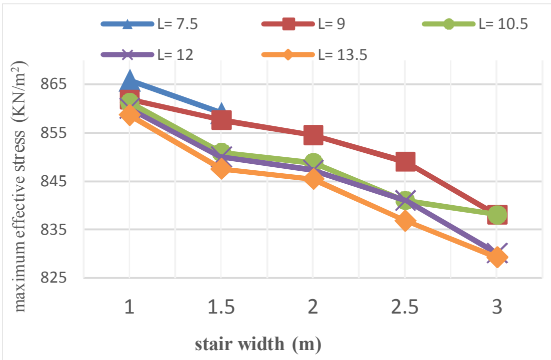

Fig.11 Maximum effective stress against step width in clay soil for different lengths of geogrid

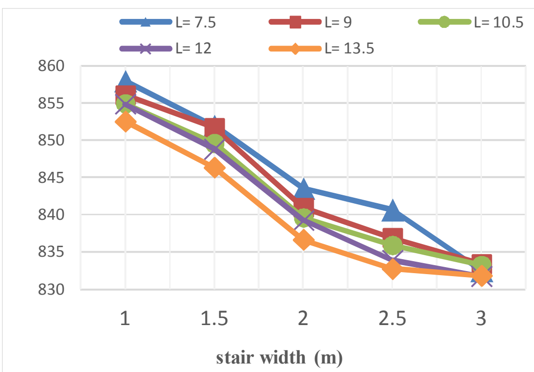

Fig.12 Maximum effective stress against step width in clay soil for different lengths of geogrids.

Effect of Geogrid Length, Step Width, and Soil Type on Safety Factor

Safety factor is the most important factor in examining stability of reinforced soil walls [1]. As it can be observed in figure 13 and 14, the extent of increase of width of wall step does not have a noticeable effect on changes of the safety factor, and anyway, increase of width of wall step causes a trivial decrease in the safety factor. Also by increase of the length of geogrids, because of increase of capacity of reinforcements and transmission of a higher force to the reinforcement and also reinforcement of a larger volume of soil, safety factors and as a result of that, stability of reinforced soil wall increase.

Besides step width and length of the reinforcement, the type of soil is also effective in values of the safety factors. In sand soils, because of high interaction of soil and the reinforcement and also friction between soil grains, safety factor is higher [8].

On the whole, it can be moded that increase of length of reinforcement and using sand soil, have a noticeable effect on the reinforced soil wall stability.

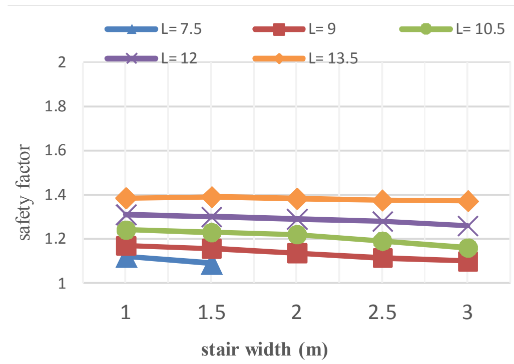

Fig.13 Safety factor against step width in clay soil for different lengths of geogrids.

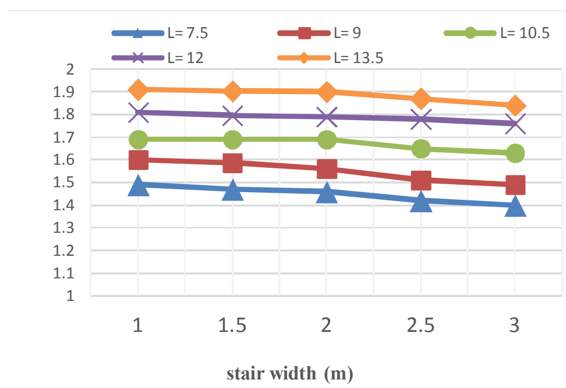

Fig.14 Safety factor against step width in sand soil for different lengths of geogrids

CONCLUSION

According to the conducted numerical models with Plaxis software and drawn diagrams based on modeling results, the following conclusions can be made:

By increase of the length of the reinforcement and increase of the step width, the maximum horizontal and vertical displacements decrease. The extent of vertical and horizontal displacements in clay soil is higher than sand soils. Under the same loading conditions, the extent of effect of displacement decrease, by increase of the length of reinforcements in clay soils, is more than sand soils. This extent of displacement decrease is noticeable in both vertical and horizontal displacements.

Increase of step width and length of the reinforcement cause transmission of situation of the maximum horizontal displacement from the central part of the wall face to the bottom part of the wall face. In other words, by increase of step width and length of the reinforcement, the deformation mode changes from bulging mode to slide mode in the toe of the wall. Maximum deformations in walls with clay soil occur at the bottom of the wall and in sand walls occur in the center of the face. Meaning that bulging mode occurs in reinforced sand soil walls and the mode of slide at the toe occurs in reinforced clay soil walls.

By increase of the length of the reinforcement and step width, the maximum effective stress decreases. The extent of effective and total stresses of wall in clay soils is more than sand soils. The effect of increase of step width in decrease of displacements is more than the effect of increase of length of geogrids in decrease of displacements.

Value of safety factor in sand soils, because of having a better interlock between grains, is more than clay soils, and also by increase of the length of the reinforcement, safety factor intensely increases.

REFERENCES

[1] Atrchian M R, Mohagheghi M and Niazi Gh, “Soil Nail Walls design and Construction Guidline FHWA” . Zanjan, Iran: Islamic Azad University of Zanjan, 2014, ch.1.

[2] Kargarian Marvasti S, komakpanah A, Dynamic analysis of soil reinforced with steel straps, Master's thesis, 2008, University of Tarbiat Modarres.

[3] Ghorbanbeigi S, Kharaghani S, Yazdan AA, Analysis and study on stability of slopes reinforced With geosynthetic, 4th International Conference on Geotechnical Engineering and Soil Mechanics (ICGESM), 2010 .Tehran, Iran.

[4] Shafabakhsh Gh and Haddad A, “Final Report of Research Project of Guides and Design and Implementation of Geosynthetic Reinforced Soil Walls”, 2005, Semnan University.

[5] Barani A and Mosallanejhad M, “ Design Optimization of Reinforced Soil Wall and Study on effect of Designing Parameters on Its Behavior and stability” 9th Congress of Civil Engineering, 2012, University of Isfahan, Iran.

[6] Niroumand H, Niroumand B, Advanced training Plaxis, publications Naghoose Andishe, 2008.

[7] Sabermahani M, Ghalandarzadeh A, Fakher A, Experimental study on seismic deformation modes of reinforced-soil walls, Geotextiles and Geomembranes, 2008.

[8] Tahouni S, “Principles of Foundation Engineering “, 2013, ch 11.

[9] Publication No. FHWA-NHI-00-043, Federal Highway Administration (FHWA), Washington (DC), 2001.

Fifth International Conference on Geotechnique, Construction Materials and Environment, Osaka, Japan,Nov. 16-18, 2015, ISBN: 978-4-9905958-4-5 C3051

THE MONITORING OF ELECTROKINETIC STABILISATION TECHNIQUE ON BATU PAHAT MARINE CLAY

Saiful Azhar Ahmad Tajudin[1,6], Nurul Syakeera Nordin[2], Aminaton Marto[3], Ian Jefferson[4], Aziman Madun[5] and Mohd Hazreek Zainal Abidin[6]

[1]Research Center For Soft Soil, Universiti Tun Hussein Onn Malaysia
[2,5,6]Faculty of Civil and Environmental Engineering, Universiti Tun Hussein Onn Malaysia
[3]Faculty of Civil Engineering, Universiti Teknologi Malaysia
[4]School of Engineering, University of Birmingham, United Kingdom

ABSTRACT

This paper outlines the monitoring results from an experimental study of electrokinetic stabilisation (EKS) technique, as those results were important in assessing the efficiency of the technique towards Batu Pahat marine clay. Two reactors were set up; 1.0 mol/liter of calcium chloride ($CaCl_2$) and sodium silicate (Na_2SiO_3) as the electrolyte and stainless steel plates as the electrodes. EKS technique was continued for 21 days with a constant voltage gradient (50 V/m). This technique was performed in two phases where the alteration of EKS was the combination of stabilizers used. The combinations of stabilizers in phase 1 and 2 were $CaCl_2$ – distilled water (DW) and $CaCl_2$ – Na_2SiO_3, respectively. The technique was monitored using electric current, total inflow and outflow of electrolytes and pH of electrolytes. It showed fluctuated profiles of electric current for both phases, attributed by the introduction of calcium ions from the anode compartment. The inflow and outflow of electrolytes results showed that electromigration and electroosmosis occurred during EKS and it indicated the movement of anion and cation to the opposite direction. The pH of electrolytes kept constant value and balanced by electrolysis process at the cathode.

Keywords: Electrokinetic stabilisation, marine clay, calcium chloride, sodium silicate.

INTRODUCTION

Marine clay is an uncommon type of clay and normally possesses a soft consistency. Batu Pahat marine clay is classified as clayey silt with low organic content [1] and usually found in the ocean bed [2]. It can be found onshore as well. Their properties rely on their initial conditions, where the saturated marine clay soil differs significantly from moist and dry soil. Marine clay is microcrystalline in nature. Clay minerals and non-clay minerals are also present in the soil. The clay minerals contained in marine clay are chlorite, kaolinite and illite while non-clay minerals found in marine clay are quartz and feldspar. Furthermore, the higher proportion of organic matter in the soil acts as a cementing agent [2]. The location of marine clay deposits in Peninsular Malaysia are shown in Figure 1 [3].

Enhancing the substructure of soil is the major aspect concerned in construction work before any superstructure can be applied on it. It is important to strengthen the soil so that it can surpass the maximum imposed load to evade any failure that might occur afterwards. There are two options in ground improvement, either by physical or chemical stabilisation technique [4].

EKS is the one of the principles of chemical stabilization and has been chosen as a potential technique to enhance the characteristics of soil [5]. It is suitable for soft clayey soils which have low hydraulic conductivity and require strengthening to improve the soil condition. Furthermore, it can also be used to stabilize the over consolidated clayey soil. The advantage of EKS instead of using traditional mix-in-place chemical stabilization is that the technique allows for remote treatment through soil without any excavation work [6]. The technique can be enhanced by use of non-toxic stabilizing agents such as lime or $CaCl_2$ solutions [7-9] that can be fed either at the anode or cathode depending on the ions to be transferred into the soil. A few soil parameters such texture, plasticity, compressibility and permeability will be altered by addition of these stabilizing agents, hence it can be very effective in improving soil characteristics by reducing the amount of clay size particles and increasing the shear strength [10].

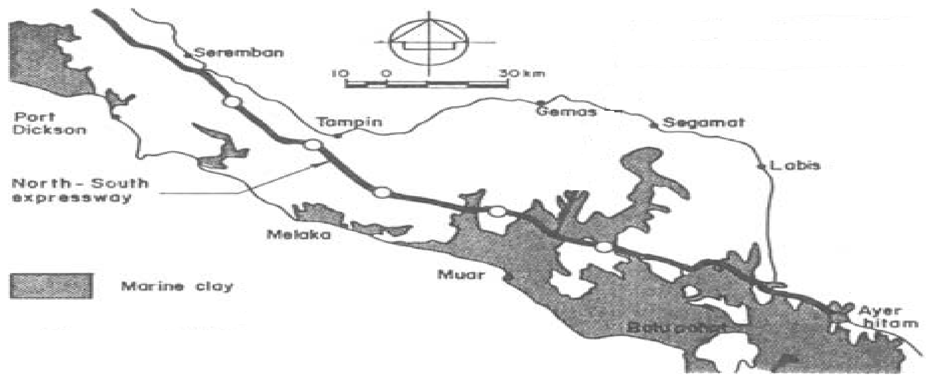

Fig. 1 Location of marine clay deposits in Peninsular Malaysia.

MATERIALS AND METHODS

Experimental apparatus

The EKS test rig was designed for this research. A schematic diagram of EKS test rig is shown in Figure 2. It was made using transparent acrylic plate with 420 mm depth, 170 mm width and 358 mm length. The thickness of the acrylic plate was 15 mm. The transparent acrylic plate for the EKS test rig was used to prevent short circuiting and to monitor the soil level during consolidation at the main compartment and level of water and/or chemical solution at the small compartments. The EKS test rig comprised of three compartments, which were separated with perforated walls. The soil sample was placed into the main compartment and the two small compartments were used to supply the chemical stabilizers into the soil.

The electrode, electrolyte and stainless steel plate were placed as shown in Figure 2. For the first phase, 1.0 mol/liter of $CaCl_2$ and distilled water (DW) were fed at the anode and cathode compartment, respectively. While in the second phase, 1.0 mol/liter of calcium chloride ($CaCl_2$) and 1.0 mol/liter of sodium silicate (Na_2SiO_3) were fed at the anode and cathode compartment, respectively. A constant voltage gradient (50 V/m) was applied to the soil sample and the experiment was performed for 21 days for both phases.

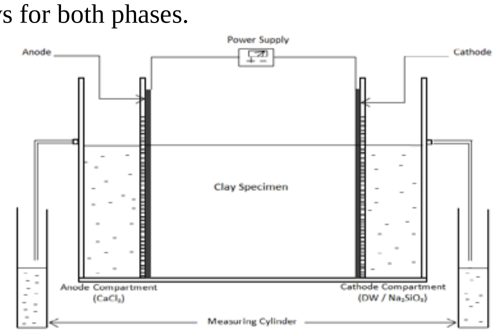

Fig. 2 Schematic diagram of EKS test rig.

Soil sample preparation

Soil sample for EKS technique was prepared consistently throughout this research for all treatment periods. Batu Pahat marine clay was dried in the oven for 24 hours. The dried sample was ground using a grinder machine to get very fine material that would pass a 425 µm sieve. The slurry sample was prepared by mixing the soil samples with distilled water to achieve 90 % of water content. The water content of the slurry sample was chosen based on 1.5 times of liquid limit (LL). Then, the slurry sample was placed inside the main compartment (278 x 165 x 413 mm) and a uniformly distributed load was applied to it by using large strain consolidation to reduce the water content resulting in a stiffer soil condition [7-9].

EKS monitoring

Throughout the EKS experiment the applied electric current, the pH of anode and cathode solutions were observed during the 21 days of EKS experiment for both phases. The total amount of stabilizers added and amount of effluent water collected from the measuring cylinder were monitored over the same period of time. On the first day of the EKS experiment, the reading of current value was taken at 1, 2, 4, 6 and 8 hours. From the second day onwards, reading of current value was taken every 24 hours. Volume of stabilizers added to the experiment was taken every 24 hours together with effluent water which was collected using measuring cylinders. The pH testing was performed on the extracted electrolytes taken from the electrolyte compartment. In addition, calcium chloride was constantly supplied at anode compartment for $CaCl_2$ – DW and $CaCl_2$ – Na_2SiO_3 systems, whereas sodium silicates were continuously supplied during the experiment in the $CaCl_2$ –

Na_2SiO_3 system to assure the effectiveness of EKS experiment towards the clay soil.

RESULTS AND DISCUSSION

Soil classifications

Table 1 shows the soil classification for untreated Batu Pahat marine clay where it was used as the control value and as the comparisons with EKS treated values. Current results and results from Abdurahman [11] were presented and compared. Those aspects measured were plastic limit (PL), liquid limit (LL), plastic index (PI), specific gravity (G_s) and pH. They showed that the current results were in range and closed as reported by Abdurahman [11]. If the plastic and liquid limit of soil were in the range of 25-40 % and 30-110 %, respectively, hence the soils are considered as kaolinite soil [4]. Kaolinite soil which has a low cation exchange capacity will exhibit high electroosmotic water transport when the soil is saturated with dilute electrolyte solution due to the high water counter ion ratio in the internal phase. Furthermore the soil is generally used in EK application. The EK technique is particularly well suited for soils of low permeability such as kaolinite in which the application of stabilizing agents by hydraulic means is impracticable [5].

Table 1 Classification of Batu Pahat marine clay.

Soil classification	**Current results**	**Results from previous study**[11]
PL	36 %	20 – 35 %
LL	61 %	37 – 65 %
PI	24.77 %	13 – 31 %
G_s	2.60	2.18 – 2.65
pH	2.73	-

(-) Not stated

Monitoring data

Figure 3 shows the profile of electric current for $CaCl_2$ – DW system during EKS experiment. On the other hand, profiles of electric current for $CaCl_2$ – Na_2SiO_3 system are shown in Figure 4. The electric current values were recorded at hour 0, 1, 2, 4, 6 and 8 on the first day of the experiment and every 24 hour afterwards for 21 days period of time.

For the $CaCl_2$ – DW system, the values on the first day of the experiment show a fluctuating trend and values remained constant afterwards until the end of the experiment. The highest value occurred at the 6th hour of experiment at 3.107 A, while the lowest value was recorded at the beginning of experiment at 3.082 A. After 8 hours the electric current values recorded were between 3.084 A to 3.094 A. In the $CaCl_2$ – Na_2SiO_3 system, a different trend was observed compared to the first phase. The profiles of electric current showed that the values increased from the beginning until the end of the experiment. At the 224th hour the electric current values started to remain constant until the end of the experiment and recorded as the highest value at 2.33 A. There was a fluctuating trend of current values that occurred at the 4th hour of experiment. The fluctuating trend that occurred in both phases was possibly caused by the introduction of additional ions by calcium chloride at the anode compartment.

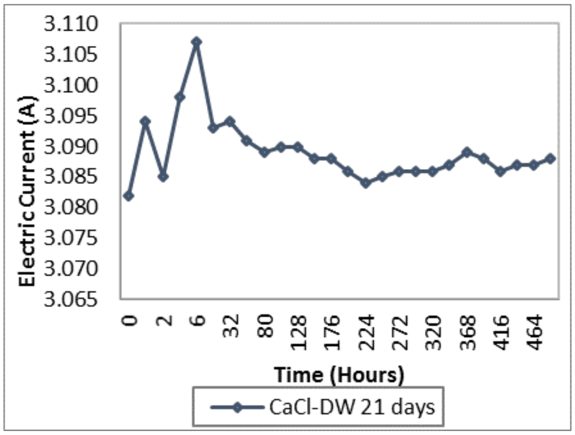

Fig.3 Electric current for $CaCl_2$ – DW system with time.

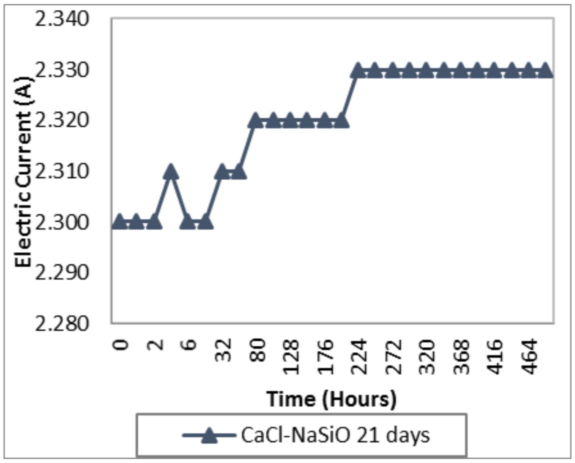

Fig.4 Electric current for $CaCl_2$ – Na_2SiO_3 system with time.

The total volume of inflow and outflow of $CaCl_2$ at anode compartment for $CaCl_2$ – DW system is presented in Figure 5. It showed that there was no outflow value of $CaCl_2$ collected by the measuring cylinder from the anode compartment where it remained zero from the beginning until the end of 21 days. At hour 224, the inflow values remained constant until the end of experiment. The total inflow and outflow values of DW at the cathode compartment for the $CaCl_2$ – DW system were shown in Figure 6. It showed that inflow of DW only occurred at 0 hour at 1705 ml, while the outflow volume increased at hour 32 of the EKS experiment. The volume of outflow was taken at the flushing chamber (cathode compartment) that was collected from the measuring cylinder. Thus, it indicated that there was no fluid discharge from the anode compartment throughout the experiment and it proved that the stabilisers have fully migrated to the soil sample.

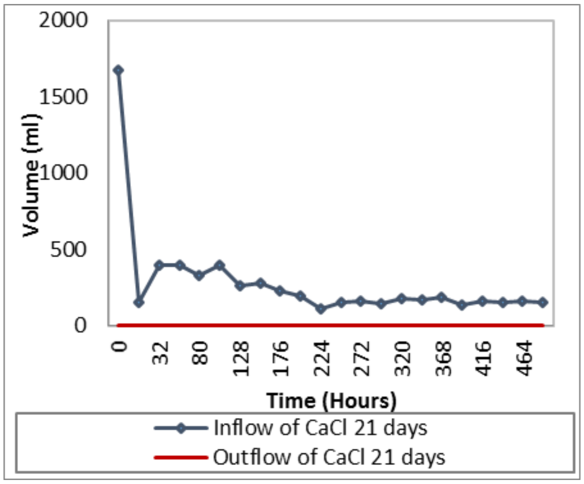

Fig.5 Inflow and outflow of $CaCl_2$ for $CaCl_2$ – DW system with time.

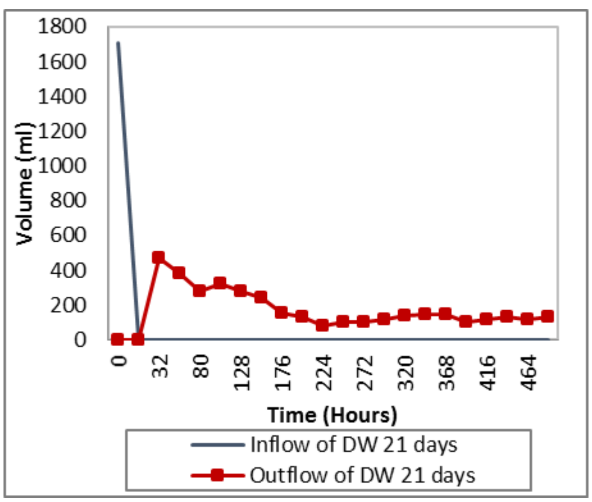

Fig.6 Inflow and outflow of DW for $CaCl_2$ – DW system with time.

Figure 7 presents the volumes of inflow and outflow of $CaCl_2$ for $CaCl_2$ – Na_2SiO_3 system. It showed that there was no outflow volume from the anode compartment from the beginning until the end of experiment where it was similar to the first phase. The inflow volume of $CaCl_2$ showed that it decreased rapidly compared to amount at the beginning of the experiment. The total inflow and outflow of Na_2SiO_3 is presented in Figure 8 and it showed that the inflow of Na_2SiO_3 occurred at 0, 152 and 320 hours. This is because the cathode compartment was cleaned every 7 days during the experiment and the empty compartment was replaced with the same amount of Na_2SiO_3 to maintain and ensure the effectiveness of the experiment. The outflow volume from the cathode compartment occurred after 32 hours of experiment and the volume was in the range of 110 – 390 ml. The results explained that the process of electromigration and electroosmosis occurred during the experiment and that the anions and cations were moving in opposite directions.

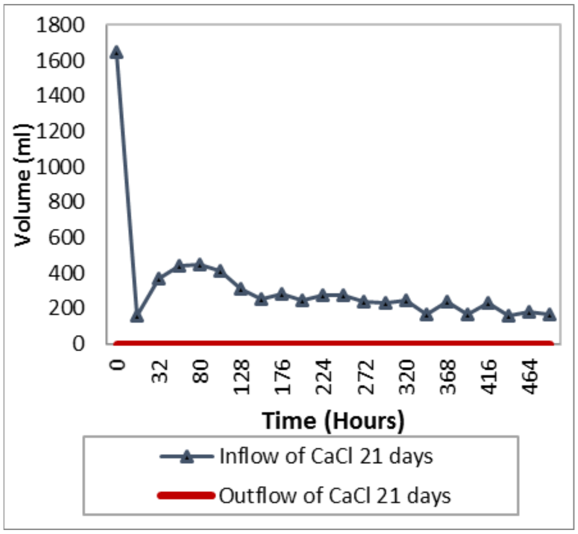

Fig.7 Inflow and outflow of $CaCl_2$ for $CaCl_2$ – Na_2SiO_3 system with time.

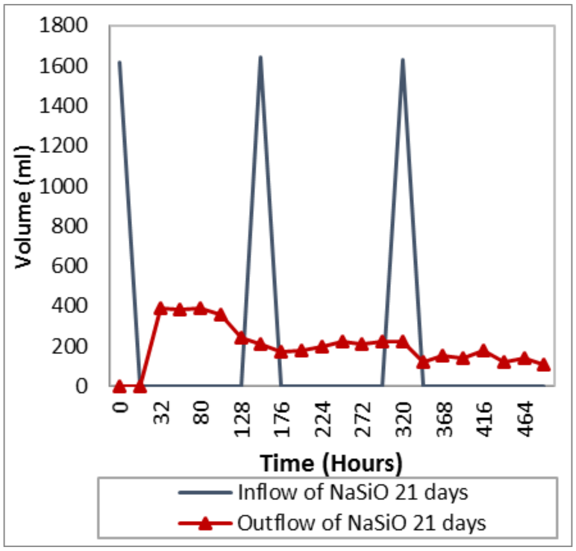

Fig.8 Inflow and outflow of Na_2SiO_3 for $CaCl_2$ – Na_2SiO_3 system with time.

The variation of pH of electrolytes for the $CaCl_2$ – DW system for the 21 day experiment is shown in Figure 9. The fluids from the anode and cathode compartment were extracted to obtain the pH values of the electrolytes. It showed that the pH of $CaCl_2$ inside the anode compartment remained constant starting from the 80th hour of the experiment. Meanwhile, the pH for DW inside the cathode compartment or the flushing chamber shows a fluctuating trend from hour 0 until hour 104. It showed that the pH value increased at hour 32 and dropped at hour 56 and hour 80 of the experiment. The pH values for the $CaCl_2$ for 21 days of the experiment ranged between pH 3.9 to pH 5.5, while for DW the value were between pH 7 to pH 13.

Figure 10 presented the variations of pH of electrolytes for $CaCl_2$ – Na_2SiO_3 system. The pH value for $CaCl_2$ dropped considerably starting from hour 56 and stabilized until the end of the experiment. The highest value recorded was pH 6.06 at hour 56 and the lowest value was pH 3.09 at hour 464. The pH value of Na_2SiO_3 showed that almost the entire specimen was subjected to alkaline conditions showing a constant trend with a pH of around 13 during the experiment. The constant value of Na_2SiO_3 showed its continuous supply at the flushing chamber where it was cleaned and replaced every 7 days during the experiment to stabilise the pH value and balance the pH changes via electrolysis process at the cathode.

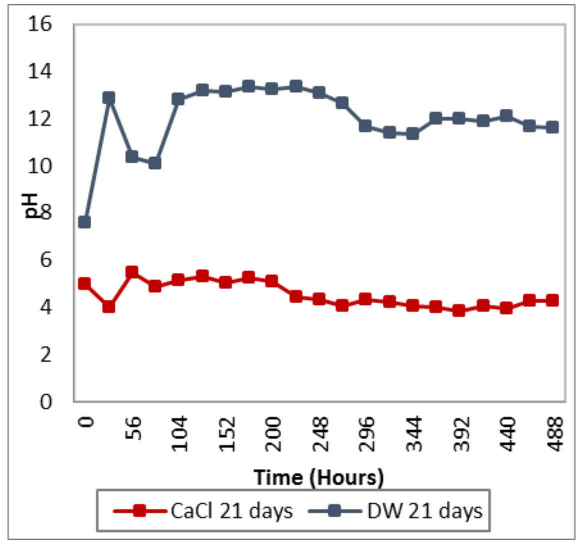

Fig.9 pH of electrolytes for $CaCl_2$ – DW system with time.

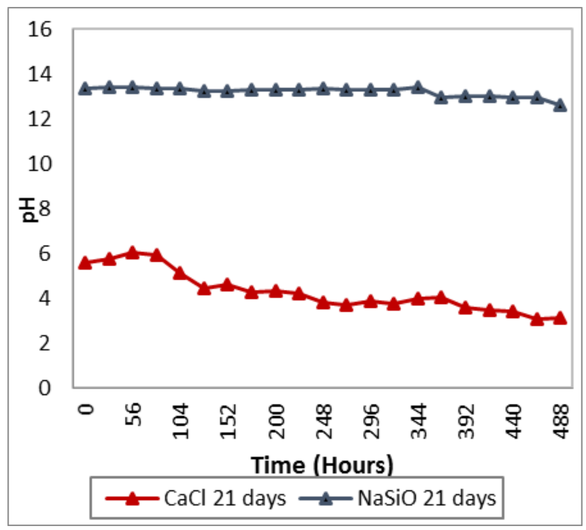

Fig.10 pH of electrolytes for $CaCl_2$ – Na_2SiO_3 system with time.

CONCLUSIONS

A 50 V/m of voltage gradient or equal to 14 V was applied towards the soil in the EKS experiment. The electric current values were strongly affected by the chemical composition of soil and influenced by the ionic concentration of the pore fluid within the soil matrices [12]. The electric current generated in the experiment was due to the existence of inorganic soil elements in high concentration for example iron, calcium and magnesium. The inflow and outflow volumes of the stabilizing agents towards the soil were affected by the physicochemical characteristics of soil, applied current and the pH. Those values were important in assessing the efficiency of electromigration and electroosmosis process in migrating stabilizing agents into the system hence improving the soil properties after EKS. The monitored pH values relied on the pH of electrolytes that was continuously supplied to the electrolyte compartment in the experiment since there were small changes of pH value shown during EKS. Monitoring data provided information on the efficiency of the EKS experiment as it proved that there were electric current and stabilizing agents being continuously supplied until the end of the experiment. It also acts as a precaution if any failure or error occurs during the experiment so that it could be detected immediately.

ACKNOWLEDGEMENT

The authors would like to thank the Ministry of Higher Education and Universiti Tun Hussein Onn Malaysia for supporting this research under Fundamental Research Grant Scheme (FRGS) Vot. 1455.

REFERENCE

[1] Rahman ZA, Yaacob WZW, Rahim SA, Lihan T, Idris WMR and Mohd Sani WNF, “Geotechnical characterization of marine clay as potential liner material”, Sains Malaysiana, Vol. 42(8), 2013, pp. 1081–1089.

[2] Basack S and Purkayastha RD, “Engineering properties of marine clays from the eastern coast of India”, Journal of Engineering and Technology Research, Vol. 1(6), 2009, pp. 109–114.

[3] Indraratna B, Balasubramaniam AS and Balachandran S, “Performance of test embankment constructed to failure on soft marine clay”. Journal of Geotechnical Engineering, Vol. 118(1), 1992, pp. 12–43.

[4] Mitchell JK and Soga K, “Fundamentals of Soil Behavior. 3rd ed.” Berkeley: University of California, 2005.

[5] Asavadorneja P and Glawe U, “Electrokinetic strengthening of soft clay using the anode depolarization method”, Bulletin Engineering Geology and Environment, Vol. 64, 2005, pp. 237-245.

[6] Barker JE, Rogers CDF, Bordman DI and Peterson J, “Electrokinetic stabilisation: an overview and case study” Ground Improvement, Vol. 8(2), 2004, pp. 47-58.

[7] Nordin NS, Ahmad Tajudin SA and Abdul Kadir A, “Physical properties of treated soft clay by using electrokinetic stabilisation method” Soft Soil Engineering International Conference, 2013.

[8] Nordin, NS, Ahmad Tajudin SA and Abdul Kadir A, “Stabilisation of soft soil using electrokinetic stabilisation method”, International Journal of Zero Waste Generation, Vol. 1(1), 2013.

[9] Nordin NS, Ahmad Tajudin SA, Abdul Kadir A, Yunus R, Mohammad Azmi MA and Mohamed Hanif MNS, “Effect of calcium and sodium ions in soft clay using electrokinetic stabilisation technique”, Applied Mechanics and Materials, 773-774, 2015, pp. 1433-1437.

[10] Nasim, M, Erwin O and Gary C, “A review of electrokinetic treatment technique for improving the engineering characteristic of low permeable problematic soil”, Int. J. of GEOMATE, Vol. 2(2), 2011, pp. 266-272.

[11] Abdurahman MN, “Short term performance evaluation of a rural road embankment with different reinforcement constructed on soft soil pertaining to vertical settlement”, Master of civil engineering, KUiTTHO, 2005.

[12] Ahmad Tajudin SA, Jefferson I, Madun A, Zainal Abidin MH, Baharuddin MFT and Mohammad Razi MA, “Monitoring of electric current during electrokinetic stabilisation test for soft clay using EKG electrode”, Applied Mechanics and Materials, 773-774, 2015, pp. 1560-1564.

Fifth International Conference on Geotechnique, Construction Materials and Environment, Osaka, Japan, Nov. 16-18, 2015, ISBN: 978-4-9905958-4-5 C3051

USING 3DEC TO SIMULATE FRACTURES AND CANISTERS INTERSECTIONS AND THEIR APPLICATIONS FOR REPOSITORY LAYOUT

Chi-Jen Chen[1], Yuan-Chieh Wu[1], Meng-Hsiu Hsieh[1]
[1]Institute of Nuclear Energy Research

ABSTRACT

Taiwan is in the Pacific earthquake ring, and seismicity is high. It's important to evaluate effects of large earthquakes on high level waste disposal. Many studies show that canisters could failure due to fracture shear displacement induced by earthquakes. The most crucial step for long term safety assessment of repository is evaluating the fractures and canisters intersections. This paper follows the methodology of Swedish SKB report and calculates number of canisters intersected by fractures by using 3DEC, and discusses the implications of intersection for repository layout. The results show our 3DEC simulation method is available in comparison with SKB's result and their applications are also illustrated for repository layout by using visualization tools of 3DEC.

Keywords: Earthquake, 3DEC, Repository layout, DFN

INTRODUCTION

There are many factors may influence repository, e.g. shaking, rock failure, pore pressure change or aftershock etc., see figure 1. But "The major damage mechanism is induced slip along pre-existing joints and secondary faults due to an earthquake. [4]" for assessing KBS-3V (engineer barrier system developed by Sweden) post-closure canister damage.

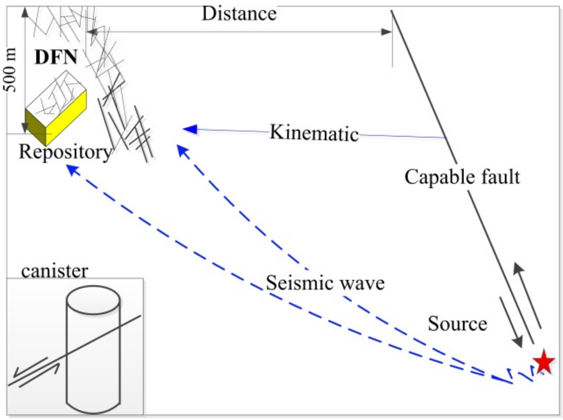

Fig. 1 Schematic diagram illustrates effects of large earthquakes on deposition holes.

Description of fractures (dip, dip direction, size, position etc.) is using DFN (Discrete Fracture Network) model, based on geological investigation. Fractures are defined as any discontinuous in rock mass, e.g. joint, fault, bed plane etc. and scale is tens to hundreds meters. "The DFN models required for earthquake studies differ from the DFN models used for fluid flow modeling [5]."

One of the most important steps for evaluation of effects of large earthquakes on repository is to calculate number of canisters intersected by fractures. There is a commercially software develop by SKB using Microsoft Excel.

In order to localize technique and optimize the visualization, this study developed the methodology of number of canisters intersected by fractures simulation by using 3DEC code.

METHODOLOGY

Creating DFN can be simplified to 4 parts, fracture orientation, fracture size distribution, fracture density and fracture spatial pattern.

The most common fracture orientation equation is Fisher distribution [6] in geologic literature:

$$f(\theta) = \frac{K \sin\theta e^{K\cos\theta}}{e^{K} - e^{-K}} \quad (1)$$

where θ is angular deviation from the mean vector, and K is the Fisher constant or dispersion factor.

The fracture size distribution is determined from probability function, including power-law, Gauss, lognormal and exponential distributions etc. It's generally accepted that fractures follow a power-law distribution in nature. Fracture power-law probability density function is formulated as [2]:

$$f(r) = \frac{k r_0^k}{r^{k+1}} \qquad r0 \le r < \infty \quad (2)$$

where r_0 is the smallest fracture radius, r is the fracture radius and k is a shape parameter.

Fracture density is using P_{32} (m^2/m^3), which is expressed as total fracture area per volume unit for specific shape and size range of fracture. Fracture spatial pattern is simply assumed that locations of fracture centroids are uniform distribution.

Fracture shear displacement of earthquakes effects is function of driving stress, shear modules, Poisson's ratio and radius [1]. Canisters are designed to afford 10 cm shear displacement in SR-CAN report. It means there is a minimum fracture size, r_{Min} that has to be avoided:

$$r_{Min} = \frac{d_{Crit}}{b} \tag{3}$$

where d_{Crit} is 0.1 m and b is typically 0.001 [3].

When fracture radius is larger than r_{Min}, the fracture is available to shear 10 cm from a centroid point to a circle. The radius of circle is defined as critical radius:

$$r'_{Crit} = \sqrt{r^2 - r_{Min}^2} \qquad r > r_{Min}$$

(4)

SIMULATION STEPS

First of all we create a hypothetical full model of repository geometry at 500 m depth in 3DEC, see figure 2, and repository can accommodate 2728 canisters. Using 3DEC to generate DFN and generating domain is extended maximum fracture radius from each edge of repository to make sure every effective fracture was simulated.

Finally, we identify the canisters intersected by fractures and eliminate the canisters outside critical radius of fractures.

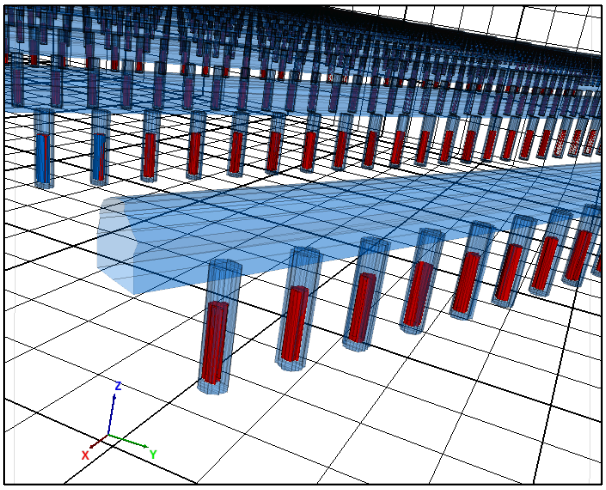

Fig. 2 Full model of repository geometry.

PARAMETERS

There are assumptions need to be declare. The fracture spatial pattern is assumed centroid of fractures to be uniform position. Fracture shape is assumed infinite thin circular discs. Fracture orientation distribution and fracture size distribution are assumed Fisher and power-law respectively.

For comparison purpose, we refer to parameters of Swedish SKB report [3], see Table 1 and Table 2. There are 5 clusters of fractures, represented by parameters, pole (trend and plunge) and kappa for orientation and by fracture intensity, shape parameter and r_0 for size distribution. Minimum fracture radius is 100 m, calculated by Eq. (3).

Table 1 DFN parameters, from R-05-29.

	NS	NE	NW	EW	SubH
Trend	87.2	135.2	40.6	190.4	342.9
Plunge	1.7	2.7	2.2	0.7	90
Kappa	21.66	21.54	23.9	30.63	8.18
k	2.88	3.02	2.81	2.95	2.92
r_0	0.318	0.318	0.318	0.318	0.318
$P32(r_0, r_\infty)$	0.602	2.07	0.448	0.226	0.605

Table 2 Additional parameters, from R-05-29.

Maximum fracture radius	500 m
Canister diameter	1.05 m
Canister height	4.833 m
Constant, *b*	0.001
Critical shear distance at deposition hole	0.1 m

RESULTS

The average number of intersected canisters is 60.2 canisters by 500 times simulations. The probability of canister intersected by fracture is 60.2/2728 ≒ 2.21 %, each probability of single cluster is shown in table 3. Apparently, results is similar and little larger compared to Swedish SKB report [3]. Furthermore, the distribution of 500 times simulations, figure 3, has the similar trend, but the distribution is more concentration in this study.

Table 3 3DEC simulations result in comparison with R-05-29

	All	NS	NE	NW	EW	SubH
Average (canisters)	60.2	10.1	16.4	10.9	2.3	19.9
Probability (%)	2.21	0.37	0.60	0.40	0.09	0.73
Probability of [3] (%)	1.91	0.32	0.51	0.34	0.08	0.66

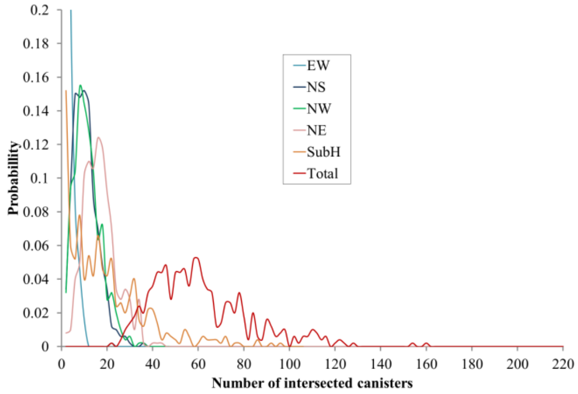

Fig. 3 Distribution of 500 times simulations.

APPLICATIONS FOR LAYOUT

When we can estimate the number of number of intersected canisters before underground construction, it's great help for feasibility assessment stage of chosen candidate repository sites. Repository layout could be design more accommodation to make sure all canisters could be loaded with relevant margin.

However, we can simulate fractures by DFN model; it's hardly to measure the size of a fracture essentially. Where we can see fractures is only on borehole and tunnel wall. Therefore, SKB develop the rejection criteria of deposition holes, FPC (Full Perimeter Criteria), to conservatively identify the deposition holes that potentially be intersected by large fracture [7].

If tunnel is full intersected by fracture, it's defined as Full Perimeter Intersection (FPI) [7]. FPC means that any deposition holes will be considered for rejection regardless of true fracture size, if canisters were intersected by the extrapolation of FPI, see figure 4. Consequently, deposition hole location is adjusted to avoid intersection.

There is a case from 3DEC simulation, see figure 5. Canisters along deposition tunnel are intersected by large fracture. In this case, FPI could be identified in main tunnel before excavation of deposition tunnel. FPI become a rick-informed and decision-making technique preventing large amount rejection deposition holes. FPI also provide information that we should do more investigation or adjust layout design.

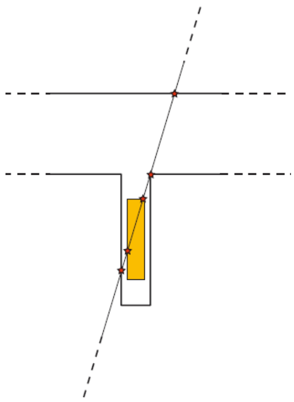

Fig. 4 Full perimeter criteria, from TR-10-21 .

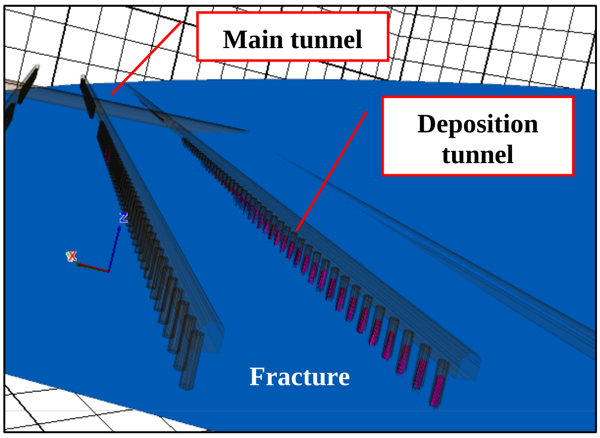

Fig. 5 Large fracture intersects canisters along whole deposition tunnel, example from 3DEC simulation.

CONCLUSIONS

The simulation results are similar to Swedish SKB report. 3DEC can simulate fracture/canister intersection and present results with powerful visualization function. The distribution of number of intersected canisters has thick tail, which increases the uncertainty. This technique is useful not only for earthquake effects but also for underground construction and repository layout configuration. It's necessary to combine deposition holes rejection criteria in simulation to reduce the uncertainty in future work.

REFERENCES

[1] Atkinson BK, Fracture Mechanics of Rock. Asn Diego: Academic Press Inc. Ltd, 1987, ch. 8.

[2] Evans M, Hastings N and Peacock B, Statistical distributions, New York: John Wiley & Sons, Inc.

[3] Hedin A, An Analytic Method for Estimating the Probability of Canister/Fracture

Intersections in a KBS-3 Repository, Stockholm: Svensk Kärnbränslehantering AB, 2005.

[4] La Pointe P, Wallmann P, Thomas A and Follin S, A Methodology to Estimate Earthquake Effects on Fractures Intersecting Canister Holes, Stockholm: Svensk Kärnbränslehantering AB, 1997.

[5] La Pointe P and Cladouhos T, Calculation of Displacements on Fractures Intersecting Canisters Induced by Earthquakes: Aberg, Beberg and Ceberg Examples, Stockholm: Svensk Kärnbränslehantering AB, 1999.

[6] R. Fisher, "Dispersion on a Sphere", Royal Society of London Proceedings, Vol. 217, 1953, pp. 295-305.

[7] Munier R, Full Perimeter Intersection Criteria, Definitions and Implementations in SR-Site, Stockholm: Svensk Kärnbränslehantering AB, 2010.

Fifth International Conference on Geotechnique, Construction Materials and Environment, Osaka, Japan, Nov. 16-18, 2015, ISBN: 978-4-9905958-4-5 C3051

EVALUATION OF GEOTECHNICAL CORRELATIONS USING ATIC METHOD

Waled A. Daoud[1], Kiyonobu Kasama[2], Naser M. Saleh[3], Abdelazim M. Negm[4]

[1,4] Egypt-Japan University of Science and Technology, Egypt
[1,2] Faculty of Engineering, Kyushu University, Japan
[1,3] Faculty of Engineering at Shoubra, Benha University, Egypt

ABSTRACT

Geotechnical correlations are widely used because it can provide fast and cost-effective means of parameter estimation using simple tests. Most of the current correlations were derived from data fitting of measurements for specific site conditions and need to be evaluated before used in other sites. During the correlation development, the deviation of the correlation from the measured values was evaluated using simple statistical measures. A better method of correlation evaluation may reduce the overall deviation of the Geotechnical parameter. Amended Theil Inequality Coefficient (ATIC) is proposed as an evaluation tool because it has the advantage that it considers both position and trend conformities between observed and correlated values. To address the efficiency and rationality of ATIC, evaluation of, 92 compression index correlations by ATIC and different statistical measures was carried out. Comparison between the results showed that ATIC is efficient in assessing the best and worst correlations and it can be considered a good tool for correlations evaluation.

Keywords: Compression Index Correlations, Statistical Evaluation, Position and Trend Conformities

INTRODUCTION

The estimation of soil parameters using empirical correlations is widely used in geotechnical engineering [1]. Most important reasons are; direct measurements contains uncertainty, not always applicable, costly, and time-consuming [2], [3]. Thus, empirical correlations can provide fast and cost-effective means of parameter estimation using simple tests [4]. Most of these correlations were derived from data fitting of measurements at specific site conditions that may cause large deviation if used for other sites [5]–[7].

During the correlation development, the deviation of the correlation from the measured values was evaluated using simple statistical measures such as correlation coefficient (R) and determination coefficient (R^2) [5]–[11]. Better statistical evaluation may reduce the overall deviation of the estimated geotechnical parameter. Evaluation of different geotechnical correlations using statistical measures grabs the attention of many researchers for decades.

For shear strength parameters correlations; Hatanaka and Ushida [12] evaluated internal friction angle correlations with standard penetration test (SPT) results and proposed a rectified correlation that consider the effect of in-situ confining pressure. Nassaji and Kalantari [13] evaluated different undrained shear strength correlations with SPT N-Value. The authors used the standard deviation and visual inspection to evaluate different correlations.

Compression index (Cc) correlations were evaluated by many researchers. Nagaraj and Murthy [14] used experimental results to evaluate the applicability of 14 correlations using analytical examination. Giasi et al. [8] evaluated 32 correlations using experimental results for 46 soil samples from Italy. The authors used both ranking distance (RD) and Ranking Index (RI) to evaluate these correlations. The authors highlighted the accuracy problems of using RD and RI in correlations evaluation.

Yoon et al. [15] evaluated the results of using 15 empirical correlations to predict Cc of Korean coast marine clay using experimental results for more than 1200 consolidation tests. The authors used R to evaluate the newly, site-specific correlations and correlated/observed ratio (K-factor) for literature correlations. Rani and Rao [16] evaluated 12 correlations using one way and two way ANOVA along with mean absolute difference (MAD) to rank these correlations. Onyejekwe et al. [1] assessed the applicability of using 18 correlations for the estimation of Cc for Missouri region. The authors used the root mean square of deviation (RMSD), K-factor, RD, and RI to evaluate the correlations. Lee et al. [17] used R^2 and MAD to evaluate 29 correlations based on experimental results in South Korea.

Most of the above used statistical measures shortcoming that it considers position conformity or trend conformity separately. This shortcoming may cause misjudgment and wrong selection of best correlation. This paper introduced Amended Theil Inequality Coefficient (ATIC) method as a tool for correlation evaluation. ATIC method has the advantage that it considers both position and trend conformities in the overall ranking process. The viability of using ATIC method to evaluate geotechnical correlations is addressed and compared with other statistical evaluation measures.

The Cc correlations shall be considered in this paper as test-case. The reasons are: Cc determination is complex and time consuming that made empirical correlations more important; many correlations for different soil conditions; previous attempts of correlation evaluation were done; and its development starts as early as 1944 and new correlations still being developed [17].

USED DATA

Subsurface investigation reports were collected from reputable geotechnical firms in Egypt, UAE, Iraq, and Indonesia. The collected reports contained field and laboratory tests results for more than 35,000 boreholes collected during the last three years. The most reliable boreholes were entered with consistent and unified units into customized geotechnical database. The data were checked with the source data to ensure the quality and consistency of information. To serve the research needs, only 27 tables were filled with 5087 boreholes

Data for this study was collected from the database with the condition that the sample has the all needed independent parameters to maintain same level of consistency and accuracy. Data was validated and only true outliers were excluded considering the very different characteristics of soils in the above countries. A total of 82 records was found to be eligible for the research needs. Table 1 shows descriptive statistic for the used soil properties.

Table 1 Used soil properties descriptive statistics

Property	Range	Mean	Std. Dev.
Initial Voids Ratio	0.32 - 4.35	1.58	0.84
Bulk Density (t/m^3)	1.04 - 2.29	1.61	0.31
Water Content (%)	11.9 - 168.1	57.15	31.09
Liquid Limit (%)	17.1 - 166.2	62.68	25.22
Plasticity Index (%)	2.48 - 113.9	30.71	17.84
Compression Index	0.07 - 1.66	0.57	0.3

Std. Dev. is the standard deviation

STUDIED CORRELATIONS

Compression index of soil depends on both field state and intrinsic properties. Main field state properties are field density, water content, and voids ratio. Main intrinsic property is soil plasticity. Several correlations were developed to relate Cc with field state properties and intrinsic properties. A total of 92 correlations were considered in this study as shown in Table 2.

Table 2 Studied Cc correlations

Cor. ID	Formula [Ref.]	Cor. ID	Formula [Ref.]
C01	$C_C = 0.29(e - 0.27)$ [18]	C47	$C_C = 0.01(L_L - 10.9)$ [15]
C02	$C_C = 0.156e + 0.0107$ [1]	C48	$C_C = 0.0037(L_L + 25.5)$ [6]
C03	$C_C = 1.21 + 1.005(e - 1.87)$ [19]	C49	$C_C = 0.0063(L_L - 10)$ [5]
C04	$C_C = 0.35\,(e - 0.5)$	C50	$C_C = 0.0075L_L$ [11]
C05	$C_C = 0.43(e - 0.25)$	C51	$C_C = 0.012L_L$ [11]
C06	$C_C = 0.54(e - 0.23)$	C52	$C_C = 0.018\,(L_L - 20.7)$ [7]
C07	$C_C = 0.4(e - 0.25)$ [21]	C53	$C_C = 0.014I_P + 0.02$ [15]
C08	$C_C = 0.256 + 0.43(e - 0.84)$ [19]	C54	$C_C = 0.0104I_P + 0.046$ [22]
C09	$C_C = 0.434(e - 0.336)$ [23]	C55	$C_C = 0.014I_P + 0.165$ [15]
C10	$C_C = 0.208e + 0.0083$ [24]	C56	$C_C = 0.0042I_P + 0.165$ [6]
C11	$C_C = 0.75(e - 0.5)$ [21]	C57	$C_C = 0.0115W_c$ [25]
C12	$C_C = 0.2e^{1.6}$ [26]	C58	$C_C = 0.01\,(W_c - 5)$ [21]
C13	$C_C = 1.15(e - 0.35)$ [27]	C59	$C_C = 0.01\,(W_c - 7.594)$ [28]
C14	$C_C = 1.15(e - 0.91)$ [27]	C60	$C_C = 0.0093\,W_c$ [7]
C15	$C_C = 1.15e$	C61	$C_C = 0.015\,(W_c - 8)$ [20]
C16	$C_C = 0.54(e - 0.37)$ [15]	C62	$C_C = 0.001766\,W_c^{2} + 0.00593\,W_c - 0.135$ [24]
C17	$C_C = 0.39(e - 0.13)$ [15]	C63	$C_C = 0.013\,(W_c - 3.85)$ [15]
C18	$C_C = 0.37(e - 0.28)$ [15]	C64	$C_C = 0.01\,(W_c + 2.83)$ [15]
C19	$C_C = 0.46(e - 0.28)$ [6]	C65	$C_C = 0.01\,(W_c - 11.22)$ [15]
C20	$C_C = 0.39e$	C66	$C_C = 0.0135W_c - 0.1169$ [6]
C21	$C_C = 0.42(e - 0.5)$ [5]	C67	$C_C = 0.01\,W_c$ [21]
C22	$C_C = 0.2608e$ [11]	C68	$C_C = 0.85\left(\frac{W_c}{100}\right)^{1.5}$ [29]
C23	$C_C = 0.3921e$	C69	$C_C = 0.0066W_c$ [5]
C24	$C_C = 0.2237e_L$ [8]	C70	$C_C = 0.014\,(W_c - 22.7)$ [7]
C25	$C_C = 0.2343e_L$	C71	$C_C = 0.005\,G_S\,I_P$ [1]
C26	$C_C = 0.274e_L$ [8]	C72	$C_C = 0.4(e + 0.001W_C - 0.25)$
C27	$C_C = \frac{0.0018n}{1-0.0109n}$ [9]	C73	$C_C = 0.489\left[\ln(G_S)\left(\frac{1+e}{G_S}\right)^2 + 0.296\right]$ [23]
C28	$C_C = \frac{0.00269n}{1-0.0115n}$ [9]	C74	$C_C = 0.1525G_S\left(\frac{1+e}{G_S}\right)^2$ [23]
C29	$C_C = 1.0584n^2 + 0.0885n$ [11]	C75	$C_C = 0.46e - 0.049G_S + 0.0023$
C30	$C_C = 0.5\left(\frac{\gamma_w}{\gamma_d}\right)^{2.4}$ [23]	C76	$C_C = 0.411e + 0.00058L_L - 0.156$ [28]
C31	$C_C = 2.4 - 1.66\,\gamma_d$	C77	$C_C = 0.37(e + 0.003L_L - 0.34)$
C32	$C_C = 1.15 - 0.66\,\gamma_d$ [15]	C78	$C_C = 0.37(e + 0.003L_L + 0.0004W_C - 0.34)$ [21]
C33	$C_C = 1.1014 - 0.579\gamma_d$ [6]	C79	$C_C = 0.4965e - 0.0014W_C - 0.123$ [6]
C34	$C_C = 0.0046(L_L - 9)$ [19]	C80	$C_C = 0.247e + 0.004L_L + 0.01W_C + 0.021$ [6]
C35	$C_C = 0.006(L_L - 9)$ [21]	C81	$C_C = 0.185\left(G_S\left(\frac{\gamma_w}{\gamma_d}\right)^2 - 0.144\right)$ [23]
C36	$C_C = \frac{(L_L-13)}{109}$ [28]	C82	$C_C = 0.141\,G_S\left(\frac{1+e}{G_S}\right)^{2.382}$ [23]
C37	$C_C = 0.0186(L_L - 30)$ [19]	C83	$C_C = 0.141\,G_S\left(\frac{\gamma_{sat}}{\gamma_d}\right)^{2.4}$ [23]
C38	$C_C = 0.009(L_L - 10)$ [1]	C84	$C_C = 0.173\,(1 + e)\,(\ln(L_L) - 3.01)$ [7]
C39	$C_C = 0.007(L_L - 7)$	C85	$C_C = 0.002343\,L_L\,G_S$ [14]
C40	$C_C = 0.017(L_L - 20)$ [7]	C86	$C_C = (1 + e)\,(0.095 + 0.00114W_C)$ [5]
C41	$C_C = 0.013(L_L - 13.5)$ [7]	C87	$C_C = 0.1905\,(1 + e)\,(\ln(W_C) - 3.03)$ [7]
C42	$C_C = 0.009(L_L - 8)$ [1]	C88	$C_C = 0.194e - 0.0025I_P + 0.0098W_C - 0.256$ [15]
C43	$C_C = 0.009L_L$ [1]	C89	$C_C = 0.538e + 0.002L_L - 0.0003W_C - 0.3$ [15]
C44	$C_C = 0.007(L_L - 10)$ [10]	C90	$C_C = 0.12e + 0.0065L_L + 0.0038W_C - 0.248$ [15]
C45	$C_C = 0.012(L_L + 16.4)$	C91	$C_C = 0.009W_C + 0.005L_L$ [7]
C46	$C_C = 0.011(L_L - 6.36)$	C92	$C_C = 0.009W_C + 0.002L_L - 0.1$

Where e: voids ratio, n: porosity, γ_d: dry density (g/cm^3), L_L: liquid limit, I_P: plasticity index, W_C: natural water content, and G_S: specific gravity

QUANTITATIVE STATISTICAL ANALYSIS

The maximum, minimum, mean, and standard deviation of the correlated values were compared to those of the observed values as shown in Fig. 1. No general conclusion can be made based on the above measures except the scatter of the correlated values around the observed values.

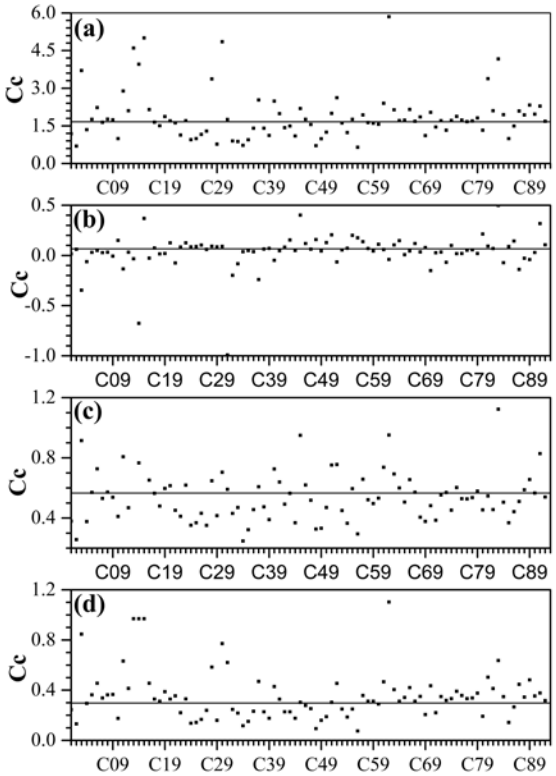

Fig. 1 Correlated values (a) Maximum, (b) Minimum, (c) Mean, and (d) Standard deviation with those of the observed values (solid line).

CORRELATIONS EVALUATION

Till now, there are no formal standards for evaluating the goodness-of-fit between the observed and correlated values, either visually or numerically [30]. In this section, ATIC method as a tool for correlation evaluation is introduced and compared with different statistical measures.

ATIC Method

Theil inequality coefficient (TIC) is widely used since 1977 because it is simple and easy to understand. However, it suffers of many flaws that have been discussed in detail by Song et al. [31] who proposed ATIC method. The ATIC covers many of the TIC method flaws; especially it considers both position and trend differences between the observed and correlated values using principle component analysis approach. The standard procedures and equations for correlations ranking based on ATIC method are given in Fig. 2.

Both position conformity coefficient, $\mathrm{D}(\mathrm{X_o}, \mathrm{X_c})$, and trend conformity coefficient, $\mathrm{T}(\mathrm{X_o}, \mathrm{X_c})$, ranges between 0 and 1. When the value is close to 1, it indicates better consistency between the observed and correlated values.

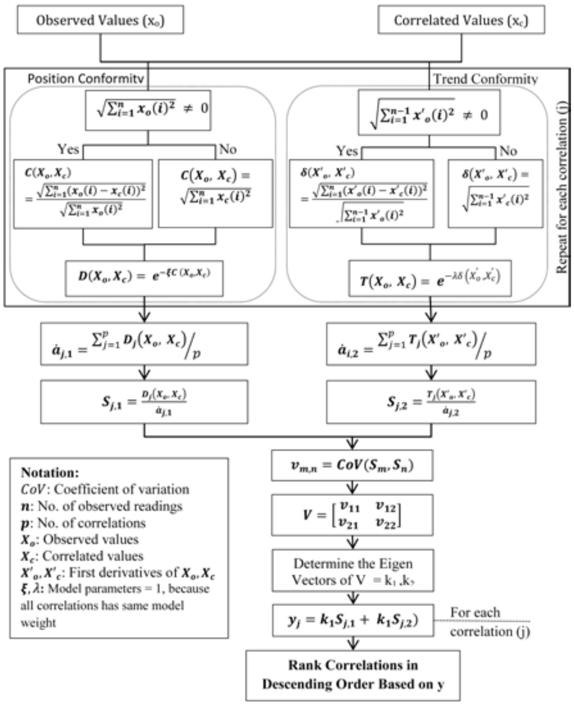

Fig. 2 Correlations ranking based on ATIC method.

ATIC method was used to rank the 92 Cc correlations. Summary of the results for the 5 top-most and bottom-most ranked correlations considering both position and trend is given in Table 3. If position conformity was considered separately; C60 and C67 will be considered the best ranked, and C13 and C15 are the worst ranked correlations. When considering the trend conformity; C26 and C22 are the best ranked, and C62 and C15 are the worst ranked correlations.

Table 3 ATIC results summary for the 10 top-most and 10 bottom-most ranked correlations

	Rank	Cor. ID	$\mathbf{D}(\mathbf{X_o}, \mathbf{X}$	$\mathbf{T}(\mathbf{X_o}, \mathbf{X_c}$	y_j
5 Top Cor.	1	C22	0.6474	0.4607	1.6259
	2	C80	0.6475	0.4566	1.6182
	3	C43	0.6405	0.4602	1.6175
	4	C10	0.6484	0.4557	1.6173
	5	C50	0.6346	0.4586	1.6077
5 Bot. Cor	88	C03	0.2969	0.1419	0.6089
	89	C14	0.2710	0.1025	0.5025
	90	C13	0.1607	0.1025	0.3803
	91	C62	0.1980	0.0565	0.3310

92	C15	0.0980	0.1025	0.3108

Correlation and Determination Coefficients

Correlation (R) and determination coefficients (R^2) give an indication about the strength of linear association between the correlated and observed data [30]. Both R and R^2 were calculated between the observed and correlated values using Eq. (2) and Eq. (3) [32].

$$R = \frac{\sum_{i=1}^{n}(x_{oi}-\overline{x_o})(x_{ci}-\overline{x_c})}{\sqrt{\sum_{i=1}^{n}(x_{oi}-\overline{x_o})^2 \ \sum_{i=1}^{n}(x_{ci}-\overline{x_c})^2}} \quad (2)$$

$$R^2 = \left[\frac{\sum_{i=1}^{n}(x_{oi}-\overline{x_o})(x_{ci}-\overline{x_c})}{\sqrt{\sum_{i=1}^{n}(x_{oi}-\overline{x_o})^2 \ \sum_{i=1}^{n}(x_{ci}-\overline{x_c})^2}}\right]^2 \quad (3)$$

Where x_{oi}, x_{ci} observed and correlated value for each point i, n: number of points, $\overline{x_o}$, $\overline{x_c}$: average of observed and correlated values, respectively.

The Cc correlations were ranked based on both coefficients and the best correlation is C29 that was ranked the 12th best based on ATIC method, the worst correlations are C53, C54, C55, and C56. Fig. 4.a and 4.b shows the values for the best and worst ranked correlations based on ATIC and R&R^2 values, respectively with the observed values.

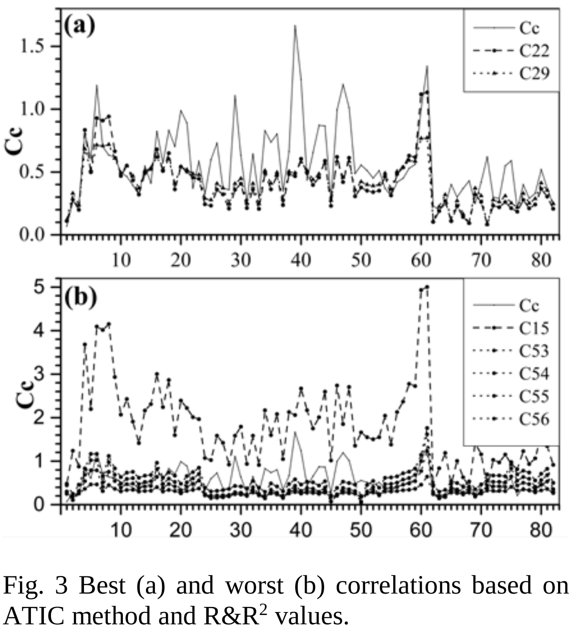

Fig. 3 Best (a) and worst (b) correlations based on ATIC method and R&R^2 values.

Figure 4.a shows that both correlations are nearly accurate to predict the observed values nevertheless; C22 is more accurate especially at the extreme values. From Fig. 4.b it can be seen that the ATIC worst correlation (C15) is too far from the observed values in contrast to the worst correlations based on R&R^2. The main reason for that the R and R^2 coefficients are sensitive for abrupt changes of the values and they only evaluate the trend of the values without considering their relative positions.

Mean Squared Deviation, Root Mean Squared Deviation, and Mean Absolute Difference

The Mean Squared Deviation (MSD), its square root (RMSD), and Mean Absolute Difference (MAD) are indicators of the difference between the positions of correlated values from the observed values. MSD, RMSD, and MAD were calculated between the observed and correlated values based on Eq. (4), Eq. (5), and Eq. (6), respectively [30].

$$MSD = \frac{\sum_{i=1}^{n}(x_{oi}-x_{ci})^2}{n} \quad (4)$$

$$RMSD = \sqrt{\frac{\sum_{i=1}^{n}(x_{oi}-x_{ci})^2}{n}} \quad (5)$$

$$MAD = \frac{\sum_{i=1}^{n}|x_{oi}-x_{ci}|}{n} \quad (6)$$

Where x_{oi} observed value for each point i, x_{ci}: correlated value for each point i, n: number of points

The Cc correlations were ranked based on those coefficients. The best correlation is C60 same results of ATIC method when considering only the position conformity. Fig. 5 shows the correlated values for the C22 and C60 in-line with the observed Cc values. It can be seen that both correlations are nearly accurate nevertheless C60 is not accurately follow the observed values trend. The worst correlation is C15 same as ATIC method rank.

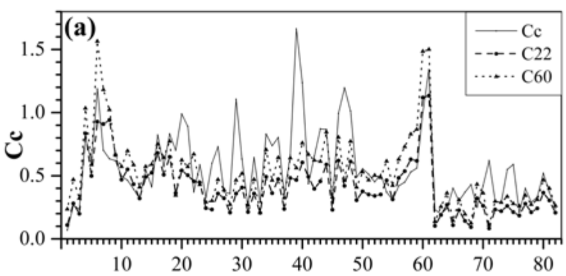

Fig. 4 Observed C_C values and correlated values for best correlations based on ATIC and MSD-RMSD-MAD values.

Ranking Index

The ranking index (RI) is proposed by Briaud and Tucker [33] to rank different methods of pile capacity determination as given in Eq. (9). The authors suggested that the lower the value of RI the better rank of the correlation.

$$RI = \mu\left|\ln\left(\frac{x_c}{x_o}\right)\right| + \sigma\left|\ln\left(\frac{x_c}{x_o}\right)\right| \quad (9)$$

Where μ, σ: represents mean and standard deviation; and x_o, x_c: observed and correlated values

Some correlation resulted illogical negative values that can't be used in the normal log function in Eq. (9) that prevents successful ranking of all correlations. When ranking the other correlations, the best correlation was C67 that was ranked the 2nd best in ATIC method when considering only the position conformity. The worst correlation is C15, same as ATIC rank. Fig. 6 shows Correlations C67 and C22 in line with the observed C_C values.

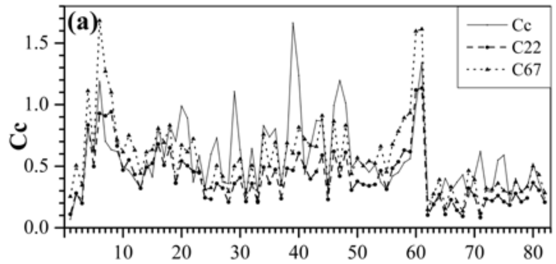

Fig. 5. Observed C_C values and correlated values for best correlations based on ATIC and RI.

Ranking Distance

The ranking distance (RD) was proposed by Cherubini and Orr [34] as a rational approach to compare between observed and correlated data as given in (10). The authors suggested that the lower the value of RD the better the accuracy and precision of the correlation.

$$RD = \sqrt{\left[1 - \mu\left(\frac{x_c}{x_o}\right)\right]^2 + \left[\sigma\left(\frac{x_c}{x_o}\right)\right]^2} \qquad (10)$$

All variables as defined in Eq. (9)

The best correlation based on RD values is correlation C02 that was ranked 58th best based on ATIC method. The worst correlation is C15, same as ATIC rank. During the data analysis, it was noted that the RD is biased for the odd ratios between correlated and observed values. Also, it considers only the position of the values without considering its trend. This may be the reasons for the large difference between the results of the ATIC method and RD. Correlations C02 and C22 are shown in Fig. 7 in-line with the observed C_C values.

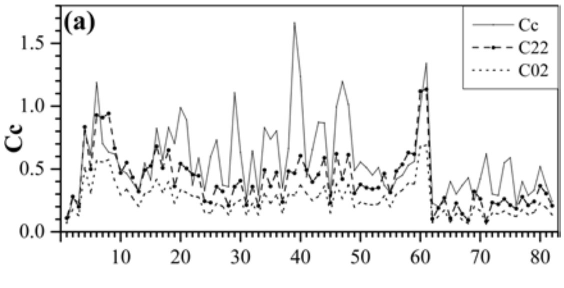

Fig. 6 Observed C_C values and correlated values for best correlations based on ATIC and RD.

CONCLUSION

This paper focused on the study of the validity and efficiency of Amended Theil Inequality Coefficient (ATIC) method for geotechnical correlations evaluation. ATIC has the advantage that it considers both position and trend conformities between the observed and correlated values. Total of 92 compression index correlations were used as test-case. Different statistical measures results that were used in the literature were compared with the results of the ATIC method.

The best correlation based on ATIC method was C22 and worst correlation was C15, both correlations relate compression index value with the initial voids ratio of the soil.

Based on R and R^2 coefficients, the best correlation is C29 and the worst correlations are C53, C54, C55, and C56. When visually inspect these correlations with the worst correlation based on ATIC, it was concluded that ATIC is more accurate. Both coefficients have shortcoming that they consider only the trend of the values without considering their relative position.

The best and worst correlations based on MSD, RMSD, and MAD is C60 and C15 respectively. When comparing these results with ATIC results, both methods give the same worst correlation, but different results for the best correlation. The MSD, RMSD, and MAD values have the shortcoming that they evaluate only the values' position around the average without considering its trend.

The RI best correlation was C67 that was ranked the 2nd best when considering only the position conformities in the ATIC method. The worst correlation was C15, same as ATIC rank. The RI considers only the position of the data that limits its ability for efficient correlation evaluation.

The RD best correlation was C02 that was ranked the 58th best based on ATIC method. The worst correlation was C15, same as ATIC rank. It was noted that RD is biased for the odd ratios between the correlated and observed values and it considers only values' position that may be considered the reason for the large difference between ATIC method results and RD results.

Based on the results of this paper, ATIC can be considered a good method of geotechnical correlations evaluation. Future research will concentrate on how to integrate ATIC method with expert knowledge to validate geotechnical correlations.

ACKNOWLEDGMENTS

Waled A. Daoud is thankful to the Egyptian Ministry of Higher Education and Egypt-japan University of Science and Technology for funding his PhD studies. Also, he would like to thank Dr. Hazem Barakat for his technical and financial support during the data collection period and special thanks to Kyushu University for offering the tools and equipment needed for the research.

REFERENCES

[1] S. Onyejekwe, X. Kang, and L. Ge, "Assessment of empirical equations for the compression index of fine-grained soils in Missouri," *Bull. Eng. Geol. Environ.*, 2014.

[2] K.-K. Phoon and F. H. Kulhawy, "Evaluation of geotechnical property variability," *Can. Geotech. J.*, vol. 36, no. 4, pp. 625–639, 1999.

[3] K.-K. Phoon and F. H. Kulhawy, "Characterization of geotechnical variability," *Can. Geotech. J.*, vol. 36, no. 4, pp. 612–624, 1999.

[4] G. A. Fenton, "Probabilistic Methods in Geotechnical Engineering," 1997.

[5] F. M. Abdrabbo and M. A. Mahmoud, "Correlations between index tests and compressibility of egyptian clays.," *Soils Found.*, vol. 30, no. 2, pp. 128–132, 1990.

[6] N. Dayal, "Consolidation analyses of greater Cincinnati soils," University of Cincinnati, 2006.

[7] B. A. McCabe, B. B. Sheil, M. M. Long, F. J. Buggy, and E. R. Farrell, "Empirical correlations for the compression index of Irish soft soils," *Proc. ICE-Geotechnical Eng.*, vol. 167, no. 6, pp. 510–517, 2014.

[8] C. I. Giasi, C. Cherubini, and F. Paccapelo, "Evaluation of compression index of remoulded clays by means of Atterberg limits," *Bull. Eng. Geol. Environ.*, vol. 62, no. 4, pp. 333–340, 2003.

[9] J. H. Park and T. Koumoto, "New compression index equation," *J. Geotech. Geoenvironmental Eng.*, vol. 130, no. 2, pp. 223–226, 2004.

[10] A. W. Skempton and O. T. Jones, "Notes on the compressibility of clays," *Q. J. Geol. Soc.*, vol. 100, no. 1–4, pp. 119–135, 1944.

[11] B. Tiwari and B. Ajmera, "New correlation equations for compression index of remolded clays," *J. Geotech. Geoenvironmental Eng.*, vol. 138, no. 6, pp. 757–762, 2011.

[12] M. Hatanaka and A. Uchida, "Empirical correlation between penetration resistance and internal friction angle of sandy soils.," *Soils Found.*, vol. 36, no. 4, pp. 1–9, 1996.

[13] F. Nassaji and B. Kalantari, "SPT capability to estimate undrained shear strength of fine-grained soils of Tehran, Iran," *Electron. J. Geotech. Eng.*, vol. 16 N, pp. 1229–1238, 2011.

[14] T. S. Nagaraj and B. R. S. Murthy, "A critical reappraisal of compression index equations," *Géotechnique*, vol. 36, no. 1, pp. 27–32, 1986.

[15] G. L. Yoon, B. T. Kim, and S. S. Jeon, "Empirical correlations of compression index for marine clay from regression analysis," *Can. Geotech. J.*, vol. 41, no. 6, pp. 1213–1221, 2004.

[16] C. S. Rani and K. M. Rao, "Statistical evaluation of compression index equations," *Int. J. Civ. Eng. Technol.*, vol. 4, no. 2, pp. 104–117, 2013.

[17] C. Lee, S.-J. Hong, D. Kim, and W. Lee, "Assessment of compression index of Busan and Incheon Clays with sedimentation state," *Mar. Georesources Geotechnol.*, vol. 33, no. 1, pp. 23–32, 2015.

[18] B. K. Hough, "Basic soils engineering.," 1957.

[19] V. M. Cozzolino, "Statistical forecasting of compression index," in *Proceedings of the 5th international conference on soil mechanics and foundation engineering Paris*, 1961, vol. 1, pp. 51–53.

[20] Z.-C. Moh, C.-T. Chin, C.-J. Liu, and S.-M. Woo, "Engineering correlations for soil deposits in Taipei," *J. Chinese Inst. Eng.*, vol. 12, no. 3, pp. 273–283, 1989.

[21] A. S. Azzouz, R. J. Krizek, and R. B. Corotis, "Regression analysis of soil compressibility.," *Soils Found.*, vol. 16, no. 2, pp. 19–29, 1976.

[22] A. Nakase, T. Kamei, and O. Kusakabe, "Constitutive parameters estimated by plasticity index," *J. Geotech. Eng.*, vol. 114, no. 7, pp. 844–858, 1988.

[23] O. Rendon-Herrero, "Closure to 'Universal compression index equation' by Oswald Rendon-Herrero (November, 1980)," *J. Geotech. Eng.*, vol. 109, no. 5, pp. 755–761, 1983.

[24] R. B. Peck and W. C. Reed, "Engineering properties of Chicago subsoils," *Univ. Illinois. Eng. Exp. Station. Bull. no. 423*, 1954.

[25] M. & R. Moran Proctor, *Study of deep soil stabilization by vertical sand drains*. Bureau of Yards and Docks, Department of the Navy, 1958.

[26] G. G. Shorten, "Geotechnical analysis of recent estuarine organo-calcareous silts, Fiji: New considerations for investigations of soft marine clays," University of Sydney, 1995.

[27] Y. Nishida, "A brief note on compression index of soil," *J. Soil Mech. Found. Div.*, vol. 82, no. 3, pp. 1–14, 1956.

[28] A. W. N. Al-Khafaji and O. B. Andersland, "Equations for compression index approximation," *J. Geotech. Eng.*, vol. 118, no. 1, pp. 148–153, 1992.

[29] K. V Helenelund, "On consolidation and settlement of loaded soil layers.," *Soil Sci.*, vol. 73, no. 2, p. 154, 1952.

[30] C. D. Schunn and D. Wallach, "Evaluating goodness-of-fit in comparison of models to data," 2005.

[31] J. Song, L. Wei, and Y. Ming, "A method for simulation model validation based on Theil's inequality coefficient and principal component analysis," in *AsiaSim 2013*, Springer, 2013, pp. 126–135.

[32] G. B. Baecher and J. T. Christian, *Reliability and statistics in geotechnical engineering*. Wiley, 2003.

[33] J.-L. Briaud and L. M. Tucker, “Measured and predicted axial response of 98 piles,” *J. Geotech. Eng.*, vol. 114, no. 9, pp. 984–1001, 1988.
[34] C. Cherubini and T. L. L. Orr, “A rational procedure for comparing measured and calculated values in geotechnics,” *Coast. Geotech. Eng. Pract. Yokohama*, vol. 1, pp. 261–265, 2000.

Construction Materials

STRUCTURE OF SUPERCONDUCTING CABLE COMPONENTS

Svetlana Barannikova[1,2,3], Anatoly Malinovsky[3] and Dmitrii Pestsov[3]

[1]Institute of Strength Physics & Materials Science, SB RAS, Russia; [2]National Research Tomsk State University, Russia; [3]Tomsk State University of Architecture and Building, Russia

ABSTRACT

Using atomic force, optical and electron microscopy methods, the changes in the microstructure and phase composition were investigated for the alloy Nb47%Ti used for the manufacture of superconducting cable employed as current-carrying elements in the magnetic system for International Thermonuclear Experimental Reactor. The test samples were prepared from the superconducting wire at an intermediate step of the drawing process for the area reduction Ø1.3→Ø1.2 mm. The effect of cold drawing and intermediate annealing on the properties of as-worked Nb-Ti alloy was assessed. Local strain zones were found to occur in the rupture area. The shape and chemical composition of Nb-Ti wire was examined for both a defect-free area and the rupture area. A Nb diffusion barrier was found to occur in the copper matrix of Nb-Ti wire.

Keywords: Superconductors, microstructure, plastic strain localization

INTRODUCTION

Materials traditionally used in electrical engineering have been to some extent supplanted by superconductive materials, which are cost-effective and suitable for a wide range of applications, in particular, nuclear energetics [1]. Thus Nb-Ti alloys are worthy of special attention [2]-[4]. These are used for the manufacture of superconducting cable employed as current-carrying elements in the magnetic system for International Thermonuclear Experimental Reactor. The cable houses several thousand strands of superconducting wire in a copper matrix, each strand being 2…5 mμ in diameter [2]. Such cables must be capable of meeting a number of stringent requirements, i.e. stability of criticality parameters and of current-voltage characteristics, strength-resistance to breaking and structural uniformity of the superconducting wire, uniform cross-section geometry of wire [5]-[7].

By the manufacture of superconducting Nb-Ti wire, the most important stage is cold drawing with the area reduction of the original bar Ø60 …70 mm→Ø0.1…1.0 mm [8]. As-produced superconducting wire is expected to have high strength resistance to breaking as well as structural uniformity, i.e. pre-set density of micro-defects for controlling formation of pinning centers. The goal of the given work is examination of the influence of the severe plastic deformation (SPD) treatment by drawing on the structure of superconducting Nb-Ti wire.

MATERIALS AND METHODS

The structural investigations were performed using test samples of the Nb-Ti alloy containing 47.5% Ti (by mass) or 63.7% Ti (at. percent). The test samples were prepared from the superconducting cable wire at the intermediate stage of cold drawing with the area reduction of the original bar Ø1.33→Ø1.2 mm. To provide for high space resolution level, several methods were used for investigation of the composition and structure of the alloy: optical microscopy (Olympus GX 71 units); raster electron microscopy (Philips SEM 515 unit); atomic force microscopy (Solver PH47-PRO unit) and contact method. The element distribution was determined for material on the border of copper matrix and Nb-Ti cable core, using the method of raster electron microscopy (Quanta 200 3D ion-electron unit equipped with detectors of secondary and back-scattered ions).

RESULTS AND DISCUSSION

The coated cable construction houses several thousand strands of superconducting Nb-Ti wire in composite copper matrix (Fig. 1). The composite might contain resistive or diffusion barriers, stabilizing coating or armoring [2]. Metallography investigation was performed using cross-sections of superconducting Nb-Ti wire strands, which had a round form with the average diameter ~10 µm. However, the intermediate layer adjacent to the copper matrix all the Nb-Ti wire strands have rhomb-like shape with13-µm and 11-µm diagonals, which might be attributed to the SPD treatment by cold drawing.

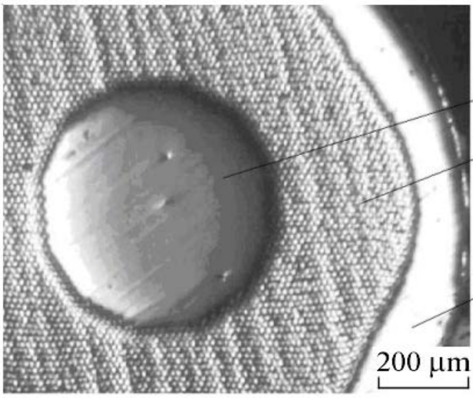

Fig. 1 The cross-section of superconducting Nb-Ti cable wire strands at the intermediate stage of cold drawing with the area reduction Ø1.3→Ø1.2 µm: 1 – copper matrix; 2 – Nb-Ti wire strands and 3 – copper core.

Using atomic force microscopy in conjunction with contact method in constant force mode, cross-section relief was examined for different cable zones [9], [10]. The scanning revealed a diffusion Nb barrier, which is clearly defined by the relief hills observed in the area of Nb-Ti strands and copper matrix (Figs. 2*a* and *3a*). A profilogram plotted by the linear-intersept method shows a smooth relief of low-amplitude lines of Ni-Ti strands and copper matrix (Fig. 2*b* and *3b*), which separate high-amplitude maximums 250…260 nm wide corresponding to the Nb barrier (Fig. 2*c* and *3c*).

The SPD treatment would cause grain refinement in the copper matrix. As a result, a submicrocrystalline structure is formed with average grain size ~800 nm, which also contains individual grains and conglomerates composed of up to eight grains. The most heavily deformed area is located along the copper core-intermediate Ni-Ti layer border with the grain sizes varying from ~2120 nm to ~310 nm. The intermediate copper matrix layers separating Nb-Ti wire strands contain equiaxed grains having average size ~800 nm, while the outer copper layers have average grain size ~1050 nm.

Using electron microscopy methods, material structure was examined in the intermediate layer on the Ni-Ti strands-copper core border; a specific defect was found to occur in the material (Fig. 4), which is due to the rupture of superconducting strands. The investigations were carried on using a raster electron microscope Carl Zeiss EVO 50, which was equipped with an attachment designed for X-ray dispersion microanalysis (Oxford Instruments). It was found that the outer layer and the core are comprised of copper; however, elements from the intermediate Ni-Ti layer would penetrate into the cable's copper core as well as intermediate-outer layer interphase. The chemical composition of intermediate layer wire strands on the core border is 35.66% (at) and 63.07% (at) for Nb and Ti, respectively; the wire strands in the point of rupture have the same chemical composition. In the former case, intermediate layer wire strands have a round form and in the latter, an elongated one.

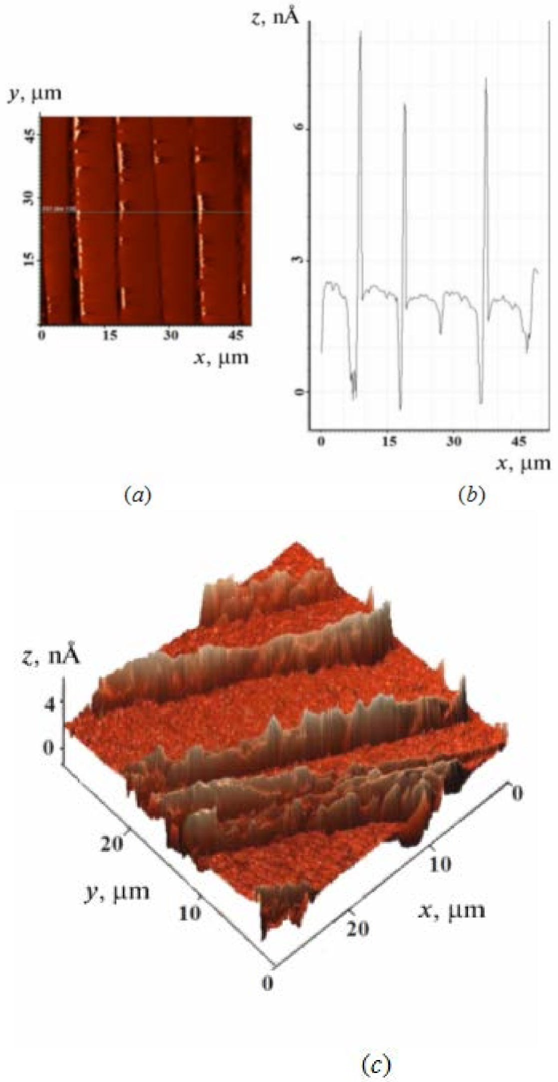

Fig. 2 The relief of longitudinal cross-section showing diffusion Nb barrier within unpolished defect-free area of Nb-Ti strands and copper matrix (*a*); a profilogram of the same area (*b*); 3D image (*c*).

Using scanning microscopy in secondary electrons mode in conjunction with characteristic X-ray radiation on a unit Quanta 200 3D, the composition of Nb-Ti strands was examined and found to be uniform.

Energy dispersive X-ray composition microanalysis was used to identify the elemental composition of material. In the area examined, i.e. intermediate Nb-Ti strands layer-copper matrix-intermediate Nb-Ti strands layer, the following elements were found to occur: Nb, Ti and Cu.

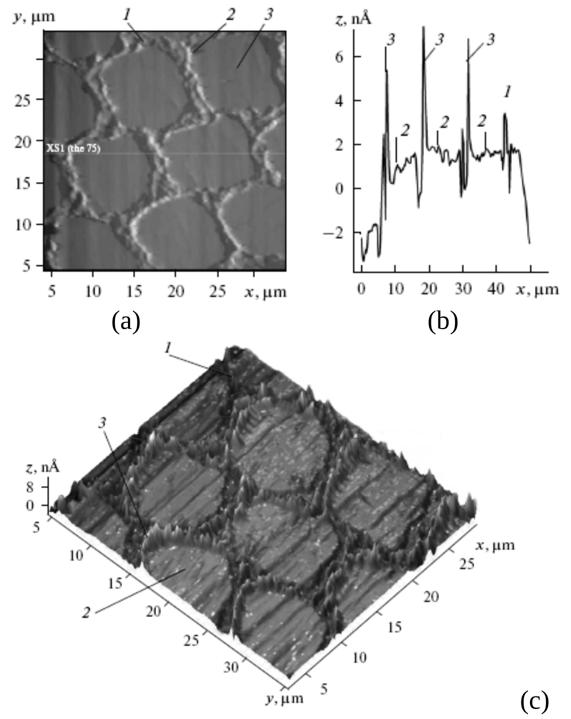

Fig. 3 The relief of transverse cross-section showing Nb barrier around the wires in a conductor matrix: (*a*), (*c*) 2D and 3D images, respectively; (*b*) profilogram of a 30 × 30 µm region. (*1*) Copper matrix, (*2*) Nb–Ti wires, and (*3*) niobium barrier.

The non-homogeneous space distribution of characteristic X-ray photons of Ti, Nb and Cu in the Nb-Ti strands and the copper matrix suggests that a diffusion layer occurs in the direction across the Nb-Ti strands-copper matrix border. The maximal and the minimal number of characteristic X-ray photons of Nb and Ti are observed, respectively for the Nb-Ti strands and the copper matrix. Exactly the converse situation is observed for the copper matrix, i.e. the maximal number of characteristic X-ray photons is observed for Cu and the minimal number of the same photons, for Ti and Nb. In the case of intermediate diffusion layer, the number of characteristic X-ray photons of Nb would first remain constant, which supports the evidence for the occurrence of Nb barrier, which was obtained by the AFM method. Then the number of characteristic X-ray photons of Nb and Ti would either grow or decrease depending on whether the number of the same photons of Cu grows or decreases.

Using ion beam, the fine structure of cable components was examined by the thin-foil method. The Nb-Ti strands are found to have a heavily deformed structure; grain boundaries were indistinct, evidence of relaxation unavailable. Individual dislocations within the grains of Nb-Ti strands could not be resolved. The Nb barrier on the Nb-Ti strands-copper matrix border could be defined only partially in the point of rupture. The material within the matrix was in a deformed and relaxed state. Individual dislocations would occur within the grains; however, no dislocation clusters are observable.

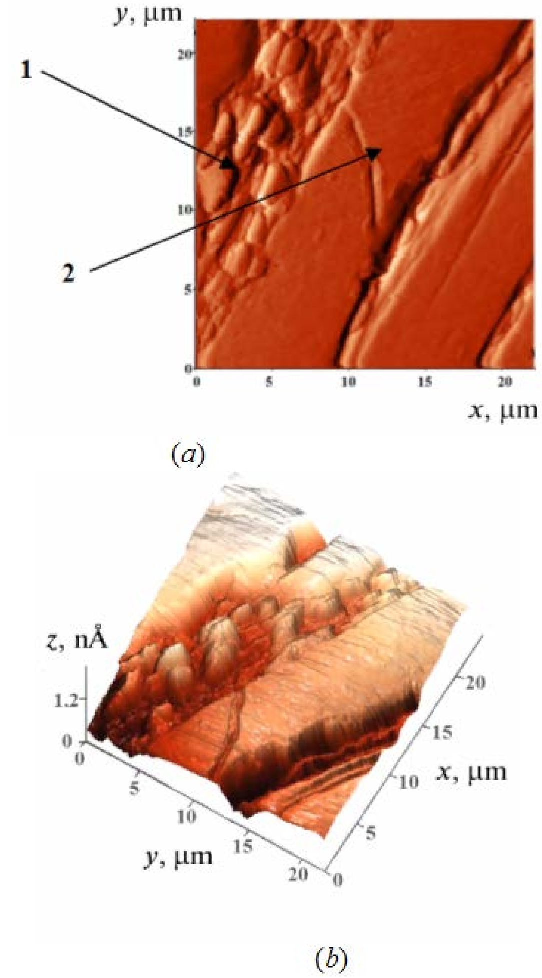

Fig. 4 Longitudinal section showing rupture of unpolished Nb-Ti strands in as-received defect-free state (*a*); 3D image (*b*); 1– copper matrix; 2 –Nb-Ti strands.

The Nb barrier would become noticeable on going along the Nb-Ti strands-copper matrix border; it has submicrocrystalline structure, small-size grains have a low degree of non-equiaxiality (Fig. 5).

The morphology of material within the localized plastic deformation zone was investigated. Several layers of material 0.5-mm each were removed with the aid of abrasive from the latter zone to be examined by metallography technique. It was found that all the Nb-Ti strands of the inner layer adjacent to the copper core have a round shape. The SPD treatment by drawing has left traces in the intermediate layer of the region adjacent to the copper core. The Nb-Ti strands in the outer layer are rhomb-shaped.

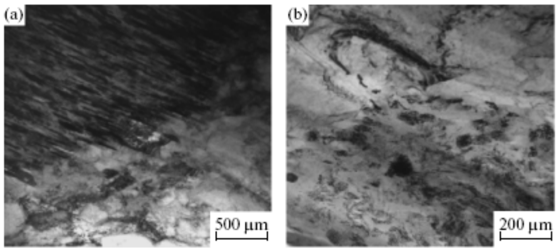

Fig. 5 Fine structure of superconducting cable: (a) boundary between Nb–Ti fiber and matrix; (b) boundary between copper matrix and niobium barrier.

The cross-section topography was examined by the methods of optical and atomic-force microscopy. After the region adjacent to the copper core had been polished with abrasive to a depth of 0.5 mm, Nb-Ti strands on its border would assume irregular shape and would form a localized deformation zone similar to that observed for as-received Nb-Ti strands which have not been polished (Fig. 6*a*, *b* and Fig. 7*a*, *b*). In the point of rupture the intermediate copper matrix layer separating Nb-Ti strands had average grain size ~850 nm.

The statistic treatment data suggests that the average grain size of the defect-free zone of the copper matrix has average grain size ~800 nm, which is comparable to that of copper in the point of rupture, i.e. ~850 nm. The profilogram obtained for the cross-section polished to a depth of 0.5 mm shows a Nb barrier in the point of rupture, which surrounds Nb-Ti strands within the copper matrix. This presents a series of high-amplitude sharp maxima having width ~250 nm, which is similar to that observed for as-received material without polishing. A similar Nb barrier surrounding Nb-Ti strands in the location of breakage was observed for material that had been polished to a depth of 1 mm.

Metallography investigation was performed for Nb-Ti strands cross-sections, which were subjected to etching and polishing to a depth of 1 mm. It was found that Nb-Ti strands appear to be unchanged by comparison with as-received unpolished material. However, the localization zone has a different aspect (Fig. 6*c* and Fig. 7*c*). The lobe-like strands coalesce to form one strand, which suggests that the strands are of different thickness. The Nb-Ti strands within the localization zone assume a round shape.

The structure of section surface, which had been polished to a depth of 2mm, was examined in an optical microscope. The general aspect of localization zone is found to have changed significantly relative to as-received defect-free state. The Nb-Ti strands in the point of rupture gradually form a conglomerate (Fig. 6*d* and Fig. 7*d*); the near-lying Nb-Ti strands have a round shape, which is characteristic for defect-free zones. It should be noted that another defect was found to occur in the vicinity of boundary between the intermediate layer of Nb-Ti strands within the copper matrix and the copper core, i.e. two Nb-Ti strands of irregular shape, which had smaller size relative to the near-lying ones.

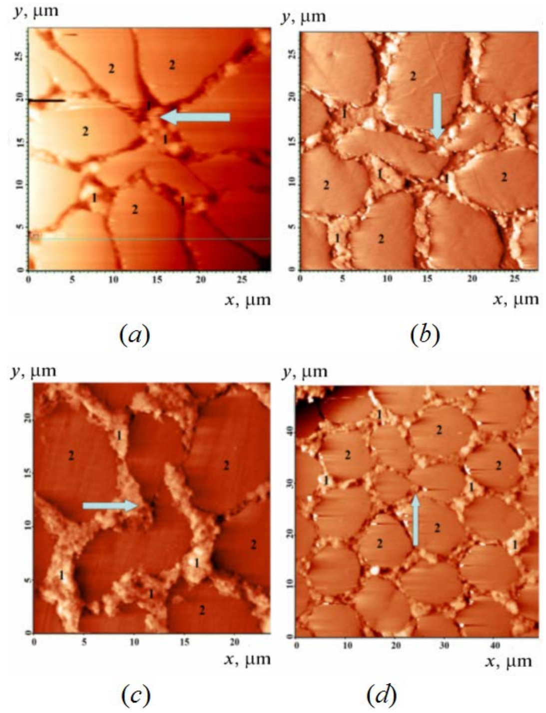

Fig. 6 The AFM image of the zone of localized plastic deformation at the point of breakage of Nb-Ti strands (designated by arrows): 1–copper matrix; 2–Nb-Ti strands; depth of polishing: (*a*) 0 mm; (*b*) 0.5 mm; (*c*) 1 mm; (*d*) 2 mm.

Using the contact method of AFM technique, we examined the cross-section surface of Nb-Ti strands which had been subjected to etching an polishing to a depth of 2 mm.

In this case, a Nb barrier is found to occur on both the inner and the outer surface of the Nb-Ti strands in copper matrix. As noted above, a similar Nb barrier had been observed previously in a defect-free area of as-received material; this shows in profilograms as a series of high-amplitude narrow maxima having width ≤ 250 nm.

The evolution of localized plasticity zone is illustrated in Figs. 6 and 7. Analysis of the curve was made in order to define in what way a change in the cross-section area of Nb-Ti strands in the point of rupture is affected by the depth of polishing (Fig. 8). The sections of Nb-Ti strands polished to a depth of 2mm were examined; the results obtained suggest that the SPD treatment by drawing caused neck formation within the localization zone observed for the Nb-Ti strands.

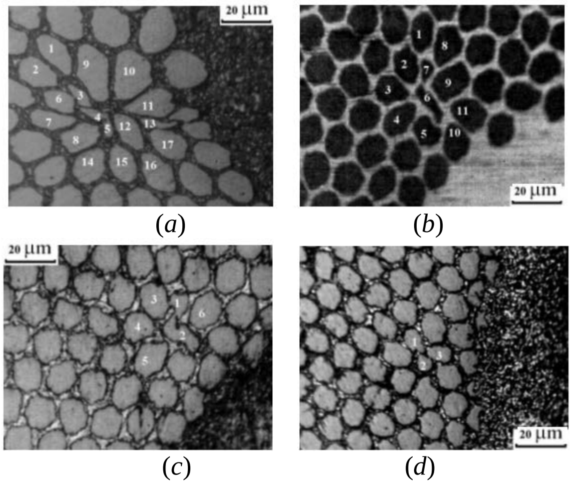

Fig. 7 The optical microscopy image of the localized plastic deformation zone in the site of breakage of Nb-Ti strands; depth of polishing: (*a*) 0 mm; (*b*) 0.5 mm; (*c*) 1 mm; (*d*) 2 mm.

Thus, the area next to the cable copper core is found to contain localized deformation zone in the point of rupture of Nb-Ti strands. Moreover, the Nb barrier is present only partially in the same area, which is indicative of a varying extent of deformation in the sections, which were polished to depths varying from 0.5, 1 and 2 mm. A major drawback to the conventional approach employed in the analysis of the ultimate tensile strength of superconductors on the base of Nb-Ti alloy is the conceptual representation of plastic deformation as a steady-state and homogeneous process [11].

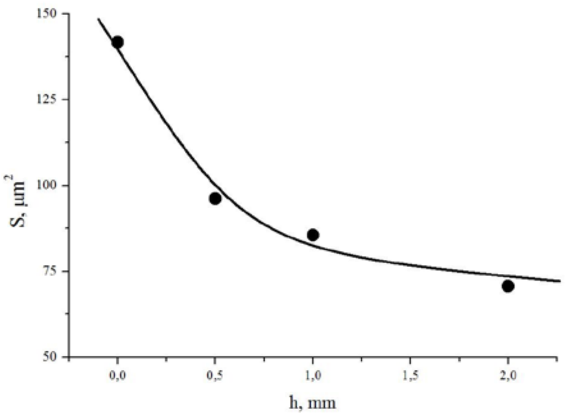

Fig. 8 A change in Nb-Ti strands cross-area (S) in the point of rupture (within the localization zone) *vs* depth of polishing: h = 0 mm; 0.5 mm; 1 mm; 2 mm.

The experimental evidence for the nature of plastic deformation strongly suggests that at the early stages of straining the plastic deformation would exhibit an inhomogeneous behavior, which is liable to cause formation of localized plasticity nuclei [12]; in one of these nuclei rupture of cable strands would occur. The macro-scale localization of deformation has been studied in sufficient detail. On the base of experimental evidence a one-to-one correspondence has been established between the work hardening law, which is acting at the given flow stage of the stress-strain curve, on the one hand and the space-time distribution plastic distortion tensor components observed for the deforming material on the other hand [12].

CONCLUSION

Analysis was made of the effect of the SPD treatment by drawing on material structure of the multi-strand superconducting cable on the base of Nb-Ti alloy. The following results have been obtained.

- Deformation localization zones are found to occur in the point of rupture of the cable. Sections of Nb-Ti strands were polished to a depth of ≤ 2 mm to reveal that the adjacent Nb-Ti strands have irregular shape.
- A variation in the shape and size of Nb-Ti strands is found to occur in a defect-free area of the intermediate layer; on the copper core border Nb-Ti strands have a round shape and diameter ~ 10 μm and those on the copper matrix border are rhomb-shaped with diagonals ~ 13 and 11 μm.
- The SPD treatment by drawing causes grain refinement; a submicrocrystalline structure will form in cable components: the copper core and the intermediate layer of material between the strands within the matrix has grain size ~800 nm; material in the point of rupture and in the intermediate layer between the strands within the matrix has grain size ~850 nm and material of the upper layer has grain size ~1050 nm.
- A diffusion Nb barrier about 250 nm wide is found to occur around the Nb-Ti strands in the copper matrix in a defect-free area; using step-by-step polishing to the depth of 2000 μm, a similar barrier was discovered within a localized deformation zone.
- A change in the chemical composition and shape of Nb-Ti strands in the intermediate layer was observed; in a defect-free area all the Nb-Ti strands have a round shape and the following chemical composition: 35.66 at.% Nb and 63.07 at.% Ti; in the area of rupture the Nb-Ti strands have a regular shape and the following chemical composition: 35.57 at.% Nb and 63.33 at.% Ti.

ACKNOWLEDGEMENTS

The work was performed in the frame of the Tomsk State University Academic D.I. Mendeleev Fund Program (No. 8.1.18.2015) and the Program of Fundamental Research of State Academies of Sciences (No. III.23.1.2) for the period 2013-2016 yrs.

REFERENCES

[1] Wilson MN, “NbTi conductors with very low loss: a review”, Cryogenics, Vol. 48, 2008, pp. 381-395.

[2] Kozlenkova N, Vedernikov G, Shikov A, Potanina LV, Filatov AV, Vorobieva AE, Pantsyrnyi VI, Gubkin I.N, ”Study on Ic (T, B) for the Nb-Ti strand intended for ITER PF insert coil”, IEEE Transactions on Applied Superconductivity, Vol. 14, 2004, pp. 1028-1030.

[3] Lu B, Luongo CA, “Parametric estimation study of interstrand conductance in multi-strand superconducting cables”, Cryogenics, Vol. 47, 2007, pp. 546-552.

[4] Ochiai S, Oki Y, Sekino F, Hojo M, Tanaka M, Okuda H, Moriai H, Sakai S, Watanabe K, “Fracture of filaments and its influence on critical current and residual strength of fatigued Nb–Ti/Cu superconducting composite”, Cryogenics, Vol. 43, 2003, pp. 45-51.

[5] Beloshenko VA, Chishko VV, Matrosov NI, Dyakonov VP, Szymczak R, Pietoza J, Puzniak R, Szymczak H, Gaida D, Zaleski A, “Effect of deformation and heat treatment with equal-channel, multiple-angle pressing on the superconducting properties of NbTi alloy”, Low Temperature Physics, Vol. 36, 2010, pp. 1045-1048.

[6] Lee PJ, Larbalestier DC, McKinnel JC, “High titanium Nb-Ti alloys initial microstructural studies”, Advances in Cryogenic Engineering, Vol. 34, 1988, pp. 967-974.

[7] Cherny OV, Andrievskaya NF, Ilicheva VO, “The microstructure and critical current density of Nb-48 wt.%Ti superconductor with very high alpha-Ti precipitate volume and very high critical current”, A Advances in Cryogenic Engineering, Vol. 48B, 2002, pp. 883-890.

[8] Cherny OV, Storozhilov GE, Andrievskaya NF, Ilichova VO, Starodubov YD, Volchok OI, Chirkina LA, Lazareva MB, Okovit VS, “Structure and properties of differently directed deformed niobium-titanium alloy”, IEEE Transactions on Applied Superconductivity, Vol. 15, 2005, pp. 3502-3505.

[9] Zuev LB, Shlyakhova GV, Barannikova SA, Kolosov SV, “Microstructure of elements of a superconducting alloy Nb-Ti cable”, Russian Metallurgy (Metally), Vol. 2013, 2013, pp. 229-234.

[10] Shlyakhova GV, Barannikova SA, Zuev LB, “On structure of localization zones of plastic deformation in superconductive cable based on Nb-Ti alloy”, Metallofizizika i Noveishie Tekhnologii, Vol. 35, 2013, pp. 453 – 465.

[11] Zuev LB, Barannikova SA, Zavodchikov SYu, “Localization of tensile deformation in a polycrystalline Zr-based alloy”, Physics of Metals and Metallography, Vol. 87, 1999, pp. 244-246.

[12] Zuev LB, Danilov VI, Barannikova SA, Gorbatenko VV, “Autowave model of localized plastic flow of solids”, Physics of Wave Phenomena, Vol. 17, 2009, pp. 1–10.

A FRESH APPROACH TO CHARACTERISATION OF HOT MIX ASPHALTS

Yeaman J[1], Yeaman S.D 1Queensland Pavement Centre, University of the Sunshine Coast, Australia; [2,3] Jacobs Engineering, Australia

ABSTRACT

Pavement Management embraces the full range of engineering activities (Design, Construction, Operation, Maintenance and Renewal), throughout the life cycle.
Over the past 4 years, The Queensland Pavement Centre at the University of the Sunshine Coast, Australia, has been studying the various parameters that influence pavement behaviour for the whole of life of a road pavement, under real operational conditions.
Pavement Design requires an in depth understanding of the properties of the component materials. Hot Mix Asphalt (HMA) is the most important component of a pavement since it provides the strength and flexibility to support the loads it is intended to carry; waterproofing of the unbound components and a smooth, safe riding surface for all users.
Hot Mix Asphalt is one of the most complex materials that an engineer can engage, it is brittle at low temperatures and will flow at high temperatures, The performance of HMA depends of the pavement temperature and the rate and magnitude of loading, all of which will vary many times in any 24 hours, yet we assume one value for "stiffness" through the resilient modulus for perhaps the next 20 years.
This paper examines how the Dynamic Modulus (|E*| can be developed in the Laboratory as a Master Curve, coupled with temperature gradient parameters to provide characterization for Dynamic Modulus that can be used in a simulation method to determine the Number of Cycles to fatigue failure for a pavement lifetime spectrum of environment and traffic

Keywords: Asphalt, Master Curves, Dynamic Modulus, Emissivity, Conductivity

INTRODUCTION

The Engineering Science of Pavement Management has stagnated for the past 20 years, with practioners reducing the Science to becoming an inventory of the stock of road assets and a means of justifying decisions that are often based on very little knowledge of the performance of the asset under an extensive range of conditions and manufacturing methods.
The design of a pavement to meet the conditions of its use must be paramount**,** since if the design is unsuitable or simply incorrect then the remainder of the management process is useless
Mathematics and computing power mean that we no longer have the need to design pavements for one season (The Mean Monthly Average Pavement Temperature), One Load (An equivalent Standard Axle) and one material (defined by Stiffness at one temperature and one time of loading).
This paper will examine the use of mathematical simulation process, using statistical data from data collected from operational pavements and materials to determine the probability of a pavement meeting its whole of life expectancy, for the conditions pertinent to its use.

TRANSFER EQUATION

In Australia, we use one transfer function, to link Asphalt properties to the Number of fatigue cycles (Nf) Reference 1

$$\mathbf{N}= \left\lceil \frac{\mathbf{6918(0.856}Vb\mathbf{+1.08)}}{S\ Mix^{\mathbf{0.36}}\mu\varepsilon} \right\rceil^{\mathbf{5}} \text{Equation 1}$$

We could, as easily, use (Reference 2

$$\boldsymbol{Nf = 18.4\ (18.4(0.00432\varepsilon^{-3.291})E^{-0.654}}$$
Equation 2

Where.
S mix, E are the HMA Stiffness, (Modulus)
E, με are the strain relevant to the study
Vb is the Volume of Bitumen in the HMA.
From which it can be seen that there is no reference to traffic , with the only material constant being the Modulus, Stiffness of the Mix which is strongly correlated to temperature.

DEVELOPMENT OF MASTER CURVES FOR

HOT MIX ASPHALT (HMA)

The development of Master Curves for HMA is fully described in three University of Sunshine Coast, final year projects (2014) by McPherson, James-Johnson and Jopson these publications are available through the University Library. Papers from this research will be submitted for publication during 2015

The Equipment

In the above studies, students prepared 100mm diameter by 150mm high asphalt samples An IPC Global Shear Box Compactor was used to compact A thirty kg billet 450mm x 200mmx200mm compacted to 95% solids. Three test cylinders were created from the one billet and trimmed with an IPC Global diamond saw

The Materials

For this study two materials were chosen A standard Brisbane City Council Mix B771 18mm Maximum Size with 15% FRAP (Fine Recycled Asphalt Product) and a standard 35mm, Brisbane City Council Mix D771 with a substitution of 20% FRAP and 10% fine recycled Glass

The Testing Regime

Each Core was fitted with 3 Linear Variable Distance Transducers (LVDT) spaced at 120° and with gauge points at 70mm. In the case of the Marshall specimens a set of gauging points were manufactured so that the adjusted evenly across the glued joint. Each set of test specimens were placed in the Environmental Chamber .Each sample was tested under repeated loading cycles at Temperatures of 10°, 20°C, 30°C, and 40°C ± 1 °C and Frequencies (in Hertz) of 0.1, 0.5, 1, 3, 5.10,15,20 with a Contact Stress of 45 KPa

Computation of the Master Curve

The Modulus of each specimen is calculated directly from the data obtained from the Asphalt Mixture Performance Tester (IPC Global) as effective stress / strain (within the Elastic limit as given by Hooke's law) for each of the test temperatures and frequencies.

Complex Modulus:

$$|E^*| = \frac{\sigma}{\varepsilon} = \frac{\sigma 0 \; sin(\omega t)}{\varepsilon 0 \; sin\;(\omega t - \phi)} \quad \text{Equation 3}$$

Where:

σ_0 = peak (maximum) stress
ε_0 = peak (maximum) strain
Φ = phase angle, degrees
ω = angular velocity
t = time, seconds

The Dynamic Modulus |E*| for each temperature is shifCobber_03
ted to the one curve Figure 1 This is "The Master Curve.

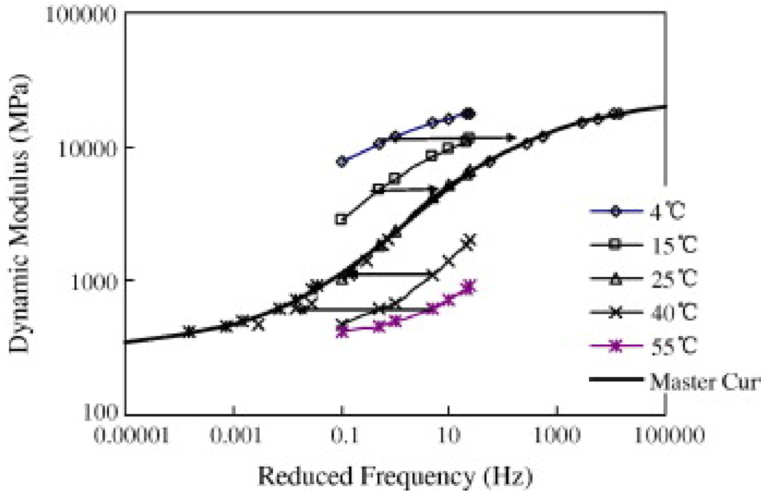

Figure 1 Example Master Curve Construction after Yanqing Shao, Jimin Tang and Liu (Reference 1)

The format of the Master Curve

The Asphalt Master Curve is of the form:

$$\boldsymbol{Log}|(\boldsymbol{E}^*|) = \boldsymbol{\delta} + \frac{\boldsymbol{\alpha}}{\boldsymbol{1+e^{\beta+\gamma\,log\,t}}} \quad \text{Equation 4}$$

Where

|E*| is the Dynamic Modulus of the Asphalt
t is the reduced time (the inverse of frequency)
α, γ, δ are Material constants
β is a temperature dependent variable
T is the required Temperature in degrees Celsius

For Example from Experimentation (McPherson) we have for Mix 2 (above – the Glass substitute mix and 20% FRAP)

Table 1 Value of Master Curve Variables by Experimentation

Temperature	10°C	20°C	30°	40°C	MEAN
Alpha	2.331	2.597	2.342	2.774	2.473
Beta	-1.521	-1.096	-0.491	-0.305	
Gamma	0.315	0.299	0.315	0.290	0.307
Delta	2.278	2.026	2.267	1.857	2.142

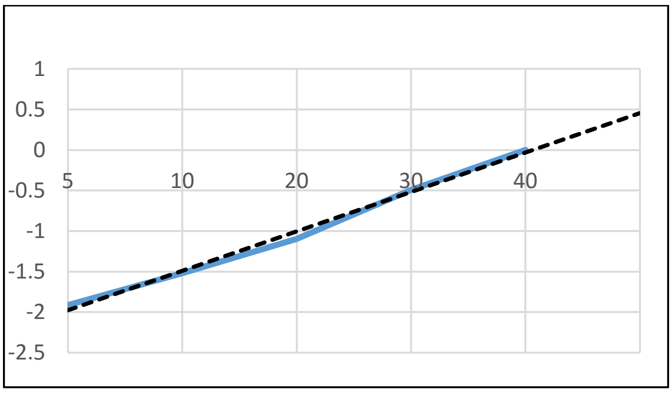

Figure 2 Beta (β) as a function of temperature

Clearly Equation 4 (above) can be used to calculate the Dynamic Modulus E=|E*| with α, β, γ, and δ being obtained from testing and t being calculated as the time of loading the function

$$t = \frac{l+2h}{S} \qquad \text{Equation 5}$$

Where
t = loading time (secs)
l= length of tyre contact area (mm)
h= thickness of asphalt layer (mm)
S = speed of vehicle (mm/sec)

The frequency time relation is given by:

$$f = \frac{1}{t} \quad \text{Equation 6}$$

Where
F= frequency (Hz)
T= time (secs)

To give a typical Performance Characteristics

Table 2 Performance Characteristics for D771G HMA

Temperature (°C)	Frequency (Hz)		Velocity (km /hr.)	S Mix (MPa) Modulus |E*|
45	0.015	High	120	3,800
	0.04	Med	45	3,250
	0.01	Slow	18	2,750
30	0.015	High	120	9,500
	0.04	Med	45	8,250
	0.01	Slow	18	7,150
25	0.015	High	120	10,600
	0.04	Med	45	9,250
	0.01	Slow	18	8,100
20	0.015	High	120	16,300
	0.04	Med	45	14,700
	0.01	Slow	18	13,250

RELATIONSHIP BETWEEN SOLAR RADIATION AND ROAD SURFACE TEMPERATURE

The University of the Sunshine Coast has had a fully instrumented section of road on Sippy Downs Drive, adjacent to the Campus since December 2012 (750 days). This site essentially consists of the following elements Table 3:
Solar Radiation is a critical parameter impacting on the pavement's environment. The quantum of solar radiation drives the pavement surface temperature, oxidation and polymerisation of the bitumen binders in HMA mixtures and surface treatments, the predominate pavements adopted in Queensland. Fortunately Solar Radiation is an unique commodity in that it can be calculated for any point on the earth's surface for any time of the day and day of the year, for example at the Sippy Downs site at Latitude 26° 43'23" South and Longitude 153° 05'02"East – Solar Radiation is at its peak at 12:03 pm every day.
Moisture content also has a serious impact on pavement performance. In Queensland we are not subjected to Freeze Thaw cycles but the State is subject to "drought and flooding rains". Pavements can be dried by the environment to well under optimum and can be totally inundated for weeks. The test runs for 24 hours including both heating and cooling cycles data is downloaded for analysis.

Table 1 Elements of Pavement Monitoring Site at Sippy Downs Drive

Weather Station	**Air temperature**	**In Pavement**	**Horizontal Strain Gauge @ 75mm**
	Relative Humidity		**Vertical Strain Gauge @ 650mm**
	Atmospheric Pressure		**Thermocouple on Surface**
	Rainfall		**Thermocouple @ 75mm**
	Wind Speed		**Moisture Gauge @**
	Wind Direction		**Moisture Gauge @**
	Solar Radiation		**Camera**
Solar panels provide electrical energy			
Data are collected every minute 24/7 and transferred daily at 6:am to the researcher's computer			
The camera records a photograph of the road surface every day at 10:00 am and a photograph of any vehicle that exceeds a nominated strain level			

Relationship between Surface Temperature and depth into pavement

Equations were developed for each of the HMA mixes ,as above with the following relationships HMA BCC B771 (18mm Max Size with 15% FRAP)
Winter T = 0.025z2- 0.069z +DMPT Equation 7

Summer T = 0.033z2 – 0.094z +DMPT Equation 8

Where T =Asphalt Temperature at depth z (°K) DMPT is Daily Maximum Pavement Surface Temperature

CYCLES TO FAILURE N_F

Miners hypothesis and the linear summation of Cycle Ratios

Miners Hypothesis is one of the most frequently used tools for understanding the mechanism for failure in the fatigue mode. Developed in 1945, the model was originally used to understand pressure vessels.

Simply stated if there are k different levels of Strain then the average number of cycles to failure at the i^{th}, ε_i is Ni. The damage factor D is given by $\boldsymbol{D = \sum_1^m \frac{ni}{Ni}}$ Equation 10

Where n_i is the number of cycles accumulated at Strain ε_i

D is the fraction of life consumed by cycles at the different strain levels. In general if the damage fraction reaches 1 failure occurs.

This linear summation of cycle ratios is fundamental to understanding pavement analysis

PAVEMENT DESIGN THROUGH SIMULATION

Monte Carlo Simulation is a computational method that is based on taking random readings from a physical law or mathematical model numerous times in order to obtain a numerical integration, an optimum value or a probability distribution.

The forensic examination of a premature failure of an Urban Collector Road is fully described in the Final Year Project thesis of Kristopher Jopson – available through USC library. This thesis will be published as a technical paper during 2015

In this application Monte Carlo Simulation was used to determine the values for Smix from the HMA Master Curves and the temperature at depth obtained calorimeter box tests

These values together with volumetric properties of the HMA (obtained from the HMA catalogue – Example Appendix A), such as Volume of Bitumen in the HMA (Vb) were used within the Transfer function (Equation 3) to determine the number of cycles to failure (Nf). The damage factor (Nf) calculated by this method divided but the design life The probability density function was determined to determine the probability of failure within the design This analysis returned an expected time to failure under actual traffic of 6 years compared ith an actual result of 7 years; at an 80% level of confidence.

CONCLUSION

The development of Hot Mix Asphalt Master Curves through the Superpave studies has provided a powerful tool, enabling the determination of Mix Stiffness (Dynamic Modulus) to be determined mathematically at temperature and time of loading. Pavement temperature at depth as a function of actual diurnal solar radiation, under laboratory conditions, enables prediction of pavement temperature for a nominated HMA

Simulation techniques enables the prediction of the Number of Cycles to failure using Asphalt Master Curves and temperature prediction at depth.

FUTURE DIRECTION

The Queensland Pavement Centre at the University of The Sunshine Coast, Australia continues to progress this approach with final year students building a catalogue of both HMA Master Curves and Temperature at depth as a function of Solar Radiation.

Samples compacted in the Shear Box Compactor to 95% solids (5% air Voids) provide analysis of both Master Curves and Thermal Conductivity

Structure through the use of micro CT (x-ray based) imaging system, (CAT scans) will soon be added to the suite of techniques.

This data will ultimately find its way into USC's Engineering Learning Hub through Simulation and Visualization technology to become a new method for pavement design and analysis

REFERENCES

[1] Austroads "Guide to Pavement Technology- Part2 : Pavement Structural Design , 2008 pp 76

[2] Tanquist, BA August 1, 2001, "Development of a Quick Reliability Method for Mechanistic-Empirical Asphalt Pavement. , Minnesota Department of Transportation

[3] James-Johnson, 2014 "Master curve production of a typical Queensland HNA compacted using varying for Mechanistic- Empirical Analysis. Final Year Thesis – University of the Sunshine Coast, Australia

[4] Gray C.J. , 2014 "the Development of a procedure to determine temperature of Asphalt at Depth" Final Year Thesis – University of the Sunshine Coast, Australia

[5] Jopson K "A forensic analysis of premature pavement failure of a road pavement using Asphalt Master Curves and Computer simulation-"Final Year Thesis , University of the Sunshine Coast, Australia

Mix Description: BCC Type 3: 18mm Dense Graded Asphalt
Mix Name: B771 Maximum Size: 18mm
Features: Mix B771 has incorporated the addition of 15% Fine Reclaimed Asphalt Product (FRAP) as an aggregate substitute within the mix
Compaction Method: Shear Box Compaction **Tested by – Cody James-Johnson**
Master Curve: **Time-Temperature Shift Method**
Sigmoidal Model **:** **Williams-Landel- Ferry**

Volumetric Properties

Sample Density:	**2.397**	**Bitumen Content (by Weight)**	**4.3%**
Maximum Theoretical Density	**2.503**	**Volume of Bitumen**	**10.1%**
Solids	**95.8**	**Voids in Mineral Aggregate**	**14.4%**
Percent Air Voids	**4.2**	**Voids filled by Bitumen**	**70.4 %**

Aggregate Gradation

Sieve Size	Per Cent Passing	Mix Design
37.5mm	100	100
26.5mm	100	100
19.0mm	100	100
13.2mm	95	90 – 100
9.5mm	76	68 – 82
4.75mm	46	42 -54
2.36mm	34	30 – 40
1.18mm	26	22 -30
0.600mm	20	16 -24
0.300mm	14	10 -16
0.150mm	7.2	6.0 – 10.0
0.075mm	5.5	4.0 – 6.0

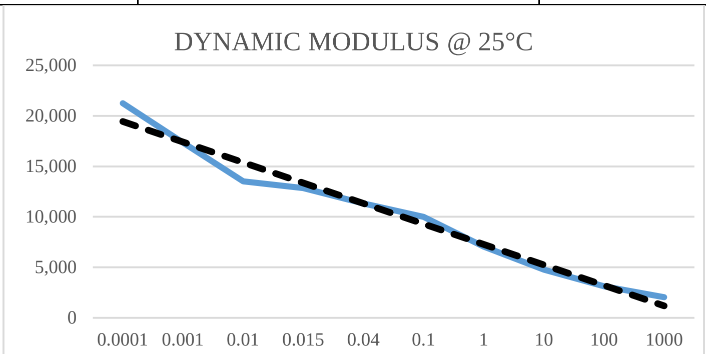

Properties

Shift Factor Type WLF

Temperature	5	10	20	30	40
alpha	2.324	2.331	2.597	2.342	2.317
beta	-1.814	-1.521	-1.096	-0.491	-0.026
gamma	0.316	0.315	0.299	0.315	0.316
delta	2.285	2.278	2.026	2.267	2.290

Performance

Temperature (°C)	Frequency (Hz)		Velocity (km /hr)	S Mix (MPa) Modulus |E*|
45	0.015	High	120	4,645
	0.04	Med	45	3,892
	0.01	Slow	18	3,290
30	0.015	High	120	9,975
	0.04	Med	45	8,640
	0.01	Slow	18	7,500
25	0.015	High	120	12,800
	0.04	Med	45	11,325
	0.01	Slow	18	9,980
20	0.015	High	120	17,090
	0.04	Med	45	15,430
	0.01	Slow	18	10,350

A STUDY RELATING SOLAR RADIATION, ROAD SURFACE TEMPERATURE AND TEMPERATURE AT DEPTH IN HOT MIX ASPHALT

John Yeaman[1],
[1]Queensland Pavement Centre, University of the Sunshine Coast, Australia;

ABSTRACT

Solar Radiation is a computable commodity, it is a function of a point on the earth's distance from the sun. For the past two years the Queensland Pavement Centre has been measuring Solar Radiation at a permanent monitoring station and comparing that with Road Surface temperatures every minute of every day. Some surprising results have been observed. It is postulated that Pavement Surface Temperatures increase by 5% for every Kilowatt per square metre of impact radiation, heat at twice the rate at which they cool during the hours of sunlight and emit heat beyond an equilibrium at the sun's zenith. Surface temperature will fall even though solar radiation is still impacting on the site. This data has been programmed into an asphalt calorimeter and temperature at depth in the pavement determined as a function of road surface temperature. These are all important factors when deciding on pavement design temperatures.

Keywords: Solar Radiation, Emissivity, Thermal Gradient in Asphalt

INTRODUCTION

Queensland, Australia is an area of diverse climatic conditions stretching from Latitude 28°South to Latitude 11°South (approximately 2000 km long) and Longitude 153° East to Longitude 138° East (approximately 1600 km wide) and covering 1,852,642 square kilometers . Queensland is larger than many countries of Europe. Climatic conditions, therefore can vary from moderate climate of South East Queensland to that of desert and tropical rain forest.

Hot Mix Asphalts (HMA) are designed principally with respect to the Number of Cycles to fatigue failure computed via a transfer function used throughout Australia: Reference [1]

$$\mathbf{N}= \left[\frac{6918(0.856Vb+1.08)}{S\,Mix^{0.36}\mu\varepsilon}\right]^{5} \quad (1)$$

Where N= the number of cycles of Equivalent Standard Axles
Vb = the volume of binder in the HMA
S Mix= the Stiffness of the Mix at a given temperature and time of loading
$\mu\varepsilon$ = the horizontal tensile strain at the base of the bound layer. It is important for pavement managers and design engineers to understand the temperature of the HMA at the critical depth in the pavement (the depth where strain is being measured) yet we adopt one value (the Weighted Mean Annual Pavement Temperature- WMAPT). The Queensland Pavement Centre at the University of the Sunshine Coast, Australia, installed a full pavement monitoring site and weather station on a collector road adjacent to the University Campus in May 2013. This site has been monitoring 14 pavement associated parameters minute by minute since that date.Of particular interest has been the effect of critical strains, with respect to temperature and moisture content, where it has been shown Reference [2] that there are both diurnal and seasonal variations impacting on the magnitude and nature of strain.

This study examines the impact of Solar Radiation on Road Surface Temperature and the subsequent impact on temperatures throughout the mix thickness. An example of Modulus' dependency on temperature follows (figure 1)

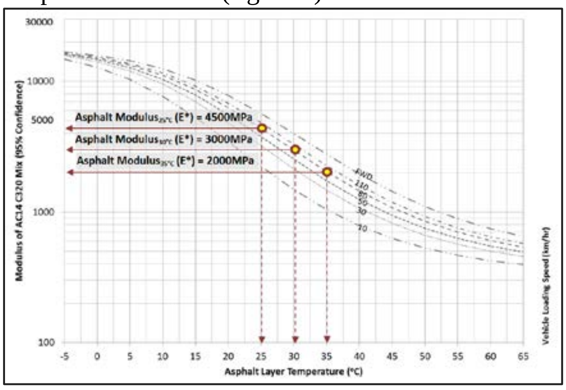

Figure 1 Modulus of Hot Mix asphalt as a function of temperature

Source: Supplement to the Austroads Pavement Design Guide, for Long Life Asphalt Pavement Design, AAPA, 2015)

THE SITE

Sippy Downs Pavement Monitoring Site, situated at Latitude 26° 43’23” South and Longitude 153° 05’02”East was initiated by Sunshine Coast Council. Sippy Downs Drive is a Sub-arterial connecting the Sunshine Coast Motorway to the Bruce Highway and was being upgraded to a 4 lane separated carriageway. The installation was to be part of that upgrade. The site is described elsewhere and consists of the following elements

Weather Station	**Air temperature**	**In Pavement**	**Horizontal Strain Gauge @ 75mm**
	Relative Humidity		**Vertical Strain Gauge @ 650mm**
	Atmospheric Pressure		**Thermocouple on Surface**
	Rainfall		**Thermocouple @ 75mm**
	Wind Speed		**Moisture Gauge @**
	Wind Direction		**Moisture Gauge @**
	Solar Radiation		**Camera**
Solar panels provide electrical energy			
Data are collected every minute, 24/7, and transferred dally at 6:am to the researcher’s computer			
The camera records a photograph of the road surface every day at 10:00 am and a photograph of any vehicle that exceeds a nominated strain level			

THE IMPACT OF SOLAR RADIATION ON ROAD SURFACE TEMPERATURE

Let us consider two different months June 2013 Early Winter, clear Sky. During the 11 hours 11 Minutes of sunlight (06:15 to 17:26) we have

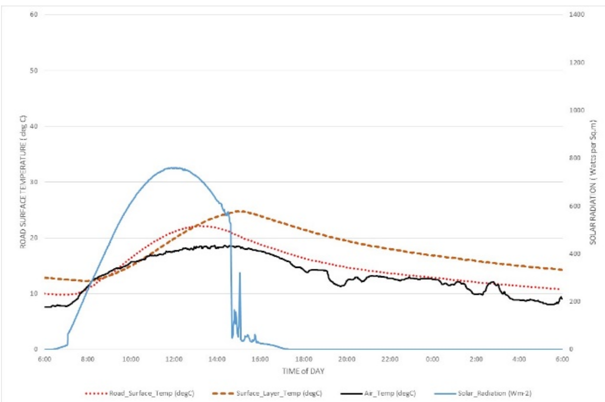

Figure 2 Radiation & Temperatures for 13 June 2013

From which the data can be summarized as follows :

Table 1 Comparison of Radiation & Road Surface Parameters for Mid-Winter

Radiation		Road Surface Temperature	
Maximum Value@ 11:58	760 Watts per Sq.m	Maximum Value @ 15:06	24.8°C
Quantum of Radiation	262,036	Area under Curve	11,577
MEAN	390 Watts per Sq.m	MEAN	18.7°C
Standard Deviation	299 Watts per Sq.m	Standard Deviation	4.2°C

Similarly for 26th December 2013 Mid-Summer - a hot cloudy day we have For the 14 hours 23 Minutes (04:36 to 18:59) of Sunlight to give:

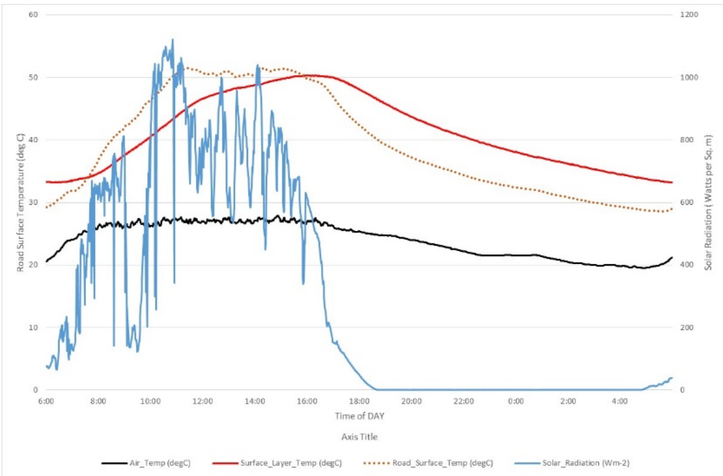

Figure 3 Radiation & Temperature for 26 December 2013 - Mid-Summer

From which the data can be summarized as

Table 2 Comparison of Radiation & Road Surface parameters for Mid-Summer

Radiation		Road Surface Temperature	
Maximum Value@ 10:51	1,122 Watts per Sq.m	Maximum Value @ 14:21	51.5
Area under Curve	409,014	Area under Curve	35,090
MEAN	524 Watts per Sq.m	MEAN	45.0°C
Standard Deviation	330 Watts per Sq.m	Standard Deviation	6.8°C

Table 3 Side by Side Comparison of Solar Radiation for a full year

Month	Radiation					
	Sunlight hours (h:min)	Maximum (Watts per m²)	@time (h:min)	Total for sunlight hours	Mean	Standard Deviation
May 13	11:22	902	12:35	268,837	390	304
June 13	11:11	760	11:58	262,036	390	299
July 13	11:20	845	12:09	175,672	258	197
August 13	11:49	892	12:02	350,594	493	323
September 13	12:15	1,203	11:13	356,406	492	347
October 13	12:20	1,050	12:04	128,400	173	138
November 13	12:37	1,139	12:33	463,505	612	377
December 13	12:59	1,121	10:51	409,104	524	330
January 14	13:06	1,571	12:41	307,571	393	291
February 14	12:44	1,033	12:03	375,266	491	379
March 14	12:17	1,345	12:25	321,820	437	356
April 14	11:43	1,125	12:08	284,315	404	318
May 14	11:14	992	10:59	184,607	273	243

Table 4 Side by Side Comparison of Temperatures for a full year

Month	Road Surface Temperature		
	Max.	Min	Difference
May 2013	27.1	15.1	12.0
June 2013	24.8	12.2	12.6
July	29.1	19.1	10.0
August	30.1	10.9	19.2
September	38.3	19.1	19.2
October	31.5	25.5	6.0
November	49.2	22.1	27.1
December	51.5	29.3	17.6
January	45.1	27.5	17.6
February	51.0	30.2	20.8
March	40.7	24.8	16.0
April	36.0	20.6	15.4
May	28.4	18.3	10.1

An analysis of the relationship between the impact of solar radiation on the road surface temperature is shown in figure 3 following

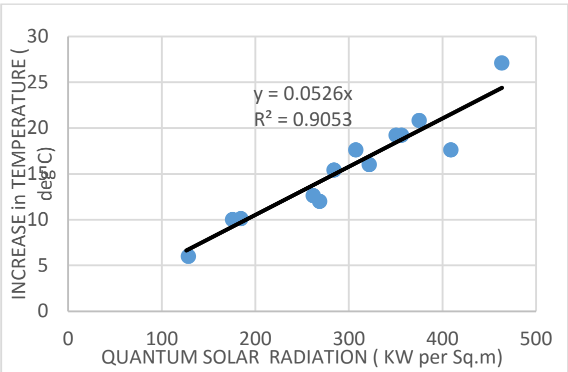

Figure 4 The impact of Solar Radiation on road Surface Temperature

From which we can derive the following hypothesis. It is important to note that this study is limited to a study of a site at Latitude 26° 45 S, Longitude 150 East, and this relationship may not hold for elsewhere in the world. It is however a good starting point and one from which it is expected other researchers will add to the knowledge.

Hypothesis

Road Surface Temperature increases by 5% for every Kilowatt per Square Metre of Solar Radiation at longitude 153° E.

HEATING & COOLING

An analysis of the road surface, during each diurnal cycle brought to light an apparent hysteresis loop between heating and cooling. From Table 3 (above) it can be observed that the hours of sunlight in winter are approximately 11 hours 11 minute compare with summer (December) where the hours of sunlight are close to 13 Hours. Over the same period the quantum of Impact Solar Radiation varies from 260 K Watts in June to over 400 K Watts in December.

Peak Radiation occurs around 12 to 12:30 each day whilst peak road surface temperature occurs anywhere between 11:00 am and 3:30 pm depending on the effect of cloud cover

Clearly there must be some period where the road surface is getting cooler even though solar radiation is still impacting on that surface.

Let us consider the Heating and Cooling effect for June and December 2013.

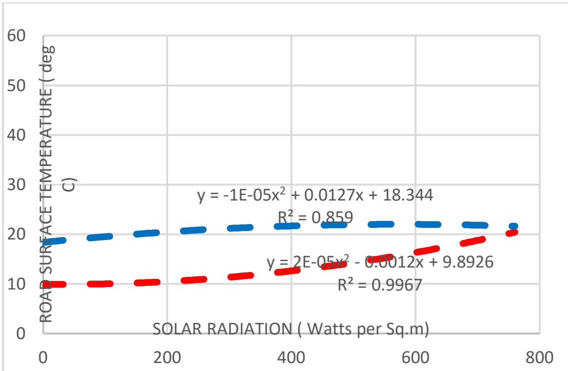

Figure 5 Effect of Solar radiation on Road Surface Temperature for June 2013

Here we can see that the road surface heats from around 10°C to 20°C, but then starts to cool even though there is some solar radiation input

If we look at the same conditions for December 2013 we see the same pattern, albeit a larger range of temperature and quanta of solar radiation

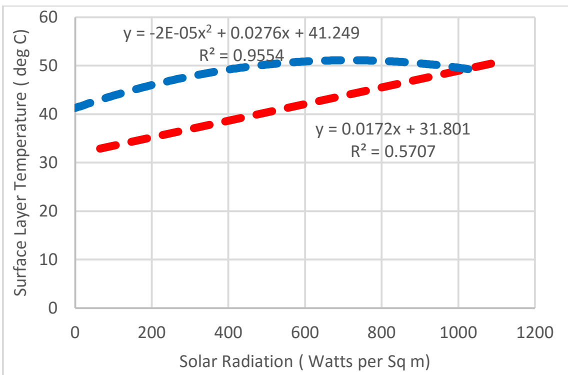

Figure 6 Effect of Solar Radiation on Road Surface Temperature for December 2013

Here we can see on the same scale that the magnitude of the results is much greater but that the shape of the curves are similar

Ratio of Heating & Cooling Results

The best way to consider the ratio of heating to Cooling in terms of solar radiation is to examine the rate of change by taking the first derivative of the trend equation. From above it will be observed that the trend equation is in fact a quadratic equation and the first derivative is in fact a function of the solar radiation. |If however we plot the relationship as a linear equation, which is close to the quadratic, then the slope of the equation of the form: $Y = mx+b$
Where m = the slope (or first derivative)
The following table lists the results for month by month for both the heating and cooling cycles

Table 5 Ratio of Heating to Cooling Cycles for Monthly Radiation & Temperature data

Month	Heating	Cooling	RATIO Heating to Cooling
May-13	0.0131	0.005	2.6
Jun-13	0.0142	0.0046	3.1
Jul-13	0.0123	0.0102	1.2
Aug-13	0.019	0.0085	2.2
Sep-13	0.0109	0.0072	1.5
Oct-13	0.003	0.004	0.8
Nov-13	0.0111	0.0122	0.9
Dec-13	0.017	0.01	1.7
The value of albedo	0.008	0.005	1.6
Feb-14	0.01	0.006	1.7
Mar-14	0.01	0.006	1.7
Apr-14	0.013	0.007	1.9
May-14	0.009	0.012	0.8
		MEAN	1.7

Hypothesis

During hours of Sunlight at Longitude 153°E road surface temperatures heat at twice the rate at which they cool.

DEFINITIONS OF APPLICABLE TERMINOLOGY

Albedo

The value for Albedo represents a reflected percentage of a surface when exposed to thermal radiation. The ratio of reflected thermal radiation is dependent on the material, its effective colour and texture. The coarse texture and dark colour of hot mix asphalt is typically low, however an asphalt surface changes to grey with time, which will impact on the Albedo value with time. Albedo is a factor of the theory of energy balance where Radiation in = Radiation out for an asphalt surface.

Emissivity

Emissivity is a factor for diffusion heat transfer within the pavement model and represents the effective radiation (out) emission properties. Understanding the emissive properties in a Hot Mix Asphalt is essential to understanding the incoming heat flow throughout a pavement and is required to model the temperature variation of conductivity.

Conductivity

Conductivity is an associated factor of diffused heat transfer within the pavement model, representing the heat flow through the material. Fourier's Law (1878) relates the change in temperature as a function of distance from the heat source, when heating is in a steady state condition. Here the heat flow in the reference direction is proportional to the thermal coefficient of conductivity. The conductivity coefficient of asphalt material will depend on the constitutive material, which in most cases will be the coarse aggregate. Therefore for Hot Mix Asphalt the pavement- depth relationship will vary according to the material composition.

Road Surface temperatures were charted against cumulative radiation during sunlight hours for the months of June (winter), September, April and December (summer) 2013 (Figure 6) from which it can be seen that there is a defined point of maximum road surface temperature. This maximum occurs between 11:30 am and 1:00 pm on each occasion i.e. the sun's zenith ± 1 hour. This time at a maximum is related to the amount of cloud cover at that time, given that at longitude 153°E the sun is at its zenith at 12:03.

Examination of this data indicates that at around midday, during any season, the HMA pavement is emitting heat at the same rate as it is being radiated by the sun. Road Surface temperature is now falling even though solar radiation is impacting on the surface. This is an important consideration when choosing a design temperature for the design of asphalt pavement thickness

Hypothesis

Road Surface temperature will reach a maximum value beyond which further irradiation by the sun will not produce higher temperatures

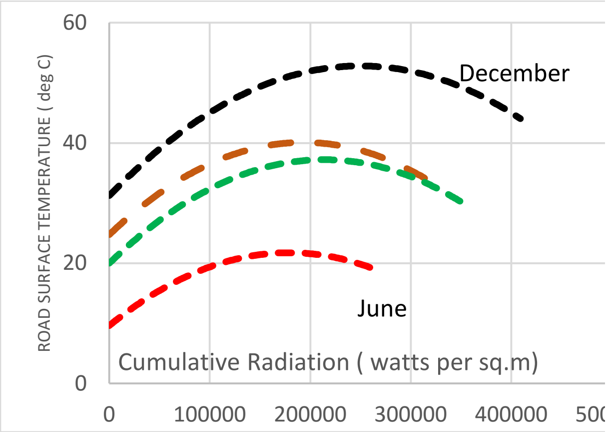

Figure 7 Comparison of Cumulative Radiation and Road Surface Temperatures June, April, September and December 2013

MEASUREMENT OF ASPHALT TEMPERATURE AT DEPTH

This information, compounded over 1 year, provided an impetus for the development of a method to measure the temperature at depth within an asphalt pavement, permitting the calculation of stiffness (modulus) and therefore the number of cycles to failure in the fatigue mode (equation 1) and figure 1. Gray (Reference [3] designed and built an asphalt calorimeter which enabled the determination of temperature at depth for any day in the year. He was able to establish a relation for temperature as a function of depth on a seasonally adjusted basis.
This data was then used Reference [5] to compare the thickness requirement for any asphalt (as characterised by the so called "Master Curve" Reference [4] for any specific location.
Gray has demonstrated (reference [4] savings in asphalt thicknesses, for the same criteria of 7% of thickness.
An extension of this work is recommended.

CONCLUSION

It must be understood that these conclusions refer to data from a specific site at Latitude 23°S, Longitude 153° E.
Further studies at other locations are being undertken to test the following hypotheses .
Researchers should add to this knowledge by evaluating these conclusions at different geographical locations
From this study it is concluded:

1. Road surface temperatures increase by 5% for every Kilowatt per square metre of impact radiation
2. A Hot Mix asphalt pavement will heat at twice the rate at which it cools
3. A heat transfer relation can be established in the laboratory using actual solar radiation data to determine temperature at depth for a specific Hot Mix Asphalt composition

REFERENCES

[1] Austroads "Guide to Pavement Technology- Part2 : Pavement Structural Design , 2008 pp 76

[2] Yeaman J, Yeaman S & Yeaman JW 2015 A New Look at Pavement Management a paper submitted to Fifth International Conference on Geotechnique, Construction Materials and Environment, Osaka, Japan, Nov. 16-18, 2015

[3] Gray C.J. , 2014 "the Development of a procedure to determine temperature of Asphalt at Depth" Final Year Thesis – University of the Sunshine Coast, Australia

[4] James- Johnson C, 2015 "Asphalt Laboratory compaction methods – Do they really impact the Master Curve?" – Proceedings 16th AAPA International Pavements Conference – Gold Coast , Australia

[5] Gray C.J 2015 "The Development of a Procedure to Determine Asphalt Temperature at Depth and Three Season Pavement Modelling - Proceedings 16th AAPA International Pavements Conference – Gold Coast , Australia

Fifth International Conference on Geotechnique, Construction Materials and Environment, Osaka, Japan, Nov. 16-18, 2015, ISBN: 978-4-9905958-4-5 C3051

EXPERIMENTAL STUDY ON THE EPS-BASED SHOCK ABSORBING MATERIAL FOR THE ROCK-SHED

Shen-Hsiang Hsu[1], Koji Maegawa[2], Li-Hsien Chen[3]
[1] Graduate student, Graduate School of Natural Science and Technology, Kanazawa University, Japan
[2] Faculty of Environmental Design, Institute of Science and Engineering, Kanazawa University, Japan
[3] Faculty of Department of Civil Engineering, National Taipei University of Technology, Taiwan

ABSTRACT

Shock absorbing material made of piled up expanded polystyrene (EPS) placing above the roof of the rock-shed was commonly used to advance the impact capacity against rockfall, but the required thickness increased with the rockfall energy and resulted in high construction cost and gradually led to the decrease of building amount. Though rock-net and rock-fence are widely applied to rockfall mitigation constructions in recent years, the rock-shed, which has characteristic of the highest rockfall energy resistance, is still irreplaceable. For this reason, a new type of EPS-based shock absorbing material that composed of two EPS-blocks, surrounded by cage wire netting, then a steel grid placed onto was tested under a series of static load and impact load tests in this study to make a rock-shed more cost effective and have better performance. Test results of static load test showed that the equipping of cage wire netting and the size of specimen contribute to 20% strength increase at the later stage, and force diffused more uniform due to the stiffness of the steel grid. And the results of impact load test indicated that the limit capacity of energy absorbing amount in the EPS-based shock absorbing material was around 490.0-627.2 kJ, which was 50% less than the empirical formula suggested by a rockfall mitigation code.

Keywords: Rockfall, Rock-shed, Shock absorber, EPS

INTRODUCTION

Rockfall is one of natural disasters that often occurs and strikes to the transportation routes and the underlying infrastructures in mountainous terrain. Despite usually impacting to small region, the rapid and occasional characteristic of rockfall often results in severe consequents of the same level as loss of lives induced by the other slope disasters. For this reason, various rockfall prevention and protection methods had been developed and increased rapidly in recent years, but the rock-shed, however, is still referred to as the most secure, reliable method due to its shelter-shaped structure and the highest rockfall energy capacity among all [1].

The rock-shed, a structure that is made up of reinforced concrete or shaped steel, is usually installed at steep slope area where the space alongside the road is insufficient to protect from direct rockfall, and is especially efficient against a rockfall of large energy. However, as the rock volume or falling height increases, enlarging the cross section of the rock-shed structure itself or gaining the thickness of the shock absorbing material on the roof above are some general ways to withstand higher rockfall impact, but the bulk volume also incurs high construction cost. On this condition, a more effective shock absorbing material of which having characteristics of easy installation, maintenance, and superior energy absorbing function is expected to be developed to lower the impact load from rock-fall, and to further reduce the cross section of the rock-shed to cut down the total construction cost.

To distribute and absorb an impact load of rock-fall, and consequently transmit a less impact load to the main structure of the rock-shed, a new type of shock absorbing material dominated by expanded polystyrene (also known as EPS) with combination of steel material is introduced in this study. The design of this EPS-based shock absorbing material is eager to promote the distribution effect by the stiffness of the steel material, to simplify the reconstruction work by the modular design, and to cut down the lifecycle cost by the reduction of material. Thus, a series of static load and impact load tests had been conducted to the EPS-based shock absorbing material to confirm the basic properties in this study.

COMPOSITION OF THE EPS-BASED SHOCK ABSORBING MATERIAL

EPS was generally used as a shock absorbing material on the roof of the rock-shed due to its light weight, easily deformed, and durable characteristics. However, despite having great advantage of shock absorption, the EPS material was still limited in load distribution effect. Furthermore, because of the joints implanted between EPS-blocks offered insufficient connection, EPS-blocks were easy to spread around while being impacted by rockfall. Thus, to improve those disadvantages, an EPS-based shock absorbing material has been developed. Figure 1 shows a basic unit of the EPS-based shock absorbing material, it is composed of two EPS-blocks, surrounded by cage wire netting (hereinafter referred to as framed EPS), piling up from 1 to 3 layers in a crisscross way, then a steel grid is placed onto the framed EPS. The adoption of steel grid here is used to widen the distribute range of impact load due to its great stiffness, whereas the cage wire netting is expected to connect several framed EPS together, and to offer better coverage to prevent EPS-blocks from spreading around while being impacted.

Configurations of the main components in the EPS-based shock absorbing material are listed below. EPS of which unit weight is 16 kg/m^3 is used and the size of an EPS-block is 2.0 m long, 1.0 m wide, and 0.5 m thick. A framed EPS approximately becomes the size of length 2.05 m, width 2.05 m, and thickness 0.52 m. The cage wire netting is made of 300 g/m^2 aluminum-zinc coating steel wires to withstand the natural corrosion and with size of 4.0φ-75×75. The steel grid is composed of several sheets of SS400 and steel bars and the size is 2.05 m long, 2.05 m wide, and 0.1 m high.

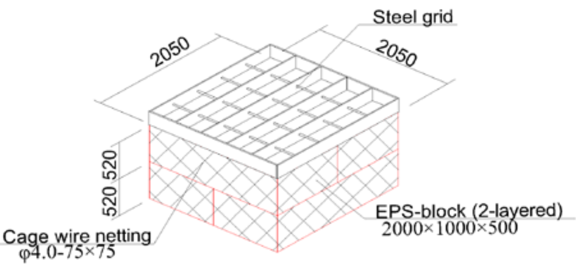

Fig. 1 A basic unit of the EPS-based shock absorbing material

OUTLINE OF THE EXPERIMENTS ON THE EPS-BASED SHOCK ABSORBING MATERIAL

Static Load Tests

Static load tests were carried out on the EPS-based shock absorbing material by using a testing machine loading at the center position of test specimens as shown in Fig. 2. Since a rockfall having weight of 1.0 ton has an equivalent diameter of about 0.9 m, a loading plate of 1.0 m in diameter was conservatively adopted.

Eight specimens of different composition were carried out and were categorized into three test series as shown in Table 1. Test specimens applied in series SE1 are framed EPS, but are different in piling layers. A steel grid is placed onto a framed EPS in series SE2 and a difference in this series is the number of layers of framed EPS. And in series SE3, an extra framed EPS is set in each layer, and a longer steel grid with size of 4.0 m long, 2.0 m wide, and 0.1 m thick is applied. The static load was applied through the loading plate and was gradually increased until EPS-block approached 80-90% strain, which regarded to be as the limit state in accordance with the former research [2].

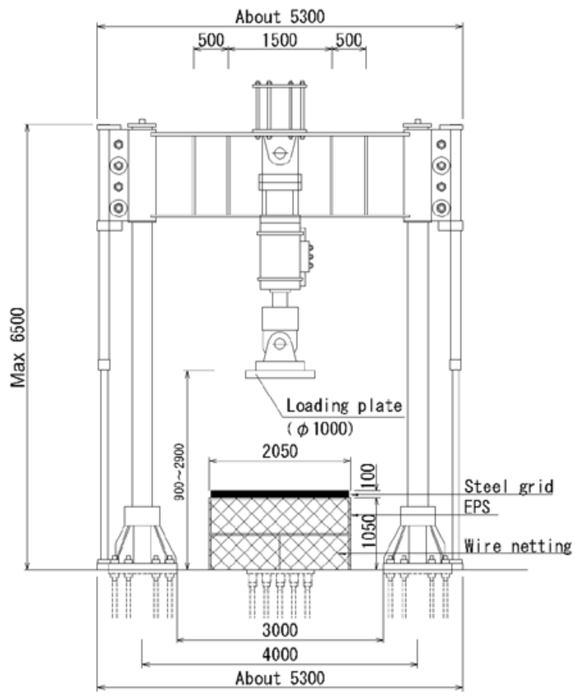

Fig. 2 Test method of static load test on the EPS-based shock absorbing material

Table 1 Static load test cases of the EPS-based shock absorbing material

Case No.	Composition of specimen	Layer of framed EPS	Remark
SE1-1	Framed EPS	1	1 framed EPS in each layer
SE1-2		2	
SE1-3		3	
SE2-1	Framed EPS & Steel grid	1	1 framed EPS in each layer
SE2-2		2	
SE2-3		3	
SE3-1	Framed EPS & Steel grid	1	2 framed EPSs in each layer
SE3-2		2	

Impact Load Tests

The shock absorbing material of pure EPS had been investigated under impact load tests so far [2]. In this study, the impact load test was carried out by dropping a block vertically onto a test specimen as

Fig. 3. On the other hand, Fig. 4 shows the specimen composed of framed EPSs which are assembled in a 3 by 3 way and piled up crisscross with two layers. Then six pieces of bolt-connected steel grids with each size of 2 m × 3 m are placed on the framed EPSs and a sand cushion of 0.5 m thick is set on the top of those steel grids to cut off the ultraviolet from sunlight which might do harm to the EPS material. Three impact load tests have been carried out on specimens of the same spec, but the applied impact energies are different as shown in Table 2, because the masses and falling heights of blocks are 2.5 ton-20 m, 3.2 ton-20 m, and 4.2 ton-25 m in cases No. DE1, DE2, and DE3, respectively. The block of which shape is specified in the guideline ETAG 027 [3] is used in the tests and made of reinforced concrete wrapped with steel plates.

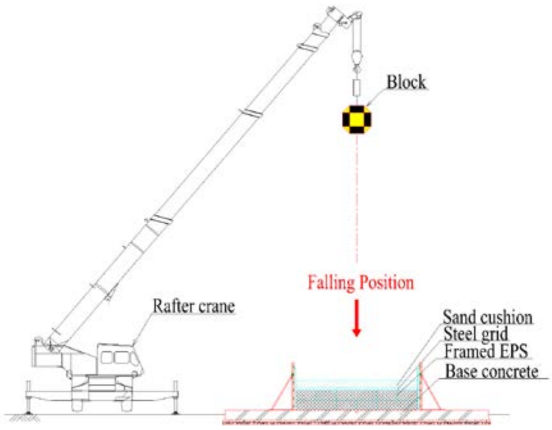

Fig. 3 Test method of impact load test on the EPS-based shock absorbing material

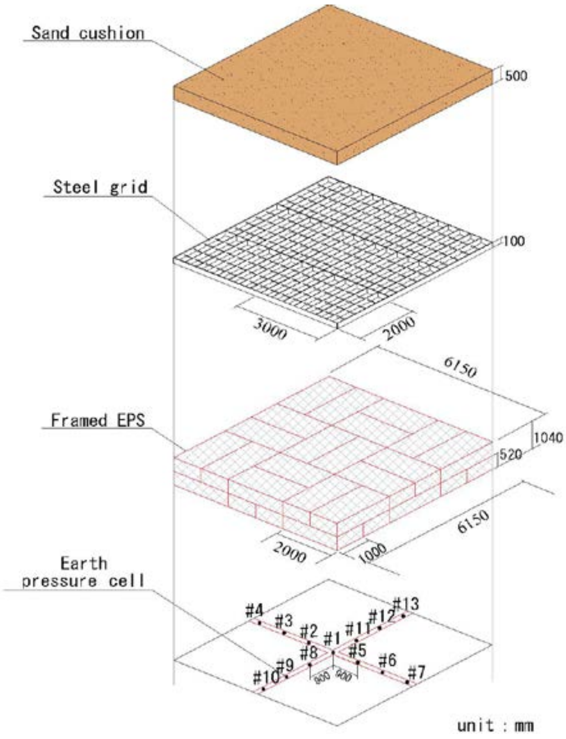

Fig. 4 Configuration of the specimen under impact load test

Table 2 Impact load test cases of shock absorbing material

Case No.	Block mass (ton)	Falling height (m)	Impact energy (kJ)
DE1	2.5	20.0	490.0
DE2	3.2	20.0	627.2
DE3	4.2	25.0	1029.0

Measurement

The main measuring item and measuring method in the static load test on shock absorbing material are listed below:

1. Load: measured by the load cell built inside the testing machine with hydraulic servomechanism.
2. Displacement: measured by the stretch of the stroke of the testing machine.
3. Deformation of steel grid: measured by a measuring tape.

Additionally, in the impact load test on shock absorbing material:

1. Acceleration of a block: a transceiver, a tri-axial accelerometer and an amplifier-recording device were set into the center of the block to receive a trigger signal and record the acceleration data at a sampling rate of 2 kHz.
2. Transmitted impact load to floor concrete: 13 earth pressure cells were set on the base concrete at 900 mm interval as shown in Fig. 4 and covered with sand layer of 50 mm thick.
3. Moreover, several normal and high speed video

cameras were set up in the front and the lateral sides to record the test condition.

RESULTS

The EPS-based Shock Absorbing Material under Static Load Test

Figures 5, 6, and 7 show the stress-strain relationships of test series SE1, SE2, and SE3, respectively, where the stress is obtained from dividing the applied load by a loading plate area of 1.0 meter in diameter. In addition, the stress-strain curve of a pure EPS-block with size of 80 mm long, 80 mm wide, and 160 mm high, which has been measured under a compression test, is also plotted as a dotted line for comparison.

Firstly, comparing the results of Pure EPS and the 1-layered framed EPS (case SE1-1) in Fig. 5, the tendencies of those two curves are similar, but the framed EPS has relatively weak stiffness at the early stage of loading due to the gap between the cage wire netting and EPS-block. However, after the cage wire netting is embedded into EPS-block in the test process, the stress of framed EPS slightly expands in elastic domain, and eventually is approximately 20% higher than that of Pure EPS at 70% strain. Hence we speculated that a cage wire netting might cause the difference of stresses between SE1-1 and Pure EPS, but the difference must be caused by the force diffused inside SE1-1 due to the specimen dimensions of SE1-1 being considerably larger than that of a loading plate. The reason is evident as follows.

After the tests of cases SE1-1 to SE1-3, a L_1=1100 mm diameter punching shear failure area was found on the top surface of the 1st framed EPS layer (counted from the top) in all cases as shown in Fig. 8. On the surface of the 2nd layers in cases SE1-2 and SE1-3, L_2=1600-1700 mm diameter deformation area were observed. And on the 3rd surface layer of framed EPS in case SE1-3, an entire smooth deformation was observed (L_3=2000 mm diameter). According to these results, the area changing between the layers were restricted by the boundary of the specimen among the 2nd and the 3rd layers, but an approximately 30 degree stress distribution angle which was the same as in the Pure EPS [2] could still be found in the framed EPS.

From Fig. 6 of test series SE2 for which a steel grid was placed onto framed EPS, the stresses in elastic domain increases about 4-5 times due to the high stiffness of the steel grid, and the strain in elastic domain becomes 10-20 %. On the other hand, the effect of piling amount of framed EPS is not obvious in SE2-2 and SE2-3 of Fig. 6 compared with test series SE1 of Fig. 5 because of the force spread sufficiently on the framed EPS owing to a steel grid. These facts are also clear from visual recognition. For example uniform deformation substituted for punching shear failure on each top surface of framed EPS and Photo 1b shows a continuous deformation in the entire EPS-based shock absorbing material, and is different from the discontinuous deformation result in series of SE1 (Photo 1a).

In test series SE3, the stress-strain curves in Fig. 7 show almost the same results with SE2. However, during the test, both longitudinal ends tilted and made discontinuous deformation (Photo 1c). The deformation area on the surface of framed EPS was about 2000 mm diameter, which indicate that steel grid extended about 1000 mm wider than the loading plate.

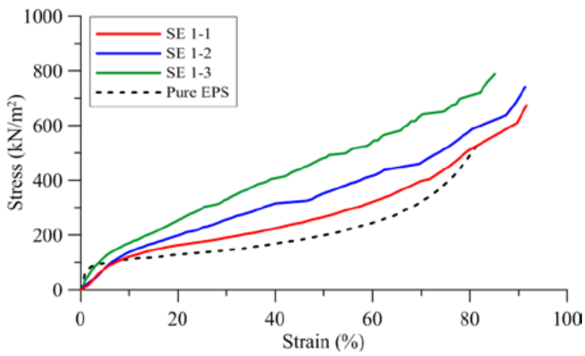

Fig. 5 Stress-strain curves of framed EPS and Pure EPS

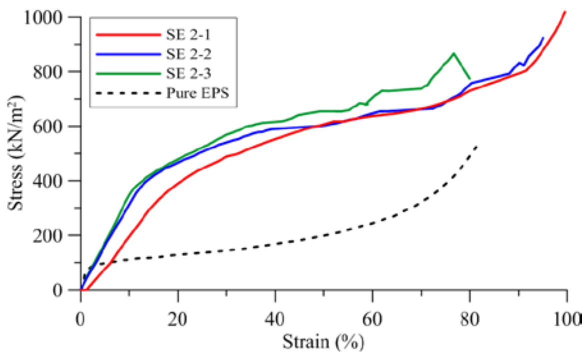

Fig. 6 Stress-strain curves of framed EPS with 2000mm×2000mm steel grid and Pure EPS

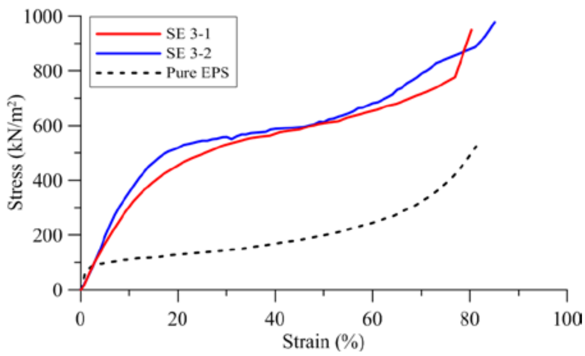

Fig. 7 Stress-strain curves of framed EPS with

2000mm×4000mm steel grid and Pure EPS

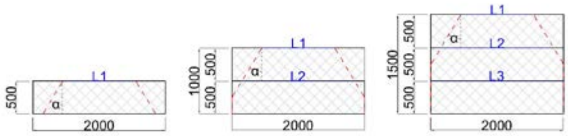

Fig. 8 Stress distribution inside framed EPS

(a) Case SE1-2

(b) Case SE2-2

(c) Case SE3-2

Photo 1 Loading condition of the EPS-based shock absorbing material

Table 3 Deformation range in each component of the EPS-based shock absorbing material

Case No.	Projected block area (m^2)	Deformation range (m2)											
		Sand cushion			Steel grid			Framed EPS (top layer)			Framed EPS (bottom layer)		
		L (m)	W (m)	A (m^2)	L (m)	W (m)	A (m^2)	L (m)	W (m)	A (m^2)	L (m)	W (m)	A (m^2)
DE1	1.16	2.0	2.1	4.2	2.3	2.3	5.3	2.0	2.0	4.0	2.0	2.0	4.0
DE2	1.37	2.2	2.3	5.1	2.2	2.9	6.4	2.0	2.0	4.0	2.0	2.0	4.0
DE3	1.64	2.9	2.9	8.4	3.5	3.4	11.9	2.0	2.0	4.0	2.0 (0.8)*	2.0 (1.0)*	4.0 (0.8)*

L=length, W=width, A=area, ( )*=range of local failure

The EPS-based Shock Absorbing Material under Impact Load Test

Table 3 shows the deformation range of each component in shock absorbing material. After a block falls to the specimen, the impact load is transmitted to the base concrete through a sand cushion, a steel grid, and two framed EPS layers orderly. The data show that the expansion of deformation range becomes wider in order of a block, a sand cushion, and a steel grid, but then reduces to 4 m^2 at both two layers of framed EPS. This indicates that most of the load concentrated in a limited range around impact location, then caused plastic deformation to the framed EPS. Additionally, a local failure of 0.8 m^2 deformation range was found at the surface of the 2^{nd} layer of framed EPS in case DE3.

For the data measured by the accelerometer and earth pressure cells, two quantities are defined as follow. (1) Impact load: acquired from multiplying block mass by block acceleration. (2) Transmitted impact load: acquired from the integration of earth pressure. A combination of load and time curves of cases DE1 to DE3 are shown in Fig. 9, where the solid curves represent impact load and the dotted curves represent transmitted impact load. Here, t=0 is the moment that a block comes in contact with the surface of the sand cushion.

For the impact load and time curves in Fig. 9, about two waves are found in each case. The first wave begins at t=0, reaches to the peak at t=6 ms, and ends at t=10-20 ms. The second wave begins at t=20-30 ms, reaches to the peak at t=70-90 ms, and ends approximately at t=150 ms. Thus the duration of the second wave is much longer than the first wave, which means the shock absorption function mainly operate in this period. Moreover, the entire waveforms of cases DE1 and DE2 are similar, both the maximum impact loads occur at the first wave which valued 985.2 and 1052.9 kN respectively, as shown in Table 5. But in case DE3, the maximum impact load 1644.5 kN appears at the moment of maximum penetration depth in the second wave. It is supposed that the local failure has occurred on the surface of the 2^{nd} layer of framed EPS due to the limit state of the material. However, comparing the EPS-based shock absorbing material with a 90 cm-thick sand cushion which commonly used on the roof of the rock-shed in the past [4], a theoretical impact load equation is adopted [1]:

$$P_{max} = 2.108 \cdot (m \cdot g)^{\frac{2}{3}} \cdot \lambda^{\frac{2}{5}} \cdot H^{\frac{3}{5}} \cdot \alpha \quad (1)$$

$$\alpha = (T/D)^{-0.5} \quad (2)$$

where P_{max}, m, g, λ, H, T and D represent impact load [kN], mass of a block or a falling rock [t], gravitational acceleration [m/s^2], Lame's constant [kN/m^2], falling height [m], thickness of sand cushion [m], and diameter of a block [m], respectively. Lame's constant equals to 1000 kN/m^2 while using a soft material such as sand cushion. Besides, the overdesign factor α should be considered in the circumstances that the equivalent diameter of a block is greater than the thickness of the sand cushion. Applying the block mass and falling height conditions of 2.5 ton-20 m, 3.2 ton-20 m, and 4.2 ton-25 m from cases DE1 to DE3, the results of the theoretical impact load are 1977, 2429, and 3483kN in case of the thickness of 90 cm of the sand cushion which is doubly greater than that on the EPS-based shock absorbing material.

And for the transmitted impact load and time relationships in Fig. 9, the curves start early with the increase in block mass: t=18, 15, and 6.5 ms in cases DE1, DE2, and DE3, respectively. Furthermore, the maximum transmitted impact load 718.7, 1263.0, and 2959.1 kN listed in Table 4 are observed at about t=90 ms in all cases. As a result, the falling energy around 490.0-627.2 kJ is speculated to be the limit capacity that the shock absorbing material could still remain its function.

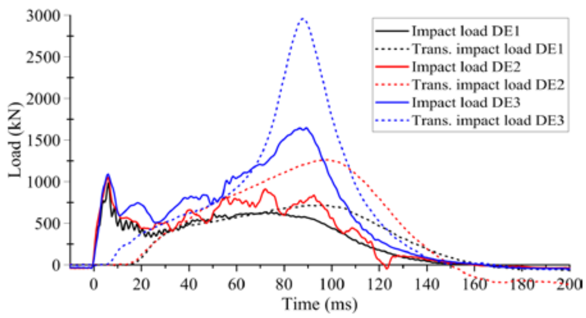

Fig. 9 Load-time curve of block impact

Table 4 Results of impact load test

Case No.	Maximum impact load (kN)	Maximum transmitted impact load (kN)
DE1	985.2	718.7
DE2	1052.9	1263.0
DE3	1644.5	2959.1

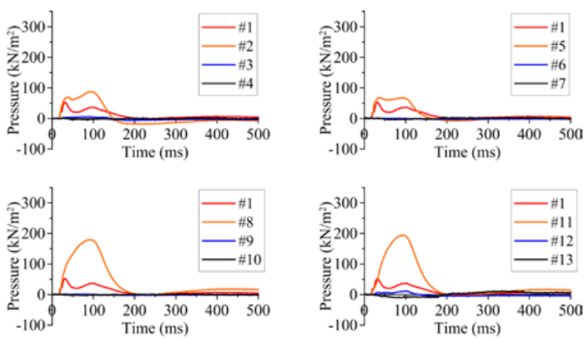

Fig. 10 Earth pressure in case DE1

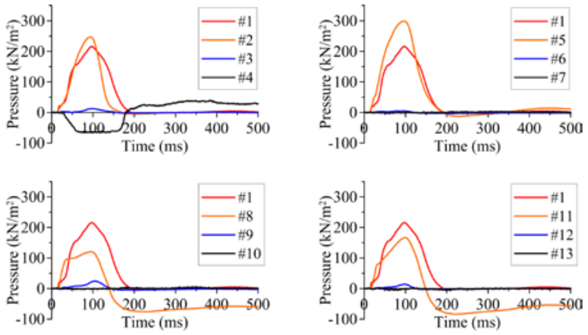

Fig. 11 Earth pressure in case DE2

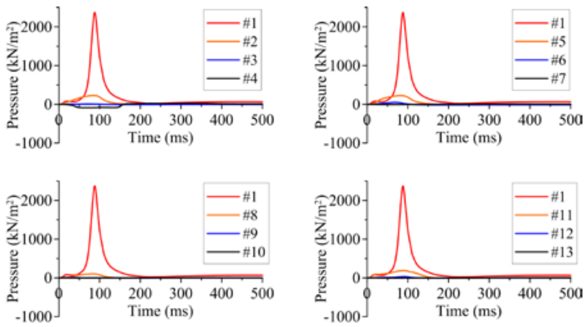

Fig. 12 Earth pressure in case DE3

The arrangement of earth pressure cells are shown in Fig. 4, and the measured earth pressure in each case are shown in Fig. 10, 11, and 12. Since the block impacted at the center of the specimen, the maximum earth pressure is supposed to be detected by the center earth pressure cell #1. But in fact, the location of earth pressure cell #1 was exactly beneath the interface of two EPS-blocks inside a framed EPS, which may have received insufficient earth pressure, such as the results appear in cases DE1 and DE2 (Fig. 10 and Fig. 11). But in case DE3, the earth pressure is significantly large in earth pressure cell #1. It is speculated that a 0.8m^2 local failure area on the surface of the 2nd layer of framed EPS could induce stress concentration, and the range of stress concentration contains only earth pressure cell #1.

CONCLUSION

The experiment results of static and impact load tests on the EPS-based shock absorbing material are listed below.

1. The stress measured in the framed EPS was approximately 20 % greater at 70 % strain than in Pure EPS in this study. The adoption of wire netting might made influence on that result, but we speculated that it was mainly cause by the dimensions of the framed EPS being

considerably larger than that of a loading plate.

2. The force spread sufficiently on the framed EPS owing to the placing of a steel grid, and the stress increased about 4-5 times in elastic domain of the EPS-based shock absorbing material.
3. The limit capacity of energy absorbing amount in the EPS-based shock absorbing material was around 490.0-627.2 kJ.
4. The impact load on the EPS-based shock absorbing material was 50% less than the empirical formula suggested by a rockfall mitigation code.

ACKNOWLEDGEMENTS

Special thanks to Raiteku Company and the relevant partners for the cooperation and all kinds of support during these tests.

REFERENCES

[1] Japan Road Association, "Rockfall Mitigation Handbook (in Japanese)", Maruzen, 2000.

[2] Yoshida H., Fujii T., Minami K. and Maegawa K., "Experimental Study on Shock Absorbing Characteristic of Reinforced Expanded Polystyrol against Falling Rocks (in Japanese)", Proceedings of the Symposium on Impact Problems in Civil Engineering, Vol. 4, pp.6-11, 1998.

[3] ETAG 027, "Guideline for European Technical Approval of Falling Rock Protection Kits", European Organisation for Technical Approvals (EOTA), 2000.

[4] Kishi N., Nakano O., Matsuoka K. and Nishi H., "Field Test on Absorbing Capacity of Sand Cushion (in Japanese)", Journal of Structural Engineering, Vol. 39 A, pp.1587-1597, 1993.

Fifth International Conference on Geotechnique, Construction Materials and Environment, Osaka, Japan, Nov. 16-18, 2015, ISBN: 978-4-9905958-4-5 C3051

A STUDY FOR SEISMIC IMPROVEMENT OF CONCRETE FRAME WITH PERFORATED WALLS
A CASE OF A STAIRCASE WITH GIRDERS AND SLABS AT MID-STORY

Ryota Ishii[1], Tetsuya Ohmura[1]
[1]Graduate School of Engineering, Tokyo City University, Japan

ABSTRACT

The Japanese building standard act was revised in 1981 considered non-linearity. However, a number of buildings built before 1981 are existing, seismic evaluations for those building have actively been assessed based on the seismic evaluation standard published by The Japan Building Disaster Prevention Association after especially 1995 Kobe Earthquake. In practical seismic evaluation works, it is relatively simple and easy to make models of general buildings, but unconventional frames are complex such as a staircase or a frame with different level girders. A perforated concrete wall is modeled as a shear wall, if the opening ratio is 0.4 and less. On the other hand, one with more than the opening ratio of 0.4 is modeled as a column with a wing wall. The modeling concept is simplified to smoothly assess the seismic performance of a building even though it is not confirmed that the models is suited to their actual behavior. In this paper, FE analyses were performed, and their results were examined. Finally, partially closing the openings down to an opening ratio of at least 0.4 is recommended because seismic slits could fail to work well.

Keywords: Wall with openings, Lateral force resist mechanism, Ratio of openings, Compressive strut

INTRODUCTION

The Japanese building standard act was revised in 1981 considered non-linearity. However, a number of buildings built before 1981 are existing, seismic evaluations for those buildings have actively been assessed based on the Seismic Evaluation Standard [1] published by The Japan Building Disaster Prevention Association after especially 1995 Kobe Earthquake. This standard takes the strength and ductility into account and defines three grades of seismic assessments to evaluate the seismic index. The modeling for columns and walls is extremely important in particularly the second grade of the seismic evaluation often taken, because the girders are assumed as rigid, and the strength and ductility of columns and walls directly influence on the seismic index.

This standard also corresponds to diversified buildings. However, for a frame of such as a staircase with beams located mid-story, the modeling concept depends on a judgment by an engineer.

In practical seismic evaluation works, it is relatively simple and easy to make models of general buildings, but when dealing with unconventional frames such as staircases or a frame with different level girders as mentioned above, it is much more complex.

First of all, the ratio of opening for a perforated wall should be calculated based on the standard. The ration of openings is defined as the square root of the openings area divided by the wall area as follows

$$r_0 = \sqrt{\frac{\sum h_i \cdot l_i}{h \cdot l_w}} \tag{1}$$

where r_o *is* the ratio of opening; h_i and l_i are the height and width of the opening; h is the height of the story; l_w is the bay.

A perforated concrete wall is modeled as a shear wall, if the opening ratio is 0.4 and less. On the other hand, one with more than the opening ratio of 0.4 is modeled as a column with a wing wall. The modeling concept is simplified to smoothly assess the seismic performance of a building even though it is not confirmed to be suited to their actual behavior. However, in order to secure the flexible length for seismic improvement, a seismic slit is often located at the edge of a column or a window in a practical seismic improvement work.

In this paper, an actual frame with a perforated wall was modeled and FE analyses were performed. To be compared with the original model, also three models with seismic slits mentioned above were analyzed.

FRAME PROPERTIES

Fig.1, 2 and 3 show the focused frame in a three-story concrete school building built in 1973. The seismic index of 1st , 2nd and 3rd story was respectively 0.53 , 0.40 , 0.84 in the longitudinal direction, and more than 1.0 in every story in the span direction. Some mullion walls and spandrel walls located between the columns 1 to 2 in Fig.1

were ignored when the frame was modeled, because only the behavior of the perforated wall located between columns 3 to 4 in Fig.1 should be focused.

The building was damaged by the 3.11 earthquake. The cracking condition is shown in Fig.1. The crack width without any note was 0.3mm. Diagonal cracks were observed at around the edge of openings. 20.7 N/mm^2 of the concrete strength was assumed in the models, because the effect of the concrete strength difference in each story should be eliminated at first in this paper.

The wall had 120mm of thickness and 9mm of longitudinal and transverse rebar with 200mm space. The orthogonal frame were ignored.

MATERIAL PROPERTIES IN THE ANALYSIS

Material properties in the analysis is shown in Fig.4. Parabolic model for a compressive concrete, the Hordiji's model for a tensile concrete and Von Mises criterion were adopted. Rebars were modeled as a bi-liner model with perfect bond.

ANALYSIS

The model is shown in Fig.5. A four nodes and quadrilateral isoparametric plane stress element was applied to concrete meshed about 100mm square. Longitudinal rebar in columns and girders was embedded and only axial stress was considered. All rebar in wall and the transverse rebar in columns and girders was smeared and layered.

Table 1 shows analysis models and Fig 6 shows slits location. Model #1 has no slit. Model #2 has *1 of the slits at the edges of the windows as shown Fig.6. Model #3 has *2 of slits at the edges of the columns as shown Fig 6. Model #4 has *2 and *3 of slits. The lateral force from the left to the right was applied for Model #1 to #4 and that from the right to left for Model #1(－) to #4(－).

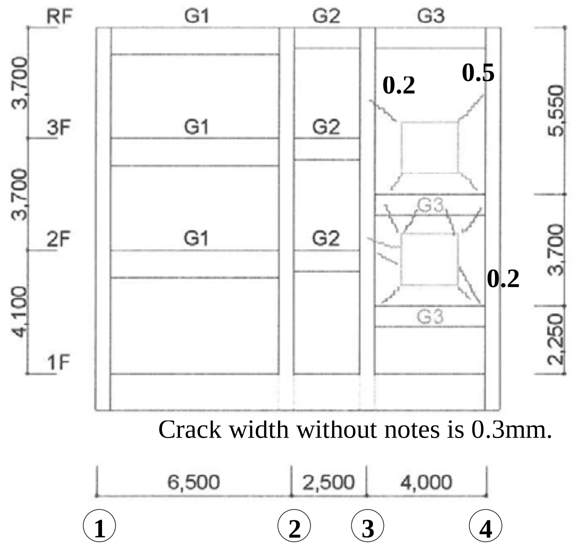

Fig.1 Elevation and crack patern damaged by 3.11 EQ

Section	500 × 500
Rebar	10-D22
Hoop	□-9φ @100

	$_2G_1$	$_2G_2$	$_2G_3$
Section	900 × 300	700 × 300	700 × 300
Upper	4-D19	5-D19	4-D22
Lower	4-D19	3-D19	2-D22
STP	□ -9φ @200		

Fig.2 Column and girder

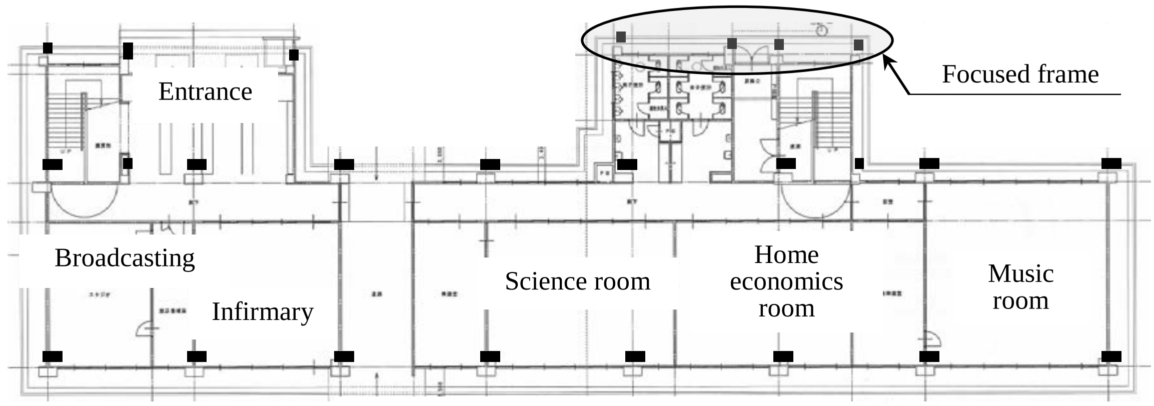

Fig.3 Plan

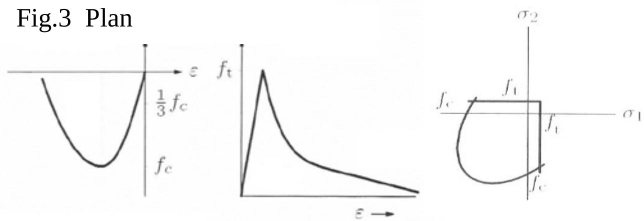

(a) Compression (b) Tension [3] (c) Criterion

Fig.4 Concrete model [2]

Table 1 Models

No.	Slit	Loading direction
#1	N/A	Left to right
#2	At windows (*1)	
#3	At left columns (*2)	
#4	At both columns (*2 and 3)	
#1 (−)	N/A	Right to left
#2 (−)	At windows (*1)	
#3 (−)	At left columns (*2)	
#4 (−)	At both columns (*2 and 3)	

*1 , *2 and *3 are indicated in Fig.7

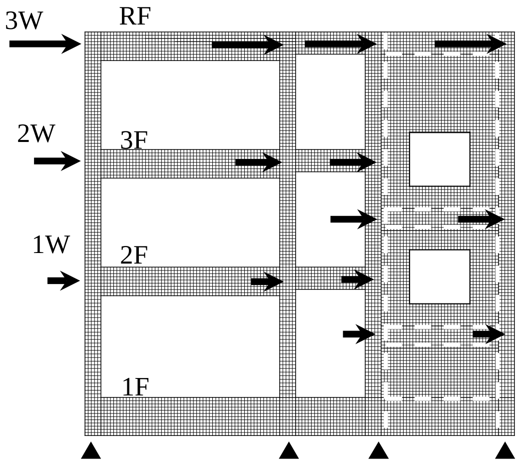

Fig.5 Mesh and lateral load

The lateral forces was applied to the each slab. The amount of the lateral force depend on their rule floor area and the lateral force distribution factor was 3, 2 and 1 respectively. In addition, 12kN/m2 of the gravity load was applied at first. The foundation girders were supported by pin supports and the uplifting of the foundation girders wasn't taken into account.

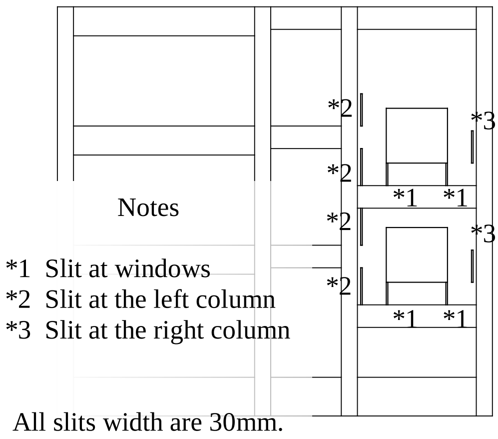

Fig.6 Slit plan

BASE SHEAR FORCE AND WHOLE DRIFT

Fig.7 shows the base shear force and whole drift of Model #1 to 4. The whole drift was calculated by the lateral displacement divided by the height of the center of the roof girder. The maximum base shear force of Model #1 which had no slit was the largest and the others showed approximately the same base shear force. About 20% of the maximum base shear force reduction was shown because of the effect of their slits. On the other hand, the difference of the maximum base shear force between #2 to 4 which had slits was extremely small value. Therefore, it could be considered there is only a slight effect of the slit pattern difference.

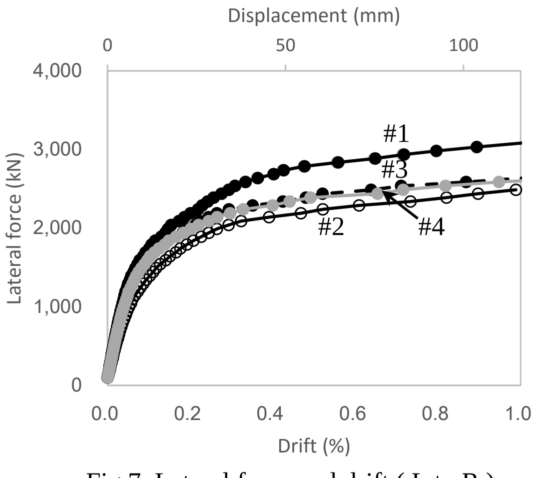

Fig.7 Lateral force and drift (L to R)

Fig.8 shows the base shear force and whole drift of Model #1(−) to #4(−) which from the right to the left of lateral force were applied. The maximum base shear force of #1(−), #3(−) and #4(−) were approximately the same. In other words, the effect of the slits at the edges of the columns is extremely small. In addition, about 13% of the maximum base shear force reduction was shown because of the effect of the slits at the edges of the windows.

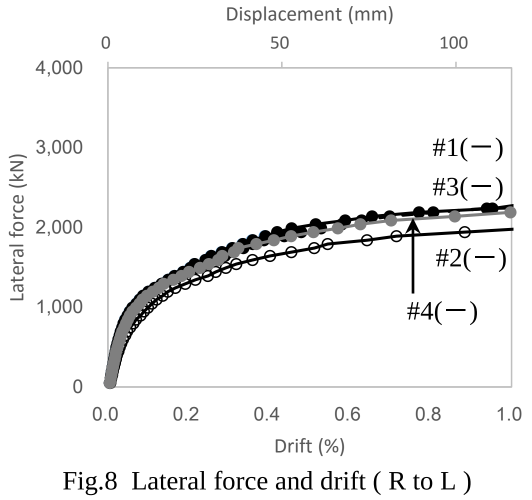

Fig.8 Lateral force and drift (R to L)

Fig.9 shows the comparison of the difference of the lateral force direction. The maximum base shear

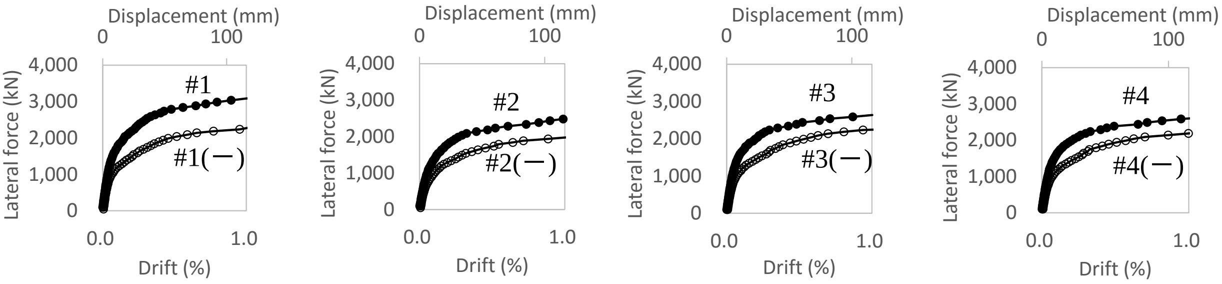

(a) #1 and #1(−) (b) #2 and #2(−) (c) #3 and #3(−) (d) #4 and #4(−)

Fig.9 Lateral force and drift (L to R)

force in the model which from the left to the right lateral force was applied is larger than that in the model which the backward lateral load was applied in all comparisons.

The maximum difference of the maximum base shear force was 26% between Model #1 and #1(−) as shown Fig.9 (a).

When slits were put into a perforated wall, the stiffness and strength should be appropriately evaluated, because the seismic evaluation of the whole building depends on the stiffness and the lateral strength of the frame with perforated walls. And the maximum lateral strength could be not the same as one under the backward lateral load.

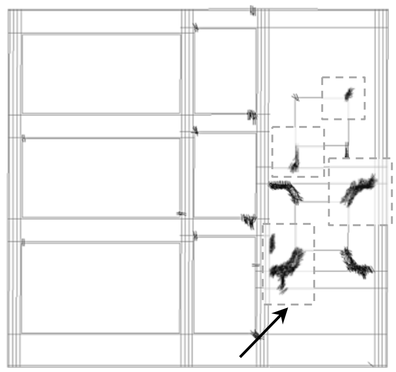

At −0.04%

Fig.10 Crack strain vector at 0.04% drift

CRACK STRAIN VECTOR

Fig.10 shows the crack strain vector at 0.04% of drift of Model #1 and #1(−). The range of dash lines shows the result of Model #1(−). The crack strain vector in our analysis was observed at the edges of the windows and similar to the crack observation damaged by 3.11 as shown Fig. 1. Our analysis result of this showed approximate good agreement with the crack observation.

Generally, in a seismic evaluation based on the Seismic Evaluation Standard, a perforated wall with over 0.4 of opening ratio is modeled as a column with wing wall having a flexible length as shown Fig.11.

The modeling concept is simplified to smoothly assess the seismic performance of a building even though it is not confirmed that the models is suited to their actual behavior, since the ground for the research and test data is insufficient.

Therefore, the flexible length as shown Fig.12 should be improved in a seismic evaluation. We suggest that a perforated wall with over 0.4 of opening ratio should be modeled as not a column with wing walls but a perforated wall with low stiffness and strength.

On the other hand, girders are ignored in the second grade of the seismic evaluation based on the Seismic Evaluation Standard. If seismic slits would be located at the edges of columns, the flexible length would be long in the same as Model #2. In addition, also a girder damage evaluation could be ignored even though the girder would be significantly damaged at the edge of seismic slits. It is caused by spandrel and hanging walls with the slits at the edges of openings.

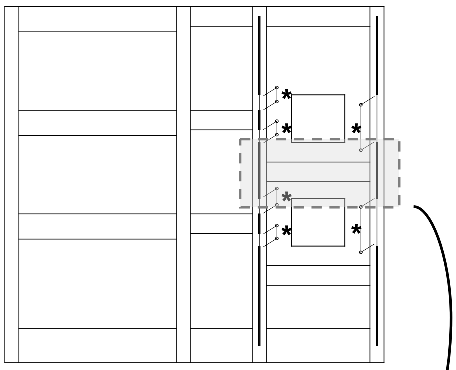

Fig.11 Flexible and rigid length

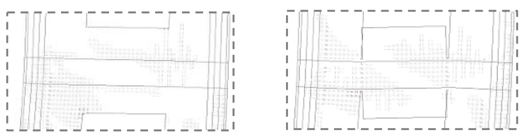

(a) #1 (0.4%) (b) #2 (0.4%)

Fig.12 Deformation

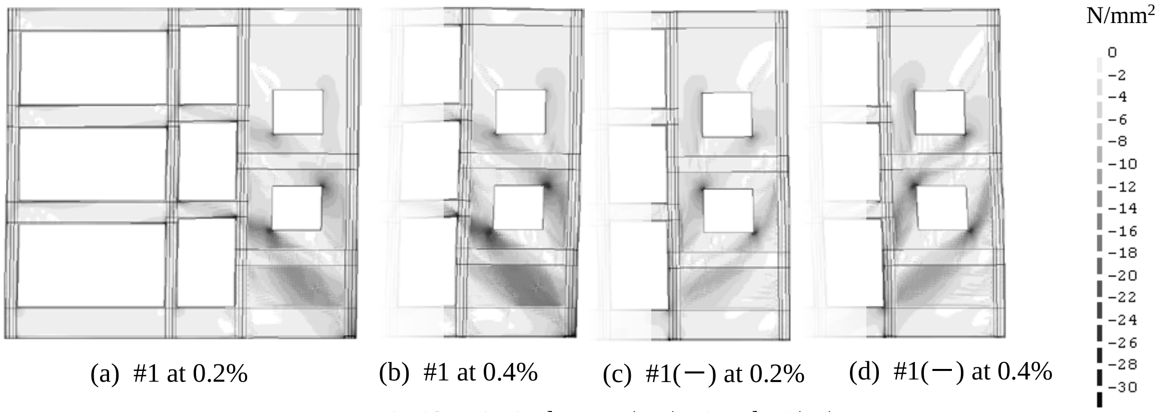

(a) #1 at 0.2% (b) #1 at 0.4% (c) #1(−) at 0.2% (d) #1(−) at 0.4%

Fig.13 Principal stress (σ_2) #1 and #1(−)

PRINCIPAL STRESS

Fig.13 shows the compressive principal stress distribution of Model #1 with no slit. The flexible length based on the compressive principal stress distribution shown in Fig.13 is similar to a general perforated wall than the assumed flexible length shown in Fig.11.Although the opening ratio is more than 0.4, the concrete compressive struts were formed. It showed lateral force was transmitted in the diagonal direction.

As mentioned above, the flexible length as shown Fig.11 should be improved in a seismic evaluation, and a perforated wall with over 0.4 of opening ratio should be modeled as not a column with wing walls but a perforated wall with low stiffness and strength in view of the results in this chapter.

In case of a concrete frame with different level girders such as the models in this paper, the stiffness, strength and damage should be properly evaluated, because the compressive principal stress distribution diagram in the positive was different from one in the negative.

Fig.14 shows the compressive principal stress distribution of Model #2, 3 and 4. As shown Fig.13(b), the concrete compressive struts were formed, however, slits prevent from forming a diagonal compressive strut such as Fig.14(b) in Model #1 with no slit, because the slits were located to interrupted the diagonal compressive strut.

In addition, even if slits were located to lengthen the flexible length of the column, only two columns enclosed by the dot line expectedly deformed as shown Fig.14(b) and (c). Therefore, the slits in this models didn’t work not effectively and unexpectedly.

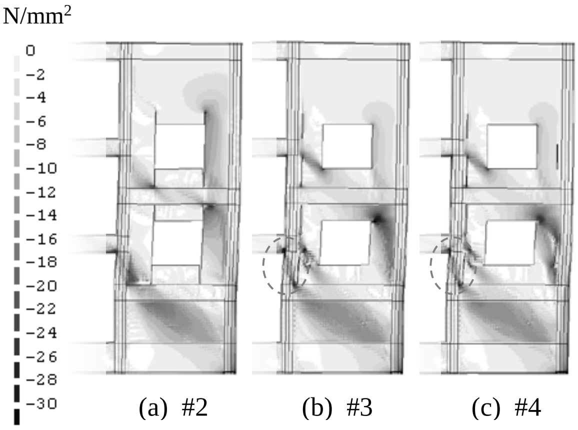

(a) #2 (b) #3 (c) #4

Fig.14 Principal stress (σ_2) at 0.4%

CONCLUSION

In case of a concrete frame with different level girders and symmetric openings such as the models in this paper, the stiffness, strength and damage should be properly evaluated, because the hysteresis curve and the compressive principal stress distribution diagram in the positive was different from one in the negative.

In a seismic improvement, not only seismic sits location planning but also the damage of girders at the edges of the slits should be examined when slits would be located at windows, because the damage would be concentrated to the both end of the seismic slits.

Closing the openings down to 0.4 of opening ratio is recommended based on the improving ways in the seismic evaluation standard, because the seismic slits would work unexpectedly and the strut forming was obstructed in the models with seismic slits.

REFERENCES

[1] Japan Building Disaster Prevention Association (2001), Seismic Evaluation Standard and Commentary for Existing Concrete buildings

[2] Diana User’s Manual (2002), Material Library

[3] Hordiji, D.A. (1991), Local approach to fatigue of concrete, PhD thesis, Delft University of Technology

Fifth International Conference on Geotechnique, Construction Materials and Environment, Osaka, Japan, Nov. 16-18, 2015, ISBN: 978-4-9905958-4-5 C3051

EVALUATING CONCRETE PROPERTIES USING RECYCLED GLASS SAND FOR RIGID PAVEMENT APPLICATIONS

Hadi Khabbaz[1], Abraham Khoury[2]
[1,2]School of Civil and Environmental Engineering, University of Technology Sydney (UTS), NSW, Australia

ABSTRACT

This study investigates the influence of using recycled glass as part of fine aggregates on the performance of pavement concrete. The properties of fresh and hardened concrete included recycled glass are compared to a control mix design not containing any glass sand. Hence, trends in concrete performance associated with different fine aggregate replacement by incorporating recycled glass are studied to verify the optimal glass replacement content in rigid pavement base mixes. The findings of this project indicate that using recycled glass sand in rigid pavement applications can yield not only more sustainable concrete at a 40% replacement content, but also induce improvements in drying shrinkage behaviour and concrete workability. The neutral effects of glass sand on air entrainment and marginal reductions in hardened concrete properties yielded from this study further supports the use of glass sand in this type of application.

Keywords: Recycled Glass Sand, Rigid Pavement, Drying Shrinkage

INTRODUCTION

Concrete can be viewed as a non-sustainable building product due to its reliance on incorporating non-renewable raw material components in its production process. The reality is that, "concrete is the world's most used construction material: over 25 billion tons of concrete are used worldwide each year, and this number continues to increase"[1]. The major components of basic concrete are sand, aggregates, water and cement. Aggregates are usually quarried materials from the earth's surface. The fact that the earth contains a finite amount of suitable aggregate sources with desirable properties for concrete production highlights its limited capacity to serve infinite concrete production for future generations. Cement production also heavily rely on the use of non-renewable resources in its production process. According to CCAA [2], limestone, clay, shale and sand represent the main raw materials required for cement production. Such raw feed is available in limited quantities, possibly restricting the production of cement in the future.

The rising difficulties associated with escalating carbon dioxide emissions and the increasing demand for more sustainable building solutions are concurrently placing pressures on the concrete industry to amend traditional concrete mix design practices. Concrete manufacture is not only profoundly reliant on the use of earth's scarce resources, but also an intensive energy process leading to the generation of undesirable greenhouse gases. Such characteristics define the unsustainable nature associated with traditional concrete manufacture. Researchers [3], [4] have investigated the fine aggregate replacement with waste materials such as recycled glass or crumb rubber.

The utilization of post-consumer glass in concrete manufacture is another industry initiative to promote concrete sustainability. There is an estimated 75,000 tonnes of crushed glass fines in New South Wales (NSW) [5] that is available for use in concrete production. Initially, such glass waste was intended to be disposed of in landfills. However, the potential to incorporate such by-product glass waste in concrete production has depicted the potential alternative application of waste glass products [6]. Waste reduction and recycling are very important elements in a waste management framework because they help to conserve natural resources and reduce demand for valuable landfill space [7].

Boral Australia, the Australia's largest construction materials and building products group, has recognised the importance of development of environmentally sustainable concrete. The organisation has introduced a recycled glass sand product into its standard 32 MPa concrete mixes.

In addressing the sustainability concern associated with concrete production, this study examines the viability to introduce recycled glass sand as a sustainable alternative to natural fine aggregate used in concrete mixes. In this experimental study the fresh and hardened concrete properties are examined in relation to performance tolerances depicted in the RMS-R83 specification [8] (the Road and Maritime Services of New South

Wales, Australia specification for paving mix design).

Incorporation of recycled glass at replacement contents of 10%, 20% and 40% of the fine aggregate contents in a paving base concrete mix is enabled the determination of how recycled glass interacts within the concrete matrix at various intensity volumes. The key aim of this study is to assess the effect of introducing 30% glass replacement content in the new revision of the RMS-R83 specification [8].

EXPERIMENTAL INVESTIGATION

The experimental procedure has been conducted to examine the influence of using a recycled material referred to as glass sand produced from a recycling firm called Benedict's in a concrete production application. It is a 50/50 blend of recycled glass with excavation sand. The main objective of this project has been to assess the effect of using this recycled glass on various quantities on fresh and hardened concrete properties. The assessment of suitability was examined on its viability to be used in standard 32-MPa grade concrete as well as the Roads and Maritime Services (RMS) pavement base concrete. However, only the results for the latter presented in this paper due to the paper length limitation.

Raw Materials

The properties of materials were determined in accordance to the relevant Australian Standards. General purpose cement was sourced from Boral Cement in Berrima NSW, Australia for use in this experimental investigation. Fly ash was utilized as a supplementary cementatious material in trialed concrete mixes. The fly ash utilized in this experimental investigation was purchased from Fly Ash Australia, sourced this by-product from Eraring Power Station located in Morisset, NSW, Australia. Eraring fly ash is classified as class F fly ash. 20 mm and 10mm crushed river gravel sourced from Boral's Emu Plains Quarry in NSW, Australia constituted as the coarse aggregate fraction blend utilized in the trialed paving mixes. A triple blend of sands was utilised in all conducted trial mixes. The RMS paving base mixes were characterised with a blend of Emu Coarse Sand, Kurnell Fine Sand and Benedict's 50/50 blend of recycled glass sand. The standard 32 grade trialed concrete mixes were characterised with a blend of Emu Coarse Sand, Dunmore Fine Sand and Benedict's 50/50 blend of recycled glass sand. Clean Sydney tap water was utilized in batching of the conducted trialed concrete mixes.

Three admixtures, products of Sika Australia, were used, including (1) Plastiment 10 is a water reducing admixture utilized in this experimental investigation. The use of such water reducing admixture in trialed concrete mixes allowed for the facilitating a more workable concrete without adding excessive quantities of water and compromising strength development. (2) Retarder N, a retarding admixture, was applied in this experimental investigation. The incorporation of this admixture in trialed concrete mixes allowed the retardation of time to initial set as well as prolonging the consistency of fresh plastic concrete. (3) Sika Air, an air entraining admixture, was also employed in this experimental investigation.

Developing Mix Designs

In examining the performance of the recycled glass sand on concrete performance, it was essential to develop a reference mix that did not contain glass sand. Hence its performance provided the benchmark to allow us to assess the viability of mixes incorporating recycled glass sand as a replacement of the fine aggregate component in concrete mixes. The reference mix design was adopted from Boral's current supply of RMS R83 concrete. The adopted mix design was then utilized to introduce the variable component of glass sand to be introduced into the mix. Three additional mix designs were developed at the different replacement rates of 10%, 20% and 40% of the fine aggregate component in a concrete mix. The proposed testing regimes are illustrated in Table 1 for fresh and hardened concrete. In determining the hardened concrete properties of mixes, it was necessary to prepare and cast the required moulds to yield test specimens. This involved preparing and curing test specimens in accordance to AS1012.8.1 [9] (for compressive and indirect tensile test specimens) and AS1012.8.2 [10] (for flexural specimens).

Table 1 Testing regime agenda

Test Descriptions	Standard [11]
Compressive Strength (1, 3, 7, 28, 56 days)	AS1012.9
Indirect Tensile Test (28 days)	AS1012.10
Flexural Strength (7, 28, 56 days)	AS1012.11
Drying Shrinkage (7, 14, 21, 28, 56 days)	AS1012. 13
Chlorides (%)	AS1012.20
Sulphates (%)	AS1012.20
Air Content (%)	AS 1012.4.2
Plastic Density	AS 1012.5
Bleeding Rate (%)	AS 1012.6
Slump	AS 1012.3.1
Setting Time of Fresh Concrete	AS 1012.18

One day prior to the mixing being conducted, batching of concrete constituents was undertaken. This involved measuring required concrete constituents as defined in proposed mix designs from stored stockpiles. Obtained samples from stockpiles were well mixed to ensure homogeneity in the retrieved samples. The measured quantities were stored in sealed containers ready to be placed in the mixing drum once ready to conduct the operation. In preparing the aggregates to be batched for use in the proposed trial mixes, the aggregates were moistened to visually prepare all aggregate sources to be in a moisture condition just over saturated surface dry (SSD) condition. Samples were then obtained from the prepared batches to determine the actual moisture conditions of the fine and coarse aggregates. The measuring laboratory conditions were set at 23°±1° degree with a relative humidity of 50±5%. The air flow in the drying room is also controlled by the degree of water evaporation from beakers filled with 375ml of water. The rate of water evaporation from such beakers shall be within the tolerance of 12±5 mL per 24-hour period.

Fig. 1 Positioning of marked points on flexural machine depicting equal distances between supports.

EXPERIMENTAL RESULTS

This section highlights key findings, obtained from conducting the proposed trial mixes. The main results are summarised in Tables 2-4.

Table 2 Test results of reference trial mix incorporating no glass sand

Test Descriptions	Results
Compressive Strength (MPa) (1, 3, 7, 28, 56 days)	14.5, 30.5, 39, 52, 60.5
Indirect Tensile Test (MPa) (28 days)	5.1
Flexural Strength (MPa) (7, 28, 56 days)	4.8, 6.1, 6.6
Drying Shrinkage (μs) (7, 14, 21, 28, 56 days)	270, 350, 410, 450, 540
Chlorides (%)	0.004
Sulphates (%)	0.77
Air Content (%)	3.6
Plastic Density (kg/m^3)	2340
Slump	60

The results, generated from each conducted mix were obtained as per specifications detailed in the relevant Australian standards. Results obtained from conducting RMS concrete trial mixes to assess the influence of incorporating glass sand (10%, 20% and 40%) as a partial replacement of the fine aggregate component are presented in Tables 2, 3 and 4, respectively.

Table 3 Test results of reference trial mix incorporating 10% glass sand

Test Descriptions	Results
Compressive Strength (MPa) (1, 3, 7, 28, 56 days)	16.5, 28.5, 37, 50.3, 57.5
Indirect Tensile Test (MPa) (28 days)	4.3
Flexural Strength (MPa) (7, 28, 56 days)	4.6, 6, 7.1
Drying Shrinkage (μs) (7, 14, 21, 28, 56 days)	280, 370, 420, 460, 550
Chlorides (%)	0.005
Sulphates (%)	0.75
Air Content (%)	3.6
Plastic Density (kg/m^3)	2340
Slump	60

Table 4 Test results of reference trial mix incorporating 20% glass sand

Test Descriptions	Results
Compressive Strength (MPa) (1, 3, 7, 28, 56 days)	17.5, 28, 38, 50, 54
Indirect Tensile Test (MPa) (28 days)	4.47
Flexural Strength (MPa) (7, 28, 56 days)	4.7, 6.1, 6.4
Drying Shrinkage (μs) (7, 14, 21, 28, 56 days)	290, 370, 430, 470, 550
Chlorides (%)	0.007
Sulphates (%)	0.75
Air Content (%)	3.6
Plastic Density (kg/m^3)	2360
Slump	55

Table 5 Test results of reference trial mix incorporating 40% glass sand

Test Descriptions	Results
Compressive Strength (MPa) (1, 3, 7, 28, 56 days)	16.5, 28.5, 36.5, 49.7, 55
Indirect Tensile Test (MPa) (28 days)	4.3
Flexural Strength (MPa) (7, 28, 56 days)	4.85, 5.43, 6.5
Drying Shrinkage (μs) (7, 14, 21, 28, 56 days)	260, 350, 400, 440, 530
Chlorides (%)	0.005
Sulphates (%)	0.75
Air Content (%)	3.6
Plastic Density (kg/m^3)	2340
Slump	65

DISCUSSION

Paving Base Concrete Trial Mixes

The results of fresh and hardened concrete samples are separately discussed in this section.

Fresh concrete properties

Air content remained constant at a value of 3.6 % across all trialed paving mixes, which were characterised with various glass replacement contents. This indicates that the quantity of introduced glass in concrete had no influence on the air entrainment of the inherent concrete and yielded air content results that were within the R38 tolerance of 4.5 ± 1.5%.

An increase in free water, associated with recycled glass aggregate as the replacement rate, was noticed. This resulted in a reduced water demand of the introduced mix water to ensure a constant water to cement ratio was maintained. The consideration of such aggregate moisture and introduction of a constant water reducing admixture yielded the development of concrete slumps in all trialed paving mixes that were within the R83 tolerance values of 55-65mm. This indicates the introduction of glass had minimal influence on workability of trialed concrete mixes due to being a fine aggregate replacement, thus influences due to physical characteristics of glass particles were minimal.

Bleed water increased relatively with a rise in the introduced glass content in a concrete mix. The impermeable nature of glass mainly contributed to this phenomenon occurring. The highest recorded bleed rate of 0.7% at a 20% glass replacement rate was well-below the 3% bleed limit specification in the R83 paving concrete specification.

The setting time of trialed paving mixes remained relatively constant. The consistency indicated the amount of utilized glass in a concrete mix had insignificant influence on varying concrete set times. The experienced trend can mainly be attributed to the constant amount of free water maintained in all trialed paving mixes.

Hardened concrete properties

Table 6 highlights the average compressive strength of samples as paving mixes incorporating glass sand at the various maturity dates. Even though, the introduction of glass sand reduced the experienced compressive strength exhibited by the inherent concrete, all trialed mixes where characterised with a compressive strength value that surpassed the RMS-R83 requirement of compressive strength at 28 days. The R83 specification calls for a minimum compression strength value of 40 MPa at 28 days. From the conducted experimental investigation, it was determined that incorporating glass at a rate of 40% of the fine aggregate component in a paving mix yielded a compressive strength value of 49.7 MPa, which surpasses RMS requirements.

Table 6. Compressive strength (MPa) of RMS R83 mixes with different sand glass replacement percentages at the various maturity days

Rep. (%)	1 d	3 d	7 d	28 d	56 d
0%	14.5	30.5	39	52	60.5
10%	16.5	28.5	37	50.3	57.5
20%	17.5	28	38	50	54
40%	16.5	28.5	36.5	49.7	55

The compressive strength the of control samples and samples with 40% replacement of fine aggregate with glass sand are shown in Fig. 2. This high glass replacement content (40%) has been the highest trialed value and still complies with the RMS specifications.

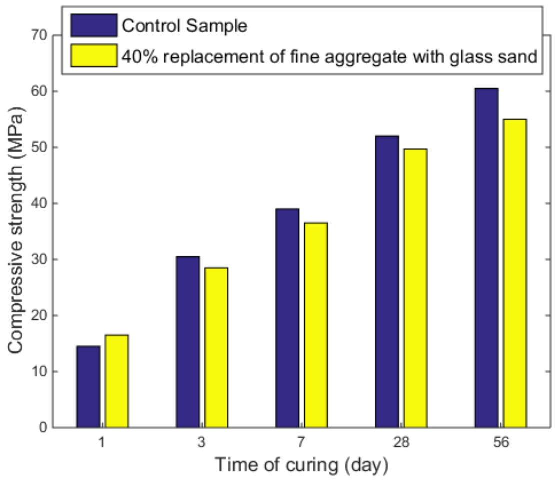

Fig. 2 Comparison of the compressive strength the of control samples with samples with 40% replacement of fine aggregate with glass sand.

The one day compressive strength of trialed paving mixes incorporating 10%, 20% and 40% glass replacement contents, where all higher than the control mix containing no glass sand. A 20% increase in one day compressive strength was achieved by the mix containing a 20% glass replacement rate. The observed behaviour can be attributed to pozzolanic reactivity of the glass promoting early strength development.

The compressive strength of trialed paving mixes incorporating 10%, 20% and 40% glass replacement contents from 3-day testing all experienced strength results that were slightly lower than the control mix. Additionally, compressive strength of concrete decreased with an increase in the glass content introduced in the mix at each tested curing period. The phenomena of changing compressive strength behaviour from 3-day testing suggested that the relative weaknesses characterising glass aggregate due to its inherent recycling process dictated concrete strength. In essence, micro-cracks in the glass aggregate facilitated the early failure of concrete. Such failure mechanism becomes the prime mode of failure at relatively later ages of testing, when cement strength exceeds the strength capacity of glass aggregates. Hence, it has been concluded that the relative weakness of glass aggregates in the concrete matrix facilitates early concrete failure.

All trialed paving mixes where characterised with compressive strength values that surpassed the R83 requirement of a 40 MPa compressive strength value at 28 days. The paving mix containing 40% glass replacement content yielded an average compressive strength value of 49.7 MPa.

The average 28 day indirect tensile strength reduction was approximately 15% when a glass replacement rate of 10% and 40% was utilized in comparison to the control mix. A 20% glass replacement rate yielded an approximate strength reduction of 12%. This experienced indirect tensile strength reduction at 28 days may again be attributed to inherent cracks in glass aggregate facilitating early concrete failure.

The 28 day flexural strength results of trialed paving mixes indicated that the flexural strength decreased with a relative increase in the glass content introduced in the mix. This trend indicated that the inherent cracks in glass aggregate become more prevalent to causing early concrete failure when the dosage rate is increased.

All trialed paving mixes where characterised with a flexural strength at 28 days that surpassed the 4.7MPa tolerance depicted by the R83 specification. The mix containing a 38.5% glass replacement rate achieved a flexural strength of 5.43MPa.

Negligible drying shrinkage variation was examined in mixes containing a 10% and 20% glass replacement rate at all dates of testing. The mix containing 40% glass replacement content achieved reduced drying shrinkage results at all dates of testing in comparison to the control mix. This reduction in drying shrinkage could be attributed to the ability of glass in a mix to increase the effective water content in the matrix due to its impermeability.

Glass aggregate contributed to increasing the chloride content characterising a concrete mix. A relative rise in chloride content was examined with increase in the glass replacement content. Meanwhile, it is found that the glass aggregate had negligible influences on the inherent sulphate content of the concrete samples.

The presented discussion above suggests that a 40% incorporation of recycled fine glass in R38-RMS paving mix designs can yield concrete that exhibits fresh and hardened properties, which surpasses the tolerances depicted in the R83 specifications. Considering the high variability in glass product quality, due to varying original sources of glass to be recycled and the inherent recycling process that crushes glass, a factor of safety should be applied to the determined 40% glass replacement rate that deemed concrete performances surpassing R83 requirements. As such, the proposed 30% glass replacement rate to be introduced in the new revision of the R83 specification is regarded to be acceptable from findings of this experimental investigation. The 30% replacement rate provides a sense of security in the mix design to accommodate for any inconsistencies associated with the recycled glass products.

CONCLUSIONS

The proposed experimental investigation was conducted to examine the feasibility of incorporating a recycled glass sand product as a partial replacement of the fine aggregate component in paving mixes in promoting the development of sustainable concrete pavement. This assessment included to analyse fresh and hardened concrete properties of many trialed RMS paving mixes incorporating glass sand at various replacement contents. The findings of this experimental investigation clearly indicated that even up to 40% incorporation of recycled fine glass in the paving mix designs can produce concrete with fresh and hardened properties, which exceeds the minimum requirements specified in the Road and Maritime Services (RMS) of New South Wales, Australia specifications, which is called RMS-R38 [8] for paving mix design.

For further research, it is recommended to conduct an experimental investigation quantifying the durability of glass aggregates, when incorporated in concrete. Although the influence of glass sand on the chloride and sulphate contents of concrete was studied in this experimental study, a major area of durability, concerned with the introduction of glass aggregate in concrete, pertains to the facilitation of the alkali-silica reaction. This is due to the relatively high silica content of glass aggregates, which facilitates the occurrence of this reaction in concrete. The occurrence of this reaction in concrete may severely degrade concrete durability.

It can be noted that, this study investigated the influence of incorporating recycled glass as a fine aggregate in paving concrete applications. Future study should investigate the influence of incorporating waste glass as a replacement for the coarse aggregate component

ACKNOWLEDGEMENTS

The Authors would like to express their appreciation to David Hocking from Boral Australia, for his technical support and provision of Boral Australia's Concrete Laboratory Testing Facility for completing this research project. Furthermore, the authors extend their appreciation to Boral Concrete Laboratory technicians for their assistance in completing the experimental test procedures.

REFERENCES

[1] Schokker, AJ, 2010, "The Sustainable Concrete Guide", The Green Concrete Council of the United States of America, 2010.
[2] Cement Concrete and Aggregates Australia (CCAA), "Sustainable Concrete Materials" Sydney, 2010.
[3] Madandoust, R, Ghavidel, R "Mechanical properties of concrete containing waste glass powder and rice husk ash", J. of Biosystems Engineering, Vol. 116, 2013, pp. 113-119.
[4] Mohammadi, I, Khabbaz, H and Vessalas, K, "In-depth Assessment of Crumb Rubber Concrete (CRC) Prepared by Water-Soaked Treatment Method for Rigid Pavement Use" is submitted to the journal of "Construction & Building Materials", Vol. 71, 2014, pp.456-471.
[5] Wood, M., Jeffreys, C. and Richardson, P. "National Waste Policy", Department of Sustainability, Environment, Water, Population and Communities, Waverly, 2011.
[6] Ling, TC, Poon CS and Wong, HW, "Management and recycling of waste glass in concrete products: Current situations in Hong Kong". J. of Resources, Conservation and Recycling, Vol. 70, 2013, pp. 25-31.
[7] Ling, TC, Poon CS and Kou SC Kou, "Feasibility of using recycled glass in architectural cement mortars". J. of Cement and Concrete Composites, Vol. 33, 2011, pp. 848-854.
[8] RMS-R83 specification, "Concrete Pavement Base", Roads and Maritime Services, IC-QA-Specification R83, 120 p., 2013.
[9] AS 1012.8.1, Standards Australia, "Methods of testing concrete - Method of making and curing concrete: Compression and indirect tensile test specimens", Publisher: Standards Australia, Sydney, 2000.
[10] AS 1012.8.2, Standards Australia, "Methods of testing concrete - Method of making and curing concrete: Flexure test specimens", Publisher: Standards Australia, Sydney, 2000.
[11] Standards Australia 1012, "Methods of testing concrete", Publisher: Standards Australia, Sydney, 2000.

AN EXPERIMENTAL INVESTIGATION OF PHYSICAL, CHEMICAL AND RHEOLOGICAL PROPERTIES OF RAP MODIFIED ASPHALT BINDER

Ashwini Shanbhag[1], Dinesh S V[2], H S Lalithamba[3] and Anand Tadas[4]
[1] Post Graduate Student, [2]Professor, [3]Associate Professor, [1,2,3]Siddaganga Institute of Technology, India;
[4]Product Specialist Nanometrics, Malvern Aimil Instruments Pvt Ltd, India.

ABSTRACT

Due to high price of crude oil, and asphalt binder, the application of reclaimed asphalt binder is widely considered. Very few investigations are related to Rheological and Chemical properties of RAP modified asphalt binders with Waste Engine Oil (WEO) as a rejuvenator. The present paper reports the results of a laboratory research, carried out to investigate the effects of addition of a rejuvenating agent to HMA with RAP. Test samples comprised of Virgin bitumen, Aged Asphalt Binder that were extracted from RAP, together with WEO were added in different ratios. Optimal amount of oil was determined by conducting basic tests. Rheological properties were then determined for samples containing optimal rejuvenator content. The physio chemical analysis of RAP modified asphalt binder was carried out using Fourier Transform Infrared Spectroscopy. The main concern of using WEO is stripping of the binder from the aggregate for which all the RAP modified samples containing optimal WEO were tested.

Keywords: Waste Engine Oil; Hot Mix Asphalt; Reclaimed Asphalt Pavement; Fourier Transform Infrared Spectroscopy.

INTRODUCTION

Asphalt binder is chemically composed of asphaltenes and maltenes. The maltenes fraction dissipates during oxidation causing a change in asphaltene –maltene ratio, which affects the stiffness properties of the asphalt [2]. This is called aging and it leads to an increase in stiffness and brittleness at intermediate and low temperatures, resulting in reduced resistance to fatigue and low temperature cracking. The process that restores aged asphalt's properties to a point considered to be comparable to a virgin material is called as asphalt rejuvenation. This process is done by adding rejuvenating agents to RAP mixtures. Some of the rejuvenating agents are industrial process oil, "softer" Performance Grade binders (PG binders), asphalt flux oil, engine oil and waste cooking oil. Increasing the RAP content in a mixture increases its stiffness and reduces its shear strain, indicating the increased resistance to rutting. Adding rejuvenators can balance the asphaltene- maltene ratio of aged asphalt in RAP mixtures.

Using RAP in HMA applications could possibly present a lower performance due to the behavior of the aged binder, which loses its lighter fractions with time. A binder rejuvenator is used in order to improve the mixture properties. This allows the modification of the aged binder, restoring some of its original properties and promoting an adequate performance of the mixture. The rejuvenator percentage affects greatly the performance based properties of the blended aged asphalt binder and the rejuvenator [3,4,5,6,]. The performance evaluation of asphalt mixtures with high rap content using a warm mix asphalt (WMA) additive, Sasobit H8, HMA with 75% RAP recycled at lower temperature show performance nearly equivalent to that of a conventional mixture [7,8]. The physical and rheological properties of bitumen change with time. It may become harder or less elastic. The RAP modified binder chemistry before and after aging process is very important. The process of aging chemically alters the structure of the RAP modified binders [9].

It is observed that, majority of the investigators have focused on physical properties of binder and mechanical properties of mixes but the rheological and chemical characteristics are the main pointers to the material performance in actual practice. The objective of the present study is to investigate the chemical and rheological changes occurring in virgin binders blended with RAP binders extracted from cold milled RAP. And also, to study the effect of rejuvenators on the performance based properties of the rejuvenated aged binder, i.e., the blends of the aged binder (RAP) containing the rejuvenator, using a series of dynamic shear rheometer tests. The characteristics of RAP modified binders are investigated in terms of chemical properties, its composition and binding parameter of modified binders for rutting.

EXPERIMENTAL INVESTIGATION

Materials

Materials used in this study include 60/70 grade bitumen, recovered rap binder and waste engine oil (WEO) as rejuvenator. WEO is the engine oil used in the vehicle during a routine oil change. Large quantities of engine oil on pavements impose damage on the asphalt pavement. However, small amounts of oil well blended in the mix may prove beneficial when combined with rap by offsetting the increased stiffness in order to produce a pavement with performance similar to one made of virgin materials.

.

Methods

Bitumen extraction

In this study, the extraction of bitumen from the used HMA was done based on the ASTM D2172 procedure, using centrifuge extractor and benzene as the solvent. The used HMA was obtained from Bangalore-Mysore NICE road which was paved 5 years ago and had deteriorated to a considerable extent. It was made using 60/70 grade of bitumen and it served heavy traffic volume.

Test methods

Binders are tested as per the procedure laid in the IS: 73:2006 for their physical properties. Rheological properties are determined using DSR according to AASHTO T315-08 [1] and are widely used to characterize the viscous and elastic behavior of asphalt binders at high and intermediate service temperatures. The DSR measures the complex modulus (G*) and phase angle (δ) of the asphalt binders at the desired temperature and frequency of loading. The sample is prepared by heating the binder until it becomes fluid to pour. The heated binder is poured into a rubber mould and allowed to cool until it attains solid consistency. Then the sample is removed and placed between the fixed plate and oscillating spindle of the DSR. The excess binder beyond the edge of the spindle is trimmed. Frequency sweep tests are performed on RAP modified binders containing optimal WEO. The samples are poured and trimmed at around 90°C. The frequency sweep tests are performed from 1 to 10 Hz under a stress of 120 Pa for temperature varying from 50 to 80ºC. For MSCR test, one-second creep load is applied to the above mentioned samples. After one-second load is removed, the sample is allowed to recover for 9 seconds. The test is started with the application of a low stress (0.1 kPa) for 10 creep/recovery cycles then the stress is increased to 3.2 kPa and repeated for an additional 50 cycles. Fourier transform spectrometry measures the infrared (IR) light absorbed by a material. This absorption depends on the chemical functional groups present in the material. Technically an infrared light beam is charged through the dissolved material. This energy causes bonds in molecules to vibrate and rotate at distinct frequencies. The energies absorbed at given frequencies are identified with a detector, and a spectrum of absorbance versus wavenumber is obtained.

The RAP is mixed with virgin bitumen in different percentages varying from 0 to 100%. WEO is also added in percentage varying from 0 to 25%. Basic tests are carried out on all these samples and optimal WEO for all the samples is determined. Rheological and chemical analysis is further carried out for the samples containing optimal WEO. Figure 1 shows the details of experimental investigations.

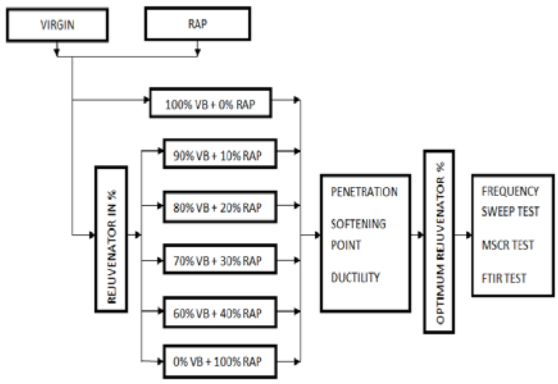

Fig. 1 Details of Experimental Investigation

RESULTS AND DISCUSSION

Basic Test Results

Basic tests were conducted on RAP modified samples containing WEO varying from 0 to 25% and optimal WEO was determined. The results of basic tests are shown in Table 1.

The penetration decreases as the percentage of RAP binder increases due to the loss of volatiles in the aged RAP binder. The penetration value of virgin bitumen is 64 mm. With the increase of RAP % penetration decreases and for 100% RAP bitumen after the long term ageing penetration value is 23mm, the lowest. But with the addition of optimum oil content, the RAP modified binders showed penetration values in the permissible limit of 60/70 grade bitumen.

The softening point of all RAP binder proportions increase as they undergo ageing because of hardening. 100% RAP bitumen exhibits the highest softening point at 64°C after being subjected to long term ageing, whereas virgin bitumen has a softening point of 45°C. But with the addition of optimum oil content, the values of all the RAP modified binders reduced to the permissible limit of 60/70 grade bitumen.

The ductility decreases as the percentage of RAP binder increases due to the loss of volatiles in the aged RAP binder. The ductility value of virgin bitumen is 80 cm. With the increase of RAP % ductility decreases and for 100% RAP bitumen after the long term ageing ductility value is 5 cm, the lowest. But with the addition of optimum oil content, the ductility values of the binders with 10 to 40% RAP increased to the permissible limit of 60/70 grade bitumen. But there was not much improvement in the 100% RAP.

Table 1 Basic test results

Bitumen	Penetration test	Softening Point test	Ductility test
IS Limit (60/70)	60-70 mm	45-55^{0}C	Min of 75 cm
Virgin Bitumen	64 mm	45^{0}C	80 cm
10% RAP	58 mm	48^{0}C	62 cm
10% RAP + 4% EO	65 mm	45^{0}C	82 cm
20% RAP	52 mm	50^{0}C	58 cm
20% RAP + 4% EO	64 mm	46^{0}C	81 cm
30% RAP	42 mm	53^{0}C	54 cm
30% RAP + 6% EO	68 mm	46^{0}C	88 cm
40% RAP	32 mm	58^{0}C	25 cm
40% RAP + 8% EO	66 mm	45^{0}C	84 cm
100% RAP	23 mm	64^{0}C	5 cm
100% RAP + 25% EO	64 mm	47^{0}C	10 cm

Thus, from the above basic tests, the optimal content of WEO for all the RAP modified binders was determined. Table 2 shows the optimal WEO for varying percentages of RAP.

Table 2 Optimal WEO for varying RAP content

Bitumen	10% RAP	20% RAP	30% RAP	40% RAP	100% RAP
Optimal WEO	4%	4%	6%	8%	25%

Stripping test is carried out on the optimally rejuvenated samples and there was no evidence of stripping.

Rheological Test Results

Frequency sweep test

Tests are conducted on samples containing optimal WEO. It is observed from Fig. 2, the general trend is that the complex modulus (G*) decreases with the increase in temperature due to visco elastic nature of bitumen. The RAP modified binders have high complex modulus than virgin bitumen due to incorporation of aged binder in increasing percentages of 10 to 40, because the bitumen becomes more viscous. Also, RAP modified binders have less phase angle than virgin bitumen which directly affects the elastic recovery properties. In conclusion, the addition of RAP binder to the base bitumen produces stiff and tough bitumen.

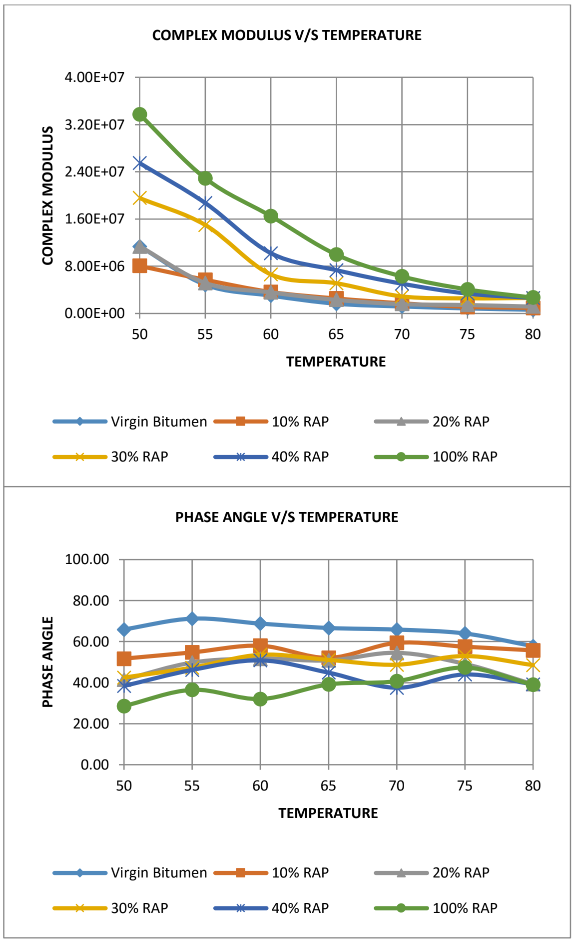

Fig. 2 Variation of complex modulus and phase angle with respect to temperature

In order to replace the lost lighter fractions in the aged RAP binder WEO is used as a rejuvenator.

Optimal content determined from the basic tests is added and test is conducted. From Fig. 3,4,5,6 and 7, it can be observed that there is a significant improvement in the complex modulus of all the RAP modified binders, but not much in case of phase angle of all the RAP modified binders. Hence, it can be concluded that addition of optimal WEO can restore the lost fractions, thus improving its rheological properties.

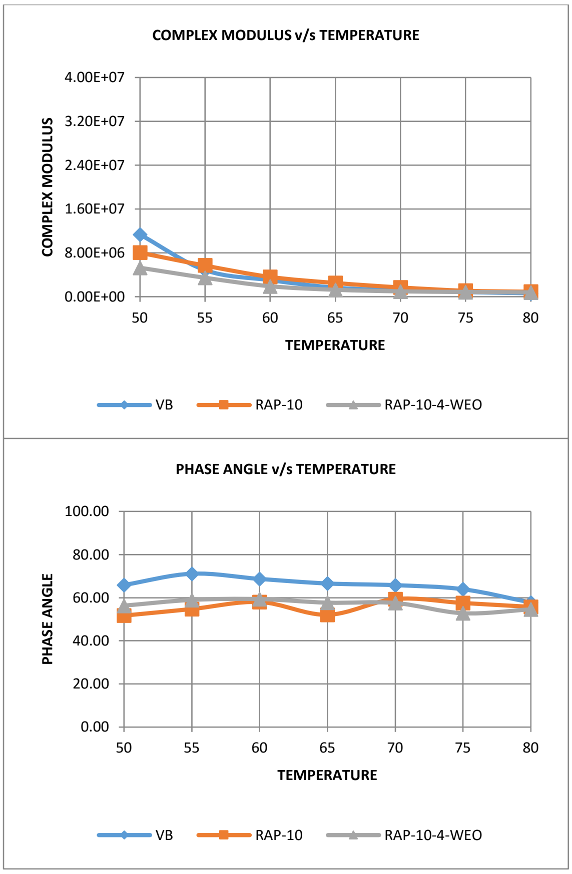

Fig. 3 Variation of G* and δ with respect to temperature for 10% RAP with 4% oil

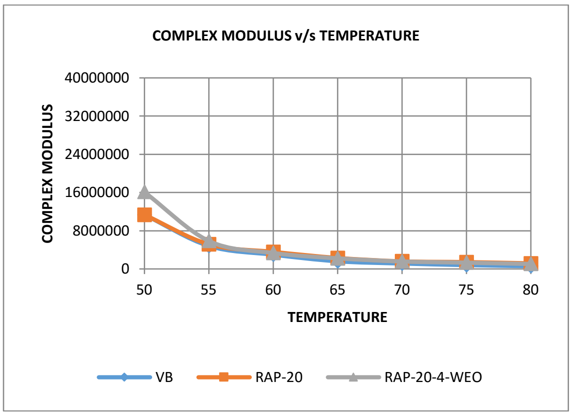

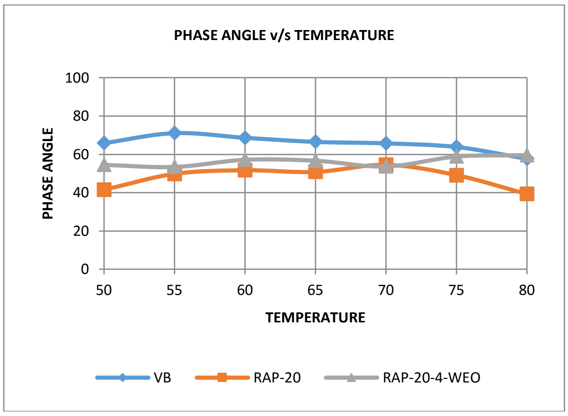

Fig. 4 Variation of G* and δ with respect to temperature for 20% RAP with 4% oil

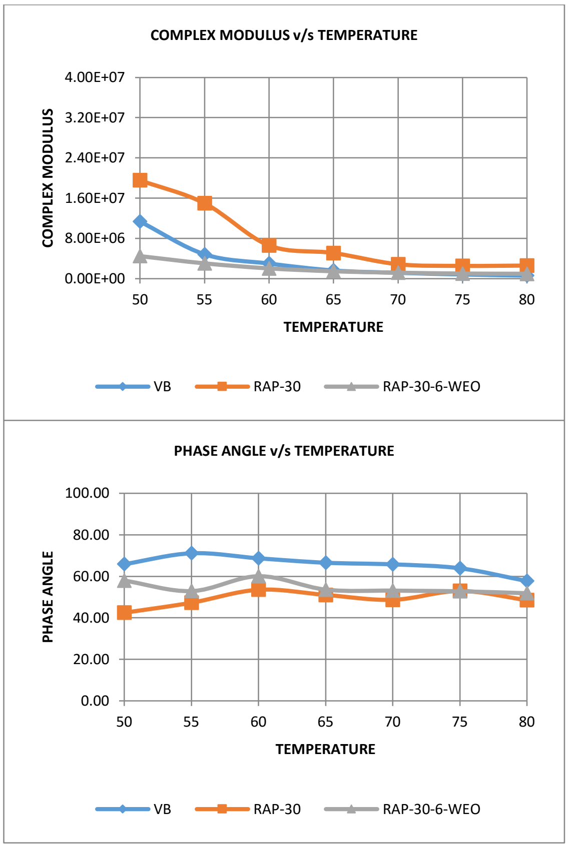

Fig. 5 Variation of G* and δ with respect to temperature for 30% RAP with 6% oil

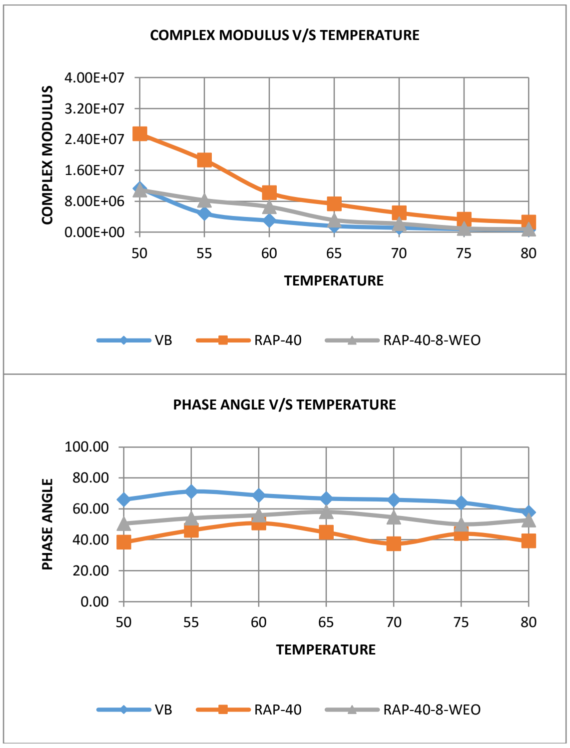

Fig. 6 Variation of G* and δ with respect to temperature for 40% RAP with 8% oil

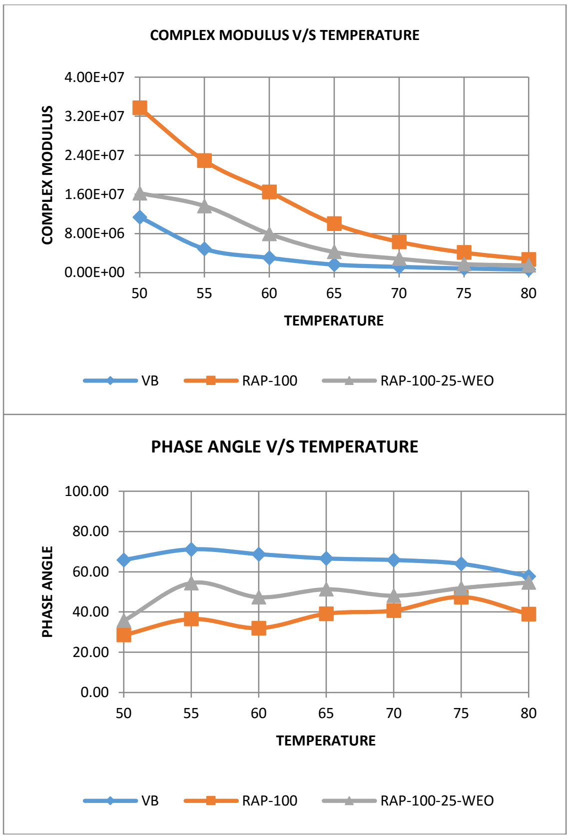

Fig. 7 Variation of G* and δ with respect to temperature for 100% RAP with 8% oil

Multiple Stress Creep Recovery Test

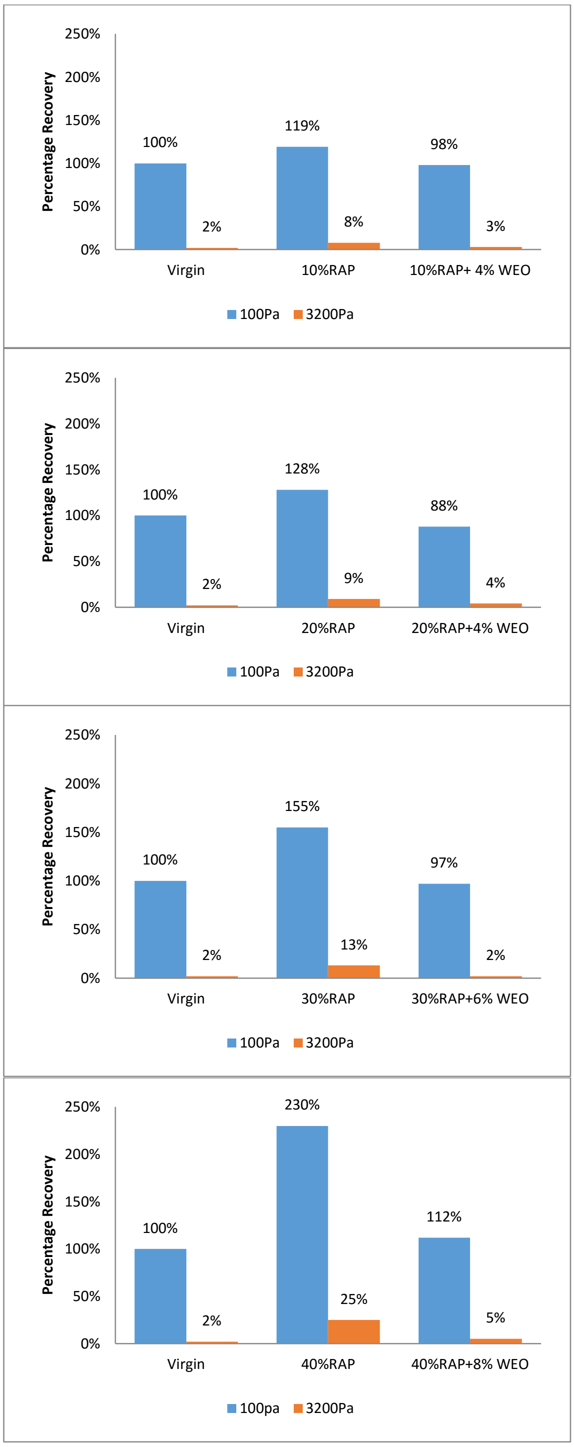

Fig. 8 Variation of percentage recovery with applied stress

MSCR could not be performed on 100%RAP binder due to its stiffness.

It is clear from Fig. 8 that, RAP infused binders show higher percentage recovery both at high and low stress levels. At lower stress levels virgin bitumen showed fair percentage recovery, at higher stress levels the percentage recovery of virgin bitumen was found to reduce. The addition of RAP to the bitumen results in the higher percentage of recovery, higher the percentage recovery better is the material in terms of rutting. And, with the addition of optimum WEO, the percentage of recovery reduced nearly to that of virgin bitumen indicating reduced resistance to rutting.

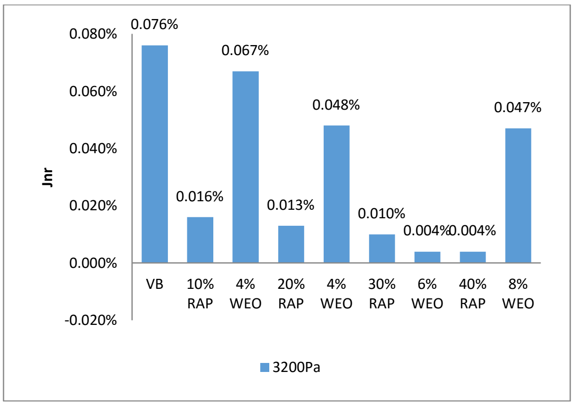

Fig. 9 Variation of Non Recoverable Creep Compliance with applied stress

From Fig. 9 it can be observed that the virgin bitumen has higher non recoverable compliance (J_{nr}) when compared to modified bitumen. Higher non-recoverable compliance can possibly increase the magnitude of rutting in the actual service life. However, addition of RAP reduces the J_{nr} thus reducing the possibility of rutting. Inclusion of optimal WEO increases the non recoverable creep compliance, but when compared to the virgin bitumen, it is less. Hence, the possibility of rutting is less when compared to that of virgin bitumen.

Fourier Transform Infrared Spectroscopy

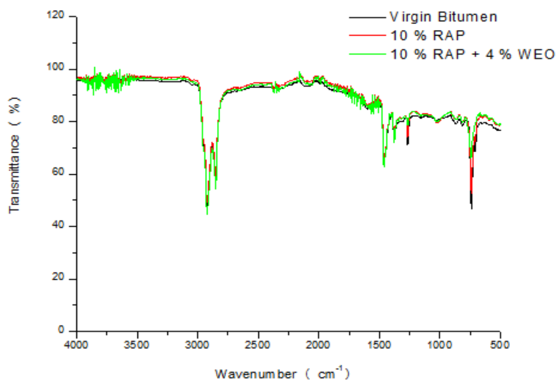

Fig. 10 IR Spectrum of 10%RAP modified bitumen with 4%WEO content

Fig. 11 IR Spectrum of 20%RAP modified bitumen with 4%WEO content

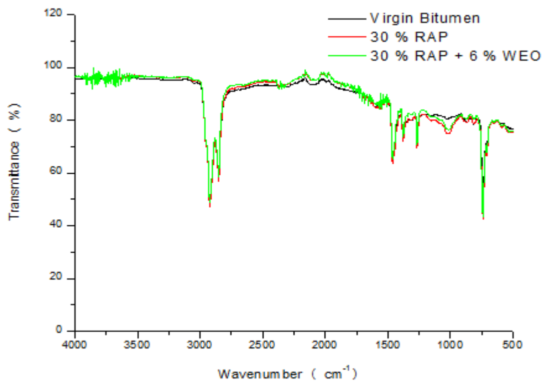

Fig. 12 IR Spectrum of 30%RAP modified bitumen with 6%WEO content

Fig. 13 IR Spectrum of 40%RAP modified bitumen with 8%WEO content

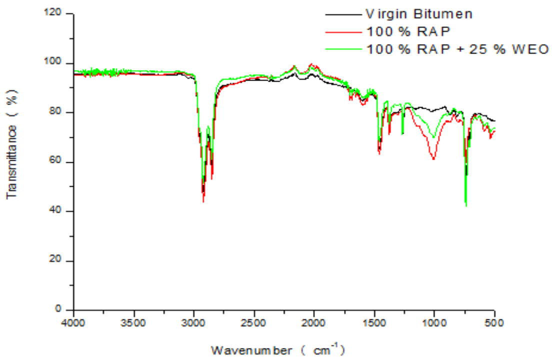

Fig. 14 IR Spectrum of 100%RAP modified bitumen with 25%WEO content

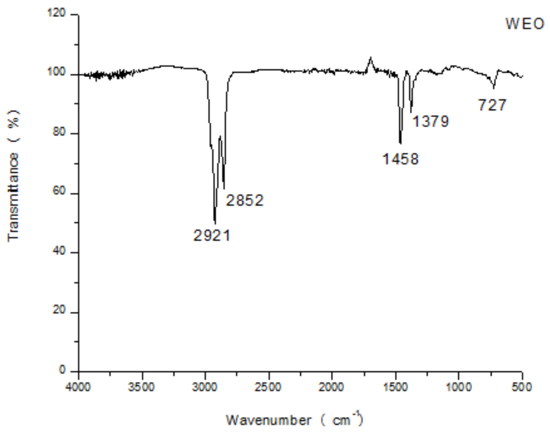

Fig. 15 IR Spectrum of WEO

FTIR is a tool to identify chemical evolution in bitumen and indicate severity of oxidation experienced by bitumen after ageing. It measures Infrared light transmitted by sample materials. FTIR is useful in identifying the presence of certain functional groups which transmit at definite frequencies. The FTIR spectra of asphalt binders and waste engine oil are shown in Fig. 10, 11, 12, 13, 14 and 15. Since both asphalt and WEO are hydrocarbons, the samples are generally comprised of saturated and aromatic hydrocarbons. The absorption peaks at 2923 cm^{-1} and 2852 cm^{-1} are associated with C-H stretching of alkane and O-H stretching of carboxylic acids respectively. A stretching vibration of C-C in the aromatic ring is detected at 1469 cm^{-1} and it also represents the bending of C-H indicating the group of $-CH_2$- and –C-CH_3. The peaks at 1271 represent C-N stretch in the aromatic ring and C-O stretch containing alcohols, carboxylic acids, esters and ethers. A stretching vibration of S=O and C-N is detected at 1030 cm^{-1} representing sulphoxides and amines. Two compounds of most interest are the sulphoxides and carbonyls showing peak at 1030 cm^{-1} and 1700 cm^{-1} respectively. These two compounds are commonly used as an indication of the aging, asphalt binder has undergone. Generally, both WEO and asphalt binder consist of similar functional groups and molecular structures. Oxidised components are introduced into virgin asphalt binder by both WEO and aged asphalt. This inclusion increases the relative oxidation of asphalt blend. Hence, it is clear from the figure above, that there is not much significant improvement in the performance of RAP modified samples even with optimal amount of WEO as they oxidise at a faster rate. However, an aging performance study on these RAP modified samples containing optimal WEO would show the rate of oxidation.

CONCLUSION

A comprehensive experimental investigation was carried out to evaluate the physical, rheological and chemical properties of RAP modified asphalt binder. From the analysis of the results, the following conclusions are drawn.

1) With the inclusion of RAP binder into the virgin the penetration and ductility consistently decrease whereas softening point consistently increase.
2) The complex modulus increases with increase in percentage of RAP binder. However, phase angle decreases with increase in percentage of RAP binder.
3) With the addition of optimum content of WEO to the RAP modified binder, the characteristics of virgin bitumen were obtained (60/70 grade).
4) Complex modulus of RAP binder with WEO decreased when compared to that without WEO. But, there was not much improvement in the phase angle with the addition of WEO.
5) The addition of RAP results in higher percentage of recovery, higher the percentage recovery better is the material in terms of rutting.
6) The virgin bitumen has higher non recoverable compliance (J_{nr}) when compared to modified bitumen. Higher J_{nr} can possibly increase the magnitude of rutting in the actual service life. However, addition of RAP reduces the J_{nr} thus reducing the possibility of rutting. Inclusion of optimal WEO increases the J_{nr}, but when compared to the virgin bitumen, it is less. Hence, the possibility of rutting is less when compared to that of virgin bitumen.
7) The infrared spectra illustrated that both asphalt binder and waste engine oil consist of similar functional groups and molecular structures. The inclusion of WEO into asphalt binder did not show much improvement in the chemical structure of the binder.

REFERENCE

[1] AASHTO T 315: Determining the Rheological Properties of Asphalt Binder Using a Dynamic Shear Rheometer (DSR).

[2] O'Sullivan, K. A. (2011) "Rejuvenation of reclaimed asphalt pavement (RAP) in hot mix asphalt recycling with high RAP content".

[3] Junan Shen, Serji Amirkhanian and Boming Tang (2006) "Effects of Rejuvenator on Performance based properties of Rejuvenated Asphalt Binder and Mixtures", Construction and Building Materials 21 (2007) 958–964.

[4] J.R.M. Oliveira, H.M.R.D. Silva and C.M.G. Jesus (2011) "Asphalt Mixtures Produced With 100% Reclaimed Materials", WASTES: Solutions, Treatments and Opportunities, 1St

International Conference, September 12th – 14th 2011.

[5] Ehsan Yaghoubi, Mohammad Reza Ahadi, Mohsen Alijanpour Sheshpoli and Hamid Jahanian Pahlevanloo (2013) "Evaluating the Performance of Hot Mix Asphalt with Reclaimed Asphalt Pavement and Heavy Vacuum Slops as Rejuvenator", International Journal of Transportation Engineering, Vol.1/ No.2/ Spring 2013.

[6] Xiaoyang Jia, Baoshan Huang , Benjamin F. Bowers and Sheng Zhao (2014) "Infrared spectra and rheological properties of asphalt cement containing waste engine oil residues", Construction and Building Materials 50 (2014); 683-691.

[7] Rajib B. Mallick, Prithvi S. Kandhal and Richard L. Bradbury (2008) "Using Warm-Mix Asphalt Technology to Incorporate High Percentage of Reclaimed Asphalt Pavement Material in Asphalt Mixtures", Transportation Research Board, Transportation Research Record 2051, 2008.

[8] Luis Loria, Elie Y. Hajj, Peter E. Sebaaly, Matt Barton, Said Kass, and Tara Liske (2011) "Performance Evaluation of Asphalt Mixtures with High Recycled Asphalt Pavement Content", *Journal of The Transportation Research Board, No. 2208*, Transportation Research Board of the National Academies, Washington, D.C., 2011, pp. 72–81.

[9] Meor Othman Hamzah and Zulkurnain Shahadan (2011) "Effects of Aging on the Physical, Rheological and Chemical Properties of Virgin Bitumen Incorporating Recovered Reclaimed Asphalt Pavement Binder", Australian Journal of Basic and Applied Sciences, 5(5): 1323-1331, 2011, ISSN 1991-8178**.**

[10] Khanna.S.K and Justo.C.E.G (2001), "*Highway Engineering*", 8th Edition, Nemchand and Brothers Publications, Roorkee.

Fifth International Conference on Geotechnique, Construction Materials and Environment, Osaka, Japan, Nov. 16-18, 2015, ISBN: 978-4-9905958-4-5 C3051

EXPERIMENTAL STUDY ON LOAD-DEFORMATION-TEMPERATURE BEHAVIOUR OF POLYMER GEOGRID

Thitapan Chantachot [1], Warat Kongkitkul [2] and Fumio Tatsuoka [3]
[1,2] Department of Civil Engineering, Faculty of Engineering,
King Mongkut's University of Technology Thonburi, Thailand;
[3] Department of Civil Engineering, Tokyo University of Science, Japan

ABSTRACT

To evaluate the effects of ambient temperature on the load - deformation behaviour of polymer geosynthetic reinforcement, a series of tensile loading tests was performed on two types of geogrid using a wide variety of load and temperature histories. The loading schemes included monotonic loading and sustained loading under different controlled ambient temperature conditions. With an increase in the ambient temperature, the rupture strength and stiffness decreased. The creep strain increased with an increase in temperature, associated with a decrease in the stiffness. The creep strain by sustained loading during which the temperature was elevated from 30^{o}C to 50^{o}C was significantly larger than the one by sustained loading during otherwise monotonic loading at the constant temperature equal to either 30^o C or 50^o C. The residual tensile strength observed at the same ambient temperature was rather independent of pre-rupture loading histories.

Keywords: Geosynthetic reinforcement, Temperature, Tensile loading test, Creep, Residual strength

INTRODUCTION

The effects of ambient temperature on the strength and stiffness of geosynthetic reinforcement is one of the important factors to be taken into account in the design of geosynthetic-reinforced soil (GRS) structures. Moreover, to prevent long-term creep rupture of geosynthetic reinforcement, allowable tensile strength of geosynthetic reinforcement is used in design, as suggested by Koerner and GRI Standard Practice [1]-[3]. The allowable tensile strength is obtained by reducing the tensile rupture strength by fast loading tests using a creep reduction factor, which is typically between 1.5 to 4.0, depending on the type of geosynthetic and application [1]-[3].

The creep reduction factor is evaluated from a creep rupture curve formulated by analysing results originally from a set of conventional creep tests. However, this type of tests is extremely time-consumption, therefore extremely costly. To shorten the time required for the entire test program, the creep tests are often conducted at elevated temperatures in order to accelerate the creep process. In the method called the time-temperature superposition (TTS), a set of creep tests are performed on geosynthetics specimens until rupture at a set of constant but different ambient temperatures. The TTS can expedite the creep, but it requires multiple replicated specimens to obtain a reliable result. Then, the stepped isothermal method (SIM) was developed in order to avoid the effect of multiple specimens [4], in which the creep test is performed with a series of elevated constant temperatures on a single geosynthetic specimen.

To understand the load-deformation behaviour during creep of geosynthetics affected by temperature, a number of temperature-accelerated creep tests on geosynthetic reinforcements have been performed [5]-[8]. However, in these tests, only load-deformation responses during sustained loading are evaluated, while the behaviour after monotonic loading is restarted following sustained loading are not. Moreover, experiments to evaluate the effects of temperature on the tensile strength are limited. The study to evaluate the combined effects of sustained loading and temperature changes cannot be found in the literature.

In view of the above, in this study, a series of tensile loading tests were performed on two types of geosynthetic reinforcement. Various loading schemes and temperature changes were applied to evaluate the effects of load - temperature histories on the load-deformation behaviour and rupture tensile strength.

APPARATUSES AND MATERIALS

Loading and Heating Apparatuses

The tensile loading tests on polymer geosynthetic reinforcements were performed by using a load-controlled loading system [9]. The tensile load was applied by controlling the air pressure in the air cylinder. The loading direction (load/unload) and load rate were controlled by means of an electro pneumatic transducer (EP).

The temperature surrounding the specimen was controlled by using a heating unit connected to a temperature-controlled chamber containing a test specimen (Fig. 1). The heating unit consists of a heater, a network of air-pipes and a temperature controller. The heater provided hot air to the chamber via the air-pipes. By using this apparatus, the temperature inside the chamber can be controlled as planned [10].

Measuring Devices

A load cell was connected to the loading piston to measure the tensile load (Fig. 1). A displacement sensor was arranged on a tiny frame that was attached on the central part of the specimen to sensitively measure the local tensile deformation of the specimen. The ambient temperature surrounding the specimen was measured by using a thermo-couple that was installed inside the temperature-controlled chamber.

Test Materials

Two different polymer geogrids were used (Fig. 2): i) high-density polyethylene (HDPE); and ii) polypropylene (PP). HDPE geogrid is a uniaxial type designed for use as reinforcement in one direction. The aperture shape is long-elliptical shape. On the other hand, PP geogrid is a biaxial type. The size of aperture is 35 mm (centre-to-centre of the members) in both longitudinal and transverse directions. The mechanical properties of these two geogrids according to their manufacturers are listed in Table 1.

TEST METHOD

Specimen Preparation

The top and bottom ends of respective specimens were clamped by using a pair of gripping device connected to the loading piston. The roller-clamps of each gripping device consists of a steel cylinder with a groove made to grip the specimen with a steel rod. A sheet of sand paper was glued on the surface of the roller-clamp to avoid slippage of the specimen around the roller clamp during testing (Fig. 1). Prior to the start of each tensile loading test, a very small preload of 20 N was applied to minimize the settling error of specimen.

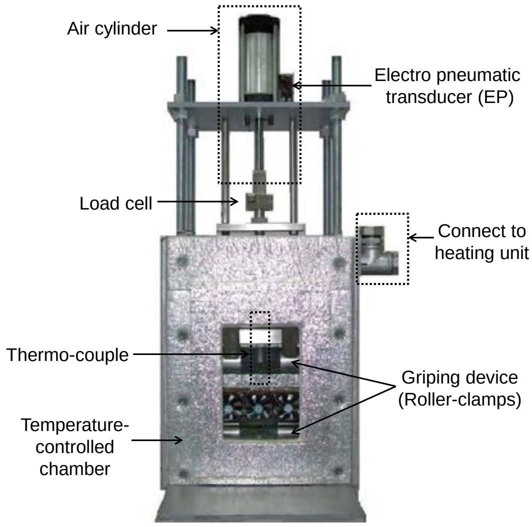

Fig. 1 Tensile loading apparatus and measuring devices

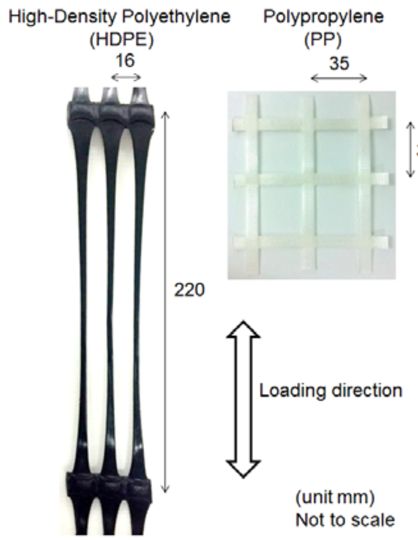

Fig. 2 Geosynthetic reinforcements

Table 1 Mechanical properties of geogrids

Type	Ultimate tensile strength (kN/m)	Yield point elongation (%)
HDPE	90	13
PP	≥ 40	≤ 8

Test Program

The following three different loading and temperature histories shown in Fig. 3 were employed:

(1) ML-CT: Monotonic loading was performed at a constant load rate of 0.6 kN/m/min towards the specimen's rupture. The ambient temperature was kept constant between 30^o C and 50^o C throughout each test.

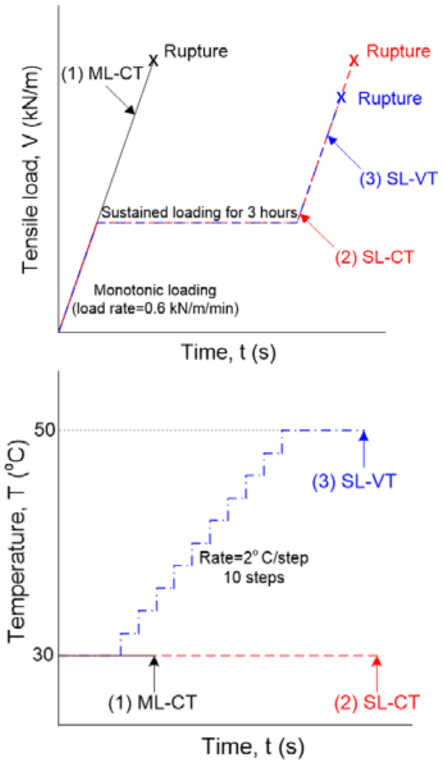

a) b)

Fig. 3 Loading and temperature histories:
(1) ML-CT tests were performed at constant temperature equal to 30º, 35º, 40º, 45º or 50º C.
(2) SL-CT tests were performed at constant temperature equal to either 30º or 50º C.
(3) SL-VT tests were performed with the temperature during sustained loading that was increased from 30º C to 50º C
In this figure, for ML-CT and SL-CT, only tests at T=30º C are depicted.

(2) SL-CT: Monotonic loading was continuously applied at a constant load rate of 0.6 kN/m/min until the tensile load was reached a certain value where sustained loading was performed for a period of three hours, followed by the restart of monotonic loading at the original load rate. The ambient temperature was controlled to be constant, either 30º C or 50º C, throughout the entire test.
(3) SL-VT: This loading type is similar to (2) SL-CT except that the temperature during sustained loading was increased from 30º C to 50º C in 10 steps at a rate of 2º C/step.

TEST RESULTS AND DISCUSSIONS

Temperature Effects on Rupture Strength

Figs. 4(a) and 4(b) show the relationships between tensile load (V) and tensile strain (ε) from (1) ML-CT tests on HDPE and PP geogrids, respectively. In these tests, HDPE geogrid did not

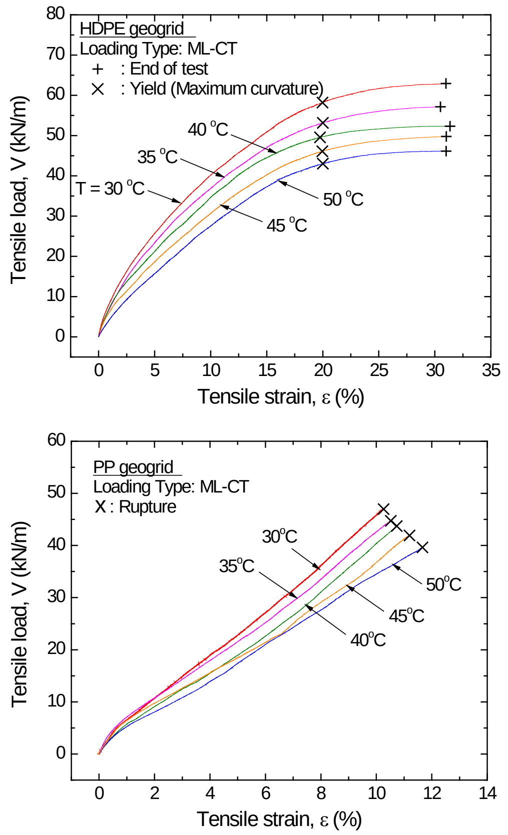

a) b)

Fig. 4 Tensile load and strain relations from (1) ML-CT tests: (a) HDPE; and (b) PP

reach the peak tensile load states at the largest strain applied, about 30 %. Hence, the rupture strength was defined by the yield load at the point of maximum curvature along the V-ε relation.

As the effects of strain rate on the tensile rupture strength (V_{max}) of geosynthetic reinforcement are significant [11], the measured values of V_{max} were corrected to the value at a strain rate of 0.1 %/min (selected as a reference strain rate). As the loading apparatus used is of load-controlled type, the strain rate at rupture along different V-ε relations were different, controlled by the tangential stiffness at the moment of tensile rupture. The values of V_{max} at a strain rate of 0.1 %/min, $V_{max,cor}$, were evaluated from the measured values by numerical simulations based on the non-linear three-component model assuming that the viscous behaviour of the tested geogrids is of isotach type. The details of the correction are described in Kongkitkul et al. (2012) [10].

The values of $V_{max,cor}$ and rupture strain (ε_{rup}) are summarised in Table 2. The secant modulus at rupture (E) of V-ε relation, defined as $E = V_{max,cor}/\varepsilon_{rup}$, is also listed in Table 2. Obviously, the values of V_{max} and E decrease significantly with an increase in the ambient temperature from 30º C.

Table 2 Test results from ML-CT loading type

Types	T (° C)	$V_{max,cor}$ (kN/m)	ε_{rup} (%)	E (kN/m)
HDPE	30	53.14	19.98	266.01
	35	48.09	20.01	240.36
	40	44.88	19.75	227.20
	45	41.82	19.96	209.57
	50	39.05	20.00	195.19
PP	30	44.00	10.27	428.29
	35	43.20	10.52	410.57
	40	41.88	10.74	390.12
	45	40.47	11.20	361.49
	50	38.42	11.66	329.47

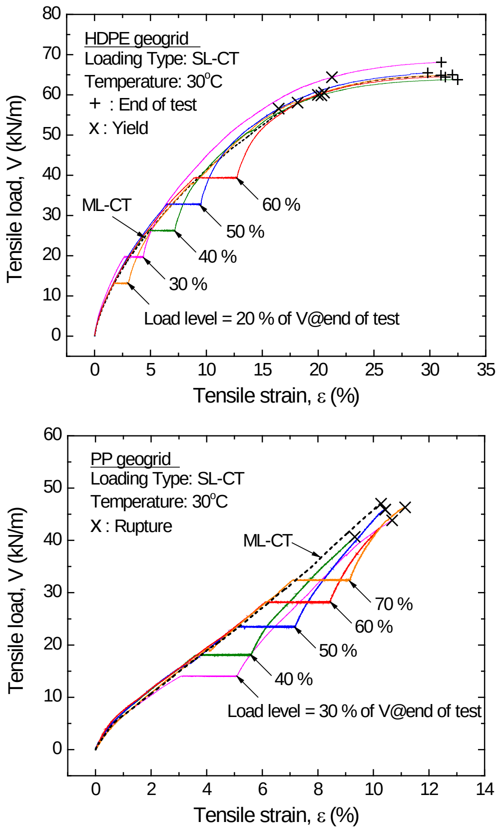

a)

b)

Fig. 5 Tensile load and strain relations at T = 30° C from (2) SL-CT tests: (a) HDPE; and (b) PP

Creep Deformation Characteristics

The V-ε relations obtained from (2) SL-CT tests at T = 30° C and 50° C are shown in Figs. 5 and 6, respectively. The V-ε relations from (3) SL-VT tests are shown in Fig. 7. It may be seen from these figures that the V-ε curves before the start of sustained loading in SL-CT and SL-VT tests are nearly the same as those from ML-CT tests at the same temperature. This result indicates a high repeatability of test in this study.

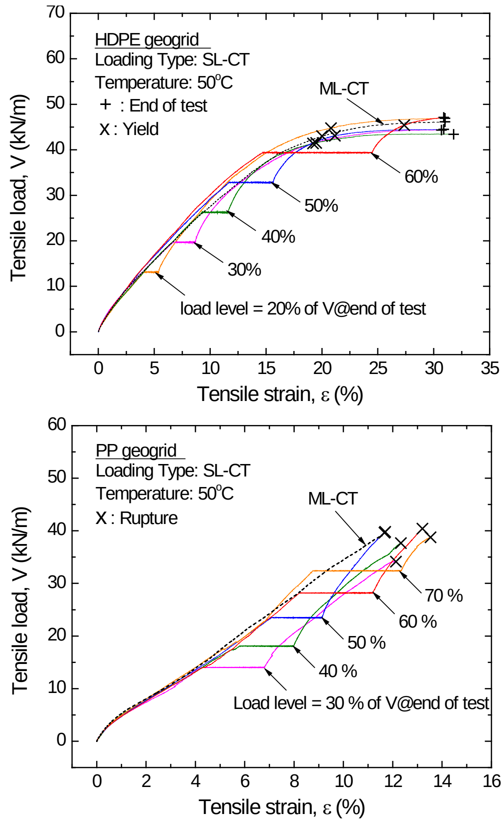

a)

b)

Fig. 6 Tensile load and strain relations at T = 50° C from (2) SL-CT tests: (a) HDPE; and (b) PP

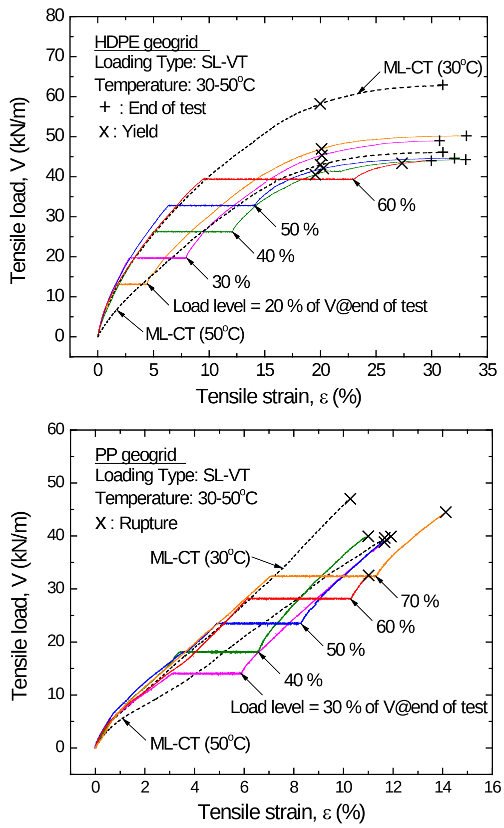

a)

b)

Fig. 7 Tensile load and strain relations from (3) SL-VT tests: (a) HDPE; and (b) PP

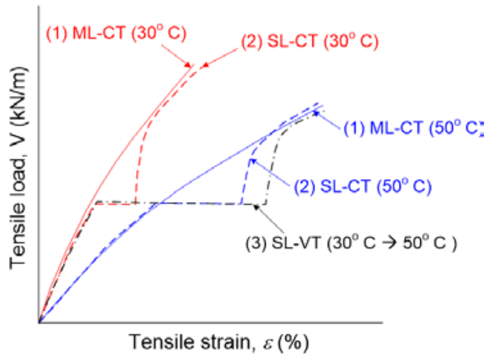

Fig. 8 Schematic diagram showing the trend of behaviour in SC-VT tests

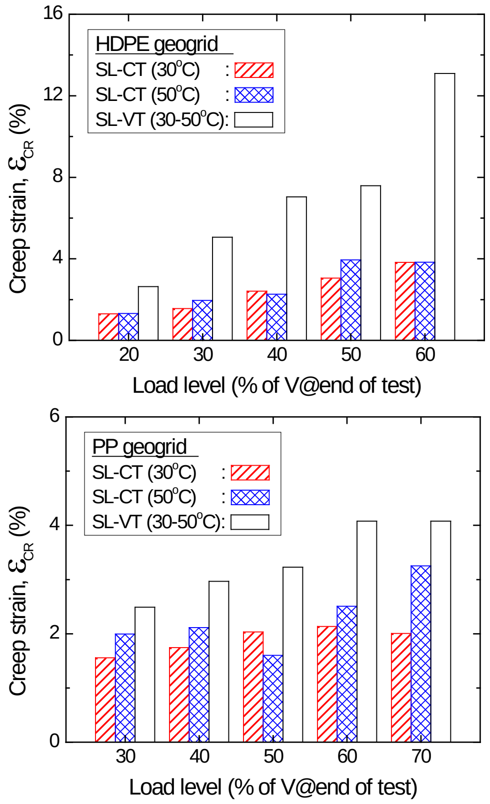

a)

b)

Fig. 9 Comparison of creep strains for: (a)

The following trends of behaviour, as schematically illustrated in Fig. 8, are also seen:

1. In Fig. 7, the *V*-ε curves immediately after the restart of monotonic loading at T = 50º C, following sustained loading, in SL-VT tests are stiffer, while exhibiting larger strains, than those in ML-CT tests at T = 50º C.
2. As seen by comparing Figs. 6 and 7, the *V*-ε curves immediately after the restart of monotonic loading at T = 50º C in SL-VT tests are as stiff as those in SL-CT tests at T = 50º C, although the strains are different.

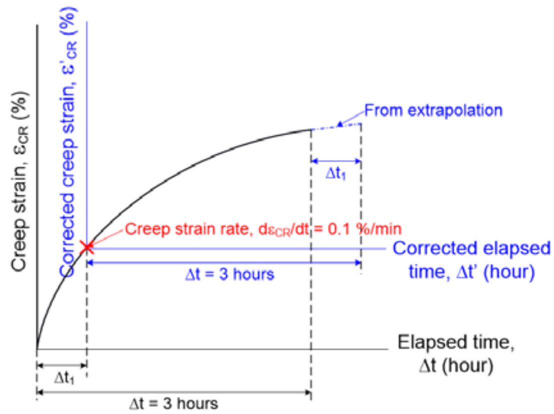

Fig. 10 Defining creep strain for the same initial strain rate

3. The subsequent *V*-ε curves approaching the ultimate failure at T = 50º C in SL-CT and SL-VT tests tend to re-joins those in ML-CT tests at T = 50º C.
4. Reflecting the trends described above, the creep strain by sustained loading during which the temperature increased from 30º C to 50º C in SL-VT tests is significantly larger than the one in SL-CT at T = 30º C or 50º C.

Fig. 9 compares the creep strains (ε_{CR}) defined as the strain increment by sustained loading for a period of 3 hours observed at different load levels from SL-CT and SL-VT tests. These ε_{CR} values have been corrected to those when the initial creep strain is 0.1 %/min (Fig. 10). That is, in this study, the actual initial creep strain rate at the start of respective sustained loading stages was different due to different load levels and temperatures. On the other hand, the ε_{CR} for a given period decreases with a decrease in the initial creep strain rate and vice versa [11]. Therefore, to remove the effects of initial creep strain rate, the start of sustained loading was redefined at the moment when the strain rate was 0.1 %/min and the total creep strain for a period of three hours were estimated by slightly extrapolating the measured time history of creep strain.

Effects of sustained load level on creep strain

It may be seen from Fig. 9 that the creep strain increased with an increase in the sustained load level. This trend is obvious particularly with HDPE geogrid.

Effects of temperature on creep strain

It may be seen from Fig. 9 that, in SL-CT tests at different constant temperatures, with an increase in the temperature, the creep strain increases associated with a decrease in the stiffness (Table 2). Kongkitkul and Tatsuoka (2007) [13] has shown that this trend of behaviour can be simulated based on the non-linear three-component model taking into account the temperature effects.

It may also be seen from Fig. 9 that the creep strain increment by sustained loading during which the temperature increased from 30° C to 50° C in SL-VT tests is significantly larger than both of those at T = 30° C and 50° C in SL-CT tests. Besides, the creep strain increment in SL-VT tests is not a simple summation of those at T = 30° and 50° C in SL-CT tests, but it is the creep strain that developed due to the viscous property coupled with temperature effects in a non-linear manner affected by load-temperature history. In this respect, Fig. 11 shows the time histories of creep strain rates ($d\varepsilon_{CR}/dt$) during sustained loading at the same load level in SL-CT and SL-VT tests of HDPE geogrid. In this figure, the moments when the temperature was changed in the SL-VT case are marked “x”. It may be seen that, as far as the load and temperature are kept constant in SL-CT tests, the creep strain rate consistently and smoothly decreased with time towards a value much lower than the initial value. On the other hand, in SL-VT tests, the relationship between the creep strain rate and the elapsed time exhibits a discontinuous decrease in the decreasing rate of creep strain rate at the moments when the temperature changed. Importantly, the creep strain rate during the last stage at 50° C in SL-VT test is significantly higher than that at the same temperature (50° C) for the same period in SL-CT test, associated with a much higher strain rate at the start of that stage. This trend indicates that the instantaneous creep strain rate is not a unique function of current load, strain and temperature, but it is controlled by loading and temperature history. It will be reported in the near future that these trends of behaviour can be simulated by the non-linear three-component model taking into account the temperature effects.

Effects of Loading and Temperature History on Residual Rupture Strength

Fig. 12(a) and 12(b) show the residual tensile rupture strengths plotted against the temperature at the end of the respective tests (i.e., the temperature when the residual strength was measured) of HDPE and PP geogrids, respectively. The data from ML-CT tests at different constant temperatures are denoted by solid squares. A line is depicted connecting these data points. Two other lines above and below this central line denote the rupture strengths that are 90 % and 110 % of the values from ML-CT tests. The other data points denote the residual strengths obtained by restarting monotonic loading following sustained loading in SL-CT and SL-VT tests. It may be seen that, under the same temperature at rupture, the residual tensile strengths

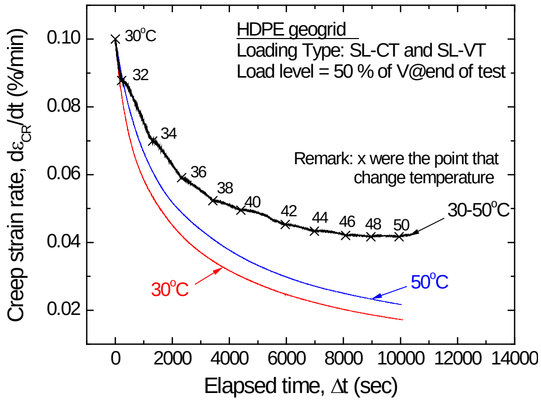

Fig. 11 Creep strain rate vs. time for different test conditions

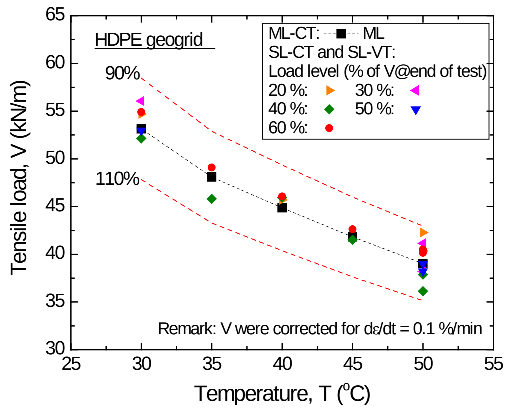

a)

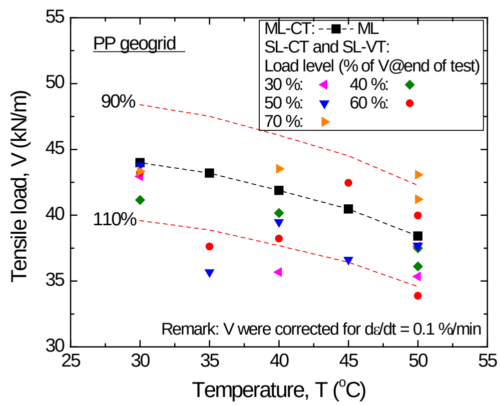

b)

Fig. 12 Residual rupture strength

for different pre-rupture loading and temperature histories are generally similar. With PP geogrid, the scatter of data is relatively large. However, there is no systematic trend due to any specific pre-rupture loading/temperature history. Therefore, it can be concluded that the residual strength of the geogrids tested is a rather unique function of temperature and strain rate at rupture, while independent of pre-rupture loading/temperature history. That is, the rising of ambient temperature exhibits negative effects on the load-deformation behaviour of geogrid. On the other hand, creep by sustained loading is not a degrading phenomenon for the rupture strength of geogrid.

CONCLUSIONS

The following conclusions with respect to the temperature effects on the load-deformation behaviour of polymer geosynthetics can be derived from the test results presented in this paper:

1. The rupture tensile strength and stiffness of the tested two geogrids decreased while the creep strain increased significantly with an increase in the ambient temperature.
2. The creep strain increment by sustained loading during which the temperature was elevated from 30º C to 50º C was significantly larger than the one by sustained loading during otherwise monotonic loading at the constant temperature equal to either 30º C or 50º C.
3. The residual strengths that were obtained with and without pre-rupture sustained loading were essentially the same, showing that creep is not a degrading phenomenon.

ACKNOWLEDGEMENTS

The authors are grateful to the National Research Council of Thailand (NRCT), the Commission on Higher Education, the Thailand Research Fund (TRF) and the National Research University (NRU) Project for financial support. Thanks are also extended to Vigor Merger Co., Ltd and Tencate Geosynthetics (Thailand) Co., Ltd who provided geogrids for this study.

REFERENCES

[1] Koerner RM, Designing with Geosynthetics. New Jersey: Pearson Education, Inc., 2005, ch. 3.
[2] Geosynthetic Institute, "Determination of the Long-Term Design Strength of Stiff Geogrids", GRI Standard Practice GG4(a), 2012.
[3] Geosynthetic Institute, "Determination of the Long-Term Design Strength of Flexible Geogrids ", GRI Standard Practice GG4(b), 2012.
[4] Thornton JS, Paulson JN, and Sandri D, “Conventional and Stepped Isothermal Methods for characterizing long term creep strength of polyester geogrids”, in Proc. 6th Int. Conf. on Geosynthetics, 1998, pp. 691-698.
[5] Jeon HY, Kim SH, and Yoo HK, “Assessment of long-term performances of polymer geogrids by accelerated creep test”, J. of Polymer Testing, Vol. 21, Aug. 2002, pp. 489-495.
[6] Bueno BS, Costanzi MA, and Zornberg JG, “Conventional and accelerated creep tests on nonwoven needle-punched geotextiles”, J. of Geosynthetics International, Vol. 12, Nov. 2005, pp. 276-287.
[7] Jones CJFP and Clarke D, “The residual strength of geosynthetic reinforcement subjected to accelerated creep testing and simulated seismic events”, J. of Geotextiles and Geomembranes, Vol. 25, Feb. 2007, pp. 155-169.
[8] França FAN and Bueno BS, “Creep behaviour of geosynthetics using confined accelerated tests”, J. of Geosynthetics International, Vol. 18, Oct. 2011, pp. 242-254.
[9] Kongkitkul W, Hirakawa D, Tatsuoka F, and Uchimura T, “Viscous deformation of geosynthetic reinforcement under cyclic loading conditions and its model simulation”, J. of Geosynthetics International, Vol. 11, Apr. 2004, pp. 73-99.
[10] Kongkitkul W, Tabsombut W, Jaturapitakkul C, and Tatsuoka F, “Effects of temperature on the rupture strength and elastic stiffness of geogrids”, J. of Geosynthetics International, Vol. 19, Apr. 2012, pp. 106-123.
[11] Hirakawa D, Kongkitkul W, Tatsuoka F, and Uchimura T, “Time-dependent stress-strain behaviour due to viscous properties of geogrid reinforcement”,J. of Geosynthetics International, Vol. 10, Dec. 2003, pp. 176-199.
[12] Tatsuoka F, Benedetto D, Kongkitkul W, Kongsukpraserat L, Nishi T and Sano Y, “Modelling of ageing on the elasto-viscoplastic behaviour of geomaterial”, J. of Soils and Foundations, Vol. 48, Apr. 2008, pp. 155-174.
[13] Kongkitkul W and Tatsuoka F, “A theoretical framework to analyse the behaviour of polymer geosynthetic reinforcement in temperature-accelerated creep tests”, J. of Geosynthetics International, Vol. 14, Feb. 2007, pp. 23-38.
[14] Zornberg JG, Byler BB, and Knudsen JW, “Creep of geotextiles using Time-Temperature Superposition methods”, J. of ASCE, Vol. 130, Nov. 2004, pp. 1158-1168.

Fifth International Conference on Geotechnique, Construction Materials and Environment, Osaka, Japan, Nov. 16-18, 2015, ISBN: 978-4-9905958-4-5 C3051

MANAGING VALORIZATION OF DREDGED SEDIMENTS VIA AN INNOVATIVE MATHEMATICAL MODEL USED FOR CIVIL ENGINEERING APPLICATION

M.Benzerzour[1], N.Abriak[1], I.Khezami[1], R.Mansi[1],
[1] Civil & Environmental Engineering department, Ecole Mines Douai, 59500 Douai, France

ABSTRACT

Several years ago, global consumption of materials used in the field of Civil Engineering and especially materials for public works, has strongly growth. The use of marine and/or river dredged sediments presents a promising alternative to deal with the problematic of sustainable development. In this paper, we study a management problem of existing treatments for these sediments. Looking to the economical and legislative obligations associated with the treatment process, these operations present one of the main encountered problems during the valorization process of sediments. The solution for this problem is to find an optimal set of treatments respecting these economical and legislative constraints. This optimal solution is obtained by solving a non-linear mathematical model with binaries variables. The proposed resolution algorithm for this model is based on a linearization of the nonlinear constraints in order to solve a simple problem using a solver.

Keywords: dredged sediments, valorization, mathematical model, civil engineering

Introduction

The exploration and the exploitation of existing and future fields are increasingly regulated looking to the economic, social and environmental reasons. The important need to conserve environment and to manage the valorisation of wastes, presents an unavoidable industrial stakes looking to its financial and environment impact.

Each year, huge quantity (600 million m3/year [4]) of sediments and sands resulting from the dredged operations executed to maintaining and to ensure the accessibility of ports and waterways. Port authorities have to find solutions for integrated and enduring managements of these sediments. Several ways of valorization in Civil Engineering applications are possible, such as the foundation of roads, dikes and landscaped mounds, concrete and artificial aggregates [6,8]. However, this management remains complex and mainly depends on several principals parameters environmental, mechanical and economic parameters.

1 Scientific approach

Several experiments of valorization are realized in the context of European research projects such as: experimental roads based on marine sediments (ex: experimental road of 200 m in Caen, France (project SETARMS [1]); implementation of dikes with river sediments (Project PRISMA[2]).

These scientific researches currently instrumented give very good results, but the sustainability of the valorization processes is not acquired and meets strong mechanical, economic and environmental challenges. Indeed, these valorizations in road construction require many specific treatments such as dehydration, de-pollution mineralogical and organic treatments, and reinforcement treatment by adding hydraulic binders and/or granules. Moreover, these valorizations process should deal with the optimizations problems of deposits sediments available locally and costs of treatment.

In the diagram below, we present the global scientific approach for the development of dredged sediments in road applications.

The valorisation of dredged sediment is composed on six main steps:

1. Zoning: localization of the potential deposit to be dredged
2. Dredging: which can be mechanical or hydraulic
3. Storage: according to the environmental nature of the sediment
4. **Treatment / formulation**
5. Laboratory validation
6. In-situ validation

One of the most important and delicate steps in the valorisation process is the treatment and the formulation of new materials based on sediments. It requires a process of optimization and reflection, often difficult. It also requires different treatments to improve sediment characteristics respecting mechanical, environmental and economic constraints of feasibility. Several treatment techniques exist such as reducing the pollution using electrokinetic methods [2]; reducing the organic matter by bioremediation technical or by calcinations [11]; reducing the water content by filter press or natural settling [7].

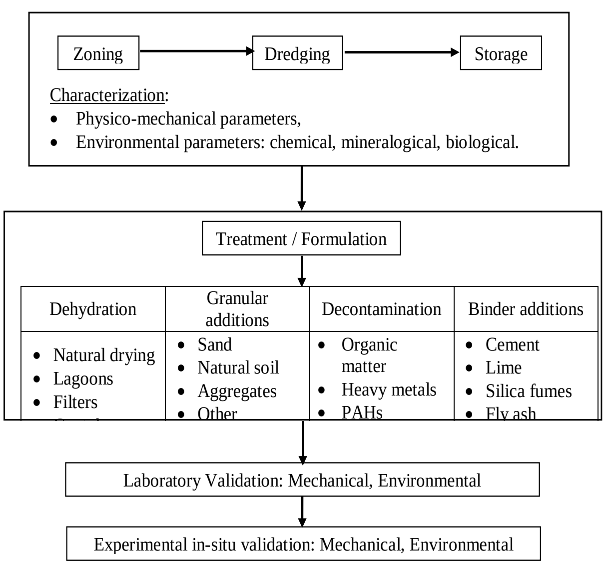

Figure 1: Valorization process

Formulation's methods look to increase the resistance of the material. These formulations are mainly done by granular additions [6] and also by addition~~s~~ of hydraulic binder [12, 13]. The optimization of these treatment methods and formulation is mainly based on the economic, mechanical and environmental criteria.

2 Mathematical Model

The objective of our research is to find a solution that provides an acceptable material for valuation in road construction. This solution is in the form of a mixture of sediment with one or more noble materials (ex: sand) which is subjected to a set of physical and chemical treatments in order to respond to requirements and normative constraints. We are interested only by the chemical part in order to solve a choice treatments problem.

Before presenting the different constraints of our model, we introduce a set of variables X associated with each sediment. $x_i \in X$ is a binary variable which equal to 1 if the sediment i is used and equal to 0 else, for $i = 1, \ldots, n$ where n is the number of sediments. The first constraint should ensure the choice of one ~~and~~ only ~~one~~ sediment. The mixture of several sediments can activate a chemical interaction between elements witch disturbs strongly the efficiency of any programmed treatment. This constraint can be presented by:

$$\sum_{i=1}^{n} x_i = 1 \qquad (1)$$

The set of treatments applied on sediment depends principally on its pollution and on the field of valorisation. In this paper we consider the case of road application.

2.1 Chemical constraints

The environmental aspect in the construction of roads based on a sub product or waste is one of the most important constraints according to the regulation (Guide SETRA [3]). Each country requires some limit values for polluting elements in the raw materials used for construction. The acceptability limits to use materials in road application are mainly concerning the concentration of contaminants elements in these materials. For example, the limits required in France are given in the next table.

Elements	Limit (mg/kl)
TOC: total organic carbon	60000
BTEX : Benzene, toluene, ethylbenzene and xylenes	6
PCB : Polyvinyl biphenyls	1
HCT : total hydrocarbons	500
PAH : Polycyclic aromatic hydrocarbons	50
As	2
Ba	100
Cd	1
Cr : total	10
Cu	50
Hg	0.2
Mo	10
Ni	10
Pb	10
Sb	0.7
Se	0.5
Zn	50
Fluoride	150
chloride	15000
Sulfate	20000
fraction soluble	60000

Table 1: Legislative limits for chemical elements in France

These limits can change from a country to another, but the constraints are always present. To make an acceptable material (sediment in our case) for road construction, it must be cleaned. In other world, it must be exposed to a set of known techniques of pre-treatment and treatment to reduce the concentration of contaminants elements if necessary. We know that each treatment has an impact on all contaminant elements. For example, the electrokinetic treatment can reduce the concentration percentage of some heavy metals such as Zn up to 32% [2] and the treatment with remediation can reduce it further to 10% [3]. Therefore, the application of the two previous treatments can reduce the concentration of Zn until (32% × 10% = 3.2%) of its initial concentration. We note that in practice rarely are the cases where the sediment requires multiple treatments.

To model this constraint, we introduce the binary variables T_T for $t = 1, \dots, |T|$ where $|T|$ is the number of treatments:

$$T_t = \begin{cases} 1 & \text{for treatment t} \\ 0 & \text{else} \end{cases}$$

$q_i^j \in [0,1]$ is a continuous value that indicates the quantity of the contaminant element j in the used sediment *i* and Q^j presents the limit associated with the element *j*. Denote by $|Q|$ the number of elements. The parameter δ_{ti}^j represents the reduction percentage associated with the element *j* and resulting by the application of treatment t on the sediment$i$. Environmental constraints can then be written as follows:

$$q_i^j \prod_{t=1}^{|T|} \left(1 - \delta_{ti}^j T_t\right) \leq Q^j + (1 - x_i)M \quad (2)$$

$$i = 1, \dots, n, \quad j = 1, \dots, |Q|$$

With M is a large positive constant which helps to relax the constraint when the sediment i is not used ($x_i = 0$). The product $\prod_{t=1}^{|T|} \left(1 - \delta_{ti}^j T_t\right)$ models the reduction of the percentage of the concentrationq_i^j.

Other constraints should be respected concerning the incompatibility of using two or more treatments together.

$$\sum_{t \in C_T^k} T_t \leq 1 \qquad (3)$$

$$k = 1, \dots, |C_T|$$

For the constraint (3), suppose that there are two possible treatments, the first one is based on the acid chemical treatment and the second uses the bacteria to reduce the organic matter.
The mixing of these two treatments cancels the role of the bacteria treatment. In order to efficiently use every treatment and then reduce the cost we should use at most one of these two treatments.

2.2 Objective function

The objective of our mathematical model is to find an acceptable solution for road application with a minimum costs. These costs are divided into two parts. The first one is concerning the acquisition and/or the dredging operations, presented by the vector $C^1 = (c_1^1, \dots, c_n^1)$ and the second one is the cost of treatments presented by the vector $C^2 = (c_1^2, \dots, c_{|T|}^2)$. The objective function is presented then by:

$$Min \quad \sum_{i=1}^{n} c_i^1 x_i + \sum_{t=1}^{|T|} c_t^2 T_t \qquad (4)$$

2.3 General Presentation of mathematical model

The mathematical model for the problem of valorization of sediments is presented by the following Quadratic MIP 0-1 problem. This model is non-linear because of constraints (2).

$$Min \ \sum_{i=1}^{n} c_i^1 x_i + \sum_{t=1}^{|T|} c_t^2 T_t \qquad (4)$$

$$\text{s.t.} \quad \sum_{i=1}^{n} x_i = 1 \qquad (1)$$

$$q_i^j \prod_{t=1}^{|T|} \left(1 - \delta_{ti}^j T_t\right) \le Q^j + (1 - x_i)M \quad (2)$$

$$i = 1, \dots, n, \quad j = 1, \dots, |Q|$$

$$\sum_{t \in C_T^k} T_t \le 1 \qquad (3)$$

$$k = 1, \dots, |C_T|$$

3 Heuristic

3.1 Linearization of nonlinear constraints (2)

Constraints (2) are nonlinear. They pose a particular difficult to solve our problem. In order to simplify our model, it is necessary to linearize these constraints, i.e. the quadratic expression $\Phi_i^{|T|} = \prod_{t=1}^{|T|} (1 - \delta_{ti} T_t)$. So we list all the combinations of variables T_t. This expensive process ($2^{|T|}$ cases) is justified by the limited number of possible treatments (at most $|T| = 20$). The linearization of $\Phi_i^{|T|}$ requires the introduction of new variable y_h associated with the combination of variables C_h^T (h is the index of the combination):

$$y_h = \begin{cases} 1 & \text{if } \forall t \in C_h^T,\ T_t = 1;\ \forall t \notin C_h^T, T_t = 0 \\ 0 & \text{else} \end{cases}$$

The associated cost with y_h is calculated then by $c_h^2 = (\sum_{t \in C_h^T} c_t^2)$ and the coefficients of y_h are $a_{ih}^j = \prod_{t \in C_h^T} (1 - \delta_{ti}^j)$. For example: the combination $C_h^T = \{2,3,4\}$ of variables is presented by the new binary variable y_h with cost $c_h^2 = (c_2^2 + c_3^2 + c_4^2)$ and coefficients $a_{ih}^j = (1 - \delta_{2i}^j) \times (1 - \delta_{3i}^j) \times (1 - \delta_{4i}^j)$.

To finalize this linearization, we add the constraint (5) to impose the choice of a single treatment combination as possible.

$$\sum_{h=1}^{2^{|T|}} y_h \qquad \le 1 \qquad (5)$$

In similar cases in the literature, an alternative approach based on the column generation algorithm [1] is adopted i.e. only promising variables (combinations) will be generated. This is difficult in our case because of the non-linearity of $\Phi_i^{|T|}$. So to solve our problem, we will use the opposite approach of the column generation algorithm. More specifically, we will generate all the variables (combinations). Note that the variables y will not be generated at the same time, but they will be added to the model step by step during the resolution. In practice, the number of treatments for sediment is very limited, which leads us to give priority to the small combinations of treatment. Then, we will consider in the beginning a combination of two treatments and after we generate a combinations of three, four and five treatments if not more. This proposal linearization for the constraint (2) allows us to eliminate the constraint (3). This constraint will be respected during the generation of different combinations. The new linear model is presented below.

$$Min \ \sum_{i=1}^{n} c_i^1 x_i + \sum_{t=1}^{|T|} c_t^2 T_t \qquad (4)$$

$$\text{s.t.} \quad \sum_{i=1}^{n} x_i = 1 \qquad (1)$$

$$q_i^j \sum_{h=1}^{2^{|T|}} a_{ih}^j y_h \le Q^j + (1 - x_i)M \qquad (2)$$

$$i = 1, \dots, n, \quad j = 1, \dots, |Q|$$

$$\sum_{h=1}^{2^{|T|}} y_h \le 1 \qquad (5)$$

$$x \in \{0,1\}^n, \quad y_h \in \{0,1\},$$

$$h = 1, \dots, 2^{|T|}$$

The resolution of this mathematical model can be done using an approximate method (heuristic for MIP 0-1 problems) or using an exact algorithms. The latters can spend a large execution time. To solve our model, we used a free solver Lpsolve. Other more efficient commercial solvers can also be used; for example Cplex. These solvers are principally based on exact algorithms.

4 Conclusions

In this paper, we proposed a mathematical model that optimizes the management and the choice of used treatments for a decontamination of marine and/or river sediments. This problem has been modelled as a nonlinear mathematical model with mixed variables. Our solving approach is mainly based on a linearization of this model. This linearization is based on the enumeration of all non-linear combinations. Finally, the simplified mathematical model is solved using a numerical solver. This mathematical model can be widened to other parameters, in particular, physical and mechanical parameters, in order to use sediments as alternative materials.

References

[1] George, B, Dantzig and Philip, Wolfe Decomposition Principle for Linear Programs. Operations Research, 8(3): 101–111, 1960.

[2] Kim, K.J., Kim, D.H., Yoo, J.C., Baek, K. Electrokinetic extraction of heavy metals from dredged marine sediment. Separation and Purification Technology, 79: 164–169, 2011.

[3] Lors, C., Tiffreau, C., Laboudigue, A. Effects of bacterial activities on the release of heavy metals from contaminated dredged sediments. Chemosphere, 56: 619–630, 2004.

[4] Jones-Lee, A., Lee, G.F. Water Quality Aspects of Dredged Sediment Management, Water Encyclopedia: Water Quality and Resource Development. Wiley, Hoboken, NJ: 122-127, 2005.

[5] Chen, H.J., Yang, M.D., Tang, C.W., Wang, S.Y. Producing synthetic lightweight aggregates from reservoir sediments. Construction and Building Materials, 28: 387-394, 2012.

[6] Zentar, R., Dubois, V., Abriak, N Mechanical behavior and environmental impacts of a test road built with marine dredged sediments. Resources, Conservation and Recycling, 52: 947–954, 2008.

[7] Dubois, V., Abriak, N., Zentar, R., Ballivy, G The use of marine sediments as a pavement base material. Waste Management, 29: 774-782, 2009.

[8] Miraoui, M., Zentar, R., Abriak, N Road material basis in dredged sediment and basic oxygen furnace steel slag. Construction and Building Materials, 30: 309-319, 2012.

[9] Tang, C.W. Chen, H.J., Wang, S.Y., Spaulding, J. Production of synthetic lightweight aggregate using reservoir sediments for concrete and masonry. Cement and Concrete Composites, 33: 292-300, 2011.

[10] Troalen, J.P., Duron, C., Hagnere, C. Traitement de vases de l’estuaire de la Seine. Revue Française de Géotechnique, 77: 31-36, 1996.

[11] Lafhaj, Z., Samara, M., Agostini, F., Boucard, L., Skoczylas, F., Depelsenaire, G Polluted river sediments from the North region of France: Treatment with Novosol process and valorization in clay bricks. Construction and Building Materials, 22: 755-762, 2008.

[12] Tremblay H., Leroueil S., Locat J. Influence of the nature of organic matter on the soil stabilization with cement. Canadian Geotechnical Journal, 39: 535-546, 2002.

[13] Satone, H., Mamiya, T., Harunari, A., Mori, T., Tsubaki, T. Solidification Mechanism of the Sediment Formed by

Particle Settling — Analysis of the Final State of the Sediment. Original Research Article Advanced Powder Technology, 19(3): 293-306, 2008.

[14] Levacher, D., Sanchez, M. Characterization of marine sediments for a reuse inland disposal land embankment. European Journal of Environmental and Civil Engineering, 15: 167-178, 2011.

Fifth International Conference on Geotechnique, Construction Materials and Environment, Osaka, Japan, Nov. 16-18, 2015, ISBN: 978-4-9905958-4-5 C3051

AN INVESTIGATION OF POLYURETHANE FOAM WITH A VAPOUR PHASE CORROSION INHIBITOR AS CORROSION PROTECTION SYSTEM

Steve Hecker[1] and Vanissorn Vimonsatit[2]
Department of Civil Engineering, Curtin University, Western Australia

ABSTRACT

Polyurethane (PU) foam is currently being explored by local corrosion consultants as a corrosion protection method. Vapour phase Corrosion Inhibitors (VpCI) are successfully being used for internal airtight spaces like electrical cabinets and PU foam has been successfully used as vehicle for certain additives such as flame retardants. The purpose of this study is to provide scientific data to develop an initial understanding of the characteristics of using VpCI as an additive to PU foam. This research is divided into two parts: Part I investigates the effects of adding a VpCI additive to PU foam and compares it to natural PU foam, and Part II is to conduct a life cycle cost analysis of PU foam to compare against existing method of replacement. The findings indicate that VpCI additive has a dramatic effect on the foams properties. This study enables corrosion experts and future researchers a foundation to explore other areas to develop this proposed corrosion protection method.

Keywords: Corrosion Protection, Polyutrethane Foam, Corrosion Inhibitor, VpCI

INTRODUCTION

The nature and extent of any corrosion is linked to the amount of time and severity that the steel has been exposed to moisture and air pollution [1]. These environments have been identified and classified in AS2312:2002 [2], which cover the guide to the protection of steel against atmospheric corrosion for Australia and New Zealand. These classifications aid in assisting designers in selecting an appropriate coating system as a hostile environment such as acidic environments (Category F in clause of 2.3 AS2312:2002) will require a much higher standard of protection than one in a placid environment (Category A in clause 2.3 of AS2312:2002).

Internal corrosion of steel hollow section is preventable if the section is sealed [3]. However evidence shows corrosion still occurred overtime due to fatigue cracks.

Polyurethane (PU) foam consists of its two main ingredients, isocyanate and polyol. However many additives have been used in a variety of applications. These additives that may be required can be used to modify reaction conditions, change the finish of the final product or control the foam. These additives include, but are not limited to catalysts, chain extenders, cross linkers, fillers, moisture scavengers, colorants and others [4].

Different additives are well tried and tested in PU foam however they can potentially have varying effects on the desired performance. Using corrosion inhibitors in PU foam as an additive in principal is not new however data is required to assess its adequacy as per the required objectives of the PU foam for this application and in accordance with AS1366:1992 [5].

Adhesion of PU foam is used extensively throughout the construction and transport industries [6]. Researcher [7] and many other PU foam institutes such as Evonik [8] have researched and tested not only the adhesion of PU foam naturally but also with adhesion additives. The adhesion strength of unmodified PU foam was found to be 0.144 N/mm^2 to 0.232 N/mm^2 depending on formulation used. However, in addition, it was found that adding a primer to the surface of the steel dramatically increased the adhesion strength by up to 300%. What effects will another additive such as polyurethane foam have on the adhesion strength of PU foam is another un-researched area of interest of this study.

Vapour Phase Corrosion inhibitors (VpCI) excel in closed situations, as such are perfect for this application [9]. Past researches [10], [11], [12] that have looked at the effect of pre-corrosion on VpCI performance were concluded that whilst it had a negative effect, it could be controlled, and as such it was shown [13] that even some inhibitors performed better with pre-corrosion. PU foam can be very resilient to moisture absorption, this is critical to the success of this study proposed application. Moisture is bad for VpCI effectiveness and is the cause of corrosion. Literature showed how to model moisture absorption [14] and it was found that PU foam samples could absorb 8 to 10% moisture [15]. Water absorption of the PU foam has to meet AS2498.8 [16].

The use of higher compressive strength type PU foams are highly recommended, whilst understanding the effects of temperature on the compressive strength is critical [17]. The effect of temperature on PU foam can result in change in volume and mass and subsequent density [18].

In Part I of this paper the objective is to investigate the quality of PU foam with a VpCI additive to existing steel hollow sections, in accordance with AS1366.1:1992 [19] and AS2498.0:1993 [20], through analysing the physical appearance (i.e. cell density, cracks, splits, voids) and water absorption of PU foam with and without a VpCI additive. Part II presents a life cycle cost analysis of PU foam. Life-Cycle Cost in accordance with AS4536:1999 [21] which outlines a detailed estimation into the cost of this proposed corrosion protection method was conducted. This was achieved using engineering economic models such as Net Present Values (NPV) and Annualized Net Present Value (ANPV) to determine direct costs of the cash flow. Values have been defined in order to compare against current and future corrosion protection systems to the internals of hollow sections.

PU FOAM WITH VPCI ADDITIVE

The quality of PU foam with and without VpCI additive as corrosion protection of steel hollow section is tested in accordance with AS1366.1:1992 and AS2498.0:1993. Steel sections used in the test are 100x100x2.0mm SHS, 40x40x2.0mm SHS, 88.9x3.0mm CHS, and 42.4x2.0mm CHS Section. Each section has been orientated at both 90º and 45º to simulate differing positions typically seen on conveyor systems.

Density

The density of PU foam depends on section size and subsequent volume. The density of natural PU foam varies from 24.5 kg/m3 to 53.2 kg/m^3; the density of PU foam with the VpCI additive varies from 24.8 kg/m^3 to 60.1 kg/m^3. The overall results are shown in Fig. 1. The scatter of the test data was due to inconsistency during the application of the foam therefore the test on the same section was conducted twic for accuracy. The linear trends have been added to show an average of the densities for sections for both types of foam from all the tests. VpCI additive represented by linear blue line shows an increase in foam density over natural PU foam. The average density of natural PU foam is 34.1 kg/m^3 and of VpCI additive is 42.3 kg/m^3, giving an increase in the density of 24%. Physical observation confirms the notion that the vapour phase corrosion inhibitor has repressed the polyurethane's expansion chemical reaction and created a more dense and heavier polyurethane foam.

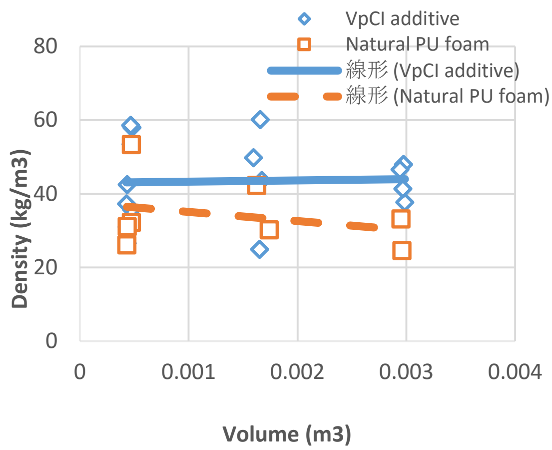

Fig. 1 Density of PU foam with and without VpCI

Physical Appearance

The physical appearance of the polyurethane foam specimens with and without a vapour phase corrosion inhibitor has been conducted in accordance with AS1366.1:1992 guidelines.

Cracks

Cracks were less prominent with natural polyurethane foam with an average rating of low to very low (0.88). With Corrosion inhibitor the cracks were more present with an appearance rating of 1.06 (20.5% difference). However with the additive, crack score was still varying from low to very low and was not of significant interest.

Internal Voids

Internal voids between the two types of PU foam presented in Fig. 2 show a 19% difference (1.56 VpCI to 1.31 Natural) in score values with range being for both of low to medium. Internal voids are not detrimental to the success of the VpCI additive as internal voids are sealed off to the atmosphere resulting in no moisture penetration and subsequently no corrosion.

External Voids

External voids are critical to the efficiency of a VpCI additive. If the foam cannot be fully adhered to the steel and leaves external voids then corrosion inhibitor will not easily create a protective barrier against moisture corrosion. In addition, external voids will easily allow the "pooling" of water and moisture penetration further exacerbating the corrosion problem. Natural PU foam scored an average of 1.43 varying from low to medium with the VpCI additive actually scoring lower with 1.23 (difference of 16.5%). Again both scores were from low to medium and as such no significantly difference is present. The extra denseness can explain the slight decrease in external voids as more space is being inhabited by foam.

Elongated voids

Elongated voids were present in both types of polyurethane foam. It was apparent that whenever there were voids in the VpCI specimens that they were elongated style voids. This was also further reinforced with a 45% more elongated cells with an average score of 1.18 scoring low to medium compared to natural foam which had an average of 0.81 (very low to low). Again however elongated voids were only present with internally voids, and as a result, elongated voids are not detrimental to the success of the VpCI additive as internal voids are sealed off to the atmosphere resulting in no moisture penetration and subsequently no corrosion.

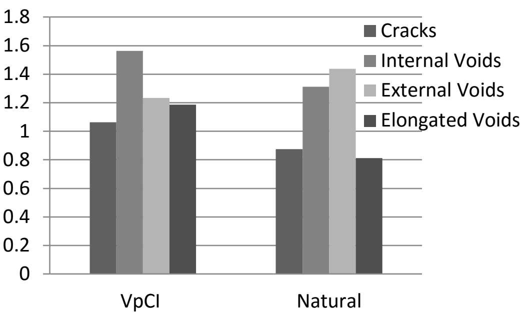

Fig. 2 Physical appearances index

Colour

The colour although not critical to this application, however when considering further uses in insulation and construction the colour has an off white colour compared to the natural yellowish colour known to polyurethane foam. Figure 3 shows the difference in colour; colour is something that should be agreed upon by both client and supplier and as such does not have a required standard to adhere to.

Water Absorption

Table 1 presents the water absorbed as a percent (%) and water absorbed per unit of surface area (g/mm^2) as per ASTM D 2842 [22]. Test on each material was conducted twice.

Water absorbed in PU specimens 1 and 2 with a VpCI additive are 9.76% and 10.71% water moisture, respectively, i.e., an average of 10.23%. In Natural PU specimens 1 and 2 with no additive, water absorbed are 13.04% and 14.81% water moisture respectively, i.e., an average of 13.92%.

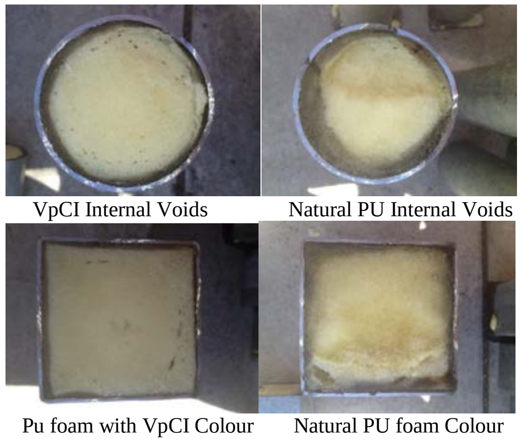

Fig. 3 Voids and Colours

Table 1 Water absorption

Items	Surface area m^2	Initial Weight g	Weight 96hr g	Water Absorbed % [g/mm^2]
VpCI 1	0.05	41.0	45.0	9.76 [79.26]
VpCI 2	0.04	28.0	31.0	10.71 [69.48]
PU 1	0.04	23.0	26.0	13.04 [70.11]
PU 2	0.05	27.0	31.0	14.81 [83.62]

From these values, it is apparent that with the addition of a VpCI additive the PU foam samples prevented the absorption of water by 3.70%. As described previously, an objective of the PU foam in this study is to prevent water moisture to the internals of hollow sections, these results are beneficial to this study. When considering water absorbed per unit of surface area (g/m^2), specimens with the VpCI additive averaged a water absorbed/unit of surface area (g/m^2) of 74.37 g/m^2 whilst the natural PU foam specimens averaged 76.86 g/m^2. These results show the natural PU foam specimens absorbed slightly more water per unit of surface area (3.35% more water absorption), which does not present an abnormal or major differing result.

LIFE CYCLE COST

Maintenance to steel structures includes all activities throughout the design life of the structure that are performed to mitigate corrosion, to repair corrosion-induced damage, and to reinstate the structure, which has become unusable as a consequence of corrosion. These activities come together to form Corrosion Management. Whilst corrosion management and its activities differ depending on the type of structure and environment it is a recognised and practiced way of planning and facilitating for corrosion [23], [24].

When dealing with corrosion on existing structures or for the design of new structures some form of corrosion management and corrosion design is required. These ideas are used to forecast costs to corrosion and determine the best corrosion practice for the specific steel structure.

In the present study, the following 8 cost elements, in no particular order (cf. Section 4.3 (a) of AS4536:1999), are considered.

1. Polyurethane Material Supply: The cost and supply of PU foam for site use.
2. Vapour Phase Corrosion Inhibitor Powder Supply: The cost and supply of VpCI for site use.
3. Surface preparation and external paint coatings: Abrasive blast cleaning, Protective primer and paint coating system to externals of the sections being maintained.
4. Metalwork to Members: This task includes the welding, cutting, grinding and any additional work to repair extremely degraded members to raise the health to a level of quality required for PU foam injection.
5. Preparation of mixing the PU foam and VpCI: On-site mixing and preparation required pre-installation.
6. Installation of PU foam with Injection Machine: Injection of Polyurethane foam into the steel hollow sections. This task mainly includes the man and machine labour required to fulfil task. Machine injection is considered the most efficient and practical way to install polyurethane foam in large quantities.
7. Setting Period: This task includes cream time, Gel time and Tack-free setting time.
8. Cleaning: Spillage, off-cutting required and general cleaning required for external paint and coating systems.

The cost element assumptions and exclusions are according to Section 4.3(b) of AS4536:1999. The following points identify cost elements that will not vary between comparing alternatives, therefore will be excluded.

- Any structure consisting of hollow sections could be used, however in this study, the structure considered in the cost analysis is a truss system as typically seen on processing plant conveyor systems.
- The size and number of members do not vary from method to method and therefore any sections' and subsequent area properties and lengths can be used to estimate absolute cost.
- Working at heights or other conditions that require extra costs have been excluded; these costs would need to be added on if required. This can be done as no matter the protection system it will be same condition
- The protective coating system VpCI has a life of 2 years as per Cortec recommendations for VpCI 609/609S used for this study
- Using Boddington gold mine as an example the expected mine life is approximately 20 years [25]. Mines life vary from mine to mine and as it is a constant variable regardless of the corrosion protection method, 20 years will be used.
- All prices exclude Goods and Services Tax.
- Overhead costs such as administration work, Occupational Health & safety and design work such as drawings have been excluded.

The obtained cost in this study is from using 500m length of 110 circular hollow sections to determine a $/m of the protection system. All costs are in Australian dollars.

Direct Cost of PU Foam

Direct cost includes material and construction cost. This section estimates the direct cost of using PU foam as the corrosion protection material. The unit costs of PU and VpCI are from local suppliers in Western Australia; other cost items such as the surface preparation and external paint coatings, metalwork, materials preparation and installation, setting and cleaning, are taken from SPON:2012 [26].

Material

1. PU foam ($/per m3): $465.00/m^3
2. VpCI ($/per m3): $48.91/m^3

Construction

1. Surface preparation and external paint coatings: $50.03/m^2
2. Metalwork to Members: $25.60/m
3. Preparation of mixing the PU foam and VpCI: $0.66/m^3
4. Injection machine hire costs: $20.00/m^3
5. Setting Period: $13.80/m^3
6. Cleaning: $39.90/m^3

Net Present Values of this corrosion method cash flow has considered a 1 metre length of 114.3 x 4.50 CHS as discussed in section 5.1.3 of this report. Using the area units, a cost per metre of 114.3x4.5CHS is $35.56/m.

Using 114.3 x 4.5 CHS, with the internal volume per metre of 0.00871 m^3/m, the total cost of this protection method is $35.56/m.

Direct Cost of Replacement

Without application of corrosion protection to steel members, it might be inevitable to replace the corroded steel with a new member. The cost of replacement is estimated in this section.

Material

For a new member, fabrication and supply costs obtained from a supplier's quotes are used to determine an accurate estimate (in year 2014) of steel sections; cost per tonne is $2145/tonne.

Construction

1. Surface preparation and external paint coatings: \$50.03/m^2 Abrasive blast clean, Primer and Paint coating materials and Labour.
2. Metalwork to remove Members: $10.25m.
3. Metal work to install new members: $25.63/m

For the net Present Values of this replacement method, the cost is considered per a 1 metre length of 114.3 x 4.50 CHS as to keep it consistent with PU/VpCI corrosion protection method. Using the above steel areas, a cost per metre is: $61.91/m.

Net Present Values and Annualised Values

Net present value (NPV) is used to determine if a proposed project is of cost benefit to the stakeholders. It uses a cash flow model based on what future monies are worth today. The annualised value (AV) is the economic figure which will be used to fairly and accurately compare PU with VpCI method against replacement of corroded members. Subsequently NPV and annualised value were estimated for the replacement option and were used to compare the results.

PU Method

With the guidelines and parameters considered, a cost of coating was estimated as $39.94/m of 110x4.5 CHS section. Subsequently Present Day Value (PDV) of this method was calculated at $154,179.00. When considering lifetime of structure and life of protection method as the two methods have different protection periods, annualised Value (AV) was estimated at $12,372.00

Replacement Method

A cost of coating was established of $39.94/m of 110x4.5 CHS section. Subsequently Present Day Value (PDV) of this method was calculated at $175,675.00. When considering lifetime of structure and life of protection method as the two methods have different protection periods, annualized Value (AV) was estimated at $14,096.00.

Uncertainties associated with the cost estimation are beyond the control of the estimation. The effectiveness of the Vapour phase inhibitor to prevent degradation is uncertain and may affect the lifetime of product but is neglected in this study. Weather constraints placed on construction may affect the time and subsequently the cost of the construction.

CONCLUSION

The findings of this study show that vapour phase corrosion inhibitors have a high potential of being a successful corrosion protection method in industry for steel hollow sections. This study presents, for corrosion consultants, the effects of the VpCI on polyurethanes behaviour and properties with no stand out concerning results which is a promising outcome. These results enable corrosion experts and future researchers a foundation to explore other areas, which are recommended as follows:

(1) The effectiveness of the VpCI to prevent further corrosion when using a polyurethane based foam as a vehicle requires further research, not only to the protection of bare steel, but also to slightly corroded steel.

(2) Vapour phase corrosion inhibiters typically have a design life of 6 to 24 months depending on the type as recommended by inhibitor suppliers. Further research needs to be conducted to ensure that this design life can be achieved as it directly effects the annualized value of this method.

(3) If maintenance or re-installation of the foam is required, a methodology with guidelines should be investigated.

(4) Due to constraints on this research, only part of the properties required to comply with AS 1366.1:1992 (Rigid cellular plastics sheets for thermal insulation, Part 1: rigid cellular polyurethane) have been investigated and subsequently tested. It is recommended that all properties required by AS1366:1992 to be tested in accordance with AS2498.0:1993 should be tested.

(5) Currently, no formal standard exists for the application of polyurethane foam to enclosed spaces. As a result this study referred to Australian Standards for polyurethane insulation. It is recommended further research with the help of this study should be conducted to develop a set of guidelines to ensure this application meets installation quality as regarded by industry experts and research.

(6) Investigations on the structural effects of polyurethane expandable foam with and without a VpCI additive on steel hollow sections should be conducted to include the structural dynamic changes (effects) induced by structure as a result of filling the steel hollow sections with expandable polyurethane foam.

If future investigations include, but not limited to, these recommendations are achieved, constraints such as financial ones can be eased off allowing polyurethane foam and VpCI to be applied as a corrosion protection method. More specifically in regards to practicality, this method is highly desirable to process plant operators as no downtime to structure is necessary when retro-fitting the foam increasing effectiveness of resources which can be used in a more sustainable manner.

REFERENCES

[1] Mandeno WL, Sarraf RI, Protective Coatings for Steel Bridges - a Guide for Bridge and Maintenance Engineers, NZ Transport Agency, Wellington, 2014, 53pp.

[2] AS2312:2002 As/Nzs 2312: Guide to the Protection of Structural Steel against Atsmopheric Corrosion by the Use of Protective Coatings. Standards Australia.

[3] Tournay M, Internal Resistance to Corrosion in Steel Hollow Sections, France, CIDECT Final Report 10B-78/3, 1978.

[4] Sharmin E, Zafar F, Polyurethane: An Introduction, INTECH, New Delhi, India. http://dx.doi.org/10.5772/51663, 2012, pp. 3-16.

[5] AS1366:1992 Rigid cellular plastics sheets for thermal insulation Part 3: Rigid cellular polystyrene—Moulded (RC/PS—M), Standards Australia.

[6] Siversten K, "Polymer Foams", 2007, //ocw.mit.edu/courses/materials-science-and-engineering/3-063-polymer-physics-spring-2007/assignments/polymer_foams.pdf

[7] Schiller C, Glos M, Gahrens S, Eilbracht C, Aesthetics and Adhesion Behavior of Pu Foam Based Composites with Rigid Facer Materials. Germany, available on line at //www.pu-additives.com/product/pu-additives/en/about/downloads/technical-papers-presentations/Documents/Aesthetics_and_Adhesion_Behavior_of_PU_Foam_based_Composites_with_rigid_Facer_Materials.pdf.

[8] Evonik, Creating high performance polyurethane foams, http://www.pu-additives.com/product/pu-additives/en/Pages/default.aspx

[9] Prenosil M, Volatile Corrosion Inhibitor Coatings, Cortec Corp, Supplement to Materials Performance, January 2001, pp. 14-17.

[10] Kowata K and Takahashi K, Interaction of Corrosion Inhibitors with Corroded Steel Surface, Annual Corrosion Conference and Exposition: Water and Waste Water Industries, Denver, CO, 24-29 Mar 1996, NACE International, Houston, TX, 1996.

[11] Gulbrandsen E, Nesic S, Stangeland A, Burcbardt T, Sundfaer B, Hesjevik SM, Skjerve S, Effect of Precorrosion on the Performance of Inhibitors for CO_2 Corrosion of Carbon Steel, Corrosion 98, Norway, NACE International, 1998, Paper 13.

[12] Paolinelli LD, Perez T, Simison SN, The Effect of Pre-Corrosion and Steel Microstructure on Inhibitor Performance in Co2 Corrosion." Corrosion Science, 50 (9), 2008, pp. 2456-2464.

[13] Dougherty JA, Stegman, DW, "The Effects of Flow on Corrosion Inhibitor Performance", CORROSION 95, paper no. 113, (Houston, TX: NACE International, 1995) and Materials Performance 35, 4(1996): p. 47.

[14] Hearle JWS, Polymers and Their Properties, Vol. 1: Fundamental of Structure and Mechanics, Ellis Horwood Ltd., 1982, 437p.

[15] Saha MC, Mohan S, Hickman D, Balakrishnan A, Moisture Absorption Behavior and Its Effect on Flexure Properties of Polyurethane Foams, in Proceedings of the XIth International Congress and Exposition June 2-5, 2008 Orlando, Florida USA, Society for Experimental Mechanics Inc.

[16] AS2498.8

[17] Batallas M, Yih H, Singh P, Determining the Performance of Polyurethane Foam Pipe Insulation for High Temperature Service, NACE International, Northern Area Western Conference Calgary Alberta, Feb 6-9, 2006.

[18] Zarr RR, Nguyen T, "Effects of Humidity and Elevated Temperature on the Density and Thermal Conductivity of a Rigid Polyisocyanurate Foam." Journal of cellular plastics 30: 9, 1994, pp. 422-430.

[19] AS1366.1:1992 Rigid cellular plastics sheets for thermal insulation Part 1: Rigid cellular polyurethane (RC/PUR), Standards Australia.

[20] AS2498.0:1993 Methods of testing rigid cellular plastics - General introduction and list of methods, Standards Australia.

[21] AS4536:1999, As/Nzs 4536 - Life Cycle Costing-an Application Guide. Standards Australia International, 1999.

[22] ASTM D 2842 [21].

[23] Balvanyos T, Lave L, "Appendix B - Economic Analysis Methods." Carnegie Mellon University, Pittsburgh, Pennsylvania, 2004, //www.corrosionda.com/pdf/economicanalysis.pdf.

[24] Kogler R, Corrosion Protection of Steel Bridges. Pittsburgh, PA, FHWA-IF-12-052, Vol. 19, 2012, 21pp.

[25] Mining Technology, Boddington Gold Mine (BGM), Western Australia, available in http://www.mining-technology.com/projects/boddington/, 2014

[26] SPON, Price Books Update, Langdon D, editor, Taylor & Francis, 2012.

Fifth International Conference on Geotechnique, Construction Materials and Environment, Osaka, Japan, Nov. 16-18, 2015, ISBN: 978-4-9905958-4-5 C3051

USE OF DESIGN OF EXPERIMENT IN SEISMIC VULNERABILITY ASSESMENT FOR EXISTING RC BUILDINGS BY JAPANESE METHOD

Naveel Islam[1], Kshama S. Roy[2] and Kamrul Islam[3]
[1,2]Faculty of Engineering and Applied Science, Memorial University of Newfoundland, Canada
[3]Department of Civil Engineering, Military Institute of Science and Technology (MIST), Bangladesh

ABSTRACT

The paper provides an overview on the Japanese Method of seismic vulnerability assessment where Design of Experiment (DOE) methodology was applied to investigate the most significant parameters that affect the seismic performance indices of an existing reinforced concrete (RC) building. The assessment emphasized on a region of recently constructed but densely populated RC buildings having uniformity in building height and surface area. Minimum Run Characteristic V Factorial Design was used to study the controlling factors which were largely dependent on the structural dimensions of a building. The results show that, lengths of the wall in X and Y directions, length of wall effective to the story concerned, total floor area supported by the story, total cross sectional area of columns in the story, time index and grade index are the most influencing parameters for Japanese method. A linear regression equation including the significant factors is developed by Design Expert software version 9.0.3.1 for computing the seismic indices. The results are also compared with the seismic indices obtained by the Japanese Method in the surveyed area.

Keywords: Japanese Method, Seismic Vulnerability, DOE, Reinforced Concrete building, Factorial Design

INTRODUCTION

The rush of urbanization has produced some of the most dangerous built environments: multi-story buildings, over-reliance on concrete and a loss of knowledge that protected previous generations. The pressure to meet the needs of growing populations leads to improperly implemented building regulations. Around three-quarters of all deaths in earthquakes are due to building collapse (www.theguardian.com). Low-cost and informal buildings are most likely to fail, meaning that earthquakes disproportionately affect the developing countries. In recent years, damage in buildings with low seismic capacities has occurred in a number of earthquake prone countries like Nepal (2015), Japan (2011), New Zealand (2010 & 2011), Mexico (2011), Indonesia (2010 & 2011), China (2010), Haiti (2010). Most building codes in the world explicitly or implicitly accept structural damage to be occurred in a building during strong earthquakes as long as hazard to life is prevented [1]. But dealing with these structural damages, under the effect of natural hazards like earthquake to predict the potential damage before its occurrence is still considered as a major scientific challenge. Almost all of the developing countries have underlined the need for seismic evaluation of existing buildings due to massive damage caused by recent earthquakes to modern reinforced concrete buildings [2]. In regions where earthquake occur in intervals measured in centuries, there is a need for a simple evaluation method that focuses on selection of buildings with high vulnerability rather than those with a high probability of survival [3]. Over the last decade, significant efforts have been devoted in devising reliable estimates incorporating the various uncertainties and randomness involved in seismic demand and capacity. Thus assessment of potential damage should be carried out based on statistical and probabilistic techniques [4].

The “Standard for Seismic Evaluation and Guideline for seismic retrofit of existing RC buildings” developed by the Japan Building Disaster Prevention Association is popularly known as the Japanese Method of Seismic Vulnerability Assessment. The underlined target of the standard was to assist other earthquake–prone countries those face similar problems (e.g. earthquake disaster prevention efforts) like Japan. [5]. Japanese method evaluates seismic performance indices for each building comparing seismic demand index of the localized region. As the evaluation process involves a number of empirical equations and standardized tables for determining the indices, finding the most significant factors that affect the seismic performance index is a major challenge. The present study aims to describe a novel statistical approach using Design of Experiment (DOE) for investigating the significant factors in Japanese Method. The paper also focuses on developing a linear regression equation for determining the seismic indices from DOE method and compares the results with actual empirical equations.

JAPANESE METHOD

The Japanese seismic performance evaluation is based on both site inspection and structural calculation to represent the seismic performance of existing medium and low–rise reinforced concrete buildings in terms of seismic performance index of structure, I_s. Three levels of screening procedures, namely the first, the second, and the third level screening, have been prepared for the seismic evaluation. Any level of the screening procedures may be used in accordance with the purpose of evaluation and the structural characteristics of the building [5]. Building inspections are conducted to check the structural characteristics of the building which are necessary to calculate the seismic index of structure, I_s. Appropriate methods for inspection are selected in accordance with the screening level, such as site inspection, collection of design drawings, and material test. In case, design drawings of the building are not available, inspections on the structural dimensions, diameters and arrangements of reinforcing bars need to be examined on site, which are necessary for seismic evaluation of the building in accordance with the screening level [5].

The seismic performance index of structure (I_s) is evaluated by the following equation at each story and to each direction,

$$I_s = E_0 * S_D * T \tag{1}$$

Where,
E_0 = Basic seismic index of structure,
S_D = Irregularity index and T = Time index

Seismic safety of structure is judged by the following Equation,

$$I_s \geq I_{so} \tag{2}$$

Where, I_s = Seismic index of structure and
I_{so} = Seismic demand index of structure

If Eq. (2) is satisfied, the building is assessed as 'Safe - the building possess the seismic capacity required against the expected earthquake motions'. Otherwise, the building is assessed as 'Uncertain' in seismic safety. The thorough procedure can be found in the Standard for seismic evaluation and Guideline for Seismic Retrofit of existing reinforced concrete building revised from the general outline given by Umemura [6] and by Japan Building Disaster Prevention Association in 1990 [5].

A detailed spreadsheet using Microsoft Excel software program has been developed for calculating the seismic index considering all the tables and empirical equations. Authors were successful in similar analysis for other seismic vulnerability assessment methods and details of the analyses can be found at Roy et al. [7]-[8] and Ahmed et al. [9]

DESIGN OF EXPERIMENT METHODOLOGY

Design of Experiment (DOE) methodology [10]-[12] is used for finding the most significant factors that affect the seismic index of the structure in the Japanese Method. DOE provides a quick and cost effective method to understand and optimize products and processes [13]. DOE lets experimenters develop a mathematical model that predicts how input variables interact to create output variables or responses in a process or system [14]. DOE method was used previously for other seismic vulnerability assessment methods i.e. Turkish method [8]. The present study is based on a survey (detailed site inspection) conducted in DOHS Mirpur area of Dhaka, the capital city of Bangladesh. The particular location was chosen because of its uniformity in the height and surface area of the buildings. Most of the buildings were seven (7) storied and from the seismic evaluation, it was found that, the top story has the lowest seismic index. For the aforementioned reasons, the experiment is based on the data that was collected from the top story of each building. Factorial design is conducted in this experiment by Design Expert 9.0.3.1[15] to find the most significant factors that affect the Japanese method of vulnerability assessment. A linear regression equation is obtained from the design of experiment methodology and the regression equation is validated using a typical survey data of a building different from the initially selected buildings. Similar analyses for other seismic vulnerability assessment methods can be found in authors' previous studies [7]-[8].

Factors and Responses

Based on the empirical equations and tables, nine (9) parameters are identified as the controlling parameters and are used as factors in the experiment. The factors and its levels are shown in Table 1. The levels of the first seven factors (A, B, C, D, E, F and G) are based on the structural dimension of the building. The levels of the last two factors (H and I) are set based on the tables given in the standard for seismic evaluation. The seismic demand index along the two directions, namely I_sX and I_sY are set as the responses of the experiment.

Experimental Design and Procedure

A regular two level factorial design with nine (9) factors would require $2^9 = 512$ runs for a complete replicate. To minimize the runs, a Minimum Run Characteristic V Design which is a Resolution V design where the two factors interactions (2FI) are aliased with three factor (3FI) and single factor is aliased with four factors interaction was used. One (1) center point was considered for checking the existence of curvature in the model. The final design includes 47 runs. The low, center and high coded values for the factors are shown in Table 1.

RESULTS

The responses obtained for the 47 runs were analyzed by Design Expert 9.0.3.1 [15]. The terms with the significant effects were determined using half normal plot. It is found that for I_sX, the factors A, C, F, G, H and I are significant while for I_sY, the factors B, C, F, G, H and I are the significant as shown in Fig. 1.

The analysis of variance (ANOVA) was conducted with the significant terms found from Figs. 1&2. Table 2 & 3 show the ANOVA tables for I_sX and I_sY respectively. The analyses show that the responses need a power transformation after checking the assumption of ANOVA, the R^2 and adjusted R^2. The model with natural log

Table 1 Factors and their levels

Factors	Name	Symbols	Units	Low Actual	Center Actual	High Actual	Low Coded	Center Coded	High Coded
A	Length of wall in the X Direction	lw_1 (X)	mm	5000	52500	100000	-1	0	+1
B	Length of wall in the Y Direction	lw_1 (Y)	mm	6000	78000	150000	-1	0	+1
C	Length of wall effective to the story concerned	lw_3	mm	20000	110000	200000	-1	0	+1
D	Thickness of peripheral wall	t_p	mm	127	190.5	254	-1	0	+1
E	Thickness of interior wall	t_i	mm	127	190.5	254	-1	0	+1
F	Total floor area supported by the story	ΣA_f	mm^2	100	400	700	-1	0	+1
G	Total cross sectional area of columns in the story	A_c	$*10^6$ mm²	1.00	3.05	6.00	-1	0	+1
H	Time Index	T	_	0.70	0.90	1.00	-1	0	+1
I	Grade Index	G	_	0.80	0.90	1.00	-1	0	+1

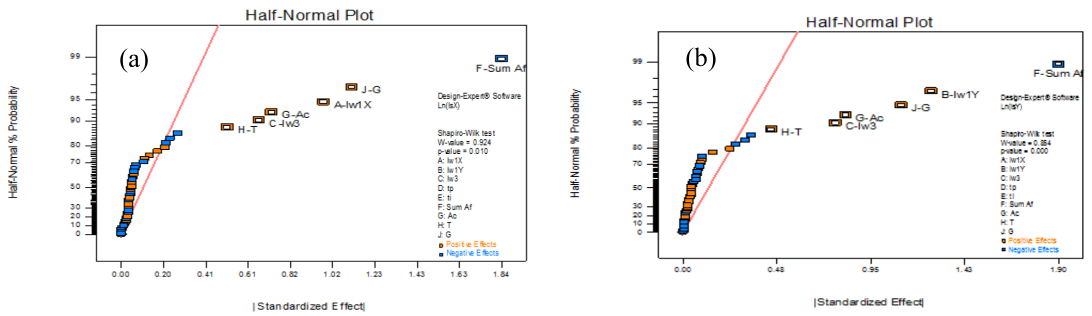

Fig. 1 Half Normal Plots for (a) I_sX and (b) I_sY

transformation gave the higher R^2. The results given in Tables 2 & 3 are obtained after the natural log transformation. Tables 2 & 3 also show that, there is curvature effect on both the responses but it is not much significant compared to the other significant factors. *MS* (treatment) is also larger than *MS* (residuals) which may have resulted in larger *F* values. As the *p*–values are << 0.05 for the factors in Tables 2 & 3, all the selected effects are highly significant. The values of R^2 for both of the responses (0.9035 for I_sX and 0.9065 for I_sY) are almost near to 1 which means the model is fairly good enough and about more than 90% of variability of data can be explained by the model.

Statistical Testing

The following four assumptions must be satisfied for ANOVA:

1. All samples are random samples from their respective populations.
2. All samples are independent of one another.
3. Departures from group mean are normally distributed for all groups.
4. All groups have equal variance.

Table 2: ANOVA Table for Seismic Index, I_sX

ANOVA for selected factorial model : I_sX
Analysis of variance table [Partial sum of squares - Type III]

Source	Sum of Squares	d_f	Mean Square	F Value	p–value, Prob > F	
Model	72.28	6	12.05	62.41	< 0.0001	
A-lw_1X	10.87	1	10.87	56.32	< 0.0001	
C-lw_3	5.05	1	5.05	26.16	< 0.0001	
F-ΣA_f	38.51	1	38.51	199.50	< 0.0001	Significant
G-A_c	6.01	1	6.01	31.15	< 0.0001	
H-T	2.99	1	2.99	15.48	0.0003	
I-G	14.13	1	14.13	73.19	< 0.0001	
Residual	7.72	40	0.19			
Cor. Total	80.00	46				
Std. Dev.		0.44			R–Squared	0.9035
Mean		0.40			Adj R–Squared	0.8890
C.V. %		108.70			Pred R–Squared	0.8643
PRESS		10.85			Adeq Precision	34.807

Table 3: ANOVA Table for Seismic Index, I_sY

ANOVA for selected factorial model : I_sY
Analysis of variance table [Partial sum of squares - Type III]

Source	Sum of Squares	d_f	Mean Square	F Value	p–value, Prob > F	
Model	89.57	6	14.93	64.66	< 0.0001	
B-lw_1Y	18.06	1	18.06	78.21	< 0.0001	
C-lw_3	6.79	1	6.79	29.39	< 0.0001	
F-ΣA_f	41.30	1	41.30	178.91	< 0.0001	Significant
G-A_c	7.73	1	7.73	33.48	< 0.0001	
H-T	2.28	1	2.28	9.90	0.0031	
I-G	13.93	1	13.93	60.34	< 0.0001	
Residual	9.23	40	0.23			
Cor. Total	98.80	46				
Std. Dev.		0.48			R–Squared	0.9065
Mean		0.49			Adj R–Squared	0.8925
C.V. %		98.16			Pred R–Squared	0.8700
PRESS		12.85			Adeq Precision	32.001

Checking Model Adequacy

Variation for Normality and Constant Variance

The normal plot of residuals in Fig. 2 shows that, most of the points follow the normal distribution line for both of the responses and thus satisfy the first assumption of ANOVA: residuals are normally distributed. The data points in Fig. 3 are well scattered which concludes that the data points have a constant variance.

Variation for Randomness and Goodness of Fit

Most of the data in the Residual vs. Run plots (Fig 4) are randomly scattered which indicates that the sequence of runs is random. In the Predicted vs. Actual plots (Fig. 5), most of the points lie on the 45˚ line, which also satisfies the assumption of ANOVA.

ANOVA RESULTS

All the assumptions of ANOVA are satisfied and the model is used for further analysis to determine the predicted model in the form of equations.

The predicted equations from the model in terms actual factors are as follows:

$$ln\,(I_sX) = -6.28284 + 1.02832E\text{-}05 * lw_1X + 3.72996E\text{-}06 * lw_3 - 3.13609E\text{-}03 * \Sigma A_f + 1.48625E\text{-}07 * A_c + 1.71844 * T + 5.56512 * G \quad (3)$$

$$\ln (I_sY) = -6.21238+8.74274E\text{-}06* lw_1Y+4.32366E\text{-}06*lw_3-3.24721E\text{-}03* \Sigma A_f+1.68552E\text{-}07*A_c +1.50194*T+5.52780*G \quad (4)$$

Equations (3)-(4) in terms of actual factors will be used to make predictions of the Seismic Index of the structure based on the significant factors in the equations.

VALIDATION OF PREDICTED MODEL

The validity of the proposed equations in terms of actual factors for predicting seismic index is done by detailed inspection on random buildings (different from the 47 building data) on the same area. Equations (3)-(4) are used for determining the predicted responses. Comparisons between the predicted and actual responses are presented in

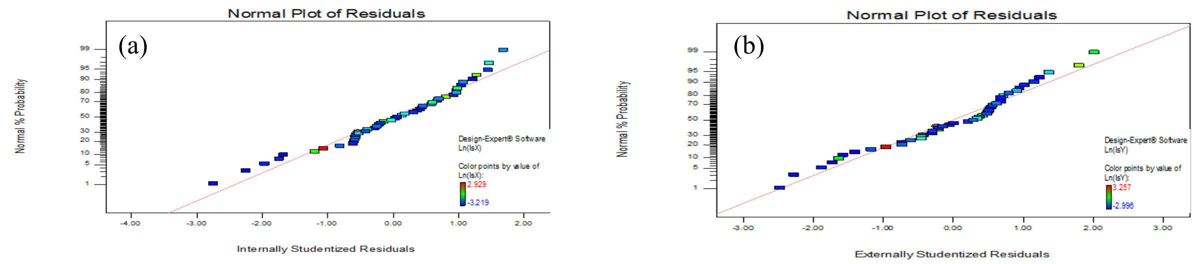

Fig. 2 Normal Plot of Residuals for (a) I_sX and (b) I_sY

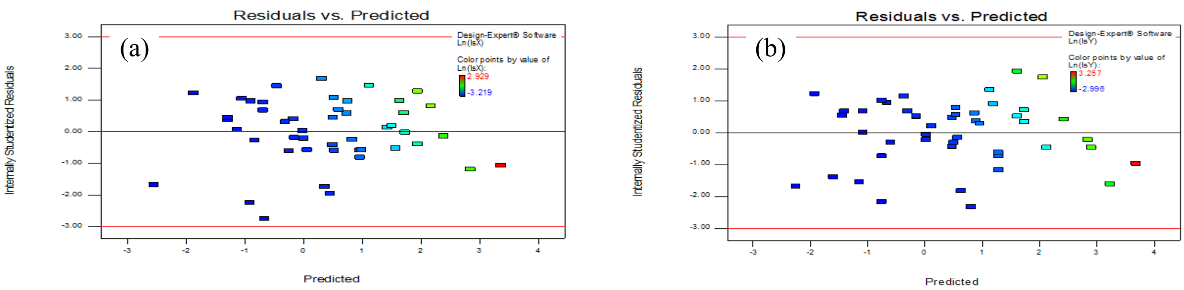

Fig. 3 Residuals vs. Predicted for (a) I_sX and (b) I_sY

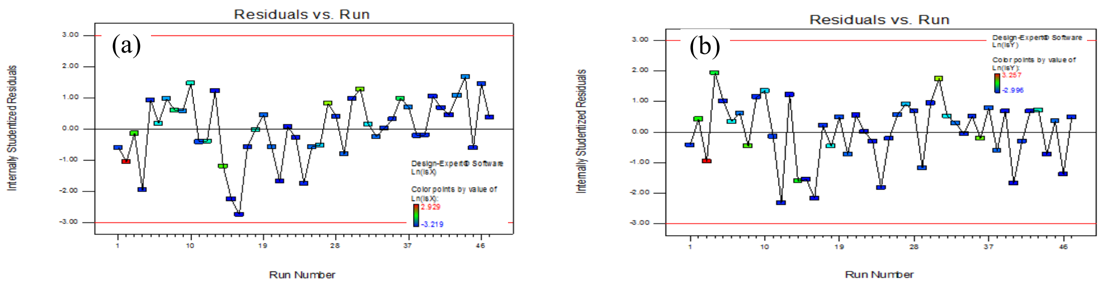

Fig. 4 Residual vs. Run for (a) I_sX and (b) I_sY

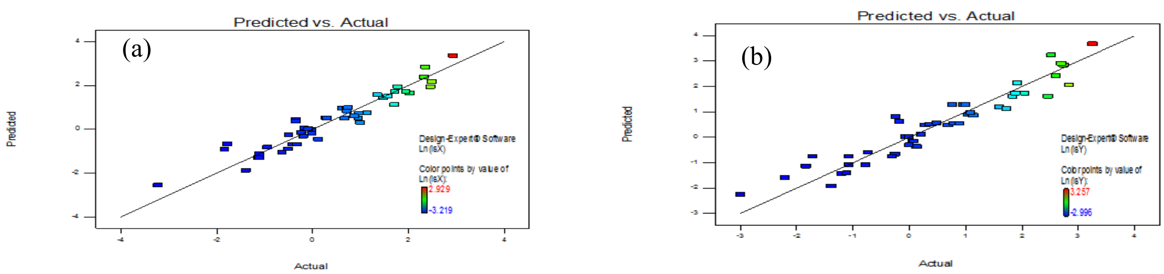

Fig. 5 Predicted vs. Actual for (a) I_sX and (b) I_sY

Table 5. The results for both of the responses, I_sX and I_sY for the predicted model are in good agreement with the actual model. The predicted equations from the model are found to give almost similar results as found by the actual Japanese method.

Table 5 Comparison of Predicted & Actual Responses

No. of Buildings Surveyed	Building Number	Predicted Response		Actual Response	
		I_sX	I_sY	I_sX	I_sY
1	165	1.43	1.18	1.25	0.86
2	188	1.15	1.10	1.46	1.89
3	310	2.48	2.06	2.25	2.13
4	450A	1.37	1.08	1.95	1.55
5	519	1.77	1.63	1.26	1.66
6	545-547	1.66	1.70	1.12	1.49
7	548	1.98	1.86	1.45	1.85
8	581-582	0.88	1.16	0.70	1.39
9	652-654	1.37	1.04	1.57	1.24
10	698	1.38	1.32	1.35	1.69
11	781	0.96	0.83	0.86	0.79
12	1047	1.11	1.04	1.16	1.27

CONCLUSIONS

The present study is conducted to find the significant factors that affect the Japanese method and thereby forming linear regression models including only the significant factors in determining the seismic performance indices of Japanese method. The experiment was started with nine (9) factors relating with each other with a group of empirical equations and tables (Japanese method) and finally ended up with six (6) significant factors for each responses along with two (2) prediction equations (DOE) which can predict identical responses to that of the actual responses. The paper also verifies the adequacy of the regression equations by several diagnostic plots which are in good agreement with the model equations. The validation runs of the experiment show that the anticipated model has high accuracy with mere variation on the results. Further validation runs can be conducted by making detailed inspection from a number of buildings to foresee the true validity of the predicted equations.

ACKNOWLEDGEMENT

The authors are very grateful to Dr. Leonard Lye who is a pioneer in using the Design of Experiment method [14].

REFERENCES

[1] Otani, S. 2000. "Seismic vulnerability Assessment Methods for Buildings in Japan", Earthquake Engineering and Eng. Seismology, 2 (2): 47-56

[2] Nanda, R.P and Majhi, D. R. 2013. "Review on Rapid Seismic Vulnerability Assessment for Bulk of Buildings", Journal of Inst. of Engineers (India), 94(3): 187-197

[3] Sozen, M. A., and Hassan, A. F. 1997, "Seismic Vulnerability Assessment of Low-Rise Buildings in Regions with Infrequent Earthquakes", ACI Structural Journal, 94 (1), 31 -39.

[4] Ozcebe, G., Yucemen, M. S., Aydogan, V., and Yakut, A. 2004. "Statistical Seismic Vulnerability Assessment of Existing Reinforced Concrete Buildings in Turkey on a regional scale", Journal of Earthquake Eng., 8(5): 749-773

[5] Standard for Seismic Evaluation and Guidelines for Seismic Retrofit of Existing Reinforced Concrete Buildings, 2001 (English Edition), Japan Building Disaster Prevention Association.

[6] Umemura,H., 1980 "A Guideline To Evaluate Seismic Performance of Existing Medium and Low Rise RC Buildings And Its Application", Proc. of The 7th World Conf. on Earthquake Eng., Istanbul, Turkey, 4: 505-512

[7] Roy, K. S., Islam, K. and Arafat, M. S. 2010. Seismic Risk Assessment of Existing Low-rise Buildings in Unplanned Urban Regions of Dhaka City, *Proceedings of the 2nd International Conference on Construction in Developing Countries (ICCIDC-2)*, Cairo, Egypt.

[8] Roy, K. S., Islam, K. and Arafat, M. Shams. 2011. A Novel Statistical Approach for Investigating the Significant Factors that Influence the Performance Score of the Turkish Method, *Proceedings of International Conference on Geotechnique, Construction Materials and Environment (GEOMAT-2011),* Tsu City, Mie, Japan.

[9] Ahmed, M.Z., Islam, K., Roy, K. S., Arafat, M. S. and Al-Hussaini, T.M. 2010. Seismic Vulnerability Assessment of RCF Buildings in Dhaka City, *Proceedings of the 3rd International Earthquake Symposium (IESB-3)*, Dhaka, Bangladesh.

[10] Montgomery, D.C. 2013. Design and analysis of experiments 8th ed., John Wiley & Sons Incorporated, New York, NY, USA

[11] Box, G.P., Hunter, J., Hunter W. 2005 Statistics for experimenters design innovation and discovery. 2nd ed. Wiley and Sons

[12] Lye, L. 2014. ENGI 9516: Similitude, Modeling and Data Analysis –Course Note, Memorial University of Newfoundland, Canada

[13] Antony, J. 2002. Training For Design of Experiment Using a Catapult. Journal of Quality and Reliability Eng. International, 18: 29-35

[14] Lye, L. M., 2003. Some Applications of Statistical Design of Experiment Methodology in Civil Engineering. *Annual Conference of the Canadian Society for Civil Engineering, Moncton, Nouveau-Brunswick, Canada*

[15] Stat. Ease, 2014 Design Expert 9.0.3.1 Design of Experiment software developed by Stat-Ease, Inc.

THE ROLE OF POLYPROPYLENE FIBERS IN IMPROVING HIGHLY PLASTIC CLAY INTEGRITY

Muawia A Dafalla [1], Arif Ali Baig Moghal[1] and A. Obaid[1]
[1] Department of Civil Engineering, College of Engineering, King Saud University, Riyadh.

ABSTRACT

The geotextile industry research and development is growing at a fast rate and new products of variable specifications are now available for earthworks and design engineers. The polypropylene fiber material is non-biodegradable which can stand aggressive chemical exposure when placed along with soil media. This research is conducted on a polypropylene fiber reinforced ~~s~~oil treated with chemical admixture in order to study the interlocking mechanism and to study the extent of improvement on their tensile behaviour. Locally available plastic clay was selected for this investigation. The extent of improvement by the polypropylene fibre~~s~~ inclusion on the tensile behaviour was evaluated by carrying out a series of brazilian tensile strength tests. The dominant mechanism responsible for the increase in tensile strength properties has been proposed. The effect of various geotechnical parameters like grain size distribution, density and moisture content on the tensile strength improvement has been discussed. The study shows that the addition of polypropylene fibers alone to highly plastic clay will not suffice the tensile strength requirements. The polypropylene fibers when added with lime of 6% can improve the tensile strength by further by 13 to 28% depending on the dose or fiber content.

Keywords: Polypropylene fiber, Clay, Expansive soil, Bonding mechanism

INTRODUCTION

The clay or intact soil material remains intact when a sufficient cohesive or attraction force is holding the grains together. The material is disintegrated when this force is not sufficient to hold the grains particularly when the material is subjected to pull, bending or even temperature gradient. This study is performed to measure the tensile strength of polypropylene fiber reinforced highly plastic clay treated or untreated with lime additive.

The idea of computing tensile test strength indirectly goes back to 1943 as quoted by reference [1]. Tensile strength of compacted clays was investigated in the literature since the seventies of the twentieth century. Reference [2] presented a method for measuring tensile strength of soils. This test became popular and many versions were introduced to measure the tensile strength indirectly. [2] and [3]. The procedure is standardized by the ASTM (ASTM Standard Test Method D3967-81) [4] and suggested by the International Society for Rock Mechanics in 1981[5]. It is either carried out as direct measurement of tension or indirectly by calculating bending stresses. This study considered flattened Brazilian test similar to the approach of reference [6]. Introduction of fibers to soil mixtures and clay is an ancient technique used to enhance the adhesion and erosion resistance properties. Natural fibers or organic straw material derived from dried plants or grasses can provide more tensile strength by bonding clay lumps or clay particles with additional link. The natural organic material is not expected to hold strong for extended periods. Adding polypropylene fibers is thought to be of advantage due to uniformity and better control. Works of reference [7] provided evidence that clays reinforced with fibers can have reduced crack sizes and reduced crack depths but it did show that the number of surficial crack is increased. The polypropylene fibers produced as an additive to concrete is too smooth to be bonded to clay particles. Adding extra cementing agent like lime or cement is believed to overcome this problem.

MATERIAL AND METHODS

Clay material from Al-Qatif town located in the Eastern province of Saudi Arabia was used in this study. Al Qatif clay as classified in accordance with ASTM D2487 is highly plastic clay (CH). This clay is known of its high expansion and shrinkage properties. Several research studies were performed to characterise and evaluate this type of clay [8]-[10]. The standard proctor maximum dry density is measured at 11.5 to 12 kN/m^3[11]. The optimum moisture content is reported as 30 to 32%. Al Qatif clay indicated liquid limit of 130 to 150 with plasticity index is in the order of 60 to 70 [12],[13]. The lime material used in this investigation is an analytical grade Calcium Hydroxide, supplied by Winlab Chemicals, UK.

The polypropylene material used in this study is 12mm in length produced by a United Kingdom manufacturer (Propex concrete systems). A fine monofilament with a melting point of 162 º C (324 º

F) and ignition point of 593º C (1100º F). The material is of low electrical and thermal conductivity. The specific gravity is in the order of 0.91. The guidelines as specified in ASTM D 3967 were followed. Each and every sample was carefully prepared in a mould of inner dimension of 50 mm and length of 100mm. In order to have a uniform density static compaction was applied using two piston rods; at top and at the bottom. The samples prepared at dry densities of 12 kN/m^3 were kept for 7 days curing at room temperature. The testing frame used is a Wykhamm Farrance system shown in Figure 7. Samples were loaded through a spacer applying load through a flat surface. The machine is equipped with a calibrated proving ring and displacement dial gauge. Failure tensile strength T is calculated using the following formula:

$$T = 2P/\pi DL \quad (1)$$

Where
P = applied load
D = diameter of the specimen
L = length of the specimen

3 EXPERIMENTAL PROGRAM

The investigation program included two sets of sample prepared in cylindrical moulds in order to assess the influence of fibers in reinforcing the clay. One set was Al-Qatif clay reinforced with fibers using three different dosage ; 600 gm, 900 gm and 1200 gm in addition to plain clay. The other set was similar to the first set but included addition of 6% lime. The tensile strength of clay is extremely low and hardly taken into account in practice. It is widely variable and dependant on the structure, state of packing and soil suction [14]. The material was proportioned and prepared as a homogeneous mix and then statically compacted in a cylindrical mould of 5 cm diameter and 10 cm length. The two sets of samples were left to cure for 7 days period. Each mix was prepared in two samples and the results were reported as an average value. In order to view the profile of stress strain relationship of fiber reinforced clay the tensile strength was recorded at fixed intervals. The strain rate used was 0.3 mm/min.

4 RESULTS AND DISCUSSIONS

The test results indicated that adding fibers without a cementing agent is unlikely to add any tensile strength to the clay material. The tensile strength reported for clays without reinforcement with fibers was 54.4 kPa. This value did not increase when adding 600 gm/m^3 fiber dose and even went lower for 900 gm/m^3. A very slight increase is shown with the high dose of 1200 gm/m^3. This can be understood due to the fact that fibers can be of non-straight stretch and not cemented to the clay particle. On adding lime the tensile strength jumped to more than double. The addition of fibers with lime improved the tensile strength by 13 to 28%. This study suggests that the use of fibers without a cementing agent is of little or no benefit to highly plastic clay and clays in general. Observations on modes of failures indicate a ductile nature which is facilitated by the fibers. Failure plains started close to the edges before the major splitting failure plain is developed at the central zone of the sample. The load application angle determines the location of crack initiation [15]. Edge cracks are sometimes referred to as wing cracks in the literature and claimed that they normally stop when the central cracks are initiated. The bond between fibers and the clay is dependent on the geometry of clay particles, grain size distribution, void ratio and state of compaction. The influence of these parameters can be judged theoretically based on contact areas between fibers and clay particles. The moisture content can also have a role as it is related to the level of compaction.

Table 1 Splitting tensile strength (kPa) for fiber reinforced clay

Fiber amount gm/m3	0%lime	6% Lime
0	54.43	133.43
600	54.06	150.46
900	53.37	165.87
1200	56.59	171.16

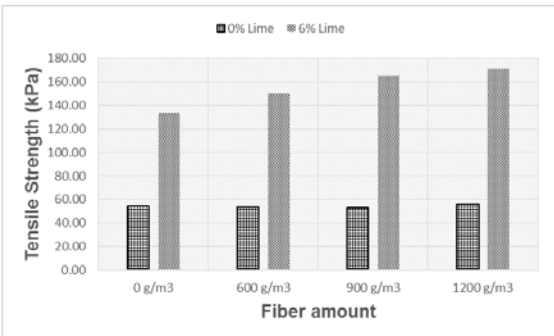

Fig 1. Tensile strength of fiber reinforced and non-fiber reinforced clays.

Table 2. Splitting tensile strength profile for fiber

reinforced clay with 900 gm per cubic meter.

Deformation Dial Reading	Load Dial Reading	Displacement (mm)	Applied Loading (kg)	Applied Loading (N)	Spilitting tensile strength (kPa)
0	0	0	0	0	0
20	6.2	0.2	4.57	44.81	5.71
40	12	0.4	8.84	86.73	11.04
60	18	0.6	13.27	130.10	16.56
80	22.5	0.8	16.58	162.62	20.71
100	27.5	1	20.27	198.76	25.31
120	34	1.2	25.06	245.74	31.29
140	40.5	1.4	29.85	292.71	37.27
160	45.5	1.6	33.53	328.85	41.87
180	49.5	1.8	36.48	357.76	45.55
200	51.3	2	37.81	370.77	47.21
220	53.8	2.2	39.65	388.84	49.51
240	54.5	2.4	40.17	393.90	50.15
260	55.8	2.6	41.12	403.29	51.35
280	56.5	2.8	41.64	408.35	51.99
300	58	3	42.75	419.20	53.37
320	57	3.2	42.01	411.97	52.45
330	57	3.3	42.01	411.97	52.45
340	56.5	3.4	41.64	408.35	51.99

Strain rate = 0.3 mm/min. Deformation Dial: 1 unit = 0.01 mm; Proving Ring. Load Dial: 1 unit = 0.737 Kg

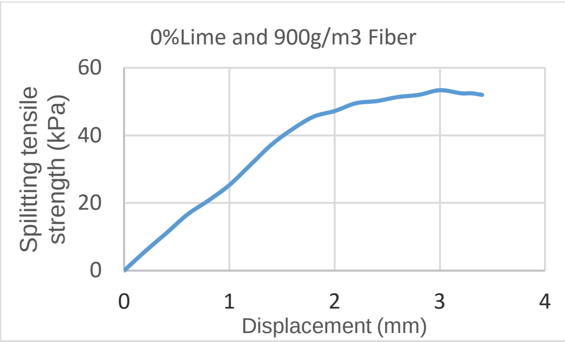

Fig. 2 Profile of splitting tensile strength of fiber reinforced clay.

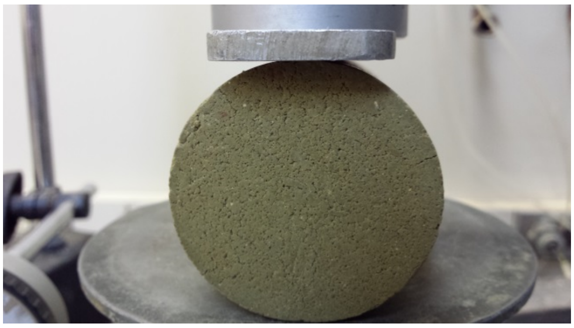

Fig. 3 Failure planes starting at the edges of the sample.

Fig. 4 Main central splitting area starts showing.

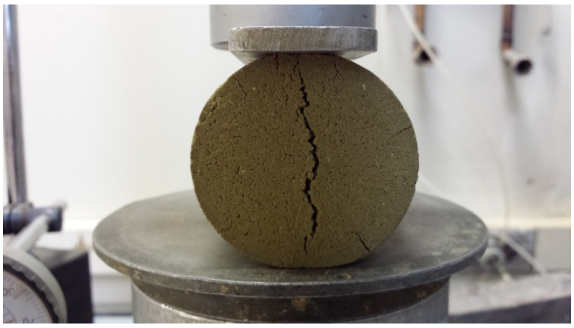

Fig. 5 Splitting progress retarded by fibers

Fig. 6 Failure state reached.

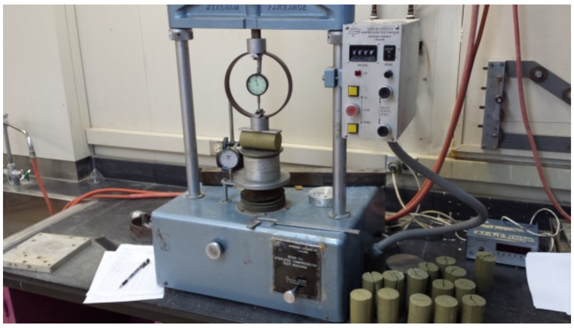

Fig. 7 Equipment used


Fig 8. View of failed samples

CONCLUSION

The study shows that the addition of polypropylene fibers alone to highly plastic clay will not suffice the tensile strength requirements. The bond between the fibers and clay cannot be established without considering a cementing agent. Lime addition of 6% to Al-Qatif clay indicated improvement in the tension capacity of the clay by more than 100%. The polypropylene fibers when added with lime of 6% can improve the tensile strength by further by 13 to 28% depending on the dose or fiber content. The fiber addition is also found to give the clay a ductile state where large deformation can be reported beyond the elastic or semi-elastic zone. Failure was found typical to Brazilian tests of various materials. It is noted that cracking starts at the rim of the sample until a major splitting failure plain is developed at the central zone.

ACKNOWLEDGEMENTS

This project was funded by the National Plan for Science, Technology and Innovation (MAARIFAH), King Abdulaziz City for Science and Technology, Kingdom of Saudi Arabia, Award Number (11BUI1489-02).

REFERENCES

[1] Li, Diyuan, and Louis Ngai Yuen Wong(2013). "The Brazilian Disc Test for Rock Mechanics Applications: Review and New Insights." Rock Mechanics and Rock Engineering 46 (2013): 269-87.

[2] Fang, H. Y. and Fernandez, J. (1981). Determination of tensile strength of soils by unconfined penetration test, ASTM STP 740, pp. 130-144.

[3] Favaretti, M. (1996). Tensile strength of compacted clays. State of the art in Unsaturated Soils. First international conference on unsaturated soils UNSAT95 edited by . Alonso and P. Delage, eds, Balkema, Rotterdam: 51-56.

[4] ASTM D3967 - 08. Standard Test Method for Splitting Tensile Strength of Intact Rock Core Specimens.Book of Standards Volume: 04.08

[5] International Society for Rock Mechanics (1981).Suggested Methods "Rock Characterisation, Testing and Monitoring" Editor E.T. Brown, Pergamon Press 1981, pages 119 to 121.

[6] Agaiby, Shehab Sherif Wissa (2013).Fracture characterization of clays and clay-like materials using flattened Brazilian Test. Massachusetts Institute of Technology. http://hdl.handle.net/1721.1/85819. Master Thesis.

[7] Freilich, B.J.,Kuhn,J.A.and Jorge, G. Zornberg (2008). Desiccation of Fiber-Reinforced Highly Plastic Clays. The First Pan American Geosynthetics Conference & Exhibition, Cancun, Mexico

[8] El-Junaid, M., Shamrani, M. A., Puppala, A. J., & Dafalla, M. A. (2011). Evaluation of chemical stabilization of a highly expansive clayey soil. Transportation Research Record: Journal of the Transportation Research Board, 2204(1), 148-157.

[9] Elkady T. Y., Dafalla, M. A., Al-Mahbashi A. M. and Al-Shamrani M. A. (2013) "Evaluation of Soil Water Characteristic Curves of Sand-Clay Mixtures." International Journal of GEOMATE, June, 2013, Vol. 4, No. 2 (Sl. No. 8), pp. 528-532. Geotec., Const. Mat. & Env. , ISSN: 2186-2982(P), 2186-2990(O), Japan.

[10] Dafalla, M. A., Elkady, T. Y., Al-Shamrani, M. A. and Shaker, A. A. (2013). "An Approach to Rank Local Clays for Use in Sand Clay Liners", Third International Conference on Geotechnical Engineering, Tunisia Feb 2013.

[11] ASTM D 698 (2000), "Standard Test Methods for Laboratory Compaction Characteristics of Soil Using Standard Effort (12 400 ft-lbf/ft3 (600 kN-m/m3))", Vol. 4.08. D-18 Committee on Soils and Rocks. West Conshohocken, PA.

[12] ASTM, D 4318-00 (2003), Standard test methods for liquid limit, plastic limit, and plasticity index of soils. Annual Book of ASTM standards, 582-595.

[13] ASTM D 422 (2002) Standard Test Method for Particle-Size Analysis of Soils, Vol. 4.08.D-18 Committee on Soils and Rocks. West Conshohocken, PA.

[14] Rainer M. Zeh and Karl Josef Witt (2007). The tensile strength of compacted clays as affected by suction and soil structure. Experimental Unsaturated Soil Mechanics Springer

Proceedings in Physics Volume 112, 2007, pp 219-226 .
[15] Wang QZ, Xing L (1999) Determination of fracture toughness Kjc by using the flattened Brazilian disk specimen for rocks. Eng Fract Mech 64:193-201

Fifth International Conference on Geotechnique, Construction Materials and Environment, Osaka, Japan, Nov. 16-18, 2015, ISBN: 978-4-9905958-4-5 C3051

PARAMETRIC STUDY OF REINFORCED CONCRETE SLABS UNDER BLAST LOADS

Mujtaba M. N. Shuaib[1], Osama M. A. Daoud[2]
[1]Faculty of Engineering, University of Khartoum, Sudan; [2]Building and Roads Research Institute, University of Khartoum Sudan

ABSTRACT

This paper includes an investigation for the deformations, including deflections and damage modes, which occur in reinforced concrete (RC) slabs when subjected to blast loads of explosions. The slab considered was subjected to close-in detonations of three different charge weights for a constant standoff distance. For the study, the slab was analysed using the numerical method by means of nonlinear finite element analysis. The slab was modelled as 3-D structural continuum using LS-DYNA software. For concrete modelling, two constitutive models were selected, namely the KCC and Winfrith concrete models. Blast loads were applied to the slab through the Lagrangian approach, and the blast command available in the software, namely LOAD_BLAST_ENHANCED, was selected for the application. Also, slab was analysed using the single-degree-of-freedom method in UFC 03-340-02 manual. The deflections and damage modes results obtained were compared to those from a previously published experiment. In addition, a parametric study was made which investigate changing reinforcement ratio and explosive standoff distance.

Keywords: blast, reinforced concrete, slab, finite element, deformation.

INTRODUCTION

Nowadays, the protection against the effects of blast loads has become an essential need. Explosions can be seriously harmful towards humans as well as structures. Currently, blast applications are not restricted to military use only; the destructive use of blast has become a main technique that used in terrorist attacks against civilians. In other hand, blast application has spread to include the beneficial use as in some industry applications. In this field, many blast accidents have occurred during handling and storing of explosive materials. In general, explosion accidents may cause a serious impact on societies and economies. This has led to develop studies and methods that evaluate blast effects on structures which will be beneficial for their mitigation.

Reinforced concrete (RC) is one of principal material used for blast mitigation because it encompasses good characteristics in blast resistance. Among the RC structural elements, slabs are used widely for both structural and non-structural purposes. Blast wave generated in an explosion imposes a short duration dynamic loads on structures. In general, materials including concrete and steel behave differently under dynamic loads. They experience an increase in strength under rapidly applied loads [1]. RC elements possess different general behaviours depending on the intensity and standoff distance of the explosive.

The effect of blast loads on reinforced concrete structures had been investigated in many works and studies. Deformations which occur in a structural member due to blast can be assessed by applying either the experimental or the analytical approach. The later approach includes computational difficulties normally encountered with material nonlinearities in dynamic analysis. Several empirical simplified methods were introduced, and the most widely used one is the single-degree-of-freedom (SDOF). This method is known to be simple, inexpensive and reliable tool to evaluate the dynamic structural response [2].

Finite element (FE) method of analysis is an advanced method which is commonly applied recently to solve complex structural analysis problems including blast problems. Many works such as those carried out by Hao and Zhongxian [3], Wang et al [4], Zhao and Chen [5], Tai et al [6] and others have proved that by using the FE method of analysis, the local deformation occurs in concrete due to blast loads can be successfully and satisfactory assessed. The blast on structures in FE method can be applied and simulated using several approaches such as the Lagrangian and Multi-Material Arbitrary Lagrangian Eulerian (MM-ALE) approaches [7].

This paper provides comparative and parametric studies for slabs under blast loads. First, deformation results for one-way RC slab subjected to blast in previously conducted experiment, done by Wang et al [4], were compared to those obtained by analysis. Methods used for this purpose were FE and SDOF methods. Afterwards, a parametric study was made. This investigated the effect of changing reinforcement ratio and standoff distance of charge on slab deflection. Model description and analysis results are addressed in the following sections.

MODEL DESCRIPTION

The model was similar to the slab in Ref. [4], one-way RC slab supported at two opposite sides and subjected to close-in detonation of TNT explosives. The charge weights considered for the detonations were 0.2, 0.31 and 0.46kg, and their configuration is as shown in Figure 1. The RC used for slabs in the experiment had the properties of 39.5 MPa compressive strength (fc), 4.2 MPa tensile strength (ft'), and 28.3 GPa Young's modulus (Ec). The slab dimensions were 1000 mm x 1000 mm x 40 mm, and it was reinforced at its both directions by 6 mm steel bar reinforcement mesh with 75 mm spacing and 20 mm concrete cover from slab top. These are as shown in figure 2.

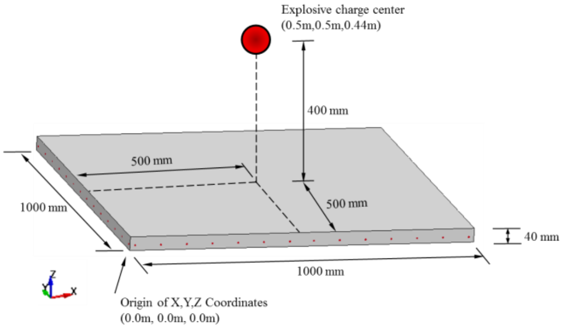

Fig. 1 Configuration of the explosive charge.

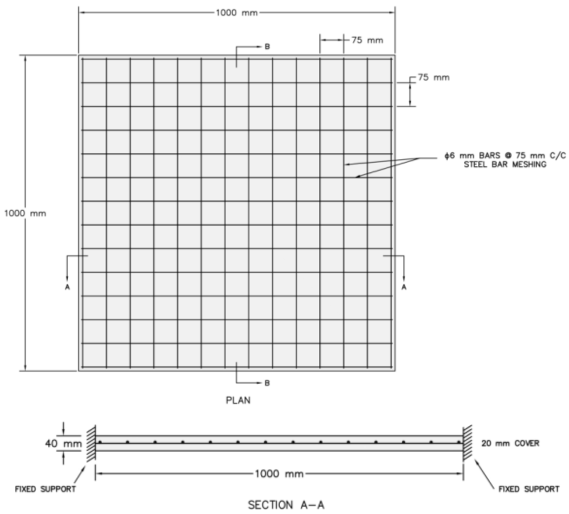

Fig. 2 RC slab geometry and reinforcement details.

FINITE ELMENT MODELING

The software used for modelling was LS-DYNA software, and the program library was used for the selection of element types and constitutive models for concrete and steel. The simulation of blast loading was carried out using the blast command available in the software. Slab was assumed to be fixed at the two supporting sides, although it was partially fixed in the experiment. A schematic finite element detail for RC slab is shown in figure 3.

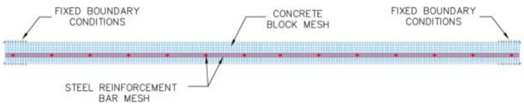

Fig. 3 Schematic finite element detail for RC slab

Slab Modeling and Meshing

The concrete of the RC slab was modelled as a solid box of dimensions 1000mm x 1000mm x 40mm which was composed of 8-node hexahedron solid elements with constant stress solid element formulation. The size of each element is 5mm x 5mm x 5mm which results in a number of 8 elements through the slab thickness. In the model, the total number of solid elements is 320,000 consisting of 363,639 nodes.

The steel reinforcement mesh was modelled as one layer of 6 mm diameter reinforcement bars and spaced at 75 mm. The type of element assigned to bars was Hughes-Liu beam element with mesh size of 5 mm, knowing that either truss or beam element can be used to model reinforcement bars. The total number of beam elements is 6,000 consisting of 5,835 nodes.

Material Constitutive Models

For concrete modelling, two constitutive models were selected. These models are namely Karagozian & Case Concrete (KCC) (MAT072R3) and the Winfrith concrete (MAT084) models. Both KCC and the Winfrith concrete models are invariant isotropic plasticity models, and they are suitable for blast problems, as they can capture the keys of concrete behaviours such as strain rate enhancement effect; however, the former proved to have better prediction for the localized shear. Both models take relatively simple input [8][9].

The KCC Concrete Model

The KCC (MAT072R3), is one of the material models that commonly used for concrete modelling. The main advantage offered by the KCC model that it allows the automatic generation of all the parameters by inputting only the unconfined compressive strength and the density of concrete [8]. The KCC model has three independent strength surfaces which are generated based on parameters calibrated from test data. The failure surface is interpolated between maximum strength surface and either the yield strength surface or residual strength surface.

For modelling, the default model parameter generation feature was used. This required the specification of the unconfined compression strength and density of concrete. For 39.5MPa concrete, the inputs in the model cards were as follows: concrete density (R0) 2400 kg/m3, negative of the unconfined compressive strength (A0) -39.5 MPa, conversion factors for length factors for length (inches-to-meters) and pressure (psi-to-MPa) (RSIZE & UCF) 39.72 and 145 for respectively. The remaining parameters were generated and determined automatically by the software.

The Winfrith Concrete Model

The Winfrith concrete model (MAT084) is a smeared crack model implemented in the 8-node single integration point continuum element. The shear surface in the Winfrith model is generated based upon four-parameter model developed by Ottosen. Similar to MAT072R3, it also allows the automatic generation of all the parameters by inputting certain parameters [9]. Those imported to the software were as follows: mass density of concrete (R0) 2400 kg/m3, initial tangent modulus of concrete (TM) 28.3 GPa, Possion's ratio (PR) 0.29, uniaxial compressive strength (UCS) 39.5 MPa, uniaxial tensile strength (UTS) 4.2 MPa and aggregate size (ASIZE) 16 mm (assumed). The remaining parameters were generated and determined automatically by the software.

Steel Constitutive Model

The steel material properties in the slab reinforcement used in the experiment were as follows: 600 MPa yield stress (fy), 200 GPa Young's modulus (Es) and 0.29 Poisson's ratio (υ). MAT003, which suited to model isotropic and kinematic hardening, was selected for steel modelling, and the previously mentioned variable values were used as input.

Blast Modeling

For blast simulation, the Lagrangian approach was used for applying the blast loads on the RC slab by means of LOAD_BLAST_ENHANCED (LBE) keyword provided by LS-DYNA. The air blast pressure is computed empirically with ConWep [10] data which is a collection of conventional weapons effects calculation from the equations and curves of TM 5-855-1 manual (similar to UFC 03-340-02 [11]) [12] [13]. To estimate the pressure time history, ConWep uses the Friedlander curve represented by the following equation:

$$P_{so}(t)=P_{so}(1-\frac{t}{t_o})e^{\frac{-\alpha t}{t_o}} \quad (1)$$

This equation represents an idealization for actual pressure time history. Curve shape resulting from applying this equation and its parameters are as shown in figure 4.

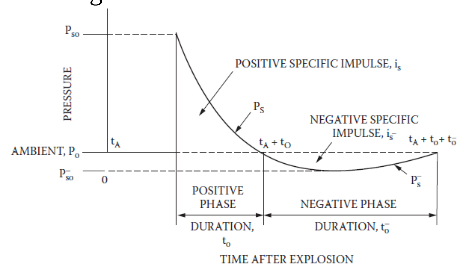

Fig. 4 Idealized pressure-time variation

SINGLE-DEGREE-OF-FREEDOM MODELING

To calculate deflection, RC slab was also analysed using the single-degree-of-freedom (SDOF) simplified method. Deflection results obtained using this method are known to be conservative compared to actual deflections. The procedure in UFC 03-340-02 manual was used for this purpose. This method is similar to the one developed by Biggs [14] in which the principles of SDOF system (shown in figure 5(a)) were applied. Since the analysed slab is one-way, the failure pattern anticipated and SDOF developed are assumed to be at the middle of slab as shown in figure 5(b).

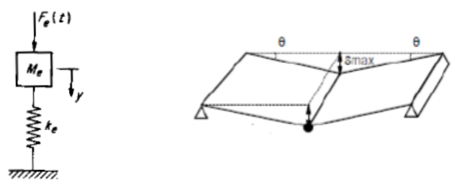

(a) (b)

Fig. 5 (a) SDOF system, (b) Failure pattern in one-way slab

For simplification, factors required for computing slab deflection (including elastic stiffness K_e, maximum resistance R_u, natural period T_n) were calculated by applying formulas for simply supported one-way structural elements. Furthermore, dynamic strength properties were considered for concrete and steel. This was through multiplying strengths by the dynamic increase factors (DIF), which are 1.25 and 1.23 for concrete and reinforcing steel bar respectively for the case of close-in detonations.

For simplification, the average overpressure was assumed to be uniformly distributed in order to calculate peak load P_o. In UFC, the maximum deflection X_m, can be obtained from curves having t_d/t_n and R_u/P_o values. When these values were calculated for the case investigated, small values were obtained for these ratios which were out of curves range. Therefore, the following equation in Ref [1] was used to estimate X_m

$$\mu_d = X_m / X_e = \frac{1}{2}\left[\left(\frac{I_0 * 2\pi * f}{R_u}\right)^2 + 1\right] \quad (2)$$

were μ_d is ductility demand, X_e maximum elastic deflection, I_o loading impulse and f frequency.

RESULTS AND DISCUSSIONS

Blast Results

The general blast wave characteristics provided by LBE were verified by observing the pressure-time histories which proved to follow the Friedlander curve as shown in figure 6. The scaled distance Z for the 0.2, 0.31 and 0.46 kg TNT charge weights and 0.4 m standoff distance was 0.68, 0.59 and 0.52 m/kg1/3 respectively. Since Z values are less than 0.71 m/kg1/3, the detonation type for all charges is close-in [11]. The pressure contours on slab for W_{TNT}=0.2 kg at different time steps are shown in figure 7.

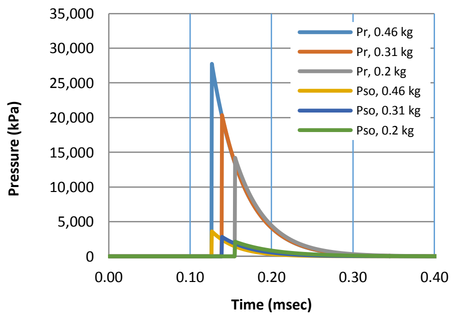

Fig. 6 Pressure-time histories of reflected and incident pressures

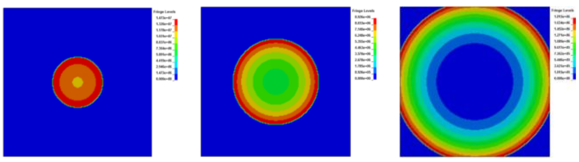

(a) 0.16 msec (b) 0.20 msec (c) 0.40 msec

Fig. 7 Pressure contours for applied reflected pressure on slab top, for pressure for W_{TNT}= 0.31 kg and R = 0.4 m (Z = 0.59m/kg$^{1/3}$)

Deflection Results

The FE analysis indicated the pattern of deflection for the one-way square slab under blast loading through time. Before RC slab reached the one-way slab failure pattern, the square slab went through different stages before reaching the one-way failure pattern. Both the KCC and Winfrith Concrete material models exhibited a similar behaviour. Graphical presentations for the slab deflection contours at different time instants for 0.2 kg TNT charge weight for the KCC material model is shown in figure 8, and cross section of the slab at maximum deflection for KCC and Winfrith concrete models are shown in figure 9(a) and (b) respectively for W_{TNT} = 031 kg.

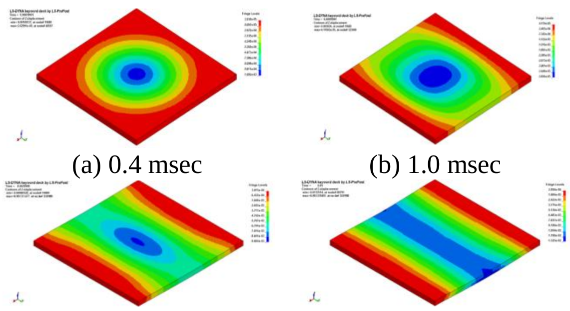

(a) 0.4 msec (b) 1.0 msec

(c) 3.0 msec (d) 10.0 msec

Fig. 8 Contours of Z-displacement in the RC slab model using the KCC Concrete for W_{TNT}= 0.20 kg at different time instants

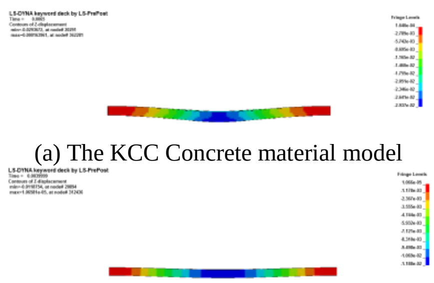

(a) The KCC Concrete material model

(b) The Winfrith Concrete material model

Fig. 9 Cross sections at the middle of slab model along supports direction for maximum deflection. W_{TNT}= 0.31 kg

Deflections were measured at the slab surface mid-point, and the displacement-time histories at this point for slabs with different concrete models are shown in figure 10. In general, the maximum deflection, shown in this figure was noticed to be increased when the TNT charge weight was increased. Besides the FE method, slab was also analysed by means of SDOF method. The maximum slab deflection was calculated for different charge weights.

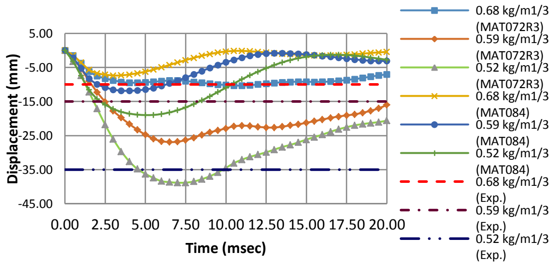

Fig. 10 Displacement-time histories at middle of slab for the KCC (MAT072R3), the Winfrith concrete models (Exp. Max: maximum displacement in the experiment)

Comparing results obtained from KCC and the Winfrith models with those form the experiment (as shown in Table 1, it was noticed that both materials estimated the maximum slab deflection effectively, and the former appeared to estimate it more effectively. In other hand, the SDOF appeared to be conservative as it overestimated the maximum slab deflection by almost twice the actual one. The variation in deflection can be observed in figure 11.

Slab No.	W_{TNT} (kg)	R (m)	Z (m/kg$^{1/3}$)	Maximum Deflection (mm)			
				Experiment	FEM		SDOF
					KCC (MAT072R3)	Winfrith (MAT084)	
1	0.2	0.40	0.68	10.00	10.36	7.41	20.94
2	0.31	0.40	0.59	15.00	26.92	11.87	36.09
3	0.46	0.40	0.52	35.00	38.84	18.99	62.27

Table 1 Summary of slab maximum deflection for charge weights

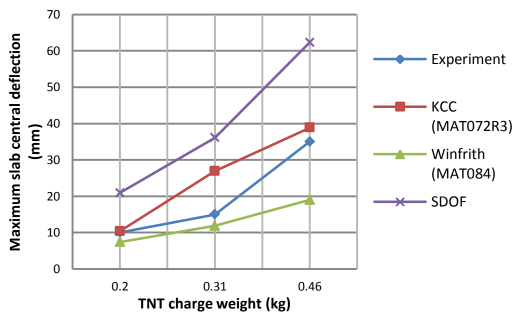

Fig. 11 Variation in maximum slab central deflection

Damage Modes Results

FE analysis using LS-DYNA, damage modes were captured by observing the effective plastic strain contours of the material which grows whenever the material is actively yielding. The slab damage modes at maximum deflection for the different scaled distances obtained from LS-DYNA models were compared to the actual modes in the experiment. The damage modes for 0.2, 0.31, 0.46 kg TNT charge weight and 0.4 m standoff distance for the KCC and Winfrith concrete material models are shown in figure 12. The damage modes can be effectively estimated by using the KCC model compared to Winfrith. In the actual slab, spallation occurred at top of slab which caused from non-uniform with high intensity pressure of the close-in detonation [11]. This could not be effectively assessed in KCC model because the LBE command applies blast loading using the Lagrangian approach in which the interaction between the ambient air and solid slabs is not considered. ALE approach considers this interaction.

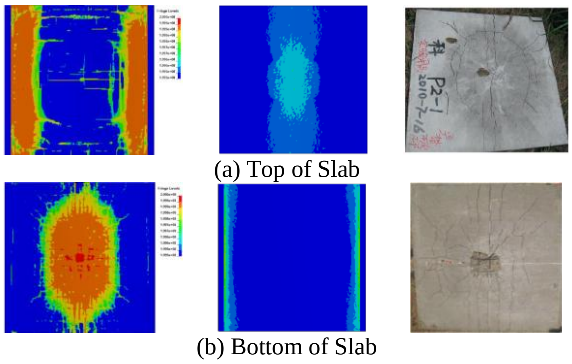

Fig. 12 Damage mode of the slab for 0.31 kg, and R = 0.4 m (Z = 0.59 m/kg$^{1/3}$). KCC (left), the Winfrith (middle) the experiment [4] (right).

PARAMETRIC STUDY

Two parameters were chosen to investigate their effect on slab deflection namely the reinforcement bar spacing (or ratio) and standoff distance. The effect of these two parameters was investigated and by means of FE analysis using the KCC and Winfrith concrete models.

Effect of Reinforcement Ratio (Bar Spacing)

The effect of reinforcement spacing was studied by means of FE analysis, in which the LS-DYNA concrete models namely the KCC and Winfrith models were used. The reinforcement used previously was 6 mm bar mesh spaced 75mm (1.3% reinforcement ratio). For investigation, additional three reinforcement bar spacing were chosen: 50mm, 100mm and 125mm responding to reinforcement ratios of 1.95, 0.975 and 078% respectively. These were investigated for the 0.2, 0.31 and 0.46 TNT charge weight and 0.4m standoff distance. The variations in maximum displacement for different charge weights and bar spacing for the KCC and Winfrith concrete models are shown in figure 13 and 14 respectively. Generally, it was observed that increasing the bar spacing has its effect as the maximum displacement was increased by an amount that varies depending on the charge weight and the bar spacing.

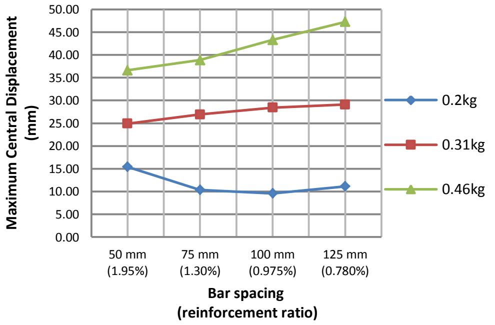

Fig. 13 Variation of slab maximum central displacement for different reinforcement ratios using the KCC concrete model (MAT072R3).

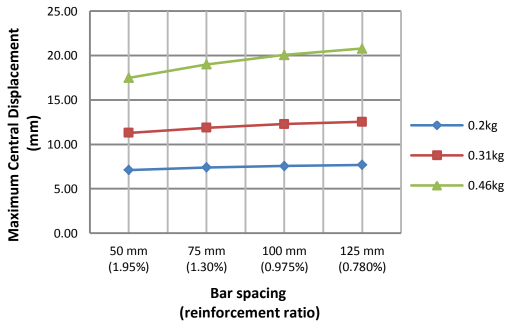

Fig. 14 Variation of slab maximum central displacement for different reinforcement ratios using the Winfrith concrete model (MAT084)

Effect of Standoff Distance

The effect of standoff distance was investigated by studying its effect in the applied pressure and the displacement behaviour of slab. Three standoff distances were considered: 0.40, 0.75 and 1.00 m for 0.2, 0.31 and 0.46 kg TNT charge weights. Varying the standoff had effects by changing the type of detonation from close-in to far range detonation. This had its impact on the blast characteristics and its parameters. For the 0.2 kg TNT charge weight, reflected and incident pressure time histories obtained for 0.40, 0.75 and 1.00 standoff distances from centre of slab are shown in figure 15. The variation in scaled distance and reflected pressures for charge weights and standoff distances are shown in figure 16 and figure 17.

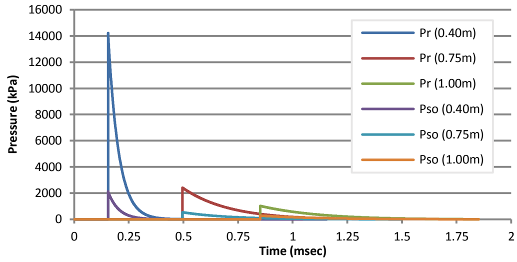

Fig. 15 Pressure-time histories of reflected and incident pressures for W_{TNT} = 0.2kg at different standoff distances

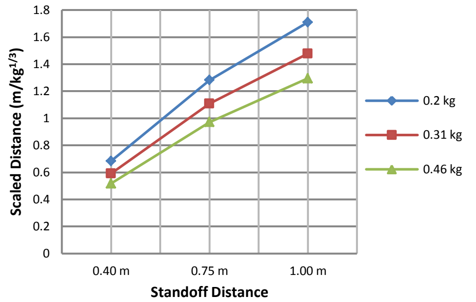

Fig. 16 Variation of scaled off distance for different TNT charge weights and standoff distances

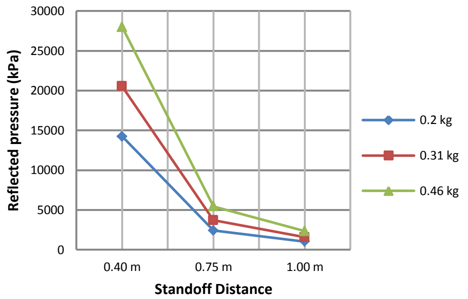

Fig. 17 Variation of reflected pressure for different TNT charge weights and standoff distances

The displacement time histories for the KCC concrete slab model were obtained for 0.40, 0.75 and 1.00 standoff distances. For 0.2 kg TNT charge weight, displacement time history is as shown in figure 18).

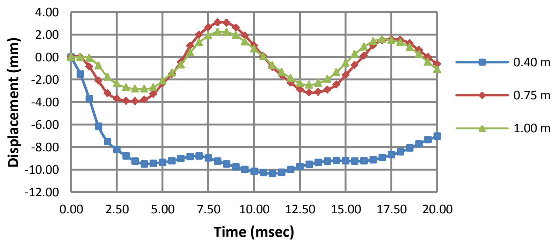

Fig. 18 Displacement-time histories at middle of slab for the KCC (MAT072R3) for different standoff distances, W_{TNT} = 0.2 kg

In the case of 0.40 m standoff distance, the loading took the form of relatively high reflected pressure and small impulse, while in the 0.75 and 1.00m the loading were having lower reflected pressures with greater impulses. This difference had its effect on the maximum deflection attained by slab in addition to the pattern of the displacement time histories. For the 0.2 kg charge weight and 0.40 m standoff distance, the slab centre displacement time history indicated that it responded plastically (displacement did not spring back after reaching the maximum deflection). When the standoff distance was changed to 0.75 m and 1.00 m, the slab responded differently as the displacement time history took the form of damped harmonic oscillator (figure 18). Also, it can be observed that by decreasing standoff distance, the displacement was decreased greatly compared to the one in 0.40 m standoff distance (figure 19). Similarly, the slab behaved in models for the 0.31 and 0.46 kg charge weight for the considered standoff distances.

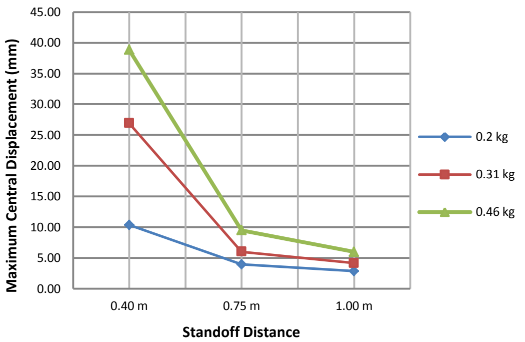

Fig. 19 Variation of slab maximum deflection for different TNT charge weights and standoff distances

CONCLUSION

The numerical models of the one-way RC slab subjected to blast loads, which are applied using Lagrangian approach, for close-in detonations indicated that the slab deflection can be estimated satisfactorily. Both KCC and the Winfrith concrete model can indicate the slab deflection effectively, while the SDOF appeared to obtain conservative results. Damage modes obtained by applying the Lagrangian approach may not indicate the local shear which occurs in the tension zone. From the parametric studies, it can be inferred that slab deflection can be controlled by adjusting slab reinforcement ratio or explosive standoff distance.

REFERENCES

[1] ASCE Task Commitee on Blast Resistant Design of the Petrochemical Committee of the Energy Division of the American Society of Civil Engineers, Design of Blast Resistance Buildings in Petrochemical Facilities, New York: American Society of Civil Engineers (ASCE), 1997.

[2] T. Krauthammer, S. Shahriar and H. M. Shanaa, "Response of Reinforced Concrete Elements to Severe Impulsive Loads," Journal of Structural Engineering, vol. 116, no. 4, pp. 1061-1079, April 1990.

[3] D. Hao and L. Zhongxian, “Numerical analysis of dynamic behavior of RC slabs under blast loading,” Transactions of Tianjin University, vol. 15, no. 1, pp. 61-64, February 2009.

[4] W. Wang, D. Zhang, L. Fangyun, S.-C. Wang and F. Tang, “Experimental study and numerical simulation of the damage mode of a square reinforced concrete slab under close-in explosion,” Engineering Failure Analysis, vol. 27, p. 41–51, 2013 .

[5] C. F. Zhao and J. Y. Chen, “Damage mechanism and mode of square reinforced concrete slab subjected to blast loading,” Theoretical and Applied Fracture Mechanics , vol. 63–64, p. 54–62, 2013.

[6] Y. S. Tai, T. L. Chu, H. T. Hu and J. Y. Wu, “Dynamic response of a reinforced concrete slab subjected to air blast load,” Theoretical and Applied Fracture Mechanics, vol. 56, p. 140–147, 2011.

[7] Z. S. Tabatabaei and J. S. Volz, "A Comparison between Three Different Blast Methods in LS-DYNA: LBE, MM-ALE, Coupling of LBE and MM-ALE," in 12th International LS-DYNA Users Conference, Dearborn, Michigan, USA, 2007.

[8] L. Schwer and L. Malvar, “Simplified Concrete Modeling with *MAT_CONCRETE_DAMAGE_REL3,” in JRI LS-DYNA User Week 2005, Nagoya, Japan, 2005.

[9] L. Schwer, “The Winfrith Concrete Model : Beauty or Beast ? Insights into the Winfrith Concrete Model,” in 8th European LS-DYNA Users Conference, Strasbourg, 2011.

[10] D. W. Hyde, "User's Guide for Computer Programs CONWEP and FUNPRO. Applications of TM 5- 855-1, "Fundamentals of Protective Design for Conventional Weapons"," Washington, DC, 1988.

[11] USA Department of Defence, “Structures to Resist The Effect of Accidental Explosions - Unified Facilities Criteria (UFC) 3-340-02”, Department of Defence, 2008.

[12] G. Randers-Pehrson and K. A. Bannister, “Airblast Loading Model for DYNA2D and DYNA3D,” Adelphi, Maryland, 1997.

[13] L.S.T.C., LS-DYNA Keyword User's Manual, Livermore: Livermore Software Technology Corporation (LSTC), 2007.

[14] J. M. Biggs, Introduction to Structural Dynamics, New York: McGraw-Hill, 1964.

[15] M. M. N. Shuaib, "Numerical Modeling of Reinforced Concrete Slab under Blast Loads", M.Sc. Thesis, University of Khartoum, Khartoum, Sudan, 2014.

SOME ASPECTS OF PHYSICAL AND MECHANICAL PROPERTIES OF SAWDUST CONCRETE

A.S.M. Abdul Awal[1], A.A.K. Mariyana[2] and M.Z. Hossain[3]
[1,2] Faculty of Civil Engineering, Universiti Teknologi Malaysia, Johor, Malaysia [3]Faculty of Bioresources, Mie University, Japan

ABSTRACT

This paper presents experimental results on some physical and mechanical properties of concrete containing sawdust. Concrete specimens having various cement to sawdust ratios of 1:1, 1:2 and 1:3 by volume were made and tested for workability, density, water absorption, strength and modulus of elasticity at different curing periods of 7, 14 and 28 days. It has been found that with the increase in the amount of sawdust, the workability and density of concrete decreased; the water absorption capacity of concrete, however, increased with the increase in volume. Although, the strength of sawdust concrete increased with curing period, the strength and the corresponding modulus of elasticity decreased with the increasing amount of sawdust in the mix. The results obtained and the observations made in the short-term investigation suggest that sawdust concrete can suitably be used as a building material in construction.

Keywords: Timber waste, Sawdust concrete, Physical properties, Strength, Deformation.

INTRODUCTION

Vast quantities of waste materials and by-products from various sources are generated from the manufacturing process, service industries and municipal solid waste. As a result, solid waste management has become one of the major environmental concerns in the world. With the increasing awareness of the environment protection, significant research has been going on globally on the utilization of waste materials and by-products as construction materials [1]. Recycling of such wastes into new building materials could be a viable solution not only to the pollution problem, but also to the challenge of high cost of building materials currently faced by both the developed and developing nations [2][3]. One of such potential waste material is sawdust which is relatively abundant and inexpensive.

Sawdust or wood dust is an industrial waste obtained as by-products from cutting, sawing or grinding of timber in the form of fine particle (Fig. 1). Sawdust bonded with cement is also known as ‘sawdust cement’ [4]. Although sawdust consists largely of cellulose (Fig.2), it also contains soluble sugar, acids, resins, oils and waxes, and

Fig. 1 Sample of sawdust used in the study

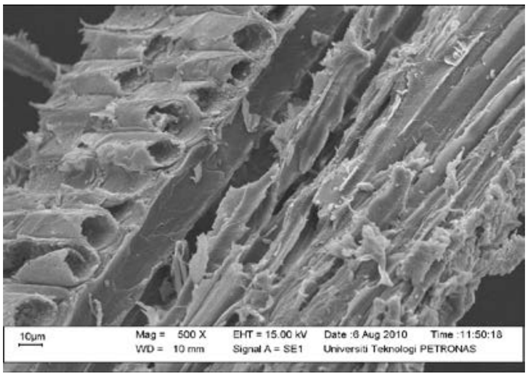

Fig.2 Scanning electron micrograph (SEM) of sawdust particles [5].

other organic substances which have an inhibiting effect on the setting and hardening of the cement. Despite setting and hardening problems, most of the softwood sawdust is rendered compatible with the cement if a mixture of lime or cement is used as the binder [6]. Eventually, the strength of concrete reduces with the increase in sawdust volume. Paramasivam and Loke [7] found that sawdust concrete with a cement to sawdust ratio of 1:1 has good bond strength and comparable to the normal concrete. The drying shrinkage, however, is very high; almost 10 times as great as in most other lightweight concretes, and thus greatly limits the usefulness of this material. In spite of the limitations, sawdust concrete has a good insulation value, resiliency, low thermal conductivity and can be sawed and nailed [8].

With the advancement in concrete technology, the utilization of sawdust in the manufacture of building materials has received some attention over the past years in many places of the world. Other than in concrete, recent studies on the use of wood sawdust wastes as a new brick material supplement appears to be viable solution not only to the environmental problem but also to the problem of economic design of buildings [9]. Considering the availability and the inherent quality of this waste material, this study aims at exploring the suitability of sawdust as building material through investigation of physical and mechanical properties of concrete.

MATERIALS AND TEST METHODS

Sawdust and Concrete Mix Proportions

Sawdust used in this study was collected from a local plank and furniture market of Johor Bahru, Malaysia. The sawdust consisted mostly of fine chippings from rubber tree (Fig. 1). In the case of light weight aggregate, it is generally recommended that the proportions are specified in terms of volume rather than by weight because the bulk specific gravities are not in the same order due to different sizes of grains [7]. In this study, three mix proportions of cement to sawdust in the ratio of 1:1, 1:2 and 1:3 by volume were utilized. Ordinary Portland cement (ASTM Type I) was used throughout the research work.

By nature, sawdust particles are porous and absorb most of the water leaving insufficient water for the setting of cement. The water cement ratio of sawdust concrete usually varies from 0.4-1.2 depending on the mix proportions [7]. In this investigation the sawdust particles were treated to saturated surface dry state to reduce the effect of water absorption by the particles. Following several trials, the water-cement ratio of 0.6 was adopted for the study. Throughout the study, supplied tap water was used for mixing of concrete.

Casting and Testing of Concrete Specimens

Concrete specimens comprising of cube (100 mm), cylinder (100x200 mm) and prism (100x100x500 mm) were cast for determining compressive, tensile and flexural strength respectively. The specimens were cast in metal moulds and were demoulded after 24 hours, and cured by polythene sheeting until testing time. Casting and testing of concrete specimens were done in the Structure and Materials laboratory of the Faculty of Civil Engineering, Universiti Teknologi Malaysia. The ambient temperature and relative humidity in the laboratory were 27 ± 3˚C and 85 ± 5% respectively.

The strength tests for compression, tension and flexure were conducted according to BS 1881: Part 116 [10], ASTMC496-05 [11] and BS1881: Part118 [12] standards respectively. While the tests on modulus of elasticity of concrete were conducted in accordance with the standard stipulated in ASTM 469-05 [13]. Along with strength measurement, ultrasonic pulse velocity (UPV) was also measured on the test specimens.

RESULTS AND DISCUSSION

Physical Properties

The physical properties of sawdust concrete are presented in Table 1. The consistency of the fresh mix, tested in terms of slump has been found to vary depending on the amount of sawdust in the mix. In general, higher the amount of sawdust lower was the slump. Slump values of 40, 15 and 5 mm were obtained for mix ratios of 1:1, 1:2 and 1:3 respectively, and were found to fall within the medium, low and no-slump ranges according to Euro code Standard classifications (BS EN 206-1) [14]. Similar observation has been made by Oyedepo et al. [15]

The density of sawdust concrete measured at 28 days for the mix ratios of 1:1, 1:2 and 1:3 are 1450, 1280 and 1065 kg/m^3 respectively. The test results show that the density values are inversely proportional to the volume of sawdust content. By assuming the average density of OPC concrete to be 2400 kg/m^3, the mix proportion of 1:1 provides about 40% reduction in density. This reduction highlights the potentials of sawdust concrete to be used as lightweight building material in construction.

The water absorption, expressed as percentage, was obtained by measuring the amount absorbed against the dry mass. Unlike slump and density, the water absorption of sawdust concrete was found to increase with the increasing amount of sawdust in the mix. This is obvious, because sawdust is relatively porous than the aggregates like sand, stone etc. used in normal concrete [16].

Table 1 Physical properties of sawdust concrete

Mix ratio	Slump (mm)	Density (kg/m^3)	Water absorption (%)
1:1	40	1450	13
1:2	15	1280	15
1:3	5	1065	19

Compressive Strength

The compressive strength test was conducted on concrete cube specimens (Fig. 3) and the results obtained for the three mixes are illustrated in Fig. 4. The results presented in the figure showed an average strength development of 14.45, 13.60 and 8.40 MPa obtained at the age of 7 days for the mix ratios of 1:1, 1:2 and 1:3 respectively. A slight increase in the strength was found to occur after 14 days.

Fig. 3 Testing of concrete cube specimen for compressive strength.

At the age of 28 days there was a significant increase in compressive strength in all the mixes. Strength values of 18.65, 17.20 and 12.80 MPa, for instance, were obtained for the mix ratios of 1:1, 1:2 and 1:3 respectively. From the results obtained it is clear that the strength of sawdust concrete decreases with an increase in the volume of sawdust in the mix proportions.

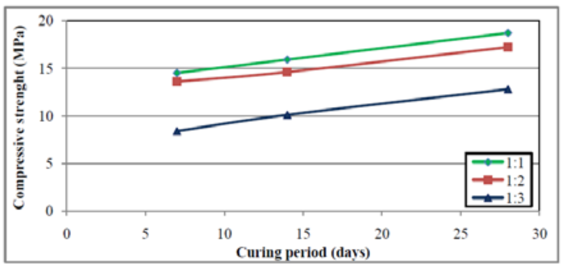

Fig. 4 Development of compressive strength of concrete.

Figure 5 illustrates a liner relationship between the compressive strength and ultrasonic pulse velocity (UPV) of sawdust concrete at the age of 28 days. Even though the UPV values increased with the increase in compressive strength, the highest value of 2620 m/s obtained for 1:1 ratio falls within the low quality range [8].

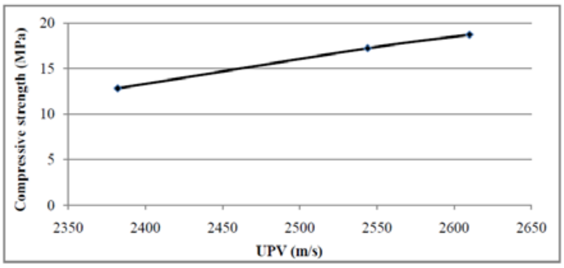

Fig. 5 Relationship between compressive strength and ultrasonic pulse velocity (UPV) of concrete.

Tensile Strength

The splitting tensile strength of sawdust concrete was also determined (Fig. 6) at the age of 7, 14 and 28 days, and the results are presented in Fig. 7. The development of splitting tensile strength was somewhat similar to that observed in the case of compressive strength i.e. splitting tensile strength decreased with the increase in the amount of sawdust. For example, at 28 days the strength values of 2.05, 1.95 and 1.30 MPa were obtained for mixes of 1:1, 1:2 and 1:3 respectively.

The relationship between the 28-day compressive and tensile strength of sawdust concrete is shown in Fig. 8. It can be observed that the relationship is somewhat liner i.e. compressive strength is proportional to the tensile strength; however, the value of the relationship diminishes with the increase in sawdust mix ratio.

Flexural Strength

The flexural strength test was conducted on concrete prism specimen (Fig. 9) at the age of 28 days and the results are presented

Fig. 6 Determination of tensile strength.

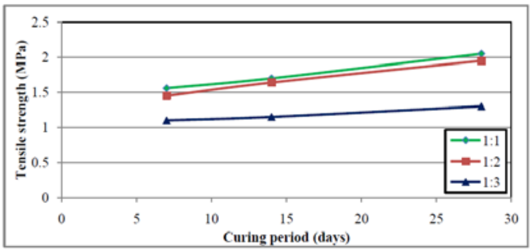

Fig. 7 Development of tensile strength of concrete.

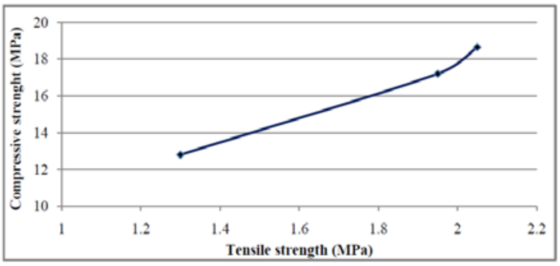

Fig. 8 Relationship between compressive and tensile strength of concrete.

in Fig. 10. It has been found that like that of compressive and tensile strength, the flexural strength of sawdust concrete also followed the same trend. For example, when the mix proportions changed from 1:1 to 1:2, the flexural strength decreased from 2.75 to 2.20 N/mm^2, which represents a decrease of about 35%, while a loss of about 30% occurred with the lean mixes from a ratio of 1:2 to 1:3.

Fig. 9 Determination of flexural strength of concrete

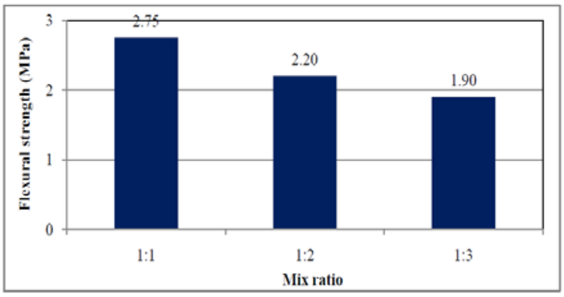

Fig. 10 28-day flexural strength of sawdust concrete.

The relationship between 28-day compressive strength and flexural strength of sawdust concrete is demonstrated in Fig. 11. Although there was a progressive increase in the two parameters, as can be seen in the figure, the relationship is not liner as observed in case of compressive and tensile strength.

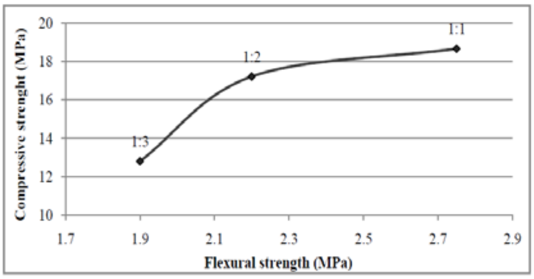

Fig. 11 Relationship between compressive strength and flexural strength.

Modulus of Elasticity

The modulus of elasticity of sawdust concrete was experimentally determined (Fig. 12) at the age of 28 days. Along with the experimental investigation, theoretical models were also studied in predicting the modulus of elasticity following the British Standard for the structural use of concrete BS 8110-2:1985 [17, 18]. Data presented in Fig. 13 reveal that the elastic modulus of 17.10, 16.40 and 11.95 GPa were obtained for the mixes of 1:1, 1:2 and 1:3 respectively while 20.30, 19.50 and 16.0 GPa were calculated using theoretical model for the same mix ratios. Although the predicted values were somewhat higher, data obtained from the limited experimental work are quite satisfactory.

Fig. 12 Determination of modulus of elasticity of concrete.

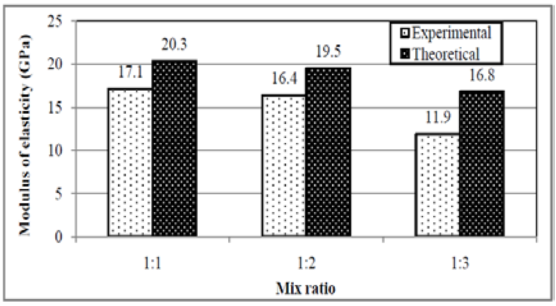

Fig. 13 Modulus of elasticity of sawdust concrete.

CONCLUSION

In this study sawdust concrete with various cement to sawdust ratios, by volume was made and the physical and mechanical properties were investigated. This paper highlights the potential benefits of sawdust concrete in terms of physical and mechanical properties. The results obtained and the observations made in this study conclude that sawdust concrete can be used as light weight concrete with a satisfactory strength performance. Long-term strength development including durability aspects has been put forward as recommendation for future study in order to explore better understanding of sawdust as a sustainable building material in construction.

ACKNOWLEDGEMENTS

The financial support received from the Universiti Teknologi through Research Management Centre (Cost Center No. Q.J130000.2522.10H06) is gratefully acknowledged.

REFERENCES

[1] Siddique R, Waste Materials and By-Products in Concrete. Springer-Verlag Berlin Heidelberg, 2008.

[2] Chandra S, Waste Materials Used in Concrete Manufacturing. Noyes Publications, New Jersey, 1997.

[3] Udoeyo F F and Dashibil PU, "Sawdust ash as concrete material', J. of Materials in Civil Engineering, Vol.14, 2002, pp.173-176.

[4] Short A and Kinniburgh W, Lightweight Concrete. CR books Ltd, London, 1968.

[5] Shaaban A, Se-Meng M, and Dimin MF, Characterization of biochar derived from rubber wood sawdust through slow pyrolysis on surface porosities and functional groups, Procedia Engineering, Int Tribology Conference Malaysia 2013, Vol. 68, pp. 365-371.

[6] Aigbomian EP and Fan M, "Development of wood-concrete building materials from sawdust and waste paper", Construction and Building Materials, Vol. 40, 2013, pp. 361-366.

[7] Paramasivam P and Loke Y O, "Study of sawdust concrete". The International Journal of Lightweight Concrete, Vol.1, No. 2, 1980. pp. 57-61.

[8] Nevillie A M, Properties of Concrete. 4th ed. ELBS Pitman, 2000.

[9] Halil MA and Turgut P, "Limestone dust and wood sawdust as brick material", Construction and Building Materials, Vol. 22, 2007, pp. 3399-3403.

[10] BS1881-116, Testing concrete. Method for determination of compressive strength of concrete cubes, 1983.

[11]ASTMC496, Test for splitting tensile strength of cylindrical concrete specimens, 2005.

[12] BS1881-118, Testing concrete. Method for determination of flexural strength, 1983.

[13] ASTM C469, Test for static modulus of elasticity and Poisson's ratio of concrete in compression, 2002.

[14] BS EN 206-1, Concrete. Specification, performance, production and conformity, 2000.

[15] Oyedepo OJ, Oluwajana SD and Akande SP, "Investigation of properties of concrete using sawdust as partial replacement of sand", Civil and Environmental Research, Vol. 6, No.2, 2014, pp.35-42.

[16] Mageswari M and Vidivelli B, "The use of sawdust ash as fine aggregate replacement in concrete". J. of Environmental Research and Development, Vol. 3, No.3, 2009, pp.720-726.

[17] BS 8110-2, Structural use of concrete. Code of practice for special circumstances, 1985.

[18] Neville AM and Brooks JJ, Concrete Technology, 2nd ed. Longman Group UK limited, 1987.

DAMAGE INVESTIGATION AND RETROFITTING OF WEST SUMATRA GOVERNOR'S OFFICE BUILDING

Fauzan[1], Febrin Anas Ismail[2], Zaidir[3], Nugrafindo Yanto[4]
[1,2,3,4]Civil Engineering Department, Andalas University, Indonesia

ABSTRACT

West Sumatra Governor's office building is one of the buildings that damaged by September 30, 2009 Sumatra Earthquake. Damage of the building structure was identified after demolition of all the partitions and column cover panels. In order to know the cause of the damage, an investigation has been done. This paper discusses the result of a building assessment to find the causes of the damage and proposes the recommendation method for retrofitting the building structure. Based on field investigation, structural damages occurred on almost all columns in first floor due to lack of shear reinforcement. A numerical simulation was carried out to evaluate the capability of building structures to resist loads, especially earthquake load based on Indonesian Standard Code, SNI 03-1726-2012. The result of simulation indicates that the damage of the columns was shear failure due to the big distance of shear reinforcement. Retrofitting of the structure was proposed using concrete jacketing for all columns in first floor and installed shear wall in the corners of the building until third floor.

Keywords: Column, Shear failure, Earthquake Load, Jacketing, Shear wall

INTRODUCTION

Indonesia is in the confluence of four major tectonic plates, i.e. the Eurasian, the Indo-Pacific, Australia, and the Philippines plates so it is known as the Ring of Fire that caused many of the earthquakes occurred due to the movement of the plate. On September 30, 2009, the 7.6 SR tectonic earthquake have hit the West Sumatra Province [1]. The earthquake was centered at coordinates 0 ° 50 ' 24 "South latitude and 99 ° 39 ' 0" East longitude. The damage was very severe in the area along the coast of West Sumatra Province. Padang as the capital city of West Sumatera with a distance of 100 km from the epicenter could not escape from severe damage. The quake with a depth of 70 km was recorded as the strongest earthquake ever to hit the city of Padang since this city stand [2].

One of the buildings that could not escape the damage is West Sumatra Governor's Office Building (Figure 1), located in the center of Padang City. This building was reinforced concrete structure, built in 1961. Damage to the structure of the building was identified after a demolition of all the partitions and column cover panel when the building repair will be started. The columns were covered by wood panels, which are not monoliths with columns so the crack occurred in the columns was not visible from the outside. The crack visually can be observed after the demolition of the wooden panels that covering the column, as can be seen in Figure 2.

There are two kinds of retrofitting can be done to damaged buildings, i.e. local retrofit and global retrofit [3]. Local retrofit was conducted by strengthening the structural elements, such as column and beam jacketing, while Global Retrofit was conducted by installing shear wall and bracing on the structure. Based on the results of research conducted by Fauzan et.al [4], the capacity of circular columns after jacketing increased significantly.

Figure 1. West Sumatra Governor's office building

In this study, retrofitting using combined concrete jacketing and shear wall was proposed to retrofit the West Sumatra Governor's office building.

a. Wooden panels covering the columns

b. Shear cracks of columns after demolition of the wooden panels

Figure 2. Damage of the columns on first floor

EVALUATION OF EXISTING BUILDING

A building assessment was carried out on West Sumatra Governor's office building to investigate the cause of damage. In addition, detail of dimensions of structural elements (column, beam etc) and other data for structural analysis was collected in the field because the building was old and no data available from the government.

Damage to the columns and Beams

The damage of columns mostly shear crack that occurred on the middle of the columns. As seen in Figure 3a, the concrete cover of the column was spalling and the steel reinforcement can be seen visually. In addition, the distance of shear reinforcement was bigger which are not following the current standard code. The shear cracks occurred at almost all columns in first floor, as shown in Figure 3b. The location of damaged columns in the 1st floor can be seen in Figure 4.

(a) (b)

Figure 3. Damage of the column on first floor

Based on visual investigation, it is found that the lack of shear reinforcement contribute to the shear failure of the columns.

Concrete and steel reinforcement

Hammer test was carried out to know the quality of concrete on the building. The result indicates that compression stress of the concrete (fc') was 22,2 MPa (225 kg/cm2). Meanwhile, Yield stress of reinforcement (fy) was around 240 MPa from the tensile test of steel reinforcement.

The damage of several beams was also observed on 2nd floor, as shown in Figure 5.

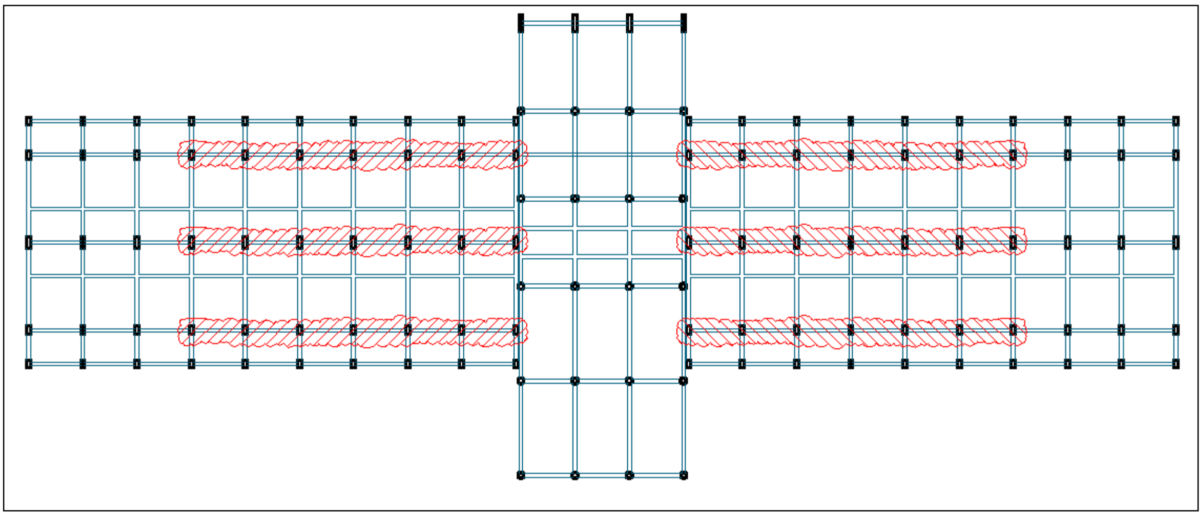

Figure 4. Location of damaged columns

Figure 5. Damaged of beam on second floor

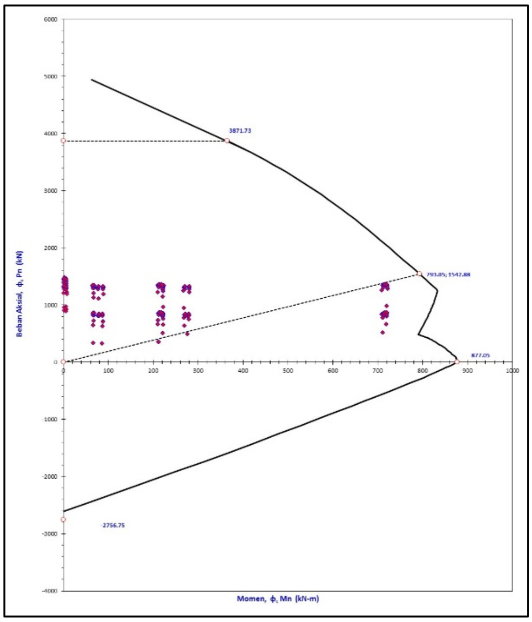

Figure 6. Interaction Diagram P-M (30/80 Column)

Structural Analysis of Existing Building

Structural analysis of existing building was conducted using computer software ETABS 9.7.4 [5]. The earthquake load applied based on current Indonesia standard code (SNI 03-1726-2012) [6]. Result of analysis shows that the capacity of all columns to resist the axial load was strong enough (Figure 6) however the shear capacity of the columns was not sufficient, as shown in Table 1.

Table 1. Shear Capacity of Column 30/80

NOMINAL SHEAR CAPACITY OF COLUMN		
⦿ Nominal Shear Capacity : Vn = Vc + Vs	(kN)	229.51
SHEAR CAPACITY DESIGN OF COLUMN		
⦿ Shear Capacity Design : Vr = ϕ_s Vn	(kN)	172.13
SHEAR CAPACITY ULTIMATE OF COLUMN		
⦿ Shear Capacity Design : Vu	(kg)	20630.10
(from structural analysis)	(kN)	202.38
SHEAR CAPACITY CONTROL		
⦿ Vr ≥ Vu		
172.13 kN < 202.38 kN		... NOT OK !!

RETROFITTING STRUCTURE

Jacketing

Jacketing of columns was proposed to retrofit West Sumatra Governor Office building. The cross-sectional dimension of columns was enlarged from 30/80 to 40/90 and the number of reinforcement was increased by installing a wire mesh type M5-150, as seen in Figure 7.

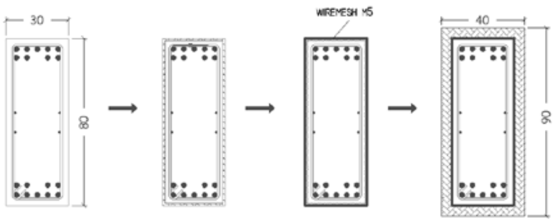

Figure 7. Jacketing methods of column

Re-analysis of structure after jacketing was conducted in order to know the capacity of jacketed columns. The result shows that the shear capacity of columns increased by around 50 - 60 %, as shown in

Table 2. The use of wire mesh contributes to the increase of shear capacity of the column.

Table 2. Comparison of column capacity

Type	Force	Ex	Jc	Ratio (%)
K5	M (kNm)	550.65	630.82	14.56
	P (kN)	2974.55	3999.05	34.44
	V (kN)	165.62	248.668	50.14
K4	M (kNm)	346.37	370.47	6.96
	P (kN)	2312.35	3122.10	35.02
	V (kN)	121.45	190.15	56.57
K3	M (kNm)	276.05	300.6	8.73
	P (kN)	2069.42	2798.20	35.22
	V (kN)	99.37	160.90	61.92

Installing Shear Wall

West Sumatra Governor's office building consists of three blocks separated by dilatation. Dilatation between the building blocks currently is about 5 cm which is very small. In order to reduce the displacement as well as the shear force of the building, reinforced concrete shear wall (Figure 8) were proposed for additional retrofitting on the building. The thickness of shear wall was 25 cm using two layers reinforcement bar D16-150. The location of the shear wall allocation can be seen in Figure 9.

Results of analysis of the structure with the shear walls shows that the displacement of the building on the top floor reduced significantly as shown in Figures 10 and 11.

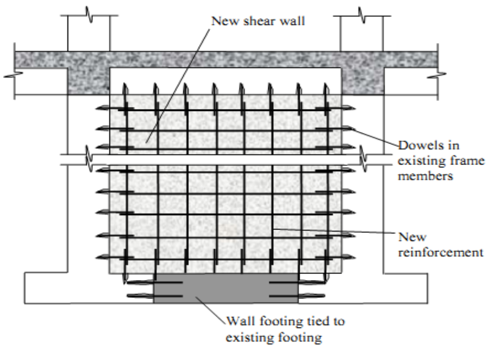

Figure 8. Shear wall

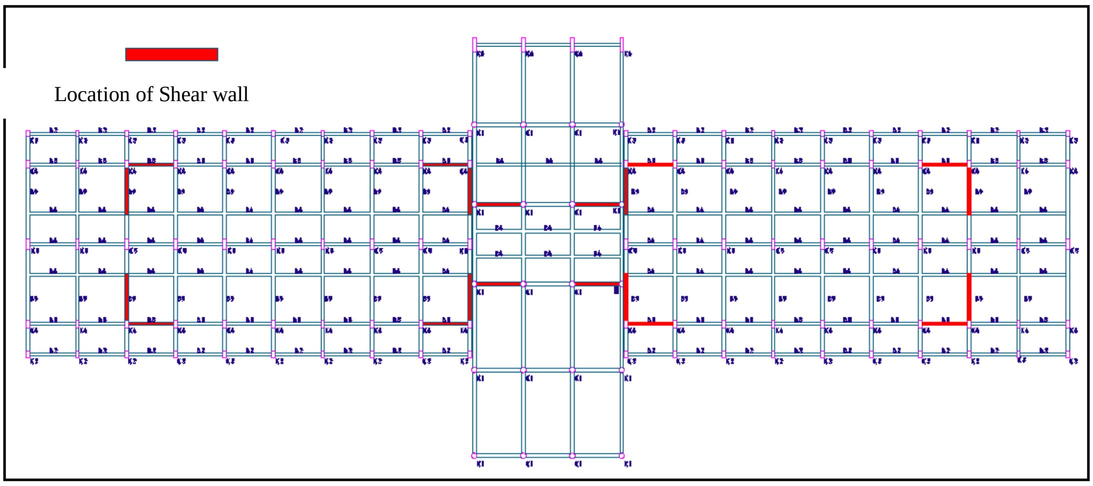

Figure 9. Location of shear wall on left/right building and center building

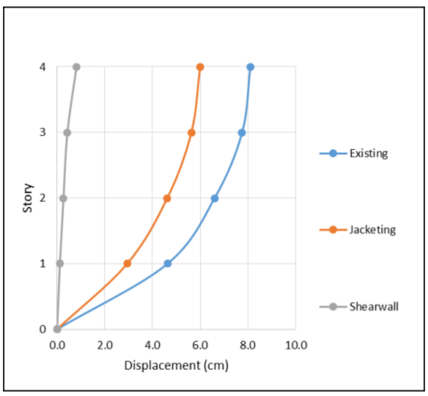

Figure 10. Displacement of Left/right Building

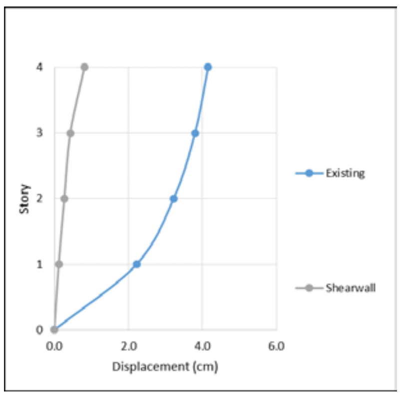

Figure 11.Displacement of Centre Building

In the SNI 1726-2012 explained that the building is separated structurally should have reasonably sufficient distance to avoid a damaging collision. The separation of the structure must be able to accommodate the maximum displacement with equations that are already set out in the regulations. From Figure 10, it can be seen that the maximum displacement after installing shear wall at the left/right building is 0.81 cm and the maximum displacement of the central building is 0.40 cm (Figure 11).

Minimum dilatation according SNI 1726-2012 is:
Left/Right building :
S_1 = 0,81 cm
Sm_1 = 4,06 cm
Center Building :
S_2 = 0,40 cm
Sm_2 = 2,00 cm
Minimum dilatation space :
$\delta m = \sqrt{Sm1^1 + Sm2^2}$
δm = 4,54 cm < 5,00 cm (ok)

Retrofitting Implementation Methods

The first step that needs to be done to the West Sumatra Governor's office building are doing the restoration actions on the elements of structure. Restoration can be implemented as follows [7]:

1. Small cracks on the beams and columns injected with cement or epoxy materials. Small cracks are cracks that have wide gaps less than 0.6 cm.
2. The elements of the structure that had large cracks should be dismantled and replaced with a new concrete.

After the restoration, the retrofitting of structure using jacketing and shear wall was conducted.

CONCLUSION

1. The damage on the Office of the Governor of West Sumatra was shear failure due to the lack of shear reinforcement.
2. Retrofit of the West Sumatra Governor's office building can be carried out using a combination of jacketing and installation of shear wall.
3. Installing shear wall on the building reduced the displacement of the buildings so it can meet the requirement of dilation space based on SNI 1726-2012
4. Retrofitting of West Sumatra Governor's office building can be done after a restoration of each structural elements.

ACKNOWLEDGEMENTS

Thanks to the Building Assesment Team of Andalas Disaster Study, Material Structure Laboratory of Civil Engineering Andalas University and Public Works Department, West Sumatra over the support and help of the required data.

REFERENCES

[1] Meteorology and Geophysics Department of Indonesia. 2009.
[2] Ismail, Febrin Anas et.al. “The Bumiminang Hotel’s building damage due to the Padang Earthquake September 30, 2009". Journal Of Civil Engineering, Bandung Institute Of Technology. Vol. 10 No. 2, pp. 119-125, August 2011, ISSN 0853-2982.
[3] Public Works Department dan Indian Building Congress. *Handbook on Seismic Retrofit of Buildings. Association Indian Institute Technology.*2007.
[4] Fauzan, et al. "Structure Analysis of Retrofitting the Andalas Mosque after earthquake 30 Sept 2009". Journal Of Civil Engineering, Andalas University. Volume 7 No. 1 February 2011, ISSN 1558-2133.
[5] Computers and Structures, Inc. *ManualETABS* (*IntegratedBuildingDesignSoftware*). California, USA. 2005.
[6] State Standardization Department. Earthquake Resistance Planning for Building and Non-Building Structures. SNI 1726:2012. Jakarta.
[7] Boen, Teddy. “How to repairing simple buildings damaged by the earthquake”. Jakarta. 2009.

HORIZONTAL PERMEABILITY OF CLAY MIXTURES UNDER LARGE SHEAR DEFORMATIONS

Po- Hao Hsu[1], Yohei Katayama[1], Takashi Tsuchida[1] and Athapaththu A.M.R.G.[1]
[1] Hiroshima University, Japan

ABSTRACT

After Tohoku Earthquake, a huge amount of disaster waste including radioactive substances was released to the environment due to the accident of Fukushima No.1 nuclear power plant. This study is related to offshore waste disposal facility for storing the waste materials. A sealing layer is one of the major component in a disposal facility. Previous studies by some of the co-authors in this paper revealed that the coefficient of permeability of 5 x 10^{-10} m/s was achieved on a predesigned clay mixture. This research was focused to examine the change of permeability characteristics under shear deformations due to earthquakes, and Tsunami. Hollow Cylinder Torsional Permeability Test (HCTPT) was conducted to examine the effect of shear deformation on permeability characteristics of the various clay mixtures. The coefficients of permeability in the horizontal direction were in the range of 1.5 - 2.0 times that of coefficient of permeability in the vertical direction. It was found that there is no considerable increase of coefficient of permeability due to the change of shear deformations.

Keywords: Permeability, Hollow Cylinder Torsional Permeability Test, Clay Mixture, Shear deformation

INTRODUCTION

After Tohoku Earthquake in Japan, a huge amount of disaster waste including radioactive substances was released to the environment due to Fukushima No.1 nuclear power plant at the east coast of Honshu Island, Japan. These wastes possess a great concern to the local people though the government carried out measures on decontamination. A huge amount of waste was generated and remained in Fukushima prefecture.

The Ministry of Environments, Government of Japan started to build an interim storage facility near Fukushima No.1 nuclear power plant. The volume is about 15 million to 28 million m^3. Area of the facility is estimated to be about 3-5 km^2. It is expected that the waste will go through the final treatment outside Fukushima Prefecture within the next 30 years (Ministry of Environments, 2013). However, no technical surveys have been carried out officially on the sites and the structures of the final disposal facility. This study is related to the possibility of constructing offshore disposal facility for these wastes.

Sealing layer is the major component in a disposal facility and its function is to make sure that the radioactive substances to become an innocuous level after passing of it. Previous studies showed that the coefficient of permeability should be less than 5.0 × 10^{-10} m/s to achieve the targets of the sealing layer and this condition can be achieved by nixing marine clays with bentonite (Murakami et al.,2015)

The permeability may be changed by deforming effect in natural hazard, such as earthquakes,

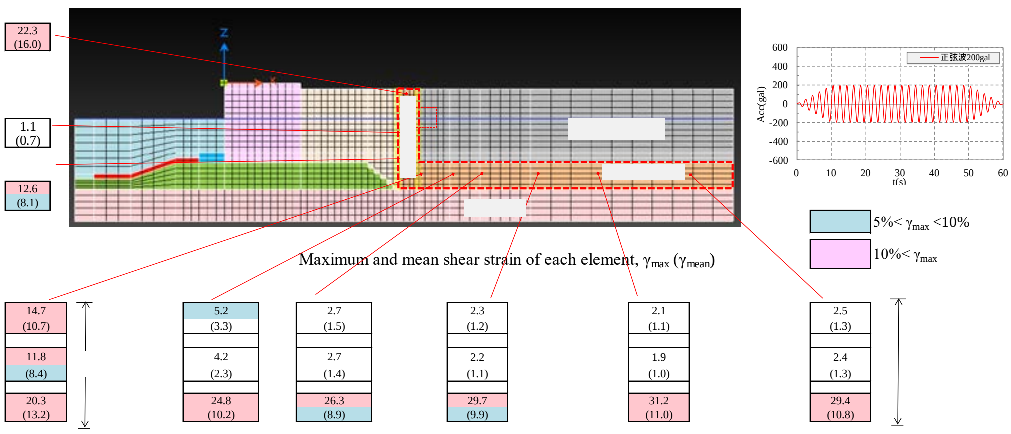

Fig. 1 Deformation Analysis based on FLIP (Tsuchida et al., 2013)

tsunami etc. When an earthquake occurs, huge force may act on the sealing layer. There is a possibility to form cracks and hence the permeability may increase by this phenomenon.

Japan located near plate boundaries and therefore earthquakes occur frequently. These earthquakes ~~would~~ may affect the safety of waste disposal facility. Some analyses were done based on FLIP (Finite element analysis of Liquefaction Program). FLIP is a well-known program and has been extensively used for the design of port and harbor structures in Japan (Iai et al., 1998, Ichii et al., 2002). A result of a deformation analysis of an offshore waste disposal facility is shown in Fig. 1 (Tsuchida et al., 2013), in which 4 m thick sealing layer was considered on the seabed. In the analysis, multiple shearing spring model was used as stress-strain model of soils (Iai et al.,1992). It was assumed that sealing layer is completely resting on the sea bed and liquefaction would not occur because of the dense sandy seabed. 20 sine waves of 200 gal were applied to the structure. The results shown inside the frame are the maximum and mean shear strains (mean value is in parentheses). It can be found that about 20-30% shear stain generated in the sealing layer of the disposal facility. Between the sheet piles which was constructed for lateral sealing, over 10% shear strains acted. The result showed that, when a strong earthquake occurs, considerable shear deformation may be generated in the sealing layers. Therefore, it is necessary to study the permeability characteristics of sealing layer under large shear strains.

METHOD OF STUDY

Experiment setup

A series of experiments was conducted on a newly developed hollow cylinder torsional permeability test (HCTPT). As the triaxial test cannot simulate the real condition of shear deformation of horizontal ground under dynamic loadings, this test becomes a very common test for simulating the real condition when disasters such as earthquake occurs. However, this time, we add some function on the device so that it can test the permeability when applying torsion. The details will be furnished later in this paper.

Fig. 2 shows that the schematic view of a HCTPT. In order to carry out permeability tests, two porous stone and the pipes were instrumented to the apparatus. The detail of this mechanism is shown in Fig. 3. In the permeability test, arrows are the direction of water. -Water comes from one ~~of~~ burette to another burette. By recording the time and flow of water , coefficient of permeability can be determined and shearing displacement on the specimen can be given through a torsion by a motor equipped in the apparatus.

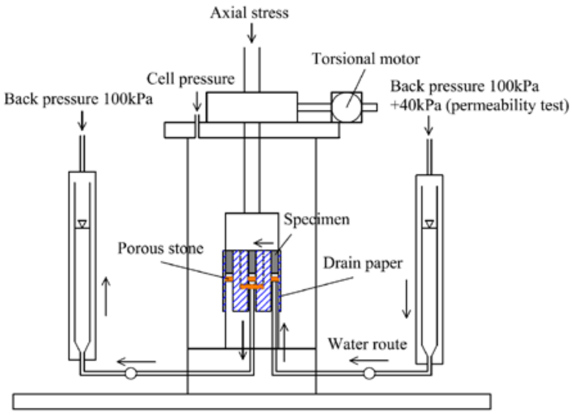

Fig. 2 Hollow cylinder torsional permeability device

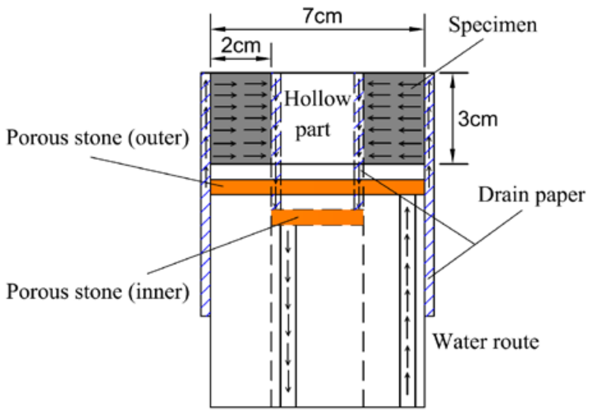

Fig. 3 Concept of permeability test

Table 1 Properties of raw materials

Material	Density (g/cm^3)	Liquid limit (%)	Plastic limit (%)
Tokuyama clay	2.616	110.6	40.0
Bentonite	2.898	510.6	44.0

Table 2 Mixing conditions of experiments

Case	Bentonite[1)] (kg/m^3)	Water content[2)] (%)
T0	-	165.9
T25	25	192.6
T50	50	205.6

Preparation of the specimens

The specimens of this experiment were made from marine clay mixed with bentonite and Portland cement. Marine clay was dredged from Tokuyama Port in Yamaguchi Prefecture, Japan. Bentonite was imported from Wyoming (America). Table 1 shows the properties of clay and bentonite.

Clay and bentonite Mixture

Sealing material is made from a clay mixture. This time, the experiment adopt clay and bentonite as raw materials. The procedure of preparing samples are as following.

1) Mix clay and bentonite according to JGS 0821. Table 2 shows the mixing conditions used in the experiment.
2) Remold the specimens by pre-consolidation. There are three step in this procedure as mentioned in the text below.
3) After consolidation, trim the specimen as in Fig. 4.

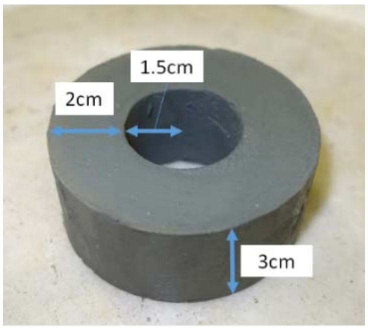

Fig. 4 Dimensions of the specimen

Cement treated soil

Cement treated clay is easier to handle than clay-bentonite mixture. To study the possibility of using cement treated clay as sealing material, the comparison was made with clay mixture. The clay is Tokuyama port clay and the cement is normal Portland cement. The specimen of cement treated soil is called C180. The unconfined compressive strength at 7 days of C180 was 180kPa.

EXPERIMENTAL PROCEDURE

Hollowed cylinder torsional permeability test was conducted to measure the coefficient of permeability of clay mixtures under different stages of shear deformation. The following is the procedures of the experiment.

1) Preparation of the specimen

Clay and bentonite were mixed with artificial sea water, which was made by adding sodium chloride and other components. The sample was remolded and reconsolidated in the laboratory. The consolidation pressure was given in stages as 12.3kPa, 24.5kPa and 49kPa. Finally, the specimen was trimmed to a hollow shape as shown in Fig.4.

2) Setting up the specimen

The rubber membrane was placed to protect specimen from water invasion. The photo is shown in Fig. 5. Fig. 6 shows the final setting of the specimen in the triaxial cell.

3) K_0 consolidation

In the experiment, it was hoping to simulate real condition when build the offshore waste disposal facility. Considering the typical structure of offshore disposal facility as shown Fig.1, ~~the~~ representative effective consolidation pressure of sealing layer was calculated to be 150 kPa. The K_0 consolidation was adopted to the specimen until the σ_v' =150 kPa. The σ_h was given by increasing the cell pressure, and the deviator stress was given to make the vertical displacement of specimen accompanied with the K_0 condition. The relationship between volume change and vertical displacement is shown in Fig.7. The cell pressure was applied in steps as shown in Fig. 8. After the K_0 consolidation was finished, back pressure was given to make the specimen saturated.

Fig. 5 Setting the sample in membrane

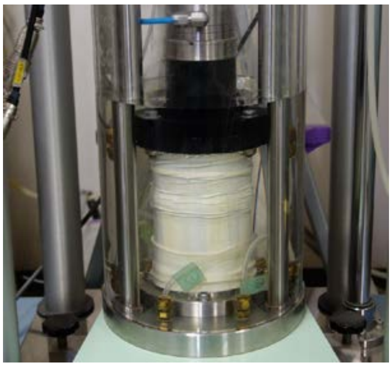

Fig. 6 Sample in a Tri-axial Cell

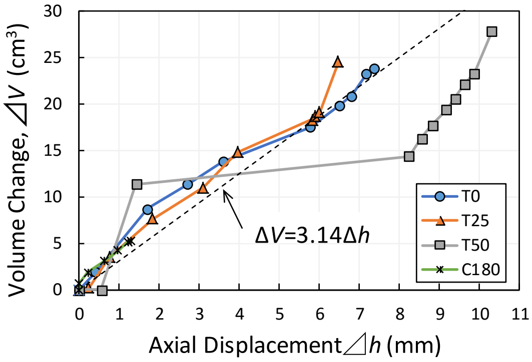

Fig. 7 Relationship between volume change and vertical displacement

4) Permeability test before shearing

The main purpose of this research is to measure coefficient of permeability. The following is a new equation, Eq. (1), derived by Darcy's law.

$$k = \frac{\Delta q}{2\pi H t \Delta P_B \times \frac{1}{9.81} \times 10^4} \ln\left(\frac{R_2}{R_1}\right) \qquad (1)$$

where Δq is the total flow, H is height of the specimen(cm), Δt is the period of the test (sec), ΔP_B is the difference of air pressure (kPa), R_1 and R_2 are the inner and outer radius of the specimen (cm), respectively. After the accurate values were confirmed, we calculated average value of them.

5) Application of shear deformation and permeability test

The purpose of this research should know the phenomenon of shearing deformation effect on the -permeability. Some shearing deformations were given on specimen by torsion. Apply the shearing deformation from 0% to 20%, and examine the permeability every 5% of deformation. The speed ~~is~~ was about 0.1% per minute. When the shear strain was determined, the calculation was based by outer radius. Therefore, in this case, the shear strain is the maximum shear strain. The stress-strain curve is shown in Fig. 9. In the figure, it can be found that every step have a peak value and the strength decreases later. It means specimen had undergone a failure.

RESULTS AND DISCUSSION

Results of Permeability Test

The results are shown in Fig. 10. It was observed that the coefficient of permeability does not increase when the shear strain increases. Permeably was shown to be slightly decreased when strain increases. This is assumed to be due to restructuring of the void or assembly change. The change of permeability ratio is shown in Fig. 11. According to the results above, it shows that there is a small possibility that permeability of sealing material increase by shearing deformation due to a natural disasters.

The value of coefficient of permeability is higher than about 100 times for cement treated clays. As no pre-consolidation was given in making specimen of cement treated soil, the void ratio e of cement treated soil was larger than that of clay bentonite mixture. This is the reason for higher permeability value of cement treated soil.

Ueno et al. (2008) carried out laboratory model test on sealing layer using Nagoya port clay mixture and cement treated clay on shear deformation. Fig.12 illustrated the model used by Ueno et al. (2008) to examine the permeability of sealing materials. Fig.13 shows the result of model

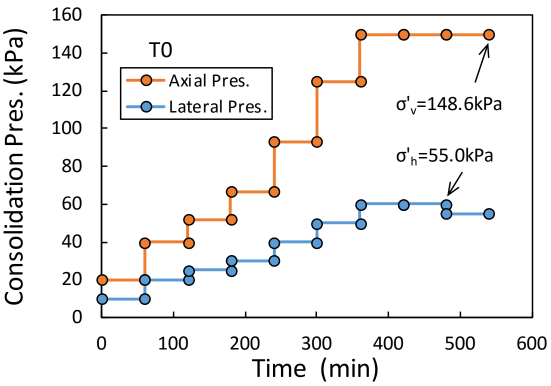

Fig. 8 Consolidation pressure with time

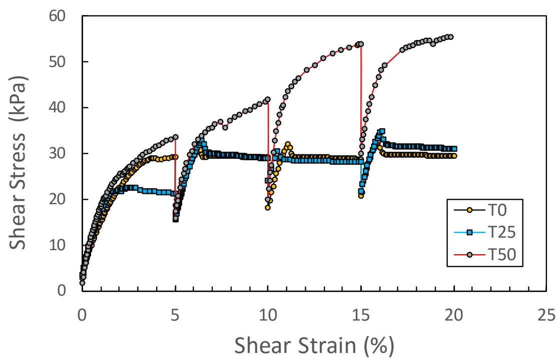

Fig. 9 Stress-strain curve (T0)

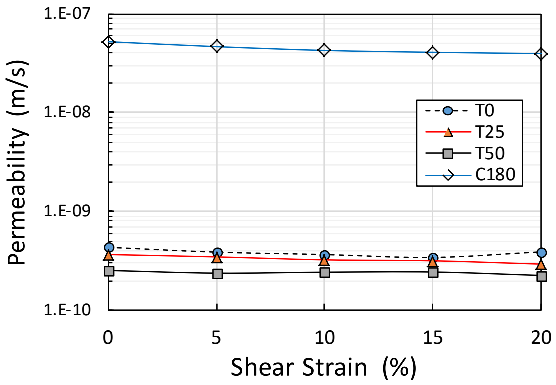

Fig. 10 Relationship of horizontal permeability and shear strain

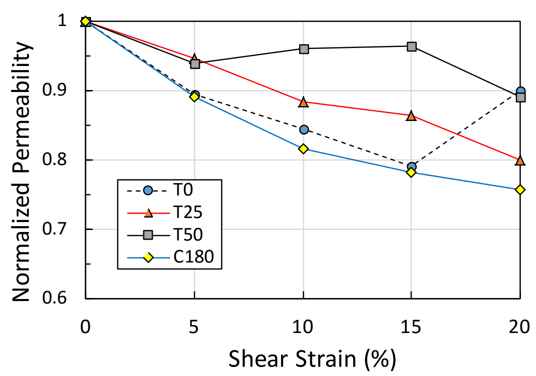

Fig. 11 Normalized horizontal permeability with shear strain

experiment (Ueno et al., 2008). The permeability of cement treated soil increased rapidly with shear strain, however, Nagoya port clay mixture did not show the increase with shear strain of 4%. The present study showed no considerable change of permeability to shear strain within 20%.

Feasibility of New Testing Method

The coefficients of vertical permeability, k_v of Tokuyama clay-bentonite mixtures, which were obtained by conventional consolidation tests are shown in Fig.14 for comparison (Murakami et al., 2014). As shown in Fig.14, k_v decreases with the consolidation pressure. The value of k_v when the effective consolidation pressure was 150 kPa was compared with the horizontal coefficient of permeability, k_h measured in this study as shown in Fig. 15. The result showed that the k_h values ranged from 1.5 to 2.0 times the k_h values. Mizukami et al. (1996) carried out a series of laboratory consolidation test of Osaka Bay Clay to compare the coefficients of consolidation c_v for vertical flow and c_h for horizontal flow. The results are shown in Fig. 16. In the figure, the values of c_h is from 1.5 to 2.0 times to the values of c_v. The coefficient of permeability k is given as Eq. (2).

$$k = c_v \times m_v \times \gamma_w \tag{2}$$

where c_v is coefficient of consolidation, m_v is coefficient of volume compressibility, and γ_w is unit weight of water. m_v can be calculated by Eq. (3) as follows.

$$m_v = -\frac{\Delta V / V}{\Delta \sigma'} \tag{3}$$

where ΔV is changing of volume, V is original volume, and $\Delta\sigma'$ is changing of stress. No matter horizontal or vertical direction, m_v would not change as the different direction. According to above equations, the relationship of coefficients of consolidation c_h and c_v ~~is~~ are similar with the relationship of coefficient of permeability k_h and k_v.

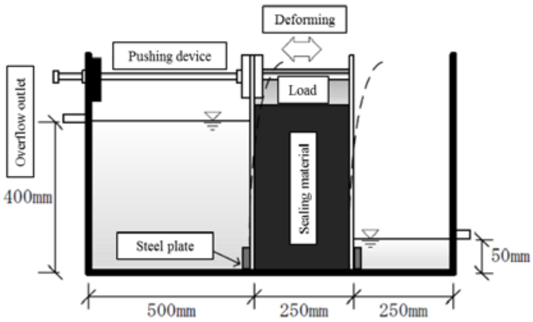

Fig.12 Model test adapted by Ueno et al.(2008)

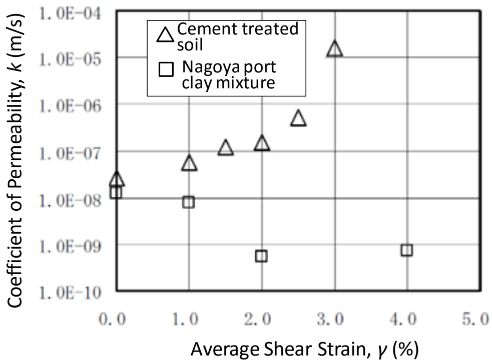

Fig. 13 Change of permeability with average shear strain for Nagoya clay mixture measured by laboratory model test (Ueno et al., 2008)

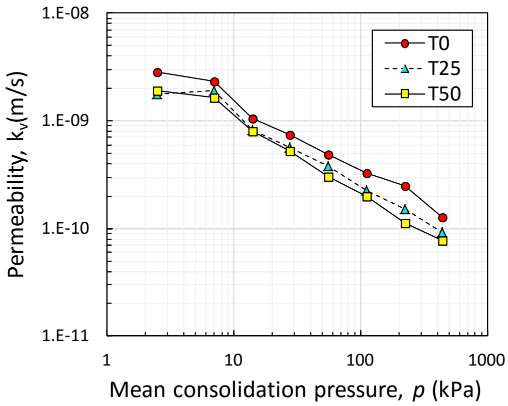

Fig. 14 Vertical permeability of Tokuyama port clay mixture (Murakami et al, 2014)

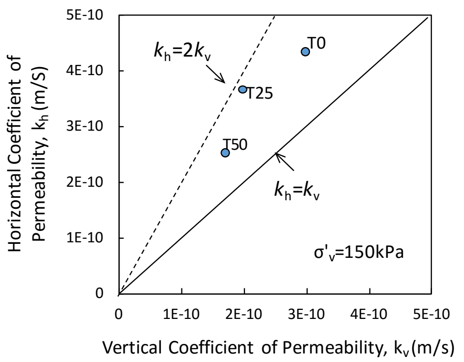

Fig. 15 Relation of horizontal and vertical permeability

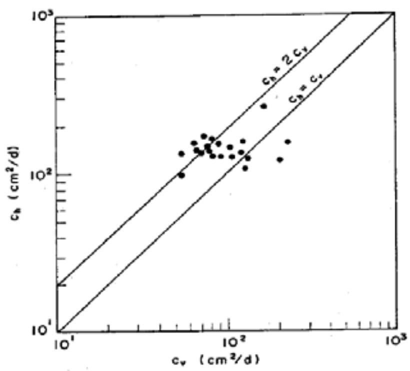

Fig. 16 Horizontal and vertical coefficient of consolidation (Mizukami et al.,1996)

From the research of Mizukami et al.(1996), it was suggested that the k_h is about 1.5-2.0 times to the values of k_{vv}. According to the above, this new testing method for measuring horizontal coefficient of permeability seems to be appropriate.

CONCLUSIONS

1. It was found that mixing of bentonite considerably decrease the permeability of Tokuyama port clay.
2. A new testing method to measure the horizontal coefficient of permeability was developed and it is called as hollow cylinder torsional shear test. The measured horizontal coefficient of permeability k_h ranged from 1.5 to 2.0 times to the vertical coefficient of permeability k_v.
3. After applying the K_0 consolidation, torsional shear was given to the specimen and k_h was measured. As the measured value of k_h did not increase~~,~~ there is no considerable change in permeability of the sealing material when maximum shear deformation of 20% is applied.

ACKNOWLEDGEMENTS

This research was supported by Environment Research and Technology Development Fund (No. 3K122109) by Ministry of Environments, Japan.

REFERENCES

[1] Iai,S. ,Ichii,K., Liu,H. and Morita, T.,"Effective stress analyses of port structures", Special issue of Soils and Foundations, Japanese Geotechnical Society, pp.97-114, 1998.

[2] Ichii, K., Iai, S., Sato., Y., and Liu, H., "Seismic Performance Evaluation Charts for Gravity Type Quay Walls," Journal of Japan Society of Civil Engineers, Vol. 19, No. 1, pp. 21s-31s, 2002.

[3] Iai,S., Matsunaga, Y. and Kameoka, T.,"Strain space plasticity model for cyclic mobility, soils and Foundations, Vo,No.2, pp.1-15, 1992.

[4] Katayama, H., Murakami, H, and Tsuchida, T., "Study of Permeability for Geo-material in Giving Shearing Deformation", Ground Engineering; Joural of Chugoku Branch of Japanese Geotechnical Society, Vol. 32, No. 1, 2014, pp. 111-116. (in Japanese)

[5] Mizukami, J., Kobayashi, M., and Tsuchida, T., "The Horizontal Coefficient of Consolidation c_h", Journal of Japan Society of Civil Engineers, Vol. 34, No. 535, 1996, pp. 1-12. (in Japanese)

[6] Murakami, H., Tsuchida, T., and Katayama, Y., "Study of Geo-material Used for Coastal Disposal Facilities for Waste Including Cesium", Journal of Japan Society of Civil Engineers B3, Vol. 70, No. 2, 2014, I_846-I_851. (in Japanese)

[7] Ministry of Environment, 2013. On the investigation of interim storage facility, 1st version, Jan. 2013. http://josen.env.go.jp/ material/pdf/dojyou_cyuukan.pdf.

[8] Tsuchida, T., Watabe. Y., Shizuma, K., Endo, S., and Ueno, K., Development of Offshore or Onshore Disposal Facility for Disaster Waster and Decontamination Waster Polluted by Radiation, Integrated Research Report of Environment Research and Technology Development Fund, Japan, 2013, pp. 1-69. (in Japanese)

[9] Ueno, K., Yamada, K., and Watabe Y., "Proposal of Sealing Geomaterial for Waste Disposal Sites in Coastal Area", Journal of Japan Society of Civil Engineers, Vol. 64, No. 2, 2008, pp. 177-186. (in Japanese)

[10] Wakioka, H., Tsuchida, T., and Kang, G., "Study of Strength Properties for Cement Treated Soil", 50th Symposium on Geotechnical Engineering, 2014, pp. 646-650. (in Japanese)

Fifth International Conference on Geotechnique, Construction Materials and Environment, Osaka, Japan, Nov. 16-18, 2015, ISBN: 978-4-9905958-4-5 C3051

EXPERIMENTAL STUDY OF INFLUENCE OF SEAWATER ON STRENGTH OF CONCRETE STRUCTURES

Moshood N.TIJANI[1], James I. INIM[2] and Saheed O. ADETU[1]
[1]Department of Geology, University of Ibadan, Ibadan - Nigeria
[2]Department of Geology, Akwa Ibom State University, Uyo - Nigeria

ABSTRACT

Against the background of direct and indirect action of physical and chemical deterioration of coastal and offshore infrastructures, the potential influence of seawater on the strength and durability of concrete structures were investigated. Cement concrete cubes of 150mm x 150mm x 150mm with cement, sand and aggregate mix ratio of 1:2:4 (mix-1) and 1:1.5:3 (mix-2) were prepared. A total number of 96 concrete cubes of different water cement ratio (w/c) of 0.4, 0.45 and 0.5 by weight were moulded. For the two mix ratios, casts in triplicate were cured in both freshwater (as control) and seawater for different periods of times (i.e. 14, 21, 28, and 90 days) followed by crushing-compressive strength tests. The study shows a proportionate increase in strength in the control casts from 17,286 to 23,673KN/m^2 and from 21,599 to 29,555KN/m^2 for mix-1 and mix-2 respectively as the curing time increased from 14 to 90 days. High compressive strengths observed for mix-2 casts compared to those of mix-1 casts was attributed to higher proportion of cement employed. In addition, the strength development for all cubes cured in seawater were relatively lower compared to those cured in freshwater at the end of the different testing periods until after 90 days; hence indications of possible negative impacts of salinity on the coastal concrete infrastructures and the need for protection measures.

KEYWORDS: Seawater, Freshwater, Cement concrete, Curing; Compressive strength

INTRODUCTION

Concretes, a combination of cement, sand and aggregates and water mixed in different proportion have received wide applicability in the construction industry. Concrete is one of the major building materials in modern day constructions both for in-land and coastal/offshore projects such as buildings, dams, foundations, columns, beam and slab in shell structures, bridges, highways, sewage- treatment works, railway sleepers, cooling towers, dams, chimneys, harbours, off-shore structures, coastal protection work among others [1]–[3]. For several reasons, effect of seawater on concrete deserves special attention due to apparent impacts on strength and durability of concrete structures. This is more obvious in coastal and offshore structures which are usually exposed to the simultaneous action of a number of physical and chemical actions of seawater. Concrete structures and walls (either with or without reinforcements) are critical components of infrastructural developments in coastal areas. Thus, there is the need to understand the complexity of concrete durability problems in coastal environment.

Coastal environments are characterized by urban, industrial and economic activities, with major metropolitan cities located along coastal areas world-wide. Consequently, in such coastal cities a large number of infrastructures like jetties, harbours and dockyards that are concrete-based (e.g. concrete piles, decks, break-water, or retaining walls) are usually exposed to impacts of seawater either directly or indirectly. Furthermore, in many developed countries, in order to relieve land from pressures of urban congestion and pollution, floating offshore platforms made of concrete are being considered for location of new airports, power plants, and waste disposal facilities etc. while the use of concrete offshore drilling platforms and oil storage tanks is already on the increase.

Consequently, the long-term durability of concrete-based infrastructures and installations in coastal environments (in the face of impacts of seawater) are of concerns to geoscientists, civil / structural engineers especially with respect to the physical and geotechnical properties of the component earth materials, choice of reinforcement as well as mixing ratio in order to avoid failure (geotechnical and structural wise). The pioneering work of J. Smeaton and L. J. Vicat on the effects of seawater on concretes as reported in [4] revealed that a large number of coastal concrete structures in the United States, Canada, Cuba and Parama are exposed to chemical deterioration.

However, the effects of seawater on concretes are usually related to factors characteristics of seawater exposure impacts on concretes and the elements of specific concrete to be affected as well as the consequences of interactions of seawater with the concretes [5]. Hence factors inherent in seawater exposure impacts on concrete are wetting and drying as well as chemical reactions of chlorides, sulphates and alkalis while the elements of concrete that can be affected these are cement, aggregates and reinforced steel components [5].

Consequently, a number of studies had reported the vulnerability of the section of concrete above high-tide to cracking and spalling [6], while deterioration due to stresses caused by crystallization pressure of salts within concrete under wetting and drying conditions were also observed [7]–[9]. In addition, a number of studies had also reported deterioration of concrete in marine environment due to the effects of chemical reaction of seawater constituents with cement hydration products, reactive alkali aggregate expansion as well as corrosion of embedded steel in reinforced or pre-stressed members [1]; **[**10]–[11]. In the light of the foregoing, the properties of concrete structures, such as strength, durability, stability, resistance to chemical attacks of seawater under wetting and drying conditions among others requires thorough investigations.

Hence, over the years, it has become imperatives to ascertain the qualities of properties of coastal structures in contact with seawater in course of their design life-span. Based on the above background, this experimental study is aimed at assessing the influence of seawater on the concrete/construction structures for purposes of highlighting the controlling factors in respect of the dynamics of impacts on strength and durability of concrete structures on one hand. On the other hand to give insight into the possible modifications to the moulding parameters in order to mitigate the negative influence of seawater and enhance durability of concrete structures under seawater attacks.

MATERIALS AND METHODS

The materials used in this study include the so-called Portland cement type, fine and coarse aggregates as well as fresh and seawater used for mixing and curing. The cement was stored under dry condition and free of lumps in conformity with BS 12. The fine aggregate consist of stream-bed washed sand deposit (free of organic matters), while the coarse aggregate consist of crushed granite rock of 3/4 inch size. Fresh tap-water in the laboratory was used for mixing while seawater from Atlantic Ocean at Bar-Beach in Lagos, Nigeria was used for curing.

Preparation and Casting of Concrete Cubes

The test specimen cubes for the determination of compressive strength of concrete were prepared using the standard metallic moulds with dimensions of 150×150×150mm adopting the procedure of rodding and hard compactions. Two mixing proportions of cement, sand and aggregate at ratios 1:2:4 and 1:1.5:3 (hereinafter referred to as mix-1 and mix-2) were employed in this study. Both mixes were prepared separately with water/cement ratio of 0.4, 0.45, and 0.5. The concrete casts were then cured in seawater while additionally mix-1 and mix-2 of 0.4 water/cement ratio (w/c) were cured in freshwater as control casts.

Batching of concrete materials by weight was adopted as the standard mode of quantifying materials, using weighing balance. The mixing was done such that the already batched fine aggregate (sand) were first spread on a clean levelled hard surface. The measured cement was then spread on the fine aggregate and dry mixed uniformly. The mixed sand and cement was again spread and the already batched coarse aggregate (granite) was spread on top. The correct quantity of water, based on the water/cement ratio, was then gradually added at interval during mixing until all the components are properly and uniformly blended. The details of the mixing ratio with respect to the weights of the different components of the concrete are presented in Table 1.

Table 1: Mixing ratios and weight of different components employed in casting of concrete cubes

Mix	W/C ratio	Water (kg)	Cement (kg)	Sand (kg)	Aggr. (kg)
1	0.40	12.5	30	60	120
2	0.40	12.5	30	60	120
3	0.45	6.75	15	30	60
4	0.50	7.5	15	30	60
5	0.40	12.0	30	66	132
6	0.40	12.0	12	66	132
7	0.45	6.75	15	33	66
8	0.50	7.5	15	33	66

W/C = Water-cement ratio; Aggr = Aggregates

For this study, the fresh concrete was placed in already lubricated and carefully prepared standard moulds which were filled in three successive layers. Each layer was compacted with 35 strokes with a 25mm high yield iron rod. The cast cubes (96 in all) were labeled and appropriately stored for 24 hours to avoid vibration or any form of impact.

Curing and Compressive Strength Tests

Subsequent to the casting, the specimen cubes were carefully stripped and placed in fresh and sea waters for curing at different time durations of 14, 21, 28 and 90 days. At the end of the respective time durations, triplicate cubes of mix-1 and mix-2 were removed from the different solutions and kept in open dry environment to allow for draining of excess water after which the weights of the cubes were recorded. Then, load was applied, with the respective cube placed with the cast face in contact with the platens of the crushing machine for the different cube after 14, 21, 28 and 90 days respectively. The crushing was done at the Geotechnical laboratory of the Ministry of Works and Transport, Secretariat, Ibadan. The characteristics compressive strengths of the concrete cubes were later determined through calculation using the already determined crushing loads and the cross-sectional area of the cube. Three specimens were used in each test, and the averages were used for analyses.

RESULTS AND DISCUSSIONS

Grain-size Distribution of Materials

The results of the grain-size distribution analyses for the gravel and sand aggregate used in this study are presented in Table 2 and 3. With coarse sand and fines size fraction of 87% and 8.1% respectively.

Table 2: Sieve analyses of the gravel aggregate employed in casting of concrete cubes

Diameter (mm)	Mass of Soil Retained (g)	% Retained	% Passing
25	0.0	0.0	100
19	144	14.4	85.6
12.5	424	42.2	43.4
9.5	272	27.2	16
4.75	95	9.5	6.5
Pan	65	6.5	0.0

Table 3: Sieve analysis of sand aggregate employed in casting of concrete cubes

Diameter (mm)	Mass of Soil Retained (g)	% Retained	% Passing
4.75	0.0	0.0	100
2.36	21.0	4.3	95.7
0.85	54.0	11.1	84.6
0.43	73.0	14.8	69.8
0.30	84.0	17.0	52.8
0.212	73.5	14.9	37.9
0.150	61.5	12.5	25.4
0.106	47.5	9.6	15.8
0.075	38.0	7.7	8.0
Pan	39.6	8.0	0.0

The aggregate fall under the zone two of the calibration graph considered suitable for concrete setting for underwater construction. The low percentage of the fine fraction (about 8%) is also considered advantageous, as excessive fine particles would easily be affected by the effect of flowing water or wave actions despite a cementing medium [12].

Chemical Characters of Fresh- and Seawaters

In addition, the results of the physico-chemical analysis of the curing (seawater) and mixing (fresh) water are presented in Table 4. Expectedly, the values of pH, EC and TDS are 6.7, 1,352µS/cm and 1,014ppm for freshwater and 9.2, 57,733µS/cm, 47,330ppm for seawater indicating relatively high dissolved solids and more free mobility of the ions in the seawater vis-a vis the freshwater. This is also consistent with the relatively higher concentrations of the major cations (Na, Mg and K) and anions (Cl and SO_4) in the seawater compare to the lower concentration in the freshwater (Table 4). Hence, it is quite possible to infer the possible types of seawater attacks to include sulphate attacks (magnesium and potasium sulphates) of the constituents of the hardened concrete cement; chloride corrosion of reinforced steel metals and alkalis-aggregate reaction: all of which will lead to deterioration or damage to concrete structures as pointed out by a number of previous studies such as [5]; [13]–[15].

Table 4: Physiochemical and chemical analyses of the fresh water and seawater

Parameters	Mixing freshwater	Curing seawater
EC (µS/cm)	1,352	57,733
TDS (mg/l)	1,014	47,330
pH	6.7	9.2
Ca^{2+} (mg/l)	8.3	415
Mg^{2+} (mg/l)	1.4	1,350
Na (mg/l)	3.2	11,041
K^{+} (mg/l)	1.8	406
Cl^{-} (mg/l)	220	22,500
SO_4 (mg/l)	110	1,475

The attack of magnesium sulphate on concrete can be attributed to two principal reactions [5]; [16]–[18]: the first involves reaction with calcium hydroxide $Ca(OH)_2$ or with calcium silicate hydrate (as component of Portland cement) to form soluble magnesium hydroxide ($Mg(OH)_2$) leading to the formation of hydrated calcium sulphate (gypsum - $CaSO_4.2H_2O$) and silica gel ($SiO_2{\cdot}nH_2O$). The second reaction involves reaction of magnesium hydroxide and silica gel to form magnesium silicate hydrate ($MgSiO_2{\cdot}nH_2O$). In both cases, white mushy substance usually appears on the surface of concrete [16], a situation that was also observed in the course of this experimental study.

Furthermore, it had been reported that, in most cases, the loss of adhesion and strength is the primary manifestation of sulphate as $MgSO_4$ attack leading to decalcification of calcium-silicate-hydrate (C-S-H) to form magnesium-silicate hydrate (M-S-H) followed by the formation of expansive salt crystals causing concrete deterioration through expansion and cracking [5]–[6]. For chloride attack, the common impact is the penetration of the chloride ions into the concrete and attendant acceleration of reinforcement corrosion [18]. However, since the plain concretes were used in this study, further discussion in the subsequent section with respect to the impacts of seawater chemistry are limited to sulphate attacks.

Results of Compressive Strength Tests

Table 5 and 6 show the average compressive strength of mix-1 and mix-2 cubes cured in freshwater and seawater for 14, 21, 28 and 90 days and at different water-cement (w/c) ratios.

Table 5: Compressive strength (in MPa) of mix1 concrete cubes cured in fresh water and seawater

Curing time (days)	FW @0.4 w/c	SW @0.4 w/c	SW @0.45 w/c	SW @0.5 w/c
14	17.29	13.51	13.10	12.92
21	19.11	12.31	11.66	11.91
28	20.76	14.74	13.39	12.86
90	23.67	31.85	30.67	30.22

FW= Freshwater; SW= Seawater

Table 6: Compressive strength (in MPa) of mix2 concrete cubes cured in fresh water and seawater

Curing time (days)	FW @0.4 w/c	SW @0.4 w/c	SW @0.45 w/c	SW @0.5 w/c
14	21.60	25.24	21.18	20.62
21	24.44	20.28	15.85	15.85
28	25.10	21.67	18.15	17.41
90	29.56	38.96	36.37	33.33

FW= Freshwater; SW= Seawater

As presented, the compressive strength for the concrete cured in freshwater at 0.4w/c expectedly increases with increase in curing time (Fig. 1) from 17.2MPa at 14 days to 23.7MPa at 90 days for mix-1 while with mix-2 showed a relatively higher values of 22MPa to 30MPa which is clearly an indication of higher cement content. The observed increase in strength of concrete cubes cured in freshwater is expected as strength of concretes increase with increase in curing time and cement setting until equilibrium is reached [19]–[20]. This situation is also clearly reflected by the curves in Fig. 1 as there seems to apparent tendency towards stable constant strength or equilibrium leading to 90 days curing time.

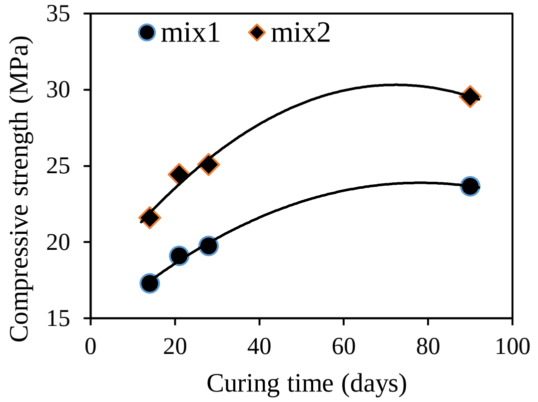

Fig. 1: Plot of compressive strength against curing time for w/c of 0.4

However, in comparison to the strength development revealed by the freshwater cured concretes as presented in Fig.1, the compressive strength for concrete cubes cured in seawater at w/c ratio of 0.40 reduced from 13.51MPa at 14 days to 12.31MPa at 21 days and later increased to 31.85MPa at 90 days for mix-1 (Fig. 2).

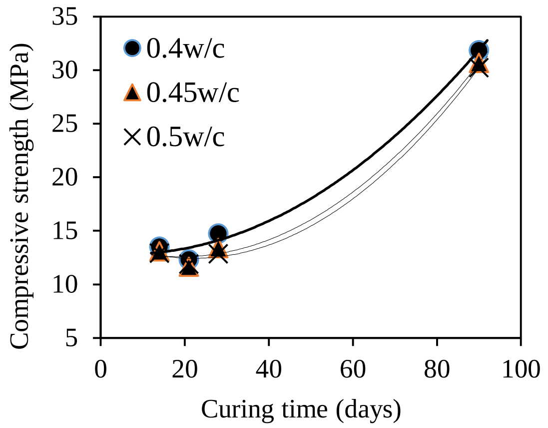

Fig. 2: Plot of compressive strength against curing time for mix-1

Similar trend with decrease in strength from 25.24 MPa at 14 days to 20.28MPa at 21 days and later increase to 38.96MPa at 90 days were observed for mix-2 as shown in Fig. 3. The decrease in strength in the first 21 days can be attributed to possible chemical reaction or sulphate attack by seawater (in form of cation exchange process) which caused the formation of soluble magnesium hydroxide ($Mg(OH)_2$) and subsequently hydrated calcium sulphate (gypsum - $CaSO_4.2H_2O$) among others.

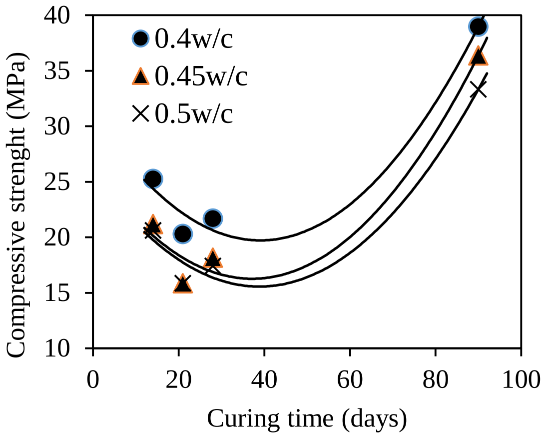

Fig. 3: Plot of compressive strength against curing time for mix-2

However, it had been reported that magnesium sulphate rather than sodium sulphate is more often responsible for sulphate attack of the several constituents of Portland cement [5]. According to the ACI Building Code 318-83, sulphate attack is classified as severe, when the sulphate ion concentration is higher than 1,500 mg/l [18]. Hence with sulphate concentration of 1,475 mg/l for the curing seawater used in this study and alongside with magnesium concentration of 1,350 mg/l, it possible to infer the dominance of $MgSO_4$ attack as the major causes of concrete deterioration in this study.

The evidence of such sulphate attack was clearly observed on the surfaces of the moulded concrete cubes after few weeks (Day 21) of this experimental study as traces of white mushy substances / crystallized salts were observed till the end of the experiment. Chemical equations of this deterioration process can be outlined as follows:

$Ca(OH)_2 + MgSO_4{\cdot}7H_2O \rightarrow CaSO_4{\cdot}2H_2O + Mg(OH)_2 + 5H_2O$ ....(1)

$3CaO{\cdot}2SiO_2{\cdot}nH_2O + MgSO_4{\cdot}7H_2O \rightarrow CaSO_4{\cdot}2H_2O + Mg(OH)_2 + SiO_2{\cdot}nH_2O$ ...(2)

$4MgSO_4 + SiO_2{\cdot}nH_2O \rightarrow 4MgO{\cdot}SiO_2{\cdot}8{\cdot}5H_2O + n\text{-}4{\cdot}5H_2O$ ....(3)

For this study, it is possible to assume that due reactions represented by Eq. (1) and Eq. (2) are the most likely processes observed due to limited duration of the study that may not allow for completion of reaction process in Eq. (3). Moreover, it had been reported that the reduction in the amount of free $Ca(OH)_2$ due to pozzalanic reaction usually limits the degree of reaction of $Ca(OH)_2$ and sulphate [21]–[22]. In addition, the presence of chlorides, as in seawater, is said to also inhibit the expansion and swelling of concrete due to sulphate attack while the greater solubility of hydrated $CaSO_4$ in chloride solution also prevented swelling in deteriorated concretes [5]; [21]. Hence, these and apparently the limited duration of this study explain why no swellings or expansions were observed in the cured concrete cubes, despite the apparent sulphate attacks.

The strength development for all cubes cured in sea water were lower than those of the cubes cured in fresh water until after 50 to 60 days of curing when the strength of the cubes cured in seawater at various w/c ratios increased more than that of cubes with freshwater water (Table 5 and 6). Furthermore, it can be observed that for the seawater cured cubes at different w/c ratios the strength development for mix-2 revealed higher strengths compared to those of mix-1 (Figs. 2 and 3). This is a clear reflection of the positive impacts of higher cement ratio in mix-2. In other words, appropriate cement to aggregate ratio of concrete structures can enhance strength and ensure resistance against deterioration in the face of seawater attacks.

SUMMARY AND CONCLUSION

Experimental studies of the influence of seawater on the strength of concrete structures involved various laboratory and experimental works in which concrete cubes was cast and subjected to various laboratory work and analysis in other to assess the controlling factors in respect of dynamics on strength of concrete.

Strength development of cubes cured in fresh water was significantly different from concrete cubes cured in seawater throughout the 90-day period of curing while the strength development in concretes cured in seawater was not significantly different from each other at 90 days of curing. At 90 days of curing, all the cubes cured in seawater had increased far more than cubes cured in freshwater. The increase in strength was highest in cubes with mix 2 at 0.4w/c. On the other hand, a decrease in compressive strength as the amount of water to cement ratio increased through the 90-day curing period, was observed.

All the concretes cured in sea water showed lower compressive strength with decrease in cement mixture on one hand and on the other hand, a decrease in compressive strength were also observed as the amount of water to cement ratio increased through the 90-day curing period. This signifies that increase in the water to cement ratio reduces the strength of concrete, and could greatly affect the resistance to the aggressive elements in the seawater.

Nonetheless, based on the chemistry of the curing seawater, it can be inferred that, at the early stage of curing, the concrete deterioration is associated with the reaction of cement matrix and calcium hydroxide forming magnesium hydroxide ($Mg(OH)_2$) and later hydrated calcium sulphate (gypsum) with an appearance of white, mushy substance as noticed on the concrete cubes.

In addition, the lost in strength of concrete cubes cured in seawater can be attributed to impacts of high Na^+ and K^+ ions (11,041 mg/l and 406 mg/l respectively) causing aggressive alkali-aggregate reaction on one hand and the weakening of the cement paste by Mg and SO_4 ions (sulphate attack) on the other hand. However, this study revealed that higher cement ratio can reduce impacts of the seawater attacks and enhance durability of coastal concrete structures. Further studies in respect of impacts of chloride on corrosion potential of reinforced concretes are recommended.

REFERENCES

[1] Kaushik, SK, and Islam, S, Suitability of seawater for mixing structural concrete exposed to a marine environment. Cement and Concrete Composites, 17 (3), 1995; pp. 177–185.

[2] Neville, A, Water, Cinderella ingredient of concrete. Concrete International Vol. 22(9); 2000; pp. 66-71.

[3] Olutoge, FA, and Amusan, GM, The Effect of Seawater on Compressive Strength of Concrete. International Journal of Engineering Science Invention, Volume 3(7); (2014); pp. 23-31.

[4] Tibbetts, DC, Performance of Concrete in Seawater. Canadian Building Series, No.2, 1968; pp. 159 – 180.

[5] Mather, B. Effects of Seawater on Concrete. Symposium on Effects of Aggressive Fluids on Concrete at the 44th Annual meeting of Highway Research Board (Committee MC-B2 on Performance of Concretes: Chemical Aspects). Publ. US Army Engineers Waterways Experiment Station, 1964: 19p.

[6] Mehta PK., Sulfate attack on concrete: A critical review. In: R.R. Villarreal (Ed.), Concrete Durability, Univ. Autonoma de Nuevo Leon, 1993; pp. 107– 132.

[7] Kumar, S, Influence of water quality on the strength of plain and blended cement in marine environments, Cement and Concrete Research, Vol. 30; 2000; pp 345-350

[8] Mehta, PK and Monteiro, P, Concrete: microstructure, properties, and materials. 3rd ed. New York: McGraw-Hill Professional, 2005. 135–136.

[9] Akinkurolere, OO, Jiang, C, and Shobola, OM, The influence of salt water on the compressive strength of concrete. Journal of Engineering Applied Science, Vol. 2(2), 2007; pp. 412–415.

[10] Mohammed, TU, Hamada, H, and Yamaji, T, Performance of seawater-mixed concrete in the tidal environment. Cement and Concrete Research, Vol. 34 (4), 2004; pp.593–601.

[11] Aburawi, MA, and Swarmy, RN, Influence of Salt Weathering on the properties of Concrete. Arabian Journal for Science and Engineering, Vol. 33 (No. 1B); 2008; pp. 105-115.

[12] Zaher, K. and Shihada, S, Effect of Gaza seawater on concrete strength for different exposures. Journal of the Islamic University of Gaza, 11 (20), 2003; pp. 156–172.

[13] Benstend J, A discussing if the paper “Magnesium sulphate attack on Portland cement: Part II. Chemical and mineralogical analysis,” by Bonen D and Cohen MD; Cement and Concrete Res. Vol. 23 (30) 1993; pp. 743-744.

[14] Bonen D, A microstructure study of the effect produced by magnesium sulphate on plain and silica fumes-bearing Portland cement mortars, Cement and Concrete Res. Vol. 23 (30) 1993. pp. 541-553.

[15] Wakeley, D, Poole, TS. Ernzen, JJ, Neeley, BD, Salt saturated mass concrete under chemical attack, in: P. Zia (Ed.), High Performance Concrete in Severe Environments, Am. Concr. Inst. SP-140, 1993, pp. 239– 267.

[16] Skainy J, Marchand J, Odier I, Sulphate attack on Concrete. London: 2002. Spon Press.

[17] Hill J., Byars, EA, Sharp, JH, Lynsdale, CJ, Cripps, JC, Zhou, Q,. An experimental study of combined acid and sulphate attack of concrete. Cement & Concrete Composites 25; 2003; pp. 997–1003, Elsevier Science Ltd.

[18] Wegian, FM, Effect of seawater for mixing and curing on structural concrete. The IES Jour. Part A: Civil and Structural Engineering; Vol. 3, (4): 2010; pp. 235-243.

[19] Kaushik, SK, and Islam S, Suitability of seawater for mixing structural concrete exposed to a marine environment. Cement & Concrete Composites, Vol. 17(3); 1995; pp.177-185.

[20] Al-Amoudi OSB, Perfomance of 15 reinforced concrete mixtures in magnesium –sodium sulphate environments, Construction and Building Materials, 9 (3); 1999; pp 149-158.

[21] Lea, FM, The Chemistry of Cement and Concrete. St. Martin's Press, New York, N. Y., 1956.

[22] Massazza, F, Pozzolanic Cements. Cement & Concrete Composites, Vol. 15(4); 1993; pp. 185– 214.

Environment

Fifth International Conference on Geotechnique, Construction Materials and Environment, Osaka, Japan, Nov. 16-18, 2015, ISBN: 978-4-9905958-4-5 C3051

POTENTIAL USE OF SILT AND SLUDGE AS LANDFILL CAPPING MATERIAL

Hamidi Abdul Aziz[1,2], Wong Chin Yik[1], Muhd. Harris Ramli[1], Salem S. Abu Amr[1]

[1]School of Civil Engineering,
Engineering Campus, Universiti Sains Malaysia,
14300 Nibong Tebal, Penang, MALAYSIA
[2]Solid Waste Management Cluster, Engineering Campus, Universiti Sains Malaysia

Abstract

Landfills have been the most common methods in municipal solid waste disposal in developing countries. Landfill capping is a containment technology that forms a barrier between the contaminated media and the surface. Presently, the commonest capping materials for landfills are sandy material and laterite soil. The objective of this research was to study the suitability of silt from Ulu Kinta dam in Malaysia and sludge (domestic wastewater sludge and water treatment sludge) as landfill capping material. The 2 materials were mixed with varying proportions of pure silt, 20, 40, 60, 80 and 100 percent of sludge. The results showed that silt material has moderate hydraulic conductivity with k of value 4.81x10-04 cm/s, poor cohesion strength, 7.64kN/m^2 and good friction angle, 36.22°. Sewage sludge has the best properties among the 3 materials, good hydraulic conductivity with k of 2.07 x10-06 cm/s, moderate cohesion strength, 8.95kN/m^2 and very high friction angle of 45.73°. Water treatment sludge's hydraulic conductivity, k was 2.9 x10-06 cm/s which is good but having poor cohesion strength and friction angle of 6.16kN/m^2 and 6.13°, respectively. Silt and sludge were also mixed to test whether the method improves the properties of the final product. The result was negative. The use of 100% sewage sludge exhibited better results than others.

Keywords: silt, sewage sludge, hydraulic conductivity landfill capping

INTRODUCTION

A landfill site is a site for the disposal of waste materials by burial and is the oldest form of waste treatment. Historically, landfills have been the most common methods of organized waste disposal and remain so in many places around the world. Many of the old landfills that are problems today were constructed in this fashion. When hazardous waste was disposed, it was placed in metal drums that rusted through in a few years, leaving the waste to seep through the landfill. Water was allowed to seep through the cover of the landfill, saturate the wastes, and come out the bottom or sides as leachate (liquid that leaches through the landfill and collects in pockets in the landfill material or below the landfill). Landfill must have a capping system. Landfill capping is a containment technology that forms a barrier between the contaminated media and the surface, thereby shielding humans and the environment from the harmful effects of its contents and perhaps limiting the migration of the contents.

A cap must restrict surface water infiltration into the contaminated subsurface to reduce the potential for contaminants to leach from the site. Presently, the commonest capping materials for landfills are sandy material and laterite soil. Most wastewater treatments process produce sludge, which has to be disposed. Conventional secondary sewage treatment plants typically generate a primary sludge in the primary sedimentation stage of treatment and a secondary, biological, sludge in final sedimentation after the biological process. The characteristics of the secondary sludge vary with the type of biological process and, often, it is mixed with primary sludge before treatment and disposal. Sanitary landfill is one of the secure and safe facilities for the disposal of MSW; it needs high standard of environment protection in the operation of landfill [2, 3].

To investigate the performance of sanitary landfill the behavioral patterns namely; leachate generation, landfill gas (LFG) emissions, etc. are required [4, 5]. Sanitary landfill plays a significant role in the disposal of MSW in most of the developing countries like Bangladesh. Most of the landfill in developing countries does not have any liners at the base or proper top covers, which results in the potential problems of ground water/surface water contamination due to the leachate generated from solid waste landfill. The assessment of environmental risks associated with leachate contamination of water resources requires the understanding of the transport of contaminants along the river networks and into the aquifer [6, 7].

The main objective of covering systems is to reduce or eliminate the transport of fluids through the waste. Covering systems must function with minimum maintenance, promote drainage, minimize erosion of the cover, accommodate settling, and have hydraulic conductivity less than or equal to that of any bottom liner system or natural soil present. In humid climates, cover and/or re-vegetation are usually required for erosion protection and infiltration control. The regulations do, however, permit alternative designs if they can achieve erosion and infiltration protection equivalent to an acceptable conventional cover system. This indicates the significance of searching different alternatives to compacted clay-based barriers in arid areas and evaluates their performance under various environmental conditions [8]. In the present day, the available capping materials consist of sand material and laterite soil. Most wastewater treatments process produce sludge, which has to be disposed. Conventional secondary sewage treatment plants typically generate a primary sludge in the primary sedimentation stage of treatment and a secondary, biological, sludge in final sedimentation after the biological process. The characteristics of the secondary sludge vary with the type of biological process and, often, it is mixed with primary sludge before treatment and disposal. Approximately one-half of the costs of operating secondary sewage treatment plants can be associated with sludge treatment and disposal.

Many laboratory tests are needed to ensure that the materials being considered for each of the landfill cap components are suitable. Landfill instability can be solved by understanding interface friction properties between all material layers, natural or synthetic. The major engineering soil properties that must be defined are the shear strength and hydraulic conductivity. Shear strength may be determined with the unconfined compression test, direct shear test, or triaxial compression test. The study aimed to find an alternative capping material which has little commercial value thus saving the cost of landfill capping material without neglecting the strength properties of the landfill capping for safety purposes. In this regard, the performance of silt and sludge as capping material for landfill in comparison with sand and laterite soil is evaluated. Both are considered as waste materials with no commercial values. Their usefulness as capping material either as an individual or in a mixed, form has not been well investigated, The performance in terms of the hydraulic conductivity and shear strength of silt, sludge and a mixture of sludge and silt are determined.

MATERIALS AND METHODS

MATERIALS AND SAMPLING

The main focus of this study is to find an alternative landfill capping material that uses various soil mixtures; specifically a mixture of silt and sludge. The geotechnical characteristics of the mixture were also compared with other different types of soil. Therefore, silt, sludge, sand and laterite soil were used in this study.

The silt used in this study was obtained from the Perak Water Board (LAP) dam in Ulu Kinta, Perak. The silt is basically sediment transported by the flow of river water into the dam. Approximately 15 kg of silt was taken from piles of excavated silt with a shovel. The sludge was obtained from the Bayan Baru wastewater treatment plant and the LAP Jalan Baru water treatment plant. Approximately 15 kg of fresh sludge were taken from sludge piles under the dewatering machine.

The sand used in this study had a fine texture and it was purchased from a nearby sand mining quarry. The purpose of the sand in this study is to compare the strength properties of sand with a silt and sludge mixture. The laterite soil used in this study was material that was available locally. It is commonly found in hot and wet tropical regions such as Malaysia. Laterite soil, which is rich in iron and aluminum, develops through an intense and lengthy weathering process of the parent rock. This process influences its soil characteristics and makes it a reddish, clayey soil due to iron oxides. The purpose of the laterite soil is to compare the strength and hydraulic conductivity of laterite with the silt and sludge mixture.

EXPERIMENTAL PROCEDURES

In selecting a suitable landfill capping material, there are several important geotechnical characteristics that merit consideration. Since a landfill should be able to contain waste material, it is very important to ensure that the soil's permeability is able to perform according to the landfill's designed concept. Besides the permeability of the capping material, the geotechnical strength characteristics of the material is also important in order to ensure that the landfill is structurally stable and able to perform according to its design specifications for many years. If this can be achieved, any geotechnical structure failure, such as slope failure, ground depression, deferential settlement and tension crack, can be prevented. Therefore, the main characteristics; permeability and strength of the soil mix material were studied in order to assess the suitability of the landfill capping material.

As a standard practice in soil mechanics, before any soil characteristic test is conducted, the sample must be classified. The classification of the sample is required in order to choose the suitable soil characteristic test. The classification test starts with sieve analysis, as grain particle-sorting was perform on sand, silt and laterite soil to determine the grain size distribution curve. The sieve analysis test was performed according to the ASTM C136-06 standard test method for sieve analysis of fine and coarse aggregates. Based on the standard sieve analysis, the particle size analysis for finer material that is available in silt and laterite soil was assessed by using a hydrometer test in accord with the ASTM D422-63 standard.

The changes in water content can also alter the mechanical properties of a clay material. Therefore, the liquid limit test based on the BS 1377 standard and the plastic limit test based on the ASTM D4318 standard were conducted on silt and laterite soil to understand this change in mechanical properties. Based on the information obtained from sieve analysis, liquid limit and plastic limit tests, the soil classification group was determined by using the unified soil classification system (USCS) based on the ASTM D2487 standard practice for the classification of soils for engineering purposes. The specific gravity of sand, silt and laterite were determined in accord with the ASTM D854-00 standard test for specific gravity of solids by water pycnometer.

Once the soil had been classified and its characteristics were identified, the permeability and shear tests were conducted. Prior to these assessments, the maximum dry density of the sample was determined. The maximum dry density values of the sample are required in order to ensure that the sample prepared for the permeability and shear tests were able to simulate the actual compacted soil at the site. The sand, silt and laterite maximum dry densities were determined by using the modified proctor test based on the ASTM 1557 standard.

Since the landfill capping material requirement required low permeability of the material, the falling head permeability tests were conducted. The permeability tests were performed on silt, laterite and a silt-sludge mixture of soil. The ratios of the silt and sludge mixture are 0, 20, 40, 60, 80 and 100%. Two types of sludge, as mentioned in the materials and sampling section, were use in this study. In order to assess the strength of the silt and sludge mixture, a direct shear test was conducted based on the ASTM D3080 standard test method for the direct shear test of soils under consolidated drained conditions. The same tests were also conducted on sand, silt and laterite soil for comparison. Based on the tests that were conducted, the alternative landfill capping material capability of various soil mixtures was assessed.

RESULTS AND DISCUSSIONS

Both table1 and figure1 shows the results of modified proctor test. Table 1 shows the maximum dry unit weight (g/cm^3) ratios for silt, sand and laterite soils. Referring to the graph above, the result of hydraulic conductivity is as plotted. The hydraulic conductivity of sludge regarding whether its sewerage or water treatment sludge, it is better than the hydraulic conductivity of silt. The mixing ratio of silt to sludge is 0, 20, 40, 60, 80 and 100 percent of sludge. As the sludge percentage increases the hydraulic conductivity drops which represent a drop in permeability. It is good since the landfill capping requires low permeability material.

Table 1: Summary result for the modified proctor test

	Silt	Sand	Laterite
Maximum dry unit weight(g/cm^3)	1.8	1.98	1.85

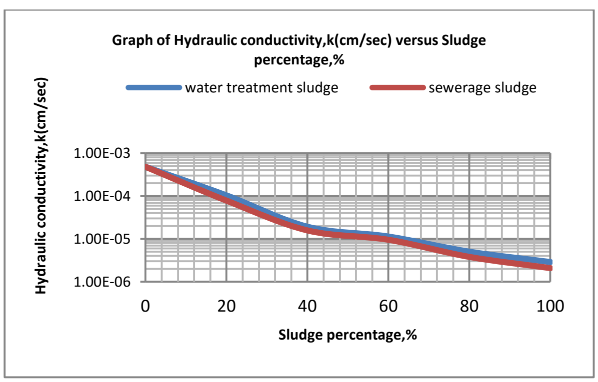

Figure 1: Graph of Hydraulic conductivity, k(cm/sec) versus Sludge percentage,%

Comparing both water treatment and sewerage sludge, the *k* value of sewerage sludge has a better advantage. The permeability of sewerage sludge is lower than water treatment sludge, which makes it a more ideal material for landfill capping. Laterite soil which is the currently used capping material has a *k* value of 8.24 e^{-08} cm/sec, which none of the combined sludge/silt samples nor did pure sludge could achieve such low hydraulic conductivity. The lowest achievable is 2.07 e^{-06} cm/sec by 100% sewerage sludge, which is still quite a significant difference, compared to laterite soil.

The result of the direct shear test can be referred in tables 2 - 7, which shows the c-value (cohesion strength) and phi value (soil friction angle) of each soil sample, including the combined sample of silt/sludge of 0, 20, 40, 60, 80 and 100% sludge. There is a significant difference between sewerage sludge and water treatment sludge. By mixing silt with sewerage sludge, it tends to weaken the cohesive strength and friction angle. Whereas the silt strengthens the cohesive strength and friction angle of the water treatment sludge. The highest strength of all the mixed samples is the pure sewerage sludge sample, with a c value of 8.95 kN/m^2 and a friction angle of 45.73°. The friction angle of pure sewerage sludge exceeds both laterite and sand material, which means the failure plane is more stable compared to both laterite and sand material; however, the *c* value (cohesion) is lower than both sand and laterite. Laterite has the highest *c* value, 13.72 kN/m^2, whereas sewerage sludge's *c* value is 8.95 kN/m^2. The experiment suggests that the best material to replace the current landfill capping material would be 100% pure sewerage sludge with no mixed silt in it.

Laterite soil with a *k* value of 8.24 e^{-08} cm/sec tends to resist water infiltration into the sample, thus enhancing the surface water runoff. The *k* value of silt is 4.81 e^{-04} cm/sec, the significant difference of hydraulic conductivity between both samples concludes that silt will not provide surface water runoff as effectively as laterite soil. From the lab tests' results, the hydraulic conductivity of sewerage sludge is 2.07 e^{-06} cm/sec. Although the hydraulic conductivity of sewerage sludge is not as low as the laterite sample, it is sufficient to support surface water runoff as the hydraulic conductivity value of sewerage sludge is considered as low permeability. The hydraulic conductivity of water treatment sludge, *k* is 2.9 e^{-06} cm/sec, which is just slightly higher than sewerage sludge. Nevertheless, it is considered as low permeability. The permeability level of water treatment sludge would be sufficient to support surface water runoff. In terms of shear strength resistance, referring to table 2, silt has a *c* value of 7.64 kN/m^2, whereas laterite soil and sand sample has a *c* value of 13.72 kN/m^2 and 11.17 kN/m^2 respectively. This proves that the bond strength of silt is not good at all. Silt is very weak in bond strength, when held in hand it tends to only stick to the hand a little. Whereas the friction angle value, Ø of silt is 36.22°. The friction angle value is in between laterite and sand sample. 41.91°< 36.22°< 34.12°. Laterite < silt < sand is the sequence of friction angle value. This means that the failure plane of silt is on the acceptable region, and the results are satisfactory.

Table 2: C and Phi value of laterite, sand and silt sample in direct shear test

	laterite	sand	silt
c	13.72	11.17	7.64
phi	41.91	34.12	36.22

Table 3: C and Phi value of mix sample of sewerage sludge and silt in direct sheartest

Sewerage sludge(%)	100	80	60	40	20	silt
c	8.95	8.9	8.77	7.88	7.74	7.64
phi	45.73	43.83	40.03	39.56	37.77	36.22

In terms of shear strength resistance, referring to table 3, sewerage sludge has a *c* value of 8.95 kN/m^2. The results proved the fact that sewerage sludge does not have good bonding properties. Whereas the friction angle value, Ø of sewerage sludge is 45.73°. The friction angle value is higher than laterite and sand sample, 45.73° < 41.91° < 34.12°. Sewerage sludge < laterite < sand is the sequence of friction angle value. This means that the failure plane of sewerage sludge is better than both laterite and sand sample which makes sewerage sludge a very good material to replace the current landfill capping.

Table 4: C and Phi value of mix sample of water treatment sludge and silt in direct shear test

Water treatment sludge(%)	100	80	60	40	20	silt
c	6.16	5.21	5.82	6.44	7.02	7.64
phi	6.13	27.7	30.07	31.5	33.36	36.22

Referring to table 4, the water treatment sludge has a low *c* value of 6.16 kN/m^2. The difference between the cohesion strength is approximately two times compared water treatment sludge with laterite and sand sample, proving that the bond strength in water treatment sludge is poor. The friction angle value, Ø of water treatment sludge is 6.13°. The friction angle value is very much lower than laterite and sand sample, 41.91°and 34.12°. Pure water treatment sludge would not be a good option for capping material since both the cohesion strength and friction angle value is too low compared to laterite and sand sample.

Table 5: Hydraulic conductivity, k(cm/s) of silt, laterite and sewerage sludge sample

	Silt	Laterite	Failed Sewerage Sludge
Hydraulic conductivity (cm/s)	4.81E-04	8.24E-08	2.66E-02

Table 6: Hydraulic conductivity, k(cm/s) of mix sample of sewerage sludge and silt

	100	80	60	40	20	silt
Hydraulic conductivity (cm/s)	2.07E-06	3.78E-06	9.50E-06	1.57E-05	7.79E-05	4.81E-04

Table 7: Hydraulic conductivity, k(cm/s) of mix sample of water treatment sludge and silt

Water treatment sludge(%)	100	80	60	40	20	silt
Hydraulic conductivity (cm/s)	2.90E-06	5.05E-06	1.14E-05	1.93E-05	1.04E-04	4.81E-04

CONCLUSION

Based on this study, silt is considered not suitable for landfill capping due to its moderate permeability and low bond strength. Although the bond strength of sewerage sludge is not desirable, the hydraulic conductivity and friction angle value shows satisfying results. Judging from the strength and permeability properties of sewerage sludge, it can be accepted as the replacement for landfill capping material. The ratios of mixed samples are the same in both types of sludge, which are 0%, 20%, 40%, 60%, 80% and

100% sludge. In the sewerage sludge, the hydraulic conductivity, cohesion strength and friction angle in sludge itself is better compared to silt. In the water treatment sludge sample, the hydraulic conductivity shows low permeability, which is good. But its cohesion strength and friction angle has very weak value. By mixing the silt in the water treatment sludge, the cohesion strength increased slightly whereas the friction angle improved a lot. Hydraulic conductivity of the water treatment sludge increases as silt is added in it. The case is the same with sewerage sludge. Among all the samples of mixture, 100% sewerage sludge poses the best and suitable properties for landfill capping usage.

REFERENCES

[1] Tubtimthai O, Landfill lysimeter studies for leachate characterization and top cover methane oxidation. Resources and Development, Master thesis, Asian Institute of Technology, School of Environment, Resources and Development, Thailand, 2003,

[2] Davis ML, Cornwell DA, Introduction to Environmental Engineering: Third Edition. New York, McFraw-Hill International, ISBN 0-07, 1998, 115237-4.

[3] Weand B L"Landfill Covers for Use at Air Force Installations." Report for the Air Force Center of Environmental Excellence. Mitretek Systems , 2010.

[4] Visvanathan C, Trankler J, Kuruparan P, Xiaoning Q, "Influence of landfill operation and waste composition on leachate control: lysimeter experiments under tropical conditions, Urban Environmental Engineering and Management Program,Asian Institute of Technology, Thailand, 2002.

[5] Fatta AP, Loizidou MA, study on the landfill leachate and its impact on the groundwater quality of the greater area, 2011, 175–190.

[6] Bodzek J SG, Hung YT, "Treatment of landfill leachate." Handbook of Industrial and Hazardous Wastes Treatment, 2004, 1155–1208.

[7] Barker JEB, Labonte M, "Groundwater contamination at a landfill sited on fractured carbonate and shale, 1988, 1–25.

[8] Blight G, (2008). "Slope failures in municipal solid waste dumps and landfills." Waste Management and research, 26, 2008, 448 - 463.

OPTIMAL DESIGN OF RAIN GAUGE NETWORK IN JOHOR BY USING GEOSTATISTICS AND PARTICLE SWARM OPTIMIZATION

Mohd Khairul Bazli Mohd Aziz[1], Fadhilah Yusof[2], Zalina Mohd Daud[3], Zulkifli Yusop[4], Mohammad Afif Kasno[5]
[1]Centre of Preparatory and General Studies, TATI University College, Malaysia, [1,2]Department of Mathematical Sciences, Faculty of Science, Universiti Teknologi Malaysia, Malaysia, [3]UTM Razak School of Enggineering and Advanced Technology, Universiti Teknologi Malaysia, Malaysia, [4]Institute of Environmental and Water Resource Management (IPASA), Faculty of Civil Enggineering, Universiti Teknologi Malaysia, Malaysia, [5]Malaysia – Japan International Institute of Technology (MJIIT),Universiti Teknologi Malaysia, Malaysia.

ABSTRACT

This study proposes particle swarm optimization (PSO) approach to determine the optimal number and locations for the optimal rain gauge network in Johor state. The existing network of 84 rain gauges in Johor is also restructured into new locations by using daily rainfall, humidity, solar radiation, temperature and wind speed data collected during the monsoon season (November – February) of 1975 until 2008. This study used the combination of geostatistics method (variance-reduction method) and particle swarm optimization as the algorithm of optimization during the restructured proses. The numerical result shows that the new rain gauge location provides minimum value of estimated variance. This shows that the proposed method can serve as an analysis tool for a decision making to assist hydrologist in the selection of prime sites for the installation of rain gauge stations.

Keywords: Rainfall Network, Geostatistics, Particle Swarm Optimization

INTRODUCTION

Collectively, rainfall data deliver important input for effective planning, designing, operating and managing of water resources projects. Rainfall data are employed in numerous water resources management tasks such as water budget analysis and assessment, flood analysis and forecasting, streamflow estimation, and design of hydraulic structures. A reliable and optimal rain gauge network can provide accurate and precise rainfall data that is crucial for effective and economic design of hydraulic structures for flood control. This will help the researchers to minimize the hydrological and economic risk and errors involved in different water resources projects. Rain gauge network is usually installed to facilitate the direct measurement of rainfall data that characterize the spatial and temporal variations of local rainfall patterns in a catchment [14]. A rain gauge network should be denser than networks used to measure other meteorological elements (e.g. temperature), because the highly variable rainfall patterns and its spatial distribution cannot be represented effectively without having a network of enough spatial density [2]. A well-designed rain gauge network thus should contain a sufficient number of rain gauges, which reflect the spatial and temporal variability of rainfall in a catchment [3].

In hydrological studies, the rain gauge network used is often sparsed and thus incapable of providing adequate rainfall estimation necessary for effective hydrological analysis and design of water resources projects. Significant design errors in the water resources projects will eventually cause in the immense loss of lives and property damages resulted from use of inaccurate rainfall data.

Thus, identification and selection of the optimal rain gauge network configuration with optimal number and locations of rain gauge stations is the main objective of the network design. Hence, the optimal rain gauge network should contain the number and locations of rain gauge stations in such a way that it can produce optimum rainfall information and data with minimum uncertainty and cost [2,4]. One can approach the problem either by removing redundant stations from the network to minimize the cost or by expanding the network with installation of additional stations to reduce the estimation uncertainty [5]. Some studies applied the kriging technique in combination with other techniques such as entropy [3] and multivariate factor analysis [7] for the network design. A few studies also combined optimization method based on simulation tools (e.g. simulated annealing) with the kriging technique [2, 8, 9] to obtain the optimal rain gauge network.

A network design methodology was developed in this study to determine optimal number and locations of the existing stations in the current rain gauge network located in the Johor state, Malaysia. The procedure involves a methodical search for the optimal number and locations of rain gauge stations in the network that minimize estimated variance. The methodology presented in this study is in line with that of [2] who used the kriging-based geostatistical and simulated annealing as an optimization method to determine the optimal number and location of rain gauge stations in the existing The major contribution here is that unlike the work of [2], the developed methodology considered the particle swarm optimization technique as an optimization method to provide fast convergence optimization procedure. The rest of the paper has been organized as follows. First, details of the study area and datasets used are presented, which is followed by the methodology. The results are summarized next and finally, the conclusions are drawn.

STUDY AREA AND DATA DESCRIPTION

Johor is the second largest state in the Malaysia Peninsular, with an area of 18,941 km^2. The rivers in Johor and its streams are important sources of water supply for the people of Johor. The catchment area contains a dense rain gauge network, 84 rain gauges covering 19,210 km^2 in Johor (see Figure 1). The current overall network density for the whole of Johor state is about 194 km^2 per gauge, which surpasses even the ideal WMO recommendation of one gauge per 600 – 900 km^2 for flat areas. In fact, it also fulfills the ideal density for mountainous region of 100 – 200 km^2 per gauge. The data used to perform the analysis was from the daily rainfall, elevation, humidity, temperature, solar radiation and wind speed measurement from November until February of 1975 through 2008 from 84 rain gauge stations that are located all over Johor. Figure 4 shows the mapping of the humidity, temperature, solar radiation, wind speed and elevation in Johor. From Figure 4, the highest humidity area is the centre of Johor, west side of Johor receives more heat based on the solar radiation and the temperature, and the wind speed is highest along the coast. The data was obtained from Department of Irrigation and Drainage (DID) Malaysia and Malaysia Meteorological Department (MMD).

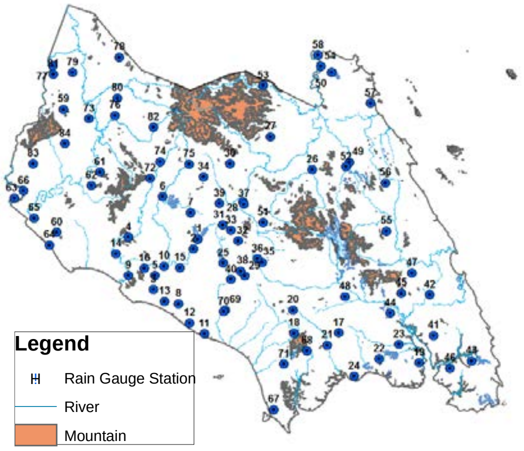

Fig.1 Rain gauge locations

METHODOLOGY

Geostatistical Method

The network design problem consists in obtaining the number N and the location of rain gauges stations that give the best estimate areal mean rainfall. The estimation variance σ^2 is a basic tool of variance reduction techniques for optimal selection of sampling locations. For the application of the variance reduction method to optimal location of sampling sites, a semivariogram must be modelled.

A semivariogram, $\gamma(h)$ is one of the significant functions to indicate spatial correlation in observations measured at sample locations. Semivariogram is represented as a graph that shows the difference in measure with distance between all pairs of sampled locations. The estimated variance depends on the semivariogram model, the number N of rain gauges and its spatial location. Therefore, choosing an appropriate semivariogram model is vital in determined the optimal estimation variance.

Let h be the lag or distance, and Z be an intrinsic random function and let $Z(x_i)$, for $i = 1,2,\ldots,N$ be a sampling of size N. Then the following expression is an unbiased estimator for the semivariogram of the random function:

$$\gamma(h) = \frac{1}{2n(h)} \sum_{i=1}^{n(h)} \left[Z(x_i + h) - Z(x_i) \right]^2 \tag{1}$$

Equation 1 is used to compute experimental semivariogram from the data under study. By changing h, both in distance and direction, a set of the sample (or experimental) semivariograms for the data is obtained [10].

The exponential semivariogram models are selected to fit the data. The exponential semivariogram model equation is as follow:

$$\gamma(h) = C\left(1 - e^{-\frac{3h}{a}}\right) \tag{2}$$

where C is the sill and a is the range.

Once the model of the semivariogram is fixed, the estimation variance only depends on the number N and the location of the rain gauges. To calculate the estimation variance using ordinary kriging,

$$\sigma^2(x_0) = 2\sum_{i=1}^{k}\lambda_i\gamma(x_i, x_0) - \sum_{i=1}^{k}\sum_{j=1}^{k}\lambda_i\lambda_j\gamma(x_i, x_j) \tag{3}$$

Where

$$\hat{Z}(x_0) = \sum_{i=1}^{k}\lambda_i Z(x_i) \tag{4}$$

Subject to $\sum_{i=1}^{k}\lambda_i = 1$.

This is an algorithm for the ordinary kriging estimation to calculate the estimation variance (Olea, 2003):

1. Calculate each term in matrix *G*.
   Let x_i's be the sampling sites of a sample subset of size k, $i = 1,2,\ldots,k$ and let $\gamma(x_i, x_j)$'s be the experimental variogram. Then the *G* is the matrix

$$G = \begin{bmatrix} \gamma(x_1,x_1) & \gamma(x_2,x_1) & \cdots & \gamma(x_k,x_1) & 1 \\ \gamma(x_1,x_2) & \gamma(x_2,x_2) & \cdots & \gamma(x_k,x_2) & 1 \\ \cdots & \cdots & \cdots & \cdots & \cdots \\ \gamma(x_1,x_k) & \gamma(x_2,x_k) & \cdots & \gamma(x_k,x_k) & 1 \\ 1 & 1 & \cdots & 1 & 0 \end{bmatrix} \tag{5}$$

2. Calculate each term in matrix g.
   Let x_0 be the estimation location, then the g is the matrix

$$g = [\gamma(x_0,x_1) \quad \gamma(x_0,x_2) \quad \cdots \quad \gamma(x_0,x_k) \quad 1]' \tag{6}$$

3. Solve the system of equations

$$GW = g,$$
$$W = gG^{-1},$$

   Where $W = [\lambda_1 \quad \lambda_2 \quad \cdots \quad \lambda_k \quad -\mu]'$.

4. Calculate the ordinary kriging estimation variance

$$\sigma^2(x_0) = g'W = g'G^{-1}g. \tag{7}$$

Partical Swarm Optimization

PSO was developed by Kennedy and Eberhart, [12] in 1995, inspired by the social behavior of bird flocking. The movement of each swarming particle is determined by a combination of a stochastic element and a deterministic element, [1]. A population (swarm) of particles is initialized in an n-dimensional search space in which each particle $x_i = (x_{i1}, x_{i2}, \ldots, x_{in})$ represents a possible solution. Each particle is aware of its current position, its own personal best position, its current velocity and the single global (or local) best position. The global best position is represented as $g_i = (g_{i1}, g_{i2}, \ldots, g_{in})$ and symbolizes the best position of all particles in the population (swarm). The personal best position represents the best position found by a particle so far and is denoted as $p_i = (p_{i1}, p_{i2}, \ldots, p_{in})$.

The velocity $v_i = (v_{i1}, v_{i2}, \ldots, v_{in})$ gives the position change of a particle. In the original proposed PSO of Kennedy and Eberhart, the new velocity for each particle is calculated according to Eq. (1). To update the new position of each particle, Eq. (2) is used:

$$v_i = v_i + c_1.r_1.(p_i - x_i) + c_2.r_2.(g - x_i) \tag{8}$$

$$x_i = x_i + v_i \tag{9}$$

where $i = 1,2,\ldots,N$, with N as population size. c_1 and c_2 are two positive constants; r_1 and r_2 are two random numbers with range (0,1).

In PSO, Eq. (8) is used to calculate the new velocity according to its previous velocity and to the distance of its current position from both its own best historical position and the best position of the entire population or its neighbourhood. Generally, the value of each component of v can be constricted by setting the maximum velocity $v_{\max}$ to the upper and lower bounds of the decision variable range. Then the particle flies toward a new position according to Eq. (9). This process is repeated until a user-defined stopping criterion is reached.

The minimisation of objective function given in Eq. (3) is a problem of combinatorial optimization.

A typical procedure of rain gauge network design has to look for a combination among all rain gauge stations in such a way that minimizes the estimation variance and/or maximizes the information content for the observed data. This can be achieved either by optimal positioning of additional and redundant stations or simply removing redundant stations that forms the scope of this paper.

The steps of PSO algorithms applied for determined optimal rain gauge network as follow:

1. Randomly initialize the *x* particles each representing different combinations of *N* rain gauge placements.
2. Evaluate each particle in the population using the fitness function, Eq. (3) and minimum fitness function is set as *pbest*.
3. Compare particle's fitness evaluation with particle's *pbest*. If current value is < than *pbest*, then set *pbest* as *gbest*.
4. Generate a new set of *x* particles by Eq. (8).
5. Stop the algorithm if the stopping criterion is satisfied or maximum number of iterations is reached.

RESULTS AND DISCUSSION

The variance reduction technique requires an appropriate semivariogram model that fitted the observed data. Initially, an experimental semivariogram from the experimental data is derived. Then, a functional semivariogram model is fitted to the experimental variogram. The obtained semivariogram model has essential information to be used in kriging interpolation of observed data. Fitting and selection of suitable semivariogram model can be accomplished through the variogram modelling technique. Once a proper semivariogram model is selected for the observed dataset, kriging is applied for the generation of interpolated surfaces and the estimation of the corresponding kriging error. The semivariogram model fitted to the experimental data is shown as in table below:

Table 1 Exponential semivariogram model

Nugget	Sill	Range
0.93917	1.5568	1.05449

When the semivariogram is successfully fitted to the empirical rainfall data, the particle swarm optimization method is applied to find the minimum objective function (equation 3) in order to get the optimum number and location of rain gauge stations. The optimization technique done based on the steps mentioned earlier. The results of the optimization process were shown in Figure 1 and Table 2.

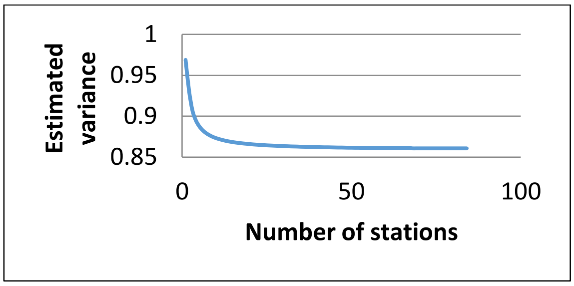

Fig. 2 Estimation variance versus number of stations

Table 2 Estimated variance value with optimal number of stations

Estimated variance	Stations selected	Stations removed
0.8618	67	17

This new optimal rain gauge network demonstrates that the high density of existing rain gauge in Johor has been reduced by removing several stations. Fig. 2 depicts that the estimated variance value decreased as the number of rain gauges increased. This value approach optimal value when the optimization process gives the number of optimal rain gauge stations. In Table 2, it is shown that the optimal number of rain gauge stations is 67 stations with estimated variance value 0.8618. The locations of the 67 selected locations are as shown in Fig. 3 below. From Fig. 3, most of the removed stations are redundant stations that are unnecessary needed.

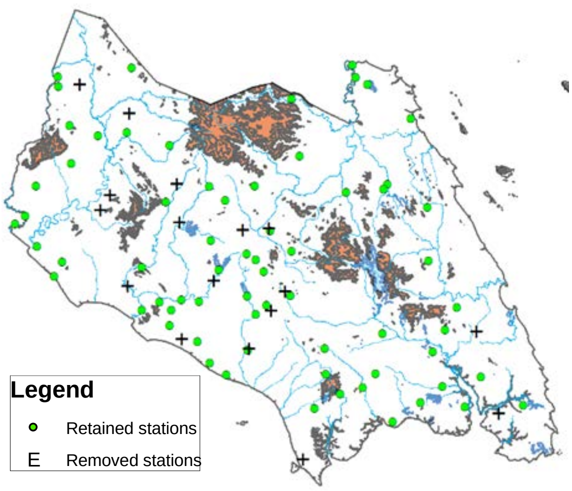

Fig. 3 Optimal locations for 67 selected rain gauge stations.

Table 3 shows the comparison of observed and estimated areal average rainfall for the existing and new optimal rain gauge stations. It shows the new optimal rain gauge stations manage to increase the mean areal rainfall despite the increase in the error due to the lack number of stations.

Table 3 Comparison between observed and estimated areal average rainfall

Estimated Mean Areal Rainfall (mm) for the rain gauge network		Error (%) obtained for the rain gauge network	
Existing	Optimal	Existing network	Optimal Network
5.562404	5.5721	2.83	3.35

After the execution of the optimization process, two scenarios were considered for the 17 removed stations in Table 2.

- Scenario-1: Optimal positioning of 17 removed stations fitted into Figure 3 to find their optimal locations.
- Scenario-2: All 84 existing stations were reset into new optimal locations

For the redesignation purpose of the network, the whole study area is discretized into 250 square grids with each unit equivalent to 100km² (Fig. 4f). This is in line with the criterion set by the World Meteorological Centre [11] which stated that every rain gauge in the mountain region of temperate, Mediterranean and tropical zone need to be in the area of 100-250km² each. In order to redesign the network, the following criteria were also considered and the design is based on these criteria:

1. Each selected grid cannot have more than one station.
2. The new rain gauge must be put in an area where it is not more than 100 meters above sea level. This is because most of the existing rain gauge stations in Johor are located not more than 100 meters above the sea level as can be seen in Fig. 4(e).
3. The new rain gauge must be put in an area with high humidity reading value as this shows that the area receives more rainfall.
4. The new rain gauge must be put in an area with low temperature as lower temperature shows that the area is humid and receives more rainfall.
5. The new rain gauge must be put in an area where the value solar radiation is low as this shows that the area is humid and has low temperature.
6. The new rain gauge must be put in an area that is protected from the wind in all direction. Area with low wind speed ensures that the collected data is not influenced by the wind speed.

The PSO algorithm is applied once again to determine the optimal rain gauge location for the existing 84 stations from the 250 possible sites. The humidity, temperature, solar radiation, wind speed and elevation data in Fig. 4 will help the algorithm locates suitable locations for the rain gauges.

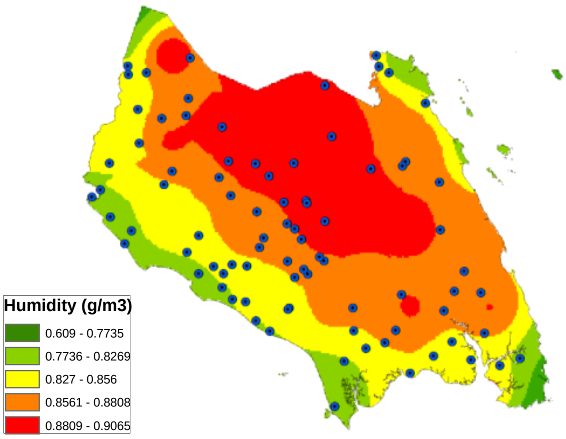

a. humidity

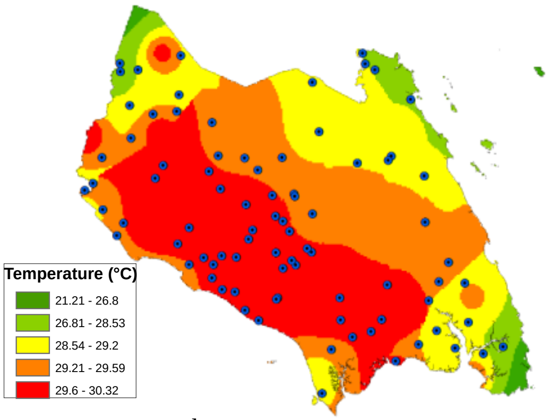

b. temperature

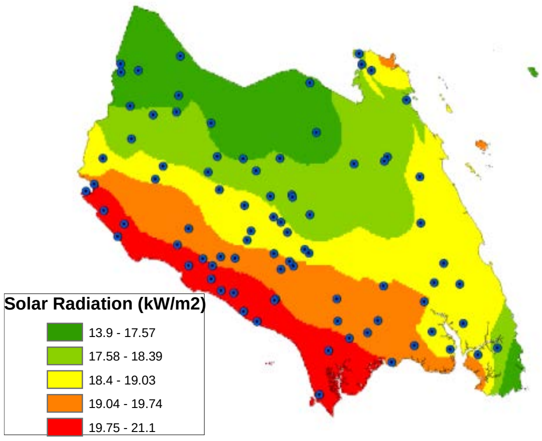

c. solar radiation

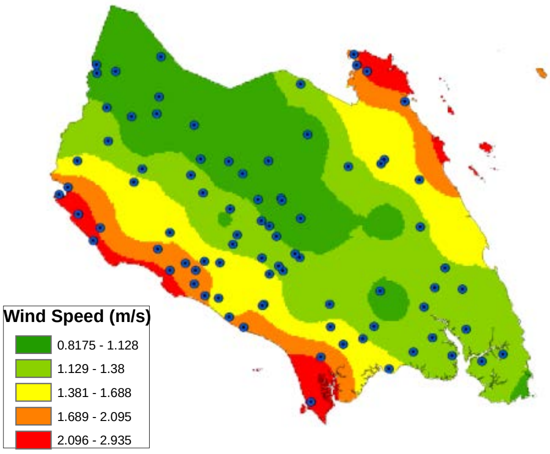

d. wind speed

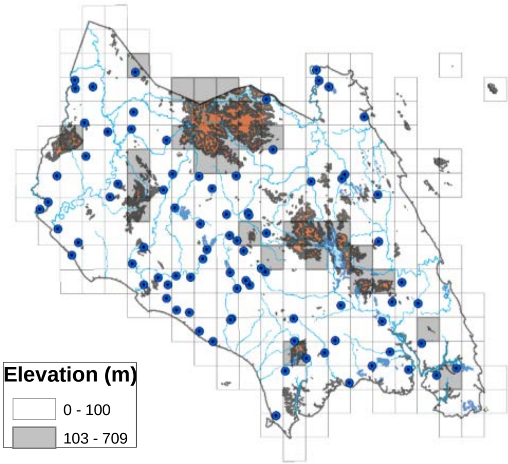

e. elevation

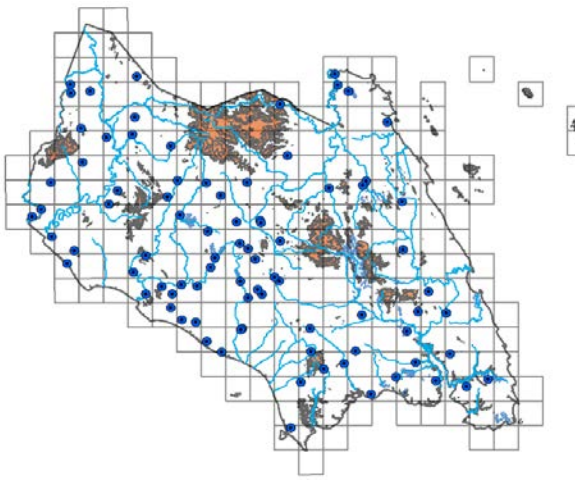

f. Johor with grids

Fig. 4 Humidity, Temperature, Solar Radiation, Wind Speed, Elevation and Grids

Table 4 shows the resulted estimated variance for both scenarios. For scenario 1, the estimated variance value reduces when the removed stations were located into new optimal locations. This shows that the removed stations were able to improve the accuracy of the network by placing it in an optimum location. For scenario 2, the estimated variance decreases lower than scenario 1 and previous estimated variance. This shows that in order to achieve an optimal network with the existing stations, all stations must be reorganized and relocated into new locations. Elevation, temperature, wind speed, solar radiation and humidity data has help in identifying the optimal locations in the discretized Johor.

The new locations of the restructured rain gauge networks for both scenarios are as shown in Fig.5. In Fig. 5a, the 17 removed stations were relocated into new optimal locations. The placements of the 17 removed stations allow the stations to fill the gap in empty potential grid in Fig. 4f. These 17 stations will act like an additional stations to already optimal 67 stations obtained in the first process. The placements of these additional stations will improve estimation accuracy that leads to an optimal rain gauge network.

In Fig. 5b, the 84 existing rain gauge stations were restructured into a whole new optimal rain gauge network. This process considered the number of existing stations but need to be located into a new possible optimal location. Figure 5b also depicts locations of all rain gauge stations in Johor that are no longer with redundant stations located into new locations which are complied with the criterion to not have stations located in one same grid. The PSO algorithm managed to determine a new site for each rain gauge stations and it is well placed into a flat and terrain area with elevation not more than 100m above sea level. It is because, when determining the theoretical placement of any rain gauge, the manufacturer often assumes the absence of any physical obstacles that could reduce or obstruct the rainfall. Placing a rain gauge close or on a hilly area will severely alter the rainfall data.

Table 4 Estimated variance

	Scenario 1	Scenario 2
Estimated Variance	0.8473	0.7163

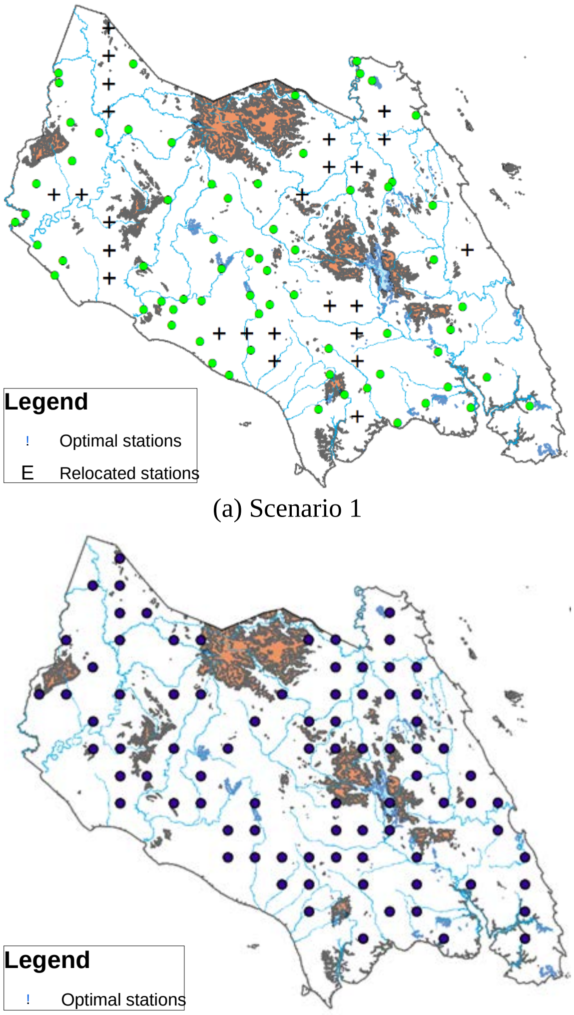

(a) Scenario 1

(b) Scenario 2

Fig. 5 New optimal locations for 84 rain gauge stations

CONCLUSIONS

Combination of geostatistics methods and particle swarm optimization as an algorithm of optimization can be used as a framework for rain gauge network design models as it improves the existing rainfall network by minimizing the variance of estimation value. Through this study, it was found that the optimal number of stations for Johor is 67 stations with the estimated variance of 0.8618. Particle swarm optimization as an algorithm of numerical optimisation also improves the optimal network of rain gauge stations in Johor by variance reduction method with the help of rainfall, elevation, humidity, solar radiation, temperature and wind speed data. From the data analysis, it was also found that the 17 stations were either removed or relocated into new locations. This study considered two scenarios. Scenario 1 consideration was to optimally relocate the 17 removed stations to new locations and scenario 2 considerations was to redesign all the existing stations. Scenario 1 was most likely to be applied when the rain gauge network need an additional stations while scenario 2 was more practical in the early planning and designing of an optimal rain gauge network. Redesignation of all 84 stations depicts the minimum optimum estimated variance compare to only 17 relocated stations in scenario 1. This approach is more expensive because it requires a completely new network to be established but the accuracy and the reliability of the rain gauge network is surely improved.

Overall, this study has illustrated that the geostatistics method with particle swarm optimization can be used as the optimization method to provide the solution in designing an optimal rain gauges network system. This optimal network also is essential in providing better rainfall data. This model and methodology can provide information that will help decision makers to understand the relationship between numbers and locations of rain gauge stations in order to provide a better and more accurate rainfall data. Further researches on the optimization technique are required for better results.

ACKNOWLEDGEMENTS

The authors would like to thank the Malaysian Ministry of Higher Education, TATI University College and Universiti Teknologi Malaysia for their financial funding and support.

REFERENCES

[1] Yang, X. S., Enggineering optimization: An introduction with metaheuristics applications. Wiley Publications. 2010.

[2] Pardo-Igúzquiza, E. Optimal selection of number and location of rainfall gauges for areal rainfall estimation using geostatistics and simulated annealing. Journal of Hydrology 210: 206–220. DOI: 10.1016/S0022-1694(98)00188-7. 1998.

[3] Yeh, H. C., Chen, Y.C., Wei, C., Chen, R. H., Entropy and kriging approach to rainfall network design. Paddy and Water Environment 9: 343–355. DOI: 10.1007/s10333-010-0247-x. 2011.

[4] Kassim, A. H. M., Kottegoda, N.T. Rainfall network design through comparative kriging methods. Hydrological Sciences Journal 36: 223–240. DOI: 10.1080/02626669109492505. 1991.

[5] Mishra, A. K., Coulibaly, P. Developments in hydrometric network design: a review. Reviews of Geophysics 47: RG2001. DOI: 10.1029/2007RG000243. 2009.

[6] Chen, Y. C., Wei, C., Yeh, H. C. Rainfall network design using kriging and entropy. Hydrological Processes 22: 340–346. DOI: 10.1002/hyp.6292. 2008.

[7] Shaghaghian, M. R., Abedini, M. J. Rain gauge network design using coupled geostatistical and multivariate techniques. Scientia Iranica 20: 259–269. DOI: 10.1016/j.scient.2012.11.014. 2013.
[8] Barca, E., Passarella, G., Uricchio, V. Optimal extension of the rain gauge monitoring network of the Apulian regional consortium for crop protection. Environmental Monitoring and Assessment 145: 375–386. DOI: 10.1007/s10661-007-0046-z. 2008.
[9] Chebbi, A., Bargaoui, Z. K., Cunha, M. D. C., Optimal extension of rain gauge monitoring network for rainfall intensity and erosivity index interpolation. Journal of Hydrologic Engineering 16: 665–676. DOI: 10.1061/(ASCE)HE.1943-5584.0000353. 2011.
[10] Burrough, P. A. Principles of Geographical Information Systems for Land Resources Assessment. Clarendon Press, Oxford, pg. 147-165. 1987.
[11] Guide to Meteorological Instruments and Methods of Observation, (WMO-No.8, Seventh edition), WMO, Geneva, 2008.
[12] Eberhart, R. and Kennedy, J. A new optimizer using particle swarm theory. In Proceedings of the Sixth International Symposium on Micro Machine and Human Science (MHS '95), pages 39–43. IEEE Press, 1995.
[13] Olea, R. A. *Geostatistics for Engineers and Earth Scientists*, Kluwer Academic Publishers, ISBN 0-7923-8523-3, Massachusetts, 2003.
[14] Sajal, K. A., Abdullah, G. Y. and Nitin, M. Optimal design of rain gauge network in the Middle Yarra River catchment, Australia. Hydrol.Process.2014.

EFFECTIVENESS OF JACKFRUIT SEED STARCH AS COAGULANT AID IN LANDFILL LEACHATE TREATMENT PROCESS

Mohd SuffianYusoff [1], Noor Aina Mohamad Zuki [1] and Mohd Faiz Muaz Ahmad Zamri[1]
[1]School of Civil Engineering, Universiti Sains Malaysia, Malaysia.

ABSTRACT

Aluminium sulphate (alum), ferric chloride and polyaluminium chloride (PAC) are the most common coagulants being used for leachate coagulation-flocculation treatment. However, the impact of these residual's coagulants have sparked huge concern ceaselessly. Therefore, development of natural coagulant as an alternative coagulant for treatment process has been given full attentions. In this attempt jackfruit seed starch (JSS) which produce by extraction method was used as coagulant aid with PAC. The removal efficiency was determined using jar test method. The removal of leachate pollutants was compared between PAC coagulant with and without JSS. Interestingly the JSS coagulant aid has succeed to reduce the dosage of PAC from 900 mg/L to 600 mg/L by increasing the removal of COD, colour and ammonical nitrogen (NH_3-N) up to 33.6%, 93.6%, and 13.1 % respectively. While the removal for turbidity and suspended solid (SS) were maintained at 94% and 92 % respectively. The addition of JSS has succeeded to reduce 33.3% the usage amount of PAC in treatment process of landfill leachate. The result proved that JSS was effective to be used as coagulant aid landfill leachate treatment.

Keywords: Landfill Leachate, Natural Coagulant, Jackfruit Seed and Starch.

INTRODUCTION

Leachate is highly contaminated liquid that defined as the aqueous effluent generated through precipitation, degradation and percolating process of landfill storage (waste) within period time [1]. Leachates usually contain large amounts of organic and inorganic matter [2], which are toxic to living organisms and ecosystems. Generally the physical-chemical treatment is effective method for old and stabilized leachate. One of common physical-chemical method that used was coagulation-flocculation.

Coagulation-flocculation is a relatively simple physical–chemical technique that may be employed successfully for the treatment of stabilized and old landfill leachate [3]. Nevertheless the performances of the treatment are varies and depending on the type of process parameter implemented.

Jackfruit (Artocarpus heterophyllus Lam.) is an important naturalized plant of Southeast Asia which rich with starch sources. There are various natural based coagulants or flocculants has been explored in water and wastewater treatment applications. Jackfruit seed starch has not been considered and exploited as a potent source of starch. However, only a few published articles are available on this material. Thus this paper is focused on landfill leachate treatment using JSS as coagulant in Kuala Sepetang Landfill Sites. The efficiency of removal of organic matter and ammonia in leachate were investigated by comparing between powder and dilution of JSS using jar test.

METHODOLOGY

Leachate Sampling and Characterization

The leachate samples were collected from a Kuala Sepetang Landfill Sites,Taiping, Perak. The characteristics of raw leachate collected are shown in Table 1.

Preparation of Jackfruit Seed Starch (JSS)

Preparation of JSS is used from a modified method of Tulyathan, Mukprasit and Sajjaanantakul [4,5]. Method of isolation of JSS is based on modified method of Bobbio, Dash, and Rodrigues [6]. Slurries of JSS was prepared in 0.05 M sodium hydroxide (NaOH) solution and constantly stirred for 6 h. The slurries were centrifuged for 20 min at 4°C. The supernatant was drained and the upper brown sediment was scraped and followed by a second extraction with a 0.05 M NaOH solution. The remaining sediment was mixed with distilled water and filtered by a sieve (0.15 mm mesh size) to eliminate fibers. The filtrate was neutralized with 0.1 M hydrochloric acid (HCl) to pH 7.0 and the slurries were centrifuged for 20 min at 4°C. The supernatant was drained and the upper brown sediment was scraped and the remaining was washed with distilled water and centrifuged for 20 min at 4°C. The starch cake was dried at 50°C for 12 h.

Jar Test

Coagulation test was performed by using jar test equipment (SW6 Stuart Bibby Scientific Limited, UK). 3M NaOH and 3M HCl were used to adjust the pH sample. 500 ml of leachate samples were filled into six beakers and agitated simultaneously with combination of rapid mixing speed of 200 rpm in 3 min and 40 rpm in 30 minutes for slow mixing, and settling time was 60 minutes.

RESULTS AND DISCUSSION

Characteristics of Raw Leachate

Characteristics of leachate at Kuala Sepetang landfill was summarized in Table 1. The obtained pH (8.16) agrees with the other studies conducted for stabilized leachate characteristics in Malaysia [7, 8]. However, according to BOD5/COD ratio below, the leachate showed higher biodegradability than expected.. Although the age of the leachate is already more than 10 years. The value obtained indicates that the leachate are partially stabilized leachate (0.1< BOD5/COD<0.3) This probably happened because the landfill is still under operating and producing young leachate which is mixed together with old leachate and this may effects the biodegradability of the leachate itself. Therefore, biological degradation is still occurring in the leachate [8].

Table 1 Characteristics of Kuala Sepetang raw leachate

No	Parameters	Value
1	pH	8.16
2	Turbidity(NTU)	106
3	Colour (Pt Co)	4588
4	Suspended Solid (mg/L)	187
5	Ammonia-N (mg/L)	264
6	BOD_5 (mg/L)	100
7	COD (mg/L)	898
8	BOD_5/COD	0.11
9	pH	8.16

Removal Rate

In this study, the optimum dosage of PAC was investigated at the optimum pH (pH5). The percentage removal of COD, colour, turbidity, SS and NH_3-N the dosage range were tested from 400mg/L until 1100 mg/L. Table 2 shows the optimum percentage removal of pollutants. Based on the result obtained, the optimum dosage for pollutants removal was 900 mg/L. This optimum dosage was successfully removing 13.9% of COD, 93.5% of colour, 90.3% of turbidity, 95.6% of SS and 9.7% of NH_3-N.

This result displayed high removal of efficiency of contaminants which conforming that stabilized leachates are rich with organic matters [9] such as humic substance (measured as COD intensity) and fulvic like fraction [7, 10]. The removal of substance can be explained by the charge neutralization mechanism in coagulation-flocculation process. Basically, the amount of coagulant added depends on the magnitude of electrical charge surrounding the colloidal particles (zeta potential) in samples. Since the charge of PAC (Al^{3+}) is positive, the negative charges of particles in leachate are neutralized by the addition of PAC during coagulation flocculation process [11]. Furthermore, as the landfill getting older, more organic matter with negatively charged particles exists in the leachate.

Table 2 PAC-leachate coagulation performance at selective coagulation

Parameter	Removal (%)	Supernatant concentration (mg/L)	Standard*
Chemical oxygen demand (COD)	13.9	720.0	400
Colour (Pt Co)	93.5	323.0	100 ADMI
Turbidity (NTU)	90.3	9.0	-
Suspended solids (SS)	95.6	8.2	50.0
Ammoniacal-nitrogen (NH_3-N)	9.7	2170.0	5.0

* Malaysian Environment Quality Regulations 2009

Figure 1 shows the effect of JSS dosage as coagulant aid on the removal of COD, colour, turbidity, SS and NH_3-N by using PAC (900 mg/L, pH 5) as coagulant in leachate treatment. The percentage removal of COD, colour, turbidity, SS and NH3-N the dosage range were tested from 500mg/L until 3000 mg/L. Table 3 shows the optimum percentage removal of JSS dosage as coagulant aid at optimum dosage of PAC (900 mg/L, pH 5). Based on the result obtained, the optimum dosage for pollutants removal was 500 mg/L for colour, turbidity and suspended solid removal. While the optimum dosage

COD and NH_3-N removal were 1000 mg/L and1500 mg/L respectively. This optimum dosage was successfully removing 31.6% of COD, 93.3% of colour, 92.3% of turbidity, 94.5% of SS and 13.1% of NH_3-N.

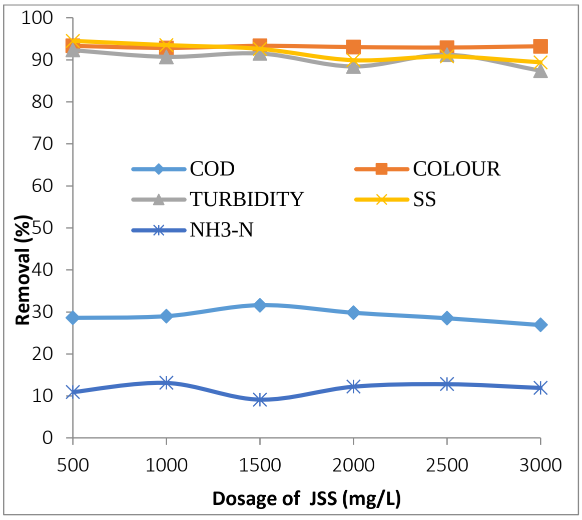

Fig. 1 Effect of JSS dosage as coagulant aid on the removal of COD, colour, turbidity, SS and NH_3-N by using PAC (900 mg/L, pH 5) as coagulant in leachate treatment.

The implementation of JSS as coagulant aid with PAC displayed improvement for the pollutants removal compared to PAC without JSS. The removal of COD turbidity, SS and NH_3-N has increased to 31.6%, 92.3%, 94.5% and 13.1 % respectively. The removal of substance can be explained by the bridging mechanism in coagulation-flocculation process. Basically, the flocculation process promoted the agglomeration of flocs with the polluted particles. The addition of JSS has increased the agglomeration within the flocs and the size of floc formation. The agglomerations of the flocs provide strong attraction to the suspended particles and increased the floc size for settlement. Thus the addition of JSS with PAC (900mg/L at pH 5) has improved removal of the pollutants.

Figure 2 shows the effect of PAC dosage as coagulant on the removal of COD, colour, turbidity, SS and NH_3-N at optimal dosage of JSS (500 mg/L) as coagulant aid leachate treatment. The percentage removal of COD, colour, turbidity, suspended solid and NH_3-N the dosage range were tested from 300mg/L until 1000 mg/L. Table 4 shows the optimum percentage removal of PAC dosage as at optimum dosage of JSS. Based on the result obtained, the optimum dosage for PAC was 600 mg/L for COD, color and NH_3-N removal. While the optimum dosage for turbidity and suspended solid removal was 500 mg/L. This optimum dosage was successfully removing 33.5% of COD, 93.6% of colour, 92.3% of turbidity, 94.5% SS and 14.1% NH_3-N.

Table 3 PAC- JSS leachate coagulation performance at selective coagulation.

Parameter	Removal (%)	Supernatant concentration (mg/L)	Standard*
Chemical oxygen demand (COD)	31.6	636.0	400
Colour (Pt Co)	93.3	335.0	100 ADMI
Turbidity (NTU)	92.3	10.3	-
Suspended solids (SS)	94.5	12	50.0
Ammonical-nitrogen (NH_3-N)	13.1	2780.0	5.0

* Malaysian Environment Quality Regulations 2009

The effect of optimal dosage of JSS as coagulant aid at optimal dosage PAC displayed good improvement for the pollutants removal. The removal of COD, colour and ammonical nitrogen has increased to 33.6%, 93.6%, and 13.1 % respectively. While the optimum dosage for turbidity and suspended solid removal were remain the same. This proved that the addition of JSS as coagulant as coagulant aid has succeeded to reduce 33.3% the usage amount of PAC in treatment process of landfill leachate.

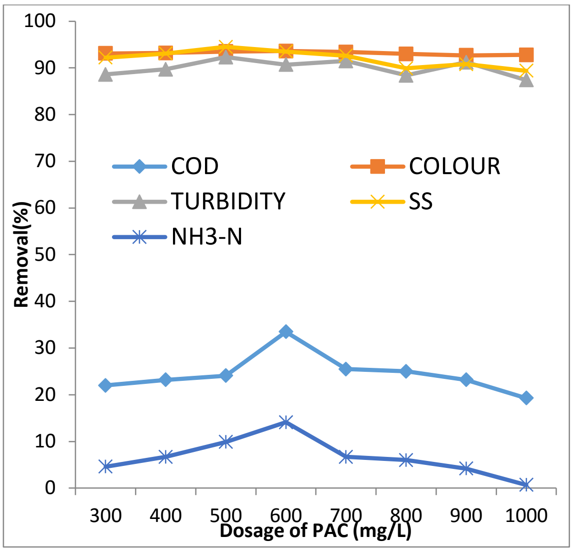

Fig. 2 Effect of PAC dosage as coagulant on the removal of COD, colour, turbidity, SS and NH_3-N by using JSS (500 mg/L) as coagulant aid in leachate treatment.

Table 4 The optimal dosage of PAC- JSS removal performance**.**

Parameter	Removal (%)	Supernatant concentration (mg/L)	Standard*
Chemical oxygen demand (COD)	33.5	580.0	400
Colour (Pt Co)	93.6	318.0	100 ADMI
Turbidity (NTU)	92.3	10.3	-
Suspended solids (SS)	94.5	12	50.0
Ammoniacal-nitrogen (NH_3-N)	14.1	2430.0	5.0

*Malaysian Environment Quality Regulations 2009

CONCLUSION

The performance of JSS with PAC coagulant was further optimized. The results shows the dosage optimization of PAC at optimal dosage of JSS was achieved 600mg/L. The addition of JSS has succeeded to reduce 33.3% the usage amount of PAC in treatment process of landfill leachate. Therefore, this study suggests that starch from the jackfruit seed has a potential to be used as coagulant aid in removing organic matter and ammonia present in the landfill leachate.

ACKNOWLEDGEMENTS

The writers would like to express their heartiest thanks to Universiti Sains Malaysia for the financial support funded under the RUI USM grant (1001/PAWAM/814166).

REFERENCES

[1] Clarke, B.O., Anumol, T., Barlaz, M., Snyder, S. A, “Investigating landfill leachate as a source of trace organic pollutants”. Chemosphere. Vol. 127, 2015, pp. 269–275.

[2] Liu, Z.P., Wu, W.H., Shi, P., Guo, J.S., Cheng, J. “Characterization of dissolved organic matter in landfill leachate during the combined treatment process of air stripping, Fenton, SBR and coagulation”. Waste Management. In Press. April 2015.

[3] Amor, C., Torres, S.E.D., José, A.P., Maldonado, M.I., Oller, I., Malato, S., Lucas, M.S. “Mature landfill leachate treatment by coagulation/flocculation combined with Fenton and solar photo-Fenton processes”. Journal of Hazardous Material. Vol 286, April 2015, pp.261-268.

[4] Tulyathan, V., Tananuwong, K., Songjinda, P., & Jaiboon, N. “Some physicochemical properties of jackfruit (Artocarpus heterophyllus Lam) seed flour and starch”. Science Asia, Vol 28, 2002, pp. 37-41

[5] Mukprasit, A., Sajjaanantakul, K. “Physico-chemical properties of flour and starch from jackfruit seeds (Artarpus heterophyllus Lam.) compared with modified starches”. International Journal of Food Science & Technology, Vol. 39, 2004, pp. 271-276.

[6] Bobbio, F. O., El-Dash, A. A., Bobbio, P. A., Rodrigues, L. R. (1978). Isolation an characterization of the physiochemical properties of the starch of jackfruit seeds (Artocarpus heterophyllus). Cereal Chemistry, Vol. 55, 1978, pp.505–511.

[7] Zainol N. A., Aziz H. A., and Yusoff M. S. “Characterization of Leachate from Kuala Sepetang and Kulim Landfills, A comparative Study” . Energy and Environment Research, Vol. 2, 2012, pp. 45.

[8] Aziz H. A., Alias S., Assari F., Adlan M. N. “The use of alum, ferric chloride and ferrous sulphate as coagulants in removing suspended solids, colour and COD from semi-aerobic landfill leachate at controlled pH”. Waste Management & Research, Vol. 25, 2007, pp. 556-565

[9] Tats, A. A., Zouboulis A. I., MAtis K. A., and Samaras P.“Coagulation-flocculatio pretreatment of sanitary landfill leachates”. Chemosphere, Vol. 53, 2003, pp. 737-744.

[10] Kulikowska D., and Klimiuk E. “The effect of landfill age on municipal leachate composition, Bioresource Technology”. Vol 99, 2008, pp. 5981-5985.

[11] Al-Hamadani Y. A. J., Yusoff M. S., and Umar M., Bashir M. J. K., and Adlan M. N."Application of psyllium husk as coagulant and coagulant aid in semi-aerobic landfill leachate treatment". Journal of Hazardous Materials, Vol.190, 2011,pp. 582-587.

Fifth International Conference on Geotechnique, Construction Materials and Environment, Osaka, Japan, Nov. 16-18, 2015, ISBN: 978-4-9905958-4-5 C3051

WATER QUALITY AND COMPOSITIONS OF THE PHYTOPLANKTON AND ZOOPLANKTON BEFORE AND AFTER BUILDING A BULKHEAD MAINTENANCE CONSTRUCTION IN LAKE FUKAMI-IKE, JAPAN

Hiromi Suda [1], Masaaki Tanaka [2] , Maki Oyagi [2], Megumi Nobori [1] and Akihiko Yagi [1]
[1] Faculty of Civil Engineering Department of Urban Environment, Aichi Institute of Technology, Japan;
[2] Faculty of Environmental and Information Sciences, Yokkaichi University, Japan

ABSTRACT

Lake Fukami-ike is a small monomictic and eutrophic lake, located in southern Nagano Prefecture in central Japan. Water quality improvement was expected from maintenance of farm village drainage and waterfront function was carried out for town activation in 1992. However, no blue-green algal bloom outbreak had occurred before. We studied the water quality and compositions of the zooplankton and phytoplankton before and after building a bulkhead maintenance construction.

Large decreased values for NO_3-N, NH_4-N and NO_2-N were 1.87→0.50 gNm^{-2} (26.7%), 1.49→0.78 gNm^{-2} (52.3%) and 0.085→0.030 gNm^{-2} (35.3%), respectively. *Aphanizomenon flos-aquae* (Cyanophyceae) were dominant in the summer; some species of the genus *Synedra* were dominant among phytoplankton during study periods. The dominant species of zooplankton during study periods were *Keratella cochlearis* (Rotatoria); smaller than *Cyclops vicinus* (Crustaceae) were dominant species of zooplankton before the construction.

Keywords: Building a Bulkhead maintenance construction, Water quality, Phytoplankton, Zooplankton

INTRODUCTION

Water pollution is worldwide problem, and control of river inflow that is the source of nitrogen and phosphorus is important for the water quality improvement [1]-[2].

Lake Fukami-ike is a small monomictic and eutrophic lake, located in southern Nagano Prefecture in central Japan. The studies in the lake were begun from 1978, and it is continuing now mainly about water quality roughly once a month.

Maintenance of farm village drainage and waterfront function and water quality expectations became better. However, although water color stays a dark green or brown, the transparency variation for 35 cm - 470 cm in the 1992 - 2010s was larger than that of 50 cm - 150 cm in the 1980s - 1992. Moreover, no blue-green algal bloom (*Microcystis aeruginosa*) outbreak had occurred before, and high chlorophyll-a concentration (357 μgL^{-1}) and low transparency (35 cm) was observed in June 2000.

We studied the water quality in the water column and compositions of zooplankton and phytoplankton before and after building a bulkhead maintenance construction.

METHODS

Study Area

Lake Fukami-ike is located in southern Nagano Prefecture in central Japan; north latitude 35°32′55″77, east longitude 137°81′93″56. The surface area of the lake is about 2.0 ha, with a maximum depth of 7.75 m, and volume 1.0×105 m^3 and with a small diameter: 150 m, 300 m. (Fig. 1 and Fig. 2) [3].

The lake is eutrophic lake because of having 12 units considering inflow nutrients from surrounding paddy fields. The maximum depth was reported 9.3 m in 1951 [4], 8.1 m in 1993 [5], and 7.75 m in recently [3].

The lake has five inflow rivers and the lake water exits from an outflow river. These rivers receive the runoff sewage water from around houses.The lake water is not dry up because there is a lot of spring water which become a source of inflow water having less than 30 cm wide.

Circulation periods were in November to March, and stagnation periods were in April to October; the dissolved oxygen concentration was zero in about the 4 m to 5 m deeper layer in mid-summer [6].

Water plants (such as *Phragmites australis*; Poales, *Typha latifolia*; Typhales) live around the lakeshore. Local residents mow these weeds on a regular basis.

Lake Fukami-ike has been described in previous studies about manganese, purple nonsulphur bacteria, microbial sulfur cycling, dial vertical migration of *Chaoborus flavicans* (Diptera) [3],[7]-[9]. It is interesting to note that the chlorophyll-a amount in the winter was higher than that of summer caused the interruption of upward nutrient transportation from the tropholytic layer due to distinct stagnation of water and the consumption of nutrients by photosynthetic sulfur bacteria (as bacteriochlorophyll-c) growing near the top of the anoxic layer in summer [10].

Chlorophyceae (classes of green algae) reached a rich "Vegetationstrübung" condition, and no water bloom occurred in the lake [11].

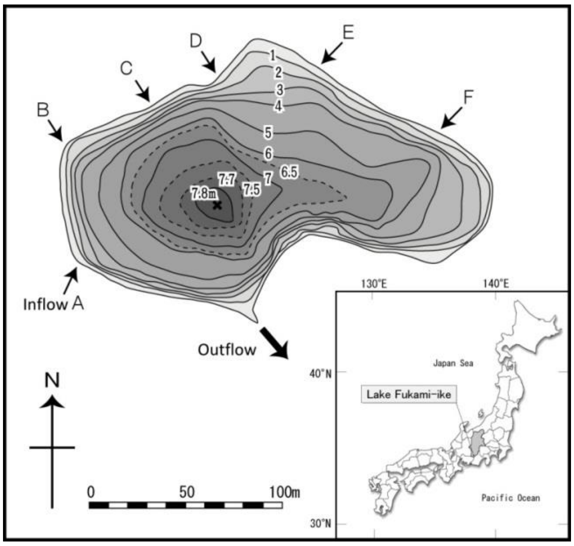

Fig. 1 Bathymetrical map of Lake Fukami-ike.

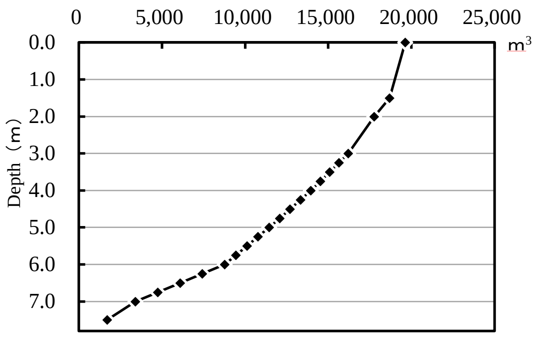

Fig. 2 Stratified volume amount of Lake Fukami-ike.

Sampling and analysis

Lake water samples were collected at the deepest point with a hand-operation water pump connected to a polyvinylchloride tube from every 0.25 m depth during the period of water stratification from April to October or from every 50 cm - 1 m depth in other months.

Part of the water samples was filtered through a glass fiber filter (Whatman, GF/F, 47 mm) immediately after the sampling. The samples were stored at -20 ℃ until chemical analysis in the laboratory.

The filtrate was used for the determination of inorganic nitrogen (NO_3-N, NH_4-N and NO_2-N) were measured by ion chromatography analysis (DKK-TOA CORPORATION, PCI-311S).

Total phosphorus and total dissolved phosphorus were measured by the molybdenum blue colorimetric method [12].

Chlorophyll-a was measured by the fluorometric method [13].

Water temperature was measured with a thermistor thermometer, and dissolved oxygen was determined with a DO meter (HORIBA DO Meter OM-12).

Plankton samples were taken with a Van Dorn water sampler (10L, Rigo Co., Ltd., Tokyo Japan) every 1 m from the upper to bottom layer. All samples were preserved in 1% formalin in the field immediately, then counted and identified using an optical microscope (BX51, OLYMPUS Optical Co., Ltd., Tokyo, Japan) in the laboratory.

RESULTS AND DISCUSSION

Inflow and Outflow rivers

The interannual variability of the inflow rate data were shown in Table 1. Before building the bulkhead maintenance, inflow data were 4 LS^{-1} in 1973, 9.9 LS^{-1} in 1979, 5.7 LS^{-1} in 1980. However, 0.52 LS^{-1} and 0.62 LS^{-1} in 2008 were measured after, the mean values were dramatically decreased from 6.5 LS^{-1} to 0.57 LS^{-1}.

Table 1 Mean abundance of flow rates in inflow and outflow rivers

maintenance construction	Observation day	Inflow (LS^{-1})	Outflow (LS^{-1})
Before	Nov 2, 1973	4	14.4
	Sep 15, 1979	9.9	19.5
	Feb 15, 1980	5.7	7.7
	Means (LS^{-1})	6.5	13.8
After	Feb 15, 2008	0.52	0.68
	Oct 22, 2008	0.62	0.46
	Means (LS^{-1})	0.57	0.57

Outflow data 14.4 LS^{-1} in 1973, 19.5 LS^{-1} in 1979 and 7.7 LS^{-1} in 1980, 0.68 LS^{-1} and 0.46 LS^{-1} in 2008. Mean values were 13.8 LS^{-1} before construction, and 0.57 LS^{-1} after. Because the inflow river course had a bypass to avoid the lake for the bulkhead construction in 1992, inflow and outflow dramatically decreased one-twentieth and one twenty-fourth respectively.

Nutrients

Nitrogen

Seasonal depth-time diagram distribution of inorganic nitrogen from 1978 to 1980 and 1999 to 2000 was shown in Fig. 3 (NO_3-N), Fig. 4 (NO_2-N) and Fig. 5 (NH_4-N).

All inorganic nitrogen (NO_3-N, NH_4-N and NO_2-N) concentrations in the lake were decreased after maintenance construction than before it; in particular, NO_3-N concentrations from 0 m to 3 m in the epilimnion were much decreased.

The interannual mean values of NO_3-N, NH_4-N and NO_2-N in the water column before (1979-1992) and after (1992-2013) for NO_3-N, NH_4-N and NO_2-N were 1.87 → 0.50 gNm^{-2} (26.7 %), 1.49 → 0.78 gNm^{-2} (52.3 %) and 0.085 → 0.030 gNm^{-2} (35.3 %), respectively. In particular, NO_3-N value decreased one fourth before the maintenance construction. Because inflows contain from paddy fields and orchards (allochthonous inorganic matter) stop to significantly reduce, NO_3-N value decrease largely after the construction.

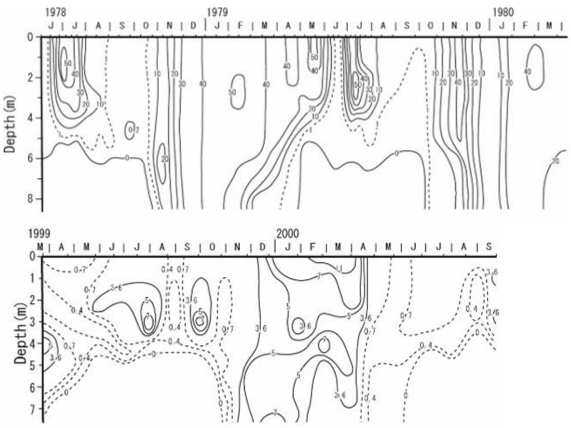

Fig. 3 Depth-time diagram distribution of NO_2-N (μg at. N l^{-1}) concentrations in 1978-1980 (above) and 1999-2000 (below). (Modified from [14].)

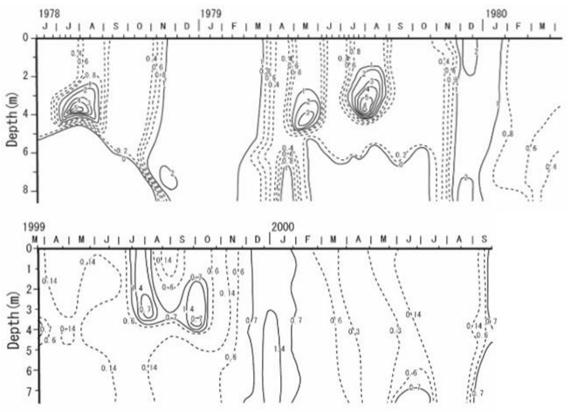

Fig. 4 Depth-time diagram distribution of NO_3-N (μg at. N l^{-1}) concentrations in 1978-1980 (above) and 1999-2000 (below). (Modified from [14])

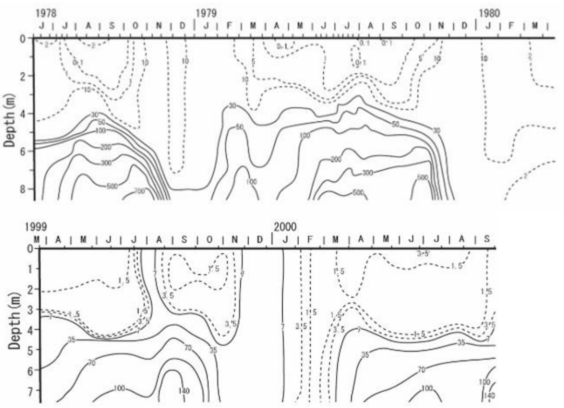

Fig. 5 Depth-time diagram distribution of NH_4-N (μg at. N l^{-1}) concentrations in 1978-1980 (above) and 1999-2000 (below). (Modified from [14])

Phosphorus

The mean total phosphorus (TP) amounts in the lake before the construction (1979-1992) and after (1992-2013) were shown in Fig. 6.

TP in the oxic layer increased about 1.2 times from 0.95 gPm^{-2} (before) to 1.12 gPm^{-2} (after), and particulate organic phosphorus amounts were decreased from 0.28 gPm^{-2} (before) to 0.19 gPm^{-2} (after), respectively.

On the other hand, the mean TP amounts in the anoxic layer were almost equal to 1.84 gPm^{-2} (before) and 1.80 gPm^{-2} (after), and particulate organic phosphorus (POP) amounts were increased from 0.09 gPm^{-2} (before) to 0.45 gPm^{-2} (after). The POP amounts in the anoxic layer increased 5-fold because it was associated with the increase of photosynthesis sulphur bacteria.

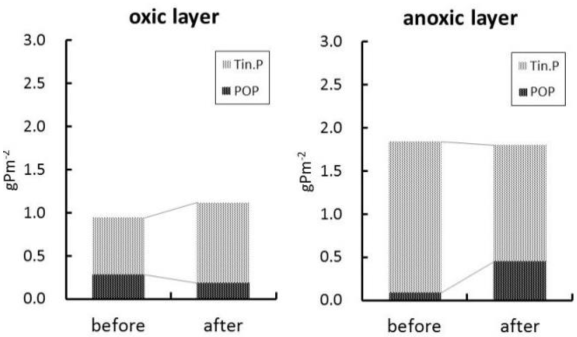

Fig. 6 Mean amount of total phosphorus in the oxic and anoxic layer of the water column before and after maintenance construction.

Chlorophyll-a

Monthly mean chlorophyll-a amounts in the oxic layer in the lake before (1979-1992) and after (1992-2013). The values from April to November (stagnation periods) were 167.6 mg m^{-3} (maximum 321.5 mgm^{-3}, minimum 50.1 mgm^{-3}) before construction and 188.5 mg m^{-3} (max 378.0 mgm^{-3}, minimum 50.1 mgm^{-3}) after it.

The values from December to March (circulation periods) were 353.3 mg m^{-3} (maximum 642.9 mgm^{-3}, minimum 179.6 mgm^{-3}) before construction and 557.1 mgm^{-3} (maximum 730.1 mgm^{-3}, minimum 246.0 mgm^{-3}) after it. The values in the circulation periods after the construction were slightly higher before. The tendency the for values to be low in the stagnation period and high in the circulation period was the same before and after the maintenance construction.

Plankton

Phytoplankton

Seasonal changes in the abundance of phytoplankton found from April 2013 to March 2014 were shown in Fig. 7.

Bacillariophyceae were dominant from April to May, and from the beginning November to March. Chlorophyceae were dominant from spring to summer, and Cyanophyceae were dominant in July.

Aphanizomenon flos-aquae (Cyanophyceae) were dominant in July. Bacillariophyceae were included *Fragilaria construens* and *F. crotonensis*, *Synedra rumpen*s and some species of the *Synedra*. Chlorophyceae were included *Gleocystis* sp., *Oocystis* sp. and *Crucigenia tetrapedia*.

The phytoplankton found in Lake Fukami-ike was previously reported [4],[15]-[16]. The dominant species of seasonal changes was reportedly, *Synedra acus* from middle of March to the middle of September, and *Aulacoseira ambigua* (Bacillariophyceae) from the end of September to the beginning of March, and others (Chlorophyceae and Bacillariophyceae) were found in 1978-1979 [16].

Chlorophyll-a amounts in the lake before and after the building construction did not change greatly previously; chlorophyll-a contents (phytoplankton) showed little change.

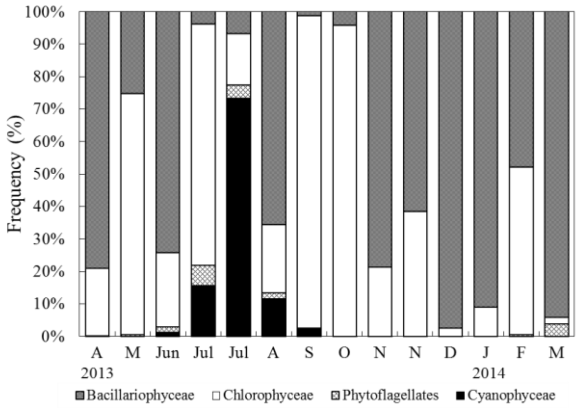

Fig. 7 Seasonal changes in the abundance of phytoplankton group found.

Zooplankton

Seasonal changes in the abundance of zooplankton found from April 2013 to March 2014 were shown in Fig. 8.

Rotatoria were dominant from April to May, from the beginning of July to the beginning of November, in January and March. Protozoa were dominant in June, and from the end of November to December, and February. As for the dominant Protozoa the end of November, the upwelling water from the bottom layer included Protozoa carried up from all layers, because observations were conducted and zooplankton were collected just at the beginning of circulation periods.

About *Keratella cochlearis* (Rotatoria) became dominant from April to May, followed by *Trichocerca similis* and *Keratella cochlearis* var. *tecta* (Rotatoria) in summer, *Tintinnopsis lacustris* (Protozoa) in autumn, and *Filinia longiseta* (Rotatoria) in winter. Crustaceae were found Nauplius of Cyclops in the beginning of July, *Bosmina longirostris* were found in January.

In 1978-1979, the dominant species were *Cyclops vicinus* in the beginning October to the middle of February. *Bosmina longirostris* (Cladocera), *Mesocyclops Leuckarti* (Cyclopoida), and *Filinia longiseta* (Rotatoria) were found [16]. However, in 2013-2014, a few Crustaceae, larger than Rotatoria, were found.

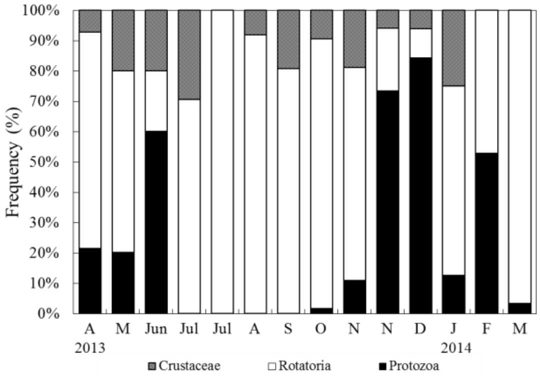

Fig. 8 Seasonal changes in the abundance of zooplankton group found.

CONCLUSION

NO_3-N amounts were largely reduced after the construction, this results suggested that the inflow water from paddy fields and orchards has stopped by the construction. However, Chlorophyll-a amounts not changed before and after the construction. Phytoplankton it believed to using nitrogen (ammonium and phosphorus) which have accumulated in the bottom. Water quality is not improved even stop the inflow of nutrients because the nutrients have already accumulated in the bottom [17].

Recently, Cyanophyceae has dominant in early-midsummer, it seems that chlorophyll-a contents (phytoplankton species) only changed before and after the construction. One should consider the possibly that Cyanophyceae can make advantage the competition for nutrients (NO_3-N) to be used for growth [18].

Rotatoria were dominant recently because that they were released from predation pressure of large size (Cyclopoida). Fish predation has emphasized as a factor to determine the species composition of the zooplankton community [19]. These problem need more investigation and is still open to discuss. We found that there is significant difference for long-term changes of plankton in the Lake Fukami-ike.

ACKNOWLEDGEMENTS

We are grateful to the Anan-cho authorities in Shimoina-gun, Nagano Prefecture, who generously provided research facilities. We especially thank Sohey Hane and Seiya Kato for their help in the field.

REFERENCES

[1] Schwoerbel J., "Materials budget of natural waters", I, Handbook of Limnology, John Wiley & Songs, 7, 1978, pp.67-94.

[2] Wetzel, R. G., "Lake and River Ecology", Limnology, 3th ed., Academic Press, Tokyo., 2001, pp.298-301.

[3] Yagi A, "Biological manganese cycle in the oxic and anoxic layers of Lake Fukami-ike", Limnology in Tokai Region of Japan, Vol.43, 2010, pp.51-60.

[4] Ueno M, "Lake Fukami-ike in Shimoinagun, Nagano Prefecture", Iida, An educational association of Shimoinagun (in Japanese), 1952, pp.120.

[5] Yagi A, Miyachi S and Shimodaira I, "Change in depth by sedimentation of Autochonous organic substances in eutrophic lake", Journal of Nagoya Women's university, Home Economics・Natural Science, No.39, 1993, pp.77-82.

[6] Yagi A, Funahashi J, Nishio N, and Umemura M, "Seasonal changes of methane and organic acid in Lake Fukami-ike", Verh. Internat. Verein. Limnol., Vol.30, 2009, pp.878-883.

[7] Yagi A, Miyachi S and Terai H, "Vertical distribution of purple nonsulphur bacteria and their utilization of dissolved organic carbon in Lake Fukami-ike" Archiv für Hydrobiologie, 1991, 121: pp.307-317.

[8] Nakagawa M, Ueno Y, Hattori S, Umemura M, Yagi A, Terai K, Koba K, Sasaki Y, Makabe A and Yoshida N, "Seasonal change in microbial sulfur cycling in monomictic Lake Fukami-ike, Japan", Limnology and Oceanography. Vol.57, No.4, 2012, pp.974-988.

[9] Nagano M, Yagi A, Yoshida T, "Seasonal pattern and induction cues of dial vertical migration of *Chaoborus flavicans* in Lake Fukami-ike, Nagano, Japan" Springer., Ecological Research, 2014, pp.145-152.

[10] Yagi A, Shimodaira I, Terai H and Saijo Y, "Seasonal Change of Chlorophyll-a and Bacteriochlorophyll-c in Lake Fukami-ike" Jpn. J. Limnol., Vol. 44, 1983, pp.283-292.

[11] Tanaka M, "The current state of the eutrophication of Japan lakes and marshes judged from plankton lakes (in Japanese) [Translated from Japanese]", Water, Vol.23, No.9, 1981, pp.90-95.

[12] Murphy J, J.P. Riley, "A modified single solution method for the determination of phosphate in natural waters", Analytica Chimica Acta, Vol.27, 1962, p.36.

[13] Holm-Hansen O., et al., "Fluorometric determination of Chlorophyll", J. of Cons. perm. int. Explor. Mer, Vol. 30, pp.3-15.

[14] Limnology of committee of Shimoina kyoiku-kai, "Shimoina-shi", Shimoina Editorial Committee of Shimoina-shi edited, (in Japanese) [Translated from Japanese], 2009, pp.338-339.

[15] Tanaka M, "11-18. Lake Fukami-ike", The lakes in Japan (in Japanese), 1th ed. Nagoya, The University of Nagoya Press., 1992, pp.417-421.

[16] Sakurai Y, Watanabe Y, "Lake Fukami-ike", Limnology of Shinshu, 1, 1974, pp.117-128.

[17] Japan Society On Water Pollution Res,. edited, marsh environment survey guideline (in Japanese), pollution control technique association of corporate executives, 1982, pp.153-166

[18] Horne Alexander J. and Goldman Charles R., "Phytoplankton and periphyton", "Limnology", Kyoto, Kyoto University Press., 2th ed., 1999, pp.243-275.

[19] Benndorf, J., "Possibility and limits for controlling eutrophication by biomanipulation", International Revue gesamten, Hydrobiologie, 1995, Vol.80, pp.519-534.

NEW MICROBIAL-FUNCTION-BASED REINFORCEMENT METHOD FOR SLOPES

Toshiro HATA[1], Kazuhiro KANEDA[2] and Tomohiro TANIKAWA[3]
[1]Faculty of Engineering, Toyama Prefectural University, JAPAN;
[2,3] Takenaka Research & Development Institute, JAPAN

ABSTRACT

In recent years, erosion control has been increasingly implemented for the land slopes of public roadways (e.g., express highways). The development of an easy-to-use maintenance method for such slopes based on a natural process is an important subject in geo-environmental engineering. The aim of this research is to develop an eco-friendly maintenance method for land-slope management that is low cost and protects the natural eco-system. In this paper, the general concept of the newly proposed method tested in the laboratory and the results of a numerical simulation are presented. The most important advantage of this technique is the enhancement of urease activity in the in-situ microorganism community. Normally, this technique requires a two- to three-month cultivation term prior to the maintenance work. During the construction phase, only spraying of the microbial culture medium and solidification substance mixture is carried out. The results of the numerical simulation demonstrate the slope control achieved because of the reinforcement effect of the proposed method.

Keywords: Erosion control, Microbial function, Urease activity

INTRODUCTION

In Japan, the maintenance cost of infrastructure facilities has been increasing. In addition, the amount of carbon dioxide emissions from construction and maintenance activities has been increasing in recent years. Therefore, low-cost eco-friendly maintenance techniques need to be developed in the near future. Urea is a very popular agricultural material used for supplying nutrients from soil to plants. In this study, we developed a slope maintenance method that uses in-situ urease-producing bacteria. These bacteria live in normal soil (pH = around 7 and electrical conductivity = 0.6 mS/cm). The advantage of the proposed technique is that it is eco-friendly and low cost.

Soil whose strength is enhanced by using microbial functions is called "Bio-Soil." In past research, specific bacteria isolated from Yagaji island in Okinawa were found to enhance soil strength to up to 2 MPa after cultivation for 2 months [1]. In another study, potato extract solution was injected into the soil column to control the soil permeability; that is, an in-situ leakage repair method that uses in-situ microorganism activity was employed [2]. The present paper describes the experimental results of the analysis of Bio-Soil's physical properties and the effect of the soil on slope stability based on numerical simulations.

OVERVIEW OF THE PROPOSED METHOD

In this research, we developed a new eco-friendly maintenance method to increase the surface soil strength based on a microbial function (hydrolysis of urea). The mechanism of hydrolysis of urea and the precipitation of calcite are represented by equations (1), (2), and (3).

(Hydrolysis of urea)

$$CO(NH_2)_2 + 2H_2O \rightarrow 2NH^+_4 + CO^{2-}_3 \;\; pH\,(\uparrow) \qquad (1)$$

(Precipitation of calcite (calcium carbonate))

$$CO_2 + H_2O \rightarrow HCO^-_3 + H^+ \qquad (2)$$

$$HCO^-_3 + Ca^{2+} + OH^- \rightarrow CaCO_3\,(\downarrow) + H_2O \qquad (3)$$

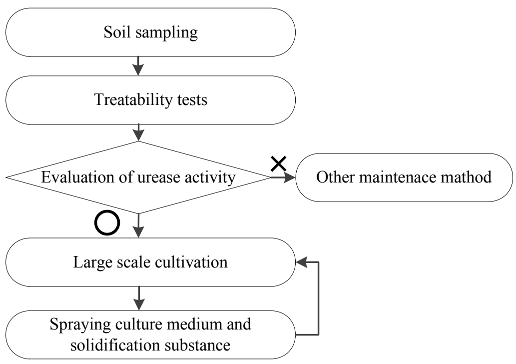

Fig. 1 Process of the maintenance method

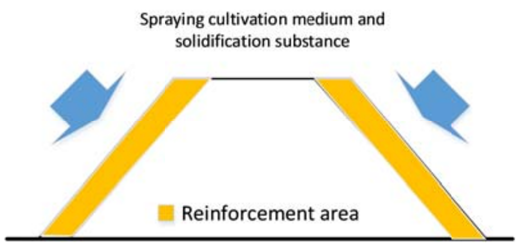

Fig. 2 Schematic diagram of the maintenance work

These reactions require urea, a calcium source (calcium chloride, calcium nitrate, etc.), and urease-producing bacteria [2], [3]. In this study, we selected a specific microorganism named *Bacillus pasteurii*, which has high urease activity and salt tolerance [4]. The process of the proposed eco-friendly maintenance method is shown in Fig. 1, and a schematic diagram of the remediation system is shown in Fig. 2. Before initiating this type of maintenance work, treatability tests were performed using in-situ soil microorganisms. Then, another treatability test was performed in a laboratory to evaluate the urease activity with various combinations of nutrients and calcium sources. A combination of nutrients and a calcium source was selected according to the treatability test, and this combination was sprayed on the surface soil to accelerate the reinforcement activities of microorganisms. During the maintenance work, microbial monitoring was also carried out to ensure that the conditions were optimal for the entire microbial community in general and for the microorganisms in particular.

LABORATORY TESTS

Material and methods

The soil used in the experiments was Toyoura sand. Aerobic urease-producing alkaliphilic bacteria named *Bacillus pasteurii* (ATCC11859) were used as the microorganisms in this study. Calcite precipitation was carried out using the following procedure. The bacterial culture medium was infiltrated with a solidification medium. The soil columns were immersed in a solution with 1 L of the solidification medium containing 0.30 M $CaCl_2$ and urea thrice per 24 h. The soil columns were then removed from the solution for one day before being used for strength testing. Cyclic triaxial tests and consolidated-drained (CD) triaxial compression tests were performed using a compression machine to test the physical properties of microbial carbonate precipitation (MCP) sand and the liquefaction strength. After the strength tests, the $CaCO_3$ weight was measured as follows: (1) After oven drying (110°C, 24 h), the weight of the soil samples was measured. (2) The soil samples were washed with 1 N HCl twice or thrice to dissolve precipitated carbonates. (3) The soil samples were rinsed with ion exchange water, drained, and oven dried (110°C, 24 h). (4) The weight of the rinsed soil samples was measured. Three samples each were prepared for MCP sand and control sand.

Results

The physical properties of the sand samples are listed in Table 1. The dry density of the two sand types was measured to be 1.364 and 1.472 g/cm^3. The experimental results showed that MCP-treated sand increased the dry density of Toyoura sand. That is, the precipitation of calcite in the sand pore increased the soil density. The same results were obtained when the cohesion (C) value of the MCP-treated sand was used. However, the internal friction angle (φ) remained constant after the MCP process. These results suggested that the increase in the sand strength increased the C value, similar to what happens in the case of cement-treated soil. The results of the CD triaxial compression tests (confining pressure of 100 kPa) are shown in Fig. 3. The use of the MCP-treated sand increased the peak strength by approximately 20%.

Table 1 Physical properties of sand sample

Item	ρ_d (g/cm^3)	C (kN/m^2)	φ (°)
Toyoura sand (control)	1.364	3.3	36.5
MCP sand	1.472	11.9	36.9

The cyclic axial load of a sinusoidal wave with a frequency of 0.1 Hz was applied to the soil. The cell pressure and water pore pressure were measured. Table 2 shows the comparison of the results for MCP-treated soil and untreated soil. The results showed the MCP-treated soil had higher E_0 and G_0 values than the untreated (control) sand.

NUMERICAL SIMULATIONS

Outline of numerical simulations

Figure 4 shows the numerical mesh and boundary conditions. The side and bottom of the ground were adopted as the repeated boundary and viscosity boundary, respectively. The embankment was 3.0 m in height, 16 m in width, and 4.0 m in width at the crest. First, self-gravity analysis was performed for both the ground and embankment. Then, dynamic

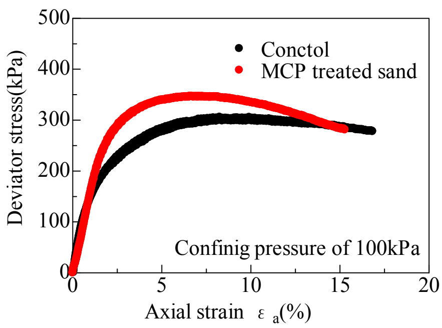

Fig. 3 Process of the maintenance method

Table 2 Results of cyclic triaxial cell tests

	E_0 (MN/m^2)	ε_r (%)	G_0 (MN/m^2)	γ_r (%)
MCP sand	435.5	1.84E-02	145.4	2.76E-02
Untreated sand	106.0	5.43E-02	35.4	8.14E-02

analysis was performed. Table 3 lists the material constants. Figure 5 shows the initial Vs, shear stiffness, yield stress, and reference strain after the self-gravity analysis at the area with no embankment. Assuming Vs = 150 m/s at the ground surface, the shear stiffness G is calculated from equation (1). The yield stress and reference strain are calculated from equations (2) and (3). The strength of the ground is given by the cohesion c = 50 kPa and friction angle φ = 40° (Table 3).

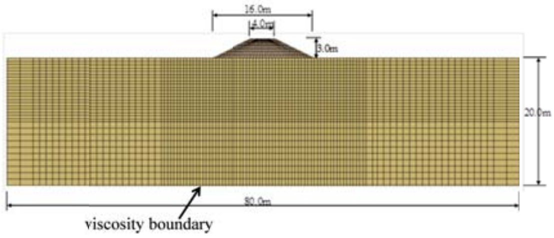

Fig. 4 Analysis mesh

$$G_0 = G_{ref}\left(\frac{\sigma'_{m0}}{\sigma_{ref}}\right)^n \quad (1)$$

where G_{ref} : initial shear stiffness for the test

σ_{ref} : initial constraint stress for the test

σ'_{m0} : mean effective stress at each element

n: material constant ($n = 0.5$)

$$\tau_y = \sigma'_m \sin\phi + c\cos\phi \quad (2)$$

$$\gamma_r = \frac{\tau_y}{G_0} = \frac{\sigma'_m \sin\phi + c\cos\phi}{G_{ref}\left(\frac{\sigma'_m}{\sigma_{ref}}\right)^n} \quad (3)$$

where c: cohesion

φ: friction angle

The dynamic deformation characteristic (G/G_0) and damping ratio h are calculated from equations (4) and (5). For the ground, h_{max} is assumed to be 20.0%.

$$\frac{G}{G_0} = \frac{1}{1+\frac{\gamma}{\gamma_r}} \quad (4)$$

$$h = h_{max}\left(1-\frac{G}{G_0}\right) \quad (5)$$

Figure 6 shows the G/G_0,h~γ curve obtained using experimental data at the embankment for both treated and untreated soil at a constraint pressure of 50 kPa.

Figure 7 shows the embankment area with treated and untreated soil. The surface of the embankment is treated with urease.

Table 3 Material constants

Self-gravity analysis

	ρ (t/m3)	G_{ref} (kPa)	σ_{ref} (kPa)	ν	c (kPa)	φ
Embankment	1.95	70800	200	0.49	3.3	36.5
Ground	1.8	304934	500	0.49	50	40

Dynamic analysis

	ρ (t/m3)	G_{ref} (kPa)	σ_{ref} (kPa)	ν	c (kPa)	φ	α	β
Embankment	1.95	70800	200	0.3	3.3	36.5	0.595	0.000614
Treated-embankment	1.94	292000	200	0.3	11.9	36.5	0.595	0.000614
Ground	1.8	304934	500	0.3	50	40	0.595	0.000614

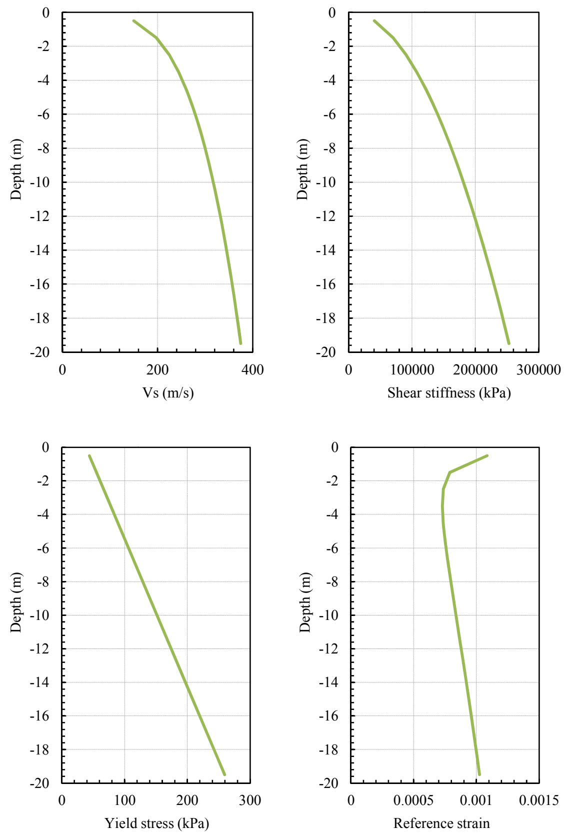

Fig. 5 Initial states after self-gravity analysis

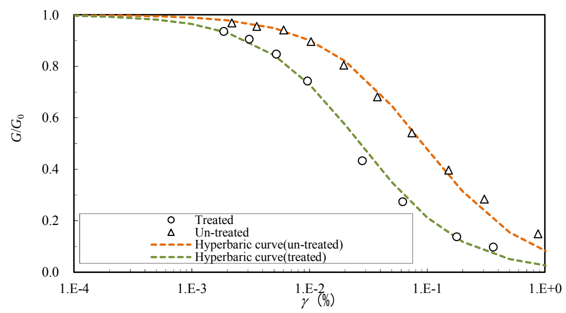

Fig. 6 $G/G0$,h~γ curves

The change in input acceleration is shown in Fig. 8. The maximum acceleration is 7.95 m/s, and the time duration is 50 s. The earthquake wave is applied to the bottom as 2E.

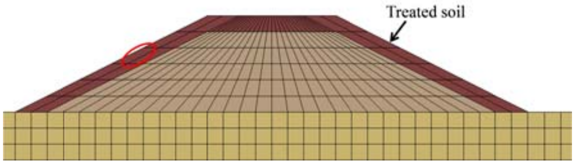

Fig. 7 Treated and untreated soil at the embankment

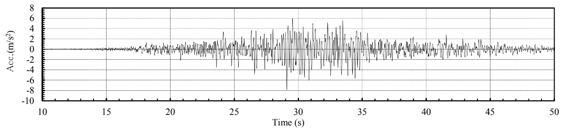

Fig. 8 Changes in input acceleration

Numerical results

Figure 9 shows the distribution of the equivalent strain at 50.0 s. In the untreated case, failure is observed at the top of the embankment. On the other hand, in the treated case, no failure is observed even when the input maximum acceleration is approximately 8.0 m/s.

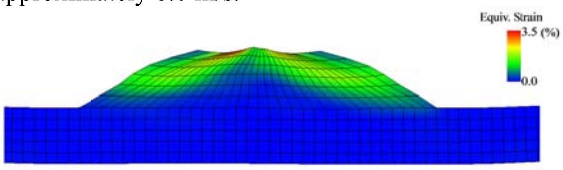

Untreated case

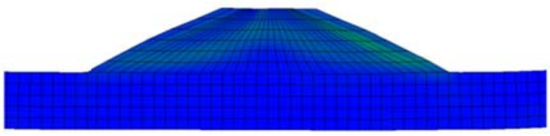

Treated case

Fig. 9 Distribution of equivalent strain (50 s)

Figure 10 shows the time history of the settlement at the top of the embankment. One can see that the settlement of treated soil is smaller than that of the untreated soil. Figure 11 shows the time history of the shear strain of the element circled in red in Fig. 8. In the treated case, for high shear stiffness, the shear strain is smaller than that in the untreated case. One can see that the surface treatment of the embankment by urease is effective for suppressing shear strains caused by an earthquake.

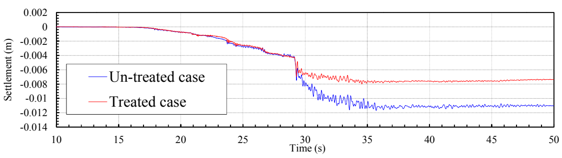

Fig. 10 Time history of settlement

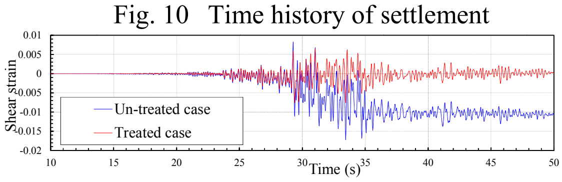

Fig. 11 Time history of shear strain

CONCLUSION

In this study, laboratory tests and numerical simulations were performed to study a new microbial-function-based reinforcement method for slopes. The main conclusions of this study are as follows:

1) The MCP method can improve the physical properties of Toyoura sand.
2) MCP-treated Toyora sand increases the peak strength by approximately 20% based on the production of calcite in the sand pore.
3) MCP can increase the cohesion value of Toyoura sand.
4) The MCP treatment of the surface of the embankment can increase the surface soil strength and change the no-failure condition for an earthquake.

In this research, we performed laboratory tests and two types of numerical simulation. Some of our results show that the surface soil properties are improved. However, the application of specific microorganisms (such as *Bacillus pasteurii*) to actual sites is difficult. Furthermore, the in-situ urease-producing activity of the bacteria should be enhanced by controlling the physical and chemical properties of the soil.

ACKNOWLEDGEMENTS

This research was partially supported by a Japan Society for the Promotion of Science (JSPS) Grant-in Aid for Scientific Research (B) and Center for Revitalization Promotion of the Japan Science and Technology Agency for providing funds

REFERENCES

[1] T.Danjo and S.Kawasaki, "Formation mechanisms of beachrocks in Okinawa and Ishikawa, Japan, with a focus on cements"< Materials and Transactions, Vol.55, No.3, 2014, pp.493-500.

[2] Guo HX,Cheng XH and Li.M,"Experimental analysis of bio-stimulated sealing process in environmental getotechnical engineering", Science China Technological Sciences,Vol.56, No.3,2013. pp.732-738.

[3] Fujita Y. et al, "Stimulation of microbial urea hydrolysis in groundwater to enhance calcite precipitation", Environmental Science Technology Journal, Vol.42, No.8, 2008, pp. 3025-3032.

[4] Victoria S.W, Leon A.V.P and Marien P.H," Microbial Carbonate Precipitation as a Soil Improvement Technique", Geomicrobiology Journal,No.24,2007, pp.417-423.

[5] Keri L.B et al," Urease activity in microbiologically- induced calcite precipitation, Journal of Biotechnology, Vol.93, 2002, pp.171-181.

Fifth International Conference on Geotechnique, Construction Materials and Environment, Osaka, Japan, Nov. 16-18, 2015, ISBN: 978-4-9905958-4-5 C3051

ANALYSIS OF EVACUATION BEHAVIORS IN DIFFERENT AREAS BEFORE AND AFTER THE GREAT EAST JAPAN EARTHQUAKE

Tetsuo Morita[1], Shinya Tsukada[2] and Akira Yuzawa[3]
[1] Graduate School of Engineering, Tohoku Institute of Technology, Japan; [2] Maebashi City, Japan,
[3] Graduate School of Engineering, Maebashi Institute of Technology, Japan

ABSTRACT

This study aims to obtain the insights necessary for future disaster prevention planning and management in Japan. To this end, a questionnaire survey on evacuation behaviors was administered to the residents of Yamada-machi in Iwate Prefecture and Ishinomaki-shi in Miyagi Prefecture, which had been stricken by the Great East Japan Earthquake. The obtained data were analyzed on the basis of the regional differences in said behaviors. The analytical results are summarized as follows. (1) Prevention measures, such as earthquake drills and occasional discussions regarding earthquakes, tended to be implemented in areas facing the Rias coast before the Great Earthquake occurred. (2) The interval between the occurrence of the earthquake and the initiation of evacuation was shorter in the regions fronting the Rias coast and in those located along a coastline than in areas situated on a plain and along a river. (3) Residents of the regions facing the Rias coast and the areas located along a river tended to evacuate by foot, whereas people living in other areas favored evacuation by automobile.

Keywords: Great East Japan Earthquake, evacuation behavior, Yamada-machi, Ishinomaki-shi

INTRODUCTION

Purpose of the study

The Great East Japan Earthquake (hereinafter referred to as the Great Earthquake) that occurred on March 11, 2011 severely damaged East Japan. The epicenter of seismic activity was located in Tohoku district and resulted in a casualty of approximately 20,000 people. Given the necessity for safety and prevention arising from the disaster, this study aims to acquire the information essential for future disaster prevention planning and management in the country. To achieve this goal, a questionnaire survey on evacuation behaviors was administered to the residents of Yamada-machi in Iwate Prefecture and Ishinomaki-shi in Miyagi Prefecture, which had been seriously stricken by the Great Earthquake. The obtained data were analyzed on the basis of the regional differences in evacuation behavior.

Overview of the study

Research on the Great Earthquake has only recently been initiated, with several researchers comprehensively examining the evacuation behaviors of residents in disaster-stricken areas [1]-[5]. In addition, the study on simulation of the evacuation behaviors is pushed forward [6]-[7]. Previous studies focused on specific areas, but the current research deviates from the typical approach by dividing the regions of interest into four areas according to distance from a coast or a river and accordingly analyzing the dissimilarities in evacuation behaviors across the different areas. In this study, we use basic analysis technique without simulating the evacuation behaviors.

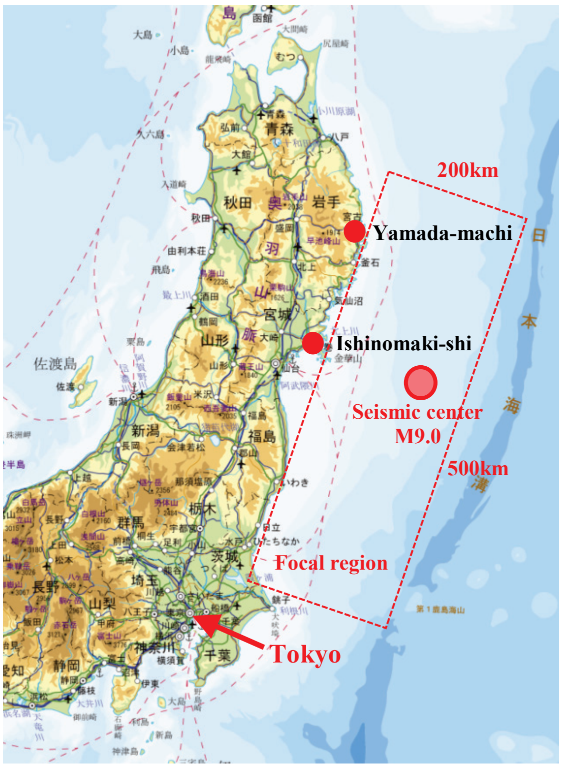

Source: Geospatial Information Authority of Japan

Fig. 1 Study regions

STUDY REGIONS AND SURVEY METHODS

Study regions

As previously stated, the study sites chosen for this research are Yamada-machi located in Iwate Prefecture and Ishinomaki-shi situated in Miyagi Prefecture (Fig. 1). These two regions were chosen because (1) they differ in terms of geographical characteristics but (2) are similar with regard to tsunami height witnessed in the regions and building damage ratio. The locations were therefore deemed suitable for the analysis of variances in evacuation behaviors across different areas.

The study regions experienced several times of great earthquakes in the past: 1896(Meiji Sanriku earthquake), 1933(Showa Sanriku earthquake) et al. In these earthquakes, the East Japan great earthquake disaster brought the heaviest damage.

Fig. 2 shows the tsunami inundation ranges of the two regions. The ratios of tsunami inundation area to inhabitable land in Yamada-machi and Ishinomaki-shi were 19.2% and 30.1%, respectively. The number of casualties in the former was 825 (4.3% of the total population) and that in the latter was 3,957 (2.5% of the total population).

Table 1 and Fig. 3 show the situation of the damage of the study regions.

Table 1 Damage of the study regions

	Yamada-machi	Ishinomaki-shi	
Population	19,270	160,826	2001, Before earthquake
Household	7,192	57,871	
Area	263 km^2	556 km^2	
Geographical features	Rias coast	Plains	
Height of tsunami	6-19 m	5.8-10.4 m	
Inundation area	5 km^2	73 km^2	
Death person	676	3,512	
Missing person	149	445	
Rail	Senseki Line, Isinomaki Line	Yamada Line	
Road	Route 45	Route 45, Route 108	

Yamada-machi

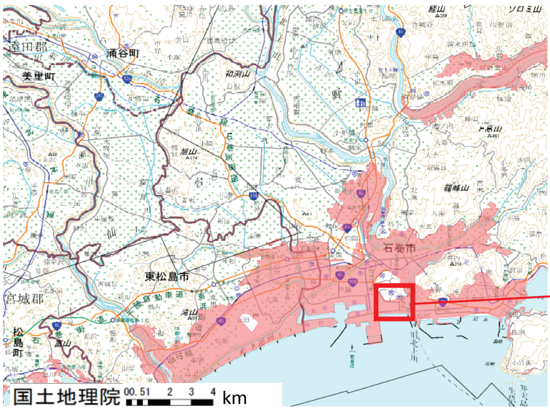

Ishinomaki-shi

: Inundation range

Source: Geospatial Information Authority of Japan

Fig. 2 Tsunami inundation ranges

Yamada-machi

Ishinomaki-shi

Source: Geospatial Information Authority of Japan

Fig. 3 Damaged areas in study regions

Survey methods

Table 2 presents core information on the questionnaire survey administered in the investigated localities.

Table 2 Details regarding the questionnaire survey

	Yamada-machi	Ishinomaki-shi
Period	June-September, 2011	October-December, 2011
Number of respondents	184 (approximately 1.6% of the population in the tsunami inundation range)	279 (approximately 0.2% of the population in the tsunami inundation range)
Data collection method	Hearing survey	
Location of data collection	Places of refuge and temporary dwellings	
Items	(1) Personal attributes (sex, age, and occupation) (2) Situation immediately after the occurrence of the Great Earthquake (3) Tsunami evacuation behaviors	
Investigator	The Great East Japan Earthquake Disaster Tsunami Evacuation Joint Survey Group (number of members: 30)	

EVACUATION BEHAVIORS IN DIFFERENT AREAS

Area classification

To understand the evacuation behavior patterns across the regions of interest, these were separated into different zones. Ishinomaki-shi was classified into zones A (along a coast), B (on a plain), and C (along a river), as determined according to distance from a coast or a river, and Yamada-machi was set as zone D, in accordance with its position fronting the Rias coast (Table 3). Table 4 lists the population in the localities, the number of responses received from the participants, the response rates of the questionnaire, and the disaster mortality rates in the regions (the number of deaths in the area divided by the total population of the area). The disaster mortality rate was highest in zone C, followed by zones A, D, and B.

Table 3 Details of classification

Zone A (along a coast)	Ishinomaki-shi: Direct distance from a coast, less than 300 m (less than 3 m above sea level)
Zone B (on a plain)	Ishinomaki-shi: Direct distance from a coast, 300 m or higher (3 m or higher above sea level)
Zone C (along a river)	Ishinomaki-shi: Direct distance from the Old Kitakami River, less than 300 m
Zone D (facing the Rias coast)	Yamada-machi

Table 4 Details of survey responses

	Population	Number of responses	Response rate (%)	Mortality rate (%)
Zone A	10,833	105	0.97	5.83
Zone B	30,333	113	0.37	2.33
Zone C	7,085	61	0.86	8.07
Zone D	15,084	184	1.22	4.44

Table 5 Pre-earthquake behaviors in different areas

Survey items		Zone A	Zone B	Zone C	Zone D
(1) I have participated in disaster prevention drills every year.	Expected frequency	28	30	17	54
	Actual frequency	11	30	11	77
(2) I can recognize a hazard map.	Expected frequency	15	16	9	30
	Actual frequency	7	9	8	46
(3) My family has occasional discussions regarding earthquakes.	Expected frequency	43	46	27	85
	Actual frequency	41	35	16	109
(4) I evacuated from my home during/after the 2010 Chilean tsunami.	Expected frequency	41	44	25	75
	Actual frequency	41	30	19	95
(5) Estimated tsunami arrival time	[Min]	18.6	19.7	56.1	23.8
(dark shading)	Items in which the actual frequency was smaller than the expected frequency				
(light shading)	Items in which the actual frequency was larger than the expected frequency				

Pre-earthquake behaviors

To examine the differences in behaviors across various areas before the Great Earthquake, a chi-square test was performed to determine the plausibility of the null hypothesis that no differences exist among the regions. Table 5 lists the survey items, for which the chi-square test revealed a significant difference at the 5% level.

The number of responses was compared with the expected frequency, which was obtained on the assumption that no differences in evacuation behaviors exist among the studied areas. With regard to item #1, the actual frequency of participation in disaster prevention drills every year in zone D (fronting the Rias coast) was larger than the expected frequency; the actual frequency was smaller than the anticipated frequency in zones A (along a coast) and C (along a river). In terms of item #2, the actual number of people who could recognize a hazard map was larger than the expected number only in zone D; the values obtained for the rest of the areas were smaller than the expected values. Concerning item #3, the number of families who had occasionally discussed earthquakes was larger than the expected number only in zone D; the rest of the areas exhibited values smaller than those anticipated. With respect to item #4, the actual number of people who had evacuated from the 2010 Chilean tsunami was larger than the predicted number in zone D, whereas the expected number was smaller than the anticipated number in zones B and C. The estimated tsunami arrival time was around 20 min before the Great Earthquake in zones A, B, and D, but this estimate was more than twice as long (56 min) in zone C.

Behaviors immediately after the Great Earthquake

With respect to immediate behaviors after the Great Earthquake, Fig. 4 shows the interval between disaster occurrence and evacuation initiation in each area, and Fig. 5 indicates the ratio of residents who returned home to the total population (returnee ratio hereafter) in each area after the occurrence of the Great Earthquake. The interval between the occurrence of the Great Earthquake and the initiation of evacuation was shortest in zone D, followed by zones A, B, and C. The returnee ratio was lowest in zone B and highest in zone D.

To examine the differences in evacuation methods among the areas, a chi-square test was carried out to determine the plausibility of the null hypothesis that no differences exist across the studied regions. Table 6 lists the survey items, for which the chi-square test indicated a significant difference at the 5% level. With regard to "means of evacuation," the people in zones A and B tended to evacuate by automobile, those in zone C favored both evacuation by car and by foot, and those in zone D tended to evacuate by foot. In terms of "evacuation sites," the people in zone A tended to evacuate to bridges and places that were located at

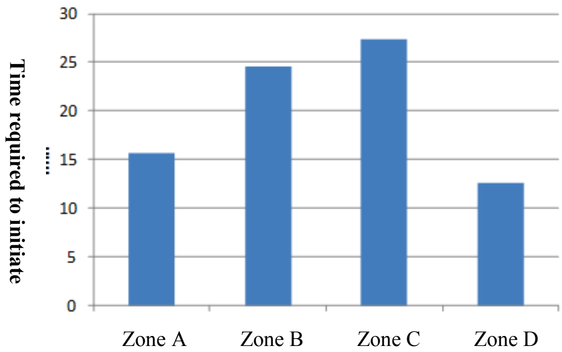

Fig. 4 Time taken to initiate evacuation

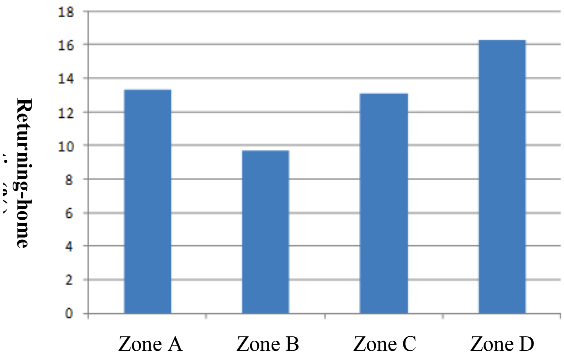

Fig. 5 Returnee ratio to Houses

Table 6 Analytical results on evacuation methods

Survey items		Zone A	Zone B	Zone C	Zone D
Means of evacuation	By foot			○	○
	By car	○	○	○	
Evacuation sites	Bridges and places located at higher elevations	○			
	Upper floors of houses and office buildings		○	○	
	Upward slopes or hills				○

○ = items that exceeded the expected values higher elevations to avoid the erosion caused by the earthquake; the residents of zones B and C preferred evacuating to the upper floors of their houses and office buildings; and the residents of zone D tended to evacuate to upward slopes or hills.

CONCLUSION

Analytical results

The analytical results are summarized as follows.

(1) With regard to pre-earthquake behaviors, prevention measures, such as earthquake drills and occasional discussion on earthquakes, tended to be implemented in areas facing the Rias coast. No prevention measures were taken in Ishinomaki-shi.

(2) The interval between the occurrence of the Great Earthquake and the initiation of evacuation was shortest in zone D, followed by zones A, B, and C. The people living in these four areas tended to return home, even though they had evacuated early after the occurrence of the Great Earthquake.

(3) The people living in the areas fronting the Rias coast and those located along a river favored evacuation by foot, whereas the residents of other regions tended to evacuate by car. With reference to evacuation sites, the people living in the four studied areas tended to evacuate to easily accessible sites.

Future tsunami disaster prevention and management measures

On the basis of the analytical findings, the following recommendations for future tsunami disaster prevention and management were formulated.

The analytical results on the evacuation behaviors indicate that participation in earthquake drills, the recognition of a hazard map, and in-family discussions of earthquakes are important preventive measures that increase survival rates. In relation to means of evacuation, the facilities to be occupied by evacuees should be examined to determine whether these are accessible by automobile or other means. An important requirement for facilitating auto-based evacuation is the construction of roads that are easily cleared of traffic jams even after a given area is struck by an earthquake. With reference to evacuation by other means, safe evacuation sites must be established within walking distance given the travel constraints imposed by disasters. For houses and office buildings located on plains, an essential measure is to design effective anti-tsunami measures, in addition to constructing tsunami evacuation buildings.

The strongest tsunami waves caused by the Great Earthquake arrived approximately 30 min after the occurrence of the earthquake. In the case of Tokai, Tonankai, and Nankai consolidated earthquakes, the strongest tsunami wave is predicted to arrive less than 30 min after earthquake occurrence. Therefore, people living in areas susceptible to such earthquakes must be evacuated within a short period. Achieving this goal necessitates prevention and management measures that are specific to the evacuation behaviors of residents in different regions.

REFERENCES

[1] Kanai M and Katada T, “Decision-Making of Evacuation from Tohoku Tsunami in 2011”, Japan Society for Disaster Information Studies, No. 10, 2012, pp. 91-102.

[2] Urata J and Hato E, “An Analysis of Evacuation Timing with Pre-Activities in Tsunami Disasters: With a focus on the evacuation behaviors in the city of Rikuzentakata during the 2011 Great East Japan Earthquake”, Journal of the City Planning Institute of Japan, Vol. 48, No. 3, 2013, pp. 807-812.

[3] Kikuchi Y and Minami M, “Study on the Tsunami Evacuation Behavior of the School in the Great East Japan Earthquake: A Case of the Elementary and Junior High Schools in the Iwate Coast”, Journal of the City Planning Institute of Japan, Vol. 49, No. 3, 2014, pp. 333-338.

[4] Fujiu M, Ishikawa T and Takada K, Language Analysis of Tsunami Evacuation Behavior in Kesennuma City During the 2011 off the Pacific Coast of Tohoku Earthquake, Journal of JSCE, A1, Vol. 69, No. 4, 2013, pp. 798-806, 2013.

[5] Yanagihara S and Murakami H, A Study on Travel Means and Distances of Tsunami Evacuation in Ishinomaki Urban Area After the 2011 Great East Japan Earthquake Disaster, Journal of JSCE, A1, Vol. 69, No. 4, 2013, pp. 1013-1020, 2013.

[6] Takada K, Fujiu M and Onomura K, Research on Reproduction Method of the Situation of Tsunami Evacuation with Car – Case Study of Kesennuma City -, Journal of JSCE, A1, Vol. 69, No. 4, 2013, pp. 973-979, 2013.

[7] Morita T, Hasegawa H, Tsukada S, Hashimoto T and Yuzawa A, Analysis on Effects of Disaster Prevention Measures Based on Refuge Behavior Data - A Case Study of Ishinomaki City -, Socio Technology Research, Vol. 12, 2015, pp. 51-60.

Fifth International Conference on Geotechnique, Construction Materials and Environment, Osaka, Japan, Nov. 16-18, 2015, ISBN: 978-4-9905958-4-5 C3051

AN APPROACH TO ASSESS PERFORMANCE OF SEWER PIPES SUBJECTED TO BOULDER IMPACT

Thayalan Nall, and TaeWoo Eom
Coffey International Pty Ltd, Brisbane, Australia;

ABSTRACT

Design studies are now underway to rehabilitate concrete sewer pipes in the city of Brisbane which are over 100 year old. Some sections of the sewer have been laid in an unlined, hand dug rock tunnel excavated by uncontrolled blasting. It is believed that due to the construction technique used, the rock in the tunnel roof region may have been highly fractured, and the loosely wedged boulders may fall in the event they are disturbed. Parallel to this sewer alignment, a major road widening is now being proposed involving construction of deep foundations. Consequently, there are concerns that potential vibration from such activities may trigger rockfalls and potentially damage the dilapidated sewer pipes.

For health and safety reasons it was not possible to inspect the conditions of the ailing tunnel roof conditions. Hence, a desk study was undertaken to assess the performance of the sewer pipe if it were subjected to rockfall. For this study, the impact load due to free fall of rock boulders was computed using simple but adequate methods. They were then modelled using finite element techniques to assess the behaviour of the sewer pipe. This paper describes the assessment techniques adopted in the desk study and how the outcomes helped to plan further investigations for conclusive results.

Keywords: Boulder impact, Sewer pipe, Tunnel, Sewer rehabilitation

INTRODUCTION

Concrete sewer pipes in the city of Brisbane are over 100 years old and will be rehabilitated with a flexible internal liner and by grouting the annular space between the liner and the pipe. Some sections of them lay in an unlined, hand dug rock tunnel then excavated by uncontrolled blasting. It is believed that due to the construction technique used, the rock in the tunnel roof region may have been highly fractured and the loosely wedged boulders may fall in the event they are disturbed.

Prior to the commencement of sewer rehabilitation, a potential road upgrade project was proposed near the sewer alignment. The project was to involve activities of some deep foundation construction, and there were concerns that potential vibration from such activities may trigger rockfalls and may damage the dilapidated sewer pipes. In this context a desk study was undertaken to assess the behaviour of the sewer under rock impact loading and on the integrity of the proposed rehabilitation.

METHOD OF ASSESSMENT

This study was performed in four stages: In stage one, the impact load due to free fall of rock boulders on the sewer pipe was computed using established expressions. In the absence of detailed information on degree and extent of blast induced fractures on the tunnel roof, tunnel geometry and size of loosely wedged boulders; it was difficult to predict the potential size of boulders that are susceptible to fall and their height of drop. Hence a scenario study with boulder weighing up to 250kg and them falling over a range of heights from 0.25m to 0.75m have been considered.

In stage 2, structural behaviour of the existing sewer pipe was assessed under rockfall impact loading. For this assessment, the geometry of the existing dilapidated concrete pipe as described in Fig. 1 has been considered.

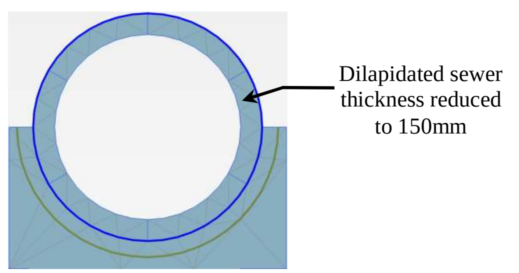

Fig. 1: Existing Dilapidated Sewer Pipe

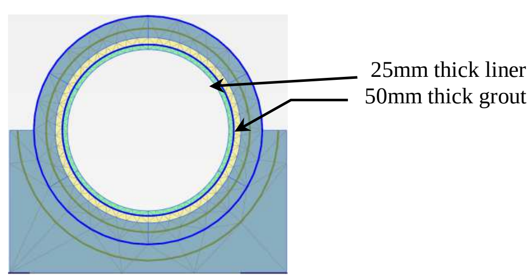

Fig. 2: Proposed Rehabilitation

In stage 3, the structural behaviour of the dilapidated sewer pipe was evaluated with the proposed rehabilitation (with internal flexible liner) as described in Fig. 2. The existing dilapidated concrete pipe has been considered as the 1st line of defence against rockfall in this evaluation (i.e. the maximum allowable stress of the dilapidated pipe as the limiting value).

The stage 4 assessment is very similar to stage 3, but the flexural strength of the liner has been considered as the limiting stress. This is to reflect the scenario of potential subsequent hits by boulders after breaking of the outer pipe.

DYNAMIC BEHAVIOUR OF STRUCTURES UNDER IMPACT LOADING

The kinematic or potential energy of a moving object can be computed using well established expressions. However, the resulting impact force on a structure, is not straightforward as it involves aspects of geotechnical, structural and material engineering. This subject has been widely studied by two scientific communities in general. One by the military for their applications and the other for the development of protective structures to withstand impacts either due to civil activities or those of natural origin such as rockfalls, wave action, etc. Findings from the latter are more freely available in the public domain, and therefore used in this study. Further, the developed procedures for design of rockfall galleries being closely resemble this study; approaches from those studies are incorporated in the assessment.

In general, impact problems are classified by the impact velocity, either as low (up to 50m/s) or high velocity impact and by the way the kinetic energy is dissipated, either as a soft or hard impact. The assessment of impact load on a sewer pipe would be considered to be in the low velocity regime, and it is reasonable to consider that the material behavior will remain largely in the elastic stage and yielding may only occur locally.

By this definition, rockfall on concrete pipe should be treated as a hard impact, and the sewer pipe has to dissipate the impact energy by means of deformations. It is also possible that deposited sediments around the sewer pipe over flood events since construction may have formed a cushioning layer, and may contribute towards a softer impact. However for a conservative estimate of impact load, this option had been ignored.

Computation of Impact Load

The impact load from the free fall of boulders was assessed using some of the existing design guides developed for rockfall galleries. They are described below;

The Japanese design guide for design of rockfall impact structure by the Japan Road Association [1]-[2] – this approach is referred to as Method 1. The impact force is computed using the expression:

$$P = 2.108(mg)^{2/3}\lambda^{2/5}H^{3/5}(T/D)^{-0.58} \tag{1}$$

Design guide from Switzerland Federal Road Office (ASTRA) for the design of rockfall protection galleries [3]-[7] – this approach is referred to as Method 2. The impact force is computed using the expression:

$$P = 2.8T^{-0.5}r^{0.7}M^{0.4}\tan\phi\,[(m \times v^2)/2]^{0.6} \tag{2}$$

Where; P - Impact force (kN), m - Mass of falling rock (t), g – gravitational acceleration (m/s^2), v - Impact velocity (m/s), M - Modulus of the cushion layer (kPa), ϕ - Internal friction angle of the cushion layer (°), T - Thickness of the cushion layer (m), λ - Lame's constant proposed as 1000kPa, r or D - Radius or Diameter, respectively, of an equivalent sphere representing the boulder (m), and H - Height of free fall.

Although there are a number of other guides that provide expressions to compute P, design guides from Japan and Switzerland have been adopted, primarily because both countries have made significant advances in designing rockfall protection galleries, and also share similar levels of risk acceptance as Australia.

For this assessment, where the formulae adopted to compute the impact force involve a cushioning layer with its stiffness, then the dilapidated pipe wall has been considered as a hard cushion with a modulus of 11GPa and a friction angle of 30 degrees.

Published studies indicate that the material behaviour under dynamic loading is different to that under static loading, and plays an important role in the structural performance. In this study however, the dynamic material behaviour has not been considered since the expected impact velocity is relatively low.

Estimation of Static Equivalent Force

Both design guides considered prescribe a method to estimate a static equivalent force to represent the impact force. This is expressed in equation 4.

$$F_{se} = PC \tag{4}$$

For the constant 'C', the Japanese guide recommends values between 1.2 and 2.0, while the Swiss guide suggests values of 0.4 and 1.2 for ductile and brittle failures respectively. For this assessment a value of 1.2 has been adopted for 'C'.

The computed static equivalent forces (SEF) using these methods are shown in Fig. 3. It should be noted that although these approaches are simple to use, they do not fully incorporate the dynamic behaviour of the structure in arriving at SEF.

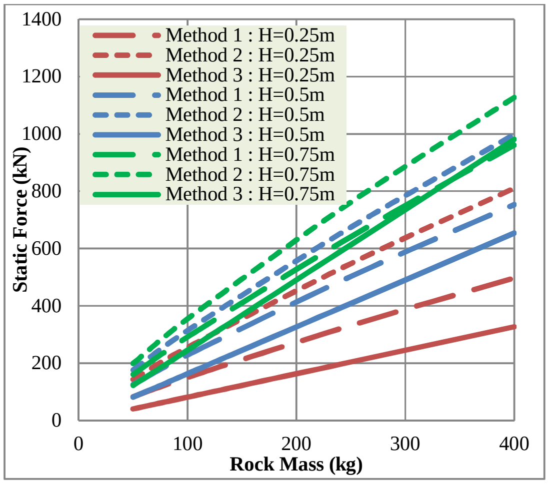

Fig. 3: Computed static equivalent forces

STRUCTURAL PERFORMANCE OF THE EXISTING SEWER PIPE WITHOUT THE LINER

By undertaking finite element modelling using the commercially available software 2D-PLAXIS, the structural performance of the sewer pipe was assessed, subjecting the sewer pipes to the static equivalent force computed.

The sewer pipe section as shown in Fig. 1 was modelled in PLAXIS within a tunnel section for a given ground model, where the overlying rock layer is not in contact with the pipe. The static equivalent force calculated by these methods was applied as a point load on the crown of the sewer pipe, and the resulting shear force, bending moment and stress in the sewer pipe have been computed. For modelling:

- The rock layer beneath the sewer pipe was modelled as a homogeneous Mohr-Coulomb material with a Young's modulus of 600MPa, cohesion of 75kPa and friction angle of 35 degrees.
- The sewer pipe was modelled as a tunnel element. It was considered that the pipe thickness has been reduced to 150mm from its initial thickness of 225mm, after being subjected to internal erosion and gas attack over time. Although it was constructed with a 25MPa concrete then, a reduced modulus of 11GPa, corresponding to 5MPa concrete has been adopted.
- Concrete supporting the sewer pipe was modelled as a linear elastic material, also with a Young's modulus of 11GPa.

The performance of the pipe was evaluated by assessing bending moments, shear forces and major principal stresses in the pipe. Typical plots of shear force, bending moment distributions and stress contours under a static point load are shown in Fig. 4 to Fig. 7.

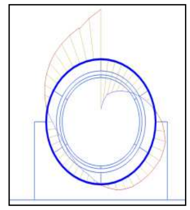

Fig. 4: Typical Shear Force Distribution

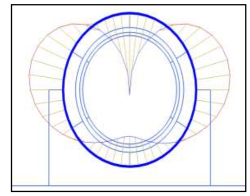

Fig. 5: Typical Bending Distribution

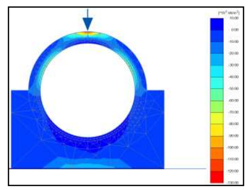

Fig. 6: Typical Distribution of Principal Stress (σ_1)

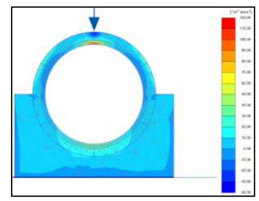

Fig. 7: Typical Distribution of Principal Stress (σ_3)

Computed Shear Force

The shear force distribution on the composite sewer pipe due to static equivalent force from boulders dropping from a height of 0.25m, 0.5m and 0.75m was evaluated. For the case of 0.5m free fall, the computed maximum shear forces are presented in Fig. 8.

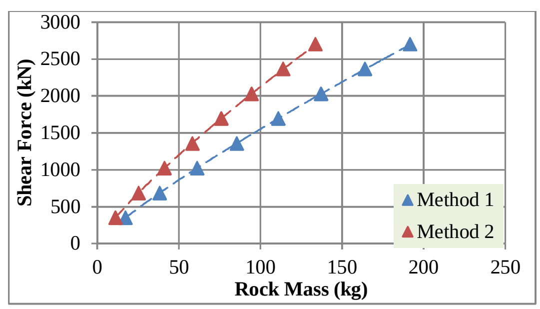

Fig. 8: Maximum Shear Force for 0.5m Free Fall

Computed Bending Moments

The computed maximum bending moments on the sewer pipe due to static equivalent force from boulders dropping from a height between 0.25m and 0.75m were evaluated. For the case of 0.5m free fall, computed maximum bending moments are presented in Fig. 9.

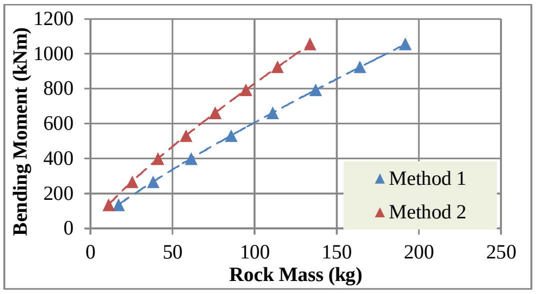

Fig. 9: Max. Bending Moment for 0.5m Free Fall

Stress on Pipe

The maximum stresses on the sewer pipe wall due to static equivalent force from boulders dropping from a height between 0.25m and 0.75m were evaluated without the proposed flexible liners. The ultimate compressive strength of the dilapidated concrete pipe was considered as 5MPa (limiting stress) to arrive at the maximum size of boulders that would impart that order of stress. They are tabulated in Table 1 and are also shown in Fig. 10, for Method 2 for the case without the liner.

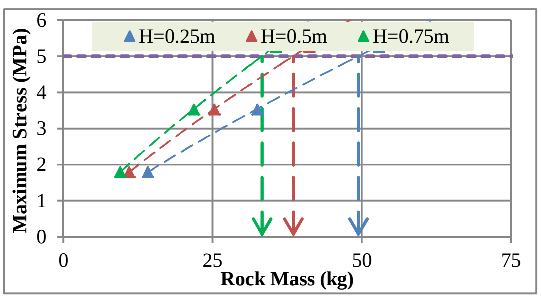

Fig. 10: Maximum Compressive Stress and Limiting Rock mass – Computed by Method 2

Table 1: Limiting Boulder Size without Liner

Method	Limiting Size of Boulder in Mass (kg)		
	Height of Fall = 0.25m	Height of Fall = 0.5m	Height of Fall = 0.75m
1	93	57	43
2	49	38	33
Average	71	48	38

STRUCTURAL PERFORMANCE OF THE SEWER PIPE WITH THE LINER

To assess the structure performance of the dilapidated concrete sewer under a static equivalent point load, similar numerical analyses were undertaken through PLAXIS 2D modelling of a tunnel cross-section with the composite pipe. The composite pipe was modelled in a similar manner as above, but with the additional components to it as described below:

- Flexible liner was modelled as a 25mm thick tunnel element having stiffness values of 1.8 and 6.5GPa.
- The grout infill within the annular between the pipe and the liner was considered 50mm thick and modelled as a liner elastic material with a Young's modulus of 16GPa, corresponding to 10MPa concrete.

Computed Shear Force

The shear force distribution on the composite sewer pipe due to static equivalent force from boulders dropping from a height between 0.25m and 0.75m was evaluated for the two proposed liners. The order of difference between the computed maximum shear force with the liner having a modulus of 6.5GPa and 1.8GPa was found to be less than 10kN. Hence, the computed average maximum shear forces are presented in Fig. 11 for a 0.5m free fall height. This indicates that the introduction of liner has reduced the shear force by around 10%

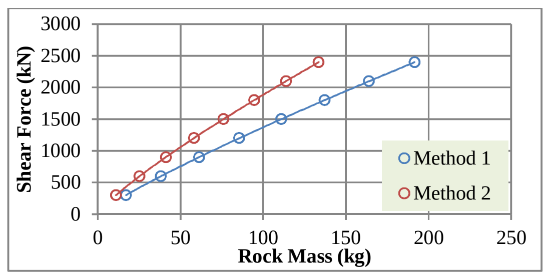

Fig. 11: Computed Max. Shear Force under Static

The maximum bending moments on the composite sewer pipe due to static equivalent force from boulders dropping from a height between 0.25m and 0.75m were evaluated with both flexible liners proposed. The maximum bending moment for a free fall height of 0.5m are shown in Fig. 12. This indicates that the introduction of liner has reduced the bending moment by around 40%

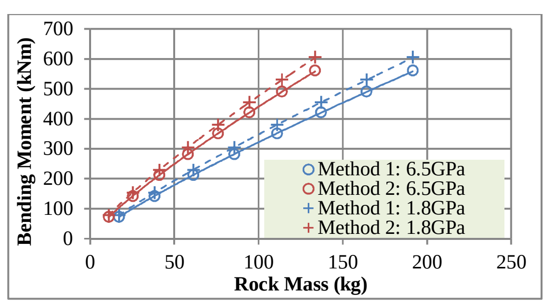

Fig. 12: Computed Bending Moment under Static

Stress on Pipe

The maximum stresses on the sewer pipe wall due to static equivalent force from boulders dropping from a height between 0.25m and 0.75m were evaluated with the proposed flexible liners. The computed maximum stresses with the 6.5GPa liner by Method 2 are shown in Fig. 13.

Since the dilapidated concrete pipe will act as the 1st line of defence, the ultimate compressive strength (5MPa) of the dilapidated concrete pipe as the limiting stress to arrive at maximum size of boulder that would impart that order of stress. They are tabulated in Tables 2 and 3. This indicates that the introduction of liner has increased the tolerable boulder size by around three fold.

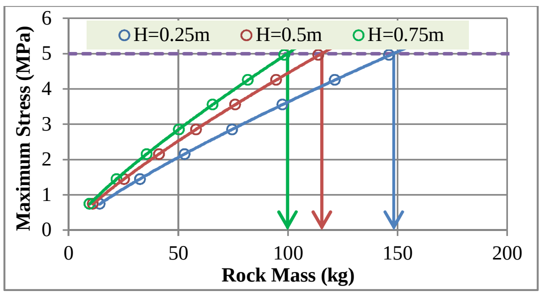

Fig. 13: Maximum Compressive Stress and Limiting Rock mass – Computed by Method 2

Table 2: Limiting Boulder Size with 6.5GPa liner

Method	Limiting Size of Boulder in Mass (kg)		
	Height of Fall = 0.25m	Height of Fall = 0.5m	Height of Fall = 0.75m
1	270	166	125
2	148	115	100
Average	209	141	113

Table 3: Limiting Boulder Size with 1.8GPa liner

Method	Limiting Size of Boulder in Mass (kg)		
	Height of Fall = 0.5m	Height of Fall = 1.0m	Height of Fall = 1.5m
1	246	152	114
2	135	105	91
Average	191	129	103

STRUCTURAL PERFORMANCE OF THE FLEXIBLE LINER

For the assessments of required minimum stiffness and thickness of the liner, a two stage analysis similar to those described before has been considered.

In stage 1, for larger size boulders with rock mass between 1000kg and 1750kg, the potential impact load was computed. Since the above study indicated that among the two methods considered, the impact loads estimated using the Swiss Guideline resulted in the highest value, the Swiss approach has been adopted in the assessment to arrive at reasonably conservative outcomes. Further, among the three free fall heights considered, the mid value of 0.5m which is likely to be the clearance between the pipe and tunnel crown was selected to compute the impact loads on the pipe.

In Stage 2, finite element analyses using 2D PLAXIS, similar to models described previously, have been undertaken to assess the stresses on the liner with the following changes:

- Recent CCTV investigations undertaken within the sewer pipes, suggest that in some sections of the pipe the crown regions of the sewer pipes have undergone more damage compared to the sides and would be conservative to adopt a wall thickness of 100mm in place of 150mm. Taking this into account the concrete sewer pipe was modelled as a tunnel element of 100mm thick with a Young's modulus of 11GPa, corresponding to 5MPa concrete.
- Flexible liner was also modelled as a tunnel element. For this study liner thickness of 25mm and 35mm has been considered and a range of stiffness values varying from 1.8GPa to 20GPa have been examined. The flexural strength was considered to be linearly proportional to its stiffness as shown in Fig. 14.
- The grout infill within the annulus between the sewer pipe and the liner was considered 25mm thick and modelled as a liner elastic material with a Young's modulus of 11GPa, corresponding to 5MPa concrete.

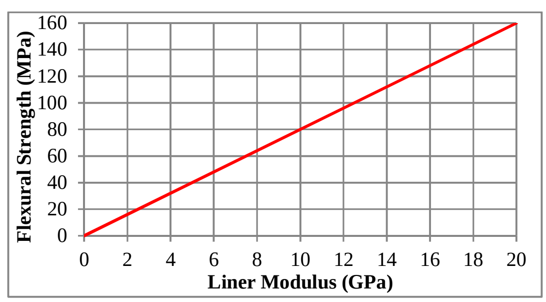

Fig. 14: Young's Modulus and Flexural Strength of Liner

The static equivalent force calculated as per the Swiss guideline for dislodged boulders falling from a height of 0.5m was applied as a point load at the crown of the sewer pipe and the resulting maximum stresses in the flexible liner instead of in the sewer have been computed through PLAXIS modelling. The computed maximum stress was compared with the flexural strength of the liner to arrive at suitable stiffness values for the proposed liner. They are presented in Figs 15 and 16 for 25mm and 35mm thick liners respectively and summarised in Table 4.

Table 4: Boulder Size and Liner Stiffness

Boulder Mass (kg)	Required Minimum Liner Stiffness (GPa)	
	25mm Liner	35mm Liner
750	8.6	7.9
1000	10.6	9.7

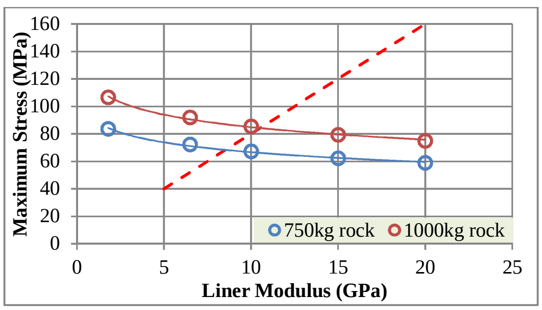

Fig. 15: Maximum Stress on 25mm thick Liner

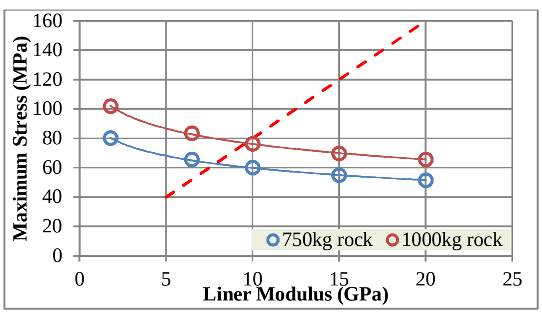

Fig. 16: Maximum Stress on 35mm thick Liner

The above results indicate that, for the free fall height considered (0.5m), if the liner stiffness is less than 10.6GPa and 9.7GPa respectively for 25mm and 35mm thickness, any boulder of mass greater than 1000kg ($0.4m^3$) would potentially cause damage to both the pipe and the liner. It should be noted that this assessment does not cover localised punching failures.

CONCLUDING COMMENTS

It should be noted that the analyses and outcomes presented above are based on an equivalent static loading corresponding to an impact load, and ignoring the time-dependent dynamic behaviour of the pipe following an impact.

The conclusions are only based on tolerable compressive stress on the sewer pipe and the liner. At the time of preparation of this paper no information available on the bending and shear capacities of the sewer pipe.

The methodology discussed in this paper should be complemented with laboratory load testing on the composite sewer pipes, in consultation with structural engineers, to assess shear and bending capacities, and to further interpret their ability to withstand the estimated shear forces and bending moments.

Introduction of liner with grout filled in the annular space would improve the capacity to withstand 3 times larger size boulders compared to the unlined sewer pipe.

To withstand boulders of size larger than 1000kg falling from a height of 0.75m, the internal liners have to be stronger and at least have a Young's Modulus of 10.6GPa.

REFERENCES

[1] Ishikawa N. Recent progress on rock-shed structures studies in Japan. In: Joint Japan-Swiss Scientific Seminar on Impact Load by Rockfalls and Design of Protection Structures, 1999, Kanazawa, Japan.

[2] Jacquemoud J. Swiss guideline for the design of rockfall protection galleries: Background, safety concept and case histories. In: Joint Japan-Swiss Scientific Seminar on Impact Load by Rockfalls and Design of Protection Structures, 1999, Kanazawa, Japan.

[3] Chikatamarla R, Laue J, Springman S M. Rockfall impact on protection galleries. Zingoni, A. (edition.): Progress in Structural Engineering, Mechanics and Computation, Taylor & Francis, London; 2004.

[4] Schellenberg K, Vogel T. Swiss Rockfall Galleries - Impact Load. In: Proceedings IABSE Symposium Lisbon 2005, 'Structures and Extreme Events', Zurich, 2005.

[5] Chikatamarla R, Laue J, Springman SM. Rockfall on protection galleries. SEMC, 2004, Cape Town, South Africa.

[6] Chikatamarla R. Rockfalls on slopes and structures, PhD Thesis, Swiss Federal Institute of Technology, Zurich, 2005.

[7] Schellenberg, K. On the Design of Rockfall Protection Galleries. Swiss Federal Institute of Technology, Zurich, Switzerland, 2009.

Fifth International Conference on Geotechnique, Construction Materials and Environment, Osaka, Japan, Nov. 16-18, 2015, ISBN: 978-4-9905958-4-5 C3051

STUDY ON ASSESSING THE VALUE OF THE TENGUIWA IRRIGATION CANAL

Shinya Tsukada[1], Tetsuo Morita[2], and Akira Yuzawa[3]
[1] Maebashi City Office, Japan, [2] Graduate School of Engineering, Tohoku Institute of Technology, Japan;
[3] Graduate School of Engineering, Maebashi Institute of Technology, Japan

ABSTRACT

In Japan, following changes in socioeconomic conditions, such as financial deterioration, an increase in social capital, and a decrease in population, ideas about infrastructure improvement have greatly changed. Recently, irrigation canals possessing historic value have attracted the attention of the public as assets for community development. The present study focused on the Soja district, in which many historical and cultural resources exist but where these resources have not been developed. A questionnaire was administered to the local residents and revealed the value of the Tenguiwa Irrigation Canal as an environmental asset. The present study also examined the relationship between the value of the Tenguiwa Irrigation Canal as an environmental asset and the direction of community development in the Soja district.

Keywords: Irrigation canal, historic value, environmental asset, Maebashi-shi,

INTRODUCTION

Purpose of the study

In Japan, following changes in socioeconomic conditions, such as financial deterioration, an increase in social capital stock, and a decrease in population, ideas about infrastructure improvement have greatly changed. Recently, irrigation canals possessing historic value have attracted the attention of the public as assets for community development. The aim of the present study is to understand the residents' awareness of the value of the Tenguiwa Irrigation Canal as an environmental asset and the direction of community development in the Soja district.

Overview of the study

There have been previous studies on irrigation canals. First, Marumo et al. assessed the value of the Yanagawa canal [1]. Second, Maki et al. assessed the value of the Old Mita Channel [2]. Third, Yamashita et al. assessed the value of the Tamagawa Channel [3]. However, only a few studies have assessed the value of an irrigation canal as an environmental asset, and comprehensively and quantitatively examined the residents' awareness of the direction of community development. The present study focused on the Tenguiwa Irrigation Canal in the Soja district, Maebashi City, assessed the value of the Tenguiwa Irrigation Canal, and quantitatively examined the direction of community development in the Soja district.

STUDY REGIONS AND SURVEY METHODS

Study regions

The present study investigated the Tenguiwa Irrigation Canal in the Soja district, Maebashi-shi, Gunma Prefecture, in which urban development had not been carried out. The Tenguiwa Irrigation Canal is an agricultural water channel passing through Maebashi-shi, Takasaki-shi, and Tamamura-machi from the Tone River (Fig. 1).

In 1604, Nagatomo Akimoto, the lord of Soja Castle, dammed up the Tone River to create the Tenguiwa Irrigation Canal. Therefore, the canal has a history of more than 400 years. Flower beds and promenades have been prepared along the canal, and the local residents enjoy walking along the promenades. A volunteer organization was established to protect the environment around the

Fig. 1 Tenguiwa Irrigation Canal

Tenguiwa Irrigation Canal, and the organization has been inspecting facilities and maintaining the flower beds and promenades by weeding, planting, and seeding.

Survey methods

Table 1 presents core information about the survey administered in the investigated localities.

Table 1 Details regarding the questionnaire survey

Date of survey	- Distribution: July 24-27, 2010 - Collection: August 15, 2010 (latest posting date)
Location of data collection	Soja district, Maebashi-shi, Gunma Prefecture
Data collection method	- Distribution: Putting in mailbox - Collection: Mailing
Items	(1) Satisfaction levels about the Tenguiwa Irrigation Canal and the surrounding environment (2) Direction of community development
Distribution and collection	- Number of questionnaire cards distributed: 1,000 - Number of questionnaire cards collected: 253 - Recovery: 25.3%

VALUE ASSESSMENT OF THE TENGUIWA IRRIGATION CANAL

Assessment of the environment around the Tenguiwa Irrigation Canal

Regarding the environment around the Tenguiwa Irrigation Canal, the residents were asked to evaluate the items shown in Table 2 using a five-point scale from “very good” to “very bad”.

Extraction of environmental factors regarding the Tenguiwa Irrigation Canal

To summarize the assessment results of the above 20 items, a factor analysis was performed. Table 3 shows the results of the factor analysis. Four environmental factors, i.e., “facility improvement,” “natural landscape,” “regional characteristics,” and “safety and security” were extracted from the factor analysis.

Model for assessing the Tenguiwa Irrigation Canal as environmental assets

Fig. 2 shows a model for assessing the Tenguiwa Irrigation Canal as an environmental asset using

Table 2 Assessment items

C1	Management of fences
C2	Management of trees and plants
C3	Garbage scattering
C4	Crime-free
C5	Sidewalk construction
C6	Walking safety
C7	Nighttime illumination
C8	Traffic safety
C9	Safe playground
C10	Rest facility
C11	Waterside organisms
C12	Rich in nature
C13	Quality of landscape
C14	Bird-watching
C15	Water sanitation
C16	Rich in trees
C17	Peace of mind
C18	Region exchange
C19	Local history
C20	Community symbol

Table 3 Results of the factor analysis

	Facility improvement	Natural landscape	Regional characteristics	Safety and security
C5	0.7901	0.1707	0.1805	0.0994
C6	0.7195	0.0934	0.1568	0.3377
C3	0.6811	0.1349	0.1691	-0.0656
C1	0.6189	0.2047	0.0466	0.0878
C2	0.6154	0.2070	0.1764	0.1140
C8	0.5976	0.0333	0.0629	0.1798
C13	0.2340	0.7264	0.1977	0.0023
C12	0.1752	0.7227	0.1715	-0.0341
C14	0.1045	0.6993	0.0036	0.1294
C16	0.2765	0.5987	0.1618	0.0921
C17	0.3116	0.5920	0.3706	0.2734
C15	0.2145	0.5100	0.3189	0.2162
C11	-0.1119	0.4239	0.0378	0.2374
C20	0.2015	0.2017	0.8283	0.1793
C19	0.1721	0.2436	0.7927	0.1138
C18	0.2634	0.3908	0.4556	0.3177
C9	0.1330	0.0649	0.1296	0.8251
C7	0.2445	0.0383	0.1372	0.4249
C4	0.3535	0.1817	-0.1078	0.3936
C10	0.0196	0.1282	0.1033	0.3837

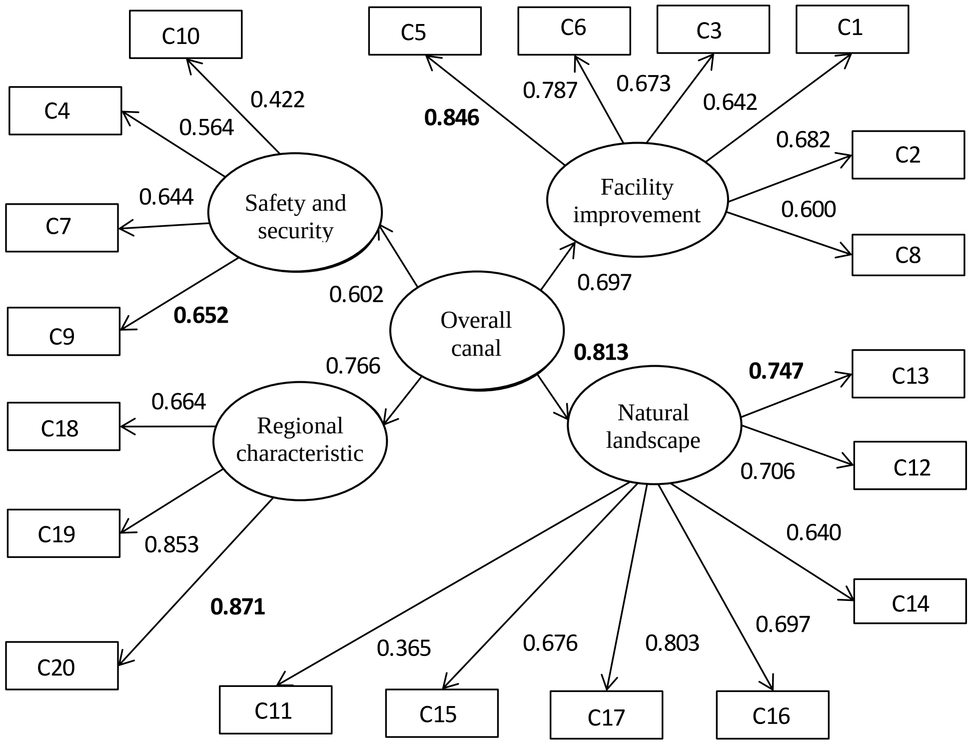

Fig. 2 Model for assessing the Tenguiwa Irrigation Canal as an environmental asset

satisfaction levels. In this model, "overall canal" represents a comprehensive assessment of the environment of the Tenguiwa Irrigation Canal. Under "overall canal," four environmental factors, i.e., "facility improvement," "natural landscape," "regional characteristics," and "safety and security," that were extracted in the factor analysis were allocated as potential factors (level 1). Under these four potential factors, assessment items shown in Table 2 were allocated as observation variables (level 2). The adjusted goodness of fit index of the model was 0.765. The t-values of all path coefficients satisfied a level of significance at 0.1%.

A covariance structure analysis was performed for this model. The values of the path coefficients indicated that the effect of "natural landscape" (0.813) on "overall canal" was the greatest. Of the items under "natural landscape," the effect of "C13: Quality of landscape" (0.747) was the greatest.

Of the items under "facility improvement," the effect of "C5: Sidewalk construction" (0.846) was the greatest. Of the items under "regional characteristics," the effect of "C20: Community symbol" (0.871) was the greatest. Of the items under "safety and security," the effect of "C9: Safe playground" (0.652) was the greatest.

VALUE ASSESSMENT OF THE TENGUIWA IRRIGATION CANAL AND THE DIRECTION OF COMMUNITY DEVELOPMENT

Assessment of the Tenguiwa Irrigation Canal

The results of the covariance structure analysis revealed that the effect of "natural landscape" on the value of the Tenguiwa Irrigation Canal as an environmental asset was larger than that of other environmental factors. Of the items under "natural landscape," the effect of "quality of landscape" was the greatest.

The direction of community development

Table 4 shows the results of the regression analysis, in which the comprehensive assessment of the environment of the Tenguiwa Irrigation Canal was used as an objective variable and "community development using regional history and culture" and five other items were used as explanatory variables. These explanatory variables were expressed in terms of a five-level assessment of the residents' intensity in considering the direction of community development.

Table 4 Results of the regression analysis

Variable	Partial regression coefficient	Standard regression coefficient	T-value	Judgment
Community development using regional history and culture	0.1358	0.1770	2.4093	* 5%
Community development performed mainly by local residents	0.0061	0.0093	0.1286	
Assignment of traditional buildings as to be preserved	0.0250	0.0297	0.3270	
Community development using ancient tombs and castle sites	0.1034	0.1302	1.5080	
Development of streets and parks by performing land readjustment	-0.0760	-0.0901	-1.0098	
Conservation of landscapes, stores, and houses although it may be inconvenient	0.0039	0.0053	0.0640	
Constant term	2.4499		7.7161	** 1%

The result of the regression analysis, the item of the comprehensive assessment of the environment of the Tenguiwa Irrigation Canal, the effect of "Community development using regional history and culture" (0.1770) was the greatest. And, t-values satisfied a level of significance at 0.5%.

Consequently, the value of the Tenguiwa Irrigation Canal as an environmental asset was closely related to the direction of community development in the Soja district.

CONCLUSION

This study focused on the Soja district, in which many historical and cultural resources exist but where these resources have not been developed. A questionnaire was administered to the local residents and revealed the value of the Tenguiwa Irrigation Canal as an environmental asset. The present study also examined the relationship between the value of the Tenguiwa Irrigation Canal as an environmental asset and the direction of community development in the Soja district.

The results of the covariance structure analysis revealed that the effect of "natural landscape" on the value of the Tenguiwa Irrigation Canal as an environmental asset was larger than that of other environmental factors. And, the result of the regression analysis revealed that the effect of "Community development using regional history and culture" on the value of the Tenguiwa Irrigation Canal as of the residents' was larger than that of other directions of community development in the Soja district.

Previously, land for roads had been prepared by laying irrigation canals underground in Japan because social infrastructure, such as urban roads, had not been sufficiently provided. Recently, irrigation canals have been reassessed as environmental assets.

Consequently, the present study created a model for assessing the Tenguiwa Irrigation Canal as an environmental asset, and quantitatively analyzed the effects of assessment items on environmental factors.

The present study also quantitatively analyzed the relationship between the value of the Tenguiwa Irrigation Canal as an environmental asset and the direction of community development using regional history and culture.

REFERENCES

[1] Marumo Y, Kikuchi S, "The situations of the Present Waterway in Canaltown 'Yanagawa' and the influence of Measures Adopted Improve Waterways", J. Archit. Plann., AIJ, No.603, 2006, pp.1-7.

[2] Maki H, Ishikawa M, "A Study on the Cultural Landscape of Mita Waterway and its Historical Transformation", Journal of the City Planning Institute of Japan, Vol. 45, No. 3, 2010, pp. 397-402.

[3] Yamashita Y, Ito H, Ono R, Shimomura A, "Changes of the Relationship between Green Spaces and Residents on Tamagawa Josui Green Way", LRJ, 75(5), 2012, pp.677-682.

Fifth International Conference on Geotechnique, Construction Materials and Environment, Osaka, Japan, Nov. 16-18, 2015, ISBN: 978-4-9905958-4-5 C3051

THE EFFECT OF FLOODING ON THE INTEGRITY OF ROAD SUBGRADE

Abdul Naser Abdul Ghani[1], Nur Izyan Roslan[2] and Ahmad Hilmy Abdul Hamid[3]
[1,2,3] School of Housing Building and Planning, Universiti Sains Malaysia, Malaysia

ABSTRACT

Deterioration of road structural integrity because of flooding may cause huge expenditure for rehabilitation and maintenance of roadway. In principle, the design of pavement structure is based on the strength of compacted soil known as the subgrade or road foundation. Therefore, subgrade is a significant part of the road structural system. When roads are inundated for a long time or repeatedly, the materials in each layer of road structure become saturated, and the original condition of subgrade soils will be compromised. This study investigated the effect on sub-grade strength and properties due to road submergence period and repeated submergence of the road structural systems. Two types of soil that are normally used as the embankment material in road construction, which can be categorized as cohesive and cohesionless materials, were used in this study. California Bearing Ratio (CBR) test and consolidation settlement test were carried out on various categories of inundation and loading conditions including repeated inundation. The findings indicated that the strength of subgrade materials were affected differently depending on the inundation period and number of repeated inundation. These findings are useful for road design and maintenance strategies of flood affected road links.

Keywords: Flooding, Road Sub-grade, Pavement

INTRODUCTION

Floods have resulted in many undesirable outcomes on human and the environment. This is mainly due to their adverse impacts on humans, properties, environmental surrounding, road structures and many forth. Additionally, human activities can also contribute to the flooding event which include: (i) farming and deforestation that exposes the soil to erosion and increases surface runoff, (ii) urbanization by unplanned building construction in vulnerable areas without following the regulations of town planning, poor watershed management and failure to control the flooding promptly, and (iii) obstruction of natural flow of water through drainage modification [1]. The impact of flood disaster can be significant after the event since it may impact the whole infrastructure involved as well as can have long term effect in terms of the maintenance work. In the long run, flooding can bring the deterioration to road pavement foundation when the phenomenon keeps repeating. Continuous flood submersion of roads could bring damage on large part of the road infrastructure, thus affecting the stability of asphaltic concrete pavement layer [2].

Damages of roads structure due to flood event are commonly causing a huge expenditure for the rehabilitation and maintenance works of roads. Recently, Malaysian federal government has allocated RM42 million to repair the embankment collapsed in federal roads damaged by floods in the state of Kelantan. Previously, Bernama [3] reported that the state of Terengganu spent more than RM 74 million for flood damaged roads of only one flood event.

Similarly in town of Sibu in the state of Sarawak it was reported that the city requires RM 500 million to repair road related infrastructure damaged by flooding [4]. Malaysian federal government has also allocated RM 106 million [5] to repair federal roads damaged by flash floods in between October 2012 and January 2013 (monsoon season). Figure 1 is a typical road inundated during flash flood.

Fig.1: Typical road inundation during flash flood

Monsoon season will always come every year and it is only logical to expect the same or more amount of money will be required to reinstate the damaged roads annually. On the other hand, when the roads are inundated for a long time, the materials in each layer for road pavement become saturated, and then as floodwaters drained, the sub-grade soils began to shrink and subside. The excessive water can drain into the foundation reducing its load bearing efficiency. Thus, this situation can cause the strength of road pavement systems to be compromised.

The Sub-grade

The sub-grade is a foundation for the pavement structure to support the load from upper layer to the beneath soil. Basically, sub-grade must be stable in performance to carried load in any weather conditions. Generally in road engineering, CBR test is performed to determine the strength of sub-grade soil and these CBR values will be used to design the thickness of flexible pavement [6]. As soil is a highly variable engineering material due to its composition and the dependence of its properties on environmental conditions, it is logical to evaluate the effect of the variability associated with sub-grade strength on pavement design and performance [7], [8]. Generally, no systematic study has been performed to evaluate the effects of weak, variable sub-grade conditions on pavement design, construction, and performance prediction [9], [10]. Change of the properties of sub-grade soil is definitely affecting the performance of pavement structure.

Fairweather and Yeaman [11] recently studied the influence of flooding on road pavement deterioration and recommended further research to better predict pavement failure.

EXPERIMENTAL SETUP

The samples of sub-grade soil were taken from two different quarries that supply soil which is usually used as the embankment soil in road works. The soil samples were categorized as cohesive material and cohesionless material according to Standard Specification for Road Works by Public Work Department (JKR), Malaysia. The properties of soil are shown in Table 1.

Table 1 Properties of Soil

Soil	Properties	Values
Soil 1 (Well-graded sand with clay and gravel)	Liquid limit	78.5
	Plastic limit	34.2
	Plasticity index	44.3
Soil 2 (Silty clay and gravel)	Liquid limit	88.8
	Plastic limit	38
	Plasticity index	50.8

Sample Preparation

Initially, the experiments such as grain size distribution and index properties were conducted to find out the different properties of soil. After that, the CBR test was performed on unsoaked and soaked specimens in different days of submergence as well as the soil samples were kept submerged in water for certain period in the case of repeated flooding in order to determine the strength of subgrade soil. Finally, the Odometer consolidation tests were carried out to determine the settlement of soil.

CBR Test

CBR test was carried out according to the BS1377. 4300g of soil was compressed in the mould and assign to unsoaked, soaked and repeated submerged condition. The unsoaked soil sample is tested immediately after the soil being compressed into mould, while soaked soil sample is tested for its strength after being soaked for 1, 3 and 7 days. Furthermore, to simulate the effect of repeated inundation the samples were kept in water for 1 hour on Day 1, Day 3 and Day 7. The penetration was measured using a dial gage which has accuracy 0.01mm.

Oedometer Consolidation Test

The Odoemeter test was carried out according to the ASTM D2435. In this research, the Oedometer was modified by using data logger for data recording. The standard Oedometer test is carried out on a cylindrical specimen of saturated soil with the dimension of 75 mm diameter and 20 mm thick. The soil sample is enclosed in a metal ring and is placed on a porous stone. The soil samples were prepared for 1-day submerged and 3-days submerged before tested. The test involves applying increments of 1kg, 2kg, 4kg, 8kg, 16kg and 32kg of vertical static load to the sample and recording the corresponding settlement. The time intervals were 6s, 15s, 30s, 60s, 120s, 240s, 480s, 900s, 1800s, 3600s, 7200s, 14400, 28800s and 86400s.

RESULTS AND DISCUSSION

The mechanical and physical properties for the two types of the tested soils were determined and the particle size distribution for the tested soils, according to American Association of State Highway and Transportation Officials (AASHTO), is shown in Fig. 2 indicating that the percentage passing no. 200 sieve for Soil 1 and Soil 2 are 0.6% and 1% respectively. Based on the AASHTO soil classification system, both soils belongs to soil group which usual types of significant constituent materials are silty or clayey gravel and sand. Moreover, according to the Unified Soil Classification System (ASTM D2487), the tested soils were found and can be classified in group name of "well-graded sand with clay and gravel" for the Soil 1, whereas for the Soil 2 is "poorly graded silty clay and gravel".

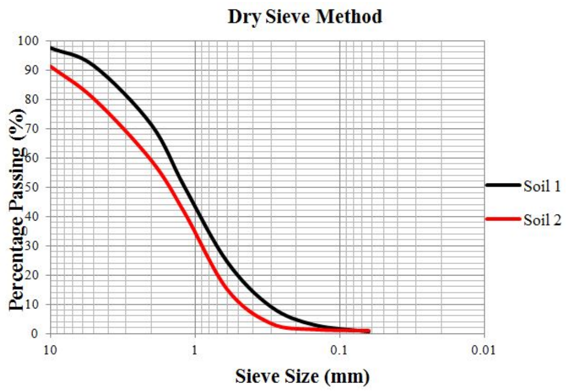

Fig. 2 Particle Size Distribution Curve

CBR Performance

Soil 1

The result of CBR strength presented in Fig. 3 illustrated the comparison of soil strength for unsoaked and soaked condition. The soil samples were inundated for 1, 3 and 7 days for soaked condition. From the bar chart, it shows the CBR value for unsoaked condition relatively higher than CBR value for soaked condition due to the saturated period for soaked soil samples. It shows that the CBR value for unsoaked condition was 35.7% and on submerging the soil samples for 1, 3 and 7 days, the CBR values were 15%, 12.2% and 8.6% respectively. Generally, the soil strength has been reduced by 76% from the condition of unsoaked sample to the 7-day soaking sample. Obviously, the presence of water when the soil had been soaked for 1, 3 and 7 days contributes to the decreasing of soil strength. Soil had been loss strength starting on 1-day soaking when it compared to the unsoaked condition. Soil sample in unsoaked condition show its capability to sustain the higher load since it is evident that there have no subsequent loss of strength. The unsoaked sample basically showed better performance on their strength and the CBR strength probably can be increased with well compacted on soil tested.

However, the CBR value for soaked condition decreased with the strength accordingly due to the number of inundation days for each soaked soil samples. It was found that further increase in the number of days of soaking decreases the CBR value gradually and it is also observed that the loss of CBR value between conditions of 1 day until 7 days soaking. Significant loss of strength was observed caused by inundation and subgrade soil becomes saturated within the soaking period. From the results, it is concluded that the value of CBR for the given soil sample decreases rapidly from unsoaked condition to 1 day of soaking. Additionally, it is also observed that the variation between 1-day and 7-day soaking values are quite different. Soil had been loss more strength on 7-day soaking compared to 3-day soaking since the percentage of CBR value decrease from 12.2% to 18.6% respectively. The volume of soil has been changed effect from the soaking condition, thus the strength of soil become less due to number of inundation days.

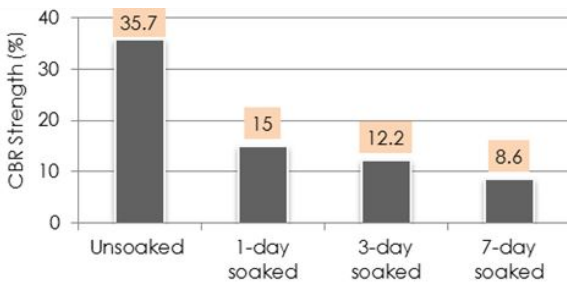

Fig. 3 Comparison of CBR values of inundated samples (Soil 1)

Meanwhile, the bar chart in the Fig. 4, for the repeated submerged condition has shown different result of unsoaked and soaked condition. The soil samples were submerged for 1 hour only on day-1, day-3 and day-7. It shows that the CBR value for unsoaked condition was 35.7% and on repeated submerging for 1 hour on day-1, day-3 and day-7, the CBR values were 25%, 15.9% and 18.5% respectively. Basically, the result shows that unsoaked condition still have the higher CBR strength value when it compared to the repeated submerged condition of soil samples. In the repeated submerged case, the CBR strength was reduced on day-1 after submerged for 1 hour and subsequently the CBR value also reduced on day-3 compared to the unsoaked sample. However, on the day-7, the soil sample was gaining its strength again when inundated for 1 hour after on the day 3. The CBR strength was increased by 16% after submerged for 1 hour on day-7.

Soil sample in unsoaked condition show its capability to sustain the higher load since it is evident that there were no subsequent loss of strength. Moreover, the CBR values for repeated submerged condition is higher than soaked condition since the soil was only inundated for short period when it compared to the soaked condition which the soil has been inundated for a longer period. CBR values were strongly affected by the long-term inundation compared to the case of repeated submerged condition. Since the soil 1 was categorized as well-graded sand with clay and gravel, the possibility of soil to gain the strength on day-7 after submerged on 1 hour is easier because of the soil particle and lower pore water pressure itself.

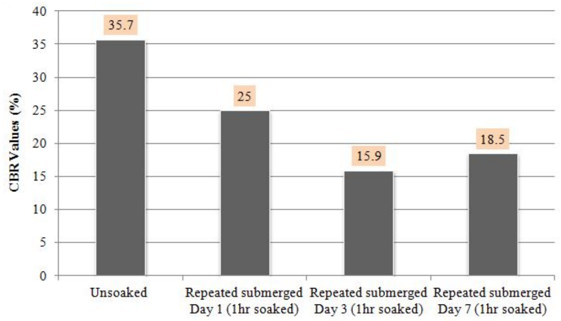

Fig. 4: Comparison of CBR of repeated submergence samples (Soil 1)

Soil 2

Figure 5 presented the result of CBR value for the second soil samples which comparing between unsoaked and soaked condition of soil samples. The test and soil conditions were conducted similar with the first soil samples. From the bar chart, it shows the CBR value for unsoaked condition relatively higher than CBR value for soaked condition due to the saturated period for soaked soil samples. It shows that the CBR value for unsoaked condition was 22.9% and on submerging the soil samples for 1, 3 and 7 days, the CBR values were 10.7%, 6.84% and 3.42% respectively. Generally, the CBR value for both conditions on second soil quite different from soil 1 since the soil 2 was categorized as silty clay and gravel. CBR strength has been reduced by 85% from the condition of unsoaked sample to the 7-day soaking sample. Basically, the second soil sample in unsoaked condition shows its capability to sustain the higher load similar with the first soil samples since it is evident that there has no subsequent loss of strength. However, the CBR strength of soil samples for soaked condition was decreased due to submerging time.

The unsoaked sample basically showed better performance on their strength and the CBR strength probably can be increased with better compaction before the soil will be tested. Meanwhile, soil that soaked for 7 days show the deterioration of its strength performance compared to the 1 and 3 days of soaking condition. Significant loss of strength was observed caused by inundation and subgrade soil becomes saturated within the soaking period. From the results, it is concluded that the value of CBR for the given soil sample decreases rapidly from unsoaked condition to 1 day of soaking. Soil had been loss more strength on 7-day soaking compared to 3-day soaking.

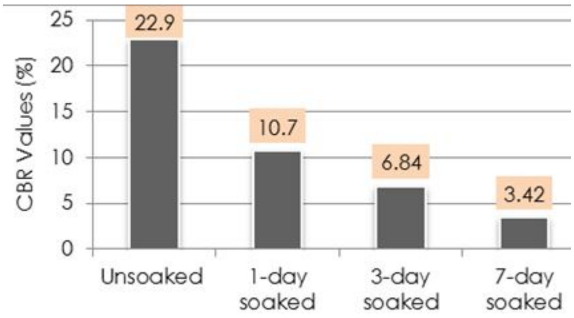

Fig. 5: Comparison of CBR values of inundated samples (soil 2)

On the other hand, the bar chart in the Fig. 6 shows the repeated submerged condition seen differently compared to the unsoaked and soaked condition. The soil samples were submerged similar with soil 1 condition which is the soil samples were submerged for 1 hour only for 1, 3 and 7 days. It shows that the CBR value for unsoaked condition was 22.9% and on repeated submerging for 1 hour on day-1, day-3 and day-7, the CBR values were 13.5%, 8.05% and 5.25% respectively. Basically, the result shows that unsoaked condition still have the higher CBR strength value when it compared to the repeated submerged condition of soil samples. In the repeated submerged case, the CBR strength was reduced on day-1 after submerged for 1 hour and subsequently the CBR value also reduced on day-3 and day-7 compared to the unsoaked sample. The reduction of strength was 61.1% from day-1 submerged for 1 hour to day-7 submerged for 1 hour. This condition occurs probably due to clay condition which its properties consist of small particle size which tends to be very dense. The density of clay that thicker and heavier than other soil types will takes longer time to clay particles absorb this water, and further slowing the flow of water through the soil.

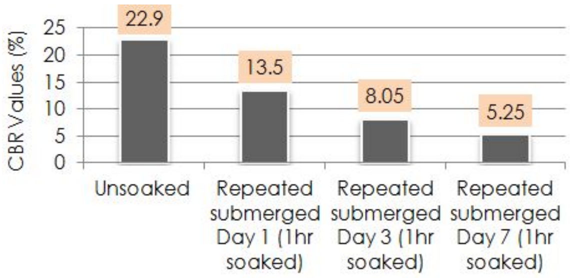

Fig. 6 Comparison of CBR values of repeated submergence samples (Soil 2)

Consolidation Performance

Consolidation is a process by which soils decrease in volume. In this study, the focus is to observe the settlement effect from various loading capacity. Figure 7 and Figure 8 show the graph of settlement against time for soil condition of 1-day submerged and 3-days submerged respectively. For 1 day submerged condition, as shown in Fig. 7, the settlement increases due to the increment of loading. Generally, the load of 1kg, 2kg and 4 kg obtain quick initial settlement at 60s before the soil reached at the optimum settlement. In addition, the load for 8kg, 16kg and 32kg take longer time to reach the constant settlement. The average time to soil reached the constant settlement was about 2 hours. The higher settlement takes places when 32kg load was applied and reach the constant settlement at 1.52mm.

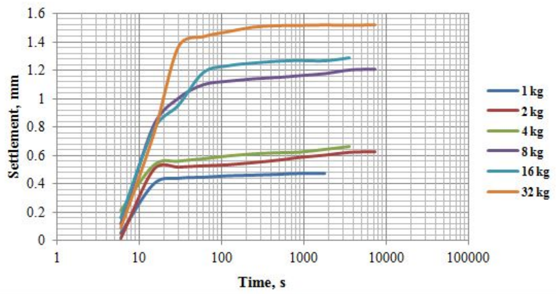

Fig. 7 Graph of settlement against time for 1-day submerged sample

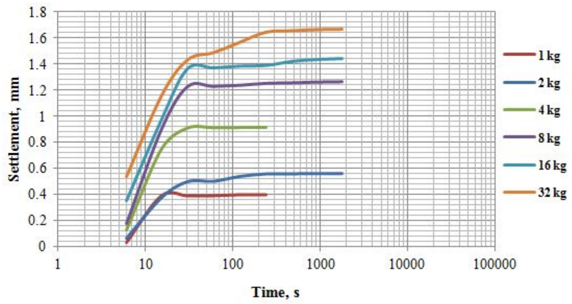

Fig. 8 Graph of settlement against time for 3-days submerged sample

Figure 8 shows the settlement of soil against time for the 3-days submerged condition. The pattern line of graph can be seen quite different when compared to soil samples of 1-day submerged condition since the initial settlement occurs for each load is higher than 1-day submerged condition. This is because the longer period of inundation cause the quick and higher initial settlement. The higher settlement takes places when 32kg load was applied and reach the constant settlement at 1.70mm which higher than the 1-day submerged condition but the consolidation occur in a relatively short time to reach the constant settlement.

The test provides a reasonable estimate of the amount of settlement on soil samples However, the rate of settlement is often underestimated, that is, the total settlement is reached in a shorter time than that predicted from the test data. This is largely due to the size of sample which does not represent soil fabric and its profound effect on exact conditions. Besides the natural condition of the sample, sampling disturbance will have a more pronounced effect on the results of the test done on small samples. Furthermore, the boundary effect from the ring enhances the friction of the sample. The friction reduces the stress acted on the soil during loading and reduces swelling during unloading.

CONCLUSION

Experimental study has been carried out to determine the strength of soil samples when tested in different inundation conditions. The CBR strength for both soils samples indicated the decreases of its strength due to higher increment number of inundation days. It can be concluded that the strength of soil further decrease when they are inundated for a longer period. Similarly, consolidation test also prove that higher settlement could occur when the soil is inundated for a longer period. A more extensive testing will provide the basis for the inclusion of inundation effect in the road design procedures.

ACKNOWLEDGEMENTS

The authors gratefully acknowledge financial support from FRGS research grant no. USM/203/PPBGN/6711257 and NAPREC grant no. USM/401/PPBGN/510059/I-124.

REFERENCES

[1] Adedeji, A. A. and Salami A. W., (2008): Environmental hazard: Flooding and Its Effects on Residential Buildings in Ilorin, Nigeria. http://www.scribd.com/doc/9268022/ . Date Accessed Jan 29 2015.

[2] Bowoputro, H. et al. (2009): Temperature Influence and Lapindo Mud Submersion towards the Stability Value of Asphaltic Concrete Mix, Rekayasa Sipil Journal, Volume 3, No.3 1978 – 5658.

[3] Bernama (2009): RM 21 Juta Untuk Baiki Jalan Rosak Akibat Banjir. Bernama.Com. December 22, 2009.

[4] mySarawak (2009): RM 500 juta bina infrastruktur rosak akibat banjir di Sibu. mySarawak, February 8 , 2009

[5] The Star (2013): RM 106 Juta Diperuntuk Untuk Baik Pulih Jalan Persekutuan Rosak Akibat Banjir. The Star, Jauary 11, 2013.

[6] Naagesh, S., Sathyamurthy, R., Sudhanva, S. (2013): Laboratory Studies On Strength and Bearing Capacity Of GSB-Soil Sub-Grade Composites.

[7] Deshpande, V. P., Damnjanovic, I., and Gardoni, P. (2008): *Modeling The Effects of Rehabilitation Actions on The Reliability of Flexible Pavements*, Proc., Transportation Research Record 87th Annual Meeting, Transportation Research Board, Washington, D.C.

[8] Tarefder, R. A., Saha, N., Hall, J. W., and Ng, P. T. T. (2008): *Evaluating weak subgrade for pavement design and performance prediction: A case study of US 550,* Journal of GeoEngineering, 3(1), 13–24.

[9] Khogeli, W. E. I. and Mohamed, E. H. H. (2004): *Novel Approach for Characterization Of Unbound Materials.* Journal of the Transportation Research Board, No. 1874, Washington, D.C., 38-46.

[10] Theyse, H. L., Hoover, T. P., Harvey, J. T., Monismith, C. L. and Coetzee, N. F. (2006): *A Mechanistic-Empirical Subgrade Design Model Based On Heavy Vehicle Simulator Test Results,* Geotechnical Special Publication No. 154, Pavement Mechanics and Performance, B., Huang, R., Meier, J., Prozzi, E., Tutumluer, Geo Institute, ASCE, 195-202

[11] Fairweather, H. and Yeaman, J. (2014). “A study of the parameters affecting the performance of roads under extreme rainfall event”. Int. J. of GEOMATE, Sept., 2014, Vol. 7, No. 1 (Sl. No. 13), pp.955-960

Fifth International Conference on Geotechnique, Construction Materials and Environment, Osaka, Japan, Nov. 16-18, 2015, ISBN: 978-4-9905958-4-5 C3051

ARSENIC RELEASE PROCESSES INTO CONFINED AQUIFERS OF THE SEINO BASINS, NOBI PLAIN, JAPAN

Yusuke Kawai[1], Masahiko Katoh[2, 3], Ryuki Mori[3], Yu Otake[4], and Takeshi Sato[3]
[1]Graduate School of Engineering, Gifu University, Japan; [2] School of Agriculture, Meiji University, Japan; [3] Faculty of Engineering, Gifu University, Japan; Faculty of Engineering, Niigata University, Japan

ABSTRACT

To understand the mechanisms of arsenic release from the sediment of the Seino Basins, Nobi Plain, Japan, the present study investigated the characteristics of arsenic dissolution and arsenic phases in the sediments of the G_1 and G_2 aquifers and their upper layers. No significant, direct positive relationship between the total and water-soluble arsenic was found. The results of sequential extraction showed that the main sources of water-soluble arsenic were the non-specifically and weakly bound arsenic phases. In addition, a small portion of the arsenic specifically sorbed on the surface of the sediment was dissolved by water extraction. Multiple regression analyses demonstrated that high pH, total arsenic content, and water-soluble organic carbon (WSOC) content strongly contributed to the enhancement of arsenic release from the specifically bound arsenic fraction. These results suggest that high levels of total and non-specifically bound arsenic are responsible for higher levels of arsenic release. In addition, high pH and WSOC content facilitate arsenic release.

Keywords: Alluvial Plain, Arsenic Release, Confined Aquifer, Groundwater

INTRODUCTION

Arsenic is hazardous to human and animal health. Because of its potential migration into groundwater and subsequent plant uptake, it may also be detrimental to plant growth. High groundwater arsenic concentrations, above the World Health Organization (WHO) standard of 0.01 mg/L, have been observed in many areas of the world, particularly in Asian countries. The Bengal Delta Plain in Bangladesh and West Bengal, India, has been recognized as the most serious case of groundwater arsenic contamination. In this region, serious problems caused by arsenic contamination have risen. It is estimated that in Bangladesh, 20 to 50 million people are at risk from drinking water with a high arsenic concentration [1], and in West Bengal, 180 thousand people were found to have suffered from arsenic poisoning [2]. Therefore, much international and local research has been undertaken to elucidate the mechanisms of arsenic release into groundwater [3]–[5].

Similar to the areas mentioned above, arsenic concentrations exceeding the WHO standard have been found in groundwater from alluvial plains in Japan [6], [7]. One such plain is the Nobi Plain, which is located in central Japan. The Seino Basins that are located in the south-west region of the Nobi Plain have two Pleistocene aquifers: the upper, G_1, aquifer exists at a depth of 50–80 m and the lower, G_2, aquifer exists at a depth of 170–200 m. Arsenic concentrations above the WHO standard have been frequently detected in the G_1 aquifer. However, arsenic has not been detected in the G_2 aquifer despite the upper layer of both aquifers (a sedimentary layer accumulated during the Pleistocene age) containing arsenic-contaminated sediment.

The observation of high arsenic concentrations in such sedimentary aquifers provides impetus for research focused on the sources of arsenic and the mechanisms of arsenic release. In many cases, including the Seino Basins, the minerals that compose the sedimentary layer are considered to be the most probable sources of dissolved arsenic in groundwater [8]. The mechanisms of arsenic release into groundwater have been studied by many researchers, e.g., the oxidation of arsenic-containing sulfide [2], [9] and the dissolution of sorbed iron hydroxide arsenic [10], [11]. In addition, the chemical characteristics of groundwater such as pH [12], phosphate ion concentration [12], bicarbonate ion concentration [13] affect arsenic dissolution.

Arsenic release greatly depends on the site characteristics; therefore, the mechanisms of arsenic release at one site may not be applicable to another. For some alluvial plains in Japan, arsenic release mechanisms have been proposed [7], [14]; however, little information is available on arsenic release at the Seino Basins [8], [15]. In particular, it is not understood why high arsenic concentrations are detected in groundwater from the G_1 aquifer, but not from the G_2 aquifer.

The present study investigated the characteristics of arsenic dissolution and arsenic phases in the sediments of the G_1 and G_2 aquifers and their upper layers, using samples from boring cores. The aim of the study was to elucidate the reasons why arsenic is released into the G_1 aquifer but not the G_2 aquifer.

MATERIALS AND METHODS

Study Area and Sample Preparation

This study was conducted using sediment samples from boring cores, which were collected from the Seino Basins located at 35° 9′ 37″ N and 136° 39′ 56″ E in Kaizu, Gifu prefecture, Japan. The following eight sediment samples were selected for chemical analysis: the Nobi layer at depths of 46 and 52 m, the G_1 aquifer at depths of 60 and 64 m, the Atsuta layer at depths of 167 and 173 m, and the G_2 aquifer at depths of 180 and 184 m. The sediment samples of the Nobi and Atsuta layers were mainly composed of silt and clay; in contrast, those of the G_1 and G_2 aquifers were sand and gravel. The samples were air-dried and passed through a 2- or 0.45-mm sieve prior to analysis.

Water-Soluble and Total Arsenic Contents and Arsenic Phases by Sequential Extraction of Sediment

Total water-soluble arsenic in the sediment samples was extracted using ultra-pure water (1:10 solid/liquid ratio). The inorganic and organic arsenic fractions in the water extraction were determined because arsenic behavior was considered likely to differ markedly between these fractions. The fractions were separated by a permeable membrane with a molecular weight cut off of 1,000 (Spectra/Por 7, SPECTRUM). Arsenic concentrations in the total and organic fractions of the water extraction were measured, and the inorganic arsenic concentration was calculated by difference. The total arsenic content of the sediment sample was determined by acid microwave digestion with 14.5 M HNO_3 and 12 M HCl. Sequential extraction was performed on the sediment sample following the procedure described in Wenzel et al. [16]. A 1.0 g, < 0.425-mm sample was extracted with 25 ml of 0.05 M $(NH_4)_2SO_4$ solution (non-specific phase). The sediment remaining after the first extraction procedure was extracted with 25 ml of 0.05 M $(NH_4)H_2PO_4$ solution (specific phase). The sediment remaining after the second extraction was further extracted with 25 ml of 0.2 M NH_4/oxalate buffer at pH 3.25 by shaking for 4 h in the dark (amorphous Fe/Al oxide bound phase). The sediment remaining after the third extraction was extracted with 0.2 M NH_4/oxalate buffer including 0.1 M ascorbic acid at pH 3.25 in a 95 °C water bath with occasional agitation (crystalline Fe/Al oxide bound phase). The remaining sediment was then digested with 5 ml HNO_3 and 2 ml 30% H_2O_2 using a microwave oven, and diluted in a 50 ml measuring flask (residual phase). All extracted or digested solutions were passed through a 0.45-µm filter. The arsenic concentrations of the water soluble fraction were measured by inductively coupled plasma mass spectrometry (ICP-MS; 7500cx, Agilent Technologies Inc., USA), and those of the remaining fractions by ICP atomic emission spectrometry (ICP-AES; ULTIMA2, HORIBA Ltd., Japan) equipped with a hydride generator.

Chemical Properties of the Sediment

The pH and water-soluble organic carbon (WSOC) content were determined in the same solution used for water-soluble arsenic, using a pH meter (MM-60R, DKK-TOA Co., Japan) and a total organic carbon (TOC) analyzer (TOC-V_{WS} Shimadzu Co. Japan), respectively. The amorphous and crystalline forms of metals in the sediment samples were extracted according to the method of Shuman [17], and the iron, manganese, and aluminum concentrations were measured by ICP-AES.

RESULTS AND DISCUSSION

Water-Soluble, and Total Arsenic Contents, and Arsenic Phases by Sequential Extraction of Sediment

The highest water-soluble arsenic concentration (0.64 mg/kg) was found in the sediment sample of the Nobi layer at a depth of 52 m. The second highest was found in the sediment sample of the G_1 aquifer at a depth of 64 m (Fig. 1a). In the sediment samples of

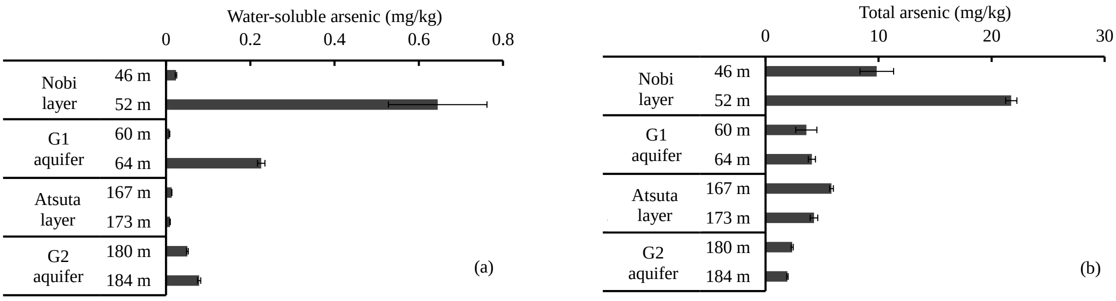

Fig. 1 Water-soluble (a) and total (b) arsenic contents in sediment sample.

the G_2 aquifer at depths of 180 and 184 m, a relatively high level of water-soluble arsenic was observed; however, these values were less than 0.1 mg/kg, the equivalent value of the Japanese environmental standard (converted using the standard value of 0.01 mg/L and the solid/liquid ratio of the water extraction). The total arsenic contents in the sediment samples of the Nobi layer, particularly at a depth of 52 m, were higher than those in the other sediment samples (Fig. 1b). The total arsenic contents in the sediment samples of the G_1 aquifer, the Atsuta layer, and the G_2 aquifer ranged from 1.9 to 5.8 mg/kg. The relationship between the total and water-soluble arsenic contents was investigated, and the result is shown in Fig. 2. When all the samples were included, a significant relationship was found ($r^2 = 0.716^{**}$). However, if the highest concentration sample (open circle in Fig. 2) was excluded, no relationship was found. These results indicate that arsenic release from the sediment was not fully explained by total arsenic content, and that physicochemical characteristics and arsenic phases in the sediment likely controlled

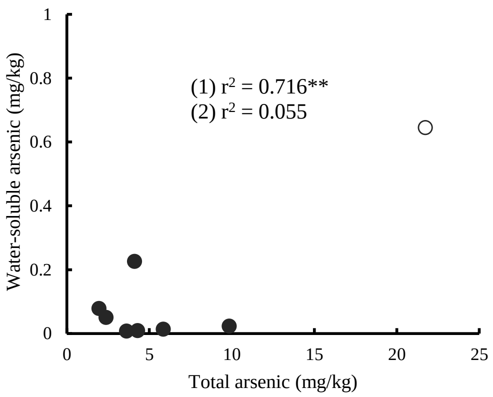

Fig. 2 Relationship between total and water-soluble arsenic contents in sediment sample.
A correlation coefficient (1) was evaluated including all the samples. A correlation coefficient (2) was evaluated in the case of removing an open-circled plot.

arsenic release. The percentage of organic and inorganic arsenic in the water extractions is shown in Fig. 3. The percentage of organic arsenic differed greatly among the sediment samples, ranging from 1 to 68%. In addition, it was not significantly related to the total amount of water-soluble arsenic ($r^2 = 0.001$, data not shown). The water-soluble organic arsenic would be easily desorbed from the surface of the sediment because the complexation of arsenic with organic matter enhances its mobility [3], [18], [19]. However, the poor relationship between the total amount of water-soluble arsenic and the percentage of water-soluble organic arsenic suggests a low contribution of arsenic-organic matter complexation to arsenic release in this study.

Figure 4 shows the arsenic contents of the various fractions in the sequential extraction. The average recovery ratio, which is defined as the ratio of the sum total of each fraction after sequential extraction to the total arsenic content in the sediment sample, was 88 ± 13%. In all samples, except those of the Atsuta layer, the dominant fraction in the sequential extraction was the amorphous Fe/Al oxide bound fraction, in which arsenic concentrations ranged from 1.44 to 8.86 mg/kg. The non-specifically bound fraction, which is the most soluble fraction, showed relatively low arsenic content, 1% or less of the total arsenic content. Figure 5 shows the relationship between the amount of non-specifically bound arsenic and the amount of water-soluble arsenic in the sediment samples. In some samples, which are shown under the broken line, the amount of water-soluble arsenic was lower than the amount of non-specifically bound arsenic, demonstrating that the main sources of water-soluble arsenic were the non-specifically and weakly bound arsenic phases on the surface of the sediment. However, in other sediment samples, shown above the broken line, the amount of water-soluble arsenic was higher than that of the non-specifically bound fraction, indicating that a small amount of arsenic that was specifically sorbed on the surface of the sediment was dissolved during the extraction at the same time

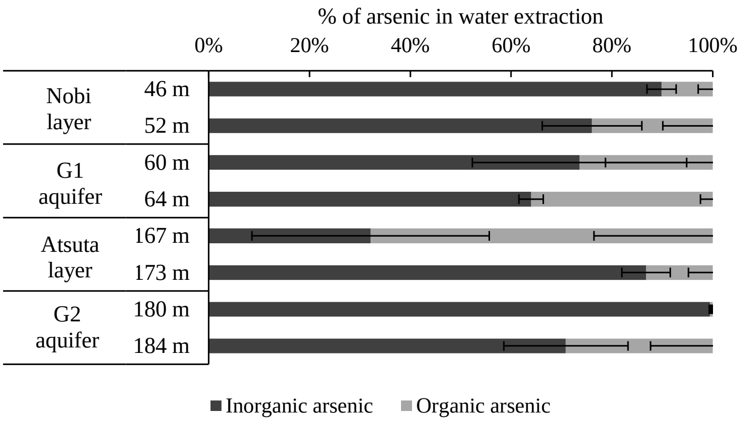

Fig. 3 Percentage of inorganic and organic arsenic fraction in water extraction of sediment sample.

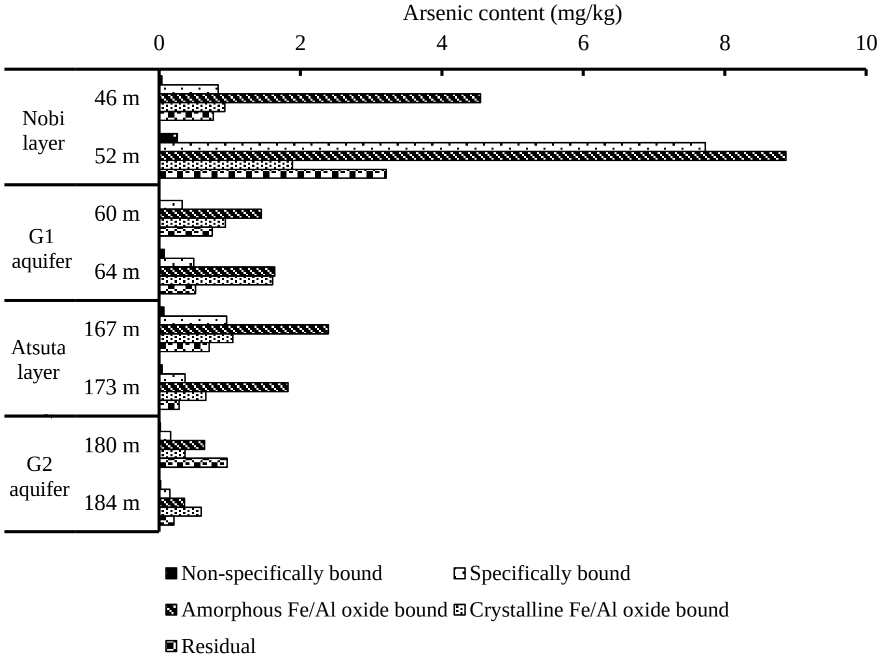

Fig. 4 Sequential extraction of arsenic from sediment sample.

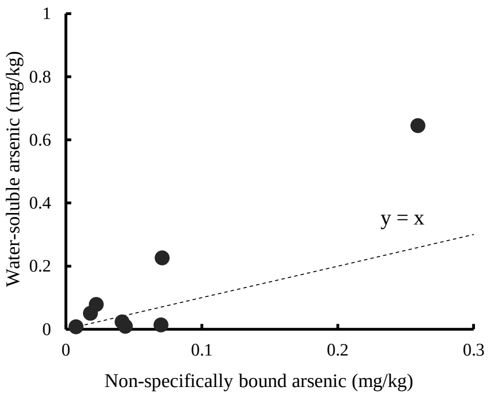

Fig. 5 Relationship between non-specifically bound and water-soluble arsenic contents in sediment sample.
A broken line indicates y = x.

as non-specifically sorbed arsenic was released. Specifically sorbed arsenic can be desorbed by changes in chemical properties of the sediment such as pH, redox condition, and dissolved organic carbon (DOC) concentration [3], [12], [19]. Therefore, the chemical properties of such sediments would lead to an enhancement in the release of arsenic from specifically sorbed phases. In the following section, we investigated the relationship between the amount of water-soluble arsenic and the chemical properties of the sediment samples.

Chemical Characteristics of Sediment Sample

Values of pH in the sediment samples are shown in Table 1. The pH values of the G_2 aquifer at depths of 180 and 184 m were higher than those of the G_1 aquifer at depths of 60 and 64 m, respectively. Similarly, the pH values of the Atsuta layer at depths of 167 and 173 m were higher than those of the Nobi layer at depths of 46 and 52 m, respectively. These results suggest that arsenic would be released more readily from the sediment of the Atsuta layer and the G_2 aquifer compared with the sediment of the Nobi layer and the G_1 aquifer because higher pH induces an increase in the surface net negative charge of sediment, which leads to desorption of oxyanions such as arsenate and arsenite [20]. Figure 6 shows the WSOC contents of the sediment samples. The highest WSOC content of 735 mg/kg was observed in the Nobi layer at a depth of 52 m, and the second highest

Table 1. pH of sediment sample.

	Depth (m)	pH
Nobi layer	46	4.4±0.0
	52	6.1±0.2
G_1 aquifer	60	6.3±0.1
	64	7.2±0.1
Atsuta layer	167	5.9±0.0
	173	6.4±0.1
G_2 aquifer	180	7.2±0.1
	184	8.6±0.7

values were in the Nobi layer at a depth of 46 m and the G_2 aquifer at depths of 180 and 184 m. In the other samples, the WSOC content ranged from 33 to 49 mg/kg. The presence of DOC can enhance arsenic release due to the competition for sorption sites [18], [20]; thus, high WSOC concentrations likely induce arsenic release. The amorphous and crystalline metal contents of the sediments are summarized in Table 2. These greatly depended on the metal species and the depth of the sample, particularly for amorphous iron and crystalline aluminum. However, no significant, positive correlations between the amount of water-soluble arsenic and these chemical properties were found (data not shown). Therefore, the multiple regression analysis between water-soluble arsenic content and the chemical characteristics and total arsenic content of the sediment samples was conducted using forward and backward selections for the choice of explanatory variables to identify the most influential chemical properties on the enhancement of arsenic release. The model fitting was evaluated by determining the *t* value of each variable, the coefficient of determination, the *F* value, and Akaike's information criterion (AIC); the parameters obtained from these analyses are listed in Table 3. According to the results of the analyses, sediment pH, total arsenic content, WSOC, amorphous iron, and crystalline aluminum were extracted as the variables. However, the sensitivity

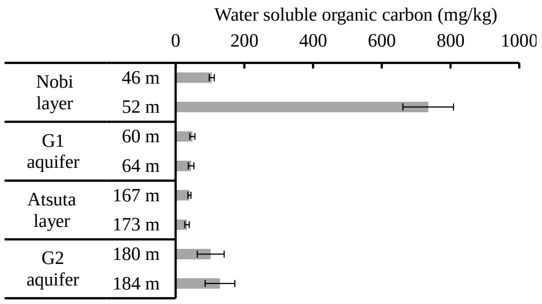

Fig. 6 Water soluble organic carbon in sediment sample.

(calculated by dividing coefficient by average value of variable), where a higher sensitivity indicates a greater contribution to the model, was not high for all variables. The sediment pH showed the highest sensitivity; second was total arsenic content, and third was WSOC. These results demonstrate that these three variables mainly induced the enhancement in release of water-soluble arsenic from the sediment.

As mentioned in the previous section, a portion of the specifically-bound arsenic phase was water-extractable, although the main source of water-soluble arsenic was the non-specifically bound fraction. Samples having a higher level of water-soluble arsenic than non-specifically bound arsenic were found at depths of 52, 64, 180, and 184 m (Figs. 1a and 5). At 52 m, the high total arsenic and WSOC contents would be responsible for the high level of water-soluble arsenic. However, the level of water-soluble arsenic in the sediment sample at 46 m was low, even though the levels of total arsenic and WSOC were high. This can be explained by the low pH of the sediment sample at a depth of 46 m (Table 1), because arsenic sorption on sediment surfaces increases at low pH [20]. The second highest level of water-soluble arsenic was found in the sediment sample at a depth of 64 m, whereas total arsenic and WSOC contents here were comparable to other low-level samples. The pH of the sediment sample at 64 m was 7.2 (Table 1), and this relatively high pH likely led to an enhancement in the level of water-soluble arsenic. The levels of water-soluble arsenic in the sediment samples of the G_2 aquifer at depths of 180 and 184 m were also relatively high, but were lower than the Japanese environmental standard. Despite the high pH and WSOC content potentially enhancing the level of water-soluble arsenic, the low total and non-specifically bound arsenic contents would lead to its suppression, resulting in the preservation of a relatively low level of water-soluble arsenic.

In the Seino Basins, arsenic is detected at levels higher than the Japanese environmental standard in groundwater from the G_1 aquifer, but is not detected

Table 2. Amorphous and crystalline metal contents of sediment sample (mg/kg).

	Depth (m)	Amorphous			Crystalline		
		Fe	Mn	Al	Fe	Mn	Al
Nobi layer	46	7875±740	378±37	1488±72	10552±1335	165±19	4758±626
	52	4648±424	100±7	1380±38	13419±811	226±16	8576±560
G_1 aquifer	60	2638±163	63±8	383±40	8305±398	101±4	1907±163
	64	1431±120	66±23	153±124	6905±214	96±2	1046±47
Atsuta layer	167	4089±569	256±97	685±44	10345±967	148±8	4160±327
	173	8392±556	467±31	1060±75	7945±287	161±7	2564±171
G_2 aquifer	180	4449±1098	374±130	443±24	5414±285	109±6	1437±93
	184	10099±1955	299±97	1706±120	5473±230	103±5	1736±140

Table 3 Multiple regression analysis between water-soluble arsenic and chemical characteristics in sediment.

	Coefficient	*t* value	Sensitivity[1)]
Intercept	-0.2845	-2.017	-
pH	0.0492	2.771	7.56×10^{-3}
Total arsenic	0.0323	3.384	4.81×10^{-3}
WSOC	0.0005	2.541	3.23×10^{-6}
Amorphous iron	-0.0001	-2.488	-1.80×10^{-8}
Crystalline aluminum	-0.0001	-2.205	-3.10×10^{-8}
Coefficient of determination	0.9522		
Adjusted coefficient of determination	0.9389		
F value	71.66		
AIC	-135.96		

1) Coefficient/average

in the G_2 aquifer. As mentioned above, this study demonstrates that non-specifically bound arsenic was the main source of water-soluble arsenic, and chemical characteristics such as pH, WSOC, and total arsenic content in the sediment caused specifically bound arsenic to become water-soluble. Therefore, the results suggest that in the sediment of the Nobi layer and the G_1 aquifer, the high levels of total and non-specifically bound arsenic (as compared with those of the Atsuta layer and the G_2 aquifer, respectively), are responsible for a higher level of arsenic release. In addition, high pH and WSOC content would facilitate the release of arsenic from the specifically bound fraction in the Nobi layer and the G_1 aquifer. This study used only a small number of sediment samples; therefore, in future work, numerous samples should be used to gain a more complete understanding of arsenic release from sediment in the Seino Basins.

CONCLUSION

The present study investigated the characteristics of arsenic dissolution and phases in the sediment of the G_1 and G_2 aquifers and their upper layers, the Nobi and Atsuta layers, respectively, in order to understand the mechanism of arsenic release from the sediment in the Seino Basins, Nobi Plain, Japan. A high level of water-soluble arsenic (over 0.1 mg/kg) was found in the sediment samples of the Nobi layer and the G_1 aquifer, but not in those of the Atsuta layer and the G_2 aquifer. No significant, direct positive relationship between total and water-soluble arsenic contents was found. In some sediments, the amount of water-soluble arsenic was lower than that of the non-specifically bound fraction, demonstrating that the main source of water-soluble arsenic was the non-specifically and weakly bound arsenic phases. However, in other sediments, the amount of water-soluble arsenic was higher than that of the non-specifically bound fraction, indicating that a small portion of the arsenic specifically sorbed on the surface of the sediment was dissolved during the extraction. The results of chemical analyses and multiple regression showed that high pH, total arsenic content, and WSOC content strongly contributed to the enhancement of water-soluble arsenic. These results suggest that in the sediment of the Nobi layer and the G_1 aquifer, the high levels of total and non-specifically bound arsenic would be responsible for the higher level of arsenic release. In addition, high pH and WSOC content would facilitate the release of arsenic from the specifically bound fraction.

ACKNOWLEDGEMENTS

The ICP-AES used for the chemical analysis in this study was made available by the Division of Instrumental Analysis at Gifu University. The authors are grateful to Prof F. Li and Prof T. Yamada (Gifu University) for allowing the use of the TOC analyzer and ICP-MS. This study was supported by Japan Society for the Promotion of Science (JSPS) KAKENHI (grant number 26420481).

REFERENCES

[1] Bhattacharya P, Welch AH, Stollenwerk KG, McLaughlin MJ, Bundschuh J, Panullah G, “Arsenic in the environment: Biology and chemicsty”, Sci. Total Environ., Vol. 379, 2007, pp. 109–120.

[2] Das D, Samanta G, Mandal BK, Chowdhury TR, Chanda CR, Chowdhury PP, Basu GK,

Chakraborti D, "Arsenic in groundwater in six districts of West Bengal, India", Environ. Geochem. Health, Vol. 18, 1996, pp. 5–15.

[3] Anawar HM, Akai J, Komaki K, Terao H, Yoshioka T, Ishizuka T, Safiullah S, Kato K, "Geochemical occurrence of arsenic in groundwater of Bangladesh: sources and mobilization processes", J. Geochem. Explor., Vol. 77, 2003, pp. 109–131.

[4] Seddique AA, Masuda H, Mitamura M, Shinoda K, Yamanaka T, Itai T, Maruoka T, Uesugi K, Ahmad KM, Biswas DK, "Arsenic release from biotite into a Holocene groundwater aquifer in Bangladesh", Appl. Geochem., Vol. 23, 2008, pp. 2236–2248.

[5] Polizzotto ML, Harvey CF, Li G, Badruzzman B, Ali A, Newville M, Sutton S, Fendorf S, "Solid-phases and desorption processes of arsenic within Bangladesh sediments", Chem. Geol., Vol. 228, 2006, pp. 97–111.

[6] Shimada N, "Geochemical conditions enhancing the solubilization of arsenic into groundwater in Japan", Appl. Organomet. Chem., Vol. 10, 1996, pp. 667–674.

[7] Kaneko E, "Arsenic concentration in groundwaters in Sendai City", Chikyukagaku (Geochemistry), Vol. 13, 1979, pp. 1–6. (in Japanese with English abstract)

[8] Nishizawa T, Katoh M, Kitazawa H, Sato T, "Chemical speciation and release of arsenic to groundwater in Seino Basins, Nobi Plain", J. Japan Society Civil Engineering, Ser. G, Vol. 68, 2012, pp. 670–679. (in Japanese with English abstract)

[9] Mandal BK, Chowdhury TR, Samanta G, Mukherjee DP, Chanda CR, Saha KC, Chakraborti D, "Impact of safe water for drinking and cooking on five arsenic-affected families for 2 years in West Bengal, India", Sci. Total Environ., Vol. 218, 1998, pp. 185–201.

[10] Nickson RT, McArthur JM, Ravenscroft P, Burgess WG, Ahmad KM, "Mechanism of arsenic release to groundwater, Bangladesh and West Bengal", Appl. Geochem., Vol. 15, 2000, pp. 403–413.

[11] McArthur JM, Ravenscroft P, Safiullah S, Thirlwall MF, "Arsenic in groundwater: Testing pollution mechanisms for sedimentary aquifers in Bangladesh", Water Res., Vol. 37, 2001, pp. 109–117.

[12] Smedley PL, Kinniburgh DG, "A review of the source, behavior and distribution of arsenic in natural waters", Appl. Geochem., Vol. 17, 2002, pp. 517–568.

[13] Anawar HM, Akai J, Sakugawa H, "Mobilization of arsenic from subsurface sediments y effect of bicarbonate ions in groundwater", Chemosphere, Vol. 54, 2004, pp. 753–762.

[14] Masuda H, Ibuki Y, Tonokai K, "Mechanism of natural arsenic pollution of shallow groundwater in the northern part of Osaka prefecture, Japan", Journal Groundwater Hydrology, Vol. 41, 1999, pp. 133–146. (in Japanese with English abstract)

[15] Nishizawa T, Katoh M, Hori A, Sato T, "Mechanisms of arsenic release into groundwater in Seino Basins, Nobi Plain", J. Japan Society Civil Engineering, Ser. G, Vol. 68, 2012, pp. III_507–III_515. (in Japanese with English abstract)

[16] Wenzel WW, Kirchbaumer N, Prohaska T, Stingeder G, Lombi E, Adriano DC, "Arsenic fractionation in soils using an improved sequential extraction procedure", Anal. Chim. Acta., Vol. 436, 2001, pp. 309–323.

[17] Shuman LM, "Fractionation method for soil microelements", Soil Sci., Vol. 140, 1985, pp. 11–22.

[18] Redman AD, Macalady DL, Ahmann D, "Natural organic matter affects arsenic speciation and sorption onto hematite", Environ. Sci. Technol., Vol. 36, 2002, pp. 2889–2896.

[19] Bauer M, Blodau C, "Mobilization of arsenic by dissolved organic matter from iron oxide, soils and sediments", Sci. Total Environ., Vol. 354, 2006, pp. 179–190.

[20] Grafe M, Eick MJ, Grossl PR, Saunders AM, "Adsorption of arsenate and arsenite on ferrihydrite in the presence and absence of dissolved organic carbon", J. Environ. Qual., Vol. 31, 2002, pp. 1115–1123.

ARSENIC FIXATION STUDIES ON LIME STABILIZED SEMI ARID SOILS

Arif Ali Baig Moghal[1], Krishna R Reddy[2], Syed Abu Sayeed Mohammed[3], Mosleh Ali Al-Shamrani[1] and Waleed M Zahid[1]

[1]Department of Civil Engineering, College of Engineering, King Saud University, Riyadh – 11421, Saudi Arabia

[2]Department of Civil and Materials Engineering, University of Illinois at Chicago, Chicago, IL 60607, USA.
[3]Department of Civil Engineering, HKBK College of Engineering, Bangalore 560045, India.

ABSTRACT

Fine-grained geologic materials are potential barriers for preventing the migration of contaminants from waste disposal sites into local hydrogeological regimes. They have excellent potential to retard the movement of contaminants, they come into contact with. The release of arsenic from dam tailings, spent heap, leach operations and other mining wastes constitutes a major problem owing to its acute toxicity. In this study, locally available semi-arid soils (Al-Ghat and Al-Qatif) having different chemical and mineralogical characteristics are considered as barrier materials, and their response to arsenic adsorption at varying initial concentrations, pH conditions, temperature and dilution ratios is studied. Empirical models (Langmuir and Freundlich) are applied to ascertain monolayer or heterogeneous adsorption. Lime is added to these soils in order to enhance their geotechnical properties. As such, the arsenic adsorption studies are also performed on these soils in the presence of lime. Kinetic models are employed to validate the type and nature of arsenic sorption onto these soils (whether pseudo first-order or second-order). It is found that both Al- Ghat and Al- Qatif soils when amended with lime can attenuate arsenic, and the experimental results correlate well with selected empirical models.

Key Words: Sorption, Arsenic, Langmuir isotherm, Elovich model, Intraparticle diffusion model, Pseudo second order model, Pseudo first order model.

Introduction

Soil is a basic building block for the most terrestrial ecosystems and a complex heterogeneous medium consisting of both solid and fluid phases. The ability of these soils to adsorb and desorb metal ions from the aqueous phase is of great importance when dealing with both the environmental and agricultural issues. The clay fraction predominantly affects the metal ion concentrations in environmental systems owing to their ability to adsorb these ions and any release in part or whole when subjected to varying natural conditions. Heavy metal and metalloid removal from aqueous solutions can be achieved through processes such as chemical precipitation, solvent extraction, ion-exchange, reverse osmosis, and adsorption. However, adsorption process, with the selection of a suitable adsorbent, is commonly used as it is a simple and effective technique for the removal of heavy metal ions. Soils and soils amended with additives have also been used as an adsorbent to remove many heavy metals. The efficiency of retention is found to vary considerably with the nature of soil, type of heavy metal (including oxidation state and concentration), pH of the solution, and other environmental factors [1-2].

Arsenic is one of the most commonly found metal contaminants in wastes and at waste disposal sites. Arsenic can occur naturally in rocks and soil, water, air, plants and animals, or it can be released into the environment through natural activities such as volcanic action, erosion of rocks, and forest fires. Moreover, anthropogenic contributions of arsenic in the environment can occur through its use as wood preservatives in paints, dyes, metals, drugs, soaps and semi-conductors. High arsenic levels can also be released from certain fertilizers and animal feeding operations. Industry practices such as copper smelting, mining and coal burning also contribute arsenic to our environment. Higher levels of arsenic tend to be found in ground water sources than in surface water sources (i.e., lakes and rivers) of drinking water. The demand on ground water from municipal systems and private drinking water wells may cause water levels to drop and release arsenic from rock formations and exacerbate the arsenic levels in ground water [3]. Arsenic exposure can result in carcinogenic and non-carcinogenic responses in humans. Inorganic arsenic compounds are known human carcinogens; USEPA ascertained this designation based on increased lung cancer mortality in multiple human populations exposed primarily through inhalation, increased mortality from multiple internal organ cancers (liver, kidney, lung and bladder), and increased incidence of human cancer in populations consuming drinking water high in inorganic arsenic. The critical effects are hyper pigmentation, keratosis, and possible vascular complications based on human chronic exposure The maximum limit for human consumption of arsenic is limited to 10 ppb by USEPA.

Arsenic speciation can be quite complex in soils. As^{+3} or As(III) is the dominant form under reducing conditions, while As^{+5} or As(V) is generally the stable form in oxidizing environments. Arsenic compounds adsorb to soils, clays, organic matter and metal oxides/ hydroxides [4]. Arsenic is challenging to treat, and some of the common remediation methods may include containment using barriers, soil washing/flushing, electrokinetics, solidification and stabilization [5]. Solidification and stabilization (S/S) is considered to be the cost effective method for treating high levels of arsenic in soils [6]. Additives and binders used in S/S oxidize As^{+3} and As^{+5} and form insoluble complexes or become immobilized due to formation of strongly adsorbed species or form co-precipitates with calcium or iron [7]. Calcium has been found to retain arsenic by replacing itself for arsenic in a ratio of 1: 1 mole [8]. However, a sufficient amount of $Ca(OH)_2$ is also required for the hydration to proceed in the system [9,10,11].

In this study, the retention of As in two semi-arid soils, originating from Al-Ghatt and Al-Qatif, is investigated to evaluate their suitability as barrier materials. Further, the effects of amending these soils with lime on enhanced arsenic retention are explored. Several series of batch equilibrium tests are conducted to systematically investigate the effects of initial concentration, solution pH, temperature, and time dependent kinetics on arsenic retention in the soils with and without lime amendment.

MATERIALS AND METHODS

Materials

Soil samples collected from Al-Ghatt and Al-Qatif are selected for testing in this study. Al-Qatif is a historic coastal oasis region located on the western shore of the Persian Gulf in the Eastern Province of Saudi Arabia (26° 56′ 0″ N, 50° 1′ 0″ E). Al-Ghatt is a town located 270 km to the Northwest of Riyadh at latitude 26° 32' 42" N and longitude 43° 45' 42" E. The physicochemical properties of soils were determined and the USCS (Unified Soil Classification System) classified both soils as CH (clay with high plasticity) with specific gravity of 2.84 and 2.71, respectively. It was found that Al-Ghat soil to be a kaolinitic soil and Al-Qatif soil to be a montmorillonitic soil. Lime was used as soil amendment (6% by dry weight of the soil), and the lime used was obtained as AR grade calcium hydroxide from Qualigens Company. Arsenic was obtained as arsenic trioxide (AR- grade) supplied by Qualigens Company, which was used as source chemical for arsenic in this study.

Batch Equilibrium Test Procedure

Batch adsorption experiments were conducted by shaking mechanically a series of bottles containing the soil sample and heavy metal ion solutions maintained at different pH values. Soil sample of 5g was mixed with 100 ml of the solution maintained at a particular pH in 500 ml polyethylene bottles to obtain the soil slurry. In all the tests, the liquid to solid dilution ratio was maintained at 20. This slurry was agitated with a mechanical shaker at room temperature (25±2°C) for 2 h until the pH was stabilized. The pH of the slurry was adjusted to the desired value in the range of 2 to 10 with 0.1M HNO_3 and NaOH [12].

Predetermined amounts of source chemical were added to the bottles to result in the desired arsenic concentrations (10, 15, 20, 25 and 30 mg/l), and the bottles were further agitated until equilibrium concentrations were attained. The slurry was filtered using Whatman 42 ashless filter paper and the residual concentration of arsenic in the filtered solution was measured using atomic absorption spectrophotometry (AAS). The amount of arsenic adsorbed by the clay fraction was taken as the difference between the initial and residual concentrations of the arsenic in the solution. In order to determine the removal by hydroxide precipitation at various pH values, a set of blank tests were also conducted using solutions maintained at different pH values without soil. Tests were conducted in triplicates and the average concentrations are calculated. In order to investigate the effect of temperature on adsorption of arsenic, a series of tests was conducted in controlled constant water bath conditions following the same adsorption testing procedure [13].

The effects of solids to liquid ratio on adsorption results was assessed by preparing the samples with solid to liquid (S/L) ratios of 1:20, 1:30, 1:40, 1:100, and 1:200 and shaking them for 24 hours. Then, 100 mgL^{-1} equivalent arsenic mass was added to all samples and again shaken for 24 hours. The samples were then removed, filtered and the filtered liquid was analyzed for arsenic concentration. Another series of experiments was conducted to investigate pH effects by employing the similar procedure except the pH of the contaminant solution was first adjusted to the required level and then the adsorbent was added while maintaining a constant S/L ratio of 1:20 throughout the procedure.

Adsorption Kinetics Test Procedure

A series of kinetic adsorption tests was conducted to study the time dependent arsenic adsorption and help determine the time necessary to achieve the maximum removal capacity. For this test series, batch experiments were conducted for different predetermined time intervals in different polyethylene bottles prepared and maintained under similar conditions. At the end of each fixed time interval, the soil slurry was filtered and the concentration of arsenic was determined as above. This procedure was repeated till the concentration of arsenic in the filtrate remained unchanged with time. The experimental results were validated by applying them to isotherm and kinetic models. Table 1 gives details of all the models used.

RESULTS AND DISCUSIONS

The results obtained from batch equilibrium and kinetic adsorption experiments are assessed to study the adsorption behavior of arsenic in the tested two soils.

Effects of Initial Concentration, Dilution Ratio and pH on Arsenic Adsorption

Results in Fig.1 show that sorption coefficient increases with initial concentration, with the increase in concentration the competition from other ions reduced resulting in an efficient sorption of arsenic. A decrease in soil amount decreases the number of active sites that are available for sorption and the amount of sorption decreases. This is evident from Fig.2 in that as dilution ratio increases, more amount of metal ion become available for sorption. Only stable metal ions get sorbed leading to an effective and permanent sorption. Heike [14] also reported similar results in that an increase in the solids results in an increase in retention. This is attributed to an increase in the available surface area and thus an increase in active sites. However, the increase in contaminant retention is not proportional to the amount of the solids; which is attributed to the decrease in the mass transfer gradient as the remaining concentration of contaminant diminishes.

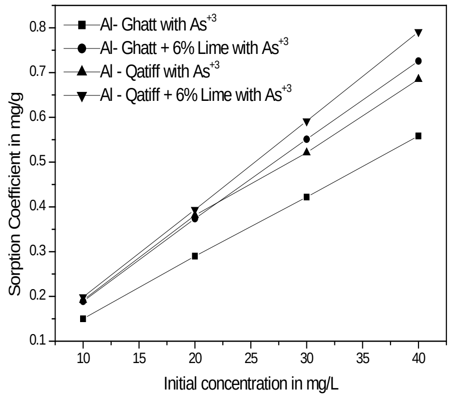

Fig. 1 Sorption of As in soils with and without lime amendment under different initial concentration

The pH plays a major role in sorption of arsenic, and the results showed a gradual increase in the amount of sorbed arsenic with the increase in pH. This increase in sorption can be explained by the changes that occur to the sorbate (soils and their oxide surfaces) and the formation of hydroxides of metal complexes under different pH conditions. The pH of the solution affects the protonation of the functional group on the adsorbent surface of soils as well as metal complexation. At low pH values, adsorbed protons that are exchanged on surface can form proton bonds between surface and metal complexes. The sorbed protons, also, generate positive charges at the surface repelling or attracting positively or negatively charged metal complexes respectively. It was found that the presence of calcium in lime played a major role in sorption as it increased the pH of the solution there by precipitating the As ions. It was found that the effective sorption took place at a pH range of 4.5 to 8.5 which can be attributed to the formation of As-Ca complexes at this pH range [15].

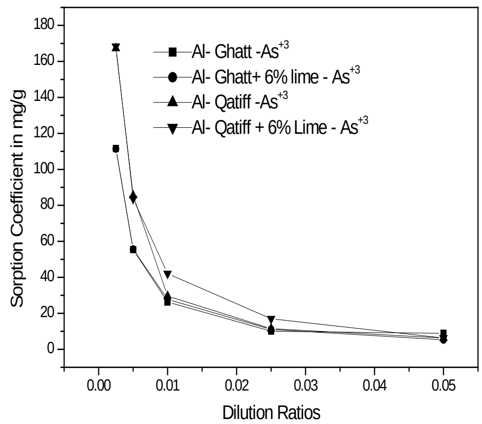

Fig. 2 Sorption of As in soils with and without lime amendment under different solids to liquid ratios

Effect of Temperature on Arsenic Adsorption

Temperature is known to affect the complexation of metal ions. The influence of the temperature on retention of arsenic was investigated in the range from 25° to 55°C. The selected temperature range encompasses the typical temperature expected during the course of the year in Saudi Arabia. The average temperature of 25°C corresponds to winter, while 55°C is the maximum possible temperature during the summer. All the tests were conducted at neutral pH value (6.8 to 7.2). The effect of temperature under different pH conditions was beyond the scope of this study. For a given initial concentration, the amount of arsenic retained increased considerably with increase in temperature. This effect was more pronounced at higher initial concentration values. The increase in retention levels for arsenic could be attributed to conditions favoring enthalpy and entropy changes in both Al-Ghat and Al-Qatif soils. The increased retention capacity at elevated temperatures is primarily due to entropy increase arising due to increased disorder of water molecules and respective cations in the soil slurry. The results obtained indicate that for both Al-Ghat and Al-Qatif, the increase in temperature aids in higher arsenic removal capacity.

Sorption Isotherms

Batch equilibrium sorption data was modeled using two common sorption isotherm models, namely Langmuir model and Freundlich model. The isotherm parameters were calculated and are summarized in Table 2. The values of monolayer sorption capacity calculated using Langmuir isotherm are in the similar range for all the soil lime mixtures. For Freundlich isotherm, the R^2 is close to one, but its adsorption values are unrealistic. Hence, Freundlich isotherm does not hold good for these samples. The Langmuir isotherm may be expressed in terms of equilibrium parameter R_L which is a dimensionless constant referred as separation factor. R_L value indicates the sorption nature to be unfavorable if $R_L > 1$; linear if $R_L = 1$; favorable if $0 < R_L < 1$; and irreversible if $R_L = 0$. A separation factor of less than one is obtained for all the samples, which indicates that Langmuir isotherm is favours this sorption.

Adsorption Kinetics of Arsenic in Soils

It can be observed from Fig. 3 that significant sorption occurs immediately and it increases with time with maximum sorption levels in 30 minutes, and thereafter it remains constant till 1440 minutes (24hrs). Sorption increased with time as well as with initial arsenic concentration.

The sorption versus time data was used to test different kinetic models such as pseudo first order, pseudo second order, Elovich, and intraparticle diffusion. The results obtained are summarized in Table 3. It was observed from regression analysis that pseudo second order kinetic model was better than the first order kinetic model as its regression coefficient was closer to one. Also for a heterogeneous material like soil, monolayer sorption alone does not occur. Instead, a number of processes such as chemi-sorption, ion exchange and precipitation occur simultaneously. Pseudo second order being a better model reinforces this assertion and this conclusion is also in general agreement with previous studies [15]. Elovich kinetic model tries to model the processes of desorption and chemisorption. It can be seen from the regression analysis, as given in Table 3, that the regression coefficient is closer to 1 which indicates that chemisorption is also possibly occurring, where the ά and β values represent sorption and desorption. Further, sorption increases with concentration, while desorption decreases with concentration [16].

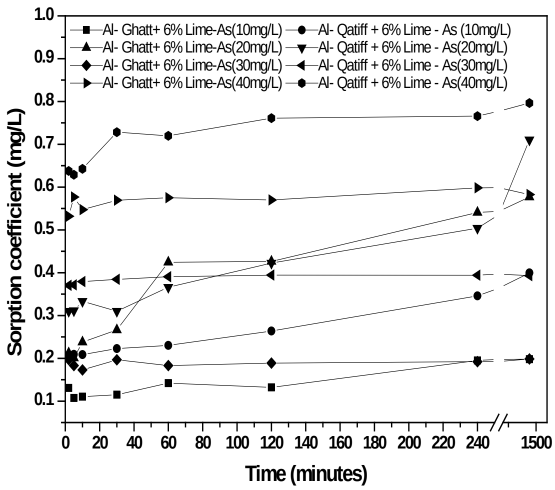

Fig. 3 Time dependent adsorption of As soils with and without lime amendment

At a higher concentration, sorption takes place predominantly on sorption sites whereas at lower concentration desorption is dominant as competing ions predominate the sorption sites. Similarly, intra particle diffusion model tries to predict the phenomenon of diffusion in the sorption process. If the results follow a linear fit passing through the origin, then it implies that only diffusion acts as the predominant phenomenon. It can be observed from Table 3 that, the regression value is closer to 1, but the regression line does not coincide with the origin which shows that along with sorption, diffusion is also active, but it is not the dominant process in sorption.

Table 1 Linear forms of Models used

Sl No.	Name	Linear Form	Plot	Slope	Intercept
1.	Sorption Coefficient	$q_e = \frac{(C_o - C_e)V}{m}$	-	-	-
2.	Langmuir Isotherm	$\frac{C_e}{q_e} = \frac{1}{K V_m} + \frac{C_e}{V_m}$	Versus C_e	$\frac{1}{V_m}$	$\frac{1}{K V_m}$
3.	Freundlich Isotherm	$Log\ q_e = \log K_f + \frac{1}{n}\log C_e$	Versus	K_F	$\frac{1}{n}$
4.	Pseudo First Order Kinetic Model	$Ln(qe - qt)_1$	Versus t	K_1	q_e
5.	Pseudo Second Order Kinetic Model	$\left(\frac{t}{qt}\right) = \frac{1}{K_2\ qe^2} + \frac{1}{qe}(t)$	vesus t	q_e	K_2
6.	Elovich Kinetic Model	$qt = \frac{1}{\beta}\ln(\alpha\beta) + \frac{1}{\beta}\ln(t)$	versus	$\frac{1}{\beta}$	$\frac{1}{\beta}\ln(\alpha\beta)$
7.	Intraparticle Diffusion Model	$qt = K_{dif}\ t^{0.5} + C$	versus $t^{0.5}$	K_{dif}	C

Table 2 Langmuir and Freundlich Isotherm Parameters for Arsenic Sorption in Soils with and Without Lime Amendment

Parameters Sorbent	Initial Conc in mg/L	Langmuir isotherm: Monolayer Adsorption Capacity in mg/g	K	R^2	Separation factor R_L	K_f	Freundlich Isotherm: n adsorption intensity	R^2
Al- Ghatt Soil + As	10	1.483	$4.50 X10^{-2}$	0.95	0.6897	0.1852	0.0053	0.98
	20	1.462			0.5269		0.0018	
	30	1.472			0.4251		0.0009	
	40	1.586			0.3576		0.0006	
Al- Ghatt Soil + 6% Lime + As	10	2.011	$1.89 X10^{-1}$	0.9512	0.3454	0.9160	0.3251	1
	20	1.874			0.2089		0.2399	
	30	1.452			0.1492		0.1980	
	40	1.758			0.1164		0.1742	
Al- Qatiff + As	10	3.785	0.126	0.904	0.4429	0.8400	0.2699	0.588
	20	3.610			0.2849		0.1897	
	30	1.571			0.2095		0.1548	
	40	1.633			0.1629		0.1375	
Al- Qatiff + 6% Lime + As	10	3.060	1.157	0.96	0.0795	0.5120	0.5287	0.95
	20	1.510			0.0425		0.5687	
	30	1.812			0.0234		0.5297	
	40	2.310			0.0216		0.5346	

Table 3 Kinetic model parameters for Arsenic Sorption in Soils with and Without Lime Amendment

Parameters		Pseudo first order		Pseudo Second Order		Elovich			Intra Particle Diffusion		
Sorbent	Initial Conc(mg/l)	K_1 per min	R^2	K_2(g/mg/min)	R^2	β g/mg	α mg/g/min	R^2	K_{dif} mg/g/min$^{0.5}$	C mg/g	R^2
Al- Ghatt Soil + As	10	0.0062	0.9800	4.26×10^{-6}	1.02529	49.4559	0.0928	0.9912	0.0032	0.07337	0.8330
	20	0.0058	0.9600	9.056×10^{-2}	1.00	25.6410	0.4626	0.9928	0.0050	0.2683	0.8049
	30	0.0185	0.9885	4.82×10^{-6}	1	22.7842	3.2682	0.9762	0.0044	0.2621	0.9613
	40	0.0024	0.9871	1.839295	0.9999	19.688	4.4788	0.9538	0.0148	0.2316	0.9833
Al- Ghatt Soil + 6% Lime + As	10	0.0119	0.97276	2.91×10^{-8}	1	48.0769	0.0627	0.9653	0.0035	0.0755	0.9768
	20	0.00374	0.99063	1.88×10^{-8}	1	35.8551	1.56204	0.8737	0.0053	0.1627	0.9839
	30	0.00407	0.9916	1.92×10^{-9}	1	26.7952	37.9274	0.9400	0.0061	0.2709	0.9363
	40	0.00359	0.99532	5.76×10^{-7}	1	24.9812	638.9750	0.8603	0.0075	0.4206	0.9129
Al- Qatiff + As	10	0.00221	0.9416	5.43×10^{-10}	1	74.6825	34.1722	0.9805	0.0036	0.1240	0.8727
	20	0.00126	0.99644	1.33972	1	59.2417	882.4575	0.9297	0.0031	0.2137	0.9391
	30	0.00051	0.78949	3.05×10^{-9}	1	36.8052	1337.9876	0.9725	0.0047	0.3468	0.9084
	40	0.000955	0.98272	1.91682	0.99999	28.2167	920.4580	0.9163	0.0069	0.4202	0.9714
Al- Qatiff+ 6% Lime + As	10	0.00304	0.96947	5.76×10^{-9}	1	236.9668	12.8765	0.9206	0.0041	0.1711	0.8854
	20	0.00499	0.99175	0	1	65.4450	166.3907	0.9714	0.0158	0.2827	0.9714
	30	0.00363	0.99085	6.16×10^{-9}	1	53.3617	369.5565	0.9368	0.0199	0.4453	0.9678
	40	0.00316	0.98837	4.77073	1	42.4448	1925.9	0.9218	0.0054	0.6091	0.9602

CONCLUSIONS

The retention of metal ions by soils is a complex process involving complex mechanisms, and is controlled by different variables that can interact. In this study, two field soils (Al-Ghat and Al-Qatif soils) having variable chemical composition were selected and amended with 6% lime to enhance their retention capacity of arsenic. The results obtained indicate that both initial concentration and rise in temperature favor the retention characteristics for both soils with lime quite significantly. Surface adsorption is known to be dominant at lower pH levels, while precipitation favored at higher pH levels. The presence of calcium in lime played a major role and formed stable precipitates of calcium arsenate at highly oxidizing conditions and moderate pH conditions of 4.5 to 8.5. At elevated temperatures the hydration of calcium occurs efficiently which contributed to efficient sorption of arsenic. The addition of lime in soil to retain arsenic creates a solidified monolith where the mobility is diffusion controlled [17]. This reduces the leaching of arsenic significantly and this soil lime mixture can be considered to suitable barrier material (e.g. soil liner for a landfill) Relatively higher retention of arsenic was recorded in case of Al-Qatiff (montmorillonitic soil) with lime than Al-Ghatt (kaolinitic soil) with lime due to difference in chemical composition, entropy and enthalpy changes. This is also consistent with the published studies that montmorillonitic soils retain arsenic better than kaolinitic soil.

The following specific conclusions can be drawn from this study:

1. Al- Ghatt soil and Al- Qatiff soil amended with 6% lime were found to be good sorbents for arsenic. Al-Qatiff is a better adsorbent than Al- Ghatt soil.
2. Sorption is pH dependent and the maximum sorption occurs over a pH range of 4.5-8.5 for arsenic in both the soils. Retention of arsenic increased with increase in initial concentration, dilution ratio, and pH.
3. Langmuir monolayer sorption capacity is shown to decrease with concentration, whereas Elovich's model sorption is found to increase with concentration and desorption to decrease with concentration.
4. The adsorption kinetic experiments show for both soils that the maximum sorption occurs within an hour and thereafter reaches equilibrium.

   Arsenic retention in soils us attributed to several processes such as sorption, chemisorptions, ion exchange, precipitation and diffusion occurring simultaneously, with no one process is being dominant.

ACKNOWLEDGEMENTS

This project was funded by the National Plan for Science, Technology and Innovation (MAARIFAH), King Abdul Aziz City for Science and Technology, Kingdom of Saudi Arabia, Award Number (12ENV2583-02).

REFERENCES

[1] Ladeira A, C. Q. and V. N S. T. Ciminelli, "Adsorption and desorption of arsenic on oxisol and its constituents" Water Research, Vol. 38(8), 2004, pp. 2087-2094.

[2] Leist, M, R J Casey, et al. "The management of arsenic wastes: problems and prospects"Journal of Hazardous Materials, Vol. 76(1), 2000, pp. 125-138.

[3] Jia Y, and G. P. Demopoulos, "Coprecipitation of arsenate with iron(III) in aqueous sulfate media Effect of time, lime as base and co-ions on arsenic retention." Water ResearchVol. 42(3), 2008, pp. 661-668.

[4] Battaglia-Brunet F, C Crouzet, et al. "Decreased leachability of arsenic linked to biological oxidation of As(III) in solid wastes frombioleachingliquors" Hydrometallurgy, Vol. 107(1–2) , 2011, pp. 34-39.

[5] Shih, CJ, and CF Lin, "Arsenic contaminated site at an abandoned copper smelter plant: waste characterizationand solidification/stabilizationtreatment"Chemosphere,Vol.53(7),2003,pp.691-697.

[6] Lenoble V O, Bouras, etal. "Arsenic Adsorption onto Pillared Clays and Iron Oxides." Journal of Colloid and Interface Science, Vol. 255(1), 2002, pp. 52-58.

[7] Jing C, S. Liu, et al. "Arsenic leachability and speciation in cement immobilized water treatment sludge." Chemosphere Vol.59(9), 2005, pp. 1241-1247.

[8] Dermatas D, DH Moon, et al. "An evaluation of arsenic release from monolithic solids using a modified semi-dynamic leaching test" Journal of Hazardous Materials Vol. 116(1–2), 2004, pp.25-38.

[9] Dusing D C, P L Bishop, et al. "Effect of Redox Potential on Leaching from Stabilized/Solidified Waste Materials" Journal of the Air & Waste Management Association,Vol. 42(1), 1992, pp. 56-62.

[10] Randall PM, "Arsenic encapsulation using Portland cement with ferrous sulfate/ lime and terra bond technologies- Microcharacterization and leaching studies", Science of total environment, Vol. 420, 2012, pp.300-312.

[11] Mohammed S, Moghal A, "Soils Amended with Admixtures as Stabilizing Agent to Retain Heavy Metals", ASCE Geotechnical Special Pub No. 234, 2014, pp.2216-2226.

[12] Moghal B, Sivapullaiah P, "Retention Characteristics of Cu^{2+}, Pb^{2+} and Zn^{2+} from Aqueous Solutions by Two Types of Low Lime Fly Ashes", J. Toxic. Environ. Chem. Vol. 94-10, 2012, pp.1941-1953.

[13] DutréV,andCVandecasteele,"Solidification/stabilisation of arsenic-containing waste:

[14] Leach tests and behaviour of arsenic in the leachate" Waste Management. Vol. 15(1), 1995,pp. 55-62.

[15] Heike B, "Adsorption of Heavy metal ions on soils and soils constituents". J. Colloid and Interface Sci, Vol. 277, 2004, pp. 1 -18.

[16] Ho Y, Mc Kay G, "Pseudo –second order model for sorption processes". J. Process Biochem,Vol. 34, 1999, pp.451 – 465.

[17] Kim, MJ, J Nriagu, et al., "Carbonate Ions and Arsenic Dissolution by Groundwater." Environmental Science & Technology,Vol. 34(15), 2000, pp 3094-3099.

[18] Daniels J L, and GP Das, "Leaching Behavior of Lime–Fly Ash Mixtures" Environmental Engineering Science, Vol. 23(1), 2006, pp. 42-52.

Fifth International Conference on Geotechnique, Construction Materials and Environment, Osaka, Japan, Nov. 16-18, 2015, ISBN: 978-4-9905958-4-5 C3051

INVESTIGATION ON THE ARSENIC POLLUTION AROUND THE DOMESTIC WASTE DISPOSAL SITE IN SUZUKA CITY

Masaaki Takahashi[1], Yukimasa Takemoto[1]

[1]Faculty of Environmental and Information Sciences, Yokkaichi University, Japan

Abstract

Recently, arsenic pollution in the ground water has been widely found around the domestic waste disposal site of Suzuka city which is situated in the central part of Japan. In order to identify the source of this pollution, we have investigated the ground water and the leachate at eleven observation sites around this landfill site. Concentrations of the following parameters such pH, EC, arsenic, Cl ion and ionic balance were analyzed. A slight relationship between the arsenic, Cl ion and EC was found. However, the source of the arsenic pollution was not apparent from the analysis on ionic balance, and further investigations are considered to be necessary.

Keyword: Arsenic pollution, Ground water, Disposal site, Suzuka City

INTRODUCTION

Arsenic is known as one of the harmful elements, and in recent years, as for the arsenic, an environmental standard became severer in Japan.. A significant amount of arsenic has been found in natural soils, and much pollution of arsenic has been reported [1], especially in the ground water [2, 3] in Japan. Five years ago, arsenic pollution was found in the Fukaya waste disposal site in Suzuka situated in the central part of Japan, 50km south west from Nagoya. Almost all of the incinerated ash discharged from Suzuka city has been disposed. The pollution which corresponds two or three times higher than the Japanese water environmental standard was found at two monitoring stations, and it has continued today. The arsenic pollution was found in a limited area of this landfill site and also was found about 30 years later after the construction of this site.

In order to solve the cause of this pollution, some investigations were carried out from the request of the Suzuka municipal government. .

INVESTIGATION METHOD

The feature of this dumping site

The Fukaya disposal site was constructed in 1972 on the valley of a hill (altitude about 30m) in Hachino town, Suzuka city , and was used till 1997. The disposal site is divided into two sections (No.1 and No.2). The size of the dumping area is 53480 m^2 (in area) and 728355 m^3 (in volume) respectively. The total amount of the waste in the disposal site is estimated to be 710,000 tons.

This waste site was filled on a natural clay bed in Neogene period [4], and enclosed by a clay levee (in No.1) and concrete levee (in No.2) at the each lower reach. The feature of the dumping site is shown in Fig.1. Almost all rain fall moves into the layer of the waste, and deposited inner part of the levee, and evacuated outside using the electric pumping. The small amount of water , however, is expected to pass through the clay bed.

In order to check the ground water pollution, some monitoring stations (monitoring wells or leaching water) were prepared around the dumping site, and monitoring of this site has been carried out for a long time. .

Monitoring stations

The monitoring was carried out at seven stations as shown in Table 1 and Fig.1.

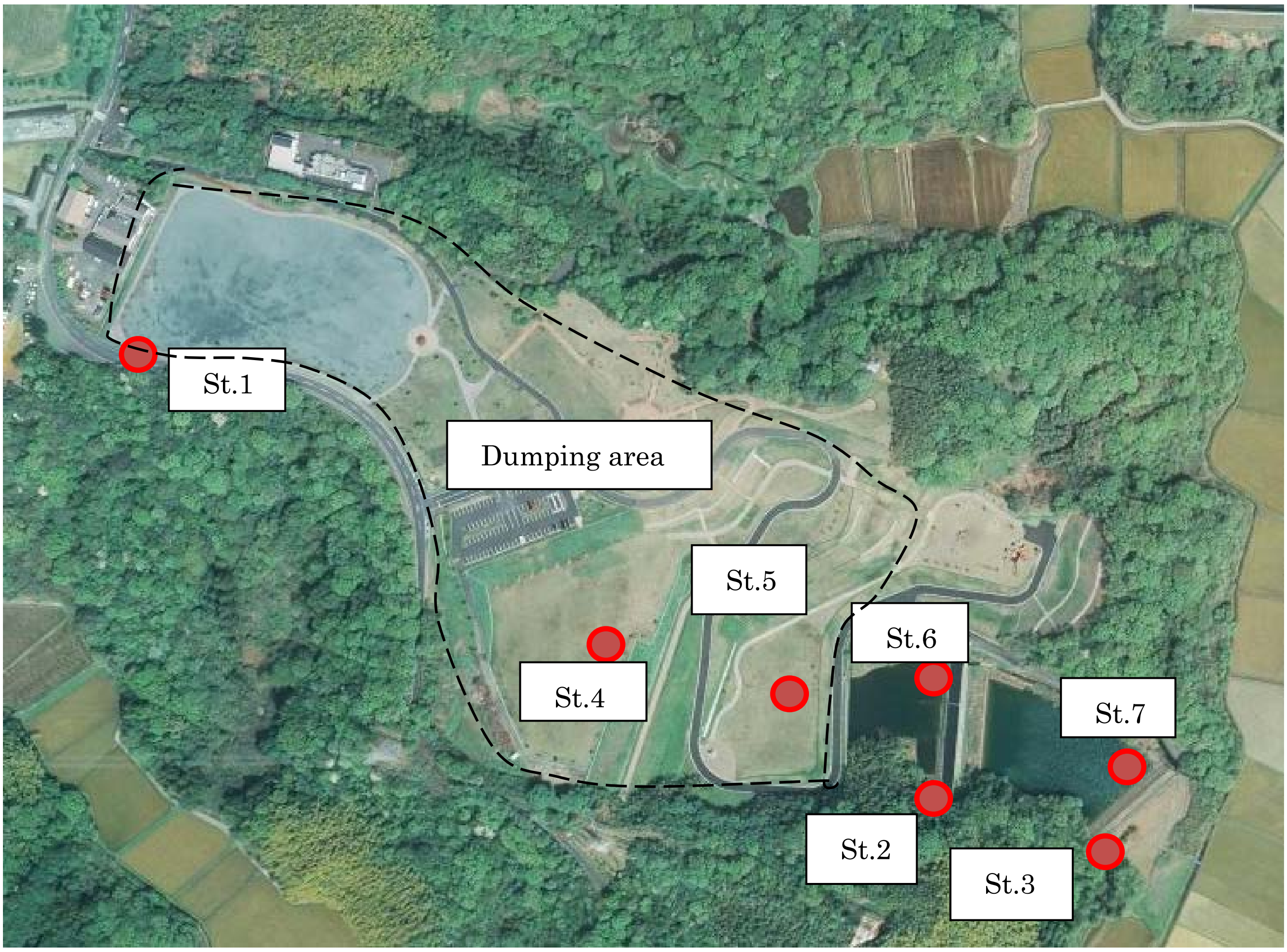

Fig. 1 The dumping site and monitoring stations

Table 1 Monitoring stations

No.	Type	Situation
St.1	Well	West part of the disposal site
St.2	Well	Well near of reservoir(old one)
St.3	Well	Well at the down stream
St.4	Well	Well in the dumping site
St.5	Well	Well in the dumping site
St.6	Reservoir	The water from the reservoir(old one)
St.7	Reservoir	The water from the reservoir(new one)

Table 2 Parameters and analytical methods

Analysis kinds and analytical methods :

Parameter	analytical method
As	ICP-MS
Cl	Ion chromatograph
SO_4	Ion chromatograph
NO_3	Ion chromatograph
HCO_3	Ion chromatograph
Na	Ion chromatograph
Mg	Ion chromatograph
K	Ion chromatograph
Ca	Ion chromatograph

Analysis parameters and analytical methods

Parameters and analytical methods are shown in table 2

RESULTS AND DISCUSSIONS

The trend of the arsenic pollution

At first, the arsenic pollution was found at St.2 and St.3 in Jun. 2010, and it has been continuing today. At St.3, a higher concentration of arsenic pollution was found than at St.2 as shown in Fig. 2. Arsenic pollution was not found in other monitoring stations where all domestic disposal waste have been buried.

From the monitoring data of EC and Cl ion, the slight increases of EC and Cl ion were found at St.3 in the last four years. The relation between arsenic pollution and Cl concentration is not evident.

Ion balance

As mentioned above, almost of all rain fall is removed from the dumping site. However, a small amount of water passes through the clay bed, and flows out of the dumping site. In order to find a leaching of the water from dumping site, ion balances were investigated. The same patterns are found into two groups (group A: St.1 and St.2, group B: St.4, St.5, St.6). A different pattern was found in St.3. This result indicates that the water of St.3 has little relation with the dumping site. A lot of arsenic pollution is found around these areas, and the arsenic pollution is thought to be come from the other natural sources. In the future ,widely survey will be needed.

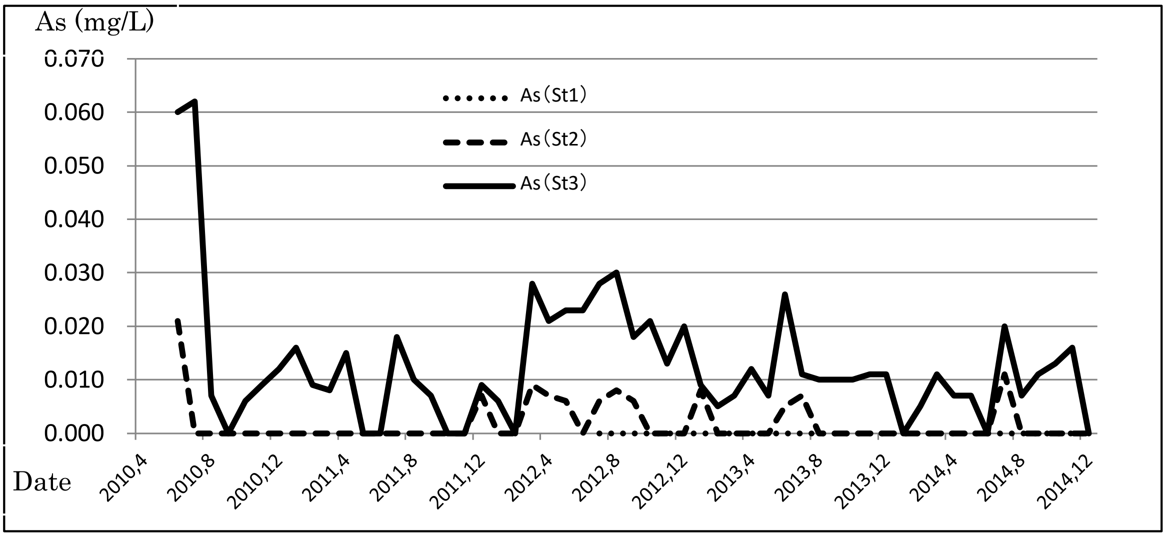

Fig. 2 The trend of the As(arsenic) pollution of the three sites

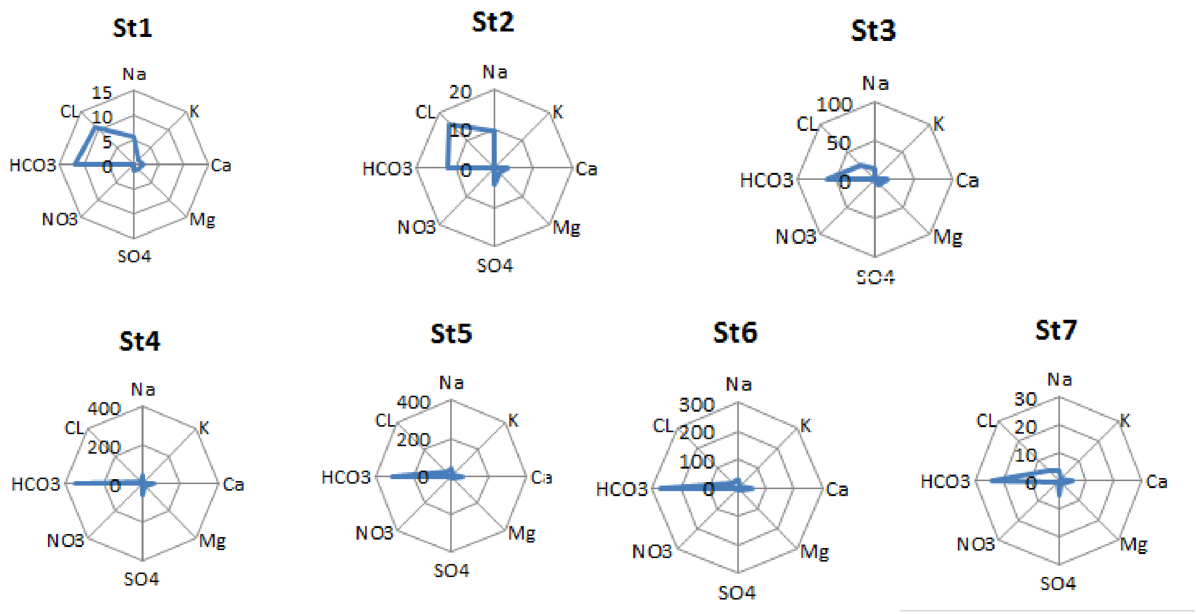

Fig. 3 Radar chart of the ion composition.

CONCLUSION

In order to find a cause of arsenic pollution, the ionic distribution of the arsenic concentration, and the ionic balance analysis were carried out. Results of these investigations indicate that the arsenic polluted water did not come from the dumping site, but from other sources. The arsenic pollution of ground water is found in the northern area of Mie prefecture [5], almost of all are considered from natural origin. Therefore, widely expanded surveys will be needed in the near future.

ACKNOWLEGEMENTS

We express much thanks to the Suzuka city municipal government who have offered the data for this research. .

REFERENCE

[1] Environmental Geochemical Science: Chikyu Kagaku Kouza 7, Japan Geochemical Society Edit., Nagoya University Publish, Baihukan Co. , LTD, 135-136 (2007) (in Japanese)

[2] Senichi Ebise and Kazuyoshi Miki: Evaluation on characteristic of heavy metals in the R. Yodo and its tributary stream by high frequency observations, Journal of Japan Society on Water Environment Vol. 24, No.11, 715-723 (2001) (in Japanese)

[3] Yukiko Hamatani, Satoko Tomimori, Kiyoshi Hashizume, Takako Aizawa and Mari Asami: Ground water features relation to arsenic – the relation to the strata in northern part of Mie prefecture, Journal of Japan Society on Water Environment Vol. 24, No.11, 739-744 (2001) (in Japanese)

[4] The survey report on the ground water of Suzukacity-Hukaya Syorizyou: Nakanihon Engineering Consultants Co., LTD. Mar., 2013 (in Japanese)

[5] Masaaki Takahashi, Yukimasa Takemoto, Kayoko Awaya, Mikihiro Ioka and Peng Guo: Ground water pollution around the northern part of Yokkaichi City, Journal of Geological Resource and Engineering Vol.2, No.3 (2014) 174-179

CHANGES OF CHLOROPHYLL-A, BACTERIOCHLOROPHYLL-C AND DOC BEFORE AND AFTER REVETMENT WORK IN LAKE FUKAMI-IKE, JAPAN

Megumi NOBORI[1], Hiromi SUDA[1], Maki OYAGI[2], Akiko YOKOYAMA[3], Akihiko YAGI [1]

[1]Aichi Institute of Technology (AIT), Faculty of Civil Engineering, Department of Urban Environment, 1247 Yachigusa, Yakusa-cho, Toyota 470-0392, Japan.
[2]Yokkaichi University
[3]Water Agency Inc.

ABSTRACT

Lake Fukami-ike is a small eutrophic lake of 2.1 ha with a maximum depth of 7.70 m in central Japan and water stratified from March to October. Anoxic conditions prevailed below 4-5 m depth from April to October and a photosynthetic green sulfur bacteria (BChl.c) accumulated in the hypolimnion. In Lake Fukami-ike, the revetment work was environment maintenance for activation of the town in 1992, and the water quality of this lake was considered to be clean. However, fluctuation in the transparency became larger than before. Data before and after revetment work (1992) was studied.

Keywords: Chlorophyll-a, bacteriochlorophyll-c, DOC, eutrophic lake

INTRODUCTION

Lake Fukami-ike is a small eutrophic lake of 2.1 ha with a maximum depth of 7.70 m in central Japan (Fig. 1). The lake is well protected from the wind and lake water stratified from March to October. Anoxic conditions prevailed below 4-5 m depth from April to October and a photosynthetic green sulfur bacteria (BChl.c) accumulated in the hypolimnion [1], [2]. Transparency, dissolved oxygen, hydrogen sulphyde and vertical distributions of nutrients have been observed in detail since 1978 in Lake Fukami-ike [1]-[9]. In Lake Fukami-ike, the revetment work was environment maintenance for activation of the town in 1992, and the water quality of this lake was expected to be clean. However, fluctuation in the transparency became larger than before.

PURPOSE

The chlorophyll-a amounts in winter were higher than in summer. The reason for such a difference was considered because of the long stagnation period [1]-[4]. Transparency was clearly changed before and after revetment work (1992), 70-280 cm in 1950s, 50-150 cm in 1970-’80s, and 35-470 cm in 1990s-2000s (Fig. 2). Thus recent transparency changes have remarkably high values. Stable state of the lake water was obtained so that the inflow of nutrient amount was stopped and had been disturbed in water column after the revetment work. Differences before and after the data were studied to clarify the influence of revetment work.

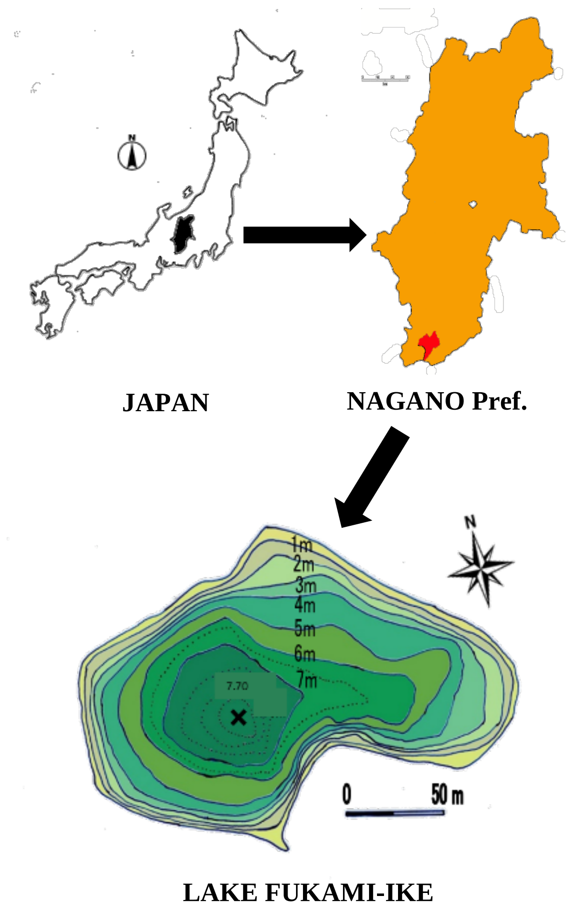

Fig. 1 Investigation spot

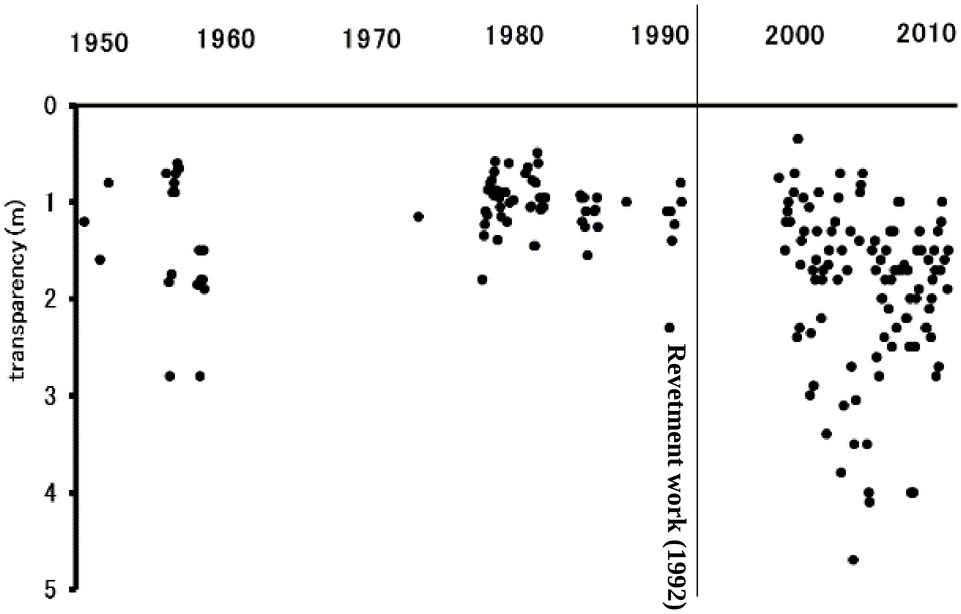

Fig. 2 Transition of transparency

METHODS

Investigation Spot

Lake Fukami-ike is located in Nagano Prefecture, Japan (North latitude 35° 32′ 55″ 77, East longitude 137°81′93″56) and has an area of 2.1 ha (maximum depth of 7.7) [7]-[8]. There are 6 inflowing streams and one outflow. The lake receives the runoff water from orchards and domestic sewage.

Water Sampling Method

Water samples were taken with a polyvinylchloride tube and a hand pump. In principle, the water was taken at 25-cm intervals in redox interface and 50~100 cm intervals in the other layer. Water samples were filtered with glass filter (GF/F, 47 mm). Water sample which was not filtered was total and the filtrated sample was dissolved, respectively. Chlorophyll-a and bacteriochlorophyll-c were determined by the spectrophotometric method [1].

Measuring Method

Water temperature (WT), Dissolved oxygen (DO)

WT and DO were measured by a DO meter (input electrode type, fluorescence method, HACL Inc., turned electrode type).

Chlorophyll-a (Chl.a) and bacteriochlorophyll-c (BChl.c)

Chl.a and BChl.c were measured by colorimetric method; Chl.a by using 663, 645, 630 nm wavelength, and BChl.c by using 662 nm [10]. BChl.c was photosynthetic sulfur bacteria and it grew extensively at the boundary layer of the oxic and anoxic layers.

Total organic carbon (TOC) & dissolved organic carbon (DOC)

Water samples were placed in 10 mL plastic bottle and mixed after adding in 0.1 mL of 1N H_2SO_4. Five minutes after, the inorganic carbon was completely expelled from water samples. The DOC was filtered. The TOC and DOC were quantified by total organic carbon meter (TOC-V (SHIMAZU)) [6], [7].

Picture 1 Lake Fukami-ike (20 Jul 2013)

RESULT & DISCUSSION

Water Temperature (WT), Dissolved Oxygen (DO)

Water temperature in 1979 of 4.5℃ in winter circulation period, gradually became 8℃ up in water stratification. 28℃ in the epiliminion of the summer stratification period and 10 ℃ under the water temperature stratification reached the stable state in the hypolimnion. In 2014, 4℃ in winter circulation period besides water temperature in the hypolimnion increased to 12℃. Low DO 1 mgL^{-1} concentration was obtained below 6 m depth in April and below 3.5 m because of stable water temperature stratification in August of 1979, respectively. An anoxic layer started previously below 5.75 m depth at the end of March and the uppermost anoxic layer appeared at 4 m depth in July, 2014. Decreases in the oxic and anoxic layers were measured.

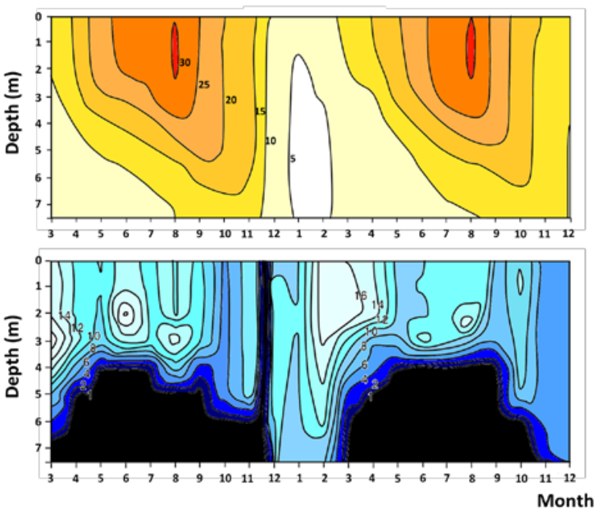

Fig. 3 Isotherm (℃) and DO isosmotic line (mgL^{-1})

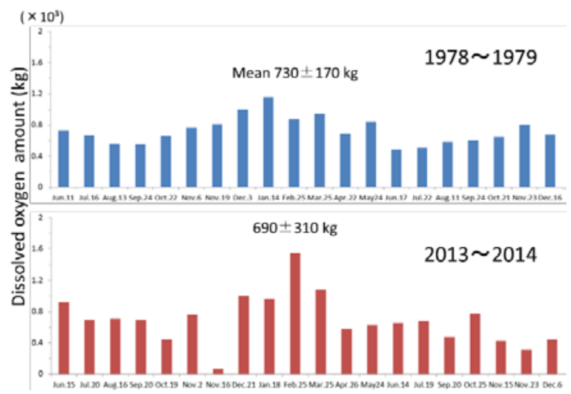

Fig. 4 Monthly changes of dissolved oxygen amount (kg)

Amount of DO in Lake Fukami-ike was measured by the depth and each volume to obtain the difference before and after revetment work. Maximum value of 1978-79 and 2013-14 were 1150 kg in January and 1550 kg in February, respectively. Minimum value of 1978-79 and 2013-14 were also 490 kg in June and 70 kg in November, respectively. 1978-79 and 2013-14 for maximum value minus minimum value were 660 kg and 1480 kg, respectively. Mean value was not different, but standard deviation was larger.

Chlorophyll-a (Chl.a) and Bacteriochlorophyll-c (BChl.c)

Figure 5 shows the aging of Chl.a amount and transparency in the oxide layer. Compared before and after revetment work, the mean of Chl.a amount before revetment work was 109 mgm^{-2}, and 174 mgm^{-2} after that work. It was 1.6 times. And the mean before that in the circulation period was 243 mgm^{-2}, 427 mgm^{-2} after the work. It was 1.8-fold. The Chl.a amount in the circulation period was larger than that of the stratification period, and this trend did not change before and after work.

Figure 6 shows the monthly variation of Chl.a in the water column in the oxidized layer. The amount in winter was more than in summer. It was the trend from ancient times of Lake Fukami-ike. The change to the circulation period from the stagnation period was calm before that work. In contrast, the fluctuation increased after that work.

Figure 7 shows monthly variation of Chl.a and BChl.c. The Chl.a and BChl.c value showed no difference in 1979 (before revetment work), but BChl.c increased in 2008 & 2013 (after revetment work). Maximum Chl.a amounts were 0.5 gm^{-2} and 0.7 gm^{-2} in 1979 and 2008, respectively. It had increased 1.4 times, but decreased 0.4 gm^{-2} in 2013. Maximum BChl.c amounts were 0.18 gm^{-2} in 1979, 2.6 gm^{-2} in 2008, and 2.9 gm^{-2} in 2013. The average Bacteriochlorophyll-c amounts in the water column in 1979 (before revetment work), 2008 & 2013 (after revetment work) were 74.4 mgm^{-2} in 1979, 1576 mgm^{-2} in 2008 and 1081 mgm^{-2} in 2013, respectively. That data in 2008 and 2013 increased 21 times and 15 times that in 1979, respectively.

As a feature of the internal production, phytoplankton and photosynthetic green sulfur bacteria amounts in the water column were 209 mgm^{-2} and 1081 mgm^{-2}. Therefore, the photosynthetic green sulfur bacteria amount was 5 times more than that of phytoplankton in Lake Fukami-ike in 2013.

Chl.a concentration decreased a little after work in the stagnation period, but increased after work in the circulation period. Bchl.c maximum value before work in August was 100 μgL^{-1}, after work it was 702 μgL^{-1}, growing 7 times. Similarly, in September, it increased 100 μgL^{-1} to 664 μgL^{-1} (Fig. 8).

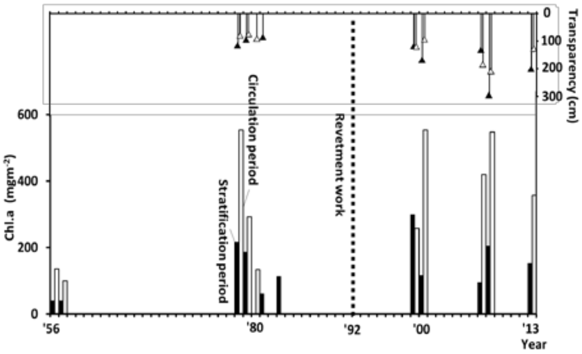

Fig. 5 Aging of the Chl.a amount and transparency in the oxide layer (1959-2013)

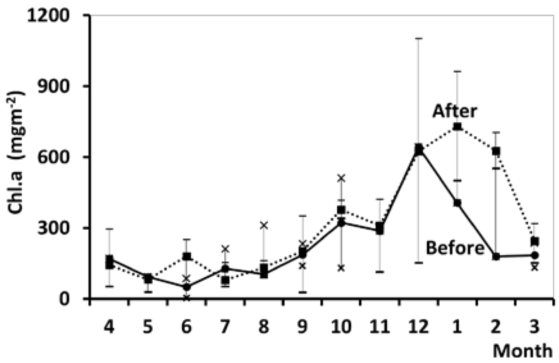

Fig. 6 Monthly variation of Chl.a in water column in oxidized layer

Table 1 Chl.a (mgm^{-2}) maximum, minimum and average value before and after revetment work.

	Before			After		
month	max	min	ave	max	min	ave
4	171	171	171	294	50	144
5	92.9	92.9	92.9	100	26.8	81.9
6	85.6	3.4	50.1	250	56.7	180
7	212	124	128	153	50	79.9
8	312	104	104	159	88.2	133
9	233	139	186	350	24.4	201
10	512	131	321	416	340	378
11	288	288	288	420	112	311
12	643	643	643	1101	150	626
1	406	406	406	960	500	730
2	180	180	180	703	550	627
3	237	133	185	319	150	246

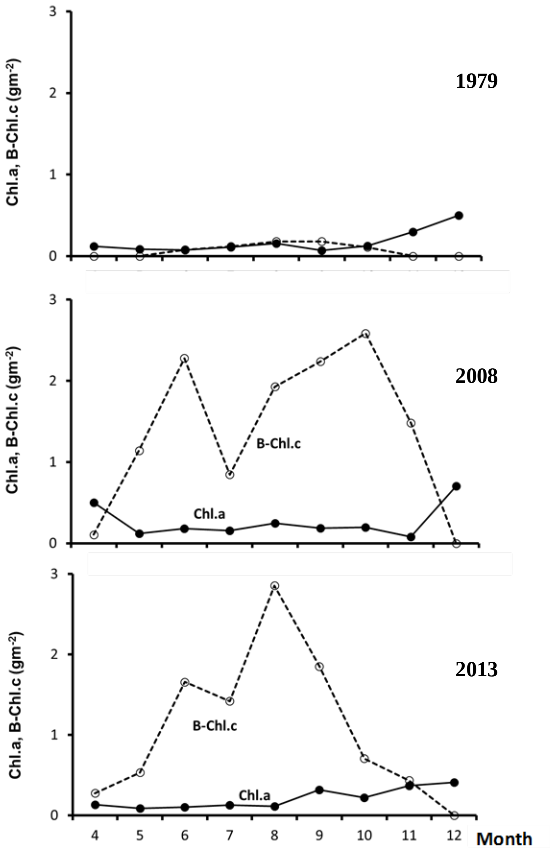

Fig. 7 Monthly variation of Chl.a and BChl.c in water column.

Dissolved Organic Carbon (DOC)

Figure 9 shows aging of the DOC in the water column in the stagnation period. Figure 10 shows monthly changes of the DOC in the water column. Fluctuations of DOC amounts were observed before work, but not after it. The mean DOC amount before work was 4.24 gm^{-2}, against 9.05 gm^{-2} after work. It became 2-fold. The difference between maximum and minimum value was up to 1.9 gm^{-2} before work, and 5.5 gm^{-2} after work. Therefore, Lake Fukami-ike was stable throughout the year before work. There was the rice field around the lake before revetment work and the runoff inflowed directly. Lake Fukami-ike is stable because the purifying effect of rice field was acting on influent water such as household waste water (low C/N ratio) and precipitation. But after the work it was not stable. It seems possible that some domestic wastewater (low C/N ratio) was still flowing into this lake.

Figure 11 shows vertical distribution of the DOC. Change of the DOC was not observed before revetment work, but a high concentration was noted in the hypolimnion from June to September. A uniform concentration was observed from epilimnion to hypolimnion before work, but different values were seen at each depth after work.

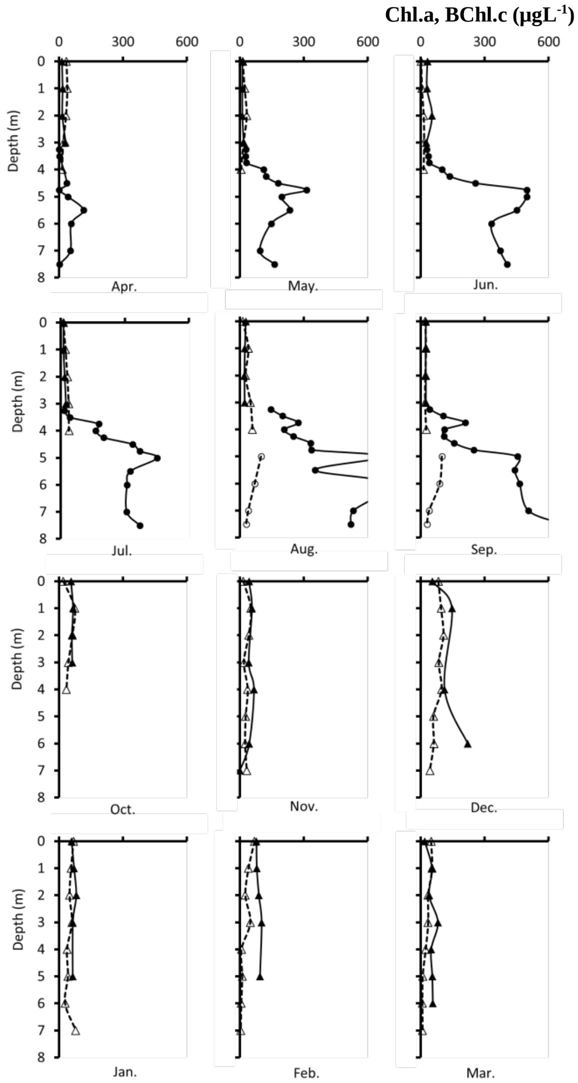

Fig. 8 Monthly vertical distribution of Chl.a and BChl.c (μgL^{-1}) (before and after revetment work)

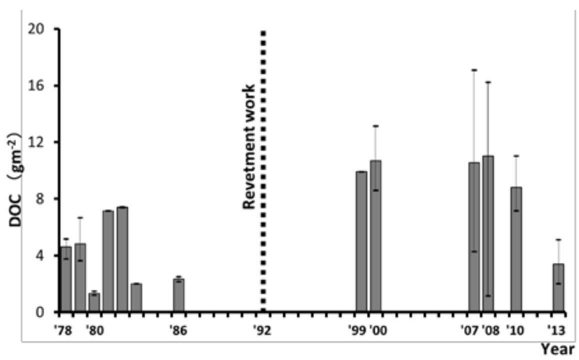

Fig. 9 Aging of the DOC in the water column in stagnation period

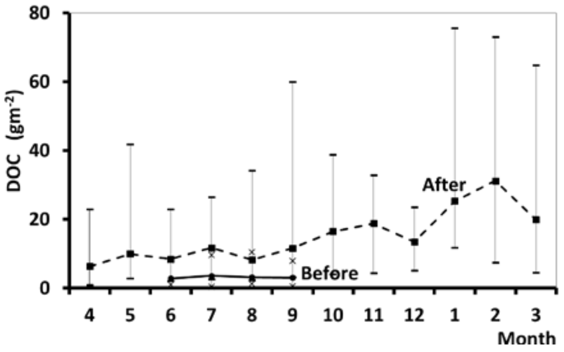

Fig. 10 Monthly changes of DOC in the water column (before and after revetment work).

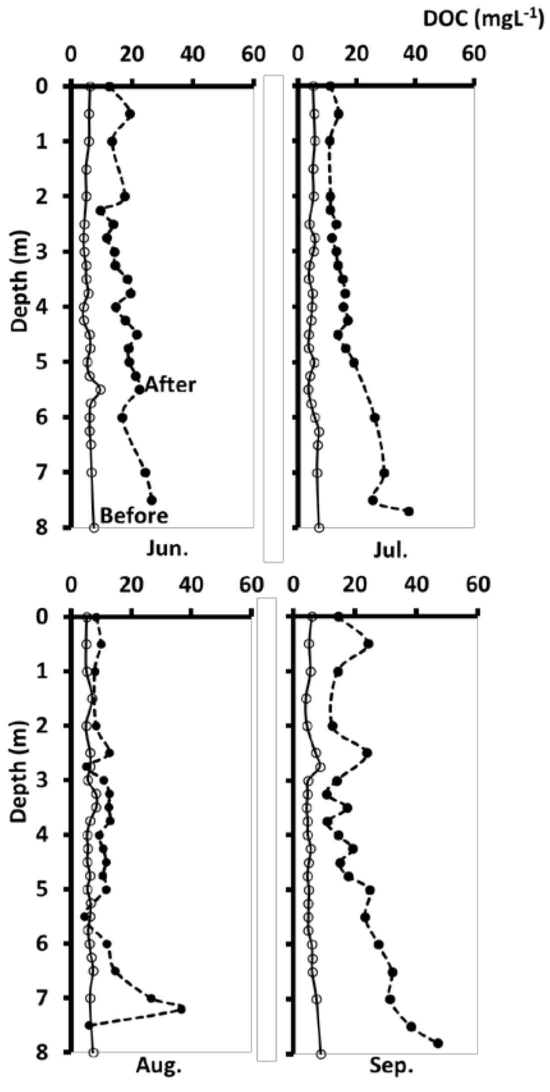

Fig. 11 Vertical distribution of DOC (before and after revetment work)

Table 2 DOC amounts (gm^{-2}) in the water column in the stratification period (maximum, minimum and average)

year	ave	max	min
1978	4.6	5.2	3.8
1979	4.8	6.7	3.6
1980	1.3	1.5	1.2
1981	7.2	7.2	7.2
1982	7.4	7.4	7.4
1983	2	2	2
1986	2.3	2.5	2.2
1999	9.9	9.9	9.9
2000	10.7	13.1	8.6
2007	10.6	17.1	4.3
2008	11	16.2	1.2
2010	8.8	11	7.1
2013	3.4	5.1	2

CONCLUSION

Chl.a was increased in both water concentration and the water column. The DOC amount of stagnation period was increased after revetment work more than before it, and the difference between maximum and minimum values also increased. BChl.c had been confirmed to increase concentration and biomass. The revetment work was environment maintenance for activation of the town in 1992, and the water quality of this lake was expected to be clean. However, the inflow of domestic wastewater did not stop; nutrients increased and Chl.a, BChl.c and the DOC also increased. Such a phenomenon is considered to be one of the factors in the variation in the transparency increase.

ACKNOWLEDGEMENTS

Assistance of the Town authorities of Anan-cho, Shimoinagun, Nagano Prefecture is also gratefully acknowledged in kindly providing the facilities for our research.

REFERENCES

[1] Yagi A, Shimodaira I, Terai H and Saijo Y, “Seosonal Changes of Chlorophyll-a and Bacteriochlorophyll in Lake Fukami-ike”, The Japanese Journal of Limnology, 1983, Vol. 44, No. 4, pp. 283-292

[2] Takahashi K, Wada E and Sakamoto M, “Carbon isotope discrimination by phytoplankton and photosynthetic bacteria in monomictic Lake Fukami-ike”, Arch Hydrobiol., 1990, Vol. 120, No. 2, pp. 197-210

[3] Yagi A, Miyachi S and Nagoya university, “Vertical distribution of purple nonsulphur bacteria and their utilization of dissolved organic carbon in Lake Fukami-ike”, Arch Hydrobiol., 1991, Vol. 121, No. 3, pp. 307-317

[4] Yagi A, “Manganese cycle in Lake Fukami-ike”, Verh. Internat. Verein. Limnol., Sep. 1993, No. 25, pp. 193-199

[5] Yagi A, “Manganese flux associated with dissolved and suspended manganese forms in Lake Fukami-ike”, 1996, Vol. 30, No. 8, pp. 1823-1832

[6] Yagi A, Funahashi J, Nishio N and Umemura M, “Seasonal changes of methane and organic acid in Lake Fukami-ike”, Jan. 2009, Verh. Internat. Verein. Limnol., Vol. 30, Part 6, pp. 878-883

[7] Yagi A, “Biological manganese cycle in the oxic and anoxic layers of Lake Fukami-ike”, Limnology in Tokai Region of Japan, 2010, Vol. 43, in Japanese

[8] Nakagawa M, Ueno Y, Hattori S, Umemura M, Yagi A, Takai K, Koba K, Sasaki Y, Makabe A and Yoshida N, “Seasonal change in microbial sulfur cycling in monomictic Lake Fukami-ike, Japan”, Limnol. Oceanogr., 2012, Vol. 57, No. 4, pp. 974-988

[9] Yokoyama A, Oyagi M, Nakagawa M and Yagi A, “Existent state of iron and manganese in inflow, outflow and inside of Lake Fukami-ike”, Limnology in Tokai Region of Japan”, 2013, Vol. 60, pp.1-6

[10] Takahashi M, and Ichimura S, “Vertical distribution and organic matter production of photosynthetic surfur bacteria in Japanese lakes”, Limnol. Oceanogr., 1968, 13: pp. 644-655.

Fifth International Conference on Geotechnique, Construction Materials and Environment, Osaka, Japan, Nov. 16-18, 2015, ISBN: 978-4-9905958-4-5 C3051

GENETIC DIVERSITY OF RESTORED ENDANGERED SPECIES, PENTHORUM CHINENSE IN THE RIVERBED

Michiko Masuda[1] and Fumitake Nishimura[2]
[1] Department of Civil Engineering, Nagoya Institute of Technology, Japan; [2] Department of Environment Engineering, Kyoto University, Japan

ABSTRACT

The Ministry of Land, Infrastructure and Transport has done the business of digging on the river road to increase the flowing quantity of Ibi River every year since 2000. It is reported to the dug region the *Penthorum chinense* populations which is the threatened species the restored in 2001. Digging is done from 2000 to 2010 every year. Therefore, we investigated *P. chinesne* population of which extent to which region grew. As a result, it was shown some the growth of the plant of 200 individuals in the 2002 digging region, 4000 individuals in the 2001 digging region and 1000 individuals in the 2000 digging region, and so on. Though it is thought that the population formed in 2000 is seed bank origin, whether the populations formed in 2001 and later the burial seed origin or formed with the seed of an existing population, it is uncertain. Then we sampled 8 populations of the species form these areas, and studied them for allelic variation at 16 enzyme loci. There was no significant correlation between the actual population size and genetic diversity parameters, suggesting that the effective population size was very small even for the large populations. However, population that restored at the riverbed and population that approved on the embankment were able to distinguish obviously in the populations that had been approved in 2002. As for the population approved to the embankment, it was shown that genetic variation was very high in the population approved to the riverbed thought it was hardly admitted.

Keywords: Population size, Burial seeds, Restorelation, Endangered species, River management

INTRODUCTION

The Ministry of Land, Infrastructure and Transport has dug up the river in Ibi River (Center of Japan) for the flood prevention every year since 2000 to 2010. This area has been disturbed by flood damage, so the digging can make the flow rate of the river increased and stop a flood, and provide the low marsh area in the river. In the new marsh area by the 2000 digging it was observed that a population of *Penthorum chinense* recovered in 2001. From 2000 to 2010 the digging was done by The Ministry of Land, Infrastructure and Transport every year, and new populations of *P. chinense* were appeared in new marsh area. And sometime new populations were appeared on the bared embankment. *P. chinense* has been described to the red list as vulnerable level (VU). A few studies reported that the populations of *P. chinense* have restoration by buried seeds [1]–[3]. In general, the populations restored it from the buried seeds are thought that genetic diversity is high. However, the character of the genetic diversities was hardly reported.

On the other hand, the natural population of *P. chinense* was observed in the river. The seeds of the species is so small that dispersed very long distance easily. It was suggested the new population was constructed by the seeds from natural population. Then, it paid attention to genetic diversities of the *P. chinense* populations approved by digging in the river in this research. Then we investigated the genetic diversity of the species with three questions, 1) Is there a relationship between the location and genetic distance? 2) Are the new populations appeared from burial seeds? 3) Is there a relationship between population size and genetic diversity? It was paid attention to these three points and analyzed.

MATERIALS AND METHODS

The Study Site and field census

The study was carried out on the Ibi River at Gifu Pref. (from 35° 20’ 25’’N, 136° 38’ 92’’E, altitude 9.3 m to 35° 17’ 50’’N, 136° 37’ 7’’E, altitude 0.2 m). The Ibi River is very steep and wide range river system, water system of the extension 121km and 1840 km^2 in the valley area. Because this river region had frequently received the flood damage, bank repair and a river dredge are continuing. Our study was dome the area 36.2km to 32.3km from the mouth of the river (Table 1).

We counted the number of P. chinense on 20th, Oct. in 2004, when the leaves of the species turned red and yellow, so we can find the species easily to find out.

The Study Plant

Penthorum chinense Pursh (Fig. 1) is a polycarpic herb plant distributed in eastern Asia [4], but its population has been decreasing in Japan and Red Data Book of Japanese vascular plants listed the species a 'vulnerable' level species [5][6]. This species is often distributed in marsh river flood plain, salt marsh area, wetland around paddy fields, and abandoned paddy fields in Japan. The species is reproduces both sexually by seeds and vegetatively by rhizomes [7].

Table 1 The characters of study site, established year, habitat condition, the distance from the mouth of the river

Study site	Established year	habitat	distance (km)
A	2001	Marsh	32.2-32.6
B	2002	Bank	32.6-33.0
C	2002	Marsh	32.6-33.0
D	2003	Bank	34.6-35.8
E	2003	Marsh	34.6-35.8
F	2002	Marsh	32.8-33.8
G	2002	Marsh	36.2-37.0
H	Natural	marsh	18.8

Fig. 1 The flowers of *P. chinense*.

Electrophoresis

Fresh leaves were collected from 30 individuals per population at August in 2003. Leaves were kept on ice during 4 hours transportation to the laboratory, after which they were refrigerated 2 days until electrophoresis. The following enzyme systems were examined: malate dehydrogenase (MDH), phospho-glucose isomerase (PGI), phospho-glucomutase (PGM), aldolase (ALD), triose-phosphate isomerase (TPI), alcohol dehydrogenase (ADH), acid phosphate (ACP), iso-citrate dehydrogenase (IDH) and malic enzyme (ME). Leaves were used to resolve the following 16 putative loci: mdh-1, mdh-2, mdh-3, pgi-1, pgi-2, pgm, ald, tpi-1, tpi-2, adh, acp-1, acp-2, acp-3, idh, me and mr. Samples were ground in a cold extraction buffer described by Odrzykoski and Gottlieb [8]. The enzymes were resolved on 10.8% starch gel. System 5 of Soltis et al. [9] were used. Staining procedures followed previous works [9]-[11].

The Statistical analysis

For each populations we calculated the number of alleles per locus (*A*), percentage of polymorphic loci (*P*), and gee diversity (*h*). We used all loci data in the calculation of *A*, and regarded a locus as polymorphic if the frequency of its most frequent alleles is under 0.95. In addition, total gene diversity [12] was calculated for species level. The population genetic structure was analyzed by initially calculating Nei's G_{ST} value [12]. Values for genetic indentities (*I*) and standard genetic distance (*D*) were computed for each pairwise comparison of all populations. The neighbor joining method [13] based on *D* was used for constructing a phenogram for *P. chiense.*

RESULTS

Field Census

The number of individuals was shown in Table 2. The numer of individuals ranged from 85 to 11000.

Table 2 The number of *P. chinense* in 2004.

Population	A	B	C	D	E	F	G	H
No. of individuals	412	45	950	120	1780	850	312	52

Genetic Diversity

Sixteen loci were scored: mdh-1, mdh-2, mdh-3, pgi-1, pgi-2, pgm, ald, tpi-1, tpi-2, adh, acp-1, acp-2, acp-3, idh, me and mr. In all populations, mdh-1, pgi-1, pgi-2, adh, acp-1 and acp-2, six loci were polymorphic. In all population mdh-3, tpi-2 and acp-3 were monomorphic. Allele frequencies at the polymorphic loci are listed in Appendix 1.

Table 3 summarizes the resultant values of *A*, *P* and *h* for each population. And total gene diversity (H_T) of P. chinense was 0.487. The levels of genetic diversity in *P. chinense* was higher than that of other endangered species, for example, *Aster kantoensis* growing in the river bed were 1.53 (*A*), 0.36(*P*) and 0.142 (*h*) [14]. And other endangered species showed *A* (1.44 to 2.01), *P* (0.199 to 0.65) and *h* (0.037 to 0.43) [15]-[18].

Table 3 Mean number of polymorphic loci (*A*), proportion of polymorphic loci (*P*), and gene diversity within a population *(h)* at 16 loci for examined populations of *P. chinense*.

Population	*P*	*A*	*h*
A	0.538	2.385	0.210
B	0.769	2.385	0.286
C	0.923	2.615	0.286
D	0.769	2.846	0.343
E	0.692	2.538	0.334
F	0.692	2.154	0.383
G	0.846	2.385	0.413
H	0.769	2.077	0.208

Population structure

The value of *I* and *D* was shown in Table 4. There is no relationship between real distance and genetic distance. It is suggested that new constructed populations result from burial seeds previous population. Fig. 3 showed the genetic distance among established populations and natural population. The genetic distance between the nearest populations were small, but the longest distant population H was not out of the phenogram.

Table 4 Estimated values of genetic identity (I) (upper) and standard genetic distance (D) (under triangle).

Poplation	A	B	C	D	E	F	G	H
A	-	0.976	0.982	0.943	0.959	0.924	0.892	0.930
B	0.024	-	0.990	0.954	0.965	0.942	0.919	0.953
C	0.018	0.010	-	0.962	0.974	0.940	0.918	0.952
D	0.057	0.046	0.038	-	0.980	0.936	0.917	0.936
E	0.041	0.035	0.026	0.020	-	0.956	0.937	0.958
F	0.076	0.058	0.060	0.064	0.044	-	0.964	0.968
G	0.108	0.081	0.082	0.083	0.063	0.036	-	0.965
H	0.070	0.047	0.048	0.064	0.042	0.032	0.035	-

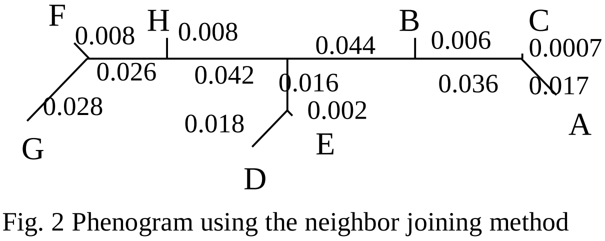

Fig. 2 Phenogram using the neighbor joining method based on Nei’s (1987) standard genetic distance.

The result of total population genetic structure G_{ST} was 0.339. The value of G_{ST} suggested the high level differentiation was occurred. It is always observed long distance populations. (no differentiation: 0-0.05, low level differentiation: 0.05-0.15, middle level: 0.15-0.25, high level: 0.25-).

DISCUSSION

In this study, genetic diversity of the populations of *P. chinense* that restored by the excavating work of the river for the flood prevention was clarified. Because the flowing quantity of the river has been made constant by the construction of dams for decades, the disturbance in the river has been suppressed. Therefore, the transition of the vegetation of the river proceeds, and the growth of a peculiar plant in the river that depends on the disturbance has been suppressed. However, if the excavating work of the river was done at moderate frequency, the effect similar to the disturbance was brought, and the restoration of the endangered species can be done. Moreover, it was shown that it was thought that the approval of the populations by digging was a burial seed origin, and genetic diversity was also not low than that of endangered species.

Some highly suggestive research [3][19][20] showed that the soil seed bank could restore the genetic diversity. But the cost of the restoration is high. In our research, the adaptive moderate excavation can be restored the endangered species population with high genetic diversity. The Ministry of Land, Infrastructure and Transport conducted the excavation at winter season when the seedlings were not occurred. And the depth of excavation was 0 to 3m, with loose slop to the low embankment. So, the gradient with water containing was made. The condition could serve the adaptive condition of *P. chinense.* This is suggested that the design of excavation can support the habitat of disturbance dependent species.

In addition, restored populations surprisingly tended to be different according to dug depth and place. It is thought that the populations is adjacent and approved can admit, and each population has been approved from a slightly different seeds at the age by the dug depth region.

Three genetic diversity indexes were very high in all restored populations. Sometimes, endangered species has low genetic diversity and the cause of low genetic diversity lead to extinction vortex. But there is no relationship between population size and genetic diversity, so the condition of the genetic diversity is curious condition. The genetic diversity from the C population that was made at 2002 digging is higher than that of B in this study. The populations of B and C were at the position placed between two spur dikes. Spur dikes were made for the protection of the embankment. It lowers the current velocity of the river. Therefore, the piling up action works, the condition of being easy to retire from a lot of seeds arises. And there is a possibility that the populations with high genetic diversity restored it from the burial seed in population C. Because it is the population B approved to a position that is about 2m higher than C, the piling up of the seed is thought to be only an increase of the flowing quantity of the river though population B is located in similar, too. And the same condition was occurred between population D and E.

The real distance of the population C and F was shorter than that other population. But the genetic distance is very large, 0.058-0.060. So the real distance cannot affect the genetic structure. It suggested that the condition of excavation depth and time of seeds accumulation. And the natural population H is very close to population G, where is the farthest from natural population. Moreover all populations are high differentiation. This sort of differentiation is usually observed among islands [21].

It was shown that the *P. chinense* populations restored it by the river construction as a result of this research. Moreover, it was shown that the genetic diversity of restoration populations was different from that of the natural populations. It will be suggested that attention be necessary for the populations that appears when constructing it like this managing in the future.

CONCLUSION

We get three main conclution.

1) There is no relationship between the real distance and genetic distance. The populations at the same position with different water level showed small genetic distances.
2) The genetic construction of natural population was very different from restored populations. So the restored populations appeared from burial seed banks.
3) There is no relationship between population size and genetic diversity.

Based on the conclusion, two proposals about the management method of the excavation.

1) The excavation for the flood management should be done with loose slope provide the different water level habitat.
2) The excavation should be done in winter when the endangered species is dormant.
3) The excavation area should not be large to avoid the uniformity is occurred, that can be provide the genetic diversity.

ACKNOWLEDGEMENTS

We wish to thank the member of Ministry of Land, Infrastructure and Transport Kiso River Office for research support and permission to work in the river. We also thank the members of our laboratory for their assistance in the field works.

REFERENCES

[1] Imahashi M & Washitani I, “Evaluation of soil seed banks as plant materials for the restoration of flood plain vegetation”, Japanese J. Conservation Ecology, 1996, Vol. 1, pp. 131-147.

[2] Kimura Y et al., “Possibility of restoration of Penthorum chinense Pursh by using soil seed bank”, Japanese J. Conservation Ecology, 2000, Vol. 5, pp. 197-204.

[3] Honnay O et al., “Can a seed bank maintain the genetic variation in the above ground plant population?”, Oikos, 2008, Vol. 117, Jan. pp. 1-5.

[4] Ohwi J, Kitagawa M, New Flora of Japan, Tokyo: Shibundo, 1983. (in Japanese)

[5] Endangered Plant Survey Group, The Red Data Book of Japanese Vascular Plants. Tokyo: Nature Conservation Society of Japan, 1989. (in Japanese)

[6] Kato T & Ota H, Endangered Wild life of Japan. Osaka: Hoikusha Pubulishing Co., 1993. (in Japanese)

[7] Kimura Y, et al., “The life history of Penthorum chinense Pursh and its growth traits in experimentally different water condition”, Bulletin of Water Plant Society, Japan, Vol. 66, 1999, pp. 15-18.

[8] Odrzykoski IJ & Gottlieb LD, “Duplications of gene coding 6-phosphofluconate dehydrogenase in Carkia (Onagraceae) and their phylogenetic implications” Systematic Botany, 1984, Vol. 9, pp. 479-486.

[9] Soltis DE et al., “Starch gel electrophoresis of ferns: a compilation of grinding buffers, gel and electrode buffer and staining schedules”, American J. of Botany, 1983, Vol. 73. Jan. pp. 9-27.

[10] Wendel JF & Weeden NF, “ The effect of serpentine on the population structure of Silene

dioica (Caryophyllaceae)", Evolution, 1989, Vol. 46, pp. 1537-1548.

[11] Chepliak WM & Pitel JA, Techniques for starch electrophoresis of enzymes from forest tree species. Information report PI-X-42. Penthawana: Penthawana National Forestry Institute, Canadian Forestry Service, 1984.

[12] Nei M, Molecular evolutionary genetics. New York: Columbia University Press, 1987.

[13] Saitou N & Nei M, "The neighbor joining method: a new method for reconstructing phylogenetic trees", Molecular Biology and Evolution, 1987, vol. 4, pp. 106-425.

[14] Maki M et al., "Genetic diversity and hierarchical population structure of a rare autotetraploid plant, Aster kantoensis (Asteraceae)", American J. of Botany, Vol. 83, Mar. 1996, pp. 296-303.

[15] Soltis DE & Soltis PS, "Genetic consequences of autotetraploidy in Tolmiea (Saxifragaceae), Evolution, Vol. 43, 1989, pp.586-589.

[16] Ness BD et al., "Autotetraploidy in Heuchera micrantha (Sazifragaceae)", American J. of Botany, Vol. 76, 1989, pp. 614-626.

[17] Wolf PG et al. "Chloroplast-DNA and electrophoretic variation in diploid an autotetraploid Heuchera grossularifolia", American J. of Botany, Vol. 77, 1990, pp. 232-244.

[18] Shore JS, " Tetrasomic inheritance and isozyme variation in Turnera ulmifolia vars. elegance Urb. and intermedia Urb. (Turnraceae)", Heredity, 1991, Vol. 66, pp.305-312.

[19] Macgraw JB et al., "Ecological genetic variation in seed banks I. Establihsment of a time transect", J. of Ecology, 1991, Vol. 79, pp. 617-625.

[20] Baskin JM & Baskin CC, "The seed bank in a population of an endemic plant species its ecological significance", Biological Conservation, Vol. 14, 1978, Sep. pp. 125-130.

[21] Tomaru N, "Genetic diversity and population structure in widespread deciduous broad-leaved trees in Japan", Earth Environment, 2013, vol 18. Pp.119-126.

Appendix 1. Allele frequencies at 13 polymorphic loci of 8 examinied populations of P. chinense

Locul	Allele	A	B	C	D	E	F	G	H
mdh - 1	N	48	45	33	45	40	40	38	40
	a	0.323	0.167	0.439	0.044	0.075	0.100	0.197	0.300
	b	0.500	0.644	0.561	0.256	0.825	0.813	0.645	0.375
	c	0.135	0.189	0.000	0.500	0.100	0.088	0.158	0.325
	d	0.042	0.000	0.000	0.200	0.000	0.000	0.000	0.000
mdh - 2	N	16	30	32	39	30	34	34	31
	a	0.563	0.000	0.531	0.180	0.117	0.706	0.529	0.903
	b	0.313	1.000	0.469	0.423	0.417	0.235	0.471	0.097
	c	0.125	0.000	0.000	0.308	0.367	0.059	0.000	0.000
	d	0.000	0.000	0.000	0.090	0.100	0.000	0.000	0.000
pgi - 1	N	48	44	30	45	43	32	35	40
	a	0.177	0.295	0.050	0.056	0.047	0.469	0.443	0.288
	b	0.698	0.636	0.850	0.411	0.640	0.406	0.514	0.663
	c	0.115	0.068	0.100	0.444	0.256	0.125	0.043	0.050
	d	0.010	0.000	0.000	0.089	0.058	0.000	0.000	0.000
pgi - 2	N	48	45	30	44	42	38	35	40
	a	0.063	0.222	0.117	0.216	0.357	0.145	0.386	0.200
	b	0.771	0.567	0.750	0.682	0.536	0.684	0.529	0.788
	c	0.146	0.211	0.133	0.080	0.095	0.118	0.086	0.013
	d	0.021	0.000	0.000	0.023	0.012	0.000	0.000	0.000
pgm	N	30	38	27	40	66	32	34	40
	a	1.000	0.237	0.463	0.738	0.530	0.453	0.088	0.150
	b	0.000	0.658	0.500	0.163	0.462	0.484	0.897	0.850
	c	0.000	0.105	0.037	0.100	0.008	0.063	0.015	0.000
ald	N	30	30	25	20	21	32	30	40
	a	0.047	0.033	0.200	1.000	1.000	1.000	1.000	1.000
	b	0.938	0.783	0.500	0.000	0.000	0.000	0.000	0.000
	c	0.016	0.183	0.300	0.000	0.000	0.000	0.000	0.000
tpi - 1	N	23	34	27	28	38	25	35	40
	a	1.000	0.559	0.593	0.071	0.711	1.000	1.000	1.000
	b	0.000	0.441	0.407	0.893	0.289	0.000	0.000	0.000
	c	0.000	0.000	0.000	0.036	0.000	0.000	0.000	0.000

Appendix continued.

Locus	Allele	A	B	C	D	E	F	G	H
adh	N	31	32	30	35	40	40	35	40
	a	1.000	1.000	0.883	0.543	1.000	0.075	0.114	0.600
	b	0.000	0.000	0.117	0.457	0.000	0.925	0.657	0.400
	c	0.000	0.000	0.000	0.000	0.000	0.000	0.229	0.000
acp - 1	N	47	45	30	45	44	32	35	39
	a	0.085	0.178	0.067	0.133	0.216	0.594	0.414	0.295
	b	0.809	0.789	0.750	0.600	0.511	0.406	0.586	0.705
	c	0.106	0.033	0.167	0.133	0.273	0.000	0.000	0.000
	d	0.000	0.000	0.017	0.133	0.000	0.000	0.000	0.000
acp - 2	N	47	44	30	44	45	40	39	40
	a	0.185	0.125	0.133	0.091	0.144	0.188	0.410	0.125
	b	0.554	0.795	0.783	0.443	0.356	0.750	0.090	0.875
	c	0.250	0.080	0.067	0.432	0.200	0.063	0.500	0.000
	d	0.011	0.000	0.017	0.034	0.300	0.000	0.000	0.000
idh	N	23	35	30	25	32	40	34	40
	a	1.000	1.000	0.883	1.000	1.000	1.000	0.546	1.000
	b	0.000	0.000	0.117	0.000	0.000	0.000	0.544	0.000
mr	N	29	33	25	36	27	32	35	40
	a	1.000	1.000	1.000	1.000	1.000	1.000	0.543	0.425
	b	0.000	0.000	0.000	0.000	0.000	0.000	0.457	0.575
me	N	24	22	32	27	32	32	32	40
	a	0.000	0.318	0.313	0.333	0.234	0.781	0.875	0.688
	b	1.000	0.682	0.500	0.667	0.766	0.219	0.094	0.125
	c	0.000	0.000	0.188	0.000	0.000	0.000	0.031	0.000
	d	0.000	0.000	0.000	0.000	0.000	0.000	0.000	0.188

Fifth International Conference on Geotechnique, Construction Materials and Environment, Osaka, Japan, Nov. 16-18, 2015, ISBN: 978-4-9905958-4-5 C3051

EARTH QUAKE AND SPATIAL TSUNAMI MODELLING FOR THE SOUTH JAVA COASTAL AREA – INDONESIA

Agus Hartoko[1]*, Muhamad Helmi[2], Mujahid Sukarno[3], Hariyadi MT[2]
[1]Dept of Fisheries. Fac of Fisheries and Marine Science & Postgraduate Progamme-Coastal Resources Management. Diponegoro University. Semarang - Indonesia
[2]Dept of Marine Science. Fac of Fisheries and Marine Science. Diponegoro University. Semarang.Indonesia
[3]Waindo SpecTerra. Jakarta. Indonesia

ABSTRACT

Long history of Indonesia with many event in experiencing tsunami, with the fact the country position surrounded by plate tectonic subduction zone (ring of fire) with very high frequency recorded tectonic earth quake and risk of tsunami. The need of reliable tetonic plate earth quake and risk of tsunami spatial data base model was inavitable.

The paper built neccesary numeric and spatial data base, analysis and develop tsunami modelling for three sites of south Java (Serang – west of south Java, Bantul - central and Banyuwangi - east of south Java) which were regarded as the most dense populated island. Phase one steps were built spatial database of the tectonic plate subduction zone with variable of depth, distance and ocean floor topography using ETOPO-2 USGS bathymetric data. Phase two steps including the development of tectonic plate earth quake history data base with above 6 Richter scale for the past five years. Development of numeric tsunami spatial model using MIKE-21 software (Evaluate License) with variable of tectonic plate earth quake coordinate, magnitude of 8 Richter scale and depth. Followed with detail analysis of the tsunami waves characters such as the height and travel time and direction towards coastal area, tsunami wave oscilation, time and run-up height and distance in reaching the coastal area. Phase three steps including development of spatial data base of contur Digital Elevation Model (SRTM-data), run-up model and wave height in reaching the dense population area and detail village and sub-district boundary, population, number of house and buildings, infrastructure and landuse of the affected area and finally followed by escape route scenario and site-selection for possible community gathering building.

Key words : earth quake, tsunami, south-Java, Indonesia

*Corresponding author : Postgraduate Building 3rd Floor. Coastal Resources Management Study Programme. Diponegoro University. Jl. Imam Barjo SH. Semarang. Indonesia. agushartoko@gmail.com

INTRODUCTION

Indonesia as the most vulnerable country for tectonic erathquake surounded with 'ring of fire' of the Eurasian, Indo-Australian and Pacific plate, espescially at the west coas of Sumatra, south coast of Java, along the south coast of West and East Nusa Tenggara, north Papua, Sulawesi/ Celebes and Molucas. The discrepancies in the past view year in spatial modelling for marine risk and hazards including risk of tsunami waves is especially due to the limitation of spatial data-base [1], analysis method and lack of a holistic point of view that an ecological spatial distribution state and analysis should be based on the whole ecosystem parameters itself as a unity, and should not be analyzed partially [2]. After three earthquakes with 8.4, 7.9 and 7.0 magnitude occurred along the coast of Mentawai islands West Sumatra since the last quake with 8.9 magnitude in 1833 the region might still hold enough energy to release 9.0 magnitude tremor that could produce deadly tsunami echoing the Aceh 2004 tsunami that klled more than 230,000 people in southeast Asia [3]

Great extensional faulting events in the shallow outer trench-slope region seaward of subduction zones are relatively rare, with the three largest-known events being the 1933 Sanriku, Japan, earthquake (moment magnitude Mw58.4), the 1977 Sumbawa, Indonesia,earthquake (Mw58.3). These huge intraplate earthquakes all had relatively high stress drop and strong tsunami genesis, with ruptures extending through the oceanic crust and at least 15–20 km into the uppermost mantle. These extensive fractures of the oceanic lithosphere are a result of plate bending and slab-pull forces. The deep faulting probably facilitates hydration of the lithosphere before subduction, enabling intermediate-depth and deep earthquakes once the plate subducts. The Sanriku and Sumbawa events occurred seaward of subduction zones for which the largest interplate thrust events are small, suggesting weak frictional coupling of the megathrusts. The 2009 Samoa event, with a seismic moment that places it among the four largest known trench-slope events, thus appears similar to the 1933 Sanriku and 1977 Sumbawa earthquakes, with the Tonga subduction zone megathrust apparently having weak frictional coupling [4]. The paper aimed to built spatial database, tsunami wave numeric modelling at along the south coast of Java. As well as to plann of escape zone for the worst tetonic earthquake scenario above 8 magnitude, for dense populated area of south Java coast at Serang (sout of west Java) , Bantul (south of central Java) and Banyuwangi regency (south of east Java).

METHOD

Ocean floor morphology analysis using ETOPO2. v2 2006, USGS USA with 2-minute Gridded Sea Floor Topography to generate 2D-ocean floor morphology. Data base of tectonic earthquake history was compilled for ten years periode, consisting of coordinates, magnitude and tectonic earthquake depth (Km). Spatial tsunami wave modelling was built using MIKE-21 software (evaluaton license, Waindo SpecTerra Company) with variable of tectonic earthquake such as Initial rupture time [hh:mm:ss - UTC], Dip-angle (δ) : 35, Slip-angle (α) : 90, Strike angle (θ) : 315, , Fault mechanism : subduction dip-slip, Mw [-] : 8.4, Shear Modulus [Gpa] : 29.4 , Lambda [Gpa] : 25.9, with vertical deformation of tsunami wave generations. Three area of south Java coast tsunami model were made with scenario of earthquake magnitude of 8.4 Richter scale, depth (Km) was 23 Km for Serang coast latitude : 06° 32'09.60" S, longitude : 103° 34'19.20" E (south of west Java), with 315 degree of earthquake slope angle. Magnitude of 7.9 Richter scale, depth of 20 km for Bantul coast (south of central Java) with 300 degree of earthquake slope angle and magnitude of 7.0 Richter scale, depth of 15 km for Banyuwangi (south of east Java) with 270 degree earthquake slope angle. All the three model with geodetic datum of WGS1984. Magnitude of earthquake was made based on range of ten years data 6.1 – 8.7 Richter scale) based on ten years earthquake recorded data along the west Sumatra and south of Java. Analysis on predicted impact to coastal region using DEM-SRTM and Geo-Eye satellite data, tsunami run-up model, demographic or district population density data, coastal infrastructure such as roads and buildings.

RESULT and DISCUSSION

The spatial affection of the possible tsunami waves generation after plate tectonic earthquake on the coastal for coastal area zonation and risk and hazards aspects antisipation in order to minimise human lost, coastal infrstuctural damages and coastal management purposes were the main focus of the paper. Analysis of ocean floor morphology was cansidered as one of important point, where as also in the case of Aceh Tsunami 2004 that there is actually present a deep bottom channel structure infront of Banda Aceh region [2] and in this case is the presence of steep slope of bottom morphology reach to Sunda strait and approaching near to Lampung Bay (Fig. 1). That both we can use to anticipate and take into account the strength of tsunami wave striking energy since there was no ocean floor barrier structure in reducing the tsunami wave energy striking to the coastal area. Based on bathymetric and ocean morphology analysis we can identify the depth at subduction zone at Sunda strait is 6,453 m with distance to the most dense population district of Serang regency is 291.7 Km (Fig. 1). Scenario for tsunami wave model for Serang was set with 8.4 Richter scale at coordinate for tectonic earthquake at latitude : 06° 32'09.60" S, longitude : 103° 34'19.20" E located at the outer part of Sunda strait, inline with subduction zone (Fig. 2). Lesson learned based on the west Sumatra earthquake that the region might still hold enough energy to release a magnitude-9.0 tremor that could produce a deadly tsunami, echoing the 2004 tsunami that killed more than 230,000 people in southeast Asia. The earthquakes released pressure from a 700-kilometre-long region, known as the Mentawai section, which had been building since the last quake, an event of magnitude 8.6–8.9 in 1833 [5]

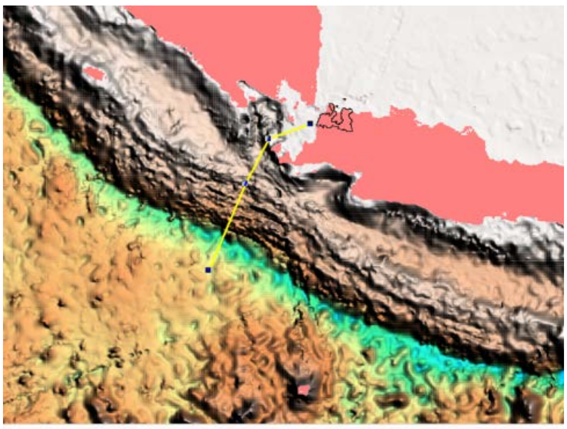

Fig. 1. Ocean morphology and the subduction zone of Serang south of West Java.

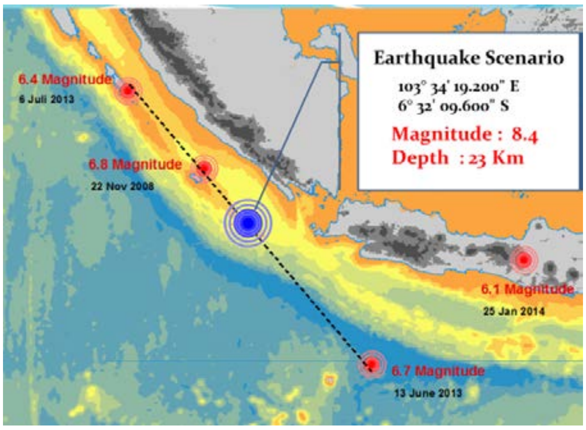

Fig. 2. Tectonic database and tectonic earthquake scenario of 8.4 Richter scale and depth 23 km

After running the numerical spatial tsunami wave model, when the tsunami waves reach the coastal area then most dense population coastal district as the most vulnerable coastal zone was identified at 1 hour and six minute with two big tsunami wave up to 10 m height (Fig. 3) with 30 minute lag-time followed with a 3 m low-seawater between the two big tsunami waves.

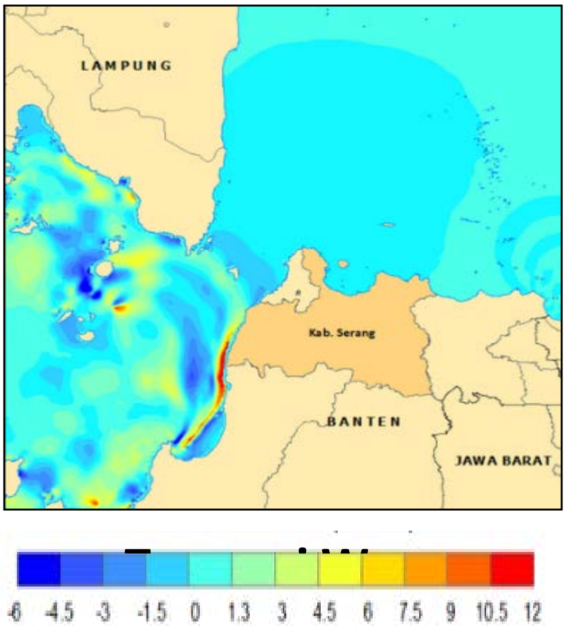

Fig. 3. Tsunami wave run-up (m) to reach the dense coastal population zone of Serang coastal area.

Based on the tsunami wave model that reach to the Serang west Java, about 231.63 Km long of coastal area was affected by tsunami waves (Fig 3). Two most dense populated district at Serang were detected at the most vulnerable coastal zone with population density between 6,413 - 8,437 per hectare (Fig.4). The area was highly packed with the existance of many important and large scale industrial zones, industrial and passenger harbour, power plants, luxurius resetlements, resorts and hotels. Tsunami escape point scenario was made with radius from 200 up to 800 meter radius zone (Fig.5) characterised with hill and flat coastal area and alluvial soil type. Spatial model of run-up height and zone was used to set based on maximum tsunami wave elevation plus 30% and plus 3m height for safe escape building height plann.

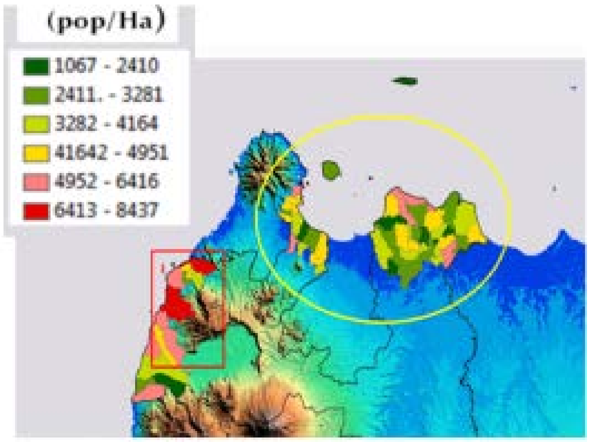

Fig. 4. High population density at most vulnerable coastal districts of Serang regency – Banten Province

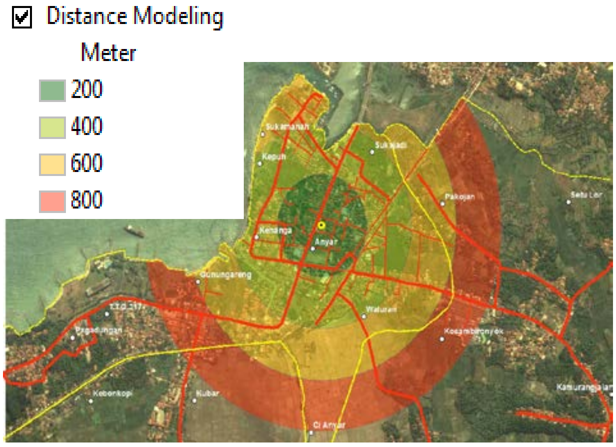

Fig. 5. Distance and analysis for the escape zone and building at Serang coastal zone

Bathymetry analysis made at south Bantul coast (south central Java) indicates the presence of relatively more gentle slope of ocean floor comparred to Banyuwangi (south east Java) with a more steep ocean floor (Fig.6) as assumed relatively will have a beter bottom resistance for tsunamy wave energy. Distance from subduction zone to the coast of Bantul is 247.2 Km, while distance at Banyuwangi is 257.8 Km. After running in the tsunami wave model for these two coast, about

79.42 Km long at Bantul coast and about 111.16 Km long coastal area at Banyuwangi which mainly would be affected by high tsunami run-up model (Fig 7 and Fig 9) up to 8m high with 2m low-water cycle (Fig 8 and Fig 10). Time lag in between high and low water run-up model at Bantul coast was about 30 minutes, while at Banyuwangi coast was only 10 minutes delay. The difference of high-low water time lag at Bantul and Banyuwangi was considered due to the difference of ocean floor morphology, where more gentle slope identified at Banyuwangi. The two coastal area were mostly flat with sandy soil type (Fig 11). Population density at these coastal districts were less than 100 people per hectare and much less coastal infrastructure such as harbour, electricity plant, highway and big roads, comparred to Serang coast.

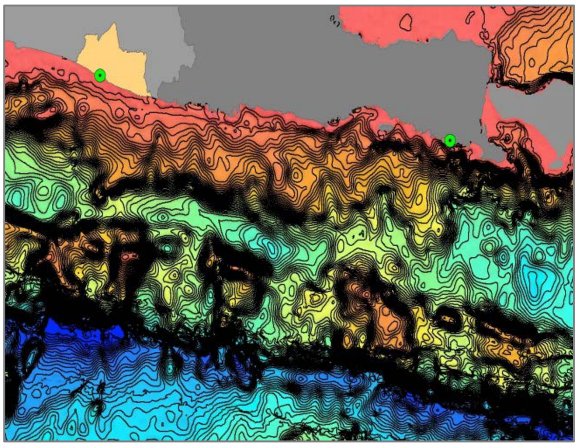

Fig. 6. Bathymetry at south Bantul (south central Java) and Banyuwangi (south east Java)

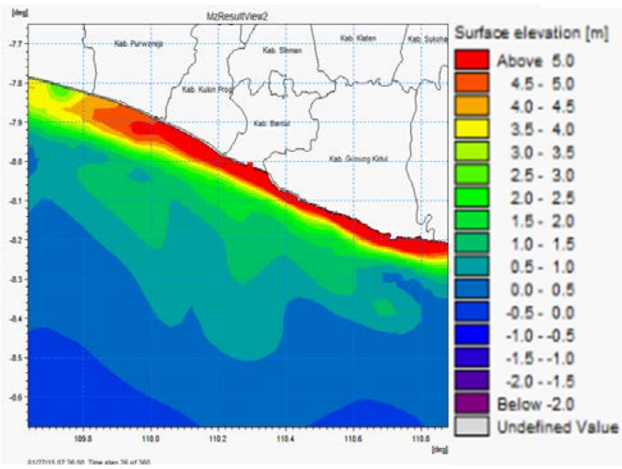

Fig. 7. Tsunami wave model at Bantul south of central Java coastal area

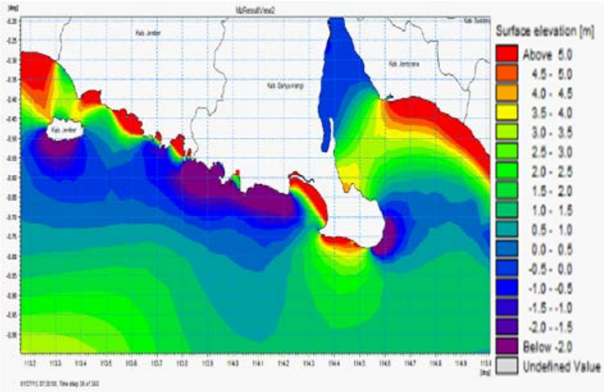

Fig. 8: Run-up numerical model at Bantul south of central Java coastal area

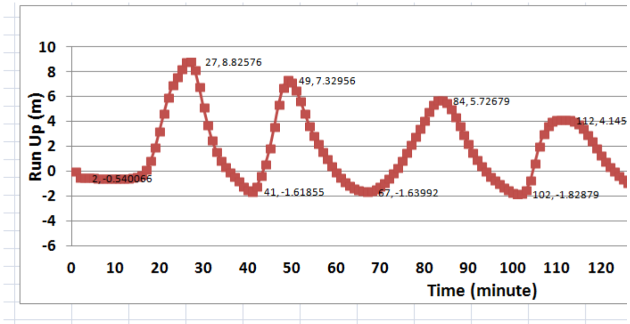

Fig. 9. Tsunami wave model at Banyuwangi south of east Java coastal area

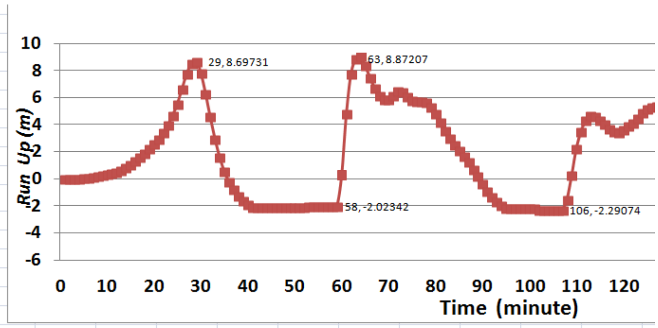

Fig. 10 : Run-up numerical model at Banyuwangi south of east Java coastal area

Fig. 11. Escape zone at the south of Banyuwangi coastal area

Refer to the world's largest earthquakes occur along the contact between subducting and overriding tectonic plates in subduction zones. Rock and sediment properties near this plate interface exert important controls on the frictional behaviour of faults and earthquake rupture dynamics. An important material property to define along the plate interface is the rigidity (the resistance to shear deformation). Rigidity affects the degree of earthquake shaking generated by a given fault displacement through its influences on seismic wave speed and earthquake rupture velocity. Hundreds of subduction zone events had been analysed from northern Japan, the Alaska and Aleutian islands region, Mexico, Central America, Peru and Chile satisfying the following criteria: (1) close proximity to the interplate contact, (2) faulting geometry consistent with interplate thrusting, (3) moment magnitude (Mw) between 5.0 and 7.5, and (4) availability of at least four high-quality teleseismic digital P-wave recordings with good azimuthal coverage and high signal to noise ratio. If stress drop is assumed constant, rigidity appears to increase with depth in each seismogenic zone by a factor of 5 between depths of 5 and 20 km. This fact is consistent with the hypothesis that `tsunami' earthquakes (characterized by large slip for a given seismic moment and slow rupture velocity) occur in regions of low rigidity at shallow depths 3 - 5m. The rigidity trends should provide an important constraint for future fault-zone and earthquake-modelling efforts [4]-[5].

The Indian Ocean has experienced, along with three main phases of seafloor spreading, two major plate reorganizations from the late Jurassic to the present. With the first phase of spreading started in northwest (NW)–southeast (SE) direction and resulted in India's movement away from Antarctic-Australia during the early Cretaceous. During the middle Cretaceous, it appears that the Indian plate rotated from its early NW–SE to north (N)–south (S) direction and moved at a slow spreading rate. The second phase of spreading started in the N–S direction and during this period, India drifted in N–S direction from Antarctica with a rapid speed of 11 to 7 cma21. The Indian and Australian plates merged and formed as a single Indo-Australian plate during the middle Eocene. The third phase of spreading initiated in northeast (NE)–southeast (SE) direction and appears to continue since then where Java island characterised with mainly North-South plate tectonic movement and fault zones [6]-[9].

Rigidity, extent of rupture of any mega tectonic fault, coastal deformation [10] combined with analysis on spatial in the future would be next important for coastal area risk and hazard zonation and planning.

CONCLUSION

Based on the running of tsunami wave model gererated, the three coastal area at the south of Java (Serang, Bantul and Banyuwangi coastal area) would be characterised with two up to 8 m high tsunami waves coupling with a 2m of low-water striking to the coastal area after 60 minutes travel time, with average of 30 minutes time-lag in between.

ACKNOWLEDGEMENTS

The authors would like to tank to Waindo Specterra Company who had provide some Geo-Eye satellite data. Also special thanks to the grant from Directorate General of Higher Education, Ministry of Research and Technology and Higher Education – Indonesia for presentation at Osaka Geomate 2015.

REFERENCES

[1] Hartoko,A. Supply of Thematics Data Sets of Coastal Resources of West Sumatra Provinces. *Report. Ministry of Marine and Fisheries, Asian Development Bank.& Bappeda of West Sumatra Province. 2004. Chapter IV. Pp 150 - 160*

[2] Hartoko,A and M Helmi. Tsunami Aceh : The Role of Marine Geomatics for Science and Society. *Proceeding. Joint Working Committe for Scientific Cooperation. Indonesia and The Netrherlands. Open Science Meeting III. Science and Society : New Challenges and Opportunities. 2005 pp : 225 - 230*

[3] Lay.Thorne, Charles J Ammon, Hiroo Kanamori, Luis Rivera, Keith D Koper, Alexander R Hutko. The 2009 Samoa-Tonga Great Earthquake Triggered Doublet. Letters. Nature. 2010. Vol. 466 : 964-968

[4] Cyranoski,David. Worse Quake to Come, Indonesia Warned. NATURE. 2007. Vol. 449: 270-278

[5] Susan L. Bilek & Thorne Lay. Rigidity variations with depth along interplate megathrust faults in subduction zones. Institute of Tectonics and Earth Sciences Department, University of California, Santa Cruz, California 95064, USA. NATURE. 1999. Vol 400 : 443 - 446

[6] Bemmelen, R.W., The Geology of Indonesia. The Hague, Martinus Nijhoff, Vol.IA. 1970. Pp : 565 - 570

[7] Bhattachary, G.C and Chaubey,A.K. Western Indian Ocean-a glimpse of the Tectonic Scenario. The Indian Ocean – A Perspective. R Sen Gupta and E Desa (Eds). New Dlhi India : Oxford and IBH Publishers. 2001. pp : 691-729.

[8] Ramana, M.V Khrisnha, K.S. Ramprasad,T, Desa, M. Subrahmanyam, V and Sarma, K.V.L.N.S,. Structure and Tectonic Evolution of the Norteastern Indian Ocean. in The Indian Ocean - A Perspective. R Sen Gupta and E Desa (Eds). New Dlhi India : Oxford and IBH Publishers. 2001. pp:731-816

[9] Chatterjee.S, R. Bhattacharyya and T.J. Majumdar. Generation and study of high-resolution satellite gravity over the Sumatran earthquake region. Earth Sciences and Hydrology Division, Marine and Earth Sciences Group, Remote Sensing Applications and Image Processing Area, Space Applications Centre (ISRO), Ahmedabad – 380 015, India. *International Journal of Remote Sensing*. 2007. Vol. 28 : 2915–2925

[10] Subarya.Cecep, Mohamed Chlieh, Linette Prawirodirdjo, Jean-Philippe Avouac, Yehudja Bock, Kerry Sieh, Aron J Meltzer, Danny H Natawidjaja, Robert McCaffrey. Plate-boundary deformation associated with the great Sumatra-Andaman earthquake. Nature. 2006. Vol. 440 : 46-51

MODELLING OF PERMEABILITY CHARACTERISTICS OFSOIL-FLY ASH-BENTONITE CUT-OFF WALL USING RESPONSE SURFACE METHOD

Joenel G. Galupino and Jonathan R. Dungca[2]
[1,2]Faculty, De La Salle University, Philippines

ABSTRACT

In order to prevent the contamination of the groundwater by restricting the horizontal movement of water, cut-off walls were recommended. Currently, one of the factors in designing cut-off walls is to provide efficient and relatively inexpensive means of containing contaminants. In order to obtain acceptable permeability, it was suggested to provide a mix of 96% soil and 4% bentonite in the design of cut-off walls, but bentonite is relatively expensive, thus the viability of fly ash as a replacement for bentonite was considered. Soil mixtures were proposed and rigorous laboratory tests was performed to determine the individual properties. Tests for specific gravity, soil index property, relative density, microscopic characterizations, elemental composition and permeability were performed to garner data that were utilized for the model. Permeability models were generated using Response Surface Method. The minimum permeability requirement for the cut-off wall was achieved by providing various mixtures for soil-bentonite-fly ash.

Keywords: Permeability, Fly Ash, Bentonite, Waste Utilization, Environment

INTRODUCTION

Nearly a decade ago, the World Bank found that the San Mateo Landfill located in Rizal Province and Carmona Landfill in Cavite Province of the Philippines containing over 23 million cubic meters of corrupting waste were contaminating the ground water of their nearby Barangays [2]. The Philippines was given financial incentives to manage their landfills [9] but still, these landfills still pose threat to the groundwater supply their nearby barangays. In order to prevent the contamination of the groundwater by restricting the horizontal movement of water, cut-off walls were recommended. Currently, one of the factors in designing cut-off walls is to provide efficient and relatively inexpensive means of containing contaminants.

In order to obtain acceptable permeability, it was suggested to provide a mix of 96% soil and 4% bentonite in the design of cut-off walls [1], but bentonite is relatively expensive, thus the viability of fly ash as a replacement for bentonite was considered. Permeability refers to the susceptibility of a material to allow fluid to move through its pores. In the context of soil, permeability generally relates to the propensity of a soil to allow fluid to move through its void spaces [5].

It was proposed that fly ash is mixed with silty sand since power plants discharge large amounts of fly ash as waste but only half of them are used and the remaining half is trashed to land and sea, its disposal became an environmental concern. The utilization of fly ash may be a viable alternative for porous backfill material because fly ashes generally consist of silt-sized particles and consequently possess high permeability [7]. Tests were performed to determine the viable mixture, and data garnered were utilized for the permeability model.

METHODOLOGY

Fly ashes generally consist of silt-sized particles and consequently possess high permeability [7]. To check the effect of the different soil, varying mixtures were tested, shown on Table 1.

Table 1. Soil Mixtures

Soil Mixture	Fly Ash (%)	Soil (%)	Bentonite (%)
100FA	100	0	0
75FA25S	75	25	0
50FA50S	50	50	0
25FA75S	25	75	0
100S	0	100	0
100B	0	0	100
96S4B	0	96	4
96S4FA	4	96	0
96S2B2FA	2	96	2

Each soil mix underwent rigorous laboratory tests: specific gravity test based on ASTM D854 was utilized, it is the standard of determining the density of the soil. Atterberg limit tests based on ASTM D4318 for determining the Liquid Limit, Plastic Limit and the Plasticity Index of the Soil. For emax and emin Tests and Relative Density, ASTM D4253 and ASTM D4254 were used to determine the maximum and minimum index densities for soils. Particle size analysis uses ASTM D422 to determine the percentage of different grain sizes in a soil.

The scanning electron microscopy (SEM) was used to evaluate the microscopic characterization of each soil mixture. Scanning electron microscopy (SEM) with energy dispersive X-ray spectroscopy (SEM/EDX) is the best known of the surface analytical techniques. High resolution images of surface topography are produced using these tests. Using the Energy Dispersive X-ray Spectroscopy (EDX), chemical composition of soil is determined to give information on the elements present in the soil.

Permeability of the different soil mixes were determined by the constant head test method and falling head test method. The direction of flow of water is also important, thus, vertical and horizontal orientations of permeameter were used. A proposed set-up for permeameter was used and modified to determine the horizontal permeability [8] of the soil mixtures, shown on Fig. 1. The equation utilized for the permeability set-up is Eq. 1.

A proposed Response Surface Methodology (RSM) model based on the data garnered was formulated. Response Surface Methodology (RSM) modelling is a statistical process for estimating the relationships among variables. It includes many techniques for modeling and analyzing several variables, when the focus is on the relationship between a dependent variable and one or more independent variables.

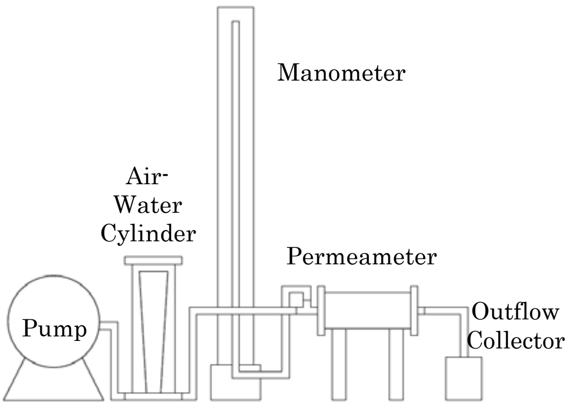

Fig. 1: Horizontal Permeability Set-up

Line and other Models. Validation using equality line usually involves a 45-degree line as a guideline that provides insight into the measured variables and as a critical part of the analysis. When the data are near the 45-degree line, this means that the residual is small and the predicted coefficient of permeability is near the measured coefficient of permeability.

$$k=Ql/Aht \quad (1)$$

where:

k = coefficient of permeability, cm/s; Q= quantity (volume) of water discharged during test, cm^3; l= length between manometer outlets, cm; A = cross-sectional area of specimen, cm^2; h = head (difference in manometer levels) during test, cm; t = time required for quantity Q to be discharged during test, s.

RESULTS AND DISCUSSIONS

Physical and Chemical Properties

Using ASTM D854 the specific gravity of each soil blend was determined. The summary of the specific gravity of various soil mixtures are shown in Table 2:

Table 2. Summary of Specific Gravity

Soil Mixture	G_s
100FA	2.02
75FA25S	2.11
50FA50S	2.31
25FA75S	2.49
100S	2.58
100B	2.75
96S4B	2.61
96S2B2FA	2.6
96S4FA	2.52

The specific gravity of the soil mixes was reduced by the addition of fly ash [6] since the usual of the specific gravity of fly ash is low. With the results shown on Table 1, the addition of fly ash reduces the specific gravity of a soil mixture, this is due to the light weight property of fly ash.

ASTM D4253 and ASTM D4254 were used to determine the maximum and minimum void ratios of the different mixes.

It can be noticed from Table 3, the Maximum Void Ratio (e_{max}) ranges from 1.78 to 1.99 because the fine contents of the fly ash contributed to the percentage of voids. 100S has the lowest value while 100FA has the highest, also from Table 3, 100S has the lowest fines content, while 100FA garners the highest. Their fines content and microfabric may have contributed to the minimum and maximum void ratio.

Table 3. Summary of e_{min} and e_{max}

Soil Mixture	e_{min}	e_{max}
100S	0.84	1.78
100FA	0.27	1.99
100B	0.36	1.98
96S4B	0.8	1.80
50FA50S	0.47	1.94
75FA25S	0.37	1.98

Soil Mixture	e_{min}	e_{max}
25FA75S	0.72	1.93
96S4FA	0.76	1.80
96S2B2FA	0.78	1.81

These minimum and maximum void ratios together with the target relative density of 90% were used to determine the void ratio to be utilized for the permeability specimens.

Table 4. Summary of Particle Size Analysis Results

Soil Mixture	% Passing #200	D_{10}	D_{30}	D_{60}
100S	21.84	0.01	0.4	1.2
100F	61.83	0.029	0.03	0.04
100B	58.36	0.0022	0.0055	0.032
96S4B	29.33	0.018	0.043	0.125
50FA50S	29.79	0.032	0.0375	0.12
75FA25S	50.78	0.019	0.032	0.06
25FA75S	25.79	0.015	0.042	0.15
96S4FA	22.27	0.035	0.09	0.13
96S2B2FA	23.82	0.03	0.08	0.25

Summary of results from the particle size analyses are shown on Table 4. 100FA has the greatest percentage of fines compared with other blends. Fly ash and soil are considered fines but the classification differ, fly ash is silt and soil is plastic. It can also be noticed that mixing fly ash with other soils increases the fines content.

In the Energy Dispersive X-ray Spectroscopy (EDX), chemical composition of soil is determined to give information on the element present in the soil. Oxygen (O) is very abundant, followed by Silicon (for Silty Sand) and Calcium (for Fly Ash). Silicon and Calcium are predominant in the soil elemental composition. Due to the presence of Oxygen and other dominant elements: Silica (from Silicon), Lime (from Calcium) and Alumina (from Aluminum) are the dominant minerals in the soil sample.

Most of the soil properties and characteristics like strength, compressibility and permeability are ascribed by its microfabric or microstructure. The scanning electron microscopy (SEM) was used to evaluate the microfabric of soil, fly ash and bentonite. Scanning electron microscopy (SEM) with energy dispersive X-ray spectroscopy (SEM/EDX) is the best known of the surface analytical techniques. High resolution images of surface topography, are produced using these tests.

Pure soils were initially tested to check their microscopic characteristics, mixed soils were also tested thereafter.

As shown in Fig. 2, with 500x magnification for 100S, it is a combination of extremely strandy grains, large angular grains and abundant silt grains formed the micro fabric. The silt grains have a rough surface. The particles are well-graded microscopically. The smaller particles tend to fill the voids created by the larger particles shown in the figure, thus creating a smaller inter-particle void. Looking closer to magnification of 1000x and 5000x, strand-like particles are present, his indicates that these elongated particles also fill the voids, giving small passageways for water to permeate.

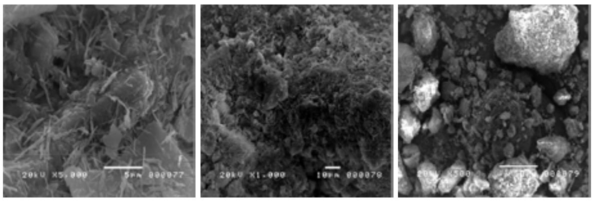

Fig. 2. Microfabric of 100S (5000x, 1000x and 500x Magnification)

As shown in Fig. 3, with 500x magnification for fly ash, it is a combination of larger silt grains and smaller silt grains to form the micro fabric. Fly ash is a silt thus normally 0.002-0.05 mm in size. As seen on the 500x magnification, particles have almost similar size, forming larger inter-particle void, compared with silty sand and bentonite, to allow water to pass through. On the 1000x and 5000x magnification, the surface of the particle is not smooth, this create passageway/voids for water to pass through.

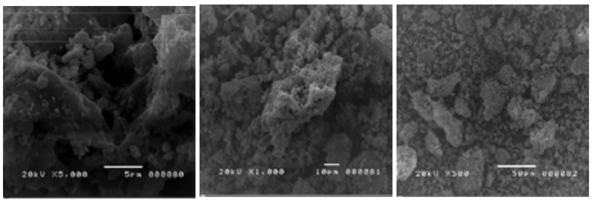

Fig. 3. Microfabric of 100FA (5000x, 1000x and 500x Magnification)

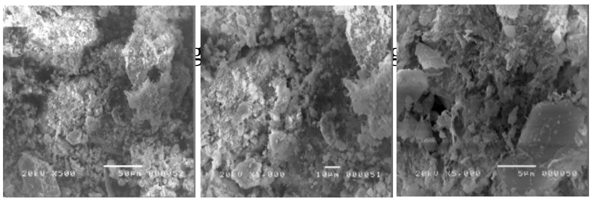

Fig. 4. Microfabric of 50FA50S (5000x, 1000x and 500x Magnification)

50FA50S, it is a combination of extremely strandy grains, large angular grains and abundant larger silt grains and smaller silt grains formed the micro fabric. The silt grains have a rough surface. Looking closer to magnification of 1000x and 5000x, strand-like particles are present but noy prevalent compared with the pure soil, the soil particles may contribute to the reduction of permeability but the silt grains of fly ash will counteract to allow water to drain faster.

As shown in Figure 5, with 500x magnification for 96S2F2B, it is a combination of extremely strandy grains, large angular grains, silt grains and elongated smooth grains formed the micro fabric. The particles are still well-graded microscopically. Looking closer to magnification of 1000x and 5000x, strand-like particles are present, this indicates that these elongated particles also fill the voids, giving small passageways for water to permeate. Also the smooth surface of bentonite particles gave a smaller inter particle-void which the permeability is reduced but counter-acted by the presence of fly ash's silt grains which contributed to additional drainage.

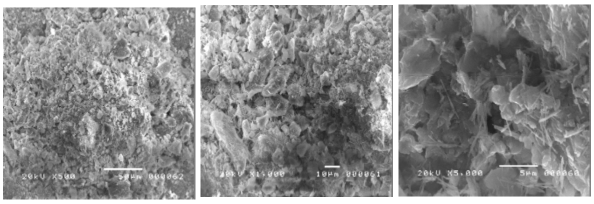

Fig. 5. Microfabric of 96S2F2B (5000x, 1000x and 500x Magnification)

Permeability Characteristics

A proposed approach in determining the vertical permeability of the various soil mixtures was utilized, it was referred on the study of Smith (2010) and was modified. Shown in Table 5, are the range of permeability values gathered for the vertical oriented constant head permeability test.

Table 5. Range of permeability values for vertical oriented permeability test

Soil Mixture	Min K, cm/s	Max K, cm/s
100FA	4.51E-05	5.35E-05
75FA25S	2.93E-05	3.97E-05
50FA50S	2.81E-05	2.98E-05
25FA75S	2.05E-05	2.50E-05
100S	1.66E-05	1.90E-05
100B	6.13E-09	2.48E-08
96S4B	1.16E-07	2.98E-07
96S2B2FA	6.90E-07	7.79E-07
96S4FA	1.93E-05	2.40E-05

It is prevalent that the permeability is increased when the amount of fly ash is increased. It now agrees with the study of Prashanth (2001) that fly ashes generally consist of silt-sized particles and consequently possess high permeability. Thus, the amount of fly ash increase the permeability of the soil mixes.

Table 6. Range of permeability values for horizontal oriented permeability test

Soil Mixture	Min K, cm/s	Max K, cm/s
100FA	6.15E-05	7.29E-05
75FA25S	4.19E-05	5.46E-05
50FA50S	3.70E-05	4.34E-05
25FA75S	3.39E-05	3.49E-05
100S	2.25E-05	2.66E-05
100B	1.30E-08	3.53E-08
96S4B	1.65E-07	2.72E-07
96S2B2FA	8.04E-07	9.87 E-07
96S4FA	2.52E-05	2.70E-05

The horizontal permeability of the various soil mixtures is important because it can discerned how long the contaminated water penetrated in the horizontal direction. Shown in Table 6, are the range of permeability values gathered for the horizontal oriented constant head permeability test.

It can also be noticed that the horizontal permeability values are larger than the vertical permeability values. This agrees with the collected data of Das (2008), where he stated that the horizontal permeability is always larger than the vertical permeability. This is due to the pressure head induced during the permeability test. The specimen is laid in a horizontal position, which experiences no pressure drop within its body, unlike the vertical specimen, which experiences pressure drop, resulting to a slower flow of water.

The permeability of silty sand ranges: (1) vertical oriented 1.47×10^{-05} cm/s to 2.09×10^{-05} cm/s and (2) horizontal oriented 2.21×10^{-05} cm/s to 2.70×10^{-05} cm/s. 100S' microfabric having a combination of extremely strandy grains, large angular grains and abundant rough-surfaced silt grains contributed to the drainage.

Fly ash is the recommended addition to the soil mixtures since waste materials are aimed to be utilized and the addition of fly ash to soils changes the inter-particle void ratio [6], which is prevalent to the microscopic characterization test for 100F.

It is a combination of larger silt grains and smaller silt grains to form the micro fabric. Silt particles have almost similar size, forming larger inter-particle void, contributing to a much larger inter-particle voids. Due to a larger inter-particle voids, the permeability of pure fly-ash ranges: (1) vertical oriented 4.51×10^{-05} cm/s to 5.35×10^{-05} cm/s and (2) horizontal oriented 1.93×10^{-05} cm/s to 7.29×10^{-05} cm/s.

Bentonite has a hydraulic conductivity of 1×10^{-6} cm/s to 1×10^{-12} cm/s (IBECO, 1998). Its microfabric usually composed of a combination of smooth elongated grains and smaller grains, thus, smaller inter-particle voids are present. In the study permeability of pure bentonite ranges: (1) vertical oriented 6.13×10^{-09} cm/s to 1.97×10^{-08} cm/s and (2) horizontal oriented 1.30×10^{-08} cm/s to 3.30×10^{-08} cm/s. Bentonite is a viable candidate for the cut-off wall since it attained the minimum permeability requirement of 9.9×10^{-7} cm/s for a cut-off wall. The price of 100B is relatively high that is why pure bentonite is not recommended for a cut-off wall.

96S2B2FA was the soil mix proposed in the study, its permeability ranges: (1) vertical oriented $6.29\text{x}10^{-07}$ cm/s to $9.60\text{x}10^{-07}$ cm/s and (2) horizontal oriented $8.04\text{x}10^{-07}$ cm/s to $9.87\text{x}10^{-07}$ cm/s. The main objective of the study is to determine the most viable permeability characteristic of the various soil mixes of soil, fly ash and bentonite for cut-off wall. Thus, this mixture of soil, fly ash and bentonite is a viable candidate for the cut-off wall. The addition of fly ash may reduce the permeability of the 96S4B mixture, but still, incorporating the 2% fly ash as the replacement of bentonite, the minimum requirement of $9.9\text{x}10^{-7}$ cm/s for the permeability of cut-off wall is still attained.

Response Surface Methodology (RSM) Model

To check the effect of fly ash and bentonite when added to soil, the mixtures were tested. Their permeability values were used to generate RSM models. The said models were able to establish a relationship between the percentage of fly ash, bentonite, soil and permeability. The delineated RSM models are shown on Figs. 6 and 7.

It can be noticed that the RSM models follow the trend that was observed with the experimental values of the soil-fly ash-bentonite mixtures - because of the silty property of fly ash, once it is increased, the drainage is also increased. The increase in drainage is due to its microfabric, which is a combination of extremely strandy grains, large angular grains and abundant larger rough-surfaced silt grains and smaller rough-surfaced silt grains that contributes to a much larger inter-particle void.

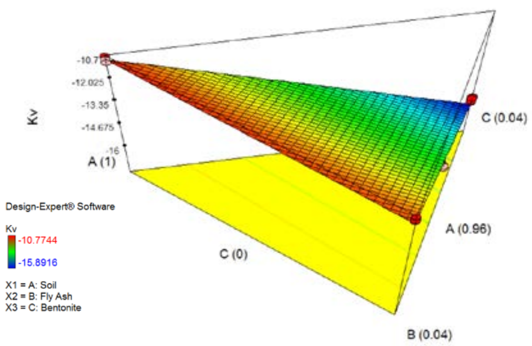

Fig. 6. RSM Model for Kv

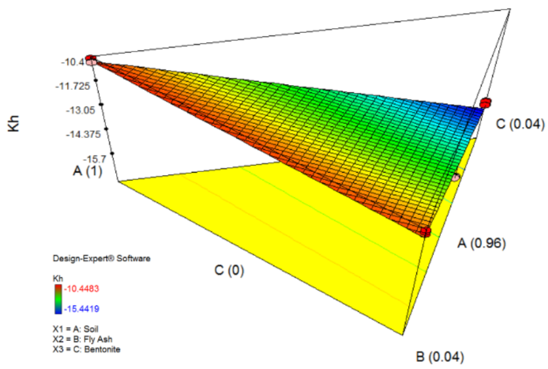

Fig. 7. RSM Model for Kh

The models utilize the percentage of fly ash, bentonite and soil as the independent variables, while the vertical and horizontal permeabilities, kv and kh, are the dependent variables, respectively. These models can predict the permeability (vertical or horizontal oriented) of any soil-fly ash-bentonite mix, once the percentages of fly ash, soil and bentonite are available.

$$k_v = exp^{-10.943*\%S} * exp^{-16.795*\%FA} * exp^{-136.648*\%B} \tag{2}$$

$$k_h = exp^{-10.644*\%S} * exp^{-16.191*\%FA} * exp^{-136.853*\%B} \tag{3}$$

where:

kv = vertical permeability, cm/sec; kh = horizontal permeability, cm/sec; %S = percentage of soil; %FA = Percentage of fly ash; %B = Percentage of bentonite.

Validation

To check the Experimental Data vs. RSM Model, the measured Coefficients of Permeability for each soil mix were compared with the predicted Coefficient of Permeability of RSM Model.

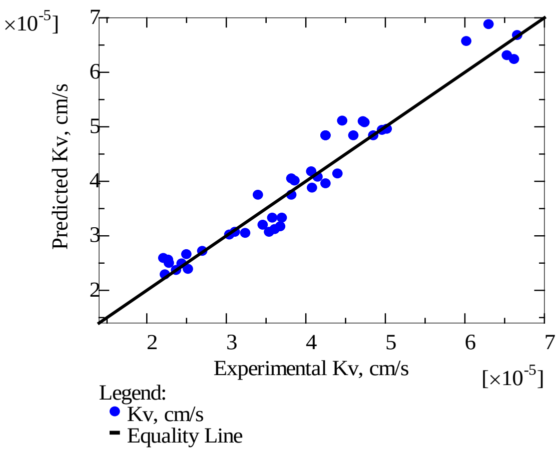

Fig. 8. Regression Model Equality Line for Kv

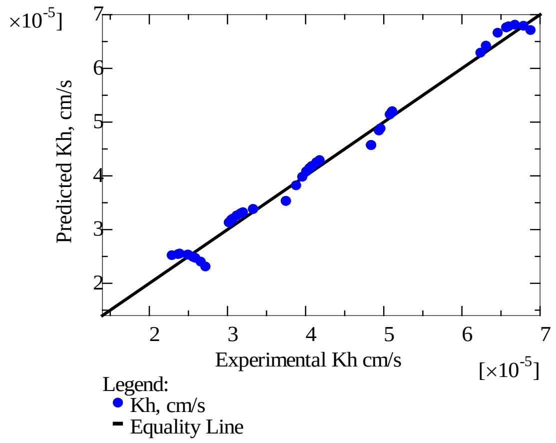

Fig. 9. Regression Model Equality Line for Kh

A line that shows equality between the variable measured (Experimental Data) on the horizontal axis of a diagram and the variable predicted (RSM Model Data) on the vertical axis. The equality line graph is shown on Fig. 8 and 9.Furthermore, the capability of our proposed Regression model of permeability may be validated by various references.

CONCLUSION

Each soil mixture underwent rigorous laboratory tests such as specific gravity tests, particle size analysis, Atterberg limit tests (liquid limit and plastic limit), relative density tests (e_{max} and e_{min} tests) and permeability tests to determine the most viable permeability characteristic of the various soil mixes of soil, fly ash and bentonite for cut-off wall.

As a criterion in selecting the viable mixture for the cut-off wall, it was recommended that the minimum permeability requirement of $x10^{-7}$ cm/s for a cut-off wall. Baxter (2004) suggested to provide a mix of 96% soil and 4% bentonite (96S4B) in the design of cut-off walls, but bentonite is relatively expensive, thus the viability of fly ash as a replacement for bentonite was considered. Fly ash is the recommended addition to the soil mixtures, since waste materials are aimed to be utilized. But the addition of fly ash to soils changes the inter-particle void ratio [6], it increases the permeability, thus, the microscopic characteristics of the soil mixtures may contribute to the increase in permeability.

Since, 96S4B's attained permeability is above the minimum required value, fly ash was incorporated in the mix. Fly ash may increase the drainage but a certain amount of fly ash can be added and still attaining the minimum required permeability [1]. 96S2B2FA was tested, it uses 2% fly ash, which replaces half of the recommended bentonite percentage of Baxter (2004). 96S2B2FA's permeability ranges: (1) vertical oriented $6.29x10^{-07}$ cm/s to $9.60x10^{-07}$ cm/s and (2) horizontal oriented $8.04x10^{-07}$ cm/s to $9.87x10^{-07}$ cm/s which is relatively above the minimum requirement. Thus, 96S2B2FA is a viable mixture for the cut-off wall.

ACKNOWLEDGEMENTS

The researchers would like to express their gratitude to those individuals who helped them accomplish this research: Dr. Mary Ann Q. Adajar, Dr. Lessandro Estelito O. Garciano, Dr. Bernardo A. Lejano, Engr. Irene Ubay-Anongphouth, Engr. King Anongphouth, Dr. Renan T. Tanhueco, Engr. Erica Elice S. Uy, Engr. Patrick B. Taclibon, Engr. Edrick P. Lim, Ms. Ma. Dianne J. Buagas, Ms. Ioulany Nayre, Engr. Jamiel L. Jayme, Engr. Daniel Valerio, Engr. Jason Maximino C. Ongpeng, Engr. Raymund P. Abad, Engr. Melody S. Doliente, Mr. Antonio Kalaw, and Mr. Miller Cutora for their guidance, support and generosity.

REFERENCES

[1] Baxter, D. Y. (2000, April 14). Mechanical behavior of soil-bentonite cut-off wall. Virginia Polytechnic Institute and Stat University, Department of Civil Engineering. Blacksburg, Va.

[2] Caplano, J. (2001, December 30). Closed landfills contaminating groundwater, World Bank warns. (Philippine Star) Retrieved November 2013, from Philippine Star: http://www.philstar.com/nation/145333/closed-landfills-contaminating-groundwater-world-bank-warnsAnnnn B, "Unpublished work but accepted", accepted, Year.

[3] Das, B. M. (2008). Advanced soil mechanics. New York: Taylor & Francis.

[4] IBECO. (1998). Bentonit-Technologie. Bentonit im Tiefbau GmbH, 1.

[5] Liu, C., & Evett, J. B. (2000). Soil Properties: Testing, Measurement and Evaluation. (E. Francis, Ed.) Charlotte, North Carolina, USA: Prentice Hall.

[6] Prabakar, J., Dendorkar, N., & Morchhale, R. (2004). Influence of fly ash on strength behavior of typical soils. Construction and Building Materials, 18, 263-267.

[7] Prashanth, J., Sivapullaiah, P., & Sridharan, A. (2001). Pozzolanic fly ash as a hydraulic barrier in landfills. Engineering Geology, 60, 245-252.

[8] Smith, C. B. (2010). Horizontal Permeameter. Magna Cum Laude Honors Research Project, University of Florida, Department of Civil and Coastal Engineering, Gainesville, Florida.

[9] World Bank. (2012, October 24). Philippines: Toward Greener Waste Management. Retrieved November 2013, from World Bank: http://www.worldbank.org/en/news/press-release/2012/10/24/philippines-toward-greener-waste-management

VEGETATION RECOVERY PROCESS ON LANDSLIDE STEEP SLOPE AFTER *Alnus sieboldiana* AND *Miscanthus condensatus* PLANTING WITH SIMPLE TERRACING WORK IN MIKURA-JIMA ISLAND, JAPAN

Tetsuo Okano and Teruo Arase
Faculty of Agriculture, Shinshu University, Japan

ABSTRACT

Typhoon 9512 hit the island of Mikura-jima in 1995, causing many landslides and destruction of forest vegetation. For long-term observation of vegetation change, a research plot was established on a landslide slope in 2003. A simple terrace was built on this slope, which was planted with native species (*Alnus sieboldiana* and *Miscanthus condensatus*) in 2000 to accelerate vegetation recovery. From 2003 to 2012, a vegetation survey of the plot was conducted to elucidate the vegetation recovery process at an early stage. *A. sieboldiana* grew steadily and its density of individuals decreased. The number of species gradually increased due to invasion of new seedlings from adjacent forests, i.e. *Castanopsis cuspidata*, *Persea thunbergii*. We found some differences in vegetation recovery from another research site, which is a landslide slope seeded with exotic pasture grasses by helicopter in 2002. Seeding of exotic pasture gasses prevented the establishment of trees and reduces successional velocity.

Keywords: Vegetation recovery, Species composition, Species diversity, Exotic pasture grasses

INTRODUCTION

Revegetation in isolated ecosystems should be carried out in ways that restore and do not disrupt the native ecosystem. In an insular ecosystem, habitat for wildlife can easily be destroyed due to disaster or development. Island ecosystems are generally rich in endemic species but tend to be homogeneous in habitat, making them vulnerable to invading species [1-3].

Mikura-jima island is 20.58 km^2 in area, located ca. 180 km south of Tokyo, and is one of the isolated volcanic islands of the Izu islands in the Pacific Ocean off the main island of Japan. The island has sea cliffs more than 100 m in height and steep slopes less than 700 m above sea level. The highest peak, Mt. Oyama, is 850 m. The annual mean temperature is 17.9 ° C and the annual precipitation is 2910 mm [3]. It is covered with natural or secondary vegetation. The main vegetation of the island is an evergreen broad-leaved forest, Carci-Castanopsietum sieboldii (Arachniodo-Castanopietum sieboldii [4]) below 500 m and Daphniphyllo-Trichodendretum aralioideae above 500 m [5].

In September 1995, Typhoon 9512 hit Mikura-jima island (Fig. 1) and produced many landslide slopes in mature forests. The bedrock and solid soil were exposed on the landslide slopes from the surface soil being washed away. After the typhoon, vegetation recovery efforts were begun with projects to put in simple terracing to retain the soil and to transplant locality-certified seedlings of native species (*A. sieboldiana* and *M. condensatus*) [6]. On some landslide slopes, exotic pasture grasses were seeded by helicopter after the transplanting of these two species.

Seeding of herbaceous species, especially exotic pasture grasses, forms a dense, carpet-like community in the short term, and this community prevents the germination and the growth of tree species [7-9]. However, there are few studies of the influence of seeding of herbaceous species on ecological succession in isolated ecosystems. In this paper, we show clearly the effect of seeding of exotic pasture grasses on ecological succession in a mature natural forest area with data from 10 years of continuous monitoring.

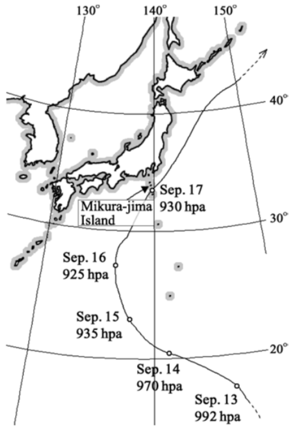

Fig. 1 Path of Typhoon 9512 [3] and location of Mikura-jima island.

METHODS

Sites and monitoring plots

Two study sites were selected to examine the influence of exotic pasture grass seeding on ecological succession on landslide slopes. One was Ofunato No. 2 slope and the other was Torino-o No. 3 slope. Both slopes are located at an elevation ranging from 500 to 550 m above sea level. Slope direction and average angle are respectively NW and 37° for Ofunato No. 2, and N and 27° for Torino-o No. 3. The distance between the two sites is about 1 km.

On both slopes, landslides were caused by Typhoon 9512 (precipitation: 648.5 mm, maximum wind velocity: 67.8 m/s) in 1995. From 2000 to 2002, simple terracing was placed and *A. sieboldiana* and *M. condensatus* seedlings were transplanted to each slope. Planting densities of these species were 1.0 seedling per square meter for *A. sieboldiana* and 1.5 stumps per square meter for *M. condensatus*. In 2002, exotic pasture grasses (including *Agrostis stolonifera*, *Festuca* sp. and *Lespedeza cuneata*) were seeded on the Torino-o No. 3 slope.

In August 2003, two monitoring plots were established in Ofunato No. 2. One was on the upper part of the slope, the other one was on the lower part of the slope, with a plot size of 62.3 m^2 and 84.0 m^2, respectively. In August 2004, one monitoring plot was established in Torino-o No. 3. Plot size was 47.15 m^2. In subsequent years, growth and species composition were investigated in summer (early August).

Growth of *A. sieboldiana*

Transplanted *A. sieboldiana* was measured for plant height (H) and diameter at the base (D_0), and the parameter D_0^2H was calculated as an estimate of aboveground biomass. Since self-thinning was observed, we estimated the regression as follows:

$$1/x = a + by \quad (1)$$

where x is the tree density, y is the mean individual D_0^2H, and a and b are constants [10].

Species composition and diversity

To assess species composition, invading and regenerated trees more than 5 cm in height were investigated for each species. For ten years (Ofunato No. 2: 2003–2012, Torino-o No.3: 2004–2013), the emergence pattern was investigated thoroughly for each species, and all species were divided into several groups. Tree species diversity was indicated by the Shannon diversity index (H') [11] as follows:

$$H' = -\mathrm{SUM}[(pi)\cdot\ln(pi)] \quad (2)$$

where SUM is a summation and *pi* is the proportion of the total number of individuals that is represented by species *i*. Based on the characterized species groups and the diversity index, differences in the change in species composition over ten years was clearly observed between Ofunato No. 2 and Torino-o No. 3, indicating an influence of exotic pasture grasses on ecological succession.

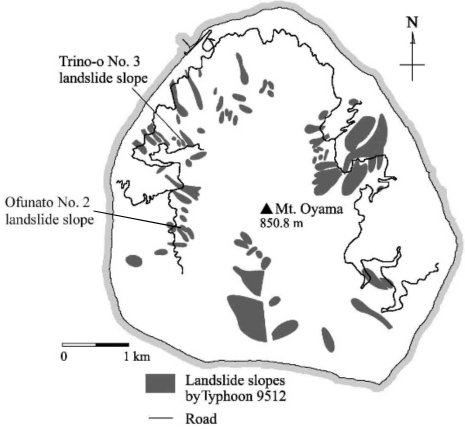

Fig. 2 Location of landslide slopes formed by Typhoon 9512 on Mikura-jima island.

RESULTS

Growth of *A. sieboldiana*

Figure 3 shows the growth of *A. sieboldiana* over a period of 9 years. In each of the Ofunato and Torino-o plots, a phenomenon resembling self-thinning was confirmed for *A. sieboldiana*: the mean plant density decreased yearly, while individual D_0^2H values increased. Although the mean plant density seemed to be greater and individual D_0^2H values smaller in 2004 in the Torino-o plot than the Ofunato plots, the progress of values tended to converge after several years. Analysis of co-variance detected no significant differences in the regression coefficients (F-test, p = 0.113 and 0.867 for a and b, respectively) among the three plots.

Density and number of species of invading trees

Figure 4 shows the density per 100 m^2 of the

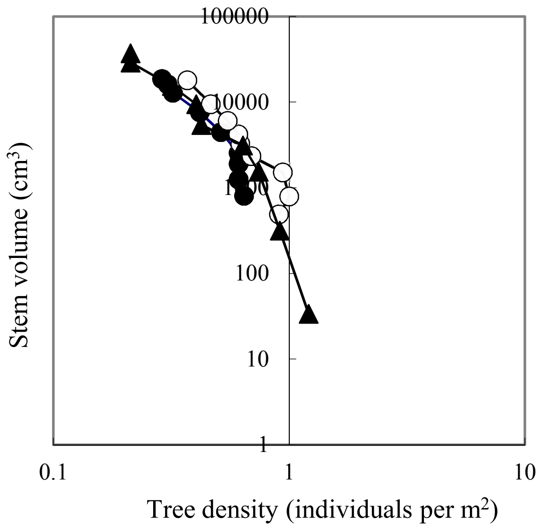

Fig. 3 Changes in the density and stem volume per individual of transplanted *Alnus sieboldiana*. Solid and open circles indicate upper and lower plot of Ofunato. Solid triangle indicates Torino-o plot.

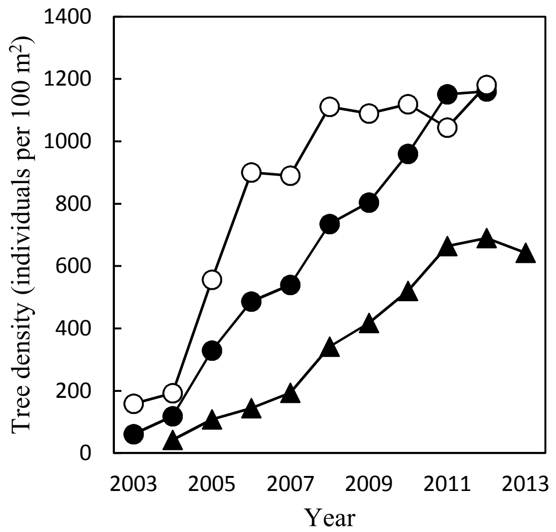

Fig. 4 Changes in the density of invading trees in each plot. Solid and open circles indicate upper and lower plot of Ofunato. Solid triangles indicate Torino-o plot.

invading trees over a period of 10 years in each plot. Until 2010, the density increased in all plots. In the lower plot of the Ofunato site, the density was higher than in the upper plot. In 2012, the density of both plots was similar, ca. 1200/100 m^2. On the other hand, until 2012, the density in the Torino-o plot was about half that in the upper plot of the Ofunato site, although the density increased. After that, the density decreased.

Figure 5 shows the number of species per plot of invading trees over a period of 10 years in each plot. The number of species indicates the species richness. These numbers increased with small fluctuations. The species richness in the Torino-o plot were about half that of the lower plot of Ofunato site. The species richness of the upper plot of the Ofunato site was in between that of the lower plot and Torino-o plot.

Species composition and diversity

Table 1 shows the species composition, the number of individuals in the study period from 2003 to 2013 and the species groups of the invading trees at each site. Thirty-nine invading tree species were confirmed and divided into four groups. Species of Group A (13 species) were present from the first year and had a tendency to increase in number yearly. Species of Group B (18 species) appeared after monitoring began. Group C (4 species) varied in tendency, increasing or decreasing in number depending on species. Group D (4 species) did not show any obvious tendencies.

At the Ofunato site, 13 species were included in Group A. Nine of these species were also growing at the Torino-o site, but only two species (*E. japonica* and *Trachelospermum asiaticum* var. *intermedium*) were included in the same group at both sites; other species, *Hydrangea involucrata* f. *idzuensis*, *Rubus trifidus* and *Stachyurus praecox* var. *matsuzakii* belonged to Group C, and *P. thunbergii*, *Rubus*

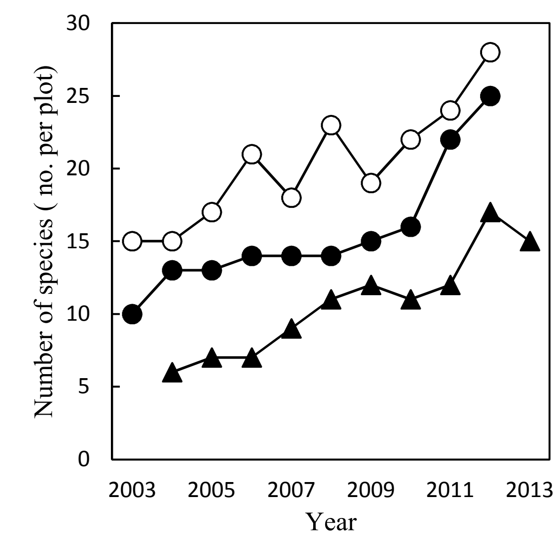

Fig. 5 Changes in the number of tree species in each plot. Solid and open circles indicate upper and lower plot of Ofunato. Solid triangles indicate Torino-o plot.

Table 1 Individual density of invading trees and species groups for each species from 2003 to 2013.

Species	Species group		Site	Year										
	Ofunato	Torino-o		2003	04	05	06	07	08	09	10	11	12	13
Castanopsis cuspidata var. *sieboldii*	A		O	2	2	2	1	1	2	2	1	2	8	
Morus kagayamai	A		O	1	0	0	1	0	0	1	1	4	4	
Persea thunbergii	A	D	O	2	6	4	4	13	12	11	12	13	16	
			T		0	0	0	0	0	0	0	0	2	0
Hydrangea involucrata f. *idzuensis*	A	C	O	4	3	2	5	14	24	37	47	59	86	
			T		0	0	0	0	2	15	15	25	15	15
Rubus trifidus	A	C	O	7	11	35	50	31	65	50	60	65	69	
			T		6	23	30	28	59	59	49	51	38	32
Rubus ribesioideus	A	D	O	25	27	41	64	151	217	244	305	297	290	
			T		6	6	15	2	4	4	8	6	21	13
Prunus lannesiana var. *speciosa*	A	D	O	3	4	10	12	16	26	37	35	41	38	
			T		2	2	0	0	0	0	0	0	0	2
Mallotus japonicus	A		O	7	6	12	12	11	14	14	20	26	28	
Eurya japonica	A	A	O	19	26	53	73	72	107	154	190	198	238	
			T		21	55	66	72	91	151	210	288	299	246
Stachyurus praecox var. *matsuzakii*	A	C	O	1	2	1	8	7	8	7	9	11	18	
			T		0	0	0	0	2	4	6	4	4	4
Styrax japonica var. jippei-kawamurae	A		O	1	1	1	1	2	3	2	3	5	4	
Trachelospermum asiaticum var. *intermedium*	A	A	O	2	3	7	10	11	23	23	27	79	93	
			T		0	8	11	4	23	8	36	93	68	91
Callicarapa japonica var. *luxurians*	A	D	O	0	3	2	5	2	3	4	5	10	8	
			T		2	0	0	0	2	2	2	2	2	2
Podocarpus macrophullus	B		O	0	0	0	1	1	1	0	1	1	3	
Ficus erecta	B		O	0	0	0	0	0	0	0	0	0	1	
Akebia trifoliata	B		O	0	0	0	0	0	0	0	0	0	0	
Rubus buergeri	B	B	O	0	0	0	0	0	1	0	1	4	3	
			T		0	0	0	21	21	34	19	51	108	153
Ilex crenata var. *hachijoensis*	B	B	O	0	0	0	1	0	0	0	0	2	2	
			T		0	0	0	0	0	0	0	0	2	4
Ilex integra Thunb.	B	B	O	0	0	0	0	0	0	0	0	1	0	
Microtropis japonica			T		0	0	0	0	0	0	0	0	2	2
Euonymus japonicus		B	T		0	0	0	2	2	2	2	2	2	2
Elaeocarpus sylvestris var. *ellipticus*	B		O	0	0	0	0	0	1	1	1	1	1	
Camellia japonica	B	B	O	0	0	0	0	0	0	0	1	1	2	
			T		0	0	0	0	0	0	0	0	2	0
Cleyera japonica	B		O	0	0	0	0	0	1	0	0	0	1	
Dendropanax trifidus	B		O	0	0	0	1	0	0	0	0	0	3	
Cornus controversa	B		O	0	0	0	0	0	0	0	0	1	0	
Ardisia japonica	B	B	O	0	0	0	0	0	0	0	0	0	1	
			T		0	0	0	0	0	0	0	0	2	0
Ardisia crenata	B	B	O	0	0	0	0	0	0	0	0	1	6	
			T		0	0	0	0	0	0	0	2	2	0
Symplocos prunifolia	B		O	0	0	0	0	0	0	0	0	1	1	
Osmanthus insularis	B		O	0	0	0	0	0	1	1	1	1	19	
Clerodendrum izuinsulae		B	T		0	0	0	0	0	0	0	0	0	2
Alnus sieboldiana	C	C	O	11	17	188	266	195	160	147	82	51	32	
			T		0	2	4	8	11	8	0	0	0	0
Hydrangea macrophylla f. *normalis*	C	C	O	11	17	30	83	100	141	127	159	155	138	
			T		0	0	13	53	123	125	168	131	112	68
Hydrangea involucrata	C		O	0	2	3	2	1	2	0	0	0	0	
Weigela coraeensis var. *fragrans*	C	C	O	13	24	49	91	84	110	83	76	64	58	
			T		0	0	0	0	0	4	0	0	0	0
Illicium religiosum	D		O	0	0	0	0	0	1	0	0	0	0	
Buxus microphylla f. *major*	D		O	1	2	1	2	2	1	1	1	1	1	
Elaeagnus macrophylla	D		O	1	1	1	1	2	1	1	2	2	1	
Damnacanthus major		D	T		4	11	6	2	0	0	4	6	6	6

Site O: Ofunato, T: Torino-o.

ribesioideus, *Prunus lannesiana* var. *speciosa* and *Callicarpa japonica* var. *luxurians* belonged to Group D. Group B included 18 species (Ofunato: 15 species, Torino-o: 8 species). Most species of this group germinated in 2011 or 2012; only 5 species were found at both sites, *Rubus buergeri*, *Ilex crenata* var. *hachijoensis*, *C. japonica*, *Ardisia japonica* and *Ardisia crenata*. Group C included 4 species (Ofunato: 4 species, Torino-o: 3 species). A clear peak in the number of *A. sieboldiana* was noted only at the Ofunato site in 2006. A peak in the individual density of *Hydrangea macrophylla* f. *normalis* was noted in 2010 at both sites. A clear peak of *Weigela coraeensis* var. *fragrans* density was noted only at the Ofunato site in 2008. Group D included 4 species (Ofunato: 3 species, Torino-o: 1 species). Fluctuation in the density of *Buxus microphylla* f. *major* was small and constant after 2008, whereas the density of *Elaeagnus macrophylla* and *Damnacanthus major* continued to fluctuate.

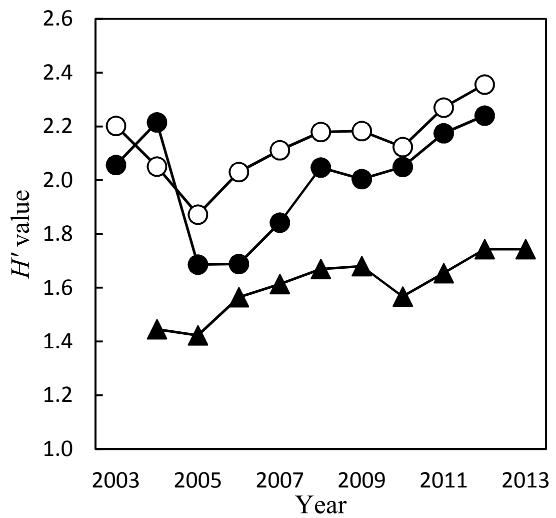

Fig. 6 Changes in tree species diversity (*H'*) in each plot. Solid and open circles indicate upper and lower plot of Ofunato. Solid triangles indicate Torino-o plot.

Tree species diversity

Figure 6 shows the tree species diversity (*H'*) over a period of 10 years in each plot. *H'* values of all plots decreased in 2005. This phenomenon was remarkable in the upper plot of the Ofunato site. After that, *H'* values of all plots increased with small fluctuations. In 2012, the Ofunato plots reached *H'* values greater than 2.2, but the value for Torino-o was less than 1.8. Therefore, tree species diversity of recovered vegetation at the Ofunato site was higher than at the Torino-o site.

DISCUSSION

For *A. sieboldiana*, the tree density decreased yearly, while the individual D_0^2H values increased (Figure 3). Although the mean plant density seemed to be greater and the individual D_0^2H value smaller in 2004 in the Torino-o plot than the Ofunato plots, these values tended to converge after several years. There are allometric relationships between stem size and biomass of each organ (stem, branch and leaf) in *A. sieboldiana* [12]. The dry weight of leaves per unit area of *A. sieboldiana* in each plot would be nearly equal because no significant differences were noticed among plots in tree density and individual D_0^2H values. Therefore, we concluded that the light environment under *A. sieboldiana* canopies did not differ remarkably among the three plots.

The density of invading trees in the three plots increased yearly, but the density in the Torino-o plot was lower than in other plots (Figure 4). The coverage percentage of exotic pasture grasses was more than 80% in 2004. The percentage decreased rapidly to less than 40% by 2008 and to less than 5% in 2011 [3]. This phenomenon indicated that interference by exotic pasture grasses didn't affect the germination of invading seeds or growth of seedlings after 2008. On the other hand, mean plant height of *M. condensatus* increased and tended toward a plateau in 2008 (ca. 170–200 cm) [3]. Therefore, the establishment of invading trees might be prevented by existing exotic pasture grass communities in the initial stage, and by *M. condensatus* communities in the next stage. The extent of changes in number of species was similar to the changes in invading tree density in the survey plots. The increasing number of species might be affected by the community dynamics of exotic pasture grasses and *M. condensatus*.

Species composition could be characterized by defining A, B and C species groups (Table 1). *C. cuspidata* var. *sieboldii*, *P. thunbergii*, *E. japonica*, *Styrax japonica* var. *jippei-kawamurae* and *T. asiaticum* var. *intermedium*, assigned to Group A in the Ofunato plot, were more frequent tree species in mature natural forests on Mikura-jima island [5], [13], [14]. The former three species in particular were abundant in mature forest stands adjacent to the Ofunato and Torino-o landslide slope sites. Other species in this group were mid-successional deciduous trees or shrubs with a wide distribution on Mikura-jima island. *H. involucrata* f. *idzuensis*, *R. trifidus* and *S. praecox* var. *matsuzakii* increased and often later decreased in individual density at the Torino-o site. The density of *P. thunbergii*, *R. ribesioideus*, *P. lannesiana* var. *speciosa*, and *C. japonica* var. *luxurians* were lower at the Torino-o site than the Ofunato site. The characteristic behavior of these seven species suggests that the expansion of exotic pasture grasses or the *M. condensatus* community prevented germination or growth of the invading tree species. Most of the species in Group B were evergreen broad-leaved and late-successional species occurring in mature natural forests on Mikura-jima island. The number of species at the Torino-o site (8 species) was smaller than at the Ofunato site (15 species). The difference of species composition between plots may be relate to the speed of ecological succession. At the present time, the successional change to the mature stage at the Torino-o site will be slower than at the Ofunato site. It is expected that the number of species represented in Group C, including *A. sieboldiana*, will decrease because these are pioneer species.

The trend in tree species diversity on both landslide slopes was similar to changes in the tree density and the number of species. However, the *H'* values of all plots decreased remarkably in the Ofunato plots in 2005 (Figure 6), although the number of species increased. This decrease was caused by a change in evenness of the species composition. Due to a rapid increase in the number of individual *A. sieboldiana* seedlings, evenness declined.

CONCLUSION

The seeding of exotic pasture grasses prevents the establishment of trees that invade landslide slopes from adjacent mature forests. Moreover, ecological successional velocity will be reduced due to the dominance of exotic pasture grasses and *M. condensatus*. When soil erosion is controlled by simple terracing, the seeding of exotic pasture grasses is unnecessary for recovery of the native vegetation.

ACKNOWLEDGEMENTS

The authors would like to thank the staff of Mikura-jima Village office and Mr. Masayuki Hino for their friendly assistance, and Mr. Tadao Hiraoka for his unfailing support.

REFERENCES

[1] Loop LL, Hamann O and Stone CP, “Comparative conservation biology of oceanic archipelagoes – Hawaii and the Galapagos”, Bio Science, Vol. 38, 1988, pp. 272-282.

[2] Ono M, Wildlife in solitary island. Tokyo: Iwanami Shoten, 1994, 239 pp.

[3] Arase T and Okano T, “Influence of fertilization on native plants and exotic pasture grasses on the fascined landslide slopes in Mikura-jima Island, Japan”, GEOMATE, Vol. 8, June. 2015, pp. 1316-1322.

[4] Miyawaki A, Vegetation of Japan Kanto. Tokyo: Shibundo, 1986, 641 pp.

[5] Ohba T, “Die Vegatation von Mikura-Insel leight 200km südlich von Tokyo”, Bull. of Kanagawa Prefectural Museum, Vol. 1(4), Feb. 1971, pp.25-53.

[6] Kyoju no Kai ed., Saving earth (1) Practices to restore nature in Mikura-jima Island. Tokyo: Kyoju no Kai, 2004, 48 pp.

[7] Yoshida H, “Stratificational revegetation of arboreous plant community by deeding method”, J. of the Japanese Society of Revegetation Technology, Vol. 24, Nov. 1998, 90-98.

[8] Arase T, Okano T, Kimura T and Inoue S, “Influence of seedling exotic pasture grasses on the vegetation recovery of landslide slopes formed by typhoon 9512 in Mikura-jima Island, Izu Islands, Japan”, J. of the Japanese Society of Revegetation Technology, Vol. 35, Feb., 2010, pp. 448-461.

[9] Holl KD, Loik ME, Lin EH and Samuels IA, “Tropical montane forest restoration in Costa Rica: overcoming barriers to dispersal and establishment”, Restoration Ecology, Vol. 8, 2000, pp.339-349.

[10] Yoda K, Forest ecology. Tokyo: Tsukiji Shokan, 1971, 331 pp.

[11] Shannon CE, “A mathematical theory of communication”, Bell System Technical Journal, Vol. 27, 1948, pp. 379-423.

[12] Saito H, “Some features of dry-matter production in a young Alnus siebodiana community on dumped detritus with special reference to reproductive parts”, Japanese J. of Forest Society, Vol. 72, 1990, pp. 208-215.

[13] Kamijo T, Isogai T, Hoshino Y and Hakamada H, “Altitudinal zonation and structure of warm-temperate forests on Mikura-jima Island, Izu Islands, Japan”, Vegetation Science, Vol. 18, 2001, pp.13-22.

[14] Hoshino Y, Nozaki R, Isogai T, Maesako Y, Kamijo T, Kobayashi H and Watabe Y, “Studies for ecology Island Mikura-jima Area”, Report of Pro Natura Fund, http://www.nacsj.or.jp/pn/houkoku/h01-08/h05-no03.html.

QUANTIFICATION OF PATHOGENIC BACTERIA IN FLOOD WATER IN MALAYSIA

Zummy Dahria Mohamed Basri[1], Zulhafizal Othman[2] and Marfiah Ab. Wahid[3]
[1,2,3]Faculty of Civil Engineering, Universiti Teknologi Mara, Malaysia

ABSTRACT

The monsoon season occurs every end of year in the east coast states of Peninsular Malaysia’s brings more rain than usual and eventually suspected annual floods on low altitude areas. However flood in late 2014 in Malaysia bring severe destruction as compared to its normal yearly floods. Besides unusual rainfall recorded, uncontrolled deforestation was said as major factors of this flood. Problem arises when floods with high water flow carried with it large leavings including logs. It washed away homes and destroyed other amenities including septic tanks. As we know septic tanks impacted by flood were containing wastewater contaminated with harmful bacteria. Water samples taken during this flood indicated the presence of up tp 800 cfu/ml of *Pseudomonas Aeruginosa*, 650 cfu/ml of *Salmonella typhi* and 1700 cfu/ml of *E.coli*. In soil samples also showed higher presence of bacteria levels where as many as 6750 cfu/ml of *E.coli* and 1500 cfu/ml of *Salmonella typhi* were detected. Post-flood showed a decreasing trend and lower concentration of bacteria present in water samples which 25 cfu/ml of *Pseudomonas aeruginosa*, 75 cfu/ml of *E.coli*, 625 cfu/ml of *Salmonella typhi* and 475 cfu/ml of *Shigella* were detected. The presence of pathogenic bacteria will affect the health of the population live where the flood and post-flood seasons showed an increase in waterborne diseases as reported by the press.

Keywords: Flood, Pathogenic bacteria

INTRODUCTION

The devastating floods in Kelantan at the end of 2014 brought great destruction to property. Monsoons that hit the east coast every end of the year also led Pahang flooded. The dirty flood water caused many victims suffered from infectious diseases. The most health risks related to the flood are water and vector borne diseases [1].

2014 flood in Kelantan is the worst since 1967. Kuala Krai is the worst area hit by the floods. Crossing the river from upstream systems that meet at the confluence Kuala Krai quickly cause overflow (see Fig. 1).

Fig. 1 Bank of the river after flood

According to a report released by the department of irrigation and drainage, rain of 850mm for 10 days in Kelantan is more than the normal rate of 100 mm. Coupled with a static clouds situation that should move to Johor brought heavier rain than usual [2]. Besides heavier rain factor, there is also deforestation factor. Some deforestation even occurred in the catchment area or waterway. Logging activities from the deforestation explained why a lot of facilities damaged [3].

Some private septic tank and sewage systems were found in a central residential area, schools and government and private buildings were shattered (see Fig. 2). It makes all the dirt out of septic tanks swept. Faeces usually bring impurities containing pathogenic bacteria. When the tank burst, these harmful bacteria are spread through the air. In the event of direct contact to human, it will cause disease.

Great dangers of flood not only the physical damage from floodwaters but also the health hazards of large-scale contamination of water for human consumption [4]. Among the diseases that are commonly encountered when flooding is food poisoning or diarrhea due to the use of uncooked water and direct contact will cause skin disease.

Fig. 2 Facilities damaged in flood

Table 1 shows several microorganisms found in floodwaters in previous study. During flood, general health condition become worst and the most prevalent condition was fever, continued by diarrhea and skin diseases [5].

Table 1 Types of microorganisms in floodwaters

Microb.	References
Shigella sp., Lestospira sp., Vibrio cholerae	[4]
Shigella flexneri, E.coli, Salmonella typhimurium	[6]
E.coli, Intestinal enterococci	[7]
Campylobacter,Legionella pneumophila	[8]

This study was conducted to investigate the occurrence of harmful bacteria in floodwater and post-flood water in Pahang and Kelantan, Malaysia.

MATERIAL AND METHODS

Study Area

Kuala Krai is the place most affected by the flood end of 2014 in Kelantan. Floodwater sampling had been done in two places namely Sungai Nal and Sungai Lebir (Fig.3 and Fig. 4).

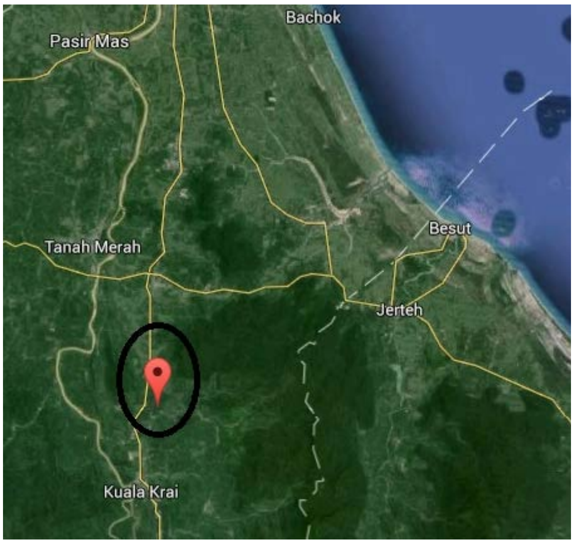

Fig. 3 Sungai Nal

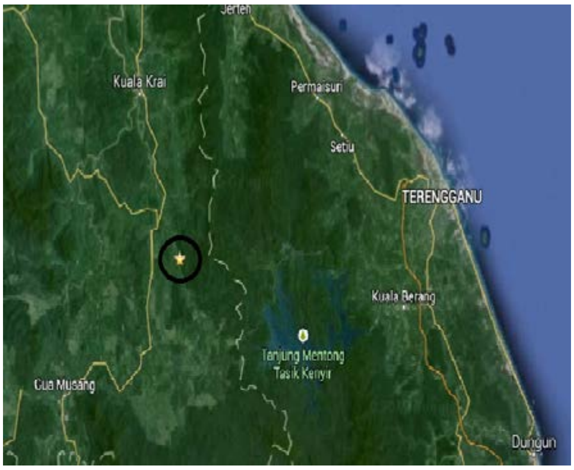

Fig.4 Sungai Lebir

Sungai Lebir and Sungai Nal are streams which located 53 meters above the sea level. The coordinates of Sungai Lebir are 5°31'0" N, 102°12'0" E and Sungai Nal are 5° 35' 0" N, 102° 11' 0" E. Both Sungai Lebir and Sungai Nal are populated place.

For Pahang case, Kampung Teluk Sentang (Fig.5) was also affected by flood in the end of 2014. The sampling area is near Pahang River. This residential area chosen for floodwater sampling suffered major flooding.

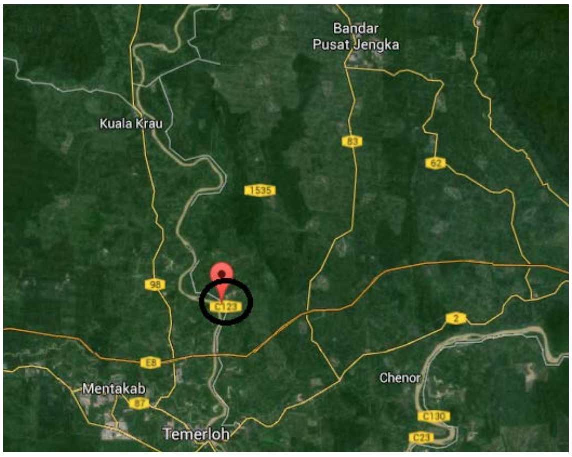

Fig. 5 Kampung Teluk Sentang, Sungai Pahang

Collection of Water Sample and Analysis

Water samples were collected during and after flooding in December 2014 and January 2015. Samples were collected from two areas affected by flooding Kelantan and one area in Pahang. In Pahang, there were two points of sample collected along Pahang River. All water samples had been collected in sterile bottle, stored in 4ºC ice box and brought to laboratory for analysis within 24 hours.

All tests were done according to Standard Method using MacConkey agar for *e.coli* and *Salmonella* concentration, and Cetrimide agar for detection of *Pseudomonas Aeruginosa*. For each sample, one series of dilution had been made and streak on the specific agar. The plate had been incubated for 24 hours at ±35ºC. The pathogenic bacteria had been counted after removing the plate from incubator.

E.coli had been known as familiar pathogenic bacteria that exists in floodwater. On MacConkey agar, *E.coli* will showed 1-3mm pink colonies. On the same agar, 1-2mm colourless colonies indicated the presence of *Salmonella typhimurium*. The occurrence of *Pseudomonas aeruginosa* showed the colourless appearance on Cetrimide agar.

RESULTS AND DISCUSSION

Floodwater both in Kelantan and Pahang were found contaminated with pathogenic bacteria (Fig. 6). The figure showed that the mud in Sungai Pahang and Sungai Lebir was fecally contaminated up to 6750 cfu/ml of *E.coli*. High concentrations of *E.coli* were detected in Kelantan and were caused by ruptured sewage tank located at the upstream. The concentration of *E.coli* in the floodwater exceeded the limit (1 cfu/ml) for criteria of recreational water (full body contact), according to [9].

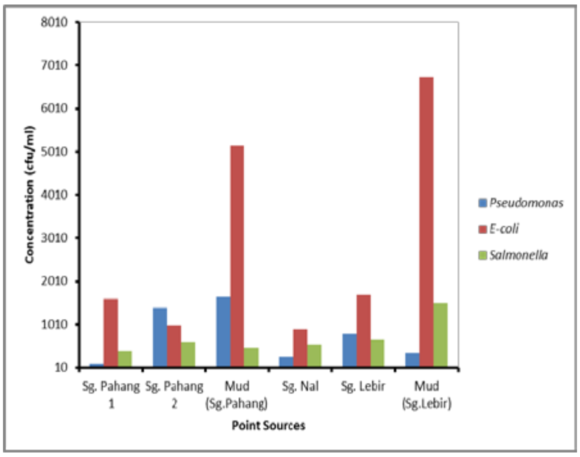

Fig. 6 Pathogenic bacteria detected in Kelantan and Pahang floodwater

The data indicates there are more harmful bacteria present in the sludge compared to floodwater. This probable the bacteria that found in the flood water, trapped in the crevices of solid particles in water flooding. With the presence of more harmful bacteria in the mud, it can be said that mud brought by flood can be more dangerous than the flood water itself.

In addition to *E.coli*, *Salmonella typhi* and *Pseudomonas A.* also detected in floodwater and in the mud. The pathogenic *Salmonella* can cause diseases like fever to those who are infected. There were 400 – 1500 cfu/ml of Salmonella detected during the water sampling in the infected area. It shows that the occurrence of the pathogenic bacteria higher than detected in floodwater in Pahang during 2013 flooding [6]. These pathogenic bacteria can cause infectious diseases to human. Not only during flooding, but the harmful bacteria can be detected after-flood water In Kelantan (Fig. 7).

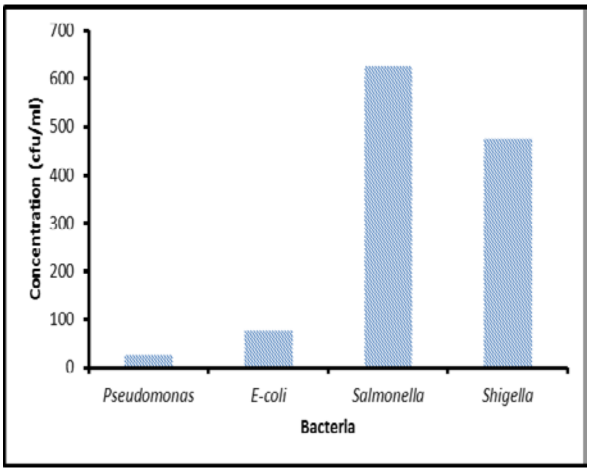

Fig. 7 Pathogenic bacteria detected in Kelantan river post-flood water

25 cfu/ml of *Pseudomonas*, 75 cfu/ml of *E.coli*, 625 of *Salmonella typhi*. and 475 cfu/ml of *Shigella* were detected in post-flood water in Kelantan. Occurrence of the pathogenic bacteria detected showed the degradation trend, but it still harmful to those directly exposed to the contaminated water.

In Kelantan, Kuala Krai Hospital (the most affected place) had the largest number of patients being medevac during flood [10]. It shows that more diseases occurred and some of them associated to the floodwater. Infectious diseases during flood should be taken seriously by the relevant parties because damaged sanitation systems lead to more infections occurred.

According to the Pahang Health Department, 28 from 1,220 cases of infectious diseases detected in 6 days of flooding are listed under the Communicable Disease Control and Prevention, 1988. There were 27 cases of food poisoning while the rest involve mild infectious diseases such as skin and eye diseases.

CONCLUSION

From the study indicated that

1. *Pseudomonas Aeruginosa*, *E.coli* and *Salmonella typhi* were found in floodwater.
2. Pathogenic bacteria mostly found in the mud compared in floodwater itself.
3. Pathogenic bacteria were higher during flood compared to post-flood event.

REFERENCES

[1] Haitham BA, Jayant KR, "Assessing factors affecting flood-induced public health risks in Kassala State of Sudan", J. of Operations Research for Health Care 3, 2014, pp. 215-225.

[2] Malaysian Meteorological Department (MET), Monthly Weather Bulletin, retrieved at http://www.met.gov.my.

[3] Wardah T, "Banjir kuning bagai tsunami ancam Kelantan", retrieved on Jan 17th at http://www.bharian.com.my/node/29743.

[4] Yuphakhun C, Punnida T, Hajime T, Bon K and Suwimon K, "Microbiological evaluation of water during the 2011 flood crisis in Thailand", J. of Science of the Total Environment, 463-464, 2013, pp. 959-967.

[5] O Kunni, Nakamura S, Abdur R, Wakai S, "The impact on health and risk factors of the diarrhea epidemics in the 1998 Bangladesh floods", Public Health, 116, 2002, pp. 68-74.

[6] Zummy Dahria, MB, Zulhafizal, O, Marfiah, AW, "Detection of pathogenic bacteria in flood water", Proceeding of International Symposium on Flood Research and Management, 2015.

[7] Helen DM, Imke L, Frans VK, Ana MDRH, "Potential health risk associated with exposure to microorganisms in urban floods", Novatech, 2013, Pathogens, 1-4.

[8] Helena S, Gertjan M, "Microbial health risks associated with exposure to stormwater in a water plaza", J. of Water research, 74, 2015, pp. 34-46.

[9] EPA, "Bacterial Water Quality Standards For Recreational Waters (Freshwaters And Marine Waters) Status Report", 2003.

[10] Kamarul AB, Shaik FAB, Nik Hisamuddin NAR, Nik Arif NM, Tuan Hairulnizam, TK, Abu Yazid MN, Mohd Roslani AM, "The record-setting flood of 2014 in Kelantan: Challenges and Recommendations from an emergency medicine perspective and why the medical campus stood dry", Malays J. Med Sci., Mar-Apr 2015, 22(2), pp. 1-7.

CONVERSION OF A DECOMMISSIONED OXIDATION LAGOON INTO A FUNCTIONAL WETLAND

Jeram Mallis[1], Rhiannon Hamilton[2], Scott Rayburg[3], Melissa Neave[4]
[1]City West Water, [2]Phoenix Mecano Australia, [3]Faculty of Engineering, Science and Technology, Swinburne University of Technology, [4]School of Global, Urban and Social Studies, RMIT University

ABSTRACT

Wetlands in Australia have immense ecological value and are known for both the diversity of their habitats and the biota they support. Wetlands in the Altona region, 15 km southwest of Melbourne, are of international significance due to the threatened and endangered biota that inhabits (and or migrates through) them. This study focuses on the conversion of a decommissioned oxidation lagoon at the Altona Treatment Plant in Victoria, Australia, into a wetland ecosystem. Throughout Victoria and most of Australia, there is an ongoing and progressive tightening of the regulation for sewage treatment. These regulatory changes are placing pressure on the water industry to improve the quality of treated effluent discharges to local waterways, bays and oceans. This is resulting in the gradual decommissioning of oxidation lagoons in favor of more technically advanced alternatives. This study proposes an ecologically valuable reuse for a decommissioned oxidation lagoon, which could be replicated elsewhere. Previous design attempts for this project had failed due to the potential risk they posed to both the surrounding environment and the Altona Treatment Plant itself. Therefore one of the objectives of this project was to undertake multiple assessments to mitigate these risks. The most important of these, and the focus of this paper, was the determination of the optimal source and quantity of water needed to sustain the wetland. Potential water sources included: water from a nearby estuarine swamp; treated class C or class A effluent from the treatment plant; and rainfall-fed runoff from the treatment plant site. Through an analysis of cost and quality of the available water sources, it was determined that locally captured rainfall-fed runoff with Class-A recycled water as a backup supply was the most feasible. In addition, hydrologic modelling revealed that this source could maintain flow in the wetland year round, even in drought years. These findings mitigate the concerns raised in association with previous designs and demonstrate that the proposed wetland is viable.

Keywords: Constructed Wetland, Recycled Water, Asset Recycling, Water Reuse

INTRODUCTION

Wetlands in Australia have immense ecological value and are known for both the diversity of their habitats and the biota they support. Moreover, the high biological productivity of wetlands and the strong selection pressures of an aquatic existence produce a rich biota associated only with wetlands [1]. This distinct and unique wetland biota includes communities of birds, reptiles, amphibians, fish, mammals and invertebrates which both live and breed in wetlands as a consequence of the shelter they provide from predators and the availability of abundant food sources. In addition to the ecological benefits, wetlands also serve a hydrological function by retaining flood waters, improving water quality and in the case of tidal wetlands, protecting coasts from erosion.

Despite their inherent importance, wetlands throughout the world have been extensively degraded and actively removed for various reasons, ranging from urbanisation to war. Wetland ecosystems in Europe, North America, Australia and China have faced, or are currently facing, substantial threats to their existence with the number of wetland ecosystems in these nations being halved in the 20th Century [2]. For example, in North America in the early 1900's, wetlands were drained by the federal government in the interests of urban and agricultural expansion, and for the eradication of mosquitoes [3]. Meanwhile, in Iraq in the late 20th century, the nation's leader at the time committed what was described by [4] as 'ecogenocide' by draining the marshlands of Iraq to destabilise the human inhabitants of an area which had revolted against the regime. In both examples, one deliberately (Iraq) and the other inadvertently (USA), the vital functions of wetlands and their associated benefits to humanity were lost, a pattern that has recurred all too frequently around the world. Throughout Australia, extensive wetland removal occurred over much of the 19th and 20th centuries.

It is only in the last 30-40 years that the ecological value of wetlands has been recognised at the global level [5]. This became formalised, for the first time in international law, in 1971 with the introduction of the Ramsar Convention. This convention was introduced as an instrument to encourage conservation of habitat with a focus on the conservation of wetlands from a legal perspective. The convention aims at protecting habitats rather than a particular species [6], which was a new concept at the time of its implementation. However, as many wetlands had already been lost by the time the Ramsar Convention was enacted (and continued to be), mitigation strategies for wetland replacement are still needed in many parts of the world. In an effort to redress some of the damage caused by wetland destruction, the use of artificial or constructed wetlands has become increasingly popular, especially in urban areas where nearly 100% of natural wetlands have been lost. In 1996 there was an estimated 1,000 constructed wetlands world-wide ranging in size from 500 m^2 to 4000 ha [7]. Since this time, the number of constructed wetlands has vastly increased as awareness of the need for wetlands habitats has become more apparent.

Throughout Victoria and most of Australia, there is an ongoing and progressive tightening of the regulation for sewage treatment. The Victorian EPA expects the water industry to work towards a future way of operating that has little to no impact, or a net benefit to the environment [8]. These regulatory changes are placing pressure on the water industry to improve the quality of treated effluent discharges to local waterways, bays and oceans. The pressure on the industry is resulting in the gradual decommissioning of oxidation lagoons in favour of more technically advanced alternatives. This study proposes an ecologically valuable reuse for a decommissioned oxidation lagoon, which could be replicated elsewhere.

The purpose of this project is to investigate the design of a constructed wetland to replace a decommissioned oxidation lagoon and to assist with the development of a project that meets pre-determined design criteria. Specific objectives associated with this project are to:

1) ensure that the wetland would complement the other wetland habitats in the area; and
2) select a preferred water source for the new wetland that ensures the wetland has good water quality and that the wetlands hydrology is consistent with surrounding natural wetlands.

SITE DESCRIPTION

The City West Water’s Altona Treatment Plant is located 15 km southwest of Melbourne’s city centre (Fig. 1). This plant was built in 1968 and is comprised of a series of trickling filters and a large oxidation lagoon. In 2005 the plant received a significant upgrade to a more modernized treatment facility, built around a central IDEA rector that currently treats up to 20 ML of sewage per day. Consequently, the existing treatment system, including the oxidation lagoon was decommissioned.

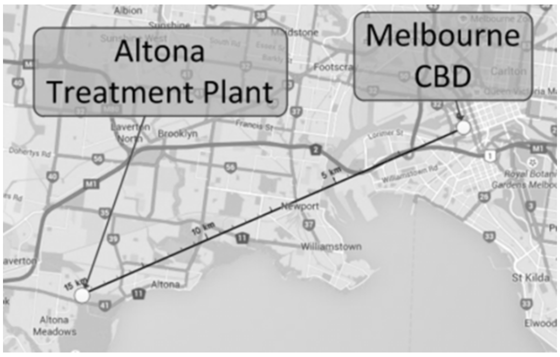

Fig. 1 Map, showing the Altona Treatment Plant relative to the Melbourne CBD.

On the eastern side of the treatment plant site is the 90,000 square meter decommissioned oxidation lagoon which is surrounded by a concrete covered retaining bank. The base of the lagoon in its current state is located at an elevation of approximately 1 m on the Australian Height Datum (AHD) while the surrounding natural surface sits at between 2.5 and 2.6 m (AHD). The lagoon has a thick clay liner to prevent groundwater contamination. This liner dates back to the treatment plant’s construction in 1968, therefore its current condition is unknown. Beneath the liner are substantial quantities of volcanic basalt and dense clay. The water table in the area is at approximately 1 m AHD and is highly saline due to the close proximity of the site to Port Phillip Bay. Currently an estimated 10,000 cubic meters of biosolids is located within the lagoon and this has been moved into ‘windrows’ in anticipation of its removal at a later date. Historically (since 2005) the lagoon fills from rainfall-fed runoff in late winter and early spring (July-September) to a depth of 400-600 mm and evaporates in the summer months until dry. The lagoon also acts as an emergency overflow storage unit for the sewerage treatment facility. The location of the proposed wetland is show in Fig. 2.

Fig. 2 The Altona Treatment Plant site showing the large decommissioned oxidation lagoon which is the proposed site for the new constructed wetland.

METHODS

To begin the process of determining how best to convert a decommissioned oxidation lagoon into a fully functioning wetland, it was required to identify which type of wetland would be most suitable for the site and its surrounds. Specifically, this involved a series of site visits to both the decommissioned lagoon and nearby natural and artificial wetland ecosystems. At each site a visual survey was conducted to determine the species of flora and fauna present. An assessment was also carried out to classify the types of wetlands present in the local area and how the proposed wetland might interact with these as part of a localised wetland matrix.

Another important consideration was the availably of a suitable water source for the proposed wetland and the associated quality of that water. There are four potential water sources in the vicinity of the proposed wetland, including: 1) Truganina swamp, a saline estuary that forms part of Laverton Creek and is located outside of the boundary to the east of the treatment plant; 2) treated effluent from the waste water treatment plant that can supply large volumes of class C water to the wetland; 3) rainfall-fed runoff from the large treatment plant site which is estimated to have 80,000 square meters of catchment area; and 4) a supply of class A recycled water from the Altona Recycled Water Plant. The approximate locations of these water sources are presented in Fig. 3.

RESULTS AND DISCUSSION

The proposed wetland, as part of the Altona wetlands region, is expected to primarily interact with the two closest freshwater wetlands: 1) Truganina Wetland, which is a small storm water wetland 1 km south of the treatment plant; and 2) Cherry Lake, a large storm water retaining basin 3 km north of the treatment plant (Fig. 4). These two wetlands are inhabited by existing metapopulations and migrating flocks of birds that are expected to utilise the Altona Treatment Plant wetland to some extent. However, as part of a greater wetland mosaic, the proposed wetland is also expected to interact with both the freshwater and saline wetland environments within close proximity to the site, including the region’s many saline wetlands, estuaries and beaches. Depending on the behavior of individual species, some birdlife may prefer to feed or nest in one particular wetland type over another; for example, the purple swamp-hen (*Porphyrio porphyrio*) has been shown to prefer wetlands that are densely planted with the Common Reed (*Phragmites australis*) and bulrush [9]. Although similar observations have been made for other wetland species in natural systems there is currently no information available to aid in the prediction of wetland mosaic alterations and metapopulation interactions in constructed wetland projects. Hence, although it is assumed that certain species will visit the proposed wetland at different times, it is impossible to know, *a priori*, which species these might be and what uses they will make of the wetland habitat.

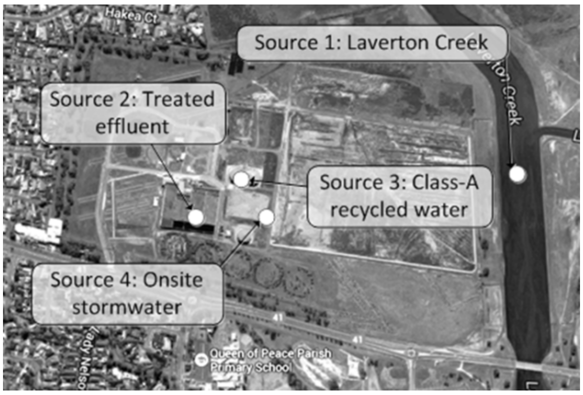

Fig. 3 Potential water sources for the new wetland.

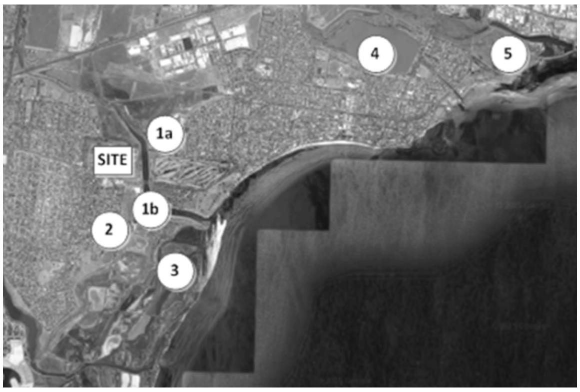

Fig. 4 Natural wetlands in the vicinity of the proposed constructed wetland: 1a) Westona Wetlands as part of Laverton Creek; 1b) Truganina Swamp as part of Laverton Creek; 2) Tuganina Swamp; 3) Cheetham Wetlands; 4) Cherry Lake; and 5) Altona Coastal Park.

Bird surveys in the existing oxidation lagoon however, have shown that as many as 16 different bird species regularly visit the existing wetland with several of these being threatened and/or endangered. In addition, other biota types in the Altona region that are of high importance might use this site. For example, [10] suggests that due to the halving of habitat area in Altona over the past 40 years, the threatened Altona skipper butterfly (*Hesperilla flavescens*) is facing extinction, because the specific sedgelands (*Gahnia filum*) that it inhabits have become isolated. This prevents metapopulations of the butterfly from developing due individual colonies of the species being unable to interact. One of the aims of the current project is to provide habitat for the Altona skipper butterfly by planting clusters of the Chaffy Saw-sedge (*Gahnia filum*). It is hoped that these new sedgelands would assist in closing the gaps between the existing sedgelands at the treatment plant site and nearby wetlands. This will allow for interactions between colonies of the butterfly, thereby creating a new metapopulation.

This information was used to design vegetation plans for the proposed wetland that aim to meet three objectives: 1) to be consistent with the native species that occur in and around the site; 2) to include species that provide favourable habitat for the 16 species that visit the current decommissioned oxidation lagoon; and, 3) to provide significant habitat for the Altona skipper butterfly.

Once the vegetation plans were developed, the next step in the design process was to determine the best water source(s) for the proposed wetland. The potential water sources included: water from a nearby estuarine swamp (Laverton Creek); treated class C or class A effluent from the treatment plant; and rainfall-fed runoff from the treatment plant site. To determine which one of these would be the best water supply source, locally available water quality samples (from Laverton Creek and the recycled water supplies) were laboratory tested and these were then assessed to determine if they were suitable for the proposed wetland.

The results of these analyses showed that the water quality of Laverton Creek was poor for multiple parameters when compared to ANZECC trigger values, Melbourne Water mean values and other known water standards. In particular, 1) the mean measured turbidity was 460% higher than the given ANZECC trigger value; 2) the peak measured salinity was of a similar salinity to sea water; 3) the mean metal content including Aluminium, Boron, Chromium and Zinc where significantly higher than the ANZECC trigger values; and 4) the mean measured E.coli was 1137 organisms/100 ml which is more than seven times the mean value as measured by Melbourne Water for E.coli across Melbourne's waterways. In addition, the nutrient levels were very high, although this observation is based on anecdotal evidence as there are no existing trigger values or averages for nutrient levels that are applicable. Hence, although Laverton Creek is able to supply the volume of water required to meet the wetland's demands, this water source is not of a sufficient quality and is therefore excluded as a potential source.

The second considered water source was treated effluent from the Altona Treatment Plant (either class C or class A). The effluent quality was available from regular sampling and testing programs that already occur at the treatment plant (Table 1).

There was limited data available to compare the treated effluent quality with, because the ANZECC trigger values are not applicable to treated effluent. Consequently, the quality of the effluent was assessed against a consultancy report by [11], commissioned by City West Water to investigate the potential for using this water in artificial wetlands. A risk assessment within this report concluded that the water quality of the treated effluent was poor due to elevated salinity, nutrients, dissolved solids and sulphates. The risks were identified as moderate and high and included; 1) odour, which posed a risk to the treatment plant's EPA licence agreement; and 2) eutrophication, which could potentially be harmful to the treatment facility if treated effluent containing toxic algae was returned to the plant for re-treatment. It was therefore concluded that although the treated effluent was of a higher water quality than the water from Laverton Creek and could provide a sufficient quantity of water to meet the proposed wetland's needs, it was unsuitable as a water source and was therefore excluded as a potential source for the wetland.

Table 1 Altona Treatment Plant effluent discharge quality.

Parameter	Average value
TN	6 mg/L
TP	3 mg/L
TDS	4600 mg/L
EC	7500μS/cm
SS	5 mg/L
BOD	3 mg/L
Sulphate	430 mg/L

This left rainfall-fed runoff as the only remaining potentially viable water source for the proposed wetland. To determine if this source would be able to meet the wetland's requirements, a flow balance model was created to determine the frequency and duration of wetting that could be achieved by capturing this water and routing it to the wetland. As the water source in this case would be rainfall runoff, it was assumed that the runoff would be of sufficient quality.

The inputs into the flow-balance model included rainfall and evaporation rates that were sourced from Bureau of Meteorology records (1976-1999), rainfall catchment area, estimated runoff coefficients, wetland volume and wetland surface area. The model simulated a 24 year period (the period for which input data existed) in 24 hour iterations to identify the seasonal variation in wetland volume and retention times. This long term dataset is of sufficient duration that it included both wet and dry periods that are representative of local rainfall variability and as such should be a valid surrogate for future conditions.

The modelling scenario involved the supply of rainfall-fed runoff from a catchment area of 85,000 square m (the area available on the grounds of the Altona Treatment Plant from which water could easily be routed to the proposed wetland) into the wetland as the only water source. The model assessed the viability of rainfall-fed runoff as the only water source and allowed for the following conclusions to be drawn: 1) the optimum volume of the wetland for the utilisation of rainfall-fed runoff was found to be 6600 kL with a surface area of 13,700 sq m, these were the largest dimensions possible without extending the longest dry period beyond 90 days; 2) the wetland displayed characteristics similar to that of an ephemeral wetland, with the water body being full for the majority of the year and having healthy retention times but drawing down below 50% capacity during an average summer period; 3) in a hot, dry summer the wetland had the potential to completely dry off; and 4) during periods of prolonged drought the wetland would remain empty or near empty (<1 ML) for extended periods of up to 90 days, completely removing the wetland as an aquatic ecosystem and aesthetic amenity for this period as well as increasing the risk of odour through the exposure of the wetland's base to the atmosphere. The results of the simulation are presented in Fig. 5.

To minimise the potential for the wetland to dry completely, a Class A recycled water supply was introduced to the model to supplement the rainfall-fed runoff. In the model, recycled water was made available when the wetland water level dropped below two-thirds capacity and was then delivered in 100 kL allocations for each day the wetland remained below this capacity.

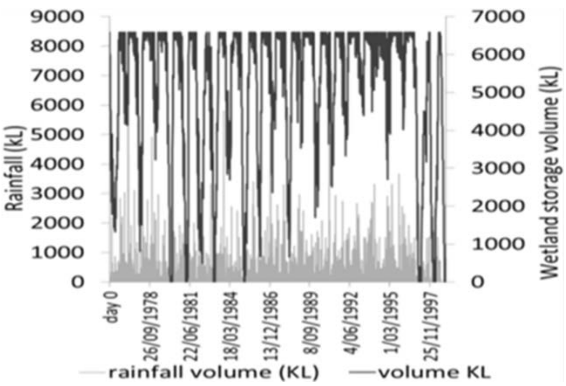

Fig. 5 Simulation of wetland storage levels over time using the rainfall-runoff water supply option.

All other parameters for the model remained the same as in the first scenario. From the model outputs, the following conclusions can be drawn: 1) the wetland displayed characteristics of a permanent wetland amenity, where the water body remained at greater than 60% capacity for the full duration of the simulation; 2) the average volume of recycled water required per year for the wetland was 3.9 ML which is estimated to cost approximately $10,000 pa to supply; 3) the full wetland permanently retains its ecosystem benefits and aesthetic amenity; and 4) the retention time was estimated to be 18 days on average over the 24 year period. The results of the simulation are presented in Fig. 6. Given the potential risks associated with the wetland drying out and the ecological benefits of a permanent wetland amenity, it was determined that the recycled water supplementation scenario was most viable.

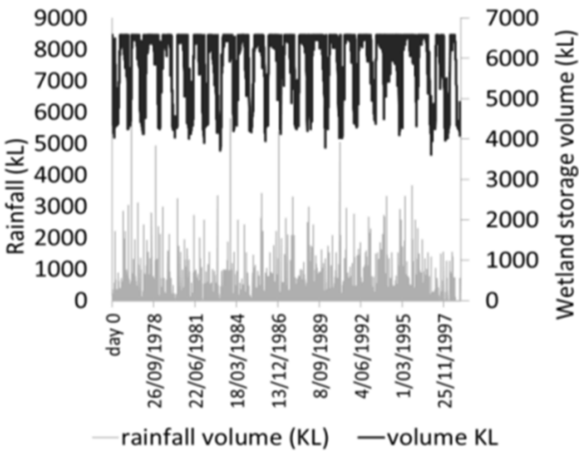

Fig. 6 Simulation of wetland storage levels over time using the rainfall-runoff water supply option with a recycled water top-up.

Once both the vegetation plan and the most favourable water source were identified, the next step was to complete a risk assessment to determine how well the proposed wetland would perform across a broad spectrum of potential threats to itself and to the surrounding local community. The results of this assessment are provided in Table 2. Table 2 also summarises proposed control measures to help minimize potential risks associated with the wetland. These control measures include: using rainwater as the primary source of inflows to the wetland; maintaining perennial flow in the wetland using recycled water top-ups as needed; optimizing wetland layout to minimize stagnant areas; using mechanical aeration to further prevent stagnant water; and optimizing plant selection to suit the needs of locally important animal species and to limit other threats. It is anticipated that these control measures will reduce all potential threats to be of moderate consequence or better, an unlikely occurrence or better and a medium risk or better.

CONCLUSION

A design is proposed to replace a decommissioned oxidation lagoon with a constructed wetland at the Altona Treatment Plant in Altona, Victoria. The design accomplished all of its key objectives. Thus, the proposed wetland will provide meaningful habitat for locally relevant species, including rare and endangered populations

Table 2 Risk assessment for the proposed wetland [11].

Risk category	Impact on	What can happen & how can it happen	Control measures	Cons.	Like.	Risk
Water source	Wetland health	Drought causes the wetland to dry harming the ecosystem	Top up rainfall with recycled water	MO	UN	M
Odour	Local resident amenity	Development of odour in the wetland.	1. Wetland layout; 2. Plant selection; 3. Mechanical aeration	MI	UN	L
Algae	Wetland health	Toxic algal blooms harm the ecosystem	1. Wetland layout; 2. Plant selection; 3. Mechanical aeration; 4. Action plan	MI	UN	L
Mosquitos	Local resident amenity	Increased mosquito population	1. Wetland layout; 2. Plant selection; 3. Mechanical aeration	I	LI	L
Weed management	Wetland health and aesthetic amenity	Weed proliferation harms the ecosystem	Weed management plan	MO	UN	M
Dust	Local resident amenity	Dust production from a dry wetland disrupts the local community	Top up rainfall with recycled water	MI	R	L
Heavy metals	Wetland health	Bioaccumulation of metals and other compounds harms the ecosystem	Use rainfall as primary water source; limit top-ups with recycled water to times of need	I	R	L

Note: Cons. = consequence: I = insignificant; MI = minor; MO = moderate. Like. = likelihood: UN = unlikely; L = likely; R = rare. Risk: L = low; M = medium.

of birds and other wildlife; the wetland will contain high quality water (supplied by local rainfall-fed runoff) and will stay wet perennially with needs-based recycled water top-ups; and a risk assessment identified potential threats and elucidated a series of control measures that minimised potential risks to the wetland habitat itself and the surrounding community. This proposal demonstrates how artificial wetlands can help to reverse the worldwide decline in wetland habitats and that decommissioned oxidation lagoons present opportunities for redevelopment into artificial wetlands.

ACKNOWLEDGEMENTS

The authors gratefully thank City West Water for their financial backing of this study and their provision of site access and data.

REFERENCES

[1] Gibbs, JP 2000, Wetland Loss and Biodiversity Conservation, Cons. Bio., 14, 314-317.

[2] Moreno-Mateos, D, Power, ME, Comin, FA & Yockteng, R 2012, Structural and functional loss in restored wetland ecosystems. Plos Bio., 10, e1001247.

[3] Carlson, AE 2010, The other kind of reclamation: Wetlands drainage and national water policy, 1902-1912, Ag. Hist., 84, 451-478.

[4] Dellapenna, JW 2007, Ecocide and genocide in the Iraqi Marshlands, Ramsar Convention, 104, 401-409.

[5] Dale, PER & Knight, JM 2008, Wetlands and mosquitoes: A review, Wetl. Ecol. and Mgmt, 16, 255-276.

[6] Ansari, AHI, Irini, A, Jariah, I & Ismail, I 2011, Ramsar convention and convention on biological diversity as mechanism for promoting biodiversity conservation of Malaysian Wetlands, J. of App. Sci. Res., 7, 2385-2393.

[7] Kadlec, R.H., Knight, R.L., 1996, Treatment Wetlands, Lewis Publishers, Boca Raton, FL.

[8] EPA Victoria 2011, EPA Water Plan 3 Guidance, Publication 1406.1, pp1

[9] Grussu M 1999, Status and breeding ecology of the Purple Swamphen in Italy. British Birds 92, 183–192.

[10] Relf, M & New, T 2009, Conservation needs of the Altona skipper butterfly, Hesperilla flavescens flavescens Waterhouse (Lepidoptera: Hesperiidae), near Melbourne, Victoria, J. Insect Cons., 13, 143-149.

[11] SKM 2011, Altona Wetland Aesthetic Amenity Study Risk Assessment. Sinclair Knight Merz, Melbourne Victoria pp 28.

Fifth International Conference on Geotechnique, Construction Materials and Environment, Osaka, Japan, Nov. 16-18, 2015, ISBN: 978-4-9905958-4-5 C3051

DESIGNING URBAN RIVERS TO MAXIMISE THEIR GEOMORPHIC AND ECOLOGIC DIVERSITY

Melissa Neave[1], Scott Rayburg[2]
[1]School of Global, Urban and Social Studies, RMIT University, Australia; [2]Faculty of Engineering, Science and Technology, Swinburne University of Technology, Australia

ABSTRACT

River geomorphic complexity is vital to support abundant and diverse ecological assemblages in river environments. With the ever increasing population of global cities, and the consequent spread of urbanized land, pressures on engineers and land planners to modify and control urban rivers channels could be detrimental to their ecological diversity. This research project provides an analysis of the geomorphic complexity and heterogeneity of an urban stream. The study compares different sections of Orphan School Creek in western Sydney, Australia to investigate how channelization and/or alternations in riparian vegetation impact on geomorphic heterogeneity. The sections of Orphan School Creek examined range from freely meandering to fully concrete channelized reaches. The results of this research project clearly show that urbanization has detrimental effects on the geomorphic complexity of urban streams, due to both catchment urbanization and channelization. Through the analysis of Orphan School Creek it was concluded that channelization reduces river geomorphic complexity, with concrete channels providing little or no geomorphic complexity or diversity. However, if managed and/or designed with a view towards optimising geomorphic complexity, urban rivers can attain meaningful ecological benefits while still being controlled to prevent damage to the urban environment from flooding and/or erosion.

Keywords: Pools and riffles; geodiversity; channelization; asymmetry

INTRODUCTION

Urban rivers are often extremely compromised, having dramatically altered flow regimes, geomorphologies, and ecologies in comparison to their non-urban counter-parts [1]-[3]. This occurs because urbanization within river catchments is typically associated with increases in impervious surface area that cause the adjacent rivers to be ‘flashy’ (i.e., have relatively high peak discharges and short flow periods), while most urban rivers are physically transformed (i.e., channelized) in some way to reduce both flooding and erosion. This channelization typically involves channel straightening and smoothing, and the reinforcement of the bed and banks with a non-erodible material that both enhances smoothness and prevents ongoing channel migration. In addition to these impacts, stormwater runoff from the catchment transports high pollutant loads that degrade water quality.

One of the most obvious outcomes of stream channelization is a loss of physical diversity that further manifests itself in the river through reduced hydraulic and habitat diversities. Morphologic adjustments to rivers can greatly affect the availability of physical habitats, particularly in association with the simplification of fluvial structures (e.g., bed features) in the down- and cross-stream directions [4]. Indeed, there is a strong link between biotic diversity and spatial heterogeneity [5] and it is generally expected that geomorphically variable and complex landscapes will have a higher chance of supporting diverse ecologic assemblages by providing a greater selection of niche spaces [6]. Conversely, geomorphically simple rivers, such as those created through channelization, will have fewer available habitats and an associated reduction in aquatic ecologic diversity.

There are several ways to compare the physical diversities of channelized and non-channelized river reaches, perhaps the most obvious of which is to consider channel planform, or the view of a channel from above. Natural river planforms vary from straight to highly sinuous or meandering, although natural straight systems are not particularly common and occur mostly when a river is constrained in some way (e.g., by geologic structure). In contrast, channelized rivers are often straight or only mildly sinuous, which is designed to increase flow velocities and thereby reduce flooding [7], [8]. Straightening a channel however, also reduces its geomorphic and hydraulic complexity, which means such a channel typically exhibits limited physical diversity. Planform is relatively easily investigated, using parameters that quantify the degree of meandering [9], such as sinuosity (SI) which is the ratio of the channel length to the long valley length [10], [11]. Meandering reaches are generally defined as having a sinuosity ratio of at least 1.05 whereas heavily channelized reaches have a sinuosity of less than 1.05 and often close to 1.0.

The physical diversity of a river channel can also be considered in terms of longitudinal variations in its bed. Many natural rivers have alternating deeps and shallows (or undulations) on their bed. These features, typically identified as pools and riffles (especially in gravel-bed systems), are thought to reduce the rate of energy expenditure by increasing flow length [12], [13], but are often removed during channelization. Thus, most channelized rivers have a smooth bed with a constant slope in the downstream direction [8], [9]. Pools and riffles create non-uniform flow conditions [14] that offer a range of habitats for aquatic organisms. Thus, the removal of pools and riffles (or bed undulations) from streams results in a concomitant loss of habitat variability. The geomorphic complexity and diversity of rivers in the longitudinal direction can be assessed using several bedform parameters, such as the extent to which a bed varies from a straight condition in the downstream direction and undulation asymmetry [15]-[17].

A final characteristic of river channels that can be used to assess physical diversity is cross-sectional variation in channel form. Indeed, [18] argues that cross-sectional asymmetry and variability imply a tendency towards irregularity and complexity. Natural streams typically have highly asymmetric cross-sections along much of their length, whereas urban or channelized systems are often highly symmetrical to ensure the rapid throughflow of water [19]. Cross-sectional asymmetry can be quantified using a number of indices, most of which represent some form of comparison between left and right channel areas [19].

This research investigates relationships between the physical diversity (i.e., geomorphic complexity and heterogeneity) of an urban stream, its degree of channelization and the general condition of its riparian vegetation. These findings are further considered in terms of the stream's habitat potential. Thus, the specific aim of the research is to establish a link between urbanization, channelization and geomorphic complexity in an urban river system.

STUDY SITE

To assess the relationship between urban river complexity and/or heterogeneity and urbanization and/or channelization, survey data were collected from Orphan School Creek in western Sydney, Australia (Fig. 1a). Orphan School Creek is approximately 12.5 km long and is a tributary of Prospect Creek, which flows into the Georges River and Botany Bay. Orphan School Creek has two small tributaries, Clear Paddock Creek (~5 km in length) and Green Valley Creek (~5.6 km in length), and a total catchment area of 34.3 km^2 [20]. The catchment is highly urbanised and the creek itself has been extensively modified over the last 50 years. Thus, the creek is 'naturally' vegetated at both its upstream and downstream ends but has an approximately 1.5 km long section in the middle where it runs through firstly a pipe and then a concrete lined trapezoidal channel.

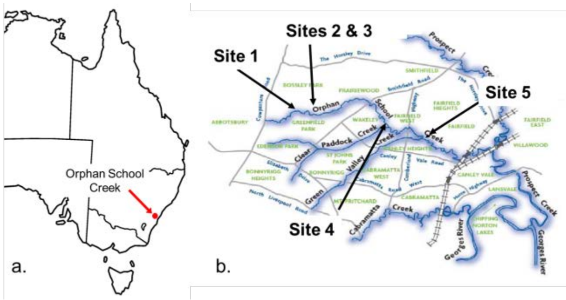

Fig. 1 Position of Orphan School Creek in western Sydney, Australia (a) and location of the five study sites used in this research [21].

The Orphan School Creek system is managed by the City of Fairfield, who balances a need for flood protection with a desire to improve the overall health of its river systems in general. The mean annual maximum temperature of the region is 23.1 ºC while the mean minimum temperature is 12.2 ºC [22]. The average annual rainfall is approximately 870 mm, the majority of which falls in January through March, although all months average at least 45 mm [22]. Major floods in 1986, 1988 and 2001 caused significant damage in the catchment and increased community pressure to develop and implement flood protection measures. At the same time, the Council has instigated a Creek Care Program that aims to produce river environments that support biodiversity and provide for community engagement [23]. Activities under this program include cleaning (e.g., direct litter removal and stormwater quality improvement), weed control, bush regeneration and stream channel rehabilitation.

METHODS

Orphan School Creek exhibits a variety of conditions along its length, ranging from naturally vegetated to fully channelized. Five sections within the first 7 km of the creek, which differed both in terms of channel form and condition and the type and extent of surrounding vegetation, were investigated for this study (Fig. 1b, Fig. 2). Site 1 is in the most upstream section of the creek and is extensively vegetated, with native trees and shrubs (dominated by *Eucalyptus* and *Casuarina* species) on both banks. This site is positioned about 900 m downstream of the creek headwaters. Site 2 is approximately 800 m downstream of Site 1. The creek in this region is grassed on both sides, although there are trees relatively close to the southern bank. This site is immediately downstream of a culvert and, subsequent to the present study, has been partially rehabilitated by the Council who reinforced the banks for erosion control. Site 3 is approximately 200 m downstream of Site 2 and is positioned within a narrow (approximately 50 m) but dense patch of native trees. The channel in this region has not been extensively modified. Site 4 is a further 2.5 km downstream and is a trapezoidal concrete channel running through a grassed parkland. Site 5 is another 2.3 km downstream and sits adjacent to a sports reserve. A ranking of these sites from best to worst, in terms of vegetation cover and degree of channelisation, would be as follows: Site 1 ('best'), Site 3, Site 2, Site 5 and Site 4 ('worst').

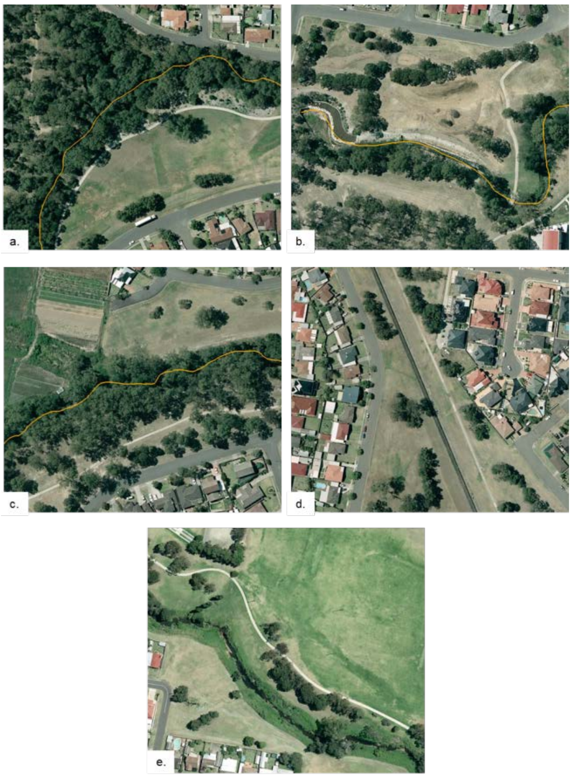

Fig. 2 Aerial views of Sites 1 (a), 2 (b), 3 (c), 4 (d) and 5 (e) on Orphan School Creek.

Within each of these five sites both cross-sectional and downstream surveys were performed using an automatic level. The cross-sectional surveys were collected along an approximately 80 m channel length and positioned roughly 10 m apart, depending upon channel conditions. The downstream surveys were taken along the thalweg, with data points collected every 1-2 m.

The survey data were used collectively to compute a series of cross-sectional, planform and longitudinal variables. These variables include bankfull width (W), depth (d), area (A) and hydraulic radius (R) and sinuosity (SI) and bed elevation range. In addition, cross-sectional thalweg asymmetry (A_t from [16]) was calculated using Eq. (1)

$$A_t = (A_{rt}-A_{lt})/A \quad (1)$$

Cross-sectional centerline asymmetry (A^* from [18],[19]) was calculated using Eq. (2)

$$A^* = (A_{rc}-A_{lc})/A \quad (2)$$

Two longitudinal asymmetry parameters (A_a and A_{L2} from [17] were calculated using Eq. (3) and Eq. (4)

$$A_a = (A_p-A_r)/A_{pr} \quad (3)$$

$$A_{L2} = (L_p-L_r)/L \quad (4)$$

Where: A is the cross-sectional area; A_{rt} and A_{lt} are the cross-sectional areas to the right and left of the thalweg, respectively; A_{rc} and A_{lc} are the cross-sectional areas to the right and left of the middle of the channel, respectively; A_p and A_r are the areas below and above a longitudinal trendline, respectively; A_{pr} is the total area around a longitudinal trendline; L_p and L_r are the pool and riffle lengths, respectively; and L is the total longitudinal length. Both A^* and A_t have limits of -1 to 1, with 0 being symmetrical and 1 or -1 being extremely asymmetrical.

Thus, ten variables were calculated for each survey site, six of which were cross-sectional, three of which were longitudinal and one of which was planform. These variables were subsequently compared between the five survey sites using Mann-Whitney U and Levene's W tests to examine means and standard deviations, respectively.

RESULTS

Representative cross-sectional surveys for each of the five sites on Orphan School Creek are presented in Fig. 3. Averages and standard deviations for the six cross-sectional variables that were calculated at each site are presented in Table 1 and statistics comparing results between sites are presented in Table 2. These data indicate that the sites that have been more extensively modified (4 & 5) are deeper, have larger channel areas and are smoother. In addition, for most parameter values there is a statistical difference between the more modified sites and the less modified sites.

Longitudinal surveys for each of the five sites on Orphan School Creek are presented in Fig. 4. Averages for the longitudinal asymmetry variables and ranges of depths are provided in Table 3. These data suggest that the bed is less regular in the downstream direction in the unmodified reaches than the modified reaches.

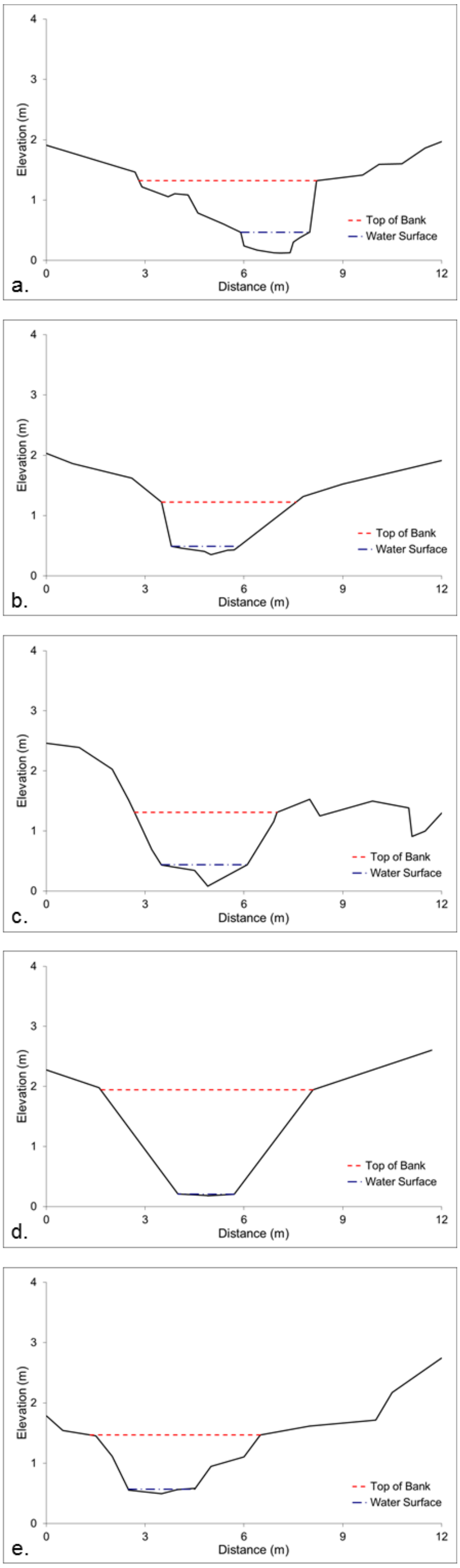

Fig. 3 Representative cross-sections for Sites 1 (a), 2 (b), 3 (c), 4 (d) and 5 (e) on Orphan School Creek, Australia.

Table 1 Averages (Avg) and standard deviations (SD) for six cross-sectional variables at five sites on Orphan School Creek, Australia.

Site	W (m)		d (m)		A (m)	
	Avg	SD	Avg	SD	Avg	SD
1	6.05	1.66	0.40	0.09	2.45	0.95
2	4.21	1.68	0.41	0.25	1.53	0.61
3	4.55	1.19	0.49	0.12	2.16	0.51
4	6.13	0.42	0.82	0.10	4.99	0.49
5	6.30	2.29	0.37	0.09	2.34	1.12
Site	R (m)		A*		A_t	
	Avg	SD	Avg	SD	Avg	SD
1	0.34	0.07	0.28	0.23	0.35	0.22
2	0.27	0.07	0.18	0.10	0.23	0.23
3	0.36	0.06	0.19	0.19	0.38	0.23
4	0.69	0.08	0.00	0.00	0.00	0.00
5	0.31	0.06	0.16	0.15	0.22	0.26

Table 2 Statistically different cross-sectional parameter comparisons between sites (e.g., Sites 1 v 2 were statistically different only for W) based on the Man Whitney U analyses.

Mann Whitney U					
Site	1	2	3	4	#
1					8
2	W				8
3	W	A			6
4	D,A,R,A_t,A^*	All 6	All 6		20
5	A^*	W,A		D,A_t,A^*	4
Levene's W					
Site	1	2	3	4	#
1					3
2					2
3	A^*	A^*			7
4	D,A,A_t,A^*	D,A_t,A^*	D,R,A_t,A^*		17
5			W,A	All 6	6

Note: # is the number of statistically significant differences observed for each site.

Table 3 Averages for two longitudinal asymmetry variables and ranges for flow depth at five sites on Orphan School Creek, Australia.

Site	No.	A_a	A_{L2}	Range (m)
1	2	0.05	0.00	0.73
2	1	0.00	0.26	0.91
3	4	0.18	0.28	1.38
4	0	0.00	0.00	0.14
5	1	0.29	0.19	0.54

Note: No. = the total number of deviations above and below the bed observed at each site.

Finally, in terms of planform Site 1 had a sinuosity ratio (SI) of 1.21. Sites 2 and 3 each had an

SI of 1.14. Site 4 had an SI of 1.00 and Site 5 had a SI of 1.10. This indicates that the more modified reaches (e.g., Sites 4 and 5) were straighter than the well vegetated and unconfined reaches.

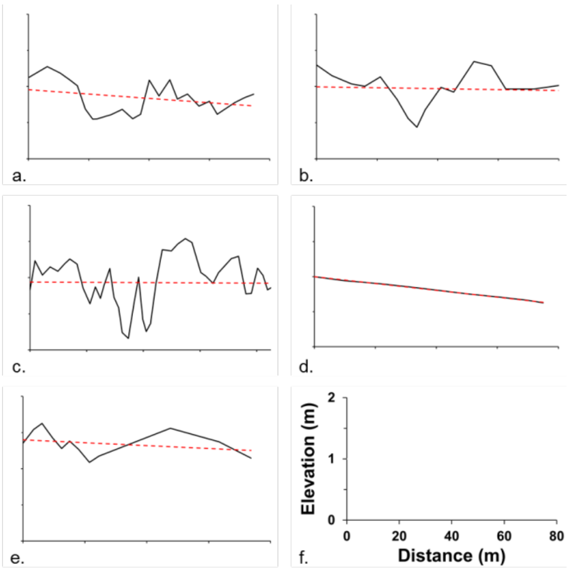

Fig. 4 Longitudinal streambed profiles for Sites 1 (a), 2 (b), 3 (c), 4 (d) and 5 (e) on Orphan School Creek, Australia. All profiles were on the same axes (f).

DISCUSSION

This research analysed and contrasted data from five sites along an urban stream in Sydney's western suburbs, ranging from a 'natural' (unconfined) reach with relatively dense native riparian vegetation (i.e., trees) on both banks (Site 1) to a straight concrete channel flanked by grass covered surfaces (Site 4). The objective was to identify differences in the geomorphic complexities of these channel types and to try and explain these differences in terms of channelization and bank vegetation. Statistical comparisons between the average cross-sectional parameters for the five sites (Table 2 Mann-Whitney U) indicate that Site 4 (channelized) was the most different in terms of physical character. It was typically larger (both deeper and wider) than the other sites, especially Sites 1, 2 and 3 which were better vegetated and had not been channelized. Site 4 differed the least from Site 5, which also lacked a dense vegetation cover and was relatively straight. Indeed, Sites 4 and 5 were statistically different only in terms of depth. This confirms previous research that indicates that urbanisation and channelization lead to both channel widening and deepening as a result both of human intervention (i.e., channelization and devegetation) and changes in runoff from urbanising catchments [24], [25].

The Levene's tests, which compare the variances between samples, reinforced that Site 4 was significantly different to the other sites for virtually all cross-sectional parameters. The low standard deviations for this site for most parameters indicate that this reflects a lack of variability of form.

An assessment of the cross-sectional asymmetry parameters (A^* and A_t) for the five sites on Orphan School Creek shows a clear trend of declining asymmetry with channelization. The highest cross-sectional asymmetry values were recorded at Sites 1 and 3, which had the densest vegetation covers and were the least confined. In contrast, Sites 4 and 5, which were the most altered reaches, had the most symmetrical cross-sections. This finding is relevant to discussions of fluvial ecologic diversity, with asymmetrical systems offering greater diversity in terms of flow and habitat than symmetrical ones. Thus, these findings support previous work that shows that an increase in urbanisation can lead to more uniform channels and [26] and that this has implications for aquatic biodiversity.

In addition to channel cross-sectional form, urbanisation and channelization have the potential to influence a river's planform and longitudinal structure. The sinuosity of Orphan School Creek decreased with increasing channelization, with Sites 1-3 having the highest sinuosity ratios. This confirms the trend evidenced in the cross-sectional asymmetry data of decreasing channel diversity with increasing intervention.

The longitudinal asymmetry data (Table 3) are a little more difficult to interpret. Sites 3 and 1 show the greatest variability in bed structures in the downstream direction (Fig. 3), although this isn't necessarily reflected in the longitudinal asymmetry results (Table 5). Indeed, Site 5, which had limited riparian vegetation and a relatively low SI, returned the largest A_a value, which suggests that it has the greatest longitudinal variability. However, the bed survey data (Fig. 3) indicate that this isn't necessarily the case and points to a need to examine the data in concert with a visual assessment. Likewise, the total variation in bankfull depth along these channels (as indicated by Range in Table 3) was considerably lower for the more modified sites (4 & 5) than the less modified sites (1, 3 & 2).

CONCLUSIONS

This research identifies some of the impacts of urbanization and channelization on urban streams, particularly in terms of geomorphic complexity and heterogeneity. The study examined five sites along Orphan School Creek in western Sydney, Australia. Overall, unconfined sites with relatively dense native vegetation covers exhibited higher diversities in their in-channel physical form (in both the cross-sectional and downstream dimensions). In contrast, as the impacts of channelization became more apparent, through direct interventions in the channel (e.g., straightening and enforcement) and alterations in the type and density of riparian vegetation (e.g., transformations to grass covered banks), there was a reduction in the physical diversity in the channel. These findings have important implications for fluvial ecosystems, with increased geomorphic complexity and heterogeneity known to support increased biodiversity through the provision of diverse niche spaces for organisms to occupy. Recognizing the importance of geomorphic diversity for biota should help those designing urban rivers to make more informed decisions about their systems.

REFERENCES

[1] Baer KE, Pringle CM, “Special problems of urban river conservation: The encroaching megalopolis”, Global perspectives on river conservation: Science, Policy and Practice. Boon PJ, Davies, BR, Petts, GE. Eds. John Wiley & Sons, 2000, pp. 385-402.

[2] Roesner LA, Bledsoe BP, “Physical effects of wet weather flows on aquatic habitats”, Final Report to Water Environment Research Foundation, 2002, WERF Project Number 00-WSM-4. 250 pp.

[3] Vaughan IP, Diamond M, Gurnell AM, Hall KA, Jenkins A, Milner NJ, “Integrating ecology with hydromorphology; a priority for river science and management”, Aquatic Conservation, Vol. 19, pp. 113-125.

[4] Gregory KJ, Davis RJ, Downs PW, “Identification of river channel change due to urbanization”, Applied Geography, 1994, Vol. 12, pp. 229-318.

[5] Huston M, “Biological diversity: the coexistence of species on changing landscapes”, Cambridge University Press, 1994, 681 pp.

[6] Hunter ML, Jacobson GL, Webb T, “Paleoecology and the coarse-filter approach to maintaining biological diversity”, Conservation Biology, Vol. 4, 1988, pp. 375-385.

[7] Emerson JW, “Channelization: a case study”, Science, Vol. 173, 1971, pp. 325-326.

[8] Brooker MP, “The ecological effects of channelization”, The Geographical Journal, Vol. 151, 1985, pp. 63-69.

[9] Lofthouse C., Robert A, “Riffle-pool sequences and meander morphology”, Geomorphology, Vol. 99, 2008, pp. 214-223

[10] Mueller JE, “An introduction to the hydraulic and topographic sinuosity indexes", Annals of the AAG, Vol. 58, 1967, pp. 371-378.

[11] Boano F, Camporeale C, Revelli R, Ridolfi, L, “Sinuosity driven hyporheic exchange in meandering rivers”, Geophys. Res. Lett., Vol. 33, 2006, L18406.

[12] Yang CT, “Formation of riffles and pools, Water Resources Research, Vol. 7, 1971, pp. 1567-1574.

[13] Wohl EE, Vincent KR, Merrits D, “Pool and riffle characteristics in relation to channel gradient”, Geomorphology, Vol. 6, 1993, pp. 99-110.

[14] Julien PY, “River Mechanics”, Cambridge University Press, 2002, 434 pp.

[15] Richards KS, “The morphology of riffle-pool sequences”, Earth Surface Processes, Vol. 1, 1976, pp. 71-78.

[16] Rayburg SC, Neave M, “Morphologic complexity and diversity in natural and channelized streams”, Engineers Australia, Vol. 4, 2008, pp. 1902-1911.

[17] Rayburg SC, Neave M, “Assessing morphologic complexity and diversity in river systems using three-dimensional asymmetry indices for bed elements, bedforms and bar units”, River Research and Applications, Vol. 24, 2006, pp. 1343-1361.

[18] Leopold LB, Wolman MG, Miller JP, “Fluvial processes in geomorphology”, Freeman, 1964, 522 pp

[19] Knighton AD, “Asymmetry of river channel cross-sections: Part I. Quantitative indices”, Earth Surface Processes and Landforms, Vol. 6, 1981, pp. 581–588.

[20] Sinclair Knight Merz, “Flood study for Orphan School Creek, Green Valley Creek and Clear Paddock Creek. Final Report”, 2008, http://www.fairfieldcity.nsw.gov.au/upload/dkryh96595/FinalReport3TribsOct08Part1.pdf.

[21] Fairfield City Council State of the Environment Report 2005-2006: Chapter 2: Creeks, http://www.fairfieldcity.nsw.gov.au/upload/tilhz85984/soe0506_Creeks_ch2.pdf.

[22] Australian Government Bureau of Meteorology, http://www.bom.gov.au.

[23] City of Fairfield, Catchments Creeks and Wetlands, http://www.fairfieldcity.nsw.gov.au/default.asp?iNavCatId=2181&iSubCatId=2194.

[24] Douglas I, “The impact of urbanization on river systems”, Proceedings of the International Geography Union Regional Conference, 1974, pp. 307-317.

[25] Roberts CR, “Flood frequency and urban-induced change: some British examples”, Floods: Hydrological, sedimentological, and geomorphological implications. Beven K, Carling P, Eds. John Wiley & Sons, 1989, pp. 57-82.

[26] Hammer TR, “Stream channel enlargement due to urbanization”, Water Resource Research, Vol. 8, 1972, pp. 1530-1540.

CHANGES IN DEPTH AND THE SEDIMENT RATE BEFORE AND AFTER THE LAKESHORE DEVELOPMENT IN LAKE FUKAMI-IKE, JAPAN

Maki Oyagi[1], Megumi Nobori[2], Hiromi Ssuda[2], Akiko Yokoyama[3] , Akihiko Yagi [2]
[1]Yokkaichi University, JAPAN, [2]Aichi Institute of Technology(AIT), JAPAN, [3]Water Agency Inc, JAPAN

ABSTRACT

Changes in depth and decrease of the sediment rate before and after a building breakhead maintenance construction were studied in small monomictic and eutrophic Lake Fukami-ike in central Japan. The maintenance of farm village drainage and the waterfront function was carried out for the activation of the town in 1992, and the water quality improvement was expected. However, variations of transparency were observed and no blue-green algal bloom outbreak had occurred before recently observed. Maximum depth changed from 9.3 m (1951), 8.5 m (1979), 8.1 cm (1992) to 7.8 m (2012), respectively. Changes in the autochthonous and allochthonous matters in the lake were thus considered. Sediment rates of 19.5 ± 10.19 $gm^{-2}d^{-1}$ (1978 to 1979) and 4.40 ± 2.27 $gm^{-2}d^{-1}$ (2007 to 2008) were observed, and decreased 22.6%. These deposition rate data corresponded to 3.1 cm $year^{-1}$ (1979) and 1.2 $cmyear^{-1}$ (2009), respectively. The decreased percentage of organic matter and the reduced deposition rate were because rice fields and forest around the lake give way to take concrete roads. It was considered to be because the inflow of sediment stopped when it rained, and allochthonous inorganic matter was significantly reduced.

Keywords: Eutrophic lake, Sediment rate, Ttransparency and Lakeshore development

INTRODUCTION

Fukami-ike is a natural eutrophic lake located in Oshimojo, Anan-cho, Shomoina-gun, Nagano prefecture, specifically, N35°19’ and E137°49’, and a sea level of 484 m. The minor axis of the lake is 150 m, and the major axis of the lake is 300 m. The area of the lake is 2.1 ha (Figure 1). The catchment area is 0.247 km^2 [1], and there were 12 residences within the catchment in 2008. As for land use prior to lakeshore development involving fertilization and nutrient salt influx, the land was used as an orchard. However, presently the land is only used as rice paddies (4% of the catchment area: 0.010 km^2) and for farm use (65%: 0.16 km^2). There are 10 inlets (7 locations have continuous influx) and one outlet.

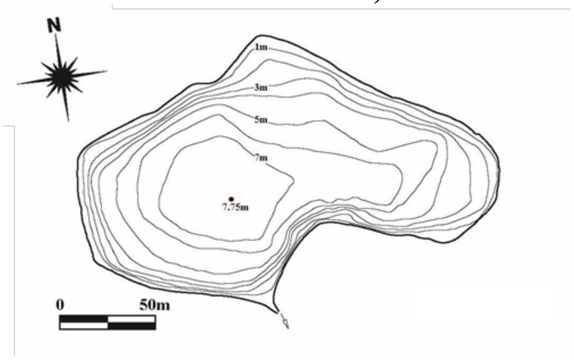

Fig.1 Lake basin of lake Fukami-ike

With Fukami-ike as the central point, Mount Hanso, the highest point in the surrounding area and located on the north side, and Senkizawa river on the south side were connected with a north-south line [2].

Fukami-ike is surrounded by mountains, and is located in a basin. It is affected little from the wind, and its depth is significant compared to the surface area. Therefore, temperature stratification of water occurs in the lake from April to November. Especially in midsummer, there is absence of oxygen under 4 m [3].

In this paper, we present several scientific characteristics of Fukami-ike. First, it is a natural eutrophic lake, rich in nutrient salt. Therefore, the lake water is cloudy, and dark or faded green in color. The values of pH and dissolved oxygen are high during the summer season. Furthermore, this lake has a high primary production which is produced by a large number of phytoplankton. Especially, during the autumn circulation period, chlorophyll a concentrations of 80 to 100 mg m^{-3} was measured throughout all the layers. Even during the winter season, phytoplankton bloom occurs, and chlorophyll a concentrations become higher than the summer [3].

At Fukami-ike, as a water environment improvement project (Led by Nagano prefecture), lakeshore construction began in November 1992. The two main goals of this water environment improvement project were (1) maintenance of farm village drainage and (2) landscaping as a hydrophilic function. As a result, due to maintenance of farm village drainage, gray water influx to the lake from the surrounding area stopped, and due to landscaping, boardwalks were built around the lake, and influx of surface water from water catchment area was almost eliminated. Afterwards, experts' opinions were taken into account, and the construction was carried out with the water depth lowered to 5 m instead of the usual 7.75 m, and instead of draining the whole lake water. Also, before and after the lakeshore development, there were no changes to the position and the height of the outlet. In this report, this water environment improvement project is defined as the lakeshore development of Fukami-ike and issues are discussed.

To determine whether internal production volume changed due to the lakeshore development of Fukami-ike, transparency and deposition rate were discussed based on the values reported in the literature in the past 50 years and the new observation results.

METHODS

Use at most three levels of headings that correspond to chapters, sections and subsections. The first level headings for chapter titles should be in 10pt, bold, justified, and upper case font. Leave one-blank line before and after the first level headings, respectively. Transparency was observed by secchi disk from 1978 to 2009. Precipitated matter were collected in sediment bottles each depth (3m, 5m and 7m) and recovery one month. Bottom sediment were collected by Ekman-Birge grab from 2007 to 2009. Water content ratio and density of bottom sediment were measured to find sediment rate. The formula [4] of the sediment rate was indicated.

$$h = (b / a c) \times (100 / (100 - w))\times 365$$

h:sediment rate (cm year^{-1}), w:average water contents of surface sediment (0-10cm depth), a:mouth area of sediment trap bottle (cm^2), b:dry weight of precipitated matter (g), c:density of sediment, t:total days

RESULTS AND DISCUSSIONS

Transparency

Transparency of Fukami-ike has been reported since July, 1950 [5]. Though there are many gaps, there are accumulated data of over half a century until December, 2009 [5],[6]. In this report, characteristics of transparency over each generation will be discussed based on these data (Figure 2).

Transparency of Fukami-ike was 0.7 m - 2.8 m (average value ± standard deviation, 1.38 ± 0.67 m) during 1950's. Later on, (1970's), prior to the lakeshore development (April 1992), values ranged

Fig.2 Changes of transparency

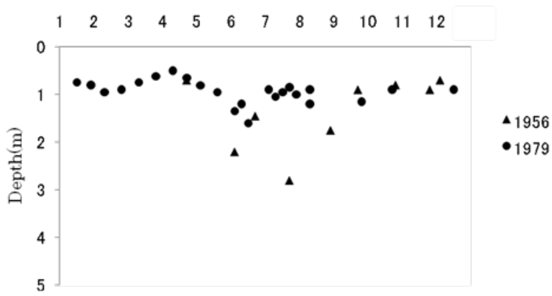

Fig.3 Seasonal changes of transparency (before lakeshore development)

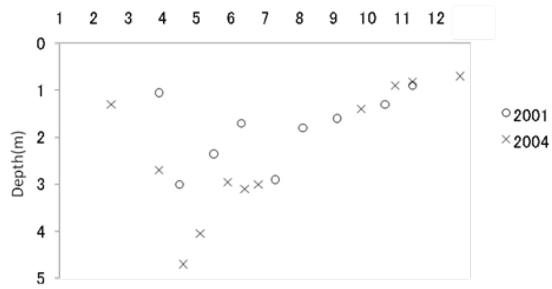

Fig.4 Seasonal changes of transparency (after lakeshore development)

from 0.50 m to 2.30 m (1.04 ± 0.30 m). Compared to during 1950s, both average value and seasonal changes are lower. After the lakeshore development (data from July 1999 to December 2009), average values increased significantly (0.35 m - 4.70 m : 1.93 ± 0.88 m).

Generally, primary production is high in lakes during the summer season when the water temperature is high, and low during the winter season when the water temperature is low. However, Fukami-ike has unusual characteristics as reported by [3]. There is little regression of nutrient salt from deep to surface water layers occur during the summer stratification period. During the autumn circulation period, nutrient salt is carried to the surface layer, and primary production is high even during the winter. Seasonal changes in transparency prior to the lakeshore development are shown in Figure 3, and after the development are shown in Figure 4. Average values and seasonal changes show some variations. But in both before and after the development, transparency is high during the stratification period when regression of nutrient salt from deep-water layer is low, and transparency is low during the circulation period when primary production is high. These results confirmed the unusual characteristics of Fukami-ike.

The highest value of transparency during 1950 to 2009 was 4.70 m in April 2004, and the lowest value was 0.35 m in June 2000. At that point, the presence of blue-green algae was visually confirmed. Until then, the presence of blue-green algae has not been confirmed. But since the latter half of 1990s, it was confirmed several times, and even local residents reported the presence of blue-green algae. All the observations were made after the lakeshore development, thus the presence of these algae is assumed to be related to the lakeshore development, and will be discussed in detail later. The lowest value of chlorophyll a concentration, 357 μg L^{-1}, was observed in the surface layer, and was determined to represent the decreased depth due to phytoplankton bloom. Though it is a eutrophic lake, Fukami-ike did not have notable occurrence of blue-green algae in the past, and was considered an unusual lake. But after the lakeshore development in 2000, blue-green algae were noted often.

The distribution of nitrate nitrogen concentration is shown in Figures 5 and 6 as water quality data of nutrient salt before and after the lakeshore development. During 1978 to 1979 before the lakeshore development, high NO_3-N values of 10 to 50 μgat L^{-1} (0.14～0.70mg L^{-1}) were observed during October to May. From August to early October, values remained low at around 1 μgat L^{-1} (0.014 mg L^{-1}). From 1999 to 2000, a period after the lakeshore development, values ranged from 0.4 to 7 μgat L^{-1} (5.6～98μg L^{-1}). Before and after the lakeshore development, seasonal changes have a similar trend, but the concentration of nitrate nitrogen dropped significantly to about 10%. At Fukami-ike, it was shown by [7] that nitric acid flows in from the water catchment area after precipitation. This may indicate an influx of surface water from orchards and rice paddies around the lake prior to the lakeshore development, but after the lakeshore development, concrete block boardwalks were built around the lake shore and thus direct influx of surface water ceased. Furthermore, after the lakeshore development, influx of sewage ceased as well. In Washington Lake, USA, since sewage influx to the lake ceased, a significant increase in transparency was observed. This is due to the change in composition of zooplankton community from the decreased nutrient salt [8]. Based on these understandings, we believe that the decreased concentration of nitric acid after the lakeshore development contributed to the increased transparency of Fukami-ike.

Next, seasonal changes in chlorophyll a per unit area before and after the lakeshore development are shown (Figures 7 and 8). During 1978 to 1979, a period before the lakeshore development, the values ranged from 45 to 260 mg m^{-2}, and during 1999 to 2000, a period after the lakeshore development, values ranged from 25 to 965 mg m^{-2}. Blue-green algae were noted in July 1999 (844 mg m^{-2}) and June 2000 (233 mg m^{-2}). The highest value was noted in January 2000, but no blue-green algae were noted at that time. Seasonal changes of chlorophyll a before and after the lakeshore development had low values during the stratification period, and a trend of high values during the circulation period. These results agreed well with the seasonal changes of transparency. However, chlorophyll a concentrations roughly increased after the lakeshore development, and do not agree with the increasing trend of transparency. It's been suggested that the changes in transparency may be caused by changes in size compositions (zooplanktons changing from small to large ones) [9]. These results indicate that at Fukami-ike, the cause is the size composition of zooplanktons instead of phytoplankton concentrations.

The cause of the increased average transparency value at Fukami-ike is as follows: First, before the lakeshore development, sewage influx and surface water influx from rice paddies and orchards of water catchment area during precipitation were occurring. But all of that ceased after the development, leading to a decrease in concentration of nitric acid, a nutrient salt. Secondly, a chrolyphyll concentration increase after the lakeshore development was confirmed, and the possibility of the size composition of zooplankton was pointed out. However, the lowest value was observed after the lakeshore development, and increased chlorophyll a concentration and presence of blue-green algae were observed; thus, significant decrease in nutrient influx led to a decreasing trend in internal production volume. Yet it is believed that the material circulation in the lake has changed.

Depth variation

Bathymetric maps were drawn three times for Fukami-ike in 1951, 1978 and 2004. The maximum depth was of the pond reported to be 9.3 m in 1951 by Ueno (1952), and was reported to be 8.5 m in 1979 (1993) and 7.85 m in 2004 (Figure 9) by Yagi, et al. Although bathymeric maps were not prepared, the maximum depth was determined to be 7.85 m in 2009. Decrease in depth from 2004 to 2009 cannot be confirmed, but the survey determined there had been a significant decrease of 1.45 m in depth over a period of 58 years.

The rate at which sedimentation built up in the pond prior to lakeshore development was shown to be 3.1 cm y^{-1} by [10] based on 1978-1979 data. Also,

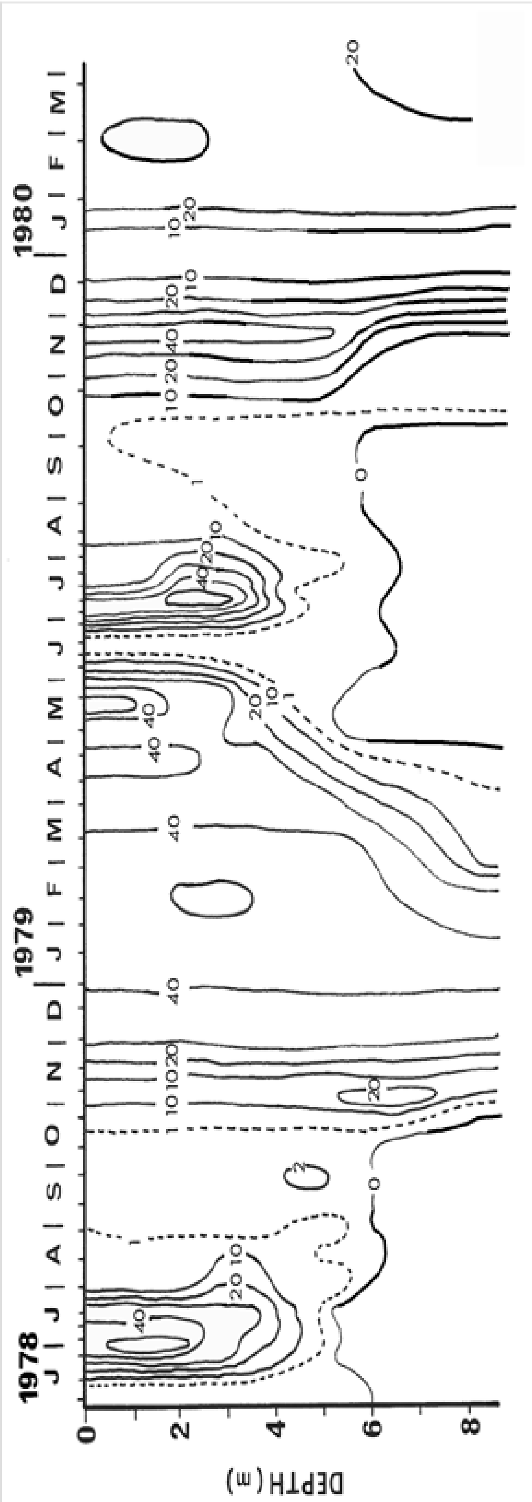

Fig.5 Seasonal changes of nitrate (before lakeshore development) unit: μ gat L^{-1}

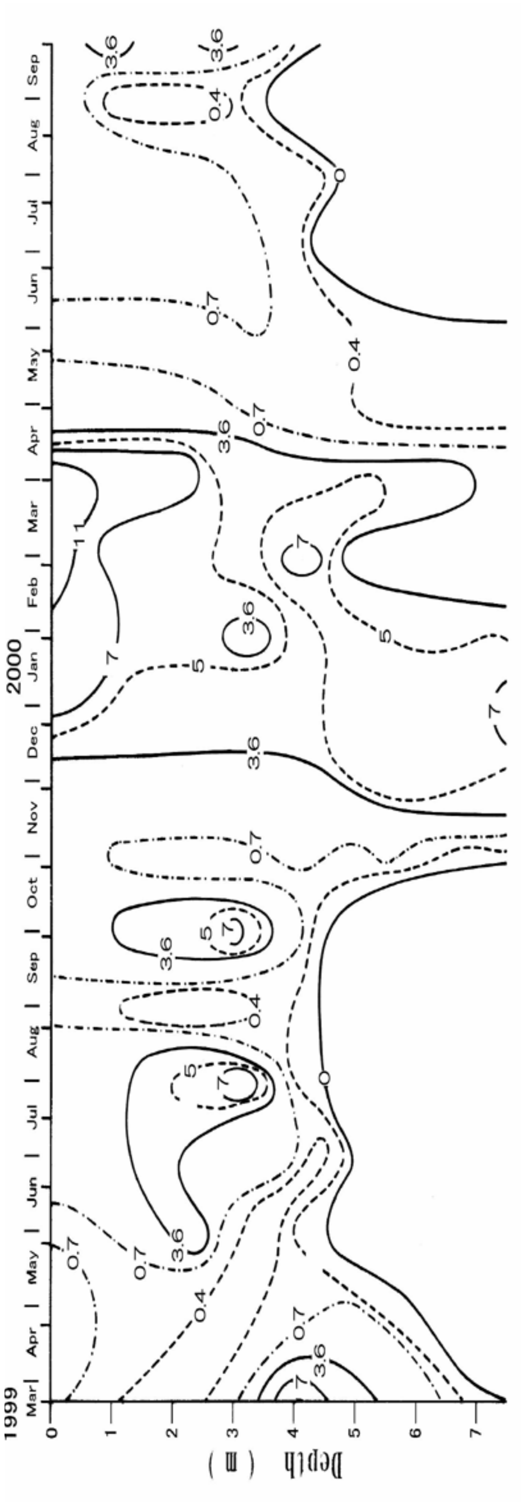

Fig.6 Seasonal changes of nitrate (after lakeshore development) unit: μ gat L^{-1}

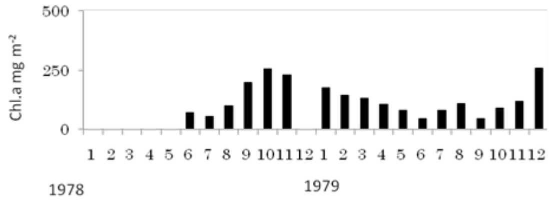

Fig.7 Seasonal changes of chloropfll-a (before lakeshore development)

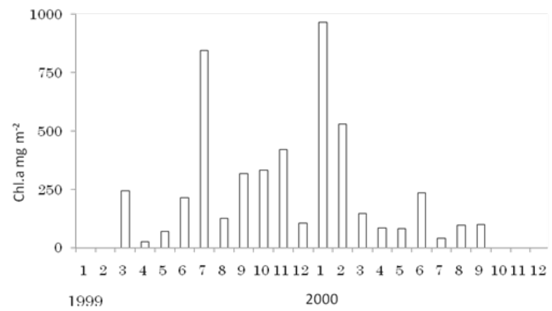

Fig.8 Seasonal changes of chloropfll-a (after lakeshore development)

sedimentation rate after improvement of lakeshore drainage facilities was calculated based on 2007-2008 data. Figure 10 shows sedimentation rate for each month from January 2007 to December 2008. It was 0.69 cm/yr^{-1} during the stratification period (late March to early October) and 1.24 cm yr-1 for circulation period (mid October to mid March), presenting a higher value during the circulation period. This corresponded well with the decreasing trend of transparency during the circulation period. Newly obtained average sedimentation rate was 1.17 cm/yr^{-1}about 37% of the sedimentation rate from 1978 to 1979 prior to the lakeshore development. This clearly shows that sedimentation rate significantly decreased after improvement of lakeshore wastewater treatment facilities.

The annual average of ignition loss for new sediments (IL) was 37.9 ± 9.94%. To understand the movement of load to Fukami-ike, total organic carbon (TOC), total nitrogen (TN), and total phosphorus (TP) load for the total inflow and outflow were obtained (Table 1). For each item, the outflow load was lower than the inflow load. TOC (113.8 g C day^{-1}), TN (100.3 g N day^{-1}), and TP (10.4 g P day^{-1}) accumulated in the lake due to internal production. These results conclude that the new sediments derived from internal production of the lake.

Firstly, depth decrease measured during 1951 to 1979 was 80 cm over 28 years. When this value is compared to the sedimentation rate obtained by [10] by trap experiments, the results were consistent with the actual measurement of 80 cm (3.1 cm x 28 years = 86.8 cm over 1951 to 1979). Depth decrease measured over 30 years (1979 to 2009) was 65 cm. From 1979, until the lakeshore development

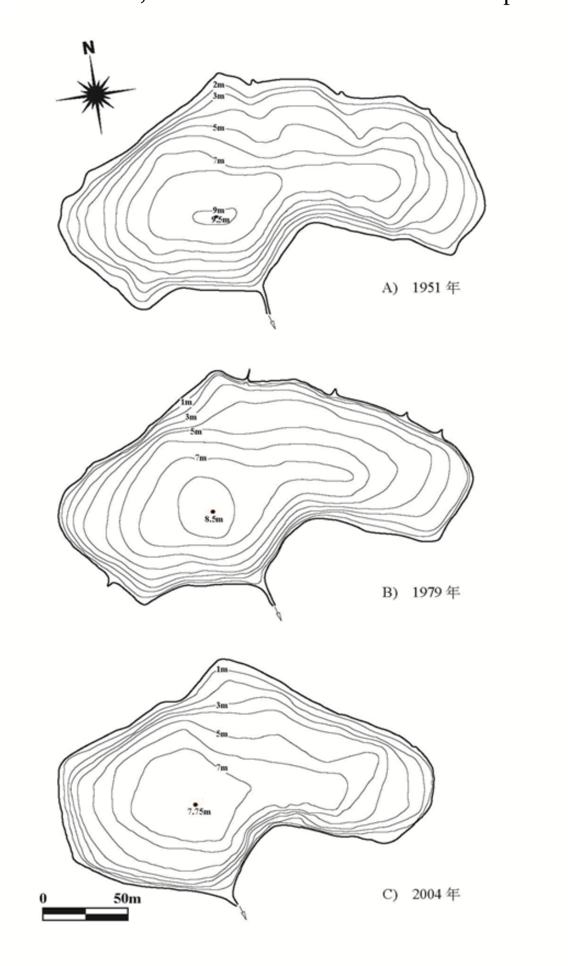

Fig.9 Changes of maximum depth at lake Fukami-ike

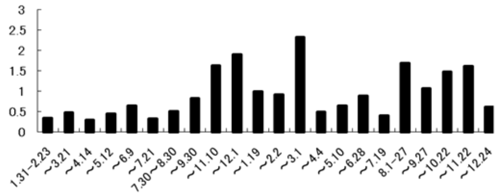

Fig.10 Seasonal changes of sediment rate (from 2007 to 2008)

in 1992, sedimentation rate of 3.1 cm yr^{-1} [10] was used. Up to 2009, after improvement of lakeshore wastewater drainage facilities, depth decrease was calculated using the newly obtained sedimentation rate of 1.17 cm/yr-1. Results were 40.3 cm (3.1 cm x 13 years) for 1979 to 1992, and 19.9 cm (1.17 cm x 17 years) for 1992 to 2009. A total depth decrease of 60.2 cm was estimated by calculation. The calculated value is approximately the actual 65 cm depth decrease. And these results show that before and after improvement of lakeshore facilities, Although eutrophication did progress, the rate of depth decrease became more gradual.

This report focuses on transparency and sedimentation rate of Fukami-ike, an eutrophic lake. Using long-term data over half a century, changes in internal production before and after the lakeshore development were investigated. Although long-term variation has been monitored in extensive lake and marsh areas, there has currently not been much research data from long-term monitoring of small lakes. This lake, however, has been affected by lakeshore development; through transparency and sedimentation rate changes, we were able to show that the resulting cessation of sewage introduction by improvement of farm village drainage facilities had a large effect on internal production of the lake. Although eutrophication has advanced despite increased annual average transparency and decreased sedimentation rate, it has become more gradual following lakeshore drainage facilities improvement. Since blue-green algae was still observed following lakeshore facilities improvement, it would not be accurate to assume that man-induced eutrophication problems have been solved. By continuing the observation, we hope to more clearly understand the effect of the improving lakeshore wastewater facilities on lakes and marshes.

REFERENCES

[1] Nagano pref. ``Improvement project of water environment report", 1991 (in japanese). sedimentation rate decreased considerably in the pond, decreasing the internal production significantly.

[2] Limnology Comittee of Shimoina Kyoiku-kai ``Shimoina-shi". Editorial Committee of Shimoina-shi 2009 (in Japanese).

[3] Yagi, A., I. Shimodaira, H. Terai and Y. Saijo, `` Seasonal change of chlorophyll-a and Bacteriochlorophyll in Lake Fukami-ike". Jpn. J. Limnol, 1983 44:283-292.

[4] Koyama T., Handa N. and Sugimura Y. ``Analysis of lake and sea water", Kodansya scientific 1983 (in Japanese).

[5] Ueno, M. ``Lake Fukami-ike in Shimoinagun, Nagano Prefecture", An educational association of Shimoninagun, IIda. 1952 (in Japanese).

[6] Sakurai Y. and Watanabe Y. ``Limnoligy of Shinsyu area", No.1, Society for scientific study of environmental chemistry 1974 (in Japanese).

[7] Terai, H. ``Influence of precipitation on development of the denitrification process in Lake Fukami-ike", Jpn. J. Limnol., 1988, 49:87-92.

[8] Edward A. Laws ``Basic sience of water environment", Gihodo shuppan Co., Ltd, 1996 (in Japanese).

[9] Haga H. and Otsuka T. ``Changes in transparency (Secchi disk reading) of the pelagic zone of the main basin of Lake Biwa over a span of 73 years", The Japanese Society of Limnology, 2003, 64:133-139. (Translated from Japanese with English abstract)

[10] Yagi A., Miyachi S. and Shimodaira I ``Change in depth by sedimentation of autochtonous organic sunstances in eutrophic lake", Journal of Nagoya Women's University, 1993, No.39:77-82 (in Japanese).

Fifth International Conference on Geotechnique, Construction Materials and Environment, Osaka, Japan, Nov. 16-18, 2015, ISBN: 978-4-9905958-4-5 C3051

MODELING OF FLUID INTRUSION INTO POROUS MEDIA WITH MIXED WETTABILITIES USING PORE NETWORK

Junichiro Takeuchi, Wataru Sumii and Masayuki Fujihara
Graduate School of Agriculture, Kyoto University, Japan

ABSTRACT

Water or air intrusion into a porous medium filled with the other fluid is affected by many factors such as size, configuration, and connectivity of pores as well as the contact angle of grain. To deal with these pore-scale factors, a pore network model is utilized. According to the modified Delaunay method, pore networks are extracted from randomly packed spherical grains computed by the distinct element method. Displacement processes of two immiscible fluid in a porous medium with mixed wettabilities, are modeled in an invasion percolation manner, in which simultaneous invasion is allowed, and water retention curves in drainage and imbibition processes are computed. The results obtained show that hydrophobic grains do not have just a strong effect on the water retention properties, but also the amount of water/air residue after a drainage/imbibition process depends on the invasion rate.

Keywords: Water Retention Curve, Residual Water, Trapped Air, Invasion Percolation

INTRODUCTION

Soil is an essential medium for plants and animals, because it does not only supports primary producers physically, but is also a supply source of water and nutrients through its pores. So, a large amount of works have involved figuring out the mechanism of soil properties such as the permeability and the water retention properties. While such hydraulic properties of porous media are macroscopic, they originate from microscopic structures such as pore size, configuration, connectivity, and wettability as well as fluid physical properties. Further, the fact that the constitutive relation depends on the history of fluid distribution and the direction of fluid movement complicates matters. One of the methodologies that estimate soil's properties is based on the pore network model, which treats a pore space in a porous medium as an assemblage of pore segments and incorporates pore-level mechanisms like capillary phenomena. Since the network model for porous media was firstly proposed by Fatt (1956) [1], the pore network approach has been applied in many disciplines, such as the petroleum engineering, e.g., [2]-[4], the hydrology and soil physics [5]-[9]. Through a series of works, the structure and generation methods of pore networks, and the algorithms for transport of fluids have evolved by new findings and the development of high-spec apparatuses [10]-[12].

Fatt (1956) [1] was the first to utilize a two-dimensional regular cubic network of cylindrical tubes joining at volumeless junctions. After Mohanty and Salter (1982) [2] introduced, a pore network comprised of relatively large pore bodies connected by narrower pore throats are generally utilized up to the present. The topology of a network can also be represented by a regular two- or three-dimensional lattice, in which sites (pore bodies) have a common coordinate number, which is the number of bonds (pore throats) connected to the site. But real porous media have more irregular structures regarding the coordinate number, pore size, and bond length. And so, several network extraction methods from pixelated images of pores and grains by X-ray tomography or a randomly packed spheres that are simulated by numerical models such as the discrete element method (DEM) have been developed [11]-[12].

Percolation theory, which is a branch of probability theory dealing with properties of a network media [7], is used to analyze the connectivity of a network when sites or bonds have two different states: 'open' or 'close', with a certain probability. For two-phase immiscible displacements governed by capillary effects in a pore network, a special version of the percolation theory known as the invasion percolation is often applied, e.g., [6]-[9]. The invasion percolation originally proposed by Wilkinson and Willemsen (1983) [3] is a dynamic percolation process, and accessibility rule is imposed for movement of interfaces between invading and defending fluids. Accessibility to an outside fluid reservoir through sites or bonds filled by the same kind fluid is required to both invading and defending fluids, or to either fluid, depending on the materials and situations of interest.

Water-repellent soils, which have resistance to spontaneous water intrusion, have been reported from the early 1900's in various countries such as New Zealand, Australia, and Netherlands [13]. Many works revealed that hydrophobic grains mixed into normal (hydrophilic) grains have potential to change the hydraulic properties drastically [14], [15]. Ustohal et al. (1998) proposed a functional model to predict the hydraulic properties of porous media variously mixed with hydrophobic grains by stochastically integrating clusters that contain multiple grains, based on the Brooks-Corey model [15]. Takeuchi et al. (2014) extended the model by Ustohal et al. (1998) and developed a distributed model to estimate the water retention properties [16]. However, in the cluster-based models the influences by hydrophobic grains are blunted when larger clusters are used. Moreover, the distribution of pore sizes, which is essential for estimating the hydraulic properties, must be identified with observed data indirectly or from literature.

The objective of this study is to develop a pore network model for predicting the hydraulic properties of porous media mixed with hydrophobic grains at various fractions, incorporating pore-level capillary actions. In this paper, changes of water retention properties by mixed hydrophobic grains are investigated, focusing on the algorithm used in the invasion percolation. While invading fluid enters only the most invadable pore in one step in the ordinary invasion percolation, simultaneous invasions are allowed in this study, and the effects are examined through numerical experiments.

MODEL DESCRIPTION

Generation of Pore Network Model

In this study, the modified Delaunay-tessellation approach proposed by Al-Raoush et al. (2003) [11] is employed to generate pore networks. Delaunay tessellation is a widely used spatial segmentation method for generation of computational meshes used in numerical simulations. After a 3-D domain is discretized into tetrahedral subdomains, based on the spherical grain's centers as nodes, a network is generated by connecting inner points of neighboring subdomains. But the network has two significant problems. First, the network has a fixed coordination number, which equals to four since a tetrahedron has four faces. Second, the location and size of pore bodies are not correct. To overcome these problems, a modified approach in which multiple subdomains are merged for identification of pore body's location and size is proposed. A realistic irregular pore network of randomly packed spherical grains could be obtained by this modification.

Here, virtual porous media randomly packed with equally-sized spherical grains are produced by DEM. To obtain relatively dense porous media, a small value was given to the friction coefficient in this study. About 58 hundreds grains are packed in a cuboidal container as shown in Fig. 1 (a). The length of horizontal edge corresponds to the length of 16 straightly lined grains, and the size of a network is derived from the required minimum network size [6]. The extracted pore network is also shown in Fig. 1 (b), and the pore network consists of 14,522 pore bodies and 36,761 pore throats. The spheres in Fig. 1 (b) represent pore bodies, and the pipes connecting pore bodies are pore throats. The shape of a pore throat cross-section is given as the void surrounded by grains as shown in Fig. 2, in which cases of three and four grains are illustrated.

Figure 3 shows the distributions of the coordinate number, the radii of pore body and throat, and the length of pore throat in the extracted pore network. The radius of a pore throat is represented as that of the maximum inscribed circle locating

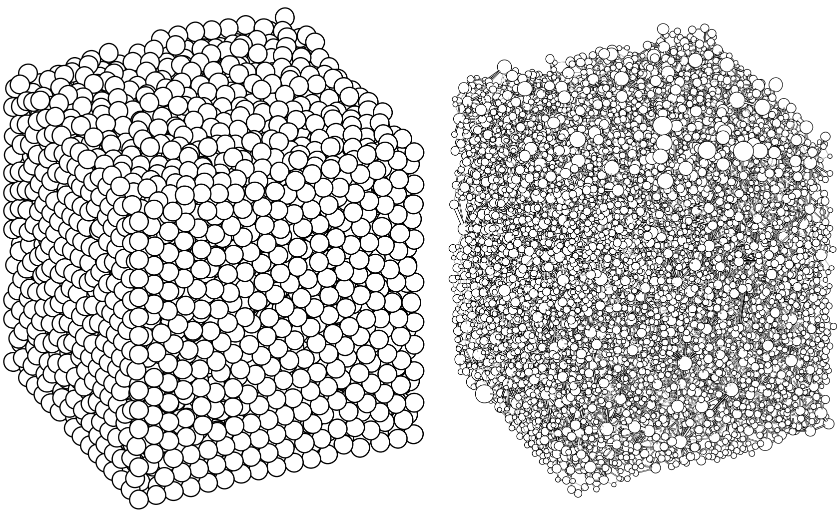

(a) Porous medium model (b) Pore network model

Fig. 1 Extraction of pore network

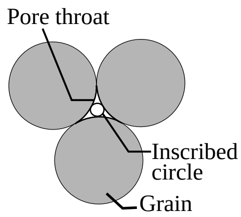

(a) Three grains

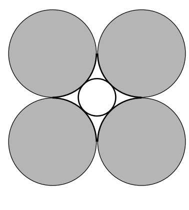

(b) Four grains

Fig. 2 Cross-section of pore throat

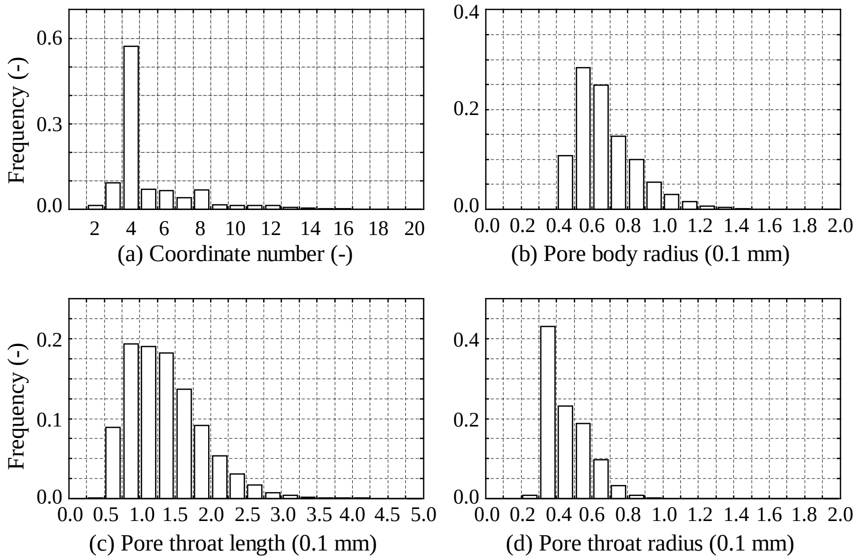

Fig. 3 Histograms of coordinate number and pore sizes

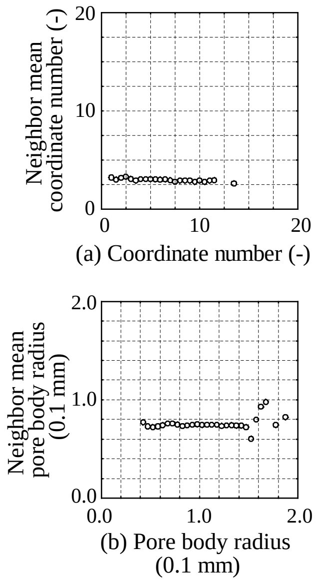

Fig. 4 Correlation of neighbor pore body

inside the void surrounded by grains as illustrated in Fig. 2. The radius of a pore body is also represented as that of the maximum inscribed sphere locating inside the void in the same way. The length of a pore throat represents the length between the centers of pore bodies connected by the pore throat.

Figure 4 shows the correlations of the coordinate number and pore body size between pore bodies connected by a throat. The graphs in both figures are almost flat, and this means that there is no spatial correlation in the coordinate number and the size between pore bodies.

Pore-level Description

In this study, it is assumed that one fluid displaces the other fluid at a sufficiently low capillary number. So, the movement of an interface between two immiscible fluids occurs quasi-statically by capillary forces. In addition, only piston-like displacements are assumed in both drainage and imbibition processes. According to Dullien et al. (1989) [17], water residue in a porous medium packed with glass beads with smooth surface was approximately 10% after a drainage process, while that in a medium with roughened glass beads by etching was approximately 1%. This result indicates that the effects of wetting layers and films are negligible when smooth glass beads are used.

Furthermore, neither residue in a drainage process nor pre-invasion in an imbibition process along the corners of hydrophilic pore throats and bodies by wetting fluid are considered in this study. Accordingly, pendular rings of wetting fluid around the two grains contact are not considered in this model.

Pores, which represents both of pore bodies and throats here, have two states: 'Water' and 'Air'. The Water/Air state represents the pore is filled with water/air. Therefore, the meniscus is formed on a boundary of a pore body in one state and a neighbor pore throat in the other state. Whether one fluid can intrude into the other fluid or not depends on the magnitude relationship between the capillary pressure P_{C} on the interface and the capillary entry pressure P_{E} assigned to all pores. These are given by the following equations.

$$P_{\mathrm{C}} = P_{\mathrm{a}} - P_{\mathrm{w}} \tag{1}$$

$$P_{\mathrm{E}} = \frac{\sigma \cos \varphi_{\mathrm{e}}}{R} \tag{2}$$

where P_{a} and P_{w} are the air and water pressures at the vicinity of the interface, respectively, σ is the interfacial tension, φ_{e} is the equivalent contact angle of the pore, and $R\ (= A/L)$ is the hydraulic radius, A is the cross-section area of the pore, and L is the perimeter of the pore cross-section. In this study, a pore body are represented as a sphere, which is the maximum inscribed sphere in the void surrounded by multiple grains as described in the subsection of 'Generation of Pore Network Model'. A pore throat is represented by a tube with constant cross-section, and the shape of the cross-section is represented as a grain boundary void, which has more than three cusps, as illustrated in Fig. 2.

The equivalent contact angle φ_{e} of a pore is assumed to be given by the Cassie-Baxter equation. When the pore is composed of multiple grains with two types of wettability, the equivalent contact angle is described as follows.

$$\cos \varphi_{\mathrm{e}} = \frac{N_1}{N_1 + N_2} \cos \varphi_1 + \frac{N_2}{N_1 + N_2} \cos \varphi_2 \tag{3}$$

where N_1 and N_2 are the numbers of hydrophilic and hydrophobic grains surrounding the pore, respectively; and φ_1 and φ_2 are the contact angles of hydrophilic and hydrophobic grains, respectively.

In addition to these equations, invadability I, which is an index that represents the degree of easiness when one fluid invades a pore filled with the other fluid, is defined as follows.

$$I = P_C - P_E \tag{4}$$

In a drainage process, invading fluid (air) can intrude into a pore, only when the invadability is positive. On the other hand, invading fluid (water) can intrude in an imbibition process, only when the invadability is negative.

Generalized Invasion Percolation

Two types of boundary are given to the pore network: one is a no-flow boundary, and the other is an open-flow boundary. A sufficiently large reservoir which is a supply source or sink is connected to the open-flow boundary. In this study, the no-flow boundary is given to the four lateral faces, and the open-flow boundary to the top and bottom faces. The top face contacts with an air reservoir, and the bottom with a water reservoir. The air pressure inside and outside of the pore network is set as a constant, and the water pressure inside of the pore network is determined by the pressure imposed on the bottom, assuming the hydrostatic pressure.

Drainage and imbibition processes are described in an invasion-percolation manner. In the invasion percolation, fluids are required to satisfy an accessibility rule in addition to the invadability condition. In this study, the accessibility rule is imposed to both invading and defending fluids to connect to each other's reservoir through pores filled with the same fluid, when the interface moves. The algorithm of the invasion percolation for computation of one sample in a drainage process is described as follows:

1. All the pore bodies and throats are filled with water, and a certain water pressure is imposed on the bottom of the pore network.
2. Produce a list of all the pore bodies and throats which are defending against air intrusion and satisfy the accessibility rule, and sort these in descending order based on the invadability value.
3. Among the listed pore bodies and throats, the interfaces of the top N^{IP} in the list are moved simultaneously (the state in the pores is changed from Water to Air) if the invadability value is positive.
4. Iterate the processes 2 and 3 until no state change occurs, and saturation of the pore network is calculated when a steady state is achieved.

If the next sample is computed continuously, the obtained result is used as an initial condition and the water pressure imposed on the bottom is decreased in a stepwise manner, and go back to 2. This process corresponds to the suction method and pressure plate method, in which one sample is used continuously under a gradually changing pressure condition. In contrast, in the soil column method, different samples are used for each pressure condition. So, if the soil column method is supposed, go back to 1 and start from the dry condition for the next pressure.

In an ordinary invasion percolation process, invading fluid is allowed to intrude into only one pore that have the largest invadability, i.e., $N^{IP} = 1$. In this study, simultaneous intrusions into multiple pores are allowed, and this type of invasion percolation is termed as a generalized invasion percolation here. The simultaneous intrusions are considered to correspond to a drainage process with relatively large capillary number.

In a case of an imbibition process, the algorithm is described in the same way with the drainage process. The main difference is in the list of candidates. The list in an imbibition process is sorted in an ascending order of the invadability, while it is sorted in a descending order in a drainage process. Then the top N^{IP} of pores would be invaded by water if the invadability value is negative.

WATER RETENTION PROPERTIES

Experimental Results

Toyoura standard sand and glass beads are used as materials. The mean diameter of Toyoura sand is

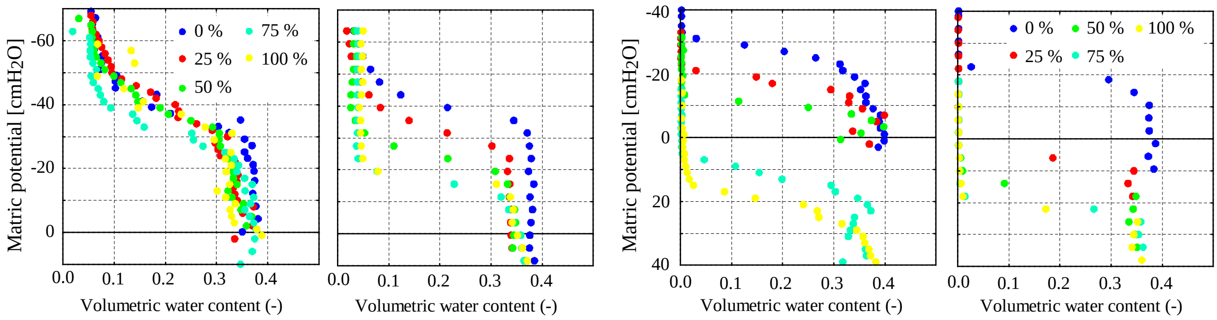

(a) Toyoura sands (b) Glass beads

5-1 Drainage process

(a) Toyoura sands (b) Glass beads

5-2 Imbibition process

Fig. 5 Water retention curves

about 0.25 mm, and that of glass beads is 0.2 mm. Toyoura sand and glass beads are hydrophobized by perfluorooctylethltrichlorosilane ($CF_3(CF_2)_7(CH_2)_2SiCl_3$) and octyltrichlorosilane ($CH_3(CH_2)_7SiCl_3$), respectively. Figure 5 shows the measured water retention curves of each material mixed with hydrophobic grains at various mixture fractions by the soil column method [16]. From these figures, it is found that water retention curves are largely altered by the mixed hydrophobic grains, and that the degree of the alteration depends on the mixture fraction.

Computational Results

Water retention curves are computed using the above mentioned pore network model in the generalized invasion percolation manner. The contact angles of the hydrophilic and hydrophobic grains are given as 58 degrees and 102 degrees, based on the measurement of the apparent contact angles of glass beads with the sessile drop method [18]. And common values are used for drainage and imbibition processes without considering receding and advancing contact angles. Several options can be considered in the computational settings about the number of simultaneous intrusions N^{IP} and the initial condition of each sample. Here two options are given in each setting. Regarding the intrusion number, N^{IP} is limited to ten in one case, and no limitation is given in the other case. Regarding the initial condition, the previous computed result is given as an initial condition in one case, and the saturated/dry condition is given in a drainage/imbibition process in the other. Therefore, four cases are considered by the combination of these options. Among these four cases, two cases are shown below: one is the combination of 'limited to ten' and 'previous result', and the other is the combination of 'no limitation' and 'saturated/dry condition'. The former is referred to as Case 1, and the latter as Case 2 in this study. The results of the rest two cases were pretty much the same with Case 1. It is considered that these three cases correspond to a relatively small capillary number, and that Case 2 to a relatively large capillary number.

The computed water retention curves of Case 1 and Case 2 are shown in Fig. 6, and the computed states of pores in the pore network are shown in Fig. 7, where the black pores represent ones occupied by water and the white pores by air. Figure 6 shows that the water retention curves are altered by

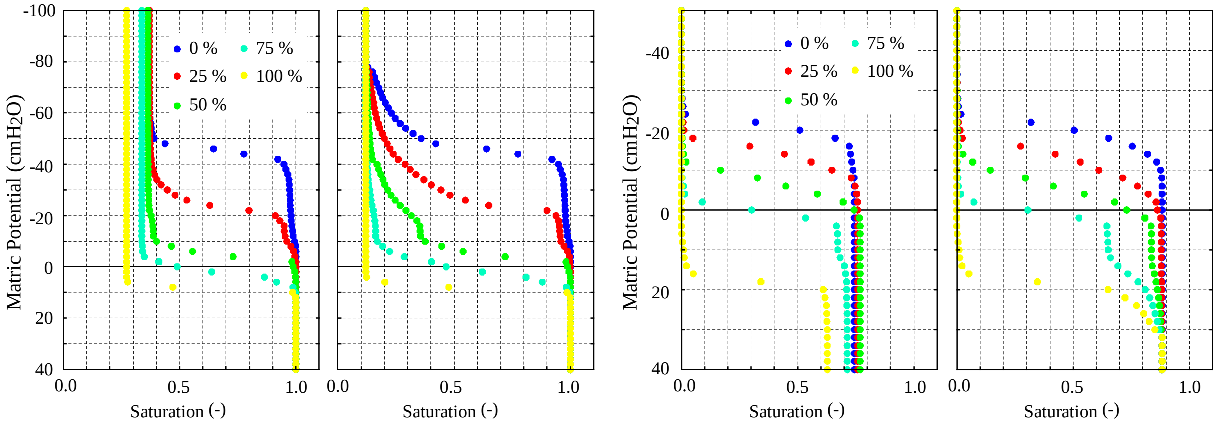

(a) Case 1 (b) Case 2

6-1 Drainage process

(a) Case 1 (b) Case 2

6-2 Imbibition process

Fig. 6 Computed Water Retention Curves

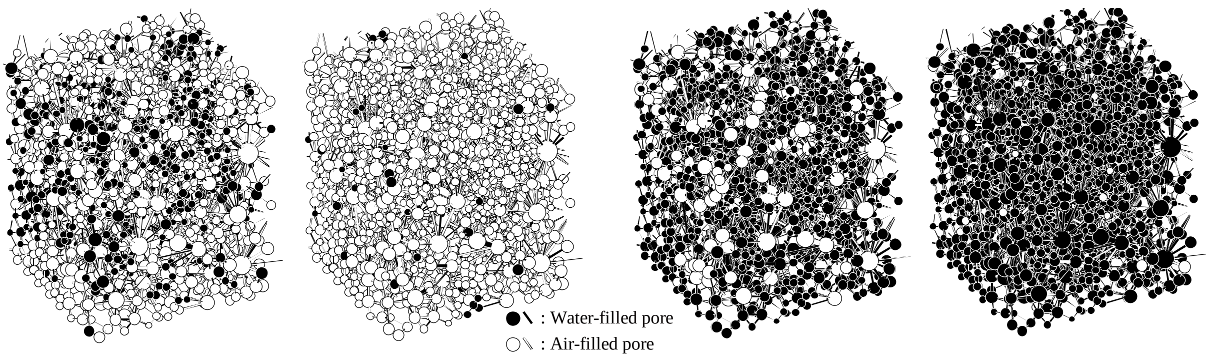

(a) Case 1 (b) Case 2

7-1 Drainage process
(Pressure on bottom = -100 cmH2O)

(a) Case 1 (b) Case 2

7-2 Imbibition process
(Pressure on bottom = 0 cmH2O)

Fig. 7 Trapped Water/Air in Pore Network (Mixture Fraction = 0%)

hydrophobic grains in common with the experimental results. Some discrepancy is seen especially in the drainage process between the experimental and computational results. While relatively small differences among the various mixture fractions are seen in the experimental results (Fig. 5-1), relatively large differences are seen in the computational results (Fig. 6-1). This suggests that different contact angles, or receding and advancing contact angles, should be used for evaluating the drainage and imbibition processes.

The main difference between Case 1 and Case 2 is seen in residual water in the drainage process and in trapped air in the imbibition process. While 10% of water or air remains after each process in Case 2, 30% to 40% is left behind in Case 1. From Fig. 7, residual water is seen in clusters of relatively small pore bodies, and trapped air are seen in clusters of relatively large pore bodies in Case 1. In a drainage process, such clusters of smaller pore bodies are formed because water is drained firstly from a sequence of larger pore bodies ahead of smaller ones and the connectivity between the clusters of smaller pore bodies and the outside reservoir is cut off. In the case of the imbibition process, clusters of relatively large pore bodies are formed in the same way.

CONCLUSION

Numerical experiments for water retention properties of porous media with mixed wettabilities were conducted, using an extracted pore network from randomly packed spherical grains. The air/water intrusion process are modeled by the generalized invasion percolation, in which simultaneous intrusions are allowed. Single or a small number of simultaneous intrusions correspond to a relatively small capillary number, and all or a large number of simultaneous intrusions corresponds to a relatively large capillary number. The computational results showed a similarity to the experimental ones in regard to the dependence of the mixture fraction, and that the amount of residual water and trapped air depends on the invasion rate.

ACKNOWLEDGEMENTS

This work was supported by JSPS KAKENHI Grant Number 24780232.

REFERENCES

[1] Fatt I, “The network model of porous media”, Trans. AIME, Vol. 207, 1956, pp. 144-181.

[2] Mohanty KK and Salter SJ, “Multiphase flow in porous media: II. Pore-level modeling”, SPE 11018 the 57th Tech. Conf. at SPE-AIME, New Orleans, Sep., 1982, pp. 26-29.

[3] Wilkinson D and Willemsen JF, “Invasion percolation: a new form of percolation”, J. Phys. A: Math. Gen., Vol. 16, 1983, pp.3365-3376.

[4] Piri M and Blunt MJ, “Pore-scale modeling of three-phase flow in mixed-wet systems”, SPE 77726 the SPE Annual Tech. Conf. and Ex., San Antonio, Texas, Sep., 2002.

[5] Jerauld GR and Salter SJ, “The effect of pore-structure on hysteresis in relative permeability and capillary pressure: pore-level modeling”, Transport in Porous Media, Vol. 5, 1990, pp. 103-151.

[6] Soll WE and Celia MA, “A modified percolation approach to simulating three-fluid capillary pressure-saturation relationships”, Adv. Water Resour., Vol. 16, 1993, pp. 107-126.

[7] Berkowitz B and Ewing R, “Percolation theory and network modeling applications in soil physics”, Surveys in Geophysics, Vol. 19, 1998, pp. 23-72.

[8] Raoof A and Hassanizadeh SM, “A new formulation for pore-network modeling of two-phase flow”, Water Resour. Res., Vol. 48, 2012, W01514, doi: 10.1029/2010WR010180.

[9] Yang Z, Niemi A, Fagerlund F, and Illangasekare T, “Two-phase flow in rough-walled fractures: comparison of continuum and invasion-percolation models”, Water Resour. Res., Vol. 49, 2013, doi: 10.1002/wrcr.20111.

[10] Blunt MJ, “Flow in porous media – pore-network models and multiphase flow”, Current Opinion in Colloid & Interface Science, Vol. 6, 2001, pp. 197-207.

[11] Al-Raoush R, Thompson K, and Willson CS, “Comparison of network generation technique for unconsolidated porous media”, Soil Sci. Soc. Am. J., Vol. 67, 2003, pp. 1687-1700.

[12] Ngom NF, Garnier P, Monga O, and Peth Stephan, “Extraction of three-dimensional soil pore space from microtomography images using a geometrical approach”, Geoderma, Vol. 163, 2011, 127-134.

[13] DeBano LF, “Water repellency in soils: a historical overview”, J. Hydrol., Vol. 231-232, 2000, pp. 4-32.

[14] Annaka T, “Wettability indices and water characteristics for sands of mixed wettability”, J. Jpn. Soc. Soil Phys., Vol. 102, 2006, pp. 79-86.

[15] Ustohal P, Dtauffer F, and Dracos T. “Measurement and modeling of hydraulic characteristics of unsaturated porous media with mixed wettabilities”, J. Contam. Hydrol., Vol. 33. 1998, pp. 5-37.

[16] Takeuchi J, Takahashi T, and Fujihara M, “Sub-Darcy scale modeling of non-uniform flow through porous media with mixed wettabilities”, Int. J. GEOMATE, Vol. 6, 2014, pp. 840-847.

[17] Dullien FAL, Francis Lai FSY, and Macdonald IF, “Hydraulic continuity of residual wetting

phase in porous media", J. Colloid Interface Sci., Vol. 109, 1986, pp. 201-2018.

[18] Bachmann J, Ellies A, and Hartge KH, "Development and application of a new sessile drop contact angle method to assess soil water repellency", J. Hydrol., Vol. 231-232, 2000, pp. 66-75.

Fifth International Conference on Geotechnique, Construction Materials and Environment, Osaka, Japan, Nov. 16-18, 2015, ISBN: 978-4-9905958-4-5 C3051

DEVELOPMENT OF TERRESTRIAL AND HYDROPHYTIC FLORA IN RELATION TO WATER MANAGEMENT IN OBASUTE-OIKE IRRIGATION POND IN JAPAN

Teruo Arase[1], Tetsuo Okano[1], Yoshiyuki Uchikawa[1] and Taizo Uchida[2]
[1]Faculty of Agriculture, Shinshu University, Japan; [2]Faculty of Engineering, Kyushu Sangyo University, Japan

ABSTRACT

In order to clarify the factors affecting the species diversity of plant communities around an irrigation pond, we surveyed Obaste-oike Irrigation Pond in Nagano Prefecture, Japan. The pond is comprised of three subdivided ponds, Kami-ike, Naka-ike, and Shimo-ike. Despite being adjacent to each other and connected by streams, the water levels in the three ponds differ. Five plant communities were studied, and one or two survey plots were selected in each community along each subdivided pond. A 32-m^2 quadrat was established in each plot of grassland, and a 400-m^2 quadrat was established in each plot of forest. The results of the distribution of species revealed that approximately 40% of the species were endemic to each subdivided pond in the terrestrial communities, whereas over 60% were endemic in the hydrophytic communities. To increase species diversity in irrigation ponds, especially in hyrdophytic communities, we suggest that dividing the ponds into several zones with distinct water levels and managing them in a sustainable manner is important.

Keywords: Obaste-oike Irrigation Pond, Water Level, Hydrophytic Plant Community, Species Diversity

INTRODUCTION

Recently, irrigation ponds are expected to have various functions, such as ecological conservation, disaster damage prevention, and scenic health resorts [1]. In ecological conservation, it is desirable that ecosystems include numerous plants and animals with high species diversity. However, according to the species-area curve theory, the number of species generally increases and reaches a maximum as the area increases [2], [3]; it follows as a consequence that a small area may include a low number of species. Is there anything that can be done to increase species diversity around an irrigation pond besides increasing its area?

Irrigation ponds are artificial reservoirs that hold water, and in Japan, they are mainly connected with rice paddy fields. Water demands in downstream areas regulate the water level of irrigation ponds. For example, in rice paddy fields, fine adjustments are made to control the water level to suit the growth of rice. Thus, the water level of irrigation ponds fluctuates largely within a year compared with natural water bodies that maintain an almost constant water level [1].

To date, many reports on species diversity in irrigation ponds have focused on hydrophytic vegetation, but most underrate the influence of water level. For example, a study by Shimoda and Kagawa concentrated on conventional water quality analyses [4]. However, since the function of supplying water for agriculture is more important than all other irrigation pond functions, we should pay close attention to the impact that water use for agriculture or other human uses has on the ecosystem around irrigation ponds. Therefore, we decided to focus on the fluctuation of water levels rather than water quality since water levels are directly linked to the distinctiveness of irrigation ponds. A better understanding of the influence of water levels in irrigation ponds will facilitate comprehension of how plant communities develop, and also provide information on how to maintain and control irrigation ponds from the viewpoint of plant communities with high diversity.

We studied Obaste-oike Irrigation Pond (Fig. 1 and Table 1), which experiences large fluctuations in water level. The pond is comprised of three subdivided adjacent ponds (Kami-ike, Naka-ike, and Shimo-ike). Since both the spilled water (through a sluice gate) and the deep water (through a bottom sluice) are led into the adjacent subdivided ponds (Fig. 1), the three subdivided ponds are estimated to have little differences in water quality. On the contrary, large fluctuations in the water levels of the subdivided ponds occur because water is used from each pond in a pre-defined order (firstly from Shimo-ike, next from Naka-ike, and last from Kami-ike) owing to water shortage (Table 1) [5], [6]. Consequently, it is appropriate to assume that the fluctuation in water level would be larger in Shimo-ike than Naka-ike, and Naka-ike than Kami-ike.

As for hydrophytic plant communities in Obaste-oike Irrigation Pond, a previous study found that

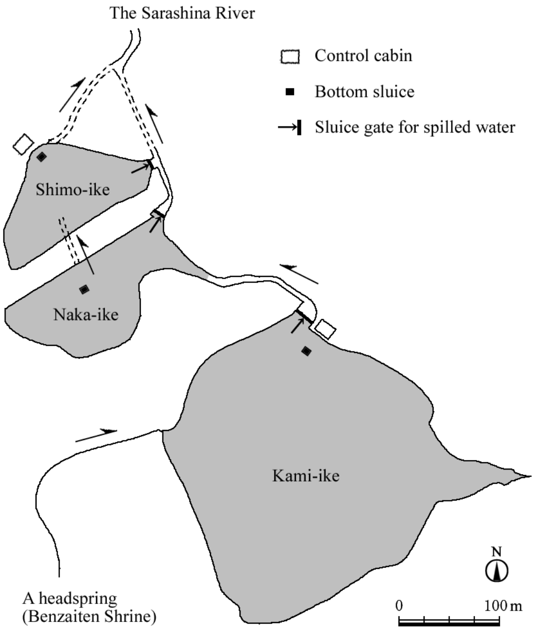

Fig. 1 The water system of Obaste-oike Irrigation Pond.

approximately 66% of the species surveyed were endemic to each subdivided pond [5]. The low species similarity among the three subdivided ponds implies that the hydrophytic communities in each subdivided pond appear to have developed independently [5]. However, since the flora of the terrestrial plant communities surrounding the pond was not studied in the previous report [5], it cannot be confirmed whether water level fluctuations caused endemic hydrophytic flora to develop independently in each subdivided pond.

Thus, in the present study, we investigated both hydrophytic and terrestrial plant communities surrounding the subdivided ponds of Obaste-oike Irrigation Pond. By analyzing the species distribution among the three subdivided ponds, we aimed to gain information on the development of flora and the influence water level fluctuations. We also aimed to offer technical recommendations for maintaining and controlling irrigation ponds with high-diversity plant communities.

METHODS

Investigation Site

Obasute-oike is located at an elevation of 820 m in Chikuma Heights, Chikuma City, Nagano Prefecture, Japan. It irrigates the Obaste-tanada area, which contains famous terraced paddy fields with an area of about 820,000 m^2.

This pond was originally constructed in the Edo period (1600-1868), encouraging the use of water collected in a hollow formed by a landslide. The banks were raised in the Taisho period (1912-1926),

Table 1 Comparison of the three subdivided ponds of Obasute-oike Irrigation Pond.

Items	Kami-ike	Naka-ike	Shimo-ike
Water reserves (m^3)	191,500	28,900	40,000
Maximum filling area (m^2)	61,000	15,000	12,000
Maximum water depth (m)	5.1	2.8	8.1
Order of water use	last	↔	first
Frequency of sluice control	low	↔	high
Fluctuation of water level	(small)	↔	(large)

Note: This information was previously tabulated by the authors [5].

but water shortages were still so severe that irrigation disputes occasionally took place among villages. In 1946, Shimo-ike was added to help alleviate water shortages.

Vegetation Survey

The vegetation of the investigation site was classified into five plant communities (Fig. 2) as follows: A) terrestrial plant communities composed of A1) short grasslands on the banks, and A2) mountainside forests; and B) hydrophytic plant communities composed of B1) marshes at the foot of a mountain, B2) grasslands along the shores, and B3) the water area.

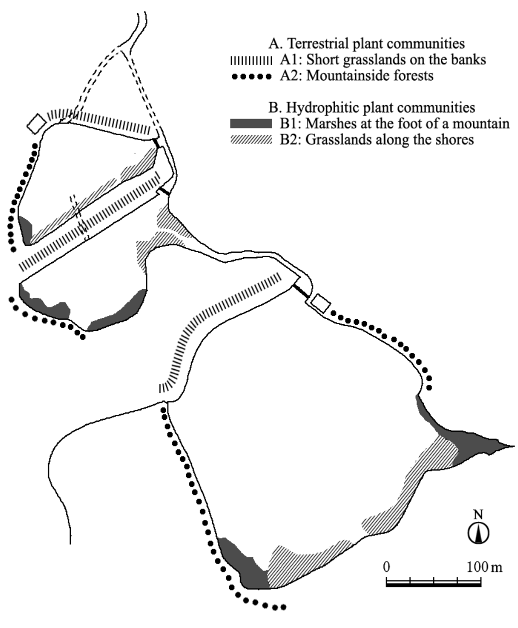

Fig. 2 Distribution of plant communities.

Table 2 Number and distribution of plant species in the three subdivided ponds of Obaste-oike Irrigation Pond.

Plant community	Endemic species			Common species				Total
	Kami-Ike	Naka-ike	Shimo-ike	Kami-ike Naka-ike	Naka-ike Shimo-ike	Kami-ike Shimo-ike	All the 3 ponds	
A: Terrestrial								
A1	5	6	5	3	7	3	12	41
%	12.2	14.6	12.2	7.3	17.1	7.3	29.3	
subtotal %			39.0				61.0	100.0
A2	22	21	23	17	17	14	45	159
%	13.8	13.2	14.5	10.7	10.7	8.8	28.3	
subtotal %			41.5				58.5	100.0
B: Hydrophytic								
B1	31	27	6	16	4	2	6	92
%	33.7	29.3	6.5	17.4	4.3	2.2	6.5	
subtotal %			69.6				30.4	100.0
B2	7	10	20	8	3	3	7	58
%	12.1	17.2	34.5	13.8	5.2	5.2	12.1	
subtotal %			63.8				36.2	100.0
B3	1	2	1	1	0	0	1	6
%	16.7	33.3	16.7	16.7	0.0	0.0	16.7	
subtotal %			66.7				33.3	100.0

The sizes of the investigation plots were 32 m^2 (4 m × 8 m) for A1, B1, and B2, and 400 m^2 (20 m × 20 m) for A2. As for B3, we observed the whole water area from the shores and used a boat to create a list of the plant species present because of its sparse vegetation. Two investigation plots were established in each of A2, B1, and B2 in Kami-ike and Naka-ike. Only one investigation plot was established in each of the other plant communities because of their limited area.

Vegetation surveys of hydrophytic plant communities (B1, B2, and B3) were conducted in 2010, and those of terrestrial plant communities (A1 and A2) in 2014 and 2015. The plant coverage of each plant species was measured in the plots of A1, A2, B1, and B2. We employed the following classes of plant coverage in each plot for the field survey: +, the plant species covered less than 1% of the plot area; 1, the plant species covered from 1 to 9%; 2, the plant species covered from 10 to 24%; 3, the plant species covered from 25 to 49%; 4, the plant species covered from 50 to 74%; and 5, the plant species covered from 75 to 100%.

To determine the number and distribution of plant species, the plant coverage data were converted into presence or absence data (1 or 0, respectively), and categorized by subdivided pond. Species found in only one of the subdivided ponds were considered "endemic species", while those found in two or three of the subdivided ponds were considered "common species". The difference in the categorized totals among plant communities was tested using the χ^2-test performed with a spreadsheet program (Microsoft Excel 2007).

RESULTS

Vegetation

Terrestrial plant communities

Short grasslands on the banks (A1) along each subdivided pond were dominated by orchard grass (*Dactylis glomerata*) and tall fescue (*Festuca arundinacea*). This plant community seemed to be cut frequently.

In mountainside forests (A2) along each subdivided pond, the tree stratum was dominated by Japanese red cedar (*Cryptomeria japonica*) and deciduous broad-leaved trees such as Japanese chestnut (*Castanea crenata*), a species of willow (*Salix* sp.), and konara oak (*Quercus serrata*). The herbaceous stratum was dominated by ferns such as *Dryopteris crassirhizoma*, a bamboo grass (*Sasamorpha borealis*), and sedges such as *Carex stenostachys*.

Hydrophytic plant communities

Marshes at the foot of a mountain (B1) were colonized by the common reed (*Phragmites australis*), but its coverage class ranged from + to 3 among plots. *Leersia japonica* and *Impatiens textori* were also found in each subdivided pond.

Grasslands along the shores (B2) were colonized by some emergent plants such as *Leersia japonica*, *Scirpus wichurae*, and *Scirpus triqueter*, but their coverage class ranged from + to 4 among plots.

In the water area (B3), only water chestnut (*Trapa japonica*) was observed to be a common species. Some submerged plants such as *Potamogeton crispus* were present, but existed very sparsely in the plant community.

Number and Distribution of Plant Species

Table 2 shows the number and distribution of plant species in the three subdivided ponds of Obaste-oike Irrigation Pond. The number of species was different among plant communities; mountainside forests (A2) had the highest number of species at 159, whereas the water area (B3) had the least at 6. The grasslands of A1, B1, and B2 had 41, 92, and 58 species, respectively (Table 2).

In terrestrial plant communities (A1 and A2), the percentages of endemic and common species were nearly 40% and 60%, respectively. On the contrary, these percentages were reversed in hydrophytic communities (B1, B2, and B3) where the percentages of endemic and common species were less than 40% and over 60%, respectively (Table 2). A significant difference in the categorized totals was detected between terrestrial and hydrophytic communities (χ^2-test, p<0.0001).

DISCUSSION

From the results of the percentages of endemic and common species, a reversal and a similarity were detected among the five plant communities in Obasute-oike Irrigation Pond. It is important to note that the majority of species in terrestrial plant communities (A1 and A2) were common species whereas endemic species were more prominent in hydrophytic plant communities (B1, B2, and B3). The percentages were relatively close between A1 and A2, and also among B1, B2, and B3, although the landscape and the total number of species were distinct in each plant community (Table 2).

The most intrinsic difference between the terrestrial and hydrophytic environment is whether ordinary water flooding occurs or not. Since the subdivided ponds are estimated to have little differences in water quality, it can be assumed that water level would be a significant factor in the regulation of plant communities. In terrestrial plant communities, relatively similar soil environments would allow many common species throughout the area. However, in hydrophytic plant communities, fluctuations in water level strongly increase the mortality of plants and influence their growth, which results in a flora with many endemic species in response to the microenvironment.

Based on the results of the present study, some technical recommendations can be made to maintain and control irrigation ponds with high-diversity plant communities. If the environment of a pond is homogeneous, the number of plant species will be limited by its area, as a consequence of the species-area curve theory [2], [3]. It seems difficult to increase species diversity in terrestrial plant communities because of the lack of regulating factors as substantial as water. However, in hydrophytic plant communities, dividing the area into several zones with different microenvironments (i.e. different water depths or flooding frequencies) is expected to increase species diversity beyond the capacity of its area, as demonstrated in the subdivided ponds of Obasute-oike Irrigation Pond. It is important to create a heterogeneous environment throughout the area, and to establish and maintain several zones of distinct microenvironments.

However, the water level in an irrigation pond can be maintained on the assumption that someone regulates it. In Obaste-oike Irrigation Pond, the most fundamental method of adjusting the water level is the indispensable water demand of continuing traditional rice cultivation in the downstream areas.

REFERENCES

[1] Uchida, K., Irrigation ponds: the multifaceted functions and application. Tokyo: Norin Tokei Kyokai, 2008, 171pp.

[2] Arrhenius, O., “Species and area”, Journal of Ecology, Vol. 9, 1921, pp. 95−99

[3] Preston, F.W., “The canonical distribution of commonness and rarity: part I”, Ecology, Vol. 43, 1962, pp. 185−215

[4] Shimoda, M. and Kagawa, H., ”Aquatic plant distribution of irrigation ponds in relation to land use and water quality in an agricultural landscape dominated by citrus orchards in Hojo area, Shikoku Island, southwestern Japan”, Vegetation Science, Vol. 26, 2009, pp. 65−78.

[5] Arase, T., Kumagai, M., Uchikawa, Y., Okano, T., Maruyama, K. and Uchida, T., “Growth of hydrophytic communities in relation to water management in Lake Obasute-oike, Nagano Prefecture, central Japan”, Bulletin Shinshu University Alpine Field Center, No. 10, 2012, pp. 91-100.

[6] Takeshita, H., “The true state of water use and landscape conservation in Obasute-tanada terrestrial paddy fields”, Master Thesis of Shinshu University, 2010, pp. 27−34.

EFFECTS OF WATER FLOW RATE ON RIVER WATER PURIFICATION BY ATTACHED GROWTH MICROORGANISM ON RIVER BED

- AN EXPERIMENTAL STUDY ABOUT NITRIFICATION -

Fumitake Nishimura[1] and Michiko Masuda[2]
[1] Department of Environmental Engineering, Kyoto University, Japan; [2] Department of Civil Engineering, Nagoya Institute of Technology, Japan

ABSTRACT

Activity or growth of microorganisms is the key factor for river water purification. Especially the activity of attached growth microorganism on river bed plays important roles for the purification. The activity can be affected by several factors such as water temperature, dissolved oxygen concentration, pH, and some other physical conditions. Understanding these effects can lead to the effective design and operation to enhance self-purification ability of rivers.

In this study water flow rate is focused as one of the factors affecting activity or growth of microorganisms on river bed. Water flow is necessary for growth of microorganisms because material exchange such as supplying substrate and removal of metabolite can be caused by water flow. However large flow rate can be promote detachment of microorganisms from river bed and it can result in deterioration of Water Purification activities.

Experimental study was conducted and it was shown that bacterial growth(nitrifying bacteria) was affected by water flow rate and the growth rate increased with increase of water flow rate under the condition that the flow rate(water velocity) was within 219(cm/min).

Keywords: Nitrification, Attached growth media, Water flow rate, Water velocity, Bacterial growth

INTRODUCTION

The key concepts for operating bioreactor are both concentration of bacteria working on the biological reaction and enhancement of its biological activity. For this purpose, attached growth media such as polyurethane foam, activated carbon and immobilized PVA were applied for accomplishing long term solid retention time(SRT), and suitable environmental conditions about water temperature, pH, dissolved oxygen(DO) and so on were investigated. Usually, these information were obtained through experiments of which scale were smaller than that of actual plants, and as results of the experiment, operational parameters such as hydraulic retention time(HRT), loading rates and biological activities were presented which could be considered applicable regardless the scale of bioreactor. However, some physical parameters don't seem to be constant regardless the reactor size, for example, water flow rate in a reactor and shearing stress on bacterial attached growth media caused by water flow can be different even if HRTs are the same. Therefore, in order to indicate the suitable design and operational parameters, not only factors which seem to be constant regardless of reactor size such as pH, DO, HRT or loading rate, but also factors which can be affected by the reactor scale.

In this study, water flow rate in a reactor was focused as a factor which can be affected by the reactor size, and experimental investigation was conducted. Polyurethane foam was used as an attached growth medium. Nitrifying bacteria were targeted as attached growth bacteria on the media. The media were fixed in the reactor and the water flow rate on the media was changed by controlling the water recirculation rate. It can be expected that material penetration into the biofilm and its exchange between biofilm and bulk-water are promoted with the increase of water flow rate, which can enhance bacterial activity. On the other hand, shearing stress on the biofilm will also increase as water flow rate becomes larger, that can promote detachment of bacteria from the media. Therefore, it is considered that water flow rate can have both positive and negative effects on the bacterial activity of the biofilm, and there would be some range which enhance the activity the most. These effects were investigated with chemostats.

MATERIALS AND METHODS

The schematic diagram of the reactor used in this study is shown in Fig. 1. The reactor was composed of two tanks; one was used for DO supplier where air diffuser was incorporated at the bottom, the other tank was used as bioreactor(nitrifying tank) where attached growth media were fixed. Both tanks were made of acrylic material. The effective volume of DO supply tank was 2.8L with height of 280mm and surface area of 100*100mm, whereas that of nitrifying tank was 2.0L with height of 320mm and surface area of 80*80mm. The two tanks were connected with a pipe between the bottoms, and liquid was recirculated from the DO supply tank to nitrifying tank by a water pump connected on the pipe. An acrylic plate with small pores(φ=5mm) were placed at the bottom of the nitrifying tank as current plate in order to moderate stream current from the water pump, 92 pierces of cubic polyurethane foam with dimensions of 15*12*12mm was connected by the stainless needles and fixed in the nitrifying tank. The apparent total volume of the cubic polyurethane foam was corresponded to 10% of nitrifying tank.

Artificial wastewater was shown in table 1, which was synthesized from the typical data of NH_4^+-N concentration in Japan. It was supplied

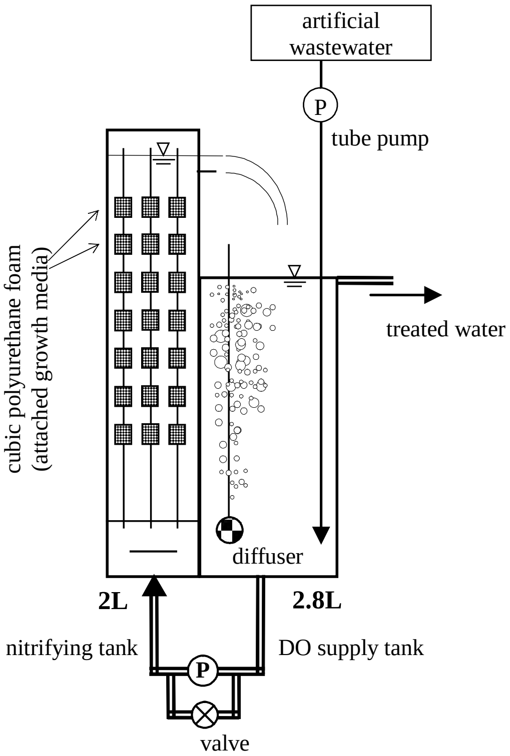

Fig.1 Schematic diagram of experimental apparatus

with a designed flow rate(HRT 6hr; reactor base) in to the bottom of the DO supply tank. The liquid was recirculated between two tanks and discharged from the top of the DO supply tank. The recirculation rate was regulated by controlling the valve settled beside the pump. Three cases of different recirculation flow rate were set for the experiment. Before starting the experiment, the attached growth media were submerged into mixed liquor with activated sludge from a domestic wastewater treatment plant. for one day in order to add bacteria into the reactor. Water samples are periodically collected from influent and effluent, and water quality indexes such as NH_4^+-N, NO_2^--N, NO_3^--N, T-N, S-N, pH, and alkalinity were confirmed to the methods described in Standard Methods(APHA, AWWA, WEF, 1998) or Methods for the Examination of Sewage(Japan Sewage Works Association, 1997). DO and water temperature at the bulk water in both tanks were also measured and influent water flow rates of all experimental cases were checked at the same time.

After the day when sufficient amount of bacteria seem to attach on the media, SS on the surface of attached growth media and some of the attached growth media were sampled from reactors, and SS amount and bacterial activity were measured by batch tests. Bacterial activity was evaluated by oxygen utilization rate(OUR), OUR with allylthiourea(ATU-OUR) which can relate to the biological activity without nitrifying bacteria. Bacteria in the reactors were roughly categorized into two groups based on the location of the attached growth media. One was the group of bacteria locating on the surface of the media(surface bacteria), and the other was these locating in the inner part of the polyurethane foams(inner bacteria). At 65 days after the start up, there were some amount of bacterial floc around the polyurethane foam. At that time, bacteria in the reactors were

Table 1 composition of artificial wastewater

chemicals	concentration
NH_4Cl	30(mgN/L)
KH_2PO_4	5(mgP/L)
$MgSO_4$	5(mgMg/L)
$NaHCO_3$	257(mg$CaCO_3$/L)
Tap water	-

Table 2 experimental condition

Case No.	recirculation water flow rate (L/min)	water velocity (cm/min)
1	3.0	46.9
2	6.0	93.8
3	14.0	219

sampled for check of the bacterial activity. The surface bacteria which locate more than about 0.5mm away from the media surface was collected with a pipette carefully, and remaining bacteria with the polyurethane foam was also sampled separately. The sampled polyurethane foam was put into an Erlenmeyer flask of 200mL and agitated slowly. Separated bacteria by this agitation were also used as surface bacteria, and other bacteria was used as inner bacteria.

The reactors were operated almost successfully under the designed conditions. The water temperature in each reactor was controlled between 22°C and 26°C during the experimental period, and the difference among the reactors was less than 1°C. DO concentration at the bulk water in all of three reactors were kept more than 6.3 mg/L, and the difference among the reactors was less than 0.5 mg/L. pH was also kept between 7.5 and 8.2, which doesn't seem to affect nitrifying activities(U. S. EPA, 1975), because of the sufficient amount of $NaCO_3$ as a pH buffer in the wastewater. Therefore, the effect of these factors were considered to be enough small to give any deference in bacterial activities among the experimental cases. Time course of NH_4^+-N,

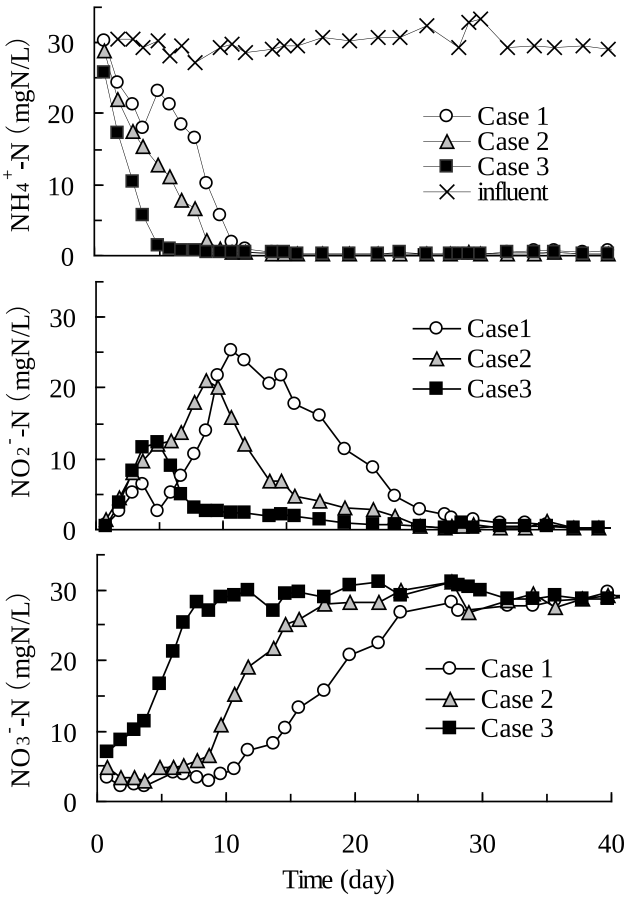

Fig.2 Time course of nitrogenous compounds

NO_2^--N, and NO_3^--N are shown in Fig. 2. There were clear differences among three experimental cases. Ammonium oxidation was accomplished within 5 days after start-up in the case 3 where water flow rate was the highest, whereas the day when complete oxidation of ammonia attained was 10 days and 12 days in the case 2, and the case 3, respectively. Similar phenomena were observed in the nitrite oxidation, and nitrite accumulation was the most in the case 2 as a result. Biological oxidation of nitrogenous compounds increases with the increase of water flow rate under the experimental conditions of water velocity between 46.9 and 219 cm/min. Average SS concentrations in the effluent were 0.54, 0.29, and 1.22 mgSS/L, in the case 1, 2, and 3, respectively. Although SS concentration in the effluent itself was enough small, that of the case 3 was the highest. It is suggested that shearing force by water flow caused the difference.

With these results, it was shown that water flow rate can give several affects on bacterial growth. Therefore, the effect will be considered from the viewpoints of bacterial growth. Biological reaction in the reactor can be modelled in the way described in Fig. 3. According from the diagram, material balance equations of NH_4^+-N, NO_3^--N, and nitrifying bacteria can be described as follows;

$$V\frac{dN_1}{dt} = QN_{10} - QN_1 - VR_1 - VY_2R_2 \quad (1)$$

$$V\frac{dN_3}{dt} = QN_{30} - QN_3 + VR_2 \quad (2)$$

If there are enough amount of substrates and nutrients, bacteria are in log growth phase. The growth pattern can be described with exponential functions;

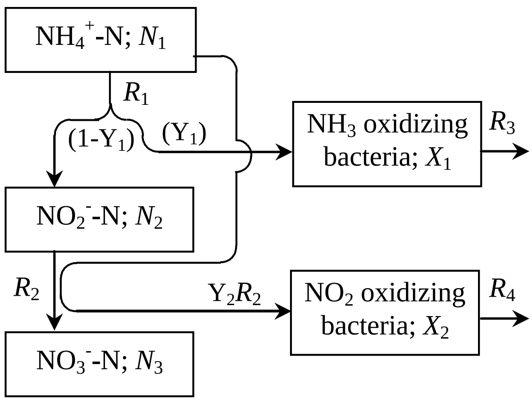

Fig.3 Schematic diagram of biological reaction in the reactor

$$V\frac{dX_1}{dt} = VY_1R_1 - VR_3 = V\mu_1 X_1 = VX_{1,t=0}\mu_1 e^{\mu_1 t} \quad (3)$$

$$V\frac{dX_2}{dt} = VY_2R_2 - VR_4 = V\mu_2 X_2 = VX_{2,t=0}\mu_2 e^{\mu_2 t} \quad (4)$$

where

R_1: NH_4^+-N oxidation rate by ammonium oxidizing bacteria (mg/L/hr)
R_2: NO_2^--N oxidation rate by nitrite oxidizing bacteria (mg/L/hr)
R_3: detachment rate of ammonium oxidizing bacteria (mg/L/hr)
R_4: detachment rate of nitrite oxidizing bacteria (mg/L/hr)
μ_1, μ_2: net specific growth rate of nitrifying bacteria (1/hr)
$X_{1,t=0}$, $X_{2,t=0}$: initial concentration of nitrifying bacteria (mg/L)
X_1, X_2: concentration of nitrifying bacteria (mg/L)
Y_1, Y_2: Yield (mg-assimilated N/mg-oxidized N) Suffix 1,2 means ammonium oxidizing bacteria, nitrite oxidizing bacteria, respectively
N_{10}, N_{30}: concentration of NH_4^+-N, NO_3^--N in influent, respectively (mgN/L)
N_1, N_3: concentration of NH_4^+-N, NO_3^--N in effluent, respectively (mgN/L)
t: time (hr)
V, Q: reactor volume (L), influent and effluent flow rate (L/hr)

If the value of Y_2R_2 is so smaller than R_1 that Y_2R_2 can be neglect in the equation (1), N_1 and N_3 can be expressed as follows;

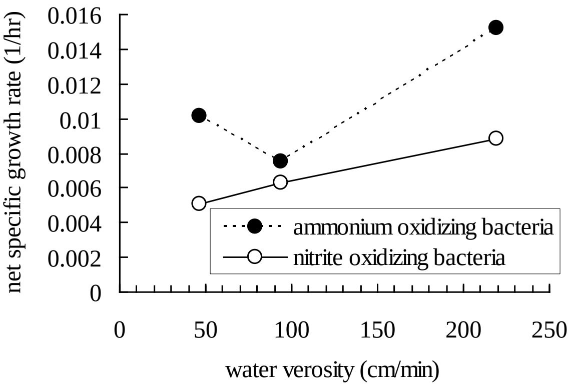

Fig.4 Net specific growth rate of nitrifying bacteria

$$N_1 = e^{-\frac{Q}{V}t}\alpha_1 + N_{10} - \frac{V\mu_1 X_{2,t=0}}{QY_1 + V\mu_1 Y_1}e^{\mu_1 t} \quad (5)$$

$$N_3 = e^{-\frac{Q}{V}t}\alpha_2 + N_{30} + \frac{V\mu_2 X_{2,t=0}}{QY_2 + V\mu_2 Y_2}e^{\mu_2 t} \quad (6)$$

α_1, α_2 : constants determined by initial conditions

The first terms of right side in the equations (5) and (6) can be neglect according to the passage of treatment time. Therefore, net specific growth rate of nitrifying bacteria(μ_1, μ_2) can be expressed as a slope in single logarithmic chart of t-(N_{10}-N_1) or t-(N_3-N_{30}) curve. Net specific growth rate of nitrifying bacteria calculated with this methods are shown in Fig. 4. It is shown that net specific growth rate becomes larger with the increase of water velocity. The values were between 0.0075 and 0.0152(1/hr) in ammonium oxidizing bacteria, whereas these of nitrite oxidizing bacteria were in a

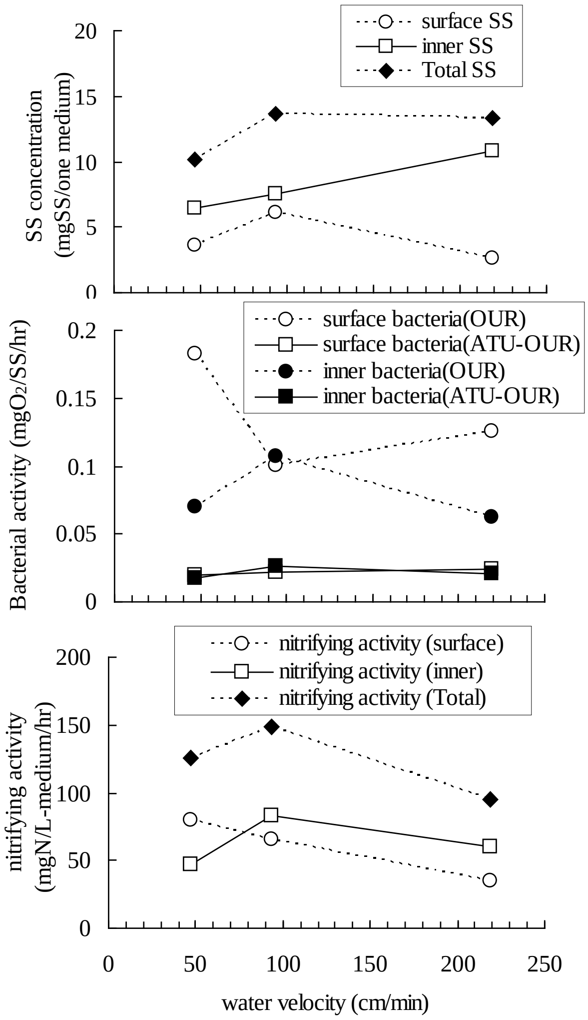

Fig.5 Results of batch test

range from 0.0051 to 0.0088(1/hr). Bacterial activity and SS concentration both inside and around the attached growth media are shown in Fig. 5. Bacterial activity of unit SS weight did not increase with the increase of water velocity. However, inner SS concentration increased as water velocity increased. It is considered that material penetration into the inside of the media was promoted as the water velocity increased, therefore, it could be easier for bacteria to exist at the inside. The results of bacterial activities shown in Fig. 5 were the potential activities, therefore the actual bacterial activities in the case of low water velocity might be lower. It is also suggested that penetration of materials such as substances and DO affect the treatment efficiencies. Operational and design parameters from these point of views also should be investigated quantitatively.

CONCLUSION

In this study, effects of water flow rate on bacterial growth at attached growth media were investigated. The results obtained in this study were summarized as follows;

1) In each case, complete nitrification was obtained under the conditions that HRT, influent NH_4^+-N concentration, volumetric incorporative ratio were 6hr, 30mgN/L, and 10%, respectively, where NH_4^+-N loading rate was 50 (mgN/L-media/hr).
2) Specific growth rate of ammonium oxidizing bacteria was in the range of 0.0075 to 0.0152(1/hr), whereas that of nitrite oxidizing bacteria was in the range of 0.0051 to 0.0088(1/hr). Specific growth rate of nitrifying bacteria increased with the increase of water velocity of which value was between 46.9 and 219 (cm/min).
3) SS concentration inside the media increased with the increase of water velocity.
4) Potential nitrification rates were in the range of 95.2 to 148 (mgN/L-media/hr)

In this study, it was certainly shown that water flow rate can have effects on bacteria, therefore, these effects should be taken into account when experimental data would be applied to the different scale reactor and system.

ACKNOWLEDGEMENTS

This research was partially supported by the grants from the Maeda Engineering Foundation (2015).

REFERENCES

[1] APHA, AWWA, WEF, Standard Methods for the Examination of Water and Wastewater 20th Edition, Washington D. C.: American publish health association, (1998), ISBN 0-87553-235-7.

[2] Hisashi, S., Satoshi, O., Yoshimasa, W., Ammonium Oxidation in Mixed-population Biofilms Determined with the Use of Microelectrodes and in situ Hybridization, J. of Japan Society on Water Environment, Vol.22, No.3, 206-214(1999). (in Japanese)

[3] Japan Sewage Works Association, Methods for the Examination of Sewage(1997). (in Japanese)

[4] Satoshi, O., Hatsuka, N., Yoshimasa, W., Spatial Distributions of Ammonia-Oxidizing Bacteria in wastewater Biofilms Analyzed by Fluorescent in situ Hybridization, J. of Japan Society on Water Environment, Vol.22, No.3, 191-198(1999). (in Japanese)

[5] U.S.EPA, Process design manual for nitrogen control, (1975).

[6] Chen Y, Wang L, Ma F, Yang JX, Qiu S., Tracking composition of microbial communities for simultaneous nitrification and denitrification in polyurethane foam, Water Science and Technology, Vol. 69, No.9, 1788-1797(2014).

[7] Aure´ lie Ce´bron1, Josette Garnier, *Nitrobacter* and *Nitrospira* genera as representatives of nitrite-oxidizing bacteria: Detection, quantification and growth along the lower Seine River (France), Water Research, Vol. 39, 4979-4992(2005).

[8] Mélanie Raimonet, Lauriane Vilmin, Nicolas Flipob, Vincent Rocher, Anniet M. Laverman, Modelling the fate of nitrite in an urbanized river using experimentally obtained nitrifier growth parameters, Water Research, Vol. 73, 373–387(2015).

[9] Deepshikha Sharma, Arun Kansal, Assessment of river quality models: a review, Reviews in Environmental Science and Bio/Technology, Vol. 12, Issue 3, 285-311(2013).

BIODIESEL INDUSTRY WASTE RECOVERY IN AGRICULTURE

Mariana Ferreira Rabelo Fernandes[1], Essaid Bilal[1, 2], Regynaldo Arruda Sampaio[1], Jatnel Alonso Lazo[3] Luiz Arnaldo Fernandes[1], Adolf Heinrich Horn[4] and Najla Lassoued[5]

[1] Instituto de CiênciasAgrárias, Universidade Federal de Minas Gerais, Caixa Postal 135, CEP 39404-006, Montes Claros, MG, Brasil; [2] Ecole Nationale Supérieure des Mines de Saint Etienne, CNRS UMR 5600, F42023 Saint Etienne, France; [3] Instituto de Ciência Animal, Apartado Postal 24, San José de las Lajas, Mayabeque, Cuba; [4] Instituto do Geociência, Universidade Fédérale de Minas Gerais, Brasil; [5] National Agronomic Institute of Tunisia, Tunis, Tunisia.

ABSTRACT

We examine in this study the possibility of using biodiesel industry waste mixed with urban sewage sludge as a source of nutrients for the production and seedling development in agriculture. Biodiesel industry waste is diatomaceous earth (DE) compounds and paraffin. We added DE with urban sewage sludge. The advantage of this operation is to eliminate the two wastes, residues of the biodiesel industry and sludge from wastewater treatment plants. We studied the behavior of Camaldulensis Eucalyptus and white mulberry (Morus Alba Yu vc-62).

The Dickson Quality Index (DQI) of White Mulberry and Eucalyptus Camaladulensis plants tested in different substrates (urban sewage sludge and DE) are all above the minimum recommended value of 0.2. The Camaladulensis eucalyptus and white mulberry (Morus Alba) plants have good growth in substrates containing urban sewage sludge and diatomaceous earth compared to commercial substrate used as control. Biodiesel industry waste can used up to 50% by volume of the substrate without compromising the quality of the plants with a reduction in the cost of production.

Keywords: Biodiesel, Diatomaceous earth, Sewage sludge, Eucalyptus, Morus Alba

INTRODUCTION

Recently, with the growing demand for biodiesel in the world, several plants for biofuel production, mainly from vegetable oils, are being installed in Brazil. For the elimination of various impurities, both the first and itself biodiesel material, these industries use filters of various types, particularly those using diatomaceous earth (D.E.) as a filter element.

The organic compounds formed from industrial waste can be used as sources of organic matter and nutrients in a substrate [1]. They increase the water retention capacity by improving aeration of the roots of plants and they increase the availability of nutrients from the growth of beneficial microorganisms. Can interfere with the increase of pH and levels of exchangeable cations of substrates.

To avoid environmental problems associated with deposits of residues biodiesel industry, we can use as a source of nutrients for the production and development of plants seems like a very good option. The residue D.E. has specific physical properties that can improve the soil properties.

The D.E. is a naturally occurring, soft, siliceous sedimentary rock, consisting of shells or frustules seaweed, which has many properties. It is a lightweight material with low-density porous structure with low thermal conductivity and non-toxic [2], [3]. At the end of the production, process of biodiesel, it is as a residue impregnated of organic material.

We added the DE residues of Biodiesel with sludge from urban wastewater treatment or manure to stimulate the activity of soil bacterial [4]. The advantage of this operation is to eliminate both wastes, residues Biodiesel industry and sludge treatment plants.

Given the economic and environmental importance of reusing these resources considered as waste, this study aims to evaluate substrate test (DE and sludge sewage) as an alternative for improving the composition of soils for plant production.

MATERIAL AND METHODS

The study was conducted in the period May-August 2014 at the Institute of Agricultural Sciences - ICA, of the Federal University of Minas Gerais - UFMG, Montes Claros, located in northern Minas Gerais state. The climate of the region is semi-arid, hot and dry tropical. The rainy season is concentrated between Octobers to March. The average annual rainfall is 1060 mm and uneven [5]. The experimental substrate was prepared from different proportions of commercial substrate control (Bioplant), DE, sewage sludge (SS) or manure (M) (table 1). Manure from breeding ICA-UFMG. Sewage sludge from the treatment plant wastewater Montes Claros - MG. Diatomaceous earth from the disposition of Petrobras biodiesel plant in Montes Claros, after use as a filtering agent of vegetable oils (soybean). Diatomaceous earth, before use, was submitted to the combustion process for the removal of residual oil.

The pots had a volume of 55 cm3 and the species studied were Camaladulensis Eucalyptus and white mulberry (Morus Alba Yu vc-62). The seeds of Eucalyptus Camaladulensis foram obtained from the ICA / UFMG and seeds of white mulberry Morus Alba vcYu-62 were CIA / Cuba. At the time of sowing three seeds were placed in each pot and 21 days after sowing took place clarified leaving only one plant per pot. The experiment consisted of two tests, one for each species. The experimental design was a randomized complete block design with three replications and four pots per experimental unit.

The composition of the pots were made on April 30 and May 1, 2014. The plants were sown on May 2. A shade sail was used with a rate 30% and 50% shade and was placed 1.5 m above the ground, oriented east-west to provide shade from the experimental unit. This shade sail was removed 30 days after the lifting of plant. Both treatments were irrigated three times daily.

Scanning electron microscopy (SEM) coupled with energy dispersive spectroscopy (EDS). Observations and elemental analyzes were performed on a scanning electron microscope Jeol JSM 6400 coupled to an Oxford EDS analyzer (ENSM-SE). Observations were carried out on secondary electrons mode in the case of granular raw unpolished samples and backscattered electron mode.

Table 1 The materials used and their proportions by volume for each substrate tests

	Substrate Tests (ST)
ST1	100% SC substrate control (Bioplant)
ST2	75% SC + 12.5% SS + 12.5% DE
ST3	75% SC + 12.5% SS + 12.5% DE
ST4	50% SC + 25% SS + 25% DE
ST5	50% SC + 16.7% SS + 33.3% DE
ST6	75% SC + 12.5% M + 12.5% DE
ST7	75% SC + 8.3% M + 16.7% DE
ST8	50% SC + 25% M + 25% DE
ST9	50% SC + 16.7% M + 33.3% DE

Physical and chemical analyzes of different substrates tests and control substrate (commercial substrate Bioplant) were performed at the Laboratory of Solid Waste UFMG following the methodology of Embrapa [6]. The diameter and height of the stem of the plants were measured from the 49th day to the 118th day. Starting at thirty days, we calculated the rate of emergence of two cultures. Where the species reached a height greater than 10 cm and 42 days after planting, we add the ammonium sulfate fertilizer.

The number of leaves per plant was calculated. Fresh weight of shoots, leaves and roots were measured by weighing. After drying in an oven at 65 ° C for 72 hours to constant weight, the dry weight matter was weighed.

We evaluated the relationship between shoot dry weight and root dry weight. All data were subjected to analysis of variance and means were compared by the Scott-Knott test at 5% probability.

Table 2 The chemical characteristics of substrate tests (ST2 to ST9) and substrate control (ST1)

ST	pH	CE										
		dS m^{-1}	P	K	Ca	Mg	H + Al	SB	t	T	V	MO	C
ST1	6.4	1.54	- mg dm^{-3} --		------------------------ $cmol_c$ dm^{-3} -------------						%	--- dag kg^{-1} --	
ST2	6.4	1.72	900	249	7.3	5.4	0.91	13.34	13.34	14.25	94	18.57	10.79
ST3	6.4	1.68	1.020	497	8.2	3.4	2.32	12.88	12.88	15.2	85	38.44	22.34
ST4	6.4	1.64	980	298	9.3	3.0	2.32	13.07	13.07	15.38	85	18.19	10.57
ST5	6.7	1.71	960	497	9.6	3.5	1.38	14.38	14.38	15.75	91	13.6	7.9
ST6	6.9	1.82	880	895	8.0	3.0	1.39	13.30	13.3	14.69	91	14.6	8.48
ST7	6.8	1.78	510	970	7.0	3.6	1.55	13.09	13.09	14.64	89	16.34	9.5
ST8	7.6	1.65	960	990	6.0	4.0	1.55	12.54	12.54	14.09	89	16.7	9.7
ST9	7.5	1.35	960	846	4.0	4.8	0.85	10.97	10.97	11.82	93	16.34	9.5

RESULTS

The pH in the control substrate ST1 chosen as substrates tests mixtures of ST2 to ST4 is the same 6.4; it passes to 6.7 in the mixture T5 (33% of DE). The pH was higher in mixtures with manure between 6.9 and 7.6. The electric conductivity (1.64 to 1.82 dS / m) in the mixtures ST2 to ST8 is higher, compared with control substrate (1.54 dS/m). Except for the case ST9, manure mixture, is very low 1.35 dS/m. K is high 880 mg/dm3 in the mixture T5. K remains high in the mixtures Manure (647-990 mg/dm3) compared with the control substrate (249 mg/dm3). The organic matter (OM), total porosity, water holding capacity (WHC) and density decrease significantly in mixtures ST4, ST5 and ST9 (table 2 and 3).

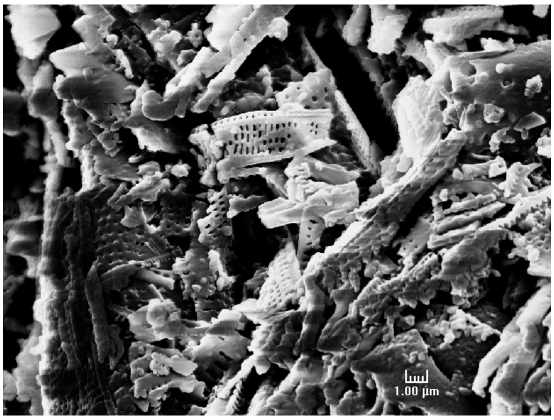

Fig. 1 Image scanning electron microscopy of biodiesel industry waste from Petrobras plant in Montes Claros, MG, Brazil.

The root volume of Eucalyptus Camaldulensis is very low in the ST5 (2.5 cm^3) compared to the control substrate ST1 (3.69 cm^3) or ST2 (5.42 cm^3), ST3 (4.92 cm^3) e ST4 (4.53 cm^3). It is similar to the root volume of Eucalyptus Camaldulensis growing in substrates with manure (1.69 to 3 cm^3). The heights of rods, the diameter, number of leaves and the root volume are determines the seedling quality higher in all the substrates tests than in the control substrate. However, all the morphological characteristics and weight biomass of the seedling in substrates with manure are less than those seedlings growing in substrates tests with sewage sludge and diatomaceous earth. Seedlings treatments ST4 and ST5 have the largest diameter 4.46 mm and 4.76 mm respectively. All other values are higher than the minimum required (2.0 to 2.5 mm). DQI [7] seedlings Morus Alba is high in the treatment with sewage sludge and diatomaceous earth T4 (0.42) and T5 (0.55) and very low in treatment with manure T7 (0.13), T8 (0.18) and T9 (0.11).

Table 3 Water retention capacity (WHC), density (ρ) and total porosity (TP) of substrate tests (ST2 to ST9) and substrate control (ST1).

Substrate tests	WHC	ρ	TP
	mL g^{-1}	gcm^{-3}	%
ST1	0.56	0.35	64.7
ST2	0.49	0.46	73.4
ST3	0.42	0.47	62.2
ST4	0.38	0.55	58.4
ST5	0.43	0.55	56.3
ST6	0.60	0.43	63.5
ST7	0.53	0.43	64.3
ST8	0.57	0.46	64.4
ST9	0.44	0.50	62.6

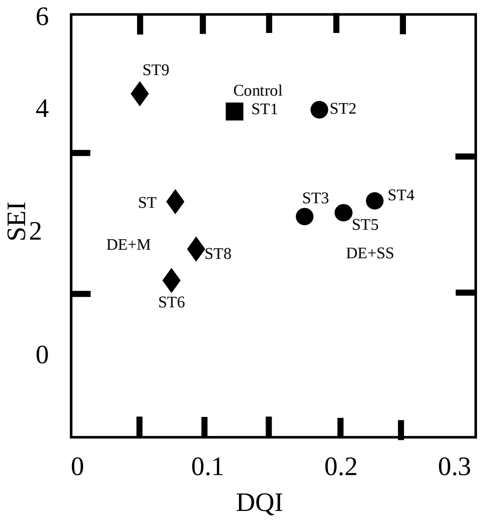

Fig. 2 Dickson Quality Index (DQI) versus Speed Emergency Index (SEI) of Eucalyptus Camaldulensis seedlings from different substrates tests and control substrate.

DISCUSSION AND CONCLUSION

Eucalyptus Camaladulensis

The observed values of the plant height, diameter of the stem and the fresh and dry weight of roots and shoots in the treatment with a manure and diatomaceous earth were statistically lower, compared with the control substrate (fig. 1). Whereas the physical and chemical properties of the substrates were similar in all treatments (Table 2 and 3), with the exception of pH, the effects observed may be attributed to the higher pH (higher than 6.5) of these substrates.

In more alkaline pH conditions, there may be nutrients and micronutrients are not available which will cause a physiological disequilibrium plants. The pH should be in the range of pH 5.5 to 6.5 to obtain the recommended quality of seedlings. According to [8] and [9], the precipitation of the solution of aluminum ground causes, among other effects, the increase of pH. Moreover, the application of manure may cause complexing Al by organic acids released by these materials. The high acidity of the soil caused by the sludge can be associated with the nitrification of ammonium nitrogen and the oxidation of sulfites and feasible production of organic acids during the degradation by microorganisms of the residue [10]. If we consider that seedlings good quality must have a minimum stem diameter of 2.0 to 2.5 mm [11], [12], the treatment with the substrate containing sludge sewage and diatomaceous earth corresponds to the desired quality (fig. 2).

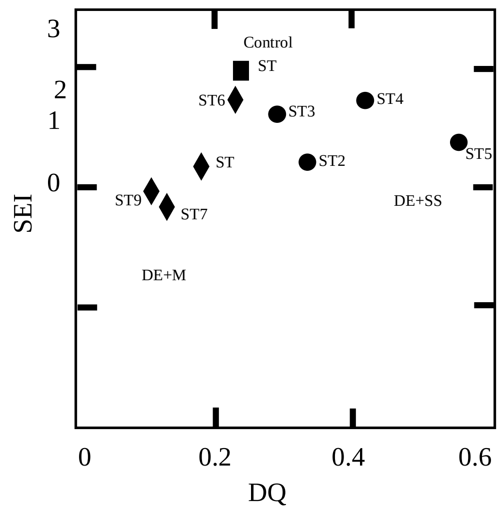

Fig. 3 Dickson Quality Index (DQI) versus Speed Emergency Index (SEI) of Morus Alba seedlings from different substrates tests and control substrate.

The seedlings may be placed on the field after 120 days of growth, with an average diameter stem from 2.65 to 2.95 mm. The emergency speed index of T2 and T9 is statistically equivalent to treatment with substrate control (Table 4). This result differs from that observed by [13]; these authors studied the value of speed emergency index based on mixtures of the substrate with rice husk, cow manure, powdered coconut and fine vermiculite.

Different mixtures had no effect on the speed emergency index of Eucalyptus urophylla. It should be noted that the decline in the rate of seedling emergence is an undesirable feature, because most of the time in the early stages of growth, it makes plants more vulnerable to adverse environmental conditions [14]. The faster root development is important, the better the vegetative development and stability of the plant [15].

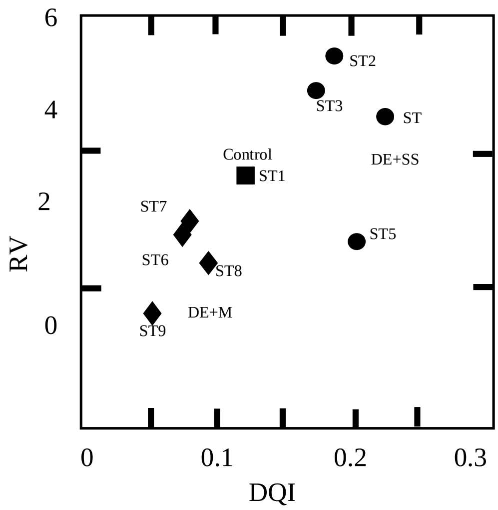

Fig. 4 Dickson Quality Index (DQI) versus root volume (RV cm^3) of Eucalyptus Camaldulensis from different substrates tests and control substrate.

The GPDM/RDM ratio showed no statistical difference between the different substrates (Table 5). However, DQI is more important in the substrate test mixture of sludge sewage and DE (0.17-0.23), whereas it is very low in substrates based on manure and DE (0.05-0.09) and in the order of 0.12 in the control substrate (fig. 2, 3 and 4); we have a good correlation with total dray matter TDM and DQI. This links up the observations [16] and [17] found that on the field the best results in the survival of eucalyptus seedling are those substrates containing sewage sludge. These authors also noted that 2/1 of GPDM/RDM is a good balance for the growth of plants. In our case, the values are slightly higher but still reasonable for the different substrates tests. We find that the ratio between the stem height and diameter of the plant did not differ significantly between the substrates tests studied (Table 4), but the root volume of Eucalyptus Camaldulensis is higher (more 4 cm^3) in blended substrate with DE and SS comparatively to control substrate and amended substrate with manure (fig. 4). Greater the value of this ratio is, the better the ability to survival and establishment of seedlings in the field [18]. The best treatments are those with sewage sludge and diatomaceous earth (fig. 4). The DQI is above the recommended minimum [19]. These authors argue that DQI should be greater than 0.2. DQI than, the higher the quality standards seedlings. The study of seedlings of Eucalyptus urophylla by [19] showed higher values for the DQI treatments with manure than what we got.

Morus Alba Yu vc-62

Tests substrates with sewage sludge and diatoms favor the growth of white mulberry (Morus Alba) seedlings (fig. 5). They are usually better than the control substrate (Table 5). For all treatments the chemical and physical properties were similar except for pH (Tables 2 and 3), we can consider that sewage sludge played an important role in nutrient level and diatoms have improved physical properties including porosity, water capacity and density of retention substrates tested.

These observations are consistent with the Maia [20] found that sewage sludge should not be used pure, despite its relative fertility [21], sewage sludge cause compression of the substrate. Diatomaceous earth is an important addition to the growth of seedlings.

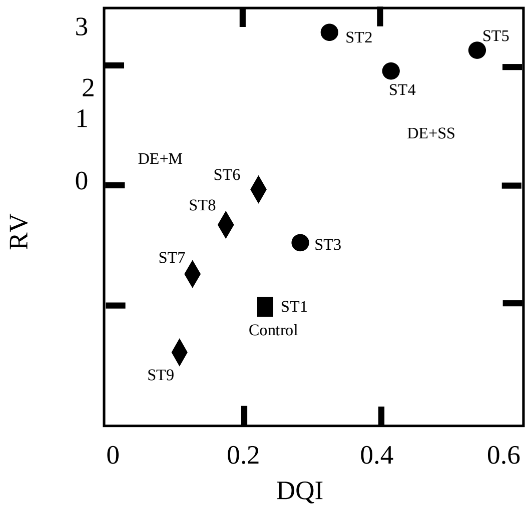

Fig. 5 Dickson Quality Index (DQI) versus root volume (RV cm^3) of Morus Alba from different substrates tests and control substrate.

All treatments showed levels of potassium (Table 2) very good according to the classification of [22], which explains the high values of stem diameter of seedlings. Valeri and Corradi [23] showed that the potassium regulates the opening of the stomata and promotes the thickening of the stem of the seedling. According to Daniel [24], the diameter of the stem is the most appropriate to evaluate the ability of seedling survival. It is also the most widely used to help determine the doses of fertilizer must be applied in the production of seedlings.

The speed emergence index of Morus Alba show (fig. 3) no statistical difference between treatments. At the stage of the germination and emergence of seeds, nutrients are not necessary for the reactions leading to the formation stem and root (fig. 5). Only hydration and aeration of the substrate and good porosity of the substrate allows a movement of the air and water favoring the quickest germination [25].

The GPDM/RDM ratios of Morus Alba seedling are not statistically different for all treatments. They indicate that the seedlings have the same probability of survival. The GPDM/RDM ratio and TDM is directly related to the composition of substrate tests strongly influenced by the availability of water, which favors the flow of nutrients and seedling growth.

The HI ratio (H/D stem height /stem base diameter) of seedlings Morus Alba shows no statistically significant difference 2.35 to 3.12. This ratio is less than that observed for the Eucalyptus (7.47 to 9.63) for the same experimental conditions. The HI ratio and root volume are likely to depend on the species of seedlings because in spite of the low values, seedlings showed good conditions for adaptation and resistance on the ground. The DQI values Morus Alba seedlings growing in test substrates with sewage sludge and diatomaceous earth, are all higher than the recommended minimum value of 0.2, with high value for ST4 and ST5 rich substrate diatomaceous earth (fig. 5). Treatments with manure does not meet the desired quality standard.

The DQI is obvious that the morphological parameters' used to evaluate the quality of seedlings and morphological parameters should not be analyzed separately to determine the quality level.

The Eucalyptus and Morus Alba seedlings produced with test substrates (sewage sludge, diatomaceous earth and commercial substrate) showed similar results to those obtained with the use only commercial substrate.

The Eucalyptus and Morus Alba seedlings have good growth in substrates containing sewage sludge and diatomaceous earth. They show better results than using only the commercial substrate. They can be used up to 50% by volume of the substrate without compromising the seedlings quality with a reduction of cost of seedlings production.

Table 4 Means of the variables total height (H), collar diameter (D), number of branches (NB), number of leaves (NL), root volume (RV), fresh biomass of the above ground part, (GPFM), root fresh matter (RFM), dry biomass of the above ground part (GPDM) and root dry matter (RDM) seedlings of Eucalyptus Camaldulensis from different substrates tests and control substrate.

Substrates tests	H	D	NB	NL	RV	GPFM	RFM	GPDM	RDM
	cm	mm	-- -- nº /seedling --		Cm3	------------------ g ----------------------------			
T1	22.03	2.43	1.62	5.12	3.69	2.59	1.14	0.86	0.45
T2	24.51	2.95	1.60	5.85	5.42	3.96	1.57	1.50	0.54
T3	23.25	2.65	1.75	5.49	4.92	3.83	1.39	1.41	0.54
T4	20.34	2.75	1.85	6.08	4.53	4.24	1.58	1.52	0.65
T5	21.98	2.89	1.79	5.97	2.72	4.15	1.43	1.36	0.61
T6	16.55	1.78	1.65	4.78	2.83	1.89	0.65	0.55	0.27
T7	16.97	2.02	1.55	4.57	3.00	1.86	0.80	0.55	0.26
T8	13.49	1.85	1.62	5.05	2.44	1.93	0.69	0.61	0.27
T9	15.36	1.59	1.66	5.03	1.69	1.57	0.58	0.39	0.20

Table 5 Means of the variables total height (H), collar diameter (D), number of leaves (NL), root volume (RV), fresh biomass of the above ground part, (GPFM), root fresh matter (RFM), dry biomass of the above ground part (GPDM) and root dry matter (RDM) seedlings of Morus Alba from different substrates tests and control substrate.

Substrates tests	H	D	NL	RV	GPFM	RFM	GPDM	RDM
	cm	mm	-- nº /seedling ---		Cm³	------------------g----------------------		
T1	7.49 C	3.04 C	2.75 A	1.00 B	1.00 C	1.45 B	0.35 B	0.43 C
T2	7.96 A	3.83 B	2.47 B	3.28 A	1.61 B	2.01 A	0.57 B	0.63 B
T3	10.10 A	3.78 B	2.67 B	1.50 B	1.47 B	1.75 B	0.48 B	0.56 B
T4	12.38 A	4.46 A	2.48 B	2.92 A	2.27 A	2.51 A	0.83 A	0.78 A
T5	11.11 A	4.76 A	2.54 B	3.11 A	2.19 A	2.90 A	0.82 A	0.94 A
T6	9.06 B	3.53 B	2.84 A	1.67 B	1.28 B	1.55 B	0.37 B	0.43 C
T7	7.96 C	2.90 C	2.86 A	1.25 B	1.03 C	0.99 C	0.29 B	0.23 D
T8	8.98 B	3.49 B	2.91 A	1.67 B	1.31 B	1.35 B	0.38 B	0.30 D
T9	9.24 B	2.99 C	3.06 A	0.64 B	1.12 C	0.92 C	0.28 B	0.20 D

Note: Means without letters or followed by the same letter are not statistically different according to the Scott-Knott test at 5% probability

ACKNOWLEDGEMENTS

This work supported by FAPEMIG (Fundação de Amparo a Pesquisa de Minas Gerais) and the Institute of Agricultural Sciences of the Federal University of Minas Gerais (UFMG), Regional Campus Montes Claros. We also thank the French Embassy and the Rectorat of UFMG for the grant of a visiting professor Essaid Bilal (ENSMSE, France) in the framework of the France-UFMG Academic Chair; and Ecole Nationale Supérieure des Mines for chemicals analyses support. The authors are grateful to Prof. Monica Butnariu for their assistance and for useful discussions.

REFERENCES

[1] Wendling, I.; Gatto, A. (2002) Substratos, adubação e irrigação na produção de mudas. Viçosa: Ed. Aprenda Fácil, 160pp.

[2] Meisiner, A. C. (1981) Diatomite, Mineral Commodity Summaries, USA, 1981, Pp. 46-47.

[3] Souza, G. P.; Filgueira, M.; Rosenthal, R.; Holanda, J. N. F. (2003) Caracterização de material compósito diatomáceo natural. Cerâmica, 49, pp. 40-43.

[4] Joseph S. D., Camps-Arbestain M., Lin Y., Munroe P., Chia C. H., Hook J., van Zwieten L., Kimber S., Cowie A., Singh B. P., Lehmann J., Foidl N., Smernik R. J., Amonette J. E., An investigation into the reactions of biochar in soil. Soil Research, 2009, 48(7), pp. 501–515.

[5] Eloi, C.M.A. (2001) Enquadramento das “zonas de vida” de HOLDRIDGE na classificação climática de Minas Gerais. Ms thèse Meteorlogy agrícola, Viçosa Univesity Federal, 48pp.

[6] EMBRAPA. (1997) Manual de métodos de análise do solo. 2 eds. Rio de Janeiro: EMBRAPA - Centro Nacional de Pesquisa de Solos. 1997. 247pp.

[7] Dickson, A.; Leaf, A.L.; Hosner, J.F. (1960) Quality appraisal of white spruce and white pine seedling stock in nurseries. Forest Chronicle, v. 36, p.10-13.

[8] Mello, S. C.; Vitti, G. C. (2002) Influência de materiais orgânicos no desenvolvimento do tomateiro e nas propriedades químicas do solo em ambiente protegido. Horticultura Brasileira 20: 452-458.

[9] Miyazawa, M., Pavan, M.A., Franchini, J.C. (2000). Neutralização da acidez do perfil do solo por resíduos vegetais, Informações Agronômicas, Piracicaba: POTAFOS, 92: 1-8.

[10] Simonete, M. A.; Kiehl, J. C.; Andrade, C. A.; Teixeira, C. F. A. (2003) Efeito do lodo de esgoto em um argissolo e no crescimento e nutrição de milho. Pesquisa Agropecuária Brasileira, v. 38, n. 10, 1187-195.

[11] Wendling, I.; Dutra, L. F. (2010) Produção de mudas de eucalipto por estaquia e miniestaquia. In: WENDLING, I.; DUTRA, L. F. Produção de mudas de eucalipto Colombo. Ed. Embrapa Florestas, 2010. Chap.2, 50-80.

[12] Lopes, J. L. W; Guerrini, I. A.; Saad, J. C. C. (2007) Qualidade de mudas de eucalipto produzidas sob diferentes lâminas de irrigação e dois tipos de substrato. Revista Árvore, Viçosa, v. 31, n. 5, 845-853.

[13] Oliveira Júnior, O. A. de; Cairo, P. A. R.; Novaes, A. B. de. (2011) Características morfofisiológicas associadas à qualidade de mudas de Eucalyptus urophylla produzidas em diferentes substratos. Revista Árvore, Viçosa, v. 35, n. 6, p. 1173-1180.

[14] Martins, C. C.; Nakagawa, J.; Bovi, M. L. (1999) Efeito da posição da semente no substrato e no crescimento inicial das plântulas de palmito-vermelho (Euterpe espirito santensis Fernandes Palmae). Revista Brasileira de Sementes. v.21, n. 1, 164-173.

[15] Soares, E. R. Da Rui, T. L. R.; Braz, R. F.; Kanashiro Junior, W. K. (2008) Desenvolvimento de mudas de pepino em substrato produzidos com resíduos de algodão e de poda de árvores. In: Encontro Nacional sobre substratos para plantas materiais regionais como substratos, 6, Fortaleza, 2008. Anais. Fortaleza, Ed. Embrapa Agroindústria Tropical/ SEBRAE/CE/UFC.

[16] Caldeira Júnior, C. F.; Souza, R. A.; Santos, A. M.; Sampaio, R. S.; Martins, E. R. (2009) Características químicas do solo e crescimento de Astronium Fraxinifolium Schott em área degradada adubada com lodo de esgoto e silicato de cálcio. Revista Ceres, v. 56, n. 1, 213-218, 2009.

[17] Caldeira, M. V.; Delarmelina, W. M.; Peroni, L.; Gonçalves, E. O.; Silva, A. G. (2013) Lodo de esgoto e vermiculita na produção de mudas de eucalipto. Pesq. Agropec. Trop., Goiânia, v. 43, n. 2, 155-163, abr./jun. 2013.

[18] Carneiro, J. G. A. (1983) Influência dos fatores ambientais, das técnicas de produção sobre o desenvolvimento de mudas florestais e a importância dos parâmetros que definem sua qualidade. In: Florestas plantadas nos Neotrópicos como fonte de energia, 1983. Anais Viçosa. p. 10-24.

[19] Gomes, J. M. Souza, A.L. DE; Paula Neto, F. DE; Resende, G.C. DE. ... Couto, L.; Leite, H. G.; Xavier, A.; Garcia, S. L. R. (2002) Parâmetros morfológicos na avaliação da qualidade de mudas de Eucalyptusgrandis. Revista Árvore, Viçosa, v. 26, n. 6, 655-664.

[20] Maia, C. M. B. F. (1999) Uso da casca de Pinus e o lodo biológico como substrato para produção de mudas de Pinus taeda. Boletim de Pesquisa Florestal, Colombo, n. 39, 81-82.

[21] Caldeira MVW, Peroni L, Gomes D. R., Delarmelina WM, Trazzi PA. (2012) Diferentes proporções de biossólido na composição de substratos para a produção de mudas de timbó (Ateleia glazioviana Bail). Scientia Forestalis 2012; 40(93) 15-022.

[22] Alvarez V., V. H; Novais, R. F.; Barros, N. F.; Cantarutti, R. B.; Lopes, A. S. (1999) Interpretação dos resultados das análises de solos. In: RIBEIRO, A. C.; GUIMARÃES, P. T. G.; ALVAREZ, V. H. (Org.). Recomendações para o uso de corretivos e fertilizantes em Minas Gerais: 5ª aproximação. Viçosa: Ed. CFSEMG, 25-32.

[23] Valeri S. V. and Corradini L. (2005) Fertilização em viveiros para a produção de mudas de Eucalyptus e Pinus. In: GONÇALVES J. L. M.; BENEDETTI V, Ed. Nutrição e fertilização florestal. Piracicaba: Instituto de Pesquisas e Estudos Florestais; 2005. 167-190.

[24] Daniel, O.; Vitorino, A.C.T., Aloisi, A.A.; Mazzochin, L.; Tokura, A.M.; Pinheiro, E.R.; Souza, E.F. (1997) Aplicação de fósforo em mudas de Acacia mangium. Revista Árvore, v.21, p.163-168.

[25] Simãon, S. (1971) Manual de fruticultura. São Paulo: Ed. Agronomia Ceres, 1971. 530pp.

Fifth International Conference on Geotechnique, Construction Materials and Environment, Osaka, Japan, Nov. 16-18, 2015, ISBN: 978-4-9905958-4-5 C3051

LESSONS FROM THE INTERNATIONAL COMPARISON OF CONTAMINATED LAND POLICIES WITH RISK GOVERNANCE IN JAPAN, THE NETHERLANDS, AND THE UK

Tomoko Miyagawa[1], Noriko Otsuka[2] and Hirokazu Abe[3]
[1]Faculty of Systems Engineering, Wakayama University, Japan; [2]ILS Institut für Landes- und Stadtentwicklungsforschung gGmbH, Germany; [3]Cyber Media Center, Osaka University, Japan

ABSTRACT

After the Great East Japan Earthquake and Fukushima Daiichi nuclear disaster, decontamination has been undertaken primarily to remediate residential areas. Therefore, it is necessary to consider risk governance in decontamination process. This paper aims to examine contaminated land policies by comparing Japan, the Netherlands, and the UK by literature reviews from the aspects of risk governance towards sustainable decontamination process. The results clarified that policies in Japan is disintegrated and sectionalised by separate acts. Contrastingly, integrated contaminated land regimes are practiced in the Netherlands and the UK on contaminated risks from current land uses. In terms of risk governance in contaminated land policies, although the Netherlands has a limited application, Japan and the UK have a certain degree of community participation in recent policies. Thus, recent contaminated land policy frameworks are adapting to promote risk governance in decontamination process by introducing statutory requirements. However, there is a limitation to ensure risk governance by statutory actions and more support to voluntary actions is needed.

Keywords: Contaminated Land, Brownfields, International Comparison Of Policies, Risk Governance

INTRODUCTION

Four years had passed from the Great East Japan Earthquake and Fukushima Daiichi nuclear disaster. At present, decontamination is in process with the Act on Special Measures concerning the Handling of Environment Pollution by Radioactive Materials Discharged by the Nuclear Power Station Accident Associated with the Tohoku District –Off the Pacific Ocean Earthquake that Occurred on March 11, 2011(After that, Act on Special Measures concerning the Handling of Environment Pollution by Radioactive Materials; 2011) released from the Fukushima Daiichi nuclear power plant which is caused by the Great East Japan Earthquake. However, contamination is widely spread into vast areas and it is not possible to decontaminate to its original condition in a short time [1].

Moreover, in the decontamination process, communication and community participation is a key aspect in the case of remediation sites to be located nearby residential areas. Additionally, in the case of severe contamination, it may take longer period for remediation, therefore, communication and community participation needs to be integrated in long term remediation. Hence, decontamination process in Fukushima applies to the above situation with primarily targeted to remediate residential areas, thus, risk governance is necessary.

The definition of risk governance is a 'collective decisions' through an interactive decision making process, which includes 'the totality of actors, rules, conventions, processes, and mechanisms' with its relevance in its collection, analysis, communication, and management decisions, due to 'the nature of the risk requires the collaboration of, and co-ordination between, a range of different stakeholders' [2], [3]. It is a dynamic continuous process with understanding gradually and adjusting to manage carefully of 'complexity, scientific uncertainty, and/or socio-political ambiguity' which needs to be 'flexible', 'interactive and inclusionary' [4]. It also aims to consider 'institutional agreements (the regulatory and legal framework that determines the relationship, roles and responsibilities of the actors and co-ordination mechanisms)' and 'political culture', to overcome differences in risk perception [2].

The Public Concerns Of Risk Governance In Fukushima City, Japan

On the other hand, according to the report on consciousness of citizens for radioactivity by postal questionnaire survey to a random selection of people who are living in Fukushima city and living elsewhere to escape from the city in May, 2014, there was a tendency to have more concerns on anxiety on health risks from radiation, i.e., families than themselves [5]. From the opinions of citizens on what should be prioritized in actions in the future by local authorities, prefecture, and central government had highlighted the highest concerns on the disclosure of accurate information at 68.8 per cent, and the health management of citizens at 64.6 per cent to follow [5]. Another investigation on perceptions of Japanese parents by online survey at four groups of Tohoku, Kanto, and Kansai regions and Fukushima prefecture in March, 2012 summarized that reasons for feelings of anxiety to be mainly from distrust of the outlook and actions by the central government, and secondly from 'uncertainty about scientific data disseminated in the past about low dose radiation' as well as 'invisible risks' , i.e., spots with high dose of radiation or food produced without monitoring from radiation [6]. Furthermore, improvement of the quality of information and disclosing information completely was strongly requested for information providers [6].

Above situations may illustrate the public concern on communication and community participation, therefore, it is necessary to consider risk governance in decontamination process. Until present, international comparison of contaminated land policies have been explored from environmental and spatial planning perspectives, i.e., US and Europe [7], North America and Europe [8], the UK and China [9], and England and Japan [10], however, discussions on incorporating social aspects of community participation is rather limited. Thus, this paper aims to examine contaminated land policies by literature reviews from the aspects of risk governance towards sustainable decontamination process by comparing Japan with separate set of acts, the Netherlands with the risk assessment system, and the UK with the planning system.

THE SIGNIFICANCE OF RISK GOVERNANCE IN DECONTAMINATION PROCESS

Environmental risk communication is recognized its importance by legislator, environmental groups and citizens that extra effort is needed to change plans in order 'to provide citizens with more meaningful input' [7], i.e., participation of the community in the early stages of the process [7], [11]-[13]. Moreover, communication should be undertaken continuously in the whole process of activities [13]. It is also suggested that 'meaningful community engagement' takes a highly influential part of actions for the public health in a case of contaminated land [11]. Therefore, the impact of effective communication on stakeholders needs to be considered, since it is 'critical to the successful delivery of remediation projects' [14]. From the above, communication and community participation can be said to be one of the most important issues for sustainable decontamination process.

The framework of risk governance comprises of four phases; 'pre-estimation', 'interdisciplinary risk estimation', 'risk characterization', and 'risk evaluation and risk management'; pre-estimation stage is a screening of actions and problems which are related to risks; interdisciplinary risk estimation is to undertake both scientifically based risk assessment and concern assessment to include socio-economic issues; risk characterization is an element based on evidence, while risk evaluation is an element based on the value to make decisions on the 'tolerability and /or acceptability of a risk'; and risk management is to re-examine 'all relevant data and information generated in the previous steps' to decide adequate actions in consideration of 'societal acceptability and tolerability' [4]. In risk governance, stakeholder and public involvement has been stated as a core feature [3], [4], and constant companions to all phases [2], [4] for transparent process, supervision by the public, and understandings among each other about the risks and their governance [2] should be ensured.

In the decontamination process, both the direct toxicological impacts and indirect affects to health, i.e., stress and anxiety, should be considered for residents living on or near in case of higher risks of contamination [11], [12]. Public concerns on contaminated land and its risks are identified as a scientific issue of 'health of self and family', as well as a range of socio-economic issues, 'property values', 'amenity', 'liability', 'level of confidence in government' s ability to protect', and 'damage to environment' [15]. It is also discussed further that the indirect affects to residents in ways of physiological, economic and psychological, in 'a less certain and less transient way than observed pollution incidents' [14]. Furthermore, it has been reported that 'more open and proactive style of risk communication and consultation' had led to less dissatisfaction in the community on brownfield land with contamination [16]. For radioactive contaminated land, 'a systematic consideration of ethical and social issues' is going to make a selection of countermeasures 'more transparent and less controversial for society' and assist in sustainable restoration and long-term management [17]. Therefore, social and economic factors need to be discussed not only to examine the decontamination approaches from the aspects of its technological effectiveness [1]. To ensure the long-term sustainability, public acceptance and social sustainability need to be undertaken in the decontamination process [18].

CONTAMINATED LAND POLICIES IN JAPAN, THE NETHERLANDS AND THE UK

Japan has similarities with the Netherlands and the UK that central governments are having a majority of role in setting and enforcing contaminated land policies [8], i.e., severely

Table 1 Comparison of contaminated land policies

Level of contamination	Japan	the Netherlands	the UK
Severely contaminated	Agricultural Land Soil Pollution Prevention Law(1970) [19] Law Concerning Special Measures against Dioxins(1999) [20] Act on Special Measures concerning the Handling of Environment Pollution by Radioactive Materials (2011) [21]	Soil Protection Act (1987) with Risk assessment [23], [24]	Special Site [25]-[27]; Part IIA to include radioactively contaminated land (2006) [26], [27]
Contaminated	Soil Contamination Countermeasures Act(2002) [22]	Soil Protection Act (1987) [23], [24]	Part IIA (2000) in Environmental Protection Act (1990) and Environment Act (1995) [25]

contaminated sites are dealt by the central governments or governmental organizations of Environment Agency as such in the UK. However, contaminated land regime in Japan had developed differently. In Japan, contaminated land regime is dealt by separate acts for specific land uses and substances which are introduced after the severe contaminated land cases, i.e., acts for agricultural lands, dioxins, and radioactive materials (Table 1). For example, for agricultural land, Agricultural Land Soil Pollution Prevention Law (1970) was introduced to deal with the 'Itai-Itai disease' in the Jinzu River Basin area in 1968 to cause soil pollution on agricultural land by chronic cadmium [19], and for dioxins, Law Concerning Special Measures against Dioxins (1999) has been introduced to deal with dioxins which is emitted from waste incinerators which became to cause pollution problems in recent years [28]. Thus, it can be said to be disintegrated and sectionalized from Soil Contamination Countermeasures Act (2002) that covers contaminated land in general.

Although EU has a number of directives to bridge the gaps between environmental laws among member states, individual member states are having a key role in policy-making [8]. The Netherlands is one of the countries to introduce contaminated land policies in early periods in 1983 with Interim Soil Remediation Act, owing to its dense population and being as an industrial country [24]. In case of severe contamination, it is dealt by Soil Protection Act (1987) with risk assessment supported by web based decision making support systems 'to combine scientific aspects of risk assessment with policy choices' [23], [24].

In the UK, contaminated land regime came into force in 2000 by part IIA of the Environmental Protection Act (1990) and the Environment Act (1995) in a case of causing or having a potential to cause significant harm, or causing or likely to cause pollution of controlled waters [25]-[27].

For severe contamination, Part IIA has been extended to include Special Site which Environment Agency to be responsible for the remediation [25], [27] under the conditions stated in circular 01/2006 [26], as well as radioactively contaminated land in 2006 [26], [27]. Contamination risks from its current use is dealt by the above system, by contrast, such risks for proposed use is controlled by Town and Country Planning Act (1990) [25]-[27]. Contamination is a 'material consideration' which requires planning authorities to consider them through development planning and development control [25], [26], i.e., remediation can be the condition before granting planning permission by the local authorities for new proposed land uses. Therefore, the UK approach is regarding contamination under the condition of 'only in relation to particular sites and particular end-uses' [29].

Japan developed separate acts concerning each environmental issue, contrastingly, the Netherlands and the UK has an integrated contaminated land regime to extending and enhancing the current acts to deal with soil contamination by Soil Protection Act (1987), and Part IIA of Environmental Protection Act (1990) and Environment Act (1995) to include severely contaminated sites (Table 1) [23]-[27]. Furthermore, the Netherlands has a national inventory of contaminated sites based on the risk of 'health and the environment or potential impact on key resources' including groundwater [8], while Japan and the UK have not been establishing the equivalent inventories. However, the UK had developed contaminated land policies from the aspects of 'recycling brownfields sites' due to pressures on efficient land uses, rather than focusing on the public health and environmental quality which can be seen in other countries [30]. For instance, concerning risks of contamination from proposed land uses, the UK has a separate system by Town and Country Planning Act (1990) [29], [30], [31] to bring 'operational tensions' by the differences of each system professionally and technically [30].

COMPARISON OF RISK GOVERNANCE IN CONTAMINATED LAND POLICIES

Steps And Opportunities Of Risk Governance

There are a number of steps and opportunities which enables better communication and participation as followings; disclosure of the information; consultations with residents associations and interest groups; community participation to consultative, decision making meetings; and correspondences during the decontamination process [32]. First and foremost, disclosure of the information is necessary for citizens to have a chance/opportunity to participate in the process, because it is considered as a highly important factor in risk communication [5], [6]. It does not directly engage with 'affected parties or the wider public', and becomes 'a critical first step' in case of a need of communication with complexity [13]. Then, consultations and participations of residents and interest groups are important for improving communication between stakeholders and to activate participation in decision making process [32]. It is a direct involvement with stakeholders, and by ensuring to listen and take into account of their opinions from these opportunities, it can be a help to smooth the process [13]. Moreover, the reflective involvement enables to 'pursue the purpose of finding a consensus on the extra margin of safety that potential victims would be willing to tolerate and potential beneficiaries of the risk would be willing to invest in order to avoid potentially critical and catastrophic consequences' [4]. During the decontamination process, involvement of all stakeholders needs to be considered in order to provide access to advice at most [14], which also enables 'to build confidence and trust between all parties' by working together to maintain consistency and approachability [12]. In risk governance, mutual actions between actors from scientists, public and private sectors, and citizens are undertaken in accordance with 'public participation, stakeholder involvement and governance structures' horizontally and vertically [2]. Furthermore, correspondences for residents during the process should also be considered in terms of the health and safety and after the process to meet with the local needs [32]. In addition, correspondences after the decontamination process may be also necessary since some of them require management on sites or have limitations on land uses due to the remediation methods [32], particularly for the long term cases i.e. in Fukushima.

Statutory Requirements Of Contaminated Land Policies With Risk Governance

In Japan, Agricultural Land Soil Pollution Prevention Law (1970) and Law Concerning Special Measures against Dioxins (1999) both have not been defined in terms of the aspects of communication and community participation, therefore, it is not mandatory to include such action in the decontamination process [19], [20]. However, there is some advancement in contaminated land policies on this issue in recent years. For example, Soil Contamination Countermeasures Act (2002) states that the public are available to browse the registry of designated areas [22]. Furthermore, Act on Special Measures concerning the Handling of Environment Pollution by Radioactive Materials (2011) includes several steps as follows; disclosure of the information which is available to browse the registry of sites under management for soil removal of areas in action for decontamination; consultations with residents associations and interest groups to create opportunities to deliver opinions from land owners; and admitted parties (stakeholder but was not included by the previous system/law, i.e., residents) by the governor (leader/chairman of the state/county council) are able to participate if necessary [21].

In the Netherlands, Soil Protection Act (1987) states various entitled parties should be communicated before making decisions in case of seriously contaminated cases [33].

In the UK, disclosure of the information is statutory that local authority should make additions to public register of contaminated land which is available to browse by the public [26].

It is also stated that consultations with residents associations and interest groups and correspondences during the decontamination process to be statutory [26]. Therefore, local authority has to arrange and plan procedures of remediation strategies by communicating, and catering for the information of parties involved including owners, occupiers of land, and other relevant interested parties; as well as information and complaints from the public, businesses and voluntary organizations [26].

Comparison And Applicability Of Contaminated Land Policies With Risk Governance

From the comparison of contaminated land policies among the three countries regarding on risk governance, it became clear that aspects of risk communication are rather limited in the Netherlands. However, recent policies in Japan and the UK are shifting to include some perspectives of community participation by incorporating disclosure of the information for the public to access the registry of contaminated sites and consultations of stakeholders. In addition, there are advancements to include community participation to consultative, decision making meetings in Japan, and correspondences during the decontamination process in the UK. However, in practice, application of policies has a limitation that became evident from a case in Fukushima to have a problem of disclosure of accurate information.

According to the framework of risk governance comprising of the four main phases from pre-estimation to management has been proposed [4], however, contaminated land policies have stated none of the actions dedicated to risk governance in the statutory process. This may be due to the fact that contaminated land policies are based on scientific data and information, and lacking to incorporate socio-economic aspects in the process. However, communication has been partially stated as a part of statutory actions, which is undertaken throughout the process in parallel to the four phases. Thus, there is a limitation to ensure risk governance by statutory actions, and many set of actions needs to be dealt by voluntary. This may be because the concept of risk governance is a continuous set of inclusive and consolidative actions, while contaminated land policies are scientifically based and has a tendency to follow administrative procedures and not to be interactive. Therefore, to fill the gap, guidelines have been provided to demonstrate best practices as a way of recommendation to support voluntary actions, i.e., SNIFFER [13], [15]. In addition, promoting further integration between the four phases of risk governance and communication may also lead to enhancement of actions on risk governance in contaminated land policies.

CONCLUSION

In this paper, it had examined contaminated land policies in Japan, the Netherlands, and the UK from the aspects of risk governance towards sustainable decontamination process to incorporate social aspects. From the comparison, Japan had developed contaminated land regime in a way of disintegrated and sectionalized, owing to separate sets of acts had been introduced to cover each specific and severely contaminated land cases. By contrast, the Netherlands and the UK has an integrated contaminated land regime by extending and enhancing the current acts to cover both severely contaminated and contaminated sites on contamination risks from current land uses. Although the above regime of the Netherlands covers both current and future proposed land uses, the UK has a separate system for future proposed land uses by town and country planning system.

Thus, the differences of contaminated land policies in the three countries may be illustrating the differences of having measures of generic numerical values of environmental quality which requires a set of soil values to have disintegrated and sectionalized in Japan, whereas the idea of risk assessment/management can be applied to various cases to allow the enhancement and integration of the current system. In order to consider the integration in contaminated land policies in Japan, it may be necessary to examine the current system which has a limitation to extend or enhance. However, risk assessment/management also require to set clear goals and to be measurable for achieving the effectiveness [34], therefore, clarification of goals may be one of the key issue for smooth implementation of contaminated land policies and sustainable decontamination process.

In terms of the comparison of risk governance in contaminated land policies, the Netherlands has a system with limited application, while the aspects of community participation has been incorporated to some extent in recent policies in the UK and Japan, i.e., disclosure of the information for the public to browse the registry of contaminated sites and consultations of stakeholders. Furthermore, community participation to consultative and decision making meeting in Japan as well as correspondences during the decontamination process in the UK should be also considered as good practices.

Therefore, recent contaminated land policy frameworks are adapting to promote risk governance in decontamination process by introducing statutory requirements. However, there is a limitation to ensure risk governance by statutory actions, and many set of actions needs to be dealt by voluntary. This may be because of the concept of risk governance is a continuous set of inclusive and consolidative actions, while contaminated land policies have a tendency to follow administrative procedures and not to be interactive. Thus, to fill the gap, guidelines have been provided to demonstrate best practices as a way of recommendation to support voluntary actions.

ACKNOWLEDGEMENTS

The authors acknowledge the financial support provided by the Japan Society for the Promotion of Science (no. 25289207), and grants from the Obayashi Foundation (research grant, no.10, 2012).

REFERENCES

[1] Yasutaka T et al., “A GIS-based evaluation of the effect of decontamination on effective doses due to long-term external exposures in Fukushima”, Chemosphere, Vol. 93, Issue 6, 2013, pp. 1222-1229.

[2] Renn O, “White Paper on Risk Governance: Toward an Integrative Framework in Global Risk Governance”, Renn O and Walker K, Ed. Springer, 2008, pp. 3-73.

[3] Aven T and Renn O, “Risk Management and Governance: Concepts, Guidelines and Applications”, Springer, 2010, pp. 1-70.

[4] Renn O and Klinke A, “A Framework of Adaptive Risk Governance for Urban Planning”, Sustainability, 5, 2013, pp.2036-2059.

[5] Fukushima city, "The second report on consciousness survey of citizens for radioactivity" (in Japanese), 2014, pp.1-11.
[6] Tateno S and Yokoyama MH, "Public anxiety, trust, and the role of mediators in communicating risk of exposure to low dose radiation after the Fukushima Daiichi Nuclear Plant explosion", J. of Science Communication, Vol. 12, No. 2, Jun. 2013, pp. 1-22.
[7] Meyer PB, Williams RH and Yount, KR, "Contaminated Land: Reclamation, Redevelopment and Reuse in the United States and the European Union", Edward Elgar, 1995, pp. 71-202.
[8] De Sousa C, "Contaminated sites: The Canadian situation in an international context", J. of Environmental Management, Vol. 62, 2001, pp. 131-154.
[9] Qishi L, Catney P, and Lerner D, "Risk-based management of contaminated land in the UK: Lessons for China?", J. of Environmental Management, Vol. 90, 2009, pp. 1123-1134.
[10] Takahashi A, et al., "Legal framework and estimated stock measurement on brownfield as contaminated land in England and Japan" (in Japanese), J. of Architecture and Planning, Vol.78, No.687, 2013, pp. 1077-1085.
[11] Barnes GJ, Litva A and Tuson S, "The Social impact of land contamination: reflections on the development of a community advocacy and counselling service following the Weston village incident", Advance Access Publication, Vol. 27, No.3, 2005, pp. 275-280.
[12] Atenstaedt RL et al., "Good practice in risk communication: A case study related to people residing on an infilled clay pit", Vol. 10, Issue 1, J. of Environmental Health Research, 2010, pp. 57-63.
[13] SNIFFER, "Risk Communication Booklet: Communicating understanding of contaminated land risks", 2010, pp. 1-24.
[14] Cross M, "Effective communication in contaminated risk management", Proc. of the Inst. of Civil Engineers, Municipal Engineer, Vol. 164, Issue ME4, 2011, pp. 229-239.
[15] SNIFFER, "Communicating understanding of contaminated land risks", Project UKLQ13, Final Report, 2010, pp. 3-51.
[16] Eiser JR, et al., "Risk perception and trust in the context of urban brownfields", Environmental Hazards, 7, 2007, pp.150-156.
[17] Oughton D, et al., "An ethical dimension to sustainable restoration and long-term management of contaminated areas", J. of Environmental Radioactivity, Vol. 74, No.1-3, Special Issue, 2004, pp.171-183.
[18] Yasutaka T, Naito W and Nakanishi J, "Cost and effectiveness of decontamination strategies in radiation contaminated areas in Fukushima in regard to external radiation dose", PLOS ONE, Vol. 8, Issue 9, Sept. 2013, pp. 1-11.
[19] Ministry of the Env., "Conservation of Soil Environment", undated, Available at: www.env.go.jp/en/water/wq/wemj/soil.html (accessed 3 Mar. 2015).
[20] Ministry of the Env., "Law Concerning Special Measures against Dioxins", 1999, pp. 1-20.
[21] Ministry of the Env., "The Act on Special Measures concerning the Handling of Environment Pollution by Radioactive Materials" (in Japanese), 2011, pp. 1-59.
[22] Ministry of the Env., "Soil Contamination Countermeasures Act" (in Japanese), 2005, pp. 1-25.
[23] Ministry of Infrastructure and the Env., "Soil Remediation Circular 2009", 2009, pp. 3-78.
[24] Swartjes FA, et al., "State of the art of contaminated site management in The Netherlands: Policy framework and risk assessment tools", Science of The Total Environment, Vol. 427-428, Jun. 2012, pp. 1-10.
[25] Env. Agency, "Dealing with contaminated land in England", 2002, pp. 1-39.
[26] Department for Env., Food and Rural Affairs, "Defra circular 01/2006", Environmental Protection Act 1990: Part 2A, Contaminated land, 2006, pp. 5-190.
[27] Env. Agency, "Dealing with contaminated land in England", 2009, pp. 1-38.
[28] Ministry of the Env., "Countermeasure for Dioxins" (in Japanese), undated, Available at: www.env.go.jp/chemi/dioxin/(accessed 3 March 2015).
[29] Cullingworth B and Nadin V, "Town and Country Planning in the UK", 13th ed., Routledge, 2002, pp. 186-188.
[30] Catney P, et al., "Dealing with Contaminated Land in the UK through 'Development Managerialism' ", J. of Environmental Policy and Planning, Vol. 8, Issue 4, 2006, pp. 331-356.
[31] Rydin Y, "Urban and Environmental Planning in the UK", 2nd ed., Palgrave Macmillan, 2003, pp. 290-291.
[32] Miyagawa T, and Nakayama T, "Study on care for the public in land contamination treatment and redevelopment for contaminated land such as brownfields in the U.K." (in Japanese), Reports of the City Planning Institute of Japan, No. 35, 2000, pp. 253-258.
[33] Ministry of Infrastructure and the Env., "Soil Protection Act", 2013, pp. 1-36.
[34] Evans J, Wood G, and Miller A, "The risk assessment-policy gap: An example from the UK contaminated land regime", Environment International, Vol. 32, No. 8, 2006, pp.1066-1071.

OCEAN DECONTAMINATION: REMOVAL EFFICIEMCY OF RADIOACTIVE CESIUM FROM OCEAN SLUDGE BY USING MICRO BUBBLES AND ACTIVATING MICROORGANISMS

Kyoichi OKAMOTO[1] and Takeshi TOYAMA[1]
[1] CST, Nihon University, JAPAN

ABSTRACT

The Fukushima nuclear accident of March 11, 2011, soil and water had been contaminated by radioactive cesium. Moreover, radioactive cesium was found in the ocean sludge in Tokyo Bay by flowing from rivers. Here, it cannot be easily removed the cesium which is adsorbed to the sludge. On the other hand, one of the authors had developed the decomposition system for ocean sludge with circulation type by micro-bubbles, which decompose and purification sludge by activating the aerobic bacteria, after creating an aerobic state by micro-bubbles. Here, based on the hypothesis that radioactive cesium is adsorbed on the surface of the sludge deposition. It is considered that radioactive cesium can be eluted, after decomposing the deposited sludge by using the decomposition system for ocean sludge with circulation type. If the cesium will be eluted in the water, we can fix the cesium to existing technology such as "Zeolite". In this study, our objects is to check the removal performance of cesium after the decomposition and elution of the sludge and then fix of cesium by setting zeolite in the decomposition system with circulation type by micro-bubbles and activating microorganisms. As the results, we obtained the removal efficiency of cesium was 62.7%.

Keywords: Decontamination, Radioactive Cesium, Ocean Sludge, Micro-bubble, Microorganism, Zeolite

INTRODUCTION

The Fukushima nuclear accident on March 11, 2011, soil and water had been contaminated by radioactive cesium. Moreover, radioactive cesium was found in the ocean sludge in Tokyo Bay by flowing from rivers. A report says it becomes 13 times of the cesium for 7 months from August, 2011 in [1]. Here, it cannot be easy to remove the cesium which is adsorbed to the sludge.

On the other hand, one of the authors had developed the decomposition system for ocean sludge with circulation type by micro-bubbles, which decompose and purification sludge by activating the aerobic bacteria, after creating an aerobic state by micro-bubbles.

Here, based on the hypothesis that radioactive cesium is adsorbed on the surface of the sludge deposition in [2], it is considered that radioactive cesium can be eluted, after decomposing the deposited sludge by using the decomposition system for ocean sludge with circulation type.

If the cesium will be eluted in the water, we can fix the cesium by the existing technology such as "Zeolite".

In our past research in [3], removal performance of cesium was 30.9% by using the decomposition system for ocean sludge with circulation type by micro-bubbles and activating microorganisms. But Measurement of cesium by the iron chromatography was very sensitive so that we had to carry out the several experiments.

In this study, our objects is to check the removal performance of cesium after the decomposition and elution of the sludge and then fix of cesium by setting "Zeolite" in the decomposition system for ocean sludge with circulation type by micro bubbles and activating microorganisms.

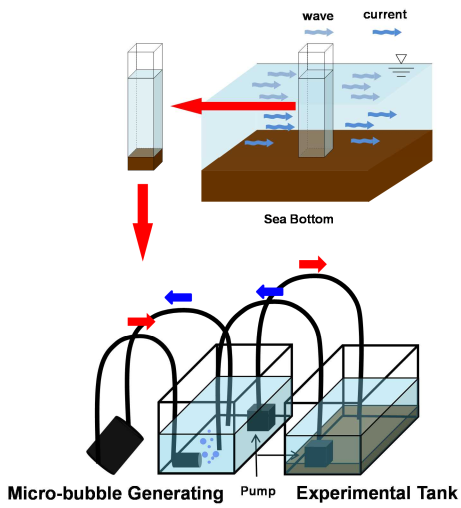

Fig. 1 Purification System of Circulation Type.

DECOMPOSITION SYSTEM WITH CIRCULATION TYPE

It is very important to reduce sedimentary sludge in the ocean. Plans to reduce the sludge are usually dreading or sand covering. Dredging is a simple way and aims to cut off the sludge. But after cutting off, treating the dredged sludge takes much more time and, of course, cost. Sand covering, in general, gives a big load to living organisms and the ecological system.

So that, a more efficient way is needed to reduce the sludge while not imparting environmental load in the local sea area. Here, attention was paid to micro-bubble technology for application to the purification of the sludge. The important point in this technique is to activate the bacteria existing in the area by micro-bubbles. Micro-bubbles (that is MB) can change conditions into an aerobic state. If the bubbling stops, the situation changes into anaerobic state, according to recent research. So, we selected a method for decomposing the sludge by microorganisms.

One of the authors had developed the decomposition system for ocean sludge with circulation type by micro-bubbles, shown in Fig.1, which decompose and purification sludge by activating the aerobic bacteria, after creating an aerobic state by micro-bubbles.

MECHANISM ON FIXING OF CESIUM FROM ELUTION

In general, ocean sludge has a negative charge. When cesium with a positive charge flows from river, sludge was adsorbed cesium, shown in Fig 2. So that, sludge adsorbed cesium cannot eliminate by usual way.

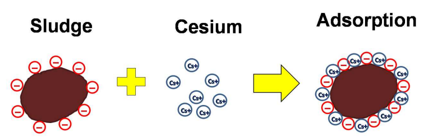

Fig.2 Mechanism on Adsorption of Cesium

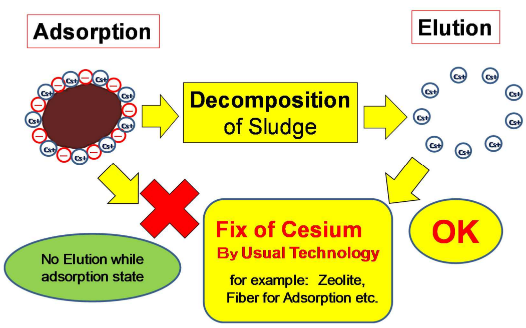

Fig.3 Mechanism on Fixing of Cesium from Elution.

Here, we have a way by using of the decomposition system for ocean sludge with circulation type. After decomposition of the sludge adsorbed cesium by our system, cesium is eluted into water, shown in Fig 3. That is our hypothesis.

ELUTION EXPERIMENTS FOR CESIUM

Procedure of Experiment

The experimental devices consist of two parts, shown in Fig. 4. The water circulates through two tanks. In one tank (Width40xLength28x Hight28cm), micro-bubbles are generated. The micro-bubbles have micro-size diameter and high solubility. This means the water with high concentration of dissolved oxygen circulates through these tanks. The other part is the experimental tank (W60xL29xH35cm). We used sea-water 30(litter) and sludge 1(kg). Here, a micro-bubble generator is based on [4], [5] and the flow rate is 900 (litter/hour). The flow rate of water pumps connected each tanks are 300 (litter/hour).

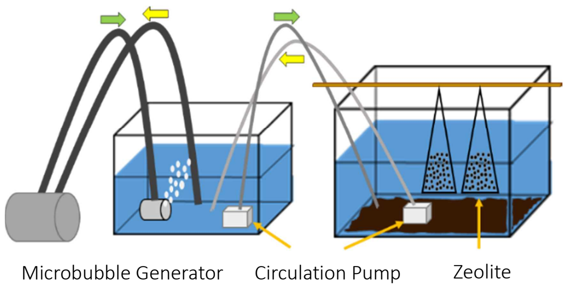

Fig.4 Experimental System for Elution of Cesium.

We had caught the sludge and the sea water at Funabashi Port in Chiba Prefecture in JAPAN, as shown in Fig.4 and 5. Here, we had removed under 10cm of the sludge from seabed before sampling as experimental procedure, because we have to remove the initial value of cesium in the sludge, from [3].

We used the cesium chloride before 24 hours of starting time and the concentration of cesium ion is 100 (ppm). A cooler for water tank was set at side of the tank for generating microbubbles, for the purpose of setting water temperature 30 degree centigrade.

After setting the decomposition system with circulation type by micro-bubbles, experiment starts at the same time of generating micro-bubble device and also the zeolites were set in the tank.

After 6 hour, the microorganism activator was put in the experimental tank. Main staff of the activator is Kelp and including nutrients and some enzyme. Our used activator is reported to show effective results in purification for grease trap.

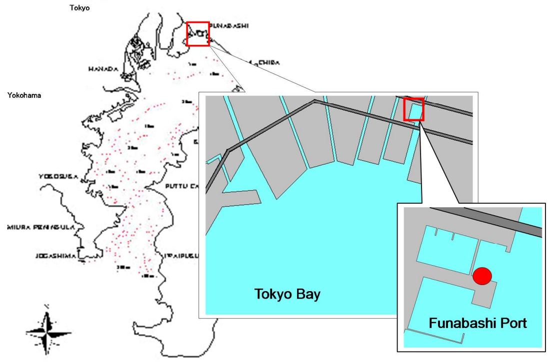

Fig.5 Catching Point of Sludge and Sea Water at Funabashi Port in Tokyo Bay.

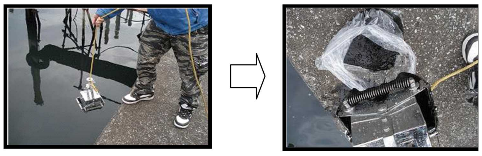

Fig.6 Scene of Catching Sludge.

Dissolved oxygen (DO), water temperature and pH are measured by using of multi-parameter water quality meter. Ammonium nitrogen (NH_4-N), total nitrogen (T-N) and total phosphorus (T-P) are measured by using of digital-water-analyzer by digital "Packtest", by water filtered after sampling in experimental tank.

Experimental Conditions

Basically, zeolite have small and so many halls. As the results, it can fixed the cesium. We used the zeolite by composed type for experiment. Since the diameter of cesium is in general about 0.338(nm), we selected 4A type which has nearly diameter, and also 3A and 5A type of zeolite. And more selected Z13 type which has not uniform diameter, 0.2 to 1.0(nm). From the above, these are experimental conditions, shown in Table.1.

Table 1 Experimental Conditions

	Kinds of Zeolite
Case 1	3A(≒0.3nm)
Case 2	4A(≒0.4nm)
Case 3	5A(≒0.5nm)
Case 4	Z13(≒0.2-1.0nm)

Results and Discussions

Results of water temperature, pH and DO as environmental condition

Fig.7-9 show the water temperature, pH and DO (Dissolved Oxygen) as the results of environmental condition of this experiment.

Water temperature is almost constant about 30 degree centigrade after 6 hours, by setting the cooler for water tank in the experimental system. pH is also constant about 7.5 to 8.7. The difference between Case 1,2 and Case 3,4 is caused by zeolite adsorb some ion when sludge is decomposed. DO in all cases is saturation state after 24 hours.

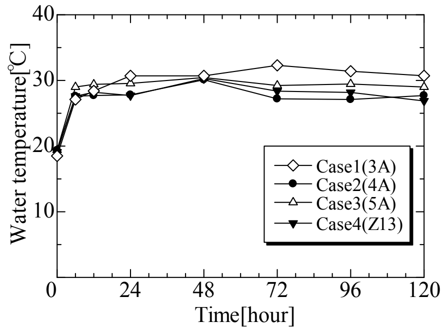

Fig.7 Changes in Water Temperature as Environmental Conditions.

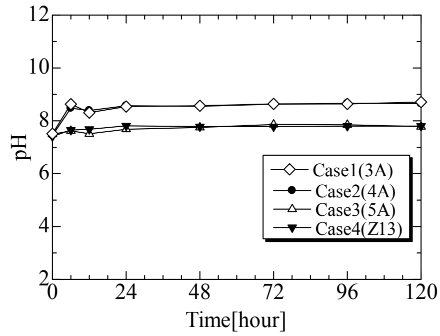

Fig.8 Changes in pH as Environmental Conditions.

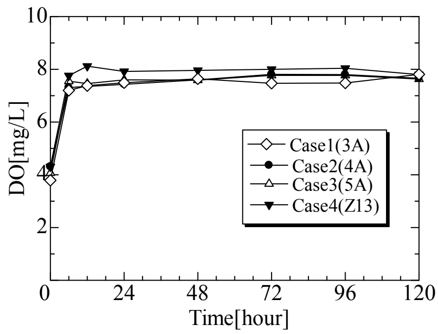

Fig.9 Changes in DO as Environmental Conditions

Results of H_2S, NH_4-N, DIN and T-N

Fig.10-13 are shown in results of H_2S (Hydrogen sulfide), NH_4-N(Ammonium nitrogen), DIN (Total inorganic nitrogen) and T-N(Total nitrogen).

H_2S in all cases decrease rapidly. It seemed by the supply of oxygen, and also another reason is zeolite can adsorb the H_2S. NH_4-N in all cases has tendency of decrease by 12 hours and then decrease slowly. DIN (= NH_4-N+NO_2-N+NO_3-N) shows 60% decrease. It seems it happen to denitrification by microorganisms from [7]. T-N in case 3 at 72 hours only increase. This reason is not clear but including measurement error. But, T-N in all cases decrease over 50% or maximum 75.0% by 120 hours. This purification efficiency is very good.

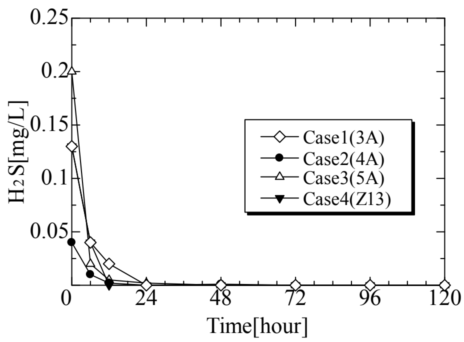

Fig.10 Changes in H_2S.

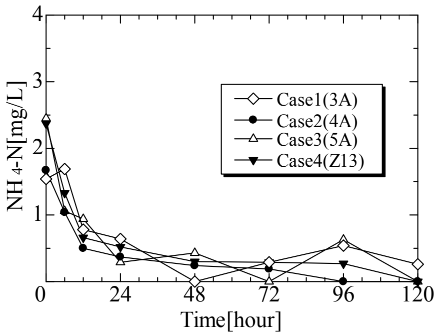

Fig.11 Changes in NH_4-N.

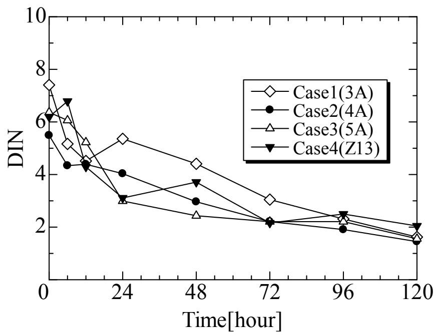

Fig.12 Changes in DIN.

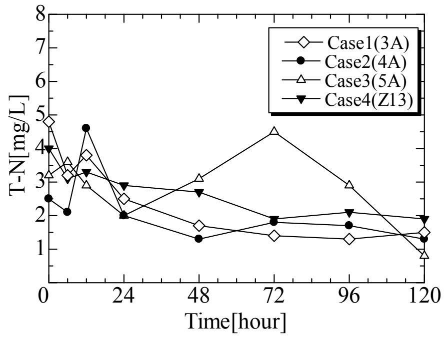

Fig.13 Changes in T-N.

Results of Cesium (liquid)

The results cesium were obtained by the iron chromatography shown in Fig 14.

The result of cesium is zero at 48 hours in case of 3A, and also is zero at 24 hours over in the other cases. It is especially very good the result of cesium in case 4A becomes zero until 12 hours. As the results of the above, fixed values of cesium by zeolite in all cases are 100 %.

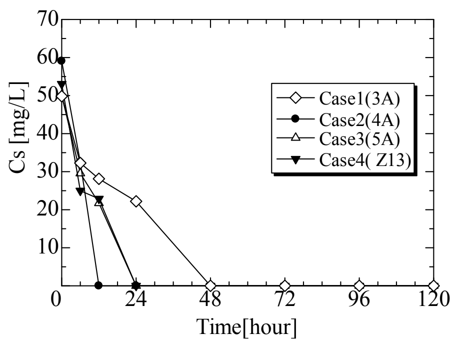

Fig.14 Changes in Cesium in Water.

Results of Cesium (solid)

We paid attention to cesium and silica (Si), as there are many chemical element in sludge. We used the energy dispersion type X-ray analysis device (EDX), because we can measure by the solid state. Weight ratio of cesium and silica (CS/Si) in solid of dry sludge are shown in Fig.15.

Ratio of decontamination of cesium was calculated from ratio of content of beginning and final value measured by EDX, as the standard values including silica in dried sludge after measuring the weight of dried sludge.

Ratio of decontamination is obtained over 50% in all cases. Especially in case of 4A, the efficiency of decontamination is obtained 62.7%.

It seemed this experimental system including zeolite was obtained very good results and the mechanism on fixing of cesium from elution by decomposition of the sludge.

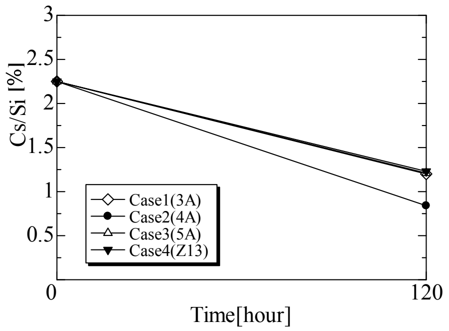

Fig.15 Changes in (Cesium)/(Silica).

CONCLUSION

We had carried out the elution and fixing cesium by setting zeolite, after decomposing the deposited sludge, by using the decomposition system for ocean sludge with circulation type by micro-bubble and activating microorganisms.

From the results by measurements for water qualification,

(1) T-N decreases maximum 75.0% in case of 3A. Purification efficiency is very good.

From the results by iron chromatography,

(2) Fixed values of cesium by zeolite in all cases are 100 % and cesium in case 4A becomes zero until 12 hours.

From the results of the energy dispersion type X-ray analysis device, the weight ratio of cesium and silica (CS/Si) in solid of dry sludge is denoted,

(3) The efficiency of decontamination is obtained over 62.7% in cases of 4A.

ACKNOWLEDGEMENTS

The authors would like to express sincere thanks for executing the experiments to Ayato INAMURA, Takayuki HORIUCHI and Kazuhiro NAKAMURA, Students of Nihon University, and for chemical analysis to Hirosuke HIRANO, Graduate student of Nihon University, in Japan.

This work was supported by KAKENHI (Grant-in-Aid for Scientific Research (C-26420831)).

REFERENCES

[1] Yomiuri News Paper, 13 times by 7 months about cesium in ocean soil in Tokyo Bay, May, 13th, 2012.

[2] Okamoto Kyoichi, Hotta Kenji, Toyama Takeshi and Kohno Hideki, Purification System of Ocean Sludge by Activating Microorganisms, International Journal of GEOMATE (Geotec, Const. Mat. & Env.), Vol.6, No.1, pp.791-795, March, 2014.

[3] Okamoto Kyoichi and Toyama Takaeshi: Ocean Decontamination: Removal of Radioactive Cesium from Ocean Sludge by Using Micro bubbles and Activating Microorganisms, The Japan Society of Naval Architects and Ocean Engineers, May, 2014.

[4] Imai, T, Shioshige, K, Ukita, M, Sekine, M, Higuchi, T, Fukagawa, K and Fujisato, T. Development of Device for Dissolving High Concentration Gas for Purification at bottom layer around enclosed water area like Dam Lake, Proc. 39th Forum on Environmental Engineering of Civil Engineering Society, 10-12, 2002.

[5] Matsuo, K, Maeda, K, Ohnari, H, Tsunami, Y, and Ohnari, H., “Water Purification of a Dam Lake Using Micro Bubble Technology”, Progress in Multiphase Flow Research I, pp.279-286, 2006.

[6] Okamoto Kyoichi and Hotta Kenji, Purification System of Ocean Sludge by Using Coagulants and Activating Microorganisms, International Journal of GEOMATE (Geotec, Const. Mat. & Env.), Vol.4, No.2, pp.574-579, June, 2013.

[7] Sone Takaaki, Yamashita kazuhiro and Okamoto Kyoichi, Identification of Microorganism in Purification Process for Ocean Sludge by using Purification System with Circulation Type, Japan Association for Coastal Zone Studies, July 2014

Fifth International Conference on Geotechnique, Construction Materials and Environment, Osaka, Japan, Nov. 16-18, 2015, ISBN: 978-4-9905958-4-5 C3051

THE CHOICE FACTOR OF THE SLOPE PROTECTION METHOD OF RICE TERRACE

Shoko Nishiwaki[1], Kenji Okaima[1]
[1]Graduate school of Bio resources, Mie University, 1577 Machiyacho, Kurima, Tsu, Mie 514-8507, JAPAN

ABSTRACT

Rice terrace which are one of the farmland using the slant ground has slopes between each terrace field. In slope protection methods of the rice terrace, there are fundamental two types of “earth slope” and “stone wall”. Some research suggested that the type of the slope protection method of rice terrace depended on the presence or absence of unearthed rocks at the time of the paddy field reclamation.

In this paper, we analyzed the type of the slope protection method of rice terrace in the point of one hundred selection of Japanese rice terraces using a subsurface geological map drawn on a scale of 1 to 200000. The geology in each point of one hundred selection of Japanese rice terrace was classified into three main groups as volcanic rock, sedimentary rock and metamorphic rock. Three main groups were further classified by rock types or geological timescale.

We formed clear that rock types or geological timescale of the subsurface geology in the point was related to the choice of the slope protection method of rice terrace. Stone walls were chosen at most points in the area of volcanic rock, sedimentary rock before Mesozoic era and metamorphic rock. Earth slope was chosen at majority points in the area of sedimentary rock in Cenozoic era. In addition, we showed the possibility that the geographical location relation to surrounding geology and the mason culture affected choice of the stone wall.

Keywords: Rice terrace, Slope protection method, Subsurface geological structure, Stone wall

INTRODUCTION

Rice terrace is one of the farmland in the slant ground that has slopes between each terrace field. Slope protection methods of rice terraces are one of the landscapes to create a regional identity. The slope protection methods have fundamental two types of “earth slope” and “stone wall”. [1] Reported that the two types slope protection methods depended on presence or absence of unearthed rocks at the time of the paddy field reclamation. However, the report was not a quantitative results based on the data.

The purpose of this study was to indicate the selective factor of slope protection methods quantitatively using geological data in major rice terrace regions in Japan. The geological data as the presence or absence of unearthed rocks was described on geologic maps. In addition, major rice terrace regions are “one hundred selection of Japanese rice terraces.”

The slope protection methods were investigated by “one hundred selection of Japanese rice terraces” designated by [2]. The rice terrace regions were classified according to geological types. The relationship between the slope protection methods and geological types of rice terrace regions was analyzed. We conducted field investigations to some rice terrace regions to verify the results of these analyses.

EXAMINATION OF THE SLOPE PROTECTION METHOD

The slope protection methods were investigated by data of “one hundred selections of Japanese rice terraces”. [2] designated 134 major rice terrace regions as “one hundred selections of Japanese rice terraces” in 1999. These rice terraces were recommended by local governments. It has been desirable to maintain beautiful landscapes at these rice terraces in future. Figure1 shows the distributed condition of rice terrace. It can be seen that many rice terraces are distributed over West Japan. This distribution applies to the entire rice terraces in Japan. [1] pointing out that the cause of this distribution is caused by the difference in the landform. There are many small alluvial plains in West Japan. On the other hand, there are many large-scale alluvial plains in the East Japan. Data of “one hundred selections of Japanese rice terraces” are consisted of mean gradient of the rice terrace, the area of the region, the number of rice terrace, size of farm per household, kind of water resources, kind of slope protection method, the origin of paddy field reclamations, and harvested quantity.

In this paper, kind of slope protection method of the data was used to analysis. Slope protection methods are classified into “earth slope”, “stone wall”, and combination of “earth slope” and “stone wall”. Figure 2 shows the composition of slope protection methods in “one hundred selections of Japanese rice terraces”. It is clear from Figure 2 that “earth slope”, “stone wall” were almost the same number. From this fact, there was no bias in the selection of the slope protection method.

Stones were used in the slope protection at the rice terraces which have combination of “earth slope” and “stone wall”. Therefore, we regarded that these rice terraces chose “stone wall” in the slope protection.

GEOLOGIC CLASSIFICATION OF RICE TERRACES

The geologic map indicates what type of stone and stratum are distributed under the surface soil. In this paper, we used a one-200,000th Japanese seamless geologic map which National Institute of Advanced Industrial Science and Technology published.

In this geologic map, color legend series is uniform in Japan. And this geologic map is updated based on the latest results of research at any time.

In this paper, the rocks which of the subsurface geological structures on the geological map are classified into three general classes of rock: igneous, sedimentary (sediment) and metamorphic.

・*Igneous rock*

Igneous rock is formed through the cooling and solidification of magma or lava. Igneous rock may form with or without crystallization, either below the surface as intrusive (plutonic) rocks or on the surface as extrusive (volcanic) rocks. The volcanic rock includes andesite, basalt, rhyolite, and so on. Plutonic rock includes granite, gabbro, serpentine, and so on. These rocks are used as stone wall and construction materials. However, there is difference in the importance of the construction.

In the fresh igneous rock, change of physical properties is little over time. However, igneous rocks change to gravel or sand by weathering.

・*Sedimentary rock*

Sedimentary rock is formed of compressed sediment by time progress. The sediment consists of mud, sand, organic remains and volcanic ashes. Sedimentary rock’s strength is further increased by cementation and consolidation. Therefore, sedimentary rock is become harder and denser with the passage of time. Table 1 shows the relationship about geological epoch and sedimentary rock’s strength. [3] reported that semimetal rock (or sediment) deposited in the Cenozoic of Holocene and Pleistocene has not yet been consolidated.

Fig. 1 The distributed condition of “one hundred selection of Japanese rice terraces”

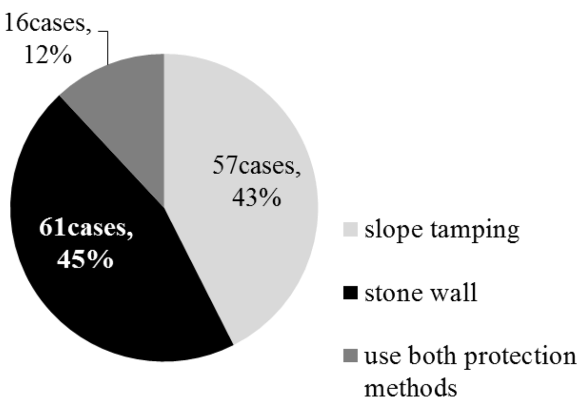

Fig. 2 The composition of slope protection methods in “one hundred selections of Japanese rice terraces”

The sedimentary rock (or sediment) which deposited in Pliocene epoch and Miocene does some compaction and is called “soft rock”. The sedimentary rock (or sediment) which deposited before the Mesozoic era does compaction strongly and called “hard rock”. In this paper, we hypothesize that the rice terraces whom there were in the subsurface geological structures deposited before Pliocene epoch making ends meet as a rock have chosen “stone wall” in a slope protection method. Therefore, we hypothesize that “earth slopes” were chosen in a slope protection method in rice terraces that have the geological feature that had deposited after Pleistocene which had not yet become hard rock.

・*Metamorphic rock*

Metamorphic rock was formed recrystallizes material in the sedimentary rock and igneous rock.

The formation of the metamorphic rock has a thing by contact metamorphism and a thing by regional metamorphism. Contact metamorphism is the name given to the changes that take place when magma is injected into the surrounding solid rock (Contact metamorphic rock). Regional metamorphism is the name given to changes in great masses of rock over a wide area. Rocks metamorphosed simply by being at great depths below the Earth's surface, subjected to high temperatures and the pressure caused by the immense weight of the rock layers above (Regional metamorphic rock).

In this paper the classification, only regional metamorphic rock had existence among metamorphic rocks. Furthermore, only schist was seen among wide area metamorphic rocks.

Regional metamorphic rocks have not been applied to important constructions for stone wall. For that reason many of these rocks split readily in one direction along mica-bearing zones (schists). But they are used for stone wall use and flat stones in private houses and farmlands. Therefore in this paper, regional metamorphic rock was regarded as rock suitable for stone wall. Furthermore, schist was only confirmed in metamorphic rocks of “one hundred selections of Japanese rice terraces”.

Fig.3 shows a ratio of igneous rock, sedimentary rock (sediment) and metamorphic rock in the subsurface geological structures of “one hundred selection of Japanese rice terraces”. In Figure 3, 64% (86/134 cases) of the “one hundred selection of Japanese rice terraces” of the rice terraces was present in the subsurface geological structures on sedimentary rocks. [4] says that, rice terraces were reclamation in landslide topography. The subsurface geological structures that a landslide happened are classified as a sedimentary rock of Cenozoic era. Therefore, it was thought that there was much existing rice terrace on the subsurface geological structures of the sedimentary rock.

RELATIONS OF THE SLOPE PROTECTION METHODS AND THE SUBSURFACE GEOLOGICAL STRUCTURES

The results of organized data about the subsurface geological structures in the cases of igneous rocks are indicated in Figure 4.

As the Figure 4 indicates the subsurface geological structures in the cases of igneous rock, tend to choose a stone wall (98% 41/42 cases). The igneous rocks are used as stone wall and construction materials. For that reason, the results of Figure 4 are proper. For example the rice terrace that chosen the “earth slope” despite the subsurface geological structure is granite, we will discuss in the next chapter.

Table.1 Relations of the geological epoch and the hardness of sedimental rock

A geological epoch			sedimentary rocks(sediment)
the Cenozoic era	the Quaternary period 1.7 million years ago	Holocene	Unconsolidated sediment
		Pleistocene	
	the Neogene period 24 million years ago	Pliocene epoch	Soft rock
		Miocene	
	The Paleogene period 65 million years ago		
the Mesozoic era	Cretaceous Jurassic Triassic 250 million years ago		Hard rock
the Palaeozoic era	Permian period		

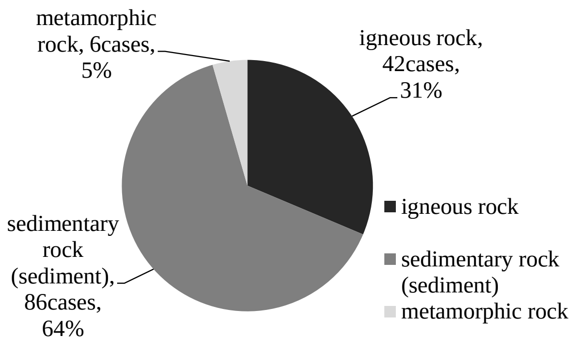

Fig. 3 the ratio of the subsurface geological structures of “one hundred selection of Japanese rice terraces”

Similarly, the results of organized data about the subsurface geological structures in the cases of sedimentary rock are indicated in Figure 5.

Figure 5 indicates that most of the rice terraces to select “earth slope” were present in Cenozoic the subsurface geological structures. The sedimentary rock formed before the Mesozoic becomes the hard rock. Most of rice terraces whom there were in area that subsurface geological structure is “hard rock” chose a “stone wall” in a slope protection method of construction.

Furthermore, the subsurface geological structures of most of the rice terraces that have selected the “earth slope”(98% 55/56 cases) were Cenozoic sedimentary rocks (sediments). The probability is that the Cenozoic sedimentary rocks (sediments) are too soft to use as the material of stone wall. Therefore, the rice terraces in the Cenozoic sedimentary rocks (sediments) area chose “earth slope”.

The results of organized data about the subsurface geological structures in the cases of metamorphic rock are presented in Figure 6.

Figure 6 indicates that most of the regions of the metamorphic rock in the subsurface geological structures have selected the stone wall. Metamorphic rocks are used for not only “stone wall” of slope protection method of rice terraces but stone-wall of private house.

CONSIDERATION OF EXCEPTION REGION

In Figures 4-8, we formed four kinds of rice terrace the exception area.

・*Choose “earth slope” and the subsurface geological structures is granite*

“Yamabuki Rice terrace” in Iwate Prefecture has been classified this case. Granite is distributed widely around “Yamabuki rice terrace”. However, “Yamabuki rice terrace” have selected the earth slope for the slope protection method. [5] reported that, this area can’t produce rocks because granite weathers deeply in this area. That is to said, there was no stone that can be building materials for “stone wall” in this region. It was considered that “Yamabuki Rice terrace” was not able to choose the “stone wall”.

・*Choose a stone wall with Cenozoic sedimentary rock (23 cases)*

Rice terraces that were selected the "stone wall" to the slope protection method in spite of the subsurface geological structures of Cenozoic sedimentary rock are classified two cases.

The first case was that the subsurface geological structures were consolidated to the extent available in “stone wall” material. (8/23 cases)

The other case was that stone that can be used as a stone wall material (hard sedimentary rock, igneous rock, or metamorphic rock) at the position of higher altitudes than the rice terrace. (15/23 cases) Cobbles or boulders of higher altitudes are used as farmland stone wall material has been reported by [6]. For field survey of the rice terrace that applies to this case will be introduced in a later chapter.

・*Choose “earth slope” with metamorphic rock (3 cases)*

Rice terraces classified in this case were existed in the area that was difficult to produce stone wall materials. [7] reported that metamorphic rocks of these areas are easy to peel. For this reason, metamorphic rocks of these areas cannot be used to “stone wall” material.

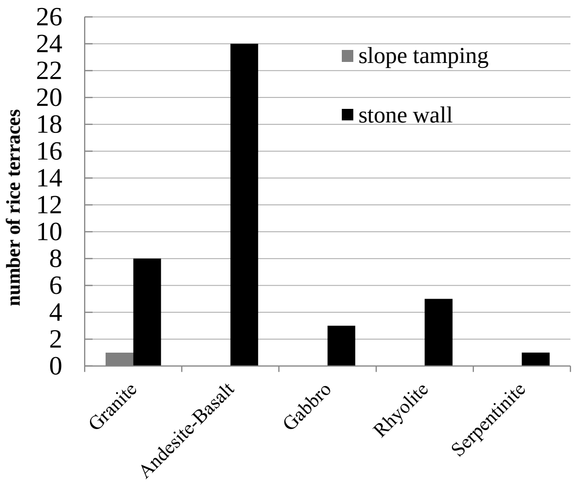

Fig. 4 The subsurface geological structures of rice terrace in the cases of igneous rock

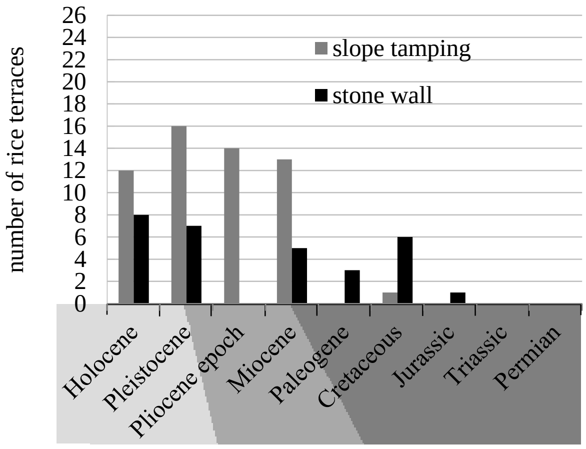

Fig. 5 The subsurface geological structures of rice terrace in the cases of sedimentary rocks

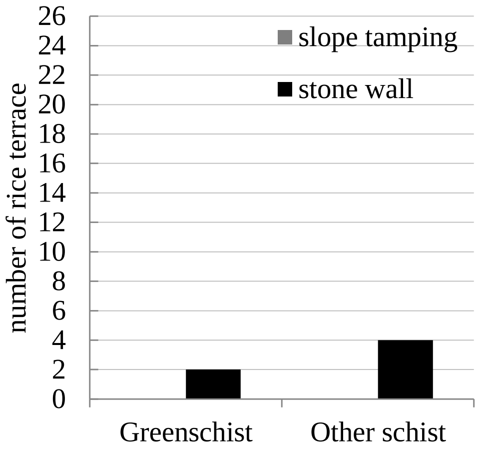

Fig. 6 The subsurface geological structures of rice terrace in the cases of metamorphic rocks

・*Choose "earth slope" with Mesozoic sedimentary rock. (2 cases)*

Sedimentary rocks that formed in the Mesozoic are "hard rock". Therefore, we considered that the rice terraces exist in such surface geological structures have chosen "stone wall" to the slope protection method. Against all expectations, these rice terraces chose "earth protection" to the slope protection method. According to the investigation with the telephone to the management group, one case of the fourth exception area use not only "earth slope" but also "stone wall". This result was in close agreement with our consideration previously described. Field investigation is necessary to the other case of rice terrace.

VERIFICATION BY FIELD INVESTIGATION

Based on the above-mentioned consideration, we did some field investigations. As an example of the field investigation, we show "Maruyama rice terrace." The field investigation was conducted on April 1, 2014. The field investigation aims were two. First, the data of slope protection method of "Maruyama rice terrace" registered in data of "one hundred selection of Japanese rice terraces" was whether correct.

The second was to know the kind of the stones that were used to "stone wall" material.
Maruyama rice terrace" is in the Mie Prefecture, and has consisted of "stone wall" to slope protection methods.

By way of example, the subsurface geological structures of "Maruyama rice terrace" and that neighboring area are given in Figure 7. Location of the survey point of Figure 8 and location of the slope failures point of Figure 11 are given triangle and circle symbols in Figure 7. According to Figure 7, the subsurface geological structure of "Maruyama rice terrace" was the soft sedimentary rock of the Miocene.

However, the data of "one hundred selection of Japanese rice terraces" registered as "stone wall". In other words "Maruyama rice terrace" was classified to the case of ・Choose a stone wall with Cenozoic sedimentary rock (32 cases).
In fact, the subsurface geological structure of higher altitudes mountain adjacent to the "Maruyama rice terrace" was the rhyolite. Rhyolite is a kind of igneous rock, and that is a rock which may be used as a building stone.

According to the field investigation, stone wall had been selected certainly in "Maruyama rice terrace" to slope protection method.

Therefore, the rhyolite that produced at a higher altitude was used in stone wall material. This fact conforms to our consideration.

Rhyolite had been used as material of the stone wall in the "Maruyama rice terrace".

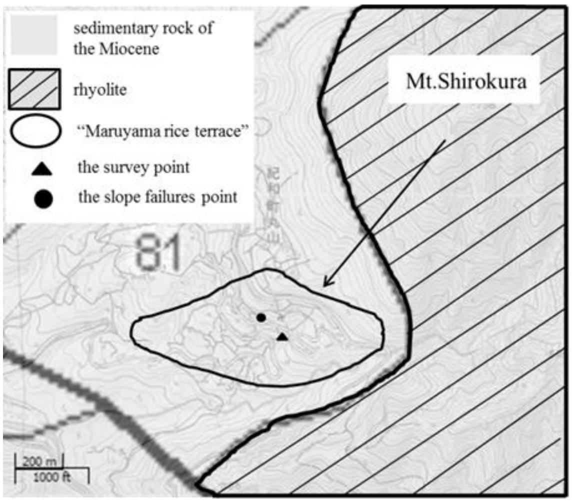

Fig. 7 The subsurface geological structures of "Maruyama rice terrace" and that neighboring area

Fig. 8 The subsurface geological structures of rice terrace in the cases of sedimentary rocks

Fig. 9 Slope failures point appearance in the "Maruyama rice terraces"

Figure 8 shows the stone wall of "Maruyama rice terraces." From Figure 8, the stone wall was formed of a uniform rock. These rocks are rhyolite that had become the stone wall. Figure 11 shows the appearance of the slope failure in the "Maruyama rice terrace". According to Figure 11, the subsoil layer in "Maruyama rice terrace" has many boulder stones of rhyolite. It is probable that the boulder stones of rhyolite were fell from the adjacent mountain, and were used as material for stone wall in "Maruyama rice terrace". The field investigation supports the consideration of "*choose a stone wall with Cenozoic sedimentary rock*".

CONCLUSION

The purpose of this paper is to clear the relationship of the subsurface geological structures and the choice factor of the slope protection method of rice terrace.

As a result, 96% (54areas/56 areas) of regions of selected "earth slope" existed in the area of the subsurface geological structures in the cases of sedimentary rocks of the Cenozoic.

In addition, the subsurface geological structures whether igneous rock, or hard sedimentary rock that formed previously Mesozoic, or metamorphic rock, "stone wall" had been chosen to slope protection method in 96% (54areas/56 areas) of the rice terraces.

However, in the following cases on the subsurface geological structures had weather or metamorphic, it was not a "stone wall", even if the subsurface geological structures of the area with rice terraces were igneous rock or hard sedimentary rock that was completed in Mesozoic previous or metamorphic rock.

In case of the subsurface geological structures enough to use as building materials or rock exists around, tend to select "stone wall".

To further verify the results, future work should perform more field investigation of various rice terrace area.

We can safely say that there were close relation at the choice factor of the slope protection method of rice terraces and the subsurface geological structures.

REFERENCES

[1] Nakashima M, "Distribution and Characteristic of Rice Terraces", J. of, JSIDRE, Vol. 70 (3), Mar. 2002, pp.195-198

[2] Ministry of Agriculture, Forestry and Fisheries, "one hundred selection of Japanese rice terraces"1999

[3] Arai T, "Origins of Japan's geotechnical", The geology to learn in case, 2005, The Japanese Geotechnical Society

[4] Shida M, "What is the rice terraces", Rice terrace Introduction, 2014, pp.3-14

[5] **I** Mekata Y, Sasaki N, Land classification basic research of Kamikitayama development area Rikutyuohhara 1/50000, 1973, pp.18-22, pp.23-27

[6] Nishiwaki S, "Tendency of distribution of stone in the farmland stone wall when limestone is used as an index", presented at JSIDRE, 2014, 522-523

[7] Inazumi H, Hidaka M, Momoi H, Moriyama Y, " II The subsurface geological structures", Land classification basic research of Kusumi:Iida Wide-area agricultural development area Beppu 1/50000, 1972, pp14-24

Fifth International Conference on Geotechnique, Construction Materials and Environment, Osaka, Japan, Nov. 16-18, 2015, ISBN: 978-4-9905958-4-5 C3051

OXYGEN AND HYDROGEN ISOTOPE STUDY FOR PRECIPITATION SAMPLED AT OSAKA AND MATSUE IN JAPAN

Tetsuya Fukano[1], Hiroyuki Ii[2]
[1]Graduate School of Systems Engineering, Wakayama University, Japan
[2]Faculty of Systems Engineering, Wakayama University, Japan

ABSTRACT

Oxygen and hydrogen isotopic ratios in precipitations at Matsue and Osaka are high around March. Isotopic ratio in each precipitation was clarified to depend on altitude at the dew point calculated from meteorological data. When the calculated altitude at the dew point is high, isotopic ratio of the precipitations is high. Rain particle evaporates from the altitude at a dew point during falling because air was saturated with water above the altitude at the dew point and then isotopic ratio changes with evaporation. Then, altitude at the dew point was important to determine the isotopic ratio of precipitation.

Keywords: Isotope ratio, Precipitation, Altitude at a dew point

INTRODUCTION

To study about oxygen and hydrogen isotope ratio of rain is important for the discussion about global environment. It is known isotopic ratios of precipitation change with temperature, amount of precipitation, sea level, distance from sea, and latitude. [1]

But it is not reported comparing isotopic ratios of precipitation at the Japan Sea side and inland of the Japan Island for long term.

From March 2012 to June 2013, we measured oxygen and hydrogen isotopic ratios at Matsue and south aria of Osaka to study about the characteristic difference, and found it was important to think about the altitude at a dew point.

A METHOD OF MEASUREMENT

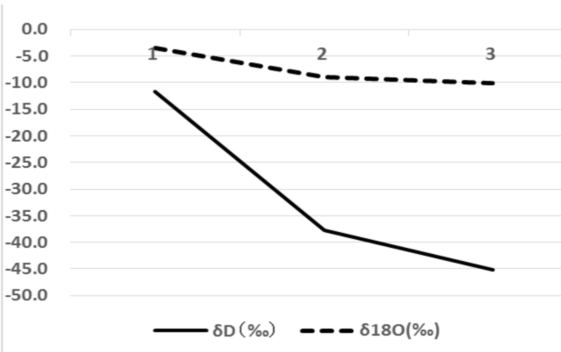

Fig. 1 Change of isotopic ratios
Isotopic ratios gradually change.
1, 2, 3 are sampled in a session, each 50ml.
Almost precipitations show the same result.

$$\delta^{18}O = (R\,sample / R\,std - 1) \times 1000 \ [‰]$$
$* \ R\,std = {}^{18}O/{}^{16}O$ of SMOW
$$\delta D = (R\,sample / R\,std - 1) \times 1000 \ [‰]$$
$* \ R\,std = D/{}^{1}H$ of SMOW

Fig.1 shows isotopic ratios gradually change.

We sampled only first 9 mm of precipitation for each event. Diameter of sampler's funnel is 18cm. So sampler can get about 50 ml of precipitation.

Photo: Rain fall sampler

After the equilibrium method, the oxygen and hydrogen isotopic ratios of the sampled water were measured with mass spectrometer (Sercon). The measurement error of isotope ratio is ± 0.100 [‰].

SEASONAL CHANGE

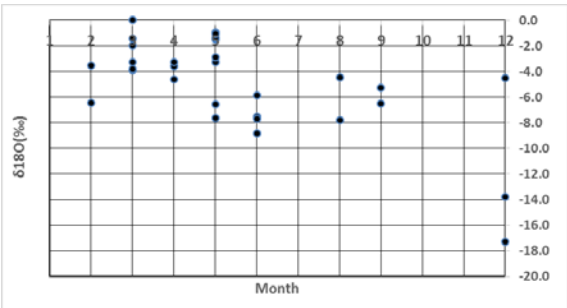

Fig. 2 Seasonal change of $\delta^{18}O$ at Osaka

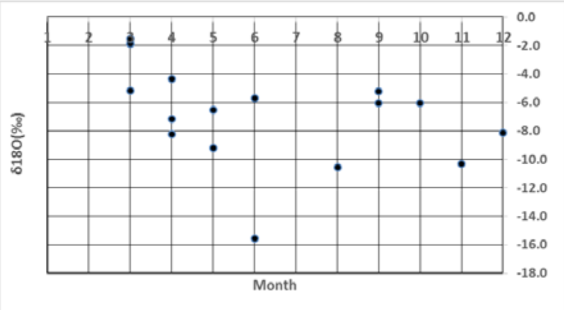

Fig. 3 Seasonal change of δ18O at Matsue

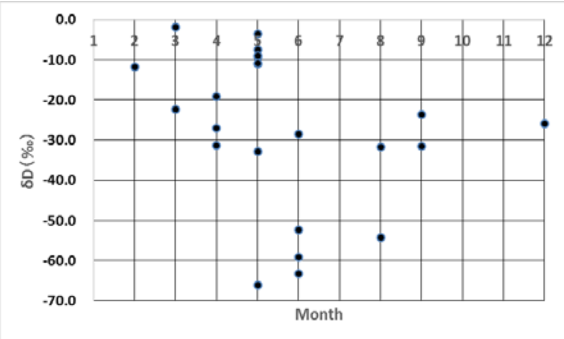

Fig. 4 Seasonal change of δD at Osaka

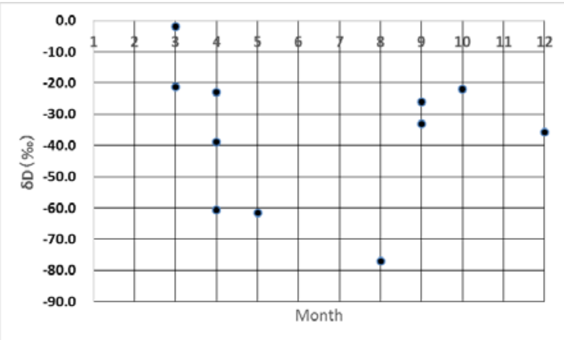

Fig. 5 Seasonal change of δD at Matsue

Fig.2-5 show both oxygen and hydrogen isotopic ratios at Matsue and Osaka are high around March.

And rough appearance on both oxygen and hydrogen isotope ratios at Matsue and Osaka are low in summer and high in winter.

Isotopic ratios of precipitations were usually low in summer and high in winter [2].

To study about these results, we checked altitude at the dew points. In this case, "Altitude at the dew point" means the lowest altitude reached to 80-90% of humidity.

Upper air observation is announced by the Meteorological Agency. We refer to the upper air datas of Shionomisaki and Matsue at 9:00 [3].

Shionomisaki, the most south aria of Wakayama, is the nearest to Osaka of the announced points.

ISOTOPE VALUES DEPEND ON ALTITUDE AT DEW POINT

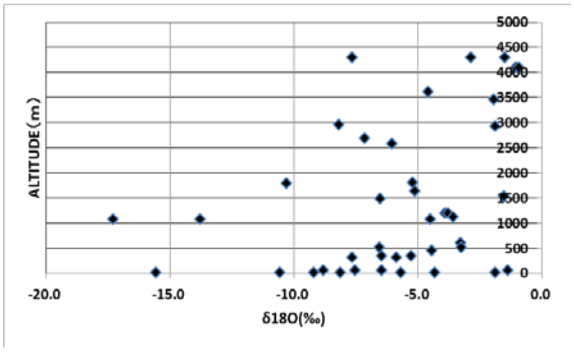

Fig. 6 Altitude at dew point and δ18O

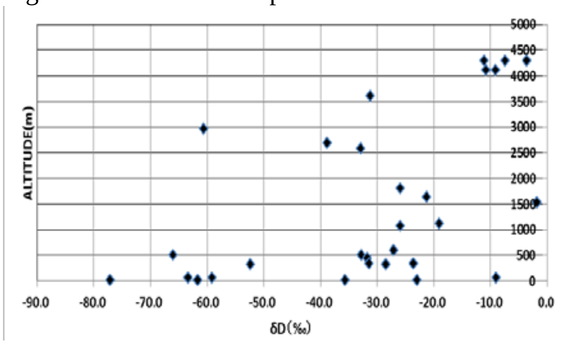

Fig. 7 Altitudes at dew points and δD

From Fig.6-7, when the altitude at the dew points are high, isotope ratios are high.

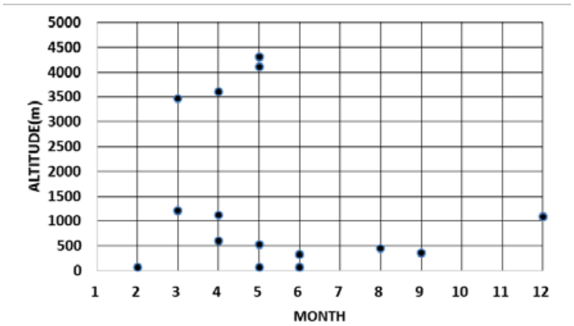

Fig. 8 Seasonal change of Altitude at a dew point at Osaka

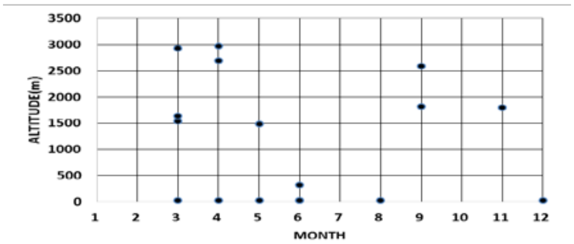

Fig. 9 Seasonal change of Altitude at a dew point at Matsue

Fig.8-9 show altitude at the dew points are high around March at Matsue and Osaka.

CONCLUSION

Oxygen and hydrogen isotopic ratios at Matsue and Osaka showed high values around March.

And rough appearance on both oxygen and hydrogen isotope ratios at Matsue and Osaka are low in summer and high in winter.

To study about these results, we checked altitudes at the dew points. And we found isotope values at each precipitations depend on altitude at each dew point.

When the altitude at the dew point is high, isotope value is high.

As rain water starts to evaporate from the altitude at a dew point and light isotope, ^{16}O and ^{1}H, starts to evaporate selectively. This is why fall distance of rain from the altitude at a dew point is thought to increase with isotope values.

Around March, the season of “Kosa”, altitudes at dew points are high. It is well known yellow sand from China often blows to Japan in the spring by the upper stream.

REFERENCES

[1] Isao MACHIDA, Akihiko KONDOH ”Stable Isotope Ratios of National Water in Japan-The Analysis by Using Environmental Isotope Database” J. Japan Soc. Hydrol. & Water Resour. Vol.16. No.5. (2003). pp. 556-569.

[2] Hiroyuki Ii, Tatemasa HIRATA, Naomi SAHARA, Kunihiko Fukushi “Chemical Composition, Hydrogen and Oxygen Isotopic ratios of Precipitation in Wakayama and Osaka Prefectures” Annual Journal of Hydraulic Engineering. Vol.45. (2001). pp.289-294.

[3] Hitoshi SAKAI, Yukihiko MATSUHISA “Stable Isotope Geochemistry” University of Tokyo Press. (1996). ISBN4-13—60713-8. PP.93-100.

[4] www.data.jma.go.jp/obd/stats/etrn/upper/index.php

Fifth International Conference on Geotechnique, Construction Materials and Environment, Osaka, Japan, Nov. 16-18, 2015, ISBN: 978-4-9905958-4-5 C3051

IMPORTANCE OF ROOM VENTILATION FOR MAINTAINING HEALTHY CO2 CONCENTRATIONS

Hiroyuki Ii[1], Kazuki Taguchi[2], and Masahiro Yamashita[3]
[1]Faculty of Systems Engineering, Wakayama University, Japan; [2]Wakayama Prefecture, Japan; [3]Graduate School of Systems Engineering, Wakayama University, Japan

ABSTRACT

Using a portable CO_2 sensor, the CO_2 concentration in a classroom at Wakayama University was measured and "natural ventilation", the open door or window effect was evaluated based upon the number of persons, room size, door or window condition and CO_2 concentration. Under a closed door and window condition, CO_2 production per person per hour in the room due to respiration was 0.01 to 0.02 for a private house under relaxed conditions and 0.005 to 0.015 m^3/hour/person for a classroom during a lecture. Maximum CO_2 concentration reached 1,300 ppm after 100 minutes in the private house and over 4,000 ppm in the classroom after 90 minutes. The amount of CO_2 gas exchanged outside through doors or windows was in agreement with the amount of CO_2 gas produced by respiration in the room with open doors or windows whose sizes were 1.6 to 8 m^2 or whose total room size per open door or window size was 32 to 180.

Keywords: Carbon dioxide concentration, classroom, ventilation, respiration

INTRODUCTION

CO_2 concentrations in classrooms using air conditioners are based on the Japanese School Environmental Standard. The Ministry of Education, Culture, Sport, Science and Technology propose that the CO_2 concentration in classrooms be less than 1,000ppm [1]. Classrooms are likely to have a high number of person present and regularly ventilating classrooms is not commonly done at Universities. In addition, buildings in recent years often have high air tightness because of improvements in building technologies [2].

Recently, reducing the use of air conditioners has been practiced to save electricity. However ventilation fans work in conjunction with air conditioners in recently constructed buildings. In most classrooms at Wakayama University, a ventilation fan does not work separately with an air conditioner. In particular, air conditioners are not used during spring and autumn time because of moderate temperatures, thus CO_2 concentration was thought to be high. The purpose of this study was to evaluate the "natural ventilation" effect of opening a door or window.

METHOD AND CONDITION

CO_2 gas measurement in the air was performed in the room at a private house in August and October 2014, and in a classroom at the faculty of Systems Engineering at Wakayama University from December 2013 to January 2015. The room size of the private house was 23.5 m^2 with 6 tatami mats. The size of the classrooms were 1,297 m^2 for A101, 430 m^2 for A103, 413m^2 for A104, 522 m^2 for A202, 416 m^2 for A203, 286 m^2 for A204, 551 m^2 for B101, and 260 m^2 for B202 as shown in Table 1. For all classrooms both air conditioners and ventilation worked together. The size of the door and window in the classroom were 1.9 m^2 and 1.5 m^2.

Table 1 Room size of house and classroom

Room name	Size m^3
Private house	23.5
A101 classroom	1,297
A103 classroom	430
A104 classroom	413
A202 classroom	522
A203 classroom	416
A204 classroom	286
B101 classroom	551
B202 classroom	260
B203 classroom	260

A portable sensor, GCH-2018, was used for measuring CO_2 concentrations in the air as shown in Fig1. The measuring place was in the center of the room for the private house and at the back side at 80 cm in height of the each classroom.

Fig. 1 Portable sensor

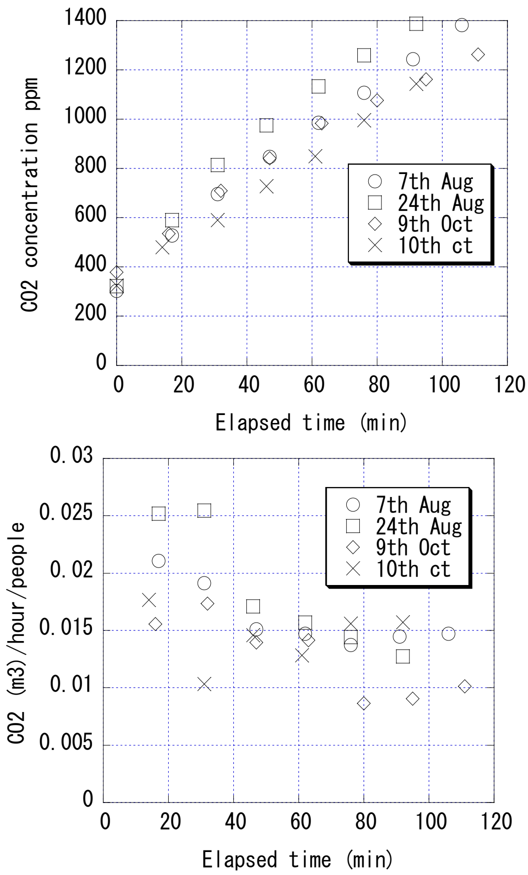

Fig.2 CO_2 concentration in room and production of private house.

RESULTS

House Room per Person with No Ventilation

Fig.2 shows CO_2 concentrations in the room under quiet conditions after the windows and door were closed. CO_2 concentrations in the air increased from 300 to 1,300 ppm at 100 minutes each time. The results showed that CO_2 concentration in the air under a no ventilation condition reached over 1,000 ppm and ventilation was necessary for normal life.

From the results, CO_2 production per hour per person by respiration was calculated in the house room as shown in Fig.3. The CO_2 production per hour per person decreased 0.02 to 0.01 m^3/hour/person with time. The calculated values with 56 kg weight and 175cm in height were average values per hour per person under normal conditions [2]. The decrease with time was thought to depend on the respiration activity of humans. High CO_2 production per hour per person from the start of measurements till the 40 minute mark was thought to be due to the still high respiration activity for preparation of experiment.

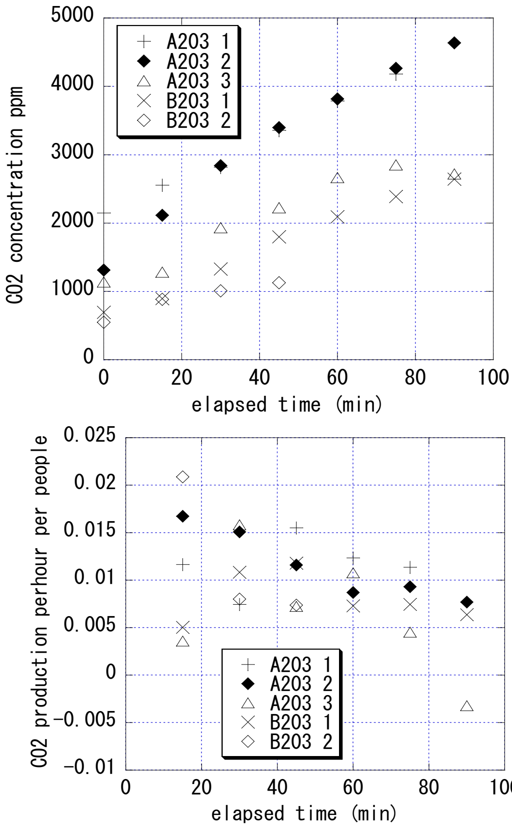

Fig. 3 CO_2 production per hour per person in classroom (A203, B203) with no ventilation and closed doors and windows from autumn 2013 to spring 2014.

Classroom on University with No Ventilation

Fig. 3 shows that CO_2 concentration and CO_2 production in the classroom during a lecture with no ventilation after the windows and doors were closed from 2013 to June 2014 for the A203 and B203 classrooms. The CO_2 concentrations increased with time and were over 2,000 ppm after one lecture time of 90 minutes. Maximum values reached over 4,000 ppm with 80 persons and a 416 m^3 volume. CO_2 production values in the classroom decreased with time as well as the private room and they were lower than those in the private room.

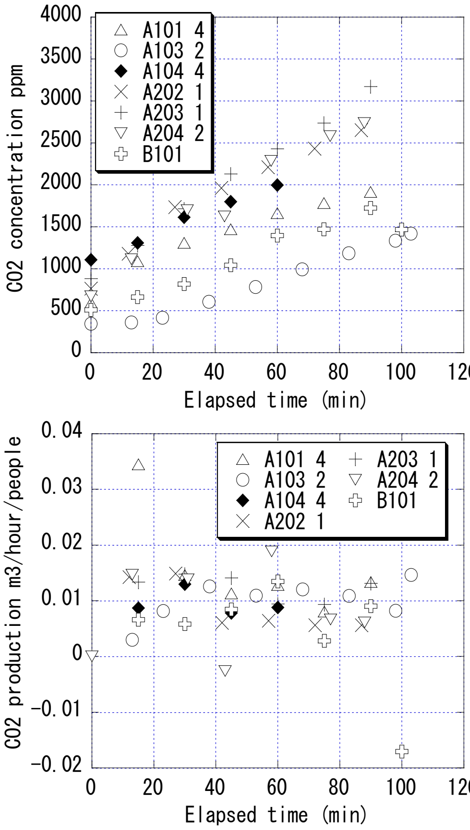

Fig. 4 CO_2 concentration and CO_2 production per hour per person in classroom (A101, A103, A104, A202, A203, A204, B101) with no ventilation and closed doors and windows from spring 2014 to autumn 2014.

Fig.4 shows CO_2 concentration and CO_2 production per hour per person in classroom (A101, A103, A104, A202, A203, A204, B101) with no ventilation and closed doors and windows from spring 2014 to autumn 2014. CO_2 concentrations increased with time and were over 1500 ppm after one lecture time of 90 minutes. Maximum values reached over 3,500 ppm with 110 persons and a 522 m^3 volume. Therefore, the CO_2 concentration of the classroom with no ventilation reached over 1,000 ppm which was the recommended maximum value. During spring and autumn seasons, air conditioners are not employed because temperatures in the classroom are moderate. Therefore, the ventilation fan did not work because it was on the same switch of the air conditioner. As a result, in spring and autumn high CO_2 conditions were sometimes observed.

CO_2 production values in the classroom were uniform with time but not as uniform as the private house room and were 0.005 to 0.015 m^3/hour/person, lower than those in the private room. Both CO_2 production values were lower than those in the private room. One possibility was because of exchanging air when some students entered into the room through the door.

University Classroom with One Open Door

Fig.5 shows CO_2 concentration and CO_2 production per hour per person in classroom (A203, B203) with an air conditioner and one open door from autumn 2013 to spring 2014. CO_2 concentrations increased with time and were over 1,000 to 3,000 ppm after one lecture time of 90 minutes. Maximum values reached over 3,000 ppm with 76 persons and a 416 m^3 volume. CO_2 concentration depended on room size and number of people however the CO_2 production per hour per person in classroom was calculating from person number and room size and it was directly evaluated each time.

CO_2 production values in the classroom under one open door decreased with time as well as the private room and they were lower than those values in the classroom under the condition of no open doors nor windows. Even though some CO_2 production values were less than 0 after 60 minutes, CO_2 concentration in the classroom exceeded 1000 ppm after 90 minutes. Therefore, one open door ventilation was not enough to reduce CO_2 concentration.

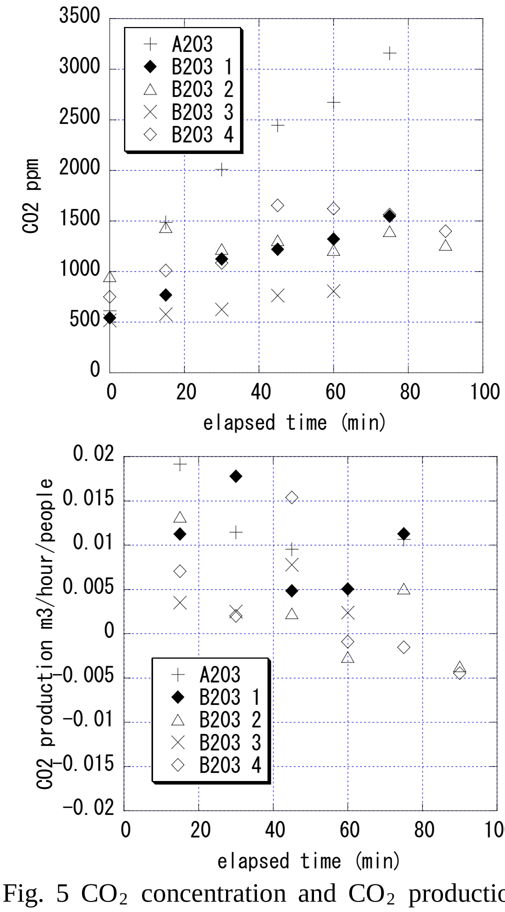

Fig. 5 CO_2 concentration and CO_2 production per hour per person in classroom (A203, B203) with no air conditioner and one open door from autumn 2013 to spring 2014.

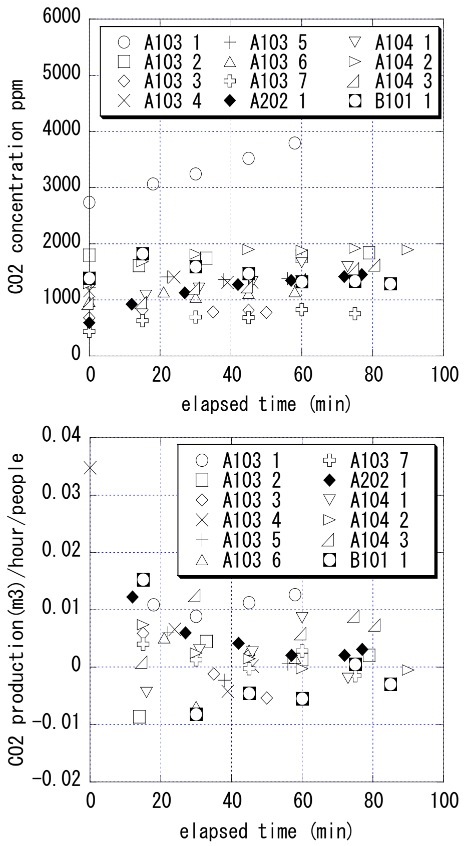

Fig. 6 CO_2 concentration and CO_2 production per hour per person in the classroom (A103, A202, A104, B101) with no air conditioner and one open door from spring 2014 to autumn 2014.

Fig.6 shows CO_2 concentration and CO_2 production per hour per person in classroom (A103, A202, A104, B101) with air conditioner and one opened door from spring 2014 to autumn 2014. The CO_2 concentrations increased with time and increases were over 1,000 ppm after one lecture time of 90 minutes. Maximum values exceeded 4000 ppm with 43 persons and 430 m^3 volume. Therefore, CO_2 concentration in a classroom with one open door for ventilation exceeded 1,000 ppm which was the recommended maximum value.

CO_2 production values under one open door varied from –0.01 to 0.015 m^3/hour/person. The difference of CO_2 production values between one door being open and no door being open was small therefore one door being open had little effect in reducing CO_2 concentration.

University Classroom with One Open Door and one Open Window

Fig.7 shows CO_2 production per hour per person in classroom (B101, B203, A202, A204) with no air conditioner and one open door and one open window. The CO_2 production values were variable with half of values were minus values showing a

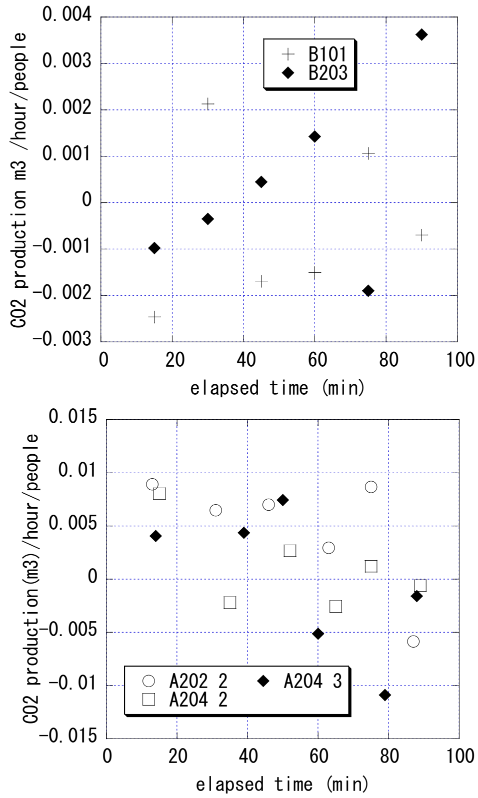

Fig. 7 CO_2 production per hour per person in classroom (B101, B203, A202, A204) with no air conditioner and one open door and one open window.

CO_2 concentration decrease and plus showing a CO_2 concentration increase. Therefore, open one door and one window was not enough to provide ventilation for reducing CO_2 concentration in the classroom.

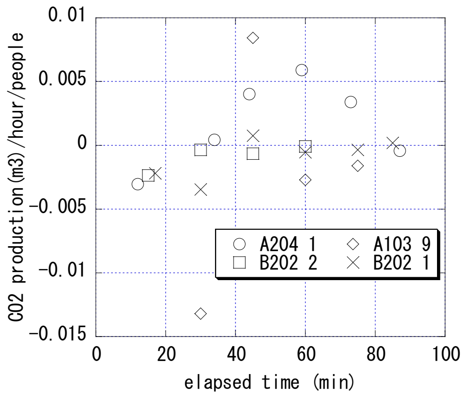

Fig. 8 CO_2 production per hour per person in classroom (A103, A204, B202) with no air conditioner and one open door and two open windows.

University Classroom with One Open Door and Two Open Windows

Fig. 8 shows CO_2 production per hour per person in classroom (A103, A204, B202) with no air conditioner and one open door and two open windows. CO_2 production values varied with most of the values being minus values. Therefore, open one door and one window was enough for providing ventilation for reducing CO_2 concentration in the classroom.

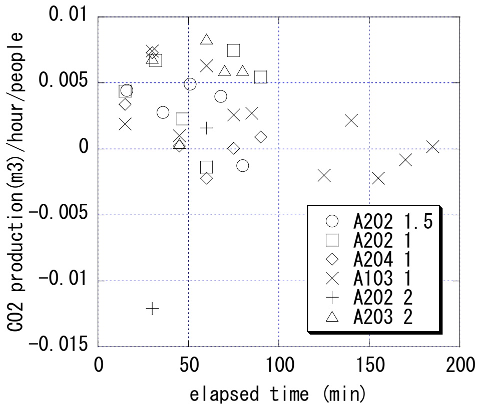

Fig.9 CO_2 production per hour per person in classroom (A103, A202, A203, A204) with no air conditioner and no open door and one or two open windows.

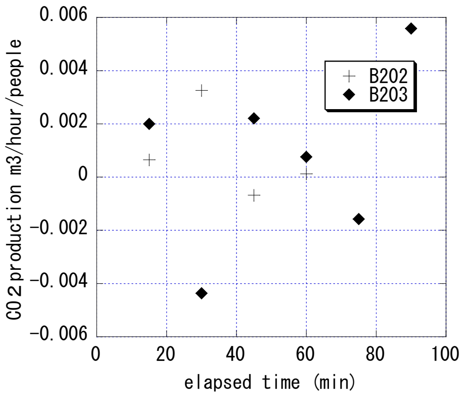

Fig.10 CO_2 production per hour per person in classroom (B202, B203) with no air conditioner and two open doors.

University Classroom with One or Two Open Windows

Fig. 9 shows CO_2 production per hour per person in classroom (A103, A202, A203, A204) with no air conditioner, no open door and one or two open windows. Most of the CO_2 production values were plus. Therefore, open one door and one window was not enough ventilation for reducing CO_2 concentration in the classroom.

University Classroom with One or Two Open Windows

Fig. 10 shows CO_2 production per hour per person in classroom (B202, B203) with no air conditioner and two open doors. Most of the CO_2 production values were minus. Therefore, opening two doors was enough ventilation for reducing CO_2 concentration in the classroom.

DISCUSSION AND CONCLUSION

Table 1 shows CO_2 production 1/1,000 m^3 /hour/person at the 15 minute mark (beginning of lecture) and the 75 minute mark (end of lecture). The size of the door and window were 1.9 and 1.5 m^2. The window was facing outside and the door was facing the floor. Comparing each CO_2 production value under the condition of no open door and window, most CO_2 production values from the small size, private house room with 23.5 m^2 to the big classroom, A101 with 1,297 m^2 were 0.010 to 0.015 m^3/hour/person not depending on time and room size. These were a little lower than the average production values of respiration under relaxed condition.

Next, the effect of doors and windows was estimated. For A103, the difference (D) of one door, one door and two windows, and one window compared with no door and window were 1 to -11× 1/1,000 m^3/hour/person and the difference per unit size of door and window (D/a) were -5.8 to 0.5× 1/1,000 m/hour/person/size. D/a shows the effect to reduce CO_2 concentration by the door or window. As a result, the effect of door and window per size, D/a, was variable however for A103, original CO_2 production with no ventilation was 2 to 11×1/1,000 m3/hour/person. Then to keep uniform CO_2 concentration, the open door or window size was 6.5(average)×1/1,000/ 2.7(average)×1/1,000, 2.4 m^2.

As well as for A104, the difference (D) of one door compared with no door and window were -8.5 to -6 ×1/1,000 m^3/hour/person and the difference per unit size of door and window (D/a) were -4.5 to -3.5×1/1,000 m/hour/person/size. Similarly, as for A104, original CO_2 production with no ventilation was 9×1/1,000 m^3/hour/person. Then to keep uniform CO_2 concentration, the open door size was 9×1/1,000/ 3.8(average)×1/1,000, 2.4 m^2. For A202, the difference (D) of one door, one door and one window, and one window compared with no door and window were -5 to 2×1/1,000 m^3/hour/person and the difference per unit size of door and window (D/a) were -1.6 to 0.6×1/1,000 m/hour/person/size. As for A203, original CO_2 production with no ventilation was 9×1/1,000 m^3/hour/person. Then to keep uniform CO_2 concentration, open door or window size was 10×1/1,000/ 1.3(average)×1/1,000, 7.7 m^2.

As for A203, the difference (D) of one door compared with no door and window were 3 to 8 ×1/1,000 m^3/hour/person and the difference per unit size of door and window (D/a) were -4.2 to 1.6×1/1,000 m/hour/person/size. As for A203, original CO_2 production with no ventilation was

9×1/1,000 m^3/hour/person. Then to keep uniform CO_2 concentration, open door or window size was 10×1/1,000/ 1.3(average)×1/1,000, 7.7 m^2. For A204, the difference (D) of one door and one window, one door and two windows, and one window compared with no door and window were -4 to -18×1/1,000 m^3/hour/person and the difference per unit size of door and window (D/a) were -0.8 to -8.0×1/1,000 m/hour/person/size. As for A204, original CO_2 production with no ventilation was 11×1/1,000 m^3/hour/person. Then to keep uniform CO_2 concentration, open door or window size was 11×1/1,000/ 4.4(average)×1/1,000, 1.6 m^2. For B101, the difference (D) of one door, one door and one windows compared with no door and window were -31 to 9×1/1,000 m^3/hour/person and the difference per unit size of door and window (D/a) were -0.9 to 4.7 × 1/1,000 m/hour/person/size. As for B101, original CO_2 production with no ventilation was 4×1/1,000 m^3/hour/person. Then to keep uniform CO_2 concentration, open door or window size was 4×1/1,000/ 0.5(average)×1/1,000, 8 m^2.

For B202 or B203, the difference (D) of one door, one door and one window, one door and two windows, and two doors compared with no door and window were 3 to -16×1/1,000 m^3/hour/per/person and the difference per unit size of door and window (D/a) were -4.2 to 1.5×1/1,000 m/hour/person/size. As for B202 or B203, original CO_2 production with no ventilation was 11×1/1,000 m^3/hour/person. Then to keep uniform CO_2 concentration, open door or window size was 11×1/1,000/ 1.4(average)×1/1,000, 7.9 m^2. As a result, open door or window size for each room was estimated and total volume of room per the open door or window size were 430/2.4 =180 for A103, 413/2.4=173 for A104, 522/7.7= 68 for A202, 416/7.7=54 for A203, 286/1.6=180 for A204, 551/8=69 for B101, and 260/7.9=32 for B202.

Table 1 CO_2 Production (1/1,000 m3 /hour/person)

Room Size m3	Time (min)	CO_2 Production 1/1,000 m^3 /hour/person					
		No	1D 1.9 m^2	1D1W 3.4 m^2	1D2W 4.9 m^2	1,2W 1.5~3m^2	2D 3.8m^2
P.H. 23.5	15	15~25					
	75	13~16					
A101 1297	15	34					
	75	8					
A103 430	15	2	-9~15			2 1.3	
	D	-	1			-0.5	
	D/a		0.5			0.3	
	75	11	-2~2		-2	3	
	D	-	-11		-13	-8	
	D/a		-5.8		-2.7	-5.3	
A104 413	15	9	-5~8				
	D	-	-6				
	D/a		-3.2				
	75	9	-1~0				
	D	-	-8.5				
	D/a		-4.5				
A202 522	15	14	12	9		4	
	D	-	-2	-3		-5	
	D/a		-1.0	-0.9		-1.6	
	75	6	3	8		-2~7	
	D	-	-3	2		-1	
	D/a		-1.5	0.6		-0.3	
A203 416	15	4~17	19				
	D	-	8				
	D/a		4.2				
	75	4~12	11				
	D	-	3				
	D/a		1.6				
A204 286	15	15		4~8	-3	3	
	D	-		-9	-18	-12	
	D/a			-2.6	-3.7	-8	
	75	7		-11~1	3	0	
	D	-		-12	-4	-7	
	D/a			-3.5	-0.8	-4.7	
B101 551	15	6	15	-25			
	D	-	9	-31			
	D/a		4.7	-0.9			
	75	2	1	1			
	D		-1	-1			
	D/a		-0.5	-0.3			
B202 B203 260	15	5~21	3~13	-1	-3		1~2
	D	-	-8	-14	-16		-12
	D/a		-4.2	-4.1	-3.3		-3.2
	75	7	-2~12	-2	0		-2
	D	-	3	-9	-7		-9
	D/a		1.5	-2.6	-1.4		-2.4

REFERENCES

[1] Noriko Ochiai, Kazunari Yamashita, "Indoor carbon dioxide of Shimane University lecture room and control of air quality", Shimane Prefecture University Bulletin, Vol.4, 2010, pp. 39-45.

[2] Homepage of Ministry of Education, Culture, Sport, Science and Technology

[3] Masahiro Yamashita1 and Hiroyuki Ii, "Unexpected high CO_2 concentration in classrooms of Wakayama University", in Proc. forth Int. Conf. on GEOMAT, 2014, pp. 572-577.

OPTIMUM CONDITIONS OF OYSTER SHELLS AS MATERIAL COVERING SEDIMENT AND INHABITATION SIMULATION OF INTERNAL LOAD USING ECOSYSTEM MODEL

Masaaki KONDO[1], Yuji KATO[2] and Takamitsu KAJISA[3]
[1,2,3]Graduate School of Bioresources, Mie University, Japan

ABSTRACT

A remediation program for a canal with water quality problem will be carried out in the future, and internal load from the bottom sediment can be new problem. Remediation measure against internal load was investigated by using oyster shells as covering material. So that shell-covered sediment experiments and numerical experiments were carried out. Pre-treatment such as graining and heating might be in vain, and non-heated shells of chip or powder size will be optimum. Properties of nutrient elusion were also obtained at the experiments. Numerical experiment was investigated on reducing patterns against external load and internal load to evaluate the various remediation measures by using ecosystem model added shell-covered sediment model. Only shell covering might have the small effect of water quality improvement. Good water quality is expected to be archived in the long period by a combination of reducing external load and applying bioresources.

Keywords: Oyster shell, Shell-covering effect, Internal load, Ecosystem model, Simulation

INTRODUCTION

Areas lower than sea level tend to have the water quality problems due to water retention because water drainage can barely proceed by gravity in low-lying areas. Water quality has deteriorated in the main drainage canal that runs through K. Town, Mie Prefecture, Japan. Due to topography constraints drainage does not flow like a river in low-lying areas such as K. Town, so the town must depend on pumping machines. Aquaculture effluent containing feed residue from fish has been dumped into the canal in addition to agricultural effluent containing soil particles from paddy fields. A remediation program has been discussed and planned for a long time to improve the water quality. While this program will be carried out in the future, by then, the internal load from the canal sediment could be greater than the improvement to the water quality in the canal.

Changes in the domestic production of oyster shells in the last decade are shown in Fig. 1 [1]. The weight ratio of oyster shells divided by oysters is 0.8 according to [2]. Shell weight was estimated by multiplying the oyster weight by the ratio of 0.8. The average annual production of oyster shells amounts to approximately 160,000 tons within Japan. There is a yield of 4,000 tons of oyster shells per year in Mie. Disposing the shells, which are industrial waste, is a major matter in any other producing areas as well as Mie. The aftermath of the 2011 Tohoku earthquake and tsunami led to a considerable decline of oyster shells containing Miyagi's production as shown in Fig.1. However, the disposal of oyster shell still remains a large problem.

Uses for oyster shell have been studied to improve various bad environments. First, improving bottom sediment was investigated. It was found that oyster shells adsorb the hazardous sulfurated hydrogen in river-mouth mud [3]. Oyster shells decrease the sulfide in brackish-lake mud as in [4]. Second, using oyster shells as material for purifying water was investigated. Oyster shells were immersed in water for agriculture, decreasing the total amount of nitrogen, especially ammonia nitrogen, in water [5]. Oyster shells were used in the process of changing ammonia nitrogen into nitrate nitrogen and denitrifying [6]. Last, oyster shells were used as material covering sediment. Sediment areas covered with oyster shells and without shells were set up in Lake Hamanako, and the concentrations over these areas were measured as in [7]. They showed that the sulfide concentration over the test area was a tenth of the concentration over the control area. Reference [8] measured the concentrations of PO_4-P and NH_4-N over sediment covered with both shells and without shells in the laboratory. The sediments were sampled from the bottom of Lake Kojimako. The concentrations of the covered sediment were lower than those of the control. Reference [9] indicated that another kind of shells led to similar results. Almost all previous research was done in areas with brackish water and salt water. Thus, it will be necessary to investigate applications for freshwater areas.

It is important to evaluate the impact of sediment on water qualities in order to calculate these concentrations in water area. The nutrient exchange

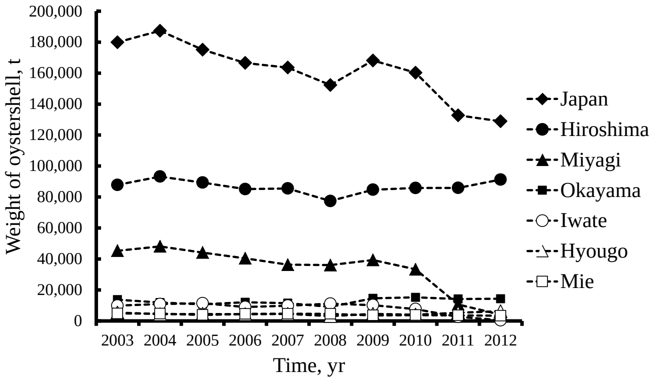

Fig. 1 Changes of annual production of oystershell with time [1].

processes between sediment and its above water, especially sedimentation process and decomposition process of phosphorus, were focused and investigated. Elution of phosphorus was calculated by using the phosphorus elution model from sediment, then various remediation measures against phosphorus release from sediment were estimated [10]. However, it is not easy to fractionate phosphorus components in sediment for the modeling, and a simple elution model appears to be needed.

In this study, experiments on internal load from shell-covered sediment were carried out under various shell conditions in order to apply the oyster shells as material covering the sediment in freshwater areas, and the optimum condition for the pre-treatment of oyster shells was investigated. Furthermore, this was done on the assumption that oyster shells would be used as covering material in the main drainage canal, and how shell-covered sediment could impact water quality in the field was investigated. A shell-covered sediment model was added to a known ecosystem model, and numerical simulations were carried out. The essential results of shell-covered sediment experiments were used to consider the model parameters and simulation patterns.

METHOD

Method of numerical experiment

Calculation model

The main drainage canal in K. Town is T-shaped and is about five kilometers long water area. Water, especially rainfall runoff, flows into the main drainage canal though not only the upstream edge of the canal but also many branch drainage canals. Two drainage pump station are located at the other downstream edge of the canal. Besides rainfall runoff, water in the main drainage canal consists of agricultural effluent from paddies, treated water

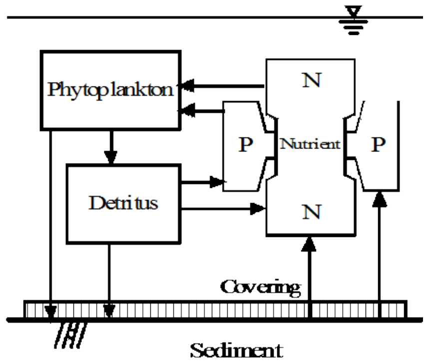

Fig. 2 Water qualities and ecosystem model with oyster shell covering

from wastewater treatment plants, and food factory effluent. The concentrations had a similar trend with each other in the main canal. Therefore, the entire main drainage canal was simplified as a single layer model.

The water quality and ecosystem model based on algal shown in Fig. 2 was used for analysis. It was added to this model that oyster shells covering the sediment inhibited nutrient elution from sediment. The model equations Eq. (1)-(4) are ordinary differential equations. The variables and constant are indicated together at the end of this paper.

$$\frac{\mathbf{d}\boldsymbol{A}}{\mathbf{d}\boldsymbol{t}} = \boldsymbol{\mu}\cdot\boldsymbol{A} - \boldsymbol{k_d}\cdot\boldsymbol{A} - \frac{\boldsymbol{v_A}}{\boldsymbol{z}}\boldsymbol{A} + \{\textstyle\sum(\boldsymbol{A_{in}}\cdot\boldsymbol{q}) - \boldsymbol{A}\cdot\boldsymbol{Q}\}/\boldsymbol{V} \quad (1)$$

$$\frac{\mathbf{d}\boldsymbol{D}}{\mathbf{d}\boldsymbol{t}} = \boldsymbol{r_D}\cdot\boldsymbol{k_d}\cdot\boldsymbol{A} - \frac{\boldsymbol{v_D}}{\boldsymbol{z}}\boldsymbol{D} - \boldsymbol{k_M}\cdot\boldsymbol{D} + \{\textstyle\sum(\boldsymbol{D_{in}}\cdot\boldsymbol{q}) - \boldsymbol{D}\cdot\boldsymbol{Q}\}/\boldsymbol{V} \quad (2)$$

$$\frac{\mathbf{d}\boldsymbol{N}}{\mathbf{d}\boldsymbol{t}} = -\boldsymbol{r_N}\cdot\boldsymbol{\mu}\cdot\boldsymbol{A} + \boldsymbol{r_{ND}}\cdot\boldsymbol{k_M}\cdot\boldsymbol{D} + (\mathbf{1} - \boldsymbol{\Phi_{inhN}})\frac{\boldsymbol{IR_N}}{\boldsymbol{z}}\boldsymbol{\theta_N}^{\boldsymbol{T}-\boldsymbol{T_c}} + \{\textstyle\sum(\boldsymbol{N_{in}}\cdot\boldsymbol{q}) - \boldsymbol{N}\cdot\boldsymbol{Q}\}/\boldsymbol{V} \quad (3)$$

$$\frac{\mathrm{d}P}{\mathrm{d}t} = -r_P\cdot\mu\cdot A + r_{PD}\cdot k_M\cdot D + (1 - \Phi_{inhP})\frac{IR_P}{z}\theta_P{}^{T-T_c} + \{\textstyle\sum(P_{in}\cdot q) - P\cdot Q\}/V \quad (4)$$

The time integration method of Eq. (1)-(4) was the fourth order Runge-Kutta method. The time step was set to be one day. It was supposed that the water volume *V* of the main drainage canal was constant in these equations. In low-lying areas, water such as rainfall runoff gathers through a hydraulically continuous lateral drainage canals. Drainage pumped at each downstream edge daily causes only a small flow in the main drainage canal, and consequently, a small fall in the water level rapidly returns to normal.

Input data for calculation model

Monthly input data used for the calculation are shown in Figs. 3 and 4. Shown are the discharges of various influents, chlorophyll-a concentrations A_{in}, suspended solids D_{in}, total nitrogen concentrations N_{in}, total phosphorus concentrations P_{in}, water temperature T in the main drainage canal, and the illuminance L around the field. These input data were determined by a committee [11] between April 2002 and March 2003, except for the illuminance. Illuminance data were quoted from a data book [12].

Waters influent into the main drainage canal consist of rainfall runoff from a basin, agricultural effluent from paddies and upland farms, treated water from the wastewater treatment plants, and food factory effluent. Each influent discharge q was monthly calculated on the basis of the water balance in the basin. Suspended solids SS were substituted for detritus concentrations D_{in} of each of the influent waters.

Rainfall runoff, calculated on the basis of rainfall, appears to flow into the main canal through the hydrological continuum of branch drainage canals. Since the daily drainage done by two pump stations pulls only a small volume of water into the main canal, the pollutant runoff coefficient could be great because the pollutant settles under slow water movement, and inflow loads associated with rainfall runoff were supposed to be zero for all water quality items.

Agricultural water supplied into the basin caused the agricultural effluent to discharge. The irrigation period was between April and August in K. Town. Agricultural effluent corresponds to almost all of the agricultural water supply and period. Inflow load associated with agricultural effluent was calculated on the basis of observed concentrations at paddies.

Since the wastewater treatment plants deal with household effluent, the plants have monthly constant discharges and regular concentrations. The inflow load was calculated by using constant discharges and observed concentrations.

Discharge of food factory effluent was incommensurably small value, as shown in Fig.3 (A). Furthermore, since the waste outlet of the food factory is very close to the pump station at the downstream edge in the main canal, the effluent has no effect on the whole of the main canal. Consequently, all inflow loads for factory effluent were supposed to be zero.

Chlorophyll-a, total nitrogen, total phosphorus, and water temperature were determined in the main drainage canal. The observed date of the water temperature was fit as a five order polynomial equation, shown in Fig.4 (A), to be used for model calculation.

Instead of illuminance, the amount of global solar radiation was used to calculate influence

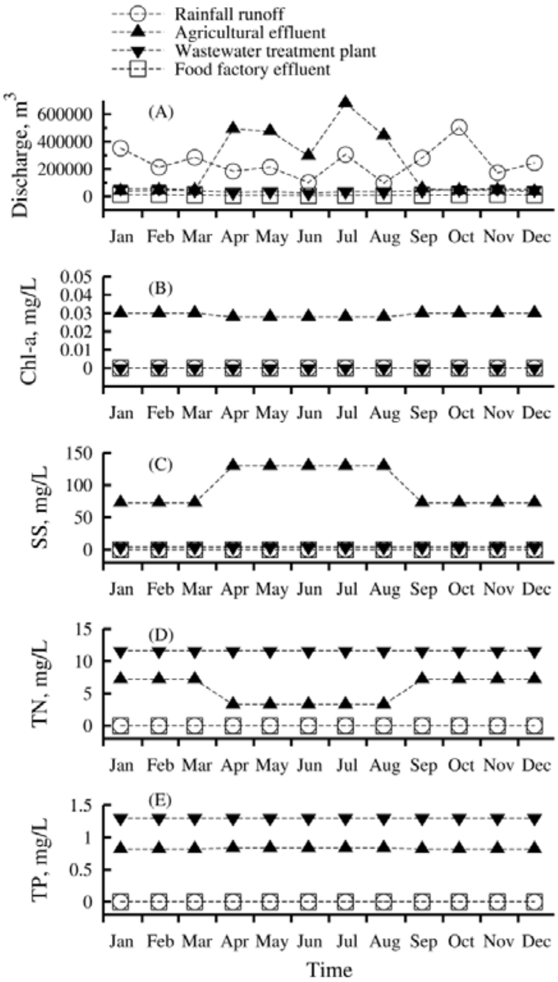

Fig. 3 Changes of influent discharges into the main drainage canal and their water qualities

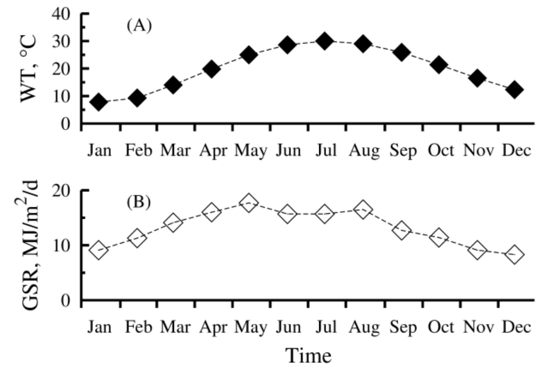

Fig. 4 Changes of (A) water temperature in the main drainage canal, and (B) amount of global solar radiation.

function Φ_s. The monthly amount of global solar radiation shown in Fig.4 (B) was measured near K. Town [12].

Table 1 List of reduction ways of external load and internal load.

External load		Internal load	
Reduction ratio	Symbol	Reduction ratio /inhibition ratio, Φ_{inh}	Symbol
000% off	E-1	No remedy (000% off constant)*	I-1
025% off	E-2	Perfect dredging (100% off constant)*	I-2
050% off	E-3	Covering type 1 (stepwise decrease)**	I-3
-	-	Covering type 2 (linear decrease)**	I-4

*) Φ_{inh}s of N, P are the same. **) Φ_{inh}s are different as shown in Fig.7.

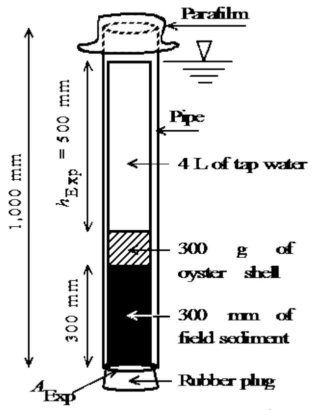

Fig. 5 Experimental arrangements for shell-covered sediment experiment.

Table 2 Numerical experiment patterns.

External load	Internal load			
	I-1	I-2	I-3	I-4
E-1	Run01	Run02	Run03	Run04
E-2	Run05	Run06	Run07	Run08
E-3	Run09	Run10	Run11	Run12

Simple model equation for covering elution from sediment

Experimental equations for nutrient elution from sediment are often expressed as a function of water temperature T [13]. The author modifies and proposes new experimental equation Eq. (5) and (6) with inhibition ratio Φ_{inh}, which shows that shell covering inhibits nutrient elution from sediment. The variables IR_N, IR_P were calculated with the data of the shell-covered sediment experiment in the next chapter. The time series of Φ_{inh} were set up as imaginary patterns.

$$(1-\Phi_{inhN})\frac{IR_N}{z}{\theta_N}^{T-T_c} \tag{5}$$
$$(1-\Phi_{inhP})\frac{IR_P}{z}{\theta_P}^{T-T_c} \tag{6}$$

Design for numerical experiment patterns

Table 1 indicates the various ways to reduce external load and internal load in the main drainage canal. The experimental patterns listed in Table 2 were generated by combining these ways, and numerical experiments were carried out.

Three ways of reducing external load are shown in Table 1, and the contents are as follows. The symbols are E-1 for reducing external load by 0%, E-2 for reduction by 25%, and E-3 for reduction by 50%. Reduction by 0% means no remediation measure. Preliminary numerical experiments resulted in deciding reduction values such as 25% and 50%. While the reduction values are not based on any theory, the author will ensure that the external load is reduced by 25% or 50%. It was expressed in the calculation for the reduction of external load that the concentrations of all effluents like rainfall runoff were equally decreased.

Four kinds of ways to inhibit nutrient elution are shown as remediation measures against internal load in Table 1. Inhibition ratio Φ_{inh} here means how much oyster-shell covering inhibits nutrient elution from sediment compared with non-covered sediment. No remedy, shown by I-1, means that Φ_{inh} is zero. Perfect dredging of I-2 was supposed that all sediment was clear off in canal bottom, then Φ_{inh} was 100%. The patterns of covering types 1 and 2, shown by I-3 and I-4, both mean that the sediment was covered with oyster shells. Both patterns were different in the variation of Φ_{inh}. The inhabitation ratio Φ_{inh}s of covering type 1 decreased in a stepwise fashion, and those of covering type 2 decreased linearly. These patterns reflected the elution properties of the shell-covered sediment experiment.

Material and methods for shell-covered sediment experiment

Oyster shells for experimental material

Barnacles and muddy blobs were adequately washed out of oyster shells by using a lot of fresh water. Long immersion in fresh water eliminated the salt content in the shells, and the shells were then dried in the sun. Three types of shell sample sizes were arranged for the experiment. The samples were called “original size”, “chip size”, and “powder size”. Chip size samples were kept on a sieve with a mesh size of 4.5 mm after granulating the dried original shells with a hammer. The powder size samples were fine shells passed through the sieve. The shell samples were heated at various high temperatures for six hours in an electric furnace. From a study on the removal of various ions using heated oyster shells, reference [14] confirmed the optimum heated temperature to be 600°C. Therefore, the three types of shells were heated at four calcination temperatures, 100°C, 200°C, 400°C, and 600°C, except for non-heated oyster shells kept at room temperature. Shell-covered sediment experiments were carried out. The water used for measurement was sampled at the upper part of a pipe used in the experiments. Water samples were subject to an absorptiometer to determine the concentrations of

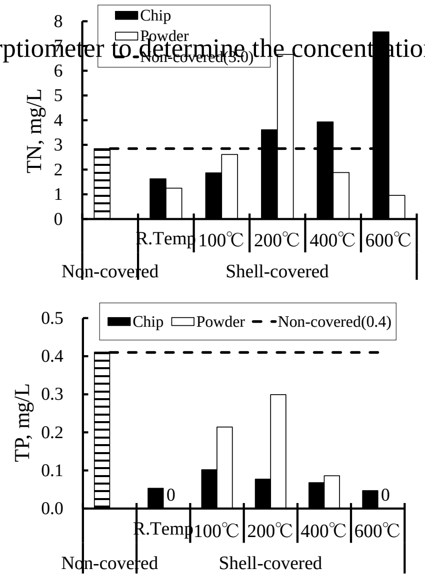

Fig. 6 Result of shell-covered sediment experiment after 10 days. Dashed lines show each concentration under the non-covered.

total nitrogen (TN) and total phosphorus (TP).

Experimental procedure

For the experiments, lumps of sediment 300 mm high were placed into the bottom of a clear PVC pipe, and the air in the sediment was let out (Fig.5). Sediment sampled at the main drainage canal in K. Town was used. Three hundred grams of shells were put over the sediment, and 4 L of tap water was funnelled with as little erosivity as possible. The upper water in the pipe was periodically sampled, non-filtered, and measured for a period of up to ten days. The shells used were the chip and powder types and were heated at all calcination temperatures. The following experimental processes were not carried out. We did not beat the water in a pipe to make it homogeneous, and we did not control the quality of the water associated with the elution of nutrients such as dissolved oxygen. Elution of nutrients from sediment was supposed to be maximum with tap water containing no nutrients. To make sure there was no phytoplankton growth from the sediment, the experiments were conducted in a darkened room.

RESULTS AND DISCUSSION

Results of shell-covered sediment experiments

Results under non-shell-covered condition

Figure 6 shows the water quality of the water column after ten days for the shell-covered sediment experiments. Under non-shell-covered condition, elution amounts were different in nitrogen and phosphorus. Thus, total nitrogen TN_{10} was 3 mg/L,

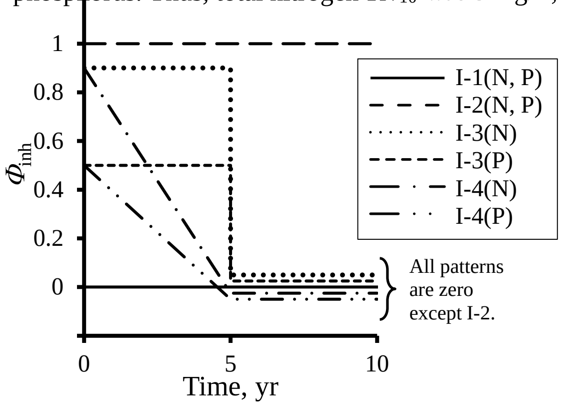

Fig. 7 Changes of inhibition patterns on internal load from sediment.

and total phosphorus TP_{10} was 0.4 mg/L after 10 days.

Results under shell-covered condition

As shown in Fig. 6, both the chip and powder samples had a similar tendency of nutrient elution from the sediments except for the chip sample heated at a temperature of 600°C. While the inhabitation ability of the shell covering diminished in the range from room temperature to 200°C, shells heated over 200°C inhibited the elution from the sediment. The concentrations of nitrogen and phosphorus with no heated shells was as low as those with shells heated in a high temperature range of 400 - 600°C, except for TN at 600°C in the experiments. Therefore, pre-treatment such as graining and heating might be in vain, and non-heated shells at both sizes will be optimum.

The elution of nutrients such as nitrogen and phosphorus was different depending on inhibition ratio. First, the nitrogen concentrations with chip and powder samples at room temperature were determined to be 1.63 mg/L and 1.25 mg/L, respectively. Therefore, shell covering inhibited elution by 50% compared with the non-shell-covered condition. Second, the phosphorus concentrations of the chip and powder were 0.05 mg/L and 0.00 mg/L, respectively. These differences mean that the shell covering inhibited elution by 90% compared with the non-shell-covered condition.

The experiments were carried out at the longest for 10 days, and not long term such as for months or years. According to elution tests worked out using many sediment samples from different irrigation ponds in Japan [15], elution concentrations such as of nitrogen and phosphorus indicated that concentration peak within 10 days or so. If long-term experiments were carried out, it would be necessary to discuss that the nutrients eluted from sediment may change or settle in water in addition to the elution. Ten days is enough for discussing elution from sediment. Consequently, the inhibition ratio for the long period was set as an imaginary time, as shown in Fig.7.

Parameters for model nutrient elution from sediment

The variables of IR_N and IR_P used in Eq. (5) and (6) were calculated like Eq. (7) and (8) by using parameters under the non-shell-covered condition. According to the specifications of apparatus used in the experiment and experimental conditions, water column h_{Exp} was 0.5 m long, as shown in Fig.5, and experiment time D_u was 10 days as mentioned above. For the non-shell-covered condition, the concentrations of TN_{10} and TP_{10} were 3 mg/L and 0.4 mg/L, respectively. The values of IR_N and IR_P, assessed at 0.15 and 0.02 g/m^2/d, respectively, were in good agreement with those of Lake Suwa [16].

$$IR_N = \frac{TN_{10} \cdot A_{\mathrm{Exp}} \cdot h_{\mathrm{Exp}}}{A_{\mathrm{Exp}} \cdot Du} = \frac{3 \times 0.5}{10} = 0.15\ (\mathrm{g/m^2/d}) \quad (7)$$

$$IR_P = \frac{TP_{10} \cdot A_{\mathrm{Exp}} \cdot h_{\mathrm{Exp}}}{A_{\mathrm{Exp}} \cdot Du} = \frac{0.4 \times 0.5}{10} = 0.02\ (\mathrm{g/m^2/d}) \quad (8)$$

Two things were simplified in the paper. First, elution test as non-shell covered sediment experiment under various water temperatures was not carried out for elution model equation. Though the IR_N and IR_P were obtained under one temperature condition, these values were in good agreement with those of a Japanese lake. Thus, the third terms of Eq. (3) and (4) were corrected by using each one experimental data of nitrogen and phosphorus, respectively. Second, not the undisturbed sediment samples but disturbed samples were applied to elution tests. Oyster-shell covering condition might be severe as elution condition in the respect of using disturbed samples in addition to use tap water not field water. It was again noticed that the values of IR_N and IR_P obtained under this experimental condition were in the proper range of a Japanese lake.

Results of numerical experiment

Figure 8 introduced several simulation results for the concentration of chlorophyll-a. For Run01, there was no remediation measure against both external and internal loads. While Run09, Run10, Run11, and Run12 were in common reduction series of external load by 50%, these series were different in terms of remediation measure against internal load. For Run09, there was no remedy, I-1, against internal load. For Run10, there was perfect dredging against internal load, I-2. Run11 and Run12 for covered sediment mean covering type 1, I-3, and covering type 2, I-4.

The concentrations of chlorophyll-a for Run10, Run11, and Run12 under the reduction of internal

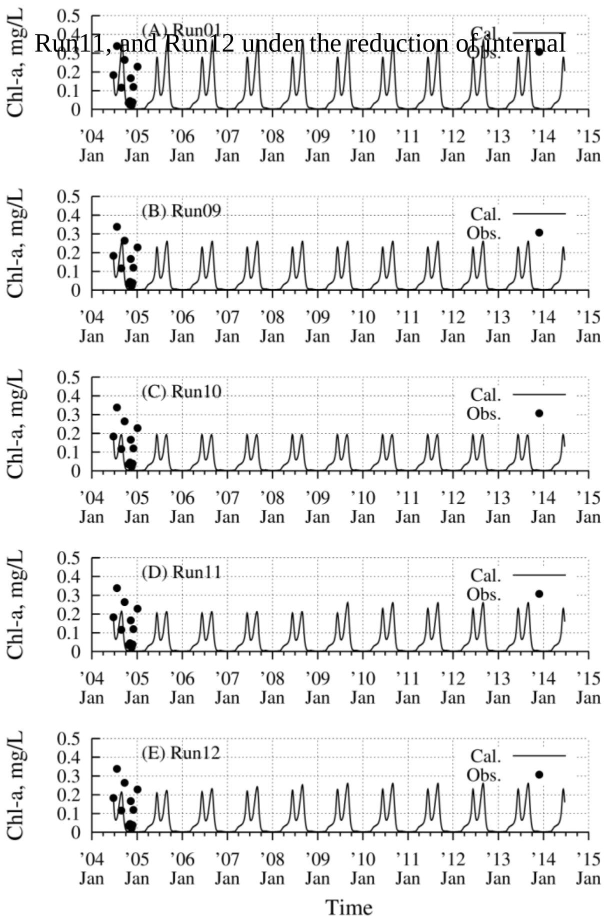

Fig. 8 Several results of numerical experiments.

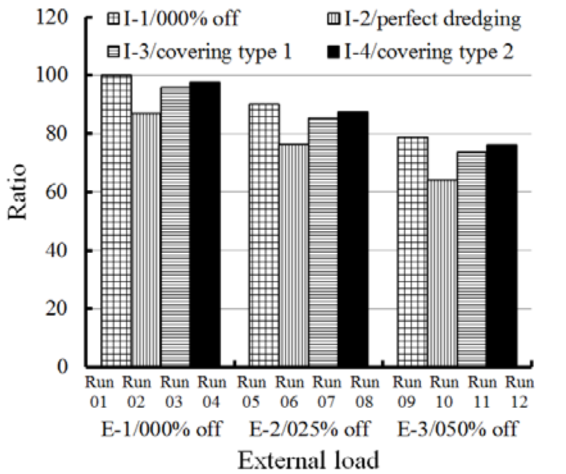

Fig. 9 Comparison of integrated concentration of chlorophyll a during 10 years shown in Fig.8.

load demonstrated the same concentrations as Run09 for 10 years except for Run10. If the bottom sediment is ideally dredged and sustained to be dredged, then a concentration of chlorophyll-a like that of Run10 might be kept much lower than the others. While the concentration of chlorophyll-a for covering type 1 like Run11 was inhibited the same as that by the dredging of Run10 for the first half of ten years, the latter concentration of chlorophyll-a was the same level as that of Run09, which had no remedy.

The concentration of chlorophyll-a for covering type 2 such as Run12 gradually became the same as that of Run09 with no remedy over 10 years. Figure 8 presented a 50% reduction of the external load mentioned above, except for Run01. The results for a reduction of 25% had similar tendency. As you can see, only a simple interaction was shown, and simulation is different from the actual world. For example, it is very difficult to keep the perfect dredging condition.

Estimation of remediation measure

To evaluate various remediation measures, the concentration $A(t)$ of chlorophyll-a was integrated over the 10 years. The integration result is shown in Fig. 9, in which each integration results is recalculated with a value of 100 representing the concentration load of Run01.

It was predictable that perfect dredging would have the best effect for the various remediation measures against internal load. Comparing Run02 with Run05, it was better to dredge than to reduce external load somewhat. The problem with actual dredging is that careful work is needed not to return. In addition, the reduction of external load was also needed to sustain the inhabitation effect of dredging. Another problem remains of how to deal with dredged sediment.

Only shell covering might have a small effect on water quality improvement. Good water quality is expected to be achieved through a combination of reducing external load and this shell covering. The water quality problem cannot be corrected in a short time, so it is a problem that should be continued to be tackled over a long period of time. One approach would be to use various kinds of bioresources, and prolonged activity is needed to do. In the author's experience, application to the field is often quite tough. It was tried that aquatic plants were grown in style of floating island, and nutrient in water was imbibed by the plants in the pursuit of clear water in the main drainage canal. Many turtles eat up aquatic plant rootage growing out of floating island, which results in aquatic plants not growing.

If concentrations at various times instead of concentration integration were used for judgement, then it would be convenient to compare the concentrations with water quality standards. In this paper, the concentration above was not selected, because a complex simulation model or enough input data was not required for calculation. Integration of concentration over 10 years would cover the various shortages of the simulation.

CONCLUSION

An oystershell-covered sediment experiment was carried out, and the properties of nutrient elution from sediment and experimental parameters were obtained. The shell-covered sediment model, which reflects the experimental parameters of elution, was added to the ecosystem model. A numerical experiment was investigated on reducing patterns against external load and internal load to evaluate the various remediation measures.

Sample graining such as chip and powder and various heated temperatures were investigated in the experiment. Pre-treatment such as graining and heating might be in vain, and non-heated shells at chip or powder size are optimum.

Under non-shell covered condition, TN and TP concentrations for 10 days were determined, and IR_N and IR_P were 0.15 g/m^2/d and 0.02 g/m^2/d, respectively. These values of IR_N and IR_P were used as parameters of the numerical model.

Experiments under the non-shell covered condition resulted in elution nutrients such as nitrogen and phosphorus being different in inhibition ratio. First, for the nitrogen concentration of the chip and powder samples, shell covering inhibited elution by 50% compared with the non-covering condition. Second, the covering on phosphorus inhibited elution by 90% compared with non-covering.

Twelve reducing patterns in the combine of external load and internal load were investigated in a numerical experiment. The ways of reducing external load consisted of no remedy, reduction by 25%, and reduction by 50%. The remediation measures of internal load had four kinds: no remedy, dredging, covering type 1, and covering type 2. The inhibition ratio of covering type 1 followed a stepwise decrease. The ratio of covering type 2 decreased linearly. The concentration of chlorophyll-a was integrated over 10 years to evaluate various remediation measures.

It was predictable that perfect dredging would have the best effect on various remediation measures against internal load. If dredging work is properly accomplished, then its performance will have a profound effect on water quality improvement. Only shell covering might have a small effect on water quality improvement. Good water quality is expected to be archived through a combination of reducing external load and this shell covering. While bioresources such as water plant is planned to be promoted, other living things and conditions could disturb the system.

A remediation program for external load is ongoing in the field. While oyster shell covering is only proposed to be one of remediation measures in this paper, the investigation results are expected to be useful of remediation.

ACKNOWLEDGEMENTS

The author is indebted to the local public officials and the committee for providing their cooperation and the valuable data for the study.

List of variables

Variable	Explanation
A	conc. of chl.-a in main drainage canal
D	conc. of detritus in main drainage canal
N	conc. of nitrogen in main drainage canal
P	conc. of phosphorus in main drainage canal
t	Time
Q	total influent discharge, $Q=\Sigma q$
q	individual influent discharge
V	total water volume of main drainage canal
μ	$\mu=\mu_{\max}\cdot\Phi_I\cdot\Phi_A\cdot\Phi_S\cdot\Phi_T$
$\mu_{\max}$	maximum specific growth rate
Φ_I	$\boldsymbol{\Phi_I=\frac{N}{k_N+N}\cdot\frac{P}{k_P+P}}$
k_N, k_P	half saturation constant of N and P
Φ_A	$\boldsymbol{\Phi_A=1}$
Φ_S	$\boldsymbol{\Phi_S=(L/L_c)\exp(1-L/L_c)}$
L	Illuminance
L_c	critical illuminance
Φ_T	$\boldsymbol{\Phi_T=T/T_c}$
T	water temperature
T_c	T_c =20°C
k_d	death factor of phytoplankton
υ_A, υ_D	settling velocity of phytoplankton and detritus
z	mean depth of main drainage canal
r_D	conversion factors between phytoplankton and detritus
k_M	decomposition and mineralization constant for detritus
r_N, r_P	conversion factors between phytoplankton and N, P
r_{ND}, r_{PD}	conversion factors between detritus and N, P
Φ_{inhN}, Φ_{inhP}	inhibition ratio of N and P from sediment
IR_N, IR_P	elution rate of N, P from sediment
A_{in}, D_{in}, N_{in}, P_{in}	conc. of A, D, N and P in influent waters
TN_{10}, TP_{10}	conc. of total-N and total-P after 10 days
A_{Exp}, h_{Exp}	sectional area and water column long of experimental cylinder
D_u	experimental time

REFERENCES

[1] Ministry of Agriculture, Forestry and Fisheries, "Statistics report on production of fisheries and aquaculture 2003-2012", Association of Agriculture and Forestry Statistics, 2005-2014.

[2] Noguchi H, "Guideline of shell recycle for fishing ground development", Monthly Construction, 51(10), 2007, pp.27-29.

[3] Asaoka S, Yamamoto T, Kondo S and Hayakawa S, "Removal of hydrogen sulfide using crushed oyster shell from pore water to remediate organically enriched coastal marine sediments", Bioresource Technology, 100, 2009, pp.4127-4132.

[4] Fujisawa K and Miyake Y, "Effects of shell of oyster scattered at the bottom mud in Kojima Lake -1", Bull. of Fisheries Experiment Station Okayama Prefecture 1979, 1980, pp.30-32.

[5] Sasaki C, Enari K, Koseki K, Ito T and Nakayama M, "The water purification test using oyster shells as industrial waste", Trans. of the Japanese Society of Irrigation, Drainage and Reclamation Engineering, Vol.67, No.2, 1999, pp.233-241.

[6] Konishi H, Makino M and Miyama T, "Research on small-scale wastewater treatment for utilizing the waste （3rd report）－ Advanced wastewater treatment utilizing nitrification - denitrogenation and phosphorus removal", Research Report from Ishikawa Prefectural Institute of Public Health and Environmental Science, 46, 2009, pp.9-14.

[7] Fukuro S and Shimada Y, "Development of technology which improves water quality by using oyster shell", Fujita Technical Research Report, 41, 2005, pp.63-68.

[8] Fujisawa K and Miyake Y, "Effects of crushed shells of oyster scattered at the bottom mud in Kojima Lake -2", Bull. of Fisheries Experiment Station Okayama Pref. 1980, 1981, pp.18-20.

[9] Agatsuma S, Murakami K, Gomyo M and Amano Y, "Influence analysis of sediment treatment using shell fragment as regional unused resources on sedimental environment", The 48th Annual Conf. of Japan Society on Water Environment 2014 in Sendai, 2014, p.132.

[10] Hosomi M, "Release and control on nitrogen and phosphorus from sediment material", Journal of Japan Society on Water Environment, Vol.16, No.2, 1993, 91-95.

[11] Mie Pref., "Handout of the second exploratory committee for K. district", Local Water Environment Development Program, 2006.

[12] National Astronomical Observatory of Japan, "Chronological scientific tables", Maruzen Publishing, 1993, p.263.

[13] Shiratani E, "Water quality analysis (4) -water quality analysis by ecosystem model-", Journal of the Japanese Society of Irrigation Drainage and Reclamation Engineering, Vol. 62, No. 1, 1994, pp.47-53.

[14] Nishioka H, Uchida T, Muramatsu Y, Yazawa T and Amako T, "Optimization of heat treatment conditions for oyster shells to increase their ability to remove ions with negative environmental impacts", Journal of the Japan Society of Material Cycles and Waste Management, Vol.22, No.4, 2011, pp.276-283.

[15] Hiramatsu K and Suzuki H, "Experiments in sediment-desiccation effect on phosphorus and nitrogen dynamics within irrigation ponds", Irrigation, drainage and rural engineering journal, Vol.75, No.4, 2007, 411-418.

[16] Tanaka T and Okino T, "Modeling the circulation of substances in Lake Suwa", Studies on the ecosystem of the watershed area of Lake Suwa, No.1, 1978, pp.73-90.

Fifth International Conference on Geotechnique, Construction Materials and Environment, Osaka, Japan, Nov. 16-18, 2015, ISBN: 978-4-9905958-4-5 C3051

ESTIMATION OF USEFUL SPECIES OF RIVER INSECTS AND WATER PLANTS AS AN INDEX OF METAL CONTAMINATION IN THE KINOKAWA RIVER CATCHMENT

Takuma Kubohara[1], Hiroyuki Ii[2]
[1]Graduate School of Systems Engineering, Wakayama University, Japan;
[2]Faculty of Systems Engineering, Wakayama University, Japan

Abstract

Heavy metals in river insects, Japanese fresh water crabs, caddice-worms, dobsonfly larvae, dragonfly larvae, stonefly larvae, crane fly larvae, mayfly larvae and corixidae and water plants, reeds, fern, moss, Japanese knotweed and coix in the contaminated area and non-contaminated area were studied in order to evaluate useful species that can serve as good indicators of metal contamination. Moss was useful as an indicator for Cu, Co and Ni contamination because moss had the highest concentration factor among river insects and water plants and a wide range of concentration depending on contamination level for Cu, Co and Ni. Fern leaf was useful as an indicator for Cd contamination because fern leaf had the highest concentration factor among river insects and water plants and a wide range of concentration depending on contamination level for Cd.

Keywords: Useful Species, Moss, Fern Leaf, Heavy Metals

INTRODUCTION

Even if there is a metal contamination source from metal mines in a catchment, metal concentrations of river water in the catchment is not always high because of dilution of rain water [1]. Therefore, metal concentration of river water is not always useful for evaluating metal contamination in a catchment. On the other hand, metal concentrations of insects and plants are often higher than those of river water because of high bioconcentration factor.

Metal concentrations for many river insects and water plants have been studied in metal contamination areas and non-contamination areas. At past, concentrations of river insects, caddice-worm [2]-[3], dobsonfly [4], stonefly [5], mayfly [5], water plants, fern [6], moss [7], and reed [8] have been studied. However, useful species for metal contamination index using river insects and water plants have not been determined because no comparison of contaminated and non-contaminated areas, although some caddice-worm were shown possibility as index of metal contamination.

Therefore, comparing metal concentrations of river insects and water plants sampled at the contaminated area and non-contaminated area, useful species as a good indicator of metal contamination was determined.

STUDY AREA

Fig.1 shows the study area. The Kinokawa River is located in the center of Kinki district and flows into the Kii Channel through the Kii plain. The Kinokawa River is classified into A river based on the Ministry of Land, Infrastructure, Transport and Tourism of Japan. Length and total area of the Kinokawa River are 136 km and 1,750 km^2 [9].

Izumi Group composed of sedimentary rocks, sandstone, mudstone and conglomerate is distributed in the northwest part of the catchment. Sanbagawa Belt composed of metamorphic rocks, serpentinite and crystalline schist is distributed in the southwest part and the northeast part of the catchment. Hidakagawa Group composed of sedimentary rocks, sandstone and shale is distributed from the southern part to the northeast part of the catchment. Chichibu Belt composed of sedimentary rocks, sandstone, mudstone, limestone and chert is distributed in the eastern part of the catchment [10]. Ryoke Complex composed of plutonic rocks, granite and gneiss is distributed in the northeast part of the catchment.

The Kinokawa River catchment has serpentinite and the closed Cu mines. The chemistry of serpentinite is quite different from another rocks, in particular, serpentinite has high concentration of Mg, and Ni. The closed Cu mine produced a lot of Cu and Fe sulfide ore and waste water was low pH and high concentration of sulfate with metal. Then, in this study, catchments were divided into three groups, serpentinite area, Cu mine area and normal area based on the geological aspect.

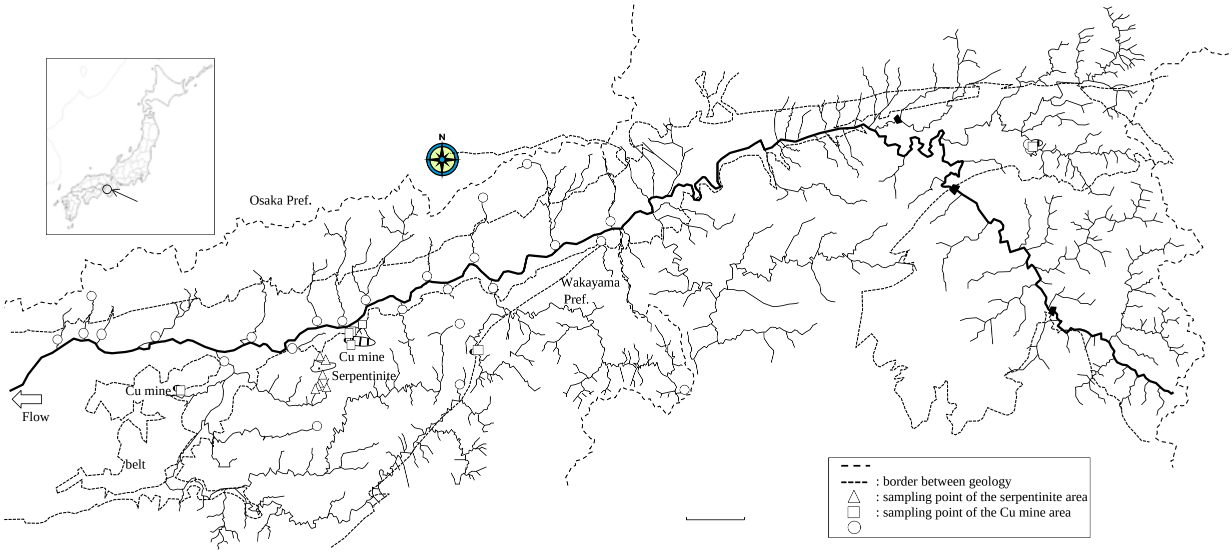

Fig.1 Study area

STUDY METHOD

River water, river insects and water plants were sampled in the Kinokawa River catchment. Sampling points were shown in fig.1. Cu, Co, Ni and Cd concentrations of river water, river insects and water plants were measured. River water samples were filtered with the membrane filter with 0.45 micrometer of pore size in site and concentrated nitric acid was added in laboratory. They were kept cool until analyzing. The sampled river insects and water plants were desiccated by dryer at first. After drying, they were dissolved with concentrated nitric acid and it was filtered with the membrane filter with 0.45 micrometer of pore size before analysis. Their Cu, Co, Ni and Cd concentration were measured by ICP-AES. The actual detection limit of ICP-AES is 0.01ppm for Cu, Co, Ni and Cd.

The species of sampled river insects were Japanese fresh water crab, caddice-worm, dobsonfly larva, dragonfly larva, stonefly larva, crane fly larva, mayfly larva and corixidae. The species of sampled water plants were reed, fern, moss, Japanese knotweed and coix. Water plants excluding moss were divided into leaf, upper part stem, middle part stem, lower part stem and root and each part is separately analyzed.

RESULTS AND DISCUSSION

Evaluation for Cu

Figs.2 and 3 show Cu concentrations of river insects and water plants. “N.D.” means under detection limit in the figure. Cu concentrations of Japanese freshwater crab, dobsonfly larva, dragonfly larva, crane fly larva and corixidae in the Cu mine area were 114 to 241 mg/kg-dry, 590 mg/kg-dry, 70 to 440 mg/kg-dry, 50 to 1,400 mg/kg-dry and 520 mg/kg-dry, respectively. Cu concentrations of Japanese freshwater crab, dobsonfly larva, dragonfly larva, crane fly larva and corixidae in another area were 45 to 73 mg/kg-dry, 16 to 81 mg/kg-dry, 18 to 59 mg/kg-dry, 11 to 130 mg/kg-dry and 77 to 190 mg/kg-dry, respectively. Cu concentrations of reed, fern, moss, Japanese knotweed and coix in the Cu mine area were 8 to 700 mg/kg-dry, 10 to 10,000 mg/kg-dry, 31 to 21,000 mg/kg-dry, 18 to 2,900 mg/kg-dry and under detection limit to 100 mg/kg-dry, respectively. Cu concentrations of reed, fern, moss, Japanese knotweed and coix in another area were under detection limit to 24 mg/kg-dry, under detection limit to 150 mg/kg-dry, under detection limit to 87 mg/kg-dry, under detection limit to 10 mg/kg-dry and under detection limit to 23 mg/kg-dry, respectively. Then, their Cu concentrations in the Cu mine area were higher than another area. In the past study, it was clarified that Cu of river insects and water plants in the Cu mine area in the Kinokawa River catchment were affected by Cu mine [1]. Therefore, their Cu concentrations in the Cu mine area were affected by Cu mines.

Cu concentrations of river insect species, moss and water plant species excluding moss influenced by the Cu mine were 11 to 1,400 mg/kg-dry, under detection limit to 21,000 mg/kg-dry and under detection limit to 10,000 mg/kg-dry, respectively. Then, moss had the highest and a wide range of Cu concentration. Figs.2 and 3 show Cu concentration factors of river insects and water plants. The concentration factor was regarded as 1 when the concentrations were under detection limit. Maximum Cu concentration factors of river insect species, moss and water plant species excluding moss influenced by the Cu mine were 66,300, 160,000 and 70,000, respectively. Then, Cu concentration factor of moss was the highest among them. Therefore, moss was a useful species for indicator of Cu contamination.

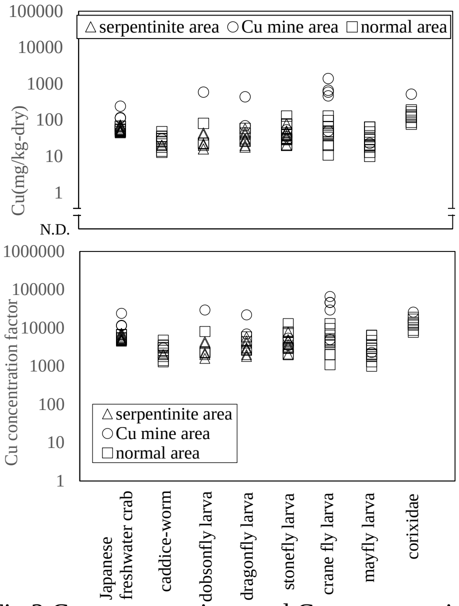

Fig.2 Cu concentrations and Cu concentration factors of river insects.

Evaluation for Co

Figs.4 and 5 show Co concentrations of river insects and water plants. "N.D." means under detection limit in the figure. Co concentrations of Japanese freshwater crab, dobsonfly larva, dragonfly larva, crane fly larva and corixidae in the Cu mine area were under detection limit to 2 mg/kg-dry, 26 mg/kg-dry, 7 to 30 mg/kg-dry, under detection limit to 82 mg/kg-dry and 20 mg/kg-dry, respectively. Co concentrations of Japanese freshwater crab, dobsonfly larva, dragonfly larva, crane fly larva and corixidae in another area were under detection limit, under detection limit to 6 mg/kg-dry, under detection limit to 23 mg/kg-dry, under detection limit to 10 mg/kg-dry and under detection limit, respectively. Co concentrations of reed root, fern root, moss, Japanese knotweed root and coix root in the Cu mine area were under detection limit to 30 mg/kg-dry, under detection limit to 21 mg/kg-dry, under detection limit to 200 mg/kg-dry, 36 to 38 mg/kg-dry and under detection limit to 5 mg/kg-dry, respectively. Co concentrations of reed root, fern root, moss, Japanese knotweed root and coix root in another area were under detection limit to 6 mg/kg-dry, under detection limit to 10 mg/kg-dry, under detection limit to 33 mg/kg-dry, under detection limit to 25 mg/kg-dry and under detection limit, respectively. Then, their Co concentration in the Cu mine area were higher than another area. In the past study, it was clarified that Co of river insects and water plants in the Cu mine area in the Kinokawa River catchment were affected by Cu mine [1].

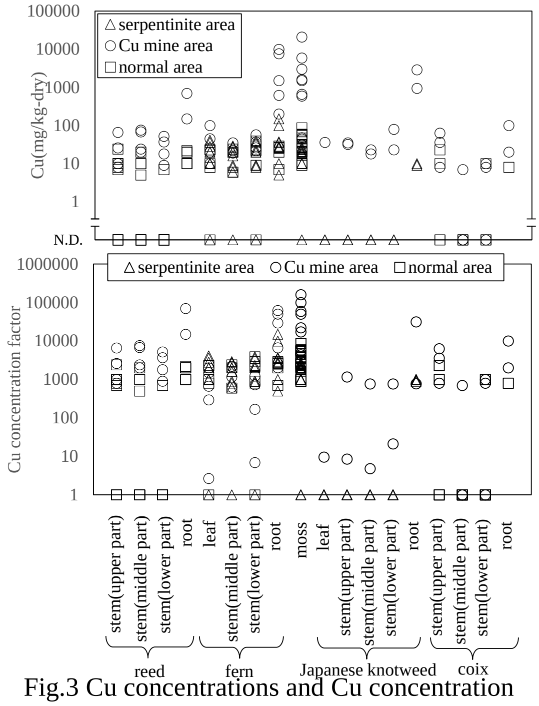

Fig.3 Cu concentrations and Cu concentration factors of water plants.

Therefore, their Co concentrations in the Cu mine area were affected by Cu mines.

Co concentrations of river insect species, moss and water plant species excluding moss influenced by the Cu mine were under detection limit to 82 mg/kg-dry, under detection limit to 200 mg/kg-dry and under detection limit to 38 mg/kg-dry, respectively. Then, moss had the highest and a wide range of Co concentration. Figs.4 and 5 show Co concentration factors of river insects and water plants. The concentration factor was regarded as 1 when the concentrations were under detection limit. Maximum Co concentration factors of river insect species, moss and water plant species excluding moss influenced by the Cu mine were 2,733, 3,666 and 3,000, respectively. Then, Co concentration factor of moss was the highest among them. Therefore, moss was a useful species for indicator of Co contamination.

Evaluation for Ni

Figs.6 and 7 show Ni concentrations of river insects and water plants. "N.D." means under detection limit in the figure. Crane fly larva, mayfly larva, corixidae, reed and coix cannot be sampled in the serpentinite area. Ni concentrations of Japanese freshwater crab, caddice-worm, dobsonfly larva, dragonfly larva and stonefly larva in the serpentinite area were under detection limit to 39 mg/kg-dry, 150 to 220 mg/kg-dry, under detection limit to 83 mg/kg-dry, under detection limit to 60 mg/kg-dry and under detection limit to 20 mg/kg-dry, respectively. Ni

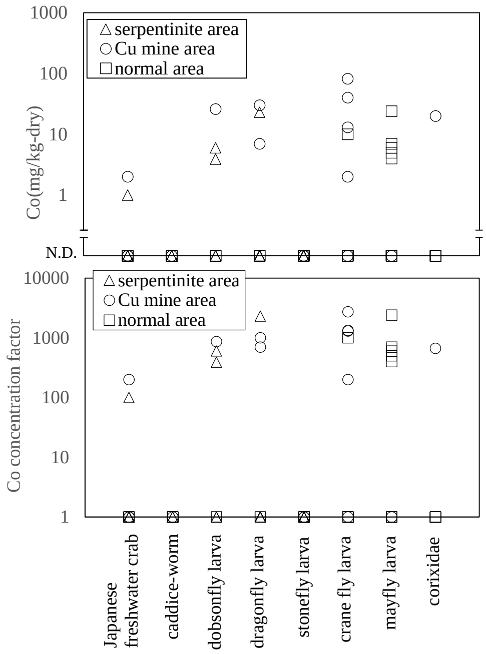

Fig.4 Co concentrations and Co concentration factors of river insects.

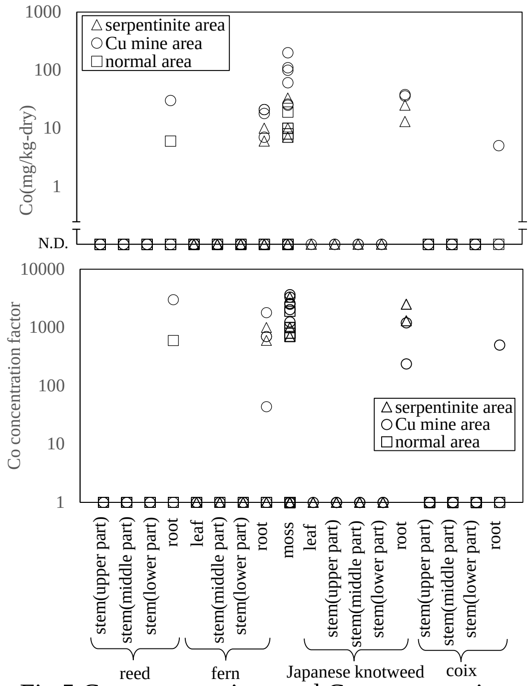

Fig.5 Co concentrations and Co concentration factors of water plants.

concentrations of Japanese freshwater crab, caddice-worm, dobsonfly larva, dragonfly larva and stonefly larva in another area were under detection limit to 1 mg/kg-dry, under detection limit to 20 mg/kg-dry, under detection limit, under detection limit to 10 mg/kg-dry and under detection limit, respectively. Ni concentrations of fern, moss and Japanese knotweed in the serpentinite area were under detection limit to 270 mg/kg-dry, 9 to 590 mg/kg-dry and 7 to 320 mg/kg-dry, respectively. Ni concentrations of fern, moss and Japanese knotweed in another area were under detection limit to 30 mg/kg-dry, under detection limit to 50 mg/kg-dry and under detection limit to 23 mg/kg-dry, respectively. Then, their Ni concentrations in the serpentinite area were higher than another area. In the past study, it was clarified that Ni of river insects and water plants in the serpentinite area in the Kinokawa River catchment were affected by serpentinite [1]. Therefore, their Ni concentrations in the serpentinite area were affected by serpentinite.

Ni concentrations of river insect species, moss and water plant species excluding moss influenced by the serpentinite were under detection limit to 220 mg/kg-dry, under detection limit to 590 mg/kg-dry and under detection limit to 320 mg/kg-dry, respectively. Then, moss had the highest and a wide range of Ni concentration. Figs.6 and 7 show Ni concentration factors of river insects and water plants. The concentration factor was regarded as 1 when the concentrations were under detection limit. Maximum Ni concentration factors of river insect species, moss and water plant species excluding moss influenced by the serpentinite were 22,000, 59,000 and 32,000, respectively. Then, Ni concentration factor of moss was the highest among them. Therefore, moss was useful species for indicator of Ni contamination.

Evaluation for Cd

Figs.8 and 9 show Cd concentrations of river insects and water plants. “N.D.” means under detection limit in the figure. Cd concentrations of Japanese freshwater crab, dobsonfly larva and crane fly larva in the Cu mine area were 0.2 to 7.4 mg/kg-dry, 10 mg/kg-dry and under detection limit to 7 mg/kg-dry, respectively. Cd concentrations of Japanese freshwater crab, dobsonfly larva and crane fly larva in another area were under detection limit, under detection limit to 2 mg/kg-dry and under detection limit, respectively. Cd concentrations of lower part stem and root of reed, fern excluding middle part stem, moss, Japanese knotweed root and upper part stem and root of coix in the Cu mine area were under detection limit to 5 mg/kg-dry, under detection limit to 96 mg/kg-dry, under detection limit to 10 mg/kg-dry, under detection limit to 7 mg/kg-dry and under detection limit to 9 mg/kg-dry, respectively. Cd concentrations of lower part stem and root of reed, fern excluding middle part stem, moss, Japanese knotweed root and upper part of stem and root of coix in another area were under detection limit, under detection limit to 2 mg/kg-dry, under detection limit to 2 mg/kg-dry, under detection limit and under detection limit, respectively. Then, their Cd concentrations in the Cu mine area were higher than another area. It is known that Cd was drained from mines [11]. Therefore, their Cd concentrations in the Cu mine area were affected by Cu mines.

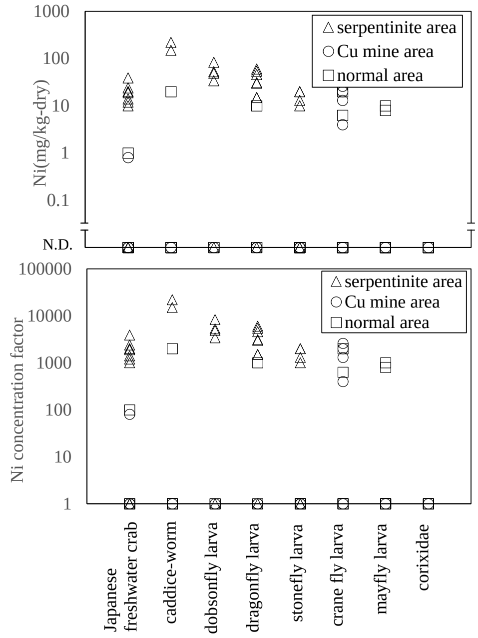

Fig.6 Ni concentrations and Ni concentration factors of river insects.

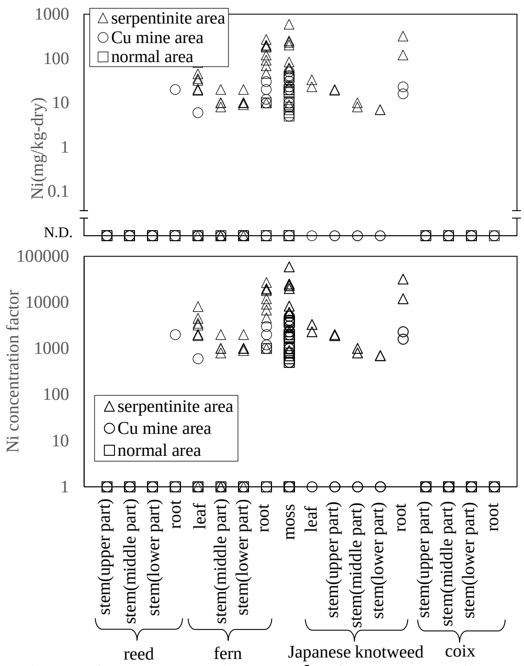

Fig.7 Ni concentrations and Ni concentration factors of water plants.

Cd concentrations of river insect species, fern leaf and water plant species excluding fern leaf influenced by the Cu mine were under detection limit to 10 mg/kg-dry, under detection limit to 96 mg/kg-dry and under detection limit to 61 mg/kg-dry, respectively. Then, fern leaf had the highest and a wide range of Cd concentration. It is reported that Cd concentration of fern leaf is higher than Cd concentration of another part [12]. Figs.8 and 9 show Cd concentration factors of river insects and water plants. The concentration factor was regarded as 1 when the concentrations were under detection

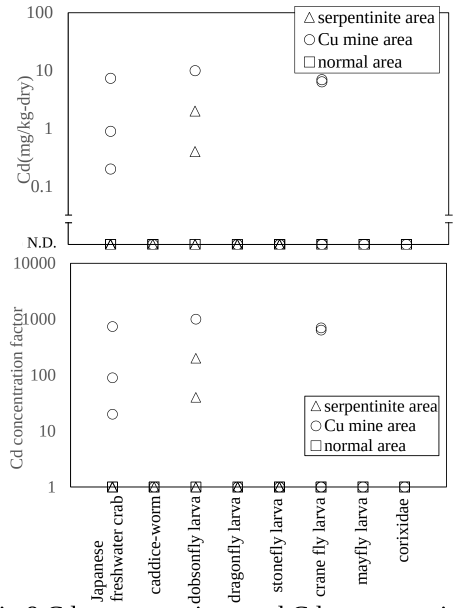

Fig.8 Cd concentrations and Cd concentration factors of river insects.

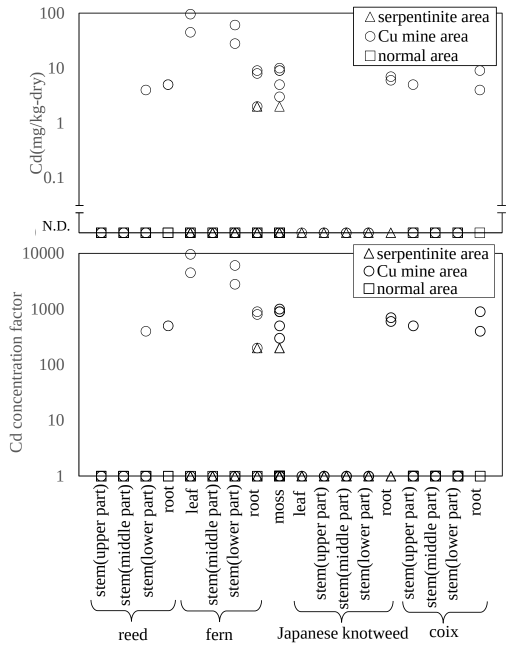

Fig.9 Cd concentrations and Cd concentration factors of water plants.

limit. Maximum Cd concentration factors of river insect species, fern leaf and water plant species excluding fern leaf influenced by the Cu mine were 1,000, 9,600 and 6,100, respectively. Then, Cd concentration factor of fern leaf was highest among them. Therefore, fern leaf was a useful species for indicator of Cd contamination.

CONCLUSION

In this study, Cu, Co, Ni and Cd concentrations of river water, river insects and water plants were studied in the serpentinite area, the Cu mine area and normal area of the Kinokawa River catchment in order to evaluate useful species that can serve as good indicators of metal contamination.

Cu, Co and Cd concentrations of Japanese freshwater crab, dobsonfly larva, crane fly larva and moss in the Cu mine area were affected by Cu mines because their concentrations were high in the Cu mine area. Cu concentrations of dragonfly larva, corixidae, reed, fern, Japanese knotweed and coix were affected by Cu mines because their concentrations were high in the Cu mine area. Co concentrations of dragonfly larva, corixidae, reed root, fern root, Japanese knotweed root and coix root were affected by Cu mines because their concentrations were high in the Cu mine area. Ni concentrations of Japanese freshwater crab, caddice-worm, dobsonfly larva, dragonfly larva, stonefly larva, fern, moss and Japanese knotweed in the serpentinite area were affected by serpentinite because their concentrations were high in the serpentinite area. Cd concentrations of lower part stem and root of reed, fern excluding middle part stem, root of Japanese knotweed and upper part stem and root of coix in the Cu mine area were affected by Cu mine because their concentrations were high in the Cu mine area.

Moss had the highest concentration factor among Japanese fresh water crab, caddice-worm, dobsonfly larva, dragonfly larva, stonefly larva, crane fly larva, mayfly larva, corixidae, reed, fern, moss, Japanese knotweed and coix and a wide range of concentration for Cu, Co and Ni. Therefore, moss was useful as an indicator for Cu, Co and Ni contamination.

Fern leaf had the highest concentration factor among them and a wide range of concentration for Cd. Therefore, fern leaf was useful as an indicator for Cd contamination.

REFERENCES

[1] Kubohara T and Ii H, "CU, CO, CR AND NI OF RIVER WATER, RIVER INSECT AND WATER PLANT IN THE KINOKAWA RIVER CATCHMENT", Int. J. of GEOMATE, Vol.10, No.1, Feb.2016, pp.1600-1606.

[2] Tochimoto H, "Study of Aquatic Insect, Caddisfly, *Stenopsyche marmorata* as a Bio-monitor of Trace Element Contamination in Rivers and Streams: Cadmium and copper", Journal of Japan Society on Water Environment, Vol. 17, No.11, 1994, pp. 737–743.

[3] Aizawa S, Tsunoda K and et al., "Evaluation of Trichoptera as an indicator organism for environmental pollution by heavy metals." BUNSEKI KAGAKU, Vol.43, 1994, pp.865-871.

[4] Fujino A and Ii H, "IMPORTANCE OF CORYDALIDAE AS AN INDEX OF METAL CONTAMINATION OF RIVER", Int. J. of GEOMATE, Vol.9, No.2, Dec. 2015, pp.1483-1490.

[5] Nehring R.B., "Aquatic insects as biological monitors of heavy metal pollution.", Bull. Environ. Contam. Toxicol. , 15 (2), Feb. 1976, pp. 147-154.

[6] Nishioka H and Kodera H, "Heavy metal content in fern plants", Journal of Environmental Conservation Engineering, Vol.34, No.4, 2005, pp. 301-305.

[7] Satake K, Shibata K and et al., "Copper accumulation and location in the moss Scopelophila cataractae", Journal of bryology, Vol.15, No.2, Jan. 1988, pp.353-376.

[8] Sasaki S, "Environmental Characteristics around River Area Based on Analysis of Chemical Contaminants in Reed", Soil mechanics and foundation engineering, 55 (8), Aug. 2007, pp.28-30.

[9] River Bureau Kinki Regional Development Bureau Ministry of Land, Infrastructure, Transport and Tourism, Kinokawa Basin, http://www.kkr.mlit.go.jp/river/kasen/kinokawa.html

[10] Wakayama City Children's Science Museum, http://www.city.wakayama.wakayama.jp/kodomo/sassi/ganseki/chizu/wakayama.htm

[11] Ministry of Land, Infrastructure, Transport and Tourism of Japan, http://www.mlit.go.jp/sogoseisaku/region/recycle/pdf/recyclehou/manual/sizenyuraimanyu_zantei_honbun.pdf, Mar.2010, pp.11-12.

[12] Hikichi H, "Plant and Metals", EQUAL, Vol.2, May 1988, pp.34-37.

ESTIMATION OF EVAPORATION RATE OF SURFACE WATER TO USING HYDROGEN AND OXYGEN ISOTOPIC RATIO

Masahiro Yamashita[1], Hiroyuki Ii[2]
[1]Graduate School of Systems Engineering, Wakayama University, Japan;
[2]Faculty of Systems Engineering, Wakayama University, Japan

ABSTRACT

Hydrogen and oxygen isotopic ratios increased with evaporation rate and the slope, δD/δ^{18}O was found to decrease with temperature. The δD/δ^{18}O was estimated by the experiment. Changes of both δD and δ^{18}O values per evaporation rate were uniform values under the condition of variable humidity and temperature. δD value per evaporation rate was determined to be 0.6 to 2.6 per mile /% andδ^{18}O value per evaporation rate was determined to be 0.09 to 0.26 per mile /% experimentally. Then, evaporation rate can be calculated from change of δD or δ^{18}O value per evaporation rate and difference of isotopic ratios between before evaporation and after evaporation.

Keywords: Evaporation rate, Hydrogen isotopic ratio, Oxygen isotopic ratio, Evaporation experiment

INTRODUCTION

It is concern that depletion of water resource will occur as one of the biggest environmental problems in the 21st century. It is considered that the amount of water that we can use will decrease because the amount of evaporation of water from the ground increases further by global warming. So, it is very important to grasp the evaporation rate for managing of water resource in about dam, reservoir and irrigation water, etc. There are various methods to calculate evaporation rate such as Thornthwaite method [1] and the Penman method [2], etc. The relation between evaporation and isotope is discussed [3], [4]. The estimation method of evaporation rate using isotopic ratio was made by Allison et al. [5] or Gibson et al. [6]. However the application of their method is not straightforward because they need complex parameters as for example expression (1) [7], [8].

$$\frac{d\,\delta_L}{d\ln f} = \frac{h_A(\delta_L - \delta_A)/(1+\delta_L) - \varepsilon^*}{(a-h_A)(a\cdot\alpha_{vap-liq}\cdot e_{i,L}/e + e_i/e)} \qquad (1)$$

δ_L : isotopic ratio of water
f : ratio of water that remains for the first water
δ_A : isotopic ratio of vapor
h_A : humidity
a : water activity
ε^* : $a\varepsilon + \triangle\varepsilon$ (ε : equilibrium vapor pressure ratio, $\triangle\varepsilon$: amount of change equilibrium vapor pressure ratio)
$\alpha_{vap-liq}$: partition coefficient
$e_{i,L}$: diffusion resistance of heavy water in water
e : diffusion resistance of steam in atmospheric (Constant)
e_i : diffusion resistance of heavy water in atmospheric

Past, using oxygen isotopic ratio, simple estimation of evaporation was carried out [9] but both oxygen and hydrogen isotopic ratios have not been clarified.

The purpose of this study was to clarify relationship between evaporation rate, isotopic ratios, humidity and temperature and to propose a simple estimation method.

METHOD

Experiment was performed at thermostatic chamber (SANYO MIRI153: Fig.1). In this experiment, temperature of the thermostatic chamber was changed from 20 degree C to 50 degree C. Temperature and humidity during the experimental period were recorded every 30 minutes by the storage meter (SATO METER WORKS SK-L200TH2: Fig.2). Tap water amount of about 2000g put in polyethylene bottle of capacity 2L evaporated. Detail of the polyethylene bottle is 126mm of diameter, 245mm of height and 75mm of diameter of the mouth. Weight of residual tap water was measured and tap water was sampled once a few days until dried up. Experimental process is as shown in Fig.3.

Fig. 1 Thermostatic chamber.

Fig. 2 Storage meter of temperature and humidity.

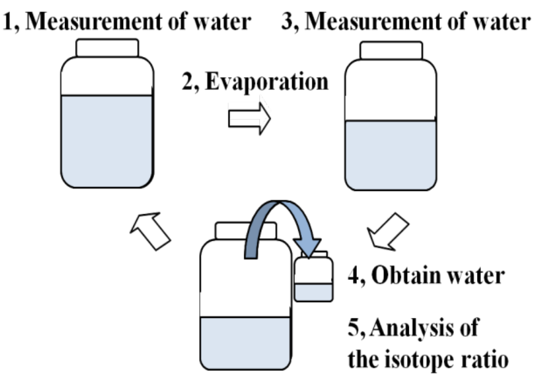

Fig. 3 Process of evaporation experiment.

Measurement of hydrogen and oxygen isotopic ratios was carried out in isotopic ratio measurement system (Sercon Geo Wet System: Fig.4). Hydrogen and oxygen isotopic ratio is presented in per mil (‰) of the standard average seawater (SMOW: Standard Mean Ocean Water). The formulas are shown in equation (2) and (3). Hydrogen and oxygen isotopic ratio of SMOW are denoted as $(D/H)_{SMOW}$, $(^{18}O/^{16}O)_{SMOW}$ and hydrogen and oxygen isotopic ratio of sample are denoted as $(D/H)_{Sample}$, $(^{18}O/^{16}O)_{Sample}$. Measurement error of hydrogen isotopic ratio δD is ±1.0‰ and oxygen isotopic ratio is ±0.1‰.

$$\delta D = [(D/H)_{Sample} / (D/H)_{SMOW} - 1] \times 1000: \quad (2)$$

$$\delta^{18}O = [(^{18}O/^{16}O)_{Sample} / (^{18}O/^{16}O)_{SMOW} - 1] \times 1000: \quad (3)$$

Fig. 4 Isotopic ratio measurement system (Sercon Geo Wet System).

RESULTS

The temperature in the thermostatic chamber was varied in 5 degree C interval from 20 degree C to 50 degree C. Tap water amount of about 2000g was evaporated and taken until dried up at each temperature condition. Water sampling period at each temperature are as follows.

- 20 degree C: 16/04/2014~01/07/2014
- 25 degree C: 17/12/2014~03/03/2015
- 30 degree C: 04/03/2014~15/04/2014
- 35 degree C: 28/07/2014~29/08/2014
- 40 degree C: 16/01/2014~04/02/2014
- 45 degree C: 13/05/2015~04/06/2015
- 50 degree C: 20/10/2014~09/12/2014

Table1 shows number of collected samples, average measured temperature and average humidity at each temperature. Total number of evaporation experiments was 122.

Table1 Summary of each temperature.

preset temperature	20℃	25℃	30℃	35℃	40℃	45℃	50℃
number of sumples	40	18	19	7	22	9	7
average temperature (℃)	19.7	23.8	29.8	34.9	39.3	44.6	49.1
average humidity (%)	64.2	32.6	29.6	43.9	29.0	26.1	30.3

Fig. 5-10 show relationship between evaporation rate and the hydrogen isotopic ratios excluding 45 degree C. And Fig. 11-16 show relationship between evaporation rate and the oxygen isotopic ratios excluding 45 degree C. Samples under 45 degree C condition have not been analyzed.

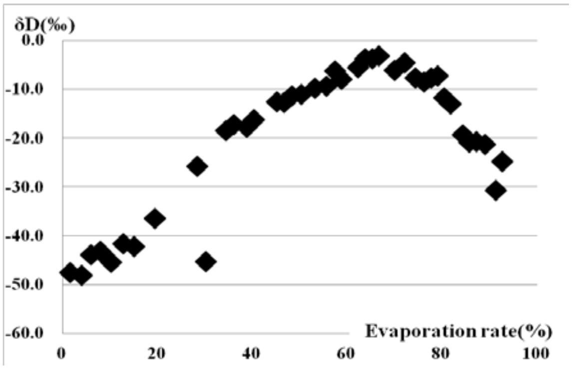

Fig.5 Relationship between evaporation rate and δD at 20 degree C.

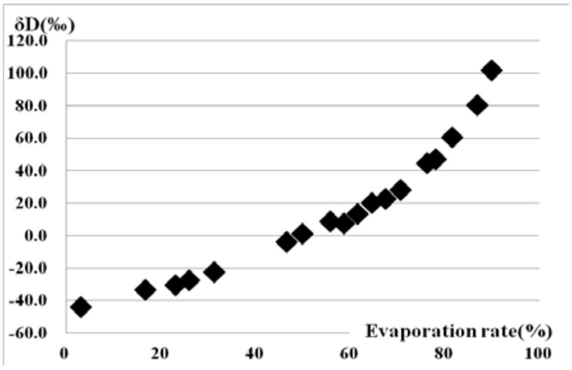

Fig.6 Relationship between evaporation rate and δD at 25 degree C.

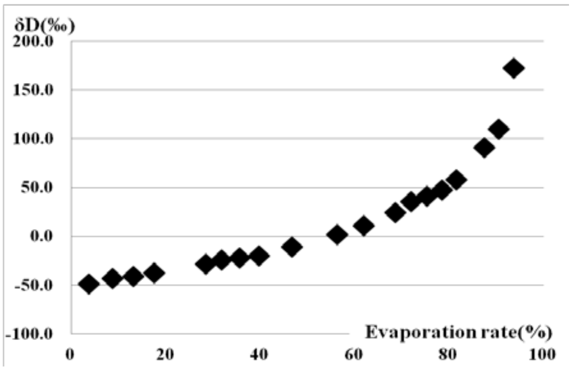

Fig.7 Relationship between evaporation rate and δD at 30 degree C.

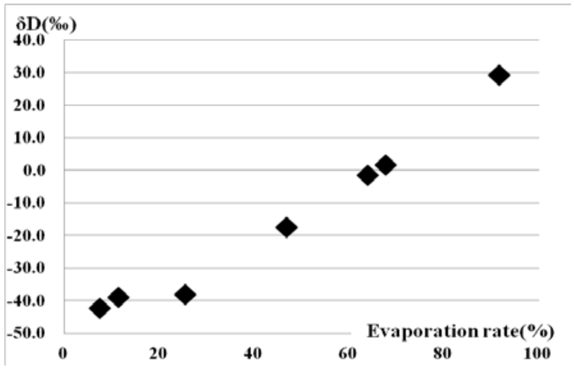

Fig.8 Relationship between evaporation rate and δD at 35 degree C.

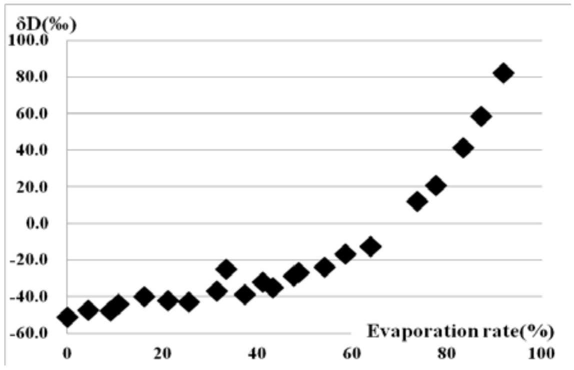

Fig.9 Relationship between evaporation rate and δD at 40 degree C.

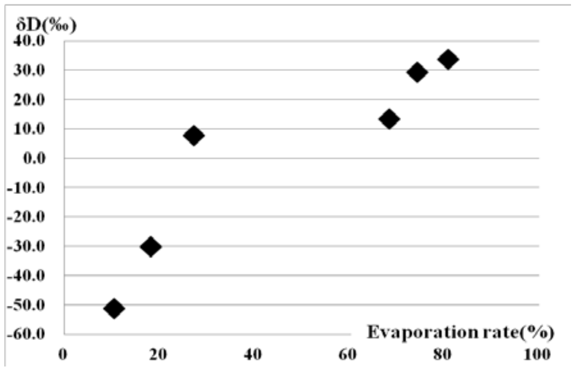

Fig.10 Relationship between evaporation rate and δD at 50 degree C.

Fig. 5-10 show relationship between evaporation rate and the hydrogen isotopic ratios at 20, 25, 30, 35, 40 and 50 degree C. δD value of the tap water before evaporation was -52.3 to -50.3‰. In four experiments excluding 20 and 50 degree C, δD values increased and in particular after 60 to 80% evaporation rate, they remarkably increased. However, at 20 degree C, although δD values increased in the same way until 60% evaporation rate, they decreased with evaporation after 70% evaporation rate. δD values at 30 degree C in Fig.7

rose to 172.1‰ finally, it was the largest increasing among all the 113 samples.

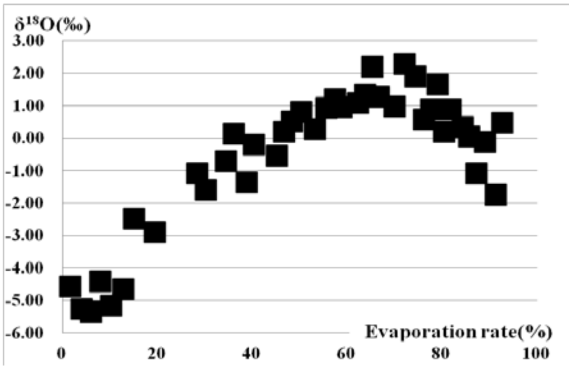

Fig.11 Relationship between evaporation rate and $\delta^{18}O$ at 20 degree C.

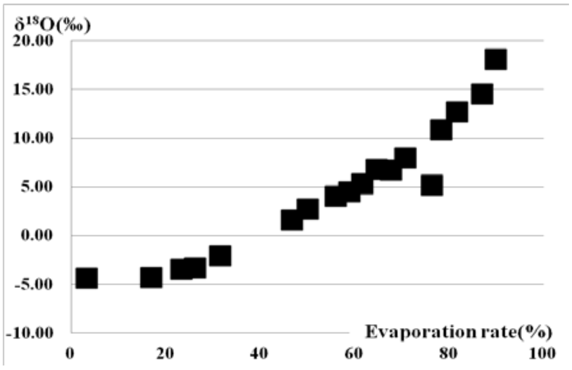

Fig.12 Relationship between evaporation rate and $\delta^{18}O$ at 25 degree C.

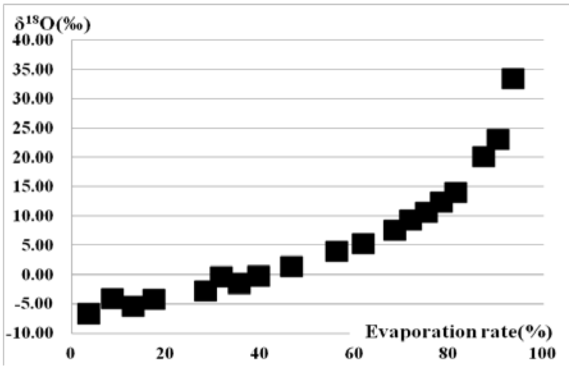

Fig.13 Relationship between evaporation rate and $\delta^{18}O$ at 30 degree C.

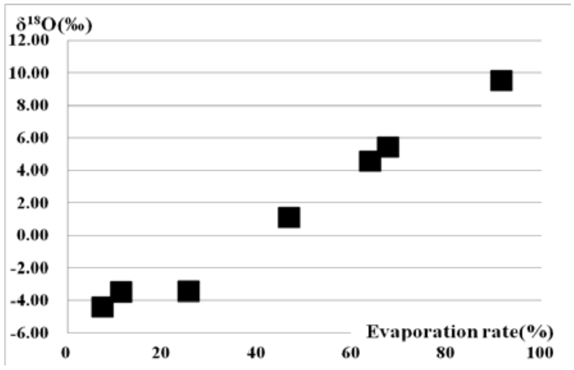

Fig.14 Relationship between evaporation rate and $\delta^{18}O$ at 35 degree C.

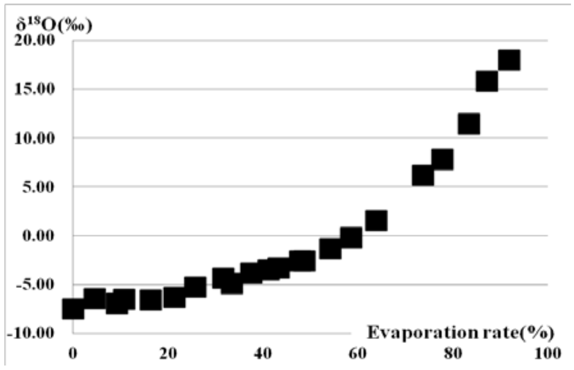

Fig.15 Relationship between evaporation rate and $\delta^{18}O$ at 40 degree C.

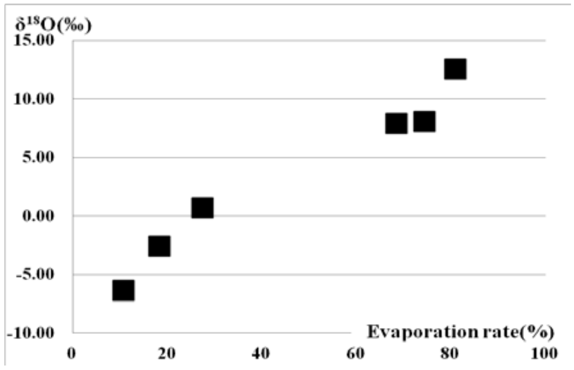

Fig.16 Relationship between evaporation rate and $\delta^{18}O$ at 50 degree C.

Fig. 11-16 show relationship between evaporation rate and the oxygen isotopic ratios at 20, 25, 30, 35, 40 and 50 degree C. $\delta^{18}O$ value of the tap water before evaporation was -7.66 to -7.39‰. $\delta^{18}O$ at 30 degree C in Fig.13 rose to 33.44‰ finally, it was the largest increasing among all the 113 samples. $\delta^{18}O$ values at 25, 30, 35, 40 and 50 degree C increased with evaporation rate and in particular after 50% evaporation rate remarkably increased as well as δD values. At 20 degree C, $\delta^{18}O$ values decreased after 70% evaporation rate. Typically, hydrogen and oxygen isotopic ratio increased when evaporation proceeds. However, decreasing with evaporation rate of both δD and $\delta^{18}O$ values was observed at 20 degree C. Comparing 20 degree C and other temperature condition, humidity of the experiment of 20 degree C was 64.2%, higher than those under other temperature condition. Therefore, humidity was also thought to be critical parameter controlling δD and $\delta^{18}O$ values. Then, it is necessary to consider the influence under high humidity condition.

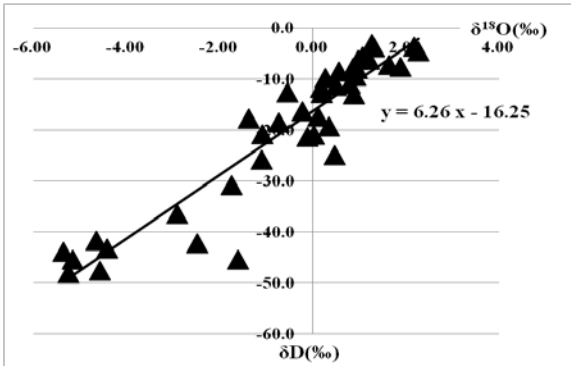

Fig.17 Relationship δD and $\delta^{18}O$ at 20 degree C.

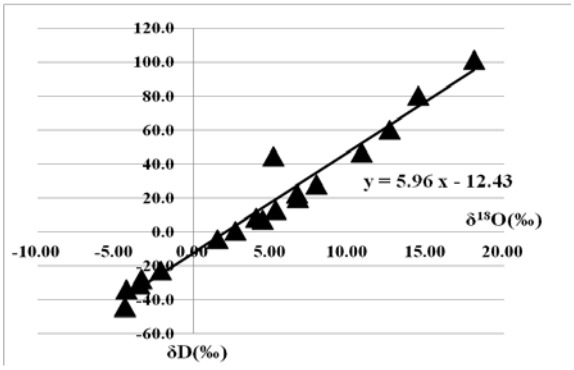

Fig.18 Relationship δD and $\delta^{18}O$ at 25 degree C.

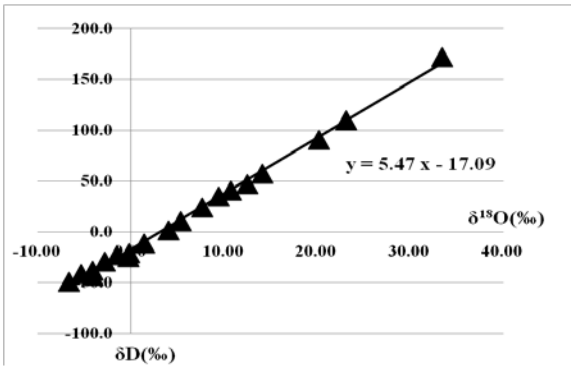

Fig.19 Relationship δD and $\delta^{18}O$ at 30 degree C.

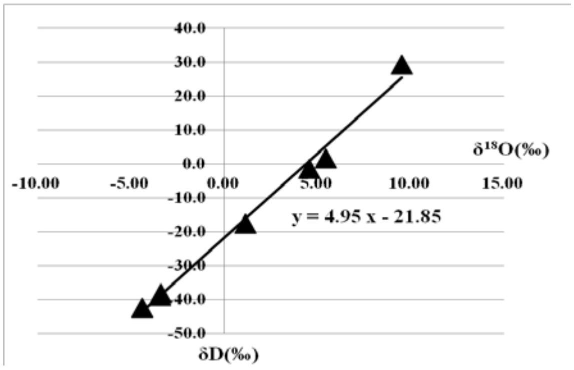

Fig.20 Relationship δD and $\delta^{18}O$ at 35 degree C.

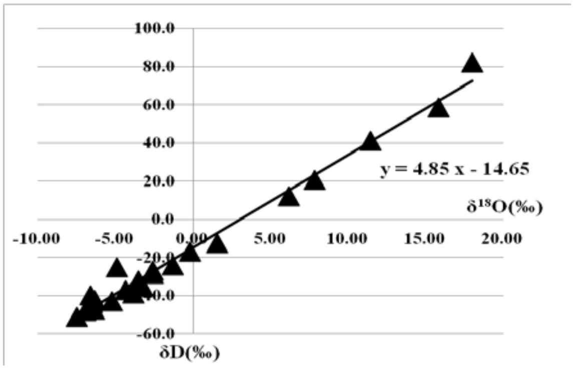

Fig.21 Relationship δD and $\delta^{18}O$ at 40 degree C.

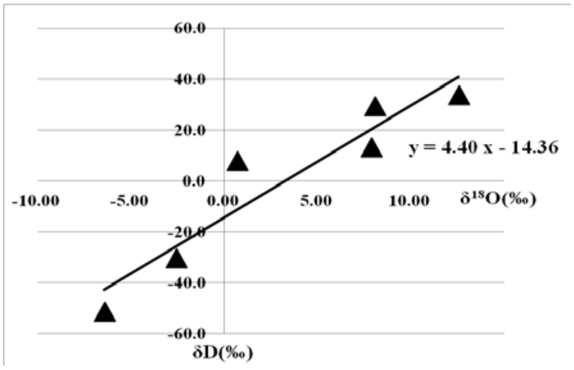

Fig.22 Relationship δD and $\delta^{18}O$ at 50 degree C.

Fig. 17-22 show relationship between δD and $\delta^{18}O$ at each temperature. Most of δD/$\delta^{18}O$ values were distributed on one straight line. However, each slope, δD/$\delta^{18}O$ at each temperature was different. The slope value depended on temperature and it varied from 4.40 at 50 degree C to 6.26 at 20 degree C. The slope of the meteoric water line ($\delta D=8\times\delta^{18}O+10$) is 8. It was found that δD/$\delta^{18}O$ values decreased from 8 for meteoric line with the temperature rising. δD/ $\delta^{18}O$ values were 6.26 at 20 degree C, 5.96 at 25 degree C, 5.47 at 30 degree C, 4.95 at 35 degree C, 4.85 at 40 degree C and 4.40 at 50 degree C.

As a result of regression analysis, equation {$y=-0.064x+7.45$ (x: temperature, y: δD/ $\delta^{18}O$)} was determined. Moreover, from Fig.23, it was found that all lines intersected at -52.3 to -50.3‰ for δD and -7.66 to -7.39‰ for $\delta^{18}O$ which were isotopic ratios of original water before evaporation.

Table2 The changes of δD values per evaporation rate at each humidity.

Evaporation rate(%)	δD(‰)/Evaporation rate(%)		
	0-30 % humidity	31-50 % humidity	51-100 % humidity
0-20	0.75	1.02	0.57
21-40	0.6	0.63	2.63
41-60	0.94	0.95	0.42
61-80	2.08	2.51	-0.33
81-100	7.97	4.98	-1.22

Table3 The changes of $\delta^{18}O$ values per evaporation rate at each humidity.

Evaporation rate(%)	$\delta^{18}O$(‰)/Evaporation rate(%)		
	0-30 % humidity	31-50 % humidity	51-100 % humidity
0-20	0.13	0.14	0.14
21-40	0.13	0.2	0.09
41-60	0.19	0.26	0.1
61-80	0.42	0.21	-0.03
81-100	1.35	0.66	-0.12

DISCUSSION AND CONCLUSION

Tables 2 and 3 show the changes of δD and $\delta^{18}O$ values per evaporation rate at 0 to 30%, 31 to 50% and 51 to 100% humidity. From tables 2 and 3 indicate that the changes of δD and $\delta^{18}O$ values per evaporation rate were not uniform however both the changes of δD and $\delta^{18}O$ values per evaporation rate were uniform less than 60% evaporation rate. After 60% evaporation rate, at 0 to 50% humidity, both the changes of δD and $\delta^{18}O$ values per evaporation rate increased however at over 50% humidity, the changes of δD and $\delta^{18}O$ values per evaporation rate decreased. Therefore, the changes of δD and $\delta^{18}O$ values per evaporation rate were uniform, at the less than 60% evaporation rate. The change of δD value per evaporation rate was 0.6 to 2.6 per mile /%. The change $\delta^{18}O$ value per evaporation rate was 0.09 to 0.26 per mile /%. However over 60% evaporation rate, they were variable and depended on humidity. The variation was thought to be caused by air isotopic ratios because residual liquid water is small volume at high evaporation rate and its isotopic ratios were apt to be influenced by air isotopic ratios. Therefore, from this result, both the changes of δD and $\delta^{18}O$ values per evaporation rate at low evaporation rate were able to use as an evaporation parameter. From the changes of δD or $\delta^{18}O$ values per evaporation rate, difference of isotopic ratios between before evaporation and after evaporation, evaporation rate can be calculated.

REFERENCES

[1] Thornthwaite, C.W.: An approach toward a rational classification of climate. Geographical Review, 38, pp.55-94, 1948

[2] Penman, H.L.: National evaporation from open water, bare soil and grass. Proceedings of the Royal Society of London. Ser. A., Mathematical and Physical Science, 193, pp.120-145, 1948.

[3] Machida I, Kondoh A: Stable Isotope Ratios of Natural Water in Japan –The Analysis by Using Environmental Isotopes Database, J. Japan Soc. Hydrol. & Water Resour. Vol.16, No.15, pp556-569, 2003.

[4] Yoshimura K, Fujita K, Kurita N, Abe O: International Workshop on Isotopic Effects in Evaporation, -Revisiting the Craig-Gordon Model Four Decades after its Formulation - Participation report, Journal of Japan Society of Hydrology & Water Resources.19, pp.420-423, 2006.

[5] Allison, G.B., Brown, R.M. and Fritz, P: Estimation of the isotopic composition of lake evaporate., Jour, of Hydrol. , 42, pp.109-127, 1979.

[6] Gibson, J.J., Edwards, T.W.D., Bursey, G.G. and Prowse, T.D. : Estimating evaporation using stable isotopes: quantitative results and sensitivity analysis for two catchments in northern Canada, 24, pp.79-94, 1993.

[7] Fontes, J. –ch. and Gonfiantini, R.: Comportment isotopique an ocours de levaporation de deux basins Sahariens, Earth Plan.Sci. Letters, 3, pp.277-374, 1967.

[8] Pupezin, J., Jancso, G. and Van Hook, W.A.: Vapor pressure isotope effect in aqueous systems. I, Jour. Phys. hem. , 76, pp.743-762.

[9] Miyahara S and Ii H,"Proposal of simple measurement method for evaporation rate by using oxygen isotopic ratio" Int. J. of GEOMATE, Vol. 9, No.1, 2012, pp. 318-324.

EXAMINING THE IMPACT OF THE 120-DAY WINDS ON EVAPOTRANSPIRATION CONSIDERING PAN EVAPORATION COEFFECIENT IN WEST REGION OF AFGHANISTAN

Homayoon Ganji[1] Takamitsu Kajisa[1] Masaaki Kondo[1] Behroze Rostami[1]
[1]Graduate School of Bioresources, Mie University, 514-8507 Kurima-machiya-cho 1577, Tsu, Japan

ABSTRACT

Evapotranspiration (*ET)* as important applications in irrigation planning plays a significant role in regional and global climate, through the hydrological cycle. *ET* adversely affected by the "120-day winds" in west region of Afghanistan. In this study, by examining the impact of metrological factors on evaporation process, the relationship of the wind speed (u_2) and pan coefficient (K_p) with reference evapotranspiration (ET_0) is examined. Penman-Monteith Method is used to estimate (ET_0-PM), whereas pan evaporation (E_{pan}) data, which is measured directly at the site, with experimental coefficient K_p is used to estimate (ET_{pan}). K_p is presented as K_p-S, which is obtained from Snyder (1992) equation and K_p-D, which is derived from ET_{pan} and ET_0-PM equations. As results, by comparing ET_0-PM with ET_{pan} and E_{pan}, it has been found that, in windy season from June until September, the ET_0-PM is lower than the E_{pan}. Whereas, the ET_0-PM is smaller when compare with ET_{pan}. Contrary to what is expected, determination coefficient (R^2) of E_{pan} shows higher value with ET_0-PM than the ET_{pan}. Furthermore, standard error estimation (SEE) of E_{pan} with ET_0-PM is obtained larger than that of the ET_{pan}. On the other hand, by considering R^2, effect of temperature is fond more significant on ET_{pan} than the wind speed (u_2) and relative humidity (*RH*). K_p-S and K_p-D show similarity only in windy season from June until September. On the other hand, by increasing u_2, K_p-S decreases. Hence, the effect of strong wind on K_p-S is more than the *RH* in windy area like Herat.

Keywords: Reference Evapotranspiration, Pan Evaporation, pan Evaporation Coefficient

INTRODUCTION

Afghanistan, as a dry country, is characterized by extremes of climate and weather that can be counted as continental climate [2].

The climate variation is observed arid in the south and southwest and to semi-arid in the most other parts of the county.

Agriculture as a main source of income in Afghanistan has been facing challenges since decades. Water scarcity is the extreme challenge which threatening the agricultural production.

The main consumer of fresh water in Afghanistan is Agricultural irrigation. There in Afghanistan, both rain fed and irrigated cropping agriculture is practiced. A land use survey was conducted on 1990s which estimated 3.2 million ha was irrigated of which 48 percent was intensively irrigated and 52 percent was intermittently irrigated with one or more crops [12].

Spatial distribution of water availability is not equal among the regions in Afghanistan.

Western region consists of four provinces such as Herat, Farah, Badghis and Ghour province, is characterized with semi-arid climate that has low precipitation, as the total precipitation was 345.6mm in 2009.

Many various factors influence water availability at the region as one of the main factor is strong winds locally known as "120-day winds".

The "120 day winds" usually begin in early July and go on until late September with a great force 7m/s averagely [6]. This period is cover entire of the summer season as this time is the main season of crop growing. According to the data measured in 2009, the precipitation is almost zero at the windy season and daily average temperature is high as 17.5 °C. The ET_0 in Herat has the highest rate in compare to the other cities in Afghanistan, as the daily average value is more than 10 mm [5]. One of the factors among the all other factors which adversely affect the irrigation is the "120-day winds". The great impact of wind velocity is increasing *ET* which can have profound implications for hydrologic processes and agricultural crop performance [3].

ET estimation has important applications in irrigation planning as it plays a significant role in regional and global climate, through the hydrological cycle [9] [10] [11].

Many different concepts are used for defending the *ET* term, as one of them is reference evapotranspiration (ET_0). The evaporative demand of atmosphere apart from the crop type, crop development and management practices is introduced by ET_0 [1]

For estimating the ET_0, many different methods have been developed based on their daily performance under the given climatic condition worldwide, of which six well known methods has been examined by H. Ganji et al. (2015) to estimate ET_0 value for the west region. By considering pan evaporation (E_{pan}) as indicator, the Penman-Monteith method is confirmed the most accurate model for estimating the ET_0 among the six well known models in the west region of Afghanistan.

For estimating the ET_0 using E_{pan} value, considering appropriate coefficient (K_P) is important in calculation.

The empirically derived coefficient K_p is a correction factor which depends on the prevailing upwind fetch distance, average daily wind speed, and relative humidity conditions associated with the sitting of the evaporation pan [4].

The K_P is ranged from 0.35 to 0.85 depends on deferent conditions [1]. Many various equations have been presented for calculating the K_P in the world, but dose equations cannot cover the effective environmental factors on K_p compatibly, as the local estimation is necessary for estimating the accurate value of ET_0.

Among the all K_P estimated equations that presented till now, Snyder (1992) equation Eq. 3 is used for estimating the ET_0 in this study Table 1.

The proposed equation by Snyder (1992) is a simpler equation for calculation daily K_P as a function of daily mean wind speed, measured at 2 meter height (Km/day), daily mean relative humidity (RH) (%) and upwind distance fetch of low growing vegetation (m).

In this paper, emphasize is focused on effect of K_P in estimation of the ET_{pan} using E_{pan} measured data, especially in windy season. Estimating the ET_{pan} using E_{pan} measured data is related to the Eq. 2 which requires the coefficient K_P [1].

It's hypothesized that, K_P is effected more than relative humidity as well as, ET_{pan} is effected by the wind speed more than the other required factors.

METHODS AND DATA

Site

The only official center where is appropriate for researching is Urdu khan Regional Agricultural Research Station. This station is the largest station in the west region which was considered as study area in this research. Urdu khan research center with a total area of 225 hectares, located in a latitude of 39° 11' N and a longitude of 68° 13' E with an elevation of 964 meters in Urdu khan village, at 5.8 kilometers southeast of Herat city. The station is bounded by Urdu khan right canal on the north and east canal on the east. In 1968 approximately 15 hectares of the total area were cultivated for the first time and extended until now as a research center [11].

According to the measured data of climatic factors in 2009, shown in Fig. 1 to 4, the maximum mean annual temperature is around 37.5°C and minimum mean temperature is 0.5°C, the total precipitation is 345.6 mm, the daily average relative humidity is 41.3 % and the daily average wind speed is 271.7 km.

Metrological Data

Many different sources are used for data collection Table 2 [5]. The metrological data is collected for year 2009, which includes the daily E_{pan}, sunshine hours, daily values of precipitation, maximum and minimum temperatures daily average relative humidity and daily average wind speed.

Mostly the climatic data is provided by Urdu Khan Research center where has not been equipped with standard and modern measurement devices yet. (I.e. the E_{pan} is measured through a very simple pan apart from standard A- class pan or etc.). Furthermore, data missing is occurred sometimes as there were some missing data for some days in 2009. Thus, interpolation method is sued to cover missing data.

Table 1 Accessible online database for irrigation planning [5].

Name	Features
CROPWAT (FAO)	Data of mean ET_0
CLIPWAT (FAO)	Component data of ET_0
NCDC (NOAA)	Air temperature, dew point, and wind velocity
Weatherspark.com	Basic daily data. Cloud cover, wind velocity, air temperature and humidity at the airport. Hourly data may be available.
Urdu khan Research center	Data of E_{pan}, temperature, sun shine and precipitation

Calculation equations

The Equations that have been used in calculation are listed in Table 2 as:

1. ET_0 and ET_{pan} have been estimated by using Penman-Monteith methods and E_{pan} data Eq. (1and 2 respectively).
2. Kp-S and Kp-D were calculated by using Eq. (3 and 4 respectively)
3. SEE is calculated by sing Eq. (5).

Table 2 Calculation equations

Model	Equation	No
Penman-Monteith (ET_0 -PM)	$\boldsymbol{ET_0 - \mathrm{PM} = \dfrac{0.408\Delta(R_n - G) + \gamma \dfrac{900}{T+273} u_2 (e_s - e_a)}{\Delta + \gamma(1 + 0.34u_2)}}$	1
ET_{pan}	$\boldsymbol{ET_{Pan} = K_p \times E_{pan}}$	2
Derived Pan Coefficient	K_{p}-D= $\boldsymbol{ET_0 - \mathrm{PM} \div E_{pan}}$	3
Snyder Pan Coefficient	$\boldsymbol{K_p - \mathrm{S} = 0.0482 + [0.24ln(F)] - 0.000376u_2}$ $+0.0045\,RH$	4
Standard Error Estimation (SEE)	$\boldsymbol{\sigma_{est} = \sqrt{\dfrac{\sum(Y - Y')^2}{N}}}$	5

Where:
ET_0 *is* grass reference evapotranspiration (mm day^{-1}), R_{n} is net radiation (MJ m^{-2} day^{-1}), G is soil heat flux (MJ m^{-2} day^{-1}), γ *is* the psychometric constant (kPa °C^{-1}), *es* is the saturation vapor pressure (kPa), *ea* is the actual vapor pressure (kPa), Δ is the slope of the saturation vapor pressure-temperature curve (kPa °C^{-1}), T is the average daily air temperature (°C), u_2 is the mean daily wind speed at 2 m (m s^{-1} except in Eq. 4 is Km/day) [2] [14]. T is the mean monthly temperature (°C), K_{P}-S and K_{p}-D is the pan coefficient, E_{pan} is the pan evaporation (mm day^{-1}), F is the fetch (m), RH is the daily average humidity (%), σ_{est} is the standard error of the estimate, Y is an actual score (ET_{pan}), Y' is a predicted score (ET_0-PM), and N is the number of days.

RESULT AND DESCUSSION

1) daily variation of metrological variables for year 2009 is shown in (Fig. 1 to 4).

Wind speed is seen high from around June until end of September, as the peak occurred in August more than 500 km/day Fig. 1. This period is known as the “120-day winds” in the west region of Afghanistan, especially in Herat province.

Temperature increases from January on, until medal of August, as the peak is seen over 30 °C. From August on, the temperature decreases as the lowest rate is seen in December and January less than 5 °C Fig 2.

Relative humidity is one of the requirements factor for K_{p} calculation. Humidity decreases from April on, as the lowest daily average rate is seen in July less than 20 %. The peak occurred in December more than 80 % Fig. 3. Furthermore, Precipitation (PRCP) occurs mostly from December until May as the peak is seen in March more than 8 mm/day, but from May on, there is no any PRCP Fig. 4. This period coincides with windy season “120-day winds”.

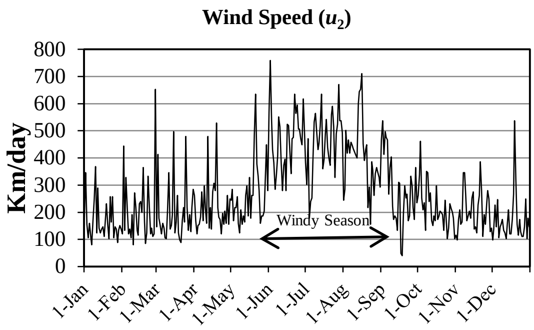

Fig. 1 Daily average wind speed, 2009

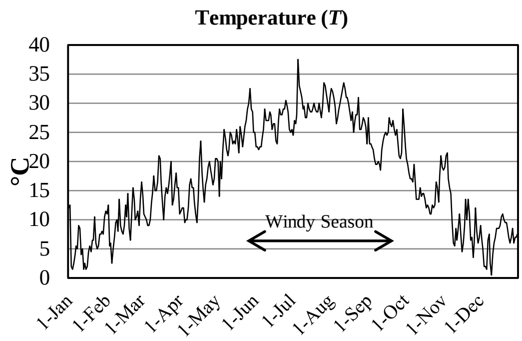

Fig. 2 Daily average Temperature, 2009

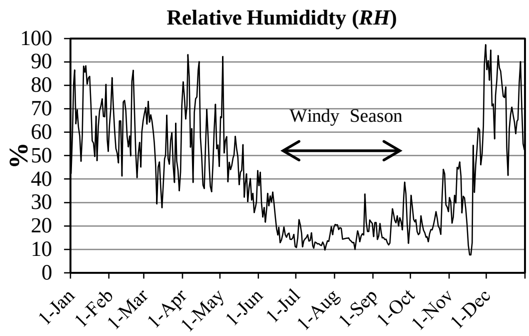

Fig. 3 Daily average relative humidity, 2009

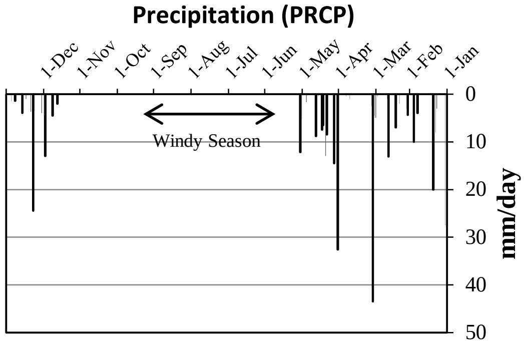

Fig. 4 Daily average precipitation, 2009

2) Compression of E_{pan} and ET_{pan} with ET_0-PM.

By comparing them, it has been found that, in the windy season, form June until September, the ET_0-PM is lower than the E_{pan}, which was measured directly at the site Fig. 5, whereas the difference is smaller when ET_0-PM compared with ET_{pan} Fig. 6.

The reason refers to the K_p application. ET_{pan} is estimated by using the Eq. 2. K_p as a correction factor is recommended for accurate estimation of ET_{pan} value.

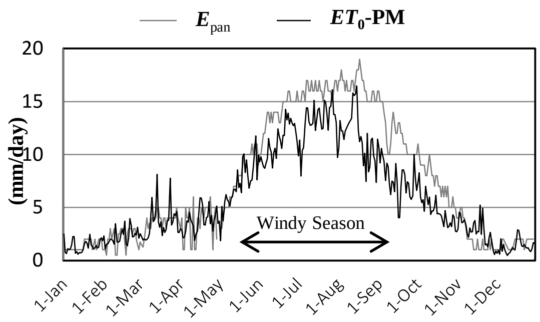

Fig. 5 Daily average E_{pan} and ET_0 PM, 2009

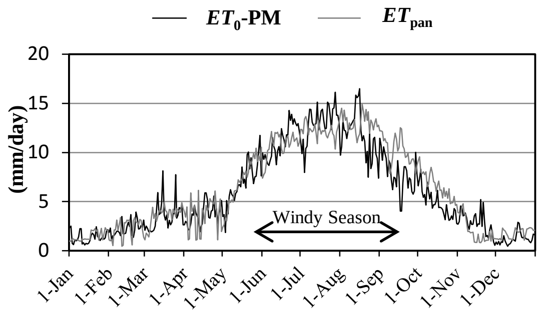

Fig. 6 Daily average ET_{pan} and ET_0 PM, 2009

It was expected that, the ET_{pan} has higher correlation with ET_0-PM than the E_{pan}, but contrary to what is expected, determination coefficient (R^2) of E_{pan} shows higher value with ET_0-pM (Fig 7 and 8). Furthermore, by using the Eq. 5, SEE of E_{pan} is obtained less than the SEE of ET_0-PM Table 3.

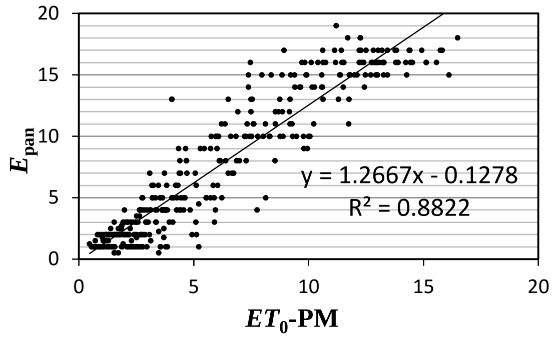

Fig. 7 Regression between E_{pan} and ET_0-PM, 2009

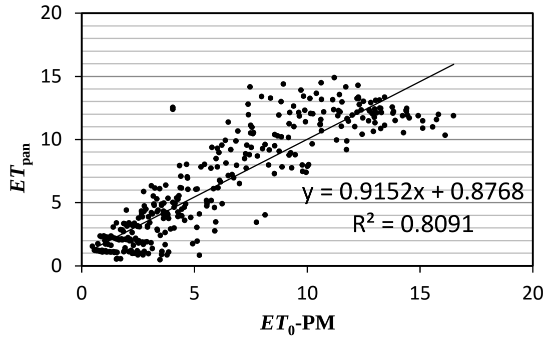

Fig. 8 Regression between ET_{pan} and ET_0-PM, 2009

Table 3 Correlated coefficient of E_{pan} and ET_{pan} with ET_0-PM including standard error estimation value

Models	coefficients R^2	coefficients a	SEE mm/day
ET_{pan}	0.8091	0.915	2.0
E_{pan}	0.8822	1.267	2.7

3) In this study, K_p is presented as K_p-S, obtained by using Eq.3, which is proposed by Snyder (1992) and K_p-D, which is calculated by using Eq. 3. Both Kp are compared between each other, as they show similarity only in windy season from June until September Fig. 9. By using correlation method, it has been found that, the coefficient R^2 is 0.0108 Fig. 9.

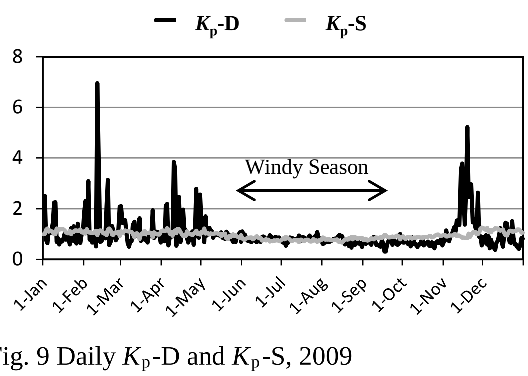

Fig. 9 Daily K_p-D and K_p-S, 2009

According to the Allen et al. (1998), K_p is ranged from 0.35 to 0.85 depends on deferent conditions, but the K_p-S has been found ranged from 0.66 to 1.25. On the other hand, as shown in Fig. 11, by increasing u_2 K_p-S and *RH* decrease. Therefore, the relationship between K_p-S and u_2 is shown in Fig. 12, as the R^2 value is 0.5986.

Effect of strong wind on K_p-S is more than the *RH* in windy area like Herat. As it is seen in Fig. 13, at the windy season, impact of wind factor is larger than *RH*.

It was expected that, the effect of u_2 on ET_{pan} is more than the effect of *T* and *RH*, but contrary to what is expected, by correlating them with ET_{pan}, it was found that, *T* has highest R^2 which is 0.7981 and *RH* has the second R^2 value which is 0.6137, Whereas the u_2 has the lowest R^2 value which is 0.3631(Fig. 14 to 16).

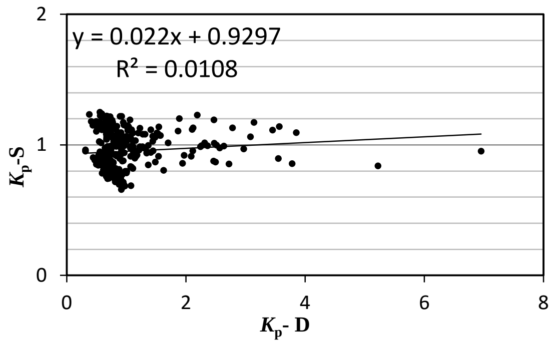

Fig. 10 Correlation between K_p-D and K_p-S

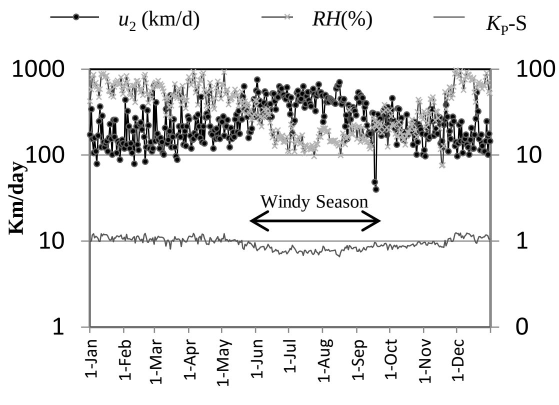

Fig. 11Daily average of u_2, RH and K_p-S in 2009

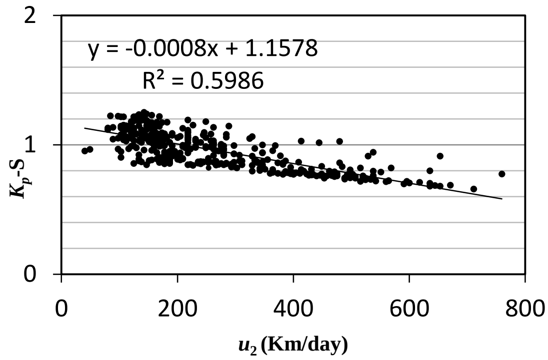

Fig. 12 Correlation between K_p-S and u_2, 2009

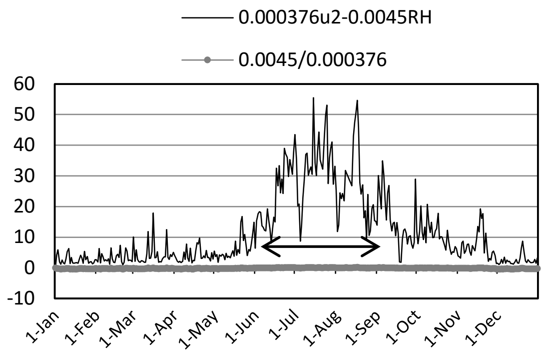

Fig. 13 Comparing of u_2 and *RH*, 2009

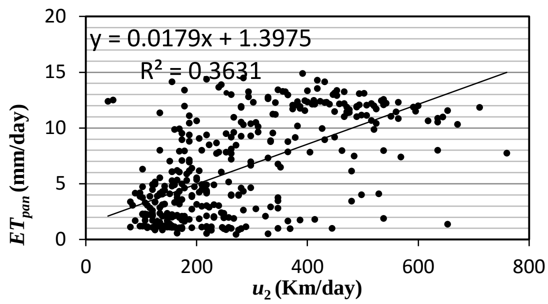

Fig. 14 Correlation between ET_{pan} and u_2, 2009

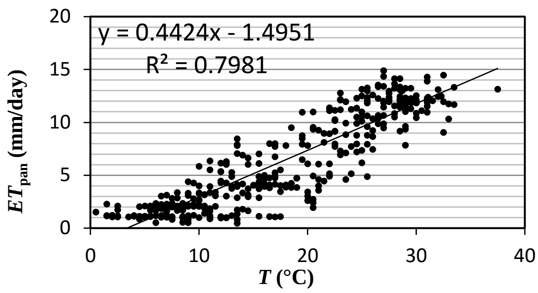

Fig. 15 Correlation between ET_{pan} and *T*, 2009

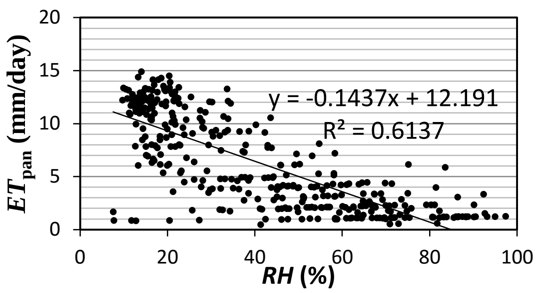

Fig. 16 Correlation between ET_{pan} and T, 2009

CONCLUSION

ET adversely affected by strong wind "120-day winds" as the daily average ET_0 is more than 15 mm. the reason refers to the climate condition as in the summer season, the wind speed is strong high, the humidity is low as less than 20%, Temperature is high more than 30 °C and the precipitation is almost zero.

ET_{pan} is found closer to the ET_0-PM than that of E_{pan}. Hence, SEE of ET_{pan} with ET_0-PM is smaller than that of the E_{pan}.

For daily accurate estimating of ET_{pan} in the west region of Afghanistan, appropriate K_p as a correction factor is needed. In this study, K_p-S, which is calculated through Snyder proposed equation, is confirmed appropriate coefficient for ET_{pan} calculation as it ranges from 0.66 to 1.25. it has been found that, effect of u_2 on K_p-S is more than *RH* in windy condition like Herat. Furthermore, K_p-S decreases in windy season when the wind speed is strong.

ACKNOWLEDGEMENTS

Access to the accurate data is still a challenge in Afghanistan due to the luck of modern stations, but recently, the obtained data is more accurate than the last decades.

REFERENCES

[1] Allen, Richard G., et al. "Crop evapotranspiration-Guidelines for computing crop water requirements-FAO Irrigation and drainage paper 56" FAO, Rome , Vol. 300(9), year 1998.

[2] A Qureshi, Asad Sarwar. Water resources management in Afghanistan: The issues and options. Vol. 49. IWMI, 2002.

[3] Bandyopadhyay, A., et al. "Temporal trends in estimates of reference evapotranspiration over India." Journal of Hydrologic Engineering 14.5 (2009): 508-515.

[4] Doorenbos, Jan. "Guidelines for predicting crop water requirements." FAO irrigation and drainage paper 24, Revised 1977, pp. 15-29.

[5] Ganji H, Rahmany Ab. S, Kajisa T, Kondo M, Hajime N, "Effect of the 120-day winds" on Agriculture and Environmental Condition in Herat, Afghanistan". Brisbane, Australia. 4th Int. Conf. on International Conference on Geotechnique, Construction Materials and Environment, 2014, pp. 500.

[6] Ganji H, Rahmany Ab. S, Kajisa T, Kondo M, Hajime N, "Comparison of the Crop Water Need between Actual Wind Condition and Zero Wind Simulation; Wind Velocity within 24-Hour Interval in Herat, Afghanistan". In Tokyo University of Agriculture. 20th Int. Conf. on ISSAAS, 2014, pp. 91.

[7] Ganji H, Kajisa T, Kondo M, Rostami B, "Examining the six well known equations for estimating reference evapotranspiration in Herat Afghanistan". In Tsu City, Japan. 1th Int. Conf. on Science & Environment, 2014.

[8] J. M. Norman, 1996: Use of remote sensing for evapotranspiration monitoring over land surfaces. Hydrol. Sci.—J. Sci. Hydrol., 41, 495–516.

[9] Kalma, J. D., and I. R. Calder, "Land surface processes in large scale hydrology", World Meteorological Organization Operational Hydrology Rep, 1994, pp. 40, 60.

[10] Kustas, W. P., and C. S. T. Daughtry, 1990: Estimation of the soil heat flux/net radiation ratio from spectral data. Agric. For. Meteor., 49, 205–223.

[11] Osmanzai, M. 2009. Annual Report. CIMMYT, Afghanistan.

[12] Rout, Bob, and Cynthia Lee. How the water flows: a typology of irrigation systems in Afghanistan. Kabul: Afghanistan Research and Evaluation Unit, 2008, pp 13.

[13] Snyder, Richard L. "Equation for evaporation pan to evapotranspiration conversions", J. of Irrigation and Drainage Engineering, Vol. 118.6. 1992, pp. 977-980.

Fifth International Conference on Geotechnique, Construction Materials and Environment, Osaka, Japan, Nov. 16-18, 2015, ISBN: 978-4-9905958-4-5 C3051

HEAVY METAL CONCENTRATIONS OF SEAWEED FROM OSAKA BAY TO SOUTH OF KII PENINSULA, JAPAN

Hiroyuki Ii[1] and Miho Kohara[2]
[1]Faculty of Systems Engineering, Wakayama University, Japan; [2]Nishimatsu Construction, Japan

ABSTRACT

Seaweed from locations ranging from Osaka Bay to the southern top of the Kii Peninsula facing the Kurosio Current at the Kii Peninsula were measured for concentrations of arsenic (As), strontium (Sr), zinc (Zn), iron (Fe), manganese (Mn), and lead (Pb). Except for one location at Kanayama neighboring a closed Pb mine, concentrations in seaweed were variable but their average values agreed with world data. Fe concentration in brown algae and Sr concentrations in green algae were high at the northern Kii Peninsula while As concentrations in seaweed and Zn concentrations in red and green algae were also high. Other seaweed metal concentrations at both the south and north sections of Kii Peninsula had almost the same values. On the whole, As and Sr concentrations in brown algae and Fe concentrations in green algae were high. Zn, Mn, and Pb concentrations in brown, red and green algae had almost the same values. Zn and Fe concentration in seaweed at Kanayama was remarkably high being 10 to 100 times that of the world value. Mn and Pb concentrations in seaweed at Kanayama were also 10 times higher than world values.

Keywords: Seaweed, metal concentration, mine waste, Kii Penisula and Kanayama

INTRODUCTION

Many papers detailing metal concentrations in various kinds of seaweeds have been published [1]–[2]. The relationship between time or sea metal concentration and the bio-concentration factor was clarified. Metal concentrations in seaweed at heavily contaminated areas were published and metal concentrations in water and contaminated soil were also described [3]–[5]. The Kii Peninsula in central Japan, neighbors the metropolises of Osaka and Kobe at the north and contacts the Kuroshiro Current in the south. Two different water resources, metropolitan sewage water and the Kuroshio Current, flow past the Kii Peninsula. Waste water from the now closed Pb Kanayama mine, located to the south, flows directly into Kanayama Bay [6]. Metal concentrations in seaweed were measured under several different sea conditions to clarify their relationship with that particular sea condition.

METHOD AND CONDITION

Fig.1 shows 14 sampling points, Ozaki, Misaki, Tomogasima Island north, Tomogasima Island west, Tomogasima Island south, Kada, Saikasaki, Tagui, Senjyo north, Senjyo, Kanayama, Hachijyuu, Susami, Tako and Kiitahara at the Kii Peninsula. All sampling points, except for Kanayama, were on the coast facing the outside sea.

Sampling dates were Ozaki March 2015, Misaki and Tomogasima January 2015, Kada March 2014, Saikasaki May 2014, Tagui, February 2015, Senjyo and Senjyo N April 2013, Kanayama May 2013, Hachijyuu June 2014, and Susami, Tako and Kiitahara April 2015. Sampled seaweed was dried then dissolved with a concentrated nitric acid solution. Metal concentrations in the solution after filtration were analyzed by ICP-AS.

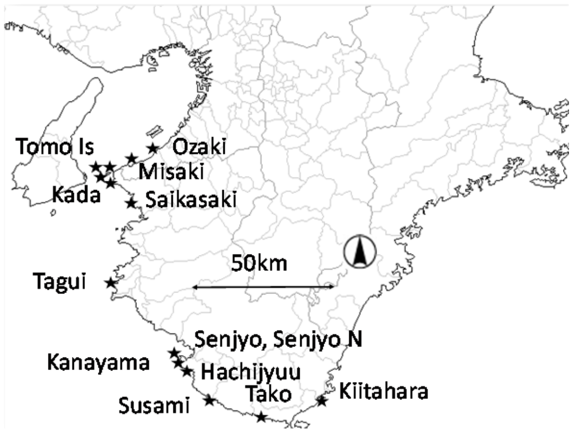

Fig. 1 Sampling points at the Kii Peninsula

Kanayama Sampling Point

Kanayama sampling point was inside Kanayama Bay. Drainage water from two veins of Kanayama mine flows into Kanayama Bay. One drainage water pathway flows into the bay through the river.

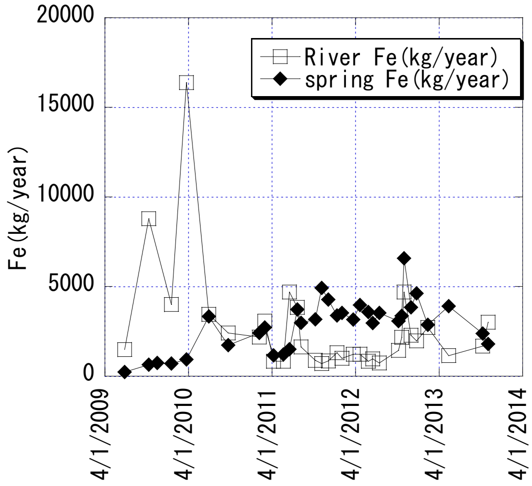

Fig. 2 Fe load of Kanayama mine.

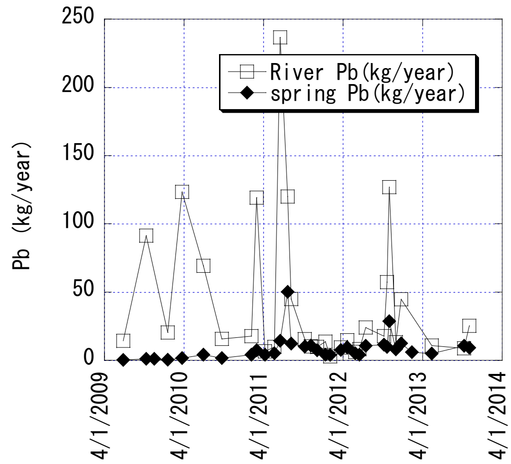

Fig. 3 Pb load of Kanayama mine.

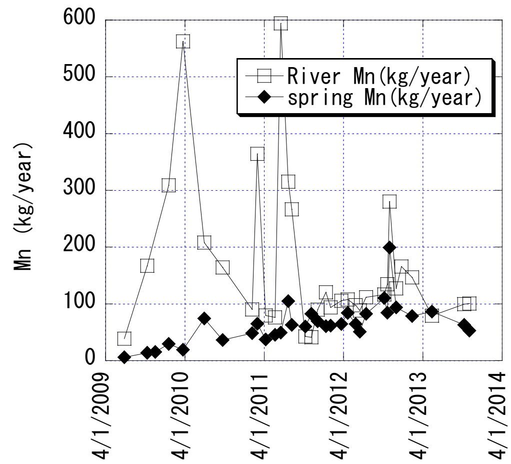

Fig. 4 Mn load of Kanayama mine.

The other drainage pathway is a spring on the coast facing the bay. Total Zn and Cu loads were 3,000 to 5,000 kg per year and several kg per year [6]. Fig 2, 3 and 4 show the Fe, Pb and Mn loads of river and spring. Fe load from the spring increased, from 2,000 to 4,000 kg per year and Fe load from the river varied at about 2,000 kg per year. Then total Fe load was about 4,000 to 6,000 kg per year. Pb load from the spring was stable, 10 kg per year and Pb load from the river varied around 10 kg per year. Then total Pb load was about 20 kg per year. Mn load from the spring was stable at 80 kg per year and Mn load from the river varied around 100 kg per year. Then total Mn load was about 180 kg per year.

Order and Species of Sampled Seaweed

Many kinds of seaweed were sampled and the order of representative seaweed was listed as shown in Fig, 5, 6, 7, 8, 9, and 10. Order (species) of sampled brown algae were Laminariale 1 (Undaria pinnatifida), Laminariale 2 (Ecklonia cava, Undaria undarioides, Agarum clathratum), Fucales 1 (Sargassum muticum, Myagropsis myagroides, Sargassum ringgoldianum), Fucales 2 (Sargassum fusiforme), Fucales 3 (Sargassum thunbergii), Fucales 4 (Sargassum piluliferum), Dictyotales 1 (Dictyota dichotoma), Dictyotales 2 (Dictyopteris undulata, Dictyopteris prolifera), Ishigeales (Ishige foliracea, Ishige okamurae), Dictyotales 3 (Padina arborescens), Scytosiphonales 1 (Myelophycus simplex), Scytosiphonales 2 (Scytosiphon lomentaria), Scytosiphonales 3 (Colpomenia sinuosa, Colpomenia peregrine), and Scytosiphonales 4 (Petalonia binghamiae).

Order (species) of red algae was Gigartinales 1 (Chondracanthus tenellus, Chondracanthus intermedius), Gigartinales 2 (Grateloupia asiatica, grateloupia livida), Gigartinales 3 (Grateloupia lanceolata, Polyopes affinis, Polyopes prolifer, Polyopes lancifolius), Gigartinales 4 (Grateloupia elliptica, Chondrus ocellatus, Chondrus verrucosus), Gigartinales 5 (Gloiopeltis complanata), Gigartinales 6 (Ahnfeltiopsis flabelliformis), Gigartinales 7 (Gloiopeltis furcata), Gigartinales 8 (Caulacanthus ustulatus), Gigartinales 9 (Bonnemaisonia hamifera), Gelidiales (Gelidium crinale, Gelidium japonicum, Pterocladiella tenuis), and Bangiales (Pyropia yezoensis, Pyropia suborbiculata).

Order (species) of green algae were Cladophorales 1 (Cladophora wrightana), Cladophorales 2 (Chaetomorpha gracilis), Ulvales 1 (Ulva intestinalis, Ulva prolifera), and Ulvales 2 (Ulva pertusa, Monstroma nitidum).

RESULTS

As Concentration in Seaweed

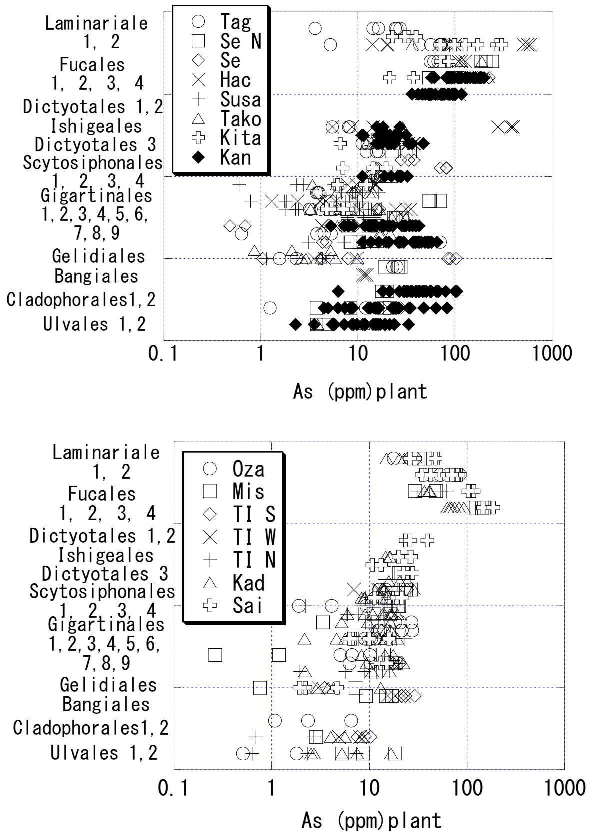

Fig.5 As concentrations in seaweed at north and south Kii Peninsula.

As concentrations in brown algae at the north and south Kii Peninsula were 10 to 300 ppm and 4 to 1,000 ppm as shown in Fig.5. As concentrations in red algae at the north and south Kii Peninsula were 0.3 to 40 ppm and 0.4 to 100 ppm. As concentrations in green algae at the north and south Kii Peninsula were 0.5 to 20 ppm and 1 to 100 ppm. As concentration in seaweed at the South Kii Peninsula was higher than that at the north of Kii Peninsula and As concentrations in brown algae was higher than those in green and red algae.

As concentration in brown algae, a kind of Fucales 1, Sargassum muticum, Myagropsis myagroides, and Sargassum ringgoldianum and a kind of Fucales 2, Sargassum fusiforme and a kind of Fucales 3, Sargassum thunbergii were much high, several 100 ppm. Sargassum fusiforme is a very popular brown algae food known as “Hijiki” in Japanese. Furthermore, As concentration in a kind of Laminariale 1, Undaria pinnatifida or “Wakame”, a very popular seaweed food, in Japanese was 10 to less than 100 ppm. As concentrations in another brown algae, Dictyotales, Ishigeales and Scytosiphonales were several to several 10s ppm and not very different from those of red and green algae.

As concentration in a very popular red algae food, a kind of Bangiales, Pyropia yezoensis, called “Nori” in Japanese were several10 ppm. As concentration in the very popular green algae food, Ulvales 1, Ulva intestinalis, Ulva prolifera and Ulvales 2, Ulva pertusa, Monstroma nitidum, called “Aonori” in Japanese was 0.4 to 100 ppm. In particular, As concentrations in seaweed at Kanayama were not high compared to other areas.

Sr Concentration in Seaweed

Sr concentrations in brown algae at the north and south Kii Peninsula were 50 to 4,000 ppm and 70 to 4,000 ppm as shown in Fig.6. However, they were very high, 500 to 4,000 ppm and 400 to 4,000 ppm excluding Scytosiphonales 3 and Scytosiphonales 4. Sr concentrations in red algae at the north and south Kii Peninsula were 30 to 1,000 ppm and 30 to 1,000 ppm however most Sr concentrations in red algae were 30 to 200 ppm and 30 to 300 ppm. As concentrations in green algae at the north and south Kii Peninsula were 40 to 2,000 ppm and 70 to 400 ppm.

Sr concentration in brown algae was much high. Therefore, analysis of brown algae for concentrations of Sr was found to be an effective method of determining levels of radioactive Sr contamination in seawater surrounding atomic power stations.

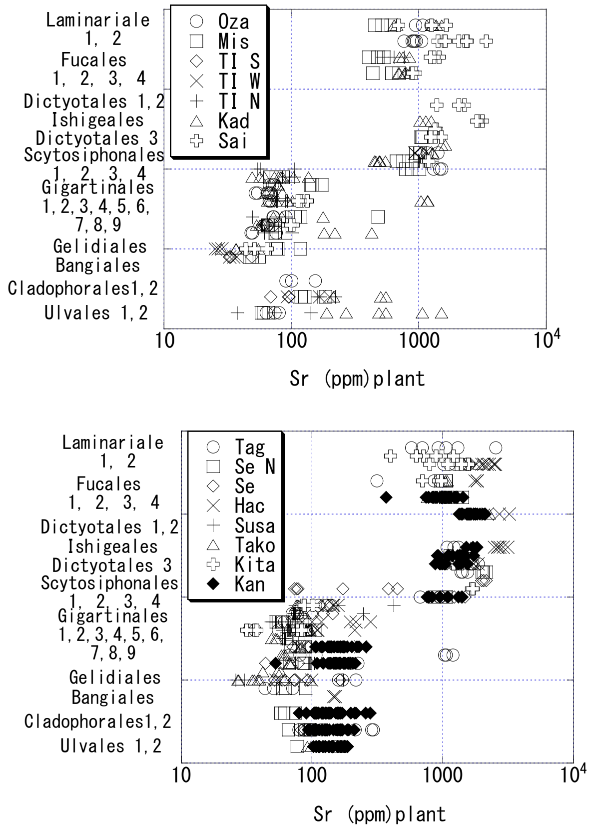

Fig.6 Sr concentrations in seaweed at north and south Kii Peninsula.

On the whole, Sr concentrations at the south Kii Peninsula were as the same as those at the north Kii Peninsula excluding Ulvales 1,2 at Kada. In particular, Sr concentration in seaweed at Kanayama was not high compared to other areas. Sr concentrations of green algae at Kada were moderate to high.

Zn Concentration in Seaweed

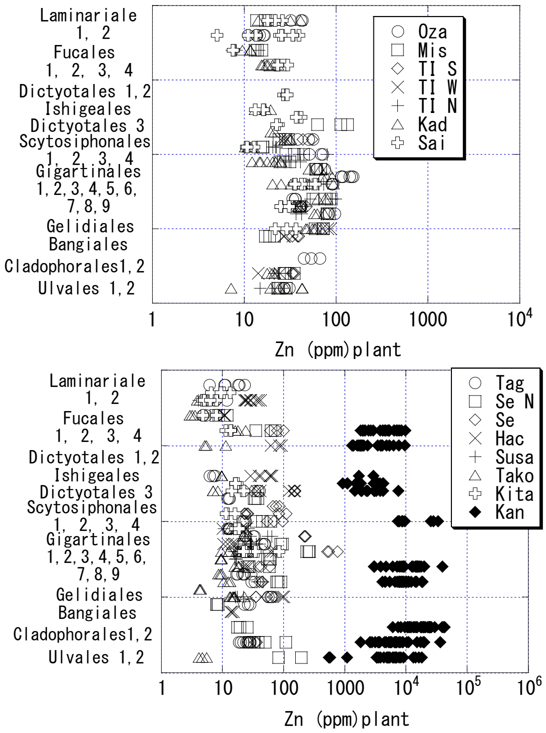

Fig. 7 Zn concentrations in seaweed at north and south Kii Peninsula.

As shown in Fig.7, Zn concentrations in brown, red, and green algae at Kanayama were several 1,000s to 30,000, 2,000 to 30,000, and 500 to 30,000 ppm. These values were much higher than those at other areas. On the whole, Zn concentrations in seaweed at the Senjyo and Senjyo N were 10s to several 1,000s ppm and higher than those at the other area. The Senjyo and Senjyo N points were 1.2 km north of Kanayama sampling point and close to a large hot spring. The Hachijyu point was 1.6 km south of Kanayama sampling point. Zn concentration at Hachijyu was not as high compared to other areas.

Total Zn load into Kanayama Bay was 3,000 to 5,000 kg per year, influence of mine waste water on Zn concentration in seaweed in Kanayama Bay was found. Zn concentrations in seaweed at the Senjyo and Senjyo N were thought to be influenced by mine waste water or hot spring water. Zn concentrations in brown algae at the north and south Kii Peninsula were 5 to 200 ppm and 3 to 200 ppm excluding seaweed at Kanayama. Zn concentration in red algae at the north and south Kii Peninsula were 10 to 200 ppm and 4 to 1,000 ppm excluding seaweed at Kanayama. Zn concentration of green algae at the north and south Kii Peninsula were 7 to 70 ppm and 5 to 200 ppm excluding seaweed at Kanayama. Therefore Zn concentrations at the south Kii Peninsula were as the same as those at the north Kii Peninsula and the Zn concentration difference between brown, red and green algae were found to be small excluding seaweed at Kanayama.

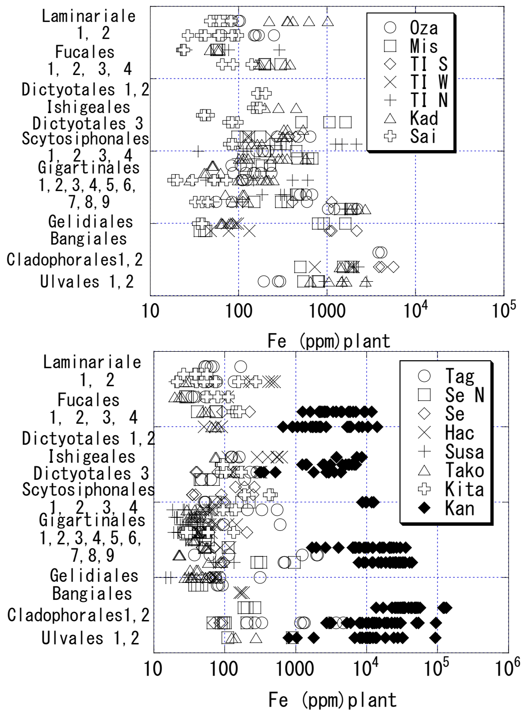

Fig. 8 Fe concentrations in seaweed at north and south Kii Peninsula.

Fe Concentration in Seaweed

Fe concentrations in brown, red, and green algae at Kanayama were several 400 to 10,000, 2,000 to 50,000, and 1,000 to 200,000 ppm and much higher than those at other areas as shown in Fig.8.

Total Fe load into Kanayama Bay was 4,000 to 6,000 kg per year and large as was the Zn load. However, Fe concentrations in seaweed at the Senjyo, Senjyo N and Hachijyu were not always high relative to other areas. Therefore, high Fe concentration in seaweed was found to be just at Kanayama Bay in spite of large amount of Fe load.

Fe concentrations in brown algae at the north and south Kii Peninsula were 30 to 3,000 ppm and 20 to 800 ppm excluding seaweed at Kanayama. Fe concentration in red algae at the north and south Kii Peninsula were 20 to 3,000 ppm and 10 to 3,000 ppm excluding seaweed at Kanayama. Fe concentration in green algae at the north and south Kii Peninsula were 200 to 7,000 ppm and 80 to 4,000 ppm excluding seaweed at Kanayama.

Therefore, Fe concentrations at the south Kii Peninsula were the same as those at the north Kii Peninsula excluding seaweed at Kanayama and in general, Fe concentrations in green algae was higher than those in brown and red algae at the both Kanayama and other areas. “Aonori”, Ulvales 1, Ulva intestinalis, Ulva prolifera and Ulvales 2, Ulva pertusa, Monstroma nitidum, was relatively high, 100 to several 1,000s ppm.

Mn Concentration in Seaweed

Total Mn load into Kanayama Bay was 180 kg per year. Mn concentrations in brown, red, and green algae at Kanayama were 7 to 500, 40 to 8,000, and 4 to 8,000 ppm and much higher than those at other areas as shown in Fig.9. Mn concentrations in brown algae at the north and south Kii Peninsula were 4 to 300 ppm and 2 to 400 ppm excluding seaweed at Kanayama.

Mn concentrations in red algae at the north and south Kii Peninsula were 5 to 400 ppm and 1 to 300 ppm excluding seaweed at Kanayama. Mn concentrations in green algae at the north and south Kii Peninsula were 20 to 700 ppm and 6 to 200 ppm excluding seaweed at Kanayama. Therefore, Mn concentrations at the south Kii Peninsula were the same as those at the north Kii Peninsula excluding seaweed at Kanayama and generally Mn concentrations in green, brown and red algae at the both Kanayama and other areas were the same.

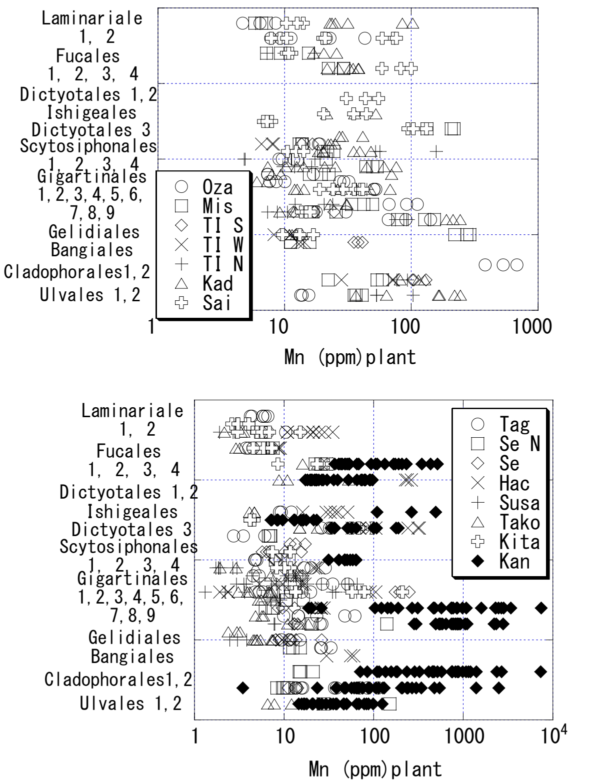

Fig. 9 Mn concentrations in seaweed at north and south Kii Peninsula.

Pb Concentration in Seaweed

Total Pb load into Kanayama Bay was 20 kg per year. Pb concentrations in brown, red, and green algae at Kanayama were 4 to 400, 30 to 1,000, and 4 to 1,000 ppm and much higher than those at other areas as shown in Fig.10. Pb concentrations in brown algae at the north and south Kii Peninsula were 0.2 to 20 ppm and 0.2 to 10 ppm excluding seaweed at the Kanayama. Pb concentration in red algae at the north and south Kii Peninsula were 0.3 to 40 ppm and 0.1 to 10 ppm excluding seaweed at Kanayama. Pb concentrations in green algae at the north and south Kii Peninsula were 2 to 40 ppm and 0.5 to 20 ppm excluding seaweed at Kanayama.

Therefore, Pb concentrations at the south Kii Peninsula were lower than those at the north Kii Peninsula excluding seaweed at Kanayama in spite of Pb load, 20kg at Kanayama, south Kii Peninsula and Pb load at Kanayama was found to be small at the Kii Peninsula. On the whole Pb concentrations in brown algae were lower those in green and red algae at Kanayama however no clear differences between brown, red and green algae were found in the other areas.

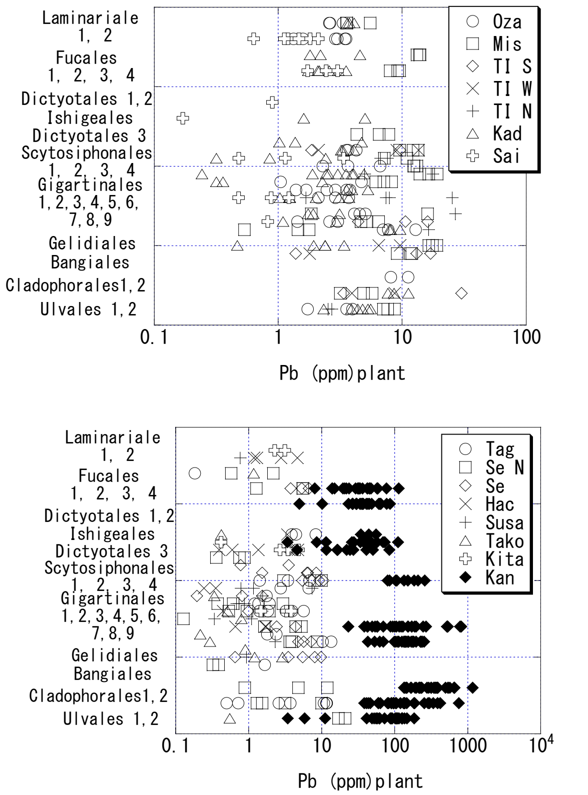

Fig.10 Pb concentrations in seaweed at north and south Kii Peninsula

Table 1 Metal concentration (ppm) of seaweed at north and south Kii Peninsula

	site	brown	red	green
As	north	10~ 300	0.3~40	0.5~ 20
	south	4 ~ 1000	0.4 ~ 100	1 ~ 100
	Ref	62	6	1.2~6
Sr	north	50~4,000	30~1,000	40~2,000
	south	70~4,000	30~1,000	70~ 400
	Ref	800~ 1,600	95~450	60~220
Zn	north	5 ~ 200	10 ~ 200	7~ 70
	south	3 ~ 200	4 ~ 1,000	5 ~ 200
	Kan	1,000~ 30,000	2,000~ 30,000	500~ 30,000
	Ref	20~140	21~150	6~260
Fe	north	30~3,000	20~3,000	200~ 7,000
	south	20~800	10~3,000	80~ 4,000
	Kan	400~ 10,000	2,000~ 50,000	1,000 ~ 200,000
	Ref	13~1,900	200~ 1,800	160~750
Mn	north	4 ~ 300	5 ~ 400	20 ~ 700
	south	2 ~ 400	1 ~ 300	6 ~ 200
	Kan	7~500	40~8,000	4~ 8,000
	Ref	1~400	16~500	16~300
Pb	north	0.2 ~ 20	0.3 ~ 40	2 ~ 40
	south	0.2 ~ 10	0.1 ~ 10	0.5 ~ 20
	Kan	4 ~ 400,	30~1,000	4~ 1,000
	Ref	2~38	2.9	40

DISCUSSION AND CONCLUSION

Table 1 shows As, Sr, Zn, Fe, Mn, and Pb and concentrations in brown, red and green algae between the north Kii Peninsula (north), the South Kii Peninsula (south) excluding Kanayama, Kanayama (Kan) and the world values (Ref) [7].

Metal concentrations in seaweed at Kanayama showed abnormally high values. The Kanayama sampling point was inside the bay and total Fe, Zn, Mn, and Pb loads of mine waste water from the closed mine into the bay were 4,000 to 6,000, 3,000 to 5,000, 180, and 20 kg per year. Zn and Fe concentrations in seaweed at Kanayama were 10 to 100 times relative to the world value. Mn and Pb concentrations in seaweed at Kanayama were 10 times higher than the world values. Fe concentrations in brown algae and Sr concentrations in green algae at the north Kii Peninsula were higher than at the south Kii Peninsula and As concentrations in seaweed and Zn concentrations in red and green algae at the south Kii Peninsula were higher than at the north Kii Peninsula. Other seaweed metal concentrations at both the south and north Kii Peninsula had almost the same values.

Although As, Sr, Zn, Fe, Mn, and Pb concentrations in seaweed from Osaka By to south top of the Kii Peninsula facing the Kurosio Current at the Kii Peninsula were very variable, their average values were in good agreement with the world data except for Kanayama. Therefore, As, Sr, Zn, Fe, Mn, and Pb concentrations in seaweed at the Kii Peninsula were normal values. In general, metal concentration distribution was uniform therefore the influence of the Kuroshiro Current and Osaka Bay facing the metropolis on metal concentration in seaweed was found to be small. As and Sr concentrations in brown algae were higher those in red and green algae and Fe concentrations in green algae were higher than those in brown and red algae. Zn, Mn, and Pb concentrations in brown, red and green algae were all the same.

REFERENCES

[1] Lunde G, “Analysis of trace elements in seaweed”, J. of Sci. Fd. Argic., Vol. 21, Aug. 1970, pp. 416-418.

[2] Yamamoto T, and Ishibasi M, “The Content of Trace Elements in Seaweeds”, in Proc. 7th Int. Seaweed Symposium, 1971, pp. 511-514

[3] Ghada F El-Said and Amany El-Sikaily, “Chemical composition of some seaweed from Mediterranean Sea coast, Egypt”, Environmental Monitoring and assessment, July 2013, Vol. 185, Issue7, pp 6089-6099

[4] Alahverdi M and Savabieasfahani M, “Metal Pollution in Seaweed and related Sediment of the Persian Gulf, Iran”, Bull Environ. Contam. Toxicol, Vol. 88, 2012, pp. 939-945.

[5] Griselda MRF, Evgueni S and Ignacio SR, “Heavy metal Pollution monitoring using the brown seaweed Padina durvillaei in the coastal zone of the Santa Rosalia mining region, Baja calfornia Peninsula, Mexico”, J. Appl. Phycol., Vol. 21, 2009, pp. 19-26.

[6] Ii H, “Cu, Zn and As contamination of seaweed beside Shizuki and Kanayama metal mines in Japan”, Int. J. of GEOMATE, Vol. 9, No.1, Sep. 2015, pp. 1411-1417.

[7] Asami T. and Chino M., “Elements in organism”, Environmental Chemistry of the Elements, 1st ed. Hakuyusha, 1983, pp. 101–105. In Japanese.

Fifth International Conference on Geotechnique, Construction Materials and Environment, Osaka, Japan, Nov. 16-18, 2015, ISBN: 978-4-9905958-4-5 C3051

DISTRIBUTION CHARACTERISTICS OF THE LOAD AMOUNT OF NUTRIENTS, INCLUDING AT THE FLOODS TIME IN YAMATO RIVER BASIN

Masanobu Taniguchi[1] ,Hiroyuki Ii[1], Tatemasa Hirata[1]
[1]Facult of Systems engineering,Wakayam University, Japan;

ABSTRACT

It is important that outflow to the Osaka Bay at the time of the flood of nutrients in the Yamato River. In order to the form of nitrogen and phosphorus nutrition is changed by Purification treatment of sewage treatment plant and purifying effect of rivers, it is necessary to clarify the distribution of nutrients amount in Yamato River. Until now load analysis using LQ formula and intensity method has been carried out, the error is large. This study clarify the runoff characteristics of nutrients at the time of the flood using the data of automatic stations of government, and suggested new method of calculation of flow rate. As a result, the nitrogen load of the Yamato River basin was calculated. As a result, the flood condition of nitrogen load accounts for 45% of annual. The nitrogen load of treated water of sewage system is 23%.
Keywords: the Yamato River, nitrogen load, flow rate, distribution, flood

INTRODUCTION

The Yamato River had problem of water quality in 1970s by High-growth period. In the resent years, the water quality is improved by installation of sewage system in the whole of the Nara Basin. However, the total of nitrogen load is not reduced in the Yamato River, the river has been eutrophication. The riverbed of part region of the river basin is discolored black, so it is estimated that oxygen in the water is insufficient. It is important to understand the distribution of amount of nitrogen load.

The nitrogen load in flood condition is unknown. The organic component is collected by low flow in fine day at spot. The riverbed of high nitrogen concentration flows by the flood, and the amount of water is much, so the nitrogen load in the flood condition is estimated high. The survey in the flood condition is danger, and automatic observing station is not measured the total nitrogen concentration. Therefore the total nitrogen concentration is estimated by another data, and analyzed relation between the nitrogen concentration and the other water quality data.

The research object is the distribution of total nitrogen load including the flood condition.

THE SERARTH AREA AND THE METHOD

Figure 1 shows research area information of the Yamato River Basin. The land use map uses Ministry of Land, Infrastructure and Transport Ministry of Land numerical information

Land use mesh (Heisei 18, 2006)

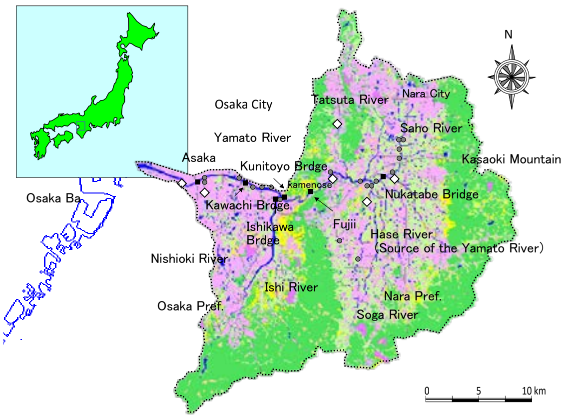

Fig. 1 Research area information of the Yamato River Basin

The area of the Yamato River basin is 1070km^2. The population of the basin is 200 million people. The basin has big cities in upper stream, and the population of the Nara basin is 109 million people. Population has increased significantly in high-growth period. Therefore the sewage system is established from 1970s. The sewage system diffusion rate is 7.4% in 1975, and is 33% in 1990, and is 58.7% in 2000, and is 85.3% in 2013. The river purification facilities are established as the water quality of improvement from 1994.

The analysis of nitrogen load uses the water information system of Ministry of Land, Infrastructure, Transport and Tourism, Japanese Government. To calculate the correct flow rates, Wakayama University surveyed the river cross section and flow velocity. The flow rate of null data are calculated by the new manning method that is suggested in this research. Some observing stations have both of water level and flow rate, and the recent data are not updated in near 2 or 3 years. It is necessary to interpolate the flow rate, to calculate the nitrogen load in whole a year. The calculated flow rate is compared with the upper stream and the lower stream, it confirmed the consistency.

THE TIME SERIES OF FLOW RATE AND NITROGEN LOAD IN REAL DATA

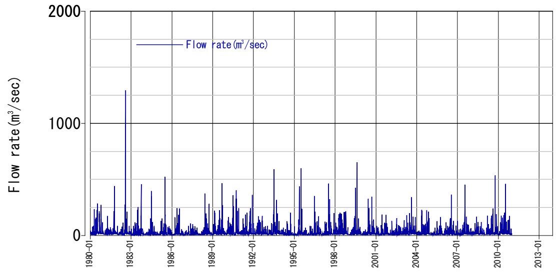

Fig. 2 The time series of flow rate at Fujii(lower stream in Nara Basin)

Figure 2 shows the time series of flow rate in Fujii. The observing station is lower stream in the Nara Basin, and this point is all collected water in the Nara Basin. The observing station have both of water level and flow rate, and have automatic water quality measurement, and many water quality items. The max of flow rate is about 1200m^3/sec in 1982. The usual flow in fine day is about 13m^3/sec, and the monthly data is measured by around the value of flow rate. The value is calculated by 50% of the rank of the flow rate, as the value is less than at 185 days in 365 days. The most new data is the data in 2010, is no data in after 2011.

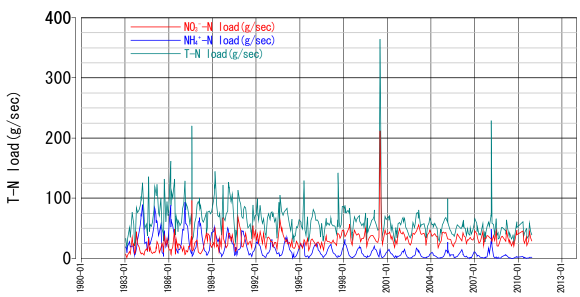

Fig. 3 The time series of nitrogen load at Fujii

Figure 3 shows the time series of the nitrogen load at Fujii. The nitrogen load is calculated by the real measured data, and not include the nitrogen load in the flood condition. So, it is estimated that nitrogen load is more big value in annual. The usual total nitrogen load in fine day is average 63g/sec, and is tend to decrease mostly from 1975 to 2010. The usual nitorete nitrogen load in fine day is average 29g/sec, and is tend to increase mostly from 1975 to 2010. The usual ammonia nitrogen load in fine day is average 16g/sec, and is tend to decrease mostly from 1975 to 2010. The sewage system diffusion rate is increased from 7% to 85% in this term, however the total nitrogen load is not little changed constantly. The cause is estimated that ammonia nitrogen is changed to nitrate nitrogen, total nitrogen is not changed.

THE ANALYSIS OF T-N LOAD AT FUJII AND ESTIMATION OF FLOW RATE

The Fujii observing station is important for calculate the runoff of the whole Nara Basin , as the lowest point in the Nara Basin. However the Fujii has no flow rate data in 2011. It is necessary to estimate the flow rate.

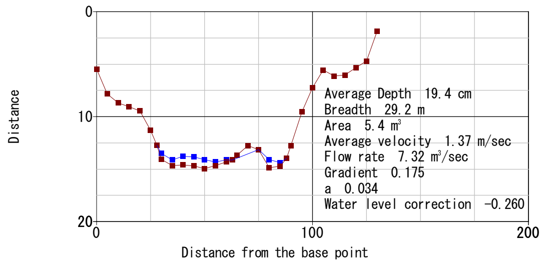

Fig. 3 The river cross section at Fujii

The actuary cross section is possible to calculate the flow rate from water level. The velocity is calculated from follow equation.

$$v = \frac{1}{n} a^{\frac{1}{2}} H^{\frac{1}{6}}$$
(1)

v:velocity, n:Roughness coefficient, a:Eigenvalue of observatory, H:water depth

The equation is derived by the Manning equation. The Manning method uses Hydraulic radius(R), it is possible to R replace H in generally in big rivers. The Manning equation can be modified the following equation. ,

$$v^2 = \frac{1}{n^2} H^{\frac{1}{3}} H^{\frac{3}{3}} I^{\frac{2}{2}}$$
(2)

$$a = HI$$
(3)
I: Hydraulic gradient

Equation (1) is made by substituting the equation (3) into equation (2).As the bot of flow rate and water level is measured in Fujii, the area of the river across section is calculated by the water level. The average velocity of the river cross section in a day is determined by dividing the flow rate in the area. Unknowns become one of parameter *I*. The parameter *I* is calculated by the Manning method. The parameter a is calculated by equation (3), and figure 4 shows the relation between average water depth and Hydraulic gradient (*I*).

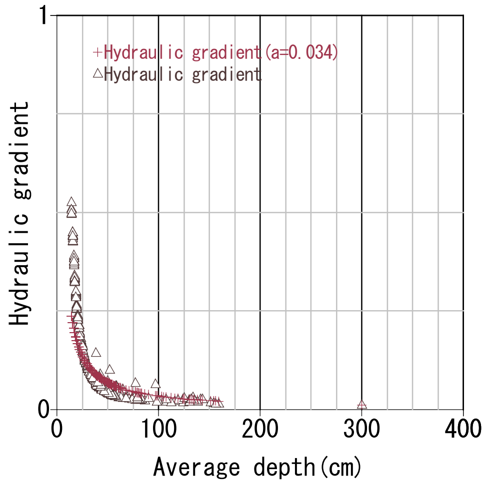

Fig. 4 The relation between average water depth and Hydraulic gradient (*I*) at Fujii in 2010

The average parameter a can be calculated by annual data or some major depth. Now is annual data, parameter *a* is determined 0.034 at Fujii. The water level is fitting to the survey depth, the current value is -0.26m, and the roughness coefficient (n) is 0.100 in general apply for the natural river.

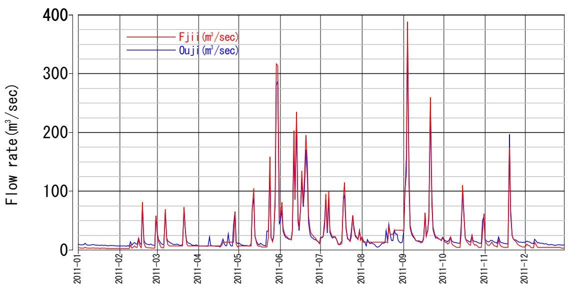

Fig. 5 The time series of the flow rate at Fujii and at Oji

Figure 5 shows the time series of the flow rate at Fujii and at Oji. Oji is upper stream of Fujii, and a small river flows into between Oji and Fujii. It was confirmed the calculated flow at Fujii is almost exactly.

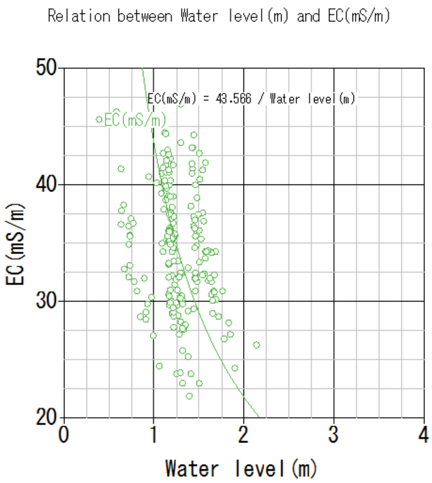

Fig. 6 The relation between water level and EC by monthly data from 1989 to 2011 at Fujii

Figure 6 shows the relation between water level and EC by monthly data from 1989 to 2011 at Fujii. T-N concentration is not measured every day, moreover there are little data in annual. However EC value is measured every day by automatic observing station. EC value is measured at flood time. EC value is decrease with water level and the relation between water level and EC showed the same tend from 1989 to 2011.

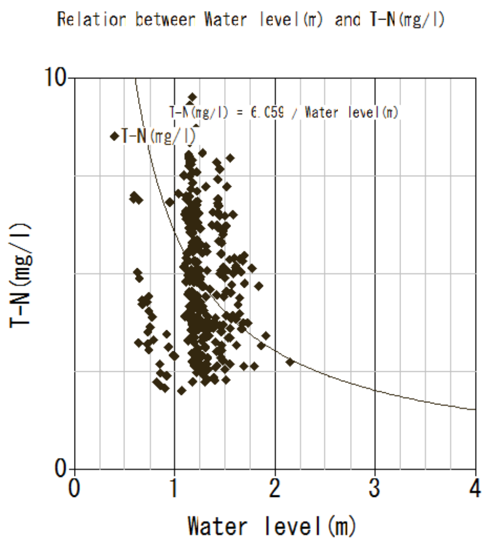

Fig. 7 The relation between water level and T-N concentration by monthly data from 1989 to 2011 at Fujii

Figure 7 shows the relation between water level and T-N concentration by monthly data from 1989 to 2011 at Fujii. T-N concentration is decrease with water level and the relation between water level and EC showed the same tend from 1989 to 2011 Therefore T-N concentration and EC value is same Tend, T-N concentration and EC value is are dependent on the water level.

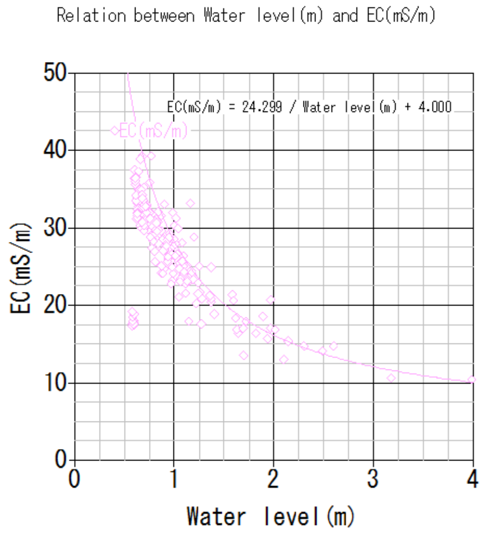

Fig. 8 The relation between water level and EC by every day data in 2011 at Fujii

Figure 8 shows the relation between water level and EC value by every day data in 2011 at Fujii. The EC value is decrease with Water level. The approximate line between Water level and EC value shows by next equation.

$$EC = \frac{24.229}{WL} + 4 \quad (4)$$

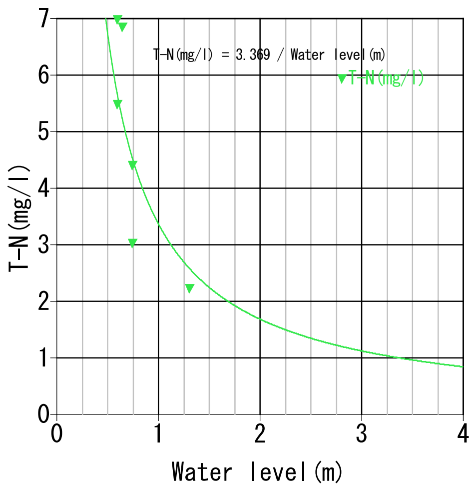

Fig. 9 The relation between water level and T-N concentration by every day data in 2011 at Fujii

Figure 9 shows the relation between water level and T-N concentration by every day data in 2011 at Fujii. The T-N concentration is decrease with Water level. The approximate line between Water level and EC value shows by next equation.

$$WL = \frac{3.369}{TN} \quad (5)$$

$$TN = 0.139 \times EC - 0.556 \quad (6)$$

Equation (6) is made by substituting the equation (4) into equation (5).

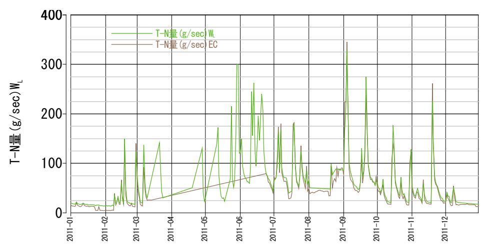

Fig. 10 The time series of T-N load (g/sec) at Fujii

Figure 10 shows the time series of T-N load at Fujii calculated from EC value. The annual T-N load is calculated by the sum of the flow rate times the T-N concentration. The result of annual T-N load at Fujii is calculated as 1501t/year.

T-N LOAD AT KASHIHARA

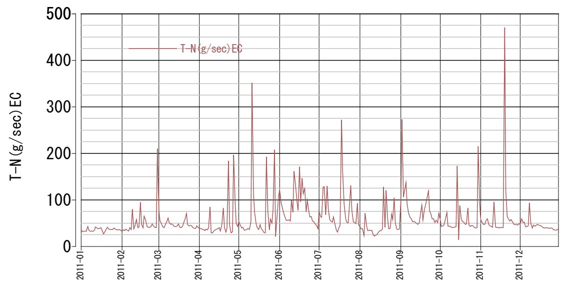

Fig. 9 The time series of T-N load (g/sec) at Kashihara

The Kashihara observing station is located at lowest stream in the Yamato River as non-influence of sea. The Kashihara station has both of the flowrate and the water level. The approximate line between T-N concentration and EC value shows by next equation.

$$TN = 0.186 \times EC - 2.064 \quad (7)$$

The result of annual T-N load at Kashihara is calculated as 1836t/year. The flow rate in fine day means the flow rate (75% flow) not less than this 95 days through 1 year. The nitrogen load in flood condition is calculated by divided by 75% flow. As a result, the nitrogen load in flood condition is 835t/year, and average load is 108g/sec. The nitrogen load in fine day is 1021/year, and average load is 43g/sec. The nitrogen load in flood condition is more 2 times of nitrogen load in fine day, and flood condition is 89 days in 2011. The flood condition of nitrogen load accounts for 45% of annual.

THE EC VALUE INFLUENCE RATE FOR THE DISSOLVED ION

In generally, the 80% of water of Yamato River is sewage. So it is estimated that water of same origin is mostly same water quality. The EC value is increased for constant rate by ion concentration of 1mg/L. Table 1 shows EC value for ion concentration of 1mg/L.

Table 1 EC value for ion concentration of 1mg/L

Ion concentration	EC value per 1mg / L (mS/m)	Ion concentration	EC value per 1mg / L (mS/m)
Na^+	0.213	K^+	0.184
NH_4^+-N	0.524	Ca^{2+}	0.260
Mg^{2+}	0.382	Cl^-	0.214
NO_3^--N	0.510	HCO_3^-	0.0715
CO_3^{2-}	0.282	SO_4^{2-}	0.154

The sewage water includes salt and nitrogen origin of organic compound, so the water is rich in Na^+, Cl^-, NO_3^-, NH_4^+. Na^+ of EC value per 1mg/l is 0.213mS/m, Cl^- is 0.214mS/m, NH_4^+-N is 0.524mS/m, NO_3^--N is 0.510mS/m. The dissolved ions of EC value is high response in the all of ions in the figure.

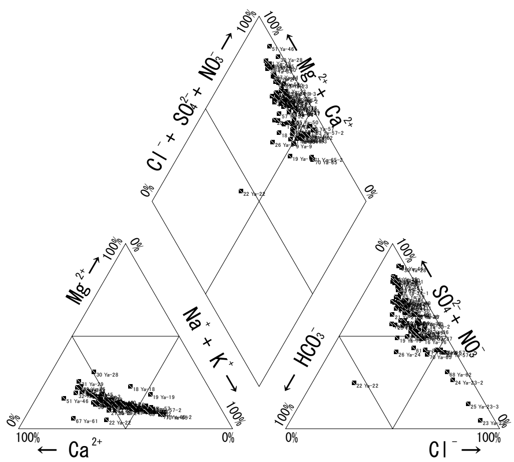

Fig. 10 The triennia diagram of the Yamato River Basin in 1999

The Yamato River Basin of water is rich in Na+K, Cl by more than 70%. The distribution is concentration in one point, Type of water quality is divided in Alkaline earth non-carbonated salt. So, the type of water quality is same mostly in the whole basin, the nitrogen concentration is possible to estimate by EC value.

THE ESTIMATION OF FLOW RATE UPPER STREAM FROM FUJII

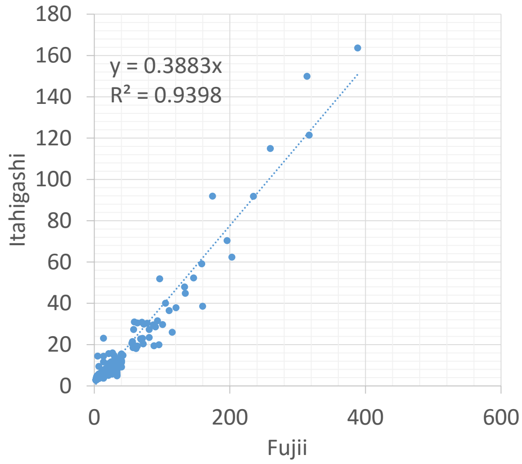

Fig. 11 The Relation between the flow rate of Fujii and Itahigashi in 2011

Itahigashi observing station has a little water quality data, and the data is not enough to estimate nitrogen load. Figure 11 shows The Relation between the flow rate of Fujii and Itahigashi in 2011. The nitrogen load is calculated by ratio of the flow rate of Fujii and Itahigashi. The flow Rate of Itahigashi is 38% of Hujii, and some rivers flow into between Fujii and Itahigashi. Assuming flowing at the same rate, the nitrogen load is estimated 570t/year.

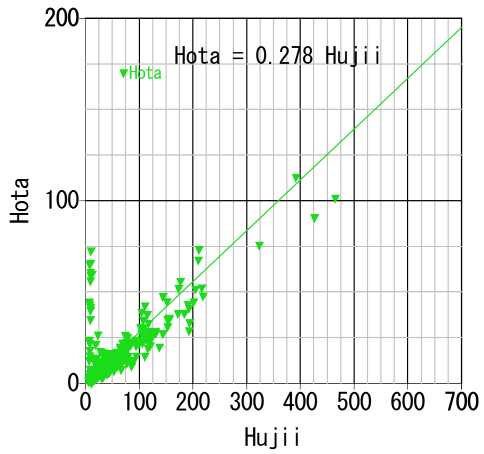

Fig. 12 The Relation between the flow rate of Fujii and Hota from 1997 to1999

Figure 12 shows The Relation between the flow rate of Fujii and Hota from 1997 to 1999. The data is most new in Hota. To account for errors, it is shown three-year relationship of the flow rate. The flow Rate of Hota is about 28% of Hujii, and some rivers flow into between Fujii and Hota. Assuming flowing at the same rate, the nitrogen load is estimated 417t/year.

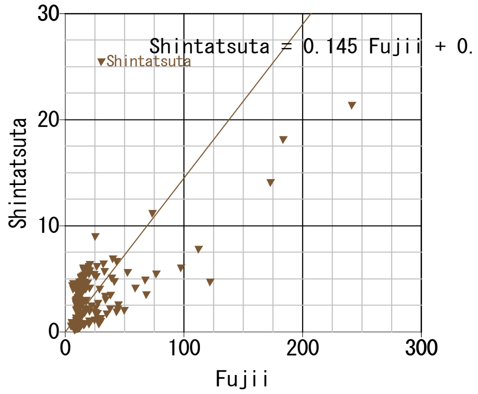

Fig. 13 The Relation between the flow rate of Fujii and Shintatsuta from 1986 to1989

Figure 13 shows The Relation between the flow rate of Fujii and Shintatsuta from 1986 to 1989. The data is most new in Shintatsuta. To account for errors, it is shown three-year relationship of the flow rate. The flow Rate of Shintatsuta is about 15% of Hujii, and some rivers flow into between Fujii and Shintatsuta. Assuming flowing at the same rate, the nitrogen load is estimated 218/year.

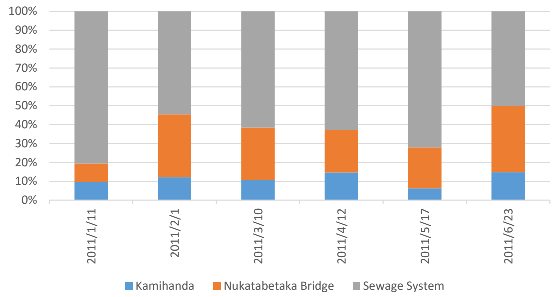

Fig. 14 The ratio of flow rate in Itahigashi upper

The two rivers and treated water of sewage system flow into the Itahigashi observing station. Figure 14 shows The ratio of flow rate in upper stream of Itahigashi. The ratio of flow rate of the two rivers are less than 50% of all flow rate, and the amount of treated water of sewage system is more than 50% constantly. It is estimated that the influence of treated water of the sewage system is big at whole.

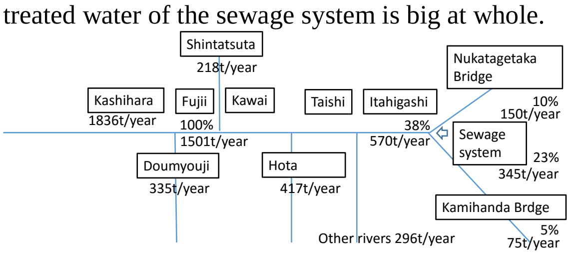

Fig. 15 The schematic diagram of the Yamato River in 2011

Figure 15 shows the schematic diagram of the Yamato River in 2011. The flow rate of upper stream was estimated by compare with the flow rate of Fujii observing station. The flow rate of Itahigashi is 38% of Fujii. Nukatabetaka Bridge and Kamihanda Bridge flow into Itahigashi, and treated water from sewage system flows into Itahigashi. The ratio of flow rate is calculated by monthly few data, because data is little. As a result, the nitrogen load is calculated to dividing the nitrogen load of Fujii by the ratio of flow rate. The flow rate of Nukatabetaka Bridge is 10% of Fujii, and Kamihanda Bridge is 5% of Fujii, and the treated water from the sewage system is 23%. Therefore the nitrogen load at Nukatabetaka Bridge is estimated as 150t/year, Kamihanda Bridge is 75t/yea and the treated water from sewage system is 345t/year.

CONCLUSION

Since there is not enough data in the upstream, it was difficult to estimate the nitrogen load of the upstream. Moreover new data is not aligned, it is necessary to predict by using other data. This study improve the accuracy of load amount calculated by interpolation of the data of the up and down stream observation stations and apply flow rate calculation from the water level using by the new Manning equation. In other less data observing station, the nitrogen load is calculated by ratio of flow rate for Fujii of flow rate. The nitrogen load of the Yamato River basin was calculated. As a result, the flood condition of nitrogen load accounts for 45% of annual. The nitrogen load of treated water of sewage system is 23%.

REFERENCES

[1] Masanobu Taniguchi, Hiroyuki Ii, Tatemasa Hirata, Analysis of organic nitrogen compound in domestic sewage in Yamato River using a social experimental test, 2010, vol. 30, Part 10, p. 1587–1590, Stuttgart, April 2010

[2] Ministry of Land, Infrastructure and Transport, Japan, Water information system, http://www1.river.go.jp/

[3] Yamato River construction office, http://www.yamato.kkr.mlit.go.jp/YKNET/index.html

[4] Masanobu Taniguchi, Hiroyuki Ii, Tatemasa Hirata, The development of water resource system – The Water balance of Yamato River Baisin, Environmental Engineering Research Papers Vol. 48,2011.

Fifth International Conference on Geotechnique, Construction Materials and Environment, Osaka, Japan, Nov. 16-18, 2015, ISBN: 978-4-9905958-4-5 C3051

SEDIMENT IMPROVEMENT MATERIALS COMPARISON APPLIED TO EUTROPHICATED SEASIDE PARK POND

Kazuhito Murakami[1], Saki Agatsuma [1,2] and Akiko Inoue-Kohama[3]
[1]Department of life and Environmental Sciences, Chiba Institute of Technology, Japan; [2]Mikuniya Corporation, Japan; [3]Department of Environment and Energy, Tohoku Institute of Technology, Japan

ABSTRACT

This study was aimed to analysis the influence on bottom sediment environment by sprinkling shell as regional unused resources. In addition, adsorption isotherm was calculated by culture experiments of bottom sediment material improvement. And adsorption effect of the nutrient in each processing was assessed. Water quality of pore water was as follows; T-N in pore water showed the low concentration with sprinkling shells as regional unused resources. As reason for this, NH_4-N eluted from sediment into water by the influence of sprinkled CaO. T-P in pore water also showed the low concentration with sprinkling shells, and moreover it was remarkable that in burning-treated system more than in non-treated system. By sprinkled, $Ca_3(PO_4)_2$ was formed with Ca^{2+} and PO_4^{3-} bonding on the shell surface, and PO_4-P in the pore water decreased. As assessment by adsorption isotherm; NH_4-N and T-N showed the negative adsorption isotherm. As reason for this, NH_4-N eluted in water by sprinkled bottom sediment improvement materials, and nitrogen in the pore water decreased. For T-P and PO_4-P, all bottom sediment improvement materials showed positive adsorption effects. CRM treatment using CaO showed the highest effect

Keywords: Bottom Sediment Improvement, Langmuir's Adsorption Isotherm, Pore Water, Nutrient, Eutrophicated Brackish Pond

INTRODUCTION

With the population growth, eutrophication in enclosed water bodies is progressing by inflows of domestic wastewater into rivers. Therefore, lakes are the environment susceptible to nutrient load and organic matter. Some eutrophication measures have been implemented. However, problems such as the collapse of the ecosystem issues and maintenance and the cost has occurred. Shells were used as the sprinkled material in this study is a principal component of calcium carbonate, it is considered that the influence on the ecosystem is less. Then, the Ca of the components of the shell, also has the ability of adsorbing the nutrients.

Hasunuma Seaside Park pond in Sanmu city of Chiba prefecture locates at 350m inland from Kujyukurihama coast line. This pond is strong enclosed, and its surface area is about 10,000m², water volume is about 7,400m^3, the water depth is 0.74m in average (Fig.1) [1]. In past, a rental boat shop opened in this pond, but the problem of stink and deterioration of landscape occurred because of Aoko in summer. Improvement trials of drying in the sun and drainage work conducted, but Aoko occurred again in summer of next year (Fig.2) [2]. Therefore, the eutrophic cause in these ponds is the elution of the nutrients from bottom sediment.

Dominant species of Aoko in this pond is *Anabeana spiroides*, and it has "air nitrogen fixation

Fig.1 Hasunuma seaside park pond

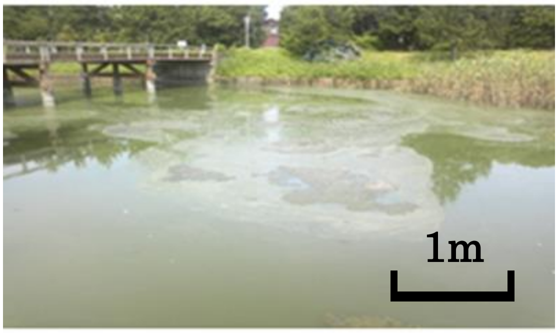

Fig.2 Aoko occurred in Hasunuma

ability", therefore, they can multiply explosively if there is even phosphorus in water. The other side, many shells are scattering in Kujyukurihama coast on nearly of Hasunuma Seaside Park pond.

This study was aimed to analysis the influence on bottom sediment environment of sprinkling shell as regional unused resources. In addition, adsorption isotherm was calculated by microcosm culture experiments of bottom sediment material improvement. And adsorption effect of the nutrient in each processing was assessed

MATERIALS AND METHODS

Regional Unused Resources

In this study, *Anadara broughtonii* bivalves was supplied as a regional unused resources. This shell was broken into 1-3mm size fragment (Fig.3). More than 90% of shell body component is made from $CaCO_3$. It sprinkled on the bottom mud of the pond where is nutrient resource. Shells are scattered much in Kujyukurihama coast of neighboring of Hasunuma Seaside Park pond. And when the fragment sprayed on bottom mud, the surface of sediment looks bright by a reflection of the sun light.

Culture Method

Water volume in the microcosm test is generally 300-1,000 ml [3]. From this reason, clear glass container (volume: 470ml, height: 14cm, diameter: 7cm,) was supplied to this study. 100g of bottom sediment collected from the pond was put in the bottom of the container to be flat, and 380mL of pond water was poured without disturbing the sediment. Crashed shells were sprinkled on the surface of bottom sediment.

The microcosm systems were cultured in incubator. Culture period was set to 20 days, and culture system were no-treated system as control and sprinkled systems of 50, 100g/m² of shell fragment. Culture condition was 25 degrees (Celsius) in temperature and 2,400lux in illuminance (L/D＝12/12hr.). Measuring parameters were T-P, PO_4-P, T-N, NH_4-N, NO_2-N, NO_3-N, COD, pH and T-S.

Extraction of pore water

50-100g of bottom sediment was sampled into precipitation tube, and centrifuged under 2,000-3,000rpm for 10min.

Evaluation by the adsorption isotherm

This study evaluated CRM (Chemical Remediation Materials) treatment (MgO and/or CaO) (Fig.4, 5), hybrid treatment (DAF treatment plus CRM treatment) and the shell sprinkled as regional unused resources treatment (non-burning

Fig.3 Shell fragment as regional unused resources

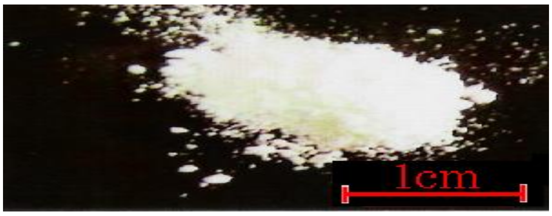

Fig.4 Magnesium oxide (MgO)

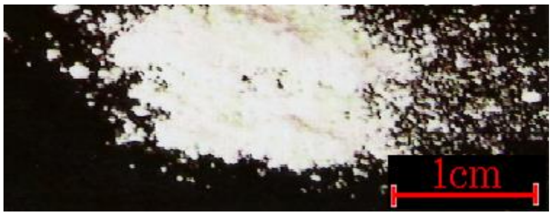

Fig.5 Calcium oxide (CaO)

treated and burning-treated) (Fig.3). MgO can be suppressed occurrence of Chl.a and elution of phosphorus. Therefore, it is expected to be viable in the bottom mud treatment of enclosed lakes [4]. CaO is possible to suppress the elution of phosphoric acid from the bottom mud. However, NH_4 washout from the bottom sediment and rapid rise in pH occurs. That impact on the ecosystem is considered large in a concern. DAF process is a method for making the aerobic condition sediments.

Adsorption isotherm was calculated using Langmuir's adsorption isotherm as formula (1) as below [5].

$$W=a \cdot Ws \cdot C \qquad (1)$$

RESULTS AND DISCUSSION

Water quality of pore water

Concentration ratio of nitrogen

NH_4-N (Fig.6a): In 10g/m^2 and 20g/m^2 sprinkled system, no change was observed in the concentration ratio either of the burning system and a non-burning system. In 50g/m^2 and 100g/m^2 sprinkled system, reduction of 40-50% concentration was observed in the non-burning system, and 60-70% concentration ratio recreased in burning-treated system. Thus, due to the sprinkling of calcium, by increasing the pH of the sediment, NH_4-N elution occurred by washout effect. In a system that has been subjected to a burning treatment in particular, shows a high value of pH11, pore water of the bottom mud is inclined to alkaline. It is thought that the elution amount of NH_4-N was greater than in the non-burning system.

NO_2-N (Fig.6b): As with NH_4-N, there was no change in 10g/m^2 sprinkled systems and the non-burning system of 20g/m^2 sprinkled system. In burning-treated system of 20g/m^2 sprinkled system, 50g/m^2 and100g/m^2 sprinkled system reducing the concentration of 20-30% has occurred in a non-burning system. And concentration was decreased by 20-40% of the burning-treated system.

NO_3-N (Fig.6c): In 100g/m^2 sprinkled system, it has become a high concentration of 2.5 times of the NO_3-N concentration in the overlying water in comparison with a non-dusting system. Nitrification reaction of just above water has been promoted in the elution of NH_4-N from the sediment. Therefore, it is eluted from the bottom mud NH_4-N of a large amount compared to the non-dusting system, nitrification reaction amount of sediment has been suppressed. Therefore, it thought that change was not observed in the NO_3-N concentration in the pore water.

In this way, the promotion of a series of processes of nitrification denitrification has been suggested by sprinkling shells and burning process. For a porous material is widely used for denitrification and nitrification promote, further study is necessary in the future.

T-N (Fig.6d): Pore water showed the low concentration of T-N by sprinkled shells as regional unused resources. As reason for this, NH_4-N eluted from sediment into water with the influence of sprinkled CaO.

Concentration ratio of phosphorus

PO_4-P (Fig.6e): In PO_4-P, adsorption effect has not been seen in 10g/m^2 sprinkling system and 20g/m^2 sprinkling system. However, gradually concentration decreased from 50g/m^2 sprinkling system and high adsorption effect has been shown in the burning system than non-burning system. By sprinkled shells, $Ca_3(PO_4)_2$ was formed with Ca^{2+} and PO_4^{3-} bonding on the shell surface, and PO_4-P in the pore water decreased..

T-P (Fig.6f): As with T-P, as the application rate is large, the concentration of the pore water is reduced in a system subjected to a burning treatment was shown.

Concentration ratio of total sulfide

T-S (Fig.7): The decrease of sulfide amount was observed by sprinkled the shells, and moreover it

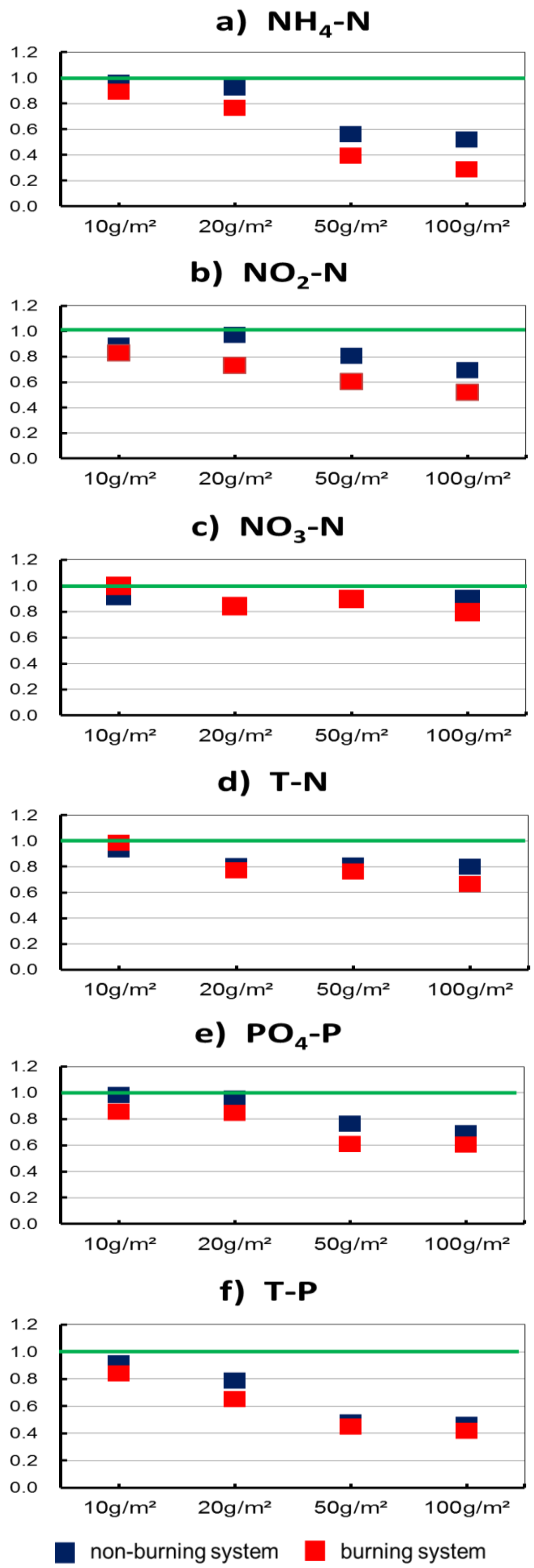

Fig.6 Nutrient concentration ratio in the pore water with shell sprinkling

was remarkable in burning-treated system more than in non-treated system, as same as T-P. In 100 g/m^2 sprinkled system, sulfide concentrations were decreased by about 1.3 times more in burning system than non-burning system. As reason for this, $CaSO_4$ was formed with Ca^{2+} and SO_4^{2-} bonding. As reason adsorption force was higher in the system that has been subjected to a burning treatment, porosity of the shell is increased by burning [6][7]. Thus, the surface area of the suction surface increases than non-burning system.

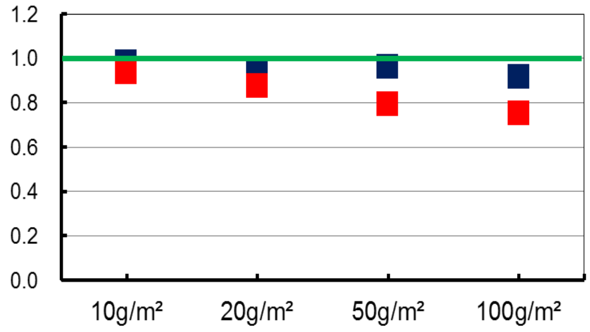

Fig.7 Total Sulfide concentration ratio in the pore water in the shell sprinkled

Assessment by adsorption isotherm

Comparison of CRM treatment and hybrid treatment

Fig.8-11 shows the adsorption of various nutrients of CRM treatment and hybrid treatment.

NO_3-N (Fig.8): The adsorption equation of NO_3-N showed below.

MgO: $W=1.6\times10^{-2}C$
CaO: $W=3.2\times10^{-3}C$
DAF+Mg: $W=1.4\times10^{-2}C$
DAF+CaO: $W=1.3\times10^{-3}C$

From these equations, adsorption effect was shown to be higher in the following order.

MgO＞DAF+MgO＞CaO＞DAF+CaO

The highest adsorption effect was showed in MgO. MgO showed higher adsorption effect than 12.1 times of that of DAF+CaO.

NH_4-N (Fig.9): The adsorption equation of NH_4-N showed below.

MgO: $W= 1.1\times10^{-4}C$
CaO: $W=-2.2\times10^{-4}C$
DAF+MgO: $W= 2.4\times10^{-5}C$
DAF+CaO: $W=-1.5\times10^{-4}C$

From these equations, adsorption effect was shown to be higher in the following order.

MgO＞DAF+MgO＞DAF+CaO＞CaO

Adsorption isotherm of CaO and DAF+CaO showed negative adsorption. As reason for this, wash out effect occurred that weakly basic of NH_4-N is eluted into water by sprinkled Ca.

T-N (Fig.10): The adsorption equation of T-N showed below.

MgO: $W= 1.5\times10^{-5}C$
CaO: $W=-2.6\times10^{-4}C$
DAF+MgO: $W= 7.3\times10^{-5}C$
DAF+CaO: $W=-1.7\times10^{-3}C$

From these equations, adsorption effect was shown to be higher in the following order.

DAF+MgO＞MgO＞DAF+CaO＞CaO

PO_4-P: Similarly, it became negative adsorption equation in a system that was sprinkled with CaO.

T-P (Fig.11): The adsorption equation of T-N showed below.

MgO: $W=9.7\times10^{-3}C$
CaO: $W=5.6\times10^{-2}C$
DAF+MgO: $W=4.0\times10^{-2}C$
DAF+CaO: $W=5.0\times10^{-2}C$

From these equations, adsorption effect was shown to be higher in the following order.

CaO＞DAF+CaO＞DAF+MgO＞MgO

CaO showed higher adsorption effect 5.81 times higher than MgO. As reason for this, binding force of CaO is higher than that of the MgO [3][8]. CaO showed higher adsorption effect 1.14 times higher than DAF+CaO. As reason for this, organic matter is reduced by applying the DAF process.

From the results above, high adsorption effect in nitrogen was obtained in MgO sprinkled system that was sprinkled. And that adsorption is highly effective in a system that was sprinkled with CaO has been shown in phosphorus.

Comparison with Regional unused resources

Fig.12 shows the adsorption of various nutrients by regional unused resources.

It compared the adsorption isotherm in the case of using the shells and adsorption isotherm of bottom sediment improvement process adsorption effect was highest.

In NO_3-N, non-burning system showed adsorption effect of 16.5 times compared to MgO but showed adsorption effect of 2.8 times compared with MgO at the burning treated system.

In NH_4-N, non-burning system showed adsorption effect of 0.18 times compared higher with MgO but showed adsorption effect of 40 times lower compared with MgO at the burning treated system.

In T-N, non-burning system showed adsorption effect of 43.8 times higher compared with DAF+MgO it showed adsorption effect of 54.8 times compared to DAF+MgO at the burning treated

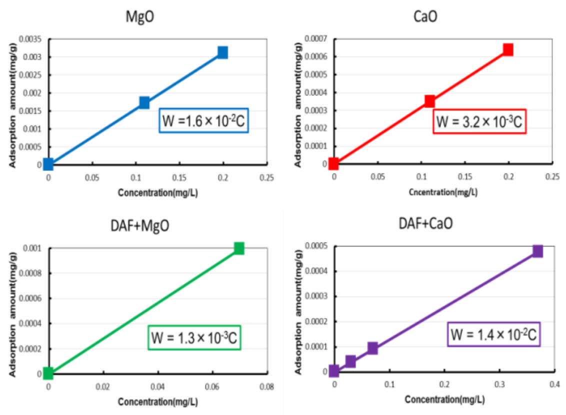

Fig.8 Adsorption characteristics of NO_3-N in various sediment material improvement

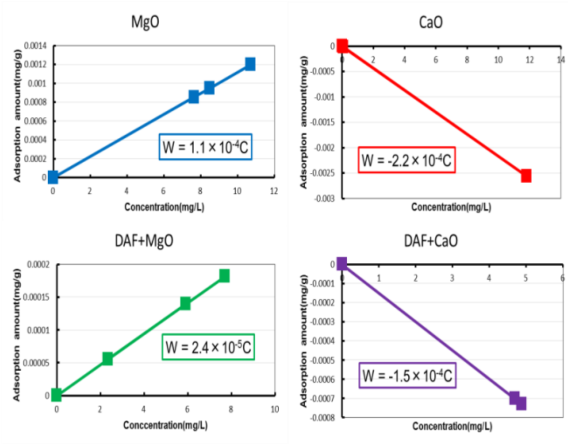

Fig.9 Adsorption characteristics of NH_4-N in various sediment material improvement

system.

In T-P, non-burning system showed adsorption effect of 13.8 times lower compared with CaO but showed adsorption effect of 11.3 times compared to CaO at the burning treated system. Adsorption effect of regional unused resources sprinkled in T-P is about 1/10 of CaO treatmemt has been shown.

By CaO sprinkling, elution of NH_4-N was observed from the bottom mud due to the rise in pH. It has resulted that affect possibility is suggested to ecosystem

In this study, culture period of microcosm system was set to 20 days, and this was too short for saturated adsorption. The values of adsorption capacity are important, but it was not detected in this study. Furthermore, studies followings are required to practice in action the shells spraying as regional unused resources. Some growth suppression effect on the benthos which play an important role of consumer of sediment ecosystem directly affected by sediment material improvement [9], need to

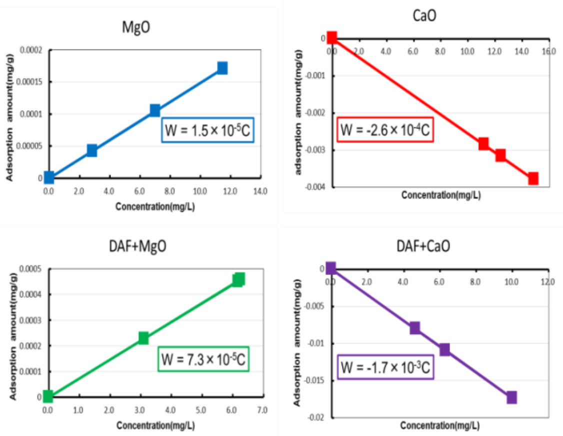

Fig.10 Adsorption characteristics of T-N in various sediment material improvement

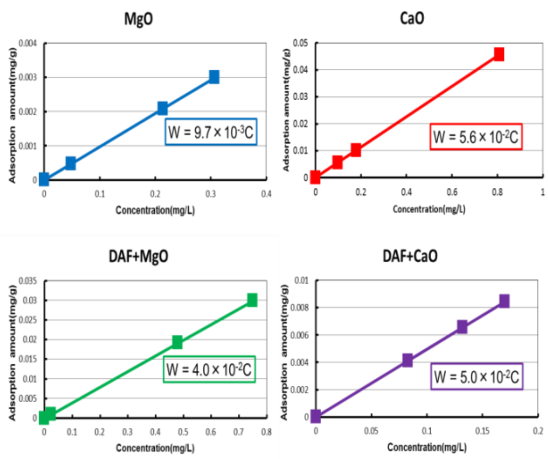

Fig.11 Adsorption characteristics of T-P in various sediment material improvement

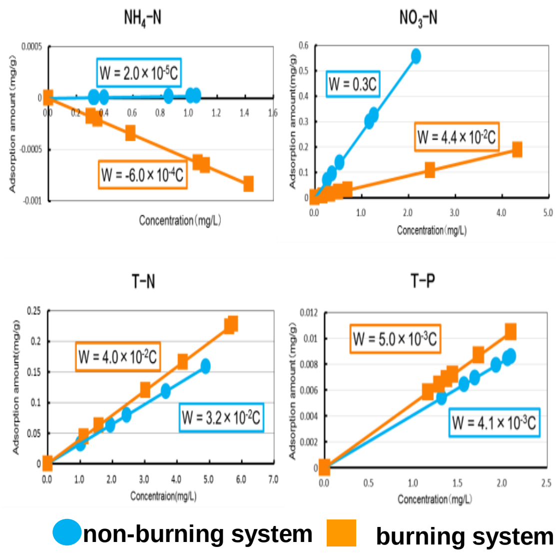

Fig.12 Adsorption characteristics of various nutrients in the shell

continue considering about what would affect the ecosystem structure consisting of complex food chain. To investigate these problems, on-site scale mesocosm system experoment should be conducted, and from the comparison between laboratory scale microcosm system and on-site scale mesocosm system, the results obtained from this study can be implemented in the field.

CONCLUSIONS

Pore water quality analysis of bottom sediment where the shell sprinked treatment as regional unused resources and the comparison of the adsorption characteristics using Langmuir's adsorption isotherm with a variety of sediment improvement materials were conducted. Results can be concluded as follows.

1) In sediment pore water, NH_4-N is eluted into upper water by wash-out effect especially in the burning treatment system, and the concentration of nitrogen in the pore water was reduced. T-P and PO_4-P also reduced the concentration in pore water, with combine of phosphate and Ca as the main component of the shell. T-S also reduced in pore water as same as phosphate.

2) In adsorption characteristics calculated using Langmuir's adsorption isotherm as various sediment improvement materials, nitrogen was reduced in MgO sprinkled treatment (MgO and DAF+MgO), and phosphate was reduced in CaO sprinkled treatment (CaO and DAF+CaO). In shell fragment sprinkled treatment, higher adsorption effect was demonstrated in nitrogen, but only 1/10 adsorption effect in phosphorus.

From these outcomes, shell fragment as regional unused resources can be considered as one of the effective tools for sediment eutrophication remediation.

ACKNOWLEDGEMENT

Special thanks for the cooperation of Sanmu Local Maintenance Center of Chiba prefecture, and this study was partly supported by grant-in Aid for Scientific Research of JSPS (KAKENHI) (24651029).

REFERENCES

[1] Murakami K, Ishii T, Taki K and Matsushima H, "Internal Production Control by Sediment Treatment in Eutrophicated Lakes using Experimental Mesocosm System", Papers on Environmental Information Science, Vol.22, 2008, pp.487-492.

[2] Murakami K, Ishii T and Taki K, "Re-eutrophication caused by bottom sediment sun-drying in shallow and strongly enclosed park pond", Papers on Environmental Information Science, Vol.23, 2009, pp.435-440.

[3] Amano Y, Taki K, Murakami K, Ishii T and Matsushima H, "Sediment remediation for ecosystem in eutrophicated lakes", The Scientific World, Vol.2, 2002, pp.885-891.

[4] Kanda R, Nakazawa Y, Inamori R, Suzuki R, Murakami K, Xu K Q and Inamori Y, "Effects of magnesium hydroxide as an environmental improvement agent on the survival and viability of aquatic organisms", Journal of Bioindustrial Science, in press, 2015.

[5] Kondo S, Ishikawa T and Abe I, "Science of Adsorption", Maruzen, 2001, 236pp.

[6] Yavitt J B and Fahey T J, "Peat and solution chemistry responses to $CaCO_3$ application in wetland next to woods lake", Experimental Watershed Liming Study, Kluwer Academic Publishers Biochemistry, 1996, pp.103-121.

[7] Crimo P C and Driscoll C T, "The impacts of a watershed $CaCO_3$ treatment on stream and wetland biogeochemistry in the adirondach mountains", Experimental Watershed Liming Study, Kluwer Academic Publishers, 1996, pp.123-156.

[8] Murakami K, Agatsuma S, Gomyo M and Inoue-Kohama A, "Eutrophicated sediment remediation using shell fragment as regional unused resources for nutrients elution control", International Journal of GEOMATE, Vol.8, 2015, pp.1239-1244.

[9] Murakami K, Gomyo M, Agatsuma S, Amano Y and Inoue-Kohama A, "Environmental condition index for estimation on eutrophic state of enclosed aquifer ecosystem", International Journal of GEOMATE, Vol. 5, 2013, pp.706-711.

Fifth International Conference on Geotechnique, Construction Materials and Environment, Osaka, Japan, Nov. 16-18, 2015, ISBN: 978-4-9905958-4-5 C3051

RISK-BASED ENVIRONMENTAL PREPAREDNESS FOR DEALING WITH DEBRIS AND WASTE FROM GREAT TSUNAMI

Keiichi KITAZUME[1], Taira OZAKI[2] and Toru MORIOKA[3]
[1]Faculty of Environmental and Urban Engineering, Kansai University, Japan; [2,3] Kansai University, Japan

ABSTRACT

In Japan, the government predicts that a large earthquake and tsunami will occur in high probability. Therefore, people have to prepare for the disaster and well treat debris and waste generated by this. This paper develops a framework of the risk-based environmental preparedness. First, areas along the coast of the Japan's island are categorized from the geographical, demographic and social point of view. Second, the key factors which significantly affect the length of dealing time and amount of emissions are revealed and structured respectively by the case of the Great East Japan Earthquake and Great Hanshin-Awaji Earthquake for reference. Third, pass ways for considering the resilient management of areas with large amount of debris and waste are developed. As results of this research, the method of risk-based environmental preparedness which enables to have merits both before and after a great earthquake is proposed.

Keywords: Preparedness, Earthquake, Waste Management, Risk Management

INTRODUCTION

The Earthquake Research Promotion predicts that a great earthquake will occur in approximately 70% of the probability within 30 years along the Nankai Trough located south of the Japan's island of Honshu. Great Tsunami will also attack the areas and generate large amount of debris and waste. On the other hand, the areas include not only metropolitan areas but also depopulated towns and villages with fishing ports, sightseeing areas and so on. In addition the compact city policy will continue to change the distribution of population, facilities and land use in next 30 years and therefore the volume and distribution of debris and waste will be different in timing of earthquake, land condition, city policy and so on. The difference will effect on the methods of treating them and we recognize these differences as risks. Despite these difficulties, these should be cleared soon for developing national resilience policy. Therefore, a concept of risk-based environmental preparedness is required as an effective approach to this issue.

The purpose of this paper is to develop a framework of the risk-based environmental preparedness for dealing with debris and waste considering the diversity of timing of earthquake, land condition and city policy.

EARTHQUAKE AND TSUNAMI

Figure 1 shows the areas where the Nankai Trough earthquake and following Tsunami will attack reported by the Cabinet Office of Japan. These areas are inundated more than 30 cm within 30 minutes after the earthquake or municipalities located between designated ones considering integration. The area is 27,186 km^2 and consists of 14 prefecture (or 139 cities, towns and villages) and population is 10,346 thousand in 2010. There is a diversity in this area and meticulous policy measures are required.

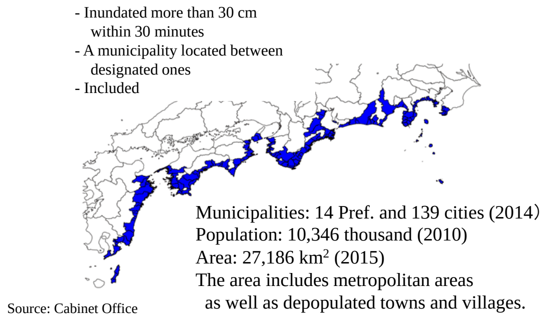

Fig. 1 Designated areas of policy measures

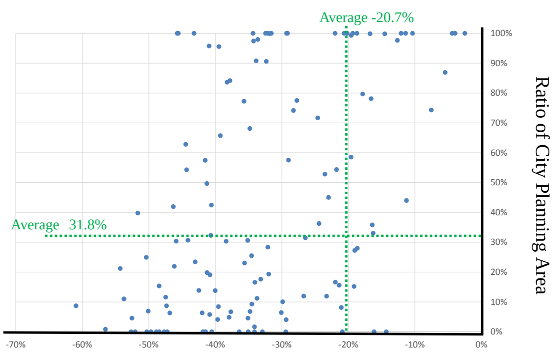

Fig. 2 Data of municipalities in the area

Figure 2 shows data of target municipalities. Horizontal axis shows ratio of depopulation in 2040 to that in 2010 and vertical axis shows ratio of city planning area [1]. The average of ratio of depopulation is -20.7% while less than -50.0% is observed in some municipalities. In these depopulated municipalities, ratios of city planning area are very low and the volume and distribution of houses and buildings will be expected to radically change. On the other hand, the average of ratio of city planning area is 31.8% and 100 % is observed in some municipalities. Even though the city planning area consists of urbanization control area as well as promotion area, high ratio represents high density of population and facilities. In addition, population in some cities with 100 % of city planning area also will decrease from -20 % to -50 %. We can divide these municipalities into three categories, one is high ratio of city planning area and low ratio of depopulation, second is high ratio of city planning area and high ratio of depopulation and the last one is low ratio of city planning area and high ratio of depopulation. The amount of population which may be related to hierarchy of city such as designated, core, or special city and metropolitan area or not and so on, also effect on the difference. However, both of the ratio of city planning area and depopulation represents well the estimated volume and distribution of debris and waste.

Experiences of former earthquakes

Table 1 shows experiences of former two earthquakes in Japan, one is the Great Hanshin-Awaji earthquake in 1995 and the other is the Great East Japan in 2011.

In Great East Japan earthquake, Tsunami attacked sea coast areas and generated not only waste but also debris from cars, ships and others and the amount of debris and waste was larger than the Great Hanshin-Awaji earthquake. Thus the cost was also higher. The main stakeholder of the Great Hanshin-Awaji case was cities and towns, mainly Kobe city, because Kobe was the main disaster area and had much power and capability of governance. On the other hand, in the Great East Japan case, stakeholders were not mainly municipalities but prefectures, the upper level of local government, because the disaster areas were very wide and included many types of cities, towns and villages. Small municipalities could not treat the large amount of debris and wastes by themselves, therefore prefectures arranged the co-relations among them and advised them methods. Accordingly, the ratio of cross border treatment of debris and waste was lower in the Great Hanshin-Awaji case than in the Great East Japan case. In Japan, the usual basic concept is that a municipality should treat the waste from the own area there. However, in the emergency case many towns and villages could not treat almost of all debris and waste and some other municipalities helped them. Recycle ratios between the two cases are also different. The ratio in the Great East Japan case was higher than that in the Great Hanshin-Awaji case since the capacity of disposal plants which treat mainly municipal solid waste was very low. Finally, as shown in figure 3, the term of clearance of waste and debris were both two years, but the timing of start in the Great East Japan case was 1 year later for arrangement of co-operation among municipalities.

Table 1 Experiences of former two earthquakes

	Great Hanshin-Awaji	Great East Japan
Contents	debris	Debris, Cars, Ships, others
Volume of Waste (million t)	14.30(Hyogo)	Waste 20.19(13Pref.) Deposit 11.02
Cost (thousand Yen/t)	19	37
Main Stakeholder	City and Town	Prefecture and City
Term(plan) Approximately	2 years	within 3 years
Term(real)	98% finished in 2 years	3 years(Iwate, Miyagi) Continue(Fukushima)
Recycle Ratio (%)	38	Waste 82, Deposit 99 (13pref.)
Cross border Treatment	Within the Prefecture Out of Prefecture (10%)	Requested to other Prefecture

The Nankai Trough case will be relatively similar to the Great East Japan case. The disaster area will widely spread over and consist of many types of municipalities which includes small towns and villages. For fast start treatment, prefecture or national government must arrange co-operation of treatment of waste and debris smoothly.

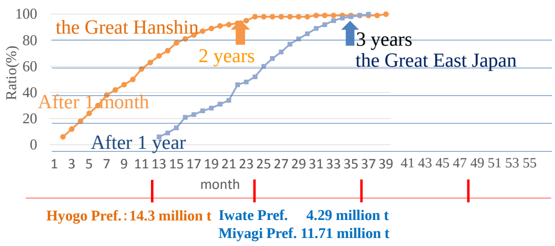

Fig. 3 Ratio of treatment of disaster waste

SCENARIO

Concept of compact city

The national government and many researchers propose the concept "Compact City". Although the concept has many meanings, commonly narrower area for residents and urban activities should be required for a depopulated city. Most of urban areas will be controlled to be narrow, in other word compact, since the number of population will be reduced 20% on average in the next 30 years.

In Sendai, for example, which is the largest city in the disaster area of the Great East Japan earthquake, the center of city is located relatively far from the sea coast and main public transportation system is also. Therefore, main urban activities were safe while other cities which are located just on the sea coast received much damage. In a compact city of the future, some residences and urban facilities will get concentrate into the center of the city along the next 30 years, the debris and waste by Tsunami will decrease in volume. This means that distance between the city center and sea coast is one of the important factor to evaluate the volume of debris and waste.

Locations of sites for treatment

Figure 4 shows typical step of treatment of waste. Debris and waste are generated everywhere in urban areas and their distribution may have much relation to the distribution of buildings, houses, urban facilities and infrastructures. After the lifesaving activities and other emergency works, smoothly these are transported to primarily temporarily storage sites. Because of required smoothness, the location of the sites are near the built areas. After sorting work, these are carried to the secondarily temporarily storage sites. These sites should be located far from residential areas, because wastes and garbage may stink bad smell or become any reasons of troubles. The sites also require wide area. Therefore, these sites are located mainly by the sea coast or other low urban activity areas. After more sorting works, debris and wastes are carried to depots which are located in available areas. After that, they are treated into fracture, incineration, reuse or recycle or final disposal.

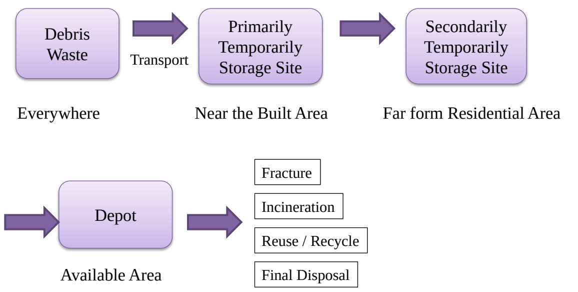

Fig. 4 Steps of treatment of waste

Since it was very difficult to get the sites for primarily/secondarily temporarily storage and depot, the local government should prepare candidates of the sites. However, the locations have relation to distribution of urban areas in the next 30 years. Depopulation and compactness will effect on the distribution of population and urban facilities. Therefore, the candidates for sites will also change along time passing. This matter will be risk for a prepared plan for disaster.

Scenarios

Figure 5 shows some scenarios along the next 30 years according to the factors this paper discussed. In the BaU case, urban facilities and houses will spread over the city area while the population will decrease in number. In the scenario 1, the center of city or the main urban facilities will remain in low lying area just on sea coast despite of depopulation. The city center or main urban facilities are originally located there and no relocation policy measures will be introduced. In this case, tsunami will directly attack these facilities and generate large amount of debris and waste.

In the scenario 2, some people will move to upland area and will be followed by some daily facilities. Since the relocation to upland area will be carried out along 30 years passing, the timing of occurrence of earthquake will be key factor to evaluate the volume and distribution of debris and waste. If an earthquake will occur in the near future, the volume will be larger and required sites for storage sites and depots will be wider. Furthermore, the candidates of them will not easier be prepared because many inhabitants still live in the low lying area and daily facilities will also be located there.

In the scenario 3, co-relational measures will be introduced between municipalities in an upland area and a low lying area. In this case, demands or usage of some public facilities will decrease because of depopulation. Relocation of these facilities should be planned. If the new facility will be selected to be located in upland area or the existed facility in the upland area will be selected as an integrated one, people will also be expected to move there and the volume of debris and waste will decrease. However, the relocation will be also made along the time passing, therefore the timing of earthquake will be key factor for the evaluation.

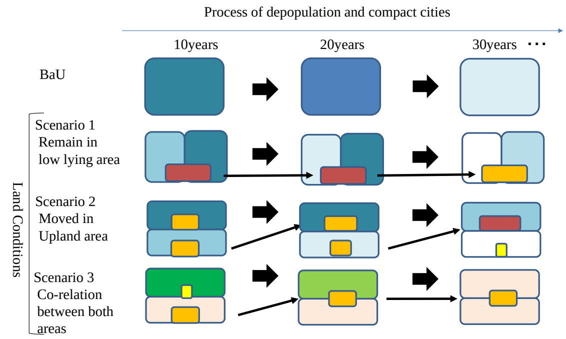

Fig. 5 Scenarios by timing of earthquake

CONCLUDING REMARKS

Pass way management

Depopulation and relocation of residents and urban facilities which will effect on the volume and distribution of debris and waste, will gradually proceed. Therefore, the timing of earthquake is important not only for the volume and distribution of debris and waste but also the treatment after the occurrence of earthquake. These problems depend on pass way to relocation because of timing in progress.

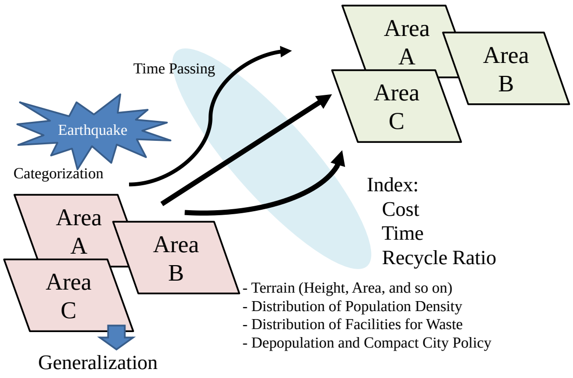

Fig. 6 Concept of pass way management

Figure 6 shows a concept of pass way management for policy measures. As a result of this research, the author proposes requirement of the pass way management to make a plan for the disaster. The dominant factors will be terrain, for example height, distance from the sea coast and so on, distribution of population density which are affected by the geographical matters of each city, distribution of facilities and infrastructures which is effected by that of residential areas and land use policy, and progress of depopulation and compact city policy. Furthermore, more important factor is the timing of occurrence of an earthquake. Especially occurrence in the near future, the volume of debris and waste will be large and the treatment will be more difficult because of difficulty to obtain the sites for temporary storage and depot. The local government in the designated areas reported by the Cabinet Office of Japan already prepare plans for treatment for disaster waste and debris. However, most of them do not consider these differences depend on the timing and the concept and more analytical approach to pass way management will be required as described in figure 7.

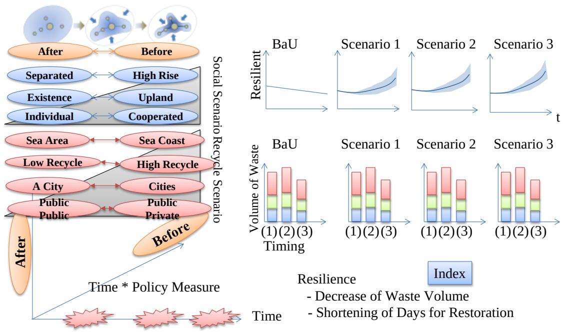

Fig. 7 framework of pass way management

This research presents the only framework of the pass way management policy. The analysis of concrete policy measures and their benefits and costs are required as future researches.

ACKNOWLEDGEMENTS

This paper is a part of research (3K153008) funded by the Environment Research and Technology Fund of Ministry of the Environment of Japan. The authors acknowledge this grant with deep gratitude.

REFERENCES

[1] National Institute of Population and Social Security Research, Population Projections for Japan -2011 to 2060 -, 2012.
[2] City Planning Association of Japan, Annual Report of City Planning, 2012.

MATHEMATICAL MODELING OF CONTAMINANT FLOW IN CLOSED RESERVOIR

Valeriy Perminov[1], Alexander Goudov[2]
[1]Department of ecology and basic safety, Tomsk Polytechnic University, Russia
[2]Department of UNESCO, Kemerovo State University, Russia

ABSTRACT

A mathematical model of the impurity distribution in a flooded mine due to allocation of groundwater is under consideration. The boundary-value problem is solved numerically by using the finite volume method. Distribution of the main functions of the process (the velocity field, the concentration of the pollutant components, etc.) over time was obtained with the help of numerical solution. The ecological situation in Kuzbass and many other mining regions can be characterized by the problem of water body pollution with harmful substances. Light and heavy materials (with density that is less or greater than the density of water) such as oil products, coal particles and stones eventually either float or collect at the bottom of a coal mine. Mathematical modeling is used to solve practical problems associated with the distribution of such impurities in a closed reservoir and water treatment.

Keywords: Water Pollution, Coal Mine, Mathematical Modeling, Finite Volume

INTRODUCTION

Water body pollution by mining and quarry waters is a typical problem for Kuzbass and many other mining regions [1]. Mining waters usually contain particles of coal dust, clay, calcium compounds, magnesium, oil products, etc. Light substances (which density is less than water density) such as oil products accumulate on water surface while other particles remain suspended or sediment gradually. The problem of mining water treatment by pumping into abandoned mines and further use of the water after precipitation of impurities (for heavy materials) or impurity floating up (for light particles) is of great interest.

PHYSICAL AND MATHEMATICAL SETTING

The paper considers the process of fluid flow containing impurity particles in a flooded mine shown in Fig.1.

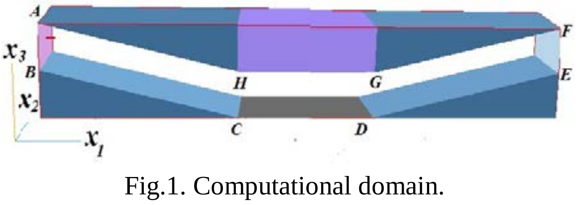

Fig.1. Computational domain.

Water with impurities inflows into a mine thorough the boundary *AB* (KD, CI, GN). Water leaves the domain under consideration though the boundary *EF* and ground water inflow though *HG*. Influenced by flow some impurities partially leave the mine while the remaining part gravitates to the bottom. To describe this transfer process differential equation system is used. They express the laws of conservation of mass, momentum and elements concentration in the domain. Mathematically the following differential equation system for turbulent flow should be solved. Many practical problems are devoted to such impurity distribution in an enclosed water body.

$$\frac{\partial \rho}{\partial t} + \frac{\partial}{\partial x_j}(\rho u_j) = 0 \qquad (1)$$

$$\frac{\partial}{\partial t}(\rho u_i) + \frac{\partial}{\partial x_j}(\rho u_i u_j) = -\frac{\partial p}{\partial x_i} + \frac{\partial}{\partial x_j}(-\overline{\rho u_i' u_j'}) - \rho S C_d u_i |\vec{u}| - \rho g_i, \qquad (2)$$

$$\rho\left(\frac{\partial Y_k}{\partial t} + u_1 \frac{\partial Y_k}{\partial x_1} + (u_3 - u_{3k})\frac{\partial Y_k}{\partial x_3}\right) = \frac{\partial}{\partial x_j}(-\overline{\rho Y_k' u_j'}), \qquad (3)$$

$$p = \rho R_0 T \sum_k \frac{Y_k}{M_k} \qquad (4)$$

$$\vec{g} = (0, g), u_{3k} = \frac{g d_k^{\,2}}{18\nu}\left(\frac{\rho_k}{\rho} - 1\right). \qquad (5)$$

The following symbols are used in the equation system above: t, x_i – time and spatial coordinates ($i=1,\ 3$); u_i – velocity vector projection on the corresponding axis of cartesian reference system, p

– pressure; g – gravitational acceleration, R_0 – absolute gas constant, M_k – molecular weight k – components, ρ – density of the mixture of fluid with particles, ν – kinematic viscosity coefficient, D_t – diffusion coefficient, d_k, $\rho_{k,}$ u_{3k} - diameter, density and velocity of particle settling, Y_k – mass concentrations k – components ($k=1$ – water, 2 – solid particles). Equation system (1)-(4) contains elements related to turbulent convection and needs a closing equation. Tensor components of turbulent stresses - $\rho\overline{v_i' v_j'}$ are described with the help of mean floatation gradients according to the formulas:

$$-\rho\overline{u_i'u_j'} = \mu_t\left(\frac{\partial u_i}{\partial x_j} + \frac{\partial u_j}{\partial x_i}\right) - \frac{2}{3}k\delta_{ij} \qquad (6)$$

Taking into account that the flow is turbulent, the coefficient of turbulent viscosity is used $\mu_t = \rho C_\mu k^2/\varepsilon$, where: $k = \overline{u_i'}\overline{u_i'}/2$ – turbulent kinetic energy; ε – its dissipation, C_μ- constant. The flow -$\rho\,\overline{u_i'}\overline{Y_k'}$ is modeled with the help of assumption concerning gradient diffusion $-\overline{\rho u_i' Y_k'} = \Gamma_k \frac{\partial Y_k}{\partial x_i}$, where Γ_k – coefficient of turbulent transport, corresponding to scalar function Y_k. At this point the assumption concerning the all-around isotropic turbulence is implicitly mentioned. Transfer coefficient Γ_k for scalar functions is considered to be equal to ratio of turbulent viscosity to turbulent Prandtl number $\Gamma_k = \nu_t/\mathrm{Pr}_t$. The equation for turbulent kinetic energy k is as follows [2]:

$$\frac{\partial}{\partial t}(\rho k) + \frac{\partial}{\partial x_i}(u_i\rho k) = \frac{\partial}{\partial x_i}\left[\left(\frac{\mu_t}{\sigma_k} + \mu\right)\frac{\partial k}{\partial x_i}\right] - \qquad (7)$$

$$-\mu_t\left(\frac{\partial u_i}{\partial x_j} + \frac{\partial u_j}{\partial u_j}\right)\frac{\partial u_i}{\partial x_j} - \beta\rho g_i\frac{\mu_t}{\mathrm{Pr}}\frac{\partial T}{\partial x_i} - \rho\varepsilon,$$

where $\beta = -\frac{1}{\overline{\rho}}\left(\frac{\partial\overline{\rho}}{\partial\overline{T}}\right)_p$.

The equation for dissipation of turbulent kinetic energy ε is as follows:

$$\frac{\partial}{\partial t}(\rho\varepsilon) + \frac{\partial}{\partial x_i}(u_i\rho\varepsilon) = \frac{\partial}{\partial x_i}\left[\left(\frac{\mu_t}{\sigma_\varepsilon} + \mu\right)\frac{\partial\varepsilon}{\partial x_i}\right] + \qquad \mathbf{(8)}$$

$$+C_1\frac{\varepsilon}{k}(G_k + G_B) - C_2\rho\frac{\varepsilon^2}{k},$$

where σ_k, σ_ε, C_1, C_2 – empirical constants, and G_k, G_B – turbulence generation because of forced and natural convection.

NUMERICAL SOLUTION AND RESULTS

Based on mathematical statement of the problems (1)–(7) numerical calculations were made to determine the pattern of impurity distribution process in a flooded mine with the help of **PHOENICS** [2-3]. Vector fields of velocity and impurity distribution at different time moments were obtained as the result of numerical integration. Taking into account three dimensional domain side walls are considered not to influence the impurity distribution process and fluid flow. Thus the problem is solved in the two-dimensional domain. A flooded mine (length -100 meters horizontally, depth- 10 meters) is under consideration. Water with impurity concentration 0.5 and particle sizes d_k= $5\cdot10^{-5}$ - 10^{-4} м enters this flooded domain through the left boundary. Impurity particles density is 2000 kgs/m^3 that is twice as much as water density. The rate of groundwater inflow from the upper layer HG is 0.1 m/s. Fig.2-3 show distribution of impurity concentration at different time moments.

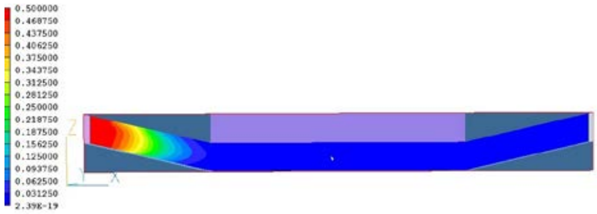

Fig.2
Impurity distribution in a flooded mine (t=115 sec.)

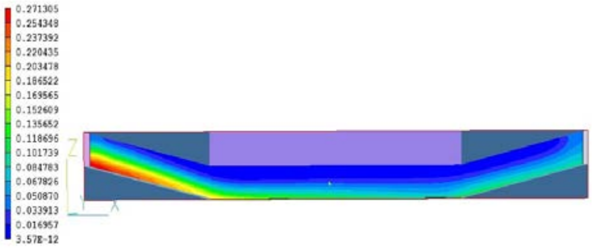

Fig.3
Impurity distribution in a flooded mine (t=900 sec.)

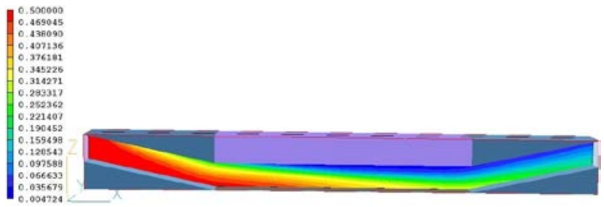

Fig.3
Impurity distribution in a flooded mine (t=900 sec.)

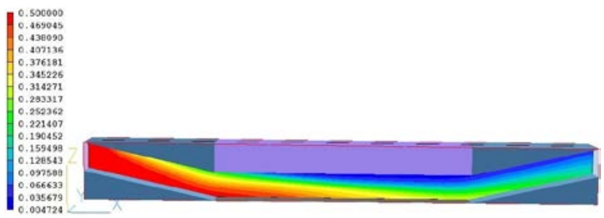

Fig.4
Impurity distribution in a flooded mine (t=4000 sec.)

According to the distributions of impurity concentration displayed above the impurities gradually distribute in the mine by gravitating to the bottom. While carrying out numerical calculation with t=6000 sec. (Fig.5) two last figures show that steady flow and impurity distribution at the bottom were identified. Fig.5 shows the impurity distribution.

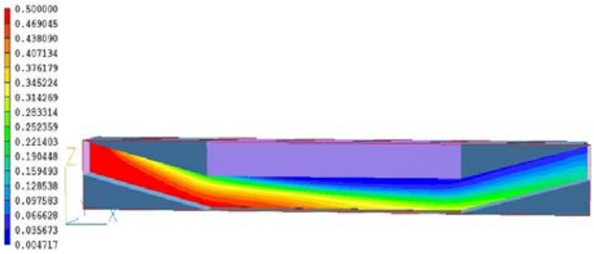

Fig.5
Impurity distribution in a flooded mine (t=6000 sec.)

Fig.6 shows the field distribution of flow velocity in a flooded mine at *t*=6000 sec.

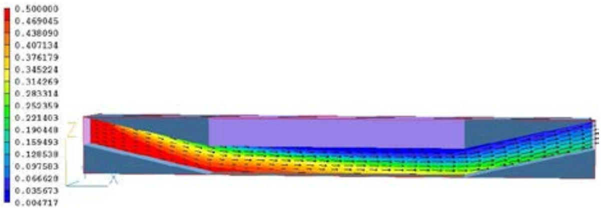

Fig.6
Field distribution of velocity and impurity concentration (t=6000 sec.).

If the fluid velocity at the entrance of the domain is doubled then the impurity distributes more evenly at the bottom compared to the previous case.

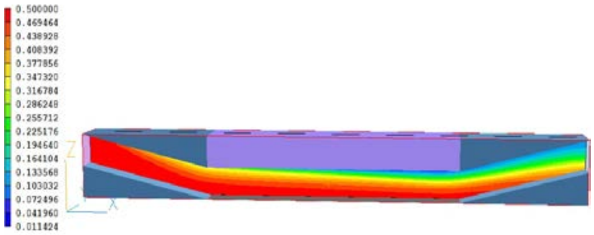

Fig.7
Impurity distribution in a flooded mine (t=6000 sec.)

The results of calculation showed if the sizes of particles are decreased then the deposition rates are decreased too. So, water with strong impurity concentration leaves the domain under consideration (Fig.8).

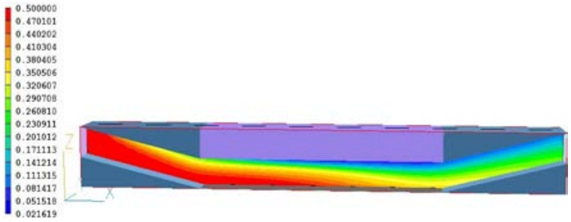

Fig.8
Impurity distribution in a flooded mine (t=6000 sec.).

In other words, in order to decrease impurity concentration on the outflow boundary it's necessary to prolong impurity residence time in the domain or change the pumping rate of polluted fluid at the entrance of the domain under consideration.

CONCLUSION

The general-purpose CFD software PHOENICS has been customized and validated for modeling contaminant transfer in a flooded mine due to ground waters allocation. The influence of flow velocity and size of particles at the entrance of the domain on the distribution impurity concentration in a reservoir as well as on the outflow boundary was under consideration by using this software.

REFERENCES

[1] Y.N.Zakharov, Potapov V.P., Schastlivtsev E.L., Chiryukina A.V. Simulation of impurity distribution in flooded mine working \\ Vestnik NGU. Information technologies . 2009. Volume 7,4, P.66-72

[1] PHOENICS On-Line Information System: www.cham.co.uk/ChmSupport/polis.php.

[2] Patankar S.V., Numerical Heat Transfer and Fluid Flow. New York: Hemisphere Publishing Corporation, 1981.

Fifth International Conference on Geotechnique, Construction Materials and Environment, Osaka, Japan, Nov. 16-18, 2015, ISBN: 978-4-9905958-4-5 C3051

FUZZY RANKING FOR LANDFILL SITE SELECTION IN INDIAN CONTEXT

J.E.M. Macwan and Hecson Christian

CED, S V National Institute of Technology, Surat-395007 Gujarat, India

ABSTRACT

Landfill site selection in an urban area is critical issue in the urban planning process. It creates major impact on economy, ecology, and the environmental health of the region. With the growth of urbanization as well as the desire to live in cities, larger amount of wastes are produced. Therefore, unfortunately the problem gets bigger every day. A selection of proper waste disposal site is a function of many parameters pertaining to urban planning and Environmental aspects. The normal practice is to select a site where open space is available. Parameters pertaining to above aspects are hardly attended to. The right method of selection should have been based upon correct assessment of parametric evaluation. All parameters have various scales and values too. In order to integrate these values, fuzzy approach seems to be the reasonable selection method. Thus, the objectives of this paper are to highlight solid waste scenario in Indian context, to present the assessed parameters and to present a model of fuzzy ranking approach to solve the problem. The fuzzy multi criteria decision making (FMCDM) is used to rank different land fill sites. Site II is best, if we look for environmentally safe site criteria. Site I is having most favorable accessibility criterion. Overall output suggest that site I is the best site for landfill with 0.6705 index and site III is least preferable site with 0.4243 indexes. Site II and site IV are having 0.5900 and 0.5183 index respectively. The solution suggested shall be a useful tool for urban environmental applications.

Keywords: Urbanization, Municipal Solid Waste, Fuzzy logic, analytical hierarchy process, landfill,

INTRODUCTION

Municipal Solid Waste (MSW) is key environmental issues for soaring urban centres. During the early period, MSW was conveniently disposed in low lying areas with large open land space. The population growth leads to increase in Solid Waste generation. The problem of waste disposal and its adverse impact on the environment is matter of great concern. Municipal Solid Waste in India has created many environmental imbalances. Unfortunately environmental planning as well as socio-economic factors are hardly quantified and considered to decide disposal locations. An approach based on fuzzy analysis is presented considering Indian situation.

In India, the growth of cities is taking place from two major perspectives. Firstly,in a natural and uncontrolled way, without following scientific principles of urban development. Secondly, few cities are growing by following certain scientific principles adopted by urban planners based on urban theories and development experiences.

India's urban population is growing at the fastest rate globally. Therefore, it is difficult to combat the urban challenges and scientific growth pattern. A scientific decision making approach needs to be adopted for disposal of municipal solid waste, where environmentally safe landfill site selection is significant. Four sites are proposed, out of which the best site is to be identified. Fuzzy logic approach has given ranks of proposed four sites, to make decision. Analytic Hierarchy Process (AHP) is used to evaluate parametric weights. The city under study is the fastest growing urban centre in India.

STUDY AREA

Surat city is selected for this research work, which is a major industrial up and fastest growth centre.
For the study area, it is proposed to include 4 sites located at various zones of the city for the purpose of Solid Waste Landfill disposal.
The locations of the sites (as shown in the map) are as follows:

Site I- South-Zone	Site II East-Zone
Site III-North-Zone	Site IV-West-Zone

OBJECTIVES

Objectives of this research are as follows

- To evaluate urban planning parameters, influencing solid waste landfill site selection.

- To determine weights of each parameters by AHP.
- To identify ranks of each landfill site by using fuzzy approach.

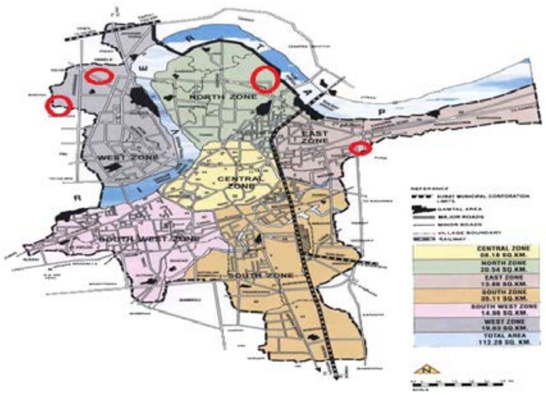

Fig 1 Proposed Location of Landfill Site

Review of Literature

S.M Issa et.al.[2] used eight parameters to identify landfill site in Abudhabi using similar approach,while Afzali et al[4] carried scientific studies in selecting suitable sites for landfill.V.Akbari et.al.[6] advocated for ranking based on decision making method ,zeinhom EL Alfy[3] used weighed linear combination (WLC)and AHP to rank the landfill sites, GH.R.Dini [1] used the Boolean process and followed by fuzzy approach to identify fuzzy land fill site, A.Karkazi[5] took 6 input parameters, used fuzzy logic for analysis of data and the evaluation of the final results. Juan M.SAchez[7] used MCDM method for locations while Mehnaz Eskandari and Mehndi Homaee[8]used integrated approach for environmental and socio cultural data.

Fuzzy Composite Programming Approach

This multi-objective analysis of site selection includes uncertainties in terms of fuzzy membership function. The membership in the sets cannot be defined on a scale of yes/no in fuzziness as the boundaries of the sets are unclear. The membership degree for a vague value can be found by expert's judgment based on knowledge and practical experience (Stan bury et al., 1991). Uncertainty analysis or fuzziness in site selection was included to take into account the vagueness in the data range.

Figure: 2 shows the composite structure of the basic indicators, selected for site selection from urban planning point of view.

The membership function for each of the basic criteria can be constructed, where Zi,h(x) is an interval value of the basic criteria at the confidence level (membership degree) h, [i.e., a≤ $Z_{i,,h}$ (x) ≤b].

Level-I Level II Level III

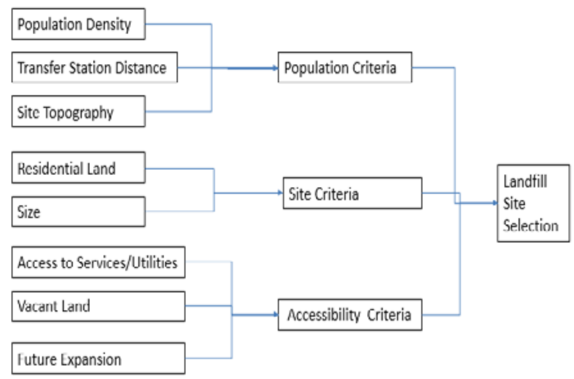

Fig 2 Fuzzy Composite Structure

The best and worst value for the basic criterion is determined by expert's perceptions. Using the best value of Z_i($BESZ_i$) and the worst value of Z_i($WORZ_i$)for the i^{th} basic indicator, the actual value $Zi,_h(x)$ is transformed into an i^{th} normalized basic criterion value. The actual value $Z_{i,\ h}(x)$ is transformed into an index value denoted by $S_{i,\ h}(x)$. In the model Z_{imin} is minimum value and Z_{imax} is maximum value in observed data. The normalized values for field data are determined by the following equation. (Bogardi,1992).

$$Si = \frac{(Zi - Zimin)}{(Zimax - Zimin)} \quad \text{(When } Z_{imax} \text{ is best)}$$

$$Si = \frac{(Zimax - Zi)}{(Zimax - Zimin)} \quad \text{(When } Z_{imin} \text{ is best)}$$

Where Si is normalized i^{th} fuzzy indicator; Zi is value of i^{th}fuzzy indicator; Z_{imax} is maximum possible value of i^{th} indicator and Z_{imin} is minimum possible value of i^{th} indicator. The composite distance was computed by the following equation (Bogardi, 1992)

$$Lijk_{(x)} = \left[\sum_{j}^{n} (W_{ij} \left[S_{ij}(x)\right]^{bj} \right]^{1/bj}$$

Where Lj, h(x) is fuzzy composite distance in group j, Nj is the number of elements in the first level group j; Si, hj(x) is the index value for the ith indicator in the first level group j of basic indicators; wij is the weight reflecting the importance of each basic indicator in the first level group. Pj= the balancing factor for the first level group j. The index values, Lj, h(x) of the second and third level indicators respectively can be calculated.

To calculate the weight for different indicators, (parameters) weights are selected as per Saaty's scale. Pair wise comparisons are used to determine the relative importance of each alternative. To compare indicator i with indicator j, the decision maker assigns values aij suggested in AHP method. If the degree of importance of the aji= (1/r). If i = j, then aij= aji=1. Saaty (1988) has shown that the eigen vector corresponding to the maximum Eigen value of matrix A is a cardinal ratio scale for the indicators compared.

$$AXW = f_{max} XW$$

Moreover, the unit eigenvector, (W) corresponding to f_{max}yields the preference weights for the criteria compared. The maximal deviation is presented by balancing factor p between the indicators of same group. The normal values used for balancing factors in equation are one and two. In this study balancing factor considered is 1.

RESULTS AND DISCUSSIONS

On the basis of survey collected from 20 experts weights of each criteria is determined using AHP. A weight of each criterion is shown in Table 1. Population criteria are having maximum weights among second level parameters.

Table 1: Weights for each criteria

Level	Indicators and Criteria	Weights
1	Population Density	0.6746
	Transfer station distance	0.0757
	site topography	0.2495
	residential land	0.7248
	size	0.2751
	access to services/utilities	0.0444
	vacant land	0.581
	future expansion	0.374
2	Population Criteria	0.4425
	Site Criteria	0.2627
	Accessibility Criteria	0.2948

Determination of best and worst values for first-level indicators is based on design standards suggested by Ministry of Environment and Forest, Government of India. The Best/Worst value of each of the indicator is shown in Table 2.

Table 2: Best and Worst Indicator Values for Criterion

Criteria	Best Value	Worst Value
Population density (ppha)	0	100
Transfer station distance(km.)	5	15
Site topography	1/10	1/1
Residential land (%)	0	35
Size (ha.)	250	100
Access to services/utilities (Km.)	0	5
Vacant land(Ha.)	50	25
Future expansion(Ha.)	25	0

Table 3 is showing existing site parameters values for all four sites under consideration.

Table 3: Values of Parameters for sites

Criteria	Site-I	Site-II	Site-III	Site-IV
Population density (ppha)	48	12	60	55
Transfer station distance (km.)	12	10	13	8
Site topography	1:5	1:4	1:6	1:8
Residential land (%)	20	10	32	30
Size (ha.)	175	200	175	150
Access to	2	3.5	1.6	0.8

services/utilities (Km.)				
Vacant land (Ha.)	50	30	35	40
Future expansion (Ha.)	25	20	15	20

Output of the model is tabulated in Table 4. Result shows that on the basis of population criteria, site III is least suitable; all other sites are having almost favorable conditions. Site II is best, if we look for environmentally safe site criteria. Site I is having most favorable accessibility criterion. Overall output suggest that site I is the best site for landfill with 0.6705 index and site III is least preferable site with 0.4243 indexes. Site II and site IV are having 0.5900 and 0.5183 index respectively.

Table 4: $L_{i, j, k}$, Second and Third Stage parameters for all Sites

Site	I	II	III	IV
Population Criteria	0.2634	0.2794	0.2282	0.2651
Site Criteria	0.1177	0.1841	0.0524	0.5130
Accessibility Criteria	0.2893	0.1264	0.1435	0.2020
Selection index	*0.6705*	*0.5900*	*0.4243*	*0.5183*

CONCLUSION:

1**.** Population criteria plays major role for decision makers for urban planning process.

2. Site I is environmentally safe, as it is least populated and other factors are favorable for solid waste disposal.

3. Once site I is filled than other sites may be considered as per rank.

ACKNOWLEDGEMENT

Authors are grateful to local municipal authorities for help in supplying necessary data. Experts are also acknowledged for their kind suggestions. Institute authorities were also kind in co-operating this research.

REFERENCES

1. GH. R. Dini, M. Amini, P. Zieaean Firooz Abadi, Seid Ramezan Mousavi. “GIS–Based Site Selection for Solid Waste Landfill Using Fuzzy Logic Case Study: Sari City, Iran,” *Queensland Spatial Conference, (2008).*
2. Zeinhom El Alfy & Rasha Elhadary,” Integrating GIS with MCDM to Deal with Landfill Site Selection”, *International Journal of Engineering & Technology IJET-IJENS Vol:10 No:06, (2010).*
3. Afzali, J. M. V. Samani, M. Rashid,” Municipal Landfill Site Selection For Isfahan City By Use Of Fuzzy Logic And Analytic Hierarchy Process”, *Iran. J. Environ. Health. Sci. Eng., 2011, Vol. 8, No. 3, pp. 273-284, (2011).*
4. A.Karkazi, T. Hatzichristos, A. Mavropoulos, B. Emmanouilidou, Ahmed Elseoud, “ Landfill Siting using GIS & Fuzzy Logic”, *Springer Publications, (2011).*
5. V. Akbari, M.A. Rajabi, Chavoshi, Shams, “Landfill Site Selection by Combining GIS and Fuzzy Multi Criteria Decision Analysis, Case Study: Bandar Abbas, Iran”**,** *World Applied Sciences Journal 3 (Supple 1):pp 39-47, (2008).*
6. Juan M.Sánchez-Lozano & JerónimoTeruel-Solano, “Geographical Information Systems (GIS) and Multi-Criteria Decision Making (MCDM) methods for the evaluation of solar farms locations: Case study in south-eastern Spain”, *Elsevier Journal, (2013).*
7. Mahnaz Eskandari & Mehdi Homaee, “An integrated multi criteria approach for landfill siting in a conflicting environmental, economical and socio-cultural area”, *Elsevier Journal, (2012).*
8. André L. O. Melo, Maria Lúcia Calijuri, Shahla Mahmodi, “Strategic Decision Analysis for Selection of Landfill Sites”, *Journal of Survey Engg, ASCE,(2006).*

TOURISM PLANNING PROPOSAL FOR VISAKHAPATNAM CITY, ANDHRA PRADESH, INDIA

Dr. Krupesh A. Chauhan [1], Y. Pavan Teja [2]

1 Asso. Professor, PG in-charge, M. Tech (urban planning**)**, Department of Civil Engineering, Sardar Vallabhbhai National Institute of Technology, Surat, Gujarat, India
2 Research Student, Department of Civil Engineering, Sardar Vallabhbhai National Institute of Technology, Surat, Gujarat, India

ABSTRACT

Tourism industry plays an important role in developing economy, especially in some cities where there are different historical, landscape and other natural attractions. Visakhapatnam City, Andhra Pradesh, India is one of the major city in south east coast of India has outstanding natural landscapes, moderate weather especially in spring and summer. The main aim of this study is to evaluate the strengths, weaknesses, opportunities, and threats (SWOT) in tourism Development in the city of Visakhapatnam and giving suitable proposals to enhance tourism. It is supported with various case studies on global & national level. The analysis of tourist profile is carried out in different occasion in different months to know about the present situation and various Issues performed. A SWOT and analytical hierarchical process (AHP) method analysis is formulated to analyze the data.This Proposals will benefit local area in which various tourist Infrastructures attract more tourist in Visakhapatnam, Andhra Pradesh, India

Keywords: Tourism Development, SWOT, AHP, Proposal

1.0 INTRODUCTION

The World Tourism Organization defines Tourism is an activity done by an individual or a group of individuals, which leads to a motion from a place to another. From a country to another for performing a specific task, or it is a visit to a place or several places in the purpose of entertaining, which leads to an awareness of other civilizations and cultures, also increasing the knowledge of countries, cultures, and history. Tourism as a whole is a booming industry and particularly offers a lot of varieties in terms of activities. Offshore and onshore activities have attracted tourist to coastal areas all around the world. In India tourism activities, policies are boosting economic growth and economic activities in many regions and many local governments are using tourism policy to boost their economic growth and raise income level for local people and local business. Visakhapatnam is one of the major city in the state of Andhra Pradesh located at south east coast of India attracts many travelers from tourism perspective who visit and sightsee. The city has a potential to serve as a center of tourism in the region as it has beautiful beaches, pilgrimage centers, recreational parks, heritage sites, etc. There is a lack of facilities at some places and need for up gradation.Therefore study is very much required for proper development and to attract more number of tourists in city data collection is made by interviewing experts and tourists in Visakhapatnam city respectively, and based on that SWOT analysis is formulated and different proposals are prepared for the up gradation of tourism in the Visakhapatnam city

2.0 OBJECTIVES AND SCOPE

The objective of this study is to assess the present situation of Tourism development in Visakhapatnam City, analyze the present situation based on SWOT analysis and to provide future proposals.
The Scope of this study is limited to tourist places in Visakhapatnam City area which is under Greater Visakhapatnam Municipal Corporation limits.

3.0 STUDY AREA PROFILE

Visakhapatnam is the largest city in Andhra Pradesh, a sprawling industrial city and one of the emerging metropolis*.* Visakhapatnam city lies between 17.6883° N latitude, and 83.2186° E longitude. Its periphery consists of plains along the coastline while the interior boast of the beautiful hills of the Eastern Ghats, which surround it on the North and the West. The City is located on the sea shore of Bay of Bengal in the East, with a population of **20.91 lakhs** and occupying **530 sq.km**

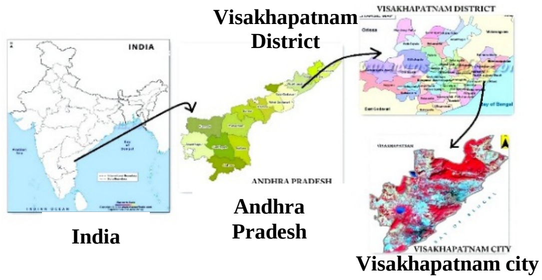

Fig 1: Location of Visakhapatnam city

Visakhapatnam city is divided into 6 zones and 72 Wards

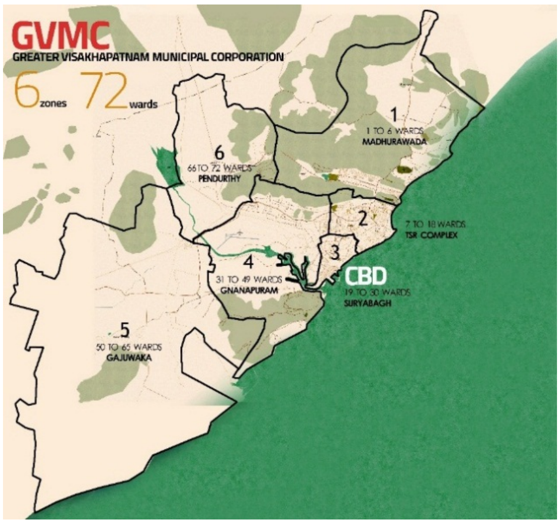

Fig.2 Zone map of Visakhapatnam City

4.0 METHODOLOGY

The methodology adopted for the study and the sequence of various steps undertaken is shown in the fig 3. The first stage is selection of the study area with aim, objectives. In second stage literature review has been done. Third stage followed by collection of inventory and field data. Fourth stage consists of analysis and calculation for future requirements. In fifth stage proposals has been given in various locations to enhance tourism

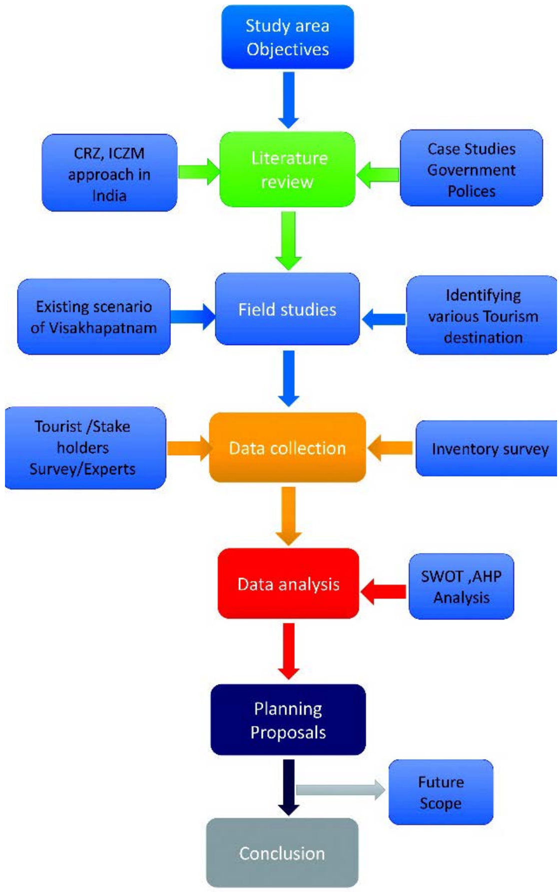

Fig.3 showing the methodology adopted

5.0 DATA COLLECTION AND ANALYSIS

The Inventory data is collected from different sources like Tourism department, Visakhapatnam Urban Development authority and Municipal Corporation and the field data are collected from tourists, Experts and Stakeholders

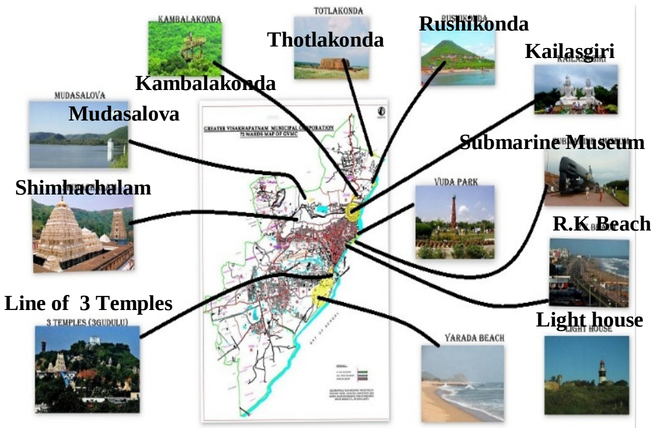

Fig.4 Map showing tourism location in Visakhapatnam City

SWOT analysis is developed following an integrative procedural model that includes the tourists, stakeholders, and experts

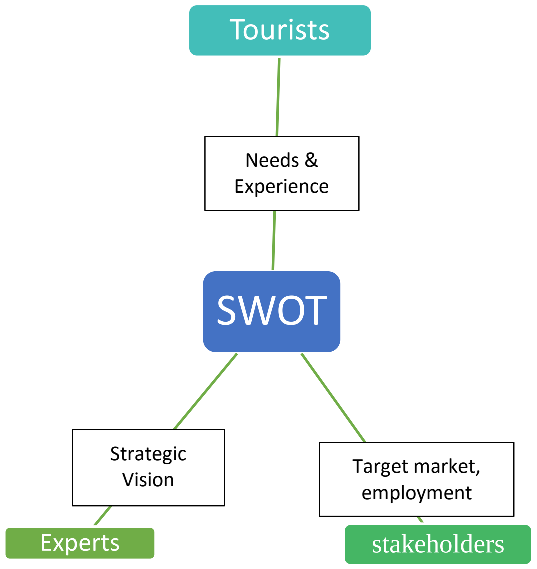

Fig. 5 Data collection procedure

5.1 Analysis

The analysis gives a complete understanding to identify behaviors of tourists, stakeholders and experts for existing situation in tourism of Visakhapatnam city which is followed by comparative analysis, sentimental analysis, gap analysis and SWOT analysis.

5.1.1 Purpose of Visit:

From the fig 6, it is shown that 29 % tourists come Visakhapatnam for Rest and relaxation While 25% come for Religious. And 11 % tourists coming for Recreation .Therefore tourists willing to come Visakhapatnam for mostly relaxation and enjoy over ere and religious because of important Pilgrimage also study includes general characteristics like purpose of visit, Duration of Stay, Mode of transportation and other related information like expenditure pattern which will affect the Local Economy in Visakhapatnam city

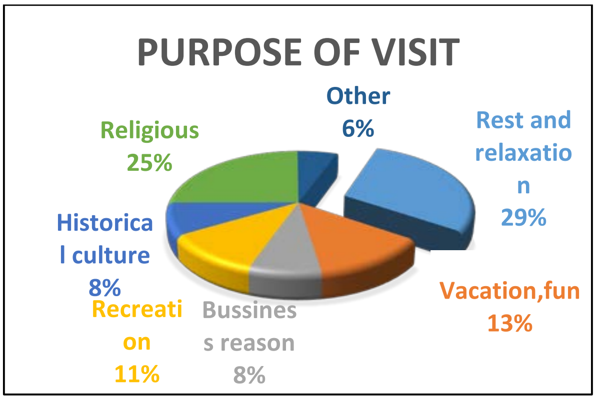

Fig. 6 Chart showing purpose of visit

5.1.2 Comparative analysis:

In the fig 7 the comparison between different tourism resources like facilities, connectivity and accommodation is shown and it clearly shows tourists are mostly satisfied with the accommodation but when comes to facilities there are somehow dissatisfied in some tourist spots .

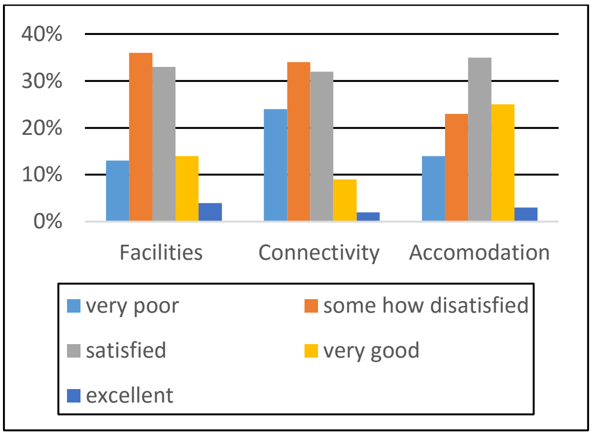

Fig. 7 Comparison chart

The comparison of other tourism resources like infrastructure, management and maintenance is also included in the study

5.1.3 Sentiment Analysis:

In the Fig 8 shows the perception of the tourists is taken into consideration how there sentimental feel about the religious & pilgrimage places in Visakhapatnam city. Nearly 34% of the people were satisfied and 26% people are somehow dissatisfied and 17 % feels the condition is very good and 15 % says excellent and 8 % people says the condition is poor

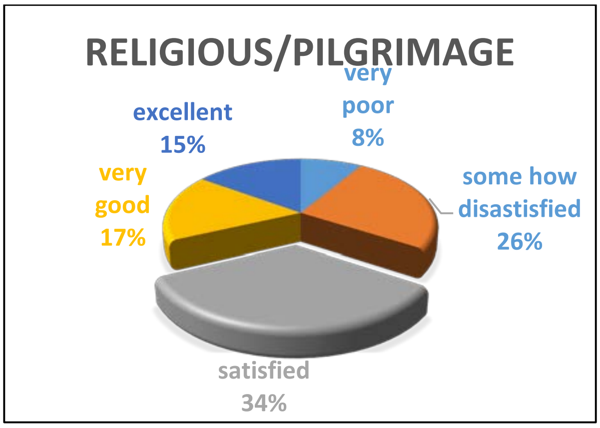

Fig .8 Sentimental analysis of Pilgrimage

The Sentimental analysis also done for knowing the tourists perception of beach and heritage spots in Visakhapatnam city.

5.1.4 Gap Analysis:

The gap analysis is done on the basis of standard norms considering current scenario for up-gradation of future tourism in Visakhapatnam city

Table 1 Gap analysis of recreation

Existing Recreational			
Year	Percentage of Recreational	Minimum Requirement of Percentage	Gap(N-M)
2011	12.54	15	2.54

Where,
P = Recreational facilities gap.
M = Existing Recreational
N =Required Recreational facilities

Based on Urban and Regional development plans Formulation and Implementation URDPFI Norms India 2015 for a port city the recreation area can be minimum 15 to 20 percent of the total land use of the city

5.1.5 Facilities to be upgraded:

From the fig 9 it is shown that parks and also the requirement of amusement is suggested by the maximum number of Tourists with 35% of them giving various opinions the improvement of sanitation and toilet Facilities is second with 18% of the tourists. Also,15 % of the tourists felt that the Availability of water facility must be improved and 13 % of tourist feel that water sports at beach must be improved and 10 % people feel that there must be a cycling track enabled a beach

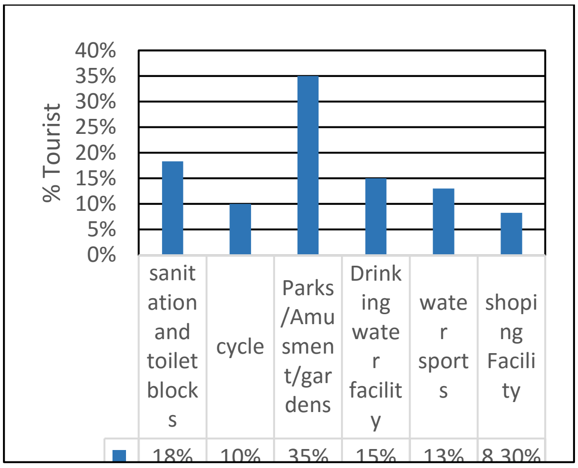

Fig .9 Facilities to be upgraded

5.1.3 SWOT Analysis

Based on the Survey with 358 stakeholders and 8 experts SWOT was formulated

Strengths:

- Good rail and road connectivity to Visakhapatnam city
- Well road networks to connect almost all the main tourist destinations.
- The Visakhapatnam is one among very few which has both lined up hills on one side and stretches of sandy beaches
- Mix of destinations and attractions of all types- Beach tourism, hill stations, religious, Heritage with immense natural beauty. The majority of the tourists visit for its breath taking and inspiring natural beauty
- Tourists have choice to see different beaches, different places like Simhachalam, Sri Kanaka Mahalaxmi temple, kailasigiri recreational park on hill etc.

Weaknesses:

- Lack of proper Skill man power in the tourism department.
- Lack of facilities and wayside amenities for tourist in Visakhapatnam city
- Lake of Maintenance at some tourist spots
- Lack of adequately trained guides and information

Opportunities:

- Government of India has declared Visakhapatnam for developing as smart city Expand current offerings
- Ecotourism sites in and around the city
- Many Archaeological Buddhists sites around the city
- Increasing the employment opportunity for local people.

- Tourism has been declared as an industry by the Government of Andhra Pradesh. This makes the sector eligible for a host of incentives and concessions
- Accommodations are sufficient to support tourists.
- The highway passes through the city and connects to Kolkata on the north east and Chennai on the south of the city
- Visakhapatnam is on track for the development of the Metro rail and BRTS

Threats

- Sometime the environmental conditions, Nature calamities also giving threat to the tourism actives
- Lack of proper vision and mission
- Increasing lack of user friendliness
- Competing wild life sanctuaries in the vicinity
- There are no activity programs that support Tourism

6.0 PLANNING PROPOSALS

Proposals are made for vision of future development of tourism in Visakhapatnam city. The proposals are given based on the existing situation in the city

6.1 Proposal -I

For the proposal of amusement park the vacant lands are chosen based on the growth patterns in the city and availability of urban space. Their vacant lands are chosen in different zones of Visakhapatnam city All the sites which are chosen are having good strength for setting up the amusement park but for better approach of assessment seeking the view of experts is taken into consideration and giving ranking based on AHP and choosing the best site for proposal

Table 2 Ranking analysis based on AHP

	site 1	site 2	site 3
Aesthetics	3.63	3.48	1.63
Traffic condition	3.75	3.06	1.20
Accessibility	2.07	3.81	2.17
Pedestrian	3.11	2.99	1.89
services	3.25	3.45	1.27
Open space	3.07	3.47	1.44
Green space	2.15	4.02	1.81
Total	21.03	24.28	11.42

The selected site is located towards north direction of the city in the zone 1. The site is having a land of approximately 15 hectors and this zone there are many Government vacant lands .This zone is also known as an educational hub of Visakhapatnam

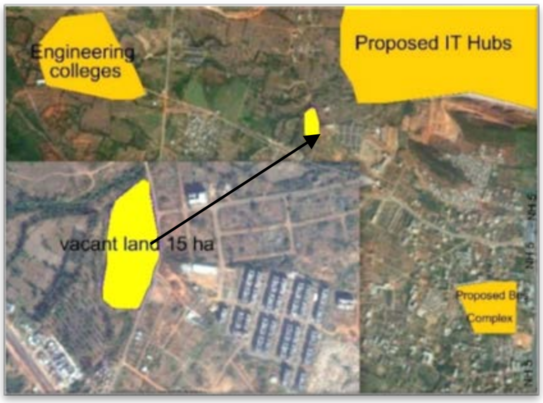

Fig. 12 Vacant land site in North zone

Below fig 14 showing the proposed amusement park .The park is mainly having the features of beautiful green infrastructure and water rides

Fig. 14 Proposed Amusement Park

6.2 Proposal -II

Kailasigiri Recreational park is one of the most attracting tourist spot in Visakhapatnam was recently badly affected by Hud Hud Cyclone has lost the green infrastructure. The park has a potential to attract many tourists

Fig. 15 Existing situations at Kailasgiri Park

According to the report of ministry of tourism Andhra Pradesh 2012, where there have carried out potential carrying capacity and estimated that by the year 2021 the dwell unit will be 12591persons per day which is presently 2850 per day. So giving proposal further hopes for the betterment of recreation in the park.

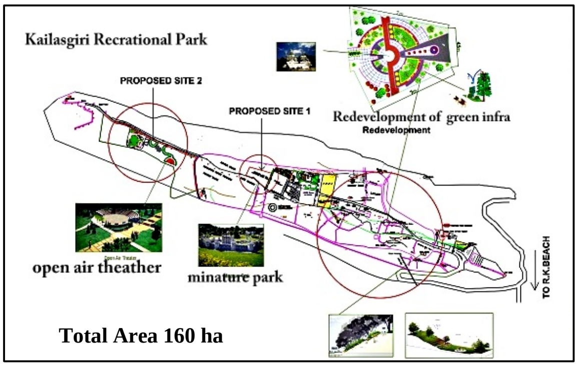

Fig. 16 Proposed Amusement Park

6.3 Proposal-III

Towards North east of the selected area, there are many private resorts and recreation clubs. Between the hills and with a sea coast , the area has a lot of potential to develop as a recreational area for new aqua sports can be launched like beach volley ball and speed boating.

Fig. 17 Proposed Cycle track and water sports region

7.0 CONCLUSION

In this paper, it has been presented the main objective of the study to analyze the strengths, weaknesses, opportunities, and threats of tourism in Visakhapatnam City, India. On the basis of analysis. It is concluded that strengths and more opportunities are more comparable to threats and weakness. Which gives a positive approach for encouraging future tourism development and also the proposed study of this paper is included with proposals like amusement park, Redevelopment of Kailsigiri recreational park and proposal for development of aqua sports are given for vision of future which led to the growth of economy and also helpful for employment generation

8.0 ACKNOWLEDGEMENT

We earnestly wish to express our heartfelt thanks and a sense of gratitude to all the officials of Visakhapatnam Urban Development authority, Municipal Corporation Tourism Department and stakeholders for providing the information.

9.0 REFERENCES

[1] Archana Bhatia, “SWOT Analysis of Indian tourism Industry”, IJAIEM , Volume 2, 2012

[2] Asia pacific economic cooperation, the economic impact of travel & tourism 2013, travel & tourism economic impact

[3] K.Mythili , “Tourism-impact on Environmental-observation for north costal Districts of Andhra Pradesh.”International journal of Social management Economics and Business Engineering, 2012, Vol. 7

[4] Iis P. Tussyadiah ,“ The City Of Cape May Tourism Plan National Laboratory for Tourism & ecommerce (NLTeC)”, 2012

[5] Kamran Noori1, Farhad Zand (2013)“Rural Tourism Development Based on SWOT Model” (Case Study: Paveh Township, Kermanshah)

[6] KomainKantawateera, AreeNaipinit, Thongphon Promsaka Na Sakolnakorn, “A SWOT Analysis of Tourism Development in khonkean, Thailand”. Asian Social Science; Vol. 9, 2013,No. 17.

[7] Mohammad Ali Firoozia, Majid goodarzi, Abdolmotalleb Akbaric, “ Analyzing the role of Bavan Valley in Mamasani as tourists attraction” Management Science Letters Management Science Letters 2 (2012) 2449–2456.

[8] Salma Begum, “Revitalizing Public Open Space-The Case of Dhakeshwari ” Proceedings of the 1st National conference of Sustainable and Smart cities,2015, Surat.

[9] TCPO, Government of India Ministry of Urban Development. “Urban and regional development plans formulation and implementation” (URDPFI) guidelines volume1”,january 2015.

SOLID WASTE MANAGEMENT IN DHAKA CITY CORPORATION

Md. Aminul Islam and Zakaria Hossain

Faculty of Bioresources, Mie University, Japan

ABSTRACT

Unplanned urbanization and inadequate collection of municipal waste are the main problems for solid waste management in Dhaka City Corporation. Due to rapid urbanization, expanding economic activity and consumption of consumer items; quantities of municipal solid waste is increasing rapidly. Domestic or household waste is the largest amount of municipal solid wastes. In this paper, a model has been developed to determine if the population is known and the increasing rate of waste generation remain same. As the results, average generation rate of domestic waste has been determined 0.36 kg per capita per day and in general average waste generation rate has been determined 0.56 kg per capita per day. It is observed that most of the domestic wastes can be recycled or reused. In data analysis from the field survey, it is found that most of the recyclable materials were collected by the waste pickers. It is concluded that the scenario of waste disposal facility in Bangladesh is not satisfactory. A typical suggestion for a well-established waste management system has been recommended at the end of this paper.

Keywords: Population, Urbanization, Dhaka City, Municipal Waste Generation, Waste management.

INTRODUCTION

The population of Dhaka is now nearly 10 million within its city area of 360 sq. km. In addition to this, about one million commuters visit the city every day in search of their livelihood. The population of Dhaka city has increased rapidly, with a growth rate of 3.72% per year. In Dhaka City Corporation (DCC) area, 60% houses are of low income, 37% middle income and the rest 3% constitutes high-income houses. The old part of Dhaka is more densely populated than the new part of Dhaka. There are over 1,000 small and large industries including 149 tanneries, about 500 clinics and hospitals in Dhaka Metropolitan area [1]. Solid wastes make an incredible environmental hazard and social problem in city lives. A massive volume of solid waste is generated every day in the city areas. Now, solid waste management has become a serious problem due to the limited resources and lack of proper management system for handling the increasing rate of generated waste.

Rapid urbanization has made solid waste management (SWM) a serious problem today [5]. The urban area of Bangladesh generates approximately 16,015 tons of waste per day, which adds up to over 5.84 million tons annually. It is projected that this amount will grow up to 47,000tons/day and close to 17.16 million tons per year by 2025, due to growth both in population and the increase in per capita waste generation. Based on the present total urban population, per capita waste generation rate is found at 0.41 kg/capita/day in urban area of Bangladesh.

Existing infrastructure for waste management showed that waste collection efficiency in different urban areas varies from 37% to 77% with an average of 55% [2]. The overall waste collection situation is not satisfactory. Huge amount of uncollected waste, a high proportion of which is organic, makes nuisance and pollutes the local environment rapidly.

Solid waste disposal poses a greater problem because it leads to land pollution if openly dumped, water pollution if dumped in low lands and air pollution if burnt [3]. Dhaka, the capital city of Bangladesh is facing serious environmental degradation and public-health risk due to uncollected disposal of waste on streets and other public areas, clogged drainage system by indiscriminately dumped wastes and by contamination of water resources near uncontrolled dumping sites. The study concentrated on municipal solid waste management of Dhaka City Corporation. It has identified the existing recycling condition of domestic waste and the scope of further recycling or reuse of domestic waste, present condition of municipal solid waste management and survey on waste pickers. The study also dealt with future prediction of municipal solid waste generation with a view to proposing a better municipal waste management system.

METHODOLOGY

To pursue this study, a few questionnaire surveys were conducted on the type and rate of generation of domestic solid waste, collection and recycling condition of municipal solid waste and field visits were paid to some waste treatment centers and disposal sites. Another questionnaire survey was also conducted on the waste pickers in Dhaka City Corporation. The secondary data were collected from the different published sources like newspapers, books, journals, research reports etc.

Site Selection of Study Area

The study site was selected with a view to determine the type and rate of generation of domestic wastes, collection disposal and recycling. The purpose of such selection was to obtain a scenario of existing waste management and recycling situation of Dhaka City Corporation for proposing a better municipal waste management system.

Present Scenario of SWM in Dhaka City

The present scenario of Municipal Solid- Waste Management in Dhaka City Corporation is not satisfactory at all. With the increasing population, expansion of the city- without proper planning the situation aggravated further. It has been found that the household solid constitute the largest volume of municipal solid wastes. But they are not properly segregated at sources and it makes the task of waste management more difficult. With the scanty resources in terms of money, skilled manpower and logistics support, it is very difficult to handle the bulk volumes of solid wastes in Dhaka City where about 4,500 tons of waste per day generated by more than 10 million people. As a result more than half of the city's daily generated wastes remain uncollected and more disposed locally and informally making the environment and health of the metropolis quite gloomy and dismal. The city-dwellers seem to have accepted to live with garbage scattered around along with strong stench and severe health and environmental hazards; not only basic civic sense of throwing of wastes are lacked in city but also there is tremendous lack- in part of both citizen and the government to come up with alternative plans to manage the huge amount of solid wastes produced in the city.

COMPOSITION OF MUNICIPAL SOLID WASTE

The following Figure 1 shows the composition of municipal solid waste in Dhaka city Corporation. Food waste constitute 78.87%, Glass/metal/ Construction 8.17%, paper and cardboard 4.29%, and plastic 4.1%, textiles 4.57%. Here, food waste is the largest amount of solid waste generated in the study area.

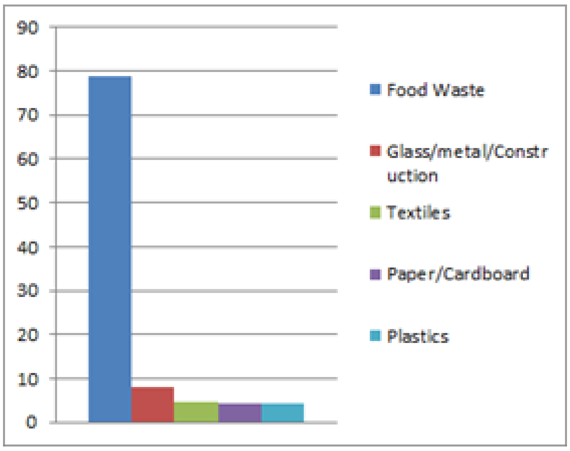

Fig-1 Composition of Municipal solid waste

CLASSIFICATION OF MUNICIPAL SOLID WASTE

The classification of municipal solid waste is given in Table 1 showing component and its description and rate of waste generation is given in Table 2.

Table-1 Classification of municipal solid waste

Items	Description
Food wastes	The animal, fruit, or vegetable residues (also called garbage) resulting from the handling, preparation, cooking, and eating of foods, Because food wastes are putrescible, they will decompose rapidly, especially in warm weather.
Rubbish	Combustible and noncombustible solid wastes, excluding food wastes or other putrescible materials. Typically, combustible rubbish consists of materials such as paper, cardboard, plastics, textiles, rubber, leather, wood, furniture, and garden trimmings. Noncombustible rubbish consists of items such as glass, crockery. Tin cans. Aluminum cans. Ferrous and nonferrous metals, dirt, and construction wastes.
Ashes and residues	Materials remaining from the burning of oil, coal, coke, and oilier combustible wastes. Residues from power plants normally are oil included in this category. Ashes and residues are normally composed of fine. Powdery materials, cinders, clinkers, and small amounts of burned and partially burned materials.
Demoli-tion and construc-tion wastes	Wastes from razed buildings and other structures are classified as demolition wastes. Wastes from the construction, remodeling, and repairing of residential, commercial field industrial buildings and similar structures are classified as construction wastes. These wastes may include dirt, stones, concrete, bricks, plaster, lumber, shingles, and plumbing, heating, and electrical parts.
Special wastes	Wastes such as street sweepings, roadside litter, catch-basin debris, dead animals, and abandoned vehicles are classified as special wastes.
Treat-ment plant wastes	The solid and semisolid wastes 'from water, wastewater, and industrial waste treatment facilities are included in this classification.

Table: 2 Waste Generation Rate (WGR) and Total Waste generation (TWG) in Dhaka City and other cities, 2004

City/Town	WGR(kg/ cap/day)	No. of City/Town	Total	Population	TWG(ton/day)		Average (TWG)
			Population	-2005	Dry season	wet season	
Dhaka	**0.56**	**1**	**6,116,731**	**6728404**	**3,767.91**	**5,501.14**	**4,634.52**
Chittagong	0.48	1	2,383,752	2,622,098	1,258,.61	1,837.57	1,548.09
Rajshahi	0.3	1	425,798	468,378	140.51	205.15	127.83
Khulna	0.27	1	879,281	967,365	261.19	381.34	321.26
Barisal	0.25	1	397,724	437,009	109.25	159.51	134.38
Sylhet	0.3	1	351,724	386,896	116.07	169.46	142.76
Pourasavas	0.25	298	13,831,187	15,214,306	3,803.58	5,553.22	4,678.40
Other urban Centres	0.15	281	8,379,647	9,217,612	1,382.64	2,018.68	1,700.65

Waste generation per capita for residential, commercial and public areas are given in Table 3 showing different places of Dhaka city.

Table: 3 Waste generation per capita (residential, commercial and public areas)

Category	No Of House	Contributing Population	Quantities of Waste(kg)		Total waste(kg)	KG/C		Composite (KG/C	Average Contribution(kg/ C/day)	Average Generation
			organic	inorganic		organic	inorganic			
Gulsan-1	1	3	1.1	0.56	1.66	0.37	0.18	0.55	0.48	
	1	4	1.08	0.54	1.62	0.27	0.14	0.41		
Green Road	1	2	0.5	0.24	0.74	0.25	0.12	0.38	0.36	
	1	4	0.96	0.48	1.44	0.24	0.12	0.36		**0.36**
	1	6	1.32	0.66	1.98	0.22	0.11	0.34		
Mirpur	1	5	1	0.5	1.5	0.2	0.1	0.31	0.33	
	1	4	0.92	0.44	1.36	0.23	0.11	0.34		
Badda	1	7	1.17	0.58	1.75	0.166	0.083	0.25	0.25	
Restaurant	1	1200	171.42	8.75	180	0.142	0.007	0.149	0.15	0.15
School	1	250	17.5	35	52.5	0.07	0.14	0.21	0.21	
College	1	450	37.8	56.7	94.5	0.084	0.12	0.204		0.25
MMDL	1	150	8.5	23	31.5	0.057	0.15	0.207		

CURRENT STATE OF SOLID WASTE MANAGEMENT

Dhaka City Corporation collects municipal wastes which are accumulated in DCC's bins or containers.

About 7,146 cleaners are employed for street sweeping and collection of waste found in places other than dustbin, road side, open spaces, ditches etc. by hand trolley. It has 2,080 hand trolleys for primary collection of waste. DCC has 128 demountable container carrier trucks for collection of accumulated waste in 414 container and 242 open trucks to collect waste from municipal bins at different locations. In some residential areas like Kalabagan, Dhanmondi, Banani, Gulshan, Baridhara and Uttara; 'house to house' waste collection service has been organized by some private initiative [4]. Rickshaw vans are used for collection of waste from houses to municipal containers. 50% of population are using waste enclosure or bins, 20% of population using roads to dispose of waste, 20% of population using drains to dispose of waste and 10% of population using open ground to dispose of waste.

The total amount of solid waste generated every day in DCC area is about 4500 to 5000 tons. According to Mott Macdonald International Ltd report of 1991, waste stream fraction of Dhaka city is 46.8% domestic, 21.8% street sweeping, 19.2% commercial, 12.9% industrial and 0.5% clinical. Solid waste flow of a residential area is 58.7% domestic, 33.08% street sweeping, 7.9% commercial and 0.32% clinical (Salam,2001).Analysis of physical composition of domestic waste show that the primary component is food waste covering 78.87%, Glass/metal/ Construction 8.17%), paper and cardboard 4.29%, and plastic 4.1%, textiles 4.57%. There is a variation of waste composition between down town and residential area of new parts of Dhaka. Domestic waste generation rate for residential area is 0.60 kg per person a day (Salam, 2001)

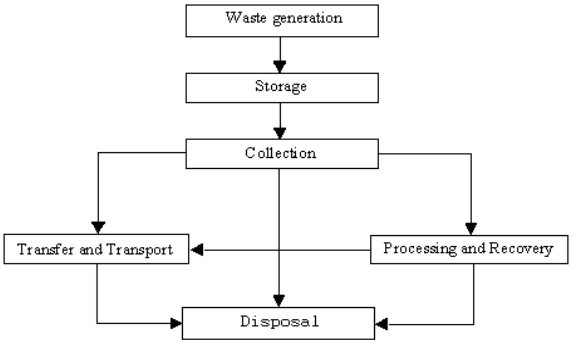

Fig 2 :Existing waste collection and management system

The figure 2 shows the general waste collection process and management system in Dhaka City Corporation.The DCC is responsible for collecting the solid wastes from municipal collection points and for disposal of the wastes in the disposal sites.But the DCC openly states that the collection system cannot cope with the task of handling the large volume municipal wastes produced by the ever-growing number of city dwellers.It has been found that only 40-50% daily generated solid wastes is being collected (DCC 2011) [6].On the other hand ,the uncollected wastes are badly contributing to environment pollution and deteriorating the public health and sanitation.

RESUL TAND DISCUSSION

Categorozation and Composition of Solid waste

Categorization and composition of solid wastes are very important for the proper management of municipal solid wastes. From the study it has been found that food waste constitutes the largest amount of solid wastes in Dhaka City Corporation. It is estimated that around 78% of the total solid is food wastes. On the contrary, plastic waste is the lowest amount of daily produced solid waste. The DCC collects only 40 -50% solid wastes. As a result, the uncollected wastes are badly polluting the environment and thereby creating a risk for public health and sanitation.

Generation Rate of Solid Wastes

Estimating the generation rate of daily produced municipal solid wastes is very significant for a better waste management system. In this paper, average generation rate of domestic waste in Dhaka City Corporation has been determined 0.36 kg per capita per day and in general average solid waste generation rate has been determined 0.56 kg per capita per day. There is a very close connection between the increase of population and the generation rate of solid wastes. The waste generation rate increases with increase of population .The projection of future population is very essential to estimate the exact generation rate of solid wastes for a better waste management system. With the help of the following equation, the future population can be projected and the generation rate of solid waste can be predicted.

$P=P_0 (1+r)^n$

Where, P= Expected Population
P_0=Present Population
R= Growth Rate
N= Year

CONCLUSION

The Dhaka City Corporation with a large number of population is facing a serious problem to manage the huge amount of daily generated solid wastes. Due to the lack of manpower; absence of modern tecknology; most importantantly, the lack of proper estimation of the generation rate of solid waste. It is unable to collect and properly manage the solid waste.The categorization and exact estimation of the total amount of solid waste generation is very significant for a better waste management system. Average generation rate of domestic waste has been determined 0.36 kg per capita per day and in general average waste generation rate has been determined 0.56 kg per capita per day.

REFERENCES

[1] JICA, Clean Dhaka Master Plan, The Study On The Solid Waste Management In Dhaka City. Final Report, Volume-i Summary Japan International Cooperation Agency, March 2005.
[2] Ahmed, M.F., "Municipal Waste Management in Bangladesh with Emphasis on Recycling" Aspects of Solid Waste Management: Bangladesh Context, German Culture Centre, 1991.
[3]. Hasan, S. Problems of Municipal Waste Management in Bangladesh: An Inquiry into its Nature, in Habitat International, 22(2): 191-202, 1998.

[4] Ashfaq, K. N. Analysis of Heavy Metals in Bed Sediments of Dhanmondi Lake in Dhaka City, M Engineering Thesis, Dcpl. of Environmental Engineering, BUET, Dhaka.
[5] Enayetullah, I., Sinha, A. H. M. M. and Khan, S. S. A. 'Urban Solid Waste Management Scenario of Bangladesh: Problems and Prospects', Waste Concern Technical Documentation, Dhaka, Bangladesh, pp.3-18, 2000.
[6] DCC, Solid Waste Management by Dhaka City Corporation, Dhaka City Corporation, Dhaka, 2011.

INFLUENCE OF SOIL REPLACEMENT ON BEARING CAPACITY AND DEFORMATION OF SOFT CLAY IN ARABIAN GULF

Nuri al- Mohamadi [1] and Vahik K. Bedrosian [2]
[1]Civil Engineering, Applied Science University, Amman, Jordan
[2]Vahik K. Bedrosian

ABSTRACT

The major part of the present research was directed to the evaluation of ultimate bearing capacity (qu) and soil displacement (ρ) by performing loading tests on rigid circular model footings founded on the surface of laboratory prepared soft clay layer overlained by a dense sand layer. A special device is developed to measure pore water pressure in the clay layer during the loading tests. The prepared soil properties were measured, including; Atterberg limits and indices, undrained shear strength Cu and modulus of deformation Es. The influence of model footing diameter B, the replacement ratio R= H/B, (where H= thickness of sand layer) and load increment (L.I) on the bearing capacity and displacement was studied. The main findings of this study are; qu increased by a ratio of 21.5% to 82% and the displacement decreased by 19.4% to 97% depending on the replacement ratio (R). This improvement was most beneficial at the range of: $1 \leq R \leq 2$, which give an increase in qu of (59% to 82%) and decrease in displacement of (68% to 97%). qu and displacement of larger footings were mostly affected by soil replacement. The comparison between the measured pore water pressure values and the theoretical values were in good agreement. The experimental results were compared with the theoretical values proposed by Meyerhof (1974) good agreement was achieved. Experimental results of soil displacement were compared with those obtained from linear elastic finite element analysis, very good agreement was observed. The difference between the two analyses was only 4.4%.

Keywords: soft clay, soil replacement, sand layer, bearing capacity, displacement, foundations.

INTRODUCTION

The formation of the triangular Fao peninsula in southern Iraq was a result of changing the course of Shattal-Arab River during the past 6000 years. This area is composed mainly of: normally consolidated (N.C) young clay along the present river course, N.C aged clay along the old river trace near Um – Qasir and surrounding area. These clayey soils are considered as the most soft and compressible in Iraq. Soil properties are summarized in table [1],

Table 1 Average properties of soft clay from Fao region

Property	Range
Specific gravity; G.s	2.72
Water content, w%	46-48
Liquid limit; L.L%	48-50
Plastic limit; P.L	24
Plasticity index;Ip%	24-26
Total unit weight; γt	16.3-17.78 KN/m^3
Dry unit weight; γd	11.2-12.2 KN/m^3
Initial void ratio; e	1.13-1.39
Compression index; Cc	0.24-0.27
Activity; A	0.86
Clay fraction; %	28-30

The reconstruction of Fao town has imposed complicated problems on the main author studying the appropriate foundations for different types of structures. It was decided to improve the top soil beneath foundations by replacing it with 1.0 m thick of compacted sand layers stabilized with cement. Therefore, it was essential to study this proposal theoretically and experimentally and to compare the results with available theories to reach to a satisfactory method for design and construction of foundations in soft clay.

THEORETICAL CONCEPTS

Meyerhof [2], proposed a semi empirical theory for the estimation of ultimate bearing capacity qu for a soft clay layer. The assumption evolved from punching shear theory is that; at the ultimate load, A soil mass in the upper sand layer (friction angle ϕ1) of roughly truncated pyramidal shape is pushed in the lower soft clay layer (cohesion C_2) in the direction of applied load.

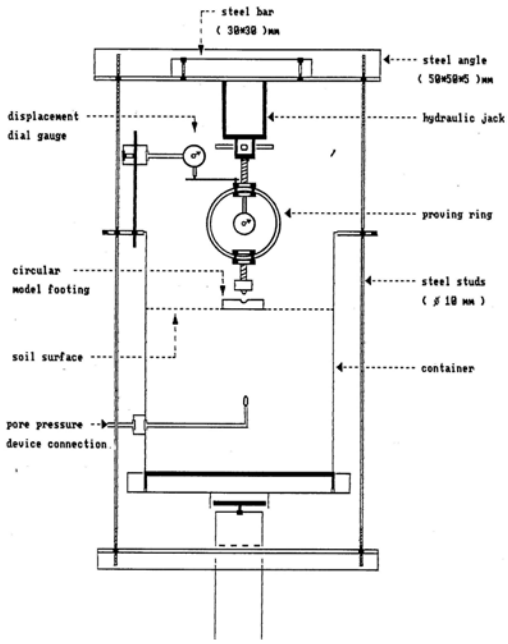

Fig.1 Details of loading apparatus for the model footing tests

According to Myerhof [2], qu of a rough strip footing of width B and depth D_f is given by Eq. (1).

$$q_{u=} q_b + 2P_p \sin\delta/B - \gamma 1H \qquad \le q_t \tag{1}$$

Where:

$$P_{p=}0.5\gamma_1 H^2\left((1+\frac{2D_f}{H}) * K_p/\cos\delta\right) \tag{2}$$

For practical purpose $\delta = 0.5\phi_1$ and $K_s \tan\phi_1 = K_p \tan\delta$.

Where: K_s is coefficient representing punching shear resistance on the vertical plane through footing edge. Eq. (1) can be rewritten as follows

$$q_{u=} q_b + \gamma_1 H^2(1+2D_f/H) * \left(SoK_s \tan\frac{\phi_1}{B}\right) - \gamma_1 H \quad \le q_t \tag{3}$$

S_o is a shape factor = 1.10-1.27, for Conservative design S_o= 1, [3].

In the above equation q_t is the ultimate bearing capacity of a homogeneous thick bed of the upper sand layer, and q_b is the ultimate b.c of the footing on a very thick bed of clay layer.

TESTING EQUIPMENTS

The testing equipment shown on Fig. (1) consist of four main parts;

(i) Containers for sample preparation made of galvanized perforated steel plate cylinders 450mm in diameter, 500mm high with collar 400 mm high to prepare samples from slurry.

(ii) Aluminum model footings 50, 75,100 mm in diameter, 25 mm thick.

(iii) Specially built loading apparatus to allow consolidation of sample before testing using lever arm system, during load test a dead weight system is used.

(iv) Pore water pressure device, specially developed for this work.

TESTING PROGRAM

A total of 14 loading tests on model footings 50mm and 75mm in diameter, including 2 tests subjected to cyclic loading as shown on table (2).

Table 2 Model footing test results

Test No.	B mm	R	L.I KPa	q_e KPa	ρ_e mm	q_y KPa	ρ_y mm	P.S
1	75	0	4	24	9.6	13.5	0.64	1
2	75	0	4	36	12.5	22.4	2.27	2
3	50	0	4	52	6.05	30.3	1.39	2
4	50	0.5	4	52	5.85	38.6	1.95	2
5	75	0.5	4	52	6.0	36.7	1.99	2
6	75	1	4	52	1.75	--	--	2
7	75	1	8	96	7.5	75.4	2.08	3
8	50	1	8	96	7.5	74.5	2.19	3
9	50	2	8	104	2.52	--	--	3
10	75	2	8	104	2.10	--	--	3
11	50	2	16	160	7.05	116.0	1.99	4
12	75	2	16	160	6.4	127.4	2.30	4
13c	50	0.5	8	64	8.43	48.0	3.17	4
14c	75	0.5	8	56	7.25	47.6	2.60	4

SAMPLE PREPERATION AND TESTING PROCEDURE

The soil from Fao town area was mixed with water to form slurry. Sample container warped with filter paper and 25mm sand drainage layer was placed at bottom of container. The container is then filled with slurry to top of collar to allow for consolidation. The pore pressure initial value is recorded as u_o.

Consolidation process is carried out under a stress of 38.4 KPa to obtain a void ratio e = 1.2 to 1.33 and a moisture content ω = 46% to 48% which represent properties of the natural Fao clay. The consolidation process lasted for 20 to 22 days. Loading stage started by applying load increments scheduled for each test, which was 4, 8, or 16 KPa, until failure occurred when excessive settlement was observed. After loading tests were completed, samples were obtained for engineering and physical properties tests.

ANALYSIS OF TEST RESULTS

Ultimate Load Criterion

Soil failure under a loaded footing is clearly defined in the case of general shear failure mode, in the case of other failure mode; local and punching shear, failure point is difficult to establish [6]. A very consistent ultimate load criterion that is adopted in this paper defines the ultimate load at the point of break of the load-displacement curve in a log-log plot Fig.(3b). Although some researchers refer this point as "Yield point load q_y**"**, and consider that the total failure is still beyond this point.

Model Footing Test Results

Fig. (2) shows typical results of loading test of 75mm diameter footing resting on soft clay,

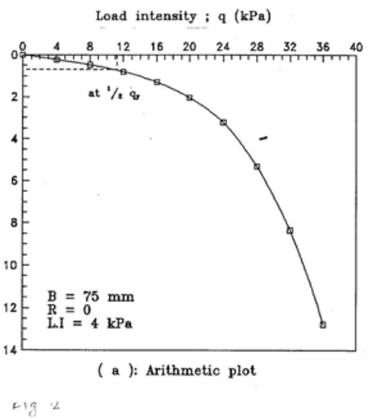

Fig.2 load-displacement relationships for test No. 2 on natural clay

Results obtained are: qu= 22.4KPa and vertical settlement ρ_y= 2.27mm. To study the effectiveness of soil replacement on qu and ρ_y, the same soil is used and the test is repeated with sand layer thickness H= 0.5B, i.e a replacement ratio R= H/B = 0.5. Results of this test are shown on fig. (3).

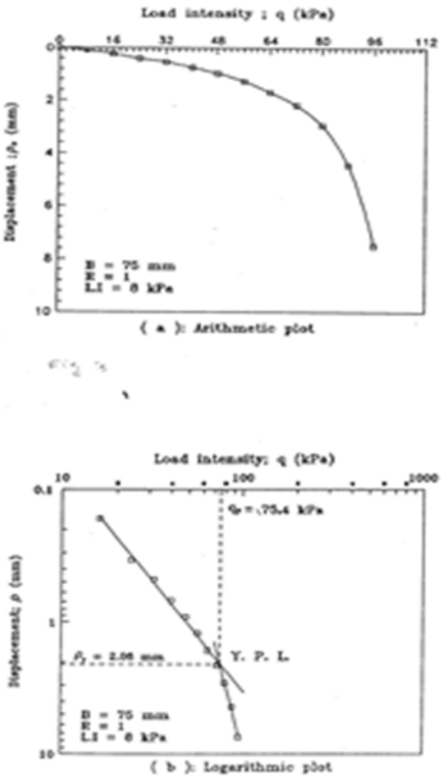

Fig.3 load –displacement relationships for test No.7

Values obtained are: qu = 36.7 KPa and ρ_y = 1.99mm. This result indicates an improvement in qu of 39% and ρ_y of 12.3%. Similar results were observed for 50mm diameter footing, but with different improvement values due to scale effect. Sand replacement ratio R was increased in other tests to R=1 and R=2. Values obtained are: qu= 75.4 KPa ρ_y = 2.08mm and qu= 127.4 KPa, ρ_y = 2.32mm for the two ratios respectively. These results impliy that an extremely large improvement in ultimate bearing capacity qu is obtained as the thickness of sand replacement layer is increased. This effect is clearly shown on fig. (4).

Results of cyclic loading tests, pore water pressure measurement could not be presented in this paper due to space limitation.

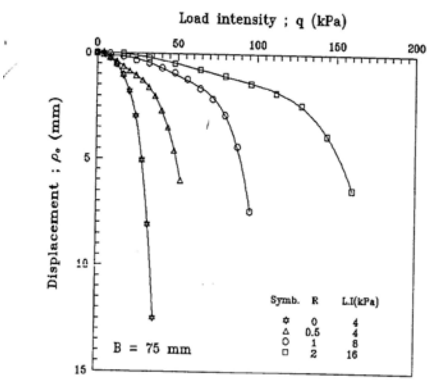

Fig.4 load vs displacement relationships for model footing tests; 2, 5, 7 &12

Modulus of subgrade reaction

An attempt has been made to estimate the modulus of subgrade reaction Ks from model footing load tests. Terzaghi [7], defined Ks as:

$$Ks = {}^{q}/_{\rho} \tag{4}$$

Where q and ρ are obtained from load displacement relationship at 0.5 q_y. Values of Ks can be used to calculate modulus of soil deformation Es from Eq. (5), [8]

$$Ks = \frac{Es}{B(1-\mu^2)} * I_w \tag{5}$$

Where I_w is a factor depending on shape and rigidity of the footing. For circular rigid footing I_w=0.88. Adopting values for Poisson's ratio μ = 0.45 for clay and μ =0.30for sand, Es can be calculated from Eq. (5), and presented in table (3). Values of Es for soft clay ranged from 1185 KPa to 1474 KPa, while for sand Es ranged from 4645 KPa to 5465 KPa. These values are rather low if compared with typical values.

Modulus of subgrade reaction Ks ranged from 28000 KN/m^3 to 33778 KN/m^3 for soft clay and from 91000 KN/m^3 to 116000KN/m^3 for sand. The calculated values of Ks showed good comparison with those proposed by [7] especially for dense sand. While for soft clay they were slightly overestimated.

Theoretical Estimation of Ultimate Bearing Capacity

According to Meyerhof [2] proposed theory qu of circular model footing founded on surface of dense sand layer overlying soft clay layer, can be estimated from Eq.(6), which is a modification of Eq.(3) to suit a circular footing:

$$qu = 1.2CuNc + \frac{2\gamma_1 H^2 (Ks\tan\emptyset 1)}{B} \le q_t \tag{6}$$

Where Nc=5.14 for Φ=0, γ_1=18 KN/m^3, φ_1=45° Ks = $Kp\tan\delta / \tan\emptyset'$, δ= 0.5 φ_1, Kp = 21.38 (columb eq.).

In the present study; Eq. (6) to analyze the ultimate bearing capacity qu and to compare it with observed ultimate load intensities q_y from load tests for various values of replacement ratio R. this comparison is presented in table (4) and on Fig.(5).

Table (4) Analyses of ultimate bearing capacity

Test No.	B mm	R	H mm	Su KPa	qu KPa	q_b KPa	q_t KPa	q_y KPa	Δ %
2	75	0	0	5.33	32.9	32.9	---	22.4	31.9
3	50	0	0	=	32.9	32.9	---	30.3	7.9
4	50	0.5	25	=	36.9	33.35	118.2	38.6	-4.6
5	75	0.5	37.5	=	38.9	33.58	177.4	36.7	5.6
7	75	1	75	9.66	83.5	60.9	177.4	75.4	9.7
8	50	1	50	=	75.5	60.5	118.2	74.5	1.3
11	50	2	100	8.75	117.7	55.8	118.2	116.0	1.4
12	75	2	150	=	149.6	56.7	177.4	127.4	14.8
13c	50	0.5	25	=	58.0	54.5	118.2	48.0	17.2
14c	75	0.5	37.5	=	59.9	54.7	177.4	47.6	20.5

Values of qu from Eq.(6) and q_y from land tests showed good agreement, with qu values are a bit higher than q_y. This is expected since q_y does not represent the actual failure values as mentioned before.

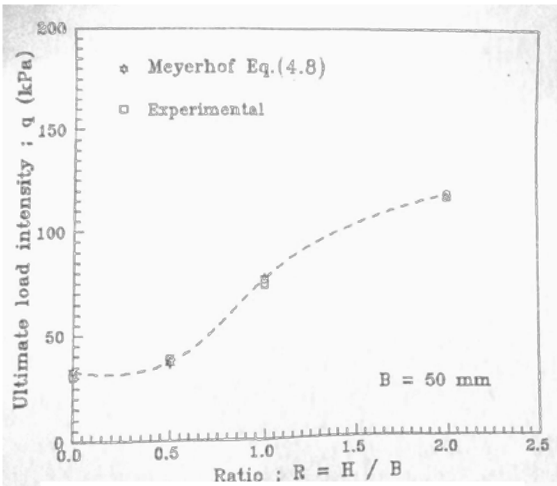

Fig.(5) Theoretical and experimental results of ultimate bearing capacity

CONCLUSIONS

Based on the results obtained from this research, the following conclusions can be drawn:

1. The partial replacement process of soft clay by a dense layer improves qu and decrease Po. For replacement ratios R= 0.5, 1.0 and 2.0 the increase in qu was = 39.0%, 70.3% and 82.4% respectively, while footing settlement were reduced by 19.4%, 68.7% and 85.0%. These settlement values were compared for a stress level of 32.0KPa, to obtain valid comparison for all tests. Similar conclusion was reported by a recent study [7].
2. The relative thickness of replaced soil in the order of ($1.0\ B \leq H \leq 2.0B$) was found to give the most beneficial effect on qu.
3. Comparison between qu obtained from model footing tests and those theoretically calculated from Meyerhof (Eq.3) showed excellent agreement with a difference in the order of 1.3% to 14.8%.
4. Apparently the most beneficial results for qu and ρ_y in construction of foundations of Fao city structures, were for footings width B= 1.0m. For larger footings the improvement will be less effective, since R < 1.

ACKNOWLEDGEMENT

Main author would like to acknowledge the support of Applied SCIENCE University, Amman, Jordan to participate in this conference.

REFERENCES

[1] Al – Mufty, A. (1990); "Analysis of stress deformation behavior of Fao soil" M.Sc. thesis, Univ. of Baghdad.

[2] Meyerhof, G.G. (1974) "Ultimate Bearing Capacity of Footings on Sand Layer Overlying Clay" Geotechnical J. Vol.11, Ohawa, Canada.

[3] Hanna, A.M. and Meyerhof, G.G. (1980), "Design Charts for Ultimate Bearing Capacity of Foundations on Sand overlying Soft Clay" Canadian Geot.J., Vol.15.

[4] Meyerhof, G.G. and Hanna, A.M. (1978), "Ultimate Bearing Capacity of Foundations on Layered Soil Under inclined Load" Canadian Geot.J., Vol.15.

[5] Brown, J.D. and MEYERHOF, g.g. (1969) "Experimental Study of Bearing Capacity in Layered Soil", Proc. 7th ICMFE, Vol.2.

[6] Vesic, A.S. (1975): "Bearing Capacity of Shallow Foundations" ch.3 in: Foundation Engineering Hand Book, by Winterkorn, H.F. and Fang, H., Van Nostrand Reinhold Ltd.co.

[7] Murat, A., Ahmet, D., Mustafa, L., an Abdulazim,Y. (2012) "Numerical Analysis of circular Footings on Natural Clay Stabilized with a Granular Fill" Acta Geotechnical, Slovenia.

Authors Index

GEOMATE 2016

Sixth International Conference on

Geotechnique, Construction Materials & Environment

14-16 November 2016, Bangkok, Thailand

Invitation to participate

- The "International Journal of GEOMATE" is a Scientific Journal of the GEOMATE International Society that encompasses a broad area in Geotechnique, Construction Materials and Environment.
- The key objective of this journal is to promote interdisciplinary research from various regions of the globe.
- The editorial board of the journal is comprised of extensively qualified researchers, academicians, scientists from Japan and other countries of the world.
- It is peer-reviewed Journal that is published quarterly till 2015 and now bimonthly. All articles published in this journal are available on line.
- Contributors may download the manuscript preparation template for submitting paper or contact to the Editors-in-Chief

  [editor@geomatejournal.com].